XXV Russian Particle Accelerator Conference RuPAC-2016

21-25 November 2016
St. Petersburg, Russia

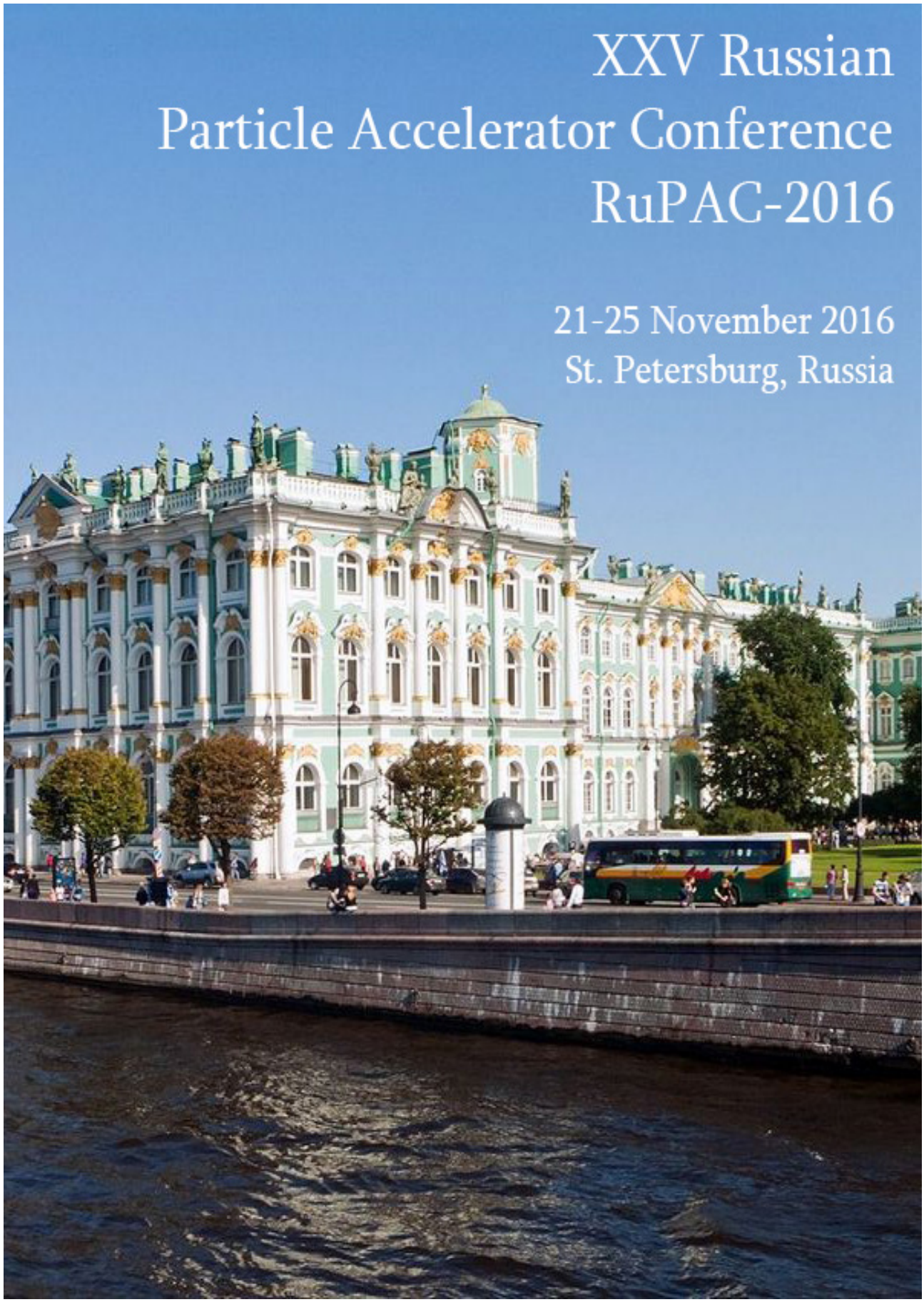

PREFACE

The XXV Russian Particle Accelerator Conference (RuPAC–2016) was held in a renovated state-of-the-art campus of Saint Petersburg State University, the "Mikhailovskaya Dacha" premises (Petergof, Saint Petersburg), on November 21 –25, 2016. Hosted by Saint Petersburg State University (SPbSU), it was co-organized by Joint Stock Company "D.V. Efremov Institute of Electro-Physical Apparatus" (JSC "NIIEFA"), Scientific Council of Russian Academy of Sciences on Charged Particle Accelerators and Interregional Innovative Development Center (INNO-MIR) with the assistance of Joint Institute for Nuclear Research (JINR, Dubna), Budker Institute of Nuclear Physics SB RAS (BINP, Novosibirsk), and Institute for High Energy Physics of National Research Center "Kurchatov Institute" (IHEP, Protvino). The Conference was supported in part by the Russian Foundation for Basic Research (under RFBR grant #16-02-20815) and LLC NIIEFA-ENERGO.

The event has provided a forum for exchange of new information and discussion in the field of accelerator science and engineering: particle beam physics, new projects for particle colliders, new accelerator projects and modernization of existing accelerator facilities for basic research and applications (with an emphasis on medical applications). The scientific program covered the following topics:

- Modern trends in accelerators
- Colliders
- Particle dynamics in accelerators and storage rings, cooling methods, new methods of acceleration
- High intensity cyclic and linear accelerators
- Heavy ion accelerators
- Synchrotron radiation sources and free electron lasers
- Magnetic and vacuum systems, power supplies
- Superconducting accelerators and cryogenics
- RF power structures and systems
- Control and diagnostic systems
- Ion sources and electron guns
- Medical and industrial applications
- Radiation problems in accelerators

RuPAC–2016 was attended by more than 260 full-time delegates from 13 countries and 67 organizations. Among the attendees, there were 75 students and young scientists under 35 years old. The Organizing Committee decided to maintain the conference tradition of the best youth's scientific works award. This year, the contest winners are: Florian Dirk Dziuba (GSI, Helmholtz-Institute Mainz, Mainz, Germany) for his oral report "First Cold Tests of the Superconducting CW Demonstrator at GSI", Vladislav Altsybeev (SPbSU, Saint Petersburg, Russia) for his poster presentation "Modeling of Triode Source of Intense Radial Converging Electron Beam", and Yuri Rogovsky (BINP SB RAS, Novosibirsk, Russia) for his talk "Recommissioning and Perspectives of VEPP-2000 Complex", Andrey Bondarchenko and Konstantin Kuzmenkov (JINR, Dubna, Russia) for their joint poster presentations "Production of Intense Ion Beams from ECR Ion Source using

MIVOC Method". The Prizes were awarded by the decision of the Selection Committee summoned at the Conference and chaired by academician Sergey Ivanov (IHEP of NRC KI, Protvino, Russia).

An Industrial Exhibition took place during the whole conference period. This year, 8 companies presented their high-technology products and services to the delegates in an excellent atmosphere conducive to discussions.

The RuPAC–2016 scientific program was compiled by the Program Committee. It spanned over three full days and halves of the first and the last days of the Conference. There were plenary sessions only on Monday, November 21. Poster sessions were scheduled stand-alone at the end of each full day afternoon, from Tuesday, November 22 till Thursday, November 25. On Friday, November 26 special session dedicated to the Russian large-scale NICA project was convened.

27 invited talks, 49 contributed oral reports and 197 posters (273 in total) were presented at the Conference.

Processing of the electronic files of about 300 contributions, during and after the Conference, was accomplished by Maxim Kuzin and his team from BINP SB RAS. The final version of the Proceedings is published at the JACoW site (www.jacow.org).

The success of the RuPAC–2016 was due to the joint efforts of the Program and Organizing Committees, the local staff of the host University – SPbSU, and, of course, due to all participants who had shown high level of involvement, motivation and enthusiasm during the Conference.

Dmitri Ovsyannikov, Chair of RuPAC-2016 Organizing Committee

Igor Meshkov, Co-Chair of RuPAC-2016 Program Committee

Contents

Preface

Foreword . . . iii
Contents . . . v
Committees . . . xi
Pictures . . . xii

Papers

MOZMH01 – CEPC-SppC Accelerator Status . . . 1
MOZMH03 – Search for the Charged Particle Electric Dipole Moments in Storage Rings . . . 6
TUXMH01 – The European XFEL - Status and Commissioning . . . 11
TUXMH02 – Novosibirsk Free Electron Laser: Terahertz and Infrared Coherent Radiation Source . . . 16
TUCAMH01 – Planar Superconducting Undulator With Neutral Poles . . . 21
TUCAMH02 – CW 100 mA Electron RF Gun for Novosibirsk ERL FEL . . . 24
TUCBMH01 – Status of the Kurchatov Synchrotron Light Source . . . 27
TUCBMH02 – Numerical Analysis of the Effective Width of the Spectrum of Synchrotron Radiation . . . 30
TUYMH01 – Status of the Future Circular Collider Study . . . 34
TUYMH03 – Recommissioning and Perspectives of VEPP-2000 Complex . . . 39
TUZMH01 – Status of U-70 . . . 44
TUZMH02 – INR High Intensity Proton Linac. Status and Prospects. . . . 48
TUZMH03 – Status of IFMIF-EVEDA RFQ . . . 51
WEXMH01 – Feeding BINP Colliders with the New VEPP-5 Injection Complex . . . 56
WECAMH01 – Some Problems of the Beam Extraction from Circular Accelerators . . . 61
WECAMH03 – Analysis of the Particle Dynamics Stability in the Penning-Malmberg-Surko Trap . . . 64
WECAMH04 – Recent Experiments With High Energy Electron Cooler in COSY . . . 67
WECAMH05 – Optimization and Simuations of Beam Dynamics in APF Accelerators . . . 70
WEYMH01 – Development of MHF Conception at ITEP . . . 73
WEYMH02 – A Radioactive Ion Beam and Isotope Production Facility for iThemba LABS . . . 78
WECBMH01 – First Cold Tests of the Superconducting cw Demonstrator at GSI . . . 83
WECBMH02 – Collector Ring Project at FAIR: Present Status . . . 86
WEZMH01 – Spallation Neutron Source at the 1 Gev Synchrocyclotron of PNPI . . . 90
WEZMH02 – Radiocarbon analysis of different samples at BINP AMS . . . 95
WECDMH01 – Commissioning of High Efficiency Standing Wave Linac for Industrial Applications . . . 99
WECDMH03 – A 5 to 20 MeV Electron Linear Accelerator for Metrology . . . 102
THCAMH01 – Universal Proton and Neutron Centre for Radiation Resistance of Avionic, Space Electronics and Other Applications at 1 Gev Synchrocyclotron in PNPI . . . 105
THCAMH02 – Electron Accelerators Series ILU and Prospects of Their Application in the Food Industry . . . 108
THCAMH03 – The Target Development For Medical Radionuclides 67Cu and 82Sr Production . . . 111
THCAMH04 – MCC-30/15 Cyclotron-based System for Production of Radionuclides Project. . . . 114
THCAMH05 – The CC-18/9M Cyclotron System for Production of Isotopes for PET . . . 117
THCAMH06 – Gantry Free Transport Line for a Proton/Ion Therapy . . . 120
THYMH02 – Hadron Therapy Research and Applications at JINR . . . 123
THZMH01 – SC and HTS-related Activity at IHEP . . . 128
THZMH02 – Status of Superconducting ISAC-II and eLinac accelerators, and SRF Activities at TRIUMF . . . 133
THCDMH01 – Conceptual Design of Superconducting Combined-Function Magnets for the Next Generation of Beam Cancer Therapy Gantry . . . 138
THCDMH02 – Recent Optimized Design of ILC Cryomodule With Explosion Welding Technology . . . 141
THCDMH03 – The Progress on Manufacturing and Testing of the SC Magnets for the NICA Booster Synchrotron 144
THCEMH01 – Vacuum Insulation Tandem Accelerator: Progress and Prospects . . . 147
FRCAMH01 – Status of the Nuclotron . . . 150
FRCAMH02 – Commissioning of New Light Ion RFQ Linac and First Nuclotron Run with New Injector . . . 153
FRCAMH03 – Commissioning of the New Heavy Ion Linac at the NICA Project . . . 156
FRCAMH05 – Booster Synchrotron at NICA Accelerator Complex . . . 160
FRCAMH06 – Simulation of Two-Plane Painting Multiturn Injection into BRing with Space Charge Effect . . . 163
FRCAMH07 – NICA Collider Lattice Optimization . . . 166
FRCAMH08 – Dynamic Aperture Optimization of the NICA Collider . . . 169

TUCASH02 – Commissioning and First Tests of the New Standing Wave 10 Mev Electron Accelerator 173
TUCASH03 – High Efficiency Stripping Extraction on 80 MeV H-minus Isochronous Cyclotron in PNPI 176
TUCASH04 – Physical Start-up of the C-80 Isochronous Cyclotron 179
TUCASH05 – The CC1-3 Cyclotron System. Installation and Test Results 182
TUCASH06 – Progress in CW Mode Electron Resonance Accelerator BETA-8 Development 185
TUCASH07 – HF Structure of BETA-8 Electron Resonance Accelerator 188
THXSH01 – Development of the INR Linear Accelerator DTL RF System 191
THXSH02 – Three Transverse Deflecting Systems for Electron Beam Diagnostics in the European Free-Electron Laser XFEL 196
THCASH01 – Effective RF Deflecting Structures for Bunch Rotation and Deflection 201
THCBSH01 – INR RAS Instrumentation for Bunch Shape and Beam Cross-Section Monitoring 204
THCBSH02 – Structure and Hardware of LIA-20 Control System 207
THCBSH04 – The Monitoring of the Effects of Earth Surface Inclination With the Precision Laser Inclinometer for High Luminosity Colliders 210
TUPSA001 – Commissioning of e^+/e^- Transfer Line from BINP Injection Complex to VEPP-2000 Facility 213
TUPSA004 – Proposal of the Accelerating Structure for the First Cavity of the Main Part of INR Linac 216
TUPSA006 – Development of RF Accelerator on Parallel-Coupled Structure - Trend in Accelerator Technique . 219
TUPSA007 – New Experimental Results on RF Accelerator with Parallel-Coupled Structure and RF Controlled Gun 222
TUPSA008 – Gradient Limitations for RF Accelerator on Parallel-Coupled Structure 225
TUPSA009 – Electron Beam Dynamics Calculation and Accelerating Structure Geometry Design in 10 MeV Hybrid Electron Linac 228
TUPSA010 – Electron Linear Accelerator with the Variable Energy from 6 to 11 MeV 231
TUPSA011 – Matching the Proton Beam by Means of Independently Phased Bunchers in CYCLINAC Concept 234
TUPSA012 – Superconducting Stored Energy RF Linac as Free Electron Laser Driver 237
TUPSA013 – Investigation of a Second Order Method of RFQ Channel Optimization 240
TUPSA014 – A Simple Model for Electromagnetic Field in RFQ Channel 244
TUPSA015 – Acceleration of Deuterons and Protons in Single RFQ Strucrure 247
TUPSA016 – Beam Simulation and Measurements at Beam Line to RADEX Experimental Area of INR Linac . 250
TUPSA018 – Experimental Facility for E-Beam Irradiation Test of Prototype IF Target in RISP 253
TUPSA019 – Upgrade of the RF System on the LUE-200 256
TUPSA020 – Installation for the Research of Z-Pinch Plasma Initiated by the Electron Beam 258
TUPSA024 – On Stabilization of Systems of Linear Equations with Linear Increasing Time Delay by Observation 261
TUPSA025 – First Results of Beam Dynamics Simulation in electron injector linac for FCC-ee 264
TUPSA026 – Beam Dynamics Study for the New CW RFQ 267
TUPSA027 – The Study of the Helical RF Resonator for the 300 keV Nitrogen Ion CW Implanter 270
TUPSA028 – QWR resonator Cavities Electrodynamics Simulations for new Nuclotron-NICA Injector 273
TUPSA029 – High Power Solid State RF Generator for Neutral Beam Injector 276
TUPSA030 – Regulation of the Waveguide Coupling Factor of Standing Wave Linear Accelerator 279
TUPSA031 – The Cascade Interference Switch Comprising a Transmission Resonator 282
TUPSA034 – 520 MeV TRIUMF Cyclotron RF System: Maintenance, Tuning and Protection 285
TUPSA035 – Estimation of Multipacting in CDS Structure 288
TUPSA036 – Manufacturing Tolerances Estimation for Proton Linac Cavities 291
TUPSA037 – Powerfull RF Triode as Anode Modulator Vacuum Tube 294
TUPSA038 – The RF Power System for RFQ-Injector of Linac-20 297
TUPSA040 – S-Band Choke Mode Cavity for Low Energy Storage Ring 300
TUPSA041 – High-Energy Micro-Buncher Based on the mm-Wavelength Dielectric Structure 303
TUPSA042 – Software Complex "Dynpart" for the Calculation of Self-Consistent Beam Dynamics in Dielectric Wakefield Accelerating Structures 307
TUPSA043 – Wake Field Components in a Rectangular Accelerating Structure With Dielectric Anisotropic Loading 310
TUPSA046 – Experimental Analysis of Dipole Modes in Elliptical Cavity 313
TUPSA049 – Electromagnetic Field in Dielectric Concentrator for Cherenkov Radiation 316
TUPSA050 – Electron Beam Stability in the Energy Recovery Linac for the Lithographic Free Electron Laser . . 319
TUPSA051 – Form-factor Determination of an Arbitrary Bunch Sequence for the Coherent Radiation Calculation 322
TUPSA052 – First Order Perturbation Theory Evaluation of Initial Stage of Self Amplified Crystal-Based X-Ray Emission 325

TUPSA058 – Production of Intense Beams of Iron Ions from ECR Ion Source by MIVOC Method at the Cyclotron DC-60 . . . 328
TUPSA059 – Production of Intense Metal Ion Beams From ECR Ion Sources Using the MIVOC Method . . . 330
TUPSA061 – Comparative Research of Low Energy Beam Transport Systems for H-minus Ion Beam . . . 333
TUPSA062 – Modeling of Triode Source of Intense Radial Converging Electron Beam . . . 336
TUPSA063 – The Electron Trajectories Construction in the System With a "Real" Geometry of the Field Cathode 339
TUPSA064 – The Infinitely Thin Field Emitter Mathematical Modeling . . . 342
TUPSA068 – Simulation of S-Band RF Gun with RF Beam Control . . . 345
TUPSA069 – Optimization of an RF Probe Vicinity for RF Gun Cavities . . . 348
WEPSB002 – First Experimental Demonstration of the Extraction of Low Energy Beams from the ESR to the CRYRING@ESR . . . 351
WEPSB003 – Design Relativistic Charged Particle Beam Transportation Channels . . . 354
WEPSB004 – The Intelligent Object-oriented Interface in the Design Environment of The Charged Particles Relativistic Beams Transport Channels . . . 357
WEPSB005 – On the Minimax Problem of Beam Dynamics Optimization . . . 360
WEPSB006 – On Modeling and Optimization of Intense Quasiperiodic Beam Dynamics . . . 363
WEPSB007 – On Application of Monte Carlo Method for Poisson Problem Solving . . . 367
WEPSB008 – About Behavior of Electrons and Ions in the Accelerating Interval . . . 371
WEPSB009 – The Behavior of Powerful Relativistic Electron Beam With Elliptical Cross-Section in Longitudinal Magnetic Field . . . 373
WEPSB010 – The Use of Multi-Objective Genetic Algorithms for Accelerator and Light Source Optimization . . . 376
WEPSB011 – About Development System for the Analysis of Charged Particle Beam Dynamics . . . 379
WEPSB012 – On The Beam Dynamics Simulation In The Injection System . . . 382
WEPSB013 – On Approach for Resonant Frequency Tuning in Drift Tube Structures on the Designing Stage . . . 386
WEPSB014 – Symmetrical Parameterization for 6D Fully Coupled One-Turn Transport Matrix . . . 389
WEPSB015 – On the Integro-Differential Equations for Dynamics of Interacting Charged Particles Modeling . . . 392
WEPSB016 – Coupled Bunch Instabilities in the Storage Rings . . . 395
WEPSB017 – Chromatic and Nonlinear Dynamics of Antiprotons Injected to Collector Ring at FAIR . . . 398
WEPSB018 – Beam Dynamics Calculation of Electron Bunch Sequence Passing Through Dielectric . . . 401
WEPSB019 – Orbital Motion in Multipole Fields via Multiscale Decomposition . . . 404
WEPSB020 – On a New Approach for Description of Self-Consistent Distributions for a Charged Particle Beam 407
WEPSB023 – Formation of a Given Distribution of the Beam in the Periodic Channel . . . 411
WEPSB024 – Program Complex for Modeling of the Beam Transverse Dynamics and Orbit Correction in Nuclotron, LHEP JINR . . . 414
WEPSB025 – Application of GPGPUs and Multicore CPUs in Optimization of Some of the MpdRoot Codes . . . 416
WEPSB026 – Dynamical Aperture Beyond Perturbations: From Qualitative Analysis to Maps . . . 419
WEPSB028 – Computer Simulation of the Slow Beam Extraction From Nuclotron . . . 422
WEPSB030 – Parallelization of Envelope Dynamics of High Intensive Beams . . . 425
WEPSB032 – Numerical Analysis of Cavity Mode Operation and Electron Beam Dynamics in Lebedev Institute Microtron . . . 428
WEPSB033 – Focusing of Charged Particles by Magnetic Dipoles . . . 431
WEPSB034 – The Electromagnetic Field Structure in the Circular Waveguide with Transverse Boundary . . . 434
WEPSB035 – Model of the Optimal Parameters Choice for the Charged Particles Beam . . . 437
WEPSB036 – Gold Ions Beam Losses at the Nuclotron Booster . . . 440
WEPSB037 – Beam Transfer From Heavy-Ion Linear Accelerator HILAC Into Booster of NICA Accelerator Complex 443
WEPSB038 – Multigap and Polyharmonic Bunching Systems at FLNR Cyclotrons . . . 446
WEPSB039 – New Techniques for Operation and Diagnostics of Relativistic Electron Coolers . . . 449
WEPSB040 – Commissioning of the 60 keV Electron Cooler for the NICA Booster . . . 452
WEPSB041 – Stochastic Cooling System at NICA Project . . . 455
WEPSB042 – Commissioning of Electron Cooling Devices at HIRFL-CSR . . . 458
WEPSB044 – Design and Calculation of Cylindrical Electrostatic Deflector for the Transport Channel of the Heavy Ion Beam . . . 461
WEPSB045 – The Way To Improve Conformity Of Proton Therapy . . . 464
WEPSB046 – A Cyclotron Complex for Acceleration of Carbon Ions . . . 467
WEPSB048 – Beam Shaping Assembly Optimization for Boron Neutron Capture Therapy . . . 471
WEPSB049 – Temperature Control System for Thermoradiotherapy Facilities . . . 474

WEPSB050 – Laboratory Model of Thermoradiotherapy Facility: Experimental Results . . . 477
WEPSB051 – Mathematical and Computer Methods of Data Processing in Nuclear Medicine Studies . . . 480
WEPSB052 – The Use of Graphene as Stripper Foils in the Siemens Eclipse Cyclotron . . . 483
WEPSB055 – The Problems of Accelerator-Driver Design for ADS . . . 486
WEPSB056 – Study of Oil Wells With the Use of Accelerator Tubes, Time and Energy Spectrometers of Neutrons and Gamma Rays in a Single Geophysical Complex . . . 490
WEPSB057 – Beam Dynamics in New 10 Mev High-Power Electron Linac for Industrial Application . . . 493
WEPSB059 – Realization of Positron Annihilation Spectroscopy at LEPTA Facility . . . 496
WEPSB060 – Development of Positron Annihilation Spectroscopy at the LEPTA Facility . . . 499
WEPSB061 – Neutron Generators of the NG-10 Series for Metrology . . . 502
WEPSB064 – Modifications of Electron Linear Accelerators Produced in NIIEFA for Sterilization . . . 505
WEPSB065 – Development of the Beam Diagnostic System for the Radiobiological Research at the Proton Linear Accelerator I-2 . . . 508
WEPSB067 – Modeling of ADSR Dynamics With Proton Linac in Multi-Point Approximation . . . 511
WEPSB068 – Radiation From Open-Ended Flanged Waveguide With Dielectric Loading . . . 515
WEPSB069 – Radiation of a Bunch Flying from the Open End of a Waveguide with a Dielectric Loading . . . 518
WEPSB071 – Charged Beams Optical Properties of Scattering Media . . . 521
WEPSB073 – Design Study of the Proton Linac for Radiopharmaceuticals Production . . . 524
WEPSB074 – High Current Pulsing Deuteron Accelerator with Energy of 500 keV . . . 527
WEPSB075 – Beam Injector for Vacuum Insulated Tandem Accelerator . . . 529
WEPSB077 – High Speed Cryogenic Monodisperse Targets for High Intensity Cyclic and Linear Accelerators . . . 532
THPSC001 – The Multipole Lens Mathematical Modeling . . . 535
THPSC002 – Use of Structural-Variational Method of R-functions in Mathematical Modeling of Magnetic Systems 538
THPSC003 – The Design of Permenant Magnet Spread System for 0.5 MeV Irradiation Accelerator . . . 541
THPSC004 – Measuring System for FLNR Cyclotrons Magnetic Field Formation . . . 544
THPSC005 – Magnetic Measurement System For the NICA Collider Dual Dipoles . . . 547
THPSC006 – Simulation of Precision Magnetic Shielding System for Beam Injectors in Tokamaks . . . 550
THPSC007 – Modeling Magnetic Effects of Steel Rebar of Concrete Surroundings for Electrophysical Apparatus 553
THPSC008 – Magnetic Systems for Beam Transport at Extraction Channels of ILU Accelerators . . . 556
THPSC010 – Magnetic Measurement System For The NICA Quadrupole Magnets . . . 559
THPSC012 – First Experience of the HTS-II Dipole Type Magnets Development at NIIEFA . . . 563
THPSC013 – The Nonsymmetrical Variant of the Nonferromagnetic Extraction Kicker Magnet of the NICA Booster 566
THPSC014 – Fast Kicker for High Current Electron Beam Manipulation in Large Aperture . . . 569
THPSC017 – A Synchrotron Radiation Beamline Installed at BINP to Study the High Luminosity LHC Vacuum System . . . 572
THPSC018 – Achievement of Necessary Vacuum Conditions in the NICA Accelerator Complex . . . 575
THPSC019 – Hardware for Increasing Reliability of the Power Supply System for Corrector Magnets of the European XFEL . . . 578
THPSC020 – Electromagnetic Compatibility of the Power Supply System for Corrector Magnets of the European XFEL . . . 581
THPSC021 – Corrector magnet power supplies of the European XFEL . . . 584
THPSC022 – High-Voltage Power Supply for GOG-1001 . . . 587
THPSC023 – Automated System for Precision Current Sources Testing . . . 589
THPSC024 – The Pulsed High Voltage Power Supply for the NICA Booster Injection System . . . 592
THPSC025 – Generator of High-Voltage Pulse for High-Current Accelerator of Deuteron With Laser Starts . . . 594
THPSC026 – The Automation of Energy Ramping for the Main Storage Ring of KSRS . . . 597
THPSC027 – Solid-State Modulators for Particle Accelerators . . . 600
THPSC028 – Switching Network Units for High Currents and Voltages or Plasma Applications . . . 603
THPSC029 – 300 kV High-Voltage Source With Up to 15 kW Output Power . . . 606
THPSC030 – High-Precision Ramped High-Voltage Source With Up to 50 kV Output Voltage . . . 609
THPSC031 – Power Supplies for IHEP Negative Hydrogen Ions Source . . . 612
THPSC032 – The Study of the Electrical Strength of Selected Insulators With a Different Shape of the Surface 615
THPSC033 – Obtainment of 5 mA 2 MeV Proton Beam in the Vacuum Insulation Tandem Accelerator . . . 618
THPSC037 – Loss Analysis of Insulated Core Transformer High Voltage Power Supply . . . 620
THPSC038 – A Novel Design of Insulated Core Transformer High Voltage Power Supply . . . 623
THPSC041 – New Superconducting Linac Injector Project for Nuclotron-Nica: Current Results . . . 626

THPSC043 – Series Magnetic Measurements Of NICA Booster Dipoles . . . 629
THPSC046 – High-Power High-Temperature Graphite Beam Dump for E-Beam Irradiation Test of Prototype IF Target in RISP . . . 632
THPSC047 – A Faraday Cup for a Low Charge LWFA Electron Beam Measurement . . . 635
THPSC048 – Measurement of Gamma Beams Profile by Cherenkov Radiation in Fibers . . . 638
THPSC049 – Dielectric Chart as a Tool for Diagnosis of Dielectric Materials . . . 641
THPSC050 – Possibilities of Diffraction Radiation Non-Destructive Diagnostics for Non- and Moderately Relativistic Beams . . . 644
THPSC051 – The Magnetic Energy Analyzer for Electron Beam Of LUE-200 Linac of IREN Facility . . . 647
THPSC052 – The Longitudinal Broadband Impedance and Energy Spread Measurements at VEPP-4M . . . 650
THPSC053 – The Pepper-Pot Emittance Measuring Device at the 400 keV H-minus LEBT Channel . . . 653
THPSC054 – Modernization of the Electron Beam Stabilization System in the KSRS . . . 656
THPSC055 – Electrodynamic Characteristics of RF-Deflector for Bunch Shape Monitor . . . 659
THPSC056 – Proposal to Symmetric Quench Detection at Superconducting Elements by Bridge Scheme Usage 662
THPSC057 – Application of Model Independent Techniques at VEPP-2000 and SIS100 . . . 664
THPSC058 – Beam Diagnostics and Instrumentation Upgrade for Multipurpose Research Complex of INR RAS 667
THPSC059 – Thermal Loads of Wire-Based Beam Instrumentation at Ion Linacs . . . 670
THPSC060 – The Longitudinal Distribution and Bunch Length Measurements at VEPP-2000 Collider . . . 673
THPSC061 – Beam Diagnostics Overview for Collector Ring at FAIR . . . 676
THPSC063 – System of Thermomonitoring and Thermostabilizing of Kurchatov Synchrotron Radiation Source . 680
THPSC064 – Monitoring of Low Intensity Ion Beams at FLNR Accelerator Complex . . . 683
THPSC065 – Diagnostics of Accelerator Beams by the Dependence of the Vavilov-Cherenkov Radiation Intensity on the Refractive Index of the Radiator "n" . . . 686
THPSC067 – Coaxial Quarter Wavelength Impedance Converter for Coupling Control of Triode Cavity . . . 689
THPSC068 – Integrated Inspection Method of Motor Transports Based on Acceleration Technology . . . 692
THPSC069 – Measurement of the Ion Beam Profile with the D-Pace Wire Scanner . . . 695
THPSC070 – Measurement of the Proton Beam Profile via an Activation Method of Diagnostics . . . 698
THPSC072 – Digital-to-Analog Beam Energy and Current Stabilization of ELV Accelerators . . . 700
THPSC073 – Development of the Hardware-Software Complex PIRS-5 for Field Measurements in Accelerating Structures . . . 702
THPSC074 – Longitudinal Beam Distribution Measurements in Damping Ring of VEPP-5 Injection Complex . . 705
THPSC076 – Host-Based System to Control the Accelerator . . . 709
THPSC077 – Control System for the 1 MW Neutral Beam Injector . . . 712
THPSC078 – Controller of Power Supplies for Corrector Magnets of European XFEL . . . 715
THPSC080 – Data Processing Automatization for Gamma-Spectrometry Diagnostics of Neutron Accelerator BNCT 718
THPSC081 – VME Based Digitizers for Waveform Monitoring System of Linear Induction Accelerator LIA-20 . . 721
THPSC083 – System of Geodetic Measurements for LIA-20 . . . 724
THPSC084 – The New Control for Magnet System of KSRS . . . 727
THPSC085 – Present Status of VEPP-5 Injection Complex Control System . . . 730
THPSC086 – Development and Implementation of the Automation System of the Ion Source for BNCT . . . 733
THPSC087 – Stabilization of the Equilibrium Position of a Magnetic Control System with Delay . . . 736
THPSC088 – Software and Computational Infrastructure of LIA-20 Control System . . . 739
THPSC090 – The Stochastic Characteristics Stability in the Problem of Observation and Estimate of the Charged Particles Movement . . . 742

Appendices

List of Authors . . . 745
Institutes List . . . 755

PRORGAM COMMITTEE

Chairman: S. Ivanov (Institute for High Energy Physics, Protvino, Russia)
Co-chairman: I. Meshkov (Joint Institute for Nuclear Research, Dubna, Russia)
Secretary: E. Akhmanova (Joint Institute for Nuclear Research, Dubna, Russia)

N. Alexeev (Institute for Theoretical and Experimental Physics, Moscow, Russia)
A. Golubev (Institute for Theoretical and Experimental Physics, Moscow, Russia)
E. Kotina (Saint Petersburg University, Saint-Petersburg, Russia)
L. Kravchuk (Institute for Nuclear Research, Troitsk, Russia)
T. Kulevoi (Institute for Theoretical and Experimental Physics, Moscow, Russia)
E. Levichev (Budker Institute of Nuclear Physics SB RAS, Novosibirsk, Russia)
D. Ovsyannikov (Saint Petersburg University, Saint-Petersburg, Russia)
V. Parkhomchuk (Budker Institute of Nuclear Physics SB RAS, Novosibirsk, Russia)
S. Polozov (National Research Nuclear University MEPhI, Moscow, Russia)
V. Romanov (Institute for Physics and Power Engineering, Obninsk, Russia)
B. Sharkov (FAIR-Russia Research Center, Moscow, Russia)
G. Shirkov (Joint Institute for Nuclear Research, Dubna, Russia)
A. Skrinsky (Budker Institute of Nuclear Physics SB RAS, Novosibirsk, Russia)
G. Trubnikov (Joint Institute for Nuclear Research, Dubna, Russia)
M. Vorogushin (Joint Stock Company "D.V.Efremov Institute of Electrophysical Apparatus", Saint Petersburg, Russia)

ORGANIZATION COMMITTEE

Chairman: D. Ovsyannikov (Saint Petersburg University, Saint-Petersburg, Russia)
Co-chairman: O. Filatov (Joint Stock Company "D.V.Efremov Institute of Electrophysical Apparatus")
Co-chairman: G. Shirkov (Joint Institute for Nuclear Research, Dubna, Russia)

Scientific secretary: E. Kotina (Saint Petersburg University, Saint-Petersburg, Russia)
Main coordinator: A. Golovkina (Saint Petersburg University, Saint-Petersburg, Russia)

N. Alexeev (Institute for Theoretical and Experimental Physics, Moscow, Russia)
S. Andrianov (Saint-Petersburg University, Saint Petersburg, Russia)
N. Egorov (Saint-Petersburg University, Saint Petersburg, Russia)
A. Feschenko (Institute for Nuclear Research, Troitsk, Russia)
Yu. Gavrish (Joint Stock Company "D.V.Efremov Institute of Electrophysical Apparatus", Saint Petersburg, Russia)
V. Glukhikh (Joint Stock Company "D.V.Efremov Institute of Electrophysical Apparatus", Saint Petersburg, Russia)
A. Golubev (Institute for Theoretical and Experimental Physics, Moscow, Russia)
O. Drivotin (Saint-Petersburg University, Saint Petersburg, Russia)
L. Kravchuk (Institute for Nuclear Research, Troitsk, Russia)
M. Kuzin (Budker Institute of Nuclear Physics SB RAS, Novosibirsk, Russia)
O. Lebedev (Institute for High Energy Physics, Protvino, Russia)
E. Levichev (Budker Institute of Nuclear Physics SB RAS, Novosibirsk, Russia)
V. Matveev (Joint Institute for Nuclear Research, Dubna, Russia)
I. Meshkov (Joint Institute for Nuclear Research, Dubna, Russia)
B. Sharkov (FAIR-Russia Research Center, Moscow, Russia)
Yu. Shatunov (Budker Institute of Nuclear Physics SB RAS, Novosibirsk, Russia)
O. Patarakin (ROSATOM, Moscow, Russia)
G. Trubnikov (Joint Institute for Nuclear Research, Dubna, Russia)
M. Vorogushin (Joint Stock Company "D.V.Efremov Institute of Electrophysical Apparatus", Saint Petersburg, Russia)









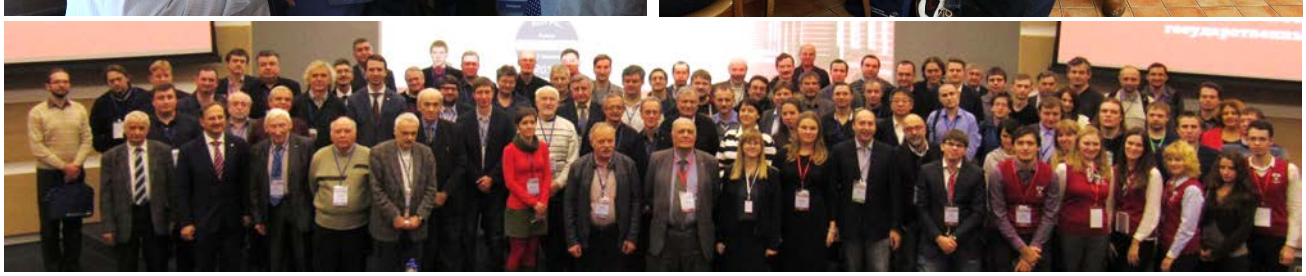

CEPC-SPPC ACCELERATOR STATUS*

J. Gao†, IHEP, Beijing 100049, China

Abstract

In this paper we will give an introduction to Circular Electron Positron Collider (CEPC). The scientific background, physics goal, the collider design requirements and the conceptual design principle of CEPC are described. On CEPC accelerator, the optimization of parameter designs for CEPC with different energies, machine lengthes, single ring and crab-waist collision partial double ring options, etc. have been discussed systematically. The subsystems of CEPC, such as collider main ring, booster, electron positron injector, etc. have been introduced. The detector and MDI design have been briefly mentioned. Finally, the optimization design of Super Proton-Proton Collider (SPPC), its energy and luminosity potentials, in the same tunnel of CEPC are also discuss. It is decided that CEPC-SppC CDR baseline will be of 100km circumference, and the corresponding designs are underway.

INTRODUCTION

With the discovery of the Higgs particle at the Large Hadron Collider at CERN in July 2012, after more than 50 years of searching, particle physics has finally entered the era of the Higgs, and the door for human beings to understand the unknown part of the Universe is wide open! Thanks to the low energy of Higgs, it is possible to produce clean Higgs with circular electron positron colliders in addition of linear colliders, such as ILC and CLIC, with reasonable luminosity, technology, cost, and power consumption.

In September 2012, Chinese scientists proposed a Circular Electron Positron Collider (CEPC) in China at 240 GeV centre of mass for Higgs studies with two detectors situated in a very long tunnel more than twice the size of the LHC at CERN. It could later be used to host a Super Proton Proton Collider (SppC) well beyond LHC energy potential to reach a new energy frontier in the same channel.

After ICFA Higgs Factory Workshop held at Fermi Laboratory in Nov 2012, CERN proposed also a similar one, Future Circular Collider (FCC) with a much longer tunnel than that of LHC. From 12 to 14 June 2013, the 464th Fragrant Hill Meeting was held in Beijing on the strategy of Chinese high energy physics development after Higgs discovery, and the following consensuses were reached: 1) support ILC and participate to ILC construction with in kind contributions, and request R&D fund from Chinese government; 2) as the next collider after BEPCII in China, a circular electron positron Higgs factory (CEPC) and a Super proton-proton Collier (SppC) afterwards in the same tunnel is an important option as a historical opportunity, and corresponding R&D is needed. ICFA has given two successive statements in Feb. and July of 2014, respectively, that ICFA supports studies of energy frontier circular colliders and encourages global coordination; ICFA continues to encourage international studies of circular colliders, with an ultimate goal of proton-proton collisions at energies much higher than those of the LHC. During the AsiaHEP and ACFA meeting in Kyoto in April 2016, a positive statement of AsiaHEP/ACFA Statement on ILC+CEPC/SppC has been made with strong endorsement of the ILC and encouraging the effort led by China on CEPC/SppC. On Sept 12, 2016, during the meeting of the Chinese High Energy Physics of Chinese Physics Society, a statement on the future Chinese high energy physics based on accelerator has been made that CEPC is the first option for future high energy accelerator project in China as a strategic action with the aim of making CEPC as a large international scientific project proposed by China. The 572th Fragrant Hill Meeting dedicated to CEPC has been held from Oct. 18-19, 2016, and it is concluded that CEPC has a solid physics reason to be built with big physics potential in SppC. The optimization design, relevant technologies and industry preparation could be ready after a five years dedicated R&D period before CEPC starts to be constructed around 2022 and completed around 2030. CEPC will operate 10 ten years with two detectors to accumulate one million Higgs and 100 million of Z particle.

In the beginning of 2015, Pre-Conceptual Design Reports (Pre-CDR) of CEPC-SppC [1] have been completed with international review. The International Advisory Committee (IAC) of CEPC was also established in 2015. At the end of 2016 a CDR Status Report will be finished before finishing of the CDR at the end of 2017. In 2016, Chinese Ministry of Science and Technology has allocated several tens of million RMB on CEPC R&D to start with.

Finally, it is decided that CEPC-SppC CDR baseline will be of 100km circumference, and the corresponding designs are underway.

CEPC ACCELERATOR DESIGN

According to the physics goal of CEPC at Higgs and Z-pole energy, it is required that the CEPC provides e^+e^- collisions at the center-of-mass energy of 240 GeV and delivers a peak luminosity of 2×10^{34} cm$^{-2}s^{-1}$ at each interaction point. CEPC has two IPs for e^+e^- collisions. At Z-pole energy the luminosity is required to be larger than 1×10^{34} cm$^{-2}s^{-1}$ per IP. Its circumference is around 60 k-

* Work supported by National Key Programme for S&T Research and Development (Grant NO.: 2016YFA0400400) and National Natural Science Foundation of China (NO.11575218, 11505198, 11605211).

† gaoj@ihep.ac.cn

ISBN 978-3-95450-181-6

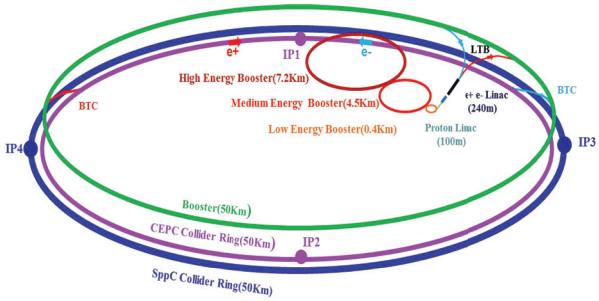

Figure 1: CEPC-SPPC schematic layout.

m in accordance with SppC, which has 70 TeV of center of mass proton proton collision and 20 Tesla superconduction magnet dipole field. The schematic layout of CEPC-SppC is shown in Fig. 1, and CEPC accelerator complex is composed of a 6 GeV electron and positron linac injector with a 1 GeV positron damping ring, a booster from 6 GeV to 120 GeV in the same channel of 120 GeV collider rings.

Main Parameters and Main Ring Designs

To make an optimization a collider, started from the goals, such as energy, luminosity/IP, number of IPs, etc, one has to consider very key beam physics limitations, such as beam-beam effects [2] and Beamstrahlung [3], and also take into account of economical and technical limitations, such synchrotron radiation power and high order mode power in each Superconducting rf cavity. By taking into account all these limitations in an analytical way, an analytical electron positron circular collider optimized design methods have been developed both head-on collision and crab-waist collision. The CEPC parameters of single ring head-on collision scheme as used in CEPC-SppC Pre-CDR and the crab-waist collision designs are shown in Tab. 1 [4].

In Pre-CDR, single ring head-on collision scheme has been studied with Pretzel scheme. The apparent low cost single ring Pretzel scheme has many problems, such as not flexible lattice solution, small dynamic aperture, low Z-pole energy luminosity (around 10^{32} cm$^{-2}s^{-1}$), and very high AC power consumption (around 500MW). To solve these critical problems, a Partial Double Ring (PDR) scheme has been proposed independently [5][6]. In Tab. 1 we could find that with crab wait collision, one could reduce synchrotron radiation power from 50 MW to about 30MW, and with Z-pole luminosity to satisfy the design requirement. In fact, in addition to single ring and partial double ring schemes, there are two other types of schemes, i.e. Advanced Partial Double Ring (APDR) [7] and Double Ring (DR) scheme [8]. In fact, in principle, the crab-waist CEPC parameters could be realized by PDR, APDR and DR schemes. PDR, APDR and DR are also called options to a crab-waist collision scheme. However, if one take synchrotron radiation effect and the collective effect of superconducting accelerator system taking into account, the three options are quite different from one from another. Apparently, DR is the most expensive and relative easy option, APDR as shown in Fig. 2(PDR is a special case of APDR, only two partial double ring sections at two IPs) is most possible economic option overcoming the difficulties from PDR, i.e., beam loading and sawtooth effects, which should be studied carefully before a reasonable choice among differen options.

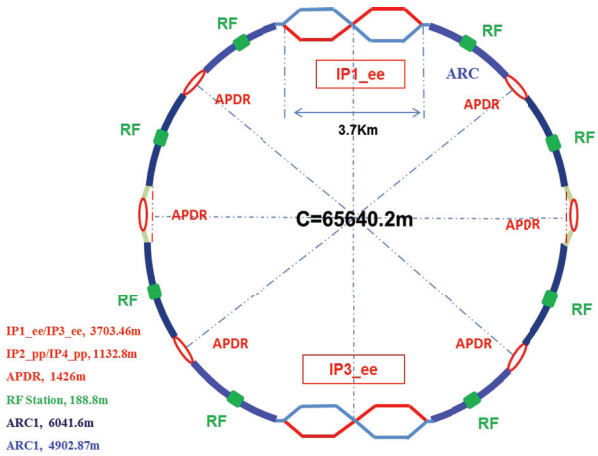

Figure 2: CEPC advanced partial double ring scheme.

As for PDR (APDR) lattice design, in the Arc region, the FODO cell structure is chosen to provide a large filling factor. The 90/90 degrees phase advances is chosen to achieve a very small emittance of 2 nm. The non-interleaved sextupole scheme [9] was selected due to its property of small tune shift. Considering the symmetry of two IPs and two beams, the lattice CEPC PDR scheme has a four-fold symmetry and the maximum number of sextupole families in the ARC region is 96 [10].

The CEPC interaction region (IR) was designed with modular sections including the final transformer, chromaticity correction for vertical plane, chromaticity correction for horizontal plane and matching transformer. To achieve a momentum acceptance as large as 2%, local correction of the large chromaticity from final doublet is necessary.

The dynamic aperture of the ring is optimized by SAD and goal is to have dynamic aperture in both transverse planes lager than 5σ including all effects with energy spread of from $+2\%$ to -2%.

The advantage of PDR and APDR over DR is the cost saving, if beam loading and sawtooth effects related to PDR (APDR) are not to be the showstoppers, which need detailed studies before making a final decision.

Injector

To reduce the cost of the whole system, the length of the Linac is chosen to be as short as possible, and a booster ring is used to ramp the beams from the Linac energy to the full injection energy of the main collider. Therefore, the whole CEPC system is composed of three parts: a linac, a booster, the main collider ring. The Linac injector system

ISBN 978-3-95450-181-6

Table 1: Main parameters of CEPC

	Pre-CDR	H-high lumi.	H-low power	W	Z
Number of IPs	2	2	2	2	2
Energy (GeV)	120	120	120	80	45.5
Circumference (km)	54	61	61	61	61
SR loss/turn (GeV)	3.1	2.96	2.96	0.58	0.061
Half crossing angle (mrad)	0	15	15	15	15
Piwinski angle	0	1.88	1.84	5.2	6.4
N_e/bunch (10^{11})	3.79	2.0	1.98	1.16	0.78
Bunch number	50	107	70	400	1100
Beam current (mA)	16.6	16.9	11.0	36.5	67.6
SR power /beam (MW)	51.7	50	32.5	21.3	4.1
Bending radius (km)	6.1	6.2	6.2	6.2	6.2
Momentum compaction (10^{-5})	3.4	1.48	1.48	1.44	2.9
β_{IP} x/y (m)	0.8/0.0012	0.272/0.0013	0.275 /0.0013	0.1/0.001	0.1/0.001
Emittance x/y (nm)	6.12/0.018	2.05/0.0062	2.05 /0.0062	0.93/0.0078	0.88/0.008
Transverse σ_{IP} (um)	69.97/0.15	23.7/0.09	23.7/0.09	9.7/0.088	9.4/0.089
ξ_x/IP	0.118	0.041	0.042	0.013	0.01
ξ_y/IP	0.083	0.11	0.11	0.073	0.072
V_{RF} (GV)	6.87	3.48	3.51	0.74	0.11
f_{RF} (MHz)	650	650	650	650	650
Nature σ_z (mm)	2.14	2.7	2.7	2.95	3.78
Total σ_z (mm)	2.65	2.95	2.9	3.35	4.0
HOM power/cavity (kw)	3.6	0.74	0.48	0.88	0.99
Energy spread (%)	0.13	0.13	0.13	0.087	0.05
Energy acceptance (%)	2	2	2		
Energy acceptance by RF (%)	6	2.3	2.4	1.7	1.2
n_γ	0.23	0.35	0.34	0.49	0.34
Life time due to beamstrahlung_cal (minute)	47	37	37		
F (hour glass)	0.68	0.82	0.82	0.92	0.93
L_{max}/IP (10^{34}cm^{-2}s^{-1})	2.04	3.1	2.01	4.3	4.48

is composed of a 6 GeV S-band linac with positron source and a 1 GeV positron damping ring with two stage bunch compressors.

Booster The booster provides 120 GeV electron and positron beams to the CEPC collider for top-up injection at 0.1 Hz. The Booster is in the same tunnel as the collider, placed above the collider ring and has about same circumference. The design of the full energy booster ring of the CEPC is especially challenging due to the injected beam only 6GeV, which might cause difficulties. As an alternative design we studied also a wiggler dipole magnets to raise the initial magnetic field [11].

Detector and MDI

The CEPC conceptual detector takes the ILD detector as starting point [12][13]. Similar to the ILD, the core part of this conceptual detector is a solenoid with 3.5 Tesla Magnet Field. To minimize the dead zone, the entire ECAL, HCAL and the tracking system are installed inside the solenoid. The tracking system is composed of a large volume TPC as the main tracker and the silicon tracking system. The interaction region of the CEPC partial double ring consists of two beam pipes, of which the crossing angle is 30mrad, surrounded by silicon tracker, luminosity calorimeter and the final quadrupoles QD0 and QF1, with L* is 1.5m [14]. The inner radius of the vacuum chamber should be larger than the beam-stay-clear region. We chose 17 mm (2 mm for safety) both for QD0 and QF1. On the other hand, the collision environment of CEPC is significantly different from that of the linear colliders. Therefore, mandatory changes have been included into the CEPC conceptual detector design. The entire Machine Detector Interface (MDI) has been re-designed, to achieve the nominal luminosity and to keep the radiation at the IP at acceptable level for the electronics. The distance between the final focusing quadrupole magnet (QD0) and the interaction point have been changed from 3.5 meter to 1.5 meter. In the original design, the ILD uses extremely heavy Yoke system, to shield the B-field since Linear Collider requires the Push-Pull scenario. On the contrary, CEPC has 2 interaction points and a much thinner return Yoke could serve. Beside these changes, dedicated simulation and optimization studies has been established, to test new ideas and designs. Hopefully, these studies will eventually leads to a detector design that further balances the construction cost and physics performance.

ISBN 978-3-95450-181-6

Table 2: SPPC parameter list

	SPPC (Pre-CDR)	SPPC 61Km	SPPC 100Km	SPPC 100Km	SPPC 82Km
Main parameters and geometrical aspects					
Beam energy[E_0]/TeV	35.6	35.0	50.0	64.0	50.0
Circumference[C_0]/km	54.7	61.0	100.0	100.0	82.0
Dipole field[B]/T	20	19.81	15.62	19.98	19.74
Dipole curvature radius[ρ]/m	5928	5889.64	10676.1	10676.1	8441.6
Bunch filling factor[f_2]	0.8	0.8	0.8	0.8	0.8
Arc filling factor[f_1]	0.79	0.78	0.78	0.78	0.78
Total dipole length [L_{Dipole}]/m	37246	37006	67080	67080	53040
Arc length[L_{ARC}]/m	47146	47443	86000	86000	68000
Straight section length[L_{ss}]/m	7554	13557	14000	14000	14000
Physics performance and beam parameters					
Peak luminosity per IP[L]/ $cm^{-2}s^{-1}$	1.1×10^{35}	1.20×10^{35}	1.52×10^{35}	1.02×10^{36}	1.52×10^{35}
Beta function at collision[β^*]/m	0.75	0.85	0.99	0.22	1.06
Max beam-beam tune shift per IP[ξ_y]	0.006	0.0065	0.0068	0.0079	0.0073
Number of IPs contribut to ΔQ	2	2	2	2	2
Max total beam-beam tune shift	0.012	0.0130	0.0136	0.0158	0.0146
Circulating beam current[I_b]/A	1.0	1.024	1.024	1.024	1.024
Bunch separation[Δt]/ns	25	25	25	25	25
Number of bunches[n_b]	5835	6506	10667	10667	8747
Bunch population[N_p] (10^{11})	2.0	2.0	2.0	2.0	2.0
Normalized RMS transverse emittance[ε]/μm	4.10	3.72	3.59	3.11	3.35
RMS IP spot size[σ^*]/μm	9.0	8.85	7.86	3.04	7.86
Beta at the 1st parasitic encounter[$\beta 1$]/m	19.5	18.67	16.26	69.35	15.31
RMS spot size at the 1st parasitic encounter[σ_1]/μm	45.9	43.13	33.10	56.19	31.03
RMS bunch length[σ_z]/mm	75.5	56.69	66.13	14.62	70.89
Full crossing angle[θ_c]/μrad	146	138.03	105.93	179.82	99.29
Reduction factor according to cross angle[F_{ca}]	0.8514	0.9257	0.9247	0.9283	0.9241
Reduction factor according to hour glass effect[F_h]	0.9975	0.9989	0.9989	0.9989	0.9989
Energy loss per turn[U_0]/MeV	2.10	1.98	4.55	12.23	5.76
Critical photon energy[E_c]/keV	2.73	2.61	4.20	8.81	5.32
SR power per ring[P_0]/MW	2.1	2.03	4.66	12.52	5.90
Transverse damping time [τ_x]/h	1.71	1.994	2.032	0.969	1.32
Longitudinal damping time [τ_ε]/h	0.85	0.997	1.016	0.4845	0.66

SPPC DESIGN

The design goal of the SPPC is about 70 TeV, using the same tunnel as the CEPC of 61 km, with SC dipole magnet field of about 20 Tesla of luminosity of 1.2×10^{35}/cm$^{-1}s^{-1}$. If 100km ring is adopted a proton beam of 128 TeV of luminosity of 1×10^{36}/cm$^{-1}s^{-1}$ at 20 Tesla could be obtained, and parameter choice and optimization process is given in Tab. 2 [15].

The injector chain pre-accelerates the beam to injection energy with the required beam properties such as bunch current, bunch structure, and emittance. The injection chain determines the beam fill period. To reach 2.1 TeV, we have designed a four-stage injector chain: a linac (p-Linac) to 1.2 GeV, a rapid cycling synchrotron (p-RCS) to 10 GeV, a medium-stage synchrotron (MSS) to 180 GeV, and finally the super synchrotron (SS) to 2.1 TeV. High repetition rates for the lower energy stages help reduce the SS cycling period. This is important because the SS uses superconducting magnets and also to reduce the beam fill period of the SPPC. The beams can also be used for other applications or research purposes when the accelerators are not preparing beam for injection into the SPPC.

As for the circumference of SppC is concerned, to explore a center-of-mass energy of 100 TeV while keeping the dipole field at 20 T, the circumference should be 82 km at least. With this condition, there is hardly any space to upgrade, so a 100 km SPPC is much better because the dipole field is then only 15.62 T.

CONCLUSIONS

In this paper we have briefly reviewed the CEPC-SppC projects history, design philosophy and actual status. A dedicated R&D program both on accelerator and detectors has started with support of Chinese MOST. The beam loading and sawtooth effects have to be studied carefully to before the final choice between partial double ring (PDR and APDR) and double ring schemes. It is decided that CEPC-SppC CDR baseline will be of 100km circumference, and the corresponding designs are underway.

ACKNOWLEDGMENT

The author thanks CEPC-SppC design groups' hard works and their international collaborators's contributions.

REFERENCES

[1] The CEPC-SPPC Study Group, "CEPC-SPPC Preliminary Conceptual Design Report, Volume II-Accelerator," IHEP-AC -2015-01, March 2015.

[2] J. Gao, "Review of some important beam physics issues in

ISBN 978-3-95450-181-6

electron positron collider designs," Modern Physics Letters A, Vol. 30, No. 11, p. 1530006, 2015.

[3] V. Telnov, arXiv:1203.6563v, 29 March 2012.

[4] D. Wang, J. Gao et al., "CEPC partial double ring scheme and crab-waist parameters," International Journal of Modern Physics A, Vol. 31, (2016) 1644016.

[5] J. Gao, IHEP-AC-LC-Note 2013-012.

[6] M. Moratzinos and F. Zimmermann, "Mitigatng performance limitations of single beam pipe circuar e+e- colliders," IPAC 2015.

[7] J. Gao, "The advanced partial double ring scheme for CEPC," IHEP-AC-LC-Note2016-002.

[8] K. Oide, "FCC(ee) Status", ICHEP2016.

[9] Yukiyoshi Ohnishi et. al, "Accelerator design at SuperKEKB," Prog. Theor. Exp. Phys. 2013, 03A011.

[10] Yiwei Wang et.al, "Dynamic Aperture study of the CEPC main Ring with Interaction Region," THPOR012, IPAC2016.

[11] T.J. Bian, J. Gao, et al., "Design study of CEPC alternation magnetic field booster," THPOR011, IPAC2016.

[12] The CEPC-SPPC Study Group, "CEPC-SPPC Preliminary Conceptual Design Report, Volume I-Physics and Detector," IHEP-EP -2015-01, March 2015.

[13] M. Ruan, "Higgs measurements at e+e- Circular Colliders," Proceeding of ICHEP 2014, arXiv 1411.5606v1.

[14] Sha Bai et al., "MDI Design in CEPC partial double ring," THPOR014, IPAC2016.

[15] F. Su, J. Gao et al, "SPPC Parameter Choice and Lattice Design," TUPMW001, Proceedings of IPAC2016.

ISBN 978-3-95450-181-6

SEARCH FOR THE CHARGED PARTICLE ELECTRIC DIPOLE MOMENTS IN STORAGE RINGS

Y. Senichev#, IKP, Forschungszentrum Jülich, Germany
on behalf of the JEDI Collaboration

Abstract

The idea of searching for the electric dipole moment (EDM) of the proton and the deuteron using polarized beams in a storage ring was originally proposed at Brookhaven National Laboratory (BNL), USA. Currently, the "Jülich Electric Dipole Moment Investigations" (JEDI) collaboration is developing the conceptual design of such a ring specifically for the search of the deuteron electrical dipole moment (dEDM). The idea is that the oscillation of spin due to a possible finite electric dipole moment is separated from the influence of the magnetic dipole moment (MDM), and the behavior of spin indicates the existence of dEDM. In connection with this problem, two questions arise: (i) how to create conditions for maximum growth of the total EDM signal of all particles in the beam bunch, and (ii) how to differentiate the EDM signal from the induced MDM signal. For the design of such a ring, we need to address three major challenges:

- the ring lattice should meet the conditions of beam stability, and it has to have incorporated straight sections to accommodate the accelerating station, equipment for injection and extraction of the beam, a polarimeter, and sextupoles;
- the beam polarization lifetime must be around ~1000 seconds;
- systematic errors have to be minimized to eliminate the induced fake EDM signal.

In my contribution, I will present the current status of the project.

INTRODUCTION

One of the essential problems of modern physics is the baryon asymmetry of the Universe that represents the prevalence of matter over antimatter [1]. In addition, cosmic detectors, whose purpose is to search for antimatter, PAMELA and AMS haven't found any significant amount of it in the Universe yet [2]. The development of the new idea that claims one of the reasons for the baryon asymmetry is the breaking of CP invariance, has begun soon after its discovery. A. Sakharov established three necessary conditions for baryogenesis (initial creation of baryons) in 1967 [3]:

- Baryon number violation;
- C-symmetry and CP-symmetry violation;
- Interactions out of thermal equilibrium.

Many theories beyond the SM have been proposed and all of them of so-called "New Physics" are able to remove the difficulties that one meets in the Standard Model, but their experimental confirmation has yet to be found. One of the possible arguments for the breaking of CP-invariance is the existence of non-vanishing electric dipole moments (EDM) of elementary particles.

Currently, the "**J**ülich **E**lectric **D**ipole Moment **I**nvestigation" (JEDI) collaboration works in two directions: first on the existing accelerator COSY the precursor experiment is carried out to prove the feasibility of EDM measurement using the storage ring [4,5,6], and secondly the conceptual design of the ring specifically for search of the deuteron electrical dipole moment (dEDM) is being developed [7]. At present the RF flipper for installation on COSY ring is progressing successfully. Besides, we have already obtained very important experimental results with precise measurements of the spin precession frequency [4,5] which will allow calibrating the particle energy using the clock-wise and counter clock-wise procedure, and we have reached the longest spin coherence time ~1000 sec in horizontal plane [6].

This article is devoted mainly to the dEDM ring development. For the design of such a ring, we need to address three major challenges:

- the lattice should meet the conditions of stability of motion, minimization of beam loss, and it has to have incorporated straight sections to accommodate the accelerating station, equipment for injection and extraction of beam, a polarimeter, and sextupoles;
- using an RF cavity and a certain number of sextupole families, the beam polarization lifetime must be around ~1000 seconds;
- systematic errors have to be minimized to eliminate the induced fake EDM signal.

FROZEN AND QUASI-FROZEN SPIN CONCEPTS

In this paper, we will analyze two types of structures: the frozen spin (FS) and the quasi- frozen spin (QFS) lattices described in [7]. The concept of "frozen spin" lattice has been suggested by BNL [8], and it is based on the elements with incorporated electric and magnetic fields in one element, when the spin of the reference particle is always orientated along the momentum. Using this concept, a lot of lattice options for its implementation were proposed for protons and deuteron, in particular by R. Talman [9].

In the "frozen" spin method the main objective is to maximize the EDM signal growth, which is provided by the frozen orientation of spin along the momentum, i.e. by zero spin frequency $\vec{\omega}_G = 0$ relative to the momentum

#y.senichev@fz-juelich.de

ISBN 978-3-95450-181-6

due to the magnetic dipole moment (hereinafter called MDM precession) in $\vec{E}\times\vec{B}$ fields:

$$\vec{\omega}_G = -\frac{e}{m}\left\{G\vec{B} + \left(\frac{1}{\gamma^2 - 1} - G\right)\frac{\vec{\beta}\times\vec{E}}{c}\right\}, \qquad (1)$$

where $G = \frac{g-2}{2}$ is the anomalous magnetic moment and g is the gyromagnetic ratio. The expression (1) defines the ratio between electric and magnetic fields in "E+B" elements.

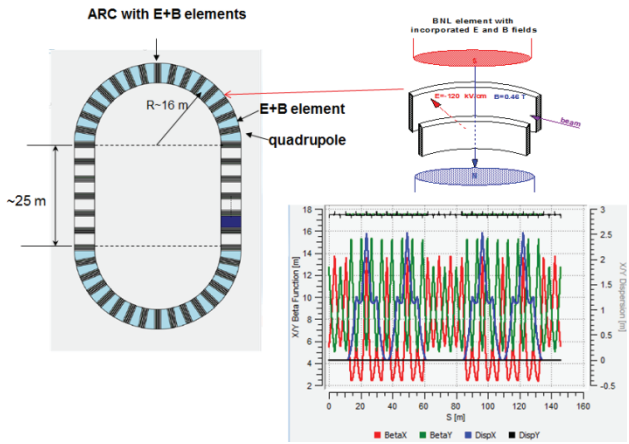

Figure 1: FS lattice with TWISS functions.

We have developed a custom option of FS lattices for the EDM deuteron measurement, which is based on "E + B" elements. The FS lattice has the racetrack shape and contains two arcs and two zero-dispersion straight sections (see fig.1). The TWISS functions show the beam envelope and dispersion along circumference. We have studied the spin-orbital dynamics in this ring with sextupoles, which would allow us to get the spin coherence time of more than 1000 seconds.

Studying the FS structure, we have paid attention to the fact that the frozen spin condition is performed only for the reference particle, and the spin vector of all other particles oscillates relative the frozen direction. But if so, it might not be worth it to strictly fulfill the frozen spin condition even for the reference particle. If the spin oscillates in the horizontal plane with respect to the frozen spin direction with amplitude Φ_s, then the EDM growth decreases proportionally to the factor $J_0(\Phi_s) \approx 1 - (\Phi_s)^2/4$. Taking into account that the deuteron's anomalous magnetic moment $G = -0.142$ has a small value and the fact that the spin oscillates around the momentum direction within half value of the advanced spin phase $\pi \cdot \gamma G/2$ in the magnetic arc, each time returning in the elements with electrical field on the straight sections, it is obvious that the effective contribution to the expected EDM effect is reduced only by a few percent. This allows us to proceed to the concept of quasi-frozen spin QFS [10], where the spin is not frozen with respect to the momentum vector, but continually oscillates around momentum with small amplitude of few degrees.

In case of the quasi-frozen spin lattice, we have two options. In the first option (see fig.2), the electrical and magnetic fields are fully spatially separated in arcs and straight section elements.

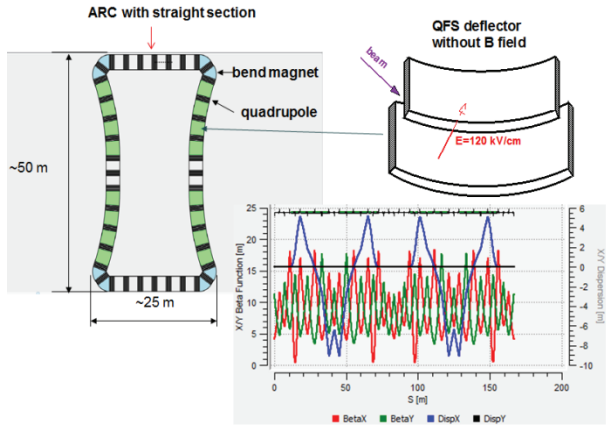

Figure 2: First option of ring lattice based on QFS concept with TWISS.

However, this concept inherits the drawback of cylindrical electrodes, namely the whole set of high-order nonlinearities. Therefore, in second option of QFS lattice we introduced a magnetic field of small value ~100 mT, compensating the Lorentz force of the electric field on arcs (see fig.3). Both QFS lattices consist of two arcs and two straight sections with approximately similar circumference to that of the FS lattice.

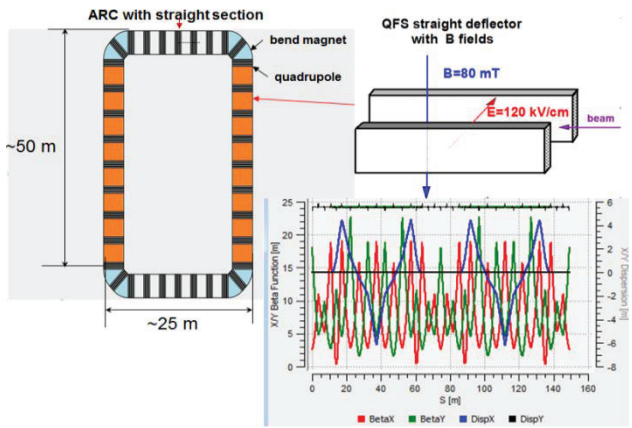

Figure 3: Second option of ring lattice with TWISS functions.

In both cases the lattice includes the straight sections with zero dispersion in the middle of the magnetic arcs for installation of the polarimeter, the beam extraction and injection systems, and the RF cavity.

SPIN TUNE DECOHERENCE

To discuss the effect of spin decoherence, it is reasonable to consider the spin tune, which is the number of spin oscillations in one revolution of the particle around the ring. Initially, the problem of spin tune

ISBN 978-3-95450-181-6

decoherence arose due to the requirement of having a maximum EDM signal. For horizontally oriented spin, the spread of spin tune leads to a multi-directional EDM signal for different particles and ultimately to a reduction of the total EDM signal. Later on, this problem gained salience due to understanding the fact that considering systematic errors, in particular due to misalignment of the electric and magnetic elements, spin decoherence can be transferred from the horizontal plane into the vertical plane, where we expect to see the EDM signal, that is, we get the "fake" EDM signal. The latter is a stronger argument than the geometric phase considered in [8], and it puts forward much greater demands on the limitation of the spin tune decoherence.

Now let us briefly mention the main causes of decoherence. Expanding in Taylor series the well-known expression for the spin tune in electric field $\nu_s^E = \left(1/(\gamma^2-1) - G\right)\cdot \gamma\beta^2$ and in magnetic field $\nu_s^B = \gamma G$ in the vicinity of an arbitrary point γ_0

$$\begin{aligned} \Delta\nu_s^B &= \Delta\gamma \cdot G \\ \Delta\nu_s^E &= \Delta\gamma \cdot \left[-G-(1+G)/\gamma_0^2\right] + \Delta\gamma^2 \cdot (1+G)/\gamma_0^3 + .. \end{aligned} \quad (2)$$

we see that the spin tune spread $\Delta\nu_s^E$ in an electric field has all orders of non-linearity. Obviously, the linear term $\Delta\gamma \cdot G$ in both fields gives the maximum contribution to the spin tune decoherence, and a simple estimate shows that the spin coherence time is limited to a few milliseconds.

Introduction of the RF cavity allows averaging and practically reducing the linear term contribution to zero. However, it has been shown in [11] that the $\Delta\gamma(t)$ deviation follows the expression:

$$\Delta\gamma(t) = \Delta\gamma_m \cos\Omega_s t - \frac{\beta^2}{\eta}\left[\left(\alpha_1 - \frac{\eta}{\gamma^2}\right)\cdot\frac{\Delta\gamma_m^2}{\beta^2} + \gamma^2\left(\frac{\Delta L}{L}\right)_\beta\right] (3).$$

where $(\Delta L/L)_\beta = \left[\left\langle p_{xm}^2\right\rangle + \left\langle p_{ym}^2\right\rangle\right]/4$ is the orbit lengthening due to the betatron motion with amplitude of transverse momentum deviation in horizontal p_{xm} and vertical p_{ym} planes, $\Delta\gamma_m$ is amplitude of $\Delta\gamma(t)$ synchrotron oscillation for arbitrary particle, $\eta = \alpha_0 - 1/\gamma^2$ is the slip factor, $\alpha_0 = 1/\gamma_{tr}^2$ is the first order momentum compaction factor, α_1 is the second order momentum compaction factor, and Ω_s is the synchrotron frequency.

Despite that the linear term in (3) is practically reduced to zero with RF, the time independent term and the term proportional to $\Delta\gamma^2$ in equation (3) restrict the spin coherence time to a few hundred seconds.

The final step to reduce the spin tune decoherence is based on the sextupoles, which change the orbit length dependent on the momentum deviation and the dispersion [11]. Detailed numerical consideration of decoherence effects [12] has been done using COSY Infinity [13] and MODE code [14].

SYSTEMATIC ERRORS

Generally, the measurement errors can be divided into two components: random errors and systematic errors. The systematic error is called the error component, which remains constant in repeated measurements and is caused by imperfections of the physical facility. In the EDM ring experiment, the systematic error arises due to the misalignments of electric and magnetic elements in the ring and causes a "fake" EDM signal. The nature of origin being random errors, the misalignments create conditions for systematic errors in EDM experiments. The installation errors (misalignments) are associated with limited capabilities of the geodetic instruments. As is known, the bending magnet (or the electric deflector) can be rotated in three planes. We consider only the rotation around the longitudinal and transverse axis, because the rotation around the vertical axis does not introduce a systematic error. First, let us consider the case of the magnet rotated relative to the longitudinal axis (see Fig.4). Due to such rotation, a horizontal component of

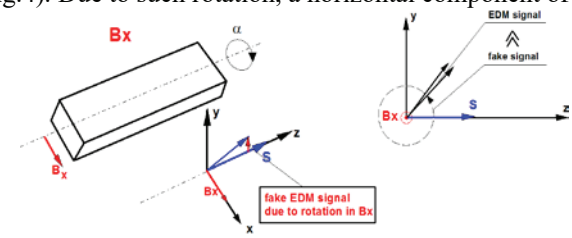

Figure 4: Magnet rotating relative to longitudinal axis.

the magnetic field B_x arises and causes the spin rotation $\Omega_x = \Omega_{\mathrm{Bx}}$ in the same plane where we expect the EDM rotation. To illustrate, let us write the solutions of T-BMT equations with initial condition $S_x = 0,\ S_y = 0,\ S_z = 1, \Omega_z = 0$ and $\Omega_x \neq 0$ in simplest form:

$$S_x(t) = \frac{\Omega_y \sin(\sqrt{\Omega_x^2+\Omega_y^2}\,t)}{\sqrt{\Omega_x^2+\Omega_y^2})}; S_y(t) = -\frac{\Omega_x \sin(\sqrt{\Omega_x^2+\Omega_y^2}\,t)}{\sqrt{\Omega_x^2+\Omega_y^2})} (4).$$

Taking into account the above, we can present components: $\Omega_x = \Omega_{EDM} + \Omega_{\mathrm{Bx}}$ and $\Omega_y = 0 + \delta\Omega_{\mathrm{decoh}}$, where Ω_{EDM} is the frequency of spin rotation due to the presence of an EDM, B_x is the horizontal component induced by the magnet rotation (misalignments), and $\delta\Omega_{\mathrm{decoh}}$ is the spin tune decoherence in the horizontal plane, and it is allowed to reach an rms value of 1 rad for spin coherence time t_{SCT}>1000 sec, that is the rms value of $\left\langle \delta\Omega_{\mathrm{decoh}}\right\rangle \approx 10^{-3}$ rad/sec.

ISBN 978-3-95450-181-6

The magnets are supposed to be installed at the technically realized accuracy of 10μm, which corresponds to the rotation angle of the magnet around the axis of about $\alpha_{\max} = \pm 10^{-5}$ rad. Using COSY Infinity [13] and MODE [14], we have calculated the MDM spin rotation due to B_x, which is $\Omega_{Bx} \approx 3$ rad/sec. At the same time, at presumable EDM value of 10^{-29} e·cm, the EDM rotation should be $\Omega_{EDM} = 10^{-9}$ rad/sec, that is $\Omega_{EDM}/\Omega_{Bx} \approx 10^{-9}$, and the expression (4) can be simplified without loss of measurement accuracy of possible signal EDM at the level of 10^{-9}:

$$\langle S_x(t)\rangle = \frac{\langle \delta\Omega_{decoh}\rangle}{\Omega_{Bx}} \sin\Omega_{Bx} t;\ S_y(t) = -\sin(\Omega_{Bx} + \Omega_{EDM})t\ . \quad (5)$$

We can see from the first equation of (5) that the spin decoherence in the horizontal plane is not growing and is stabilized at the level of $\langle S_y\rangle \sim \langle \delta\Omega_{decoh}\rangle/\Omega_{Bx} \approx 10^{-3}$. This is a significant positive feature. But to be fair, we should understand that, since $\Omega_{Bx} = \frac{e}{m\gamma}(\gamma G + 1)B_x$, we will now get due to $\gamma = \gamma_0 + \Delta\gamma$ the spin frequency decoherence $\Omega_{Bx} = \Omega_{x,\gamma=\gamma_0} + \Delta\Omega_{x,\Delta\gamma}$ in the vertical plane around horizontal axis, which one we can minimize by the same methods (sextupoles, RF) as in horizontal plane. In addition, we are really deprived of ability to measure the accumulated EDM signal by growth of the vertical component of spin suggested in [8], since the spin rotation due to the magnet errors is much faster than due to possibly existing EDM $\Omega_{Bx} >> \Omega_{EDM}$. That is S_y reach a maximum for very short time meanwhile the signal EDM does not have time to be accumulated.

Therefore, the only solution is to measure the total frequency $\Omega_{Bx} + \Omega_{EDM}$, but in order to split out the EDM signal from the sum signal, we need an additional condition. Such a condition is to measure the total spin frequency in the experiment with a counter clock-wise (CCW) direction of the beam $\Omega_{CCW} = -\Omega_{Bx}^{CCW} + \Omega_{EDM}$ and compare with clock-wise (CW) measurements $\Omega_{CW} = \Omega_{Bx}^{CW} + \Omega_{EDM}$. Simultaneously, we must understand that the accuracy of the frequency measurement of $\Omega_{CW}, \Omega_{CCW}$ determines the precision of the EDM measurement. In [5], we achieved the precision of the spin frequency measurements that agrees well with the statistical expectation: $\sigma_\Omega = 2\sqrt{6/N}/(\tilde{\varepsilon}T)$ where N is the total number of useful events, $\tilde{\varepsilon} \approx 0.27$ is the oscillation amplitude of measured asymmetry of polarization, and T is the measurement duration. In a 1000 s time interval with an initial detector rate of 5000 s^{-1}, one would expect an error of the spin frequencies $\Omega_{CW}, \Omega_{CCW}$ of 10^{-5} rad/sec. Taking into account the average accelerator beamtime of 6000 hours per year, we can reach $\sigma_\Omega \approx 5\cdot 10^{-8}$ rad/sec with one-year statistics. Assuming that we can measure the spin frequencies $\Omega_{CW}, \Omega_{CCW}$ with such an accuracy, we will be able to determine the EDM signal $\Omega_{EDM} = (\Omega_{CW} + \Omega_{CCW})/2 + (\Omega_{Bx}^{CCW} - \Omega_{Bx}^{CW})/2$ at the level of $10^{-27} \div 10^{-28}$ e·cm. The lacking one orders of magnitude can be obtained by the time modulation of the "diamond pellets" target (frequency of following diamonds) and higher detector rate [16]. It would allow having bigger number of useful events in the interval when the polarization asymmetry changes faster and having the smaller statistic errors. Thus, such an approach looks promising.

However, we need to be sure that when the sign of the driven magnetic field B_y for the CW-CCW is changed, the magnetic field component B_x is restored with the required relative precision of not lower than 10^{-10}. Therefore, we suggest calibrating the field in the magnets using the relation between the beam energy and the spin precession frequency in the horizontal plane, that is, determined by the vertical component B_y. Since the magnet orientation remains unchanged, and the magnets are fed from one power supply, the calibration of B_y will restore the component B_x with the same relative accuracy 10^{-10}, which applies to the difference $\Omega_{Bx}^{CCW} - \Omega_{Bx}^{CW}$ as well. Besides, we should mention that the calibration in the horizontal plane does not involve the EDM signal. Thus, this calibration will allow using one-year statistics with a limit of EDM on the level up to $10^{-27} \div 10^{-28}$ e·cm. Figure 5 shows the results of a numerical simulation of the EDM measurement procedure. We purposely took the initial EDM value 10^{-21} when $\Omega_{EDM} = 0.1$ rad/sec in order to reduce the duration of the simulation. Then, following the above described procedure, we have "measured" EDM and got EDM= 10^{-21}. Thus, we have proved the method of EDM measurement.

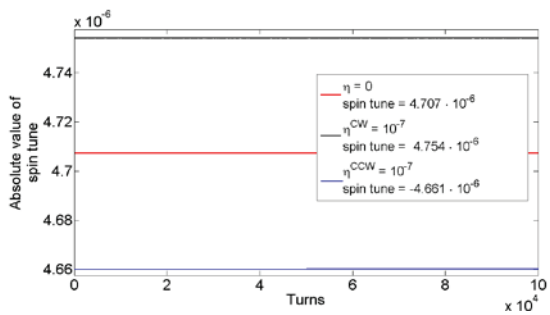

Figure 5: Results of numerical simulation of EDM measurement.

Nevertheless, the fundamental question of how to calibrate the field B_y using the spin tune measurement in a

ISBN 978-3-95450-181-6

horizontal plane, if due to misalignments the spin rotates in the vertical plane with the relatively high frequency of Ω_{Bx}~10 rad/sec, remains. To solve this problem, we plan for the calibration mode only to introduce the inhibitory vertical field, for example by means of a horizontal coil. Having inhibited rotation in the vertical plane to the reasonable value of Ω_{Bx}~0.1 rad/sec and calibrated, we turn off the coil. In this case, we do not need to know the value of the field in the coil.

Up to this point, we have discussed only how to calibrate the magnetic field. But our ring consists of magnetic and electrical elements. Here we rely on the fact that calibrating the magnetic field and taking into account that the electric polarity is not changed and the unique connection of the magnetic field with the electric field for each energy value, we calibrate the electric field as well.

We have to mention that the idea of measuring EDM by introducing a horizontal coil with magnetic field and measuring the spin precession in the vertical plane has been proposed in the wheel concept by I. Koop [17], but it differs from the method considered here. The wheel method uses a special horizontal coil, assuming calibration of the field in the coil by splitting of CW and CCW trajectories and measuring the distance between the separated beams. Besides, in the wheel concept, the issue with the change of field direction in presence of misalignments remained to be unresolved.

Finally, let us consider the case where systematic errors arise due to magnet rotation around the transverse axis, and we get the longitudinal component $B_z \neq 0$. The longitudinal component is not mixed with the EDM signal directly, but it can transform by spin decoherence from the horizontal plane into the vertical plane where we expect an EDM signal. Now, let us suppose that we do not have the systematic errors B_x=0 in vertical plane, but B_z≠0. The solution of the T-BMT equations with initial condition $S_x = 0,\ S_y = 0,\ S_z = 1,\ \Omega_x = 0$ at condition $\Omega_z = \Omega_{Bz}$, $\Omega_y = 0 + \delta\Omega_{decoh}$ and $\Omega_{Bz} << \delta\Omega_{decoh}$ is:

$$S_x(t) = \sin\Omega_{decoh}t;\ S_y(t) = \frac{\Omega_{Bz}}{\Omega_{decoh}}\left[1 - \cos\Omega_{decoh}t\right]. \quad (6)$$

How to see the fake signal depends on the ratio between $\langle\Omega_{decoh}\rangle$ and Ω_{Bz}. Therefore, the only way is to minimize the longitudinal component of the magnetic field with $\Omega_{Bz} \sim 10^{-9}$ rad/turn, using additional trim coils with the longitudinal magnetic field.

CONCLUSION

In the paper, we analyzed the frozen and quasi-frozen spin structures, taking into account the effect of spin decoherence and systematic errors. It has been shown how you can measure the EDM in an imperfect ring using achieved the experimental results of spin tune measurement and the beam polarization lifetime of 1000 sec. In the proposed conception we use: the calibration energy in horizontal plane and measurement in vertical plane, the invariability of ratio B_x to B_y after change of polarity in all elements. These estimates show that the lower limit of detection of presumably existing EDM can be as low as ~$10^{-27} \div 10^{-28}$ e·cm.

REFERENCES

[1] Canetti L., Drewes M., Shaposhnikov M. (2012). "Matter and Antimatter in the Universe", New Journal of Physics, 14, 095012.

[2] Aguilar M., Alberti G., Alpat B. et al., (2013) "First Result from the Alpha Magnetic Spectrometer on the International Space Station: Precision Measurement of the Positron Fraction in Primary Cosmic Rays of 0.5 - 350 GeV", Phys. Rev. Lett., 110, 141102.

[3] Sakharov A. (1967). "Violation of CP Invariance, C Asymmetry, and Baryon Asymmetry of the Universe", Letters to Jounal of Experimental and Theoretical Physics, 5, 24- 26.

[4] Z. Bagdasarian et al., Measuring the polarization of a rapidly precessing deuteron beam, Phys. Rev. ST Accel. Beams 17, 052803 (2014).

[5] D. Eversmann et al., New method for a continuous determination of the spin tune in storage rings and implications for precision experiments, Phys. Rev. Lett. 115, 094801 (2015)

[6] G. Guidoboni, et al., How to reach a thousand-second in-plane polarization lifetime with 0.97-GeV/c deuterons in a storage ring, Phys. Rev. Lett. 117, 054801, (2016).

[7] Y.Senichev et al., Investigating of lattice for deuteron EDM ring, Proceedings of ICAP 2015, Shanghai, China, pp. 17-19.

[8] D. Anastassopoulos et al., "AGS Proposal: Search for a permanent electric dipole moment of the deuteron nucleus at the 10−29 e · cm level", BNL, 2008.

[9] R.Talman et al., Beam and spin dynamics in electric proton EDM, Proceedings of IPAC2012, New Orleans, Louisiana, USA.

[10] Yu.Senichev et al., Quasi-frozen Spin Method for EDM Deuteron Search, Proceedings of IPAC2015, Richmond, VA, USA.

[11] Y. Senichev et al., Spin Tune Decoherence Effects in Electro- and Magnetostatic Structures", Proceedings of IPAC 2013, Shanghai, China, pp. 2579-2581.

[12] E. Valetov et al., Search for optimal spin decoherence effect in QFS lattice, these proceedings.

[13] M. Berz, "Computational Aspects of Design and Simulation: COSY INFINITY", NIM A298, (1990).

[14] Ivanov A. et al., (2014), "Matrix Integration of ODEs for Spin-orbit Dynamics Simulation", Proc. of IPAC2014, Dresden, Germany, 400-402.

[15] Yu.Senichev, et al., Systematic Errors Investigation in Frozen and Quasi-Frozen Spin Lattices of Deuteron EDM Ring, Proceedings of IPAC2016, Busan, Korea.

[16] I.Keshelashvili, Towards JEDI Polarimetry, XVIth International Workshop in Polarized Sources, Targets, and Polarimetry, PSTP2015, Bochum, Germany.

[17] I. Koop et al., Asymmetric Energy Colliding Ion Beams in the EDM Storage Ring, Proceedings of IPAC 2013, Shanghai, China.

ISBN 978-3-95450-181-6

THE EUROPEAN XFEL – STATUS AND COMMISSIONING*

H. Weise, Deutsches Elektronen-Synchrotron, Hamburg, Germany
on behalf of the European XFEL Accelerator Consortium

Abstract

The European XFEL under construction in Hamburg, Northern Germany, aims at producing X-rays in the range from 260 eV up to 24 keV out of three undulators that can be operated simultaneously with up to 27,000 pulses per second. The FEL is driven by a 17.5 GeV superconducting linac. Installation of this linac is now finished and commissioning is next. First lasing is expected for spring 2017. The paper summarizes the status of the project. First results of the injector commissioning are given.

INTRODUCTION

The accelerator complex of the European XFEL [1] is being constructed by an international consortium under the leadership of DESY. Seventeen European research institutes contribute to the accelerator complex and to the comprehensive infrastructure. Major contributions are coming from Russian institutes. DESY coordinates the European XFEL Accelerator Consortium but also contributes with many accelerator components, and the technical equipment of buildings, with its associated general infrastructure. With the finishing of the accelerator installation, the commissioning phase is now starting, with cool down of the main linac scheduled for end of November 2016.

LAYOUT OF THE EUROPEAN XFEL

In the following the overall layout of the European XFEL is given with emphasis on the different sections of the accelerator complex.

Introduction to the Accelerator

The European XFEL with its total facility length of 3.4 km follows the established layout of high performance single pass Self-Amplified Spontaneous Emission (SASE) FELs. A high bunch charge, low emittance electron gun is followed by some first acceleration to typically 100 MeV. In the following, magnetic chicanes help to compress the bunch and therefore increase the peak current. This happens at different energies to take care of beam dynamic effects which would deteriorate the bunch emittance in case of too early compression at too low energies. Thus the linac is separated by several of such chicanes. The European XFEL main linac accelerates the beam in three sections, following the first acceleration in the injector.

Injector

The injector design of the European XFEL is visibly affected by the need of long bunch trains which are required for the efficient use of superconducting linac technology. Like many other FELs it starts with a normal-conducting 1.6 cell radio frequency (RF) electron gun but here the source has to deliver 600 µs long trains i.e. the rf-on time is equivalently long, and not just some few µs. The produced 6 MeV electron beam is almost immediately injected into the first superconducting accelerator section which allows efficient acceleration of bunch trains. This first linac section consists of a standard eight cavity XFEL module, followed by a harmonic 3.9 GHz module. The latter is needed to manipulate the longitudinal beam profile together with the later bunch compression in magnetic chicanes. Beam diagnostics is used to verify the electron beam quality at energy of about 130 MeV. The in total 50 m long injector installation ends with a beam dump being able to take the full beam power.

The injector of the European XFEL was commissioned and operated during the installation period of the main linac sections. First beam was accelerated in 12/2015. At the end of the injector, 600 µs long electron bunch trains of typ. 500 pC bunches are available with measured projected emittances of 1 to 1.5 mm mrad. Most relevant for the FEL process is the slice emittance which was found to be of the order of 0.5 mm mrad for 500 pC.

The next section downstream of the injector is a warm beam line including a so-called dogleg and the first bunch compressor, for historical reasons named BC0. The dogleg takes care of the vertical offset between the injector tunnel and the main linac tunnel.

Compression in all bunch compressors is reached by creating different path lengths in a four dipole magnet chicane. Electrons with slightly lower beam energy are deflected stronger and thus pass the chicane on an ‘outward curve’. The acceleration in the injector section is done slightly off-crest, i.e. the energy of the leading electrons in the bunch is intentionally lower. The above mentioned 3.9 GHz harmonic system helps to get the proper energy modulation along the bunch. Since all electrons have essentially the same speed, the leading ones travel slightly longer, and the bunch is compressed.

The XFEL bunch compressor BC0 does a first slight compression by roughly a factor 2. The bunches ready for further acceleration reach 1 mm length, approx. 100 A peak current, with an energy spread of 1.5% at 130 MeV beam energy.

At present the European XFEL uses the lower of two injector tunnels. The second one was originally built to install a copy of the first injector – availability depending on reliable injector operation was the issue. Meanwhile it seems to be more adequate to aim for a different injector favoring longer pulse or even continuous wave (CW) operation.

* Work supported by the respective funding agencies of the contributing institutes; for details please see http:www.xfel.eu

ISBN 978-3-95450-181-6

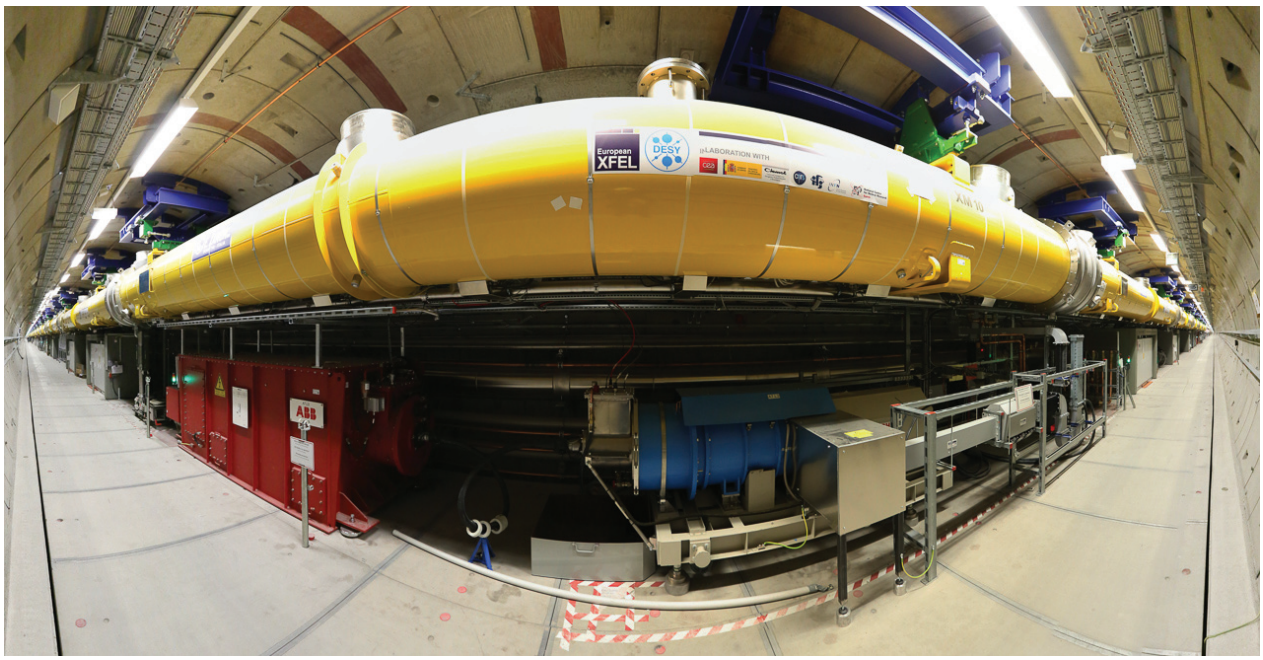

Figure 1: Wide angle photography showing some few meters of the in total almost 1 kilometer long superconducting linac of the European XFEL. The yellow accelerator module (length 12.2 m) is suspended from the ceiling. It houses eight superconducting structures. All installed 96 main linac modules are the result of a strong collaborative effort. Subcomponents were contributed by different partners, assembly [2, 3] was done at Saclay, France, and final cold testing [4] was carried out in the accelerator module test facility at DESY, Hamburg.

The First Linac Section L1

The first section of the main linac consists of four superconducting (s.c.) XFEL accelerator modules operated at 1.3 GHz. Since each module houses eight approx. 1 m long s.c. structures, and since the required energy increase is 470 MeV only – the bunch compression scheme asks for approx. 600 MeV at BC1 - , the accelerating gradient in the first linac section is very moderate and very well below the XFEL design gradient of 23.6 MV/m. In fact, the failure of some few cavities could be easily compensated. With respect to the rf operation, the first four modules are representing a standard XFEL unit since all four are connected to one single 10 MW multi-beam klystron [5]. While the injector klystrons are located outside the accelerator tunnel, the configuration of this first RF power station is identical to all other downstream stations: the modulator is installed outside the tunnel, the pulse transformer and the klystron with its waveguide distribution is located below the accelerator modules (see also Fig 1). Special care is taken to improve the availability of the first linac section. The low-level rf control, installed in shielded compartments next to the klystron, is duplicated with the possibility to switch between the two systems without tunnel access.

Bunch Compression in BC1

The next section, starting at approx. 100 m deep in the main linac tunnel (called XTL), is the bunch compression chicane BC1.

The BC section needs four dipole magnets, further focusing elements, and beam diagnostics. Since this warm beam line section is close to the preceding as well as to the succeeding cold linac section, particle free preparation of ultra-high vacuum systems is essential. Here the work started already during the design phase of all respective beamline components. Cleaning methods had to be considered early on, and movable parts are to be avoided wherever possible. In consequence, the chicane vacuum chambers are wide and flat (in the vertical plane), changing the compression factor by shifting the beam to different paths does not require mechanically moving the vacuum chambers. Here the European XFEL design differs from normal conducting linac designs which are usually less restrictive with respect to particle cleanliness.

The Second Linac Section L2

The BC1 compressor is followed by a twelve accelerator module section (called L2). This altogether 150 m long superconducting linac is supposed to increase the electron beam energy to 2.4 GeV. The required average gradient is with 18.75 MV/m still moderate. Also here a conservative design gradient was chosen. On the other hand, the installation of intentionally high performance modules – accelerating gradients around 30 MV/m were reached in many module tests – can be and in fact was done to again increase the availability of a beam with sufficiently high energy, here at bunch compressor BC2. Also an energy increase at BC2 during parameter optimization becomes possible. From the rf station point of view the linac section L2 consists of three identical rf stations with pulse transformer and klystron every 50 m. Cryogenic-wise L2 forms a stand-

ISBN 978-3-95450-181-6

ard unit. Altogether 12 modules are connected to one cryogenic string, i.e. one long cryostat without intermediate separation valves. All linac sections have a cryogenic feed- and end-box, both connecting to the cryogenic bunch compressor bypass lines linking the different linac sections.

Final Bunch Compression in BC2

Downstream of L2 the last bunch compressor BC2 is installed which basically repeats the functionality of BC1, here with the goal to produce the final electron bunch length required for lasing. A bunch length of 0.02 mm corresponding with 5 kA peak current, with a relative energy spread of 0.3% at 2.4 GeV beam energy will be reached. The section includes a transverse deflecting system as an essential beam diagnostic device. Single bunches are picked and deflected transversely which converts the short bunch length into a corresponding transverse beam size which then can be measured.

The Main Linac Section L3

Downstream of BC2 the linac L3 starts with a design length of more than 1 km. The actually installed length including the cryogenic string connection and end boxes is 984 m. Taking into account all installed main linac accelerator modules – four in L1, twelve in L2, and 80 in L3 – the achievable electron beam energy is above the European XFEL design energy of 17.5 GeV. The exact number will depend on the optimization of the LLRF control, and here especially on the regulation reserve needed as a function of the electron beam current.

The main linac ends after 96 accelerating modules, which corresponds to 9 cryogenic strings, or 24 RF stations. The shortening by four accelerating modules was due to beam line vacuum leaks in two modules which could not be repaired in a timely manner. A third module suffers from a small leak in one of the cryogenic process lines. Thus one rf station equivalent to four modules was left out which was legitimated by the excellent performance of many accelerator modules. A temporary transport beam line was installed which then is followed by some further transport and a collimation beam line protecting the downstream undulator beam lines from beam-halo and mis-steered beams in case of linac problems.

Beam Transport, Collimation and Distribution to the Different Undulators

Downstream of the linac the electron beam line is also supported from the ceiling, over a length of 600 m. This keeps the tunnel floor free for transports and installation of electronics. Especially at the end of the 5.4 m diameter tunnel, where 3 beamlines (to SASE 1 & 3, SASE 2 and into the linac dump) run in parallel, installation and maintenance of the components posed a considerable challenge. During accelerator operation the electrons are distributed with a fast rising flat-top strip-line kicker into one of the two electron beam lines. Another kicker system is capable of deflecting single bunches in a dump beam line. This allows for a free choice of the bunch pattern in each beam line even with the linac operating with constant beam loading.

All undulators and photon beamlines are located in a fan-like tunnel. Figure 2 shows the arrangement of two hard x-ray undulators (SASE 1 und SASE 2), and a soft x-ray undulator (SASE 3) installed downstream of SASE 1. Each undulator provides x-ray photon beams for two different experiments. The time structure of the photon beams reflects the electron bunch pattern in the accelerated bunch trains, affected by the kicker systems.

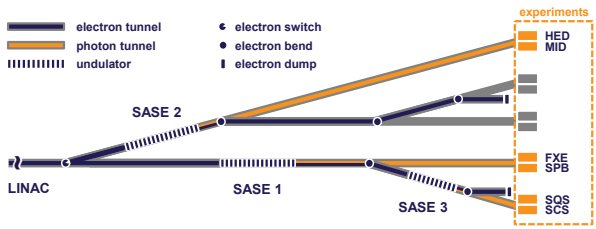

Figure 2: arrangement of two hard x-ray undulators (SASE 1 und SASE 2), and a soft x-ray undulator (SASE 3) installed downstream of SASE 1.

The fan-shaped tunnel system houses two electron beam dumps. Here the electrons are stopped after separation from the photon beams. Each dump can handle up to 300 kW beam power. An identical beam dump is located further upstream, at the end of the main linac tunnel (not shown in Fig. 2). Thus accelerator commissioning and also beam operation is possible while installation or maintenance work in the undulator and photon beam tunnels is ongoing. All five photon beam tunnels end at the experimental hall. During initial operation two experiments each are set up at three beamlines.

OVERVIEW ABOUT ACCELERATOR IN-KIND CONTRIBUTIONS

As described above the European XFEL project benefits from in-kind contributions provided by many partners. In the following an overview is given which allows understanding the responsibilities within the project. The description essentially follows the project structure, i.e. contributions to the superconducting linac are listed first, followed by assignments related to the other sections of the accelerator complex. Infrastructure tasks are described also.

Cold Linac Contributions

Building the worldwide largest superconducting linac was only possible in collaboration. Sufficiently developed SRF expertise was required. Major key-player already working together in the TESLA linear collider R&D phase joined the European XFEL in an early phase. During the XFEL construction phase DESY had several roles. The accelerator complex including the superconducting linac required coordination. At the same time large in-kind contributions in the field of SRF technology were contributed. Work packages contributing to the cold linac are in all cases co-led by a DESY expert and a team leader from the

ISBN 978-3-95450-181-6

respective contributing institute. Integration into the linac installation and infrastructure was another task. The commissioning and operation of the accelerator complex is delegated to DESY.

The accelerator of the European XFEL is assembled out of superconducting accelerator modules being contributed by DESY (Germany), CEA Saclay, LAL Orsay (France), INFN Milano (Italy), IPJ Swierk, Soltan Institute (Poland), CIEMAT (Spain) and BINP, Russia. The overall design of a standard XFEL module was developed in the frame of TESLA linear collider R&D. Final modifications were done for the required large scale industrial production. Further details about the contributions to the superconducting accelerator modules can be found in [3].

Contributions to the Cold Linac Infrastructure

The operation of the superconducting accelerator modules requires the extensive use of dedicated infrastructure. DESY provided the RF high power system which includes klystrons, pulse transformers, connection modules and matching networks, high voltage pulse modulators, preamplifiers, power supplies, RF interlocks, RF cables, and waveguide systems. During the design & development phase, the used 10 MW multi-beam klystrons were developed together with industrial partners. In total 27 klystrons were finally ordered at two vendors. Pulse transformers were procured as one batch from one company. The modules connecting klystron and pulse transformer were developed and built in collaboration with BINP Novosibirsk. Each klystron supplies RF power for 32 superconducting structures, i.e. four accelerator modules. The used waveguide system takes care of a sophisticated rf power matching [6]. The from module tests known individual accelerating gradients are considered for a special tailoring of the distribution system. In order to optimize the rf control, both outputs of the multi-beam klystron deliver roughly the same power which is realized by a sorting of the accelerator modules before tunnel installation.

The Low Level RF System (LLRF) controlling the accelerating RF fields of the superconducting modules is another major DESY contribution. Precision regulation of the RF fields inside the accelerating cavities is essential to provide a highly reproducible and stable electron beam. RF field regulation is done by measuring the stored electromagnetic field inside the cavities. This information is further processed by the feedback controller to modulate the driving RF source. Detection and real-time processing are performed using most recent field programmable gate array (FPGA) techniques. Performance increase demands a powerful and fast digital system, which was found with the Micro Telecommunications Computing Architecture (MicroTCA.4). Fast data transfer and processing is done by FPGAs within one crate, controlled by a CPU. In addition to the MicroTCA.4 system, the LLRF comprises external supporting modules also requiring control and monitoring software. During the XFEL construction phase DESY was operating the Free Electron Laser (FLASH), which is a user facility of the same type as the European XFEL but at a significantly lower maximum electron energy of 1.2 GeV. The LLRF system for FLASH is equal to the one of European XFEL, which allowed for testing, developing and performance benchmarking in advance of the European XFEL commissioning [7].

BINP Novosibirsk produced and delivered major cryogenic equipment for the linac such as valve boxes and transfer lines. The cryogenic plant itself was an in-kind contribution of DESY.

Contributions to the Warm Linac Sections

The largest visible contributions to the warm beam line sections are the over 700 beam transport magnets and the 3 km vacuum system in the different sections. While most of the magnets were delivered by the Efremov Institute, St. Petersburg, a smaller fraction was built by BINP Novosibirsk. Many meters of beamline, be it simple straight chambers or the quite sophisticated flat bunch compressor chambers, were also fabricated by BINP Novosibirsk. DESY took care of a careful incoming inspection, whenever necessary including particle cleaning.

State of the art electron beam diagnostics is of essential importance for the success of an FEL. Thus 64 screens and 12 wire scanner stations, 460 beam position monitors of eight different types, 36 toroids and 6 dark-current monitors are distributed along the accelerator. Longitudinal bunch properties are measured by bunch compression monitors, beam arrival monitors, electro-optical devices and most notable transverse deflecting systems. Production of the sensors and read-out electronics is basically finished. Prototypes of all devices have been tested at FLASH. BPM electronics was developed by the Paul-Scherrer-Institut, Villigen and showed, together with the DESY built pick-ups, performance exceeding the specifications [8, 9].

ACCELERATOR STATUS AT THE START OF COMMISSIONING

As of fall 2016 the installation work in the main accelerator tunnel will be finished. All linac sections but the last cryogenic strings (8 accelerator modules) will be ready for cold commissioning. The complete linac will be cooled down to operating temperature. The last cryogenic string (CS) requires final actions like finishing the waveguide systems, commissioning of the technical interlock system or for some few components even finishing of signal cables installation. The respective work will be done during maintenance access.

Cold Linac Status

Installation of in total 96 main linac accelerator modules was finished in 9/2016. The original plan to get one module per week ready for tunnel installation was basically fulfilled. Modules assembled at CEA Saclay came to DESY and were tested. Test results were used to define the rf power distribution, which was then realized by a proper tailoring of the waveguide system (see above). Sorting of modules helped to find an optimum in the grouping of for modules each connected to one multi-beam klystron. Finally some prognosis with respect to the achievable linac energy can be made. Neglecting the working points of the

ISBN 978-3-95450-181-6

bunch compressors, and only looking at the accelerator modules' usable gradients as determined during the cold test after arrival at DESY, the sum of all individual accelerator modules' usable gradients is about 22 GeV. Respecting the constraints of the possible rf power distribution leads to a reduction to 21 GeV corresponding with an average gradient of 27.5 MV/m. The European XFEL linac by far exceeds the design gradient of 23.6 MV/m. Details are given in [4].

It is expected that during cold commissioning some accelerator cavities or the respective associated systems (rf power coupler, waveguide, LLRF) will show some unforeseen limitations. The European XFEL design included one rf station (i.e. four modules) as spare. Thus it is correct to conservatively state that the designed 17.5 GeV final energy can be safely reached. The excess in energy will give a higher availability.

The nominal working point of BC2 is 2.4 GeV, while the at present highest possible working point is 3.3 GeV, which would bring the final energy to about 19.5 GeV, assuming all systems in operation and close to their limit.

Completing the picture of the accelerator module performance it can be stated:

- In order to make 808 superconducting cavities available for 101 accelerator modules less than 1% extras were required. This based on indispensable quality measures in the full production chain [10].
- Although many accelerator modules needed correction of non-conformities (component or assembly related), discovered either during assembly or even later during test at DESY, at the end only three modules were not ready for installation in time. Nevertheless, sufficient expertise was required at all partner laboratories.
- Most challenging for the cold linac team was the availability of the rf power couplers. Quality issues often but not exclusively related to the copper plating of stainless steel parts, and the resulting schedule challenges were faced. The experienced supply chain risk required a lot of flexibility and willingness to find corrective measures.

Other Sections of the Accelerator Complex

The installation of all beamline sections from the injector to the end of the main linac tunnel XTL will be finished at the time of linac cool-down. Beam transport to the linac commissioning dump after 2.1 km will be possible.

After the linac almost 3 km of electron beam lines distribute the beam through the SASE undulators to the three different beam dumps. In the northern branch, housing the SASE1 and SASE3 undulators, most of the beamline sections are ready. All undulators are in place. During the last quarter of 2016 the northern branch of tunnels will be completed. The southern branch, housing SASE 2, is scheduled for Q1/2017.

CONCLUSION

The installation of the European XFEL accelerator complex comes to an end. While the linac sections are finished and cooldown / commissioning is next, the remaining beam line sections will be finalized in the next months. First lasing in the SASE 1 undulator is expected for spring 2017, about 6 month after start of the linac cool-down

ACKNOWLEDGEMENT

The European XFEL was built in a great collaborative effort accompanied by an immense team spirit of the involved partners. The author would like to thank all colleagues working as work package leader, as supervisor, as key expert, as field worker, or as backstage helper. Useful information about the project structure and an overview about in-kind contributions are available [11].

REFERENCES

[1] "The European X-Ray Free-Electron laser; Technical Design Report", DESY 2006-097 (2007);
http://xfel.eu/en/documents

[2] S. Berry, "Assembly of XFEL Cryomodules: Lessons and Results", in *Proc. LINAC'16*, East Lansing, MI, USA, Sep. 2016, paper WE1A02, this conference.

[3] H. Weise, "How to Produce 100 Superconducting Modules for the European XFEL in Collaboration and with Industry", in Proc. *IPAC'14*, Dresden, Germany, 2014.

[4] N. Walker, "Performance Analysis of the European XFEL SRF Cavities, From Vertical Test to Operation in Modules", in *Proc. LINAC'16*, East Lansing, MI, USA, Sep. 2016, paper WE1A04, this conference.

[5] V. Vogel et al., "Summary of the Test and Installation of 10 MW MBKs for the XFEL Project", in *Proc. LINAC'16*, East Lansing, MI, USA, Sep. 2016, paper TUPLR017, this conference.

[6] S. Choroba, V. Katalev, E. Apostolov, "Series Production of the RF Power Distribution for the European XFEL", in *Proc. LINAC'16*, East Lansing, MI, USA, Sep. 2016, paper THPLR067, this conference.

[7] C. Schmidt et al., "Performance of the microTCA.4 based LLRF System at FLASH", in Proc. *IPAC'14*, Dresden, Germany, 2014.

[8] M. Stadler et al., "Beam test Results of Undulator Cavity BPM Electronics for the European XFEL", in Proc. *IPAC'14*, Dresden, Germany, 2014.

[9] D.M. Treyer et al., "Design, and Beam test Results of Button BPMs for the European XFEL", in Proc. *IPIC2013*, Oxford, Great Britain, 2013.

[10] W. Singer et al., "Production of superconducting 1.3-GHz cavities for the European X-ray Free Electron Laser", PRSTAB 19, 092001 (2016).

[11] http://www.xfel.eu/project/organization
http://www.xfel.eu/project/in_kind_contribution

ISBN 978-3-95450-181-6

NOVOSIBIRSK FREE ELECTRON LASER: TERAHERTZ AND INFRARED COHERENT RADIATION SOURCE*

N.A. Vinokurov#, I.V. Davidyuk, Ya.V. Getmanov, Ya. I. Gorbachev, B.A. Knyazev, E.V. Kozyrev, S.S. Serednyakov, V.S. Arbuzov, K.N. Chernov, O.I. Deichuli, E.N. Dementyev, B.A. Dovzhenko, E.I. Kolobanov, A.A. Kondakov, V.R. Kozak, S.A. Krutikhin, V.V. Kubarev, G.N. Kulipanov, E.A. Kuper, I.V. Kuptsov, G.Ya. Kurkin, L.E. Medvedev, S.V. Motygin, V.N. Osipov, V.K. Ovchar, V.M. Petrov, A.M. Pilan, V.M. Popik, V.V. Repkov, T.V. Salikova, M.A. Scheglov, I.K. Sedlyarov, O.A.Shevchenko, A.N. Skrinsky, S.V. Tararyshkin, V.G. Tcheskidov, P.D. Vobly, V.N. Volkov, A.G. Tribendis, Budker INP SB RAS, Novosibirsk, Russia

Abstract

High-power free electron laser (FEL) facility NovoFEL has been created at Budker INP. Its wavelength can be tuned over a wide range in terahertz and infrared spectrum regions. As a source of electron bunches this FEL uses multi-turn energy recovery linac which has five straight sections. Three sections are used for three FELs which operate in different wavelength ranges (the first one - 90-240 microns, the second - 37-80 microns and the third - 5-20 microns). The first and the second FELs were commissioned in 2003 and 2009 respectively. They operate for users now. The third FEL is installed on forth accelerator track which is the last one and electron energy is maximal here. It comprises three undulator sections and 40 m optical cavity. The first lasing of this FEL was obtained in summer, 2015. The radiation wavelength was 9 microns and average power was about 100 watts. The designed power is 1 kilowatt at repetition rate 3.75 MHz. Radiation of third FEL has been delivered to user stations recently. The third FEL commissioning results as well as current status of the first and second FELs and future development prospects are presented.

OVERVIEW OF THE NOVOSIBIRSK FEL FACILITY

Accelerator and Two Old FELs

The Novosibirsk FEL facility [1] includes three FELs. All the FELs use the electron beam of the same electron accelerator. It is a multi-turn energy recovery linac (ERL). A simplified scheme of the four-turn ERL is shown in Fig. 1. Starting from low-energy injector 1, electrons pass four times through accelerating radiofrequency (RF) structure 2. After that they loose part of their energy in FEL undulator 4. The used electron beam is decelerated in the same RF structure, and low-energy electrons are absorbed in beam dump 5.

The Novosibirsk ERL has three modes, one mode for operation of one of the three FELs. The first FEL is installed under the accelerating (RF) structure (see Figs. 2 and 3). Therefore, after the first passage through the RF structure, the electron beam with an energy of 11 MeV is turned by 180 degrees in the vertical plane. After the use in the FEL, the beam returns to the RF structure in the decelerating phase. In this mode, the ERL operates as a single-orbit linac.

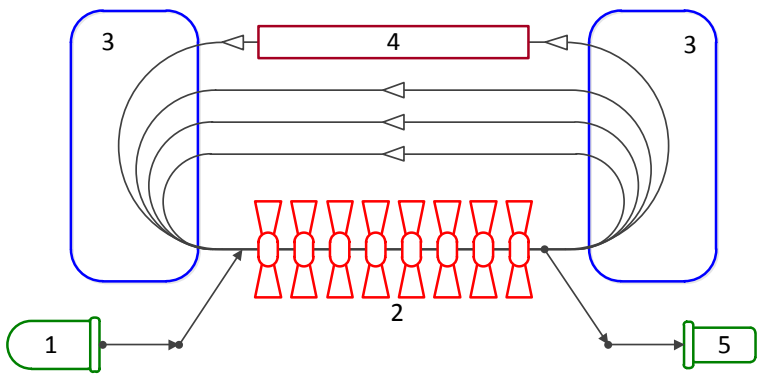

Figure 1: Simplest multi-turn ERL scheme: 1 – injector, 2 – linac, 3 – bending magnets, 4 – undulator, 5 – dump.

*Work supported by Russian Science Foundation project N 14-50-00080. #vinokurov@inp.nsk.su

ISBN 978-3-95450-181-6

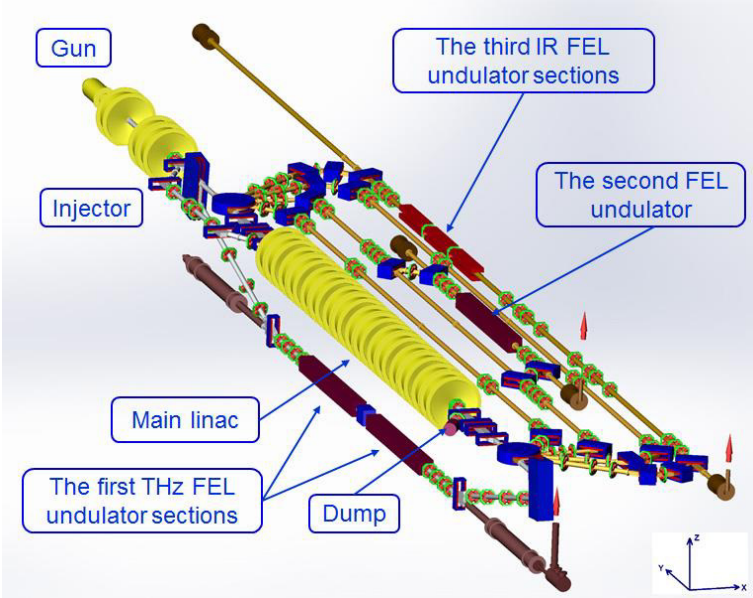

Figure 2: The Novosibirsk ERL with three FELs (top view).

The first FEL has been in operation since 2003 [2]. It provides a narrow-band (less than 1%) terahertz radiation in the wavelength range of 80 – 240 μm at an average power of up to 0.5 kW and a peak power of up to 1 MW (100-ps pulses at a repetition rate of 5.6 MHz). About 30 user research projects in different fields of science were carried out at the facility in recent years, see e.g. [3 – 8].

For operation with the second and third FELs, two round magnets (a spreader and a recombiner) are switched on. They bend the beam in the horizontal plane, as shown in Fig. 2. After four passes through the RF accelerating structure, the electron beam is in the undulator of the third FEL. The used beam is decelerated four times and goes to the beam dump.

If four magnets on the second track (see Fig. 2) are switched on, the beam with an energy of 20 MeV passes through the second FEL. It generates a narrow-band (less than 1%) far infrared radiation in the wavelength range of 40 – 80 μm at an average power of up to 0.5 kW and a peak power of up to 1 MW (50-ps pulses at a repetition rate of 7.5 MHz). We plan to consider an option of using a new type of variable-period undulator at this FEL [9]. It will allow us to expand significantly the wavelength tuning range.

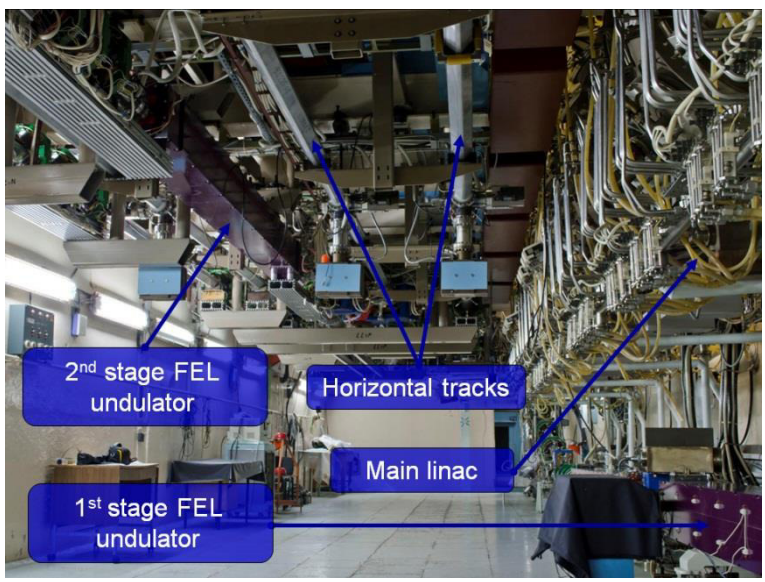

Figure 3: Accelerator hall.

ISBN 978-3-95450-181-6

Figure 4: Optical beamline for FELs. Radiation of all FELs is delivered to the same user stations. Switching between FELs is done using retractable mirrors.

Unlike other ERLs [10, 11], the Novosibirsk one is the world's only multi-turn ERL.

A photo of arrangement of the accelerator hall with accelerating RF cavities and the FELs is shown in Fig. 3.

The radiation of all the three FELs is directed to the same nitrogen-filled beamline to the user stations. The radiation combiner is shown in Fig. 4.

The Third FEL Design

The energy of electrons in the third FEL is about 42 MeV as the beam is accelerated four times. The undulator of the FEL is installed on the fourth track, as shown in Fig. 5 and Fig. 6. The whole undulator is composed of three 28-period sections. Each of them is a permanent magnet undulator with a period of 6 cm and a variable gap. Now the section in the middle is used for phasing of the two other sections.

The wavelength range of this FEL will be 5-20 μm.

The optical cavity of this FEL is about 40 m long. It is composed of two copper mirrors. The radiation is out-coupled through the holes in the mirror center. We can also implement an electron out-coupling scheme here [12] (see Fig. 7), and we are going to try it in future. In this scheme, the beam is bunched in the first undulator and then the achromatic bend slightly deflects it in the transverse direction, so that its radiation in the second undulator goes off the axis and past the front mirror. It should be noted that this scheme is advantageous only with high power radiation. Usually, the users do not need much power and the out-coupling through the holes is much simpler.

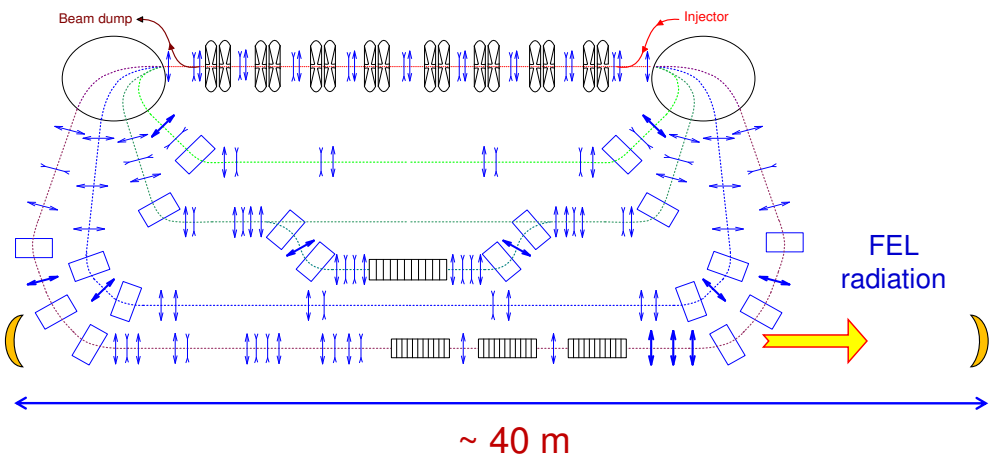

Figure 5: The third stage ERL with FEL undulators and optical cavity.

ISBN 978-3-95450-181-6

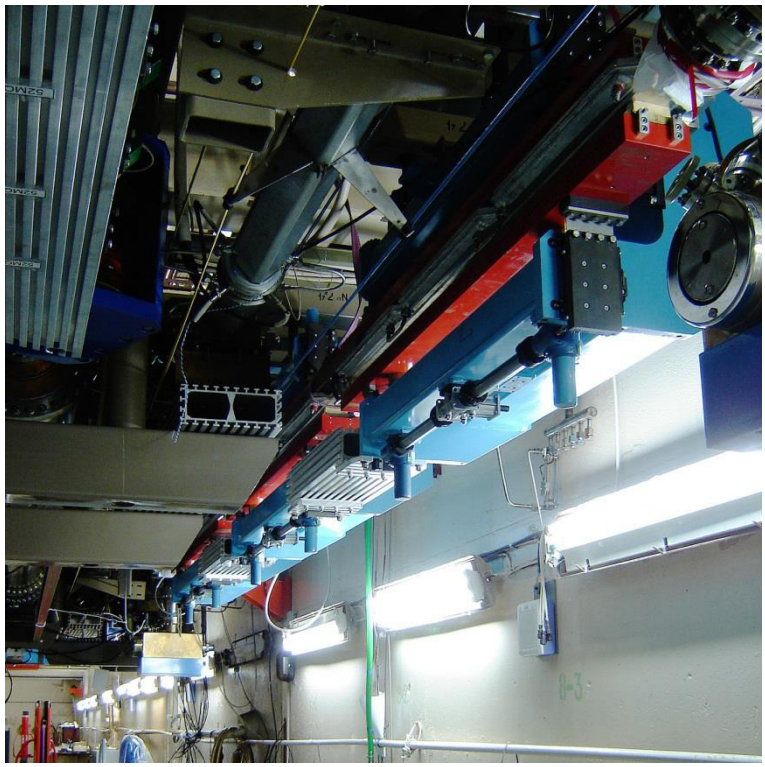

Figure 6: The third stage ERL with FEL undulators.

COMMISSIONING OF THE THIRD FEL - CHALLENGES, FIRST EXPERIMENTS AND FUTURE PROSPECTS

The commissioning of the third stage FEL would be impossible without solutions to some physical and technical problems. The first task was attaining high recovery efficiency in the multi-turn ERL. Without it, the quite high bunch repetition rate, which is required for lasing, would be impossible. Adjustment of the ERL lattice made it possible to decrease the beam losses down to 10 %. As a result, an average current of 3.2 mA was achieved. It should be noted that the commissioning of this ERL was a challenge itself as being accelerated and decelerated bunches use the same tracks. The experience attained here can be used in design of future ERL-based facilities [13].

Alignment of the 40-m optical cavity was another problem. The distance between the mirrors had to be adjusted with accuracy better than 0.3 mm. It was also necessary to align the beam trajectory in the undulator with submillimeter accuracy. When all the requirements were fulfilled, the lasing became a simple task.

The first experiment with the FEL radiation included measurement of the radiation power and wavelength. The maximum power was 100 W at a wavelength of about 9 μm. When we had installed remote control units for the undulator gap and delivered the FEL radiation to the existing user stations, the first user shift took place on the third FEL. The first use of this FEL radiation was done recently in experiments of our colleagues from the International Tomography Center (ITC SB RAS). They studied the influence of intense IR radiation on the spin state of a photoswitchable magnetoactive compound based on copper ions and nitroxide radicals. The spin state of the complex was controlled by EPR spectroscopy, the EPR spectra before and after IR excitation being compared. The obtained results are quite interesting, but they require further investigations. In these experiments we swept the IR-light wavelength in the range from 8.5 to 9.6 μm.

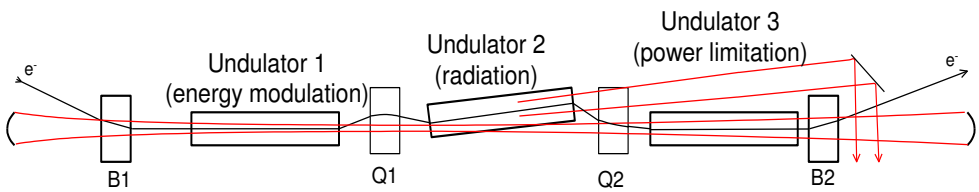

Figure 7: Electron out-coupling scheme.

ISBN 978-3-95450-181-6

Future experiments at the third stage FEL will include study of selective photochemical reactions, infrared laser catalysis and separation of isotopes. In the nearest future, we are also going to improve the x-ray and neutron radiation shielding, decrease beam losses, increase the average current and the DC gun voltage, improve the beam quality in the injector, and optimize the electron efficiency of the FEL. The regular user shifts at the first stage FEL will be also continued.

ACKNOWLEDGMENT

This work was supported by the Russian Science Foundation (project No. 14-50-00080).

The work was done using the infrastructure of the Shared-Use Center "Siberian Synchrotron and Terahertz Radiation Center (SSTRC)" of Budker INP SB RAS.

REFERENCES

[1] Kulipanov, G.N. et al. Novosibirsk Free Electron Laser - Facility Description and Recent Experiments. IEEE Transactions on Terahertz Science and Technology, 5(5) (2015) 798–809.

[2] Antokhin, E. et al. First lasing at the high-power free electron laser at Siberian center for photochemistry research. Nucl. Instr. and Meth. A 528(1) (2004) 15–18.

[3] Knyazev, B.A. et al., 2015. Generation of Terahertz Surface Plasmon Polaritons Using Nondiffractive Bessel Beams with Orbital Angular Momentum. Physical Review Letters, 115(16) (2015) 163901.

[4] Choporova, Y.Y. et al. Classical Holography in the Terahertz Range: Recording and Reconstruction Techniques. IEEE Transactions on Terahertz Science and Technology, 5(5) (2015) 836–844.

[5] Komlenok, M.S. et al. Fabrication of a multilevel THz Fresnel lens by femtosecond laser ablation. Quantum Electronics, 45(10) (2015) 933–936.

[6] Agafonov, A.N. et al. Control of transverse mode spectrum of Novosibirsk free electron laser radiation. Applied Optics, 54(12) (2015) 3635.

[7] Chesnokov, E.N. et al. Non-Faraday rotation of the free induction decay in gaseous NO. Chemical Physics Letters, 636 (2015) 203–207.

[8] Gerasimov, V.V. et al. Experimental investigations into capability of terahertz surface plasmons to bridge macroscopic air gaps. Optics Express, 23(26) (2015) 33448.

[9] Vinokurov, N.A. et al. Variable-period permanent magnet undulators. Physical Review Special Topics - Accelerators and Beams, 14(4) (2011) 040701.

[10] Neil, G.R. et al. Sustained Kilowatt Lasing in a Free-Electron Laser with Same-Cell Energy Recovery. Physical Review Letters, 84(4) (2000) 662–665.

[11] Minehara, E.J. Highly efficient and high-power industrial FELs driven by a compact, stand-alone and zero-boil-off superconducting RF linac. Nuclear Instruments and Methods in Physics Research Section A: Accelerators, Spectrometers, Detectors and Associated Equipment, 483(1) (2002) 8–13.

[12] Matveenko, A. et al. Electron outcoupling scheme for the Novosibirsk FEL. Nucl. Instr. and Meth. A 603 (2009) 38 – 41.

[13] Socol, Y. et al. Compact 13.5-nm free-electron laser for extreme ultraviolet lithography. Physical Review Special Topics - Accelerators and Beams, 14(4) (2011) 040702.

ISBN 978-3-95450-181-6

PLANAR SUPERCONDUCTING UNDULATOR WITH NEUTRAL POLES

N.A. Mezentsev, S.V. Khruschev, V.A. Shkaruba, V.M. Syrovatin, V.M. Tsukanov,
Budker Insitute of Nuclear Physics, Novosibirsk, Russia

Abstract

Superconducting undulator with use of neutral poles was proposed in Budker INP. Period of the undulator is 15.6 mm. Pole gap and magnetic field are equal to 8 mm and 1.2 T correspondingly. A prototype of the undulator with 15 periods was fabricated and successfully tested. Calculations, design and test results of the prototype in the report are presented. The cryogenic and vacuum system of the undulator are discussed.

INTRODUCTION

The development and creation of new magnetic structures for bright synchrotron radiation sources, the emittance of which is close to the diffraction limit, makes high demands on the creation of an adequate generators radiation , such as short period undulators with minimal phase error. Creation of this type of an undulator with a short period, with undulator strength parameter K~2 and with phase error <3° gives the opportunity to work on high harmonics. Widespread currently received undulators based on permanent magnets as radiation sources in the centers of synchrotron radiation. Despite the fact that there is progress in the production of new materials for permanent magnets the use of magnets based on superconductors has advantages in creating a higher field with less period, and less the value of the phase errors.

Several groups in the world [1-7] are busy the problem of a superconducting undulator with short period and with K~2. A variant of the arrangement of the windings in the vertical plane – the "vertical racetrack" is commonly under development.

In this paper we propose a variant of placing of the windings in the horizontal plane – "horizontal racetrack", which differs from the standard solutions used in the superconducting wigglers [8].

MAGNET DESIGN

The transverse electromagnetic field in the undulator, which are used for the generation of radiation, are created by transverse currents in coils near an electron beam orbit . The question of how these currents are closed is minor and relates more to technological solutions from the point of view of higher-quality fields with smaller phase errors. The most widely spread method of closing currents is the method of "vertical racetrack". In the article the method of close of the currents for the superconducting undulator is suggested as horizontal racetrack (Fig. 1). A key element of the undulator is a single magnetic pole (Fig. 2), consisting of a single section coil wound on an iron core.

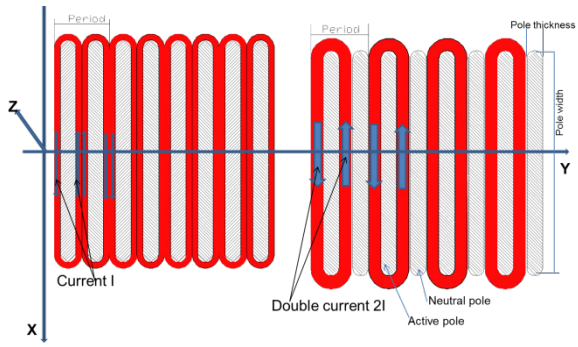

Figure 1: Schematic view of the location of poles and the currents in them for an undulator with horizontal racetrack coils: on the left the standard set of coils with standard of currents closing (coils type of a wiggler), right – set of coils with the neutral poles.

The period of the undulator is formed by magnetic pole with superconducting coil (active pole) and neutral pole, which is an iron core without windings. The undulator magnet consists of two identical halves which are located one above the other.

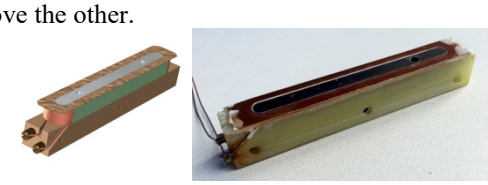

Figure 2: A separate pole is the basic element of the superconducting undulator

All the windings of the upper and lower parts of the magnet are connected in series with the same direction of the currents. The dimensions of the neutral poles and the active poles optimized with respect to the minimum of undesirable components of the magnetic field in the horizontal transverse region of ± 20 mm. When the currents are applied, the magnetic fields of each part of the magnet should be directed in opposite directions so that if you align the two halves in the longitudinal direction, in this case the transverse magnetic field should be zero on the median plane of the magnet. To create the transverse components of the magnetic field in the undulator, it is necessary to shift the top and bottom of the magnet on half period in the longitudinal direction (Fig. 3).

To check the possibility of the creation of this type of undulator, a prototype undulator was designed, manufactured and tested with 15 periods and period length of 15.45 mm. The prototype was performed as standard blocks containing five periods each, made of a soft magnetic iron (Fig. 4). Separate active poles were embedded in the grooves of these blocks. The role of the neutral poles played a rib of iron blocks.

ISBN 978-3-95450-181-6

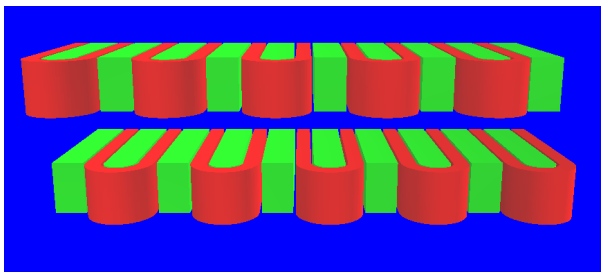

Figure 3: Layout top and bottom halves of the undulator to generate a transverse magnetic field.

The blocks were mounted on steel frames that made up the upper and lower halves of the magnet of the undulator (Fig. 5).

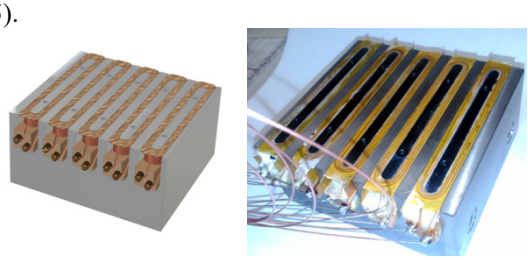

Figure 4: 3D model (left) and photograph (right) of a block of 5 periods.

TEST RESULTS OF THE PROTOTYPE UNDULATOR

The prototype of superconducting undulator with the period of 15.45 mm is designed, fabricated and successfully tested in BINP. Windings type of the prototype are made as horizontal racetrack. Pole gap - 8 mm, number of the periods 15, maximal field was achieved 1.2 T. The superconducting NbTi/Cu wire with diameter of 0.5/0.55 mm was used for production of single-section windings. The maximum current 500 A that corresponds to a magnetic field of ~1.2 T in the median plane. Cooling of undulator is proposed to use of cryocoolers with heat tubes and materials with high heat conductivity.

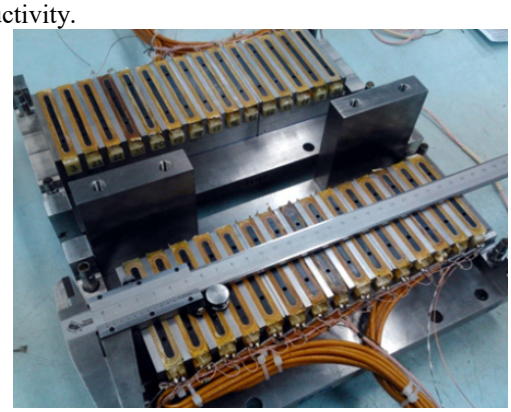

Figure 5: Photo of the halves of the magnet of the prototype undulator before final assembly.

MAGNETIC MEASUREMENTS

Testing of the prototype undulator was carried out in a bath cryostat at liquid helium temperature. The cryostat is equipped with a scanning system that has the ability to scan the magnetic field in the longitudinal direction by means of Hall sensors. Quench training of the undulator magnet has shown that the magnet quickly goes on the calculated field that was calculated based on the properties of superconducting wire (Fig. 6).

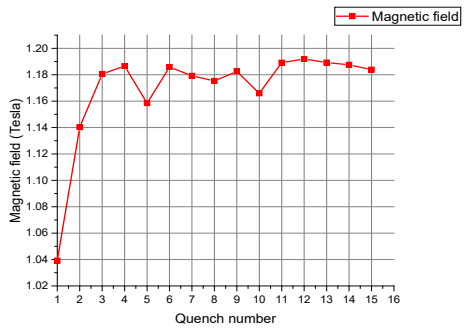

Figure 6: Quench history of the undulator prototype inside vacuum cryostat with indirect cooling system

The distribution of magnetic field along the prototype undulator was carried out in a bath cryostat using a carriage with five Hall sensors. The measurement results showed that the longitudinal field distribution corresponds to a calculated field excluding ends of the prototype for which was not provided special conditions for obtaining the zero field integrals in the longitudinal direction.(Fig. 7)

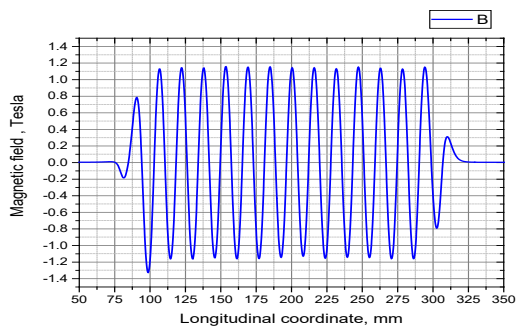

Figure 7: Longitudinal scan of the prototype undulator magnetic field with the Hall probe.

However, testing revealed some negative effects of this design. Magnetic field components as a skew quadrupole and skew octupole are presented in the median plane, which significantly worsen the first field integral of horizontal field for the transverse horizontal displacement of the orbit. To compensate for the skew quadrupole it is necessary to make a correct relation between the transverse dimensions of the iron cores of active and neutral poles. Figure 8 shows the relationship between the widths of the active and neutral poles for zero gradient of the skew quadrupole in the case that the poles are made of iron with a saturation field of 2 T.

When the width of the active pole of 150 mm the width of the neutral pole should be in range of 85-89 mm for compensation of skew quadrupole gradient in order to meet the requirement of field uniformity in the magnet for horizontal displacement of ±6 mm..

ISBN 978-3-95450-181-6

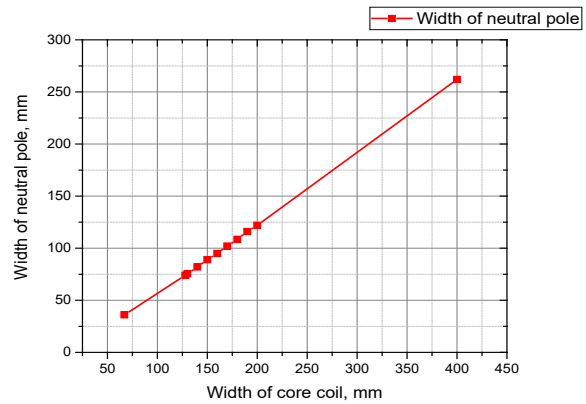

Figure 8: Width of neutral pole versus width of active pole for compensation of skew quadrupole field component in the undulator.

In order to extend the horizontal region, where the horizontal magnetic field does not exceed 10^{-5} T, up to ±20 mm, it is required the use of special compensating windings, located at the top and bottom parts of the undulator magnet.

CRYOGENIC AND VACUUM SYSTEM

An indirect cooling system with use of nitrogen heat-pipe for primary cooling of the magnet and closed loop system with helium for cooling and maintaining low temperature of the magnet are assumed. For efficient cooling of the magnet support elements of the magnet is made of durable aluminum alloy. The cryostat is equipped with four 2-stage cryocoolers to maintain the 3 temperature levels: 4 K- temperature of the magnet, 10-20 K is the temperature of the vacuum chamber and 40-70 K – temperature of a thermal shielding [4]. The beam vacuum chamber has an internal size 6x60 mm and it is made of aluminum alloy. The temperature of the vacuum chamber is keeping 2 cryocoolers at level of 10-20 K. Vacuum chamber is placed between the two halves of the magnet undulator with a gap of 0.5 mm by means of adjustable mounting fixtures rigidly attached to the magnet with use of low heat conductive materials.

CONCLUSION

- The test results and the further calculations of the magnetic system of superconducting undulator with individual magnets and the neutral poles (horizontal racetrack) demonstrated the possibility of creating a system which has advantages compared to similar systems used vertical winding racetrack;
- no restrictions on the length of the magnet;
- the ability to minimize phase errors at the expense of making a more accurate winding;
- all poles are individually produced in mass production, which improves their precision manufacturing, to carry out selection on identity and individual test at the maximum field.

ACKNOWLEDGEMENTS

This work was supported by grant 14-50-00080 of the Russian Science Foundation.

REFERENCES

[1] Richard P. Walker, Phase errors and their effect on undulator radiation properties, Physical Review Special Topics - Accelerators And Beams 16, 010704 (2013).
[2] Ben Shepherd, SCU Magnet Modelling: Tolerances and Beam Trajectories, Superconducting Undulator Workshop, RAL, 28-29 April 2014.
[3] D. Wollmann et Al, A new concept for reducing phase errors in superconductive undulators: induction-shimming, Proceedings of epac08, Genoa, Italy.
[4] Y. Ivanyushenkov et al, Development of a superconducting undulator for the APS, 11th International Conference on Synchrotron Radiation Instrumentation (SRI 2012).
[5] S. Chunjarean et al, Field error correction for a superconducting undulator, Slac-Pub-15320.
[6] Katherine C. Harkay et al, APS superconducting undulator beam commissioning results, Proceedings of PAC2013, Pasadena, CA USA.
[7] R. Kinjo et al, A bulk high-TC superconductor staggered array undulator, Proceedings of FEL08, Gyeongju, Korea.
[8] S. Khrushchev, N. Mezentsev, V. Lev, V. Shkaruba, V. Syrovatin, V. Tsukanov, Superconducting multipole wigglers: state of art. Proceedings of IPAC2014, Dresden, Germany, 4103-4106.

ISBN 978-3-95450-181-6

CW 100 mA ELECTRON RF GUN FOR NOVOSIBIRSK ERL FEL

V. Volkov#, V. Arbuzov, E. Kenzhebulatov, E. Kolobanov, A. Kondakov, E. Kozyrev, S. Krutikhin, I. Kuptsov, G. Kurkin, S. Motygin, A. Murasev, V. Ovchar, V.M. Petrov, A. Pilan, V. Repkov, M. Scheglov, I. Sedlyarov, S. Serednyakov, O. Shevchenko, S. Tararyshkin, A. Tribendis, N. Vinokurov, BINP SB RAS, Novosibirsk, Russia

Abstract

Continuous wave (CW) 100 mA electron rf gun for injecting the high-quality 300-400 keV electron beam in Novosibirsk Energy Recovery Linac (ERL) and driving Free Electron Laser (FEL) was developed, built, and commissioned at BINP SB RAS. The RF gun consists of normal conducting 90 MHz rf cavity with a gridded thermionic cathode unit. Bench tests of rf gun is confirmed good results in strict accordance with our numerical calculations. The gun was tested up to the design specifications at a test bench that includes a diagnostics beam line. The rf gun stand testing showed reliable work, unpretentious for vacuum conditions and stable in long-term operation. The design features of different components of the rf gun are presented. Preparation and commissioning experience is discussed. The beam test results are summarized.

INTRODUCTION

Recent projects of advanced sources of electromagnetic radiation [1] are based on the new class of electron accelerators where the beam current is not limited by the power of rf system – energy recovery linacs (ERLs). Such accelerators require electron guns operating in continuous wave (cw) mode with high enough average current. The only solution is an rf gun, where the cathode is installed inside the rf cavity. The advantages of the rf guns are higher accelerating field, which is desirable to obtain low beam emittance. It has no problem with degradation of the cathode due to poor vacuum in the gun. The considered rf gun if it be used in the most power Novosibirsk FEL can increase it`s power by one order on magnitude more.

In this paper we describe the beam test results of our low-frequency rf gun (see [2-4]) built as the new electron source for ERL of the Novosibirsk FEL facility (see [5]). Measured rf gun characteristics are in Table 1.

Table 1: Measured rf Gun Characteristics

Name	Value
Average beam current, mA	0.003-100
Bunch energy, keV	100 ÷ 400
Bunch duration (FWHM), ns	0.2 ÷ 2.0
Bunch emittance, mm mrad	10
Bunch charge, nC	0.3 ÷ 3.8
Bunch repetition frequency, MHz	0.01 ÷ 90

#v.n.volkov@inp.nsk.su

RF GUN AND DIAGNOSTIC STAND

Here we shortly describe the rf gun and diagnostic stand presented by sketches of Figs. 1 and 2. Detailed information sees in [2-4]. Perfections of the stand are following: 30 kW water cooled beam dump, 5 cm lead radiation shield, wideband Wall Current Monitor (WCM2), new scheme of cathode-grid modulator with GaN rf transistor, Transition Radiation Sensor, and pair of standard WCM.

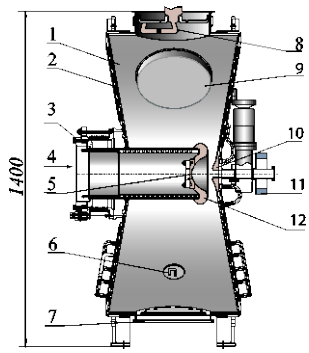

Figure 1: Rf gun sketch.

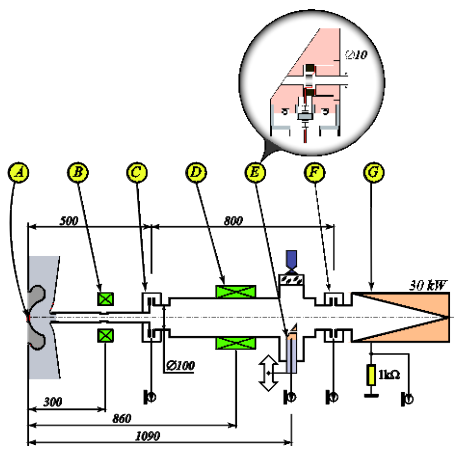

Figure 2: The stand layout.

In figures: 1- Cavity bi-metallic shell; 2-Cavity back wall; 3-Cathode Insert; 4-Cathode injection/extraction channel; 5-Thermionic cathode-grid unit (can be replaced by EIMAC); 6-Loop coupler; 7-Vacuum pumping port; 8-Power input coupler; 9-Sliding tuner; 10-Cone like nose; 11-Peripheral solenoid; 12-Concave focusing electrode.

A-Thermionic cathode-grid unit; B-Emittance compensation solenoid; C-First Wall Current Monitor (WCM1); D-Solenoid ; E-Wideband WCM and transition radiation sensor; F-third WCM; G-Faraday cup and Water-cooled beam dump.

ISBN 978-3-95450-181-6

STAND TESTING RESULTS

Beam Current vs Repetition Frequency

The running for a full beam current is made by repetition frequency rising. There must be changed the bias DC voltage (V_{bias}) on the grid to preserve a bunch charge be constant if it be required. Also bunch charge depends on Modulator pulse voltage (V_{pulse}), the pulse duration (τ_{FWHM}=1÷2 ns), and the heating voltage (V_{heat}, see Fig 3). The last is because the cathode-grid distance is changed inversely of heating power due to the cathode unit thermal elongation. Optimal heating voltage for maximal cathode life time is 14 ÷ 15 V instead of 12.6 V established for rf tubes due to the presence of heat reflected anode surface there.

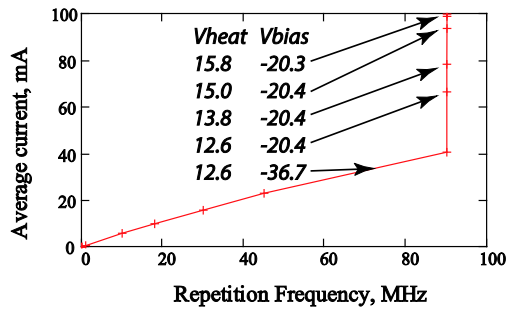

Figure 3: Typical mode of current rising.

Calibration of Cavity Voltage Meter

In order to produce accurate measured data, the calibration of the cavity voltage meter is made with using of two wall current monitors by time delay measuring between them for different cavity voltages. The fitting of measured date by relativistic energy dependency on particle velocity (see Fig.4) gives a perfect accuracy. Numerically calculated beam energy dependency on cavity voltage (*E(keV)=0.9991137·V(kV)-0.96419*) was used there.

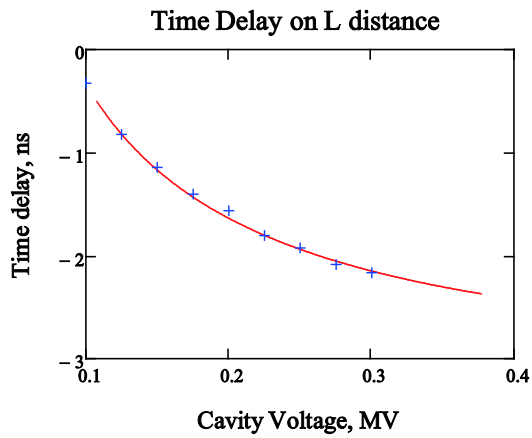

Figure 4: Measured data fitting by theory curve.

Cavity Testing up to 400 kV

The cavity voltage was raised to 400 kV step by step during 5 hours because ½ hour operation time needs to normalize pressure level after the each step (see Fig.5). Then the beam current up to 47 mA limited by maximal beam dump power was getting on in the typical rising mode as shown in Fig. 3.

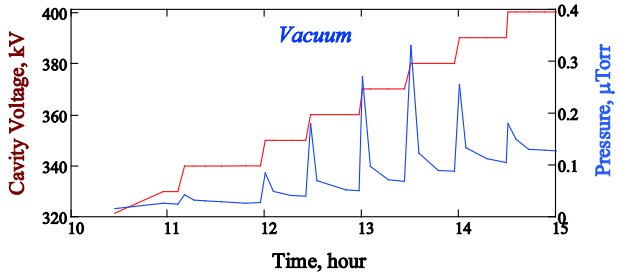

Figure 5: Cavity testing process behavior.

Launch Phase Functions

In order to explain effects of beam bunching, modulator jitter compensation, and other effects in the rf gun, the numerically calculated (by ASTRA cod [6]) launch phase functions are presented. There are launch phase (68°) with maximal bunch energy shown in Fig. 6. At smaller phases, the bunch`s length grow short because its tail having more energy catch up with their head having smaller energy. Also, those bunches launched a little bit earlier/later (jitter) will be late/lead so the jitter will be decreasing.

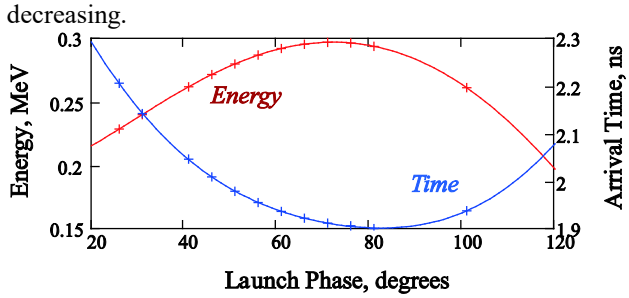

Figure 6: Launch phase functions.

Velocity Modulation Bunching

The numerically calculated r.m.s. bunch duration behaviour on the drift space after the rf gun is presented in Fig.7.

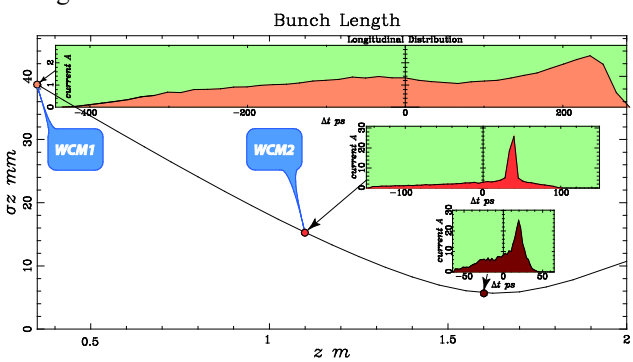

Figure 7: Bunch duration behaviour on the drift space.

Current distributions along bunches are shown by insertions. Frontal spike is formed into cathode-grid gap due to bunching effect there. Then it grows short to be of 20 ps FWHM duration at the distance of 1.1 m where the wide band WCM2 is placed. Unfortunately, our 4 GHz oscilloscope cannot show pulses with τ<200 ps, it all viewed as τ≈200 ps as shown in Fig.8.

ISBN 978-3-95450-181-6

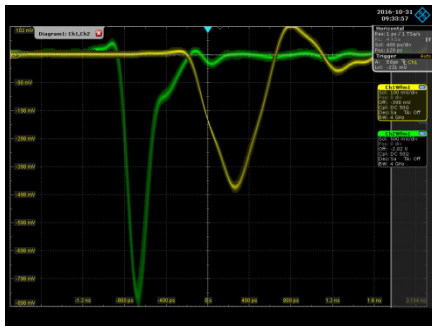

Figure 8: WCM1 (yellow) and WCM2 (green) pulses.

Modulator Jitter Compensation

The jitter compensation effect has confirmed by time delay dependency on launch phase measured between two WCMs with 1.2 m distance (see Fig. 9). Maximal bunch energy is at $\Phi_e=68°$ where it equal to the arrival phase by accurate within some constant. At all other launch phases the arrival phases are behind of it because lower bunch energies (or velocities). Arrival pulse phase becomes independent on Launch phase at $\Phi_j=27°$, i.e. the jitter is compensated there (modulator jitter is ~ $\pm 1 \div 2°$).

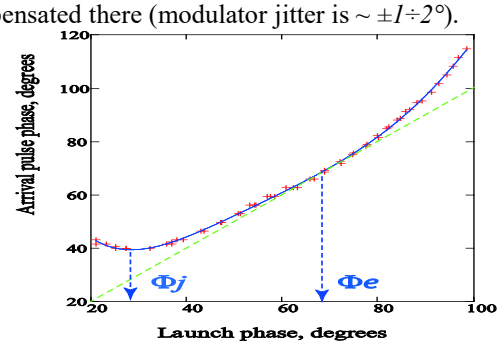

Figure 9: Arrival pulse phase behavior.

Emittance Measurements

Bunch emittance was measured by solenoid focusing method when the spot size of the beam focussed to a target is measured through CCD camera registering the transition radiation. Then the measured data behaviour on the focusing solenoid strength is compared with ASTRA numerically calculated behaviour (see Fig. 10). The deviation is only 9% so we can trust to our calculations.

As the calculation predicts, the measured normalized emittance of ε=15.5 mm mrad can be compensated by a proper solenoid focusing scheme to ε=10 mm mrad.

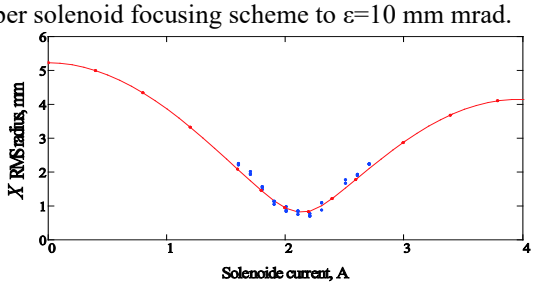

Figure 10: Measured and calculated beam behaviors.

Dark and Leakage Currents

Two places with peak surface field of 10-14 MV/m only can be the sources of field emitted dark currents (see Fig. 11). As we see from Fig. 11, there are no dark currents in the beam absolutely that confirms definitely.

Leakage current source is the cathode oneself at some bias voltages. There is depending on heating voltage because cathode-grid gap depended. To exclude leakage current from the beam we must chose proper bias voltage.

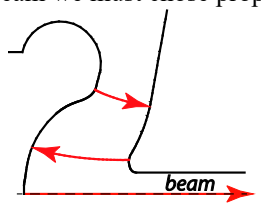

Figure 11: Dark current trajectories in cavity geometry.

Radiation Background

Radiation background was measured during cavity testing from 320 to 400 kV with radiation sensors at 1.5 m. The data exactly coincides with R_{15} is presented in Fig.12 by Fouler-Nordheim (F-N) coordinates in view of straight lines having the enhancement factor of $\beta=628$. The accurate calculations of this field emission process have shown surprisingly things: all calculated values have F-N nature, i.e. have view of straight lines (see Fig. 12) having different β: *I*-dark current, $\beta_I=1250$; P_e-dark current power, $\beta_e=1003$; P_γ-bremsstrahlung power, $\beta_\gamma=865$; R_d-Radiation doze power shielded by Cu with d thickness in mm, $\beta_{3,5,10,15}=721,695,649,628$.

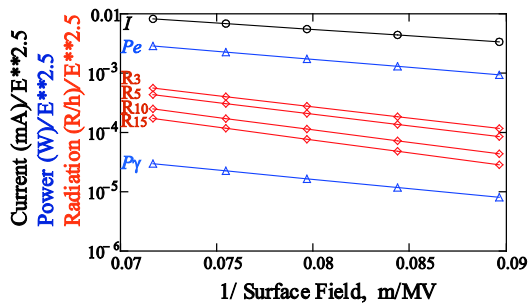

Figure 12: Calculated field emission process.

REFERENCES

[1] Vinokurov, N. A., Levichev, E. B., 2015. Undulators and wigglers for the production of radiation and other applications, Physics-Uspekhi. 58 850–871.

[2] Volkov V.N., et al., First test results of RF gun for the Race-Track Microtron Recuperator of BINP SB RAS. RuPAC2012, 2012, Saint-Petersburg, Russia.

[3] Volkov V., et al., Thermionic cathode-grid assembly simulations for rf guns. PAC2009, 2009, Vancouver, British Columbia, Canada.

[4] V. Volkov, et al., Thermocathode Radio-Frequency Gun for the Budker Institute of Nuclear Physics Free-Electron Laser. ISSN 1547-4771, Physics of Particles and Nuclei Letters, 2016, Vol. 13, No. 7, pp. 827–830.

[5] Kulipanov, et al., Novosibirsk Free Electron Laser—Facility Description and Recent Experiments, IEEE TRANSACTIONS ON TERAHERTZ SCIENCE AND TECHNOLOGY. 5. doi:10.1109/ TTHZ.2015.2453121.

[6] K. Flottmann, ASTRA User`s Manual, http://www.desy.de~mpyflo/Astra_docomentation .

ISBN 978-3-95450-181-6

STATUS OF THE KURCHATOV SYNCHROTRON LIGHT SOURCE

V. Korchuganov, A. Belkov, Y. Fomin, E. Kaportsev, Yu. Krylov, V. Moiseev, K. Moseev, N. Moseiko, D. Odintsov, S. Pesterev, A. Smygacheva, A. Stirin, V. Ushakov, V. Ushkov, A. Valentinov, A. Vernov,
NRC Kurchatov Institute, Akademika Kurchatova Sq., 1, Moscow, 123182 Russia

Abstract

The Kurchatov synchrotron light source operates in the range of synchrotron radiation from VUV up to hard X-ray. To improve facility capabilities in the last few years technical modernization of all facility systems is underway and new beam lines are constructed. In this report the present status and future plans of the Kurchatov synchrotron light source are presented.

INTRODUCTION

The Kurchatov synchrotron light source [1] includes 80 MeV electron linear accelerator, 450 MeV storage ring Siberia-1 with the horizontal emittance 800 nm·rad, the 2.5 GeV storage ring Siberia-2 with the horizontal emittance 78-100 nm·rad and two transport lines. Siberia-2 supplies users' experimental stations by synchrotron radiation in photon energy range 4-40 keV from its bending magnets. Siberia-1 is mostly used as a booster for Siberia-2 but also as an independent SR source.

KSRS OPERATION

The Siberia-2 operates nine months per year in around the clock mode. Within one week 9 working 12-hour shifts are provided. One more shift is dedicated to accelerator physics and machine tuning. As a rule there is one beam storing per day, typical electron current is 100 – 150 mA. Beam lifetime is equal 15 – 20 hours at 100 mA level and defined by vacuum conditions. Injection process at 450 MeV usually takes about 1 hour, energy ramping takes 3 minutes with 2-3% beam loss.

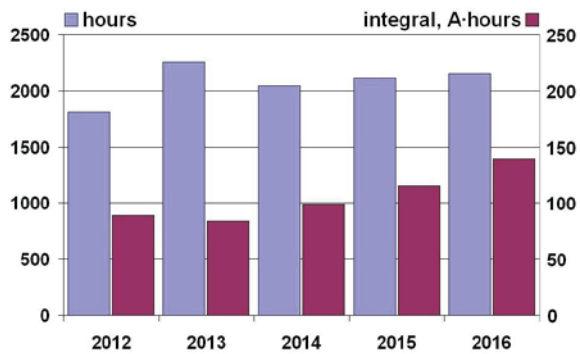

Figure 1: Total time used for experiments and beam current integral at 2.5 GeV for Siberia-2.

Fig. 1 demonstrates total time devoted for SR experimental work at Siberia-2 and electron current integral at 2.5 GeV during last 5 years.

A magnetic lattice of Siberia-2 provides horizontal emittance equal to 98 nm at 2.5 GeV. Betatron coupling is maintained at very small level of 0.001 so vertical beam size is determined by non-zero vertical dispersion function. At injection energy betatron coupling is artificially increased up to 10-15% in order to enhance beam lifetime.

There are 11 experimental stations using SR at Siberia-2 and 4 stations at Siberia-1. Three stations were put into operation during last year (Photoelectron spectroscopy, Phase-sensitive solid-state research, X-ray structure analysis). Two other stations will be commissioned next year (moved from DESY).

Siberia-2 Closed Orbit Distortions

Serious problem for users is slow drift of photon beam in vertical direction. It is caused by heating of machine basis from thick aluminum conducting bar of bending magnet power supply. This induces a progressive slope of magnets and vertical close orbit distortion as a result. We observe the slope with two time constants. First one is equal to approximately one hour and acts just after energy ramping. Second one is equal to one day and is observed during whole working week. As a result we must correct vertical orbit each time before beam storing and jus after energy ramping. As a rule we have RMS distortion of closed orbit about 40 microns in vertical plane and 500 microns in horizontal plane.

In order to stabilize photon beam position feedback system is used. Every beamline has luminophor sensor with TV camera for fixing beam image on luminofor strip. The feedback provides local orbit bump to stabilize photon beam with accuracy of 2-4 microns in sensor location. Plans for future are to improve cooling of power supply conductor by increasing of water flow using more powerful pumps.

DEVELOPMENT OF KSRS IN 2015-2016

The purpose of works in 2015-2016 was both modernization of the existing equipment and introduction of new diagnostics systems on Siberia-2 storage ring. Much attention was paid to developing of KSRS control system.

Siberia-2 New High Voltage Generators

Two new generators based on pseudo-spark switches (a thyrotron TPI1-10k/50) and RLC resonant circuits with a semi-sinusoidal form of currents were produced on "Pulse

ISBN 978-3-95450-181-6

Systems" Ltd. (Ryasan) and installed inside machine tunnel. Total pulse duration is equal 1 μsec.

Due to the excitations of multibunch instabilities by long pulses of kickers the maximum injection efficiency factor is limited near 50-60% (with 10 kV on "kicker" and 6 kV on "prekicker"). To avoid the excitations we shall continue the generator scheme modernization to shorten the pulse duration.

Feedbacks for Instabilities Suppression In Siberia-2

Longitudinal and transverse feedback systems (KCSR and IT, Slovenia) for damping the beam excitations are now under commisionning.

A special small RF cavity is intended as a kicker for suppression of coherent synchrotron excitations. Its own measured frequency is 954.7 MHz and a quality factor is equal to 9.1 [2]. The longitudinal kicker reflectivity measurement and resulting reflectivity dependence on the frequency of the excitation are shown in Fig.2.

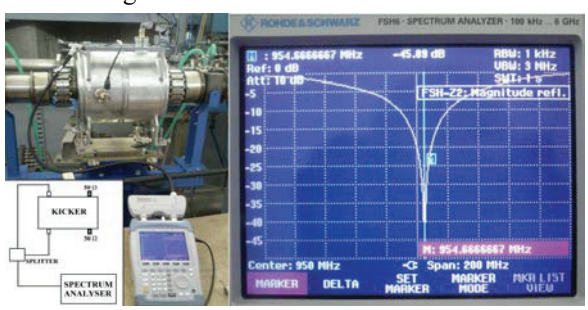

Figure 2: The reflectivity measurement of longitudinal kicker at the Siberia-2 straight section.

Strip lines existing on Siberia-2 ring are used as transverse kickers for suppression of coherent betatron oscillations in X- and Y- plane. One of BPM is used as a sensor. The digital electronics, broadband amplifiers (25 W and 100 W), phase detectors, the modulator, RF control are installed in the rack outside Siberia-2 tunnel.

Siberia-2 Station Of Optical Supervision

The station of optical supervision (SOS) [3] was mounted outside to biological protection of Siberia-2 in 2013. Now all six SOS diagnostic systems are in operation. They permit to measure transverse (resolution is ~1μm) and longitudinal (resolution is 40 psec) bunch sizes, beam dynamics TV monitoring, relative beam displacement (1280×960 pixels CCD camera, 100 Mbit Ethernet interface), a turn-by-turn registration of a chosen bunch transverse profile, synchrotron and betatron frequencies. An example of obtained data is given in Figure 3. Lengthening of the bunch is caused by microwave instability and Touchek effect (at 450 MeV).

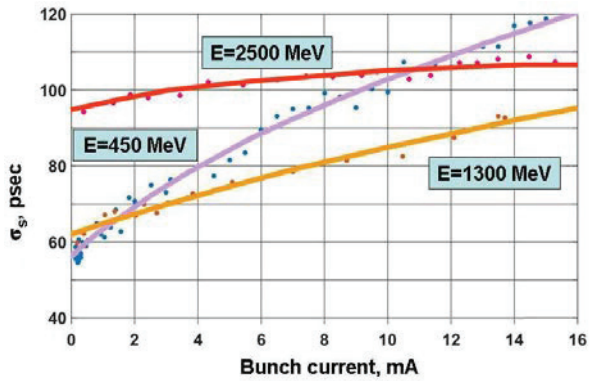

Figure 3: Bunch length vs. beam current in single-bunch mode for different machine energies (approximated dissector data).

Control System

Upgrade of CS consists in changeover of the old CAMAC equipment on modern one and the organization of new architecture. The full-function monitoring system and controls - CitectSCADA works at the top level [4]. CitectSCADA provides visualization of processes, automated workplace control, tracing of systems in real time in a graphic form and access to contemporary records, preparation of the detailed reports, execution of the sub-programmes developed on CitectVBA and CiCode. Now CitectSCADA controls number of subsystems:

- Vacuum system.
- Temperature measurements and temperature stabilization of linac structure.
- Siberia-2 RF generators measurements.
- Siberia-2 magnetic system control, including ramping process, cycle of remagnetization, betatron tune correction and so on.
- Control of photon absorbers in SR beamlines from bending magnets.
- Control of equipment in superconducting wiggler beamline.

At present main goal of KSRS control system staff is to provide CitectSCADA control over all machine systems.

Superconducting Wigglers

SC wiggler (SCW1) with maximum field 7.5 T is installed on Siberia-2 ring. Unfortunately we cannot reach this field with electron beam current value more than 7-10 mA. Rapid beam lifetime decreasing took place for larger values of electron current. The lifetime didn't restore after beam loss. We suggest that ion trapping occurs inside wiggler vacuum chamber because of insufficient pumping rate near wiggler position.

SR users plan to limit maximum field value by 4 T. Earlier there were 3 beamlines of SR from the wiggler, now only one will stay. 100 mA electron current was received with this value of the magnetic field.

At present 2 new superconducting wigglers are fabricated for KSRS in BINP (Novosibirsk). They will be ready to

ISBN 978-3-95450-181-6

install on the ring in the end of 2018. Parameters of all wigglers are presented in Table 1.

Table 1: Wiggler's Parameters

SCW parameters	SCW1	SCW2,3
Max field	7.5 (4) T	3 T
Field period	164 mm	46 mm
Number of poles	19+2	50+4
Undulator parameter	115 (61)	12.9
Emitted energy at 100 mA	35 (10) kW	4.1 kW

KSRS MODERNIZATION

KSRS accelerators and their supply systems will be upgraded according to Federal Program of modernization of synchrotron and neutron laboratory of NRC Kurchatov Institute. General scheme of KSRS will stay unchanged. The modernization will provide an improvement in all valuable machine parameters such as electron current, lifetime, operation time, SR spectral range and flux. Main features of the program are:

- Additional RF generator for Siberia-2, new system of power supply and cooling for all three RF generators. New scheme for RF system: separate generator for every RF cavity instead of old scheme (2 generators for 3 cavities). Three new waveguides.
- New pneumatic vacuum valves, additional vacuum monitors, ion pumps, BPM monitors, eliminating of "hot spots" in the vacuum chamber near inflectors and superconducting wiggler.
- New power supply for bending magnets and quadrupole lenses of Siberia-2, bending magnets of Siberia-1 and transfer lines.
- Two new 3 T superconducting wigglers and their beamlines.
- New generators for linac klystron station and pulse magnets.
- Upgrading of the accelerators' control system and safety system of the facility.
- New water cooling and air-cooling systems for all equipment, new air conditioning for accelerator and experimental halls.
- New beamlines and experimental stations. Total number of stations will achieve 21.

KSRS parameters after modernization are given in Table 2.

Table 2: KSRS Parameters Before And After Modernization

Siberia-2 parameters	2016	2020
Time for users per year, hours	2000 - 2400 (in 24/5 mode)	3000 (4200 in 24/7 mode)
Maximal current, mA	200	300
Maximal total RF voltage, MV	2.0	2.7
Lifetime, hours (at 100 mA)	20 - 25	35 - 40
Lifetime restoring after vacuum chamber repair	2 weeks	3 – 4 days
Number of wigglers	1	3
Number of experimental stations	11	21

CONCLUSION

KSRS continues to work as the only dedicated SR source in Russian Federation. An improvement of accelerators' parameters is a result of continuous efforts in the solution of scientific and technical problems. KSRS modernization will allow to achieve new quality of facility operation.

REFERENCES

[1] V.Korchuganov, A.Belkov, Y.Fomin et al., "The Status of the Facilities of Kurchatov's Synchrotron Radiation Source", RUPAC'14, Obninsk, THY02, p. 290, http://www.JACoW.org.

[2] A.Smygacheva, A.Valentinov, V.Korchuganov et al., NRC KI, Russia and D. Tinta, R. Hrovatin, R. Cerne, IT, Slovenia, "The Feedback System for Damping Coherent Betatron and Synchrotron Oscillations of Electron Beam at Dedicated SRS Siberia-2", ICALEPCS'13, San Francisco, p.1359 THPPC128, http://www.JACoW.org.

[3] A.Stirin, G.Kovachev, V. Korchuganov et al., NRC KI, O. Meshkov, V.Dorohov, A.Khilchenko et al., BINP, "New Station for Optical Observation of Electron Beam Parameters at Electron Storage Ring SIBERIA-2", IPAC'14, Drezden, p.3611, THPME151, http://www.JACoW.org.

[4] Y.Fomin et al., "New Automated Control System At Kurchatov Synchrotron Radiation Source Based On SCADA System Citect", Proceedings of ICALEPCS'13, San Francisco, p.97, MOPPC020, http://www.JACoW.org.

ISBN 978-3-95450-181-6

NUMERICAL ANALYSIS OF THE EFFECTIVE WIDTH OF THE SPECTRUM OF SYNCHROTRON RADIATION

V. G. Bagrov, A. S. Loginov, A. D.Saprykin, Tomsk State University, Russia
D. M. Gitman, A. D. Levin, Institute of Physics, University of Sao Paulo, Brazil

Abstract

For an exact quantitative description of spectral properties in the theory of synchrotron radiation, the concept of effective spectral width is introduced. In the classical theory, numeric calculations of effective spectral width (using an effective width not exceeding 100 harmonics) for polarization components of synchrotron radiation are carried out. The dependence of the effective spectral width and initial harmonic on the energy of a radiating particle is established.

INTRODUCTION

As one of the major quantitative characteristics of spectral distributions for electromagnetic radiation, one commonly uses the concept of spectral half-width. For spectral distributions having a sharp maximum, spectral half-width is the most informative physical characteristic.

However, once a spectral distribution has no pronounced maximum, spectral half-width ceases to be an adequate quantitative characteristic. In particular, this is exactly the case of spectral distributions for synchrotron radiation (SR), and therefore SR spectral half-width has neither been calculated theoretically, nor measured experimentally.

Instead of spectral half-width, the present study proposes to introduce a new precise quantitative characteristic of SR spectral distributions: effective spectral width. It is shown how this quantity can be calculated theoretically, and which physically relevant information can be obtained using this quantity.

In order to set up the problem, we now present some well-known expressions of the classical SR theory for the physical characteristics of synchrotron radiation, which can be found in [1–7].

The spectral-angular distribution for radiation power of SR polarization components can be written as

$$W_s = W \sum_{\nu=1}^{\infty} \int_0^{\pi} f_s(\beta;\, \nu,\, \theta) \sin\theta d\theta. \qquad (1)$$

Here, the following notation is used: θ is the angle between the control magnetic field strength and the radiation field pulse; ν is the number of an emitted harmonic; the charge orbital motion rate is $v = c\beta$, where c is the speed of light; W is the total radiated power of unpolarized radiation, which can be reveled in [1–7]. The index s numbers the polarization components: $s = 2$ corresponds to the σ-component of linear polarization; $s = 3$ corresponds to the π-component of linear polarization; $s = 1$ corresponds to right-hand circular polarization; $s = -1$ corresponds to left-hand circular polarization; $s = 0$ corresponds to the power of unpolarized radiation. The form of functions $f_s(\beta;\, \nu,\, \theta)$ can be founded in [1–7].

SPECTRAL DISTRIBUTION FOR POLARIZATION COMPONENTS OF SYNCHROTRON RADIATION IN THE UPPER HALF-SPACE

It is well known [1–7] that the angle range $0 \leqslant \theta < \pi/2$ (this range will be called the upper half-space) is dominated by right-hand circular polarization, and the angle range $\pi/2 < \theta \leqslant \pi$ (this range will be called the lower half-space) is dominated by left-hand circular polarization (exact quantitative characteristics of SR properties were first obtained in [8–11]). To reveal these features, the expressions (1) can be represented as

$$W_s = W\left[\Phi_s^{(+)}(\beta) + \Phi_s^{(-)}(\beta)\right],$$
$$\Phi_s^{(\pm)}(\beta) = \sum_{\nu=1}^{\infty} F_s^{(\pm)}(\beta;\, \nu),$$
$$F_s^{(\pm)}(\beta;\, \nu) = \int_{0\mp\pi/2}^{\pi/2\mp\pi/2} f_s(\beta;\, \nu,\, \theta) \sin\theta d\theta, \qquad (2)$$

and it suffices to study the properties of functions $F_s^{(+)}(\beta;\, \nu)$ (respectively, the properties of functions $\Phi_s^{(+)}(\beta)$), due to the evident relations

$$F_s^{(-)}(\beta;\, \nu) = F_s^{(+)}(\beta;\, \nu), \quad \Phi_s^{(-)}(\beta) = \Phi_s^{(+)}(\beta)\ {}_{s=0,\,2,\,3};$$

$$F_{\pm1}^{(-)}(\beta;\, \nu) = F_{\mp1}^{(+)}(\beta;\, \nu), \quad \Phi_{\pm1}^{(-)}(\beta) = \Phi_{\mp1}^{(+)}(\beta).$$

The exact form of the functions $F_s^{(\pm)}(\beta;\, \nu)$ and $\Phi_s^{(\pm)}(\beta)$ was revealed in [8–11].

EFFECTIVE SPECTRAL WIDTH FOR POLARIZATION COMPONENTS OF SYNCHROTRON RADIATION

As one of the quantitative characteristics of physical properties for spectral distributions of SR polarization components, it is proposed to introduce the concept of effective spectral width $\Lambda_s(\beta)$. Let us define $\Lambda_s(\beta)$ as follows.

For each fixed value of β, we examine the quantities of partial contributions $P_s(\beta;\nu)$ for individual spectral harmonics, introduced in [12].

ISBN 978-3-95450-181-6

$$P_s(\beta;\nu) = \frac{F_s^{(+)}(\beta;\,\nu)}{\Phi_s^{(+)}(\beta)}\,. \tag{3}$$

Then (2) implies the property

$$\sum_{\nu=1}^{\infty} P_s(\beta;\nu) = 1\,. \tag{4}$$

We choose some values $\nu_s^{(1)}(\beta)$ and $\nu_s^{(2)}(\beta)$ such that the minimum difference $\nu_s^{(2)}(\beta) - \nu_s^{(1)}(\beta)$ should provide the minimum of the non-negative value

$$\sum_{\nu=\nu_s^{(1)}(\beta)}^{\nu_s^{(2)}(\beta)} P_s(\beta;\nu) - \frac{1}{2} \geqslant 0\,. \tag{5}$$

The effective spectral width $\Lambda_s(\beta)$ is defined by the expression

$$\Lambda_s(\beta) = \nu_s^{(2)}(\beta) - \nu_s^{(1)}(\beta) + 1,\;\; \Lambda_s(\beta) \geqslant 1\,. \tag{6}$$

we arrive at the following definition: effective spectral width is the minimum spectral range at which the sum of partial contributions for individual harmonics is not less than $1/2$.

In practice, the most interesting case is the ultrarelativistic limit ($\beta \approx 1$, equivalent to $\gamma \gg 1$). In this case, the analytical study of effective spectral width and other physically interesting quantitative characteristics for spectral distributions of SR polarization components can be significantly extended. This study was carried out in [13].

Given a particular value of β (or γ), it is a purely computational task to obtain the exact values of $\Lambda_s(\beta)$ and $\nu_s^{(1)}(\beta)$. In this article, we present a numerical study of the region $1 \leqslant \Lambda_s(\beta) \leqslant 100$. The effective width $\Lambda_s(\beta)$ is a positive integer, so there exists a range of β (corresponding to a range of γ; hereinafter, we only indicate γ) in which $\Lambda_s(\beta)$ is constant.

ANALYSIS OF NUMERICAL RESULTS FOR EFFECTIVE SPECTRAL WIDTH OF SYNCHROTRON RADIATION

The main results of a numerical study for effective spectral width of SR polarization components are given by our Table 1.

The numerical study is carried out as follows. For each type of polarization s, we examine the sequences of integers $\Lambda_s = 1\,,2\,,3\,...$ and $\nu_s^{(1)} = 1\,,2\,,3\,...$ (it is evident that $\nu_s^{(2)} = \nu_s^{(1)} + \Lambda_s - 1$) and determine the regions of values γ_s for which the condition (5) is satisfied. It is clear that the boundary points of possible regions for γ_s can be found, according to (5), as solutions of the equations

$$\sum_{l=0}^{\Lambda_s-1} P_s(\beta;\nu_s^{(1)}+l) - \frac{1}{2} = 0\,. \tag{7}$$

The roots $\beta_s = \beta_s(\Lambda_s, \nu_s^{(1)})$ of these equations determine the boundary points $\gamma_s = \gamma_s(\Lambda_s, \nu_s^{(1)})$.

In general, for given column s (given polarization component) of the Table 1 indicates for each Λ_s the smallest possible value $\nu_s^{(1)} = \nu_s^{(1)}(\Lambda_s)$ and the corresponding largest value $\gamma_s = \gamma_s(\Lambda_s, \nu_s^{(1)}(\Lambda_s))$, as well as the largest possible value $\tilde{\nu}_s$ for this Λ_s and the corresponding smallest value $\tilde{\gamma}_s$. Possible intermediate values $\nu_s^{(1)}$ between the smallest $\nu_s^{(1)}(\Lambda_s)$ and the largest $\tilde{\nu}_s$, as well as the respective intermediate values γ_s, are not specified. The intermediate values of γ_s always satisfy relations (8). Besides, for a given width Λs following inequalities are true

$$\gamma_s(\Lambda_s\,,k) < \gamma_s(\Lambda_s\,,n)\,,\;\; k > n. \tag{8}$$

Consequently, in the column for given s we indicate the regions of values γ

$$\gamma_s(\Lambda_s - 1, \nu_s^{(1)}(\Lambda_s - 1)) < \gamma \leqslant \gamma_s(\Lambda_s, \nu_s^{(1)}(\Lambda_s)), \tag{9}$$

for which the effective spectral width for the s-component of polarization for SR equals to Λ_s. We also indicate the initial points of the effective spectral width. These points are not determined uniquely. For the smallest initial value $\nu_s^{(1)}$, the range of values (9) taken by γ is the largest one, while this region is the smallest one for the largest possible value $\tilde{\nu}_s$.

For the other polarization components, the results of calculation are given in the respective columns of the Table 1. In particular, the Table 1 shows that for equal values Λ_s the corresponding values γ_s obey the inequalities

$$\gamma_3 > \gamma_1 > \gamma_0 > \gamma_2 > \gamma_{-1}\,. \tag{10}$$

At a fixed energy γ, the corresponding values of Λ_s are restricted by

$$\Lambda_3 < \Lambda_1 < \Lambda_0 < \Lambda_2 < \Lambda_{-1}\,. \tag{11}$$

In this way, for each polarization component of synchrotron radiation we have found energy regions at which the effective spectral width equals to Λ_s, and the initial harmonic of this effective width is determined. Numeric calculations have been carried out in the case $\Lambda_s \leqslant 100$.

In the ultrarelativistic case, the corresponding results have been obtained in [13].

ACKNOWLEDGMENTS

The work of Bagrov and Gitman is partially supported by RFBR research project No. 15- 02-00293a and by Tomsk State University Competitiveness Improvement Program. Gitman thanks CNPq and FAPESP for their permanent support. Levin thanks CNPq for permanent support.

ISBN 978-3-95450-181-6

Table 1: Bondary harmonics and respective energy of effective spectral width for polarization component of SR

Λ	$\nu_2^{(1)}$	γ_2	$\tilde{\nu}_2$	$\tilde{\gamma}_2$	$\nu_3^{(1)}$	γ_3	$\tilde{\nu}_3$	$\tilde{\gamma}_3$	$\nu_0^{(1)}$	γ_0	$\tilde{\nu}_0$	$\tilde{\gamma}_0$	$\nu_{-1}^{(1)}$	γ_{-1}	$\tilde{\nu}_{-1}$	$\tilde{\gamma}_{-1}$	$\nu_1^{(1)}$	γ_1	$\tilde{\nu}_1$	$\tilde{\gamma}_1$
1	1	1.1434	1	1.1434	1	1.2363	1	1.2363	1	1.1592	1	1.1592	1	1.1062	1	1.1062	1	1.1712	1	1.1712
2	1	1.2955	1	1.2955	1	1.4519	1	1.4519	1	1.3204	1	1.3204	1	1.2348	1	1.2348	1	1.3411	1	1.3411
3	1	1.4179	2	1.3237	1	1.6126	1	1.6126	1	1.4476	1	1.4476	1	1.3440	2	1.3233	1	1.4737	1	1.4737
10	1	1.9566	3	1.9286	1	2.2680	2	2.2161	1	1.9986	3	1.9482	2	1.8655	4	1.8455	1	2.0416	2	2.0225
11	1	2.0120	3	1.9906	1	2.3329	2	2.2868	1	2.0550	3	2.0131	3	1.9197	5	1.8721	1	2.0995	3	2.0448
12	2	2.0657	4	2.0129	1	2.3949	2	2.3537	1	2.1084	3	2.0731	3	1.9711	5	1.9353	1	2.1542	3	2.1072
20	2	2.4168	5	2.3807	1	2.7998	2	2.7779	2	2.4603	4	2.4313	4	2.3049	7	2.2738	1	2.5141	3	2.4967
21	2	2.4538	5	2.4215	1	2.8422	2	2.8217	2	2.4980	4	2.4716	4	2.3402	7	2.3139	1	2.5522	4	2.5154
22	2	2.4895	5	2.4608	1	2.8831	2	2.8636	2	2.5345	4	2.5104	4	2.3744	7	2.3521	1	2.5891	4	2.5556
30	3	2.7443	6	2.7193	1	3.1728	3	3.1407	2	2.7937	5	2.7685	5	2.6176	9	2.5933	2	2.8530	4	2.8350
31	3	2.7731	6	2.7499	1	3.2053	3	3.1740	2	2.8227	5	2.7992	5	2.6449	9	2.6233	2	2.8828	4	2.8659
32	3	2.8012	6	2.7797	1	3.2374	3	3.2078	2	2.8512	5	2.8292	5	2.6716	9	2.6525	2	2.9119	4	2.8960
40	3	3.0078	7	2.9869	1	3.4723	3	3.4511	2	3.0601	6	3.0371	6	2.8684	11	2.8465	2	3.1258	5	3.1063
41	3	3.0316	7	3.0121	1	3.4998	3	3.4793	2	3.0842	6	3.0625	6	2.8911	11	2.8712	2	3.1505	5	3.1319
42	3	3.0550	7	3.0367	1	3.5270	3	3.5074	2	3.1079	6	3.0875	6	2.9133	11	2.8953	2	3.1748	5	3.1572
50	4	3.2309	8	3.2126	1	3.7286	3	3.7123	3	3.2864	6	3.2728	7	3.0811	12	3.0670	2	3.3567	6	3.3363
51	4	3.2515	8	3.2342	1	3.7528	3	3.7383	3	3.3074	6	3.2944	8	3.1007	13	3.0814	2	3.3781	6	3.3585
52	4	3.2720	8	3.2555	1	3.7757	3	3.7619	3	3.3281	7	3.3078	8	3.1202	13	3.1022	2	3.3992	6	3.3805
60	4	3.4267	9	3.4098	1	3.9502	3	3.9402	3	3.4849	7	3.4705	9	3.2675	14	3.2529	3	3.5590	6	3.5458
61	4	3.4450	9	3.4289	1	3.9700	4	3.9502	3	3.5035	7	3.4897	9	3.2851	14	3.2714	3	3.5781	6	3.5653
62	4	3.4634	9	3.4480	1	3.9911	4	3.9704	3	3.5219	7	3.5087	9	3.3024	14	3.2896	3	3.5969	6	3.5846
70	5	3.6025	10	3.5866	1	4.1489	4	4.1321	3	3.6625	8	3.6477	10	3.4347	16	3.4193	3	3.7409	7	3.7258
71	5	3.6191	10	3.6039	1	4.1678	4	4.1513	4	3.6794	8	3.6651	10	3.4505	16	3.4361	3	3.7581	7	3.7434
72	5	3.6356	10	3.6210	1	4.1844	4	4.1703	4	3.6961	8	3.6823	10	3.4662	16	3.4526	3	3.7751	7	3.7610
80	5	3.7624	11	3.7472	1	4.3263	4	4.3122	4	3.8246	8	3.8140	11	3.5868	17	3.5749	3	3.9061	7	3.8952
81	5	3.7776	11	3.7631	1	4.3432	4	4.3295	4	3.8400	9	3.8249	11	3.6013	17	3.5901	3	3.9219	7	3.9114
82	5	3.7931	11	3.7788	1	4.3601	4	4.3466	4	3.8554	9	3.8406	11	3.6157	17	3.6051	3	3.9375	8	3.9220
90	6	3.9105	11	3.9002	1	4.4884	4	4.4763	4	3.9736	9	3.9622	12	3.7268	19	3.7140	3	4.0582	8	4.0459
91	6	3.9247	12	3.9107	1	4.5039	4	4.4919	4	3.9879	9	3.9768	12	3.7403	19	3.7281	3	4.0727	8	4.0609
92	6	3.9386	12	3.9253	1	4.5192	4	4.5074	4	4.0021	9	3.9914	12	3.7536	19	3.7420	4	4.0872	8	4.0757
98	6	4.0214	12	4.0105	1	4.6089	4	4.5976	5	4.0851	10	4.0723	13	3.8317	20	3.8202	4	4.1722	8	4.1623
99	6	4.0349	12	4.0244	1	4.6232	4	4.6121	5	4.0987	10	4.0861	13	3.8444	20	3.8334	4	4.1860	8	4.1764
100	6	4.0482	12	4.0381	1	4.6374	4	4.6263	5	4.1121	10	4.0999	13	3.8570	20	3.8465	4	4.1997	9	4.1860

ISBN 978-3-95450-181-6

REFERENCES

[1] A. A. Sokolov, I. M. Ternov, Synchrotron Radiation, (Akademie - Verlag, 1968), 202 p.

[2] Herman Winick, S. Doniach, Synchrotron Radiation Research, (Plenum Press, 1980), 754 p.

[3] A. A. Sokolov, I. M. Ternov, C. W. Kilmister, Radiation from Relativistic Electrons, (American Institute of Physics, 1986), 312 p.

[4] V. G. Bagrov et al., Synchrotron Radiation Theory and Its Development, (World Scientific, Singapore New Jersey London, 1999), 447 p.

[5] P. J. Duke, Synchrotron Radiation: Production and Properties, (Oxford University Press, 2000), 251 p.

[6] Helmut Wiedemann, Synchrotron Rdiation, (Springer, 2003), 274 p.

[7] Albert Hofmann, The Physics of Synchrotron Radiation, (Cambridge University Press, 2004), 323 p.

[8] . V. G. Bagrov, M. V. Dolzhin, V. B. Tlyachev, A. T. Jarovoi. "Evolution of the Angular Distribution of Circularly Polarized Synchrotron Radiation with Charge Energy", Russian Physics Journal. 2004, v. 47, No. 4, pp. 414-423, doi:10.1023/B:RUPJ.0000042770.97166.87

[9] V. G. Bagrov, D. M. Gitman, V. B. Tlyachev, A. T. Jarovoi, "Evolution of Angular Distribution of Polarization Components for Synchrotron Radiation under Changes of Particle Energy", in Proc. 15th International Summer School - Seminar "Volga - 15" on Recent Problems in Teoretical and Mathematical Physics (Recent Problems in Field Theory. V. 4), Petrov School (Kazan, June - July 2003), Ed. A. V. Aminova, Published by Organizing Committee of Petrov School, Kazan. Heter, 2004, pp. 9-24. (In Russian).

[10] V. G. Bagrov, D. M. Gitman, V. B. Tlyachev, A. T. Jarovoi, "Evolution of Angular Distribution of Polarization Components for Synchrotron Radiation under Changes of Particle Energy", in Proc. 11th Lomonosov Conference on Elementary Particle Physics (Particle Physics in Laboratory, Space and Universe),Moscow State University, Faculty Physics,(August 2003), Ed. A. I. Studenikin, World Scientific. New Jersey London Singapor, 2005, pp.355-362.

[11] V. G. Bagrov, D. M. Gitman, V. B. Tlyachev, A. T. Jarovoi, " New Theoretical Results in Synchrotron Radiation". Nuclear Instruments & Methods in Physics Research B. 2005, v. 240, No. 3, pp. 638-645, doi:10.1016/j.nimb.2005.03.286

[12] V. G. Bagrov, M. V. Dolzhin, K. G. Seravkin, V. M. Shakhmatov, "Partial Contributions of Individual Harmonics to the Power of Synchrotron Radiation", Russian Physics Journal. 2006, v. 49, No. 7, pp. 681-689, doi:10.1007/s11182-006-0162-1

[13] V. G. Bagrov, D. M. Gitman,A. D. Levin, A. S. Loginov, A. D. Saprykin, "Effective Spectrum Width of the Synchrotron Radiation", The European Physical Journal. C. 2015, v. 75, No. 11, 555 (6 pages), doi:10.1140/epjc/s10052-015-3798-6

ISBN 978-3-95450-181-6

STATUS OF THE FUTURE CIRCULAR COLLIDER STUDY*

M. Benedikt†, F. Zimmermann, CERN, Geneva, Switzerland

Abstract

Following the 2013 update of the European Strategy for Particle Physics, the international Future Circular Collider (FCC) Study has been launched by CERN as host institute. Its main purpose and long-term goal is to design an energy-frontier hadron collider (FCC-hh) with a centre-of-mass energy of about 100 TeV in a new 80–100 km tunnel. The FCC study also includes the design of a 90–350 GeV high-luminosity lepton collider (FCC-ee) installed in the same tunnel, serving as Higgs, top and Z factory, as a potential intermediate step, as well as an electron-proton collider option (FCC-he). The physics cases for such machines are being assessed and concepts for experiments will be developed by the end of 2018, in time for the next update of the European Strategy for Particle Physics.

This overview summarizes the status of machine designs and parameters, and it discusses the essential technical components being developed in the frame of the FCC study. Key elements are superconducting accelerator-dipole magnets with a field of 16 T for the hadron collider and high-power, high-efficiency RF systems for the lepton collider. In addition, the unprecedented beam power presents particular challenges for the hadron collider. First conclusions from geological investigations and implementation studies are available. We report the status of the FCC collaboration and outline the further planning.

INTRODUCTION

The Large Hadron Collider (LHC) presently in operation at CERN, and its high-luminosity upgrade, the HL-LHC, have an exciting physics program, which extends through the mid 2030's, i.e., covering the next 20 years. From the initial proposal in 1983, it has taken more than 30 years to design, build and fully commission the LHC. In view of such time scales, it is urgent for the community to start preparing the next accelerator for the post-LHC period.

European studies for a large post-LHC physics-frontier machine began in 2010–2013, for both lepton and hadron colliders (at the time called LEP3/TLEP and VHE-LHC, respectively). In response to the 2013 Update of the European Strategy for Particle Physics [1]. in early 2014 these efforts were combined and expanded as global Future Circular Collider (FCC) study [2, 3], hosted by CERN.

FCC STUDY SCOPE & TIME LINE

A large circular hadron collider seems to be the only approach to reach, during the coming decades, energy levels far beyond the range of the LHC. The long-term goal and focus of the FCC study [3], therefore, is a 100-TeV hadron collider (FCC-hh), which determines the infrastructure needs of the new facility. The energy reach of a high-energy hadron collider is simply proportional to the dipole magnetic field and to the bending radius: $E \propto B \times \rho$. Assuming a dipole field of 16 T, expected to be achievable with Nb_3Sn technology, the ring circumference must be about 100 km in order to reach the target value 100 TeV for the center-of-mass energy.

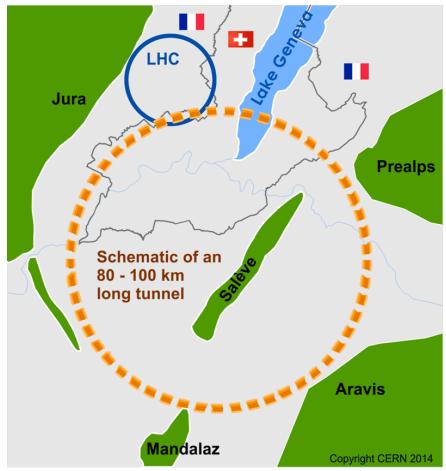

Figure 1: Schematic of a 100 km tunnel for a Future Circular Collider in the Lake Geneva basin.

Figure 1 presents a schematic of the FCC tunnel. Prior to FCC-hh installation, this new tunnel could host a high-luminosity circular e^+e^- collider (FCC-ee). Concurrent operation of hadron and lepton colliders is not foreseen, however. In addition, the FCC study considers aspects of *pe* collisions, as could be realized, e.g., by colliding the electron beam from an energy recovery linac with one of the two FCC-hh hadron beams. The FCC study also includes the design of a High-Energy LHC (HE-LHC) realized by installing 16 T magnets developed for FCC-hh in the existing 27 km LHC tunnel, so as to approximately double the energy of the LHC.

The FCC study has launched international R&D efforts on key enabling technologies through dedicated collaborative programmes, e.g. on high-field magnets, advanced cryogenics, superconducting radiofrequency systems (e.g. thin film coating) and highly efficient radiofrequency power sources. The FCC R&D includes the design of a 100 km tunnel infrastructure in the Geneva area, linked to the existing CERN accelerator complex, as requested by the European Strategy. The FCC study further explores the particle-physics opportunities and discovery potentials for the hadron, lepton and lepton-hadron colliders. The results of these physics studies drive the collider performance targets (e.g. luminosity, energy, lepton polarization). In addition, the FCC study is developing experiment concepts for the three types of colliders, addresses machine detector interface, and defines further R&D needs for detector technologies. Last not least,

* This work was supported in part by the European Commission under the HORIZON 2020 project EuroCirCol, grant agreement 654305.
† michael.benedikt@cern.ch

ISBN 978-3-95450-181-6

the FCC study aims at establishing an overall cost model for the various collider scenarios — including infrastructure and injectors —, at formulating global realization concepts, and at forging early partnerships with key industries.

Figure 2 shows the FCC time line in relation to previoun collider projects at CERN.

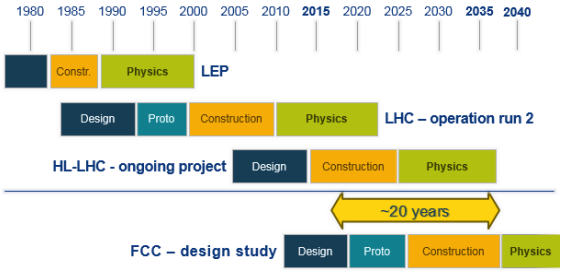

Figure 2: Time line of CERN circular colliders with the Future Circular Collider (FCC) as the next step.

MACHINE DESIGNS

An explorative study of the geology in the Lake-Geneva basin has concluded that a tunnel circumference of 90–100 km would fit the geological situation well (Fig. 3). From the technical point of view, the LHC would be suitable as a potential injector [4], with an injection energy around 3.3 TeV [5–7]. Two possible configurations of the FCC-hh and its LHC injector are illustrated in Fig. 4. A 100 km tunnel version intersecting the LHC is now being studied in greater detail. Injecting into the FCC-hh from a new fast-cycling superconducting machine located in the SPS tunnel would also be permitted by the chosen configuration. In this case the injection energy would be about 1.5 TeV.

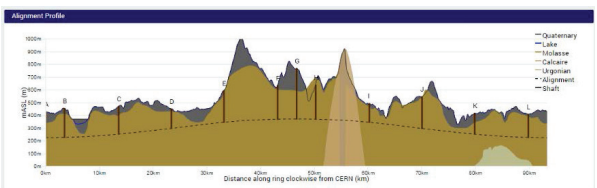

Figure 3: Example placement of a tunnel with a 93 km circumference in the Geneva region, together with geological layers and access shafts; obtained from a tunnel optimization tool developed in the frame of the FCC study [4].

Figure 4: Two configurations of FCC-hh and LHC [7].

Common layouts and consistent optics footprints for the hadron and lepton colliders have been established. Figure 5 shows two main interaction points located at positions 'A' and 'G', for both machines.

Table 1 compares key parameters of FCC-hh and HE-LHC with those of LHC and HL-LHC. The FCC-hh design

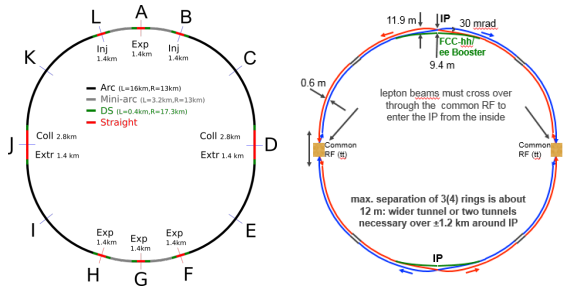

Figure 5: Layouts of hadron (left) and lepton collider (right). The optics of FCC-ee [8] was designed so as to exactly agree with the footprint of the hadron collider [9], except for the intreaction regions, where the collision points are offset by about 9 m, and only the lepton injector (top-up booster) follows the path of the protons.

considers parameter sets for two phases of operation [11, 12]: Phase 1 (baseline) aims at a peak luminosity of 5×10^{34} cm^{-2}s^{-1}, and should deliver about 250 fb^{-1} per year on average. In phase 2 (ultimate) the peak luminosity is increased by almost a factor of six, to 2.9×10^{35} cm^{-2}s^{-1}, and the integrated luminosity by a factor of four to 1000 fb^{-1} per year. The daily luminosity evolution for these two phases is illustrated in Fig. 6.

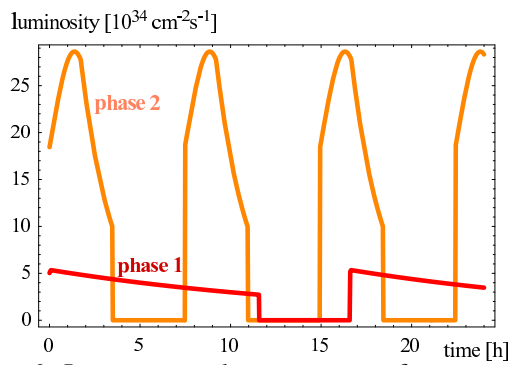

Figure 6: Instantaneous luminosity as a function of time during 24 hours for FCC-hh phases 1 and 2 [12].

The transition from FCC-hh phase 1 to phase 2 is realized without any increase in the beam current, primarily by reducing β^* from 1.1 to 0.3 m, and by accepting a three times larger beam-beam tune shift ($\Delta Q_{\text{tot}} = 0.03$ instead of 0.01 [11, 12]; the larger value of 0.03 has been demonstrated at the LHC [13]).

The total integrated luminosity of FCC-hh over 25 years operation is estimated as about 20 ab^{-1} per experiment, which matches the particle-physics goals [14]. The FCC-hh physics programme covers standard-model processes, Higgs physics and electroweak symmetry breaking studies, phenomena beyond the standard model, physics with heavy ions, and physics opportunities at the FCC-hh injectors [14].

A full ring optics design is available for the FCC-hh, comprising arcs, intereaction regions, injection region combined with radiofrequency section, momentum collimation, betatron collimation, and extraction. Example optics segments are displayed in Fig. 7.

ISBN 978-3-95450-181-6

Table 1: Key parameters of LHC, HL-LHC, FCC-hh, and HE-LHC

parameter	FCC-hh phase 1	FCC-hh phase 2	HE-LHC	HL-LHC	LHC (*pp*)
c.m. energy [TeV]	100	100	25	14	14
ring circumference [km]	100	100	26.7	26.7	26.7
arc dipole field [T]	16	16	16	8.33	8.33
initial bunch intensity [10^{11}]	1.0	1.0 (0.2)	2.5	2.2	1.15
beam current [A]	0.5	0.5	1.27	1.11	0.58
peak luminosity/IP [10^{34} cm^{-1}s^{-1}]	5	30	34	5 (lev.)	1
events / crossing	170	1020 (204)	1070	135	27
stored energy per beam [GJ]	8.4	8.4	1.4	0.7	0.36
arc synchrotron radiation [W/m/ap.]	28.4	28.4	4.1	0.35	0.18
bunch spacing [ns]	25	25 (5)	25	25	25
IP beta function $\beta^*_{x,y}$ [m]	1.1	0.3	0.25	0.15	0.55
initial normalized rms emittance [μm]	2.2	2.2 (0.45)	2.5	2.5	3.75
transv. emittance damping time [h]	1.1	1.1	4.5	25.8	25.8

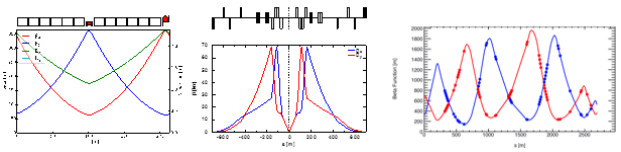

Figure 7: Optics for the FCC-hh arcs (left), interaction region (center) and betatron collimation (right) [9].

In Table 2 key parameters for the electron-positron collider FCC-ee [10] are compared with those of LEP2. The FCC-ee design exploits the lessons and recipes from past and present colliders (synchrotron radiation, high beam current, crab waist, ultralow β^*_y, polarization. etc.), as is sketched in Fig. 8. The present optics design of FCC-ee achieves the required

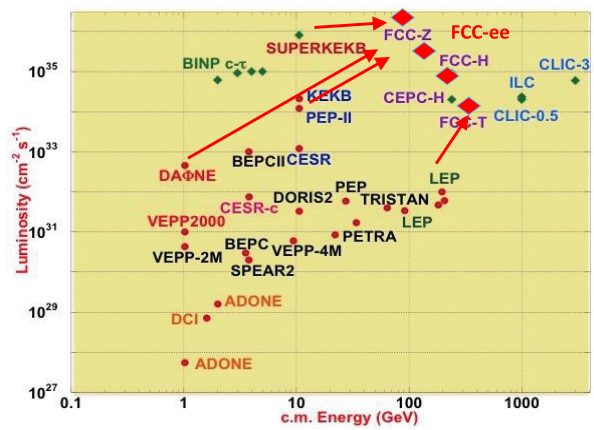

Figure 8: Luminosity as a function of c.m. energy for past, present and future e^+e^- colliders (M. Biagini).

performance for all four target energies [8]. The interaction-region optics and geometry are asymmetric (Fig. 9), to limit the amount and energy of synchrotron-radiation photons emitted towards the physics detector. Sufficient dynamic aperture and a ±2% off-momentum acceptance are obtained at all working points.

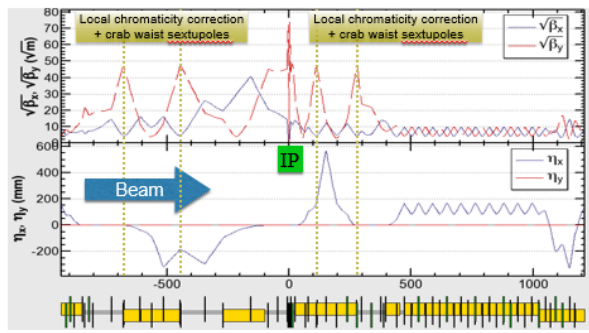

Figure 9: Asymmetric final-focus optics for the FCC-ee interaction region [8].

TECHNOLOGIES

At the FCC-hh an unprecedentedly large synchrotron radiation power of about 2.3 MW per beam is emitted in the cold arcs. To efficiently absorb this synchrotron radiation, a new beam screen, inserted inside the cold bore of the magnets, is proposed [16,17]. As is shown in Fig. 10, it features two slits with an integrated wedge such that most primary photons are deflected upward and downward behind the beam screen, where pumping holes are placed. Very few photoelectrons are generated inside the beam screen proper. First FCC-hh beam screen prototypes have been fabricated. Their cryogenic and vacuum behaviour will be tested at the synchrotron light source ANKA at KIT Karlsruhe, in the presence of synchrotron radiation resembling the conditions expected in the FCC-hh arcs. At the FCC-hh, the beam screen temperature will be raised, from 5–20 K at the LHC to 40–60 K. The higher temperature improves the Carnot efficiency and, thereby, facilitates the removal of the synchrotron radiation heat load. The effect of beam-screen temperature on total refrigerator power is illustrated in Fig. 11.

The key technology R&D for the FCC-hh comprises superconductor (SC) development and high-field magnet design. Nb_3Sn is one of the major cost & performance factors for FCC-hh and requires highest attention. The main development goals until 2020 are: (1) an increase of the critical current density J_c (at 16 T, 4.2 K) to above 1500 A/mm^2

ISBN 978-3-95450-181-6

Table 2: Key parameters for the FCC-ee, at three beam energies, compared with those achieved at LEP2. The FCC-ee parameters refer to a crab-waist scheme [15], with constant, energy-independent arc-cell length.

parameter	FCC-ee					LEP2
circumference	100					26.7
energy / beam [GeV]	45.6		80	120	175	105
bunches / beam	30180	91500	5260	770	78	4
beam current [mA]	1450		152	30	6.6	3
luminosity / IP [10^{34} cm^{-2}s^{-1}]	207	90	19	5.1	1.3	0.0012
energy loss / turn [GeV]	0.03		0.3	1.67	7.55	3.34
total synchrotron radiation power [MW]	100		100	100	100	22
RF voltage [GV]	0.4	0.2	0.8	3.0	10	3.5
rms horizontal emittance ε_x [nm]	0.2	0.1	0.26	0.6	1.3	22
rms vertical emittance ε_y [pm]	1	1	1	1	2.5	250
horizontal IP beta function β_x^* [m]	0.5	1	1	1	1	1.2
vertical IP beta function β_y^* [mm]	1	2	2	2	2	50
rms bunch length (SR) σ_z [mm]	1.2	1.6	2.0	2.0	2.1	12
full crossing angle θ_c [mrad]	30	30	30	30	30	0
longitudinal damping time [turns]	1320		243	72	23	31
beam lifetime from radiative Bhabha scattering [min.]	94	185	90	67	57	434

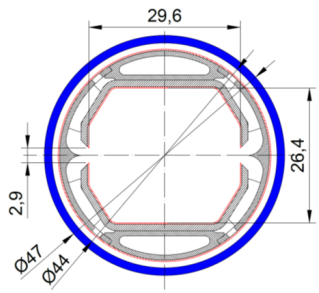

Figure 10: FCC-hh beam-screen design with integrated "folded" antechamber [16, 17].

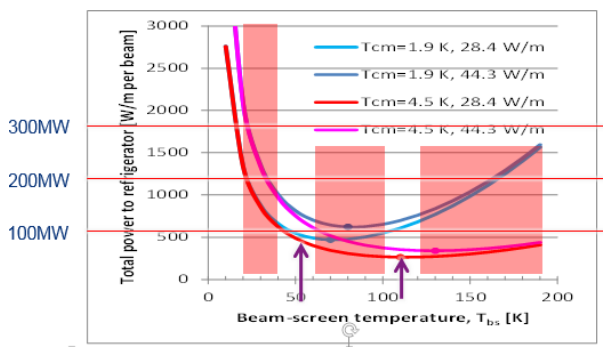

Figure 11: Total cryogenics power in units of Watt per meter per beam as a function of beam-screen temperature, for two different temperatures of the magnet cold bore and two different synchrotron-radiation power loads [18]. Regions excluded by vacuum considerations are shaded in red.

i.e. a 50% rise with respect to the HL-LHC wire [19, 20] (see Fig. 12), (2) a reference wire diameter of 1 mm, and (3) preparing the ground for large scale production and cost reduction.

To accomplish these goals, various international collaborations have been set up. The FCC Nb_3Sn conductor program

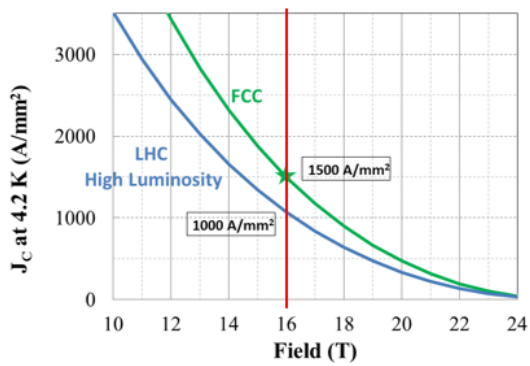

Figure 12: Critical current versus magnetic field for the HL-LHC Nb_3Sn conductor at 4.5 K, and the FCC-hh target curve together with the planned operating point [19, 20].

has started with the procurement of state-of-the-art conductor for prototyping from European (Bruker) and US industry (OST). FCC conductor development is planned, or already underway, in Japan, Russia, Korea, and Europe.

A new US DOE magnet development program [21] directs joint activities of US industry (OST) and US laboratories. A project 'EuroCirCol', supported in the frame of the EU's HORIZON2020 programme, contributes to core elements of the FCC-hh hadron collider (optics, cryo-vacuum system, and 16 T dipole design including a construction folder for demonstrator magnets). Four different design approaches for 16 T dipole magnets are shown in Fig. 13. In Europe three of these designs are pursued by EuroCirCol, the fourth one by PSI/Switzerland. A down-selection of options by mid 2017 will allow for detailed design work. This will be followed by model production (2018–2022) and prototype production (2023–2025). A parallel US magnet program advances the cosine theta and canted cosine theta designs.

The radiofrequency (RF) system for the lepton collider must cover a large range of operation parameters, ranging

ISBN 978-3-95450-181-6

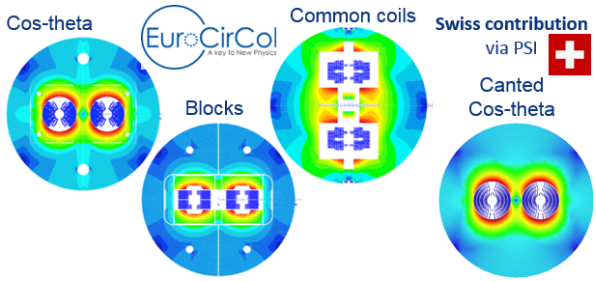

Figure 13: Four different design concepts for 16 T magnets.

from Ampere beam currents to high accelerating gradients. The RF voltages and beam currents span more than two orders of magnitude. No well-adapted single RF system solution is available to satisfy all the requirements. Instead, two separate sytems are being considered [22, 23], as is illustrated in Fig. 14. For both FCC-ee Z operation (45.6 GeV/beam with RF gradients of a few MeV/m) and the hadron collider FCC-hh, 400 MHz single-cell cavities are preferred. For these cavities, the baseline choice is Nb/Cu at 4.5 K. This development also has ample synergies with HL-LHC and HE-LHC. The associated R&D must address the power coupling for up to 1 MW/cell, and HOM power handling (damper, cryomodule). For the higher-energy operation modes of FCC-ee (ZH, $t\bar{t}$ and WW), 400 or 800 MHz multi-cell cavities would be suitable. Two possible options for these cavities are either 400 MHz of Nb/Cu at 4.5 K, or an 800 MHz bulk Nb system at 2 K. The pertinent R&D focuses on high Q_0 cavities, coating, and, in the long term, on Nb_3Sn-like components.

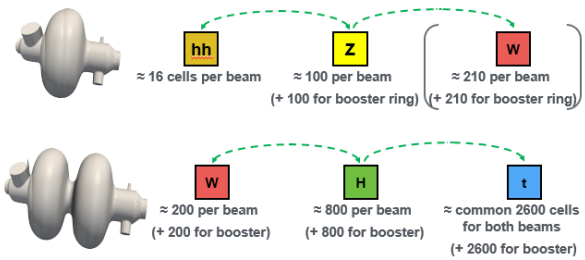

Figure 14: Single- and multi-cell SC cavities for different FCC collider branches [22, 23].

ORGANISATION & COLLABORATION

Since February 2014, a total of 88 institutes from 28 countries and four continents have joined the FCC collaboration, including BINP Novosibirsk, JINR Dubna, MEPHi Moscow, and NUST MISiS Moscow. The latest status can be found on the FCC web site [3]. One major FCC conference — the "FCC Week" — is being organized every year. The next one will be held in Berlin, Germany, from 29 May to 2 June 2017 [24].

SUMMARY

The FCC study is advancing well towards the delivery of a Conceptual Design Report for end of 2018. Consolidated parameter sets exist for both hadron (FCC-hh) and lepton machines (FCC-ee). These are supported by complete baseline optics designs, assessment of beam dynamics, and estimated performance compatible with the physics requirements. A first round of geology, civil engineering and infrastructure studies have been completed. Superconductivity is the key enabling technology for FCC. The Nb_3Sn program towards 16 T model magnets is of prime importance for the FCC-hh and the development of high-efficiency superconducting radiofrquency systems is critical for FCC-ee. International collaboration is essential to advance on all the challenging subjects, and the community is warmly invited to join the FCC efforts.

REFERENCES

[1] European Strategy Session of Council, 30 May 2013, CERN-Council-S/106 (2013).

[2] Future Circular Collider Study Kickoff Meeting, University of Geneva, 12–15 February 2014, http://indico.cern.ch/e/fcc-kickoff.

[3] FCC web site http://cern.ch/fcc.

[4] C. Cook et al., Proc. IPAC'15 (2015) 2079.

[5] B. Goddard, W. Bartmann, W. Herr, P. Lebrun, and A. Milanese, CERN-ACC-2015-030 (2015).

[6] A. Milanese, B. Goddard, and M. Solfaroli Camillocci, CERN-ACC-2015-133 (2015).

[7] W. Bartmann et al., Review of the FCC-hh Injection Energy, CERN, 16 October 2015, http://indico.cern.ch/event/449449.

[8] K. Oide, Phys. Rev. Accel. Beams 19, 111005 (2016).

[9] A. Chancé et al., Proc. IPAC'16 (2016) p. 1470.

[10] J. Wenninger et al., FCC-ACC-SPC-0003, Rev. 3.0, EDMS no. 1346081 (2016).

[11] M. Benedikt et al., Proc. IPAC'15 (2015) p. 2173.

[12] M. Benedikt, D. Schulte, F. Zimmermann, Phys. Rev. ST – Accel. Beams 18, 101002 (2015).

[13] W. Herr et al., Proc. IPAC'11 (2011) p. 1936.

[14] Physics at the FCC-hh, https://twiki.cern.ch/twiki/bin/view/-LHCPhysics/FutureHadroncollider.

[15] A. Bogomyagkov, E. Levichev, and D. Shatilov. Phys. Rev. ST Accel. Beams 17, 041004 (2014).

[16] R. Kersevan, Review of the FCC-hh Injection Energy, CERN, 16 October 2015.

[17] C. Garion, FCC Week 2016, Rome.

[18] P. Lebrun, L. Tavian, Proc. ICEC/ICMC 2014, Twente, Enschede, CERN-ACC-2014-0220 (2014).

[19] D. Schoerling et al., Proc. EPS-HEP 2015, Vienna, 2015.

[20] D. Tommasini, private communication (2015).

[21] S.A. Gourlay et al., "The U.S. Magnet Development Program Plan," June 2016.

[22] R. Calaga et al., "SRF for Future Circular Colliders," Proc. SRF2015 Whistler (2015) p. 1474.

[23] O. Brunner, "FCC RF System Parameters for Z, W, H and tt," eeFACT2016 Daresbury, October 2016.

[24] http://cern.ch/fccw2017

ISBN 978-3-95450-181-6

RECOMMISSIONING AND PERSPECTIVES OF VEPP-2000 COMPLEX

Yu. Rogovsky#[1], V. Anashin, D. Berkaev, A. Kasaev, I. Koop[1], A. Kenzhebulatov, A. Krasnov, G. Kurkin, A. Kyrpotin, A. Lysenko, S. Motygin, E. Perevedentsev[1], V. Prosvetov, A. Semenov, A. Senchenko[1], Yu. Shatunov, P. Shatunov, D. Shwartz[1], A. Skrinsky, I. Zemlyansky, Y. Zharinov,
Budker Institute of Nuclear Physics, Novosibirsk, Russia
[1]also at Novosibirsk State University, Novosibirsk, Russia

Abstract

VEPP-2000 is electron-positron collider exploiting the novel concept of round colliding beams. After three seasons of data taking in the whole energy range of 160-1000 MeV per beam it was stopped in 2013 for injection chain upgrade. The linking to the new BINP source of intensive beams together with booster synchrotron modernization provides the drastic luminosity gain at top energy of VEPP-2000. Recommissioning status, fist results and perspectives of the VEPP-2000 complex will be presented.

VEPP-2000 OVERVIEW

The VEPP-2000 collider [1] exploits the round beam concept (RBC) [2]. The idea of round-beam collisions was proposed more than 25 years ago for the Novosibirsk Phi-factory design [3]. This approach, in addition to the geometrical factor gain, should yield the beam-beam limit enhancement. An axial symmetry of the counter-beam force together with the X–Y symmetry of the transfer matrix between the two IPs provide an additional integral of motion, namely, the longitudinal component of angular momentum $M_z = x'y - xy'$. Although the particles' dynamics remain strongly nonlinear due to beam–beam interaction, it becomes effectively one-dimensional. The reduction of degrees of freedom thins out the resonance grid and suppress the diffusion rate resulting finally in a beam-beam limit enhancement [4].

The layout of the VEPP-2000 complex as it worked before shutdown for upgrade in 2013 is presented in Fig. 1.

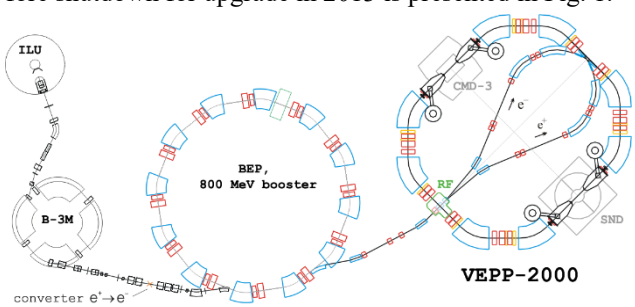

Figure 1: VEPP-2000 complex layout.

VEPP-2000 collider used the injection chain of it's predecessor VEPP-2M [5]. It consisted of the old beam production system and Booster of Electrons and Positrons (BEP) with an energy limit of 800 MeV. Collider itself hosts two particle detectors [6], Spherical Neutral Detector (SND) and Cryogenic Magnetic Detector (CMD-3), placed into dispersion-free low-beta straights. The final focusing (FF) is realized using superconducting 13 T solenoids. The main design collider parameters are listed in Table 1. In Fig. 2 one can find a photo of the collider ring.

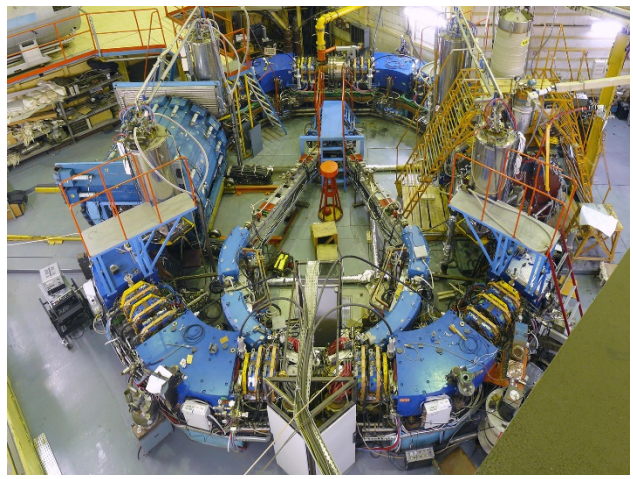

Figure 2: VEPP-2000 collider photo.

The density of magnet system and detectors components is so high that it is impossible to arrange a beam separation in the arcs. As a result, only a one-by-one bunch collision mode is allowed at VEPP-2000.

Table 1: VEPP-2000 Main Parameters (at E = 1 GeV)

Parameter	Value
Circumference, C	24.39 m
Energy range, E	150–1000 MeV
Number of bunches	1 × 1
Number of particles per bunch, N	1×10^{11}
Betatron functions at IP, $\beta^*_{x,y}$	8.5 cm
Betatron tunes, $\nu_{x,y}$	4.1, 2.1
Beam emittance, $\varepsilon_{x,y}$	1.4×10^{-7} m rad
Beam–beam parameters, $\xi_{x,z}$	0.1
Luminosity, L	1×10^{32} cm^{-2} s^{-1}

EXPERIMENTAL RUNS

VEPP-2000 started data-taking with both detectors installed in 2009 [7]. The first runs were dedicated to experiments in the high-energy range [8, 9], while during the last 2012 to 2013 experimental run the scan to the lowest energy limit [10, 11] was done (see Fig. 3). Apart from partial integrability in beam-beam interaction, the RBC gives a

#rogovsky@inp.nsk.su

ISBN 978-3-95450-181-6

significant benefit in the Touschek lifetime when compared to traditional flat beams. This results in the ability of VEPP-2000 to operate at an energy as low as 160 MeV — the lowest energy ever obtained in e^+/e^- colliders.

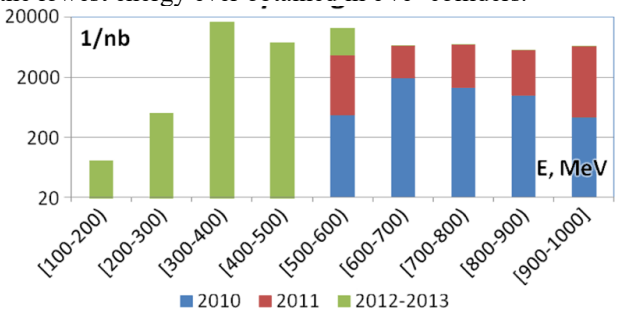

Figure 3: Delivered luminosity in 2010 – 2013.

The averaged over 10% of best runs luminosity obtained by CMD-3 detector during the last three seasons is shown in Fig. 4 with red points. The red lines overestimate the hypothetically achievable peak luminosity with jumps corresponding to possible shortening of FF solenoids by feeding only half of coils. The blue dashed line shows the beam-beam limited luminosity for a fixed machine lattice (energy scaling law $L \propto \gamma^4$). It was successfully exceeded due to β^* reduction to 4÷5 cm available at low energies.

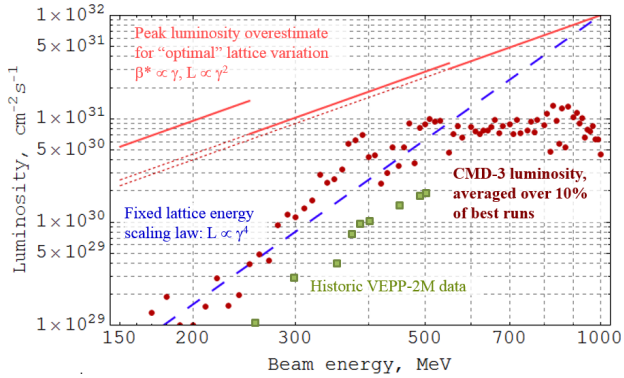

Figure 4: Achieved VEPP-2000 luminosity.

At high energies (> 500 MeV) luminosity was limited mostly by an insufficient positron production rate. At energies over 800 MeV the necessity of energy ramping in the collider storage ring additionally restricts the luminosity. Only for middle energy range 300÷500 MeV the luminosity is really limited by the beam–beam effects, especially by the flip-flop effect. At the lowest energies the main limiting factors are the small DA, IBS, weak radiation damping, and low beam lifetime as a result.

At middle energies, after thorough machine tuning, the beam-beam parameter achieved the maximal value of $\xi \sim 0.12$ per one IP during regular work breaking a world record [12,19].

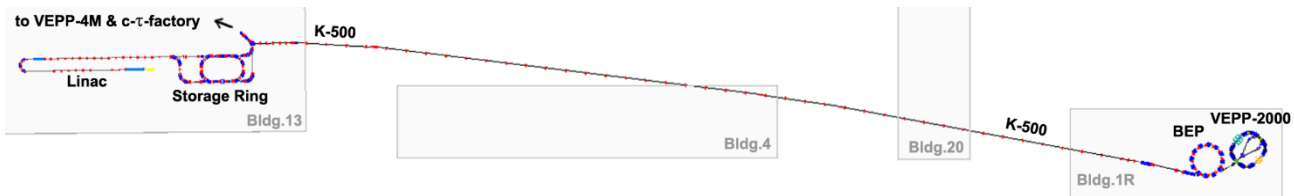

Figure 5: VEPP-2000 linked to the new Injection Complex.

VEPP-2000 COMPLEX UPGRADE

During first phase of operation, the luminosity of VEPP-2000 at top energies (see Fig. 3, left) was limited by: 1) insufficient e+ production rate and 2) necessity of acceleration at VEPP-2000 ring. In order to achieve the design luminosity the machine was stopped in 2013 for upgrade of the whole injection chain.

Firstly, the complex was linked up via a 250 m beamline K-500 to the new BINP Injection Complex (IC) providing e^+/e^- beams at energy of 400 MeV (see Fig. 5). In addition, BEP was upgraded to provide top-up injection up to 1 GeV.

The transfer channels to VEPP-2000 ring were also reconstructed in order to cope with 1 GeV beam.

IC consists of electron gun, 270 MeV driving electron linac, 510 MeV positron linac and damping ring (see Fig. 6). Damping ring stores and cools down both electron and positron beams for the next extraction to K-500 beam transfer line [13].

The K-500 beam transfer line was turned into operation in the end of 2015 [14]. This 250 m beamline consists of three parts: descent from DR to K-500 tunnel, regular FODO structure in the tunnel and ascent to the BEP hall. The fragment of the K-500 is shown in Fig. 7 (left).

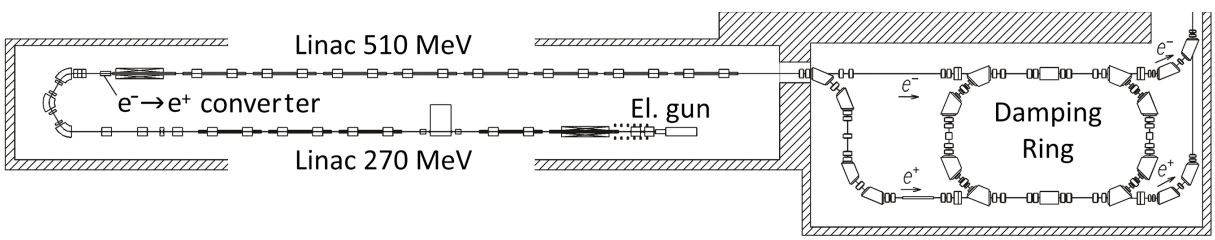

Figure 6: VEPP-5 Injection Complex Layout.

ISBN 978-3-95450-181-6

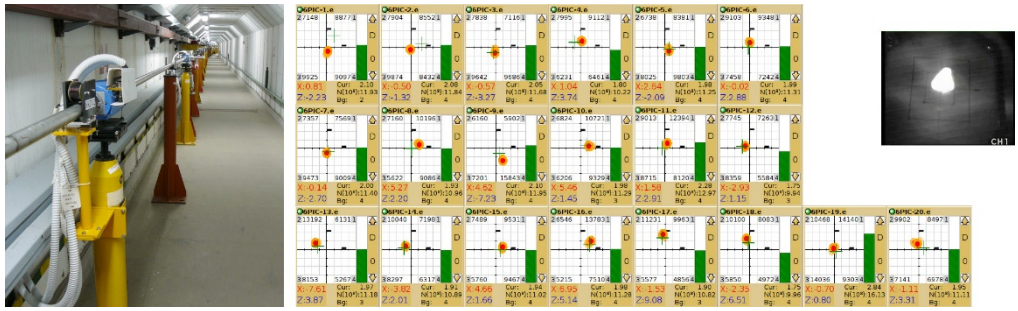

Figure 7: K-500 tunnel (left). Beam at BPMs along K-500 (center) and at scintillator screen (up-right).

Booster BEP Upgrade

Booster BEP dedicated to capture, cooling and stacking of hot 125 MeV positrons from old conversion system operated since 1991. It consists of 12 FODO cells. Each cell houses 30° sector dipole, two quads and straight, used for RF-cavity, kickers, injection/extraction septum, diagnostics and vacuum pumping (see Fig. 8). Booster layout is presented in Fig. 2, main parameters are listed in Table 2.

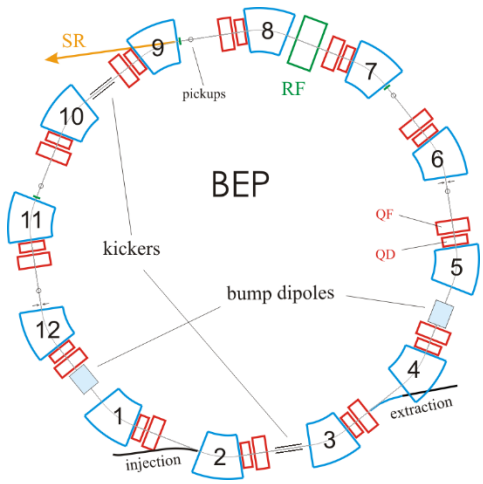

Figure 8: Booster synchrotron BEP layout.

Table 2: Modified BEP Main Parameters @ 1 GeV

Parameter	Value
Perimeter, Π	22.35 m
Revolution frequency, f_0	13.414 MHz
Bending radius, r_0	128 cm
RF harmonic, q	13
Synchrotron radiation loss	70 KeV/turn
Emittances, ε_x, ε_y	$8.6 \cdot 10^{-6}$, 10^{-8} cm
Betatron tunes, ν_x, ν_y	3.4, 2.4
Momentum compaction, α_p	0.06

To achieve the 1 GeV all magnetic elements were strengthened during upgrade. The field of 2.6 T was achieved in the normal conducting dipole magnets [15] both by 20% reduction of gap and feeding current increase up to 10 kA. Due to feeding in series with dipoles by accurate return yoke profiling quads' excitation curve was fitted to the dipoles' one in whole energy range (see Fig. 9, left). The poles of quadrupoles also were remachined to increase the sextupole component needed for chromaticity compensation. (see Fig. 9).

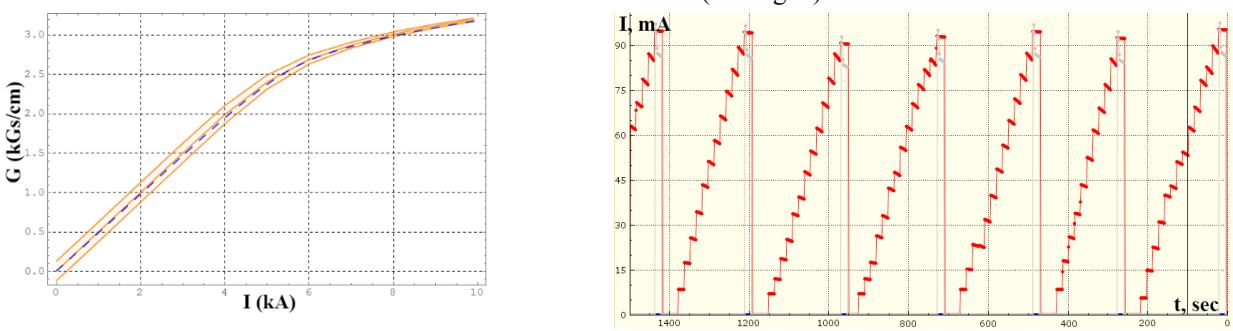

Figure 9: F-quad excitation curve compared to dipole's one (left). e+ stacking @ BEP (right).

The aluminum vacuum chamber was deformed locally inside the dipoles and D-quads due to aperture reduction. In order to increase RF voltage up to 110 kV new 174.376 MHz cavity was installed (see Fig. 10, left). Beam diagnostic system based on six CCD-cameras and old-fashioned BPMs was improved with 2 new sensitive calibrated electrostatic pickups (see Fig. 11).

The upgrade was finished in the beginning of 2016. VEPP-2000 injection chain was successfully recommissioned [16]. The achieved positron stacking rate at BEP amounts to 2×10^8 e+/sec that exceeds corresponding value before upgrade in one order of magnitude (see Fig. 9, right).

ISBN 978-3-95450-181-6

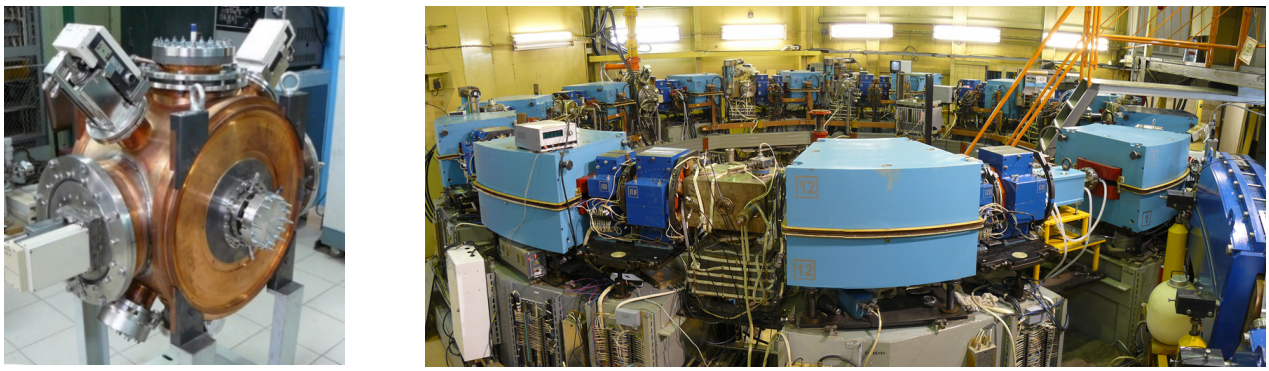

Figure 10: BEP new RF-cavity (left). BEP after assembly (right).

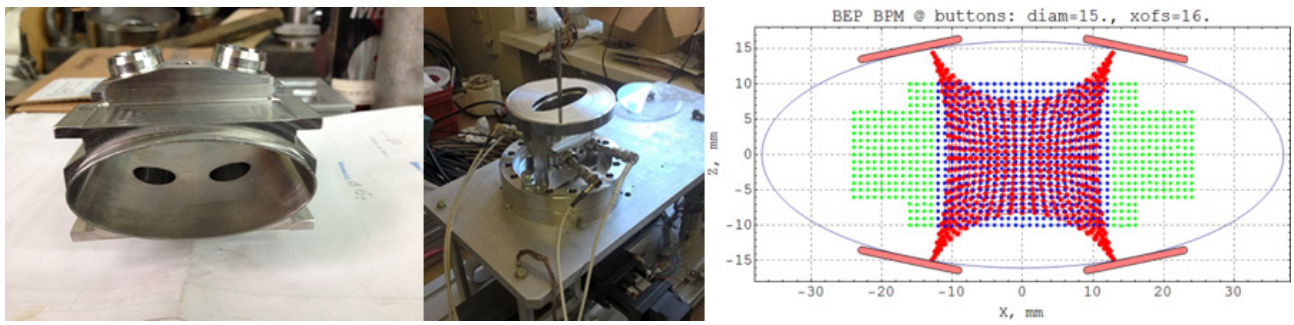

Figure 11: BEP new electrostatic BPM: production (left), test stand (middle), nonlinear calibration (right).

VEPP-2000 Collider Upgrade

Relatively small modifications were done in VEPP-2000 storage ring. Two additional kickers were installed to provide 1 GeV beam injection. All 8 two-sided copper mirrors used to extract the synchrotron light to CCD cameras were replaced. In 2016 the collider passed through the beam scrubbing procedure (see Fig. 12, right) working with switched-off SC solenoids. In addition, in this regime two beams e^+/e^- with low intensity were obtained to carry out the beam diagnostics alignment and tuning.

In 2016 the collider passed through the beam scrubbing procedure working in so called "warm mode" with switched off FF solenoids. In this regime two beams e^+/e^- with infinitesimal intensity were obtained to carry out the beam diagnostics alignment and tuning.

During upcoming new run (end of 2016, beginning 2017) we intend to achieve target luminosity and start it's delivery to detectors SND/CMD-3 with ultimate goal to deliver at least 1 fb^{-1} [17] with luminosity close to project value $L = 1 \times 10^{32}$ cm^{-2} s^{-1}.

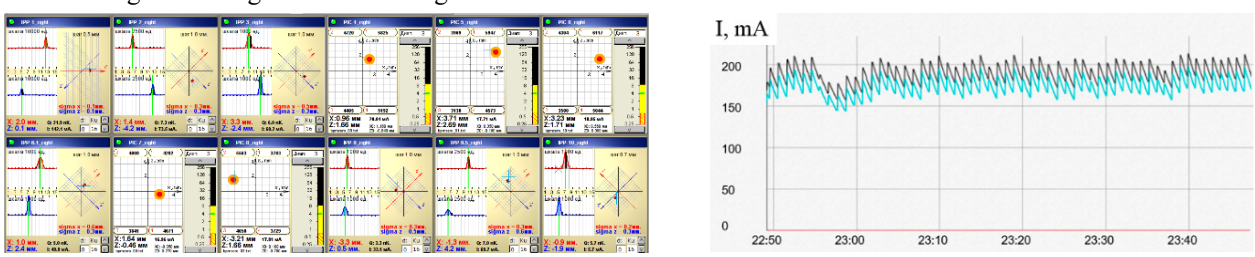

Figure 12: BEP-VEPP beam transfer (left). Beam scrubbing at VEPP-2000 (right).

CONCLUSION

Round beams give a serious luminosity enhancement. The achieved beam-beam parameter value at middle energies amounts to $\xi \sim 0.1$–0.12. VEPP-2000 was successfully taking data with two detectors across the whole designed energy range of 160–1000 MeV with a luminosity value five times higher than that achieved by its predecessor, VEPP-2M [18]. To reach the target luminosity, injection chain upgrade was done. Upgraded complex is now at the finish of the commissioning phase and ready to deliver luminosity at the design level for the next 5-10 years.

ACKNOWLEDGEMENT

We are grateful to A. Andrianov, A. Batrakov, O. Belikov, E. Bekhtenev, M. Blinov, D. Burenkov, F. Emanov, A. Frolov, V. Gambaryan, K. Gorchakov, G. Karpov, S. Krutikhin, I. Korenev, P. Logachev, Yu. Maltseva, D. Nikiforov, N. Pimonov, A. Romanov, V. Raschenko, I. Sedlyarov, D. Shatilov, A. Tribendis, V. Veremeenko, V. Volkov, for continuous support.

ISBN 978-3-95450-181-6

REFERENCES

[1] Yu.M. Shatunov *et al.*, "Project of a New Electron-Positron Collider VEPP-2000", in *Proc. EPAC'00*, Vienna, Austria, 2000, pp. 439-441.

[2] V.V. Danilov *et al.*, "The Concept of Round Colliding Beams", in *Proc. EPAC'96*, Sitges, Spain, 1996, pp. 1149-1151.

[3] L.M. Barkov *et al.*, "Phi-Factory Project in Novosibirsk", in *Proc. 14th HEACC'89*, Tsukuba, Japan, 1989, p. 1385.

[4] K. Ohmi, K. Oide and E.A. Perevedentsev, "The beam-beam limit and the degree of freedom", in *Proc. EPAC'06*, Edinburgh, Scotland, 2006, pp.616-618.

[5] G.M. Tumaikin *et al.*, in *Proc. HEACC'1977*, Serpukhov, USSR, 1977, p.443.

[6] T.V. Dimova *et al.*, "Recent Results on $e^+e^-\to$hadrons Cross Sections from SND and CMD-3 Detectors at VEPP-2000 collider", *Nucl. Part. Phys. Proc.*, vol. 273-275, pp. 1991-1996, 2016.

[7] M.N. Achasov *et al.*, "First Experience with SND Calorimeter at VEPP-2000 Collider," *Nucl. Instrum. Meth. A* vol. 598, pp. 31–32, 2009.

[8] D.N. Shemyakin *et al.*, "Measurement of the $e^+e^- \to K^+K^-\pi^-$ cross section with the CMD-3 detector at the VEPP-2000 collider", *Phys. Let. B,* vol. 756, pp. 153-160, 2016.

[9] M.N. Achasov *et al.*, "Study of the process $e^+e^- \to \omega\eta\pi^0$ in the energy range $\sqrt{s} < 2$ GeV with the SND detector", *Phys. Rev. D,* 94, 032010, 2016.

[10] M.N. Achasov *et al.*, "Search for the $\eta' \to e^+e^-$ decay with the SND detector", *Phys. Rev. D,* 91, 092010, 2015.

[11] V.E. Shebalin *et al.*, " Calorimetry of the CMD-3 detector", *J NIM 824, DOI: 10.1016/j.nima.2015.11.128*, 2016.

[12] D. Shwartz et al., Recent Beam-Beam Effects at VEPP-2000 and VEPP-4M, Proc. ICFA Mini-Workshop BB2013, CERN-2014-004, pp. 43-49.

[13] F.A. Emanov *et al.*, "Feeding BINP Colliders by the New VEPP-5 Injection Complex", in proc. RuPAC-2016, paper id WEXMH01.

[14] P.Yu. Shatunov *et al.*, "Commissioning of e+/e- Transfer Line from BINP Injection Complex to VEPP-2000 Facility", in proc. RuPAC-2016, paper id TUPSA001.

[15] D. Shwartz *et al.*, "Booster of Electrons and Positrons (BEP) Upgrade to 1 GeV", in *Proc. IPAC'14*, Dresden, Germany, pp. 102-104.

[16] D. Berkaev *et al.*, "Comissioning of Upgraded VEPP-2000 Injection Chain", in *Proc. IPAC'16*, Busan, Korea, pp. 3811-3813.

[17] I. Logashenko *et al.*, "Measurement of hadronic cross-sections with CMD-3 at VEPP-2000", in *Proc. ICHEP'16*, 2016, to be published.

[18] P.M. Ivanov *et al.*, "Luminosity and the Beam-Beam Effects on the Electron-Positron Storage Ring VEPP-2M with Superconducting Wiggler Magnet", in *Proc. 3rd Advanced ICFA Beam Dynamics Workshop on Beam–Beam Effects in Circular Colliders*, Novosibirsk, USSR, 1989, pp. 26-33.

[19] P.Yu. Shatunov *et al.,* "Status and perspectives of the VEPP-2000", *at. Phys. Part. Nuclei Lett. (2016) 13: 995. doi:10.1134/S154747711607044X.*

ISBN 978-3-95450-181-6

STATUS OF U70

S. Ivanov, on behalf of the U70 staff#
Institute for High Energy Physics (IHEP) of NRC "Kurchatov Institute"
Protvino, Moscow Region, 142281, Russia

Abstract

The report overviews present status of the Accelerator Complex U70 at IHEP of NRC "Kurchatov Institute". The emphasis is put on the recent activity and upgrades implemented since the previous conference RuPAC-2014, in a run-by-run chronological ordering.

History of the foregoing activity and upgrades is recorded sequentially in Refs. [1].

GENERALITIES

Layout of the entire Accelerator Complex U70 is shown in Fig. 1. It comprises four machines — 2 linear (I100, URAL30) and 2 circular (U1.5, U70) accelerators. Proton mode (default) employs a cascade of URAL30–U1.5–U70, while the light-ion (carbon) one — that of I100–U1.5–U70.

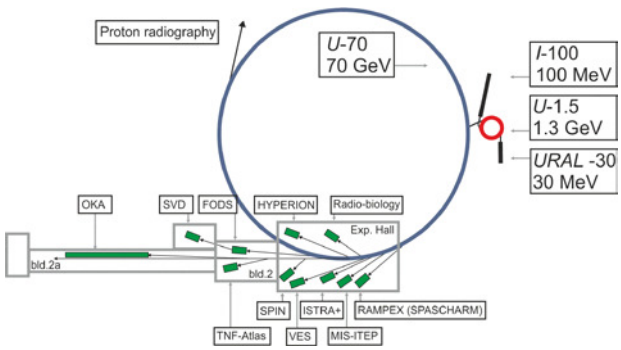

Figure 1: Accelerator Complex U70, beam transfer line network and fixed-target experimental facilities included.

Since the previous conference RuPAC-2014, the U70 complex operated for four runs in total. Table 1 lists their calendar data. The second run of 2016 was being launched during compiling this report.

Details of the routine operation and upgrades through 2014–2016 are reported in what follows run by run.

RUN 2014-3

It was the 3rd run per year of 2014 which has broken the long-term tradition of two annual (spring and autumn) runs of U70. The run had its specific features:

On the one hand, it was the 1st run of U70 for fixed-target physics when the machine was operated under the upgraded 1.5 km ring magnet main power supply plant equipped with the up-to-date static thyristor AC-DC convertors. The relevant upgrade activity took 1½ years.

The *B*-field ramping quality attained ensured safe acceleration (at least, in the single-particle limit) which is illustrated by Fig. 2.

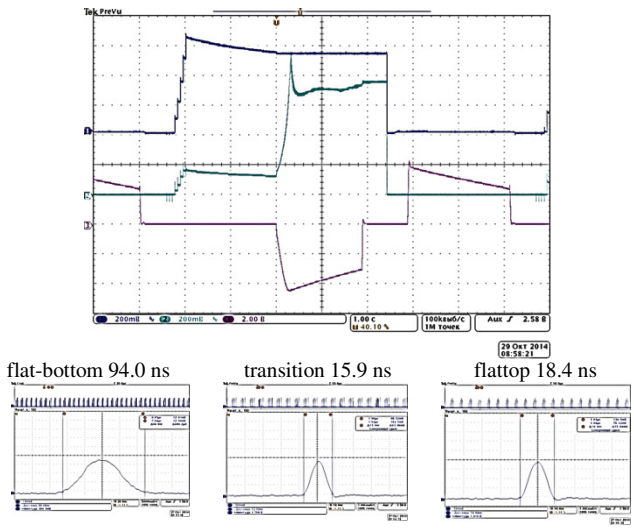

Figure 2: Acceleration in U70 with a new ring magnet power supply plant. Traces from top to bottom: beam DC current (5 bunches injected); bunch peak current (spike occurs at transition); *B*-field ramp rate (0.82 T/s max); bunch evolution through a cycle.

On the other hand, it was the 1st ever run when the 50 GeV proton beam was directed with the highest priority to the topical applied fixed-target research. It was ejected to the full-scale Proton-Radiographic Facility, named PRGK-100, operated jointly with RFNC–VNIIEF (Sarov, N. Novgorod Region).

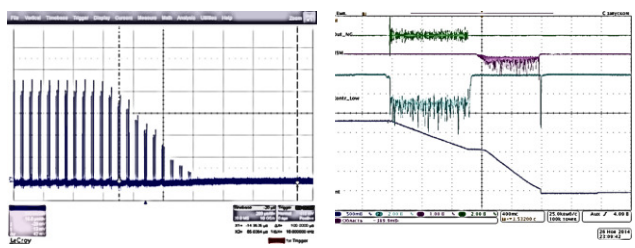

Figure 3: Beam extractions from U70. Left: 10-turn fast extraction of a short train of bunches. Right: Sequential beam sharing at flattop with slow extractions. Traces from top to bottom: AM-modulated feeding noise, spill to internal target IT35, stochastic slow spill, and waiting beam DC current decay (piecewise-linear).

To this end, the beam was extracted either with the conventional 1-turn fast (in 5 μs) or with the multi-turn (3–10 turns) fast extractions (refer to Fig. 3, left). The

N. Tyurin, A. Zaitsev, O. Lebedev, V. Kalinin, V. Lapygin, D. Demihovskiy, Yu. Milichenko, I. Tsygankov, I. Sulygin, N. Ignashin, S. Sytov, Yu. Fedotov, A. Minchenko, A. Maksimov, A. Afonin, Yu. Antipov, and D. Khmaruk.

ISBN 978-3-95450-181-6

latter was due to the new FE scheme implemented that involves fast dipole magnet deflectors to drive a rising lumped horizontal orbit bump around the thin-wire electrostatic deflector for incremental beam shaving.

In course of operation for particle physics, U70 has delivered $3{\cdot}10^{12}$ ppp (average), $3.8{\cdot}10^{12}$ ppp (max) to 7 experimental facilities. Stochastic slow extraction (refer to Fig. 3, right) has attained 80–85% in-out transfer ratio for the beam fraction extracted. Fractional beam availability was about 83.8% which figure complies with the 10-year-long operational statistics.

By end of the run, the machine was switched to carbon-beam mode at intermediate energy 456 MeV/u (specific kinetic). The beam of bare carbon nuclei was stretched in and then extracted from the U-70 ring at flat-bottom. The intensity stored was $1–2.8{\cdot}10^{9}$ ipp of which $1.2–1.9{\cdot}10^{9}$ ipp were extracted for applied methodical and radio-biology research. Pulse-to-pulse period was 8.2 s.

The beam was extracted slowly with a stochastic extraction scheme capable of yielding 0.6–1 s long square-wave spills. The in-out transfer ratio amounted 55-57%, close the top expected value of around 68%.

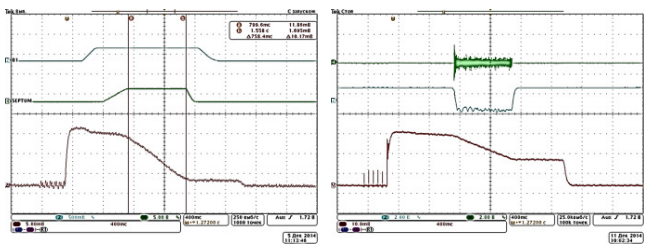

Figure 4: Stochastic slow extraction of carbon beam at flat-bottom of U70.

Fig. 4, left, illustrates the attractive, quasi-static nature of the stochastic slow extraction involved. Indeed, the linear decay of circulating beam DC current (bottom trace; 90% extracted, ca) is maintained under steady-state currents through closed-orbit bump coils and the 1st (upstream) deflecting magnet windings (two top traces).

Fig. 4, right, plots the feeding noise AM-modulated with a dedicated beam feedback (top trace), resultant square-wave spill monitored with a smoothing ionization chamber (central trace), and circulating beam DC current (bottom trace; about 50% of beam extracted in this case).

It is the adequate quality of carbon beam extracted that allowed a team from the Medical Radiological Research Center of the Russian Ministry of Health (MRRC, Obninsk, Kaluga Region) to accomplish the 2nd round of carbon-beam radio-biology studies with biological objects and structures at U70.

RUN 2015-1

While planning this run, the U70 personnel had encountered a noticeable competition between divergent demands of beam users. The compromise was settled with a complicated operational schedule composing various machine regimes overloaded by interfacing periods in between.

First, the machine was operated with the proton beam at 25 GeV. Such a routine regime was the first in U70 record. Still, in despite of complications in tuning the hardware, the beam was ultimately accelerated to the non-standard 25 GeV flattop and extracted successfully to the experimental facilities. Use was made of the stochastic slow extraction (up to 90% in-out), of internal targets and bent-crystal deflectors. The average beam intensity was not high, $2{\cdot}10^{12}$ ppp in 10–12 bunches (of 29 max available).

Second, the machine was operated at the conventional 50 GeV (protons). The beam has fed up to 7 experimental facilities (refer to Fig. 5) and, under the top priority, the Proton-Radiographic Facility. Beam intensity was $3–6{\cdot}10^{12}$ ppp, which was not so high due to troubles at the proton linac URAL30 at front end of the accelerating cascade in the proton mode. There is definitely a room for improvement left since occasionally the machine has yielded promising values of intensities per bunch amounting at max to 4.5 (U1.5), 3.8 (U70)$\cdot 10^{11}$ ppb.

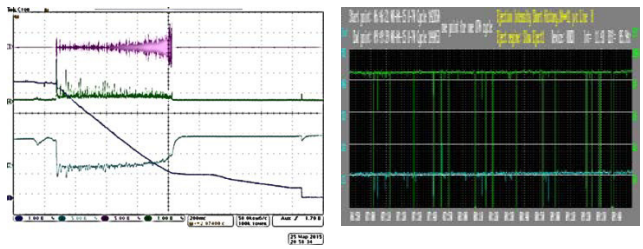

Figure 5: Stochastic slow extraction of protons from U70. Left, traces from top to bottom: AM-modulated feeding noise, low-ripple stochastic slow spill, waiting beam DC current, and beam feedback signal to modulate amplitude of noise. Right, monitor of slow extraction: bottom trace is spill intensity in relative units; top trace is in-out transfer ratio varying from 80 to 93% (at this plot).

Third, U70 was switched to high-energy carbon-beam mode at 25 GeV/u (the same magnetic rigidity and compliable kinematics as those for 50 GeV protons for future complementary hadron-nuclei and nuclei-hadron experiments). In course of a very short MD session the three issued extraction systems available were re-tuned to service carbon nuclei — (i) fast extraction to beam transfer line BTL#8, (ii) stochastic slow extraction to BTL#22, and (iii) slow extraction via bent-crystal deflectors to BTLs#22 and #8. Beam intensity varied in between $3–6.5{\cdot}10^{9}$ ipp.

There were two beam observations reported that are crucial for further advance of light-ion experimental program at U70. These are high quality (purity) of the high-energy carbon beam at the exit faces of beam transfer lines and negligible fragmentation the carbon nuclei in and after bent-crystal deflectors.

Fourth and finally, U70 was switched over to 456 MeV/u carbon beam storage and stretcher mode feeding BTL#25 ended by Interim Radio-Biological Workbench. Stored beam intensity amounted to $3–6.5{\cdot}10^{9}$ ipp. The end-user off-site experimentalist community at U70 has been joined by a new member — a

ISBN 978-3-95450-181-6

team from Institute for Theoretical and Experimental Biophysics the Russian Academy of Science (ITEB, Pushchino, Moscow Region). The intermediate-energy slowly-extracted carbon beam is thus well in-demand.

RUN 2015-2

In course of this run, U70 was again employed in two modes — proton (50 GeV) and carbon (456 MeV/u) ones.

To meet beam user demand, proton part of the run was broken into 3 segments with different priorities assigned either to fundamental or to applied fixed-target research. These used to call for a non-compliant set of beam structure, extractions and the BTLs involved.

During the shutdown, a crush program to improve functionality of proton source and URAL30 linac had been accomplished to attain reliable operation with $4{\cdot}10^{11}$ ppb in a variable number of bunches (up to 29).

Major bulk of fixed-target fundamental research was arranged, as usual, with sequential and parallel beam sharing at flattop. Occasionally, 5 experimental facilities were fed by the beam simultaneously in a cycle which constitutes a clear example of an efficient multi-user regime.

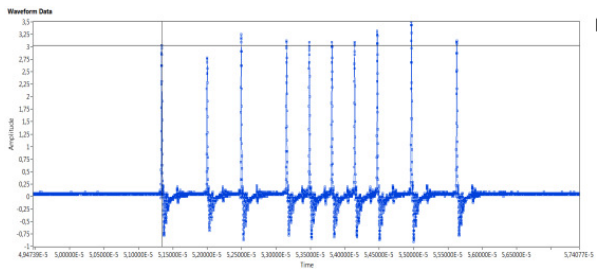

Figure 6: Beam train of 10 bunches in U70 for fast single-turn extraction for applied research. Bunch intensity is $3{\cdot}10^{11}$ ppb (marked with horizontal line).

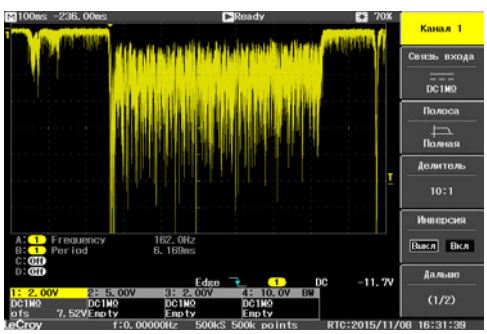

Figure 7: Stochastic slow spill of 50 GeV protons to the OKA experimental facility (study of rare kaon decays). Spill intensity $4{\cdot}10^{12}$ ppp.

In total, the 50 GeV proton beam was consumed by 6–8 beam users. Beam intensities were $3{\cdot}10^{12}$ ppp (average), $8.2{\cdot}10^{12}$ ppp (max), $5.3{\cdot}10^{12}$ ppp (stochastic slow extraction @ max 91% in-out transfer).

In the 456 МэВ/u carbon beam mode, U70 accepted 3–$5{\cdot}10^{9}$ ipp and delivered beam to radio-biological research. The two off-site research teams engaged in this activity were already mentioned (MRRC and ITEB).

Figures 6–9 illustrate a few milestones of the run at issue. Its tasks were accomplished.

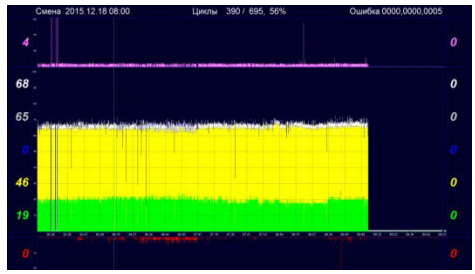

Figure 8: End of run 2015-2. Numerical data at the intensity monitor screenshot: $1.9{\cdot}10^{12}$ ppp to internal targets (green), $4.6{\cdot}10^{12}$ ppp to stochastic slow extraction (yellow), $6.5{\cdot}10^{12}$ ppp of total extracted intensity, 4% of integral start-to-end beam losses, transition crossing included (purple). Notice smooth sustained operation of U70 prior to scheduled shutdown at 09:00 of December 18, 2015.

RUN 2016-1

In course of this run, U70 was employed in two modes and with four beam energies — proton (40 and 50 GeV) and carbon (20 GeV/u and 456 MeV/u).

The machine was launched and tuned with 40 GeV proton beam at 3 s long flattop. Essentially, it was a test pilot beam to adjust injection systems and beamlines to the non-standard energy. The goal was to accommodate the machine to accept the much-less-intensive 20 GeV/u carbon-nuclei beam of the same magnetic rigidity.

In the aftermath of such a pre-tuning, the machine was switched to carbon mode. Thus, the 1st in record lengthy (23 days) run of U70 for fixed-target physical program with high-energy carbon beam had started. Peak intensity observed was $7{\cdot}10^{9}$ ipp (one bunch).

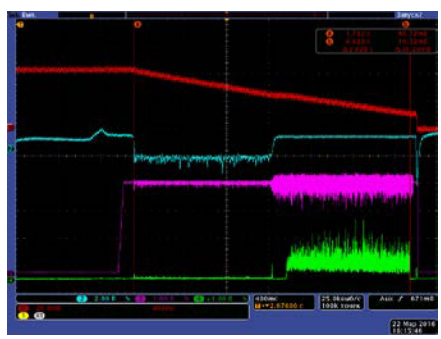

Figure 9: Sequential slow extraction of high-energy (20 GeV/u) carbon nuclei to FODS (via bent-crystal deflectors) and VES (stochastic) experimental facilities at the 1st and 2nd halves of the U70 flattop, respectively. Net intensity is $6.7{\cdot}10^{9}$ ipp.

Upon acceleration, the beam was de-bunched at flattop and extracted to existing FODS, SPIN and VES experimental facilities. To this end, two extraction schemes were employed — via noise-diffusive feeding the 3rd order horizontal resonance (stochastic slow extraction) or via bump-translational feeding bent-crystal

ISBN 978-3-95450-181-6

Table 1: Four runs of the U70 in between RuPAC-2014 and -2016

Run	2014-3	2015-1	2015-2	2016-1
Launching linac URAL30, booster U1.5 and U70 sequentially (I100 in parallel with a delay)	October, 06	February, 09	September, 29	February, 15
Beam in the U70 ring since	October, 23	March, 03	October, 29	February, 29
Fixed-target physics program with extracted top-energy beams (either of protons or of carbon nuclei)	November, 06 – December, 01, 25 days	March, 10 – April, 20 32 days	November, 09 – December, 18, 39 days	March, 03 – April, 11, 31 day
No. of multiple beam users (of which the 1st priority ones)	9 (7)	9 (8)	9(9)	6(6)
MD sessions and R&D on beam and accelerator physics, days	14	12	14	11
Light-ion acceleration program, intermediate energy only	December, 12–22, 11½ days	April, 20–24, 4½ days	December, 18–25, 7½ days	April ,14–25, 11 days

deflectors. Both the extractions succeeded which is confirmed by Fig. 9.

By end of the high-energy part of the run, U70 was again re-tuned to standard 50 GeV protons to yield the beam for other fixed-target research: proton radiography (daytime); TNF-ATLAS and ISTRA (nights).

Traditionally now, the run had ended with the 456 MeV/u carbon beam mode for radio-biological studies. Still, it is worth noting that one more off-site team of experimentalists had applied for and got the intermediate-energy carbon beam from U70 — the scientists from Joint Institute for Nuclear Research (JINR, Dubna, Moscow Region) irradiated nuclear emulsions thereby.

This run deserves a dedicated comment from the standpoint of experimental physics.

Indeed, it has launched a systematic experimental fixed-target research in the field of relativistic nuclear physics with the formerly entirely-proton machine. It was its first-in-record run when experimental facilities where fed mostly by high-energy beams of carbon nuclei. There were three major physical facilities involved – FODS, SPIN and VES. Beam energy was 20 GeV/u or 240 GeV in total. (To remind, the top magnetic rigidity of the U70 synchrotron allows gaining proven 35 GeV/u or 420 GeV total). Beam intensity varied from 10^5 to $4 \cdot 10^9$ nuclei per cycle (9.5 s), on demand of experimentalists.

The FODS facility was engaged in observation of fragmentation processes of high-energy carbon nuclei projectiles impacting other fixed-nuclei and studies of generating secondary particles in a deep cumulative region.

The SPIN facility studied spectra of secondary particles with large transverse momenta in course of impact of the high-energy carbon nuclei against nuclear (hydrogen included) fixed targets. Implementation of hydrogen target allows acquiring carbon-proton interaction data for subsequent cross-analysis with the complementary inversed-kinematics proton-carbon interaction data recorded in the earlier proton runs of U70.

The VES facility was engaged in a survey hadron-spectroscopy experiment to study specifics of meson states showing up in carbon-carbon interactions. Another topic was a search for bounded meson-nuclei states

Thus, run 2016-1 has de-facto opened a new direction of experimental research in IHEP of NRC “Kurchatov Institute”.

CONCLUSION

Accelerator Complex U70 at IHEP of NRC “Kurchatov Institute” is maintained in a healthy functional status, have noticeably improved its functionality due to recent upgrades and provides beams for ongoing topical fixed-target research, both fundamental and applied, with protons and carbon nuclei of high and intermediate energies, slowly or fast extracted.

REFERENCES

[1] S. Ivanov, on behalf of the U70 staff. Proc. of RUPAC-2008, Zvenigorod, 2008, p. 130–133; Proc. of RUPAC-2010, Protvino, 2010, p. 27–31; Proc. of RUPAC-2012, St.-Petersburg, 2012, p. 85–89; Proc. of RUPAC-2014, Obninsk, 2014, p. 1–5.

ISBN 978-3-95450-181-6

INR HIGH INTENSITY PROTON LINAC. STATUS AND PROSPECTS.

A. Feschenko, L.V. Kravchuk, V.L. Serov,
Institute For Nuclear Research, Moscow 117312, Russia

Abstract

The status and the prospects of High Intensity INR Linac are presented. The routine beam intensity is equal to 130 μA. The annual accelerator run duration is about 1600 hours. The main beam user facilities are multipurpose complex for neutron science, isotope production facility and proton therapy facility. The primary activities are accelerator maintenance, modernization of accelerator systems and beam transportation channels, increasing of accelerator reliability, improvement of beam parameters.

INTRODUCTION

The detail information on INR Linac has been given previously [1, 2, 3]. The current report repeats some basic information about the accelerator and describes the current status, prospects and latest activities.

INR Accelerator Complex is located in science city Troitsk (Moscow) 20 kilometers to the south-west from Moscow circular road. It includes the high-intensity proton Linac, Experimental Area with three neutron sources and Beam Therapy Complex as well as Isotope Production Facility (IPF).

In nineties INR accelerator was the second large high intensity and medium energy linac after LANSCE (former LAMPF) at LANL, Los Alamos, USA. Since that time two new linacs of this type with improved parameters have been put in operation (SNS and J-PARC) and several more ones are being constructed or designed now. This activity shows the urgency of the researches made at the accelerators of this type and confirms extreme topicality of the INR research complex.

LINEAR ACCELERATOR

General Description and Parameters

The simplified diagram of the accelerator is shown in Fig. 1. The accelerator consists of proton and H-minus injectors, low energy beam transport lines, 750 keV booster RFQ, 100 MeV drift tube linac (DTL) and 600 MeV coupled cavity linac (CCL, Disk and Washer accelerating structure). There are seven 198.2 MHz RF channels for five DTL tanks and RFQ cavity (including one spare channel) as well as thirty two 991 MHz RF channels for 27 CCL accelerating cavities and one matching cavity (including three spare channels and one channel for equipment tests). Design, obtained and currently available operational Linac parameters are summarized in Table 1.

The accelerator is in regular operation since 1993. 123 accelerator runs with total duration of 45000 hours have been carried out so far including 55 runs of total duration of 16000 hours within the last decade. The availability of the beam for the users is 80÷90 % of the total beam time.

Table 1: Main Accelerator Parameters

Parameter	Design	Obtained	November 2016
Particles	p, H-minus	p, H-minus	p
Energy, MeV	600	502	247
Pulse current, mA	50	16	15
Repetition rate, Hz	100	50	50
Pulse duration, μs	100	200	0.3÷200
Average current, μA	500	150	130

Resent Modifications

The main isotope produced at INR IPF is Sr-82 used for positron emission tomography. The efficiency of isotope production depends on proton beam intensity at the target. The limitation of beam intensity is set taking into account several effects. One of the effects is heating of the target including that within the beam pulse. To decrease the pulse heating the fast raster system has been developed, built and implemented in the beam line to IPF [4]. The system provides a circular scan with adjustable amplitude and the frequency of 5 kHz thus providing one turn of the beam on the target within the 200 μs beam pulse. Due to implementation of this system the tolerable beam intensity for 143 MeV beam has been increased from 100 μA to 130 μA.

In order to increase the beam intensity twice the efforts to increase the beam pulse repetition rate from 50 Hz to 100 Hz have been undertaken. Doubling of the repetition rate will also give the possibility to effectively split the beam between the IPF and the experimental area with the help of the pulsed magnet installed several years ago in the intermediate beam extraction area (160 MeV) providing the 50 Hz beam to each facility pulse by pulse [5]. Though the whole problem has not yet been solved several intermediate results have been obtained:

- The proton injector beam pulse repetition rate has been doubled and reliable operation of the injector has been achieved at 100 Hz [6].
- Accelerating system and RF power supply systems have been tested at 100 Hz.

When testing the RF power supply systems the effect of bi-periodicity of the RF pulses has been found. The effect was due to mains supply and was observed in both accelerator parts. The problem has been investigated and

ISBN 978-3-95450-181-6

generally solved [7]. However the task of replacement of the powerful modulator vacuum tubes by powerful RF tubes arose [8] and the problem of bi-periodicity will have to be newly investigated and solved in future for new vacuum tubes.

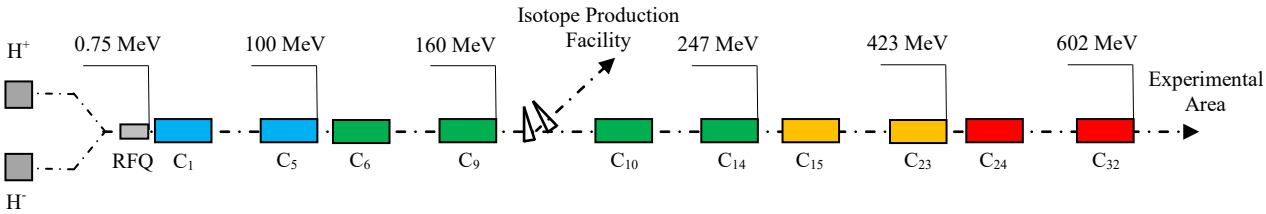

Figure 1: Simplified diagram of the accelerator (C_1÷C_{32} – accelerating cavities). The sectors of the accelerator are marked with different colors (five sectors totally).

The tests of the accelerating system with 100 Hz repetition rate revealed a catastrophic problem with the first CCL Disc and Washer cavity (100÷113 MeV). Number of RF breakdowns in the cavity increases drastically which makes practically impossible its operation at 100 Hz with the required pulse duration of more than 200 μs. The activity to develop the new cavity based on the novel Cut Disk Structure has started [9].

As mentioned above the accelerator includes the intermediate extraction area where the Isotope Production Facility is located. The IPF is a stationary installation and is foreseen to work with high intensity beam. However the tasks to irradiate different items with low intensity beams arise regularly. Recently a decision to build an irradiation channel for low intensity beams (up to 1 μA) with the energies from 100 MeV up to maximum possible energy has been done and the construction has started at the exit of the accelerator.

EXPERIMENTAL AREA

Experimental Area is shown in Fig. 2. All the equipment of experimental area is foreseen to work with the beam of 600 MeV but now the power supply system is restricted and enables to work with the energies up to 300 MeV. At present the following facilities are in operation: Spallation neutron source IN-06 with a number of multipurpose instruments, 100-ton spectrometer LNS-100 on slowing down in lead, RADEX facility (a modified beam stop) with neutron guides and stations for time-of-flight spectrometry, Beam Therapy Complex.

Initially the main beam for the Experimental Area was foreseen to be H-minus. Splitting of the primary beam into several ones by stripping and further separation in vertical plane was intended. The separated beams were planned to supply to different experimental installations simultaneously. As the beams appeared to be displaced with respect to each other their further transportation was not an easy task as no one beam moved along the axis of the magnetic system. Moreover optimum position of the magnetic elements was not at the same level and they were displaced vertically. In this configuration transportation of even one high intensity beam was not an easy task.

After restructuring in 2014 the transportation channels of the experimental area from the accelerator exit to the experimental facilities have been passed to the accelerator division. After careful analysis of the current status of the channels, available possibilities and the realistic tasks a decision to abandon the multi beam mode with simultaneous beam transportation to several experimental installations has been done. All the electromagnetic equipment has been realigned and installed on one level thus enabling to simplify beam tuning, to reduce requirement to beam parameters, to decrease beam losses and to improve reliability.

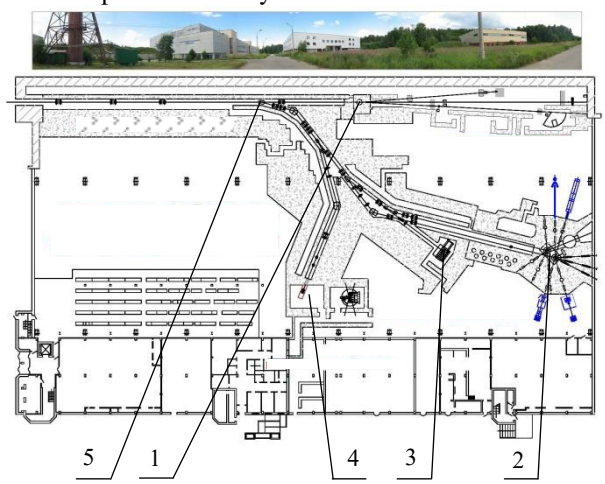

Figure 2: Experimental Area (1 - RADEX facility, 2 - Spallation neutron source IN-06, 3 - LNS-100 spectrometer, 4 – Beam Therapy Complex, 5 – beam separation area).

PROSPECTS

Due to several reasons the design parameters of the linac have never been obtained. Meanwhile some accelerator systems including vacuum system, focusing system, control, diagnostics and conventional facilities work practically in the design mode. At present the accelerator regularly works with the energy of 209 MeV. The available amount of klystrons enables to accelerate the beam up to 247 MeV with minor efforts. It is quite realistic to obtain the energy of 300÷350 MeV but

ISBN 978-3-95450-181-6

essential efforts and expenditures are needed. Increasing the beam intensity above 130÷150 mA requires doubling of the beam pulse repetition rate up to 100 Hz. To solve this task the first accelerating cavity of the high energy part of accelerator must be replaced by a new one and the RF power supply system of the low energy part must be modernized.

Building the irradiation channel at the exit of the accelerator is also considered as a promising improvement enlarging the accelerator functionality.

However the most promising task being discussed and negotiated with international Thorium Energy Committee (iThEC) is an ADS experiment based on INR linac and spallation neutron source IN-06. According to iThEC, INR facility is the most suitable place in the world where the demonstration ADS experiment can be performed at a relatively modest cost and on a relatively short time scale. The subcritical ADS core can be installed in the second compartment of the spallation source which is empty now. The formulated requirements to the accelerator beam do not seem unattainable: proton beam energy 247÷350 MeV, beam intensity up to 250 μA, beam power 25÷90 kW. With these characteristics, it will be possible to study ADS properties up to a thermal power of 2.5 MW, varying the neutron multiplication factor k_s up to 0.98. For the minimum required beam power of 25 kW the thermal power of 1 MW can be obtained with k_s=0.972.To supply the beam to the second compartment of the neutron source the beam line with the length of near 40 m must be built. The main electromagnetic equipment for this line is in hands.

CONCLUSION

The scientific facility based on 600 MeV Proton Linac is in operation at the Institute for Nuclear Research. Permanent modernization of the accelerator and the Experimental Area enables not to only maintain the complex in operational state but also to improve beam parameters and complex capabilities. The existing experimental facilities are the basis for variety of both basic and applied researches.

ACKNOWLEDGMENT

The authors acknowledge the personnel of accelerator division for their contribution to the work.

REFERENCES

[1] L.V.Kravchuk. INR proton Linac operation and applications. Nucl. Instr. and Meth. A 562, (2006), 932-934.
[2] L.V.Kravchuk. Operation and Research Activities at the INR accelerator complex. Proc. of RUPAC2008, pp.137-140.
[3] A.Feschenko et al. Multipurpose Research Complex based on the INR High Intensity Proton Linac. Proc. of RUPAC2012, pp.90-94.
[4] O.Volodkevich et al. Use of Fast Magnetic Beam Raster System for INR Isotope Production Facility. Proc. of RUPAC2014, pp.426-428.
[5] N.I.Brusova et al. Beam Pulse Separation System of INR Linac, Proc. of RUPAC2012, pp.451-452.
[6] E.S.Nilulin et al. INR RAS Proton Injector 100 Hz PRR Operation Mode. Proc. of RUPAC2014, pp.306-308.
[7] A.N.Drugakov et al. Investigation of INR Linac DTL RF System Operation at 100 Hz Repetition Rate, Proc. of RUPAC2012, pp.296-298.
[8] A.Kvasha et al. Development of the INR Linear Accelerator DTL RF System, THXSH0, these proceedings.
[9] I.Rybakov et al. Proposal of the Accelerating Structure for the First Cavity of the Main Part of INR Linac, TUPSA004, these proceedings.

ISBN 978-3-95450-181-6

STATUS OF IFMIF-EVEDA RFQ

E. Fagotti, L. Antoniazzi, A. Baldo, A. Battistello, P. Bottin, L. Ferrari, M. Giacchini, F. Grespan, M. Montis, A. Pisent, F. Scantamburlo, D. Scarpa, INFN/LNL, Legnaro (PD), Italy
D. Agguiaro, A.G. Colombo, A. Pepato, l. Ramina, INFN/PD, Padova, Italy
F. Borotto Dalla Vecchia, G. Dughera, G. Giraudo, E.A. Macrì, P. Mereu, R. Panero, INFN/TO, Torino, Italy
T. Shinya, K. Kondo, QST, Rokkasho, Japan

Abstract

All IFMIF – EVEDA RFQ modules were completed in summer 2015. In the previous year the last three modules were RF tested at LNL at nominal power up to cw operation. At the beginning of this year all the modules were assembled in three 3.3 m long super-modules structures that were shipped to Japan. RFQ was then installed and tuned with provisional aluminum tuners and end plates to nominal frequency and field distribution. Replacement of movable aluminum components with copper fixed ones increased cavity quality value not affecting field flatness and frequency.

INTRODUCTION

The required acceleration in continuous wave (CW) of 125 mA of deuterons up to 5 MeV poses IFMIF RFQ at the forefront frontier of high intensity injectors [1].

This RFQ is indeed meant to be the injector of a 5 MW deuteron linac (40 MeV final energy) for fusion material irradiation tests. The International Fusion Materials Irradiation Facility (IFMIF) [2] project aims at producing an intense (about 10^{17} s^{-1}) neutron source facility, with spectrum up to about 14 MeV, in order to test the materials to be employed in the future fusion reactors. The facility will be based on two high power CW accelerator drivers, hitting a single liquid lithium target (10 MW power) to yield neutrons via nuclear stripping reactions.

The IFMIF-EVEDA project was funded at the time of the approval of ITER construction (2007); the task is to validate the IFMIF design by the realization of a number of prototypes, including a high-intensity CW deuteron accelerator (called LIPAc, Linear IFMIF Prototype Accelerator) for a beam power exceeding 1 MW.

LIPAc is being installed at the QST site in Rokkasho (Japan). Accelerating structures of the prototype linac, operating at 175 MHz, are the RFQ and the first Half Wave Resonator cryomodule (Fig. 1).

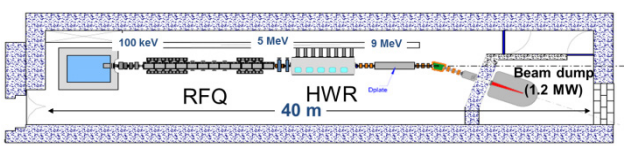

Figure 1: Schematic layout of the IFMIF-EVEDA prototype linac (125 mA, 9 MeV deuterons).

LIPAc realization is a strict collaboration between Japan and Europe. The detailed organization of such challenging project is discussed in [3].

Presently injector commissioning data are under evaluation, RFQ is assembled and tuned, MEBT and diagnostic plate are under set up and RF system is under completion [4]. The commissioning plane foresees four phases: Phase A that is the production of 140 mA deuteron current at 100 keV in CW; Phase B that is acceleration of 125 mA deuteron current at 5 MeV at 0.1% duty cycle; Phase C that is acceleration of 125 mA deuteron current at 9 MeV at 0.1% duty cycle; Phase D that is the ramping up of the duty cycle up to CW. In all phases it is planned to characterize and use, together with the deuteron beam, a proton beam with half energy, half current and similar space charge.

Phase A commissioning was concluded first week of November. Such phase was extremely important to establish the correct RFQ input conditions and guarantee the required LIPAc performances [5-7]. Unfortunately injectors didn't reach specifications at 100% DC. However, considering that a low duty cycle operation for the injector was demonstrated, it was decided to conclude phase A2, that is the characterization of injector parameters at the RFQ input location and move towards phase B. Possibility to have additional time for a phase A3, that is the characterization of injector parameters in the middle of the LEBT, was maintained.

During phase A2 commissioning, RFQ was installed 3.3 m downstream its nominal position for assembling and tuning allowing, in parallel, injector commissioning. At the beginning of November, RFQ was finally installed in its final position (Fig. 2) in view of RF conditioning and beam commissioning (phase B).

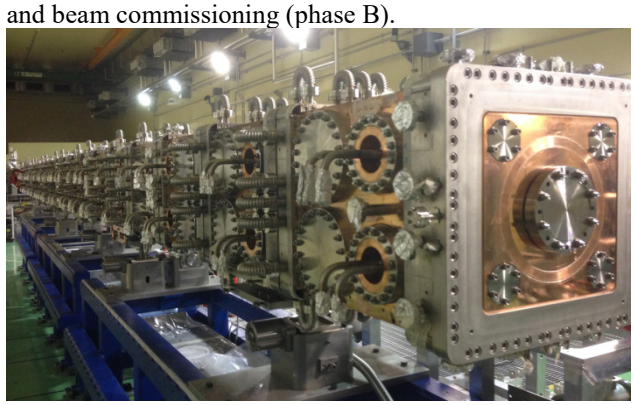

Figure 2: RFQ fully assembled and aligned in the final position.

ISBN 978-3-95450-181-6

RFQ CONSTRUCTION

INFN was in charge of the design and construction of the RFQ system, namely the accelerator structure, the vacuum system, the cooling system used for slow frequency tuning and the local control system. This activity was developed through the INFN Legnaro National Laboratories, by an accelerator physics group with previous experience in RFQ realization and through Padova, Torino and Bologna INFN sections, with previous experience for mechanical development and realization in large international experiments (like for CERN LHC). The responsibilities were distributed accordingly, with Padova and Torino in charge of the RFQ module mechanical development and engineering integration respectively. About 30 people including physicists and engineers have been involved in RFQ realization.

A specific characteristic of this development has been the use of internal resources and installations, not only for the physical and local control design, but also for all the other realization steps, like mechanical design, high precision machining of critical components, QA and measurements, vacuum brazing and high power RF testing. This allowed the best efficiency when processes were given to industry, plus an important flexibility to solve the problems that sometimes occurred. Moreover, the various steps of the development have been openly discussed within the accelerator community and published in order to share opinions and have the best result for our difficult task [8-29].

The specifications of IFMIF-EVEDA RFQ are very challenging, since the 650 kW beam should be accelerated with low beam losses and activation of the structure should allow hands-on maintenance of the structure itself. Beam losses less than10 mA in total and less than 0.1 mA between 4 MeV and 5 MeV are allowed.

The beam dynamics optimization led to a solution with high focussing parameter B, high voltage ramped in the middle part of the structure up to 132 kV. The design approach followed the standard subdivision in shaper (approx. 1.5 m), gentle buncher (approx. 1.5 m) and accelerator (approx. 7 m). The accelerator, with a linear synchronous phase variation from -60° to -32°, was optimized cell by cell, keeping the maximum surface field and increasing the acceptance up to 2 mm-mrad norm. A strong focussing factor (B = 7) is necessary in the gentle buncher section in order to keep the tune depression above 0.4 in order to avoid the main space charge driven resonances. The focusing in the shaper rises from B = 4 to B = 7 allowing an input beam with smaller divergence and an easier matching from the LEBT.

The inter-vane voltage in the accelerator section is ramped using a V(z) law in closed-form and continuous up to the 2nd derivative; it is possible in this way to have continuous cut-off frequency variations along the RFQ, as well as limited frequency excursions, keeping at the same time the maximum surface field below 1.8 Ekp along the structure.

The four vane resonator was the only practical solution for such high inter-vane voltage. The cross section was optimized for high shunt impedance and about 86 kW/m maximum dissipated power.

The mechanical design is based on a brazed structure and metal sealing to guarantee the necessary high reliability. These two choices determined many aspects of the design, for example the use of 316LN stainless steel for most of the interface points. The brazed approach for a structure with such a large cross section was developed by choosing 18 relatively short modules, about 550 mm long; the square shape has many mechanical advantages and good shunt impedance. Finally, efficient water cooling channels were needed to maintain geometry despite intense RF dissipation.

Due to the extremely high beam current, the attainment of beam loss control is of paramount importance in such a structure. Beam losses are basically related to geometrical tolerances and in particular can be affected by: vane modulation machining, beam axis accuracy along the accelerator and voltage law accuracy along the structure.

The electrode machining was very accurate and it was verified with continuous scanning CMM of each of the 72 electrodes (20 μm max error in the modulation geometry of each module was achieved).

The beam axis accuracy requires quadrupole center maximum misalignment of 0.1 mm. This was achieved with proper module characterization after brazing (CMM measuring), precise transverse alignment using laser tracker and precise longitudinal positioning determined by calibrated spacers machined according to laser tracker analysis of the modules connecting surfaces.

As for the third aspect, in few words it is related to the global deformation of the module mainly during brazing. The effect of part of this deformation can be recovered by tuners but the geometry of the module should be good enough to remain in the tuning range, ±1 MHz in our case. This is the most demanding aspect for the mechanical design and quality management of the module production since the brazing process has to guarantee electrode displacements below 50-100 μm, depending on modulation amplitude.

So the mechanical design was based on vacuum brazing with very strict tolerances on relatively large and heavy structures. Even the procurement of the CUC2 raw material blocks was limited by the total mass amount and calls for a maximum longitudinal dimension of about 550 mm. The accelerator is therefore composed by 18 modules.

The blocks undergo deep drilling of the cooling channels, EDM rough machining, to minimize stresses and possible deformations in the oven, annealing, final machining and brazing cycles. After the first prototypes and modules, produced with two brazing cycles, INFN developed the procedure used for the production of most of the modules: single brazing cycle (Fig. 3).

The four electrodes of each module were joined in vertical position together with SS components like head flanges, lateral flanges and cooling tube connectors. It

ISBN 978-3-95450-181-6

was very important to develop the correct fixture, so to keep the pieces with the right tolerance during brazing, leaving the differential elongation possibility during the oven thermal cycle.

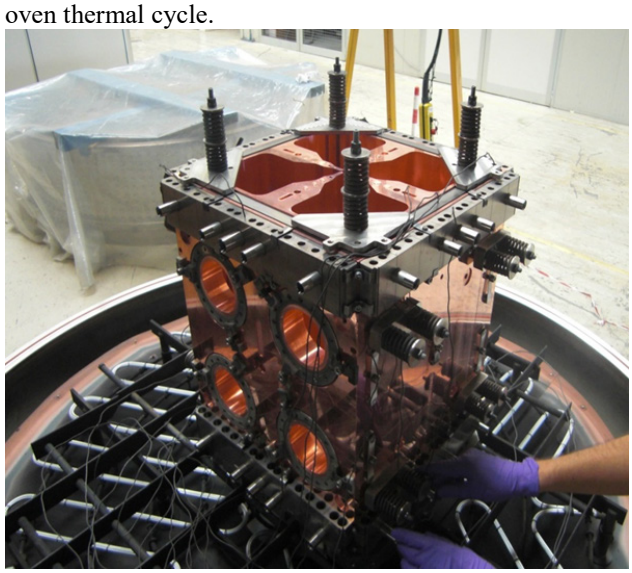

Figure 3: The RFQ module (550 mm long) in the vacuum oven

Subdivision in many modules has various advantages: each module can be machined with very precise and common milling machines; vacuum ovens for limited dimensions are also major spread. The cavity wall interruption has almost no consequence on power consumption due to TE operating mode, while the vane interruption with a gap of about 100 μm can be realized without too large increasing of the local surface field.

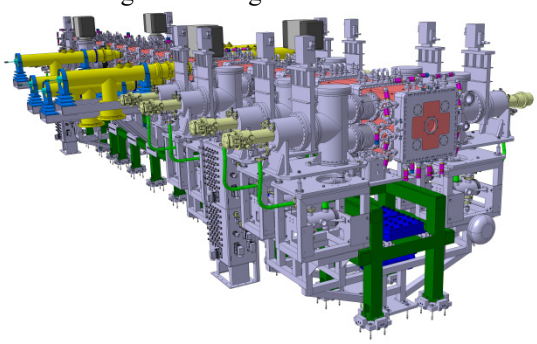

Figure 4: The three SMs integrated with the ancillaries

Modules are coupled in three groups of six modules each constituting "super-modules"(SM). Each SM has its own support (Fig. 4). The cooling system follows this architecture, with two cooling circuits one for the vanes and one for the tank skin, for each SM. The resonant frequency is controlled acting on the difference between vane and tank temperature. The thermal deformation of the cavity has been extensively simulated with 3D FEM to take into account the actual channel distribution, the stiffening determined by the head flange of each module, the lateral flanges for tuning, pumping and power coupling [26]. The most severe hot spots are foreseen in the vane undercut on the high energy side [27].

The vacuum system layout is based on cryogenic pumps mounted on pumping manifolds able to use two vacuum ports each. The nominal pressure with full power beam is lower than $5x10^{-7}$ mbar.

The RFQ is fed by eight independent RF chains and eight power couplers, 200 kW each: 650 kW for beam loading, 600 kW for power dissipation in copper plus margin for regulation.

The 18 modules were produced in three sets, corresponding to the three SMs; 6 machined and brazed in house, 12 in the industry by two different companies. The first produced SM was the high energy one. The intermediate energy SM, with most demanding machining due to the voltage ramping, was built internally by INFN. The in house capability to entirely produce a module was also important to recover the production problems for one of the two external contractors.

In the production the constant quality control was clearly very important. Each module was tested with CMM and RF in various phases. In ref [25] the details of this comparison are shown, with a remarkable coherence of the results of the two methods. Overall the production showed an average spread of 350 kHz, or 46 μm in average aperture R_0. These values can be well compensated by the tuner (range ±1MHz).

After brazing, each module needed to be mounted again on the milling machine. In this phase, the final machining of the reference plane was particularly important. It allows, via calibrated spacers, the proper closing of the head flange and relative positioning of the modules.

HIGH POWER TEST IN EU

A very important step of our risk reduction strategy was the implementation of high power tests in Europe. Indeed one of the problems encountered was the lack of experience in CW RFQ operation and the necessity to validate the design and the construction technique, in view of the construction of 18 RFQ modules to be installed about 10000 km far away.

As a preliminary step in 2010, in collaboration with CEA, two modules of TRASCO RFQ (352 MHz designed by LNL and built in Italy for a different project) were installed at Saclay and operated CW. The RF system of IPHI project and an INFN cooling skid for frequency regulation were used [28]. Nominal field in CW mode was reached.

In 2012 it was decided to test in Italy at LNL a 2 m long structure, corresponding to the last three elements of IFMIF RFQ, assembled with a prototype module used for RF field matching. The assembly, the alignment, the tuning and the transportation with a truck to a different building were important procedures test. This structure could be driven by a single 200 kW RF chain. In this way we could check the condition of maximum voltage, maximum field and maximum power density.

For this purpose, a specific test stand was built at LNL, with a light bunker and approximately 600 kW power installed, mainly for RF system and refrigerator.

ISBN 978-3-95450-181-6

Elements of the RFQ local control and cooling systems were used for this test as well as a circulator kindly borrowed by Ciemat. Unfortunately, just before test starting, a problem was discovered on the high power couplers produced by QST, which caused the impossibility to use those couplers for a power test. In order to keep the schedule and validate the design during module production, two new RF power couplers, both rated 200 kW, were developed at LNL and procured by Italian industry in few months.

As a result, it was possible to condition the RFQ in CW mode up to the operating field. In Fig. 5, the log of 5 operation hours at full power is reported. This corresponds to a field of 1.8 Ekp and to a power density of 86 kW/m [27].

Moreover, from the measurement of the pick-ups field it was possible to verify that the field distribution remained stable, with an error lower than 0.5%, from low field up to nominal field. Finally, it was possible to close the RF frequency feed-back loop and stabilize the natural frequency of the cavity by means of the temperature difference between vanes and external structure checking the resonance control system.

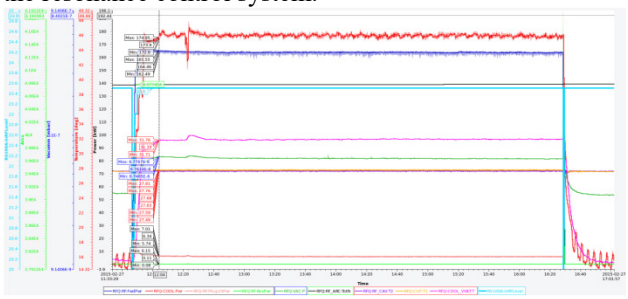

Figure 5: RFQ stayed at nominal power and CW operation for 5 hours. Then test was considered successfully concluded

RFQ ASSEMBY AND TUNING

The RFQ was assembled in Italy in three SMs. Each SM was mounted on an independent support. During assembly, each module was mounted on a temporary six degree of freedom support with sliding capability, aligned by means of the laser tracker and connected to the next one. Transverse position was determined by alignment while tightening the bolts, the longitudinal position by calibrated spacers inserted at the level of bolts. After each step a vacuum test was done to check the correct operation of the squared metallic seal.

The three SMs were completely assembled at LNL in January 2016. Before careful packaging, all the SMs were successfully tested in vacuum and filled with nitrogen gas. Shock recorders were screwed on the top of each SM to monitor various transport steps: from LNL to Milan airport by truck, from here to Frankfurt airport by aircraft, from here to Tokyo airport by aircraft and from here to Rokkasho site by truck. After SM unpacking, vacuum tests confirmed a vacuum leak lower than 2×10^{-10} mbar-l/s.

SMs and their associated support stands were pre-aligned using the rough alignment system able to regulate position with 0.5 mm precision over ±20 mm range in all directions. SMs were then precisely aligned within 0.05 mm respect to nominal references using the precise alignment system.

It is important to notice that during coupling of the SMs, alignment of the interface modules axes has higher priority respect to alignment of the SMs respect to reference beam axis. This means that low energy plate and high energy plate of the RFQ are forced to be on beam axis while single modules axes can be as far as 0.2 mm from the nominal beam axis in the vertical component.

Just after RFQ assembly, dummy tuners and bead pull system were installed on the RFQ cavity to find the optimum configuration for cavity tuning. Bead-pull campaign to optimize end plates and 108 tuners penetrations started at the end of April 2016 and took two weeks.

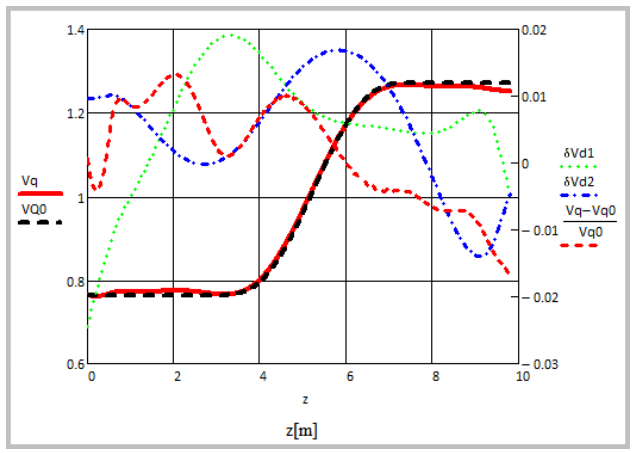

Figure 6: Bead pull measurement of the IFMIF RFQ field. VQ0 is the nominal field; Vq is the measured field (left scale); the dipole components and the relative error on the right.

From the first measurement with flush tuners the good quality of the cavity appeared, since dipole field components were below 2% and the frequency corresponded to 3D simulations. The geometry of the end plates without dipole correcting fingers was confirmed. After several iterations on dummy tuners positions, nominal field distribution was established, with spurious mode components below 2% target limit (Fig. 6).

Final tuners and final end plates were machined at required quotes according to RFQ bead pull measurements results. Machining was done in three steps in order to maintain enough tuning margin up to the conclusion of the process. In the first step copper termination plates and 16 copper tuners were replaced to dummy termination plates and dummy tuners. Bead pull measurements showed that final low energy termination plate caused a small change in the field flatness that was recovered by changing the penetration of the four tuners located near the plate. In the second step, 43 aluminum

ISBN 978-3-95450-181-6

tuners were substituted with copper ones and no changes appeared on the field flatness. At the end, the remaining 49 aluminum tuners were replaced with the copper ones without affecting the field.

Finally the frequency, rescaled for vacuum and nominal temperature, was measured to be equal to 175.014 MHz and the quality factor Q_0 was equal to 13200±200, 82% of SUPERFISH value with flash tuners, corresponding to a shunt impedance R_{sh} = 201 kΩ*m.

The shunt impedance is clearly a very important parameter for a CW RFQ operating at high inter-vane voltage. The confirmation of the very good design value, in the presence of all the 3D and "as built" details, was an extremely good result.

CONCLUSIONS

The RFQ construction was concluded, all the modules were accepted after RF and CMM tests completion.

The CW RF performances of the RFQ such as maximum field, power density, water temperature frequency control loop, were achieved in the high power test in Italy.

The air-transportation in three SMs and the assembly in Japan were successful. The RF field was tuned to the nominal shape with specified accuracy (2%).

The excellent shunt impedance of the design has been achieved (Q_0=13200). Conditioning and beam commissioning will start on May 2017.

REFERENCES

[1] A. Pisent, "High Power RFQs" in Proc. of PAC09, Vancouver, Canada, May 2009, p. 75.

[2] J. Knaster, et al., "Materials research for fusion," Nat. Phys., vol. 12, p. 424, 2016.

[3] J. Knaster, et al., "Challenges of the High Current Prototype Accelerator of IFMIF/EVEDA," in Proc. IPAC2016, Busan, Korea, May 2016, p. 52.

[4] P. Cara, et al., "The linear IFMIF Prototype Accelerator (LIPAC) design development under the European-Japanese Collaboration," in Proc. IPAC2016, Busan, Korea, May 2016, p. 985.

[5] B. Bolzon, et al., "Intermediate Commissioning Results of the 70 mA/50 keV H+ and 140 mA/100 keV D+ ECR Injector of IFMIF/LIPAC," in Proc. IPAC2016, Busan, Korea, May 2016, p. 2625.

[6] L. Bellan, et al., "Source and LEBT beam preparation for IFMIF-EVEDA RFQ," presented at LINAC'16, East Lansing, USA, Sept. 2016.

[7] M. Comunian, et al., "IFMIF-EVEDA RFQ, Measurement of Beam Input Conditions and Preparation to Beam Commissioning," in Proc. HB2016, Malmö, Sweden, p. 338.

[8] A. Pisent, et al., "IFMIF-EVEDA RFQ Design," in Proc. EPAC08, Genoa, Italy.

[9] M. Comunian, et al., "Beam dynamics design of IFMIF-EVEDA RFQ," in Proc. EPAC08, Genoa, Italy.

[10] M. Comunian, et al., "Beam dynamics redesign of IFMIF-EVEDA RFQ for a larger input beam acceptance," in Proc. IPAC'11, San Sebastian, Spain, p. 670.

[11] F. Grespan, et al., "RF design of IFMIF-EVEDA RFQ," in Proc. LINAC'08, Victoria, Canada.

[12] A. Pepato, et al., "Mechanical Design of the IFMIF-EVEDA RFQ," in Proc. PAC09, Vancouver, BC, Canada, p. 4923.

[13] A. Pepato, et al., "Engineering Design and First Prototype Tests of the IFMIF-EVEDA RFQ," in Proc. IPAC'10, Kyoto, Japan, p. 600.

[14] P. Mereu, et al., "Mechanical integration of the IFMIF-EVEDA Radio Frequency Quadrupole," in Proc. IPAC2016, Busan, Korea, May 2016, p. 3712.

[15] F. Grespan, A. Pisent, A. Palmieri, Nucl. Instr. Meth. A, vol. 582, pp. 303-317, 2007.

[16] A. Palmieri, et al., "The IFMIF RFQ real scale aluminum model: RF measurements and tuning," in Proc. IPAC'10, Kyoto, Japan, p. 603.

[17] A. Pepato, et al., "Construction of the Modules of the IFMIF-EVEDA RFQ," in Proc. LINAC'14, Geneva, Switzerland, p. 256.

[18] E. Fagotti, et al., "The Couplers for the IFMIF-EVEDA RFQ High Power Test Stand at LNL: Design, Construction and Operation," in Proc. LINAC'14, Geneva, Switzerland, p. 643

[19] F. Scantamburlo, et al., "Production and Quality Control of the First Modules of the IFMIF-EVEDA RFQ", Proc. LINAC'12, Tel-Aviv, Israel, p. 38.

[20] A. Palmieri, et al., "3D Aspects of the IFMIF-EVEDA RFQ: Design and Optimization of the Vacuum Grids, of the Slug Tuners and of the End Cell," in Proc. LINAC'10, Tsukuba, Japan, p. 533.

[21] F. Scantamburlo, et al., "3D Thermo Mechanical Study on IFMIF-EVEDA RFQ," in Proc. LINAC'10, Tsukuba, Japan, p. 539.

[22] F. Grespan, "RF Design of the IFMIF-EVEDA RFQ," in Proc. LINAC'08, Victoria, Canada, p. 148.

[23] M. Comunian, et al., "The IFMIF-EVEDA RFQ: Beam Dynamics Design," in Proc. LINAC'08, Victoria, Canada, p. 145.

[24] A. Fagotti, et al., "Preparation and installation of IFMIF-EVEDA RFQ at Rokkasho site," presented at LINAC'16, East Lansing, USA, Sept. 2016.

[25] L. Ferrari, et al., "IFMIF RFQ module characterization via mechanical and RF Measurements," presented at LINAC'16, East Lansing, USA, Sept. 2016.

[26] A. Palmieri, et al., "Tuning the IFMIF %MeV RFQ accelerator," presented at LINAC'16, East Lansing, USA, Sept. 2016.

[27] E. Fagotti, et al., "High power RF test of IFMIF-EVEDA RFQ," presented at LINAC'16, East Lansing, USA, Sept. 2016.

[28] E. Fagotti, et al., "High-Power RF Conditioning of the TRASCO RFQ," in Proc. LINAC'12, Tel Aviv, Israel, p. 828.

[29] A. Palmieri, et al., "Preserving Beam Quality in Long RFQs on the RF Side: Voltage Stabilization and Tuning," in Proc HB2014, East Lansing, USA, p. 345.

ISBN 978-3-95450-181-6

FEEDING BINP COLLIDERS WITH THE NEW VEPP-5 INJECTION COMPLEX

F. Emanov*, A. Andrianov, K. Astrelina, V.V. Balakin, A. Barnyakov, O.V. Belikov, D.E. Berkaev, M. Blinov, Yu.M. Boimelshtain, D. Bolkhovityanov, A.G. Chupyra, N.S. Dikansky, A.R. Frolov, Ye.A. Gusev, G. Karpov, A. Kasaev, V. Kokoulin, A.A. Kondakov, I. Koop, I. Kuptsov, G.Ya. Kurkin, R. Lapik, N. Lebedev, A. Levichev, P. Logatchov, Yu. Maltseva, P. Martyshkin, A. Murasev, D. Nikiforov, A.V. Pavlenko, V. Pavlov, A. Petrenko, V. Podlevskih, V. Rashchenko, S. Samoylov, S. Shiyankov, A. Skrinsky, A. Starostenko, D.P. Sukhanov, A.G. Tribendis, A.S. Tsyganov, S. Vasiliev, V. Yudin, I. Zemlyansky, Yu. Rogovsky, A. Novohatsky,
BINP, Novosibirsk, Russia
A.L. Romanov, Fermilab, USA

Abstract

VEPP-4 and VEPP-2000 e+e- colliders are switching to feed from VEPP-5 Injection Complex via newly constructed K-500 beam transfer line. Since first operation of K-500 at the end of 2015 injection complex delivered e+ and e- beams to VEPP-2000 facility and is getting ready to work with VEPP-4. Upgraded injection chain demonstrated ability to provide design luminosity to VEPP-2000 and techniques of reliable operation are now under development. The design and operation experience of Injection Complex and transfer lines will be presented.

INTRODUCTION

Injection complex was introduced in 1994 as e+/e- beam source of VEPP-5 project [1], which also included VEPP-3/4M electron-positron collider complex, charm-tau factory, phi-factory(abandoned collider project), linear accelerator (or synchrotron as alternative) for increasing injection complex beam energy to VEPP-4M and charm-tau factory experiments energy and beam transfer lines. It was later decided to build 250 m beam transfer line from injection complex to BEP in order to provide particles for VEPP-2000 [2].

First 2010-2013 run of VEPP-2000 showed 30 time lower luminosity than designed value $10^{32} cm^{-2} \cdot c^{-1}$, which was limited by insufficiency of positrons. Since injection complex had demonstrated acceptable performance by 2013/2014 season [3] upgrade of VEPP-2000 injection chain was performed in 2014-2015 [4]. VEPP-3 injection systems were switched to injection complex in summer 2016. The resulting layout of BINP colliders with injection complex is shown on Fig. 1

INJECTION COMPLEX

Injection complex is linear accelerator based e+/e- beams source with damping ring (see Fig. 2). It consists of electron gun, bunchers, 270 MeV electron linac, conversion system, 510 MeV positron linac, injection channels and dumping ring. Key designed parameters of VEPP-5 Injection Com-plex are presented in Table 1.

Table 1: VEPP-5 Injection Complex Design Parameters

parameter	value
Max. Beam Energy	510 MeV
Max. number of e- or e+ per bunch	$2 \cdot 10^{10}$
Energy spread in the bunch	0.07%
Longitudinal bunch sigma	4 mm
Horizontal emittance	0.023 mm mrad
Vertical emittance	0.005 mm mrad
beam transfers rate	1 Hz

Linear Accelerator

Linear accelerator is S-band and consists of four modules. Each module includes SLAC 5045 klystron, SLED-type [5] power compressor and 3 or 4 accelerating structures. Both linacs include 14 accelerating structures [6], which are round disk-loaded waveguide (see Fig. 3). The main design parameters of linear accelerators is presented in Table 2.

Table 2: Injection Complex Linear accelerators design parameters

parameter	value
Max. Beam Energy	280, 500 MeV
RF frequency	2855.5 MHz
Max. number of e- in beam	10^{11}
Max. number of e+ in beam	$6.3 \cdot 10^9$
Energy spread e+, e-	3%, 1%
repetition rate	50 Hz

Conversion System

In order to produce positrons we accelerate electron beam to 270 MeV and send it to tantalum conversion target.

* F.A.Emanov@inp.nsk.su

ISBN 978-3-95450-181-6

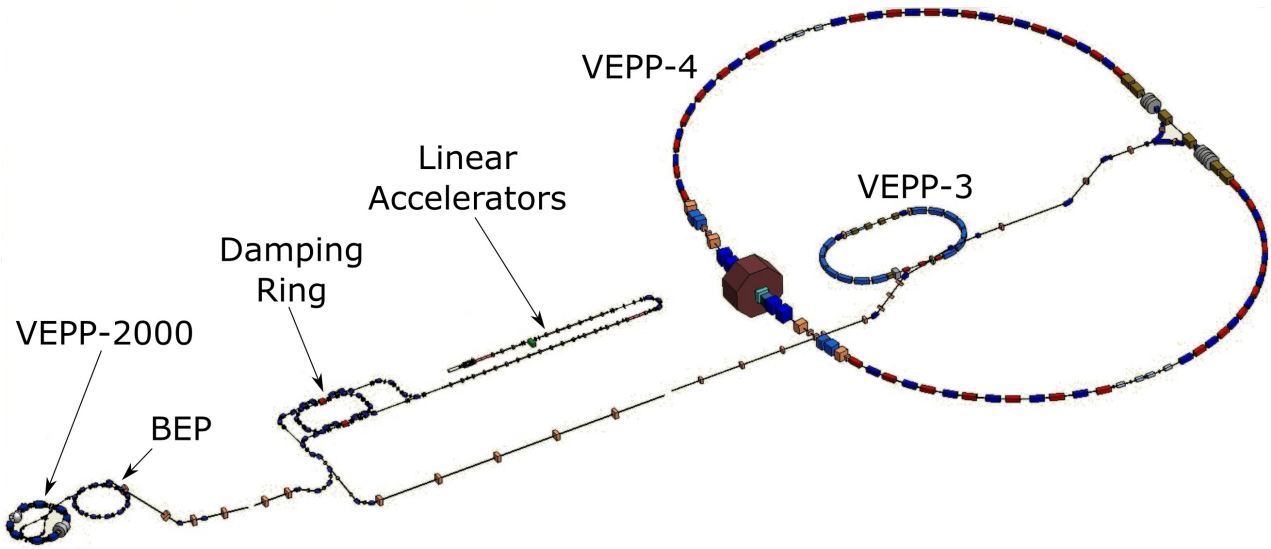

Figure 1: Injection complex and colliders.

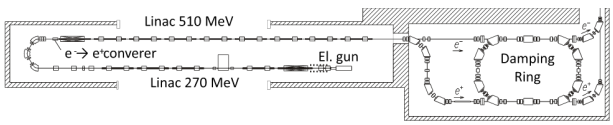

Figure 2: Layout of injection complex.

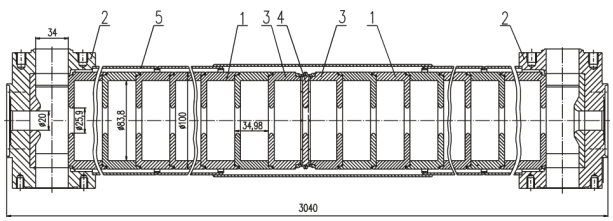

Figure 3: Linac RF structure. 1 regular cell, 2 wave type transformer, 3 junction cell, 4 junction diaphragm, 5 cooling circuit.

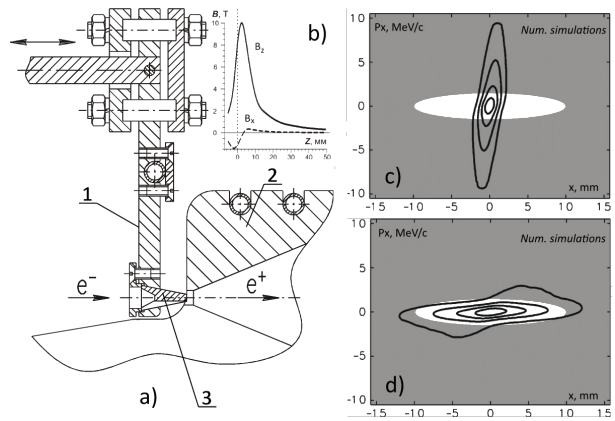

Figure 4: VEPP-5 Conversion system (e focusing not shown). a) 1 movable target holder, 2 magnet flux concentrator, 2 target; b) magnetic measurements; c) positron beam phase portrait after the target (inacceptable linac area is in grey); d) positron beam phase portrait after the flux concentrator.

Then secondary particles pass to flux concentrator (matching device), which is pulsed magnet with 10 T at maximum "axial" magnetic field (see Fig. 4). We are running flux concentrator at about 7.3 T since increased field just slightly increases number of collected positrons [7] and significantly decreases the device lifetime. Main operating parameters of the flux concentrator are presented in Table 3.

Damping Ring

Injection complex damping ring [1, 8] (see Fig. 5) was designed to inject beams into S-band linear accelerator, accordingly designed longitudinal bunch sigma is 4 mm. Hence damping ring RF frequency was selected to be 700 MHz (frequency ratio is 64). Klystron 100 kWt was used in the damping ring RF system as power amplifier. It was possible to achieve 400 kV resonator voltage being limited to 230 kV due to possible damages to klystron or waveguide. The last klystron failed in 2016 and 1 kWt semiconductor amplifier had been used for a few months. We are now switching to 20 kWt semiconductor amplifier, so 230 kV resonator voltage will be achievable. Since current beam users do not require short beams it is possible to increase injection complex productivity by exchanging 700MHz to 11.94 MHz (RF ratio is 1). This upgrade is under consideration now.

One turn injection with pre-kick of a stored beam is used in a damping ring. Injection system consists of four kickers (see Fig. 5) and their high voltage generators [10]. Designed kickers repetition rate is 50 Hz and it is currently limited to 12.5 Hz due to issue of loads cooling.

Key designed parameters of damping ring are shown in table 4. Electron-optical model of the damping ring was calibrated during initial commissioning [9]. Then orbit was

ISBN 978-3-95450-181-6

Table 3: Injection Complex Conversion System parameters

parameter	value
Max. magnetic field	10 T
Common current on the cone surface	120 kA
Max. voltage of the capacitor	1.2 kV
Pulse energy	90 J
Pulse duration	26 mks
Repetition frequency	50 Hz
Max. average power	4 kW

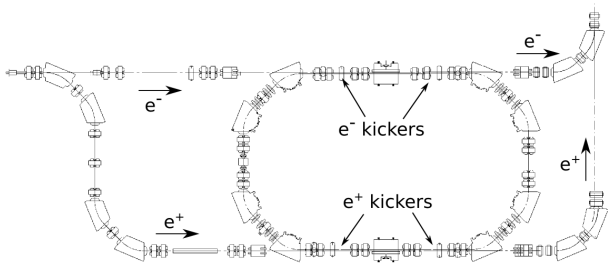

Figure 5: Damping ring layout.

corrected in order to increase available aperture [3].

Table 4: Damping Ring Designed Parameters

parameter	value
Max. energy	510 MeV
Perimeter	27.4011 m
RF ratio	64
RF frequency	700 MHz
Max. beam current	35 mA
damping times h,v,l	11.3, 17.5, 11.9 ms
Energy spread in the bunch	0.07%
Longitudinal bunch sigma	4 mm
Horizontal emittance	0.023 mm mrad
Vertical emittance	0.005 mm mrad

K-500 Beam Transfer Line

K-500 beam transfer line was turned into operation at BINP at the end of 2015. It includes two beamlines: line about 160 m to VEPP-3 and another one about 250m to VEPP-2000. Each of beamlines consists of three main sections: descent from damping ring to K-500 tunnel, regular FODO structure in the tunnel and ramp to corresponding facility. K-500 designed energy is 510 MeV. Electron beams are routinely transferred to VEPP-3 and BEP with transfer coefficient up to 70%. Positrons were transferred only to BEP.

K-500 magnets and power supplies limit minimal switching time of particles or direction to about 30 s and time between beam transfers is limited to about 1 s.

Beam Users Requirements

There are two beam users now: VEPP-2000 and VEPP-3/4. It is required to load $4 \cdot 10^{11}$ electrons or positrons to VEPP-3. VEPP-3 acceleration and polarity change time is 7 minutes, then other particles need to be loaded. Beam loading is followed by the experiment time from 40 minutes to a few hours. Beam for VEPP-2000 is to be injected to BEP. 10^{11} electrons and positrons are required to be injected in VEPP-2000 as a full load. Since there are transfer losses it is required to pass twice more particles to BEP. In order to avoid very high beam currents in BEP it is going to be done in 8 injections to VEPP-2000. BEP uses 30 s to accelerate, transfer particles and change polarity. After initial load beam charge should not be reduced more than 10%. Since expected lifetime is about 500 s it is required to reload beams with 10^{10} electron and positrons in about 50 s. Since BEP and K-500 polarity change time is about 30 s it is required to refill each beam in about 30s.

Control System Changes

In order to support joint operation with colliders the following steps are made:

- Common synchronization system was deployed in order to synchronize beam transfers. Reference frequency and "transfer solution" signals are encoded and transmitted over optical cable from injection complex site to collider site. Returned signal used to implement cable thermal drift compensation. In order to synchronize transfer accepting machine shift RF frequency to meet designated ratio with ramping ring.
- Machine mode control services and GUI applications was implemented as centralized tool to save and control injection complex state and related information.
- Basic semi-hardware automatic tools and procedures implemented for beam storage and transfer.
- Injection complex servers and network infrastructure are preparing to provide high availability.

High-level services and tools are implemented using Python, PyQt, CXv4 [11] control system framework and PostgreSQL databases. The instruments described above allow us to run injection-extraction cycle automatically while we need to manually switch beam user on particles type. This operation mode is acceptable to start operation and accumulate operation data for implementation of full set of automatic procedures.

OPERATION EXPERIENCE

Since VEPP-2000 facility requires to refill each beam every 30 seconds injection complex has to switch between particles much faster in order to have a time for beam storage. An ideal solution is to create electron beam at the same point where positrons are produced. Then both beams will be accelerated in the same fields and almost nothing is to be done to switch between particles. In fact 270 MeV electron beam bypasses the conversion target and hence can

ISBN 978-3-95450-181-6

not be guided by the same fields as a positron beam. In order to reduce time to switch between particles we need to consistently avoid changing modes of "slow" elements and make equal energy for both beams at linac exit. There are three ways to reduce electron beam energy: to shift accelerating field phase in positron linac, to reduce accelerating field amplitude, and to under fill accelerating structures by starting RF earlier for some linac module. The first way leads to increasing beam energy spread and hence decreasing captured beam charge in the damping ring. We consider this way as unacceptable. The second approach leads to average power difference for electron and positron modes. Hence accelerating structures thermal conditions may be different for electron and positron modes. The last approach is the best but more complicated to implement with injection complex control system. According to our tests both acceptable approaches is good for linac shots repetition rates up to 12.5 Hz. For 25 Hz repetition rate average power difference leads to increasing of mode switching time. Since repetition rate is limited to 12.5 Hz we are reducing accelerating field now to make electron beam energy equal to positron beam energy.

It was not possible to transport electron and positron beams through linacs and inject to damping ring with the same magnetic system setting. In order to reduce particles switching time we achieved electron and positron modes which differs only on fast enough linac quadrupole magnets and linac and damping ring magnetic correctors. This modes was made with energy 395 Mev. Switching between modes can be done within 10 seconds by loading required mode.

The following main parameters were achieved:

- Beam energy is about 395 MeV for electrons and positrons.
- linac electron production rate is $3 \cdot 10^{10}$/shot.
- Linac positron production rate is $6.3 \cdot 10^{9}$/shot.
- Electron beam storage rate is 10^{10}/shot.
- Positron beam storage rate is $2.5 \cdot 10^{8}/s$ at 12.5 Hz repetition rate.
- Transfer coefficient is up to 70% in both directions with 50% typical value.

Current peak production rates are about 10 times greater then former BINP colliders sources. It is enough to start feeding colliders with injection complex but it is steel required to increase positron productivity in order to support high VEPP-2000 luminosity.

CHARGE PRODUCTIVITY

Positron refill required to be done in 30 s and about 10 s injection complex is switching from electron storage mode. Hence there are 20 s to store 10^{10} positrons to support VEPP-2000 luminosity. Therefore required positron storage rate at least 5^{8}/s not taking to account beam transfer losses. Then positron storage rate should be grater than 10^{9}/s.

According to our calculations most of positrons are lost during injection to damping ring due to high positron beam energy spread. In order to reduce energy spread we can maximize linac energy or install a debucher in positron injection channel [7]. There are some extra injection losses due to linac single bunch mode is not implemented and hence linac beam is longer than damping ring RF bucket. Since current beam users do not require short beams it was proposed to change 700 MHz cavity to 10.94 MHz one, which allow to accept much longer beam from linac. In that case implementation of linac single bunch mode is not required. Available positron productivity increasing ways with estimated maximum gains is shown in table 4. According to estimations it is possible to achieve positron storage rate about 10^{9} with already planned upgrades and about $4 \cdot 10^{9}$ with all the considered ways.

Table 5: Positron Productivity Increasing Ways

Action	Gain
Switch to 10.91 MHz RF station	2
Increase gun pulse duration	2
Increase operating energy to maximum	1.5
Increase repetition rate	1.5-2
Implement linac single bunch mode	2
Install debuncher	1.5

CONCLUSION

Injection complex achieved acceptable performance for begining of operation and successfully transported beams to BEP and VEPP-3. Charge productivity and operation stability improvement approaches is under consideration now.

REFERENCES

[1] "Physical project VEPP-5," BINP SB RAS, 1995.

[2] Yu. Shatunov et al., "Project of a New ElectronPositron Collider VEPP-2000," EPAC'2000, Vienna, Austria, p.439

[3] P. Logatchev et al., "Status of Injection Complex VEPP-5", Proceedings of RuPAC2014, Obninsk, Kaluga Region, Russia, p. 11-13, TUY02

[4] D. Shwartz et al., "Booster of Electrons and Positrons (BEP) Upgrade to 1 GeV", IPAC'2014, Dresden, Germany, p. 102.

[5] Z.D. Farkas et al., "SLED: Method of Doubling SLACs Energy," HEACC74, p 597.

[6] V.V. Podlevskih, "Accelerating structure and RF load for VEPP-5 injection complex," Dissertation, Novosibirsk, 2003

[7] K.V. Astrelina et al., "Production of intence positron beams at vepp-5 injection complex," JETP 2008, vol. 106, issue 1, pp 77-93.

[8] V.V. Anashin et al., "Damping Ring for VEPP-5 Injection Complex," BINP Preprint, Novosibirsk, 1992, no 9244, http://15.inp.nsk.su/injector/docs/DampingRing.pdf

ISBN 978-3-95450-181-6

[9] A.V. Petrenko, "Calibrating of the electron-optical model of the VEPP-5 damping ring," Instruments and Experimental Techniques, 2011, Vol.54, issue 1, pp 8-15.

[10] A.I.Butakov, B.I. Grishanov, F.V. Podgorny, "Injection system to damping ring of an electron-positron injection complex VEPP-5," Proceedings of RuPAC XIX, Dubna 2004.

[11] D. Bolkhovityanov, P.B. Cheblakov, F.A. Emanov, "CXv4, a Modular Control System," ICALEPCS2015, Melbourne, Australia, WEPGF093.

ISBN 978-3-95450-181-6

SOME PROBLEMS OF THE BEAM EXTRACTION FROM CIRCULAR ACCELERATORS

Serge N. Andrianov*, Nikolai Edamenko,
St. Petersburg State University, 7/9 Universitetskaya nab., St. Petersburg, 199034 Russia

Abstract

In this article some problems of optimizing the output beam of particles from the circular accelerator are discussed. In particular, we consider some problems of matching the booster, Nuclotron and collider in the NICA project. The main attention is paid to matching of the extraction beam systems. The proposed approach allows providing qualitative and quantitative analysis of the impact of various factors of the corresponding control systems.

INTRODUCTION

The problems of long time evolution of particles in cyclic accelerators arise not only in the implementation of the extraction of the particles. As an example, we should mention the problem of injection of particles into the accelerator, and also the problem of long time evolution (over millions of revolutions) of the particle beam in the storage rings and colliders. Let us look at the main types of problems that arise in similar types of tasks:

• construction of closed orbits in ideal and non-ideal machines;
• the problem of stability of the closed orbits in the framework of the linear and non-linear approximation of the control fields including possible deviations from the ideal parameters;
• problems of the beam injection and extraction from circular accelerators

It should be noted that when modeling of the long-time evolution (more than one billions revolutions) it is necessary to perform huge number of steps of integration and guarantee preserving both the energy of the particles and property of the symplecticity of corresponding mapping.

It is known that knowledge is information about control elements allows you to find the stable fixed points and areas (islands) with steady evolution in its neighborhoods. Knowing the location of these areas and their characteristics allows managing (using additional controls) during of extraction or injection processes using the information about topology of the corresponding closed orbits. Controlling by the corresponding classes of stable orbits can be carried out regardless. In particular, it allows not to use septum-magnets, which are traditionally used for extraction of the beam (see, eg, [**?**]). Note that the trend of development of modern circular accelerators leads to the need to include among the objects of control nonlinear control field with increasingly nonlinearity. The transition to an essentially nonlinear dynamics leads to the need for new and effective methods of mathematical modeling of long-term evolution of the beam in the accelerator channel. Increasing order nonlinear effects on the one hand allows you to "improve the quality of the beam" but to a significant complication of corresponding mathematical models and as a consequence corresponding algorithms and programs.

The purpose of this paper is to present the basic principles that not only form the basis of the proposed approach but and realized as special software and demonstrated effectiveness for a number of tasks [2]. The problems of extraction and injection of beam particles in cyclic accelerators included in the NICA complex, should be consider accurately enough, due to the peculiarity of the complex [3].

A study of the dynamic system in this case is carried out in terms of the map $\mathcal{M}_k$, generated by the control elements on the k-th step iteration $\mathbf{X}_{k+1} = \mathcal{M}_k \circ \mathbf{X}_k$, where $\mathbf{X}_k$ is the phase vector on k-th step of the iterative process, where $\mathbf{X}_k$ is phase vector on k-th step of the iterative process wich generated by the periodic dynamic system, where $\mathcal{M}_k$ is an operator of the evolution of a dynamical system corresponding to k-th period.

If $\mathcal{M}_k = \mathcal{M}$, then for any k we can talk about periodic mapping. In this case, the full map for k-th turns (for periodical channel) one can write

$$\mathcal{M}(s + kL|s) = \underbrace{\mathcal{M} \circ \ldots \circ \mathcal{M}}_{k \text{ times}} = \mathcal{M}^k,$$

where $\mathcal{M} = \mathcal{M}(s + L|s)$.

Before constructing the computational process for evolution of the beam, we should not only carefully examine the properties of the map $\mathcal{M}$, but also to ensure the fulfillment of these conditions in all stages of the computational experiment. Here we have in mind the preservation of the properties of symplecticity for the map $\mathcal{M}$ throughout interval solutions of the problem In particular, namely similar approach is implemented in a rather numerous modern works on the generation of symplectic difference schemes or integrators for Hamiltonian systems. In a number of previous works (see for example [4]) we considered the method of symplectification of block matrices included into the matrix solutions of Hamiltonian dynamical equations. Similar approach allows not only use unified mathematical tools, but create efficient algorithms and derive interpretable results.

* s.andrianov@spbu.ru

ISBN 978-3-95450-181-6

MATHEMATICAL MODELS

The Main Types of the Tasks for Long-Term Evolution

Let us point out the following (related) types of beams physics problems arising in the study of the evolution of the long beam in cyclic accelerators:

1) search periodic orbits of the beam control systems and studying of their stability;
2) study of resonances (especially nonlinear): search resonance regions, the separatrices construction , the determination of their configuration, and so on;
3) the construction of the dynamic aperture, its maximization by introducing non-linear correctors;
4) the study of the conditions of formation of the beam halo and its characteristics.

These and other tasks require the creation of efficient methods, algorithms and computer codes. First of all we should pick out several levels of increase of efficiency of computer modeling (namely computer modeling as symbolic and numerical, is the main means of solving the problems stated above). Methods of the *first level* are based on the use of effective (from computational point of view) mathematical methods. Methods of the *second level* are based on algorithms that efficiently implement the selected mathematical methods. From the point of view of the used matrix formalism, it is primarily the various accelerators" matrix algebra. We also should use parallel algorithms and computation distribution, intended for realization on high-performance computers. The *third-level methods* are based on the use of various types of data and knowledge bases, allowing the use of the knowledge gained in the study of similar systems. Of great importance at this stage of play the methods and means of artificial intelligence, such as computer algebra, graph theory, computational intelligence and so on. It should be noted that this ideology should be included in the computer simulation circuit at an early stage selection of mathematical methods and appropriate software.

The Equations of Motion

Before derivation of the equations it is necessary to do some number of assumptions. In particular, in this article we will suggest: 1) absence of any interaction between the particles in the beam;
2) for external fields we limit ourselves to magnetic fields and and will consider the adiabatic nature of the magnetic field changes with time;
3) the development of resonance occurs in the median plane, as evidenced by preliminary calculation non-linear equations taking into account experimental data along the reference trajectory.

The computational experiments demonstrated that the initial transverse phase portraits circulating beam in the horizontal plane x, x' and the vertical plane y, y' are images that differ little from the ellipse. But in the process resonance the phase portrait of the beam is in the horizontal plane x, x' radically deformed, although in the vertical plane the deformation is negligible. Thus, the resonant members practically no effect on the phase portrait of the beam in the plane y, y'. This is confirmed by calculations carried out in view of the experimental data. All our assumptions correspond to the real processes taking place at resonant multi-turn (slow) extraction, and thus provide sufficient adequacy of the approximating model under consideration. Given the above assumptions the equations of motion of particles in a magnetic field up to terms of the second order have the form

$$x'' + (1-n)h^2 x = (2n-1-\beta)h^3 x^2 + h' x x' + \frac{h}{2}(x')^2 + \frac{1}{2}(h'' - nh^3 + 2\beta h^3)y^2 + h' y y' - \frac{1}{2}h(y')^2 + \mathcal{O}(3), \quad (1)$$

$$y'' + nh^2 y = 2(\beta - n)h^3 xy + h' x y' - h' x' y + h x' y' + \mathcal{O}(3), \quad (2)$$

where $' = d/ds$, s is the independent variable which measured along the reference orbit, $\mathcal{O}(3)$ are members of the third and higher orders on the variables x, x', y, y'. Here we are considering the monoenergetic beam and that the equilibrium trajectory is a reference orbit. In equations (1) and (2) used standard for this class notation tasks.

Note 1. The curvature of the base curve (equilibrium trajectory in our case) is h and the maximum value of x, defined by the position of the septum magnet. We should note that In our case the members of the third order of smallness give about a few percent compared to the second order.

The Investigation of Motion Equations

Preliminary there was carried out computing experiment using for several hundreds of turns in two planes (that ensures a reasonable global error under using conventional numerical methods, such as Runge-Kutta methods). The results showed that resonance phenomena develop mainly in the plane $\{x, x'\}$, so henceforth consider the equation for beam evolution only in this plane:

$$x'' + (1-n)h^2 x = (2n-1-\beta)h^3 x^2 + h' x x' + \frac{h}{2}(x')^2 + \mathcal{O}.$$

We should note that the terms containing x' no effect on development of resonance, and only lead to slight deformation of the beam phase portrait during slow extraction (in particular, there is a certain rotation around a center point). Therefore, these members may also be discarded. The complete equations in the plane x, x' can be written in the matrix form

$$\mathbf{X}(s) = \mathbb{M}^2(s|s_0)\mathbf{X}_0^2 = \mathbb{M}^{11}\mathbf{X}_0 + \mathbb{M}^{12}(s|s_0)\mathbf{X}_0^{[2]}, \quad (3)$$

where $\mathbb{M}^2(s|s_0)$ is the full matrix of the evolution of nonlinearities up to second order, $\mathbb{M}^{11}$ is a matriciant of lin-

ISBN 978-3-95450-181-6

earized equation, $\mathbb{M}^{12}$ is the matrix corresponding to nonlinear second-order fields. Adiabatic changes of coefficients ν^2 and α_1 allow replacing them by piecewise constant functions. Then on the entire interval of permanence for the equation (3) we can obtain a solution manually or by using one of the systems computer algebra codes (in this paper were used Reduce system codes, Maple V and Wolfram Mathematica). In the calculations we also used another (smoothed) representation of the motion equations. The results showed that a smooth approximation is a very workable model, while the computing speed many times more than the speed of calculations with using other models. We note that usage of other models for computation of the full cycle is almost impossible due to a time-consuming and the unacceptable exactness of the numerical calculations [2]. Thus, the desired solution can be represented in the form

$$\mathbb{M}^{11} = \begin{pmatrix} C_1 & S_1/\nu \\ -\nu S_1 & C_1 \end{pmatrix},$$

$$\mathbb{M}^{12} = \frac{\alpha_1}{6\nu^4}\begin{pmatrix} \varkappa_{11}^1 & \varkappa_{12}^1 & \varkappa_{13}^1 \\ \varkappa_{21}^1 & \varkappa_{22}^1 & \varkappa_{23}^1 \end{pmatrix} + \frac{\alpha_2}{\nu_1}\begin{pmatrix} \varkappa_{11}^2 & \varkappa_{12}^2 & \varkappa_{13}^2 \\ \varkappa_{21}^2 & \varkappa_{22}^2 & \varkappa_{23}^2 \end{pmatrix}.$$

Here, the matrices $\mathbb{M}^{11}$ and $\mathbb{M}^{12}$ can becalculated in , in particular, symbolical form (see, [4]) that allows you to not only significantly reduce the computing time, but also to realise study of the effect of control parameters on the beam dynamics. We should note that there occur resonance phenomena, however it can be shown that the elements of the matrix $\mathbb{M}^{12}$ have a finite value on the resonance, but there appear secular terms. In a periodic structure of cyclic accelerators we should for each turn to repeat calculations very large number of times (in particular more than 10^9 times). But the procedure of exponentiation allows (given the structure of the accelerator) significantly reduce the time required of computing. The matrix $\mathbb{M}$ is an upper triangular block-matrix consisting of $\mathbb{M}^{11}$, $\mathbb{M}^{12}$ and $\mathbb{M}^{22} = \mathbb{M}^{11[2]}$, and is responsible for translating the beam for a single turn. Since $10^9 = ((10)^3)^3$ then the number of required operations is significantly reduced. We note to further speed up the computation we can calculated the matrix $\mathbb{M}^(3)$ in advance in a symbolical form, to store in a special database and then use on demand for numerical computation of the corresponding matrices.

According to the [3] the optical structure of the booster has FODO periodicity and consists of four superperiods, each of which consists of 5 regular periods and a interval which does not contain the dipole magnets. Regular period includes quadrupole lenses, two dipole magnets and four free period, designed to accommodate multipole correctors, collimators and special diagnostic equipment. The beam injection system from the Nuclotron into the accelerator complex consists of two parts. The first part provides output of the beam from the booster into the matching channel and then the beam is injected into the Nuclotron. The matching channel (represented in Fig. 1, see [5]), and performs the beam focus using six quadrupoles. The turns in the horizontal and vertical directions are realized using dipole magnets. The channel also has elements of exercising "stripping" beam and separators for spurious charge states.

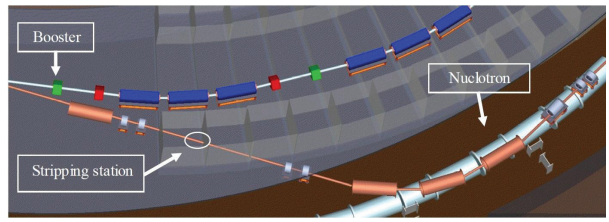

Figure 1: Injection system layout and beam orbits and envelopes: 1 - injected beam, 2 - bumped one, 3 - circulated beam after first turn injection, 4 - after accumulation; BM $1 \div 3$ - magnets for the bump formation, SM - injection septum magnet.

The second variant of the beam output (slow extraction) used for medical-biological and applied research on the beams from booster. This problem also makes special demands on the beam. In this case the operating point of the booster shifts into the area of nonlinear resonance. It should be noted that this process takes place over a large number of turns. Thus, both types of output beam makes it necessary to ensure the implementation of restrictions of the beam at the stage of its evolution from booster. We note that similar restrictions also lead to the need for detailed investigation of the formation of the beam in the case of multiturn evolution.

CONCLUSION

In this study we conducted a testing of different regimes of beam extraction from the particle accelerator. Results of the study demonstrated high efficiency from a computational point of view and the correctness of the results.

REFERENCES

[1] A.Franchi, M. Giovannozzi Novel technique for injecting and extracting beams in a circular hadron accelerator without using septum magnets. Physical Review Special Topics - Accelerators and Beams 18(7),July 2015. DOI: 10.1103/PhysRevSTAB.18.074001.

[2] D. Zyuzin, R. Maier, Yu. Senichev, A. Ivanov, S. Andrianov, M. Berz, Comparison of different numerical modelling methods for beam dynamics in electrostatic rings Proceedings of IPAC2012, New Orleans, Louisiana, USA TUPPC071 P. 1335–1337

[3] Design and Construction of Nuclotron-based Ion Collider fAcility (NICA). Conceptual Design Report. Dubna 2008. http://nica.jinr.ru/files/NICA-CDR.pdf

[4] Andrianov S.N. Dynamic modeling of control systems particle beams. SPbGU, SPb P. 373. 2004 (in Russian).

[5] A.V.Tuzikov, V.A.Mikhailov The transport channel of the Booster-Nuclotron NICA project. Physics of Elementary Particles and Atomic Nuclei, Letters. 2010. Vol. 7,N 7 (163). P. 781-787 (in Russian).

ISBN 978-3-95450-181-6

ANALYSIS OF THE PARTICLE DYNAMICS STABILITY IN THE PENNING-MALMBERG-SURKO TRAP

I.N. Meshkov, JINR, Dubna, Moscow Region; Saint Petersburg State University, Saint Petersburg
M.K. Eseev, NAFU, Arkhangelsk
A.D. Ovsyannikov*, D.A. Ovsyannikov, V.A. Ponomarev,
Saint Petersburg State University, Saint Petersburg

Abstract

Problem of stability of charged particle dynamics in the Penning-Malmberg-Surko trap is considered. It is shown that, magnetron motion is unstable for sufficiently small value of parameter a (which is the amplitude related parameter of the Rotating Wall (RW) electric dipole field). This contradicts the conclusion of the article [1] that there is a possibility of the compression of magnetron motions in the case of $\mid a \mid \rightarrow 0$. So it may indicate that the simplified model of the dynamics used by the author of the article is not accurately enough to describe the dynamics of the original system.

INTRODUCTION

Present report refers to the problem of the study of charged particle dynamics in the Penning-Malmberg-Surko trap. Various models of particle dynamics describing the magnetron and cyclotron motions are considered. The problems of the stability of the magnetron motion are investigated. In articles [1,2] the compression and expansion rates of the magnetron radius are discussed. Compression rates have been presented. The particle does not leave the area of the rotating field, and the bunch is compressed. These results are questionable.

PROBLEM STATEMENT

We consider a charged particle in the field of the potential

$$\Phi(z) = \frac{m}{q} \cdot \frac{\omega_z^2}{2} \cdot (z^2 - \frac{r^2}{2}) + \\ + \frac{m}{q} a \cdot z \cdot r \cdot cos(\theta + \omega_r t), \quad (1)$$

and homogeneous longitudinal magnetic field $\vec{B} = \vec{e_z} B$. Here m and q are the mass and the charge of the particle, ω_z is the frequency of the particle longitudinal oscillations in the axially symmetric electric field of the trap electrodes, a and ω_r is amplitude related parameter and the frequency of the Rotating Wall (RW) electric dipole field asymmetric in the z-direction, z and r are the axial and radial coordinates with the axis coinciding with symmetry axis of the trap electrodes.

* a.ovsyannikov@spbu.ru

The magnitude of the parameter a can be estimated as

$$a = \frac{q}{m} \cdot \frac{U_r}{2RL}, \quad (2)$$

where U_r is the maximum of the potential difference between the segmented electrode plates, $2L$ is the length of the dipole RW field and R is the curvature radius of the cylindrical plates.

The charged particle motion in these fields is described by the following system of equations:

$$\ddot{x} = \frac{\omega_z^2}{2} \cdot x - a \cdot z \cdot cos(\omega_r t) + \Omega_c \dot{y} - k\dot{x}, \quad (3)$$

$$\ddot{y} = \frac{\omega_z^2}{2} \cdot y + a \cdot z \cdot sin(\omega_r t) - \Omega_c \dot{x} - k\dot{y}, \quad (4)$$

$$\ddot{z} = -\omega_z^2 \cdot z - k\dot{z} - a(x \cdot cos(\omega_r t) - y \cdot sin(\omega_r t)). \quad (5)$$

Here $\Omega_c = qB/m$ is the particle cyclotron frequency, the parameter k presents the friction force related to the particle scattering by the trap buffer gas molecules.

Further, we transform the system (3-5) to the complex form. Multiplying the equation (4) by imaginary unit i and adding it with equation (3) we come to the equation for the complex function

$$\xi(t) = x + iy, \quad (6)$$

$$\ddot{\xi} + i\Omega_c \dot{\xi} + k\dot{\xi} - \frac{\omega_z^2}{2} \cdot \xi = -a \cdot z \exp(-i\omega_r t). \quad (7)$$

The equation (7) together with the equation (5) describes the particle motion in the trap.

FREE PARTICLE MOTION IN THE TRAP

The *general solution of the homogeneous differential equation* in (7) is the following

$$\xi(t) = A_1 \cdot \exp(i\omega_+ t) + A_2 \cdot exp(i\omega_- t), \quad (8)$$

where

$$\omega_\pm = -\frac{\Omega_c - ik}{2} \mp \frac{1}{2}\sqrt{(\Omega_c - ik)^2 - 2\omega_z^2}. \quad (9)$$

The constants A_1, A_2 should be found using the initial conditions.

ISBN 978-3-95450-181-6

At the typical values of the trap parameters we have the relations between the frequencies:

$$\mid \omega_+ \mid \sim \Omega_c \gg \omega_z \gg \mid \omega_- \mid \sim \omega_m \equiv \omega_z^2/(2\Omega_c) \gg k. \quad (10)$$

Here ω_m is so called *magnetron frequency*: the frequency of the particle rotation in the crossed fields of the trap – longitudinal magnetic field B and radial component of the electric field (1) at $a = 0$. The relations (10) allow us to find the approximate values of the frequencies ω_- (lower sign in (9)) and ω_+ (upper sign in (9)).

Rewrite the equation (9) as following:

$$\omega_\mp = -\frac{\Omega_c - ik}{2} \pm \frac{\Omega_c}{2}\sqrt{1 + (-\frac{2ik}{\omega_c} - \frac{k^2}{\Omega_c^2} - 2\frac{\omega_z^2}{\Omega_c^2})}. \quad (11)$$

One can show that

$$\omega_+ \approx -(1-\alpha)\Omega_c + i(1+\alpha)k \approx -\Omega_c + ik, \quad (12)$$

$$\omega_- \approx -\alpha\Omega_c - i\alpha k \approx -\omega_m - i\frac{k\omega_m}{\Omega_c}, \quad (13)$$

$$\alpha = \frac{\omega_z^2}{2\Omega_c^2}.$$

Then the solution (8) can be presented as following:

$$\xi(t) = A_1 \exp(-i\Omega_c t - kt) + A_2 \exp(-i\omega_m t + \quad (14)$$
$$+(k\omega_m/\Omega_c)t),$$
$$A_1 \approx 2\omega_m\xi_0 - \frac{\dot{\xi}_0}{\Omega_c}, \quad A_2 \approx \xi_0 - \frac{\dot{\xi}_0}{\Omega_c}.$$

The first term in (14) describes a free *cyclotron rotation* of the particle in the field $\vec{B}$ damped with the decrement k. The second term describes the particle rotation around the trap axis with the angular frequency ω_m, i.e. the *magnetron rotation*. Its amplitude increases in time with the increment $k\omega_m/\Omega_c$ the magnetron orbit expansion related to the particle scattering by the buffer gas molecules (the parameter k).

PARTICLE MOTION STABILITY IN THE TRAP WITH RW DIPOLE FIELD

In case of time-dependent linear differential system to investigate a stability of system (3-5) one should consider the set of characteristic indices of the system (which are the same in stationary case as real parts of characteristic numbers of the system with $a = 0$). Obviously, if at least one of characteristic indices of the system is positive then it is unstable in the Lyapunov sense.

In view of the stability of the characteristic indices of linear system (3-5) with respect to small perturbations [3], the system (3-5) has a positive characteristic index for sufficiently small $a \neq 0$ because it has the characteristic number with a positive real part for $a = 0$ (as it was shown above) and should be unstable in the Lyapunov sense at least for

$$\mid a \mid < k\frac{\omega_m\omega_z}{\Omega_c\sqrt{2}}. \quad (15)$$

It should be noted that the stability of the characteristic indices of the system (3-5) means their continuity respectively to a parameter a.

DECOUPLING THE MAGNETRON AND CYCLOTRON MOTIONS

The authors [1,2] perform the change of variables in the equations (3-5) defined by the equality

$$\boldsymbol{V}^\pm = \frac{dr}{dt} + \omega_\mp \hat{z} \times r, \quad (16)$$

where $\hat{\boldsymbol{z}} = \begin{pmatrix} 0 \\ 0 \\ 1 \end{pmatrix}$ is a unit vector, $\boldsymbol{r} = \begin{pmatrix} x \\ y \\ 0 \end{pmatrix}, \boldsymbol{V}^\pm = \begin{pmatrix} V_x^\pm \\ V_y^\pm \\ 0 \end{pmatrix}, \omega_\pm = \frac{1}{2}(\Omega_c \pm \sqrt{\Omega_c^2 - 2\omega_z^2})$.

Then, the equations (3-5) take the following form:

$$\dot{V_x^\pm} = \omega_\pm V_y^\pm - k\Big(V_x^\pm + \frac{\omega_\mp}{\omega_+ - \omega_-}(V_x^+ - V_x^-)\Big) - \quad (17)$$
$$-a \cdot z \cdot cos(\omega_r t),$$
$$\dot{V_y^\pm} = -\omega_\pm V_x^\pm - k\Big(V_y^\pm + \frac{\omega_\mp}{\omega_+ - \omega_-}(V_y^+ - V_y^-)\Big) - \quad (18)$$
$$-a \cdot z \cdot sin(\omega_r t),$$
$$\ddot{z} = -\omega_z^2 z - k\dot{z} - \frac{a}{\omega_+ - \omega_-}\Big[(V_y^- - V_y^+)cos(\omega_r t) - \quad (19)$$
$$-(V_x^- - V_x^+)sin(\omega_r t)\Big].$$

Transforming of the system (17-19) by introducing the complex variables

$$V_c^+ = V_x^+ + iV_y^+;$$
$$V_c^- = V_x^- + iV_y^-. \quad (20)$$

$$\dot{V_c^+} = -\Big(k\frac{\omega_+}{\omega_+ - \omega_-} + i\omega_+\Big)V_c^+ + k\frac{\omega_-}{\omega_+ - \omega_-}V_c^- - \quad (21)$$
$$-a \cdot z \cdot \exp(-i\omega_r t),$$
$$\dot{V_c^-} = -k\frac{\omega_+}{\omega_+ - \omega_-}V_c^+ + \Big(k\frac{\omega_-}{\omega_+ - \omega_-} - i\omega_-\Big)V_c^- - \quad (22)$$
$$-a \cdot z \cdot \exp(-i\omega_r t),$$
$$\frac{d^2}{dt^2}z = -\omega_z^2 z - k\frac{dz}{dt} - \frac{a}{\omega_+ - \omega_-} \times \quad (23)$$
$$\times Re\Big[i(V_c^+ - V_c^-)\exp(i\omega_r t)\Big].$$

The characteristic equation of system (21,22) for $a = 0$ has the form

ISBN 978-3-95450-181-6

$$\lambda^2 + (k + i(\omega_+ + \omega_-))\lambda - \omega_+\omega_- = 0. \quad (24)$$

Defining the roots $\lambda_{1,2} = i\omega_{1,2}$ via the "frequencies"$\omega_{1,2}$, we obtain

$$\omega_{1,2} = -\frac{(\omega_+ + \omega_-) - ik}{2} \pm \pm \frac{1}{2}\sqrt{((\omega_+ + \omega_-) - ik)^2 - 4\omega_+\omega_-} = = -\frac{\Omega_c - ik}{2} \pm \frac{1}{2}\sqrt{(\Omega_c - ik)^2 - 2\omega_z^2}. \quad (25)$$

Let us note that characteristic indices of the systems (3-4) and (21-22) for $a = 0$ are the same (do compare (11, 12, 13, 25)). Indeed $\omega_+ + \omega_- = \Omega_c$ and $\omega_+\omega_- = \omega_z^2/2$ so formulae (25) and (9) are the same. So it is obvious that the system (21-22) at $a = 0$ has characteristic root with a positive real part and thus is unstable $(Re(i\omega_1) > 0)$.

By the property of the stability of the characteristic indices the system (21-23) is unstable also at sufficiently small $a \neq 0$, at least for $\mid a \mid < k\frac{\omega_m\omega_z}{\Omega_c\sqrt{2}}$ (the condition (15)), i.e. similar to the system (3-5).

CONCLUSION

Given the stability of characteristic indices of the linear systems under consideration with respect to small perturbations, magnetron motion is unstable for sufficiently small $a \neq 0$ (the condition (15)). This contradicts the conclusions of the article [1] that there is a possibility of the compression of magnetron motions in the case of $\mid a \mid \to 0$ ($\mid a \mid \ll k\sqrt{\omega_z\Omega_c}$). The contradiction may indicate that the simplified model of the dynamics and the approach used by the author [1] of the article do not accurately describe the dynamics of the process, because it leads to qualitative discrepancies in the behavior of the original system and simplified system. And, as shown above, at least for $\mid a \mid < k\frac{\omega_m\omega_z}{\Omega_c\sqrt{2}}$ magnetron motion is unstable and the compression is impossible.

It is also doubtful that a positron bunch compression may occure when the rotating electric field is applied on the all length of the storage area (see eq.(1)). It was observed in the experiment [4] that good compression can be achieved as long as the axial extent of the RW electrode is less than half of the plasma length. We also observed [5] the inability of accumulation region in the case where the rotating electric field length coincides with the length of the storage region.

It should be noted that the existence of compression found in experiment can not be explained with the analysis presented in [1,2]. There is other explanation [6] of the rotating electric field effect on the charged particles accumulation in traps at large and small particle densities [5,6].

REFERENCES

[1] C.A. Isaac, Phys. Rev. A 87, 043415 (2013).

[2] D.P. van der Werf, C.A. Isaac, C.J. Baker, T. Mortensen, S. J. Kerrigan and M. Charlton, New Journal Phys. 14, 075022 (2012).

[3] N.A. Izobov, Lyapunov exponents and stability. Stability Oscillations and Optimization of Systems. Cambridge: Cambridge Scientific Publishers. 380 p. (2013).

[4] J.R. Danielson and C.M. Surko, Phys. Plasmas, 13, 055706 (2006).

[5] M.K. Eseev, A.G. Kobets, I.N. Meshkov, A.A. Sidorin, O.S. Orlov, JETP letter 102, 261 (2015)

[6] M.K. Eseev, I N. Meshkov, Phys. Usp. 59, 304 (2016)

ISBN 978-3-95450-181-6

RECENT EXPERIMENTS WITH HIGH ENERGY ELECTRON COOLER IN COSY

V. B. Reva, V.V. Parkhomchuk, BINP, Novosibirsk, Russia and Novosibirsk State University, Novosibirsk, Russia
M.I. Bryzgunov, BINP, Novosibirsk, Russia and FSBI "SSC RF ITEP" of NRC "Kurchatov Institute, Moscow, Russia
D.N. Skorobogatov, BINP, Novosibirsk, Russia
V. Kamerdzhiev, IKP FZJ, Jülich, Germany
I.N. Meshkov, JINR, Dubna, Russia

Abstract

The 2 MeV electron cooling system for COSY-Julich started operation in 2013 years. The cooling process was observed in the wide energy range of the electron beam from 100 keV to 1.256 MeV. Vertical, horizontal and longitudinal cooling was obtained at bunched and continuous proton beam. This report deals with electron cooling experiments at COSY with proton beam at energy 1.66 and 2.3 GeV. The proton beam was cooled at different regimes: RF on and off, barrier bucket RF, and cluster target on and off.

SETUP DESCRIPTION

The COSY cooler (see Table 1) may be used in experiments with polarized and unpolarized protons and deutrons with energies of up to 2880 MeV/u on the internal target or with extraction of the beam to the external target. In experiments with the internal target, the possibility of cooling the beam (i.e., of decreasing the spread of the particle momenta to suppress “warming effects”) is of great importance. Today, three cooling systems are already used in the COSY. Electron cooling to low electron energies (about 200 MeV) allows researchers to accumulate charged particles and raise the phase density of the beam prior to subsequent experiments. Stochastic cooling [1, 2] prevents the quality degradation of a beam interacting with a target at typical experimental energies. Unfortunately, stochastic cooling suffers from natural limitations, which hinder the operation of the synchrotron at a high intensity of the cooled beam and a small spread of the cooled particle momenta. Electron cooling at experimental energies can effectively prevent small angle scattering and ionization losses. Both factors are most probable when the energy of particles interacting with a material is high. When combined with stochastic cooling, electron cooling is expected to greatly enhance the luminosity in experiments with the internal target.

The schematic design of the high-voltage cooler is shown in Fig. 1. The design of the cooler and its main parameters are described in [3-5]. The electron beam is accelerated by an electrostatic generator that consists of 33 individual sections connected in series. Each section has two high-voltage power supplies with maximum voltage 30 kV and current 1 mA. The electron beam is generated in electron gun immersed into the longitudinal magnetic field. After that the electron beam is accelerated, moves in the transport line to the cooling section where it interacts with protons and deuterons of COSY storage ring. After interaction the electron beam returns to electrostatic generator where it is decelerated and absorbed in the collector.

Table 1: COSY Regime Parameters

Parametere	Value
Gamma transition	2.26/2.287
Proton numbers	10^8-10^9
Kinetic energy	1.66/2.3 GeV
Vacuum	10^{-9}-10^{-10} mbar
Qx	3.59-3.65
Qy	3.675-3.64
Slip-factor	-0.066/-0.1
Perimeter	183.5 m
Revolution frequency	1.524/1.564MHz
Electron energy	909/1265 kV
Electron current	0.5-0.8 A
Radius of electron beam in the cooling section	0.5 cm

EXPERIMENTS SETUP

The diagnostic of the proton beam was based on IPM (ionization profile monitor) and pickup of the stochastic cooling system. The proton current is measured by DCCT.

The transverse profiles of the beam were determined in real time with a profile monitor that measures the profiles of ions produced by electron beam ionization of residual gas. The momentum distribution was measured with pickup of the stochastic cooling system. The harmonic for Schotky noise detection was 1250.

The main parameters of COSY regime are listed in Table 1 for the regime with proton energy 1.66 and 2.3 GeV.

EXPERIMENTS WITH ENERGY 1.257 MEV

The most experiments in run 2014-2015 were carried out with electron energy 908 keV. The next step to high-voltage was done to energy 1.257 MeV. Before the cooling process the training of the high-voltage column was

ISBN 978-3-95450-181-6

done (see Fig. 2). During this process leakage current through SF_6 gas decreased from 20 uA to 9 uA. The black lines show the level of the leakage currents in the different moment of the time.

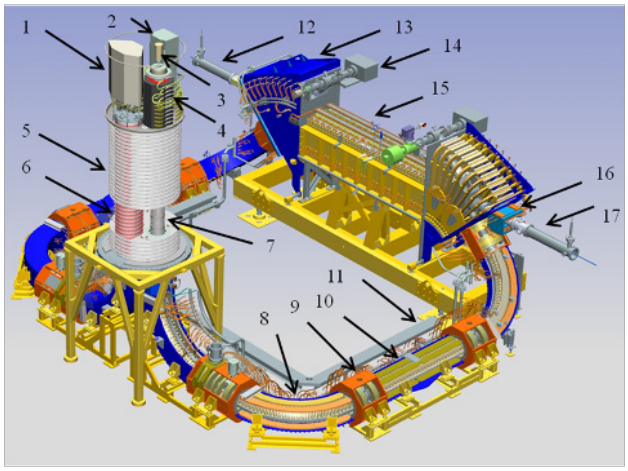

Figure 1: 3D design of 2 MeV COSY cooler. Collector PS is 1, gun and collector PS is 2, ion pumps are 3,14, collector is 4, HV section is 5, cascade transformer is 6, acceleration tube is 7, bend 90 is 8, straight section is 9-10, cable path is 11, proton beam in/out are 12,17, toroid 45 is 13, cooling section is 15.

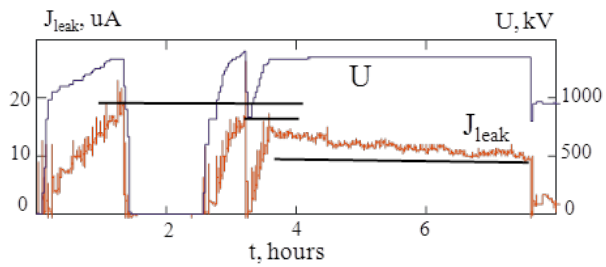

Figure 2: Training procedure of high voltage for 1.257 MeV.

After training the first electron beam with current 0.5 A was obtained. The electron energy was calculated initially from storage ring parameters as 1256.6 kV. The first the obvious shift in Schottky spectrum was observed induced by the electron cooling force. The spectrogram of this process from Schottky pickup is shown in Fig. 3 (left). The mismatch between the electron and ion velocities is large but the cooling force enough for changing revolution frequency of the proton beam. The proper value of the electron beam was found at 1259.5 kV by experimental way (see Fig.3, right). The duration of both spectrograms is about 570 s .

The Parkhomchuk' equation [6] can be rewritten in the form

$$\frac{\delta p_{//}}{p_0} = \gamma^2 \beta L_N \left(\frac{m_e c^2}{\delta E_e} \right)^2 r_e r_p n_e \tau c f_0 \Delta T$$

for large deviation between particle velocities. Here r_e, r_p are the classical radiuses of proton and electron, f_0 is the revolution frequency, ΔT is duration of the cooling, $m_e c^2$ is the rest energy of electron, δE_e is the difference between electron energy and its optimum value for cooling, n_e=4·10^7 cm^{-3} is the electron density in co-moving system. The Coulomb logarithm is

$$L_N = \ln\left(1 + \frac{\delta V \cdot \tau}{\rho_L}\right),$$

where $\delta V \cdot \tau = \delta E_e \cdot \tau / (\gamma \beta m_e c)$ is maximum impact factor, ρ_L is Larmour radius that can be estimated for first experiments as $\rho_L = 100$ μm, $\tau = l_{cool}/(\gamma \beta c)$ is flight of the cooling section with length l_{cool} .The cooling rate from this estimation gives changing the proton momentum about 2.1·10^{-4} during 300 s that is close to observed effect in Fig. 3. In the case of the matched velocity the cooling process is faster (see Fig. 3, right).

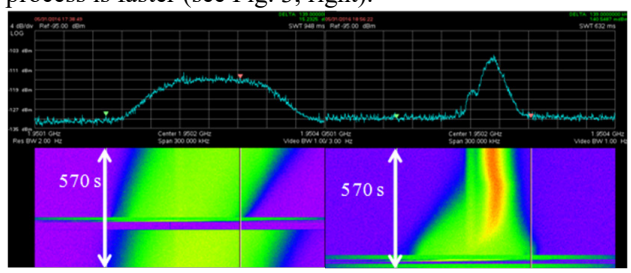

Figure 3: Spectrogram of the cooling process with strong (left) and small (right) difference between the electron and ion velocities. The electron energy is 1256.6 kV, electron current is 0.5 A. The span of the longitudinal momentum is δp/p=1.5·10^{-3}.

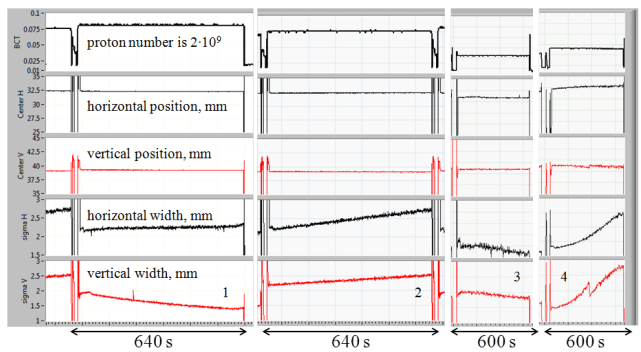

Figure 4: Changing transverse size during cooling experiments. Curve 1 is cooling at energy 909 kV, curve 2 is reference cycle without cooling, curve 3 is cooling at energy 1259 keV, curve 4 is growth of the transverse size at changing working point (tune) despite of electron cooling action.

The transverse cooling in the run 2016 is demonstrated in Figure 4. The results became more inconsistent than the transverse cooling obtained in runs 2014/2015. The possible reason is dependence of the cooling process from the working point of the storage ring. Figure 4 shows the transverse size of the proton beam with e-cool and without it. The curve 2 shows the transverse dynamic of the proton beam without cooling process. One see growth of the beam emittance that nature wasn't clear. The curve 4 shows the worse situation with emittance growth at changing working point from local optimum at $\Delta Qx/\Delta Qy$ = 0.02/-0.01. The similar effects were observed in electron cooling experiments at injection energy [7]. The best

ISBN 978-3-95450-181-6

electron cooling at energy 909 kV was obtained in the run 2015 (see Fig. 5). The cooling time about 100 s was obtained.

The electron cooling at presence of target and barrier bucket RF was investigated at energy 909 kV. Figure 6 shows that the barrier bucket RF and electron cooling suppress the longitudinal action of the target. The presence of target did not change the longitudinal momentum spread and the longitudinal shape of the proton bunches. The barrier bucket itself (see Fig. 7) wasn't able to suppress the target ionization loss. The particle escapes from the bucket.

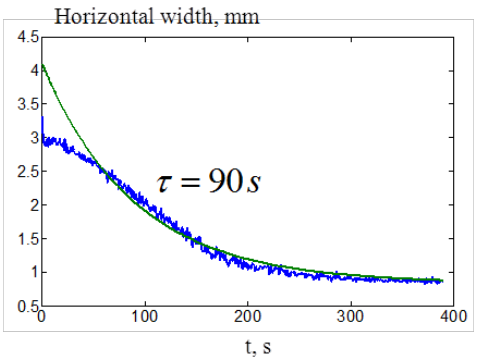

Figure 5: Horizontal cooling at electron energy Ee=909 kV. Number of the proton is $3 \cdot 10^8$, the electron current is 800 mA.

The strength of the electron cooling enough to suppress of the ionization loss and straggling without help of the barrier bucket. Figure 8 shows the experiment with cooling of the proton beam with target without barrier bucket. One can see that the electron cooling practically suppressed longitudinal and transverse growth induced by target but the more precise tuning storage ring and e-cooler is necessary.

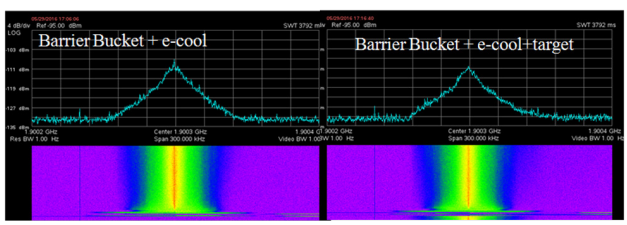

Figure 6: Spectrogram of Schotkky signal at the combine action barrier bucket RF and electron cooling (left picture) and barrier bucket, electron cooling and target (right picture). The electron energy 909 kV, electron current is 570 mA, the proton number is $2 \cdot 10^9$, $U_{RF} \approx 200$ V. The duration of the spectrum is about 300 s.

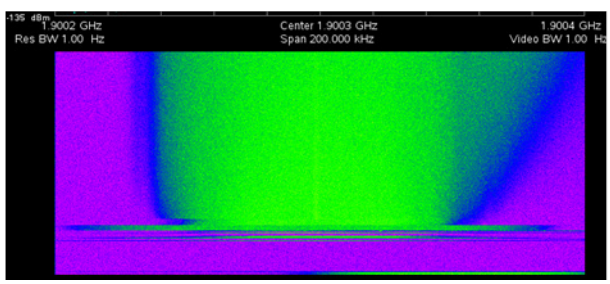

Figure 7: Spectrogram of Schottky signal at the simultaneously action barrier bucket and target. The spectrum duration is about 550 s.

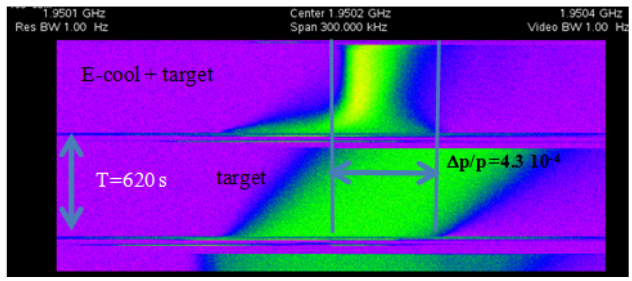

Figure 8: Spectrogram of the cooling process with electron cooling and target. The electron energy 1259.6 keV, the electron current is 500 mA, target with density is $n_a = 2 \cdot 10^{14}$ cm^{-2}.

CONCLUSION

The first successful experiment was carried out in COSY with electron energy 1257 keV. The experimental results show usefulness the electron cooling device with strong longitudinal magnetic field for improving quality of the proton beam. The electron cooling may be useful in combination with barrier bucket and usual RF. The electron cooling suppresses the action of the target with density $n_a = 2 \cdot 10^{14}$ cm^{-2}. The role of the working point and optics of the storage ring at cooling process should be investigated more carefully

ACKNOWLEDGEMENT

The authors would like to thank the members of the project teams at BINP and at COSY for their cooperation and support.

REFERENCES

[1] N. D. Prasuhn, J. Dietrich, R. Maier, et al., Nucl. Instrum. Methods Phys. Res. A 441, 167 (2000).
[2] R. Stassen, U. Bechstedt, J. Dietrich, et al., in Proceedings of the 6rd European Particle Accelerator Conference (EPAC 98), Stockholm, Sweden, 1998, pp. 553–555.
[3] N. Alinovsky et al., "The first commission results of the high-voltage magnetized cooler for COSY" Proc. COOL-11, Alushta, THIOA02, p. 37-42.
[4] V. B. Reva, N.I. Alinovskiy, T. V. Bedareva et al. Proc. COOL-13, Murren, Switzerland, 2013, p.79-83
[5] C. Bohme, J. Dietrich, V. Kamerdzhiev, et al., in Proceedings of the 9th European Workshop on Beam Diagnostics and Instrumentation (DIPAC'09), Basel, Switzerland, 2009, pp. 191–193.
[6] V.V.Parkhomchuk. "New insights in the theory of electron cooling". Nucl. Instr. Meth. A 441 (2000), p. 9-17.
[7] Yu.Korotaev, I.Meshkov, A.Sidorin, et al. "Intensive ion beam in storage rings with electron cooling" BProceedings of RuPAC XIX, Dubna 2004, p. 13-17.

ISBN 978-3-95450-181-6

OPTIMIZATION AND SIMULATIONS OF BEAM DYNAMICS IN APF ACCELERATORS

D. A. Ovsyannikov, V. V. Altsybeyev*,
Saint-Petersburg University, 7/9 Universitetskaya nab., St. Petersburg, 199034 Russia

Abstract

Design problem of APF accelerator for ensure enough high quality of output beam is considered. As we know, this problem is not easy because we have to achieve stability of longitudinal and transversal motions simultaneously. One of the first significant results in this subject were obtained by V. V. Kushin [1]. In the work [2] the problems of optimizations of ion beam are considered. The optimization approaches for some beam characteristics improving (acceleration and transmission ratios) are considered. Obtained results are confirmed by particle in cell simulations.

INTRODUCTION

Linacs with focusing by an accelerating field have long been part of the composition of any modern accelerating complex. In particular, the combination of radio frequency quadrupole (RFQ) [3–5] and APF linacs [1, 2, 6, 7] is a good decision for the initial part of the accelerating channel for high energies. In this case an ion beam is bunched in the RFQ and injected into a resonator with APF. A linac with APF has a high acceleration rate and no focusing magnetic elements. Therefore, the development of these linacs and the improvement of the beam quality remain important and current problems. When a linac is developed, parameters such as the linac length, beam current, current flow, effective emittance, etc. should be taken into account. These parameters can be improved using different optimization methods. Thus, the development of a linac based on the optimization approach can be of wide practical importance.

THE MAIN STAGES

Let us give a brief description of the main stages of accelerator modelling and optimization process.

1. Synchronous phase sequence calculation. At this stage we have to obtain a first approximation of a synchronous phase sequence. For example, application of a some analytical approximation (e. g. proposed be Jameson [8]) and swarm optimization methods may give a good enough results at this stage.

2. Cell lengths calculation and Drift tube structure generation. The lengths of accelerator cells are determined by the synchronous phase sequence. The diversity of cells lengths causes the deviation from the particular value of the resonant frequency. So the distribution of accelerating field may be non-uniform. This aberration can be eliminated by the adjustment of other geometry parameters period's length, gap ratio and drift tube diameter. For calculation of gaps lengths we use approach based on the tuning of resonant frequency of each cell on the operating frequency [9]. Follow this approach we calculate preliminary the set of dependences of resonant frequency of separate accelerator cell on the main parameters of this cell (cell length, gap length, drift tubes radii). These simulations are performed using COMSOL Multiphysics using Comsol API for Matlab in automatical mode. In following using these precalculated dependences one can choose a gap length and a drift tubes radii for a arbitrary cell length in order to tune a resonant frequency of each separate cell on the operating frequency.

3. PIC simulations. Then drift tube structure is generated one can compute the distribution of electric field and simulate particle dynamics with taking into account the space charge for the beam quality evaluation. Particle-in-cell simulations can give the most accurate result. At this stage we use the DAISI code [10–14].

4. Render decision on the optimization. If after simulations one detect that beam quality is not good enough (e. g. low transmission) we can render decision on the optimization of the synchronous phase sequence.

5. Optimization can be conducted using different approaches. In this report in follow we will consider optimization based on gradient descent method.

6. After optimization one have to regenerate the drift tubes structure and repeat the PIC simulation in order to estimate optimization process advances.

GRADIENT DESCENT OPTIMIZATION

Let us denoted $\tau = ct$, $\psi = \varphi - \varphi_s$, $p = \gamma_s - \gamma$, $\alpha_{tr} = eE_{max}/(2m_0c^2)$. Here c is the light velocity; φ and φ_s is the phases of synchronous particle and beam particle; γ and γ_s is the Lorentz factors of synchronous particle and beam particle; E_{max} is the accelerating wave amplitude. The approximation of accelerating field as an cos standing wave allows to accept the following mathematical model of beam dynamics in the an equivalent traveling wave:

$$\frac{d\beta_s}{d\tau} = \frac{\alpha_{tr}}{\gamma_s}\cos(\varphi_s(\tau)),$$
$$\frac{d\psi}{d\tau} = -2\pi\frac{\beta - \beta_s}{\lambda\beta_s},$$
$$\frac{dp}{d\tau} = \alpha_{tr}(\beta_s\cos(\varphi_s(\tau)) - \beta\cos(\varphi_s(\tau) + \psi)),$$

* v.altsybeev@spbu.ru

ISBN 978-3-95450-181-6

$$\frac{dS_{11}^x}{d\tau} = 2S_{21}^x, \quad \frac{dS_{11}^y}{d\tau} = 2S_{21}^y,$$
$$\frac{dS_{21}^x}{d\tau} = QS_{11}^x + S_{22}^x, \quad \frac{dS_{21}^y}{d\tau} = QS_{11}^y + S_{22}^y,$$
$$\frac{dS_{22}^x}{d\tau} = 2QS_{21}^x, \quad \frac{dS_{22}^y}{d\tau} = 2QS_{21}^y,$$
$$Q = -\frac{\alpha_{tr}\pi}{\lambda\beta_s\gamma}\sin(\varphi_s + \psi).$$

Here six variables $S_{11}^{x,y}$, $S_{21}^{x,y}$, $S_{22}^{x,y}$ are the elements of the matrixes $G^{x,y} = \begin{pmatrix} S_{11}^{x,y}, & S_{21}^{x,y}, \\ S_{21}^{x,y}, & S_{22}^{x,y}, \end{pmatrix}$, that describe dynamics of the initial transversal distribution ellipses $G_0^{x,y}$ in the phase planes $(y,\ dy/dt)$,$(x,\ dx/dt)$. The phase of synchronous particle is the following step-wise function

$$\varphi_s(\tau) = \varphi_{s_i} \in [-2\pi; 2\pi], \qquad \tau \in [\tau_i; \tau_{i+1}),$$
$$\tau_{i+1} - \tau_i = \lambda(\varphi_{s_{i+1}} - \varphi_{s_i} + \pi)/2\pi.$$

Thus, the set of parameters φ_{s_i} determines the beam dynamics in this approximation. For evaluation the quality of the beam we have to introduce some fitness function. For example for improving the beam transmission the following function may be used [7]

$$I = \int\limits_{M_{T,u}} (c_1F_1(\psi_T) + c_2F_2(S_{11}^{x,y})) \times$$
$$\times d\psi_T dp_T dS_{11}^{x,y}{}_T dS_{12}^{x,y}{}_T dS_{22}{}^{x,y}{}_T,$$

$$F_1 = \begin{cases} (\psi_T + \psi_1)^2, & \psi_T < -\psi_1; \\ 0, & \varphi_T \in [\psi_1, \psi_2]; \\ (\psi_T - \psi_2)^2, & \psi_T > \psi_2. \end{cases}$$

$$F_2 = \begin{cases} 0, & S_{11}^{x,y} < S; \\ (S_{11}^{x,y} - S)^2, & S_{11^{x,y}} > S. \end{cases}$$

Here c_1, c_2, ψ_1, ψ_2, S are non-negative constants, $M_{T,u}$ is the set of the beam positions in the phase space. On the base of the analytical representation presented in works [15] the representation of the partial derivatives $\frac{\partial I}{\partial \varphi_{s_i}}$ were obtained. Thus the gradient descent optimization may be constructed and applied for correction the sequence of the parameters φ_{s_i}.

RESULTS OF OPTIMIZATION

By using the proposed gradient descent optimization approach, an optimization of synchronous phase sequence was carried out for APF linac. The main resonator parameters are presented in Table 1. We assume that input bunches for APF are extracted from RFQ linac without any matching section. It is possible on the considered frequency 433 MHz. The optimized synchronous phase sequence is presented in Fig. 1. The electric field distributions calculated using electrodynamic (COMSOL) and electrostatic approximations (DAISI) are presented in Fig. 2. From Fig. 2 one can conclude that the electric field distribution is enough uniform. It has been achieved using the described above approach of the resonant frequency tuning on the design stage. The dependences of transmission ratio on input impulse current before and after optimization are presented in Fig 3.

Table 1: Main Parameters of Optimized Accelerator

Ion type	deuteron
Operating frequency, MHz	433
Input emittance (XdX, YdY), cm·mrad	0.02π
Input impulse current, mA	$0 - 35$
Voltage between drift tubes, kV	185
Number of cells	60
Input energy, MeV	4.1
Output energy, MeV (before optimization)	9.1
Accelerator length, m (before optimization)	1.72
Acceleration rate, MeV/m (before optimization)	2.89
$E_{max}/E_{kilpatric}$ (before optimization)	1.81
Output energy, MeV (after optimization)	8.35
Accelerator length, m (after optimization)	1.64
Acceleration rate, MeV/m (after optimization)	2.57
$E_{max}/E_{kilpatric}$ (after optimization)	1.95

From presented results one can the conclude the following observation:

1. it is possible to improve a capture ratio for the intense beam using the proposed optimization approach;

2. acceleration rate after a capture ratio optimization may rather decreases;

3. rather short gaps and drift tubes after optimization may be appears, it results in increasing the maximal electric field on the resonator surface. It is possible to eliminate this effect by increasing the length of short cells up to $1.5\beta\lambda$.

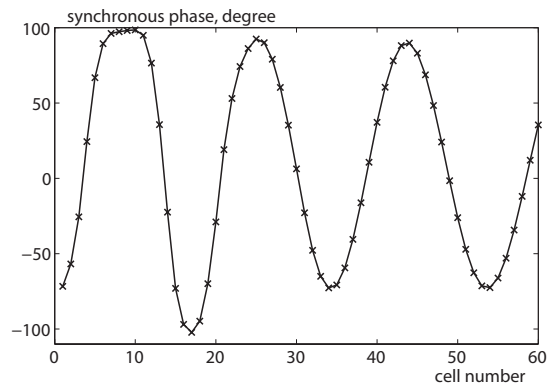

Figure 1: Synchronous phase sequence after optimization.

ISBN 978-3-95450-181-6

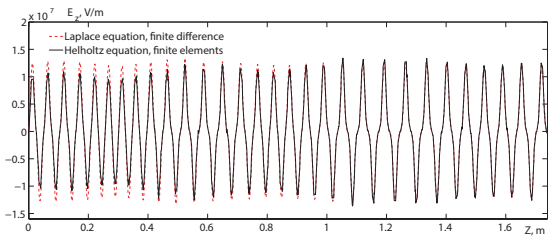

Figure 2: Electric filed distribution on the resonator axis.

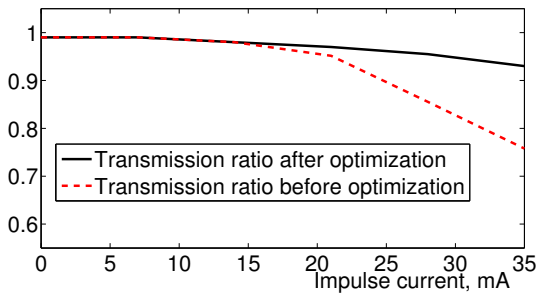

Figure 3: Transmission ratios before and after optimization.

CONCLUSION

In this paper the problem of optimizing the parameters of longitudinal and transverse motion of the beam in an APF accelerator is considered. The solution based on analyzing the beam dynamics in an equivalent traveling wave is proposed. This approach allows to provide tuning of resonator to produce the uniform field distribution. Analytic representation of the gradient of the fitness function allows us to provide the numerical optimization by different motion parameters. For instance it can be the width of the output energy and phase spectrum, the radial divergence of the beam, the effective emittance or the acceleration rate.

REFERENCES

[1] V. V. Kushin. “On improving the phase-alternating focusing in linear accelerators”. In: *Nuclear Energy* 29.2 (1970), pp. 123–124.

[2] Ovsyannikov, D. A. and Papkovich, V. G. “On the design of structures with accelerating field focusing”. In: *Problems of Atomic Science and Technology* 2.3 (1977), pp. 66–68.

[3] A. D. Ovsyannikov et al. “Application of optimization techniques for RFQ design”. In: *Problems of Atomic Science and Technology* 3.91 (2014), pp. 116–119.

[4] O. I. Drivotin and D. A. Ovsyannikov. “Stationary Self-Consistent Distributions for a Charged Particle Beam in the Longitudinal Magnetic Field”. In: *Physics of Particles and Nuclei* 47.5 (2016), pp. 884–913.

[5] Ovsyannikov, A. D. and Durkin, A. P. and Ovsyannikov, D. A. and Svistunov, Yu. A. “Acceleration of different ion types in single RFQ structure”. In: *Problems of Atomic Science and Technology* 3.103 (2016), pp. 54–56.

[6] D. A. Ovsyannikov and V. V. Altsybeyev. “On the Beam Dynamics Optimization Problem for an Alternating-Phase Focusing Linac”. In: *Physics of Particles and Nuclei Letters* 13.8 (2016), pp. 805–809.

[7] D. A. Ovsyannikov and V. V. Altsybeyev. “Optimization of APF accelerators”. In: *Problems of Atomic Science and Technology* 6.88 (2013), pp. 119–122.

[8] R. A. Jameson. “Design and Simulation of Practical Alternating-Phase-Focused (APF) Linacs - Synthesis and Extension in Tribute to Pioneering Russian APF Research”. In: *Proceedings of RuPAC-2012*. 2012, pp. 12–14.

[9] I. S. Skudnova and V. V. Altsybeyev. “On Approach For Resonant Frequency Tuning In Drift Tube Structures On The Designing Stage”. In: *Proceedings of RuPAC-2016*, these proceeding.

[10] V. Altsybeyev et al. “Numerical simulation of a triode source of intense radial converging electron beam”. In: *Journal of Applied Physics* 120.14, 143301 (2016). DOI: http://dx.doi.org/10.1063/1.4964335.

[11] V. V. Altsybeyev. “Numerical Simulations of the Charged-Particle Flow Dynamics for Sources with a Curved Emission Surface”. In: *Physics of Particles and Nuclei Letters* 13.8 (2016), pp. 801–804.

[12] V. V. Altsybeyev and V. A. Ponomarev. “Application of Gauss’s law space-charge limited emission model in iterative particle tracking method”. In: *Journal of Computational Physics* 324 (2016), pp. 62–72. DOI: http://dx.doi.org/10.1016/j.jcp.2016.08.007.

[13] V. Altsybeyev and V. Ponomarev. “Development of 2D Poisson equation C++ finite-difference solver for particle-in-cell method”. In: *Stability and Control Processes in Memory of V.I. Zubov (SCP), 2015 International Conference*. 15637294. 2015, pp. 195–197.

[14] V. Altsybeyev et al. “Numerical simulations of the radial convergent electrons and ions flows for cylindrical pulsed source”. In: *Stability and Control Processes in Memory of V.I. Zubov (SCP), 2015 International Conference*. 15637218. 2015, pp. 138–141.

[15] D. A. Ovsyannikov. *Modeling and Optimization of Charged Particle Beam Dynamics*. Leningrad State University, Leningrad, 1990, p. 312.

ISBN 978-3-95450-181-6

DEVELOPMENT OF MHF CONCEPTION AT ITEP

N.N. Alexeev, V.A. Andreev, M.M. Kats, A.A. Kolomiets, V.I. Nikolaev, Yu.A. Satov,
A.V. Shumshurov, V.S. Stolbunov, A.B. Zarubin,
ITEP, B. Cheremushkinskaya 25, 117218, Moscow, Russia

Abstract

The conception of Multi-purpose Hadrons Facility (MHF) began to be discussed at ITEP in the late ~2010s [1] when ITEP-TWAC facility was intensively exploited for physical and applied research with the use of accelerated proton and ion beams varied in a wide range of operating parameters. Technological developments have continued to expand the scope of beams utilizing in diverse fields of science, medicine, industry and education. The ITEP-TWAC facility was decommissioned in 2012 and continues to remain in a state of waiting for reasonable decision on its recovery and upgrade, but conception of MHF is alive and aims at reviving in ITEP a technological base of particle accelerator technique intended for generation of proton and ion beams, covering the needs of many areas of fundamental, applied and technological research and industrial applications, represents a significant scientific and practical interest for modern and future engineering community. Created MHF environment should obviously be friendly and flexible for collaboration with industry, universities, and other national and foreign labs to provide continuous intelligent and technological progress. The key components of the MHF mission and vision are presented.

INTRODUCTION

The history of accelerator science and technology in our country, spanning more than seven decades, contains many glorious pages of the extraordinary contribution of national research institutions, scientists and engineers in the development and implementation of new ideas and the creation of unique installations.

ITEP is historically related to innovative accelerator center and it has been one of the basic institutions of the accelerator industry which specialized on the technological peculiarities of proton and ion beam accelerators. The ITEP School of accelerator science and technology has a long tradition and is focused on studying, invention, construction, creation, mastering and implementation to operation of equipment, systems and installations providing proton and ion beams for usage in physical experiments and applied research works.

Main accelerator facility of ITEP until 2012 was ITEP-TWAC which decommissioning not only significantly reduced the innovative ability of the Institute in the field of accelerator technology, but also virtually terminated all experimental work with usage of accelerated beams. The creation of MHF as a new generation of accelerator facilities would help to restore and significantly expand the accelerator technological base of the Institute and to bring the possibility of physical experiments and application works in usage of hadrons beams

TRENDS IN ACCELERATOR TECHNIQUE DEVELOPMENT

The project of MHF has to be elaborated on a base of world trends in accelerator development. The main motivation for the promotion of accelerator technologies remains still high energy physics which after the discovery of the Higgs boson has charted new frontiers of research on the accelerated beams in two main ways: the study of the properties of known and search for new particles at increasingly high both energies of interaction and luminosity; precision measurements of known processes to look for possible, tiny deviations from the SM expectations which require primarily high intensity beams [2]. At a time when accelerator projects at the high-energy frontier are experiencing difficulties in gaining financial support, projects at the high-intensity frontier are flourishing worldwide [3].

Super High Energy Colliders

There is international consensus that the priority for the short and medium term future is the full exploitation of LHC, including its luminosity upgrade (project HL-LHC). Two similar projects of colliders are currently being considered: SppC in China and FCC-hh in CERN [4]. The conceptual design for both projects foresees to 100 km ring equipped with 16-20 T magnets, to reach a pp centre-of-mass energy 100 TeV. Two projects of linear colliders being considered are: ILC [5], for which Japans has expressed interest as host country; and the CLIC [6], being developed at CERN. The needed RF gradients is 31 MV/m for 500 GeV ILC and 100 MV/m for 3 TeV CLIC.

High Intensity Proton Accelerators

Proton beam intensity is one of frontiers in advance of physics research including [7]: neutrino experiments (experimental studies of neutrino oscillations and neutrino interaction physics); kaon, muon, nucleon, and neutron precision experiments (studying ultra-rare kaon decays, searching for muon-to-electron conversion and nuclear electron dipole moments, exploring neutron properties at very high precision); material science and nuclear energy applications (critical input into the design of future energy systems, including next generation fission reactors, nuclear waste transmutation systems and future thorium fuel-cycle power systems).

During the past decades, accelerator-based neutron-generating facilities like SNS [8], J-PARC [9], PSI [10] and LANSCE [11] advanced the frontier of proton beam intensity to 1 MW power level. There are a number of different types of accelerators running at 100 kW or more today (TRIUMF, ISIS, FNAL MI, AGS, SPS). Many of these involve rapid cycling synchrotrons (RCS) as part of the acceleration chain. Many of these operate, or have

ISBN 978-3-95450-181-6

operated, as part of a higher energy collider chain. There are two accelerators that operate at the MW level: the PSI cyclotron chain and the SNS linac. Many of the existing accelerators have plans and on-going design for further power increases more than 1 MW: ESS (5 MW, 2 GeV), SPL (4 MW, 5 GeV), Project-X (3 MW, 3 GeV), MYRRHA (2.4 MW, 0.6 GeV), Daejalus (3 MW, 0.8 GeV). Visible trend of reducing the energy of powerful proton beam.

Main Some Key Technical Challenges for high power proton accelerators are: management of beam loss to very low fraction levels and improvements simulations to predict beam behavior to the level $<10^{-6}$; increase gradients in SRF linacs, development of high power coupler, high power RF sources, minimize cryogenic loads; improvement charge exchange injection techniques of ring injection; for ADS high reliability is a major consideration.

High Intensity Heavy Ion Accelerators

Extremely high energies of heavy ions (HI) is achieved in hadron colliders (LHC) in which HI are used in the experiments, a fraction of the time, for colliding with protons [12]. The only collider, specialized for HI, is RHIC operating successfully for over 10 years and continuing to improve their operational parameters [13]. RHIC's main objective is to increase its ability to study quark-gluon plasma and the rare processes associated with it. The project of HI collider NICA, which is realized in JINR, Dubna, complements RHIC in the range of extremely low for the quark-gluon plasma energies [14].

The largest HI project under construction is FAIR [15] that allows acceleration of intense beams of stable elements from protons (30 GeV) to uranium (10 GeV/u) to be used for research in several scientific areas: physics of hadrons and quarks in compressed nuclear matter (CBM experiments); atomic and plasma physics; applied sciences in the bio, medical, and materials sciences (APPA); hadron structure and spectroscopy; strange and charm physics; hypernuclear physics with antiproton beams (PANDA) and the structure of nuclei; physics of nuclear reactions and nuclear astrophysics with RIBs (NuSTAR).

The main purpose of other high intensity HI accelerators is rare isotope production using the projectile fragmentation method (RIKEN [16], FRIB [17], SPIRAL2 [18]). Deuteron beams are effectively used for neutron production (SAFAR [19], IFMIF [20], SPIRAL2). For HI, the power frontier is supposed to be advanced to 400 kW with the construction of FRIB currently underway at Michigan State University [21].

Key Technical Challenges for high intensity HI accelerators includes: High Intensity (CW) and High charge state Ion Source, Superconducting RF, Integrated Cryogenics, Loss Detection and Machine Protection, Collimation, Normal - and Superconducting RFQ, Charge Stripping, High Vacuum, RCS Technology for heavy ions, Accumulator Technology etc.

Accelerators for Applications

About 30,000 accelerators are in use in the world, but only few dozen of them are high energy and used for scientific purposes [22]. All known methods of particle acceleration are used for applied purposes:

Direct Voltage: DC voltage to accelerate either electrons or ions (Dynamitron & Cockcroft Walton generator, energies to 5 MeV and currents up to 100 mA; Van de Graaff, energies from 1 to 15 MeV at currents of a few nA to a few mA; Inductive Core Transformer (ICT), energies to 3 MeV at currents up to 50 mA)

RF Linacs: in a wide range of operating rf frequencies for any charged particles (Electron linacs., standing wave and traveling wave cavities from 0.8 to 9 GHz, energies from 1 to 16 MeV at beam powers to 50 kW.; Proton and Ion linacs, frequencies at 80 to 600 MHz, energies from 1 to 70 MeV at beam currents up to >1 mA)

Circular Accelerators (Betatrons, electron energies to 15 MeV at few kW beam power; Cyclotrons.,ion energies from 10 to 70 MeV at beam currents to several mA; Rhodotrons, electron energies from 5 to 10 MeV at beam powers up to 700 kW; Synchrotrons, electron energies to 3 GeV, proton and ion energies to 300 MeV/u).

Energy, current, and beam power of application accelerators span many orders of magnitude (10^2 – 10^9 V, 10^{-8}-10^2 A, 10^{-6}-10^9 W).

Well established commercial applications of accelerators are the following : Proton and C-ion therapy for cancer treatment, medical isotopes, electron microscopes, etc; Ion implantation for semiconductors and materials; Electron beam irradiators and material processing; Production of radioisotopes; Ion beam analysis; Analysis using neutron generators; Non-destructive testing & inspection; Synchrotron radiation application in many areas.

Sales of accelerators for applications in the world is >$5B/yr and growing ~10%/yr in products.

MHF: CONCEPTION

Following the trends of development and use of accelerator technologies in the world, strategic goal of MHF is aimed to revive at ITEP technological base of accelerator science and technique for fundamental and applied nuclear research and innovative development, using beams of protons and heavy ions of intermediate energies. Integration of technological base with educational process will allow to train the skilled workforce for accelerators construction and related technologies development in the future.

The key objectives of the MHF mission and vision are:

- maintenance, improvement and expanding of ITEP accelerator facility infrastructure as the basis of the scientific and technological base;
- fundamental and applied research and technological development using relativistic proton and ion beams with energy to 10 GeV for protons and to 5 GeV/u for ions;
- applied research, technological development and industrial application using proton and ion beams with energy to 1 GeV/u;

ISBN 978-3-95450-181-6

- fundamental research and technological development using high power pulsed nuclei beams with energy of <1 GeV/u;
- technological research and development in the field of generation, acceleration, accumulation, cooling, compression, extraction and sharp focusing of high intensity hadrons beams;
- expansion of scientific and educational activity in the areas of nuclear technologies.

The concept is based on the core capabilities available at ITEP and focuses on the multi-purpose use and development of accelerator facilities, highlighting priority and demanded activities, appropriate qualification of staff and infrastructure capabilities, expanding within existing constraints. The main competences required for the implementation of the accelerator projects are: Accelerator Science (beam dynamics, theory, simulation, beam experiments); Technology (proton and ion sources, linacs, RF systems, kickers, ring lattice, beam lines, injection/extraction, correction systems, high vacuum); Engineering (design, construction, integration of electrical, RF, electronics, mechanical, cooling, vacuum systems, etc.); Particle Detectors (advanced detector development, beam test pickups, devices, tools and instruments); Controls (processor control, interlock & DAQ systems, machine adjustment, etc).

MHF: IMPLEMENTATION

The first phase MHF is implemented in the existing infrastructure of the accelerator complex (Figure 1). Five upgraded accelerator facilities will determine the technological capabilities of MHF listed in Table 1.

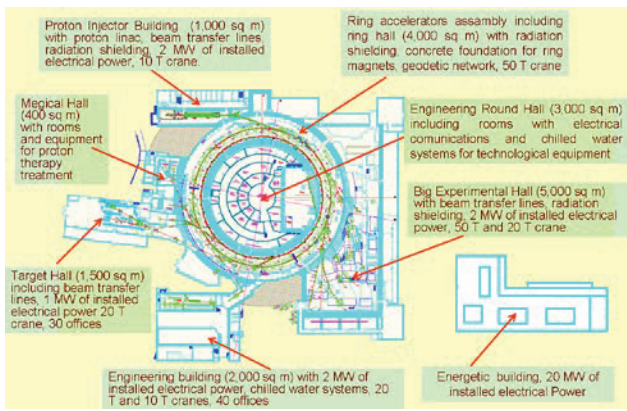

Figure 1: Existing Infrastructure of MHF.

Table 1: Expected Parameters of MHF

Accel. Type	Beam	Beam Duty	Energy MeV/u	Beam Intens., s^{-1}
I2	p	$2x10^{-5}$	25	$2x10^{14}$
I2/U10	p	$4x10^{-6}$;0.3	50-9300	$1x10^{12}$
I2/UK	p	$4x10^{-6}$;0.5	50-3000	$1x10^{12}$
I3M	Fe to U	$1x10^{-5}$	12xZ/A	$(2-8)x10^{9}$
I3M/UK	Fe to U	$5x10^{-6}$;0.5	10-1000	$(1-4)x10^{9}$
I4	d to Fe	$1x10^{-4}$	7	10^{10}-10^{12}
I4/UK	d to Fe	$5x10^{-6}$;0.5	10-1000	10^{10}-10^{11}
UK/U10	C to U	pulse, cw	100-900	to 10^{14} p/p

The MHF project can be built in two phases. The first phase includes the revival of ring accelerators with upgraded injection facility: intensity of proton injector I2 will be increased by order-of-magnitude to $1.2x10^{14}$ s^{-1}; energy of HI in injector I3 will be raised to 12xZ/A MeV (A/Z=3÷10); new injector I4 accelerating ions at A/Z≤3 to 7 MeV/u will be installed [23].

Phase two should advance MHF to the frontier of high intensity hadrons facilities providing a radical increase of the beam intensity and expansion of infrastructure for activation of a new actual scientific research and applications.

Relativistic Proton and Ion Beams

Beams of protons and ions, accelerated up to relativistic energies, can be used for generation of secondary beams on internal targets or directly at slow extraction of particles to the Big Experimental Hall (BEH) in particular, for the previously planned experiments: FLINT - Search for and study of cold dense baryonic matter; EPICURUS - Baryon spectroscopy; FRAGM - Cumulative nuclear fragments [23].

Beams for Applications

Proton and ion beam applications are performed in the energy range from 1 MeV/u up to 1GeV/u in different modes of accelerator facilities operation (Table 2).

Table 2: Use of Beams For Applications

Application	Beam	Accel. Type	Energy MeV/u	Place
Proton therapy	p	I2/UK	50-250	MB
Ion therapy	C	I4/UK	90-400	MB
Implantation	p, P, B	I2, I4	10-25	SI2, SI4
Protonography	p	I2/UK	1000	TH
Rad. effects on Comp and Sys	p, Fe, Ag, U	I2/UK I3M/UK	10-800 90-500	BEH
Radiobiology	p, C, Fe	I2/UK I4/UK	50-250 90-400	MB
Material properties	p	I2	25	SI2
Radioisotopes Production	p	I2	25	SI2

High Power Pulsed Nuclei Beams

A beam of high density nuclei of elements from C to Ni is accumulated and formed in the Ring U10 using technologies of multiple charge exchange injection, stochastic cooling and longitudinal compressing. The beam power of 10^{11}-10^{12} W can be reached at the beam energy ~1 GeV/u in pulse length of (50-100) ns.

Technological Research And Development

Ongoing technological research focuses on the development of promising projects for modernization of existing accelerators and creation of new equipment components corresponding global trends and cardinally expanding experimental and productive possibilities of MHF. The main areas of technological research are the key technical challenges for high power proton and heavy ion accelerators.

ISBN 978-3-95450-181-6

Scientific and Educational Activity

Expanding of educational activity is one of the most important functions of MHF. On the basis of existing relations with Universities (MEPhi, MIPT, MSU) will be established practical classes, engineering and scientific training of: engineers (bachelors, masters) in many fields; physicist-experimenters; medical physicists and radiation therapists for clinics; postgraduate and doctoral students.

The infrastructure of facility allows organizing the work of interns in research groups and collaborations: participation in the creation of installations, in physics experiments, in commercial project.

Scientific and Educational Activity includes lectures, symposia, technical meetings and seminars on issues related to technical and methodological basis of engineering developments, physics experiments and implementation of physical research.

PERSPECTIVES-NEW PROPOSAL

Phase two of the concept will bring MHF to the level of the next generation of accelerator facilities with enhanced functional capabilities allowing a large variety of frontier research in physics and applied science. New 200 MeV/1 mA proton linac I2M, which will be installed instead of existing I2, will be used as the driver injector for the updated synchrotron UK to RCS UKM operated at the rep. rate of 25 Hz and delivering 1 GeV/100 kW proton beam for nuclear physics, neutron and RIB experiments.

Infrastructure

Enhanced infrastructure of MHF (Figure 2) includes the following new buildings :

Proton Injector Building (PIB), reconstructed and enlarged for installation of new proton injector I2M;

Isotope Production Building (IPB) adjacent to PIB;

Neutron Stand Building (NSB) for I2M beam;

Medical Building (MB), reconstructed and enlarged for proton and ion therapy;

Special-Purpose Building (SPB) to be used for testing of radiation effects on components and systems;

Radiation Protected Area (RPA) of BEH.

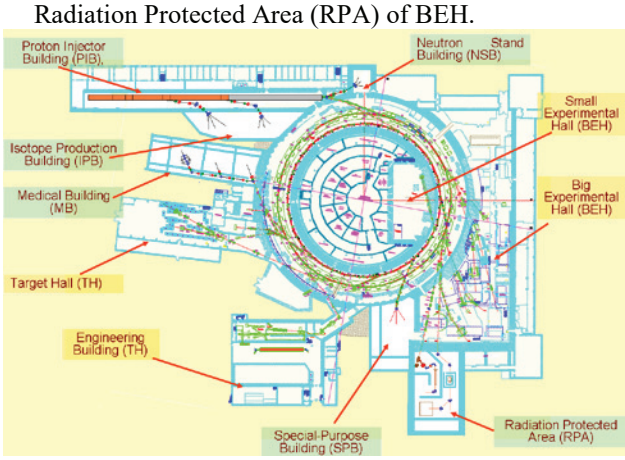

Figure 2: Enhanced Infrastructure of MHF.

High Current Proton Linac-Injector

The driver proton linac I2M (Figure 3) includes duel-beam H^+/H^- injection scheme for the 4 m long, 4-vane, 3MeV RFQ operating at 300 MHz with a high duty factor or in CW mode. The H^+ injector includes a duoplasmatron proton source delivering CW beam current of 1 mA . The H^- beam injector includes a cesiated, multicusp – field, surface – production ion source with beam current ~10 mA at 25 Hz x 500 μsec. pulse length. The MEBT line will transport and match the beam to the DTL which is ~40 m long and accelerates the beam to 80 MeV in five tanks. A FODO focusing lattice is used in DTL assumes permanent magnet quadrupoles.

The rest of the acceleration in the I2M linac will be provided by superconducting cavities. Double spoke cavities [24] can be used to accelerate the beam from 80 MeV to 200 MeV. The most prominent arguments for spoke cavity are large aperture, operational flexibility, high gradient, less real estate, lower operating costs, small wakefields, excellent vacuum, and very high efficiency.

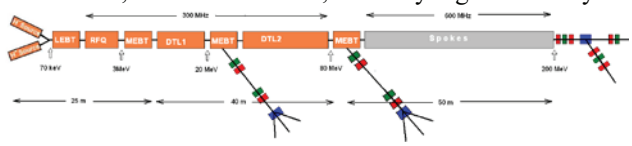

Figure 3: Scheme of proton injector-driver I2M.

The H^- beam from linac is delivered to the RCS UKM injection point, where it is multi-turn charge-exchange injected with a carbon stripper foil.

Rapid Cycling Synchrotron

The UKM (Figure 4) is upgraded synchrotron UK to 25 Hz RCS accelerating proton beam to 1 GeV with intensity 2.5×10^{13} p/p corresponding to the beam power 100 kW. Ceramic vacuum chambers will be used in the RCS dipole and quadrupole magnets, injection bumps and extraction kickers to avoid the eddy current.

Circumference, m	222.768
Superperiods	21
Max. magnetic field, T	1.31
Max. Bρ, T·m	12.89
Inj. proton energy, MeV	200
Inj. ion energy, MeV/u	12xZ/A (I-3) 7 (I-4)
Max. beam intensity for ions, p/p	6×10^9
Max. proton energy, GeV	3.04
Max. repetition rate, Hz	25
Max. intensity for protons, p/p	2.5×10^{13}
Tune shift $Q_{x,z}$	5.75
Hor. acceptance, π mm mrad	200
Ver. acceptance, , π mm mrad	120
Required vacuum pressure, Torr	$<10^{-11}$

Figure 4: Scheme and parameters of RCS UKM.

Auxiliary Ring

The Ring U-10 will be used as Accelerator–Stretcher–Accumulator (ASA) and equipped with two injection and three extraction systems (Figure 5). The proton beam, injected from linac I2M or UKM Ring can be accelerated in ASA to relativistic energy with following throwing on the internal target or extraction (fast or slow) to BEH. The proton beam in the energy range of 50-250 MeV will delivered at slow extraction to MB. The ion beam injected from UKM Ring can be accelerated up to relativistic energy and extracted to BEH. Using multiple charge

ISBN 978-3-95450-181-6

exchange injection technique, the beam of nuclei from C to Ni in the energy range <1 GeV/u can be accumulated and compressed to the extremal power level for extraction to TH. The same technique will be used for stretching of ion beam to duty factor of 1 and slow extraction to MB or TH.

Circumference, m	251.15
Superperiods	8
Max. magnetic field, T	1.01
Max. Bρ, T-m	34.1
Inj. proton energy, MeV	200
Inj. ion energy, MeV/u	50-1000
Max. proton energy, GeV	9.3
Max. repetition rate, Hz	0.5
Max. intensity for protons, p/p	1.5×10^{12}
Max. intensity for stacked nuclei beam	2.7×10^{13} (Co)
Max. power of nuclei beam, TW	2.4 (Co)
Tune shift $Q_{x,z}$	9.3
Hor. acceptance, π mm mrad	250
Ver. acceptance, , π mm mrad	120

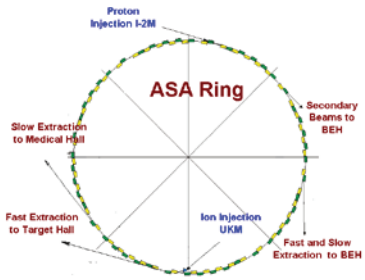

Figure 5: Scheme and parameters of ASA Ring.

Isotope Production

The I2M accelerator will be designed to host six beamlines to IPB for isotope production: three for 40-MeV and other three for 80-MeV beam utilization. Large variety of radio-isotopes can be produced by using the high power accelerator. Among them, F-18 for PET application, Sr-82 to monitor the blood flow in cardiac tissue and can be produced by using RbCl as a target, Cu-67 for cancer therapy and can be produced using ZnO as a target [25].

Proton and C-Ion Therapy Facility

New medical facility will have three treatment rooms and one for research. One treatment room equipped with isocentric gantry for proton therapy. The other treatment rooms for proton and ion therapy and equipped with planar irradiation systems with a dedicated pencil beam scanning nozzle.

The proton beam will be delivered to MB from ASA Ring in the energy range of 50-250 MeV for protons and 100-450 MeV/u for C-ions with high duty factor or CW mode.

Testing of Radiation Effects On Components

Radiation effects on microelectronic components and systems, including single-event upsets in microprocessors will be tested and studied with beams of proton and ions to U delivered to SPB at slow extraction from ASA Ring in the energy range up to 3 GeV for proton, and 100 (U) – 800 (C) MeV/u for ions.

Experiments with an Intense Beam

Accelerators of MHF will deliver for high intensity experiments proton beams with energy 40, 80, 200 MeV and 1 GeV.

Usage area of 40 MeV and 80 MeV proton beams is IPB, where in addition to the isotopes production will be experiments with material neutron irradiation.

The 200 MeV proton beam will be used in NSB for basic energy science and applications.

The proton beam accelerated in UKM up to 1 GeV will be delivered to RPA for experiments with rare isotope beams and study of nuclear structure, reactions and astrophysics.

High intensity beams will be used also for generation data required in applications like the transmutation of nuclear waste (ADS), design of future fission and fusion reactors, nuclear medicine (production of radio nuclei) and biology (cell irradiation), basic data for evaluated data bases.

CONCLUSION

The main goal of the presented concept is to call attention to the absolute necessity of the forced development the accelerator-technological base in the country. Disengagement of Rosatom from the management of the accelerator area in science and industry was a serious mistake that destroyed the Foundation of nuclear energetic of the future, which is impossible without solution to global problems of nuclear safety, transmutation of nuclear waste and closed cycle. The purpose of MHF is to solve these and other problems of nuclear science, and realization of this project at ITEP is a strategically optimal for this time.

. REFERENCES

[1] N.Alexeev at al. RuPAC2014, p. (2014).
[2] F.Gianotti, IPAC2014, p.4079 (2014).
[3] J. Wei et al, IPAC'14, 17 (2014).
[4] F.Zimmermann, IPAC2014, p.1-6 (2014).
[5] ILC Technical Design Report (2013); http://www.linearcollider.org/ILC/Publications/Technical-Design-Rep
[6] CLIC Conceptual Design Report (2012); http://project-cliccdr.web.cern.ch/project-clickcdr/
[7] S. Holmes et al., Project X Reference Design Report, http://projectx-docdb.fnal.gov/cgibin/
[8] S. Henderson, LINAC'10, 11 (2010); J. Galambos, PAC'13, 1443 (2013).
[9] Y. Yamazaki, PAC'09, 18 (2009); K. Hasegawa et al, IPAC'13, 3830 (2013).
[10] M. Seidel et al, IPAC'10, 1309 (2010); P.A. Schmelzbach et al, HB'06, 274 (2006).
[11] D.E. Nagle, LINAC'72, 4 (1972); R.W. Garnett et al, PAC'11, 2107 (2011).
[12] J.M. Jowett, IPAC2016, p. 1493 (2016).
[13] G.Robert-Demolaize, IPAC2015, p.4091 (2015).
[14] G. Trubnikov, IPAC2016, p. 2061.
[15] FAIR Green Paper-The Modularized Start Version, October 2009.
[16] O. Kamigaito et al, IPAC'13, 333 (2013).
[17] J. Wei et al, NA-PAC'13, 1453 (2013).
[18] R. Ferdinand et al, IPAC'13, 3755 (2013).
[19] D. Berkovits et al, LINAC'12, 100 (2012).
[20] J. Knaster et al, Nucl. Fusion 53, 116001 (2013).
[21] Y. Yamazaki et al, NA-PAC'16, 2039 (2016).
[22] R.W. Hamm IPAC'13.. (2013).
[23] Upgrade of ITEP AC. Int. report 1127. (2014).
[24] M. Eshraqi, IPAC'16. 948 (2016).
[25] M.S. Gulley, PAC'09, 1337 (2009).

ISBN 978-3-95450-181-6

A RADIOACTIVE ION BEAM AND ISOTOPE PRODUCTION FACILITY FOR ITHEMBA LABS

J. L. Conradie, L. S. Anthony, F. Azaiez, S. Baard, R. A. Bark, A. H. Barnard, P. Beukes, J. I. Broodryk, J. C. Cornell, J. G. de Villiers, H. du Plessis, W. Duckitt, D. T. Fourie, P. Gardiner, I. H. Kohler, J. Lawrie, C. Lussi, N. R. Mantengu, R. H. McAlister, J. Mira, H. W. Mostert, C. Naidoo, F. Nemulodi, M. Sakildien, G. F. Steyn, R. W. Thomae, M. J. van Niekerk, P. A. van Schalkwyk, iThemba LABS, Somerset West, South Africa
A. Andrighetto, A. Monetti, G. Prete, M. Rossignoli, INFN, Laboratori Nazionali di Legnaro, Viale dell'Università, 2 - 35030 Legnaro, Padova, Italy

Abstract

iThemba LABS is a multidisciplinary research facility that provides accelerator-based facilities for physical, biomedical and material sciences, treatment of cancer patients with neutrons and protons and the production of radioisotopes and radiopharmaceuticals. The demand for beam time by the 3 main users, namely radioisotope production, nuclear physics research and medical applications, exceeds the available time by far.

During the past 3 years a feasibility study for a new radioactive ion beam and radioisotope production facility at iThemba LABS has been in progress. A dedicated isotope production facility is proposed which will free up the existing K=200 separated-sector cyclotron facility for nuclear physics research with stable beams. A facility for the production of low-energy radioactive ion beams is planned using the K=200 cyclotron as driver for the production of radioactive beams. A technical overview of the proposed isotope production and radioactive-ion beam facility will be given.

INTRODUCTION

iThemba LABS, located at Faure near Cape Town, operates a number of accelerators of which the Separated-Sector Cyclotron (SSC) is the largest. The SSC, a variable-energy machine, is extremely versatile and capable of producing high-intensity proton beams, a large variety of heavy ions and polarized protons at energies sufficient to probe the structure of sub-atomic matter. The SSC is primarily shared by three disciplines: nuclear physics research, proton/neutron therapy – along with radiation biology research – and radioisotope production. Over the past number of years it has become increasingly evident that the current beam allocation schedule is counterproductive and cannot satisfy the high demand for beam time from both research disciplines and radioisotope production.

The usual mode of operation is that nuclear physics research is conducted over weekends, while the rest of the week is scheduled for radiotherapy and the production of both short- and long-lived radioisotopes. iThemba LABS uses a 66 MeV proton beam from the SSC with currents of up to 250 μA to produce radioisotopes. The available beam time for radioisotope production is essentially fixed due to the current schedule and in order to expand the isotope production capacity, it became necessary to introduce a number of innovations. These include the installation of flat-topping systems for the injector cyclotron (SPC1) and the SSC, a new vertical-beam target station and beam-splitting. For operation with higher beam currents it also became essential to develop and implement non-destructive beam diagnostic equipment. Since, under present operating conditions, any further increase in the beam time for radioisotope production can only be achieved at the expense of one or more of the other programmes, it has now become essential to acquire a dedicated cyclotron for radioisotope production.

The long-term research strategy for the SSC includes the study of neutron-rich nuclei, which is rapidly becoming the focus of international research in order to understand how the elements were formed in astrophysical environments such as stars and supernovae. A forerunner to the long-term strategy is the already partially funded Low-Energy Rare Isotope Beam (LERIB) project, which aims at understanding the astrophysical processes that led to element formation. LERIB will make use of a high intensity 66 MeV proton beam from the SSC to produce different neutron-rich species. For the second phase it is envisaged that low-energy RIBs (<50 keV) will be accelerated to high energies, using a post accelerator.

The various projects will be carried out in phases. Phase 1 will involve the installation of a dedicated 70 MeV H-minus cyclotron for radioisotope production and the LERIB project. During Phase 2, a post-accelerator capable of accelerating radioactive beams from the LERIB project to an initial energy of ~ 5 MeV per nucleon will be installed.

RECENT INFRASTRUCTURE UPGRADE

Cooling Towers and Chillers Upgrade

The facility relies on a central cooling plant comprising four water-cooled chillers, seven cooling towers and associated pumps to supply chilled water at 6 °C with a cooling capacity of 4.4 MW. Chillers are operated in parallel and switched on demand as the heat load increases. During 2011 the cooling towers were replaced. Subsequently funds have been approved to replace the chillers and pumps this year. The new equipment will not only be more reliable, but will also offer a sustainable

ISBN 978-3-95450-181-6

energy saving due to the high Coefficient of Performance (COP) of the modern technology chiller units.

4 MVA Uninterruptable Power Supply Battery Replacement

A total of 4 banks, each consisting of 264 X BAE 25 OGI 2000 batteries, were installed. The new installation of low-antimony alloy, vented lead-acid batteries has a lifespan of 20 years. The capacity of the installation is designed to keep the accelerator facilities operational for 20 minutes at full load.

New Digital Low-Level RF Control System

A new digital low-level RF (DLLRF) control system to replace the 30-year-old analogue RF control systems has successfully been developed. The system [1] shown in Fig. 1 is field-programmable-gate-array (FPGA) based and is capable of synthesizing RF signals between 5 MHz and 100 MHz in steps of 1 µHz. It can achieve a closed-loop amplitude stability of better than 1/10000 and a closed-loop phase stability of less than 0.01°. Six of the systems are currently in operation on the two injector cyclotrons. In total, 35 production systems have been manufactured and installation will be completed during the coming months.

Figure 1: The new digital, low-level RF control system.

THE RADIOISOTOPE PRODUCTION FACILITY

To increase beam time for research and to the production capacity of radioisotopes, a dedicated production facility is proposed. Full use will be made of existing building infrastructure to establish an independent radioisotope production facility. A commercial 70 MeV H-minus cyclotron will be installed in the current underutilised neutron therapy vault, while the proton therapy vault and a third redundant vault will house a number of isotope production target stations (see Fig. 2). Repurposing of existing building infrastructure makes this configuration the least complex and potentially realises significant savings from an investment and future maintenance point of view. The existing radioisotope production facilities will provide increased opportunities for research regarding new radioisotopes and will also be available as an emergency backup for the new facilities. With this proposal, beams from the 70 MeV cyclotron could also service all the nuclear physics vaults as well as the target ion source of the LERIB project. An additional vault can be added next to the current proton therapy vault for dedicated radiation biology research. This approach is preferred, because of the cost saving aspect and the versatility of delivering beams to a large number of different end users and it also does not preclude neutron and proton therapy research from continuing. The department concerned is currently drafting long-range plans to support the continuation of the research, closely linked to radiation biology and radioisotopes research.

The proposed timeline realises the completion of Phase 1 in four years, i.e. three years to build the cyclotron and the fourth year for installation, testing, commissioning and ramping up of the beam intensities to the required levels for routine radioisotope production and research.

70 MeV H-Minus Cyclotron

The 70 MeV cyclotron will be procured from a commercial manufacturer. The cyclotron will have a dual beam delivery system with beam current up to 350 µA on each delivery port. Preliminary studies and discussions with two manufacturers have shown that it will be possible to fit the cyclotron from either manufacturer into the neutron therapy vault, as shown in Fig. 2. Detail information regarding the two commercially available cyclotrons can be found in references [2, 3]. Procurement will be done by means of a tender process that will request the 70 MeV cyclotron to be supplied inclusive of the switching magnets at the two extraction ports. Determining factors for a successful bid will include aspects like the maximum beam current delivery per extraction port, beam loss in the cyclotron and beamlines, ease of maintenance/service of cyclotron and final cost.

The components required for the beamlines that will deliver the beams to the four target stations will be designed and manufactured by iThemba LABS.

Radionuclide Production Target Stations

The design of the bombardment stations for radionuclide production with 70 MeV proton beams of high intensity will be similar (but not identical) to the existing horizontal-beam target station (“Elephant”) that has been in routine operation at iThemba LABS for 26 years [4]. The targets will be irradiated outside the beamline vacuum, surrounded by a composite radiation shield during bombardment (see Fig. 3). A helium-cooled, double-foil Havar window will serve to isolate the vacuum from the station. A four-sector graphite collimator located in the radiation shield immediately upstream of the double-foil window will assist with the beam focusing and centering, by providing current read-out on each sector. The beam will be swept in a circular mode around the beam axis in order to spread the thermal load over a larger surface area of the target. An electro-pneumatically controlled pusher arm will connect the cooling water to a target holder.

ISBN 978-3-95450-181-6

All target stations will be serviced by an electrically-driven target transport trolley which moves on rails, connecting the irradiation vaults to a hot-cell complex, target loading facility and a target store. The transfer of target holders to and from a target station and the transport trolley will be facilitated by means of a remote-controlled robot arm. Each target station will be electrically isolated from earth and the beam transport infrastructure in order to permit accurate measurement of the beam current and accumulated charge. Each target station will therefore act as a faraday cup.

Development of new targetry, compatible with a 70 MeV proton beam and intensities up to 350 µA, has commenced. An optimized tandem target for the simultaneous production of 82Sr and 68Ge will consist of a stainless-steel (S316) encapsulated Rb disc in the high-energy slot and a Nb-encapsulated Ga disc in the low-energy slot. The relevant energy windows of the Rb and Ga target materials will be 61.8 – 37.7 MeV and 24.8 – 0 MeV, respectively. The "dead layers" in the target are due to the encapsulation materials, cooling water layers and the beam entrance window located on the target holder: such dead layers are unavoidable.

The evaluation of the local radiation shield has recently been performed by means of Monte Carlo simulations with the code FLUKA [5]. The cylindrical geometry of a target station and the off-centre location of the target holder were modelled accurately, as shown in Fig. 3. Also, the tandem target described above was accurately modelled, including the cooling-water. Fig. 4 shows the results of a neutron fluence scan when a 70 MeV proton beam of 350 µA is incident on the target. The origin was defined as the center of the beam spot on the front face of the target, the z-axis along the beam direction, a vertical y-axis and a horizontal x-axis. The scan shown in Fig. 4 is along the positive x-axis. A similar plot is shown with the local radiation shield omitted. The vertical dashed lines indicate the intersection of the shielding material boundaries and the x-axis. It is clear that at the location of the outer surface of the target station, the neutron fluence is between 2 and 3 orders of magnitude lower than what would be the case if the shielding is omitted. Inside the station, the presence of the shield leads to a build-up of the neutron fluence. Most of the attenuation and absorption occurs in the paraffin wax layer (20 cm thick, containing 4% B4C by weight). This hydrogenous layer, however, is only effective for thermalizing neutrons entering with relatively low energies (below about 4 MeV) and finally capturing more than 99% of them. This is why a 50 cm thick inner Fe layer is required. The Fe layer effectively slows down fast neutrons to intermediate energies by inelastic scattering. The outer Pb layer mainly serves to attenuate gamma-rays, in particular the 2.2 MeV photons emitted in the capture of thermal neutrons by hydrogen. The total thickness of the local radiation shield is largely dictated by the available space, while the optimum thicknesses of the three complementary shielding materials have been determined by means of Monte Carlo simulations.

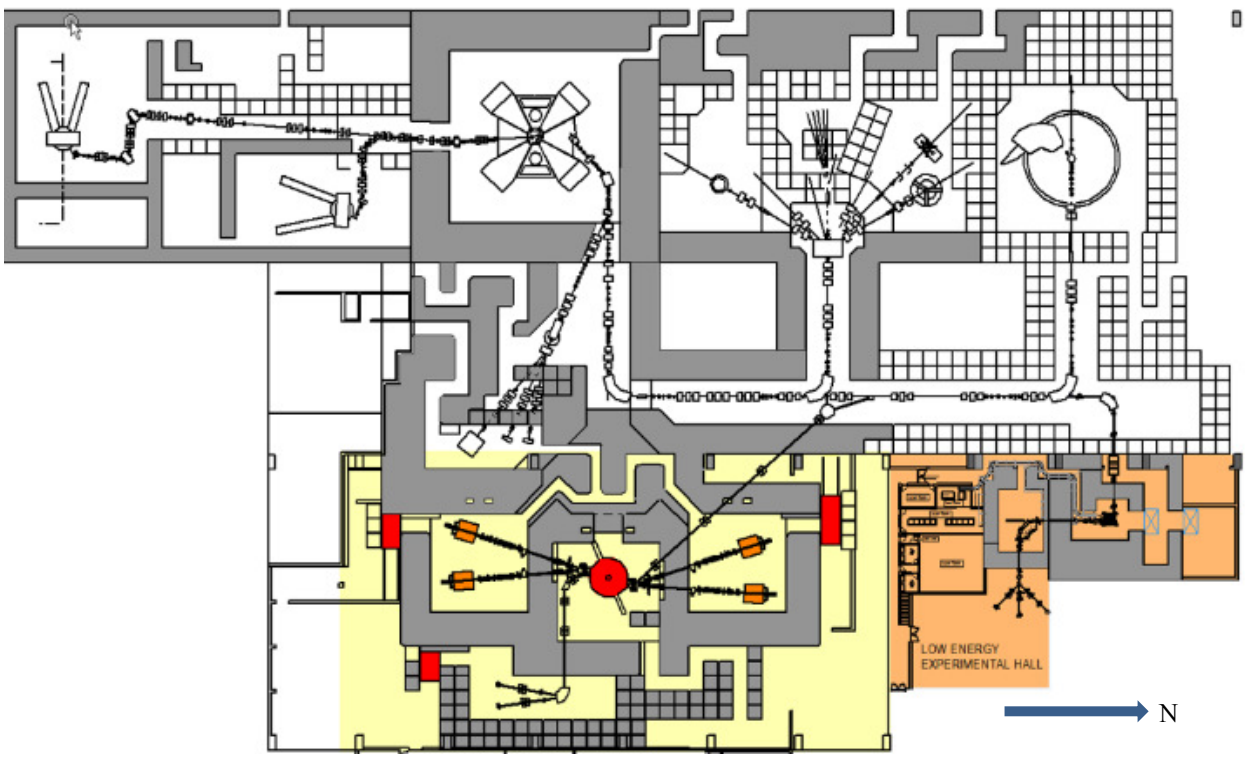

Figure 2: Layout of the new cyclotron and radioisotope production facilities utilising the existing and redundant therapy vaults shown on yellow background. The 70 MeV cyclotron is shown in red and the 4 target stations are shown in brown. The LERIB facility in relation to the existing infrastructure is shown on the brown background.

ISBN 978-3-95450-181-6

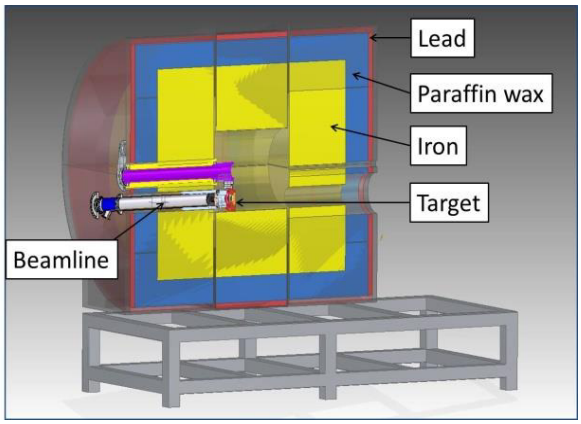

Figure 3: A vertical section along the beam axis through the local radiation shield of the target station.

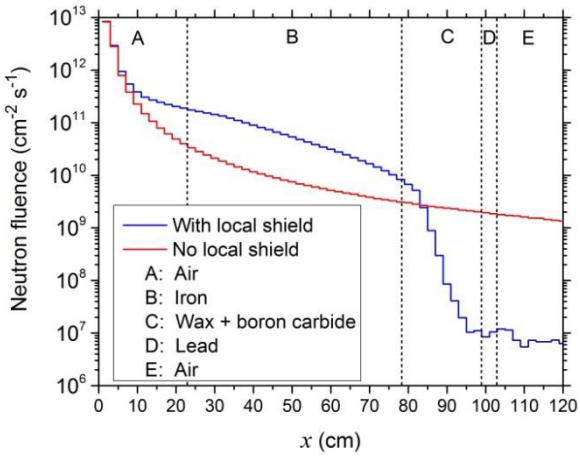

Figure 4: Neutron fluence scan, performed with the FLUKA code, along the x-axis (see text) through the target station for the case of an incident 70 MeV proton beam of 350 μA intensity on a tandem Rb/Ga target.

Shielding/Radiation Safety

To accommodate the cyclotron, beamlines and target stations, extensive modifications have to be made to the shielding of therapy vaults. To enlarge the vaults parts, mainly corner sections, of the vault walls will have to be modified. Because the planned beam intensities are much higher and the beam directions will be different, additional shielding, in the form of large blocks, will have to be attached to some walls. For the same reasons the existing labyrinths, for access of staff and equipment, will no longer provide sufficient shielding and they also partly block the installation route for the cyclotron. Some of the existing blocks will be rearranged to form a new, much narrower, labyrinth for the cyclotron vault. For the two production vaults lack of space does not allow the use of labyrinths and a combination of movable doors and blocks is planned. An essential requirement is provision for transport of the targets from the four target stations through labyrinths to the existing radioisotope production vault.

The existing air-conditioning equipment and ducts in the shielding walls will be used. The installed cooling capacity allows nine air changes per hour. In the existing radioisotope production vault the air is changed six times per hour. The only modification required is installation of HEPA filters and extraction fans in the air outlets from the vaults.

A radiation and equipment safety-interlocking system will monitor the status of vaults, doors, faraday cups, neutron shutters, radiation monitors and power supplies to prevent unsafe conditions and interrupt the beam in case of equipment failure.

Tentatively, the maximum permitted dose rate in areas where radiation workers will regularly work has been specified as 2.5 μSv/h. In less accessible regions, such as on top of the roof beams, at a height 7 m and more, a dose rate of 15 μSv/h is considered acceptable.

It is foreseen that during the early stages of operation, beam currents of several tens of micro-amperes will be stopped on copper faraday cups to optimize the cyclotron and beamline settings. In the cyclotron vault, it will sometimes be necessary to insert faraday cups in the beamlines from both ports. Because of the low beam losses in the cyclotron and its self-shielding characteristics, radiation from the faraday cups will be the determining factor for the shielding dimensions.

The present design of the new shielding layout, taking into account access for services, equipment and personnel, is based on reports about the design of the existing facilities [6, 7, 8, 9] and more recent data [10, 11], as well as on radiation dose rate measurements at iThemba LABS. Scaling and interpolation of the data, as well as calculations, led to the present design.

To verify that the calculations are not too crude, measurements of the dose rates were made, using a 10 μA, 66 MeV proton beam on faraday cups in vaults with different roof beam dimensions. The results were compared with calculations based on the graphs and table of Chen et al. [11], from which the neutron source term and attenuation lengths in concrete were determined. For comparison with results in the literature it is important to note the differences in concrete densities that are used.

Neutron dose rates of 21 μSv/h and 0.6 μSv/h per μA were measured for 1.5 m and 2 m thick roof beams, respectively, for a beam height of 1.5 m and a roof height of 3 m, below the concrete beams, which have a density of 2.35 g/cc. The copper thickness of the faraday cup and its support from the beam position to the top is 5 cm. The wall thickness of the stainless steel vacuum chamber is 3 mm.

For the cyclotron vault, 4 layers of roof beams with a total thickness of 3 m are planned. For the production vaults three layers with a total thickness of 2.25 m will be sufficient. The foundations of the vault basements consist of an 800 mm thick layer of concrete which can be increased to a total thickness of 2 m to limit ground water activation. Finally, Monte Carlo simulations will be done to determine whether the objectives have been met and if significant savings can be made by reducing the number of roof beams and simplifying the labyrinth of the cyclotron vault. The maximum permitted dose rates and beam currents that will be stopped on the faraday cups have to be reconsidered and finally specified.

ISBN 978-3-95450-181-6

LOW-ENERGY RARE ISOTOPE BEAM FACILITY

To enhance and supplement existing research platforms and to stay globally competitive through the promotion of new research opportunities in the field of nuclear physics, iThemba LABS initiated a flagship project to establish a Rare Isotope Beam (RIB) facility. Specific areas of interest include the study of neutron-rich nuclei, which is only achievable by way of the production and analysis of RIBs.

A Strategic Research Infrastructure Grant from the National Research Foundation (NRF) had been approved to fund a pilot project for the construction of a Low-Energy RIB (LERIB) facility. The facility will be used to develop and refine the techniques for RIB production and analysis. Knowledge, experience and equipment gained through this endeavour will be carried forward into a full-fledged RIB facility that will include beam cooling, high-resolution mass separation, charge-breeding and post-acceleration.

The LERIB facility and infrastructure will be housed in a new building as illustrated in Fig. 2. The new building will be strategically placed to allow the SSC to be used as a driver to deliver high intensity 66 MeV proton beams to the LERIB test facility. The location of the new building is such that future expansion to the north of the current accelerator complex will be possible. A number of end-stations for low-energy (<50 keV) experiments will be provided. The isotope of interest will be transported to the end-stations after passing through magnetic mass separator with a mass resolution of 1 in 3000.

Target Ion Source

A formal collaboration agreement between the NRF and the Instituto Nazionale di Fisica Nucleare (INFN) in Legnaro, Italy had been signed in February 2015. As part of the collaboration a replica of the fully developed Front End containing the Target Ion Source (TIS) which had been developed by Laboratori Nazionali di Legnaro (LNL) in Legnaro, Italy for their SPES project, has been constructed for iThemba LABS. The TIS exploits the Isotope Separation On-line (ISOL) method of producing neutron-rich radioactive ions and will form the basis of the proposed LERIB test facility at iThemba LABS.

The required characteristics of the ISOL target are both a high fission production yield and the capability to release the fission products as fast as possible. The most critical element of the TIS unit is the Multi-Foil Direct Target. The target configuration consists of several thin disks suitably spaced in the axial direction in order to improve the cooling of the UCx target by thermal radiation and to avoid large temperature differences with respect to the graphite box containing the target discs. The open structure of the target assembly also promotes the quick release of fission products. The advantage of this configuration is the simplicity of the cooling system and the consequent relatively low cost.

To guarantee an efficient RIB production rate the TIS target has to work at elevated temperature levels up to 2200°C. The proton beam power is not sufficient to heat the graphite box and the target discs in a uniform temperature profile. Therefore it was crucial to introduce an additional and independent electrical heating system.

Neutral atoms diffuse from the target assembly into the hot-cavity surface ionizer via a transfer tube. The surface ionization mechanism produces mainly singly charged particles that are accelerated up to 50 keV by the extraction electrode assembly. Accelerated particles then enter the low-energy beam transport system for transportation via a mass separator to the low-energy experimental areas.

During 2014 an online test had been performed at iThemba LABS [12] to validate the theoretical results of the thermal finite element simulations of the multi-foil target system. A 60 μA, 66 MeV proton beam from the SSC was stopped on the target assembly comprising 13 thin silicon carbide discs housed in a graphite container. The test results confirmed that the power dissipation capability of the multi-foil target system is suitable for ISOL-RIB production.

REFERENCES

[1] W. D. Duckitt, et al., “A new Digital Low-Level RF Control System for Cyclotrons”, Cyclotrons’16, Zurich, Switzerland, Sep. 2016, this conference
[2] F. Poirier, et al., “Studies and Upgrades on the C70 Cyclotron Arronax”, Cyclotrons’16, Zurich, Switzerland, Sep. 2016, TUD02.
[3] V. Sabaiduc, et al., “BEST 70P Cyclotron Commissioning at INFN LN Legnaro”, Cyclotrons’16, Zurich, Switzerland, Sep. 2016, TUD04.
[4] G.F. Steyn et al., Nucl. Instrum. Meth. A 727 (2013) 131.
[5] A. Ferrari et al., FLUKA: a multi-particle transport code, (CERN-2005-10, INFN/TC_05/11, 2005)
[6] J.C. Cornell, “Shielding Walls“, NAC-SH 77-1 internal report (1977).
[7] J.C. Cornell, “Labyrinth Design“, NAC-SH-78-2 internal report (1978).
[8] J.C. Cornell, “Neutron Therapy Vault“, NAC-SH-78-3 internal report (1978).
[9] J.C. Cornell, “Neutron Shutters“, NAC-SH 82-1 internal report (1982).
[10] L. Sarchiapone and D. Zafiropoulos, “Radiation Protection Aspects of the SPES Project at LNL”, LNL Technical Design Report, Chapter 10, 2008.
[11] C.C. Chen et al., “Calculations of Neutron Shielding Data for 10-100 MeV Proton Accelerators”, Radiation Protection Dosimetry, Volume 116, No. 1-4, 2005, p. 245.
[12] A Monetti et al., “On-line test using multi-foil SiC target at iThemba LABS”, Eur. Phys. J. A (2016) 52: 168.

ISBN 978-3-95450-181-6

FIRST COLD TESTS OF THE SUPERCONDUCTING CW DEMONSTRATOR AT GSI

F. Dziuba[1,*], M. Amberg[1,3,†], K. Aulenbacher[1,4], W. Barth[1,2,5], M. Basten[3], M. Busch[3], V. Gettmann[1], M. Heilmann[2], S. Mickat[2], M. Miski-Oglu[1], H. Podlech[3], M. Schwarz[3], S. Yaramyshev[2,5]

[1]HIM Helmholtz Institute Mainz, 55099 Mainz, Germany
[2]GSI Helmholtzzentrum für Schwerionenforschung GmbH, 64291 Darmstadt, Germany
[3]IAP Goethe University Frankfurt, 60438 Frankfurt am Main, Germany
[4]KPH Johannes Gutenberg University Mainz, 55128 Mainz, Germany
[5]MEPhI National Research Nuclear University, 115409 Moscow, Russia

Abstract

The future experimental program of super heavy element synthesis at GSI desires high intense heavy ion beams at or above the coulomb barrier, exceeding the capabilities of the GSI-UNILAC (Universal Linear Accelerator). Additionally, the existing GSI accelerator chain will be used as an injector for FAIR (Facility for Antiproton and Ion Research) primarily providing high power heavy ion beams at a low repetition rate. Due to this limitations a new dedicated superconducting (sc) continuous wave (cw) linac is proposed to keep the Super Heavy Element (SHE) research program at GSI competitive. The construction of the first linac section has been finished in the 3rd quarter of 2016. It serves as a prototype to demonstrate its reliable operability in a realistic accelerator environment. This demonstrator cryomodule comprises the sc 217 MHz crossbar-H-mode (CH) multigap cavity as the key component of the whole project and two sc 9.3 T solenoids. The performance of the cavity has been extensively tested at cryogenic temperatures. In this contribution the measurement results of initial cold tests will be presented.

INTRODUCTION

Regarding the future construction of a sc cw linac at GSI an R&D program has been initiated. It is intended to build and test the first linac section with beam [1]. In this context, a sc 217 MHz CH cavity [2] with 15 equidistant accelerating cells, $\beta = 0.059$ was built (see Table 1). The beam dynamics layout of the cavity is based on the special EQUUS (EQUidistant mUlti-gap Structure) [3]. Three dynamic bellow tuners inside the cavity adjust frequency changes during operation [4]. Furthermore, a helium vessel made from titanium provides a closed helium circulation around the cavity. Several flanges in each quadrant of the cavity allow an adequate surface processing. For future beam tests a 5 kW cw power coupler is available. After final surface preparation steps the new cavity has been extensively tested with low level rf power at 4.2 K.

* f.dziuba@gsi.de
† out of business

Table 1: Main parameters of the cavity

β (v/c)		0.059
Frequency	MHz	216.816
Accelerating cells		15
Effective length ($\beta\lambda$)	mm	612
Diameter	mm	409
Tube aperture	mm	18 / 20
G	Ω	52
R_a/Q_0		3240
$R_a R_S$	kΩ^2	168
E_a (design)	MV/m	5.5
E_p/E_a		6.3
B_p/E_a	mT/(MV/m)	5.7

RF TESTS OF THE CAVITY

A first rf test of the sc 217 MHz CH cavity (without helium vessel) at the Institute of Applied Physics (IAP) of Goethe University Frankfurt has been performed beginning of 2016 [5]. At that time the performance of the cavity was limited by field emission caused by insufficient surface preparation. Regarding this, rinsing could be performed along the beam axis only. Due to a technical re-

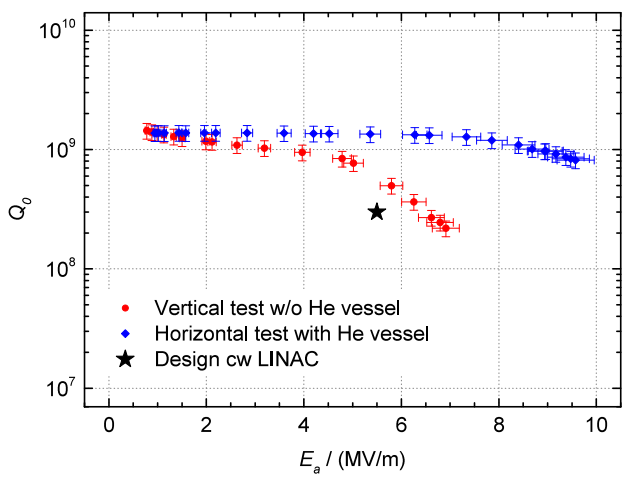

Figure 1: Q_0 vs. E_a curves at 4.2 K for two different rf tests.

ISBN 978-3-95450-181-6

striction of the provided High Pressure Rinsing (HPR) device, rinsing was not possible inside each quadrant of the cavity. Nevertheless, a maximum accelerating gradient of $E_a = 6.9\,\mathrm{MV/m}$ at $Q_0 = 2.19 \cdot 10^8$ was reached (see Figure 1).

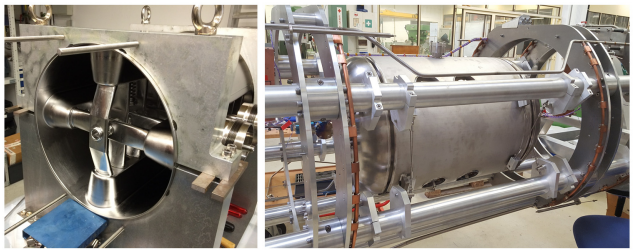

Figure 2: Superconducting 217 MHz CH Cavity during manufacturing (left) and finally mounted into the support frame (right).

After the final assembly of the helium vessel and further HPR preparation the cavity was delivered to GSI and prepared for a second rf test in a horizontal cryomodule (see Figure 2). A 50 W broadband amplifier was used to deliver the required rf power. The cavity was operated as a generator driven resonator directed by an rf control system. Further equipment, namely a network analyzer, three power meters and a scope has been used for rf measurements. To validate the measuring system all power meters have been calibrated via the X-ray spectrum of the cavity recorded at a gradient of 5.5 MV/m. X-rays arise from field emission; it is assumed that electrons, coming from the drift tube where the highest voltage is located, are accelerated to the neighbouring tube inside the cavity. Consequently, a continuous Bremsstrahlung spectrum is generated by hitting the neighbouring drift tube. The maximum energy as well as the maximum electron energy of the measured sprectrum was 574 keV (see Figure 3), confirmed by the related absolute voltage determined by the power meters (567 ± 7 kV).

Initially, the cavity has been passively precooled down to 218 K by the N_2 shield of the cryostat. Hereafter, the temperature was quickly lowered (3 K/min in average) applied by liquid helium to 4.2 K avoiding hydrogen related Q-disease. A mean residual pressure of $4 \cdot 10^{-9}$ mbar could be achieved applying evacuation by a turbomolecular and an ion getter pump. Subsequently, rf conditioning has been performed. All multipacting barriers up to 4 MV/m could permanently be surmounted.

In a next step the rf performance of the cavity was reviewed. Figure 1 shows the related Q_0 vs. E_a curves measured in vertical position (without helium vessel, red curve) and in horizontal orientation (with helium vessel, blue curve), respectively. The maximum Q-value at a low field level (Q_0^{low}) was measured for $1.37 \cdot 10^9$ which is 4.9 % lower in comparison to the first vertical test. This minor discrepancy is caused by worse magnetic shielding leading to a less residual surface resistance R_S (38 nΩ instead of 36 nΩ, see Table 2). Nevertheless, recently the cavity showed an improved performance due to an advanced HPR treatment. The initial design quality factor at 5.5 MV/m has been exceeded by a factor of 4. Furthermore, a maximum accelerating gradient of $E_a = 9.6\,\mathrm{MV/m}$ at $Q_0 = 8.14 \cdot 10^8$ was reached, which is a promising result considering the complex multigap structure of the cavity. The maximum gradient is limited by cavity quenches presumably caused by a thermal defect since the degeneration of the Q-value is still quite low. Table 2 summarizes the main measurement results of both rf tests.

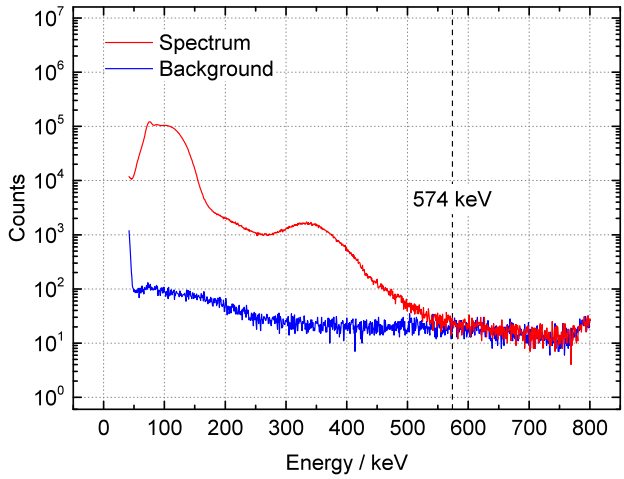

Figure 3: X-ray spectrum of the cavity at $E_a = 5.5\,\mathrm{MV/m}$.

Table 2: Main results of the vertical and horizontal rf test

		Vertical test w/o He vessel	Horizontal test with He vessel
Q_0^{low}		$1.44 \cdot 10^9$	$1.37 \cdot 10^9$
R_S	nΩ	36	38
R_{BCS}	nΩ	15	15
R_{mag}	nΩ	9	12
R_0	nΩ	12	11
E_a	MV/m	6.9	9.6
Q_0		$2.19 \cdot 10^8$	$8.14 \cdot 10^8$
V_a	MV	4.2	5.9
E_p	MV/m	43	60
B_p	mT	39	55

FURTHER ANALYSIS

Respectively the evaluation of the power consumption shows that the cavity was no longer limited by field emission at low field levels contrary to earlier measurements. Figure 4 shows the total power losses inside the cavity as function of the gradient in comparison to the expected ohmic losses asuming a constant Q-value. Related to the previous test (red curve) the total losses increase due to field emission from $E_a = 2\,\mathrm{MV/m}$ while the related peak electric field E_p is estimated in the range between 12 MV/m or 43 MV/m referred to the maximum gradient. At $E_a = 5\,\mathrm{MV/m}$

ISBN 978-3-95450-181-6

repectively at E_p = 32 MV/m the total power consumption increases rapidly suggesting an activation of a field emitter. This behaviour can be confirmed by considering the corresponding non-ohmic losses which increase exponentially starting at the same field level as shown in Figure 5. After the cavity's surface was rinsed again a central field emitter could be removed or at least significantly smoothed. Thus, extremely reduced non-ohmic losses occur and a minor field emitter activation only beyond E_a = 7.8 MV/m can be observed (see Figure 5, blue curve). In that case E_p is 49 MV/m or up to 60 MV/m at the maximum accelerating gradient. Figure 6 shows the corresponding Fowler-Nordheim plot illustrating the different enhancement factors β_{FN} of the emitting spots for the two different surface qualities. Due to the extensive HPR treatment and the resulting improvment of the surface quality the enhancement factor could be decreased from β_{FN} = 403 to β_{FN} = 176 reflecting a distinct difference in emitter activity.

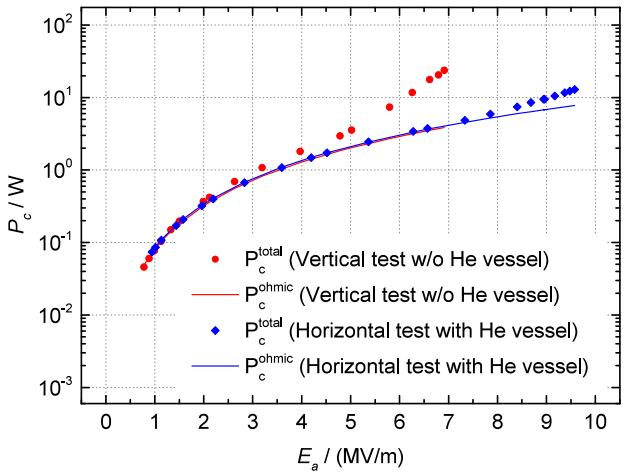

Figure 4: Total losses inside the cavity in comparison to pure ohmic losses for the vertical and horizontal rf test.

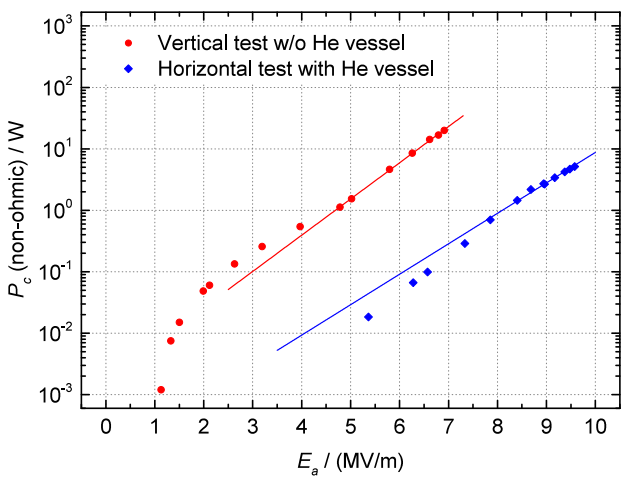

Figure 5: Non-ohmic losses inside the cavity before and after the improved surface preparation.

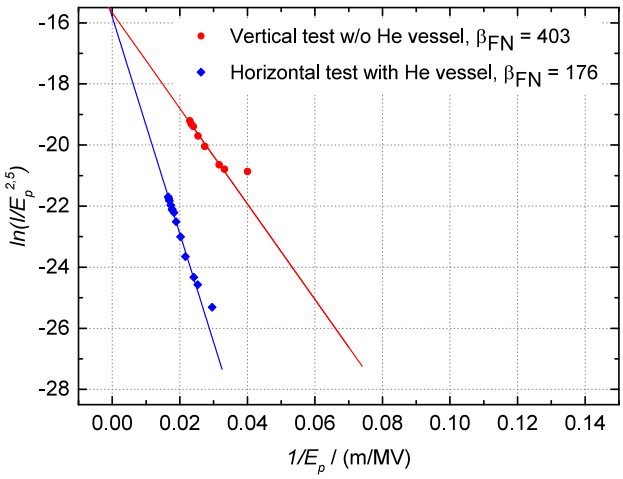

Figure 6: Fowler-Nordheim plot for the two different surface qualities.

SUMMARY & OUTLOOK

The sc 217 MHz CH cavity has been successfully tested at GSI with low level rf power at 4.2 K. A very promising gradient of 9.6 MV/m could be reached after an advanced surface preparation. In a next step a full performance test with beam is planned for the 1st quarter of 2017. Afterwards an optimized HPR device will be used allowing to rinse the cavity additionally inside each quadrant. Other methods, like an argon plasma discharge or a 300°C bake-out, are foreseen to improve the surface quality of the cavity. Furthermore, two short sc 217 MHz CH cavities [6] with a simplified geometry for the advanced demonstrator [7,8] are currently under construction, at least reproducing or probably improving the excellent results made so far.

REFERENCES

[1] V. Gettmann et al., in Proc. of SRF2011, Chicago, Illinois, USA, MOPO030 (2011).

[2] F. Dziuba et al., Phys. Rev. ST Accel. Beams 13, 041302 (2010).

[3] S. Minaev et al., Phys. Rev. ST Accel. Beams 12, 120101 (2009).

[4] M. Amberg et al., in Proc. of LINAC2014, Geneva, Switzerland, MOPP068 (2014).

[5] F. Dziuba et al., in Proc. of LINAC2016, East Lansing, Michigan, USA, THPLR044 (2016).

[6] M. Basten et al., in Proc. of IPAC2016, Busan, Korea, MOPOY019 (2016).

[7] W. Barth et al., in Proc. of IPAC2014, Dresden, Germany, THPME004 (2014).

[8] W. Barth et al., in Proc. of Baldin ISHEPP XXIII, Dubna, Russia, EPJ Web of Conferences (in press) (2016).

ISBN 978-3-95450-181-6

COLLECTOR RING PROJECT AT FAIR: PRESENT STATUS*

P. Shatunov, D. Berkaev, A. Kasaev, Yu. Rogovsky, D. Shwartz, Budker Institute of Nuclear Physics SB RAS, Novosibirsk, Russia and FSBI "SSC RF ITEP" of NRC "Kurchatov Institute", Moscow, Russia
V. Anashin, E. Bekhtenev, M. Bryzgunov, D. Gurov, V. Kolmogorov, I. Koop, A. Krasnov, O. Meshkov, T. Rybitskaya, A. Semenov, Yu. Shatunov, S. Shiyankov, A. Starostenko, A. Sukhanov, A. Tsyganov, A. Utkin, Budker Institute of Nuclear Physics SB RAS, Novosibirsk, Russia

Abstract

In November 2013, the FAIR management delegated the responsibility for the technical design, construction, installation, and commissioning of the whole Collector Ring and its components from GSI to Budker Institute of Nuclear Physics (BINP). Since that time a lot of modifications of the original design were made aiming to improve the beam parameters and the machine performance. This work shows the present status of the development.

INTRODUCTION

Collector Ring (CR) is one of the key installations of the FAIR project (Darmstadt, Germany). It is dedicated for stochastic cooling (SC) of incoming beams of antiprotons and rare ions. The cycle of the CR operation consists of injection, RF stretching, SC and finally extraction towards the HESR. Additionally there is a mode of operation for experiments with precise mass measurements of the particles in the ring. Main parameters of the storage ring for three main modes of operation are shown in Table 1. The sketch of the ring is presented in the Figure 1.

Table 1: The CR Main Parameters

	Antiprotons	Ions
Perimeter, Π	221.451 m	
Rigidity, Bρ	13 T·m	
Number of particles, N	10^8	10^9
Kinetic energy, K	3 GeV	740 MeV/u
Velocity, v	0.971c	0.830c
Relativistic factor , γ	4.20	1.79
Betatron tunes, ν_x, ν_y	4.39, 3.42	3.40, 3.44
Revolution frequency, ω_0	1.35 MHz	1.16 MHz

The work of BINP was based on the final version of the Technical Design Report (TDR) for the CR that was released by the GSI team in February 2014 [1]. Since that time a lot of modifications of the original design were made aiming to improve the beam parameters and the machine performance. All these changes were reported to the Machine Advisory Committee (MAC) in 2014 and 2015 and following its recommendations were published as a TDR Annex in 2016 [2]. These two Annexes to the TDR summarize all changes to the CR design made since February 2014. Here the part of the work done in BINP is presented.

*The work is carried out with the financial support of FAIR-Russia Research Center

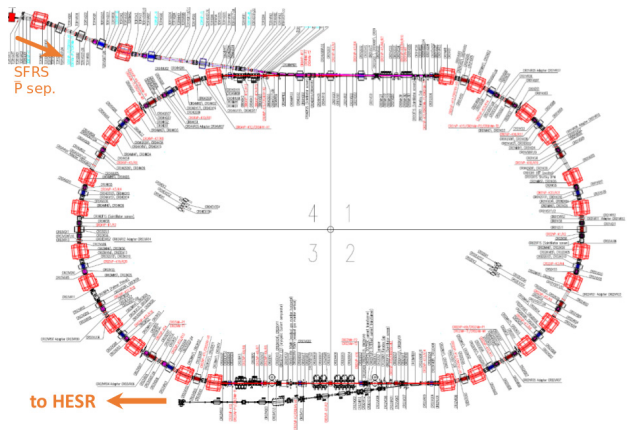

Figure 1: The Collector Ring overview.

LATTICE

The huge work was done to adopt the projects lattice to various demands coming from RF-system, SC-system, Injection/Extraction system and HESR team, taking into account all modes of operation. The apertures and lengths of magnets as well as conceptual design of all the correctors and beam diagnostic components were changed. Some magnetic elements were rearranged. Totally new concept for vacuum system was proposed.

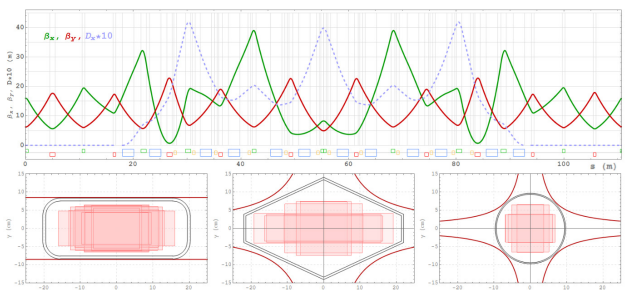

Figure 2: The lattice functions of the CR for the anitproton mode of operation and matching of the beam sizes to the aperture in the elements: the bending magnet, wide quadrupole and narrow quarupole (from left to right).

All these numerous changes were supported by adaptation of linear lattice with control of self-consistence of beam sizes, betatron phase advances between key azimuths, magnets apertures etc. Finally, in the end of 2015 the acceptable solution of overall CR conceptual design was found and the lattice (for all three operation modes) was frozen (see Fig. 2).

Since the momentum spread is very large in injected beam the natural betatron tunes chromaticity must be

ISBN 978-3-95450-181-6

compensated to fit beam footprint between resonances. Also it is important to control second-order chromatic effects (second-order dispersion function, lattice function chromaticity) to avoid strong chromatic variation of beam sizes where the aperture is limited, and variation of betatron phase advances between SC components.

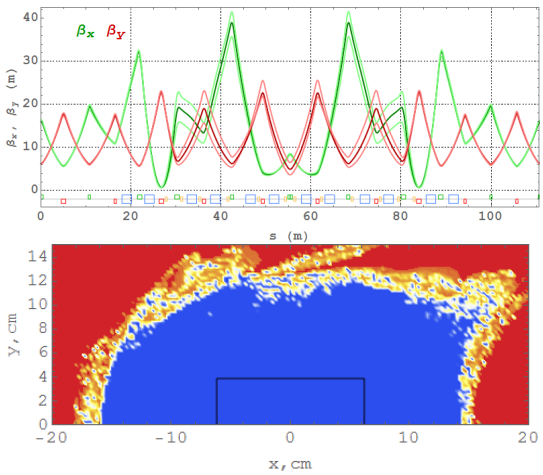

Figure 3: The chromatic effects of the lattice functions in one half of the ring (up) and the dynamic aperture estimation for the CR in the antiproton mode (bottom). The black rectangle in the middle matches to the physical aperture of the ring.

There was found a scheme to suppress these effects with use of 6 families of sextupole magnets [3]. However sextupole magnets are the main source of nonlinear fields. The dynamic aperture was checked for this scheme taking into account the nonlinearities of main magnetic elements and random deviations in strength and rotation of the quads and sextupoles (see Fig. 3).

MAGNETIC ELEMENTS

Extremely high acceptance of the ring (240 mm*mrad) leads to large apertures of all magnetic elements including the septum magnets. Meanwhile desired parameters of the magnetic field and magnetic field quality are comparatively strict. All magnets are iron dominated with laminated yoke. The standard production technology will be used while the quality is achieved by the yoke geometry. Here the short review of all the magnetic elements is given.

Bending Magnet

The CR will use normal conducting dipole magnets (see Fig. 4). There will be 24 H-type sector magnets with a deflection angle of 15° with a maximum field value of 1.6 T. The usable magnet gap will be 140 mm, while the horizontal good field region amounts to 380 mm. The integrated 5,37 см over the length of the magnet field quality as a function of radius is $\Delta B \cdot l / B \cdot l = \pm 1 \times 10^{-4}$ as required from the beam dynamics simulations. This challenging field quality is necessary mainly for precise experiments with ion beam in ISO regime. Below 1.6 T the value $\Delta B \cdot l / B \cdot l$ can be higher with a linear approximation up to $\pm 2.5 \times 10^{-4}$ at the field level of 0.8 T.

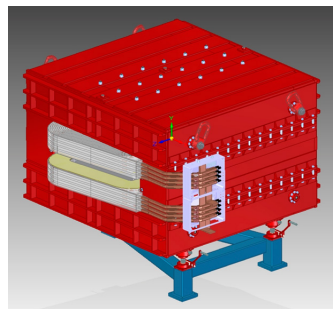

Figure 4: The 3D model of the designed dipole.

The present layout proposes a coil with total current of 88×1420 A. The required DC power for this magnet amounts to 126 kW. To change the polarity between maximum field levels within a minute the ramp rate of 0.054 T/s is required presently for the dipole power converter.

Quadrupole Magnets

Because of the large acceptance of the CR, it is important to use large aperture magnets only where they are needed.

Table 2: Main Parameters of the CR Quarupole Magnets

	Wide	Short Wide	Extended Wide	Narrow
Number of magnets	14	12	3	11
Maximum gradient [T/m]	4.7	4.7	3.5	6.2
Inscribed radius [mm]	160	160	185	100
Effective length [m]	1.0	0.7	1.0	0.5
Integrated gradient [T]	4.7	3.29	3.5	3.1
Field homogeneity $\Delta B/B$	$\pm 5 \times 10^{-4}$	$\pm 5 \times 10^{-4}$	$\pm 1 \times 10^{-3}$	$\pm 5 \times 10^{-4}$
Coil current [A]	1470	1480	1470	1210

The extremely wide aperture quadrupole magnets with useful aperture 450 mm × 180 mm are used for the injection section (inscribed to poles radius 185 mm) (see Table 2). In the arcs two other types of wide aperture quadrupoles with pole radius 160 mm will be installed. One group of 14 quadrupoles has the useful aperture 400 mm × 180 mm and the effective magnetic length 1 m. The other group of 12 quadrupoles has the same aperture but shorter effective length equal to 0.7 m. The narrow quadrupole magnets (useful aperture 180 mm × 180 mm, pole radius 100 mm) are installed only in the straight sections.

ISBN 978-3-95450-181-6

Sextupole Magnets

24 sextupole magnets are used in CR. 3D modelling (see Fig. 5) was done to achieve the desired parameters: the maximum strength of 10 T/m^2, the effective length of 500 mm, the inscribed radius of 201 mm, the useful aperture of 430 × 180 mm^2, the field uniformity of $\pm 5\times10^{-3}$. Coils have 22 turns for each pole with the maximum current of 500 A.

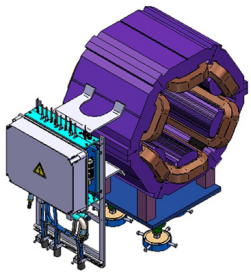

Figure 5: The 3D model of the sextupole magnet.

Dipole Correctors

Three types of steering magnets for orbit correction are proposed in the CR: additional separately powered coils embedded into dipoles; wide-aperture vertical; narrow-aperture combined-functions X/Y steering magnets.

The embedded correctors should provide angle of ±3 mrad with use of 270 turns coils with maximum current of 5.5A. The vertical correctors are of a frame type and envelope the beam position monitors. With maximum current density of 1.7 A/mm^2 the maximum field is 0.045T over the effective length of 740mm.

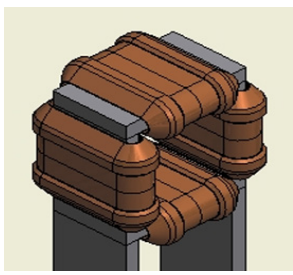

Figure 6: The 3D model of the combined steering magnet.

Combined Steering Magnets (see Fig. 6) with narrow aperture are window-frame magnets with two pairs of separately powered coils. The maximum field of 0.067 T over the effective length of 300 mm is achieved with the current density of 1.9 A/mm^2 and gives the maximum angle of ±1.5 mrad.

Octupole Correctors

Octupole correction coils will be installed into 12 wide quadrupoles of the CR arcs (see Fig. 7) to increase the parameters of the experiment in the isochronous mode. The maximum achievable octupole gradient is 13 T/m^3 with 268 turns of the coil and the current of 6 A.

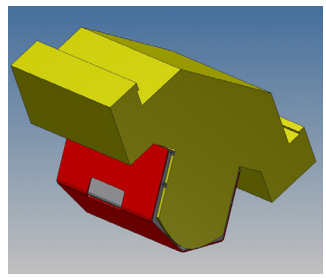

Figure 7: 3D model of the one quarter of the quad yoke with octupole coils.

Injection Septum Magnet

Three pulsed magnets (see Fig. 8) form the Injection Septum Magnet (IJS) and bend the beam for 124 mrad. C-type laminated yoke is used [4]. Magnetic field in the gap is formed with two coils – primary multiturn coil connected to the power source and secondary one-turn coil connected to the knife. The length of the pulse is 3ms. Maximum magnetic field of 0.6T is reached with the current of 5kA. The ceramic vacuum tube is used to reduce the heat losses of eddy currents.

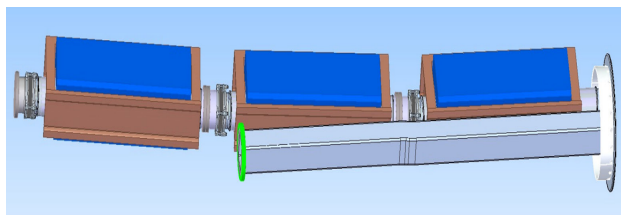

Figure 8: The magnets of ISM with the vacuum chamber.

Injection-Extraction Kicker Magnets

There are 6 kicker magnets (KM) grouped in two vacuum tanks (see Fig. 9) [5]. Same KM are used for both injection and extraction. The length of the pulse is variable from 150 to 1500 ns. The pulse of 70kV produces integrated magnetic field of 1944 mT×m that allows the kick of 15mrad in the beam. Ferrite yoke forms the magnetic flux.

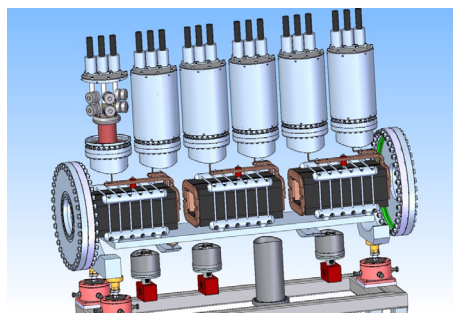

Figure 9: The set of the 3 KM in the vacuum tank.

PRODUCTION PLANS

Production plans for the elements of the ring are mainly dictated by the production of the bending magnets. According to the design 65 months are needed. It matches to the schedule of the FAIR installation procedure. All other elements fit into these dates.

ISBN 978-3-95450-181-6

REFERENCES

[1] A. Dolinksy et al. “Technical Design Report of the CR, v.15”, 2014.
[2] V. Anashin et al., “CR TDR Annex-1”, 2016.
[3] D. Shwartz et al., “Chromatic and Nonlinear Dynamics of Antiprotons Injected to Collector Ring at Fair”, WEPSB017, these proceedings.
[4] P. Yu. Shatunov et al., “The Injection Septum Magnet for the Collector Ring (FAIR)”, Proc. IPAC’16, p.1145.
[5] A. Kasaev et al., “The Kicker System for the Collector Ring Project (FAIR)”, THPSC016, these proceedings.

ISBN 978-3-95450-181-6

SPALLATION NEUTRON SOURCE AT THE 1 GeV SYNCHROCYCLOTRON OF PNPI

O.A. Shcherbakov#, E.M. Ivanov, G.F. Mikheev, G.A. Petrov, G.A. Riabov, A.S. Vorobyev, B.P. Konstantinov Petersburg Nuclear Physics Institute, NRC "Kurchatov Institute", Gatchina, Leningrad district, 188300, Russia

Abstract

A description of the spallation pulsed neutron source and neutron TOF spectrometer GNEIS based on the 1 GeV proton synchrocyclotron of PNPI in Gatchina is presented. The main parameters of the GNEIS are given in comparison with the analogous world-class facilities. The experimental capabilities of the GNEIS are demonstrated by the examples of some nuclear physics and applied research experiments carried out during four decades of its operation.

DESCRIPTION OF NEUTRON SOURCE

The 1 GeV proton synchrocyclotron SC-1000 at the PNPI was commissioned in 1970 [1]. A few years later (1975), spallation neutron source and TOF spectrometer GNEIS have been developed at the accelerator and put into operation [2]. Since that time GNEIS was effectively used for neutron-nucleus interaction studies utilizing the time-of-flight technique over a wide range of neutron energies from thermal up to hundreds of MeV, both for basic nuclear physics and applied research.

The water-cooled lead target (40×20×5 cm^3) of the GNEIS neutron source is located inside the accelerator vacuum chamber (Fig. 1) below the median plane of the accelerator magnet magnetic field.

When the circulating proton bunch is deflected to strike the target, the short (~10 ns) pulses of fast neutrons are produced at a repetition rate of ≤50 Hz. At the average internal proton current of 3 μA and neutron yield of ~20 n/p for 1GeV protons, the average intensity of fast neutrons is equal to ~$3 \cdot 10^{14}$ n/s. Neutron source is supplied with a polyethylene moderator (30×10×5 cm^3) located above the target and median plane. The target and moderator are moved remotely in vertical and radial directions for optimum position during the accelerator and neutron source tuning. Five neutron beams are transported using evacuated flight tubes through the 6 m thick heavy concrete shielding wall of the accelerator main room into the experimental hall of the GNEIS. The beams are equipped with brass/steel collimators, steel shutters and concrete/steel beam dumps. Measurement stations for experimental installations are located in the GNEIS building (15×30 m^2) at the flight path distances of 35-50 m. Neutron beams #1- 4, whose axes pass through the moderator, are characterized by a $1/E^{\alpha}$ (α = 0.75-0.95) neutron spectrum shape (Fig. 2) being well suited for measurements at resonance energies (1 eV – 100 KeV). Neutron beam #5, whose axis "looks" at the surface of "bare" lead target, has a typical spectrum shape with spallation and cascade components in the neutron energy

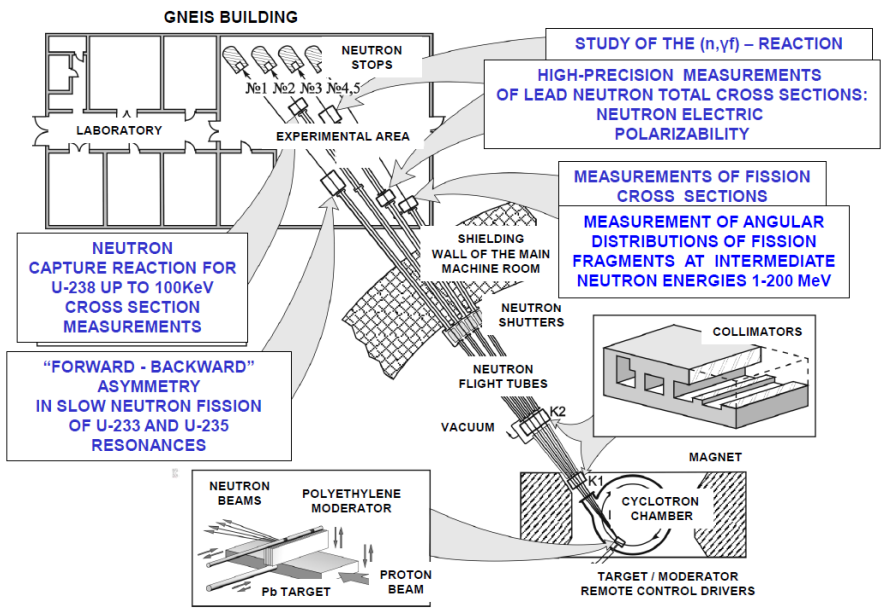

Figure 1: General layout of the GNEIS facility.

#shcherbakov_oa@pnpi.nrcki.ru

ISBN 978-3-95450-181-6

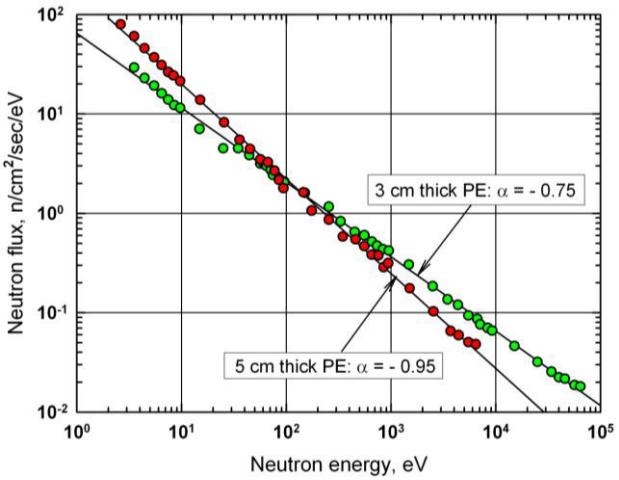

Figure 2: The neutron spectra of the beam #3 measured at the 40 m flight path station with 3 cm and 5 cm thick polyethylene (PE) moderators. The data are normalized to an average neutron production rate of $1.5 \cdot 10^{14}$ n/s.

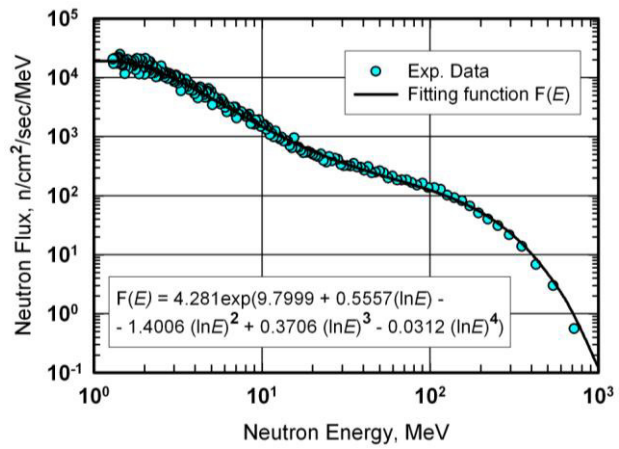

Figure 3: Neutron spectrum from the "bare" lead target measured at the 36.5 m flight path station of the beam #5. The data are normalized to an average neutron production rate of $2.5 \cdot 10^{14}$ n/s.

range 0.1-1000 MeV (Fig. 3). The cascade component extends up to the energy of the incident protons (1 GeV) and is strongly peaked in the forward direction. The evaporation component which is dominant below ~ 20 MeV has the shape of a Maxwell distribution with a characteristic temperature of 1-3 MeV and is practically isotropic.

For non-relativistic neutron energies below ~ 10 MeV, the commonly used expression for evaluation of the energy resolution of a neutron TOF-spectrometer is

$$\Delta E / E = 2.78 \cdot 10^{-2} E^{1/2} (\Delta t / L), \qquad (1)$$

where E (eV) is the neutron energy, L (m) is the flight path length and Δt (μs) is the total timing uncertainty. It is convenient to approximate the resolution function by a Gaussian-type curve

$$R(E / E') = \frac{1}{W\sqrt{\pi}} \exp\left(-\frac{(E - E')^2}{W^2}\right). \qquad (2)$$

The relation of the practically used quantity H (full width at half-maximum) and parameter W is defined by

$$H = 2W\sqrt{\ln 2}. \qquad (3)$$

The basic components of the total width of resolution function are as follows

$$W^2 = W_D^2 + W_M^2 + W_T^2, \qquad (4)$$

where W_D is the width of Doppler broadening due to the thermal motion of investigated nuclei, W_M is the moderator contribution, and W_T is determined by the various timing uncertainties, such as the neutron burst width τ_n, the TDC's channel width τ_{ch}, the electronic jitter τ_j, etc. The energy resolution of the GNEIS (relative half-widths of the resolution function) and its basic components are shown in Fig. 4 for the 40 m flight path length, the 5 cm thick PE moderator, and the accelerator burst width of 10 ns. For comparison, the resolution functions for similar TOF facilities with 100 ns and 1μs neutron burst widths are also shown. It should be noted that inclusion of other timing uncertainties mentioned above leads to the broadening of resolution function.

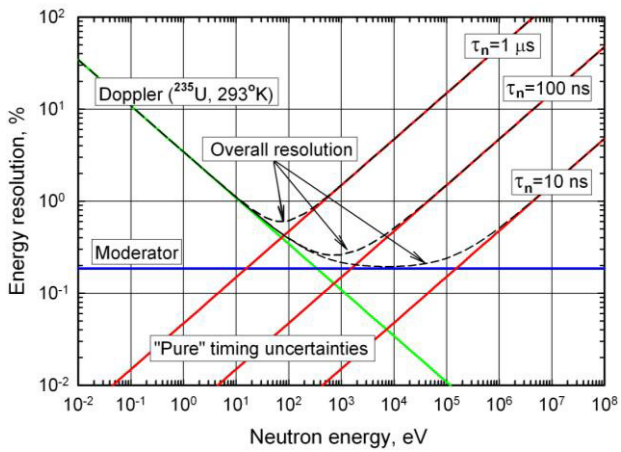

Figure 4: The energy resolution of the GNEIS facility.

COMPARISON WITH OTHER FACILITIES

At present, on the European neutron landscape, 4 pulsed neutron sources located in Russia can be specified, namely: GNEIS (Gatchina), IREN and IBR-2 (Dubna), IN-06 (Troitsk). Currently, only first 2 facilities are used for neutron resonance TOF spectroscopy and only the GNEIS can effectively compete with the best neutron sources/TOF facilities operated in other countries. In a Table 1 below, a comparison of the GNEIS with the

ISBN 978-3-95450-181-6

world-class facilities is given. It should be emphasized that the GNEIS and other spallation neutron sources have much higher upper limit of neutron spectra (up to 1 GeV) than those based on the electron Linacs (below 100 MeV). This feature makes spallation neutron sources indispensible for investigations at intermediate energies (several hundred MeV).

Table 1: Parameters of the GNEIS and other neutron sources. The quality coefficient of the neutron source is defined as: intensity/(pulse width)^2. The quality coefficient value marked by *) corresponds to 10 ns pulse width.

Neutron source (laboratory)	Intensity (10^{15} n/s)	Pulse width (ns)	Quality (10^{30} n/s^3)
GNEIS (PNPI, Gatchina, Russia)	0.3	10	3.0
IREN (JINR, Dubna, Russia project)	1.0	400	0.0062
n_TOF (CERN, Switzeland)	0.4	6	11
LANSCE (LANL, USA)	10	1-125	100*)
ORELA (ORNL, USA)	0.13	2-30	1.3*)
GELINA (IRMM, Belgium)	0.025	1	25

EXPERIMENTS AT THE GNEIS

High intensity and energy resolution of the GNEIS enable to perform measurements of neutron total and partial cross sections (e.g. capture, fission, etc.) with high precision and reliability. In the inserts of Fig. 1 are shown titles of the main experiments carried out at the GNEIS. The first one was dedicated to study of the (n,γf)-reaction in ^{235}U and ^{239}Pu in energy range 1-200 eV, which means a neutron-induced fission after preliminary emission of one or more γ-quanta [3-5]. In the other experiment, a so-called "type-II" 720 eV-resonance was investigated in the subthreshold fission of ^{238}U [4]. An accuracy of the cross section measurements of the next experiment was increased from 1-2% to 0.2-0.5 % with the aim to evaluate effect of "forward-backward" asymmetry of fission fragments and parameters of the very weak p-resonances non-observed by usual methods in slow neutron fission of ^{233}U and ^{235}U [6, 7]. A value of neutron electric polarizability was reliably obtained from the results of high-precision measurements of the total cross sections of lead isotopes ^{204}Pb, ^{206}Pb, ^{207}Pb and ^{208}Pb below 10 keV [8, 9]. The unique experimental data for a number of actinides (^{232}Th, ^{233}U, ^{235}U, ^{238}U, ^{237}Np, ^{239}Pu, ^{240}Pu, ^{243}Am) and non-fissile nuclei (^{nat}Pb, ^{209}Bi, ^{nat}W) have

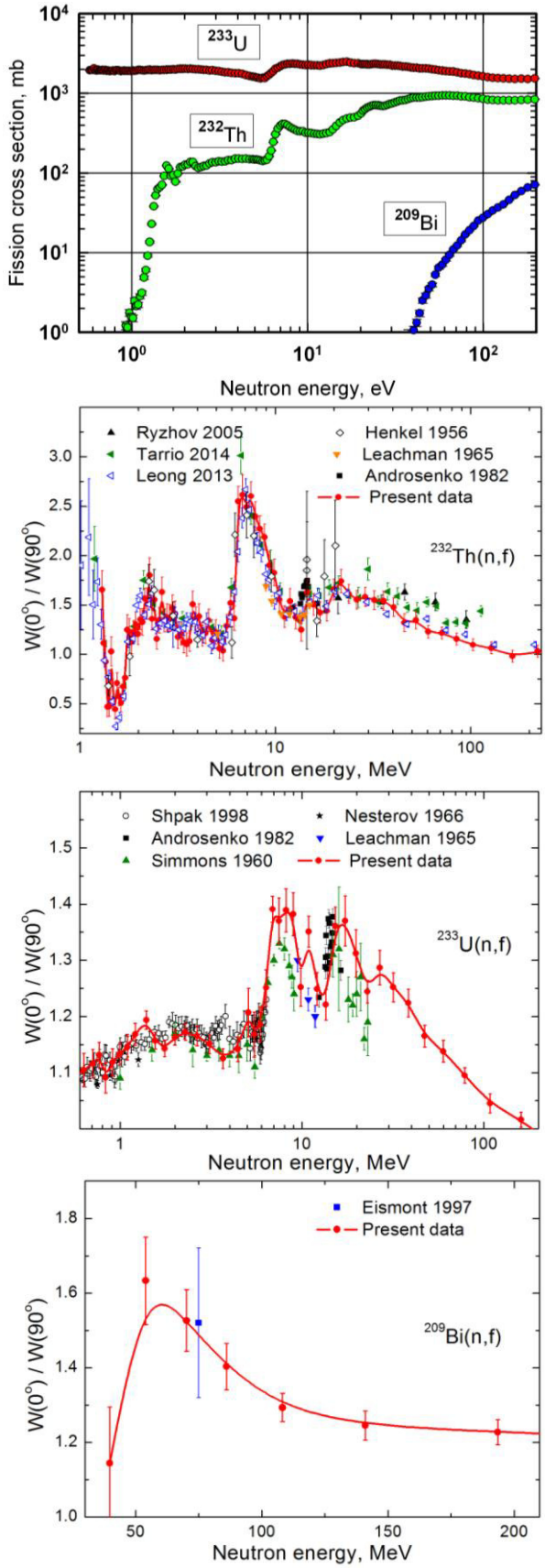

Figure 5: Fission cross sections and fission fragment anisotropy measured at the GNEIS spectrometer.

ISBN 978-3-95450-181-6

been obtained from the measurements of fission cross sections [10-12] and fission fragment anisotropy [13,14] in the energy range 1-200 MeV (Fig. 5), where the GNEIS facility successfully competes with LANSCE and n_TOF. During the last years, a neutron beam #5 of the GNEIS with atmospheric-like neutron spectrum is intensively used for SEE (single event effect) radiation testing of the electronic components.

NEUTRON TEST FACILITY

The ISNP/GNEIS test facility is operated since 2010 at the neutron TOF-spectrometer GNEIS [15, 16]. The main feature of this facility is a neutron spectrum resembling that of terrestrial neutrons in the energy range of 1-1000 MeV. The ISNP/GNEIS test facility is located inside the GNEIS building on the neutron beam #5, which has the following parameters:

- neutron energy range: 1-1000 MeV;
- neutron flux: $4 \cdot 10^5$ n/cm^2·s (at 36 m flight path);
- beam diameter: 50-100 mm (at 36 m flight path);
- uniformity of the beam profile plateau: ± 10%.

The neutron beam profile (Fig. 6) is measured by means of MWPC - the 2-coordinate position sensitive multiwire proportional counter used for registration of fission fragments from the ^{238}U target deposited on the MWPC's cathode. The neutron flux of $4 \cdot 10^5$ n/(cm^2·s) is an integral over neutron spectrum in the energy range 1-1000 MeV. It corresponds to the maximum value of 3μA of the internal average proton beam current. The neutron flux and shape of the neutron spectrum are measured using FIC (neutron monitor) and TOF-technique (Fig. 7). The FIC is a fast parallel-plate ionization chamber which contains two targets of ^{235}U and ^{238}U. The neutron fission cross sections of these nuclei are recommended standards in the energy range 1-200 MeV. These data are taken

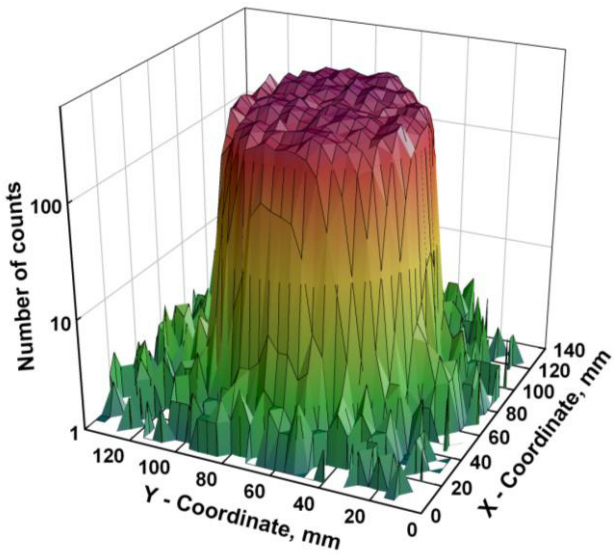

Figure 6: Neutron beam profile measured using MWPC.

from the ENDF/B-VII.1 Library [17] while the data above 200 MeV are taken from the JENDL High Energy Library [18]. The neutron spectrum of the ISNP/GNEIS is shown in Fig. 7 together with the JEDEC standard terrestrial neutron spectrum from JESD89A [19] referenced to New York City and multiplied by scaling factor $7 \cdot 10^7$, as well as the neutron spectra of leading test facilities [21-25]. The corresponding values of 1-hour neutron fluence in the energy range above 1 MeV are given in Table 2. Both the shape of the neutron flux and neutron intensity demonstrate that the ISNP/GNEIS is successfully competing with the other first-grade test facilities with the atmospheric - like neutron spectrum. It should be noted that presently in Russia the ISNP/GNEIS test facility is the only one with atmospheric-like neutron spectrum.

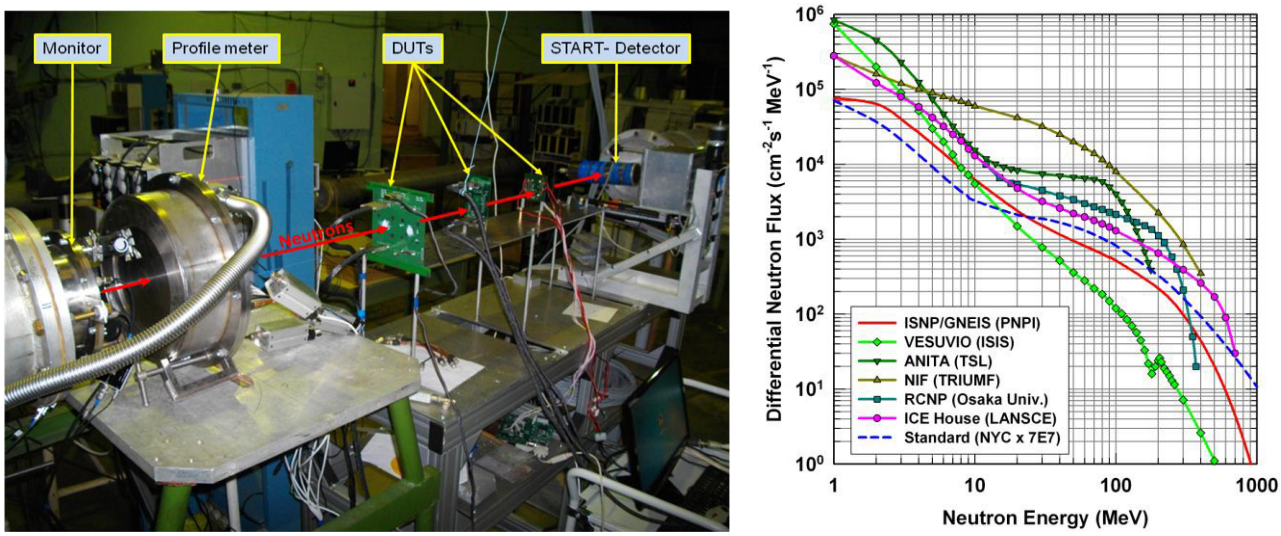

Figure 7: Left: General layout of the ISNP/GNEIS test facility. Right: Neutron spectrum of the ISNP/GNEIS comparison with standard terrestrial neutron spectrum [5] and spectra of other world-class test facilities [6-10].

ISBN 978-3-95450-181-6

Table 2: Integrated (E_n > 1 MeV) neutron flux of various neutron test facilities and Standards.

Standard/Facility (location, proton energy, target material)	Neutron Flux (n/cm^2 hour)
JEDEC (NYC, sea level, outdoors, mid. solar activity) JESD89A [19]	20
IEC (altitude 12 km, latitude 45°) IEC TS 62396-1 [20]	8760
ISNP/GNEIS (PNPI, Gatchina, 1000 MeV, lead)	$1.5 \cdot 10^9$
ICE House (LANSCE, Los Alamos, USA, 800 MeV, tungsten) [21]	$3.4 \cdot 10^9$
RCNP (Osaka University, Japan, 180 MeV, lead) [23]	$5.4 \cdot 10^9$
ANITA (TSL, Uppsala, Sweden, 400 MeV, tungsten) [22]	$9.9 \cdot 10^9$
NIF (TRIUMF, UBC, Vancouver, Canada, 500 MeV, aluminum) [24]	$1.3 \cdot 10^{10}$
VESUVIO (ISIS, RAL, Chilton, UK, 800 MeV, tungsten/tantalum) [25]	$2.5 \cdot 10^9$

The SC-1000 possesses a potential of the neutron intensity growth. A new irradiation station located at a distance of 5-6 m from the neutron-production target operated on the extracted proton beam enables to increase neutron flux at least 10 times at the DUT (device under test) position. Simultaneously, an irradiation of the bulky equipment will be possible.

CONCLUSION

Four decades of operation have showed that owing to its unique parameters, the GNEIS neutron source and TOF spectrometer still occupy an important place in the world list of neutron facilities effectively used for science and technology. High neutron intensity up to $3 \cdot 10^{14}$ n/s and short neutron burst of 10 ns, as well as a convenient repetition rate of 50 Hz, enable to cover neutron energy range from thermal up to hundreds of MeV in a single TOF-measurement. At present, the same experimental conditions are achievable only at the n_TOF facility at CERN. Also, it is important that both low-energy (< 10 KeV) and high-energy (above 10 MeV) measurements are carried out simultaneously due to availability of a few flight paths with different neutron spectra. Nuclear data measured using the GNEIS, primarily the high accuracy neutron cross sections, demonstrate the unique experimental capabilities of this spallation neutron source.

ACKNOWLEDGMENT

The authors express their sincere gratitude to all colleagues from the B.P. Konstantinov Petersburg Nuclear Physics Institute participated in development of the neutron source and TOF-spectrometer GNEIS, as well as the radiation test facility ISNP/GNEIS. They also thank the staff of the synchrocyclotron for their permanent efforts to provide stable operation of the accelerator during experimental and irradiation works. The financial support and cooperation with the Branch of Joint Stock Company "United Rocket and Space Corporation"-"Institute of Space Device Engineering (Moscow) in the development of the ISNP/GNEIS facility are highly appreciated.

REFERENCES

[1] N.K. Abrosimov et al., Zh. Tekhn. Fiz. 41 (1971) 1769.
[2] N.K. Abrosimov et al., Nucl. Instr. Meth. A. 242 (1985) 121.
[3] O.A. Shcherbakov, Sov. J. Part. Nucl. 21 (1990) 177.
[4] O.A. Shcherbakov and A.B. Laptev, "Prefission and capture gamma-rays in neutron resonances of ^{235}U, ^{238}U and ^{239}Pu," CGS-10, Santa Fe, Aug-Sept. 1999, AIP Conf. Proc. 529 (2000) 710.
[5] O.A. Shcherbakov, "Measurement and evaluation of (n,γf)-reaction effects in resonances of ^{235}U and ^{239}Pu", Int. Conf. "Nuclear Data for Science and Technology", Julich, May 13-17, 1991. Conf. Proc., Springer-Verlag, p. 918 (1992).
[6] A.M. Gagarski et al., JETP Letters. 54 (1991) 7.
[7] A.M. Gagarski et al., "Investigation of the p-resonance properties in slow resonance fission of ^{235}U", Int. Conf. "Nuclear Data for Science and Technology", Julich, May 13-17, 1991. Conf. Proc., Springer-Verlag, p. 134 (1992).
[8] A.B. Laptev et al., J. Nucl. Sci. Tech. Suppl. 2, 1 (2002) 327.
[9] O.A. Shcherbakov et al., "Nuclear physics investigations at the time-of-flight spectrometer GNEIS with spallation neutron source", ASAP 2002 Workshop, Oak-Ridge, March 11-13, 2000. Proc., World Scientific, p. 123 (2002).
[10] O.A. Shcherbakov et al., J. Nucl. Sci. Tech. Suppl. 2, 1 (2002) 230.
[11] A.B. Laptev et al., Nucl. Phys. A 734 (2004) E45.
[12] A.B. Laptev et al., "Fast neutron-induced fission of some actinides and sub-actinides", Int. Conf., Sanibel Island, USA, November 11-17, 2007. Conf. Proc., World Scientific, p. 462 (2008).
[13] A.S. Vorobyev et al., JETP Letters. 102 (2015) 231.
[14] A.S. Vorobyev et al., JETP Letters. 104 (2016) 365.
[15] N.K. Abrosimov et al., Instr. Exp. Tech. 53 (2010) 469.
[16] O.A. Shcherbakov et al., IEEE Trans. Nucl. Sci. 63 (2016) 2152.
[17] Evaluated Nuclear Data Library ENDF/B-VII.1 (2011).
[18] JENDL High Energy File 2007 (JENDL/HE-2007).
[19] JEDEC Standard JESD89A, Oct. 2006.
[20] IEC Technical Specification TS 62396-1, May 2006.
[21] The ICE House at LANSCE (available on line): http://lansce.lanl.gov/NS/instruments/ICEhouse/index.html.
[22] A.V. Prokofiev et al., "Characterization of the ANITA neutron source for accelerated SEE testing at the Svedberg laboratory," RADECS-2008, Jyvaskyla, Sept. 2008, Conf. Proc. p. 260 (2008).
[23] T. Nakamura et al., *Terrestrial Neutron-Induced Soft Errors in Advanced Semiconductor Devices* (World Scientific, Singapore, 2008).
[24] E.W. Blackmore et al., "Improved capabilities for proton and neutron irradiation at TRIUMF," IEEE Nuclear and Space Radiation Effects Conf., Radiation Effects Data Workshop, Monterey, 2003, Conf. Proc. p. 149 (2003).
[25] C. Andreani et al., Appl. Phys. Lett. 92 (2008) 114101.

ISBN 978-3-95450-181-6

RADIOCARBON ANALYSIS OF DIFFEREENT SAMPLES AT BINP AMS

S.A. Rastigeev, V. V. Parkhomchuk, BINP SB RAS, Novosibirsk, Russia and
NSU, Novosibirsk, Russia
A.R. Frolov, A.D. Goncharov, V. F. Klyuev, E.S. Konstantinov, N. A. Petrishchev,
A. V. Petrozhitskii, BINP SB RAS, Novosibirsk, Russia,
L. A. Kutnykova, IAE SB RAS, Novosibirsk, Russia

Abstract

The accelerator mass spectrometer (AMS) created at BINP is used for biomedical, archaeological and other applications. Present status and experimental results are described.

INTRODUCTION

The accelerator mass spectrometry is an ultra-sensitive method of isotopic analysis for archaeology, geology, biomedical science and other fields. It's based on measurements of the ratio between isotopes. The ratio between isotopes in sample can be less than 10^{-15}. So, the counting methods are used for detection of such low radiocarbon concentration [1-5]. The AMS is based on the electrostatic tandem accelerator. The AMS system consists of the ion source, low energy channel, tandem accelerator and high-energy channel [6-8]. The low energy beam line is used for initial isotopes selection. The tandem accelerator is applied for rejection of the molecular ions and of course for obtaining necessary beam energy for radioisotopes detector. The high-energy beam line is used for the subsequent ions selection and for radioisotopes detection.

. The most distinguishing feature of our AMS machine is the use of additional electrostatic separator of ion beam, located inside the terminal. In this configuration of the AMS, the ions background is significantly reduced by the energy filter in the high voltage terminal. Interfering isobaric molecules are destroyed by collisions in the stripper into the terminal and are selected immediately after the stripping process. It is important to decrease the background from molecular fragments before the second stage of acceleration [9-10], because the energy of fragments is always less then the ion energy (at this moment). The next important distinguishing feature is magnesium vapours stripper [11] instead of the gas stripper. The gas flow into the accelerator tubes leads to big energy spread in the beam thus limiting the sensitivity and accuracy of spectrometer. The molecular destruction and ion recharging by magnesium are localized into the hot tube of the stripper. Moreover, the moment of time for ion detection can be registered with 16 μs channel width by TOF detector [12,13]. This data is used for calculation of number of detected ions per unit time, allowing filtering the background ions from electrical breakdowns.

AMS ANALYSIS ALGORITHM

During the measurements of user samples, the injection energy of radiocarbon beam was about 25 keV. The terminal voltage of tandem accelerator was 1 MV. The 180° electrostatic bend was set to transmit the ions with charge state 3+. The magnesium vapors stripper was heated for obtaining the equilibrium charge state distribution, but not more. The vacuum in the beam line was about 10^{-6} Torr.

The 20 graphitized samples are setted in the ion source sample wheel to measure the concentration of radiocarbon. Furthermore, the 3 control sample with a known concentration of radiocarbon is setted in ion source sample wheel for control and normalization of the measurement samples. Typically, this sample are two carbon wire with a carbon concentration on the natural content of modern plants and one sample of graphite MPG with radiocarbon concentration at $2*10^{-3}$ compared to modern plants. It should be noted that the control samples did not require the procedure of graphitization and setted in the sample wheel in natural form.

When measuring the concentration of radiocarbon in the samples, the switching algorithm is used. The isotope ^{14}C is detected by TOF telescope and ^{13}C currents are measured at the exit of AMS. For switching algorithm the high voltage of ion source is changed. The energy of the cesium ions remains constant. The electrostatic lens and correctors at the exit of the ion source are changed for each isotope. Thus, the passage of isotopes is carried out through a first dipole magnet, without changing the magnetic field. The magnetic field in high energy magnet is not changed to, because the radial aperture is wide enough for passing radiocarbon ions to TOF detector and ^{13}C ions to shifted FC.

The cycle of AMS-analysis of samples is represented as follows. For each sample, the ^{14}C ions are counted four times (10 seconds each) and twice the ^{13}C currents are measured for each 10 seconds counting. After that, the samples wheel is turned to the next sample for process repetition. Measuring of whole graphitized sample wheel (20 samples) takes about 15 minutes. For a set of statistics the wheel are moving to the second turn, third, etc. Typically, the measurement will take approximately 5 hours, with a statistical error of measurement for modern samples less than 1%. The process of isotope measuring and sample changing (wheel rotation) is fully automated.

ISBN 978-3-95450-181-6

SAMPLES FOR AMS ANALYSIS

For AMS analysis, all samples must be converted to so-called "graphite". For these purposes, a sample is combusted in vacuum. Then the carbon from formed CO_2 gas catalytically deposited on iron powder. The Fe-C mixture is pressed in aluminum sample holder (cathode for ion source) for AMS analysis.

Now at BINP AMS used two types of sample holders: with inner diameter of 2 mm (for about 3 mg of carbon sample) and with inner diameter of 1 mm (for 1 mg or less of carbon sample). The 1 mm and 3 mm samples can be installed in the sample wheel together. The sputtering by Cs beam region of the sample is about 0.5 mm in diameter. The new alignment system was manufactured for the Cs beam hitting in the center of the 1 mm target.

Now at BINP AMS used graphitized samples from NGU and LAE SB RAS chemists and a number of samples graphitized at IG RAS. Samples are produced from a variety of natural materials: bone, charcoal, wood etc.

The quality of sample preparation is crucial for formation of negative carbon ions from ion source, because sufficiently good thermal conductivity of samples is needed. The sputtered carbon atoms capture electrons from the cesium, which was accumulated on the surface of the sample. If thermal conductivity of samples is low, the cesium atoms are evaporated from sample surface. Typically, the maximum current is obtained from graphite without sample preparation. The currents from graphitized natural samples are in the range from graphite currents level to much smaller level.

Contamination during sample preparation can significantly affect to the dating results. The "dead" carbon pollution (for example, the carbon from technical oil) increases the age of dating objects. The "modern" carbon pollution (for example, the carbon from atmospheric CO_2) decreases the age of dating objects.

RADIOCARBON MEASUREMENTS

Over the last year, more than 1000 samples were analyzed at BINP AMS. The typical carbon beam currents from samples during samples wheel rotation are present at the Fig. 1 (a). As seen, the beam current of sample from sample position 14 (sp14) is so much smaller than the other. The vacuum is worse, when the sp14 sample is sprayed by cesium beam Fig. 1 (b). The vacuum remains good enough and does not affect to the beam transmission efficiency. During the measurement, the gassing from such sample is reduced, but the carbon current is not increased significantly. The mean currents for the time of AMS analysis are present at the Fig. 1 (c). Typically, the currents from samples can differ twice. The carbon beam current ratio from the different samples can be changing during the measurement. This depends on the special features of graphitization for each sample. However, beam current from some samples can be very small (as from sp14 sample). Significant number of the samples with a small current is contaminated by external carbon during graphitization. The radiocarbon dating of samples with small current is not reliable and usually necessary graphitize additional sample. Moreover, the statistical error of measurements for such samples is significantly greater than for the other samples.

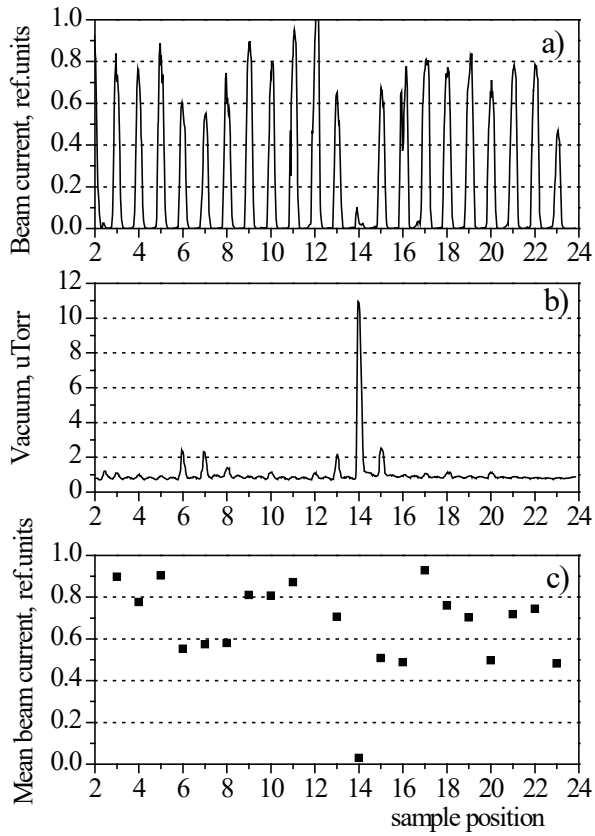

Figure 1: The carbon beam current a), mean current c) and the residual gas pressure b) for samples.

The kinds of pollution can differ in the graphitized samples. The oxygen current from samples during sample wheel rotation are present at the Fig. 2. The AMS was tuned to the passage of oxygen beam. The sample in position 2 is a graphite MPG (without sample preparation), the samples in positions 1, 12 are carbon wires (without sample preparation), the other samples - graphitized natural objects. As seen, the oxygen content in graphitized samples is significantly higher than in technical graphite MPG. Many other chemical elements can be present even in "clean" samples. For example, the boron concentration normalized to the carbon is about 10^{-6} in graphite MPG without sample preparation, the lithium concentration - about 10^{-9}. But, if the radiocarbon selection in AMS is good enough, it is not a problem for radiocarbon dating. The light atoms can pass the injection magnet as part of the molecule 14 a.m.u. mass as if radiocarbon ions. Such atoms are separated from radiocarbon beam by energy filter in the high voltage terminal at BINP AMS.

ISBN 978-3-95450-181-6

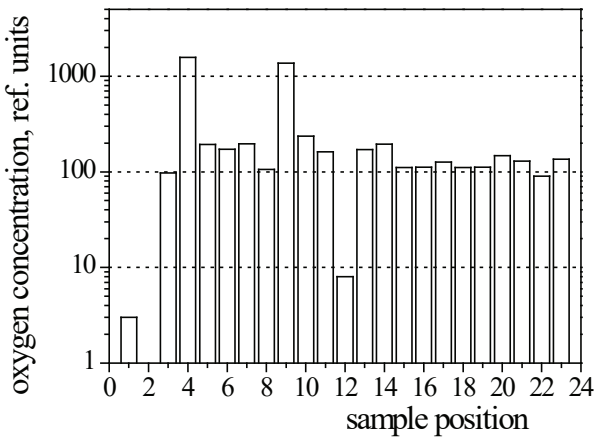

Figure 2: The oxygen beam currents from the samples.

The isotope ratio may differ significantly before and after graphitization (fractionation effect). The measured radiocarbon concentrations in graphitized samples of OXII (oxalic acid natural standard) are present at the Fig. 3. The data are normalized to the radiocarbon concentration in carbon wire (without sample preparation). As seen in Fig. 3, the radiocarbon concentration in the samples is less for sample preparation by NSU than by IG RAN. This should be considered when calculating the radiocarbon age of the samples. So, the concentration of radiocarbon in the unknown samples is normalized to the radiocarbon concentration in standards prepared by the same laboratory. This is necessary for the correct dating of the samples.

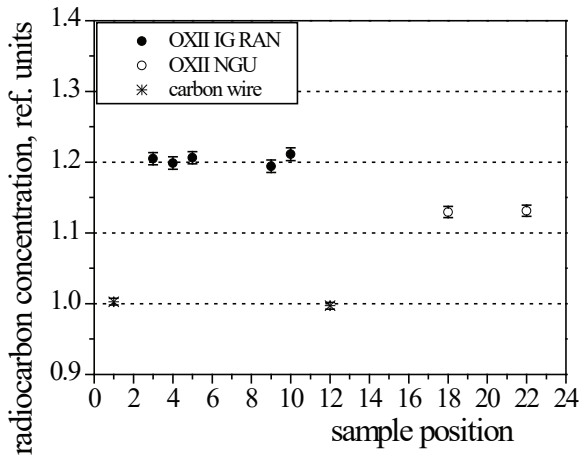

Figure 3: The radiocarbon standards from different laboratories.

Atmospheric carbon is permeated into the samples during graphitization. Samples used for radiocarbon dating must be handled carefully to avoid contamination. The contamination level in the samples during the sample preparation procedure is estimated by the radiocarbon content in graphite after combustion and graphitization (the radiocarbon concentration in graphite is insignificant before this procedure). The concentration of radiocarbon in the prepared graphite depending on the weight of the sample is presented in Fig.4.

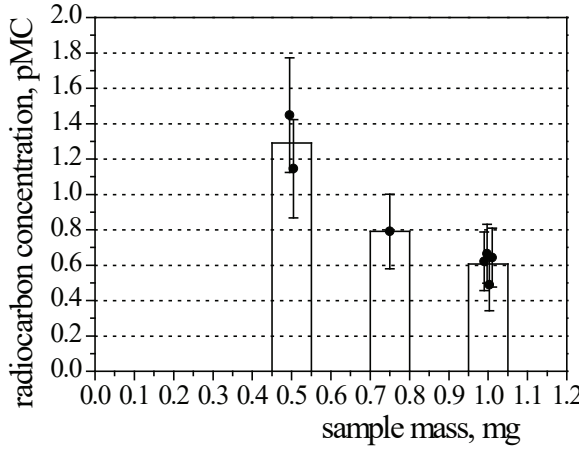

Figure 4: The concentration of radiocarbon in the prepared graphite as a function of sample mass.

The results are reported using the unit pMC (percent modern carbon). The radiocarbon concentration in atmospheric CO_2 is about 100 pMC. As seen from Fig. 4, the level of sample contamination decreases with increasing of sample mass. Moreover, the contamination level depends on the sample type and the technology being used for sample graphitization. It is different for different sample preparation laboratories. Typically, the contamination level is about 1 pMC. Note that the radiocarbon concentration of graphite MPG without sample preparation procedure is about 0.2 pMC.

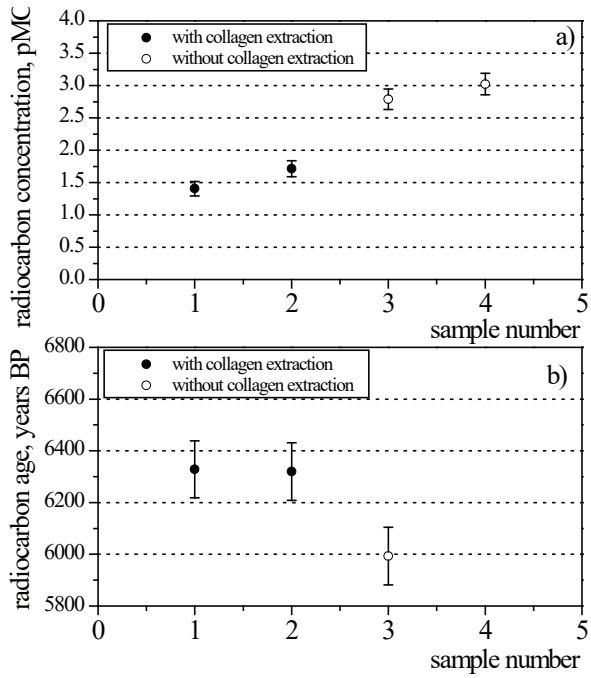

Figure 5: The radiocarbon concentrations in old rhinoceros with and without collagen extraction (a), the radiocarbon age of young mammoth with and without collagen extraction (b).

ISBN 978-3-95450-181-6

Usually, the specific functions of natural samples are used for graphitization. For example, collagen is used for the bone samples or cellulose - for wood samples. This reduces the influence of natural pollution on the radiocarbon dating. The results of AMS measurements of old rhinoceros with and without collagen extraction are presented in Fig.5 (a). As seen, the radiocarbon concentration in samples is smaller with collagen extraction than without. This is because the rhinoceros bone is contaminated by modern carbon. Similarly, for a young mammoth: the measured mammoth age is older with collagen extraction than without. As is known, the radiocarbon dating of bone is more correct with collagen extraction from natural samples than without.

As an example of AMS-analysis, the data from geological samples - lake Sargul sediments, depending on the depth from surface level (samples of Krivonogov S.K., IGM SB RAS), presented in Fig. 6. Such analyzes are necessary to obtain a timescale for lake sediments. Such results are quite revealing, since in the absence of mixings deposits should be observed dependence - the deeper the ancient.

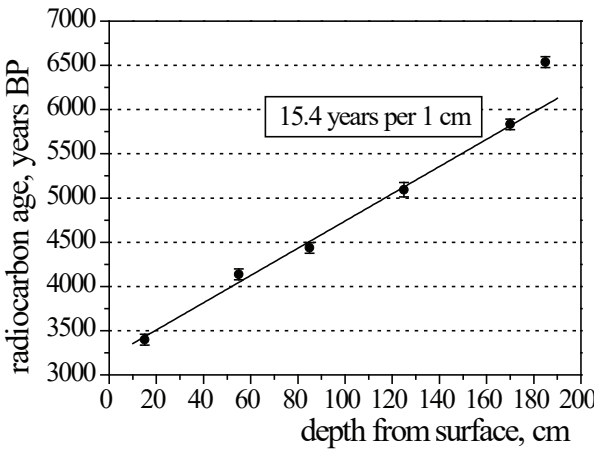

Figure 6: The radiocarbon age of lake sediments, depending on the depth from surface level.

SUMMARY

The BINB AMS is used for radiocarbon analysis of graphitized natural samples. The algorithm of the AMS analysis was described. Currently, the samples measured by BINB AMS are prepared from some independent chemical laboratories. The natural and chemical contamination of samples can be detected at BINB AMS.

REFERENCES

[1] S.A. Rastigeev et al, “Operation and development of the BINP AMS facility “, Proceedings of RuPAC-2014, Obninsk, Russia, 2014, p. 134.

[2] S.A. Rastigeev et al, Acceleration Mass Spectrometer of the Budker Institute of Nuclear Physics for Biomedical Applications // Physics of Particles and Nuclei Letters, 2014, V. 11, № 5, p. 642

[3] S.A. Rastigeev et al, “First radiocarbon measurements at BINP AMS“, Proceedings of RuPAC-2010, Protvino, Russia, 2010, p. 309.

[4] S.A. Rastigeev et al, Accelerator mass spectrometer SB RAS // Problems of Atomic Science and Technology/ Series “Nuclear Physics Investigation”. 2013, №6(88), p. 16.

[5] Parkhomchuk, V. V., Rastigeev S.A., Accelerator mass spectrometer of the center for collective use of the Siberian Branch of the Russian Academy of Sciences // Journal of Surface Investigation. X-ray, Synchrotron and Neutron Techniques, 2011, V. 5, Issue: 6, p.1068

[6] N.I. Alinovskii et al, Accelerator mass spectrometer for the Siberian Branch of the Russian Academy of Sciences. // Technical Physics, 2009, Vol. 54, No 9, p 1350.

[7] S.A. Rastigeev et al, Development of the BINP AMS complecs at CCU SB RAS. // Problems of Atomic Science and Technology/ Series “Nuclear Physics Investigation”. 2012, №3(79), p. 188.

[8] S.A. Rastigeev et al, Recent results in accelerator mass spectrometer construction at BINP. // Problems of Atomic Science and Technology/ Series “Nuclear Physics Investigation”. 2008, №5, p. 8.

[9] Parkhomchuk, V. V., Rastigeev S.A., Ion selection in accelerator mass spectrometer at the Budker institute of nuclear physics // Physics of Particles and Nuclei Letters, 2012, V. 9, Issue 4-5, p. 406

[10] V.V. Parkhomchuk and S.A. Rastigeev, Analysis of the ion background in an acceleration mass spectrometer of the Siberian Division of the Russian Academy of Sciences. // Technical Physics, 2009, Vol. 54, No. 10, p 1529.

[11] V.F. Klyuev, V. V. Parkhomchuk, S.A. Rastigeev, A magnesium vapor charge-exchange target for an accelerator mass spectrometer. // Instruments and Experimental Techniques, 2009, Vol. 52, No. 2, p. 245.

[12] N.I. Alinovskii et al, A time-of-flight detector of low-energy ions for an accelerating mass-spectrometer. // Experimental Techniques, 2009, Vol. 52, No. 2, p. 234.

[13] V. V. Parkhomchuk et al, Thin-film detector for ion registration in accelerator mass spectrometers // Physics of Particles and Nuclei Letters, 2012, V. 9, Issue 4-5, p. 448

ISBN 978-3-95450-181-6

COMMISSIONING OF HIGH EFFICIENCY STANDING WAVE LINAC FOR INDUSTRIAL APPLICATIONS

A.N. Ermakov*, V.V. Khankin, A.S. Alimov, L.Yu. Ovchinnikova, N.I. Pakhomov, N.V. Shvedunov, V.I. Shvedunov, Skobeltsyn Institute of Nuclear Physics, MSU, Moscow, Russia and Laboratory of Electron Accelerators MSU, Ltd., Moscow, Russia
V.V. Klementiev, Yu.N. Pavshenko, A.S. Simonov,
Laboratory of Electron Accelerators MSU, Ltd., Moscow, Russia

Abstract

We present the results of the commissioning of the pulsed linear electron accelerator with beam energy of 10 MeV, developed with the participation of scientists and engineers of the SINP MSU, LEA MSU Ltd. and JSC "RPE "Toriy". The source of RF power for accelerator is a multibeam klystron KIU-147A operating at 2856 MHz with pulse output power 6 MW and an average power of 25 kW. As a result of commissioning we received at the output of accelerator scanning system an electron beam with an energy of 10 MeV and an average power of more than 15 kW. Capture ratio and electronic efficiency of 1.24 m long accelerating structure are greater than 60% and 75%, respectively.

INTRODUCTION

Described in this paper a prototype of industrial electron linear accelerator for beam energy and average power of 10 MeV and 15 kW is based on our previous studies [1,2].

We describe the main accelerator systems: accelerating, RF, high-voltage power supply, beam scanning and diagnostic. Finally, a description of methods and results of measurements of the basic beam parameters is given.

ACCELERATING SYSTEM

Our linear accelerator is based on a standing wave bi-periodic on-axis coupled accelerating structure. In the process of the accelerating structure optimization we chose sufficiently large beam hole diameter and large webs thickness, thus increasing the vacuum conductivity, reducing the beam losses and increasing the limit of average RF losses in the walls. These features of accelerating structure are reason of a moderate value of the effective shunt impedance $Z_{eff} \approx$ 70 MOm/m. High overall efficiency of the accelerator is achieved by high value of accelerated pulse current.

The next relations provide rough estimation of accelerator parameters. Pulsed RF power required to get beam energy E = 10 MeV is:

$$P_w = \frac{E^2}{Z_{eff} L} \approx 1.14 \text{ MW} \qquad (1)$$

for accelerating structure electrical length L = 1.25 m. With maximum klystron pulsed RF power $P_{kl} = 6$ MW, taking into account losses in the waveguide system, about $P_b =$ 4.5 MW pulsed beam power can be reached which corresponds to pulsed beam current $I_b = 450$ mA and average beam power 18 kW with maximum duty cycle of klystron KIU-147A D_{max} = 0.4 % [3].

Electronic efficiency of accelerating structure thus is:

$$\eta = \frac{P_b}{P_b + P_w} \cdot 100\% = 80\ \%, \qquad (2)$$

which is obtained with optimal coupling coefficient of the accelerating structure with waveguide:

$$\beta = 1 + P_b/P_W = 4.94. \qquad (3)$$

Detailed computer simulation of accelerating structure and beam dynamics was done in [4]. Parameters of the first three accelerating cells were optimized to provide high capture efficiency and proper beam focusing with space charge forces taken into account. The rest 21 accelerating cells are $\beta = 1$. With total electric length of the accelerating structure is L = 1.24 m, RF power losses in the walls necessary to reach 10 MeV are 1.5 MW.

About 60% of nominal 750 mA electron gun current is accelerated to final energy within energy spread of ±0.3%. Beam current losses take place mainly in the initial part of accelerating structure, so beam power losses in the structure do not exceed 1.4% of accelerated beam power.

Two more features of our accelerating structure should be mentioned. First, if a focusing coil is installed at the initial part of accelerating structure, then the beam energy can be changed in the range 5 – 10 MeV by regulation of accelerating field level within 70%, wherein the capture efficiency is varied in the range 45 – 60% (for energy spectrum width ±0.3 MeV).

Second, for pulsed RF power losses in the walls 1.5 MW and duty cycle 0.4%, average RF power losses per unit of accelerating structure length are 4.8 kW/m. Due to large webs thickness cooling channels can be drilled in them as described in [1]. In this case, the limit for RF power dissipation is about 200 kW/m [5] and maximum possible average beam power with appropriate RF source is above 700 kW.

Three electrodes electron gun operating at -50 kV cathode voltage is used as an injector. Injected beam current can be regulated between 200 – 900 mA by changing control electrode voltage in the range 2 – 15 kV with respect to cathode.

* a_ermak1978@mail.ru

ISBN 978-3-95450-181-6

TEST STAND

The accelerator commissioning was done at a stand shown in Fig. 1. Besides the accelerating structure with electron gun, manufactured by JSC "RPE "Toriy" [6], the stand included low and high power RF systems, high voltage klystron modulator and gun power supply, vacuum system, cooling system, beam scanning, beam diagnostic and control systems.

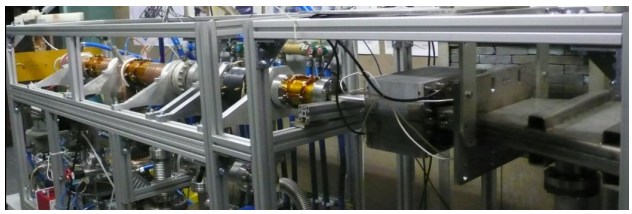

Figure 1: Test stand photo.

High power RF system consisted of klystron, ferrite isolator, directional coupler and isolating gas system.

Two variants of low power RF systems were tested: one based on an autooscillation principle with the accelerating structure in the klystron feed-back loop [7], and another with external excitation by master oscillator with adjustable frequency, and with a p-i-n attenuator followed by a solid state amplifier at klystron RF input.

To power klystron we used solid-state modulator [8] with pulsed/average power supplied to klystron 13.2 MW/60 kW, high voltage pulse length regulated in the range 6 - 12 μs and pulse repetition rate regulated from 10 to 400 Hz. Photo of modulator pulses is shown in Fig. 2.

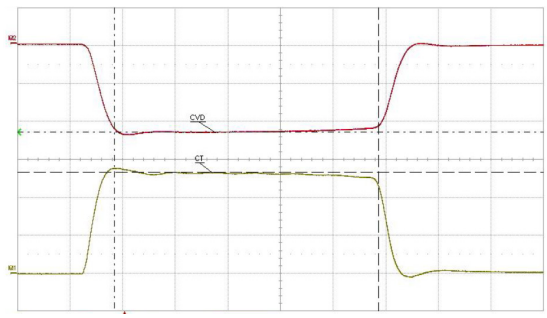

Figure 2: Modulator high voltage (upper trace) and current pulses with amplitudes 50 kV/270 A, respectively. Time scale is 2 μs/div.

Electron gun was powered by -50 kV DC power supply, current pulses were produced by providing regulated in the range 2 – 15 kV pulsed voltage to control electrode. Gun current pulse duration and position with respect to RF pulse can be regulated in a wide range.

Two configurations of the stand we used during the accelerator commissioning: one with cooled high power Faraday cup (FC) at accelerator exit (Fig. 3) and another with scanning magnet and scanning horn with 50 μm Ti foil window followed by cooled beam dump.

We used two methods to control accelerating field level: measurement of RF signal from antenna, installed in coupler cell, and measurement of average power losses in accelerating structure walls. To estimate pulsed RF power dissipated in the wall via antenna signal, the average power measured by power meter was divided by duty cycle, determined with RF diode, and multiplied by known attenuation factor of antenna and RF cable.

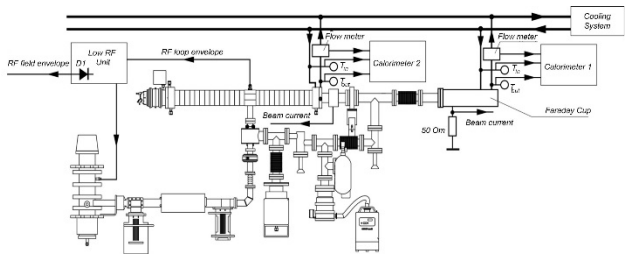

Figure 3: Stand configuration with FC at exit.

To estimate pulsed RF power dissipated in the structure walls by another method we measured average power using data from temperature sensors installed at structure cooling circuit inlet and outlet and from flowmeter. Pulsed power value was obtained by dividing average power by duty cycle. The results obtained by two methods were in good agreement and were used to estimate beam energy via a calibration curve found in beam dynamics calculations.

We controlled pulsed accelerated beam current also by two methods (Fig. 3): by beam current transformer (BCT) with sensitivity about 5 V/A, installed at accelerating structure exit, and by current of FC (or beam dump) loaded by 50 Ohm resistor. Example of signals from BCT and from FC, corresponding to about 430 mA current, is given in Fig. 4.

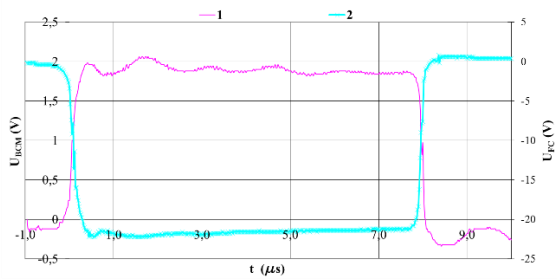

Figure 4: BCT (read curve) and FC (blue) pulses. Time scale is 2 μs/div.

We measured average beam power absorbed by FC or by beam dump using precise calorimeter consisting of inlet and outlet water temperature sensors, flowmeter and power calculator. The beam power measured by this method is somewhat underestimated (up to 10%) due to power escaped via bremsstrahlung radiation.

Average beam power, $\bar{P}_b$, and average beam current, $\bar{I}_b$, were used to estimate average beam energy:

$$\bar{E}_b = \bar{P}_b / \bar{I}_b \quad (4)$$

Beam scanning along the horn exit window following a saw-tooth law with a frequency in the range 0.5 – 30 Hz and scanning width, regulated in the range 400 – 600 mm, was reached by powering the scanning magnet by a fast four-quadrant programmable power supply. We controlled current density distribution at the horn exit by measuring average current from 20 mm diameter cooled cylinder

ISBN 978-3-95450-181-6

remotely movable along the exit window. Finally, to check the beam spot dimensions and form during the scanning we covered the beam dump wall by luminophore, tilted it for 450 and registered moving beam image with CCD camera synchronized with the beam pulses.

THE MAIN RESULTS

After accelerating structure training with FC at exit and reaching the average beam energy, estimated with expression (4), in the range 9.8 – 9.9 MeV for average beam power of a few kW, we installed scanning horn and did following measurements of beam power with the beam dump. Keeping constant average beam energy, we gradually increased the duty cycle by increasing the pulse length and pulses repetition rate. Dependence of the beam power on the duty cycle is shown in Fig. 5. To get the project value of beam power 15 kW it took about 16 hours of accelerator operation. Given value of maximum beam power does not include more than 1 kW of power escaped with bremsstrahlung radiation.

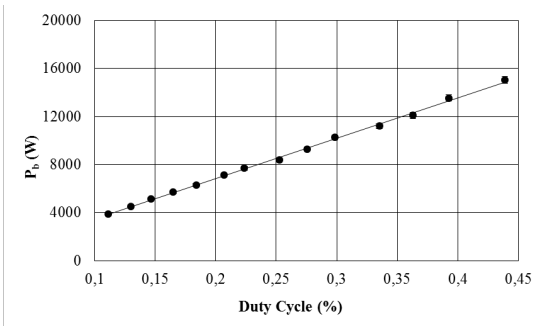

Figure 5: Dependence of measured beam power on the duty cycle.

In Fig. 6 we show results of measurement of the beam current distribution along the scanning horn exit window at 10 cm from the exit for two amplitudes of scanning magnet coils current. Current distribution uniformity is about ±3%.

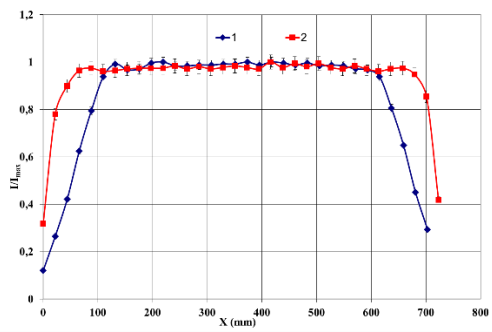

Figure 6: The beam current distribution at the scanning horn exit for two amplitudes of scanning magnet coils current.

Instantaneous beam images registered during the scanning at three positions along the exit window are shown in Fig. 7. Central image corresponds to about zero scanning magnet field. Two symmetrical images at upper and lower pictures correspond to beam position at exit window of about ±150 mm with respect to center. One can clearly see the beam dispersion due to energy spread. The dispersion, which can influence on the dose distribution during irradiation process, can be decreased by decreasing the energy spread. The energy spread is defined in part by specific of beam dynamics in accelerating structure, but the main contribution is due to variation of accelerating field at front and rear edges of the RF pulse. This contribution can be decreased by proper positioning of the gun current pulse with respect to RF pulse.

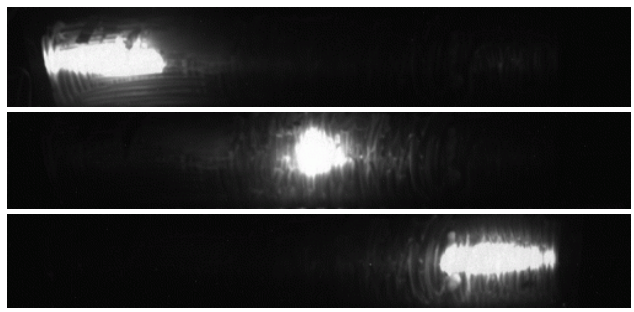

Figure 7: The moving beam spot images during the scanning.

CONCLUSION

The design accelerator parameters: beam energy of 10 MeV and average beam power of 15 kW have been reached during the accelerator commissioning. Electronic efficiency of accelerating structure of about 75 % have been obtained. Taking into account the efficiency of the klystron and modulator the overall efficiency of accelerator is close to 30% in nominal mode.

As the next series of experiments we plan to conduct beam parameters measurements in the range of energy regulation 5 – 10 MeV and to measure the beam energy spread depending on relative position of the gun current pulse with respect to RF pulse.

REFERENCES

[1] A.V. Grizlov, V.N. Iliin, S.V. Lamonov et al., in Proc. the XI Int. Conf. on Charged Particle Accelerators Applied in Medicine and Industry, St. Petersburg, Russia, October 10-14, 2005, p. 132.
[2] A.S. Alimov, E.A. Alimov, A.N. Kamanin, et al, in Proc. RuPAC08, p.267.
[3] I.A. Frejdovich, P.V. Nevsky, V.P. Sakharov, et al, in Proc. RuPAC06, p. 100.
[4] A.V. Poserjaev, Calculation of dynamics and optimization of parameters of different purpose accelerator complexes, Ph.D. Thesis, Moscow, 2006.
[5] J.-P. Labrie, in Proc. PAC85, p.2775.
[6] http://www.toriy.ru
[7] A.N. Ermakov, D.I. Ermakov, B.S. Ishkhanov et al, , Instr. and Exp. Tech., Vol. 45, No. 4 (2002) 482.
[8] www.sc-nova.com

ISBN 978-3-95450-181-6

A 5 TO 20 MEV ELECTRON LINEAR ACCELERATOR FOR METROLOGY

Yu.V. Zuev, Z.A. Andreeva, M.A. Kalinichenko, A.P. Klinov, A.S. Krestianinov,
O.L. Maslennikov, A.V. Tanchuk, V.V. Terentyev, NIIEFA, St. Petersburg, Russia
S.G. Trofimchuk, I.I. Tsvetkov, VNIIM, Saint-Petersburg, Russia

Abstract

The paper outlines design parameters and construction features of an electron linear accelerator to be operated in the Mendeleyev Institute for Metrology (VNIIM). The accelerator system is intended to form bremsstrahlung and electron radiation fields of variable intensity.

INTRODUCTION

A designed facility should be included into the National standard of units, which is used for metrological assurance of measurements in the nuclear-physical instrumentation, ship and aircraft building, rocket production, radiation processing and in the accelerating equipment for industry and medicine [1].

The accelerating facility consists of an electron source, accelerating structure, magnet–separator, and radiation head with an electrically-operated mechanism used for replacement of bremsstrahlung targets, foils and collimators. Table 1 presents the main design characteristics of the facility designated as follows: W_B is the energy of electrons in the spectrum maximum, ΔW is the energy spread, I_0 is the average electron current, D_B is the beam diameter in the plane of an extraction window. A required range of radiant flux is obtained by changing the pulse-repetition frequency and fine adjustment of the beam current in a pulse. This imparts a high spatial stability to radiation fields.

Table 1: Specification of the Facility

Radiation head input:	
W_B, MeV	5-20
$\Delta W/W_B$, %	±5
I_0, μA	0.1-10
D_B, mm(FWHM)	≤ 5
Electron radiation field at the 100 cm SSD:	
Area, cm^2	10x10
Flatness, %	≤ 2
Particle flux density (aver.), $c^{-1}\cdot cm^{-2}$	$6\cdot10^{11}$ - $6\cdot10^{13}$
Bremsstrahlung field at the 100 cm SSD:	
Area, cm^2	10x10
Flatness, %	≤ 2
Energy flux density (aver.), W/cm^2	0.5-200

ELECTRON SOURCE

The accelerator is equipped with a three-electrode electron source of a typical construction. Electrons are emitted from an oxide-nickel hot cathode 5 mm in diameter. The control electrode is closed with a grid of 0.1 mm-thick wires. The geometric transparency of the grid is 73 %. The grid voltage of 250-300 V provides 70-90 mA current at the gun output. Under these conditions, the electron beam has a minimum emittance well matched with the accelerator acceptance, Fig. 1. The energy of the beam injected into the accelerator is 50 keV. A separate gun modulator specifies the beam pulse duration of 5 μs; the pulses follow with a frequency from 2 up to 200 Hz.

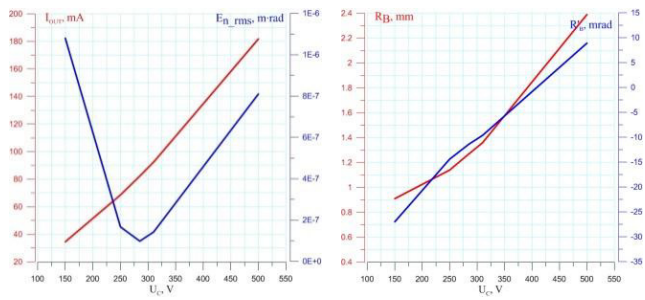

Figure 1: Calculated characteristics of the beam at the electron source output. I_{OUT} is the beam current, E_{n_rms} is the rms emittance (norm.), R_B, R'_B are the envelope size and slope, U_C is the grid voltage.

ACCELERATING STRUCTURE

A biperiodic electrodynamic structure with internal coupling cells is used for acceleration of electrons. The structure operates in the π/2 standing wave mode at 2856 MHz and comprises sixty one cells. The first ten bunching cells have cylindrical shape optimized for a minimum of high-energy particle losses over the whole beam line. The rest elements of the structure are standard Ω-shaped accelerating cells alternating with cylindrical coupling cells. The total length of the accelerating structure is 1.5 m.

The electric field of the structure is used both to accelerate particles and to confine transverse dimensions of the beam, consequently there are no external focusing elements. Energy of electrons is varied by changing the accelerating field amplitude (the field excitation power) and is accompanied with some degradation of the electron spectrum [2].

ISBN 978-3-95450-181-6

Design parameters of the structure are given in Table 2 and are designated as follows: P_{RF} is the pulsed RF power consumption; E_M is the maximum field strength on the beam axis; I_{INP} (I_{OUT}) is the pulsed beam current at the structure input (output); I_W is the pulsed working current, i.e. the current being in the energy interval ± 5% relative to W and passing through the magnet–separator; $\kappa = I_{OUT} / I_{INP}$ is the beam transmission; $\eta = I_W / I_{OUT}$ is the fraction of the working current in the output one; VSWR is the voltage standing wave ratio in a supplying waveguide.

Table 2: Design Parameters of the Accelerating Structure

W_B, MeV	P_{RF}, MW	E_M, MV/m	I_{INP}, mA	κ	η	I_W, mA	VSWR
5	1.59	17.7	86	0.65	0.36	20	1.50
8	1.86	18.7	80	0.69	0.65	36	1.38
11	2.31	20.4	80	0.73	0.71	41	1.28
14	2.95	22.7	80	0.78	0.77	48	1.18
17	3.95	26.2	80	0.84	0.84	57	1.08
20	5.00	29.8	80	0.88	0.87	61	1.01

Computational distribution of the accelerating field on the structure axis is shown in Fig. 2. The maximum average lost power in resonator walls is 1.3 kW, the pulsed power loss is 3.7 MW.

An amplifying klystron KIU-168 is planned to be used for excitation of the accelerating structure. The RF line of the facility also comprises a circulator, 2 waveguide loads and 2 dielectric RF windows; the RF power pulse duration is 6 μs.

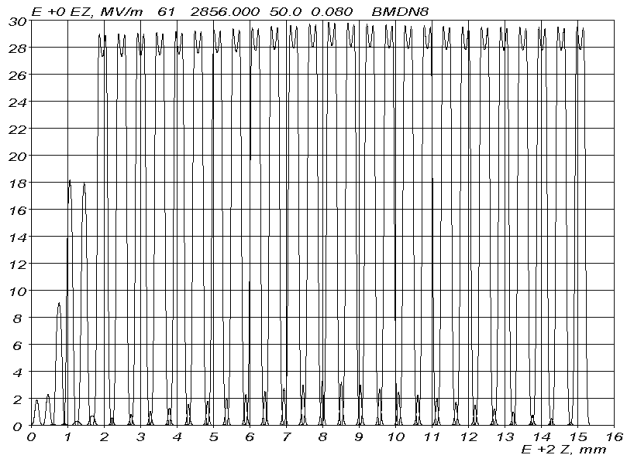

Figure 2: Accelerating field on the structure axis.

MAGNET-SEPARATOR

The beam-bending magnet-separator (MS), Fig. 3, is intended to change the travel direction of electrons (horizontal instead of vertical) and to remove the non-working part of the spectrum from the beam. The magnet-separator is installed between the accelerating structure and the radiation head. The distance from the structure to the MS input is 700 mm; that from the MS output to the extraction window, behind which the radiation head will be placed, is 525 mm.

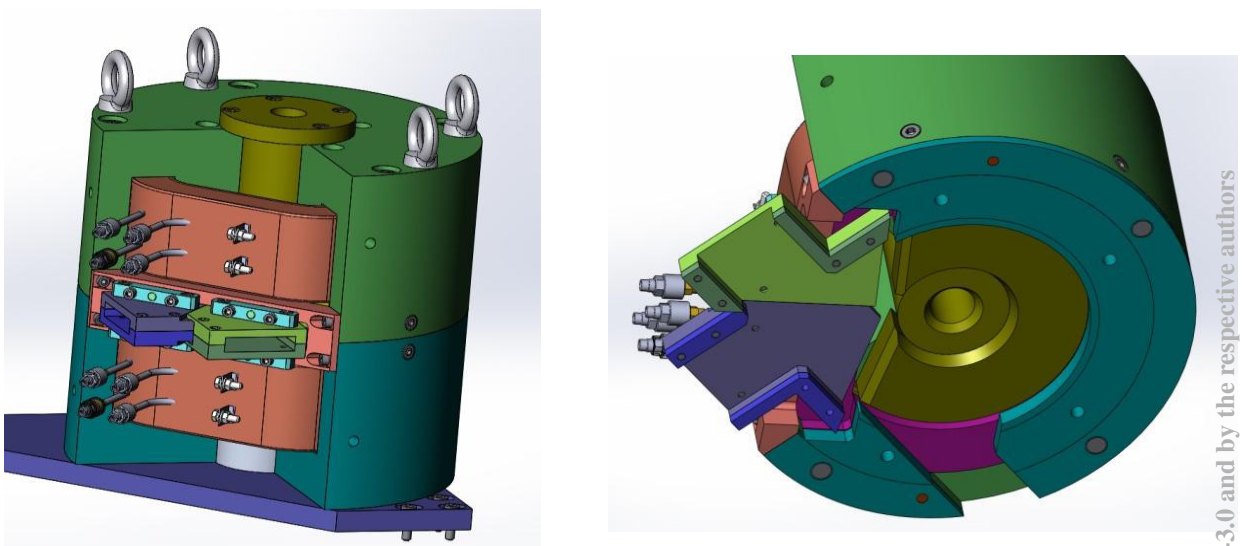

Figure 3: 3D model of the magnet-separator.

ISBN 978-3-95450-181-6

The separator consists of 1 electromagnet with an angular length of 270° and a constant pole gap of 14 mm. To make the system stigmatic and non-dispersive, which is necessary to keep the azimuthal symmetry of the radiation field, pole face angles are chosen to match with the working position of the bremsstrahlung target. The electromagnet bends the beam with energies 5-20 MeV along the circumference with a radius of 70 mm and consequently provides a change in the guiding magnetic field in the range of 0.26-0.97 T.

To restrict the extent of stray fields around the beam path, the MS is equipped with two field clamps. The clamp is a split-type thick-walled magnetic shielding jacket put on the vacuum chamber. The construction allows the gap between the clamp and poles to be adjusted within the limits of 5-20 mm.

A maximum power consumed by the magnet is 2×500 W, the excitation coil voltage amounts to 20 V and current is equal to 45-50 A. A required stability of the coil power supply is $1 \cdot 10^{-3}$ ($\Delta I / I$).

A prescribed momentum acceptance determines a minimum width of the MS working area and the distance between the walls of the vacuum chamber, onto which the non-working part of the beam will be dumped [2]. The power of the heat released in the walls depends on the current flow and spectrum of accelerated electrons. In the nominal operating mode of the accelerator the power is lower than 140 W. The distance between the walls is 16 mm, and it is the same over the whole bend length.

The vacuum chamber walls are made of tinless bronze, Fig. 4. Both the walls and the magnet excitation coils are cooled with water. The beam is extracted into the atmosphere though a titanium foil.

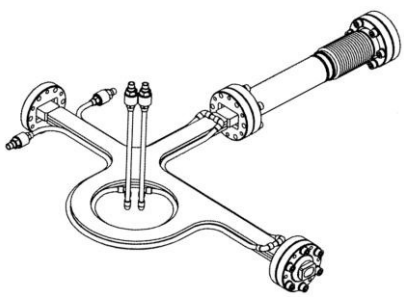

Figure 4: Vacuum chamber with cooling channels.

COMPONENTS OF LOCAL RADIATION SHIELDING

The non-working part of the beam dumped on the vacuum chamber walls is a source of high-energy background ionizing radiation. The magnet yoke, excitation coils, clamps and vacuum chamber walls attenuate the radiation in part. For this reason, special absorbers made of non-magnetic material were provided in the magnet-separator. Lead absorbers meet the customer requirements for the maximum level of the induced (residual) radioactivity, which is 2-6 μSv/h on the magnet-separator surface, Fig. 5.

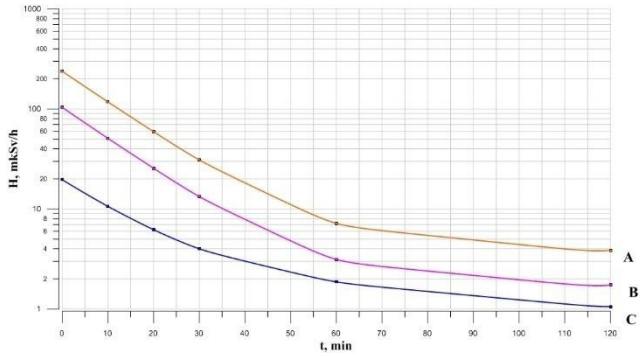

Figure 5: Calculated data on the induced activity of the magnet-separator. A – magnet separator without special radiation shielding. B – magnet separator with added Al absorbers. C – magnet separator with added Pb absorbers.

RADIATION HEAD

To form bremsstrahlung fields, a system of replaceable units is installed in the radiation head. It consists of a tungsten-rhenium target, cone-shaped collimator made of W-Ni-Cu alloy and copper flattening filter. To form electron radiation fields, the radiation head houses replaceable units comprising a primary collimator made of aluminium, and a pair of foils: tantalum scattering foil and aluminium compensating foil. To define the shape of flattening filters and compensating foils, we used the GEANT4 code.

STATUS OF THE PROJECT

The electron source has passed testing, and design parameters were confirmed. The accelerating structure has been manufactured (see Fig. 6) and RF-tuned. All the main systems of the facility are ready for delivery to the customer.

Figure 6: Accelerating structure with cooling jacket.

REFERENCES

[1] I.A. Kharitonov, I.I. Tsvetkov, Proc. X-th Int. Conf. on Appl. Charged Particle Accelerators, Saint-Petersburg, 2001, pp.257-261.

[2] The adopted engineering solution has resulted from the financial resources of the customer.

ISBN 978-3-95450-181-6

UNIVERSAL PROTON AND NEUTRON CENTRE FOR RADIATION RESISTANCE OF AVIONIC, SPACE ELECTRONICS AND OTHER APPLICATIONS AT THE 1 GEV SYNCHROCYCLOTRON IN PNPI

S.A. Artamonov#, D.A. Amerkanov, E.M. Ivanov, J.S. Lebedeva, G.F. Mikheev, G.A. Riabov, O.A.°Shcherbakov, A.S. Vorobyev, B.P. Konstantinov Petersburg Nuclear Physics Institute, NRC "Kurchatov Institute", Gatchina, Leningrad district, 188300, Russia
V.S. Anashin, P.A. Chubunov, L.R. Bakirov, A.E Koziukov, Branch of the JSC "United Rocket and Space Corporation" – "Institute of Space Device Engineering", Moscow, 111250, Russia

Abstract

In PNPI RNC KI a universal center for testing electronic components for the needs of aviation and space and other applications is created on the synchrocyclotron SC-1000 with the proton energy of 1 GeV. The center consists of two protons and one neutron stands for test facilities developed at the PNPI in collaboration with the ROSCOSMOS Interagency Testing Center. The PNPI center is equipped with all necessary systems of diagnostics and monitoring of a beam, installation of targets on a beam. There is an opportunity to vary temperature of exemplars in the wide range. A unique conjunction of proton beams with variable energy 60-1000 MeV and atmospheric like neutron beam with broad energy range (1-1000 MeV) spectrum enable to perform complex testing of the semiconductor electronic devices at the SC-1000 within a single testing cycle.

INTRODUCTION

The proton synchrocyltrotron SC-1000 with the proton energy of 1 GeV and intensity of extracted proton beam of 1 μA [1] is one of the basic installations of the PNPI NRC "Kurchatov Institute". It was commissioned in 1970 and during exploitation it was significantly modernized. The experimental complex of the SC-1000 is used for investigations in fields of elementary particle physics, atomic nucleus structure and mechanisms of nuclear reactions, solid state physics and for the purposes of applied physics and nuclear medicine. Radiation resistances testing of electronics are conducted at the SC-1000 during more than two decades. Sharp growth of the needs in accelerated Single-Event-Effect (SEE)-testing of electronic components and systems intended for avionic/space and other applications has led to the development of new test facilities at the high-energy accelerators used as powerful sources of protons and neutrons.

In present report, a short description is presented of the proton (IS SC-1000 and IS OP-1000) and neutron (IS NP/GNEIS) test facilities developed at the PNPI in collaboration with the Branch of JSC "United Rocket and Space Corporation" - "Institute of Space Device Engineering", a Head Organization of the ROSCOSMOS Interagency Testing Center. A unique conjunction of proton beams with variable energy 60-1000 MeV and atmospheric like neutron beam with broad energy range (1-1000 MeV) spectrum enable to perform complex testing of the semiconductor electronic devices at the SC-1000 within a single testing cycle.

PROTON TEST FACILITIES

At present, 2 of 3 proton beam lines of the SC-1000 are used for radiation testing of electronics. The IS SC-1000 test facility has fixed proton energy of 1000 MeV and is located on the P2 beam line. At the IS OP-1000 facility located on the P3 beam line, proton energy can be varied from 1000 MeV down to 60 MeV by means of a system of copper degrader (absorber) of variable thickness from 73 mm (at 900 MeV) to 530 mm (at 60 MeV). A scheme of the proton beams and irradiation workstations placed in the experimental room, as well as a photo of the degrader system located in the SC-1000 main room are shown in Fig.1. The parameters of both proton test facilities are given in Table 1.

An adjustment of the proton beam profile is carried out roughly by means of quadrupole lenses whereas for final tuning a 2m-long steel collimator with 20 mm aperture is used. All irradiations are carried out at open air and room temperature. Both proton and neutron beam lines are equipped with a remotely controlled system intended for positioning the device under test (DUT) and heating in 20°-125°C temperature range.

Table 1: Parameters of the Proton Test Facilities

Parameter	IS SC -1000	IS OP - 1000
Irradiation conditions	Atmosphere	Atmosphere
Particle	Protons	Protons
Energy, MeV	1000	60 -1000
Flux, protons/cm^2 s	10^5 - 10^8	10^5 - 10^8
Irradiation area, mm	Ø ≥ 25	Ø ≥ 25
Uniformity, %	≤ 10	≤ 10
Status	In operation (1998)	In operation (2015)

#artamonov_sa@pnpi.nrcki.ru

ISBN 978-3-95450-181-6

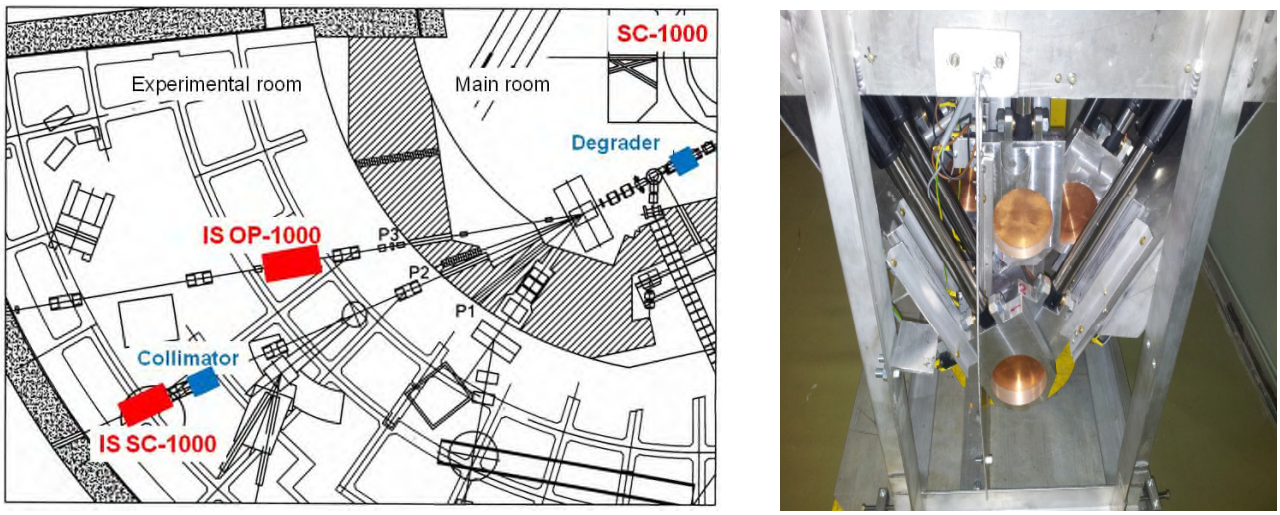

Figure 1: Left: scheme of the proton beam lines, P2 - protons with the energy of 1000 MeV, P3 – protons with variable energy of 60 – 1000 MeV. Right: device for remote variation of the absorber length and the proton energy.

Parameters of the proton beam at the outlet of copper absorber of variable thickness have been evaluated by means of the Geant-4 code calculation. Energy distribution of the initial proton beam was supposed to be of Gaussian-type with the parameters of 1000 MeV and 3.84 MeV for proton energy and standard deviation, respectively. The results of Geant-4 calculations are given in Table 2 and Figure 2. Both incoming and outcoming proton beam parameters have been verified experimentally by means of the TOF-measurements carried out using microstructure of the proton beam (~73 ns between proton micropulses).

Table 2: Parameters of the proton beam after transmission through the copper absorber (Geant-4 calculation).

Proton energy, MeV	Standard deviation, MeV	Absorber thickness, mm	Absorber transmission, %
62.1	28.20	530.5	1.6
100.09	24.63	521.2	2.3
197.93	15.77	490.8	3.4
300.21	12.12	448.7	5.4
399.12	10.24	398.0	8.4
499.24	8.92	340.9	13.5
601.03	7.89	279	22.0
699.88	7.01	213.1	35.6
800.18	6.13	144.3	56
899.85	5.13	73.11	82.1

Beam diagnostics is carried out using a set of standard tools which includes: (1) thin scintillator - screen coupled with a CCD-sensor for rapid evaluation of the beam profile image; (2) 2D-moving Se-stripe-type beam profile meter; (3) double-section ionization chamber for "on-line" control of the proton intensity (fluence); (4) Al-foil activation technique in conjunction with a high-resolution HPG-detector as absolute "off-line" monitor of proton fluency.

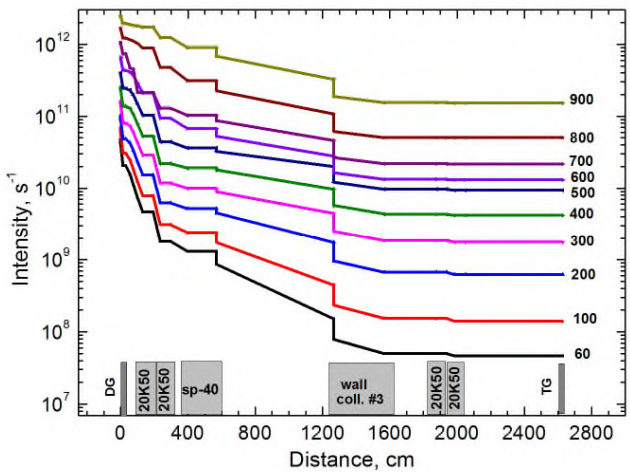

Figure 2: Dynamics of protons losses at different energies along a beam line P3: DG – absorber, 20K50 – quadrupole, SP – 40 – bending magnet, wall, coll. 3 – a wall with the collimator #3 between the main and experimental room of the accelerator, TG – target.

NEUTRON TEST FACILITY

The ISNP/GNEIS test facility is operated since 2010 at the neutron TOF-spectrometer GNEIS [2,3]. Its main feature is a spallation source with neutron spectrum resembling that of terrestrial neutrons in the energy range of 1-1000 MeV. The water-cooled lead target located inside the accelerator vacuum chamber (Fig. 3) produces short 10 ns pulses of fast neutrons with a repetition rate of 45-50 Hz and average intensity up to $3 \cdot 10^{14}$ n/s. The ISNP/GNEIS test facility is located inside the GNEIS building on the neutron beam #5, which has the following parameters:

- neutron energy range: 1-1000 MeV;
- neutron flux: $4 \cdot 10^5$ n/cm^2·s (at 36 m flight path);

ISBN 978-3-95450-181-6

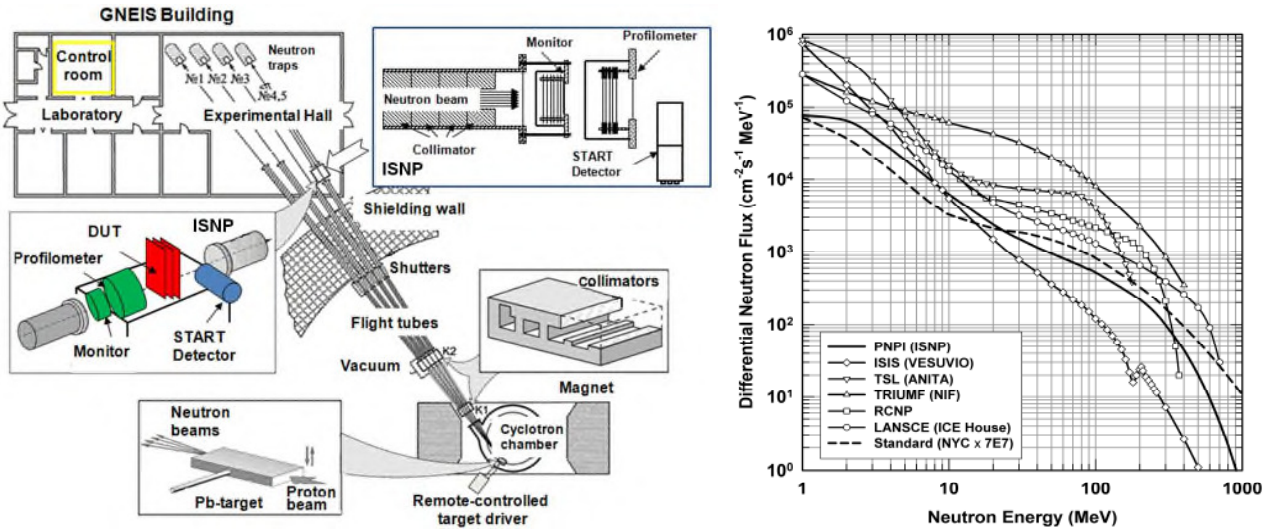

Figure 3: Left: General layout of the neutron time-of-flight spectrometer GNEIS and ISNP test facility. Right: Neutron spectrum $F_{ISNP}(E)$ of the ISNP/GNEIS facility in comparison with standard terrestrial neutron spectrum and spectra of other world-class test facilities.

- beam diameter: 50-100 mm (at 36 m flight path);
- uniformity of the beam profile plateau: ± 10%.

The neutron flux of $4 \cdot 10^5$ n/(cm^2·s) is an integral over neutron spectrum in the energy range 1-1000 MeV. It corresponds to the maximum value of 3μA of the internal average proton beam current. The neutron flux and shape of the neutron spectrum are measured using FIC (neutron monitor) and TOF-technique (Fig. 4). The FIC is a fast parallel-plate ionization chamber which contains two targets of ^{235}U and ^{238}U. The neutron fission cross sections of these nuclei are recommended standards in the energy range 1-200 MeV. The neutron beam profile is measured by means of MWPC - the 2-coordinate position sensitive multiwire proportional counter used for registration of fission fragments from the ^{235}U target deposited on the MWPC's cathode [4].

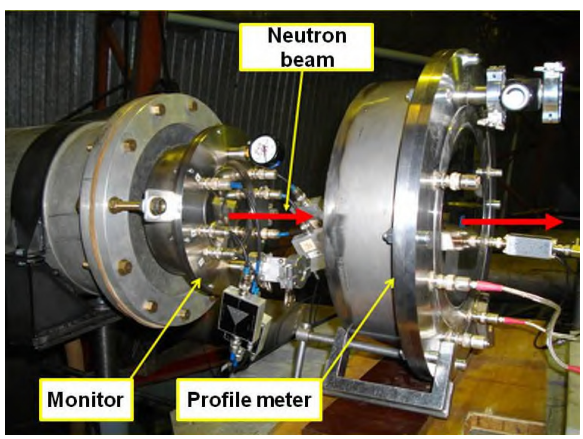

Figure 4: FIC (neutron monitor) and MWPC (profile meter).

The neutron spectrum $F_{ISNP}(E)$ is shown in Fig. 3 together with the JEDEC standard terrestrial neutron spectrum from JESD89A referenced to New York City and multiplied by scaling factor $7 \cdot 10^7$, as well as the neutron spectra of leading test facilities. Both the shape of the neutron flux and neutron intensity demonstrate that the ISNP/GNEIS is successfully competing with the other first-grade test facilities with the atmospheric - like neutron spectrum. The SC-1000 possesses a potential of the neutron intensity growth. A new irradiation station located at a distance of 5-6 m from the neutron-production target operated on the extracted proton beam enables to increase neutron flux at least 10 times at the DUT position. Simultaneously, an irradiation of the bulky equipment will be possible.

CONCLUSION

A versatile complex of test facilities has been developed at the SC-1000 accelerator of the PNPI. At present, a growing number of Russian research organizations specialized in radiation testing of the electronics conduct their research on the proton and neutron beams under direct agreements with the PNPI or with the Branch of JSC "URSC" - "ISDE".

ACKNOWLEDGMENT

The authors express their sincere gratitude to all colleagues from the PNPI who participated in development of the radiation test facilities at the SC-1000 synchrocyclotron.

REFERENCES

[1] N.K. Abrosimov et al., Zh. Tekhn. Fiz. 41 (1971) 1769.
[2] N.K. Abrosimov et al., Nucl. Instr. Meth. A. 242 (1985) 121.
[3] N.K. Abrosimov et al., Instr. Exp. Tech. 53 (2010) 469.
[4] O.A. Shcherbakov et al., IEEE Trans. Nucl. Sci. 63 (2016) 2152.

ISBN 978-3-95450-181-6

ELECTRON ACCELERATORS SERIES ILU AND PROSPECTS OF THEIR APPLICATION IN THE FOOD INDUSTRY

A. A. Bryazgin, V.Bezuglov, B.L. Faktorovich, E.N. Kokin, M.V. Korobeynikov, A.N. Lukin, V. E. Nekhaev, A. D. Panfilov, V.M. Radchenko, A.V. Sidorov, E. Shtarklev V. O. Tkachenko, L.A. Voronin, A. Vlasov, BINP, Novosibirsk, Russia

Abstract

This report describes industrial accelerators type ILU as well as their basic parameters and characteristics. Their current applications in a cable industry, medicine and other fields are outlined. Recent experiments with food products irradiation are described, new features and ILU machines application in food industry are discussed. Some information about problems in the Russian legislation related tofoodstuff treatment by ionizing radiation is given.

INTRODUCTION

Research results in fields of radiation physics, chemistry and biology are a basis for the development of many industrial technologies. At present, the application of radiation technologies has been expanding in many developed and developing countries, such as USA, Japan, South Korea, China and others. Cost-effectiveness of the radiation technologies is attractive for industrial use.

Development of new technologies creates a demand for new industrial electron accelerators with improved parameters, namely increased energy and electron beam power, while maintaining operation ease and management.

Table 1: Basic Parameters of the ILU-type Accelerators

Parameters	ILU-6	ILU- 8	ILU-10	ILU-14
Energy of electrons, MeV	1.2-2.5	0.6-1.0	3.0-5.0	7.0-10.0
Average beam power (max), kW	20	25	50	100
Average beam current (max), mA	20	30	10	10
Power consumption, kW	100	80	150	450
Accelerator weight, tons	2.2	0.6	2.9	5
Weight of local protection, t	-	76	-	-

Budker Institute of Nuclera Physics (BINP) is one of the largest Russian research centers, it is widely known in Russia and abroad. BINP is known for fundamental works on problems of high energy physics, plasma physics and controlled thermonuclear fusion physics.

Applied works are also carried out in the BINP, namely creation and use of synchrotron radiation sources and powerful electron accelerators.

Powerful industrial electron accelerators type ILU are working round the clock operation in industrial lines for decades since 1970-s.

The ILU machines cover the energy range from 0.7 to 10 MeV at an accelerated beam power of up to 100 kW. The intrinsic features of these accelerators are simple design, ease in maintenance and a long term reliable operation under conditions of industrial production. Table 1 shows the basic parameters of the ILU-type accelerators produced by BINP [1-3].

GENERAL DESCRIPTION OF ILU MACHINES

A basic model of the ILU accelerators is the ILU-6 accelerator [1]. This machine has rather high parameters at modest dimensions and can be used for wide spectrum of technological processes. The protected hall with inner dimensions 3*4*5 m is big enough for its placement. The required volume of concrete for construction of such hall is about 180 m^3 (the required wall thickness is of about 1.5 m).

The model ILU-6 is widely used as in our country and abroad. A principle of high-voltage acceleration is used in majority of modern accelerators, i.e., the energy of electrons corresponds to the voltage generated by the rectifier. The industrial accelerators type ILU are an exception of this rule. A principle of acceleration of electrons in the gap of radio frequency (RF) resonator is used in the ILU machines. Such accelerator does not contain details, potentials of which in respect to the ground is comparable to accelerating voltage. So the complex high-voltage units (accelerating tubes, sections of rectifiers and etc.) which are damaged by the occasional discharges are not used in ILU machines. And so there is also no necessity to use insulating gas and high-pressure vessels.

RF acceleration has allowed us to create rather simple design of the machine having modest dimensions and weight. As a result the machine can be placed inside the hall of smaller dimensions comparing with the halls for high-voltage accelerators having the same parameters.

ISBN 978-3-95450-181-6

The model ILU-8 is the result of further development. It is designed mainly for processing of cables and tubes. This accelerator does not require construction of a special protected premise (hall) as it can be placed in usual industrial shop due to local biological shield hosting the machine and equipment for products transportation. The local shield is designed as a box made from steel plates. Inside the box is divided into two parts (Fig. 1). The top part is used to place accelerating system with RF resonator, spallation vacuum pumps and some other systems. A beam extraction device, ventilation system air pipes and technological equipment are placed in the bottom part of the shield. A back wall of the shield has the channels (labyrinths) for input of cables, air and water pipes.

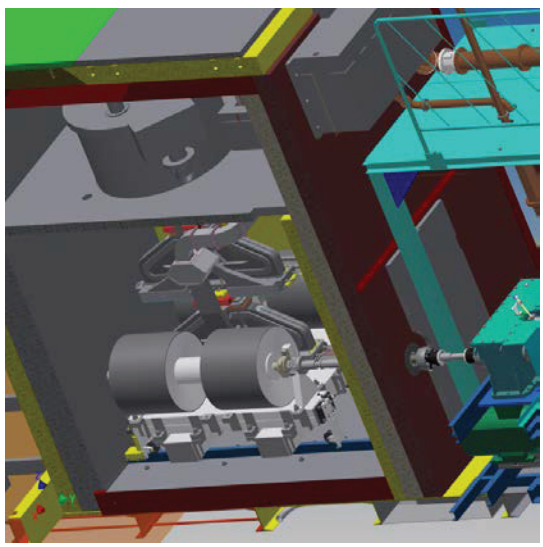

Figure 1: ILU-8 accelerator inside the local biological shield.

The removable front wall serves as a door of a protective box. The thickness of radiation shield in side walls part is 330 mm and in top is 240 mm. Gross weight of shield is 76 tons. The reduction factor for brake radiation (Bremsstrahlung) at electron energy of 1.0 MeV is not less than $5*10^7$.

On the base of the ILU-6 accelerator, an ILU-10 accelerator was developed to satisfy the needs of technological processes requiring the energies up to 5 MeV (Fig. 2).

A basic component of the accelerator is a toroidal copper cavity with an operating frequency of 116 MHz with axial protrusions forming the accelerating gap having length of 270 mm.

The protrusion shape was chosen from the conditions of the formation and focusing of an electron beam in the processes of its injection, acceleration and further passage through the extraction system with minimum losses.

Figure 2: ILU-10 accelerator.

The ILU-10 accelerator is a pulse machine, maximum pulse repetition rate is 50 Hz, pulse duration is 400-500 mks. It can be supplied with a tantalum X-ray converter, a rather homogeneous dose distribution on irradiated material surface can be obtained. At the scanning width of 60 cm, the average dose value was 17 kGy with the conveyor equivalent speed of 1 mm/s [4].

APPLICATION OF ILU ACCELERATORS FOR MEDICAL PRODUCT STERILIZATION AND FOOD TREATMENT

The important directions in BINP works are medical, biological and pharmacological applications of our accelerators. The electron beam sterilization technology for medical single use products is well studied and widely used both in our country and abroad [1]. The ILU-10 machine that can reach maximum energy of 5.0 MeV ideally suits for the irradiation centers purposed for treatment of wide spectrum of goods. The electron energy of 5 MeV permits to treat the products that can have the surface density up to 4 g/cm^2 if the two-sided irradiation is organized. It means that the products can be treated in the packed form – in the cartoon boxes containing the several sets of products.

The maximum beam power of ILU-10 machine is 50 kW, so the productive rate of the irradiation facility can be up to 1000-2000 kg per hour assuming the sterilization dose of 25 kGy.

Now one ILU-10 machine in BINP is regularly used for sterilization of single use medical cloths and sets of instruments (Fig. 3). The market for sterilization services is now actively growing and the demand for the irradiation of different products is constantly increasing. A phytogenous raw materials (herbs, ground roots, etc.) are efficiently sterilized by electron beam treatment without loosing of their medicinal action.

ISBN 978-3-95450-181-6

Figure 3: Box of disposable medical linen on the line under the exhaust device of the accelerator ILU-10.

In recent years, many countries in addition to sterilization develop the use of radiation technologies in industry for pasteurization of food products. However, some problems arise. For example, the penetrating power of electron beam is relatively small, which puts limits on the volume of the irradiated material.

In some cases it may be necessary treatment of food products having a complex geometry and with a large mass thickness (20 g/cm2 or more). For this treatment, the use of accelerated electrons is inefficient (their penetration is of the order of 4 g/cm2 for two-sided irradiation and energy 5МэV). As according to IAEA recommendations, the energy of the electron accelerators shall not exceed 10 MeV when using the electron beam tretment and 5 MeV when using X-rays (7.5 MeV in the USA).

ILU machines suits for pasteurization of food products, they can operate in the electron beam mode and can generate X-rays having penetration depth of 40 g/cm^2 for two-sided irradiation. This allows to cover whole range of processed food products using electron beam or X-rays treatment The performance of the accelerator when operating in X-ray generation mode can be up to 300 kg/hour at dose of 10 kGy. Operation mode change (from electron beam treatment to X-rays and back) recquires not more than 30 minutes. This technique significantly expands treated products range.

Electron beam treatment of food products (cool pasteurizatrion process) by ILU machines gives a number of positive effects: reduction of pathogenic microorganisms, an increase in products storage time, insects desinfestation, increase in amount of consumed food due to the increased storage period (import substitution), cheaper products pasteurization compared to traditional methods (for example, the possibility of production of canned meat and canned goods in a plastic bag), improve population health and reduce disability by improving the quality of food consumed.

International studies show that currently about 40% of food is thrown away by customers or sales networks due to the expiry of their shelf life. Pasteurization of food by X-rays generated by ILU machines will help to significantly reduce these losses. It's important to consider the impact of this radiation on the properties of food. In 1980-s the joint Committee of experts (FAO, IAEA and who) reviewed the international research project on the toxicity of irradiated foods and concluded that they are no more harmful than regular foods containing volatile small amounts of mutagen, the dose not exceeding 10 kGy. The doses required for food products pasteurization are usually in a range from 1 to 6 kGy.

REFERENCES

[1] V.L. Auslender. ILU-type electron accelerator for industrial technologies. Nuclear Instruments and Methods in Physical research, B 89 (1984), 46-48.

[2] V.L. Auslender, A.A. Bryzgin, L.A. Voronin, G.A. Vasiliev, V.A. Gorbunov, M. Korobeinikov, V.N. Kokin, S.A. Maximov, V.E. Nekhaev, A.D. Panfilov, V.M. Radchenko, V.O. .Tkachenko, A.A. Tuvik, B.L. Factrovich. ILU-type electron accelerators with energies higher than 5.0 MeV and power over 50 kW, Abstracts of Proceedings of XVII Workshop on accelerators of charged particles, Protvino, 2000.

[3] Auslender, R.A. Salimov. Electron accelerators of INP SB AS USSR for national economy, Atomnaja energija, v.44, issue 5, 1978. – pp. 403–408.

[4] V.L. Auslender et al. Electron Accelerator for Energy up to 5.0 MeV and Beam Power up to 50 kW with X-ray Converter, in XVIII Int. Workshop on Charged Particle Acc. Proc., Alushta, 2003.

ISBN 978-3-95450-181-6

THE TARGET DEVELOPMENT FOR MEDICAL RADIONUCLIDES ^{67}CU AND ^{82}SR PRODUCTION

V. N. Panteleev, A. E. Barzakh, L. Kh. Batist, D. V. Fedorov, V. S. Ivanov, S .A. Krotov, F. V. Moroz, P. L. Molkanov, S. Yu. Orlov, and Yu. M. Volkov,
NRC "Kurchatov Institute" PNPI, 188300 Gatchina, Russia

Abstract

The RIC-80 (Radioactive Isotopes at cyclotron C-80) radioisotope complex which is constructed at the beam of cyclotron C-80 at the Petersburg Nuclear Physics Institute for the production of a wide spectrum of medical radionuclides for diagnostics and therapy has been discussed. The results of a new method utilization for the target development for the production of generator PET radioisotope ^{82}Sr and radionuclide ^{64}Cu are presented.

INTRODUCTION

The production of radionuclides that decay with emission of positrons, allowing their use for PET (Positron Emission Tomography), is very important for diagnostics of different diseases. The nuclear physics experimental methods, combined with very sensitive detectors of nuclear radiation, give a very good possibility for modern medicine in diagnostics and therapies.

In this paper the first results on the development of a new method of a high temperature separation of radioisotopes from different kind of target materials are presented, which has been worked out in the Petersburg Nuclear Physics Institute.

THE RIC-80 FACILITY

The proton beam energy of the C-80 [1] can be varied in the interval 40-80 MeV. The proton beam intensity will be up to 200 μA. This cyclotron is intended mainly for the production of a wide spectrum of medical radionuclides for diagnostics and therapy. A photograph of the C-80 cyclotron with three proton beam lines to the target stations is presented in fig.1. The RIC-80 radioisotope complex [2,3] is being constructed in the cellar of the experimental hall of the PNPI synchrocyclotron. The proton beam line is directed from the ground floor to the cellar where it can be deflected and focused to one of three target stations. The mass-separator with its target station [3] will allow for the production of separated medical radionuclides of a high purity, which will be implanted into corresponding collectors from which they can be easily extracted. The target stations will be equipped with special devices to transfer the highly radioactive targets into protection containers so that they can be transported safely to special storage places, or to hot cells for the after-treatment and corresponding preparations for pharmaceutics. The proton cyclotron C-80 gives a possibility to obtain sources of a high activity practically for the whole list of radionuclides produced at accelerators.

Figure 1: Cyclotron C-80 (ground floor) with three proton beam lines to the target stations (cellar).

These are ^{64,67}Cu, ^{68}Ge, ^{82}Sr, ^{111}In, ^{123,124}I, ^{223,224}Ra and others, which are at present under discussion in corresponding publications as perspectives for diagnostics and therapy. The mass-separator method [3] will give the possibility of the production of very pure beams of some radioisotopes. As the first steps they can be ^{81}Rb, ^{82}Sr, ^{111}In, ^{223,224}Ra, as radionuclides with respectively low ionization potentials, which can be produced by a mass-separator method with a high efficiency.

Experiment Description and Experimental Results of ^{82}sr Production and Extraction From RbCl Target Material

In the experimental tests for the production of ^{82}Sr the powder of RbCl was used as a target material. Radionuclide ^{82}Sr with a half-live $T_{1/2}$ = 25.55 days is a generator for its daughter isotope ^{82}Rb ($T_{1/2}$ = 1.25 min) which is widely used in PET diagnostics. For separation of the target material and produced strontium isotopes a new developed, high temperature method was utilized [4]. After irradiation by the 1 GeV proton beam at the PNPI synchrocyclotron RbCl powder was placed into a vessel manufactured from stainless steel which was put into Ta-

ISBN 978-3-95450-181-6

W oven heated by the direct current. In a high vacuum the powder was heated slowly to the temperature up to 900 °C to be evaporated to a separated volume specially constructed to minimize the waste of irradiated material in the process of its evaporation. At that temperature the process of complete evaporation of the target material of one gram mass took about one hour. For the evaporation process control the γ-spectrum of the vessel with irradiated RbCl was measured before and after each stage of the heating process. Additionally after each heating the vessel was weighted for the evaporated material mass control. In fig. 2 a), b) a part of gamma-spectra of the irradiated sample of rubidium chlorine is presented. They were measured with a high purity germanium detector. The gamma-line of the energy 552 keV belongs to the decay of ^{83}Rb with half-life 86.2 days and its decreasing indicates the efficiency of the target material evaporation. The gamma-line of the energy 776 keV belongs to the decay of ^{82}Rb with half-life 1.27 min, which is the daughter isotope of ^{82}Sr and its decreasing indicates the strontium radionuclide evaporation. In Fig. 2 by squares the spectrum of the vessel with the irradiated RbCl before the heating is shown. The spectrum after one hour vessel heating at a temperature 500 °C is shown by circles. In Fig. 3 comparison of the spectra after the heating at a temperature 500 °C (circles) and at a temperature 900 °C (triangles) are shown.

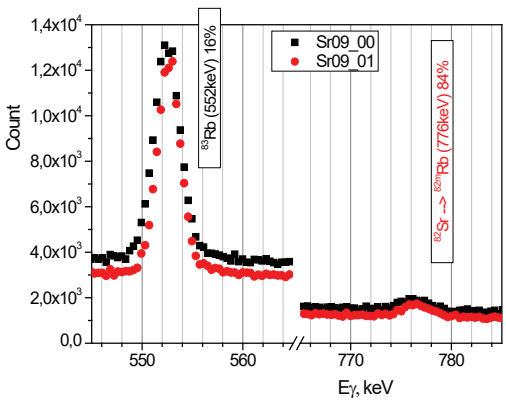

Figure 2: Gamma spectrum of RbCl before heating.

As one can see from Fig. 2, the heating of the irradiated sample at a temperature 500 °C for one hour does not give any effect on the target material evaporation. The same result was obtained by the sample weighting before and after its heating at 500 °C. At the same time Fig. 3 shows, if the vessel with the RbCl is heated up to 900 °C, the target material has been evaporated completely with almost hundred percent conservation of strontium. The fact of complete evaporation of the irradiated target material has been confirmed by the sample weighting before and after its heating at 900 °C. Finally conserved radioactive Sr atoms can be evaporated from the vessel at higher temperature, or washed by a small amount of an acid solution.

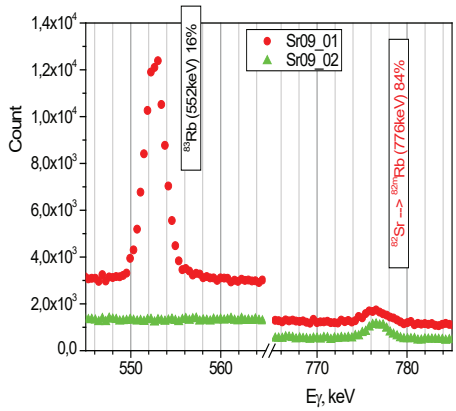

Figure 3: Gamma spectrum after 1 hour heating.

Therefore, as one can see from Fig. 2, 3 for the separation of strontium isotopes, should be some stages of the evaporation of the target material and produced species in the process of the target heating in a high vacuum at different temperatures. To separate strontium from the rubidium chloride target, the target heating was started at a low temperature (500 - 900) °C to evaporate the target material RbCl which has considerably lower boiling point, than strontium. After that, strontium was selectively extracted by washing of internal vessel volume by the HCl solution. Another way of strontium extraction was the niobium or tantalum vessel use with the heating it up to 1700 °C after the target material evaporation at 900 °C. The evaporated strontium atoms were directed to the collector cooled by floating water. The experiments carried out gave the efficiency of the target material separation better than 99,9%. The efficiency of the strontium radionuclide extraction was about 95%.

Experiment Description and Experimental Results of ^{67}Cu Production and Extraction from Zn Target Material

In the experimental tests for the production of ^{67}Cu natural metallic Zn was used as a target material. Radionuclide ^{67}Cu with a half-live 2.57 days is considered as a very perspective radioisotope for therapy of some kinds of malignant tumours. For separation of the target material and produced ^{67}Cu radionuclide a new so called "dry", high temperature method, similar to the described method of strontium isotope extraction [4] was utilized. After irradiation by the 1 GeV proton beam at the PNPI synchrocyclotron metallic zinc was placed into a vessel manufactured from tantalum, which was put into Ta-W oven heated by the direct current. In a high vacuum irradiated zinc was heated slowly up to the temperature 700 °C to be evaporated to a separated volume specially constructed to minimize the waste of irradiated material in the process of its evaporation. At that temperature the process of complete evaporation of the target material of one gram mass took about one hour. For the evaporation

ISBN 978-3-95450-181-6

process control the γ-spectrum of the vessel with irradiated zinc was measured before and after the heating process. Additionally after the heating the vessel was weighted for the evaporated material mass control. In Fig. 4, 5 a part of gamma-spectra of the irradiated sample of zinc is presented. The gamma-line of the energy 1115 keV belongs to the decay of ^{65}Zn with half-life 244.3 days and its disappearance indicates the efficiency of the target material evaporation. The fact of complete evaporation of the irradiated zinc material has been confirmed by the sample weighting before and after its heating at 700 °C. The gamma-line of the energy185 keV belongs to the decay of ^{67}Cu ($T_{1/2}$=2.57 days), which is the produced required radioisotope. In Fig. 4 by squares the spectrum of the vessel with the irradiated Zn before the heating is shown. The spectrum after one hour vessel heating at a temperature 700 °C is shown by circles.

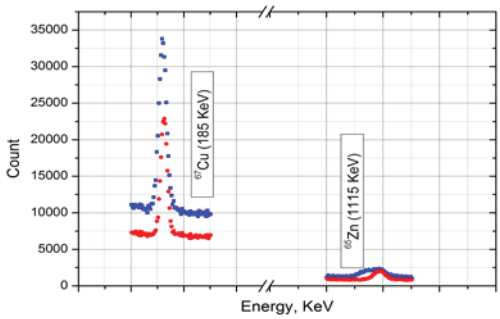

Figure 4: Gamma spectrum of the vessel before and after heating at 700 °C.

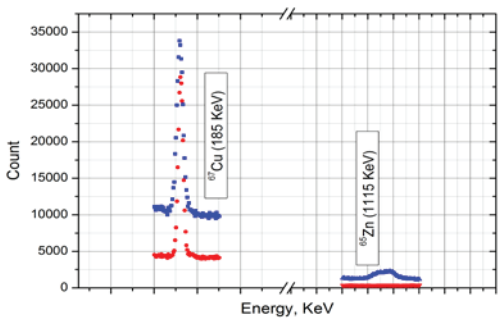

Figure 5: Gamma spectrum before and after heating at 1460 °C.

As one can see, after the heating the target material has been completely evaporated, that was confirmed by the weighting the vessel before and after heating. At the same time radioactive atoms of cooper, having considerably higher boiling point (2562 °C), than the target material zinc (907 °C), remained in the vessel. Also the presence of the gamma-line of the energy1121 keV of ^{46}Sc ($T_{1/2}$=83.8 days) at the spectrum measured after the target material evaporation demonstrates, that atoms of scandium, which is a rather hard volatile element (boiling point 2830 °C) does not evaporate from the target vessel at a temperature of 700 °C. In Fig. 5 in lower part the spectrum of evaporated cooper atoms collected at the cold finger cooled by floating water after the vessel heating at a temperature 1460 °C in two hours (circles) is presented. For comparison by squares the spectrum of the vessel with the irradiated Zn before the heating is shown. Therefore, as one can see from Fig. 4, 5 for the separation of cooper radionuclides and zinc target material should be two stages: the first one is a slow evaporation of the target material at a temperature about 700 °C; the second one is the evaporation of produced cooper species in the target heating process at a temperature 1460 °C.

The first experiments carried out gave the efficiency of the target material separation better than 99%. The efficiency of the cooper radionuclide extraction and collection was about (90 ± 15)%.

SUMMARY

At PNPI a high current cyclotron C-80 with the energy of extracted proton beam of 40-80 MeV and the current up to 200 μA will be put into operation at the end of 2016 – beginning of 2017. One of the main goals of C-80 is production of a large number of medical radio nuclides for diagnostics and therapy. At present time the construction of radioisotope complex RIC-80 at the beam of C-80 is carried out. The peculiarity of the proposed radioisotope facility is the use of the mass-separator with the target-ion source device as one of the target stations for on-line, or semi on-line production of a high purity separated radio isotopes. The important part of the work was devoted to the target and ion source developments for the new project RIC-80. The tested target materials and developed ion sources will be used for manufacture real target prototypes for PNPI radioisotope complex. R@D of new high temperature methods of separation of produced radionuclides ^{82}Sr and ^{67}Cu from rubidium and zinc irradiated targets has been carried out. The following stage of the work will be the target unit prototype construction with the amount of the target material 40-60 grams, which is required for the effective medical radionuclide production at the RIC-80.

REFERENCES

[1] S.A. Artamonov et al., (National Research Center "Kurchatov Institute" B.P. Konstantinov Petersburg Nuclear Physics Institute, High Energy Physics Division. Main scientific Activities, Gatchina 2013) p.332, see http://hepd.pnpi.spb.ru/hepd/articles/PNPI_2007-2012.pdf..
[2] V.N. Panteleev et al., (National Research Center "Kurchatov Institute" B.P. Konstantinov Petersburg Nuclear Physics Institute, High Energy Physics Division. Main scientific Activities, Gatchina 2013) p.278, see http://hepd.pnpi.spb.ru/hepd/articles/PNPI_2007-2012.pdf.
[3] V.N. Panteleev et al., Rev. Sci. Instrum. **86**, 123510 (2015).
[4] V. N. Panteleev, Patent for an invention # 2598089 "The production method of radionuclide strontium-82".

ISBN 978-3-95450-181-6

MCC-30/15 CYCLOTRON-BASED SYSTEM FOR PRODUCTION OF RADIONUCLIDES PROJECT

A.P. Strokach, Yu.N. Gavrish, S.V. Grigorenko, V.I. Grigoriev, M.L. Klopenkov, R.M. Klopenkov,V.G. Mudrolyubov, G.V. Muraviov, V.I. Nikishkin, V.I. Ponomarenko, JSC "NIIEFA", St. Petersburg, Russia

Abstract

The projected MCC-30/15 cyclotron system is intended for operation in high-technology nuclear medicine centers. The system consists of a cyclotron, target systems for production of radionuclides in liquid, gaseous and solid states and a system for transport of accelerated ions to final units. The updated MCC-30/15 cyclotron with new systems for external injection, RF power supply and acceleration will ensure production of accelerated proton and deuteron beams in energy ranges of 18-30 and 9-15 MeV and currents not lower than 200 and 70 μA, respectively. Target systems are equipped with mechanisms for remote replacement of gaseous and liquid targets. Modular configuration of the beam transport system will allow the production of isotopes and carrying out of researches to be performed in separate experimental halls.

INTRODUCTION

The strategy for the development of nuclear medicine in RF is aimed at solving import substitution problems and providing international competitiveness of the equipment, which is one of the most high-technology products of industry. One of the main purposes of nuclear medicine is early diagnostics of diseases, which can significantly increase the efficiency of treatment and reduce the time needed. The most important tool for early diagnostics is functional diagnostics based on application of modern radiopharmaceuticals and apparatus for visualization of radionuclides' distribution in a patient' s body. Diagnostic studies in cardiology, oncology, neurology, etc. need a wide assortment of radiopharmaceuticals, for which purpose radioisotopes of high purity and a possibility for their production in close vicinity to a consumer must be provided. It is evident that organization of studies aimed at the development and application of new radiopharmaceuticals is possible only in research centers equipped with cyclotron equipment generating accelerated beams of hydrogen ions in a wide energy spectrum, which is proved by the world practice. The most expedient seems the use of a cyclotron with the energy of protons ranging from 18 to 30 MeV and that of deuterons varying from 9 to 15 MeV.

THE MAIN OBJECTIVES OF THE PROJECT

Prototype of the MCC-30/15 cyclotron has been designed and manufactured in the Efremov Institute (JSC "NIIEFA"). Put into operation in 2010 (see Fig. 1) [1-2].

Figure 1: General view of the MCC-30/15 cyclotron.

The experience gained in the process of the cyclotron operation has demonstrated the correctness of engineering solutions made at stages of its designing, development and manufacturing. However, more stringent current requirements for such facilities brought into being an urgent need for updating the cyclotron equipment while keeping unchanged its basic concept, namely, vertically located median plane, shielding-type magnet (which requires a radiation-shielded hall of a minimum size and offers easy maintenance/repair), combined functions of the magnet yoke and vacuum chamber, acceleration of H^- and D^- ions at one operating frequency (the 2nd and 4th harmonics).

The main purpose of the updating is attaining of higher intensity of accelerated ion beams and reliability of the system under long-term operation modes as well as designing of a new project of a system for beam transport to six remote targets. The main parameters and characteristics, which are supposed to be attained as a result of the updating are shown in Table 1.

Table 1: The main parameters of the cyclotron with updated systems.

Parameters	Values
Type of ions	
• Accelerated	H^-/D^-
• Extracted	H^+/D^+
Energy of accelerated ions, variable, MeV	
• Protons	18-30
• Deuterons	9-15
Number of devices for simultaneous beams extraction.	2
Total current of extracted beam, not less than, μA	
• Protons	200
• Deuterons	70
Power consumption, no more than, kW	
• Stand-by mode	30
• Operating mode	120

ISBN 978-3-95450-181-6

The main tasks to be solved in the course of updating:

- ***External injection system***.Development of a new source of hydrogen ions based on a cold cathode, which will allow an increase in the time of its continuous operation (with a heated cathode it is not more than 500 hours).
- Attaining of higher injection energy up to 24-26 keV, which will improve conditions of the beam forming in the injection line and increase the ion beam capture in the acceleration process.
- ***Resonance accelerating system.*** Development of new dee and dee stems constructions with an enhanced mechanical strength and thermal stability.
- Development of a new construction of the central cyclotron region providing higher capture of the ion beam in the acceleration process and offering enhanced mechanical strength.
- Development of a new construction of the AFT trimmer with the frequency tuning maximally close to linear.
- Development of an additional system for water cooling of the resonance accelerating system meeting more stringent requirements for thermal stabilization compared to the water cooling of the whole cyclotron system (water temperature stabilization at the resonance system output is in the range of±1°C).
- ***Main electromagnet.*** Modification of shims' construction to simplify the correction of the magnetic field topology when changing the type of ions to be accelerated.
- Modification of the vacuum chamber casing and central region of pole pieces with allowance for the new construction of the resonance system.
- ***The RF power supply system***. Designing of a new specialized RF generator adapted for the cyclotron equipment. This necessity results from a negative experience gained in installation and operation of the purchased equipment including foreign firms.
- Using of a home-made 4 kW transistor amplifier as the 1st stage of the power amplifier seems reasonable.
- Designing of a module for control and stabilization of the signal amplitude on the basis of positive experience gained at designing and installation of similar equipment of the C-80 cyclotron system.
- ***Vacuum system***. Keeping in mind requirements for import substitution, we made a decision to stop using of foreign high-vacuum pumps and apply diffusion and cryopumps of home manufacture.
- Pressure sensors with an extended service life will be used in measurements (possibility for long-term failure-free operation under intensive neutron fields and γ-radiation).
- ***Hookup elements***. When designing hookup elements (probes, stripping devices, trimmer), vacuum linear translators are provided for to ensure a high positioning accuracy and reliability under long-term operation.
- ***The beam transport system*** is built by the modular principle using standard electromagnets, quadrupole lenses, diagnostic devices designed in the Efremov Institute. Any beam transport to remote targets meeting the requirements of the End User can be provided.
- ***Target systems.*** Development of a mechanism for remote replacement of liquid and gaseous targets (up to five targets of different yields and applications), (see Fig. 2).
- Designing of a liquid target for production of ^{18}F isotope with a yield of not less than 8 Cifor 2-hour irradiation. Possibility for work at an accelerated proton beam current up to 100 μA.
- Designing of a special system for irradiation of solid targets (production of ^{64}Ci, ^{67}Ga, ^{111}In, ^{124}I isotopes, etc.), which allows an irradiated target to be automatically discharged to a shielded box or to a system delivering an irradiated material to this box.

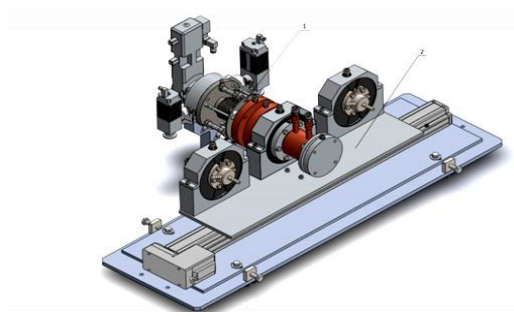

Figure 2: System for remote replacement of liquid and gaseous targets (three in total).

Systems of power supply, water cooling and automatic control will undergo no fundamental updating. Their final configuration is defined at the stage of approval of the beam transport system and target systems' composition by the End User. The cyclotron system to be updated meets to the utmost the needs of university centers planning a wide spectrum of researches in the fields of nuclear medicine, neutron and radiation physics, beam neutron therapy, diagnostic and therapeutic practice applying nuclear medicine methods as well as training of specialists in all the aforementioned fields.

An example of such a research center is a center created by cooperative efforts of specialists from the Efremov Institute, Russia and the Jyvaskula University, Finland. The equipment of the MCC-30/15 cyclotron system was designed in parallel with the elaboration of construction documents; manufacturing of the equipment and construction works were finished simultaneously. The whole cycle of works has been performed within 2 years, (see Figs. 3 and 4).

ISBN 978-3-95450-181-6


Figures 3, 4: Works on creation of a research center on the site of the University in Jyvaskula, Finland.

CONCLUSION

Guided by far-reaching plans of a number of Universities, both in Russia and abroad, to date we have designed several possible layouts of cyclotron centers equipped with a cyclotron with a maximum energy of 30 MeV. The main lines of activities of similar centers will be the following:

- Development and testing of new radiopharmaceuticals on the basis of promising isotopes for PETand SPECT diagnostics.
- Carrying out of a wide range of applied researches on the practical use of neutron therapy methods for the treatment of especially dangerous oncologic diseases.
- Preparation of radiopharmaceuticals obtained on the basis of radioisotopes produced by cyclotron for routine diagnostics by nuclear medicine methods.
- Production of radioisotopes, synthesis of radiopharmaceuticals on their basis and commercialization, which will provide income and profitability of a center.
- Studies, including those on a commercial basis, on the effect of radiation on radio - electronic components and units.
- Research studies in the radiation material science using high-energy flows of hydrogen ions, neutrons and γ-radiation.

Such centers will prove rather important in training and re-training of specialists for nuclear medicine, applied physics, etc. One of possible layout of the cyclotron system is shown in Fig. 5.

REFERENCES

[1] P.V. Bogdanov et al., “MCC-30/15 Cyclotron - parameters, adjusting works and their results”, RuPAC-2010, Protvino, September - October 2010, FRCHA03, pp. 408-410; http://www.JACoW.org

[2] P.V. Bogdanovet al., “The MCC-30/15 medical cyclotron with variable energy of accelerated ions”,Voprosy Atomnoi Nauki i Tekhniki, series “Electrofizicheskaya apparatura”, V. 5(31), St. Petersburg, 2010, pp. 32-43.

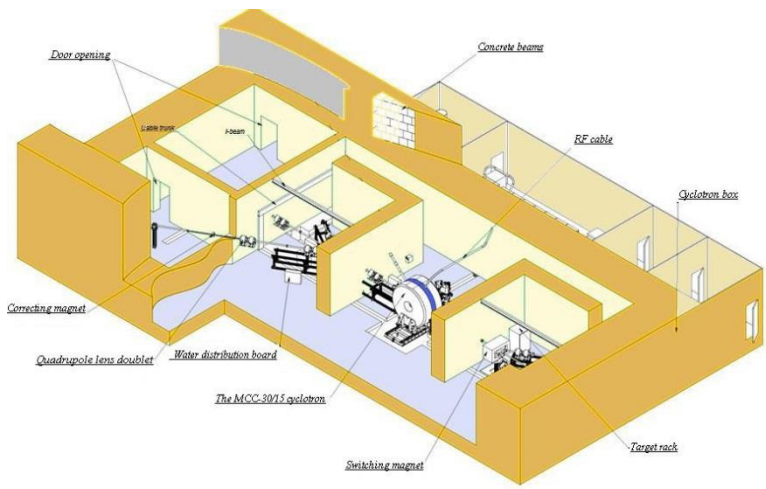

Figure 5: One of possible layouts of the cyclotron system.

ISBN 978-3-95450-181-6

THE CC-18⁄9M CYCLOTRON SYSTEM FOR PRODUCTION OF ISOTOPES FOR PET

R.M. Klopenkov, O.L. Veresov, Yu.N. Gavrish, A.V. Galchuck, P.A. Gnutov, S.V. Grigorenko, V.I. Grigoriev, M.A. Emeljanov, M.L. Klopenkov, L.E. Korolev, A.N. Kuzhlev, A.G. Miroshnichenko,V.G. Mudroliubov, G.V. Muraviov, V.I. Nikishkin, V.I. Ponomarenko, K.E. Smirnov, Yu.I. Stogov, A.P. Strokach, S.S. Tsygankov, JSC "NIIEFA", St. Petersburg, Russia
A.S. Guchkin, I.A. Ashanin, I.P. Grigoryev, CHTD-Ltd, Moscow, Russia

Abstract

The CC-18/9M cyclotron system has been designed, manufactured and delivered to JSC "NIITFA", Moscow to be operated in a pilot PET center. Acceptance tests have been conducted. Design parameters of the updated cyclotron have been obtained: energy of accelerated proton and deuteron beams was varied within the ranges of 12-18 and 6-9 MeV with currents of 150 and 50μA, respectively. For the first time in NIIEFA practice the cyclotron is equipped with a target system intended for production of F-18 and C-11 radionuclides for PET. At present, the cyclotron system is put into commercial operation in the PETcenter.

INTRODUCTION

Successful treatment of a series of diseases in cardiology, oncology and neurology to a great extent depends on their early diagnostics, which provides a significantly higher efficiency and less time needed for treatment. Nuclear medicine is an undisputable leader in early detection of diseases, and wide application of nuclear medicine methods is proved by the fact that more than a half of radioactive isotopes produced in the world are intended for medicine. Absolute leaders in introduction of nuclear medicine into practice are the USA, Japan and some European countries. In particular, in the USA the nuclear medicine methods were used in 46% of the total diagnostic studies performed in cardiology, 34% in oncology and 10% in neurology.

Establishing of centers rendering high-tech medical assistance based on modern methods of nuclear medicine allowing us to make an early diagnosis of the most important socially significant diseases is highly urgent in the Russian Federation is highly urgent in the Russian Federation.

A pilot PET-center primarily intended for further development and optimization of the home-made equipment with the future aim of its serial production has been created in the JSC"NIITFA", Moscow. A CC-18⁄9M cyclotron system was designed and manufactured in JSC "The D.V. Efremov Scientific Research Institute of Electrophysical Apparatus" (NIIEFA) to be used in this PET-center. The machine was put into operation in 2014.

NEW ENGINEERING SOLUTIONS. COMPARATIVE CHARACTERISTICS

The cyclotron system is based on an updated CC-18⁄9M machine, which prototype is the CC-18/9 cyclotron [1, 2]. Three CC-18/9 cyclotrons have been previously manufactured and delivered to PET-centers of the Turky University, Finland (2005), the Russian research Center for Radiology and Surgical Technologies, Pesochny, St. Petersburg, Russia (2006) and Snezhinsk town, Chelyabinsk region, Russia (2010). In the updated cyclotron, the energy of accelerated proton and deuteron beams is varied in the ranges 12-18 and 6-9 MeV respectively, which widens fields of its application and raises its competitiveness. Simultaneously the design current of protons increased half as much compared to that of the basic model

It was for the first time in the NIIEFA practice that the cyclotron was delivered together with the target system providing the production of isotopes necessary for PET-diagnostics. The general view of the cyclotron [3] is shown in Fig. 1.

Figure 1: The CC-18⁄9M cyclotron system.

When designing the updated machine, the major engineering solutions proved by practice when operating CC-18⁄9 cyclotrons were kept unchanged:

- Shielding-type electromagnet with vertically located median plane to give an easy access to in-chamber devices by moving apart the movable part of the magnet along the guides (see Fig. 2). In addition, the radiation exposure of the operating personnel in the process of scheduled maintenance and repair works is significantly reduced.

ISBN 978-3-95450-181-6

- Choice of negative hydrogen and deuterium ions as particles to be accelerated and extraction of proton and deuteron beams practically without loss of the beam intensity by stripping negative ions on thin carbon foils.
- Use of the external injection system [4], which appreciably reduces the inflow of the working gas from the source to the vacuum chamber, makes easier the high vacuum production and consequently reduces ion losses in the process of acceleration by charge exchange on the residual gas molecules.
- Acceleration of hydrogen and deuterium ions at a fixed frequency (the 2-nd and 4–th harmonics, respectively).

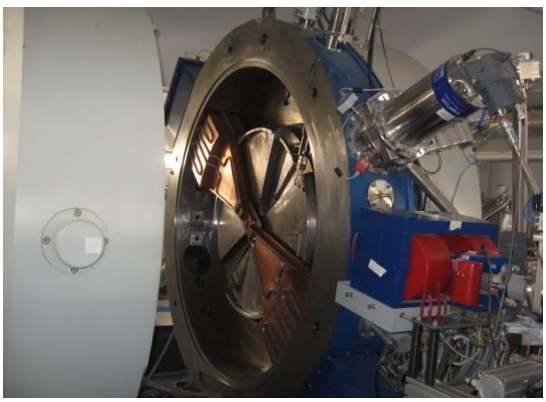

Figure 2: The CC18/9M cyclotron with an open vacuum chamber.

When designing the CC-18/9M cyclotron, special attention was paid to upgrading of output parameters as well as making easier its maintenance/repair.

- A new resonance accelerating system allowing the power losses to be reduced from 18 to 13 kW has been designed. The operating frequency of the RF power supply system is 40.68 MHz.
- A new manufacturing technology of the main magnet yoke was developed, which made easier the process of the electromagnet assembly and obtaining a necessary topology of the magnetic field.
- A new system was designed for on-line correction of the magnetic field topology when changing the type of particles to be accelerated.
- A new construction of hookup elements was designed providing a reduction in their cost, lower labor expenditures and less working hours needed for their manufacturing.

The main characteristics of the cyclotron system are given in Table 1.

TARGET SYSTEM

The target system designed and manufactured in the Efremov Institute is adapted to parameters of the CC-18/9M cyclotron beam. The system comprises water and gaseous target devices (see Fig.3 and Fig.4) [5] providing production of radioisotopes for PET-diagnostics.

Target devices can be mounted both directly on the output flanges of cyclotrons and on the end flanges of beamlines. Each target device comprises a unit providing targets' loading with a target material, system to deliver the activity to shielded boxes and system for monitoring the target status under irradiation.

Control of the target system is completely automated and is performed from the operator workstation [6]. Screens of the user interface are shown in Fig. 5.

The target system is designed by the modular principle. This allows a larger number of targets to be used and a wider assortment of radioisotopes to be produced. The target system is a completely self-contained system and can be adapted to any cyclotron used for commercial production.

Table 1: Main Characteristics of the CC-18/9M Cyclotron System Compared with Available Analogues

Main parameters	**CC-18/9 JSC "NIIEFA", Russia**	**CC-18/9M JSC "NIIEFA", Russia**	**Cyclone 18/9 IBA, Belgium**	**PET trace GE, Great Britain**	**TR-19/9ACS, Canada**
Type of accelerated particles	H^-/D^-	H^-/D^-	H^-/D^-	H^-/D^-	H^-/D^-
Type of extracted particles	H^+/D^+	H^+/D^+	H^+/D^+	H^+/D^+	H^+/D^+
Beam energy, MeV	18/9	12-18/6-9	18/9	16.5/8.4	19/9
Max beam current, μA, not less than	100/50	150/50	150/50	150/60	300
Energy variation	-	+	-	-	+
Number of simultaneously irradiated targets	2	2	2	2	2
Total power consumption, kW, no more than	60	60	55	70	65

ISBN 978-3-95450-181-6

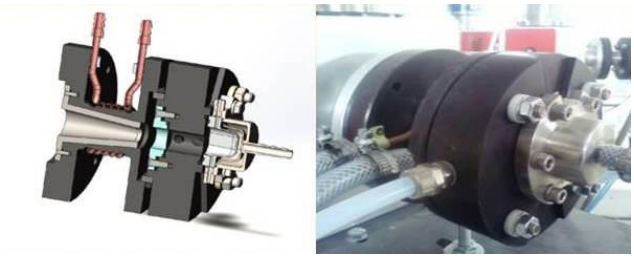

Figure 3: Target device for production of fluorine-18 (^{18}F) radionuclide.

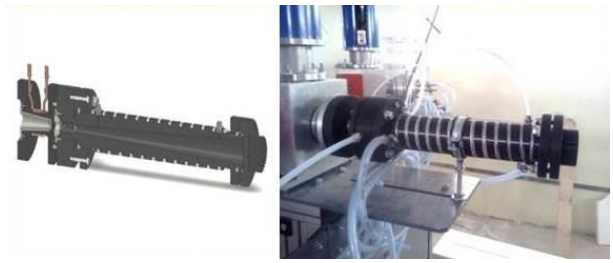

Figure 4: Target device for production of carbon-11 (^{11}C) radionuclide.

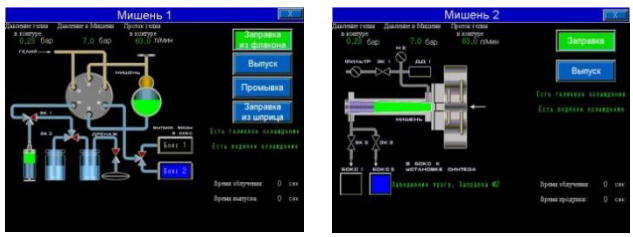

Figure 5: Status of water and gaseous targets on the monitor of the target system operator.

CURRENT STATUS AND PROSPECTS

In the tests of the target system with a proton beam current of 50 μA, the 5 Ci activity yield was attained with a 3 ml water target device for 2 hours of irradiation (production of ^{18}F). In this case, pressure in the working cavity of the target was 8 bars, which allows us to expect a higher yield after testing at a higher current of the beam of protons.

During 2016, the cyclotron system was operated in the mode of routine production of ^{18}F. More than 100 irradiation sessions were performed, and 7500 μAh of the beam time was used. The average proton beam current was 40 μA, average activity after 2-hour irradiation was 4.5 Ci and average yield of FDG was 70%.

As this cyclotron system is a pilot project, works to upgrade the performances of the external injection system, RF power supply system and automated control system were performed in parallel with its commercial operation. The near-future task to be solved is reduction of the beam intensity loss in the process of acceleration and beam transport through the beam line. Solution of this problem will allow us to increase the extracted proton beam current and to define the maximum and recommended yields of water targets.

The system comprising the cyclotron and target devices successfully demonstrated its service capability and proved an opportunity for commercial production of the radionuclides used in PET diagnostics.

REFERENCES

[1] P.V. Bogdanov et al., The RF patent №2373873 H05H, “Isochronous cyclotron for acceleration of several types of charged particles”, Bulletin № 32, 20.11.2009.

[2] P.V. Bogdanov et al., “Novel Compact cyclotrons for production of radionuclides”, RuPAC2008, Zvenigorod, September-October 2008, Proc. of Conf., pp. 361-363; http://www.JACoW.org

[3] P.V. Bogdanov, V.G. Mudrolyubov, S.A. Silaev. “Specific features of accelerating systems of compact cyclotrons CC-18/9, CC-12, MCC-30/15,” Voprosy Atomnoi Nauki i Tekhniki, series “Elektrofizicheskaya apparatura”, V.5 (31), St. Petersburg, 2010, pp. 65-74.

[4] P.V. Bogdanov et al., “Systems for external injection of negative ions for compact cyclotrons,” Voprosy Atomnoi Nauki i Tekhniki, series “Elektrofizicheskaya apparatura”, V.5 (31), St. Petersburg, 2010, pp. 74-83.

[5] P.V. Bogdanov et al., “Medical compact cyclotron MCC-30/15 with variable energy of accelerated ions,” Voprosy Atomnoi Nauki i Tekhniki, series “Elektrofizicheskaya apparatura”, V.5 (31), St. Petersburg, 2010, pp. 32-43.

[6] E.N. Abramov et al., “Target System for the CC-Series Cyclotrons Designed and Manufactured in NIIEFA”, Problems of Atomic Science and Technology, Series “Nuclear Physics Investigation” (61), 2013, V. 6(88), pp. 201-204.

ISBN 978-3-95450-181-6

GANTRY FREE TRANSPORT LINE FOR A PROTON/ION THERAPY

M.M. Kats#
FSBI SSC RF ITEP "Kurchatov Institute", Moscow

Abstract

For a long time a gantry was considered as a mandatory element for proton/ion therapy facility. However medics from MGH (Boston) suggested alternative concept which leads to decrease both cost and size of the facility [1]. The concept is based on the following provisions:

- immovable isocenter;
- active scanning of a target volume;
- different positions of patients at different fractions:
- using CT on the place of irradiation after each change of positions of the patient for improvement plan;
- using small change direction of the beam (like $\pm 10^0$).

The "Planar isocentric system" developed by author can be used to enlarge the flexibility of the concept [2]. It's relatively chip, small and can be realized for short time. It can be used for treatment for 90% of localizations. The system can replace gantry in centers of proton/ ion therapy providing significant decreasing of treatment price. The details of the system are presented and discussed.

INTRODUCTION

A therapy by beams of protons and ions is the technology of the twenty-first century. It is effective and necessary method to save human life. Its benefits in a cancer radiation therapy were known for a long time (see Figure 1). It is implemented in the radiation treatment for 20 years. But with the current technology today and in two years later the proportion of patients to whom it can be applied is about 1% of patients who are treated with beams of gamma rays [1-3].

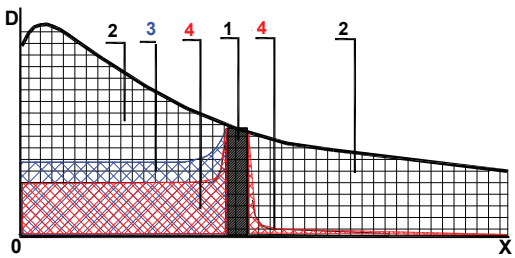

Figure 1: A scheme of energy distribution in the patient's body at irradiation by one direction at using different beams. 1 - target, 2 – gamma, 3 - protons, 4 - ions.

To generate beams of protons and ions useful for the treatment and for the further transportation of the beams to the patient it is necessary to use expensive and bulky equipment. Therefore, the treatment by proton and ion beams is significantly more expensive in a comparison with the treatment by gamma rays. In USA insurance companies pay now for the use of this treatment only for certain cancer locations, which need particularly important accuracy dose distribution (e.g., eyes), or for children treatment in order to prevent (on many years) reactions on small doses in healthy parts of the body.

In the world specialists are searching for more compact and less expensive equipment for proton and ion therapy. Compact and easy to use accelerators with superconducting magnets have been proposed. But beam transportation systems to the patient from different directions stay still bulky and expensive. Why a choice of directions of irradiation is necessary? In order not to irradiate those parts of body that must not be irradiated, and to spread the inevitable release of the energy in healthy parts of the body in a large volume, to different organs, in order to remain them at a relatively safe level.

Many years ago doctors formulated requirements for such equipment: the patient lies horizontally, motionless, the beam is transported from any direction of the plane perpendicular to the longitudinal axis of the patient. Systems that implement these requirements are generally called as a gantry. The gantry is expensive and bulky equipment because conventional electromagnets can rotate a beam of protons with a radius of about 1.5m and a beam of ions with a radius of about 4m. As a result, the standard gantry for proton's has a size of about $10m^3$ and the weight of the equipment rotated precisely in this volume is about 100t. Similar parameters of the HIT gantry for ion beam transport is 13m*13m* 18m and 660t. An optimal scheme for the proton's gantry is shown in Fig. 2.

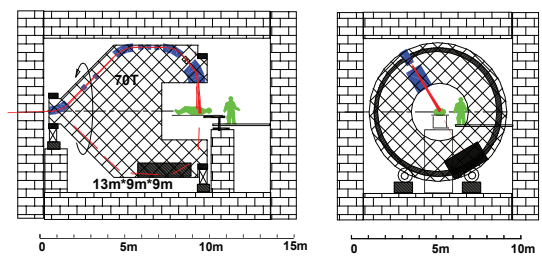

Figure 2: An optimal scheme of the gantry for a proton beam.

A significant part of the cost of a treatment is associated today with gantry systems (up to 70% for centers with four gantries). Attempts to develop a simple low-cost compact gantry based on superconductivity had not real success so far. A special conference of experts of this topic took place in the autumn of 2015 in Switzerland [4]. The problem is the necessity of fast enough distribution of the beam energy for the target volume ("scanning").

It were proposed in the form of compact "one room's" complexes by IBA, VARIAN, MEVION firms during recent years. But these complexes with one accelerator

#markmkats@gmail.com

ISBN 978-3-95450-181-6

and one treatment room can work only with beams of protons, have a limited annual productivity and can not significantly reduce the price of the treatment.

Does a therapy by proton and ion beams have a real future in a competition with a gamma therapy? Yes, if its treatment cost will be comparable to the cost of treatment by gamma rays. Much less expensive and more compact equipment is necessary instead of the gantry.

PREVIOUS SOLUTIONS WITHOUT GANTRY

V.E. Balakin proposed a system with a fixed horizontal beam, which is directed to the standing or sitting patient (see Figure 3). An initial horizontal beam is focused by quadrupole lenses and deflected by scanning magnets. The patient turns around a vertical axis in this system to change the direction of irradiation. A CT scanner with vertical displacement was proposed to control the shape of the body and of the target.

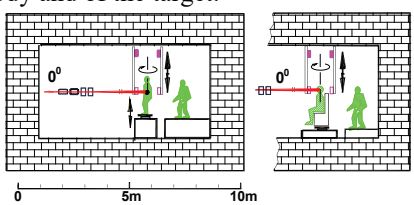

Figure 3: Balakin's scheme of changing the direction of irradiation.

In 2002 we proposed a "Simple Planar System" - "SPS (F)" [5]. Initial horizontal beam is focused by quadrupole lenses and deflected by scanning magnets too. A fixed magnet with increased gap is used to bend the beam in a vertical plane at an angle of less than F. A treatment table (with the patient fixed on it) is shifted in the vertical plane so as the rotated beam hits the target (see Figure 4). It is compact system with a possibility to change direction of the irradiation in the interval (–F<f<+F). A CT scanner shifted vertically together with the treatment table was proposed to control the shape of the body and the target. The scanner has additional possibilities of horizontal displacements.

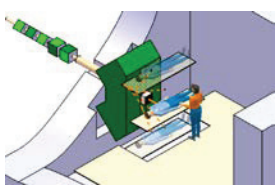

Figure 4: Three dimensions scheme of a simple planar system.

NEW REQUIREMENTS AND A NEW SOLUTIONS

In 2016, the doctors of MGH (Boston) analyzing the experience of a treatment of 4300 patients with different cancer localization [6], take thought about the appropriateness of the cumbersome and expensive gantry and its replacement by a new equipment with the following requirements to it:

1. Motionless irradiation center.
2. An active dose distribution in the target volume (scanning).
3. The admissibility of various positions of the patient in different fractions (the patient lying with limited (<± 15^0) turns of the table relative to the horizontal longitudinal axis of the patient or if the patient is sitting under rotations around of the vertical axis).
4. The use of a CT scanner in the place of irradiation after each change of the position of the patient.
5. The use of beam direction changes in a small interval (like <± 10^0).

In addition to the new doctor's requirements we proposed in 2016 the use of a "Planar Iso-centric System" with a fixed irradiation center and with three significantly different fixed beam directions in the vertical plane ("PIS"). The patient in this system can be irradiated both in lying and sitting positions. Each additional magnetic channel has small magnets and a simple optic. The patient can be irradiated from its second side in the next fraction. (About 20 fractions are in treatment process). A lot of designs versions are possible (see Figure 5 for example).

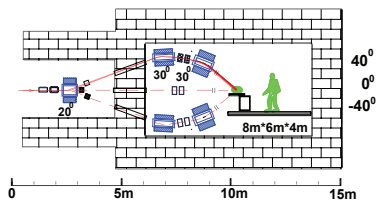

Figure 5: A scheme the PIS for a proton beam with three fixed directions.

Compared with the conventional gantry system in PIS at the beam direction of ±40^0 the beam rotation into PIS is decreased from 180^0 to 80^0. There is no complex and expensive mechanical system for precision turns of heavy magnets in a large volume and no complex magnetic focusing of a beam. There is no practically power consumption at the irradiation in a horizontal direction. The position of the scanning magnets allows reduce the weight, power and cost of the last magnet at saving scanning distance of about 3m. This limits the weight, power and cost of the entire PIS system. Dimensions of a treatment rooms with the PIS system are mainly determined by the patient's comfort transportation and installation to the working position. They are 5-10 times smaller than the dimensions of the room for the gantry.

Small rotations (like <± 15^0, without discomfort to the patient) of the treatment table around a horizontal axis with the fixed lying patient can be used under the control of a body shape and a target by sliding horizontally the CT scanner to increase a possibility directions of the irradiation (see Figure 6).

ISBN 978-3-95450-181-6

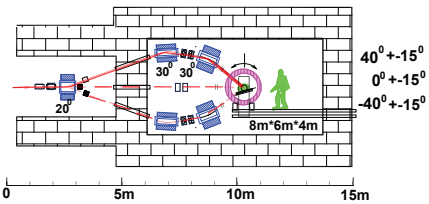

Figure 6: A scheme of the PIS with the patient lying on an inclined table under the control by a CT scanner.

A treatment armchair with sitting fixed patient can be rotated around a vertical axis under the control of the body shape and the target with shifted vertically CT scanner (see Fig. 7) for the expansion of choices of the irradiation direction in addition to three fixed directions.

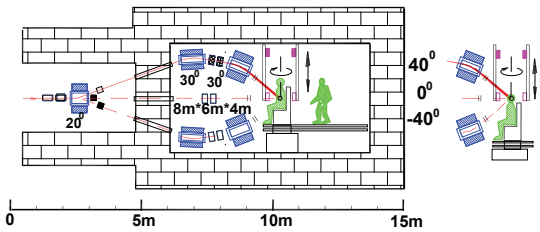

Figure 7: The scheme of PIS with sitting patient and with a CT scanner sliding vertically.

Using the PIS allows for any selected fixed position of the patient after one application of a CT scanner to clarify irradiation plans for all three possible directions of the irradiation. The proposed system allows to choose different directions of the irradiation in different fractions in a rather wide spread for the treatment of any cancer sites.

PIS SYSTEM FOR ION TRANSPORT

The same system can be easily realized by using more long warm magnets for the transport of ion beams. It has low cost, small size and low power consumption compared with all versions of a gantry (see Fig. 8), even in comparison with HIMAC gantry based on superconductive magnets.

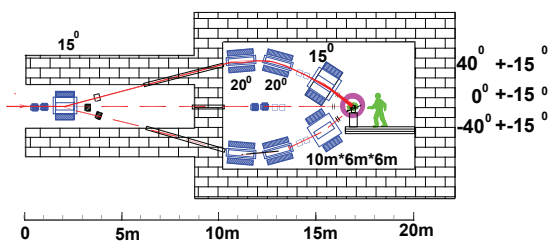

Figure 8: The scheme of PIS for ion beam with warm magnets.

CONCLUSIONS

The main progress in the radiation treatment in the future can be produced by a wide use of a proton therapy instead of a gamma therapy. For this purpose it is necessary to design compact and not expensive systems for the beam transportation to a patient by many spatial directions, to reach the price for a treatment by a proton beam comparable with the price of a treatment by a gamma equipment. Construction of a new gantry is not useful for this aim. New solution of a transport system (PIS) was suggested here instead of a gantry according of a new medical requirements. It used three beam directions in vertical plane with fixed center of irradiation at scanning the target volume. It used different positions of the patient in different fractions under the CT scanner control. For change direction of irradiation at sitting position of a patient the treatment chair can be rotated around of the vertical axis. For change direction of irradiation at a lying position of a patient the treatment table can be rotated on limited angels around of the horizontal axis. Three independent directions of irradiation are possible in any fraction at any fixed patient position. PIS ideas can be used to design more compact systems for ion transport by usual magnets.

An future equipment for low cost cancer therapy by proton beam can be designed on base of one simple accelerator with transport its slowly extracted beam to many (4-6) treatment rooms equipped by PIS systems.

The center of proton therapy with similar equipment is necessary in Moscow now.

ACKNOWLEDGEMENTS

The author expresses his deep gratitude to proff. J.Flanz (MGH, Boston) and to proff. E.V.Khmelevski (Herzen's hospital, Moscow) for helpful advices.

REFERENCES

[1] Particle Therapy Patient Statistics (per end of 2015). http://www.ptcog.ch/archive/patient_statistics/Patientstatistics-updateDec2015.pdf

[2] Particle therapy facilities *in operation (last update: Sep-2016).* https://www.ptcog.ch/index.php/facilities-in-operation

[3] M.Durante, H.Paganetti Nuclear physics in particle therapy: a review Rep. Prog. Phys. 79(2016) 096702

[4] Gantry Workshop II (Gantry with s-c. magnets) EuCARD 09.2015. https://indico.psi.ch/contributionListDisplay.py?confId=3575

[5] M.M.Kats New schemes for irradiation patients by proton and ion beams ITE, 2, p.126-135, 2002 (in Russian).

[6] Susu Yan et al, MGH Reassessment of the Necessity of the Proton Gantry: Analysis of Beam Orientations From 4332 Treatments at the Massachusetts General Hospital Proton Center Over the Past 10 Years, Radiation Oncology, May 1, 2016 V. 95, Issue 1, P.224.

[7] M.M.Kats. Planar system for transport proton and ion beams to immovable center from different directions Medical physics 2016, 2, 82-87 (in Russian).

ISBN 978-3-95450-181-6

HADRON THERAPY RESEARCH AND APPLICATIONS AT JINR

G. Shirkov†, G. Karamysheva, S. Gurskiy, O. Karamyshev, N. Morozov, D. Popov, E. Samsonov, S. Shirkov, G. Trubnikov, JINR, Dubna, Russia

Abstract

JINR has the unique experience in cancer treatment with proton beam during about 50 years. In 2005 the collaboration with IBA (Belgium) was established. During these years, the technical design of the first carbon superconducting cyclotron C400 was successfully created, the construction of serial proton cyclotron C235 was significantly improved and the fist modernized cyclotron C235 was assembled, debugged and put in the test operation in Dubna in 2011. This C235 will be used soon in the first Russian medical center with proton therapy in Dimitrovgrad. In 2015 the joint project with ASIPP (Hefei, China) on design and construction of superconducting proton cyclotron SC202 was started. Two copies of SC202 shall be produced, according to the Collaboration Agreement between JINR and ASIPP. One will be used for proton therapy in Hefei and the second one will replace the Phasotron to continue the proton therapy at JINR.

PROTON THERAPY IN JINR

The history of proton therapy in JINR began 50 years ago:

- 1967 – the beginning of the research on proton therapy;
- 1968 –1974 – first 84 patients treated with protons;
- 1975 –1986 – upgrading of accelerator and construction of a multi -room Medico -Technical Complex (MTC);
- 1987 -1996 – treating of 40 patients with protons;
- 1999– inauguration of a radiological department of the Dubna hospital;
- Since 2000 - regular treating of patients with tumors seated in the head, neck and thorax.

The modern technique of conformal three-dimensional proton therapy was realized firstly in the JINR Medical-technical accelerator complex which includes the Phasotron, the beam delivery systems and medical cabins.

Now JINR is the leading research centers of proton therapy in Russia. About 100 patients take a course of fractionated treatment in Dubna every year. During last 14 years from the startup of the Dubna radiological department more than 1000 patients were treated with proton beams [1].

The initial operation of the accelerator took place in 1949. In 1979-1984, the synchrocyclotron was converted into azimuthally varying field Phasotron. Now it is heavily depreciated and out of date, so it is important to replace it with the modern accelerator.

JINR (DUBNA) –IBA (BELGIUM) COLLABORATION

Superconducting C400 Cyclotron

IBA, the world's industrial leader in equipment of the proton therapy centers, in collaboration with JINR has designed the first superconducting carbon C400 cyclotron [2].

Most of the operating parameters (particle energy, magnetic field, RF frequency) of the C400 cyclotron are fixed. Small main field and RF frequency variation are necessary for the switching from one element to another. It is relatively small (6.6 m in diameter) and cost effective.

It offers very good beam intensity control for ultra-fast pencil beam scanning (PBS). But it requires an energy selection system (ESS) in order to vary the beam energy. The efficiency of the ESS for carbon is better than for protons due to lower scattering and straggling of carbon ions in the degrader.

The key parameters of the 400MeV/u superconducting cyclotron are listed in Table 1. The view of the cyclotron is presented in Fig.1.

Table 1. Main Parameters of the C400 Cyclotron

General properties	
accelerated particles	H_2^+, $^4He^{2+}$, $^6Li^{3+}$, $^{10}B^{5+}$, $^{12}C^{6+}$
injection energy	25keV/Z
final energy of ions, protons	400 MeV/u 265 MeV/u
number of turns	1700
Magnetic system	
total weight	700 t
outer diameter	6.6 m
bending limit	K = 1600
RF system	
number of cavities	2
operating frequency	75 MHz, 4 th harmonic

† email address: shirkov@jinr.ru

ISBN 978-3-95450-181-6

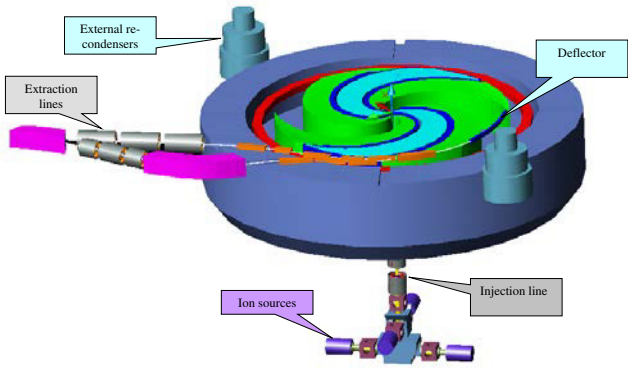

Figure 1: View of the median plane in the C400 superconducting cyclotron.

Three external ion sources are mounted on the switching magnet on the injection line located below the cyclotron. $^{12}C^{6+}$ are produced by a high-performance ECR at current 3 μA, alphas and H_2^+ are also produced by a simpler ECR source. All species have a Q/M ratio of 1/2 and all ions are extracted at the same voltage 25 kV, so the small retuning of the frequency and a very small magnetic field change achieved by different excitation of 2 parts in the main coil are needed to switch from H_2^+ to alphas or to $^{12}C^{6+}$. We expect that the time to switch species will be no longer than two minutes, like the time needed to retune the beam transport line between different treatment rooms.

Acceleration of the beam will occur at the fourth harmonic of the orbital frequency, i.e. at 75 MHz, and will be obtained through two normal conducting cavities placed in the opposite valleys.

Extraction of protons supposed to be done by means of the stripping foil. Deflector extraction is supposed to be used for the carbon beam. It is possible to extract the carbon beam by means of one electrostatic deflector (located in the valley between the sectors) with a 150 kV/cm field inside.

C235-V3 Proton Cyclotron for Dimitrovgrad

In Russia, construction of several centers of proton and ion therapy within the next few years is planned. The center of proton therapy in Dimitrovgrad will be the first Russian hospital center of the proton therapy, it was approved in 2010. The JINR-IBA collaboration has developed and constructed the C235-V3 proton cyclotron [3] for this center.

This cyclotron is a substantially modified version of the IBA C230 cyclotron (see Fig.2). Its characteristics exceed the series cyclotrons IBA of the previous modifications, already established in eleven hospital oncologic centers of the different countries of world.

JINR specialists examined the reasons for the losses of beam during the process of acceleration, the influence of the radial component of magnetic field in the median plane of accelerator, analyzed the influence of main resonances and carried out the calculations of the beam extraction system.

In Dubna, during 2011-2012 years had been carried out assembling of the cyclotron, shimming magnetic field, optimization of the acceleration modes and testing with the extracted proton beam. Proton transmission from radius 300mm to 1030 mm is 72% without beam cutting diaphragms. This allows reduce irradiation dose of the machine elements in comparison with serial C235 with extraction efficiency is 62%.

For performance assembly and beam tests of C235 V3 the building 5 in JINR was refurbish and adapt. That time connection of electricity, water cooling, ventilation, radiation safety and fire alarm were organized. Building floor reinforcement, vault shielding by concrete blocks, technological pit were prepared.

Figure 2: C235 cyclotron in JINR.

New technologies realized in JINR:

- Special compact (1m size) platform designed and manufactured for mechanical fabrication of the pole edges.
- Special 3D Carl Special 3D Carl Zeiss machine used to measure of the pole edged profile with μm accuracy during shimming of the magnetic field.
- New JINR calibration dipole magnet with field up to 2.9 T used for calibration of the Hall probes.
- The new system of the axial magnetic field measurements was tested.

The cyclotron is delivered to Dimitrovgrad and it's assembling in the hospital is underway now.

The JINR experience and technologies on design and construction of cyclotrons for hadron therapy can be used for creation and development of any accelerators for medicine such as SC202 for proton therapy.

JINR (DUBNA)–ASIPP (CHINA) COLLABORATION

Superconducting SC202 Cyclotron

The SC202 superconducting cyclotron for hadron therapy is under development by collaboration of ASIPP (Hefei, China) and JINR [4]. Superconducting cyclotron SC202 will provide acceleration of protons up to 202 MeV with maximum beam current of 1 μA in 2017-2018. We are planning to manufacture in two cyclotrons: one will operate in Hefei cyclotron medical center, the other will replace Phasotron in Medico-technical center to continue the proton therapy research at JINR in the near future.

ISBN 978-3-95450-181-6

The results of simulation of magnetic, accelerating and extraction systems are presented here. The cyclotron is compact and relatively light, the estimate total weight is less than 55 tons and extraction radius is 60 cm only. We have performed simulations of all systems of the SC202 cyclotron and specified the main parameters of the accelerator. Average magnetic field of the cyclotron is up to 3.6 T and the particle revolution frequency is 45.5 MHz. These parameters determine the requirements for the accuracy of all simulation to be unprecedented high.

The Medico-technical complex (MTC) JINR uses proton beam with energy up to 200 MeV specializing mainly on treatment of head localizations. The 200 MeV final energy has been chosen for SC202 cyclotron based on the experience of work of the MTC JINR and statistics for necessary depth of treatment provided by HIMAC (Japan) concerning the treated patients from 1995 to 2001 [5].

The proton beam with energy 200 MeV can irradiate all of the tumor localizations with a maximum depth of 25 cm. SC202 cyclotron will also be used for eye melanoma treatment at energies 60-70 MeV after degrading beam energy. Degrading the 200 MeV energy to 60-70 MeV would provide better beam quality compared to degrading from conventional energy 250 MeV.

SC202 is an isochronous superconducting compact cyclotron. Superconducting coils will be enclosed in cryostat, all other parts are warm. Internal ion source of PIG type will be used. It is a fixed field, fixed RF frequency and fixed 202 MeV extracted energy proton cyclotron. Extraction will be organized with an electrostatic deflector and magnetic channels. For proton acceleration we are planning to use 2 accelerating RF cavities, operating on the 2nd harmonic mode.

Magnet System of Cyclotron SC-202

The design of the SC202 magnetic system is described in details in [6].

Most accurate results of simulations were received in the parametrized model of the magnet (see Fig.3) created in CST studio and COMSOL Multiphysics.

Results of simulations are exporting to MATLAB for analyzing by conventional CYCLOPS-like code and for particle acceleration in 3D fields.

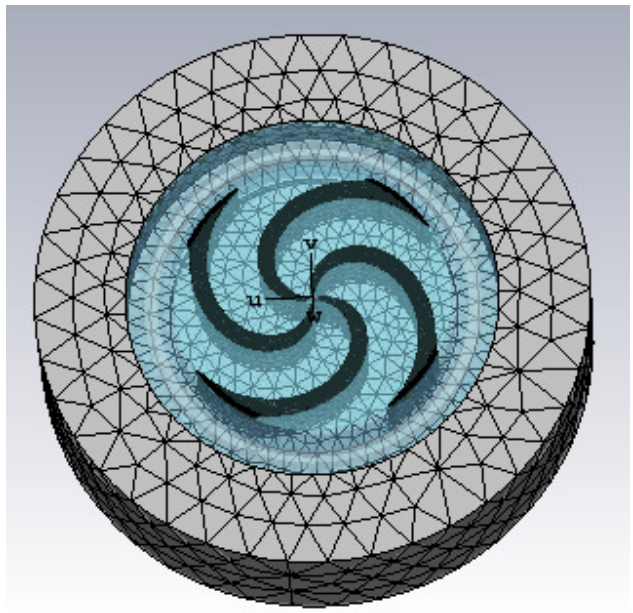

Figure 3: Model of the magnet.

Isochronism of the average field was achieved by decreasing of the sector width correspondently to orbital frequencies in closed orbits. Azimuthal width of sector against radius which provide isochronous field shown in Fig. 4. Orbital frequency of the final average field (Fig. 5.) is presented in Fig. 6. From Fig. 6 one can estimate that difference between mean field and isochronous is about 3-4 Gauss in accelerating region.

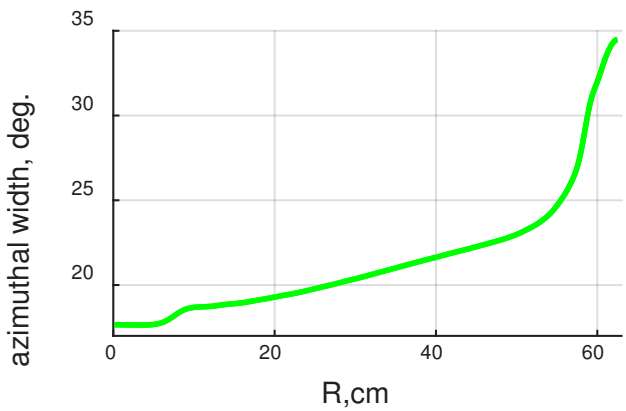

Figure 4: Azimuthal width of sector.

ISBN 978-3-95450-181-6

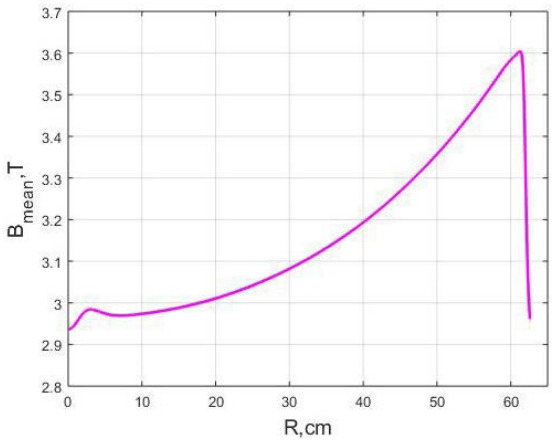

Figure 5: Average magnetic field along the radius.

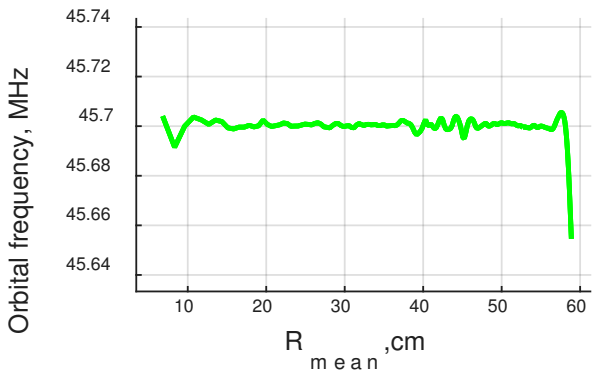

Figure 6: Orbital frequency against mean radius.

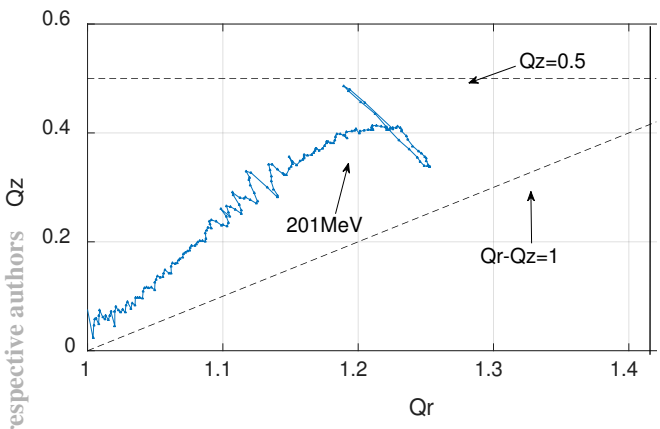

Figure 7: Working diagram in SC202.

CYCLOPS-like code was used to calculate the betatron tunes. Working diagram is presented in Fig. 7.

We are going to use 2 RF cavities operating on 2nd harmonic mode, each 50 degrees in azimuthal length, the acceleration is going to be relatively week on each turn. That is why, avoiding resonances is crucial for the design of the SC202 cyclotron.

Many efforts have been done to avoid the most dangerous resonances during acceleration Qr-Qz=1 and 2Qz=1. One can see that the first resonance is avoided completely while the second one is close at the end of acceleration.

RF System

Two RF cavities, connected in the center will be working on the 2nd harmonic on approximately 91.4 MHz.

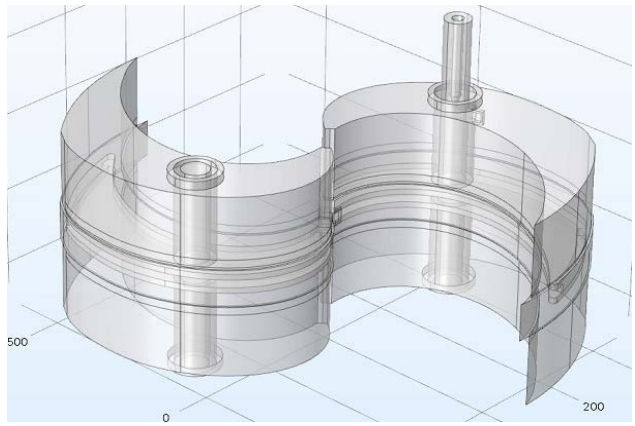

Figure 8: Overview of 3D model of RF system.

From the beam dynamics point of view the choice of 2nd harmonic is not the best solution, as the acceleration rate will be lower compared to 4th harmonic which seems like a natural choice for a cyclotron with 4 sector structure. However, operating on 182.8 MHz would raise problems with the extraction of particles from the ion source and the generators on 182.8 MHz are not widely available as compared to 91.4 MHz ones. As we avoid all critical resonances and extraction scheme does not require high acceleration rate we are able to use just 2 cavities on the 2nd harmonic. Computer simulations of the cavity was performed (see model in Fig. 8) Suitable accelerating frequency and voltage along radius (Fig. 9) were achieved. Accelerating system is described more detailed in report [7].

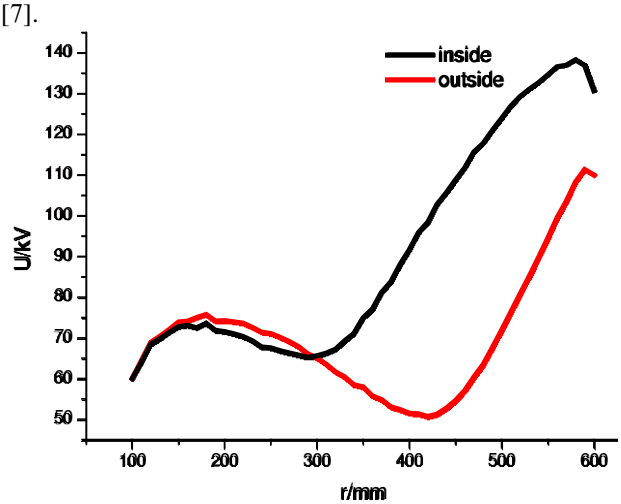

Figure 9: Mean acceleration voltage along radius.

Central Region Studies

Internal PIG proton source will be used in our cyclotron, so our simulations start from the inside of the source. We have built a 3D model of the source and the central region. In order to increase the efficiency of the extraction of the

ISBN 978-3-95450-181-6

protons from the source the first accelerating gap between the tip of the RF dee and the source should be kept as small as possible. However, sparking must be prevented, so we need to provide safe distance in both vertical and horizontal directions. The compact size of the accelerator is the major challenge in the design of the central region.

It was chosen to use 60 kV in the central region, and in this case, the major problem was to bypass the source on the first turn. In order to do so, we had to shape the dee tips in the center in such way to provide optimal acceleration rate.

We have used our 3D model of the RF system and the magnet in order to simulate the particle trajectories in the central region. It is clear that focusing and the energy gain using are good enough. However, it is very important to keep in mind that the final design will be strongly affected by the changes in magnet model, when we will get the measured BH curve of the steel, that will be used in the SC202 magnet.

Extraction

Simulations show that the extraction can be provided by deflector with electric field 150 kV/cm and focusing magnetic channels (see Fig. 10).

Extraction efficiency has been estimated for different changes of the septum thickness along its length and for different values of the beam radial oscillations during acceleration.

Maximum attainable extraction efficiency ~75% is achieved if amplitude of radial oscillations does not exceed 2 mm and septum has constant thickness 0.1 mm.

The collimator will be used to match the beam parameters with requirements imposed by a transport system.

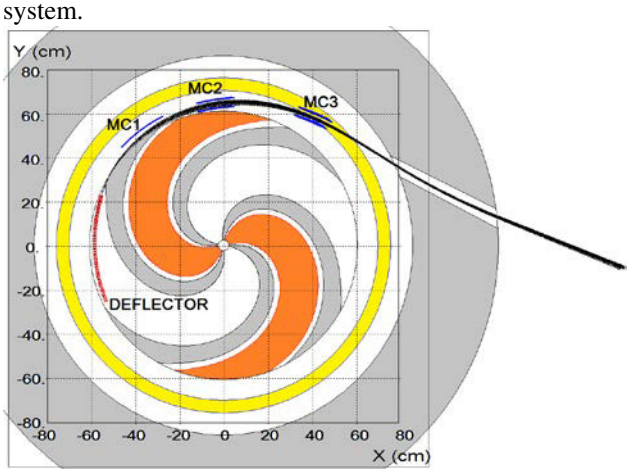

Figure 10: Plan view of the cyclotron with extracted beam.

Both copies of the SC202 will be manufactured in China, JINR and ASIPP will perform together the assembly, field measurements and shimming, RF ion source and beam tests of the both cyclotrons. Works on cyclotron for Dubna can be performed partially in JINR engineering center for the assembling and testing of the medical accelerator equipment.

CONCLUSION

JINR experience in proton therapy and cyclotron design is very important for the development of the new compact superconducting accelerator SC202 for proton therapy. The technical design of the cyclotron should be finished in 2016. The systems and components for SC202 will be manufactured by Institute of Plasma Physics in 2017 and assembling in China should be completed by the end of 2018.

REFERENCIES

[1] E.M. Syresin et al., Project of the demonstration center of proton therapy at DLNP JINR, Physics of Particles and Nuclei Letters, July 2015, Volume 12, Issue 4, pp 628–636.

[2] Y. Jongen et al. Compact Superconducting Cyclotron C400 for Hadron Therapy // Nuclear Instruments and Methods in Physics Research Section A. 2012. V. 624, Issue 1. pp. 47–53.

[3] G.A. Karamysheva, O.V. Karamyshev, S.A. Kostromin, N.A. Morozov, et al., Beam dynamics in a C253-V3 cyclotron for proton therapy, Technical Physics 57 (1), pp 106-112, 2012.

[4] G.A. Karamysheva, et al., Compact Superconducting Cyclotron SC200 for Proton Therapy, International Conference on Cyclotrons and Their Applications 2016.

[5] Yasuo Hirao, Results from HIMAC and other Therapy Facilities in Japan, International Conference on Cyclotrons and Their Applications 2001, AIP Conference Proceedings; 2001, Vol. 600 Issue 1, p 8.

[6] Morozov N.A. et al., Computer Modelling of Magnet for SC202 Superconducting Cyclotron, International Conference on Cyclotrons and Their Applications 2016.

[7] Gen Chen et al., Preliminary Design of RF System for SC202 Superconducting Cyclotron, International Conference on Cyclotrons and Their Applications 2016.

ISBN 978-3-95450-181-6

SC AND HTS-RELATED ACTIVITY AT IHEP

S. Kozub, A. Ageyev, I. Bogdanov, E. Kashtanov, V. Pokrovsky, P. Shcherbakov, L. Shirshov, V. Shuvalov, P. Slabodchikov, M. Stolyarov, V. Sytnik, L. Tkachenko, O. Trusov, S. Zinchenko
State Research Center of Russian Federation - Institute for High Energy Physics (IHEP) of National Research Centre "Kurchatov Institute", Protvino, Moscow region, Russia

Abstract

The SC program at IHEP of NRC "Kurchatov Institute" has been developed intensively in the 1980s in the framework of the UNK project. More than a hundred of models of the SC magnets of various designs, and then the pilot batch consisting of 25 full-scale dipoles and 4 quadrupoles have been designed, manufactured and tested at IHEP. Two SC magnetic systems of Electron Lens for the Tevatron collider (USA) were developed, manufactured and successfully brought into operation. Development of fast-cycling SC magnets for SIS300 accelerator and wide-aperture high gradient quadrupole magnets for Plasma Experiments within the FAIR project (European Research Centre of Ions and Antiprotons, Germany) is discussed. Racetrack and annular coils from HTS-2G tape for electrical machines that were developed, manufactured and tested are reported. Test and trial results with HTS dipole magnets employing Bi2223 as well as second-generation HTS are also reviewed.

SC MAGNETS FOR UNK PROJECT

New generation of high energy proton accelerators is based on superconducting (SC) magnets. In the early eighties of the last century the special cryogenic and superconducting facilities have been created at IHEP in frame of UNK project. In collaboration with Bochvar's institute SC NbTi wire of 0.85 mm diameter with 8910 of 6 micron filaments was developed. More than 100 SC magnet models and pilot batch consisting of 25 full scale 6 m dipoles (Fig. 1) as well as four quadrupoles were developed, produced and tested at IHEP [1] - [2]. The main characteristics of the magnets are presented in Table 1.

Table 1: The Main Characteristics of UNK SC Magnets

Parameters	Dipole	Quad
Magnetic field, T	5.11	
Field gradient, T/m		97.4
Operating current, kA	5.25	5.25
Field ramp rate, T/s	0.11	
Rate of central gradient, T/m/s		2.1
Number of layers	2	2
Strand number in cable	19	19
AC losses, W	5.5	2
Stored energy, kJ	570	180
Inductance, mH	45	13
Coil inner diameter, mm	80	80
Length of the coil, mm	5800	3100
Length of the cryostat, mm	6420	4165
Mass of magnet, kg	6000	1600

Figure 1: UNK SC dipole magnet.

SC MAGNETIC SYSTEM OF TEVATRON ELECTRON LENS

In 1999 – 2003 two SC magnetic systems of Tevatron Electron Lens for Fermilab, USA were developed and produced. These systems were placed and operated at TEVATRON accelerator (Fig.2). The system consisted of seven SC and ten copper magnets [3]. Main SC solenoid had 6.5 T nominal magnetic field, 2.5m length, 152 mm coil inner diameter. The solenoid coil was wound by the Rutherford type cable from 10 SC wires of 0.85 mm diameter. Turn number of the solenoid is 7238 and nominal current – 1800 A. Six SC steering dipoles were placed over the solenoid. Two dipoles of 1840 mm length were arranged in the centre and four dipoles of 250 mm length in the end parts of the solenoid. The central dipole produced 0.2 T magnetic field at 50 A current and end dipole – 0.8 T at 200 A. All dipoles were wound by cable transposed from 8 SC wires of 0.3 mm diameter.

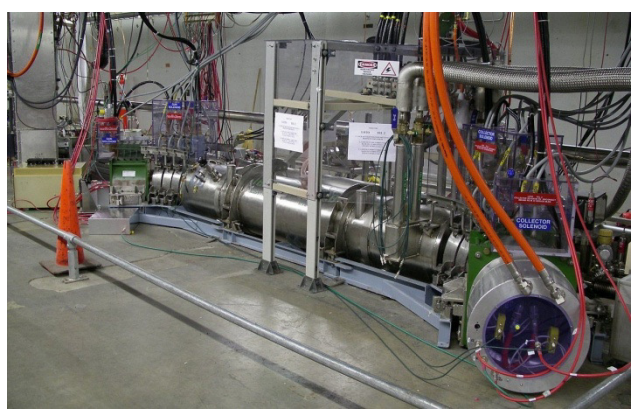

Figure 2: SC magnetic system of Tevatron Electron Lens.

ISBN 978-3-95450-181-6

The system included gun and collector solenoids with 250 mm inner diameter, 474 mm outer diameter, 300 mm length which produce 0.4 T magnetic field in aperture. Copper corrector coils were inside these solenoids. Three bending electron beam solenoids with 390 mm inner diameter, 500 mm outer diameter, 72 mm length were between cryostat and gun solenoid and the same between cryostat and collector solenoid. Turn number and nominal current of the solenoid were 48 and 357 A. Gun, collector and bending solenoids were produced from copper cable with 8.25×8.25 mm^2 cross-section with 5.5 mm diameter hole for water cooling.

HIGH FIELD FAST CYCLING SPERCONDUCTING MAGNETS

High field fast cycling magnets were developed and produced for the SIS300 accelerator of the FAIR project, Germany. The high field fast cycling dipole for the SIS300 is shown in Fig. 3 and its parameters are presented in Table 2 [4].

Figure 3: High field fast cycling dipole magnet.

Table 2: Parameters of the High Field Fast Cycling Dipole

Parameter	Value
Magnetic field, T	6
Operating current, kA	6.72
Field ramp rate, T/s	1
Number of layers	2
Strand number in cable	36
AC losses (calc.), W/m	4.7
In the coil	3.4
In the iron yoke	1.3
Stored energy, kJ	260
Inductance, mH	11.7
Coil inner diameter, mm	100
Length of SC coil, m	1
Mass of magnet, ton	1.8

A special design of SC wire and cable with stainless steel core was developed for this dipole. 6.8 T magnetic field in aperture of the dipole was reached and the magnetic field did not reduced up to 1.2 T/s ramp rate (Fig.4). The dipole with these parameters is unique in a world practice.

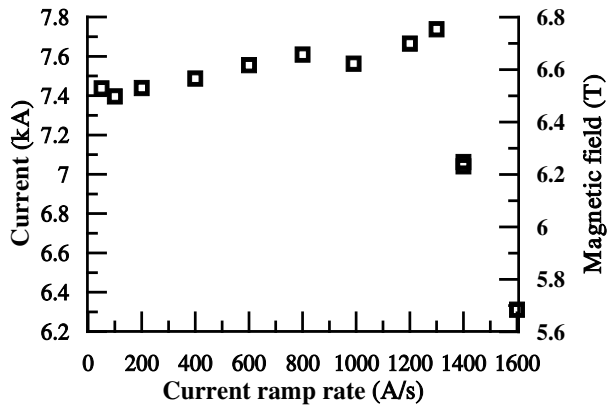

Figure 4: Ramp rate dependence of the high field fast cycling dipole.

A prototype of the SIS300 fast cycling quadrupole was produced and tested in 2011. Design parameters of the quadrupole are 45 T/m central gradient, 10 T/m/s ramp rate, 125 mm inner diameter and 1 m effective length [5]. Fig. 5 shows a general view and Table 3 presents main parameters of the quadrupole.

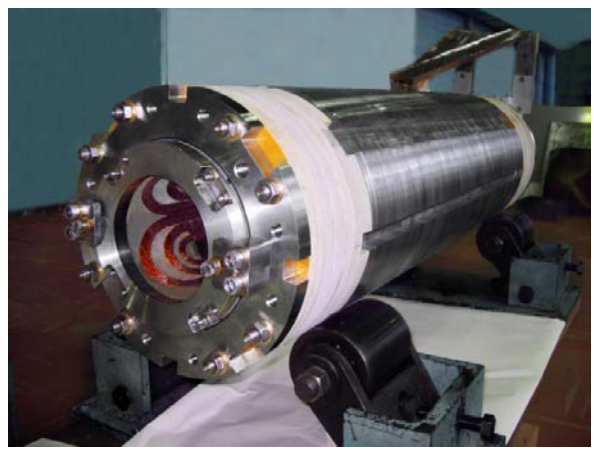

Figure 5: SIS300 fast cycling quadrupole prototype.

Table 3: Parameters of the SIS300 Quadrupole Prototype

Parameter	Value
Central gradient, T/m	45
Rate of central gradient, T/m/s	10
Operating current, kA	6.26
Maximum magnetic field on coil, T	3.51
Temperature margin in SIS 300 cycle, K	1.54
Stored energy, kJ	3.8
Inductance, mH	2
Number of turns in coil	80
Inner diameter of coil, mm	125
Thickness of collars, mm	22
Thickness of iron yoke, mm	52
Effective length, m	1

The quench current of the quadrupole reached 8.734 kA in fifth quench that corresponds to 40% current margin. Measurements of the quench current of the quadrupole at various ramp rates showed that the quench current was higher than 8.5 kA up to 5 kA/s (2.8 T/s) ramp rate.

ISBN 978-3-95450-181-6

At present a design of wide-aperture high gradient quadrupole magnets for Plasma Experiments in the FAIR has been developed [6]. The quadrupole cross section and main parameters are shown in Fig.6 and Table 4.

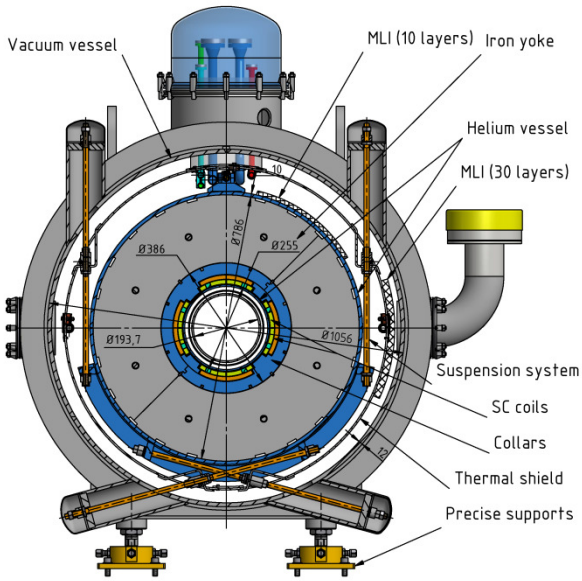

Figure 6: Wide-aperture quadrupole cross section.

Table 4: Parameters of the Wide-Aperture Quadrupole

Parameter	Value
Central gradient, T/m	37.6
Inner diameter, mm	260
Maximal field, T	5.9
Operating current, kA	5.73
Total magnetic force/octant, kN/m	1454
Total energy in the magnet, kJ/m	613.5
Inductance, mH/m	36.5
Length of magnet, m	1.89

DEVICES ON THE BASIS OF FIRST GENERATION HTS

In 1998 – 2000 first in Russia 600 A HTS current leads on basis of Bi2223 were developed in collaboration with Bochvar's institute in frame of contract with CERN, Switzerland [7]. First current lead had 33 HTS tapes with Ag+10%at.Au matrix, second - 16 HTS tapes and third current leads – 14 HTS tapes with Ag+1%at.Au matrix (Fig.7). These current leads consist of resistive part cooled by 20K helium gas and HTS part cooled by helium vapor. The resistive part consists of 2300 copper wires of 0.13 mm diameter which are placed into stainless steel tube of 11 mm inner diameter and 500 mm length. HTS part is 400 mm length. The third current leads had characteristics qualified for LHC: Heat leak to liquid helium is 0.08W at 600A current; resistance of HTS – resistive contact equals 220 nohm, resistance of HTS – NbTi wire contact – 6 nohm; helium flow rate cooling the resistive part – 0.04 g/s; pressure drop of the helium flow –5 kPa.

Figure 7: 600 A HTS current leads.

The next step in application of HTS is development of first in Russia HTS dipole in 2001 [8]. The dipole has 280x345 mm^2 cross section and 590 mm length (Fig. 8). 1T magnetic field was reached at 25 A current and 65 K temperature in 21×70 mm^2 aperture of the dipole. "Race-track" type coil was wound by 3.8×0.25 mm^2 HTS tape which consists of Bi2223 filaments in silver matrix. The coil was placed into yoke made from electric steel.

Figure 8: HTS dipole magnet on Bi2223 basis.

DEVICES ON THE BASIS OF SECOND GENERATION HTS

Full-scale racetrack coils for the rotors of the prototype of 200 kW SC synchronous motor (Fig.9) and the prototype of 1 MVA SC synchronous generator were produced and tested at IHEP [9]. The second generation (2G) HTS tape of the "American Superconductor Corporation" with cross section with insulation 4.93×(0.32 – 0.40) mm^2 was used. Insulation of HTS tape was made of a polyimide film, the total thickness of the insulating layer on one side was 76 microns. Critical current of the HTS tape (1 μV/cm, 77 K, self field) was equal 94 – 116 A. Basic parameters of the SC synchronous motor and generator coils are presented in Table 5.

ISBN 978-3-95450-181-6

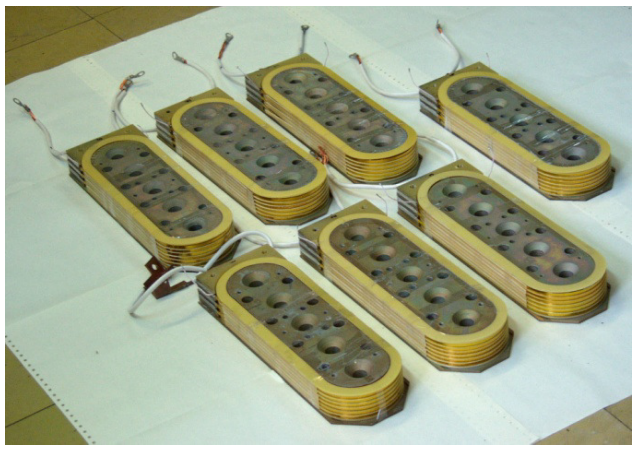

Figure 9: The HTS coils of SC 200 kW motor.

Because of the above mentioned dispersion of tape thickness from 0.32 to 0.40 mm the number of turns in motor coils was in the range of 188 - 205 and 381 - 393 in generator coils. Critical current of motor and generator coils at the coil voltage drop corresponding to 1 μV/cm was in the range of 46 – 53 and 42 – 47 A respectively.

Table 5: Basic parameters of the coils of the SC synchronous 200 kW motor and 1 MVA generator

Parameter	Motor 200 kW	Generator 1 MVA
Length, mm	334	587
Width, mm	114	187
Height, mm	40	50
Number of layers	6	6
Number of turns in the coils	188-205	381-393
Critical current of the coils (1 μV/cm, 77 K), A	46-53	42-47
Inductance, mH	45-51	42-43
Weight of coil with pole, kg	13	51
Number of coils	6	10

Two annular 2G HTS excitation coils for a 1 MVA superconducting synchronous generator were manufactured and successfully tested in a forced liquid nitrogen flow cooling mode inside their own cryostats (Fig.10) [10]. The coils were wound using 2G HTS tape produced by "SuperOx". The tape had cross section without insulation 12.0×0.15 mm^2. IHEP developed equipment and technology of 2G HTS tape insulation. The "SuperOx" HTS tape was insulated with a polyimide film, the thickness of the tape insulation was 26 microns. Minimum critical current of the HTS tape (1 μV/cm, 77 K, self field) was equal 300 A. Main parameters of the annular excitation coil are presented in Table 6. The measured values of the critical current of 116 A and 126 A at 78 K temperature and the voltage drops on coils corresponding to 1 μV/cm criterion are in line with the current threshold for thermal runaway and the increase of the normal zone. Critical current value for the coil #1 is slightly lower than that for the coil #2. We believe that this difference can be explained by variation of the characteristics of the particular HTS tape used in these coils. The threshold current values for both coils exceed the maximum operating design current of 115 A.

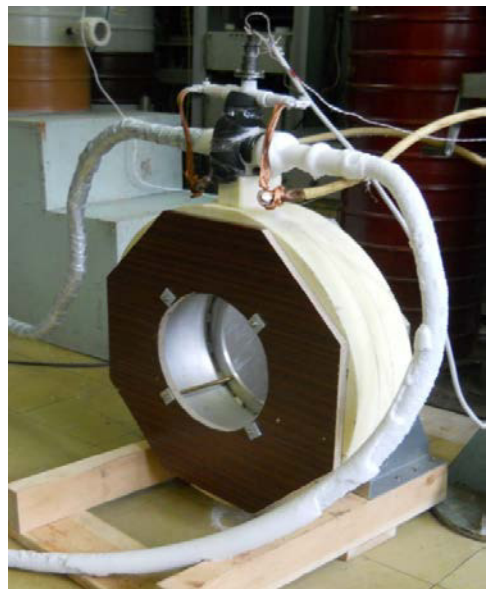

Figure 10: Test of cryostat with 2G HTS annular coil for the 1 MVA superconducting synchronous generator.

Table 6: Main Parameters of the HTS Annular Coil

Parameter	Value
Coil axial thickness, mm	25
Coil inner diameter, mm	491
Coil outer diameter, mm	557
Number of layers	2
Number of turns in the coil	306
Maximum operating current, A	115
Inductance, H	0.4
Axial magnetic field, T	0.25
Weight of the coil with cryostat, kg	28

A HTS dipole magnet (Fig.11) with a 1 T central field in 80×40 mm^2 aperture has been designed fabricated and successfully tested [11].

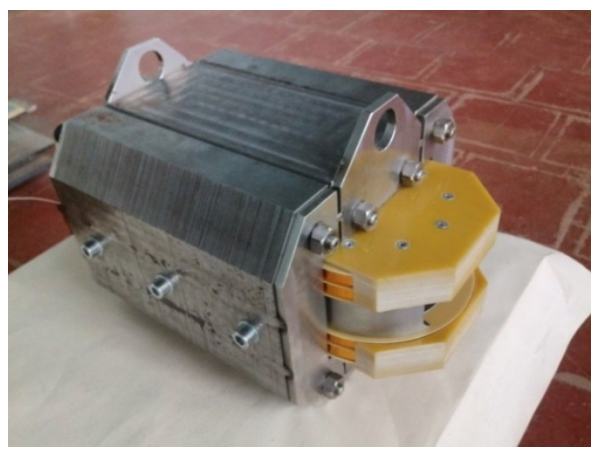

Figure 11: Dipole on the basis of second generation HTS.

The magnet coils were wound using 2G HTS tape produced by "SuperOx" (Table 7). IHEP insulated the HTS tape with a polyimide film, the thickness of the HTS tape insulation was 40 microns. Table 8 shows main design parameters of the HTS dipole.

ISBN 978-3-95450-181-6

Table 7: Properties of the SuperOx 2G HTS Tape

Parameter	Value
Substrate	Hastelloy C276
Min critical current (77 K, self-field)	400 A
Tape width	12 mm
Tape thickness without insulation	100 μm
Silver coating	1.5 μm
Copper coating	20 μm per side

Table 8: Design Parameters of the HTS Dipole

Parameter	Value
Nominal magnetic field in aperture	1 T
Operating current	100 A
Number of coils	2
Number of layers in each coil	2
Number of turns in each coil	180
Total number of turns	360
Longitudinal magnet length	425 mm
Longitudinal coil length	418 mm
Coil straight section length	250 mm
Longitudinal yoke length	250 mm
Aperture dimensions	40×80 mm^2
Magnet mass	103 kg

Fig. 12 presents a result of the magnet test at various temperatures. At 77 K and 10 μV/cm the current in the HTS coil reached 113 A, generating the central field of 1.12 T. At 65 K and 10 μV/cm, the HTS coil current was 228 A and the central field was 1.66 T. In liquid helium bath, the maximum injected current of 847 A was limited by the power supply, and the central field was 3.03 T.

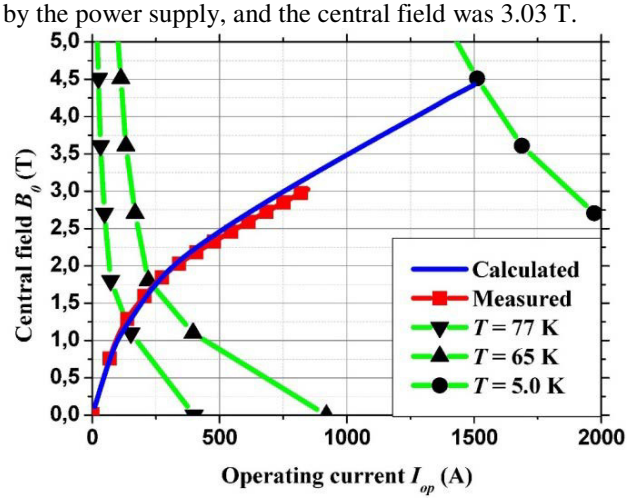

Figure 12: Measured and calculated dependences of the magnet central field on the operating current and field dependences of the 2G HTS tape critical current at 77, 65 and 5 K (green curves).

CONCLUSION

IHEP has meaningful experience and equipment for development and production of accelerator magnets on basis of superconductors. More than 100 SC magnet models and pilot batch consisting of 25 full scale 6 m dipoles as well as 4 quadrupoles were developed, produced and tested at IHEP. Two SC magnetic systems of Electron Lens were produced and operated at Tevatron, Fermilab, USA. High field fast cycling dipole with unique parameters in a world practice and quadrupole were developed and produced for the SIS300 accelerator of the FAIR project, Germany. Design of a wide-aperture high gradient quadrupole for final focus system of the HEDgeHOB beam line has been developed. First in Russia HTS current leads and dipole on the Bi2223 basis were manufactured and successfully tested. 2G HTS racetrack and annular coils for electrical machines were produced and tested at IHEP. Dipole on the basis of second generation HTS has been designed fabricated and successfully tested. At 77 K the central field of 1.12 T and 1.66 T at 65 K was reached. In liquid helium bath, the maximum injected current of 847 A was limited by the power supply and the central field was 3.03 T.

REFERENCES

[1] N.I Andreev et al. Development and Study of the Superconducting Quadrupole Magnet for the UNK. European Particle Accelerator Conference EPAC'94', London, June, 1994, p.p.2280-2282.

[2] A.I Ageev et al. The development and study of superconducting magnets for the UNK. IEEE Transactions on Magnetics, V.28, Issue 1, 1992, p. 682-685.

[3] Vladimir Shiltsev et al. Tevatron electron lenses: Design and operation. Phys. Rev. ST Accel. Beams 11, 103501, 2008.

[4] S. Kozub et al. SIS 300 Dipole Model, IEEE Transaction on Applied Superconductivity, V20, N3, June 2010, pp. 200- 203.

[5] S. Kozub et al. SIS300 fast-cycling superconducting quadrupole prototype. IEEE Transaction on Applied Superconductivity, v. 22, 2012, number 3, 4001104.

[6] L. Tkachenko et al. Development of Wide-Aperture Quadrupole Magnets for Plasma Experiments in the FAIR Project. IEEE Transaction on Applied Superconductivity, v. 23, 2013, number 3, 4000204.

[7] I. Bogdanov et al. Design and Test of High Temperature Superconductor Current Lead. IEEE Transactions on Applied Superconductivity, March 2000, V. 10, N 1, p.p. 1485-1488.

[8] A. Ageyev et al. Test Results of HTS Dipole. IEEE Transaction on Applied Superconductivity, vol. 12, no. 1, pp. 125-128, March 2002.

[9] I. Bogdanov et al. HTS racetrack coils for application in electrical machines. Proceedings of National Conference of Applied Superconductivity, November 2015, Moscow, p.p. 258-264.

[10] A. Ageyev et al. HTS Annular Field Coils of the Synchronous Generator. Proceedings of National Conference of Applied Superconductivity, November 2015, Moscow, 269-275.

[11] I. Bogdanov et al. Design, fabrication and testing of a dipole magnet made with 2G HTS wire. Superconductor Science and Technology. V. 29, N.10, 105012, October 2016.

ISBN 978-3-95450-181-6

STATUS OF SUPERCONDUCTING ISAC-II AND ELINAC ACCELERATORS, AND SRF ACTIVITIES AT TRIUMF

V. Zvyagintsev, Z. Ang, K. Fong, T. Junginger, J. Keir, A. Koveshnikov, C. Laforge, D. Lang, R.E. Laxdal, Y. Ma, N. Muller, R. Nagimov, D.W. Storey, E. Thoeng, B. Waraich, Z. Yao, Q. Zheng,
TRIUMF, Vancouver, BC, V6T 2A3, Canada

Abstract

The development for superconducting accelerators has been started at TRIUMF in 2000. The main milestones and material implementations are: 2006 - commissioning of Phase-I of the heavy ion superconducting accelerator ISAC-II, 2010 - Phase-II, 2014 - commissioning of Phase-I of the superconducting electron linear accelerator eLinac. We are using the accumulated experience and resources for farther SRF development at TRIUMF and external projects VECC, RISP, FRIB and SLAC. TRIUMF is also running fundamental studies for SRF and educational program for universities. Status of Superconducting ISAC-II and eLinac accelerators and SRF development aspects, results and plans are discussed.

ISAC-II

SRF at TRIUMF began in 2000 with cavity and infrastructure development in support of the ISAC-II heavy ion linac as an extension of ISAC facility for ISOL based on radioactive ion beam production and acceleration. In 2006 Phase-I of ISAC-II with acceleration voltage of 20 MV was commissioned for operation [1]. In 2010 the design goal of ISAC-II for 40 MV of acceleration voltage was achieved with completion of Phase-II [2]. ISAC became a leading ISOL facility supporting a full physics program with both stable and radioactive beams being delivered: stable beams of 16O5+, 15N4+, 20Ne5+ and radioactive beams (and their stable pilot beams) of 26Na, 26Al6+, (26Mg6+), 6He1+, (12C2+), 24Na5+, (24Mg5+), 11Li2+, (22Ne4+) including 74Br14+ from the charge state booster.

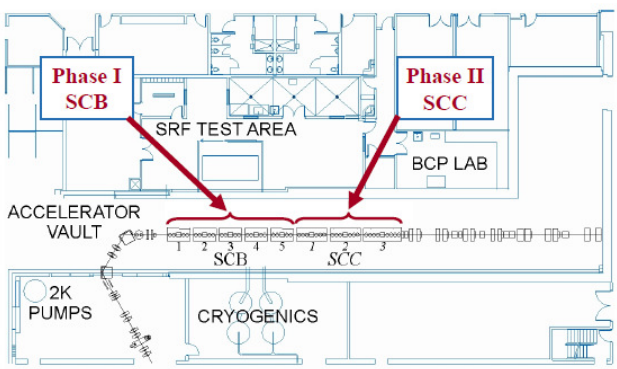

Figure 1: Layout of ISAC-II linac and SRF infrastructure.

*TRIUMF receives federal funding via a contribution agreement through the National Research Council of Canada

The Phase-I segment (SCB section of Fig. 1) consists of twenty 106 MHz quarter wave cavities housed in five cryomodules with four cavities per cryomodule.

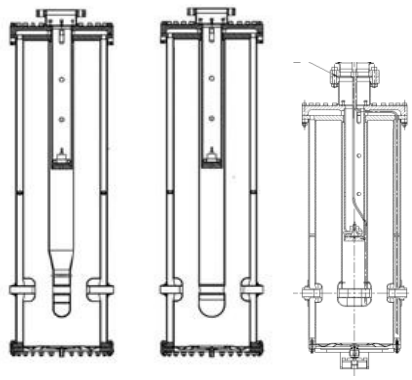

Figure 2: ISAC-II β=0.057, 0.071 and 0.11 cavities.

The Phase-II consists of twenty 141 MHz QWR cavities at β=0.11 in three cryomodules with six cavities in each of the first two modules and eight cavities in the third (SCC section in Fig. 1). Both Phase-I and Phase-II cryomodules have one 9T superconducting solenoid symmetrically placed in the cryomodule.

Cavities

The first eight of Phase-I cavities have a geometric β of 0.057 and the remainder a geometric β of 0.071 (Fig. 2). The cavity design was conducted in collaboration with INFN-LNL (Italy) with adoption of ALPI INFN-LNL coaxial bulk Nb cavities concept with vacuum volume open to cryomodule isolation vacuum; the cavities are specified to operate at 106MHz and to provide an effective acceleration of 1.1MV for a cavity power of 7W at 4.2K and corresponding peak surface fields of 30MV/m and 60mT [3]. 20 Phase-I cavities were fabricated at Zanon (Italy) and assembled in 5 cryomodules designed and fabricated at TRIUMF.

The Phase-II 141 MHz superconducting cavity with β of 0.11 is shown in Fig. 2. It was developed at TRIUMF and has a similar structure to the ISAC-II Phase-I linac cavity. The chief difference here besides the frequency is the inner conductor beamport region is outfitted with a donut style drift tube to improve the transit time factor. The Phase-II cavity has the same specification as the Phase-I cavities [4]. Twenty Phase-II cavities were produced by PAVAC Industries in Canada. Three cryomodules with high beta cavities were successfully commissioned in April 2010 [2]. An SRF infrastructure for SC development including SRF test area, clean room

ISBN 978-3-95450-181-6

and chemical laboratory (Fig. 1) was created at TRIUMF.

Tuning of the cavities is provided with deformation of Nb plates bolted to the bottom flange. A mechanical damper installed inside of the inner conductor provides >10 dB attenuation of microphonics noise. The cavities operate in strong overcoupled regime (coupling ~50-100) to provide enough bandwidth to maintain stable operation from microphonics. The LN2 cooled coupling loop produces <0.25 W power dissipation in helium system at 200W forward power.

Operating experience

The performance of the cavities is monitored periodically during start-up after shutdown. The linac is warmed up once per year for three months as part of the site maintenance shutdown.

The linac cavities operate with an average gradient corresponding to a peak surface field of 32 MV/m for Phase-I and 28.5 MV/m – Phase-II without any discernible reduction in performance. The reasons why Phase-II cavities performance is lower could be:

- Q-disease. Tests show that Phase-II cavities start degrading performance after 1h in the range of temperatures 200-100K, for Phase-I cavities it occurs after 10h. It could be due to higher hydrogen content in the Nb.
- During production of Phase-II cavities 2 of them were rejected due to vacuum leaks that opened in the donut weld after a final BCP of 100μm. Due to the tight schedule we limited BCP (in the beam tube region) to 60μm on subsequent cavities. All leaking cavities were successfully repaired and tested. Another four cavities were installed in cryomodules without single cavity cryostat tests due to time constraints.

We experience some cavity failures for different reasons but it doesn't stop operation. Since every cavity has an independent RF system, we can compensate the performance of the unavailable cavities by increasing the gradient in other cavities (at power dissipation >7W).

We are conducting continuous development to upgrade the cavities systems and mitigate failures

- Replacement of coupler loop mechanical joints
- We experienced with several failures of internal cables due to RF glow discharge in vacuum. Hermetic cable assemblies were unavailable at that time due to a long delivery time. Since 2015 we started replacing 3/8" for ½" ANDREW HELIAX cables. It works fine so far.
- We replace Phase-I couplers that use a rack and pinion mechanical arrangement and Teflon guide bearing for Phase-II couplers with design with non-magnetic cross-roller bearings and symmetric loading – this has improved the mechanical motion which is important because of ½" cable is more rigid and provides more side load for the coupler mechanism.
- During maintenance we are doing high pressure rinsing and sometimes light etch to recover the cavities performance.

During operation cryogenics failures cause cavity recoverable degradation.

- Trapped magnetic flux from short interruption of LHe supply. Full recovery (~two hours activity) involves degaussing the solenoid and environs, then warming cavities and solenoid to 30K to quench all solenoid trapped flux, then recooling the cold mass [5].
- Q-disease due to long interruption of LHe supply. Full recovery requires cavity warmup to room temperature.

Low level multipacting in some cavities is responsible for delay of start-up and tuning. It is three orders of magnitude less than the operational field level and doesn't affect performance. Pulse RF conditioning in self-excited loop is required to start these cavities, sometimes it takes a significant time. We implemented driven option for multipacting conditioning from a signal generator and apparently we see that it is more efficient. Multipacting disappears during cavity operation and reappears after warmup.

The Phase-I system uses tube amplifiers and they have been a source of downtime due to tube aging issues causing phase drift and non-linear output affecting LLRF operation. We started replacement for solid state amplifiers.

For the future we intend to make a development for degassing of Phase-II cavities to eliminate Q-disease issue and increase the cavities operational gradient.

ELINAC

The ARIEL project [6] will allow an increase in the radioactive ion beam (RIB) hours with the addition of a new electron linac driver of 50 MeV (0.5 MW), a new proton line from the 500MeV cyclotron and new production target stations. Accelerated electrons can be used to generate RIBs via the photo-fission process. The electrons are stopped in a converter to generate bremsstrahlung photons for fission in actinide target material. An electron beam intensity and energy of 10 mA and 50 MeV is required for a fission rate of 10^{13} fissions/sec.

The electron linac is housed in a pre-existing shielded experimental hall adjacent to the TRIUMF 500 MeV cyclotron that has been re-purposed as an accelerator vault. The elinac is being installed in a phased way with stages shown schematically in Fig. 3.

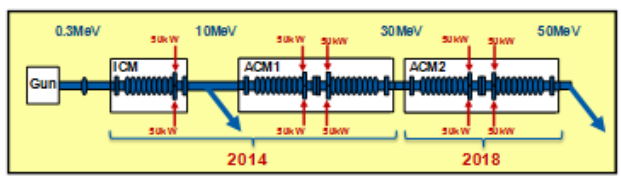

Figure 3: The stages of the eLinac project.

ISBN 978-3-95450-181-6

A first phase consisting of a 300 kV 16 mA electron gun, an injector cryomodule, ICM, containing one 1.3 GHz nine-cell cavity and an accelerating cryomodule, ACM1, that now contains one 1.3 GHz nine-cell cavity (and eventually two cavities) plus associated beamlines is now installed and is being commissioned [7]. This first phase is designed to accelerate CW up to 10 mA of electrons at 30 MeV. The initial beam dumps and production targets will only be compatible with 100 kW operation. A second phase, dependent on funding, will see the addition of a second accelerating module, ACM2, and a ramp up in beam intensity to the full capability of 50 MeV 0.5 MW.

eLinac Design

An RF frequency for accelerating cavities of 1.3 GHz is chosen to take advantage of the considerable global design effort at this frequency both for pulsed machines (ILC) but also for CW ERL applications (KEK, Cornell, BerlinPro). The linac architecture was determined by the final CW beam power of 500 kW (10 mA/50 MeV electron beam) and the available commercial CPI VWP3032 couplers for 75 CW RF at 1.3 GHz. The cavity design allows two couplers per cavity arranged symmetrically around one end delivering a total of 100 kW of beam loaded power. This sets the number of cavities at 5 with a maximum gradient per cavity of 10 MV/m. It is our intention to install a future ERL ring with injection and extraction between 5-10 MeV and so a single cavity off-line injector cryomodule was chosen plus two 2-cavity accelerating modules. The electron hall is shown in Fig. 4 as it would appear at the end of Phase-I stage of the project.

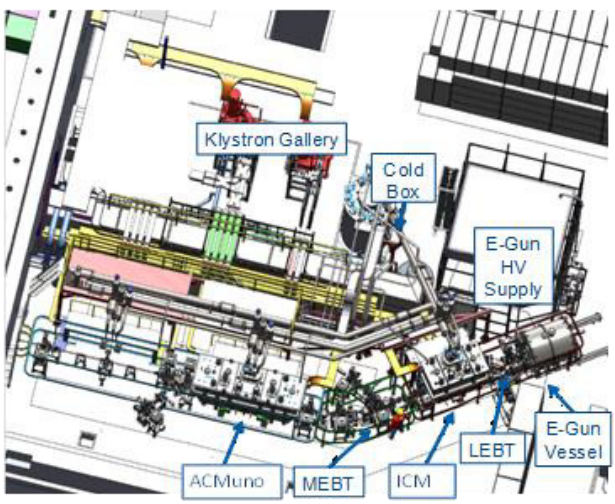

Figure 4: The Phase-I configuration of the eLinac.

The electron source provides electron bunches with charge up to 15.4 pC at a repetition frequency of 650 MHz. The main components of the source are a gridded dispenser cathode in a SF6 filled vessel, and an in-air high voltage power supply. The beam is bunched by superimposing a RF modulation to overcome a DC suppression voltage on the grid. The source is installed and conditioned to 320 kV with beam extracted at 300 kV up to the full CW intensity of 10mA.

The LEBT straight section contains three solenoids to provide transverse matching and transportation. The LEBT is now installed and commissioned [7].

Cavities

The cavity design parameters include f_o=1.3 GHz, L=1.038 m, R/Q=1000, E_a=10 MV/m. For Q_o=1•10^{10} the cavity power is P_{cav}=10 W at 2 K that sets the active load requirement for the cryogenics system. A rendering of the jacketed cavity is shown in Fig. 5.

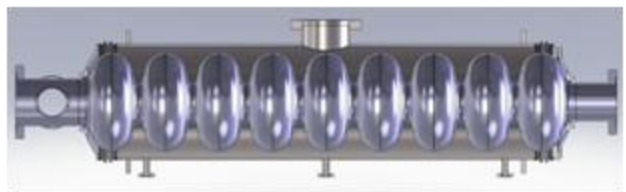

Figure 5: The e-Linac nine cell cavity with jacket.

The inner cells take their shape from the Tesla nine cell cavities but the end groups are modified to accept the two power couplers and to help push HOMs to dampers located on each end. On the power coupler end there is a stainless steel damping tube coaxial with the beam tube and extending into the beam pipe. On the opposite end of the cavity a coaxial CESIC tube is used. Each tube is thermally anchored at 77 K and thermally isolated from the cavity by a thin walled stainless steel bellows. The dampers are sufficient to reduce the HOMs to meet the BBU criterion of Rd/Q•QL<10^7. The beam tube diameters on the coupler end and opposite end are 96 mm and 78 mm respectively. The vacuum jacket is made from Ti with a machined two convolution flexure on either end. A single 90 mm diameter chimney allows for large CW RF load of up to 60 W per cavity assuming a conservative heat transfer of 1 W/cm^2.

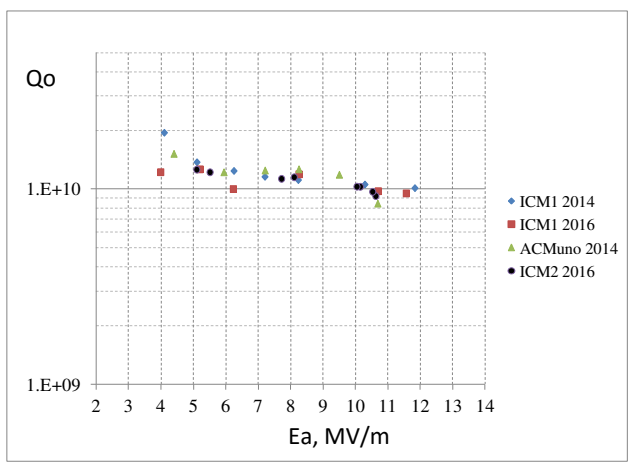

Figure 6: Q-curves of the cavities in eLinac cryomodules.

The ARIEL cavities have been fabricated by PAVAC [7]. To date four cavities have been received. The cavities are tuned, degreased then given a 120 μm BCP before

ISBN 978-3-95450-181-6

final tuning. After the initial cold test all ARIEL cavities were each degassed at FNAL at 800 C for four hours. All the cavities exhibit similar test results. The cavities reach, during 'vertical' tests, the specified gradient of 10 MV/m but at a Q_0 of $6•10^9$. So far 3 ARIEL cavities after jacketing were installed in cryomodules: ICM, ACMuno and ICM2 (for VECC). All of them in, 'horizontal' mode, shown $Q_0 > 1•10^{10}$ at E_a=10 MV/m (Fig. 6). Cavity jacketing was done at PAVAC. Due to problems with Ti-bellows from the sub-contractor PAVAC proposed to machine Ti flexures into the jacket. These work well with no significant increase to the cavity stiffness of 1800 N/mm.

Cryomodules

In brief the module is a top-loading box-like structure with a stainless steel vacuum chamber (Fig. 7). The cold mass is suspended from the lid and includes a stainless steel strongback, a 2 K phase separator pipe, cavity support posts and the cavity hermetic unit. The hermetic unit consists of the niobium cavities, the end assemblies, an inter-cavity transition (ICT) with a stainless steel HOM damper, the power couplers (FPC) and an RF pick-up. The end assemblies include the warm-cold transition (WCT), CESIC HOM damping tubes and beam-line isolation valves. Other features include a scissor jack tuner and warm motor, LN2 cooled thermal isolation box and two layers of mu metal and alignment monitoring via a WPM diagnostic system.

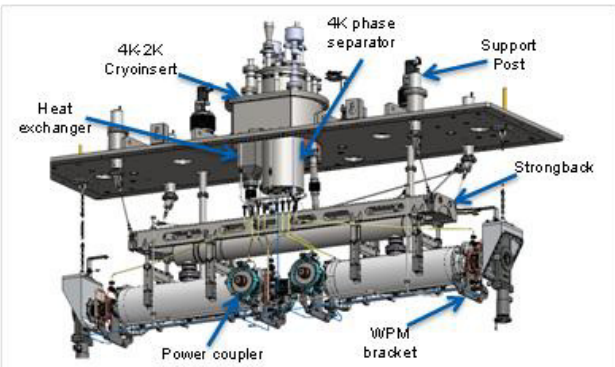

Figure 7: Accelerating cryomodule for ARIEL eLinac.

Each cryomodule is outfitted with an on-board 4 K to 2 K cryogenics insert. The insert consists of a 4 K phase separator, a 2.5 gm/sec heat exchanger and a JT expansion valve, a 4 K cooldown valve and a 4 K thermal intercept syphon supply and return. During cooldown the 4K valve is used to direct LHe to the bottom of the cold mass until 4 K level is reached. The level in the 4 K reservoir is regulated by the LHe supply valve, the level in the 2 K phase separator is regulated by the JT valve and the 2 K pressure is regulated by the sub-atmospheric line valve. Piping within the module delivers the syphon supply to a number of 4 K thermal intercept points (WCT, ICT and FPC) and then returns the two phase LHe back to the top of the 4 K phase separator.

In 2014 the second cavity for ACM1 was not ready and it was decided for installation along with a `dummy' cavity that occupies the second cavity space in the cryomodule and the RF System was adapted accordingly. The 'dummy' cavity contains all the interfaces to the helium system so that all helium piping surrounding the dummy will be final. In addition the 'dummy' cavity is installed with a DC heater to replicate cavity active loads and WPM brackets to permit alignment studies. The one cavity ACM variant we term 'ACMuno'. This configuration allows a full cryo-engineering characterization of the cryomodule. Both cryomodules are equipped with protection systems developed and fabricated at TRIUMF for fast trip of RF drive in case of cavity quench and threshold signals for RF power, vacuum and temperature.

Cryogenics characterization. The static heat loads are measured by observing the rate of falling LHe level after the supply valves are closed to the volume and noting the volume change of LHe per unit time and the heat of vaporization. The rate of 2 K production is measured by closing the 4 K supply valve while regulating the JT valve to keep the level constant in the 2 K space. In this case the falling level in the 4 K space is a combination of the static loads of the 4 K and 2 K space plus the vapour lost due to expansion from atmosphere to 31.5 mbar. The 77 K static load is measured by noting the warmed GN2 flow required at the exhaust side in order to keep the LN2 thermal shield cold. In this case the measurement is an overestimate since it was difficult to regulate the LN2 at a lower level but the thermal shield was always cold. Measured values for the ICM are pretty close to design: static load for 4K, 2K are 6.5, 5.5 W correspondingly. The 2 K production efficiency improves as a function of mass flow as the temperature of the heat exchanger and JT valve decreases: 70% at 0.5 g/s, 80% at 1g/s and 86% at 1.5 g/s. The ACMuno cryogenics test with one cavity and one 'dummy' show 6.4 W of static load for 4 K and 6.5 W of static load for 2 K.

RF characterization. The test includes cavity turn on and phase/amplitude lock, tuner frequency range and tuner lock, microphonics measurements and beam acceleration. The tuner range was measured at +400 kHz – the tuner motion was very stable. Due to the excellent frequency stability and broad bandwidth phase lock could be obtained with stable forward power even without the tuner but the tuner lock was easily achieved in any case. Cavity quality factors were estimated based on calorimetric measurements. The Q-curves of ARIEL1, ARIEL2 and ARIEL3 cavities installed in ICM, ACMuno and ICM2 cryomodules are presented in Fig. 6. The Q_0 values in the cryomodules are higher than the values measured in the vertical test. This can be due to an additional BCP of 20 μm that each cavity received after vertical test or an improved magnetic environment or both. The cavities meet ARIEL specifications of $Q_0=10^{10}$ corresponding to power dissipation of 10 W at 2 K for E_a=10 MV/m. The results indicate that the magnetic shielding is sufficient and that the HOM dampers do not

ISBN 978-3-95450-181-6

load the fundamental mode. The goal RF coupling for ARIEL cavities for 10mA/10MV performance at $Q_0=10^{10}$ is $Q_{ext}=10^6$. The coupling adjustment is in the range of $Q_{ext}=7•10^5…3•10^6$. For the initial beam test we set the minimum coupling of $Q_{ext}=3•10^6$.

Cryogenics System

The design of the cryomodules allows a simplified cryogenics system. A standard commercial 4 K ALAT LL Cold Box is employed delivering 4 K liquid to a supply dewar near atmosphere. The LHe in the dewar is pushed through the cold distribution with slight overpressure (1.3 Bar) and delivered to the cryomodule 4 K reservoir with parallel feed from a common distribution trunk and cold return back from each cryomodule to the exhaust side of the trunk. Specification for a pure refrigeration performance of 600 W and a pure liquefaction performance of 280 l/h was defined. The final commissioning produced a pure refrigeration performance of 837 W and a pure liquefaction performance of 367 l/h comfortably above the criteria. Four sub-atmospheric pumping units rated at 1.4 g/s each are installed. More can be added as the 2 K production increases in Phase-II.

RF System

The RF system includes one high power RF source for each cryomodule. In Phase-I each cryomodule is driven by a dedicated klystron. For Phase-II one of these klystrons will drive ACM2 while the ICM will be driven by a 150 kW power source to be determined. The ACM RF power feed is split to feed each of the cavities equally. A further splitting is required to feed each of the power couplers while phase shifters in each leg are used to achieve the proper phase conditions. One LLRF system is used for each cryomodule with a vector sum compensation of voltage and phase drifts in the ACM.

Two CPI VKL7967A 290 kW CW 1.3 GHz klystrons and two 600 kW 65 kV klystron power supplies from AMPEGON are now installed. Waveguide elements have been installed and tested. The power couplers have been conditioned by two couplers at once at room temperature in a Power Coupler Test Station (PCTS) using a 30 kW IOT.

Beam Acceleration Test

A ‘23 MeV Beam Test’ of the front end unit is a project milestone to validate cryogenics, HLRF, LLRF, e-Gun operation, LEBT, ICM, ACMuno engineering and overall synchronization [7].

The beam energy was estimated based on the dipole setting at the maximum current intensity into the dump Faraday cup. Beam simulations were done to calculate the final energy assuming a certain cavity gradient. For the beam tests a gradient of 12 MV/m is achieved for the ICM and 11 MV/m for the ACM cavity. The required forward powers are 18 kW and 14 kW CW respectively.

EXTERNAL PROJECTS

In frame of collaboration agreement with VECC (India) TRIUMF developed and successfully commissioned a copy of the eLinac injector cryomodule ICM2 and 30 kW CW IOT Transmitter which was used for eLinac power coupler conditioning. The IOT Transmitter was used also for 4kW 1.3GHz couplers conditioning for the SLAC LCLS-II project.

TRIUMF SRF infrastructure is extensively involved in testing of SC QWR and HWR cavities for RISP. We are conducting development of novel Spoke cavity for RISP.

We developed and fabricated variable test couplers for SRF tests of FRIB SC QWR and HWR cavities.

SRF DEVELOPMENT

TRIUMF is developing design and ‘in house’ fabrication of SC Deflecting cavity for eLinac ERL separator. We are conducting a series of developments for SRF technology: μSR material samples study, vertical electro polishing, induction oven for cavities degassing and doping, T-map for SRF cavities tests.

SUMMARY

Next year we are going to complete Phase-I of eLinac with installation and commissioning of second cavity in ACM cryomodule and completion of the RF System.

We are going to proceed with development for ISAC-II cavities performance and reliability.

External projects and collaborations help to raise expertise and extend competency of TRIUMF SRF team. The TRIUMF SRF team was honoured to host the SRF 2015 Conference.

REFERENCES

[1] R.E. Laxdal, “Commissioning and Early Experiments With ISAC-II,” PAC’07, Albuquerque, New Mexico, USA, June 2007, THXAB01, p. 2593-2597 (2007)

[2] R.E. Laxdal et al., “Operating Experience of the 20MV Upgrade Linac,” LINAC’10, Tsukuba, Japan, September 2010, MO202, p. 21-25 (2010)

[3] A. Facco et al., “The Superconducting Medium Beta Prototype for Radioactive Beam Acceleration at TRIUMF,” PAC’01, Chicago, USA, June 2001, MPPH134, p. 1092-1094 (2001)

[4] V. Zvyagintsev et al., “Production and Testing Results of Superconducting Cavities for ISAC-II High Beta Section,” PAC’09, Vancouver, Canada, June 2009, TU4PBC04, p. 786-788 (2009)

[5] R.E. Laxdal, et al, “Cryogenic, Magnetic and RF Performance of the ISAC-II Medium Beta Cryomodule at TRIUMF”, PAC’05, Knoxville, May 2005, TPPT052, p. 3191-3193 (2005)

[6] L. Merminga et al., “ARIEL: TRIUMF’s Advanced Rare Isotope Laboratory”, WEOBA001, IPAC’11, San Sebastian, Spain, September 2011, p. 1917-1918 (2011)

[7] V. Zvyagintsev et al., “Commissioning of the SRF Linac for ARIEL”, TUAA02, Whistler, September 2015, p. 457-461 (2015)

ISBN 978-3-95450-181-6

CONCEPTUAL DESIGN OF SUPERCONDUCTING COMBINED-FUNCTION MAGNETS FOR THE NEXT GENERATION OF BEAM CANCER THERAPY GANTRY

S. Sanfilippo, C.Calzolaio, A.Anghel, A. Gerbershagen and J.M.Schippers,
Paul Scherrer Institut, Villigen PSI, Switzerland

Abstract

An increasing number of proton therapy facilities are being planned and built at hospital based centers. Many facilities use rotatable gantry beamlines to direct the proton or ion-beam at the patient from different angles. A key issue is the need to make future gantries lighter and more compact with the use of cryogen-free superconducting magnets, in particular for the final bending section which can be of large aperture. Benefits of using the superconducting technology are: (1) the possibility to have a large momentum acceptance, hence reducing the need to ramp the magnet and enabling new treatment techniques, (2) the size reduction due to a lower bend radius and (3) the weight reduction up to a factor ten. The latter will also significantly reduce the costs of the supporting structure. We present a conceptual design based on Nb_3Sn superconducting combined function magnets (dipole, quadrupole, sextupole). The geometry using racetracks, the superconducting strand and cable parameters and the results of the thermal and the mechanical studies are reported. These magnets will work at a temperature of about 4.2 K cooled with cryocoolers.

INTRODUCTION

The number of the centres offering proton therapy has grown significantly over the past years and the number of hospitals and research institutions delivering protons or carbon ions for tumour treatment is following also an increasing trend. For the next generation of these machines, the superconducting technology applied to magnet development will play a key role as it will enable developping compact and light gantries. A gantry is the final section of a proton therapy facility, which consists of beamline magnets, beam diagnostics elements and the mechanical support structure. The gantry rotates around the patient and irradiates the tumour from different directions. The increased field strengths using superconducting magnets will decrease the bending radius, decrease the overall weight of the system and reduce the demands on the mechanical structure. Moreover superconducting magnets allow increasing the momentum acceptance, hence reducing the need to ramp the magnet and enabling new treatment techniques [1].

The present concept is based on an isocentric gantry design with the transverse scanning performed downstream of the final bending magnet (Fig.1). A transverse scanning field of 30 cm x 40 cm with a beam spot size of $2\sigma r \approx 5$ mm at the isocenter is required. The gantry should also allow a beam energy modulation between 70 MeV and 230 MeV (corresponding to a magnetic rigidity Bρ of 1.2 Tm and 2.3 Tm, respectively). In our gantry layout, the last bending section aims at deflecting the proton beam by 135°. An achromatic layout is chosen with a very large momentum acceptance ($\Delta p/p \sim \pm 12\%$). Energy change between two layers will be performed in less than 100 ms, within the momentum acceptance window, keeping a ramping speed of magnetic field between these windows below 0.1T/s.

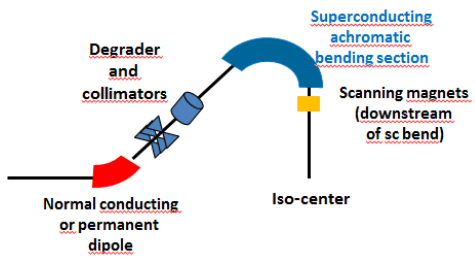

Figure 1: Gantry based on achromatic superconducting combined function magnets for the bending section.

The bending section consists of a series of superconducting combined function magnets described in this work, resulting from the conclusions of a preliminary study based on an upstream design [2]. The magnet geometry, the field maps, the conductor characteristics and the results of the thermo-mechanical calculations are discussed. Each dipole is cooled using two stage cryocoolers working at 4.2 K. To enable a sufficient temperature margin avoiding quenches after four consecutive current cycles (the treatment for the maximal target size), Nb_3Sn cables are used in the coils.

LAYOUT AND MAGNET DESIGN

Bending Section layout

The transport section is a curved, compact and locally achromatic, to minimize the proton beam dispersion. The section consists of three types of combined function magnets: (1) two superconducting combined dipoles-quadrupole and sextupole magnets (SDC1, SDC2), (2) a superconducting combined quadrupole-sextupole magnet (SCQ), (3) two tuneable normal conducting quadrupoles (Q1&2) at each side to meet with the beam optic conditions [1]. All the geometries are based on racetrack coils to keep the manufacturing as easy as possible. The design is optimized in different steps. From the magnets 3D field maps, the field harmonics are calculated and compared with the ones required by theoretical first order

ISBN 978-3-95450-181-6

calculations. Tracking simulations including all orders are then performed and the beam parameters are analysed.

Magnet Specifications

Table 1 describes the specifications of the three types of magnets (x and y directions are shown in Fig.2).

Table 1: Magnet specifications

Type	Q1&2	SDC1&2	SCQ
Length (cm) /bending angle (°)	10	67.5	35
Bending radius (m)		0.8	
Half-aperture (cm) (Half good field region)	25	10 (x) 4 (y)	12.5(x) 2 (y)
Dipole field (T)	0	2.57	0
Quadrupole (T/m)	25.7	-5.3	21.4
Sextupole (T/m^2)	0	-9.8	21.9
Operating current in superconducting magnets (A)		1700	1700
Number turns / turns per layers		36/28	20/30

Magnet Design and Field quality

The field distribution of the bending section magnets is calculated using OPERA3D^{TM} and the positioning of each component is optimized through tracking studies using OPAL, a tool for charged-particle optics in accelerator structures and beam lines [3]. Fig.2 shows the field map in each magnet of the bending section.

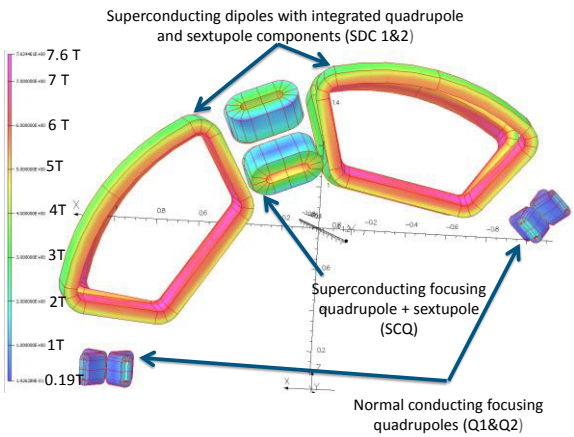

Figure 2: Field distribution in the Q1&2, SDC1&2 and SCQ magnets at operating current.

Peak fields at the conductor location are 7.62 T and 7.12 T for the SDC1&2 and SCQ respectively, three times higher w.r.t the average magnetic field in the good field region (GFR). Field quality is evaluated in several transverse cross sections with respect to the beam path. The multipole expansion was calculated in a circle of diameter equal to the smaller side of the GFR. The three components of the fields along the circle were projected onto the radial direction and using the Fourier transformation, the normal and skew multipoles were obtained. More details on the field quality determination can be found in [2]. The field quality in the superconducting magnets displays octupoles and 14-poles below 0.4% of the dipole field, matching well with the specifications.

SUPERCONDUCTING CABLE

The peak field values, the additional effect of the losses when the magnets are ramped up and down and the practical need of using dry systems for the cooling, have led to select Nb_3Sn for the coils. A reasonable temperature margin of about 4 Kelvins at operating conditions (fields of 7-8 T and temperature of 4.2 K) is pursued. In addition Nb_3Sn strands are well characterized by now. Accurate critical current scaling laws are available in the literature and the conductor is available on the market in large quantities. The Bronze routed Nb_3Sn strand developed for the ITER project [4] by the company Bruker-EAS is selected because it has shown good mechanical properties and low filament size. It withstands an axial tensile stress up to 180 MPa and bending strain up to 0.4-0.5% without breakages. Such strands feature also small filaments size, below 10 μm, minimizing the hysteresis losses. The strand parameters are summarized in table 2. For one single turn carrying 1.7 kA, a cable has to be wound. Rutherford cables provide a good current distribution reducing the field errors and guaranteeing a sufficient stability during operation. The cable will be made by 12 Nb_3Sn strands.

Table 2: Strand parameters for SDC and SCQ magnets

Parameter	Value
Strand diameter (mm)	0.82
Filaments twist pitch (mm)	14
Filaments diameter (μm)	≈6-7
N. of filaments	8305
Cu to non-Cu ratio	0.93
RRR	>100
I_c @ 4.5 T, 4.2 K and 0.2% strain (A)	200

The coils will be layer wound and impregnated to guarantee a good mechanical stability. The coils operating current was optimized aiming at a peak voltage in case of quench below 1.5 kV (per coil). A corresponding operating current value of 1700 A was selected, which allows also keeping the hot spot temperature below 150 K in case of quench. The J_c limits are based on the ITER Nb_3Sn critical surface parametrization [5] and the fields evaluated with the program OPERA 3D^{TM}. The proposed operating point corresponds to a magnetic field at the conductor position of 7.62 T (for a current of 1.7 kA) and an operating temperature of 4.2 K. For an intrinsic strain value below 0.3% the margin along the load-line is more than 25 % and in temperature around 5 K.

ISBN 978-3-95450-181-6

THERMO MECHANICAL STUDY

Mechanical Analysis

The critical current of the strain-sensitive Nb_3Sn is strongly reduced under the applied mechanical load; therefore, the right choice of the mechanical support and a careful estimation of the deformations on the coils are carried out. The winding pack is wound around a stainless steel (316 LN) former. CuBe rings are placed around the coil to give a pre-compression and guarantee a thermal path to the cryocoolers cold heads. The two parts of the support structure are maintained by four 316LN stainless steel columns and anchored to the gantry through six G10 supports, four on the bottom and two on the sides. The (von Misses) stress distribution on the coil is calculated using the Multiphysics Code COMSOL (see Fig.3).

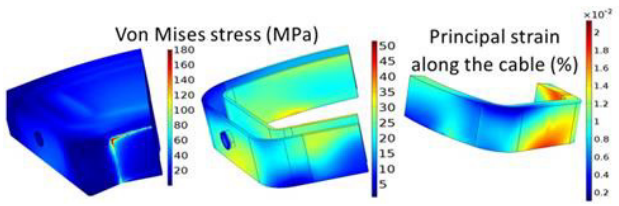

Fig.3: Von Mises stress distribution in MPa calculated in a SDC magnet support structure (left and middle) and principal strain along the cable direction (on the right).

The stress seen by the structure is below 180 MPa. This stress level leads to strain on the strands of the superconducting Nb_3Sn wires of around below 0.1%.

Thermal Analysis

Bath cooling at saturation temperature and ambient pressure is the most efficient cooling solution. The manufacturing of a rotating cryostat with inlet and outlet cold connections and an external re-condensing unit that liquefies the helium vapour coming from the magnet remains, however, extremely challenging. A "cryogen-free" solution is therefore adopted with all the SDC and SCQ magnets cooled by conduction using cryocoolers. The cooling sources are two stages cryocoolers producing a power of 1.4 W at 4.2 K. For the SDC, the first stage will be anchored to a Cu shield and the second stage to the CuBe rings. The first stage of the cryocooler is used to intercept the heat load from the normal conducting part of the current leads, as well as the thermal radiation from the room temperature environment. The second stage cools down the coil and intercepts the heat deposited by a pair of 2 kA high temperature superconducting current leads. In addition to the joule heating, the effect of the AC losses has to be considered. The SDC and SQC magnets will be designed to operate with typical ramp rates ranging up to 0.1 T/s. The considered treatment cycle is composed of four consecutive current cycles. Thermal analysis includes the following contributions: Losses occurring in the conductors and induced eddy currents in the structure, radiation from the thermal shield and heat input from the mechanical support. The losses in the conductor originate from a) eddy current losses in the matrix, b) hysteresis losses in the superconductor itself, and c) losses from coupling of the different strands and of the filaments of the composite conductor. The results of this study will be reported in details in a future separate contribution. In this work only the coils temperature distribution calculated after four cycles (i.e. 462 s) is presented. As shown in Fig.4 (right), the coil temperature does not exceed 6.6 K, allowing a comfortable temperature margin, well below the current sharing temperature T_{cs}. The total losses are of about 140 W/m^3, strongly dominated by the hysteresis contribution.

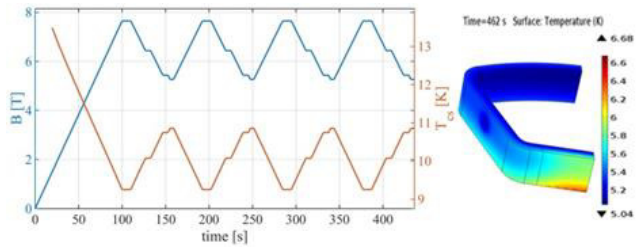

Fig.4: On the left: treatment cycle for a target of maximal size. Peak fields at the conductor along with the current sharing temperature are shown. On the right: Temperature distribution in the winding pack (only one quarter) at the end of the cycles.

CONCLUSION

The conceptual design of a superconducting achromatic bending section for a compact gantry is reported. The magnets will operate at 4.2 K, cooled down by cryocoolers. Using race-track geometry, peak fields at the conductor are showing a maximum value of 7.6 T. For the winding pack, Nb_3Sn Rutherford cables were designed to operate the magnet with a sufficient temperature margin. Thermo-mechanical analyses confirm this choice with temperatures not exceeding 6.6 K.

REFERENCES

[1] A. Gerbershagen et al. "A novel beam optics concept in a particle therapy gantry utilizing the advantages of superconducting magnets," Zeitschrift für Medizinische Physik, Volume 26, Issue 3, September 2016, p. 224–237.

[2] C.Calzolaio et al., "Conceptual design of a superconducting dipole for future compact scanning gantries for proton therapy", IEEE Trans. Appl. Supercond., vol. 26, no.3, 4401005, 2016.

[3] A.Adelmann et al., "The OPAL Framework Version 1.4.0 User's Reference Manual", http://amas.web.psi.ch/docs/opal/opal_user_guide.pdf

[4] S.A. March et al., "Results of the TFEU6 Sample Tested in SULTAN," IEEE Trans. Appl. Supercond., vol. 23, no. 3, 2013.

[5] Luca Bottura and Bernardo Bordini, "Jc(B,T,ε) parametrization for the ITER Nb3Sn production," IEEE Trans. Appl. Supercond., vol. 19,1521, 2009.

ISBN 978-3-95450-181-6

RECENT OPTIMIZED DESIGN OF ILC CRYOMODULE WITH EXPLOSION WELDING TECHNOLOGY

B. Sabirov, J. Budagov, G. Shirkov, Yu.Taran, JINR, Dubna, Russia
A. Bryzgalin, S. Illarionov, E. Pekar, PWI, Kiiv, Ukraine
A. Basti, F. Bedeschi, P. Fabbricatore, INFN, Pisa/Genova, Italy

Abstract

The past few years, we have made a great deal of progress in developing and demonstrating the enabling technology needed for a linear collider for the modernization of the cryomodule for the International Linear Collider (ILC) in the frame of collaboration JINR (Dubna, Russia), INFN (Pisa/Genova, Italy) and PWI (Kiiv, Ukraine) [1-4].

INTRODUCTION

Based on our experience, the collaboration got down to creating a transition specimens between the steel shell of the cryomodule vessel and the niobium cavity (Fig. 1). Trimetallic Nb+Ti+SS specimens were produced using the explosion welding and successfully tested at liquid nitrogen and liquid helium temperatures. This version deserves special attention for its manufacturability, simpler design, guaranteed strength and reliability of the joint and above all for an appreciably lower cost. It is a promising new transition joint technology based on cladding side surfaces of a steel flange by titanium using explosion bonding and welding a Nb pipe to titanium by EBW.

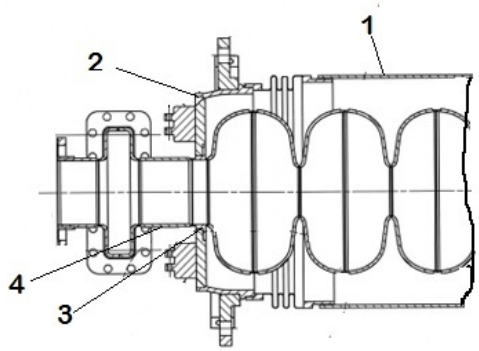

Figure 1: Scheme of combined adapter connection with a cryogenic module: 1 – steel shell; 2 - electron beam welding or argon arc welding connection of shell with steel flange of adapter; 3 - steel flange; 4 - niobium tube.

PROBLEM DEFINITION

It is known that welding of similar materials gives the best results. The adapter should consist of at least two metals, niobium and stainless steel. No fusion welding, including electron beam welding is suitable for joining niobium and stainless steel because it results in formation of intermetallic compounds like Nb_xFe_y, which do not allow the required adapter tightness to be obtained. In addition, this compound does not withstand the thermal load at cryogenic temperatures and fails.

Earlier experiments showed that electron beam welding of niobium and titanium did not result in formation of intermetallic compounds and ensured the required helium and vacuum tightness. In this connection the following adapter manufacture procedure was proposed [5]. First, the stainless steel disc is clad with titanium on both sided by explosion welding, the resulting trimetal is shaped as required (by planishing and turning to the size), and a hole is cut for the niobium pipe. The pipe is inserted in the hole and electron-beam welded to titanium (Fig. 2).

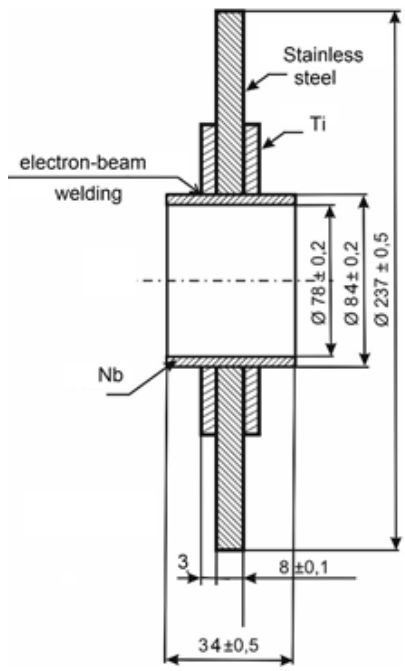

Figure 2: The design of the adapter, ensuring the absence of niobium intermetallic formations during welding.

Advantages of this adapter manufacture procedure are as follows:

- electron beam welding of niobium and titanium did not result in formation of intermetallic compounds and ensured the required helium and vacuum tightness;
- possible formation of intermetallic compounds in the explosion weld steel–titanium joint does not affect helium tightness;
- explosion welding of flat pieces is technologically much simpler than welding of pipes and allows joints with quality as much stable as possible;
- expenditure of steel and niobium decreases.

ISBN 978-3-95450-181-6

EXPLOSION WELDING OF METALS AND ITS MAIN PARAMETERS

Explosion welding is a process of making a permanent joint through metallic bonding [6]. It does not require a heat source because the energy comes to the joint area from the collision of the plates (Fig. 3). In optimum explosion welding regimes the heat-affected zone is very small, as is the existence time of high temperature.

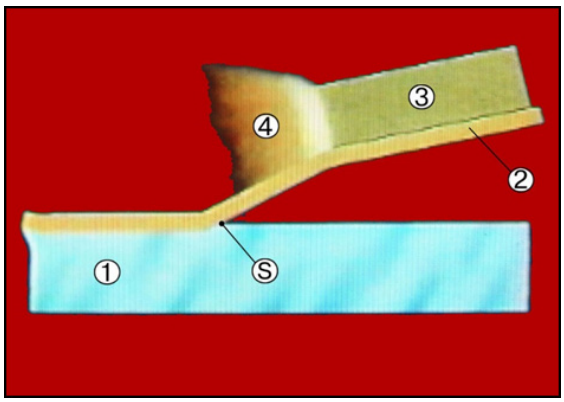

Figure 3: Principal schemes of explosion welding process with an angle between metal sheets 1 - base plate; 2 – cladding plate; 3 - explosive; 4 - detonation products; S - point (line) of contact of surfaces during welding.

The surfaces of the metals to be joined suffer plastic deformation creating a wave pattern bond line. An increase in the welding energy (collision energy of plates) increases wave parameters.

Since explosion welding is a complicated and high-velocity process, there is so far no universal mathematical model capable of precisely describing all its details. It is worth noting that titanium forms intermetallic compounds with almost all metals except niobium, tantalum, and vanadium

Explosion welding regimes for fabricating the titanium–steel–titanium trimetal were selected experimentally. The titanium was 3 mm thick and the steel was 8 mm thick. Plates with dimensions 250x250 mm (Ti) and 300x700 mm (SS) were welded. After the explosion and after the fabrication of the trimetal the planishing was performed on an industrial rolling mill to eliminate local deformation to make the billet flat.

Discs 237 mm in diameter with a central hole 84 mm in diameter for the niobium pipe were cut and electron beam welding (EBW) process of niobium tube with titanium clad occurs in a high-vacuum chamber in the deepest penetration regime (Fig .4).

The Vickers microindentation test was performed. The results of measuring microhardness at a load of 100 g are presented in Fig. 5.

The layer shear tests (Fig. 6) showed the strength at a level of 350 MPa considered satisfactory.

Obtained test results are rather optimistic and encouraged : the joining density characterized by absence of leak at background leak rate ~$4.7 \cdot 10^{-9}$ mbar·l/sec, measured at variety extreme conditions: thermocycles at temperature 77K and 2K, at pressure 6.5 atm; test at high temperature thermoload, exposure to ultrasonic radiation.

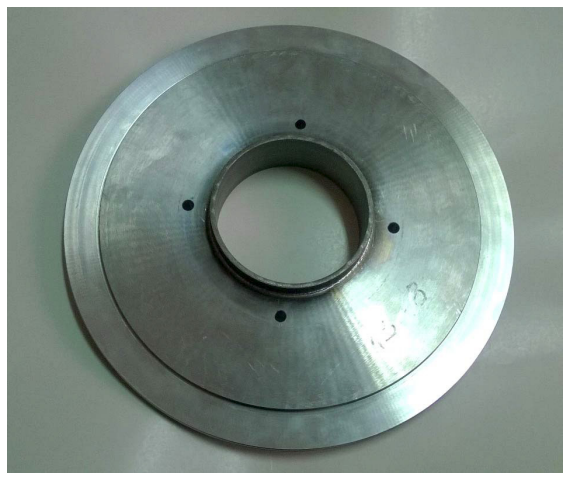

Figure 4: Appearance of combined adapter.

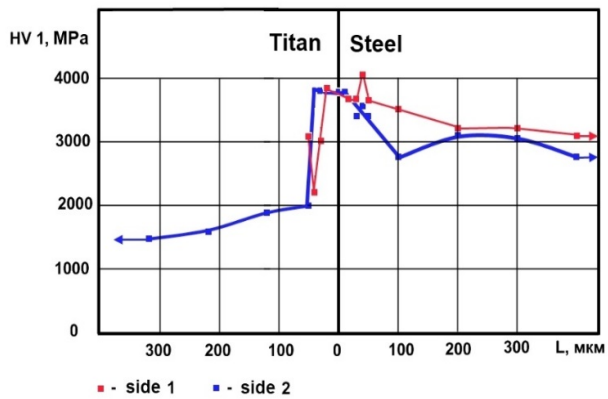

Figure 5: The microhardness of the steel-titanium boundary after explosion welding.

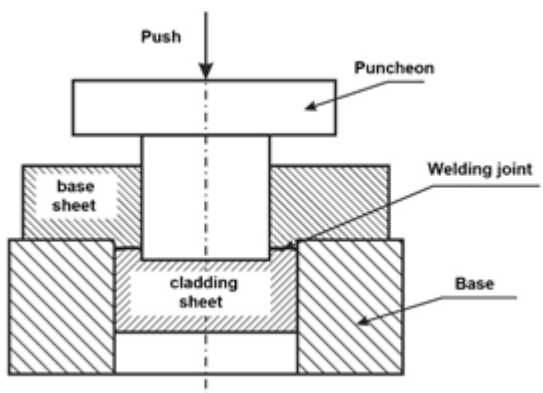

Figure 6: The scheme of layer tear test.

The next test is **main crusial** one: for imitation of use transition sample in real working position, connected with Nb cavity, Nb rings were joint with Nb pipe of samples by EBW. The welded joint experienced various internal stresses, first, due to the explosion welding, then due to the

ISBN 978-3-95450-181-6

thermal load from the electron beam welding (niobium melting point is 2460°C), and ultimately due to the thermal load at an extreme low helium temperature of 4°K. Superposition of all these residual stresses may result plastic deformation, failure of welds, and consequently occurrence of a leak. Test result ussued absence of leak at background leak rate $\approx 0.5 \cdot 10^{-10}$atm·cc/sec.

We have measured residual stresses in Ti+SS joint using the neutron diffraction method. Measurements were carried out with the POLDI stress diffractometer on the neutron beam from the ISIS reactor of the Paul Scherrer Institute (Switzerland) [4].

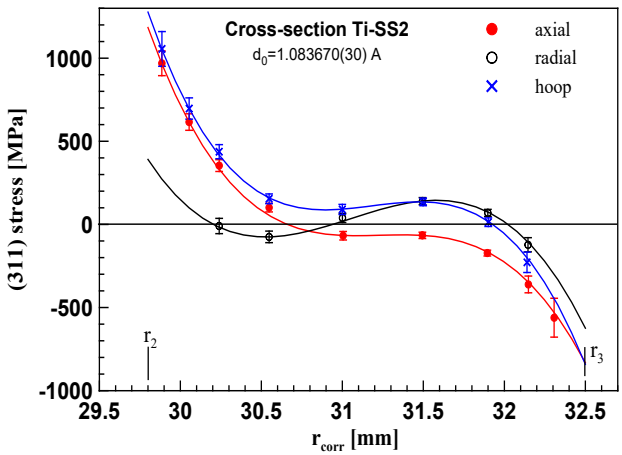

Figure 7: Measured (points) and fitted (curves) radial dependence of the stress . tensor components obtained for the peak (311) in the Ti+SS cross section.

Measured (points) and fitted (curves) radial dependences of the stress tensor components obtained for the peak (311) in the Ti+SS cross section ultimate result of residual stress measurements in the bimetallic Ti+SS joint in the process of scanning the titanium-to-stainless steel joint (Fig.7). As is evident from the plot, the residual stress is quite considerable, amounting to ≈1000 MPa. Considering that foregoing residual internal stresses superposition can make titanium turn into the state which corresponds to the deep plastic region. This may cause local microcracks in the Ti+SS (or Nb+SS) joint, which in turn may adversely affect tightness of the transition element when it is used in the cryomodule.

CONCLUSION

The adapter is designed which is suitable for manufacturing a linear collider cryomodule and eliminates the necessity to weld niobium to steel.

An explosion welding technology is developed that allows a trimetallic billet for manufacturing an adapter to be made such that the niobium–titanium bond is free of intermetallic compounds and the effect of the difference in the linear expansion coefficients of the ensemble components is eliminated. Regimes for EBW of steel to niobium and titanium are chosen which tentatively meet the adapter operation requirements.

The results showed the full eligibility of suggested design Nb+Ti+SS transition sample not for only Linear Collider, but for any cryogenic systems [7,8].

REFERENCES

[1] Sabirov B. “Explosion welding: New Design of the ILC Cryomodule”. JINR NEWS, 3/2010, p.16, Dubna,2010.

[2] “Electric welding technology of metalls and alloys by melting”(rus) By edition of B.E.Paton. Moscow: “Mashinostroenije”, 1974.

[3] B.Sabirov et al., “Recent Advances in Ti and Nb explosion welding with stainless steel for 2K operating (ILC Program)”, Proceedings of the International Workshop on Future Linear Colliders (LCWS11), Spain, Granada, 26-30 September, 2011, arXiv:1201.3472.

[4] Taran Yu.V. et al. Residual Stresses in an Explosion Welding Titanium-Steel Bilayer Pipe by Neutron Diffraction // JINR News. 2011. No.4. P.16.

[5] B.Sabirov et al.,”Modernisation of the ILC Cryomodule using High-Tech Technology — Explosion Welding”, XXIV Russian Particle Accelerator Conference (RuPAC’2014), Obninsk, Russia, 6-10 October, 2014.

[6] Lisak V.I., Kuzmin S.V. “Explosion welding” (rus). Moscow, “Mashinostroenie”, 2005, 511 p.

[7] Basti A., Sabirov B., et al., ”Optimization of ILC Cryomodule Design Using Explosion Welding Technology”, International Particle Accelerator Conference (IPAC’15), Richmond, Virginia ,3-8 May, 2015.

[8] Sabirov et al. “High Technology Application to Modernization of International Electron-Positron Linear Collider (ILC)”, International Conference “New Trends in High-Energy Physics”, Montenegro, Budva, 2-8 October, 2016.

ISBN 978-3-95450-181-6

PROGRESS ON MANUFACTURING AND TESTING OF THE SC MAGNETS FOR THE NICA BOOSTER SYNCHROTRON

H.G. Khodzhibagiyan#, N.N. Agapov, P.G. Akishin, V.V. Borisov, A.V. Bychkov, A.R. Galimov, O.V. Golubitskiy, A.M. Donyagin, V.N. Karpinskiy, B.Yu. Kondratiev, S.A. Korovkin, S.A. Kostromin, A.V. Kudashkin, G.L. Kuznetsov, D.N. Nikiforov, A.V. Shemchuk, S.A. Smirnov, A.Yu. Starikov and G.V. Trubnikov, JINR, Dubna, Russia

Abstract

NICA is a new accelerator collider complex under construction at the Joint Institute for Nuclear Research in Dubna. The facility is aimed at providing collider experiments with heavy ions up to Gold in the centre of mass energy from 4 to 11 GeV/u and an average luminosity up to $1 \cdot 10^{27}$ cm^{-2} s^{-1} for Au^{79+}. The collisions of polarized deuterons are also foreseen. The facility includes two injector chains, a new superconducting booster synchrotron, the existing 6 AGeV superconducting synchrotron Nuclotron, and a new superconducting collider consisting of two rings, each 503 m in circumference. The booster synchrotron is based on an iron-dominated "window frame"- type magnet with a hollow superconductor winding analogous to the Nuclotron magnet. The design of superconducting magnets for the NICA booster synchrotron is described. The progress of work on the manufacturing and testing of the magnets is discussed. The calculated and measured values of the characteristics of the magnets are presented. The status of the facility for serial test of superconducting magnets for the NICA and FAIR projects is described.

INTRODUCTION

The NICA project [1], [2] started at the Joint Institute for Nuclear Research (JINR) in Dubna in 2007. The main goal of the project is to study hot and dense strongly interacting matter in heavy-ion (up to Au) collisions at the centre-of-mass energies up to 11 GeV/u. A study of spin physics is also foreseen with extracted and colliding beams of polarized deuterons and protons at the energies up to 27 GeV for protons. The NICA accelerator complex will consist of two injector chains, the new 600 MeV/u superconducting (SC) booster synchrotron, the upgraded SC synchrotron Nuclotron [3], and the new SC collider having two storage rings each about 503 m in circumference with luminosity up to $1 \cdot 10^{27}$ cm^{-2} s^{-1} for Au^{79+} and two interaction points. The Nuclotron-type design [4] – [6] based on a cold iron yoke and a saddle-shaped SC coil has been chosen for the booster and the collider magnet. The magnet includes a window frame yoke at 4.5 K and a SC coil made of a hollow Nb-Ti composite SC cable cooled with a two-phase helium flow. The yoke supports Lorentz forces in the coil.

DESIGN OF THE MAGNETS

The designs of the magnets for the NICA booster are given in [7] – [12]. The iron yoke of the magnet consists of two symmetric parts bolted together. The half-yokes are fabricated of the laminated isotropic 0.65 mm thick electrical steel M 530. The laminations are compressed with pressure of 5 MPa in the direction of the longitudinal axis of the magnet. The side plates 10 mm thick are welded with laminations and stainless steel end plates 20 mm thick. The magnet is 2.2 m long and has a radius of the curvature of about 14 m. Fig. 1 shows the dipole magnet for the NICA booster.

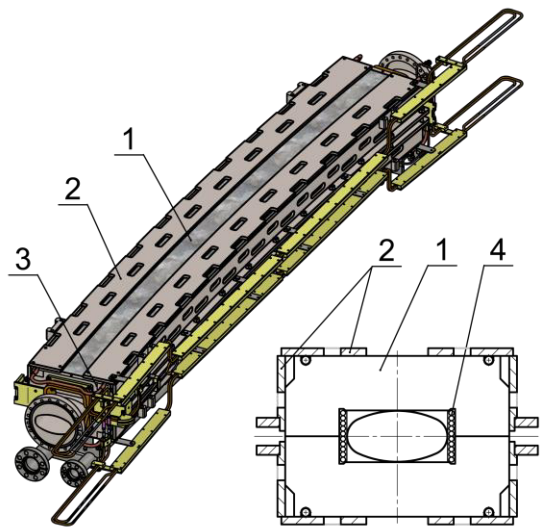

Figure 1: View of the dipole magnet. 1 – lamination, 2 - side plate, 3 - end plate, 4 – SC coil.

Each pair of lattice lenses is connected using the intermediate cylinder and form a doublet (see Fig. 2). The doublet of about 1.8 m length has a rigid mechanical design. It has a demountable construction that allows splitting the doublet into two horizontal parts to install the beam pipe. The doublet is fixed in a cryostat by means of eight suspension rods and adjusted in space as a unit.

Table 1: Main Characteristics of the Magnets

Characteristic	Dipole	Lens
Number of magnets	40	48
Max. magnetic field (gradient)	1.8 T	21.5 T/m
Effective magnetic length	2.2 m	0.47 m
Beam pipe aperture (h/v)	128 mm/ 65 mm	
Radius of curvature	14.09 m	-
Overall weight	1030 kg	110 kg

ISBN 978-3-95450-181-6

There will 32 corrector magnets of 0.32 m long in the ring of booster synchrotron. 24 corrector magnets will have two coils each (horizontal and vertical dipole coils) and 8 corrector magnets will contain four coils each (normal and screw quadrupole and sextupole coils). The characteristics of the NICA booster lattice magnet are given in Table 1.

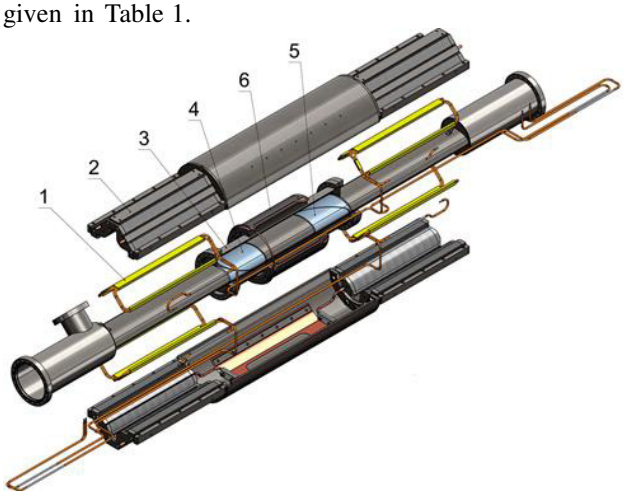

Figure 2: View of the doublet of the lenses. 1 – half-coil, 2 – half-yoke, 3 – beam pipe, 4, 5 – beam position monitors, corrector magnet.

STATUS OF MANUFACTURING THE MAGNETS

The iron yokes for the NICA booster dipole and quadrupole magnets are manufactured at SMZ (new name SSZ) plant in Savelovo town. Production of all 24 yokes for doublet of the lenses and 28 of 40 yokes for dipole magnets has been completed in this month (see Fig. 3). Production of the 32 yokes for corrector magnets is carried out at the company ATOM in Dubna. Completion of this work is scheduled for the second quarter of 2017. The vacuum shells for all booster magnets were manufactured at the company FRAKO-TERM from Poland. The thermal shields for cryostats will manufactured at the Laboratory of High Energy Physics (LHEP) of JINR. Supply of thin-walled curved beam chambers for dipole magnets and straight elliptic pipes for doublets of the lenses is scheduled for March - July 2017. The supplier of the beam pipes is FRAKO-TERM Company.

Figure 3: The yokes and vacuum shells for the magnets.

hamlet@jinr.ru

The Nuclotron-type superconducting cable and all coils for dipole and quadrupole magnets will manufacture at the Laboratory of High Energy Physics. 16 dipole and 38 quadrupole coils have been manufactured up to now. Completion of SC coils manufacturing is scheduled for mid-2017.

FACILITY FOR CRYOGENIC TESTS

A special facility [13], commissioning of which at LHEP is scheduled for the next week, is designed for assembly and cryogenic test of superconducting magnets for NICA and FAIR projects (see Fig. 4-5). JINR and FAIR / GSI participate together in funding the facility. In the period of 4 to 6 years 40 dipoles, 48 quadrupoles and 32 corrector magnets for the NICA booster, 80 twin bore dipoles, 86 twin bore quadrupoles, 12 final focus quadrupoles, 8 dipoles for bring together and separate the beams, and 48 pairs of corrector magnets for the NICA collider, as well as 170 quadrupoles and 140 corrector magnets for the FAIR project, will be assembled and tested at this facility. The total number of the superconducting magnets to be assembled and tested at this facility is 664, without spare magnets. Six cryogenic benches in parallel operating a round the clock are provided to achieve operating rate of testing two magnets per week. One of the satellite-type helium refrigerators serves each pair of benches. The Dewar vessels with liquid helium for their operation are delivered from the Nuclotron central liquefier. Two pulse power converters of 15 kA and 25 V have been designed to test the magnets. Electrical connection of the magnet to the power converter is carried out by means of current leads having a high-temperature superconductor, cooled with liquid nitrogen. The original cable machine was designed and manufactured for the production of the Nuclotron-type superconducting cable.

Figure 4: The facility for assembly and cryogenic test of superconducting magnets for the NICA and FAIR projects.

More detailed information about the results of the latest tests of the magnets is given in [14] – [19].

ISBN 978-3-95450-181-6

Figure 5: Series dipole magnet (left) and doublet (center) for NICA booster, and pre series dipole magnet for NICA collider (right).

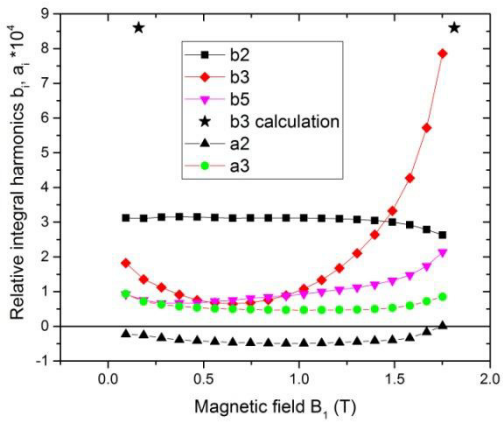

Figure 6: Relative integral harmonics of the magnetic field in the aperture of the NICA booster magnet at the radius of 30 mm as a function of the magnetic field in the magnet centre.

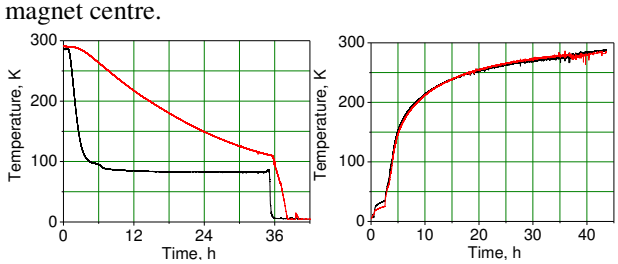

Figure 7: Cooling-down (left) and warm-up (right) of the dipole magnet for the NICA booster. Black line is inlet and red line – outlet of the magnet.

Some test results are shown in Fig. 6 and Fig. 7.

CONCLUSION

Serial production of the magnets for the NICA booster at the Laboratory of High Energy Physics of JINR has passed the halfway. Completion of manufacturing the magnets for the NICA booster synchrotron is planned for the middle of 2017. Facility for assembling and cryogenic tests of the SC magnets for the NICA and FAIR projects is prepared for commissioning in full configuration at Dubna in next week. Facility for assembling and cryogenic tests of the SC magnets for the NICA and FAIR projects is prepared for commissioning in full configuration at Dubna in next week. Serial cryogenic tests of the magnets successfully started at new test facility. Completing the cold tests of the magnets is scheduled for the end of 2017.

REFERENCES

[1] Nuclotron - based ion collider facility. Available: http://nica.jinr.ru/
[2] G. Trubnikov et al., "NICA project at JINR", Proceedings of IPAC2013, Shanghai, 2013, pp. 1343 – 1345.
[3] A. Baldin et al., "Nuclotron status report", *IEEE Trans. Nucl. Sci.,* vol. 30, pp. 3247-3249, August 1983.
[4] H. Khodzhibagiyan, and A. Smirnov, "The concept of a superconducting magnet system for the Nuclotron", *Proceedings of ICIC12*, Southampton, 1988, pp. 841-844.
[5] H. Khodzhibagiyan et al., "Superconducting Magnets for the NICA Accelerator Complex in Dubna", *IEEE Trans. Appl. Supercond*., vol. 21, pp. 1795-1798, June 2011.
[6] H. Khodzhibagiyan et al., "Development of fast-cycling superconducting magnets at JINR", Proc. of ICIC21, CRYOPrague 06, vol. 1, pp. 113-116, 2006.
[7] H. Khodzhibagiyan et al., "Status of the design and test of superconducting magnets for the NICA project," Proceedings of RUPAC2012, Saint Petersburg, 2012, pp. 149-151.
[8] H. Khodzhibagiyan et al., "Status of the development of superconducting magnets for the NICA project", IEEE Trans. Appl. Supercond., vol. 22, N3, pp. 4003004, June 2012.
[9] E. Fischer, H. Khodzhibagiyan, P. Schnizer, and A. Bleile "Status of the superconducting magnets for the SIS100 synchrotron and the NICA project", IEEE Trans. on Appl. Supercond., vol. 23, pp. 4100504, June 2013.
[10] H. Khodzhibagiyan et al., "Prototype superconducting magnets for the NICA accelerator complex", Proceedings of IPAC2013, Shanghai, 2013, pp. 3567 – 3569.
[11] H. Khodzhibagiyan et al., "Superconducting Magnets for the NICA Accelerator Collider Project", IEEE Trans. Appl. Supercond., vol.26, N3, June 2016.
[12] H. Khodzhibagiyan et al., "Superconducting Magnets for the NICA Accelerator-Collider Complex", IEEE Trans. Appl. Supercond., vol.24, N3, pp. 4001304, June 2014.
[13] Khodzhibagiyan H. et al., "Facility for Superconducting Magnet Assembling and Serial Testing", Proc. of the 13th Cryogenics 2014, IIR International Conference, Prague, April 2014, pp. 66-70.
[14] V. Borisov et al., "Magnetic Measurement System for the NICA Booster Magnets", Proceeding of IPAC2014, Dresden, 2014, pp. 2696-2699.
[15] V. Borisov et al., "Magnetic measurements system for series production of NICA superconducting magnets. Data acquisition, control and analysis", Presented at XXV International Symposium on Nuclear Electronics and Computing, Budva, 2015, http://nec2015.jinr.ru
[16] S. Kostromin et al., "Testing of SC-magnets of NICA Booster & Collider", this conference.
[17] V. Borisov et al., "Series magnetic measurements of NICA Booster dipoles", this conference.
[18] M. Shandov at al., "Magnetic measurement system for the NICA collider dual dipoles", this conference.
[19] A. Shemchuk et al., "Magnetic measurement system for the NICA booster quadrupole magnets".

ISBN 978-3-95450-181-6

VACUUM INSULATION TANDEM ACCELERATOR: PROGRESS AND PROSPECTS*

S. Taskaev#, T. Bykov, A. Ivanov, D. Kasatov, Ya. Kolesnikov, A. Koshkarev, A. Makarov, Yu. Ostreinov, I. Shchudlo, E. Sokolova, I. Sorokin, T. Sycheva,
BINP and Novosibirsk State University, Novosibirsk, Russia

Abstract

A promising method of treatment of many malignant tumors is the boron neutron capture therapy (BNCT). It provides a selective destruction of tumor cells by prior accumulation of a stable boron-10 isotope inside them and subsequent irradiation with epithermal neutrons. It is expected that accelerator based neutron sources will be created for the clinical practice. One such source could be an original source of epithermal neutrons, created in BINP. To obtain proton beam a new type of particle accelerator is used – tandem accelerator with vacuum insulation. Generation of neutrons is carried out as a result of the threshold reaction ^{7}Li(p,n)^{7}Be. Several changes were made in the construction of tandem accelerator with vacuum insulation during 2015-2016. This allowed us to suppress the unwanted flow of charged particles in the accelerator, to improve its high-voltage stability, and to increase the proton beam current from 1.6 to 5 mA. Such current value is sufficient for BNCT. The report describes in detail the modernization of the accelerator, presents and discusses the results of experiments on obtaining the proton beam and the formation of neutron flux using lithium target, and declares our prospective plans. The obtained neutron beam meets the requirements of BNCT: the irradiation of cell cultures provides the destruction of cells with boron and preservation of cells without boron. Irradiation of immunodeficient mice with grafted glioblastoma results in their recovery.

INTRODUCTION

Boron neutron capture therapy is currently considered as a promising technique for treatment of malignant tumors [1, 2]. For the widespread introduction of this technique in practice compact epithermal neutron sources based on charged particle accelerators are required. A new type of the accelerator – a tandem accelerator with vacuum insulation – was proposed [3] and constructed in BINP [4]. The accelerator is characterized by fast ion acceleration and a large distance between the ion beam and the insulator (on which electrodes are mounted). After the dark current was suppressed to an acceptable level [5], the injection of a negative hydrogen ion beam into the accelerator [6] and stripping in the gas target were optimized [7], the proton beam current was increased from the initial values of about 140 μA [8] to 1.6 mA [9], which was stable for more than one hour. In the elucidation of the reasons for the limitation of the current in the tube for accelerating negative hydrogen ions, a significant electron flow and a counter-flow of positive ions generated in the acceleration tube and in the stripping target were found and measured [10].

*Work supported by grant from the Russian Science Foundation (Project no. 14-32-00006), the Budker Institute of Nuclear Physics and the Novosibirsk State University
taskaev@inp.nsk.su

DESIGN OF THE ACCELERATOR

Figure 1 shows the accelerator. Coming from source *1* the low-energy negative hydrogen ion beam is defected in a magnetic dipole field by an angle of 15 degrees, focused by a pair of magnetic lenses *2*, injected into accelerator *3* and accelerated up to 1 MeV. In a gas (argon) stripper *7* which is installed inside a high-voltage electrode *6* negative hydrogen ions are converted into protons. Then protons are accelerated by the same 1 MV potential to an energy of 2 MeV. The potential for the high-voltage electrode *6* and five intermediate electrodes *5* of the accelerator is supplied by the sectioned rectifier *9* (most the source is not shown) through insulator *8*, wherein the resistive divider is set. Gas evacuation is performed by turbomolecular pumps *10* mounted on the ion source and at the accelerator exit and a cryogenic pump *4* via jalousies in the electrodes.

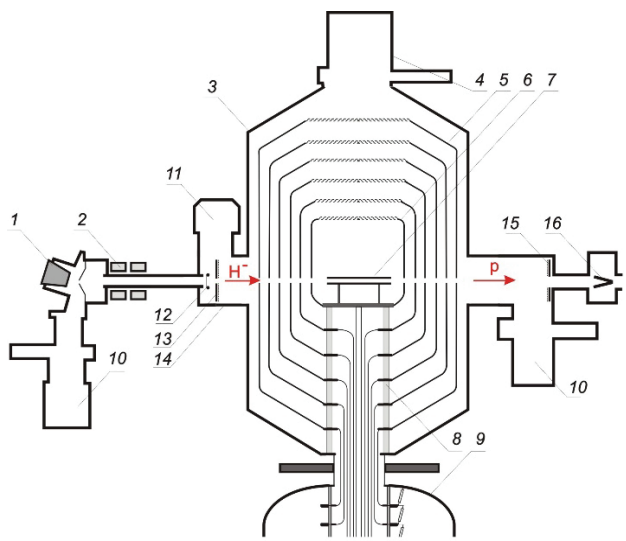

Figure 1: Modernized tandem accelerator with vacuum insulation: *1* – negative hydrogen ion source, *2* – magnetic lenses, *3* – accelerator, *4* – cryogenic pump, *5* –intermediate electrodes, *6* – high-voltage electrode, *7* – gas stripper, *8* – insulator, *9* – high-voltage sectioned rectifier, 10 – turbomolecular pumps, *11* – cryogenic pump, *12* – ring, *13* – cooled metallic diaphram and end detector with a grid, *14* – intake vacuum volume, *15* – detector with a grid, *16* – Faraday cup.

ISBN 978-3-95450-181-6

EXPERIMENTAL RESULTS

The accelerator entrance appears to be a critical point: here the injected ions still have a relatively low energy. As a consequence, there is a high probability of their interaction with atoms and molecules of the residual gas. The residual gas pressure at this point can be high because the gas flow from the stripper and the negative hydrogen ion source comes here. To prevent undesirable ion beam stripping we improved the vacuum conditions at the accelerator entrance by modernization of the accelerator. An intake vacuum volume (*14* in Fig. 1) was replaced by a new larger one. On the upper flange plate of the volume an additional cryogenic pump *11* was installed (*11* in Fig. 1). With the intent to improve the vacuum conditions within the entrance unit, diaphram *13* was mounted, which serves as vacuum resistance and limits the penetration of gas and ultraviolet radiation into the acceleration tube. The diaphram is cooled to prevent the secondary electron emission due to its heating by the peripheral part of the injected ion beam. Between the exit of the beam transport path and the diaphram, metal ring *12* is placed; a negative potential applied to this ring should suppress the flow of electrons accompanying the negative hydrogen ion beam. The entire surface of the diaphram from the accelerator side is covered by a tantalum wire grid to suppress secondary electrons, generated by positive ion irradiation, by supplying a negative potential to it. Between the diaphram and the grid, an insulated metal disk is mounted to measure the positive ion current. A similar disk with grid *15* is mounted within the exit unit of the accelerator.

The modernization resulted in drastic changes. Fig. 2 depicts the graphs of some measured parameters depending on the potential supplied to the grid in the entrance unit of the accelerator and to the ring. The measurements were carried out at an injected current of 800 μA, an accelerator voltage of 900 kV, and the gas supply to the stripping target providing 90 % beam stripping. As can be seen in Fig. 2a, the supply of the potential to the grid at the accelerator entrance significantly decreases the dose rate for bremsstrahlung, which is explained by a decrease in the current of electrons accelerated to the full voltage [11].

The current-voltage characteristic of the end detector (disk with a grid) at the accelerator entrance shown in Fig. 2c indicates that the secondary electron emission coefficient under the effect of positive ions formed is about 10. Such a high secondary electron emission coefficient is typical of many-electron ions and atoms with an energy above 100 keV [12].

The potential supply leads to an increase in the first electrode potential (Fig. 2b) given by a voltage divider and its approach to the equilibrium value of 150 kV obtained in the absence of currents in the gaps. The approach of the potential to the equilibrium value indicates a decrease in the current in the gap between the vacuum tank walls and the first electrode.

Fig. 2d clearly shows that the potential supply results in a noticeable decrease in the associated particle current.

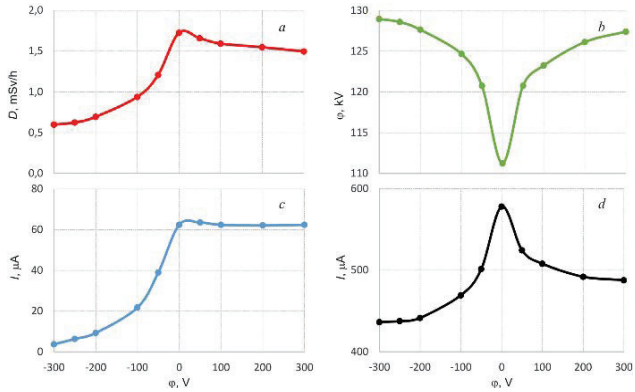

Figure 2: Dependence of the dose rate for bremsstrahlung D (*a*), the first electrode potential of the accelerator φ (*b*), the current supplied to the end detector I (*c*), and the associated particle current I (*d*) on the potential φ supplied to the ring and the grid mounted at the accelerator entrance.

The main result of the modernization is not so much a decrease in the unwanted charged particle flows [13], as a better high-voltage stability of vacuum acceleration gaps and almost complete disappearance of full-voltage breakdowns. This allowed us to raise the current of the injected negative hydrogen ion beam to the maximum and significantly increase the proton beam current, from 1.6 mA to 5 mA [14]. An accelerator with this current can be used in BNCT.

When the proton beam is dumped onto a lithium target [15], it allows us to obtain the epithermal neutron flux acceptabled for BNCT. *In vitro* and *in vivo* researches were carried out.

Human U251 and T98G glioma cells and Chinese hamster CHO-K1 and V-79 cells were incubated at various concentrations in the culture medium containing ^{10}B-enriched L-boronophenylalanine (BPA). The cells were irradiated with a neuron beam. A clonogenic assay was used to evaluate the viability of the irradiated cells. Irradiation of all four cell lines were cultured in the presence of ^{10}B was shown to reduce their colony-forming capacity compared with the control (Fig. 3) [16].

We irradiated immunodeficient mice at the 32nd day after U87MG tumor transplantation. Three of five mice became healthy.

We tested new boron delivery drugs – carbon nanohorn [17].

We have proposed a new method for measuring an absorbed dose in the BNCT [18] – delivery drug contain boron and gold. Neutron capture by boron leads to the absorbed dose, neutron capture by gold leads to activation. Measurement of activation by γ-spectrometer allows you to recover the absorbed dose. The idea was tested experimentally [19].

ISBN 978-3-95450-181-6

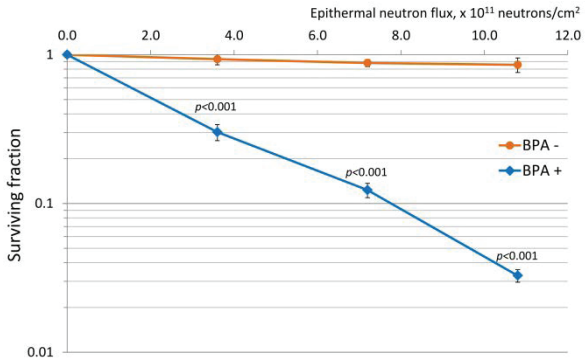

Figure 3: U251 MG cell survival ratio with and without BPA depending on neutron flux.

PROSPECTS

It is planned to replace the lithium target by the new one to set neutron beam shaping assembly [20] and to obtain therapeutic beam of neutrons that meets the requirements of BNCT to the greatest extent. New lithium neutron target [21] is a set of thin tantalum tubes with a thin lithium layer deposited. This target is characterized by maximum resistance to radiation blistering and a minimum level of γ-radiation at the absorption of protons in it.

The current understanding of the processes in tandem accelerator with vacuum insulation and the progress achieved allows us to consider the possibility of creating a specialized accelerator neutron source for the oncology clinic for the purpose of BNCT. The idea of reversing the high-voltage sectioned rectifier and insertion lower part of feedthrough insulator into it can be realized at the accelerator [22, 23]. This will reduce the facility height and make it really compact and attractive for placing in a clinic. This will significantly increase the stability of the accelerator because the potential for intermediate electrodes can be fed directly from the relevant sections of the rectifier.

CONCLUSION

The modernization significantly suppressed the unwanted charged particle flows in the tandem accelerator with vacuum insulation. This resulted in the improved high voltage stability of acceleration gaps and enabled an increase in the proton beam current from 1.6 to 5 mA that is sufficient for Boron Neutron Capture Therapy.

Prolonged stable generation of neutrons was implemented for *in vitro* and *in vivo* BNCT researches. The obtained neutron beam meets the requirements of BNCT: the irradiation of cell cultures provides the destruction of cells with boron and preservation of cells without boron. Irradiation of immunodeficient mice with grafted glioblastoma results in their recovery.

The planned modification of the facility will allow obtaining the therapeutic beam of neutrons that meets the requirements of BNCT to the greatest extent during the next year.

REFERENCES

[1] Neutron Capture Therapy. Principles and Applications. Eds.: W. Sauerwein *et al*. Springer (2012) 553 p.
[2] S. Taskaev, V. Kanygin, *Boron Neutron Capture Therapy*, (Novosibirsk: Publisher of SB RAS, 2016), 216.
[3] B. Bayanov et al., Nucl. Instrum. Meth. A 413 (1998) 397.
[4] S. Taskaev, Phys. Particles and Nuclei 46 (2015) 956.
[5] V. Aleinik et al., Instrum. Experim. Techn. 56 (2013) 497.
[6] A. Makarov et al., "Optimization of the negative hydrogen ion beam injection into the tandem accelerator with vacuum insulation", RUPAC'2012, Saint-Petersburg, Russia, Sept. 2012, WEPPD038, p. 623 (2012).
[7] A. Kuznetsov et al., "Calibration testing of the stripping target of the vacuum insulated tandem accelerator", RUPAC'2012, Saint-Petersburg, Russia, Sept. 2012, WEPPC057, p. 560 (2012).
[8] A. Kuznetsov et al., Techn. Phys. Lett. 35 (2009) 346.
[9] D. Kasatov et al, JINST 9 (2014) P12016.
[10] D. Kasatov et al., Techn. Phys. Lett. 41 (2015) 139.
[11] I. Shchudlo et al., "Measurement of the spatial distribution of gamma radiation at tandem accelerator with vacuum insulation". RUPAC'2014, Obninsk, Russia, Oct. 2014, TUPSA37, p. 116 (2014).
[12] U. Arifov et al., Proc. of the Academy of Sciences of USSR, series: Physical 26 (1962) 1398.
[13] A. Ivanov et al., JINST 11 (2016) P04018.
[14] A. Ivanov et al., Techn. Phys. Lett. 42 (2016) 608.
[15] B. Bayanov, V. Belov, S. Taskaev, J. Phys.: Conf. Series 41 (2006) 460.
[16] O. Volkova et al., Russ. J. Radiology 97 (2016) 283.
[17] K. Nakai et al., "Application of carbon nanohorn containing boron to BNCT". 17 Intern. Congress on Neutron Capture Therapy, Oct. 2016, Columbia, Missouri, USA, p. 111 (2016).
[18] A. Zaboronok, S. Taskaev, "The method of measurement of absorbed dose for boron neutron capture therapy", *Patent application for the invention*, № 2015150701, 2015 (positive decision 16.09.2016).
[19] A. Zaboronok et al., "Accelerator-based neutron source for boron neutron capture therapy: in vitro efficacy evaluation with in-sample dosimetry using gold nanoparticles", 17 Intern. Congress on Neutron Capture Therapy, October 2-7, 2016, Columbia, Missouri, USA, p. 42 (2016).
[20] L. Zaidi et al., Phys. Atom. Nuclei 80 (2017) 1.
[21] B. Bayanov, S. Taskaev, "Neutron producing target", *Patent application for the invention*, № 2015150702, 2015.
[22] I. Sorokin, S. Taskaev, Appl. Radiat. Isot. 106 (2015) 101.
[23] E. Domarov et al., Instrum. Experim. Techn. 60 (2017) 1.

ISBN 978-3-95450-181-6

STATUS OF THE NUCLOTRON

A. Sidorin, N. Agapov, A. Alfeev, V. Andreev, V. Batin, O. Brovko, V. Bugaev, A. Butenko, D.E. Donets, A. Eliseev, V. Fimushkin, E. Gorbachev, I. Gorelyshev, A. Govorov, A. Grebentsov, E. Ivanov, V. Karpinsky, H. Khodzhibagiyan, A. Kirichenko, A. Kovalenko, O. Kozlov, K. Levterov, V. Mikhailov, V. Monchinsky, A. Nesterov, Yu. Nozhenko, A. Osipenkov, A. Philippov, S. Romanov, P. Rukoyatkin, A. Shurygin, I. Slepnev, V. Slepnev, A. Smirnov, E. Syresin, G. Trubnikov, A. Tuzikov, B. Vasilishin, V. Volkov, JINR, Dubna, Russia
A. Belov, INR RAS, Moscow

Abstract

Since last RuPAC two runs of the Nuclotron operation were performed: in January – March of 2015 and June 2016. Presently we are providing the run, which has been started at the end of October and will be continued up to the end of December. The facility development is aimed to the performance increase for current physical program realization and preparation to the NICA Booster construction and Baryonic Matter at Nuclotron experiment.

INTRODUCTION

The Nuclotron is the basic facility of the Veksler and Baldin laboratory for high energy physics (VBLHEP). Its scientific program includes experimental studies on relativistic nuclear physics, spin physics and physics of flavours. At the same time, the Nuclotron beams are used for research in radiobiology and applied research.

VBLHEP accelerator complex includes Alvarez-type linac LU-20, superconducting synchrotron Nuclotron equipped with an internal target station and slow extraction system and facilities for fixed target experiments located in experimental building of about 10000 m^2.

In future the Nuclotron will be main synchrotron of the NICA facility being constructed at JINR [1]. Presently the creation of the NICA general elements is realizing in the frame of three officially approved JINR projects: “Nuclotron-NICA” (accelerator part), MPD (the project oriented to creation of one of the collider detectors) and BM@N (Baryonic Matter at Nuclotron – the fixed target experiment with heavy ions, the detector is under construction).

Last two years general attention was paid to development of the injection complex, preparation for the NICA Booster construction and BM@N experiment. The Nuclotron operational time was optimized in accordance with the JINR topical plans with account the plan of the NICA construction. During this period two Nuclotron runs were performed and the spin physics run has been started 26 of October. In this report we are concentrated on the most important results of the machine development works. Results of the injection complex development are presented in dedicated talks [2, 3].

STATISTICS OF OPERATION

During the run #51, performed in the period from 26 January to 15 March 2015, the following machine development works were provided:

- development of Q-meter hardware and software,
- put into test operation of the system for precise current measurement of the Nuclotron magnetic system,
- the works for the current stabilization in magnets of the extracted beam lines,
- put into operation new thermometry system of the Nuclotron,
- methodical investigations of stochastic cooling and different modes of the beam adiabatic capture.

Total duration of the run was about 1150 hours, about 800 hours of the beam time was spent for experimental researches in accordance with JINR topical plan. For the first time all the subsystems of the BM@N detector were tested with the beam. During the run deuteron and carbon ions were accelerating. Maximum deuteron energy was about 5.3 GeV/u (magnetic field at the extraction plateau is 1.855 T).

General task of the technological run #52 was commissioning of new fore-injector, optimization of the source of polarized ions (SPI) and test of polarimetry. The run at total duration of about 650 hours was performed from 2 to 30 of June 2016. Its main result is successive operation of the new fore-injector and acceleration of deuteron beam from SPI at intensity of 10^9 at the experiment energy. During the run the polarimeters after linear accelerator LU-20, at Nuclotron internal target station and at extracted beam line have been tested. During the machine development shifts the prototypes of the Booster magnetic system power supplies were tested at superconducting load. During a few shifts the beam injection at the field plateau with adiabatic capture into acceleration were used in routine operation. Experimental fragment of White Rabbit Network was tested at BM@N detector systems.

The run #53 was started 26 October 2016 with the scheduled duration of about 1400 hours. Main task of the run is experimental investigations in spin physics in few body nuclear systems (with polarized deuterons). Development of the diagnostics, investigations of dynamic behaviors of the Booster power supply prototypes with the beam acceleration, test of new current source for optic elements in the extracted beam lines,

ISBN 978-3-95450-181-6

investigations of stochastic cooling are the main goals of the machine development.

During all the runs the control system based on TANGO framework was in the active development [4]. To implement the Tango control system the following main tasks there were performed:

1) The control equipment database was designed and created.
2) The web-tool for using and managing of the control equipment database was developed.
3) Servers were purchased and configured.
4) The necessary toolbox for development, storing, documenting and using of Tango-based software was set up.

All new equipment is design to be compatible with the TANGO system and all old Nuclotron systems step by step are modernized in accordance with TANGO requirements.

MACHINE DEVELOPMENT

New thermometry system was put into operation during the run #51. It consists of 10 measurement loops. 8 of them correspond to structural elements of the Nuclotron octants. One loop required for the standard cell, inflector magnet and electrostatic septum. The last loop – for all inserted elements and nitrogen shield. The system is based on 608 thermo-resistors and 28 precise test resistors and include ten 64- channel switches which output signals are transferred to 24-bits registrators. The system provide additional (non-temperature) information about cryogenic system: pressure at the input and output of both helium tracts, helium level in two liquefiers and nitrogen pressure in the tank. At the Fig. 1 the TANGO web-client window of the thermometry system is presented.

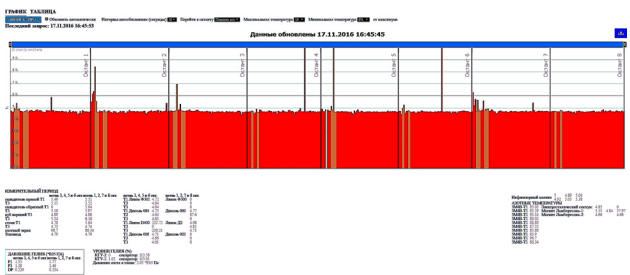

Figure 1: TANGO window of new thermometry system.

During the run #51 the system for precise current measurement in the Nuclotron magnets was put into test operation. The Nuclotron power supply system consists of main source feeding all structural elements connected in series (maximum current is 6 kA), two small units for current variation in focusing and defocusing lenses, three units for slow extraction control. All these sources were equipped with the current transformers ITZ Ultrastab (Fig. 2) with the absolute relative inaccuracy $6.5 \cdot 10^{-5}$. After ADS the signal are used in feed-back system for the current control. The system possibilities can be illustrated by the following example: during slow extraction of the beam for experiment at current at the plateau of 3741.8 A the ripple amplitude was measured as 0.071 A, that corresponds to the relative instability below $2 \cdot 10^{-5}$.

Figure 2: Current transformer ITZ Ultrastab at the current line.

For optimization of longitudinal beam dynamics the equipment for the RF amplitude control (Fig. 3) were developed. To improve the RF system performance a preamplifier based on modern technical solutions was constructed in Budker institute of nuclear physics (BINP, Novosibirsk). During the run #52 it was put into test operation. A few shifts the beam injection at the magnetic field plateau and adiabatic capture into acceleration was used in the routine operation.

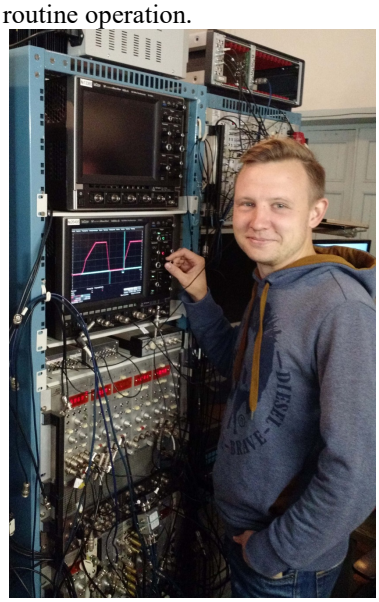

Figure 3: Equipment for the RF amplitude control during adiabatic capture.

ISBN 978-3-95450-181-6

NEAREST PLANS

Two Nuclotron runs are scheduled for 2017 before shut down for the Booster assembly and commissioning. First of them in February - March will be performed with laser ion source. It will be dedicated to experiments with light ions (d, Li, C) in accordance with the JINR topical plans. The run at the end of 2017 is aimed to test BM@N detector with heavy ions (Ar, Kr) providing by electron string ion source. The systems of the Nuclotron Booster are under construction in cooperation with BINP and scientific centers from member states of JINR. Serial production of the Booster magnets has been started in 2015. Preparations for the Booster construction and BM@N experiment were actively provided during the Nuclotron runs.

PREPARATIONS FOR THE BOOSTER ASSEMBLY AND BM@N EXPERIMENT

The BM@N detector is located inside the existing experimental building at a distance of 160 m from the exit of slow extraction. The beam line includes 8 dipole and 18 quadrupole magnets. Reconstruction of the line vacuum system is provided to diminish a material budget along the beam transfer line. For stabilisation of the current in the magnet coils new current control units were developed. One of them was tested during the run #51 and permitted to obtain relative instability during long-term operation below 10^{-3}. First prototype of the modern current source produced by LM Invertor company (Moscow) was successfully tested during the run #53.

The NICA synchronization system decided to be based on White Rabbit technology because it is developed by wide international collaboration including CERN and FAIR, based on existing standard, namely Ethernet, Synchronous Ethernet and PTP, open hardware and software and provide sub-nanosecond accuracy. Experimental segment of the White Rabbit network of about 3 km of the length was created at the Nuclotron complex and tested for BM@N sub detector operation during the run #52.

The Booster magnet power supply system will consist of three main units: for all structural elements connected in series (maximum current is 11 kA) and two small units for current variation in focusing and defocusing lenses. Three companies are participating in the tender for the power supply construction: LM Invertor, EVPUas (Slovak Republic) and Frako-Term (Poland). Prototypes of the source were installed at JINR and during the run #52 they were tested at superconducting load. Test of their dynamic properties with the beam acceleration is started in the run #53.

New helium liquefier OG1000 at capacity of 1100±100 l/h constructed especially for the NICA project was commissioned in June 2016 two days before the run #52.

Serial production of the Booster magnet was started in 2015 and now the cryogenic tests and cold magnetic measurements of the dipole magnets are in the active phase [5]. Example of TANGO based software developed for these works is presented in the Fig. 4.

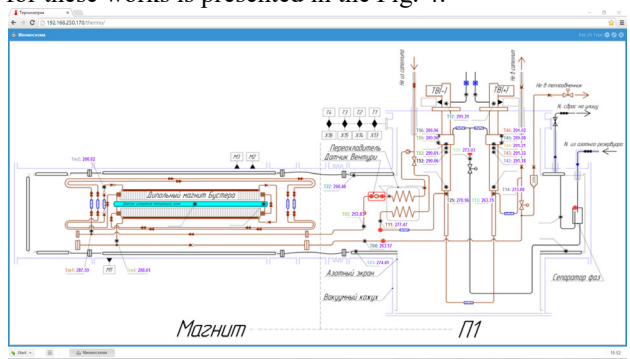

Figure 4: TANGO software for thermometry at the magnet test facility.

The Booster electron cooling system was constructed and successfully tested at BINP in May 2016 [6]. Construction of all other Booster systems is in progress.

CONCLUSION

Main result of the VBLHEP accelerator complex development during last years is commissioning of two new linear accelerators: RFQ fore-injector for LU-20 and HILac. The Nuclotron operational time is optimized in accordance with the JINR topical plans with account the plan of the NICA construction. Main attention during 2016 was paid for spin physics in few body nuclear systems (with polarized deuterons).

The beam time dedicated to the machine development is used for enhancement of the Nuclotron performance for current physics program realization and for tests of the equipment, diagnostics and operational regimes of the new NICA accelerators. Construction of the Booster elements and BM@N detector is in active phase. The Booster assembly is scheduled for 2018.

REFERENCES

[1] G.Trubnikov et. al, Status of the NICA project, these proceedings.
[2] A.Butenko et al, Commissioning of New Light Ion RFQ Linac and First Nuclotron Run with New Injector, these proceedings.
[3] H.Hoeltermann et. al, Commissioning of the New Heavy Ion Linac at the NICA Project, these proceedings.
[4] G.Sedykh, E.Gorbachev, The equipment database for the control system of the NICA accelerator complex, Proceedings of ICALEPCS2013, San Francisco, USA.
[5] H. Khodzhibagiyan, The Progress on Manufacturing and Testing of the SC Magnets for the NICA Booster Synchrotron, these proceedings.
[6] A. Bubley, Commissioning of the 60 keV Electron Cooler for the NICA Booster, these proceedings.

ISBN 978-3-95450-181-6

COMMISSIONING OF NEW LIGHT ION RFQ LINAC AND FIRST NUCLOTRON RUN WITH NEW INJECTOR

A.M. Bazanov, A.V. Butenko, A.I. Govorov, B.V. Golovenskiy,D.E. Donets, V.V. Fimushkin, V.V. Kobets, A.D. Kovalenko, K.A. Levterov, D.A. Lyuosev, A.A. Martynov, V.V. Mialkovsky, V.A. Monchinskiy, D.O. Ponkin, R.G. Pushkar, V.V. Seleznev, K.V. Shevchenko, A.O. Sidorin, I.V. Shirikov, A.V. Smirnov, G.V. Trubnikov, Joint Institute for Nuclear Research, Dubna, Moscow Region, Russia
S.V. Barabin, A.V. Kozlov, G.N. Kropachev, V.G. Kuzmichev, T.V. Kulevoy, Institute of Theoretical and Experimental Physics NRC "Kurchatov Institute", Moscow, Russia
A.S. Belov, Institute for Nuclear Research of the Russian Academy of Sciences, Moscow, Russia
S.M. Polozov, National Research Nuclear University – Moscow Engineering Physics Institute, Moscow, Russia

Abstract

The new accelerator complex Nuclotron-based Ion Collider fAcility (NICA) is under development and construction at JINR, Dubna now (Fig. 1). This complex is assumed to operate using two injectors: the Alvarez-type linac LU-20 as injector of light ions, polarized protons and deuterons and a new linac HILAc – injector of heavy ions beams. Old HV fore-injector of the LU-20, which operated from 1974, was replaced by the new RFQ accelerator, which was commissioned in spring 2016. The first Nuclotron technological run with new fore-injector was performed in June 2016 with beams of D^+ and H_2^+. The polarized deuterons beam were successfully injected and accelerated in the Nuclotron ring during the last run #53. Main results of the RFQ commissioning and the last Nuclotron run with new fore-injector are presented in this paper.

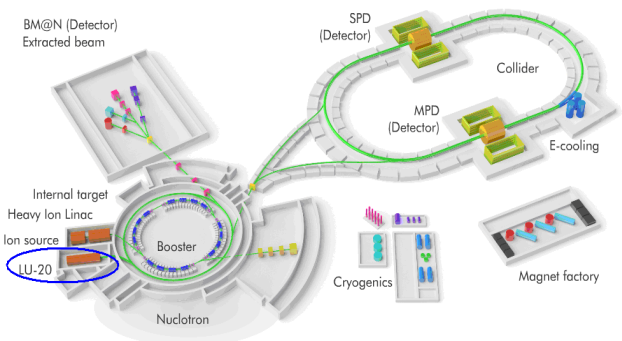

Figure 1: NICA complex. Proton, light and polarized ion linac LU-20 with new RFQ injector is marked.

INTRODUCTION

The injection system of the operating superconducting fast cycling synchrotron Nuclotron is under upgrade now.

Up to 2016 year, the charged particles for injecting into LU-20 linac were pre-accelerated with the electrostatic tube supplied by pulsed HV transformer with voltage up to 700 kV. The ion sources supply of up to 5 kW power placed at the HV "hot" platform was provided by feeding station consisting of motor and generator isolated one from the other with wood shaft. The new fore-injector of LU-20 based on the RFQ linac was constructed and put in to operation in 2016 (see Fig. 2). Pulsed HV supply up to 120 kV (based on HV pulsed transformer) was designed and assembled to provide necessary electric potential of the ion source terminal. The ion source systems supply is provided using isolation transformer on 160 kV, 35 kWA.

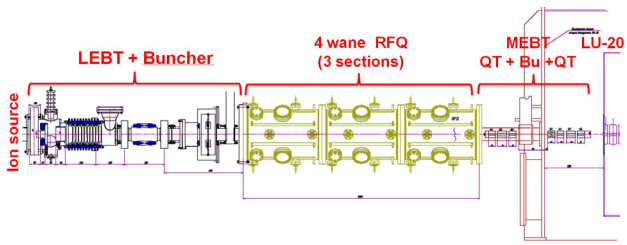

Figure 2: New fore-injector for LU-20 scheme.

New RFQ linac parameters are presented in Table 1, the project is performed in collaboration of JINR, MEPhI and ITEP. The beam dynamics simulation, the RFQ resonator simulation and design as well as RF system development were carried out in 2011-2013 [5]. The accelerator's resonator was manufactured in VNIITP (Snezhinsk).

Table 1: The LU-20 Fore-Injector Design Parameters

Z/A	0.5	0.3
RFQ input		
Injection energy, keV	61.8	103.0
Maximum current,mA	20	10
Normalized trans. emittance, π·cm·mrad	0.2	0.15
Operating frequency, MHz	145.2	
Output		
Output energy, MeV/u	0.156	0.156
Transmission RFQ, %	≥85	≥90
$\Delta p/p$, %	≤ 4	≤ 4
Normalized trans. emittance, π·cm·mrad	≤0.5	≤ 0.5
Resonator length, m	≤ 3	≤ 3
Voltage at electrodes, kV	84	140

ISBN 978-3-95450-181-6

RESONATOR TUNING AND RF COMMISSIONING

The four-vane resonator with displaced magnetic coupling windows was chosen for the NICA RFQ design. It should operate at 145.2 MHz like the LU-20 main resonator operating frequency. The LU-20 is the Alvarez-type DTL which RF system operates in self-excitation mode. Correspondingly, the new LLRF provides appropriate frequency and phase of RF oscillations in the RFQ and buncher [4].

After manufacturing and preliminary vacuum and low-power RF tests at VNIITP the resonator was transferred to ITEP and placed in tuning hall in March 2015. Resonator was excited on operating frequency and RF required field distribution in four quarters was measured (Fig. 3) [6].

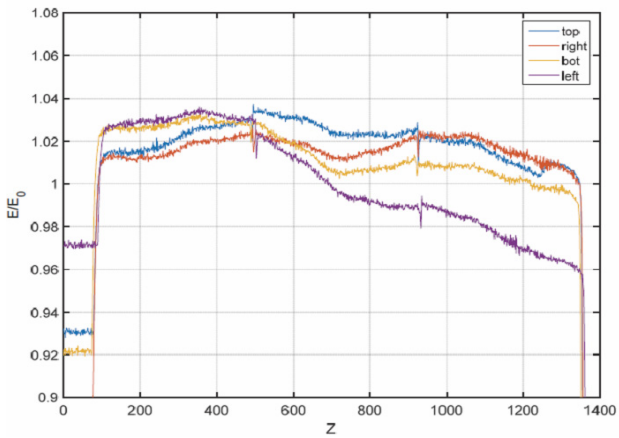

Figure 3: RF field amplitude deviation (< 2%) in four quarters of RFQ resonator.

RF power load was the next step in tuning. It was realized easily and about 380 kW was feed into RFQ resonator (~340 kW is necessary for carbon ions C^{4+} acceleration). Multiple RF sparks on the same place were not observed but training of multipactor was necessary and it was done. Vacuum of $(8\text{-}9)\cdot10^{-8}$ Torr was achieved after RF commissioning. The resonator was filled by dry nitrogen, transported to JINR and installed in test position in LU-20 injector hall (see Fig.4).

COMMISSIONING AT JINR

In injectors hall the RFQ resonator was equipped by all RF, tuning and vacuum components which were dismounted for the transportation. High power RF system was also assembled at projected place and the resonator was pumped and loaded RF power.

Further, the laser ion source, HV fore-injector (up to 120 kV) and LEBT (two focusing solenoids, two steerers and beam diagnostics box) were mounted to the linac support, tested and the deuterium beam was injected into RFQ. The magnetic separator with a special vacuum chamber for smooth angle changing was installed at the RFQ output to measure the beam spectrum for different *Z*/*A*. At the end of separator a special set of collectors and slits for the beam registration were installed.

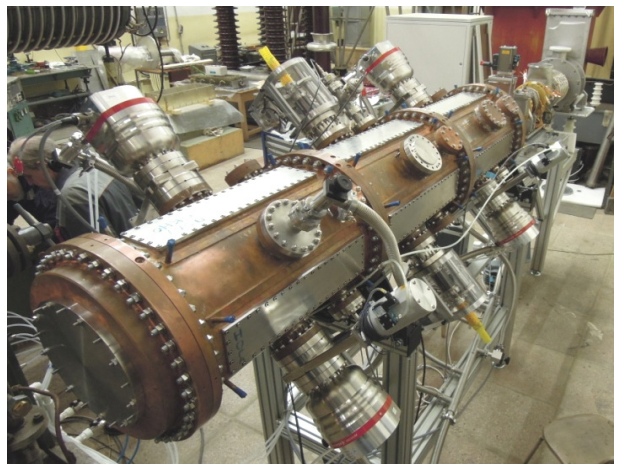

Figure 4: RFQ linac with RF and vacuum components installed on resonator on test area at JINR (Nov. 2015).

The system was calibrated using of H^+, D^+ and carbon beams, which were generated by laser ion source using different targets and accelerated by 63 kV in accelerating tube. The first beam was successfully accelerated in RFQ linac 10-12 Dec. 2015.

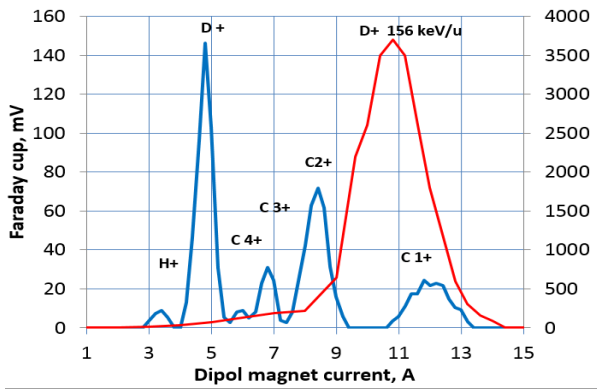

Figure 5: Measured spectrums for ions from the LIS with deuterated polyethylene target, HV = 63 kV (blue) and accelerated up to 156keV/u in RFQ deuterium beam (red).

Measured spectrums for both deuterium and carbon ion beams are presented in Figure 5, the beam current is about ~10 mA for the deuterium beam and ~5 mA for the carbon one. Good agreement of simulation and experimental results was observed for accelerated/non-accelerated carbon and deuterium beams. The current transmission coefficient through the RFQ is close to 80 % that agreed with projected value.

In February 2016, the old HV fore-injector accelerator tube was dismounted and the new RFQ fore-injector was installed on the LU-20 axis. All the systems of the accelerator were assembled, aligned and commissioned again. The new HV platform 15 m^2 for the Source of Polarized Ions (SPI) was constructed [1,2].

Two triplets of quadrupoles for the MEBT line were designed, manufactured and assembled with vacuum system between the RFQ and LU-20 resonator. All magnets of LEBT and MEBT lines are powered by pulsed power supplies with a special control system, which were designed and assembled in LHEP JINR.

ISBN 978-3-95450-181-6

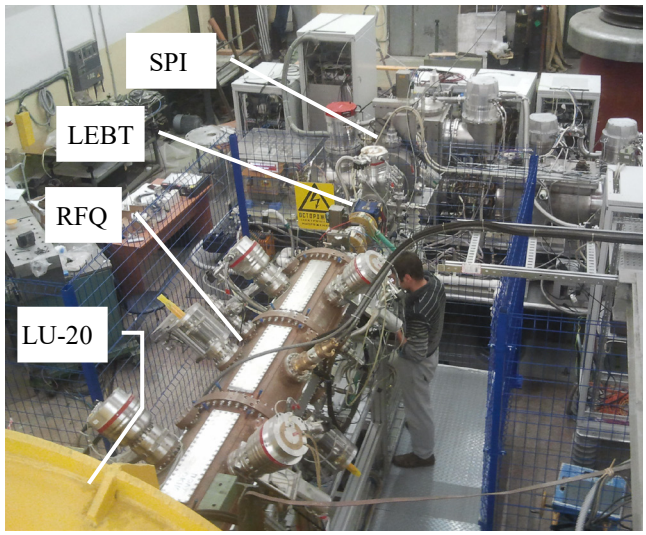

Figure 6: Source of Polarized Ions mounted on the HV terminal and RFQ connected to the LU-20

The first deuteron beam was accelerated in LU-20 with new fore-injector in March 2016 with transmission factor up to 20% thru the whole injector. To increase capture efficiency of the beam in LU-20 the new buncher in MEBT line is needed. Such cavity was designed and under manufacturing now.

NUCLOTRON RUN

During May 2016, the new SPI was disassembled, transferred and mounted on the HV terminal platform of the new fore-injector (see Fig. 6). In June 2016, the first technological Nuclotron run #52 with the deuteron beam from the new fore-injector and SPI was provided. During that run all the main systems of the ion source and injector were commissioned and put in to operation.

26 of October 2016 the next run #53 was started with the scheduled duration of about 1400 hours. Main task of the run is experimental investigations in spin physics in few body nuclear systems (with polarized deuterons). The polarized beam was successfully injected and accelerated in Nuclotron ring. Average intensity of the beam is about 5-7·10^8 particles per cycle (up to 10^9 ppc, Figure 7).

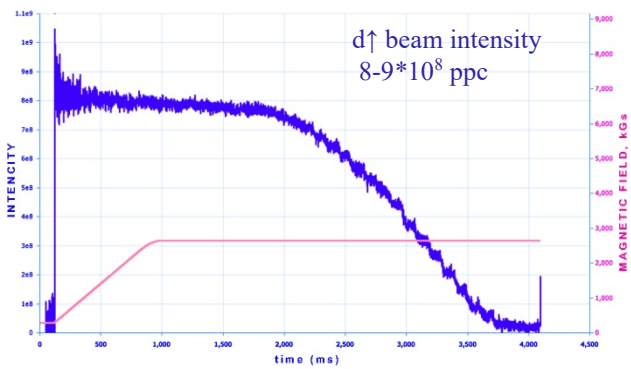

Figure 7: Polarized deuterons beam accelerated in Nuclotron ring – blue line, main magnetic field – red line.

CONCLUSION

After four years of intensive discussions, simulations, construction and manufacturing the new RFQ linac for LU-20 injection complex upgrade was installed in the Nuclotron injector's hall at LHEP JINR and put in operation (Fig. 8). Deuterium and carbon beams were successfully accelerated in new fore-injector. Stable and safety operation of the LU-20 with new RFQ and SPI during the Nuclotron superconducting synchrotron run was demonstrated. The polarized deuteron beam successfully injected and accelerated in Nuclotron for physical experiments. To increase the intensity to reach the project level of the beam the new buncher and a lot of work on optimization for all systems of accelerator is needed.

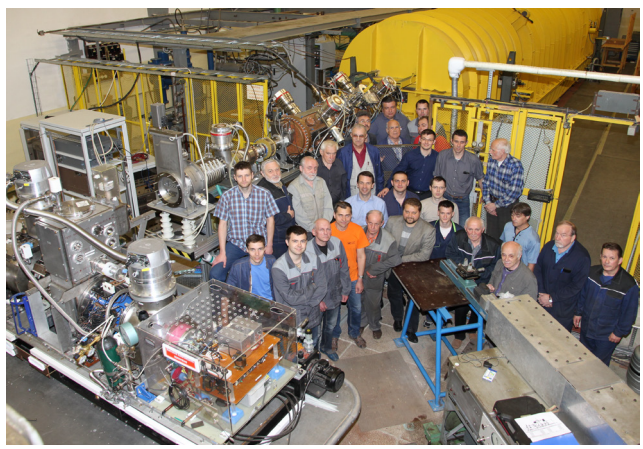

Figure 8: LINAC team during commissioning of the RFQ and the SPI.

ACKNOWLEDGEMENTS

We would like to thank all Institute of Technical Physics (Snezhinsk) specialists which are take part in resonator manufacturing and personally I.V. Mamaev, K.A. Klykov, M.Yu. Naumenko and G.N. Ostashkov.

We also would like to thank MEPhI TechnoPark and personally A.N. Petrovsky, A.P. Korotkova and S.S. Korotkov for the organization support.

REFERENCES

[1] G. Trubnikov, N. Agapov, V. Alexandrov et al., Proc. of IPAC'10, 693-695 (2010).
[2] V.Fimushkin, A. Kovalenko, A. Belov et al., Proc. of PSTP'15, PoS (PSTP2015) 041.
[3] A.V. Butenko, E.E. Donets, E.D. Donets et al., Proc. of IPAC'13, 3915-3917 (2013).
[4] A.V.Butenko, E.E.Donets, E.D.Donets et al., Proc. of IPAC'14, 2103-2105 (2014).
[5] V.A. Andreev, A.I. Balabin, A.V. Butenko et al., Problems of Atomic Science and Technology. Series: Nuclear Physics Investigations, 6 (88), 8-12 (2013).
[6] V.S. Aleksandrov, A.V. Butenko, et al., Proc. of IPAC'16, 940 - 943 (2016).

ISBN 978-3-95450-181-6

COMMISSIONING OF THE NEW HEAVY ION LINAC AT THE NICA PROJECT

A.M. Bazanov, A.V. Butenko, B.V. Golovenskiy, D.E. Donets, V.V. Kobets, A.D. Kovalenko, K.A. Levterov, D.A. Lyuosev, A.A. Martynov, V.A. Monchinskiy, D.O. Ponkin, K.V. Shevchenko, A.O. Sidorin, I.V. Shirikov, A.V. Smirnov, G.V. Trubnikov, JINR, Dubna, Russia
D.A. Liakin, ITEP, Moscow, Russia
H.Höltermann*, U.Ratzinger, A.Schempp, H.Podlech, D. Mäder, BEVATECH GmbH, Frankfurt, Germany

Abstract

The new accelerator complex Nuclotron-based Ion Collider fAcility (NICA) is now under development and construction at JINR, Dubna. This complex is assumed to operate using two injectors: The modernized Alvarez-type linac LU-20 as injector of light polarized ions and a new Heavy Ion Linear Accelerator HILAc-injector for heavy ions beams. The new heavy ion linac, which accelerates ions with q/A-values above 0.16 to 3.2 MeV/u, is under commissioning. The main components are a 4-Rod-RFQ and two IH-drift tube cavities, operated at 100.625 MHz. Most recent results of the HILac commissioning with a carbon beam from a laser ion source are discussed.

INTRODUCTION

For the NICA collider ion beams from p to Au at energies from a few hundred MeV/u up to a few GeV/u. will be delivered by two superconducting synchrotrons-the Booster (magnetic rigidity is 25 Tm) and the Nuclotron (45 Tm) and 2 injector linacs [1]. The beams will be created by three new ion sources: SPP (Source of Polarized Particles), LIS (Laser Ion Source), Krion-6T (ESIS type heavy ion source). The ion sources will feed 2 linacs: The existing linac LU-20 with a new RFQ as front-end and the new heavy ion linac – HILac. The HILac design and development was performed by Bevatech GmbH [2] and described in detail in [3]. HILac commissioning with a C^{3+} beam from the laser ion source are presented. Parameters for HILac are given in table 1.

Table 1: HILac Parameters

Target Ion	Au^{32+}
A/q	6.25
Current	< 10 emA
Pulse length	10 µs – 30 µs
Rep. rate	< 10 Hz
LEBT energy	17 keV/u.
RFQ energy	300 keV/u.
LINAC output energy	3.2 MeV/u.

ION SOURCE & LEBT

The LIS is based on a commercially available Nd-YAG laser LPY 7864-2 The laser was tested at its operational regimes producing carbon ions at a test bench (Fig. 1).

The HILac LEBT with a length of about 2 m is split into 2 main parts. Part 1. is an electrostatic section the second part uses 2 magnetic solenoids. with a maximum magnetic field of 1.23 T. The whole LEBT has been simulated for investigating the beam matching into the RFQ acceptance (Fig 2).

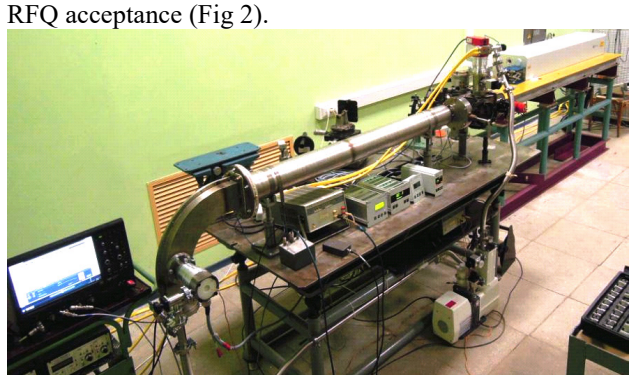

Figure 1: Nd-YAG laser at the test bench.

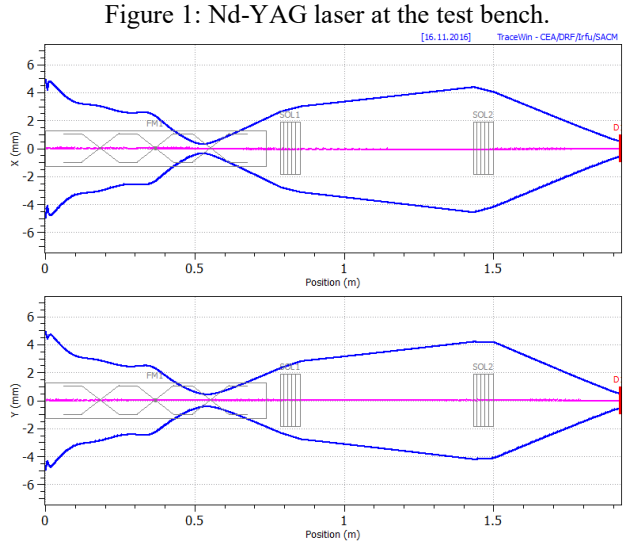

Figure 2: Matched case (rms envelope) for C^{3+} beam along the LEBT into the RFQ acceptance.

MEBT

The MEBT is equipped with two identical pulsed quadrupole-doubletts located in front and behind the

ISBN 978-3-95450-181-6

rebuncher. The rebuncher is built as a 4-gap quarter-wave resonator powered by a kW amplifier. An impulse current transformer is located directly behind the RFQ and a phase probe is located after the second quadrupole doublet. In combination with two other phase probes, one in between the 2 IH drift tube linacs and one after the second IH DTL, the probes allow TOF beam energy measurements. To overcome angular deviations from the beam axis at the MEBT entrance a magnetic-steerer has been added into the beam-line.

RFQ

The HILac RFQ is a 4-rod structure operating at 100.625 MHz. The RFQ tank is a 3.16 m stainless steel tank of 0.35 m in diameter which is copperplated inside. The RFQ was commissioned using high power up to 120 kW and is driven by a 140kW solid state amplifier

IH-DRIFT TUBE SECTION

The MEBT is followed by 2 Interdigital H-type cavities (IH) with 2.42 m and 2.15 m outer length, respectively (see Fig. 3). The first IH tank contains an internal quadrupole triplet lens. The final energies are 1.87 AMeV after IH1 and 3.2 AMeV after IH2. For the design A/q – value of 6.5 the sum voltage gain is 20.8 MV. Both IH cavities are powered by 340 kW solid state amplifiers, one for each cavity.

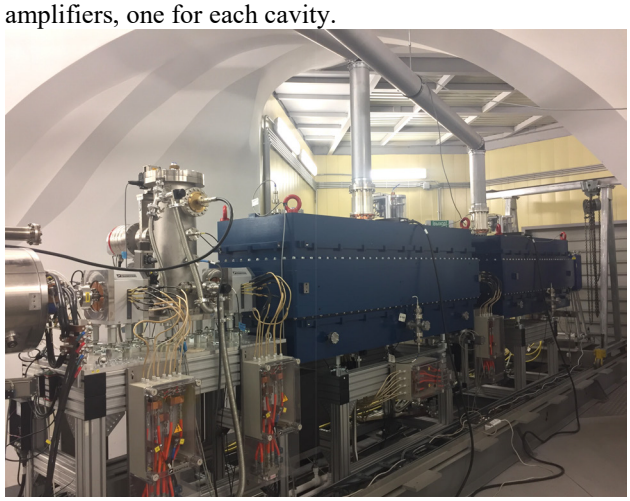

Figure 3: Interdigital H-type cavities IH1 and IH2 at JINR

COMMISSIONING

RF Commissioning

All solid state power amplifiers have been pre-tested with full power on a water load and a calibrated bi-directional coupler. Additionally a cavity with a Q factor of around 7000 has been used to test sensitivity and behavior in the matched- and unmatched case. In a stress test the 140 kW RFQ amplifier and the two 340 kW IH DTL amplifiers were driven with 5-10% excess power. Long term stability tests at 90% full power have been performed over 2 days. A digital Low Level RF system developed by ITEP [4] and also in use at LU20 of the JINR facility is providing amplitude and phase adjustments all cavities

After installation of all amplifiers, connectivity to LLRF system, rigid lines and HILac cavities at JINR, the pre-conditioned cavities were tested successfully up to full power.

RFQ Commissioning

Before installing the IH cavities the RFQ has been tested with beam. The beam energy was measured with a magnet spectrometer to be 300 keV/u ± 3% . The beam injected into the RFQ contained a mixture of carbon ion species C^{3+} and C^{2+} from LIS (Fig. 4). The total RFQ beam transmission was 90%. During daily runs in August and September the RFQ demonstrated a stable operation with good reserve of rf power when extrapolated to the A/Q design value of 6.25.

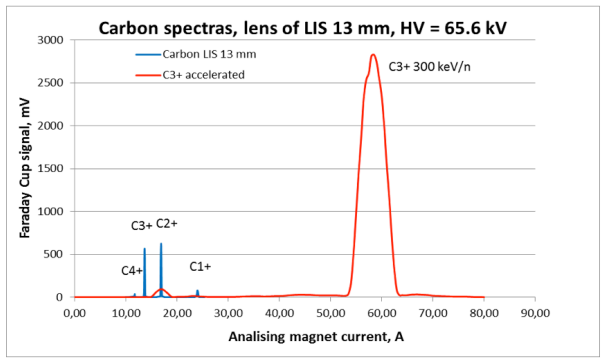

Figure 4: RFQ & MEBT with coaxial rebuncher.

MEBT Commissioning

MEBT commissioning followed beginning of October 2016. All quadrupole magnets had been tested in the factory for a alignment precision of the magnetic axis of 100 µm and a maximum tilt of 1 mrad. The alignment precision of the magnets in the beam line against the axis was validated using a laser tracker with an accuracy of 50 µm having precision markers on all beam line elements. The coaxial rebuncher showed a transient oscillation behavior with less than 5% reflected power.

IH DTL Commissioning

Phase probe signals behind the RFQ, IH1 and IH2 allowed to detect the macropulse shape as a signal envelope as well as the microbunch signal (see fig 5). Beam pulse lengths of 10 µs – 30 µs according the design specifications were measured with the phase probes. In one of the next steps these probes will also be used for TOF beam energy diagnosis during operation, once the probes and their cable lengths are calibrated and checked against the energy measurements with the magnetic spectrometer at the end of IH2. Two identical pulsed current transformers (ICT made by BERGOZ), one in the MEBT and one after IH2, allow to measure Linac beam transmission.

ISBN 978-3-95450-181-6

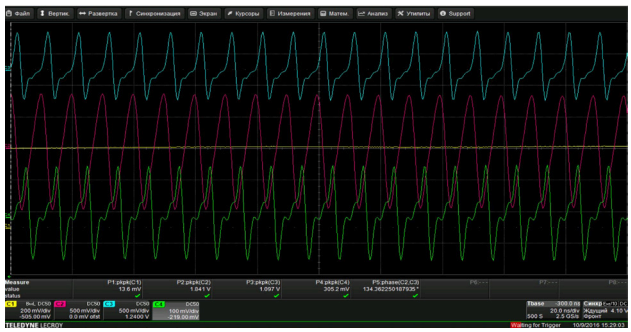

Figure 5: Phaseprobe signals: red – behind RFQ, green – behind IH1, blue – behind IH2.

Fig. 6 is from the last day of measurements on HILAc. Displayed are the signals from current transformers in MEBT and after IH2, blue line – signal from Faraday cup in the spectrometer (more than 90% of the beam accelerated in spectra is after the magnet). So the transmission factor for C3+ is about 60% from RFQ exit to IH2 exit at this stage of running in.

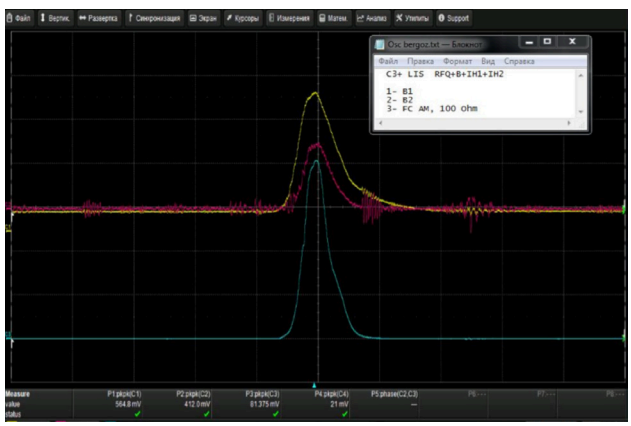

Figure 6: MEBT and IH1 ICT in yellow/red and Faraday cup at the spectrometer in blue.

Further optimization of quadrupole settings and steerer behind the RFQ allow for future improvements. In a third series of measurements the beam energy at the exit of the 2 IH cavities was validated with the magnetic spectrometer. Due to timing constraints it was not possible to optimize the spectrometer setup at its position behind IH2. The energies behind IH1 and IH2 could be verified with the spectrometer well to be at 1.87 AMeV 3.2 AMeV (Fig. 7).

SUMMARY

After 4.5 years of design and development work the Heavy Ion Linac - HILac - at JINRs new injector complex has been successfully commissioned. Ion source, LEBT, RFQ, MEBT and IH DTLs are in good agreement between simulations and measurements. The installation of the vacuum-, electrical-systems and alignment have been performed in best practice by the JINR team. Vacuum conditions were at the 10^{-8} mbar level after three days of continuous pumping. The RFQ was operated absolutely stable with a transmission of > 90% for all carbon species from the LIS mixed beam. The injector commissioning lasted 3 weeks. During this time a total transmission of accelerated beam after LEBT of more than 50% for C^{3+} was measured in first tests. The energy behind the RFQ and for each IH cavity was validated to be well in agreement with the design values. All accelerating structures, the solid state rf power amplifiers and the digital LLRF system run stable. The optimization process for HILac will start in 2017. As one of the next steps the ESIS source will be added providing beam with A/Q = 6.25 using target ions of Au^{32+} for which HILac was designed. Goal of the next steps is to optimize all settings for maximum beam transmission.

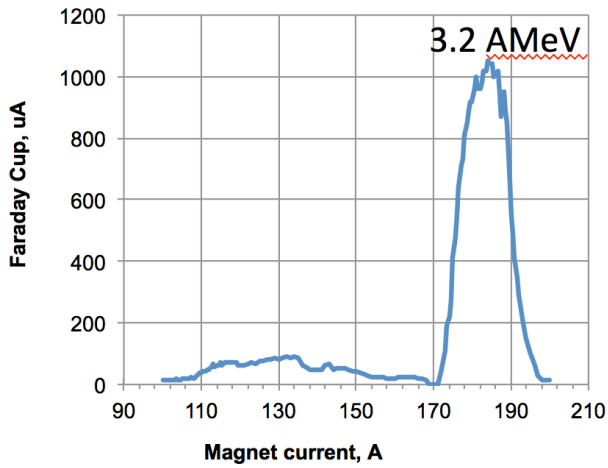

Figure 7: HILac at nominal energy.

ACKNOWLEDGMENTS

Figure 8: HILac team for commissioning.

The work on HILac has been performed in a mixed team consisting of Russian and German scientists (Fig. 8). We would like to express our best thanks for all the good work, the fruitful discussions and exchanged ideas with all team members. Our good cooperation was the basis for this successful project.

ISBN 978-3-95450-181-6

REFERENCES

[1] G. Trubnikov et al., "Heavy ion collider facility NICA at JINR (Dubna): status and development", Proceedings of ICHEP'12, Melbourne, Australia.
[2] www.bevatech.com
[3] A.V. Butenko et al, "Development of the NICA injection facility", Proceedings of IPAC2013, Shanghai, China, http://accelconf.web.cern.ch/AccelConf/IPAC2013/papers/thpwo069.pdf
[4] A.V. Butenko et al, "Development of the NICA injection complex", Proceedings of IPAC2014, Dresden, Germany, http://accelconf.web.cern.ch/AccelConf/IPAC2014/papers/wepro067.pdf

ISBN 978-3-95450-181-6

BOOSTER SYNCHROTRON AT NICA ACCELERATOR COMPLEX

A. Tuzikov, O. Brovko, A. Butenko, A. Eliseev, A. Fateev, V. Karpinsky, H. Khodzhibagiyan, S. Kostromin, I. Meshkov, V. Mikhaylov, A. Sidorin, A. Sidorov, A. Smirnov, E. Syresin, G. Trubnikov, V. Volkov, Joint Institute for Nuclear Research, Dubna, Russia
O. Anchugov, V. Kiselev, D. Shvedov, A. Zhuravlev, Budker Institute of Nuclear Physics, Novosibirsk, Russia

Abstract

NICA is the new complex being constructed on the JINR aimed to provide collider experiments with ions up to Au at energy of 4.5x4.5 GeV/u. The NICA layout includes 600 MeV/u Booster synchrotron as a part of the heavy ion injection chain of the NICA Collider. The main goals of the Booster are the following: accumulation of $2 \cdot 10^9$ Au^{31+} ions; acceleration of the heavy ions up to energy required for effective stripping; forming of the required beam emittance with electron cooling system. The layout makes it possible to place the Booster having 210.96 m circumference and four fold symmetry lattice inside the yoke of the former Synchrophasotron. The features of the Booster, its main systems, their parameters and current status are presented in this paper.

INTRODUCTION

The Booster of the NICA accelerator complex [1] is a superconducting synchrotron which will be placed inside the yoke of the former Synchrophasotron (see Figure 1). Main goals of the Booster are accumulation of $2 \cdot 10^9$ Au^{31+} ions; acceleration of the heavy ions up to energy required for effective stripping; forming of the required beam emittance with electron cooling system. The Booster has four fold symmetry lattice with DFO periodic cells (see Figure 2). Each quadrant of the Booster has 10 dipole magnets, 6 focusing, 6 defocusing quadrupole lenses and multipole corrector magnets. Missing dipole cells of the lattice are used for installation of injection, extraction, RF and electron cooling systems.

Accumulation of ions is provided by means of multivariant injection of ion beams into the Booster [2]. Main methods of beam injection into the Booster are single-turn, multi-turn and multiple injections. Ions are accumulated on the horizontal phase plane of the Booster.

Fast (single-turn) extraction provides ion stripping and transfer from the Booster into the Nuclotron. Slow extraction is not designed for the current version of the Booster and is considered to be implemented during later modernizations of the accelerator.

The Booster has working cycle of 4.02 s duration (see Figure 3). In case of necessity a technological pause between the Booster cycles of 1 s duration is presumed. Beam injection energy is equal to 3.2 MeV/amu. Electron cooling of a beam is fulfilled in the energy range from 65 to 100 MeV/amu. Maximal magnetic field in the dipole magnets is 1.8 T that corresponds to energy of Au^{31+} ions equal to 578 MeV/amu.

The design working point of the Booster is $Q_x = 4.8$, $Q_y = 4.85$. Lattice functions of the Booster are presented on Figure 4.

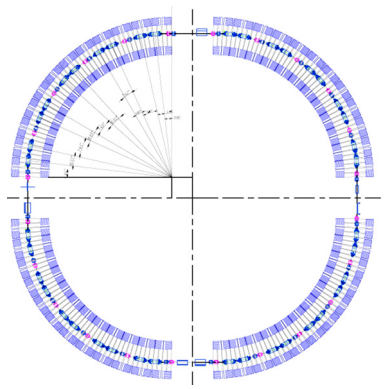

Figure 1: Layout of the Booster inside the former Synchrophasotron yoke.

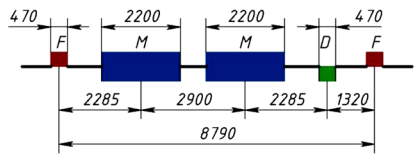

Figure 2: Regular DFO-cell of the Booster.

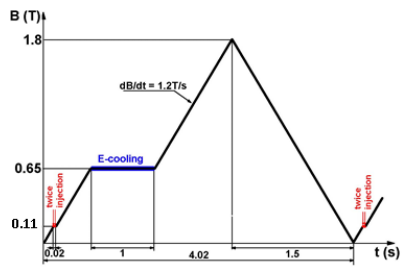

Figure 3: Working cycle of the Booster.

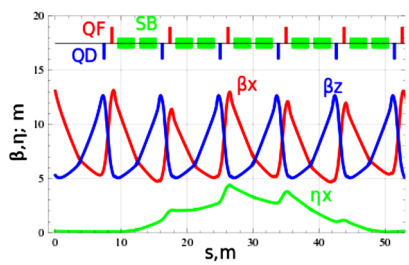

Figure 4: Lattice functions of the Booster synchrotron.

ISBN 978-3-95450-181-6

SUPERCONDUCTING MAGNETS

The magnetic system of the Booster is based on superferric Nuclotron-type magnets [3]. The Nuclotron-type magnets include a cold (4.5K) window frame iron yoke and a superconducting winding made of a hollow NbTi composite superconducting cable cooled with a two-phase helium flow.

The iron yoke of the dipole magnet consists of two symmetric parts that are bolted together. The half-yokes of the dipole are fabricated of laminated isotropic electrical steel. The sector magnet is 2.2 m long and has a radius of the curvature of about 14 m. The magnet is fixed in a cryostat with 8 suspension rods and is adjusted in relation to the adjacent magnets (see Figure 5).

Figure 5: The dipole magnet inside the Booster cryostat.

The Booster quadrupole is 0.47 m long. The quadrupoles are installed by pairs. Doublet of the quadrupoles is a single rigid mechanical construction of about 1.8 m length. A doublet consists of a focusing quadrupole lens, a defocusing lens, a cylinder for rigid mounting of lenses with each other, as well as two beam position monitors. The doublet is fixed in a cryostat with 8 suspension rods and is adjusted as a unit.

Facility for the assembly and tests of Nuclotron-type magnets is under commissioning at the Laboratory of High Energy Physics now [4]. Equipment of the facility is allocated in separate building of 2600 m^2 and provides: SC cable production; windings production; assembling yokes of magnets and winding, welding and brazing cooling channels of magnets; room temperature magnetic measurements; check of vacuum tightness of cooling channels, beam pipes and cryostats; assembling magnets in cryostats; cryogenic tests of magnets at 6 benches. At present manufacturing, testing and magnetic measurements of the Booster magnets are started in the facility.

POWER SUPPLY SYSTEM

At design of the Booster power supply system [5] the requirement of consecutive connection of lattice dipole magnets (total inductance 16.4 mH), quadrupole focusing (total inductance 0.6 mH) and defocusing (total inductance 0.6 mH) lenses is accepted for a basis. The main powerful source of the power supply system forms a demanded current (up to 12.1 kA) with the required magnetic field ramp of 1 T/s in the general chain according to a demanded cycle. Two additional power supply sources of essentially smaller power are intended for flexible adjustment of the Booster working point. One of them allows varying simultaneously the magnetic field gradient in focusing and defocusing lenses, another only in defocusing ones.

Currently power supplies from different manufacturers are tested at the Laboratory of High Energy Physics during the Nuclotron runs.

BEAM INJECTION SYSTEM

The beam injection system of the Booster [6] consists of an electrostatic septum and three electric kickers. The system's elements are located in the vicinity of the 1st straight section of the Booster (see Figure 6). The section has a bypass of cryogenic and superconducting communications and the largest part of the section including the septum and the kicker IK2 is room-temperature while the kickers IK1 and IK3 are placed inside the Booster cryostat.

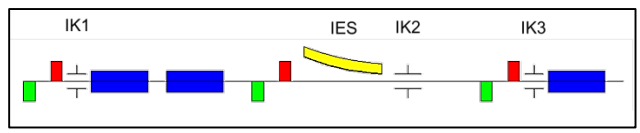

Figure 6: Layout of the beam injection system. Notation: blue – lattice dipole magnets, red – focusing quadrupole lenses, green - defocusing quadrupole lenses.

The electrostatic septum represents a pair of curved electrodes. High voltage (up to 125 kV) is applied to the cathode. Length of the IES is 1.9 m. Gap between the electrodes is 35 mm, thickness of the anode (which serves as a knife) is 1 mm. Currently the technical design of the septum is finished and its manufacturing will be started in the nearest future.

The electric kickers represent pairs of conducting plates. Lengths of the kickers IK1 and IK3 are 0.45 m, length of the IK2 is 0.8 m. Five power supplies of the kickers [7] provide independent unipolar charging/discharging of each of the plates (excluding one of the plates of the kicker IK1). Maximal voltage between the plates: IK1 – 40 kV, IK2 – 45 kV, IK3 – 60 kV. Currently the kicker prototype and the power supply (with voltage up to 60 kV) are manufactured and will be tested in the nearest months.

BEAM EXTRACTION SYSTEM

The beam extraction system of the Booster consists of a magnetic kicker, two magnetic septa, a stripping station and a closed orbit bump subsystem including four lattice dipoles with five additional HTS current leads. The system's elements are located in the vicinity of the 3rd straight section of the Booster (see Figure 7). The section has a bypass of cryogenic/superconducting communications and all the elements inside it are room-temperature.

Designs of the kicker and the septa as well as the whole system are being developed by Budker Institute of Nucle-

ISBN 978-3-95450-181-6

ar Physics (BINP, Novosibirsk) now. The kicker magnet is made of couple of conductors and the passive copper screen with opposite induced current [8]. Length of the kicker is 1.5 m. The maximum magnetic field is 0.17 T; the corresponding current in the kicker magnet conductors is 32 kA.

Two eddy-current septa have lengths of 0.4 and 1.4 m. The maximum magnetic fields of the septa are 0.5 and 1.3 T; the corresponding currents are 3 and 5.4 kA.

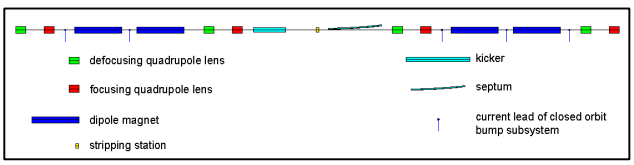

Figure 7: Layout of the beam extraction system.

RF SYSTEM

The RF system of the Booster [9] is based on amorphous iron loaded cavities. Two RF stations are to provide 10 kV of acceleration voltage. Frequency range of operation of the stations in the NICA Collider injector chain is from 587 to 2526 kHz. The provisions are made for autonomous mode of operation in the frequency range of 0.5 – 5.5 MHz at the same accelerating voltage.

The accelerating cavity consists of two coaxial quarter-wave resonators, working in push-pull mode onto a common accelerating gap (see Figure 8).

The RF stations have been designed and created at BINP (Novosibirsk). At present they have been delivered to JINR and are tested in Dubna.

Figure 8: RF station.

ELECTRON COOLING SYSTEM

The electron cooling system of the Booster [10] (see Figure 9) provides the ion beam cooling in the energy range from 65 up to 100 MeV/amu. The maximum electron energy is 60 keV.

The e-cooler have been designed and created at BINP (Novosibirsk). At present it is ready to be delivered to JINR in the nearest months.

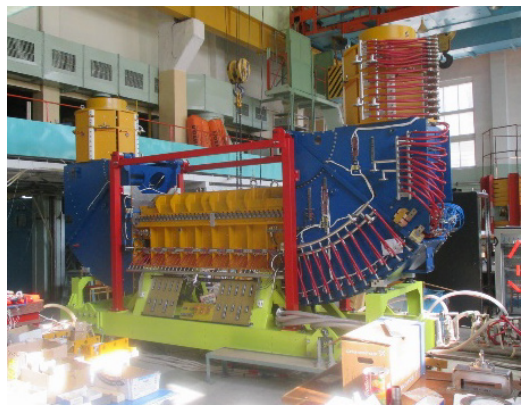

Figure 9: Electron cooling system.

REFERENCES

[1] Technical Project of NICA Acceleration Complex (Dubna, 2015).

[2] V. Volkov, I. Meshkov, V. Mikhailov, G. Trubnikov, A. Tuzikov, and A. Fateev, “Conceptual design of the system of heavy-ion beam injection into the booster of the NICA accelerator complex”, Phys. Part. Nucl. Lett. 11, 675 (2014).

[3] H. Khodzhibagiyan, P. Akishin, A. Bychkov, A. Donyagin, A. Galimov, O. Kozlov, G. Kuznetsov, I. Meshkov, V. Mikhaylov, E. Muravieva, P. Nikitaev, A. Shabunov, A. Smirnov, A. Starikov, and G. Trubnikov, “Status of the design and test of superconducting magnets for the NICA project”, Proceedings of RuPAC 2012, 149 (2012).

[4] S. Kostromin, V. Borisov, O. Golubitsky, A. Donyagin, A. Galimov, S. Korovkin, H. Khodzhibagiyan, A. Kudashkin, G. Kuznetsov, D. Nikiforov, T. Serochkina, A. Shemchuk, A. Starikov, and A. Tikhomirov, “Commisioning of facility for assembling and tests of superconducting magnets”, Proceedings of IPAC 2016, 1215 (2016).

[5] A. Kudashkin, V. Karpinsky, H. Khodzhibagiyan, and A. Sidorin, “Power supply and protection system of the Nuclotron booster in the NICA project”, Proceedings of RuPAC-2010, 83 (2010).

[6] A. Tuzikov, A. Butenko, A. Fateev, S. Kolesnikov, I. Meshkov, V. Mikhaylov, V. Shvetsov, A. Sidorin, A. Sidorov, G. Trubnikov, and V. Volkov, “Beam transfer from heavy-ion linear accelerator HILAC into Booster of NICA accelerator complex”, these proceedings.

[7] V. Bulanov, E. Gorbachev, N. Lebedev, A. Tuzikov, and A. Fateev, “A conceptual design of a power-supply system of deflecting plates for multivariate injection into the NICA accelerator complex booster”, Phys. Part. Nucl. Lett. 11, 695 (2014).

[8] V. Alexandrov, A. Tuzikov, and A. Fateev, “The nonsymmetrical variant of the nonferromagnetic extraction kicker magnet of the NICA Booster”, these proceedings.

[9] G. Kurkin, A. Batrakov, S. Krutikhin, Ya. Kruchkov, S. Motygin, and A. Pilan, “RF system of the Booster of NICA facility”, Proceedings of RuPAC 2014, 26 (2014).

[10] M. Bryzgunov, A. Bubley, V. Panasyuk, V. Parkhomchuk, V. Polukhin, V. Reva, “Low energy cooler for NICA Booster”, Proceedings of RuPAC 2012, 391 (2012).

ISBN 978-3-95450-181-6

SIMULATION OF TWO-PLANE PAINTING MULTITURN INJECTION INTO BRING WITH SPACE CHARGE EFFECT

A.V.Smirnov#, JINR, Dubna, Russia
W.Chai, G.F.Qu, L.Yao, IMP, Lanzhou, China

Abstract

The new project HIAF is under design now in IMP (Lanzhou, China) [1]. One of the aim of the project is to accumulate up to 1×10^{11} ions U^{34+} in the booster ring (BRing) at the injection energy 17 MeV/u. Two-plan painting procedure in both horizontal and vertical spaces was proposed to fill out full acceptance of BRing. The space charge effect was estimated with the molecular dynamics technique which was effectively used for the crystalline beam simulation.

TWO-PLANE PAINTING

The aim of the two-plan painting at BRing is to reach the necessary beam intensity 1×10^{11} after an injection procedure (Table 1). The transverse emittance of the injected beam is 5 π mm mrad and the horizontal ring acceptance is about 200 π mm mrad. In this case, the maximum gain for one-plan injection is about 26 what is not enough to accumulate the necessary value of the particle number. In accordance with [2] the gain factor for two-plan painting procedure can be achieved a value up to 100.

Table 1: BRing parameters for Au^{34+}

Parameter	Value
Circumference, m	473
Rigidity, T m	1 – 34
Acceptance, hor/ver, π mm mrad	200 / 100
Longitudinal acceptance, Δp/p, %	±0.5
Injection energy, MeV/u	17
Injection intensity	1.5×10^{9}
Injection emittance, π mm mrad	5
Injected momentum spread, %	±0.5
Injection cycle number	90
Extraction energy, MeV/u	800
Extracted particle number	7×10^{10}

The two-plan painting can be realized with two groups of orbit bump for both horizontal and vertical, simultaneous injection in horizontal and vertical phase spaces using tilted septum (Figure 1). During injection procedure the septum position is coming to the reference orbit and the septum angle remains constant.

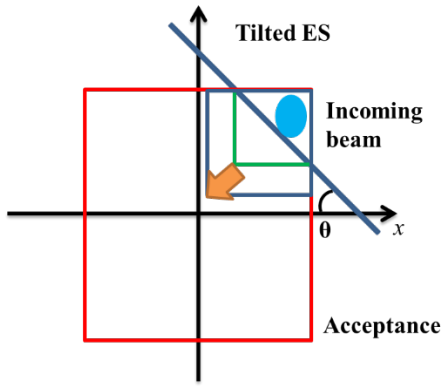

Figure 1: Scheme of injection in horizontal and vertical phase spaces using tilted septum.

The optimization of two-plan painting procedure was carried out with WinAgile [3], ORBIT [4] and BETACOOL [5] programs. The injection efficiency was optimized with the following input parameters: lattice functions at injection point, betatron values, septum angle, septum position, etc.

On Figure 2 is presented simulation results with BETACOOL for designed parameters (Table 1). Left picture is the particle distribution in the transverse plan, right picture is horizontal phase space after 90 cycles of the injection. The particle losses on the septum and transverse acceptance are taken into account. The dependence of the transverse emittances and particle number during injection procedure are presented on Figure 3.

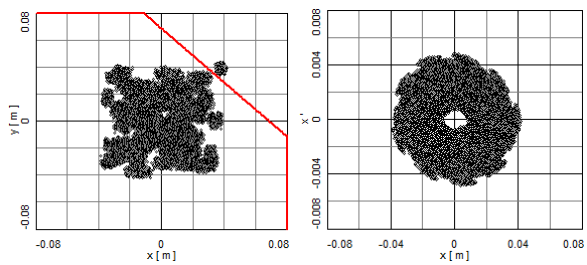

Figure 2: Particle distribution for transverse plan (left picture) and horizontal phase space (right picture) after 90 cycles of injection procedure.

Results of simulation with BETACOOL program have a good agreement with results of ORBIT program and show that without space charge effect the particle number can reach a necessary value 1×10^{11}.

#smirnov@jinr.ru

ISBN 978-3-95450-181-6

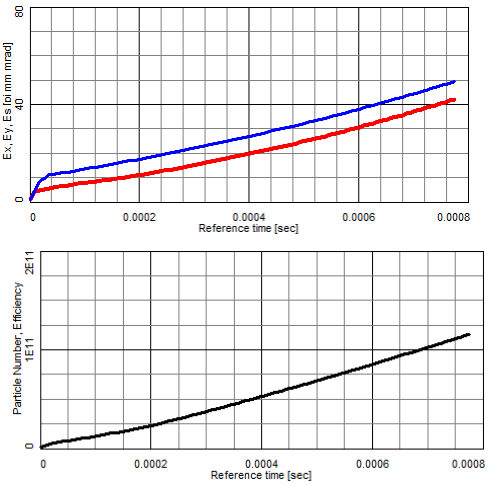

Figure 3: Transverse emittances (top picture) and particle number (bottom picture) during injection procedure. Injection efficiency 85%.

For the optimization of the working point the injection efficiency can be plotted on the tune shift diagram (Figure 4). The different colours corresponds to the particle number after injection procedure for different values of betatron tunes. The minimum injection efficiency is defined by the crossing of structure resonances.

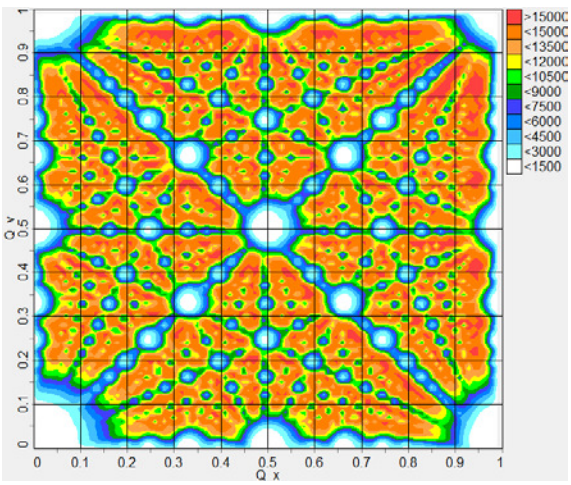

Figure 4: Injection efficiency on tune shift diagram, BETACOOL simulation without space charge effect.

SPACE CHARGE EFFECT

For the investigation of the space charge effect during injection procedure the Molecular Dynamics (MD) algorithm was applied in BETACOOL program which is successfully used for the crystalline beam simulation [6]. MD algorithm simulates direct Coulomb interactions under following assumptions:

- Particles have periodical distribution in longitudinal direction – cannot be used for bunched beam.
- No interactions with the electric field of chamber wall – only Coulomb interaction between particles.
- Very close interactions between particle does not take into account – no intrabeam scattering.

Horizontal (vertical) coordinates of particles are changed after (i+1) turn of transformation matrix as [7]:

$$\begin{bmatrix} x \\ x' \end{bmatrix}_{i+1} = \begin{bmatrix} \cos\mu + \alpha\sin\mu & \beta\sin\mu \\ -\gamma\sin\mu & \cos\mu - \alpha\sin\mu \end{bmatrix} \times \begin{bmatrix} x \\ x' \end{bmatrix}_i , \quad (1)$$

where x and x' – particle coordinates, μ – phase advance, α, β, γ – Twiss parameters. Betatron tune shifts for horizontal (vertical) plan can be calculated from the transformation matrix for each particle:

$$\Delta Q = \frac{1}{2\pi}\arctan\frac{\sin\mu}{\cos\mu} . \quad (2)$$

Tune shift distribution of particles calculated with (2) after one turn in BRing is presented on Figure 5 (right picture). Result is in a good agreement with the theoretical estimation of tune shift about ΔQ~0.3. One rhombus red point is working point; another one is the centre of tune shift distribution after one turn.

For the optimization of the injection procedure with space charge effect the tune shift diagram (Figure 5, right picture) can be overlapped with the efficiency diagram (Figure 4). It permits to avoid the crossing of structure resonances during and after injection procedure.

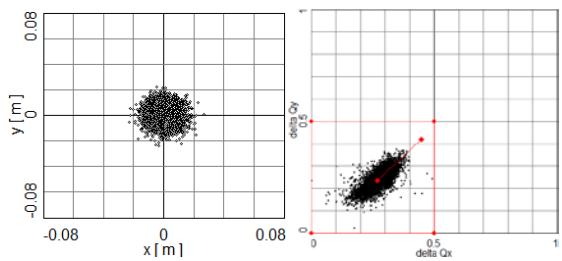

Figure 5: Numerical simulation of the tune shift due to space charge effect for Gaussian distribution. Left picture – particle distribution, right picture – tune shift distribution after turn.

The tune shift distribution after injection procedure (90 injection cycles) in BRing for designed parameters (Table 1) is presented on Figure 6 (left picture). One can see that for non-uniform distribution the tune shift much smaller in comparison with the theoretical estimation.

If the particle number increases in few times then the space charge leads to the relax of the particle distribution and the tune shift distribution seems more close to the theoretical estimation of the tune shift (Figure 6, right picture).

Injected efficiency for designed parameters of BRing (Table 1) is about 85% without space charge effect (Figure 7, zero value of particle number) and about 71% with space charge effect that is enough for HIAF project. Further increasing of the injected particle number leads to the decreasing of the injection efficiency (Figure 7) and fast increasing of the space charge effect (Figure 6, right picture).

ISBN 978-3-95450-181-6

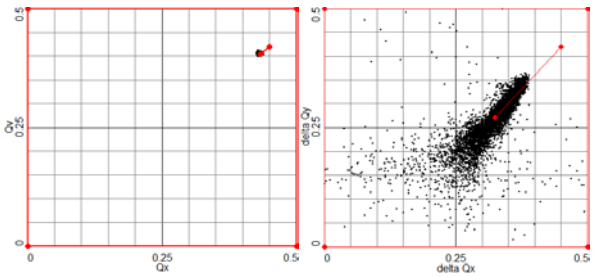

Figure 6: Numerical simulation of the tune shift due to space charge effect after two-plan painting multiturn injection, left pictures: N~10^{11} (ΔQ~0.08), right picture: N~5×10^{11} (ΔQ~0.4).

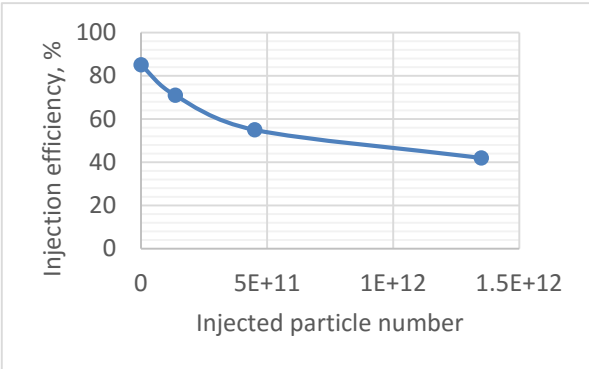

Figure 7: Dependence of injection efficiency on the total injected particle number. Zero particle number means no space effect (Figure 2).

The same effect with decreasing of the space charge effect was observed for the transverse shift of beam position (Figure 8). The area of the tune shift distribution is comparable with normal beam position (Figure 5) but shift of the tune shift distribution equal zero.

However, after a few hundred turns the particle distribution fill out all phase space around the reference orbit and the space charge comebacks to the normal value. Probably, if it possible to find way how to keep the beam in the non-uniform distribution for long time then the space charge effect can be significantly decreasing.

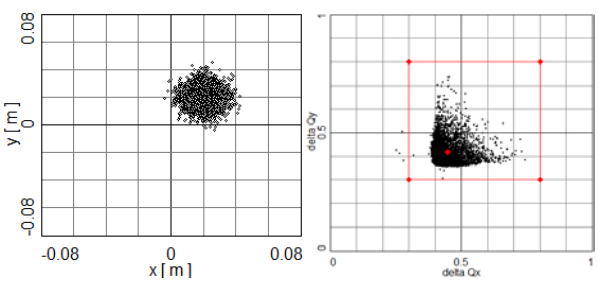

Figure 8: Numerical simulation of tune shift distribution (right picture) due to space charge effect with horizontal and vertical shifts (both are 2 cm) of the beam centre (left picture).

CONCLUSUTION

The using of Molecular Dynamics technique for the numerical simulation of the space charge effect can open new possibilities for the optimization of the intense beam dynamics in storage rings. From the present investigation can be formulated the following conclusions:

- Space charge has not large effect on injection procedure in BRing for designed parameters.
- Influence of space effect is significantly decreasing for non-uniform ion beam distribution.
- Large space charge leads to fast mixing (relax) of particles distribution and beam becomes uniform.

REFERENCES

[1] J. C.Yang. “High Intensity heavy ion Accelerator Facility (HIAF) in China”. Nuclear Instruments and Methods in physics Research B, 317:263-265 (2013).

[2] A.W.Chao, K.H. Mess, M.Tigner, F.Zimmermann. “Handbook of accelerator physics and engineering” (2nd edition). World Scientific (1999).

[3] P.J.Bryant. “AGILE, A tool for interactive lattice design”. Proceedings of EPAC (2000).

[4] J.Galambos, V.Danilov, D.Jeon, J.Holmes, D.Olsen, J.Beebe-Wang, A.Luccio “ORBIT – A Ring Injection Code with Space Charge”, Proceeding of PAC (1999).

[5] A.O.Siodrin, A.V.Smirnov. “Long term beam dynamics simulation with the BETACOOL code”. Proceedings of RUPAC (2012).

[6] T.Shirai, M.Ikegami, A.Noda, I.Meshkov, A.Smirnov, et.al. One-Dimensional Beam Ordering of Protons in a Storage Ring. Phys. Rev. Lett. 98, 204801 (2007).

[7] H.Grote, F.C.Iselin. “The MAD program”. Preprint CERN/SL/93-13.

ISBN 978-3-95450-181-6

NICA COLLIDER LATTICE OPTIMIZATION

O. Kozlov, A. Butenko, H. Khodzhibagiyan, S. Kostromin, I. Meshkov, A. Sidorin, E. Syresin, G.Trubnikov, JINR, Dubna, Russia

Abstract

The Nuclotron-based Ion Collider fAcility (NICA) [1] is a new accelerator complex being constructed at JINR. It is aimed to collider experiments with ions and protons and has to provide the ion-ion (Au^{+79}) and ion-proton collision in the energy range of 1÷4.5 GeV/u and also polarized proton-proton (5÷12.6 GeV) and deuteron-deuteron (2÷5.8 GeV/u) collisions. Two collider rings are designed and optimized to achieve the required luminosity at two interaction points (IP). Taking into account space charge effects of the intense ion beam the application of electron beam or stochastic cooling methods were proposed to provide beam or luminosity lifetime. This paper is considering one of the most challenging problems of accelerator physics that is finding the dynamic aperture (DA) of the collider ring.

INTRODUCTION

NICA collider lattice development [2] has many necessary aspects of the design. The collider should operate in the energy range for Au-ions of 1÷4.5 GeV/u, with the average luminosity about $1 \cdot 10^{27}$ cm^{-2} s^{-1}. The ring should work with the different particle species (Au^{+79}, protons and deuterons). Collider has a certain circumference limitation. The collider lattice is based on the technology of super-ferric magnets developed in VBLHE, JINR [3]. The collider optics optimization includes the certain effects which set constraints on the lattice parameters: luminosity lifetime limitation by intrabeam scattering in a bunch (IBS), space charge tune shift, threshold of microwave instability, slippage factor optimization for efficient stochastic cooling, maximum required RF voltage amplitude. The maximum energy of the experiment is determined by the Nuclotron maximum magnetic rigidity of 45 T·m. This paper considers only the most developed heavy ion mode of facility operation and the $^{197}Au^{+79}$ ions as the reference particles.

LATTICE STRUCTURE

Technical constraints were taken into account in lattice optimization: ring circumference, a number of the dipole magnets in an arc, convenience of the beam injection into the ring. The FODO optics with 12 periods is a principal choice for arc structure. Two arcs and two long straight section form the collider racetrack shape and correspond exactly to two Nuclotron circumferences. The rings are vertically separated (32 cm between axes) and use two-aperture superconducting magnets (dipoles and quadrupoles) [3]. This lattice has a large efficiency of stochastic cooling at 4.5 GeV/u. The luminosity of 10^{27} cm^{-2} s^{-1} could be reached in the wide energy range.

Table 1: Collider Ring and Beam Parameters

Ring circumference, m	503.04		
Number of bunches	22		
Rms bunch length, m	0.6		
β-function in the IP, m	0.35		
Betatron tunes, Q_x/Q_y	9.44/9.44		
Chromaticity, $\xi_{x,0}/\xi_{y,0}$	-33/-28		
Ring acceptance	40 π·mm·mrad		
Long. acceptance, Δp/p	±0.010		
Gamma-transition, γ_{tr}	7.088		
Ion energy, GeV/u	1.0	3.0	4.5
Ion number per bunch	2.0e8	2.4e9	2.3e9
Rms Δp/p, 10^{-3}	0.55	1.15	1.50
Rms emittance, hor./vert. (unnorm.), π·mm·mrad	1.10/ 0.95	1.10/ 0.85	1.10/ 0.75
Luminosity, $cm^{-2}s^{-1}$	0.6e25	1e27	1e27
IBS growth time, s	170	470	1900

The convenient injection scheme could be realized through the arc dipole-empty cell.

FODO periodic cell (12 m length) consists of four rectangular dipole magnets per cell (80 magnets per ring), two quadrupoles [3], multipole correctors and BPMs. The maximum field in 1.94 m dipole of 1.8 T and gradient in 0.47 m quadrupoles of 23 T/m are chosen to avoid the saturation effects in iron yokes at higher energies. Multipole corrector includes the several types of windings – dipole (orbit correction), quadrupole (tuning), skew quadrupole (coupling correction), sextupole (chromaticity correction) and octupole.

Arc comprises 12 FODO cells (90^0 phase advance per cell). The last 1.5 cells realize the horizontal dispersion suppressor (the effective quadrupole gradient (3 families) tuned by the nearby quadrupole corrector).

Long straight sections are matched to the arcs, contain the insertion devices, produce the betatron tune variation and the vertical beam separation and final focusing in IPs.

Collider ring general parameters are given in Table 1 and Twiss-functions for the ring are shown in Fig. 1. Two rings are separated vertically. In this scheme, two-aperture quadrupoles should have the opposite connections for upper and bottom rings in arcs and long straights, but the final focus triplets should have the antisymmetric connections with respect to IPs providing the same horizontal and vertical betatron tunes for counter circulating beams.

ISBN 978-3-95450-181-6

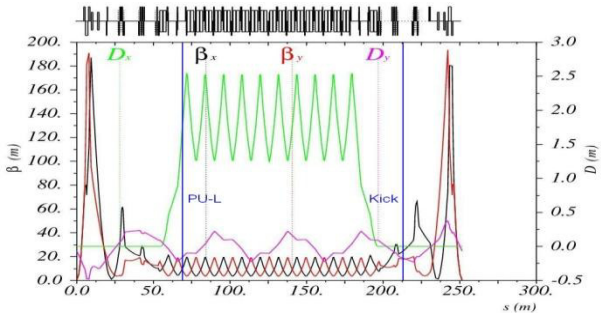

Figure 1: β-functions and dispersions for half a ring.

DYNAMIC APERTURE

In the design of a cyclic accelerator, one of the main tasks is to calculate or estimate the effect of nonlinear forces on the motion of a charged particle. One can introduce the concept of a maximum initial amplitude of particle oscillation assuming the absence of real geometrical aperture limitations or a vector in the space of transverse invariants, $E_{x,y}(s)$, so that the particle remains stably circulating in the accelerator ring within the required time or number of turns N_{tum}. The value of $E_{x,y}$ in a certain position along the accelerator ring is called the dynamic aperture (DA). The DA in an optimally designed accelerator must satisfy the condition $E_{x,y}(s) \geq A_{x,y}(s)$, where $A_{x,y}(s)$ is the acceptance of the ring at a given azimuth. In our optimizations of the collider DA we have aimed for the reasonable reserve for DA as $E_{x,y}(s) = 2 \cdot A_{x,y}(s)$. The following nonlinear fields were taken into account in DA estimations:

Nonlinear harmonics of the dipoles and quadrupoles, systematic and random, expected values are obtained from the magnetostatic calculations [3].

System of the chromaticity correction, which includes 4 families of sextupole correctors (focusing and defocusing). Sextupoles in each family are located in 180^0 betatron phase advance for the compensation of their nonlinear influence on the dynamic aperture (DA). The dependence of the collider tune on Δp/p is shown in Fig. 2 before and after chromaticity correction (maximum sextupole strength of 150 T/m^2 at the maximum energy of 4.5 GeV/u).

Fringe fields of the dipole and quadrupole magnet, in particular, the quadrupoles of the final focusing in IP.

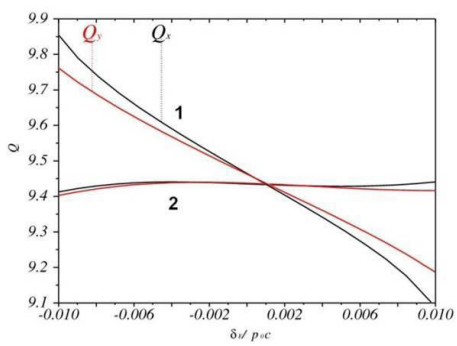

Figure 2: Tune spread over the momentum acceptance before (1) and after (2) chromaticity correction.

DA CALCULATION

The DA is calculated by the accelerator design program MAD-X [4]. Two methods for numerical integration of charged particle motion in external fields are implemented in MAD-X. One method, the thin lens model, transforms each magnet into a sequence of thin elements (slices) or, by default, one element of zero length placed in the center of the "thick" element. The other method, the Polymorphic Tracking Code (PTC) [4], is the same attempt of symplectic integration of particle motion, i.e., the motion with conservation of phase space. In this method, the ring elements are described symplectically to a certain extent, which depends on the user and the computer speed.

The collider DA calculations were carried out with and without nonlinearities of the magnetic field. The proper harmonics of the structural dipole and quadrupole magnets introduce the small influence on DA. The sextupole correction system of tune chromaticity operates anytime of particle tracking. The fringe fields of the magnetic elements show the most severe effect on the collider DA. The option of switching-on or switching-off of the fringe fields of all elements along the collider ring is realized in PTC tracking code. The particle dynamics was checked for the $N_{turn}=10^3$ number of turns in the collider ring.

The optimization of the collider optics is carried out from the viewpoint of the large DA in the limits of the designed collider geometry and concept of the 12 FODO cell bending arcs. The regulations of Q_x, Q_y betatron tunes and beta-functions $\beta^*_{x,y}$ in IPs are realized by both the trim quadrupoles in the long straight section (small regulation $\Delta Q_{x,y}=\pm 0.1$, small correction current $I_{t,max}=1$ kA) and arc quadrupoles (strong change of tunes in the range $Q_{x,y}=8.1\div 9.5$, $I_{q,max}=11$ kA). In Fig. 3 the resonance diagram and possible betatron working points of the collider ring are shown. The nominal tunes of $q=0.42\div 0.44$ are preferable for the stochastic cooling method in the energy range of $E_k=3\div 4.5$ GeV/u, but the tunes around q=0.1 could be used for electron beam cooling technique at the lower energies.

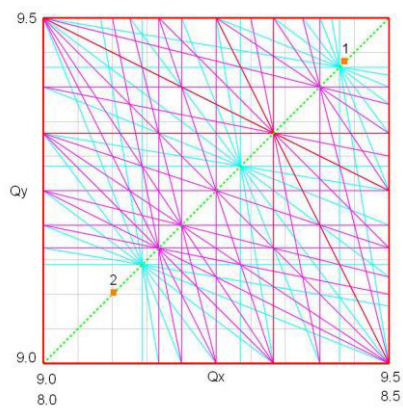

Figure 3: Resonance diagram up to 7^{th} order. Collider working points of betatron tunes.

ISBN 978-3-95450-181-6

The PTC DA calculation value for the nominal parameters of the collider (Table 1, Fig. 1) ($Q_{x,y}$=9.44, $\beta^*_{x,y}$=0.35 m) gives the averaged value of E=160 π·mm·mrad when the fringe field is off, chromaticity correction is on. The fringe fields reduce the DA below the ring's geometrical acceptance. Obviously, the increase the beta-function β^* in IPs leads to decrease the maximal beta-function β_{max} in final focusing quadrupoles and, consequently, to decrease the fringe field effect. The optics with $Q_{x,y}$=9.44, $\beta^*_{x,y}$=1.0 m provides the E=400 π·mm·mrad (no fringe field), E=100 π·mm·mrad (fringe field) and the considerable luminosity reduction as well. The next studies of the collider DA were carried out around the working point Q_x=8.44, Q_y =9.44, which is tuned by arc quadrupoles. The large number of the arc quadrupoles requires the small change in gradient. Thus, one can build the collider optics and provide the optimal chromaticity correction control (Fig. 4).

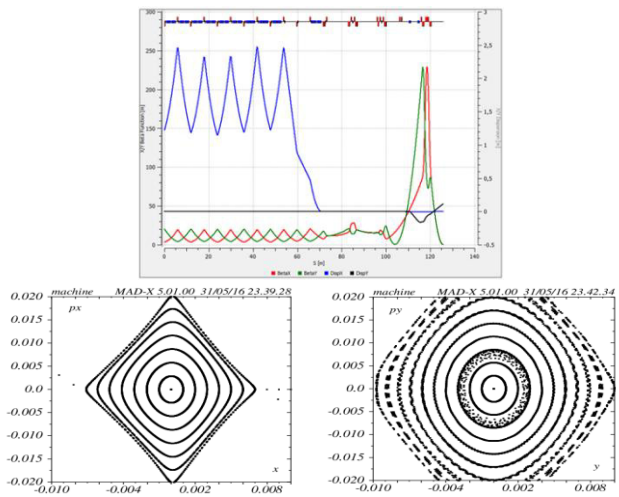

Figure 4: Collider optics, quarter of the ring, symmetric version. Phase portraits in IP (hor./vert.) with chromaticity correction.

The dependencies of the collider DA on beta-function in IP at the chosen working point are shown in Fig. 5, where the aperture presented in terms of beam amplitude and emittance. It seems the optics for β^*=0.6÷0.7 m and Q_x=8.44, Q_y=9.44 looks optimal and provide the double acceptance of the collider ring. The dominant influence of the final focusing quadrupoles fringe field on the DA could be demonstrated through the particle tracking over the system of quadrupole lens triplets having symmetric or antisymmetric connection with respect to IPs. The transverse phase space distortion appears at large amplitudes as it has shown in Fig. 6 for horizontal plane and symmetric connection. The pictures are similar for horizontal and vertical plane, symmetric and antisymmetric schemes.

CONCLUSION

The collider lattice concept – 503 m circumference with 12 cell FODO structure in the arcs has been chosen. The

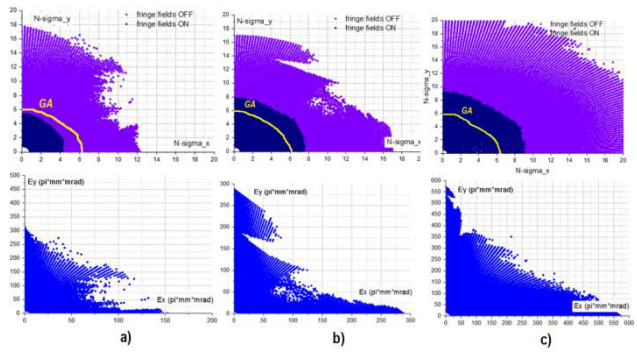

Figure 5: Collider DA in terms of beam amplitude and emittance. Q_x=8.44, Q_y =9.44, β^*=0.35 m (a), 0.5 m (b), 0.7 m (c). GA – geometrical acceptance.

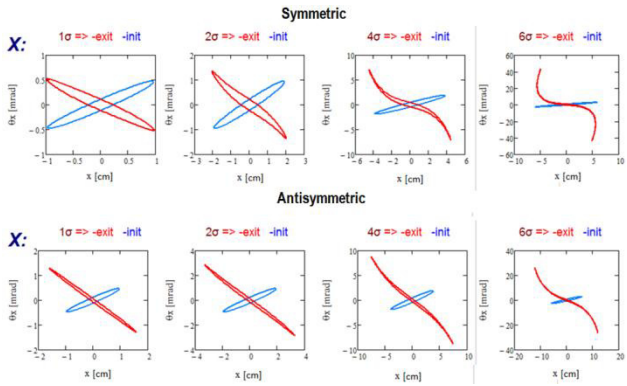

Figure 6: Particles tracking over the system of final focusing quadrupoles. Horizontal plane. Initial beam – blue, exit beam – red.

optical properties of this lattice have been optimized for the larger dynamic aperture of the ring. The variation of the betatron tunes together with the value of the beta-function in the interaction point by the arc and trim quadrupoles allows to find the new settings for the working point Q_x=8.44, Q_y =9.44, β^*=0.6 m where the DA is about the twice of ring geometrical acceptance. The some luminosity decrease is compensated by the small raise of beams intensity.

REFERENCES

[1] G.V. Trubnikov et al., "Status of NICA Project at JINR", Proc. of International Particle Accelerator Conf. (IPAC 2014), Dresden, Germany, 2014, pp. 1003-1005.

[2] O.S. Kozlov et al., "Collider of the NICA accelerator complex: optical structure and beam dynamics", Proc. of Russian Particle Accelerator Conf. (RuPAC 2012), St. Petersburg, Russia, 2012, pp. 278-280.

[3] H.G. Khodzhibagiyan et al., "Status of the design and test of superconducting magnets for the NICA project", Proc. of Russian Particle Accelerator Conf. (RuPAC 2012), St. Petersburg, Russia, pp. 149-151.

[4] MAD – Methodical Accelerator Design, http://madx.web.cern.ch/madx/.

ISBN 978-3-95450-181-6

DYNAMIC APERTURE OPTIMIZATION OF THE NICA COLLIDER*

S. A. Glukhov, E. B. Levichev, BINP, Novosibirsk, Russia

Abstract

NICA is a proton and heavy ion collider being built at JINR in Dubna, Russia. It was shown that nonlinear quadrupole fringe fields are among the main factors limiting dynamic aperture of the machine. In the present paper the following ways of dynamic aperture optimization were studied: betatron tunes optimization and placing octupole lenses to the lattice to compensate fringe fields' effect.

INTRODUCTION

Dynamic aperture (DA) optimization study for NICA lattice was started recently using the program codes MAD-X [1] and TrackKing [2]. At the moment the only nonlinearities taken into account are chromatic correction sextupoles, quadrupole nonlinear fringe fields in hard edge approximation [3] and octupoles added to compensate the latter effect. Figure 1 shows that DA is limited mainly by fringe fields of central lenses of final focus (FF) triplets (quads 2), contribution of the other triplet's lenses (quads 1, 3) is also significant. Additional DA reduction due to fringe fields of arc quadrupoles is negligible. Resulting

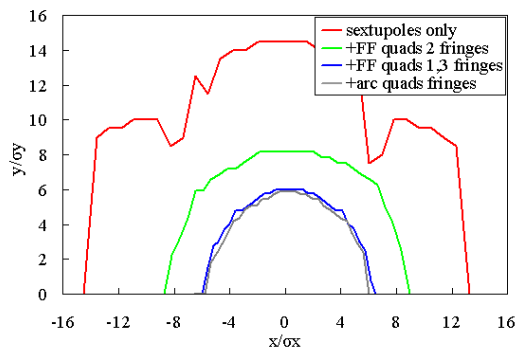

Figure 1: Effect of quadrupole nonlinear fringe fields on DA.

DA size is inacceptably small, therefore, optimization is necessary. In theoretical part of the present paper the relationship between quadrupole nonlinear fringe fields and octupole fields is shown. Then two steps of optimization are described. Firstly, we place two families of thin octupoles into the chromatic correction sextupoles and insert a "phase trombone" into the lattice (fictitious thin linear element which adjusts betatron tunes to the given values). Then we try to maximize DA with these octupoles and find the region of betatron working points where DA gain is the most significant. At the second stage we rematch the linear lattice using MAD-X to decrease influence of nonlinear fringe fields and bring working point to the previously defined region, then DA is optimized again with octupoles. Finally we make some estimations to prove that resulting increased DA is stable in the presence of magnetic field errors and misalignments.

* This work has been supported by Russian Science Foundation (project N14-50-00080).

NONLINEAR QUADRUPOLE FRINGE FIELDS AND OCTUPOLES

Hamiltonian for charged particle moving in a lattice with quadrupole and octupole fields can be written as follows

$$H = \frac{{p_x}^2+{p_y}^2}{2} + k_1(s)\frac{x^2-y^2}{2} + p_x k_1'(s)\frac{x^3+3xy^2}{12} - \\ -p_y k_1'(s)\frac{y^3+3yx^2}{12} + k_3(s)\frac{x^4-6x^2y^2+y^4}{24} \quad . \tag{1}$$

Here quadrupole gradient k_1' is introduced to take into account nonlinear quadrupole fringe fields.

If all octupoles are thin, then each of them causes the following coordinate transformation

$$(\bar{p}_x)_{\text{oct}} = p_x - (k_3 l)\frac{x^3-3xy^2}{6} \\ (\bar{p}_y)_{\text{oct}} = p_y - (k_3 l)\frac{y^3-3yx^2}{6} \quad , \tag{2}$$

where l is effective octupole length. If we also consider edges of each quadrupole as thin elements (so called "hard edge approximation" [3]), then the coordinate transformation for quadrupole fringe can be obtained

$$(\bar{x})_{\text{fringe}} = x + \Delta k_1 \frac{x^3+3xy^2}{12} \\ (\bar{y})_{\text{fringe}} = y - \Delta k_1 \frac{y^3+3yx^2}{12} \\ (\bar{p}_x)_{\text{fringe}} = \frac{p_x\left(1-\Delta k_1\frac{x^2+y^2}{4}\right) + p_y \Delta k_1 \frac{xy}{2}}{1-(\Delta k_1)^2\frac{(x^2-y^2)^2}{16}} \quad , \\ (\bar{p}_y)_{\text{fringe}} = \frac{p_y\left(1+\Delta k_1\frac{x^2+y^2}{4}\right) - p_x \Delta k_1 \frac{xy}{2}}{1-(\Delta k_1)^2\frac{(x^2-y^2)^2}{16}} \tag{3}$$

where Δk_1 is a variation of the quadrupole gradient, it has opposite signs at entrance and exit faces of the quadrupole. One can see that $\Delta(\bar{p}_{x,y})_{\text{oct}}$ and $\Delta(\bar{x},\bar{y})_{\text{fringe}}$ have similar structure but with different signs between terms. Therefore, nonlinear quadrupole fringe can be called "quasi-octupole".

ISBN 978-3-95450-181-6

There is no obvious way to improve DA, even if the sort of nonlinearities is clearly defined. One possible technique is to flatten betatron tune-amplitude dependence up to large enough apertures, because if this dependence is strong, it can limit DA by driving tunes to strong resonances. In the case of thin octupoles and quadrupole edges the following amplitude-dependent tune shifts can be obtained [4]

$$\begin{aligned}\Delta Q_x &\approx \frac{1}{16\pi}\sum_o (k_{3,o}l_o)\left(\beta_{x,o}^2 I_x - 2\beta_{x,o}\beta_{y,o}I_y\right) + \\ &+\frac{1}{8\pi}\sum_q (k_{1,q}l_q)k_{1,q}\left(\beta_{x,q}^2 I_x + 2\beta_{x,q}\beta_{y,q}I_y\right) \\ \Delta Q_y &\approx \frac{1}{16\pi}\sum_o (k_{3,o}l_o)\left(\beta_{y,o}^2 I_y - 2\beta_{x,o}\beta_{y,o}I_x\right) + \\ &+\frac{1}{8\pi}\sum_q (k_{1,q}l_q)k_{1,q}\left(\beta_{y,q}^2 I_y + 2\beta_{x,q}\beta_{y,q}I_x\right)\end{aligned}, \quad (4)$$

where summation is performed over octupoles and quadrupoles. With proper choice of octupole strenghts these terms can cancel each other exactly, but DA may be not optimal in this case because of higher order terms coming from quadrupole fringe fields. So, direct comparison of tune-amplitude plots is needed to determine optimal degree of cancellation, this can be performed using TrackKing.

WORKING POINT AND OCTUPOLE OPTIMIZATION

It is believed that working point of heavy particle collider should be near coupling resonance $Q_x = Q_y$ to keep beams round. Therefore, tune scan can be performed only in one dimension along this resonance. Results of this scan are shown in Fig. 2, they do not change with small deviations from the resonance with amplitude of $|Q_x - Q_y| < 0.01$. As we can see, DA can be improved

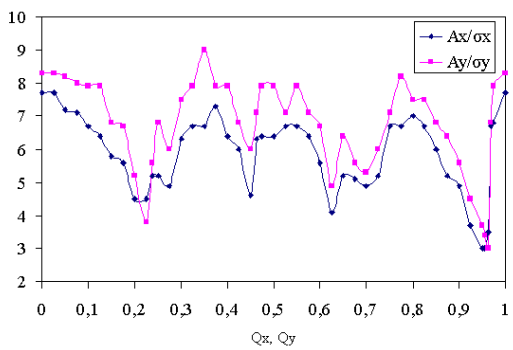

Figure 2: DA tune scan along the coupling resonance.

by shifting working point down, towards sextupole resonance, which is suppressed by octupole-like terms. New working point will be $Q_x/Q_y = 0.361/0.364$. It improves initial DA to $7.5\sigma_x \times 9\sigma_y$. Then optimal octupole strengths should be found. We have x- and y-family of octupoles, so we can optimise x-family first, because pure horizontal motion does not disturb vertical one, then optimize y-family. Tune-amplitude dependence for different octupole strengths in these two steps is shown in Fig. 3 and Fig. 4. Optimal octupole configuration is $k_{3,x}l = -9\ \mathrm{m}^{-2}$, $k_{3,y}l = -10\ \mathrm{m}^{-2}$.

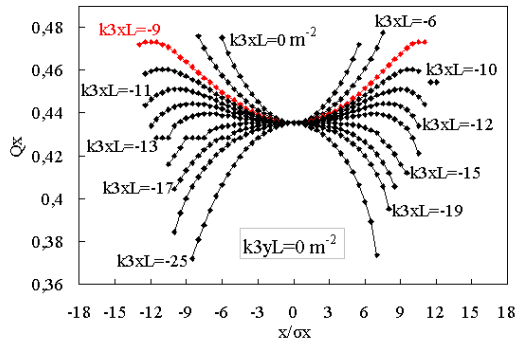

Figure 3: Tune-amplitude dependence for different strength of x-octupoles.

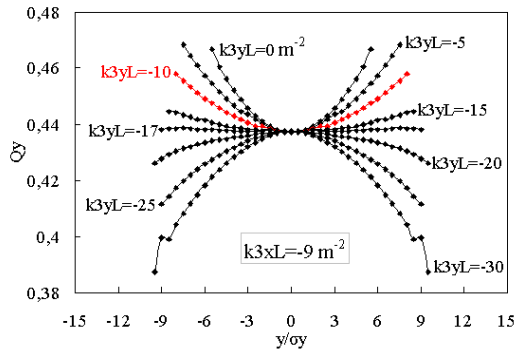

Figure 4: Tune-amplitude dependence for different strength of y-octupoles.

LATTICE OPTIMIZATION

According to (4), tune shifts depend quadratically on the quadrupole strenghts and beta-function values in them. So, the idea is to reduce $\beta_{\max}$ by adjusting straight section quadrupoles providing that their strenghts will be increased insignificantly or even reduced. Also working point should be brought to $Q_{x,y} = 0.39$.

Initial optical functions of NICA are presented in Fig. 5. Optical functions of interaction region in initial (dashed lines) and modified (solid lines) lattice of NICA are presented in Fig. 6. $\beta_{\max}$ in central quadrupole of the final focus triplet is reduced from 250 m to 200 m. Figure 7 shows DA before and after octupole optimization for both lattices.

MISALIGNMENTS AND FIELD ERRORS

Dynamic aperture shown in Fig. 7 is for ideal case. It will degrade due to magnetic field errors of the lattice el-

ISBN 978-3-95450-181-6

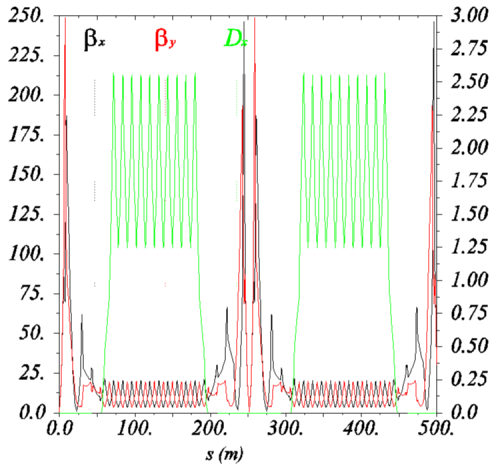

Figure 5: Optical functions of NICA (initial lattice).

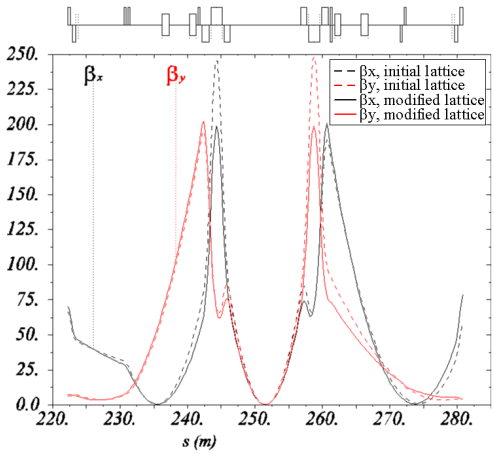

Figure 6: Optical functions of interaction region of NICA.

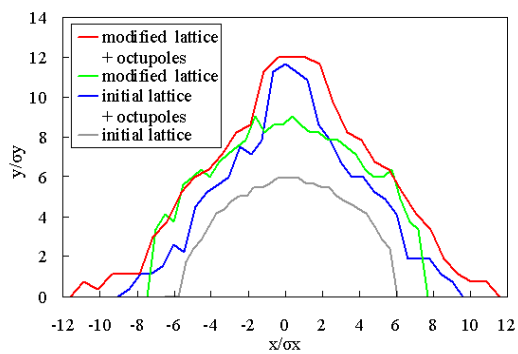

Figure 7: DA for initial and modified lattice before and after octupole correction.

ements. An attempt to estimate this effect was made in the case of pure octupole error in all quadrupoles. Integral strength of the octupole perturbation was 10^{-4} of the quadrupole gradient integral at $r = 3$ cm. Error distribution was Gaussian with a cut at 2σ. Misalignments of the beamline elements are another source of dynamic aperture degradation. Only effect of sextupoles and octupoles displacement can be estimated at the moment, because closed orbit correction module in TrackKing is still under development. Figure 8 shows DA for 10 different random seeds with octupole gradient errors in quadrupoles and transversal multipole displacements for initial and modified lattice. Misalignment distribution was Gaussian with $\sigma = 0.1$ mm and a cut at 2σ. One can see that assigned field errors and

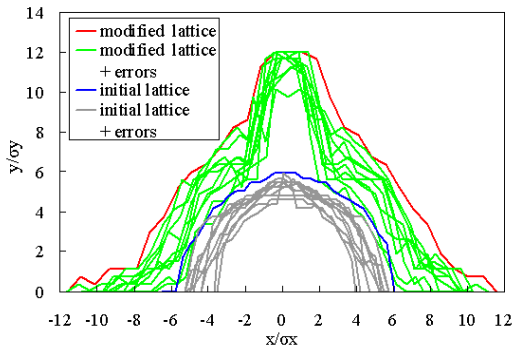

Figure 8: DA degradation due to octupole field errors in quadrupoles and multipole misalignments.

misalignments have reduced DA of modified lattice to that of initial one, whereas initial DA would be reduced to less than $4\sigma_x \times 4\sigma_y$.

FUTURE PLANS

Other factors affecting beam dynamics in NICA are intrabeam scattering and space charge effect. Simulation of these effects will be implemented in TrackKing soon. Also an attempt will be made to develop fast enough symplectic algorithm for simulation of the longitudinal kick due to space charge as well as transversal one. Closed orbit correction module also will be implemented soon, then more realistic simulation of misalignments will be available.

CONCLUSION

Simulations with MAD-X and TrackKing show that nonlinear fringe fields of FF triplet quadrupoles reduce DA of the NICA collider to $< 6\sigma$. Octupolar field errors and misalignments of chromatic correction sextupoles may reduce it further to $< 4\sigma$. Therefore, various sorts of optimization are to be done. Firstly, linear lattice should be modified to reduce strength of FF quadrupoles and beta-functions in them. Secondly, this is working point optimization, another question to answer is how far should it be from coupling resonance. And finally optimal octupole field distribution along the lattice should be found to compensate quasi-octupolar fields coming from quadrupole fringe fields.

ISBN 978-3-95450-181-6

REFERENCES

[1] H. Grote et al., "The MAD-X program (methodical accelerator design) version 5.02.06: User's reference manual", http://madx.web.cern.ch/madx/madX/doc/latexuguide/madxuguide.pdf

[2] S. Glukhov, E. Levichev, S. Nikitin, P. Piminov, D. Shatilov and S. Sinyatkin, "6D Tracking with Compute Unified Device Architecture (CUDA) Technology," doi:10.18429/JACoW-ICAP2015-WEP34

[3] E. Forest, J. Milutinovic, "Leading Order Hard Edge Fringe Fields Effects Exact (1 + Delta) and Consistent With Maxwell's Equations for Rectilinear Magnets," Nucl. Instrum. Meth. A **269** (1988) 474. doi:10.1016/0168-9002(88)90123-4

[4] F. Zimmermann, "Tune shift with amplitude induced by quadrupole fringe fields," CERN-SL-2000-009-AP, NEUTRINO-FACTORY-NOTE-18.

ISBN 978-3-95450-181-6

COMMISSIONING AND FIRST TESTS OF THE NEW STANDING WAVE 10 MEV ELECTRON ACCELERATOR

D.S. Basyl, T.V. Bondarenko, M.A. Gusarova, Yu.D. Kliuchevskaia,
M.V. Lalayan, S.M. Polozov, V.I. Rashchikov, E.A. Savin
National Research Nuclear University – Moscow Engineering Physics Institute, Moscow, Russia
M.I. Demsky, A. Eliseev, V. Krotov, D. Trifonov
CORAD Ltd., Saint-Petersburg, Russia

Abstract

A new linear electron accelerator for industrial applications was developed by the joint team of CORAD and MEPhI. It is based on conventional biperiodical accelerating structure for energy range from 7.5 to 10 MeV and beam power up to 20 kW. The use of modern methods and codes for beam dynamics simulation, raised coupling coefficient and group velocity of SW biperiodic accelerating structure allowed to reach high pulse power utilization and obtain high efficiency. The first two accelerators with the new structure have been installed and tested.

INTRODUCTION

A number of commercial S-band 10 MeV linacs for industrial applications are nowadays available on the market. These linacs are developed and produced by MEVEX, GETINGE, NUCTECH and Wuxi El Pont companies and can provide 15-30 kW of beam power . New industrial linac for average beam power up to 20 kW and variable energy range from 7.5 to 10 MeV was developed in 2014-15 by the joint team of CORAD and MEPhI. New linac has high electrical efficiency, narrow beam energy spectrum, provide energy regulation and low accelerated beam loses.

We tried to realize the following statements in our new linac design: the accelerating structure should have high coupling coefficient for maximal RF pulse power usage efficiency; the gentle buncher should be used to provide high capturing coefficient and narrow energy spectrum for all output energies.

The first two new accelerators have been produced and installed at EB-Tech Company site in Daejeon, Republic of Korea, and for company ACCENTR in "Rodniki" Industrial Park, Ivanovo Region, Russia. In this article we will briefly report the main results of linac development, manufacturing and testing.

THE LINAC GENERAL LAYOUT AND BEAM DYNAMICS

The traditional three-electrode E-gun was used for injection. It should provide up to 400-450 mA of pulse beam current to reach 300-320 mA of accelerated beam. Injection energy is equal to 50 keV.

The conventional biperiodical accelerating structure (BAS) based on Disk Loaded Waveguide (DLW) was used in linac. It operates on standing wave with resonant frequency of 2856 MHz. Wide magnetic coupling windows were used to increase the coupling coefficient which leads to low RF transient time and high group velocity. Low (~200 ns) RF filling time was realized using such idea. It also leads to the beam loading effect decrease.

Beam dynamics simulation was done using BEAMDULAC-BL code developed at MEPhI for simulations with beam loading and Coulomb field effects taken into account self-consistently [1]. Beam dynamics optimization was directed to obtain effective beam bunching for all energy range of 7.5-10 MeV and to achieve low beam energy spread. It was proposed to use a gentle buncher for these aims. The phase velocities β_{ph} and RF field amplitudes are rising for effective beam bunching. The linac consists of 28 accelerating and 27 coupling cells, its total length is 143 cm. The bunching part consists of of 6 accelerating cell with variable length. The average field in the accelerating cells should be equal to 160 kV/cm for the effective beam bunching and acceleration up to 11 MeV. Maximal on-axis RF field amplitude will be equal to 210 kV/cm in this case. One of the middle cells is used as RF power coupler.

Four short ~20 cm focusing magnetic coils are used for beam focusing, three of the coils were installed before coupler and one after it. Magnetic field of 30 mT on the linac axis is necessary for effective beam focusing.

Some main beam dynamics simulation results are presented in Table 1: E_{RF} is averaged field into accelerating cells, kV/cm; I_{out} is output current, mA; K_T is current transmission coefficient, %; N_{main} is the part of electrons in the main beam energy distribution peak, %; $\delta\gamma/\gamma$ is the energy spread on the energy distribution peak base; η, % is RF efficiency. Experimental data was defined for the first linac, which was commissioned on Sep. 2015 at EB-Tech Company site. All experimental data are presented for the beam output current of 320 mA. It is clear that linac provides effective beam bunching and acceleration for wide bands of beam currents and energies. The current transmission coefficient is close to 65-70 % for all operating modes and output energy spectrum is limited by 10 % (full width on the distribution base). It is clear that RF efficiency η slowly decreases vs. E_{max} (or vs. W_{max}) for constant current. But it increases with the beam current growth for constant W_{max}. It should be noted that E-gun provide about 450 mA of injection current and results for higher beam currents are interesting for simulation only.

ISBN 978-3-95450-181-6

Table 1: Beam Dynamics Simulation Results and Linac RF Efficiency, Initial Beam Current I_0=450 mA

		Output energy W, MeV							Power, kW				
	E_{RF}, kV/cm	Peak	Avg.	Avg. for main peak	I_{out}, mA	K_T, %	N_{main}, %	δγ/γ, %	Wall loses	Beam	Beam loses	Total	η, %
Simulation	70.0	1.93	1.59	1.60	110	24.4	-	±3.6	380	180	800	1360	13.2
	80.0	4.44	3.46	3.86	157	34.9	~ 25	±9.0	490	540	660	1690	32.0
	90.0	6.19	5.39	5.91	198	44.0	~ 40	±7.5	620	1070	490	1980	54.0
	100.0	7.05	6.76	7.20	217	48.2	~ 46	±4.6	770	1470	430	2670	55.1
	110.0	7.86	7.74	7.94	234	51.9	~ 49	±4.9	930	1800	370	3100	58.1
	120.0	8.61	8.39	8.68	256	56.8	~ 55	±4.8	1110	2150	300	3560	60.4
	130.0	9.03	9.09	9.28	275	61.2	~ 60	±4.9	1300	2500	240	4040	61.9
	140.0	9.73	9.75	9.89	293	65.2	~ 64	±3.8	1500	2860	200	4560	62.7
	150.0	10.34	10.32	10.45	306	67.9	~ 66	±3.4	1730	3160	170	5080	62.2
	160.0	11.04	10.91	11.02	320	71.2	~ 71	±3.4	2000	3500	150	5650	61.9
	170.0	11.71	11.42	11.62	326	73.4	~ 73	±4.9	2220	3720	130	6090	61.1
	180.0	12.33	12.10	12.22	316	70.3	~ 67	±5.0	2500	3820	90	6430	59.4
	190.0	13.00	12.73	12.83	306	68.0	~ 65	±6.6	2780	3900	90	6770	57.6
	200.0	13.58	13.25	13.43	294	65.3	~ 62	±5.2	3080	3900	100	7080	55.1
Experiment		**9.57**	**8.68**		**320**	**~ 55**	**~ 55**					**4600**	**60.4**

ACCELERATING STRUCTURE RF POWER SYSTEM

As it was noted above, the conventional DLW-based BAS was used in linac. The coupling cell length and diaphragm thickness were chosen constant along the structure including periods of the gentle buncher.

Traditional RF power coupler was simulated and tuned. The coupler is highly over-coupled with the structure (ρ≈4) because of the high beam pulse current. The additional auxiliary rectangular waveguide was added to the coupler cell for RF field distribution symmetrization. The main aim of cells optimization was to provide necessary RF field amplitude distribution in buncher (see Figure 1) with high and constant magnetic coupling coefficient for cells having varying length, shell radius and field. Optimization was successfully done and the following electrodynamics characteristics were obtained: resonant frequency is 2856 MHz, coupling coefficient > 10 % (this value was one of the projected parameters to limit the RF filling time), Q-factor is 16600, effective shunt impedance is 82.5 MOhm/m and maximal overvoltage on the surface is 3.6 (it is observed on the diaphragm bevels).

The accelerating cell shape was optimized to minimize multipactor discharge problem. MultP-M code was used for simulation [2].

The measured Q-factor of the manufactured section is equal to 14400.

The klystron TH2173F (Thales Electron Devices) was used for linac RF feed. It provides up to 5 MW of pulse power for 17 μs RF pulses duration and up to 36 kW of averaged power.

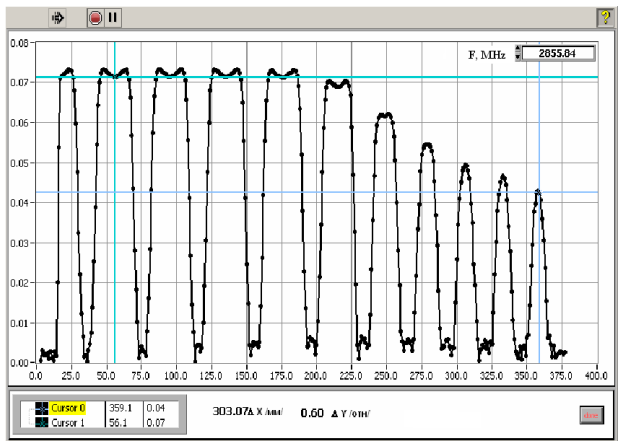

Figure 1: Measured RF field distribution in buncher and first regular cells, the amplitude deviation doesn't exceed 5 % from the simulations.

LINACS COMMISIONINGS

The first new accelerator was manufactured, assembled and successfully tested at EB Tech Company site in Daejeon, Korea (see Figure 2). Two solid-state modulators were manufactured by CORAD Ltd. to feed both klystron and electron gun.

Control system and some other accelerator components were made by EB Tech. The first accelerated beam was generated on September, 2015 [4].

The beam energy was measured by ISO/ASTM 51649:2005(E) Standard [3]. Experimental data is also presented in the Table 1. The beam energy and pulse beam power have very good correlation to simulated values. The RF efficiency is ~60.4 % and this value correlates with the simulation dates very well too. We

ISBN 978-3-95450-181-6

also confirm the achieved high total linac electrical efficiency. If we take the most probable energy for definition of the total linac electrical efficiency, latter equals to 19 % for 15 kW beam power and 17.4 % if we take the averaged beam energy value. It is high result for standing wave S-band RF linac.

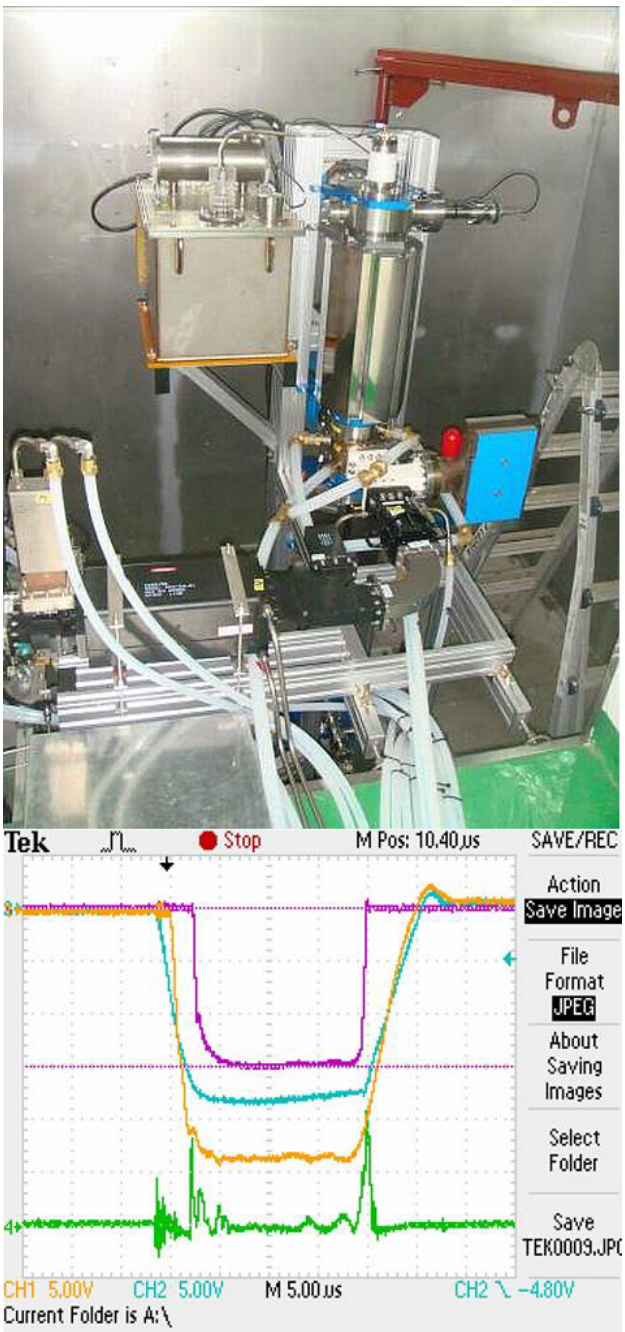

Figure 2: Photo of the assembled linac (it is installed vertically over the conveyer) at EB Tech Company site in Daejeon, Korea and experimental curves for klystron voltage pulse (yellow), E-gun pulse (cyan), beam pulse (magenta) and reflected RF wave (green).

The second linac was manufactured for ACCENTR Ltd. Company and installed at "Rodniki" Industrial Park, Ivanovo Region on September, 2016. Unlike the first linac, such accelerator has horizontally conveyor as it can be seen from Figure 3. Such linac is under commissioning at present. It will used for sterilization of medical disposable products.

Figure 3: Photo of installed linac at ACCENTR Ltd. Company site, the beam scanner is clearly seen in the right side of the photo.

CONCLUSION

The new 10 MeV linear electron accelerator for industrial applications was successfully developed by the joint team of CORAD and MEPhI. The first two accelerators have been manufactured, installed at EB-Tech Company site in Daejeon, Republic of Korea, and at "Rodniki" Industrial Park, Ivanovo Region, Russia, and successfully tested. After minor engineering enhancements and specifications corrections such linac can be produced in a series.

REFERENCES

[1] T.V. Bondarenko, E.S. Masunov, S.M. Polozov, Problems of Atomic Science and Technology. Series: Nuclear Physics Investigations, 6 (88), 114-118 (2013).
[2] M.A. Gusarova et al., NIM A, 599, 100-105 (2009).
[3] www.iso.org/iso/catalogue_detail.htm?csnumber =39027.
[4] M.I. Demsky, M.V. Lalayan, S.M. Polozov et al., Proc. of IPAC'16, 1794-1796 (2016).

ISBN 978-3-95450-181-6

HIGH EFFICIENCY STRIPPING EXTRACTION ON 80 MEV H-MINUS ISOCHRONOUS CYCLOTRON IN PNPI

S.A. Artamonov#, A.N. Chernov, E.M. Ivanov, G.A. Riabov, V.A. Tonkikh, B.P. Konstantinov
Petersburg Nuclear Physics Institute, NRC "Kurchatov Institute", Gatchina, Leningrad district, 188300, Russia

Abstract

H-minus cyclotron has the advantage that high intensity internal beam can be extracted from the acceleration chamber with practically 100% efficiency by transformation H-minus ions into H-plus ion by using thin foil. The extraction system is consists from the probe with stripping foil, extraction window in the vacuum chamber and two allaying magnets to match the extracted beam with beam transport line. The beam optics calculations in the measured magnetic field make it possible to find optimal relative position of the extraction system elements as well the parameters of the extracted beam with energy 40 - 80 MeV. At present time the beam is extracted from the chamber with efficiency about 100 % and there is good agreement with the optic calculations.

INTRODUCTION

The start up of a new high intensity isochronous cyclotron with the design beam energy from 40 up to 80 MeV and beam current of 100 microamperes was announced in November of 2016. The cyclotron is intended for production of high quality medicine isotopes, organization of eye melanoma treatment facility, treatment of surface forms of cancer and radiation resistance tests of the electronics for the aviation and space [1].

The external view of the cyclotron and the first part of the beam transport line is presented in Figure1.

Figure 1: The external view of the C-80 cyclotron and beginning part of the transport line.

Basic parameters of the cyclotron are summarized in the Table1.

Table 1: Parameters of C-80 Cyclotron

MAGNET	
Pole diameter	2.05 m
Valley gap	386 mm
Hill gap (min.)	163 mm
Number of sectors	4
Spiral angle (max.)	65°
Magnetic field in centre	1.352 Tl.
Flatter (max.)	0.025
Extraction radius	0.65-0.90 m
EXTRACTED BEAMS	
Energy	40 - 80 MeV
Method	stripping

Advantage of H – minus cyclotron is that high intensity internal beam can be extracted from the acceleration chamber with practically 100% efficiency by stripping H^- ions to H^+ ions using thin foils.

The 3D sketch of the cyclotron and extraction system is presented in Figure 2.

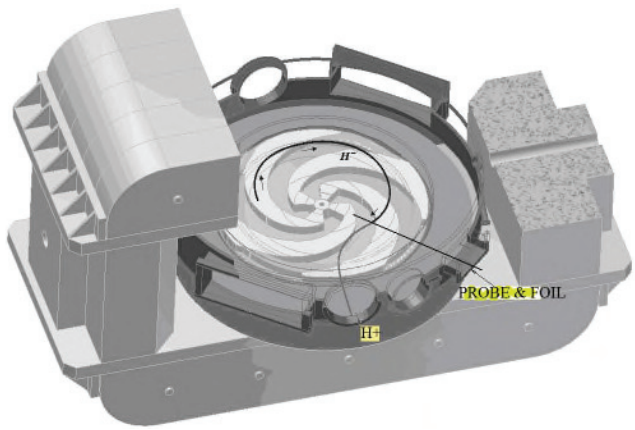

Figure 2: 3D sketch of C-80 cyclotron and the extraction system.

The extraction system consists of the probe with stripping foil, extraction window in the vacuum chamber and two correction magnets to divert the extracted beams of different energy into the transport line.

Schematic view of the extraction system is presented in Figure 3.

#artamonov_sa@pnpi.nrcki.ru

ISBN 978-3-95450-181-6

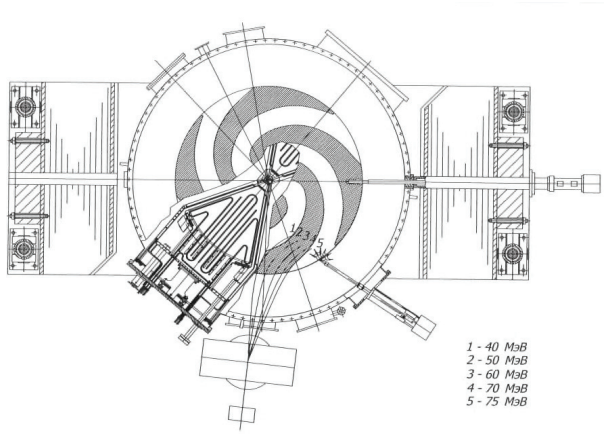

Figure 3: Schematic view of the extraction system of C-80 cyclotron.

MAGNETIC FIELD

To design the extraction system it is necessary to now magnetic field as in the acceleration region as on the edges. For that reason the residual magnetic field was measured up to a radius of 230 cm.

The C-80 cyclotron has some specific features in the magnetic structure. As can be seen from Table 1 the magnetic structure with very low flatter and very high spiral angle (up to 65 degrees) is used in the cyclotron. Such a structure makes it possible to decrease the magnetic field in the hill region to avoid beam losses due to electro-dissociation of H-minus ions. As a result it permits acceleration of H–minus ions up to an energy of 80 MeV using a magnet with the pole diameter of 2 meters and keeping the beam losses below 3 %. Detailed description of the magnetic structure can be found in RUPAC-2014 report [2]. The final magnetic field of C-80 cyclotron is presented in Figure 4.

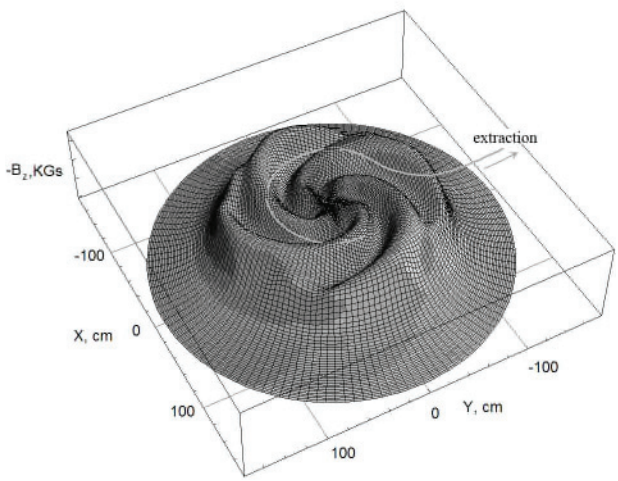

Figure 4: Magnetic field of C-80cyclotron.

REFERENCE TRAJECTORIES

One of the problems in design of the extraction system is to determine the relative positions of the extraction window in the vacuum chamber and the extraction foil. As a first approximation positions of the window and foil were estimated based on simulated closed orbits in the calculated magnetic field. The particle trajectories were started from the closed orbit. It is necessary to provide that participles of different energies pass throw the extraction window and enter the entrance of the allaying magnet. It can be achieved by varying the stripper position along the radius and azimuth. The trajectories of the extracted particles are shown in Figure 5.

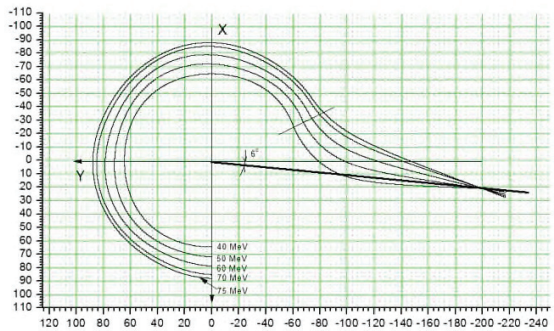

Figure 5: Trajectories of the extracted particles.

As result of these calculations it was established that the full energy in a range from 40 up to 80 MeV can be obtained when stripper foil is moved along the nearly the straight line (line equation *Y=0,88857 X – 36,27)* in the coordinate system shown in Fig.5. The maximal deviation from the straight line should not exceed a few centimeters.

Original stripper probe with tree stripper foil was designed for C-80 cyclotron. The probe can be moved along the straight line and in addition each foil can move along the azimuth by 5 cm. As a result it permits to obtain the whole energy range by moving the probe along the straight line. The reference trajectory calculations make possible to estimate the main parameters of the extraction system: position of the extraction window in the vacuum chamber, position and movement ranges of the stripper foil, arrival points of particles with the different energies at the allaying magnet entrance, direction of the extracted beam and at last the necessary angles range for the allaying magnet. The direction of the extracted beam is at 6 degrees with respect to longitudinal axis of the cyclotron magnet as it is shown in Fig.5. Deviation angle in the allaying magnet is varied from 15 up to - 4 degrees.

BEAM OPTICS CALCULATION

Besides the reference trajectory it was necessary to determine the size and divergence of the beam near the reference trajectory to design the beam transport line.

The computer simulation [3] can be used to calculate both the reference trajectory and beam optics. In the linear approximation the movements in the vertical and horizontal planes are independent and the beam behavior can be described by two independed phase ellipses. The starting ellipse size on the stripper in the vertical plane

ISBN 978-3-95450-181-6

was defined assuming that the maximum beam size in cyclotron is about 6 mm and divergence corresponds to divergence of matched with magnetic structure ellipse on the stripper position. The beam spot on the stripper is supposed to be 3 mm in horizontal plane and divergence should correspond to divergence of matched ellipse. Example of evolution of the phase ellipses in the extraction process for 70 MeV beam is shown in Figure 6.

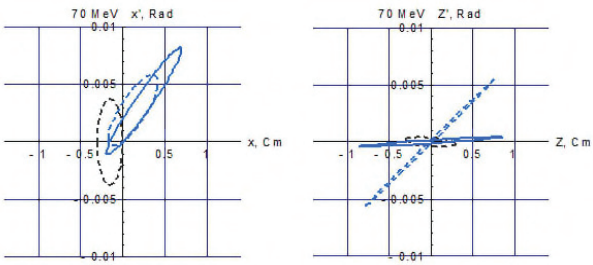

Figure 6: Phase ellipses for 70 MeV beam in the extraction process (the black dotted line corresponds to stripper position; the blue dotted line corresponds to entrance of the allaying magnet and a blue line corresponds to exit of the magnet).

Figure 7 shows evolution of the beam envelopes from stripper up to the exit from the allaying magnet for 70 MeV beam. After stripper the beam is exposed to the defocusing forces in the horizontal and vertical planes.

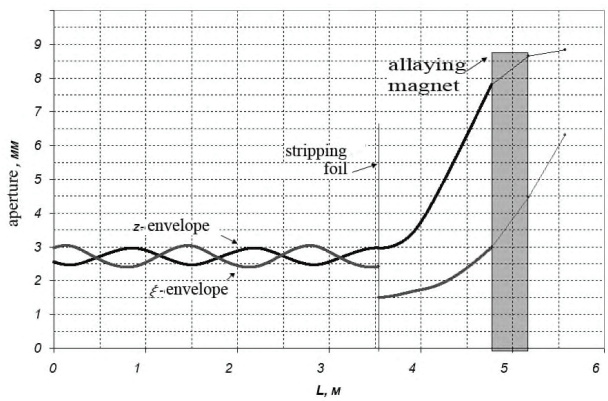

Figure7: Transformation of the beam envelopes in the extraction process.

The calculated parameters of the beam ellipses at the allaying magnet are presented in Table 2.

TRAJECTORY CALCULATIONS IN THE EXPERIMENTALLY MEASURED MAGNETIC FIELD

At the final stage it was calculated 500 particle trajectories with random start condition in the experimentally measured magnetic field map from inflector exit up to entrance of the allaying magnet. This calculation to a great extent confirmed the previous results for the extraction window and stripper position, direction of the extracted beam and the beam parameters. In addition it was found that beam spot in horizontal plane on the stripper is 3mm, as it was assumed in previous calculations. The energy uncertainty is about 1%. Furthermore it was found that internal beam quality strongly depends on the cyclotron tuning, in particular on central optic tuning, the first and third harmonics in the magnetic field. It is interesting to note that the second and fifth harmonics have no effect on the beam emittance.

Table 2: Beam Ellipse Parameters at the Allaying Magnet Entrance

T, MeV	40		70	
	ξ	z	ξ	z
α	*-1.793*	*-5.079*	-3.562	-3.123
β, mm/mrad	*5.801*	*5.010*	3.559	62.220
γ, mrad/mm	*0.727*	*5.348*	3.845	0.173
ε, mm·mrad	*5.4*	*3.8*	5.6	1.2
D, cm	105		51	
D^1, rad.	1.03		0.52	

EXPERIMENT

The physical start up of C-80 cyclotron was in summer of 2016. Design beam parameters were achieved in November. To avoid irradiation of cyclotron elements and personal it was operated in the pulse regime. The extracted beam has been obtained in the energy range from 40 up to78 MeV. Extraction efficiency estimated as a ratio of the current on the first in beam line Faraday cap and current on the internal probe is 80-100%. The beam is directed into the beam line, which position was defined from computer simulations. The energy range was obtained by moving the stripper probe along the calculated line. Results of computer simulations have been confirmed by experiment.

Optimization of the beam line and the tuning of the cyclotron regime are planned for the near future.

ACKNOWLEDGMENT

In conclusion we have a pleasure to express our appreciation to Yu.N. Gavrish, V.G. Mudrolyubov and especially to A.V. Galchuk for the help and fruitful discussions.

REFERENCES

[1] Yu.N. Gavrish et al., "Physical Start-up of the C-80 Isochronous Cyclotron," TUCASH04, these proceedings.
[2] S.A. Artamonov et al., "The Final Magnetic Field Distribution of the 80 MeV H-minus Isochronous Cyclotron at Gatchina." Proceedings of XX Int. Conf. Beam Dynamics & Optimization, BDO-2014, Saint-Petersburg, Russia, June 30-July 04, 2014, p. 18-19.
[3] N.K. Abrossimov et al., PNPI preprint - 2851, 2010.
[4] N.K. Abrossimov et al., PNPI preprint - 2858, 2011.

ISBN 978-3-95450-181-6

PHYSICAL START-UP OF THE C-80 ISOCHRONOUS CYCLOTRON

Yu.N. Gavrish, A.V. Galchuck, S.V. Grigorenko, A.N. Kuzhlev, V.G. Mudrolyubov,
JSC "NIIEFA", St. Petersburg, Russia
D.A. Amerkanov, S.A. Artamonov, E.M. Ivanov, G.F. Riabov, V.I. Yurchenko
PNPI, Gatchina, Leningrad region, Russia

Abstract

Works on the installation of a cyclotron system for the acceleration of H^- ions at energies ranging from 40 up to 80 MeV have been completed in the B.P. Konstantinov Petersburg Nuclear Physics Institute (PNPI), the National Research Centre "Kurchatov Institute". The cyclotron is intended for production of a wide assortment of radioisotopes including radiation generators (Sr-Rb, Ge-Ga) for medicine, proton therapy of ophthalmic diseases, tests of radioelectronic components for radiation resistance and studies in the field of nuclear physics and radiation material science.

In June, 2016 physical start-up of the cyclotron was realized in the pulsed mode. To date, the beam of ~38 μA was obtained at the inner probe of the cyclotron, the extracted beam at the first diagnostic device was ~28 μA. The beam transport to the final diagnostic device of the beamline (~35 m long) practically without losses was demonstrated. In the near future we plan to obtain the design intensity of 100 μA.

PURPOSE AND MAIN CHARACTERISTICS

The C-80 cyclotron system developed by specialists of PNPI and the D.V. Efremov Institute is intended for production of proton beams with energies ranging from 40 up to 80 MeV and current of up to 100 μA. The beams with such parameters will be used to finalize the development of the technology for production of a wide assortment of radioisotopes for medicine including radiation generators and for commercial production of these radioisotopes [1-3]. In the nearest future the following works are planned:

- Creation of a special line to form homogeneous proton beams of ultra-low intensity (10^7-10^9) for proton therapy of ophthalmic diseases.
- Creation of a test facility to carry out studies on the radiation resistance of radioelectronic equipment using intensive beams of protons and neutrons.

The cyclotron system equipment with the transport system of an accelerated proton beam to remote target stations is mounted in the experimental hall of building 2 and in its basement. The equipment of the cyclotron and that of the first section of the beam transport system is located on the first floor (see Fig. 1), the external injection system, the RF generator and the system for the beam transport to three targets are mounted in the basement. The main characteristics of the cyclotron are given in Table1.

The major unit of the cyclotron, an electromagnet, was designed using a model of the magnet of the synchrocyclotron operating in PNPI and further updated. Such a decision limited significantly the choice of engineering solutions when designing the cyclotron. In the process of commissioning works some structural deficiencies made at the design and manufacturing stages were detected and eliminated.

Figure 1: The C-80 cyclotron system.

Table 1: The main Characteristics of the Cyclotron

System, parameter	Characteristic, value
Type of accelerated particles	H^-
Type of extracted particles	H^+
Beam energy, variable, MeV	40-80
Beam current, μA.	100

TESTS AND RESALTS

In the process of preliminary tests of the cyclotron, appreciable losses of the beam intensity in the cyclotron central region were found out. Measurements of current performed with a three-electrode probe inside the cyclotron chamber demonstrated a noticeable beam shift relative to the median plane (see Fig. 2).

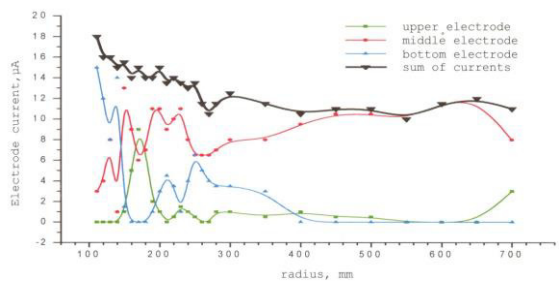

Figure 2: Results of current and beam position measurements in the process of acceleration.

ISBN 978-3-95450-181-6

To identify the reasons for such a behavior of he beam, additional magnetic measurements were carried out, which showed that the actual field in the central region exceeded significantly the calculated value and the field formed prior the vacuum chamber assembly. The main reason of such a difference is magnetic properties of non-stainless steel, which was used as a material for the vacuum chamber. Fig. 3a shows the isochronous magnetic field formed prior the vacuum chamber assembly, and Fig. 3b demonstrates the difference between the actual magnetic field and the isochronous magnetic field formed after the assembly.

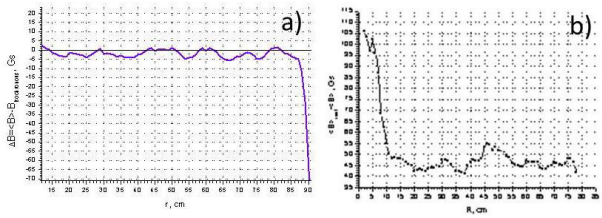

Figure 3: Difference between the actual magnetic field and calculated isochronous magnetic field: a) prior the vacuum chamber assembly; b) after the vacuum chamber assembly.

In addition, the analysis of the results obtained allowed us to suppose that large intensity losses result from the magnetic field radial component occurrence in the median plane [4]; unfortunately, there are no means to measure it correctly with account for the actual geometry of the cyclotron central region.

The use of additional valley coils did not made the situation better because of their remote location from the central axis of the electromagnet. To place the coils closer to the axis is impossible as the central region is limited in space, and sizes of the channel to input the beam from the external injection system should be kept unchanged. Therefore, the only method to reduce the intensity losses of the accelerated beam is an experimental choice of the position, size and shape of additional magnetic elements (plugs, additional rings, etc.) located in the cyclotron central region.

The resonance acceleration system consists of two symmetrical quarter-wave resonators and is placed completely inside the vacuum chamber. The system is equipped with a capacitor for frequency tuning, AFT trimmer and RF probe. The operating frequency of RF oscillations is 41.2 MHz, which corresponds to the 2nd harmonic of the ion revolution frequency. The normal value of the RF voltage amplitude is 60 kV. When manufacturing the vacuum chamber, a required rigidity of covers was not provided, and this resulted in smaller gap between them and deformation of resonator claddings in the process of pumping-down**.** This made necessary changing of vertical sizes of dee stems and resonator tanks with a subsequent radiotechnical tuning of the system. Under tests of the RF-system at a high power level, an appreciable heating of a ceramic unit of the trimmer stem took place and its illumination and subsequent destruction was observed, which resulted from a poor choice of the trimmer position in the tank of one of resonators. A new unit was designed, manufactured and installed, which allowed the trimmer location outside the resonator volume and thus its heating was excluded.

The RF power supply system consists of a stabilization and control module and RF-power amplifier. The stabilization and control module designed in the Efremov Institute provided reliable operation in the process of generating 41.2 MHz operating frequency, tuning and stabilization of the natural frequency of the resonance system and accelerating voltage amplitude.

The RF power amplifier designed and delivered by the «Coaxial Power Systems», Great Britain should provide an output power of 80 kW at a frequency of 41.2 MHz. From the results of initial tests of this equipment in operating modes, a pressing need for fundamental updating was identified. Six additional fans, each 0.25 kW, and additional partitions were installed; perforations were made in available partitions, which provided an optimal distribution of air flowsand requiredthermal mode. The insulators used by the CPS firm in the final stage were completely replaced because of their systematic breakdowns. We detected and eliminated the whole series of errors in circuitry which did not allow a necessary stability of the output signal to be obtained and prevented normal operation of the RF system:

- The high-voltage input of the final stage was re-designed, re-manufacturedand newly installed; the leading-in power cable was replaced for a shorter one.
- The circuit of transistor amplifiers' power supply was modified and one of power supply units was replaced for a more powerful.
- Voltage filters of the final stage anode were replaced.
- The fans' power supply circuit providing an effective cooling of heated electronic components after amplifier's turn-off was modified.
- The switch-on time of the power supply system of tube filaments was changed to improve their operation stability.
- The circuit-breaker for mains' power input was replaced.
- Inspection of cable inter-connections in the amplifier was conducted with subsequent replacement where necessary, etc.

Works on updating the RF power amplifier slowed down considerably the completion of commissioning works and demonstrated a pressing need for using our own efforts to design proper amplifiers for our cyclotrons.

The cyclotron is equipped with remotely-operated diagnostic probes intended to measure the beam current. In the process of commissioning works a high level of the RF noise was observed, which made difficult correct displaying of the beam current on the central monitor of the operator workstation. We managed to eliminate the observed noise by placing additional protection screens on probe electrodes.

ISBN 978-3-95450-181-6

A distributed automatic control system (ACS) is used. It consists of Mitsubishi and Fastwel IO controllers and computers, each being responsible for the control of one or several sub-systems of the cyclotron. The main unit of the control system is an industrial (host) computer, which inquires slave controllers and transmits the information acquired to computers of the operator's workstation; receives commands from the operator's workstation and performs their arbitration and distribution. Data exchange is realized via network interfaces. To ensure normal operation of the automated control system, there must be a reliable special grounding to provide electromagnetic compatibility of the cyclotron equipment. At the initial stage of works, this grounding did not meet the requirements, which resulted in failures of several controllers and made us to prolong the time for carrying out commissioning works.

The beam transport system of the C-80 cyclotron is intended to transport the extracted proton beam to final devices. Fig. 4 shows the schematic of the beam transport system layout and photos of its equipment.

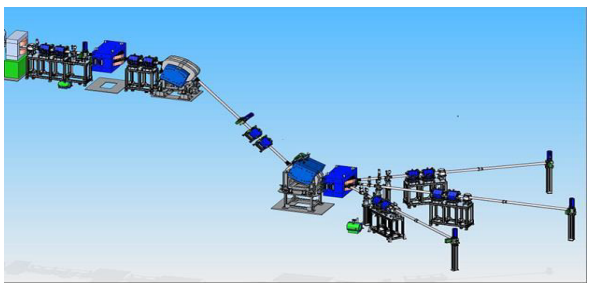

Figure 4: Layout of the beam transport system.

The first section of the beam transport system consisting of matching, correcting, switching and bending magnets, doublet of quadrupole lenses and beam diagnostics is located in the experimental hall. The second section of the beam transport system comprising bending, switching and correcting magnets, quadrupole lenses doublets and beam diagnostics is housed in the basement of the experimental hall. Because of large length of an inclined part between bending magnets in the experimental hall and in its basement, the quadrupole lenses doublet and diagnostic device are placed here.

In June, 2016 physical start-up of the C-80 cyclotron system was realized. Works were carried out in the pulse mode at low currents of the accelerated beam to exclude strong activation of the equipment to make possible safe continuation of works in the cyclotron vacuum chamber, with the components of the beam transport system, etc. When choosing the operating modes, available permissions granted by supervising authorities to carry out commissioning works were taken into account. At this stage, a beam of ~38 μA was obtained at the inner probe of the cyclotron; an extracted beam obtained at the first diagnostic device was ~28 μA. The beam transport practically without losses to the final diagnostic device of the beam transport system (~35 m) was demonstrated. Physical start-up was realized in the automated control mode under monitoring of all the systems of the cyclotron. Fig. 5 presents information on the status of all the cyclotron systems and their parameters in the process of performed works.

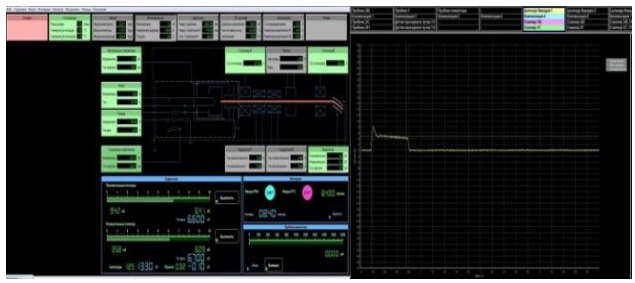

Figure 5: Information on the status of the cyclotron systems.

CONCLUTIONS

Our short-term plans include attaining of the design intensity of 100 μA by using reserves untapped so far:

- Completion of works on optimization of the electromagnetic field in the cyclotron central area.
- Increase of the injection current up to its specified value (from 900 up to 2500 μA).
- Use of the buncher potentialities with the anticipated effect of not less than two times higher current of the extracted beam; in works on the physical start-up, the buncher installed in the external injection system line was not used.

Efforts made towards these lines guarantee the attaining of design parameters of the C-80 cyclotron system and will offer opportunities for further increase of the accelerated proton beam intensity.

REFERENCES

[1] P.V. Bogdanov et al., "Major Technical Characteristics of the C-80 Cyclotron System", Problems of Atomic Science and Technologi, Series "Nuclear Physics Investigation" (58), V. 3(79), Kharkov, 2012, pp. 10-14.

[2] Yu.N. Gavrish et al. "The C-80 Cyclotron System. Technical Characteristics, Current Status, Progress and Prospects", RuPAC2012, Saint-Petersburg, September 2012, WEBOR01, pp. 106-108; http://www.JACoW.org

[3] S.A. Artamonov et al., "The Final Magnetic Field Distribution of the 80 MeV H-minus Isochronous Cyclotron at Gatchina", Proc. of XX Int. Conf. "Beam Dynamics and Optimization" (BDO-2014), Saint-Petersburg, June-July, 2014, pp. 18-19.

[4] G.A. Karamysheva et al., "Influence of the Magnetic Field Radial Component Imperfection on the Beam Dynamics in the Medical Cyclotron C235-V3", Particles and Nuclei, Letters, 2014, V.11, № 6 (190), p.1232.

ISBN 978-3-95450-181-6

THE CC1-3 CYCLOTRON SYSTEM. INSTALLATION AND TEST RESULTS

V.G. Mudrolyubov, A.V. Antonov, O.L. Veresov, Yu.N. Gavrish, A.V. Galchuck, S.V. Grigorenko, V.I. Grigoriev, M.A. Emeljanov, M.T. Kozienko, L.E. Korolev, A.N. Kuzhlev, A.G. Miroshnichenko, G.V. Muraviov, V.I. Nikishkin, V.I. Ponomarenko, K.E. Smirnov, Yu.I. Stogov, A.P. Strokach, S.S. Tsygankov, JSC "NIIEFA", St. Petersburg, Russia

Abstract

Works on the installation and adjustment of a unique CC1-3 cyclotron system in the Vinca Institute of Nuclear Sciences, Belgrade, Serbia have been finished. The cyclotron system will be used in the laboratory of nuclear-physical methods of the elemental analysis. A compact cyclotron and a beam-forming system produce an accelerated proton beam in a wide range of energies from 1 to 3 MeV with a spectrum width not more than 0.1%. Tests of the cyclotron system have been carried out at proton energies of 1.0, 1.7 and 3 MeV with the beam transport to the final diagnostic device.

PURPOSE

The CC1-3 cyclotron system has been developed and manufactured in the D.V. Efremov Scientific Research Institute of Electrophysical Apparatus. Unique parameters of accelerated proton beams (energy ranging from 1 up to 3 MeV, energy spectrum width of not more than 0.1 %) allow the use of this system as an effective technological equipment for analytical studies on the basis of nuclear-physical methods [1]. A distinctive feature of these express methods is a high sensitivity and comprehensive analysis (detection of small concentrations up to 10^{-5}–10^{-7} g/g). Possibility for non-contactnon-destructive analysis of substances or objects is of special interest.

The following fields were defined as the main applications of this system:

- X-ray method for the elemental analysis with a possible extraction of the proton beam into the atmosphere to irradiate samples for a detailed study of their surface layer.
- The method of analysis based on the Rutherford backscattering (RBS) to study both the elemental composition and the concentration profile of elements implanted into a sample.
- Spectral (Y–ray) analysis, the method based on recording of γ–radiation produced by nuclear reactions (P, X, γ).
- In future, potentialities of the system can be extended by developing a new equipment, which will make possible the realization of the method for the target potential modulation to study the concentration profile of implanted elements by recording the secondary Y-radiation produced by nuclear reactions under irradiation with an accelerated proton beam.

BRIEF DESCRIPTION

The cyclotron system consists of a compact cyclotron and a system for the beam forming and transport to remote analytical chambers including the beam extraction into the atmosphere as well as systems for power supply, automated control, vacuum pumping and water cooling [2].

The compact cyclotron provides acceleration of negative hydrogen ions to the final energy in the range of 1-3 MeV and extraction of a proton beam to the beam transport system by stripping of two electrons on a thin carbon foil. The cyclotron comprises an electromagnet with a vacuum chamber, resonance system, diagnostic devices (probes) and stripping device, external injection system and RF generator.

The major part of the cyclotron is a four-sector shielding-type electromagnet 1400 mm in diameter with a horizontally located median plane (see Fig. 1). The pole diameter is 600 mm; the average induction of 0.98 T was chosen to provide an optimal separation of orbits to minimize the energy spread. To make easy maintenance/repair of the equipment located inside the vacuum chamber, the upper beam of the magnet can be moved upward up to 500 mm.

Figure 1: Electromagnet of the CC1-3 cyclotron.

The resonance accelerating system is located completely inside the vacuum chamber of the electromagnet (see Fig. 2) and is equipped with an inductive RF power in-feeding device, AFT trimmer and RF-probe. The operating frequency is 59.7 MHz and it corresponds to the 4th harmonic of the hydrogen ions revolution frequency.

ISBN 978-3-95450-181-6

The RF generator consists of a control and stabilization module and RF-power amplifier, in which the 3CW5000A7 generator triode is used. The main parameters of the RF generator are as follows: operating frequency-59.7 MHz, frequency stability-10^{-7}, phase stability±0.5°, output power-7 kW and accelerating voltage amplitude stability-10^{-3}. The RF power is transmitted to the resonance system through a flexible coaxial feeder.

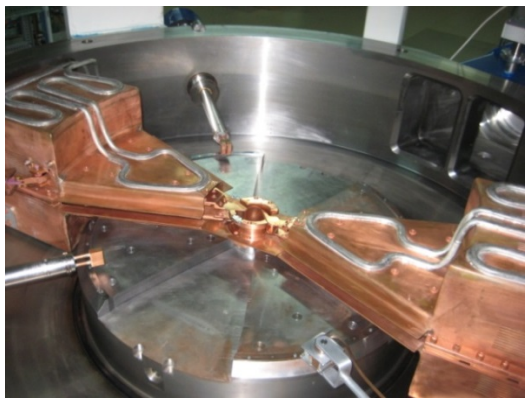

Figure 2: Resonance system.

The external injection system is located under the electromagnet (see Fig. 3). It consists of a source of negative ions with an ion-optical system for the beam additional acceleration and focusing, differential pumping chamber, two electrostatic lenses, spiral inflector and ancillary equipment.

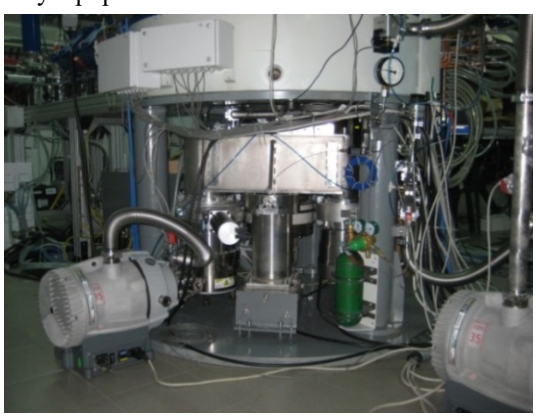

Figure 3: External injection system.

The cyclotron is equipped with remotely-operated probes, which ensures radial travel of the probes to control the beam in the acceleration area. The stripping device defining the energy of the extracted proton beam is also equipped with a drive. This allows quick installation of one of three charge-exchange foils to the working position and, in addition, variation of the foil radius and angle of location. Thickness of the charge-exchange foil should be optimized to minimize energy losses of hydrogen ions and to provide a sufficient mechanical strength. On the basis of experimental studies performed by us, thickness of a carbon film was chosen to be 0.15 mg⁄cm^2. Film samples were tested on an operating cyclotron at energies ranging from 1-3 MeV.

The beam-forming system is designed to meet the requirements for the proton beam energy spectrum, which are not typical for cyclotrons. The major part of the system is an analyzer, which consists of an analyzing magnet (see Fig. 4) with a bending angle of 270° and a bending radius of 600 mm and two collimators installed at the inlet and outlet of the analyzing magnet vacuum chamber.

Figure 4: Analyzing magnet.

A possibility to choose one of three fixed dimensions of collimator slits (without vacuum deterioration) is provided (0.5, 1 and 2 mm).The energy resolution behind the output slit is shown in Table 1.

Table 1: Energy Resolution of Magnetic Analyzer

Input slit total width, mm	Energy spread, ΔE/E, %	
	Design field index n=0.8317	Measured field index n=0.8324
2.0	0.0561	0.05587
1.0	0.02805	0.02793
0.5	0.014025	0.01397

The beam-transport system includes matching, switching and correcting magnets, a doublet of quadupole lenses and diagnostics, in particular, the Faraday cup and beam profile monitors.

The power supply system consists of a power switchboard, power supply racks for the external injection system, electromagnets and lenses as well as power supply units for step motors and a mechanism moving upward the upper beam of the main magnet.

The automatic control system is of distributed architecture. It consists of Mitsubishi and Fastwel IO controllers and computers, each being responsible for the control of one or several sub-systems of the cyclotron. The major unit of the control system is an industrial (host) computer, which inquires slave controllers and transmits the information acquired to personnel computers of the operator's workstation; receives commands from the operator's workstation and performs their arbitration and

ISBN 978-3-95450-181-6

distribution. Fig. 5 shows as an example the status of the vacuum system units displayed on the operator's monitor.

The vacuum system contains a cryopump, four turbomolecular pumps, mechanical dry pumps, gate valves, valves, leak valves and pressure gages to measure low and high vacuum.

The equipment of the cyclotron is cooled with distilled water circulating in the water-cooling loop of the cyclotron building. Four water distribution boards are used to distribute cooling water to remove the heat released by the heat-loaded components and units of the cyclotron, to control pressure and stabilize water flow rates.

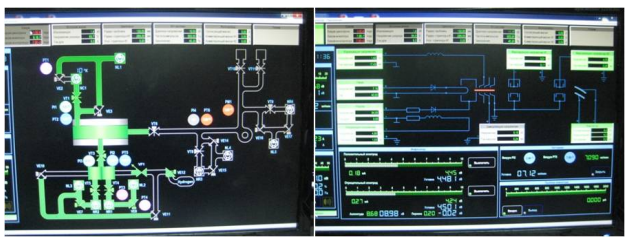

Figure 5: Status of the vacuum system and external injection system units displayed on the operator' s monitor.

In 2015 the cyclotron system was delivered to the Vinca Institute of Nuclear Sciences, Belgrade, Serbia. Installation of the equipment and separate tests of all systems have been carried out. General view of the system is given in Fig. 6.

TEST RESULTS

Tests of the whole system with the beam on were carried out for boundary values of the design range of proton energies (1 and 3 MeV) and an intermediate value of 1.7 MeV. Acceleration of negative hydrogen ions, proton beams extraction from the cyclotron and their transport through the beam-forming line, including the analyzer, up to the Faraday cup located behind the switching magnet have been implemented. The beam current of 104 nA was obtained at a maximum proton energy and collimator slits widths of 2 mm; current of 60 nA was fixed at minimum and intermediate energies, which correspond to the design value (10-100 nA). At present, the cyclotron system is ready for operation.

Figure 6: The CC1-3 cyclotron with the beam-forming line.

REFERENCES

[1] V.G. Mudrolyubov et al., "The CC1-3 Cyclotron System", RuPAC2012, St. Petersburg, September 2012, FRACH03, pp.191-193; http://www.JACoW.org

[2] O.L. Veresov et al., "The CC1-3 Cyclotron System for Non-Destruction Nuclear-Physical Methods of the Element Analysis", Problems of Atomic Science and Technology, Series "Nuclear Physics Investigation" (61), V. 6(88), Kharkov, 2013, pp. 13-15.

ISBN 978-3-95450-181-6

PROGRESS IN CW MODE ELECTRON RESONANCE ACCELERATOR BETA-8 DEVELOPMENT

A.V. Telnov*, V.S. Gordeev, N.V. Zavialov, A.M. Opekunov, S.M. Pridchin, S.A. Putevskoy, M.L. Smetanin, I.V. Shorikov, RFNC-VNIIEF, Sarov, Russia
V.S. Arbuzov, V.N. Volkov, I.A. Zapryagaev, E.A. Kenzhebulatov, V.V. Kozlov, E.V. Kozyrev, E.I. Kolobanov, A.A. Kondakov, S.A. Krutikhin, G.Ya. Kurkin, S.V. Motygin, V.K. Ovchar, V.N. Osipov, V.V. Repkov, S.S. Serednyakov, S.V. Tararyshkin, A.G. Tribendis, V.V. Tarnetskiy, K.N. Chernov, BINP SB RAS, Novosibirsk, Russia
O.K. Belyaev, S.V. Ivanov, V.G. Kudryavtsev, A.I. Lepin, E.V. Mazurov, IHEP, Protvino, Russia

Abstract

The progress in mode high-power resonance accelerator BETA-8 is presented. The accelerator operates in the mode of electron beam continuous generation and is aimed at performing radiation researches. Basic parameters of the accelerator are as follows: electron beam variable output energy 1.5 – 7.5 MeV, beam average power up to 300 kW, operating resonance frequency ≈ 100 MHz.

There were developed, produced and tested basic components of the accelerator [1]. The HF characteristics of coaxial cavity assembled with a unit of HF power input (UPI) at a low RF power level were measured. Three modules of RF generator the output power of each of them being 180 kW and the device of their power summation were tested. HF injector with electron energy up to 100keV was tested. There was developed the pattern of accelerated electrons transport making it possible to fulfill up to five successive passes through the accelerating cavity. Operative embodiments of deflecting electromagnets were designed and produced.

INTRODUCTION

Electron accelerator BETA-8 is developed to implement radiation researches and radiation tests of large-size objects in a wide energy range of accelerated electrons. It will be possible to study and elaborate with its aid the technological processes requiring high power and high values of absorbed dose of electron radiation and bremsstrahlung.

The accelerator design parameters are as follows:

- Range of accelerated electron output energy – 1.5 ÷ 7.5 MeV;
- Maximum average power of the beam– 300 kW;
- Operating resonance frequency – 100 MHz;
- Modes of operation – continuous mode and pulse-periodic regime.

TESTING OF ACCELERATOR BETA-8 SYSTEMS OPERATION

At the first stage there were performed all preparative activities in testing the systems of the accelerator which is characterized by the accelerating cavity power supply from one of the three HF generator modules. Electrons acceleration is fulfilled in a half-wave coaxial cavity (Fig.1) similar to that described in paper [2].

To the cavity there are connected the required technological systems: vacuumization system, water- and air-cooling system that make it possible to train the standard mode of operation. The elements of the channel of HF power transfer – coaxial HF feeder and unit of HF power input (UPI) – are used to feed the cavity from one generator module with the average power up to 180kW. At this level of HF supply power there can be generated a beam of accelerated electrons with the average power up to 15 kW and energy up to 7.5 MeV what is enough for experimental verification of the possibility of achieving basic design objectives.

Figure 1: Accelerator BETA-8: 1 – accelerating cavity; 2 – exhaust cart.

*telnov@expd.vniief.ru

ISBN 978-3-95450-181-6

System of the Accelerator HF Power Supply

The system of HF power supply is designed to get continuous HF power of 540 kW as well as to synchronize its operation with HF injector. HF generator represents three single type generator modules [3] and HF power combiner (Fig. 2). The generator module is a multi-stage amplifier of HF power its preliminary stage being produced on tetrode GU-92A while the output one – on tetrode GU-101A.

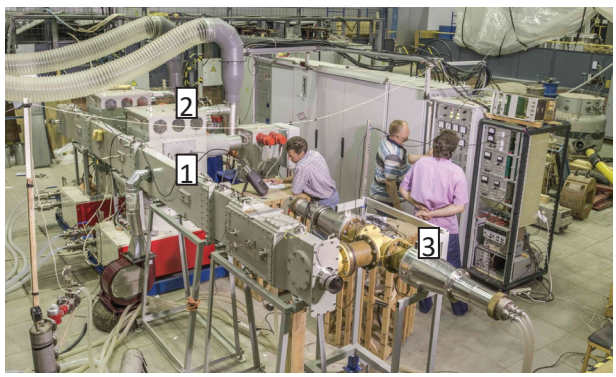

Figure 2: System of HF power supply: 1 – HF power combiner; 2 – generator module; 3 – matched load.

There was performed a matched load test for the generators. At operating on resonance frequency the measured power constituted 180 kW.

UPI and Channel of HF Power Transfer

The developed unit of HF power input (UPI) makes it possible to match HF power transfer from the generator to the accelerating cavity through HF channel power transfer. UPI can operate on the frequencies in the range from 98 to 102 MHz the interface level being no worse than 1.3. The maximal HF power transferred through UPI in the modes of pulsed and continuous generation is estimated to be 600 kW. The external view of UPI is presented in Fig. 3.

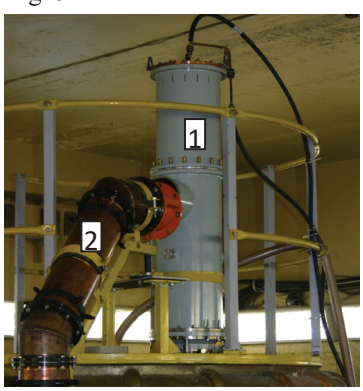

Figure 3: External view of UPI: 1 – UPI; 2 – channel of HF power transfer.

The channel of HF power transfer is developed on the base of air-filled coaxial waveguide the wave resistance being 50 Ω.

HF Injector

The grid controlled thermo-cathode HF gun based on a quarter wave coaxial cavity operating on the frequency of 100 MHz (Fig. 4) is a basic unit of the injector.

The HF injector [4] accelerates electrons up to the required energies (50 ÷ 100) keV with the average current in the continuous mode up to 40 мА and regulated bunch repetition rate (0.01–100) MHz. Thereafter the electron beam is additionally formed in the transport channel with the aid of magnetic quadrupoles and then achieves the accelerating field of the cavity.

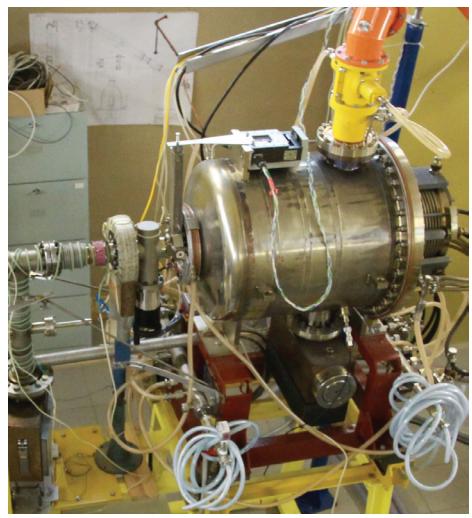

Figure 4: HF injector of electrons.

Accelerator Technological Systems

There was tested the system of accelerator cavity vaccuumization – the achieved in the system vacuum constituted 10^{-5} Pa. Two similar exhaust carts connected to the accelerator cavity make it also possible to evacuate vacuum channels of beam transport and extraction.

The system of water cooling and thermal stabilization is designed to remove heat power excess up to 400 kW from the accelerator (cavity, HF generator etc.) and to maintain the preset temperature with the accuracy up to ±1°C.

For remote control and technological process inspection there was developed the automated control system and the system of accelerator control on the base of industrial computer.

DEVELOPMENT OF A SYSTEM OF ELECTRON BEAM MAGNETIC GUIDANCE IN ACCELERATOR BETA-8

The acceleration of electrons was implemented at multiple pass of the cavity through a medial plane [4]. The cavity is computed so that at HF power supply there is formed in it the accelerating electric field increasing the energy of electrons by ≈ 1.5 MeV per one pass. The return of the beam to the cavity is provided by deflecting magnets arranged outside the cavity body.

ISBN 978-3-95450-181-6

Fig. 5 demonstrates the computed trajectory of the beam in the cavity and magnetic system of transport for each of the operating energy values. A 3D model of accelerating cavity and the system of beam magnetic guidance is available in Fig. 6.

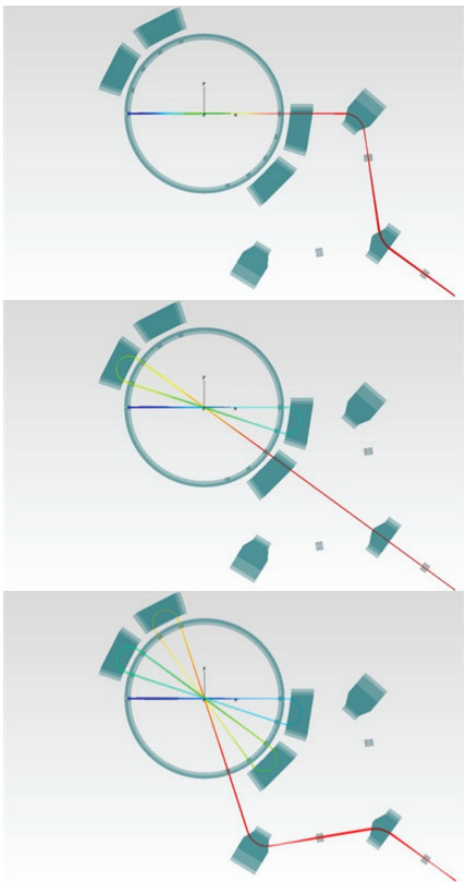

Figure 5: Three versions of electron beam computed trajectories for the following output energies: (a) – 1.5 MeV; (b) – 4.5 MeV; (c) – 7.5 MeV

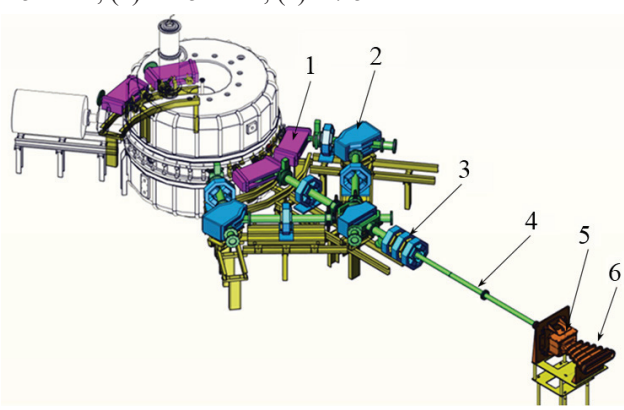

Figure 6: System of beam magnetic guidance:1 – magnets of (responsible for) beam recycling; 2 – beam transport magnets; 3 – quadrupole lenses; 4 – vacuum channel of beam guidance; 5 – scanning magnet; 6 – vacuum faucet.

At guiding a high-power beam the losses of electrons in the walls of the cavity and vacuum chambers are being constantly controlled by the automated management system with the aid of thermocouple sensors located in most critical points. The undertaken numerical three-dimensional calculations demonstrated that at beam diameter equal to (10 – 15) mm the transverse emittance should not exceed 50 mm·mrad, while the width of spectrum is – 0.1 MeV. Having provided these conditions one can implement five-fold acceleration of electron beam and its extraction to the irradiation area.

CONCLUSION

There is described the stage of creating accelerator BETA-8 on which at decreased values of HF supply power (up to 180 kW) and electron beam there should be experimentally elaborated key physical principles of the accelerator operation. At this stage there were implemented the installation and testing of basic accelerator assemblies: accelerating cavity with UPI, one module of HF generator and HF injector. The required technological systems of the accelerator were also developed and tested so that stable design parameters are achieved at the operation with the automated system of management and control.

The developed system of electron beam magnetic guidance in accelerator BETA-8 is described. There are described as well the computed beam trajectories for each of the operating energy values: 1.5, 4.5 and 7.5 MeV, obtained as a result of three-dimensional simulation of electron dynamics in the accelerator.

After this stage is completed the BETA-8 accelerator can be taken to design output parameters through the increase of HF supply power up to the expected level of 540 kW.

REFERENCES

[1] S.A. Zhelezov et al., "Design of continuous electron resonance accelerator", in Proc. VIII Int. Conf. Khariton's topical scientific readings. High energy density physics, Sarov, Russia, 2006, pp. 122–129.

[2] J. Pottier, "A new type of RF electron accelerator: the Rhodotron", Nucl. Instr. Meth.,– vol. B40/41. pp. 943-945.

[3] V.S. Arbuzov et al., "HF generator for resonance accelerator of electrons on the base of coaxial cavity", in Proc. XII Int. Conf. Khariton's topical scientific readings. High energy density physics, Sarov, Russia, 2010, pp. 28–32.

[4] V.N. Volkov et al., "CW 100 keV electron RF injector for 40 mA average beam current", in Proc. of XXIV Russian Particle Accelerator Conference (RUPAC'14), 2014, pp. 309–311.

ISBN 978-3-95450-181-6

HF STRUCTURE OF BETA-8 ELECTRON RESONANCE ACCELERATOR

M.L. Smetanin, V.S. Gordeev, N.V. Zavyalov, S.A. Putevskoy, A.V. Tel'nov, I.V. Shorikov, A.N. Shein, RFNC-VNIIEF, Sarov, Russia
O.K. Belyaev, S.V. Ivanov, V.G. Kudryavtsev, A.N. Lepin, E.V.Mazurov, National Research Center "Kurchatov Institute" FSUE SSC RF – IHEP, Protvino, Moscow region, Russia

Abstract

RFNC-VNIIEF is developing a powerful resonance electron accelerator BETA-8, operating in the mode of continuous wave generation. The accelerator is developed on the basis of half-wave coaxial cavity, excited on the wave of T1 type.

The paper presents calculation results of accelerating cavity with operating frequency 100 MHz, as well as an inductive unit of HF power input (UPI) meant for transfer of continuous HF signal on the operating frequency with an average power level 600 kW. Calculation results are proved by measurements of HF characteristics of the cavity assembled together with UPI and a coupling wave guide.

The location of an indicator loop–pickup, mounted in a coupling wave guide is computed. The given loop–pickup is meant for operation in a frequency feedback circuit for the HF generator.

INTRODUCTION

Resonance electron accelerator BETA-8 (Figure 1) is being developed in RFNC-VNIIEF. Development of an accelerating facility with average electron beam power up to 300 kW with a control range of accelerated electron energies - from 1 up to 8 MeV and meant for study of radiation resistance and radiation tests of large-scale objects is based upon requirements, specified earlier [1, 2].

Figure 1: General accelerator view.

Below are reported results of three-dimensional electrodynamic calculation of basic components of accelerator HF structure as well as calculation methods of its radioengineering tuning.

ACCELERATING CAVITY, UPI AND FEEDBACK WITH GENERATOR

A coaxial cavity, a transmitting feeder – coaxial wave guide and UPI are basic elements of BETA-8 accelerating HF structure. Estimated electric field distribution inside the cavity, in the electron acceleration region is given in fig. 2.

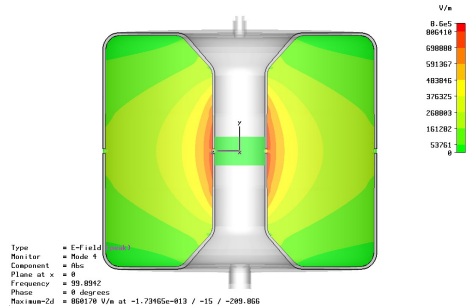

Figure 2: Waveform of electric field strength in the coaxial cavity median longitudinal plane.

The basic cavity's overall dimensions are: 1) inner conductor radius – 210 mm, 2) outer conductor radius – 1040 mm, 3) cavity height (longitudinal size) – 1626 mm. Electrons are accelerated in the cavity median transverse plane. The basic estimated electrodynamic characteristics (EDC) of the coaxial cavity comprise: resonance frequency f_0 = 99.9 MHz; kinetic energy gain per one pass We = 1.5 MeV; transit time factor T = 0.777; loss power within the cavity walls P_{loss} = 165.2 kW; resonator quality factor Q_0 = 56088; effective shunt impedance $Z_{sh.ef}$ = 15.25 MOhm.

At the first stage to supply the cavity, a single module of HF generator is used. At the matching mode it generates a signal with average power 180 kW and frequency ≈100 MHz [3].

UPI, developed in SSC RF IHEP (Protvino, Russia) is meant for operation as a connector, allowing connection of the transmitting feeder with accelerating coaxial cavity.

The main specification of UPI involves the following: coupling with the cavity – inductive; device input - coaxial, with wave resistance 50 Ohm; sizes of entrance air-filled coaxial feeder - Ø160/70 mm; UPI operates at any frequency in the range 98 - 102 MHz; operating frequency – 100 MHz; transmitting HF power in the mode of pulse and continuous generation – up to 600 kW; UPI provides an interface level of the feeder with a cavity with a voltage standing-wave ratio (VSWR) ≤ 1,2 in the frequency range 98-102 MHz.

ISBN 978-3-95450-181-6

The basic element of UPI is an inductive loop, required for magnetic coupling of the transmitting feeder and the cavity. The loop is mounted on the cavity end wall in the plane, perpendicular to magnetic field. Fig. 3 shows the place of the loop mount in the cavity.

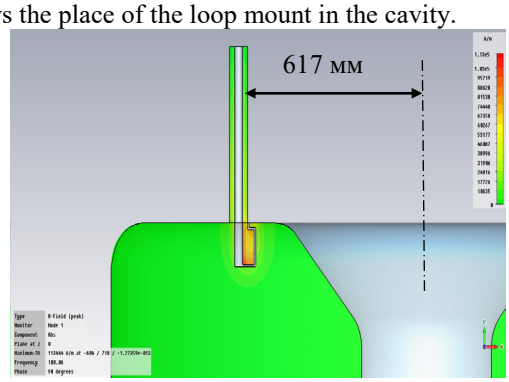

Figure 3: Place of the loop mount in the resonator.

To match the resonator input impedance and the input coaxial, a circuit with quarter-wave transformer and a parallel closed stub is chosen. Figure 4 presents equivalent UPI circuit.

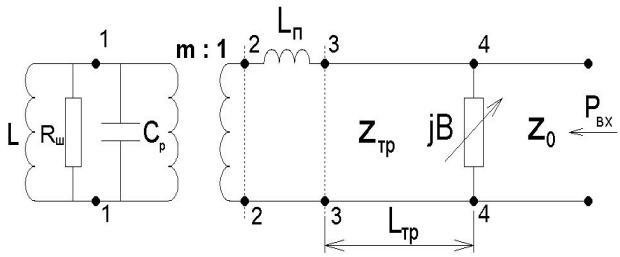

Figure 4: Equivalent UPI circuit.

The generator feeder, a nondissipative matching stub and an output line form a coaxial tee. For reasons of design, accepted is the following arrangement: two tee arms (a stub and a quarter-wave transformer) have a common axis, and HF signal is supplied from the arm side, perpendicular to this axis, (figure 5).

Figure 6 shows UPI, mounted on the accelerating cavity with a connected coaxial feeder.

VSWR measured experimentally on the input of the system, consisting of a transmitting feeder, UPI and an accelerating cavity is given in fig. 7. At resonance frequency (99.857MHz) VSWR=1.05.

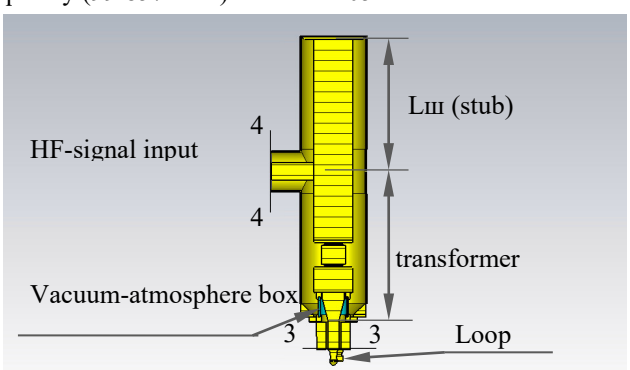

Figure 5: UPI arrangement.

Figure 6: Feeder, UPI and cavity ready-fitted.

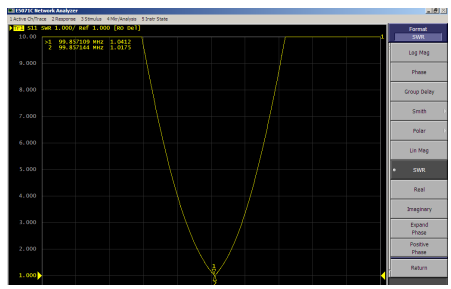

Figure 7: Experimentally measured VSWR at the UPI input assembled together with the cavity.

When switching on the HF generator with the accelerating coaxial cavity, two circuits of generator-to-cavity feedback should be put into operation. The first circuit – the frequency feedback one, allows tuning of the HF generator operating frequency to the resonance frequency of the coaxial accelerating cavity. The basic element of the given circuit is a magnetic coupling indicator loop-pickup, mounted in the transmitting feeder, connecting the HF generator and UPI, at the point of voltage node origin providing the possible mismatch.

The place of indicator loop mount in the transmitting feeder was calculated. Below are given results of three-dimension electrodynamic calculation of HF structure (Figure 8), consisting of the transmitting feeder, UPI and cavity.

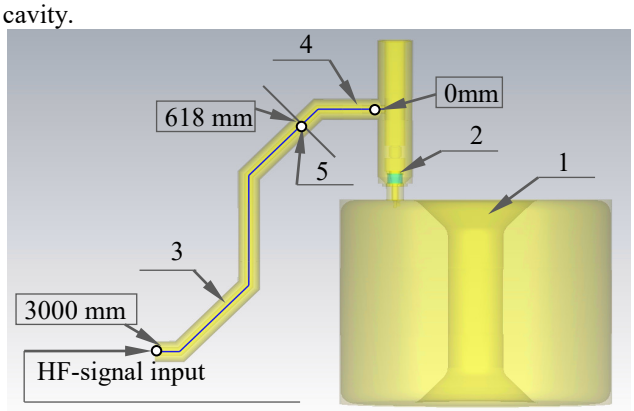

Figure 8: HF-structure design model. 1-accelerating cavity; 2- UPI; 3 – feeder; 4 – projecting line; 5 – cross-section for indicator loop mount.

ISBN 978-3-95450-181-6

Figure 9 presents distribution of electric strength in the transmitting feeder in cases of match and mismatch. In the case of mismatch the standing-wave is formed in the feeder, the first voltage node originates at a distance of 618 mm from zero on the projecting line.

Thus, there is specified a place, where it is possible to mount the indicator loop-sensor of a frequency circuit of HF generator feedback.

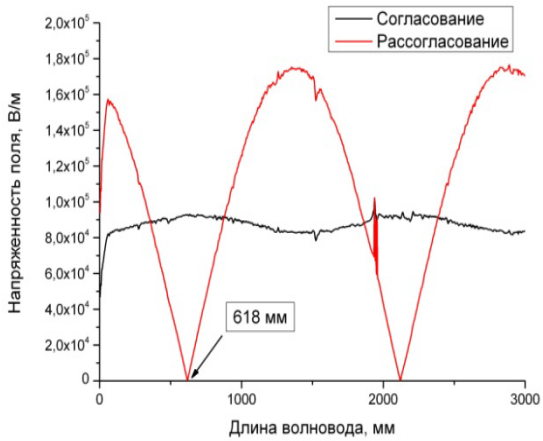

Figure 9: Calculated dependencies of electric field strength along the feeder axis at matching and mismatching.

To primarily try-out modes of functioning the feeding HF generator module (with average power up to 180 kW) and accelerating complex technology systems, there have been calculated, designed and tested a matched load (Figure 10). The load involves two resistors C2-25 (50 Ohm, 100 kW). The structure matching provides a quarter-wave transformer, experimentally measured VSWR at the input is 1.15 on the operating frequency 100 MHz.

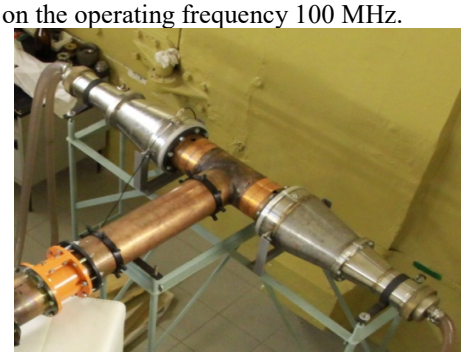

Figure 10: Matched load.

CONCLUSION

The HF-structure of BETA-8 resonance electron accelerator is represented.

The basic structure element is an accelerating coaxial half-wave cavity with operating frequency 100 MHz. At HF supply with average power more than 165 kW it allows obtaining the kinetic energy gain of 1.5 MeV accelerated electrons per a single full pass in its median transverse plane. The cavity was calculated, designed, manufactured and tested. Its experimentally obtained EDC with satisfactory precision coincides with calculated ones.

To match the resonator with the HF feeder, UPI was calculated, designed and manufactured. This unit allows practically with no power losses (with VSWR =1.05 on the resonance frequency) HF-signal transfer into the accelerating cavity.

Three-dimension electrodynamic calculations were carried out. They allowed determination of the location of the indicator loop, operating in the frequency feedback circuit, on the transmitting feeder. Such calculations significantly simplified determining of its location in practice.

There was calculated, designed, manufactured and tested the matched load, allowing tests of HF generator module and accelerator technological system at high average power up to 200 kW.

REFERENCES

[1] S.A. Zhelezov, N.V. Zavyalov, et al. Design of an electron continuous resonance accelerator.// VIII Khariton lectures on the problems of high-dense energy physics. Report Collection. 2006. Sarov – P.122-128.

[2] V. Zavyalov, S.A. Zhelezov, et. al. A CW Electron Accelerator. The Planned Design and Electro-physical Characteristics.// Problems of Atomic Science and Technology. 2006 №2 Series: Nuclear Physics Investigations (46), – P.8-10.

[3] Gladyshev E.N., Gordeev V.S. et al. Status of works on development project for continuous electron resonance accelerator BETA-8// Proceedings of RFNC-VNIIEF. Ser. Science and Research Edition. 2015. Issue 20. P. 1. P. 184–193.

ISBN 978-3-95450-181-6

DEVELOPMENT OF THE INR LINEAR ACCELERATOR DTL RF SYSTEM

A.V.Feschenko, A.I.Kvasha, V.L.Serov
Institute for Nuclear Research, RAS, Moscow

Abstract

Regular INR DTL RF system operation has started in 1992. By this point three new vacuum tubes, designed especially for INR linear accelerator, have been manufactured at "Svetlana" association in the amount sufficient for RF system operation for 20 years. Among them were two vacuum tubes for final and intermediate RF power amplifiers, GI-54A and GI-51A correspondingly, as well as one vacuum tube for powerful anode modulator – GMI-44A. In the late '80s the manufacture of these vacuum tubes was terminated and in 1990 development of new vacuum tube for RF output power amplifier instead of GI-54A has started. The new vacuum tube GI-71A with the output pulse RF power up to 3 MW, plate power dissipation up to 120 kW and power gain about 10 became simpler and less expensive in comparison with GI-54A. The transition to new vacuum tubes started in 1999 and completed in 2014. Successful test of GI-57A for preliminary RF amplifier was fulfilled in 2008 and opened the possibility to replace GI-51A. As for the modulator tube GMI-44A no vacuum tube with the required parameters produced in Russian Federation was found and a decision to use the RF power amplifier tube GI-71A instead of the modulator one has been done.

Below some problems connected with the vacuum tubes replacement and the main results of twenty years DTL RF system operation are described.

INTRODUCTION

Brief reference. *INR linear accelerator is in regular operation since 1993. The accelerator consists of two parts. The low energy part operates at the frequency of 198.2 MHz and includes RFQ, five Alvarez tanks and seven RF amplifier channels including a spare one. The second part operates at 991MHz and includes 28 disk and washer cavities. At present, the accelerator operates with beam pulse length up to 200 μs, repletion rate up to 50Hz and beam pulse current up to 15 mA.*

Each RF channel includes the following units:

- One solid state and four vacuum tube amplifiers;
- Vacuum tube plate modulator (AM) for the first and the second vacuum tube RF amplifiers;
- Powerful vacuum tube plate modulator (PAM) for the two last RF amplifiers;
- Coaxial line between the final RF power amplifier (FPA) and Alvarez tank with the switch enabling to connect any tank with the spare channel instead of a faulty one.
- High voltage power supply for powerful modulator including artificial forming line (AFL) with the impedance of 24 Ohm.

The simplified structure of RF channel is given in fig.1.

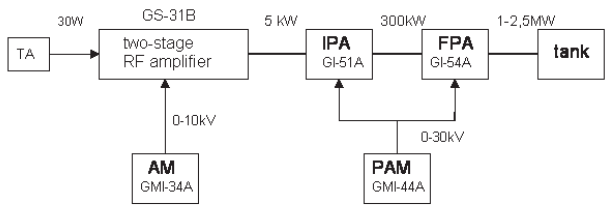

Figure1: Simplified structure of the DTL RF channel (TA – solid state RF amplifier, IPA - intermediate power RF amplifier, FPA - final RF power amplifier).

The pictures of vacuum tube RF amplifiers are shown in figures 2÷4.

Figure 2: Two-stage RF amplifier.

Except for the tubes GS-31B and GMI-34A developed earlier and being manufactured for a long time the following vacuum tubes have been specially developed for INR accelerator:

- Modulator triode GMI-44A with magnetic focusing. Due to the magnetic field the plate-grid characteristics are similar to those of tetrode with small grid current

ISBN 978-3-95450-181-6

and small plate-cathode voltage (*Uak*) of the open vacuum tube. These features enable to decrease the pre-modulator pulse power and plate voltage. Emission current of the tube is up to 500A, plate voltage - up to 60kV and plate power dissipation – up to 150 kW.

- Powerful pulse triode GI-54A for RF final power amplifier (FPA) with the output pulse power up to 4MW and pulse plate voltage up to 40kV. Average power dissipated at the plate is up to 400kW.

Figure 3: Intermediate power RF amplifier.

- Pulse tetrode GI-51A for RF intermediate power amplifier (IPA) with output pulse power up to 400kW and pulse plate voltage up to 40 kV. Average power dissipated at the vacuum tube plate is up to 30kW.

Unfortunately the above listed vacuum tubes didn't find application in other Russian accelerators. This circumstance has predetermined the termination of tube production and hence the need to rework the DTL RF system. However, the amount of tubes manufactured in 70s and 80s appeared to be sufficient for twenty years accelerator operation with 2-3 thousand hours annual accelerator run duration.

FINAL POWER AMPLIFIER

The tubes GI-54A appeared to be too expensive especially in case of small scale production (real life time of the tubes was from 5 to 6 thousand hours thus giving the annual need of only 2-3 units).

In early 90s a decision to develop a new tube with lower cost at the expense of acceptable decrease of several parameters was jointly made by INR and JSC "SED-SPb" (former "Svetlana" association). The requirement was to keep electrical and mechanical parameters of the new tube as close as possible to those of the old one with the aim to diminish reworking of the existing equipment of FPA especially the anode-grid cavity.

Figure 4: Final RF power amplifier.

Initially a pirographite grid having important advantages over the metallic one [1] was planned to be used. Unfortunately it was abandoned due to too big expenses for maintenance of pirographite grids production which is of special importance for small market of new tubes. Due to possible deformation of the cathode and the grid the gap between them influencing the gain cannot be smaller than 2-3 mm. That is why even in spite of large cathode surface the gain of new GI-71A tube appeared to be only 10 while for GI-54A this parameter was 25.

The first DTL RF channel has been reworked for the use of new tube in 1999 and the first GI-71A tube started to be used in regular accelerator runs. The process of tubes replacement lasted till 2014 when the stock of GI-54A became completely exhausted.

The biggest modifications were related with cathode-grid cavity and filament circuits. The plate voltage had to be increased by several kV as well to compensate gain reducing.

Generally there are two basic configurations of the RF amplifiers corresponding to one or two-sided arrangement of the anode-grid and cathode-grid cavities with respect to the tube (fig. 5). The one sided configuration is more

ISBN 978-3-95450-181-6

compact and easier to tune but requires special blocking capacitor to supply high voltage to the plate. The RF discharge in the grid-plate cavity does not result in high voltage breakdown between the plate to the ground and hence does not affect the HV modulator.

It is still since times of the proton linear accelerators I-2 (ITEP) and I-100 (IHEP) the second design of FPA has been chosen as the primary one (see fig.5, right). In the last case FPA design is simpler and allows increasing a gap between the inner and outer tubes of coaxial anode-grid cavity. In turn, increasing of the gap reduces the risk of RF breakdowns in plate-grid cavity. Gap size limit is determines by the wave length of the nearest high order mode H_{11} with critical wave length $\lambda_k \sim \pi (R + r)$, where R and r are outer and inner radiuses of the anode-grid coaxial cavity. Supposing equality of wave lengths of H_{11} and operation modes (λ_0) it is easy to determine possible value of the gap (g) between inner and outer tubes of coaxial cavity:

$$g = \frac{\lambda_0}{\pi} - d$$

In the last expression *d* is diameter of inner tube. Thus, as follows from fig.5, two-sided arrangement of the plate-grid cavity really decreases a danger of RF breakdowns due smaller value of *d*. The vacuum tube installation is plate down. High voltage pulse at vacuum tube plate enters at the inner tube in RF electric field node.

Disadvantage of the chosen FPA design is high voltage at the inner tube of coaxial plate-grid cavity. As the result, RF discharge in the grid-plate cavity can result in high voltage breakdown between the coaxial cavity inner tube and the ground and hence affect the HV modulator.

That is why excess pressure was foreseen in the anode-grid cavity, because increasing of outer diameter of the coaxial cavity is impossible due risk of H_{11} mode excitation.

Experience of operation with excessive pressure [3] has shown a possibility to get a pulse power at the FPA output near 4 MW in matched load. But a lack of qualified staff and the situation in the early 90s didn't allow realizing the excessive pressure in all RF channel.

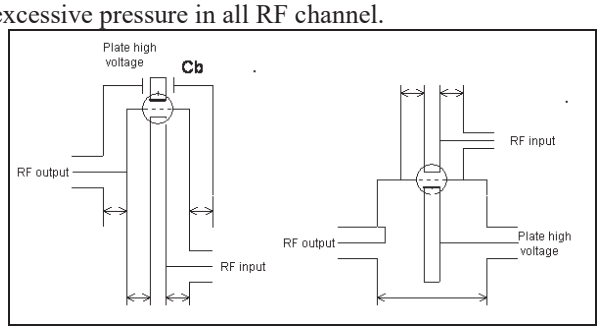

Figure 5: Drawings of two main decisions of FPA design.

So in INR FPA from the very beginning the decision was made to refuse from the excess pressure despite of possibilities, laying in design (see fig.4). At that, the procedure of vacuum tube exchange is simplified (In LANSCE FPA with excess pressure it is required about 16 hours to exchange the vacuum tube [4]), but the danger of breakdowns in the anode-grid cavity, surely, grows.

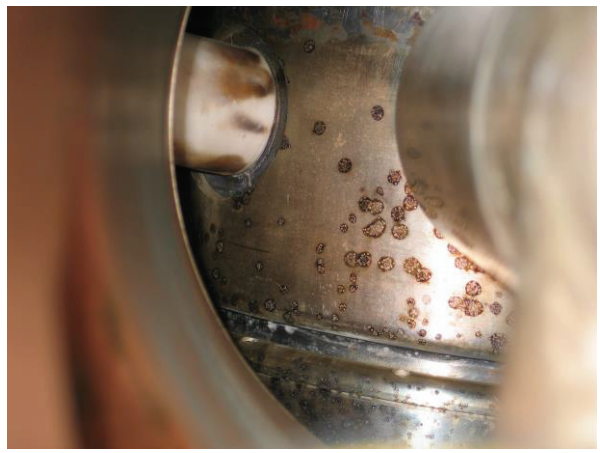

Figure 6: Traces of breakdowns in FPA plate-grid cavity.

At fig.6 picture of the plate-grid cavity inner tube in the region of the loop is shown. Shot has been made in FPA of the first RF channel that operates the longest. Breakdowns in the FPA plate-grid cavity are payment for operation without excessive pressure. At that, if sparking quantity in vacuum tube decreases in process of aging, breakdowns in the cavity, on the contrary, can grow due, for example, pollution of inner surface. The problem can be solved by means of the series crowbar system only [2].

CROWBAR

The series crowbar interrupts beam acceleration for 1-3 second, whereas the traditional crowbar, that entirely discharges the artificial forming line, stops accelerator operation for 10-15 min. The last time determines by peculiarities of the DTL tank frequency control system (FCS). The point is that during operation of the INR Linac with duty cycle value 0.02, RF power, dissipated in the DTL cavity, results in the considerable cavity detuning.

It should be noted, that frequency control system is realized by means of Alvarez cavity drift tubes temperature control. So before input RF power in the cavity drift tubes have to be warmed up to the resonance temperature.

With the rise of RF power in the tank temperature of cooling water has to be decreased so that resonance temperature of the cavity metal was unchangeable. And, on the contrary, after RF channel switching off the water temperature has to be warmed up to the resonance temperature [5]. Really it takes nearly 10-15 min for warming up drift tubes cooling water after RF channel failure. That is why the series crowbar essentially increases efficiency of accelerator operation.

ISBN 978-3-95450-181-6

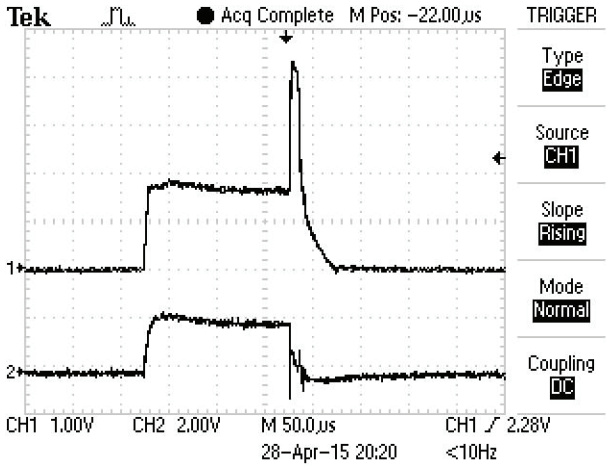

Figure 7: Series crowbar operation. Upper trace is modulator vacuum tube plate current, lower trace is modulator output pulse.

Thus, design of the FPA, quality of the FCS, and choice of crowbar system are interdependent. At fig.7 snapshots of the modulator output voltage and plate current are presented. Short time (about 10µs) between times of breakdown and interruption of FPA plate pulse is useful from the point of view FPA vacuum tube aging.

INTERMEDIATE POWER AMPLIFIER

As mentioned above, manufacture of vacuum tubes, designed especially for INR Linac, has been terminated 25 years ago. Among them was tetrode GI-51A designed for operation with common cathode and used in intermediate RF power amplifier IPA. Similarly to FPA the blocking capacitor was not foreseen in IPA and the plate high voltage was applied to the inner electrode of the coaxial cavity. The view of IPA is shown in fig. 3.

The search of a new tube for IPA has started near ten years ago. The main requirements were the capability to provide the pulse output RF power 300-400 kW and the possibility to mechanically fit with the existing equipment. The only choice was RF triode GI-57A, designed and manufactured in JSC "SED-SPb" for radar stations. Unlike GI-51A the tube GI-57A was designed to operate with the common grid. The parameters of the tubes GI-51A and GI-57A are given in table 1. One should note that the dimensions of input and output cavities of the amplifier are essentially determined by the inter-electrode capacitances grid-cathode Cgc and grid-plate Cga respectively for common grid circuit and by the capacitances grid-cathode Cgc and plate cathode Cac for common cathode circuit. The difference of the capacitances resulted in a need to fully change the dimensions of both input and output cavities. However the most complicated unit - the tank of the anode-grid cavity was succeeded to keep unchanged (fig. 8).

Generally replacement a tetrode by triode decreases a gain of RF amplifier. However in our case we succeed to keep it due two reasons. Firstly, the plate voltage was increased as IPA and FPA are powered in parallel (fig. 1).

Figure 8: Intermediate power amplifier after revision.

and increasing of plate voltage is also needed for FPA with GI-71A tube. Secondly, better matching between IPA output and FPA input has been achieved.

Table 1: Parameters of the tubes

Parameters	GI-51A	GI-57A
Pulse plate voltage, kV	40	28
Output RF power, kW	400	300
Operating life, hours	1000	3000
C_{ga}, pF	0,1	30
C_{ac}, pF	17	0,5
C_{gc}, pF	470	270

At present, two IPA with GI-57A tubes are installed and operate in RF channels and the third one is assembled, tested and is ready for installation.

MODULATOR VACUUM TUBE

All the GMI-44A vacuum tubes were manufactured in 70s-80s. Unfortunately, in the early years of RF system operation low-resistance water was used for modulator vacuum tubes cooling. Scale formation resulted in overheating of the tube elements and the lifetime of the tubes was only 1.5-2 thousand hours. After upgrading of the cooling system the lifetime increased up to 6-7 thousand hours, but significant amount of tubes has been lost by that time.

Since 2000 INR contacted "SED-SPb" several times and proposed to resume manufacture of the modulator tubes.

However due to several reasons, with the main being absence of consumers except for INR, the resumption of the manufacture was impossible. Fife years ago "SED-

ISBN 978-3-95450-181-6

SPb" agreed to start restoration procedure of the old vacuum tubes. Unfortunately, only seven tubes were restored of the whole amount about 24 vacuum tubes delivered for restoration. The quality of the restored tubes appeared to be lower than expected. For example pumping time increased from 20-30 minutes for new tubes up to several days for the restored ones. The life time of the restored tubes was less than 1000 hours. Only one of the restored tubes operated for 4000 hours.

The restoration program appeared to be unsuccessful and it was necessary to urgently find a replacement for GMI-44A. Similarly to the RF tubes the requirement to keep the existing equipment as unchangeable as possible was of importance. First of all this requirement was related to the filament power transformer and the transformer for negative grid bias. Due to series connection of modulator and FPA vacuum tubes [5] the secondary windings of the transformers are under high output pulse voltage and require HV isolation. The transformers have been produced about 30 years ago and their reproducing now is hardly possible.

After careful analysis and the consultations with "SED-SPb" a conclusion about a possibility to use RF triode GI-71A as powerful anode modulator vacuum tube has been done.

This choice simplifies several problems:

- Bias and filament transformers can be used without revision.
- GI-71A can be installed in the existing modulator rack.
- The assortment of vacuum tubes manufactured by SED-SPb for INR linear accelerator can be decreased to two items – GI-57A and GI-71A. In turn, manufacturing of GI-71A will doubled and a quality of the tubes could be improved.

The experience and the results of the studies connected with the replacement of the modulator tubes by the RF tubes are described in [6]. Several problems have been met:

- Pre-modulator power has to be clearly increased more than order of magnitude due much higher grid current of GI-71A than that of GMI-44A.
- The gain in the feedback loop of the accelerating field amplitude control decreases due to smaller GI-71A tube gain as compared with that of GMI-44A.
- Malfunctioning of the series crowbar system. Though in case of the breakdown the pre-modulator pulse is interrupted, the modulator tube GI-71A remains open.

Fig.9 demonstrates the processes which observed during breakdown in the final power amplifier, operating at pulse plate voltage 25 kV and output RF power near two MW.

From snapshot at fig.9 follows that in spite of modulator pulse interruption (middle trace) by the series crowbar system the modulator tube current (upper trace) continues up to full discharge of the artificial forming line.

At that breakdowns take place namely in the FPA plate-grid cavity, because they accompanies by sound. It means that an energy of artificial forming line discharges in the cavity but not in the FPA vacuum tube.

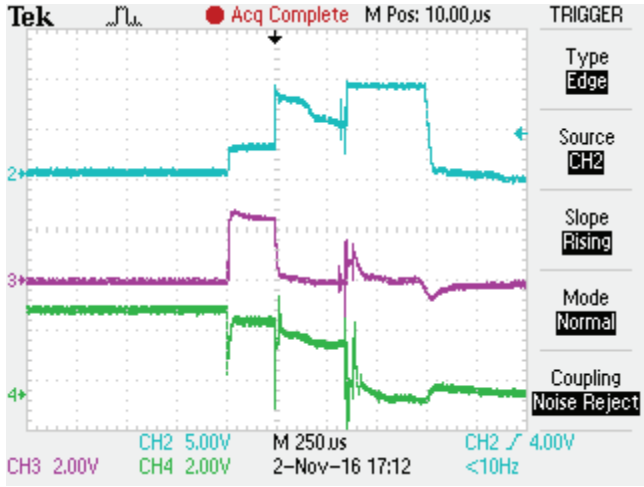

Figure 9: Processes in the PAM during FPA breakdown.

We consider several ways to overcome the problem. Among them are installation of solid-state opening switch [7] in GI-71A plate circuit and right choice of correcting circuits to limit grid-cathode gap overvoltage.

We don't also eliminate a possibility of GI-71A design changing. In particular there is agreement with SED-SPb about placing magnetic discharge vacuum pump at grid electrode of GI-71A.

REFERENCES

[1] A.I.Kvasha, etc. "A new 200MHz Powerful Pulse Triode for the Output Power Amplifier of DTL RF System", Proc. PAC2001, Chicago, p.1222.

[2] A.I.Kvasha. V.L.Serov "Development of the INR DTL RF System Crowbar Operation", Proc. of RUPAC2008, p.218.

[3] S.K. Esin, etc. "Stendovie ispitanija canala usilenija visokochastotnoy moschnosti nachal'noy chasti uskoritelja nezonnoy fabriki INR AN USSR. Trudi 3-go Vsesoyuznogo seminara "Programmaexperimentalnih issledovaniy na mezonnoy fabrike INR AN USSR", 23-27 April 1983, Moskva 1984,pp.23-30.

[4] John T.M. Lyles etc. "Progress on the new high power 200 MHz RF system for the LANSCE DTL", Proceedings of the 2001 PAC, Chicago, pp.996-998.

[5] Yu.Kiselev, A.Kovalishin, A.Kvasha, D.Hlustin "Simulation of the INR RAS DTL frequency stabilization system", Proc. of RUPAC 2006, pp.258-260.

[6] A.I.Kvasha, V.L.Serov "Powerful RF triode as anode modulator vacuum tube", these proceedings.

[7] Ian S. Roth etc. "A solid-state opening switch for crowbar replacement", Proc. of the PAC2001, Chicago, pp. 1459-1461.

ISBN 978-3-95450-181-6

THREE TRANSVERSE DEFLECTING SYSTEMS FOR ELECTRON BEAM DIAGNOSTICS IN THE EUROPEAN FREE-ELECTRON LASER XFEL*

A. A. Zavadtsev†
Institute for Nuclear Research of Russian Academy of Sciences, Moscow, Russia

Abstract

In frames of Russian in-kind contribution to European XFEL, INR in cooperation with DESY is responsible for Transverse Deflecting Systems (TDS) for special beam diagnostic in the XFEL linac. Three TDS have been developed: TDS INJ in the Injector, TDS BC1 in the Accelerator tunnel after Bunch Compressor 1 and TDS BC1 after Bunch Compressor 2. Each system includes S-band disk-loaded deflecting structure (DLS), waveguide system, klystron, pulse transformer, modulator and control system. TDS INJ has been built, assembled in the Injector building and tested. It is used to monitor the bunch length, longitudinal phase space and slice emittance now. Exceptionally small, exceeding expectations, slice emittance of electron bunch was measured using TDS INJ during the XFEL Injector commissioning. Three structures for TDS BC1 and TDS BC2 as well as the waveguide systems have been built, tested and TDS BC2 part installed in the XFEL tunnel.

INTRODUCTION

Tree Transverse Deflecting Systems operating at frequency 2998 MHz have been designed, built and installed (partially) for longitudinal electron beam diagnostics in the European XFEL at three locations: in the Injector, after BC1 and after BC2. The TDS location and corresponding electron energies are shown in the XFEL block-diagram (Figure 1).

The full scale prototype of the TDS INJ has been developed, designed, built and commissioned at DESY PITZ, Zeuthen facility [1]. It operates successfully now [2].

TRANSVERSE DEFLECTING STRUCTURE

Several travelling wave DLS operating at a hybrid mode have been considered for the XFEL TDS at the stage of development (Figure 2). These structures have been considered in details in [3] and [4]. Azimuthal inhomogeneity in these structures is used for stabilization of the azimuthal position of the deflecting field and for increasing frequency difference of two perpendicular polarizations of the hybrid mode.

All variants have very similar RF efficiency. The frequency separation of two perpendicular modes is about 40 MHz for variants A, B and D, 150 MHz for variant C and 900 MHz for variant E.

Basing on similar RF efficiency of these structures, taking into account the level of development and proven experience of high power operation at LOLA, the DLS of variant A was accepted for XFEL TDS.

The DLS of variant A has been developed in details. TDS systems include 16 cell structure for TDS INJ, 46 cell structure for TDS BC1 and two 46 cell structures for TDS BC2, so the lengths of these structures are 0.7 m and 1.7 m correspondingly. The same shape and the geometry dimensions have been chosen for all four structures to meet all requirements optimally. Therefore, the cells are the same and the couplers are the same for all structures. It simplifies the production and the tuning of the structures significantly [5].

The group velocity of the structure has been minimised to β_g=-0.018 choosing the shape of the cell. It allows us to use the TDS System for single bunch measurement.

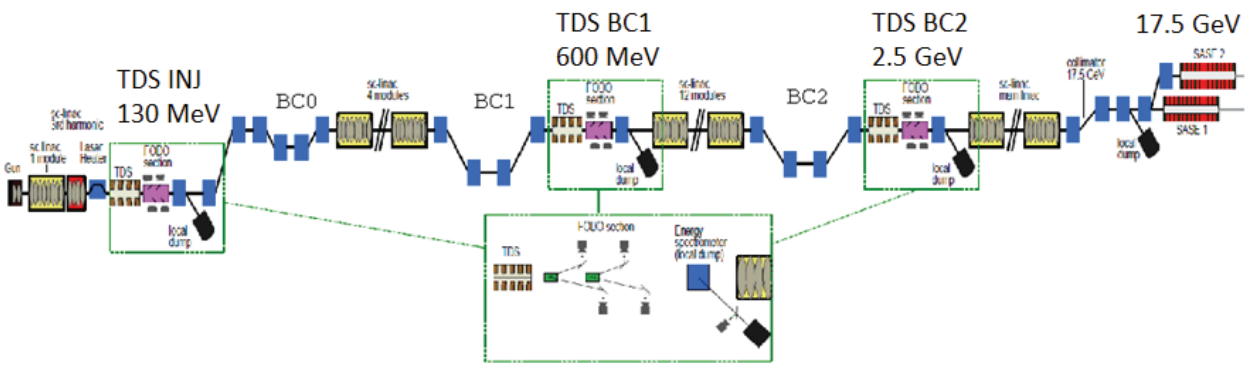

Figure 1: TDS Systems at the XFEL block-diagram.

The TDS Deflector INJ at the test stand is shown in Figure 3. The precision of the cell machining ensures the cell eigen frequency tolerance, which is equivalent to the cell

* Work supported by European XFEL GmbH and Ministry of Education and Science of Russia
† On behalf of the joint XFEL TDS team. azavadtsev@yandex.ru.

ISBN 978-3-95450-181-6

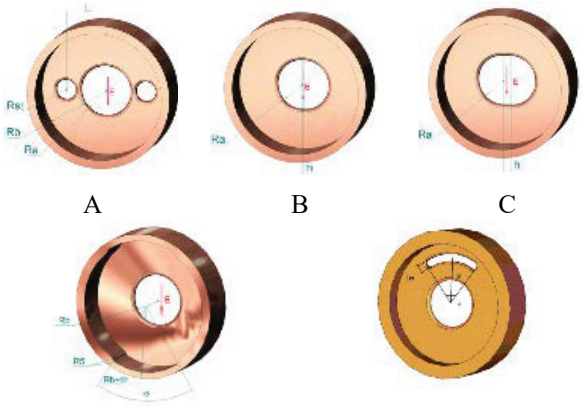

Figure 2: DLS deflecting structures.

radius tolerance of 3-5 μm. Nevertheless, each cell has been provided with two tools for tuning after brazing allowing both to increase and to decrease the frequency via the cell wall bending inside or outside the cell. The tuning tool is shown in Figure 3. The max frequency tuning range of the cell is 4 MHz at 2 mm wall bulge of two tools.


Figure 3: TDS INJ at test stand and tuning tool.

The TDS Systems BC1 and BC2 includes three the same deflecting structures 1.7 m long each. It is shown in Figure 4, including also measured amplitude and phase of the deflecting electric field.

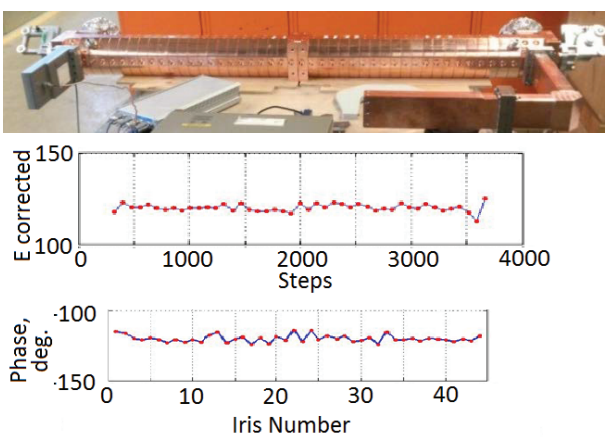

Figure 4: One of three structures for TDS BC1 and TDS BC2 at the test stand and measured amplitude and phase of deflecting electric field.

HIGH POWER RF SYSTEM

High Power RF System (HPRF) includes modulator, RF generator (pulse transformer, klystron, solenoid and local shielding) and waveguide system.

Modulator

Arkadiev type modulator is used both for TDS INJ and for TDS BC1/BC2. The capacitors are charged in parallel and discharged in series. The voltage in the load is a sum of the capacitor voltages. IGBT is used as a switch in these modulators. The modulator for TDS INJ includes six 10 kV modules. The modulator for TDS BC1 includes two dual 22 kV modules. The load of the modulator is the primary winding of the pulse transformer.

The modulator for TDS INJ is shown in Figure 5. It is assembled in the standard cabinet and includes 6 modules, 3 power supplies, 2 safety earthing units, control module, bias power supply for the pulse transformer, and low voltage filament power supply for the klystron. The control module is coupled with the modules via fiber optic lines.

Three modules produce negative voltage -24 kV with respect to the ground. Another three modules produce positive voltage +24 kV. Differential voltage 48 kV is transmitted to the primary winding of the pulse transformer via HV cables.

Table 1: Modulator Parameters

Parameter	Unit	INJ	BC1/BC2
Number of modules		6	2
Voltage of the module	kV	8	22
Voltage of the modulator	kV	48	44
Voltage in the modulator with respect to the ground	kV	24	22
Current of the modulator	A	166	1420
Ratio of pulse transformer		2.3	5.7
Max klystron voltage	kV	110	250
Nom klystron voltage	kV	101	230/232
Max klystron current	A	72	250
Nom klystron current	A	66.4	214/219

Test of the modulator with equivalent resistive load shown following results:

- output differential voltage U=50kV,
- current I=170A,
- pulse length up to τ=6 μsec,
- repetition rate F=10 Hz,
- pulse flat-top length τ_{ft}=0.1-5.5 μsec,
- pulse flat-top voltage uniformity <1%,
- pulse rise time is τ_r=0.2 μsec,
- pulse fall time is τ_f=0.2 μsec.

The modulator, developed for TDS BC1 and TDS BC2, includes two dual modules producing -22 kV and +22 kV with respect to the ground. So differential voltage of 44 kV is transmitted to the primary winding of the pulse transformer.

ISBN 978-3-95450-181-6


Figure 5: Modulator and RF generator of the TDS INJ.

Pulse Transformer

The pulse transformers for the TDS INJ and the TDS BC1/BC2 have been simulated, designed and manufactured. Figure 5 shows RF generator of the TDS INJ, including the pulse transformer, low voltage filter, bias filter, high voltage filament power supply, voltage&current monitor, located in oil tank, and klystron, solenoid, and oil circulating system, located on the top of the oil tank.

Pulse transformer of the TDS BC1 is shown in Figure 6.

Figure 6: Pulse transformer of the TDS BC1.

Klystron

CPI VKS-8262HS klystron is used for the TDS INJ, and THALES TV2002DoD klystron is used for the TDS BC1/BC2.

Table 2: Klystron Parameters

Parameter	Unit	INJ	BC1/2
Klystron		VKS-8262HS	TV2002DoD
Frequency	GHz	2.998	2.998
Peak power	MW	3	24
Voltage	kV	110	250
Current	A	72	250
Pulse length	μsec	12	6.5
Drive power	W	80	240

The test of the HPRF INJ with waveguide load shown following results:

- klystron voltage U=0…110 kV
- klystron current I=0…82 A
- pulse length τ=6 μsec
- repetition rate F=10 Hz
- pulse-to-pulse output voltage instability (peak-to-peak) 0.19%
- RMS voltage fluctuation 0.03%
- flat-top voltage non-uniformity <1%

Measured oscillograms are shown in Figure 7: in normal operation and in the fast interlock event (high voltage breakdown - high voltage interrupts within the pulse, and current is limited).

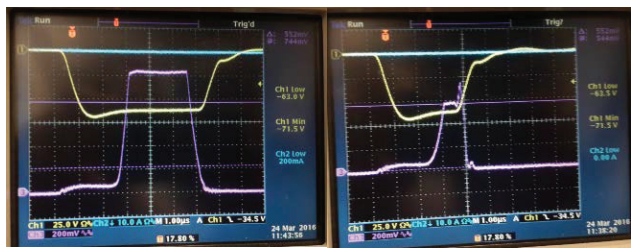

Figure 7: Measured pulses at HPRF INJ: yellow is the klystron voltage, pink is RF power in the klystron waveguide.

Waveguide System

The waveguide system connects the klystron and the deflecting structure [6]. It includes:

- directional coupler,
- waveguide window,
- waveguide load,
- spark detectors,
- waveguide adapters for ion pumps,
- E-bends,
- H-bends,
- straight waveguides.

Each directional coupler includes two channels: for forward and for reflected power. Typical parameters of the directional coupler are presented in Table 3: coupling ***S13***, isolation ***S14*** and directivity ***D***. The directional coupler is shown in Figure 8.

Table 3: Directional Coupler Parameters

Channel	*S13*, dB	*S14*, dB	*D*, dB
Forward	-65.9	-103	37
Reflected	-65.6	-100	34

Figure 8: Directional coupler.

ISBN 978-3-95450-181-6

The UHV dual mode waveguide window with ALUMINA flat disk has been developed and built for TDS Systems. It is shown in Figure 9. Measured reflection is ***S11***=-37 dB at operating frequency. The frequency band is 60 MHz at ***S11***<-20 dB.

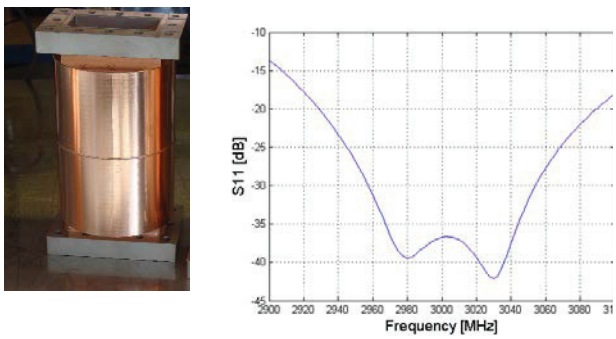

Figure 9: UHV dual mode waveguide window.

The UHV waveguide load has been developed and built. It consists of rectangular waveguide with decreasing of the height on special function covered by Sendust inside. The test of the Sundust coating, performed by DESY, confirmed its UHV compatibility. The load is shown in Figure 10. Reflection is ***S11***=-36 dB at operating frequency and ***S11***<-33 dB in frequency band 200 MHz.

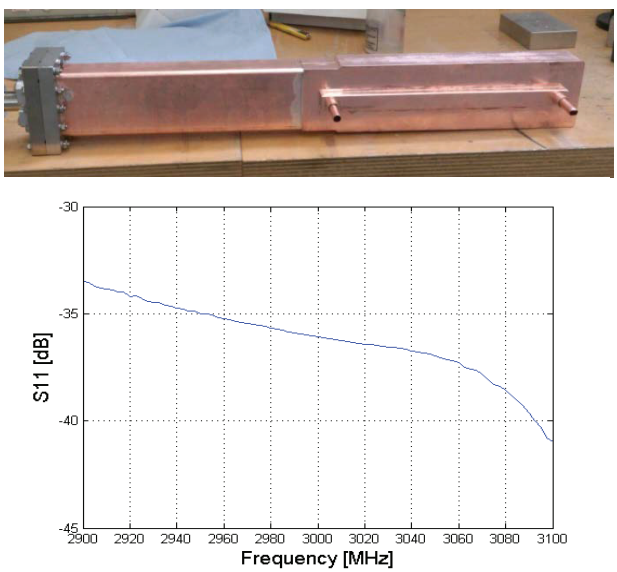

Figure 10: UHV waveguide load.

55 m long waveguide system of XFEL TDS INJ has been assembled in in XFEL Injector building. It is shown in Figure 11. Reflection from the waveguide line is ***S11***=-42 dB at operating frequency.

TDS SYSTEM DESIGN

3D design of the TDS System INJ is shown in Figures 12 and 13.

RF generator and control cabinet of the TDS INJ are located at -5 floor of the Injector building, and the deflecting structure is located in the Injector tunnel at -7 floor. 55 m long waveguide system connects the klystron and the deflecting structure.

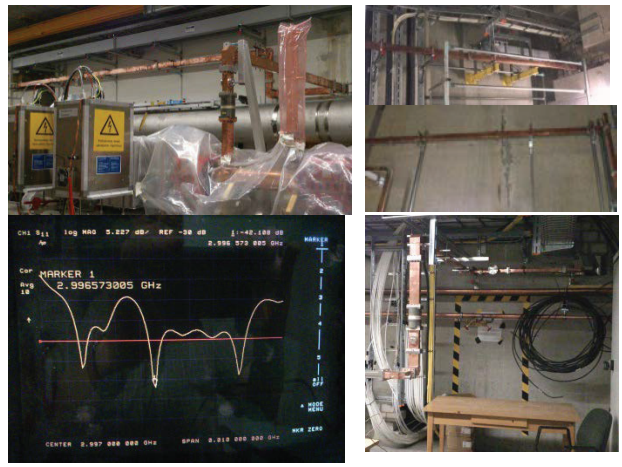

Figure 11: 55 m long waveguide system of the XFEL TDS INJ.

The whole TDS Systems BC1 and BC2 are located in local space in the accelerator tunnel. 3D design of the TDS System BC1 is shown in Figure 14.

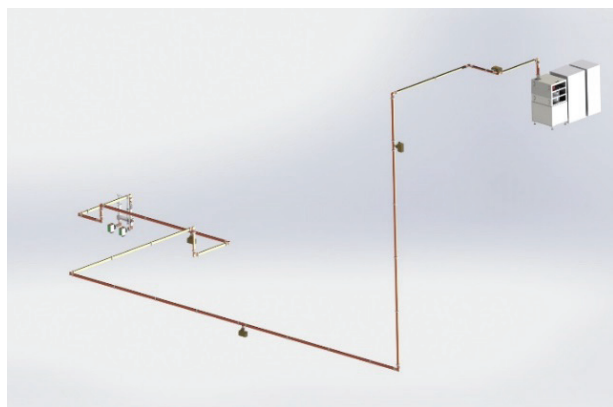

Figure 12: 3D design of the TDS INJ.

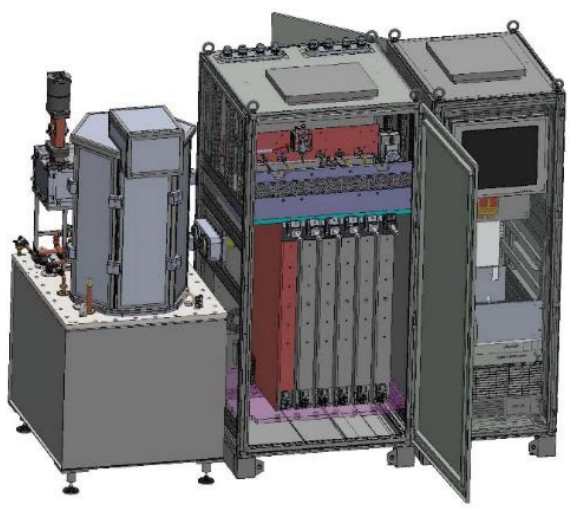

Figure 13: 3D design of the TDS HPRF INJ: RF generator, modulator and control cabinet.

ISBN 978-3-95450-181-6

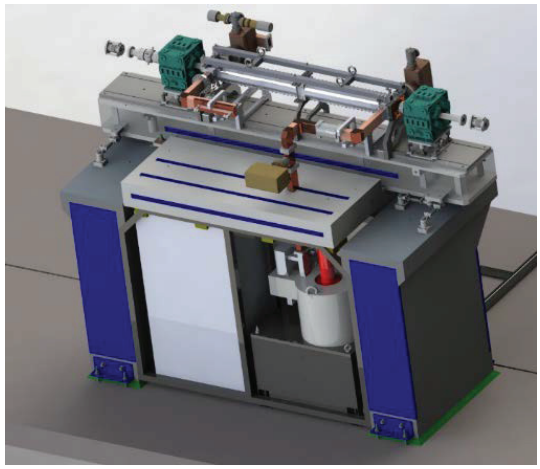

Figure 14: 3D design of the TDS BC1.

ASSEMBLING AND COMMISSIONING

The TDS System INJ has been assembled, tuned and tested. Figure 15 shows operating HPRF INJ and TDS structure INJ.

The TDS Deflector BC2 including two deflecting structures has been installed in the XFEL tunnel (Figure 16).

DESY has successfully concluded tests of the first section of the particle accelerator for the European XFEL. The TDS based diagnostic system produces elongated images of individual electron bunches and allows analysing them in slices. Measured images of individual electron bunches are shown in Figure 17 [7].

Figure 15: HPRF INJ and TDS structure INJ.

Figure 16: Two TDS structures BC2 in XFEL tunnel.

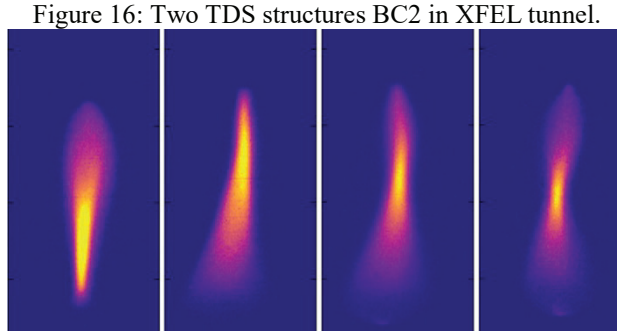

Figure 17: Bunch images produced by TDS System.

CONCLUSION

1. TDS System INJ has been tuned and installed at XFEL. It operates for the beam diagnostics.
2. TDS Structures and waveguide systems for XFEL TDS BC1 and XFEL TDS BC2 have been manufactured, tuned and supplied to DESY.
3. TDS Structure BC1 will be assembled on the girder in the XFEL tunnel in accordance with XFEL schedule.
4. The modulator for XFEL TDS BC1 is under production. It will be supplied to DESY, tested at the test stand and installed in the XFEL tunnel then.
5. Two TDS Structures BC2 have been assembled on the girder in the XFEL tunnel.

ACKNOWLEDGEMENT

Sincere appreciation to all XFEL TDS cooperation members from INR RAS, Nano Invest, DESY and MEPHI for the fruitful and interesting joint work during TDS development, construction and commissioning.

REFERENCES

[1] L. Kravchuk et al., in *Proc. LINAC'10*, *p.* 416
[2] H. Huck et al., in *Proc. FEL'15*, *p.* 110
[3] A. Anisimov et al., "Structures with a transverse deflecting field for a free-electron laser", *Instruments and Experimental Techniques*, vol. 53, p. 107, 2010.
[4] V. Paramonov et al., in *Proc. LINAC'10*, p. 434
[5] A. Anisimov et al., in *Proc. RuPAC'10*, p. 328
[6] A. Zavadtsev et al., "Components of the radio-frequency system for traveling-wave deflecting structures", Instruments *and Experimental Techniques*, vol. 57, p. 706, 2014.
[7] http://www.xfel.eu/news/2016/electron_injector_for_european_xfel_exceeds_expectations/.

ISBN 978-3-95450-181-6

EFFECTIVE RF DEFLECTING STRUCTURES FOR BUNCH ROTATION AND DEFLECTION

V.V. Paramonov*, Institute for Nuclear Research of the RAS, Moscow, Russia

Abstract

The Deflecting RF Structures (DS's) find now applications for the bunch rotation with the purposes of diagnostic for the longitudinal distribution, the emittance exchange and the luminosity improvements in colliders. Results of development DS with minimized the level of aberrations in the distribution of deflecting field are described. Applied for bunch rotation along transverse axis, such DS's provide in orders smaller emittance growth, as compared to another options. In comparison with widely used deflectors, based on the Disk Loaded Waveguide, developed DS's have, depending on modification, in $2 \div 4$ times higher RF efficiency. Structures can operate both in Traveling Wave (TW) and in Standing Wave (SW) modes. To create longer RF cavities for SW operation, compensated DS's options are developed, adding field distribution stability and saving high RF efficiency. The main solutions are described and achieved parameters are reported.

INTRODUCTION

The periodical structures with transverse components of the electromagnetic field - DS's - were introduced for charged particle deflection and separation. The bunch cross DS synchronously with the Deflecting Field (DF) Ed, corresponding the phase $\phi = 0$ in the DS and all particles get the similar increment in the transverse momentum p_t. At present, for short and bright electron bunches DS found another applications in bunch rotation, for bunch special diagnostic, luminosity improvement and emittance exchange experiments. All directions are related to the Transformation of Particle Distribution (TPD) in the $6D$ phase space and DS operates in another mode - the Central Particle (CP) of the bunch center cross DS at zero E_d value, $\phi = 90^o$. Downstream and upstream particles get opposite increments in p_t.

The applications for TPD provide an additional requirement - a DS for TPD should provide the minimal, as possible, own distortions to the original distributions. The additional limitation to known DS's design naturally results in the reduction of the other parameters, RF efficiency and dispersion properties. Results of DS's development combining both field quality and saving another parameters are presented.

METHODICAL BASEMENT

The concept of DS's with the minimized level of own aberrations in the DF distributions was introduced in [1]. The DF distribution analysis was performed, [2], using the basis of hybrid waves HE and HM, [3]. The particles dynamic for the bunch rotation is studied and compared for different DS's in [4].

The equivalent DF is defined from the transverse component of the Lorenz force F^L, where the field components are expressed by using the basis of hybrid waves HE and HM, [3]:

$$\vec{F}^L = e(\vec{E} + [\vec{v}, \vec{B}]), F_x = eE_d = e(E_x - \beta Z_0 H_y), \quad (1)$$
$$\vec{E} = A\vec{E}_{HE} + B\vec{E}_{HM}, \vec{H} = A\vec{H}_{HE} + B\vec{H}_{HM},$$

and $Z_0 = \sqrt{\frac{\mu_0}{\epsilon_0}}$.

The reasons for the emittance growth during TPD are the aberrations - the non linear additions in the E_d distribution, which take place due to not relativistic energy of particles, $\beta < 1.0$, additions from higher sextupole modes, the higher spatial harmonics in the distribution of the deflecting field. The main attention should be paid to the higher spatial harmonics, see [2], [4] for details.

In any periodical structure each field component $E_j, H_j(x, y, z)$ in the beam aperture can be represented as the set over spatial harmonics:

$$E_j, H_j(x, y, z) = E_j, \widehat{H_j(x, y, z)} e^{i\psi_j(z)} = \quad (2)$$
$$= \sum_{n \to -\infty}^{n \to +\infty} a_{jn}, b_{jn}(x, y) e^{\frac{-i(\Theta_0 + 2n\pi)z}{d}},$$

where $E, \widehat{H_j(x, y, z)}$ and $\psi_j(z)$ are the amplitude and the phase distributions, d is the structure period and $a, b_{jn}(x, y)$ are the transverse distribution for the n-th spatial harmonics, Θ_0 is the operating phase advance. The same representation is valid for E_d also.

In the periodical slow wave structure each component of original fields $\vec{E}, \vec{H}$ can not exist without the higher spatial harmonics, $n \geq 1$ in (2). It is the law for slow wave structures. But DF is composed from two components of original fields, (1), and this law, generally, has no force for E_d. During DS design we can manage A and B relation in (1) in such way, that spatial E_x harmonics a_{jn} will compensate the H_y harmonics b_{jn}. To provide such compensation, the opposite phasing of hybrid waves $\vec{E}_{HE}$ and $\vec{E}_{HM}$ is required, $A \cdot B < 0$ in equation (1).

For harmonics estimations in values, the parameters $\delta\psi_j(z)$ and Ψ_j at the DS axis are introduced, [2]:

$$\delta\psi_d(z) = \psi_d(z) + \frac{\Theta_0 z}{d}, \quad \Psi_d = max(|\delta\psi_d(z)|), \quad (3)$$

with the physical sense as the deviation and the maximal phase deviation of the total E_d distribution from the main synchronous harmonic in E_d. During bunch rotation, $\phi = 90^o$, CP sees the effect of higher spatial harmonics, [2], as:

$$E_{rot} \approx E_{d0} sin(\Psi_d) \approx E_{d0} \Psi_d, \quad (4)$$

* paramono@inr.ru

ISBN 978-3-95450-181-6

where E_{d0} is the amplitude of the synchronous E_d harmonic. Minimizing Ψ_d value, we keep CP close to DS axis, in the region of low non linear additions, and simultaneously reduce the amplitudes of these additions in the total DS aperture. As the result, we have in orders smaller emittance growth after bunch rotation.

THE FIRST STAGE RESULTS

The described procedure was applied to the classical DS, [3], based on DLW, Fig. 1a, resulting in the strong reduction of aberrations, $\Psi_d \leq 2^o$, but at the expense of reduction in the effective shunt impedance value $Z_e \approx 17\ \frac{MOm}{m}$, [5], at $\approx 6\ \frac{MOm}{m}$ lower as compared to usual DLW options.

To find a more RF effective solution, the DS with TE-

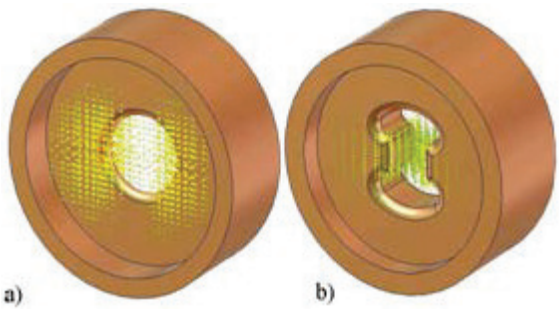

Figure 1: The DLW based DS with minimized level of aberrations, (a), and the decoupled structure, (b), [5].

like operating mode, [6], which has possible Z_e up to $\approx 80\ \frac{MOm}{m}$, but, due to the same phasing of hybrid waves, $A \cdot B > 0$ in equation (1), very bad for bunch rotation field quality, $\Psi_d \approx 70^o$, was transformed, see Fig. 2, into decoupled structure, Fig. 1b, Fig. 2c. Together with the good field quality, $\Psi_d \approx 1.87^o$, much higher, as compared to DLW, Fig. 1a, $Z_e \approx 36\ \frac{MOm}{m}$ value for RF efficiency was obtained, [5].

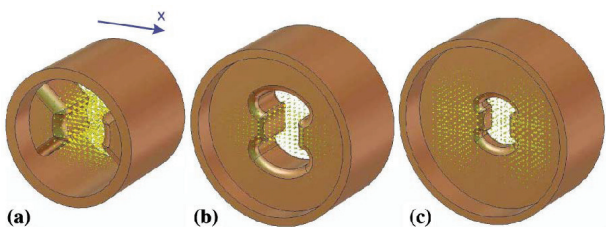

Figure 2: DS transformation from high RF efficiency and bad field quality, (a), to fine field quality and tolerable RF efficiency, (c).

EFFICIENCY IMPROVEMENT

Providing the cell shape near DS axis as a drift tube, Fig. 4a, we improve Z_e value up to $Z_e \approx 43\ \frac{MOm}{m}$, while keeping $\Psi_d \approx 1.9^o$. This DS option, named with service name $V2$, due to very specific distribution of magnetic field in the middle between disks, calculated with ANSYS, has the working name "Vanja", Fig. 4b. For the $V2$ option the field balance is achieved in average, because for synchronous harmonics in E_x and H_y the balance is of $a_0 = -1.27 b_0$. With the value $\Psi_d \approx 1.9^o$ CP moves near $V2$ axis, but higher spatial harmonics for E_d distribution in DS aperture are dumped in average, see [4].

Modifying the drift tube dimensions we come to $V3$ option,

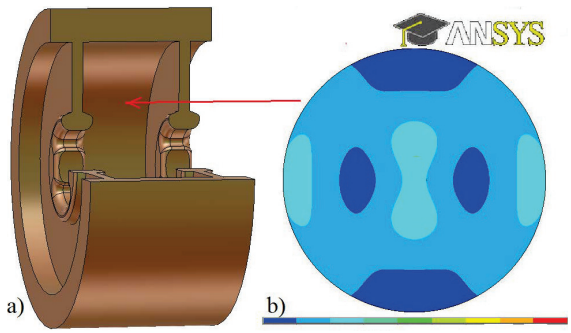

Figure 3: The shape with the drift tube - V2 option, (a), and magnetic field distribution in the plane between disks, (b).

Fig. 5a, with the fields balance in total, $a_0 = -1.007 b_0$ even with higher RF efficiency, $Z_e \approx 53\ \frac{MOm}{m}$ and similar field quality, $\Psi_d \approx 2.0^o$. For bunches with small, as compared to DS aperture, transverse dimensions, $V2$ and $V3$ options provide similar very small results in the emittance growth.

Relaxing requirement for the field quality to $\Psi_d \approx (20^o \div 4^o)$, which is typical for the classic DLW, not optimized for minimal aberrations, we can improve RF efficiency up to $Z_e \approx (93 \div 73)\ \frac{MOm}{m}$ by more complicated shape near DS axis, Fig. 5b, option $V4$. In the emittance growth option $V4$ definitely lose to $V2$ and $V3$ and is comparable to not optimized DLW, having more than 3 times higher RF efficiency.

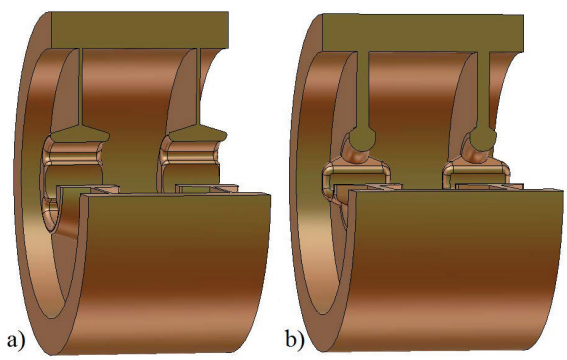

Figure 4: The cells shape for V3, (a), and V4, (b) options.

DISPERSION PROPERTIES

The opposite phasing of hybrid waves in equation (1) defines the negative DS dispersion and for TW operation structures operate in the backward wave mode. Additionally, fields balancing in (1) $a_0 \approx -b_0$ to have a minimal Ψ_d value results in a narrow passband. For SW operation it limits the number of cells in a deflecting cavity and possible

ISBN 978-3-95450-181-6

value of deflecting voltage V_d. For dispersion curve correction near operating π mode the resonant slots in DLW disks were considered, [5]. More simple and effective solution is developed now - compensated DS options. As it is known well, [7], compensated structures combine the high RF efficiency with the qualitatively higher stability of the field distribution for operating π mode.

Different technical solutions are possible. After comparison, we select the method, which can be applied to all considered DS's, results in a minimal Z_e reduction and can be mostly reliable and simple realized in practice. Two additional disks are partially inserted in the outer cylindrical DS wall in the middle between the original DS disks, Fig. 5a. With the appropriate adjustment of the cell radius and radius and depth of insertion for additional disk, the DLW dispersion curve becomes typical for compensated structures, Fig. 5b.

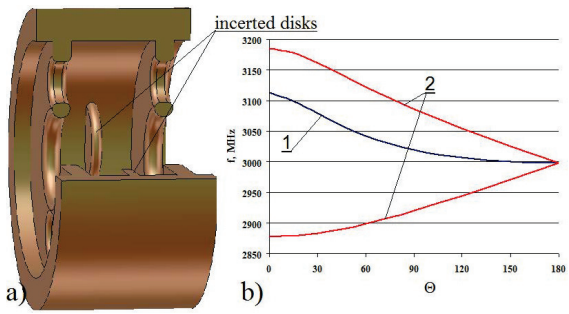

Figure 5: The compensated DLW option, (a) and corresponding dispersion curves, (b) for the simple DLW option, 1, and for the compensated one, (2).

The most important stability problem is for $V3$ option due to perfect field balance $a_0 = -b_0$. The simple $V3$ option has the passband width $\approx$ 100 MHz only for the S band operating frequency. As one can see from Fig. 6, the compensated $V3$ option solves this problem.

In compensated DS's options we switch on for DS's the new physical property - mutual compensation for contributions of adjacent modes into operating field distribution due to deviation of cell frequencies in manufacturing or RF tuning. We can also improve the passband width, see Fig. 5, Fig. 6, and control the value of coupling coefficient.

Additional elements in the compensated DS's options naturally result in Z_e reduction, which is of $(3 \div 6)\ \frac{MOm}{m}$. For the DLW such Z_e reduction is too strong. For developed $V2, V3$ and $V4$ options, at the background of the high initial Z_e, this price for the new quality is tolerable.

Due to the additional set of physical limitations the shape of cells for the developed DS's are more complicated, but realistic for manufacturing with the modern numerically controlled equipment. All DS's are developed following to the concept of domination - one free geometrical parameter in cell dimensions in times more strongly effects at the corresponding physical parameter of the DS. It allows a fast dimension adjustment in DS development and simplifies cells tuning.

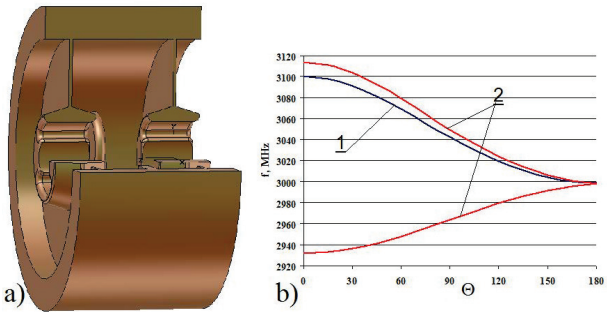

Figure 6: The compensated V3 option, (a) and corresponding dispersion curves, (b) for the simple V3 option, 1, and for the compensated one, (2).

SUMMARY

New family of deflecting structures is developed with the main feature of careful bunch handling during transformation of particle distributions due to minimized own DS aberrations. Even with this added new quality, developed structures have excellent RF efficiency and can be used for usual bunch deflection. Results of this development are requested by community and INR starts promotion of this structures now into research facilities. The first results of operation we expect soon.

ACKNOWLEDGEMENT

The author thanks colleagues, L. Kravchuk, P. Orlov, A. Skassyrskaya, INR, for joint work and support at the start of this research. Especially warm thanks to Klaus Floetmann, DESY, for support in collaboration and the beam dynamics expertise. At the initial stage this research was supported in part by RBFR grant N12-02-00654-a.

REFERENCES

[1] V. Paramonov, " Deflecting Structures with Minimized Level of Aberrations", in *Proc. Linac 2012*, Tel Aviv, Israel, September 2012, p. 445.

[2] V. Paramonov, "Field distribution analysis in deflecting structures", DESY 18-13, DESY, arXiv:1302.5306v1, 2013.

[3] H. Hahn, "Deflecting Mode in Circular Iris-Loaded Waveguides", *Rev. Sci. Inst.*, v. 34, n. 10, p. 1095, 1963.

[4] K. Floettmann and V. Paramonov, "Beam dynamics in transverse deflecting rf structures", *Phys. Rev. ST Accel. Beams*, vol. 17, p. 024001, 2014.

[5] V. Paramonov, L. Kravchuk and K. Floettmann, "Standing Wave RF Deflectors with Reduced Aberrations", in *Proc. RuPAC 2012*, St. Peterburg, Russia, October 2012, p. 590.

[6] V. Paramonov, L. Kravchuk and K. Floettmann, "RF Parameters of the TE - Type Deflecting Structure", in *Proc. Linac 2012*, Tel Aviv, Israel, September 2012, p. 366.

[7] V. Kulman, "Accelerating system", in *Ion linear accelerators*, B. Murin, Ed. Moscow, USSR: Atomizdat, vol. 2, pp. 36–46, 1978.

ISBN 978-3-95450-181-6

INR RAS INSTRUMENTATION FOR BUNCH SHAPE AND BEAM CROSS-SECTION MONITORING

S. Gavrilov†, A. Feschenko, P. Reinhardt-Nickoulin
Institute for Nuclear Research of the Russian Academy of Sciences, Moscow, Russia

Abstract

Instruments for bunch shape and beam cross-section diagnostics at ion linacs are as important as complicated devices. Widespread Bunch Shape Monitors developed in INR RAS are used during a linac commissioning and optimization of beam dynamics. Beam Cross-Section Monitor implemented at INR RAS linac provide efficient non-destructive beam tuning and control. Features of both monitors investigated in simulations and beam tests are described. A variety of experimental results are presented.

INTRODUCTION

A bunch shape is defined usually as longitudinal distribution of particle intensity in bunches *I(z)* or *I(φ)*, which is one of the most difficult to observe characteristics of a beam at ion linear accelerators.

There are several methods for bunch shape measurements, however low energy secondary electrons are used most extensively because of weak dependence of their properties both on the type of primary particles and on their energy. The technique of a coherent transformation of a temporal bunch structure into a spatial charge distribution of low energy secondary electrons through RF-modulation was initially implemented by R. Witkover [1] for BNL linac. An energy (longitudinal) RF-modulation of secondary electrons was used.

In the Bunch Shape Monitor (BSM) [2], developed in INR RAS, a transverse RF-scanning is used. The general principle of BSM operation is clear from Fig. 1.

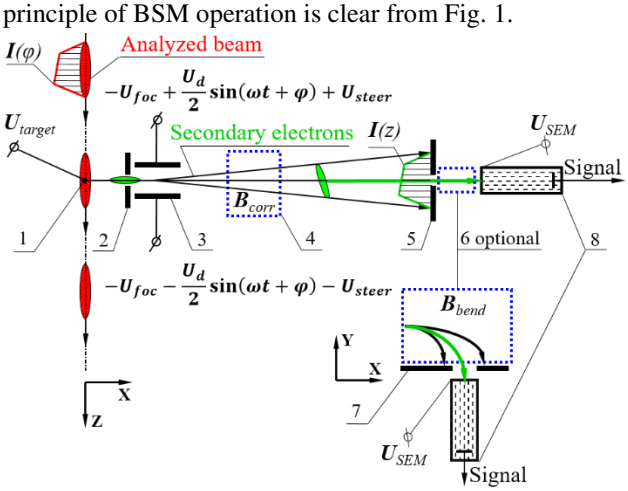

Figure 1: BSM scheme: 1 – tungsten wire target, 2 – inlet collimator, 3 – RF-deflector combined with electrostatic lens, 4 – correcting magnet, 5 – outlet collimator, 6 – optional bending magnet, 7 – registration collimator, 8 – secondary electron multiplier.

† s.gavrilov@gmail.com

Two-dimensional beam density distribution *I(x, y)* is one of the most informative beam parameters, enabling simultaneous measurements of beam position, profiles and emittance ellipses reconstructed from profiles data in combination with adjustable beam focusing elements for linear transformations in phase space. Luminescent screens, typical devices for 2D cross-section measurements, have all advantages and drawbacks of destructive diagnostics. More convenient, transparent technique of residual gas ionization, was initially proposed by V. Mihailov et al. [3] and used for both charged particle and synchrotron light beams [4].

The Beam Cross-Section Monitors (BCSMs) [5], based on ion component of the residual gas ionization, were implemented and upgraded at INR RAS linac for in-flight non-destructive diagnostics in the full range of beam parameters. The basic principle of operation is shown in Fig. 2. The energy of the ions at the slit linearly depends on their original coordinates X, hence their energy distribution downstream of the slit reproduces the transverse particle density distribution in the primary beam along X coordinate, while the distribution of the ions along Y coordinate keeps the same as that in the primary beam, similarly to 1D ionization profile monitors. In case of uniform fields the distances X_0 and X_1 are related as $X_1=2X_0(E_{ex}/E_a)$, that is independently of charge and mass of residual gas ions, and all types of ions contribute to formation of 2D image of particle density distribution in analyzing beam cross-section.

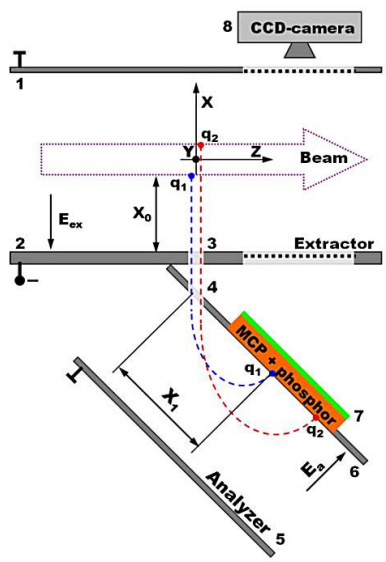

Figure 2: BCSM scheme: 1, 2 – electrodes of extractor, 3, 4 – double slit filter, 5, 6 – electrodes of analyzer, 7 – electro-optical converter, 8 – CCD-camera.

ISBN 978-3-95450-181-6

BUNCH SHAPE MONITOR

The main requirement for bunch shape measurements is a phase resolution. In ion linacs for typical bunch phase durations about several tens of degrees the resolution of 1° looks sufficient, that corresponds to a temporal resolution from several tens to hundreds of picoseconds.

The first BSM, providing such resolution, has been developed and built in INR in the eighties and the first measurements has been done in 1988 during commissioning of INR linac. Since that time various modifications of BSM have been developed and built for several accelerators [6] including SSC Linac, DESY Linac-3, SNS Linac, J-PARC Linac, CERN Linac-2/3/4.

Two groups of electrons passing the deflector with the phase shift of 180° get through the output collimator and their intensity is detected. If the bunch length is bigger than 180° then the signals corresponding to two longitudinal points, shifted by 180°, are superimposed, and the results of the measurements are distorted. Hence the typical phase range of BSM measurements is equal to half a period of the deflecting field. The range of the measurements can be increased to full period if one of the two groups of electrons is blocked. In 2016 BSM with the feature of 360° phase range and with three replaceable RF-deflectors was fabricated and tested for GSI-FAIR accelerators: UNILAC, CW- and proton linacs (Fig. 3).

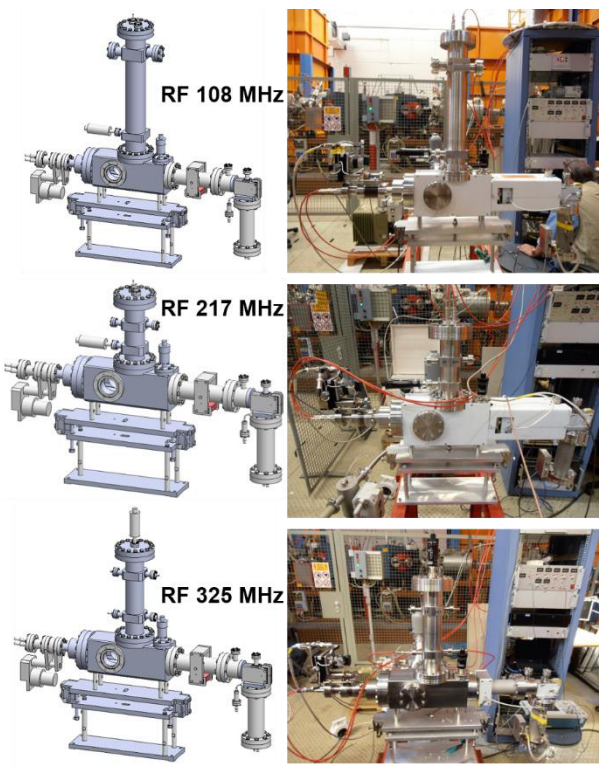

Figure 3: BSM: 108.408 MHz for UNILAC, 216.816 MHz for CW-linac, 325.224 MHz for proton linac.

To do it the flag-type movable curtain was installed at the exit of RF-deflector. Rotating the curtain one can absorb the electrons corresponding to one of the two half-periods of the deflecting field thus avoiding superimposing of the signals from particles shifted by half a period.

Modern ion linacs under construction, such as FRIB MSU or ESS ERIC are foreseen to operate with RMS bunch lengths of about 10÷20 ps at medium energies and even shorter at high energies, and at least 0.5° phase resolution is required for reliable bunch shape diagnostics. To improve the resolution of BSMs for these linacs several modifications, based on long experience, were implemented.

Firstly, to improve the uniformity of both deflecting and focusing fields in Y-direction, thus improving a phase resolution, the new λ-type symmetric RF-deflector has been developed for BSM-ESS (Fig. 4).

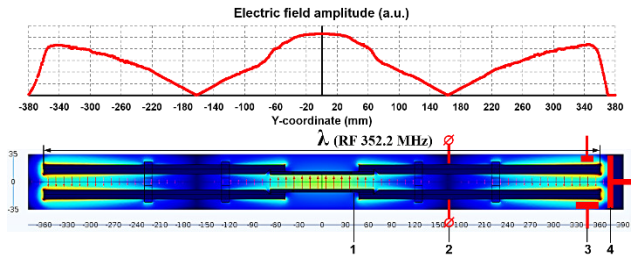

Figure 4: E-field distribution in λ-type deflector.

The symmetric deflector provides resolution about 0.5° (about 4 ps for ESS linac), in case of proper focused and oriented electron beam.

So, the second feature, foreseen for new BSM modifications, is a correcting magnet with the combination of dipole and quadrupole fields (Fig. 5a). The dipole field produced with two coils moves the electron beam along Y-axis. The quadrupole field of another four coils enables to adjust the tilt of the beam image in YZ-plane (Fig. 5b).

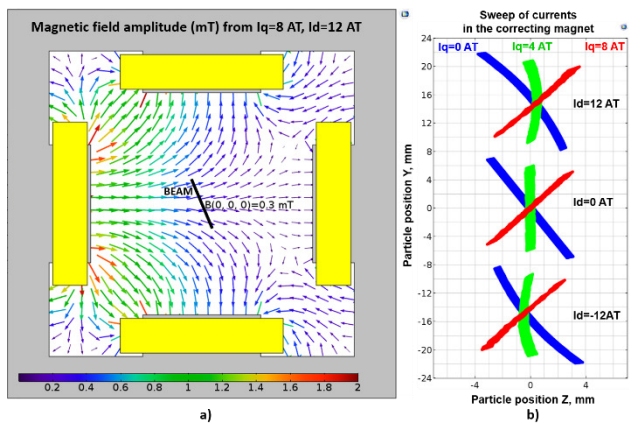

Figure 5: (a) Superposition of dipole and quadrupole fields of the correcting magnet. (b) Cross-sections of the e-beam in the plane of the outlet collimator for different quadrupole Iq and dipole Id coil currents (Ampere·Turns).

The three corrections provide an exhaustive fit of the electron beam and the outlet collimator, thus compensating misalignments and influence of external moderate static magnetic fields. To decrease strong fringe or alternating fields from magnetic focusing elements special magnetic shield is used. Typical BSM shield represents a sectional jacket made of 2 mm low-carbon steel. Additionally, the interior surfaces can be covered with a foil made of an amorphous cobalt-iron alloy with high μ_r.

ISBN 978-3-95450-181-6

BEAM CROSS-SECTION MONITOR

Non-destructive diagnostics is preferable both for high-intensity beams, which can destroy diagnostic device, and low-intensity beams, which can be destroyed totally during measurements.

Despite seeming simplicity of ionization method BCSM (Fig. 6) has a variety of realization problems: geometry and alignment of registration box interior, design of optical channel and radiation shield for CCD-camera, multilevel voltage supply for fields uniformity, lifetime of electro-optical converter etc.

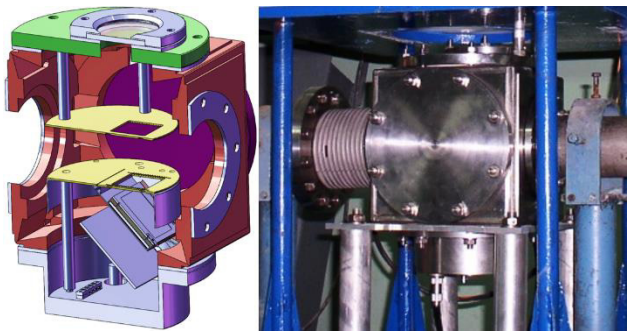

Figure 6: BCSM at the exit of INR Linac.

The main problem of BCSM operation is radiation background at the accelerator (Fig. 7). Both γ-quanta and neutron fluxes cause damages and functional disruptions of radiation sensitive BCSM electronics (CCD camera, memory chips, ADC, MCP). Besides, it is necessary to consider that, for example, reconfiguration process of INR linac for various experiments can change the beam intensity up to 10^4 times, that leads to proportional change of images brightness and losses in the same number of times. Therefore, it is necessary to protect the electronics at high beam intensity, without losing sensitivity in low intensity. So, lens-mirror periscope system was implemented at the linac for realization of these inconsistent requirements.

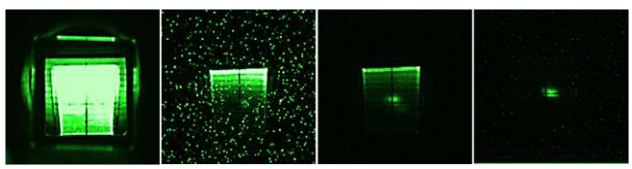

Figure 7: Beam losses decrease during beam tuning.

Now upgraded BCSM is the unique tool for observation and measurements of beam parameters both high and extremely low intensities in the wide range of energy. BCSM has high experimentally tested signal dynamic range (5 μA, 7 μs ÷ 10 mA, 120 μs) and reproduces as simple as complex beam cross-section images and profiles with resolution about 300 μm, that is quite admissible result for in-flight control and diagnostics of various beam parameters (Fig. 8). Our long experience shows, that during normal operation, the shape of the beam cross-section is close to the elliptical one and is unvaried in time. Normally the invariability of the cross-section indicates the stability of the accelerator parameters, that is why BCSM can be used as a tool for control of general beam quality.

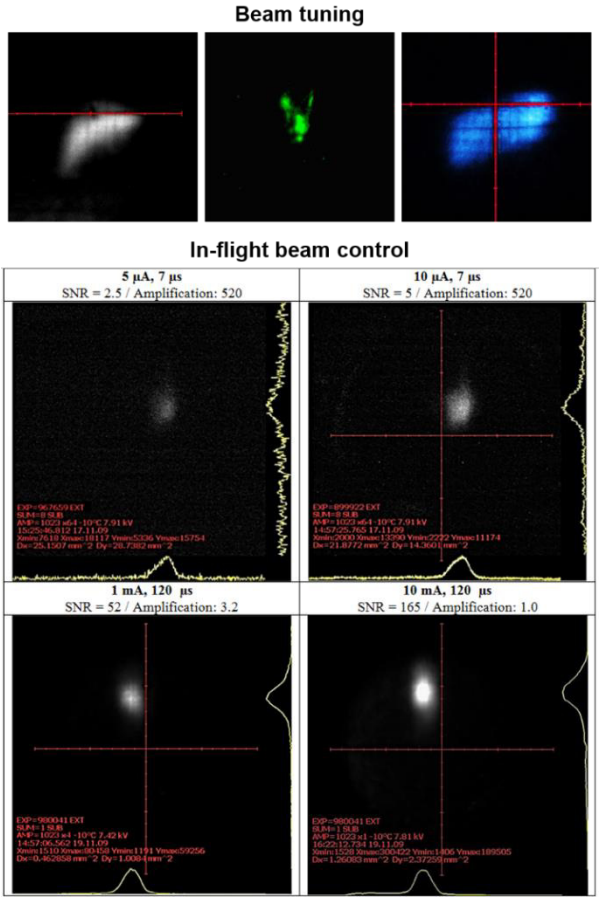

Figure 8: Experimental beam images, registered by BCSM.

ACKNOWLEDGEMENT

Such complicated beam diagnostics devices as Bunch Shape Monitor and Beam Cross-Section Monitor are tools, which developed and upgraded for years. Many people contribute to this work and it is not so easy to list all of them. Nevertheless, the authors would like to acknowledge those, who made enormous contribution during the resent years: Victor Gaidash, Yuri Gotovtsev, Yuri Kisselev, Yuri Kalinin and Ivan Vasilyev.

REFERENCES

[1] R. Witkover, "A non-destructive bunch length monitor for a proton linear accelerator", *Nucl. Instr. Meth.*, vol. 137, no. 2, pp. 203-211, 1976.

[2] A. V. Feschenko, P. N. Ostroumov, in *Proc. LINAC1986*, Stanford, USA, pp. 323-327.

[3] V. Mihailov et al., General-purpose ionization detectors for accelerated particle beams, *Instr. and Exp. Tech.* 6 (1995) 39.

[4] L. Ioudin et al., Synchrotron radiation parameters registration using beam cross-section image detector: the first experiments, *Nucl. Instr. and Meth. in Phys. Res. A*, 405 (1998) 265.

[5] S. Gavrilov et al., "Two-dimensional non-destructive diagnostics for accelerators by Beam Cross Section Monitor", 2014 *JINST* 9 P01011.

[6] A. Feschenko, "Technique and instrumentation for bunch shape measurements", in *Proc. RUPAC2012*, Saint-Petersburg, Russia, pp. 181-185.

ISBN 978-3-95450-181-6

STRUCTURE AND HARDWARE OF LIA-20 CONTROL SYSTEM

G. Fatkin*, E. Bekhtenev, E. Kotov, A. Ottmar, A. Panov, A. Senchenko, S. Serednyakov,
M. Vasilyev, BINP and NSU, Novosibirsk, Russia
A. Batrakov, A. Chupyra, Ya. Macheret, V. Mamkin, A. Pavlenko,
A. Selivanov, P. Selivanov, K. Shtro, S. Singatulin, BINP, Novosibirsk, Russia

Abstract

The control system of a linear induction accelerator LIA-20 for radiography is presented in this paper. The accelerator is designed to provide a series of three consecutive electron pulses with energy up to 20 MeV, current 2 kA and lateral size less than 1 mm. To allow reliable operation of the whole complex, coordinated functioning of more than 700 devices must be guaranteed in time frames from milliseconds to several nanoseconds. Total number of control channels exceeds 6000. The control system structure is described and the hardware in VME and CAN standards is presented.

INTRODUCTION

Linear Induction Accelerator LIA-20 (see Fig. 1) is designed to pro-vide three consecutive electron beams with an energy up to 20 MeV, current up to 2 kA and the beam lateral size after focusing on the target less than 1 mm. It is planned to pro-vide three consecutive pulses, with one of them divided into 9 angles. The accelerator will be used for the flash X-Ray radiography. Successsfully commissioned LIA-2 accelera-tor (2 MeV, 2 kA) could be considered a prototype for the injector of the 20 MeV installation [1]. The control system of the LIA-2 is described in [2]. Both accelerators consist of a large number of complex electrophysical devices that require extensive control.

To attain the minimum possible beam size the structure with low acceleration rate was chosen. The upside of this approach is that common and cheap HV technology could be used (thyratrons, cabling). The downside is a large quantity of required devices. In case of LIA-20 we have more than 6000 control and measurement channels, this is approximately ten times more than LIA-2 and all known LIA flash radiography installations (DARHT, FXR, AIRIX, DRAGON)[3]. Therefore we had to introduce a lot of new approaches for design of our control system. Structure and hardware of the control system are the scope of this paper, while the software and the computational infrastructure are described in [4].

STRUCTURE OF THE ACCELERATOR

LIA-20 consists of the injector and a number of accelerating modules. The injector has 92 inductors and generates an electon beam with the current up to 2 kA and the energy 2 MeV. 30 “short” accelerating modules (SAM) are placed after the injector. Each of them consists of 16 inductors and adds an energy of 0.33 MeV to the beam. Then 12 “long” accelerating modules (LAM) are placed each of them consists of 32 inductors. Each LAM adds an energy of 0.66 MeV to the beam. The total length of the accelerator is about 75 meters, therefore controlling the positioning of optical system is critical. The injector has individual support, two SAM’s are placed on one support and each LAM is placed on a separate one. Two position control systems are provided to control the horisontal, vertical and angular offsets of the axis of supports.

Focusing solenoidal lenses and correctors are placed between accelerating modules. The lenses are powered by pulsed power supply that provides 0.5 kA, 2.05 ms sinusoidal pulse. Beam position monitors (BPM’s) are present between accelerating modules. Several other technological sub-systems including vacuum and insulating gas pressure require control.

Accelerating pulses on the inductors are formed by the

* G.A.Fatkin@inp.nsk.su

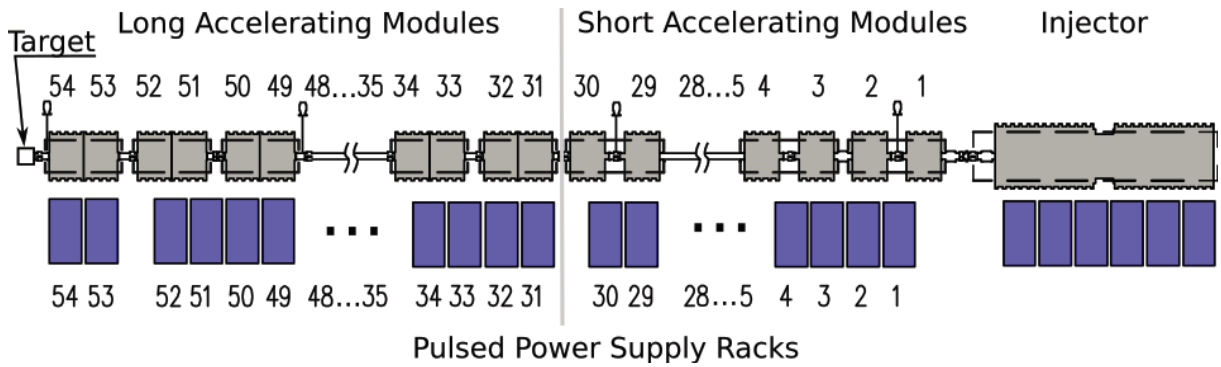

Figure 1: Scheme of LIA-20 Accelerator

ISBN 978-3-95450-181-6

modulators. Each modulator is a high-voltage device based on thyratron that provides 40 kV 60-300 ns pulse with fronts better than 5 ns for two inductors. To provide several consecutive pulses, several modulators are used. Each thyratron has it's own delay, therefore to get required accelerating voltage pulse form, starting moments must be arranged in time with accuracy better than 4 ns. The modulators are grouped in racks called pulsed power supply racks (PPSR). Eight modulators provide one pulse, 16 are used for two-pulsed regime and 24 are required for three consecutive pulses. The injector is supplied by 3 PPSR's, two SAM's are supplied by one PPSR, and each LAM is supplied by one PPSR's. PPSR's are charged by charging devices that are placed along the installation. The sinusoidal demagnetization pulse (100 A, 1 ms) is required for inductors and is provided by high-voltage demagnitizer that supplies 16 inductors.

It should be noted that to facilitate the launching process a 5 MeV version of the installation would first be assembled at BINP. Then after necessary beam parameters would be obtained, 20 MeV single-pulsed installation would be assembled. After that, several pulses and several angles are planned.

CONTROL OBJECTIVES

Let us formulate the objectives of the control system. It should be noted, that flash radiography experiments that would be held using LIA-20 are very time and resource consuming, therefore one of the main tasks is to provide reliable and coordinated functioning of all the elements of the installation. To ensure the reliability as much information as possible about the installation should be collected. Also to prohibit the experiment in case some of the subsystems are working incorrectly the fast interlock system is necessary.

Another objective of the control system is to allow the operator control such an installation. This is not an easy task. With big amount of information, human couldn't effectively control all of it, therefore automation of information processing should be introduced providing the integral indicators. But every individual channel must be tracked and controlled and the operator should be able to change single parameters manually.

Table 1 presents the summary of channels for one-pulsed version of the 20-MeV machine. "D." means a digital channel.

STRUCTURE OF THE CONTROL SYSTEM

It is reasonable to divide the control elements into the structural units and place these units along the installation. It was decided that we can have one control unit providing all necessary functions for one LAM, or for two SAM's. Three control units would be necessary for the injector. The control units are connected using Ehternet.

The control system in whole could be divided into following subsystems:

- Synchronization
- Measurement
- Fast interlock
- Slow controls

First three of them are used to control the processes during the "pulse" of the accelerator, including: charging the pulsed power supplies, forming the inductor demagnetizing and magnetic lenses current pulses, initiating the experiment, launching thyratrons and measuring all the resulting signals and pulses. The last one takes care of all the processes deemed "slow". This processes take place between the pulses and include: controlling the position of the accelerating structure, controlling vacuum pumps and vacuum quality, controlling the incandescence of the cathode, etc.

The synchronization subsystem provides all controlled and controlling devices with start pulses. The overall accuracy must be better than 4 ns across 70 m of length. This means that the propagation delays between control units must be taken into consideration and negated.

The measurement subsystem digitizes two groups of signals: the "fast" (up to several us) signals and the "slow" (up to several ms) signals. "Fast" signals include: form of the voltage on inductors, form of the current on lenses and beam positioning monitor signals. "Slow" signals are: charging device and modulator voltages and demagnetizing currents. More detailed description of the measurment subsystem could be found in [5]

Main goal of the fast interlock subsystem is to prohibit the start of the experiment if some critical component doesn't work correctly at the moment. It has to collect the interlock signals from all devices and make a fast decision.

The slow controls subsystem incorporates: vacuum and pumps controls; optical system alignment control (described in detail in [6]); control of the parameters of charging device, degauss and lense power supplies, and modulators; cathode filament power source.

HARDWARE

The slow controls is realized using CAN-BUS. Several previously developed devices: CANDAC, CANADC,[7] are used. Specialized controllers were developed for: the demagnetizing source, the cathode filament power source, modulators and optical system alignment control.

Specialized VME crate was designed for the control unit of the control system. It has the following features:

1. 21-position 2-U VME crate
2. VME-64x standard compatible
3. $\pm$ 12 V 6 A power lines
4. integrated remote power control by CAN-BUS

ISBN 978-3-95450-181-6

Table 1: Controlled Devices and Number of Channels

Name	Control	Measurement	Synchronization
Inductors	0	480	0
Modulator	0	480	0
Pulsed Power Supply	480 D.	480 + 480 D.	540
Demagnetizing	60 D.	60 + 60 D.	60
Lense power supply	60 D.	60 + 60 D.	60
Charging device	6 D.	6 + 6 D	6
BPM	0	120	0
Positioning (wire)	0	28 D.	0
Positioning (water)	0	84 D.	0
Technological and Vacuum	≈ 100	≈ 100	0
Total	706 D.	1686 + 818 D.	666

5. synchronization and clock lines on U/D pins
6. inter-module communication daisy-chain on U/D pins

A number of modules were developed specially for the control system and the VME-BINP crate. First are the two oscilloscope modules developed for the measurement subsystem.

ADC4x250VME

- 4 ADC channels
- 250 MSps
- 80 MHz bandwidth
- 0.75 MWords/Channel

ADC-32VME

- 4 8-channel ADC's (32 channels)
- 125 kSps (switchable)
- 300 kHz bandwidth
- 0.75 MWords/Channel

Next, we present two modules for the synhcronization subsystem: the delay line DL-250VME and the Timer-VME.

DL-250VME

- 16 channels (RIO) + 8 channels (Front)
- Discrete 4 ns
- Range 17 s

Timer-VME

- optical connection
- propagation delays accounting
- clock accuracy 2 ns
- low-jitter $<$ 100 ps
- VME-Binp synchronization

CAN-Bus is used for all slow and technological control needs. **VME-CAN** board provides the interface for 2 CAN-Bus networks to the VME.

CONCLUSION

Using the experience of LIA-2 the control system structure for LIA-20 was devised with focus on modularity, extensibility. The developed VME-BINP crate is a extension of VME-64x standard. A number of modules are developed and Currently an inductor test stand with 2 PPSR's and 4 SAM's is comissioned and control system elements are being tested on it. Next step is the assembly of LIA-5 – the 5 MeV linear accelerator with all control system elements. Then the 20 MeV one-pulsed version is planned.

REFERENCES

[1] Starostenko D. A. et al., "Results of operating LIA-2 in radiograph mode", Phys. of Particles and Nuclei Letters, 2014, Vol.11, No. 5, pp. 660-664.

[2] Bak P. A. et al., "Control system of a linear induction accelerator of an X-ray complex: Structure, hardware, and test performance", Optoelectron. Instrument. Proc., 2011, Vol. 47, No. 3, pp. 303-312.

[3] C. Ecdahl, "Modern electron accelerators for radiography." 2001 IEEE Pulsed Power Conference, Las Vegas, Nevada, 2001, plenary presentation.

[4] A. Senchenko et al. "Software and Computational Infrastructure of LIA-20 Control System" THPSC088, these proceedings.

[5] E. Kotov et al. "VME Based Digitizers for Waveform Monitoring System of Linear Induction Accelerator (LIA-20)" THPSC081, these proceedings.

[6] A. Chupyra et al. "System of Geodetic Measurements for LIA-20" THPSC083, these proceedings.

[7] Kozak V. R. and Kuper V. A. "Multifunctional devices for control system of accelerator facilities" Optoelectron. Instrument. Proc. 2015, Vol. 51, No 1, pp. 12-21.

ISBN 978-3-95450-181-6

THE MONITORING OF THE EFFECTS OF EARTH SURFACE INCLINATION WITH THE PRECISION LASER INCLINOMETER FOR HIGH LUMINOSITY COLLIDERS

B. Di Girolamo*, J.-Ch. Gayde, D. Mergelkuhl,
M. Schaumann, J. Wenninger, CERN, Geneva, Switzerland
N. Azaryan, J. Budagov, V. Glagolev, M. Lyablin,
G. Shirkov, G. Trubnikov, JINR, Dubna, Russia

Abstract

Earth surface movements, provoked for example by earthquakes or industrial noise, can induce a degradation of particle accelerators instantaneous luminosity or even sudden beam losses. This report presents the results from monitoring the effects of earthquakes on the present LHC beam orbit and luminosity, using a novel instrument, the Precision Laser Inclinometer (PLI). The aim is to characterize the response of accelerators to remote or nearby Earth surface movements and propose possible applications of the instrument for minimizing detrimental effects.

INTRODUCTION

The Precision Laser Inclinometer (PLI) is a novel type of instrument able to detect inclination of the Earth surface with high precision [1]. The instrument main characteristics have been studied in comparison with other known instruments and observing natural phenomena as a continuous source of calibrating events: the micro-seismic peak, the effects of the Moon attraction cycle and earthquakes. This report will briefly introduce the working principles of the PLI, the observations of relevant phenomena and finally discuss the possible applications to high luminosity colliders, which are notoriously very sensitive to Earth surface movements from natural and human (cultural noise) sources.

THE PRECISION LASER INCLINOMETER

The Precision Laser Inclinometer (PLI) is part of a large program of survey instrumentation developed at JINR - Dubna in the framework of research and developments for the ATLAS experiment in collaboration with the CERN Survey group. The deployment and the study of the results are being done in collaboration between JINR and CERN (the High Luminosity LHC Project and the Beam Operations).

A set of PLI prototypes have been installed at CERN, since 2015, in the TT1 tunnel, a former transfer tunnel of the Intersecting Storage Rings (ISR) and now used as stable environment for the development of surveyors instrumentation among other usage. The TT1 tunnel offers a suitable environment for the understanding of PLI characteristics.

The Experimental Setup and the First Measurements

The PLI setup is shown in Fig. 1. Schematically the setup is quite simple, a cuvette with liquid is placed on a very stable base plate (support S) and a Laser delivers a light ray, reflected by the surface of the liquid. The reflected light is detected by a quadrant photodiode (QPr).

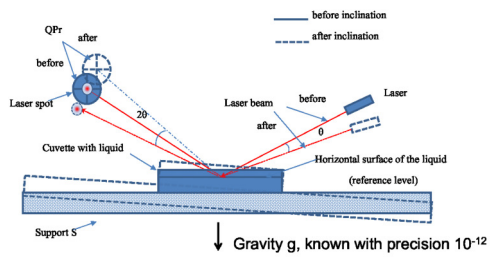

Figure 1: The PLI setup.

When the system is inclined by an angle θ, the surface of the liquid remains, by gravity, horizontal, while the Laser light is deflected by an angle $2\times\theta$ and this movement of the light spot is detected by the quadrant photodiode and recorded by the data acquisition system. The detection is in both planes and therefore it is easy to calculate the combined slope of the movement and its azimuth.

The very stable ground and temperature conditions in the TT1 transfer tunnel allowed to perform several studies of stability versus temperature, influence of industrial noise. Comparative measurements with known instruments [2, 3] allowed to to monitor, over a period of a month, a variety of phenomena inducing Earth inclinations, from industrial to natural kind, where the latter are dominated by the recording of the micro-seismic peak, the Moon attraction cycle and earthquakes. The precision of detection achieved was assessed to be better than 10^{-9} rad/Hz$^{1/2}$ in the frequency range $[3 \cdot 10^{-7}, 1]$ Hz, where $3 \cdot 10^{-7}$ Hz corresponds to one month period. For daily measurements the precision achieved has been assessed to 10^{-10} rad/Hz$^{1/2}$ in the frequency range $[10^{-3}, 1]$ Hz [2, 3]. Recently the working range of the PLI has been extended to 4 Hz via carefully selecting a liquid with lower viscosity.

*beniamino.di.girolamo@cern.ch

ISBN 978-3-95450-181-6

OBSERVATIONS OF EARTHQUAKES AT THE LHC

It is well known that accelerators and light sources are sensitive to ground oscillations. Earthquakes are rare events, but provide calibrating data to establish the sensitivity of accelerator components and of the detecting instruments (e.g. the PLI).

The effects can be quantified to determine both the impact of ground motions and the possible deployment of PLIs for their monitoring and ideas for corrective actions.

Waves from Earthquakes

During an earthquake event the different types of body (Pressure, Shear) and surface (Rayleigh, Love) waves and their path and reflections through the Earth produce a complex signature at seismic measurement stations and also at the LHC. The seismic activity in the Geneva area is very low, but distant earthquakes can affect the LHC.

During the past years of operations of the LHC at high luminosity several earthquakes had effects on the beam. Around twenty earthquakes have been observed to affect the LHC beam, during the period March 2015-November 2016. Many more earthquakes occurred in that period, but no beam was circulating during those occurrences. The effects on the earthquakes can be quantified looking at the RMS of the LHC orbit oscillations, estimating the impact as follows:

- $\Delta R \sim 50\ \mu$m: beam dump unlikely
- $\sim 200\ \mu\text{m} < \Delta R < \sim 100\ \mu$m: beam dump probable
- $\Delta R > \sim 200 \mu$m: beam dump definitive

where $\Delta R = 200\ \mu$m corresponds approximatively to 1 σ at the LHC primary collimation system (TCP).

These are qualitative limits as a beam dump for a certain orbit movement strongly depends on tail population and wave properties among other factors. The orbit stability at the TCP is constantly monitored and it is controlled to the level of $\pm 5\ \mu$m during stable collisions.

Earthquake Detection by the LHC and the PLI

About twenty earthquakes have been observed simultaneously by the LHC and the PLI, showing correlations of the effects and improving the knowledge of the response of both the accelerator and the PLI.

A recent earthquake in the Atlantic Ocean at the Ascension Islands occurred on August 29th, 2016. The earthquake magnitude was 7.1 and the ground movements were detected at CERN ten minutes after, at the distance of ~ 5600 km from the epicenter.

Looking at the effect of this earthquake it is possible to observe clear correlations between the ground motion detected by the PLI and the orbit perturbation and losses for the LHC beams. The latter mainly appear at the maximum of the amplitude of the oscillations as shown in Fig. 2. From top to bottom are shown the amplitude plots from PLI and from LHC, the plot of the RMS of the LHC orbit and finally the profile of the losses at the collimation system. It is interesting to notice that, in this occasion, the PLI starts detecting oscillations earlier than the LHC orbit starts significantly to vary.

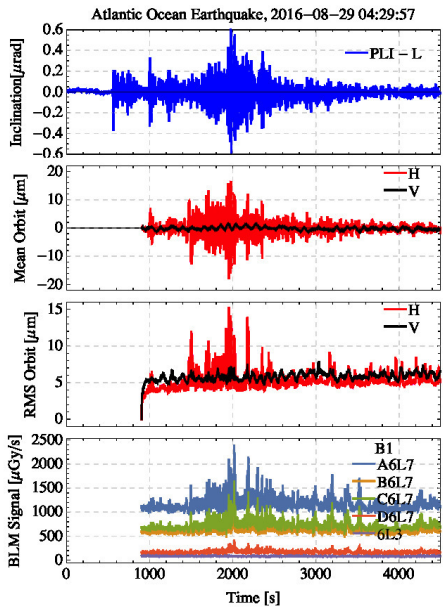

Figure 2: The amplitude plots for the PLI response, the LHC orbit perturbation, the LHC RMS of the orbit and the profile of the losses at the level of the collimation system.

The mean orbit perturbation and the PLI signal amplitude correlated, as well as how well correlated are the beam losses at the collimators and the PLI signal amplitude.

A very clear correlation between the PLI signal and the accelerator behaviour in presence of ground movements is given by looking at the instantaneous luminosity at the experiments. The Fig. 3 shows, as an example, the superimposition of the PLI amplitude signal and the instantaneous luminosity in the ALICE experiment that oscillates in phase with the ground motion and the PLI signal, in very good agreement.

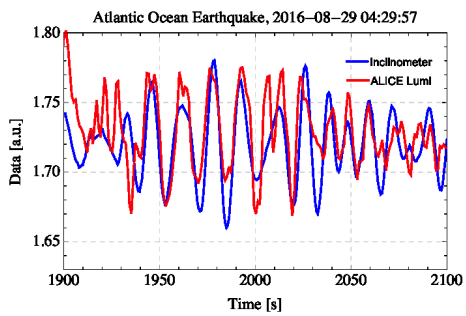

Figure 3: The PLI signal superimposed on the ALICE instantaneous luminosity showing very good agreement.

ISBN 978-3-95450-181-6

A simulation of the LHC ring response to ground movements is under active development. The simulation takes into account the measured displacement and the travel direction of the wave with respect to the LHC. The PLI provides both and it is therefore a good testbench for the simulation results.

A comparison has been done at the simulation level by comparing the current LHC optics with possible schemes of optics for the HL-LHC [4], where beams are more squeezed. The comparison indicates that the RMS orbit response is increased by a factor around two to three for the HL-LHC optics. As an example an earthquake occured in Italy in 2012 caused a RMS obit oscillation of around 60 $\mu(m)$ to which the LHC beam survived, but that would have most probably caused a beam dump with the HL-LHC optics.

APPLICATIONS FOR HIGH LUMINOSITY COLLIDERS

The PLI is a newly born instrument and the development has shown a wide range of possible applications. Concentrating on possible deployments at high luminosity colliders, based on the observations made so far, one can easily identify three possible area of application, which will be detailed here.

Monitoring activity. The monitoring of the PLI started at the beginning of 2015 in the TT1 tunnel. In the future one can propose the installation of four PLI devices in the vicinity of the Inner Triplet areas for the ALICE, ATLAS, CMS and LHCb experiments at the LHC. Relevant experience can be thus achieved.

Active feedback. Once the PLI will be fully commissioned and calibrated with comparison to known instruments it can supply a more active feedback to the operators of a high luminosity collider. It can provide warnings about the occurrence of ground movements preventing possible unwanted beam dumps.

Active stabilization. For the future of the PLI development program a very important role is played by the networking of the devices. By connecting devices in a network over a large area will allow a mapping of the ground movements and of their propagation over such a large area as for example below the LHC inner Triplet quadrupoles. With a sort of "mechanical transistor" the movement detected by each PLI can generate a command to motorised jacks to modify the height of the magnet compensating for ground movements.

NEXT STEPS AND CONCLUSIONS

Several improvements are being considered as next steps in the development of the PLI. Quite recently detailed technical specifications have been prepared for a possible industrial production.

The PLIs will then provide a systematic measurement of any ground movement in the years to come allowing to improve the knowledge of the instrument and of the seismic and micro-seismic activities and the LHC response to them. If installed in 2018 they will be able to provide a measurement during the excavation work for the underground areas for the future HL-LHC (to house power converters, superconducting links) to happen in the years 2019-2020 and will allow the inter-calibration of the PLI with other more classical instruments, like the HLS and geophones or similar.

The PLI can have several others applications in other fields, however since March 2015 is being also used as an instrument to detect ground movement that affect the LHC beams with effects on the beam losses and on the instantaneous luminosity. The beam conditions for the High Luminosity LHC will be more severe with a factor, between two and three, higher level of perturbation for the orbit and beam losses at the primary collimation system level.

The high sensitivity of the PLI (better than 10^{10} $\mathrm{rad/Hz^{1/2}}$) in the frequency range $[10^{-3}, 1]$ Hz allows early detection of events like earthquakes, allowing the PLI to be used as an active feedback system in addition to the monitoring functions already deployed. Being the earthquakes rare events, the attention is also to the monitoring of micro-seismic activities to which high luminosity and low emittance colliders might be potentially affected.The PLI can possibly provide a way of active stabilisation of large magnets by amplification of its detection to correct the position of magnets depending on the ongoing ground movements.

This novel instrument appears to have great potentialities that are being actively investigated for its optimal use.

ACKNOWLEDGMENT

The authors would like to acknowledge the very useful discussions and support provided by Gianluigi Arduini, Oliver Bruning, Paolo Fessia, Miriam Fitterer, Michael Guinchard, Helene Mainaud-Durand, Dominique Missiaen and Lucio Rossi.

The Dubna group thanks the BMBF (Germany) for the fundamental and serious financial support.

Finally a special thanks to the organiser of the RuPAC 2016 Conference in Saint Petersburg for the excellent conference spirit.

REFERENCES

[1] N. Azaryan et al., "The precision laser inclinometer long-term measurement in thermo-stabilized conditions (First Experimental Data)", Phys. Part. Nucl. Lett 12 (2015), Issue 4, 532-535

[2] V. Batusov et al., " Recent advances and perspectives of the high precision laser metrology," CLIC 2014 Workshop, CERN, February 2014, JINR E13-2014-21

[3] N. Azaryan et al., "Comparative Analysis of Earthquakes Data Recorded by the HLS and the PLI Instruments", Part. Nucl. Lett. (submitted)

[4] G. Apollinari et al. (eds), "High-Luminosity Large Hadron Collider (HL-LHC) : Preliminary Design Report", CERN, Geneva (2015) http://cds.cern.ch/record/2116337

ISBN 978-3-95450-181-6

COMMISSIONING OF e^+/e^- TRANSFER LINE FROM BINP INJECTION COMPLEX TO VEPP-2000 FACILITY*

I.M. Zemlyansky#, Yu.S. Aktershev, V.V. Anashin, A.V. Andrianov, A.M. Batrakov, O.V. Belikov, D.E. Berkaev, M.F. Blinov, B.A. Dovzhenko, F.A. Emanov, V.V. Gambaryan, V.A. Kiselev, I.A. Koop, I.A. Mikheev, D.A. Nikiforov, A.V. Otboev, V.P. Prosvetov, V.V. Rashchenko, A.M. Semenov, P.Yu. Shatunov, Y.M. Shatunov, S.S. Vasichev, V.D. Yudin, Yu.M. Zharinov,
BINP SB RAS, Novosibirsk, Russia
A.A. Krasnov, A.V. Pavlenko, Y.A. Rogovsky, D.B. Shwartz, A.A. Starostenko,
BINP SB RAS, Novosibirsk; NSU, Novosibirsk, Russia

Abstract

VEPP-2000 e^+/e^- collider [1] was constructed in 2006 at BINP. The design luminosity of 1×10^{32} $cm^{-2}s^{-1}$ may be achieved at filling rate of 1×10^8 e^+/e^- per second. Old VEPP-2M facility infrastructure provided only 1×10^7 e^+/e^- per second. We decided to use Injection Complex [2, 3]. The transfer line [4] connects Injection Complex and VEPP-2000 facility. Commissioning of e^+/e^- transfer line from Injection Complex to VEPP-2000 facility is done in 2016. Both electrons and positrons beams are injected to VEPP-2000 collider.

GEOMETRY AND OPTICS

We simulated the optics with the RING program [5]. Detailed geometry and optics are shown in Figures 1-9.

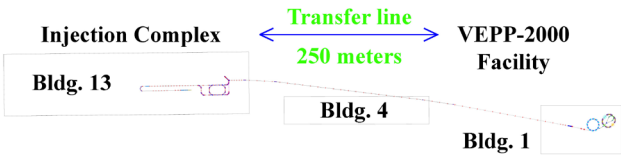

Figure 1: The transfer line location.

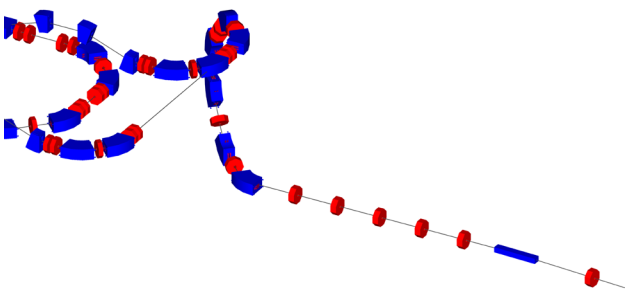

Figure 2: The descent from the storage ring.

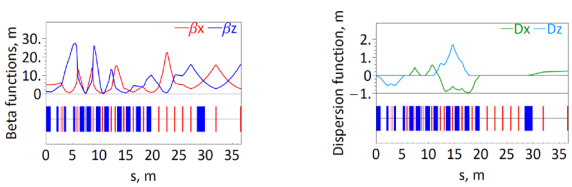

Figure 3: Lattice functions of the descent.

Figure 4: First horizontal bend.

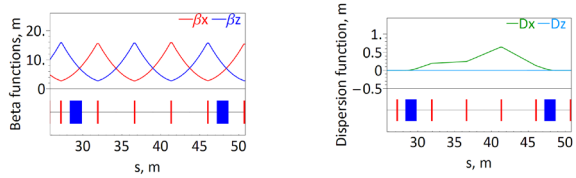

Figure 5: Lattice functions of first horizontal bend.

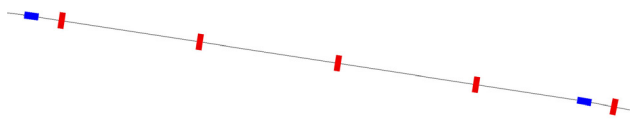

Figure 6: Second horizontal bend.

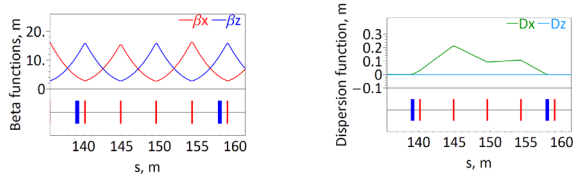

Figure 7: Lattice functions of second horizontal bend.

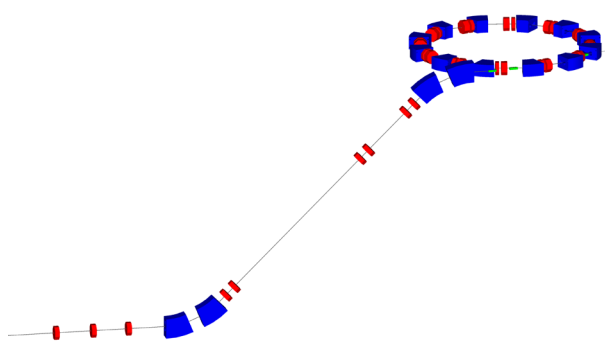

Figure 8: The ascent to booster BEP.

*The work is supported by the Ministry of Education and Science of the Russian Federation, NSh-10088.2016.2
#I.M.Zemlyansky@inp.nsk.su

ISBN 978-3-95450-181-6

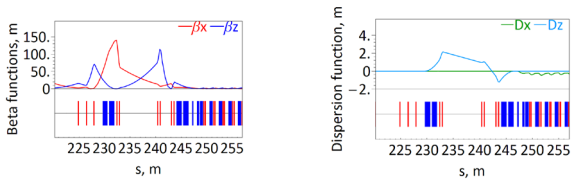

Figure 9: Lattice functions of the ascent.

MAGNETS AND POWER SUPPLIES

We calculated magnets with the aid of the MERMAID code [6]. Parameters of magnets and power supplies [7] are listed in Table 1.

Table 1: Magnetic elements and power supplies for beam energy of 510 MeV.

Element	Parameters	Power supply
6 dipoles of the descent	H=1.52T L=0.88m	2 DC, IST I=1.1kA
2 horizontal dipoles of the first bend	H=0.08T L=1.51m	1 DC, UM-20, I=20A
2 horizontal dipoles of the second bend	H=0.1T L=0.51m	1 DC, UM-20, I=20A
4 vertical dipoles of the ascent to the booster BEP	H=0.67T L=1m	1 AC, GID-3000, W=3kJ
1 horizontal dipole before the septum of BEP	H=1.74T L=0.29m	1 AC W=2.4kJ
1 septum of BEP	H=1.74T L=0.43m	1 AC W=2.4kJ
18 quadrupoles of the descent, the ascent and the matching part	G=1-16T/m L=0.2m	18 AC, GID-25, W=25J
43 quadrupoles of the regular part	G=2.59T/m L=0.2m	8 AC, GID-25, W=25J
6 dipole correctors in 6 dipoles of the descent	Hmax=0.02T L=0.88m	6 DC, PS-3A, I=3A
11 dipole correctors in 11 quadrupoles of the descent and the ascent	Hmax=0.1T L=0.2m	11 AC, GID-25, W=25J
27 dipole correctors	Hmax=0.01T L=0.1m	27 DC, PS-3A, I=3A

VACUUM SYSTEM

The vacuum chambers are made of stainless steel. The inner aperture of quadrupoles is 23 mm. Inner regular part dipole's aperture is 24 mm, inner descent and ascend dipole's aperture is 21 mm. The required vacuum level of 1×10^{-8} Torr was obtained by sputter ion pumps (quantity is 8 pcs) with pumping speed of 160 l/s (nitrogen equivalent). We located pumps at the distance of 25 meters each other.

CONTROL SYSTEM

We based the automation system [8, 9] on several PC platforms under Linux operating system. The control of power supplies is based on VsDC2 integrators [10, 11].

Some fragments of control software are shown in Figure 10-14.

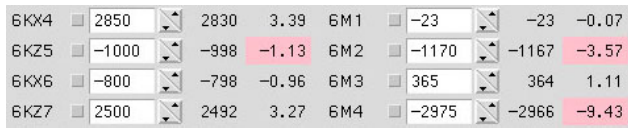

Figure 10: Control of some DC-elements.

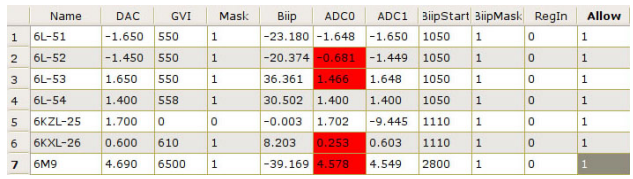

	Name	DAC	GVI	Mask	Biip	ADC0	ADC1	BiipStart	BiipMask	RegIn	Allow
1	6L-51	-1.650	550	1	-23.180	-1.648	-1.650	1050	1	0	1
2	6L-52	-1.450	550	1	-20.374	-0.681	-1.449	1050	1	0	1
3	6L-53	1.650	550	1	36.361	1.466	1.648	1050	1	0	1
4	6L-54	1.400	558	1	30.502	1.400	1.400	1050	1	0	1
5	6KZL-25	1.700	0	0	-0.003	1.702	-9.445	1110	1	0	1
6	6KXL-26	0.600	610	1	8.203	0.253	0.603	1110	1	0	1
7	6M9	4.690	6500	1	-39.169	4.578	4.549	2800	1	0	1

Figure 11: Control of some AC-elements.

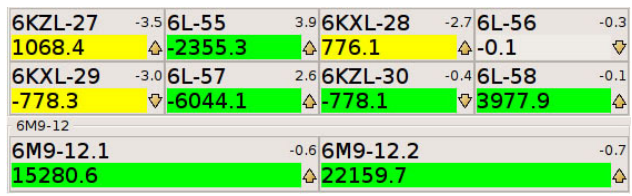

Figure12: Control of some power supplies.

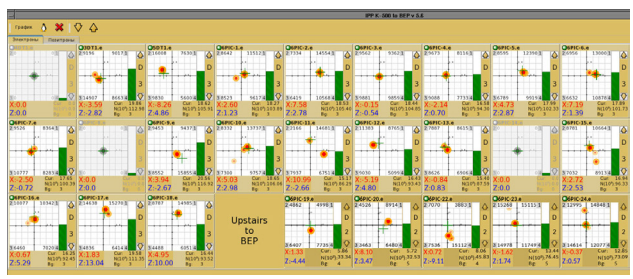

Figure 13: Image current monitors over the transfer line.

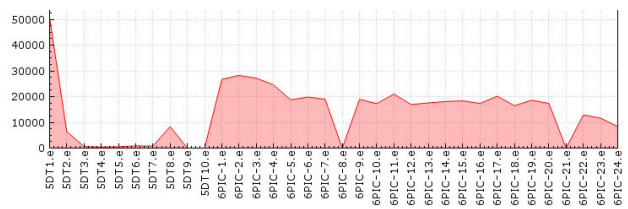

Figure 14: Current distribution over the transfer line.

BEAM DIAGNOSTICS

We used three types of sensors for beam diagnostics: 12 luminophor probes, 24 image current monitors and 1 Faraday cup. They are presented in Figures 15-17.

ISBN 978-3-95450-181-6

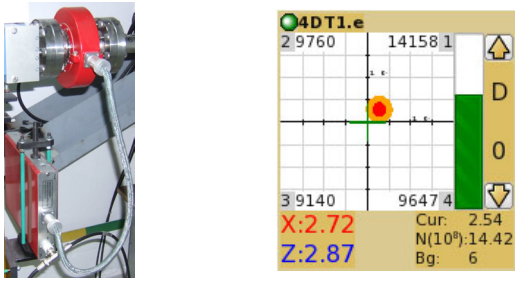

Figure 15: We used image current monitors in real time beam pass.

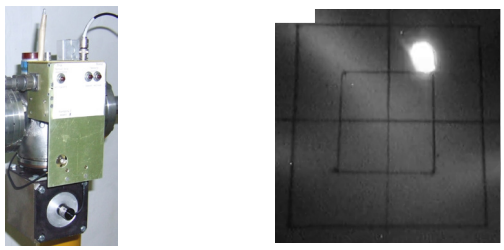

Figure 16: Luminophor probes are used for first beam-pass. Beam-picture's size is about 20 mm.

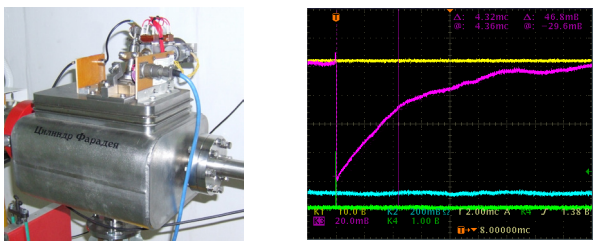

Figure 17: We use Faraday cup to determine the number of particles in the beam before the ascent. The graph shows the beam discharge.

CONCLUSION

During creation of the transfer line, a number of tasks has been solved. We created the optical scheme of the transfer line connecting Injection Complex and VEPP-2000 facility. Simulation of the acceptance of BEP [12] in the admission place for determination of optimum coordinates and inclinations of bunches is carried out. We simulated magnetic calculations of all magnetic elements, beginning from the descent. We made the analysis of possible deviations of the bunch trajectory from a design trajectory, for the reasons of instability of power supplies and possible errors of a geodetic exhibition. For correction of a trajectory, installation sites of dipole correctors are optimized. Considering an arrangement of magnetic elements and dipole correctors, we defined locations of the diagnostic equipment. Losses of positrons and electrons at design luminosity of a collider of VEPP-2000 are estimated. Proceeding from the necessary speed of replenishment of particles, we developed the working mode of the transfer line and we defined additional requirements to designs of magnetic elements and power supplies.

Transfer of bunches from Injection Complex to BEP was a lot of work. We synchronized RF systems of Injection Complex and VEPP-2000 facility. The control of power supplies and beam diagnostics are debagged. We written software applications. The bunch is transported through all turns.

The transfer line will allow us to obtain new data on detectors SND [13] and CMD-3 [14].

ACKNOWLEDGMENT

Thanks to L.N. Arapov, D.B. Burenkov, I.N. Churkin, K.V. Dyakov, Yu.I. Koysin, I.E. Korenev, N.N. Lebedev, E.B. Levichev, P.V. Logatchev, S.A. Mishin, M.I. Nepomnyaschykh, A.A. Novikov, A.V. Polyansky, R.Z. Pronik, O.A. Proskurina, A.L. Romanov, S.I. Ruvinsky, S.V. Seleznev, L.E. Serdakov, A.N. Skrinsky, V.P. Cherepanov, V.A. Shishkin, G.G. Shumakov, V.D. Yudin, V.K. Zhurba.

REFERENCES

[1] Yu.A. Rogovsky et al., "Status and perspectives of the VEPP-2000 complex," Proc. of RuPAC2014, Obninsk, Kaluga Region, Russia.
[2] A.V. Akimov et al., "Status of Injection Complex VEPP-5: machine commissioning and first experience of positron storage," Proc. of IPAC2014, Dresden, Germany.
[3] D. Berkaev et al., "Commissioning of upgraded VEPP-2000 injection chain," Proc. of IPAC2016, Busan, Korea.
[4] I.M. Zemlyansky et al., "Electron and positron beams transportation channels to BINP colliders," Proc. of RuPAC2014, Obninsk, Kaluga Region, Russia.
[5] A.P. Lysenko et al., "Program of numerical simulation of accelerator structures RING," BINP, Novosibirsk, Russia.
[6] A.N. Dubrovin, "Program of magnetic calculations MERMAID," BINP, Novosibirsk, Russia.
[7] V.V. Rashchenko, "А ГИД-25 Bipolar Pulse Generator for Energizing Elements of the K500 Beam Transportation Channel," Instrum. Exp. Tech., 2012, Vol. 55, No. 1, pp. 49–55.
[8] A. Senchenko et al., "VEPP-2000 collider control system," Proceedings of PCaPAC2012, Kolkata, India.
[9] D. Bolkhovityanov, "CXv4, a modular control system," Proceedings of ICALEPCS2015, Melbourne, Australia.
[10] A. Pavlenko, "Electronics for precise measurements of accelerator pulsed magnets," Proc. of IPAC2013, Shanghai, China.
[11] A.M. Batrakov et al., "Precision Digital Signal Integrators with Accurate Synchronization," Optoelectron. Instrument. Proc., 2015, Vol. 51, No. 1, pp. 51–57.
[12] D. Shwartz et al., "Booster of electrons and positrons (BEP) upgrade to 1 GeV," Proc. of IPAC2014, Dresden, Germany.
[13] M.N. Achasov et al., "Search for the $\eta' \to e^+e^-$ decay with the SND detector," Phys. Rev. D, 2015, Vol. 91, Iss. 9.
[14] D.N. Shemyakin et al., "Measurement of the $e^+e^- \to K^+K^-\pi^+\pi^-$ cross section with the CMD-3 detector at the VEPP-2000 collider," Phys. Lett. B, 2016, Vol. 756, pp. 153–160.

ISBN 978-3-95450-181-6

PROPOSAL OF THE ACCELERATING STRUCTURE FOR THE FIRST CAVITY OF THE MAIN PART OF INR LINAC

I.V. Rybakov†, Y.Z. Kalinin, V.N. Leontev, L.V. Kravchuk, A.N. Naboka, V.V. Paramonov, V.L. Serov, A.V. Feschenko, Institute for Nuclear Research of the RAS, Moscow, Russia

Abstract

For the improvement of beam power and operational stability of INR linac, replacement of the first four section cavity of the main linac part is required. The new cavity should not lose to the present one in beam dynamics and RF parameters with minimal modifications in the other linac systems. The results of more detailed study of possible accelerating structure are presented in this paper.

INTRODUCTION

The first cavity of the main part of INR linac works for proton acceleration in the range β=0.4313 – 0.4489 with acceleration gradient $E_0 T\cos\varphi_s$ = 2.5 MV/m and the synchronous phase φ_s=-33°. The cavity has the aperture radius r_a= 17 mm, operating frequency f_a=991.0 MHz and the required operating regime is with RF pulse length τ=200 μs and Repetition Rate (RR) up to 100 Hz, Fig. 1.

Figure 1: The existing INR DAW cavity. 1 – accelerating sections, 2 – bridge coupling cavities, 3 – RF input, 4-focusing elements.

The main part of the INR linac is based on the Disks and Washers (DAW) structure [1], Fig. 1c. After a long time after linac construction, the direct repetition of the single DAW cavity in the industry is expensive and another options should be considered. Both proven in high intensity hadron linacs and promising new developments were considered preliminary for this purpose, [2], considering parameters of the existing DAW cavity as the reference points. From the total set of required parameters the INR development – Cut Disk Structure (CDS) - was pointed out as the most effective choice. This structure already is used for electron acceleration, β=1.0, with the accelerating gradient up to E_0T= 12 MV/m as the PITZ CDS booster cavity, [3], and operates in the regime with RF pulse length up to τ=800 μs, RR =10 Hz, hence, with the heavy heat load up to 25 kW/m. Application for low β~0.4313 case is not favorable for CDS parameters. We not can scale simply solutions for β=1.0 case, and additional development is required. Results of the more detailed CDS development for applications in the intense hadron linac with a moderate velocity of accelerating particles β=0.4313 – 0.4489 are presented below.

PARAMETERS OF THE STRUCTURES

Compared structures, DAW, CDS, Side Coupled Structure (SCS) [4] and Annular Coupled Structure (ACS) [5], are shown in Fig. 2 in a common scale for the same operating frequency.

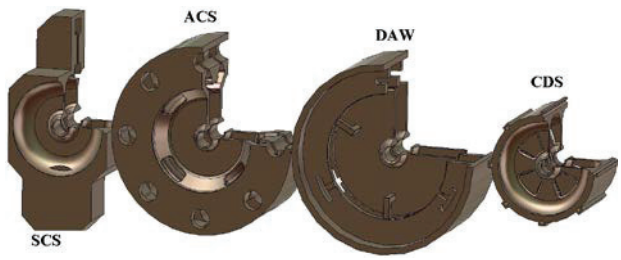

Figure 2: Considered accelerating structures: a) SCS, b) ACS, c) DAW, d) CDS.

For the proven structures DAW, SCS and ACS the key points of cavities design and parameters are known from references. Structures have a similar value of the effective shunt impedance Z_e, but strongly differ in value of coupling coefficient K_c. At the background of the known experience for DAW, there is no sense to consider structures SCS and ACS for the single cavity. But with two times smaller CDS transverse dimensions we can reduce costs of construction by less amount of raw OFE material and applying more usual Numerically Controlled (NC) equipment. Operating regime of the first cavity results in the heat load more than 7 kW/m. For such regime all considered structures require an internal cooling – cooling channels should be placed inside the structure closer to drift tube region to prevent a significant shift of operating frequency Δf_a and the temperature increase ΔT at the drift tube tip during cavity operation. In the proven structures it is realized by internal cooling channels inside web between accelerating cells and with necessity in the design there are brazed joints water-vacuum. In CDS for low β~0.44 the cooling problem is more severe.

CDS OPTIMIZATION

The schematic sketch of the CDS period is shown in Fig. 3. Internal channels should be placed in the web between coupling and accelerating cells only, see Fig. 3. It limits the web thickness to $t_w \geq 10$ mm and the total distance $d_w \sim 25$ mm becomes comparable with the period length $d=\beta\lambda/2 \sim 65$ mm. In such conditions for all structures Z_e value decreases and we can not get directly required RF efficiency.

ISBN 978-3-95450-181-6

† rybakov@inr.ru

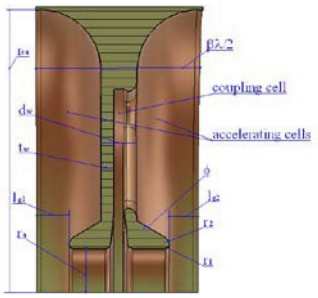

Figure 3: Schematic sketch of the CDS period.

The reference DAW design has a reserve – a single radius of the drift tube tip and the maximal electric field at the drift tubes is $E_{s.max}$=0.5 E_k where E_k =28.5 MV/m is the Kilpatrick threshold at operating frequency. It is too conservative value for present hadron linacs and there is a reserve for Z_e improvement.

CDS RF Parameters

The drift tube region for CDS structure was optimized following to the procedure, described in [6]. To improve further Z_e value the double radii tip shape is introduced for drift tube, see Fig. 3. For the accelerating cell in 2D approximation the data library was stored for different combinations of the drift tube dimensions. To have the same conditions for beam dynamics, aperture radius r_a is conserved as in reference design. In the further treatment the values of drift tube rounding r_1 and r_2 were connected to have the same $E_{s.max}$ value at both arcs and the optimal gap length was defined to have the maximal Z_e value. In each section of the cavity the cells have the same β value, which increases from first to forth sections. Taking into account the numbers of cells in each section, which is defined by lattice of particles focusing, [1], we define the total effective shunt impedance of the cavity Z_{et} and can analyze $Z_{et}(E_{s.max})$ dependencies, see Fig. 4.

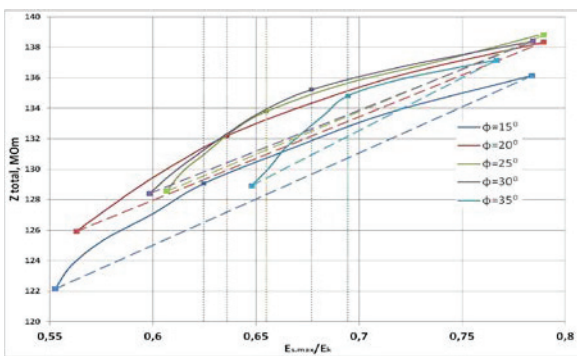

Figure 4: Plots of Z_{et} ($E_{s.max}$) for the total cavity different angles of drift tube, φ.

To reduce the cost of mechanical treatment, the main part of cells dimensions, which define CDS geometry, are the same for all four cavity sections. The fixed dimensions were defined to have the minimal Z_{et} reduction for the total cavity as compared to variable dimensions in four sections. Finally, at the expense of increasing to $E_{s.max}$=0.8 E_k, we obtain Z_{et} value for the CDS cavity at a small amount of 0.12% higher than Z_{et} for the reference DAW cavity. It is also rather conservative $E_{s.max}$ value. Further increasing is not reasonable. As can be seen from Fig. 4, Z_{et} ($E_{s.max}$) dependencies are not linear and with further $E_{s.max}$ rise, increasing a risk of electrical breakdowns, we do not have a sufficient compensation in cavity RF efficiency.

Structure Cooling

In the proven CDS booster cavity [3] the cooling circuit is realised both with internal channels, placed in webs between cells, and with outer channels along the section. For the INR cavity the operating regime results in a lower heat loading and structure cooling was reconsidered by using ANSYS software [7] and following to the procedure, described in [8]. Assuming the safe value for cooling water velocity of < 2 m/sec, the calculated distribution of the temperature at the cell surface are shown in Fig. 5 for the input water temperature of 27 C°.

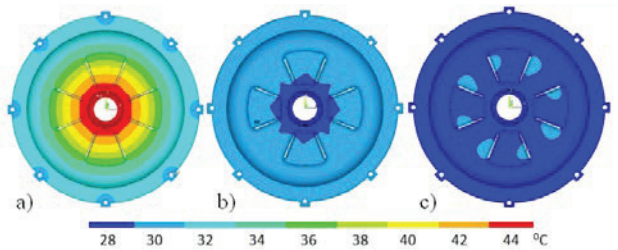

Figure 5: The temperature distributions at the CDS cell surface for cooling with external channels only, (a), internal only, (b), and for both external and internal channels, (c).

The non uniform heating due to RF power dissipation results in a non uniform temperature rise ΔT and induced thermal deformations of the cell surface, which results in frequency shifts both for accelerating Δf_a and coupling Δf_c modes. The calculated numerical results for different options of structure cooling are presented in Tab. 1. The thermal stress value is well inside elastic limit for the annealed OFE copper in all options of cells cooling.

Table 1. Calculated ΔT , Δf_a , Δf_c values for different options of the structure cooling.

Opt.\Par.	external	internal	Internal and external
ΔT, °C	15.24	3.30	2.10
Δf_a, kHz	-324.7	-49.3	-46.8
Δf_c, kHz	1131.2	171.7	165.1

Analyzing results in the Table 1 we see, that internal channels provide the major effect in the cell cooling. Addition of external channels results in very small effect on values of frequency shifts , Δf_a , Δf_c. To simplify the design of the total cavity and reduce cost of construction, in the cavity only internal cooling channels for cells cooling are foreseen. Basing on the small CDS transverse dimensions and the proven experience [3], internal cooling channels can be produced in cells without the brazed

ISBN 978-3-95450-181-6

joints water-vacuum. It strongly improves reliability of the long term cavity operation.

Multipactor Discharge

For the PITZ booster [4] CDS was designed to avoid MultiPacting (MP) in operating cavity range. For INR cavity CDS should operate with much smaller accelerating gradient E_0T and with the period length $d=\beta\lambda/2 \sim 65$ mm we are limited in the selection of dimensions for coupling cell. Possibility of MP for INR cavity is studied in [10].

Accelerating CDS cells are free from discharge all time. But in compensated structures the total field contains addition of coupling mode, which should be excited to ensure RF power flow along the cavity to compensate losses for RF power dissipation in cavity walls and for beam acceleration, [10]. This addition linearly decreases from RF input point to the cavity ends. In the INR cavity RF input is into the central bridge cavity between the second and the third accelerating sections. Results of study show MP possibility for operating regime in the first and the fourth sections, e.g. for the low level of excitation for the coupling mode. For safety we introduce for these sections enforced excitation of coupling mode to the level above the upper range of MP zone by alternating detuning of adjacent accelerating cells at the frequency $df \sim 1.2$ MHz. Such detuning of adjacent cells results in a tolerable Z_e decreasing < 0.5%. Also detuning is regular along CDS section and does not results in a significant spread of the accelerating filed distribution.

According results of simulations, for the second and the third CDS sections this detuning of adjacent cells is not necessary. The natural excitation of the coupling mode is sufficient. Application of alternating cells detuning for these sections results in a more complicated procedure of RF tuning and will be defined in the consideration of the total CDS cavity parameters, taking into account bridge coupling cavities.

Tolerances for Manufacturing and RF Tuning

For intense hadron linacs the input value for selection of tolerances for cells manufacturing is the standard deviation of the electric field distribution σ_e <1 %. This σ_e value is connected with K_c and tolerable values σ_{fa}, σ_{fc} for the spread in frequencies of accelerating and coupling modes, the stop band width $\delta f=f_c-f_a$ and the spread in coupling coefficient σ_{kc}, see [11] for details. CDS structure naturally realizes $K_c \sim 17$ % and, in comparison with SCS and ACS, $K_c \sim 5$ % already there is an one order σ_e decreasing for the same precision of cells production. Further K_c increasing, up to $K_c \sim 40$ % like in DAW, is possible for CDS at the expense of Z_e reduction, but is not so effective, because σ_{kc} contribution in σ_e dominates.

According the results of tolerances estimation, [11], for CDS cells we can apply a typical tolerance value up to +- 50 μm and relax the tolerance for the stop band width in RF tuning of sections to $\delta f \sim (200 – 350)$ kHz. It overlaps the stop band opening due to structure heating in operating regime, see Table 1. The expected spread for accelerating cells is of $\sigma_{fa} \sim 3.8\ 10^{-4}$ and the calculated value $\sigma_e \sim 0.5$ % provides some reserve and freedom in RF tuning. Together with the moderate transverse dimensions, CDS cell outer diameter is of ~ 240 mm, the mechanical tolerances of ~ 50 μm are comfortable for cells production with an usual NC equipment.

The technique of the CDS sections tuning was developed during CDS booster cavity construction, [12]. Basing on the sufficient K_c value, we avoid the individual tuning of cells frequencies and tune the section as a whole. But the intermediate Quality Control (QC) for produced cells was introduced to prevent against accidental extra spikes in cell frequencies. With the regular detuning of accelerating cells for the first and the forth sections, taking into account the expected values $3\sigma_{fa} f_a \sim df = 1.2$ MHz, QC procedure, used in [12], should be extended to have the ensured difference between frequencies of adjacent accelerating cells.

SUMMARY

The results of the detailed study show, that, instead of initial CDS proposal and proven application for high energy particles, we can adapt structure for application in the high intensity hadron linac for moderate energy range. With the tolerable increasing $E_{s.max}=0.8\ E_k$ required RF efficiency is obtained. Structure cooling can be realised without not reliable joints water - vacuum. More complicated procedure of RF tuning to prevent multipackting is the acceptable price for the single cavity. CDS structure remains the mostly cost effective choice for application in replacement of the first cavity in the main part of INR linac.

REFERENCES

[1] B. Murin, “Biperiodic accelerating structures”, in *Linear ion accelerators*, Atomizdat, Ed. Moscow, USSR: 1981
[2] I. Rybakov *et al.*, “Comparison of accelerating structures for the first cavity of the main part of the INR linac”, *J. Phys.: Conf. Ser.*, vol. 747, p. 012073, 2016.
[3] V. Paramonov et al., in *Proc. LINAC’10*, *p.* 241
[4] S. Henderson et. al. , in *NIM A*, v. 763, pp. 610-673, 2014.
[5] “Accelerator Technical Design Report for J-PARC”, KEK, Tsukuba, Ibaraki, Japan, 2003
[6] V. Paramonov, in *Proc. LINAC’96*, *p.* 493
[7] ANSYS, http://www.ansys.com
[8] A. Skassyrskaya et. al., in *Proc. LINAC’02*, p. 216
[9] I. Rybakov and I. Isaev, TUPSA035, this conference.
[10] V. Andreev and V. Paramonov, in *Proc. PAC’95*, p. 1702.
[11] I. Rybakov et. al., TUPSA036, this conference.
[12] A. Naboka et. al., "Results of CDS booster cavity RF tuning", *VANT, Series: Nuclear physics*, vol. 5, p. 35, 2008.

ISBN 978-3-95450-181-6

DEVELOPMENT OF RF ACCELERATOR ON PARALLEL-COUPLED STRUCTURE – TREND IN ACCELERATOR TECHNIQUE

Yu. D. Chernousov†, Voevodsky Institute of Chemical Kinetics and Combustion SB RAS, Novosibirsk, Russia

Abstract

Development of parallel-coupled accelerating structure (PCS), creation of RF linier accelerator based on PCS is new and rapidly developing field of accelerator technology. Compared with conventional accelerating structures with serial communication - the standard traveling and standing waves structures, the PCS has a lot of features and advantages. There are many problems in the development of RF linear accelerators: breakdowns at high power levels, the destruction of the structure due to overheating, the excitation of higher-order mode, the decline of field strength along the structure, transients, beam loading, beam focusing, multipactor, radiation accelerator cleanliness, etc. PCS - the best accelerating structure for solving these problems.

INTRODUCTION

To construct RF accelerators, accelerating structures of traveling and standing waves [1] have been used and improved for a significant amount of time. By method of excitation, these are the structures with serial communication, where the microwave power is linked up with one of the structure's cavities and then it is subsequently circulated from one cavity to another. Both the accelerating structures with serial communication and the electron linear accelerators in these structures are characterized by a significant number of scientific and technical problems. Some of the problems and the challenges set accordingly are listed below:

- Cavity RF breakdown, and reduction of breakdown influence on the structure and the accelerating beam.
- Local pulsed overheating, input elements destruction, and heat reduction.
- Excitation of higher order modes, and "decimation" of the mode spectrum.
- Decline in strength of the accelerating field along the structure's axis, and challenge on developing the specified field.
- Accelerated particles focusing at considerable beam currents, and challenge on developing the effective system of beam focusing.
- Problems of injection current control, and challenge on developing the effective control systems.
- Transient processes in the structure, and stabilization of the microwave field amplitude.
- Load of the structure by the beam current, and stabilization of accelerating voltage.
- Radiation background, and provision with a high beam capture close to 100%.
- Excitation of secondary-emission resonant discharge, and its suppression.
- Forming the electron beams of considerable average power (at least 10-100 kW) at energy over 5 MeV.

The main solutions of these problems for standard accelerating structures intended for low-energy accelerators as well as for high-energy physics seemed to be found. For example, for structures with high accelerating gradient, these are an increase in the accelerating field frequency, reduction in the pulse duration, optimization of the cavity shape, selection of the work surface materials, preparation and training of accelerating structures [2]. For the standard structures, limit operations are defined, the optimal values are found.

Recently, an interest in parallel-coupled accelerating structures has been deepened. These structures are characterized not by the consistent, but by the parallel method to supply the microwave power to the accelerating cavities. Such a circuit design makes it possible to expect for higher limit values in comparison with the standard structures with serial communication - traveling and standing waves.

PARALLEL-COUPLED STRUCTURE FOR RF ACCELERATOR

Key Idea Development

An idea of the "Parallel Coupled Structure" (PCS) in the accelerator technology occurred upon the paper [3] published which describes the structure containing the accelerating cavities powered in parallel from the lead-in coaxial waveguide. The phase velocity of the wave in the coaxial line is equal to the light speed, thereby the wave and accelerated electrons synchronization is ensured. Currently, a new focus area in the accelerator technology is being developed, various schemes of accelerating structures are being offered, features and advantages of the PCS are being investigated [3-13].

A circuit scheme disadvantage [3] was a low level of microwave power supplied to the accelerating cavities through a coaxial line. Easy replacement of the coaxial line with the hollow waveguide is impossible, since the wave phase velocity in the waveguide is bigger than the light speed, the wave "runs away" from the accelerated particles, synchronism is impossible. While developing [3], we proposed a scheme with a counter-movement of waves and particles. The a concept of reverse power input is applied, the particles and accelerating field synchronization in the PCS can be achieved under usage of the rectangular waveguide as an exciting element operating in the traveling wave regime [4]. A structure schematic diagram is shown in Figure 1.

† email address: chern@catalysis.ru

ISBN 978-3-95450-181-6

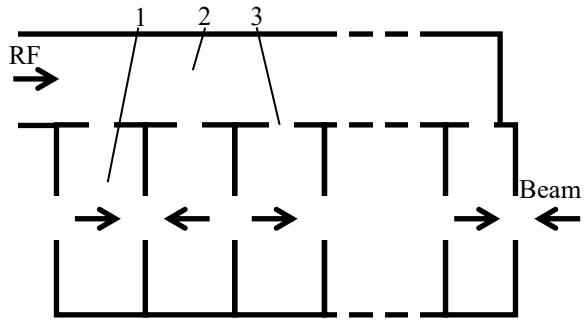

Figure1: The PCS scheme with rectangular exciting waveguide and reverse power input.

Accelerating cavities 1 are excited by the RF wave traveling along the rectangular waveguide 2 through the coupling slots 3. Microwave power and electron inputs are performed at the opposite ends of the accelerating structure. If the structure geometry is the case, the following condition is fulfilled:

$$L=\lambda_g\lambda_0(V/C)/[\lambda_g+\lambda_0(V/C)],$$
$$\Delta\varphi=2\pi\lambda_0(V/C)/[\lambda_g+\lambda_0(V/C)]. \quad (1)$$

where L - the space in between the near-by cavities' centers, $\Delta\varphi$ - the oscillation phase shift in the near-by cavities. The bunch moving towards the wave from one cavity to another one gets into the same phase of accelerating field oscillations. Under this condition, synchronism is provided, and the particles are accelerated. Here λ_g, λ_0, V, C are respectively the wave length in the waveguide, in free space, the electron velocity and the light speed. According to the accelerating cavities excitation method, such a structure is a structure with parallel connection with variable distance L between the cavities defined by the normalized particle speed V/C. For example, when $V = 0.4C$ (the electron velocity under injection of 50 kV), in the 10-centimeter wave length range, under $\lambda_0 = 10$ cm, $\lambda_g = 15$ cm, it is found that $L\approx3$ cm, the oscillation phase shift in the near-by cavities $\Delta\varphi = 2\pi/5$; at $V = C$, we obtain: $L = 6$cm, $\Delta\varphi = 4\pi/5$. This example shows that such an accelerating structure is suitable for accelerating the electron in a wide energy range. With increase in beam energy, the phase shift and the distance between the cavities (structure step) have to grow respectively (1). The structure step is suitable for the construction of its optimized cavities. For relativistic electrons at $V = C$, the structure step is $L = 6$ cm. Such a step size is close to half the wave length ($\lambda_0/2 = 5$ cm). By installing into the size L the cavity of optimized form, a structure with shunt impedance, close to the maximum value can be achieved. For non-relativistic electrons, the structure step is smaller that is also useful for installing the cavities with smaller longitudinal dimensions. In addition, magnetic field focusing elements can be installed into the free spaces among the cavities.

New Ideas at SLAC

Close to the focus area, SLAC is currently doing researches. The accelerating structures comprising of a traveling wave waveguide for supplying the microwave power to the accelerating cavities or their groups connected to the waveguide in parallel are offered. The concept is being developed rapidly [6,9,10]. These suggestions seem a repetition of our path in this area [4], including the new challenges. Thus, each cavity included into the side wall of the waveguide [4,6,9,10] reflects, so it disturbs a traveling wave mode in the waveguide, and standing wave occurs. As a result, the ratio of oscillation amplitudes in the cavities is changed. In addition, the wave amplitude falls along the excitation waveguide due to running wave mode therein and sequential power take-off. The excitation conditions for accelerating cavities are different. This makes it necessary to select an individual coupling factor for each cavity that complicates the structure construction and setting. For these reasons, serious problems may occur while implementing the conceptual circuit schemes [6,9,10] experimentally.

Conceptual RF Schematic Diagram of the New Type PCS

We proposed and are currently investigating the new type accelerating PCS comprising of the subsequently situated accelerating cavities with microwave power carried out from a common passage exciting cavity through individual coupling slots [7,8] (Fig.2).

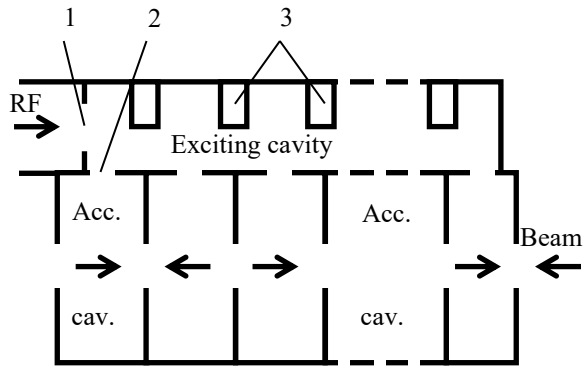

Figure 2: New conceptual PCS scheme [7,8].

Accelerating cavities of the structure are excited individually, working in a standing wave mode, communication via electromagnetic field among them is hardly seen. Microwave power from the generator is supplied to the PCS via the input inductive diaphragm 1. In the transmission-type exciting cavity constructed from the rectangular waveguide section, a standing wave is set, H_{10N-1} mode, where N - number of accelerating cavities. To reduce the wave length, the cavity is loaded by pins 3. Excitation of accelerating cavities is carried out at the standing wave maxima through the slots 2 due to magnetic-field coupling. The near-by cavities are excited in the antiphase, the structure operates on π-mode oscillations in accordance with the terminology. Due to matching pins 3, the cavity wave length is equal to a wave

ISBN 978-3-95450-181-6

length in free space λ_0. The distance between the near-by coupling holes 2 is equal to $\lambda_0/2$, the distance between the first near-by cavities is equal to $\lambda_0 V/2C$, where V - the electron speed, synchronous acceleration of electron bunches from relatively low speed to the light speed C is provided.

PCS VS STANDART STRUCTURES

The papers presented at this conference [12,13] contrast the solutions of two major problems among the given above, i.e., the breakdown problem and the problem of beam capture in the acceleration mode, the standard structure, and in the new type PCS [7,8].

Breakdown

Under the breakdown in the PCS, only one cavity is excluded from the acceleration mode, breakdowns in cavities occur independently, each breakdown is of probabilistic nature. If $\beta_{||}$ - a breakdown probability during the pulse in one specific cavity, then for the PCS consisting of N cavities, $\alpha_{||}$ breakdown probability during the same pulse in n cavities is determined by:

$$\alpha_{||} = N\beta_{||}^{n}, \quad (2)$$

If one breakdown in the PCS is assumed to be possible and a pulse is considered to be lost under simultaneous breakdowns in two cavities, then from (2) with n = 2, N = 100, $\alpha_{||} = 10^{-2}$ one finds $\beta_{||} = 10^{-2}$. The breakdown probability requirements in one specific cavity for PCS are significantly reduced; it is several orders of magnitude smaller in comparison with standard structures [12].

Capture

In electron accelerators based on the standard accelerating structures consisting of a series of subsequently excited accelerated cavities – the "series-connected structures" [1], using the diode guns for beam injection, the capture usually doesn't exceed 30-40%. In the developed microwave accelerator, one received a high capture rate close to 100% in the acceleration mode [13] due to the property of the PCS - the microwave beam focusing in the accelerating cavities, installed into PCS the magnetic system, and the use of an electron gun with injection current RF control.

CONCLUSIONS

RF accelerators tend to be characterized by a significant number of problems. The main solutions of these problems for standard accelerating structures intended for low-energy accelerators as well as for high-energy physics seemed to be found. Estimated and direct experimental comparisons show the features and advantages of the PCS versus the standard structures for low and high energy. The breakdown requirements to the cavities are significantly reduced. This makes it possible to raise the accelerating gradient [12]. It is possible to install a magnetic periodic focusing system into the microwave PCS accelerator. Along with the microwave focusing and using the electron gun with injection current microwave control, it ensures the beam capture close to 100% in the acceleration mode [13].

Development of the idea of microwave power parallel supply to the accelerating cavity, construction and investigation of RF accelerators based on the parallel-coupled accelerating structure, identification of features and benefits are a long-term trend in the accelerator technology [3-13].

ACKNOWLEDGEMENT

The author thanks his colleagues from ICKC, BINP SB RAS for cooperation and helpful discussions.

REFERENCES

[1] Th. P. Wangler, *RF Linear Accelerators*, WILEY-VCH, 2008.
[2] S. Döbert, "Gradient Limitations for High-Frequency Accelerators", *LINAC'2004*, Luebeck, Germany, p. 513.
[3] R.M. Sundelin, J.L. Kirchgessner, M. Tiger, "Parallel-Coupled Cavity Structure", *Trans. Nucl. Sci.*, vol. NS-24, pp. 1686–1688, 1977.
[4] V. I. Ivannikov, Yu. D. Chernousov, I. V. Shebolaev, "Parallel-Coupled Accelerating Structure", *Zhurnal Tekhnicheskoi Fiziki*, , vol. 56, pp. 2407–2409, 1986.
[5] O. N. Brezhnev, P. V. Logatchev, V. M. Pavlov, *et al.*, "Parallel-Coupled Accelerating Structures", *LINAC'2002*, Gyeongju, Korea, p. 213.
[6] J. Neilson, S. Tantawi, V. Dolgashev, "Design of RF Feed System for Standing-Wave Accelerator Structures", *LINAC' 2010*, Tsukuba, Japan, p. 235.
[7] Yu. D. Chernousov, "The Method Excitation of the Accelerating Structure", Pat. № RU2427112C1, B.I. 20.08.2011, №23.
[8] Yu. D. Chernousov, V. I. Ivannikov, I. V. Shebolaev, A. E. Levichev, and V. M. Pavlov, "Parallel-Coupled Accelerating Structure", Pat. № RU2472244C1, B.I. 10.01.2013, №1.
[9] V.A. Dolgashev, "Traveling Wave Linear Accelerator with RF Power Flow Outside of Accelerating Cavities", US Patent Application №US 2015/0359080 A1. Pub. Date: Dec.10, 2015.
[10] S. G. Tantawi, Z. Li, P. Borchard, "Distributed Coupling and Multi-Frequency Microwave Accelerators", US Patent Application №US 2016/0014876 A1. Pub. Date: Jan. 14, 2016.
[11] A. M. Barnyakov et al., "Transient Process in a Parallel Coupled Accelerating System with Regard to Beam Current Loading", *Technical Physics*, vol.60, pp.137-140, 2015.
[12] Yu.D. Chernousov, V., I. Shebolaev, "Gradient Limitation for RF Accelerator on Parallel-Coupled Accelerating Structure", *RUPAC'2016*, St.Petersburg, Russia, this conference.
[13] Yu. Chernousov, I. Ikryunov, I. Shebolaev, "New Experimental Results on RF Accelerator with Parallel-Coupled Accelerating Structure and RF-Control Gun", *RUPAC'2016*, St.Petersburg, Russia, this conference.

ISBN 978-3-95450-181-6

NEW EXPERIMENTAL RESULTS ON RF ACCELERATOR WITH PARALLEL-COUPLED STRUCTURE AND RF CONTROLLED GUN

Yu. D. Chernousov†, I.V. Shebolaev, I.M. Ikryanov, Voevodsky Institute of Chemical Kinetics and Combustion SB RAS, Novosibirsk, Russia

Abstract

New data on the development and experimental investigation of the RF accelerator based on the 9-cavities parallel-coupled accelerating structure that is equipped with a high-frequency grid-controlled electron gun are presented. Accelerating structure, injection system and focusing system are improved. Previously observed second emission resonant discharge - multipactor is suppressed by increasing the field amplitude in the structure first cavity and using the protector. The parameters of the accelerated beam close to the design ones, i.e. electron energy up to 8 MeV, capture to the acceleration mode up to 100%, were received. Capture is provided by the RF electron focusing of the microwave field structure with usage of the magnetic focusing system based on permanent magnets and pulsed "π-injection" of the beam by the microwave grid control in the electron gun.

INTRODUCTION

A new type RF accelerator based on the accelerating structure with parallel connection (PCS) is being developed in ICKC and BINP SB RAS. In the paper [1], the first experimental results on investigation of the RF accelerator based on the PCS - 9-cavities accelerating structure prototype are presented. The results were discouraging. The secondary emission resonance discharge interfered with achieving the designed conditions of beam acceleration. At relatively small field amplitude values, the secondary emission resonance discharge was localized in the first and second cavity of the structure. The discharge stabilized the accelerating field amplitude at a low level, the first cavities didn't accelerate the beam and the electrons fell into the third cavity with energy shortfall. Although the rest structure cavities were operating in normal mode due to the PCS properties, the capture ratio was low; the estimated value of the beam output energy wasn't achieved. It was decided to improve the accelerating structure, increase the field amplitude in the first PCS cavities, and suppress the secondary emission resonance discharge. This was achieved by increasing the communication slots between the accelerating and exciting cavities. To eliminate the secondary emission resonance discharge, a method of suppressing was developed, i.e., a protector was found and conditions of its applying to the secondary emission centers on the cavity surface were selected. The protector application is carried out in the working installation without opening and subsequent contact with the external atmosphere.

Developed by us injection system [2] contains the electron gun with grid control and microwave signal control system supplied to the gun. Previously a circuit scheme was used where the microwave signal was branched off from the main microwave tract of the accelerating structure. There were problems of controlling the signal parameters - amplitude, duration, phase. At this stage, it was decided to upgrade the system, use an additional microwave power amplifier that enables fast electronic control of all the parameters of the microwave signal.

For additional beam grouping in the injection system, a grouping cavity was used previously [1,2], it made it possible to reduce the bunch phase length and increase the beam capture in acceleration mode. The field amplitude in such a cavity was relatively small, and it became an additional place of secondary emission resonance discharge occurrence. Calculations showed that in the acceleration mode high capture close to 100% is possible due to "π-injection", microwave and magnetic focusing and without additional grouping. It was decided to simplify the beam forming system, eliminate the grouping cavity from the electron gun tract. This led to simplification of the electro-optical and magnetic focusing system.

RF ACCELERATOR

Accelerator Bench

Figure 1 shows a bench to study properties of the developed RF accelerator based on the PCS. On the bench, there are installed an improved accelerating structure with integrated focusing system, a new injection system, the measurement elements. Microwave power is supplied through the feed waveguide 1 to the accelerating structure 3. To measure the current accelerated, the Faraday cup 2 mounted on the structure output is used. Focusing of the accelerated beam is made by the installed magnetic system 4. The magnetic system consists only of permanent magnets and shunts without additional focusing coils and tuning elements. Due to the radial input and reverse, a longitudinal focusing magnetic field is generated almost exclusively on the axis of the PCS accelerating cavities, in the area of the beam span, so the magnet mass is relatively small, and in this case, the total weight of the magnetic system is less than 2 kg. Usually in the accelerators in the initial acceleration stage, a solenoid which weight is comparable with the weight of the accelerating structure is used for focusing. Probes 5 are used for measuring the form of waving microwave signals from the first and second cavities of the structure. Microwave signal is supplied via high-voltage antenna lead-in 7 [3] to the electron gun 6. One of the antennas is grounded, and the other is under injection voltage. Among the antennas there is a ceramic insulator. The gun is equipped with an isolation

† email address: chern@catalysis.ru

ISBN 978-3-95450-181-6

transformer 8. The DC high voltage from the source located in the remote control is supplied via a coaxial cable 9. To measure the pulsed injection current, an inductive sensor mounted on a wire supplying high voltage to the gun 10. High-vacuum pumping is carried out by pumps 11.

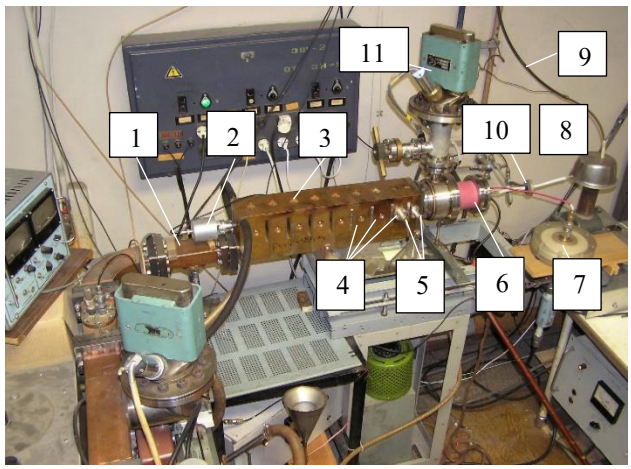

Figure 1: Experimental accelerator stand. The structure length is 0.5 m.

Injection System

Injection system includes a three-electrode electron gun with injection current grid control, an amplifier forming microwave power pulses, timing frequency synthesizer. In our device, a cathode-grid assembly of ГС-34 (GS-34) triode is used, the grid-cathode distance is about 0.1 mm. A cathode-grid unit is installed into a coaxial cavity with a grid-cathode concentrated capacitance. The controlled microwave signal under the injection voltage (about - 50 kV) is supplied via the antenna lead-in to the coaxial cavity. While delivering the controlled microwave signal in the grid-cathode gap, electrons are injected into the grid-anode gap during the half of the microwave period - at a negative cathode voltage relative to the grid. The so-

Figure 2: The gun cathode-grid subunit in the assembled condition. The focusing electrode is removed. The outer diameter is 56 mm.

called "π-mode" beam injection is implemented. The cathodic electrode of the cavity is DC isolated from the grid one and there is a negative DC voltage shift between them, hence, the gun is locked without controlled microwave voltage. This makes it possible to apply a DC-voltage source for the high-voltage power supply of the pulsed electron gun. In this case, a source providing DC high voltage up to -60 kV and current up to 1 mA is used. To generate a pulsed injection current up to 0.5A microwave power up to 0.5 kW in the pulse is required. The exterior assembly of the gun cathode-grid unit is shown in Figure 2.

EXPERIMENTAL RESULTS

The experimental results in beam acceleration were obtained on the stand, Fig. 1. Previously observed second emission resonant discharge [1] is suppressed by applying the protector and increasing the amplitude of the RF electric field in the first and second cavities of the 9-capacity accelerating structure (Fig. 3). It appears that found by us protector and a method to suppress the second emission resonant discharge are universal and applicable in other cases, they require further experimental and theoretical studies and discussions.

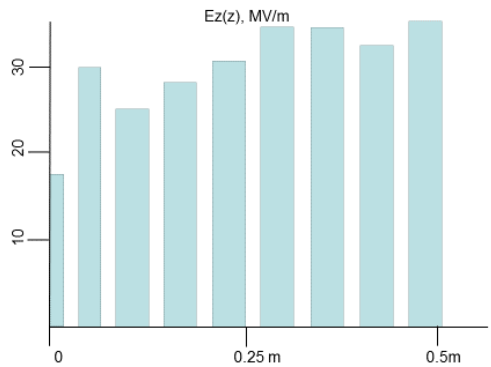

Figure 3: The accelerating field amplitude on the axis of the PCS at 3 MW generator power.

For microwave power of linear electron accelerator, a klystron КИУ-111 (KIU-111) is used [4]. The injection current pulse duration is set in the range of τ = 0.1 - 4 μs, injection current pulsed value - up to 0.3A. We measured: input current - I_{in}, and output current - I_{out}, beam energy, as well as the shape of the waving microwave power incident on the PCS and reflected. The shape detected pulses is shown in Figure 4. Sweep is 0.5 μs/div. The klystron microwave power pulse of about 2.5 MW with duration of 5 μs is shown in line 1. The reflected from the structure signal is shown in line 2. At a minimum of the reflected signal, a tuning to the structure resonant frequency is carried out. Line 3 - input current I_{in} = 200 mA (inductive sensor, 0.9 A/V), line 4 - output current = 200 mA (the Faraday cup at the output of the PCS, 20 mA/V). In this measurement, at a frequency of 2449000 kHz, the electron capture rate in the acceleration mode, $I_{out}/I_{in} \approx 100\%$.

ISBN 978-3-95450-181-6

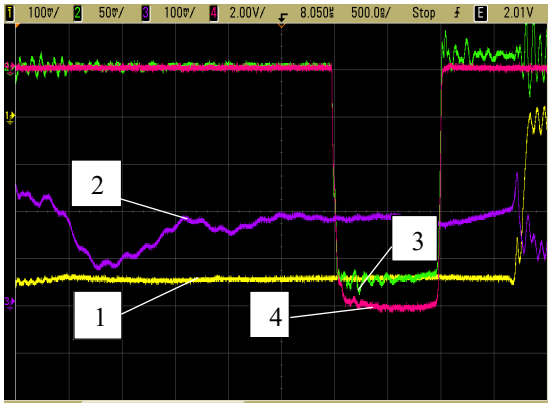

Figure 4: Oscillograms characterizing the beam acceleration mode in the PCS.

The accelerated beam energy is measured by delaying in the metal plates at the beginning of the pulse. Figure 5 shows the dependence of the capture ratio I_{out}/I_{in}, %, and the beam energy, MeV, on the frequency at I_{in} = 100mA. The beam energy is maximal at the frequency 2448950 kHz. The capture ratio is maximal at the frequency of 2449000 kHz due to, presumably, the optimal conditions of the beam microwave focusing by the accelerating electric field. This property of the PCS requires a further experimental and theoretical study. By increasing the current, the capture rate and the particles energy decrease due to the load of the accelerating structure by an electron beam and the decrease in the amplitude of the accelerating field.

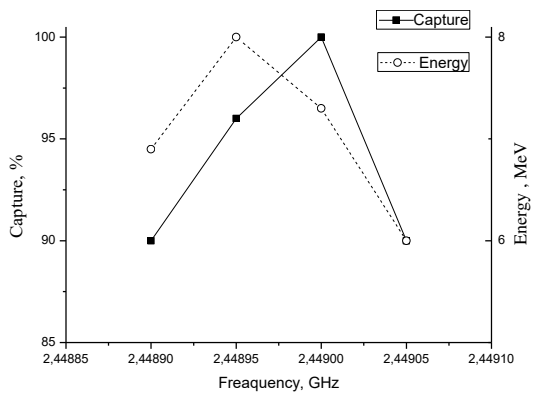

Figure 5: The dependence of the capture ratio in the acceleration and beam energy modes on the frequency.

The investigated PCS is designed to check for key properties and peculiarities of the new type accelerating structure [5,6] and is calculated on the current in the range of 0.1-0.3A in the pulse. By modifying the structure according to the calculations, it is possible to obtain high pulse currents up to 0.5-1A at high capture rate.

CONCLUSION

In the improved microwave accelerator containing the 9-cavity PCS with installed magnetic periodic focusing system based on permanent magnets and in the injection system with RF grid-controlled injection current, the parameters of accelerated electrons beam are received close to the calculated values: at "π-mode" injection, pulse duration is 0.1 - 4 μs, pulse current of the beam - up to 0.3A; beam capture in acceleration mode at currents up to 0.2A in the pulse - 100%; beam energy - up to 8 MeV. At "2p-mode" injection and the pulse duration 4 ns, the capture is about 50%, the pulse current is up to 0.6A, the beam energy is about 8 MeV. The secondary emission resonance discharge in the system is suppressed by increasing the field in the first structure cavities and developing the suppression method including the protector and its method of application to the centers of the cavity secondary emission surface. These experimentally proven properties can be attributed to advantages of the RF accelerators based on the new type PCS [5,6] in comparison with conventional accelerating structures with serial communication.

ACKNOWLEDGMENTS

These experimental works would not have been possible without the support of the BINP SB RAS, BIC SB RAS, ICKC SB RAS administration. The authors thank their colleagues from BINP SB RAS, ICKC SB RAS for fruitful cooperation, assistance in the preparation of the accelerator elements, V.M. Pavlov for the development of beam dynamics calculation program, V.Ya. Ivanov for the program of the gun electron optics calculation.

REFERENCES

[1] Yu. Chernousov, V. Ivannikov, I. Shebolaev, et al. “Experience of Operation of the Electron Linear Accelerator Based on Parallel Coupled Accelerating Structure”, *LINAC’2014*, Geneva, Switzerland, p. 281.

[2] A. S. Bogomolov, E. M. Zakutov, I. V. Shebolaev, Yu. D. Chernousov, “Installation for fast radiation-chemical processes initiation”, *Instruments and Experimental Techniques*, pp. 210-212, vol.2, 1983.

[3] A. M. Barnyakov et al., “A microwave antenna lead”, *Instruments and Experimental Techniques*, 560-564, vol. 56(5), 2013.

[4] I.A. Frejdovich et al., “Multy-Beam Klystrons with Reverse Permanent Magnet”, *RUPAC 2006*, Novosibirsk, Russia, p. 100.

[5] Yu. D. Chernousov, “The Method Excitation of the Accelerating Structure”, Pat. № RU2427112C1, B.I. 20.08.2011, №23.

[6] Yu. D. Chernousov, V. I. Ivannikov, I. V. Shebolaev, A. E. Levichev, and V. M. Pavlov, “Parallel-Coupled Accelerating Structure”, Pat. № RU2472244C1, B.I. 10.01.2013, №1.

ISBN 978-3-95450-181-6

GRADIENT LIMITATIONS FOR RF ACCELERATOR ON PARALLEL-COUPLED STRUCTURE

Yu. D. Chernousov†, I.V. Shebolaev, Voevodsky Institute of Chemical Kinetics and Combustion SB RAS, Novosibirsk, Russia

Abstract

RF breakdown is the main gradient limitation for RF accelerator [1,2]. It is believed that all the known ways to increase the accelerating gradient have been already investigated. These are increase in the frequency of the accelerating field, reduction in the pulse duration, the optimization of cavities form, selection of operating surface materials, preparation and training of accelerating structures. In this paper, we discuss the possibility of increasing the accelerating gradient due to the circuit design, i.e., the use of the parallel-coupled accelerating structure.

INTRODUCTION

To create RF accelerators, accelerating structures of traveling and standing waves are used and improved [1]. By method of excitation, these are the structure with the serial communication where the microwave energy is supplied to one of the structure cavities and then subsequently supplied from one cavity to another. For accelerating structures with serial communication and linear electron accelerators on these structures, there are a significant number of scientific and technical problems. One of them is the breakdown problem leading to a breach of the acceleration process in the structure as a whole, its destruction.

In recent years, an interest in accelerating structures with a parallel connection has been growing. The term "parallel coupled structure" (PCS) in accelerator technology came after the publication of [3] described the structure containing the accelerating cavities fed in parallel from the lead-in coaxial waveguide. Currently, a new focus area in accelerator technology is being developing rapidly, various circuit schemes of accelerating structures are offered, features and advantages of the PCS are investigated [3-11]. We have proposed a new type accelerating PCS containing successive accelerating cavities, microwave power supplied from a common passage excitation cavity through individual communication slots [7,8]. The structure accelerating cavities are excited individually; there is almost no communication along the electromagnetic field between them. While solving the problems in creating the RF accelerators, the use of these structures can produce better results than the use of conventional structures. In this paper, the features and advantages of the PCS under solving the problem of microwave breakdown are shown by calculations and experimentally on the model.

† email address: chern@catalysis.ru

PCS VS STANDARD STRUCTURES

Breakdown in Standard Structure

In the structures with the serial communication under the breakdown at any point of the structure due to a "serial communication", all the microwave energy stored in the structure is absorbed, apparently, mainly near breakdown places. The accelerating field disappears, vacuum is broken due to a discharge product and this pulse is lost. To restore the necessary vacuum conditions, a period of time is required: in the standard structure with serial communication (and consistent pumping) up to 10 seconds [2]. In the accelerators containing a significant number of accelerating structures, the structure with breakdown is disconnected from the microwave power generator and pumped to restore, and the energy shortage of the accelerated beam fills by the reserve system [2].

In the standard structure - with serial communication, α_{--} - breakdown probability during the pulse in the whole structure is N times bigger (N - number of accelerating cavities in the structure), than the β_{--} - breakdown probability in a certain cavity:

$$\alpha_{--} = N\beta_{--} \qquad (1)$$

For example, at N = 100, $\alpha_{--} = 10^{-2}$/pulse from (1), we can find $\beta_{--} = 10^{-4}$/pulse. This means that if the loss is allowed only of every hundredth impulse, at N = 100, one requires the breakdown probability in the certain cavity of such a standard structure no more than $\beta_{--} = 10^{-4}$/pulse. With the growth of the total number of cavities in the accelerator, the requirements to electrical durability of an individual cavity are increasing rapidly in accordance with the ratio (1).

Breakdown in PCS

The breakdown in the PCS occurs in a different way. We started to study the breakdown mods in the PCS in [11] on 5-cavities structure. Let us consider the results obtained in [11]. The PCS operation conditions are characterized by the pulses waveform and shown in Figure 1. Incident microwave power 1 reflected from the accelerating structure of microwave power 2 and a capacitance probe signal 3 proportional to the stored microwave power from the 5th cavity were detected (Fig.1, a - d).

The conditions without breakdown are shown in Figure 1, a. Under breakdown of the 5th cavity (Figure 1, b), all stored therein microwave energy is dissipated for 50 ns (curve 3), and is not restored till the end of the pulse.

ISBN 978-3-95450-181-6

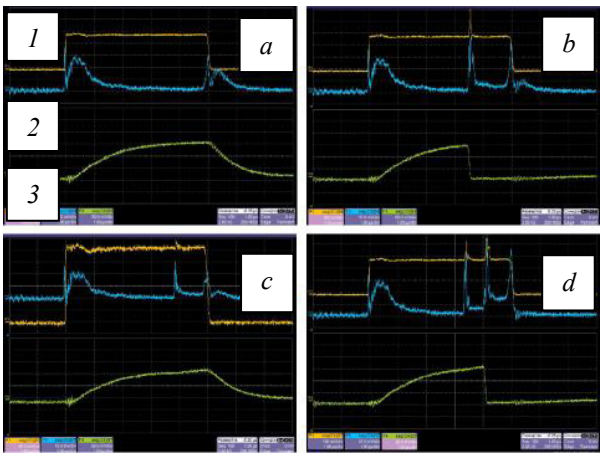

Figure1: The oscillograms descibing the PCA opearion conditions [11].

During the breakdown, the cavity quality is reduced due to losses on discharge products, the frequency seems to be heavily biased, and microwave energy is no longer supplied from the supplying excitation cavity. The cavity with breakdown is disconnected from the excitation cavity. During the breakdown, a part of the stored microwave energy from the accelerating cavity is emitted to the exciting cavity and further on, to the feed waveguide (on the reflected signal 2, a short equal to 100 ns ejection is formed). The PCS now contains only 4 accelerating cavities; the coupling coefficient at the input is changed, so the reflected signal amplitude increases slightly.

If a breakdown occurs not in the fifth cavity, but in one of the first ones, then there are the processes similar to those described above, however it is hardly reflected on the fifth cavity, as shown by curve 3, Fig.1 c. The amplitude of the pulse 3 rises slightly due to the fact that one of the structure cavities is disconnected because of the breakdown and it no longer absorbs the introduced microwave power. This power is redistributed to the remaining cavities of the structure.

Fig.1, d shows a rare case of breakdown during one pulse in two cavities that firstly occurred in one of the first cavities and then in the fifth one. The breakdown in one of the first cavities didn't influence on the stored energy value of the fifth cavity. All the energy stored in the fifth cavity is dissipated for about 50 ns.

The experimental results show that the PCS accelerating cavities influence on each other slightly. In the PCS breakdown, only one cavity is eliminated from the acceleration mode - the one with the breakdown. Remaining cavities continue to accelerate the beam. Breakdowns occur in the cavities independently and are probabilistic in nature. Accordingly, the ratio can be obtained for the probability of breakdowns in the structure.

If $\beta_{||}$ - the probability of breakdown during the pulse in one particular cavity, so for the PCS consisting of N cavities, $\alpha_{||}$ - probability of breakdown during the same pulse in n cavities is determined by the relation:

$$\alpha_{||} = N\beta_{||}^{n} \qquad (2)$$

If we assume that a breakdown in the PCS is acceptable, and under the breakdown in two cavities the pulse is considered as lost, from (2) with n = 2, N = 100, $\alpha_{||} = 10^{-2}$ /pulse, we can find $\beta_{||} = 10^{-2}$/pulse. Compared with the estimates for the β_{--} for the standard structure with serial communication, we can see that the demand on the probability of breakdown in a certain PCS cavity is significantly reduced, in this case by two orders of magnitude.

Let us estimate the requirements to accelerator cavities of considerable length, for example, to the accelerator [2], containing about 18000 standard type accelerating sections, if it is made of the PCS sections and each PCS section has 100 accelerating cavities.

For the project [2], one breakdown in one structure for 10 hours operation period is considered as acceptable at a pulse repetition frequency of 60 Hz and the total number of standard accelerating structures about 18000. This means that the maximum number (rate) of α breakdowns per one impulse is: for a standard structure $\alpha_S \approx 4.6\times10^{-7}$/pulse, for one cavity (under 100 cavities in the structure, i.e.,, 1.8×10^{6} in the accelerator cavities) $\alpha_R \approx 4.6\times10^{-9}$/pulse, and for the whole accelerator in accordance with (2), $\alpha_{ACC} \approx 8.3 \times 10^{-3}$/pulse.

Let us estimate the parameter values for the PCS. Let us assume that during one breakdown in n cavities, such a breakdown is considered as lost. Let α_n be a probability of this event. Note that α_n is equal to the maximum rate of breakdowns in the accelerator as a whole α_{ACC}. Then, assuming that $\alpha_n = 10^{-2}$/pulse, $N = 1.8\times10^{6}$ from the ratio $\beta_{||} = (\alpha/N)^{1/n}$, we will find the values $\beta_{||}$ for different n. The data are given in the Table 1.

Table 1: $\beta_{||}$ values at various n

n	1	2	5	9
$\beta_{||}$	5.5×10^{-9}	7.4×10^{-4}	2.2×10^{-2}	0.12

The table shows that the cavity parameter values $\beta_{||}$ for the PCS are rapidly increasing if n increases as well. For example, if we assume n = 2, i.e., the breakdown occurs during one pulse simultaneously in two cavities of the accelerator as a whole (that is $N = 1.8\times10^{6}$ cavities), the allowable probability of breakdown in the separate cavity $\beta_{||} = 7.4\times10^{-4}$/pulse. For the whole accelerator, such events will occur often.

The probability of α simultaneous breakdown in n cavities is determined by the relation (2). When $N = 1.8\times10^{6}$, n = 2, $\beta_{||} = 7.4\times10^{-4}$/pulse, we obtain the initial value of $\alpha \approx 10^{-2}$/pulse, i.e., every hundredth pulse will be lost. If two cavities are excluded from the acceleration mode at the same pulse, under energy set in each PCS cavity of 1 MeV, the full energy shortage will be about 2 MeV in the lost pulse. Comparing the value $\beta_{||} = 7.4\times10^{-4}$/pulse for the PCS with the values $\beta_{--} = 4.6\times10^{-9}$/pulse given earlier for the standard structure, we can see that the allowable probability of a breakdown in certain cavities under the same requirements to the accelerator generally differ by about 5 orders of magnitude.

ISBN 978-3-95450-181-6

So, under the breakdown probability in one cavity β_{II} = 7.4×10^{-4}/pulse, the breakdown will occur simultaneously in two cavities in the PCS accelerator in general with a probability $\alpha \approx 10^{-2}$/pulse, i.e., every hundredth pulse will be lost. The breakdown in one of the accelerator cavities will occur practically at each pulse.

The dependence number of the breakdowns in the structure on the field strength (breakdown rate) was thoroughly investigated for the future accelerator structures. The dependence is exponential, and in accordance with the operating schedule [2], breakdown rate increases by times with increasing intensity of the accelerating field by 10% in the working area of the accelerating field strength of 50-70 MV/m. According to these data and the estimates [2] as well as to the experimental data and the estimates given in this paper, assuming a breakdown in one cavity, i.e., considering such a pulse as a working one, and in case of breakdown in two cavities, the pulse (every hundredth one) as lost one in the PCS accelerator in comparison with the standard structures, one can increase the strength of the accelerating field by 40-50%.

CONCLUSIONS

There are a significant number of problems for RF accelerators [12]. Estimating and direct experimental comparisons show the features and advantages of the PCS in comparison with conventional structures.

The RF power supply to the PCS accelerating cavities is carried out in parallel. Therefore, after each communication slot, there is power P/N, where P - power transferred to the structure, N - number of cavities. Accordingly, input elements heating is reduced by N times, field intensity in the communication slot by $N^{1/2}$.

The PCS accelerating cavities have a slight effect on each other. The breakdown is fully localized in the certain cavity. By the breakdown, the acceleration mode is not disturbed; only one cavity is disconnected from the structure. The stored energy in the structure W may be amount at several Joules (J). By the breakdown in the certain PCS cavity, energy W/N is released. For example, at W = 10J, N = 100, the ratio W/N = 0.1J. At such a low energy released, the consequences, i.e., heat, adsorbed gases emission, melting and evaporation of surface material, are minor. For this reason, there is no significant change in the vacuum conditions in the PCS by the breakdown. The beam is accelerated in the structure both during the current pulse and all the following.

Requirements to breakdown probability of the cavities are reduced by several times in the PCS cavities. In case of allowability of one breakdown per pulse in one of the accelerator cavities and the beam energy loss equal to 1 MeV in the accelerator in general, using the PCS can significantly raise the intensity of the accelerating gradient.

The PCS is the best accelerating structure to meet the challenges arising on the way of creation of RF accelerators.

ACKNOWLEDGEMENT

The authors thank the colleagues of ICKC, BINP SB RAS for their cooperation and assistance in the preparation of the accelerator model elements.

REFERENCES

[1] Th. P. Wangler, *"RF Linear Accelerators"*, WILEY-VCH, 2008.

[2] S. Döbert, "Gradient Limitations for High-Frequency Accelerators", *LINAC'2004*, Luebeck, Germany, p. 513.

[3] R.M. Sundelin, J.L. Kirchgessner, M. Tiger, "Parallel-Coupled Cavity Structure", *Trans. On Nucl. Sci.*, vol. NS-24, pp. 1686–1688, 1977.

[4] O. N. Brezhnev, P. V. Logatchev, V. M. Pavlov, *et al.*, "Parallel-Coupled Accelerating Structures", *LINAC'2002*, Gyeongju, Korea, p. 213.

[5] J. Neilson, S. Tantawi, V. Dolgashev, "Design of RF Feed System for Standing-Wave Accelerator Structures", *LINAC' 2010*, Tsukuba, Japan, p. 235.

[6] Yu. D. Chernousov, "The Method Excitation of the Accelerating Structure", Pat. № RU2427112C1, B.I. 20.08.2011, №23.

[7] Yu. D. Chernousov, V. I. Ivannikov, I. V. Shebolaev, A. E. Levichev, and V. M. Pavlov, "Parallel-Coupled Accelerating Structure", Pat. № RU2472244C1, B.I. 10.01.2013, №1.

[8] V.A. Dolgashev, "Traveling Wave Linear Accelerator with RF Power Flow Outside of Accelerating Cavities", US Patent Application №US 2015/0359080 A1. Pub. Date: Dec.10, 2015.

[9] S. G. Tantawi, Z. Li, P. Borchard, "Distributed Coupling and Multi-Frequency Microwave Accelerators", US Patent Application №US 2016/0014876 A1. Pub. Date: Jan. 14, 2016.

[10] A. M. Barnyakov et al., "Transient Process in a Parallel Coupled Accelerating System with Regard to Beam Current Loading", *Technical Physics*, vol.60, pp.137-140, 2015.

[11] Yu. Chernousov, V. Ivannikov, I. Shebolaev, et al., "Localization of the RF Breakdown in the Parallel Coupled Accelerating Structure", *RUPAC'2012*, St.Petersburg, Russia, p.164.

[12] Yu. Chernousov, "Development of RF Accelerator on Parallel-Coupled Accelerating Structure – Trend in Accelerator Technique", *RUPAC'2016*, St.Petersburg, Russia, this conference.

ISBN 978-3-95450-181-6

ELECTRON BEAM DYNAMICS CALCULATION AND ACCELERATING STRUCTURE GEOMETRY DESIGN IN 10 MeV HYBRID ELECTRON LINAC

A.V. Bulanov, S.V. Matsievskiy, E.A. Savin, N.P. Sobenin,
National Research Nuclear University MEPhI, Moscow, Russia

Abstract

Electron linear accelerators with an energy of 10 MeV are widely used for industrial purposes. This article presents the electron dynamics calculations and the design of linac with a standing wave (SW) buncher based on the biperiodic accelerating structure and a constant impedance backward traveling wave (BTW) after it. In such accelerator, all unused RF power coming out from BTW section is used in SW section to improve the linac efficiency. Thus, no RF load is needed. Also, a beam is experiencing an RF focusing in the SW buncher. Solenoid focusing field influence on the beam dynamics in the TW section was studied.

INTRODUCTION

Electron linear accelerators to the fixed 10 MeV energy are in demand for the industrial purposes. For example, for the sterilization of medical supplies, food, cosmetics etc. [1]. One of the first choices the developer is faced – it is the choice between SW or TW operating regimes. Both options have their own advantages, disadvantages, and special issues. TW is suitable for the acceleration of high electron currents. In the meantime, SW buncher is much shorter than TW buncher and doesn't require additional focusing fields [2]. The way to combine advantages of both SW and TW structures is a hybrid linac [3], where the beam is bunching in the biperiodic accelerating SW structure (BPS) [4] and continuing to accelerate in TW structure based on the reliable diaphragm loaded structure technology.

ACCELERATOR SCHEME

We propose the hybrid structure (Fig.1), where the unused for the acceleration in BTW RF power goes not to the load but, via the rectangular waveguide, to the BPS buncher (Fig.2).

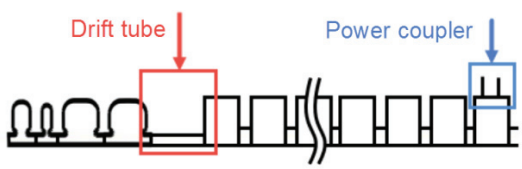

Figure 1: Hybrid linac scheme. Before the drift tube – BPS, after – BTW.

In the operating regime, power reflection from BPS, tuned to the optimal overcoupling [5], is equal to zero, thus accelerating section is operating in the TW regime. Accelerator operates at 2856 MHz frequency.

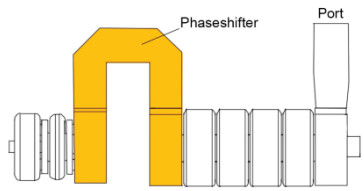

Figure 2: BTW and BPS connection.

ACCELERATOR GEOMETRY

Accelerating Section

Accelerating section for the relativistic particles is made from the disk-loaded waveguide (DLW) with an additional magnetic coupling. Magnetic coupling is designed to be higher than electric coupling, because for using BAS as a load, power flow in accelerating section should be in opposite direction to the beam propagation, i.e. negative group velocity. We studied dependencies of the main electrodynamics characteristics of BTW, such as shunt impedance r_{sh}, group velocity β_{gr}, Q-factor, attenuation coefficient α and normalized accelerating gradient $E\lambda/P^{1/2}$ as a function of phase shift per cell and normalized to the wavelength aperture radius a/λ. Shunt impedance is the highest at $2\pi/3$ mode and the optimum relative group velocity is ~1%. Table 1. shows, that shunt impedance rises with smaller aperture radius. We decided to choose $a/\lambda=0.08$ to both achieve high shunt impedance and avoid beam losses in accelerator walls.

Table 1: BTW electrodynamics parameters dependence from the normalized aperture radius at $2\pi/3$ mode, constant group velocity and 2856 MHz operating frequency.

a/λ	**0.06**	**0.08**	**0.1**
r_{sh}, MOhm/m	82.9	71.2	62.1
β_{gr}, %	1.3	1.2	1.2
Q	12500	12200	12000
α, m^{-1}	0.18	0.19	0.2
$E\lambda/P^{1/2}$	578	547	531

Phase Control Between Sections

Buncher and accelerating section are connected to each other by a rectangular waveguide with a fixed length and are separated by a drift tube. To ensure, that the accelerating mode phase difference between the last buncher cell and the first accelerating cell is suitable for the acceleration in resonance, i.e. $\Delta\varphi=180+/-2\pi$, we designed a waveguide phase shifter which allows tuning this phase difference in the whole 2π range (Fig.3). It consists of the

ISBN 978-3-95450-181-6

3dB waveguide bridge and 2 shorting plungers. While moving these plungers one changes the phase of the wave propagating through other two ports.

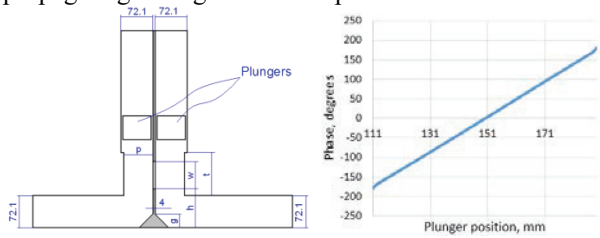

Figure 3: Waveguide phase shifter geometry (left) and transmitted wave phase dependence from the plungers position (right).

BEAM DYNAMICS

Beam Dynamics in the Accelerator

Injected beam parameters are set up by the existing gun [6] geometry. We chose the buncher cells parameters (Fig. 4) to achieve the highest capture after it which characterizes the buncher performance. Accelerator length and injected current are chosen in order to achieve 10 MeV at the end of linac and to achieve the output power from BTW equal to the required power to feed the buncher. This is an iterative process and we calculated 1.4 m length and 0.43 A injected current. Beam parameters are shown in Table 2 and Fig. 5.

Figure 4: Electric field lines in the optimized buncher.

Table 2: Beam Parameters at the End of the Accelerator

Beam power, MW	2.93
Loss power , MW	2.27
Input power, MW	5.5
Average energy, MeV	10.13
Maximum energy, MeV	11.8
Current, A	0.274
Capture, %	63.7
Efficiency, %	53.3
Beam radius/ drift tube radius	0.5
TW section length, m	1.4

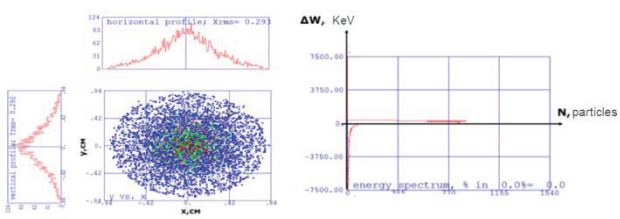

Figure 5: Beam profile (left) and it's energy spectrum (right) at the end of the linac.

Magnetic Focusing

The simulation shows that the major beam losses are in the TW section, so we can introduce the additional focusing solenoids to increase the efficiency of the LINAC. We were varying the number of magnets, its positions and magnetic field amplitude and decided that the optimum option is to use 2 magnets with 650 G maximum on-axis magnetic field (Fig.6).

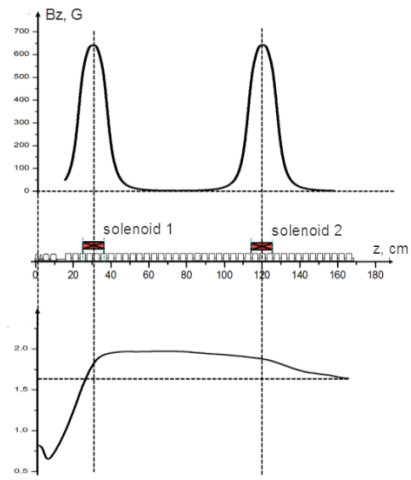

Figure 6: Focusing magnetic field length (top) and beam RMS radius (bottom) along the accelerator. Optimal solenoids centers coordinates are z_1=25 cm and z_2=120 cm.

While comparing beam parameters at the end of a linac with and without the focusing magnetic field one can see a 14% efficiency improvement with a magnetic field (Table 3).

Table 3: Beam parameters at the end of the accelerator with and without an additional focusing field

	No solenoids	2 solenoids
Beam power, MW	2.93	3.7
Current, A	0.274	0.35
Capture, %	63.7	80.8
Efficiency, %	53.3	67

EQUIVALENT CIRCUIT METHOD

To simulate the RF field distribution in the designed accelerating structure we used the software based on the equivalent circuit. A circuit shown in the Fig. 7 was used as an equivalent circuit for SW and TW cells. Its appropriateness was proven in papers [7].

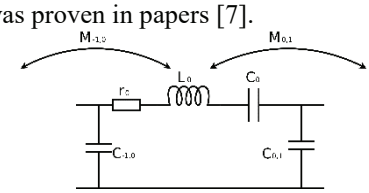

Figure 7: Equivalent circuit used to describe accelerator cells.

ISBN 978-3-95450-181-6

Buncher cells parameters were tuned according to the optimal accelerating field amplitudes in cells, obtained during the beam dynamics optimization. Tuning was done by varying electric and magnetic coupling coefficients of the buncher cells. In Fig. 8 electric field amplitude distribution in buncher (where odd cells are coupling cells and even cells are accelerating) along with the S_{11} distribution in the frequency range without the beam loading, so we can see overcoupling at the operating frequency.

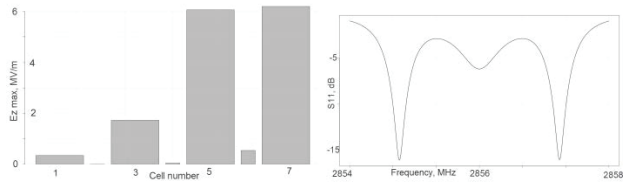

Figure 8: Distribution of the electric field (left) and S_{11} in the frequency range for the buncher (right).

When the beam loading is on, there is no reflection from the buncher, so we optimized an input coupler to minimize reflection using analytical expressions.

Results of the hybrid linac with the beam loading i.e. no reflection from buncher and TW regime in the accelerating section are shown in Fig.9. One can see that field amplitude in TW section decays according to the attenuation coefficient and phase shift per cell is $2\pi/3$.

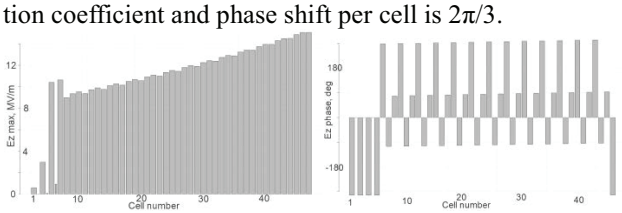

Figure 9: Electric field amplitude (left) phase (right) distribution in the hybrid linac in the operating regime.

The input impedance was calculated for two cases of the operation: with and without beam loading. Input reflection characteristic of the structure for these modes of operation is shown in Fig. 10.

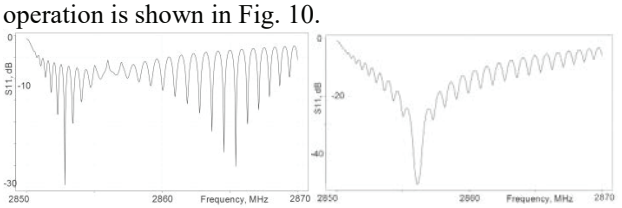

Figure 10: S_{11} in the frequency range for the hybrid linac with beam off (left) and on (right).

Fig.10 shows that without a beam power coupler sees a significant reflection because of the buncher overcoupling. When the beam and high power are on, buncher is matched with the TW section and power coupler sees no reflection.

CONCLUSION

We showed the possibility of using a hybrid electron linear accelerator as a source of 10 MeV electrons. Buncher cells are optimized to obtain the highest efficiency without an external focusing magnetic field and the connection between SW buncher and TW accelerator is optimized to use buncher as a load for the unused output power from TW section.

REFERENCES

[1] V. Shvedunov, Low energy electron accelerators application, a talk in Lomonosov State University, 10 November 2011.

[2] J. Rosenzweig, RF focusing in linear accelerator cavities, ERL 2005, JLAB, March 22, 2005.

[3] S.V. Kutsaev, N.P Sobenin et al., Design of hybrid electron linac with standing wave buncher and traveling wave structure, Nuclear Instruments and methods in Physics Research A, 636(1):13-30, April 2011.

[4] E.A. Knapp, B.C. Knapp, J.M. Potter, Standing wave high energy linear accelerator structures, Review of Scientific Instruments, 39 979 (1968).

[5] E.A. Savin et al., Design and tuning of a 40-MeV electron linear accelerator, Nuclear experimental techniques, 2013, Vol. 56, No.5, pp.506-515.

[6] S.V. Matsievskiy, E.A. Savin, "Three electrode electron gun with the decreased anode voltage geometry optimization", in *Proc. 1st Int. Particle Accelerator Conf. (RuPAC'14)*, Obninsk, Kaluga Region, Russia, October 2014, paper TUPSA05, pp. 45-47.

[7] V.E. Koluzhniy, RF characteristics of complicated multi cavity electrodynamics systems of particle accelerators (in Russian), Nuclear Physics and engineering, 2011, Vol.2, No.1, pp. 80-88.

ISBN 978-3-95450-181-6

ELECTRON LINEAR ACCELERATOR WITH THE VARIABLE ENERGY FROM 6 TO 11 MeV

A.V. Bulanov, E.A. Savin, N.P. Sobenin
National Research Nuclear University MEPhI, Moscow, Russia
A.V. Gryzlov, Research and Production Enterprise TORIY, Moscow, Russia

Abstract

A standing wave electron linear accelerator with a variable energy of 6-11 MeV was designed. Electron energy is controlled by the injected current. A buncher was designed to provide capture above 70 % for the all injected currents range. The influence of using a permanent radially magnetized toroidal magnet

INTRODUCTION

Dual energy electron linacs with an energy range up to 11 MeV found their wide range of applications in cargo inspection systems [1] [2] and industrial applications such as sterilization systems [3].

Usually, a conventional particle accelerator system works in S or C-band frequency ranges, because the installation sizes allow designing one meter – scale accelerators for 10 MeV energy. X – band is required when the space of the installation is limited and low energy is required [4]. S-band linacs simplify the manufacturing process of the complicated geometry accelerating structures, also RPE TORIY [5] already in dispose of an S-band 2856 MHz klystron with 4-6 MW variable output power, thus 2856 MHz has been chosen as an operating frequency. For the conventional purposes of the linac, the beam power must be as high as possible with a limited input power, so we designed an efficient buncher and accelerating section to obtain the accelerator efficiency, which defines as P_{beam}/P_{in}, higher than 60% in 6-11 MeV energy range. Also, we studied the decreasing of the beam radius when permanent toroidal magnets are used as a focusing system.

BEAM DYNAMICS

Accelerator was designed to fit the requirements below:

- RF power: 5.5 MW klystron with 4-6 MW variable power at 2856 MHz;
- Injection: 30 kV with 0.3-0.8 A variable current;
- Length: less than 1.4 m;
- Beam energy: 6-11 MeV;
- Efficiency >60%;
- Beam radius to the drift tube radius ratio < 0.5

Electron beam emittances at the electron gun exit were calculated for the 0.3-0.8 A injected currents range and then used as input parameters to simulate beam dynamics in 3-cells buncher. Buncher cells lengths and accelerating fields amplitudes were optimized to obtain the capture coefficient > 70 %.

Gun

Electrons are injected into the accelerating section from the 3-electrode gun (Fig. 1) with the fixed 30 kV anode potential and variable controlling electrode potential (9.4-12 kV) [6]. By varying the controlling potential value one can change the injected current (Fig. 3a). For the different currents beam Twiss parameters [7] (Fig. 2) also are different (Fig. 3b).

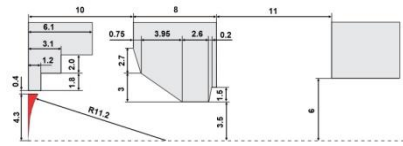

Figure 1: Electron trajectories in the gun at 0.5A current.

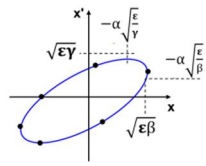

Figure 2: Twiss parameters to define a beam emittance.

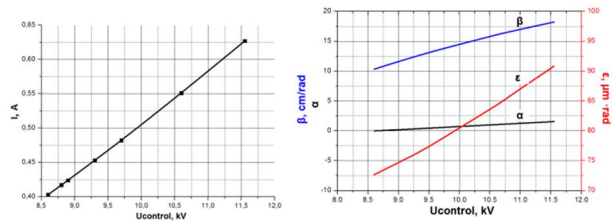

Figure 3: Electron current (a) and Twiss parameters (b) dependence in the gun from the control potential.

Buncher

Since the accelerator length is limited, standing wave is preferable because it allows getting higher energies than traveling wave structure on a shorter distance. We decided to use biperiodic structure (BPS) with inner coupling slots and nose cones [8] [9] because, even though the beam sees a π accelerating mode with a corresponding high shunt impedance (~80 MOhm/m), the RF structure itself operates at π/2 mode with a corresponding high coupling coefficient (~10%). Coupling coefficient basically describes the electric field distribution intolerance to the geometry change. Operating frequency is defined by the frequency of the klystron and is equal to 2856 MHz.

We optimized cells phase velocities and maximum electric field values on-axis (Table 1, Fig.4) both to obtain the capture >80% and energy spectrum less than 1 % after the 3rd cell with the 0.47 A injected current which corresponds

ISBN 978-3-95450-181-6

to the estimated value to obtain 10 MeV on 1.4m with 5.5 MW input power. Beam parameters after the buncher are presented in Table 2 and in Fig.5.

Table 1: Buncher Cells Parameters

Cell #	1	2	3
β_{phase}	0.5	0.42	0.75
Length, cm	2.626	2.206	3.94
Ez_{max}, MV/m	0.9	4.5	16

Figure 4: Electric field lines in the optimized buncher.

Table 2: Beam Parameters at the End of the Buncher

Beam power, MW	0.236
Average energy, MeV	0.59
Maximum energy, MeV	0.674
Current, A	0.388
Capture, %	83

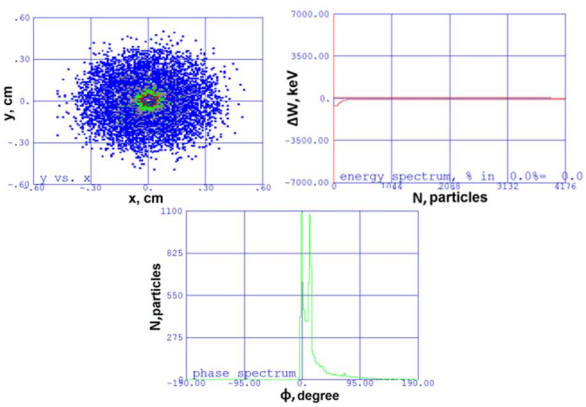

Figure 5: Beam profile (a), energy spectrum (b) and phase spectrum (c) after the buncher.

After the buncher optimization, the capture is 81% and an energy spectrum $\frac{dE}{E}$=2% . The beam radius after the buncher is equal to 0.3 cm with the 0.84 cm drift tube radius.

Accelerating Section

BPS structure allows accelerating electron beam to 10 MeV on the 1m length. It means 14 regular accelerating cells are used along with 3 bunching cells.

Table 3 and Fig.6 show the beam dynamics simulation results for the whole accelerator.

Table 3: Beam Parameters at the End of the Accelerator

Beam power, MW	3.705
Loss power , MW	1.745
Input power, MW	5.45
Average energy, MeV	10.09
Maximum energy, MeV	10.76
Current, A	0.365
Capture, %	78
Efficiency, %	68
Beam radius/ drift tube radius	0.36
Accelerator length, m	1

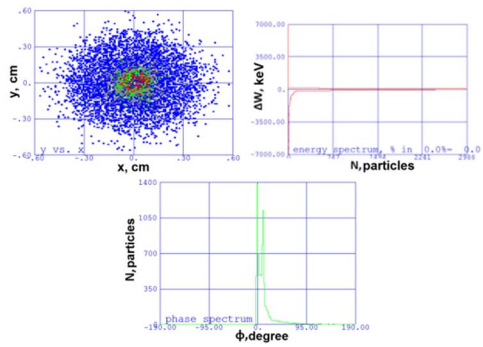

Figure 6: Beam profile (a), energy spectrum (b) and phase spectrum (c) after the buncher.

Thus we designed the 5.45 MW pulsed input power 10.1 MeV linac with further parameters:

1. Efficiency 68 % (with 78% capture);
2. Energy spectrum $\frac{dE}{E}$ = 2.5% ;
3. The difference between average and maximum energy is < 0.7 MeV;

Energy Variation

Energy variation is performed by the most convenient way – by changing the input current in the 0.3-0.8 A range changing the controlling electrode potential. 10 MeV is achieved for the ~0.4 A current and 5.45 MW input power, so the overcoupling between the power coupler and accelerating section must be tuned to β=4.44 [10] to minimize the reflected power in the operating regime. Thus, one need to assume while varying the current that the overcoupling will be not optimal for currents other than 0.4 A i.e. additional reflected power must be assumed in the power balance.

Fig.7 shows the beam energy and capture and accelerator efficiency from the injected current.

Thus, by changing the injected current from 0.4 to 0.8 A and by switching the klystron power between 4.41 and 5.45 MW one can cover the 6.7-10.3 MeV energy range keeping the efficiency higher than 60 %.

ISBN 978-3-95450-181-6

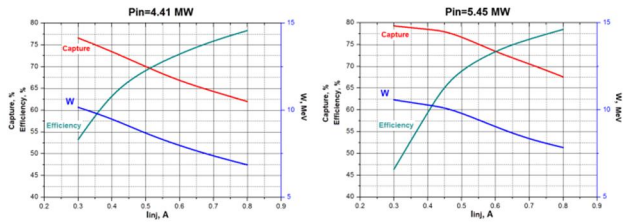

Figure 7: Average energy, efficiency and coupling coefficient dependences from the injected currents for the different power from the klystron: 4.41 MW (left) and 5.45 MW (right).

Additional Focusing

For the additional electron beam focusing one can use solenoids, but it requires an additional current source or the permanent toroidal magnets. We studied the possibility of the second option because a number of this magnet is already in TORIY disposal. Magnet geometry and it's on-axis magnetic field distribution are shown in Fig.8. The maximum B field on-axis value is 537 G.

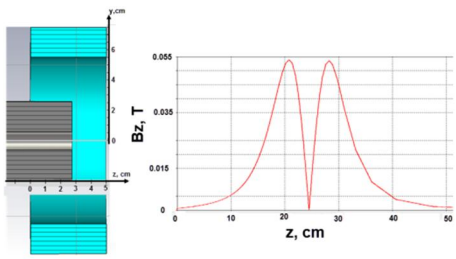

Figure 8: Magnet geometry (left) and on-axis magnetic field distribution (right).

We studied the dependence of the capture coefficient and rms beam radius from the magnet center longitudinal coordinate for the 10 MeV energy (Fig. 9a). Then, with the magnet placed at the optimum coordinate, we studied the same dependences from the second magnet center longitudinal coordinate (Fig. 9b). Simulations show that second magnet doesn't have any significant influence on the capture, i.e. having more than 1 magnet is not efficient.

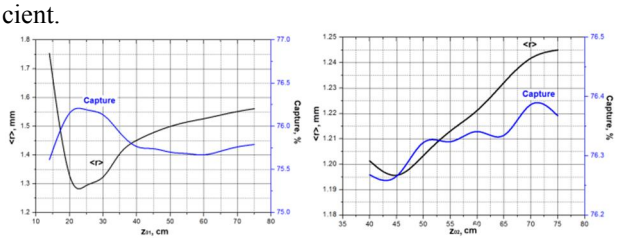

Figure 9: Capture coefficient and rms beam radius after the accelerating section dependence from the center coordinate of the first (left) and second (right, 1st magnet is in the optimum position) magnets.

When the magnet is placed at z_{01}=22 cm, rms beam radius at the end of the accelerator decreases by 20 % from 1.58 to 1.28 mm. capture coefficient is increased from 78% to 78.45 %. Fig. 10 shows the beam rms radius along the accelerator for 3 options: without magnets, with 1 magnet, and with 2 magnets. One can see once more, that the difference between options with 1 and 2 magnets is just ~4%, thus 2nd magnet is not required.

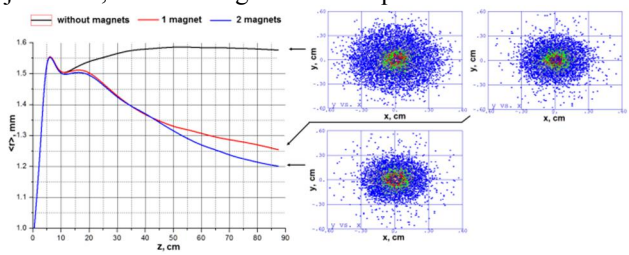

Figure 10: Beam rms radius along the accelerator without the additional focusing (black), with 1 magnet (red) and two magnets (blue).

CONCLUSION

Beam dynamics in the standing wave accelerator with 6.7-10.3 MeV variable energy was calculated. 3-cells buncher was designed to obtain the accelerator efficiency higher than 60% in the all energy range and the beam radius to the drift tube radius ratio <0.25 at the end of the accelerator. Also, the optimal longitudinal position for the permanent toroidal magnet was found to reduce the beam radius at the end of the accelerator by 20%.

REFERENCES

[1] M. Ferderer, A. A. Zavadtsev et al., Dual-energy electron linac for cargo inspection system, *Proceedings of PAC09*, Vancouver, BC, Canada.

[2] J. Shao et al., Development of a C-band 4/8 MeV dual-energy accelerator for cargo inspection system, *Proceedings of IPAC2016,* Busan, Korea.

[3] C. Tang et al., Electron linacs for cargo inspection and other industrial applications, *International topical meeting on Nuclear Research applications and Utilization of Accelerators*, Vienna, Austria, 2009.

[4] A.V. Smirnov et al., A metal-dielectric micro linac for radiography source replacement, *Proceedings of IPAC2016*, Busan, Korea.

[5] http://toriy.ru/en.html.

[6] S.V. Matsievskiy, E.A. Savin, "Three electrode electron gun with the decreased anode voltage geometry optimization", in *Proc. 1st Int. Particle Accelerator Conf. (RuPAC'14)*, Obninsk, Kaluga Region, Russia, October 2014, paper TUPSA05, pp. 45-47.

[7] E. D. Courant and H. S. Snyder, "Annals of Physics 3", p.1, 1958.

[8] E.A. Knapp, B.C. Knapp, J.M. Potter, Standing wave high energy linear accelerator structures, Review of Scientific Instruments, 39 979 (1968).

[9] N.Sobenin,B.Zverev, Electrodynamics characteristics of accelerating cavities, Foundation for International Scientific and Education Cooperation. Gordon and Breach Science Publishers, 1999

[10] V.I. Kaminskiy, M.V. Lalayan, N.P. Sobenin, Accelerating structures, Moscow 2005, in Russian

ISBN 978-3-95450-181-6

MATCHING THE PROTON BEAM BY MEANS OF INDEPENDENTLY PHASED BUNCHERS IN CYCLINAC CONCEPT

V.S. Dyubkov, S.M. Polozov, K.E. Pryanishnikov, National Research Nuclear University MEPhI, Moscow, Russia

Abstract

Nowadays a hadron therapy is one of the modern methods of a cancer treatment. For that purpose it is required that a proton beam, accelerated up to 250 MeV, penetrates on a depth about of 30 cm. It is known that linac, cyclotron and synchrotron can be used as a source of proton/ion beams. The main linac advantages are a high beam quality and a possibility of beam energy variation but, on the other hand, initial low-energy part of a linac is markedly expensive. Production of mentioned beams is possible on the base of a concept called CYCLINAC, when a commercial cyclotron is used as an injector, in which protons are accelerated up to 20-30MeV, for main linac. Matching the beam extracted from a cyclotron with a linac input is the main problem of this concept. It is caused by difference of operating frequencies of cyclotron and linear accelerator as well as a high phase size of a bunch from the cyclotron. It is proposed to use the system of independently phased bunchers for beam matching. The BEAMDULAC-CYCLINAC program is developed for simulation of the self-consistent dynamics of proton beams in a matching channel. Results of beam dynamics simulation for CYCLINAC will be presented and discussed.

INTRODUCTION

Due to the growth of cancer diseases it has recently become urgent task to develop effective methods of therapy with minimal side effects. Existing therapies such as surgery, chemotherapy, hyperthermia, radiotherapy is not completely effective in the treatment of deep-seated malignant tumours. With the development of technology accelerators, it became possible to create a complex proton and ion therapy. The expert community is actively discussing several options of implementing proton beam therapy systems. The main problem with these options is the choice of the initial part of such systems. In particular, in 1993, U. Amaldi proposed the concept of so-called CYCLINAC as the accelerator complex, in which the cyclotron used as injector in the linear accelerator [1]. Use of a PET-cyclotron for medical centres gives a significant economic effect. The most developed project concepts CYCLINAC are CABOTO [2], TULIP [3], ProTEC [4] and ProBE [5]. The main difficulty in the development of systems in accordance with the concept of CYCLINAC is the task of the transmission beam extracted from the cyclotron to the front-end of a linear accelerator, in view of the significant differences of operating frequencies of cyclotron and linac. In the present work it is compared two schemes of a beam transportation channel from the cyclotron on energy W to a linear proton accelerator energy of 250-300 MeV.

NUMERICAL SIMULATION RESULTS

At the beginning we consider a transportation channel based on three bunchers working at frequency 324 MHz that is in four times greater than cyclotron operation frequency. A schematic plot of the structure is shown in Fig. 1. It was assumed that particles continuously entered to transportation channel with average relative velocity equals to 0.248 and relative spread equals to 0.033. Beam current was presumed to be equal to 1 mA. The main transportation channel is presented in Table 1.

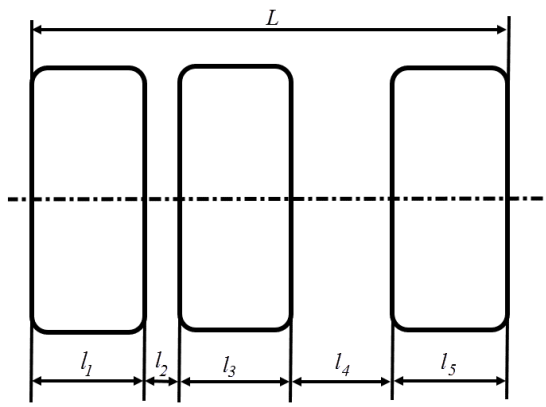

Figure 1: Layout of transportation channel.

Table 1: Main Channel Parameters

N	1	2	3	4	5
Length l, cm	34	1	16	31	16
E_{max}, kV/cm	170	–	175	–	170
Synchronous phase	π/2	–	π/5	–	π/5
Aperture, cm	5	5	5	5	5

It was obtained that the transmission coefficient was equal to 79.8% under bunch phase length equals to 2.43 (the physical length is about 6.5 cm). This bunch core conforms 70% of injected particles. Input (blue color) and output (red color) particle distributions in longitudinal phase space are presented in Fig. 2. Particle distributions in the transversal phase spaces are shown in Fig. 3 and Fig. 4. Particles spectra are shown in Fig. 5- 7. As one can see from Fig. 6 and Fig. 7 there is no significant beam envelope growth in channel without transversal focusing. In all mentioned figures blue objects are input and red are output. The above scheme allows one to decrease bunch phase width twice.

ISBN 978-3-95450-181-6

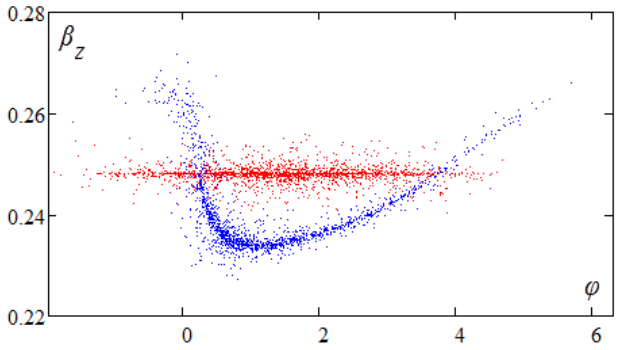

Figure 2: Longitudinal phase space.

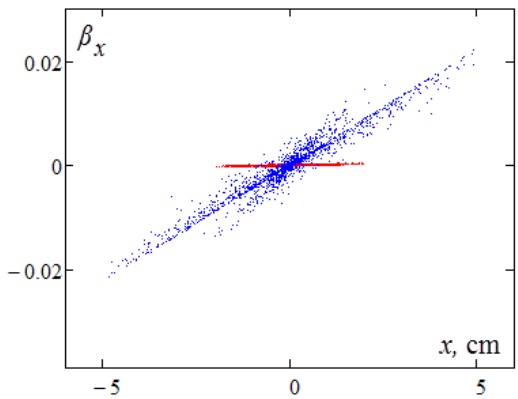

Figure 3: Transversal (x,β_x) phase space.

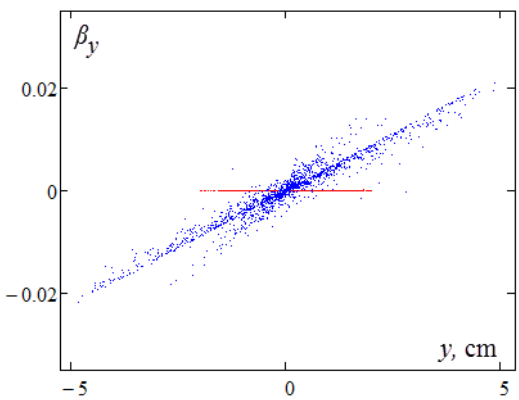

Figure 4: Transversal (y,β_y) phase space.

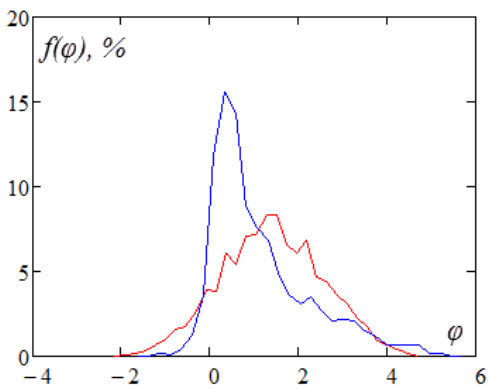

Figure 5: Particle distribution by phases.

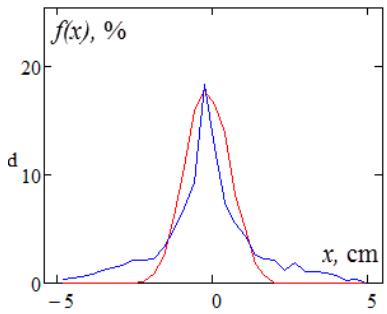

Figure 6: Particle distribution by the first transversal coordinate.

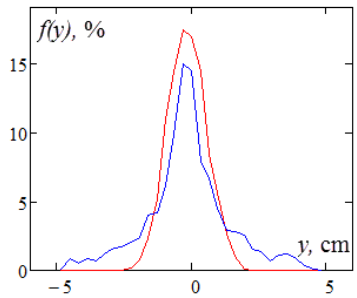

Figure 7: Particle distribution by the second transversal coordinate.

In view of improving the beam bunching quality as well as lowering particle losses in a linear accelerator, the next transportation channel scheme is proposed. This scheme consists of two resonator groups. Resonators into groups have different operating frequencies (see Table 2). A schematic plot of suggested structure is shown in Fig. 8 (the first group) and Fig. 9 (the second one). Operating frequency of the first group is 162 MHz and 324 MHz for the second one.

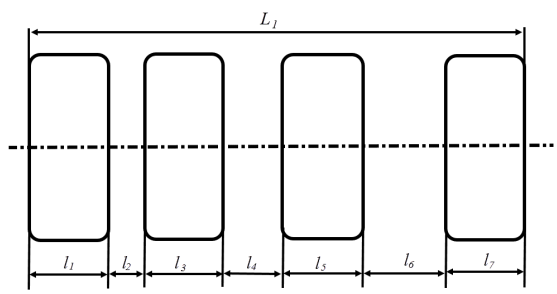

Figure 8: Layout of the 1st part of transportation channel.

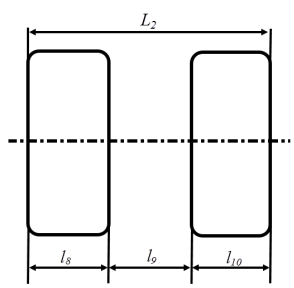

Figure 9: Layout of the 2nd part of transportation channel.

ISBN 978-3-95450-181-6

Table 2: Main Channel Parameters

	Resonators / Drift tubes									
	λ = 185.2 cm								λ = 92.6 cm	
N	1	2	3	4	5	6	7	8	9	10
Length *l*, cm	19	1	16	21	17	31	19	16	16	16
E_{max}, kV/cm	250	–	200	–	200	–	250	170	–	170
Synchronous phase	π/2	–	45π	–	π/4	–	π/5	π/5	–	π/5
Aperture, cm	5	5	5	5	5	5	5	5	5	5

This scheme allows one to decrease bunch phase width in four times.

The computer simulation results are presented in Figures 10-13. Note, that transversal phase spaces are the same that in the first scheme.

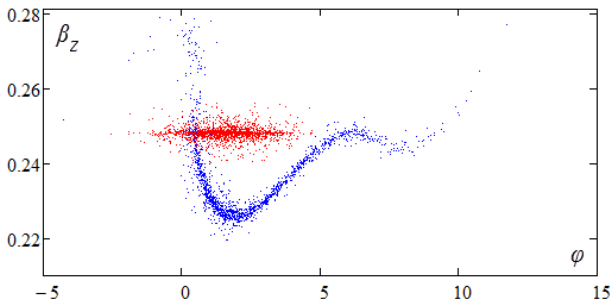

Figure 10: Longitudinal phase space.

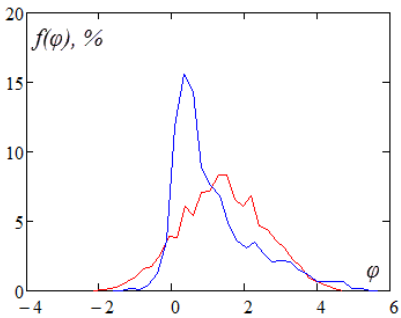

Figure 11: Particle distribution by phases.

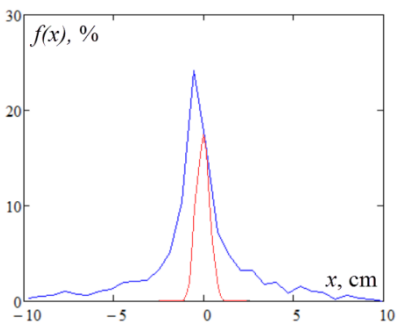

Figure 12: Particle distribution by the first transversal coordinate.

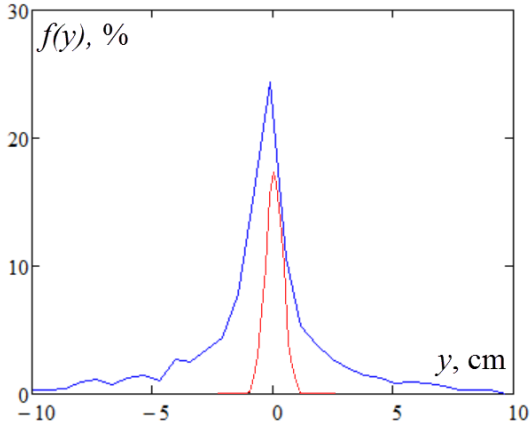

Figure 13: Particle distribution by the second transversal coordinate.

It was obtained that transmission coefficient is equal to 74%.

CONCLUSION

It is proposed to use the system of independently phased bunchers for beam matching between cyclotron and linac for CYCLINAC concept. The BEAMDULAC-CYCLINAC program is developed for simulation of the self-consistent dynamics of proton beams in a matching channel. Results of the beam dynamics simulation are presented.

REFERENCES

[1] U. Amaldi, et al., NIM A 620 (2010) 563.
[2] A. Degiovanni et al., NIM A 657 (2011) 55.
[3] A. Degiovanni, "Design of a Fast-cycling High-gradient Rotating Linac for Protontherapy", IPAC'13, Shanghai, May 2013, THPWA008, p. 3642 (2013); https://accelconf.web.cern.ch/accelconf/IPAC2013/papers/thpwa008.pdf.
[4] R. Apsimon et al., "ProTec - A Normal-conducting Cyclinac for Proton Therapy Research and Radioisotope Production", IPAC'15, Richmond, May 2015, THPF084, p. 3883 (2015); http://accelconf.web.cern.ch/AccelConf/IPAC2015/papers/thpf084.pdf.
[5] R. Apsimon et al., "ProBE - proton boosting extension for imaging and therapy", IPAC'16, Busan, May 2016, TUPOY025, p. 1963 (2016); http://accelconf.web.cern.ch/AccelConf/ipac2016/papers/tupoy025.pdf.

ISBN 978-3-95450-181-6

SUPERCONDUCTING STORED ENERGY RF LINAC AS FREE ELECTRON LASER DRIVER

V.G.Kurakin, P.V.Kurakin, Lebedev Physical Institute, Moscow, Russia

Abstract

Due to cavity losses in multi pass free electron laser (FEL), generation starts in it from definite threshold of driving electron beam current. Depending on generation wave range the threshold current strikes from fraction of ampere to dozens of amperes. In order to rich laser saturation, from hundreds to thousands electron bunches are required. Simple estimations give the value from units up to tens joules of bunches train energy in order to rich FEL saturation for infrared wave range (approximately 20 – 25 Mev of bunches energy and 3 A of pick current, bunch length being 1 cm). A beam with parameters mentioned might be obtained in rf superconducting linac operating in stored energy mode. The advantage of such approach is simplified linac power supply since dozens watts cw rf generator is required only to rich necessary accelerating voltage. At the same time the energy spread arising from beam loading may be compensated by additional cavities exited at shifted frequencies. In this paper Maxwell equations are used for beam-cavity interaction analysis. The bunch energy loss or the same the voltage induced by radiating bunch is expressed in terms of cavity external parameters. The detailed analysis of beam energy spread compensation is carried out followed by an example showing the reality of FEL schema suggested.

INTRODUCTION

Four decades of free electron lasers (FEL) development prove clearly their impressive and power status for human activity in scientific and other application. This is especially true for FELs in roentgen, ultraviolet and infrared range inaccessible for classical lasers. It is necessary to underline the main features of FELs – large power and tune ability – that are inherent to these devices due to physical mechanism of radiation generation. On the other hand FELs still are complicated and costly devises and for this reason not available for many research groups. There is no evident solution for accelerator scheme to match ridged parameters specification from light generation part and reduce simultaneously beam driver cost. Multi frequency superconducting linac that operates in stored energy mode [1] seems to be appropriate approach to drive FEL. This linac operation mode does not requires power rf source since dozens watts are necessary only in order to reach high gradient in multi cell superconducting cavity while the rf energy stored in the cavity (dozens joules) is quit sufficient to accelerate electron bunches train for laser excitation. It had been shown as well [1] that bunch train energy spread arising from beam loading might be compensated by additional cavities operating at slightly shifted frequencies.

Bunch energy and energy spread within individual bunches and in bunch train, bunch current and train length, undulator and laser cavity parameters – all these items are necessary to determine linac main parameters. For this reason we start from laser description, followed by appropriate formulae for linac parameters specification. Then appropriate formulae for bunch energy losses in cavity are derived based on solution of Maxwell equations and expressed over cavity external parameters. At last, multi frequency rf linac scheme with beam loading effect compensation is discussed followed by appropriate calculation.

FEL PARAMETERES SPECIFICATION

The processes in FEF are similar to those in traveling wave amplifier or rf linac. In latter devises electrons interact with longitudinal electric field of traveling electromagnetic wave and in the case of synchronism deliver part of their energy to field (amplifier) or take away it from a wave (accelerator). The difference is that in FEL electron interact with transverse electromagnetic wave with longitudinal electric field being equal to zero. The electrons must have transverse velocity in order to exchange their energy with the wave and for this reason a device that forces the beam to move in transverse direction – undulator - is necessary in beam environment. More over the synchronism and the energy exchange is effective when phase lag 2π between the electron and the wave takes place on one undulator period. Fig. 1 is a simple demonstration of the device just described.

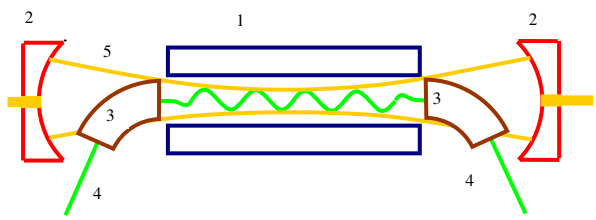

Figure 1: FEL layout. 1 – undulator, 2 – mirror, 3 – magnet, 4 – electron beam, 5 – optical mode envelope, 6 – laser radiation.

One pass of electron bunch in undulator area provides wave amplification. To transmit more energy to light train two mirror cavity is used. Twice reflected light bunch moves again in the same direction and acquires a portion of energy from new electron bunch entering the

ISBN 978-3-95450-181-6

undulator. The wave amplification continues up to the level when nonlinearity occurs and saturation takes place.

The formula for one pass gain that together with the operation principles just described is sufficient for formulation of linac parameters specification. Appropriate expression for gain G looks like [2]

$$G = 4\sqrt{2}\pi N\lambda_w^{1/2}\lambda_s^{3/2}\frac{K^2}{(1+K^2)^{3/2}}\frac{i}{si_A}\left(\frac{\Delta\omega_s}{\omega_s}\right)_t^{-2} \quad (1)$$

Here λ_w - undulator period, λ_s - generated radiation wavelength, K - undulator parameter.

$$\lambda_s = \frac{\lambda_w}{2\gamma^2}(1+K^2),\ K = eH_{W0}\lambda_w / 2\pi mc^2, \quad (2)$$

γ is relativistic factor, H_{W0} - the amplitude of periodic magnetic field on undulator axis. $\Delta\omega$ is line widening, caused by undulator finite length and non zero bunch length and its longitudinal emittance (non zero energy spread). s is bunch cross section, $i_A = mc^3/e = 17\kappa A$ and

$$\left(\frac{\Delta\omega_s}{\omega_s}\right)_t^2 = \left(\frac{\Delta\omega_s}{\omega_s}\right)_h^2 + \left(\frac{\Delta\omega_s}{\omega_s}\right)_i^2 \quad (3)$$

$$\left(\frac{\Delta\omega_s}{\omega_s}\right)_h^2 = \left(\frac{1}{N}\right)^2 + \left(\frac{\lambda_s}{2l_e}\right)^2,\ \left(\frac{\Delta\omega}{\omega}\right)_i = 2\frac{\Delta E}{E} \quad (4)$$

Keeping in mind paper motivation and running a few steps forward let us make some estimation for infrared FEL (10 μm). To make estimation more transparent we consider the contribution of finite undulator length end beam energy spread in line widening be equal end neglect the widening coursed by finite bunch length. In this case gain G_{est}

$$G_{est} \cong \pi N^3\lambda_w^2\frac{K^2}{\gamma^3}\frac{i}{si_A} \quad (5)$$

Supposing

$N = 50, \lambda_W = 3\,cm, K = 1, \gamma = 50, s = \pi\times 0.01\,cm^2$

we have $G_{est} \cong 0.05i\ (A)$. Taking into account cavity losses at the level 3-5 percent we arrive at the conclusion that bunch current of order 1 A is the FEL excitation threshold and might be referred to as reference value.

CHARGE RADIATION FIELD IN RF CAVITY

We consider that radiating charge is frozen in both direction of motion that is does not change its velocity within a cavity. To find out the field that moving charge radiates in a RF cavity we will use strict electromagnetic approach based on the theory had been developed in [3]. In this theory vortex electrical $\vec{E}(\vec{r},t)$ and magnetic $\vec{H}(\vec{r},t)$ fields are represented as derivatives of vector potential $\vec{A}(\vec{r},t)$ on time t and space $\vec{r}$ coordinates:

$$\vec{E}(\vec{r},t) = -\frac{\partial\vec{A}(\vec{r},t)}{\partial t},\ \vec{H}(\vec{r},t) = \frac{1}{\mu_0}rot\vec{A}(\vec{r},t) \quad (6)$$

where μ_0 is magnetic permeability of free space. Here and later SI units are used. Vector potential satisfies the wave equation

$$\Delta\vec{A}(\vec{r},t) - \frac{1}{c^2}\frac{\partial^2\vec{A}(\vec{r},t)}{\partial t^2} = -\mu_0\vec{j}(\vec{r},t) \quad (7)$$

$\vec{j}(\vec{r}.t)$, c being current density and the light velocity.

To find out the expressions for vector potential we will use the most direct way. Namely, we represent vector potential as an expansion on the infinite sum of RF cavity eigen functions $\vec{A}_\lambda(\vec{r})$ with time dependent coefficients $g_\lambda(t)$:

$$\vec{A}(\vec{r},t) = \sum_{\lambda=1}^{\infty} g_\lambda(t)\vec{A}_\lambda(\vec{r}) \quad (8)$$

with the boundary conditions $\vec{A}_\lambda|_\Sigma = 0$ on cavity surface.

Starting from the equation (7) and taking into account (8) one can easily obtain the equations for cavity vector eigen functions and appropriate time dependent coefficients (fields amplitudes):

$$\Delta\vec{A}_\lambda(\vec{r}) + k_\lambda^2\vec{A}_\lambda(\vec{r}) = 0 \quad (9)$$

$$\frac{d^2g_\lambda(t)}{dt^2} + \omega_\lambda^2 g_\lambda(t) = \int_V \vec{j}(\vec{r},t)\vec{A}_\lambda(\vec{r})dV \quad (10)$$

Here $k_\lambda = \omega_\lambda / c$ are eigen values of boundary values problems (4), the specific solutions for RF cavities are called cavity modes, ω_λ being the eigen angular frequencies of appropriate modes, c is light velocity. Integration in formula is assumed to be performed over cavity volume V. Last equation can be generalized up to the next one

$$\frac{d^2g_\lambda(t)}{dt^2} + \frac{\omega_\lambda}{Q_\lambda}\frac{dg_\lambda}{dt} + \omega_\lambda^2 g_\lambda(t) = \int_V \vec{j}(\vec{r}.t)\vec{A}_\lambda(\vec{r})dV \quad (11)$$

if losses in cavity and outside are taking into account. Here Q_λ stands for cavity quality factor:

$$Q_\lambda = \frac{\omega_\lambda W_\lambda}{P_\lambda} \quad (12)$$

where W_λ is the electromagnetic energy in the mode λ, stored in cavity volume and P_λ represents the total RF power losses that besides ohm losses in cavity walls includes the external losses due to cavity coupling with

ISBN 978-3-95450-181-6

external circuits. It is supposed that eigen functions are normalized by the condition

$$\int_V A_\lambda^2 = \mu_0 c^2 = 1/\varepsilon_0 \quad (13)$$

Here μ_0 and ε_0 are magnetic and electric permeability respectively.

For the analysis followed we will use the cavity excitation equation in the form with small RF losses, and this has no any influence on generality of results to be obtained. Then, all calculations will be made for a single charged particle with charge value q of zero dimensions in all directions entering cavity at moment $t = 0$. In such a case the total current density

$$\vec{j}(\vec{r},t) = q\vec{v}(\vec{r},t)\delta(x,y,vt)), \quad (14)$$

where $\vec{v}(\vec{r},t)$ stands for particle velocity being assumed constant within the cavity, and $\delta()$ is Dirac delta function: $\delta(x) = \infty$ for $x = 0$, $\delta(x) = 0$ for $x \neq 0$

$$\int_{-\infty}^{\infty} \delta(x)dx = 1 \quad (15)$$

We suppose also the case that is the most interesting for accelerator based applications – the particle moves along cavity axis where

$$x = 0, y = 0, z = vt \quad (16)$$

Starting with such assumptions and following[1,4] we arrive finally at the for the voltage induced on equivalent gap:

$$U = -\frac{q\omega}{2}\frac{R}{Q_0}\exp(-\omega t/2Q)\cos\omega t \quad (17)$$

Where R, Q_0 are cavity shunt impedance and quality factor. Very often, current value *I* averaged over RF period is used instead of charge value

$$U = -\pi I\frac{R}{Q_0}\exp(-\omega t/2Q)\cos\omega t \quad (18)$$

STORED ENERGY RF LINAC AS FEL DRIVER

If charge train is accelerated in a cavity that operates in stored energy mode charges in charge sequence move in the field that is the sum of the amplitude of stored field and radiated one. The radiated field amplitude is increased with any new bunch entering the cavity and due to this linear energy decrease takes place. To compensate this energy decrease we had suggested the linac scheme consisting of two cavities [1]. The second cavity operates at slightly higher frequency and any new charge sees higher voltage. If appropriate condition is satisfied

$$\frac{\Delta\omega}{\omega} = \frac{U_{lost}}{2\pi U_m(N-1)h}, \quad (19)$$

full compensation of energy decrease takes place. Here U_m and U_{lost} are amplitude of stored mode in the second cavity and total amplitude induced in two cavities.

It can be shown that the energy lost (in voltage units) of n-th bunch in the sequence of bunches in second rf cavity is

$$U_{lost} = -\pi I\frac{R}{Q}\times\frac{\sin\left[(n-1)\pi\left(\frac{h\Delta\omega}{\omega}\right)\right]}{\sin\pi(\frac{h\Delta\omega}{\omega})}\cos\left[\pi(n-2)(\frac{h\Delta\omega}{\omega})\right] \quad (20)$$

One has to set $\Delta\omega = 0$ for the main cavity and to sum both expressions. Thus the total induced voltage is

$$U_{lost} = \pi(n-1)I\frac{R_1}{Q_1} + \pi(n-1)I\frac{R_2}{Q_2} \quad (21)$$

if the following condition takes place

$$\pi(n-1)(\frac{h\Delta\omega}{\omega}) << 1 \quad (22)$$

Here $\omega = h\Omega$, are the main cavity frequency, the number of periods per bunch, the bunch repetition rate accordingly, $\omega + \Delta\omega$ is the frequency of the second cavity

CONCLUSION

Resonator TESLA developed for International Linear Collider one has the following parameters

$$Q = 10^{10}\ R/Q = 1kOm, U = 25MV, W \approx 80J.$$

Using half of stored energy one has the beam of 20 MeV approximately. With an optical cavity length equal to 2.3 m (10 wavelength of TESLA cavity) one has h=20 Above mentioned bunch current 1A corresponds approximately to 50 mA current averaged over rf period. At these parameters $5*10^4$ bunches may be generated.

ACKNOWLEDGMENT

The authors are grateful to all colleagues for fruitful discussion for many question touched at this article.

REFERENCES

[1] V.G.Kurakin, P.V.Kurakin. Multy Frequency Stored Energy RF Linac. Proceedings of RuPAC2012, Saint-Petersburg, 24-28 September, Russia p. 350-352.

[2] A.A.Varfolomeev. Free electron lasers and their development prospect. Moscow. 1980, 117 pp.

[3] V.M.Lopukchin. Excitation of electromagnetic oscillations and waves by electron flows. .Gostekchizdat, 1953. 324 pp., in Russian.

[4] V.G.Kurakin. Complex Shunt Impedance and Beam-RRF Cavity interaction. Proceedings of RuPAC2014. Obninsk, 6-10 October, p. 77-79.

ISBN 978-3-95450-181-6

INVESTIGATION OF A SECOND ORDER METHOD OF RFQ CHANNEL OPTIMIZATION

O.I. Drivotin*, D.A. Starikov,
St.-Petersburg State University, 7/9 Universitetskaya nab., St. Petersburg, 199034, Russia

Abstract

This report is devoted to a numerical method of solution of the RFQ structure optimization problem. The problem is considered as a control theory problem. Control functions representing geometry of the electrodes and a quality functional describing the beam are introduced. To solve the problem numerically these control functions are parametrized. The presented method is based on the computation of the derivatives of the first and the second order of the quality functional on the parameters. Results of investigation of efficiency of the method relatively to a method including computation of the derivatives only of the first order are presented.

INTRODUCTION

Methods of numerical optimization of accelerator structures were developed in the works of D.A. Ovsyannikov [1, 2, 3]. This theory was applied to the RFQ structure in the works [2, 4, 5, 6, 7, 8].

These methods have the first order, because the optimization process includes computation of derivatives of the first order of a functional describing beam quality over structure parameters. Application of these methods in practice requires a great amount of computations to achive acceptable results.

To reduce a number of computation, the method of the second order was proposed [9]. Here we present results of the second order method investigation, according to which number of computation during the process of optimization is reduced sufficiently.

FORMULATION OF THE PROBLEM

Consider a particles beam describing by the phase density [10, 11] $\varrho(x)$ defined on some surface S in the phase space $\Omega : x \in S \subset \Omega$. Coordinates on S can be taken as coordinates in the phase space. Let that at the initial instant t_0, the particle distribution density is given: $\varrho(t_0, x) = \varrho_{(0)}(x) = \varrho_{(0)\,1\ldots p}(x)\, dx^1 \wedge \ldots \wedge dx^p$, $x \in S_0 \subset \Omega$. At $t > t_0$, density $\varrho(x)$ can be found as the solution of the Vlasov equation [10, 11].

Let the trajectories of particles are described by the equation

$$\frac{dx}{dt} = f(t, x, u),$$

where $t \in T_0 = [t_0, T]$, $u \in U \subset R^r$ is a control function.

* o.drivotin@spbu.ru

Also, introduce the following functional

$$\Phi(u) = \int_S g(x_T)\varrho(T, x_T), \qquad (1)$$

where $g(x)$ is a piecewise continuous function. This functional characterizes quality of the beam at outlet of the accelerating channel. The problem of minimizing of functional (1) over control function $u \in U$ is called the terminal problem of charged particles beam control.

METHOD

Consider the equation for the first variation of x

$$\frac{d\delta x^i}{dt} = \frac{\partial f^i}{dx^j}\delta x^j + \delta_u f^i, \quad \delta x^i(t_0) = 0. \qquad (2)$$

Here and further, we apply the Einstein summation rule over repeated upper and low indices. The problem (2) has the following solution

$$\delta x^i(t) = \int_{t_0}^{t} G^i_j(t, t')\delta_u f^j(t')dt',$$

where $G(t, t')$ is the Green matrix of the system (2), satisfying to the equation

$$\frac{dG^i_j(t, t')}{dt'} = G^i_k(t, t')\frac{\partial f^k}{\partial x^j},$$

and $G(t, t) = E$, where E is identity matrix.

Then variation of the functional (1) can be written as

$$\delta_u\Phi = \int_{t_0}^{T}\int_{\Omega}\frac{\partial g}{\partial x}G(T, t')\delta_u f(t, x)\varrho(t, x)\, dt. \qquad (3)$$

Consider the differential form

$$\psi(t, x) = -\left.\frac{\partial g}{\partial x}\right|_{x=x_T} G(T, t).$$

It satisfies the following equation and conditions

$$\frac{d\psi}{dt} = -\psi\frac{\partial f}{\partial x}, \qquad \psi(T) = -\left.\frac{\partial g}{\partial x}\right|_{x=x_T}.$$

Then expression (3) can be rewritten as follows

$$\delta_u\Phi = -\int_{t_0}^{T}\int_{\Omega}\psi(t, x)\delta_u f(t, x)\varrho(t, x)\, dt.$$

ISBN 978-3-95450-181-6

Assume that the control function can be represented in parameterized form, depending on a finite number of parameters. Consider the second derivatives with respect to the same parameter $\partial^2\Phi/\partial u_i^2$. Then

$$\frac{\partial x^j}{\partial u_i}(t) = \int_{t'}^{t} G_k^j(t,t')\frac{\partial \delta_u f^k}{\partial u_i}(t')\,dt'. \quad (4)$$

Assume that $\partial^2\Phi/(\partial x^i \partial x^j) = 0$, if $i \neq j$. And then

$$\frac{\partial^2\Phi}{\partial u_i^2} = \int_{\Omega} \varrho(T)\left[\frac{\partial\Phi}{\partial x^j}\frac{\partial^2 x^j}{\partial u_i^2}(T) + \frac{\partial^2\Phi}{\partial (x^j)^2}\left[\frac{\partial x^j}{\partial u_i}(T)\right]^2\right].$$

Passing to the summation on macroparticles we get

$$\frac{\partial^2\Phi}{\partial u_i^2} = \sum_{k=1}^{N}\left[\frac{\partial\Phi}{\partial x^j}\frac{\partial^2 x^j_{(k)}}{\partial u_i^2}(T) + \frac{\partial^2\Phi}{\partial (x^j)^2}\left[\frac{\partial x^j_{(k)}}{\partial u_i}(T)\right]^2\right],$$

where the first derivatives are expressed by (4).

It can be shown that when f^j are linear on the control parameters u_i, second variation of x can be represented in the form

$$\delta^2 x^j(t) = \int_{t_0}^{t}(D^j_{kl}(t,t')\delta_u f^k(t') + G^j_k(t,t')\times$$

$$\times\delta_u\left(\frac{\partial f^k}{\partial x^l}\right)\Big|_{t'}\int_{t_0}^{t'} G^l_m \delta_u f^m(t'')\,dt''\Big)\,dt',$$

where components of the tensor D satisfy to the system of differential equations

$$\frac{\partial D^j_{kl}(t,t')}{\partial t'} = -2D^j_{km}(t,t')\frac{\partial f^m}{\partial x^l}(t') + G^i_m(t,t')\frac{\partial^2 f^m}{\partial x^k \partial x^l}(t')$$

and the condition

$$D^j_{kl}(t,t) = 0,\ \ j = \overline{1,m},\ \ k = \overline{1,m},\ \ l = \overline{1,m}.$$

OPTIMIZATION

Let the longitudinal component of electric field in the RFQ channel is

$$E_z = U_0\frac{4kT}{\pi}\cos\eta\cos\omega t, \quad \eta(z) = \int_{z_0}^{z} k(z')\,dz'. \quad (5)$$

Here $2U_0$ is the amplitude of the intervane voltage, ω is the frequency, a is the aperture, $k = \pi/L$, L is the cell length, $\eta(z)$ is the phase of electrode modulation, T is acceleration effiency.

Denote the difference between phase of synchronous particle φ_s and the phase of space modulation of the vanes η by Φ_s :

$$\Phi_s = \varphi_s - \int \overline{k}\,d\zeta. \quad (6)$$

Here $\zeta = z/\lambda$, $\overline{k} = \lambda k$, $\lambda = 2\pi c/\omega$. Take function $u_1(\zeta) = d\Phi_s/d\zeta$ as the first control function, and T as the second control function: $u_2(\zeta) = T(\lambda\zeta)$. In this model, longitudinal motion can be considered separately from the transverse one. The equations of longitudinal dynamics for a beams of low density are

$$\frac{d\varphi}{d\zeta} = 2\pi\gamma(\gamma^2-1)^{-1/2}, \quad (7)$$

$$\frac{d\gamma}{d\zeta} = C_L(2\pi\gamma_s(\gamma_s^2-1)^{-1/2} - u_1)u_2\cos\eta\cos\varphi, \quad (8)$$

where $C_L = 2eU_0/(\pi mc^2)$. Equation for η has form [6]

$$\frac{d\eta}{d\zeta} = 2\pi\gamma_s(\gamma_s^2-1)^{-1/2} - u_1.$$

Consider the case of a single scalar control function $u = T$. Then

$$\frac{dG^\varphi_\varphi}{d\zeta} = -G^\varphi_\gamma C_L\overline{k}T\cos\eta\sin\varphi, \quad \frac{dG^\varphi_\gamma}{d\zeta} = G^\varphi_\varphi\frac{2\pi}{(\gamma^2-1)^{3/2}},$$

$$\frac{dG^\gamma_\varphi}{d\zeta} = -G^\gamma_\gamma C_L\overline{k}T\cos\eta\sin\varphi, \quad \frac{dG^\gamma_\gamma}{d\zeta} = G^\gamma_\varphi\frac{2\pi}{(\gamma^2-1)^{3/2}},$$

$$\frac{\partial D^\varphi_{\varphi\varphi}(\zeta,\zeta')}{\partial\zeta'} = (2D^\varphi_{\varphi\gamma}\sin\varphi - G^\varphi_\gamma\cos\varphi)C_L\overline{k}T\cos\eta,$$

$$\frac{\partial D^\varphi_{\varphi\gamma}(\zeta,\zeta')}{\partial\zeta'} = -4\pi D^\varphi_{\varphi\varphi}(\gamma^2-1)^{3/2} - G^\varphi_\gamma C_L\overline{k}T\cos\eta\cos\varphi,$$

$$\frac{\partial D^\varphi_{\gamma\varphi}(\zeta,\zeta')}{\partial\zeta'} = 2D^\varphi_{\gamma\gamma}C_L\overline{k}T\cos\eta\sin\varphi,$$

$$\frac{\partial D^\varphi_{\gamma\gamma}(\zeta,\zeta')}{\partial\zeta'} = -\frac{4\pi D^\varphi_{\gamma\varphi}}{(\gamma^2-1)^{3/2}} + G^\varphi_\varphi\frac{6\pi\gamma}{(\gamma^2-1)^{5/2}},$$

$$\frac{\partial D^\gamma_{\varphi\varphi}(\zeta,\zeta')}{\partial\zeta'} = (2D^\gamma_{\varphi\gamma}\sin\varphi - G^\gamma_\gamma\cos\varphi)C_L\overline{k}T\cos\eta,$$

$$\frac{\partial D^\gamma_{\varphi\gamma}(\zeta,\zeta')}{\partial\zeta'} = -\frac{4\pi D^\gamma_{\varphi\varphi}}{(\gamma^2-1)^{3/2}},$$

$$\frac{\partial D^\gamma_{\gamma\varphi}(\zeta,\zeta')}{\partial\zeta'} = 2D^\gamma_{\gamma\gamma}C_L\overline{k}T\cos\eta\sin\varphi,$$

$$\frac{\partial D^\gamma_{\gamma\gamma}(\zeta,\zeta')}{\partial\zeta'} = -\frac{4\pi D^\gamma_{\gamma\varphi}}{(\gamma^2-1)^{3/2}} + G^\varphi_\gamma\frac{6\pi\gamma}{(\gamma^2-1)^{5/2}}.$$

For brevity, introduce the function $\overline{K}(\zeta) = \overline{k}\cos\eta(\zeta)\cos\varphi(\zeta)$ Second derivatives of the functional are

$$\frac{\partial^2\Phi}{\partial T_j^2} = \sum_{i=1}^{N}\Big\{\frac{\partial^2\Phi}{\partial\varphi^2}C_L^2\Big[\int_{\zeta_{j-1}}^{\zeta_j} G^\varphi_\gamma(\zeta_M,\zeta')\overline{K}(\zeta')\,d\zeta'\Big]^2 +$$

$$+\frac{\partial^2\Phi}{\partial\gamma^2}\Big[\int_{\zeta_{j-1}}^{\zeta_j} G^\gamma_\gamma(\zeta_M,\zeta')\overline{K}(\zeta')\,d\zeta'\Big]^2 +$$

ISBN 978-3-95450-181-6

$$+\frac{\partial\Phi}{\partial\varphi}\int\limits_{\zeta_{j-1}}^{\zeta_j} D^{\varphi}_{\gamma\varphi}(\zeta_T,\zeta')\overline{K}(\zeta')\int\limits_{\zeta_{j-1}}^{\zeta'} G^{\varphi}_{\gamma}(\zeta',\zeta'')\overline{K}(\zeta'')\,d\zeta''\,d\zeta'+$$

$$+\frac{\partial\Phi}{\partial\varphi}\int\limits_{\zeta_{j-1}}^{\zeta_j} D^{\varphi}_{\gamma\gamma}(\zeta_T,\zeta')\overline{K}(\zeta')\int\limits_{\zeta_{j-1}}^{\zeta'} G^{\gamma}_{\gamma}(\zeta',\zeta'')\overline{K}(\zeta'')\,d\zeta''\,d\zeta'+$$

$$+\frac{\partial\Phi}{\partial\gamma}\int\limits_{\zeta_{j-1}}^{\zeta_j} D^{\gamma}_{\gamma\varphi}(\zeta_T,\zeta')\overline{K}(\zeta')\int\limits_{\zeta_{j-1}}^{\zeta'} G^{\varphi}_{\gamma}(\zeta',\zeta'')\overline{K}(\zeta'')\,d\zeta''\,d\zeta'+$$

$$+\frac{\partial\Phi}{\partial\gamma}\int\limits_{\zeta_{j-1}}^{\zeta_j} D^{\gamma}_{\gamma\gamma}(\zeta_T,\zeta')\overline{K}(\zeta')\int\limits_{\zeta_{j-1}}^{\zeta'} G^{\gamma}_{\gamma}(\zeta',\zeta'')\overline{K}(\zeta'')\,d\zeta''\Big]\,d\zeta'\Big\}.$$

RESULTS

Test calculations were performed for accelerator structure with frequency 433 MHz and initial energy of protons 60 keV. The final energy is about 1852 MeV. Dependencies of energy of particles that have passed the accelerating structure on longitudinal coordinate after optimiztion are presented on the Fig.1

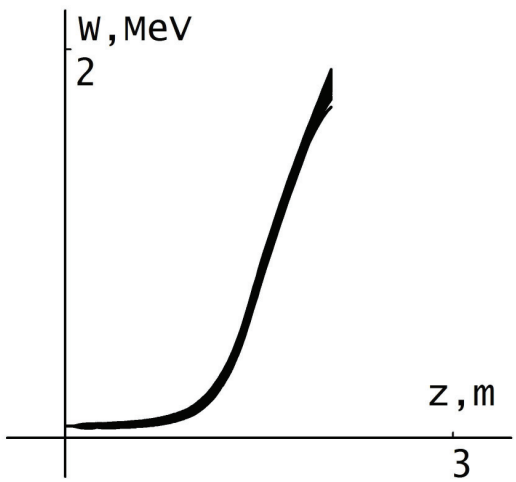

Figure 1: Energy of particles in accelerator channel

Comparison between the second order method and a method using only first order derivatives is presented on the Fig.2, and Fig.3. The dependencies of the functional quality on iteration number are shown.

The process of optimization of only one cell is shown on the Fig.2. One can see that using of the second order method speeds up the process sufficiently, as it should be.

The process of optimization of the entire structure is shown on the Fig.3. The black line describes descent by the first order method with constant step. The red line corresponds to the first order method with adaptive step. It means that the value of optimization step changes depending on changing of the functional value on this step. The

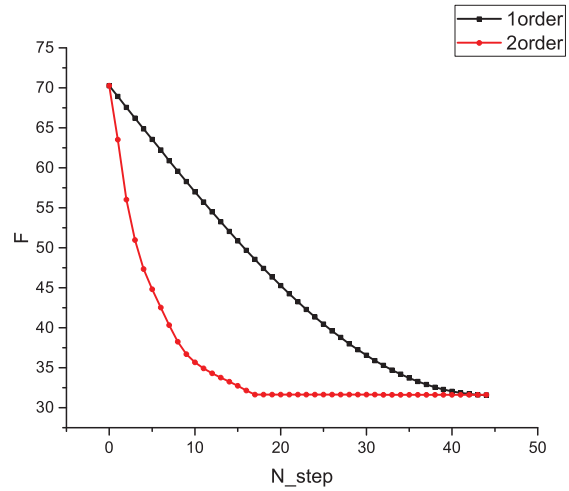

Figure 2: Changing of the quality functional during the process of optimization of the last cell

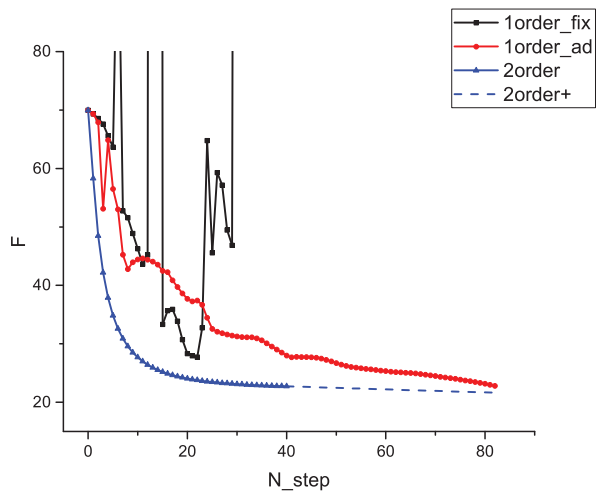

Figure 3: Changing of the functional quality during the process of optimization on the entire structure in same cases

blue line corresponds to the optimization with use of the second order method. Stroke line denotes extrapolation of the solid line.

Analyzing this result, one can see that the difference betwen the first order method an the second order one is expressed clearly. Using the second order method allows sufficiently reduce the number of computation.

REFERENCES

[1] D.A. Ovsyannikov, "Modeling and Optimization of Charge Particle Beam Dynamics", Leningrad: Publ. Comp. of Leningrad State Univ., 1990 (in russ.).

[2] D.A. Ovsyannikov, O.I. Drivotin, "Modeling of Intensive Charge Particle Beams", St.Petersburg: Publ. Comp. of St.Petersburg State Univ., 2003 (in russ.).

ISBN 978-3-95450-181-6

[3] D.A. Ovsyannikov, "Mathematical Modeling and Optimization of Beam Dynamics in Accelerator", RuPAC 2012, St.Petersburg, September 2012.

[4] O.I. Drivotin, D.A. Ovsyannikov, Yu.A. Svistunov, M.F. Vorogushin, "Modeling and Optimization of Accelerating and Focusing Structures with RFQ and APF", Problems of Atomic Science and Technology, Ser. Nuclear Physical Investigations, 2,3 (29,30), 1997, p. 93.

[5] O.I. Drivotin, D.A. Ovsyannikov, "Software for the Solving of the Problems of Optimization of Beam Dynamics in Linear Accelerating and Focusing Structure", 4th Int.Workshop "Beam Dynamics and Optimization", Dubna, Oct 1997.

[6] O.I. Drivotin, D.A. Ovsyannikov, Yu.A. Svistunov, M.F. Vorogushin, "Mathematical models for accelerating structures of safe energetical installation", 6-th Europ. Part. Accel. Conf., Stockholm, 1998, p. 1227.

[7] O.I. Drivotin, D.A. Ovsyannikov, "Modeling and Optimization of the Dynamics of High Density Beam in RFQ Channel", 6th Int. Workshop "Beam Dynamics and Optimization", Saratov, Sept. 1999, p. 31.

[8] O.I. Drivotin, K.A. Vlasova, "Numerical optimization of RFQ channel", BDO'2014, St.Petersburg, June 2014.

[9] O.I. Drivotin, D.A. Starikov, "Second Order Method for Beam Dynamics Optimization", RUPAC'2014, Obninsk, Oct. 2014.

[10] O.I. Drivotin, "Covariant formulation of the Vlasov equation", IPAC'2011, San-Sebastian, September 2011, p. 2277.

[11] O.I. Drivotin, "Degenerate Solutions of the Vlasov Equation", RUPAC'2012, St.-Petersburg, September 2012.

ISBN 978-3-95450-181-6

A SIMPLE MODEL FOR ELECTROMAGNETIC FIELD IN RFQ CHANNEL

O.I. Drivotin*, I.T. Dulatov,
St.Petersburg State University, 7/9 Universitetskaya nab., St.Petersburg, 199034, Russia

Abstract

Numerical solution of the RFQ structure optimization problem requires a great amount of computation. Each consecutive step of the numerical optimization includes modification of geometry of the channel and computation of electromagnetic field for modified geometry. Therefore, a simple model describing the field in the channel is needed for the optimization. Such model is proposed in this report. It differs from the commonly used traditional model of the field, which can be applied when profiles of the vanes are described by the harmonic functions of the longitudinal coordinate. Our model is more general and can be applied for arbitrary profiles of the vanes.

INTRODUCTION

Professor D.A. Ovsyannikov proposed an approach which consists in the optimization of accelerator channel based on control theory methods [1-3]. During the optimization the functional characterizing the beam quality and the functional gradient of parameters describing the accelerator channel are computed. After that the parameters change according to the values of functional gradient components. Then iterations repeat until the appropriate structure is found.

Since the channel parameters are changing during the optimization process, the electromagnetic field in the accelerator channel is also changing. Optimization of the RFQ channel requires a great amount of computation [4-9]. Therefore, precise computation of electromagnetic field in the channel at each step of optimization means that optimization process is not executable for a real time. By this reason we should use simple models of electromagnetic field.

Most known model of the electromagnetic field in the RFQ channel was proposed by I.M. Kapchisky [10]. But it is applicable only for the case when the vane modulation is quasi-periodic. Within the framwork of this model the field is described by piecewise harmonic functions.

Here we propose a new simple model applicable in most general case. It allows to compute the electromagnetic field dynamically for each new channel configuration. This article presents the development and the investigation of this model.

* o.drivotin@spbu.ru

ELECTRIC FIELDS MODELS

Electric field potential u satisfies to the wave equation:

$$\frac{1}{c^2}\frac{\partial^2 u}{\partial t^2} - \Delta u = 0,$$

Here t is the time, c is the light velocity.

If electromagnetic oscillation frequency is not very great, the first term in this equation is small and can be neglected and we have quasi-stationary approximation:

$$\Delta u = 0. \tag{1}$$

Assume that on the vanes surfaces the following conditions holds:

$$u_\Gamma = \pm u_0 \cos \omega t. \tag{2}$$

Here $U_0 = V/2$, and V is amplitude of intervane voltage. Assume also that the vane surfaces are described by the equations

$$r^2 \cos 2\varphi = \mu(\pm 1 - \frac{4T}{\pi} I_0(kr) \sin \eta), \tag{3}$$

where $\eta(z) = \int\limits_{z_0}^{z} k(z')\,dz'$, $k(z)$ is function specifying dependency of the vane modulation along the longitudinal axis, I_0 is the modified Bessel function of the zeroth order. The interval where η is change from $(i-1)\pi$ to $i\pi$, $i = \overline{1, N}$, corresponds to one cell of the structure, and N is the total number of the cells.

Assume that $k(z)$ and $T(z)$ slowly change when z increases:

$$\frac{dk}{dz} \ll \frac{k(z_i)}{L_i} = \frac{k(z_i)^2}{\pi}.$$

Then length of the $i-$th cell is $L_i = \pi/k(z_i)$, where z_i can be any z inside the cell.

It is easy to see that the solution of the boundary problem (1), (2) is

$$u(r, \varphi, z) = -u_0(\frac{r^2 \cos 2\varphi}{\mu} + \frac{4T}{\pi} I_0(kr) \sin \eta) \cos \omega t.$$

Denote the channel aperture by a. It is minimal with respect to all cross-section of the cell distance from the axis to the nearest vane. From the equation (3) we have

$$a^2 = \mu(1 - \frac{4T}{\pi} I_0(ka)). \tag{4}$$

From (3) we have

$$a^2 = \mu(1 - \frac{4T}{\pi} I_0(ka)). \tag{5}$$

ISBN 978-3-95450-181-6

Then

$$\mu = \frac{a^2}{\varkappa}, \qquad \varkappa = 1 - \frac{4T}{\pi} I_0(ka),$$

and the solution of the boundary problem (1), (3) can be written in the form

$$u(r, \varphi, z) = -u_0(\varkappa \frac{r^2}{a^2} \cos 2\varphi + \frac{4T}{\pi} I_0(kr) \sin \eta) \cos \omega t. \tag{6}$$

Denote the distance from the axis to another vane in the section where distance to the nearest vane is minimal. It is maximum distance for this cell. Denote it by $r_{\max}$. It is easy to see from the equation (3) that

$$r_{\max}^2 = \mu(1 + \frac{4T}{\pi} I_0(kr_{\max})). \tag{7}$$

Introducing the modulation coefficient $m = r_{\max}/r_{\min}$, we have

$$m^2 = \frac{1 - \frac{4T}{\pi} I_0(kr_{\min})}{1 + \frac{4T}{\pi} I_0(kr_{\max})},$$

$$T = \frac{\pi}{4} \cdot \frac{m^2 - 1}{m^2 I_0(ka) + I_0(mka)}.$$

The expression for the field potential (6) is valid if vane shape is described by (3), that is the vanes section are hyperbolic. Assume that the potential is described in paraxial area by the same expression also for the case when the vanes sections are not hyperbolic.

In Cartesian coordinates from (6) we have

$$u(x, y, z) = -u_0(\varkappa \frac{x^2 - y^2}{a^2} + \frac{4T}{\pi} I_0(kr) \sin \eta) \cos \omega t. \tag{8}$$

Argument of the function I_0 is less then 1. Approximating it by first two terms of its expansion into the Taylor series $I_0(kr) \approx 1 + (kr)^2/4$, and differentiating we get Cartesian components of the electric field

$$E_x = u_0(\frac{2\varkappa}{a^2} x + \frac{2k^2 T}{\pi} x \sin \eta) \cos \omega t, \tag{9}$$

$$E_y = u_0(-\frac{2\varkappa}{a^2} y + \frac{2k^2 T}{\pi} y \sin \eta) \cos \omega t, \tag{10}$$

$$E_z = u_0 \frac{4kT}{\pi} I_0(kr) \cos \eta \cos \omega t \tag{11}$$

This field model is analogous to the known model of electromagentic field [10], and is widely used for numerical solution of the optimization problem [4-8].

The characteristic feature of this model is piecewise harmonic modulation of the vane.

Here we propose another field model for arbitrary rule of modulation:

$$u(x, y, z) = u_0 \frac{d_y(z) - d_x(z)}{d_x(z) + d_y(z)} + \frac{2u_0}{d_x(z) + d_y(z)}(x - y). \tag{12}$$

Here $d_x(z)$ and $d_y(z)$ are distances from the axis to electrodes along axes x and y corresdpondingly.

The remainder of this article is devoted to the investigation of the approximation quality of this model in a real RFQ channel. It is done by numerical solution of the corresponding boundary problem.

NUMERICAL SOLUTION OF THE BOUNDARY PROBLEM

Assuming that d_x and d_y slowly vary along longitudinal axis, we reduce the boundary problem (1), (2) to a set of two-dimensional boundary problems for various cross-sections of the channel depicted on Fig.1.

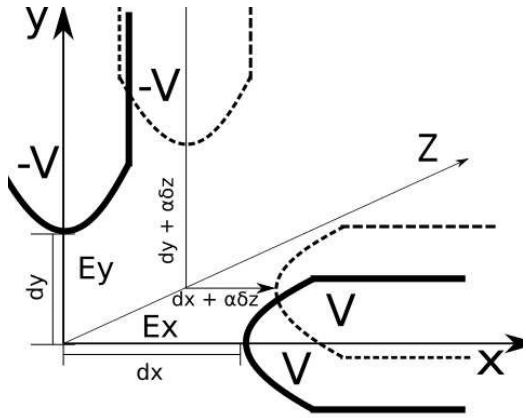

Figure 1: Cross-section of the channel.

Computation is implemented by iteration relaxation method applied for a system of finite difference equations corresponding so some grid in the region under consideration. Computational formulas correspond to various positions of a grid node where field is computed. For, example, for regular inner nodes we have the well known expression

$$U_i^j = \frac{1}{4}(U_{i-1}^j + U_{i+1}^j + U_i^{j-1} + U_i^{j+1}),$$

and for nodes adjacent to the boundary the following expressions:

$$U_i^j = \frac{(\frac{h}{\delta_x} U_0 + U_{i-1}^j)(\delta_y + h) + (\frac{h}{\delta_y} U_0 + U_i^{j+1})(\delta_x + h)}{(\frac{h}{\delta_x} + 1)(\delta_y + h) + (\frac{h}{\delta_y} + 1)(\delta_x + h)}$$

for the case $\delta_y < h$ and $\delta_x < h$,

$$U_i^j = \frac{h(\frac{h}{\delta_x} U_0 + U_{i-1}^j) + \frac{\delta_x + h}{2}(U_i^{j+1} + U_i^{j-1})}{\frac{h^2}{\delta_x} + 2h + \delta_x};$$

for the case $\delta_y \geq h$ and $\delta_x < h$,

$$U_i^j = \frac{2h(\frac{h}{\delta_y} U_0 + U_i^{j+1}) + \frac{\delta_y + h^2}{2}(U_{i+1}^j + U_{i-1}^j)}{\frac{h^2}{\delta_y} + 2h + \delta_y}.$$

for the case $\delta_y < h$ and $\delta_x \geq h$. Here h is a grid step, and δ_x, δ_y are components of displacement of the node from a nearest boundary.

RESULTS

Results of the investigation are presented on the fig.2,3. Dots represent numerically computed values of the potential at distinct cross-section. Lines represent the potential

ISBN 978-3-95450-181-6

values computed according expression (12). Distances between the channel axes and the vanes change linearly in both cases.

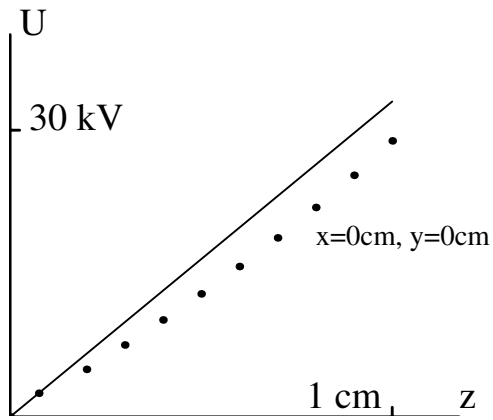

Figure 2: Variation of electric potential along beam axis at $x = 0cm, y = 0cm$.

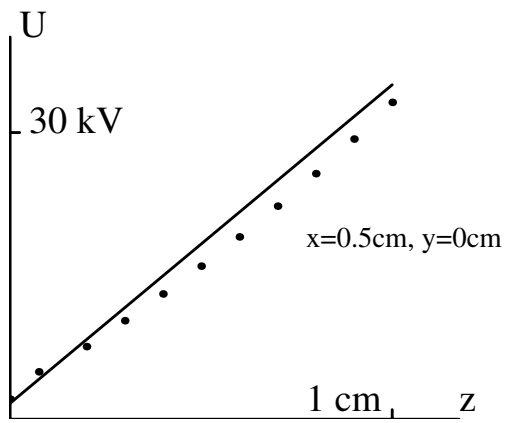

Figure 3: Variation of electric potential along beam axis at $x = 0.5cm, y = 0cm$.

One can see that difference between two models is about 10%. Therefore, the accuracy of the proposed simple model can be estimated as 10%. It means that the proposed simple linear model give good enough approximation, and can be used at an initial stage of optimization. We hope that it is possible to modify this model and to improve its accuracy.

REFERENCES

[1] D.A. Ovsyannikov, *Modeling and Optimization of Charge Particle Beam Dynamics,* (Leningrad: Publ. Comp. of Leningrad State Univ., 1990) (in russ.).

[2] D.A. Ovsyannikov, O.I. Drivotin, *Modeling of Intensive Charge Particle Beams,* (St.Petersburg: Publ. Comp. of St.Petersburg State Univ., 2003) (in russ.).

[3] D.A. Ovsyannikov, "Mathematical Modeling and Optimization of Beam Dynamics in Accelerator", RuPAC 2012, St.Petersburg, September 2012.

[4] O.I. Drivotin, D.A. Ovsyannikov, Yu.A. Svistunov, M.F. Vorogushin, "Modeling and Optimization of Accelerating and Focusing Structures with RFQ and APF", Problems of Atomic Science and Technology, Ser. Nuclear Physical Investigations, 2,3 (29,30), 1997, p. 93.

[5] O.I. Drivotin, D.A. Ovsyannikov, "Software for the Solving of the Problems of Optimization of Beam Dynamics in Linear Accelerating and Focusing Structure", 4th Int.Workshop "Beam Dynamics and Optimization", Dubna, Oct 1997.

[6] O.I. Drivotin, D.A. Ovsyannikov, Yu.A. Svistunov, M.F. Vorogushin. "Mathematical models for accelerating structures of safe energetical installation", 6-th Europ. Part. Accel. Conf., Stockholm, 1998, p. 1227.

[7] O.I. Drivotin, D.A. Ovsyannikov, "Modeling and Optimization of the Dynamics of High Density Beam in RFQ Channel", 6th Int. Workshop "Beam Dynamics and Optimization", Saratov, Sept. 1999, p. 31.

[8] O.I. Drivotin, K.A. Vlasova, "Numerical optimization of RFQ channel", BDO'2014, St.Petersburg, June 2014.

[9] O.I. Drivotin, D.A. Starikov, "Second Order Method for Beam Dynamics Optimization", RUPAC'2014, Obninsk, Oct. 2014.

[10] I. Kapchinsky, *Theory of Resonance Linear Accelerators*, (New York: Harwood Academic Publishers, 1985).

ISBN 978-3-95450-181-6

ACCELERATION OF DEUTERONS AND PROTONS IN SINGLE RFQ STRUCTURE

A.D .Ovsyannikov*, D.A. Ovsyannikov, Yu.A. Svistunov
Saint-Petersburg State University, Russia
A.P. Durkin, Moscow Radiotechnical Institute, Russia

Abstract

Some aspects of acceleration of protons and deuterons in single RFQ are considered. If effects of space charge are significantly hath nominal voltage for acceleration of deuterons can be too small to reach high efficiency of bunching and focusing of protons. It is shown that a raising of voltage up to nominal value for deuterons leads to increasing of capture and transmission for protons. Another problem is concerned with a choice of radial matching section parameters, which are optimal for both beams (proton and deuterons) simultaneously. Methods of optimization are discussed. Analysis of particles dynamics is illustrated by calculations results.

INTRODUCTION

Acceleration of ions with a different ratio of charge to mass e/m in a single channel is possible if two conditions are fulfilled:

1. longitudinal velocities at input of channel are equal for all beams,

2. for every type of ions voltage U is chosen to keep the relation eU/m is constant,

3. in case acceleration more then two types of ion with different A/Z in single RFQ one must have possibility to change intervene voltage in required diapason

$$\frac{eU}{m} = \frac{e_{nom}U_{nom}}{m_{nom}},$$

index "nom"means nominal parameters of ion, which were used in calculation of cell lengths.

So if a ratio e/m of some ion is more, than a nominal one we can use reduced voltage to copy beam dynamic when a space charge force is negligible. In our case we need to reduce voltage by one half.

However in opposite case when space charge influence is not negligible decreasing of voltage leads to weakening of external phasing and focusing forces which can compare with coulomb ones and decrease beam transmission and capture as result. On the other hand we have a reserve for doubling of voltage. So we need to estimate how we can use this reserve.

* E-mail: a.ovsyannikov@spbu.ru

CURRENT DEPENDENCE

Let consider transverse motion. Increasing voltage we move a working point on stability diagram up to its middle. Usually focusing factor is chosen as about half of value corresponding to a middle of stability interval.

In a longitudinal motion we have two opposing tendencies which counteract each other. On the one hand increasing of voltage leads to extension of separatrix for every accelerating period. On other hand a synchronization of acceleration is destroyed because we lose synchronous particle which gains given energy and phase passing the cell and which is a single center of longitudinal oscillations inside of beam. Now for every accelerating period there is its own particle, so we have additional coherent oscillation of beam inside separatrix.

As an example we used RFQ channel from the paper [1]. The main parameters of accelerator are shown in the table 1. The results are sufficient to allow conclusion: extension of separatrix is more significantly than additional coherent oscillation, transmission and capture are increased and particles does not leave separatrix. Nominal synchronous phase is changing as a smooth curve from -90 to -30 degrees. So, double voltage gives increasing of synchronous phase from -90 to -64 degrees only. As a result, current of accelerated beam depending of voltage and input current is illustrated on picture 1.

Results of these researches proves possibility of simultaneous acceleration of different types of ion with a wide spectrum of ratio e/m and with given input velocity.

Table 1: Example of RFQ Parameters

Parameters	Value
RFQ frequency (MHz)	432
Vane length (m)	6.5
Average channel radius(mm)	1.8
Vane voltage (kV)	50, 25
Injection energy of H-ions beam (KeV)	25
Injection energy of D-ions beam (KeV)	50
Initial dP/P	0
Final energy of H-ions beam (MeV)	2.5
Final energy of D-ions beam (MeV)	5
RMS emittance (cm · rad)	0.05

OPTIMIZATION PROBLEM

In general case when phase volumes of H and D beams have different orientation in phase planes xx'and yy'one

ISBN 978-3-95450-181-6

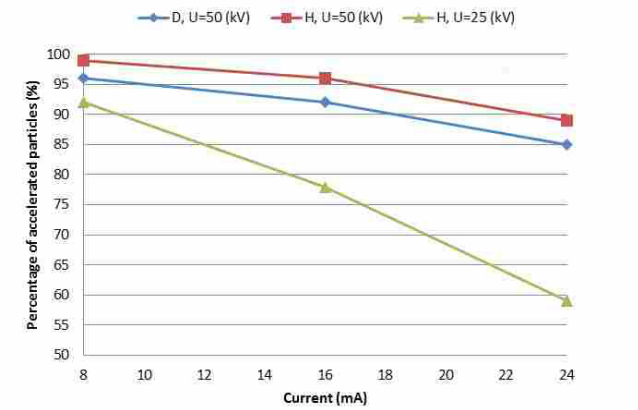

Figure 1: Dependence of ion capture effectiveness on vane voltage and beam current

can seek compromise solution using for example method presented [2,3]. In these papers matching section geometry is formed to accelerate beam, which have transversal phase volume at random oriented relatively acceptance of RFQ regular structure. It is known [4] that under some condition such as linear approximation of accelerating and focusing fields, micro canonical charge distribution and representation of bunches uniformly charged ellipsoids, equations of particle dynamics in RFQ channel may be presented in following form:

$$\frac{d^2x}{dt^2} + K_x(t, I, U, r_x, r_y, \phi_0)x = 0 \quad (1)$$

$$\frac{d^2y}{dt^2} + K_y(t, I, U, r_x, r_y, \phi_0)y = 0 \quad (2)$$

where t – time, U – vane voltage, I – average beam current, r_x, r_y – envelopes of beam in xx'and yy'planes, ϕ_0 – initial phase. Such equations may be used to describe dynamics in radial matching section too. In case of separate acceleration of two beams one need consider two of systems look like (1-2) attaching all dependent variables index H or D. To determine functions r_x, r_y in [2] used matrix algebra method. Let consider matrices A_x, A_y depending on K_x, K_y and matrices G_x, G_y which determine ellipses by filled points presented real particles in phase space, while take place conditions

$$\xi' G_x \xi \le 1, \eta' G_y \eta \le 1,$$
$$\xi = (\xi_1, \xi_2), \xi_1 = x, \xi_2 = dx/dt,$$
$$\eta = (\eta_1, \eta_2), \eta_1 = y, \eta_2 = dy/dt.$$

In case of two separate beams matrix elements G_{xH}, G_{yH}, G_{xD}, G_{yD} determine envelopes and orientation of phase ellipses in phase space. Let consider system of equations:

$$\frac{d}{dt}G_{xH} = -A'_{xH}G_{xH} - G_{xH}AxH, \quad (3)$$

$$\frac{d}{dt}G_{yH} = -A'_{yH}G_{yH} - G_{yH}AyH, \quad (4)$$

$$\frac{d}{dt}G_{xD} = -A'_{xD}G_{xD} - G_{xD}AxD, \quad (5)$$

$$\frac{d}{dt}G_{yD} = -A'_{yD}G_{yD} - G_{yD}AyD. \quad (6)$$

Optimization process includes solution of system of equations (3-6) together with auxiliary conjugate on the interval from the entrance of regular part of RFQ to the entrance of radial matching section, i.e. from $t = T$ to $t = 0$. Initial conditions for the system (3-6) are the matrices of ellipses defining acceptances of regular part of accelerator, depend on initial phase ϕ_0:

$$G_{xH}(T, \phi_0) = G_{xHT}(\phi_0), \quad (7)$$
$$G_{yH}(T, \phi_0) = G_{yHT}(\phi_0), \quad (8)$$
$$G_{xD}(T, \phi_0) = G_{xDT}(\phi_0), \quad (9)$$
$$G_{yD}(T, \phi_0) = G_{yDT}(\phi_0). \quad (10)$$

The optimization problem for the radial matching section is to find a function of radius change along the matching section, providing under condition (7 - 10) the maximum possible overlapping of family of ellipses at the entrance of the radial matching section. Optimization procedure is lead to minimization of functional

$$I(u) = c_1 \int_{\phi_1}^{\phi_2} \Phi_{xH}(\phi_0)d\phi_0 + c_2 \int_{\phi_1}^{\phi_2} \Phi_{yH}(\phi_0)d\phi_0 \quad (11)$$
$$+c_3 \int_{\phi_1}^{\phi_2} \Phi_{xD}(\phi_0)d\phi_0 + c_4 \int_{\phi_1}^{\phi_2} \Phi_{yD}(\phi_0)d\phi_0$$

where constants c_i are choose taking into account currents difference $(I_H - I_D)$. Functions $\Phi_{\chi\lambda}$ in expression (11) are determined as

$$\Phi_{xH}(\phi_0) = Sp(G_{xH}(0, \phi_0) - B_x)^2,$$
$$\Phi_{yH}(\phi_0) = Sp(G_{yH}(0, \phi_0) - B_y)^2,$$
$$\Phi_{xD}(\phi_0) = Sp(G_{xD}(0, \phi_0) - B_x)^2,$$
$$\Phi_{yD}(\phi_0) = Sp(G_{yD}(0, \phi_0) - B_y)^2.$$

Here B_x and B_y are given matrices and according to ellipses which intermediate oriented between G_{xH} and G_{xD} and G_{yH} and G_{yD}.

Functional (11) estimate the degree of mutual overlapping of ellipses corresponding to various initial phases at the entrance of matching section. ϕ_1 and ϕ_2 are limits of variation of initial phase ϕ_0; $\lambda = H, D$. Examples of choice of functionals and procedure of its minimization for similar tasks are given in [5–17].

CONCLUSION

1. Separate acceleration of two or more types of ions with different relation A/Z in single RFQ channel

ISBN 978-3-95450-181-6

may be used for example for preacceleratoin multicharged ions obtained from ECR sources before their injection into booster sinchrotron. Accelerated up to big enough energies ions are used for different applied purposes.

2. Proposed scheme optimization may be used too for RFQ output matching section optimization when one need to prepare ions of different type for further acceleration in DTL structure.

REFERENCES

[1] A.D .Ovsyannikov, A.P. Durkin , D.A. Ovsyannikov , Yu.A. Svistunov Acceleration of different ion types in single RFQ structure //Problems of Atomic Science and Technology, 2016, Vol.3(103), p. 54-56.

[2] A.D. Ovsyannikov, D.A. Ovsyannikov,S.L. Chung Optimization of a radial matching section // International Journal of Modern Physics A, 2009, Vol. 24, 5, p. 952-958.

[3] A.D. Ovsyannikov, D.A. Ovsyannikov, Yu.A. Svistunov, A.P. Durkin, M.F. Vorogushin Beam dynamics optimization: models, methods and applications // Nuclear Instruments and Methods in Physics Research, Section A: Accelerators, Spectrometers, Detectors and Associated Equipment, 2006. Vol. 558, 1. p.11-19.

[4] I.M. Kapchinsky. Theory of linear resonance accelerator. Moscow, Energoizdat, 1982, p. 240.

[5] A.D. Ovsyannikov. Mathematical models of beam dynamics optimization. Saint-Petersburg: VVM, 2014, p.181, ISBN 978-5-9651-0881-7.

[6] A.D. Ovsyannikov, D.A. Ovsyannikov, A.P. Durkin, Chang Sheng-Luen Optimization of Matching Section of an Accelerator with a Spatially Uniform Quadrupole Focusing // Technical Physics, 2009. Vol. 54, 11. p. 1663-1666.

[7] A.D. Ovsyannikov Mathematical model of charged particles dynamics optimization in RFQ accelerators // Proceedings of IPAC 2012 - International Particle Accelerator Conference, 2012, p. 298-300.

[8] D.A. Ovsyannikov, A.D. Ovsyannikov New approach to optimization of RFQ radial matching section // Proceedings of IPAC 2010 - 1st International Particle Accelerator Conference, 2010, p. 1351-1353.

[9] B.I. Bondarev, A.P. Durkin, A.D. Ovsyannikov New mathematical optimization models for RFQ structures // Proceedings of PAC99 the IEEE Particle Accelerator Conference The 18th Biennial Particle Accelerator Conference, New York, NY, USA, 1999, p. 2808-2810.

[10] D.A Ovsyannikov. Modeling and optimization problems of charged particle beam dynamics // Proceedings of ECC 1997 - European Control Conference 4, 1997, p. 1463-1467.

[11] K. Noda, T. Fujusawa, T. Furukawa et al. Proposal for carbon-beam facility for the cancer therapy in Japan // Proceedings of EPAC 2004, Lucerne, Switzerland, P.2634-2636.

[12] A.D. Ovsyannikov, D.A. Ovsyannikov, M.Yu. Balabanov, S.-L. Chung, On the beam dynamics optimization problem //International Journal of Modern Physics A, 2009. vol. A24. Issue 5, pp. 941951.

[13] D.A. Ovsyannikov, A.D. Ovsyannikov, I.V. Antropov, V.A. Kozynchenko, BDO-RFQ program complex of modelling and optimization of charged particle dynamics //Journal of Physics: Conference Series, 2016. vol. 747. 1.

[14] A.D. Ovsyannikov, D.A. Ovsyannikov, V.V. Altsybeyev, A.P. Durkin, V.G. Papkovich, Application of optimization techniques for RFQ design // Problems of Atomic Science and Technology. 2014. . 91. 3. pp. 116-119.

[15] A.D. Ovsyannikov, Transverse motion paramiters optimization in accelerators// Problems of Atomic Science and Technology.2012. 4. pp. 74-76.

[16] Y.A. Svistunov, A.D. Ovsyannikov, Designing of compact accelerating structures for applied complex with accelerators// Problems of Atomic Science and Technology. 2010. 2. pp. 48-51.

[17] D.A. Ovsyannikov. Mathematical modeling and optimization of beam dynamics in acceleratos // RuPAC 2012 Contributions to the Proceedings - 23rd Russian Particle Accelerator Conference 2012. pp. 68-72.

ISBN 978-3-95450-181-6

BEAM SIMULATION AND MEASUREMENTS AT BEAM LINE TO RADEX EXPERIMENTAL AREA OF INR LINAC

V.Aseev, S.Bragin, S.Gavrilov, P.Reinhardt-Nickoulin, O.Volodkevich

Institute for Nuclear Research of RAS, Moscow, Russia

Abstract

In 2015 the Experimental Complex beam lines of INR linac were upgraded. There is a need to study beam dynamics in these lines. The results of beam simulation at beam line to RADEX experimental area and comparison with beam measurements are presented.

INTRODUCTION

INR linear accelerator is a high-current proton beam source for researches on nuclear physics and applied researches. The Experimental Complex is the main experimental area of INR linac. The facility of Experimental Complex consists of the beam lines, the multipurpose Neutron Complex and complex of proton therapy. The Neutron Complex includes in turn: 1) the beam dump RADiation EXperiment (RADEX) facility, together with time-of-flight spectrometer; 2) the Pulsed neutron source; 3) the Lead slowing-down spectrometer.

RADEX INSTALLATION

RADEX installation makes it possible to generate high-intensity neutron fluxes in the target by high-current proton beams. It gives unique opportunities for nuclear materials testing under irradiation. For instance the radiation tests of fusion reactor candidate materials for first wall can be carried out in conditions close to the expected in reality. The installation has a vertical irradiation channel inside the beam stop for horizontally incident protons with energies up to 209 Mev. The researches in the field of neutron-nuclear interactions using the time-of-flight technique in special channels are also carried out at RADEX.

When working with a RADEX installation last time in April, 2016 the beam parameters were as follows: beam energy 209 MeV, pulse current 10 mA, pulse duration 0.3÷115 μs at pulse repetition rate 50 Hz.

The operation modes of Experimental Complex beam lines for different beam parameters are well studied [1]. But in 2015 beam lines were upgraded: re-aligning of beam line elements relative to beam axis was carried out and some new power supplies for quadrupoles were implemented. Therefore, there is a need to study beam dynamics in the new magnetic lattice of the channel to RADEX experimental area additionally.

BEAM MEASUREMENTS UPSTREAM THE EXPERIMENTAL COMPLEX

To study beam dynamics in the channel to RADEX installation it is necessary to determine correctly transverse beam parameters at its input. The measuring area at the linac exit (upstream the beam line to RADEX) is shown in Fig. 1. The following equipment is displayed at this area: 1) 8 quadrupole magnetic doublets D106÷D113 supplied from a common current source; 2) 4 quadrupole magnetic doublets D114÷D117 supplied from different current sources; 3) 3 wire scanners WS1÷WS3; 4) beam cross section monitor (BCSM).

BCSM is developed to provide non-intercepting measurements of beam parameters. Monitor operation is based on utilization of residual gas ionization. BCSM enables to observe proton distribution in beam cross section (Fig. 2) during adjustment and operation of the linac. The transverse beam profiles can be obtained from beam cross section too [2].

Wire scanners are used for transverse beam profile measurements [3]. The measurements by wire scanners may be carried out only at 1 Hz pulse repetition rate to avoid excessive equipment activation and damage of accelerator components due to their overheating in the point of significant beam losses.

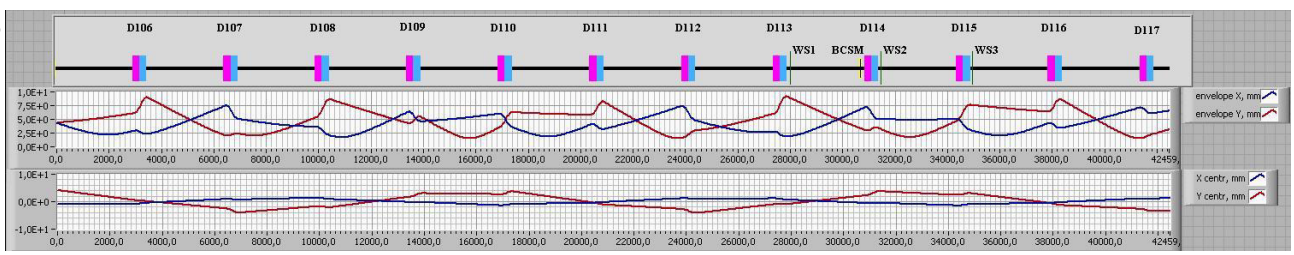

Figure 1: The accelerator area upstream the Experimental Complex beam line and beam tracing across it. D - quadrupole magnetic doublets; WS – wire scanners; BCSM – beam cross section monitor.

ISBN 978-3-95450-181-6

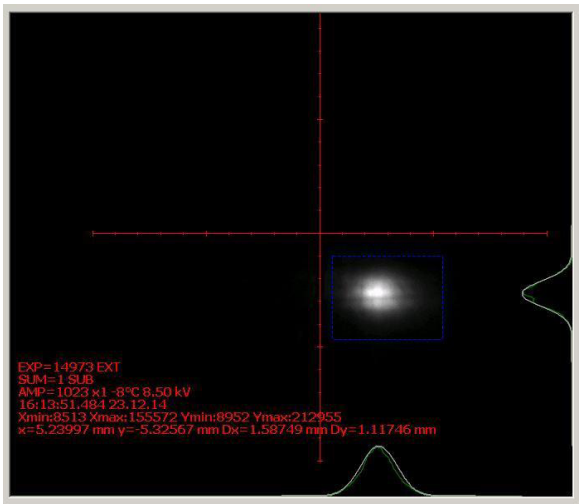

Figure 2: The example of beam cross section measurement by BCSM.

The results of rms beam size and beam centre measurement at the point of wire scanner longitudinal location for each transverse phase plane represent vertical lines. The measurements have been made for different magnetic field gradients in doublets D106÷D113 by varying the current in common current source. Then the disposition of all the lines has been transferred by matrix technique to input point of measuring area located upstream the region of variable fields. The rms phase ellipses are inscribed with the iteration algorithm in central parts of the space separated by the rms beam size lines (Fig. 3). The values of rms emittances $\varepsilon_{x\,rms}$, $\varepsilon_{y\,rms}$ and their parameters α_{x0}, β_{x0}, γ_{x0}, α_{y0}, β_{y0}, γ_{y0} are determined here graphically ($\varepsilon_{x\,rms} \approx \varepsilon_{y\,rms}$, so the notation ε_{rms} will be used). Tracing of the beam centre and beam envelope for $5\varepsilon_{rms}$ emittance containing approximately 90% of the entire beam is shown in Fig. 1. BCSM location is arbitrary chosen as an input point for beam line to RADEX. The parameters of phase ellipses in this point (α_x, β_x, γ_x, α_y, β_y, γ_y) are calculated through α_{x0}, β_{x0}, γ_{x0}, α_{y0}, β_{y0}, γ_{y0}.

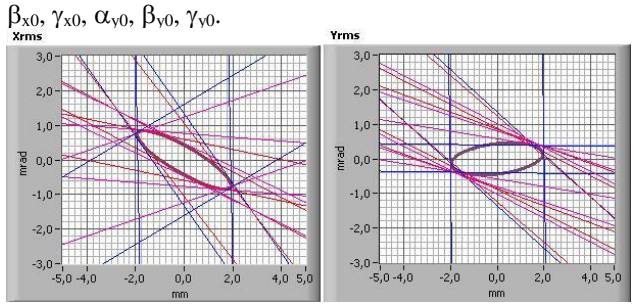

Figure 3: Determination of rms transverse emittances by wire scanners measurements.

BEAM STUDY AT RADEX BEAM LINE

The beam line to RADEX experimental area is shown in Fig.4. It stretches from BCSM location to inlet to RADEX facility. The distance from RADEX inlet to RADEX target is about 4 m. Many beam monitors are not displayed in this scheme. Multiwire secondary-electron emission monitor (SEM Grid) consisting of two mutually perpendicular grids is located 2 meters from RADEX inlet. The other elements of beam transportation line are quadrupole magnetic doublets, single quadrupole magnetic lenses and bending magnets MBV1÷MBV4. The system of four magnets elevates the beam by 4.2 m from the level of accelerator to the level of Experimental Complex.

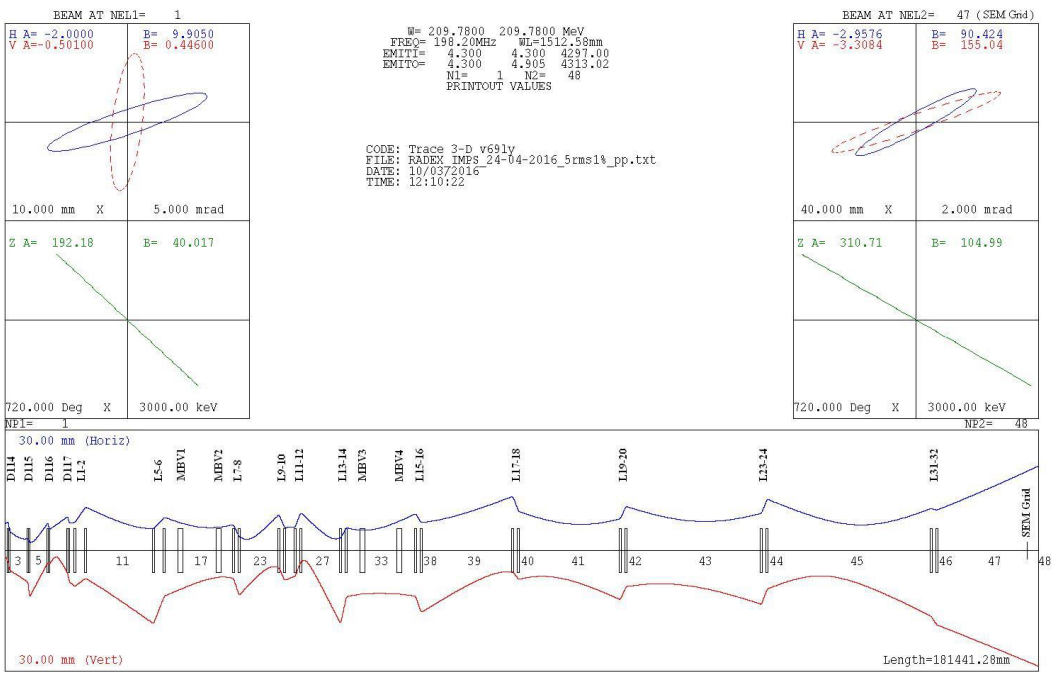

Figure 4: The beam line to RADEX experimental area and beam tracing across it. D - quadrupole doublets; L - quadrupole lenses; MBV - vertical bending magnets; SEM Grid - multiwire profile monitor.

ISBN 978-3-95450-181-6

Since the beam line has been upgraded it was necessary to study beam dynamics in modified conditions. TRACE 3-D code was used for beam dynamics simulation through magnetic elements of beam line. The value of input transverse emittances in both phase planes was assumed to be $5\varepsilon_{rms}$. The input parameters of phase ellipses (α_x, β_x, γ_x, α_y, β_y, γ_y) have been determined earlier. Series of simulation tests was carried out at different currents in focusing elements. Applicable result is shown in Fig. 4. The currents from this simulation variant were set in corresponding focusing elements. Then the currents in some focusing elements were slightly corrected to minimize beam losses along the beam line.

SEM-grid profiles presented in Fig. 5 demonstrate good agreement between simulation and measurement results.

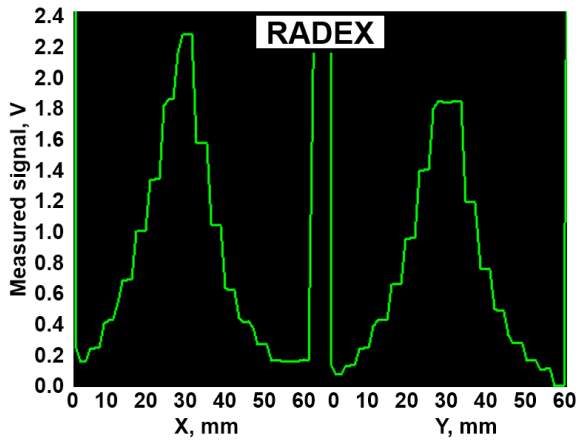

Figure 5: The result of beam profiles measurement by SEM Grid.

CONCLUSION

The considered algorithm of transverse beam profiles measurement and treatment at linac exit is actively used to get transverse beam emittances. The determination of these parameters, in turn, enables to carry out the correct beam dynamics simulation through Experimental Complex beam lines. TRACE 3-D code was used for this purpose. All the procedures in general with additional online field tuning effectively provide proper beam parameters at the target with minimal beam losses along the beam line.

REFERENCES

[1] M.Grachev, E.Ponomareva, “Optical Design of the Proton Beam Lines for the Neutron Complex INR RAS and Medical Application”, Proceedings of IPAC2011, San Sebastian, Spain, pp.2049-2051.

[2] P.Reinhardt-Nickoulin, S.Bragin, A.Feschenko, S.Gavrilov, I.Vasilyev, O.Volodkevich, “Beam Parameters Measurements by Ionization Cross Section Monitor on Proton Linac of INR RAS”, Proceedings of DIPAC2011, Hamburg, Germany, pp.161-163.

[3] P.Reinhardt-Nickoulin, S.Bragin, A.Mirzojan, I.Vasilyev, O.Volodkevich, “Emittance Measurements at the Exit of INR Linac”, Proceedings of RUPAC2012, Saint-Petersburg, Russia, pp.668-670.

ISBN 978-3-95450-181-6

EXPERIMENTAL FACILITY FOR E-BEAM IRRADIATION TEST OF PROTOTYPE IF TARGET IN RISP

K.V. Gubin, ILP SB RAS, Novosibirsk, Russia
I.K. Chakin, S.N. Fadeev, M.G. Golkovskiy, Yu.I. Maltseva, P.V. Martyshkin, BINP, Novosibirsk, Russia
J.-W. Kim, J.Y. Kim, Y.-H. Park, IBS, Daejeon, Korea

Abstract

Nowadays project RISP is developed in IBS, Daejeon. One of the main project device is graphite target system for production of rare isotopes by means of the in-flight fragmentation (IF) technique. The power inside the target system deposited by the primary beam with energy of 200 MeV/u is estimated to be around 100 kW. The target represents rotating multi-slice graphite disc cooled by thermal radiation. Necessary step of the target development is integrated test of target prototype under high power electron beam modelling real energy deposit into target. This test is planned to be held in BINP, Novosibirsk, with the use of ELV-6 accelerator.

This paper presents the design of experimental facility as well as experimental program of test. Specifications of electron beam (energy close to 800 keV, size ~ 1mm, total power 30-40 kW) are discussed. Parameters and design of basic devices and systems of facility are described.

INTRODUCTION

At the present time in IBS (Institute of Basic Since, Daejeon, Korea) the RISP (Rare Isotope Science Project) is carried out [1,2]. Project purposes are production and investigation of new isotopes of chemical elements for fundamental research. In RISP, in particular, the In Flight (IF) fragmentation method of isotope production, wherein the heavy-ion beam energy is up to 200 MeV/u and diameter is ~1 mm cracks on the solid-state target (stripper), is realized [3]. IF target represented the rotating multi-layer thin graphite disk in vacuum with cooling by its own thermal radiation [4]. Its peculiarity is high working temperature (up to 1900 °C) and temperature gradient.

Presented paper describes planned testing of multi-layer target prototype under the high-power in vacuum.

EXPERIMENTAL PROGRAM

Goal of prototype testing is experimental check of general parts of IF target under conditions as close as possible to the operational ones. Test of prototype is envisaged to clarify a series of technical and physical problems which arise designing the target, including:

- to clear up the possibility of multi-layer target construction to dissipate the beam power, its resistance to thermal and mechanical stress;
- to test the cooling panels aimed to accept and remove the heat power, heat transfer balance;
- to check up the calculations of prototype operation conditions, in particular, the temperature fields of front and rear target layers;
- to test the control, measurement and protection methods proposed for the target subsystems design.

Heavy-ion beam will be modelled by the e^- beam of ELV-6 accelerator [5-6] with diameter down to ~1 mm, energy 800 keV (minimum possible) and power up to 40 kW. Maximum beam power will be limited by the graphite beam dump ability to utilize the e^- beam energy deposit [7].

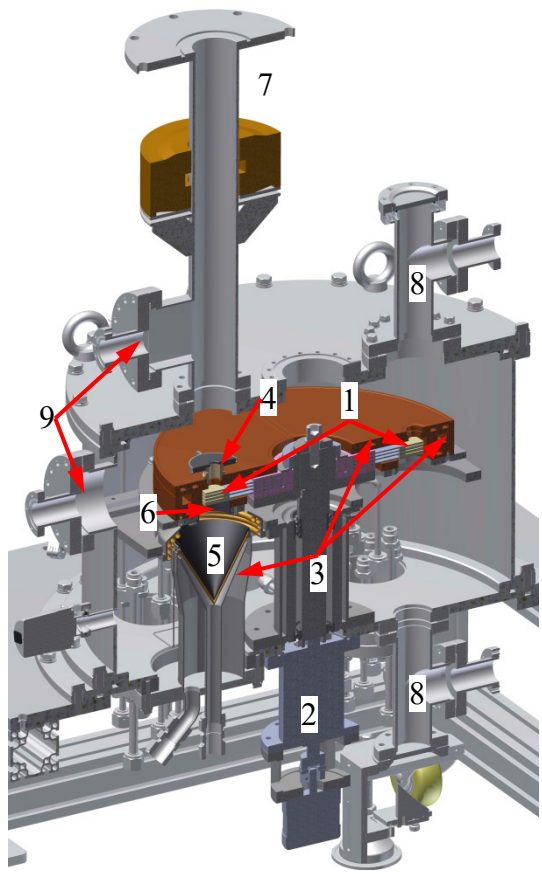

Figure 1: Experimental device. 1 – rotating target, 2 – rotary motion unit, 3 – cooling panels, 4 – protective diaphragm, 5 – graphite cone beam dump, 6 – protective graphite blanket, 7 – telescopic connecting tube to accelerator with beam control magnetic elements, 8 – optical ports, 9 – beam measurement plate ports.

ISBN 978-3-95450-181-6

PROTOTYPE DESIGN

Design of target prototype is presented in Fig. 1. Prototype represents rotating multi-slice graphite wheel (see Fig. 2) with 4 (optionally 3) layers [4] with diameter under beam 33 cm. Thickness of slice is 0.2 mm, distance between layers is 5 mm and diameter of disk is 350 mm (diameter under electron beam is 250 mm). Each layer of target is designed for beam power deposit up to 4÷10 kW. Target is covered by the water cooled copper panels. Target is mounted on the shaft with vacuum dry bearings and driven by an external electromotor via the vacuum rotary motion feedthrough. Special graphite protective diaphragm is placed before target. Conical high-temperature graphite beam dump [7] is placed after target. The prototype is housed in a water cooled, stainless steel vacuum chamber.

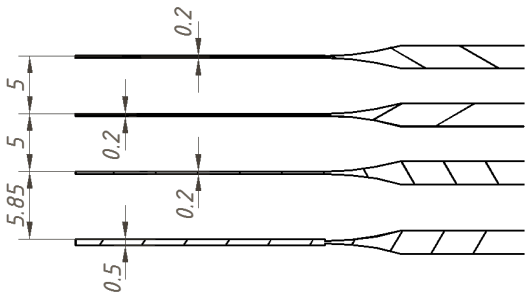

Figure 2: Layout of rotating target.

Vacuum Chamber

The vacuum chamber consists of a cylindrical volume made of stainless steel 316. Walls of chamber are equipped with cooling channels. Chamber also has the optical ports (for optical measurements of target temperature fields), electric ports (for measurement and control of different parameters) and separate pumping port. Also installation includes telescopic tube connecting the chamber and ELV-6 accelerator with the system of beam control/measurement.

Graphite Beam Dump and Protective Blanket

Beam dump with thickness 2 mm is detailed described in [7]. It is aimed to utilize the electrons passed through the target because of rotating target total thickness is not enough for full stopping the 800 keV electrons. Beam dump is insulated from installation body. The signal of current from beam dump is used for interlock unit.

Also special graphite blanket (covering outlet hole in rear cooling panel) is integral part of beam dump.

Protective Diaphragm

The protecting diaphragm is installed in order to protect the vacuum chamber and other metal parts of the construction from the e-beam hit. The diaphragm comprises (see Fig. 1) the graphite washer with 4 mm thickness, 14 mm internal diameter, and 70 mm external diameter. The washer is located right before the cooling channels and prevents the beam hit anywhere but to the prototype converter. The diaphragm is insulated from the rest part of the prototype and has the current outlet. The signal from this outlet enters the interlock unit which is described below.

Cooling Panels

Cooling panels are used to remove the excess of heat from prototype operating zone. Panels are made of copper and sectioned on top and bottom target, top and bottom beam dump panels. Thermal flow removed by the each panel can be measured. Each panel includes the covering lid and the panel body with water channels. The body and the lid are welded together. In order to provide better heat removal from the graphite plates, the panel surfaces are blackened following a custom technology.

Main Measured Parameters

- Temperature distribution over the front and rear surfaces of rotated target. Measurements are performed using the special Thermal Imaging IR Cameras, Flir (SC660) [8] and Chino (IR-CAQ2CS) [9] through the optical ports made from radiation resistant glass (see Fig. 1). Camera placed separately from vacuum chamber in the local radiation protected area. Target image transfers to camera by the optical line made from the mirrors.
- Temperature at the crucial places of the prototype body – cooling panels, target shaft, diaphragm support etc. Measurements are performed using the thermocouples.
- Measurement of heat flow from cooling panels – by the calorimeters (water flowmeters and temperature differences).
- Beam current deposit into protective diaphragm and beam dump.
- Electron beam position and current distribution.
- Measurements of the rotation speed and motor power are carried out by the motor controller.
- Measurements of beam total current and energy are performed by ELV-6 control system.

ELECTRON BEAM CONTROL/MEASUREMENT

For beam size and position the simplest magnetic system is chosen (see Fig. 3). It consists of 3 existing units: coaxial magnetic lens and 2 pairs of correctors. Lens has 80 mm, magnetic field on the lens axis can reach 0.13 T. This lens is enough for focusing the electron beam down to 1 mm on the target. Correctors have enough low inductance to be used not only for beam position control, but for beam size measurement in the scanning mode condition (see Fig. 4).

Measurements of beam position and power distribution performed using the 2 plates with thickness ~ 2 mm (not less than full stopping length). First plate has array of diagnostic holes like pepper pot. The both plates are grounded via the shunt resistor. Electron beam is linearly scanned along plates by the magnetic correctors. In this case current signal from the second plate gives us information about beam current distribution.

ISBN 978-3-95450-181-6

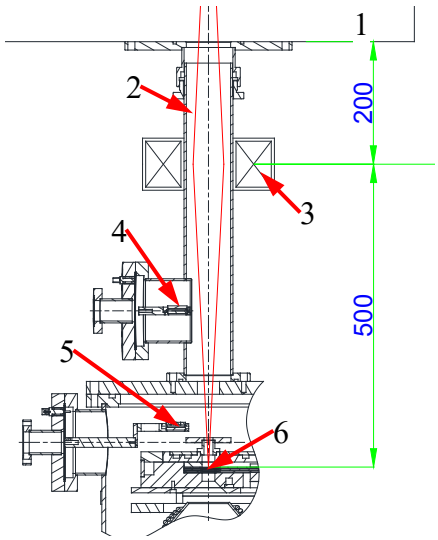

Figure 3: Magnetic system layout. 1 – ELV-6 accelerator, 2 – telescopic connecting tube to accelerator, 3 – magnetic elements, 4 – holes plate, 5 – current measuring plate, 6 – rotating target.

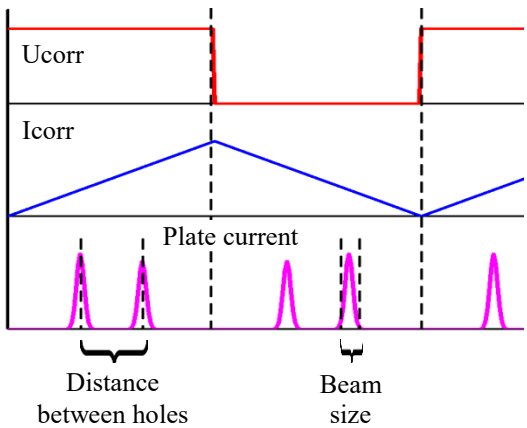

Figure 4: Time diagram of correctors parameters and measuring plate signal.

ENGINEERING AND LOCATION

Engineering includes separate control room and experimental hall with:

- biological shielding
- electrical supply 100 kW
- technical distillate up to 5 m^3/h
- ventilation system with up to 5 exchange ratio
- racks with electronics
- optical line from vacuum chamber to IR camera

Experimental equipment is located in 3 separated areas (Fig. 5):

- Vacuum chamber with internal devices, water flow meters, temperature detectors are placed directly under electron beam in the bottom floor of ELV-6 experimental hall;
- Most part of digital registration devices in cRIO-9066 format, IR camera, analogue interlock/ matching unit are placed in the top floor of ELV-6 experimental hall inside the local radiation protected area;
- Control desk and auxiliary devices are placed in ELV-6 control room.

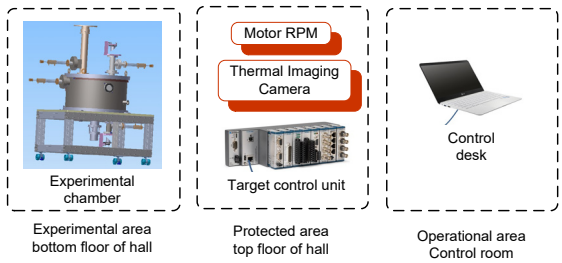

Figure 5: Experimental equipment location.

CONCLUSION, TIME SCHEDULE

By now all principal scientific and technical decisions are accepted, experimental installation is designed. Most part of equipment and devices is fabricated or purchased.

Final production and cold test of prototype is planned before end of 2016, experimental program under electron beam will be performed in BINP during march-april of 2017.

REFERENCES

[1] http://risp.ibs.re.kr/
[2] Y. K. Kwon et al., Status of Rare Isotope Science Project in Korea, Few-Body Syst (2013) 54:961–966.
[3] K. Tshoo et al., Experimental systems overview of the Rare Isotope Science Project in Korea, Nuclear Instruments and Methods in Physics Research B 317 (2013) 242–247.
[4] S.G. Hong et.al., Design and test of a graphite target system for in-flight fragment separator, Nuclear Instruments and Methods in Physics Research A 752 (2014) 1–5.
[5] R.A. Salimov et. al., DC High Power Electron Accelerators of ELV-series: Status, Development, Applications, Radiation Physics and Chemistry, 2000, Vol.57, Iss. 3-6, pp. 661-665.
[6] Yu.I. Golubenko et al., "ELECTRON ACCELERATOR OF ELV-TYPE AND THEIR WORLDWIDE APPLICATION", Proc of APAC 2007.
[7] K.V. Gubin et al., "High-power high-temperature graphite beam dump for e-beam irradiation test of prototype IF target in RISP", Proc. of this conf.
[8] FLIR systems Inc., SC660 www.flir.com
[9] CHINO Co., IR-CAQ2CS www.chino.co.jp

ISBN 978-3-95450-181-6

UPGRADE OF THE RF SYSTEM ON THE LUE-200

K.I. Mihailov, E.A. Golubkov, V.V. Kobets, A.N. Repkin, A.P. Sumbaev, JINR, Dubna, Moscow region, Russia
V.N. Pavlov, BINP SB RAS, Novosibirsk

Abstract

In the report works on upgrade of RF system of the LUE-200 (IREN) electron linac are provided. The main attention is paid to system of preliminary excitement of klystrons. After work on installation of the second accelerating section RF system of Installation it was considerably remade that allowed to carry out start-up of the second stage of the IREN installation successfully. Methods, features and problems in case of a training of two accelerating sections are discussed. Influence of the temperature and frequency modes on joint operation of accelerating sections. Results of setup of the RF system and a training of sections, and also results of posting of a bunch are given.

INTRODUCTION

Created at the Laboratory of Neutron Physics, JINR linac LUE-200 electron on the particle energy of 200 MeV for resonance neutron source (IREN) [1,2] it is based on the best world achievements in the field of accelerator technology. The pace set energy of the particles in the LUE must be 35 MeV / m, the pulse repetition frequency - 150 Hz.

The project was implemented in two stages. First it was installed and launched the first stage of the accelerator, consisting of one section of the accelerating energy of 100 MeV. Currently it implemented the second stage of the accelerator - produced by the installation of the second accelerating section and the physical start-up of accelerator. The report presents the results of the physical start-up accelerator LUE-200 of IREN.

RF SYSTEM OF THE LUE-200

Scheme of the RF system of the accelerator LUE-200 is shown in Fig. 1. The main components of the system are: two-channel sets the high-frequency generator with the ability to shift the phase of the oscillation between the channels in the 360^0 revolution and the rapid phase of both channels simultaneously vibrations 180^0, two pulse amplifier RF power for driving high-power klystron, two multiplying power system supply waveguide path RF power to the accelerating section and grouper from the powerful klystron, a directional coupler, power regulator, shifter and measuring directional couplers.

Continuous RF signal power up to 10 mW and a frequency of 2856 MHz master oscillator to the input pulse pre-amplifier driving the first and second klystron over coaxial feeders. The required phase shift between the excitation signals is carried out phase shifter.

The output klystron RF oscillation power up to 50 MW in the first pulse klystron and up to 20 MW of output from the second klystron in a rectangular waveguide evacuated arrive at 3 dB bridges. The two arms of each bridge are located high-Q resonators cumulative power of multiplication (SLED), and the fourth arm of the bridge through the waveguide and the wave type transformer is connected to the input of the accelerating section. Increasing the pulse power supplied to accelerator sections is carried out by accumulating energy in the resonator with its subsequent reradiation in going to the waveguide section when turned phase signal supplied to the resonators 180^0. Required for this switching phase of the RF oscillations carries excitation system and synchronization of the klystron at a low level RF power.

Before entering the accelerating section of the waveguide directional couplers installed H01 and H02, which signals are used to control the incident and reflected waves. Signal attenuation in the taps is about 60 dB. The output of accelerating sections unused portion of the RF power supplied to the load. Between loads and output sections mounted directional couplers (similar H01 and H02). Waveguides made of rectangular cross-section waveguides evacuated 72X34 mm. Pumping waveguides made by ion pumps in the output window of klystron and 3 dB bridges.

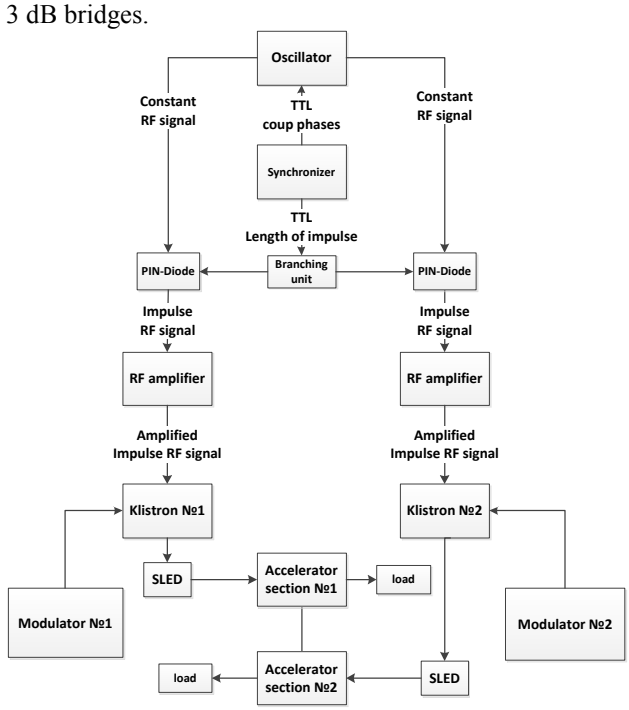

Figure 1: Scheme of the RF system of the IREN facility.

ISBN 978-3-95450-181-6

RF SYSTEM TRAINING

After the installation of the second accelerating section on the regular place and achievement in the two sections of the working vacuum accelerating work began on putting the RF power in the accelerating section and the high frequency training. This work continued for quite a long time. When workers have been achieved levels of RF power input into the accelerating section of the electron beam wiring has been made.

Figures 2 and 3 show the waveforms of the incident RF power, the klystron voltage and incident RF power from the accelerating section to the load for accelerating the first and second sections respectively. The oscillograms of the incident RF power to the load of the booster sections is visible loading of the accelerating field electron beam.

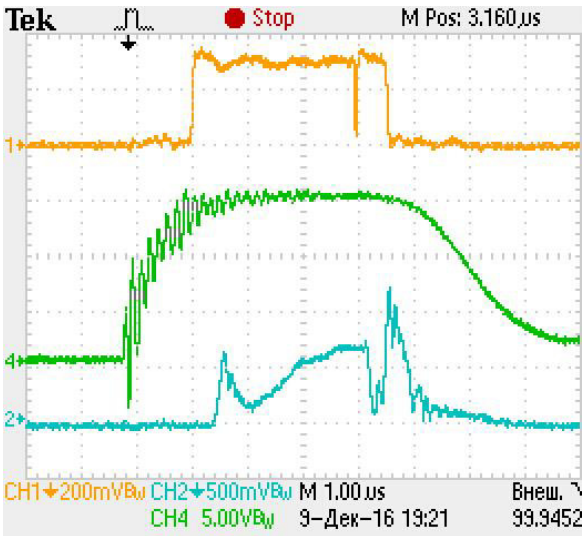

Figure 2: CH1 - the waveforms of the incident RF power, CH2 - incident RF power from the accelerating section №1 to the load, CH3 - the klystron №1 voltage.

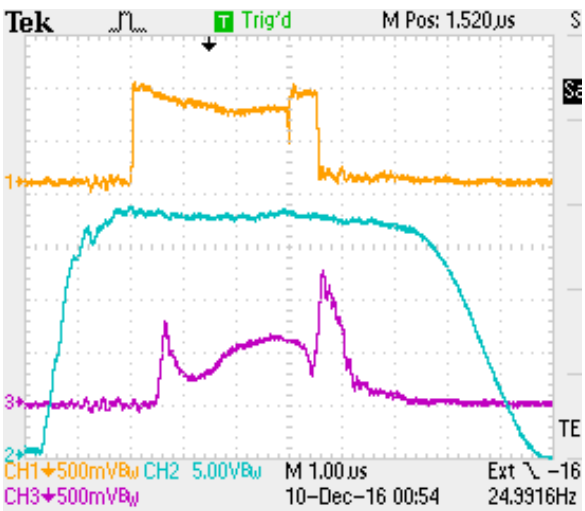

Figure 3: CH1 - the waveforms of the incident RF power, CH2 - incident RF power from the accelerating section №2 to the load, CH3 - the klystron №2 voltage.

CONCLUSION

As a result, the work was carried out a successful start up of the second stage of the LUE-200 accelerator of the IREN facility. Spend an electron beam accelerator through both sections and at a current of the electron gun 4 A on the accelerator input received accelerated output current accelerator 2 A. Work on the conclusion of the accelerator on the design parameters continues.

REFERENCES

[1] Status IREN Project, Proc. of the Conf. on Particle Acc. and High Energy, Texas, Dallas, 1995.

[2] S. Dolya at/ al. "Linac LUE-200 Test Facilities", Proc. of the XIX Int. Linac Conf. LINAC-98, (August 23-28, 1998 Chicago Illinois, U.S.A.) vol. 1, p. 52-54. ANL, Argonne, Illinois, U.S.A.

ISBN 978-3-95450-181-6

INSTALLATION FOR THE RESEARCH OF Z-PINCH PLASMA INITIATED BY THE ELECTRON BEAM

A. Drozdovsky, A. Bogdanov, S. Drozdovsky, R. Gavrilin, A. Kantsirev, V. Panyushkin, I. Roudskoy, P. Sasorov, S. Savin, V. Yanenko, SSC RF Institute of theoretical and experimental physics, Moscow, Russia

Abstract

For researches on plasma physics has been designed and constructed the electronic gun with the cold cathode on energy to 300 кэВ. The gun have the parameters: time width of pulses -100 ns, current amplitude - 100 A. The adiabatic plasma lens is developed for transportation and compression of the received electron beam. Results of researches are presented.

INTRODUCTION

At the present time, active works are underway for creating compact laser (electron and proton) accelerators [1]. For them, it is timely to solve problems of transportation and focusing of beams in discharges of the Z-pinch type, and it requires a thorough study of methods for forming such discharges. The goal of this work is to create a test installation for studying the dynamics of Z-pinch plasma with the discharge initiation by an electron beam. Typically, the discharge process begins after the high-voltage supply to the discharge tube, with the breakdown over the tube surface. It is also of interest to study the pinch development for the case when a breakdown is induced directly by an electron beam injected at the time of the application of high voltage.

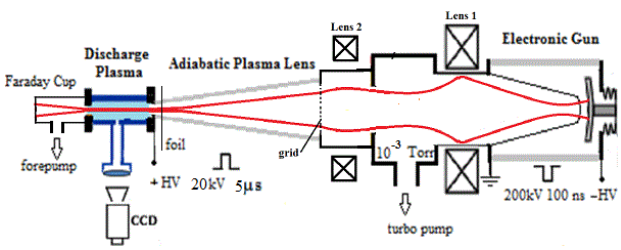

Figure 1: Installation for the research of z-pinch plasma initiated by the electron beam

THE INSTALLATION

The installation (fig. 1) consists of the electron gun [2] with magnetic lenses, experimental chamber with the scintillators located in it. Vacuum pumping of an electronic gun is conducted by the turbomolecular pump, and of plasma part of installation - the roughing-down pump. The electron beam is injected through the dividing foil into the experimental channel at a pressure of ~1 mbar. Inside the channel, the beam is compressed in the adiabatic plasma lens and then injected into the chamber of Z-pinch formation. For creation of the accelerating voltage was accepted the scheme of the generator on cable lines with use of the double forming line of Blumlein and the cable transformer of Lewis. Figure 2 shows oscillograms of the beam current and the voltage obtained on the Blumlein line with the 25 kV amplitude. The amplitude of beam current is 50 A and duration of the beam at the peak is 60 ns.

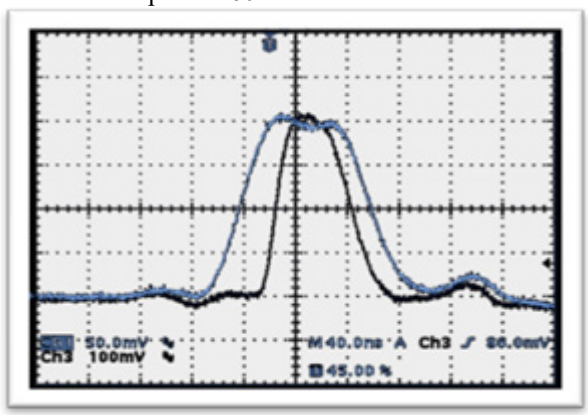

Figure 2: The electron beam current (black curve) and DFL voltage pulse signals.

Fig. 3 represents simulation results of the electron beam propagation from cathode to adiabatic plasma lens (APL). Emission current of 100 A and 50 mm cathode-anode gap under voltage of 250 kV were assumed during calculation. The simulation was performed using numerical code PICSIS-2D [3] based on use of Vlasov-Maxwell equations system with calculation of collisions of particles by Monte-Carlo method. The program enables to calculate a transportation of relativistic charged particles in arbitrary 2D electromagnetic fields taking into account its space charge and self-magnetic field.

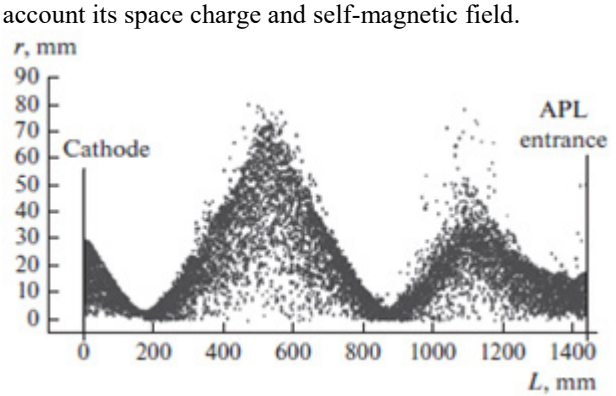

Figure 3. Calculation results of beam propagation. Concentration of dots is the product of the beam density n(r) and the coordinate r.

* Work supported by the Russian Foundation for Basic Research (grant № 16-02-01158/16)

ISBN 978-3-95450-181-6

ELECTRON DIAGNOSTICS

The Kuraray company scintillators are used for obtaining of a beam density distribution. A scintillators luminescence are registered by CCD television cameras. The last together with operating computer are in the iron boxing providing an electromagnetic shielding. Information to the central computer is transferred on optical communication. An electron beam current was measured by the current transformer which has been built in the transport channel. All measuring systems, as well as start systems, are equipped with fiber-optical devices [2].

ADIABATIC PLASMA LENS

Focusing of an charge particle beam in a plasma lens is carried out as follows (fig. 4): the z-discharge plasma current creates an azimuthal magnetic field which focuses a beam passing through the discharge tube. If a discharge tube conic, a magnetic field increase with reduction of a tube radius [4]. This of focusing can be achieved by a slow, or 'adiabatic'. Then reduction ratio of the final beam oscillation radius r_f to the initial r_i:

$$r_f / r_i = (R_f / R_i)^{1/2}$$

where R_f / R_i is the reduction ratio of final to initial diameter of discharge tube.

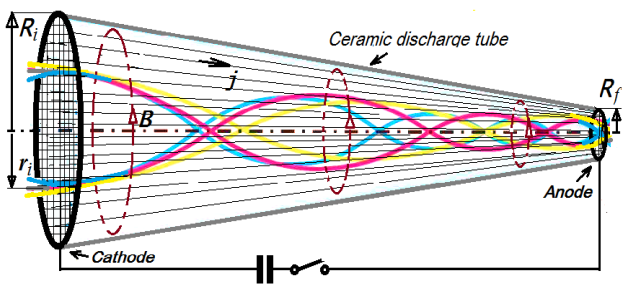

Figure 4: Schematic drawing of the principle and geometry of an adiabatic plasma lens.

Because of technological problems decided to replace a conic discharge tube with a set of cylindrical tubes. The set of tubes has length of 100 cm and their diameter decreases from 100 to 30 mm. The pulse generator with thyratron TDI1-150/25 as the switchboard on current to 30 kA was created. The current impulse duration is 5 microsec.

To choose the adiabatic plasma lens optimum operating mode were carried calculations by means of the NPINCH code [5]. It have shown (fig.5) that at peak current of 1 kA the optimum initial pressure of argon at this design of a lens lies in the range of 1-10 mTorr.

Computations of the electron beam through the APL were performed using of the data obtained on the plasma states in the applied cylindrical tubes. In a figure 6 an electron beam envelopes are given with different amplitudes of current in APL. Steps of the value decreasing from right to left correspond to the APL tubes sequence. The beam coordinate at the entrance is 900 mm and the exit coordinate is 100 mm.

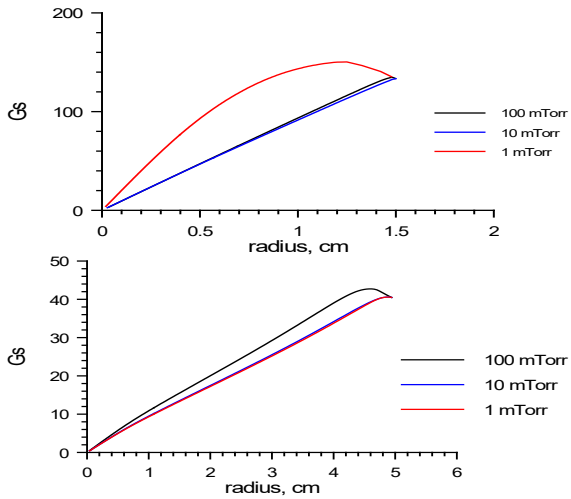

Figure 5. Azimuthal magnetic field strength (Gs) as function of radius at the time of a current maximum for a tube of diameter of 30 mm (the top drawing) and 100 mm (lower)

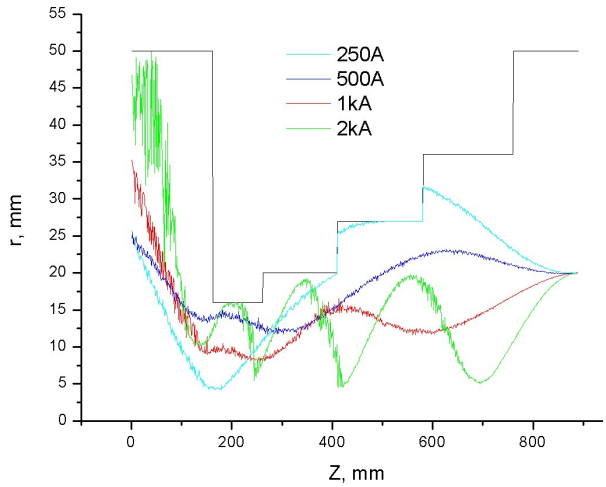

Figure 6: The electron beam envelopes for different amplitudes of current in APL.

The calculation results are given in Figs. 7 and 8 for a beam current of 10 A. The concentration of imaging dots corresponds to the product of the beam density n e (r) and the coordinate r.

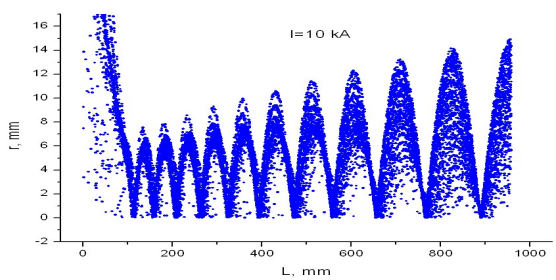

Figure 7. Results of calculation of beam propagation through APL with I = 10 kA.

ISBN 978-3-95450-181-6

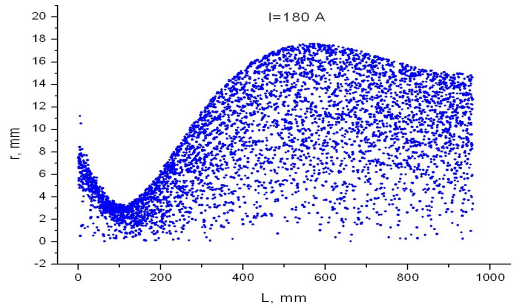

Figure 8. Results of calculation of beam propagation through APL with I = 180 A.

The first variant corresponds to the real adiabatic mode of lens operation, described at the beginning of this section, when the lens length is substantially larger than the wavelength of oscillations of the focused particles. In the second (nonadiabatic) variant, a quarter-wavelength of particle oscillations is placed on the lens length. This variant may be more preferable for use during the Z-pinch creation.

EXPERIMENTAL RESULTS

The stable discharge occurs in the APL at a pressure of ~0.1 Torr. The APL tests were conducted on the electron beam with energy of 250 keV and a current of 50 A. Figure 9 shows a luminosity of scintillators at the APL entrance and exit, as well as in the middle of the discharge tube of Z-pinch formation. The total size of the beam at the APL entrance is ~40 mm, while at the APL exit and in the discharge tube it amounts to ~10 mm.

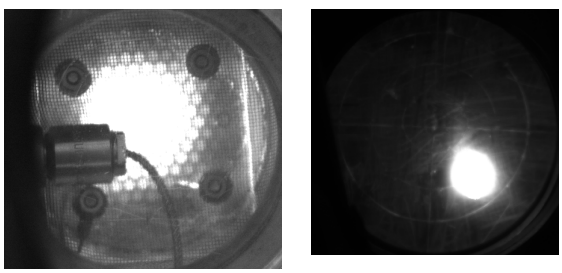

Figure 9. Glow of scintillators at the entrance and exit of APL and in the discharge tube.

The first observations of plasma luminosity in the discharge tube were conducted (Fig. 10) under the following conditions. Discharge current was ~50 kV; discharge time was ~5 μs; and beam parameters were as follows: diameter of ~1 cm, current of ~ 10 A, and duration of 100 ns. The discharge tube was located directly behind the APL. The gas was atmospheric in composition, residual, and pressure was 0.1 Torr.

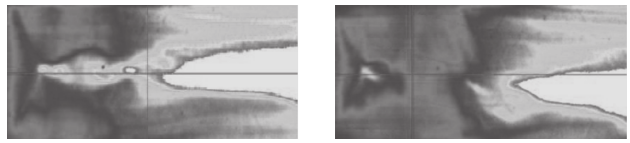

Figure 10. Plasma luminosity in the discharge tube without (on the left) and with (on the right) the beam at the first 2 μs.

CONCLUSIONS

Numerical and experimental studies of the developed system for forming an electron beam with 250-keV energy make it possible to start systematic investigation of Z-pinch creation by means of relativistic electrons. The offered method for the discharge excitation is nontraditional, which evokes interest in the search for physical distinctions of this discharges type from the traditional ones excited along the surface of the insulator. The calculations [6] show that the current distributions at the initial time instant the discharge qualitatively differ from the traditional. This leads to the smoother distribution of the current over the discharge and hence to the smaller compression ratios at the instant of maximum compression, as well as, consequently, to the lower temperatures on the discharge axis. This qualitatively corresponds to the experimental data available. Such differences will make it possible to carry out a more complete study of plasma compression in Z-pinches, as well as to better understand the dynamics of the discharge current distribution under different conditions of the process. The issue of what discharge current distributions correspond to the definite types of focusing of charged particle beams was studied in detail in our work [7].

REFERENCES

[1] W.P.Leemans et al., Phys. Rev.Lett. 113, 245002 (2014).
[2] A.A.Drozdovsky, et al., Physics of Particles and Nuclei Letters, 2014, Vol. 11, No. 5, pp. 577–580.
[3] I.Roudskoy et al., Rev. Sci. Instrum., 2008, v. 79, p. 02B313.
[4] P.Chen, K.Oide, A.M. Sessler, S.S.Yu, Phys.Rev. Lett., v. 64, 1990, 1231-1234.
[5] N.A.Bobrova, S.V.Bulanova, T.L.Razinkova, and P.V.Sasorov, Plasma Phys. Rep., 22, 349 (1996).
[6] A.Drozdowskiy et al., Physics of Particles and Nuclei Letters, 2016, Vol. 13, No. 7, pp. 847–852.
[7] A.Drozdowskiy et al., Probl. At. Sci. Technol., No. 6 (88), 39–42 (2013).

ISBN 978-3-95450-181-6

ON STABILIZATION OF SYSTEMS OF LINEAR EQUATIONS WITH LINEAR INCREASING TIME DELAY BY OBSERVATION

O.N. Chizhova, A.P. Zhabko, Saint Petersburg State University, Saint Petersburg, Russia

Abstract

In this paper we investigate a possibility of the linear differential system stabilization with time proportional delay by the linear observation. Using the sufficient conditions of asymptotic stability for the linear systems with linearly increasing delay we obtain some conditions of the asymptotic evaluation system existence for the original system. Then we use the asymptotic evaluation system for the construction of the stabilizing control and derive the sufficient conditions for the existence of such control.

INTRODUCTION

Differential-difference equations with time delay are often used in mathematical models describing the dynamics of beams of the charged particles. For example linear equation of the second order with a constant time delay describes in the smoothed approach dynamics of a beam of the charged particles in synchrotrons with a feedback system [1]. However the time delay cannot always be considered constant. The time proportional delay can occur at acceleration of beams of the charged particles in the cyclotron. It should be noted that linear increasing time delay is unbounded and well known approaches are not applicable for stability analysis such systems.

The stabilizing control for the system of linear equations could be constructed by the information on a state vector of the system. Sometimes the state vector is unknown but we know some linear combinations of its components. Then there is a problem on construction of the stabilizing control with incomplete information.

Let us consider the following linear system

$$\dot{x} = A_0 x(t) + A_1 x(\alpha t) + Bu \qquad (1)$$

$$y = Kx(t). \qquad (2)$$

Here x is n-dimensional state vector; u is r-dimensional control vector; y is scalar output; A_0, A_1, B, K are given real matrices $n \times n$; $n \times r$ and $1 \times n$; $0 < \alpha < 1$. We must construct the control $u = u\left(x(t); x(\alpha t)\right)$ using output (2).

One of the basic methods of solving such problem is the construction of the asymptotic evaluation system [2]. Some sufficient conditions of existence of this system for n scalar outputs $y_i = Rx(t - ih); i = 1; \ldots; n$ are presented in [3].

The aim of this paper is to obtain the conditions for the matrices A_0, A_1, B, K under which the stabilizing control may be constructed by output (2). The main results of the paper are construction of the asymptotic evaluation system using the output (2) and construction of the stabilizing control for the system (1).

The paper is organized as follows. The next section contains the investigation of an auxiliary system of linear differential equations. The structure of the asymptotic evaluation system for system (1) is deduced in this section. The main result is presented in section 3. A theorem about the sufficient conditions for existence of the stabilizing control is proved here. Section 4 contains a numerical example on construction of the stabilizing control.

AUXILIARY RESULT

Definition [2]. A system

$$\dot{\hat{x}} = A\hat{x} + Bu + L(y - K\hat{x})$$

is known as asymptotic evaluation system of a system without time delay

$$\dot{x} = Ax + Bu$$
$$y = Kx$$

if matrix L can be chosen such that for any $x(0); \hat{x}(0)$ the following condition is satisfied:

$$\hat{x}(t) - x(t) \to 0 \quad \text{as} \quad t \to +\infty. \qquad (3)$$

We consider a time delay system of the form

$$\dot{\hat{x}} = A_0\hat{x}(t) + A_1\hat{x}(\alpha t) + Bu + L_0\left(y - K\hat{x}(t)\right) + L_1\left(y(\alpha t) - K\hat{x}(\alpha t)\right) \qquad (4)$$

Here $L_0; L_1$ are unknown constant real vectors. Now we introduce two matrices:

$S_0 = \left(K^T; A_0^T K^T; \ldots; \left(A_0^T\right)^{n-1} K^T\right)$ and

$S_1 = \left(K^T; A_1^T K^T; \ldots; \left(A_1^T\right)^{n-1} K^T\right)$.

Theorem 1. If $rang S_0 = rang S_1 = n$ then vectors L_0 and L_1 of system (4) can be chosen so that condition (3) satisfied for any $x(0), \hat{x}(0)$.

Proof. Let $z(t) = \hat{x}(t) - x(t)$ where $x(t)$ is a solution of the system (1) and $\hat{x}(t)$ is a solution of the system (4). Then

ISBN 978-3-95450-181-6

$$\begin{aligned}\dot{z}(t)=\dot{\hat{x}}(t)-\dot{x}(t)=A_0\hat{x}(t)+A_1\hat{x}(\alpha t)+Bu+\\ L_0\big(y(t)-K\hat{x}(t)\big)+L_1\big(y(\alpha t)-K\hat{x}(\alpha t)\big)-\\ -A_0x(t)-A_1x(\alpha t)-Bu=\\ =A_0\big(\hat{x}(t)-x(t)\big)+A_1\big(\hat{x}(\alpha t)-x(\alpha t)\big)+\\ L_0K\big(x(t)-\hat{x}(t)\big)+L_1K\big(x(\alpha t)-\hat{x}(\alpha t)\big)=\\ =\big(A_0-L_0K\big)z(t)+\big(A_1-L_1K\big)z(\alpha t).\end{aligned} \tag{5}$$

So $z(t)$ is a solution of the system

$$\dot{z}(t)=Pz(t)+Qz(\alpha t), \tag{6}$$

where $P=A_0-L_0K$ and $Q=A_1-L_1K$. We now show that the vectors L_0 and L_1 can be chosen such that $z(t)\to 0$ as $t\to+\infty$.

Let us consider two functions [4]

$$f(\lambda)=\det\big(\lambda I-P\big);\quad g(\mu)=\det\big(P+Qe^{\mu\ln\alpha}\big). \tag{7}$$

Here I denotes the identity matrix. Now we introduce two sets: $\Lambda=\{\lambda|f(\lambda)=0\}$ and $\mathrm{M}=\{\mu|g(\mu)=0\}$. Then we define the following characteristics: $\overline{\lambda}=\max\limits_{\lambda\in\Lambda}\mathrm{Re}\,\lambda$ and $\overline{\mu}=\max\limits_{\mu\in\mathrm{M}}\mathrm{Re}\,\mu$ ($\overline{\mu}=-\infty$ if M is empty). Well known [4] that the system (6) is asymptotically stable if $\overline{\lambda}<0$ and $\overline{\mu}<0$.

Since $rangS_0=n$ then the system

$$\dot{x}=A_0x(t),$$
$$y=Kx(t)$$

be completely observable. Then the vector L_0 can be chosen such that the condition $\overline{\lambda}<0$ is satisfied. Moreover the eigenvalues of matrix P can be any defined in advance. Let the matrix P be constructed. Let us consider the equation

$$\det\big(P+Qe^{\mu\ln\alpha}\big)=0. \tag{8}$$

Since $0<\alpha<1$ then the condition $\overline{\mu}<0$ be satisfied for $|\alpha^{\mu}|>1$. Now we rewrite the equation (8) in the form

$$\det\big(\big(A_0-L_0K\big)+\big(A_1-L_1K\big)\beta\big)=0, \tag{9}$$

where $\beta=\alpha^{\mu}$.

Since $\det\big(A_0-L_0K\big)\neq 0$ then the equation (9) can be rewriting as

$$\begin{aligned}\det\big(I+\big(A_0-L_0K\big)^{-1}\big(A_1-L_1K\big)\beta\big)=\\ \det\big(I-\big(A_0-L_0K\big)^{-1}\big(L_1K-A_1\big)\beta\big)=\\ =\beta^n\det\big(\gamma I-\big(A_0-L_0K\big)^{-1}\big(L_1K-A_1\big)\big)=0,\end{aligned} \tag{10}$$

where $\gamma=1/\beta$.

Let $D=\big(A_0-L_0K\big)^{-1}\big(L_1K-A_1\big)$. Now we observe that the condition $|\alpha^{\mu}|>1$ is equivalent to condition $|\gamma|<1$. This means that the matrix D has to satisfy Schur-Kohn criterion.

On the other hand $rangS_1=n$ therefore the system

$$\dot{x}=A_1x(t),$$
$$y=Kx(t)$$

be completely observable too. Then the vector L_1 can be chosen such that eigenvalues of matrix L_1K-A_1 can be any defined in advance.

Let us consider the characteristic equation of the matrix D. It has a form

$$\det(\lambda I-D)=\lambda^n+d_1\lambda^{n-1}+\cdots+d_n=0, \tag{11}$$

where d_j $(j=1,\ldots,n)$ are linear function of the components of the vector L_1. Now we introduce the equation

$$\lambda^n+\nu_1\lambda^{n-1}+\cdots+\nu_n=\prod_{s=1}^{n}\big(\lambda-\lambda_s\big)=0, \tag{12}$$

where $|\lambda_s|<1$ $(s=1,\ldots,n)$ and the numbers λ_s are chosen in advance. After making the coefficients of the equations (11) and (12) equal we obtain a linear algebraic system of equations $d_j=\nu_j;\ (j=1,\ldots,n)$. The components of the vector L_1 will solutions of this system.

CONSTRUCTION OF THE STABILIZING CONTROL

Now we introduce two matrices:

$$S_2=\big(B;A_0B;\ldots;A_0^{n-1}B\big);\ S_3=\big(B;A_1B;\ldots;A_1^{n-1}B\big).$$

Theorem 2. If $rangS_2=rangS_3=n$ then the stabilizing control for the system (1) has the form

$$u=C_0\hat{x}(t)+C_1\hat{x}(\alpha t), \tag{13}$$

where $\hat{x}(t)$ is a solution of the system (4).

Proof. Let $rangS_2=rangS_3=n$. Then we can construct the matrices C_0 and C_1 such that the system

$$\dot{x}(t)=\big(A_0+BC_0\big)x(t)+\big(A_1+BC_1\big)x(\alpha t) \tag{14}$$

will asymptotically stable. Then we prove that the control (13) is the stabilizing control for the system (1). Let us consider the following system

$$\begin{cases}\dot{x}=A_0x(t)+A_1x(\alpha t)+Bu\\ \dot{\hat{x}}=A_0\hat{x}(t)+A_1\hat{x}(\alpha t)+Bu+L_0\big(y(t)-K\hat{x}(t)\big)\\ +L_1\big(y(\alpha t)-K\hat{x}(\alpha t)\big)\end{cases} \tag{15}$$

where the control has the form (13). Let the vectors L_0 and L_1 be chosen as in Theorem 1. The closed loop system has the form

ISBN 978-3-95450-181-6

$$\begin{cases} \dot{x} = A_0 x(t) + A_1 x(\alpha t) + BC_0 \hat{x}(t) + BC_1 \hat{x}(\alpha t) \\ \dot{\hat{x}} = (A_0 + BC_0)\hat{x}(t) + (A_1 + BC_1)\hat{x}(\alpha t) + \\ + L_0(y(t) - K\hat{x}(t)) + L_1(y(\alpha t) - K\hat{x}(\alpha t)) \end{cases} . \quad (16)$$

Let $z(t) = \hat{x}(t) - x(t)$ again. Here $x(t)$ is the solution of system (1) and $\hat{x}(t)$ is the solution of system (4). Then system (16) transforms to the form

$$\begin{cases} \dot{x} = (A_0 + BC_0)x(t) + (A_1 + BC_1)x(\alpha t) + \\ + BC_0 z(t) + BC_1 z(\alpha t) \\ \dot{z} = (A_0 - L_0 K)z(t) + (A_1 - L_1 K)z(\alpha t) \end{cases} . \quad (17)$$

Now note that the condition $z(t) \to 0$ as $t \to +\infty$ is satisfies in accordance with Theorem 1. The matrices C_0 and C_1 are chosen such that the system (14) is asymptotically stable. So the system (17) is asymptotically stable too. Therefore, control (13) is the stabilizing control for system (15). But system (1) is a part of system (15) therefore the control (13) is the stabilizing control for system (1).

EXAMPLE

Let the system (1) has a form

$\begin{cases} \dot{x}_1 = 2x_1(t) + x_2(t) + x_1(\alpha t) + x_2(\alpha t) \\ \dot{x}_2 = 4x_2(t) + x_2(\alpha t) + u_2 \end{cases}$, and the system (2) has a form $y = x_1(t)$.

Let $L_0 = \begin{pmatrix} l_1^{(0)} \\ l_2^{(0)} \end{pmatrix}$, then $P = \begin{pmatrix} 2 - l_1^{(0)} & 1 \\ -l_2^{(0)} & 4 \end{pmatrix}$.

Therefore

$\det(\lambda I - P) = \lambda^2 + (l_1^{(0)} - 6)\lambda + (8 - 4l_1^{(0)} + l_2^{(0)}) = 0$. Let $L_0 = \begin{pmatrix} 10 \\ 36 \end{pmatrix}$ then P is Hurwitz matrix and the condition $\overline{\lambda} < 0$ is satisfied.

Let $L_1 = \begin{pmatrix} l_1^{(1)} \\ l_2^{(1)} \end{pmatrix}$ then $L_1 K - A_1 = \begin{pmatrix} l_1^{(1)} - 1 & -1 \\ l_2^{(1)} & -1 \end{pmatrix}$

and $$D = P^{-1}(L_1 K - A_1) = \begin{pmatrix} l_1^{(1)} - 1 - \dfrac{l_2^{(1)}}{4} & -\dfrac{3}{4} \\ 9(l_1^{(1)} - 1) - 2l_2^{(1)} & -7 \end{pmatrix}.$$

Therefore

$$\det(\lambda I - D) = \lambda^2 + \left(8 - l_1^{(1)} - \frac{l_2^{(1)}}{4}\right)\lambda + \frac{1}{4}(1 - l_1^{(1)} + l_2^{(1)}) = 0.$$

Now let us consider the equation (12) in a form

$$\left(\lambda - \frac{1}{2}\right)^2 = \lambda^2 - \lambda + \frac{1}{4} = 0 .$$

The condition $|\lambda_s| < 1 \quad (s = 1,2)$ is satisfied. The components of the vector L_1 are solutions of this system

$$\begin{cases} 8 - l_1^{(1)} - \dfrac{l_2^{(1)}}{4} = -1 \\ 1 - l_1^{(1)} + l_2^{(1)} = 1 \end{cases} .$$

Therefore $l_1^{(1)} = l_2^{(1)} = 7{,}2$ and $L_1 = \begin{pmatrix} 7{,}2 \\ 7{,}2 \end{pmatrix}$. The vectors C_0 and C_1 may be similarly constructed.

CONCLUSION

The system of differential equations with linear increasing time-delay is investigated in this paper. The sufficient conditions of existence for the corresponding asymptotic evaluation system are obtained. The stabilizing control is constructed.

REFERENCES

[1] Zhabitsky V.M., Chizhova O.N. Damping of coherent betatron oscillations of a charged particle beam in synchrotrons with a feedback system. Physics of Particles and Nuclei Letters, 2014. Vol. 11, № 5. pp. 581-583.

[2] Andreev Yu. N. The finite-dimensional object control. M., Nauka, 1976, 424 p. (In Russian).

[3] Chizhova O. N. The asymptotic evaluation system construction by observation with delay. Vestnik of St. Petersburg State University, Series 1. Mathematics, mechanics, astronomy. 2002, issue 4, № 25, pp. 44-46. (In Russian).

[4] Zhabko A. P., Laktionov A.A. and Zubov V. I. Robust Stability of Differential-Difference Systems with Linear Time-Delay. In Proc. of the Second Symposium Robust Control Design. 1997, pp.101-105.

ISBN 978-3-95450-181-6

FIRST RESULTS OF BEAM DYNAMICS SIMULATION IN ELECTRON INJECTOR LINAC FOR FCC-EE

S.M. Polozov, T.V. Bondarenko,
National Research Nuclear University - Moscow Engineering Physics Institute, Moscow, Russia

Abstract

New high-energy frontier project FCC is now under development at CERN. It is planed that all three modes as ee, hh and eh will be available for FCC. New injection system for FCC-ee is planned to consist of new ~ 2 GeV electron linac and electron-positron converter. Two possible layouts for further beam acceleration are discussed. The high-energy 14 GeV linac is the first layout and the booster synchrotron is the second one. Pre-injector linac design will have two regimes: ~250 pC bunches for injection and ~6 nC bunches for e^-/e^+ conversion. In the second case we will have extreme parameters: bunch charge up to 6 nC in 10 ps, up to 10 bunches per pulse and the pulse repetition rate up to 100 Hz. Such beam parameters lead to significant design difficulties caused by very high influence of Coulomb field in the near-cathode region and high peak beam loading. First results of beam dynamics simulation in FCC-ee injection linac and near-cathode dynamics problems are discussed in the report.

INTRODUCTION

New injection system for FCC-ee [1] is now under discussion by FCC collaboration [2-3]. A number of different injection schemes are discussed: linac (from 2 to 7 GeV) with booster synchrotron, high energy linac (up to 14 GeV) and reacceleration in main collider ring, top-up injection. It is obvious that linac should include the first stage (about 2 GeV) and the electron-positron converter with damping ring to generate the necessary positron flux. Beam intensities for two regimes (electron beam acceleration for injection and for e^-/e^+ conversion) will differ very significantly: it is necessary to have up to $1.65 \cdot 10^9$ e^-/bunch (~250 pC) for injection mode [2-3] and up to $4 \cdot 10^{10}$ e^-/bunch (~6 nC) for e^-/e^+ conversion mode; 10 ps bunch duration is the same for both cases. It is planned to have 10 bunches/pulse with distance between bunches of 25 or 50 ns. The pulse repetition rate will be up to 50 Hz. The separated bunches regime facilitates RF system design and operation because of low beam loading influence compared to the bucket of bunches mode. Note that 6 nC regime is very complex and limited number of linacs are operating with such currents.

The general scheme of the CLIC linac or the new SuperKEKB injector linac [4] could be proposed to use as the base of FCC injector. New SuperKEKB injector consists of the modern RF gun commissioned in 2013-14 and traveling wave regular sections. It is very interesting idea to combine thermionic RF gun for high-intensity high-emittance drive bunch for 5 nC mode and high-quality beam generated by photogun for injection into synchrotron.

The choice of operating frequency is very important too. It is proposed to use 2000 MHz structures which will have higher acceptance compared to conventional 3000 MHz band. Two notes should be done here: i) exactly 2000 or 3000 MHz structure can give 25 (or 50) ps of bunch separation (conventional 2856 MHz can not) and ii) there are no high-power RF sources for 2000 MHz (but they are available for 1816 and 1860 MHz and can be scaled). It is important because 10 bunches/pulse regime is planned. Current pulse duration will be 250 or 500 ns, SLED or other RF pulse compression scheme can be used to reduce necessary peak RF power and RF feeding system cost. Low average pulse current (but peak is very high) give us possibility to use a standing wave structure (biperiodic accelerating structure BAS, or side-coupled one), but it should have very high coupling coefficient (10-12 %) to realize low power filling time.

Two possible layouts of linac are presented in Fig. 1. Let us discuss first results of the beam dynamics simulation and RF gun and regular section electrodynamics study.

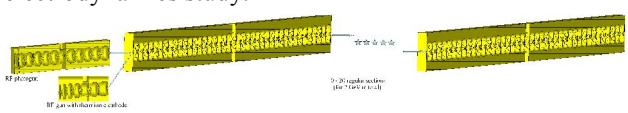

Figure 1: Two possible schemes of linac layout (RF gun with thermionic cathode is option for high intensity drive bunches production for e^-/e^+ conversion).

BEAM DYNAMICS IN PHOTOGUN

The beam dynamics simulation was done both for RF gun and regular section. The BEAMDULAC-BL code [5-7] was used for simulations. This code was developed in MEPhI for beam dynamics simulations in RF linacs and transport channels. It has modular structure and number of routines to solve different tasks: initial particles distribution (uniform, Gauss, KV, waterbag, etc.), motion equation integration (4th order Runge-Kutta method), beam emittance calculation, post processing and other. The code package has versions that take into account own space charge effects: both Coulomb part and RF part (beam irradiation and beam loading) self-consistently. The excitation equation is solved to simulate RF part of own space charge field using the method of large particles. The Poisson equation is solved on grid by fast Fourier transform (FFT) method and well-known cloud-in-cell (CIC) algorithm is used to represent particles distribution on 3D grid. The BEAMDULAC-BL code

ISBN 978-3-95450-181-6

version is discussed in detail in [7]. It was tested at a number of e-linac designs (see [8, 9] as two examples).

At first we simulated the RF photogun with 300 pC and 10 ps per bunch. Such current is not easy to generate in a photogun, but it is typical for contemporary facilities with semiconductor cathodes. A biperiodical accelerating structure (BAS) with disk-loaded waveguide (DLW) was considered. First (~56 cm in the length) version of photogun ("photogun_v1") consisting of 12 acceleration cells and 10 coupling cells (the first and the second accelerating cells are side-coupled) was presented in FCC Meeting 2016 at Rome. The first and the second accelerating cells should have a side coupling because we haven't got enough space to place it on axis: the first accelerating cell length should be enlarged to have enough space for laser port. The RF-gun accelerating structure should provide: short RF power filling time (high value of the loaded Q-factor is necessary, it can be realized in a structure with high coupling), low transverse emittance growth in first cells (where electrons are non-relativistic and the Coulomb field influence is high), the low energy spread growth (can be achieved by right choice of accelerating field profile). If we try to realize a low energy spread growth and plan to use low field value, we should provide effective capturing into acceleration mode. It was proposed to limit accelerating field by value of 400-600 kV/cm on the axis. Three cells (2nd, 3rd and 4th) having phase velocities β_{ph} =0.91, 0.98, 0.99 were used for efficient recapturing. The last accelerating cell length was enlarged because it has no coupling cell after it. All beam dynamic simulations in RF-guns were done for the operating frequency f=3000 MHz. Other structure parameters were taken for the simulation: channel aperture radius 10 mm, coupling cell length 4 mm (remind that we use side coupling for the 1st and the 2nd accelerating cells), diaphragm thickness 4 mm. The shunt impedance was defined by electrodynamics simulations (discussed below in section 4) and equals ≈80 MOhm/m. The initial transverse emittance of the bunch was taken 20 mm·mrad. The solenoid field of B_{sol} =0.1 T is enough for the effective beam focusing, the envelope of the beam will be less than 4 mm with this magnetic field value. The main beam dynamics simulation results are: capturing coefficient K_T=99.8 %, output energy 9.5 MeV, output beam spectrum FWHM ±3.9 %, bunch length 3.8 mm (initial one is 3.0 mm). Main results illustrated in Fig. 2.

The influence of beam loading was also studied. It was shown that it is not sufficient here: the accelerating field amplitude will drop for less than 0.3% for the 300 pC and 10 ps bunch due to the beam loading. It will not have any sufficient influence on the output energy: the second bunch will have energy of 9.44 MeV compared to the 9.52 MeV for the first one.

Further we tried to simulate the beam dynamics for the 1-6 nC bunch in the same structure with photocathode (we will not discuss the possibility of such charge emission from any cathode). We can simplify the general scheme of the linac (Fig. 1) if the second RF gun (with thermionic gun) is not necessary. It was shown that the current transmission coefficient decreases significantly and the energy spread growth vs. bunch charge and any other RF gun should be proposed. The capturing coefficient vs. the bunch initial current is shown in Fig. 3. It is clear that it will drop fast for high bunch charge case and the photogun has limitations for it to be used at nC drive bunches accelerator. All particle loses are occur at the first cell and are caused by longitudinal Coulomb repulsion leading to the stop of the significant part of the bunch or to the back-current formation. The capturing coefficient can grow for the higher accelerating field E_z=700-1000 kV/cm, but this growth is not higher than 7-10 %.

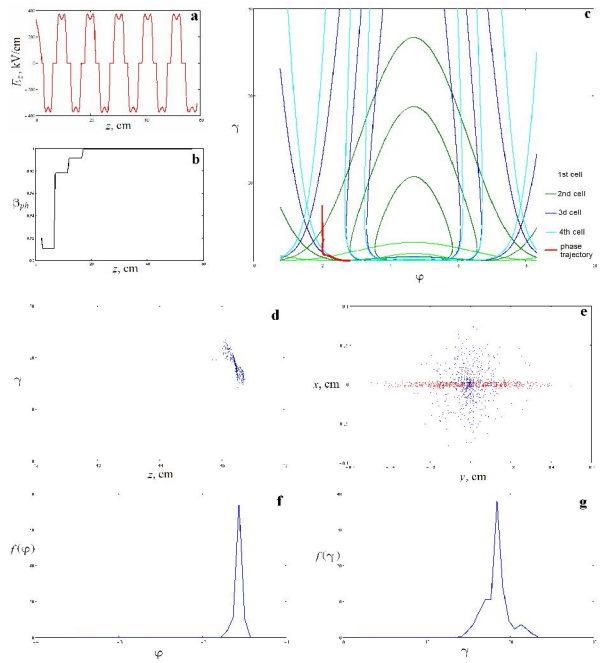

Figure 2: The RF photogun parameters: accelerating field E_z (a) and β_{ph} (b) along the longitudinal axis z; beam dynamics simulation results for the single 300 pC bunch: the center-of-mass trajectory in the (γ, φ) phase plane for first four cells (c), the phase distribution in the (γ, z) phase plane (d); the transverse emittance (e), the energy (f) and the phase (g) spectrums. All initial bunch characteristics are shown by red points and lines, output by the blue.

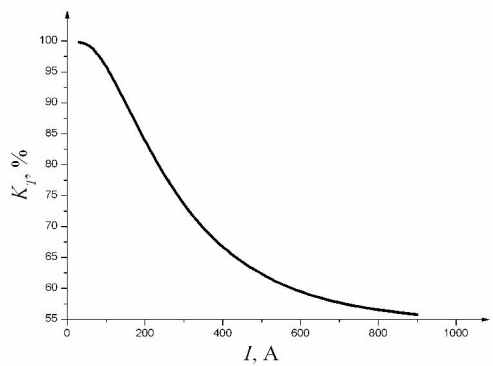

Figure 3: The capturing coefficient vs. bunch peak current for the case of using the photocathode.

ISBN 978-3-95450-181-6

As it was shown, the current transmission coefficient will drop fast for high bunch charge, as an example it will not be higher than 60 % for 6 nC bunches (see Figure 3). The photogun will have current limitations due to such results and cannot be effectively used for acceleration of bunches with population higher than 2 nC. The bunch spectrum is also rapidly increasing vs. the bunch charge. Simulations show that high bunch intensities lead to high back currents. Sufficient Coulomb "head-tail" repulsion was observed. Head-tail difference of RF field amplitude due to high bunch phase size and beam loading effect leads to energy spectrum growth. RF-gun with thermionic cathode was proposed to accelerate nC bunches with high current transmission coefficient and to have high quality bunches. First results of the beam dynamics simulations results shows that for such gun the capturing coefficient can be increased to 90-95 % for 3 nC bunches and to 85-90 % for 6 nC ones. Such studies will be done in future.

BEAM DYNAMICS IN THE REGULAR SECTION

The long (~3 m) high-coupled biperiodic accelerating structure (BAS) was discussed as a possible regular section. It will have 61 accelerating cells and 60 coupling cells (302.5 cm of the total length) at 3000 MHz. BAS operating at 2000 MHz consists of 41 accelerating and 40 coupling cells (305.0 cm). Two notes should be done here: i) 3m-length BAS is longer that it is conventionally accepted for such structures, but we could accept it because it is commonly used in high-energy travelling wave linacs, and ii) other types of high-coupled structures (disk-and-washer, modified 2π/3 travelling wave DLW, etc.) should be discussed in the future.

We discuss three power feeding scenarios: i) "low-field" scenario with E_z=400 kV/cm which is typical for industrial e-linacs, ii) "realistic" scenario, E_z=600 kV/cm and iii) "optimistic" scenario, E_z=900 kV/cm.

The main results of simulation are summarized in Table 1. Note that 2000 MHz structure has 5 % higher energy gain. It is caused by the larger effective accelerating length of such BAS: 63 mm is the accelerating cell length and 75 mm is period length with f=2000 MHz and 38 mm / 50 mm with f=3000 MHz. But this growth is not sufficient.

The beam envelope can be easily controlled in the regular section, as it is clear from Fig. 4. It was shown that the beam loading effect for 300 pC bunch is not sufficient here: accelerating field amplitude reduction is less than 0.3 % after the first bunch acceleration. Such loading influence can be easily compensated by RF system. The second bunch characteristics are also presented in the Table 1.

The beam loading influence is much more sufficient in case of the drive beam acceleration. The simulation was done for charges equal to 1-3 nC/bunch (for 6 nC it will be done in the future), RF field amplitudes in the regular section decrease is more than 3 % after the 1st bunch acceleration. Such loading must also be compensated by the RF feeding system.

Table1: The Beam Dynamics Simulations Results for One Regular Section, W_{sec} Is The Energy Gain Per Section

E_z, kV/cm	f=3000 / 2000 MHz		
	1st bunch		2nd bunch
	K_T, %	W_{sec}, MeV	W_{sec}, MeV
400	98.4 / 98.2	69.9 / 74.2	69.5 / 73.8
600	98.4 / 98.2	104.9 / 111.4	104.4 / 110.9
800	98.4 / 98.3	157.5 / 166.9	156.7 / 166.1

CONCLUSION

As it was shown by the numerical simulations, a 300 nC and 10 ps bunch can be easily accelerated in proposed scheme of the RF photogun. The current transmission coefficient is close to 100 % and the bunch energy spread FWHM is ~±3 % (or ±300 keV) and we can suppose that output energy spread after 10 or 20 regular sections with β_{ph}=1 will not be higher than 0.5-1.0 %. Beam loading effect is not sufficient here. It was shown that the current transmission coefficient will drop rapidly for nC bunch charge (RF-gun with thermionic cathode for example) accelerating structure should be proposed and studied. The first results of the bunch dynamic simulations in the first regular (BAS) section are also presented.

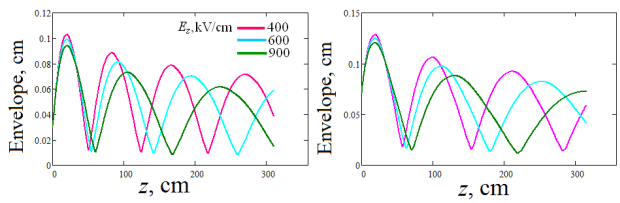

Figure 4: The beam envelope in the first regular section, bunch current is 300 pC and bunch duration is 10 ps, B_{sol} =0.1 T, f=3000 (top) and 2000 MHz.

REFERENCES

[1] K. Oide et al., FCC-ee Machine Layout and Beam Optics, FCC Meeting 2016, Rome, 11-15 Apr. 2016.
[2] Y. Papaphilippou, FCC-ee injector complex including Booster, FCC Meeting 2016, Rome, 11-15 Apr. 2016.
[3] Y. Papaphilippou et al., Proc. of the IPAC'16, 2016, 3488-3490 (2016).
[4] M. Satoh et al., Proc. of IPAC'16, 4152-4154 (2016).
[5] E.S. Masunov, S.M. Polozov, Nucl. Instrum. Methods A 558, 184 (2006).
[6] E.S. Masunov, S.M. Polozov, Phys. Rev. ST AB 11, 074201 (2008).
[7] T.V. Bondarenko et al., Problems of Atomic Science and Technology. Series: Nuclear Physics Investigations, 6 (88), 114-118 (2013).
[8] S.M. Polozov et al., Proc. of IPAC'16, 1794-1796 (2016).
[9] T.V. Bondarenko et al., Proc. of IPAC'16, 1788-1790 (2016).

ISBN 978-3-95450-181-6

BEAM DYNAMICS STUDY FOR THE NEW CW RFQ

Sergey Polozov[1,2], Winfried Barth[1,3,4], Florian Dziuba[4],
Timur Kulevoy[1,2] , Stepan Yaramyshev[1,3], Yury Lozeev[1]
[1] National Research Nuclear University - Moscow Engineering Physics Institute, Moscow, Russia
[2] Institute for Theoretical and Experimental Physics of NRC Kurchatov Institute, Moscow, Russia
[3] GSI Helmholtzzentrum fur Schwerionenforschung, Darmstadt, Germany
[4] Helmholtz-Institut Mainz, Germany

Abstract

A compact "university scale" research CW proton accelerator, as well as driver linac with three branches of experimental beam lines, delivering beam energy of 2, 10 and 30 MeV for dedicated experiments, are recently under development in Russia. A proposed front-end system of both linacs comprises a 2 MeV CW RFQ, which is foreseen to bunch and accelerate up to 10 mA proton beam. The RFQ design is presented. The beam dynamics simulation results, obtained by means of different software, are discussed and compared.

INTRODUCTION

The development of a CW high-power proton linacs is a very actual aim of crucial accelerator technology. Such linac is useful for large scale research complexes as spallation neutron sources or accelerator driven systems. Low or medium-energy linacs can be used for several applications as boron-neutron capture therapy (BNCT), high productivity isotopes generation and material science. Also compact research facilities are the modern trend for high intensity CW proton and deuteron linac development [1,2].

The Russian accelerator-driver concept has been already developed by the collaboration of researchers from MEPhI and ITEP of NRC Kurchatov Institute [3-6]. The proposed linac layout is close to the conventional scheme: an RFQ and a normal conducting DTL with transverse focusing by integrated RF sections up to 30 MeV. The independently phased SC cavities are foreseen for medium and high beam energies. Three branches of experimental beam lines, delivering a beam energy of 2, 10 and 30 MeV for dedicated experiments, are foreseen as the main feature of the proposed facility concept [7,8].

Research and development of CW applications is an important step in RFQ design. A 2 MeV RFQ is under investigation for the compact CW research proton accelerator, as well as for the planned driver linac in Russia. The maximum beam current is fixed to 10 mA; the operating frequency has been set to 162 MHz; the RF potential should be limited by 1.3-1.5 of Kilpatrick criterion for the CW mode. The main RFQ parameters are shown in Tab.1.

The beam dynamics simulations for the new RFQ channel, as well as an analysis of the RFQ characteristics, have been performed with the codes BEAMDULAC [9] and DYNAMION [10], providing for a cross-check of the design features and the calculated results. The first results of the beam dynamics simulations have been briefly discussed in [12].

Table 1. Main Parameters of the CW RFQ

Ions	protons
Input energy	46 keV
Output energy	2.0 MeV
Frequency	162 MHz
Voltage	90 kV
Length	345 cm
Average radius	0.530 cm
Vanes half-width	0.412 cm
Modulation	1.000 - 2.250
Synchr. phase	-90° - -33°
Max. input beam current	10 mA
Max. input beam emittance	6 cm·mrad (total)
Particle transmission	> 99%

A preliminary design of a CW RFQ linac has been already started at MEPhI and ITEP [11,12]. The recent detailed layout of the presented 2 MeV CW RFQ is based on a preliminary concept, exploiting long-term experience for proton and heavy ion linac development at MEPhI and ITEP [13,14], as well as decades of GSI expertise in construction, optimization and routine operation of ion linac facilities [15-21]. Most recently, the prototype for a heavy ion CW linac with a SC main part is under construction at GSI and HIM [22-26].

ANALYSIS OF RFQ CHARACTERISTICS

The maximum electrical field strength on the vane surface along the channel strongly influences on all RFQ parameters. For the presented CW RFQ design the field strength E_{max} has been limited by the 1.5 Kilpatrick criterion.

The average radius R_0 = 0.530 cm and the vanes half-width/rounding R_e = 0.412 cm have been defined together with the RFQ voltage of 90 kV. The Kilpatrick criterion E_{kp} = 148 kV/cm for the given operating frequency of 162 MHz has been calculated using modified Kilpatrick equation:

$$R_0 E_{kp}^3 \cdot \left(1 - \exp\left(-\frac{48.6 E_{kp}}{R_0 f^2}\right)\right) = 1.8 \cdot 10^5 \cdot \exp\left(\frac{170}{E_{kp}}\right)$$

with average radius R_0 given in cm, frequency f in MHz and the Kilpatrick criterion E_{kp} in kV/cm [27].

* SMPolozov@mephi.ru

ISBN 978-3-95450-181-6

The maximum electrical field on the vane surface E_{max} (Fig. 1) could be calculated for the real topology of each RFQ cell. Almost constant electrical field strength E_{max} provides the most effective focusing and acceleration along the whole channel. In particular this is important, as RF voltage and RF power should be strongly limited for a CW regime.

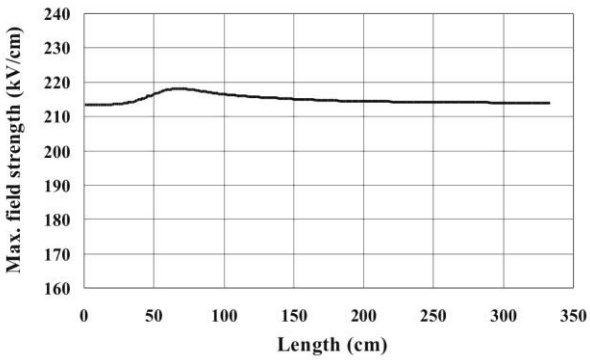

Figure 1: Maximum strength of electrical field on the vane surface along the RFQ channel, calculated for each cell separately.

Assuming a low beam current and a smooth approximation [28], the normalized local acceptance V_k for each RFQ cell can be calculated using the Floquet functions from a solution of the Mathieu-Hill equation for particle motion:

$$V_k = \nu_f \frac{a^2}{\lambda},$$

where $\nu_f = 1/\rho^2$, ρ is a module of the Floquet function, a - aperture radius of the cell, λ - wave length of the operating frequency; ν_f can be treated as a minimum of the phase advance μ on the focusing period.

Assuming a given beam current phase density (beam brilliance) for a uniformly charged beam (KV distribution), a tune depression can be calculated semi-analytically for each RFQ cell. Then a local acceptance along the channel under space charge conditions could be evaluated as:

$$V_k = V_{k0}\left(\sqrt{1+h^2} - h\right), \quad h = j \cdot \frac{B\lambda}{\mu_0 \beta I_0}$$

where the Coulomb parameter h combines parameters of the beam and the accelerating channel: $j = I / V_p$ - beam brilliance, I - beam current, V_p - normalized beam emittance, B - ratio of the peak to the pulse currents, $I_0 = 3.13 \cdot 10^7 \cdot A/Z$ - characteristic current, A, Z - mass and charge numbers, μ_0 - phase advance for low current, β - relative velocity of particle.

The lowest value of the local "cell"-acceptance estimates the transverse acceptance of the whole RFQ channel. As illustrated in Fig. 2, the RFQ acceptance under design space charge conditions (Tab. 1), is decreased on a few percent only, thus an influence of the space charge effects is neglectable. In particular, this is ensured by the chosen relatively high input particle energy of 46 keV. A lower input energy might lead to a slightly compacter RFQ, but will result in stronger space charge effects, especially inside the gentlebuncher.

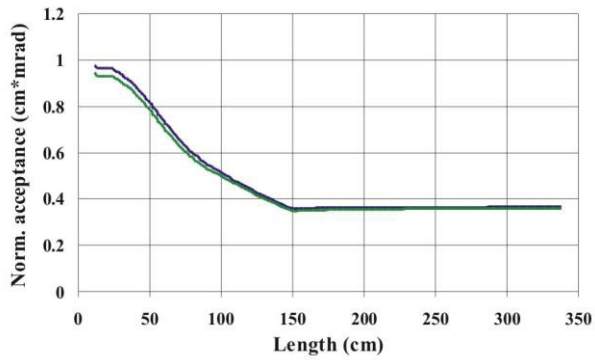

Figure 2: Normalized local acceptance for low beam current (blue) and under space charge conditions (green) along the RFQ channel, calculated for each cell separately.

BEAM DYNAMICS SIMULATIONS

The shape of the RFQ input radial matcher has been optimized for a smooth matching of the beam emittance to the RFQ acceptance. The matched Twiss-parameters have been obtained from the results of dedicated simulations for the RFQ acceptance. The same 6D phase space input macroparticle distribution (truncated Gaussian in transverse phase planes and continuous in longitudinal one) has been introduced into both codes for beam dynamics simulations with low beam current.

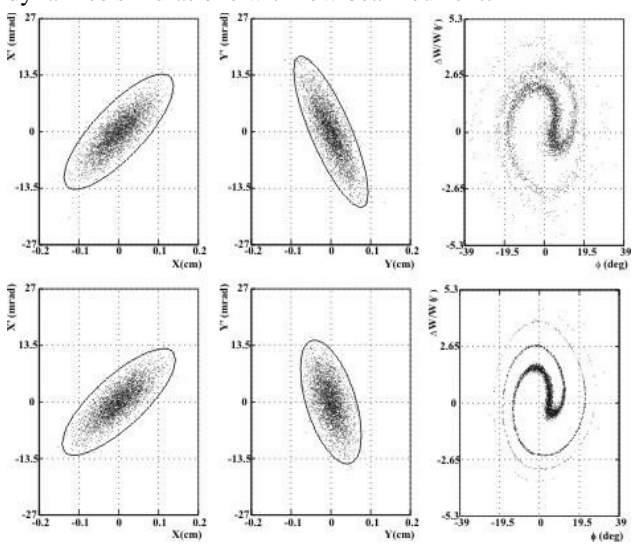

Figure 3: The beam phase portraits behind RFQ for transverse and longitudinal phase planes, simulated by the codes BEAMDULAC (top) and the DYNAMION (bottom); ellipses represent 99% of the particles.

ISBN 978-3-95450-181-6

The resulted particle distributions behind the RFQ (Fig. 3) demonstrate good coincidence between the codes BEAMDULAC and DYNAMION.

Also a set of simulations under space charge conditions, even taking low tune depression of only few percent into account, is recently under consideration together with the final optimization of the modulation and synchronous phase along the RFQ accelerating-focusing channel.

CW RFQ CAVITY

The 4-vane RFQ with coupling windows [29] can be utilized as a front-end for a high-energy high-power linac. A segmented vane RFQ type (SVRFQ), successfully commissioned in 2016 for the new NICA injector at JINR (Dubna) [30], was also proposed to be used for CW application [11].

The described RFQ cavity comprises 13 RF-cells. Magnetic coupling windows have to be optimized by six parameters to achieve high RF field uniformity and to improve the transverse shunt impedance and Q-factor: the shell radius, the transverse and conjugate diameters of windows, the transverse diameter of the endmost windows (EWs) and the lengths of both end regions.

The corresponding 3D model of the proposed SVRFQ structure with optimized elliptical vane windows is shown in Figure 4. Optimal geometry parameters for SVRFQ design normalized to the RF-cell length (L_{cell}) or shell radius (R_{shell}) as well as main electrodynamics characteristics are given in Table 2.

Table 2: Geometry for an optimal SVRFQ design and main electrodynamics characteristics

Parameter	
Frequency, MHz	162
Shell radius, mm	196
Transverse window length, $\%L_{cell}$	75.5
Transverse EW length, $\%L_{cell}$	37.0
Conjugate window length, $\%R_{shell}$	42.2
1st end region length, $\%L_{cell}$	26.3
2nd end region length, $\%L_{cell}$	26.3
Power loss, kW	61.9
Q-factor, 10^4	1.65
Transverse shunt impedance, kΩ	150.4

Figure 4: Optimized design of the SVRFQ cavity with elliptical coupling windows.

CONCLUSION

A new CW 2 MeV RFQ linac design is proposed. The maximum field strength is limited by the 1.5 Kilpatrick criterion. The proposed RFQ linac can accelerate a 10 mA proton beam with a particle transmission close to 100%. The codes BEAMDULAC and DYNAMION have been used for beam dynamics simulations. The results of the codes are in good agreement. Final optimization of the RFQ channel is in progress. The electrodynamics simulations for the RFQ resonator have been already started. The mechanical layout for a new CW RFQ cavity is recently under consideration.

REFERENCES

[1] C.R. Prior, Proc. of HB'10, MOIA02 (2010).
[2] L. Weissman et al., Journal of Instrumentation, 10, T1004 (2015).
[3] A.E. Aksentyev, P.N. Alekseev, K.A. Aliev et al., Atomic Energy, 117, Issue 4, 270-277 (2015).
[4] A.E. Aksentyev et al., Atomic Energy, 117, Issue 5, 347-356 (2015).
[5] V.A. Nevinitsa, A.A. Dudnikov, A.A. Frolov et al., Atomic Energy, 117, Issue 1, 14-18 (2014).
[6] Y.E. Titarenko, V.F. Batyaev, K.V. Pavlov, et al., Atomic Energy, 117, Issue 1, 19-28 (2014).
[7] A.E. Aksentyev et al., RuPAC'14, THPSC05 (2014).
[8] A.E. Aksentyev et al., RuPAC'14, THPSC04 (2014).
[9] S.M. Polozov, Prob. of Atomic Sci. and Tech., 3 (79), pp. 131-136 (2012).
[10] S. Yaramyshev et al., NIM A, 558/1 p. 90-94 (2006).
[11] A.E. Aksentyev, T. Kulevoy, S.M. Polozov, Proc. of IPAC'14, THPME030 (2014).
[12] S.M. Polozov et al., HB'2016, MOPL004 (2016).
[13] D. Kashinsky et al., EPAC'04, WEPLT123 (2004).
[14] V.A. Andreev, A.I. Balabin, A.V. Butenko at al., Prob. of Atomic Sci. and Tech., 6 (88), 8-12 (2013).
[15] W. Barth, W. Bayer, L. Dahl et al., NIM A, 577, Issues 1–2, 211-214 (2007).
[16] W. Barth et al., PRST AB 18(4),·040101 (2015).
[17] F. Herfurth et al., Physica Scripta, T166 (T166):014065 (2015).
[18] W. Barth et al., PRST AB 18(5), 050102 (2015)
[19] S. Yaramyshev et al., Phys. Rev. ST Accel. Beams 18, 050103 (2015)
[20] W. Barth et al., IPAC'2016, WEOBA03 (2016).
[21] W. Barth et al., HB'2016, TUAM7Y11 (2016).
[22] M. Basten et al., IPAC'2016, MOPOY019 (2016).
[23] M. Heilmann et al., IPAC'2016, MOPOY022 (2016).
[24] S. Yaramyshev et al., HB'2016, THPM9Y01 (2016).
[25] W. Barth et al., Proc. of Baldin ISHEPP XXIII (2016), EPJ Web of Conferences (in press).
[26] F. Dziuba et al., these Proceedings, WESBMH01.
[27] I.M. Kapchinsky, "About approximations of Kilpatrick criterion", PTE №1, 33-35 (1986).
[28] I.M. Kapchinsky, "Theory of linear resonance accelerators", Moscow, (1982).
[29] V.A. Andreev, Patent US5483130 (1996).
[30] V. Aleksandrov et al., IPAC'16, MOPOY041 (2016).

ISBN 978-3-95450-181-6

THE STUDY OF THE HELICAL RF RESONATOR FOR THE 300 keV NITROGEN ION CW IMPLANTER

N.V. Avreline, TRIUMF, Vancouver, B.C., Canada
S.M. Polozov, A.G. Ponomarenko, National Research Nuclear University -Moscow Engineering Physics Institute, Moscow, Russia

Abstract

The helical RF resonator for the single charged 300 keV nitrogen ion CW implanter was designed, simulated in CST Microwave Studio and the results were experimentally verified. The current setup of the implanter is described as well as possible modifications to accelerate ions of other types. The results of the field distribution's RF measurements and the results of the high-power test are also presented.

INTRODUCTION

The implanter RF system consists of the helical type accelerating resonator that is loaded by the channel of drift tubes, the Duoplasmatron source of nitrogen single charged ions with 25 keV of energy, the mechanical backing pump, the turbomolecular vacuum pump TMN-500, the ion pump Nord-250, 3 kW CW RF amplifier, the control cabinet with power supplies and the turning magnet that is used to analyze the resulting beam (Fig. 1). This implanter was primarily designed to accelerate CW beam up to 100 μA. It could accelerate ions with other charge-to-mass ratio after changing the helical inductor.

Figure 1: The 300 keV Implanter of single charged nitrogen ions.

THE DESIGN OF THE RF RESONATOR

Given a rather low operating frequency of 13.56 MHz, in the efforts to reduce the size of an accelerating structure, the resonator of a helical type loaded by an accelerating channel was selected in the design. The accelerating channel is composed of 10 drift tubes and is operating in π mode. These tubes are connected to the two longitudinal bars that are connected respectively to the ends of the half-wave length helical elements of the resonator. The main advantage of using this accelerating resonator in this implanter is that just the accelerating channel is in the vacuum chamber, but not helical inductor. This kind of a design allows to change the inductance by just replacing the helical part without opening the vacuum chamber. Specifically, the frequency of the resonator could be modified and the implanter could be used to accelerate different kinds of ions. The photo of the open resonator is presented in Fig. 2. To tune the resonance frequency of this resonator, two plates were used to shorten the windings.

Figure 2: The opened resonator with the replaceable helical part that is connected to the accelerating channel via a feedthrough.

ISBN 978-3-95450-181-6

The helical element was built out of two 12 mm diameter copper pipes that were soldered together. These pipes are water cooled. They are connected through the feedthrough insulators with the two bars that support the drift tubes. The helical element could be easily disconnected and replaced by another one as these connections are located outside of the vacuum chamber. Moreover, those connectors are of the flange type, which provide good RF connection and prevent water leaks. Indium gaskets were used to seal these connections.

The accelerating channel consists of 10 drift tubes with outer and inner diameters of 30 mm and 18 mm. The accelerating channel was designed to be inside a cradle (see Fig. 3) which allowed assembly of this channel outside of the vacuum chamber. Two longitudinal bars were supported by four insulators attached to this cradle. Drift tubes were connected to the two longitudinal bars via the supports of 5 mm in diameter. During assembly, to ensure channel's alignment, the first and the last half tubes that were soldered onto the bars first and then a stainless shaft was inserted through these tubes to provide support for the intermediate tubes. To ensure specific distance between drift tubes, washers have been used.

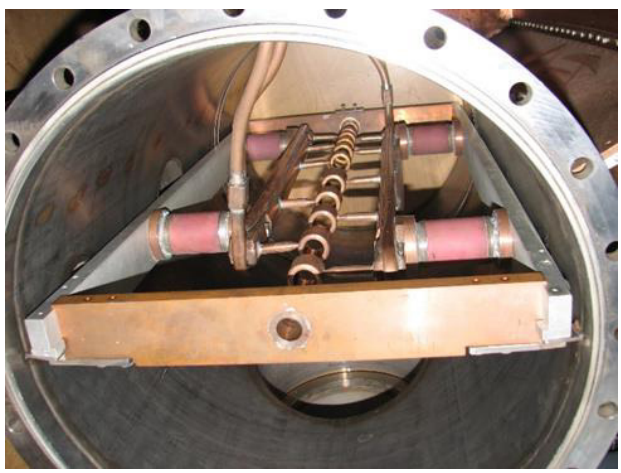

Figure 3: The accelerating channel of the implanter.

CALCULATION AND SIMULATION OF THE ACCELERATING STRUCTURE

The design and optimization of the accelerating structure were done in in the following steps: the analytical model, the study of the scalable mock-up of the resonator, simulations of the structure in the CST Microwave Studio and the experimental measurements and tests.

The analytic model was created to estimate the dimensions of the accelerating structure and to optimize its electrodynamic characteristics. The structure was represented as a resonator that consists of piece of a transmission line with a helical element instead of the inner conductor, shorted on the one end and connected to a capacitor and an inductor in series on the other end. The capacitor and the inductor represent the capacitance of the accelerating channel and the inductance of the two leads of the helical element. In the first approach this transmission line was running in the TEM mode. For the simulation, this half wavelength resonator was represented as two quarter wavelength resonators. The equivalent circuit of the quarter wavelength resonator is represented on Fig. 4.

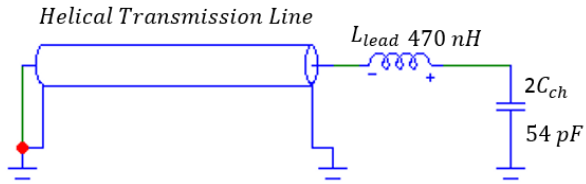

Figure 4: The model of the transmission line and the equivalent circuit of the resonator.

The helical element allows to significantly reduce the dimensions of the accelerating structure. To simulate a resonator that is based on a transmission line with the helical inner conductor, we have calculated its characteristic impedance Z_0, propagation constant γ and losses α_{loss}. In the model, an unwrapped ribbon helix was used for an equivalent representation of the transmission line geometry [1, 2] (Fig. 5).

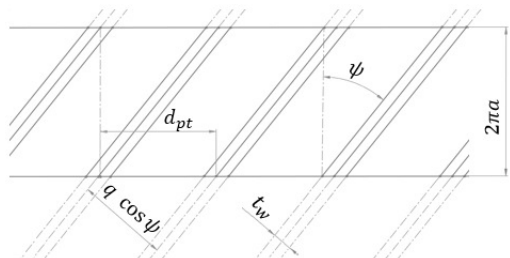

Figure 5: The model of the helical transmission line.

The model allows to find the characteristic impedance Z_0 and to minimize losses in the transmission line for different pitches and cross-sections of its helical conductor. The formula to determine α_{loss} is given by:

$$\alpha_{loss} = \frac{4}{\pi \sin\theta} \frac{F\left(\frac{\pi}{2}, \cos\theta\right)}{P_{-q}(\cos\theta) P_{-q}(\cos\theta')} \frac{R_0}{2Z_0} \quad (1)$$

where

$$Z_0 = \frac{1}{4}\sqrt{\frac{\mu_0}{\varepsilon_0}} \frac{1}{\sin(q\pi)} \frac{P_{-q}(cos(\theta'))}{P_{-q}(cos(\theta))}$$

$F\left(\frac{\pi}{2}, cos\theta\right)$ is the elliptical Integral of the first kind,

$$P_q(cos\theta) = \frac{\sin(q\pi)}{\pi} \sum_{m=0}^{\infty} (-1)^m \left(\frac{1}{q-m} - \frac{1}{q+m+1}\right) P_m(\cos\theta),$$

$P_m(\cos\theta)$ are the Legendre polynomials,

$$\theta = \pi - \theta', \quad \theta = \frac{\pi t_w}{d_{pt}}, \quad q = k\ a\ cos(\psi), \quad k = \frac{2\pi f_0}{c},$$

f_0 - operating frequency, $R_0 = \frac{\sqrt{4\pi f_0 \frac{\mu_0}{\sigma_{cu}}} ctg^2(\psi)}{2\pi a\ cos^2(\psi)}$,

a - radius of helical element, σ_{cu} - conductance of copper, ψ - angle of helical turns.

The plot of α_{loss} is presented in (Fig. 6). The minimal losses correspond to the ratio of conductor width and the helical pitch of 0.54. The conductor width was selected

ISBN 978-3-95450-181-6

based on a compromise between the losses and the dimension of the whole accelerating structure.

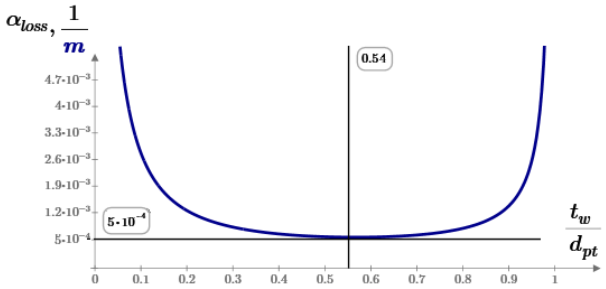

Figure 6: Losses of Helical Transmission Line.

The accelerating channel capacitance was calculated based on the formulas from [3, 4] and based on the simulation of equivalent circuit in Micro-Cap and Comsol 5.2. The equivalent circuit representing the accelerating channel is shown in (Fig. 7).

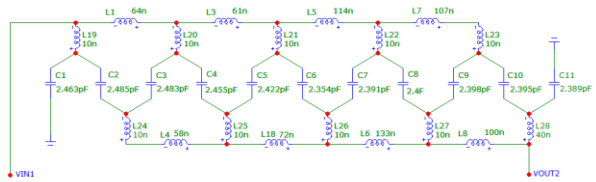

Figure 7: Equivalent Circuit of Accelerating Channel.

As a result of this calculation, the capacitance between terminals "VIN1" and "OUT2" was found to be $C_{ch} = 27\ pF$. As per the equivalent circuit presented on Fig. 4, the calculated length of the whole helical element was 239 mm and the optimal helical pitch was 43 mm.

INVESTIGATION OF THE MOCK-UP ACCELERATING STRUCTURE

Before the operational accelerating structure was manufactured, a mock-up version with a scale factor of two was designed, manufactured and investigated. The experimental investigation of this resonator determined the resonance frequency of 29.12 MHz, $Q_l = 1135$. The field distribution was measured using a complex PLC device [5] that allowed to calculate Q_l factor and shunt impedance. The measurements of the electric component distribution of the electromagnetic field, E_z along the Z axis is presented on Fig. 8.

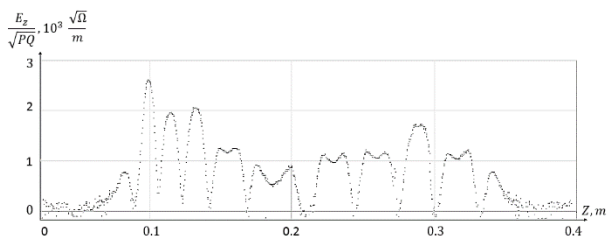

Figure 8: The distribution of E_z along of accelerating axis in the mock-up resonator.

The post processing calculation gave $R_{sh} = 163 \frac{M\Omega}{m}$ and $R_{eff\ sh} = 123 \frac{M\Omega}{m}$.

EXPERIMENTAL STUDY OF THE ACCELERATING STRUCTURE

Following the experimental investigation of the mock-up accelerating structure, the full scale accelerating resonator was manufactured and studied. The frequency of this resonator was adjusted to 13.56 MHz using the shortening plates (Fig 2.). The Q_l factor was measured using the method of resonator phase shift and the resulting value was $Q_l = 1100$. The experimental investigation and the CST Microwave Studio simulation results of the accelerating field distribution are presented on Fig.9.

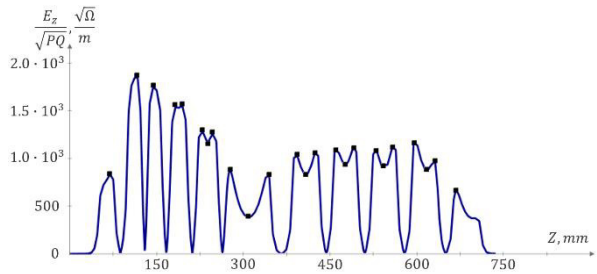

Figure 9: The distribution of E_z in the accelerating channel and the experimental extremal points (marked as "■") before the hot test.

Post processing calculations gave $R_{sh} = 167 \frac{M\Omega}{m}$ and $R_{eff\ sh} = 132 \frac{M\Omega}{m}$.

CONCLUSION

The experimental study of the accelerating resonator in the implanter showed that it has high $R_{sh\ eff}$ and Q_l factor. The implanted could be used to accelerate ions of a different type by changing helical element and could be run using a CW RF amplifier with power less than 3 kW.

REFERENCES

[1] R.A Silin, V.P. Sazonov, Moderating Systems, Sov. Radio, 1966

[2] Chiao-Min Chu, Propagation of wave in helical guides, Journal of Applied Physics, vol.29, number 1, January, 1958, pp. 88-99

[3] N.V. Avrelin et al., Calculation of Electrodynamic Characteristics of H-Resonator Based Accelerator Systems Using the Approximation Methods. Preprint 078-88, MEPhi, 1988.

[4] N.P. Sobenin, B.V. Zverev, Electrodynamic Characteristics of Accelerating Cavities, London – Moscow, 1993

[5] N.V. Avrelin, I.N. Demidov, A.G. Ponomarenko, S.V. Popov, A.E. Rodionov, Autonomous Microprocessor-based Complex for Measuring Electrodynamic Characteristics of Accelerators. Accelerator-Based Radiation Equipment, Energoatomizdat, 1987, p.31.

ISBN 978-3-95450-181-6

QWR RESONATOR CAVITIES ELECTRODYNAMICS SIMULATIONS FOR NEW NUCLOTRON-NICA INJECTOR

A.V. Butenko, Joint Institute for Nuclear Research, Dubna, Moscow Region, Russia
M.A. Gusarova, M.V. Lalayan, N.P. Sobenin, D.V. Surkov, S.A. Terekhov, S.E. Toporkov, National Research Nuclear University – Moscow Engineering Physics Institute, Moscow, Russia
T.V. Kulevoy, S.M. Polozov, National Research Nuclear University – Moscow Engineering Physics Institute, Moscow, Russia and Institute of Theoretical and Experimental Physics of NRC "Kurchatov Institute", Moscow, Russia
A.O. Sidorin, G.V. Trubnikov, Joint Institute for Nuclear Research, Dubna, Moscow Region, Russia and Saint-Petersburg State University, Saint-Petersburg, Russia
V.L. Zvyagintsev, National Research Nuclear University – Moscow Engineering Physics Institute, Moscow, Russia and TRIUMF, Vancouver, Canada

Abstract

New linac-injector for Nuclotron-NICA is planned to consist of quarter-wave coaxial cavities (QWR) having velocities of ~0.07c and ~0.12c (beam energy from 5 to 17 MeV). These cavities are to be superconducting and operating at 162 MHz. Current results of the QWR cavities electrodynamics simulations and geometry optimizations are presented.

INTRODUCTION

The joint collaboration of JINR, NRNU MEPhI, INP BSU, PTI NASB, BSUIR and SPMRC NASB started a new project on superconducting cavities design, production and test technologies development and new linac-injector design in 2015. This linac intend for protons acceleration to 25 MeV (up to 50 MeV after upgrade) and light ions acceleration up to ~7.5 MeV/u for Nuclotron-NICA injection [1-4]. The operating frequency of the linac medium energ part after RFQ is 162 MHz being further doubled to 324 MHz. Geometry choices for first group of resonators considered in this research.

The first design of the linac-injector for Nuclotron-NICA considers quarter-wave coaxial cavities (QWR) operated at 162 MHz as the best choice for velocities range of ~0.07c to ~0.14c [5-6]. QWRs are effective for frequency up to 200 MHz and velocity below 0.2c. At high velocities exceeding about 0.14c-0.15c half-wave coaxial cavities (HWR) are preferable due to many disadvantages and limitations QWRs have.

Calculations showed that for velocity 0.141c and frequency 162 MHz structure chosen as initial version, the steering effect is significant and the displacement of the beam axis is not enough to compensate it. It leads to drift tubes design modifications making cavity production more complicated.

Comparative analysis of the QWR and HWR along with beam dynamics simulation showed that there is a possibility to decrease the geometrical velocity β_G for the second group of resonators to 0.12c. It makes the cavity cheaper because less niobium is needed and also it moves the cavity design to a lower steering effect area.

The next step was to consider 162 MHz QWR for velocities 0.07c and 0.12c. Choice of optimal geometry and overall dimensions, performance, operation and maintenance issues were considered.

GEOMETRY CHOICE

Cavity basic dimensions optimization allowed us to use identical cryomodules, flanges, tuning devices etc. and minimize the number of unique parts.

Modern elliptical and conical shapes of QWR allow performance improvements, including rise in shunt impedance and decrease losses [5]. Initially simple models of cylindrical QWR based on the primary technology requirements were considered. Change of acceleration and drift sections in cavities for different β_G force us to optimize central conductor length for overall dimensions and frequency kept unchanged.

At the first stage accelerating gaps simulation for both constructions was done. Figure 1. presents acceleration path of two gap cavity, where L is resonator diameter.

According to ratio $d=\beta\cdot\lambda/2$, optimal distance between accelerating gaps was found for 0.07c and 0.12c cavities. Results presented in Table 1. According to relation $g/d = 1/3$ [6] optimal g was founded.

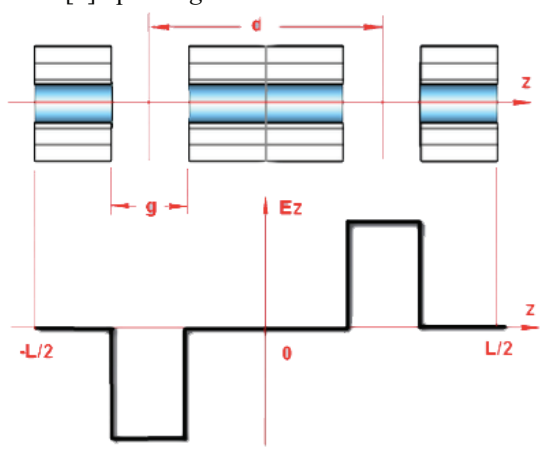

Figure 1: Acceleration path of 2-gap resonator.

ISBN 978-3-95450-181-6

Table 1: Relation velocity and dementions cavities d, g for frequency 162 MHz.

β	0.07	0.12
d, mm	63	108
g, mm	19	32

Results obtained show that minimal radius of external conductor should not exceed 90 mm keeping in mind cavities parts unification. In [6] it was shown that according to practical experience the best internal radius to external one ratio R_{in}/R_{out} should be equal to 0.3. It allows one to find an optimum between minimum magnetic field, maximum shunt impedance and geometrical factor G.

Taking into account unification requirements and sizes of internal and external conductors two different types of QWR cavities were considered: QWR with flat end of central conductor and one with donut end. Geometries presented at Figure 2.

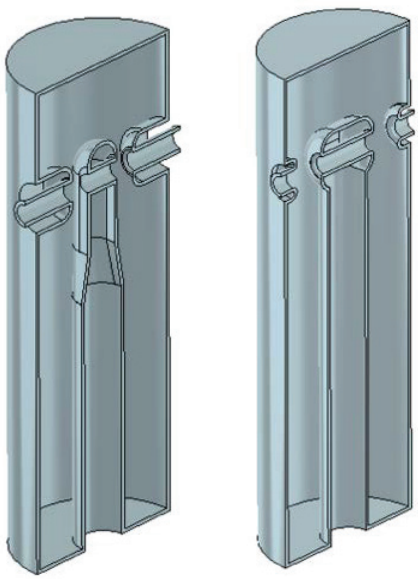

β = 0.07c β = 0.12c

Figure 2: Designs of QWRs considered.

ELECTROMAGNETIC DESIGN

Main requirements [5-6] for accelerating cavities are presented in Table 2.

Table 2: Main requirements for 162 MHz accelerating cavities.

β	0,07	0,12
Eacc, MV/m	3,08	7
Ep, MV/m	<40	<40
Bp/Eacc, mT/MV/m	<80	<80

The electromagnetic design and optimization mainly lies is to made peak surface fields both electric and magnetic as low as possible and to rise the ratio r/Q , (where r is shunt impedance and Q is quality factor) and geometry factor $G = R_sQ$ (where R_s is surface resistance).

In addition we considered easy installation and tuning, reliable operation, reasonable price. Table 3 shows results for cavities presented in Figure 2.

Table 3: RF Parameters of the 162 MHz Cavity

β	0.07	0.12
Eacc max, MV/m	3,08	7
Ep/Eacc	6.6	4.96
Ep, MV/m	20	37.1
Bp/Eacc, mT/MV/m	10.5	10.7
Bp, mT	32	72.8
r/Q_O, Ohm	517	432
G, Ohm	30,7	33
T_0	0,9	0,92

T_0 is transit time factor. There are different versions of effective length definition for accelerating field and shunt impedance per unit length. In that article data presented with $l_{eff} = L$, where L is resonator diameter.

Additional optimization towards the minimal magnetic field was carried out. It needs to tune with vertical deformation of cavity butt-end. Overall dimensions after optimization are: height 510 mm, outer radius 90 mm, inner radius 30 mm.

MECHANICAL DESIGHN

Mechanical simulations were carried out for left cavity at Figure 2. cavity. Different deformation models influence to the cavity frequency were studied:

1) Frequency change after cool down to 4 K;
2) Frequency change under helium pressure;
3) Displacement of the central conductor under helium pressure;
4) Lorentz force detuning;

Three types of cavities were considered. They are presented in Figure 3: initial reference cavity design (a), cavity with rounded end faces (b) and cavity model with fixed top and bottom (c). In (a) and (b) simulation models beam axis was fixed. At c simulation model beam axis, bottom and top of resonator were fixed. Table 4 presents results of mechanical calculations.

ISBN 978-3-95450-181-6

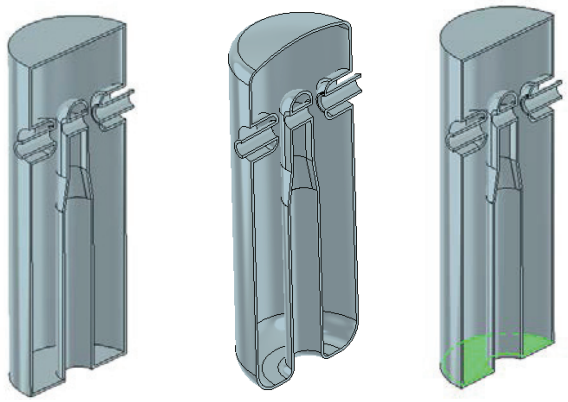

Figure 3: QWR models used for mechanical simulations: reference cavity design (a), one with rounded faces cavity (b) and cavity with fixed top and bottom(c).

Table 4: RF Parameters of the 162 MHz Cavity

Type	a	b	c
Sensitivity to external pressure, Hz/mbar	34	16	2
Vertical displacement of the stem, mm/bar	0.2	0.07	0.01
Frequency shift after cool down to 4 K, kHz	340	339	-
Lorentz force detuning, Hz/(MV/m)^2	3	0.69	0.33

Simulations show that top and bottom fixing helps to reduce sensitivity to He pressure and Lorentz detuning.

CONCLUSION

Results of SC cavities design for new JINR proton and light ion linac development for Nuclotron-NICA were discussed.

REFERENCES

[1] A.V. Butenko, E.E. Donets et al., Proc. of IPAC'13, 3915 (2013).
[2] V.A. Andreev, A.I. Balabin et al., Problems of Atomic Science and Technology. Series: Nuclear Physics Investigations, 6 (88), 8-12 (2013).
[3] M.A. Batouritski, A.V. Butenko et al., New Superconducting Linac Injector Project for Nuclotron-NICA: Current Results, Proc. of RuPAC'16, THPSC041 (2016).
[4] G.V. Trubnikov, T.V. Kulevoy et al. Proc. of IPAC'16, 941-943 (2016).
[5] M.Kelly, SRF 2013 Tutorial Program Sept. 19-21 Ganil, Caen
[6] V.L. Zvyagintsev, PhD Thesis, 2013

ISBN 978-3-95450-181-6

HIGH POWER SOLID STATE RF GENERATOR FOR NEUTRAL BEAM INJECTOR

E.I. Shubin, V.V. Kolmogorov, BINP SB RAS, Novosibirsk, Russia
A.S. Styuf, Novosibirsk State University, Novosibirsk, Russia

Abstract

Neutral Beam Heating Injector of 1 MW beam power for the TCV tokamak (Lausanne, Switzerland) was developed in BINP. The plasma is formed in a plasma box with inductively coupled RF power at frequency about 4MHz. Required RF power in the plasma box is up to 40kW during the period of 2 seconds with 5 minutes intervals [2]. Solid state RF generator with such capability has been developed in BINP. Description of the RF generator design, main features and the test results are presented in the report.

INTRODUCTION

The TCV tokamak (literally "variable configuration tokamak") is a research fusion reactor of the Federal Institute of Technology in Lausanne (EPFL). The upgrade program that is underway on TCV extends the power range of existing Electron Cyclotron Resonance Heating (ECRH) and adds direct ion auxiliary heating using Neutral Beam Injection [1]. At this time Neutral Beam Injector (NBI) is installed and the first 1 MW neutral beam is being commissioned. Plasma emitter of the NBI is powered with RF energy up to 40 kW from the solid state RF Generator.

GENERATOR LAYOUT

The Solid State RF generator is a modular system, it consists of 16 identical RF modules (placed in 2 racks), control modules, combiners, DC power supply – RFG DC PS. Output signal through coaxial feeder, matching network and decoupling HV transformer is applied to plasma emitter. Plasma emitter inductance with additional capacities form a resonant circuit tuned to the operating frequency of 4 MHz. "Matching network" converts subsequent circuit impedance to the characteristic impedance of the feeder at this frequency.

Generator's block diagram is shown in Fig. 1. Output signal is formed by summing the voltages of two identical generators RFG20 in "Final combiner". Both generators are working in-phase. The only difference is that one of them operates in "Master" mode while another one in "Slave" mode. Mode of operation is defined by operation mode of RF Control modules.

Block diagram of one of generators RFG20 is shown in Fig. 2. Generator is placed in one electronic rack and consists of 8 identical units "RF Module", output signals of which are summed in two stages of summation: first stage is Combiner1 and second is Combiner2. Both stage's combiners are implemented by identical scheme of 4-inputs combiner with 50 ohm input and output impedances. Each 4-inputs combiner of the first stage is supplied by in-phase signals from two "RF Modules" with two identical power cells inside. Similarly, the second stage's Combiner2 is supplied by signals from two combiner modules of the first stage.

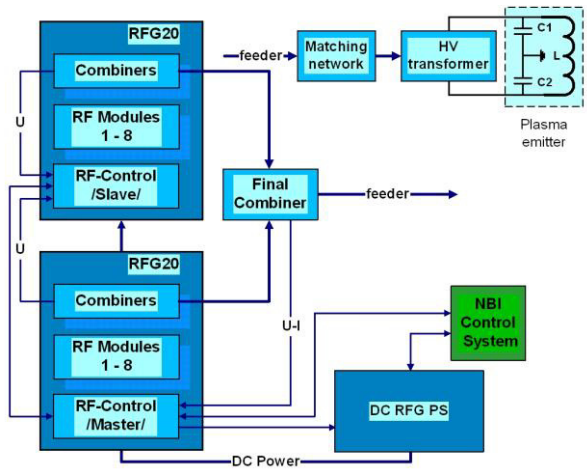

Figure 1: Generator layout.

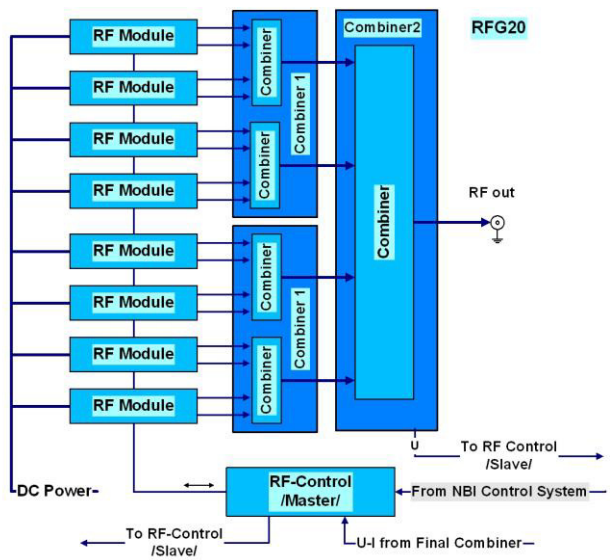

Figure 2: Block diagram of RFG20 generator.

DC power supply unit provides power cells of RF modules with adjustable power voltage. Output RF voltage of 4 MHz in the load is proportional to DC power supply voltage. The NBI system must be able to on/off modulate the beam with a minimum on/off-time of a few ms and to gradually vary the power injected into the tokamak in the range of 30-100% of full nominal power. Beam current from Injector is modulated by changing RF

ISBN 978-3-95450-181-6

power in the plasma emitter which is performed by changing the voltage of RFG DC PS.

ELEMENTS OF THE RF GENERATOR

All the elements of RF generator are placed in four 19" racks with dimensions 600*800*2000 mm. RFG20 generators are placed into two of them and DC Power supply with the Output combiner occupy the rest two. The system does not need water cooling and uses forced air cooling.

RF Modules

All RF Modules contain two identical power cells, control circuit and protection circuits. Each power cell is based on push-pull configuration with fast power transistors manufactured by IXYS RF, operating in the switching mode class DE. Such mode allows obtaining a high efficiency (about 85%). The cells have local protection from overloading by voltage, current or temperature. If one of these parameters exceeds the established threshold, transistors close. The over current protection for each cell is performed by measuring DC power current of the cell with current sensors. Fast protective diodes connected to transistor's drains with comparison circuit serve as overvoltage protection. Thermal switch mounted on the cooling radiator protects against over temperature. There is also protection from input clock signal disappearance. Control circuit accepts input signals from RF Control modules and forms signals for power cells drivers. It also provides the necessary protections and communication with RF Control modules. Every module is assembled in 3U chassis and has forced air cooling.

Combiners

The combiners of both stages of RFG20 generator are realized by cascading two 2-input combiners with current summation followed by 2-input combiner with voltage summation. This configuration forms 4-inputs combiner of in-phase signals with independent and isolated to each other 50-ohms inputs.

The final combiner circuit is based on Wilkinson schematic. At 4 MHz central frequency it has 50 ohm input impedance for the load of 50 ohm. In-phase signals from two RFG20 are applied to its inputs. Output signal is measured by current and voltage measuring transformers. Measured signals are transmitted to RF Control module for further processing.

RF Control

RF Control modules perform following tasks: distribution of the control signals, clock frequency generation for RF modules, measuring parameters of output signal and protection of the generator. Two control modules have identical structure, one of them operates as control unit in "Master" mode, and another one operates in "Slave" mode. Block diagram is shown in Fig. 3.

Module contains two fast ADCs with 100 MHz sampling frequency for voltage and current measuring, reference oscillator, DAC for making analogue signals to transfer to NBI control system and output drivers to form clock and control signals for RF modules. All necessary digital signal processing is fulfilled inside the FPGA Cyclon 3 (ALTERA).

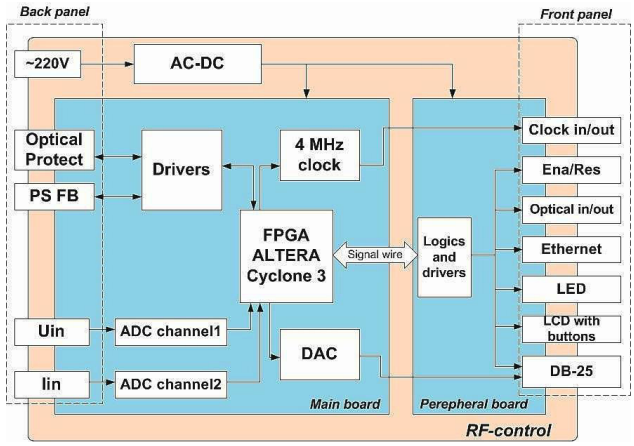

Figure 3: Layout of RF Control module.

RF Control module performs state data reading from RF modules in the case of protection take place. Every RF module has its own local protections. The single optical protection line connects all the modules serially into the ring. If protection in any block takes place RF Generator is blocked and DC power supply switches off the voltage. There is also protection against voltage disbalance between two RFG20 and against long time working without burning plasma (>50 ms).

DC Power Supply

RFG DC PS serves as the source of DC power voltage in the range of 100 ... 300 V and up to 80 kW power. Power supply is a stabilizer of two independently adjustable voltages U(LOW) and U(HIGH), which can be set by two references DAC1 and DAC2. Block diagram of the source is shown in Fig. 4.

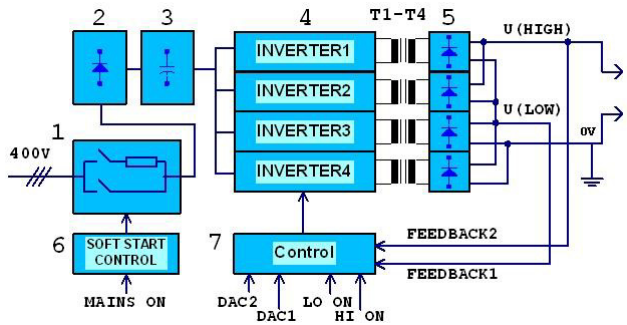

Figure 4: DC power supply layout.

Power supply consists of soft switching device of a network rectifier (1) with control (6), capacitive filter (3) of a network rectifier (2), four IGBT - inverters (4). Inverters provide a rapid regulation of the output voltage for low or base level U(LOW) and high level U(HIGH). The voltage of the inverters is regulated by pulse-width modulation at 20 kHz frequency and fed to decreasing

ISBN 978-3-95450-181-6

high-frequency transformers (T1...T4), rectified using diode rectifiers (5). Output voltage stabilization scheme (7) provides independent control for U(LOW) and U(HIGH) levels.

RF Power Ttransmission Path

The plasma is formed in a plasma box with inductively coupled RF power. Burning plasma changes parameters of plasma emitter as a load. It shifts the frequency of the resonant circuit and changes the active load depending on plasma parameters and RF power modulation. The most effective power transfer is for matched load. In this case it was decided to work at fixed frequency with fine matching at high nominal power level and tolerate degradation at lower ones. So plasma emitter resonant circuit has constant reactive elements. High voltage DC decoupling RF transformer is used for electrical insulation from the RF antenna biased to 30 kV potential during ion source operation. It has ferrite magnetic core and is placed in tank with Middel-isolating material. Matching network before the input of HV transformer has C-L-C structure with fixed elements tuned for exact matching at high power level.

RESULTS

During the period from June 2015 to January 2016 NBI was assembled and tested on TCV. In the end of January 2016 first NBI shots in TCV were made with plasma, and neutral beam heated plasma on TCV.

Photography of the RF generator is shown in Fig. 5.

Figure 5: Four cabinets of RF generator. Nearest two racks are occupied by RFG20, next two contain DC power supply and final combiner.

The generator gave RF power up to 40 kW with the pulse duration 2 sec. Fig. 6 demonstrates measured power and phase shift between voltage and current at generator output in one of the shots. Power level was modulated in steps from 15 to 37 kW by changing DC power supply

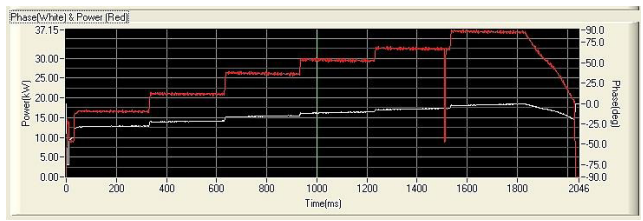

Figure 6: RF power (red) and phase shift between voltage and current (white) at generator output.

voltage. Matching is good enough at high power level and degrades at lower levels. Impedance measured at feeder input for high power level is 49.9 ohm with angle -2.2 degrees, at low level angle increases to 25 degrees. Output power and VSWR dependence from DC power supply voltage is shown in Fig. 7 where one can see good matching at Power=38 kW with VSWR=1.05. Matching was tuned at the fixed frequency of 4.022 MHz

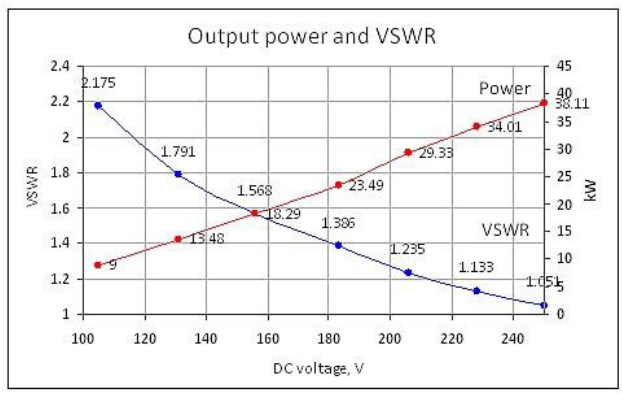

Figure 7: RF power and VSWR vs. DC power voltage.

ACKNOWLEDGMENT

Authors express thanks TCV team and our colleague Gennady Karpov for useful discussions, Vladimir Berezkin and Evgeny Sevastyanov for distribution in device assembling.

REFERENCES

[1] S. Coda et al., “Overview of the TCV Tokamak Program: Scientific Progress and Facility Upgrades,” 26th IAEA Fusion Energy Conference - IAEA CN-234, Kyoto, October 2016

[2] Alexander A. Karpushov et al., “Upgrade of the TCV tokamak, first phase: Neutral beam heating system”, Fusion Engineering and Design 96-97 (2015) 493-497.

ISBN 978-3-95450-181-6

REGULATION OF THE WAVEGUIDE COUPLING FACTOR OF STANDING WAVE LINEAR ACCELERATOR

D.S. Yurov, V.I. Shvedunov, Lomonosov Moscow State University, 119992 Moscow, Russia
also at Laboratory of Electron Accelerators MSU Ltd., Moscow, Russia

Abstract

Regulation of the waveguide coupling factor of standing wave linear accelerator allows to adjust the value of accelerated current, keeping the reflected RF power close to zero. This ensures the most efficient use of RF energy and absence of overvoltage in the waveguide elements. The paper presents studies results for various methods of coupling factors regulation with continuous wave (CW) normal conducting linear accelerator used as an example. The results of calculations and measurements on the mock-up of the accelerating structure are presented.

INTRODUCTION

Matching of the RF source and the accelerating structure (AS) of standing wave linear accelerators in traditional designs of the waveguide power coupler is ensured through selecting dimensions of the coupling iris. Iris dimensions as a rule are selected for fixed beam current loading, at that, optimum waveguide-to-AS coupling factor is determined in accordance with the following formula: $\beta = 1 + \frac{P_b}{P_w} = 1 + \frac{I_b E_b}{P_w}$, where P_w is RF power loss in the walls of the AS, I_b and E_b are current and energy of the accelerated beam. If value of the current deviates from the optimum value, a reflected wave appears, which results in lowering of the accelerator efficiency and appearance of overvoltage in the waveguide.

Industrial CW linear RF accelerators have another aspect of the matching problem. The simplest arrangement of the RF system for such accelerators is self-oscillating arrangement with AS in the feedback loop of the klystron excitation circuit [1]. In such arrangement, if the level of the reflected wave is low, klystron can operate without ferrite isolator, which simplifies the accelerator design and makes it cheaper. However, to minimize the reflected wave that adversely affects the RF source, it is necessary to be able to change the coupling factor in accordance with changes in the beam current. Possible design of the 2,856 MHz MIT storage ring cavity adjustable coupler is described in [2]. In this paper we discuss other arrangements of the coupler with coupling factor regulated over a wide range.

COMPUTER SIMULATION

We studied regulation of the coupling factor through insertion of cylindrical plungers (6 mm in diameter) to different depths into the 72x34 mm feeding waveguide perpendicular to its wide wall. Several configurations of plunger positioning were considered.

- 4 plungers near the coupling iris (Fig. 1a).
- 2 plungers opposite each other at the center of wide wall of the waveguide at some distance from the iris (Fig. 1b).
- 1 plunger at the center of wide wall.

Calculations were performed using CST Studio Suite software package [3] on the coupler model consisting of the power input cell without coupling slots in the frequency range of 2,450-2,490 MHz, which is similar to the 1 MeV CW accelerator power coupler [4].

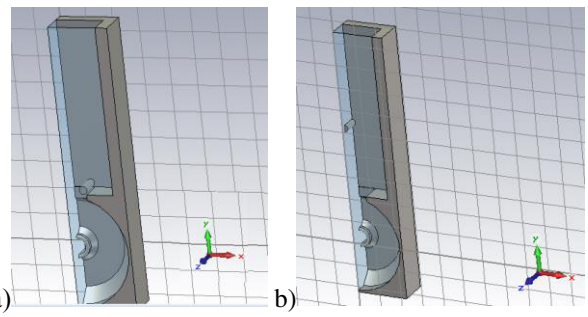

Figure 1: Models for calculating RF power coupler with adjustable coupling factor.

Feeding waveguide input port was excited by the Gaussian envelope signal. Resonance frequency f_{res} was determined by the minimum of the S_{11} parameter, and coupling factor - by the time constant τ_E of the cavity stored energy decay after the end of excitation signal: $\beta = 2\pi f_{res}\tau_E$.

One of the main criteria for evaluating calculation results was minimum shift of the resonance frequency of the power input cell and maximum range of coupling factor regulation. Resonance frequency shift results in appearance of the fields in the coupling cells located near the power input cell of the bi-periodic standing wave AS.

Calculations of the Coupler with 4 Plungers Near the Iris

Idea behind of this arrangement was regulation of the effective width of the iris by changing plunger's position. Due to symmetry a quarter of the power input cell was used in calculations (Fig. 1a). Depth of the plunger insertion L_{pl} was changed in the range of 0-17 mm (17 mm depth corresponds to closure of the opposite plungers). Fig. 2 shows the graphs of the coupling factor and resonance frequency change vs. plunger insertion depth. Without the plungers, the power coupler coupling factor was $\beta_0 = 32$, and resonance frequency was $f_0 = 2{,}486.9$ MHz.

ISBN 978-3-95450-181-6

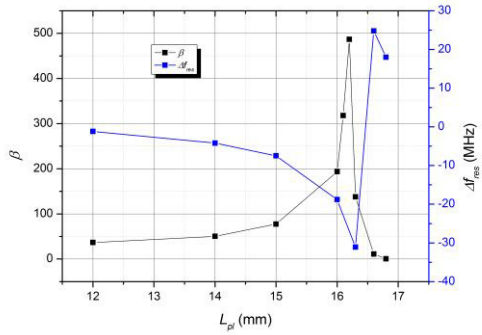

Figure 2: Dependence of coupling factor and resonance frequency shift of the power input cell vs. plunger insertion depth.

As can be seen, such plunger configuration allows to increase the coupling factor more than 10 times, however, it also causes a more than 10 MHz resonance frequency shift. To compensate the resonance frequency shift, a tuning plunger in the power coupler accelerating cell must be used.

Another problem with such plunger configuration is high strength of electric field between the opposite plungers. At the plunger insertion depth of $L_{pl} = 14$ mm (gap between plungers is 6 mm), electric field strength reaches 43% of the maximum strength of the accelerating field at the axis of the power coupler. This problem can be partially solved through increasing diameter of the plungers.

Calculations of the Coupler with 2 Plungers in the Center of Waveguide Wide Wall

Position of plungers in the waveguide was selected to minimize the power coupler accelerating cell resonance frequency shift. Figure 3 shows the graph of the resonance frequency shift vs. distance ΔY from the center of plunger to the power coupler iris at the plunger insertion depth of $L_{pl} = 13$ mm.

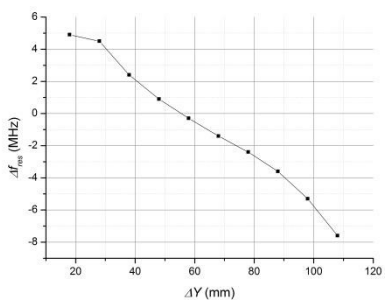

Figure 3: Resonance frequency shift vs. distance from plungers to the iris at $L_{pl} = 13$ mm.

Minimum resonance frequency shift is achieved at the distance ΔY close to a quarter wavelength in the waveguide.

Figure 4 shows graphs of the coupling factor and changes in resonance frequency vs. plunger insertion depth. As can be seen, this configuration allows to decrease the initial coupling factor by an order of magnitude with resonance frequency shift of about 1 MHz.

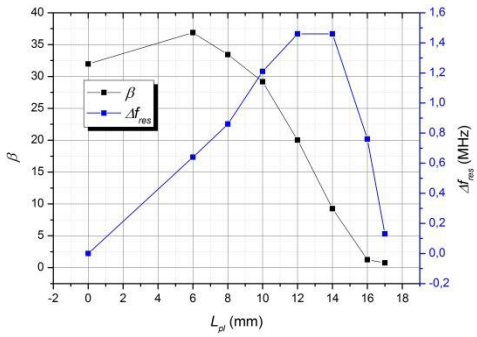

Figure 4: Dependence of coupling factor and changes in resonance frequency vs. plunger insertion depth.

Calculations done for the arrangement with one plunger located at the same distance from the iris gave similar results.

MEASUREMENTS ON A TEST STAND

To perform measurements on a real model, a mock-up consisting of 4 accelerating cells, 4 coupling cells and a power input cell located between them was assembled. Threaded holes for the plungers were made in the feeding waveguide and near the power coupler iris (Fig. 5).

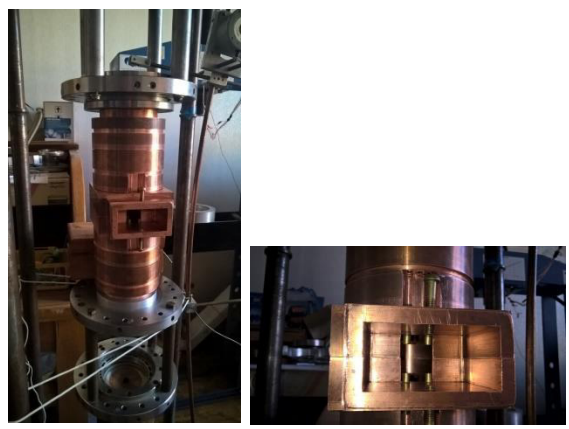

Figure 5: Picture of the mock-up.

Measurements of resonance frequency, coupling factor, loaded Q, as well as field distribution using bead pull technique were performed with Agilent HP85052C vector analyzer.

Figure 6 presents results of coupling factor and resonance frequency measurement, and Fig. 7 shows field distribution for different plunger insertions depths. Measurements with four and two plungers were done with the mock-up tuned to frequency of 2,449.3 MHz and

ISBN 978-3-95450-181-6

coupling factor of 1.81 with extracted plungers. For measurements with one plunger the iris width was increased to achieve coupling factor of 4.75 in order to get a wider range of regulation.

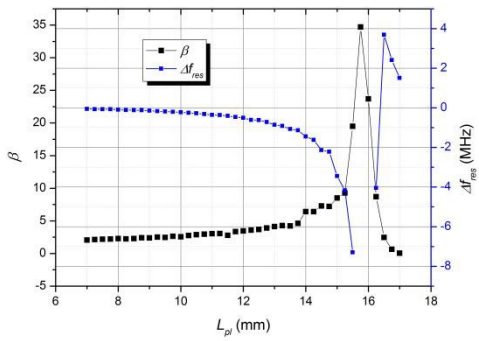

a)

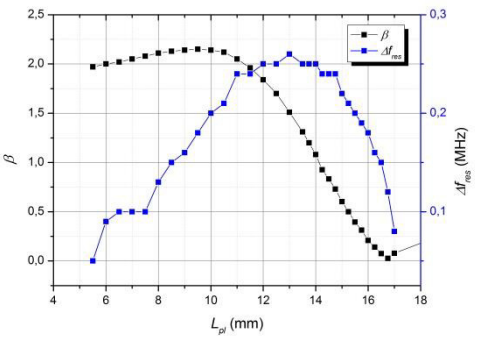

b)

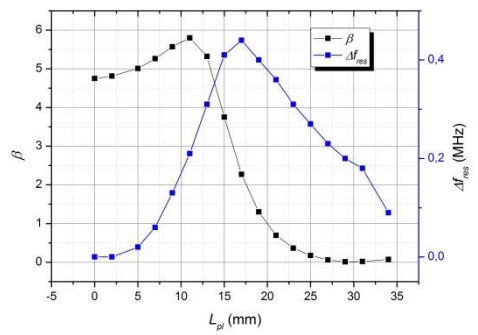

c)

Figure 6: Measured coupling factor and resonance frequency shift of the mock-up vs. plunger insertion depth for arrangement a) with plungers near the aperture, b) with two plungers in the middle of wide wall of the waveguide, c) with one plunger.

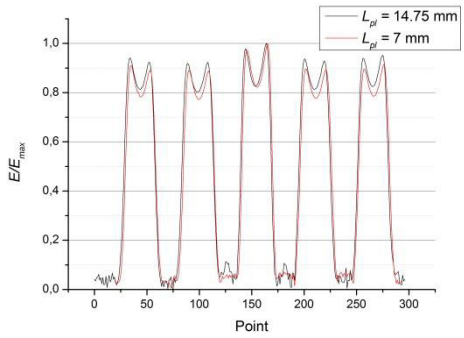

a)

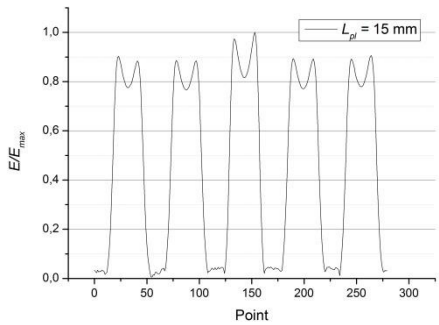

b)

Figure 7: Electric field distribution at the mock-up axis a) for arrangement with four plungers and insertion depths of 14.75 and 7 mm, b) for arrangement with two plungers and insertion depth of 15 mm.

Measurements demonstrate that configuration with plungers near the aperture results in significant fields in the coupling cells.

CONCLUSION

We examined several arrangements of the RF power coupler with adjustable coupling factor. Out of them, configuration with one plunger seems to be optimum, since it ensures tenfold changes in the coupling factor without significant effect on resonance frequency and RF power loss in the walls, besides its design is the simplest. In the near future, we plan to develop a prototype of the arrangement with one plunger for the CW linac [4].

REFERENCES

[1] D.S. Yurov et al., "Continuous-Wave Electron Linear Accelerators for Industrial Applications", IPAC'16, Busan, p. 1142 (2016).
[2] M.S. de Jong et al., "Design of a Tuner and Adjustable RF Coupler for a CW 2856 MHz RF Cavity", PAC'93, Washington, D.C., p. 829 (1993).
[3] https://www.cst.com/.
[4] D.S. Yurov et al., "Industrial Prototype of Compact CW Linac", RuPAC'14, Obninsk, p. 248 (2014).

ISBN 978-3-95450-181-6

THE CASCADE INTERFERENCE SWITCH COMPRISING A TRANSMISSION RESONATOR*

S. Artemenko, S. Gorev, V. Igumnov, Institute of Physics and Technology, Tomsk Polytechnic University, Tomsk, Russia

Abstract

The new concept of microwave interference switches is reported. Interference switch is based on series of H-plane T-junctions (cascade switch) in the view of decreasing switched power at Off state and comprises irises in both its own input and output arms. At On state the irises act as a transmission resonator localizing the nodes of the standing wave at the junctions. Such distribution is expected to decrease the plasma losses. It was shown with a simulation that the cascade switch with additional irises increases the efficiency of the active microwave compressors. The simulation was made with CST studio and COMSOL.

INTRODUCTION

The most effective way to boost microwave power feeding linear particle accelerator is usage of microwave resonant compressors. The compressor accumulates microwave energy into its cavity and rapidly discharges accumulated energy towards the load.

There are two types of resonant compressors. Passive compressors keep resonant characteristics of their resonant cavities. Passive SLED system increases an input power in factor of 4 or 9 under a condition of synchronous phase shift of a supplying generator. An active resonant compressor changes Q-factor of its resonant cavity while emitting stored energy. The ratio of Q-factors at accumulating regime and discharging regime determines amplification factor of active compressors.

The level of accumulated energy is comparable for both active and passive compressors. Active compressors have an operating power less though. The reason of it is a switching element having limited dialectical strength. Moreover, the switch has significant losses up to 3 dB.

The most frequent type of the switch is a microwave interference switch. Such switch is based on H-plane T-junction which has one direct arm coupled with a cavity and other arm short circuited. The last arm is connected to the load. A discharge gap is placed at quarter wavelength from a shorting plane. When plasma is broken down running waves from the cavity and the shorted arm add constructively and the microwave power leaves towards the load. The interference switch is simple and effective. Though, power handling capability is limited by cross-section of a waveguide. Moreover, a gas-discharger and its inner elements such as a quartz tube decrease the handling power.

To enhance the operating power a cascade interference switch was suggested [1, 2, 3]. The cascade switch divides the switching power among discharge gaps. This method allows decreasing the switching power as much as $1/2^N$, where N is number of H-tees. However, interaction between the switching wave and gas plasma discharge keeps large amount of losses.

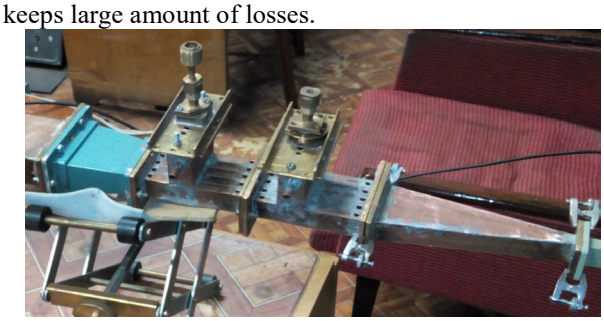

Figure 1: Overmoded cascade interference switch.

The work [4, 5, 6] proposed an overmoded microwave interference switch (Fig. 1) having enhanced handling power. Such switch has two variants of implementation an overmoded waveguide and a package of regular waveguides with a mutual side arm (Fig. 2). The cascade switch based on overmoded T-junctions brought about further enhancement of the operating power. However, interaction between plasma and the switching waves had still stood the same.

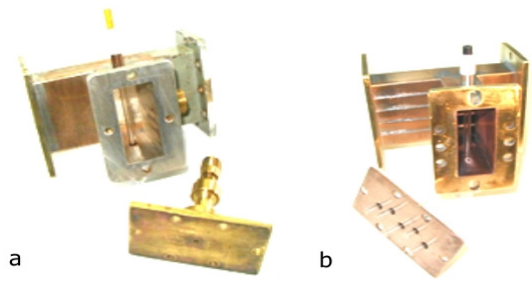

Figure 2: Overmoded interference switches (a – a switch based on overmoded waveguide; b – a package of singlemoded waveguides with a mutual side arm).

This paper concerns a method to increase the operating efficiency of the gas-discharge switches.

RESULTS OF SIMULATION AND ANALYSIS

Overmoded Cascade Switch

The singlemoded cascade switch has an interesting regularity in its act [3]. As one can see from a simulation a behavior of the overmoded cascade switch is quiet similar to the singlemoded cascade switch. Nodes of the

*The work was supported by the Program on Competitiveness Enhancement of the National Research Tomsk Polytechnic University and by Russian Foundation for Basic Research (Grant №15-08-01853).

ISBN 978-3-95450-181-6

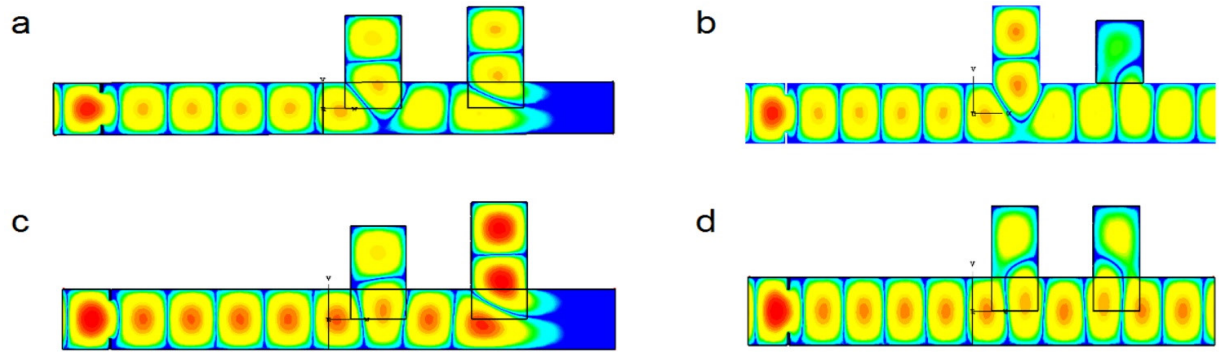

Figure 3: Field patterns of the overmoded cascade interference switch at different regimes (a – Off-state; b – the second H-tee is switched on; c – the first H-tee is switched on; c – On-state).

standing wave locate close to junctions of switched H-tees (Fig. 3 b, c) and wave amplitudes of unswitched H-tees are increasing. Such effect could locally decreases plasma losses. When the last switch is switched on a standing wave turns into a running wave (Fig. 3 d). A transmission resonator should supply a standing wave regime during all switching process.

Transmission Resonator Comprised in an Interference Switch

A regular switch with a transmission resonator was simulated (Fig. 4). This switch was switched by a wire with a low conductivity. The conductivity was chosen thus losses were equal to a half of input power for the regular switch without a transmission resonator. Such level of losses fits losses of plasma broken down in nitrogen medium.

A node of a standing wave appeared at the center of the junction when irises were connected to input and output ports at half-wave distance from the junction. Hence, a transmission coefficient became equal to ~1.

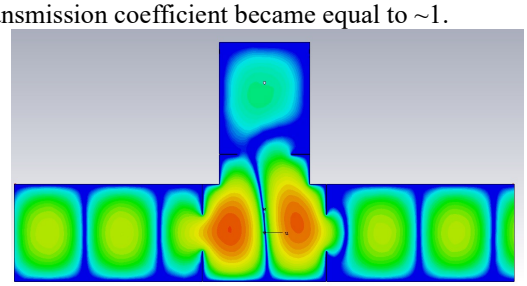

Figure 4: Field pattern in the regular interference switch comprising a transmission resonator.

There are two problems that occur when the transmission resonator is used. The first one is an increase of wave amplitudes in the discharge gaps and the second is the termination of the output pulse length. The length has to be greater than the excitation time of the transmission resonator. Long output pulses could be supplied by the compact active compressors with a variable geometry [7].

As it was estimated the electric field strength in the transmission resonator is much greater than in the regular switch at accumulating regime. Dividing accumulated energy among few H-tees (Fig. 5) one can decrease the field strength in the switch area. A distance between neighboring H-tees of the cascade switch is not equal to a half wavelength that leads to the impossibility to put wave nodes at the junctions correctly. Nevertheless, the increase of the efficiency is supposed to be significant.

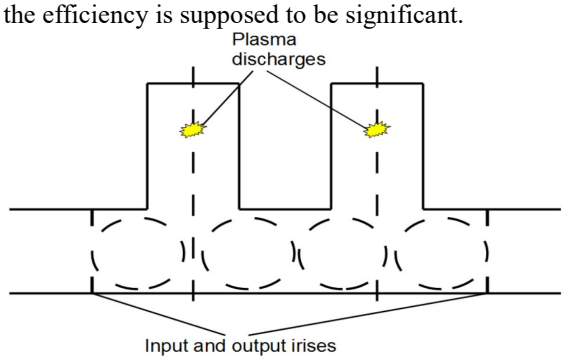

Figure 5: Scheme of the cascade interference switch with transmission resonator.

CONCLUSION

The cascade switch allows increasing the operating power at Off state and the transmission resonator allows decreasing losses at On state. So that, the switch can afford to have the greater efficiency than a conventional interference gas-discharge switch.

ACKNOWLEDGMENT

This research was performed with partial financial support from the National Research Tomsk Polytechnic University Competitiveness Programme and with support of the Russian Foundation for Basic Research (Grant No.15-08-01853a).

Authors are glad to thank Dr. Yushkov and Dr. Chumerin for supporting and helpful advises.

REFERENCES

[1] J. Guo and S. Tantawi, “Active RF pulse compression using electrically controlled semiconductor switches,” IEEE Particle Accelerator Conference, Albuquerque, 2007, vol. 1-10, pp. 4189-4191.

[2] S. Tantawi, “The design and analysis of multi-megawatt distributed single pole double throw (SPDT)

ISBN 978-3-95450-181-6

microwave switches," *8th* Workshop on Advanced Accelerator Concepts, 1998, vol. 472, pp. 959-966.
[3] S.N. Artemenko, V.A. Avgustinovich, S.A. Gorev and V.S. Igumnov, "Analysis of microwave interference switches with distributed power of switched wave and plasma gas-discharge switching," 12th International Conference on Gas Discharge Plasmas and Their Applications (GDP), 2015.
[4] V.A. Avgustinovich, S.N. Artemenko and A.A. Zhukov, "Microwave-energy extraction from a resonator via oversized interference switch," Technical Physics Letters, 2013, v. 39, pp. 492-494.
[5] S.N. Artemenko, V.A. Avgustinovich and M.S. Arteev, Technical Physics Letters, v. 39, pp. 26-32.
[6] S.N. Artemenko, V.A. Avgustinovich, S.A. Gorev, V.S. Igumnov, V.L. Kaminsky, S.A. Novikov and Y.G. Yushkov, "Oversized interference switches in microwave pulse compressors," XXIV Russian Particle Accelerator Conference, 2014, pp. 183-185.
[7] S.N. Artemenko, R. Beverly III, S.A. Gorev, V.S. Igumnov, "High power microwave pulse compressors with a variable geometry of accumulative resonant cavity," IEEE Power Modulator and High Voltage Conference, 2016.

ISBN 978-3-95450-181-6

520 MEV TRIUMF CYCLOTRON RF SYSTEM: MAINTENANCE, TUNING AND PROTECTION*

N.V. Avreline, V.L. Zvyagintsev, I.V. Bylinskii, C. Bartlett, B. Jakovljevic, T. Au
TRIUMF, Vancouver, B.C., Canada

Abstract

1 MW CW 23 MHz RF system of the TRIUMF's 520 MeV Cyclotron has been in operation for over 40 years. Continuous development of the RF power amplifiers, the waveguide system and the measurement and protection devices provides reliable operation and improves the performance of the RF System. In this article, operation and maintenance procedures of this RF system are analysed and recent as well as future upgrades are being analysed and discussed. In particular, we discuss the improvements of the transmission line's VSWR monitor and its effect on the protection of the RF system against RF breakdowns and sparks. We discuss the new version of the input circuit that was installed, tested and is currently used in the final stage of RF power amplifier. We analyse various schematics and configurations of the Intermediate Power Amplifier (IPA) to be deployed in the future.

INTRODUCTION

TRIUMF 520 MeV Cyclotron's high power RF system consists of three main parts – the 1.8 MW CW RF amplifier, the transmission line (TL) and the resonator [1]. The TL itself is composed of two coaxial lines with wave impedances of 50 and 30 ohm. The second part of the TL has three capacitor stations that match 50 ohm impedance of the TL's first part with the coupling loop port of the resonator that is at TL's terminus.

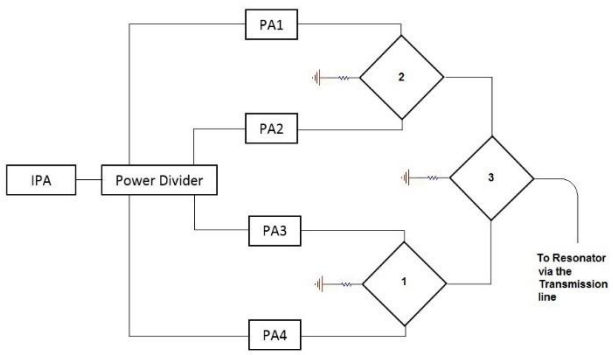

Figure 1: RF System of the 520 MeV Cyclotron.

TRANSMISSION LINE RESONATOR OPERATION AND SPARK PROTECTION

Instability in the RF system's operation appears when there are sparks, electrical breakdowns, multipactor discharge in the resonator and a presence of an essential screen current in the vacuum tubes. The VSWR monitor is used to protect the RF system. This monitor turns off the RF system, if the reflected power in one of the 12 channels exceeds a specified threshold value. The RF control system analyses the rate of the Dee voltage drop, classifies the events and then tries to recover the system. The follow up analysis of where sparks and electrical breakdowns took place is done using an oscilloscope. The oscilloscope operates in stand-by mode otherwise. An example of a typical signal pattern that illustrates a spark inside the resonator is presented in Fig. 2.

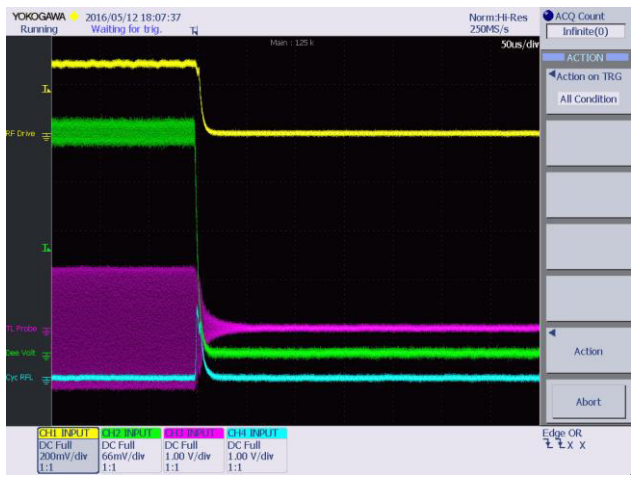

Figure 2: Resonator RF signals following a spark, when the drive is OFF (yellow – drive amplitude, green – Dee voltage, pink – RF signal, blue – rectified voltage of the reflected signal).

The rate of the Dee voltage drop allows to determine whether this spark happened inside the resonator or inside the TL and how large the spark was. The RF control system has sensors to determine the Dee voltage drop and if zero Dee voltage is detected. If either case is detected, the RF control system generates the signal to turn OFF the RF drive and to determine the time when RF system's recovery should be attempted.

However, if these sensors didn't respond properly or responded with some delay, the standing beat wave in the TL could reach double amplitude of the original signal (Fig. 3). As a result, some parts of the TL, such as matching capacitors, the water feedthrough or the TL conductors and insulators could be damaged.

To protect cyclotron's equipment in such an event, the RF switch was built into the VSWR monitor to disconnect the RF drive from the RF amplifiers (Fig. 4).

*TRIUMF receives federal funding via a contribution agreement through the National Research Council of Canada.

ISBN 978-3-95450-181-6

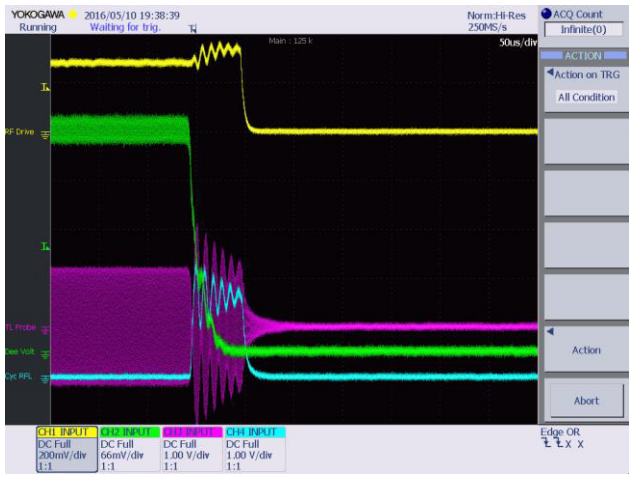

Figure 3: RF beat signals following a spark in the oscilloscope, when the drive is ON (yellow – drive amplitude, green – Dee voltage, pink – RF signal, blue – rectified voltage of the reflected signal).

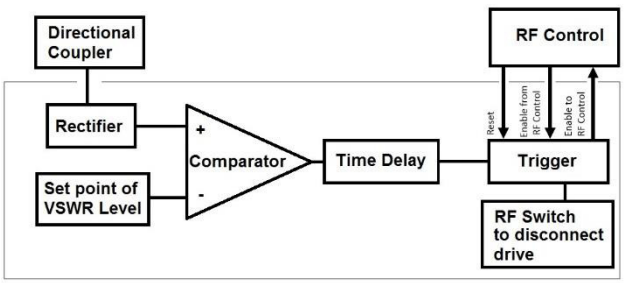

Figure 4: The Block Diagram for one of the channels of the high VSWR detector in the VSWR Monitor.

Some of the weakest parts of the TL susceptible to damage following a spark are the water hoses between the outer and the inner conductors of the TL. The water entrances into the inner conductor are simulated in HFSS v15.0 (Fig. 5).

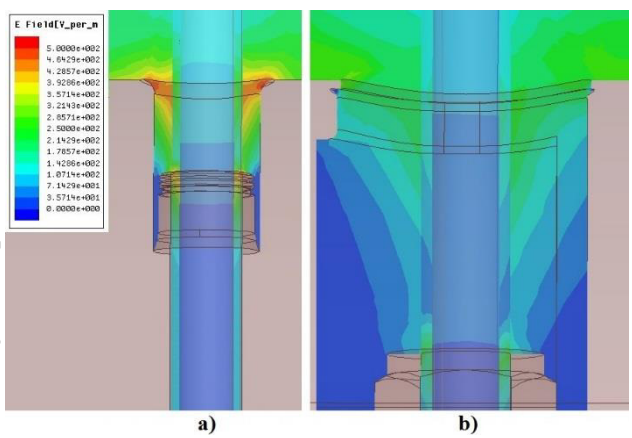

Figure 5: Simulation of the RF field near the water feedthrough in the TL for the original (a) and the new design (b).

In order to improve TL's reliability, the configuration of the conductors in the area with the highest RF field was modified. A simulation in HFSS determined that the RF field is three times higher near the water feed (ε=81) and the sharp edge of the inner conductor. As a solution, the compression fitting was moved deeper into the inner conductor.

HIGH POWER RF AMPLIFIER

The high power RF amplifier is composed of the intermediate power amplifier (IPA), the splitter, four high power amplifiers (PA) and three combiners (Fig.1). The performance and the stability of the RF system is dependent on the quality of vacuum tubes, on the amplifier fine tune and on the suppression of parasitic oscillations.

PA Tuning, Operation and Development

Each of the four PA amplifiers is composed of two 4CW250,000E tetrodes that operate in push-pull mode. Those amplifiers are designed to operate up to 450 kW CW. In order to increase the life time of these tubes they are operated at a 50% lower power and 10% lower filament current (with respect to the nominal values). As a result the tetrodes' lifetime can now reach 135,000 hours.

During the last maintenance period, the PA4 amplifier was upgraded. A new input circuit was installed in order to improve its accessibility and to reduce the downtime involved in troubleshooting as well as during input capacitor replacement.

Figure 6: Installation of a new PA4 Input circuit.

IPA Operation, Tuning and Development

The IPA consists of two stages: a pre-amplifier pentode and a final tetrode. The maximum power that could be reached under the current design is 100 kW. However, in order to increase the life time of the IPA tubes, a 4CW100,000E tetrode is used at the output stage to provide only 50 kW and is operated at 10% lower filament current.

The tetrode stage is loaded with the Pi-network which is connected to the 4-way splitter. This splitter distributes the output power between PAs inputs. To determine the impedance of this load, the method of variations of capacitances [2] was applied to the Pi-network. Independent variations of C_{37}, C_{40} (Fig. 7) from the original values allow to derive five equations for resonance conditions with C_{37}, C_{40} and L_{19} being the unknown variables.

ISBN 978-3-95450-181-6

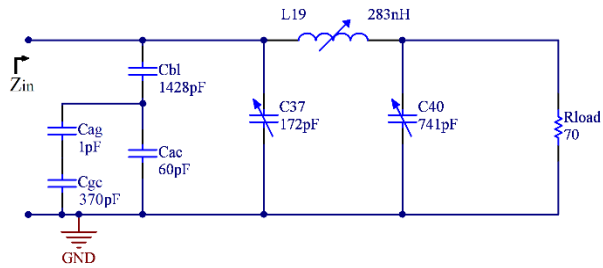

Figure 7: The load schematics setup for the variable capacitance method.

$$Im\left(Z_{inp}(\omega_1, R_{load}, C_{bl}, C_{ac}, C_{ag}, C_{gc}, C_{37}, C_{40}, L_{19})\right) = 0$$

$$Im\left(Z_{inp}(\omega_2, R_{load}, C_{bl}, C_{ac}, C_{ag}, C_{gc}, C'_{37}, C_{40}, L_{19})\right) = 0$$

$$Im\left(Z_{inp}(\omega_3, R_{load}, C_{bl}, C_{ac}, C_{ag}, C_{gc}, C_{37}, C'_{40}, L_{19})\right) = 0$$

$$C'_{37} = C_{37} + \Delta C_{37}$$

$$C'_{40} = C_{40} + \Delta C_{40}\ ,$$

where ω_1, ω_2, ω_3, R_{load}, C_{bl}, C_{ac}, C_{ag}, C_{gc} are the measured values, values of C_{37}, C_{40}, L_{19} are the unknowns. MathCAD Prime 3.1 has been used to solve this system of equations.

This more precise measurement of load impedance allowed to determine the regime of tubes. As a result, the screen current was reduced, which allowed more stable tube operation.

Currently the IPA is being planned for upgrade. The new IPA configuration will have four independent 12 kW solid state amplifiers connected directly to the inputs of PA amplifiers. The amplitude and the phase will be fixed before each IPA input. The development of a new IPA design will be carried out in several stages. Currently, the IPA is based on pentode and tetrode vacuum tubes, where the tetrode has the neutralization circuit via the pentode load. The goal of the first stage of the upgrade is to make these tubes independent. In the second stage, the pentode will be replaced by a 2 kW solid state amplifier. In order to decouple the pentode and the tetrode, a different neutralization circuit is proposed for the tetrode (Fig. 8). This circuit has been developed using the prototype that is currently used as a part of TRIUMF's ISAC-1 particle accelerator. The mechanical design and the series of

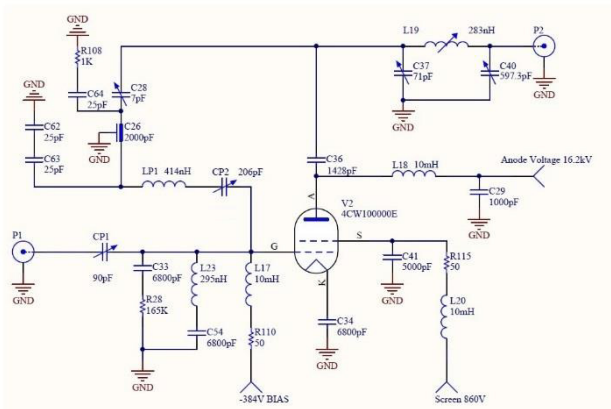

Figure 8: The tetrode stage with a new neutralization.

simulations in Micro-Cap and Altium Designer 10 have been completed. The equivalent circuit for neutralization and the results of simulation in Micro-Cap presented on Fig.9. The current timeline is to rebuild and test IPA in the winter shutdown of 2017.

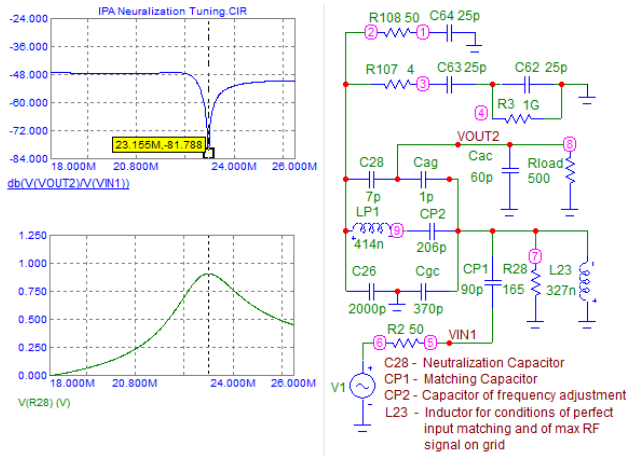

Figure 9: Simulation of neutralization tuning.

MAINTENANCE OF RF SYSTEM

All high power RF components such as vacuum capacitors of the amplifier, combiners and the TL have an annual maintenance service carried out during the 4-month winter shutdown or during 10 days of the autumn mini shutdown. A hi-pot test for the capacitors and the vacuum tubes, inspection and cleanup of the RF components, a low and high power level tunings are carried out during those maintenance periods. An inspection of the TL, the vacuum capacitors of the matching stations, the booster resonator, the water cooling pipes and hoses in the vault are also performed during every winter shutdown.

CONCLUSION

Fine tuning of PAs and the IPA, installation of the RF switch in the VSWR monitor, thermo-stabilization of the Dee voltage rectifiers improved the stability of the high power RF system.

REFERENCES

[1] Y. Bylinski, S. Calic, K. Fong, R. Poirier, "TRIUMF Cyclotron RF System Refurbishing", presented at the 17th International Conference on Cyclotrons and their Applications, Tokyo, Japan, Oct. 2004, pp. 326-329

[2] E.L. Ginzton, "Resonant-cavity characteristics: Measurements of R_o/Q_o ", in Microwave Measurements, Leonard I. Schiff, Consulting Editor, McGRAW-HILL BOOK COMPANY, INC, New York, Toronto, London, 1957, pp. 435-438

ISBN 978-3-95450-181-6

ESTIMATION OF MULTIPACTING IN CDS STRUCTURE

I.V. Rybakov†, Institute for Nuclear Research of the RAS, Moscow, Russia
I.I. Isaev[1], DESY, Zeuthen, Germany

Abstract

Within the framework of the INR's linac upgrade the Cut Disk Structure (CDS) was recommended for the linac's main part first cavity replacement [1]. The stable cavity work in operation regime requires absence of multipactor discharge. The multipactor phenomenon in a CDS structure studies are presented in this paper.

INTRODUCTION

CDS structure was first applied as a booster cavity in DESY PITZ test facility in Zeuthen [2]. For this cavity according to our analytical estimation multipaction should appear at the operating power level in coupling cells, but it was not confirmed by the numerical simulation with both accelerating and coupling modes excitation for RF energy transfer along the cavity. The multipactor appears only with the Secondary Emission Yield (SEY) growth which could happen if the inner surface of the cavity is polluted. The results of multipactor investigation in CDS PITZ were used as the reference for the CDS structure in the first cavity of the main part of INR linac. The analytical estimation and numerical simulation of multipactor in CDS INR structure shows the appearance of the discharge in coupling cells with the OFC copper SEY for the operating regime of the cavity. An option for the multipactor damping with the forced excitation of oscillations in coupling cell with voltage higher than upper multipactor limit was considered.

METHODICS OF ESTIMATION

The multipactor discharge in CDS cavity could appear in the coupling cell, which is geometrically like a flat capacitor (see Fig. 1).

The field level in the coupling cell depends on the accelerating field rate and position of the cell relative to the RF coupler.

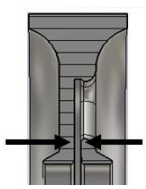

Figure 1: The design of CDS cavity.

For the power transfer through the cavity the coupling mode should be excited additionally [3]. This is the operating regime of compensated structure. The coupling mode is excited with the attenuation coefficient per period d:

$$\alpha d = (1 + \frac{I_b U_a}{P_a}) \frac{\pi \beta}{2 \beta_g Q_a} \quad , \qquad (1)$$

$$\frac{\beta_g}{\beta} = \frac{\pi k_c}{4} \, , \qquad (2)$$

where I_b is the beam current, β_g is the group velocity, β is relative phase velocity, U_a, P_a and Q_a are the accelerating voltage, power and quality factor, k_c is the coupling coefficient. For each cavity cell the αd value multiplies by coefficient N, which depends on the cell position relative to feeding waveguide.

Analytical Estimation

For the coupling cell of the CDS structure the analytical estimation of multipactor voltage level could be obtained using the flat gap approximation [4]:

$$U = 4\pi^2 (fs)^2 \frac{m}{e} \left(\frac{1+K_v}{1-K_v} \pi n \cos\psi + 2 \sin\psi \right)^{-1} \qquad (3)$$

Where f is the cavity operating frequency, s is the gap length, K_v is the relation between secondary and primary electrons velocity, ψ is the secondary electron yield phase and n is the multipactor order. The multipactor voltage levels for different f*s parameters and discharge orders could be represented by a diagram (see Fig. 2).

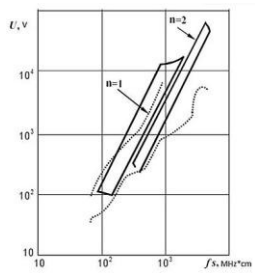

Figure 2: Multipactor voltage levels.

The analytical estimation shows the voltage levels in the gap when the multipaction is possible. We considered only 1st order discharge in case of low current in high order multipactor.

Numerical Simulations

For the numerical simulation of multipacting, the CDS structure was tuned to the secondary electron emission parameters corresponding to pure OFC copper [5]. The secondary emission yield (SEY) graph is shown at Fig. 3. All the simulations were made using the CST studio software [6], the simulation procedure is presented in [7].

† irybakov@inr.ru
[1] on leave from NRNU MEPHi, Moscow, Russia

ISBN 978-3-95450-181-6

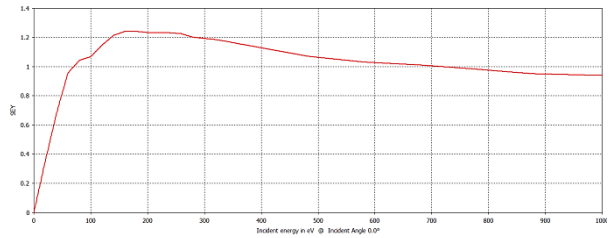

Figure 3: Secondary emission yield for pure OFC copper.

Injection of primary electrons was performed during the first RF field period of simulation. The injector of primary electrons was placed on the total inner surface of the structure.

The output of numerical simulation consists of secondary electrons counter graph, electrons number over time graph, electrons position in the structure over time and electrons energy distribution along transverse axis plots.

PITZ CDS BOOSTER

PITZ CDS booster is designed for electrons acceleration with β=1, k_c=0.08. The designed operational acceleration gradient is up to 14 MV/m [2].

The multipaction in CDS PITZ cavity was observed experimentally at 3.5 – 6.5 MV/m accelerating field rates. The analytical estimation shows the multipactor possibility in CDS PITZ structure at accelerating field rate 6 – 12 MV/m, which corresponds to the operating regime of the cavity but doesn't match the experimental results.

At the first stage of numerical investigation we performed a simulation using structure's accelerating and coupling modes separately. The acceleration rate levels were set from 0 – 14 MV/m. This simulation shows that electrons number is decaying over time at all considered accelerating voltage levels, as it is shown at Fig. 4.

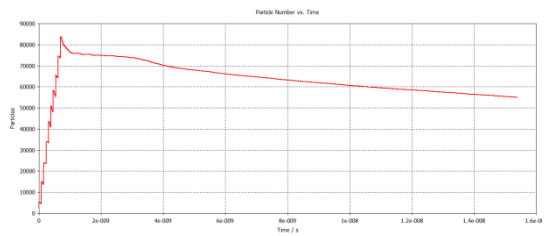

Figure 4: Total particles number over time at acceleration gradient 12 MV/m.

A simulation using the operating regime with accelerating and coupling modes both excited shows that electrons number at accelerating voltage levels 6 - 12 MV/m is growing in the first half-time of simulation with subsequent decaying. Results of this simulation for accelerating rate 12 MV/m are presented at Fig. 5.

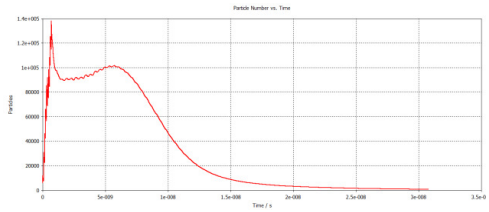

a) Total particles number over time.

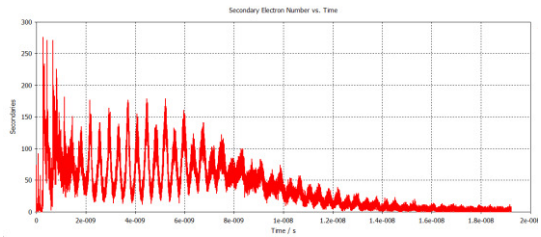

b) Secondary electrons number over time.

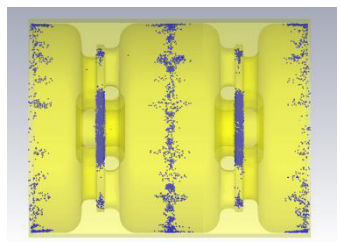

c) Remaining electrons after 25 RF cycles.

Figure 5: Results for accelerating field rate 12 MV/m.

As we can see most of secondary electrons are concentrated in coupling cells. The time distance between secondary emission pikes is ½ of RF period.

CDS PITZ booster operation has shown significant dark current (DC) [8] in the structure. The highest DC intensity has been registered in the three cells near the RF coupler. The numerical simulation shows the multipactor presence in the same cells on accelerating gradients 3.5 – 6.5 MV/m (see Fig. 6). It is a strong indication that both DC and multipactor discharge appearance could be explained as the result of cell's inner surface pollution.

For the numerical simulation with higher SEY the graph of OFC copper was point with factor 1.3.

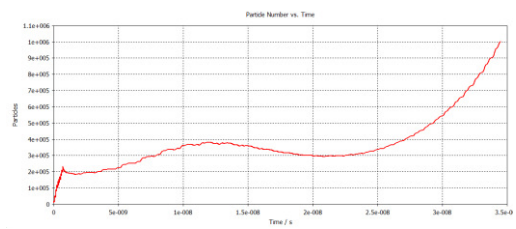

a) Total particles number over time.

ISBN 978-3-95450-181-6

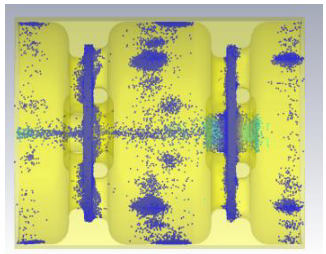

b) Remaining electrons after 25 RF cycles.

Figure 6: Results for accelerating field rate 4.5 MV/m

As we can see from Fig. 6b, simulation shows that multipacting electrons reach the acceleration axis. These electrons could provide significant contribution to DC, which is confirmed by the DC increase in the presence of multipactor during the operation of PITZ CDS booster.

INR CDS CAVITY

The first cavity of the main part of INR linac is designed for proton acceleration, β=0.4313 – 0.4489 and with significantly lower acceleration gradient 2 – 2.5 MV/m, which causes the shift of multipactor appearance levels.

Results of simulations in CDS PITZ structure were taken as reference for perspective in development structure for INR linac. The analytical estimation predicts the multipactor on accelerating field rates 2 – 2.5 MV/m, which are operating for INR linac. The first cavity of the main part consists of 4 sections with 18 – 21 CDS periods in each. The feeding waveguide is placed in sections 2 and 3. In this case the coupling mode field level in sections 1 and 4 is lower in operating regime and may produce conditions for multipactor discharge.

The results of numerical simulation for this structure are matching with analytical estimation. Multipaction appears on accelerating field levels 2 – 2.5 MV/m in coupling cells with 10*αd – 15*αd attenuation coefficient, which corresponds to cavity sections 1 and 4 (see Fig. 7).

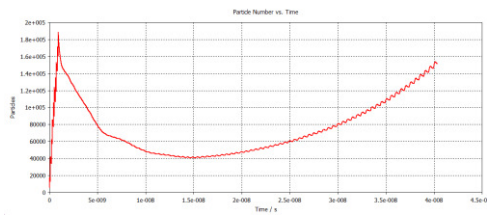

a) Total particles number over time

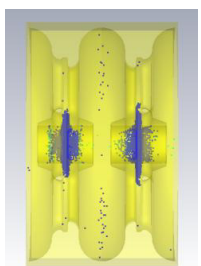

b) Remaining electrons after 25 RF cycles.

Figure 7: Results for 2.5 MV/m accelerating voltage.

In case of multipaction appearance on operating field levels an option of its damping was considered [9]. It is based on forced excitation of oscillations in coupling cell with voltage higher than upper multipactor limit. For CDS INR it is 1.9 kV. To provide this voltage the frequency of nearby accelerating cells are shifted opposite to each other. The drift tube in first cell is lingered and shortened in the next. The necessary frequency shift was obtained using the equivalent circuits method:

$$\Delta\omega = \frac{k * k_c * \omega_0}{4} \quad (4)$$

Where k is voltage multiplication factor, ω_0 is operating frequency. For CDS INR structure the frequency shift is 800 kHz. The numerical simulation with the frequency shift applied shows no multipacting on operating acceleration rate. By the application of the drift tube shift the loss in Z_e is 0.5% and <1% in Q factor.

SUMMARY

In this paper the estimation of multipacting in CDS structure is considered. For CDS PITZ structure an analytical estimation and numerical simulations were provided. The results of simulation with high SEY coefficient are matching with experimental results.

For CDS INR structure the results obtained shows the multipaction possibility on the operating field levels. In this case a method of multipactor damping was considered. The efficiency of the method was shown for CDS INR structure.

ACKNOWLEDGMENTS

The authors thank Dr. Frank Stephan and DESY PITZ group employees for help in setup of the experiment.

Special thanks to Dr. Valentin Paramonov for supervising of this work.

REFERENCES

[1] I. Rybakov et al., “Proposal of the accelerating structure for the first cavity of the main part of INR linac.”, presented at RuPAC’16, Petergof, Russia, November 2016, this conference

[2] V. Paramonov et al., in *Proc. LINAC’10,* pp. 241-243.

[3] V.G. Andreev and V.V. Paramonov, in *Proc. PAC’95*, pp. 1702-1704.

[4] I.N. Slivkov, “Multipactor discharge”, in *Isolation and discharge in vacuum*, Atomizdat, Ed. Moscow, USSR: 1972, pp. 155-163

[5] V. Baglin and J. Bojko, in *Proc. EPAC’00*, pp. 217-221.

[6] CST, http://www.cst.com

[7] G. Romanov, in *Proc. LINAC’08*, pp. 166-168.

[8] I. Isaev, “Dark current measurement at PITZ”, Humboldt-University, Berlin, Germany, Unwanted Beam Workshop, Dec. 2012.

[9] A. Yeremian et al., in *Proc. PAC’89*, pp. 657-659.

ISBN 978-3-95450-181-6

MANUFACTURING TOLERANCES ESTIMATION FOR PROTON LINAC CAVITIES

I.V. Rybakov†, V.V. Paramonov, A.K. Skasyrskaya, Institute for Nuclear Research of the RAS, Moscow, Russia

Abstract

The definition of tolerances for mechanical treatment of the cells in accelerating structures is the step in the total procedure of accelerating structures development and construction. The method of tolerances estimations for mechanical treatment is presented in this paper with examples of application for single periodic and bi-periodic structures.

INTRODUCTION

The natural deviations of the cells dimensions after manufacturing with respect to design values lead to deviations in the structure parameters. From parameters of accelerator should be limitations, which restrict possible deviations in the parameters of accelerating structure. In the case of high intensity proton linacs with long multicells structures a critical parameter is the homogeneity of accelerating field distribution, which defines the beam dynamic quality of accelerated beam. Field deviations from the designed distribution is described be standard deviation σ_E and for high intensity high energy proton linacs, [1], a typical limitation is of field $\sigma_E < 1\%$. From the theory of periodical structures are know relations between field deviations and deviations in frequencies $\sigma_{fa,c}$ and coupling coefficient σ_{kc} of cells in the accelerating structure. A method to reduce the efforts by avoiding separate simulations for each geometrical parameter of the structure cell is extended and presented. The required values could be obtained by numerical simulations only for a few the characteristic modes in the cell. After that the theory of perturbations is applied.

BASEMENT AND REALIZATION

The standard deviation of accelerating field distribution σ_E is defined as:

$$\sigma_E^2 = \frac{\sum_{i=1}^{N_p} (E_i - \bar{E})^2}{N_p}, \quad (1)$$

where N_p is the number of accelerating gaps, E_i is the filed amplitude in each gap. According to the theory, the contributions of cells deviations in frequency and in coupling coefficient contribute into field deviation independently:

$$\sigma_E^2 = \sigma_{E_f}^2 + \sigma_{E_k}^2, \quad (2)$$

where σ_{Ef}^2 is the dispersion caused by frequencies spread of accelerating and coupling modes, σ_{Ek}^2 is the dispersion caused by coupling coefficient spread [1].

Bi-periodic (Compensated) Structures

For the π/2 mode (or bi-periodic) accelerating structures the values of σ_{Ef}^2 and σ_{Ek}^2 can be obtained with expressions [2]:

$$\sigma_{E_f}^2 \approx \frac{16\sigma_{f_a}^2}{k_c^4}\left(\sigma_{f_c}^2 \frac{N_p^2+3N_p}{12} + \left(\frac{\delta f}{f_a}\right)^2 \frac{N_p^3+4N_p^2+6N_p}{3}\right) \quad (3)$$

$$\sigma_{E_k}^2 = \sigma_{k_c}^2 \frac{N_p+2}{3}, \quad (4)$$

where $\sigma_{fa,c}$ are the dispersions of frequencies for accelerating and coupling modes, $\delta_f = f_c - f_a$ is the stop band width, N_p is the number of structure periods in the cavity and k_c is the coupling coefficient. The values of $\sigma_{fa,c}$ and σ_{kc} are related with deviations in geometrical parameters of cells x_i as:

$$\sigma_{f_{a,c}} = \frac{\sqrt{\sum_i \left(\frac{\partial f_{a,c}}{\partial x_i}\right)^2 \sigma_{x_i}^2}}{f_{a,c}} \quad (5)$$

$$\sigma_{k_c} = \frac{\sqrt{\sum_i \left(\frac{\partial k_c}{\partial x_i}\right)^2 \sigma_{x_i}^2}}{k_c}, \quad (6)$$

where σ_{xi} is the dispersion of geometrical parameter x_i spread which corresponds to the tolerance value $dx_i = \pm 3\sigma_{xi}$, $\delta f_{a,c}/\delta x_i$ and $\delta k_c/\delta x_i$ are the sensitivities of frequencies and coupling coefficient to deviations in geometrical parameter x_i. In the cell geometry each parameter x_i, as a rule, defines a surface S_i, and the change in parameter δx_i means this surface displacement. The sensitivity of frequencies to the surface displacement we can define by using Slatter perturbation theorem:

† irybakov@inr.ru

ISBN 978-3-95450-181-6

$$\frac{\delta f_{a,c}}{f_{a,c}\delta x_i} = \frac{\int_{S_i} (\varepsilon_0 E_{a,c}^2 - \mu_0 H_{a,c}^2) d\vec{S}}{4W_{a,c}}, \quad (7)$$

where $W_{a,c}$ is the energy stored either in accelerating or in coupling modes.

The sensitivity for coupling coefficient k_c can be obtained from expressions for the phase velocity β and the group velocity β_g, see, for example, [3], as:

$$\frac{\beta_g}{\beta} = \frac{\pi k_c}{4} \quad (8)$$

$$\beta_g = \left| \frac{\pi\beta \int_{v_0} (\mu_0 \vec{H}_a \vec{H}_c - \varepsilon_0 \vec{E}_a \vec{E}_c) dV}{\sqrt{2W_a W_c}} \right|, \quad (9)$$

where v_0 is a volume of a half of structure period. From equations (8) and (9) the deviation of coupling coefficient k_c due to displacement of the surface S_i can be defined as :

$$\frac{\int_{S_i} (\varepsilon_0 \vec{E}_a \vec{E}_c - \mu_0 \vec{H}_a \vec{H}_c) d\vec{S}_i \delta x_i}{\sqrt{W_a W_c}} = \delta k_c \quad (10)$$

π-mode Structures

Here we consider a simple periodical structures with the single cell in the structure period, operating in π–mode or *0*- mode. The coupling coefficient is determined from the width of the structure passband as:

$$k_c = \frac{f_\pi^2 - f_0^2}{f_\pi^2 + f_0^2}, \quad (11)$$

where f_π is the π - mode frequency and f_0 is the frequency of the *0*-mode from the same dispersion curve.

The values of field perturbations caused by operating frequency spread and coupling coefficient spread are, see [2]:

$$\sigma_{E_k}^2 = \frac{2(N_p^2 - 1)}{3(2N_p - 1)} \sigma_{\frac{\delta k_c}{k_c}}^2 \quad (12)$$

$$\sigma_{E_f}^2 \approx \left(\frac{2}{k_c}\right)^2 \left(\frac{8N_p^3 + 4N_p^2 + 2}{3} - \frac{16N_p^3 - 8N_p^2 + 2N_p + 4}{6} k_c\right) \sigma_{\frac{\delta f_\pi}{f_\pi}}^2 \quad (13)$$

The value of dispersion for cell frequencies $\sigma_{f\pi}$ can be obtained in similar way equations (5) and (7). The required values for coupling coefficient sensitivities $\delta k_c/\delta x_i$ will be determined as partial derivative of expression for k_c in equation (11):

$$\frac{\partial k_c}{\partial x_i} = \frac{4 f_\pi f_0 \left(\frac{\partial f_\pi}{\partial x_i} f_0 - \frac{\partial f_0}{\partial x_i} f_\pi\right)}{(f_0^2 + f_\pi^2)^2} \quad (14)$$

Numerical Realization

The numerical technique for this procedure is realized, as before, [3], basing on ANSYS software, [4]. With the own ANSYS tools we simulate frequencies and the field distributions only for accelerating and coupling modes for bi-periodical structures or for $-\pi$ mode and *0*- mode for mono-periodical structures. According to the internal ANSYS technique, the total surface of the structure is divided into the simple numbered segments (see Fig. 1).

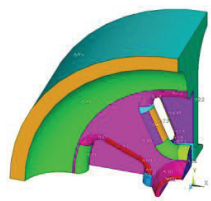

Figure 1: Structure cell surface divided into numbered segments.

A set of codes was developed to combine, if required, field distributions of simulated modes and calculate the values of deviations in frequencies and coupling coefficients for each segment, following to equations (7), (10) or (7), (14). Additionally several macros were developed for visual representation. At Fig. 2 are shown the distributions of density for sensitivities of accelerating, coupling modes and coupling coefficient for CDS cell, [5]. From such distributions the designer can clearly see the parts of structure surface, which are critical in influence on corresponding structure parameter.

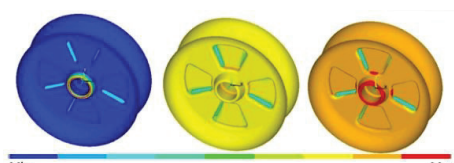

a) f_a b) f_c c) k_c

Figure 2: The distributions of the density for sensitivity of accelerating, (a), coupling, (b), modes frequencies and coupling coefficient, (c), to the displacement of the cell surface.

ISBN 978-3-95450-181-6

As we see from Fig. 2, both for frequencies and coupling coefficient, the most critical for mechanical treatment surfaces of the structure cell are placed near the drift tube.

APPLICATIONS

The required tolerances were estimated for compensated CDS structure. It is under consideration for the replacement of the first accelerating cavity in the main part of INR proton linac [5]. The structure has parameters f_a=991 MHz, k_c=17% and each section contains N_p~ 20 periods of the structure. Assuming at this stage a typical tolerance values for all cells dimensions, for the tolerances of 30, 50 and 80 μm the expected values of σ_{kc}, σ_{fa}, σ_{fc} are presented in Table 1.

Table 1: Expected standard deviations in CDS sections parameters.

Tol., μm	σ_{kc}	σ_{fa}	σ_{fc}
30	0,001143	0,000227	0,001093
50	0,001904	0,000379	0,001821
80	0,003047	0,000606	0,002914

The plot of the stop band width $\delta f/f_a$ to have the field deviation σ_E < 1% is presented at Fig. 3.

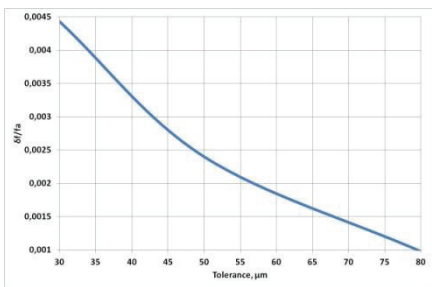

Figure 3: Plot of tolerable stop band width for different tolerances for CDS INR structure.

For tolerances ~ *50* μm, comfortable for cells treatment with numerically controlled equipment, only from field homogeneity, we can allow very large δf value ~ 2.5 MHz. In reality δf value is limited by other effects. At Fig. 4 the plot of dependence σ_E (k_c) is shown for a more real-istic δf value ~ 400 kHz. One can see clearly the im-portance of kc > 10% for the structure and reasonability of k_c=17% realized in CDS naturally.

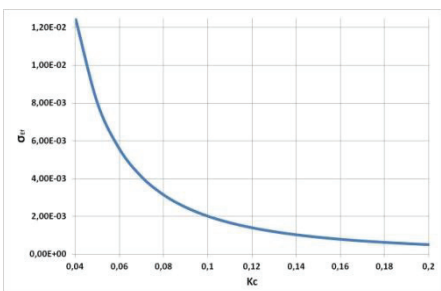

Figure 4: Plot of the σ_E (kc) dependence for δf value ~ 400 kHz and typical tolerances of 50 μm.

Results of the consideration show – with realistic for treatment tolerances, without severe requirements for RF tuning of accelerating sections, with CDS structure we can obtain required field homogeneity for INR new cavity.

π-mode Deflecting Structure

Illustrating application for mono periodical structures, tolerances for manufacturing of the S band π-mode deflecting structure, [6] the 2997 MHz were considered. The density of frequency sensitivity for operating π-mode at the structure surface is presented at Fig. 5.

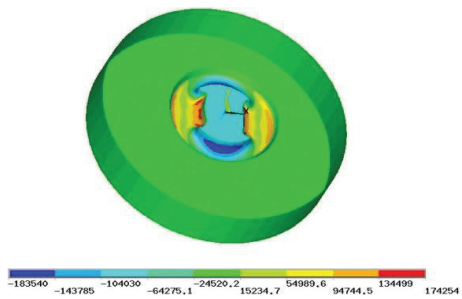

Figure 5: The density of frequency sensitivity for operating π-mode.

As it is known well, parameters of a simple mono periodical structures are much more sensitive to deviations in cells parameters. Consideration shows for the structure with k_c=4% the limitation in the cavity length up N_p~ 7 and required tolerances not more than 20 μm.

SUMMARY

The method for tolerances definition for accelerating structures construction is presented. It requires a few numerical simulations only for characteristic modes and theory of perturbations is used to obtain further results. The universality of the method and its application for π/2-wave and π-wave structures is illustrated.

The simulations for the new CDS INR structure show that the tolerance value for the cavity is 50 μm. This tolerance allows the flexible cavity tuning with the acceptable stop band width.

The simulations for π-wave deflector has shown that for mono periodic structures the value of manufacturing tolerances should essentially be not above 20 μm.

REFERENCES

[1] B. Murin, "Biperiodic accelerating structures", in *Linear ion accelerators*, Atomizdat, Ed. Moscow, USSR: 1981
[2] V.F. Vikulov and V.E. Kalyuzhny, "The influence of deviations in manufacturing at the parameters of standing wave accelerating structures", *Tech.Phys.*, v. 50, pp. 773-779, 1980
[3] V.V. Paramonov and A.K. Skassyrskaya , in *Proc LINAC'04*, pp. 812-814
[4] ANSYS, http://www.ansys.com
[5] I.V. Rybakov et al., TUPSA004, this Conference
[6] V. Paramonov, THCASH01, this Conference

ISBN 978-3-95450-181-6

POWERFUL RF TRIODE AS ANODE MODULATOR VACUUM TUBE

A.I. Kvasha, V.L. Serov, Institute for Nuclear Research, RAS, Moscow, Russia

Abstract

For 20 years modulator vacuum tube GMI-44A successfully operated in DTL RF system of INR Linac. The vacuum tube had been designed and manufactured at OKB "Swetlana" (now joint stock company SED-SPb) in the 70-ies - 80-ies of the last century. A quantity of manufactured tubes had achieved nearly 80 and allowed the accelerator operating up to date. In the middle of 80-th manufacture of the tubes was stopped. Attempts of the GMI-44A manufacture restoration or repair were unsuccessful ones.

As it is turned out, the only decision in the circumstances is use of vacuum tube GI-71A (the former name "Katran" [1]) as modulator tube. The tube GI-71A operates for the last ten years in all final RF power amplifiers (FPA) of INR Linac instead of GI-54A.

Use of RF triode GI-27A in anode modulator as control valve was considered in [2], but a creation of the HV modulator pulse was realized by means of the "soft" discharger.

ITRODUCTION

The powerful anode modulator simplified scheme is shown at fig.1, where AFL – artificial forming line (storage device), TRPM – transistor pre-modulator, TR-thyristor regulator of GI-71A filament voltage.

To simplify the subsequent discussion the modulator vacuum tube will be marked as GI-71AM though in the modulator and the FPA the same vacuum tube GI-71A sets in.

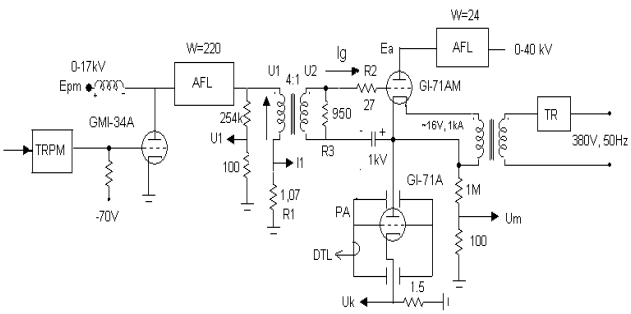

Figure1: Simplified scheme of anode modulator.

At fig.1 pre-modulator devices are additionally represented at the scheme: pulse transformer between output stage of the pre-modulator (at vacuum tube GMI-34A) and GI-71AM input, a source of negative grid bias relatively cathode, resistive dividers, which allows to measure voltages in the main point of scheme, final RF power amplifier (FPA), connected in series with modulator vacuum tube GI-71AM. Resistor R2 limits the grid current value in a case of emergency situation (short circuit of GI-71AM grid-cathode gap) and brings down oscillations in the circuit consisted from pulse transformer secondary winding inductance and capacity grid-cathode *Cgc* of the modulator vacuum tube.

It should be noted that modulator vacuum tube performs several functions such as:

- Creation of PA plate pulse voltage up to 35-40 kV with current 150-200A;
- Control of plate voltage by a signal of negative feedback from the tank;
- Interruption of pulse modulator in the case of breakdowns in PA vacuum tube [3]
- Aging of PA vacuum tube because of series crowbar operation particularities [3] - due to delay between signals from current transformer in the modulator vacuum tube plate network and at the GI-71AM input a part of energy, accumulated in AFL, is delivered in a point of break-down, destroying non uniformity at electrode surface of the FPA vacuum tube.

Before estimate problems, which are appeared after replacement of GMI-44A at GI-71A it follows to compare both vacuum tubes options (see table 1).

Table 1: Tubes Options

	GMI-44A	GI-71AM
Cag, pF	300	80
Cgc, pF	1000	200
Cac, pF	20	3
- Eg, kV	2	1.5
Ea, kV	60	45
Iem, A	500	900
Iao, A*)	140	100
Igo, A*)	1	25
Pa, kW	150	140
Pg, kW	1.5	2
Filament voltage	6V, 50Hz	16V, 50Hz
Filament current	2kA	1kA

*) At voltages Ugk = 500 V and Uak = 6kV

As can be seen from table 1 the vacuum tubes options noticeably differ in values of inter-electrode capacities and grid currents. The last one means, that pre-modulator pulse power needs to be increased 20-30 times. That can be achieved by two ways: increasing of transistor pre-modulator gain and optimization of GMI-34A mode of operation, particularly by means of plate voltage increasing.

Moreover, as follows from table 1 GI-71AM filament options demand changes of the high-voltage filament transformer. It should be noted that GI-71A modes of operation in modulator and in RF final power amplifier are significantly different ones. In FPA there is pulse plate voltage 25-30 kV and automatic pulse grid bias due small resistor in cathode circuit. Value of pulse grid bias doesn't exceed 400V. During setting GI-71A in anode modulator there are dc plate voltage up to 40kV and dc

ISBN 978-3-95450-181-6

grid bias about 1 kV. The last mode of operation is more difficult than previous one.

PRE-MODULATOR MODE OF OPERATION

Pre-modulator scheme as it looks by the secondary winding of ideal pulse transformer with transformer ratio 4:1 is shown at fig.2.

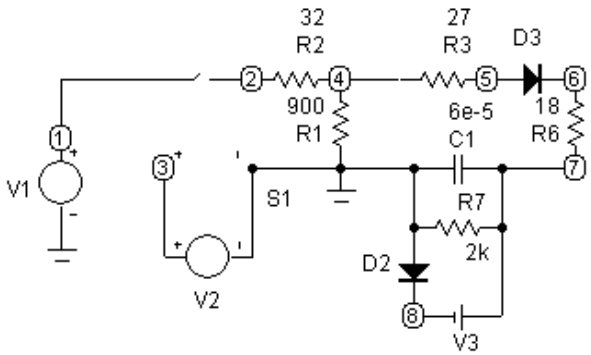

Figure 2: Pre-modulator output stage model.

At the scheme *R6* is an input impedance of the modulator vacuum tube GI-71AM, *R2* – AFL wave impedance, *V1* – GMI-34A plate voltage, *V3* – negative bias source, *V2* – *SV*-switch, operating with repetition rate 50 Hz and pulse length 400μs, *R3*-resistor limiting grid current, *R1* – additional resistor in secondary winding of pulse transformer.

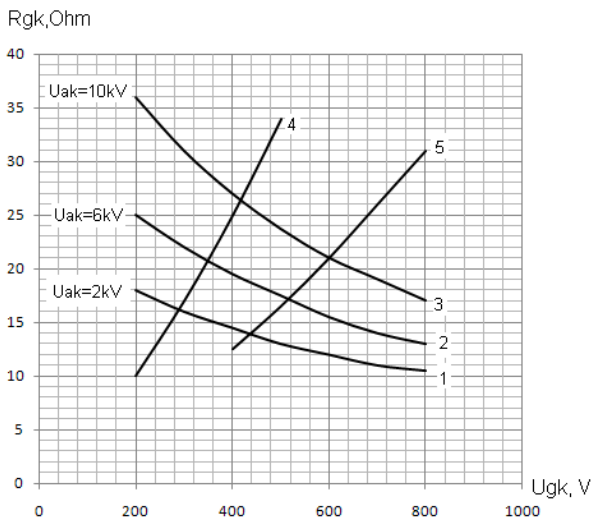

Figure 3: Example of pre-modulator options calculation.

The pre-modulator scheme allows determining real values of pulse voltage *Ugk* (U_{R6}). At that it should be noted that input impedance of vacuum tube GI-71A depends on both from grid-cathode voltage *Ugk* and anode-cathode voltage *Uak*. As a consequence, it is impossible to determine the main options of pre-modulator analytically.

Example of pre-modulator options calculation, such as GI-71A input impedance, *Ugk* voltage and plate current Iao, is shown at fig.3, where curves 1-3 represent the GI-71A input impedance as a function of the *Ugk* and *Uak* voltages.

The curves are created from known dependecies *Ig=f(Ugk)* of vacuum tube GI-71A. Curves 4,5 correspond to the pre-modulator options, presented at fig.3, where voltage *Ugk* value was calculated for different values of *R5*.

The curve 4 corresponds value of V3 = 2500V, the curve 5 – 3500V. Taking into account the pulse transformer ratio, plate voltage of vacuum tube GMI-34A for curve 4 is equal 10 kV and for curve 5 – 14 kV.

Intersection points of curves 1-3 and 4,5 determine values of *Ugk* and *Rgk* and, hence, values of grid current *Ig* = *Ugk/Rgk* and GI-71AM plate current *Iao* – from known plate-grid dependencies *Iao* = *f(Ugk)*. Below, in table 2 some results of such calculations are presented.

Table 2: Results of Calculations

	U1=2500V			U1=3500V		
Uak, kV	2	6	10	2	6	10
Rgk, Ohm	16	21	26	12.5	17	21
Ugk, V	290	350	420	400	520	600
Ig, A	18.1	16.6	16.1	32	30.6	28.5
Ia, A	50	70	120	65	120	170

It follows from table 2 that due to nonlinearity of GI-71A input impedance, *Ugk* value increases on 50%, when *Uak* value changes from 2kV to 6kV. At that, grid current value change is minor – 10% only. All this takes place at unchangeable value of GMI-34A plate voltage.

In order to move from static options to the real ones it is possible to make use the procedure, presented in [4]. According to that of it follows, first of all, to set FPA input options such as RF voltage value *Ug* at the GI-71A grid and plate voltage *Ea*, which provide required level of RF power in the DTL cavity.

Calculation model, presented in [4], allows determining FPA vacuum tube mode of operation in full, including plate current constant component *Iao*. Returning to GI-71A static options it is easy to determine *Ugk* and *Uak* values, matching calculated above value *Iao*. Then it is not difficult to define *R6* value and GMI-34A plate voltage, which provide demanded value of *Ugk*.

As to GI-71AM plate voltage *Eao* its value is determined as *Eao=Ea + Uak + W Iao*, where *W* is the wave impedance of *AFL* at GI-71AM plate.

It should be noted the increasing role of capacitor C1 in connection with grid current growth.

Values of the grid current, resister R7 and capacity C1 determine the low limit of negative bias voltage. If assume, that the external negative bias source is disconnected, then negative bias voltage will be result of capacitor *C1* charging by grid current. Really in a steady state the next ratio takes place:

$$(E_{go} + \Delta Uc)(1 - e^{\frac{-1}{FTc_c}}) = \Delta Uc\,,$$

where *Ego* – negative bias, that appears as a result of capacitor *C1* charging, *F* – a pulse repetition rate, *Tc* = *C1*R7* – capacitor *C1* discharge time constant,

ISBN 978-3-95450-181-6

$\Delta U_C = \frac{1}{C_1}\int_0^{\tau} I_g(t)dt$ where τ is the pulse length of grid current.

Assuming grid current value constant along pulse length it is easy to get an expression, determining a low level of the bias voltage:

$$E_{go} = \frac{I_g}{C_1} T_u e^{-\frac{t}{FT_C}} (1 - e^{-\frac{t}{T_C}})^{-1}$$

For example, for *Ig=30A, C1=60nF, F=50Hz, Tc=0,12s, τ = 400μs* value of negative bias achieves *Ego~ -1100V*.

SOME RESULTS OF GI-71AM TESTING

During the year new modulator vacuum tube GI-71A had been installed in four of the six regular RF channels with output pulse RF power 1MW (the fifth RF channel), 1,2 MW (the first RF channel), 1,8MW (the fourth RF channel and 2,2 MW (the sixth reserve channel).

Maximum operating time of the vacuum tube has been about 2000 hours to date. Failure of the vacuum tubes has not been noted. Unexpectedly the modulator speed of response has been noticeably increased after replacing GMI-44A at GI-71AM. It allowed giving up from additional feedback circuit around modulator [5].

The most reliable operation takes place in the first and fifth RF channels, where GI-71AM plate voltage does not exceed 28 kV. With increasing GI-71AM plate voltage the series crowbar system [3] operation can be disturbed. The fact is that crowbar operation is caused by anode-grid breakdowns in FPA vacuum tube GI-71A or anode grid cavity, whereupon open vacuum tube GI-71AM is proved under full plate voltage. If the modulator vacuum tube is not closed by the series crowbar system, plate current will be increased several times up to 400-500 A, until the artificial forming line will be discharged. It means that breakdown pulse width will achieve 400 μs instead of 10 μs in a case of proper operation of the crowbar system.

There are two main reasons of the crowbar failure.

- Lack of aged vacuum tube GI-71AM because neither manufacturer (S.E.D-S.Pb) nor user (INR RAS) has equipment for aging of vacuum tubes GI-71A. That is why vacuum tube aging takes place during beam sessions only.
- Overvoltage in pre-modulator networks as a result of GI-71AM grid current interruption by the series crowbar system.
- Unknown processes in the vacuum tube GI-71AM after breakdowns in the FPA causing short circuit vacuum tube GI-71AM cathode at the ground.

It should be recalled that FPA operates with ground grid and breakdowns take place between the inner tube of coaxial plate-grid cavity (or vacuum tube plate) and ground.

At fig.4 snapshot of processes which accompany FPA breakdown are shown. From them follows that despite of modulator input pulse cutting off modulator vacuum tube GI-71AM is open until full discharge of the forming line.

Moreover grid-cathode gap is also broken down and capacitor C1 (see fig.2) is discharged through broken gap supporting GI-7AM open.

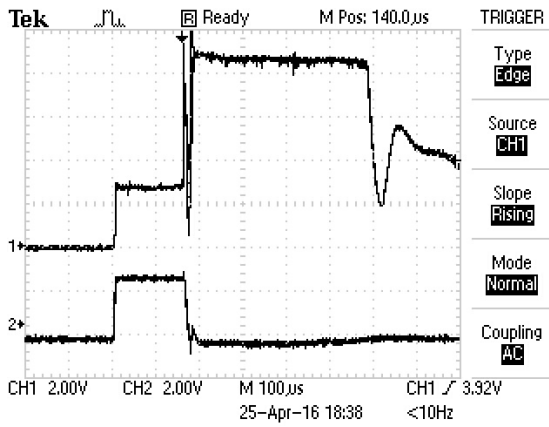

Figure 4: Snapshot of process during breakdown in FPA. Upper trace – plate current, lower trace – pulse at the GMI-34A input (see fig.1).

Unfortunately cathode and grid of vacuum tube GI-71A are under high pulse voltage and real processes at the electrodes can't be watched by the simple way.

Now we consider a few ways of the problem deciding, particularly installation of solid-state opening switch [6] in GI-71AM plate circuit and correcting circuits, limiting value of overvoltage at the GI-71AM grid. We don't also eliminate a possibility of GI-71A design changing. In particular there is agreement with SED-SPb about placing magnetic discharge vacuum pump at grid electrode of GI-71A.

REFERENCES

[1] A.I.Kvasha, etc. "A new 200MHz Powerful Pulse Triode for the Output Power Amplifier of DTL RF System", Proc. PAC2001, Chicago, p.1222.

[2] Kvasha A.I., etc. "Opiti kompensacii spadov uscorjayuschego polja v injectore Serpuhovskogo sinhrotrona pri uskorenii intensivnih puchkov", Trudi II-go Vses. Sovesch.po usk.zar. chastic, "Nauka", M, 1972, v.II, p.157.

[3] A.I.Kvasha. V.L.Serov "Development of the INR DTL RF System Crowbar Operation", Proc. of RUPAC2008, p.218.

[4] A.I.Kvasha "Numerical calculation of vacuum tube power amplifier mode of operation", Problems of Atomic Sciences and Technology (58), №3 (79), 2012, p.29.

[5 A.I.Kvasha "Improving of the DTL cavity RF voltage stability by means of anode modulator feedback", Proc. of RUPAC2010, Protvino, Russia, pp.366-368.

[6] Ian S. Roth etc. "A solid-state opening switch for crowbar replacement", Proc. of the 2001 PAC, Chicago, pp. 1459-1461.

ISBN 978-3-95450-181-6

THE RF POWER SYSTEM FOR RFQ-INJECTOR OF LINAC-20

V. Kuzmichev, A. Kozlov, Yu. Stasevich, D. Seleznev, Institute for Theoretical and Experimental Physics, Moscow, Russia
A. Butenko, Joint Institute for Nuclear Reseach, Dubna, Russia
C. Polozov, National Research Nuclear University MEPhI, Moscow, Russia
T. Kulevoy, Institute for Theoretical and Experimental Physics, Moscow, Russia and National Research Nuclear University MEPhI, Moscow, Russia

Abstract

In the frame of the NICA project the electrostatic injector of LU-20 is replaced by a RFQ accelerator, which has been developed in ITEP. The construction of 400 kW 145 MHz RF power system for RFQ-injector are described. Parameters and test results of the RF power system operated on the resistive load and on RFQ during ion beam acceleration are presented.

INTRODUCTION

In the framework of the NICA project the modernization of injection line is realized. As a result of upgrading the 700 kV electrostatic injector of the DTL LU-20 was replaced by an RFQ. It enables to decrease the potential at the ion source high voltage platform to 150 kV and as result to deliver on it the 35 kW electric power needed for the polarized ion sources operation [1].

The RFQ accelerator, RF power system and low-level RF system were developed in ITEP. The oscillating tube specially developed for application in accelerator technology is used in the RF amplification system [2].

The RF system of the existing linear accelerator LU-20 operates in self-exciting oscillation mode. This requires the dynamic phase synchronization between RFQ and DTL cavities. The RFQ cavity works at the same frequency as DTL and the stability of phase difference between the oscillations in these two cavities has to be kept within tolerance of one degree. The synchronization is provided by a high performance FPGA-based digital Low-level RF system (LLRF).

DESCRIPTION OF RF SYSTEM

RFQ is driven by an RF power system consisting of a solid-state amplifier (SSA), four-stage preamplifier and the final stage based on the high-power water-cooled GI-27AM tube. Block diagram of the RF system is presented in Figure 1.

The RF signal is generated by master oscillator. The SSA amplifies the 10 mW output signal from the master oscillator to a level of 150 W. To protect the SSA, the ferrite circulator with low insertion losses is used at its output. The preamplifier consists of four units with GI-39B triodes, RF power splitter and combiner. It provides the RF power up to 50 kW at the input of the last stage.

The resonator uses two identical RF coupling loops (Figure 2) installed symmetrically in the middle section of the RFQ. The area of loops is about 870mm^2. The non-compensated inductance of couplers leads to a resonant frequency decrease by 33kHz. Fine adjustment of the coupler input impedance is carried out by loop rotation against its axis.

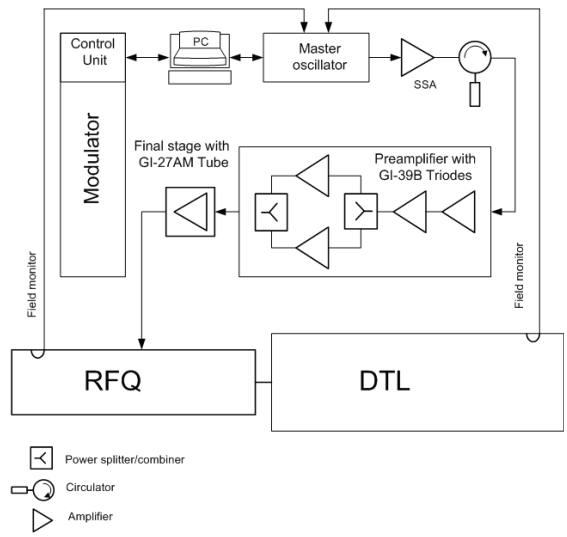

Figure 1: Block-diagram of RF system. PC-computer, SSA–solid state amplifier, RFQ- accelerator, DTL- linear accelerator LU-20.

In the final stage of RF amplifier a powerful generator tube GI- 27AM is used. To obtain the required output power, the tube the power of about 50 kW is needed at the input circuit of. The single unit with GI-39B was tested to define the output power achievable at the DTL frequency 145.2 MHz with pulse length of 150 μs. It was demonstrated that the single lamp can produce power up to 30-35 kW for routine operation.

Also it was found that the output power of two GI-39B connected in parallel get 50 kW which can be transmitted to the input circuit of GI-27AM tube.

A lay-out of the final unit based on the GI-27AM triode is shown in Figure 3. Detailed design of the generator is described in [3].

ISBN 978-3-95450-181-6

Figure 2: RF coupler.

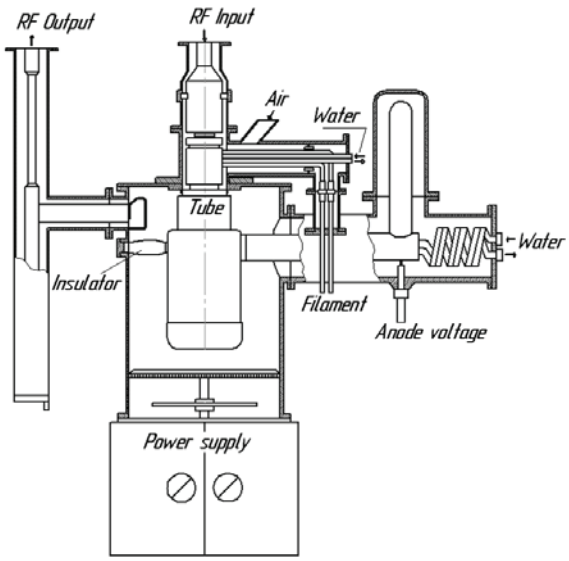

Figure 3: Design of the final stage.

MODULATOR

A high-power voltage modulator was designed to supply the anode of GI-27AM triode. The block diagram of the modulator is shown in Figure 4. A high-voltage power supply HCP700-6500 sets the voltage of the pulse-forming network in the range from hundreds volts to 6,5 kV with accuracy of 0,1%. A bank of 10 thyristor TB -143 -400- 12 in series forms a high voltage switch.

Control of modulator is carried out both in local and remote mode by programmable logic controller via Ethernet.

All components of the modulator are placed in a metallic cabinet with dimensions of 1600 × 1800 × 600 cm. The main obtained modulator parameters are given in Table 1.

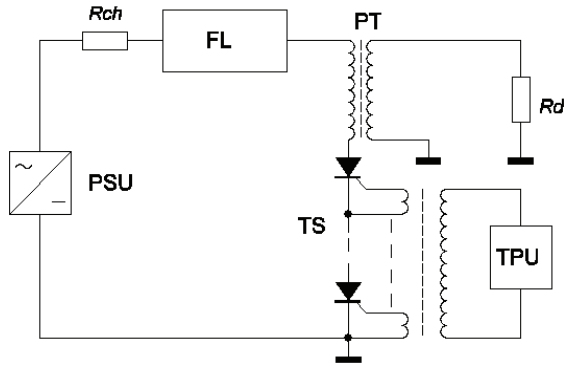

Figure 4: Block diagram of modulator. PSU - high-voltage power supply unit, FL - forming line, PT- pulse transformer, Rch- charging resistor, Rd- dummy load, TPU – trigger-pulse unit.

Table 1: Parameters of Modulator

Pulse power	800 кW
Variation ranging of output voltage amplitude	0-18 kV
Pulse duration by base	150 μs
Amplitude pulse duration	70 μs
Pulse top drop	<1,5%
Amplitude instability	< 1%
Pulse repetition frequency	1Hz
Supply voltage	220V±5%
Power consumption	2 кW

RESALTS

Two methods were used to measure the RF power at RF units. In the first method, the absorbed power meter was used. It implements the method of peak voltmeter [4].

In the second method, RF power was directed to the equal load. The pick voltmeter measured the signal from directional coupler installed at the load. The difference in the power measured by two methods is within the error of the instrument. Output power of the final stage during operation on dummy load is equal to 430 kW at an efficiency of 65%.The main parameters obtained for RF system are given in Table 2.

Table 2. Main Parameters of RF System

Operating frequency	145,2 MHz
Pulse length	150 μs
Pulse repetition rate	1p/sec
Peak output power	430 kW
Peak output power of preamplifier	50kW
Anode voltage on the final stage	18kV

Cold measurements of RFQ resonator results:

ISBN 978-3-95450-181-6

- unloaded quality factor Qo=5200,
- loaded quality factor Ql=2550,
- operational resonant frequency f=145,2 MHz.
- The amplitude of the fields in the four chambers of the RFQ resonator differ each other by less 2%.

First test of RFQ with high power were carried out in ITEP. High power test was started under of $5{,}6 \cdot 10^{-5}$ Pa. The level of input power was measured by the reflectometers installed at the output terminal loops of the final unit. The power required for the acceleration of ions with Z/M = 0.3 was achieved in one month of commissioning.

The beam test was carried in JINR in Dubna. The RFQ and RF power supply were moved and installed in the experimental hall of LU-20 (Figure 5 and 6). In one week after the start of pumping the designed RF power was delivered to the RFQ. The measured result of the RF power into RFQ versus charging voltage on modulator is given in Figure 7.

The successful commissioning of the RFQ and RF power supply was carried out with deuterium and C^+ ion beams.

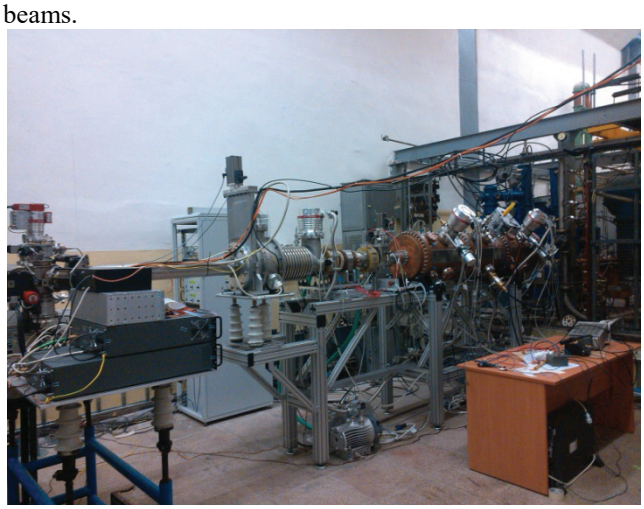

Figure 5: RFQ in experimental hall for commissioning.

Figure 6: RF power system mounted in JINR.

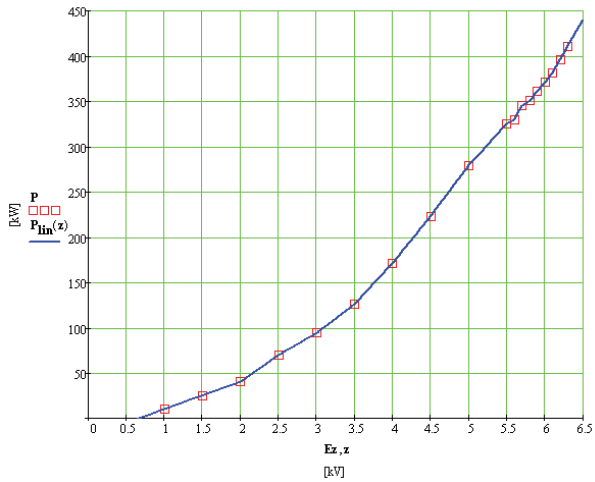

Figure 7: The RF power delivered into RFQ (P) versus charging voltage of modulator (Ez)

CONCLUSION

The RF power system developed in ITEP for new RFQ provided the successful acceleration of C^{4+} ion beam during commissioning. The required power was delivered to RFQ in one week after all system (both RFQ and RF power) was moved to JINR in Dubna and assembled at the test point (Figure 6). The successful result of RFQ test enables the replacement of old electrostatic injector by the RFQ and its commissioning with deuterium ion beam as a part of Nuclotron facility. The test turn of Nuclotron with RFQ was carried out successfully on May-June 2016.

REFERENCES

[1] A.A.Butenko, A.I. Govorov, D.E.Donets, E.D.Donets, E.E. Donets, K.A.Levterov, V.A.Monchinski, S.A. Sidorin, G.V.Trubnikov, V.V.Fimushkin. Modernization of the injection complex nuclotron // Particles and Nuclei, Letters, 2012. T. 9, № 4-5 (174-175), ss. 654-665. http://www1.jinr.ru/Pepan_letters/panl_2012_4-5/17_but.pdf

[2] A.M. Raskopin, A.M. Kozodaev, V.G. Kuz'michev, V.G. Tsar`kov. "The experience of the use GI-39B triode in the mode of increased average power." // XVIII Russian Conference on Charged Particle Accelerators. RUPAC- 2002 , October 1-4 , Obninsk.

[3] B.P.Murin, V.G. Kuhlman, L.G.Lomize, B.I. Polyakov, A.P. Fedotov. Linear accelerators ions. V.2 . Basic systems. Oxford: Clarendon Press, 1978.320 p.

[4] M.I. Bil`ko, A.K. Tomashevski. Measurement of power at microwave frequencies. - 2nd ed, Rev. and add. - M.: Radio and Communications, 1986.

ISBN 978-3-95450-181-6

S-BAND CHOKE MODE CAVITY FOR LOW ENERGY STORAGE RING

L.Yu. Ovchinnikova, V.I. Shvedunov, Skobeltsyn Institute of Nuclear Physics, Lomonosov Moscow State University, Laboratory of Electron Accelerators MSU, Moscow, Russia
A.D. Ryabov, Institute of High Energy Physics, Protvino, Russia

Abstract

Several variants of a low-energy storage ring for Thomson scattering X-ray source were considered in [1]. The most promising variant "C" of the ring with small dimensions and large dynamic aperture has also large momentum compaction factor, which would lead to too long bunches with RF cavity operating at 714 MHz, so shorter wavelength must be used. In this paper we present results of optimization of S-band double-cells cavity with parasitic mode damping by chokes similar to [2]. Interaction of the bunch circulating in the ring with cavity parasitic modes is simulated.

INTRODUCTION

Thomson scattering of laser photons on relativistic electrons enables generating monochromatic X-radiation with adjustable energy. High average intensity of radiation can be achieved through higher collision frequency of photon and electron bunches with small cross-sectional dimensions at the interaction point. High collision frequency is achieved through circulation of electron bunches in compact storage ring. Four variants of Thomson generator ring with electron energy of ~50 MeV and bunch charge of ~1 nC are presented in publication [1]. For further consideration, we selected option C with the largest dynamic aperture and smallest dimensions. A modified variant of the ring is given in Fig. 1, and its characteristics are given in Table 1.

Distinct feature of this variant is large value of the momentum compaction factor, which along with other parameters determines RMS length of the bunch circulating in the ring:

$$\Delta l_{rms} = \frac{\Delta p_{rms}}{p_s}\sqrt{\frac{cL\alpha\, E_s}{2\pi f_{RF} e V_{RF}\cos\varphi_s}}, \qquad (1)$$

where Δp_{rms} is the RMS momentum spread, and other designations are given in Table 1. To ensure acceptable length of the bunch, we increased operating frequency of the RF cavity from 714 MHz [3] to the frequency of the injector of 2,856 MHz [4]. For the ring parameters given in Table 1, such modification results in the following ratio of the bunch length and momentum spread: $\Delta l_{rms} \approx 1.75\frac{\Delta p_{rms}}{p_s}$ (m). It should be noted that such high operating frequency of the cavity was also used in the MIT-Bates storage ring [5].

In the process of the RF cavity optimization and choice of its design, a number of problems must be solved, the most significant ones being suppression of the higher order modes (HOM) and increasing of the cavity efficiency. To solve the above problems, we analyze two variants of the RF cavity: cavity with removal of the HOMs into the beam pipe which walls are covered by RF absorbing material (see e.g. [5]); and cavity with a choke suggested in [2] that has little impact on the operating mode, but ensures absorption of the HOMs.

Table 1: Storage Ring Parameters

Parameter	Value
Operating frequency of the RF cavity, f_{RF}	2856 MHz
Frequency of bunch circulation, f_0	35.7 MHz
Orbit length, L	8.397 m
Momentum compaction factor, α	0.13
RF voltage, V_{RF}	300 kV
Synchronous particle momentum, p_s	50.5 MeV/s
Synchronous phase, φ_s	0^0
Bunch charge, q_B	1 nC
Number of bunches at orbit, M	1
Bunch replacement period, τ_{ch}	20 ms
Average beam current, I_b	35.7 mA
Synchrotron tune, Q_s	0.05
β –function at cavity position,	2/2 m
Betatron tunes, Q_x / Q_y	2.7 / 1.8

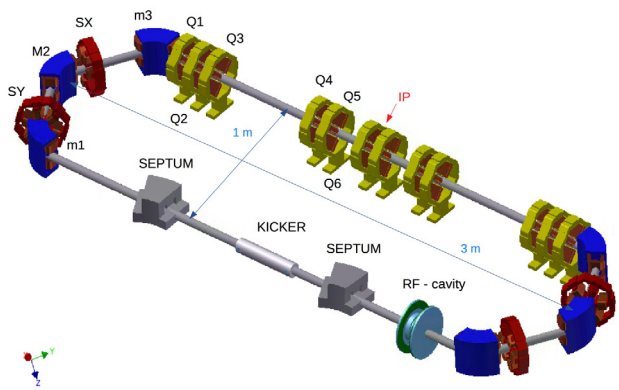

Figure 1: Storage ring layout.

HOMS SUPPRESSION CRITERION

Electron bunches circulating in the ring excite HOMs of the cavity, subsequent interaction with which at certain values of the beam current can result in two types of instability, longitudinal and transversal. In case of Thomson generator with low energy of the circulating beam (35 – 50 MeV), emittance growth due to intrabeam scattering effect stipulates the need to replace bunches in the ring with the period of τ_{ch} ≈20 ms, which is much shorter than the dumping time due to synchrotron radiation, the value of which at such low energy is > 1 s. As such, stable motion of bunches in the ring is determined by the condition that

ISBN 978-3-95450-181-6

time constant of the HOMs field amplitude growth is greater than τ_{ch}.

Based on publications [6-8], time constants for developing longitudinal ($\tau_{\parallel}$) and transverse ($\tau_{x,y}$) coupled bunch instabilities can be determined as follows:

$$\frac{1}{\tau_{\parallel}} \approx \frac{\alpha I_b}{2Q_s p_s} f_k^L R_{\parallel}(f_k^L) \quad (2)$$

$$\frac{1}{\tau_{x,y}} \approx \frac{\beta_{x,y} I_b f_0}{2p_s} R_{x,y}(f_k^{x,y}) \quad (3)$$

where f_k^L and $f_k^{x,y}$ are longitudinal and transverse harmonics of beam current: $f_k^L = (k + Q_s)f_0$, $f_k^{x,y} = (k + Q_{x,y})f_0$, k=1,2,…, $R_{\parallel}(f_k^L)$ and $R_{x,y}(f_k^{x,y})$ are values of longitudinal and transverse HOMs shunt impedance at the beam current harmonic frequencies:

$$R_{\parallel}(f_k^L) \approx \frac{R_{\parallel}(f_{HOM}^L)}{1+(2Q_{HOM}^L \delta_k^L)^2} \quad (4)$$

$$R_{x,y}(f_k^{x,y}) \approx \frac{R_{x,y}(f_{HOM}^{x,y})}{1+(2Q_{HOM}^{x,y} \delta_k^{x,y})^2} \quad (5)$$

$f_{HOM}^{L,x,y}$ are frequencies of longitudinal and transverse HOMs, $Q_{HOM}^{L,x,y}$ is their loaded quality factor, $\delta_k^{L,x,y}$, is their relative detuning: $\delta_k^{L,x,y} = (f_{HOM}^{L,x,y} - f_k^{L,x,y})/f_{HOM}^{L,x,y}$. Other designations are given in Table 1.

Using ring parameters from Table 1, we determine longitudinal and transverse stability criteria:

$$f_k^L R_{\parallel}(f_k^L) < 0.05 \text{ MHz×MΩ}, \quad (6)$$

$$R_{x,y}(f_k^{x,y}) < 2 \text{ kΩ /m}, \quad (7)$$

which should be met at beam current harmonic frequencies for all HOMs.

RF CAVITY WITH LARGE BEAM PIPE

Fig. 2 shows geometry of the cavity with large beam aperture (similar to [5]), which ensures coupling out of HOMs from the cavity. Covering of the beam pipe walls by material with high RF energy absorption coefficient ensures compliance with conditions (6), (7).

Calculations of frequencies, Q and shunt resistance values of the cavity modes were done using CST Microwave Studio code [9]. Electric wall type boundary conditions were set at the ends of the beam pipe.

The final variant of the geometry has two longitudinal and one dipole potentially dangerous modes, frequencies of which are lower than the critical frequencies of the beam pipe: 4.4 GHz for TE-waves, and 5.74 GHz for TM-waves. Presence of absorber ensures compliance with conditions (6) and (7) for these modes.

As a result of optimization, RF cavity geometry with removal of HOMs into the beam pipe was found. For the operating mode, the calculated shunt impedance is 1.6 MΩ, and Q is 16,500. To achieve design effective RF voltage of 300 kV at the gap, average RF power loss in the walls reaches ~56 kW. Removal of heat loss of such high level without substantial changes of electrodynamic characteristics of the cavity does not seem possible, moreover so high RF power consumption would drastically decrease the X-ray source efficiency.

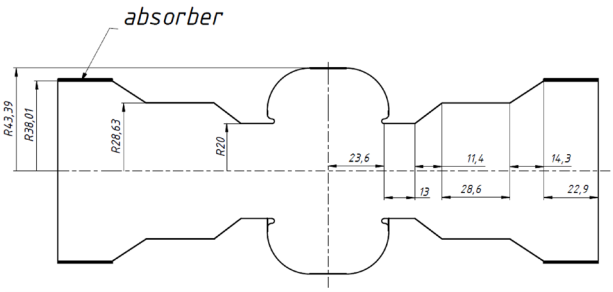

Figure 2: Geometry of the RF cavity with large diameter of the beam aperture.

RF CAVITY WITH SELECTIVE LOAD

Design of the RF cavity with a choke that has a little impact on characteristics of the operating mode, but allows to lower Q of the HOMs through use of the absorber located near the choke was proposes in [2]. The beam aperture ensuring high shunt impedance of the operating mode can be chosen for such cavity.

With the beam aperture of 10 mm the calculated shunt impedance of the operating mode is 3.8 MΩ, and Q is 14,000. So RF power losses of 24 kW are required to achieve RF voltage of 300 kV at the gap. Since there is sufficient free space in the ring design, to lower dissipated power we install two RF cavities with voltage of 150 kV at each gap. Cavities are fed from a single klystron via a 3-dB coupler, which permits to operate klystron without ferrite isolator. The proper phase difference between RF cavities field is achieved by choice of the distance between cavities. RF power consumption in proposed scheme is decreased to 12 kW.

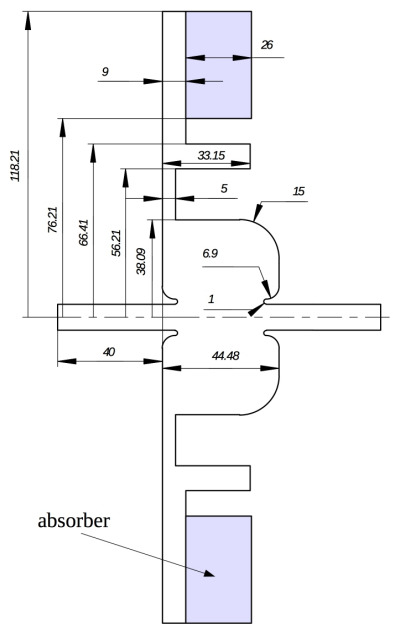

Figure 3: Geometry of cavity with a choke.

ISBN 978-3-95450-181-6

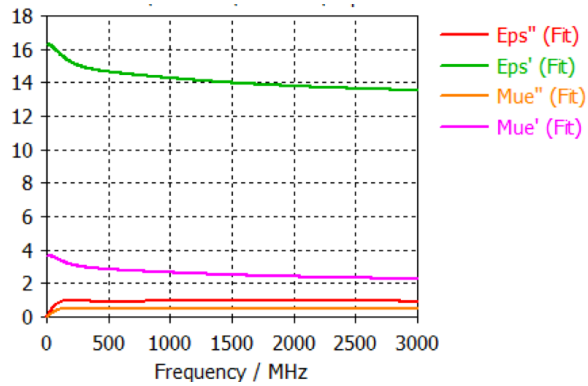

Figure 4: Characteristics of absorbing material.

Choke optimization allowed to lower Q of the HOMs through transmission of their energy to the absorber, which was considered to be a dielectric with characteristics shown in Fig. 4 [10]. Calculations demonstrated that decrease of Q of the operating mode due to presence of the absorber does not exceed 3-4%. Fig. 5 shows time constants of different cavity modes $\tau = \frac{Q}{2\pi f}$ with and without absorber. It is seen that for most HOMs, time constant is an order of magnitude lower than a bunch circulation period in the ring, which is 28 ns. Therefore, presence of such modes will not result in coupled bunch instability. Fig. 5 shows two modes with time constant exceeding the bunch circulation time. The first is the operating mode; the second one is the quadrupole mode, which is not dangerous.

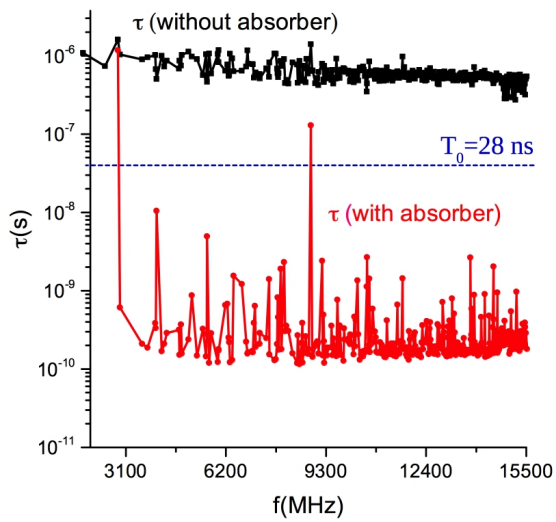

Figure 5: Dependence of cavity modes time constant on frequency without (black curve) and with absorber (red curve).

CONCLUSION

The study resulted in proposing two variants of the RF cavity for the storage ring of the X-ray Thomson generator free from dangerous longitudinal and lateral modes. From standpoint of minimum power requirements, the optimum variant is the RF cavity with selective load.

REFERENCES

[1] L. Ovchinnikova, V. Shvedunov, A. Mikhailichenko, E. Bessonov, and M. Gorbunkov. A comparative study of low energy compact storage rings for a Thomson scattering x-ray source. *Proc. of IPAC-16, 2016*, pp. 3308-3310.

[2] T. Shintake, The Choke Mode Cavity, Jpn. J. Appl. Phys, Vol. 31,1992, pp. L1567-L1570, No. 1lA.

[3] L. Ovchinnikova, V. Shvedunov, A. Ryabov. Optimization of the RF Cavity of a Low-Energy Storage Ring for Thomson Scattering X-Ray Source. *Proc. of IPAC-16, 2016*, pp. 438-440.

[4] I.Yu. Vladimirov, B.S. Ishkhanov, L.Yu. Ovchinnikova, V.I. Shvedunov, and D.S. Yurov. A High-Intensity Electron-Beam Source. Moscow University Physics Bulletin, 2016, Vol. 71, No. 3, pp. 245–252.

[5] M.S. de Jong, F.P. Adams, R.J. Burton, R.M. Hutcheon, T. Tran-Ngoc, A. Zolfaghari, P. . Demos, A 2856 MHz RF Cavity for the MIT-Bates South Hall Ring, In Proc. PAC 1993, pp. 832-834.

[6] F.J. Sacherer, A longitudinal stability criterion for bunched beams, in Proc. PAC 1973, pp. 825-827.

[7] F. Pedersen, Multibunch instability, CERN/PS 93-36 (RF)

[8] A. Fabris, C. Pasotti, M. Svandrlik, Coupled bunch instability calculations for the ANKA storage ring, In Proc. EPAC 1998, pp. 1011-1013

[9] CST, http://www.cst.com

[10] Young Joon An, Ken Nishida, Takashi Yamamoto, Shunkichi Ueda, Takesh Deguchi, Microwave absorber properties of magnetic and dielectric composite material, Electronics and Communications in Japan, Vol. 93, No. 4, 2010, pp. 441-448

ISBN 978-3-95450-181-6

HIGH-ENERGY MICRO-BUNCHER BASED ON THE MM-WAVELENGTH DIELECTRIC STRUCTURE

I. Sheinman*, Saint Petersburg Electrotechnical University
A. Petrenko, CERN, Geneva, Switzerland

Abstract

The proton-driven plasma wakefield acceleration is a recently proposed technique promising a GeV/m rate of acceleration to a TeV-scale energy in a single plasma stage. In order to excite high-amplitude plasma wakefields a long proton bunch from a synchrotron should be broken into a sequence of sub-mm long micro-bunches which can drive the plasma oscillations resonantly. We suggest a novel approach to produce the required train of micro-bunches using collinear wakefield acceleration in a dielectric-loaded structures. First the energy modulation is introduced into the proton beam with the help of the mm-wavelength dielectric accelerating structure. Then the energy modulation is transformed into the longitudinal micro-bunching using proton beamline with magnetic dipoles. Beam dynamics simulations were used to find the appropriate parameters of the dielectric accelerating structure, driving electron bunch and the beam focusing system.

INTRODUCTION

Hadron beams in high-energy synchrotrons provide the highest-energy particles available in laboratories today. Synchrotrons also hold the record for the maximum total energy stored in the beam. For example, both rings of the Large Hadron Collider currently operate at 6.5 TeV with 2200 bunches of $1.1 \cdot 10^{11}$ protons each. This beam has the total energy of 250 MJ which is equivalent to the kinetic energy of a typical fully-loaded airliner (80 t) at the take-off speed of 300 km/h (280 MJ). Even the single bunch ($3 \cdot 10^{11}$ protons at 400 GeV) in the 40 year old Super Proton Synchrotron (SPS) at CERN carries an order of magnitude more energy than the single bunch in the proposed International Linear Collider ($2 \cdot 10^{10}$ electrons or positrons at 250 GeV). Several techniques have been suggested to transfer a fraction of the proton beam energy to other particles which cannot be accelerated in a circular machine either because of the prohibitively high energy loss due to the synchrotron radiation (electrons/positrons) or because of the short life-time of the unstable particles (muons, pions) [1–3]. Such accelerated particles can be used for instance in the collider experiments which do not require high luminosity [4]. The proton-driven plasma wakefield acceleration [3] is the recently proposed method promising a GeV/m rate of acceleration to a TeV-scale energy in a single plasma stage. GV/m plasma wakefields correspond to the plasma wavelength of around 1 mm, while proton bunch in a typical synchrotron is several tens of cm long. In order to excite high-amplitude plasma wakefields the proton bunch should be either compressed longitudinally by a large factor [2, 3] (which is technically very challenging) or the single proton bunch should be broken into the sequence of sub-mm long micro-bunches which can drive the plasma oscillations resonantly. The Self-Modulation Instability (SMI) of a long proton beam in plasma has been suggested as a convenient way to create such a resonant sequence of micro-bunches [5]. The feasibility of this technique will be tested in the forthcoming AWAKE experiment at CERN [6]. However the efficiency of the SMI is low since the majority of protons are lost from the beam during the development of this instability. In this article we propose a more efficient alternative approach to create the sequence of sub-mm long proton micro-bunches via the longitudinal bunching process first described in the "proton klystron" proposal [1]. We rescale it down to the mm-wavelength using the collinear wakefield acceleration in the dielectric-loaded structures. A resulting train of sub-mm proton micro-bunches could be useful not only for the plasma wakefield acceleration but also as a powerful source of mm-wavelength radiation or as a driver for the similar dielectric accelerator.

GENERAL DESCRIPTION OF THE METHOD

The basic idea of the proposed scheme is shown in Figure 1 [7]. First the energy modulation is introduced into the proton beam with the help of a mm-wavelength accelerating structure. Then the energy modulation is transformed into the longitudinal micro-bunching using the beamline with magnetic dipoles. Proton path length inside the dipoles linearly depends on the proton momentum therefore the energy modulation is transformed into the longitudinal micro-bunching. The 400 GeV SPS proton beam used here as an example has the energy spread $\sigma_{\Delta E} = 120$ MeV (the relative value $\sigma_{\Delta E/E} = 0.03\%$). In order to produce micro-bunching suitable for the plasma wakefield acceleration the energy modulation introduced by the mm-wavelength accelerating structure should be several times larger than the uncorrelated energy spread of the incoming proton beam, – we take ±500 MeV as a typical value. The dielectric wakefield acceleration is based on excitation of electromagnetic wave with a longitudinal component of electric field by a high-current electron bunch in the vacuum channel of a dielectric wave guide. The proton beam will pass the dielectric channel behind the electron bunch. At a typical field of 100—150 MV/m the required ±500 MeV energy modulation can be obtained in 3—5 m. Since the length of the proton beam is much larger than the wavelength the wakefield should be excited in a single mode. It's important to note that the

* ishejnman@yandex.ru

ISBN 978-3-95450-181-6

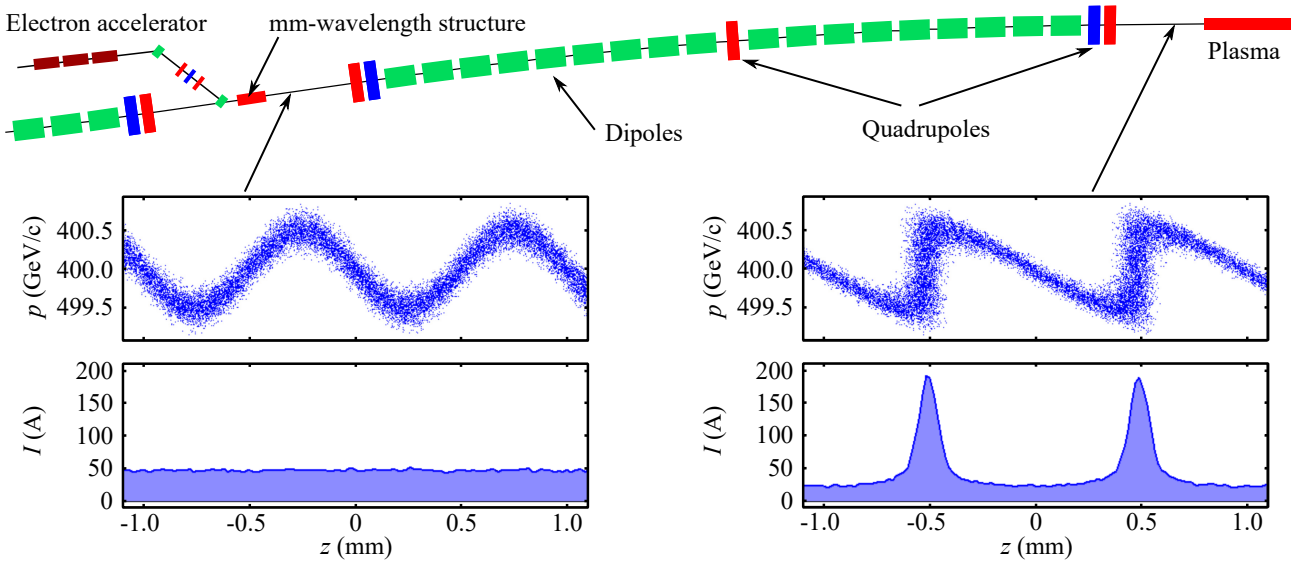

Figure 1: General layout of the proposed micro-bunching system. Proton beam current and proton momentum modulation along the beam are shown before and after the achromat. The realistic proton beam is much longer ($\sigma_z = 5 - 10$ cm) and it can produce around 100 of such micro-bunches.

proton beam does not extract energy from the wakefield in our case (i.e the wakefield is not loaded) – the energy is just redistributed within the proton beam.

THE DIELECTRIC ACCELERATING STRUCTURE

Waveguide parameters and self-consistent beam dynamics calculations were carried out in the DynPart code [9, 10]. For creation of a wakefield with the required parameters (the basic frequency of 300 GHz, electric field above 100 MV/m, we use a dielectric waveguide with an internal radius of vacuum channel $R_c = 1$ mm, dielectric permittivity $\epsilon = 3.75$ (quartz). The external radius of dielectric $R_w = 1.061$ mm, thickness of dielectric $d = 0.061$ mm. Dielectric thickness with the given frequency depends on waveguide radius (in case of $R_c = 2$ mm $d = 0.0334$ mm). Radius of the waveguide defines the amplitude of the wakefield in case of the given value of electron bunch charge and its length. We will consider a Gaussian electron bunch. Length of the bunch defines the spectrum of the excited field. Increase in bunch length leads to lower generated wakefield and, at the same time, to exponential suppression of high-frequency modes of the waveguide. Reduction of the bunch length leads to higher generated wakefield, but, at the same time, to increase in quantity of the excited waveguide modes. As a result, character of the field becomes non-uniform in amplitude. In this regard, we will select such a minimum length of the bunch which provides the maximum amplitude, but excites almost pure single-mode of the wakefield. Achieving 100 MV/m amplitude wakefield in the waveguide with $R_c = 1$ mm and length $L = 5$ m requires electron beam charge $Q = 5$ nC and energy $W_0 = 600$ MeV. The mean squared length of the bunch which meets the requirements described above is $\sigma_z = 0.1$ mm.

The initial transverse parameters of electron bunch are defined by its transverse dynamics in the dielectric waveguide. The field generated by the electron bunch affects both electron and proton beams. If electron bunch is slightly shifted from the waveguide axis the transverse component of the wakefield can reach significant values, leading to electron beam defocusing and loss due to the beam break-up instability. To keep the intense electron bunch on-axis the strong quadrupole focusing is required. The value of the focusing magnetic field for not superconducting ("warm") magnets on waveguide border, as a rule, doesn't exceed $B_0 = 1.5$ T, which we will use in these calculations. For the fixed magnetic field gradient inside the quadrupoles the maximum travel distance for the electron bunch is determined by the initial shift of the bunch from the axis as well as the length of the focusing section. There is an optimum length of the focusing section (i.e. the optimum average beta-function of the quadrupole channel). We will select the transverse size of the electron bunch $\sigma_x = \sigma_y = 0.05$ mm. The typical required beta-function of the quadrupole focusing channel is $\sim$ 10 cm meaning that the maximum normalized emittance of the matched beam $\epsilon_{nx} = \gamma\sigma_x^2/\beta_x \sim 1200 \cdot (0.05\text{ mm})^2/100\text{ mm} = 30\text{ mm}\cdot\text{mrad}$ which is around 10 times higher than the typical electron beam emittance produced by photo-injectors. This means that significant emittance blow-up in the electron bunch compression system can be tolerated.

The best electron beam transfer is achieved in our simulations with 11 cm long FODO period, while the length of every quadrupole is 4.7 cm. The magnetic field at the pole of the first quadrupole is 1.5 T. The strength of the following quadrupoles is decreasing proportional to the energy of electrons in the middle of the bunch.

ISBN 978-3-95450-181-6

The simulation is terminated as soon as the first electron beam macro-particle reaches the waveguide wall. The 5 m propagation of the driver bunch was reached for the initial 0.03 mm offset of the electron beam with respect to the waveguide axis. In this case electrons from the middle part of the drive bunch are decelerated by 450 MeV down from the initial energy of 600 MeV. In this case the maximum energy modulation is ±670 MeV in the proton beam. The initial transverse offset of 0.1 mm limits the electron beam propagation distance to 2.4 m with a corresponding energy spread in the proton beam reaching ±340 MeV.

It's important to note that the proton beam emittance is not distorted significantly by the transverse wakefields excited in the dielectric channel due to initial electron beam offset from the axis. The normalized proton beam emittance increases only by 0.2 mm · mrad (10% of the typical ϵ_n) after the dielectric section.

THE PROTON BEAMLINE

The typical normalized emittance of the proton beam extracted from the SPS is around 2 mm · mrad [8]. Taking a typical value of the proton beam beta-function equal to the length of the dielectric section (5 m) this corresponds to the transverse beam size $\sigma_x = \sqrt{\beta_x \epsilon_{nx}/\gamma} = \sqrt{5000\text{ mm} \cdot 2\text{ mm} \cdot \text{mrad}/400} = 0.16$ mm which gives us a 6 sigma aperture for the proton beam transport through the dielectric channel.

In order to transform the proton beam energy modulation into the micro-bunching and focus the beam before plasma some kind of achromatic bending system can be used. The path length difference of particles with momentum spread Δp is given by

$$\Delta z = \frac{\Delta p}{p} \int_L \frac{D(s)}{\rho(s)} ds, \qquad (1)$$

where D is the dispersion function, ρ is the bending radius. Therefore the required length of the achromat L is defined only by the value of dispersion function inside the dipoles. This value can't be too high since the dispersion-induced beam size $D\Delta p/p$ is limited by the aperture of quadrupoles and dipoles. The required energy modulation is around ±500 MeV and for the 400 GeV beam this corresponds to $\Delta p/p = \pm 1.3 \cdot 10^{-3}$. The aperture of quadrupoles used in the SPS-AWAKE transport line TT41 is 4 cm. In this case the dispersion function can't be larger than $2\text{ cm}/1.3 \cdot 10^{-3} = 15$ m.

Consider the simplest symmetric achromat with one quadrupole in the middle (as shown in Figure 1). The dispersion function before the quadrupole grows as $D(s) = [1 - \cos(s/\rho)]\rho$. The integral in Eq. 1

$$\int_L \frac{D}{\rho} ds = 2 \int_0^{L_d} \left[1 - \cos\left(\frac{s}{\rho}\right)\right] ds \approx \frac{\rho}{3}\left(\frac{L_d}{\rho}\right)^3, \qquad (2)$$

where L_d is the length of each of the two dipoles in this achromat ($L_d \ll \rho$). Assuming the momentum modulation along the proton beam after the dielectric section

$$p(z) = p_0 + \Delta p \sin(2\pi z/\lambda_{\text{rf}}), \qquad (3)$$

Eq. 1 and Eq. 2 can be used to find the required L_d:

$$L_d \approx \rho \sqrt[3]{\frac{3p}{\rho}\left(\frac{\mathrm{d}p}{\mathrm{d}z}\right)^{-1}_{\max}} = \rho \sqrt[3]{\frac{3p}{\rho}\left(2\pi\frac{\Delta p}{\lambda_{\text{rf}}}\right)^{-1}} \approx$$
$$\approx (790\text{ m}) \sqrt[3]{\frac{3}{790\text{ m}}\left(2\pi\frac{1.3 \cdot 10^{-3}}{1\text{ mm}}\right)^{-1}} \approx 60\text{ m}. \qquad (4)$$

And the full length of the achromat will be close to $2L_d$ = 120 m (15% of the TT41 beamline total length). The maximum value of the dispersion function

$$D_{\max} = \left[1 - \cos\left(\frac{L_d}{\rho}\right)\right]\rho \approx \frac{\rho}{2}\left(\frac{L_d}{\rho}\right)^2 \approx 2.2\text{ m}, \qquad (5)$$

which is below the maximum dispersion function (3 m) in the existing beamline and well below the aperture defined limit of 15 m (i.e. with more complicated achromat optics its length can be reduced). The required proton optics with low-beta insertion followed by the achromat seems possible to implement by rearranging dipoles and quadrupoles in the existing beamline.

CONCLUSIONS

We suggested a novel approach to produce the long train of high-energy proton micro-bunches using the mm-wavelength dielectric-loaded structure.

For the considered example case of the 400 GeV proton beam from the CERN SPS the requirements on electron drive beam parameters seem to be rather challenging. Such electron beams are normally produced for the soft X-ray Free Electron Lasers and require too much infrastructure investment to be considered for the AWAKE experiment now. Still such option can be very interesting for some eventual application of the proton-driven acceleration using the LHC proton beam for example.

The efficiency of electron driver can probably be improved significantly. The mm-wavelength accelerator parameters obtained in our studies are very similar to the Argonne proposal of the dielectric-based high-repetition FEL [11, 12]. However the transverse electron beam dynamics in our case is more relaxed since the required propagation length of the electron beam is many times shorter. Using the drive beam shaped similar to the FEL proposal it should be possible to reduce the electron beam energy well below 600 MeV assumed in this article.

Some kind of longitudinal proton beam cooling at high-energy (e.g. optical stochastic cooling) can reduce the random energy spread in the proton beam, so that the required mm-wavelength energy modulation can be reduced also.

ACKNOWLEDGMENTS

Authors thank Y. Sheinman and A. Yakushkin for the help in the development of the DynPart program interface and discussion of the obtained results.

ISBN 978-3-95450-181-6

REFERENCES

[1] E.A. Perevedentsev, A.N. Skrinsky, On possibility of using intense beams of large proton accelerators for excitation of linear accelerating structures, Proceedings of VI National Accelerator Meeting, Dubna, 1978; Preprint INP 79-80, Novosibirsk, 1979.

[2] V.E. Balakin, A.V. Novokhatsky, The method of accelerating electrons with maximum high gradient by a proton beam; Preprint INP 79–86, Novosibirsk, 1979.

[3] A. Caldwell, K. Lotov, A. Pukhov, and F. Simon, Proton-Driven Plasma-Wakefield Acceleration. Nature Phys. 5, 363 (2009).

[4] A. Caldwell. Collider physics at high energies and low luminosities. Eur. Phys. J. Spec. Top. (2014) 223: 1139.

[5] N. Kumar, A. Pukhov and K. Lotov, Self-Modulation Instability of a Long Proton Bunch in Plasmas. Phys. Rev. Lett. 104 255003 (2010).

[6] R. Assmann et al. (AWAKE Collaboration), Proton-driven plasma wakefield acceleration: a path to the future of high-energy particle physics. Plasma Phys. Control. Fusion 56, 084013 (2014).

[7] A. Petrenko. Proton beam micro-bunching using mm-wavelength accelerators, AWAKE Collaboration Meeting in Lisbon (2016). http://indico.cern.ch/event/484032/contributions/2002139

[8] H. Timko et al., Short High-Intensity Bunches for Plasma Wakefield Experiment AWAKE in the CERN SPS // Proceedings of IPAC'2013, Shanghai, China.

[9] I. Sheynman, A. Kanareykin, G. Sotnikov. Numerical and Analytical Methods of Modeling of Bunch Dynamics in Dielectric Filled Accelerating Structures // Proceedings Russian Particle Accelerator Conference (RuPAC-2012), MOPPA010. Saint-Petersburg, Russia, pp. 266-268. 2012.

[10] I. Sheinman, P. Kirilin. Code development for calculation of self-coordinated beam dynamics in dielectric wakefield accelerators // Proceedings of 20th International Workshop on Beam Dynamics and Optimization (BDO), Combined Conferences IVESC-ICEE-ICCTPEA-BDO'2014, W-BDO-7. Saint-Petersburg, Russia. pp. 245-247. 2014.

[11] A. Zholents et al. A Collinear Wakefield Accelerator for a High Repetition Rate Multi Beamline Soft X-Ray FEL Facility. Proceedings of FEL'2014 conference, Basel, Switzerland.

[12] A. Zholents et al. A preliminary design of the collinear dielectric wakefield accelerator. Nuclear Instruments and Methods in Physics Research A 829 (2016).

ISBN 978-3-95450-181-6

SOFTWARE COMPLEX "DYNPART" FOR THE CALCULATION OF SELF-CONSISTENT BEAM DYNAMICS IN DIELECTRIC WAKEFIELD ACCELERATING STRUCTURES

I. L. Sheinman*, A. E. Yakushkin,
Saint-Petersburg Electro-Technical University «LETI», Saint-Petersburg, Russia

Abstract

Dielectric waveguide structures are a basis for development of new generation of accelerators on the basis of a wakefield method of the charged particle acceleration, beam manipulation, and also free electron lasers. A self-coordinated dynamics of relativistic particle beams in a single layer cylindrical waveguide with dielectric filling is investigated. The computer code is developed based on mathematical expressions for the analysis of the radial dynamics. The possibility of modelling interaction of different types of particles in a bunch is realized. Influence of both own wake fields and external fields of focusing and deflection systems on bunch dynamics is analyzed.

INTRODUCTION

Wakefield acceleration principle is based on a generation by high-current charged particles bunch in the waveguide structure of an electromagnetic wave with a longitudinal component of the electric field up to 100 MV/m. This wake field is used to accelerate a following low-current bunch of high energy. In free electron lasers electromagnetic wave generated by high-current electron bunch is extracted from the waveguide and structure is used as an electromagnetic radiation source.

Dielectric wakefield accelerating structures are single or multilayer dielectric cylindrical waveguides with outer metal covering and vacuum channel along the axis. Along with the longitudinal fields there are transverse fields, leading to bunch deflection from the axis of the waveguide and subsidence of particles on its wall.

Development of new methods of acceleration based on principle of wakefield acceleration, requires a detailed analysis of the self-consistent beam dynamics taking into account both own and external focusing and deflecting fields.

Nowadays, wakefield accelerators often use light particles, electrons, as driving bunch, to generate the wakefield for acceleration of another electron bunch (which is usually called “witness”) like it is organized at AWA/APS accelerator complex in Argonne National Laboratory (USA) [1]. Wakefield acceleration of heavier particles, like protons, is not used because of traditional cyclic accelerators like synchrotrons are more effective for acceleration of heavy particles. Nevertheless wake field generated by driving electron bunch in the wakefield structure can be used for energy modulation of long proton bunch [2].

*isheinman@yandex.ru

At the same time wakefield acceleration with its high acceleration gradient would be promising in case of muons acceleration which can live in their self-reference system only 2.2 μs.

Effectiveness of wakefield acceleration is limited by “Wakefield’s theorem”. In accordance with "Wakefield's theorem" in the accelerator, where the electron bunches move along the same line, in the case of symmetric driving electron bunch accelerated bunch cannot increase its energy more than twice the value of electron energy of the driving bunch. This limit can be overcome by using a proton beam accelerated in synchrotron as a driver and electron or muon bunch as a witness.

SPECIALIZED SOFTWARE

For the analysis of the radial beam dynamics in the accelerating structure, methods of computational experiment are used. Specialized software, like CST Particle Studio [3], has been developed to aid in accelerator modelling; however, these codes based on particle-in-cell solver being universal are rather slow. Some special codes like BBU-3000 developed for self-consistent beam dynamics in wake fields uses numerical methods for differential equation solving. We decided to take a different approach and develop a software complex that uses strict analytic solutions to dynamics equations to calculate particle coordinates [4, 5].

DYNPART SOFTWARE COMPLEX

Analysis of the beam dynamics in the developed software is based on the method of macroparticles. In this method charge distribution function is realized by generating an array of particles with a given distribution in space, and field calculation is organized by summation of field generating of each macroparticle over the array. In case of high-current relativistic beams electrostatic approximation inapplicable to determine the Cherenkov wake field. Our algorithm for calculating wake fields is based on dot charge field expansion in series on waveguide eigenfunctions. That requires for the self-consistent beam dynamics calculation using the "particle – particle" method. The number of operations in this method increases with the square of the number of macroparticles that increases the calculation time and thus imposes restrictions on their accuracy. For accelerating of calculations an analytical solutions of the equations of relativistic dynamics and optimized for calculation speed algorithm for finding wake fields based on expansion on waveguide eigenfunctions were used (Fig. 1).

ISBN 978-3-95450-181-6

Developed software allows to:

1. Calculate of parameters of the cylindrical waveguide with single layer dielectric filling.
2. Simulate dynamics for any number of bunches in waveguide.
3. Solve the self-consistent equation of dynamics in 2D, and 3D models.
4. Choose parameters of alternating-gradient focusing and weak focusing.
5. Observe the transformation of the beam shape when it moves in the waveguide in the process of calculating (Fig. 2).
6. Display the field distribution in the space inside and outside the beam, and construct a vector diagram fields.
7. Identify the flight range to prevent beam touching the waveguide wall.
8. Perform optimization of the parameters of the waveguide and the beam focusing system for maximization of flying range and energy extraction from the beam.
9. Perform parallel computing based on OpenMP for shared memory systems. The result is a substantial increase in performance of about 8 times compared with the linear calculations.

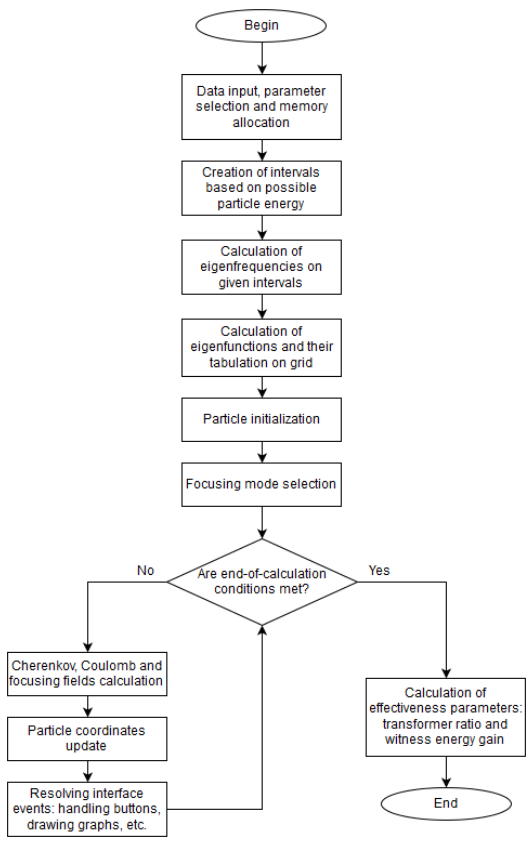

Figure 1. A workflow chart for the primary calculation process of DynPart.

New features and code optimizations

"DynPart" program [6], developed for study of beam dynamics in wakefield accelerating structures, has been revised and expanded to this day. Some parts of the code have been optimized to increase computing speed, and new features were added.

The primary feature of the new version is the ability to calculate beams made of different particles. The beams being studied can now include bunches contain different particles (see Fig. 2). Supported particles are protons, electrons, muons and their antiparticle counterparts.

New graphs are plotted, including the energy distribution within a bunch (see Fig. 3) and phase-space impulse graph.

This expanded functionality allows us to study the wakefield accelerators. Testing data shows to be consistent with real-world results obtained by Argonne National Laboratory, which leads us to the conclusion that the code developed is correct and can be used for further research.

For increasing speed of calculations optimization algorithm for wake fields calculating was developed. On the first step an array of waveguide eigenvalues and eigenfunctions is created, correspondent to different bunches with different types of particles, different charge energies and charge positions. In the course of calculation of bunch dynamics wake fields are found by the choice of an array element corresponding to type, energy and the position of a particle.

Additionally, the code is now based on Cartesian coordinates and uses them to move data between modules; the only conversion to cylindrical coordinates is made within a field calculation module for cylindrical geometry.

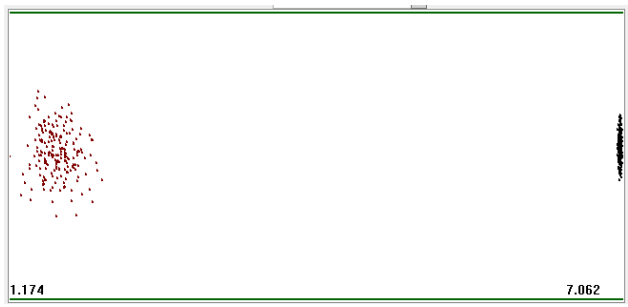

Figure 2. A screenshot illustrating an example simulation of different particles in an accelerator; painted red being the protons, and black – the electrons.

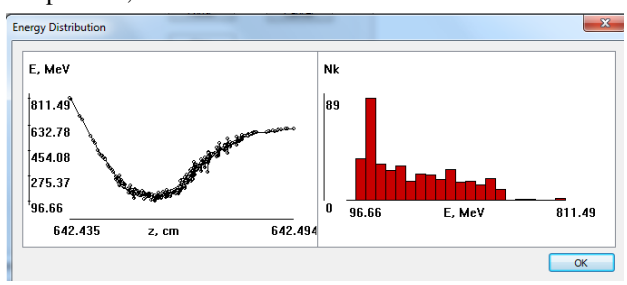

Figure 3. Driver bunch energy distribution

ISBN 978-3-95450-181-6

Perspectives

New code architecture is developed to meet the new requirement of easy expandability. The new architecture is supposed to be modular and, therefore, easily modifiable. We will be able to combine various sequences of wave guides with dielectric filling of different geometry and the focusing and rotary elements. We will also try to perform a platform abstraction – in other words, create a platform-independent program that uses a platform-dependent API for low-level operations. Primary target platforms include Windows and Linux, therefore, using Qt appears reasonable for resolving this task, as it includes features such as platform-independent multithreading and graphics.

DYNPART IN RESEARCH

DynPart code was used for calculation of beam dynamics for Argonne Wakefield Accelerator / Argonne Photon Source (AWA/APS), investigation of interaction of FODO focusing with dielectric loaded wakefield waveguides [1, 4-6]. DynPart code has also been used to calculate of electron driver beam dynamics and creating of appropriate energy modulation for an mm-wavelength proton high energy microbuncher developed in collaboration with CERN AWAKE experimental group [2].

REFERENCES

[1] M.E. Conde et al. “Argonne Wakefield Accelerator (AWA): A Facility for the Development of High Gradient Accelerating Structures and Wakefield Measurements” Proceedings of IPAC’2013, Shanghai, China, May 2013, TUOCB101, pp. 1111-1113 (2013); http://www.JACoW.org.

[2] I. Sheinman, A. Petrenko. High-energy Micro-Buncher Based on the mm-Wavelength Dielectric Structure, TUPSA041, these proceedings.

[3] https://www.cst.com/Products/CSTPS

[4] I. L. Sheinman and A. D. Kanareykin, Technical Physics, 53 (2008) 10, pp. 1350-1356.

[5] I. Sheinman et al., “Numerical and Analytical Methods of Modeling of Bunch Dynamics in Dielectric Filled Accelerating Structures,” Proceedings Russian Particle Accelerator Conference (RuPAC-2012). Saint-Petersburg, Russia, pp. 266-268. 2012.

[6] I. L. Sheinman, P. S. Kirilin. “Code development for calculation of self-coordinated beam dynamics in dielectric wakefield accelerators”. Proceedings of 20th International Workshop on Beam Dynamics and Optimization (BDO), Combined Conferences IVESC-ICEE-ICCTPEA-BDO’2014, W-BDO-7. Saint-Petersburg, Russia. pp. 245-247. 2014.

ISBN 978-3-95450-181-6

WAKE FIELD COMPONENTS IN A RECTANGULAR ACCELERATING STRUCTURE WITH DIELECTRIC ANISOTROPIC LOADING

I. L. Sheinman*, Yu. S. Sheinman,
Saint-Petersburg Electro-Technical University «LETI», Saint-Petersburg, Russia

Abstract

Dielectric lined waveguides are under extensive study as accelerating structures that can be excited by electron beams. Rectangular dielectric structures are used both in proof of principle experiments for new accelerating schemes and for studying the electronic properties of the structure loading material. Some of the materials used for the waveguide loading of accelerating structures possess significant anisotropic properties. General solutions for the fields generated by a relativistic electron beam propagating in a rectangular dielectric waveguide have been derived using the mode expansion method for the transverse operators of the Helmholtz equation. An expression for the combined Cherenkov and Coulomb fields obtained in terms of a superposition of LSM and LSE-modes of rectangular waveguide with anisotropic dielectric loading has been obtained. Numerical modeling of the longitudinal and transverse (deflecting) wake fields has been carried out. It is shown that the dielectric anisotropy influences to excitation parameters of the dielectric-lined waveguide with the anisotropic loading.

INTRODUCTION

Physics of particle accelerator now is on the edge of traditional and new accelerating methods. One of the promising directions is development of linear colliders with high acceleration rate on the base of wakefield accelerating structures. Wakefield waveguide structures can contain plasma or dielectric loading excited by laser, RF source or high current charged beam. Unlike plasma structures, dielectric filled waveguides with vacuum channel provide collisionless transport of the beam [1,2]. The cherenkov accelerating structure is a dielectric waveguide with an axial vacuum channel for beam passing covered by conductive sleeve.

Dielectric wakefield structures provide both high acceleration rate and ensure the control over the frequency spectrum of the structure by introducing additional ferroelectric layers [3] as well as a possibility using of perspective materials with unique properties like diamond and sapphire [4].

The high current short generating bunch (usually called driver) with low energy excites Vavilov-Cherenkov wake field. Generated longitudinal field accelerates a low intensive but higher energy bunch (witness). The witness is placed to a distance behind the driving bunch corresponds to an accelerating phase of the wake field.

As usual, the cylindrical geometry for structures with dielectric filling is proposed. Nevertheless, structures with a rectangular cross section and dielectric filling in some cases are also used [5–14]. Advantage in usage of this geometry is simplification of manufacturing techniques. Such structures (along with cylindrical structures) for generating electromagnetic radiation and producing wakefield acceleration in the frequency range 0.5–1.0 THz are considered [4]. In THz range, the planar geometry can be preferable because of difficulties of precise cylindrical structure manufacture. Rectangular structures can be used for test experiments in analysis of new accelerating systems [14] and for studying the properties of materials effective for producing high acceleration rates and pulsed heating of the structure (diamond, sapphire) [4].

*isheinman@yandex.ru

THEORETICAL ANALYSES OF RECTANGULAR WAVEGUIDE EXCITATION

Let us consider a rectangular waveguide with a symmetric filling in the form of dielectric transversal isotropic layers (2) parallel to the x axis and with a vacuum channel (1) at the centre (Fig. 1).

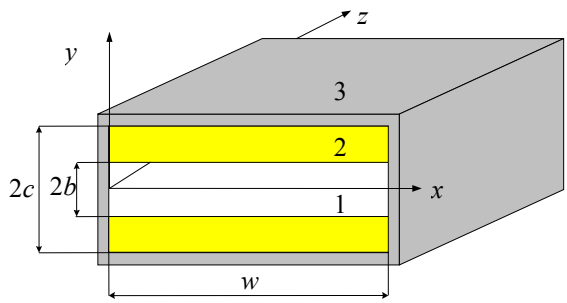

Figure 1: Rectangular waveguide.

In this case, the filling in the direction of the y axis is inhomogeneous, and the permittivity and permeability tensors are functions of y: $\hat{\varepsilon} = \hat{\varepsilon}(y)$ and $\mu = \mu(y)$.

$$\hat{\varepsilon} = \begin{pmatrix} \varepsilon_{\parallel}(y) & 0 & 0 \\ 0 & \varepsilon_{\perp}(y) & 0 \\ 0 & 0 & \varepsilon_{\parallel}(y) \end{pmatrix}, \quad \mu = \begin{pmatrix} \mu_{\parallel}(y) & 0 & 0 \\ 0 & \mu_{\perp}(y) & 0 \\ 0 & 0 & \mu_{\parallel}(y) \end{pmatrix}.$$

Let us transform initial Maxwell equations combined with material relations for this case. Equations give biorthogonality of the eigenfunctions and similarity of the operator to a self adjoint operator [15-16].

Maxwell equations can be transformed to equations for normal to dielectric layer electric and magnetic field components in isotropic [15-16] and anisotropic [17] cases.

ISBN 978-3-95450-181-6

Solutions for all field components are:

$$E_y = \sum_{n,m} \frac{\psi(x,x_0)}{\varepsilon_0} Y_{E_y n,m}(y) Y^*_{Ed}(y_0) \frac{S_{En,m}(\zeta,z_0)}{\sqrt{|\lambda_E|}},$$

$$E_z = -\sum_{n,m}^{\infty} \frac{\psi(x,x_0)}{\varepsilon_0} \left[\frac{G_E(\zeta,z_0) Y_{Ed}(y) Y^*_{Ed}(y_0)}{\left(k_{xn}^2 + \lambda_E\right)} + \right.$$
$$\left. + \frac{k_{xn}^2 \beta^2 G_H(\zeta,z_0) Y_{B_y}(y) Y^*_B(y_0)}{\left(k_{xn}^2 + \lambda_H\right)} \right],$$

$$E_x = \sum_{n,m}^{\infty} \frac{\psi'(x,x_0)}{\varepsilon_0} \left[\frac{S_E(\zeta,z_0) Y_{Ed}(y) Y^*_{Ed}(y_0)}{\sqrt{|\lambda_E|}\left(k_{xn}^2 + \lambda_E\right)} - \right.$$
$$\left. - \frac{\lambda_H S_H(\zeta,z_0) \beta^2}{\sqrt{|\lambda_H|}\left(k_{xn}^2 + \lambda_H\right)} Y_{B_y}(y) Y^*_B(y_0) \right],$$

$$H_y = -v \sum_{n,m} \psi'(x,x_0) Y_{H_y n,m}(y) Y^*_B(y_0) \frac{S_{H\,n,m}(\zeta,z_0)}{\sqrt{|\lambda_H|}},$$

$$H_z = v \sum_{n,m} \psi'(x,x_0) \left[\frac{G_H(\zeta,z_0) Y_{Hd}(y) Y^*_B(y_0)}{\left(k_{xn}^2 + \lambda_H\right)} + \right.$$
$$\left. + \frac{G_E(\zeta,z_0) Y_{D_y}(y) Y^*_{Ed}(y_0)}{\left(k_{xn}^2 + \lambda_E\right)} \right],$$

$$H_x = v \sum_{n,m} \psi(x,x_0) \left[\frac{k_{xn}^2 S_H(\zeta,z_0) Y_{Hd}(y) Y^*_B(y_0)}{\sqrt{|\lambda_H|}\left(k_{xn}^2 + \lambda_H\right)} - \right.$$
$$\left. - \frac{\lambda_E S_E(\zeta,z_0) Y_{D_y n,m}(y) Y^*_{Ed}(y_0)}{\sqrt{|\lambda_E|}\left(k_{xn}^2 + \lambda_E\right)} \right].$$

Here we used the following designations:

$$\psi(x,x_0) = q \sin(k_{xn} x) \sin(k_{xn} x_0),$$

$$G_{E,H}(\zeta,\zeta_0) = \begin{cases} \cos\left(\sqrt{\lambda_{E,H}}(\zeta-\zeta_0)\right)\theta(\zeta_0-\zeta), \lambda_{E,H} \geq 0; \\ \dfrac{\mathrm{sign}(\zeta-\zeta_0)}{2} e^{-\sqrt{|\lambda_{E,H}|}|\zeta-\zeta_0|}, \lambda_{E,H} < 0, \end{cases}$$

$$S_{E,H}(\zeta,\zeta_0) = \begin{cases} -\sin\left(\sqrt{\lambda_{E,H}}(\zeta-\zeta_0)\right)\theta(\zeta_0-\zeta), \lambda_{E,H} \geq 0; \\ \dfrac{\mathrm{sign}(\zeta-\zeta_0)}{2} e^{-\sqrt{|\lambda_{E,H}|}|\zeta-\zeta_0|}, \lambda_{E,H} < 0, \end{cases}$$

$\theta(\zeta)$ is the Heaviside function.

We denoted normalized eigenfunctions of transverse operators and their adjoint operators as $Y_{D_y}(y)$, $Y_{B_y}(y)$, $Y_{E_y}(y)$, $Y_{H_y}(y)$, $Y_{Ed}(y)$, $Y_{Hd}(y)$ and $Y^*_{Ed}(y_0)$, $Y^*_B(y_0)$.

The transversal forces operating on electrons in a waveguide can be found with use of a formula of Lorentz:

$$\frac{F_x}{-e} = \sum_{n,m}^{\infty} \frac{\psi'(x,x_0)}{\varepsilon_0} \left[\frac{S_E(\zeta,z_0) Y_{Ed}(y) Y^*_{Ed}(y_0)}{\sqrt{|\lambda_E|}\left(k_{xn}^2 + \lambda_E\right)} + \right.$$
$$\left. + \frac{S_H(\zeta,z_0) k_{xn}^2 \beta^2 Y_{B_y}(y) Y^*_B(y_0)}{\sqrt{|\lambda_H|}\left(k_{xn}^2 + \lambda_H\right)} \right],$$

$$\frac{F_y}{-e} = \sum_{n,m} \frac{\psi(x,x_0)}{\varepsilon_0} \left[\frac{k_{xn}^2 \beta^2 \mu_{\|} S_H(\zeta,z_0) Y_{Hd}(y) Y^*_B(y_0)}{\sqrt{|\lambda_H|}\left(k_{xn}^2 + \lambda_H\right)} + \right.$$
$$\left. + \left(\frac{S_E(\zeta,z_0)}{\sqrt{|\lambda_E|}} \left(\frac{1}{\varepsilon_{\perp}} - \frac{\mu_{\|} \lambda_E \beta^2}{k_{xn}^2 + \lambda_E} \right) \right) Y_{D_y}(y) Y^*_{Ed}(y_0) \right].$$

Transverse fields can be used to calculate self-consistent beam dynamics in the rectangular dielectric wakefield waveguides.

CALCULATION RESULTS

Obtained equation solutions were used for analysing of the wakefields generated by a Gaussian relativistic electron bunch in the sapphire-based rectangular sub-THz accelerating structure. The accelerating structure had the following parameters: w = 2.5 mm, b = 1.0 mm, c = 1.04 mm, $\varepsilon_{2\perp} = 11.5$, $\varepsilon_{2\|} = 9.4$, base frequency is 300 GHz. As a source of Cherenkov radiation, a generator electron bunch with a Gaussian charge distribution and energy W = 75 MeV, charge q = 10 nC and bunch length σ_z = 0.1 mm was considered. The bunch is located at point $x_0 = w/2$, $y_0 = 0$, $\xi_0 = 0$ cm; the coordinates of the observation point are $x = w/2$, $y = 0$, $\xi = z - vt$.

The dependence of the longitudinal electric field component E_z produced by the bunch on the distance $\xi = z - vt$ behind it is shown in Fig. 2. The high accelerating gradient (exceeding 100 MV/m) combined with one-mode regime of wake radiation behind the bunch is worth noting.

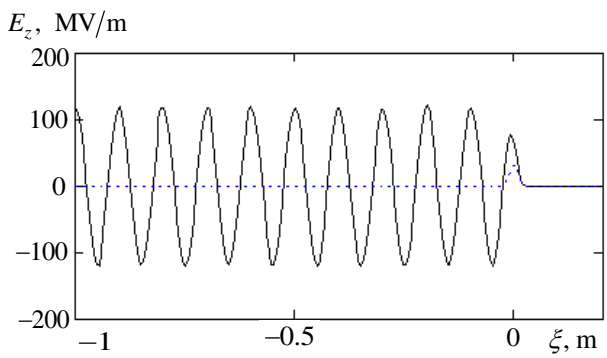

Figure 2: Dependency on the distance of the longitudinal wake field in the rectangular accelerating structure.

Dependences of electric (Fig. 3) and magnetic (Fig. 4) fields and transversal forces (Fig. 5) on coordinates were simulated. Simulation was done for z-coordinate corresponding to the first maximum of the longitudinal electric field followed the driver bunch.

ISBN 978-3-95450-181-6

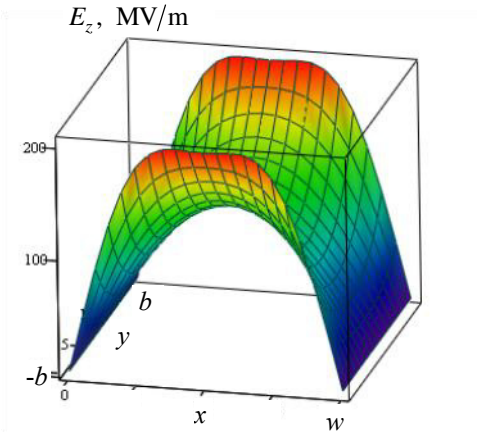

Figure 3: Spatial distribution of the electric intensity.

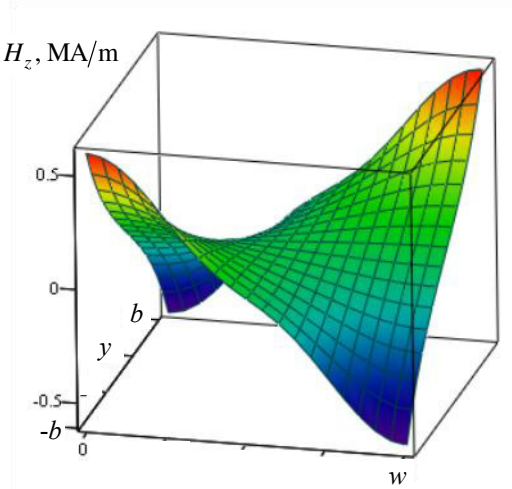

Figure 4: Spatial distribution of the magnetic strength.

Electric field strength has maximum near the borders of dielectric loading in the centre of waveguide along x-axis. It is twice higher than the field strength near the waveguide axis of symmetry. In the centre of the waveguide, accelerating gradients higher than 100 MV/m were obtained. Longitudinal magnetic field strength along the waveguide axis of symmetry is rather small – about zero, but dramatically rises as the corners of dielectric filling approached.

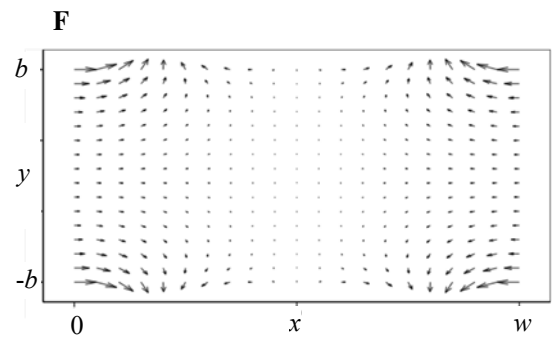

Figure 5: Transversal forces.

Transversal Lorentz forces are rather small at the center of the waveguide. Force increases as the dielectric edge is approached.

SUMMARY

We have proposed an analytic method for calculating wake fields of Vavilov – Cherenkov radiation in a rectangular accelerating structure with anisotropic dielectric filling. Using this method, we have analyzed the sapphire based dielectric structure with a rectangular cross section, in which accelerating gradients higher than 100 MV/m can be attained.

REFERENCES

[1] W. Gai, P. Schoessow, B. Cole, R. Konecny, et al., Phys. Rev. Lett. 61, 2756 (1988).
[2] W. Gai, AIP Conf. Proc. 1086, 3 (2009).
[3] A. M. Al'tmark, A. D. Kanareikin, and I. L. Sheinman, Tech. Phys. 50, 87 (2005).
[4] A. D. Kanareykin, J. Phys.: Conf. Ser. 236, 012032 (2010).
[5] A. D. Kanareikin and I. L. Sheinman, Tech. Phys. Lett. 33, 344 (2007).
[6] L. Xiao, W. Gai, and X. Sun, Phys. Rev. E 65, 1 (2001).
[7] C. Jing, W. Liu, W. Gai, L. Xiao, and T. Wong, Phys.Rev. E 68, 016502 (2003).
[8] A. Tremaine, J. Rosenzweig, P. Schoessow, and W. Gai, Phys. Rev. E 56, 7204 (1997).
[9] A. D. Bresler, G. H. Joshi, and N. Marcuvitz, J. Appl. Phys. 29, 794 (1958).
[10] A. Rowland and J. Sammut, J. Opt. Soc. Am. 72, 1335 (1982).
[11] J. W. Tao, J. Atechian, P. Ratovondrahanta, and H. Baudrand, Proc. IEE 137 (Part H), 311 (1990).
[12] S. Y. Park, C. Wang, and J. L. Hirshfield, AIP Conf. Proc. 647, 527 (2002).
[13] C. Wang and J. L. Hirshfield, Phys. Rev. ST Accel. Beams 9, 031301 (2006).
[14] G. V. Sotnikov, I. N. Onishchenko, J. L. Hirshfield, and T. C. Marshal, Probl. At. Nauki Tekhnol. Ser.: Yad._Fiz.Issled., No. 3 (49), 148 (2008).
[15] S. S. Baturin, I. L. Sheinman, A. M. Altmark, A. D. Kanareikin, Tech. Phys. 57, 5, 683 (2012)
[16] S. S. Baturin, I. L. Sheinman, A. M. Altmark, and A. D. Kanareykin. Transverse Operator Method for Wakefields in a Rectangular Dielectric Loaded Accelerating Structure. Phys. Rev. ST Accel. Beams 16, 051302 (2013)
[17] I. Sheinman, S. Baturin, A. Kanareykin. "Analysis of a Rectangular Dielectric-lined Accelerating Structure with an Anisotropic Loading" IPAC'12, New Orlean, USA, pp. 2769-2771. (2012)

ISBN 978-3-95450-181-6

EXPERIMENTAL ANALYSIS OF DIPOLE MODES IN ELLIPTICAL CAVITY*

M. Lalayan, A. Orlov, Ya. Shashkov, N. Sobenin,
National Research Nuclear University MEPhI, Moscow, Russia

Abstract

The experimental measurements of transverse shunt impedance for higher order modes TM_{110} and TE_{111} for S-band elliptical cavity were carried out. The experiments using dielectric and metallic spheres as perturbing objects and with ring probe were done.

INTRODUCTION

While studying the accelerating structures besides the calculation of electrodynamic characteristics (EDCs) at operating mode and higher order modes (HOMs) it is important to determine these parameters experimentally.

Today a considerable number of universally acknowledged numerical simulation codes used for EDCs calculation is known. Possibilities of an experimental study are modest compared to the ones of simulation approach and depend on the availability of modern measuring equipment and methods.

The most well-known field measurement method is the small perturbation technique using dielectric and/or metal perturbing bodies of different shapes. This article presents the results of measurements of the transverse shunt impedance using this method. In addition to the known approaches [1-2] application of ring-type perturbing bead is considered [3].

CAVITY MODEL

All simulations were done using software to model of elliptical harmonic cavity without drift tubes [4]. Figure 1 shows the cavity cell geometry together with basic dimensions and illustrates principle of cavity design.

We considered two dipole modes TM_{110} and TE_{111}, as they are the most dangerous for beam dynamics.

There are two methods of calculating linear transverse shunt impedance $r_{sh\perp}$ [5]:

1. By using Panofsky–Wenzel (PW) theorem one could derive the following equation:

$$r_{sh\perp} = \frac{\int_0^l \frac{1}{k_z}\frac{\partial E_z}{\partial r}\exp(ik_z z)dz}{P_{loss}*l} \qquad (1)$$

where k_z - longitudinal wave number, E_z – longitudinal component of the electric field, P_{loss} – power loss in the structure, r – transverse coordinate offset in the plane of the dipole polarization of the wave off the cavity axis, l – length of the structure.

2. The direct integration (DI) method based on the transverse components of the electric $E_y(z)$ and magnetic $H_x(z)$ fields calculation.

$$r_{sh\perp} = \frac{\left|ic*\mu_0*\int_0^l H_z(z)\exp(ik_z z)dz - \int_0^l E_y(z)\exp(ik_z z)dz\right|}{P_{loss}*l} \qquad (2)$$

where c – speed of light , μ_0 – magnetic constant.

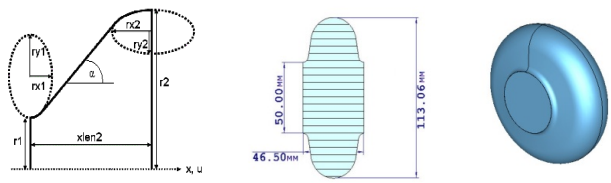

Figure 1: Geometry of elliptical harmonic cavity cell.

PERTURBING BODIES

Dielectric (DS), metallic (MS) spheres and metal wire loop probe as perturbing bodies were used for our research.

Table 1. Characteristics of Ceramic and Metallic Spheres

Parameter	simulation	experiment
Diameter, mm	1,8	1,8
DS form-factor k^E*10^{-20}, $(m^2\times s)/Ohm$	1,50	1,32
Electric constant	9,4	
MS form-factor k^E*10^{-20}, $(m^2\times s)/Ohm$	2,03	1,87
MS form-factor k^H*10^{-15}, $m^2\times s\times Ohm$	1,44	1,19

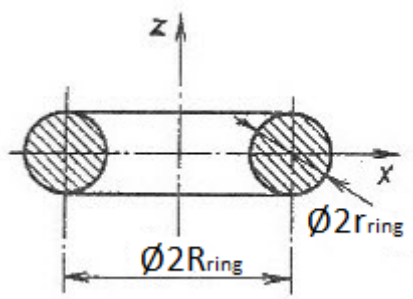

Figure 2: Geometry of ring probe.

Ring probe as bead for magnetic field and axially symmetric electric fields measurements is considered in [3]. Ring probe shape and dimensions are illustrated by

*Work supported by Ministry of Education and Science grant 3.245.2014/r

ISBN 978-3-95450-181-6

Figure 2. Electric and Magnetic form-factors for the ring probe can be calculated using the following formulas:

$$k_z^E = \varepsilon_0 \pi^2 r_{ring}^2 R_{ring} \quad (3)$$

$$k_z^M \cong \frac{\mu_0 \pi^2 R_{ring}^3}{4\ln(\frac{R_{ring}}{r_{ring}})} \quad (4)$$

The ring probe has larger orientation coefficient in a magnetic field compared to the metal sphere, i.e. ratio of the longitudinal form-factor to the transverse one.

$$k_{dir}^M = \frac{k_z^M}{k_{x,y}^M} = \frac{1}{3}\left(\frac{R_{ring}}{r_{ring}}\right)^2 \frac{1}{ln\left(\frac{R_{ring}}{r_{ring}}\right)} \quad (5)$$

Table 2. Characteristics of Metallic Ring Probe

Parameter	Simulation	Experiment
R_{ring}, mm	2,30	2,30
r_{ring}, mm	0,35	0,35
form-factor k^E*10^{-19}, (m^2×s)/Ohm	2.01	2.38
form-factor k^H*10^{-14}, m^2×s×Ohm	2,00	1,92

As it could be seen from Tables 1 and 2, the ring form-factor for the magnetic field is considerably greater than one for metallic sphere.

EXPERIMENTAL RESULTS

Ceramic and metallic spheres with the characteristics presented in Table 1 and ring probe as perturbing bodies were chosen and used for measurements. The experimental stand is described in [5].

During the pulling of perturbing body in the cavity phase change of transmission coefficient S_{21} with respect to phase, with the perturbing body is out of the cavity was measured. The corresponding change in the resonance frequency _ is calculated from the following formula (where Q_L – loaded Q-factor)

$$\frac{\Delta f}{f_0} = \frac{1}{2 * Q_L}\tan(\Delta\varphi) \quad (6)$$

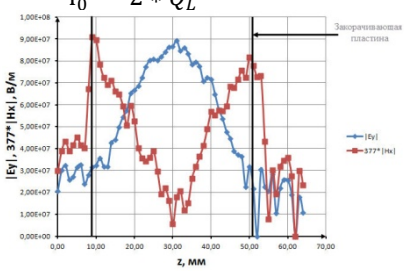

Figure 3: Distribution of fields.

Figure 3 shows the distribution of the transverse components of the electric and magnetic fields. Change in the resonance frequency was measured with ceramic and metallic spheres moved along the longitudinal cavity axis.

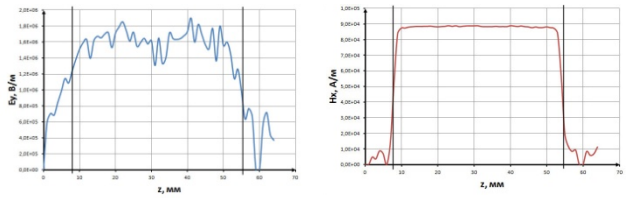

Figure 4: Distribution of transverse component of fields for TM_{110}.

Figure 4 shows the transverse field components distribution. Simulation of the experiment was carried out with ceramic and metallic spheres resulting in the same dependencies.

Figures 5 and 6 show results of experimental fields measurements using te metallic ring and ceramic sphere.

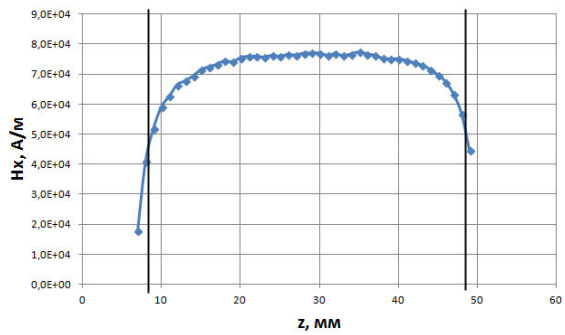

Figure 5: Distribution of magnetic field $|H_x|$ in measurements for TM_{110}.

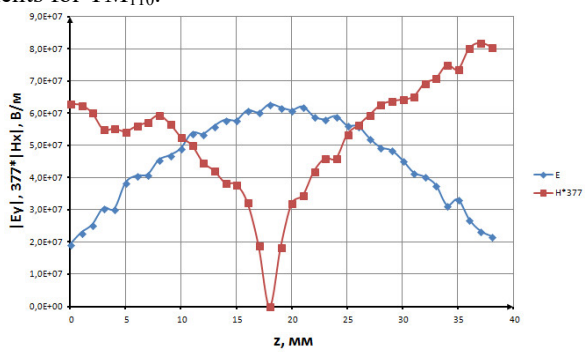

Figure 6: Distribution of fields in measurements for TE_{111}.

ERROR ESTIMATIONS

In the experiments the following uncertainty sources were considered: instrumental error, error in measurement of resonant frequency change, phase change of transmission factor, the loaded Q – factor, as well as manufacturing tolerances of perturbing bodies, perturbing body guide and positioning system.

Figures 7-8 show change form-factor of perturbing bodies when their size changes.

ISBN 978-3-95450-181-6

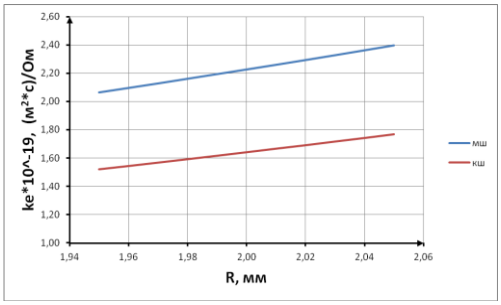

Figure 7: The dependence of the electric form-factor for spheres vs radius.

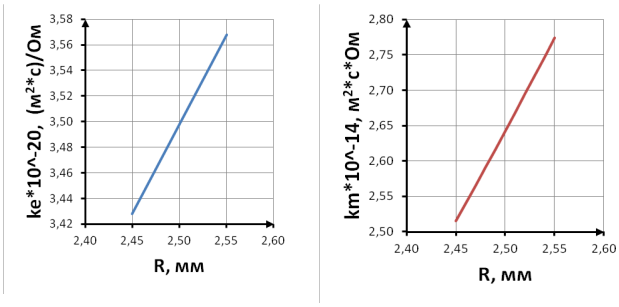

Figure 8: The dependence of form-factors for ring probe vs. radius at constant cross-section radius r = 0,4 mm.

Accuracy of the measurement fields using the ring probe was estimated in case of the ring is tilted by a small angle (10-20°) about to the magnetic field lines. The evaluation was done for TM_{110} mode. Figure 9 shows that in the case of 10 degrees deviation resulting field strength error is 1,5%, and in the case of 20 degrees it is 6%.

The total error in measurements is 11-18%.

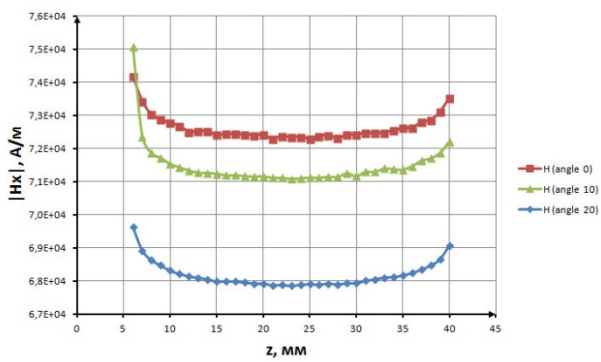

Figure 9: Transverse component of the magnetic field $|H_x|$ distribution along the structure.

TRANSVERSE SHUNT IMPEDANCE

After that based on the field measurement results the shunt impedance values were obtained and compared to the results obtained by the simulation results. The $r_{sh\perp}$ values were calculated by the the formulas (1) and (2). The comparison of the results obtained with different measurement methodics are presented in Table 3.

Table 3. Comparison of results obtained by different measurement methodics.

Wave		$r_{sh\perp}$, MOhm/m	
		TM_{110}	TE_{111}
Computer simulation	PW	17	0,76
	DI	16	0,76
Simulation of experiment	PW	14,0	
	DI (sphere)	16,0	0,89
	DI (ring)	17	0,84
Experiment	PW	13,7	
	DI (sphere)	16,9	0,77
	DI (ring)	16,5	0,86

CONCLUSION

The measurements of transverse shunt impedance for dipole modes TM_{110} and TE_{111} using ceramic, metallic spheres and ring probe were performed. The results showed the measurements done by the ring probe have the accuracy not worse than with the use of spherical probe.

REFERENCE

[1] M. Navarro-Tapia, R. Calaga, Bead-Pull measurements of the main deflecting mode of the double-quarter-wave cavity for the HL-LHC, proceedings of SRF2015, Pre-Press, Whistler, BC, Canada.

[2] H. Hahn, R. Calaga, HOM identification by bead pulling in the Brookhaven ERL cavity, Nuclear Instruments and Methods in Physics Research A 734 (2014) 72–78.

[3] B.V. Zverev, N.P. Sobenin, Electrodynamic Characteristics of Accelerating Cavities, Energoatomizdat, Moscow, 1993.

[4] Ya. V. Shashkov et al. “Comparison of higher order modes damping techniques for 800 MHz single cell superconducting cavities”, Nuclear Instruments and Methods in Physics Research A, v. 767, 2014.

[5] A.A. Zavadtsev, D.A. Zavadtsev, V.I. Kaminsky, A.Yu. Smirnov, N.P. Sobenin, “RF deflectors for the diagnostic of charged particles beams”, M:NRNU MEPhI, 2014, 180 p. (in Russian).

ISBN 978-3-95450-181-6

ELECTROMAGNETIC FIELD IN DIELECTRIC CONCENTRATOR FOR CHERENKOV RADIATION*

S.N. Galyamin†, A.V. Tyukhtin, V.V. Vorobev, A.A. Grigoreva, Saint Petersburg State University, St. Petersburg, Russia
E.S. Belonogaya, Saint Petersburg Electrotechnical University "LETI", St. Petersburg, Russia

Abstract

Recently we have reported on axisymmetric dielectric concentrator for Cherenkov radiation that focuses almost the whole radiation in the vicinity of the given point (focus) located on the trajectory of the charge [1]. Particularly, we have shown that this structure can increase the field up to two orders of magnitude. In this report we continue investigation of this concentrating target and analyse in more detail the field near the focal point depending on parameters of the target.

INTRODUCTION

Various dielectric targets are considered as candidates for development of modern non-invasive system of bunch diagnostics [2]. However, rigorous theory describing radiation processes for most of targets' geometries cannot be developed. Therefore, various approximate approaches are considered [3-6]. We have applied our original approach to calculate the shape of axisymmetric dielectric target concentrating most of generated Cherenkov radiation (CR) in a small vicinity of a focus point. We call this target "dielectric concentrator for CR" [1]. Here we proceed with investigation of this structure and perform analysis of the field components near the focal point.

THEORY

Figure 1 shows $x-z$ cut of the axisymmetric dielectric target with cylindrical channel (where a charge q passes) and specific form of the outer boundary. In the coordinate system shown in Fig. 1, this hyperbolic surface x_0, y_0, z_0 is determined as

$$\begin{aligned} x_0 &= \rho_0\cos\varphi, \quad y_0 = \rho_0\sin\varphi, \\ \rho_0 &= r(\theta)\sin\theta, \quad z_0 = z_f + r(\theta)\cos\theta, \end{aligned} \tag{1}$$

$$r(\theta) = f(1-n)\left[1+n\sin(\alpha+\theta)\right]^{-1}, \tag{2}$$

where r is a distance from $z=z_f$ to the surface, $n=\sqrt{\varepsilon\mu}>0$, $\sin\alpha=(n\beta)^{-1}$, $\beta=Vc^{-1}$ (V is a charge velocity and c is a speed of light in vacuum), f is a focal parameter, i.e. minimal distance from the focus to the surface, $f=r(3\pi/2-\alpha)$. For θ satisfying $\sin(\alpha+\theta)=-1/n$ we obtain $r\to\infty$, and this angle corresponds to the asymptote of hyperbola. In order to obtain the outer surface of the final target, we should take a piece of (2) for $\theta\in[\theta_{\min},\theta_{\max}]$, where $\rho_0(\theta_{\max})=a$ (a is a channel radius), $\rho_0(\theta_{\min})=x_{\max}$, and rotate this piece over z axis. Length of the target $z_{\max}$ is

$$z_{\max} = z_0(\theta_{\max}) - z_0(\theta_{\min}). \tag{3}$$

Consideration of the refracted rays shows that they converge exactly to the focus point, while ray optics formulas give divergent field magnitude [1]:

$$H_{\varphi\omega} \approx H^*_{\varphi\omega}\, T_{\parallel} \left|\frac{1}{1-l/r(\theta)}\right| \exp\left(\frac{i\omega}{c}l\right), \tag{4}$$

where l is a distance from the surface to the observation point along the ray, $T_{\parallel}$ is a Fresnel transmission coefficient,

$$T_{\parallel} = 2\cos\theta_i\left[\cos\theta_i + n\cos\theta_t\right]^{-1}, \tag{5}$$

and $H^*_{\varphi\omega}$ is the field at the inner side of the surface [7]:

$$H^*_{\varphi\omega} = \frac{iq}{2c}\eta s H_1^{(1)}\left(s\rho^*\right)\exp\left(i\frac{\omega}{\beta c}z^*\right), \tag{6}$$

$$s=\omega(\beta c)^{-1}\sqrt{\varepsilon\mu\beta^2-1},\ \operatorname{Im}s\ge 0,\ k=|\omega|(\beta c)^{-1}\sqrt{1-\beta^2},$$

$$\eta = \frac{-2i/(\pi a)}{\dfrac{(1-\varepsilon\mu\beta^2)}{(1-\beta^2)\varepsilon} I_1(ka) H_0^{(1)}(sa) + sI_0(ka)H_1^{(1)}(sa)}, \tag{7}$$

ρ^* and z^* are cylindrical coordinates of the ray start point at the surface. Since for the focus point there is an equality $l=r(\theta)$, we obtain divergence in (4).

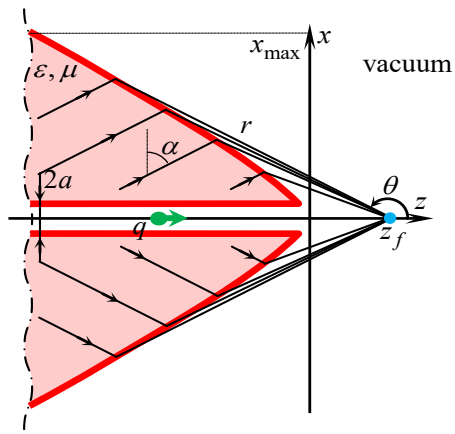

Figure 1: Geometry of concentrator ($x-z$ cut).

*Work supported by the Grant of the President of Russian Federation (No. 6765.2015.2) and the Grant from Russian Foundation for Basic Research (No. 15-32-20985).
† s.galyamin@spbu.ru

ISBN 978-3-95450-181-6

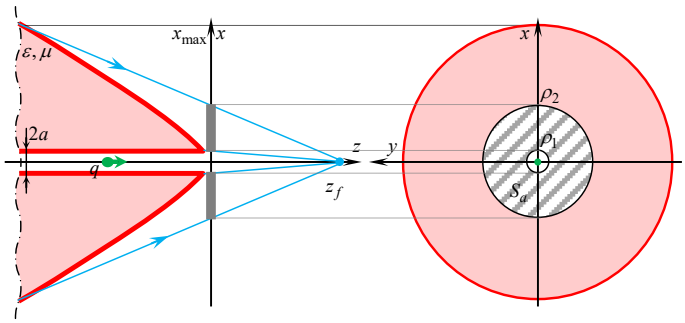

Figure 2: Ring aperture S_a for Stratton-Chu formulas.

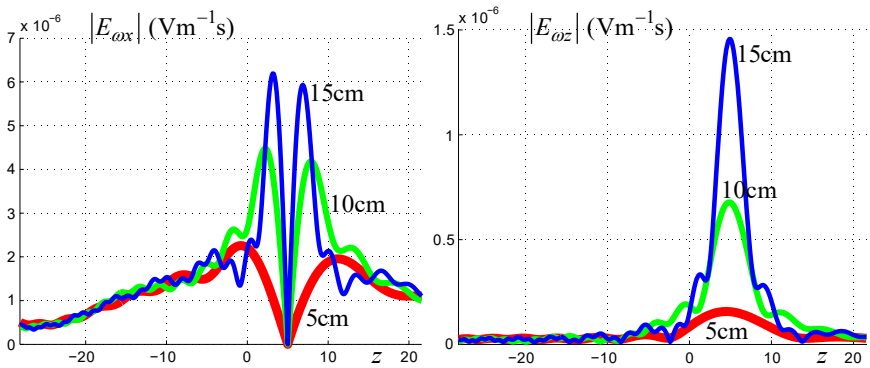

Figure 3: Behaviour of the transversal ($E_{\omega x}$) and longitudinal ($E_{\omega z}$) components of the electric field over the ray with $\theta = 178.5^\circ$. Other parameters are: $z_f = 5\,\text{cm}$, $f = 5\,\text{cm}$, $\beta = 0.8$, $\varepsilon = 2$, $\omega = 2\pi \cdot 1\,\text{THz}$. Number near curves indicates transversal target size $x_{\max}$.

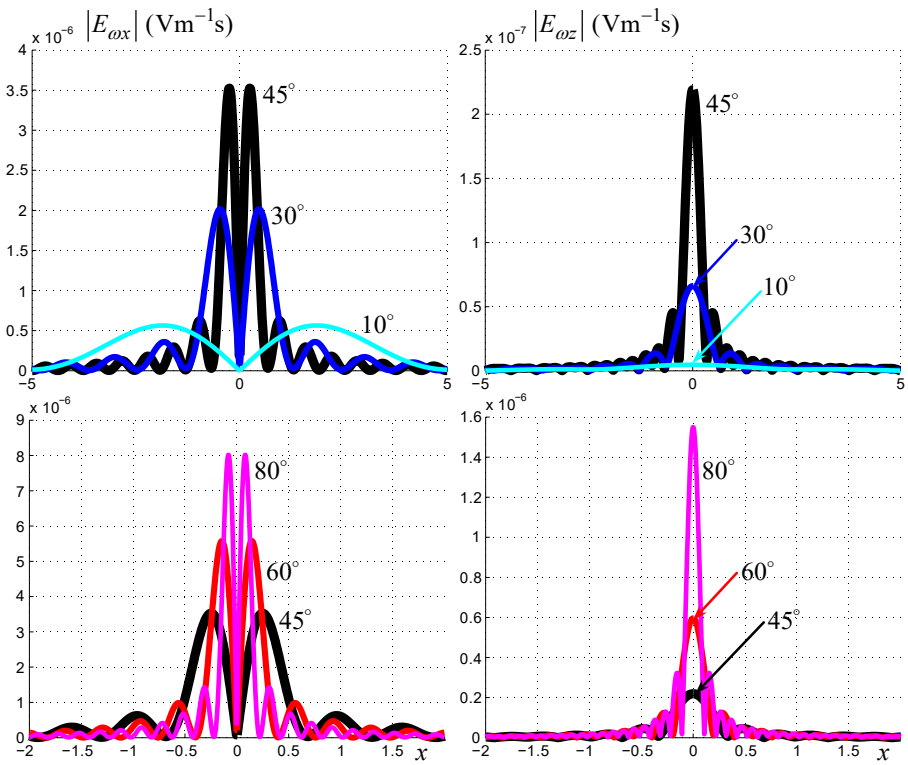

Figure 4: Transversal (left column) and longitudinal (right column) components of the electric field over line parallel to x-axis for $z = z_f = 5\,\text{cm}$, $f = 5\,\text{cm}$, $\beta = 0.8$, $\omega = 2\pi \cdot 1\,\text{THz}$, $x_{\max} = 10\,\text{cm}$. Number near curve indicates α.

ISBN 978-3-95450-181-6

In order to investigate the field near the focus, we use Stratton-Chu aperture integration formulas (which are the generalization of Kirchhoff formula for vector fields) [8] with flat aperture, as shown in Fig. 2. The aperture represents a ring enlightened by the refracted rays in the plane $z = \hat{z} = z_f - f(1-n)/(1-1/\beta)$ (curve (1) intersects z-axis in this point). Using (4), we calculate x- and y-components of electric and magnetic fields on the aperture ($H^a_{x,y}$ and $E^a_{x,y}$), electric field in arbitrary point with $z > 0$ is expressed as follows:

$$4\pi\vec{E} = \int_{S_a} \left\{ ik\,\vec{j}^s_e \varphi + \frac{i}{k}(\vec{j}^s_e, \vec{\nabla})\vec{\nabla}\varphi + \left[\vec{j}^s_m, \vec{\nabla}\varphi\right] \right\} d\Sigma, \quad (8)$$

where $\vec{j}^s_e = -\vec{e}_x \vec{H}^a_y + \vec{e}_y \vec{H}^a_x$, $\vec{j}^s_m = \vec{e}_x \vec{E}^a_y - \vec{e}_y \vec{E}^a_x$, $\varphi = \exp(ik\tilde{R})/\tilde{R}$, $\tilde{R} = \sqrt{(x-x')^2 - (y-y')^2 + (z-\hat{z})^2}$, $d\Sigma = dx'dy'$ is a surface element of S_a.

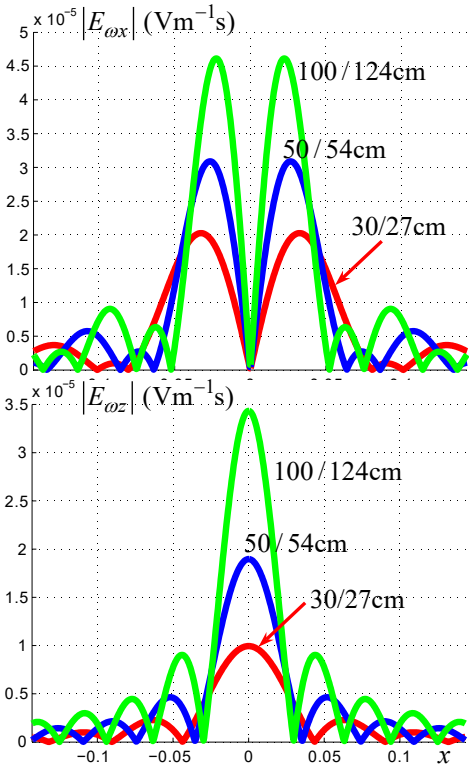

Figure 5: Electric field components over straight line parallel to x-axis, $\alpha = 88^\circ$, $x_{\max}/z_{\max}$ is indicated near curves, other parameters are the same as in Fig. 4.

NUMERICAL RESULTS

Results presented in this section were calculated using formulas (8). Figure 3 shows behaviour of the electric field over the ray. We can see a clear-cut maximum at the focus in the longitudinal component, while transversal component equals zero at this point. With an increase in target dimension, both main maximum of $E_{\omega z}$ and lateral maxima of $E_{\omega x}$ increase, ratio between these maxima also increases.

Table 1: Calculation Parameters

β	n	α°	$z_{\max}$ (cm)
0.8	7.2	10	283
	2.5	30	87
	1.77	45	52
	1.44	60	30
	1.27	80	11

Figure 4 shows the field behaviour over straight line parallel to x-axis and passing through $z = z_f$ for given β and various refractive indices n (or α). Transversal scale of the target $x_{\max} = 10$cm. Calculation parameters summarized in Table 1. As one can see, to obtain α close to $\pi/2$, one should use material with refractive index close to unity. Target prolongation in z-direction decreases with α, so that for $\beta = 0.8$ and $\alpha = 80^\circ$ longitudinal and transversal sizes are practically coincide. In all cases, maxima increase and become narrower with an increase in α. Typically, lateral maxima in $E_{\omega x}$ component are several times larger compared with maximum in $E_{\omega z}$ component (for example, they are around 1 order larger for $\alpha = 45^\circ$). However, for larger α this ratio becomes less, it is around 5 for $\alpha = 80^\circ$.

Figure 5 shows x-dependencies for $\alpha = 88^\circ$ and increasing values $x_{\max}$. As one can see, for α close to $\pi/2$ and large enough targets maximum values of $E_{\omega x}$ and $E_{\omega z}$ can practically coincide.

REFERENCES

[1] S.N. Galyamin, A.V. Tyukhtin, Phys. Rev. Lett. 113, 064802(2014).
[2] A.P. Potylitsyn et al., in Proc. IPAC'10, pp. 1074-1076.
[3] A.A. Tishchenko, A.P. Potylitsyn, M.N. Strikhanov, Phys. Rev. E 70, 066501 (2004).
[4] D.V. Karlovets, JETP 113, 27 (2011).
[5] E.S. Belonogaya, A.V. Tyukhtin, S.N. Galyamin, Phys. Rev. E 87, 043201 (2013).
[6] E.S. Belonogaya, A.V. Tyukhtin, S.N. Galyamin, J. Opt. Soc. Am. B 32, pp. 649-654 (2015).
[7] B.M. Bolotovskii, Physics-Uspekhi 4, 781 (1962).
[8] A.Z. Fradin, *Microwave Antennas* (Pergamon, New York,1961).

ISBN 978-3-95450-181-6

ELECTRON BEAM STABILITY IN THE ENERGY RECOVERY LINAC FOR THE LITHOGRAPHIC FREE ELECTRON LASER*

Ya.V.Getmanov#, N.A. Vinokurov, O.A. Shevchenko, Budker INP, Novosibirsk, Russia

Abstract

According to microelectronic production leaders the lithography based on the free electron laser (FEL) could become the main technology for the elements mass production with scale to 5 nm in the nearest future. One of the main problem is the absence of the working FEL with required parameters. The feasibility study of those FEL based on superconducting energy-recovery linac (ERL) was made in Budker INP. The ERL average current is limited by longitudinal and transverse instabilities, caused by interaction between electron beam and its induced fields in the superconducting cavities. The estimations of the threshold currents and ERL parameters were made.

INTRODUCTION

The feasibility study of high power radiation source for the lithographic applications has been discussed the last decade [1-2]. Using Free Electron Laser (FEL) based on multiturn Energy Recovery Linac (ERL) looks promising for this challenge due to high power radiation and energy efficiency in comparison to another machine types. For the industry application it is necessary to have high power laser radiation and therefore high average electron current and energy in the ERL. For the high energy of the electron beam is the most suitable to use the superconducting radio-frequency system (SRF).

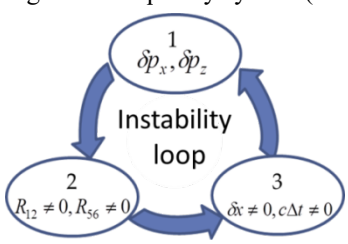

Figure 1: The threshold instability loop.

One of the main problems of the accelerator based on superconducting RF-cavities is the interaction between electron beam and long-living RF-field modes. This phenomenon could cause the degradation of the beam quality and moreover could limit the maximum achievable electron average current. Cavity modes could be spatially divided on transverse and longitudinal by the additional electron momentum obtaining. There is no fundamental difference in mechanics of the instabilities growth between them (Fig. 1): 1 – electron bunch passes through the cavity and gains additional momentum deviation from exited dipole or fundamental RF field modes; 2 – at the magnetic structure momentum deviation transforms to the coordinate, if the appropriate transport matrix elements are nonzero; 3 – electron bunch returns to the cavity and closes the instability loop enhancing dipole and deflecting fundamental RF modes.

ACCELERATOR SCHEME

The using of multiturn ERL scheme reduces the total cost of the facility. The experience with Novosibirsk multiturn ERL (NovoFEL) [3] shows one of the disadvantages the scheme with one accelerating structure. The adjusting of the electron-optical system is complicated by simultaneously pass of accelerating and decelerating beams with different energy spread due to FEL lasing. Therefore it was considered to use the scheme with separated acceleration structure (Fig. 2) [2, 4-5]. The main advantage of such structure is the possibility to independently adjust the arcs optic system for two types of beam. Principle of operation is the following: electrons from injector 1 pass to the pre-linac 2, are accelerated two times in linacs 3, are used in undulator 5, then in decelerating phase follow to the linacs, return energy to thee RF fields and drop to the dump 7. The wavelength of the first harmonic undulator radiation determines the maximum electron energy 800 MeV. For increasing the threshold value and more effective focusing it was considered to have different energy gain at main linacs 100 MeV and 275 MeV while the preliminary linac energy is 40 MeV.

TRANSVERSE STABILITY

All along of unbound arcs optical system main linacs can be considered independently. Therefore due to lower electron energy the lower threshold current is expected in the first main linac. The RF system of the first linac consists of 10 nine cell cavities with accordingly nine horizontal dipole modes. Consequently there are 90 horizontal dipole modes determine the threshold current. To determine the lowest values of the quality it was used the same parameters for the all modes $Q=5\cdot10^4$, $\rho=100$ *Ohm*.

The threshold current can be estimated using the ultra-relativistic approximation for non-overlapped modes of the accelerating structure. For the multiturn ERL it is given by

$$I_{th} = -2\frac{m_0 c^3}{e}\frac{1}{\omega_m\left(\frac{R_{sh}}{Q}\right)_m Q_m \sum_{k=1}^{2N-1}\sum_{n=k+1}^{2N} M_{12}^{kn}\sin\left(\omega_m\left(T_n - T_k\right)\right)}, \quad (1)$$

where c, m_0, e – speed of light, mass and charge of the electron, ω_m, $R_{sh,m}$, Q_m – frequency, shunt impedance and quality of the cavity dipole mode with number m, T_n is the time of the n-th pass through the cavity.

* Work supported by Russian Science Foundation project N 14-50-00080.
#y_getmanov@mail.ru

ISBN 978-3-95450-181-6

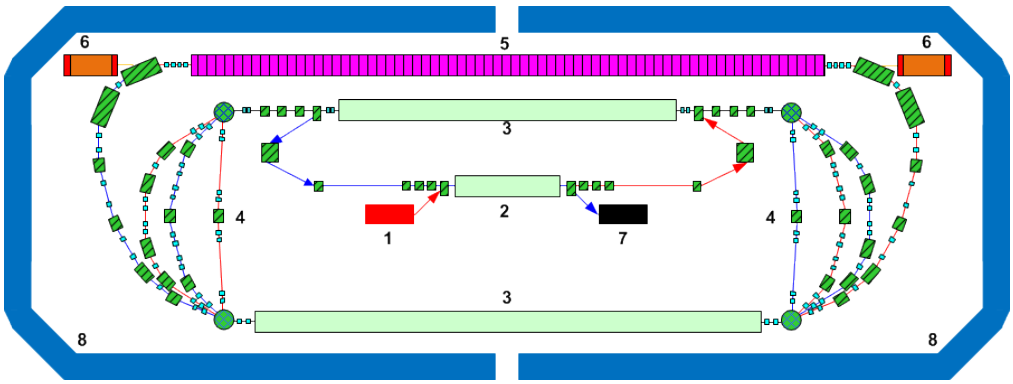

Figure 2: Scheme of ERL: 1 – injector, 2-preliminary linac, 3 – main linacs, 4 – magnetic structure, 5 – undulator, 6 – optical resonator, 7 – dump, 8 – protection walls.

The transport matrix element M_{12}^{kn} between k-th and n-th passes through the cavity depends on betatron function β_n and β_k at this passes

$$M_{12}^{kn} = \gamma_k \sqrt{\frac{\beta_k \beta_n}{\gamma_k \gamma_n}} \sin(\Delta\psi_{nk}),$$

where γ_n, γ_k – relativistic factors and $\Delta\psi_{kn}$ – phase advance. For the beam current optimization, in the first place there was used the technique of reducing the average beam sizes in the cavities by Elegant code [6]. To determine the electron optic of the linac it was used the symmetrical conditions of accelerated and decelerated beams. The second parameter affected on the threshold current is the phase advance. Since it is the periodic function and the arcs optic is independent for the accelerating and decelerating beams it is not necessary to calculate the full accelerator optical structure. After threshold current optimisation founded phase advances would be additional constraints for the focusing structures of the bending arcs. The dependence of the threshold current on the phase advances at the three bending arcs calculated by (1) is shown on the Fig. 3. From this distribution there was selected the area with the optimal threshold current (Fig. 4). The achieved parameters of the accelerator electron optical system were used for simulations in BI code [7]. The results of the simulations are presented on Fig. 5. The minimum threshold current for all modes varies between 90 to 108 *mA* from estimation by (1) to simulations.

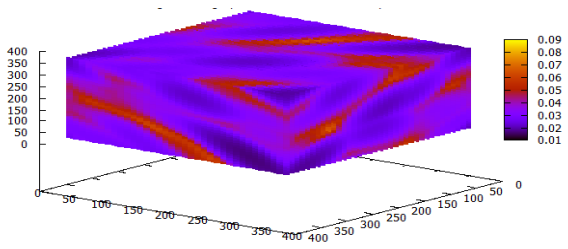

Figure 3: The dependence of threshold current and n phase advances (X,Y,Z axes – phase advance at bending arcs (degrees), colour is the current (A)).

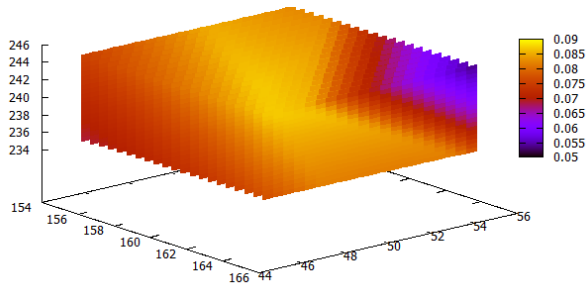

Figure 4: : The dependence of threshold current and phase advances (X,Y,Z axes – phase advance at bending arcs (degrees), colour is the current (A)).

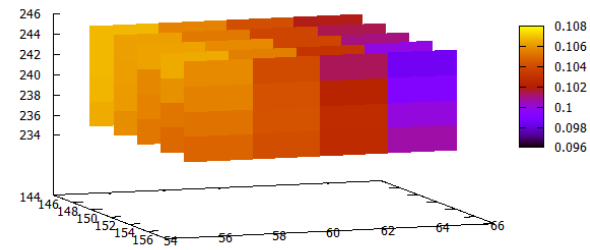

Figure 5: The dependence of threshold current and phase advances (X,Y,Z axes – phase advance at bending arcs (degrees), colour is the current (A)).

LONGITUDINAL STABILITY

To achieve the high power radiation it is necessary to group the electron bunches by motion to undulator (Fig. 2). The nonzero values of the longitudinal dispersion close the instability beam-cavity loop (Fig. 1). The longitudinal stability of multiturn ERL with one acceleration structure was considered previously [8].

Since all cavities have the same fundamental accelerating mode and R_{56} elements of transport matrixes in ultra-relativistic case between cavities in one linac are zero, it possible to use one cavity approximation with appropriate parameters. The beam-cavity interaction can

ISBN 978-3-95450-181-6

be represented as equivalent contour approximation with lumped parameters. Then electron beam and generator currents are presented as current sources. For analysis this system was used perturbation theory of stationary state [9, 10].

To check the theory conclusions there were made simulations used the wake-function of the electron bunch. The comparison of the induced voltage on the cavity calculated by theory and simulated by code is presented on Fig. 6.

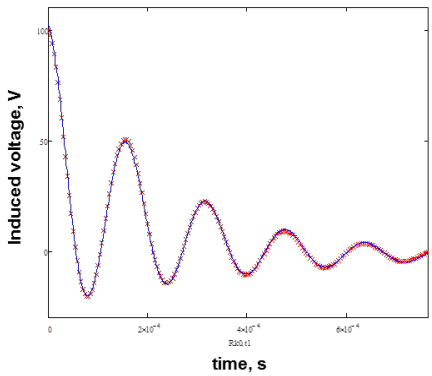

Figure 6: The illustration of the time dependence and induced voltage obtained by simulations (red colour) and by theoretical approximation (blue color).

In case of one undulator it does not necessary to group beam after lasing. Therefore two cases with different R56 were considered: the first is R_{56}=1 *m* for all bending arcs except the undulator arc with R_{56}=2 *m*, the second - R_{56}=1 *m* for all bending arcs before the undulator arc with R_{56}=2 *m* and R_{56}=0 *m* after undulator arc.

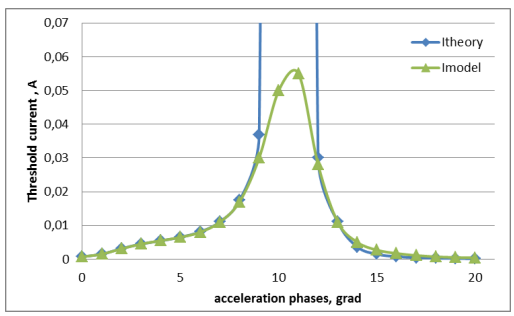

Figure 7: The illustration of the time dependence and induced voltage obtained by simulations (red colour) and by theoretical approximation (blue color).

Calculations show the structure with non-zero longitudinal dispersion at all bending arcs is more stable. The comparison of the theoretical and simulated values of the threshold current for the equal accelerating phases is presented at Fig. 7.

CONCLUSION

There were achieved the permissible quality factor values of the nonsymmetrical dipole modes in the cavities. The stable area of the beta-phase gain at the bending arcs provides the high average current 100 mA.

In case of longitudinal motion were considered two options of the bunch grouping. The nonzero values of longitudinal dispersion parameter at the bending arcs after undulator provide more stable area and higher beam threshold current. There were determined the range of the accelerating phases and cavity detunings necessary for high average current.

ACKNOWLEDGMENT

This work was supported by the Russian Science Foundation (project No. 14-50-00080).

The work was done using the infrastructure of the Shared-Use Center "Siberian Synchrotron and Terahertz Radiation Center (SSTRC)" of Budker INP SB RAS.

REFERENCES

[1] G.N. Kulipanov et al., J. of synchrotron radiation v. 5, pt 3 (1998) 176.
[2] Y. Sokol et al., PRST AB, (2011) 14 (040702).
[3] O.A. Shevchenko et al., PEPAN Letters, accepted to publication, 2016.
[4] D. Douglas, ICFA BD-Nl 26 (2001) 40.
[5] Ya.V. Getmanov et al. J. of Physics: Conference Series (2013) 4.
[6] M. Borland, “Elegant: A Flexible SDDS-Compliant Code for Accelerator Simulation”, APS LS-287, 2000.
[7] I.V. Bazarov, BI - Beam Instability BBU Code, http://www.lepp.cornell.edu/~ib38/bbucode/src.
[8] N.A. Vinokurov et al., Proc. SPIE 2988 (1997) 221.
[9] Ya. V. Getmanov et al., Proc. FEL’11 (2011) 345.
[10] Ya.V. Getmanov et al., PEPAN Letters, accepted to publication, 2016.

ISBN 978-3-95450-181-6

FORM-FACTOR DETERMINATION OF AN ARBITRARY BUNCH SEQUENCE FOR THE COHERENT RADIATION CALCULATION*

D. A. Shkitov#, A. E. Harisova, Tomsk Polytechnic University, Tomsk, Russia

Abstract

The approach how to calculate the form factor of an arbitrary bunch sequence is developed and described in this report. The form factors for different beam parameters of LUCX facility (KEK, Japan) are calculated and discussed.

INTRODUCTION

It is well known that the coherent effect occur when charged particles in a bunch radiate in phase [1]. This is accompanied by a quadratic increase in the radiation intensity and significantly influences the radiation spectrum. The coherent radiation is characterized by a form factor, which is the coefficient mainly depending on the ratio of bunch dimensions to the observed radiation wave length. The form factors will be different for the synchrotron and transition radiation because of their different nature of radiation. Now electron accelerators that produced beams with a sub-picosecond bunch length and a picosecond distance between them already exist [2]. Through the appearance of interference between radiation from such a sequence of bunches, the total intensity is no longer equal to the sum of radiation from each bunches [3, 4]. For this reason, it is essential to determine the form factor of an arbitrary electron bunch sequence. Herein the uniform bunch distribution will be the special case. One of the examples, how such a radiation from sequence can be used, is represented in [5, 6]. In this report we describe an approach to obtaining the form factor of arbitrary bunch sequence.

COHERENT RADIATION

The total radiation from a bunch of charged particles is generally considered consisting of incoherent and coherent part. Following to Ref. [7], these parts may be derived by way which described below. Assuming that electromagnetic field does not depend on the coordinates of individual particles in the bunch, we may write an expression of total bunch field as:

$$E_R = \sum_{i=1}^{N} E_i = \sum_{i=1}^{N} E_0 \, e^{i\Delta\varphi_i} = E_0 \sum_{i=1}^{N} e^{i\Delta\varphi_i}$$

Where E is an electric component of radiation field and $\Delta\varphi$ is a radiation phase shift. Throughout this report all of E and $\Delta\varphi$ are the functions of $E(r,\omega)$ and $\Delta\varphi(r,\omega)$ respectively. Further the radiation intensity from the single bunch is written as:

$$\frac{d^2W}{d\omega d\Omega} = cR^2 E_R E_R^* = cR^2 |E_R|^2 \sum_{i=1}^{N} e^{i\Delta\varphi_i} \sum_{j=1}^{N} e^{-i\Delta\varphi_j} = \frac{d^2W_0}{d\omega d\Omega} \cdot \Sigma$$

Where R is the distance to an observation point, $\frac{d^2W_0}{d\omega d\Omega}$ is the radiation intensity from single particle and sign (*) is a complex conjugate. Let's divide the sum term Σ into two parts. First part Σ_{inc}, when $j = i$, is responsible for the incoherent radiation:

$$\Sigma_{inc} = \sum_{i=1}^{N} 1 = N$$

Second part Σ_{coh}, when $j \neq i$, is responsible for the coherent radiation:

$$\Sigma_{coh} = \sum_{i=1}^{N} e^{i\Delta\varphi_i} \sum_{\substack{j=1 \\ j\neq i}}^{N} e^{-i\Delta\varphi_j} = \sum_{i=1}^{N} \int e^{i\Delta\varphi_i} \delta(r - r_i) dV \cdot \sum_{\substack{j=1 \\ j\neq i}}^{N} \int e^{-i\Delta\varphi_j} \delta(r' - r_j) dV' = \int e^{i\Delta\varphi_i} \sum_{i=1}^{N} \delta(r - r_i) dV \cdot \int e^{-i\Delta\varphi_j} \sum_{\substack{j=1 \\ j\neq i}}^{N} \delta(r' - r_j) dV'$$

Where δ is the Dirac function. In the transformations we employ the integral property of Dirac function. We have also introduced the notation: $\sum_{i=1}^{N} \delta(r - r_i) = N\rho(r)$ and $\sum_{\substack{j=1 \\ j\neq i}}^{N} \delta(r' - r_j) = (N-1)\rho(r')$, here ρ is spatial distribution of the particles in the bunch. When $N \gg 1$ we have $\rho(r) \approx \rho(r')$, then:

$$\Sigma_{coh} = N(N-1) \int e^{i\Delta\varphi} \rho(r) dV \cdot \int e^{-i\Delta\varphi} \rho(r') dV' = N(N-1) f(\omega) \cdot f^*(\omega)$$

Where $f(\omega) = \int e^{i\Delta\varphi} \rho(r) dV$ is the geometric form factor of the bunch. After all transformations we will obtain a general expression for the radiation intensity in the following form:

$$\frac{d^2W}{d\omega d\Omega} = [N + N(N-1) \cdot |f(\omega)|^2] \frac{d^2W_0}{d\omega d\Omega}$$

RADIATION FROM BUNCH SEQUENCE

Further we consider the radiation from the irregular sequence of identical electron bunches which moving along

* Work was partially supported by the grant of the President of Russian Federation No SP-261.2015.2.

#shkitovda@tpu.ru

ISBN 978-3-95450-181-6

Z axis with the same energy and with different distance between them. This radiation may be described as the sum of field from each bunches by following formula:

$$E_R = \sum_{i=1}^{N\cdot M} E_i = \sum_{i=1}^{N\cdot M} E_0 e^{i\Delta\varphi_i} = E_0 \cdot \left[\sum_{i=1}^{N} e^{i\Delta\varphi_1} + \cdots + \sum_{i=N(M-1)+1}^{N\cdot M} e^{i\Delta\varphi_M}\right] = E_0 \left[\sum_{i=1}^{N} e^{i\Delta\varphi_1} + \cdots + \sum_{j=1}^{N} e^{i\Delta\varphi_1} e^{i\frac{\omega l_M}{c\,\beta}}\right] = E_0 \sum_{i=1}^{N} e^{i\Delta\varphi}\left(1 + \cdots + e^{i\frac{\omega l_M}{c\,\beta}}\right) = E_0 \sum_{i=1}^{N} e^{i\Delta\varphi} \sum_{k=1}^{M} e^{i\frac{\omega l_k}{c\,\beta}}$$

Where N is the number of particles in each bunches, M is the number of bunches, $\Delta\varphi$ is the phase for the single bunch, $l_k = \{l_1 = 0, \ldots, l_M\}$ is the distances between 1st and kth bunches. The phase factors $e^{i\frac{\omega l_k}{c\,\beta}}$ occur due to the different distance among bunches which moving with the same velocity equal to β. Moreover, we need to clarify that these phase factors appear only for geometry of transition radiation since the radiation generates on target surface. For synchrotron radiation these factors will be depend on the observation angle and the trajectory radius of the particles.

Then we may apply the approach for the calculation of single bunch form factor described in the previous section. According to this approach the radiation intensity from irregular sequence of identical bunches will be equal to:

$$\frac{d^2W}{d\omega d\Omega} = \frac{d^2W_0}{d\omega d\Omega}\left(MN + N(N-1)\cdot|f(\omega)|^2 \cdot \left|\sum_{k=1}^{M} e^{i\frac{\omega l_k}{c\,\beta}}\right|^2\right)$$

Where factor f(ω) is the form factor of the single bunch mentioned above. If the distances between each two bunches are equal the l_0 then:

$$F(\omega) = \left|\sum_{k=1}^{M} e^{i(k-1)\frac{\omega l_0}{c\,\beta}}\right|^2 = \left|\left(e^{iM\frac{\omega l_0}{c\,\beta}} - 1\right)\Big/\left(e^{i\frac{\omega l_0}{c\,\beta}} - 1\right)\right|^2 = sin^2 M\frac{\omega l_0}{2c\beta}\Big/ sin^2\frac{\omega l_0}{2c\beta}$$

Where $F(\omega)$ is the interference factor which arises in the theory of undulator and Smith-Purcell radiation as well due to the periodical structure of magnetic field and grating respectively.

EXAMPLES AND DISCUSSION

Further, we will consider different cases of sequence form factor for LUCX beam parameters [2]. Necessary parameters to compute the form factors for sequences are listed in Table 1.

Table 1: Simulation Parameters

Name	Value
Electron energy, E_e	8.25 MeV ($\gamma \approx 16$)
Particle speeds, β	0.998
Bunch length (r.m.s.), σ_z	100 fs (30 μm)
Bunch spacing, l_0	0 – 10 ps
Number of bunches, M	2 – 16

Figure 1 shows the form factor with different number of bunches in the sequence with bunch spacing equals to 0.5 ps. Population is the same for all bunches. The form factor of the single Gaussian bunch is determined by the following expression:

$$|f(\omega)|^2 = e^{-\omega^2\sigma_z^2/\beta^2c^2}$$

Here we consider only the influence of longitudinal bunch profiles. This approximation means that $\sigma_z \gg \sigma_t$, where σ_t is the transversal bunch size. However, for more accurate calculations and for arbitrary case of σ_z/σ_t ratio the transversal size must be taken into account.

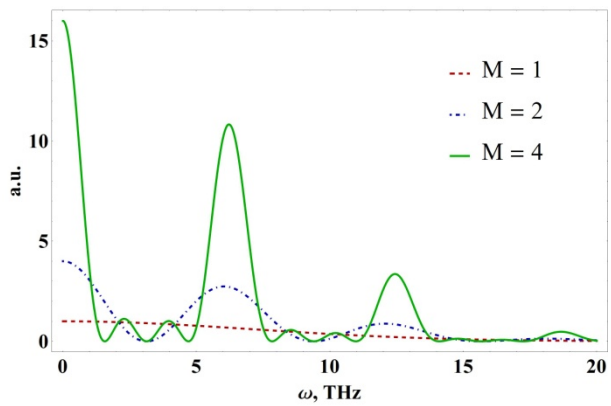

Figure 1: Form factors for different number of equal gaussian bunches (σ_z = 100 fs) in the sequence.

As it is expected the monochromaticity should be inversely proportional to the amount of bunches in the sequence, so $\Delta\omega/\omega \sim 1/M$. This dependence maybe observed in Fig. 1. The monochromaticity for the parameters of above picture with 2, 4, 8 and 16 bunches is equals to 0.243, 0.123, 0.059 and 0.029 respectively for the first radiation order, where obtained values is in a good agreement with the dependence $\sim 1/M$. Furthermore, the intensity of maxima in the spectrum increases quadratically vs. bunch number.

If the distances between bunches are equal to each other, in first approximation the spectrum maxima will be located at ω_n when denominator of $F(\omega)$ is vanished. It means that $\omega_n = 2\pi c \cdot n\beta/l_0$, where n is number of order. Figure 2 illustrates this relation. Accordingly, we can smoothly change the peak positions by varying the spacing structure

ISBN 978-3-95450-181-6

in the sequence. However, there are the peak position shifts due to the factor $|f(\omega)|^2$ which is the monotonically decreasing function. For this reason, the peaks are slightly shifted into the low frequency range.

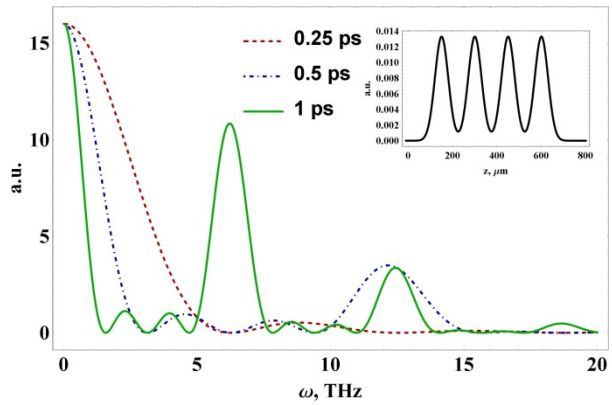

Figure 2: Form factors for 4-bunch-sequence with the same length as in Fig. 1 calculated for different bunch spacing. Insertion is the longitudinal profile of the same sequence with 0.5-ps-spacing.

Figure 3 shows the three form factors for different spacing in the sequence.

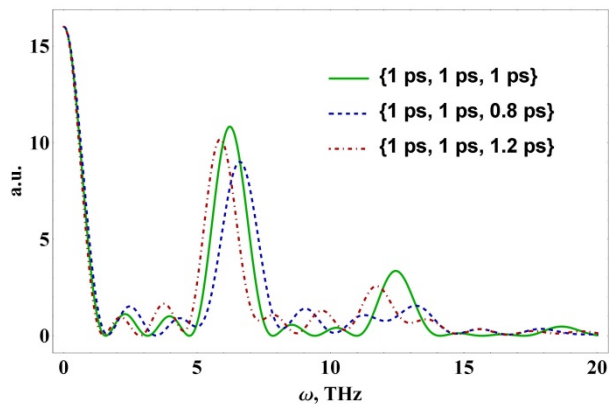

Figure 3: Form factors for different spacing structure $\{l_{12}, l_{23}, l_{34}\}$ (see the legend) with M = 4 and σ_z = 100 fs.

Due to the unequal distances between bunches, there will be a shift of radiation peak positions in the spectrum. In first approximation this shift may be estimated by expression $\Delta\omega = -(2\pi cn\beta) \cdot \langle \Delta l \rangle / \langle l_0 \rangle^2$, where $\langle l_0 \rangle$ is the average distance between bunches and $\langle \Delta l \rangle$ is the average shift between bunches.

CONCLUSION

We conclude that the new form factor for the calculation of coherent transition radiation from bunch sequence is obtained. This new form factor differs from single bunch form factor that it contains the multiplier characterizing the distribution of bunches in the sequence. Due to the radiation interference from the bunches, some of the radiation frequency is amplified in spectrum. According to the obtained calculation results, increasing the number of bunches in the sequence, the intensity is quadratically increased for the certain frequencies. Then, if the distances between bunches is equal to each other (uniform sequence), the peak positions is briefly determined by the expression $\omega_n = 2\pi cn\beta / l_0$. In the case of arbitrary bunch sequence, in general, the peak positions will be shifted by an amount depending on the number of bunches in the sequence, number of radiation order and the sequence structure. In the case of relativistic particles the small energy spread will have practically no influence to the spectrum shape and vice versa, in the non-relativistic case, the energy spread dramatically effect to the spectrum shape.

REFERENCES

[1] A. P. Potylitsyn, M. I. Ryazanov, M. N. Strikhanov, A. A. Tishcenko, Diffraction Radiation from Relativistic Particles, Berlin, Springer, 2010.

[2] A Aryshev et. al., "Development of advanced THz generation schemes at KEK LUCX facility", in Proc. 10th Annual Meeting of PASJ, Japan, August 2013, paper SUP020, p. 873.

[3] D. A. Shkitov et al., "Feasibility of double diffraction radiation target interferometry for compact linear accelerator micro-train bunch spacing diagnostics", J. of Phys.: Conf. Ser., vol. 517, p. 012024, 2014.

[4] D. A. Shkitov et al., "Double diffraction radiation target interferometry for micro-train beam diagnostics", in Proc. IPAC'14, Dresden, Germany, June 2014, pp. 3635-3637.

[5] S. E. Korbly et al., "Observation of frequency-Locked coherent terahertz Smith-Purcell radiation". Phys. Rev. Lett., vol. 94, pp. 054803-1, 2005.

[6] L. G. Sukhikh et al., "Feasibility of THz Source Based on Coherent Smith-Purcell Radiation Generated by Femtosecond Electron Bunches in Super-Radiant Regime", in Proc. IPAC'12, New Orleans, USA, May 2012, paper MOPPP005 pp. 574-576.

[7] G. Naumenko, "Form-factors of relativistic electron bunches in polarization radiation", Advanced Materials Research, vol. 1084, p. 138, 2015.

ISBN 978-3-95450-181-6

FIRST ORDER PERTURBATION THEORY EVALUATION OF INITIAL STAGE OF SELF AMPLIFIED CRYSTAL-BASED X-RAY EMISSION

A. Benediktovitch, Belarusian State University, Minsk, Belarus *

Abstract

Mechanisms of x-ray generation by relativistic electrons in the energy range below 100 MeV by interaction with crystals are discussed in view of possibility to obtain self amplification of spontaneous emission. To investigate the initial stage of self amplified spontaneous emission process the first-order perturbation theory that enables to describe the collective beam response as effective susceptibility is used. Based on this approach Cherenkov radiation in the anomalous dispersion frequency range, parametric x-ray radiation and axial channeling radiation mechanisms are considered. The axial channeling mechanism in the case of grazing incidence electrons was shown to be most promising one.

INTRODUCTION

X-ray Free Electron Lasers (XFELs) open new revolutionary opportunities for investigations in materials science, chemistry, biology and other areas. However, due to high cost of construction and maintain, the access to these facilities for wide scientific community is quite limited. This motivates search for schemes of compact bright x-ray sources. The size of X-ray Free Electron Lasers is dictated by basic properties of undulator radiation: to produce x-rays with Angstrom wavelength from cm period undulator one needs electrons with energy in GeV range. If one considers the radiation mechanisms accompanying the propagation of electron beam through a crystal structure (channeling radiation, parametric x-ray radiation, Cherenkov radiation near K-edge), one can see that to get photons in x-ray range one needs electrons with energy of tens to hundreds MeV. The dramatic 10 orders of magnitude increase of brightness of XFELs compared to III generation synchrotron became possible due to phenomenon of self amplified spontaneous emission (SASE). In the case of XFELs the spontaneous emission which is amplified is the undulator radiation, the SASE process being developed due to high charge, short duration and small emittance of the bunch as well as long undulator length. In the present paper we will investigate the possibility of SASE process for which as a spontaneous radiation mechanisms serve x-ray radiation mechanisms in crystals. The development of rigorous SASE theory in this case is extremely difficult task due to large number of phenomena accompanying electron propagation in crystals and complexity of SASE phenomena itself, however, one can use the first order perturbation theory to describe the first stage of SASE process [1] and determine the most promising radiation mechanism and experiment geometry.

* andrei.benediktovitch@atomicus.by

RADIATION MECHANISMS

One of the ways to find at which conditions x-ray radiation of electrons in crystal will take place is to find phase match between the electromagnetic field that can exist in the crystal and current of electron in the crystal. In the Fourier space this condition can be expressed as intersection of dispersion surface of electromagnetic radiation

$$k^2 - \frac{\omega^2}{c^2}(1 + \chi(\omega)) = 0 \tag{1}$$

here $\chi(\omega)$ is the susceptibility of the crystal; and condition that should be satisfied for Fourier components of a single electron current

$$\omega - \vec{k} \cdot \vec{v} = 0 \tag{2}$$

here $\vec{v}$ is the velocity of electron. In order to organize intersection of (1) and (2) one can act in two ways: either modify properties of the medium to bring (1) in intersection with (2), or modify the movement of the electron and correspondingly (2) to bring it in intersection with (1). Let us name the first scenario as case I and the second as case II.

In the x-ray domain for electrons in crystals case I can be realized if $\mathrm{Re}\chi(\omega) > 0$ that leads to Cherenkov radiation, or under the Bragg diffraction conditions under which dispersion equation (1) is modified to

$$\left[k^2 - \frac{\omega^2}{c^2}(1+\chi_0)\right]\left[(\vec{k}+\vec{H})^2 - \frac{\omega^2}{c^2}(1+\chi_0)\right] - \chi_{\vec{H}}\chi_{-\vec{H}}\frac{\omega^4}{c^4} = 0 \tag{3}$$

here $\vec{H}$ is the reciprocal lattice vector for which the Bragg condition $(\vec{k}+\vec{H})^2 = k^2$ is satisfied, $\chi_{\vec{H}}$ is the spatially periodic part of the susceptibility corresponding to crystallographic planes with reciprocal lattice vector $\vec{H}$, the polarization in the plane orthogonal to vectors $\vec{k}$, $\vec{H}$ is considered for simplicity. Under the conditions of intersection of (3) with (2) parametric x-ray radiation takes place.

The case II can be realized if one introduce oscillatory component in the electron current. In the case of relativistic electrons in the crystal, the oscillatory component can appear if the electron goes into the channeling regime, in this case (2) is modified to

ISBN 978-3-95450-181-6

$$\omega - \vec{k}\cdot\vec{v} - \omega_{if} = 0, \quad (4)$$

here ω_{if} is the frequency of transition between initial and final states of transverse channeling motion. Under the conditions of intersection between (4) and (1) the channeling radiation takes place.

SASE ESTIMATIONS FOR CHERENKOV AND PARAMETRIC X-RAY RADIATION

The SASE effect is conditioned by action of radiated electromagnetic field on the electrons and back action of the induced current on the electromagnetic field. In the frame of first order perturbation theory this process leads to component of the beam current that is proportional to the acting electromagnetic field, hence in terms of interaction with electromagnetic field the presence of the beam can be described as an active medium. Based on the Vlasov equation one can show that the induced susceptibility tensor is

$$\chi_b(\vec{k},\omega) = -\frac{4\pi e^2}{m_e\gamma\omega^2}\int d^3\vec{p} f^{(0)}(\vec{p})[1 + \frac{\vec{v}\otimes\vec{k} + \vec{k}\otimes\vec{v}}{\omega - \vec{k}\cdot\vec{v}} + k^2\frac{\vec{v}\otimes\vec{v}}{(\omega-\vec{k}\cdot\vec{v})^2}] \quad (5)$$

here $f^{(0)}(\vec{p})$ is initial distribution of electron momenta in the beam, the sign $\otimes$ denoted the diad (Kronecker) product.

Cherenkov radiation

In the x-ray frequency domain the susceptibilty of a crystal is negative and is mainly determined by total electron density. However, near frequencies corresponding to transitions from inner electron shells, e.g. K-edges, the corresponding electronic transitions give significant contribution to susceptility and in the harrow range the susceptibility can become positive. Inevitably, in the same region the imaginary part of the susceptibility responsible for absorption increases as well.

Consider a frequency at which the crystal susceptibility is positive that leads to Cherenkov radiation. The analysis of SASE possibility can be performed by means of considering the dispersion equation of electromagnetic field in the medium and active medium described by (5). The wave equation for electromagnetic field in such a medium reads

$$L(\vec{k},\omega)\cdot\vec{E}(\vec{k},\omega) = 0, \quad (6)$$
$$L(\vec{k},\omega) = k^2 - \vec{k}\otimes\vec{k} - \frac{\omega^2}{c^2}(1+\chi_0+\chi_b(\vec{k},\omega))$$

here scalar quantities entering in L are assumed to be multiplied by a unit matrix. The dispersion equation is obtained from condition $DetL = 0$. If one considers normal incidence and solve the dispersion equation in terms of deviation of the wavevector δk_z from the resonance conditions at which intersection of (1) and (2) takes place, one arrives at

$$\left(2\frac{\delta k_z}{\omega} - i\chi''\right)\frac{\delta k_z}{\omega}^2 \simeq \frac{\omega_b^2}{\gamma\omega^2}4\chi_0^2 \quad (7)$$

here one has taken into account that the beam plasma frequency is much smaller than x-ray frequency, beam emittance was considered to be infinitely small, the exact resonance conditions are fulfilled, χ'' is imaginary part of the susceptibility. If one considers very optimistic parameter for the focused electron bunch current density $j \sim 10^{10}A/cm^2$ and neglect χ'' in (7), for typical x-ray frequency of 10keV one obtains $\mathrm{Im}\frac{\delta k_z}{\omega} \sim 10^{-6}$. This value is about 3 orders of magnitude less than imaginary part of the susceptibility responsible for absorption, hence Cherenkov based SASE process in x-ray domain hardly can be expected.

Parametric x-ray radiation

In the case of parametric x-ray radiation the equation analogous to (6) takes the form

$$[k^2 - \vec{k}\otimes\vec{k} - \frac{\omega^2}{c^2}(1+\chi_0)]\vec{E}_0(\vec{k},\omega) - \frac{\omega^2}{c^2}\chi_{-\vec{H}}\vec{E}_H(\vec{k},\omega) = \frac{\omega^2}{c^2}\chi_b(\vec{k},\omega)\vec{E}_0(\vec{k},\omega)$$
$$[(\vec{k}+\vec{H})^2 - (\vec{k}+\vec{H})\otimes(\vec{k}+\vec{H}) - \frac{\omega^2}{c^2}(1+\chi_0)]\vec{E}_H(\vec{k},\omega) - \frac{\omega^2}{c^2}\chi_{\vec{H}}\vec{E}_0(\vec{k},\omega) = 0 \quad (8)$$

here $\vec{E}_H(\vec{k},\omega)$ corresponds to Bragg-diffracted wave. A detailed analysis of (8), calculation of dispersion equation, evaluation of emittance effect and analysis of SASE process based on boundary conditions can be found in [2]. The analysis shows that for optimized geometry of $\vec{k},\vec{v},\vec{H}$ direction, and under the most favorable conditions and value for the bunch current $j \sim 10^{10}A/cm^2$ one arrives at intensity e-folding crystal thickness of about 1 mm. After such distance in the crystal the beam would suffer drastic multiple scattering that would degrade the induced susceptibility due to the integration in (5). This would degrade the SASE process, hence the parametric x-ray radiation SASE scenarion has significant difficulties as well.

SASE ESTIMATIONS FOR CHANNELING RADIATION

The process of multiple scattering can be significantly changed if electrons of the beam are under conditions of channeling. In this case electrons are trapped by potential of atomic plane or atomic string, the transverse motion being described by Schrodinger equation with effective mass γm. If one is interested in x-ray radiation wavelength in the Angstrom range, the corresponding electron energy is below 100 MeV, in this energy range the quantum description

ISBN 978-3-95450-181-6

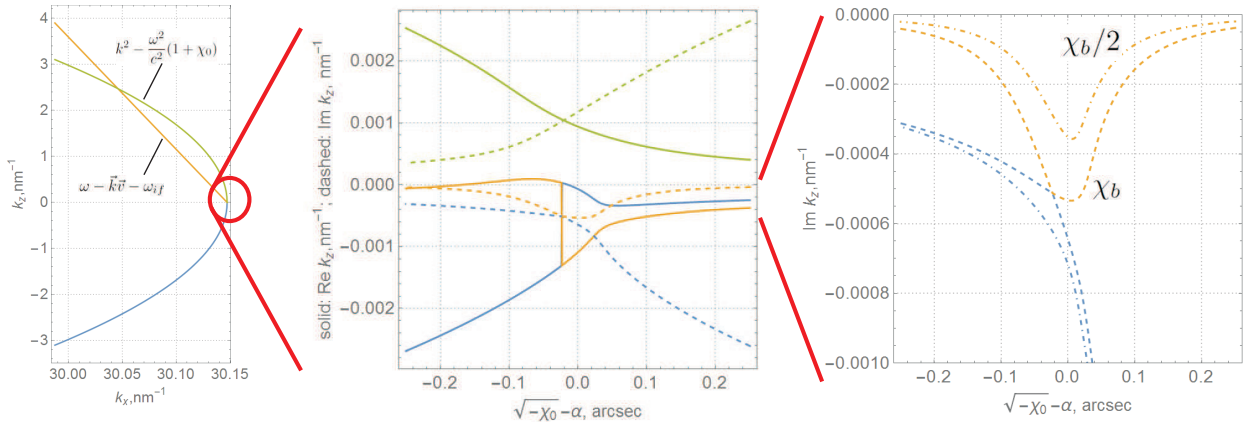

Figure 1: Dispersion surface under the grazing incidence conditions, magnified from left to right under. Parameters used: electron energy 25 MeV, bunch charge 1 nC, bunch length 0.1 ps, emittence is $\epsilon_n = 0.1\text{mm}\cdot\text{mrad}$, LiH crystal, channeling direction $< 110 >$, corresponding x-ray energy is 5.9 keV.

of electron channeling is essential. The action of electromagnetic field on channeled electrons and back within the first order quantum mechanical perturbation theory can be described by induced susceptibility as well as in the case I, the corresponding expression reads:

$$\chi^{(b)}(\vec{k},\omega) = \chi_b \frac{\omega\vec{\zeta}\otimes\vec{\zeta}}{\omega - \vec{k}\vec{v} - \omega_{if}}, \quad (9)$$

$$\chi_b = \frac{4\pi n_e e^2}{\omega^3}(P_i - P_f)\omega_{if}^2 m_{if}^2,$$

$$\vec{\zeta} = \vec{n}_c + \vec{v}\frac{\vec{k}\vec{n}_c}{\omega_{if}},\ m_{if}\vec{n}_c = \langle\phi_i|\vec{r}_\perp|\phi_f\rangle$$

here axial channeling is assumed, $\vec{n}_c$ is the crystallographic direction along which channeling is taking place, $|\phi_i\rangle, |\phi_f\rangle$ are wavefunctions of initial and final states, P_i, P_f are occupations of these states. In contrast to the case I, in order to describe the spontaneous emission of channeling radiation one has to treat the noise current of channeled particles quantum-mechanically:

$$\hat{\vec{j}}_0(\vec{k},\omega) = -ie\sum_i \hat{\sigma}_-^{(i)} e^{-i\vec{k}\vec{r}_i^{(0)}} m_{if} \times \quad (10)$$

$$\omega_{if}\vec{\zeta}\delta(\omega - \vec{k}\cdot\vec{v} - \omega_{if}) + h.c.,\ \hat{\sigma}_- = |i\rangle\langle f|$$

The electromagnetic field operators should be treated quantum mechanically as well, however if we use the Heisenberg picture one can apply boundary conditions similar to the classical case and use form similar to Maxwell equations to calculate observable values [3]. The electromagnetic field in the crystal can be presented as

$$\hat{\vec{E}}(\vec{k},\omega) = \sum_s \hat{\vec{E}}_s(\vec{k}_{||},\omega)\delta(k_z - k_z^{(s)}(\vec{k}_{||},\omega)) + \quad (11)$$

$$G(\vec{k},\omega)\frac{4\pi i\omega}{c}\hat{\vec{j}}_0(\vec{k},\omega)$$

here the first summand corresponds to homogeneous part of the electromagnetic field that is described based on equation similar to (6) with susceptibility (9) instead of (5), $k_z^{(s)}$ are the solutions of the dispersion equation $\text{Det}L(\vec{k},\omega) = 0$ as a function of frequency ω and component of the wavevector parallel to the crystal surface $\vec{k}_{||}$; the second summand corresponds to inhomogeneous part of the field due to spontaneous current, $G(\vec{k},\omega) = L(\vec{k},\omega)^{-1}$ is the Green function.

In the considered case at the intersection of (4) and (1) that corresponds to direction given by deviation from surface normal equal to $\theta = \sqrt{2\omega_{if}/\omega - 1/\gamma^2 - |\chi_0|}$, the imaginary part of the wavevector comes out to be $\delta k = \pm i\frac{\omega}{c}\sqrt{\frac{\chi_b}{2}}$ that under the conditions given at Fig.1 results in gain length about 0.8 mm that is much larger than the dechanneling length.

However, this length can become significantly smaller if larger number of dispersion surface branches are brought to resonance. This situation can take place if the dispersion surface (4) comes close to the dispersion branches corresponding to transmitted and reflected waves, see Fig.1. In this case if channeling axes makes angle $\alpha = \sqrt{|\chi_0|}$ to the sample surface and the radiation is observed at angle $\beta = \sqrt{2\omega_{if}/\omega - 1/\gamma^2 - |\chi_0|}$ one can obtain based on the dispersion equation for deviation from resonance that $\delta k_z = \pm i\frac{\sqrt{3}}{2}\frac{\omega}{c}\left(\frac{\chi_b}{\beta}\right)^{\frac{1}{3}}$ if the conditions $\left(\frac{\chi_b}{\beta}\right)^{\frac{1}{3}} \sim (\text{Im}\chi_0)^{\frac{1}{2}}$ are fullfilled. In the case of parameters of Fig.1 one can see that the gain length decreases to a quantity comparable with the dechanneling length. In the future work we plan to investigate this case in more details.

REFERENCES

[1] V. G. Baryshevsky and I. D. Feranchuk, Phys. Lett. A. 102 (1984) 141.

[2] arXiv:1509.01489 (2015).

[3] R. Matloob, R. Loundon, S. M. Barnett and J. Jeffers, Phys. Rev. A. 52 (1995) 4823.

ISBN 978-3-95450-181-6

PRODUCTION OF INTENSE BEAMS OF IRON IONS FROM ECR ION SOURCES BY MIVOC METHOD AT THE CYCLOTRON DC-60

A.E. Bondarchenko, K.I. Kuzmenkov, V.N. Loginov, Joint Institute for Nuclear Research, FLNR, Dubna, Russia
V.V. Alexandrenko, A.A. Amirova, M.V. Zdorovets, Astana branch of Institute of Nuclear Physics, Astana, Kasakhstan
I.A. Ivanov, E.K. Sambayev, A.E. Kurahmadov, S.G. Kozin, D.B. Kadyrzhanov, Astana branch of Institute of Nuclear Physics, Astana, Kasakhstan and Eurasian National University named after L.N. Gumilyov, Kazakhstan
A.E. Ryskulov, Eurasian National University named after L.N. Gumilyov, Kazakhstan

Abstract

The article describes the experiments carried out in 2015 at the accelerator complex DC-60 of Astana branch of the INP (Alma-Ata, Kazakhstan Republic), to develop methods for production of intense beams of multi charged ions of iron with the use of volatile compounds (Metal Ions from Volatile Compounds) – MIVOC [1]. As a result of performed work for the first time at DC-60 cyclotron a beam of iron ions was obtained, acceleration mode of $^{56}Fe^{10+}$ ions to the energy of 1.75 MeV/n was optimized

PRODUCTION OF IONS $^{56}Fe^{10+}$ USING VOLATILE COMPOUNDS MIVOC

For production of the iron ions from the ECR ion source DECRIS-3 [2] the ferrocene compound $Fe(C_5H_5)_2$ was used as a working substance. The working substance was put into the metallic container, which was connected to the ECR source via piezoelectric leak valve SNA-2.

The smoothly opening of the piezoelectric leak valve allows the injection of molecular flow of substance into the source. If the substance flow is not sufficient for stable source operation, helium can be used as a support gas. After optimization of the ECR ion source settings the following results were obtained: 50 eμa of Fe^{9+} ions, and 15.6 eμa of Fe^{10+} ions.

Figure 1 shows charge state distribution of iron ion beam, obtained after the bending magnet of the axial injection system of the DC-60 cyclotron, source settings being optimized for the production of Fe^{10+}.

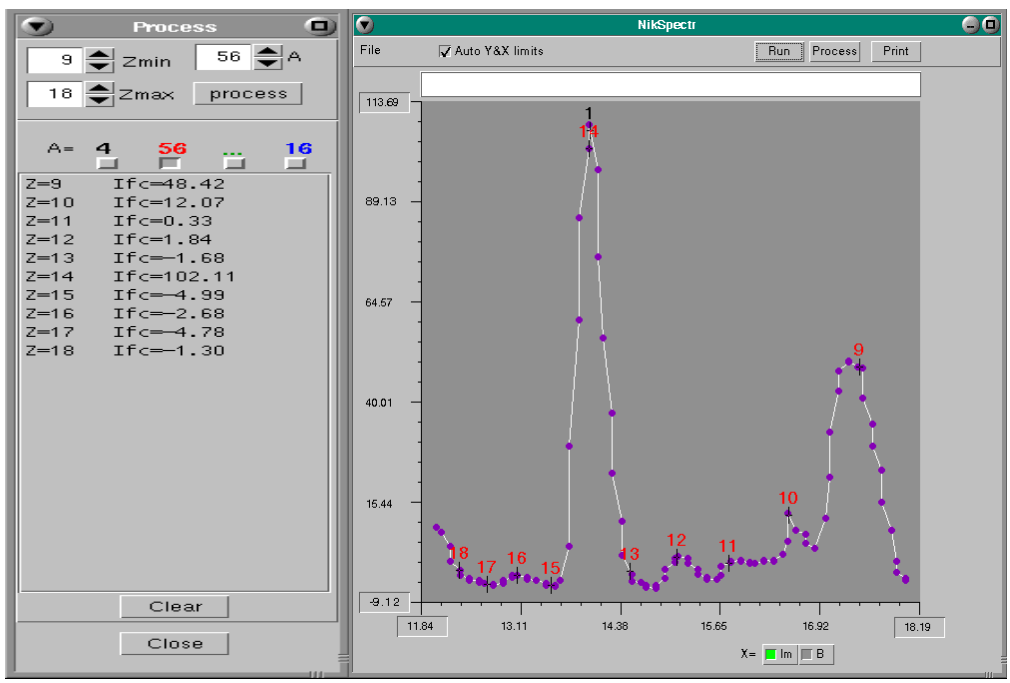

Figure 1: Charge spectrum of iron ions produced by the DECRIS-3 ion source. The position of Fe^{14+} ions coincides with the position of C^{3+} ions.

ISBN 978-3-95450-181-6

ACCELERATION OF $^{56}Fe^{10+}$ IONS

For the first time in Kazakhstan at the accelerator complex DC-60 the accelerated beam of $^{56}Fe^{10+}$ ions with the energy of 1.75 MeV/nucleon was produced. Calculated parameters of the acceleration mode are given in table 1.

After optimization of the axial injection system settings, the $^{56}Fe^{10+}$ ion beam was injected into the chamber of the cyclotron.

Table 1. Calculated parameters of the acceleration mode for $^{56}Fe^{10+}$ ions.

Atomic mass of ion	56
The charge of the ion	10
Mass to charge ratio A/Z	5.6
Field B_0, T	1.518
Field B_e, T	1.5209
The ion energy, MeV/nucleon	1.75
The current of the main magnet, A	249.2
The frequency of the RF generator, MHz	16.650
RF harmonic number	4
The injection voltage, kV	16.7
Type of inflector	"A"
Inflector voltage, kV	±6.7

In order to provide the maximum capture of the beam into the acceleration mode some improvements of the RF generator matching were performed, which result in the increase of TWR at a fixed workload of amplifying tetrode.

The optimization of cyclotron settings for the acceleration of $^{56}Fe^{10+}$ ions was performed. We investigate the influence of correction and azimuthal coils for magnetic field formation. The accelerated beam current at the extraction radius of the cyclotron obtained after optimization of operating modes of the axial injection system and of the cyclotron constitutes of 613 nA.

Figure 2 shows the radial dependence of the accelerated ion beam. It is seen, that radial distribution of the beam is almost uniform.

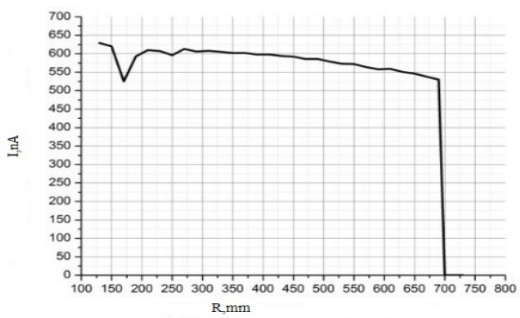

Figure 2: Radial dependence of the accelerated ion beam

Figure 3 shows the resonance curves of accelerated ion beam. The coincidence of the beam current maximum at different radial probe position indicates the correct configuration of the magnetic field.

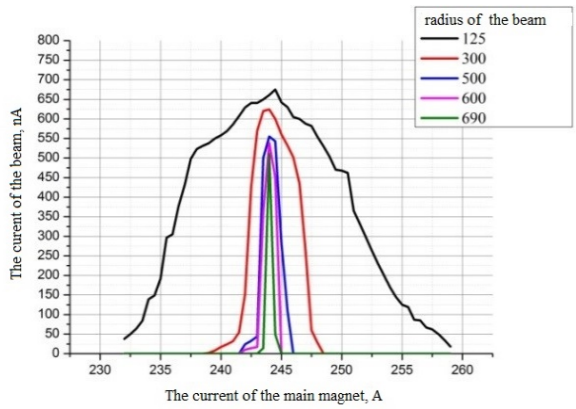

Figure 3: Dependence of $^{56}Fe^{10+}$ ion beam current from the level of magnetic field at different radius.

For production of the maximal current of the extracted ion beam the influence of the positions of the septum and potential deflector plates, and also deflector potential on the intensity of the extracted beam was studied. After optimization the extracted beam intensity of 240 nA was achieved.

$^{56}Fe^{10+}$ ion beam with the intensity of 241 nA was produced in the target chamber, thus the efficiency of beam transport from the extraction radius of cyclotron to the target constitutes of 39 percent.

CONCLUSION

As a result of performed work for the first time at the DC-60 cyclotron the accelerated beam of iron ions was obtained with the use of MIVOC method. After optimization of the ion source and acceleration mode settings 630 nA and 240 nA of $^{56}Fe^{10+}$ ions were obtained at the cyclotron extraction radius and in the transport channel correspondingly.

The widening of the range of accelerated ions increase the possibilities for the experiments in the field of nuclear physics, radiation physics of solids and various applications at the DC-60 cyclotron complex.

REFERENCES

[1] H. Koivisto, J. Arje, M. Nurmia Rev. Sci. Instrum., 69, (2). 1998, p. 785–787.

[2] A.Efremov et al. Proc. of the 14th Int. Worshop on ECRIS, CERN, Geneva, Switzerland, 1999, p.31-34.

ISBN 978-3-95450-181-6

PRODUCTION OF INTENSE METAL ION BEAMS FROM ECR ION SOURCES USING THE MIVOC METHOD

A. E. Bondarchenko, S. L. Bogomolov, K.I. Kuzmenkov, V.N. Loginov, V.Ya. Lebedev,
JINR, Dubna, Moscow Region, Russia
Z. Asfari, B. JP. Gall, IPHC, Strasbourg Cedex 2, France

Abstract

The production of metal ion beams by electron cyclotron resonance (ECR) ion sources using the MIVOC (Metal Ions from Volatile Compounds) method [1] is described. The method is based on the use of metal compounds which have high vapor pressure at room temperature, e.g., $C_2B_{10}H_{12}$, $Fe(C_5H_5)_2$, etc. Intense ion beams of B and Fe were produced using this method at the FLNR JINR cyclotrons. Experiments on the production of cobalt, chromium, vanadium, germanium, and hafnium ion beams were performed at the test bench of ECR ion sources.

Main efforts were put into production and acceleration of ^{50}Ti ion beams at the U-400 cyclotron. The experiments on the production of Ti ion beams were performed at the test bench using natural and enriched compounds of titanium $(CH_3)_5C_5Ti(CH_3)_3$. All these efforts allowed the production of accelerated titanium and chromium ion beams at the U-400 cyclotron.

PRODUCTION OF METAL IONS USING THE MIVOC METHOD

The experiments on the production of chromium, cobalt, vanadium, nickel, and hafnium ion beams were performed using the DECRIS-2m (Dubna ECR ion source) source [2] installed at the test bench. Natural compounds $Cr(C_5H_5)_2$, $Co(C_5H_5)_2$, $V(C_5H_5)_2$, $Ni(C_5H_5)_2$, and $(C_5H_5)_2Hf(CH_3)_2$ were used as working substances. For the production of germanium ions, two compounds were tested, i.e., tetraethylgermane $Ge(CH_2CH_3)_4$ and tetramethylgermanium $Ge(CH_3)_4$. Experiments with tetramethylgermanium yielded better results. The results obtained at the test bench are presented in Table 1.

Table 1. The intensity (eμA) of metal ion beams produced at the test bench using the MIVOC method (* - intensity optimisation)

Z	5+	6+	7+	8+	9+	10+	11+	12+	13+
Fe		43	93	125	172	145*	114	73	45
Co		57	80	86	98		82*	25	
Cr	50	70*	60	37	17	7			
V	75*	54	41	54	55.5*	43	34	19.5	
Ni		45*	43	48	53*		30	10	
Ge			43*	54		47*			
Z	13+	14+	16+	17+	18+	19+	20+		
Hf	31	45	50*	45*	36	27	17		

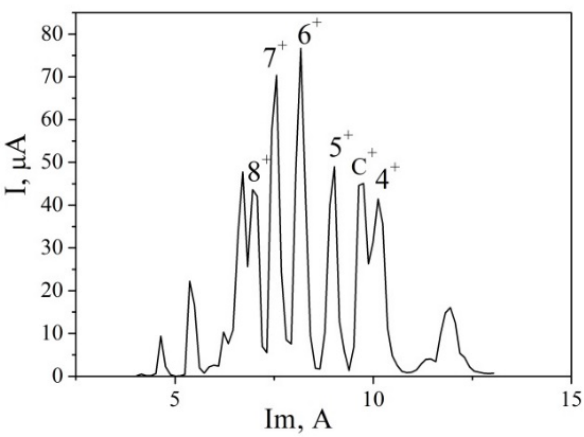

Figure 1. Charge spectrum of chromium ions produced by the ECR4M source.

After the tests ^{48}ti and ^{52}cr ions were accelerated at the u-400 cyclotron for the experiments on fission physics using the $c_5(ch_3)_5ti(ch_3)_3$ and $cr(c_5h_5)_2$ compounds as a working substances. the stable beams of ti^{5+} and cr^{6+} were produced during three weeks experiments.

Figure 1 shows charge state distribution of chromium ion beam, obtained after the bending magnet of the axial injection system of the u-400 cyclotron, source settings being optimized for the production of cr^{6+}.

ISBN 978-3-95450-181-6

PRODUCTION OF TITANIUM ION BEAMS

Major progress in the titanium-50 beam production was achieved through collaboration between IPHC (Strasbourg, France) and FLNR JINR.

Following several years of developments in chemistry carried out at IPHC, the $C_5(CH_3)_5Ti(CH_3)_3$ compound was synthesized using 92.57% enriched ^{50}Ti. Two-step chemistry was done with quite high efficiency from $TiCl_4$ to $C_5(CH_3)_5Ti(CH_3)_3$ through an intermediate $C_5(CH_3)_5TiCl_3$ organic compound.

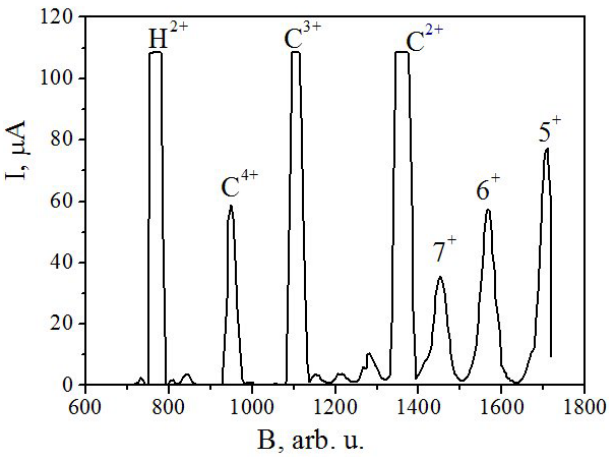

Figure 2. Charge spectrum of titanium ions produced in the ECR4M source using the MIVOC method at the microwave power of 20 W

In long-term experiments at the test bench several samples of compounds and different methods of material feeding into the source were tested. The beam currents of Ti^{5+} - 80 mkA and Ti^{11+} - 70 mkA (Fig. 2,3) were achieved at different settings of the source.

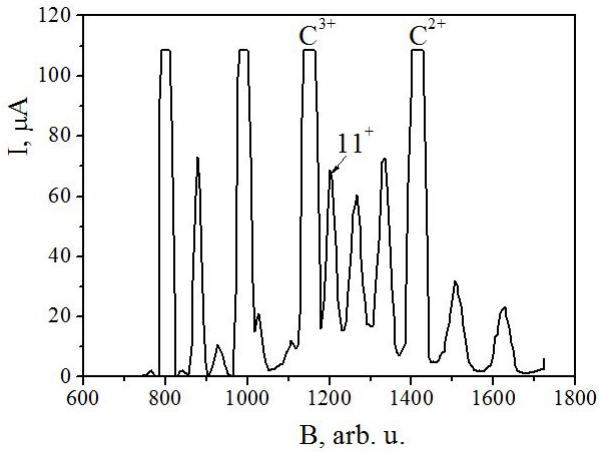

Figure 3. Charge spectrum of titanium ions produced in the ECR4M source using the MIVOC method at the microwave power of 300 W

Following successful tests, in October 2013 the first 3-week run was performed with ^{50}Ti beams at the U-400 cyclotron aimed to perform experiments on the spectroscopy of super heavy elements [3]. The intensity of the injected $^{50}Ti^{5+}$ beam was 50–60 μA. The source worked stably during experiment. The compound consumption rate was determined at about 2.4 mg/h, which corresponded to the ^{50}Ti consumption of 0.6 mg/h.

Since that, next three runs with ^{50}Ti beams were performed at the U-400 cyclotron. The durations of runs were from three to six weeks. The intensity of the ^{50}Ti beam and compound consumption were similar to those in the first run. Typically, the container with about 850 mg of compound allows the non-stop operation of the source during two weeks.

Table 2 summarizes the results of the titanium ion beam production at different laboratories using the MIVOC method (JYFL, GANIL, FLNR) and oven technique (GSI, ANL, IMP).

Table 2. The intensity (eμA) of titanium ion beams produced at different laboratories using the MIVOC[(a)] and oven[(b)] methods.

	JYFL[(a)]	GANIL[(a)]	FLNR[(a)]	GSI[(b)]	ANL[(b)]	IMP[(b)]
$^{48}Ti^{5+}$			79			
$^{48}Ti^{10+}$		20				
$^{48}Ti^{11+}$	45		68			24
$^{50}Ti^{5+}$			82			
$^{50}Ti^{8+}$				50		
$^{50}Ti^{11+}$	20					
$^{50}Ti^{12+}$					5.5	

ISBN 978-3-95450-181-6

CONCLUSION

Over the past few years, notable results and significant progress have been achieved in the production of intense multiply charged metal ion beams in ECR ion sources using the MIVOC method.

The MIVOC method was successfully used for producing and accelerating titanium-50 ion beam at the U-400 cyclotron. This method helps produce intense ion beams, provides long-term stability and is promising for experiments on synthesis of superheavy elements.

REFERENCES

[1] H. Koivisto, J. Arje, M. Nurmia, Rev. Sci. Instrum., 69, (2). 1998, p. 785–787.
[2] V.N. Loginov et al., Nukleonika 2003, Volume 48(Supplement 2), p. S853–6 S88
[3] A.V. Yeremin et al. Part. Nucl. Letters, 2015 V. 12, N1 (192), p.74 – 80.

ISBN 978-3-95450-181-6

COMPARATIVE RESEARCH OF LOW ENERGY BEAM TRANSPORT SYSTEMS FOR H-MINUS ION BEAM

B.A.Frolov, National Research Centre "Kurchatov Institute" State Research Center of Russian Federation – Institute for High Energy Physics, Protvino, Moscow Region, Russia
V.S.Klenov, Institute for Nuclear Research, Russian Academy of Science, Moscow, Russia

Abstract

The source of H-minus ions for the injection in LU-30 accelerator is constructed in IHEP. A three-dimensional simulation code IBSimu (Ion Beam Simulation) has been utilized for modeling of the transport and matching system of beam from the H-minus ion source into RFQ. A magnetic low energy beam transport (LEBT) line consisting of two solenoids and LEBT consisting of six magnetic quadrupole lenses were analyzed. The particle data from the 50 mA 100 keV ion beam extraction system simulations were taken as the starting data for the LEBT simulations. The final aim of calculations was to achieve the required Twiss parameters and to minimize emittance growth of beam at RFQ entrance. LEBT consisting of two solenoids is more convenient in adjustment and as simulation results have shown this system offers more acceptable beam characteristics at the match point in comparison with LEBT composed of quadrupole lenses.

INTRODUCTION

The collaboration of IHEP and INR is developing the source of H-minus ions for injection in the linear accelerator LU-30. The implementation of the negative ion source as the linear accelerator injector and the organization of multi-turn charge-exchange injection at the circular accelerator exit U-1.5 (buster) will allow to several times raise the intense of the IHEP acceleration complex. This will provide new possibilities for fundamental research and applied studies. For charge-exchange injection implementation the source generating H-minus ion beams with the following parameters: current ≥ 50 mA, pulse duration – 25 μs, repetition rate - 25 Hz, energy of ions -100 keV, normalized rms emittance ≤ 0.25 π mm·mrad, e/H^- ratio < 5 is being developed. The surface-plasma source with the Penning gas-discharge chamber with axially symmetric emission aperture at the ion source exit was chosen as a source of H-minus ions. The three-electrode ion-optical system (IOS) was simulated with 3D code IBSimu [1] to extract H-minus ions from plasma, form beam and accelerate it up to the energy of 100 keV in [2].

At the LU-30 accelerator entrance the ion beam with the energy of 100 keV should have the following parameters: normalized 4•rms emittance (for the 50 mA beam current) ε ≤1π mm·mrad and Twiss parameters of phase ellipse α=2.3, β=0.14. In [2] as a first approximation the beam transportation through the two solenoid matching channel to the RFQ entrance was simulated with by code TRACE-2D. Matching channel calculations done with the help of TRACE-2D do not take into consideration the fields distribution and space charge and do not allow to evaluate the beam emittance growth at its transportation to RFQ. In the current work the 3D modelling of the whole system including three-electrode IOS and two-solenoid LEBT with consideration of real field distribution for the 50 mA beam current was done with the help of code IBSimu. The matching channel consisting of the magnetic quadrupole lenses was examined. For the quadrupole lenses channel it resulted hard to provide the beam matching with the accelerator entrance because of considerable angle divergence which the beam acquires at the drift length before the channel entrance. IOS consisting of five electrodes was projected to reduce the radius and the beam divergence angle at the matching channel entrance.

IOS OF BEAM EXTRACTION AND ACCELERATION TO 100 KEV

The three-electrode IOS of H-minus ions extraction is formed by plasma, extraction and acceleration electrodes. Plasma electrode works as gas discharge anode and is at the impulse potential of 100 kV. The extraction electrode potential is +20 kV relative to the plasma electrode, acceleration electrode is ground. Emission aperture with 3 mm diameter was selected upon analog of the version of the penning source developed in BINP SB RAS [3]. The selection of the three-electrode IOS optimal geometry (radii of extraction (2 mm) and acceleration (2 mm) electrodes and lengths of extracting (3.3 mm) and accelerating (7.5 mm) gaps) was done [1] basing on a series of detailed calculation under the condition of getting minimal emittance at the matching channel entrance. 3D modeling and IOS optimization was carried out with the help of code IBSimu taking into account scattered transverse magnetic field of penning discharge for the H-minus beam current of 50 mA with the co-extracted electrons current of 150 mA.

IOS variants with additional electrodes with accelerating or decelerating potential were investigated to reduce the radius and divergence angle of the beam at matching channel entrance and to extend IOS focusing capacities. The optimal variant which ensured minimal emittance growth in such a system consisting of five electrodes with the potential of 0 kV - 20 kV - 100 kV - 50 kV – 100 kV (in the line of beam) is demonstrated in fig.1. The first three electrodes have the same geometry (diameters and gaps) as those in the 3-electrode IOS. The radius of the forth electrode is 2.5 mm and the distance from it to the third and fifth electrodes is 4 mm. The ion source magnetic field with the induction of around 0.1-

ISBN 978-3-95450-181-6

0.15 T protrudes to the beam extraction and acceleration area and deflects the negative ions off-axis in the extraction and acceleration gaps. Two corrector dipoles with the opposed fields are used to return the beam back to axis with the null angle deflection. SmCo (10×20×10 mm^3) dipole-antidipole magnet configuration (with magnetic yoke and auxiliary winding) is located in the drift gap between the acceleration electrode and LEBT.

In simulation the ions and electrons transverse temperature was set to 2 eV, plasma potential to 10 eV, the initial energy of particles to 5 eV, number of each sign particles to 25 000. The source, dipoles, solenoids and quadrupoles magnetic fields were calculated with ANSYS and the magnetic field data were imported in IBSimu. Figure 1 shows the ions (red) and electrons (yellow) trajectories in IOS considering the source and dipoles magnetic fields. The residual magnetic field of source quite properly separates the electron flux from ion beam and deflect electrons on the extraction electrode. The simulation has been carried out with gas-discharge chamber peak magnetic field of 0.1 T.

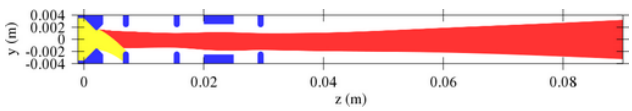

Figure 1: Trajectories of H-minus ions (red) and electrons (yellow) from 3D simulation of the five-electrode IOS.

The Einzel lens composed of the electrodes with 100-50-100 kV potentials reduces the beam radius and divergence angle at LEBT entrance for the 5-electrode IOS in comparison with the 3-electrode IOS (see below the Twiss-parameters in the table 1 and table 2). Additionally the lens makes possible tuning these parameters. Figure 2 shows the beam phase space distribution in horizontal x-plane and vertical y-plane at z = 90 mm.

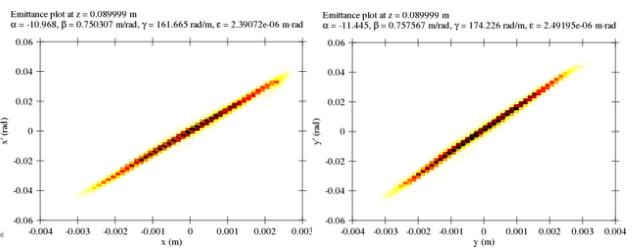

Figure 2: Calculation transverse emittance plot in xx'-plane (left) and in yy'-plane (right) from 3D simulation shown in the fig. 1 at z=90 mm.

BEAM SIMULATIONS FOR TWO-SOLENOID MAGNETIC LEBT

Constant step mesh is used for calculations in the code IBSimu. For this reason 3D simulations of IOS and LEBT were carried out in two stages. IOS was calculated with the small step (5·10^{-2} mm) of mesh, which is needed for extraction beam process simulations in the emission electrode area. LEBT simulations were carried out on a mesh with bigger step. The LEBT was simulated starting with the phase coordinates of particles from the three-electrode IOS simulation. The matching channel consisted of two solenoids, that were located at z=0.08 m and z=0.805 m respectively. The length of each solenoid with magnetic yoke is 255 mm, the aperture radius is 60 mm. The distance of 470 mm between solenoids is meant for gas evacuation and diagnostic device allocation. The whole length of two-solenoid magnetic LEBT up to RFQ entrance is 1250 mm. As a result of simulations the peak magnetic field on the axis equals 0.524 T and 0.496 T in the first and second solenoids for achieving the required Twiss parameters with minimal beam emittance growth at RFQ entrance. Figure 3 shows the H-minus ions trajectories through the LEBT for 50 mA beam current. The beam phase portraits in xx'-plane and yy'-plane at the LEBT exit are shown in figure 4.

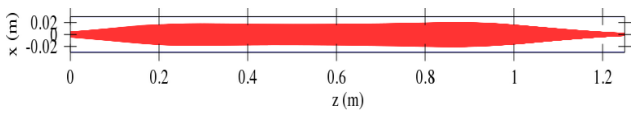

Figure 3: Trajectories of H-minus ions through two-solenoid LEBT for 50 mA beam current.

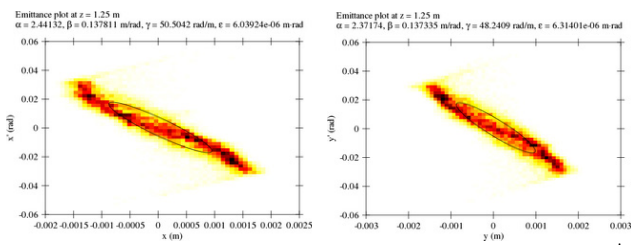

Figure 4: Calculation transverse emittance plot in xx'-plane (left) and in yy'-plane (right) at the two-solenoid LEBT exit.

Twiss-parameters and rms emittances at the two-solenoid LEBT entrance and exit are listed in the table 1. Twiss-parameters at the matching channel exit are closed to required at the RFQ entrance. Exact matching is not possible because of beam deviations at the LEBT entrance from xy-symmetry. The beam emittance value increased in 2.4 times in both planes at the LEBT exit. The normalized 4•rms emittance equals 0.35 π mm·mrad in xx'-plane and 0.37 π mm·mrad in yy'-plane at the matching point.

Table 1. Twiss-parameters and rms emittances at the two-solenoid LEBT entrance (top line) and exit (bottom line).

α_x	β_x m/rad	E_{rms}•10^{-6} m•rad	α_y	β_y m/rad	E_{rms}•10^{-6} m•rad
-19.5	1.43	2.55	-18.4	1.34	2.63
2.44	0.138	6.04	2.37	0.137	6.31

ISBN 978-3-95450-181-6

BEAM SIMULATIONS FOR QUADRUPOLE LENS MAGNETIC LEBT

The quadrupole lenses LEBT utilization instead of the two-solenoids LEBT decreases the equipment and exploitation costs. The five-electrodes IOS allows to use the system consisting of six quadrupole lenses (at reasonable lengths and diameters), bunched two triplet, for beam matching with RFQ. The phase coordinates of particles at the LEBT entrance corresponded to phase coordinates received on the five-electrode IOS exit at z=90mm. The quadrupole lenses LEBT variants with various geometry (length and diameter) and various distance between lenses were investigated. Quadrupole lenses geometry was chosen from the compromise between reasonable gradients requirement and the necessity of intensive beam transportation.

As a result of simulation and magnetic field optimization only approximate values of required Twiss parameters at the quadrupole LEBT exit were received. Figure 5 shows the H-minus ions trajectories for one of the most optimal variant of the matching channel in the xz-plane and yz-plane for 50 mA beam current. The aperture channel diameter is 80 mm, the poles length is 90 mm. The whole length of the quadrupole lenses LEBT is 1350 mm. Z coordinates of lenses are 0.07-0.16, 0.2-0.29, 0.33-0.42, 0.9-0.99, 1.03-1.12, 1.16-1.25 m. The corresponding magnetic field gradients of lenses equal ±4.156 T/m, ±5.226 T/m, ±2.731 T/m, ±2.797 T/m , ± 5.062 T/m, ±3.559 T/m (the upper sign is assigned to xz-plane, the lower sign to xy-plane). The beam phase portraits in xx'-plane and yy'-plane at the LEBT exit are shown in figure 6.

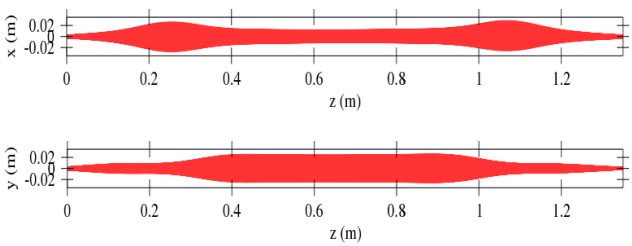

Figure 5: Trajectories of H-minus ions through quadrupole LEBT for 50 mA beam current in the xz-plane (at the top) and yz-plane (at the bottom).

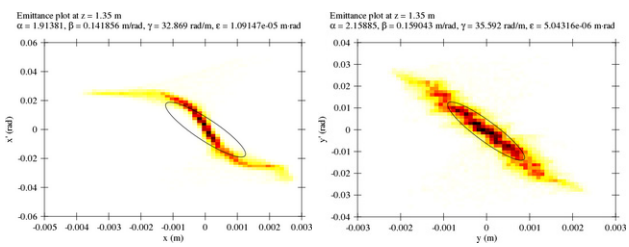

Figure 6: Calculation transverse emittance plot in xx'-plane (left) and in yy'-plane (right) at the quadrupole lenses LEBT exit.

Twiss-parameters and rms emittances at the six quadrupole lenses LEBT entrance and exit are listed in the table 2. The calculation data demonstrate noticeable aberration of the beam phase portrait and bigger growth of the emittance in xx'-plane (in 4.6 times) in comparison with yy'-plane (in 2 times) at the LEBT exit.

Table 2. Twiss-parameters and rms emittances at the six quadrupole lenses LEBT entrance (top line) and exit (bottom line).

β_x m/rad	α_x	$E_{rms}\cdot10^{-6}$ m•rad	α_y	β_y m/rad	$E_{rms}\cdot10^{-6}$ m•rad
-11.0	0.75	2.35	-11.4	0.758	2.49
1.91	0.142	10.9	2.16	0.159	5.04

CONCLUSIONS

The magnetic two-solenoid LEBT structure allows to get the beam with the close to optimal Twiss-parameters at the RFQ entrance for 50 mA beam current. In the same time the beam emittance grows in 2.4 times, which is absolutely acceptable. The magnetic quadrupole lenses LEBT allows to reach less satisfactory beam matching with bigger emittance growth in one of the planes. Let's notice that the matching channel of two solenoids is easy in tuning (by adjusting the two solenoid currents) in comparison with the six quadrupole lenses LEBT.

REFERENCES

[1] T. Kalvas, O. Tarvainen, T. Ropponen, O. Steczkiewicz, J. Ärje et.al., "IBSIMU: A three-dimensional simulation software for charged particle Optics", Rev. Sci. Instrum., **81**, 02B703 (2010).

[2] B.A. Frolov, V.S. Klenov, V.N. Mihailov, O.M. Volodkevich, "Simulation and Optimization of Ion Optical Extraction, Acceleration and H^- Ion Beam Mathing Systems", RuPAC2014-THPSC46, Obninsk, Russia, pp.429-431, (2014).

[3] Yu.I. Belchenko, A.I. Gorbovsky, A.A. Ivanov et.al., "Upgrade of CW Negative Hydrogen Ion Source" , AIP Conf. Proc.,1515, 448-455 (2013).

ISBN 978-3-95450-181-6

MODELING OF TRIODE SOURCE OF INTENSE RADIAL CONVERGING ELECTRON BEAM

V. Altsybeyev *, V. Engelko, A. Ovsyannikov, D. Ovsyannikov, V. Ponomarev
Saint-Petersburg State University, 7/9 Universitetskaya nab., St. Petersburg, 199034 Russia
R. Fetzer, G. Mueller
Karlsruhe Institute of Technology, Institute for Pulsed Power and Microwave Technology,
PO Box 3640, 76021 Karlsruhe, Germany

Abstract

The considered source of triode type produces intense radial converging electron beam for irradiation of cylindrical targets. As an electron emitter an explosive plasma cathode is used. The role of initial transverse velocities of electrons, defocusing effect of the controlling grid, the beam self-magnetic field, electron and ion emission from the controlling grid, backscattering of electrons and ion flow from the target is analyzed. Conditions for achieving required electron beam parameters (the electron kinetic energy - 120 keV, the beam energy density on the target 40 J/cm^2 on a maximum possible length of the target surface) were determined.

INTRODUCTION

In ref.[1] the design of the electron source of triode type producing an intense radial converging electron beam employed for modification of the outer surface of cylindrical targets (such, for example, as fuel element claddings) is described. In this paper we performed the set of numerical simulations and try to analyze the following physical effects arising in the considered source: the role of the initial transverse velocity of electrons, defocusing effect of the controlling grid, the beam self-magnetic field, backscatter of electrons, ion flow from the target. Using obtained results one can can determine the source parameters that ensures stable operation mode and conditions for achieving the required beam energy density on the target $\sim$ 40 J/cm^2 per 40-60 μs impulse. For numerical particle-in-cell simulations [2] the DAISI code will use [3–8].

SCHEME OF THE SOURCE

The electron source consists of the outer cylindrical cathode, anode and controlling grid [1]. The values of the main parameters are presented in Table 1.

Table 1: Parameters of the Source

Cathode length, m	$L = 0.98$ m
Cathode radius, m	$r_c = 0.15$ m
Grid radius, m	$r_g = 0.1$ m
Anode/Target radius, m	$r_a = 0.005$ m
Cathode-grid voltage, V	$U_{cg} = 20 - 40$ kV
Cathode-anode voltage, V	$U_{ca} = 80 - 140$ kV

* v.altsybeev@spbu.ru

In the new source design a multi-arc plasma cathode is applied. At such a cathode plasma is produced by a vacuum arc discharge provided by a large number of discharge gaps equally spaced on the cathode area. The space occupied by the plasma is separated from an external electric field by a separating grid. Such cathode design allows to control the value of the emission current density and to reduce the initial angular spread of electrons.

STABLE AND UNSABLE OPERATION MODES

We performed a set of simulations for different cathode–grid and cathode–anode voltages, for monopolar electron flow and bipolar electron and ion flows, for different grid electrode radius. Main results are the following. For each grid radius and cathode–anode voltage there is a critical value of the cathode-grid voltage U_{cr} dividing the mode of the source operation for stable and unstable regime (Fig. 1. As an example, $U_{cr} = 25$ kV for the grid radius $r_g = 0.1$ m and $U_{ca} = 120$ kV. If U_{cg} is less than or equal to the critical value the source operates stably, electron and ion trajectories are laminar, currents reach their stable magnitudes within several tens of nanoseconds, and the distribution of the power density on the target length 0.75 m is sufficiently homogeneous, as it is seen from.

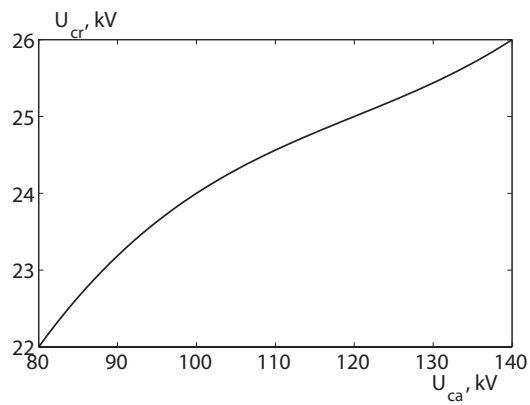

Figure 1: Dependence of U_{cr} on U_{ca} for $r_g = 0.1$ m.

When the cathode–grid voltage exceeds the critical value the source operation is unstable, electron and ion currents do not reach stable magnitudes, particle flows are not laminar. Under the influence of the beam self magnetic field electrons move from the edges of the source to its central part, which leads to inhomogeneity of the power density

ISBN 978-3-95450-181-6

distribution on the target (Fig. 2). In addition, the structure of the power density distribution is different in different moments of time, which is the consequence of unstable source operation.

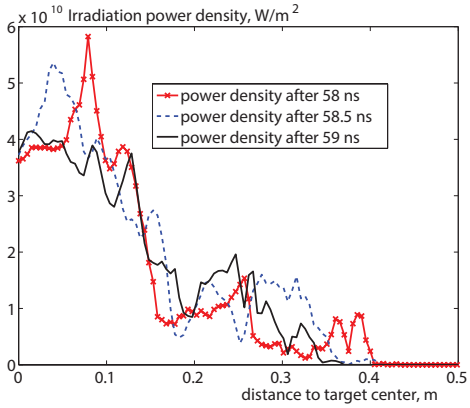

Figure 2: Power density on half of the target for different moments of time. $U_{cg} = 40$ kV, $U_{ca} = 120$ kV, $r_g = 0.1$ m.

THE ROLE OF THE TRANSVERSE VELOCITY OF ELECTRONS

Transverse velocity of electrons may be caused by the temperature of the cathode plasma or by the transverse electric field existing in the controlling grid region (108 wires with 0.2 mm in diameter). Let us consider first the grid effect. We performed simulations of electron beam dynamics in the source cross-section plane with taking into account real field distribution in the area of the controlling grid. In Fig. 3 an example of the potential distribution between wires is shown. One can see that the potential drop is rather small. Note, that the space charge of electrons slightly increases the potential drop while the space charge of ions decreases it. Fig. 4 illustrates the combined influence of the cathode plasma temperature and azimuthal electric field in the controlling grid region on the efficiency of the electron beam focusing to the target (I_e and I_t are electron emission current and current to the target correspondingly). Finally, calculations showed that the influence of the grid on the electron beam focusing can be neglected.

Calculations showed that the cathode plasma temperature significantly affects the source operation if T exceeds 30 eV. In particular, a part of electrons passes by the target and oscillates in the source volume (Fig. 5).

CONDITIONS FOR ACHIEVING THE REQUIRED BEAM ENERGY DENSITY

We performed a set of simulations for different cathode plasma temperatures, with taking into account electron backscatter from stainless steel target [9, 10], ion flow from target and beam self-magnetic field.

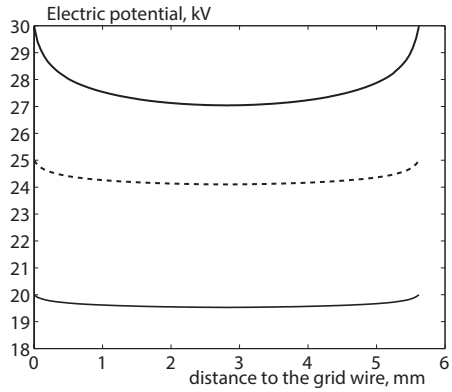

Figure 3: Distribution of electric potential between controlling grid wires for U_{cg} 20 kV, 25 kV, 30 kV, $U_{ca} =$ 120 kV, $r_g = 0.1$ m.

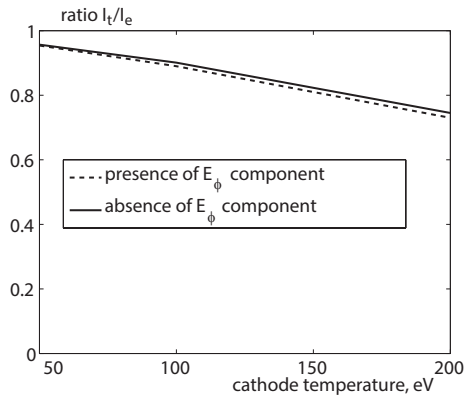

Figure 4: Dependence of the efficiency of the electron beam focusing to the target on the cathode plasma temperature and azimuthal electric field in the controlling grid region for $U_{ca} =$ 120 kV, $U_{cg} = 30$ kV, $r_g = 0.1$ m

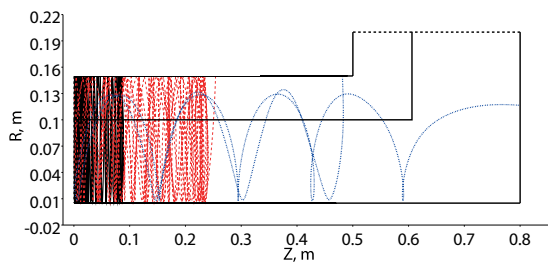

Figure 5: Examples of oscillating electron trajectories for $U_{ca} = 120$ kV, $U_{cg} = 20$ kV, $r_g = 0.1$ m. Trajectory started near cathode center (black solid line), trajectory started near cathode edge (blue dash-dot line), trajectory started between center and edge of cathode (red dashed line).

ISBN 978-3-95450-181-6

The increase of the cathode plasma temperature results in the emission current and power density suppression, especially near the target center where the density of oscillating electrons is larger. Note that in the presence of oscillating electrons, some oscillation of the electron current in time is observed (see Fig. 7). There are two types of oscillations – low-frequency and high-frequency. As the analysis shows, the low-frequency oscillations appear in the presence of backscattered electrons and high-frequency oscillations – in the presence of passing electrons. From proposed results one can conclude that the required energy density of the electron beam on the target (40 J/cm^2) can be achieved under the following conditions:

- the cathode–grid voltage value is 23–25 kV;
- the temperature of the cathode plasma is less than 50 eV;
- beam pulse duration is 30-40 μs;
- the beam current is removed from both sides of the target.

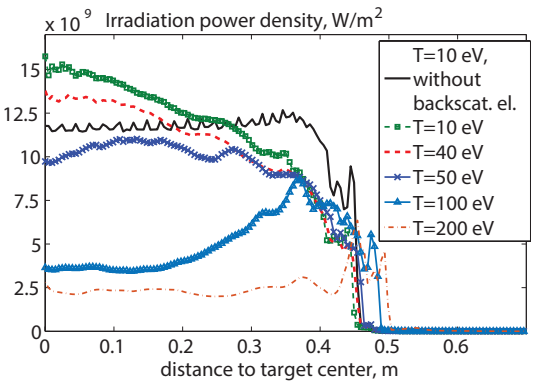

Figure 6: Power density on half of the target for different cathode temperatures for $U_{ca} = 120$ kV, $U_{cg} = 20$ kV, $r_g = 0.1$ m.

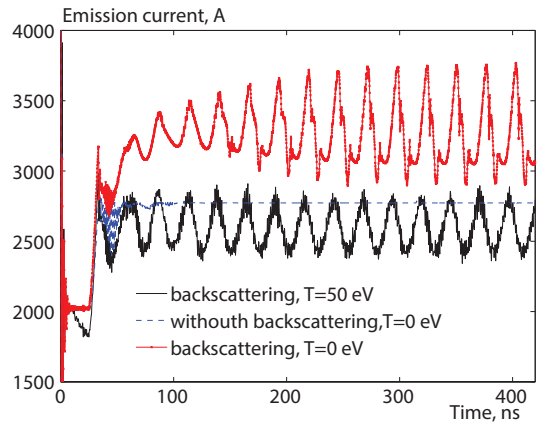

Figure 7: Dependence of emission currents on time for $U_{ca} = 120$ kV, $U_{cg} = 20$ kV, $r_g = 0.1$ m, $T = 50$ eV.

REFERENCES

[1] V. I. Engelko, V. S. Kuznetsov, and G. Mueller. "Electron source of triode type with radial converging electron flow for irradiation of cylindrical targets". In: *J. Appl. Phys.* 105 (2009).

[2] R. Hockney and J. Eastwood. *Computer Simulation Using Particles*. Francis, 1988.

[3] V. Altsybeyev et al. "Numerical simulation of a triode source of intense radial converging electron beam". In: *Journal of Applied Physics* 120.14, 143301 (2016). DOI: http://dx.doi.org/10.1063/1.4964335.

[4] V. V. Altsybeyev and V. A. Ponomarev. "Application of Gauss's law space-charge limited emission model in iterative particle tracking method". In: *Journal of Computational Physics* 324 (2016), pp. 62–72.

[5] V. V. Altsybeyev. "Numerical Simulations of the Charged-Particle Flow Dynamics for Sources with a Curved Emission Surface". In: *Physics of Particles and Nuclei Letters* 13.8 (2016), pp. 801–804.

[6] V. Altsybeyev et al. "Numerical simulations of the radial convergent electrons and ions flows for cylindrical pulsed source". In: *Stability and Control Processes in Memory of V.I. Zubov (SCP), 2015 International Conference*. 15637218. 2015, pp. 138–141.

[7] V. Altsybeyev and V. Ponomarev. "Development of 2D Poisson equation C++ finite-difference solver for particle-in-cell method". In: *Stability and Control Processes in Memory of V.I. Zubov (SCP), 2015 International Conference*. 15637294. 2015, pp. 195–197.

[8] V. Altsybeyev et al. "Numerical simulations of the radial electron flow formation for the triode type source". In: *10th International Vacuum Electron Sources Conference, IVESC 2014 and 2nd International Conference on Emission Electronics, ICEE 2014*. 6891934. 2014.

[9] V. Engelko et al. "Influence of electrons reflected from a target on the operation of triode-type electron sources". In: *J. Appl. Phys.* 88.7 (2000), pp. 3879–3888.

[10] B. V. Oliver, T. C. Genoni, and D. V. Rose. "Space-charge limited currents in coaxial diodes with electron backscattering". In: *J. Appl. Phys.* 90.10 (2001), pp. 4951–4956.

ISBN 978-3-95450-181-6

THE ELECTRON TRAJECTORIES CONSTRUCTION IN THE SYSTEM WITH A "REAL" GEOMETRY OF THE FIELD CATHODE

A. Yu. Antonov*, Saint Petersburg State University, Saint Petersburg, Russia
M. I. Varayun†, Saint Petersburg Electrotechnical University "LETI", Saint Petersburg, Russia

Abstract

The problems of the trajectories constructing for field electrons and emission images simulation are considered. As an approximation of the emitter shape an explicitly and implicitly defined surfaces are selected. Hyperboloidal, ellipsoidal and paraboloidal models are studied. Also an equipotential surface of the charged sphere-on-orthogonal-cone system is used. A simple solution of the field distribution problem is allowed to formulate the Cauchy problem for the motion equations. The shape of the anode (the projector microscope screen) can be selected in any desired form. Achieving a screen by electrons is performed with dense output technique in numerical approach to the solution. The distribution of the work function on the cathode surface is obtained. The trajectories for the projection of the field emission activity as the image are used.

INTRODUCTION

The phenomenon of field electron emission is a recognized tool for the analysis of electron sources. These sources are necessary for accelerating technology and for high-precision microscopes. Surface shape, distribution of the force field in the interelectrode space and the cathode material affect emission main characteristics. Advanced emitters search will be more relevant for a long time [1].

In this paper the number of the tasks required to build emission images are considered. Emission images show the current density distribution on the surface of the cathode. The source itself and the work function maps modeling, and the construction of electron trajectories in diode systems with elements of a statistical approach are performed.

PHYSICAL AND MATHEMATICAL MODELS

To initiate a field electron emission at low voltages V, sources are often made in the form of tips (figure 1).

Figure 1: Shapes of the real cathodes ([2], [3] and [4]).

* a.antonov@spbu.ru
† m.varayuan@spbu.ru

As the approximation of the emitter surface the part of the two-sheeted hyperboloid, prolate ellipsoid of revolution, paraboloid of revolution and sphere-on-orthogonal-cone system are utilized.

As emission control parameters of the system the radius of curvature r_0 at the top of the cathode, the distance d from the top of the cathode to the anode (screen), the voltage V between the electrodes are considered. As the example the following values were used: $r_0 = 1.00$ μm, $d = 2.00$ cm, $V = 20.0$ kV.

RESULTS AND DISCUSSION

The potential distribution is found by solving the Laplace equation. It exists in an analytical form for all of the systems in question [3], [5]. It leads us to the determination of the force field structure in the gap between the electrodes. For the example the picture of the field in the system with the paraboloidal tip is presented (figure 2).

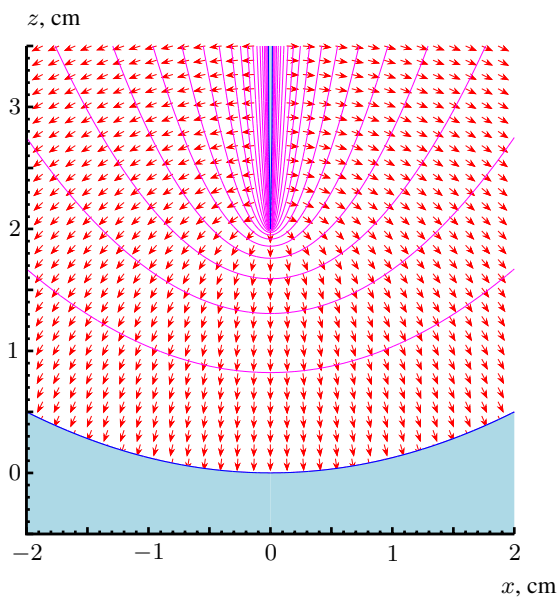

Figure 2: Equipotentials and force field.

For a single crystal cathode it is important to have an idea of the work function Φ distribution of on its surface. In the metal samples case the semi-empirical model proposed in [6] is well established:

$$\Phi = A + B\Delta t.$$

Here A and B must be found by linear regression method with the experimental data. Parameter Δt depends on the type of crystal lattice and Miller indices. The model has

ISBN 978-3-95450-181-6

successfully passed extensive statistical testing for materials such as W, Mo, Pt, Ir, Ta, Cu, Nb, Ni, Re, Ru [7], [8].

The figure 3 shows the distributions of the work function for Ni. The work function varies within regression model from 4.3 eV to 5.3 eV. Small values of Φ are colored in green, average values — in yellow, high values — in red. An algorithm for work function map constructing is published in [8].

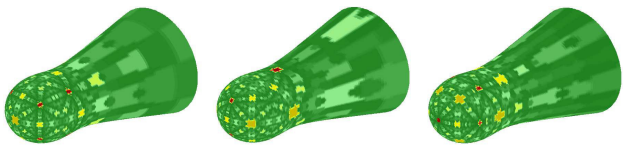

Figure 3: Maps of Φ: faces (001), (011), (111).

The basic law that reflects the dependence of the emission current density j on the electric field strength E and the work function Φ, is the Fowler—Nordheim formula [9]:

$$j = \frac{e^3}{8\pi h \Phi t^2(y_0)} E^2 \exp\left[-\frac{4\sqrt{2m}}{3\hbar e E}\Phi^{\frac{3}{2}} v(y_0)\right],$$

$$y_0 = \frac{e}{\Phi}\sqrt{\frac{eE}{4\pi\varepsilon_0}}.$$

Here e is the elementary charge, h is the Planck constant, m is the electron mass, $t(y)$ and $v(y)$ are the Nordheim's elliptic functions. One of the most successful approximations of the Nordheim functions presented in [10].

In fact, j determines the probability density of the electron escape from a specific point on the cathode surface. This value can be calculated with more accurate way to solving the Schrödinger equation and using the temperature dependence of the electron energy distribution [11]. Runge—Kutta—Nyström method with Dormand—Prince coefficients of 12-th order with embedded method of 10-th order is used [12]. Integration of the current density is performed with Simpson and Bode rules [13].

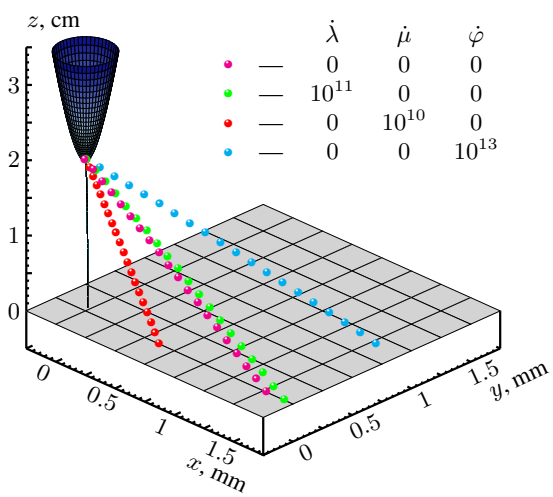

Figure 4: Electron trajectories.

The next step is the projection of the current density distribution on the screen. This procedure can be accomplished through field lines or by constructing the trajectories of emitted particles [14]. Figure 4 demonstrates the calculated trajectories for the hyperboloidal tip. Here λ, μ and φ are prolate spheroidal coordinates. Generalized velocities corresponds to the thermal values. Integration of the motion equations is carried out by Runge—Kutta method with Dormand—Prince coefficients of 8th order with two embedded methods of 5th and 3rd order [12]. Screen surface achievement is monitored by dense output based on method's continuous expansion of 7th order.

The velocity distribution of electrons required to the formulation of the Cauchy problem for the motion equations is obtained on the basis of the total and normal energy distributions (figure 5). Here $E = 5.0 \cdot 10^9$ V/m, $T = 300$ K, $\Phi = 4.5$ eV, Fermi energy $\mathscr{E}_F = 5.78$ eV (last two values corresponds to tungsten) [13].

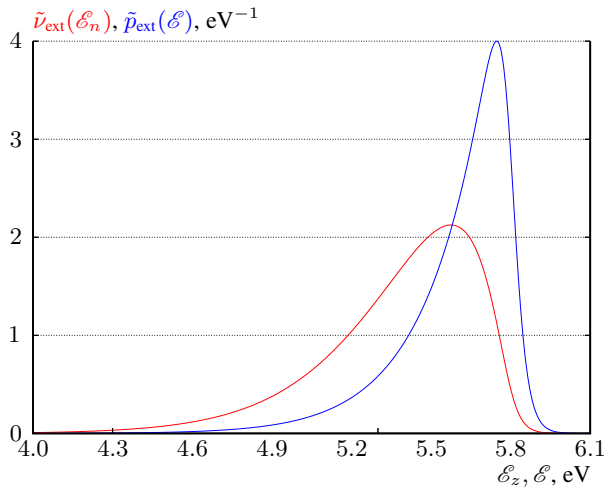

Figure 5: Normalized electron energy distributions.

Figure 6 illustrates emission images of tungsten obtained in the natural experiment.

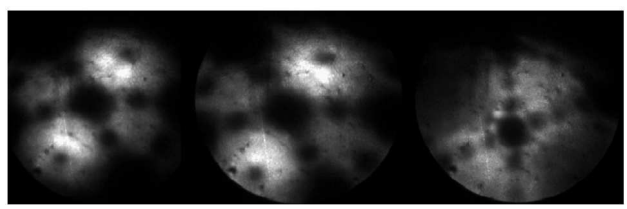

Figure 6: Tungsten emission images [15].

Figure 7 demonstrates the results of the statistical modeling for the tungsten emission image. On the top of the tip the face with Miller indices (001) is located. We can say that the picture qualitatively faithfully describes the situation (it should be noted that the real surfaces has unavoidable defects and inhomogeneities).

ISBN 978-3-95450-181-6

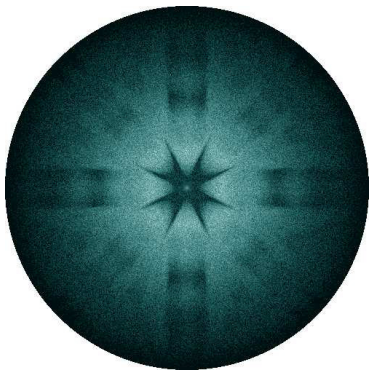

Figure 7: Emission image modeling.

CONCLUSION

In the paper the field emission images simulation of single crystal cathode of tip form is performed. The software package implements surface modeling and work function distribution algorithms. On the basis of the electric field and the current density evaluations the electron energy distributions and coordinates of escape are constructed. The projection of the emission image on the screen is carried out with the motion equations solution.

ACKNOWLEDGMENT

The study has been funded by Russian Science Foundation (Grant No. 15-19-30022).

REFERENCES

[1] K. Nikifirov, V. Trofimov and N. Egorov. Field emission spectroscopy of silicon carbide: natural modelling // "Stability and Control Processes" in Memory of V.I. Zubov (SCP), 2015 International Conference, St. Petersburg, 2015, pp. 180–182.

[2] Sh. Hasegawa and F. Grey. Electronic transport at semiconductor surfaces — from point-contact transistor to micro-four-point probes // Surface Science, Vol. 500, No. 1, 2002, pp. 84–104.

[3] W.P. Dyke, J.K. Trolan, W.W. Dolan and G. Barnes. The field emitter: fabrication, electron microscopy, and electric field calculations // Journal of Applied Physics, Vol. 24, No. 5, 1953, pp. 570–576.

[4] A.-D. Müller, F. Müller, M. Hietschold, F. Demming, J. Jersch and K. Dickmann. Characterization of electrochemically etched tungsten tips for scanning tunneling microscopy // Review of Scientific Instruments, Vol. 70, No. 10, 1999, pp. 3970–3972.

[5] C.F.A. Souza, N.P. Andion and C.M.C. de Castilho. Electric potential and field near pointed shaped surfaces // Journal de Physique IV, Vol. 6, No. 5, 1996, pp. C5-55–C5-58.

[6] S.A. Surma. Correlation of electron work function and surface-atomic structure of some transition metals // Physica Status Solidi A, Vol. 183, No. 2, 2001, pp. 307–322.

[7] N.V. Egorov, A.Yu. Antonov and I.M. Gribkova. Statistical Test of a Single Semiempirical Work Function Model // Journal of Surface Investigation. X-ray, Synchrotron and Neutron Techniques, Vol. 8, No. 1, 2014, pp. 138–143.

[8] A.Yu. Antonov, M.I. Varayun', I.M. Gribkova and E.Yu. Pigul'. Mathematical modelling of the work function distribution on a monocrystalline cathode surface // "Stability and Control Processes" in Memory of V.I. Zubov (SCP), 2015 International Conference, St. Petersburg, 2015, pp. 144–147.

[9] L.W. Nordheim. The effect of the image force on the emission and reflexion of electrons by metals // Proceedings of the Royal Society A, Vol. 121, No. 788, 1928, pp. 626–639.

[10] R.G. Forbes. Simple good approximations for the special elliptic functions in standard Fowler—Nordheim tunneling theory for a Schottky—Nordheim barrier // Applied Physics Letters, Vol. 89, No. 11, 2006, pp. 113–122.

[11] N.V. Egorov, L.I. Antonova and A.Yu. Antonov. Experimental and Numerical Investigation of the Emission Properties of a Cathode with a W-Cs3Sb Coating // Journal of Surface Investigation. X-ray, Synchrotron and Neutron Techniques, Vol. 6, No. 6, 2012, pp. 906–910.

[12] E. Hairer, S.P. Nørsett and G. Wanner. Solving ordinary differential equations I. Nonstiff problems. 2nd edition. Springer, 2008. 528 pp.

[13] N.V. Egorov, A.Yu. Antonov and N.S. Demchenko. Statistical modeling of the energy spectra for the field emission electrons // Technical Physics, Vol. 87, No. 2, 2017, pp. 175–181. (In russian)

[14] A.Yu. Antonov and N.S. Demchenko. Electron trajectory construction in the emission system // Vestnik Sankt-Peterburgskogo Universiteta. Seriya 10. Prikladnaya Matematika. Informatika. Protsessy Upravleniya, No. 3, 2010, pp. 3–12. (In russian)

[15] D.V. Zhukov, J. Plšek, Z. Knor. Metal-metal and metal-oxide-metal systems investigation with the field electron microscopy techniques // Journal of Surface Investigation. X-ray, Synchrotron and Neutron Techniques, No. 8, 2004, pp. 57–61. (In russian)

ISBN 978-3-95450-181-6

THE INFINITELY THIN FIELD EMITTER MATHEMATICAL MODELING

E.M. Vinogradova*, N.V. Egorov, E.V. Kalaturskaja,
Saint Petersburg State University,
7/9 Universitetskaya nab., St. Petersburg, 199034 Russia

Abstract

In this work an axisymmetric diode electron-optical system based on a field emitter is simulated. The field emitter in the form of a thin filament of finite length is located on the flat substrate with the dielectric layer. The anode is a plane. The electrostatic potential distribution was found in an analytical form — in the form of Fourier-Bessel series in the whole area of the system under investigation. The coefficients of Fourier-Bessel series are the solution of the system of linear equations with constant coefficients.

INTRODUCTION

The field emitters as a nanostructured materials with nanometer-scale sharp tips are extensively applied in the various domains of nano-scale electronic devices [1]– [3].

This article is devoted to the modeling of the axially symmetric emission diode system on the field emitter basis [4]. The field emitter is a thin filament of finite length on the flat substrate [5]. The cathode substrate is coated with a dielectric layer. The anode is a plane. Fig. 1 shows a schematic representation of the diode system. The potentials of the emitter and substrate are zeros.

To find the distribution of the electrostatic potential $U(r,z)$ the variable separation method in the cylindrical coordinates (r,z) for the axially symmetric system is used [6].

The problem parameters:

$r = R_1$ — the radius of the system region,

$z = 0\ (0 \le r \le R_1)$ — the surface of the emitter substrate,

$z = Z_1\ (0 \le r \le R_1)$ — the boundary between two dielectrics,

Z_2 — the emitter length,

$z = Z_3\ (0 \le r \le R_1)$ — the anode surface,

$U(r,0) = 0\ (0 \le r \le R_1)$ — the boundary condition at the substrate,

$U(0,z) = 0\ (0 \le z \le Z_2)$ — the boundary condition at the emitter,

$U(R_1,z) = f_1(z)\ (0 \le z \le Z_3)$ — the boundary condition at the surface $r = R_1$,

$U(r,Z_3) = f_2(r)\ (0 \le r \le R_1)$ — the boundary condition at the anode.

* e.m.vinogradova@spbu.ru

MATHEMATICAL MODEL

The electrostatic potential distribution $U(r,z)$ is the solution of the boundary value problem for the Laplace equation

$$\begin{aligned} &\triangle U(r,z) = 0; \\ &U(r,0) = 0, \quad 0 \le r \le R_1; \\ &U(0,z) = 0, \quad 0 \le z \le Z_2; \\ &U(R_1,z) = f_1(z), \quad 0 \le z \le Z_3; \\ &U(r,Z_3) = f_2(r), \quad 0 \le r \le R_1. \end{aligned} \tag{1}$$

The conditions on the the boundary $z = Z_1$ between two dielectrics with the the dielectric constants ε_1 and ε_0 can be written as:

— continuity conditions of the potential distribution

$$U(r,z)\Big|_{Z_1-0} = U(r,z)\Big|_{Z_1+0}, \tag{2}$$

— the normal derivative of the electric displacement vector continuity conditions

$$\varepsilon_1 \frac{\partial U(r,z)}{\partial z}\Big|_{Z_1-0} = \varepsilon_0 \frac{\partial U(r,z)}{\partial z}\Big|_{Z_1+0}. \tag{3}$$

SOLUTION OF THE BOUNDARY – VALUE PROBLEM

To solve the boundary value problem (1)–(3) the interior of the diode system can be divided into three subdomains:

1 — $(0 \le r \le R_1,\ 0 \le z \le Z_1)$ with dielectric constants ε_1,

2 — $(0 \le r \le R_1,\ Z_1 \le z \le Z_2)$ with dielectric constants ε_0,

3 — $(0 \le r \le R_1,\ Z_2 \le z \le Z_3)$ with dielectric constants ε_0.

Then the potential distribution $U(r,z)$ for $0 \le r \le R_1$ can be represented as:

$$U(r,z) = \begin{cases} U_1(r,z), & 0 \le z \le Z_1, \\ U_2(r,z), & Z_1 \le z \le Z_2, \\ U_3(r,z), & Z_2 \le z \le Z_3. \end{cases} \tag{4}$$

ISBN 978-3-95450-181-6

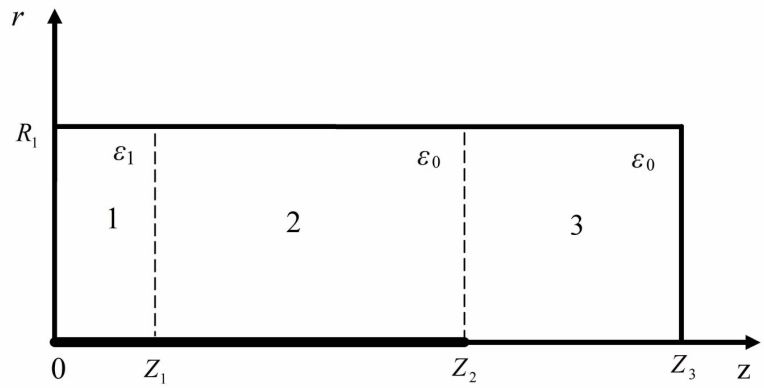

Figure 1: Schematic representation of the diode system.

According to the variable separation method functions (4) $U_i(r,z)$ $(i=1,2,3)$ are the Fourier-Bessel series:

$$U_1(r,z)=\sum_{n=1}^{\infty}A_n\frac{\sinh(\mu_{1,n}z)}{\sinh(\mu_{1,n}Z_1)}J_1(\mu_{1,n}r)+ \\ +\sum_{m=1}^{\infty}B_m\frac{I_1(\nu_m r)}{I_1(\nu_m R_1)}\sin(\nu_m z), \tag{5}$$

$$U_2(r,z)=\sum_{n=1}^{\infty}\left[A_n\frac{\sinh(\mu_{1,n}(Z_2-z))}{\sinh(\mu_{1,n}(Z_2-Z_1))}+ \right. \\ \left. +C_n\frac{\sinh(\mu_{1,n}(z-Z_1))}{\sinh(\mu_{1,n}(Z_2-Z_1))}\right]J_1(\mu_{1,n}r)+ \\ +\sum_{m=1}^{\infty}D_m\frac{I_1(\xi_m r)}{I_1(\xi_m R_1)}\sin(\xi_m(z-Z_1)), \tag{6}$$

$$U_3(r,z)=\sum_{n=1}^{\infty}\left[E_n\frac{\sinh(\mu_{0,n}(Z_3-z))}{\sinh(\mu_{0,n}(Z_3-Z_2))}+ \right. \\ \left. +F_n\frac{\sinh(\mu_{0,n}(z-Z_2))}{\sinh(\mu_{0,n}(Z_3-Z_2))}\right]J_0(\mu_{0,n}r)+ \\ +\sum_{m=1}^{\infty}G_m\frac{I_0(\eta_m r)}{I_0(\eta_m R_1)}\sin(\eta_m(z-Z_2)), \tag{7}$$

where $J_i(\mu_{i,n}r)$ — Bessel functions of the first kind,
$\mu_{i,n}=\gamma_{i,n}/R_1$, $\gamma_{i,n}$ — the zeros of Bessel functions: $J_i(\gamma_{i,n})=0$ $(i=0,1)$,
$I_1(\nu_m r)$, $I_0(\xi_m r)$, $I_0(\eta_m r)$ — modified Bessel functions of the first kind,
$\nu_m=\pi m/Z_1$,
$\xi_m=\pi m/(Z_2-Z_1)$,
$\eta_m=\pi m/(Z_3-Z_2)$.

The coefficients B_m, D_m and G_m for the potential distributions $U_i(r,z)$ (5)–(7) from the boundary conditions (1) at the surface $r=R_1$ can be calculated as:

$$B_m=\frac{2}{Z_1}\int_0^{Z_1}f_1(z)\sin(\nu_m z)\,dz, \\ D_m=\frac{2}{Z_2-Z_1}\int_{Z_1}^{Z_2}f_1(z)\sin(\xi_m z)\,dz, \\ G_m=\frac{2}{Z_3-Z_2}\int_{Z_2}^{Z_3}f_1(z)\sin(\eta_m z)\,dz. \tag{8}$$

The coefficients F_n for the potential distributions $U_3(r,z)$ (7) from the boundary conditions (1) at the anode surface $z=Z_3$ can be calculated as:

$$F_n=\frac{2}{R_1^2J_0^2(\gamma_{0,n})}\int_0^{R_1}r\,f_2(r)\,J_0(\mu_{0,n}r)\,dr. \tag{9}$$

To find the coefficients A_n, C_n, E_n the continuity conditions can be used. The condition (2) is satisfied automatically with the formulas (4)–(6).

The normal derivative continuity of the electric displacement vector continuity conditions (3) can be written as

$$\varepsilon_1\left.\frac{\partial U_1(r,z)}{\partial z}\right|_{z=Z_1}=\varepsilon_0\left.\frac{\partial U_2(r,z)}{\partial z}\right|_{z=Z_1}. \tag{10}$$

The additional conditions at the boundary $z=Z_2$ are:

$$U_2(r,Z_2)=U_3(r,Z_2), \tag{11}$$

$$\left.\frac{\partial U_2(r,z)}{\partial z}\right|_{z=Z_2}=\left.\frac{\partial U_3(r,z)}{\partial z}\right|_{z=Z_2}. \tag{12}$$

Making use of the orthogonal systems of eigenfunctions, the formulas (10)–(12) lead to the system of the linear algebraic equations in the unknown coefficients A_n, C_n, E_n.

ISBN 978-3-95450-181-6

CONCLUSION

In this article the axially symmetric emission diode system on the field emitter basis is presented. The diode system is defined as field cathode — a thin filament of finite length on the plane substrate and a plane anode. The cathode substrate is coated with a dielectric layer. The variable separation method is used in the cylindrical coordinates to find electrostatic potential distribution. To solve the boundary value problem (1)–(3) the interior of the diode system can be divided into three subdomains (4). The electrostatic potential distributions for each of the subdomain is found as the Fourier-Bessel series (5)–(7). Some of the coefficients (8), (9) are determined from the boundary conditions (1). The continuity conditions (10)–(12) on the subdomains interfaces are applied to calculate the remaining coefficients of Fourier-Bessel series as the solution of the linear algebraic equations system with the constant coefficients.

REFERENCES

[1] K. Heo et al., "Carbon and metal nanotube hybrid structures on graphene as efficient electron field emitters," Nanotechnology 27 (2016) 275301 (7pp).

[2] D. Ye et al., Nano Lett. 12 (2012) 1265.

[3] E.M. Vinogradova et al., Vacuum 127 (2015) 45.

[4] E.M. Vinogradova et al., Tech. Phys 60(2) (2015) 176.

[5] E.M. Vinogradova and V.O.Sergeev, 20th International Workshop on Beam Dynamics and Optimization, BDO 2014, Saint Petersburg, Article number 6890095.

[6] E.M. Vinogradova and N.V. Egorov, Journal of Communications Technology and Electronics, 49(2) (2004) 232.

ISBN 978-3-95450-181-6

SIMULATION OF S-BAND RF GUN WITH RF BEAM CONTROL

A. Barnyakov, A. Levichev, D. Nikiforov, BINP SB RAS, Novosibirsk, Russia
M. Maltseva, NSU, Novosibirsk, Russia

Abstract

The RF gun with RF control is discussed. It is based on the RF triode and two kinds of the cavities. The first cavity is a coaxial cavity with a cathode-grid assembly, where beam bunches are formed, the second cavity is required for the beam acceleration. The features of the gun are the following: bunched and relativistic beams in the output of the injector, absence of the back bombarding electrons, low energy spread and short length of the bunches. The scheme of the injector is shown. The electromagnetic field simulation and beam dynamics are presented.

INTRODUCTION

The RF gun with a thermionic cathode can be used as the injector. It is based on the cavity joint with the cathode-grid assembly [1, 2]. Emitted by the cathode electrons are accelerated by the cavity electric field. The main advantages of this system are the following. Firstly, the beam is immediately formed to the bunches that follow with the cavity frequency. Secondly, the particles can become relativistic at the output of the injector. This beam can be directly injected to the linear accelerator regular accelerating structures operating with a frequency of the injector cavities. But if the thermionic cathode without an additional control of the beam current is used, the electrons are emitted continuously. In this case some negative effects occur: wide energy spread of the particles at the injector output, back bombardment of the cathode and the cavity walls by the electrons, additional heating of the cathode. Besides that, output bunches have significant “tails”. Then, during the acceleration, these “tails” are usually lost. If they are of a high energy, an additional radiation background can occur when “tails” hit the inner walls of the accelerator channel.

To avoid disadvantages of the conventional RF gun the additional control cavity can be used. This cavity is coaxial type cavity with capacitance, which is based on the RF triode [3, 4]. Generating the necessary phase shift between the controlling RF signal (which is applied to the cathode-grid gap) and the electric field in the accelerating cavities, one can reduce the output bunch duration and decrease the particle spread. In case of a sufficient RF power in the accelerating cavities, particles at the injector output have ultrarelativistic velocities.

In this paper a principle scheme of the injector with a frequency of 2856 MHz is discussed. The control system of the beam current is described. Results of the output beam dynamics simulations with an emission current of 10 A are presented. The most attention is paid to the longitudinal beam dynamics. The beam emittance is unconsidered in the paper.

SCHEME OF THE INJECTOR

General scheme of the controlled RF gun is presented in Figure 1. RF power from the klystron which can also be used to feed the regular accelerating structures is transmitted to the gun accelerating cavities along the waveguide section through the isolator and the vacuum window. Part of the klystron power is derived to the coaxial cavity which is a part of the RF triode. The triode grid is the continuation of the accelerating cavity end wall. To tune the voltage amplitude on the cathode-grid gap and the phase delay relative to the accelerating cavities in the RF section of the coaxial cavity, an adjustable attenuator and a phase shifter are used. Cathode heating is realized by the power source through the inner conductor of the coaxial cavity. To compensate the accelerating cavity field which penetrates to the cathode-grid gap due to the grid transparency, an additional bias voltage can be applied.

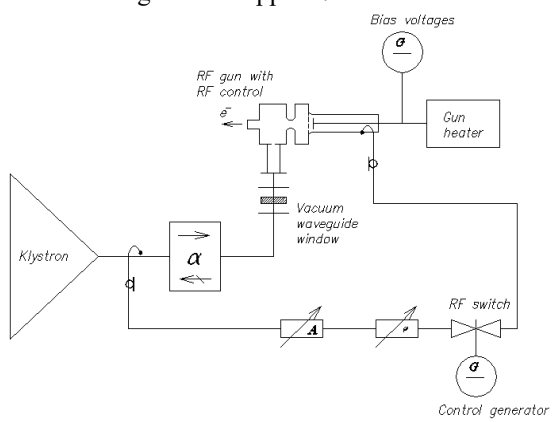

Figure 1: Scheme of the RF gun with RF control.

In the scheme of the RF gun with RF control presented in Figure 1, the common RF power generator is used to feed the accelerating cavities and the control coaxial one. In this case the beginning of the beam current pulse and its duration are always connected with the common RF pulse of the generator. For the independent control of the beam current duration without using an additional RF power source, it is proposed to use the coaxial RF switch at PIN diodes developed before [5-6]. By means of the control voltage on the diodes, one can let pass a RF signal through the coaxial line or provide its full reflection. The RF pulse edges have the duration of about 50 ns, so one can form the current with a pulse base duration of 100 ns. Also the independent RF power source for the control cavity can be

ISBN 978-3-95450-181-6

used. In this case the generator has to have an output RF power not less than 1.5 kW.

Electrodynamic characteristic calculations of the electron gun accelerating cavities were carried out by means of software package CST Studio [7]. The cavity consisting of 1.5 accelerating cells with the oscillation mode of π was used. Coaxial cavity includes the RF triode. As the triode GS-34 (developed in Russia) was used since it has the enough high emission current Pulse characteristics of the triode GS-34 are in [8].

Figure 2 shows the model of the injector with the electric field distribution inside the cavities. Coaxial cavity 1 has an inner diameter of 20 mm and the outer one of 50 mm, the length is 105 mm. Power input is implemented through the coaxial input of N-type 2 with radii of the conductors of 7 mm and 3 mm (outer and inner, respectively). Cathode-grid assembly 3 is inserted into the cathode focusing electrode 4. Parameters of the cathode-grid assembly are the following: cathode diameter is 12 mm, cathode-grid gap is 0.1 mm. Accelerating cavities 5 have a coaxial power input 6 with a waveguide port 7. This input was chosen for the electromagnetic field symmetrization inside the accelerating cavities. Waveguide 8 is an additional matching element and can serve for the vacuum pumping. The lengths of the accelerating cavities equaled 24.8 mm and 52.3 mm for the first cavity and the second one, respectively. Inner diameter of the coaxial input 6 is equal to 14 mm, the outer one is equal to 50 mm.

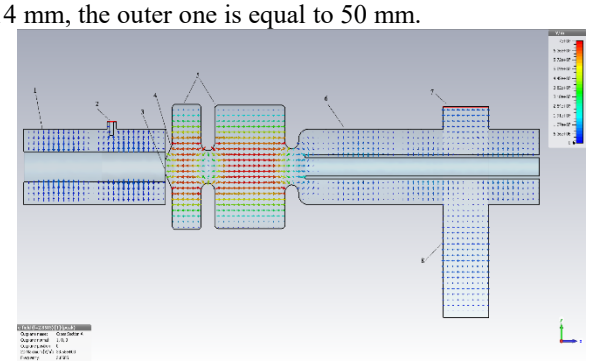

Figure 2: Model of the RF controlled RF gun. Fields agree with the power distribution: 4 MW in the accelerating cavities, 1.5 kW in the coaxial cavity.

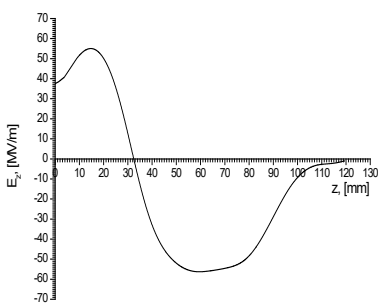

Figure 3: Distribution of the electric field amplitude on the axis of the accelerating cavities at the power of 4 MW.

Electric field distributions on the axis of the accelerating cavity is shown in Figures 3.

Figure 4 shows the electric field amplitude distribution that penetrates from the accelerating cavities to the cathode-grid gap of the coaxial cavity. According to this figure, electric field penetrates from the accelerating cavities to the cathode. Its amplitude there is not more than 2% of the field amplitude at the grid. So, the electric field with the amplitude of about 0.8 MV/m penetrates to the cathode and corresponds to the voltage at the cathode grid gap of 80 V. This additional voltage can be compensated by the bias voltage that, should not exceed 150 W by the absolute value [8].

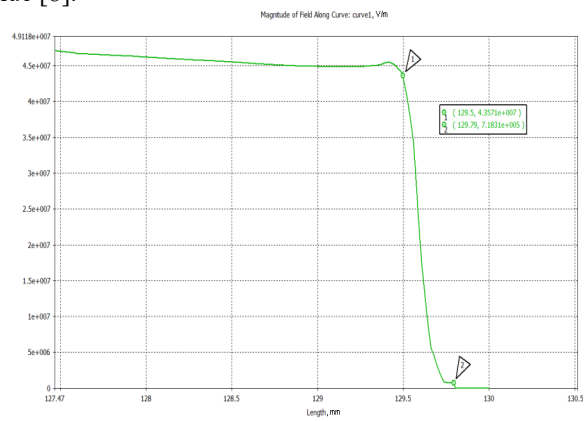

Figure 4: Electric field amplitude distribution penetrating from the accelerating cavities to the cathode-grid gap of the coaxial cavity at the excitation power of 4 MW. Marker 1 corresponds to the cathode position, marker 2 corresponds to that of grid.

PARTICLE DYNAMICS

Particle dynamics simulations were also carried out with help of CST Studio [7]. Because of computer ability limitation the accelerating cavity and the exciting one were considered to be independent in terms of the electromagnetic field. The grid was considered to be completely transparent for the beam. Phase shift between the control voltage in the coaxial cavity and the voltage in the accelerating cavities equaled about 120°. Field amplitudes are shown in Figs. 4 and 5. The cathode emission current was chosen 10 A.

Figure 5 shows the diagram of relationship between the beam current at the injector output and time. According to the figure, the beam consists of bunches with a frequency of about 2856 MHz. The phase length of a bunch is about 50°. The average output current is about 5 A that is 50% of the given cathode current. Figure 6 presents the energy spectrum of the beam at the RF power in the accelerating cavities of 4 MW. That shows the average beam energy equaled 3.1 MeV as well as the energy spread is 5% for 98% of the particles. Back travelling or lost in the cavity walls electrons are not observed. The grid influence on the angle distribution was not considered, as was already mentioned.

ISBN 978-3-95450-181-6

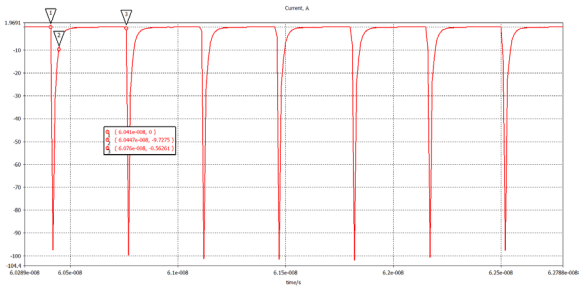

Figure 5: Beam current at the injector output.

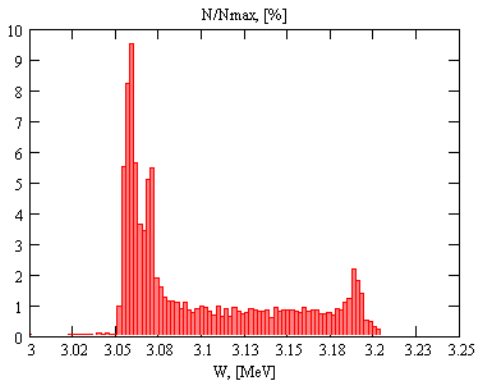

Figure 6: Energy spectrum of the beam.

Figure 7 shows the accelerated beam with the emission current of 10 A in the accelerating cavities at various moments of time. As one can see, the beam is matched with the drift channel due to using the special form of the cathode electrode.

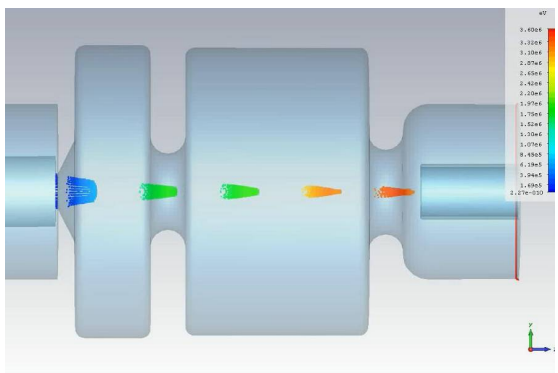

Figure 7: Transverse beam dynamics in the accelerating cavities of the RF controlled RF gun. The bunch is shown in various moments of time.

CONCLUSION

The detailed simulations show that RF gun with the RF control allows obtaining electron bunches with an operating frequency of the accelerator, relativistic velocity and small energy spread in a bunch. Besides, in this model high-energy particles that go back to the cathode or get to the injector walls are absent. The properly chosen profile of the cathode electrode is capable of focusing enough big charges without using an additional external magnetic field. The simulation of the RF power penetrating from the accelerating cavities through the grid to the exciting cavity did not show the significant voltage in the cathode-grid gap and this value can be compensated by bias voltage.

Proposed injector can be used in the complex, when the good emittance of the electron beam is not important, for example, for accelerators with conversion systems. Also this system can be applied for S-band industrial accelerators.

This work was supported by Russian Science Foundation (project N 14-50-00080).

ACKNOWLEDGMENTS

Authors would like to thank Y. D. Chernousov (Institute of chemical kinetics and combustion SB RAS), A. P. Sumbaev (Joint Institute of Nuclear Research) and V. V. Kobets (Joint Institute of Nuclear Research) for their advice and support.

REFERENCES

[1] V.L. Auslender, M.A. Batazova, G.I. Kuznetsov and et. al. Triode RF gun for linear accelerator. Proceedings of RuPAC IX, 2004, pp.**390-392**.

[2] V. Volkov, E. Kenjebulatov, S. Krutikhin and et. al. Thermo-cathode RF gun for BINP race-track microtone recuperator. Proceedings of EPAC 2008, pp. **2213-2215**.

[3] K. Masuda, K. Kusukame, T. Kii and et. al. Particle simulation of a thermionic RF gun with gridded triode structure for reduction of back-bombardment. Proceedings of the 27th FEL Conference. 2005, pp. **588-591**.

[4] S. H. Gold, A. Ting, V. Jabotinski and et al. Development of a high average current RF linac thermionic injector. PHYSICAL REVIEW SPECIAL TOPICS - ACCELERATORS AND BEAMS vol. 16, 083401, 2013.

[5] A. M. Barnyakov, A. E. Levichev, S. L. Samoilov and et al. A Microwave Coaxial Switch. Instruments and Experimental Techniques, pp.**389–394, v**ol. 58 (3), 2015.

[6] A. M. Barnyakov, Yu.D. Chernousov, V.I. Ivannikov and et al. The system of RF beam control for electron gun. JINST. 10 P06004, 2015.

[7] https://www.cst.com/

[8] Vacuum tubes. Reference lists. Electrostandart. 1989 (in Russia).

ISBN 978-3-95450-181-6

OPTIMIZATION OF AN RF PROBE VICINITY FOR RF GUN CAVITIES

V.V. Paramonov*, Institute for Nuclear Research of the RAS, Moscow, Russia

Abstract

To provide electron bunches with exceptionally high brightness, RF gun cavity should operate with the extreme electric and magnetic fields. The RF probe is required for the mostly reliable and precise measurements of the RF field phase and amplitude directly from the cavity. The implementation of an RF probe in the cavity design generates a set of coupled problems, which is analyzed and compared for different operating frequencies and different RF pulse length. Both general dependencies and particularities are considered. Some recommendations for practical choice of the RF probe are presented.

INTRODUCTION

RF gun cavities are intended for generation of high brightness electron bunches for Free Electron Lasers (FELs), based on linear accelerators. The normal conducting Fel's linacs operate in the S band frequency range with a relatively short length of RF pulse τ. For FEL's based on superconducting technology the L band range is adopted with much more long RF pulse. Instead of a large variety particular technical solutions, The major part of existing gun cavities is based on BNL concept, [1], which is shown in Fig. 1 with modern solutions. A gun cavity consists of two cells, surrounded by cooling circuit in cavity walls. The length of cells is optimized to have a small emittance of the bunch. A photo cathode is placed in the first short cell

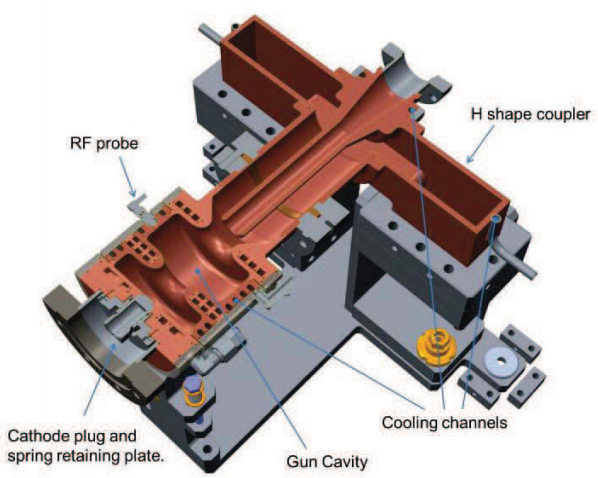

Figure 1: The modern design of RF gun cavity, [2].

of the cavity. For RF power input in Fig. 1 is shown the coaxial RF coupler to avoid an azimuthal nonhomogenuity of the cavity field. To provide electron bunches with an exceptionally high peak bunch current as well as a small transverse emittance, RF gun cavities should operate with an extreme electric field at the photo cathode E_c and, hence, in the total cavity. To provide the required performance of the FEL facility, the phase of the RF field in the gun cavity should be controlled with a maximal possible precision for synchronization with the main linac RF system. An RF probe in the cavity cell provides perturbation in the gun cavity surface resulting in perturbation of the field distribution both in the nearest probe vicinity and in the total cavity volume. It leads to a set of coupled effects, which are estimated below. To point out particularities of the cavity operating regime we will the S mode as operation with frequency $f_0 \approx 3\ GHz, E_c \approx 115\ \frac{MV}{m}, \tau \approx 3\ \mu s$ and L mode with parameters $f_0 \approx 1.3\ GHz, E_c \approx 60\ \frac{MV}{m}, \tau \approx 1000\ \mu s$.

EQUIVALENT CAVITY

For the analysis we have to know with the high precision the field distributions in a small region, compared in dimensions with a probe hole. This case the details of the total cavity design are not so important. To have the dense mesh and the high precision in numerical simulations the equivalent sector cavity was considered together with the probe hole vicinity, Fig. 2a. Simulations were performed by using ANSYS software, [3].

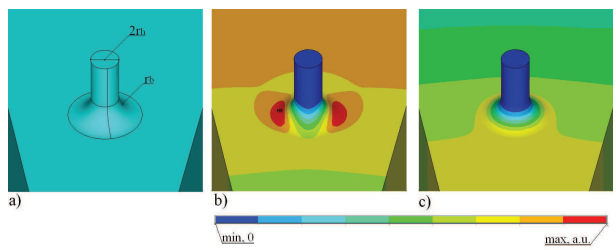

Figure 2: The equivalent cavity in with the RF probe hole, (a), and distributions of magnetic, (b), and electric, (c), fields intensity near the probe hole.

VICINITY OF THE PROBE HOLE

The set of coupled effects is estimated below.

Perturbation of the field distribution

Essential dimensions of the probe hole, the hole radius r_h and the radius of edge rounding r_b are shown in Fig. 2a. In the nearest vicinity the probe hole provides different perturbations in the distributions of electric and magnetic fields. For magnetic field the perturbation is like dipole addition, Fig. 2b, while for for electric field the perturbation is like monopole, Fig. 2c. Because the maximum values are interesting, let us consider the field enhancement, $\frac{H_{max}}{H_0}, \frac{E_{max}}{E_0}$, where H_{max}, E_{max} are the maximal values of field intensities in the probe vicinity and H_0, E_0 are the values of field

* paramono@inr.ru

ISBN 978-3-95450-181-6

intensities in case of an unperturbed cavity. The simulated results of fields enhancement are presented in Fig. 3. Until

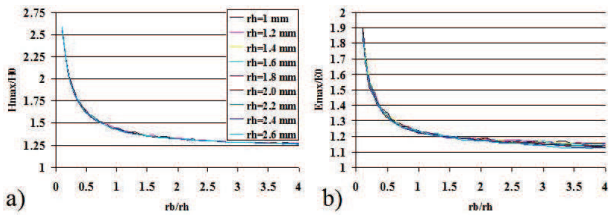

Figure 3: The plots of magnetic, (a), and electric, (b), fields enhancement in the probe vicinity.

the hole dimensions $r_h, r_b \ll \frac{\lambda}{4}$, where λ is the operating wavelength, the local field enhancement should depend on ratio $\frac{r_b}{r_h}$ only. It is the sequence of a static approximation for distributions of fields near the small hole and in Fig. 3 one can see practically merged curves for different r_h values. With $\frac{r_b}{r_h}$ increasing, for $\frac{r_b}{r_h} \geq 1.5$, the values for fields enhancement come to saturation and large r_b radius is not effective.

Together with a local perturbation of the field distribution in the nearest vicinity, the hole for the RF probe generates a field perturbation in the total cavity. The field $\vec{E}$ in a slightly deformed cavity can be described, [4], as:

$$\vec{E} \approx \vec{E}_0 + \sum_{m \neq 0} \vec{E}_m \frac{\omega_m^2 \int_{\delta V} (Z_0^2 \vec{H}_m \vec{H}_n^* - \vec{E}_m \vec{E}_n^*) dV}{W_0(\omega_0^2 - \omega_m^2)}, \quad (1)$$

where $Z_0 = \sqrt{\frac{\mu_0}{\epsilon_o}}$, $\omega_m, \vec{E}_m, \vec{H}_m$ are the own frequencies and own fields of the modes in the unperturbed cavity, δV is the volume of perturbation and W_0 is the stored energy of the fields. For the RF gun cavity the operating mode with symbol 0 in equation (1) is TM_{011} mode. The single hole couples with the operating mode all High Order Modes (HOM's) with azimuthal field dependence. For the cavity geometry, shown in Fig. 1 in the cavity spectrum below the cut off frequency of the RF coupler there are three dipole HOM's and just one quadrupole HOM with frequency $f \approx 1.7 f_0$. With two symmetrically placed holes for dipole HOM's the coupling integral over one hole in (1) cancels the integral over the second hole and dipole additions in the field disappear. Simultaneously the addition from the quadrupole HOM doubles and only the way to reduce it is to decrease the value of the coupling integral in (1). Because the hole dimensions are much less as compared to a typical distance of field variation for all HOM's, we can rewrite (1) for this single quadrupole HOM as:

$$\vec{E} \approx \vec{E}_o + \frac{\omega_q^2 (Z_0^2 \vec{H}_{qh} \vec{H}_{0h}^* - \vec{E}_{qh} \vec{E}_{0h}^*)}{W_0(\omega_0^2 - \omega_q^2)} \delta V \vec{E}_q, \quad (2)$$

where $\vec{H}_{qh}$ and $\vec{E}_{qh}$ are the HOM fields at the RF probe position. The HOM's additions in the field distributions are proportional to δV, which rises fast, $\delta V \sim r_h^3$ for $\frac{r_b}{r_h} = const$ and for $r_h = const, \delta V \sim r_b^2$, with increasing of hole dimensions.

Pulsed RF heating

The RF heating effect takes place in RF gun cavities, resulting in significant temperature rise T_{sp} at the cavity surface during the RF pulse. For an approximation of the flat surface there is well known estimation, see [6]:

$$T_{sp} = \frac{2P_d\sqrt{\tau}}{\sqrt{\pi \rho k_c C_p}} = \frac{2P_d D_p}{\sqrt{\pi} k_c}, D_p = \sqrt{\frac{k_c \tau}{\rho C_p}}, \quad (3)$$

where ρ, k_c, C_p are the density, heat conductivity and the specific heat for cavity material, which is, usually, OFHC copper, [6]. The diffusion length D_d is the effective length of heat propagation into cavity body. The temperature rise T_{sp} is proportional to RF loss density P_d. Since $P_d \sim H_{max}^2$, the local enhancement of magnetic field in the hole vicinity, Fig. 3a, leads to more sharp P_d increase, Fig. 4. For $\frac{r_b}{r_h} \leq 1$ we have strong P_d enhancement, but with r_b

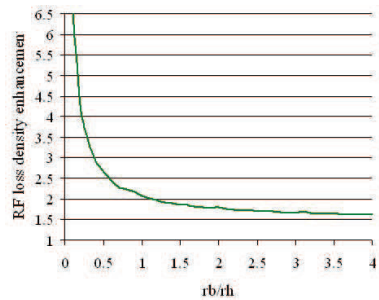

Figure 4: The plot of RF loss density enhancement.

increasing after $\frac{r_b}{r_h} \geq 2$ there is no essential decrease in P_d value.

For the S operating mode the diffusion length for OFHC

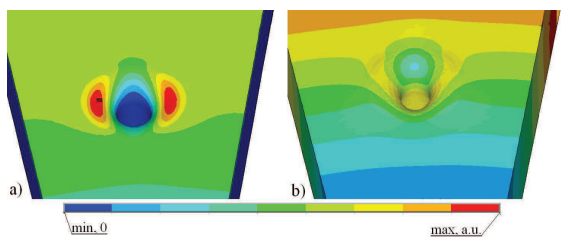

Figure 5: The distributions of the temperature rise T_{sp}, (a), and displacements, (b), in the vicinity of the hole, a.u.

copper $D_d = 19\ \mu m$ is much less than the dimensions of the probe hole. The estimation (3) works fine, the T_{sp} distribution at the cavity surface reflects P_d distribution and for induced thermal stress σ is valid well static approximation, [7]:

$$\sigma = \frac{\alpha E_{Ym} T_{sp}}{(1-\nu)}, \quad (4)$$

where α, ν and E_{Ym} are the thermal expansion, the Poisson's ratio and the elastic modulus for cavity material. For the operating L mode the diffusion length D_d is of $\approx 340\ \mu m$ and application of (3) and (4) is not so easy. Direct numerical simulations of the pulsed RF heatig for L mode

ISBN 978-3-95450-181-6

were performed following to the procedure described in [5]. The simulated distributions for T_{sp} and displacements in the hole vicinity are shown in Fig. 4.

Probe matching

For reliable RF measurements at the RF probe output the signal with RF power of $P_p \sim 1\ W$ is required. As compared to the total pulse RF power $P_i \approx (6 \div 8)\ MW$, dissipated in the cavity during RF pulse, P_p is the rather small value. We can consider the RF probe as the usual, but strongly mismatched RF coupler. Prescribing to the RF probe an equivalent external quality factor Q_e, from S parameters simulations we can define the required reflection coefficient S_{11} for this mismatched coupler:

$$Q_e = Q_0 \frac{P_i}{P_p}, S_{11} = \frac{Q_0 - Q_e}{Q_0 + Q_e} = \frac{P_i - P_p}{P_i + P_p} \approx 1 - \frac{2P_i}{P_p}, \quad (5)$$

where Q_0 is the own quality factor of the cavity. The expected Q_e value for gun cavities is of $\sim 10^{11}$ and simulations of S parameters also are sensible on an equivalent cavity, Fig. 4a, with the scaling of results to the real gun cavity. In the probe hole fields are essential at the depth $\sim r_b$, see Fig. 2b,c. Into the cylindrical part of the hole fields decay as $\approx exp(-\frac{2.6 \cdot d_i}{r_h})$ both for S and L modes, as confirmed by the slope of the straight line of $Q_e(d_i)$ dependence in Fig. 6b.

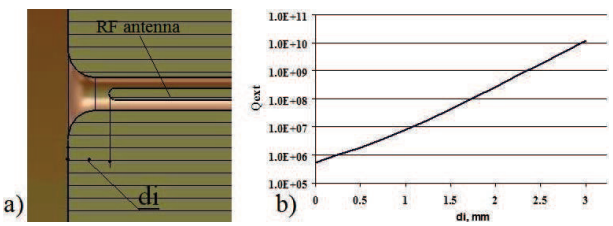

Figure 6: The model for S_{11} simulation, (a), and a typical $Q_e(d_i)$ dependence on antenna immersion, (b).

DISCUSSION AND CONCLUSION

From physical reasons the probe hole dimensions should be small, but from mechanical reasons we can not select very small values and $r_h \approx 1\ mm$ is reasonable both for L and S modes. But recommended rounding value r_b differs for these modes. Due to the short RF pulse the pulsed heating effects are not strong for S mode and at the outer cavity wall T_{sp} is of $\approx 10\ K$. The tolerable, safe, value, recommended in [6], is of $T_{sp} \approx 40\ K$. We can allow for probe vicinity to be after RF pulse a hot spot at the surface and for the rounding r_b selection the ratio $\frac{r_b}{r_h} \geq 0.5$ is tolerable. There are no limitations to place the RF probe at the outer cell surface, similar to Fig. 1.

For L mode the pulsed RF heating effects are much stronger due to the long RF pulse and after pulse already $T_{sp} \approx 40\ K$, [5]. Near the RF probe T_{sp} value should not exceed such value at the other cavity parts. The RF probe can't be place at the outer wall of the cavity with close to the maximal magnetic field. The probe should be moved to the front cavity wall with a lower $|H|$ value, simultaneously selecting $\frac{r_b}{r_h} \geq 1.5$ to restrict the local P_d enhancement. This case the diffusion length D_d is still much less than hole dimensions and expressions (3) and (4) work precisely. During the pulsed surface heating the value of the surface displacements is proportional to the heat deposited into the cavity body, [7], e.g. $\sim \tau P_i$. The simulated value of displacements with respect to unperturbed surface is of $\approx (0.12 \div 0.15)\mu m$, Fig. 5b. Taking into account $Q_e(d_i)$ dependence, Fig. 6b, we have a rough estimate for relative precision of field amplitude measurement during RF pulse as $\approx 0.1\%$. For S mode this effect is two orders less.

For the RF probe matching in S mode a smaller immersion of antenna tip d_i is required due to a smaller scaling factor from equivalent cavity. With the tip immersion in the range $1.0r_h \leq d_i \leq 2.5r_h$ the required RF power P_p can be obtained for both modes.

In ordinary simulations at the background of own numerical noises we can not distinguish the quadrupole addition in the cavity field. Just with noises filtering at the radius $r = 0.043\lambda$ we detect for L mode the quadupole additions in field components in the full cavity cell at the relative level $\leq 1.3 \cdot 10^{-4}$ along and no addition above the level of $\leq 1.0 \cdot 10^{-6}$ in the cathode cell. It is quite consistent with field distribution of the quadrupole HOM, coupled with operating mode by two holes. In S mode, for the same r_h, r_b values, the quadrupole addition is one order larger due to relative increasing of $\frac{\delta V}{V}$ in (2).

For S mode restrictions for RF probe dimensions increase come from HOM addition in the field distribution. The small rounding radius $r_b \sim 0.5r_h$ helps while keeping the effects of RF pulsed heating in tolerable limits. For L mode restrictions come form pulsed heating, require both larger hole rounding $r_b \sim 1.5r_h$ and probe position in the place with smaller magnetic field.

REFERENCES

[1] X.J. Wang *et al.*, "Design and Construction a Full Copper Photocathode RF Gun", in *Proc. PAC93*, Washington, USA, May 1993, pp. 3000–3002.

[2] B. Militsyn *et al.*, "Design of the high repetition rate photocathode gun for the CLARA project", in *Proc. LINAC14*, Geneve, Switzerland, Sep. 2014, pp. 1155–1157.

[3] ANSYS, `http://www.ansys.com`.

[4] V. Kulman, "Accelerating system", in *Ion linear accelerators*, B. Murin, Ed. Moscow, USSR: Atomizdat, vol. 2, pp. 36–46, 1978.

[5] V. Paramonov and A. Skasyrskaya, "Pulsed RF heating simulations in normal conducting L-band cavities", DESY, Hamburg, Rep. TESLA-FEL 2007-04, 2007.

[6] D. Pritzkau and R. Siemann, "Experimental study of rf pulsed heating on oxygen free electronic copper", *Phys. Rev. ST Accel. Beams*, vol. 5, p. 112002, 2002.

[7] A.D. Kovalenko, *Introduction to thermoelasticity*, Kiev, USSR, Naukova dumka, 1965.

ISBN 978-3-95450-181-6

FIRST EXPERIMENTAL DEMONSTRATION OF THE EXTRACTION OF LOW ENERGY BEAMS FROM THE ESR TO THE CRYRING@ESR

S. Litvinov, Z. Andelkovic, D. Beck, A. Braeuning-Demian, S. Fedotova, W. Geithner, R. Hess, F. Herfurth, C. Kleffner, I. Kraus, M. Lestinsky, F. Nolden, M. Steck, G. Vorobyev
GSI, Darmstadt, Germany

Abstract

The CRYRING@ESR facility [1] will provide the unique possibility for studying properties of highly charged cooled stable and short-lived ions stored at low energy for atomic and nuclear research within the FAIR project [2]. Heavy ion beams will be stored, cooled and decelerated to energies between 10 and 4 MeV/u in the ESR [3] and then delivered to the CRYRING@ESR. There is no dedicated kicker magnet for the fast extraction in this direction. However, a specially developed distorted closed orbit of the beam stored in the ESR in combination with the injection kicker has been suggested for the extraction and experimentally verified in 2014. In the first experiment the ion beam was extracted and transported over a distance of 20 m towards the CRYRING@ESR [4]. In the 2016 machine development run the heavy ion beam was successfully extracted from the ESR and delivered to the first fluorescent screen inside CRYRING@ESR for the first time. Detailed ion-optical simulations as well as the experimental results will be discussed.

CRYRING@ESR FACILITY

The Experimental Storage Ring (ESR) is a symmetric ring with two arcs and two straight sections and a circumference of 108.36 meters. The ESR consists of six 60° dipole magnets, 20 quadrupole and 8 sextupole magnets. The ESR can be operated at a magnetic rigidity in the range of 0.5 – 10 Tm. For reducing transverse and longitudinal emittances of the stored ion beams, the ESR is equipped with an electron cooler which is installed in one of the straight sections of the ring. Another straight section is foreseen for the experiments [3].

The CRYRING@ESR is a magnetic heavy ion storage ring with a circumference of 54.17 m, which corresponds to half of ESR perimeter. The CRYRING@ESR consists of twelve 30° dipole magnets connected by twelve straight sections, each of which is about 3.3 meters long. Every second section is occupied by a quadrupole triplet for the first-order focusing (18 quadrupoles in total) and 2 sextupoles (12 magnets in total) for the second-order corrections. The other straight sections are foreseen for the injection/extraction, electron-cooler, RF cavity, Schottky diagnostic and experiments. The ring will operate at a magnetic rigidity in the range between 0.054 and 1.44 Tm. Highly charged ions decelerated in the ESR to the lowest possible energy of 4 MeV/u then can be stored and decelerated in the CRYRING@ESR down to few 100 keV/u and delivered to the experiments [1].

The CRYRING@ESR is located behind the ESR and they are connected via a transfer line, which has a length of about 90 meters. The layout of the CRYRING@ESR facility is illustrated in Fig. 2.

CALCULATION

High energy ion beams are usually injected from the synchrotron SIS18 [5] into the ESR on the orbit of $\Delta p/p \approx +1\%$, and then stored and cooled with the electron cooler (solid black curve in Fig. 1). In order to keep the beam parallel to the electron beam in the cooler section, 4 horizontal correctors in 2 neighboring main dipole magnets are used. The ESR is equipped with one injection and two extraction septum magnets as can be seen in Fig. 2. The horizontal width of the beam pipe around the septa is 104 mm and in addition, there is the narrow knife of 17 mm width of each septum (see Fig. 1). The injection kicker magnet is placed after the first dipole downstream (see Fig. 2). The stored beam goes after the kick either to the northern extraction septum (towards HITRAP) or to the wall (dotted black curve in Fig. 1). In order to extract the beam properly to the CRYRING@ESR, it is necessary to change the trajectory of the kicked beam, such that it avoids the north extraction septum and the injection septum but reaches the southern extraction septum. This orbit distortion has been performed with a special bumped closed orbit, which has been calculated using 8 horizontal correctors in the 4 main dipoles, which are marked by brown boxes in Fig. 2. The corresponding trajectory is shown by the dashed black curve in Fig. 1. Applying the kick on the distorted orbit the beam can freely be extracted to the CRYRING@ESR (dotted-dashed red curve in Fig. 1).

EXPERIMENT

In August 2014, the calculations has been tested in an experiment at the ESR. Firstly, the proposed extraction scheme was verified with 100 and 400 MeV/u proton and $^{58}Ni^{26+}$ beams. The extracted beam was observed directly after the extraction septum using the TT1DF0 fluorescent screen (see Fig. 2). Later, a $^{14}N^{7+}$ beam at 30 MeV/u was injected, stored and stepwise decelerated to the final energy of 4 MeV/u ($B\rho = 0.58$ Tm), the lowest possible magnetic rigidity usable at the ESR. At each energy, the beam was successfully extracted, changing only the kick angle of the injection kicker by several tenths of a milliradian. The distortion orbit was unchanged.

ISBN 978-3-95450-181-6

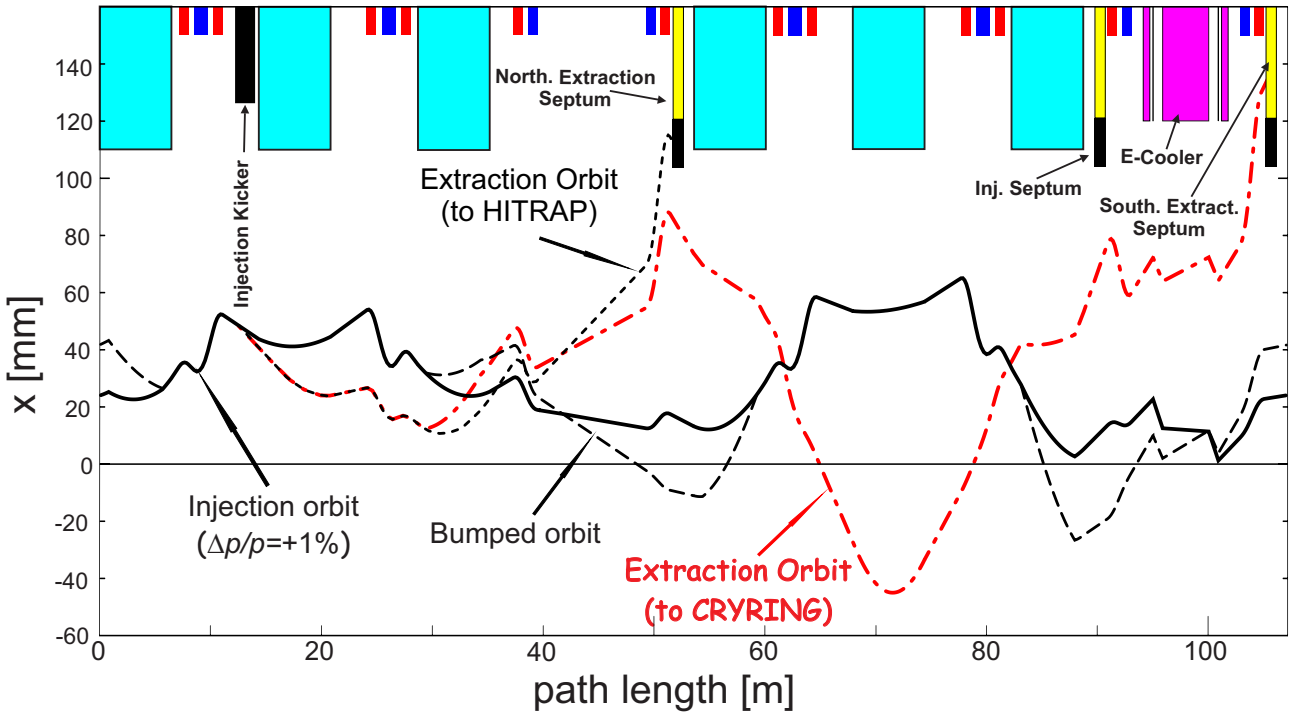

Figure 1: Calculated beam trajectories for one turn in the ESR. The injected stored and cooled orbit of $\Delta p/p = +1\%$ is indicated by the solid black curve. Its kicked orbit (extraction to HITRAP) is shown by the black dotted curve. The distorted bumped orbit is marked by the dashed black curve and its kicked orbit (extraction to CRYRING) is shown by the dotted-dashed red curve. Dipole, horizontal and vertical focusing quadrupole apertures are shown by cyan, red and blue boxes respectively.

In July 2016, during a dedicated experiment, a 6 MeV/u carbon beam using the extraction procedure described above, has been successfully extracted from the ESR. The beam transportation through the transfer channel was performed from stage to stage, observing beam spots at the fluorescent screens installed along the line, until the beam was injected into the CRYRING@ESR and detected at the last screen installed already in the ring. The corresponding beam spot images can be seen in Fig. 2. At least 60% of the ions stored in the ESR before extraction have been transmitted.

OUTLOOK

The primary goal of the experiment is reached, the low energy beam has been successfully delivered to the CRYRING@ESR. However, there is no complete ion-optical setting of the combined CRYRING@ESR structure. The rings are not ion-optically matched with the transfer line, which leads to the lack of transmission. The bottleneck of the matching is that the extraction channel goes through the ESR dipole magnet, whose stray field strongly affects the extracted beam. Its effect has been analyzed in Ref. [6] and has to be included in the matching procedure.

Instabilities of power converters of the transfer line magnets forced us to use during the experiment the ion-optical setting with stronger gradients than optimal, which however caused additional losses and requires therefore, the fine tuning of the linear optics.

REFERENCES

[1] M. Lestinsky et al., "CRYRING@ESR: present status and future research", Phys. Scr. T166, 014075 (2015)

[2] http://www.fair-center.eu/

[3] B. Franzke, "The heavy ion storage and cooler ring project ESR at GSI", NIM B 24-25, 18-25 (1987)

[4] S. Litvinov et al., "A novel scheme for fast extraction of low energy beams from the ESR to the CRYRING", GSI Report 2015-1, p. 433 (2015)

[5] K. Blasche, B. Franczak, "The Heavy Ion Synchrotron SIS", Proceedings of European Particle Accelerator Conference (EPAC), 9 (1992)

[6] B. Schillinger et al., "Ion optical stray field analysis of an ESR dipole" Proceedings in Particle Accelerator Conference, IEEE, 2594 – 2596 (1997)

ISBN 978-3-95450-181-6

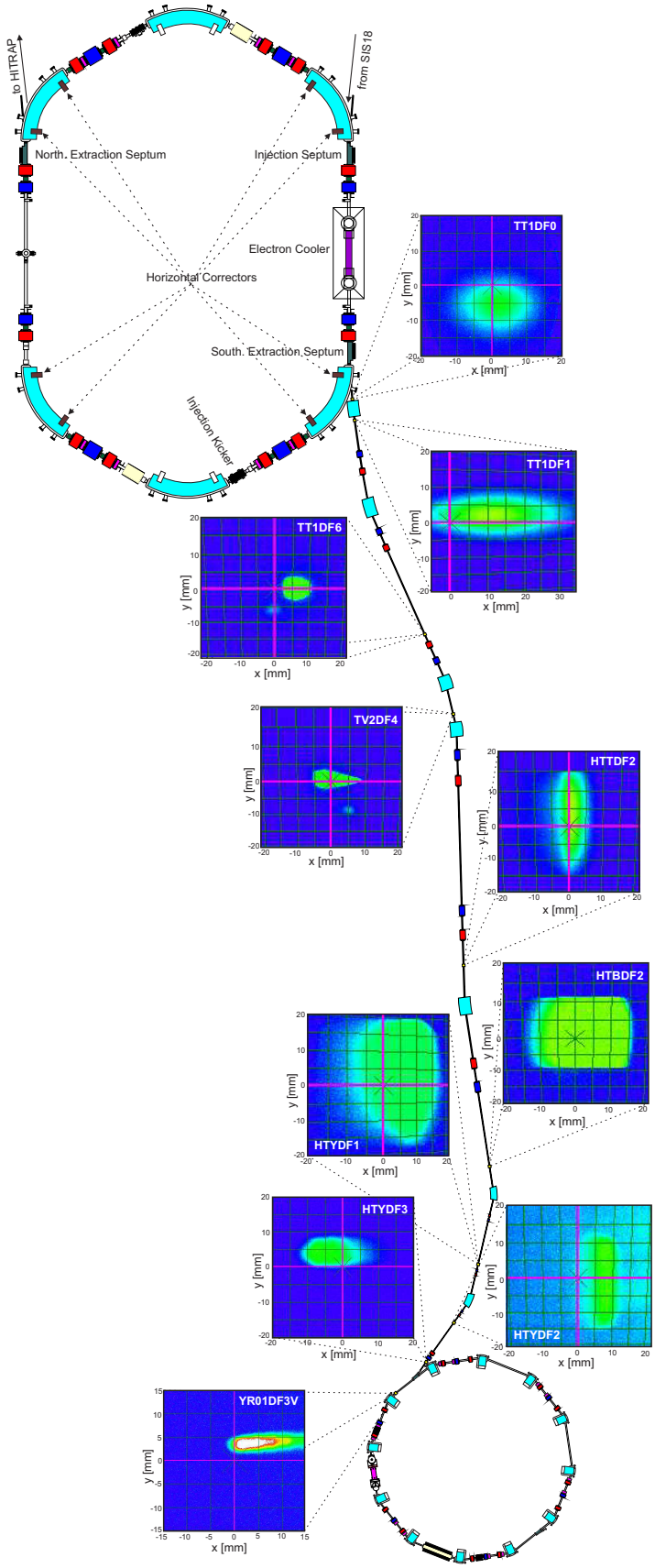

Figure 2: Layout of the CRYRING@ESR facility. The dipole, sextupole, focusing and defocusing quadrupole magnets are marked by cyan, violet, red and blue colors correspondingly. The ESR horizontal correctors used to perform the distortion orbit are indicated by brown boxes.

ISBN 978-3-95450-181-6

DESIGN RELATIVISTIC CHARGED PARTICLE BEAM TRANSPORTATION CHANNELS

G. P. Averyanov, V. A. Budkin, I.O.Osadchuk, MEPhI, Moscow, Russia

Abstract

This paper contains results of development new version (2016) of program for channels design high-energy beams of charged particles. The program includes application package modeling the dynamics of charged particles in the channel, operational tools to change the channel parameters, channel optimization tools and processing output beam parameters with graphic and digital presentation of its key features. The MATLAB (Scilab) was used as programming tools, allows to make the source code modular, compact and scalable. New object-oriented graphical user interface provides an interactive assembly of new or modernization of previously developed channel - selection and arrangement of its elements, as well as the installation and the variation of their parameters. The relational database, which is part of the new version of program, providing additional functionality to the designer. It is intended for storage of the current development, and to preserve the previously completed projects, as well as other useful designer related information. A multi-output of all the main parameters of the beam at the output, as well as anywhere in the channel. In this case, the developer has the ability to interactively search and setting the optimum mode of operation channel.

INTRODUCTION

The effectiveness of the design on the stage of computer simulation is largely determined by the convenience of the user interface of the used software package and the time of adaptation of the user to that application [1-4].

This paper presents a new approach in the implementation of interface software package KATRAN, designed for the design of channels of transportation of a relativistic charged particle beams.

THE PACKAGE STRUCTURE AND ALGORITHM DESIGN

The package contains four main modules:

- graphical interface, consisting of the Builder module of the channel and the processing module results of the calculation;
- calculation module;
- database module.

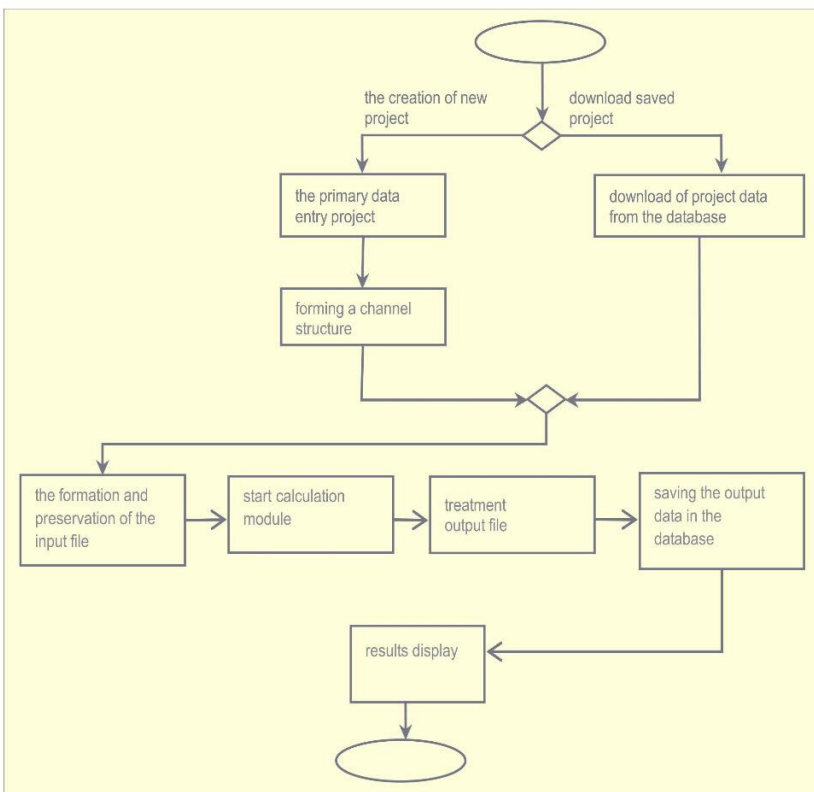

Figure 1: The package structure and algorithm design.

ISBN 978-3-95450-181-6

At System startup, initializes database, and load elements of the graphical user interface. Once launched, the user can choose from the following scenarios with the System (Fig.1):

- Create a new calculation.
- Loading a saved calculation.

Scenario 2 ("loading a saved calculation") differs from Scenario ("Create a new calculation") the fact that the input data file is generated on the basis contained in the database System the calculation data (the primary data and the structure of the channel, including the parameters of each element of the channel).

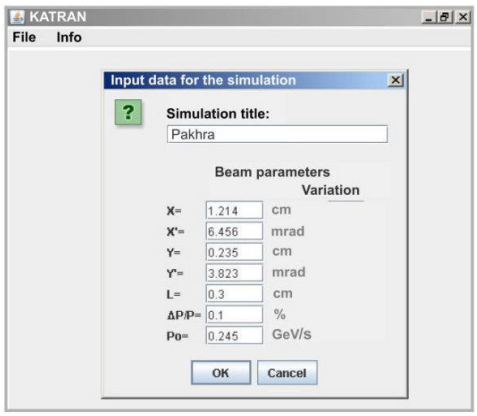

Figure 2: Setting beam parameters at the entrance of the channel.

This eliminates largely the need for immersion of the designer in the specific details of a computer environment, the features of the software package and mathematical methods of modeling channel. The generalized algorithm of the System shown in Fig. 1.

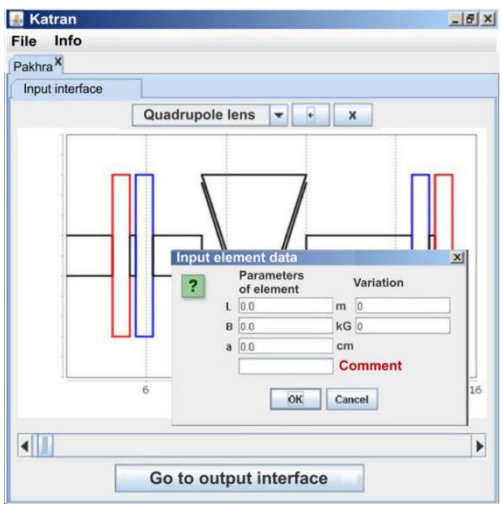

Figure 3: The visual assembly of elements of the transport channel

SIMULATION MODULE

The target feature Ft, which reflects the degree of achievement of the desired beam parameters for the experimental setup, can be written as:

$$Ft = \sqrt{\sum_{j=1}^{k} a_j \left(\varphi_j \frac{x}{x^{norm}} - \varphi_j{}^c\right)^2} \qquad (1)$$

where $\varphi_j{}^c$ – is the target value of the parameter; x^{norm} – vector of selection coefficients; parameter; a_j – weight coefficient of the parameter; x – vector space of search parameters; $\varphi_j(x)$ – the elements of the transformation matrix; k – is the number of optimized parameters. The Simplex method. (The Algorithm of Nelder-Mead) used to determine the optimal parameters of the transportation channel.

FEATURES OF THE GRAPHIC SHELL

Graphical user interface KATRAN provides high efficiency of user interaction with the program, because it implements a simple form of specifying parameters of the channel and construction of canal in General, as well as a clear presentation of the results of the calculation. The simplicity and convenience of working with KATRAN allows you to use it not only in science but also in the educational purposes, which is especially important for teaching students in specialties related to accelerator technology. The KATRAN software package includes following key interface functions:

- The design of the transport channel in visual form.
- Edit the parameters of the transport channel in the process of design.
- Displaying calculation results in visual form of the beam envelopes, and phase portraits, parameters of the elements of the channel and transformation matrix;
- Two-dimensional visualization of the canal with navigation.

The interface represents a sequence of actions of the designer for creating a virtual channel:

- Set beam parameters at the entrance of the channel (Fig. 2).
- The visual assembly of elements of the transport channel (Fig. 3).
- Parameters optimization for simulation algorithm procedure (Fig, 4).

CONCLUSION

The presented version of the environment is a continuation of earlier developments. The main advantages of this option are:

- The introduction of additional functions that extend the capabilities of study of the parameters of the transport channel and optimization of parameters;
- The accessibility to different hardware and software platforms;
- New simple multifunctional interface.

ISBN 978-3-95450-181-6

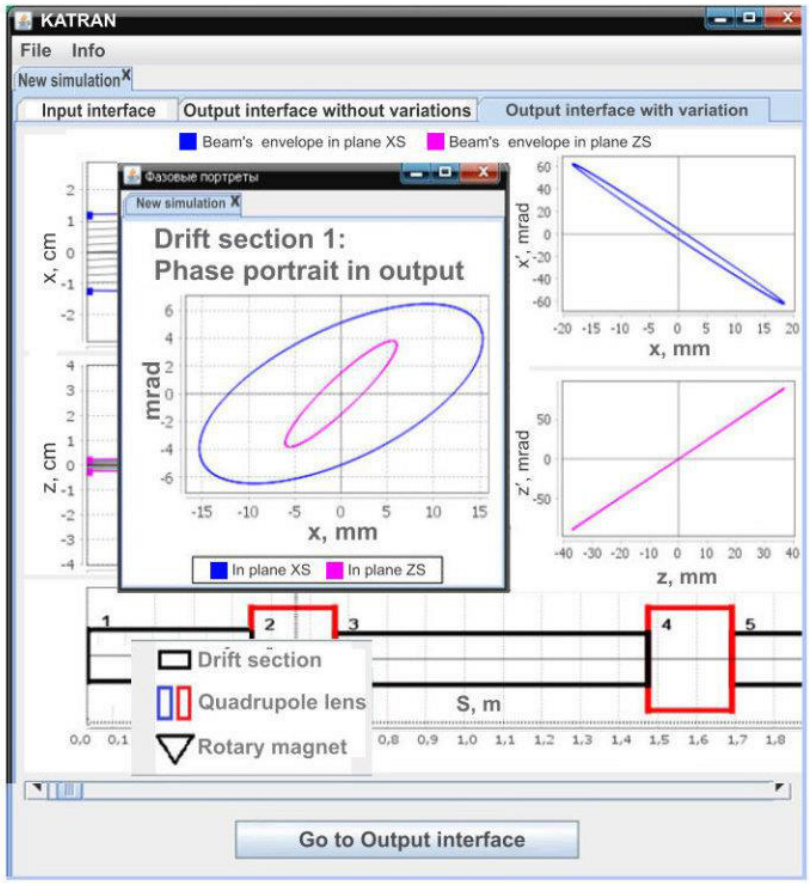

Figure 4: Parameters optimization for simulation algorithm procedure.

REFERENCES

[1] G. P. Averyanov, V. A. Budkin and V. V. Dmitrieva "CAD in Electrophysics, Part 1. Fundamentals of computer-aided design" (Moscow: MEPhI, 2011).

[2] G. P. Averyanov et al. "The Interactive Computer Environ-ment for Designing and Tuning of Charged Particle Beams Transport Channels" (Proceedings of RuPAC , Obninsk, Kaluga Region, Russia, 2014) 63.

[3] G. P. Averyanov et al. "Transportation channels calculation method in MATLAB" (Problems of atomic science and technology (PAST), № 3, 2014) 138.

[4] G. P. Averyanov et al. "Modeling the transport path of the electron beam output from "Pakhra" synchrotron" (International conference "Stability and Control Processes" is dedicated to the 85th anniversary of V.I. Zubov Isbn Isbn 978-5-9907101-1-5, 2015) 165.

ISBN 978-3-95450-181-6

THE INTELLIGENT OBJECT-ORIENTED INTERFACE IN THE DESIGN ENVIRONMENT OF THE CHARGED PARTICLES RELATIVISTIC BEAMS TRANSPORT CHANNELS

G.P. Averyanov, V.A. Budkin, A.V. Kobylyatskiy, I.O. Osadchuk, MEPhI, Moscow, Russia

Abstract

The effectiveness of the design during the computer modeling is significantly determined by the user interface convenience of the application package and the time adaptation of the user to that application. This paper presents a new approach in the implementation of KATRAN software interface for the transport channels design of the charged particles relativistic beams. The interface is a sequence of operations for the designer during the virtual channel creation setting beam parameters at the channel input, the choice of the displayed elements of the channel, the channel assembly, setting the calculation algorithm with the parameters optimization. Thus the immersion of the designer into the details of the computing environment, the features of the software and channel modeling mathematical methods is not needed. The data objects are the typical elements of the transport channels (quadrupole lenses, magnets, open intervals, etc.). The work is carried out in interactive mode. After the "build and run" of the channel is finished, the full-screen multi-factor analysis of all major parameters of the beam and channel transparency is provided.

INTRODUCTION

The channel configuration is determined by the dimensions of the accelerator hall and the experimental hall, as well as the requirements to the beam parameters and intensity [1-4]. Numerical modeling allows to identify the causes of loss of particles along the channel length and the "contribution" of each feed item in the total loss.

Adaptive modular approach to the design of channels is to pre-select separate focusing systems (modules). Preliminary optimization of the parameters of the modules based on the requirements as to the channel as a whole, and to individual modules. It defines the alignment of elements along the length of the module and the orientation of the lens (focusing-defocusing). Then, a parameter optimization of the whole channel in general. The channel calculation is performed using the software package "KATRAN" in MATLAB and Scilab.

The graphical tool environment allow you to display trajectories of individual particles, the envelopes and phase portraits of beam in horizontal and vertical plane. This information is enough to prompt the channel of the desired operation mode and adaptation of the entire focusing system to the requirements of the focusing of the beam.

The transport channel parameters

Particle dynamics in the transport channel is described by the transformation matrix in the quadrupoles, the magnets and the drifts in the horizontal m_{ij} and vertical n_{ij} plane. The relationship of the beam parameters (linear dimensions – x, z and divergence – x', z') at the output of channel (or individual element) with the input parameters is written as:

$$\begin{bmatrix} x_{out} \\ x'_{out} \end{bmatrix} = \begin{bmatrix} m_{11} & m_{12} \\ m_{21} & m_{22} \end{bmatrix} \begin{bmatrix} x_{in} \\ x'_{in} \end{bmatrix} \cdots, \cdots \begin{bmatrix} z_{out} \\ z'_{out} \end{bmatrix} =$$

$$= \begin{bmatrix} n_{11} & n_{12} \\ n_{21} & n_{22} \end{bmatrix} \begin{bmatrix} z_{in} \\ z'_{in} \end{bmatrix} \quad (1)$$

The elements of the matrices are functions of the geometric parameters of the channel and the values of the magnetic field in the quadrupole lenses and magnets. Thus, based on the values of matrix elements it is possible to form the target function Ft, which reflects the degree of achievement of the desired parameters of the beam in the plane of the experimental setup.

As an example, consider the modernization of the existing channel electron synchrotron (Fig. 1).

THE OPTIMIZATION OF CHANNEL PARAMETERS

The optimization of transportation channels includes next basic premises:

- The length of the channel and location of the bending magnets remains unchanged (determined by existing premises).
- Only the values of the magnetic fields in the lenses and doublets and their location along the channel varied.

The channel is formed from three types of focusing systems.

There are three focus system types:

- Two single quadrupole lenses
- A doublet of quadrupole lenses
- A doublet of quadrupole lenses in combination with a rotary magnet

Requirements for the beam parameters from the experiment – may be a little linear and angular dimensions of the beam at the exit of the channel.

These two requirements are competing, using methods of extreme search allows you to obtain a compromise solution. Minimum linear size of the beam in both planes at the exit of the channel is ensured by the conditions stigmatically image $m_{12} \to 0$, $n_{12} \to 0$ and about a single transformation $m_{11} \to 1$, $n_{11} \to 1$. The minimum divergence of the beam of electrons is mainly determined by the condition $m_{21} \to 0$, $n_{21} \to 0$.

ISBN 978-3-95450-181-6

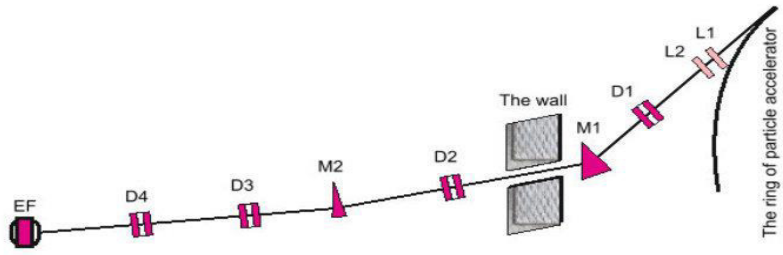

Figure 1: Scheme of the transport channel. L - quadrupole lense, D - doublet of quadrupole lenses, M - bending magnet, S - experimental installation.

The first step in the optimization of channel parameters is the choice of the schematic diagram of the position and orientation of the focusing elements along the length of the channel, which was carried out on the basis of the following provisions:

- The particle trajectories at the exit of the focusing system needs to be convergent and in between them an intermediate image of the electron beam.
- The output of the entire channel formed a stigmatic image of the electron beam.
- Linear sizes and the beam divergence at the channel outlet must be at the lowest.

A preliminary analysis of the individual modules allows more correctly generate the starting vector of the channel parameters, which are subject to optimization. As example, we present the analysis of the first focusing system (similar considered other systems of the channel).

THE FIRST SYSTEM

Range of values of the magnetic field in the lenses. Formed stigmatic image at system output (the conditions $m_{12} \to 0$, $n_{12} \to 0$). The beam at the entrance of the transport channel has an elliptical cross-section, so that with the passage of the subsequent part of the channel ellipticity of the beam is not increased, the selected orientation of the lenses $O\ D\ O\ F\ O$ (Fig.2). The criteria for assessing the quality of the focusing system are the values of the transverse dimensions of the beam, which should not exceed the size of the diameter of vacuum based (Fig.3).

Table 1: The Parameters of the First Focusing System

The structure of the first system	**Thickness (mg cm^{-2})**	**Composition**	**Matrix channel**	
			Horizontal plane	
Drift (m)	1.448	1.448	–0.63782	–0.00030
Magnetic field (kGs)	0.5	0.9577384	–1.001506	–1.56831
Drift (m)	0.81	0.81		
			Vertical plane	
Magnetic field (kGs)	0.5	0.7700728	–4.67739	0.0000096
Drift (m)	2.89	2.89	–1.47810	–0.21379

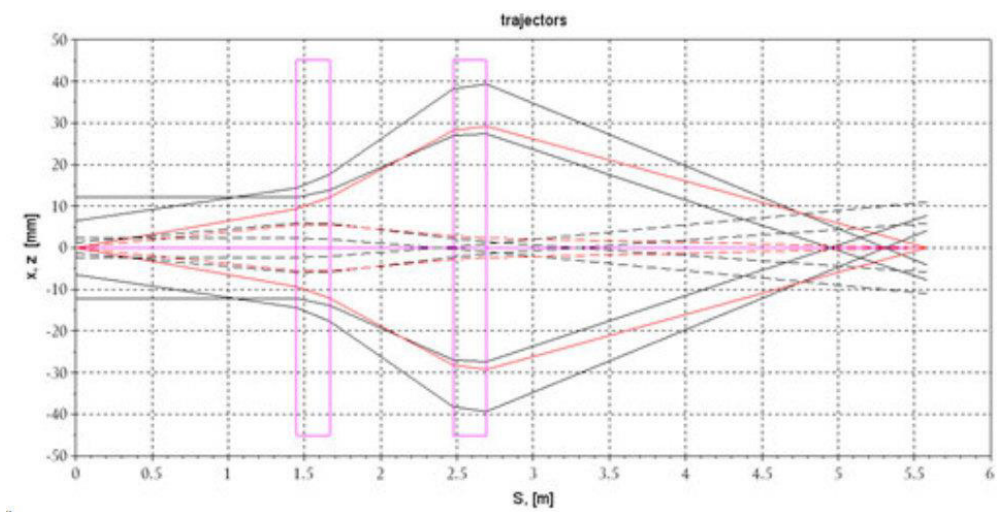

Figure 2: The particle trajectories in the horizontal (solid lines) and vertical plane (dashed line).

ISBN 978-3-95450-181-6

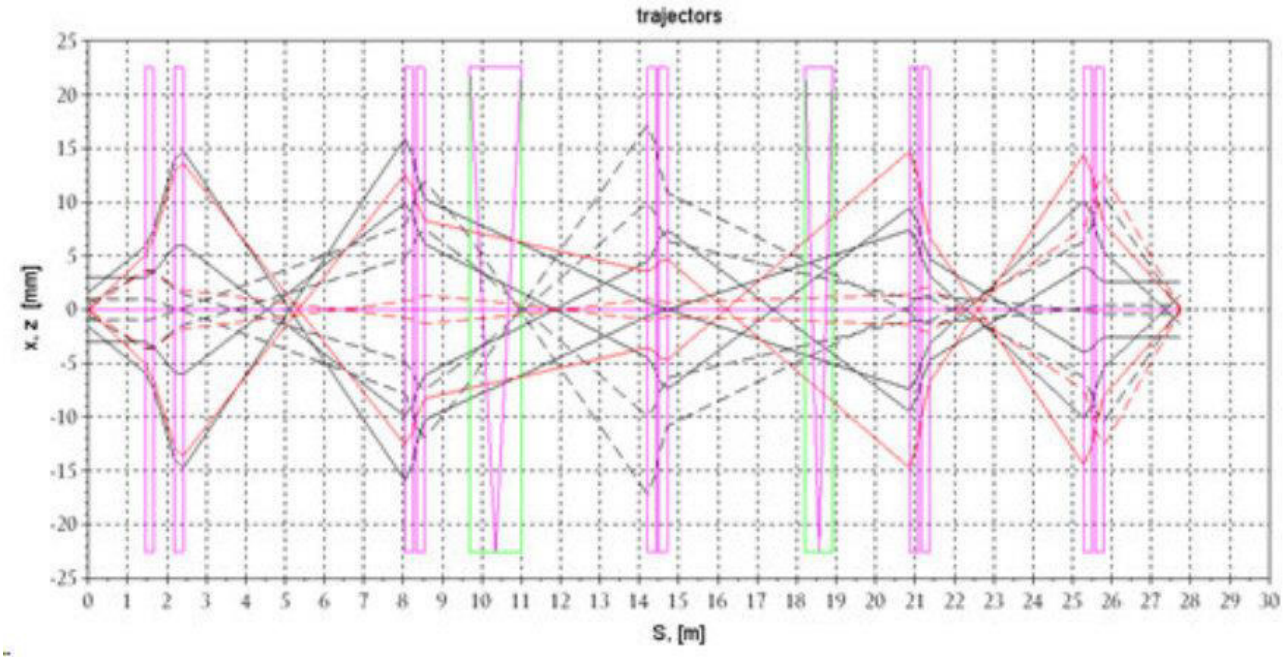

Figure 3: The particle trajectories in the horizontal (solid lines) and vertical plane (dashed line) channel as a whole.

Table 2: The Parameters of the First Focusing System

The elements of the channel	Channel structure	Length (m)	Field (kGs)
Drift		1.448	
Lens	L1(F)	0.217	1.0681174
Drift		0.532	
Lens	L2(D)	0.217	0.9053483
Drift		5.627	

As can be seen from the tables, after the optimization of channel parameters the parameters of the first focusing system (module) has undergone some correction overall.

Table 3: Matrix Transformation of the Transport channel

Horizontal plane	
0.8567355	0.0000082
0.0000067	1.1672214
Vertical plane	
–0.3863055	–0.0000569
–0.0000125	2.5886248

CONCLUSION

The presented version of the environment is a continuation of earlier developments. The main advantages of this option are:

- The introduction of additional functions that extend the capabilities of study of the parameters of the transport channel and optimization of parameters;
- The accessibility to different hardware and software platforms;
- New simple multifunctional interface.

REFERENCES

[1] G. P. Averyanov, V. A. Budkin and V. V. Dmitrieva "CAD in Electrophysics, Part 1. Fundamentals of computer-aided design" (Moscow: MEPhI, 2011).

[2] G. P. Averyanov et al. "The Interactive Computer Environ-ment for Designing and Tuning of Charged Particle Beams Transport Channels" (Proceedings of RuPAC , Obninsk, Kaluga Region, Russia, 2014) 63.

[3] G. P. Averyanov et al. "Transportation channels calculation method in MATLAB" (Problems of atomic science and technology (PAST), № 3, 2014) 138.

[4] G. P. Averyanov et al. "Modeling the transport path of the electron beam output from "Pakhra" synchrotron" (International conference "Stability and Control Processes" is dedicated to the 85th anniversary of V.I. Zubov Isbn Isbn 978-5-9907101-1-5, 2015) 165.

ISBN 978-3-95450-181-6

ON THE MINIMAX PROBLEM OF BEAM DYNAMICS OPTIMIZATION

M. Mizintseva*, D. Ovsyannikov
Saint Petersburg State University, Universitetskaya nab. 7/9, St. Petersburg, Russia

Abstract

The problem of simultaneous optimization of the ensemble of trajectories and some selected trajectory arises in the research of the charged particle beam dynamics [1–8].
The present work suggests the use of a smooth functional for the evaluation of the selected trajectories and a minimax functional for the evaluation of the dynamics of the beam of trajectories. A combination of those functionals is considered.

INTRODUCTION

In the present work a new approach to the beam dynamics optimization, based on the use of smooth and non-smooth functionals for the evaluation of the dynamics of the charged particles, is developed. The problem of simultaneous optimization of the program motion and the ensemble of trajectories is formulated. The dynamics of the program motion is evaluated using a smooth integral functional and the dynamics of the ensemble of disturbed motions is evaluated using a non-smooth functional.
In this paper the analytical form of the variation for the combination of a smooth and non-smooth functionals is presented, allowing to develop various methods of optimization. Those methods can be implemented, for instance, to the optimization of particle dynamics in a RFQ structure. It should be noted that the problems of analysis and optimization of the particle dynamics in RFQ accelerators in an equivalent running wave were explored in numerous works [9–14], but those did not utilize non-smooth functionals.

MATHEMATICAL MODEL

Let us consider the following system of differential equations

$$\frac{dx}{dt} = f(t,x,u), \qquad x(0) = x_0. \tag{1}$$

Here $t \in [0,T]$ — independent variable, $T > 0$ is a fixed moment of time; x — n–dimensional phase-vector; $u = u(t)$ — r–dimentional piecewise continuous control vector-function from a class D; $f(t,x,u)$ — n–dimentional reasonably smooth vector-function . Let us call the solution of system (1) a program motion.
At the same time we consider the so-called disturbed motions, which are the solutions of the following system of equations [1]

$$\frac{dy}{dt} = F(t,x,y,u), \qquad y(0) = y_0 \in M_0. \tag{2}$$

Here y — n–dimensional phase-vector; $F(t,x,y,u)$ — n-dimensional reasonably smooth vector-function; M_0 — a compact set.
The trajectories of system (2) are vector-functions $y = y(t, x(t,x_0,u), y_0, u)$, continuously dependent on the program motion $x(t,x_0,u)$ and initial conditions $y_0 \in M_0$.
Let us introduce the set of terminal positions of the system (2)

$$Y = \{y(T,x_0,y_0,u) \mid u \in D, x(0) = x_0, y_0 \in M_0\}.$$

On the solutions of system (1) let us introduce a functional

$$I_1(u) = \int_0^T \varphi_1(x(t,x_0,u))dt + g(x(T))$$

and on the trajectories of system (2) the following functional

$$I_2(u) = \max_{y_T \in Y} \varphi_2(Y).$$

Here φ_1 and φ_2 are non-negative smooth functions.
In the present paper the following functional is studied

$$I(u) = I_1(u) + I_2(u).$$

VARIATION OF THE FUNCTIONAL

Let us consider a variation of the control function $\Delta u(t)$, so that $\tilde{u}(t) = u(t) + \Delta u(t) \in D$.
Let us introduce a set $R_T(u)$, dependent on the control $u = u(t)$ and defined by expression

$$\begin{aligned} R_T(u) = \{\bar{y}_0 : \bar{y}_0 \in M_0, \varphi_2(y(T,x_0,\bar{y}_0,u)) = \\ = \max_{y_0 \in M_0} \varphi_2(y(T,x_0,y_0,u))\}. \end{aligned} \tag{3}$$

Following the logic of [10] lemma can be proved.
Lemma *Let us consider sets $R_T(u)$ and $R_T(\tilde{u})$, defined by the relations (3), corresponding to the allowed controls $u(t)$ and $\tilde{u}(t)$, then*

$$\max_{y_0'' \in R_T(\tilde{u})} \min_{y_0' \in R_T(u)} \|y_0'' - y_0'\| \to 0 \quad \text{when} \quad \|\Delta u\|_L \to 0.$$

The variations equations correspoding to the systems (1 –2) are as follows

$$\begin{aligned} &\frac{d\delta x}{dt} = \frac{\partial f(t,x,u)}{\partial x}\delta x + \Delta_u f(t,x,u), \\ &\delta x(0) = 0; \\ &\frac{d\delta y}{dt} = \frac{\partial F(t,x,y,u)}{\partial x}\delta x + \frac{\partial F(t,x,y,u)}{\partial y}\delta y + \\ &\qquad + \Delta_u F(t,x,y,u), \\ &\delta y(0) = 0. \end{aligned}$$

* m.mizintseva@spbu.ru

ISBN 978-3-95450-181-6

Here

$$\Delta_u f\,(t,x,u) = f(t,x,u+\Delta u) - f\,(t,x,u)\,,$$
$$\Delta_u F\,(t,x,y,u) = F\,(t,x,y,u+\Delta u) - F\,(t,x,y,u)\,.$$

Function $\varphi_2\,(y(T,x_0,y_0,\tilde{u})$ can be represented in the following form

$$\varphi_2\,(y(T,x_0,y_0,\tilde{u}) + \Delta y(T,x_0,y_0)) =$$
$$= \varphi_2\,(y(T,x_0,y_0,u)) + \frac{\partial\varphi_2\,(y(T,x_0,y_0,u))}{\partial y}\delta y + \quad (4)$$
$$+ o\,(\|\Delta y(T)\|_C)\,.$$

Using (4) the variation of the functional $I_2(u)$ can be obtained as follows

$$\delta I_2 = \max_{y_0\in R_T(u)} \frac{\partial\varphi_2\,(y(T,x_0,y_0,u))}{\partial y}\delta y(T).$$

The variation of the functional represented by a smooth function is [1, 3]

$$\delta I_1 = \int_0^T \frac{\partial\varphi_1\,(x(t,x_0,u))}{\partial x}\delta x dt + \frac{\partial g(x(T))}{\partial x}\delta x(T).$$

Then the variation of the functional $I(u)$ is

$$\delta I = \delta I_1 + \delta I_2.$$

Let us introduce functions ψ and λ

$$\psi^{*'} + \psi^*\frac{\partial f}{\partial x} = \frac{\partial\varphi_1}{\partial x} - \lambda^*\frac{\partial F}{\partial x},$$
$$\psi^*(T) = -\frac{\partial g(x(T))}{\partial x},$$
$$\lambda^{*'} + \lambda^*\frac{\partial F}{\partial y} = 0,$$
$$\lambda^*(T) = -\frac{\partial\varphi_2(Y)}{\partial y}.$$

Then the variation of the functional can be written as follows

$$\delta I(u) = \max_{y_0\in R_T(u)} \int_0^T (\,\psi^*\Delta_u f(t,x,u) - \lambda^*\Delta_u F(t,x,y,u))dt.$$

Let us introduce Hamilton's function

$$H(t,x,u,\psi,\lambda,u) = \psi^* f(t,x,u) + \lambda^* F(t,x,y,u),$$

then variation will be

$$\delta I(u) = \max_{y_0\in R_T(u)} \int_0^T \big(H(t,x,y,\psi,\lambda,u) -$$
$$- H(t,x,y,\psi,\lambda,\tilde{u})\big)dt.$$

The obtained expression for the variation of the functional can be applied to various problems of optimization in electro-physical devices.

BEAM DYNAMICS IN A RFQ STRUCTURE

Approach using systems of differential equations (1)–(2) can be applied to the modeling of beam dynamics in a RFQ accelerator in an equivalent running wave. The dynamics of a synchronous particle is described by the following equations [13, 14]

$$\frac{d\gamma_s}{dz} = u_1\frac{qU}{2m_0c^2}cosu_2,$$
$$\gamma_s(0) = \gamma_{s0}.$$

Disturbed motions are presented by the deviations in phase $\psi = \varphi - \varphi_s$ and reduced energy $p_\psi = \gamma - \gamma_s$ from the synchronous particle

$$\frac{dp_\psi}{dz} = u_1\frac{qU}{2m_0c^2}(cosu_2 - cos(\psi + u_2),$$
$$p_\psi(0) = p_{\psi 0} \in M_0,$$
$$\frac{d\psi}{dz} = \frac{2\pi}{(\gamma_s^2-1)^{3/2}}p_\psi,$$
$$\psi(0) = \psi_0 \in M_0.$$

This model quite accurately describes the dynamics of the particle beam.
Figure 1 below shows the acceleration intensity. Figure 2 shows the phase of the synchronous particle.

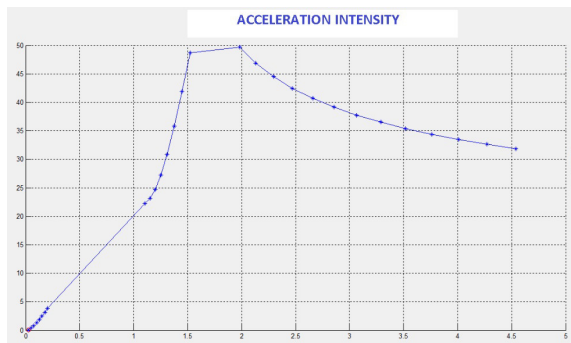

Figure 1: Acceleration intensity.

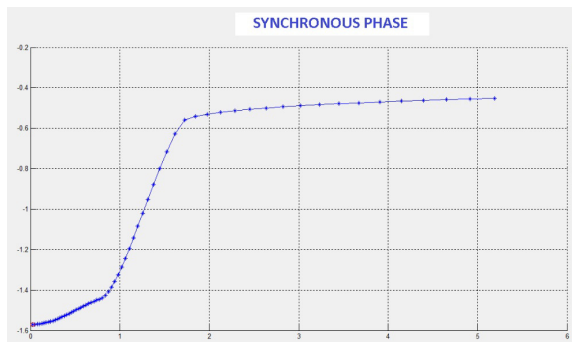

Figure 2: Phase of the synchronous particle.

ISBN 978-3-95450-181-6

Figure 3 shows reduced energy deviations from the synchronous particle. Figure 4 shows phase deviations from the synchromous particle.

Figure 3: Beam reduced energy.

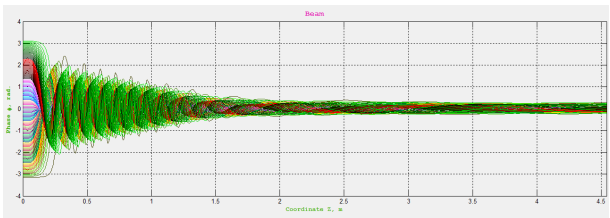

Figure 4: Deviations from the synchronous phase.

The modeling data is pretty good, but can be futher improved by implementing the proposed appoach to optimization.
The following functionals can be introduced.
Let us introduce a smooth functional $I_1(u)$

$$I_1(u) = \int_0^L \varphi_1(A_{def})dz + g(x(L)).$$

Here A_{def} — is the defocusing factor, $g(x(L)) = (\gamma_s(L) - \tilde{\gamma}(L))^2$ — in this case the aim of the optimization is the minimization of the defocusing factor and evaluation of the deviation of the reduced energy of the synchronous particle from a fixed value $\tilde{\gamma}$ at the end of the accelerating structure. The non-smooth functional $I_2(u)$ can evaluate the maximum deviation of particles in phase and reduced energy from the synchronous particle. In paticular, the following functional can be introduced

$$I_2(u) = \max_{y_T \in Y} \psi^2.$$

Resulting functional $I(u) = I_1(u) + I_2(u)$ allows to consider simultaneously the program motion and the disturbed motions in the problem of optimal control.

CONCLUSION

The proposed approach to simultaneous optimization of program and disturbed motions looks very promising in problems where it is important not just to evaluate the process in general, but also to take into account the worst, the most deviating particles.
The obtained variation of the functional can be used for construction of directed methods of minimization.

ISBN 978-3-95450-181-6

ACKNOWLEDGEMENTS

Authors would like to thank V. Altsybeyev for providing the modeling data.

REFERENCES

[1] A.D. Ovsyannikov, "Control of Program and Disturbed Motions", Vest. SpSU. Ser. 10: Applied Mathematics. Informatics. Control Proccesses N 2 (2006) pp. 111-124.

[2] D.A. Ovsyannikov. "Modeling and Optimization Problems of Charged Particle Beam Dynamics". Proceedings of the 4th European Control Conference. Brussels, Belgium, 1997, pp. 1463-1467 (1997).

[3] M. Mizintseva, D. Ovsyannikov. "On the Problem of Simultaneous Optimization of Program and Disturbed motions". Proceedings of SCP 2015 Conference. Saint Petersburg, Russia, 2015. pp. 195-196 (2015).

[4] D.A. Ovsyannikov. "Mathematical Modeling and Optimization of Beam Dynamics in Accelerators". Proceedings of the 23rd Russian Particle Accelerator Conference RuPAC 2012. Saint Petersburg, Russia, 2012, pp. 68-72 (2012).

[5] B.I. Bondarev, A.P. Durkin, A.D. Ovsyannikov. "New Mathematical Optimization Models for RFQ Structures". Proceedings of the 18th Particle Accelerator Conference. New York, USA, 1999. pp. 2808-2810, (1999).

[6] D.A. Ovsyannikov and V.V. Altsybeyev. "Optimization of APF Accelerators". Problems of Atomic Science and Technology 6.88 (2013) pp. 119-122.

[7] O.I. Drivotin, D.A. Ovsyannikov. "Modeling of Self-Consistent Distributions for Charged Particle Beam in Magnetic Field. International Journal of Modern Physics A.Vol. 24 N 5 (2009) pp. 816-842.

[8] A.D. Ovsyannikov et al. "Application of Optimization Techniques for RFQ Design". Problems of Atomic Science and Technology 3.91 (2014) pp. 116-119.

[9] D.A. Ovsyannikov, V.V. Alsybeyev. "Mathematical Optimization Model for Alternating Phase—Focusing (APF) LINAC. N 4(86) (2013) pp. 93-96.

[10] D.A. Ovsyannikov. *Mathematical Methods of Beam Control* (Leningrad: LSU Pub., 1980).

[11] A. D. Ovsyannikov, A.P. Durkin et al. "Acceleration of Different Ion Types in Single RFQ Structure". Problems of Atomic Science and Technology 3.103 (2016) pp. 54-56.

[12] D.A. Ovsyannikov, V.V. Altsybeyev. "On the Beam Dynamics Optimization Problem for an Alternating-Phase Focusing Linac". Physics of Particles and Nuclei Letters 13.8 (2016) pp. 805-809.

[13] I.M. Kapchinsky. *Theory of Resonance Linear Accelerators* (Moscow: Energoizdat, 1982), 398

[14] A.D. Ovsyannikov, A.Y. Shirokolobov. "Mathematical model of beam dynamics optimization in traveling wave". Proceedings of RuPAC 2012. Saint Petersburg, Russia, 2012. p. 355-357 (2012).

ON MODELING AND OPTIMIZATION OF INTENSE QUASIPERIODIC BEAM DYNAMICS

I. Rubtsova#, SPbSU, Saint-Petersburg, Russia

Abstract

The paper is devoted to quasiperiodic beam dynamics investigation. Particle density is modeled by trigonometric polynomial. Space charge field is represented in the similar form. This approach is applied to beam dynamics investigation in klystron-type buncher. Numerical algorithm of polynomial coefficients calculation from the positions and impulses of model particles is formalized. As a result Coulomb field intensity is expressed in the form of integral over the set of particle phase states. Integro-differential beam evolution model is presented. Analytical expression of the variation of beam dynamics quality criterion is obtained. It makes possible directed methods using for beam dynamics optimization.

BEAM DYNAMICS EQUATIONS

Consider quasiperiodic beam dynamics in accelerator or some beam forming system. Let us take klystron buncher as an example (the bunching process is supposed to be adiabatic). The channel is supposed to be cylindrical tube of radius a. Let us introduce the cylindrical coordinates r,θ,z with Oz axis coincided the channel axis.

Beam evolution is simulated on the basis of particle-in-cell method. Model particles are supposed to be "thick" disks with radius R. Dynamics equations are as follows:

$$\frac{dz_i}{d\tau}=\frac{p_i}{\sqrt{1+p_i^2}},\quad \frac{dp_i}{d\tau}=-\frac{e}{m_0c^2}\left(E_i^{(RF)}-E_i^{(int)}\right). \quad (1)$$

Here $\tau=ct\in[0,T]$, t is the time, c is the velocity of light; z_i and p_i are longitudinal coordinate and reduced impulse of i-th particle; e and m_0 are absolute charge value and rest mass of electron; $E_i^{(RF)}$ and $E_i^{(int)}$ are the intensity functions characterizing the action on model particle of RF and Coulomb fields correspondingly.

PARTICLE INTERACTION ACCOUNT

Assume that independent variable value τ is fixed. We suppose beam spatial quasiperiod to be cylinder $[0,R]\times[0,2\pi)\times[z_c-H,z_c+H)$ where z_c is center coordinate; the cylinder is charged uniformly across the radius. We presume the beam to be periodic when calculate space charge forces. Coulomb field calculation algorithm is as follows.

1. Introduction of longitudinal coordinate grid $\{\xi_j=z_c-H+2jh,\ j=\overline{0,2M}\}$, where $2h=H/M$.

2. Calculation of grid cell charges q_j, $j=\overline{0,2M-1}$ with the use of clouds-in-cells method. It is supposed that $q_{2M}=q_0$ due to beam spatial periodicity. Approximation of bunch charge density by piecewise constant function $\{\tilde{S}(z,z_c)=q_j/(2h\pi R^2),\ z\in[\xi_j-h,\xi_j+h),\ j=\overline{0,2M-1}\}$.

3. Approximation of the function $\tilde{S}(z,z_c)$ by trigonometric polynomial $S(z-z_c)$ taking the values $S_j=q_j/(2h\pi R^2)$, $j=\overline{0,2M-1}$ at grid points [1-3]:

$$S(\varsigma)=\sum_{m=0}^{M}\left[A_m\cos(m\pi\varsigma/H)+B_m\sin(m\pi\varsigma/H)\right]. \quad (2)$$

The coefficients A_m,B_m, $m=\overline{0,M}$ are expressed by trigonometric interpolation formulae:

$$A_m=\frac{(-1)^m}{M\nu_m}\sum_{j=0}^{2M-1}S_j\cos(m\,j\,\pi/M),\ m=\overline{1,M},$$
$$B_m=\frac{(-1)^m}{M}\sum_{j=0}^{2M-1}S_j\sin(m\,j\,\pi/M),\ m=\overline{0,M}, \quad (3)$$
$$A_0=Q/(2H\pi R^2),\ \nu_m=[1+m/M],$$

where Q is bunch charge value, ν_m is the integer part of the value $1+m/M$.

4. Calculation of potential field intensity characterizing the periodic beam action on the model particle. The intensity expression is derived on the basis of potential function obtained by Poisson equation solving with right-hand part proportional the polynomial $S(z-z_c)$ [2-4]. The intensity calculation formula is as follows:

$$E_i^{(int)}=C\sum_{k=1}^{\infty}D_k\sum_{m=1}^{M}C_{km}(p_c)\times$$
$$\times\left[A_m\Gamma_{sm}(z_i,z_c,p_c)-B_m\Gamma_{cm}(z_i,z_c,p_c)\right], \quad (4)$$

where

$$C=\frac{(2\pi Ra)^2H}{\varepsilon_0};\ D_k=\frac{J_1^2(\mu_kR/a)}{\mu_k^2J_1^2(\mu_k)};$$
$$C_{km}(p)=\frac{m}{(m\pi a)^2+\mu_k^2H^2(1+p^2)};$$

#rubtsova05@mail.ru

ISBN 978-3-95450-181-6

$$\Gamma_{cm}(z_i, z_c, p) = \int_{z_i-d}^{z_i+d} \cos\left(\frac{m\pi}{H}(z-z_c)\right)\chi(z-z_i, p)dz;$$

$$\Gamma_{sm}(z_i, z_c, p) = \int_{z_i-d}^{z_i+d} \sin\left(\frac{m\pi}{H}(z-z_c)\right)\chi(z-z_i, p)dz.$$

Here ε_0 is electric constant, $J_1(x)$ is first order Bessel function, $\mu_k, k = 1,2,\ldots$ are the zeros of Bessel function $J_0(x)$; p_c is the average reduced impulse of the bunch; $\chi(x, p_c)$ is model particle form coefficient; $2d$ is cloud size.

Intense beam dynamics was investigated for klystron-type buncher with following main characteristics: initial energy of electrons $W_0 = 0.5$ MeV, average beam current $I = 15$ A [2]. Beam dynamics simulation code was developed in cooperation with B.S. Zhuravlev. Two interaction account modes were realized: "disks-in-cells" model [3] using Fourier-Bessel series and described above model using trigonometric polynomial. The analysis of numerical results obtained confirms both modes validity. Clearly, "trigonometric" model provides a significant smoothing of the processes under study and is preferred to use when electron bunches are mostly formed.

COULOMB FIELD INTEGRAL REPRESENTATION

Coulomb field representation in terms of model particle positions

Let us suppose form coefficient $\chi(x, p_c)$ to be continuous function taking zero values outside the cloud. Note that the coefficients A_m, B_m, $m = \overline{0, M}$ in formulae (2)-(4) are expressed in terms of grid cell charges. In their turn, grid cell charges may be expressed in terms of model particles positions z_n, $n = \overline{1, N}$, where N is particles number. For any $j = 0,\ldots,2M-1$

$$q_j = 2h\pi R^2 Q/N \sum_{n=1}^{N} \int_{-\infty}^{\infty} \chi(x - z_n, p_c)\Pi(x - \xi_j)dx, \quad (5)$$

where $\Pi(x)$ is interpolation function defining the rule of charge distribution in grid cells.

In view of Eq. (3)-(5), beam action on the $i-$th model particle has the representation of the following form:

$$E_i^{(int)} = \frac{1}{N}\sum_{n=1}^{N} V_n = \frac{1}{N}\sum_{n=1}^{N} V(z_i, z_c, p_c, z_n), \quad (6)$$

where $V(z_i, z_n, z_c, p_c)$ is the smooth function.

Phase density and Coulomb field integral form

Now we will take into account external field dependence on control vector $\mathbf{u}$. Assume that τ value and vector function $\mathbf{u}$ are fixed. Let us consider particle distribution to be continuous; let $M_{\tau,\mathbf{u}}$ be the domain of bunch particles phase states.

Let particle phase state (z, p) be a random variable with the values in the domain $M_{\tau,\mathbf{u}}$ and $\rho(\tau, z, p)$ be probability density. Consequently, the expected value of any function $U(z, p)$ defined on beam trajectories may be presented in the form $\int_{M_{\tau,\mathbf{u}}} U(z_\tau, p_\tau)\rho(\tau, z_\tau, p_\tau)dz_\tau dp_\tau$.

Relying formula (6) and the law of large numbers, we can argue that

$$E_i^{(int)} \xrightarrow[N\to\infty]{P} \int_{M_{\tau,\mathbf{u}}} V(z_i, \mathbf{x}_c, \hat{z}_\tau,)\rho(\tau, \hat{z}_\tau, \hat{p}_\tau)d\hat{z}_\tau d\hat{p}_\tau, \quad (7)$$

where $\mathbf{x}_c = (z_c, p_c)$. The integral in right-hand part of formula (7) provides mathematical model of quasiperiodic beam Coulomb field.

INTEGRO-DIFFERENTIAL BEAM DYNAMICS MODEL

Consider beam evolution description with due account of the fields excited by the beam itself basing on the research conducted by Dmitri Ovsyannikov and his colleagues [5-11].

We will describe quasiperiodic beam dynamics by integro-differential equations. Mathematical models of such a class are widely applied in treatment of beam dynamics modeling and optimization problems [5,9,12-16].

Let us generalize beam dynamics model (1) taking into account the fields induced by moving beam itself [12]. Dynamic controlled process is described by the equations

$$\frac{d\mathbf{x}}{d\tau} = \mathbf{f}\left(\tau, \mathbf{x}, \mathbf{u}, \mathbf{F}(\mathbf{u})\right) = \mathbf{f}_1\left(\tau, \mathbf{x}, \mathbf{u}, \mathbf{F}(\mathbf{u})\right) + \int_{M_{\tau,\mathbf{u}}} \mathbf{f}_2(\tau, \mathbf{x}, \mathbf{y}_\tau)\rho(\tau, \mathbf{y}_\tau)d\mathbf{y}_\tau, \quad (8)$$

$$\frac{\partial\rho}{\partial\tau} + \frac{\partial\rho}{\partial\mathbf{x}} f\left(\tau, \mathbf{x}, \mathbf{u}, \mathbf{F}(\mathbf{u})\right) + \rho\, div_{\mathbf{x}}\mathbf{f}\left(\tau, \mathbf{x}, \mathbf{u}, \mathbf{F}(\mathbf{u})\right) = 0 \quad (9)$$

with initial conditions

$$\mathbf{x}(0) = \mathbf{x}_0 \in M_0, \quad \rho(0, \mathbf{x}) = \rho_0(\mathbf{x}). \quad (10)$$

Here $\tau \in [0, T]$ is independent variable, T is constant, $\mathbf{x}$ is phase vector; $\mathbf{u}$ is control; vector function $\mathbf{f}_1$ is

ISBN 978-3-95450-181-6

determined by the method of external fields modeling; $\mathbf{F}(\mathbf{u})$ is the vector of values of functionals defined on beam trajectories; vector function $\mathbf{f}_2$ is determined by the method of particle interaction account; $\rho(\tau,\mathbf{x},\mathbf{y})$ is phase density defined on system (8) trajectories; M_0 is the set of initial particle phase states; $\rho_0(\mathbf{x})$ is initial phase density; $M_{\tau,\mathbf{u}}=\{\mathbf{x}_\tau=\mathbf{x}(\tau,\mathbf{x}_0,\mathbf{u}):\mathbf{x}_0\in M_0\}$. Vector $\mathbf{F}(\mathbf{u})$ components are the values of the functionals

$$F_l(\mathbf{u})=\int_0^T\int_{M_{\tau,u}}\Lambda_l(\tau,\mathbf{x}_\tau,\mathbf{u})\rho(\tau,\mathbf{x}_\tau)d\mathbf{x}_\tau d\tau,\quad l=\overline{1,L},$$

describing the characteristics of RF fields excited by moving beam.

All the functions in the Eq. (8)-(10) are supposed to be rather smooth to obtain quality functional variation and gradient [5,12].

Mathematical model (8)-(9) may be applied to describe beam control process in klystron buncher. In this case we have $t=\tau$; $\mathbf{x}=(z,p)^T$. Besides, we suppose $p_c=p_{c0}$, $z_c=z_{c0}+\tau\, p_c\Big/\sqrt{1+p_c^2}$, where z_{c0} and p_{c0} are initial coordinate and initial reduced impulse of bunch centre. So the integrand in formula (7) may be presented as $V(\tau,z_i,\hat{z})$. Control vector $\mathbf{u}$ is the vector of device parameters (resonator mismatches and drift tube lengths); the components of vector $\mathbf{F}(\mathbf{u})$ are the coefficients of Fourier-series expansion of induced current in resonators;

$$\mathbf{f}_1=\left(p\Big/\sqrt{1+p^2},-\frac{e}{m_0c^2}E^{(RF)}(\tau,z,\mathbf{u},\mathbf{F}(\mathbf{u}))\right)^T,$$

$$\mathbf{f}_2(\tau,z,\hat{z})=\left(0,\frac{e}{m_0c^2}V(\tau,z,\hat{z})\right)^T.$$

The detailed RF fields description is given in [12,15-17].

OPTIMIZATION PROBLEM

The approach suggested by D.A. Ovsyannikov makes it possible to formulate different beam dynamics optimization problems as trajectory ensemble control problems; under certain conditions one can obtain quality criterion gradient. Such an approach is successfully applied by many researchers [9,13,18-27].

Let us estimate the controlled process (8)-(9) quality by the values of functional

$$I(\mathbf{u})=\int_0^T\int_{M_{\tau,\mathbf{u}}}\Phi(\tau,\mathbf{x}_\tau,\mathbf{u})\rho(\tau,\mathbf{x}_\tau)d\mathbf{x}_\tau d\tau \qquad (11)$$

with smooth integrand.

For example, when optimizing klystron buncher parameters, one can construct the integrand $\Phi(\tau,\mathbf{x},\mathbf{u})$ to be positive for the particles satisfying the requirements imposed at device exit and to be zero (or negative) otherwise. Functional (11) is to be maximized.

Using the results [5,12] we obtain nonclassical variation of the functional (11):

$$\delta I(\mathbf{u},\Delta\mathbf{u})=-\int_0^T\int_{M_{\tau,\mathbf{u}}}\left[\boldsymbol{\psi}^T(\tau,\mathbf{x}_\tau)\Delta_{\mathbf{u}}f_1(\tau,\mathbf{x}_\tau,\mathbf{u},\mathbf{F})-\right.$$
$$\left.-\Delta_{\mathbf{u}}\Phi(\tau,\mathbf{x}_\tau,\mathbf{u})-\mathbf{G}(\mathbf{u})\Delta_{\mathbf{u}}\boldsymbol{\Lambda}(\tau,\mathbf{x}_\tau,\mathbf{u})\right]\rho(\tau,\mathbf{x}_\tau)d\mathbf{x}_\tau d\tau. \qquad (12)$$

Here $\Delta\mathbf{u}$ is control $\mathbf{u}$ variation; $\Delta_{\mathbf{u}}$ designates the increment of any function with respect to argument $\mathbf{u}$ only; vector function $\boldsymbol{\psi}(\tau,\mathbf{x})$ satisfies on the trajectories of dynamic process (8)-(9) the auxiliary system of integro-differential equations

$$\frac{d\boldsymbol{\psi}}{d\tau}=\left(\frac{\partial\Phi(\tau,\mathbf{x}(\tau))}{\partial\mathbf{x}}\right)^T-\left(\frac{\partial\mathbf{f}(\tau,\mathbf{x}(\tau),\mathbf{u}(\tau),\mathbf{F}(\mathbf{u}))}{\partial\mathbf{x}}\right)^T\boldsymbol{\psi}-$$
$$-\int_{M_{\tau,\mathbf{u}}}\left(\frac{\partial f_2(\tau,\mathbf{y}_\tau,\mathbf{x}(\tau))}{\partial\mathbf{x}}\right)^T\boldsymbol{\psi}(\tau,\mathbf{y}_\tau)\rho(\tau,\mathbf{y}_\tau)d\mathbf{y}_\tau- \qquad (13)$$
$$-\left(\frac{\partial\boldsymbol{\Lambda}(\tau,\mathbf{x}(\tau),\mathbf{u})}{\partial\mathbf{x}}\right)^T\mathbf{G}^T(\mathbf{u})$$

with the following condition at $\tau=T$:

$$\boldsymbol{\psi}(T,\mathbf{x}(T))=0.$$

Vector $\mathbf{G}(\mathbf{u})$ in Eq. 12, 13 is the vector of values of functionals defined on beam trajectories:

$$\mathbf{G}(\mathbf{u})=\int_0^T\int_{M_{\tau,u}}\boldsymbol{\psi}^T(\tau,\mathbf{x}_\tau)\frac{\partial f_1(\tau,\mathbf{x}_\tau,\mathbf{u},\mathbf{F}(\mathbf{u}))}{\partial F}\rho(\tau,\mathbf{x}_\tau)d\mathbf{x}_\tau d\tau.$$

The analytical representation (12) of quality criterion variation makes it possible to use the directed optimization methods in beam dynamics optimization problems. It may be beneficial to combine the gradient optimization with random search [28].

REFERENCES

[1] I.D. Rubtsova, "Integral-differential Model of Quasi-periodic Beam Longitudinal Dynamics", Beam Dynamics & Optimization (BDO), 2014 20th International Workshop, June-July 2014, St. Petersburg, Russia, Proceedings, IEEE, p. 144 (2014).

[2] I.D. Rubtsova, "Analytical Approach to Quasiperiodic Beam Coulomb Field Modeling", II Conference on Plasma&Laser Research and Technologies (2016), Journal of Physics: Conference Series, Vol. 747, No 1, 012074 (2016); http://iopscience.iop.org/1742-6596/747/1/012074

ISBN 978-3-95450-181-6

[3] D.A. Ovsyannikov, I.D. Rubtsova, V.A. Kozynchenko, *Some Problems of Intense Charged Particle Beams Modeling in Linear Accelerators*, (SPb: VVM publishing, 2013), 144.
[4] I.D. Rubtsova, "On Quasiperiodic Beam of Interacting Particles Dynamics Modeling", Vestnik St. Petersburg University, Ser. 10, No 1, pp. 104-119 (2014).
[5] D.A. Ovsyannikov, *Modeling and Optimization of Charged Particle Beam Dynamics,* (Leningrad: Leningrad State University, 1990), 312.
[6] O.I. Drivotin, D.A. Ovsyannikov, "Modeling of Self-consistent Distributions for Longitudinally Non-uniform Beams", Nuclear Instruments and Methods in Physics Research, Section A: Accelerators, Spectrometers, Detectors and Associated Equipment, 2006, Vol. 558, No 1, pp 112-118 (2006).
[7] O.I. Drivotin, D.A. Ovsyannikov, "Self-consistent Distributions for Charged Particle Beam in Magnetic Field", International Journal of Modern Physics, Section A, 2009, Vol.24, No 5, pp. 816-842 (2009).
[8] O. Drivotin, N. Ovsyannikov, "Self-Consistent Distributions Simulation for a Charged Particle Beam", Proceedings of III International Conference "Stability and Control Processes" in Memory of V.I. Zubov (SCP), IEEE, pp. 161-164 (2015).
[9] D.A. Ovsyannikov, "Modeling and Optimization Problems of Charged Particle Beam Dynamics", ECC 1997-European Control Conference 4, pp. 1463-1467 (1997).
[10] V.A. Kozynchenko, "The Modeling of Charged Particle Interactions in the Elliptic Beam", 20th International Workshop on Beam Dynamics and Optimization (BDO 2014), pp. 94-95 (2014).
[11] V.A. Kozynchenko, S.A. Kozynchenko, "Parallel Beam Dynamics Simulation in Injection Systems Taking into Account Particle Interactions", 20th International Workshop on Beam Dynamics and Optimization (BDO 2014), pp. 98-99 (2014).
[12] I.V. Olemskoy, I.D. Rubtsova, "Modeling and Optimization of Beam Dynamics in Resonance Bunching and Decelerating Systems", First International Workshop: Beam Dynamics & Optimization, St. Petersburg, Russia, 1994, pp. 143-153 (1995).
[13] D.A. Ovsyannikov, A.D. Ovsyannikov, M.F. Vorogushin, Yu.A. Svistunov, A.P. Durkin, "Beam Dynamics Optimization: Models, Methods and Applications", Nuclear Instruments and Methods in Physics Research, Section A: Accelerators, Spectrometers, Detectors and Associated Equipment, 2006, Vol. 558, No 1, pp. 11-19 (2006).
[14] I.D. Rubtsova, E.N. Suddenko, "Investigation of Program and Perturbed Motions of Particles in Linear Accelerator", RuPAC'12, St. Petersburg, Russia, September 2012, pp. 367-369 (2012); http://www.JACoW.org
[15] I.D. Rubtsova, "Mathematical Optimization Model of Longitudinal Beam Dynamics in Klystron-type Buncher", RuPAC'14, Obninsk, Russia, October 2014, pp. 66-68 (2014); http://www.JACoW.org
[16] I.D. Rubtsova, "Optimization of Iterative Beam Dynamic Process", Proceedings of III International Conference "Stability and Control Processes" in Memory of V.I. Zubov (SCP), IEEE, pp. 198-200 (2015).
[17] B.P. Murin, A.P. Durkin, O.Ju. Shlygin, "Relativistic Electron Beams Bunching in Microwave Generator of Quasi-continuous Action", in collection of papers: Theory and Techniques of Relativistic Microwave Generators, Moscow, Radio Engineering Institute, pp.76-83 (1988).
[18] D.A. Ovsyannikov, A.D. Ovsyannikov, I.V. Antropov, V.A. Kozynchenko, "BDO-RFQ Code and Optimization Models," 2005 International Conference on Physics and Control (PhysCon 2005), Proceedings, Art. No 1513994, pp. 282-288 (2005).
[19] A.D. Ovsyannikov, D.A. Ovsyannikov, A.P. Durkin, S.-L. Chung, "Optimization of Matching Section of an Accelerator with a Spatially Uniform Quadrupole Focusing", Technical Physics, The Russian Journal of Applied Physics, 2009, Vol. 54, No 11, pp. 1663-1666 (2009).
[20] A.D. Ovsyannikov, D.A. Ovsyannikov, S.-L. Chung, "Optimization of a Radial Matching Section", International Journal of Modern Physics A, 2009, Vol.24, No 5, pp.952-958 (2009).
[21] A.D. Ovsyannikov, D.A. Ovsyannikov, M.Yu. Balabanov, S.-L. Chung, "On the Beam Dynamics Optimization Problem", International Journal of Modern Physics A, 2009, Vol. 24, No 5, pp. 941-951 (2009).
[22] S.V. Zavadsky, D.A. Ovsyannikov, S.-L. Chung, "Parametric Optimization Methods for the Tokamak Plasma Control Problem", International Journal of Modern Physics A, 2009, Vol. 24, No 5, pp.1040–1047 (2009).
[23] D.A. Ovsyannikov, "Mathematical Modeling and Optimization of Beam Dynamics in Accelerators", RuPAC'12, St. Petersburg, Russia, September 2012, pp. 68-72 (2012); http://www.JACoW.org
[24] D.A. Ovsyannikov, V.V. Altsybeyev, "Mathematical Optimization Model For Alternating-Phase Focusing (APF) Linac", Problems of Nuclear Science and Engineering, 2013, No 4, p. 93 (2013).
[25] D.A. Ovsyannikov, V.V. Altsybeyev, "Optimization of APF Accelerators", Problems of Nuclear Science and Engineering, 2013, No 6, p. 119 (2013).
[26] A.D. Ovsyannikov, D.A. Ovsyannikov, V.V. Altsybeyev, A.P. Durkin, V.G. Papkovich, "Application of Optimization Techniques for RFQ Design", Problems of Nuclear Science and Engineering, 2014, Vol. 91, No 3, pp. 116-119 (2014).
[27] D.A. Ovsyannikov, A.D. Ovsyannikov, I.V. Antropov, V.A. Kozynchenko, "Software complex BDO-RFQ", Proceedings of III International Conference "Stability and Control Processes" in Memory of V.I. Zubov (SCP), IEEE, pp. 335-337.(2015).
[28] L.V. Vladimirova, "Global Extremum Search on the Basis of Density and Its Mode Estimation", Proc. of 20th International Workshop: Beam Dynamics & Optimization (BDO), June-July 2014, St. Petersburg, Russia, IEEE, p. 186 (2014).

ISBN 978-3-95450-181-6

ON APPLICATION OF MONTE CARLO METHOD FOR POISSON PROBLEM SOLVING

L.V. Vladimirova#, I. Rubtsova, SPbSU, Saint-Petersburg, Russia

Abstract

The paper presents the application of random grid walk for Dirichlet problem solving for Poisson equation. Boundary value problem is discretized and reduced to the system of linear algebraic equations. The matrix of this system is used for stochastic matrix constructing. Thus, there is a possibility of Markov chains obtaining. The special random value is defined on Markov chain trajectories; this value is used for approximation of the desired solution. The advantages of this method are discussed in the paper.

The algorithm is applied for electric potential calculation in the cell of support lattice of exit window in large-aperture electron accelerator.

DIRICHLET PROBLEM FOR POISSON EQUATION

Consider the Dirichlet problem for electric potential. Poisson equation for unknown potential $u(x,y)$ has the form

$$\frac{\partial^2 u}{\partial x^2}+\frac{\partial^2 u}{\partial y^2}=\tilde{f}(x,y),\quad (x,y)\in G \tag{1}$$

with boundary conditions

$$u\big|_{\Gamma}=\varphi(x,y). \tag{2}$$

Here $G\subset R^2$ is some domain, Γ is the boundary of the domain G, $\tilde{f}(x,y)$ and $\varphi(x,y)$ are given functions.

Let us consider problem (1)-(2) discretization algorithm for the rectangle domain. The modification of this algorithm for the domain of any other form is given in the book [1].

For numerical solution of Dirichlet problem (1)-(2) we introduce sufficiently fine grid S with the step l: $S=\{s_{i,j}=(x_i,y_j):\ x_i=il,\ \ y_j=jl,\ \ i=\overline{0,L_x},\ \ j=\overline{0,L_y}\}$. We distinguish the set of boundary grid points $S_\Gamma=\{s_{i,j}=(x_i,y_j)\in S:\ \ i=0,L_x,\ j=0,L_y\}$. The internal grid points set is $S_G=S\setminus S_\Gamma$.

After that we introduce the following grid functions: $\{u_{i,j}=u(s_{i,j}):\ \ s_{i,j}\in S\}$, $\{\tilde{f}_{i,j}=\tilde{f}(s_{i,j}):\ \ s_{i,j}\in S_G\}$, $\{\varphi_{i,j}=\varphi(s_{i,j}):\ \ s_{i,j}\in S_\Gamma\}$.

Let us replace the equation (1) at internal grid points by the difference equation

$$u_{i,j}=(1/4)(u_{i-1,j}+u_{i+1,j}+u_{i,j-1}+u_{i,j+1}-l^2\tilde{f}_{i,j}). \tag{3}$$

At boundary grid points we assume

$$u_{i,j}=\varphi(x_i,y_j). \tag{4}$$

The solution of algebraic system (3)-(4) converges to the solution of Dirichlet problem (1)-(2) as $l\to 0$ [2,3].

Let us number all the grid points in any order (using one index) and rewrite the equations (3)-(4) in the same order. Now the grid S is described as follows: $S=\{(x_k,y_k),k=\overline{1,L}\}$, where $L=(L_x+1)(L_y+1)$. Let I_G and I_Γ be the sets of numbers of internal and boundary grid points correspondingly.

After that we introduce the grid functions $u=(u_1,...,u_L)$, $\tilde{f}=(\tilde{f}_1,...,\tilde{f}_L)$ and $\varphi=(\varphi_1,...,\varphi_L)$ representing the grid values of potential, right-hand part of equation (1) and boundary function correspondingly.

Now the system (3)-(4) takes the form

$$u=Au+f, \tag{5}$$

where A is $L\times L$ matrix of coefficients; L-vector f is determined as follows:

$$f_i=\begin{cases}(-1/4)l^2\tilde{f}_i, & i\in I_G\\ \varphi_i, & i\in I_\Gamma\end{cases}. \tag{6}$$

As for matrix A, when $i\in I_G$, the line $A_i=(a_{i,1},...,a_{i,L})$ contains four elements equal $1/4$ and other elements zero; if $i\in I_\Gamma$ the line A_i is zero.

"WALK-ON-GRID" METHOD

Stochastic Matrix

To obtain the solution of the system (5) we apply "walk-on-grid" algorithm.

Let us construct stochastic matrix P by the rule:

$$i\in I_G\Rightarrow\begin{Bmatrix}p_{i,j}>0\ \ if\ a_{i,j}>0\\ p_{i,j}=0\ \ if\ a_{i,j}=0\end{Bmatrix},\ j=\overline{1,L};\ \sum_{j=1}^{L}p_{i,j}=1;$$

$$i\in I_\Gamma\Rightarrow p_{i,j}=\delta_{i,j},\ \ j=\overline{1,L},$$

#sergvlad@sp.ru

ISBN 978-3-95450-181-6

where $\delta_{i,j}$ is Kronecker delta. Evidently, every line of matrix P presents the probability distribution. Besides, let us introduce initial probability distribution $p=(p_1,\ldots,p_L)$ ($\sum_{i=1}^{L} p_i=1,\quad p_i\geq 0$). Using the set $\{p,P\}$ we can simulate Markov chain; in this case p is initial states probability vector and P is transition matrix.

Markov chain simulation

Consider the problem of calculation of scalar product (h,u), where h is prescribed L-vector.

Markov chain may be considered to describe the evolution of the object called "particle". The particle changes its state in accordance with chain trajectory.

Let us assign the "weight" Q_k to moving particle. Suppose the "weight" to change in the process of particle movement. For "weight" determination let us introduce the values

$$q_i=\begin{cases} h_i/p_i, & p_i>0 \\ 0, & p_i=0 \end{cases},\quad q_{i,j}=\begin{cases} a_{i,j}/p_{i,j}, & p_{i,j}>0 \\ 0, & p_{i,j}=0 \end{cases}, \qquad (7)$$

where $i,j=\overline{1,L}$.

The particle is "born" at some initial grid point; we obtain its number i_0 as a result of random variable simulation with probability distribution $p=(p_1,\ldots,p_L)$.

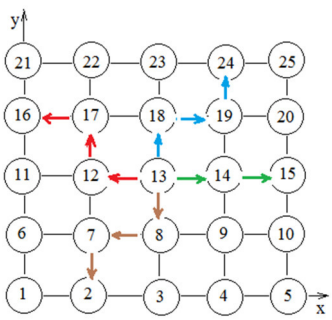

Figure 1: Random walk on grid (L=25)

The initial "weight" of particle is $Q_0=q_{i_0}$. We obtain next grid point number i_1 by random variable simulation with probability distribution $P_{i_0}=(p_{i_0,1},\ldots,p_{i_0,L})$; P_{i_0} is the line of stochastic matrix P. The particle passes to the point numbered i_1 with probability p_{i_0,i_1}. Particle "weight" becomes equal $Q_1=q_{i_0}\cdot q_{i_0,i_1}$, and so on. We calculate the "weights" by recurrent formula $Q_0=q_{i_0}$, $Q_m=Q_{m-1}\cdot q_{i_{m-1},i_m}$. If new particle state is boundary grid point with number i_μ, the particle stays at this point with probability $p_{i_\mu,i_\mu}=1$ and the chain terminates. Clearly, if one continues simulation, in view of Eq. 7 the result is $i_{\mu+1}=i_\mu$, $q_{i_\mu,i_{\mu+1}}=0$, $Q_{\mu+1}=0$ and so on. So in this case we obtain the chain of the length $\mu: i_0\to i_1\to\cdots\to i_\mu$. The example of Markov chains is depicted in Fig. 1, $L=25$.

Special random variable

Let us introduce random variable ξ_μ defined on the trajectories of the Markov chain of the length μ [1]:

$$\xi_\mu=\sum_{m=0}^{\mu} Q_m f_{i_m} \quad or \quad \xi_\mu=\sum_{m=0}^{\mu}\frac{h_{i_0}a_{i_0,i_1}\cdots a_{i_{m-1},i_m}}{p_{i_0}p_{i_0,i_1}\cdots p_{i_{m-1},i_m}}f_{i_m} \qquad (8)$$

Here $f_{i_\mu}=\varphi_{i_\mu}$ in view of Eq. 6.

For internal grid points the matching conditions are satisfied:

$$p_i>0 \ \ if \ \ h_i\neq 0,$$
$$p_{i,j}>0 \ \ if \ \ a_{i,j}\neq 0.$$

Consequently, one can argue [1] that

$$M\xi_\mu \xrightarrow[\mu\to\infty]{} (h,u). \qquad (9)$$

Consider N independent trajectories beginning at the point numbered i_0. If $h=\hat{h}=\left(0,\ldots,0,\underset{i_0}{1},0,\ldots,0\right)$, the scalar product provides the calculation of one component of the solution: $u_{i_0}=(h,u)$. In view of the statement (9) this component may be calculated by formula

$$u_{i_0}=(\hat{h},u)\underset{(9)}{\approx}M\xi_\mu\approx\frac{1}{N}(\xi_{\mu_1}+\cdots+\xi_{\mu_N}). \qquad (10)$$

Consider the following particular case. Let us take $\hat{h}$ as initial distribution vector: $p=\hat{h}$ and assume $p_{i,j}=\begin{cases} a_{i,j}, & i\in I_G \\ \delta_{i,j}, & i\in I_\Gamma \end{cases}$, $j=\overline{1,L}$. In this case the "weights" along the trajectory are as follows: $Q_0=Q_1=\cdots=Q_\mu=1$ until the chain reaches the boundary; after that $Q_{\mu+1}=Q_{\mu+2}=\cdots=0$. Consequently, calculation of the values of random variable ξ_μ (See Eq. 8) becomes especially simple:

$$\xi_\mu=\left(f_{i_0}+\cdots+f_{i_{\mu-1}}+\varphi_{i_\mu}\right). \qquad (11)$$

The formulae (10)-(11) provide the computational scheme for determination of one component of unknown vector u.

ISBN 978-3-95450-181-6

NUMERICAL RESULTS

Electromagnetic fields determination in different devices and beam evolution modelling and investigation as well as optimization of beam dynamics and device parameters often includes boundary value problems solving for Poisson equation [4-26]. Monte Carlo method provides the simple and effective algorithms for computation and parallelization [1-2, 27-32].

This paper deals with application of "walk-on-grid" method to electric potential distribution determination in the cell of support lattice of exit window in large-aperture electron accelerator [27].

The application specifics of electron sources of large cross-section beams in gas laser or radiation-chemical technologies demands beam extraction from the vacuum into the gas at atmospheric pressure (or higher). Consequently, the obligatory component of such electron source construction is a window with thin metal foil and support lattice. The foil is impermeable to gas but quite freely passes the accelerated electrons [33].

The electron accelerator provides formation, acceleration and extraction of the electron beam in the workspace of gas discharge chamber. Particle beam energy is $150keV$, beam cross-section square is $700mm^2$, current density in stationary mode reaches $0.120\,mkA/mm^2$. Support lattice bar width is 1 mm, height is 12 mm, the distance between bars is 5 mm. Charge density value in the cell is calculated using the accelerator characteristics and equal $\rho_0 = 5.19 \cdot 10^{-9}\, C/m^3$.

Let us consider the potential calculation domain to be the rectangle $G = [0,a] \times [0,b]$. We suppose the potential distribution in any cross-section $z = const$ to be identical.

Electron beam moves through the side $y = b$, so the potential distribution is prescribed on this side. The potential on remaining sides of rectangle are supposed to be zero.

Boundary conditions are as follows:

$$u(0,y) = u(a,y) = 0, \quad 0 \le y \le b,$$

$$u(x,0) = 0,\ u(x,b) = \sin\frac{\pi}{a}x, \quad 0 \le x \le a.$$

The calculation was performed for various values of grid step l and trial number N .The results are presented for $l = 0.0024$, $N = 5000$. The potential was calculated by the formula (10). The potential distribution in the cell of support lattice of exit window in large-aperture electron accelerator is presented in Fig. 2.

PARALLEL PROCESSING

Monte Carlo methods allow the perfect parallelization of the computational process.

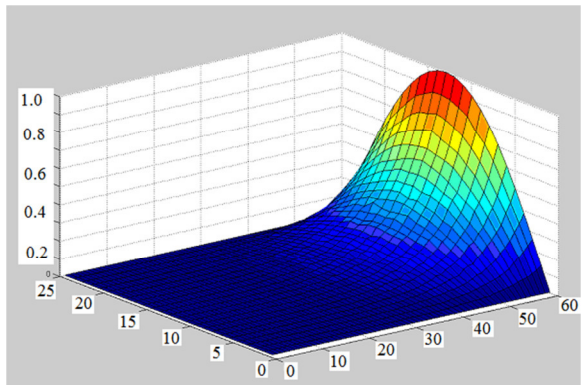

Figure 2: Potential distribution in the cell.

Parallel computing was performed for the problem under study. The numerical experiment shows that parallelization gives extremely low benefit for the grids with large step. Consequently, it is more efficient to use a fine grid.

The analysis of parallel processing efficiency is illustrated in Fig. 3. The graphs are presented for various number of threads and various number N of Markov chains. The best computing time result is achieved for 4 threads. Threads number increasing does not lead to appreciable time advantage.

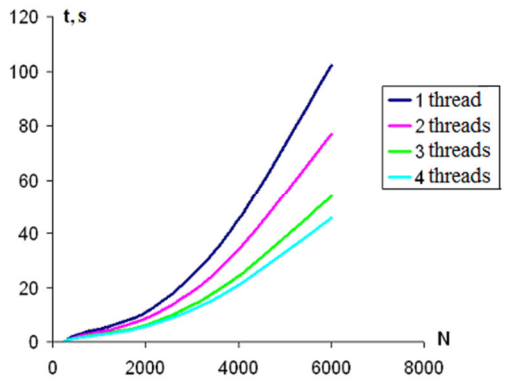

Figure 3: Parallel processing.

REFERENCES

[1] S.M. Ermakov, *Monte Carlo Method and Related Matters*, (Moscow: Nauka, 1975), 471.

[2] K.K. Sabelfeld, *Monte Carlo Methods in Boundary Value Problems*, (Moscow: Nauka, 1980), 280.

[3] V.S. Vladimirov, *Equations of Mathematical Physics*, (Moscow: Mir Publishers, 1983), 464.

[4] O.I. Drivotin, D.A. Ovsyannikov, "Modeling of Self-consistent Distributions for Longitudinally Non-uniform Beams", Nuclear Instruments and Methods in Physics Research, Section A: Accelerators, Spectrometers, Detectors and Associated Equipment, 2006, Vol. 558, No 1, pp 112-118

[5] O.I. Drivotin, D.A. Ovsyannikov, "Self-consistent Distributions for Charged Particle Beam in Magnetic Field", International Journal of Modern Physics, Section A, 2009, Vol.24, No 5, pp. 816-842.

ISBN 978-3-95450-181-6

[6] O. Drivotin, N. Ovsyannikov, "Self-Consistent Distributions Simulation for a Charged Particle Beam", Proceedings of III International Conference "Stability and Control Processes" in Memory of V.I. Zubov (SCP), IEEE, pp. 161-164 (2015).
[7] V.A. Kozynchenko, "The Modeling of Charged Particle Interactions in the Elliptic Beam", 20th International Workshop on Beam Dynamics and Optimization (BDO 2014), pp. 94-95, (2014).
[8] V.A. Kozynchenko, S.A. Kozynchenko, "Parallel Beam Dynamics Simulation in Injection Systems Taking into Account Particle Interactions", 20th International Workshop on Beam Dynamics and Optimization (BDO 2014), pp. 98-99 (2014).
[9] D.A. Ovsyannikov, A.D. Ovsyannikov, I.V. Antropov, V.A. Kozynchenko, "Software complex BDO-RFQ", Proceedings of III International Conference "Stability and Control Processes" in Memory of V.I. Zubov (SCP), IEEE, pp. 335-337.(2015).
[10] I.D. Rubtsova, E.N. Suddenko, "Investigation of Program and Perturbed Motions of Particles in Linear Accelerator", RuPAC'12, St. Petersburg, Russia, September 2012, pp. 367-369 (2012); http://www.JACoW.org
[11] I.D. Rubtsova, "Integral-differential Model of Quasi-periodic Beam Longitudinal Dynamics", Beam Dynamics & Optimization (BDO), 2014 20th International Workshop, June-July 2014, St. Petersburg, Russia, Proceedings, IEEE, p. 144 (2014).
[12] I.D. Rubtsova, "Analytical Approach to Quasiperiodic Beam Coulomb Field Modeling", II Conference on Plasma&Laser Research and Technologies (2016), Journal of Physics: Conference Series, Vol. 747, No 1, 012074 (2016); http://iopscience.iop.org/1742-6596/747/1/012074
[13] L.V. Vladimirova, "Optimization of Interacting Particle Beam Dynamics in Linear Accelerator", Journal of Computer and Systems Sciences International, 6, pp. 178-183 (1995)
[14] D.A. Ovsyannikov, "Modeling and Optimization Problems of Charged Particle Beam Dynamics", ECC 1997-European Control Conference 4, pp. 1463-1467 (1997).
[15] D.A. Ovsyannikov, A.D. Ovsyannikov, I.V. Antropov, V.A. Kozynchenko, "BDO-RFQ Code and Optimization Models," 2005 International Conference on Physics and Control (PhysCon 2005), Proceedings, Art. No 1513994, pp. 282-288 (2005).
[16] D.A. Ovsyannikov, A.D. Ovsyannikov, M.F. Vorogushin, Yu.A. Svistunov, A.P. Durkin, "Beam Dynamics Optimization: Models, Methods and Applications", Nuclear Instruments and Methods in Physics Research, Section A: Accelerators, Spectrometers, Detectors and Associated Equipment, 2006, Vol. 558, No 1, pp. 11-19 (2006).
[17] A.D. Ovsyannikov, D.A. Ovsyannikov, A.P. Durkin, S.-L. Chung, "Optimization of Matching Section of an Accelerator with a Spatially Uniform Quadrupole Focusing", Technical Physics, The Russian Journal of Applied Physics, 2009, Vol. 54, No 11, pp. 1663-1666 (2009).
[18] A.D. Ovsyannikov, D.A. Ovsyannikov, S.-L. Chung, "Optimization of a Radial Matching Section", International Journal of Modern Physics A, 2009, Vol.24, No 5, pp.952-958 (2009).
[19] A.D. Ovsyannikov, D.A. Ovsyannikov, M.Yu. Balabanov, S.-L. Chung, "On the Beam Dynamics Optimization Problem", International Journal of Modern Physics A, 2009, Vol. 24, No 5, pp. 941-951 (2009).
[20] S.V. Zavadsky, D.A. Ovsyannikov, S.-L. Chung, "Parametric Optimization Methods for the Tokamak Plasma Control Problem", International Journal of Modern Physics A, 2009, Vol. 24, No 5, pp.1040–1047 (2009).
[21] D.A. Ovsyannikov, "Mathematical Modeling and Optimization of Beam Dynamics in Accelerators", RuPAC'12, St. Petersburg, Russia, September 2012, pp. 68-72 (2012); http://www.JACoW.org
[22] D.A. Ovsyannikov, V.V. Altsybeyev, "Optimization of APF Accelerators", Problems of Nuclear Science and Engineering, 2013, No 6, p. 119 (2013).
[23] A.D. Ovsyannikov, D.A. Ovsyannikov, V.V. Altsybeyev, A.P. Durkin, V.G. Papkovich, "Application of Optimization Techniques for RFQ Design", Problems of Nuclear Science and Engineering, 2014, Vol. 91, No 3, pp. 116-119 (2014).
[24] D.A. Ovsyannikov, V.V. Altsybeyev, "Mathematical Optimization Model For Alternating-Phase Focusing (APF) Linac", Problems of Nuclear Science and Engineering, 2013, No 4, p. 93 (2013).
[25] I.D. Rubtsova, "Mathematical Optimization Model of Longitudinal Beam Dynamics in Klystron-type Buncher", RuPAC'14, Obninsk, Russia, October 2014, pp. 66-68; http://www.JACoW.org
[26] I.D. Rubtsova, "Optimization of Iterative Beam Dynamic Process", Proceedings of III International Conference "Stability and Control Processes" in Memory of V.I. Zubov (SCP), IEEE, pp. 198-200 (2015).
[27] L.V. Vladimirova, *Electromagnetic Fields Simulation by Monte Carlo Method, part I: "Walk-on-grid" Method*, tutorial (St. Petersburg: St. Petersburg State University, 2007), 31.
[28] L.V. Vladimirova, "Global Extremum Search on the Basis of Density and Its Mode Estimation", Proc. of 20th International Workshop: Beam Dynamics & Optimization (BDO), June-July 2014, St. Petersburg, Russia, IEEE, p. 186 (2014).
[29] L.V. Vladimirova, "Monte Carlo Methods in Beam Dynamics Optimization Problem", Vestnik St. Petersburg State University, Ser.10, No 1, pp. 30-39 (2014).
[30] L.V. Vladimirova, I.A. Fatyanova, "Construction of Regression Experiment Optimal Plan Using Parallel Computing", Proceedings of III International Conference "Stability and Control Processes" in Memory of V.I. Zubov (SCP), IEEE, pp. 361-363 (2015).
[31] L.V. Vladimirova, "Mixed Boundary Value Problem Solving for the Laplace Equation by Monte-Carlo Method with the Use of "Random Walk by Spheres" Algorithm, Vestnik SPGUTD, Ser. 1, Issue 2, pp. 22-28 (2016).
[32] L.V. Vladimirova, "Multicriterial Approach to Beam Dynamics Optimization Problem", II Conference on Plasma&Laser Research and Technologies (2016), Journal of Physics: Conference Series, Vol. 747, No 1, 012070 (2016); http://iopscience.iop.org/1742-6596/747/1/012070
[33] S.P. Bugaev et al., *Eelectron beams of large cross-section*, (Moscow: Energoatomizdat, 1984), 112

ISBN 978-3-95450-181-6

ABOUT BEHAVIOR OF ELECTRONS AND IONS IN THE ACCELERATING INTERVAL

A.S.Chikhachev, SSC VEI, Moscow, Russia
H.Y.Barminova, NRNI MePhI, Moscow, Russia

Abstract

The behavior of the electron-ion ensemble in accelerating gap. Hot electrons are described by the distribution function, which is a solution of the collisionless kinetic equation, which depends not only on the integrals of motion. For a description of cold ions used hydrodynamic equations. The possibility of excess ions ion-acoustic velocity. The equation that determines the relative density of the ions in the case of closed phase trajectories characterizing the dependence of the field on the coordinate

INTRODUCTION

To study the actual recovery process of heavy ions from the plasma carried out a large number of studies on the review of the process models. In [1] it was shown that the plasma leaving the ions at velocities exceeding the ion-sound velocity. Because in the real world, the electron temperature substantially greater than the temperature of the ion number of accelerated ions is exponentially small. Note, however, the work [2], to study the acceleration of a thin ion beam. In this paper we show that the ion velocity can exceed the speed of ion-sound when changing the beam radius .. In [3] studied the state of the accelerated flow of cold ions in resting, in general, the hot-electron cloud. In particular, in [3], the transition layer system "plasma-vacuum" is infinitely large. In all these works the electron current is zero. In [4] studied the equilibrium state of the system in the presence of a nonzero electron current by using hydrodynamic description of electrons. The paper [5] examines the state of the ion flux in the layer of electrons moving in a direction perpendicular to the flow of electrons. In this work, the maximum energy which can acquire ions in a layer equal to the temperature of electrons, whereas in the conditions of [4], the energy can exceed the electron temperature. problems are also considered in [6] studied in the present work.

FORMULATION OF THE PROBLEM

We shall describe the ensemble of collisionless kinetic equation for electrons and ions to describe the hydrodynamic equations, assuming for the sake of simplicity, one-dimensional problem. For electrons, the kinetic equation is:

$$\frac{p}{m}\frac{\partial f}{\partial x}+e\frac{d\Phi}{dx}\frac{\partial f}{\partial p}=0, \qquad (1)$$

where m - the mass of the electron, $-e$ the charge, Φ - the potential, x - coordinate, p - momentum, $f(x,p)$ - particle distribution function.

Let us put

$$f=\sigma\left(p-\sqrt{2m\left(C_0+e\Phi\right)}\right)\Psi\left(H\right). \qquad (2)$$

Here $\sigma(x)$ - Heaviside function., $C_0>-e\Phi(x)$ for any x. Expression (2) determines non-zero fluid of electrons: $\Gamma_e=\int\limits_{\sqrt{2m(C_0+e\Phi)}}^{\infty}\frac{p}{m}\Psi(H)\,dp=\int\limits_{C_0}^{\infty}dH\Psi(H)$. In the case of exponential distribution $\Gamma_e=\kappa_0 T\exp\left(-\frac{C_0}{T}\right)$. The electron density in this case is expressed as follows:

$$n_e=\kappa_0\sqrt{\frac{\pi mT}{2}}\exp\left(\frac{e\Phi}{T}\right)\left(1-erf\left(\sqrt{\frac{C_0+e\Phi}{T}}\right)\right) \qquad (3)$$

Here $erf(x)=\frac{2}{\sqrt{\pi}}\int\limits_0^x\exp\left(-y^2\right)dy$ - error integral.

The role of the factor $\sigma\left(p-\sqrt{2m\left(C_0+e\Phi\right)}\right)$ in the expression (2) is significant - the one hand, the particle density varies view, on the other - particle current is not zero. Using the hydrodynamic description of one-dimensional flow of cold ions, it is easy to obtain $n_i=\frac{\Gamma_i}{\upsilon_i}=\frac{n_{i0}\upsilon_0}{\sqrt{\frac{M\upsilon_0^2}{2}+e\Phi}}$

Here M - ion mass.

Put the fluid density as: $\Gamma_i=n_{0i}\upsilon_0$, n_{0i} - initial ion density, υ_0 - initial ion velocity. If we introduce the dimensionless potential $u=\frac{e\Phi}{T}$ and to identify the ion-sound velocity $\upsilon_s=\sqrt{\frac{2T}{M}}$, the ion density becomes: $n_i=\frac{n_{i0}\upsilon_0}{\upsilon_s\sqrt{\frac{\upsilon_0^2}{\upsilon_s^2}-u}}$

Let $n_{0e}=\kappa_0\sqrt{\frac{\pi mT}{2}}$

We introduce the dimensionless variables: $t=\frac{x}{l_0}$, $l_0=\sqrt{\frac{T}{4\pi e^2 n_{0e}}}$, $\frac{C_0}{T}=\zeta_0$. Then the Poisson equation becomes:

$$\frac{d^2u}{dt^2}=\exp(u(t))\left(1-erf\sqrt{\zeta_0+u}\right)-\frac{\nu_i}{\sqrt{\frac{\upsilon_0^2}{\upsilon_s^2}-u(t)}} \qquad (4)$$

Here $\nu_i=\frac{n_{0i}}{n_{0e}}\frac{\upsilon_0}{\upsilon_s}$.

ISBN 978-3-95450-181-6

Equation solution.

Equation (4) has integral looking as:

$$\frac{\dot{u}^2}{2} = \exp(u) - \exp(u)\,erf\sqrt{\zeta_0 + u} + \frac{2}{\sqrt{\pi}}\exp(-\zeta_0)\sqrt{\zeta_0 + u} + 2\nu_i\sqrt{\frac{\upsilon_0^2}{\upsilon_s^2} - u} + C_*. \qquad (5)$$

Consider solutions (5), characterized by closed phase trajectories $\dot{u}(u)$ - dependence field from the potential. There should be two points where $\dot{u}$ vanishes. If $\dot{u}(-4) = 0$, then $0 = e^{-4} + 2\nu_i\sqrt{\frac{\upsilon_0^2}{\upsilon_s^2} + 4} + C_*$, and if $\dot{u}\left(\frac{\upsilon_0^2}{\upsilon_s^2}\right) = 0$, then

$$0 = \exp\left(\frac{\upsilon_0^2}{\upsilon_s^2}\right)\left(1 - erf\left(\sqrt{4 + \left(\frac{\upsilon_0^2}{\upsilon_s^2}\right)}\right)\right) + \frac{2}{\sqrt{\pi}}e^{-4}\sqrt{4 + \left(\frac{\upsilon_0^2}{\upsilon_s^2}\right)} + C_*$$

From these equations, it follows that the ion density, characterized by a quantity ν_i is not arbitrary. Given that $\nu_i = \frac{n_{0i}}{n_{0e}}\frac{\upsilon_0}{\upsilon_s}$ we have a system of three equations for $C_*, \nu_i, \frac{\upsilon_0}{\upsilon_s}$. When $\frac{n_{0i}}{n_{0e}} = 1$ we get the equation:

$$\exp\left(\nu_i^2\right)\left(1 - erf\sqrt{4 + \nu_i^2}\right) + \frac{2}{\sqrt{\pi}}\exp(-4)\sqrt{4 + \nu_i^2} = \exp(-4) + 2\nu_i\sqrt{4 + \nu_i^2}. \qquad (6)$$

Solving (6) we obtain:

$$\nu_i \cong 0.007 = \frac{\upsilon_0}{\upsilon_s},\ C_* \cong -0.046316.$$

At Fig.1. phase trajectory $\dot{u}(u)$ is shown. Trajectory has closed character – ions are accelerated from initial point where $u = -4$ to the point where $u = 0.4 \cdot 10^{-4}$.

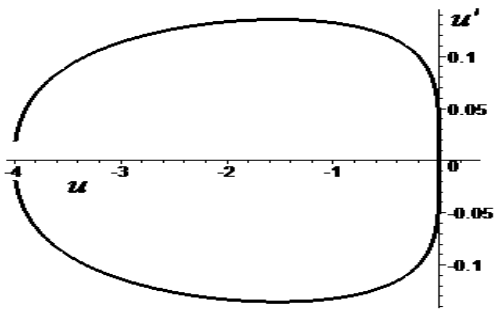

Figure 1: phase trajectory $\dot{u}(u)$.

It is possible, then, to build a relationship of ion density on the coordinate (Fig.2.).

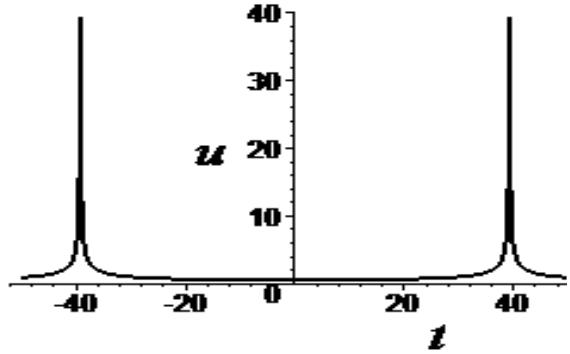

Figure 2: The dependence of ion density on the coordinate At certain points there is a maximum ion density. At these points, the ions have a minimum speed, the maximum speed - the points where the ion density is minimal.

At Fig. 3 - the dependence of the electron velocity on potential.

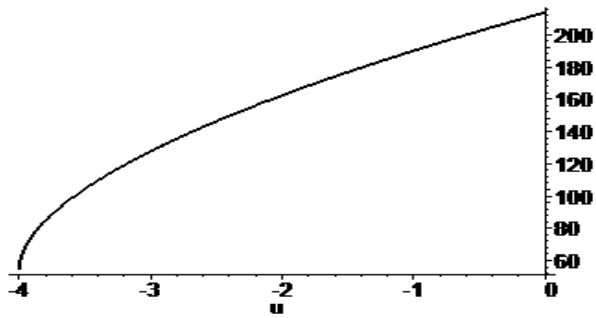

Figure 3: The dependence of electron velocity on potential.

The average hydrodynamic energy of the electrons increases with increasing potential, whereas the energy of the ions decreases when moving in the opposite direction.

CONCLUSION

Thus, in work it is shown that in case of acceleration of ions in a stream of hot electrons at a certain ratio for density of ions a phase trajectory - dependence of the field on potential - has the closed character

REFERENCES

[1] K.-U Riemann, J.Phys.D, Appl. Phys. 1991, 24, 493-519.
[2] Yu.A.Kovalenko, T.V.Chernyshev, A.S.Chikhachev, Techn.Phys.2011,v..81, №5, p.139-141.
[3] N.Sternberg, V.Godyak, IEEE Transaction on Plasma Science, **35**, N5, October 2007, pp.1341.
[4] Yu.A.Kovalenko, T.V.Chernyshev, A.S.Chikhachev, Izv. RAS, ser. Energetika, 2011, No.4, p.24-28.
[5] Yu.A.Kovalenko, A.S.Chikhachev, www.Jacow.org. RuPAC 2012. TUPPB039.
[6] A.S.Chikhachev, Cybernetics and Physics, 2014, vol.3, N4, pp161.

ISBN 978-3-95450-181-6

THE BEHAVIOR OF POWERFUL RELATIVISTIC ELECTRON BEAM WITH ELLIPTICAL CROSS-SECTION IN LONGITUDINAL MAGNETIC FIELD

A.S. Chikhachev , SSC VEI, Moscow, Russia
H.Y. Barminova, NRNU MEPhI, Moscow, Russia

Abstract

The behavior of relativistic intense electron beam with elliptical cross-section moving in a longitudinal magnetic field is investigated with the help of self-consistent model. The solutions for the beam envelopes are obtained in the case of the beam current differed from Alfven limit and the beam charge neutralized. The conditions of stationary beam propagation are determined, however it is discovered that for the case of non-zero self-consistent magnetic field the stationary beam propagation is violated, the partial emittance oscillations being observed. The found time- dependence of the partial emittances and the beam envelopes illustrates the effect of emittance transfer caused by the coupled particle motion in magnetic field.

INTRODUCTION

In [1,2,3] studied the behavior of the electron beam in a quadrupole system, the aim of this study was the possibility of compression - reducing the area of the cross-section of the beam when changing quadrupole forces. If the [1] to the transverse emittance were considered equal, in [2], these values are considered to be different, but continuing when the beam moves. In this paper we study the distribution of the electron beam decompensated with an elliptical cross-section in the absence of external quadrupole system and in the presence of a longitudinal magnetic field. The presence of the longitudinal magnetic field greatly complicates the situation - there are not two independent integrals of motion. Emittance can be converted (pumped). It is not a conserved quantity as the product of these values.

EQUATIONS

Consider a beam whose charge is compensated by the secondary particles. Lateral movement can be separated from the lengthwise when the current satisfies the following condition:

$J << J_A$, where $J_A = mc^3\gamma_0\beta_0/e$. The distribution function can be written as: $F = \delta(\beta_z - \beta_0)f(\vec{r}_\perp, z, \vec{v}_\perp)$. In this paraxial approximation the longitudinal velocity of the particles can be considered constant and equal for all particles. The stationary problem instead of the time you can use a coordinate z. In accordance with the invariant that defines the movement, should depend on $x(z), y(z), x' = \frac{dx}{dz}, y' = \frac{dy}{dz}, z$. We derive the equations of motion of particles in the laboratory frame. Consider that in the system connected to the main beam axes(x_1, y_1) have their own self-compression force directed to the beam axis: $F_{x_1} = -\frac{2ix_1}{R_x(R_x+R_y)}, F_{y_1} = -\frac{2iy_1}{R_y(R_x+R_y)}$. Here $i = J/J_A$ beam current related to Alfven,, $R_x(z), R_y(z)$ - the value of the semi-axes of the elliptic beam cross section). Calculating further, $F_x = F_{x_1}\cos\theta - F_{y_1}\sin\theta, F_y = F_{x_1}\sin\theta + F_{y_1}\cos\theta$, which should be considered $x_1 = x\cos\theta + y\sin\theta, y_1 = -x\sin\theta + y\cos\theta$, and $\theta(z)$ - angle of rotation of the principal axes of the ellipse relative to fixed axes, the equation can be obtained:

$$x'' = \omega_H y' - \alpha(z)x + \beta(z)y,\ y'' = -\omega_H x' + \beta(z)x - \gamma(z)y, \quad (1)$$

where

$$\alpha = \frac{i}{R_xR_y}\left(1 - \frac{R_x - R_y}{R_x + R_y}\cos 2\theta\right)$$

$$\beta = \frac{-i}{R_xR_y}\frac{R_x - R_y}{R_x + R_y}\sin 2\theta$$

$$\gamma == \frac{i}{R_xR_y}\left(1 + \frac{R_x - R_y}{R_x + R_y}\cos 2\theta\right)$$

In equations (1) are also taken into account the presence of an external longitudinal magnetic field, and $\omega_H = \frac{eH}{mc^2\gamma_0\beta_0}$, the dimension of this magnitude - the inverse length.Invariant system (1) can be represented as:

$$\begin{aligned} I = {} & A_1(z)x'^2 + 2A_2(z)x'x + A_3(z)x^2 + B_1(z)y'^2 + \\ & 2B_2(z)y'y + B_3(z)y^2 + C_1(z)x'y' + \\ & C_2(z)x'y + C_3(z)xy' + C_4(z)xy \end{aligned} \quad (2)$$

From condition $\frac{dI}{dz} \equiv 0$ using (1) we obtain:

$$\begin{aligned} A_1' &= -2A_2 + \omega_H C_1, \\ A_2' &= -A_3 + A_1\alpha(z) + 0.5\omega_H C_3 - 0.5C_1\beta(z), \\ A_3' &= 2A_2\alpha(z) - C_3\beta(z), \\ B_1' &= -2B_2 - \omega_H C_1 \\ B_2' &= -B_3 + B_1\gamma(z) - 0.5\omega_H C_2 - 0.5C_1\beta(z), \\ B_3' &= 2B_2\gamma(z) - C_2\beta(z), \\ C_1' &= -C_2 - C_3 + 2\omega_H(B_1 - A_1), \\ C_2' &= -C_4 + C_1\gamma(z) - 2A_1\beta(z) + 2\omega_H B_2, \\ C_3' &= -C_4 + C_1\alpha(z) - 2A_2\omega_H - 2B_1\beta(z), \\ C_4' &= C_2\alpha(z) + C_3\gamma(z) - 2B_2\beta(z) - 2A_2\beta(z). \end{aligned} \quad (3)$$

Converting, furter, I. Instead x', y' introduce variables ξ, η.

$$x' = \xi\cos\alpha + \eta\sin\alpha, \quad y' = -\xi\sin\alpha + \eta\cos\alpha \quad (4)$$

ISBN 978-3-95450-181-6

Suppose that $\tan(2\alpha) = C_1/(B_1 - A_1)$. If then assume $\xi_1 = \xi + (x\cos\alpha(A_2 + C_2/2) - y\sin\alpha(B_2 + C_3/2))/P, \eta_1 = \eta + (x\sin\alpha(A_2 + C_2/2) + y\cos\alpha(B_2 + C_3/2))/Q$, one should obtain:

$$I = P\xi_1^2 + Q\eta_1^2 + Ax^2 + By^2 + Cxy \quad (5)$$

where

$$P = A_1 + B_1 - \sqrt{(A_1 - B_1)^2 + C_1^2},$$
$$Q = A_1 + B_1 - \sqrt{(A_1 - B_1)^2 + C_1^2},$$
$$A = A_3 + K/\Lambda, B = B_3 + L/\Lambda,$$
$$C = C_4 + M/\Lambda, \Lambda = A_1B_1 - C_1^2/4,$$
$$K = A_2^2B_1 - 0.5A_2C_1C_3 + 0.25A_1C_3^2,$$
$$L = A_1B_2^2 - 0.5B_2C_1C_2 + 0.25B_1C_2^2,$$
$$M = A_1B_2C_3 + A_2B_1C_2 - A_2B_2C_1 - 0.25C_1C_2C_3. \quad (6)$$

If we assume that the distribution function is:$f = \delta(I - 1)$, the integral should be calculated for the density of the particles:

$$\int d\xi_1 d\eta_1 \delta\left(P\xi_1^2 + Q\eta_1^2 - Ax^2 - By^2 - Cxy - 1\right) =$$

$$\frac{\pi}{\sqrt{PQ}}\sigma\left(1 - Ax^2 - By^2 - Cxy\right),$$

where $\sigma(x)$ Heaviside function, $\sigma(x) = 1, x > 0, \sigma(x) = 0, x < 0$.To bring to the principal axes of the bunch should take advantage of the relations, expressing x_1, y_1 wia x, y. Supposing $\tan 2\theta = \frac{C}{B-A}$, we obtain

$$Ax^2 + By^2 + Cxy = \frac{x_1^2}{R_x^2} + \frac{y_1^2}{R_y^2},$$

$$R_x^2 = \frac{2}{A + B - \sqrt{(A-B)^2 + C^2}},$$

$$R_y^2 = \frac{2}{A + B + \sqrt{(A-B)^2 + C^2}}.$$

There remains the phase volume: $V = \Lambda(AB - C^2/4) \equiv const = \Lambda(A_3B_3 - C_4^2/4) - B_3K - A_3L + (C_4/2)M + (A_2B_2 - C_2C_3/4)^2$.Important characteristic beam are rms values. You can express the mean values through coefficient quadratic form I_{xy}. For example,

$$\overline{x'^2} = \frac{B_1}{2\Lambda}, \overline{x^2} = \frac{B}{2(AB - C^2/4)},$$
$$\overline{y'^2} = \frac{A_1}{2\Lambda}, \overline{y^2} = \frac{A}{2(AB - C^2/4)}. \quad (7)$$

Determing values:

$$E_x(z) = B_1(z)B(z)/$$

$$V, E_y(z) = A_1(z)A(z)/V,$$

beam emittance are in x and y direction. To solve the system (3) to set the initial conditions - the values of functions A_i, B_j, C_k if $z = 0$.

SOLUTION OF THE EQUATIONS

To find out the conditions under which the conditions of possible solutions for the stationary beam envelopes. Put $\omega_H = 0$ and all $C_j \equiv 0$. So invariant I mai be represented as sum of $I = I_1 + I_2$, where $I_1 = A_1x'^2 + 2A_2x'x + A_3x^2, I_2 = B_1y'^2 + 2B_2y'y + B_3y^2$. Constant solutions for R_x, R_y may be obtained if $A_2 \equiv B_2 \equiv 0$. Except initial conditions $A_2(0) = 0, B_2(0) = 0$ must be derivatives vanish at the starting point. From (3) follows: $A_3(0) = A_1(0)\alpha(0)$, $B_3(0) = B_1(0)\gamma(0)$. One can obtain:

$$A_1 = \frac{A_3}{2i\sqrt{B_3}}(1/\sqrt{B_3} + 1/\sqrt{A_3}),$$

$$B_1 = \frac{B_3}{2i\sqrt{A_3}}(1/\sqrt{B_3} + 1/\sqrt{A_3}).$$

Putting in this equalities $A_3(0) = 0.9, B_3(0) = 0.1$. Then, in the case of a force field in the solution of system (3) can be constant values$R_x \equiv \sqrt{10}, R_y \equiv \sqrt{1/0.9}, B_1(0) = 2/9i, A_1(0) = 6/i$. This is a very characteristic change of solutions when defining a small field($\omega_H = 0.003$), as shown in Figure 1.

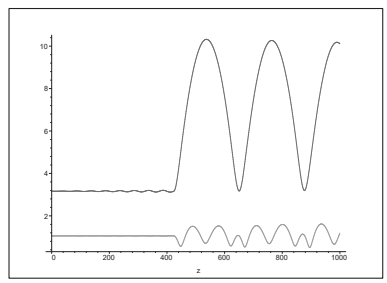

Figure 1: The dependence of the beam size $R_x(z), R_y(z)$ from coordinate.

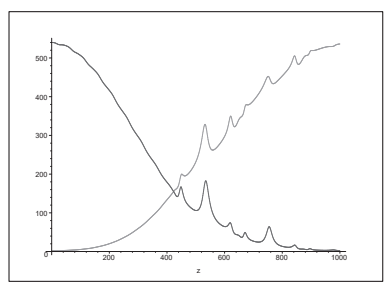

Figure 2: The dependence of emittance $E_x(z), E_y(z)$ from coordinate.

From Fig.1. It shows that the beam dimensions remain substantially constant up to a certain point (i.e. range of relatively small amplitude) after reaching these sizes vary at a constant frequency and a substantially greater amplitude. From Fig.2. You can see what is happening pumping emittance, and it was after reaching a point where the emittance compared begin intense oscillations of the transverse

ISBN 978-3-95450-181-6

dimensions of the beam. The above initial conditions under which the $A_1(0) \neq B_1(0)$ does not correspond to the conventional cathode elliptical shape whose $R_x \neq R_y$, and the spread of the initial transverse velocities are the same in the directions (ie, must be made equal $A_1(0) = B_1(0)$). Here are the results of a solution of (3) in the case of an isotropic distribution of initial velocities, assuming that $A_1(0) = B_1(0) = 25$.

In Fig. 3 dependences are given sizes $R_x(z)$ and $R_y(z)$ at isotropic distribution of initial velocities, in Fig.4 dependences are given emittances $E_x(z)$ and $E_y(z)$ at isotropic distribution of initial velocities.

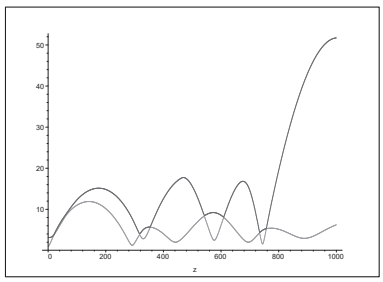

Figure 3: The dependence of the beam size $R_x(z), R_y(z)$ from the coordinates of an isotropic distribution of initial velocities.

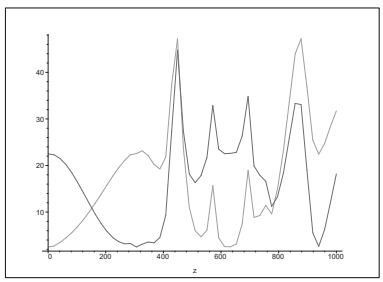

Figure 4: The dependence of emittance $E_x(z), E_y(z)$ from the coordinates of an isotropic distribution of initial velocities.

CONCLUSION

In this case, it should be noted quite chaotic dependence of the beam characteristics of the longitudinal coordinate. At the initial stage can be seen pumping emittance, and subsequently deprived of regular structure vibrations, the beam sizes also vary. Thus, in the work of the model Kapchinsky obtained system of equations that allows to study characteristics beam compensated charge with an elliptical cross-section in a constant longitudinal magnetic field. Obtained partial solutions, describing the state of the beam. It seems likely that the management performance characteristics of the beam should be used alternating field, which is supposed to study in the future.

REFERENCES

[1] A.S.Chikhachev, 1981, Tech. Phys.,**51**,p.496.

[2] A.S.Chikhachev, 1983, Tech. Phys.,**53**,p.1513.

[3] A.S.Chikhachev, 1984, Tech. Phys.,**54**, p.103.

ISBN 978-3-95450-181-6

THE USE OF MULTI-OBJECTIVE GENETIC ALGORITHMS FOR ACCELERATOR AND LIGHT SOURCE OPTIMIZATION*

Ye. Fomin#, V. Korchuganov, A. Smygacheva, NRC «Kurchatov Institute», Moscow, Russia

Abstract

The nonlinear effects are very important in development of new accelerators and synchrotron light sources. Nowadays they are one of the main factors limiting the achievement of the required facility parameters. In many cases in development of new accelerators the analytical estimations give very rough results and in some cases they don't apply at all. Therefore, the best way to research and design accelerators is to use numerical simulation. Nevertheless, very often during complex physical process simulation (taking into account many nonlinear effects) the use of classical optimization methods is difficult and does not give the desired results.

The article deals with the application of multi-objective optimization using genetic algorithms for accelerators and light sources. These algorithms allow both simple linear and complex nonlinear accelerator structures to be optimized with the same effectiveness when obtaining the required facility parameters.

INTRODUCTION

There are many methods of optimization. All of them can be divided into three groups: determinate, random (stochastic) and combined.

Most accelerator and light source optimization problems can be attributed to combinatorial problems with many different quality solutions. An exhaustive search of all solutions or only subset of solutions is the main feature of combinatorial algorithms. To find the best solution directed, random and combined an exhaustive search of all possible problem variables is used. Therefore, the search of proper solutions often becomes the art. After all, very often if you want to optimize nonlinear multi-objective problem (for example – beam emittance minimization and dynamic aperture maximization) with many variable parameters and restrictions you will face serious difficulties (most rapid and effective optimization methods can't be used, there are many local minima solutions, solving time is directly related to the number of variable parameters, etc.).

One of the effective way to solve combinatorial problems within a reasonable time is the use of genetic algorithms. Genetic algorithms are heuristic search algorithms used to solve optimization problems by random selection, combining and modification of desired parameters using process like the biological evolution.

Genetic algorithms as any other optimization algorithms have their own advantages and disadvantages.

*The reported study was funded by RFBR according to the research project No. 16-32-00336 мол_а.

#yafomin@gmail.com

Their most important advantages may be said to be:

- Any information about the fitness function behavior is not required.
- Discontinuities of the fitness function don't have a significant effect on optimization.
- Methods are relatively stable to fall into local minima.

Their most important disadvantages may be said to be:

- Methods are inefficient for optimizing fitness functions which have a long calculation time.
- A large number of parameters often turns «work with genetic algorithm» to «play with genetic algorithms».
- In the case of simple fitness functions, genetic algorithms are slower than specialized optimization algorithms.

Nowadays, genetic algorithms are powerful computing tool to solve different multidimensional multi-objective optimization problems. The use of genetic algorithms for accelerator and light source optimization allows to simplify and speed up the search of proper solutions.

The common block diagram for optimization process using genetic algorithms is shown in Fig. 1.

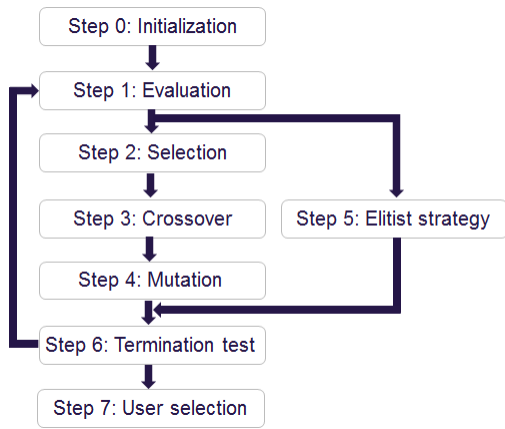

Figure 1: The block diagram of the optimization process using a genetic algorithm.

DESCRIPTION OF OPTIMIZATION METHOD

In general, all optimization problems can be divided into two groups. The first group contains only one fitness function optimization problems, the second one – at the same time two or more fitness function optimization problems. To solve the problems of each group it is advantageous to use a little different algorithms.

One fitness function optimization problem is the simplest situation with easy-to-analyse results. These kinds of problems can be efficiently solved with the help of the differential evolution method [1] is well suited.

ISBN 978-3-95450-181-6

Differential evolution is used for multidimensional real-valued functions but does not use the gradient of the problem being optimized, which means differential evolution does not require for the optimization problem to be differentiable as is required by classic optimization methods such as gradient descent and quasi-newton methods. Differential evolution can therefore also be used on optimization problems that are noisy, not continuous, changing over time, etc.

To solve two or more fitness functions optimization problems it is well suited another methods – the so-called multi-objective genetic algorithms. The aim of our multi-objective optimization problem is to find all possible tradeoffs among multiple objective functions that are usually conflicting.

Since it is difficult to choose a single solution for a multi-objective optimization problem without iterative interaction with the decision maker, one general approach is to show the set of Pareto optimal solutions to the decision maker. Then one of the Pareto optimal solutions can be chosen depending on the preference.

Pareto frontier and Pareto optimal solutions for example emittance and dynamic aperture optimization is shown in Fig 2. Blue dots – Pareto optimal (nondominated) solutions, red dots – other (dominated or not Pareto optimal) solutions.

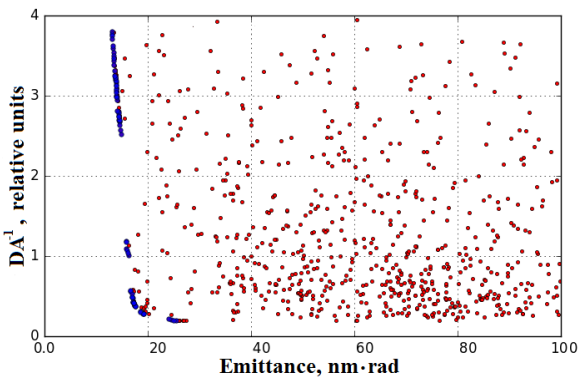

Figure 2: Pareto frontier. Blue dots – Pareto optimal solutions, red dots – other solutions.

A multi-objective optimization is an evolution of conventional numerical or combinatorial optimization, therefore many existing methods could be applied to this general case which makes defining of fitness function the main issue needs to be resolved. In recent decades, a number of approaches was developed to do it.

For solving accelerator lattice optimization problems only Step 2 (selection) and Step 5 (elitist strategy) in optimization process (see Fig. 1) are of particular interest.

For selection we chose the Nondominated Sorting Genetic Algorithm [2] as one of the most powerful and faster algorithm up to date. As an alternative, we also tried to use simpler and faster Random Weights Genetic Algorithm [3], but results were not as good as with the previous one.

In scenario when optimization is being done with smooth and continuous fitness function the genetic algorithms prove to be effective and everything works well. However, this is not the case when optimization needs to be performed for circular accelerators since its fitness function is not smooth, nor continuous, for which reason using of the genetic algorithms becomes quite problematic. Mostly because of a large amount of not periodic or incorrect solutions which means that no optimization is really accomplished.

This problem can be successfully addressed through the use of elitist strategy. During every new generation after fitness functions evaluation a certain number of best solutions are selected as elite individuals. When mutation is done N solutions are randomly removed from the current population and replaced by solutions from elite individuals. This elite preserve strategy has an effect in keeping the variety of each population.

SIMULATION RESULTS

To research genetic algorithms capabilities we used Siberia-2 storage ring lattice of Kurchatov synchrotron radiation source.

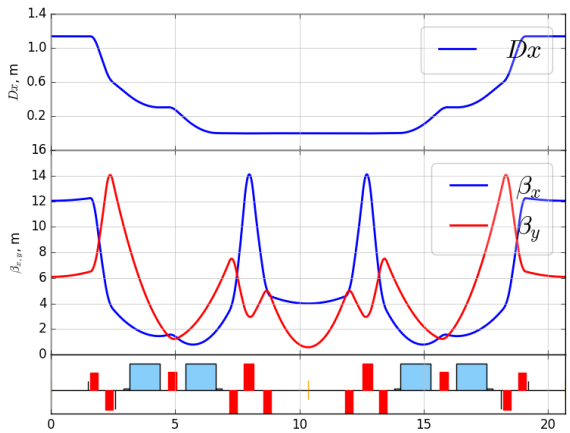

Figure 3: Optical functions for one of 6 ring cells in regular operation mode.

Optical functions of one of Siberia-2 superperiods being used in synchrotron radiation experiments are shown in Fig. 3 and the main parameters of the storage ring are presented in Table 1.

Table 1: Siberia-2 Storage Ring Main Parameters into Regular User Operation Mode

Parameter	Value
Circumference	124 m
Beam energy	2.5 GeV
Beam current	up to 150 mA
Horizontal emittance	98 nm·rad
Horizontal/vertical tune	7.775 / 6.695
Horizontal/vertical chromaticity	-16.9 / -12.9

Siberia-2 magnetic lattice consists of 6 mirror symmetric cells with 4 bending magnets and 6 quadrupole lenses. Each cell contains one nondispersive straight

ISBN 978-3-95450-181-6

section (3 m) for installing RF cavities and insertion devices and one dispersive straight section (3 m). The chromaticity is being corrected by 2 families of sextupole lenses.

Before starting an optimization process, we set following requirements and restrictions. In order for an injection into the Siberia-2 storage to stay efficient new optics must have a large dynamic aperture. Switching from the regular operation mode to the new mode should be performed only by adjusting the quadrupole and sextupole lenses strengths. As previously stated the six-fold symmetry optics is required for the new modes.

To accelerate optimization process we used initial approximation for variable parameters – the polarity of quadrupoles lenses is the same as used in Siberia-2 regular operation mode. As well, we set quadrupole lenses strengths of Siberia-2 regular operation mode as initial approximation for used optimization algorithms. Here we present the results obtained through the use of two different optimization genetic algorithms.

The first genetic algorithm applied was the differential evolution. This algorithm was used to minimize electron beam emittance in the presence of one additional condition – dispersion function should be zero in one of the two straight sections. After optimization we have that minimum emittance with the above-mentioned condition is approximately 65 nm·rad. It may be a little bit higher or lower depending on size of dynamic aperture, the precision of zeroing dispersion function and betatron tunes. Optical functions of one of the possible lattice tuning (emittance is 67 nm·rad) are shown on Fig. 4.

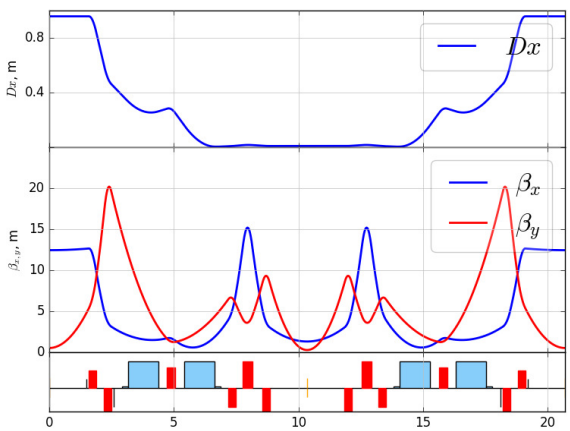

Figure 4: Optical functions for minimum emittance with zero dispersion function operation mode.

The second used genetic algorithm was multi-objective genetic algorithm with NSGA-II selection algorithm and elitist strategy. Now we will simultaneously minimize electron beam emittance and maximize dynamic aperture without any additional restrictions. Pareto frontier for emittance and dynamic aperture optimization is shown in Fig 2 and optical functions of one of the possible lattice tuning (emittance is 17 nm·rad) are shown on Fig. 5. As you can see on Fig. 2 achievable emittances are close to theoretical minimum emittance for Siberia-2 storage ring lattice. But in practice operation with such small emittance is not be possible with existing injection system due to very small dynamic aperture.

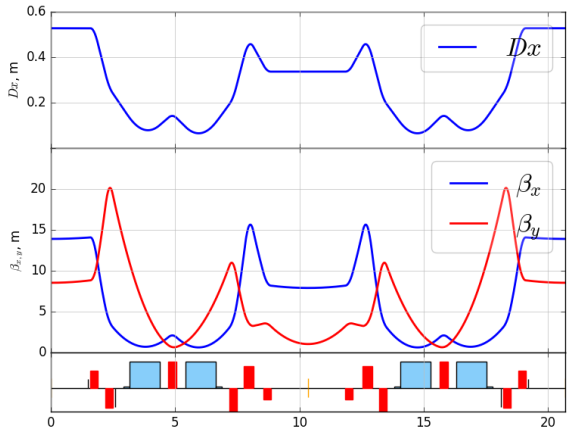

Figure 5: Optical functions for minimum operation mode.

It is also worth noting that reducing emittance to the minimum attainable level makes it impossible to keep zero dispersion function into one straight section. For that reason operating superconductive wiggler in this low-emittance mode is not advisable.

The obtained lattices look quite achievable. But before changing to the new optics tuning it is necessary to carry out more detailed research on the subject in order to obtain the optimal lattice parameters. As well, it is necessary to perform a lot of additional work at accelerating facility.

CONCLUSION

Genetic algorithms provide to be an effective optimization tool. Using these methods for solving complex accelerator lattices optimization problems yields good results. The carried out research demonstrates that when no initial approximation is made or only minimum prior information about behavior variable parameters is available using of genetic algorithms allows to provide desired results within a reasonable time.

In addition, we would like to note that it is not always possible to obtain exact optimal solution using genetic algorithm. Nevertheless, this problem can be solved by using solution obtained with the help of genetic algorithms as initial approximation for specialized optimization algorithms.

REFERENCES

[1] R. Storn, K. Price, Differential evolution - a simple and efficient adaptive scheme for global optimization over continuous spaces, Technical Report TR-95-012, ICSI, March 1995.

[2] K. Deb, A Fast and Elitist Multiobjective Genetic Algorithm: NSGA-II, IEEE Transactions on Evolutionary Computation, vol. 6, № 2, 2002.

[3] T. Murata, H. Ishibuchi, MOGA: Multi-Objective Genetic Algorithms, IEEE International Conference on Evolutionary Computation, vol. 1, 1995.

ISBN 978-3-95450-181-6

ABOUT DEVELOPMENT SYSTEM FOR THE ANALYSIS OF CHARGED PARTICLE BEAM DYNAMICS

M. Balabanov*, Saint-Petersburg State University, Saint-Petersburg, Russia

Abstract

Modern research process of scientific problems often requires large computational resources. To solve them we have to use distributed computing systems. Researcher groups need to use them simultanieously and mostly remotely. The paper describes build of the distributed system for collaborative research process. As example was chosen a problem of the optimization dynamics charged particle beams using high-performance computing systems. The solution of many topical tasks leads to nonlinear optimization problems for example the controlling beams of charged particles [1-10].

Optimization is performed by minimizing some quality functional the choice of which is a corollary fact that the control functions which provides a functional minimum should determine the accelerating structure with the desired characteristics. The problem is usually formulated as finding the control functions for which the controlled system satisfies the given constraints. There is a necessity of the quality functional choice which ensures the problem solution. Research objectives: the development of a distributed information-computational system for the analysis of charged particle beam dynamics.

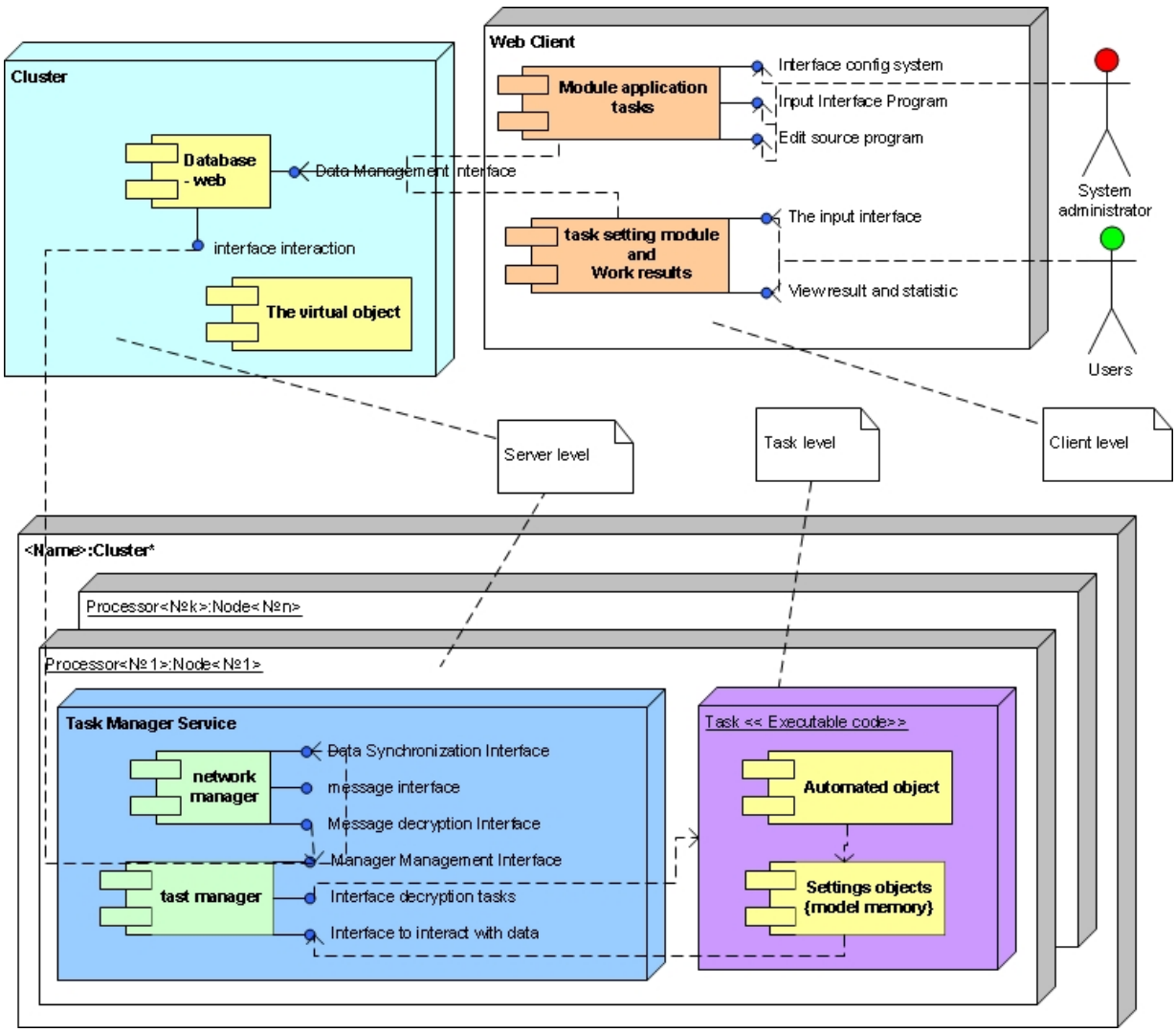

Figure 1: System architecture.

* BalabanovMYu@gmail.com

ISBN 978-3-95450-181-6

SYSTEM ARCHITECTURE

Three-tier architecture has been proposed at the design stage fig. 1. The system uses a mixed control model: centralized control manager (client-server interaction) and broadcast event management (internal client management)[11]. The main features of the system elements were determined in decomposition stages. System structure provides the problem encapsulation, virtualization of working with remote components, modularity and the external programs connect ability.

Application domain analysis allows to identify the main interaction interfaces and classes that allows to structure virtualization engine for models and methods implemented on late-binding technique. The database structure was derived from the application domain infological model.

Customer level is implemented as a web application fig. 2 and fig. 3.

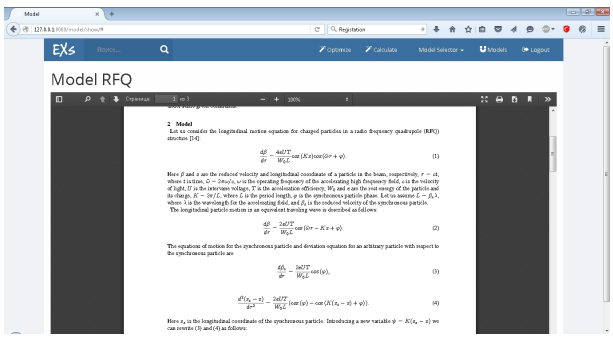

Figure 2: View web application: page about model.

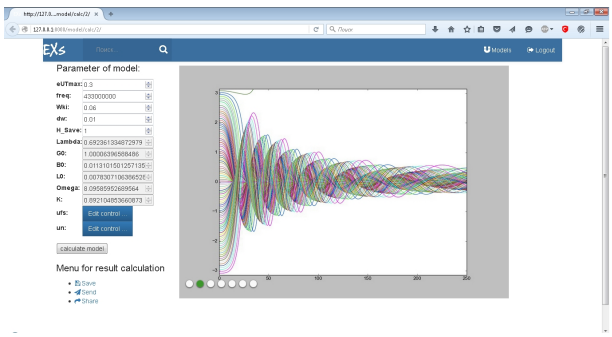

Figure 3: View web application: page calculate model.

RESULT

The system approbation had carried out: implemented the longitudinal motion model of charged particles in the structure with spatially uniform quadrupole focusing. The model optimization had carried out (with augmenting the knowledge base).

The following problem is the search admissible control. The following longitudinal motion equation for charged particles in a radio frequency quadrupole (RFQ) structure [9]. Search admissible control carried for the proton accelerator at 352 MHz frequency. The following limitations

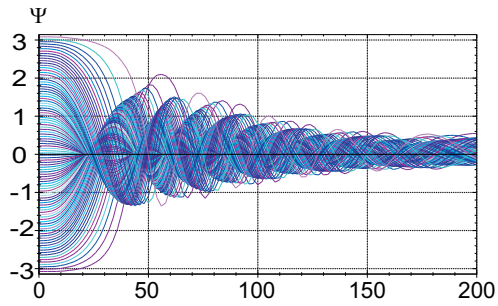

(a) phase of beam particles

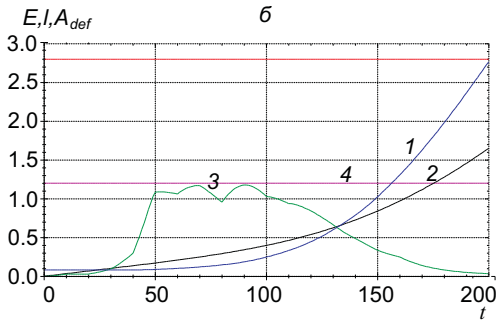

(b) *1* – energy (MeV); *2* – length of structure (m); *3* – defocusing factor; *4* – limit of defocusing factor;

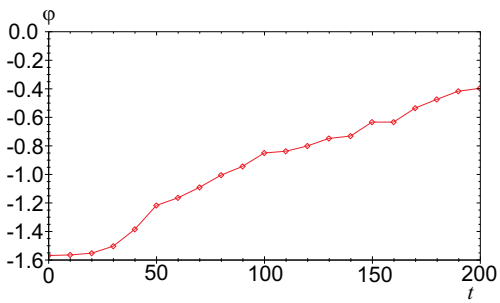

(c) acceleration intensity

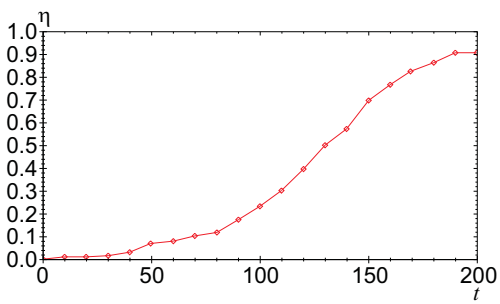

(d) synchronous phase

Figure 4: characteristics to optimize.

were taken into account: $(UT)_{\max} \leq 45$ and limitations on characteristics of the structure and controls.

At the first stage, the initial control search satisfying certain constraints extension, which is being implemented in several ways: searching in the knowledge base and applying initial control search techniques. One embodiment of the found structure has the following characteris-

ISBN 978-3-95450-181-6

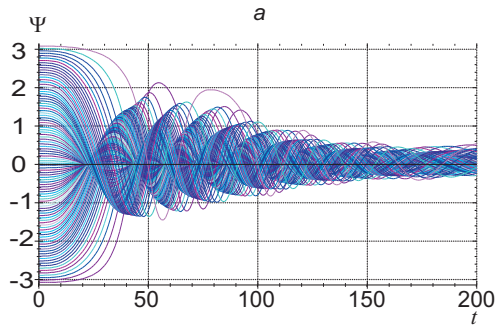

(a) phase of beam particles

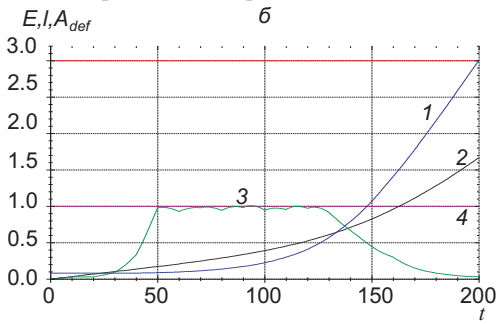

(b) *1* – energy (MeV); *2* – length of structure (m); *3* – defocusing factor; *4* – limit of defocusing factor;

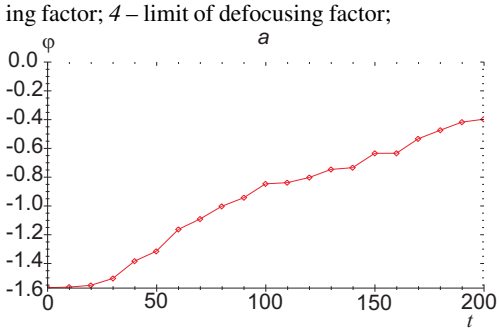

(c) acceleration intensity

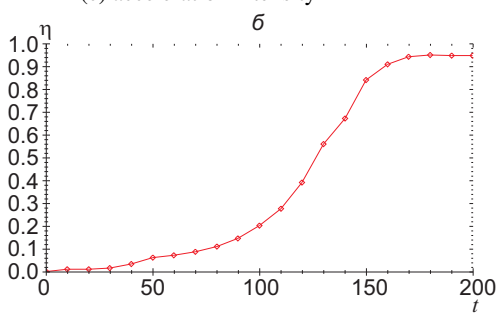

(d) synchronous phase

Figure 5: characteristics after optimization.

tics: almost 99% particles captured into the acceleration mode, maximal defocusing factor 0.012, the output energy 2.9 MeV and length of structure 1.7 m. The properties of program motions, controls, and phase space portraits of beams in separatrices are illustrated fig. 4.

At subsequent stages the iterative process of improving the solution is carried out by one of the specified methods of optimization. After a few steps is received structure satisfies the given limitations. Structure has the following characteristics: almost 100% particles captured into the acceleration mode, maximal defocusing factor 0.01, the output energy 3.1 MeV and length of structure 1.65 m. The properties of program motions, controls, and phase space portraits of beams in separatrices are illustrated fig. 5.

REFERENCES

[1] *D. A. Ovsyannikov, A. D. Ovsyannikov, Yu. A. Svistunov, A. P. Durkin, M. F. Vorogushin.* Beam dynamics optimization: models, methods and applications Nuclear Instruments and Methods in Physics Research, section A 558, 2006, pp.11-19.

[2] *A. D. Ovsyannikov.* Transverse motion parameters optimization in accelerators Problems of Atomic Science and Technology (4), 2012, pp.74-77.

[3] *Yu. A. Svistunov, A. D. Ovsyannikov.* Designing of compact accelerating structures for applied com-plexes with accelerators Problems of Atomic Sci-ence and Technology (2), 2011, pp.48-51.

[4] *B. Bondarev, A. Durkin, Y. Ivanov, I. Shumakov, S. Vinogradov, A. Ovsyannikov, D. Ovsyannikov.* The LIDOS.RFQ.Designer development Proceedings of Particle Accelerator Conference 2001, 2001, Vol.4, pp.2947-2949.

[5] *A. D. Ovsyannikov, D. A. Ovsyannikov, S. -L. Chung.* Optimization of a radial matching section International Journal of Modern Physics A, Vol. 24, Issue 5, 2009, pp.952-958.

[6] *A. D. Ovsyannikov, D. A. Ovsyannikov, A. P. Durkin, S. -L. Chung.* Optimization of matching section of an accelerator with a spatially uniform quadrupole focusing Technical Physics, The Rus-sian Journal of Applied Physics, Vol. 54 (11), 2009, pp.1663-1666.

[7] *D. A. Ovsyannikov, A. D. Ovsyannikov, I. V. Antropov, V. A. Kozynchenko.* BDO-RFQ code and optimization models Proceedings of International Conference Physics and Control, 2005, pp.282-288.

[8] *D. A. Ovsyannikov, V. G. Papkovich.* On calculation of accelerating structures with focusing by acceler-ating field Problems of Atomic Science and Tech-nology, V.2(3). Kharkov, 1977, p.66-68.

[9] *D. A. Ovsyannikov , Ovsyannikov A. D., Balabanov M. Yu., Chung S.-L.* On beam dynamics optimization problem Intern. J. of Mo dern Physics A. February 20, 2009. P. 941-951.

[10] *M. Yu Balabanov* About Choosing initial control in optimization problems of the dynamics charged particle beams St.Petersburg, Vestnik SPbGU, Vol.10 (3), 2010, pp. 82–92.

[11] *Andrew S. Tanenbaum, Maarten Van Steen* Distributed systems: principles and paradigms Upper Saddle River, NJ: Pearson Prentice Hall, 2007.

ISBN 978-3-95450-181-6

ON THE BEAM DYNAMICS SIMULATION IN THE INJECTION SYSTEM

A. D. Ovsyannikov[1], S. A. Kozynchenko, V. A. Kozynchenko
Saint-Petersburg State University, Saint-Petersburg, Russia

Abstract

When developing a particle accelerator for generating the high-precision beams, the injection system design is of importance, because it largely determines the output characteristics of the beam. At the present paper we consider the injection systems consisting of electrodes with given potentials. The design of such systems requires carrying out simulation of beam dynamics in the electrostatic fields. For external field simulation we use the new approach, proposed by A.D. Ovsyannikov, which is based on analytical approximations, or finite difference method, taking into account the real geometry of the injection system. The software designed for solving the problems of beam dynamics simulation and optimization in the injection system for non-relativistic beams has been developed. Both beam dynamics and electric field simulations in the injection system which use analytical approach and finite difference method have been made and the results presented in this paper.

INTRODUCTION

The paper mostly focuses on exploring the ways of algorithmic and software realization of the optimal design methodology in the beam dynamics area, which is proposed in [1-3] and intended to be applied in the injection systems producing the high-precision beams. The development of the optimal design methodology for beam dynamics is considered to be rather complex and laborious problem. It has given rise to a large and growing body of research [4-12].

The main issue in the optimal design techniques that we try to address in the paper consists in finding an analytical representation of both the field U_ξ inside the working domain and the control function $\phi(\eta)$ defined over the domain contour which to be used in further optimization.

$$F(\xi,\phi) \equiv \frac{1}{2\pi i}\int_L f(z)dz = \frac{1}{2\pi i}\left[\int_L u(x,y)dx - v(x,y)dy + i\int_L v(x,y)dx + u(x,y)dy\right], \quad (1)$$

where $f(z) = u(x,y) + i \cdot v(x,y)$ is a function of a complex variable $z = x + i \cdot y$. Therefore, the potential function U can be defined as a real line integral.

The paper starts with some algorithmic study relating to the numerical solution of the integral of Cauchy type that is applied in the given problem to calculate the electrostatic field. Then we consider a case study model of the axial symmetrical field in an injection system. Some numerical data obtained in the C++ computer simulation are presented.

A POSSIBLE BASIC ALGORITHM OF FINDING THE INTEGRAL OF CAUCHY TYPE

Let us consider a three-dimensional simply connected bounded domain having the axial symmetry and let G be its diametric cross section. This two-dimensional domain is bounded by a contour L that is supposed to be a smooth closed curve. Hereinafter the real plane R^2 containing the domain G will be identified with the complex plane C. Let a continuous complex function $\phi(\eta)$ be defined over the contour L. The complex potential of the external electrostatic field inside the domain G can be evaluated with the use of an integral of Cauchy type

$$F(\xi,\phi) = \frac{1}{2\pi i}\int_L \frac{\phi(\eta)}{\eta - \xi}d\eta, \quad \xi \notin L, \quad (2)$$

where $\xi = z_G + i \cdot r_G \in G$, $\eta = x_L + i \cdot y_L \in L$. Then the complex potential of the three-dimensional external field can be represented as follows (see [3], p. 97):

$$H(z,r,\phi) = \frac{1}{2\pi}\int_0^{2\pi} F(z + i \cdot r\cos\alpha, \phi)d\alpha \ .$$

The real part of H, i.e. the function $U = \mathrm{Re}\, H$, will be considered as a function determining the electrostatic field in the three-dimensional domain. The complex contour integral (1) can be written as

$$U(x,y) = \frac{1}{2\pi}\int_L v(x,y)dx + u(x,y)dy$$

taken over the same contour L as the complex integral. Let us consider the simplest case when the function $\phi \equiv \phi_0$ is a constant. Then the following expressions can be written

$$f(z) = \frac{\phi_0}{z}, \ u(x,y) = \frac{x}{x^2+y^2}, \ v(x,y) = -\frac{y}{x^2+y^2},$$

and the real part of the integral (1) is evaluated as follows

$$U \equiv \mathrm{Re}\, F(\xi,\phi_0) = \frac{\phi_0}{2\pi}\left[\int_L -\frac{ydx}{x^2+y^2} + \int_L \frac{xdy}{x^2+y^2}\right], \quad (3)$$

where $x = x_L - z_G$, $y = y_L - r_G$.

1 a.ovsyannikov@spbu.ru

ISBN 978-3-95450-181-6

Let us take the domain G as a rectangle $ABCD$ shown in Fig.1. The integral (3) can be represented as a sum of four integrals to be evaluated counter-clockwise over the horizontal and vertical segments AB, BC, CD, DA of the closed contour L. Actually, these segments can be treated as vectors. Thus, on the vector $\overrightarrow{AB}$ it turns out that $dy = 0$ and the integral (3) takes the form

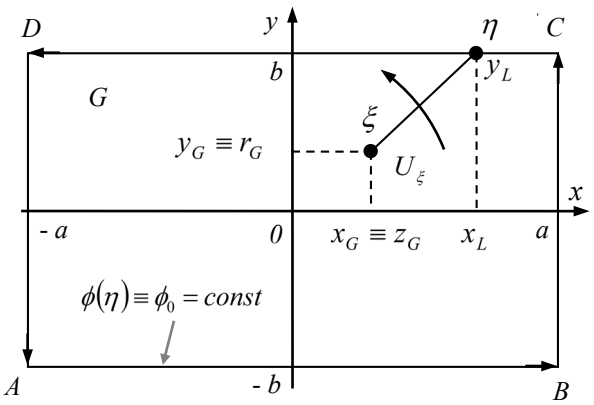

Figure 1: Finding the potential U_ξ inside the conducting rectangle with the use of integral of Cauchy type.

$$U_{AB} = -\frac{\phi_0}{2\pi}\int_{-a}^{a}\frac{ydx}{x^2+y^2}.$$

Given an arbitrary position of the point ξ in the domain G, the variables x and y are defined as $x = x_L - x_G$, $y = y_L - y_G$.

So, we have

$$U_{AB} = -\frac{\phi_0}{2\pi}\int_{-a}^{a}\frac{ydx}{x^2+y^2} = -\frac{\phi_0}{2\pi}\int_{-a}^{a}\frac{d(x/y)}{(x/y)^2+1} =$$

$$= -\frac{\phi_0}{2\pi}\arctan\left(\frac{x}{y}\right)\Bigg|_{-a}^{a} =$$

$$= -\frac{\phi_0}{2\pi}\left[\arctan\left(\frac{a-x_G}{-b-y_G}\right) - \arctan\left(\frac{-a-x_G}{-b-y_G}\right)\right]. \quad (4)$$

In a similar manner, we obtain other constituents of potential U_{BC}, U_{CD}, U_{DA}:

$$U_{BC} = \frac{\phi_0}{2\pi}\int_{-b}^{b}\frac{(x_L-x_G)\,d(y_L-y_G)}{(x_L-x_G)^2+(y_L-y_G)^2} =$$

$$= \frac{\phi_0}{2\pi}\left[\arctan\left(\frac{b-y_G}{a-x_G}\right) - \arctan\left(\frac{-b-y_G}{a-x_G}\right)\right], \quad (5)$$

$$U_{CD} = -\frac{\phi_0}{2\pi}\int_{a}^{-a}\frac{(y_L-y_G)\,d(x_L-x_G)}{(x_L-x_G)^2+(y_L-y_G)^2} =$$

$$= -\frac{\phi_o}{2\pi}\left[\arctan\left(\frac{-a-x_G}{b-y_G}\right) - \arctan\left(\frac{a-x_G}{b-y_G}\right)\right], \quad (6)$$

$$U_{DA} = \frac{\phi_0}{2\pi}\int_{b}^{-b}\frac{(x_L-x_G)\,d(y_L-y_G)}{(x_L-x_G)^2+(y_L-y_G)^2} =$$

$$= \frac{\phi_0}{2\pi}\left[\arctan\left(\frac{-b-y_G}{-a-x_G}\right) - \arctan\left(\frac{b-y_G}{-a-x_G}\right)\right]. \quad (7)$$

So, at the point ξ the potential U_ξ equals to

$$U_\xi = U_{AB} + U_{BC} + U_{CD} + U_{DA} \quad (8)$$

This expression evidently contains the pairs of terms in which the arguments of the function *arctan* are inverse ones. Taking into account the following trigonometric identity

$$\arctan x + \arctan\frac{1}{x} = \begin{cases} \pi/2, \text{ if } x > 0 \\ -\pi/2, \text{ if } x < 0 \end{cases},$$

we can represent (8) as a sum of binomials forming such a pair of terms. For instance, taking the first term from (5) and the second from (6), we get

$$\frac{\phi_0}{2\pi}\arctan\left(\frac{b-y_G}{a-x_G}\right) + \frac{\phi_0}{2\pi}\arctan\left(\frac{a-x_G}{b-y_G}\right) = \frac{\phi_0}{2\pi}\frac{\pi}{2} = \frac{\phi_0}{4},$$

as $b - y_G > 0$ and $a - x_G > 0$.

Similarly, summing the first term from (4) and the second from (5) gives

$$-\frac{\phi_0}{2\pi}\arctan\left(\frac{a-x_G}{-b-y_G}\right) + \left[-\frac{\phi_0}{2\pi}\arctan\left(\frac{-b-y_G}{a-x_G}\right)\right] =$$

$$= -\frac{\phi_0}{2\pi}\left(-\frac{\pi}{2}\right) = \frac{\phi_0}{4}, \text{ as } \frac{a-x_G}{-b-y_G} < 0.$$

Finally, the summation of all four pairs in (8) gives us the potential value in an arbitrary point ξ of the domain G:

$$U_\xi = 4 \cdot \phi_0/4 = \phi_0 .$$

This result evidently matches the electrostatics fundamentals: if a plane closed contour (e. g., made from a conducting wire) has been charged to the potential ϕ_0, then any point inside the contour has the same potential.

It seems to be worth attempting to apply the above scheme in the case of non-constant potential function $\phi(\eta)$ over the closed contour L. The possible solution could consist in representing the smooth contour by a sequence of horizontal and vertical directed segments - vectors, together with making the approximation of the function $\phi(\eta)$ by a step function $\phi_s(\eta)$ that is a constant at each segment. A contribution of each segment into the whole potential at a point ξ in G can be computed using one of the formulas (4), (5), (6), or (7) depending on the orientation of the segment.

ALGORITHM DESCRIPTION AND A CASE STUDY SIMULATION

An algorithm considered in the paper includes the following stages:

- Computing the electrostatic field in the working domain of an injection system under the given initial configuration and potentials of electrodes. The computation is carried out using, e.g., the iterative

ISBN 978-3-95450-181-6

Liebmann's procedure on a square grid, [13], as is done in the paper.

- On moving along the piece-wise contour bounding the working domain, the reference potential profile $\varphi(\eta_i)$ over the frontier of the working domain is formed. This set of exact values is used for finding the approximate boundary control function $\phi(\eta)$.
- A suitable type of an approximating function is chosen and its parameters are computed by one of the methods of solving the systems of linear equations.
- In order to find a potential at any point of the domain, the integrals of Cauchy type are computed at each grid cell side (horizontal or vertical) around the domain contour using the formulas (4-7), where $\phi_0 = 0.5 \cdot [\varphi(\eta_i) + \varphi(\eta_{i+1})]$.

Let us consider these stages in greater detail. As an example in the case study we take an axially-symmetric working domain for an injection system with three electrodes, which cross-section is shown in Fig. 2. The rectangle AFF_1A_1 of length $AF = 400\ mm$ and height $AA_1 = 80\ mm$ is covered with a square grid with a cell side $h = 0.5\ mm$. Potentials of electrodes are $U_1 = 100\ kV$, $U_2 = 45\ kV$, $U_3 = 87\ kV$.

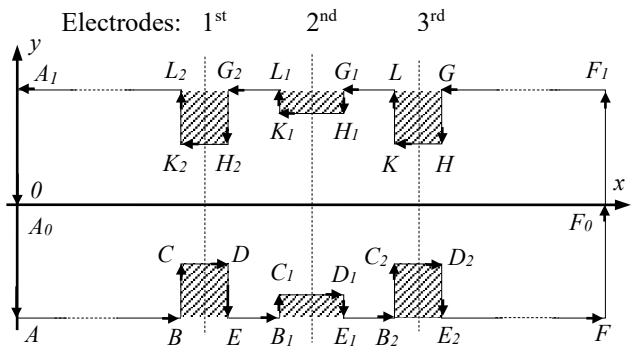

Figure 2: Cross-section of the axially-symmetric working domain of the 3-electrode injection system.

The simulation model has been developed in C++, where a class *Field* defines the model parameters and contains all necessary member functions. One of them computed the electrostatic field in a cylindrical coordinate system by the iterative Liebmann's method with the maximal error $\varepsilon = 0.001\%$. It takes ca. 88360 iterations. Another function scans the grid nodes that bound the top half of the contour, namely $A_0A_1L_2K_2H_2G_2L_1K_1\ H_1G_1LK$-$HGF_1F_0$, and collects the potentials into an array of size $n_L = 1173$. The reference profile $\varphi(\eta_i)$ is shown in Fig. 3. curve 1.

To approximate the profile of the contour potential, we have chosen a rational-fraction approximation:

$$\phi(\eta) = \left(a_0 + \sum_{i=1}^{i=4} a_i \eta^i\right) \Big/ \left(1 + \sum_{j=1}^{j=5} b_1 \eta^j\right) .$$

For finding the unknown parameters a_i, b_j, the least squares method that minimizes a weighted mean-square approximation error has been used. It handles the over-determined matrix with $M = 15$ rows (i.e., equations) and $N = 10$ columns (unknowns). The approximating function $\phi(\eta)$ is shown in Fig. 3, curve 2.

Finally, the potential function $U_{axis}(x)$ over the domain axis has been calculated using the reference profile $\varphi(\eta_i)$ (see Fig. 4, curve 1), the approximate profile $\phi(\eta)$ (curve 2) and based on the Liebmann's method (curve 3).

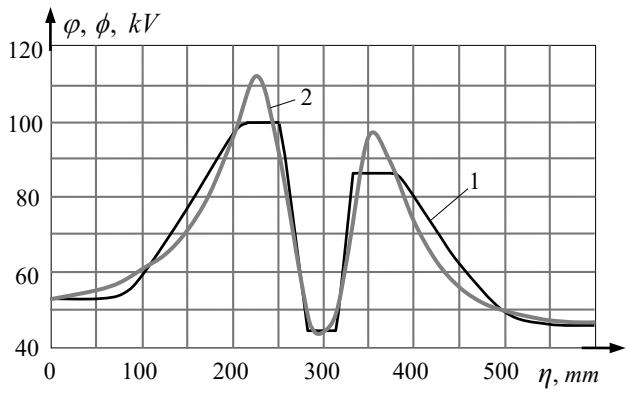

Figure 3: The reference and approximate potential profiles over the top boundary of the domain.

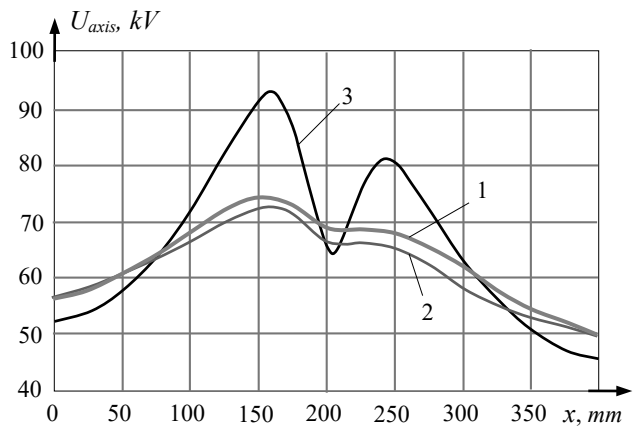

Figure 4: Different potential functions computed on the domain axis A_0F_0.

CONCLUSIONS

The numerical technique using the integral of Cauchy type and intended for calculating the electrostatic field inside the axially symmetric domain has been considered. The simulation results have shown that the given approach seems to be practicable but requires some theoretical and algorithmic studies to achieve better accuracy. The algorithm considered in the paper can be used in computing and optimization of beam dynamics in the injection systems (see, e.g., [14]).

ISBN 978-3-95450-181-6

REFERENCES

[1] Ovsyannikov A.D., On optimization of charged particle dynamics in electrostatic field //Vestnik St. Petersburg University. Ser. 10. 2013. Issue 2. pp. 54-59.

[2] Ovsyannikov A.D., Beam dynamics optimization in electrostatic field //Problems of Atomic Science and Technology. 2013. № 4(86), pp. 90-92.

[3] Ovsyannikov A.D., Mathematical models of the beam dynamics optimization, St. Petersburg State University, BBM, 2014.-181 p.

[4] Masunov E.S., Polozov S.M., High intensity ion beams in rf undulator LINAC //Physical Review Special Topics - Accelerators and Beams. 2008. vol. 11. № 7. p. 074201.

[5] Ovsyannikov A.D., Ovsyannikov D.A., Durkin A.P., Chang S.-L., Optimization of matching section of an accelerator with a spatially uniform quadrupole focusing //Technical Physics. 2009. vol. 54. №11, pp. 1663–1666.

[6] Ovsyannikov A.D., Ovsyannikov D.A., Balabanov M. Yu., Chung S.-L., On the beam dynamics optimization problem //International Journal of Modern Physics A. 2009. vol. 24. Issue 5, pp. 941–951.

[5] Ovsyannikov A.D., Ovsyannikov D.A., Chung S.-L., Optimization of radial matching section //International Journal of Modern Physics A. 2009. vol. 24. Issue 5. pp. 952-958.

[6] Svistunov Y.A., Ovsyannikov A.D., Designing of compact accelerating structures for applied complexes with accelerators //Problems of Atomic Science and Technology. 2010. № 2. pp. 48-51.

[7] Ovsyannikov D.A., Ovsyannikov A.D., New approach to optimization of RFQ radial matching section// In:IPAC 2010 - 1st International Particle Accelerator Conference 2010. pp. 1351-1353.

[8] Ovsyannikov A.D., Transverse motion paramiters optimization in accelerators// Problems of Atomic Science and Technology. 2012. № 4. pp. 74-76.

[9] Ovsyannikov A.D., On a class of optimization problems in electric field //Doklady Mathematics. 2013. vol. 88. № 3. pp. 751-753.

[10] Ovsyannikov A.D., Ovsyannikov D.A., Altsybeyev V.V., Durkin A.P., Papkovich V.G., Application of optimization techniques for RFQ design //Problems of Atomic Science and Technology. 2014. vol. 91. № 3. pp. 116-119.

[11] Kozynchenko S.A., Development of the Win 32 API-based software in C++ for beam dynamics simulation and optimization in the injection systems //2015 International Conference on "Stability and Control Processes" in Memory of V.I. Zubov, SCP 2015 – Proceedings.

[12] Ovsyannikov D.A., Ovsyannikov A.D., Antropov I.V., Kozynchenko V.A., BDO-RFQ program complex of modelling and optimization of charged particle dynamics //Journal of Physics: Conference Series. 2016. vol. 747. №1.

[13] Sadiku M.N.O., Numerical Techniques in Electromagnetics, 2nd ed., CRC Press, 2001.- 760 pp.

[14] Kozynchenko V.A., Kozynchenko S.A., Parallel beam dynamics simulation in injection systems taking into account particle interactions //2014 20th International Workshop on Beam Dynamics and Optimization (BDO).

ISBN 978-3-95450-181-6

ON APPROACH FOR RESONANT FREQUENCY TUNING IN DRIFT TUBE STRUCTURES ON THE DESIGNING STAGE

I. S. Skudnova, V. V. Altsybeyev*,
Saint-Petersburg University, 7/9 Universitetskaya nab., St. Petersburg, 199034 Russia

Abstract

Current research considers the crossbar H-mode linear resonant accelerator with drift tubes mounted inside the cavity. The focus of the study has been on the dependence of resonant frequency on the parameters of the geometry. Since Alternating-Phase-Focusing (APF) type of accelerator is investigated, the efficiency of the operation depends on the synchronization of the charged particle velocity and accelerating field oscillations. Researchers can control it by the variation of longitudinal size of the cells of the structure (periods). On the other hand, the effective performance of this resonant system requires the equality of resonant frequencies of its cells, because it affects the uniformity of accelerating field distribution along the axis. The diversity of cells longitudinal sizes causes the deviation from the particular value of the resonant frequency. This aberration can be eliminated by the adjustment of other geometry parameters period's length, gap length and drift tube radii. We have conducted the study to analyze the relation between resonant frequency and these values. Using the this dependency we can tune the geometry parameters of each period in the structure. We first create the computer-aided design (CAD) geometry model of the accelerator cavity. Then, using Comsol Multiphysics, the platform for physics-based modeling and simulation, we conduct the calculation of resonant frequencies.

INTRODUCTION

On the first steps of linear accelerator production many parameters of the structure should be considered. One of the main parameters - period's lengths L is determined by the synchronous phase sequence. It is quite difficult for analytic field approximation model to embody many other structure parameters such as drift tube inner and outer radii and holder position and thickness. Of course, one can do a numerical simulation with any given geometry. Accelerator structure usually consists of dozens of periods, each one characterized by 5-6 parameters. The field computation of all acceptable combinations of parameters is severely time-consuming. Therefore, in the study we investigate the dependencies between electric field and some particular geometry parameters.

FREQUENCY CALCULATION

The resonant frequencies of the periods can be significantly different because length of periods are not equal. In this case the amplitude distribution of the electric field in the cavity is non-uniform, which requires considerable additional tuning. However, the resonant frequency of each period can be adjusted by means of gap length, drift tube radii and holder design [1]. With the appropriate choice of this parameters period frequency of some estimated value can be obtained. If we fix values of some basic parameters like cavity radius and holder design we can calculate the dependencies of resonant frequency from period's length, gap length, drift tube radii.

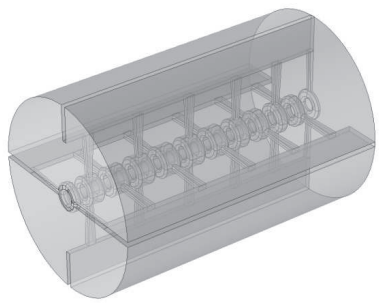

Figure 1: CAD model of the cavity with 11 periods.

In order to calculate the dependency we have created a computer-aided-design (CAD) geometry model of the cavity (figure 1). We are using COMSOL Multiphysics together with MATLAB. COMSOL Multiphysics is a general-purpose software platform, based on advanced numerical methods, for modeling and simulating physics-based problems. Its toolbox LiveLink for MATLAB allows us to utilize the full power of MATLAB as well as use COMSOL Multiphysics functions in the MATLAB script file (.m).

The volume of the cavity ω has a boundary surface S. The electric field E inside the volume satisfy the Helmholtz equation (1).

$$\nabla^2 \mathbf{E} - \left(\frac{\omega}{c}\right)^2 \varepsilon_r \mu_r \mathbf{E} = 0. \quad (1)$$

ε_r and μ_r are relative permittivity and relative permeability respectively. As for the boundary condition, we assume the perfectly conducting surface (2).

$$\mathbf{n} \times \mathbf{E}|_S = 0. \quad (2)$$

To solve the problem (1)-(2) we use the finite-element solver of COMSOL Multiphysics - Radio Frequency, Electromagnetic Waves.

* v.altsybeev@spbu.ru

ISBN 978-3-95450-181-6

DESIGN ALGORITHM

1. Assign cavity radius, drift tube inner radius and holder design. Decide on the range of geometry parameters that we want to analyze (Drift Tube Outer Radius, Pediod length and Pediod length). See Table 1.

Table 1: Analyzed Range of Geometry Parameters

Cavity radius (m)	0.0093
Pediod length (m)	0.020 : 0.01 : 0.035
Gap coefficient	0.2 : 0.1 : 0.7
Drift Tube Inner Radius (m)	0.0065
Drift Tube Outer Radius(m)	0.014, 0.017

2. Calculate the resonant frequency of one period corresponding to the each set of geometry parameters mentioned above and save all the data as a table. In this research we considered 2000 different sets.

3. Using the synchronous phase sequence calculate period's lengths.

4. From the previously made table choose the drift tube radii and gap length corresponding to the specified period's length and operational frequency (figure 2).

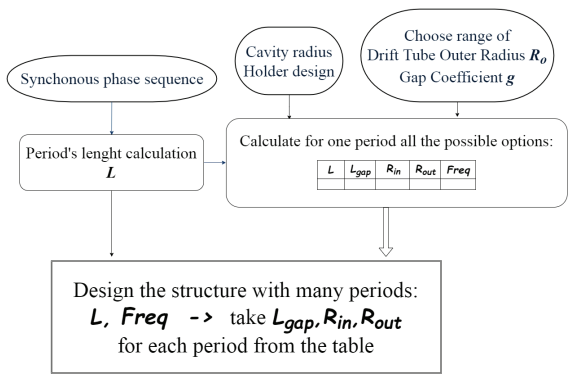

Figure 2: Design algorithm.

RESULTS

Computation of the resonant frequency for one period for 2000 different geometry parameters sets takes about 24 hours. Numerical simulation revealed that the resonant frequency of one period increases when period length and gap coefficient increases. But it diminishes with the increase of drift tube outer radius. The dependencies are shown in figure 3 and 4.

Period's length were calculated using synchronous phase sequence obtained before [2]. The questions of synchronous phase optimization are discussed elsewhere [3]. Target frequency is 433 MHz. Inner radius was fixed, gap length and drift tube outer radius of each period were chosen following Tuning Algorithm. The results are shown is the figure 5.

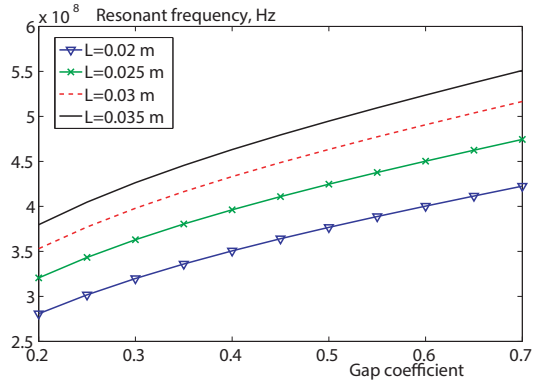

Figure 3: Dependence of resonant frequency on gap coefficient, $R_{outer} = 0.014m$ (for one period, 4 different period's lengths L considered).

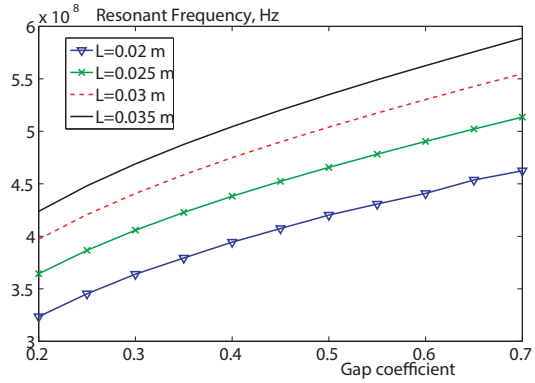

Figure 4: Dependence of resonant frequency on gap coefficient, $R_{outer} = 0.017m$ (for one period, 4 different period's lengths L considered).

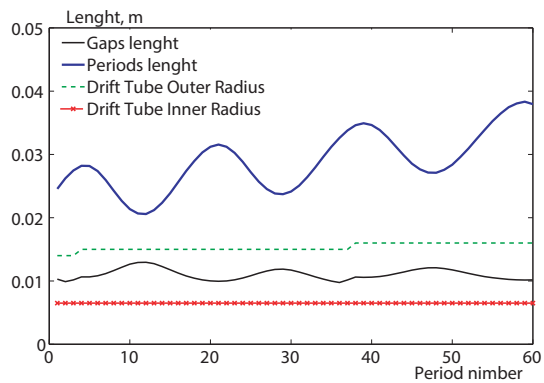

Figure 5: Calculated geometry parameters.

To check the efficiency of the method, electrical field was calculated in the obtained geometry. For the whole structure of 60 periods we made it in two ways: a) with constant gap length - figure 6 and b) with gap lengths, obtained by the algorithm - figure 7. To ensure the results, distribution of electric field was also calculated in electrostatic approximation (Poisson equation, finite difference method) using DAISI code [4]-[8].

ISBN 978-3-95450-181-6

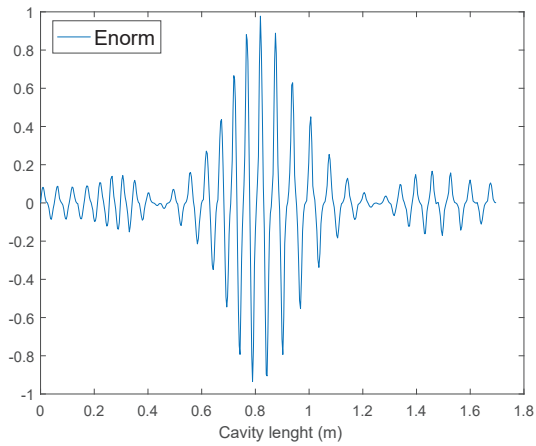

Figure 6: a) Electric field distribution, gap length = 0.01m for every period, resonant frequency 429 MHz.

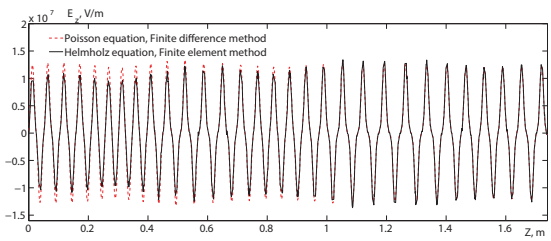

Figure 7: b) Electric field distribution, gap length chosen by the algorithm, resonant frequency 434.6 MHz. Consistent with calculation in electrostatic approximation.

With the use of the algorithm, axial distribution of the field is close to uniform which is a promising environment to gain good acceleration. Moreover, the resonant frequency of the structure (434.6 MHz) is closer to the target frequency (433 MHz) then in case of constant values (429 MHz). After assembling the cavity, a resonant frequency of a several hundred megahertz is typically within about a few megahertz of the target value [9].

CONCLUSION

The research was conducted in the area of linac resonant cavity design. The study indicated that resonant frequency increases, when periods length and gap coefficient increase. It is inversely proportional to drift tube outer radius. Based on these observations we can adjust parameters of each period so that its resonant frequency is close to the target frequency. This tuning makes electric field distribution much more uniform, which is considered to prove the effectiveness of the approach.

REFERENCES

[1] V. A. Bomko et al. "Design and investigation of electromagnetic characteristics of modified accelerating structures for heavy ions", Preprint KhFTI 82-110, Kharkov, 1982.

[2] D. A. Ovsyannikov and V. V. Altsybeyev. On the Beam Dynamics Optimization Problem for an Alternating-Phase Focusing Linac. In: Physics of Particles and Nuclei Letters 13.8 (2016), pp. 805 809.

[3] D. A. Ovsyannikov and V. V. Altsybeyev. Optimization of APF accelerators. In: Problems of Atomic Science and Technology 6.88 (2013), pp. 119122.

[4] V. Altsybeyev et al. Numerical simulation of a triode source of intense radial converging electron beam. In: Journal of Applied Physics 120.14, 143301 (2016). DOI: http://dx.doi.org/10. 1063/1.4964335.

[5] V. V. Altsybeyev. Numerical Simulations of the Charged-Particle Flow Dynamics for Sources with a Curved Emission Surface. In: Physics of Particles and Nuclei Letters 13.8 (2016), pp. 801804.

[6] V. V. Altsybeyev and V. A. Ponomarev. Application of Gausss law space-charge limited emission model in iterative particle tracking method. In: Journal of Computational Physics 324 (2016), pp. 6272. DOI: http://dx.doi.org/10.1016/j.jcp.2016. 08.007.

[7] V. Altsybeyev and V. Ponomarev. Development of 2D Poisson equation C++ finite-difference solver for particle-in-cell method. In: Stability and Control Processes in Memory of V.I. Zubov (SCP), 2015 International Conference. 15637294. 2015, pp. 195 197.

[8] V. Altsybeyev et al. Numerical simulations of the radial convergent electrons and ions flows for cylindrical pulsed source. In: Stability and Control Processes in Memory of V.I. Zubov (SCP), 2015 International Conference. 15637218. 2015, pp. 138141.

[9] T. P. Wangler, Principles of RF Linear Accelerators, Wiley, New York, 1998, p.95.

ISBN 978-3-95450-181-6

SYMMETRICAL PARAMETERIZATION FOR 6D FULLY COUPLED ONE-TURN TRANSPORT MATRIX*

S. A. Glukhov, BINP, Novosibirsk, Russia

Abstract

Symmetry properties of 6D and 4D one-turn symplectic transport matrices were studied. A new parameterization was proposed for 6D matrix, which is an extension of the Lebedev—Bogacz parameterization for 4D case. The parameterization is fully symmetric relative to radial, vertical and longitudinal motion. It can be useful for lattices with strong coupling between all degrees of freedom.

INTRODUCTION

For the case of a 2×2 transport matrix a well-known Twiss parameterization exists [1]. It can be used also in the case of 4×4 and 6×6 matrices if there is no coupling between different degrees of freedom. The usual case is when transversal modes are uncoupled but there is a small interaction between either of them (or both) and longitudinal one. But if longitudinal tune is much smaller than transversal ones, then longitudinal Twiss functions are assumed to be constant. So, longitudinal motion is eliminated and taken into account only in terms of the dispersion functions.

If there is an interaction between transversal modes, then different parameterizations for coupled motion can be used [2], [3], [4]. These parameterizations make use of the fact that horizontal and vertical degrees of freedom are identical mathematically. But this is also the case for the longitudinal one. In this paper we will derive some symmetry properties of a 6×6 transport matrix and build up a totally symmetrical parameterization for it. This parameterization can be used for lattices with strong coupling between all degrees of freedom. Then using the same approach we will reduce the dimensionality to 4×4 and derive Lebedev—Bogacz parameterization [4].

BASIC DEFINITIONS

Let us define a *block-diagonal matrix* as matrix having non-zero elements only within its 2×2 diagonal blocks. Then we introduce the following notation

$$\mathbf{I} = \begin{pmatrix} 1 & 0 \\ 0 & 1 \end{pmatrix}, \mathbf{S} = \begin{pmatrix} 0 & 1 \\ -1 & 0 \end{pmatrix}, \quad \begin{matrix} \mathbf{I}_6 = \mathrm{diag}\,(\mathbf{I} \quad \mathbf{I} \quad \mathbf{I}) \\ \mathbf{S}_6 = \mathrm{diag}\,(\mathbf{S} \quad \mathbf{S} \quad \mathbf{S}) \end{matrix}.$$

Let $\mathbf{M}$ be a 6×6 symplectic one-turn transport matrix, i.e. $\mathbf{M}^T\mathbf{S}_6\mathbf{M} = \mathbf{S}_6$. Then all the eigenvalues of $\mathbf{M}$ can be grouped into mutually inverse pairs [1]. Let λ_1 and λ_2 form such a pair, $\mathbf{v}_1$ and $\mathbf{v}_2$ be their eigenvectors, then

$$\overleftrightarrow{\mathbf{M}}\,\mathbf{v}_{1,2} = \hat{\lambda}\mathbf{v}_{1,2}\,, \tag{1}$$

where $\overleftrightarrow{\mathbf{M}} = \mathbf{M} + \mathbf{M}^{-1}$ is *recurrent matrix*, and $\hat{\lambda} = \lambda_1 + \lambda_2$. This means that $\overleftrightarrow{\mathbf{M}}$ has at most 3 different eigenvalues, each of them is degenerated at least twice. $\mathbf{M}$ describes stable motion if and only if all $|\lambda_j| = 1$ [1], so $\hat{\lambda} = 2\,\mathrm{Re}\,\lambda_{1,2}$.

For any 2×2 matrix $\mathbf{A}$ a *pseudoinversed matrix* $\hat{\mathbf{A}}$ can be defined (this operation was introduced in [1] as "symplectic conjugate")

$$\hat{\mathbf{A}} = -\mathbf{S}\mathbf{A}^T\mathbf{S}$$

with the following properties

$$\mathbf{A} + \hat{\mathbf{A}} = (\mathrm{Tr}\,\mathbf{A})\mathbf{I}\,, \quad \mathbf{A}\hat{\mathbf{A}} = |\mathbf{A}|\mathbf{I}\,.$$

Now one can write down the 6×6 transport matrix, its inverse and recurrent matrix in a blockwise form

$$\mathbf{M} = \begin{pmatrix} \mathbf{M}_{11} & \mathbf{M}_{12} & \mathbf{M}_{13} \\ \mathbf{M}_{21} & \mathbf{M}_{22} & \mathbf{M}_{23} \\ \mathbf{M}_{31} & \mathbf{M}_{32} & \mathbf{M}_{33} \end{pmatrix}, \overleftrightarrow{\mathbf{M}} = \begin{pmatrix} b_1\mathbf{I} & \mathbf{R}_3 & \hat{\mathbf{R}}_2 \\ \hat{\mathbf{R}}_3 & b_2\mathbf{I} & \mathbf{R}_1 \\ \mathbf{R}_2 & \hat{\mathbf{R}}_1 & b_3\mathbf{I} \end{pmatrix},$$
$$\mathbf{M}^{-1} = \begin{pmatrix} \hat{\mathbf{M}}_{11} & \hat{\mathbf{M}}_{21} & \hat{\mathbf{M}}_{31} \\ \hat{\mathbf{M}}_{12} & \hat{\mathbf{M}}_{22} & \hat{\mathbf{M}}_{32} \\ \hat{\mathbf{M}}_{13} & \hat{\mathbf{M}}_{23} & \hat{\mathbf{M}}_{33} \end{pmatrix},$$

where $\mathbf{R}_i = \mathbf{M}_{\overrightarrow{i}\,\overleftarrow{i}} + \hat{\mathbf{M}}_{\overleftarrow{i}\,\overrightarrow{i}}$, $b_i = \mathrm{Tr}\,\mathbf{M}_{ii}$ and $|\mathbf{R}_i| = d_i$. From now on we will assume that indices $i, j \in \{1, 2, 3\}$, also $\overleftarrow{i}$ and $\overrightarrow{i}$ mean cyclic permutation of these values (e.g. $\overleftarrow{1} = \overrightarrow{2} = \overrightarrow{3}$).

EIGENVALUES OF RECURRENT MATRIX

Our method for eigenvalues calculation is similar to the one proposed in [2]. Let $\overleftrightarrow{\mathbf{v}}$ be 6-component eigenvector of $\overleftrightarrow{\mathbf{M}}$, i.e. $\overleftrightarrow{\mathbf{M}}\overleftrightarrow{\mathbf{v}} = \hat{\lambda}\,\overleftrightarrow{\mathbf{v}}$. We split $\overleftrightarrow{\mathbf{v}}$ into 3 two-component subvectors, so as $\overleftrightarrow{\mathbf{v}}^T = (\,\mathbf{X}_1^T \quad \mathbf{X}_2^T \quad \mathbf{X}_3^T\,)^T$. Then

$$a_{ij}\mathbf{X}_i + \mathbf{R}_{\overleftarrow{i}}\mathbf{X}_{\overrightarrow{i}} + \hat{\mathbf{R}}_{\overrightarrow{i}}\mathbf{X}_{\overleftarrow{i}} = \bar{\mathbf{0}}\,, \tag{2}$$

where $\bar{\mathbf{0}}$ is a zero two-component vector, $a_{ij} = b_i - \hat{\lambda}_j$. Eliminating 2 of 3 $\mathbf{X}_i$ one can obtain

$$a_{1j}d_1 + a_{2j}d_2 + a_{3j}d_3 - a_{1j}a_{2j}a_{3j} = t\,, \tag{3}$$

where $t = \mathrm{Tr}\,(\mathbf{R}_1\mathbf{R}_2\mathbf{R}_3)$.

As we proved earlier, each eigenvalue of $\overleftrightarrow{\mathbf{M}}$ is degenerated at least twice, so its characteristic polynomial is a perfect square of some $\hat{P}(\hat{\lambda})$ with real coefficients. So, (3) can be regarded as characteristic equation of $\overleftrightarrow{\mathbf{M}}$, i.e.

$$\hat{P}(\hat{\lambda}) = \sqrt{|\overleftrightarrow{\mathbf{M}} - \hat{\lambda}\mathbf{I}|} = \hat{\lambda}^3 - (b_1 + b_2 + b_3)\hat{\lambda}^2 + \\ + (b_1b_2 + b_2b_3 + b_1b_3 - d_1 - d_2 - d_3)\hat{\lambda} + \\ + (b_1d_1 + b_2d_2 + b_3d_3 - b_1b_2b_3 - t)$$

* This work has been supported by Russian Science Foundation (project N14-50-00080).

ISBN 978-3-95450-181-6

Let us also introduce the following notation

$$p_j = \hat{P}'(\hat{\lambda}_j) = (\hat{\lambda}_{\substack{\rightarrow\\ j}} - \hat{\lambda}_j)(\hat{\lambda}_{\substack{\leftarrow\\ j}} - \hat{\lambda}_j)\,.$$

The 3 roots of $\hat{P}(\hat{\lambda})$ can be found using Cardano formulae. Matrix $\mathbf{M}$ describes stable motion if and only if all of them are real and lie inside the region $(-2; 2)$. If there are less than 3 different roots, then spectrum of $\mathbf{M}$ is degenerated, this case will not be covered in the present paper. It is important that in non-degenerated case $p_j \neq 0$.

EIGENVECTORS OF RECURRENT MATRIX

Let us reexamine the (2) system. It can be rewritten as 9 different equivalent equation pairs

$$u_{ij}\mathbf{X}_{\substack{\rightarrow\\ i}} = \hat{\mathbf{W}}_{\substack{\leftarrow\\ i\,j}}\mathbf{X}_i\,, \quad u_{ij}\mathbf{X}_{\substack{\leftarrow\\ i}} = \mathbf{W}_{\substack{\rightarrow\\ i\,j}}\mathbf{X}_i\,, \qquad (4)$$

where

$$\mathbf{W}_{ij}=\frac{1}{p_j}\left(\hat{\mathbf{R}}_{\substack{\leftarrow\\ i}}\hat{\mathbf{R}}_{\substack{\rightarrow\\ i}}-a_{ij}\mathbf{R}_i\right),\; u_{ij}=\frac{1}{p_j}\left(a_{\substack{\rightarrow\\ i\,j}}a_{\substack{\leftarrow\\ i\,j}}-d_i\right).$$

Using (4) one can write down 3 different matrices whose columns are eigenvectors of $\overleftrightarrow{\mathbf{M}}$

$$\overleftrightarrow{\mathbf{W}}_j=\begin{pmatrix} u_{1j}\mathbf{I} & \mathbf{W}_{\substack{\rightarrow\\ 3\,j}} & \hat{\mathbf{W}}_{\substack{\leftarrow\\ 2\,j}} \\ \hat{\mathbf{W}}_{3j} & u_{\substack{\rightarrow\\ 2\,j}}\mathbf{I} & \mathbf{W}_{\substack{\leftarrow\\ 1\,j}} \\ \mathbf{W}_{2j} & \hat{\mathbf{W}}_{\substack{\rightarrow\\ 1\,j}} & u_{\substack{\leftarrow\\ 3\,j}}\mathbf{I} \end{pmatrix}.$$

The following properties of $\mathbf{W}_{ij}$ and u_{ij} can be found directly

$$\begin{gathered}\mathbf{W}_{ij}\mathbf{W}_{\substack{\rightarrow\\ i\,j}} = u_{\substack{\leftarrow\\ i\,j}}\hat{\mathbf{W}}_{\substack{\leftarrow\\ i\,j}}, \quad |\mathbf{W}_{ij}| = u_{\substack{\rightarrow\\ i\,j}}u_{\substack{\leftarrow\\ i\,j}}, \\ \mathbf{W}_{i1} + \mathbf{W}_{i2} + \mathbf{W}_{i3} = \mathbf{0},\end{gathered} \qquad (5)$$

$$u_{i1} + u_{i2} + u_{i3} = u_{1j} + u_{2j} + u_{3j} = 1\,, \qquad (6)$$

then $\overleftrightarrow{\mathbf{W}}_1 + \overleftrightarrow{\mathbf{W}}_2 + \overleftrightarrow{\mathbf{W}}_3 = \mathbf{I}_6$.

One can combine u_{ij} into 3×3 *coupling matrix*. According to (6), it contains 4 independent parameters and can be parameterized with u_{11}, u_{22}, u_{33} and *coupling asymmetry* l, which is

$$l = u_{32} - u_{23} = u_{13} - u_{31} = u_{21} - u_{12}\,.$$

TWISS PARAMETERIZATION

Let $\mathbf{W}_j$ be 3 matrices whose columns are the eigenvectors of $\mathbf{M}$. System (1) means that eigenvector of $\mathbf{M}$ corresponding to eigenvalue λ is the linear combination of two eigenvectors of $\overleftrightarrow{\mathbf{M}}$ corresponding to eigenvalue $\hat{\lambda} = \lambda + \lambda^{-1}$, hence one can find such block-diagonal matrices $\mathbf{Q}_j$ that

$$\mathbf{W}_j = \overleftrightarrow{\mathbf{W}}_j\,\mathbf{Q}_j = \overleftrightarrow{\mathbf{W}}_j\cdot\mathrm{diag}\begin{pmatrix}\mathbf{Q}_{1j} & \mathbf{Q}_{\substack{\rightarrow\\ 2\,j}} & \mathbf{Q}_{\substack{\leftarrow\\ 3\,j}}\end{pmatrix}.$$

Therefore, the following matrices are also block-diagonal

$$\mathbf{T}_j = \overleftrightarrow{\mathbf{W}}_j^{-1}\mathbf{M}\,\overleftrightarrow{\mathbf{W}}_j = \mathrm{diag}\begin{pmatrix}\mathbf{T}_{1j} & \mathbf{T}_{\substack{\rightarrow\\ 2\,j}} & \mathbf{T}_{\substack{\leftarrow\\ 3\,j}}\end{pmatrix} \qquad (7)$$

with $|\mathbf{T}_{ij}| = 1$. So, well-known Twiss parameterization can be introduced for these blocks [1]

$$\begin{gathered}\mathbf{T}_{ij} = \mathbf{I}\cos\mu_j + \mathbf{J}_{ij}\sin\mu_j\,, \quad \mathbf{J}_{ij} = \begin{pmatrix}\alpha_{ij} & \beta_{ij}\\ -\gamma_{ij} & -\alpha_{ij}\end{pmatrix}, \\ \gamma_{ij} = \tfrac{1+\alpha_{ij}^2}{\beta_{ij}}\,, \quad \mu_j = \arg\lambda_j\,.\end{gathered} \qquad (8)$$

Note that since μ_j are fixed, then β_{ij} can be negative for $i \neq j$. Diagonal blocks of $\mathbf{Q}_j$ can be expressed as

$$\mathbf{Q}_{ij} = \frac{1}{\sqrt{2\beta_{ij}}}\begin{pmatrix}-\beta_{ij} & \beta_{ij}\\ \alpha_{ij} - I & -\alpha_{ij} - I\end{pmatrix},$$

where I is imaginary unit.

From (7) and (8) the following commutation rules can be obtained

$$\mathbf{W}_{ij}\mathbf{J}_{\substack{\leftarrow\\ i\,j}} = \mathbf{J}_{\substack{\rightarrow\\ i\,j}}\mathbf{W}_{ij}\,. \qquad (9)$$

Then a closed expression for $\mathbf{M}$ can be found

$$\mathbf{M} = \overleftrightarrow{\mathbf{W}}_1\,\mathbf{T}_1 + \overleftrightarrow{\mathbf{W}}_2\,\mathbf{T}_2 + \overleftrightarrow{\mathbf{W}}_3\,\mathbf{T}_3\,. \qquad (10)$$

Using (5), all $\mathbf{W}_{ij}$ can be expressed in terms of $\mathbf{W}_{11}$, $\mathbf{W}_{22}$, $\mathbf{W}_{33}$ and u_{ij} in 2 different ways

$$\begin{aligned} l\mathbf{W}_{\substack{\leftarrow\\ j\,j}} &= u_{\substack{\rightarrow\leftarrow\\ j\,j}}\mathbf{W}_{jj} - \hat{\mathbf{W}}_{\substack{\leftarrow\leftarrow\\ j\,j}}\hat{\mathbf{W}}_{\substack{\rightarrow\rightarrow\\ j\,j}} \\ l\mathbf{W}_{\substack{\rightarrow\\ j\,j}} &= -u_{\substack{\leftarrow\rightarrow\\ j\,j}}\mathbf{W}_{jj} + \hat{\mathbf{W}}_{\substack{\leftarrow\leftarrow\\ j\,j}}\hat{\mathbf{W}}_{\substack{\rightarrow\rightarrow\\ j\,j}} \end{aligned}, \qquad (11)$$

or

$$\begin{aligned} \tau_j\mathbf{W}_{\substack{\leftarrow\\ j\,j}} &= \mathbf{J}_{\substack{\rightarrow\leftarrow\\ j\,j}}\mathbf{A}_j + \mathbf{A}_j\mathbf{J}_{\substack{\leftarrow\leftarrow\\ j\,j}} \\ \tau_j\mathbf{W}_{\substack{\rightarrow\\ j\,j}} &= \mathbf{J}_{\substack{\rightarrow\rightarrow\\ j\,j}}\mathbf{B}_j + \mathbf{B}_j\mathbf{J}_{\substack{\leftarrow\rightarrow\\ j\,j}} \\ \tau_j &= \mathrm{Tr}\,(\mathbf{J}_{\substack{\rightarrow\rightarrow\\ j\,j}}\mathbf{J}_{\substack{\rightarrow\leftarrow\\ j\,j}} - \mathbf{J}_{\substack{\leftarrow\rightarrow\\ j\,j}}\mathbf{J}_{\substack{\leftarrow\leftarrow\\ j\,j}}) \\ \mathbf{A}_j &= \mathbf{W}_{jj}\mathbf{J}_{\substack{\leftarrow\rightarrow\\ j\,j}} - \mathbf{J}_{\substack{\rightarrow\rightarrow\\ j\,j}}\mathbf{W}_{jj} \\ \mathbf{B}_j &= \mathbf{W}_{jj}\mathbf{J}_{\substack{\leftarrow\leftarrow\\ j\,j}} - \mathbf{J}_{\substack{\rightarrow\leftarrow\\ j\,j}}\mathbf{W}_{jj} \end{aligned}. \qquad (12)$$

Knowing $|\mathbf{W}_{ij}|$ from (5), one can obtain the following expressions from (9)

$$\mathbf{W}_{ij} = r_{ij}(\mathbf{I}\cos\phi_j + \mathbf{J}_{\substack{\rightarrow\\ i\,j}}\sin\phi_j)(\mathbf{J}_{\substack{\rightarrow\\ i\,j}} + \mathbf{J}_{\substack{\leftarrow\\ i\,j}})$$

where $r_{ij} = \sqrt{\dfrac{u_{\substack{\rightarrow\\ i\,j}}u_{\substack{\leftarrow\\ i\,j}}}{2 - \mathrm{Tr}\,(\mathbf{J}_{\substack{\rightarrow\\ i\,j}}\mathbf{J}_{\substack{\leftarrow\\ i\,j}})}}$.

ϕ_j can be expressed as follows

$$\phi_j = \arctan\frac{f_jg'_j - f'_jg_j}{h_jf'_j - h'_jf_j} + \left(\frac{1}{2} \pm \frac{1}{2}\right)\pi\,, \qquad (13)$$

ISBN 978-3-95450-181-6

where

$$f_j = |\mathbf{C}''_j| - \tau_j^2 u^{\rightarrow\leftarrow}_{j\,j} u^{\leftarrow\leftarrow}_{j\,j} \qquad f'_j = |\mathbf{D}''_j| - \tau_j^2 u^{\rightarrow\rightarrow}_{j\,j} u^{\leftarrow\rightarrow}_{j\,j}$$
$$g_j = |\mathbf{C}'_j| - \tau_j^2 u^{\rightarrow\leftarrow}_{j\,j} u^{\leftarrow\leftarrow}_{j\,j} \qquad g'_j = |\mathbf{D}'_j| - \tau_j^2 u^{\rightarrow\rightarrow}_{j\,j} u^{\leftarrow\rightarrow}_{j\,j}$$
$$h_j = \mathrm{Tr}\,(\mathbf{C}'_j \hat{\mathbf{C}}''_j) \qquad h'_j = \mathrm{Tr}\,(\mathbf{D}'_j \hat{\mathbf{D}}''_j)$$
$$\mathbf{C}'_j = \mathbf{J}^{\rightarrow\leftarrow}_{j\,j} \mathbf{A}'_j + \mathbf{A}'_j \mathbf{J}^{\leftarrow\leftarrow}_{j\,j} \qquad \mathbf{D}'_j = \mathbf{J}^{\rightarrow\rightarrow}_{j\,j} \mathbf{B}'_j + \mathbf{B}'_j \mathbf{J}^{\leftarrow\rightarrow}_{j\,j}$$
$$\mathbf{C}''_j = \mathbf{J}^{\rightarrow\leftarrow}_{j\,j} \mathbf{A}''_j + \mathbf{A}''_j \mathbf{J}^{\leftarrow\leftarrow}_{j\,j} \qquad \mathbf{D}''_j = \mathbf{J}^{\rightarrow\rightarrow}_{j\,j} \mathbf{B}''_j + \mathbf{B}''_j \mathbf{J}^{\leftarrow\rightarrow}_{j\,j}$$
$$\mathbf{A}'_j = r_{jj}((\mathbf{J}^{\rightarrow}_{j\,j} + \mathbf{J}^{\leftarrow}_{j\,j})\mathbf{J}^{\leftarrow\rightarrow}_{j\,j} - \mathbf{J}^{\rightarrow\rightarrow}_{j\,j}(\mathbf{J}^{\rightarrow}_{j\,j} + \mathbf{J}^{\leftarrow}_{j\,j}))$$
$$\mathbf{A}''_j = r_{jj}((\mathbf{J}^{\rightarrow}_{j\,j}\mathbf{J}^{\leftarrow}_{j\,j} - \mathbf{I})\mathbf{J}^{\leftarrow\rightarrow}_{j\,j} - \mathbf{J}^{\rightarrow\rightarrow}_{j\,j}(\mathbf{J}^{\rightarrow}_{j\,j}\mathbf{J}^{\leftarrow}_{j\,j} - \mathbf{I}))$$
$$\mathbf{B}'_j = r_{jj}((\mathbf{J}^{\rightarrow}_{j\,j} + \mathbf{J}^{\leftarrow}_{j\,j})\mathbf{J}^{\leftarrow\leftarrow}_{j\,j} - \mathbf{J}^{\rightarrow\leftarrow}_{j\,j}(\mathbf{J}^{\rightarrow}_{j\,j} + \mathbf{J}^{\leftarrow}_{j\,j}))$$
$$\mathbf{B}''_j = r_{jj}((\mathbf{J}^{\rightarrow}_{j\,j}\mathbf{J}^{\leftarrow}_{j\,j} - \mathbf{I})\mathbf{J}^{\leftarrow\leftarrow}_{j\,j} - \mathbf{J}^{\rightarrow\leftarrow}_{j\,j}(\mathbf{J}^{\rightarrow}_{j\,j}\mathbf{J}^{\leftarrow}_{j\,j} - \mathbf{I})).$$

There are 3 possible ways of resolving ambiguity in (13). Firstly, ϕ_j can be introduced into parameterization as additional dependent parameters. Secondly, one can use 3 additional boolean parameters to indicate "+" or "−" in ϕ_j. And other way is to invert signs of β_{ij}, α_{ij} and μ_j, if ϕ_j has "+", then change it to "−".

Finally, resulting parameterization has 25 parameters: 3 μ_j, 9 α_{ij}, 9 β_{ij}, 3 u_{jj} and coupling asymmetry l. 21 of them are independent, and there are 4 identities which can be obtained from (11) and (12)

$$\mathrm{Tr}\,(\mathbf{W}_{jj}\mathbf{J}^{\leftarrow\leftarrow}_{j\,j}\hat{\mathbf{W}}_{jj}\mathbf{J}^{\rightarrow\rightarrow}_{j\,j} - \mathbf{W}_{jj}\mathbf{J}^{\leftarrow\rightarrow}_{j\,j}\hat{\mathbf{W}}_{jj}\mathbf{J}^{\rightarrow\leftarrow}_{j\,j}) =$$
$$= \tau_j(u^{\rightarrow\leftarrow}_{j\,j} u^{\leftarrow\leftarrow}_{j\,j} - u^{\rightarrow\rightarrow}_{j\,j} u^{\leftarrow\rightarrow}_{j\,j})$$
$$4\mathrm{Tr}\,(\mathbf{W}_{11}\mathbf{W}_{22}\mathbf{W}_{33}) = -l^2(1+s) +$$
$$+(1-s+2u_{11})(1-s+2u_{22})(1-s+2u_{33})\,,$$

where $s = u_{11}+u_{22}+u_{33}$.

4D CASE

This case can be deduced from 6D case with $\mathbf{M}_{31} = \mathbf{M}_{13} = \mathbf{M}_{32} = \mathbf{M}_{23} = \mathbf{0}$. The only nonzero $\mathbf{W}_{ij}$ are $\mathbf{W}_{32} = -\mathbf{W}_{31} = \mathbf{W}$, and all u_{ij} depend on one parameter u: $u_{11} = u_{22} = 1-u$, $u_{12} = u_{21} = u$. Then

$$\mathbf{W}\mathbf{J}_{21} = \mathbf{J}_{11}\mathbf{W}, \quad \mathbf{W}\mathbf{J}_{22} = \mathbf{J}_{12}\mathbf{W}, \quad |\mathbf{W}| = u(1-u). \tag{14}$$

If $u \neq \{0;1\}$, then this system can be solved only in the case of $\mathrm{Tr}\,(\mathbf{J}_{11}\mathbf{J}_{12} - \mathbf{J}_{21}\mathbf{J}_{22}) = 0$. So, the following identity can be derived

$$\beta_{11}\gamma_{12} + \beta_{12}\gamma_{11} - 2\alpha_{11}\alpha_{12} = \beta_{21}\gamma_{22} + \beta_{22}\gamma_{21} - 2\alpha_{21}\alpha_{22}\,. \tag{15}$$

Solution of (14) is the following

$$\mathbf{W} = k\,(\mathbf{J}_{11}\,(\mathbf{J}_{12} - \mathbf{J}_{22}) + (\mathbf{J}_{12} - \mathbf{J}_{22})\,\mathbf{J}_{21})\,,$$

where

$$k = \pm\sqrt{\frac{u(1-u)}{|\mathbf{J}_{11}\,(\mathbf{J}_{12} - \mathbf{J}_{22}) + (\mathbf{J}_{12} - \mathbf{J}_{22})\,\mathbf{J}_{21}|}}\,.$$

If of $k < 0$ then its sign should be changed along with simultaneous inversion of signs of $\{\mathbf{J}_{11}, \mathbf{J}_{21}, \mu_1\}$ or $\{\mathbf{J}_{12}, \mathbf{J}_{22}, \mu_2\}$ to resolve ambiguity.

The parameter set for 4D case is also redundant and has 11 items: 2 μ_j, 4 α_{ij}, 4 β_{ij} and u. Only 10 of them are independent because of identity (15).

RELATION TO LEBEDEV—BOGACZ PARAMETERIZATION

One can easily set up a correspondence between notations used in Lebedev—Bogacz parameterization [4] (left) and in the parameterization described above (right)

$$\begin{aligned}
\mu_{1L} &= \mu_1 \cdot \mathrm{sgn}\,\beta_{11} & \mu_{2L} &= \mu_2 \cdot \mathrm{sgn}\,\beta_{22} \\
\beta_{1x} &= |(1-u)\beta_{11}| & \beta_{1y} &= |u\beta_{21}| \\
\beta_{2x} &= |u\beta_{12}| & \beta_{2y} &= |(1-u)\beta_{22}| \\
\alpha_{1x} &= (1-u)\alpha_{11} \cdot \mathrm{sgn}\,((1-u)\beta_{11}) & & \\
\alpha_{2x} &= u\alpha_{12} \cdot \mathrm{sgn}\,(u\beta_{12}) & & \\
\alpha_{1y} &= u\alpha_{21} \cdot \mathrm{sgn}\,(u\beta_{21}) & & \\
\alpha_{2y} &= (1-u)\alpha_{22} \cdot \mathrm{sgn}\,((1-u)\beta_{22}) & &
\end{aligned}\,,$$

the "L" index of μ_{1L} and μ_{2L} is introduced to emphasize possible sign change. There are two main differences. Firstly, in [4] α_{ij} and β_{ij} depend on u, and u is dependent parameter, which, in turn, can be expressed through α_{ij} and β_{ij}. In the present paper α_{ij} and β_{ij} are independent on u, but there is identity (15). Secondly, in [4] all β_{ij} are positive, but there are 2 additional boolean parameters. In this paper these ambiguities are resolved by lifting the restriction of $\beta_{ij} > 0$.

SECOND-MOMENTS MATRIX AND EMITTANCES

If $\boldsymbol{\Sigma}$ is the second-moments matrix, then $\boldsymbol{\Sigma} = \mathbf{M}\boldsymbol{\Sigma}\mathbf{M}^T$. Using the following notation

$$\tilde{\boldsymbol{\Sigma}}_j = \mathrm{diag}\left(\tilde{\boldsymbol{\Sigma}}_{1j} \quad \tilde{\boldsymbol{\Sigma}}_{2\,j}^{\rightarrow} \quad \tilde{\boldsymbol{\Sigma}}_{3\,j}^{\leftarrow}\right), \quad \tilde{\boldsymbol{\Sigma}}_{ij} = -\varepsilon_j \mathbf{J}_{ij}\mathbf{S}\,,$$

one obtains closed expression for $\boldsymbol{\Sigma}$

$$\boldsymbol{\Sigma} = \overleftrightarrow{\mathbf{W}}_1\,\tilde{\boldsymbol{\Sigma}}_1 + \overleftrightarrow{\mathbf{W}}_2\,\tilde{\boldsymbol{\Sigma}}_2 + \overleftrightarrow{\mathbf{W}}_3\,\tilde{\boldsymbol{\Sigma}}_3\,.$$

Here ε_j are emittances of normal modes, one can calculate them from beam sizes

$$\begin{pmatrix}\varepsilon_1\\ \varepsilon_2\\ \varepsilon_3\end{pmatrix} = \begin{pmatrix}u_{11}\beta_{11} & u_{12}\beta_{12} & u_{13}\beta_{13}\\ u_{21}\beta_{21} & u_{22}\beta_{22} & u_{23}\beta_{23}\\ u_{31}\beta_{31} & u_{32}\beta_{32} & u_{33}\beta_{33}\end{pmatrix}^{-1}\begin{pmatrix}\sigma_1\\ \sigma_2\\ \sigma_3\end{pmatrix}.$$

ACKNOWLEDGEMENT

The author is grateful to D.N. Shatilov, E.B. Levichev, E.A. Perevedentzev, P.A. Piminov, N.A. Vinokurov (BINP) for review comments and discussions.

REFERENCES

[1] E. D. Courant, H. S. Snyder, "Theory of the alternating gradient synchrotron," Annals Phys. **3**, 1 (1958) [Annals Phys. **281**, 360 (2000)].

[2] H. Mais, G. Ripken, "Theory Of Coupled Synchrobetatron Oscillations. 1.," DESY M-82/05.

[3] D. A. Edwards, L. C. Teng, "Parametrization of linear coupled motion in periodic systems," IEEE Trans. Nucl. Sci. **20**, 885 (1973).

[4] S. A. Bogacz, V. A. Lebedev, "Betatron motion with coupling of horizontal and vertical degrees of freedom," eConf C **010630**, T511 (2001).

ISBN 978-3-95450-181-6

ON THE INTEGRO-DIFFERENTIAL EQUATIONS FOR DYNAMICS OF INTERACTING CHARGED PARTICLES MODELING

D.A. Ovsyannikov*, N. Edamenko,
St. Petersburg State University, 7/9 Universitetskaya nab., St. Petersburg, 199034 Russia

Abstract

In this paper we consider some integral-differential model of the dynamics of charged particles with smoothed interaction. This model is used in solving various problems of optimization of the dynamics of intense beams. Using the proposed model in optimization problems allows you to find analytical expressions for the functional variation that characterize the dynamics of the particles, and then consruct methods of directed search of extremum.

INTRODUCTION

Problems of the analysis of charged particles dynamics in view of their interaction have long been the focus of many researchers. One of the basic mathematical models describing the dynamics of the interaction of particles is the mathematical model proposed by A.A.Vlasov [1]. Vlasov equation widely used to solve a variety of application problems. Of particular interest is the finding of the self-consistent distributions to a beam of charged particles in an electromagnetic field [2-4,15]. The problems of existence and uniqueness of solutions of the Vlasov equation considered in [5,6]. It should be noted that in the numerical simulation of the dynamics of intense beams mainly smoothed interaction of charged particles is used [7-10]. In this paper we consider some integral-differential model of the dynamics of charged particles with smoothed interaction. This model is used in solving various problems of optimization of the dynamics of intense beams. Using the proposed model in optimization problems allows you to find analytical expressions for the functional variation that characterize the dynamics of the particles, and then construct methods of directed search of extremum [11-14]. The paper describes an example of the construction of such integral-differential model for the dynamics of charged particles.

INTEGRO-DIFFERENTIAL MODEL

Suppose that the dynamics of the beam of interacting charged particles is described by the system of integro-differential equations

$$\frac{dx}{dt} = f(t,x), \tag{1}$$

$$\frac{\partial \rho}{\partial t} + \frac{\partial \rho}{\partial x} f(t,x) + \rho\, div_x f(t,x) = 0, \tag{2}$$

$$f(t,x) = f_1(t,x) + \int_{M_t} \rho(t,y) f_2(t,x,y)\, dy \tag{3}$$

with initial conditions

$$x(t_0,x_0) = x_0 \in \overline{M}_0, \quad \rho(t_0,x) = \rho_0(x). \tag{4}$$

Here the nonempty open bounded set $M_0 \subset R^n$; the real-valued nonnegative continuous function $\rho_0(x)$ in $\overline{M}_0$ specifies a density of particle distribution in the phase space at the initial time t_0; the vector-function $f_1(t,x)$ is determined by the external electromagnetic fields acting on particles; the vector-function $f_2(t,x,y)$ is determined by considering the particle interaction. Solution of (1)-(4) represent a set of vector-functions $x(t,x_0)$ that determine the bundle of trajectories emanating from the set M_0. Note that $M_t = \{x(t,x_0) : x_0 \in M_0\})$ and $\rho(t,x(t,x_0))$ is the density of particle distribution along these trajectories. Equality (2) means that

$$\int_{M_t} \rho(t,y) f_2(t,x,y)\, dy = \int_{M_0} \rho_0(y_0) f_2(t,x,x(t,y_0))\, dy_0,$$

that is, we consider the system of integro-differential equations

$$\frac{dx(t,x_0)}{dt} = f(t,x(t,x_0)) = f_1(t,x(t,x_0)) + \int_{M_0} \rho_0(y_0) f_2(t,x(t,x_0),x(t,y_0)) dy_0 \tag{5}$$

with initial conditions

$$x(t_0,x_0) = x_0 \in \overline{M}_0. \tag{6}$$

Suppose that the vector real functions $f_1(t,x)$ and $f_2(t,x,y)$ are defined and continuous on the sets $(\alpha,\beta)\times\Omega$ and $(\alpha,\beta)\times\Omega\times\Omega$ respectively, where $(\alpha,\beta) \in R^1$, and Ω is a region in R^n.

Denote $R_a = \{t : |t-t_0| \le a\}$, $\overline{M}_b = \{x : ||x-x_0|| \le b,\ x_0 \in \overline{M}_0\}$, $R_1 = R_a \times \overline{M}_b$, $R_2 = R_a \times \overline{M}_b \times \overline{M}_b$.

We have the following theorem of existence and uniqueness.

Theorem Suppose the following conditions are satisfied:

1) the nonnegative function $\rho_0(x) \in C(\overline{M}_0)$ is given: $\rho_0(x) \ne 0$ for $x \in M_0$, and $\int_{M_0} \rho_0(x)dx = \rho < +\infty$;

2) numbers $a > 0$ and $b > 0$ are given, such that $R_a \subset (\alpha,\beta)$, $\overline{M}_b \subset \Omega$;

3) $M_1 = \sup_{(t,x)\in R_1} ||f_1(t,x)||$, $M_2 = \sup_{(t,x,y)\in R_2} ||f_2(t,x,y)||$;

4) the vector-functions $f_1((t,x)$ and $f_2((t,x,y)$ satisfy the Lipschitz condition in the variables x and x,y with constant L_1 and L_2 on the sets R_1 and R_2, respectively.

* d.ovsyannikov@spbu.ru

ISBN 978-3-95450-181-6

Then there exists a unique vector-function $x(t, x_0)$ that is defined and continuously differentiable with respect to t; it continuous in x_0 on $R_h \times \overline{M}_0$ and satisfies equation (5) and initial conditions $x(t_0, x_0) = x_0$. Here $h = \min(a, b/M)$ and $M = M_1 + \rho M_2$.

The proof of this theorem can be found in [9].

Let us assume that the vector-functions $f_1((t, x)$ and $f_2((t, x, y)$ are continuously differentiable with respect to x and y. Then the solution $x(t, x_0)$ of system (5) is continuously differentiable with respect to x_0. This assertion is proved just as the continuous differentiability of solutions for the systems of ordinary differential equations is proved with respect to initial data. In this case the matrix $\partial x(t, x_0)/\partial x_0$ satisfies the equation

$$\frac{d}{dt}\frac{\partial x(t,x_0)}{\partial x_0} = \frac{\partial f(t,x(t,x_0))}{\partial x}\frac{\partial x(t,x_0)}{\partial x_0} = \left(\frac{\partial f_1(t,x(t,x_0))}{\partial x} + \int\limits_{M_t} \frac{\partial f_2(t,x(t,x_0),y_t)}{\partial x}\rho(t,y_t)\,dy_t\right)\frac{\partial x(t,x_0)}{\partial x_0}$$

The existence and uniqueness of the solution $\rho(t, x)$ of equation (2) follows [9] from the equality

$$\frac{d\rho(t,x(t,x_0))}{dt} = -\rho(t,x(t,x_0))\mathrm{div}_x f(t,x(t,x_0))$$

and continuous differentiability of $x(t, x_0)$ to the initial data.

Problem (1)-(3) becomes the problem of controlling an ensemble of trajectories [9], if the function $f_1(t, x)$ depends on the control u (as a rule, the parameters of the accelerator), that is $f_1 = f_1(t, x, u)$, $x = x(t, x_0, u)$, and $M_t = M_{t,u} = \{x_t = x(t, x_0, u) : x_0 \in \overline{M}_0\}$. The quality of the beam dynamics of charged particles may be evaluated by functional such as

$$I(u) = \int\limits_0^T \int\limits_{M_{t,u}} \phi(t, x_t, \rho(t, x_t))\,dx_t dt + \int\limits_{M_{T,u}} g(x_T, \rho(T, x_T))\,dx_T, \quad (7)$$

where $\phi(t, x, \rho)$ and $g(x, \rho)$ are nonnegative continuously differentiable in its arguments functions. The control u we choose minimizing the functional (7). In the case of continuous differentiable functions f_1, f_2, $\mathrm{div}_x f_1$, $\mathrm{div}_x f_2$ it is possible to obtain an analytical expression [9] for the variation of the functional and thus construct directed methods to minimize it.

Here is an example of a model of the form (5) with smooth interaction, that is, with continuously differentiable functions $f_2(t, x, y)$, $\mathrm{div}_x f_2$. This example shows that the methods of large particles can be formulated in integro-differential form.

INTEGRO-DIFFERENTIAL DISK INTERACTION MODEL

In studies of the longitudinal motion of charged particles in axially symmetric external electromagnetic fields the particle beam is often seen as a set of N disks of radius R. Each disk moves at a time t along the axis z accelerating structure under the action of electromagnetic field generated in the accelerator and under the action of the field created by the remaining disks. The equations of motion i-th disc in dimensionless coordinates are

$$\frac{d\xi_i}{d\tau} = \frac{p_i}{\sqrt{1+p_i^2}}, \quad (8)$$

$$\frac{dp_i}{d\tau} = \alpha(\tau, \xi_i) + F_i. \quad (9)$$

Here $p_i = \beta_i/\sqrt{1-\beta_i^2}$ is the i-th particle momentum; $\beta_i = v_i/c$; v_i is the velocity of the i-th disk along the axis ξ; $F_i = \sum_{J=1}^{N} F_{ij}$, where F_{ij} is the force with which the j-th disc acts on the I-th disk. In calculating the force of one disk on the other along the ξ axis, we assume that the motion of the disk is uniform and the potential of any disk circle is given [7] by equality

$$U(r,z) = \frac{R_0}{\epsilon_0 a}\sum_{i=1}^{\infty}\frac{J_0(\mu_i R_0/a)J_0(\mu_i r/a)}{\mu_i J_1^2(\mu_i)}e^{-\mu_i|z|/a}. \quad (10)$$

Here R_0 is the radius of a charged circle; a is the radius of the tube; J_0 and J_1 are the Bessel functions; μ_i are the roots of the function J_0; r is the distance of the observation point from the tube axis, z is the longitudinal coordinate of the point at which the potential is calculated.

Expression (10) is valid for each circle in its own system of coordinates. That is, we need to calculate $-\partial U/\partial\xi$, to integrate with respect to the disk thickness and radius, and then to pass to a stationary system of coordinates.

For thin disks, the force with which the j-th thin disk acts on the i-th thin disk

$$f(\xi_i - \xi_j) = \frac{2e^2}{\pi R^2\epsilon_0}\mathrm{sign}(\xi_i - \xi_j)\times \sum_{i=1}^{\infty}\left(\frac{J_1(\mu_i R/a)}{\mu_i J_1(\mu_i)}\right)^2 e^{-\mu_i\lambda|z_2 - z_1|/a}.$$

is the discontinuous function at $\xi_i = \xi_j$, but for disks of finite thickness $2d$ the function $F(\xi_i - \xi_j)$ is continuously differentiable [9] (smoothed interaction). Here ξ_i and ξ_j are the coordinates of the centers of the thick discs in the stationary coordinate system.

In the simulation of particle dynamics taking into account the relativistic effects $F = F(\xi_i - \xi_j, p_j)$.

Thus, F_i in the equation (9) for the phase coordinate p_i has the form

$$F_i = \sum_{j=1}^{N} F(\xi_i - \xi_j, p_j)$$

ISBN 978-3-95450-181-6

Let points $\{(\xi_{i0}, p_{i0})\}_{i=1}^{N}$ are distributed in the set $\overline{M}_0$ with partial density $\rho_0(\xi, p)$, and let $(\xi_i(\tau, \xi_{i0}, p_{i0}), p_i(\tau, \xi_{i0}, p_{i0}))$ is the solution of a system (8)-(9) with the initial conditions

$$\xi_i(\tau_0, \xi_{i0}, p_{i0}) = \xi_{i0},\ p(\tau, \xi_{i0}, p_{i0}) = p_{i0},\ i = 1, 2, \ldots, N.$$

When $N \to \infty$ the sum F_i should be replaced by the integral

$$\iint\limits_{M_\tau} \rho(\tau, \xi', p') F(\xi(\tau, \xi_0, p_0) - \xi', p') d\xi dp',$$

where $\xi(\tau, \xi_0, p_0)$, $p(\tau, \xi_0, p_0)$ satisfy the system of equations

$$\frac{d\xi(\tau, \xi_0, p_0)}{d\tau} = \frac{p(\tau, \xi_0, p_0)}{(1 + p^2(\tau, \xi_0, p_0))^{1/2}},$$

$$\frac{dp}{d\tau} = \alpha(\tau, \xi_i) + \iint\limits_{M_\tau} \rho(\tau, \xi', p') F(\xi(\tau, \xi_0, p_0) - \xi', p') d\xi' dp'.$$

Here

$$M_\tau = \{(\xi(\tau, \xi_0, p_0), p(\tau, \xi_0, p_0) : (\xi_0, p_0) \in \overline{M}_0\}.$$

Note that

$$\rho(\tau, \xi(\tau, \xi_0', p_0'), p(\tau, \xi_0', p_0')) = \rho_0(\xi_0', p_0') \times \det{}^{-1} \left(\frac{D(\xi(\tau, \xi_0', p_0'), p(\tau, \xi_0', p_0'))}{D(\xi_0', p_0')} \right)$$

and, therefore,

$$\iint\limits_{M_\tau} \rho(\tau, \xi', p') G(\xi(\tau, \xi_0, p_0) - \xi', p') d\xi' dp' = \iint\limits_{M_0} \rho_0(\xi_0', p_0') F(\xi(\tau, \xi_0, p_0) - \xi(\tau, \xi_0', p_0'), p(\tau, \xi_0', p_0')) d\xi_0' dp_0'.$$

Thus, we obtain the system of the form (5):

$$\frac{d\xi(\tau, \xi_0, p_0)}{d\tau} = \frac{p(\tau, \xi_0, p_0)}{(1 + p^2(\tau, \xi_0, p_0))^{1/2}},$$

$$\frac{dp(\tau, \xi_0, p_0)}{d\tau} = \alpha(\tau, \xi(\tau, \xi_0, p_0)) + \iint\limits_{M_0} \rho_0(\xi_0', p_0') F(\xi(\tau, \xi_0, p_0) - \xi(\tau, \xi_0', p_0'), p(\tau, \xi_0', p_0')) d\xi_0' dp_0'.$$

The one-dimensional disk model is convenient in exploration of the longitudinal motion in axial symmetric structures. For exploration of three-dimensional problems¡ however, by way of example we may take a uniformly charged sphere of radius a as a large-size particle. The formula for force of interaction of two such balls is known [8] and based on this formula, we can write the system of integro-differential equations [10] for modeling and optimization of beam dynamics of charged particles in three-dimensional case.

CONCLUSION

Considered integro-differential model for the dynamics of intense charged particle beams can be used effectively and is used in the solution of simulation and optimization of beam dynamics of charged particles in the accelerating and focusing structures.

REFERENCES

[1] A.A. Vlasov, *Many-Particle Theory and Its Application to Plasma*, (Moscow-Leningrad: GITTL, 1950; Translated from the Russian, New York: Gordon and Breach, 1961), 413.

[2] R.C. Davidson, *Theory of Noneutral Plasmas*, (New York: Benjamin, 1974), 199.

[3] O.I. Drivotin, D.A. Ovsyannikov, "Stationary Self-Consistent Distributions for a Charged Particle Beam in the Longitudinal Magnetic Field". In: *Physics of Particles and Nuclei* 47.5 (2016), pp. 884-913.

[4] I.M. Kapchinsky, *Theory of Resonance Linear Accelerators*, (Moscow: Energoizdat, 1982; New York: Harwood, 1985), 398.

[5] A.A. Arsen'ev, "Unicness and Existance in the Small of the Classical Solution of Vlasov's System of equations," Dokl. Acad. Nauk SSSR 218 (1) (1974), pp. 11-12.

[6] A.A. Arsen'ev, "Existance and Unicness of the Classical Solution of Vlasov's System of equations," USSR Comput. Math. Math. Phys. 15 (5) (1975), pp. 252-258.

[7] Yu.V Batygin et al., "The formation of intense beams of nanosecond duration in linear accelerators," JTF 47 (10) (1977), pp. 2125–2131.

[8] B.P. Murin et al., *Linear ion accelerators*, (Moscow: Atomizdat, 1978), T1, 264.

[9] D.A. Ovsyannikov, *Modeling and Optimization of Charged Particle Beam Dynamics*, (Leningrad: Leningrad State University, 1990), 312.

[10] D.A. Ovsyannikov, N.S. Edamenko, "Modeling of charged particle beam dynamics," Vestnik St. Petersburg University 10 (2) (2013), pp. 60–65

[11] D.A. Ovsyannikov, "Modeling and Optimization Prblems of Charged Particle Beams Dynamics," ECC'97, Brussels, Belgium, July 1997, pp. 1463–1467.

[12] D.A. Ovsyannikov, "Mathematical Modeling and Optimization of Beam Dynamics in Accelerators," RuPAC'2012, St. Petersburg, Russia, September 2012, pp. 68–72.

[13] D.A. Ovsyannikov, V.V. Altsybeyev, "On the Beam Dynamics Optimization Problem for an Alternating-Phase Focusing Linac," Phys. Part. Nucl. Lett. 13.8 (2016), pp. 805–809.

[14] D.A. Ovsyannikov, A.D. Ovsyannikov et al., "Beam Dynamics Optimization: Methods and Applications," Nucl. Instr. Meth. Phys. Res. Section A 558 (1) (2006), pp. 11–19.

[15] O.I. Drivotin, D.A. Ovsyannikov, "Self-Consistent Distributions for a Charged Particle Beam in Magnetic Field". In: Int. Journal of Modern Physics A 24.5 (2009), pp. 941-951.

ISBN 978-3-95450-181-6

COUPLED BUNCH INSTABILITIES IN THE STORAGE RINGS*

A.S. Smygacheva#, V.N. Korchuganov, Y.A. Fomin
NRC «Kurchatov Institute», Moscow, Russia

Abstract

Coherent instabilities of the bunched beam are one of the reasons that limit a total beam current in the storage rings. Although there are solutions of this problem, the estimation and reduction of the wake-fields influence on the longitudinal beam dynamics remain important things. In the article we return to the subject of coherent instabilities of the unevenly-filled bunches in the storage rings.

INTRODUCTION

The interaction of the bunched beam with its wake-fields in the vacuum chamber of the storage ring causes the coherent single-bunch and coupled-bunch instabilities. The growth of the coherent instabilities contributes to an increase of the longitudinal and transverse emittances and the energy spread of the single bunch. Also it leads to the partial losses and to complete losses of the bunch particles in some cases. The result of this process is the limitation of the maximum synchrotron radiation brightness of a facility.

Since most of the modern storage rings operate in a multi-bunch mode, a primary task is to cure the coupled-bunch instabilities. To dump the coherent oscillations of a bunch sequence the feedback systems are used [1]. But it's not a single way to solve the problem. To increase the instability threshold and the total beam current in the storage ring, it requires the reducing the wake-fields influence. In view of this fact the RF cavities with the HOM dumping or with a good HOM frequency control and stabilization, the smoothing of a vacuum chamber structure and the using the harmonic RF cavities for Landau damping have place at the accelerators [2].

The review of bunched beam coherent instabilities can be found in [3, 4, 5, 6, 7]. In most cases authors considered the interaction of the symmetrically disposed point charge bunches with wake-fields. Whereas the operation with the non-symmetrical beam and unevenly-filled bunches allows to increase the instability threshold and the total beam current. The attempts to determine the wake-field contribution to the longitudinal dynamics and the bunch sequence have led to the development of the several calculation schemes [8, 9, 10]. But these are special cases of a symmetrically-filled ring, and in some of them estimation results not always agreed to the experiment data.

The coherent frequencies of the non-symmetrical bunched beam were found following a basic approach that uses a notion of the beam spectrum and an impedance function to describe the beam-chamber interaction. This analytical solution allows to estimate the influence of each field mode on the coherent oscillations of bunches with known mode parameters (the resonant frequency, the shunt impedance, the quality factor), the given bunch sequence and the Gauss distribution of particles in the phase plane.

*The reported study was funded by RFBR according to the research project No. 16-32-00335 мол_а.
#sasmyga@mail.ru

COUPLED BUNCH INSTABILITIES

The longitudinal dynamics of the bunched beam under the influence of the external RF fields and its own wake-fields is presented in this article.

The M electron bunches circulate in the accelerator with an angular revolution frequency ω_o. Bunches fill the orbit in the arbitrary order. Maximum number of bunches corresponds with the separatrix number of the ring, which is equal to the ratio of the RF frequency to the revolution frequency.

The appearance of the coherent oscillations adds to stationary distribution the components of the density perturbation. Then the electron distribution function can be written as:

$$\begin{cases} \Psi(\hat{\tau},\varphi,t) = \Psi_o(\hat{\tau}) + \sum_{m\neq 0}\Psi_m(\hat{\tau})e^{jm\varphi}e^{j\omega_{sm}t} \\ \tau = \hat{\tau}\cos\varphi\,,\ \frac{\dot{\tau}}{\omega_s} = \hat{\tau}\sin\varphi \\ \varphi = \omega_s t + \varphi_o \end{cases}, \quad (1)$$

where $\Psi_o(\hat{\tau})$ – the stationary distribution function of particles in the bunch, $\Psi_m(\hat{\tau})$ – the amplitude of the density perturbation component for the m-mode of oscillations, ω_{sm} – the coherent angular frequency of the m-mode of oscillations, τ – the time deviation of the particle from the reference particle place, $\hat{\tau}$ и φ – the amplitude and phase of oscillations in polar coordinates, ω_s – the incoherent synchrotron frequency taking into account the potential well distortion effect [11], φ_o – the initial phase of oscillations.

The longitudinal dynamics of electrons in the k-bunch is described by a synchrotron motion equation of the single particle and the Vlasov equation for the distribution function of particles in the bunch [3]. For small oscillations the linearized equations are:

$$\ddot{\tau} + \omega_{so}^2\tau = -2\pi\frac{e\eta}{\beta^2 T_o E}\sum_{p,m,i} j^{-m}\cdot I_b^i\cdot Z(p\omega_o+\omega_{sm})\cdot F_{pm}^i\cdot e^{-jp\omega_o(i-k)\frac{T_o}{h}}\cdot e^{jp\omega_o\tau}\cdot e^{j\omega_{sm}t}, \quad (2)$$

$$\left(\frac{\partial}{\partial t}-\omega_s\frac{\partial}{\partial\varphi}\right)\sum_m\Psi_m^k(\hat{\tau})e^{jm\varphi}e^{j\omega_{sm}t} = -(\ddot{\tau}+\omega_s^2\tau)\cdot\frac{\sin\varphi}{\omega_s}\cdot\frac{\partial\Psi_o^k(\hat{\tau})}{\partial\hat{\tau}}, \quad (3)$$

where

ISBN 978-3-95450-181-6

$$F_{pm}^{i} = \int_0^{+\infty} \hat{\tau}\Psi_m^i(\hat{\tau}) J_m(p\omega_o\hat{\tau})d\hat{\tau},$$

p,m=0,±1,±2,±3…, i=0,1,2..h-1, $h = \frac{\omega_{rf}}{\omega_o}$ – the RF harmonic number, ω_{so} – the incoherent synchrotron frequency, $\beta = {}^{v}/_{c}$ – the relativistic velocity factor, T_o – the revolution time period, $\eta = \alpha - 1/\gamma^2$, α – the momentum compaction factor, γ – the relativistic factor, E – the particle energy, $I_b = \frac{Ne}{T_o}$ – the bunch current, N – the number of electrons in the bunch, e – the elementary charge, $Z(\omega)$ – the longitudinal impedance function, $J_m(p\omega_o\hat{\tau})$ – the first order Bessel function.

The main cause of the rise of the longitudinal bunched beam instabilities is the long-range electromagnetic fields excited by bunches in the resonant structures of the vacuum chamber. As a rule these structures are the accelerating RF cavities that have them own resonant frequency spectrum, given by the cavity design.

The impedance function $Z(\omega)$ of the structures can be represented as a sum of resonant impedances of the RLC circuits with the resonant frequency ω_r, shunt impedance $R_{sh.r}$ and quality factor Q_r. In addition, if the resonant structures of the ring separate from each other as far as the electromagnetic relation is not existed, that the impedances are additive. The impedance of the structure at the beam current harmonic with coherent frequency is:

$$Z(p\omega_o + \omega_{sm}) = \sum_r -j\frac{R_{sh.r}\cdot h_r}{Q_r}\frac{p+\nu_{sm}}{(p-p_{1.r})(p-p_{2.r})}, \quad (4)$$

where $p_{1,2.r} = -\nu_{sm} + j\frac{h_r}{2Q_r} \pm \frac{h_r}{2Q_r}\sqrt{4Q_r^2 - 1}$; $h_r = \frac{\omega_r}{\omega_o}$; $\nu_{sm} = \frac{\omega_{sm}}{\omega_o}$, for small bunch current $\nu_{sm} \approx m\nu_s = \frac{m\omega_s}{\omega_o}$, the sum over r is the sum over the impedance frequency spectrum.

Rewrite the equation (3) for components of the distribution function with the view of the coherent mode coupling is absent:

$$j(\omega_{sm} - m\omega_s)\cdot\Psi_m^k(\hat{\tau}) = -\frac{e\eta}{\beta^2 E}\frac{m}{\omega_s\hat{\tau}}\frac{\partial\Psi_o^k(\hat{\tau})}{\partial\hat{\tau}}\cdot\sum_{p,i} I_b^i\cdot F_{pm}^i\cdot \frac{Z(p\omega_o+\omega_{sm})}{p}\cdot e^{-jp\frac{2\pi}{h}(i-k)}\cdot J_m(p\omega_o\hat{\tau}). \quad (5)$$

Multiply both parts of (5) by $\left(\frac{\hat{\tau}}{T_o}\right)^m$ and integrate respect to $\hat{\tau}$:

$$j(\omega_{sm} - m\omega_s) = -\frac{e\eta}{\beta^2 E}\cdot\frac{m}{\omega_s}\cdot\sum_{p,i}\frac{Z(p\omega_o+\omega_{sm})}{p}\cdot I_b^i\cdot e^{-jp\frac{2\pi}{h}(i-k)}\cdot\frac{F_{pm}^i\cdot G_{pm}^k}{F_m^k}, \quad (6)$$

where

$$G_{pm}^k = \int_0^{+\infty}\frac{\partial\Psi_o^k(\hat{\tau})}{\partial\hat{\tau}}\left(\frac{\hat{\tau}}{T_o}\right)^m J_m(p\omega_o\hat{\tau})d\hat{\tau}.$$

$$F_m^k = \int_0^{+\infty}\hat{\tau}\Psi_m^k(\hat{\tau})\left(\frac{\hat{\tau}}{T_o}\right)^m d\hat{\tau}$$

The first order Bessel function is

$$J_m(p\omega_o\hat{\tau}) = \sum_{n=0}^{+\infty}\frac{(-1)^n}{n!\cdot\Gamma(m+n+1)}\left(\frac{p\omega_o\hat{\tau}}{2}\right)^{2n+m}.$$

The most typical particle distribution for electron bunched beams is a Gaussian distribution. So the stationary distribution of electrons in the k-bunch is

$$\Psi_o^k(\hat{\tau}) = \frac{1}{2\pi\sigma_{\tau k}^2}e^{-\frac{\hat{\tau}^2}{2\sigma_{\tau k}^2}}, \quad (7)$$

$\sigma_{\tau k}$ – the RMS bunch length. The initial bunch length is set by the potential well distortion effect, the microwave instability, the Touschek effect, the quantum fluctuations and the radiation damping in the storage rings. The first free effects dominate at the low energies, and so the bunch length depends on the bunch current. The quantum fluctuations and the radiation damping determine the bunch length at the high energies. Therefore we can suppose the bunch length is independent of the current at the high energies.

We have for the Gaussian distribution

$$G_{pm}^k = -\frac{\sigma_{\tau k}^{2m-2}\cdot(2\pi p)^m\cdot e^{-\frac{(p\omega_o\sigma_{\tau k})^2}{2}}}{2\pi\cdot T_o^{2m}},$$

and

$$j(\omega_{sm} - m\omega_s) = \frac{e\eta}{2\pi\beta^2 E}\cdot\frac{m}{\omega_s}\cdot\sum_{p,i,n}\frac{(-1)^n\cdot T_o^{2n}}{n!\cdot\Gamma(n+m+1)\cdot 2^n\cdot\sigma_{\tau k}^{2n+2}}\cdot \frac{F_{nm}^i}{F_m^k}\cdot I_b^i\cdot\frac{Z(p\omega_o+\omega_{sm})}{p}\cdot\left(\frac{p\omega_o\sigma_{\tau k}}{\sqrt{2}}\right)^{2m+2n}\cdot e^{-\frac{(p\omega_o\sigma_{\tau k})^2}{2}}\cdot e^{-jp\frac{2\pi}{h}(i-k)},$$

$$F_{nm}^i = \int_0^{+\infty}\hat{\tau}\Psi_m^i(\hat{\tau})\left(\frac{\hat{\tau}}{T_o}\right)^{2n+m}d\hat{\tau}.$$

The substitution of the infinite upper limit in the integrals has place due to the density perturbation components are bounded in the phase space.

Using the method presented by B. Zotter in [12], we can find the effective impedance of the resonant structure that surrounds the beam. The final equation for the coherent frequencies of coupled bunches having the Gaussian distribution of particles is:

$$(\omega_{sm} - m\omega_s) = -\frac{e\eta}{2\pi\beta^2 E}\cdot\frac{m}{\omega_s}\cdot\sum_{r,n}\frac{(-1)^n\cdot T_o^{2n}}{n!\cdot\Gamma(n+m+1)\cdot 2^n\cdot\sigma_{\tau k}^{2n+2}}\cdot \frac{R_{sh.r}\cdot h_r}{Q_r\cdot(p_{2.r}-p_{1.r})}\cdot\left(I_b^k\cdot\frac{F_{nm}^k}{F_m^k}\cdot[S_{02}-S_{01}] + \sum_{i\neq k}I_b^i\cdot\frac{F_{nm}^i}{F_m^k}\cdot[S_{\alpha 2}-S_{\alpha 1}]\right), \quad (8)$$

where

ISBN 978-3-95450-181-6

$$S_{01,2} = \left(\left(x_{1,2}\right)^{2(m+n)} \cdot R_{01,2} + \sum_{l=0}^{m+n-1} \Gamma\left(l+\frac{1}{2}\right) \cdot \left(x_{1,2}\right)^{2(m+n)-2l-1}\right) + \nu_{sm} \frac{\omega_o \sigma_{\tau k}}{\sqrt{2}} \cdot \left(\left(x_{1,2}\right)^{2(m+n)} \cdot R_{01,2} + \sum_{l=0}^{n+m-1} \Gamma\left(l+\frac{1}{2}\right) \cdot \left(x_{1,2}\right)^{2(m+n)-2l-2}\right),$$

$$S_{\alpha 1,2} = \left(\left(x_{1,2}\right)^{2(m+n)} \cdot R_{\alpha 1,2} + \sum_{l=0}^{n+m-1} \Gamma\left(l+\frac{1}{2}\right) \cdot \left(x_{1,2}\right)^{2(m+n)-2l-1}\right) + \nu_{sm} \frac{\omega_o \sigma_{\tau k}}{\sqrt{2}} \cdot \left(\left(x_{1,2}\right)^{2(m+n)} \cdot R_{\alpha 1,2} + \sum_{l=0}^{n+m-1} \Gamma\left(l+\frac{1}{2}\right) \cdot \left(x_{1,2}\right)^{2(m+n)-2l-2}\right),$$

$$R_{01,2} = -\pi e^{-\left(x_{1,2}\right)^2} \cot \pi p_{1,2.r} + j\pi \left(w\left(x_{1,2}\right) - e^{-\left(x_{1,2}\right)^2}\right),$$

$$R_{\alpha 1,2} = -j2\pi e^{-\left(x_{1,2}\right)^2} \frac{e^{-jp_{1,2.r}2\pi\frac{i-k}{h}}}{1-e^{-j2\pi p_{1,2.r}}} + j\pi \left(w\left(x_{1,2}\right) - e^{-\left(x_{1,2}\right)^2}\right),$$

$$x_{1,2} = \frac{p_{1,2.r}\omega_o \sigma_{\tau k}}{\sqrt{2}},$$

$w(x) = e^{-x^2}\left(1 + \frac{2j}{\sqrt{\pi}} \int_0^x e^{t^2} dt\right)$ – a complex error function.

The ratio $\frac{F_{nm}^i}{F_m^k}$ is unknown in the (8). Let us assume the amplitude of particle oscillations is small as compared with the wave-length of the electromagnetic wake-field ($\frac{p\omega_o \hat{\tau}}{2} \ll 1$) to define the ratio. That in (5)

$$J_m(p\omega_o \hat{\tau}) \approx \frac{1}{\Gamma(m+1)} \cdot \left(\frac{p\omega_o \hat{\tau}}{2}\right)^m.$$

Multiplied both parts equation (5) by $\left(\frac{\hat{\tau}}{T_o}\right)^m$ and integrated respect to $\hat{\tau}$, we get

$$j(\omega_{sm} - m\omega_s) = -\frac{e\eta}{\beta^2 E} \cdot \frac{1}{\omega_s} \cdot \frac{F_{om}^k}{F_m^k} \cdot \sum_{p,i} \frac{m \cdot (\pi p)^{2m}}{p \cdot \Gamma^2(m+1)} \cdot I_b^i \cdot F_m^i \cdot Z(p\omega_o + \omega_{sm}) \cdot e^{-jp\frac{2\pi}{h}(i-k)}, \quad (9)$$

where

$$F_{om}^k = \int_0^{+\infty} \frac{\partial \Psi_o^k(\hat{\tau})}{\partial \hat{\tau}} \left(\frac{\hat{\tau}}{T_o}\right)^{2m} d\hat{\tau} = -\frac{2^m \cdot \Gamma(m+1) \cdot \sigma_{\tau k}^{2m-2}}{2\pi \cdot T_o^{2m}}.$$

Put equation (9) in (5) and find the approximate solution for functions $\Psi_m^k(\hat{\tau})$ for $\frac{p\omega_o \hat{\tau}}{2} \ll 1$:

$$\Psi_m^k(\hat{\tau}) = \frac{1}{\hat{\tau}} \cdot \frac{\partial \Psi_o^k(\hat{\tau})}{\partial \hat{\tau}} \cdot \left(\frac{\hat{\tau}}{T_o}\right)^m \cdot \frac{F_m^k}{F_{om}^k}. \quad (10)$$

Put (10) in the ratio $\frac{F_{nm}^i}{F_m^k}$, we can rewrite equation (8)

$$(\omega_{sm} - m\omega_s) = -\frac{e\eta}{2\pi\beta^2 E} \cdot \frac{m}{\omega_s} \cdot \sum_{r,n} \frac{(-1)^n}{n! \cdot \Gamma(m+1) \cdot \sigma_{\tau k}^{2n+2}} \cdot \frac{R_{sh.r} \cdot h_r}{Q_r \cdot (p_{2.r} - p_{1.r})} \cdot \left(I_b^k \cdot \sigma_{\tau k}^{2n} \cdot [S_{02} - S_{01}] + \sum_{i \neq k} I_b^i \cdot \frac{F_m^i}{F_m^k} \cdot \sigma_{\tau i}^{2n} \cdot [S_{\alpha 2} - S_{\alpha 1}]\right), \quad (11)$$

The ratio $\frac{F_m^i}{F_m^k}$ is unknown in the (11) also. Suppose here that each bunch has the same distribution function and the RMS bunch length is independent of the self-bunch current. Hence, the RMS bunch lengths are equal each other and the ratio $\frac{F_m^i}{F_m^k}$ is equal 1 for bunches oscillating in the same potential well, formed by the external RF field and wake-fields. As a result, the coherent frequencies are

$$(\omega_{sm} - m\omega_s) = -\frac{e\eta}{2\pi\beta^2 E} \cdot \frac{m}{\omega_s} \cdot \sum_{r,n} \frac{(-1)^n}{n! \cdot \Gamma(m+1) \cdot \sigma_{\tau k}^2} \cdot \frac{R_{sh.r} \cdot h_r}{Q_r \cdot (p_{2.r} - p_{1.r})} \cdot \left(I_b^k \cdot [S_{02} - S_{01}] + \sum_{i \neq k} I_b^i \cdot [S_{\alpha 2} - S_{\alpha 1}]\right). \quad (12)$$

CONCLUSIONS

The equation (12) is the approximate solution of the coherent frequencies. But it already allows to estimate the wake-fields influence and the coherent oscillations stability of the bunched beam. Also the solution for single-bunch instabilities can be found taking just term for $i=k$ in the equation (12).

REFERENCES

[1] M. Lonza, "Multi-bunch feedback systems", CERN-2008-003, 2008, p. 285

[2] A. Mosnier, "Cures of coupled bunch instabilities", Proc. of the 1999 Part. Acc. Conf., New York, pp. 628-632

[3] F. Sacherer, "Methods for computing bunched-beam instabilities", CERN/SI-BR/72-5, 1972

[4] J.M. Wang, "Longitudinal symmetric coupled bunch modes, Brookhaven National Laboratory", Report BNL 51302, 1980

[5] B. Zotter, "Longitudinal stability of bunched beams. Part III: Mode coupling and the microwave instability", CERN SPS/81-20 (DI), 1981

[6] J.L. Laclare, "Bunched beam coherent instabilities", CERN 87-03, p. 264, 1987

[7] A. Wu Chao, *Physics of Collective beam instabilities in high energy accelerators*, John Wiley&Sons Inc., 1993

[8] J. Scott Berg, "Bounds on multibunch growth rates when the bunches currents are not identical", CERN SL Note 97-72 (AP), 1997

[9] R.D. Kohaup, "On multi-bunch instabilities for fractionally filled rings", DESY 85-139, 1985

[10] S. Prabhakar, "New diagnostics and cures for coupled-bunch instabilities", Proc. of the 2001 Part. Acc. Conf., Chicago, pp. 300-304

[11] B. Zotter, "Potential-well bunch lengthening", CERN SPS/81-14 (DI), 1981

[12] B. Zotter, "The effective coupling impedance for instabilities of Gaussian bunches", CERN/ISR-TH/80-03, 1980

ISBN 978-3-95450-181-6

CHROMATIC AND NONLINEAR DYNAMICS OF ANTIPROTONS INJECTED TO COLLECTOR RING AT FAIR*

D. Shwartz#,1, I. Koop[1], P. Shatunov, BINP, Novosibirsk, 630090, Russia
[1] also at Novosibirsk State University, Novosibirsk, 630090, Russia

Abstract

Collector Ring (CR) is the storage ring for capturing and stochastic cooling of secondary beams of antiprotons or secondary ions. It is a part of a FAIR project being presently at the early start of a construction phase. Due to the proposed large acceptance in both transverse and longitudinal phase spaces, the chromatic aberrations and their correction with sextupoles are very important for capture efficiency. Calculations results for beam transfer from Pbar target to the ring are presented.

INTRODUCTION

The concept for the production of antiproton ($\bar{p}$, pbar) beams at FAIR is determined by the luminosity requirements for experiments with cooled $\bar{p}$ beams colliding with an internal H_2-target in the kinetic energy range from 0.8 GeV to 15 GeV at the High Energy Storage Ring (HESR) with $\bar{P}$ANDA [1].

Antiprotons are produced in inelastic collisions of high-energy protons with nucleons of a target. In the present accelerator layout for FAIR (see Fig.1) the SIS100 synchrotron accelerates protons to a kinetic energy of 29 GeV. Every 10 seconds the target will be hit with 2×10^{13} protons in a bunch of about 50 ns duration. The maximum yield (production and collection with reasonable emittance and momentum spread) is achieved for $\bar{p}$ kinetic energy of around 3 GeV that corresponds to 13 Tm of magnetic rigidity.

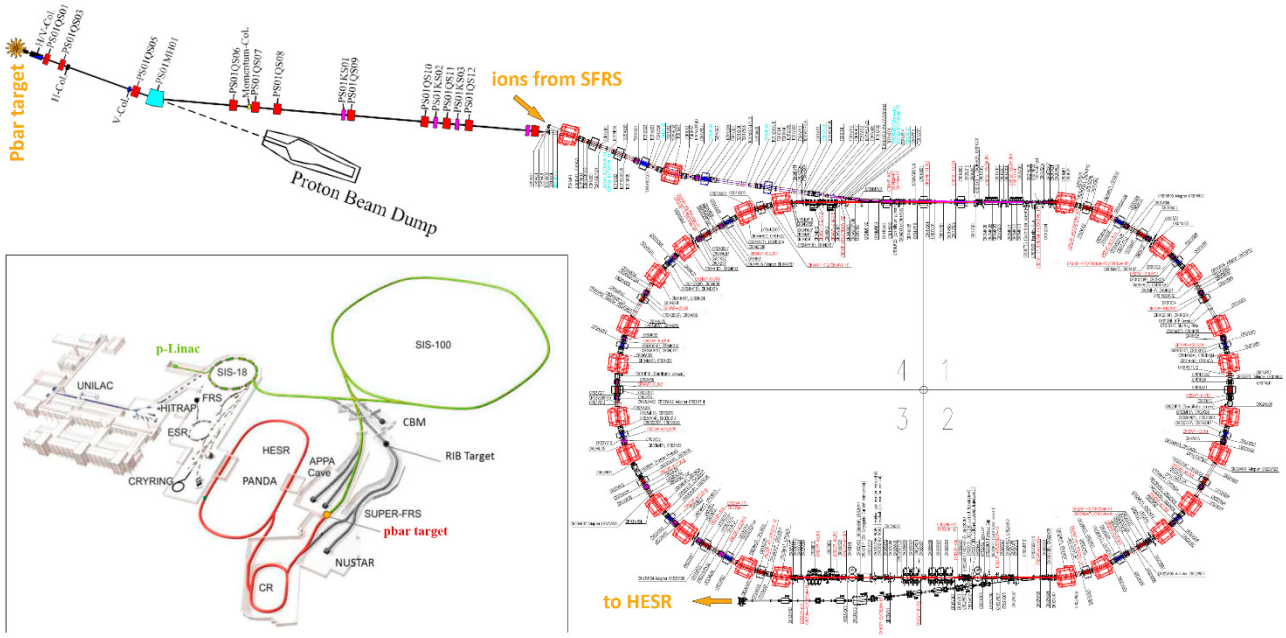

Figure 1: The overall antiproton program scheme at FAIR (left-down), and layout of AS-TCR1 beamline and Collector Ring.

TRANSPORT CHANNEL

The antiproton beam coming from target is focused by magnetic horn and passed through Antiproton Separator (AS) beamline with 4 consecutive collimators [2]. The calculated distribution of $\bar{p}$ in transverse phase space is shown in Fig.2 [3]. Only particles within aperture of first H/V collimator are shown.

The beamline following junction with path of ion beam from SFRS is called TCR1. The aim of the whole transfer line is to separate and to pass antiprotons with transverse emittance of $\varepsilon_{x,y}$ = 240 mm·mrad and momentum spread of $\Delta p/p = \pm 3\%$ that corresponds to CR acceptance.

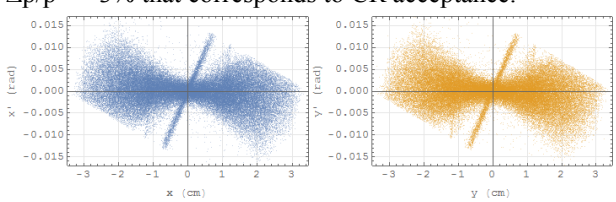

Figure 2: Transverse phase space after horn.

The lattice functions of whole transfer channel including straight section of CR ending with kickers are presented in

*Work supported by FAIR-Russia Research Center (FRRC)
#d.b.shwartz@inp.nsk.su

ISBN 978-3-95450-181-6

Fig.3. The transverse beam sizes along the channel can be found in the same figure.

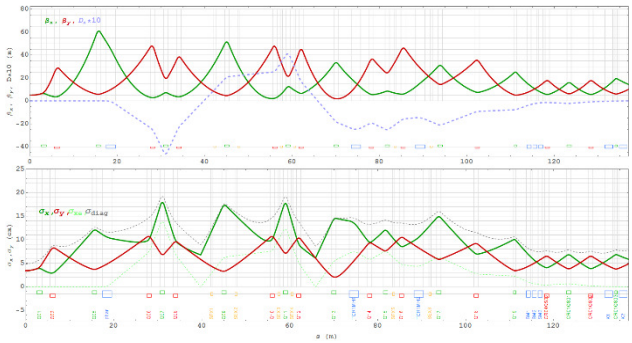

Figure 3: Lattice functions (above) and beam sizes (below) along the transverse channel.

Due to large momentum spread the second-order chromatic effects of the focusing structure are important. In Fig.4 the variation of lattice functions with momentum deviation in the range of ±3% is shown together with second-order dispersion function D_1. Both these effects leads to beam size increase and to mismatch of the lattice functions with CR ones for particles with momentum deviation. To suppress chromatic effects, shown with orange in Fig.3 6 sextupoles are foreseen.

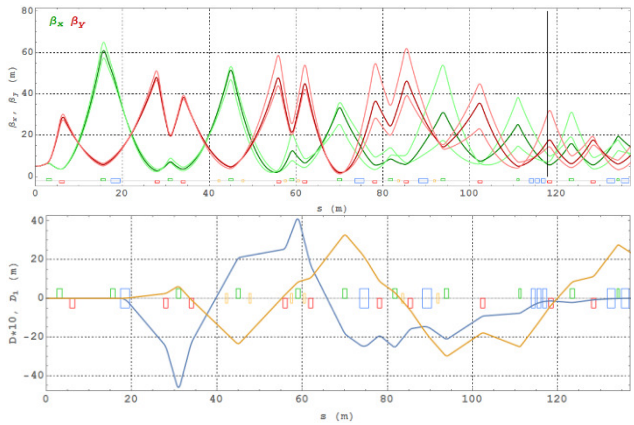

Figure 4: Beta-functions variation for Δp/p = ±3% (above) and first- and second-order dispersion-functions (below).

The careful tracking of antiprotons from magnetic horn to CR with realistic aperture limitations and collimation to given emittance and momentum spread was done with full 6D SAD code [4]. The sample of 10000 particles' tracks is shown in Fig.5.

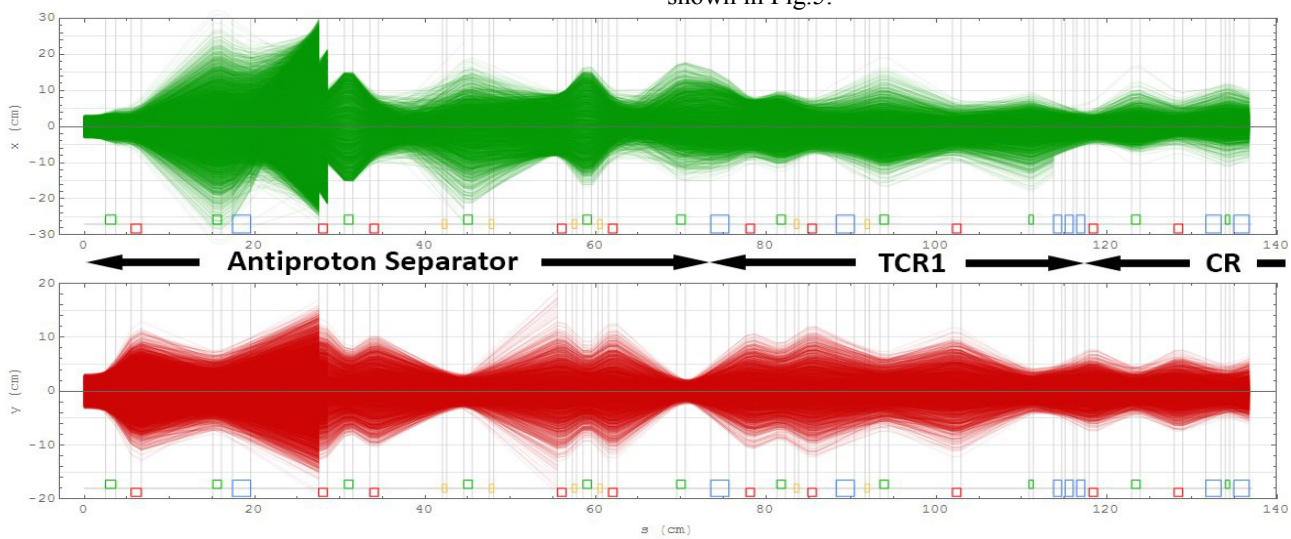

Figure 5: Horizontal (above) and vertical (below) projection of antiprotons tracks.

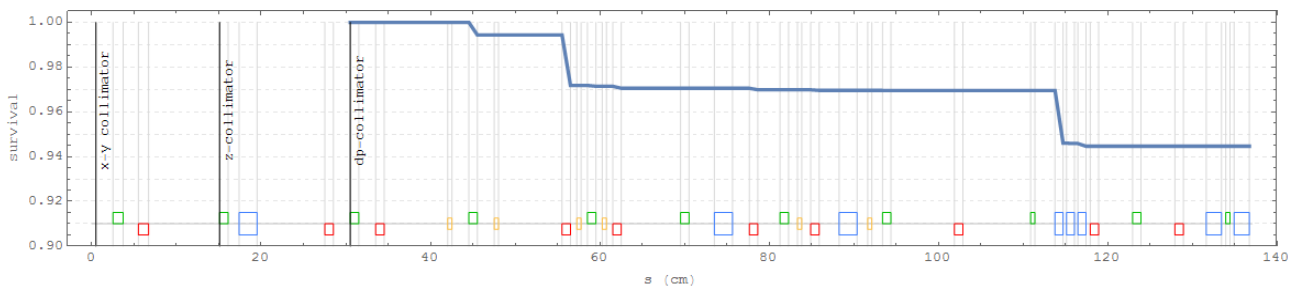

Figure 6: Beam losses along transfer channel.

The corresponding beam losses are presented in Fig.6. Here the number of particles is normalized on number of $\bar{p}$ after last collimation.

In Fig.7 the cross-section of the simulated beam is shown at the entrance of Septum Magnet (SM) [5]. With pink ellipse, the beam cross-section in linear approximation is shown. One can see, that number of particles with large momentum deviation does not fit to the SM vacuum chamber (shown with black circles), being shifted to the left. This is the result of uncompensated chromatic aberrations. The work on optimization of nonlinear

ISBN 978-3-95450-181-6

correction in channel is still in progress. The momentum spread of pbars injected to CR is shown in Fig.8.

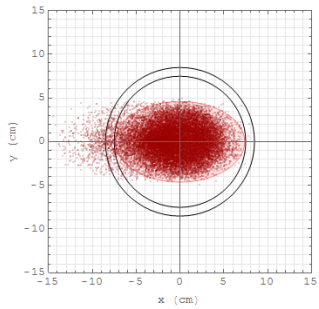

Figure 7: Beam at the entrance to CR septum.

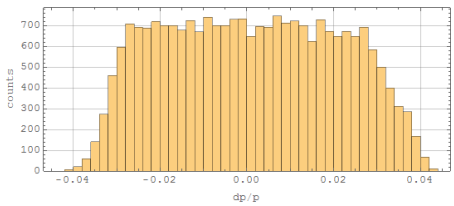

Figure 8: Momentum spread the entrance to CR septum.

COLLECTOR RING

The CR is a large acceptance storage ring designed for capturing and stochastic cooling of hot antiproton or rare isotope beams at FAIR [6, 7]. It will also operate in the isochronous mode to measure masses of short-lived secondary rare isotopes.

In Pbar regime CR should capture the beam with fixed kinetic energy of 3 GeV (γ = 4.20, $B\rho$ = 13 T·m), emittances $\varepsilon_{x,y}$ = 240 mm·mrad and momentum spread of $\Delta p/p$ = ±3 %.

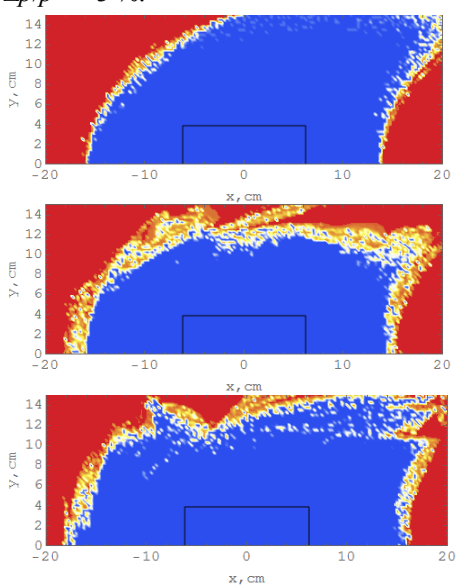

$\Delta p/p$ = –3 %

$\Delta p/p$ = 0

$\Delta p/p$ = +3 %

Figure 9: Dynamic aperture of CR.

Due to large energy spread it is important to control and tune with help of sextupoles simultaneously betatron tunes chromaticity, second-order chromatic effects, and nonlinear beam dynamics [8]. Six families of sextupoles are foreseen to optimize beam dynamics. The chosen scheme for chromaticity correction provides the sufficient Dynamic Aperture (DA) according to simulations with SAD code [4]. In Fig. 9 the calculated DA is shown. Here the chromatic sextupoles as well as high-order field harmonics of main magnetic elements (dipoles, quadrupoles) are taken into account. Also breaking ring symmetry field errors (±1% for quads, ±10% for sextupoles) and 5÷10 mrad elements rotations were included. The DA is defined as a survival during 1000 turns that corresponds to time of the injected bunch rotation in longitudinal phase space with special RF-debunchers. After rotation the momentum spread decreases significantly and possible DA limitations should be suppressed.

The chromaticity of lattice functions with the same sextupoles' distribution is suppressed to acceptable values (see Fig. 10).

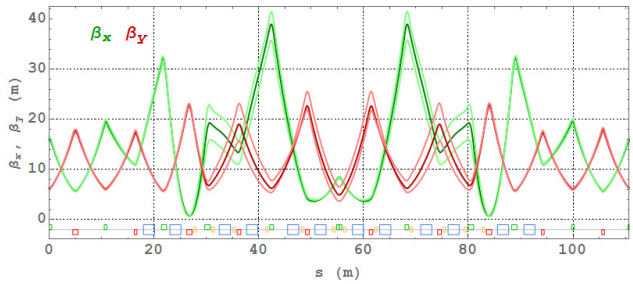

Figure 10: Beam at the entrance to CR septum.

CONCLUSION

Although the further optimization of transfer channel lattice is possible the simulations already show acceptable beam losses in range of several percent with respect to conceptual design parameters.

AKNOWLEGEMENT

We are grateful to K. Knie, V. Gostishchev, S. Litvinov, A. Dolinskii and O. Gorda for support and discussions. We would like to thank K. Oide and Yu. Rogovsky for help with SAD code.

REFERENCES

[1] E. Prencipe [P̄ANDA collaboration], "Status and Perspectives for P̄ANDA at FAIR", Nucl. Part. Phys. Proc. **273-275** (2016) 231-237.
[2] R. Bar et al., "Technical Design Report on the Antiproton Target and Separator (pbar)", Feb 2016.
[3] S.A. Litvinov et al., "Ion-Optics of Antiproton Separator at FAIR", Proc. IPAC'16, THPMR018.
[4] Strategic Accelerator Design (SAD) code homepage, http://acc-physics.kek.jp/SAD/sad.html.
[5] P. Yu. Shatunov et al., "The Injection Septum Magnet for the Collector Ring (FAIR)", Proc. IPAC'16, p.1145.
[6] P. Yu. Shatunov et al., "Collector Ring Project at FAIR: Present Status", Proc. RuPAC'16, WECBMH02, these proceedings.
[7] V. Anashin et al., "CR TDR Annex-1", 2016.
[8] O. Gorda et al., "Beam Dynamics and Closed Orbit Correction at the Collector Ring", Proc IPAC'16, p.3216.

ISBN 978-3-95450-181-6

BEAM DYNAMICS CALCULATION OF ELECTRON BUNCH SEQUENCE PASSING THROUGH DIELECTRIC *

A.Altmark, Saint-Petersburg Electrotechnical University "LETI" ,Russia,
A.Kanareykin, EuclidTechLabs LLC, Gaithersburg MD, US

Abstract

The present work involves modelling the electron beams dynamics for development of new THz source based on cylindrical dielectric waveguide. The sequence of relativistic electron bunch generates Cherenkov radiation, which is a superposition of the TM and HEM-modes. The distances between bunches is selected for creating of monochromatic THz radiation. We made calculation of beam dynamics considering the Space Charge and focusing field with help of original BBU 3000 code. The main parameter of radiation was investigated: length of wave pocket, monochromaticity and frequency.

INTRODUCTION

This work was initiated by the experimental works [1-4] aimed at exploring new sources THz sources based on dielectric waveguide. Numerical calculations of the sources are made in previous works [5].

The THz Cherenkov radiation is generated in dielectric waveguide by electron beam. Spectrum of radiation is defined by parameters of waveguide (outer and inner radius, dielectric constant). Charge profile of electron beam can be used for selecting and damping of TM-modes in Cherenkov radiation. We are considering a new method of frequency selecting based on using of bunch sequence as source of radiation, figure 1. Variation of distances between bunches allow to select radiation frequency. The main disadvantage of this method is inability of frequency variation.

The main point of present work is beam dynamics which limits way passed by bunches. This parameter limits wave pocket of radiation.

Transverse dynamics caused by influence of asymmetric HEM–modes and focusing system. The value of transverse field grows with offset increasing from the axis of waveguide. In this paper, we study the dynamics of bunch sequence and influence of the focusing system to control of the transverse instability.

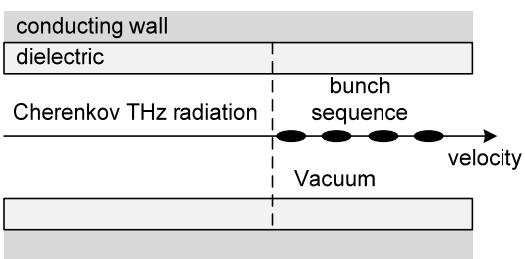

Figure 1: Longitudinal section of cylindrical dielectric waveguide with sequence of bunches.

The radiation (wakefield) with strong Ez component behind single bunch consist principally set of TM modes. One mode regime with frequency of TM_{01} mode can be realized by increasing of bunch length. The sequence of bunches permits to excite one mode radiation based on high order TM modes. This monochromatic radiation can be realized by fine tuning of distances between bunches. The sequence with founded distances allow to damp all TM mode except selected one.

INITIAL PARAMETERS

The dielectric waveguide presented in this work (Table 1) can be used as THz source for next frequencies: 142 GHz (TM_{01}-mode), 439 GHz (TM_{02}-mode), 765 GHz (TM_{03}-mode).

Parameters of bunch sequence are presented in Table 2. All bunches have same radial offset, which caused strong transverse instability particularly for low energy (15 MeV).

It is very important to consider the attenuation of the wakefield (loss tangent of dielectric and conductivity of metal wall in Table1), as well as the effect of group velocity. The group velocity grows with order of TM modes. It is means the wave pocket for high frequency will be shortest.

Table 1: Dielectric Waveguide Parameters

Waveguide	**Value**
Inner radius (um)	600
Outer radius (um)	850
Epsilon	3.8
Length (cm)	10
Loss tangent	0.001
Wall conductivity (S/m)	5.7E+07

Table 2: The Bunch Sequence Parameters

Bunch sequence	**Value**
Transverse beam size (um)	120
Longitudinal bunch length (um)	~ 100
Beam energy (MeV)	~ 15
Offset (um)	~ 100
Number of bunches	6-8
First frequency (GHz)	439
Second frequency (GHz)	765

ISBN 978-3-95450-181-6

BEAM DYNAMICS CALCULATION

We used original BBU 3000 code [5,6] for beam dynamics calculation. This code is based on Green function knowledge for different types of dielectric waveguides. Numerical calculation of dynamics is realized according to macroparticle method.

First, we used Green function for "Multibunch" module which allow to create and edit different types of sequences and calculate result wakefield. Figure 2 show example for THz radiation on frequency 765 GHz created by 8 bunches. In the next step, all founded parameters transmitted to "3D Beam Dynamics" module. The focusing system also is created before final simulation. Focusing and defocusing quadrupole sections are edited per next parameters: number of sections, values of magnetic field, lengths.

Beam dynamics calculation is based on interaction between particles and consider 4 axial monopole TM modes and four asymmetric dipole HEM modes. For each mode attenuation coefficient and group velocity are calculated.

First numerical experiment was made without focusing system. This fact led to the destruction of sequence after 3.5 cm pass. The strongest radial force experienced by bunches in middle of sequence: "head" and "tail" of bunches are displaced in opposite directions in transverse coordinate.

We suggest FDFD (Focusing-Defocusing) system to increase the way of sequence up waveguide length. Figure 3 show tracking of bunch sequence and structure of focusing system. Each quadrupole section focus bunches in one direction and defocus it in perpendicular direction. This fact causes increasing of transverse size of sequence which leads to the bunch collision with dielectric tube, figure 4. Presence of focusing system allow to pass bunch sequence up to 9.5 cm.

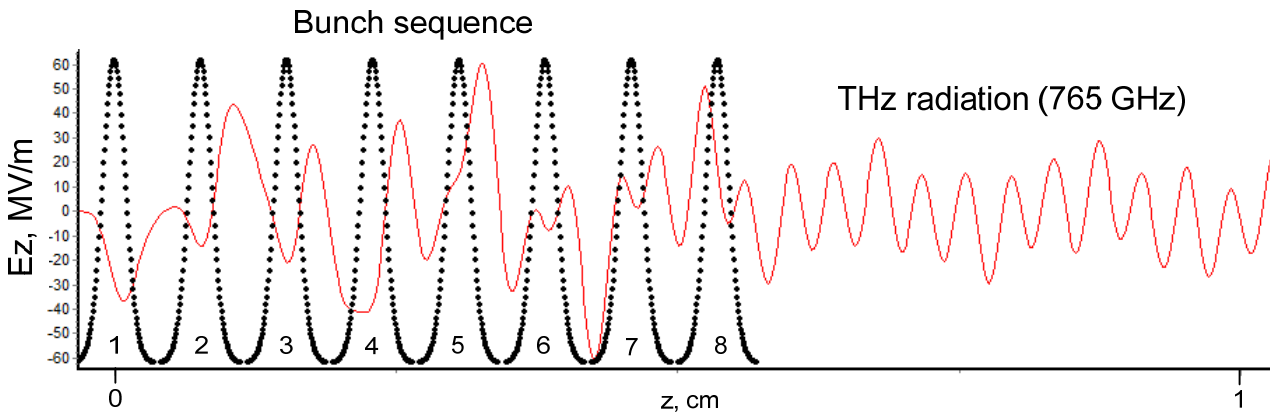

Figure 2: THz radiation inside and behind bunch sequence passing in waveguide from right to left.

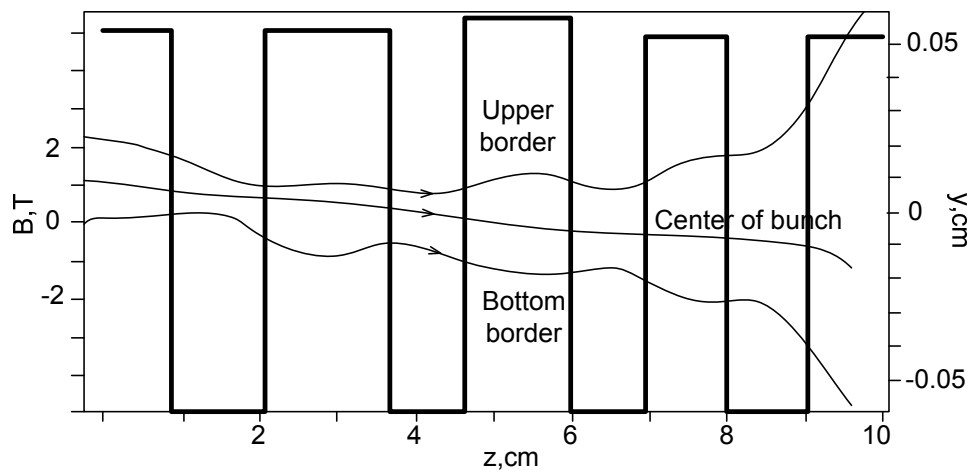

Figure 3: Results of dynamics calculation presented as dependence of sequence's borders (transverse coordinate – right axis) from passed way. Bunches are moving from left to right in presence of FDFD focusing system (left axis)

ISBN 978-3-95450-181-6

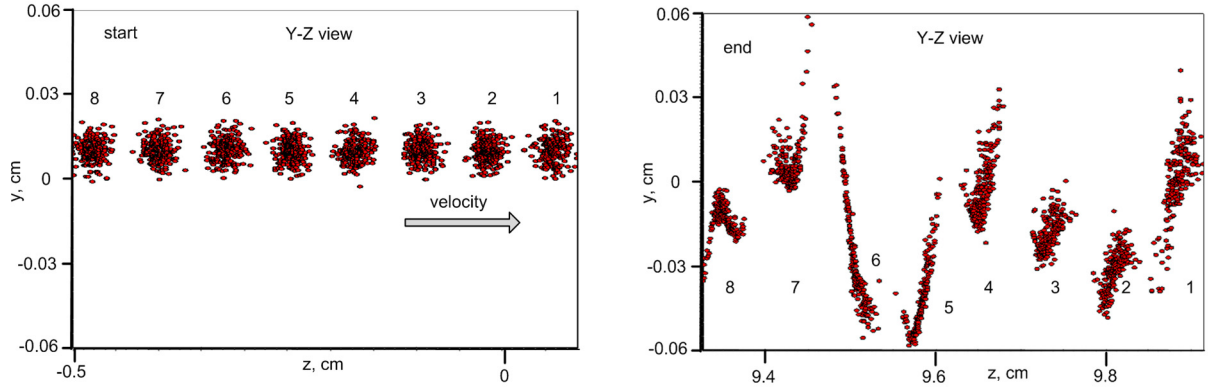

Figure 4: Results of dynamics calculation presented as image of start longitudinal view (left plot) and final longitudinal view after 9.5 cm passing inside waveguide (right view). Bunches are moving from left to right in presence of FDFD focusing system, figure 3.

CONCLUSION

We plan to develop algorithm for optimisation of focusing system parameters. Focusing system must provide of bunch sequence passing in dielectric waveguide for permissible ranges of offsets and number of bunches.

ACKNOWLEDGMENTS

This work was supported by grant 15-02-08745 from the Russian Foundation for Basic Research.

REFERENCES

[1] G. P. Gallerano, S Biedron, Proc. of FEL, (2004) 216
[2] M Lang, A Deninge, Photonik Int, (2012) 36
[3] G Andonian, O Williams, X Wei et al, Applied Physics Letters, 98 (2011) 202901
[4] S Antipov, C Jing, S Baryshev et al, Proc. of IPAC, 1929 (2015)
[5] A.Kanareykin, A Altmark, Journal of Physics Conference Series, (2016) 732
[6] P Schoessow, C Jing, A Kanareykin et al, Proc. of PAC. WEP111 (2011)

ISBN 978-3-95450-181-6

ORBITAL MOTION IN MULTIPOLE FIELDS VIA MULTISCALE DECOMPOSITION

A.N. Fedorova, M.G. Zeitlin*, IPME RAS, St. Peterburg, Russia

Abstract

We present applications of methods of nonlinear local harmonic analysis in the variational set-up for a description of multiresolution representations in polynomial approximations for nonlinear motions in arbitrary n-pole fields. Our approach is based on the methods allowed to consider the best possible dynamical beam/particle localization in phase space and provided exact multiscale represention via nonlinear high-localized eigenmodes for all observables with exact control of contributions to motion from each underlying hidden scale.

INTRODUCTION

In this paper, we consider the applications of a numerical-analytical technique based on the methods of local nonlinear harmonic analysis [1] (in the particular case of underlying affine group a.k.a. wavelet analysis) to the calculations of orbital motion in arbitrary n-pole fields. Our main generic examples here are orbits in transverse plane for a single particle in a circular magnetic lattice in case when we take into account multipolar expansion up to an arbitrary finite number, and particle/beam motion in storage rings [2]. We reduce the complicated initial dynamical problem to a finite number of algebraical problems and represent all dynamical variables via multiscale expansions in the bases of modes maximally localized in the phase space. Our methods here are based on our general universal variational-wavelet approaches considered in papers [3]. Starting in next section from Hamiltonian of orbital motion in magnetic lattice and rational approximation of classical motion in storage rings, in the subsequent part we consider very flexible variational-biorthogonal formulation for a dynamical system with rational nonlinearities and construct the explicit representations for all dynamical variables as expansions in the bases/frames of proper nonlinear high-localized eigenmodes.

MOTION IN MULTIPOLAR FIELDS

The magnetic vector potential of a magnet with $2n$ poles in Cartesian coordinates is

$$A = \sum_n K_n f_n(x, y), \tag{1}$$

where f_n is a homogeneous function of x and y of order n. The cases from $n = 2$ to $n = 5$ correspond to low-order multipoles: quadrupole, sextupole, octupole, decapole. The corresponding Hamiltonian is (ref. [2] for designation):

$$H(x, p_x, y, p_y, s) = \frac{p_x^2 + p_y^2}{2} + \left(\frac{1}{\rho^2(s)} - k_1(s)\right) \cdot \frac{x^2}{2} + k_1(s)\frac{y^2}{2} - \mathcal{R}e\left[\sum_{n\geq 2} \frac{k_n(s) + ij_n(s)}{(n+1)!} \cdot (x+iy)^{(n+1)}\right]. \tag{2}$$

Then we may take into account an arbitrary but finite number of terms in expansion of RHS of Hamiltonian (2) and from our point of view the corresponding Hamiltonian equations of motions are not more than nonlinear ordinary differential equations with polynomial nonlinearities and possibly variable coefficients. As the second generic example, we consider the beam motion in storage rings [2]. Starting from Hamiltonian described classical dynamics in storage rings, and using Serret–Frenet parametrization, we have, after standard manipulations with the truncation of power series expansion of square root, the following approximated (up to octupoles) Hamiltonian for orbital motion in machine coordinates:

$$\begin{aligned}\mathcal{H} &= \frac{1}{2} \cdot \frac{[p_x + H \cdot z]^2 + [p_z - H \cdot x]^2}{[1 + f(p_\sigma)]} \\ &+ p_\sigma - [1 + K_x \cdot x + K_z \cdot z] \cdot f(p_\sigma) \\ &+ \frac{1}{2} \cdot [K_x^2 + g] \cdot x^2 + \frac{1}{2} \cdot [K_z^2 - g] \cdot z^2 - N \cdot xz \\ &+ \frac{\lambda}{6} \cdot (x^3 - 3xz^2) + \frac{\mu}{24} \cdot (z^4 - 6x^2z^2 + x^4) \\ &+ \frac{1}{\beta_0^2} \cdot \frac{L}{2\pi \cdot h} \cdot \frac{eV(s)}{E_0} \cdot \cos\left[h \cdot \frac{2\pi}{L} \cdot \sigma + \varphi\right]\end{aligned} \tag{3}$$

and the corresponding polynomial series expansion for function $f(p_\sigma)$. We consider here only arbitrary polynomial/rational (in terms of dynamical variables) expressions.

BIORTHOGONAL VARIATIONAL APPROACH VIA LOCALIZED MODES

The first main part of our consideration is some variational approach to these problems, which reduces the initial problem to the problem of solution of functional equations at the first stage and some algebraical problems at the second stage. Multiresolution representation [1] is the second main part of our construction. As a result, the solution is parameterized by solutions of two reduced algebraical problems, one is nonlinear and others are linear problems obtained from proper multiresolution/multiscale constructions. Finally, we obtain the exact (fast convergent numerically) multiscale decomposition via high-localized modes, like compactly supported wavelets or wavelet packets. Because the integrand of our (invariant) variational functional is represented by the bilinear form, it seems more reasonable to consider the constructions which take into account

* zeitlin@math.ipme.ru

ISBN 978-3-95450-181-6

all advantages of this structure, so we will use the so-called biorthogonal decompositions [4].

Let us consider the symplectically invariant representation for our initial Hamiltonian problems (2), (3). The key ingredient of such a description is an operator S, symplectic form ω, quasicomplex structure J and proper action of operator S on dynamical variables x:

$$S(\omega(J), H, x, \partial/\partial t, \nabla, t)x = -J\dot{x}(t) - \nabla H(x(t)) \quad (4)$$

which is polynomial in x and (possibly) has arbitrary dependence on time. It provides us with the following invariant variational formulation:

$$\int_0^T < Sx, y > \mathrm{d}t = 0. \quad (5)$$

The next is based on the some version of multiresolution machinery. The non-abelian affine group of translations and dilations (it is a simple but generic case) which acts as a hidden symmetry on a proper realization of the underlying finctional space provides the contribution to exact multiscale decomposition from each scale of resolution from the whole infinite scale of spaces. More exactly, the closed subspace $V_j (j \in \mathbf{Z})$ corresponds to level j of resolution, or to scale j. We consider a r-regular multiresolution analysis (MRA) of $L^2(\mathbf{R}^n)$ which is a sequence of increasing closed subspaces V_j:

$$...V_{-2} \subset V_{-1} \subset V_0 \subset V_1 \subset V_2 \subset ... \quad (6)$$

satisfying the following properties:

$$\bigcap_{j\in\mathbf{Z}} V_j = 0, \quad \overline{\bigcup_{j\in\mathbf{Z}} V_j} = L^2(\mathbf{R}^n),$$
$$f(x) \in V_j <=> f(2x) \in V_{j+1},$$
$$f(x) \in V_0 <=> f(x-k) \in V_0, \ \forall k \in \mathbf{Z}^n. \quad (7)$$

There exists a function $\varphi \in V_0$ such that $\{\varphi_{0,k}(x) = \varphi(x - k), k \in \mathbf{Z}^n\}$ forms a Riesz basis for V_0. The function φ is regular and localized. Let $\varphi(x)$ be a scaling function, $\psi(x)$ is a wavelet function and $\varphi_i(x) = \varphi(x-i)$. Scaling relations that define φ, ψ are

$$\varphi(x) = \sum_{k=0}^{N-1} a_k \varphi(2x-k) = \sum_{k=0}^{N-1} a_k \varphi_k(2x), \quad (8)$$

$$\psi(x) = \sum_{k=-1}^{N-2} (-1)^k a_{k+1} \varphi(2x+k). \quad (9)$$

Let indices ℓ, j represent translation and scaling, respectively and

$$\varphi_{jl}(x) = 2^{j/2}\varphi(2^j x - \ell), \quad (10)$$

then the set $\{\varphi_{j,k}\}, k \in \mathbf{Z}^n$ forms a Riesz basis for V_j. The wavelet function ψ is used to encode the details between two successive levels of approximation. Let W_j be the orthonormal complement of V_j with respect to V_{j+1}:

$$V_{j+1} = V_j \bigoplus W_j. \quad (11)$$

All V_j are spanned by dilation and translations of the scaling function, while W_j are spanned by translations and dilation of the mother wavelet $\psi_{jk}(x)$, where

$$\psi_{jk}(x) = 2^{j/2}\psi(2^j x - k). \quad (12)$$

All expansions which we used are based on the following properties:

$$\{\psi_{jk}\}, \quad j,k \in \mathbf{Z} \quad \text{is a Hilbertian basis of } L^2(\mathbf{R})$$
$$\{\varphi_{jk}\}_{j\geq 0, k\in\mathbf{Z}} \quad \text{is an orthonormal basis for} L^2(\mathbf{R}),$$
$$L^2(\mathbf{R}) = V_0 \overline{\bigoplus_{j=0}^{\infty} W_j}. \quad (13)$$

According to machinery [4] we start with two hierarchical sequences of approximations spaces:

$$\ldots V_{-2} \subset V_{-1} \subset V_0 \subset V_1 \subset V_2 \ldots, \quad (14)$$
$$\ldots \widetilde{V}_{-2} \subset \widetilde{V}_{-1} \subset \widetilde{V}_0 \subset \widetilde{V}_1 \subset \widetilde{V}_2 \ldots,$$

and the corresponding biorthogonal expansions:

$$x^N(t) = \sum_{r=1}^{N} a_r \psi_r(t), \quad y^N(t) = \sum_{k=1}^{N} b_k \tilde{\psi}_k(t). \quad (15)$$

Let W_0 be complement to V_0 in V_1, but not necessarily orthogonal complement. Orthogonality conditions have the following form:

$$\widetilde{W}_0 \perp V_0, \quad W_0 \perp \widetilde{V}_0, \quad V_j \perp \widetilde{W}_j, \quad \widetilde{V}_j \perp W_j.$$

The translates of ψ span W_0, the translates of $\tilde{\psi}$ span $\widetilde{W}_0$. Biorthogonality conditions are

$$< \psi_{jk}, \tilde{\psi}_{j'k'} >= \int_{-\infty}^{\infty} \psi_{jk}(x)\tilde{\psi}_{j'k'}(x)\mathrm{d}x = \delta_{kk'}\delta_{jj'}, \quad (16)$$

where $\psi_{jk}(x) = 2^{j/2}\psi(2^j x - k)$. Functions $\varphi(x), \tilde{\varphi}(x-k)$ form dual pair:

$$< \varphi(x-k), \tilde{\varphi}(x-\ell) >= \delta_{kl}, \qquad < \varphi(x-k), \tilde{\psi}(x-\ell) >= 0.$$

Functions $\varphi, \tilde{\varphi}$ generate a (biorthogonal) multiresolution analysis. The translations of bases functions $\varphi(x-k)$, $\psi(x-k)$ are synthesis functions while $\tilde{\varphi}(x-\ell)$, $\tilde{\psi}(x-\ell)$ are analysis functions. Synthesis functions are biorthogonal to analysis functions. Scaling spaces are orthogonal to dual wavelet spaces. Two multiresolutions are intertwining

$$V_j + W_j = V_{j+1}, \quad \widetilde{V}_j + \widetilde{W}_j = \widetilde{V}_{j+1}.$$

These are direct sums but not orthogonal sums. So, our representation (15) for the solution on the level of resolution V_j has now the form

$$x_j(t) = \sum_k \tilde{a}_{jk}\psi_{jk}(t), \quad (17)$$

ISBN 978-3-95450-181-6

where synthesis wavelets are used to synthesize the decomposition. But $\tilde{a}_{jk}$ come from inner products with analysis wavelets. Biorthogonality yields

$$\tilde{a}_{jm} = \int x^j(t)\,\tilde{\psi}_{jm}(t)\,\mathrm{d}t. \qquad (18)$$

So, we may add this powerful construction, accelerating convergence, to our variational approach [3]. We have the modification only on the level of computing coefficients of reduced nonlinear algebraical system of equations (generic generalized dispersion relations). This biorthogonal construction is more flexible and stable under the action of a large class of operators while orthogonal construction (one hidden scale for multiresolution) is fragile. As a result, all computations are much more simpler and we accelerate the rate of convergence. In all types of Hamiltonian calculations based on some bilinear structures such an approach leads to greater success regarding traditional ones. In numerical modelling we considered (periodic) wavelet families/wavelet packets providing the minimum Shannon entropy property and exponential control of convergence in wide classes of underlying functional spaces. We obtain from (5) the following reduced system of algebraical equations (RSAE) on a set of unknown coefficients a_i of expansions (17):

$$L(S_{ij}, a, \alpha_I, \beta_J) = 0 \qquad (19)$$

which are the generalized dispersion relations generating spectra for comlex dynamics on a set of coexistent hidden internal subscales. Here the operator L is the algebraization (after the application of variational procedures) of the initial problem (5). $I = (i_1, ..., i_{q+2})$, $J = (j_1, ..., j_{p+1})$ are multiindexes, by which are labelled α_I and β_I, the other coefficients of RSAE (19):

$$\beta_J = \{\beta_{j_1 \ldots j_{p+1}}\} = \int \prod_{1 \le j_k \le p+1} \varphi_{j_k}, \qquad (20)$$

$$\alpha_I = \{\alpha_{i_1} \ldots \alpha_{i_{q+2}}\} = \sum_{i_1, \ldots, i_{q+2}} \int \varphi_{i_1} \ldots \dot{\varphi_{i_s}} \ldots \varphi_{i_{q+2}},$$

where p (q) is the degree of nominator (denominator) part of operator S (4), $i_\ell = (1, ..., q+2)$, $\dot{\varphi_{i_s}} = \mathrm{d}\varphi_{i_s}/\mathrm{d}t$. Now, when we solve RSAE (19) and determine unknown coefficients from formal expansion (17) we therefore obtain the solution of our initial problem. It should be noted that if we consider only truncated expansion with N terms then we have from (19) the system of $N \times n$ (n is the dimension of x (17)) algebraical equations and the degree of this algebraical system coincides with the degree of the initial differential system. The problem of computations of coefficients α_I, β_J (20) of the reduced algebraical system may be explicitly solved inside such a multiresolution approach. The bases functions $\psi_k(t)$ (15) are obtained via multiresolution expansions (14) and represented by compactly supported wavelets. Because affine group of translations and dilations is inside the approach, this method resembles the action of a microscope. So, according to the procedures described above, we compute contributions to the full multiscale decomposition/spectrum from each underlying hidden scale of the full (multi)resolution tower (or more exactly mathematically, filtration) or from the whole infinite scale of subspaces (6) or (14) of the underlying functional space of states. The solution (in case of the simplest non-abelian affine group of hidden symmetry) has the following form

$$x(t) = x_N^{slow}(t) + \sum_{j \ge N} x_j(\omega_j t), \quad \omega_j \sim 2^j, \qquad (21)$$

which corresponds to the full multiresolution expansion in all hidden scales.

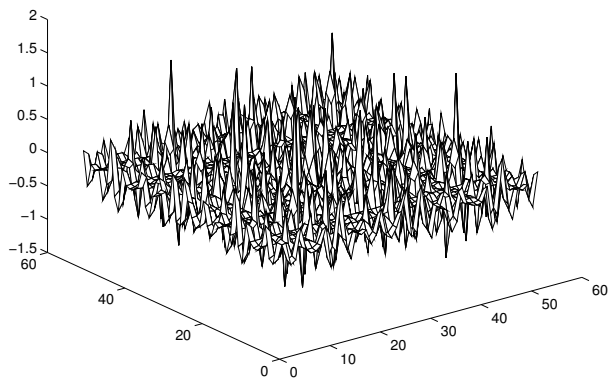

Figure 1: Multiscale representations for $x - p_x$ sections.

Formulas like (21) provide expansion into a slow part x_N^{slow} and fast oscillating parts for arbitrary N. So, we may move from coarse scales of resolution to the finest one for obtaining more detailed information about our dynamical process. The first term in the RHS of decomposition (21) corresponds on the global level of function space decomposition to the resolution space and the second one to the detail space. In this way we calculate contributions to our final decomposition (21) from each scale of resolution or each time scale. On Fig. 1 we present multiscale representations for the sections $x - p_x$ in phase space corresponding to the models (2), (3), (4) for some (multipole) parameter region. Definitely, such an analysis provides a lot of possibilities to analyze dynamics and to control the quality of particle/beam motion/orbits in accelerators.

REFERENCES

[1] Y. Meyer, *Wavelets and Operators*, CUP, 1990.

[2] A. Dragt, *Lectures on Nonlinear Dynamics*, UMD, 1996; A. Chao, *Handbook of Accelerator Physics and Engineering*, World Scientific, 1999.

[3] Antonina N. Fedorova, Michael G. Zeitlin, papers/preprints at `http://math.ipme.ru/zeitlin.html`

[4] A. Cohen, *e.a.*, *Biorthogonal bases of compactly supported wavelets*, CPAM, 45, 485, 1992.

ISBN 978-3-95450-181-6

ON A NEW APPROACH FOR DESCRIPTION OF SELF-CONSISTENT DISTRIBUTIONS FOR A CHARGED PARTICLE BEAM

O.I. Drivotin*, D.A. Ovsyannikov,
St.Petersburg State University, 7/9 Universitetskaya nab., St. Petersburg, 199034, Russia

Abstract

The present report is concerned with the problem of particle phase space distributions for a charged particle beam. A new approach is presented. It provides the possibility to specify various coordinates in the phase space. The main attention has been focused on the case where motion integrals are taken as phase coordinates. Using such coordinates, one can obtain a lot of self-consistent distributions. Some distributions for a breathing beam are considered as examples: generalized Brillouin flow, generalized KV distribution, and others. Besides, this approach allows simple graphical representation of various self-consistent distributions.

PHASE DENSITY

Main feature of the presented approach is covariant description of the particle distribution density in the phase space. The phase space particle distribution is described by a tensor density instead of the scalar distribution function. It allows specifying various coordinates in the phase space. This concept was previously formulated in the works [1, 2].

Let us consider a charged particle beam as a continuous media that occupies an open set in the phase space M. Such distribution are nondegenrate, and this cases can be regarded as most general. According to this model, particle number in an open subregion G, $G \subset M$, is a real number. Call the differential form $n(t, q)$ of degree $m = \dim M$ such that integration of the form over each open set G gives particle number in G the particle distribution density in the phase space, or the phase density:

$$\int\limits_G n = N_G.$$

Here q and t denote position in the phase space and the time correspondingly. The boundaries of G and the form n are assumed sufficiently smooth for integration being possible. Such tensor density has the following physical sense. If we take a cell in the phase space defined by m displacement vector, the density as a polylinear form acting on these displacement vectors gives us a number of particles in this cell.

Consider another case when particle are distributed on an oriented surface S in the phase space that can move, $\dim S = p$, $0 < p < m$. Call the differential form $n(t, q)$ of degree p defined on the surface S such that for any open set G, $G \subset M$,

$$\int\limits_{G \cap S} n = N_G$$

the particle distribution density for this case. This form depends on orientation of the surface. The orientation is defined by an ordered set of $m - p$ vectors. For example, orientation of a two-dimensional surface in the three dimensional space is defined by a vector, and in the four-dimensional and orientation of A change of the orientation can result in change of sign of the form components [3]. Assume that form n and the surface S are also sufficiently smooth for integration being possible.

At last, consider the case of a collection of dicrete particles. Define the scalar function

$$\delta_{q'}(q) = \begin{cases} 1, & q = q', \\ 0, & q \neq q'. \end{cases} \quad (1)$$

If q' depends on t, then this function is also function of t. All functions which values are nonzero only in finite set of points can be represented as linear combination of the functions of form (1). Restrict ourselves only to combinations with all coefficients equal to 1:

$$n(t, q) = \sum_{i=1}^{N} \delta_{q_{(i)}}(q), \qquad q_{(i)} \neq q_{(j)}, \quad \text{if} \quad i \neq j. \quad (2)$$

In this class of functions, define an operation of taking sum of function values in all points $q_{(i)}$, where the function value is nonzero:

$$\sum_{q \in G} n(t, q) \equiv \sum_{i:\, q_{(i)} \in G} n(t, q_{(i)}). \quad (3)$$

Operation defined by equation (3) is analogous to integration of the form of higher degree over G. A scalar function can be regarded as the differential form of degree 0. Therefore, equation (3) set a rule of integration of a form of degree 0 over open set G. As previously, call function of form (2) the phase density for system of pointlike particles if

$$\sum_{q \in G} n(t, q) = N_G.$$

It is easy to understand that the phase density is given by equality (2), where $q_{(i)}$ are positions of the particles in the phase space, $i = \overline{1, N}$, N is the total number of particles in the ensemble.

* o.drivotin@spbu.ru

ISBN 978-3-95450-181-6

At each instant of time t, particle dynamics equations define a vector field $f(t,q)$, which depends on the force acting on a particle.

Assume that for each t $q \in M$ there exists a unique integral line passing through point q. For example, if components of $f(t,q)$ in Cartesian coordinates are continuously differentiable with respect to coordinates and the time, it will be so. The time can be taken as a parameter for the integral lines.

In all three cases, the Vlasov equation can be written in the form

$$n(t+\delta t, F_{f\,\delta t}q) = F_{f\,\delta t}n(t,q). \tag{4}$$

Here $F_{f\,\delta t}$ denotes the operation of Lie dragging of a point or a tensor along the vector field f by the parameter increment δt.

When moving particles always lie on the same surface, that is each points of this surface belongs to the support of this distribution, equation (4) can be rewritten with use of the Lie derivative of the phase density along the vector field f, which is denoted by $\pounds_f n(t,q)$, as follows

$$\partial n/\partial t = -\pounds_f n(t,q). \tag{5}$$

SPACE OF INTEGRALS OF MOTION

Consider stationary azimuthally symmetric beam in longitudinal magnetic field in which all particles have the same longitudinal velocity v^z [4-16]. Let radius of the beam cross-section R and longituninal component of the magnetic field $B_z(z)$ slow change along beam axis: $\partial B_z/dz \ll B_z/R$. Assume also that the spatial density is uniform within each cross-section: $\varrho = \varrho_0(z), r < R$.

Under the assumptions the vector potential corresponding to the external magnetic field can be taken as

$$A_0 = A_r = A_z = 0, \quad A_\varphi = -cB_z(z)r^2/2,$$

and the vector potential of the self field of the beam as

$$A = (-U(r,z)/c, 0, 0, \beta U(r,z)/c).$$

Here r, φ, z denotes the cylindrical spatial coordinates, $\beta = v_z/c$ is reduced longitudinal velocity, $U(r,z)$ – potential of the self electric field.

Then equation of the azimuthal motion can be written in the form [3]

$$\frac{dp_\varphi}{ds} = \frac{e}{c}\frac{\partial A_j}{\partial \varphi}u^j, \tag{6}$$

and its integral in the form (6)

$$M = r^2(\varphi' + \omega_0). \tag{7}$$

Here p, u denote four-dimensional momentum and velocity of the particle, s -relativistic interval, $\omega_0 = eB_z(z)/2mc$, $M = p_\varphi/mc$, e and m charge and mass of the particle, stroke denotes differentiation with respect to s, summation over j is meant according the Einstein rule.

Equation of the radial motion has the form

$$\frac{dp_r}{ds} = -mcr\varphi'^2 + \frac{e}{\gamma c}\frac{\partial U}{\partial r} - eB_z r\varphi'. \tag{8}$$

Substituting $\varphi' = -\omega_0 + M/r^2$, $p_r = mc\,dr/ds$, and taking into account uniformity of the spatial distribution inside beam cross-section, rewrite the equation (8) in the form

$$\frac{d^2r}{ds^2} = -\omega_0^2 r + \frac{\lambda}{R(z)^2}r + \frac{M^2}{r^3} = -\omega^2 r + \frac{M^2}{r^3}. \tag{9}$$

Here

$$\omega^2 = \omega_0^2 - \frac{\lambda}{R(z)^2}, \quad \lambda = \frac{J}{J_0}\cdot\frac{1}{\beta\gamma}, \quad J_0 = \frac{2\pi\varepsilon_0 mc^3}{e},$$

J is the beam current, $\gamma = (1-\beta^2)^{-1/2}$ is reduced energy, ε_0 is electric constant.

Assume that the beam envelope $R(z)$ is determined only by particles with $M = 0$. Then the equation (9) of the radial motion can be represented in the form:

$$X' = AX, \tag{10}$$

where

$$X = \begin{pmatrix} r \\ r' \end{pmatrix}, \; A = \begin{pmatrix} 0 & 1 \\ -\omega^2 & 0 \end{pmatrix}.$$

Assume that in initial cross-section $z = z_0$ particle fill the ellipse

$$X_0^* B_0 X_0 \le 1, \; B_0 = \begin{pmatrix} a_0^{-2} & 0 \\ 0 & c_0^{-2} \end{pmatrix}.$$

Then at $z \ge z_0$, they will fill ellipses $X^* B X \le 1$, where $B = {F^*}^{-1} B_0 F^{-1}$, and F — matrizant of the system (10).

It is easy to see that

$$R^2 = (B^{-1})_{11} = a_0^{-2}F_{11}^{-2} + c_0^{-2}F_{12}^2.$$

Matrix elements F_{11} and F_{12} satisfy to the equations

$$F_{11}'' = -\omega^2 F_{11}, \; F_{12}'' = -\omega^2 F_{12}.$$

Integrating them, we get the envelope equation in the form

$$R'' = -\omega^2 R + \frac{a_0^2 c_0^2}{R^3}. \tag{11}$$

The system of equation (9), (11) can be reduced to a particular case of the generalized Ermakov system considered in the work [17]. It can be shown that

$$I = (Rr' - rR')^2 + \frac{M^2R^2}{r^2} + \frac{a_0^2c_0^2r^2}{R^2} =$$

$$(\frac{dq}{d\tau})^2 + \frac{M^2}{q^2} + a_0^2c_0^2q^2 \tag{12}$$

is integral of the motion. Here $q = r/R$, $d\tau = ds/R^2$. Integral (12) was introduced for the first time in the work [5]. When $M = 0$, $\omega = \omega(s)$ integral (12) coincides with

ISBN 978-3-95450-181-6

well known Courant-Snyder invariant [18], which is integral for the Ermakov system [19] and for its generalization [17]when $M = 0, \lambda \neq 0$.

Call the space with coordinates M and I the space of integrals of motion. It is easy to see that the set of admissible values of M and I in this space is determined by inequalities

$$2a_0c_0|M| < I \leq M^2 + a_0^2c_0^2. \qquad (13)$$

Denote this set by $\tilde{\Omega}_1$.

Consider a particle distribution of some thin slice moving along beam axis. The phase space is four-dimensional, and integrals M, I, azimuthal angle φ and particle phase on the trajectory θ can be taken as coordinates in it. Assume that particle uniformly distributed on θ and φ. Under this condition any distribution in the phase space is uniquely defined by distribution in the space of integrals of motion.

There exists a condition which should be satisfied for distribution specified in this way. Such distribution should be spatially uniform in the beam cross-section, as the integral I was obtained under this assumption.

Therefore, we should substitute a density specified in the space of integrals of motion in some integral equation.

There is a more simple way to construct new self-consistent distribution. If we know various distributions uniform inside beam cross-section, we can take their linear combination, and it will be also uniform. If a class of such distributions depends on a parameter, integrating over this parameter also gives spatially uniform distribution.

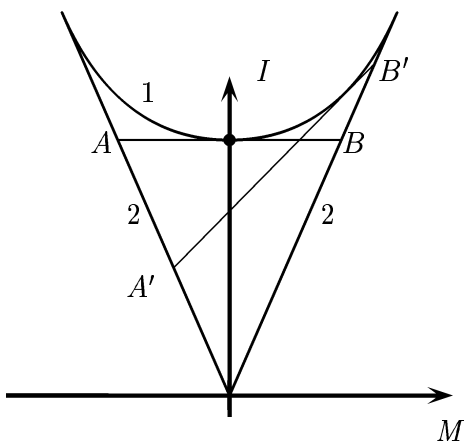

Figure 1: The set of admissible values $\tilde{\Omega}_1$ in the space of integrals of motion for a uniformly charged beam (thick lines).

SELF-CONSISTENT DISTRIBUTIONS

At first, consider a case when particles are distributed on the two-dimensional surface $M = 0$, $I = 0$. In this case the Vlasov equation (5) takes the form

$$\frac{\partial n_{\theta\varphi}}{\partial t} + \dot{\theta}\frac{\partial n_{\theta\varphi}}{\partial \theta} + \dot{\varphi}\frac{\partial n_{\theta\varphi}}{\partial \varphi} = 0.$$

The first term in the left hand side is zero as the distribution is stationary. According to the previous assumption, the second and the third terms are equal to zero. Therefore such distribution is satisfied to the Vlasov equation.

Passing to the Cartesian spatial coordinates x, y, it is easy to find that spatial distribution is uniform inside the beam cross-section. Such distribution is a generalization of the well known Brillouin flow [20].

Consider also a distribution when all particles are uniformly distributed on the segment S_k, which is tangent to upper boundary of the set $\tilde{\Omega}_1$:

$$S_k : I = kM + I_0, \quad I_0(k) = a_0^2c_0^2 - k^2/4,$$

$|k| < 2a_0c_0$, $(M, I) \in \tilde{\Omega}_1$ (segment $A'B'$ on Fig.1). Describe the particle density in the space of the integrals of motion by the differential form of the first degree $f_0 dM$, $f_0 > 0$. In the initial four-dimensional phase space such density is described by the form of degree 3 defined on the segment S_k.

As for each M, I particles are uniformely distributed on θ and φ,

$$n_{\varphi\theta M} = f_0/4\pi P(M, I),$$

where $P(M, I)$ is change of the phase θ along a half of trajectory:

$$P(M, I) = \int_{q_{\min(M,I)}}^{q_{\max(M,I)}} (I - \frac{M^2}{q^2} - a_0^2c_0^2q^2)^{1/2}\, dq = \frac{\pi}{2a_0c_0}.$$

Passing to the Cartesian coordinates $\tilde{x} = x/R$, $\tilde{y} = y/R$, we get

$$n_{\tilde{x}\tilde{y}M} = \frac{n_{\varphi\theta M}}{q|\dot{q}|}.$$

For spatial density we obtain

$$\varrho_{\tilde{x}\tilde{y}M} = \int_{M_1}^{M_2} n_{\tilde{x}\tilde{y}M}\, dM = \frac{a_0c_0f_0}{\pi} = const.$$

Therefore, for such distributions the particles are uniformely distributed inside the beam cross-section.

When $k = 0$ (segment AB on Fig.1), we have analogue of the Kapchinsky-Vladimirsky distribution for nonuniform beam. It is easy to understand that taking a linear combination of such distributions with various k we also get a solution of the Vlasov equation.

As it was mentioned before, various self-consistent distributions can be also found from the integral equation This equation can be written if we express spatial density through the density in the space of integral of motion and equate it to the density for which integrals are gotten.

REFERENCES

[1] O.I. Drivotin, "Covariant Formulation of the Vlasov equation," IPAC'2011, San-Sebastian, September 2011,

[2] O.I. Drivotin, "Degenerate Solutions of the Vlasov Equation", RUPAC'2012, St.-Petersburg, September 2012,

ISBN 978-3-95450-181-6

[3] O.I. Drivotin, Mathematical Foundations of the Field Theory, (St.-Petersburg: Publ. Comp. of St.-Petersburg State Univ., 2010) (in russ.).

[4] O.I. Drivotin, D.A. Ovsyannikov, "Determination of the Stationary Solutions of the Vlasov Equation for an Axially Symmetric Beam of Charged Particles in a Longitudinal Magnetic Field", USSR Comp. Math. Math. Phys. 27 (1987) 62-70.

[5] O.I. Drivotin, D.A. Ovsyannikov, "New Classes of Stationary Solutions of Vlasov's Equation for an Axially Symmetrical Beam of Charged Particles of a Constant Density", USSR Comp. Math. Math. Phys. 29 (1989) 195-199.

[6] O.I. Drivotin, D.A. Ovsyannikov, "On Self-Consistent Distributions for a Charged Particles Beam in a Longitudinal Magnetic Field", Dokl. Phys. 39 (1994) 1-4.

[7] O.I. Drivotin, D.A. Ovsyannikov, "New Classes of Uniform Distributions for Charged Particles in Magnetic Field", PAC'97, Vancouver, Canada, 1997, 1943-1945.

[8] O.I. Drivotin, D.A. Ovsyannikov, "Self-Consistent Distributions of Charged Particles in Magnetic Field.I", Vestnik Sankt-Peterburgskogo Universiteta, Ser.10: Applied Math. 1 (2004) 3-15 (in russ.).

[9] O.I. Drivotin, D.A. Ovsyannikov, "Self-Consistent Distributions of Charged Particles in Magnetic Field.II", Vestnik Sankt-Peterburgskogo Universiteta, Ser.10: Applied Math. 2 (2004) 70-81 (in russ.).

[10] O.I. Drivotin, D.A. Ovsyannikov, "Modeling of Self-Consistent Distributions for Longitudinnaly Non-Uniform Beam", Nucl. Instr. Meth. Phys. Res. A 558 (2006) 112-118.

[11] O.I. Drivotin, D.A. Ovsyannikov, "Self-Consistent Distributions for Charged Particle Beam in Magnetic Field", Int. J. Modern Phys. A 24 (2009) 816-842.

[12] O.I. Drivotin, D.A. Ovsyannikov, "Solutions of the Vlasov Equation for Charged Particle Beam in Magnetic Field", Izvestiya Irkutskogo Gosudarstvennogo Universiteta, Ser. Math., 6(4) (2013) 2-22 (in russ.).

[13] D.A. Ovsyannikov, O.I. Drivotin, Modeling of Intensive Charge Particle Beams, (St.-Petersburg: Publ. Comp. of St.-Petersburg State Univ., 2003) (in russ.).

[14] O.I. Drivotin, D.A. Ovsyannikov, "Exact Solutions of the Vlasov Equation in Magnetic Field", LINAC'2014, Geneva, September 2014.

[15] O.I. Drivotin, D.A. Ovsyannikov, "Space of Motion Integrals in Problems on Self-Consistent Distributions". ICAP'2015, Shanghai, 2015.

[16] O.I. Drivotin, D.A. Ovsyannikov, "Stationary Self-Consistent Distributions for a Charged Particle Beam in Longitudinal Magnetic Field". Phys.Part.Nuclei 47 (2016) 884.

[17] J.R. Ray, J.L. Raid "More exact invariants for the time-dependent harmonic oscillator", Phys.Lett. 71 (1979) 317-318.

[18] E.D. Courant, H.S. Snyder, "Theory of Alternating-Gradient Synchrotron", Annals of Physics 3 (1958) 1-48.

[19] V.P. Ermakov, "Differential Equations of the Second Order. Integrability Conditions in Finite Species", Univ. Izvestiya (Kiev) 20(9) (1880) 1-25 (in russ.).

[20] L. Brillouin, "A Theorem of Larmor and its Importance for Electrons in Magnetic Field", Phys.Rev. 67 (1945) 260-266.

ISBN 978-3-95450-181-6

FORMATION OF A GIVEN DISTRIBUTION OF THE BEAM IN THE PERIODIC CHANNEL

Serge N. Andrianov*, Nikolai Edamenko,
St. Petersburg State University, 7/9 Universitetskaya nab., St. Petersburg, 199034 Russia

Abstract

Accelerators and beam transport systems are the most widely used in various fields of fundamental and applied science. This leads to the need for construction of correct models of the corresponding objects and processes. In this paper we consider the problem of forming a beam with a given distribution. Note that similar requirement to the beam occurs in circular accelerators, and in the beam transport systems for various fields of physics, chemistry, biology and so on. Special attention is paid to the development of effective mathematical methods and computer programs to modeling of control systems to ensure the necessary requirements to the beam.

INTRODUCTION

At the moment, we have a long experience in the study of the dynamics of the distribution of particles in the beam in a periodic channel (see, eg, [1], [2], [3]). It is well known that variety of self-consistent density distributions can be built in a uniform focusing channel, see [4], [5]. However, the question of purposeful formation of the desired particle distribution (for example, in the configuration space) in our opinion was not sufficiently developed in theory and practice of accelerator systems, despite the relatively high demand for similar tasks. Requirements for particle beams in modern accelerators, are constantly increasing. First of all, it concerns aspects of modeling optimal systems. Secondly, the inclusion of non-linear control elements for targeted management to produce beams with the specified parameters.

In this direction there are some "basic" approaches. The first type (direct) is based on a careful study of the influence of various factors on the beam dynamics. The second method uses optimization techniques, in which there essentially are solved the inverse problems. Indeed, in this case, we can formalize the requirements for the beam parameters and to implement the search process of optimal solutions for ensuring specified requirements with a given accuracy. It should be noted that inverse problems are a class of ill-posed problems requiring the construction of special methods of solution. However, in both methods there are some common features. In the following we briefly describe the formalism in which the beam itself and the control system of the accelerator are described. This formalism is based on an approach based on the matrix representation for evolution operators [5] on the one hand and different forms of descriptions of the beam as a collective object.

* s.andrianov@spbu.ru

CONCEPT OF MATRIX FORMALISM

Let us briefly describe the essential features of the mathematical formalism of the matrix formalism and its features that allow realizing for effective computational experiments. Following [5] for the nonlinear ordinary differential equations describing the evolution of the particles in the accelerator we can write

$$\frac{d\mathbf{X}}{ds} = \mathbf{F}^{\rm ext}(\mathbf{B}^{\rm ext}(\mathbf{X}, s, \mathbf{E}^{\rm ext}(\mathbf{X}, s), \mathbf{X}, s) + \mathbf{F}^{\rm self}(\langle f(\mathbf{X}, s)\rangle_{\mathfrak{M}}, \mathbf{X}, s), \quad (1)$$

where $\langle f(\mathbf{X}, s)\rangle_{\mathfrak{M}}$ means that the distribution function is included in the $\mathbf{F}$ via integral and the integration is over volume occupied by particles $\mathfrak{M} = \mathfrak{M}(s)$, where s is the length measured along the reference orbit. According to [5] one can introduce the evolution operator $\mathcal{M}(t\,|\,t_0; \mathbf{F})\colon \mathbf{X}_0 \to \mathbf{X}(t)$ in by equation (1). Given the property of the evolution operator one can write

$$\mathbf{F}^{\rm self}(\langle f(\mathbf{X}, t)\rangle_{\mathfrak{M}}, \mathbf{X}, t) = \mathbf{F}^{\rm self}(\langle f_0(\mathcal{M}^{-1}(t\,|\,t_0, \mathbf{F}) \circ \mathbf{X}_0)\rangle_{\mathfrak{M}_0}, \mathbf{X}, t). \quad (2)$$

In accordance with the equations (1) and (2) one can write the following integral operator equation

$$\mathcal{M}\left(t\,|\,t_0; \mathcal{V}^{\rm ext} + \mathcal{V}^{\rm self}\right) = \mathcal{I}d + \int_{t_0}^{t} \left(\mathcal{V}^{\rm ext}(\tau) + \mathcal{V}^{\rm self}(\tau)\right) \circ \mathcal{M}\left(\tau\,|\,t_0; \mathcal{V}^{\rm ext}(\tau) + \mathcal{V}^{\rm self}(\tau)\right) d\tau. \quad (3)$$

We note that equation (3) is an integral equation of Volterra–Urysohn of type II (see, eg, [6]), as in fact the control system (the transportation system) – the control object (beam) is covered by the feedback. It proves that the sequence $\mathcal{M}^k$ converges (in some sense) to some element $\mathcal{M}^{\rm fin}$, and one can install the identity $\mathcal{M}^{\rm fin} = \mathcal{A} \circ \mathcal{M}^{\rm fin}$. We should note that similar approach not only allows us to use different forms describe the beam dynamics, taking into account the impact of its own charge but and allows us to build different methods of description of the beam dynamics, taking into account the impact of their own charge. The similar approach allows us to build different forms describe the beam dynamics, taking into account the impact

ISBN 978-3-95450-181-6

of their own charge. In particular, for a given initial distribution function we can introduce different presentation of the generalized matrix of envelopes

$$\mathfrak{S}_0^{ik} = \int\limits_{\mathfrak{M}_0} f_0(\mathbf{X})\mathbf{X}^{[i]}\left(\mathbf{X}^{[k]}\right)^{\mathrm{T}} d\mathbf{X},$$

where the $\mathfrak{M}_0$ is an initial set in the phase space.

As an example, consider the case of the elliptical beam

$$\mathbf{G}_0(\mathbf{X},\varepsilon) = \mathbf{X}^{\mathrm{T}}\,\mathbb{A}_0\,\mathbf{X} - \varepsilon, \quad 0 < \varepsilon \le 1,$$

where $\mathbb{A}_0$ is the matric defining the initial beam distribution. We shall seek the solution of equations of motion taking into account the space charge in the following form $\mathbf{X}(t) = \sum\limits_{k=1}^{N} \mathbb{M}^{1k}(t|t_0)\mathbf{X}_0^{[k]}$, and correspondingly $\mathbf{X}_0 = \sum\limits_{k=1}^{N} \mathbb{T}^{1k}(t|t_0)\mathbf{X}^{[k]}(t)$, where $\mathbb{M}^{1k}$ and $\mathbb{T}^{1k}$ are polynomials of k-th order.

In this case, the transformation matrix of the envelopes can be represented as follows

$$\mathbf{G}(\mathbf{X},t) = \left(\sum_{k=1}^{\infty}\mathbb{T}^{1k}\mathbf{X}^{[k]}\right)^{\mathrm{T}}\mathbb{A}_0\left(\sum_{j=1}^{\infty}\mathbb{T}^{1j}\mathbf{X}^{[j]}\right) - \varepsilon =$$

$$\sum_{k=1}^{\infty}\sum_{j=1}^{\infty}\left(\mathbf{X}^{[k]}\right)^{\mathrm{T}}\left(\left(\mathbb{T}^{1k}\right)^{\mathrm{T}}\mathbb{A}_0\mathbb{T}^{1j}\right)\mathbf{X}^{[j]} - \varepsilon =$$

$$\sum_{k=1}^{\infty}\sum_{j=1}^{\infty}\left(\mathbf{X}^{[k]}\right)^{\mathrm{T}}\mathbb{A}^{kj}\mathbf{X}^{[j]} - \varepsilon = \left(\mathbf{X}^{\infty}\right)^{\mathrm{T}}\mathbb{A}^{\infty}\mathbf{X}^{\infty} - \varepsilon, \quad (4)$$

$$\mathbb{A}^{\infty} = \left(\mathbb{A}^{kj}\right)_{k,j\ge 1}, \quad \mathbb{A}^{kj} = \left(\mathbb{T}^{1k}\right)^{\mathrm{T}}\mathbb{A}_0\mathbb{T}^{1j},$$

where $\mathbb{A}^{\infty}$ is a matrix definding the current distribution of particles in beam considering the nonlinear effects. The equality (4) one can write as the following equation

$$\frac{d\mathfrak{S}^{ik}}{dt} = \sum_{l=i}^{\infty}\mathbb{P}^{il}\mathfrak{S}^{lk} + \sum_{l=k}^{\infty}\mathfrak{S}^{lk}\left(\mathbb{P}^{kl}\right)^{*},$$

or by combining, for $\mathfrak{S}^{\infty}$:

$$\frac{d\mathfrak{S}^{\infty}(t)}{dt} = \mathbb{P}^{\infty}(t)\mathfrak{S}^{\infty}(t) + \mathfrak{S}^{\infty}(t)\left(\mathbb{P}^{\infty}(t)\right)^{*},$$

where, as before, $\mathbb{P}^{\infty}(t)$ is an upper triangular matrix, $\mathbb{P}^{ik}$ ($\mathbb{P}^{ik} \equiv 0\ \forall\ i > k$) are the block matrices.

The initial matrix $\mathfrak{S}_0^{ik}$ or $\mathfrak{S}_0^{\infty}$ can be calculated according to equations

$$\mathfrak{S}_0^{ik} = \int\limits_{\mathfrak{M}_0} f(\mathbf{X}_0)\mathbf{X}_0^{[i]}\left(\mathbf{X}_0^{[k]}\right)^{*} d\mathbf{X}_0,$$

$$\mathfrak{S}_0^{\infty} = \int\limits_{\mathfrak{M}_0} f(\mathbf{X}_0)\mathbf{X}_0^{\infty}\left(\mathbf{X}_0^{\infty}\right)^{*} d\mathbf{X}_0.$$

After this we implement the method of successive approximations using the method of virtual changing of beam parameters $\mathfrak{S}_1^{ik} = \alpha\mathfrak{S}_0^{ik} + (1-\alpha)\,\mathfrak{S}_0^{ik}$, $0 < \alpha < 1$. This process is ended when there the following inequality

$$2\frac{\|\mathfrak{S}_1^{ik} - \mathfrak{S}_0^{ik}\|_c}{\|\mathfrak{S}_1^{ik} + \mathfrak{S}_0^{ik}\|_c} < \varepsilon^{ik}$$

where for any enough small $\varepsilon^{ik} \ll 1$. We should note that the order of nonlinearities is defined by our knowledges about the transport system (see the next section).

We also note that one can use the some another presentatiom for beam description (see, for example, [5]), in particular using a particle distribution function $f(\mathbf{X},t)$.

BEAM FORMING WITH ALMOST UNIFORM DISTRIBUTION

Let be the next function describe some particles distribution in phase space

$$f_0(\mathbf{X}) = Q_{2m}(\mathbf{X})e^{-P_{2n}(\mathbf{X})}, \quad (5)$$

where $Q_{2m}(\mathbf{X})$, $P_{2n}(\mathbf{X})$ are polynomials of the $2m$-th and $2n$-th order correspondingly. Coefficients of these polynomials are determined from experimental data fully or partly. In the last case the free coefficients can be determined from other information or used as control parameters. At the base of our approach we use the methods which briefly described in the previous sections.

According to [5] one can write

$$f(\mathbf{X},t) = P_{N_1}\left(\sum_{k=1}^{N}\sum_{j=1}^{N}\left(\mathbf{X}^{[k]}\right)^{\mathrm{T}}\left(\mathbb{T}^{1k}\right)^{\mathrm{T}}\mathbb{A}_0\mathbb{T}^{1j}\mathbf{X}^{[j]}\right)\times$$

$$\exp\left(-\frac{Q_{N_2}\left(\sum\limits_{j=1}^{N}\left(\mathbf{X}^{[k]}\right)^{\mathrm{T}}\left(\mathbb{T}^{1k}\right)^{\mathrm{T}}\mathbb{A}_0\mathbb{T}^{1j}\mathbf{X}^{[j]}\right)}{2\sigma^2}\right). \quad (6)$$

As an example, let us consider the formation of the current distribution of the beam in the nonlinear channel (to the third order of nonlinearities). For testing (besides of the usual computer codes) we also use systems for symbolic computation (packages Mathematica and Maple) for the analysis of possible functions of beam distributions. At the first stage, we search the matrix elements included in the matrices $\mathbb{M}^{1k}$ for $1 \le k \le n$ for some n (in our example we restricted by $n = 3$). In general the researcher must solve the inverse problem of determining the values of the control parameters for the channel transport in view of the desired output beam distribution in coordinate space. This task can be formulated as a problem with the feedback and demands quite time-consuming necessary for computing that leads us to using of modern computer systems. As an example, we consider the formation of the current distribution of the beam in the nonlinear channel (up to third

ISBN 978-3-95450-181-6

order of nonlinearity). Using packages Mathematica and Maple help us to provide visual representation of the calculations for the analysis of possible beam distributions. At the first stage, the search matrix elements for the matrices $\mathbb{M}^{1k}$ for $1 \leq k \leq n$ for some n (in our example we restricted by third order). The investigator should solving the inverse problem for determining the values of the control parameters for the channel transport in view of the desired output beam distribution in coordinate space. As this problem with the feedback, then it leads us to enough time-consuming computing. That is why it is necessary usage modern computer systems with parallel and distributed operations.

CONCLUSION

In the conclusion we should note that computational accelerator physics has significantly changed and is broadened over the last years. These changes are first of all due to the advent new methods of high performance computing (parallel and distributed) and in connection with the capabilities of modern packages for symbolic computations. In particular many new mathematical methods appeared namely largely due to the packages for symbolic computations. These new models and instruments can provide not only overall accuracy of mathematical and computer modelling, but better understanding of the physical processes in accelerators. Finally, the use of modern computational frameworks provide an opportunity to developers to concentrate first of all on the mathematics and physics. In the article we give some pictures (see Fig. 1, Fig. 2, Fig. 3) that not only demonstrate possibilities of above described approaches, but and demonstrate the transfer from Gauss distribution into a distribution with a nearly uniform distribution (in the configuration space). The necessary computations were realized up to third order of nonlinearity. We also note that we considered the beam parameters and the structure of cyclic accelerator with parameters are enough close to the structure of the Nuclotron in JINR (Russia).

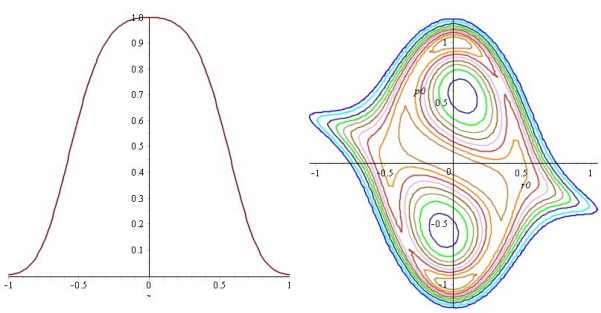

Figure 1: On the picture there are presented: on the left – an almost Gauss distribution of the beam in the x-section (as an example); on the right – the example of beam transformation after tens of thousands of revolutions in the $x - p_x$ section (view from "above").

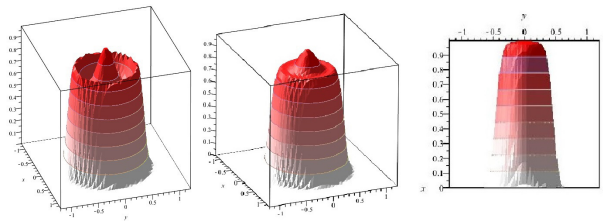

Figure 2: On the picture the successive changes of distribution of beam particles are presented (in the $x - y$ plane). The left two pictures present the sequential (in time) changing of distribution for particles of beam in x- and y-planes. The almost uniform distribution (the goal of the transformations) is demonstrated on the third picture.

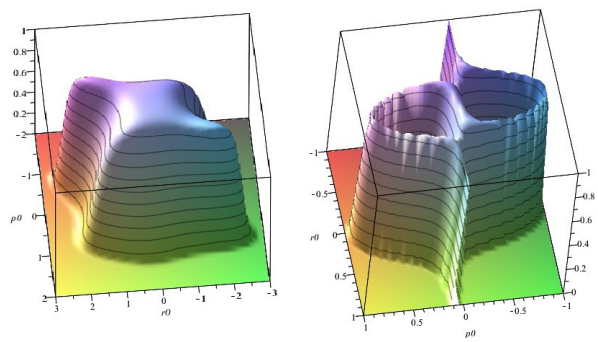

Figure 3: On the picture there are presented examples of distribution of particles in the $x - p_x$ plane. On the left picture – an intermediate stage of the fillamentation process, on the right picture – some next stage of the fillamentation process (after thousands of turns of the beam evolution).

REFERENCES

[1] N.Pichoff, G.Haouat, P.Y.Beauvais, J.M.Lagniel, R.Ferdinand, S.Nath, S.Joly Transverse-profile equilibrium in a space-charge-dominated beam 1st Asian Particle Accelerator Conference, Tsukuba, Japan, 23 - 27 Mar 1998, pp.617

[2] R.A.Kishek, S.Bernal, P.G.O Shea, M.Reiser, I. Haber Transverse space-charge modes in non-equilibrium beam Nuclear Instruments and Methods in Physics Research A 464 P. 484-492, 2001.

[3] J.Struckmeier, I.Hofmann Generation of emittance conserving non-kv distributions in periodic focusing channels. http://accelconf.web.cern.ch/AccelConf/e98/PAPERS/THP43G.PDF

[4] M.Reiser Theory and Design of Charged Particle Beams. Wiley-VCH Verlag GmbH & Co. KGaA 2008

[5] S.N. Andrianov, Dynamical Modeling of Particle Beam Control Systems. SPbSU. SPb. 2004 (in Russian).

[6] Urysohn, P. S. On a type of nonlinear integral equation. Mat. Sb., 31. P. 236–355, 1924.

ISBN 978-3-95450-181-6

PROGRAM COMPLEX FOR MODELING OF THE BEAM TRANSVERSE DYNAMICS AND ORBIT CORRECTION IN NUCLOTRON, LHEP JINR

I.V. Antropov, V.A. Kozynchenko*, V.O. Khomutova, D.A. Ovsyannikov,
Saint-Petersburg State University, Saint-Petersburg, Russia
I.L. Avvakumova, O.S. Kozlov, V.A. Mikhaylov, A.O. Sidorin, G.V. Trubnikov,
JINR, Dubna, Moscow Region, Russia

Abstract

Program complex for modelling of transverse dynamic of particle beams and orbit correction at Nuclotron synchrotron (LHEP JINR) is considered in current work. The program complex provides calculation of transverse dynamic of charged particle beams in Nuclotron and its axis, based on linear model with transport matrix of lattice elements, calculation of Nuclotron Twiss parameters, acceptance and emittance of the beam. A possibility to optimize the location of beam position monitors (pick-up) and multipole correctors is foreseen as well as calculation of the orbit with measuring data of pick-up stations of Nuclotron. Program complex includes realizations of orbit correction algorithms with response matrix and provides correction of the orbit in Nuclotron. User's graphic interface provides interaction of user with program complex, including performance on demand of the user of separate functions of the program complex, providing input and maintenance of parameters, download from file and record into the file of parameters and calculation results, graphical view of the calculations results in program complex. Program software environment is integrated with MAD-X program (upload, processing of data to and from, visualization). Format of input and output data is compatible with relevant MAD-X format.

INTRODUCTION

At present, in the Joint Institute for Nuclear Research (Dubna, Russia) successfully operates the Nuclotron – a synchrotron for accelerating beams of multicharged ions, protons and deuterons [1]. To reduce losses in the Nuclotron, various orbit correction methods are used [2]. When studying the problem of orbit correction, the necessity has arisen for creating a package of programs that would allow making cooperative use of both the accumulated experience and new developments. The program comlex considered in the paper includes an extensive graphical interface and a variety of tool kits, methods and algorithms that allows the researcher mostly to be focusing on the model development. The package also includes the BDO Nuclotron laboratory, a general description of which is the subject of this article.

DESCRIPTION OF THE PROGRAM COMPLEX

The program complex consists of a control program, laboratories and libraries.

BDO Shell [3],[4] – a control program having the rich graphical user interface, a library of model parameters, and system functions. One may refer to the specific features of this product the following:

- the possibility of dividing the calculation process into stages with specifying the groups of input and output data files;
- the ability to automate the simulation process for a given parameter ranges;
- using various case studies with pre-described sets of parameters, input and output data files, settings of calculation stages.

BDO Nuclotron - laboratory for modeling and optimization of particle beams dynamics in the Nuclotron. The laboratory consists of several models allowing computation of the linear transverse dynamics of the beam center of gravity, the beam transverse dynamics, and the structural features of the Nuclotron. There is also a library of initial distributions, and a library of the correction methods for a closed orbit.

MODULES

The Module for Calculating the Lateral Dynamics of the Center of Gravity of the Beam in the Nuclotron Based on a Linear Model

The module for calculating a transverse beam dynamics in the Nuclotron provides computing the lateral dynamics of the center of gravity of the beam at the Nuclotron that is based on a linear model and uses the transport matrices of structural elements of the Nuclotron (dipole bending magnets, focusing and defocusing quadrupole lenses, drift gaps, and multipole magnetic correctors). When calculating the dynamics, the structural elements intended for the slowed-down beam extraction from the Nuclotron channel are not considered. One can add other structural elements of the Nuclotron, as well as change the location of pick-up displays and multipole correctors. When calculating the dynamics, the own beam field is ignored. It is possible to take into account the errors of the magnetic field in the elements of the transport matrix. The module provides for the formation of the response matrix being made on the base of computing the transverse

*v.kozynchenko@spbu.ru

ISBN 978-3-95450-181-6

dynamics provided that a user specifies the locations of pick-up displays and multipole correctors in the drift gaps.

The Module for Calculating the Beam Envelope and Structural Functions of the Nuclotron

The module carries out the calculation of beam dynamics in Twiss parameterization, the calculation of the structural functions of the Nuclotron and the calculation of the acceptance channel of the Nuclotron.

The Module for Calculating the Orbits of the Nuclotron

The module calculates the Nuclotron orbits using the orbit data measured by the pick-up monitors of the Nuclotron. The orbit is calculated over the whole Nuclotron ring, including the insides of its structural elements. When calculating an orbit, it is possible to exclude the readings of some pick-up monitors.

Library of Functions Implementing the Initial Distributions

The library contains functions that implement the initial uniform and normal distributions of the beam. The transverse distribution is formed on the basis of specifying an input beam emittance.

The Module for Calculating a Transverse Beam Dynamics in the Nuclotron Using a Linear Model

The module for calculating a transverse beam dynamics in the Nuclotron calculates transverse beam dynamics in the Nuclotron on the basis of a linear model with the usage of the transport matrix of the Nuclotron structural elements (dipole bending magnets, focusing and defocusing quadrupole lenses, drift gaps and multipole magnetic correctors) without taking into account the structural elements for slowed-down beam extraction from the Nuclotron channel. The beam is represented by a set of model particles. One can add other structural elements of the Nuclotron, as well as change the location of pick-up monitors and multipole correctors. When calculating the dynamics, the own beam field is ignored. It is possible for the magnetic fields errors to be taken into account in the transport matrix elements. The initial distribution is generated using the library of the initial distribution functions. The possibility of calculating the beam emittance is provided.

Library of Functions Implementing Various Methods of the Orbit Correction

The library contains software implementations of the algorithms of orbit correction using the response matrix: SVD [2] and MICADO. The SVD method provides the possibility of determining the currents in the correctors based on the use of the pseudoinverse matrix for the response one. Pseudoinverse matrix is calculated using the singular decomposition of the response matrix. MICADO method allows determining the most effective correctors from the available ones. One can add other methods of orbit correction.

The Module of Orbit Correction Using the Response Matrix

The module provides an orbit correction in the Nuclotron using the library of correction methods. The orbit correction is made on the basis of the response matrix. The response matrix can be calculated using the results of numerical simulation of the dynamics of the beam center of gravity or can be obtained on the results of measurements of the position of a beam center of gravity in the pick-up monitors of the Nuclotron.

CONCLUSIONS

In the presented program complex, implemented are the models for calculating the transverse dynamics and the models of the beam orbit correction in the Nuclotron based on the use of the response matrix. To ensure the effective orbit correction, the suggestion has been made to complement the software package with the optimization models that allow determining the real errors of the transport matrices of the Nuclotron structural elements. It is also planned to add new optimization methods for the orbit correction.

REFERENCES

[1] A.O. Sidorin et al. “Status of the Nuclotron, ” RuPAC 2012 Contributions to the Proceedings - 23rd Russian Particle Accelerator Conference 2012. C. 117-119.

[2] Y. Chung, G. Decker, and K. Evans, “Closed orbit correction using singular value decomposition of the response matri, ” PAC 1993.

[3] D.A. Ovsyannikov, A.D. Ovsyannikov, I.V. Antropov, V.A. Kozynchenko, “Software complex BDO-RFQ,” 2015 International Conference on "Stability and Control Processes" in Memory of V.I. Zubov, SCP 2015 - Proceedings, p.335-337.

[4] D.A. Ovsyannikov, A.D. Ovsyannikov, I.V. Antropov, V.A. Kozynchenko, “BDO-RFQ Program Complex of Modelling and Optimization of Charged Particle Dynamics,” Journal of Physics: Conference Series 2016.

ISBN 978-3-95450-181-6

APPLICATION OF GPGPUs AND MULTICORE CPUs IN OPTIMIZATION OF SOME OF THE MPDROOT CODES*

A. Fatkina#, O. Iakushkin, N. Tikhonov, St. Petersburg State University, St. Petersburg, Russia

Abstract

We analyzed the ways to optimize MPDRoot algorithms using existing solutions from external libraries. We also examined the libraries designed to work with graphics accelerators and multi-core CPUs, such as cuRAND, cuFFT and OpenCL FFT.

The paper describes the ways to expedite a portion of Kalman filter by transferring it to GPUs or multi-core CPUs using the implementation included into the MPDRoot package.

INTRODUCTION

MPD (Multi Purpose Detector) is a part of NICA (Nuclotron-based Ion Collider fAcility) [1]. MPDRoot is a framework based on ROOT and FairRoot technologies. It is designed to simulate experiments conducted on MPD and to analyze the resulting data. According to the MPD documentation, collected data can be huge. Fast data processing is necessary to cope with extreme data sets. Thus it is a task of crucial importance that algorithms work well in parallel and distributed environments [2-6]

In this paper, we look into how Graphic Processing Units (GPUs) and multicore CPUs may be applied in MPDRoot project optimization.

PERFORMANCE ANALYSIS OF MPDROOT FRAMEWORK TESTS

The following methods were used to analyze MPDRoot framework:

- Doxygen utility was used to generate classes and functions dependency graphs. It was also used to code navigation.
- ValgrindCallgrind tool was used to profile the package. By using this we got callgraphs for MPDRoot tests.

We selected some algorithms that can be ported on coprocessor architectures and seems to be optimizable.

PROPOSED OPTIMIZATIONS

The following algorithms were considered:

- Fast Fourier Transform;
- Random number generation;
- Kalman Filter.

Figure 1 shows calls of the Rndm() function in the ROOT framework. It is called over 32 million times in the runMC test. The function employs MT (Mersenne Twister) algorithm described in [7].

Random Number Generation

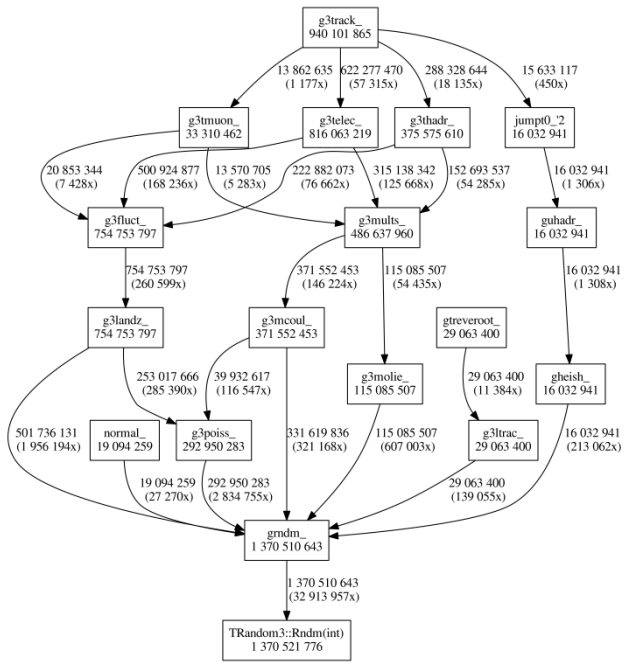

Figure 1: Profiling data - Random number generation.

There is a modified version of this algorithm — SFMT (SIMD-oriented Fast Mersenne Twister) [8], which is twice as fast owing to the SIMD (Single Instruction Multiple Data) principle. It should be noted that the version of MT described in that paper can only be executed on a CPU with a vector processing unit (VPU).

CuRAND library may be used as an alternative to ROOT-based MT. It makes it possible to generate random numbers on GPGPU (general-purpose computing for graphics processing units) using CUDA architecture. The library provides a wide range of generators including MT and MTGP (Mersenne Twister for Graphic Processors) [9].

The use of the cuRAND library to generate random numbers in the GEANT4 framework was proposed at the Annual Science Meeting in 2013 [10]. This approach can either be integrated into the MPD Root project directly with the cuRAND library or indirectly by using GEANT4.

Kalman Filter

MPD Root reconstructs the particles' tracks using Kalman filter. This algorithm is sequential and uses matrixes.

* supported by SPbU (Saint Petersburg State University) grants 9.37.157.2014, 0.37.155.2014 and Russian Foundation for Basic Research grant (project no. 16-07-01113 and no. 16-07-01111).

st035020@student.spbu.ru

ISBN 978-3-95450-181-6

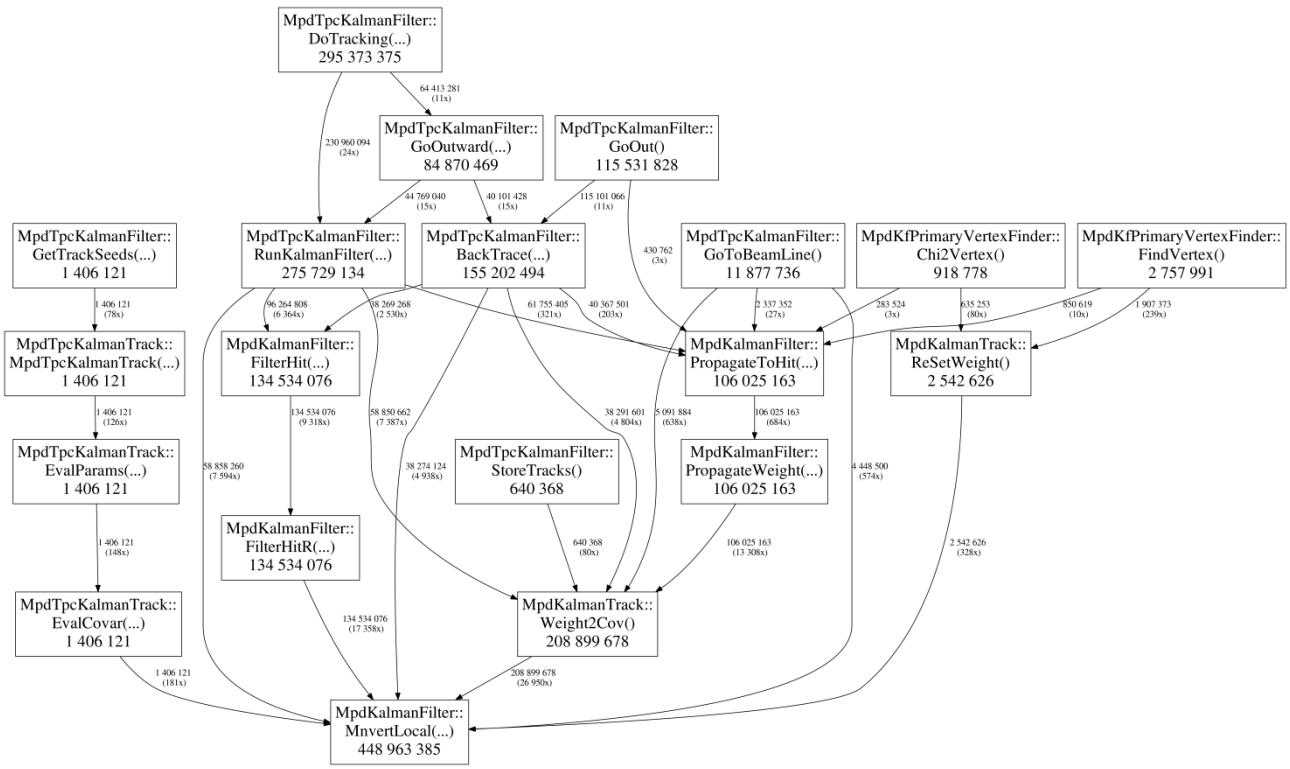

Figure 2: Profiling data - Kalman Filter: MnvertLocal function.

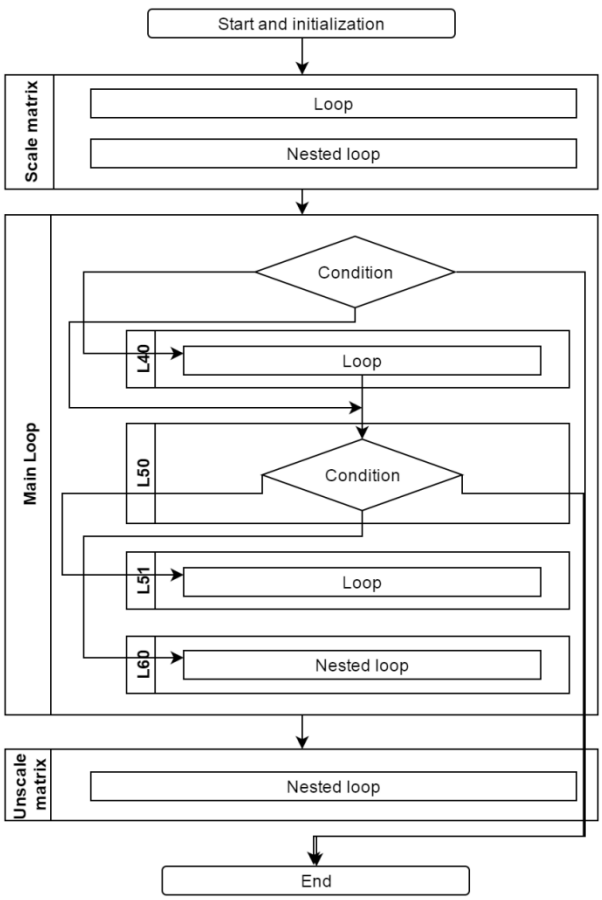

Figure 3: MnvertLocal function scheme.

Figure 2 shows the call graph of MpdKalmanFilter::MnvertLocal() function, which implements the Kalman filter algorithm. It utilizes nested loops to invert matrixes. Figure 3 shows a schematic representation of MnvertLocal function algorithm. Each loop executes similar instructions independent of the values obtained during the previous iterations. They can, therefore, be distributed to multiple cores of the CPU and vectorized, or transferred to the GPGPU.

An alternative way to expedite Kalman filter track reconstruction algorithm is described in [11]. In the paper, the authors proposed using SIMD instructions to optimize the Kalman filter in the CBM@FAIR (Compressed Baryonic Metter) experiment. They tested the algorithm before and after optimization and saw a major improvement: the authors managed to increase the algorithm execution speed by a factor of 120.

Fast Fourier Transform

FFTW library is used in the digitizing algorithm of the TPC detector in TVirtualFFT class, a Fourier transformation shell in the ROOT framework. It provides interfaces to work with OpenMP and MPI technologies. However, it does not support graphic co-processors. There are multi-core-oriented libraries, such as cuFFT and clFFT, which implement algorithms included into FFTW.

However, the use of multiple cores does not necessarily influence the execution time of code segments. In some cases, it can even increase their total processing time. For

ISBN 978-3-95450-181-6

instance, according to the available tests, Fourier transform algorithm represents a minor part of MPDRoot project compared to the other package components (less than 0.01%). This allows to conclude that running these code segments on multiple cores will not reduce the test processing time.

CONCLUSION

In this paper, we consider some of the possible optimizations for MPDRoot project with coprocessor technologies. We proposed some recommendations based on both external libraries and algorithms based on MPDRoot codes.

ACKNOWLEDGMENT

This research was partially supported by SPbU (Saint Petersburg State University) grants 9.37.157.2014, 0.37.155.2014 and Russian Foundation for Basic Research grant (project no. 16-07-01113 and no. 16-07-01111).

REFERENCES

[1] MPD Collaboration, MPD Concept Design Repot; http://mpd.jinr.ru

[2] A.Zinchenko, Y.Murin, V.Kondrat'ev, N.Prokof'ev, "Modeling of the internal tracking system of the NICA/MPD detector." Physics of Particles and Nuclei Letters, 13(4), pp.483-491 (2016).

[3] O. Iakushkin, "Intellectual scaling in a distributed cloud application architecture: A message classification algorithm", Stability and Control Processes in Memory of VI Zubov (SCP), 2015 International Conference, IEEE, p. 634-637. (2015).

[4] S. Abrahamyan, S. Balyan, A. Muradov, V. Korkhov, A. Moskvicheva, and O. Iakushkin. "Development of M-Health Software for People with Disabilities." In International Conference on Computational Science and Its Applications, Springer International Publishing, p. 468-479(2016).

[5] O. Iakushkin, O. Sedova, G. Valery, "Application Control and Horizontal Scaling in Modern Cloud Middleware.", Transactions on Computational Science XXVII, Springer Berlin Heidelberg, p. 81-96.(2016).

[6] Y. Shichkina, A. Degtyarev, D. Gushchanskiy, and O. Iakushkin. "Application of Optimization of Parallel Algorithms to Queries in Relational Databases.", International Conference on Computational Science and Its Applications, Springer International Publishing, p. 366-378 (2016).

[7] M. Matsumoto, N. Takuji, "Mersenne twister: a 623-dimensionally equidistributed uniform pseudo-random number generator", ACM Transactions on Modeling and Computer Simulation, Vol. 8 No. 1 p. 3-30 (1998).

[8] M. Saito, M. Matsumoto, "SIMD-oriented Fast Mersenne Twister: a 128-bit Pseudorandom Number Generator", Monte Carlo and Quasi-Monte Carlo Methods 2006, p. 607 — 622 (2008).

[9] M. Saito, M. Matsumoto, "Variants of Mersenne Twister Suitable for Graphic Processors" ACM Transactions on Mathematical Software, Vol. 39 No. 2 (2013).

[10] Soon Yung Jun, J. Apostolakis, "GPUs in GEANT4", Annual Concurrency Meeting, February 2013.

[11] S. Gorbunov, U.Kebschull, I. Kisel, W. F. J. Müller, V. Lindenstruth, "Fast SIMDized Kalman filter based track fit", Computer Physics Communications, Vol. 178, No. 5, p. 374-383 (2008).

ISBN 978-3-95450-181-6

DYNAMICAL APERTURE BEYOND PERTURBATIONS: FROM QUALITATIVE ANALYSIS TO MAPS

A.N. Fedorova, M.G. Zeitlin*, IPME RAS, St. Peterburg, Russia

Abstract

We start with a qualitative approach based on the detailed analysis of smoothness classes of the underlying functional spaces provided possible evaluation of the dynamical aperture in general nonlinear/polynomial models of particle/beam motion in accelerators. We present the applications of discrete multiresolution analysis technique to the maps which arise as the invariant discretization of continuous nonlinear polynomial problems. It provides a generalization of the machinery of local nonlinear harmonic analysis, which can be applied for both discrete and continuous cases and allows to construct the explicit multiresolution decomposition for solutions of discrete problems which are the correct discretizations of the corresponding continuous cases.

INTRODUCTION

The estimation of the dynamic aperture of accelerators is an important, complicated and long standing problem. From the formal point of view the aperture is some border between two types of dynamics: relative regular and predictable motion along of acceptable orbits or fluxes of orbits corresponding to KAM tori and stochastic motion with particle losses blown away by the Arnold diffusion and/or chaotic motions. According to the standard point of view this transition is being done by some analogues with map technique [1]. Consideration for aperture of n-pole Hamiltonians with kicks

$$H = \frac{p_x^2}{2} + \frac{K_x(s)}{2}x^2 + \frac{p_y^2}{2} + \frac{K_y(s)}{2}y^2 + \frac{1}{3!B\rho}\frac{\partial^2 B_z}{\partial x^2}(x^3 - 3xy^2)L\sum_{k=-\infty}^{\infty}\delta(s-kL) + \dots \quad (1)$$

is done by linearisation and discretization of canonical transformation and the result resembles (pure formally) standard mapping. This leads, by using the Chirikov criterion of resonance overlapping, to the evaluation of aperture via amplitude of the following global harmonic representation:

$$x^{(n)}(s) = \sqrt{2J_{(n)}\beta_x(s)}\cdot \cos\left(\psi_1 - \frac{2\pi\nu}{L}s + \int_0^s \frac{\mathrm{d}s'}{\beta_x(s')}\right). \quad (2)$$

The goal of this paper is two-fold and presents a sketch of alternative approaches located beyond any linearization or perturbation approaches. In the next part, we consider some qualitative criterion which is based on the attempts of more realistic understanding of the existing difference between motion in KAM region and stochastic regions: motion in KAM regions may be described by regular functions only (without the influence of complicated internal structures leading to nonuniform hyperbolicity generating chaos) while motion in stochastic regions/layers may be described by functions with internal (self-similar, e.g.) structures (definitely, created by actions of symmetry generated groups, like discrete groups, or by actions of hidden symmetries of background functional space, like affine group in the most simple case) i.e. fractal type functions which realized the proper orbits [2]. In the subsequent section according to the invariant Marsden-Veselov approach, we consider symplectic and Lagrangian background for the case of discretization of flows by the corresponding maps [3]. Affter that, in the next section, we present the construction of the corresponding solutions by applications of the multiscale approach of A. Harten [4] based on generalization of multiresolution analysis for the case of maps. Such approaches provide the principles and the possibilities for the control of aperture behaviour in the space of machine parameters. All details, constructions, and results can be found in [5].

QUALITATIVE ANALYSIS

The fractal or chaotic image is a function (distribution) which has structure at all underlying scales. Such objects have additional nontrivial details on any level of resolution. But they cannot be represented by smooth functions, because they resemble constants at small scales [2]. We need to find self-similarity behaviour during movement to small scales for the functions describing non-regular motion. So, if we look on a "fractal" function f (e.g. the Weierstrass function) near an arbitrary point at different scales, we find the same function up to the scaling factor. Consider the fluctuations of such function f near some point x_0

$$f_{loc}(x) = f(x_0 + x) - f(x_0), \quad (3)$$

then we have the renormalization (group)–like behaviour/transformation

$$f_{x_0}(\lambda x) \sim \lambda^{\alpha(x_0)} f_{x_0}(x), \quad (4)$$

where $\alpha(x_0)$ is the so-called local scaling exponent or Hölder exponent of the function f at x_0. According to [2] general functional spaces and scales of spaces can be characterized through wavelet coefficients or wavelet transforms. Let us consider continuous wavelet transform

$$W_g f(b,a) = \int_{R^n} \mathrm{d}x \frac{1}{a^n}\bar{g}\left(\frac{x-b}{a}\right) f(x),$$

* zeitlin@math.ipme.ru

ISBN 978-3-95450-181-6

$b \in R^n$, $a > 0$, w.r.t. analyzing wavelet g, which is strictly admissible, i.e.

$$C_{g,g} = \int_0^\infty \frac{\mathrm{d}a}{a} |\hat{g}(\bar{a}\, k)|^2 < \infty.$$

Wavelet transform has the following covariance property under action of the underlying affine group:

$$W_g(\lambda a, x_0 + \lambda b) \sim \lambda^{\alpha(x_0)} W_g(a, x_0 + b). \tag{5}$$

So, if the Hölder exponent of (distribution) $f(x)$ around the point $x = x_0$ is $h(x_0) \in (n, n+1)$, then we have the following behaviour of $f(x)$ around $x = x_0$:

$$f(x) = c_0 + c_1(x - x_0) + \ldots + c_n(x - x_0)^n + c|x - x_0|^{h(x_0)}.$$

Let the analyzing wavelet has n_1 ($> n$) vanishing moments, then

$$W_g(f)(x_0, a) = Ca^{h(x_0)} W_g(f)(x_0, a) \tag{6}$$

and

$$W_g(f)(x_0, a) \sim a^{h(x_0)},$$

when $a \to 0$. But if $f \in C^\infty$ at least in the point x_0, then

$$W_g(f)(x_0, a) \sim a^{n_1},$$

when $a \to 0$ [2]. This shows that the localization of wavelet coefficients at small scale is linked to local regularity. As a rule, the faster the wavelet coefficients decay, the more the analyzed function is regular. So, transition from regular motion to chaotic one may be characterised as the changing of the Hölder/scaling exponent of the function which describes motion. This gives a criterion of the appearance of fractal behaviour and may determine, at least in principle, the dynamic aperture as well as the dependence on parameters of the type of behaviour.

INVARIANT DISCRETIZATION

Discrete variational principles lead to evolution dynamics analogous to the Euler-Lagrange equations [3]. Let Q be a configuration space, then a discrete Lagrangian is a map $L : Q \times Q \to \mathbf{R}$, L is obtained by approximating the given Lagrangian. For $N \in N_+$ the action sum is the map $S : Q^{N+1} \to \mathbf{R}$ defined by

$$S = \sum_{k=0}^{N-1} L(q_{k+1}, q_k), \tag{7}$$

where $q_k \in Q, k \geq 0$. The action sum is the discrete analog of the action integral in continuous case. Extremizing S over $q_1, \ldots, q_{N-1}$ with fixing q_0, q_N we have the discrete Euler-Lagrange equations (DEL):

$$D_2 L(q_{k+1}, q_k) + D_1(q_k, q_{q-1}) = 0, \tag{8}$$

for $k = 1, \ldots, N-1$.

Let

$$\Phi : Q \times Q \to Q \times Q \tag{9}$$

and

$$\Phi(q_k, q_{k-1}) = (q_{k+1}, q_k) \tag{10}$$

is a discrete function (map), then we have for DEL:

$$D_2 L \circ \Phi + D_1 L = 0 \tag{11}$$

or in coordinates q^i on Q we have DEL

$$\frac{\partial L}{\partial q_k^i} \circ \Phi(q_{k+1}, q_k) + \frac{\partial L}{\partial q_{k+1}^i}(q_{k+1}, q_k) = 0. \tag{12}$$

It is very important that the map Φ exactly preserves the discretization of the symplectic form ω [3]:

$$\omega = \frac{\partial^2 L}{\partial q_k^i \partial q_{k+1}^j}(q_{k+1}, q_k) \mathrm{d}q_k^i \wedge \mathrm{d}q_{k+1}^j \tag{13}$$

MAPS: MULTIRESOLUTION

Our approach to solutions of equations (12) is based on applications of general and very efficient methods developed by A. Harten [3], who produced a "General Framework" for multiresolution representation of discrete data. It is based on consideration of basic operators, decimation and prediction, which connect adjacent resolution levels. These operators are constructed from two basic blocks: the discretization and reconstruction operators. The former obtains discrete information from a given continuous functions (flows), and the latter produces an approximation to those functions, from discrete values, in the same function space to which the original function belongs. A "new scale" is defined as the information on a given resolution level which cannot be predicted from discrete information at lower levels. If the discretization and reconstruction are local operators, the concept of "new scale" is also local. The scale coefficients are directly related to the prediction errors, and thus to the reconstruction procedure. If scale coefficients are small at a certain location on a given scale, it means that the reconstruction procedure on that scale gives a proper approximation of the original function at that particular location. This approach may be considered as some generalization of standard wavelet analysis approach. It allows to consider multiresolution decomposition when usual approach is impossible (singular, non-regular behaviour). We demonstrated the discretization of kick/Dirac function by wavelet packets on Fig. 1 and Fig. 2.

Let F be a linear space of mappings

$$F \subset \{f | f : X \to Y\}, \tag{14}$$

where X, Y are linear spaces. Let also D_k be a linear operator

$$D_k : f \to \{v^k\}, \quad v^k = D_k f, \; v^k = \{v_i^k\}, \quad v_i^k \in Y. \tag{15}$$

This sequence corresponds to k level discretization of X. Let

$$D_k(F) = V^k = \mathrm{span}\{\eta_i^k\} \tag{16}$$

ISBN 978-3-95450-181-6

and the coordinates of $v^k \in V^k$ in this basis are $\hat{v}^k = \{\hat{v}_i^k\}$, $\hat{v}^k \in S^k$:

$$v^k = \sum_i \hat{v}_i^k \eta_i^k, \tag{17}$$

D_k is a discretization operator. Main goal is to design a multiresolution scheme (MR) [4] that applies to all sequences $s \in S^L$, but corresponds for those sequences $\hat{v}^L \in S^L$, which are obtained by the discretization (14).

Since D_k maps F onto V^k then for any $v^k \subset V^k$ there is at least one f in F such that $D_k f = v^k$. Such correspondence from $f \in F$ to $v^k \in V^k$ is reconstruction and the corresponding operator is the reconstruction operator R_k:

$$R_k : V_k \to F, \qquad D_k R_k = I_k, \tag{18}$$

where I_k is the identity operator in V^k (R^k is right inverse of D^k in V^k).

Given a sequence of discretization $\{D_k\}$ and sequence of the corresponding reconstruction operators $\{R_k\}$, we define the operators D_k^{k-1} and P_{k-1}^k

$$\begin{aligned} D_k^{k-1} &= D_{k-1} R_k : V_k \to V_{k-1} \\ P_{k-1}^k &= D_k R_{k-1} : V_{k-1} \to V_k \end{aligned} \tag{19}$$

If the set D_k is nested [4], then

$$D_k^{k-1} P_{k-1}^k = I_{k-1} \tag{20}$$

and we have for any $f \in F$ and any $p \in F$ for which the reconstruction R_{k-1} is exact:

$$D_k^{k-1}(D_k f) = D_{k-1} f, \quad P_{k-1}^k (D_{k-1} p) = D_k p \tag{21}$$

Let us consider any $v^L \in V^L$, Then there is $f \in F$ such that

$$v^L = D_L f, \tag{22}$$

and it follows from (21) that the process of successive decimation [4]

$$v^{k-1} = D_k^{k-1} v^k, \qquad k = L, ..., 1 \tag{23}$$

yields for all k

$$v^k = D_k f \tag{24}$$

Thus the problem of prediction, which is associated with the corresponding MR scheme, can be stated as a problem of approximation: knowing $D_{k-1} f$, $f \in F$, find a "good approximation" for $D_k f$. It is very important that each space V^L has a multiresolution basis

$$\bar{B}_M = \{\bar{\phi}_i^{0,L}\}_i, \{\{\bar{\psi}_j^{k,L}\}_j\}_{k=1}^L \tag{25}$$

and that any $v^L \in V^L$ can be written as

$$v^L = \sum_i \hat{v}_i^0 \bar{\phi}_i^{0,L} + \sum_{k=1}^L \sum_j d_j^k \bar{\psi}_j^{k,L}, \tag{26}$$

where $\{d_j^k\}$ are the k scale coefficients of the associated MR, $\{\hat{v}_i^0\}$ is defined by (17) with $k = 0$. If $\{D_k\}$ is a nested sequence of discretization [4] and $\{R_k\}$ is any corresponding sequence of linear reconstruction operators, then we have from (26) for $v^L = D_L f$ applying R_L:

$$R_L D_L f = \sum_i \hat{f}_i^0 \phi_i^{0,L} + \sum_{k=1}^L \sum_j d_j^k \psi_j^{k,L}, \tag{27}$$

$$\begin{aligned} &\phi_i^{0,L} \in F, \\ &\psi_j^{k,L} = R_L \bar{\psi}_j^{k,L} \in F, D_0 f = \sum \hat{f}_i^0 \eta_i^0. \end{aligned} \tag{28}$$

When $L \to \infty$ we have sufficient conditions which ensure that the limiting process in (27, 28) yields a multiresolution basis for F (14). Then, according to (25), (26) we have a very useful representation via the multiscale form for solutions (26) of map version (12) of initial equations obtained from (1) as well as for various maps constructions which are discrete counterparts for continuous cases considered in [5].

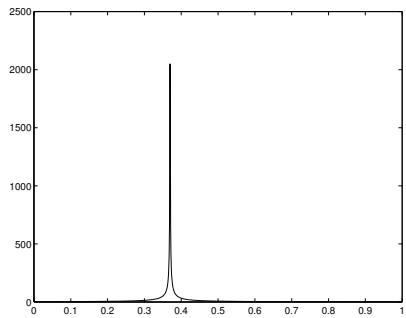

Figure 1: Kick/Delta function.

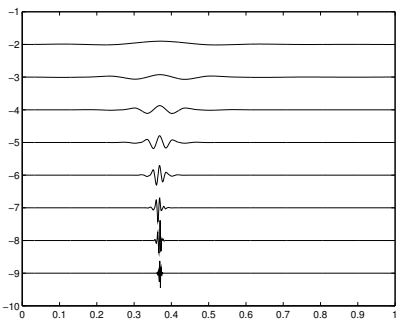

Figure 2: Discretization via wavelet packets.

REFERENCES

[1] A. Chao, *Handbook of Accelerator Physics and Engineering*, World Scientific, 1999.

[2] A. Arneodo, *Wavelets*, p. 349, Oxford, 1996; M. Holschneider, *Wavelets*, Clarendon, 1998.

[3] J.E. Marsden, *Park City Lectures on Mechanics, Dynamics and Symmetry*, Caltech, 1998.

[4] A. Harten, *SIAM J. Numer. Anal.*, 31, 1191-1218, 1994.

[5] Antonina N. Fedorova, Michael G. Zeitlin, papers/preprints at `http://math.ipme.ru/zeitlin.html`; "Orbital motion in multipole fields via multiscale decomposition", this Volume.

ISBN 978-3-95450-181-6

COMPUTER SIMULATION OF THE SLOW BEAM EXTRACTION FROM NUCLOTRON

I. Avvakumova, V. Emelianenko, A. Kovalenko, V. Mikhaylov, VBLHEP, JINR, Dubna, Russia

Abstract

The results of modelling of particles motion during slow beam extraction from Nuclotron at the energy of 6 GeV/u are analyzed. Influence of the measured sextupole component of dipole magnets and fringe fields of the Lambertson magnets on the characteristics of extracted beam is presented. The calculations have been done using the MadX package.

INTRODUCTION

The Nuclotron, superconducting heavy ion synchrotron with iron shaped magnets, has been under operation since 1993. Physics experiments were carried out only in internal circulating beams before March, 2000. Preparation of the extraction system elements [1], their final bench tests and installation in the ring were performed in 1999. In 2000 the works were completed, and the equipment was installed into the ring and put into operation that made it possible to carry out further experiments at the extracted beams as well [2], [3].

EXTRACTION SYSTEM

System of slow beam extraction from Nuclotron includes electrostatic septum (ES), pair of Lambertson magnets (LM), 4 sextupole lenses and 4 special quadrupole lenses. The sextupoles produce 22-th harmonic of sextupole nonlinearity to excite the resonance $Q_x = 22/3$. The first pair of the lenses is located in second and sixth octants of the Nuclotron lattice whereas the second pair in fourth and eighth octants respectively. Special quadrupole lenses are used to shift the horizontal tune to the resonance vicinity. The lenses are located in the first, third, fifth and seventh octants respectively. The ES and LM are located within the fifth octant. These elements provide two-stage particle deflecting system, namely: ES in horizontal plane and LM in vertical plane to the level of existing beam-transport channels in experimental halls. The LM is superferric magnet consisting of two sections 1.5 m long each. Composition of the lattice is shown in Fig. 1.

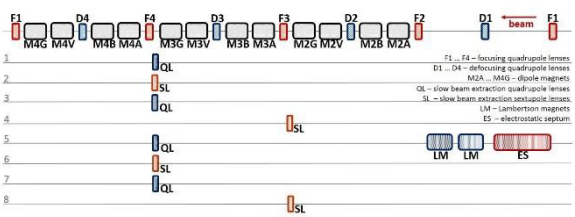

Figure 1: Composition of the Nuclotron elements.

The main task of this work is to consider how sextupole nonlinearity of dipole magnets and fringe fields of the LM disturb beam dynamics and to estimate possibility to extract the beam with high efficiency at the maximum energy. All the calculations were done for the betatron tunes $Q_x \sim 22/3$ and $Q_y = 7.4$. The gap between 3 cm and 5 cm on horizontal plane (XX' plane) is marked at each plot to show the gap of the ES. The possibility of entering this gap for the particle means its extraction.

SIMULATION AND RESULTS

At first, the case with zero nonlinearities of the structural dipoles and the other elements was considered. In this situation, there is no reason for the resonances exciting and for the extraction of the beam. Horizontal and vertical plane of the beam phase portrait at the entrance in ES are shown on Fig. 2a and Fig. 2b.

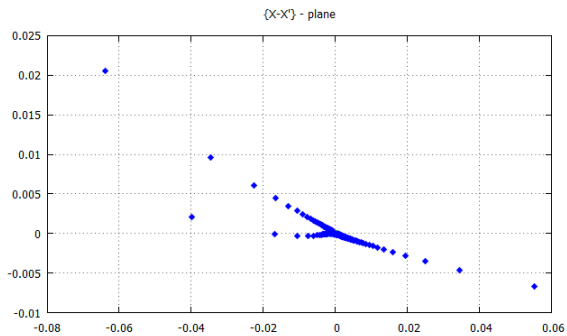

Figure 2a: XX' plane without nonlinearities

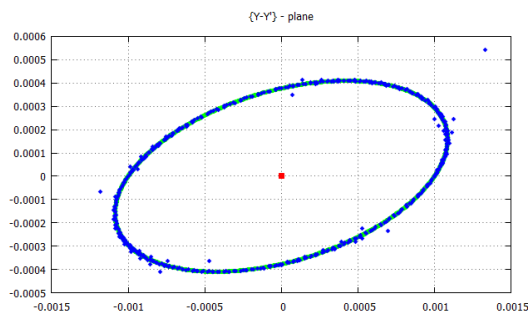

Figure 2b: YY' plane without nonlinearities.

At the next stage the sextupole nonlinearity of the dipoles was taken into account. The appearance of additional areas of stability (see Fig. 3) is observed even without switching the sextupole lenses of slow beam extraction.

ISBN 978-3-95450-181-6

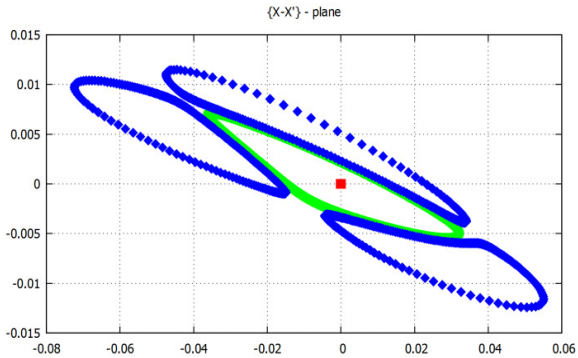

Figure 3: XX' plane with general and additional areas of stability.

At such conditions, switching of special sextupole lenses for slow beam extraction gives no the expected positive effect. There is no general or partial stable areas, however there is bending of the particle trajectories at Q_x = 22/3 (Fig. 4 and 5a, 5b).

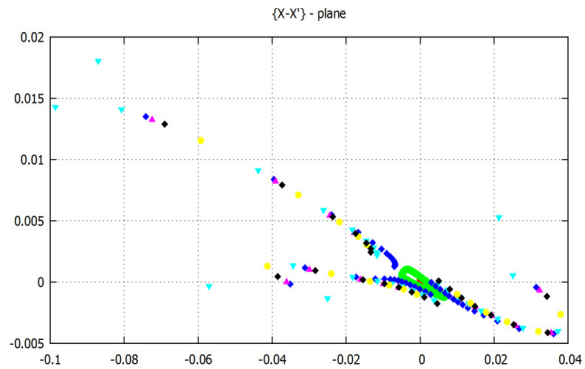

Figure 4: Bending of the trajectories caused by the sextupoles switching on.

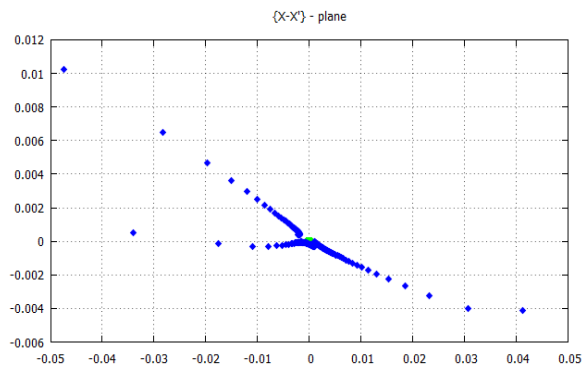

Figure 5a: XX' plane with the slow extraction sextupoles, Qx = 22/3.

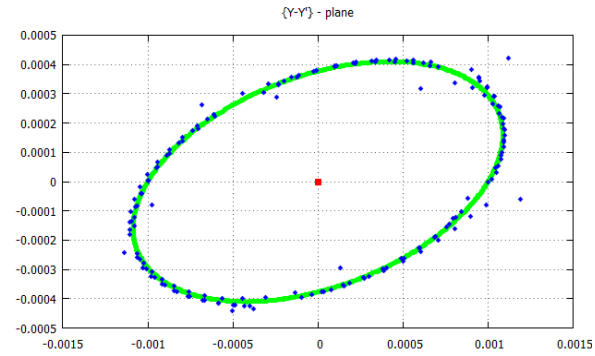

Figure 5b: YY' plane with the slow extraction sextupoles, Qx = 22/3.

The situation is improved a little bit if we shift the work point from the resonance. This case is shown at Fig. 6a calculated at Qx = 22/3 + 0,01. Phase portrait in YY' plane for the conditions mentioned above is shown in Fig. 6b.

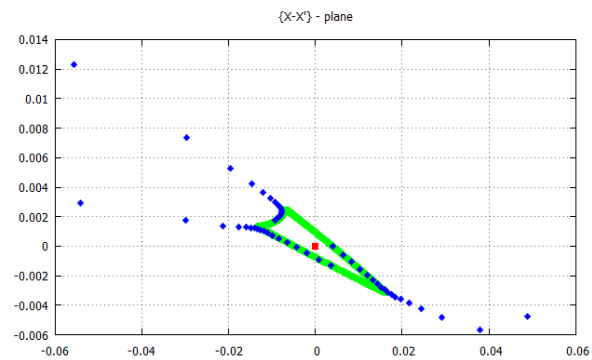

Figure 6a: XX' plane with the sextupoles nonlinearity at Qx = 22/3 + 0,01.

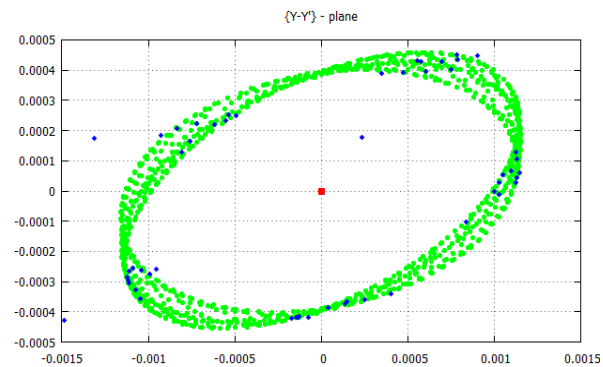

Figure 6b: YY' plane with the sextupoles nonlinearity at Qx = 22/3 + 0,01.

Influence of the LM fringe fields together with the sextupoles nonlinearity was considered in the next step. The modelling shows that directly at the resonance point (Qx = 22/3) the beam can enter to the ES gap, and slow beam extraction is possible (Fig. 7a and 7b).

ISBN 978-3-95450-181-6

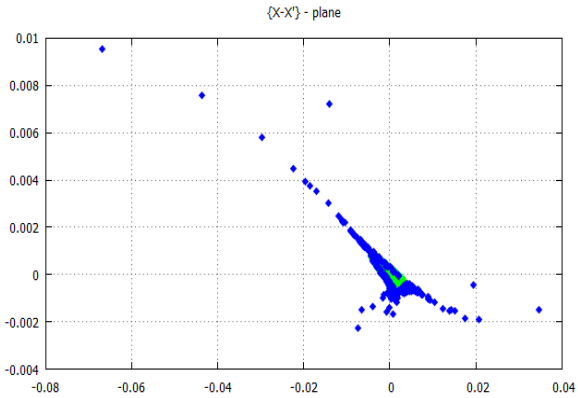

Figure 7a: XX' plane with the sextupoles nonlinearity and the LM fringe fields at Qx = 22/3.

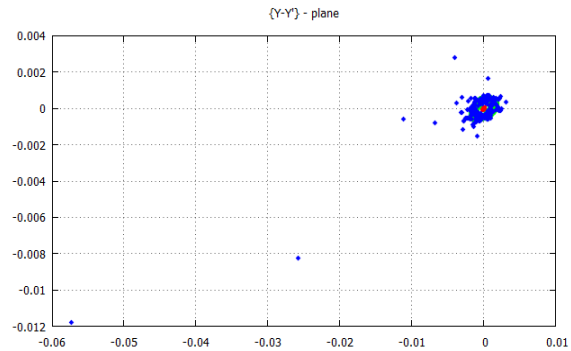

Figure 7b: YY' plane with the sextupoles nonlinearity and the LM fringe fields, Qx = 22/3.

However, trajectories of the beam motion in the limits of resonance tuning (Qx = 22/3 + 0,01) and with both sets of nonlinearities (sextupole nonlinearity and fringe fields of Lambertson magnets) show that slow beam extraction occurs under these conditions with very low efficiency (Fig. 8a, 8b and 9).

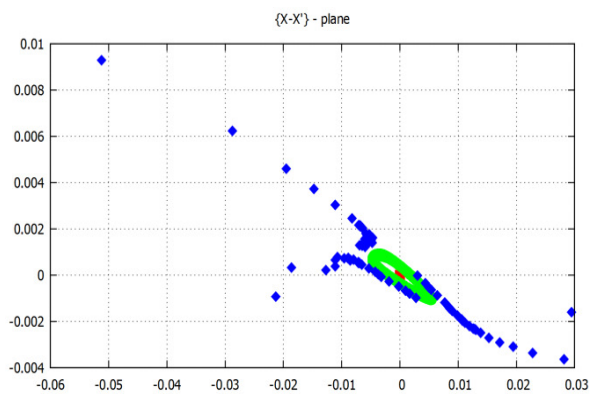

Figure 8a: XX' plane with the sextupoles nonlinearity and the LM fringe fields at Qx = 22/3 + 0,01.

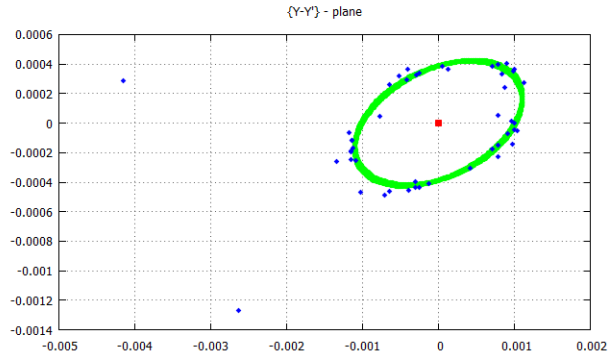

Figure 8b: YY' plane with the sextupoles nonlinearity and the LM fringe fields, Qx = 22/3 + 0,01.

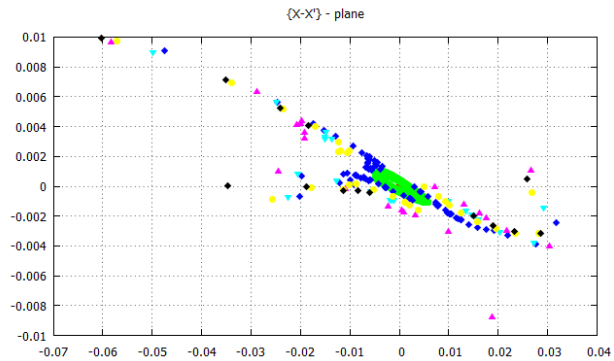

Figure 9: XX' plane with the sextupoles nonlinearity and the LM fringe fields at Qx = 22/3 + 0,01.

CONCLUSION

The obtained data demonstrate the necessity of further analysis of slow beam extraction process at Nuclotron and especially at the maximum magnetic field in lattice dipoles (2 T and over). The measured values of the sextupole component of the Nuclotron structural dipoles were used in the presented set of calculations. Nevertheless, the decapole component exists in the dipole magnetic field and its distribution was measured also. Thus, the work will be continued.

REFERENCES

[1] I. Issinsky, V. Mikhaylov, V. Shchepunov, "Nuclotron lattice", EPAC'90, Nice, June 1990, p.458 (1990).

[2] A. Kovalenko, "Nuclotron: status and future", EPAC 2000, Vienna, June 2000, p.554 (2000).

[3] N. Agapov et al. "Slow beam extraction from Nuclotron", PAC'01, Chicago, March 2001, p.1646 (2001).

ISBN 978-3-95450-181-6

PARALLELIZATION OF ENVELOPE DYNAMICS OF HIGH INTENSIVE BEAMS*

N. Kulabukhova†, Faculty of Applied Mathematics and Control Processes,
Saint-Petersburg State University, St. Petersburg, Russia

Abstract

In this work the survey of methods for high intensive beam dynamics is given. As an alternative to them the approach based on envelope dynamics was used. This method is focusing on the use of the matrix form for Lie algebraic methods for calculating the beam dynamics in the presence of self-field of the beam. In particular, the corresponding calculations are based on the predictor-corrector method. Pros and cons of using described approach on hybrid systems are discussed.

INTRODUCTION

The number of methods and software for modeling beam dynamics is out of counting. The most popular software packages are MAD, COSY Infinity, TRANSPORT, BEAMBEAM3D, IMPACT-Z, IMPACT-T and some others [1]. But the problem of gathering different packages under one software product (figure 1) is not yet solved [2, 3]. Software for modeling beam dynamics with the

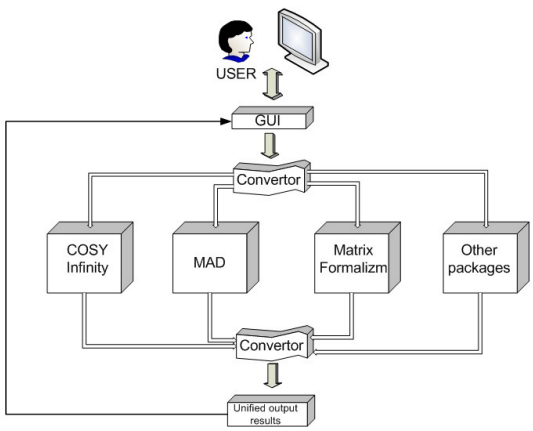

Figure 1: Unified user access.

space charge forces in the concept of matrix forms is the part of project of making a unified user interface "Virtual Accelerator Laboratory"(VAL) [4]. The main use of the VAL is simulation of beam dynamics by different packages with the opportunity to match the results (in case of using different solution methods for the same problem) and the possibility to create pipelines of tasks when the results of one processing step based on a particular software package can be sent to the input of another processing step.

However, in all these packages methods of tracking particle by particle through the whole system. The most commonly used is Particle-in-Cell method (PIC)[5, 6]. The Fortran-based environment COSY INFINITY is based on computations of perturbation expansions of Poincare maps to high orders. MARYLIE [7] is a FORTRAN program for beam transport and tracking based on a Lie algebraic formulation of charged particle trajectory calculations.

And in case of intensive beams, which can lead to the so called the filamentation effect or to the Halo, the number of particles is bigger then 1 billion. Though, the computer resources allow us to calculate large amount of data, the practice shows that it is better to have a parallel algorithm than a good and powerful machine. That was the goal: to make the algorithm that can be parallelized easily.

ENVELOPE DYNAMICS IN MATRIX FORM

It is well known that the envelope equations for continuous beam with uniform charge density and elliptical cross-section were first derived by Kapchinsky and Vladimirsky (KV). This very useful result has been put into different approaches to charged beams description with any charge distribution with elliptical symmetry. More over this is also true in practice for three dimensional bunched beams with ellipsoidal symmetry.

Matrix formalism is a high-performance mapping approach for Ordinary Differential Equation solving. It allows to present solution of the system in the following form

$$X = \sum_{i=0}^{k} R^{1i}(t) X_0^{[i]}$$

where R^{1i} are numerical matrices. As it was said above, there are different ways of modeling beam dynamics:

- Trajectory analysis. In this case the beam is presented as a particles assemble and can be written using the following matrix $X^N = \{\vec{X}^1, \ldots, \vec{X}^N\}$, where $\vec{X}^k$ is a phase vector of k-th particle and N is a number of particles.
- Beam envelope dynamics. In this case the beam is described in the terms of envelope matrices [8]. We will speak about them later.
- Distribution function dynamics. In this case one present the beam in the terms of a distribution function, which satisfies to the Maxwell-Vlasov equations system.

In this paper, we describe an approach to construct analytical expressions for the electric field produced by the

* Work supported by SPbSU 0.37.155.2014 and RFBR 16-07-01113A
† n.kulabukhova@spbu.ru

ISBN 978-3-95450-181-6

beam particles. These expressions may be derived using the matrix formalism for a trajectory analysis [8], and in terms of the envelope of the beam and/or the distribution function (in accordance with the Vlasov-Maxwell equations).

Particle Tracking

For beam without bunches the equations of motion can be written in the following form [8]

$$x'' = \frac{q}{p}T\left(y'B_s - (1+x'2)B_y + x'y'B_x + T\frac{E_x}{c\beta\gamma}\right)$$
$$y'' = -\frac{q}{p}T\left(x'B_s - (1+y'2)B_x + x'y'B_y + T\frac{E_y}{c\beta\gamma}\right) \quad (1)$$

Using the concept of matrix formalism equations (1) can be rewritten

$$\frac{d\mathbf{X}}{ds} = \sum_{k=1}^{\infty}\left(\mathbb{P}^{1k}_{ext}(s) + \mathbb{P}^{1k}_{self}(s)\right)\mathbf{X}^{[k]} \quad (2)$$

In linear case the equation of motion with the space charge effect (1) will have the following view:

$$x'' + k_x x - \frac{q}{\epsilon_0 m_0 c^2 \beta^2 \gamma^3}E^L_x = 0 \quad (3)$$
$$y'' + k_y y - \frac{q}{\epsilon_0 m_0 c^2 \beta^2 \gamma^3}E^L_y = 0$$

Matrix $\mathbb{P}^{11}$ in this case can be

$$\mathbb{P}^{11}(s) = \mathbb{P}^{11}_{ext}(s) + \mathbb{P}^{11}_{self}(s)$$

where

$$\mathbb{P}^{11}_{ext}(s) = \begin{pmatrix} 0 & 1 & 0 & 0 \\ -k_x & 0 & 0 & 0 \\ 0 & 0 & 0 & 1 \\ 0 & 0 & -k_y & 0 \end{pmatrix},$$
$$\mathbb{P}^{11}_{self}(s) = \begin{pmatrix} 0 & 0 & 0 & 0 \\ -\eta_x & 0 & 0 & 0 \\ 0 & 0 & 0 & 0 \\ 0 & 0 & \eta_y & 0 \end{pmatrix},$$

If we speak about nonlinear case the equations (1) will be

$$x'' + (k_x - \alpha k_{xx})x = a_x x^3 + B_x x x'^2 + c_x x y^2 + \\ + k'_x x y y' + d_x x y'^2 + k_x x' y y', \quad (4)$$

$$y'' + (k_y - \alpha k_{yy})y = a_y y^3 + B_y y y'^2 + c_y y x^2 + \\ + k'_y y x x' + d_y y x'^2 + k_y y' x x' \quad (5)$$

Using matrix form this equations will be

$$\mathbf{X} = \begin{pmatrix} x \\ x' \end{pmatrix}, \quad \mathbf{Y} = \begin{pmatrix} y \\ y' \end{pmatrix}, \quad (6)$$

$$\mathbf{X}^3 = \begin{pmatrix} \mathbf{X} \\ \mathbf{Y} \\ \mathbf{X}^{[3]} \\ \mathbf{X}^{[2]} \otimes \mathbf{Y} \\ \mathbf{X} \otimes \mathbf{Y}^{[2]} \\ \mathbf{Y}^{[3]} \end{pmatrix}.$$

And for matrices $\mathbb{P}$:

$$\mathbb{P}^{11} = \begin{pmatrix} \mathbb{P}^{11}_x & \mathbb{O} \\ \mathbb{O} & \mathbb{P}^{11}_y \end{pmatrix},$$
$$\mathbb{P}^{13} = \begin{pmatrix} \mathbb{Q}^{11}_x & \mathbb{O} & \mathbb{Q}^{13}_x & \mathbb{O} \\ \mathbb{O} & \mathbb{Q}^{22}_y & \mathbb{O} & \mathbb{Q}^{24}_y \end{pmatrix},$$

where, for example, for {x, x'}

$$\mathbb{P}^{11}_{ext} = \begin{pmatrix} 0 & 1 \\ -k_x & 0 \end{pmatrix},$$
$$\mathbb{P}^{11}_{self} = \begin{pmatrix} 0 & 0 \\ \alpha k_{xx} & 0 \end{pmatrix}.$$

Envelope Dynamics

The approximation of the envelope can be done by different ways (see figure 2):

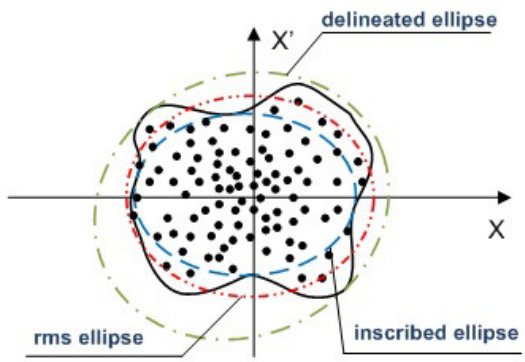

Figure 2: Types of approximated ellipses of the envelope.

- the root mean square approximation;
- approximation by delineate ellipsoid;
- approximation by inscribed ellipsoid.

The general view of envelope matrix is

$$\mathfrak{S}^{ik}_0 = \int_{\mathfrak{M}_0} f_0(\mathbf{X})\mathbf{X}^{[i]}(\mathbf{X}^{[k]})^* d\mathbf{X}$$

In linear case for delineate ellipsoid according to matrix formalizm equations can be

ISBN 978-3-95450-181-6

$$\frac{d\mathfrak{S}^{max}}{ds} = \mathbb{P}^{11}\mathfrak{S}^{max} + \mathfrak{S}^{max}(\mathbb{P}^{11})^*.$$

For root-mean-square envelope the equation with the space charge forces is

$$\frac{d\mathfrak{S}^{rms}}{ds} = \mathbb{P}^{11}\left(\langle\mathfrak{S}^{rms}\rangle_{\Delta s}; s\right) + \mathfrak{S}^{rms}\mathbb{P}^{11}\left(\langle\mathfrak{S}^{rms}\rangle_{\Delta s}; s\right)^*.$$

After that, using algorithm, described in [9] we get the envelope matrices to solve the equation of motion in the matrix form.

BENEFITS OF PARALLELIZATION

Due to the fact that the described approach is based on matrices and the main operations are multiplication and addition of them, the use of GPU programming [10, 11] seems very useful and effective. The present research is shown that there is no great benefit via parallelization of computational code for one particle by using, for example, OpenMP library (see Table 1). In this case overhead on data sending is significant and take the greatest part of time. On the other hand, matrix formalism allows to process a set of initial points as an envelope of the distribution function, where the data sending is lower. But using only GPUs is not justified. However, the results have shown that the described algorithm is well parallelizing.

Table 1: Time (sec.) in parallel code for different number of particles.

Threads/ Particles	10^7	$20 * 10^6$	$30 * 10^6$
Sequential	9,14508	18,3444	28,1367
4	13,1787	26,3788	21,5358
8	7,16977	14,5777	20,8549
16	6,8548	13,6071	20,15
64	6,70448	13,5593	20,0794
128	7,92809	14,8894	22,748

CONCLUSION

Our challenge is to provide computer simulation for developed algorithm for solving the problem of accounting space-charge forces in general and compare this algorithm with other methods. It allows simulate both long-term evolution of a set of particles, and evaluating based on envelope description. As it was said above the method can be implemented in parallel codes on GPU+CPU hybrid Cluster. That is why the future development of the research also can be based on writing software to compare different parallel techniques for Hybrid Systems, in order to effective use of described approach to compute the required number of particles in long-term evolution of the beam.

ACKNOWLEDGMENT

The author would like to express gratitude to Vladimir Korkhov for valuable help. Scientific research were performed using the equipment of the Research Park of St.Petersburg State University. The work was sponsored by the Russian Foundation for Basic Research under the projects: 16-07-01113 "Virtual supercomputer as a tool for solving complex problems" and by the Saint-Petersburg State University under the project 0.37.155.2014 "Research in the field of designing and implementing effective computational simulation for hydrophisical and hydrometeorological processes of Baltic Sea (and the open Ocean and offshores of Russia)".

REFERENCES

[1] Robert D. Ryne, Advanced Computing Tools and Models for Accelerator Physics, Proceedings of EPAC 2008, pp. 2947-2951, 2008.

[2] N. Malitsky and J. Smith and J.Wei and R. Talman, UAL-Based Simulation Environment for Spallation Neutron Sourse Ring, Proceedings of the 1999 Particle Accelerator Conference, 1999.

[3] D. Sagan and at al., Unified Accelerator Modeling Using the Bmad Software Library, Proceedings of IPAC 2011, 2011.

[4] V. Korkhov and A. Ivanov and N. Kulabukhova and A. Bogdanov and S. Andrianov, Virtual Accelerator: Distributed Environment for Modeling Beam Accelerator Control System , Lecture Notes in Computer Science, Vol. 6681116, pp. 166-169,2013.

[5] S. Paret and J. Qiang, Collisional Effects in Particle-In-Cell Beam-Beam Simulation, Proceedings of IPAC 2013, pp. 1700-1702, 2013.

[6] G. Stancari and S. Redaelli and V. Moens, "Beam Dynamics in an Electron Lens with Warp Particle-in-Cell Code", Proceedings of IPAC 2014, pp. 451-453, 2014.

[7] Alex J. Dragt and Robert D. Ryne at al., "MARYLIE 3.0 Users Manual: A Program for Charged Particle Beam Transport Based on Lie Algebraic Methods", University of Maryland, 2003.

[8] Andrianov S.N., Dynamical Modeling of Control Systems for Particle Beams, SPbSU, Saint Petersburg, 2004 (in Russian).

[9] Kulabukhova N. and Andrianov S. and A. Bogdanov and A.Degtyarev, Simulation of Space Charge Dynamics in High Intensive Beams on Hybrid Systems, Lecture Notes in Computer Science, Vol. 9786, pp. 284-295, 2014.

[10] Kulabukhova Nataliia, Space Charge Dominated Envelope Dynamics Using GPUs, Proceedings of IPAC 2013, 2013.

[11] N. Kulabukhova and A. Degtyatev and A. Bogdanov and S. Andrianov, Simulation of Space Charge Dynamics on HPC, Proceedings of IPAC 2014, 2014.

ISBN 978-3-95450-181-6

NUMERICAL ANALYSIS OF CAVITY MODE OPERATION AND ELECTRON BEAM DYNAMICS IN LEBEDEV INSTITUTE MICROTRON

V.S. Dyubkov, Yu.Yu. Lozeev, National Research Nuclear University MEPhI, Moscow, Russia
Yu.A. Bashmakov, National Research Nuclear University MEPhI and P.N. Lebedev Physical Institute of the Russian Academy of Sciences, Moscow, Russia

Abstract

Dynamics of electrons in classic microtron is studied. 3D cavity model is developed and electromagnetic field distribution is simulated. Dependence of output beam parameters on microtron operation mode is investigated and discussed.

INTRODUCTION

The microtron is a circular resonance electron accelerator that was first proposed by V.I. Veksler in 1944 [1]. Electrons are accelerated in RF cavity located inside the magnet that forms a uniform time-constant field. Electrons, captured in synchronous acceleration mode, move in circles with stepwise increasing radii. Note all these circles theoretically have a common point that located inside the cavity. The main advantages of the microtron are extremely narrow energy spectrum and small sizes of accelerated beams [2,3]. Additionally, the microtron has relatively simple design and low cost of operation. Classical microtrons are used in variety application of science, industry and medicine. Thus, microtron is used as injector for electron synchrotrons with average energy is equal to (0.250 – 1.5) GeV [4,5]. It can be an effective source of high energy photon radiation in photon and neutron activation analysis. Microtrons can be used for photonuclear reaction production [6], as well as for neutron production for pulsed fast neutron reactor [7]. Today, one of the actual problems is a design of THz FEL based on microtron [8-10], one of the first realization attempts could date to the sixties of the last century.

NUMERICAL SIMULATION RESULTS

Electron dynamics simulation in 7 MeV Lebedev Physical Institute (LPI) microtron was carried out in present paper. This accelerator is an injector for 1.3 GeV "Pakhra" electron synchrotron (LPI). This microtron is also used to study bremsstrahlung characteristics of relativistic electrons in complex structures.

Circular cylindrical cavity based on the operating mode of E_{010} (TM_{010}) type at frequency of 2856 MHz is used as an accelerating element in LPI microtron. Electron source is a thermionic cathode mounted in a wall of the resonator (the so-called intracavity injection). LPI microtron is operated with the first type of acceleration [2,11,12]. The cavity cross section in microtron median plane is shown in Fig. 1. There are the basic geometric dimensions of the cavity in Fig. 1: radius (R), cavity length (d), distance between center of thermal emitter and the resonator axis (r_{emit}). Resonator geometry has a deviation from axially symmetric because of electron dynamics feature at the first turns. We consider that cavity length d was equal to 19 mm. Note that $R = 0.383\lambda_{010}$, λ_{010} – wavelength for E_{010} mode.

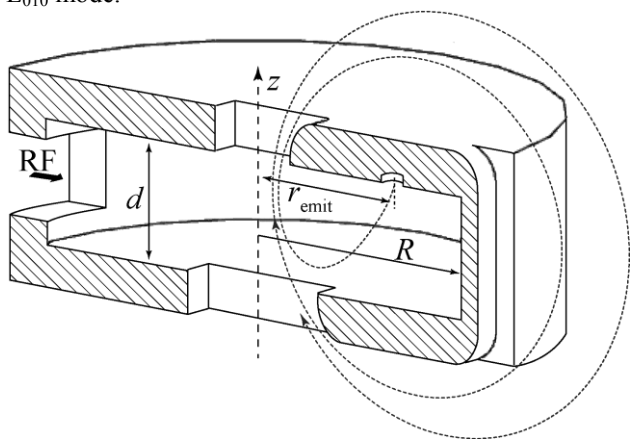

Figure 1: Cross-sectional view of RF cavity.

In the beginning 3D distribution of RF electromagnetic field (both electric and magnetic components) in microtron cavity was calculated by means of specialized code [13]. Typical spatial distribution of electric field absolute value in median plane is shown in Fig. 2. There are accelerating component of the cavity field as a function of longitudinal and transversal coordinates in Fig. 3 and Fig. 4 correspondingly.

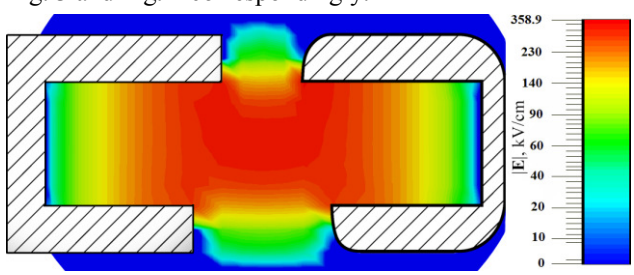

Figure 2: Typical spatial electric field distribution in median plane.

Further, dependence of output beam parameters on microtron operation mode, namely on amplitude of accelerating voltage, was investigated. In the first step it was written a special MICRO code that allowed us to carry out a two-dimensional one particle electron dynamics simulation in the field, calculated above, in microtron median plane. The energy of the emitted electrons was equal to 5 eV and r_{emit} was equal to 27 mm (shifted-emitter microtron). On simulating the electron dynamics we found that uniform magnetic field for circular motion is 0.12 T. Energy gain for one period is defined as follows

ISBN 978-3-95450-181-6

$$\Delta W_s = eU_0 T \cos\varphi_s$$

where U_0 is an accelerating voltage amplitude and transit-time factor is [14]

$$T = 2\sin(\theta/2)/\theta$$

and $\theta = \pi d/\lambda$. Note that in our case T is approximately equal to one. Thus, it was obtained that an amplitude of accelerating voltage should be equal to 660 kV in order to satisfy resonant acceleration condition.

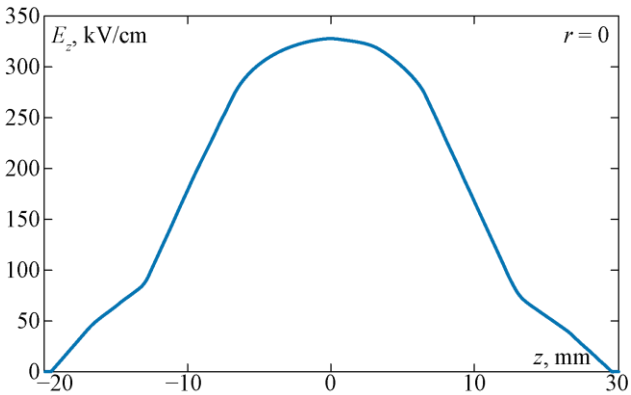

Figure 3: E_z vs z (cavity axis).

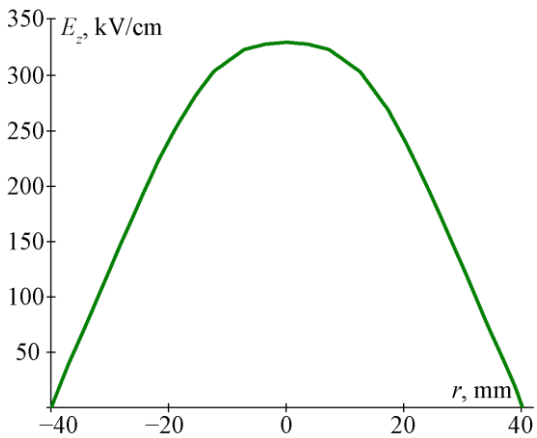

Figure 4: E_z vs r ($z = 0$).

There are several electron trajectories in Fig. 5. Each of them corresponds to different moments of electron emission from the thermionic cathode in the cavity field. One can see that a significant part of the electrons fall on the inner cavity wall and some part are lost on the outer cavity side.

In the second step 3D electron dynamics simulation in LPI microtron assuming continuous emission from thermionic cathode was carried out. Emitter spot diameter was presumed to be equal to 4 mm. For instance, dependence of normalized current on the 9th orbit on accelerating voltage amplitude is shown in Fig. 6. One can see that the maximal current value is achieved under amplitude value equal to 665 kV, but further 3D simulations have shown that this value is not optimal from the point of view of beam quality.

Thus, the optimal value of accelerating voltage amplitude is 660 kV. Dependences of electron beam core sizes on orbit number are shown in Fig. 7 and Fig. 8. As one can see from Fig. 7 & Fig. 8 the longitudinal beam size lies in the range from 2.5 mm to 4.8 mm and transversal one is not greater than 0.22 mm under chosen microtron parameters. The beam particles energy spectrum on the 9th orbit is shown in Fig. 9. There is a typical view of forming the electron bunches in Fig. 10. Note that half-width of energy spread of electron beam on the 9th orbit is about 0.3%.

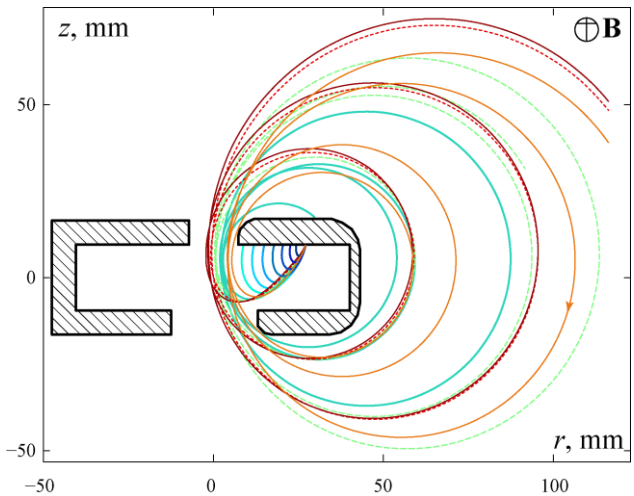

Figure 5: Typical trajectories of electrons in microtron.

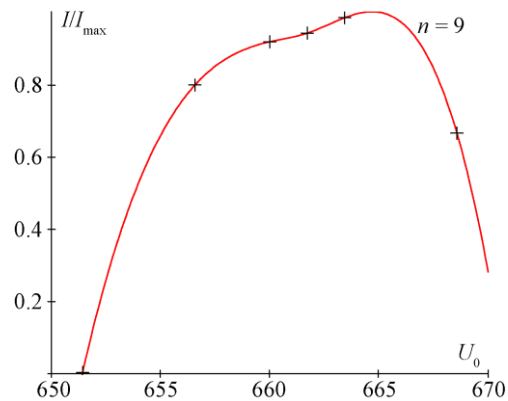

Figure 6: Normalized current on the 9th orbit vs accelerating voltage amplitude.

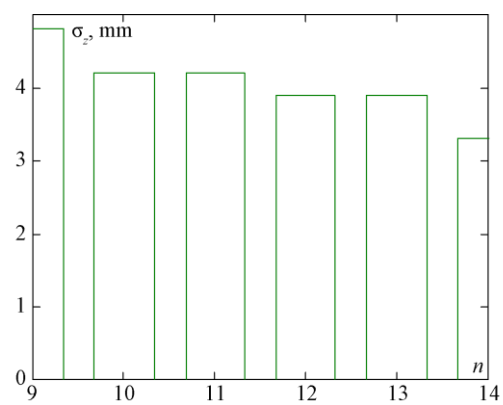

Figure 7: Longitudinal beam size vs orbit number.

ISBN 978-3-95450-181-6

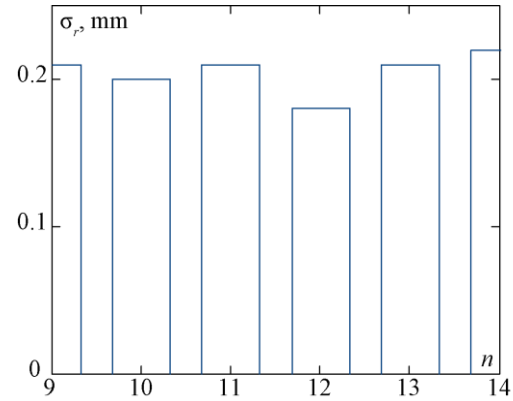

Figure 8: Transversal beam size vs orbit number.

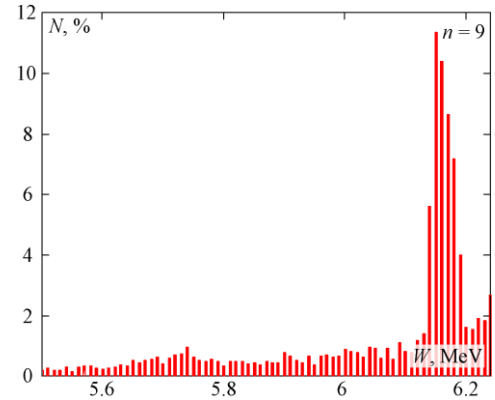

Figure 9: Particles energy spectrum on the 9th orbit.

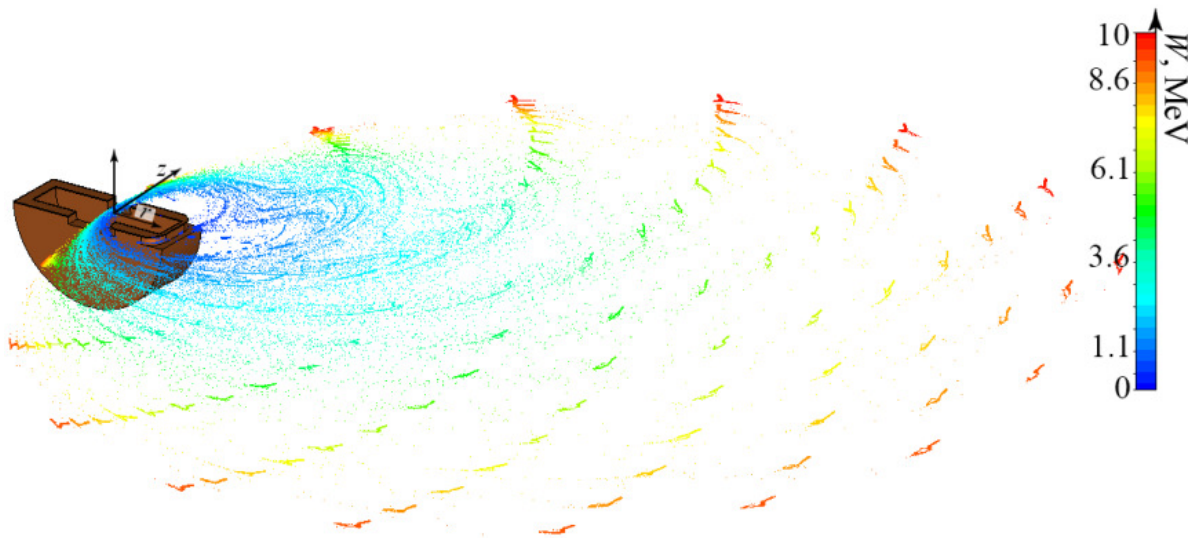

Figure 10: Typical view of forming the electron bunches in 3D space.

It was found that the maximal energy value is typical for particles that were emitted in phases of the RF field in the range approximately from −90° to −70° (for cosine voltage variation). Note also that approximately 65% of emitted particles hits the internal cavity wall during one period of RF field and only 20% are accelerated up to final energy which is equal to 10.9 MeV on the 18th orbit under magnet pole diameter is equal to 75 cm.

CONCLUSION

Dynamics of electrons in LPI microtron was studied. 3D cavity model was developed and electromagnetic field distribution was simulated. Dependence of output beam parameters on microtron operation mode was investigated. Optimal values of microtron parameters were found. It was shown that electrons can be accelerated up to 10.9 MeV under chosen parameters.

REFERENCES

[1] V.I. Veksler, Dokl. Ak. Nauk., J. Phys. USSR 9 (1945) 153
[2] S.P. Kapitza, V.N. Melekhin, The Microtron (London: Harwood Academic Publishers, 1978), 204
[3] Y.M. Tsipenyuk, S.P. Kapitza, The microtron: Development and applications (London: Taylor & Francis, 2002) 348
[4] U. Bizzarri et al., Lettere al Nuovo Cimento 1(16) (1969) 820
[5] V.G. Kurakin et al., “Automation of the Lebedev Physical Institute Synchrotron to the Energy 1.3 GeV as the First Stage of the Accelerator Upgrade”, PAC'01, Chicago, June 2001, WPPH303 p. 2778 (2001); http://accelconf.web.cern.ch/AccelConf/p01/PAPERS/WPPH303.PDF
[6] M. Kralik, et al. RSI 83 (2012) 083502
[7] P. Krist et al., J. Radioanal. Nucl. Chem. 304 (2015) 183
[8] S. Park et al., IEEE Transactions on Nuclear Sci. 63(2) (2016) 898
[9] S. Park et al., J. Korean Phys. Society 66(3) (2015) 358
[10] P.A. Cherenkov et al., NIM A 282(2) (1989) 436
[11] K.A. Belovintsev et al., Soviet Atomic Energy 14(4) (1964) 364
[12] G.G. Subbotin, A.V. Serov, LPI Preprint 19 (2007) 20070
[13] www.ansys.com
[14] A.P. Grinberg, Uspekhi Fiz. Nauk 75 (1961) 421

ISBN 978-3-95450-181-6

FOCUSING OF CHARGED PARTICLES BY MAGNETIC DIPOLES

G.V. Dolbilov, Joint Institute for Nuclear Research, Dubna, 141980, Russia

Abstract

The possibility of using magnetic dipoles for tight focusing of charged particles is discussed. Plane-parallel geometry of the magnetic poles of the dipoles greatly simplifies lens design and reduces the cost of creating a focusing system. Focusing is performed using gradient pulses of force of the magnetic dipoles.

INTRODUCTION

The strong focusing of linear beams of charged particles is performed quadrupole lenses. The magnetic fields of the quadrupole lenses can be created by the magnetic poles, the surface of which is isosceles hyperbolic cylinders. In practice, using simpler forms of poles, but this reduces the working area of the lens, and decrease the maximum value of the induction in the working area. The focusing action of the quadrupole lenses is associated with alternate deviation of the particle to the axis and off-axis focusing system. As a result of this action carried out "hard" beam focusing.

The use of dipoles with the gradient of the force impulse allows you to create lenses that strongly focus the beam in one of the mutually perpendicular direction reject particles only to the axis of the focusing system. In such lenses particles get two of the equal magnitude, but oppositely direction of the momentum force, if they are on the axis of the focusing system. As a result, the total moment of force is zero. All particles which are offset from the axis is always deflected to the axis of the focusing system. In the other direction the particles are defocused by edge fields on the boundary dipoles with opposite polarity field.

DYNAMICS OF PARTICLES IN THE BIPOLAR SYSTEM OF DIPOLES

Particle motion in a uniform field dipole is described by the equations

$$\frac{dP_y}{dt} = qv_xB_z, \quad dP_y = qB_z dx, \; dv_y = \frac{v}{R}dx,$$

$$v_{n,y} = v_{(n-1),y} + \frac{v}{R}x_n, dx = \frac{R}{v}dv_y \qquad (1)$$

were $R = M\gamma v/qB_z = P/qB_z -$ circular radius of the particle in the field B_z; $q, M, v, P -$ charge, mass, speed and momentum of the particle, respectively, $\gamma -$ the relativistic factor of the particle, $x -$ the projection length of the trajectory of a particle on the x-axis.

$$\frac{dy}{dt} = v_x\frac{dy}{dx} = v_y\,, \quad \frac{dy}{dx} = \frac{v_y}{v_x} = \frac{v_y}{\sqrt{v^2 - v_y^2}},$$

$$dy = \frac{v_y}{\sqrt{v^2 - v_y^2}}dx = \frac{R}{v}\frac{v_y dv_y}{\sqrt{v^2 - v_y^2}},$$

$$y_n = y_{(n-1)} + \frac{R}{v}\int_{v_{(n-1),y}}^{v_{n,y}} \frac{v_y dv_y}{\sqrt{v^2 - v_y^2}} =$$

$$= y_{(n-1)} + \frac{R}{v}\left(\sqrt{v^2 - v_{n,y}^2} - \sqrt{v^2 - v_{(n-1),y}^2}\right)$$

In focusing systems, transverse speed of the particles is much less than the longitudinal velocity

$$\frac{v_y}{v} = \delta \ll 1,$$

Therefore, in the first approximation, ignoring the parameter of the second order of smallness δ^2 compared to unit, have

$$y_n = y_{(n-1)}\,, \qquad v_{n,y} = v_{(n-1),y} + \frac{v}{R}x_n$$

In the second approximation, when $\sqrt{v^2 - v_y^2} \cong v\left(1 - v_y^2/2v^2\right)$

$$y_n = y_{(n-1)} + \frac{R}{2}\left(\frac{v_{n,y}^2}{v^2} - \frac{v_{(n-1),y}^2}{v^2}\right),$$

$$v_{n,y} = v_{(n-1),y} + \frac{v}{R}x_n$$

FOCUSING LENS WITH TWO DIFFERENT POLARITY DIPOLES

Changing the parameters of a particle - displacement Δy and the relative velocity $\Delta v_y/v$, , a focusing lens consisting of two dipoles with uniform, equal in magnitude, but different polarity of the magnetic field and form of magnetic poles, as shown in Fig.1, will be as follows:

In the case where the first dipole deflects particles in the of positive $y -$ direction, on the output of the first dipole change of the transverse velocity and coordinate are equal

$$\Delta v_1 = v_1 - v_0 = v\frac{x_1}{R}$$

$$\Delta y_1 = y_1 - y_0 = \frac{R}{2}\left(\frac{v_{1,y}^2}{v^2} - \frac{v_{0,y}^2}{v^2}\right)$$

If the second dipole deflects particles in the negative $y -$direction on the output of the second dipole Δv_2 *and* Δy_2 will be equal

$$\Delta v_2 = v_2 - v_0 = v\frac{x_1 - x_2}{R},$$

$$\Delta y_2 = y_2 - y_1 = \frac{R}{2}\left(\frac{v_{2,y}^2}{v^2} - \frac{v_{1,y}^2}{v^2}\right) \qquad (2)$$

where x_1 и $x_2 -$ projection of the particle trajectories in the first and second dipoles, respectively.

Particles injected into the lens parallel to the axis of the lens, $v_0 = 0$, are rejected by the lens on the angle $\Delta\varphi$ (Fig.1) .

$$tg\Delta\varphi = \frac{v_{2,y}}{v_x} \cong \frac{v_{2,y}}{v} = \frac{x_1 - x_2}{R} = -\frac{2\Delta x}{R}$$

Since (Fig.1)

$$tg\Delta\varphi = \frac{v_y}{v_x} \cong \frac{v_{3y}}{v} = \frac{1}{R}(2x_1 - x_2)$$

$$x_1 = x_0 - \Delta x, \quad x_2 = x_0 + \Delta x, \quad \Delta x = y \cdot tg\alpha$$

ISBN 978-3-95450-181-6

$$tg\Delta\varphi = \frac{2}{R} y \cdot tg\alpha$$

The angle $\Delta\varphi$ determines the focal distance of the lens (Fig.1)

$$tg\Delta\varphi = \frac{y}{F},$$

Therefore, the focal distance of the lens with two gradient dipoles is equal to

$$\boldsymbol{F = \frac{R}{2tg\alpha}}$$

In the area between the dipoles there is a y −component of the magnetic induction, which defocusing particles (boundary field defocusing [2]), with focal length equal to

$$\boldsymbol{F = -\frac{R}{2tg\alpha}}$$

The magnitude of transverse displacement of beam axis (2) at the exit of the lens when

$$v_0 = 0, \qquad x_1 = x_2 = x_0, \qquad v_2 = 0$$

In the first approximation - $\Delta y_2 = 0$

In the second approximation - $\Delta y_2 = R \cdot \delta^2$

where is the small parameter δ equal to

$$\delta = \frac{x_0}{R} \sim \frac{v_y}{v} \ll 1$$

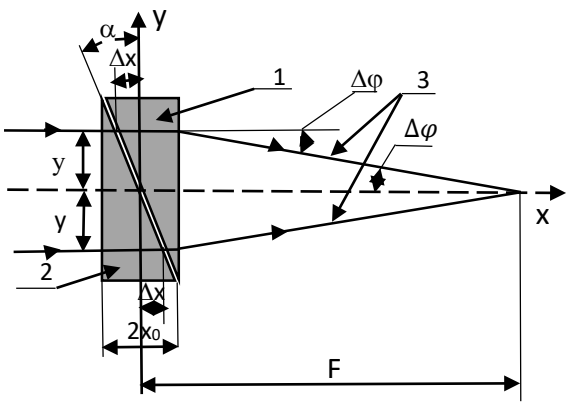

Figure 1: The scheme of gradient lens with two dipoles, where: 1 and 2 – dipoles with uniform, equal in magnitude but different in sign to the magnetic field, 3 – trajectories of particles at the exit of the lens, $2x_0 -$ longitudinal size of the lens, $(x_0 \pm \Delta x) -$ length of the projection on the x axis of particle trajectory in each dipole, $y -$ is the displacement of particle trajectory at the entrance to the lens, $\Delta\varphi -$ is the inclination of particle trajectory at the exit of the lens, $F -$ focal distance of the lens, $tg\alpha -$ the parameter of the dipoles boundary.

FOCUSING LENS WITH THREE GRADIENT DIPOLES

Diagram of the dipole gradient lens that does not shift the beam axis during the passage of the lens, shown in Fig.2. In the case where dipoles 1 and 3 reject particles in the direction of positive y, and 2 dipole deflects particles in the direction of negative y, the variation of the transverse speed and coordinates of the particle at the exit of the lens will be as follows:

$$\Delta v_1 = v_1 - v_0 = v\frac{x_1}{R}$$

$$\Delta v_2 = v_2 - v_0 = v\frac{x_1 - x_2}{R}$$

$$\Delta v_3 = v_3 - v_0 = v\frac{2x_1 - x_2}{R},$$

In order for the axial particle of the beam is not deviated by the lens, $\Delta v_3 = 0$, then it must be equality $x_2 = 2x_1$, while $\Delta v_2 = \Delta v_1$. The amount of displacement of the particles of the beam at $v_{0,y} = v_{3,y} = 0$, is

$$\Delta y_3 = y_3 - y_0 = \frac{R}{2}\left(\frac{v_{1,y}^2}{v^2} - \frac{v_{2,y}^2}{v^2}\right) = 0$$

The angle of inclination of the trajectory of the particle $\Delta\varphi$ during the passage of the lens in the region $y > 0$ is determined by the ratio

$$tg\Delta\varphi = \frac{v_y}{v_x} \cong \frac{v_{3y}}{v} = \frac{1}{R}(2x_1 - x_2)$$

Since (Fig.2) , $x_1 = x_0 - y \cdot tg\alpha$

and $x_2 = 2x_0 + 2y \cdot tg\alpha$ (3)

then $tg\Delta\varphi_- = -\frac{4}{R} y \cdot tg\alpha$ (4)

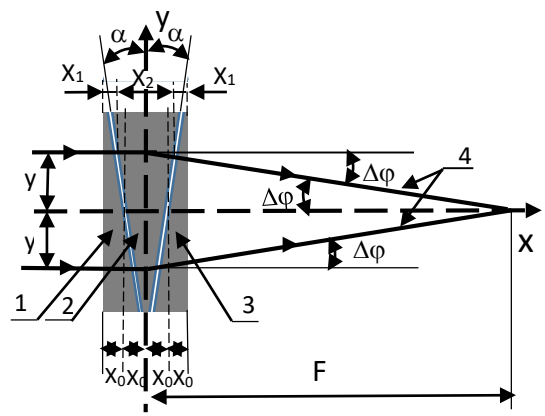

Figure 2: The scheme is gradient lens with three dipoles, where: 1 and 3 – dipoles with uniform and equal in magnitude and polarity to the magnetic field, 2 – dipole with a uniform field, equal in magnitude to the fields in the dipoles 1 and 2, but with reverse polarity, 4 – trajectory of particles in the exit lens, $4x_0 -$ longitudinal length of the lens, $x_1 -$ rojection of particle trajectory on the x-axis for the dipoles 1 and 3, $x_2 -$ projection of the trajectory in the dipole 2, and $y -$ the amount of displacement of the trajectory at the entrance to the lenses, $tg\alpha -$ parameter the geometry of the boundary of the dipoles, $\Delta\varphi -$ the angle of particle trajectory at the exit of the lens, $F -$ focal distance of the lens.

Change the angle of trajectory of particles during the passage of the lens in the regions $y < 0$ and $y > 0$ is equal in magnitude but different in sign.

$$tg\Delta\varphi_+ = +\frac{4}{R} y \cdot tg\alpha$$

The focal length of the lens (Fig.2) defined by the relation

ISBN 978-3-95450-181-6

$$F = \frac{y}{tg\Delta\varphi}$$

And taking into account equality (4) focal length is equal to

$$\boldsymbol{F = \frac{R}{4tg\alpha}}$$

In the other perpendicular direction of the focal distance of the lens is [2]

$$\boldsymbol{F = -\frac{R}{4tg\alpha}}$$

THE STIFFNESS OF FOCUSING SYSTEM WITH GRADIENT DIPOLES

Evaluation of rigidity of focusing will be made on the system consisting of short lenses, which are located at a distance $l/2$ from each other (Fig.3). When the oscillation amplitude of the particles is limited by the value $\pm y_m$, and the transverse speed of a particle is equal $\pm v_{m,y}$), the parameters of the trajectory of a particle are connected with the following ratios:

$$y_m = \frac{1}{4}L \cdot tg\Delta\varphi, \quad \frac{v_{m,y}}{v} = sin\Delta\varphi$$

Since the transverse speed of the particle after passing through the lens $v_{out,y}$ are equal in magn (5) ind opposite in sign to the velocity before passing through the lenses $v_{in,y} = v_{m,y}$

$$v_{out,y} = v_{m,y} + v\frac{2x_1 - x_2}{R} = -v_{m,y},$$

Therefore, in view of (3)

$$\frac{v_{m,y}}{v} = \frac{2y_m}{R}tg\alpha$$

In view of (5) we find

$$y_m = \frac{R}{2}sin\Delta\varphi\frac{1}{tg\alpha} = \frac{1}{4}L \cdot tg\Delta\varphi,$$

The length of the period of oscillation of a particle in a focusing system with gradient dipoles of equal

$$L = \frac{2R}{tg\alpha} \cdot \frac{1}{cos\Delta\varphi} \cong \frac{2R}{tg\alpha} = \frac{2}{tg\alpha}\frac{P}{qB_z}$$

The frequency of betatron oscillations in the system

$$\omega = 2\pi\frac{v}{L}$$

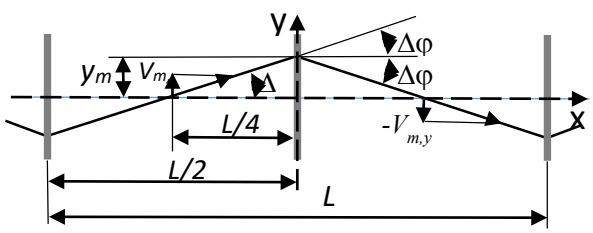

Figure 3: The particle trajectory in the focusing system with short gradient dipoles.

For comparison, the length of the period of oscillation L_0 same particles in a magnetic field B_0 with the index $n_0 = 1$ are equal (Fig. 4) and the frequency of betatron oscillations

$$\omega_0 = 2\pi\frac{v}{L_0}$$

The ratio of the frequencies of betatron oscillations

$$\frac{\omega}{\omega_0} = \frac{L_0}{L} = \pi tg\alpha\frac{B_z}{B_0} = \sqrt{\frac{n}{n_0}}$$

The equivalent index n of the focusing system with gradient dipoles of equal

$$n = \left(\pi tg\alpha\frac{B_z}{B_0}\right)^2$$

For example, if $B_z = B_o$, and $tg\alpha = 1$ $(\alpha = 45^0)$ $n = 9.87$

If $\alpha = 60^0$, $n = 29.6$

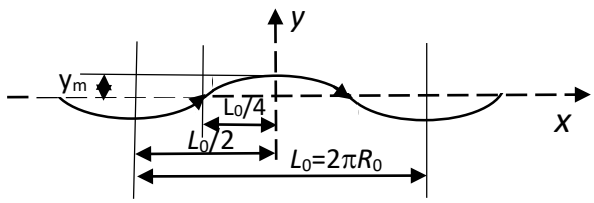

Figure 4: The particle trajectory in the magnetic field with the index $n_0 = 1$.

CONCLUSION

Magnetic dipoles, in which the momentum of the forces acting on the particles depends on the transverse coordinates can be used for tight focusing of beams of charged particles.

The use of such a gradient dipoles allows you to create lenses, which in one of the transverse coordinates rejects all particles to the axis of the system and deviate from the axis in the other transverse coordinate.

Lenses with three dipoles are characterized in that in these lenses there are no small displacement of the beam axis at the lens output.

When the orientation of the magnetic poles of the lenses in accordance with the orientation of the poles of the leading dipoles of cyclic accelerator these gradient magnetic lenses can be part of the leading dipoles.

Changing the focusing action of the lens for defocusing action and Vice versa is achieved by changing polarity of the magnetic field

Shorter focal length of these lenses with gradient dipoles allows you to create a system with the equivalent indicator field $n \gg 1$. Gradient dipoles with plane-parallel poles can provide the vertical focusing of particles in cyclic accelerators with the magnetic field index n≫1 and in the induction synchrotrons with constant magnetic field [1].

REFERENCES

[1] Dolbilov G.V. The Induction Synchrotron with a Constant Magnetic Field // Proc. of the XXIV Russian Particle Accelerator Conference RuPAC-2014, Obninsk, Russia, http://accelconf.web.cern.ch/AccelConf/rupac2014/papers/wepsb29

[2] Livingood J. Principle of Cyclic Particle Accelerators // Argonne National Laboratory.

ISBN 978-3-95450-181-6

THE ELECTROMAGNETIC FIELD STRUCTURE IN THE CIRCULAR WAVEGUIDE WITH TRANSVERSE BOUNDARY*

A.A. Grigoreva†, A.V. Tyukhtin, V.V. Vorobev, S.N. Galyamin
St. Petersburg State University, 7/9 Universitetskaya nab., St. Petersburg, 199034 Russia

Abstract

We consider the electromagnetic field structure in a circular partially regular waveguide. One semi-infinite part of the waveguide is empty and the other consists of a cylindrical dielectric layer and a vacuum channel. It is assumed that the incident field is the transverse symmetrical magnetic mode launching either from the vacuum part or from the dielectric one. The analytical investigation is performed by use the technique of mode decomposition for reflected and transmitted fields. Typical dependencies of the field excitation coefficients on the channel radius are presented and discussed. Also the comparison of analytical results with numerical simulations is adduced.

INTRODUCTION

The work is devoted to the study of the electromagnetic field in the circular infinite waveguide which has a transverse boundary between vacuum area and the dielectric area containing axisymmetric vacuum channel. Earlier the problems in sectionally regular waveguides were solved for planar waveguide [1] or for cylindrical in the absence of the coaxial channel [2, 3]. Underline that the presence of the channel leads to emergence of mode transformation effect on the transverse boundary, which in turn causes an infinite sets on eigenmodes in the reflected and transmitted fields.

The considered problem is of interests, for instance, for the wakefield acceleration technique [4], namely for the analysis of formation process of the wave field by bunch moving in a dielectric waveguide structure. Therefore it is important to consider the field excited by bunch entering into the dielectric area.

Another example relates to the problem of the terahertz radiation generation by an electron bunch in a dielectric loaded waveguide structure [5]. In this case the question of the wave field which is excited by a bunch entering into the vacuum area of the waveguide becomes critical.

Here we consider the problem where the incident field is a symmetrical TM mode. In this paper the waveguide characteristics are chosen so that the incident mode can be both propagating or evanescent.

ANALYTICAL INVESTIGATION

We consider the problem with harmonic $(exp(-i\omega t))$ axially symmetrical TM_{0i} mode undergoing transformation on the transverse boundary of the waveguide. It is assumed that the left part of the waveguide $(z < 0)$ is loaded with medium having characteristics ε_c, μ_c and the right part $(z > 0)$ contains the cylindrical dielectric layer and a coaxial channel with characteristics ε_d, μ_d and ε_c, μ_c respectively (Fig. 1). Initially it is assumed that the mediums are dissipative, that is, $Im(\varepsilon_{c,d}) > 0$ for positive frequencies. Note that the dissipation is negligible quantity and the values ε_c, μ_c are set to 1 (vacuum) for further numerical calculations. Both mediums are isotropic, homogeneous and nondispersive.

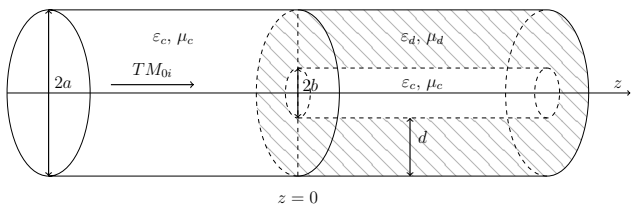

Figure 1: The case of the mode launching from the vacuum part of the waveguide

The incident field can be written by using the single-component vector-potential (the cylindrical coordinates (r, φ, z) are used):

$$A_z^{(i)} = J_0\left(\eta_i r/a\right) \exp\left(ih^{(i)} z\right), \qquad (1)$$

where η_i is the zero of Bessel function $J_0(\eta)$, $h_i = \sqrt{k_c^2 - \eta_i^2/a^2}$ is the longitudinal wavenumber and $k_c = \omega\sqrt{\varepsilon_c \mu_c}/c$. Note that the attenuation condition results in the inequality $Im\left(h^{(i)}\right) > 0$.

Analytical study is performed by using the well-known cross-linking method. According to this method the reflected and transmitted fields are written in a form of the infinite series of eigenmodes for the empty part of the waveguide and partially dielectric part respectively:

$$A_z^{(r)} = \sum_{n=1}^{\infty} R_n \frac{\eta_i}{\eta_n} J_0\left(\eta_n \rho\right) \exp\left(-ih_n^{(r)} z\right),$$
$$h_n^{(r)} = \sqrt{k_c^2 - \eta_n^2/a^2}, \quad \mathrm{Im}\left(h_n^{(r)}\right) > 0, \qquad (2)$$

$$A_z^{(t)} = \sum_{n=1}^{\infty} T_n \frac{\eta_i}{\chi_{cn}} \left\{ \begin{array}{l} J_0\left(\chi_{cn}\rho\right) \quad \text{for } \rho < b/a \\ C_{1n} H_0^{(1)}\left(\chi_{dn}\rho\right) + C_{2n} J_0\left(\chi_{dn}\rho\right) \\ \text{for } b/a < \rho < 1 \end{array} \right\}$$
$$\times \exp\left(ih_n^{(t)} z\right),$$
$$h_n^{(t)} = \sqrt{k_c^2 - \chi_{cn}^2/a^2}, \ \mathrm{Im}\left(h_n^{(t)}\right) > 0. \qquad (3)$$

* Work supported by Russian Foundation for Basic Research (No. 15-02-03913) and Grant of the President of Russian Federation (No. 6765.2015.2).

† aleksandra.a.grigoreva@gmail.com

ISBN 978-3-95450-181-6

where $\rho = r/a$, $h_n^{(r,t)}$ is the longitudinal wavenumber of reflected or transmitted TM_{0n} mode, R_n and T_n are unknown excitation coefficients of the reflected and the transmitted modes. At that the values C_{1n}, C_{2n} and χ_c, χ_d are defined by continuity conditions for the fields components $E_z^{(t)}$, $H_\varphi^{(t)}$ on the boundary between vacuum and dielectric ($r = b$).

Mode excitation coefficients R_n, T_n are obtained using the continuity condition for the fields' components E_z and H_φ on the transverse boundary ($z = 0$).

The system with infinite number of linear algebraic equations for the excitation coefficients is obtained. In the general case of arbitrary waveguides characteristics this system is analytically insoluble and a numerical algorithm should be developed for the R_n and T_n coefficients calculation.

Note that the results of the analytical studies for two dedicated cases of a narrow channel (when $b/a \ll 1$) and a thin dielectric layer (when $d/a \ll 1$), as well as the case of the mode launching from partially dielectric part of the waveguide are presented in [6].

NUMERICAL CALCULATIONS AND DISCUSSION

To analyze the electromagnetic field structure in general case the numerical algorithm for calculating excitation coefficients of the reflected and transmitted modes has been implemented in computer algebra system Mathcad. The problem is reduced to the solution of the infinite system of equation. However for the further calculations it is possible to consider the system with some finite set of modes since most of high-order reflected and transmitted modes are evanescent and they decay exponentially with increasing the distance from the transverse boundary. Therefore, the method of successive approximations is used: at first the system for excitation coefficients is solved at some finite set of modes, then the systems size is increased by a unit at every further step until the relative change of obtained result for main excited modes becomes sufficiently small (usually not more than 1%).

In the case of interaction between the evanescent incident mode and the boundary the consideration of the refraction R_{zn} and transmission T_{zn} coefficients is more convenient for the field analysis:

$$R_{zn} = \left.\frac{E_{z_n}^{(r)}}{E_z^{(i)}}\right|_{z=0,\ \rho\to 0}, \quad T_{zn} = \left.\frac{E_{z_n}^{(t)}}{E_z^{(i)}}\right|_{z=0,\ \rho\to 0}.$$

The left graphics in Fig.2 presents the absolute values of R_z and T_z coefficient for the 3rd evanescent mode launching from the vacuum part of the waveguide. It is interesting to note that this mode excites two propagating modes in the reflected field and up to four modes in the transmitted field, depending on the channel radius.

In order to verify the obtained analytical results the comparison with simulations carried out in Comsol system has been made for the cases when the incident modes are propagating ones. For this to be done, the normalized excitation coefficients corresponding to the Comsol S-parameters are used

$$W_n^{(r,t)} = \lambda_n^{(r,t)} \alpha_n^{(r,t)}, \tag{4}$$

where $\alpha_n^{(r,t)} = R_n; T_n$ and

$$\lambda_n^{(r,t)^2} = \left(\int_0^1 E_{r_n}^{(r,t)} \overline{H}_{\varphi_n}^{(r,t)} \rho d\rho\right) \cdot \left(\int_0^1 E_r^{(i)} \overline{H}_\varphi^{(i)} \rho d\rho\right)^{-1}$$

(bar means complex conjugation). Value $\lambda_n^{(r,t)^2}$ is the ratio of the averaged energy flux of the reflected or transmitted mode to the averaged energy flux of the incident mode.

The absolute values of the normalized coefficients $W_n^{(r,t)}$ obtained from the analytical expressions and absolute values of S-parameters calculated in Comsol system are shown in Fig.2.

The middle figures represent the interaction of the 1st incident mode launching from the vacuum part of the waveguide with the transverse boundary. One can see that there are two propagating modes in the reflected field. At that the 1st mode prevails in the wide range of channel radius and only for sufficiently large vacuum channel the 2nd mode becomes the main. For the considered waveguides parameters, the transmitted field can contain up to six propagating modes depending on the channel radius. However Fig. 2 illustrates only the first four modes since the 5th and the 6th modes are excited at very narrow channels and their excitation coefficients are much less than the others. So the 5th and the 6th modes do not give a considerable contribution to the transmitted field.

The right figures refer to the case of the TM_{01} mode launching from the partially dielectric part of the waveguide. Up to five propagating modes can be excited in reflected field in this case. However the 5th mode is very weak excited and exists only in the case of narrow channels (therefore it is not represented in Fig. 2). Despite of the fact that the 1st mode is the main in the reflected field for a wide range of the channel radii the TM_{03} mode can be prevailing at sufficiently large values ($7.4 \le b \le 9.3$ mm). The TM_{01} mode dominates in the transmitted field at arbitrary channel radius.

One can see that the results based on the analytical investigation and results of Comsol simulations are in very good agreement for both cases

CONCLUSION

The field structure in the cylindrical waveguide having a transverse boundary between vacuum and partially dielectric areas is considered. The analytical investigation is conducted by the expansion of the reflected and transmitted fields into a series of eigenmodes and using the continuity conditions for the tangential fields' components at the boundary. The problem has been reduced to the solution of an infinite system of linear algebraic equations that can't

ISBN 978-3-95450-181-6

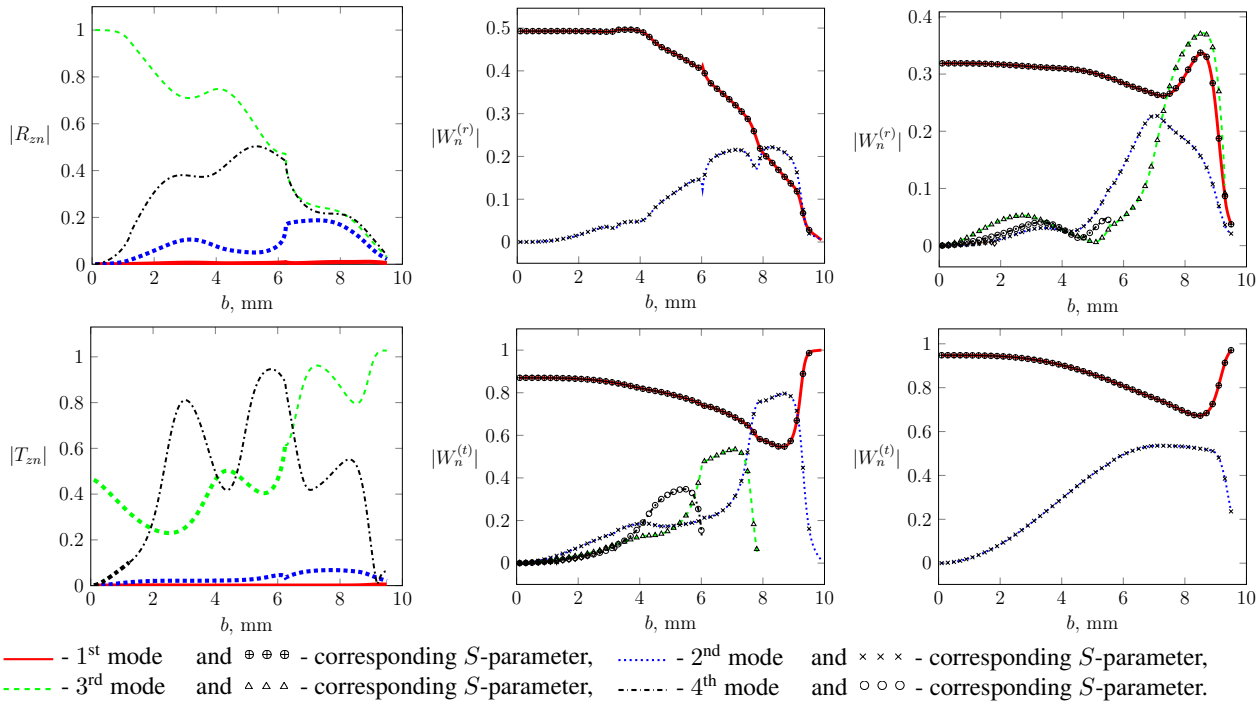

Figure 2: The left graphics correspond to the case when the incident mode is evanescent (the 3rd mode launching from the empty part of the waveguide); dependencies of the coefficients R_{zn} and T_{zn} on the channel radius b (mm) are shown; $a = 10$ mm, $\varepsilon_d = 4$, $f = 30$ GHz. Bold lines correspond to the propagating modes, thin lines correspond to the evanescent modes. The middle and the right graphics correspond to the case when the incident mode is propagating; dependencies of the coefficients $W_n^{(r,t)}$ on the channel radius b (mm) in the case of $a = 10$ mm are shown. Middle: the 1st incident mode launches from the empty part, $\varepsilon_d = 10$, $f = 30$ GHz. Right: the 1st incident mode launches from the partially dielectric part, $\varepsilon_d = 4$, $f = 40$ GHz. Lines correspond to the Mathcad results, marks correspond to Comsol results.

be solved analytically at the arbitrary waveguide parameters. The numerical solution of the obtained system is conducted in algebra system Mathcad. The typical behaviour of the normalized excitation coefficients of the reflected and transmitted modes are presented and discussed. Also the comparisons with Comsol simulations results demonstrate high accuracy of the calculations based on analytical analysis.

REFERENCES

[1] R. Mittra and S. W. Lee, Analytical techniques in the theory of guided waves, (Macmillan, 1971).

[2] T. Yu. Alekhina and A. V. Tyukhtin, "Self-acceleration of a charge intersecting a boundary surface in a waveguide", Phys. Rev. STAB. 16 (2013) 081301.

[3] T. Yu. Alekhina and A. V. Tyukhtin, "Cherenkov-transition radiation in a waveguide with a dielectric-vacuum boundary", Phys. Rev. STAB. 15 (2012) 091302.

[4] C. Jing, A. Kanareykin, J. G. Power, M. Conde, W. Liu, S. Antipov, P. Schoessow and W. Gai, "Experimental demonstration of wakeeld acceleration in tunable dielectric loaded accelerating structure", Phys. Rev. Lett. 106 (2011) 164802.

[5] A. M. Cook, R. Tikhoplav, S. Y. Tochitsky, G. Travish, O. Williams and J. Rosenzweig, "Observation of narrow-band terahertz coherent cherenkov radiation from a cylindrical dielectric-lined waveguide", Phys. Rev. Lett. 103 (2009) 095003.

[6] A. A. Grigoreva, A. V. Tyukhtin, V. V. Vorobev, T. Yu. Alekhina and S. Antipov, "Mode transformation in a circular waveguide with a transverse boundary between a vacuum and a partially dielectric area", IEEE Trans. Microw. Theory Techn. 64 (2016) 3441.

ISBN 978-3-95450-181-6

MODEL OF THE OPTIMAL PARAMETERS CHOICE FOR THE CHARGED PARTICLES BEAM

O.A.Malafeyev, S.A.Nemnyugin * SPbSU, Saint-Petersburg, Russian Federation

Abstract

Problem of the optimal parameters choice for the charged particles beam is considered. It is supposed that the beam is characterized by the set of quality characteristics and may be controlled by multiple parameters. It is assumed that in general case choice of the control parameters that is optimal for all criteria is not possible. In the article the optimization problem is formulated as the conflict control problem. The case is considered when parameters that should be optimized form the vector. Two cases are under consideration. In the first one fully optimal solution may be found. In the second case finding of the compromise solution is considered. Computing algorithms are proposed.

INTRODUCTION

The charged particles beams are used in different areas of technics, science, medicine etc. Accurate adjustment of the beam characteristics often plays crucial role in producing final results of a target irradiation. There are different approaches to the optimization of the beam parameters adjustment [1], [2], [3]. In many cases there are multiple criteria of the beam quality which should be taken into account. Some of these characteristics should be considered in tight connection with the target properties. For example in the hadron therapy among possible characteristics of the particles beam following ones may be mentioned: energy, intensity, biological efficiency, depth of the Bragg peak localization, influence of the fragmentation products and so on. Importance of the problem is confirmed by projects in hadron therapy [4], new facilities in high energy physics [5].

In the article [6] problem of the focusing system optimization was considered with the only one beam characteristic - beam divergence. The only control device was the accelerator's focusing system. In more general situations few beam characteristics may be important and few control channels may be used. For example, in stereotactic radiosurgery a set of up to few hundreds of irradiation channels are used which should be adjusted for more efficient action on tumor. In these case all optimization parameters may be considered as independent. On the other hand multiple quality characteristics may be dependent. In the hadron radiotherapy energy of the therapeutic beam is connected with its biological efficiency. But change of the beam energy influences depth and width of the Bragg peak localization. Shift of the depth-dose distribution maximum and its broadening will affect treatment effect. Also increasing of the beam energy will increase effects of fragmentation also affecting results of the hadron therapy. So some criteria of optimization may be contradictory. In this case choice of optimal parameters should be considered from the point of view of finding of a compromise of all characteristics of the particles beam.

At the present paper the problem of the beam optimization with multiple quality characteristics is considered as the problem of conflict control. Both cases of independent and conflicting characteristics are considered. Formalization of the problem and algorithms of its solution are proposed.

FORMALIZATION OF THE CONFLICT CONTROL PROBLEM

It is supposed that dynamic of the beam characteristics may be described by the system of differential equations:

$$\dot{\mathbf{X}} = \mathbf{f}(\mathbf{X}, \mathbf{u}, \mathbf{v}), \tag{1}$$

with initial condition

$$\mathbf{X}(t = 0) = \mathbf{X}_0, t \in [0, T] \tag{2}$$

Here $\mathbf{X} \in \mathrm{R}^m$ is state vector, $\mathbf{u} \in U \subset \mathrm{R}^p$ are control parameters which should be adjusted to improve the beam's quality, and $\mathbf{v} \in V \subset \mathrm{R}^q$ are control parameters, associated with uncontrollable external actions. U and V are compact sets in Euclidean spaces R^p and R^q. It is supposed that vector function $\mathbf{f}(\mathbf{X}, \mathbf{u}, \mathbf{v})$ in (1) satisfies following conditions:

1. $\mathbf{f}$ is continuous on $(\mathbf{X}, \mathbf{u}, \mathbf{v}) \in R^m \times U \times V$;
2. $\mathbf{f}$ satisfies Lipschitz condition for $\mathbf{X}$ with constant A, i.e. for any $\mathbf{u} \in U$, $\mathbf{v} \in V$ and $\mathbf{X}, \overline{\mathbf{X}} \in R^m$ the following inequality holds:
$$\left|\mathbf{f}(\mathbf{X}, \mathbf{u}, \mathbf{v}) - \mathbf{f}(\overline{\mathbf{X}}, \mathbf{u}, \mathbf{v})\right| \leq A \left|\mathbf{X} - \overline{\mathbf{X}}\right|, \tag{3}$$
3. $\mathbf{f}$ is bounded, i.e. for any $\mathbf{u} \in U$, $\mathbf{v} \in V$, $\mathbf{X} \in R^m$:
$$|\mathbf{f}(\mathbf{X}, \mathbf{u}, \mathbf{v})| \leq B, \quad (B > 0); \tag{4}$$
4. for any $\mathbf{X} \in R^m$ set
$$\{\mathbf{f}(\mathbf{X}, \mathbf{u}, \mathbf{v}) \mid \mathbf{u} \in U, \mathbf{v} \in V\}$$
is convex.

We assume that these conditions hold for a wide range of physical situations under consideration.

Definition. Measurable on the interval $[0, T]$ vector functions $\mathbf{u} = \mathbf{u}(t)$ $(\mathbf{v} = \mathbf{v}(t))$ which satisfies conditions

* s.nemnyugin@spbu.ru

ISBN 978-3-95450-181-6

$\mathbf{u}(t) \in U$ ($\mathbf{v}(t) \in V$) for any $t \in [0, T]$ are called *admissible controls*.

For any pair of admissible controls $\mathbf{u}(t),\ t \in [0, T]$ and $\mathbf{v}(t),\ t \in [0, T]$ conditions 1–3 guarantee existence and uniqueness of solution continuable to interval $[0, T]$ for the system (1), which satisfies initial condition (2).

At the moment T of achieving of required quality, process participant who makes control choice $\mathbf{v}$ gets payoff equal to $\mathbf{H}(\mathbf{X}(T))$, where $\mathbf{X}(T)$ is final system state, $\mathbf{H} : R^m \to R^n$ is uniformly continuous bounded vector-function which satisfies Lipschitz condition: for any $\mathbf{X}, \overline{\mathbf{X}} \in R^m$ there exists positive constant L, such as:

$$\left|\mathbf{H}(\mathbf{X}) - \mathbf{H}(\overline{\mathbf{X}})\right| \le L \left|\mathbf{X} - \overline{\mathbf{X}}\right|.$$

Operator's goal is getting the optimal solution for $\mathbf{H}(\cdot)$ by the choice of control $\mathbf{u}$. External factors may be considered as action of the other operator (let us call him "operator 2") with opposite goal.

Definition *Control strategy* $\varphi(\psi)$ of operator (operator 2) is called pair (σ_1, K_{σ_1}) $((\sigma_2, K_{\sigma_2}))$, where $\sigma_1 = \{t_0 = 0 < t_1 < \ldots < t_{N_{\sigma_1}} = T\}$ ($\sigma_2 = \{t_0 = 0 < t_1 < \ldots < t_{N_{\sigma_2}} = T\}$) is arbitrary partitioning of interval $[0, T]$ and $K_{\sigma_1}(K_{\sigma_2})$ is mapping that associates with state of information of operator (operator 2) at time's moments $t_i \in \sigma_1,\ i = 0, \ldots, N_{\sigma_1} - 1$ ($t_j \in \sigma_2,\ j = 0, \ldots, N_{\sigma_2} - 1$) admissible controls $u_i(\tau),\ \tau \in [t_i, t_{i+1})$ ($v_j(\tau),\ \tau \in [t_j, t_{j+1})$).

Set of control strategies of operator (operator 2) is denoted by $\Phi(\Psi)$. Trajectory $\chi(\varphi, \psi)$ is uniquely defined by the pair of strategies (φ, ψ) in the following way. Let $\sigma = \{t_0 < t_1 < \ldots < t_{N_\sigma}\}, \sigma = \sigma_1 \cup \sigma_2$ is arbitrary decomposition of the time interval $[0, T]$. At any subinterval $[t_k, t_{k+1}), k = 0, 1, \ldots, N_\sigma - 1$ images of maps K_{σ_1} and K_{σ_2} are continuous controls $\mathbf{u}(t)$ and $\mathbf{v}(t)$ so on subinterval $[t_0, t_1)$ eq.(1) has unique solution $\mathbf{X}(t) = \mathbf{X}(\mathbf{X}_0, \mathbf{u}(t), \mathbf{v}(t)), \mathbf{X}(t_0) = \mathbf{X}_0, t \in [t_0, t_1)$. After that eq.(1) should be solved with initial conditions $\mathbf{X}(t_1)$. Making iterations of the algorithm the unique trajectory $\chi(\varphi, \psi)$ of control parameters may be obtained.

Payoff function of operator for the situation (φ, ψ) is defined as follows:

$$\mathbf{K}(\mathbf{X}_0, \varphi, \psi) = \mathbf{H}(\chi(\varphi, \psi)(T)),$$

where $\chi(\varphi, \psi)(T) = \chi(\varphi, \psi)(t)\,|_{t=T}$ and $\chi(\varphi, \psi)(t)$ is trajectory of control corresponding to $(\varphi, \psi) \in \Phi \times \Psi$.

Due to antagonistic type of operators interaction payoff function of operator 2 is equal to $-\mathbf{K}(\mathbf{X}_0, \varphi, \psi)$.

In [7] it was demonstrated that ε-equilibrium exists in games in complete metric spaces, when dynamics of the game is defined by generalized dynamic system.

NUMERICAL SCHEMA FOR THE HAMILTON-JACOBY EQUATION

$\mathbf{\Omega}$ is uniform mesh in the configuration space of the system R^m. The mesh steps over spatial variables are $h_\alpha > 0$, $\alpha = 1, 2, \ldots, m$ and:

$$\omega_h = \{\mathbf{X}^j = (x_{1_{j_1}}, x_{2_{j_2}}, \ldots, x_{m_{j_m}}),\ x_{\alpha_{j_\alpha}} = j_\alpha h_\alpha,\ j_\alpha = 0, \pm 1, \pm 2, \ldots;\ h_\alpha = 1/M_\alpha,\ \alpha = 1, 2, \ldots, m\}$$

where $h = (h_1, h_2, \ldots, h_m)$, $j = (j_1, j_2, \ldots, j_m)$ and M_α are positive integers.

Let us introduce uniform mesh also on the time interval $[0, T]$ with step $\delta > 0$

$$\overline{\omega}_\delta = \{t_n = n\delta,\ t_0 = 0,\ t_{N_\sigma} = T,\ n = 0, 1, \ldots, N_\sigma\}$$

which coincides with partitioning σ.

Let us denote mesh function defined in mesh nodes $\omega_{h\delta}$ as $\overline{V}^n_{j_1, j_2, \ldots, j_m}$, where:

$$\omega_{h\delta} = \omega_h \times \overline{\omega}_\delta = \left\{(\mathbf{X}^j, t_n) |\ \mathbf{X}^j \in \overline{\omega}_\delta\right\}.$$

Change of the parameter h leads to mesh sequence $\{\omega_h\}$ which exhausts countable everywhere dense set in R^m. Let us denote this set as $X = \{\omega_h\}$.

The Hamilton-Jacoby or Bellman-Isaacs equation may be written for the value function $\overline{\mathbf{V}}(\cdot)$:

$$\frac{\partial \overline{\mathbf{V}}}{\partial \tau} = \min_{\{\mathbf{u}\}} \max_{\{\mathbf{v}\}} \left[\sum_{i=1}^{m} \frac{\partial \overline{\mathbf{V}}}{\partial x_i} \cdot f_i(\mathbf{X}, \mathbf{u}, \mathbf{v})\right] \tag{5}$$

with initial condition

$$\overline{\mathbf{V}}(\mathbf{X}, \tau)\big|_{\tau=0} = \mathbf{H}(\mathbf{X}(T)), \tag{6}$$

where $\tau = T - t, \tau \in [0, T]$.

Let us associate with the problem (5)-(6) following finite difference scheme on the mesh $\omega_{h\delta}$:

$$\begin{aligned}
\overline{V}^n_{j_1, j_2, \ldots, j_m} &= \overline{V}^{n-1}_{j_1, j_2, \ldots, j_m} + \delta \min_{\{\mathbf{u}\}} \max_{\{\mathbf{v}\}} \\
&\left[\frac{\overline{V}^{n-1}_{j_1+1, j_2, \ldots, j_m} - \overline{V}^{n-1}_{j_1, j_2, \ldots, j_m}}{h_1} \cdot f_1(\mathbf{X}^j, \mathbf{u}, \mathbf{v}) + \ldots\right. \\
&\left. \ldots + \frac{\overline{V}^{n-1}_{j_1, j_2, \ldots, j_m+1} - \overline{V}^{n-1}_{j_1, j_2, \ldots, j_m}}{h_m} \cdot f_m(\mathbf{X}^j, \mathbf{u}, \mathbf{v})\right], \\
&j_i \in Z,\ i = \overline{1, m};\ n = 1, \ldots, N_\sigma, \\
\overline{V}^0_{j_1, j_2, \ldots, j_m} &= H_{j_1, \ldots, j_m},\ j_i \in Z,\ i = \overline{1, m};\ n = 0.
\end{aligned} \tag{7}$$

Properties of the scheme (7) and amenity of its application to solve some control problems are considered in [8]-[10].

COMPROMISE SOLUTION OF THE BEAM CONTROL PROBLEM

Let us consider a situation when it is impossible to make one optimality parameter the best one without making any other optimality parameters worse off. Such kind of optimization should be considered in cases mentioned in the Introduction when improvement of some characteristic of the beam leads to worsening of other characteristics. In this case compromise solution of the beam control problem should be found.

ISBN 978-3-95450-181-6

Definition. *Compromise solution* is defined as follows. Let us $X = \{x\}$ is the set of all admissible solutions then

$$C_H = \Big\{ x \in X | \max_i (M_i - H_i(x)) \leq \leq \max_i (M_i - H_i(x')) \forall x' \in X \Big\}$$

Here

$$M_i = \max_{x \in X} H_i(x)$$

$\mathbf{H} = (H_1, H_2, ..., H_n)$ is vector-function which describes the set of optimization criteria and $H_i : X \to R^1$, $\mathbf{H} : X \to R^n$. Compromise solution C_H of the optimization problem may be found as a result of the following algorithm.

1. Find "ideal vector" $\mathbf{M} = (M_1, M_2, ..., M_n)$.
2. Fix $x \in X$ and define corresponding discrepancy vector:

   $$\mathbf{\Delta}_k = (M_1 - H_1(x), M_2 - H_2(x), ..., M_n - H_n(x)).$$

3. Rearrange vector's components on increasing:

   $$\mathbf{\Delta}'_k = (M'_1 - H'_1(x), M'_2 - H'_2(x), ..., M'_n - H'_n(x)).$$

4. Choose $x \in X$ which leads to

   $$C_H^I = arg \min_{x \in C_H^{I-1}} \max_{i \in I} \{M'_i - H_i(x)'\}$$

   where $I = \{1, 2, ..., n\}$.

5. If the set of compromise solutions includes few elements then steps should be repeated for the next beam characteristic and so on.

Usually the resulting control is the only solution of the optimization problem.

CONCLUSION

In the article problem of finding of the beam optimal parameters choice is formulated as control problem. It makes possible to use mathematical and computing techniques of dynamic programming. Computational method for the compromise solution is formulated. Some issues relating to mathematical aspects of conflict control are discussed in [11]-[14]. High-performance computing may be used to reduce computing time [15].

REFERENCES

[1] D.A. Ovsyannikov, N.V. Egorov, Mathematical Modelling of. Electron and Ion Beams Forming Systems, St.-Petersburg University. Press, 1998.

[2] E.M.Vinogradova,N.V.Egorov, Simulation of an electron gun with a field-effect cathode, Journal of Communications Technology and Electronics, v. 49, N 2, 2004, P.232.

[3] G.R.Brewer, Focusing of High-density electron beams in Focusing of Charged Particles, Ed. by A.Septier, v.11, 1967, p.23

[4] O.A.Kalatusha, O.V.Ruban, S.A.Nemnyugin, Computer simulation of radiation dose absorption in biological specimens, Mathematical Modelling and Geometry, v.4, N 1, 2016, P.41-50.

[5] S.P.Merts, S.V.Razin, O.V.Rogachevskii, Accumulation of space charge in the time-projection chamber of MPD detector, Pisma v zhurnal "Physika elementarnyh tchastic i atomnogo yadra", v.10, N 1, 2013, P.113 (in Russian).

[6] G. V. Alferov, O. A. Malafeyev, S. A. Nemnyugin. Charged Particles Beam Focusing with Uncontrollable Changing Parameters // 2014 2nd International Conference on Emission Electronics, ICEE 2014 Joined with 10th International Vacuum Electron Sources Conference, IVESC 2014, International Conference on Computer Technologies in Physical and Engineering Applications, ICCTPEA 2014, 20th International Workshop on Beam Dynamics and Optimization, BDO 2014 - Proceedings, 2014. — P. 25-27.

[7] O.A.Malafeyev. Situation of equilibrium in dynamic games, Kibernetika, N 3, 1974, P.111. (in Russian)

[8] O.A.Malafeyev, M.S.Troeva (Davydova), On the weak solution of the basic equation of differential game and its approximation. Voprosy mehaniki i processov upravleniya. 1991. N 14. P. 42 (in Russian).

[9] O.A.Malafeyev, Control in conflict dynamic systems. - Saint-Petersburg: Izdatelstvo SPbGU, 1993 (in Russian).

[10] O.A.Malafeyev, Stability of solutions of many-criterial optimization problems and conflict control processes. - Leningrad: Izdatelstvo LGU, 1990 (in Russian).

[11] V.N.Kolokoltsov, O.A.Malafeyev, Understanding Game Theory, New Jersey, London,World Scientific Publishing Company 2010.

[12] O.A.Malafeyev, A.J.Radchenko, A.F.Zubova, Idempotent analysis and many-agent interaction in sybchronization problems and production systems. Linear and non-linear systems dynamics, V.25, N 2, Works of ISI RAS, P.233.

[13] V.N.Kolokoltsov, O.A.Malafeyev, Dynamic competitive systems of many-agent interaction and their asymptotics, part 1, Vestnik of civil engineers, V.5., 2010, P.144.

[14] V.N.Kolokoltsov, O.A.Malafeyev, Dynamic competitive systems of many-agent interaction and their asymptotics, part 2, Vestnik of civil engineers, V.5, 2010, P.133.

[15] A.E.Basalaev, A.S.Bondarenko, S.P.Merts, S.A.Nemnyugin, A.N.Timofeev, Application of high-performance computing technologies in problems of high-energy physics for NICA/MPD project. Vestnik Yuzhno-Uralskogo Gosudarstvennogo Universiteta, v.2, N 1, 2013, p.17 (in Russian).

ISBN 978-3-95450-181-6

GOLD IONS BEAM LOSSES AT THE NUCLOTRON BOOSTER

A. V. Philippov†, A. V. Tuzikov
Veksler and Baldin Laboratory of High Energy Physics,
Joint Institute for Nuclear Research, Dubna, Russia

Abstract

The calculation results of the gold ions beam losses along the Nuclotron Booster perimeter are given. The presented results take the ion stimulated desorption from the cold surface of the vacuum chamber and collimation of charge-exchanged gold ions into account.

INTRODUCTION

The main goals of the Booster as the intermediate machine in NICA accelerator complex are the following [1]: to accumulate of $2 \cdot 10^9$ gold $^{197}Au^{31+}$ ions and to accelerate them from 3.2 MeV/*u* up to 578 MeV/*u* which is sufficient for their effective stripping to the bare gold nuclei state in the Booster-Nuclotron beam transport channel; forming of the required beam emittance with electron cooling system at energy 65 MeV/*u*; providing a fast extraction of the accelerated beam for its injection into the Nuclotron.

The Booster acceleration ramp is divided into four stages (see Figure 1): adiabatic ion capture into the separatrix during 0.02 s at the magnetic field plateau at injection energy of 3.2 MeV/*u*, ion acceleration up to 65 MeV/*u* during 0.4 s, electron cooling of $^{197}Au^{31+}$ ions during 1 s and ion acceleration up to energy 578 MeV/*u* during 1.3 s.

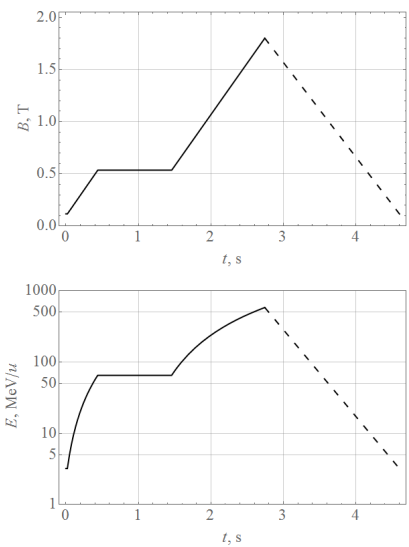

Figure 1: Booster time diagrams: magnetic field ramp (top) and acceleration ramp (bottom) of $^{197}Au^{31+}$ ions.

The vacuum system of the Booster divided into cold and warm parts. The surface of the cold part of the vacuum beam chamber has a temperature about 10 K, while the surface temperature of the warm part is close to room temperature 300 K. The cold part occupies most of the length of the Booster (circumference of the Booster is 210.96 m). Four warm straight part with a length about 7 m are present: injection (section 1); RF stations (section 2); extraction (section 3) and electron cooling system (section 4).

BEAM LOSSES MECHANISMS AND PROBLEM STATEMENT

Beam losses mechanisms are well known and studied in several number papers ([2] and references therein). The charge-exchange of accelerated ions with molecules of the residual gas and the ionization of these molecules are the primary processes that result in the loss of multicharged ions in circular accelerators and affect the vacuum pressure. In the first case, recharged ions of a beam are deflected by the lattice dipoles and hit the walls of the accelerator chamber with a higher energy at a small angle. In the second case, the residual gas ions are accelerated by the beam potential and hit the walls with a low energy (about 30 eV for the Booster case) under nearly perpendicular angle to their surface. In both cases a large amount of desorbed molecules from the chamber walls go back the chamber, however, the first process is the dominant one [3].

The charge particles beam losses are characterized by the set of differential equations based on the results presented in [2]:

$$\begin{cases} \dfrac{dN_q}{dt} = -N_q \sum\limits_{\alpha} \left\langle \Gamma_{\alpha,q\to q-1} + \Gamma_{\alpha,q\to q+1} + \Gamma^{\text{Bethe}}_{\alpha,q\to q+1} \right\rangle, \\ N_q\big|_{t=0} = N_{q,0}, \\ V\dfrac{\partial n_\alpha}{\partial t} = \dfrac{\partial}{\partial z}\left(C_\alpha \dfrac{\partial n_\alpha}{\partial z} \right) - n_\alpha S_\alpha + \dfrac{Q_\alpha A}{k_B T} + \\ \quad + N_q \left(\sum\limits_{\alpha} \left\langle \Gamma_{\alpha,q\to q-1} + \Gamma_{\alpha,q\to q+1} \right\rangle \eta_{\angle,\alpha} (1-\theta) + \right. \\ \quad \left. + \sum\limits_{\alpha'} \left\langle \Gamma^{\text{Bethe}}_{\alpha',q\to q+1} \right\rangle \eta_{\perp,\alpha'/\alpha} \right), \\ n_\alpha\big|_{t=0} = n_{\alpha,0}, \quad n_\alpha\big|_{z=0} = n_\alpha\big|_{z=L}, \quad \left.\dfrac{\partial n_\alpha}{\partial z}\right|_{z=0} = \left.\dfrac{\partial n_\alpha}{\partial z}\right|_{z=L}. \end{cases} \quad (1)$$

Here N_q — beam intensity that depends on time t only; n_α — concentration *of* α-kind of residual gas that depends on the longitudinal coordinate z and time t; V — accelerator volume; $\eta_{\angle,\alpha}$ and $\eta_{\perp,\alpha/\alpha'}$ — desorption coefficients; θ — collimation efficiency; A — the Booster vacuum chamber surface area; Q_α — outgassing rate; S_α — pumping speed; k_B — Boltzmann constant; T — temperature; $\Gamma_{\alpha,q\to q+1}$ and $\Gamma_{\alpha,q\to q-1}$ — charge-exchange rate for one electron loss and one electron capture by beam ions due to interaction with residual gas atoms or molecules; $\Gamma^{\text{Bethe}}_{\alpha,q\to q+1}$ — ionization rate of residual gas atoms or molecules by beam ions; C_α — specific conductivity of the Booster vacuum chamber; L — the Booster circumference. The values V, A and S_α are

† philippov@jinr.ru

ISBN 978-3-95450-181-6

taken per unit length. The angle brackets in the set (1) denote averaging over the longitudinal coordinate z.

The equations set (1) is supplemented by the following values: intensity at the initial time $N_{q,0}$, distributions of residual gas concentrations over the Booster ring at the initial time $n_{\alpha,0}$ and periodic boundary conditions for the residual gas concentration and its first-order derivative.

Note here that the charge-exchange rate is a product of the ion velocity, the cross section of the charge-exchange process (taken from [4]) and the residual gas concentration.

INITIAL DISTRIBUTION OF RESIDUAL GAS CONCENTRATIONS

The solution of the following system was used as the distribution of residual gas concentrations at the initial time:

$$\begin{cases} \dfrac{d}{dz}\left(C_\alpha \dfrac{dn_\alpha}{dz}\right) - n_\alpha S_\alpha + \dfrac{Q_\alpha A}{k_B T} = 0, \\ n_\alpha\big|_{z=0} = n_\alpha\big|_{z=L}, \quad \dfrac{\partial n_\alpha}{\partial z}\bigg|_{z=0} = \dfrac{\partial n_\alpha}{\partial z}\bigg|_{z=L}. \end{cases} \tag{2}$$

Let find the solution to the system (2) in two different cases: with actual pumps' layout around the Booster ring (pump is pinhole; speeds of the pumps are equal; pumps position at the centers of all intervals between the Booster lattice elements) and with averaged pumping speed in warm and cold Booster parts.

We found the solution of (3) over the Booster ring separately for warm and cold part. Let M is amount of parts of the simulated domain in case of actual pumps layout. This value includes amount of pumps, amount of additional conditions, such as defining the boundaries between warm and cold Booster parts and the periodical boundary conditions of the solution. In case of actual pumps layout for the equation set (3), we have:

$$\frac{d^2 n_{\alpha,i}}{dz^2} - \omega_{\alpha,i}^2 n_{\alpha,i} + \lambda_{\alpha,i} = 0, \quad i = \overline{1, M}. \tag{3}$$

The solution of the equation set (3) is as follows:

$$n_{\alpha,0} = \begin{cases} -\dfrac{\lambda_{\alpha,i}\left(z - z_{i-1}\right)^2}{2} + A_{\alpha,i}\left(z - z_{i-1}\right) + B_{\alpha,i}, \\ z_{i-1} \le z < z_i, \quad i \in \text{warm}, \\ \dfrac{\lambda_{\alpha,i}}{\omega_{\alpha,i}^2} + A_{\alpha,i} e^{\omega_{\alpha,i}(z - z_{i-1})} + B_{\alpha,i} e^{-\omega_{\alpha,i}(z - z_{i-1})}, \\ z_{i-1} \le z < z_i, \quad i \in \text{cold}. \end{cases} \tag{4}$$

Here z_i are the coordinates of boundaries of the domain parts. The expressions for $\omega_{\alpha,i}$ and $\lambda_{\alpha,i}$ are given in (5).

$$\omega_{\alpha,i} = \sqrt{\frac{S_{\alpha,\text{cold}}}{C_{\alpha,i}}}, \quad \lambda_{\alpha,i} = \frac{Q_{\alpha,i} A}{k_B T_i C_{\alpha,i}}, \quad \Omega_{\alpha,i} = \sqrt{\frac{S_{\alpha,i}}{C_{\alpha,i}}}. \tag{5}$$

The constants $A_{\alpha,i}$ and $B_{\alpha,i}$ are defined by crosslinking conditions at the boundaries of the simulated domain which are given in (6).

$$\begin{cases} n_{\alpha,\text{warm/cold},i}\big|_{z=z_i - z_{i-1}} = n_{\alpha,\text{warm/cold},i+1}\big|_{z=0}, \\ \Omega_{\alpha,i}^2\, n_{\alpha,\text{warm/cold},i}\big|_{z=z_i - z_{i-1}} = n'_{\alpha,\text{warm/cold},i+1}\big|_{z=0} - \\ - n'_{\alpha,\text{warm/cold},i}\big|_{z=z_i - z_{i-1}}, i = \overline{1, M-1}, \\ n_{\alpha,\text{cold},M}\big|_{z=z_M - z_{M-1}} = n_{\alpha,\text{warm},1}\big|_{z=0}, n'_{\alpha,\text{cold},M}\big|_{z=z_M - z_{M-1}} = n'_{\alpha,\text{warm},1}\big|_{z=0}. \end{cases} \tag{6}$$

In the second case with average pumping, we found the solutions of the system (2) in warm and cold parts separately:

$$\begin{cases} \dfrac{d^2 n_{\alpha,\text{warm}}}{dz^2} - \omega_{\alpha,\text{warm}}^2 n_{\alpha,\text{warm}} + \lambda_{\alpha,\text{warm}} = 0, n_{\alpha,\text{warm}}\big|_{z=0} = n_{\alpha,\text{cold}}\big|_{z=L_{\text{cold}}}, \\ \dfrac{d^2 n_{\alpha,\text{cold}}}{dz^2} - \omega_{\alpha,\text{cold}}^2 n_{\alpha,\text{cold}} + \lambda_{\alpha,\text{cold}} = 0, n_{\alpha,\text{cold}}\big|_{z=0} = n_{\alpha,\text{warm}}\big|_{z=L_{\text{warm}}}. \end{cases} \tag{7}$$

Here expressions for $\omega_{\alpha,\text{warm/cold}}$ and $\lambda_{\alpha,\text{warm/cold}}$ are given in (10) and $L_{\text{warm/cold}}$ — length of warm and cold Booster parts that were assumed equal to 7 and 98.48 m. The solution of the system (7) is as follows:

$$\begin{gathered} n_{\alpha,\text{warm/cold}} = \frac{\lambda_{\alpha,\text{warm/cold}}}{\omega_{\alpha,\text{warm/cold}}^2} + A_{\alpha,\text{warm/cold}} e^{\omega_{\alpha,\text{warm/cold}} z} + B_{\alpha,\text{warm/cold}} e^{-\omega_{\alpha,\text{warm/cold}} z}, \\ \omega_{\alpha,\text{warm/cold}} = \sqrt{\frac{s_{\alpha,\text{warm/cold}}}{C_{\alpha,\text{warm/cold}}}}, \quad \lambda_{\alpha,\text{warm/cold}} = \frac{Q_{\alpha,\text{warm/cold}} A}{k_B T_{\text{warm/cold}} C_{\alpha,\text{warm/cold}}}. \end{gathered} \tag{8}$$

Here the constants $A_{\alpha,\text{warm/cold}}$ and $B_{\alpha,\text{warm/cold}}$ are defined by crosslinking conditions (7).

The relation between pumping parameters at the warm and cold parts in the averaged model and the same parameters of the model with actual pumps layout is as follows:

$$s_{\alpha,\text{warm}} = \frac{\sum_{i \in \text{warm}} S_{\alpha,i}}{L_{\text{warm}}}, \quad s_{\alpha,\text{cold}} = S_{\alpha,\text{cold}} + \frac{\sum_{i \in \text{cold}} S_{\alpha,i}}{L_{\text{cold}}}. \tag{9}$$

Here $C_{\alpha,\text{warm/cold}}$, $Q_{\alpha,\text{warm/cold}}$, $s_{\alpha,\text{warm/cold}}$ and $T_{\text{warm/cold}}$ define the specific conductivity, outgassing rate, average pumping speed and temperature in warm and cold Booster parts (see on poster Figure 2). Also note here that the values with the second lower index warm/cold or i like C_α, Q_α, s_α, S_α and T_i or $T_{\text{warm/cold}}$ in (4), (5) and (8) are the constant and determined by the position, i.e. warm/cold or index i.

Table 1: Average Pumping Speed, Outgassing Rate And Desorption Coefficients (taken from [5])

	H_2	CH_4	CO	CO_2
s_{warm}, $l \cdot s^{-1} \cdot m^{-1}$	0.46	0.56	5.76	6.25
s_{cold}, $l \cdot s^{-1} \cdot m^{-1}$	2.41	145.81	114.26	74.94
Q_{warm}, 10^{-12} mbar$\cdot l \cdot s^{-1} \cdot cm^{-2}$	0.025	0.015	0.018	0.014
Q_{cold}, 10^{-12} mbar$\cdot l \cdot s^{-1} \cdot cm^{-2}$	0.003	0.001	0.001	0.001
$\eta_{\angle,\text{warm}}(^{197}Au^{31+})$	150	5	1000	250
$\eta_{\angle,\text{cold}}(^{197}Au^{31+})$	1500	50	10000	2500
$\eta_{\perp,\text{warm}}(H_2^+)$	0.54	0.54	0.54	0.54
$\eta_{\perp,\text{warm}}(CH_4^+)$	0.04	0.05	0.07	0.11
$\eta_{\perp,\text{warm}}(CO^+)$	0.25	0.29	0.29	0.33
$\eta_{\perp,\text{warm}}(CO_2^+)$	0.14	0.14	0.14	0.14
$\eta_{\perp,\text{cold}}(H_2^+)$	0.33	0.33	0.33	0.33
$\eta_{\perp,\text{cold}}(CH_4^+)$	0.02	0.03	0.04	0.07
$\eta_{\perp,\text{cold}}(CO^+)$	0.15	0.17	0.17	0.2
$\eta_{\perp,\text{cold}}(CO_2^+)$	0.09	0.09	0.09	0.09

For the specific conductivity C_α of vacuum chamber the Knudsen formula was used [6]:

$$C_\alpha = \frac{4}{3} \frac{u_\alpha V^2}{A}.$$

Here u_α — mean particles' speed of α-kind residual gas component. This formula is more general since it takes into account the distribution function of the residual gas atoms and molecules and varying the Booster vacuum chamber aperture.

ISBN 978-3-95450-181-6

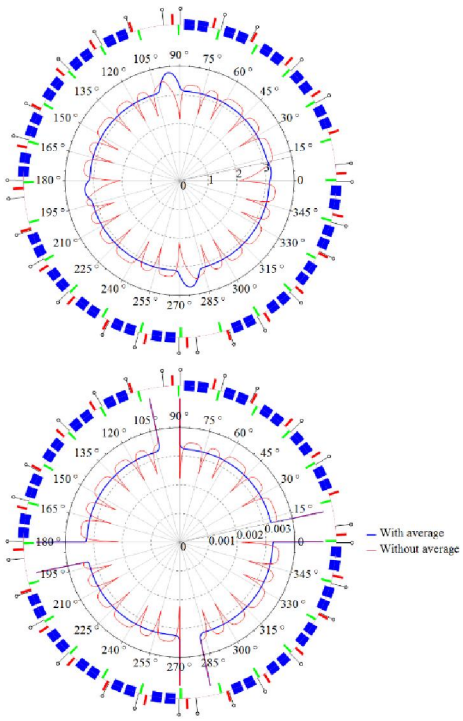

Figure 2: Total gas concentration in 10^6 cm^{-3} (top) and total static pressure in nTorr (bottom).

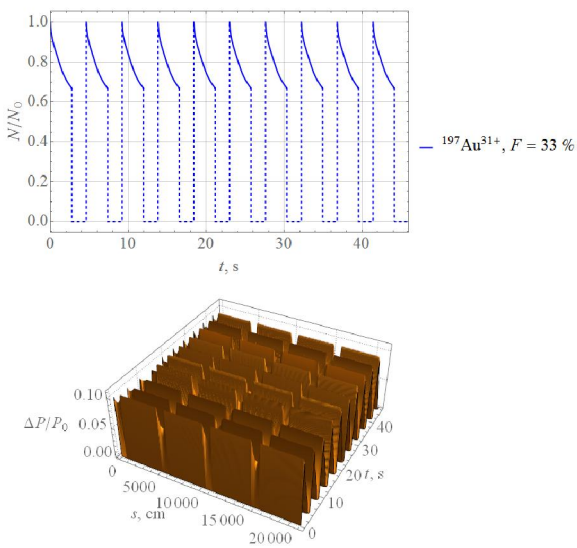

Figure 3: Time dependence of gold $^{197}Au^{31+}$ ion beam losses (top) and total dynamic residual gas pressure rises (bottom). Beam losses F are about 33% and residual gas pressure rise ΔP is not more 10% for average pressure level in the Booster vacuum chamber about 0.01 nTorr.

CALCULATION RESULTS

The solution of non-stationary problem (1) for the Booster magnetic cycle (see Figure 1) with the initial stationary distribution (see Figure 2) and parameters' list for average pumping speed, outgassing rates and desorption coefficients given in the Table 1 is shown in Figure 3. The residual gas composition is taken as follows: H_2, CH_4, CO and CO_2; initial $^{197}Au^{31+}$ ions beam intensity was $2 \cdot 10^9$; collimation efficiency was taken not more that 35%.

Two curves represented on Figure 2 correspond to (4) solution in case of actual pumps layout (2) and to (8) solution in case of average pumping speed around the Booster ring (7). The relation (9) between parameters of the problems (3) and (7) is taken into account. The Booster lattice and pumps layout are also shown on Figure 3.

CONCLUSION

The mathematical model of gold $^{197}Au^{31+}$ ions beam losses calculation due to interaction with residual gas atoms and molecules is given. The presented results are taken the ion stimulated desorption from the Booster vacuum cold surface and collimation of charge-exchanged gold ions into account.

The analytical solutions of the stationary problem for residual gas concentrations in the Booster vacuum chamber in case of two different problem statements (actual pumps layout and average over the Booster ring pumping speed) are given.

It was shown that for the values of pumping speed averaged over the Booster ring, outgassing rates and desorption coefficients in the warm and cold Booster parts close to the project expected values [1], the gold $^{197}Au^{31+}$ ions beam losses are of about 33% that corresponds to average residual gas pressure in the Booster vacuum chamber about 0.01 nTorr.

Note that in the presented simulation the residual gas composition in the warm Booster part was about 90% H_2 and about 10% totally of CH_4, CO and CO_2. The residual gas composition was approximately 100% H_2 in the cold Booster part. In general case, the proposed mathematical model provides arbitrary residual gas composition to be simulated.

REFERENCES

[1] Technical Project of NICA Acceleration Complex (Dubna, 2015)

[2] C. Omet, P. Spiller, J. Stadlmann, and D. H. H. Hoffmann, New J. Phys. 8, 284 (2006)

[3] E. Mahner, LHC-VAC/EM Vacuum Technical Note No. 2002-04

[4] I. L. Beigman, I. Yu. Tolstikhina, and V. P. Shevelko, Tech. Phys. 53, 547 (2008)

[5] A. Rossi and N. Hilleret, LHC Project Report No. 674 (CERN, Geneva, 2003)

[6] L. N. Rozanov. Vacuum Techniques. Moscow. 1990 (in Russian)

ISBN 978-3-95450-181-6

BEAM TRANSFER FROM HEAVY-ION LINEAR ACCELERATOR HILAC INTO BOOSTER OF NICA ACCELERATOR COMPLEX

A. Tuzikov†, A. Butenko, A. Fateev, S. Kolesnikov, I. Meshkov, V. Mikhaylov,
V. Shvetsov, A. Sidorin, A. Sidorov, G. Trubnikov, V. Volkov,
Joint Institute for Nuclear Research, Dubna, Russia

Abstract

Designs of systems of ion beam transfer from the linear accelerator HILAC into the Booster of the NICA accelerator complex (JINR, Dubna) [1] including the transport beam line HILAC-Booster and the beam injection system of the Booster are considered in the report. The proposed systems provide multi-variant injection for accumulation of beams in the Booster with required intensity. Special attention is paid to various aspects of beam dynamics during its transfer. Main methods of beam injection into the Booster are described. These are single-turn, multi-turn and multiple injection ones. Results of beam dynamics simulations are presented. Status of technical design and manufacturing of the systems' equipment is also highlighted.

INTRODUCTION

The systems of beam transfer from the HILAC linear accelerator to the Booster include the HILAC-Booster beam transport channel and the system of beam injection into the Booster (see Figure 1).

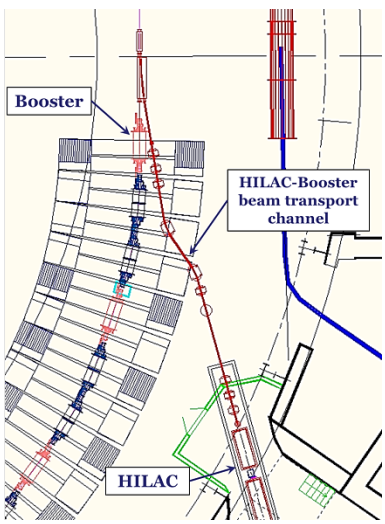

Figure 1: Layout of the HILAC linear accelerator, the Booster synchrotron and the HILAC-Booster beam transport channel.

The beam transfer in the HILAC-Booster transport channel involves beam debunching, betatron matching of ion beam of the target charge state with the Booster, separation and collimation of neighbor parasitic charge states of ions. The ion-optical system of the transport channel and the beam injection system of the Booster provide multi-variant injection for accumulation of beams in the Booster with required intensity [2]. Main methods of beam injection into the Booster are single-turn, multi-turn and multiple injections. Ions (see Table 1) are accumulated on the horizontal phase plane of the Booster.

Table 1: Main Beam Parameters

Ions	Au^{30+}, Au^{31+}, Au^{32+} (from HILAC); Au^{31+} (inside Booster)
Intensity	up to $2.5 \cdot 10^9$ (Au^{31+}); up to $6 \cdot 10^9$ (total)
Current, mA	4
Energy, MeV/amu	3.2
Repetition rate of beam injection into Booster, Hz	0.25
Repetition rate of stages of multiple injection, Hz	10 (3 injection stages per 4 s)
Transition, %	90
Transverse 95% emittance, π·mm·mrad:	
at the exit of HILAC;	10
at the entry of Booster;	15
after filamentation in Booster.	15 ÷ 135 (hor.) / 15 (vert.)

BEAM INJECTION INTO BOOSTER

Concept of multi-variant injection into the Booster synchrotron implies possibility of beam injection by means of several schemes of single-turn, multi-turn and multiple injection methods. The beam injection system of the Booster is designed to create a local closed orbit bump and also has useful feature: ability of rapid change of fields inside the system's kickers that allows ions to fill the horizontal phase plane of the Booster more compact.

Single-turn injection is a conventional method providing minimal transverse beam emittances after filamentation of phase space distribution of ions in the Booster. The beam duration in case of single-turn injection is less than 8.5 μs. Horizontal emittance of the injected beam is equal to 15 π·mm·mrad. Vertical emittance does not depend on beam injection method used and is 15 π·mm·mrad.

Multi-turn injection method involves accumulation of ions on the horizontal phase plane during 2-3 periods of the beam revolution so the beam duration is 17 or 25.5 μs. Two schemes of multi-turn injection are considered: with single-plateau (ordinary) pulses of the injection system's kickers and with double-plateau pulses formed by rapid change of fields in the kickers. Horizontal emittances of

† tuzikov@jinr.ru

ISBN 978-3-95450-181-6

the accumulated beam after filamentation in the Booster according to these beam injection schemes are 120 π·mm·mrad and 65 π·mm·mrad correspondingly.

Multiple injection method means twice or triple repetitions of single-turn beam injections (or stages of multiple injection) with periodicity of 100 ms. Modes of single-plateau and double-plateau pulses of the kickers are also used for multiple injection. Additional option is variation of the horizontal phase portrait of the injecting beam (provided by dynamic retuning of the HILAC-Booster beam transport channel in intervals between stages of multiple injection) which allows more compact filling of the phase plane. There are six schemes proposed for multiple injection which give horizontal emittances of the accumulated beam after filamentation in the Booster in the range from 55 π·mm·mrad to 135 π·mm·mrad.

BEAM INJECTION SYSTEM

The beam injection system of the Booster consists of the electrostatic septum IES and the electric kickers IK1 – IK3. The kickers serve to put the beam onto the closed orbit of the Booster (in case of single-turn injection) and to create a local bump of the closed orbit (in cases of multi-turn and multiple injection schemes).

The system's elements are located in the vicinity of the 1st straight section of the Booster (see Figure 2). The kickers IK1 and IK3 are placed inside the Booster cryostat in periodic DFO cells adjacent to the 1st straight section. The electrostatic septum IES and the kicker IK2 are positioned in the 1st straight section itself. The section has a bypass of cryogenic and superconducting communications and the largest part of the section including the septum and the kicker is room-temperature.

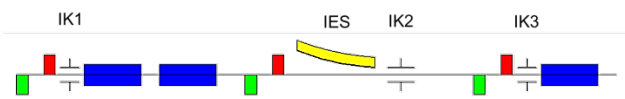

Figure 2: Layout of the beam injection system of the Booster. Notation: blue – lattice dipole magnets, red – focusing quadrupole lenses, green - defocusing quadrupole lenses.

The electrostatic septum IES (see Figure 3) is a pair of curved electrodes installed inside a vacuum box. The cathode is positioned on the outside of the anode. High voltage is applied to the cathode, the anode is grounded. Length of the IES is 1.9 m. Gap between the electrodes is 35 mm, thickness of the anode (which serves as a knife of the septum) is 1 mm.

The IES is operated in the cyclic mode. A constant voltage between the septum electrodes is maintained during the beam injection. There is capability to vary the voltage in intervals between stages of multiple injection. The range of the voltage variation is from 116 kV up to 125 kV.

Currently the technical design of the electrostatic septum IES is finished and its manufacturing will be started in the nearest future.

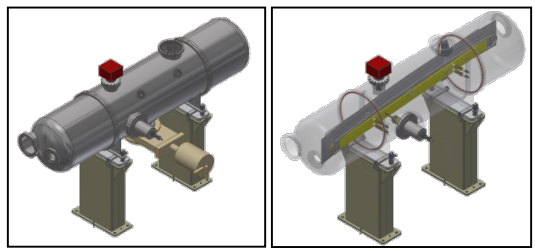

Figure 3: 3D model of the electrostatic septum IES.

The electric kickers IK1 – IK3 (see Figure 4) are pairs of conducting plates installed vertically inside vacuum boxes parallel to the Booster axis. Lengths of the kickers IK1 and IK3 are 0.45 m, length of the IK2 is 0.8 m. The plates of the kickers IK1 and IK3 are positioned symmetrically relative to the Booster axis and gaps between the plates are 102 mm. The plates of the kicker IK2 are shifted outside the Booster axis, the gap is 93 mm.

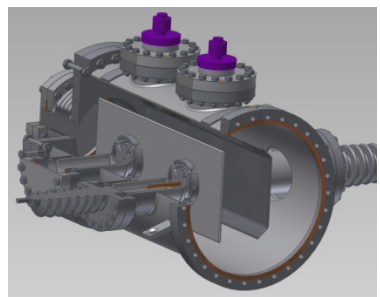

Figure 4: 3D model of the electric kicker IK1.

Five power supplies of the kickers [3] provide independent unipolar charging/discharging of each of the plates (excluding one of the plates of the kicker IK1). Two modes of the kickers' operation are considered. The single-plateau pulse mode means that electric potential is applied only on one plate of the kicker (the primary plate). In case of the double-plateau pulse mode, potentials are initially applied on both plates of the kicker then one of the plates (the secondary one) is discharged that leads to rapid change of voltage in the kicker.

Maximal voltage between the plates: IK1 – 40 kV, IK2 – 45 kV, IK3 – 60 kV. The power supplies are divided conventionally on high-voltage (up to 60 kV) ones feeding the primary plates and middle-voltage (up to 20 kV) ones feeding the secondary plates.

The kickers' pulses have a flat-top from 8 to 30 μs. The rise time of the pulse is about 1 ms, the fall time does not exceed 100 ns. Repetition rate of pulses in case of multiple injection is equal to 10 Hz, maximal number of repetitions is 3.

Currently the kicker prototype and the power supply (with voltage up to 60 kV) for its primary plate are almost manufactured and will be tested in the nearest months.

HILAC-BOOSTER BEAM TRANSPORT CHANNEL

Layout of the HILAC-Booster beam transport channel is shown in Figure 1. The beam transport channel provides the beam transfer only in the horizontal plane as the

ISBN 978-3-95450-181-6

HILAC axis is located on the median plane of the Booster.

The beam transport channel contains 2 dipole magnets, 7 quadrupole lenses, a debuncher and a set of steerers. At present all the transport channel elements (see Table 2) are available at JINR.

Table 2: Main parameters of the magnets and the debuncher of the HILAC-Booster beam transport channel.

Dipole magnets	
Effective length, m	0.65
Max. magnetic field, T	1
Gap, mm	45
Quadrupole lenses	
Effective length, m	0.29
Max. gradient, T/m	10
Gap (diameter), mm	95
Debuncher	
Length, m	0.49
Frequency, MHz	100.625
Max. effective voltage, kV	260

The beam transport channel has the following functionality: the beam matching with the Booster ring, the beam debunching, separation of neighbor parasitic charge states of ions, capability to modify position and Twiss parameters of the transferring beam at the exit of the channel (to provide different schemes of the beam injection into the Booster).

The debuncher provides reduction of longitudinal momentum spread of the beam from initial value of $5 \cdot 10^{-3}$ (at the exit of the HILAC) to $1 \div 1.5 \cdot 10^{-3}$ (the upper value is a semi-height of the Booster separatrix). To increase efficiency of the debuncher operation it is installed at the end of the 1st straight section of the beam transport channel in the non-dispersive region.

Separation of charge states of ions is fulfilled by means of the 1st dipole magnet. Separated parasitic charge states of ions (Au^{30+} and Au^{32+} for case of Au^{31+} target ions) are collimated just before the entrance of the second dipole magnet.

The steerers distributed along the channel provide the beam trajectory correction. Full correction of the trajectory (i.e. its alignment with the channel axis) is achieved inside the debuncher and in the end of the channel.

The special steerer is placed just after the final quadrupole lens. It is used for alteration of the beam position at the entry of the electrostatic septum IES which is required to perform several schemes of the beam injection into the Booster.

The vacuum chamber of the beam transport channel (except the dipole magnets) is considered to be round with radius of 35 mm. The vacuum chamber inside the dipoles is elliptical with semi-axes of 35 mm and 20 mm. Acceptance-limiting places of the channel are the collimators for parasitic charge states of ions and the vacuum chamber of the defocusing lens in the 1st triplet for horizontal and vertical acceptances accordingly (see Figure 5). Horizontal and vertical acceptances of the channel are close to each other and equal to 28 π·mm·mrad and 30 π·mm·mrad correspondingly.

Growth of effective transverse emittances of the beam in the transport channel is limited by 50%. The beam dynamics simulations have shown that the emittance growth due to the debunching and chromatic effects is perceptible but does not exceed 15% and 25% for horizontal and vertical effective emittances accordingly. Other sources of the emittance growth such as errors and space charge effects also do not lead to violation of the emittance budget.

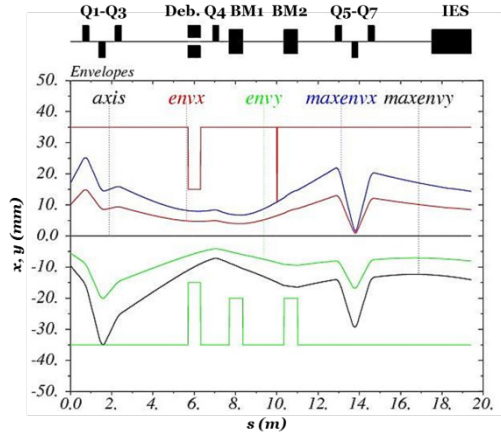

Figure 5: The beam envelopes in the HILAC-Booster beam transport channel and the electrostatic septum IES. Positive values on axis *x,y* mean horizontal coordinates, negative ones represent vertical coordinates. Notation: BM1-BM2 – dipole magnets; Q1-Q7 – quadrupole lenses; Deb. – debuncher; *envx*, *envy* – horizontal and vertical envelopes of the beam with transverse emittances equal to 10 π·mm·mrad; *maxenvx*, *maxenvy* – horizontal and vertical envelopes of the beam with transverse emittances equal to the channel acceptances.

CONCLUSION

Concept of multivariant beam injection into the Booster has been proposed. The systems of the beam transfer from the HILAC to the Booster have been developed such a way all the considered schemes of the beam injection are capable to be implemented. Technical designs of the systems' devices are near to completion and some devices are being fabricated to date.

REFERENCES

[1] Technical Project of NICA Acceleration Complex (Dubna, 2015)

[2] V. Volkov, I. Meshkov, V. Mikhailov, G. Trubnikov, A. Tuzikov, and A. Fateev, "Conceptual design of the system of heavy-ion beam injection into the booster of the NICA accelerator complex", Phys. Part. Nucl. Lett. 11, 675 (2014).

[3] V. Bulanov, E. Gorbachev, N. Lebedev, A. Tuzikov, and A. Fateev, "A conceptual design of a power-supply system of deflecting plates for multivariate injection into the NICA accelerator complex booster", Phys. Part. Nucl. Lett. 11, 695 (2014).

ISBN 978-3-95450-181-6

MULTIGAP AND POLYHARMONIC BUNCHING SYSTEMS AT FLNR CYCLOTRONS

I.V. Kalagin†, G.G. Gulbekian, B.N. Gikal, S.V.Prokhorov, N.N. Pchelkin,
Joint Institute for Nuclear Research, FLNR, Dubna, Moscow region, Russia

Abstract

Since 1997, different variants of bunching systems have been used at the axial injections of FLNR cyclotrons to increase ions capture into acceleration efficiency. Combination of two single gap Sine and Line bunchers are used at the axial injections of U400 and DC110 cyclotrons. Since 2015, a single gap double RF harmonic buncher has been installed into the upper part of the U400M injection in addition to the lower sine buncher, the experimental results is being presented. For the HV axial injection of the new DC280 cyclotron, two variants of polyharmonic bunchers will be used: a multigap buncher and a single gap one.

INTRODUCTION

At present time, axial injection systems with ECR ion sources are integral components of heavy ion cyclotrons at the Flerov Laboratory of Nuclear Reaction of the Joint Institute for Nuclear Research (FLNR, JINR). The axial injections allowed us to use bunchers for matching the longitudinal ion beam emittance with the cyclotron phase acceptance, as for linacs. The typical voltage of ion extraction from our ECR sources is U_{inj}=15÷20 kV. The typical phase acceptance (CPA) of our cyclotrons is 20°÷30°. The typical capture into acceleration efficiency (CIAE) without beam bunching is 5÷8%.

The best type of bunchers from the point of view CIAE increasing is the buncher with saw-tooth voltage in the gap (linear buncher) [1]. The calculated CIAE with the bunchers is 80÷90%, but their using is restricted by technical difficulties. The simplier type of bunchers is the buncher with sinusoidal voltage in the gap (sine buncher). The simulated CIAE for the sine buncher is about 50% [2].

Unlike linacs, the design of the sine buncher for the FLNR cyclotrons cannot been made in form of a single gap λ/4 resonant cavity because our cyclotrons use relatively low accelerating frequencies: 5.4-22 MHz (λ/4= 3.5÷14 m). Therefore, we have utilised bunchers with two grids that are fed with a special resonant system. The resonant system consists of two extended coaxial resonators (or cables), matching inductors and variable capacitors for resonance turning. The system allows us to form sinusoidal voltages at both buncher grids in anti-phases to prevent additional acceleration of ions in central phases and for decreasing influence RF fringing fields on CIAE before and after the buncher gap. The buncher can be installed into the vertical part of an axial injection at various distances from a cyclotron median plane (CMP). We received the best CIAE at the U400 cyclotron when the buncher was situated at 0.8 m above the CMP. The voltage amplitude at the gap was about 700 V (optimized by maximal CIAE). The CIAE was 15÷29% depending on ion current (the parameter decreases with ion current increasing) [3].

Experimental values of CIAE with our bunchers are typically lower than calculated ones. The reasons of it can be influence of space-charge effects. The effects become significant in vicinity of the CMP where the bunch pulse current is in one order higher than the DC ion current at the ECR exit. In addition, there are other factors such as: path difference of ions into longitudinal magnetic field of the axial channel and into the helical inflector; losses of ions at the buncher grids and at residual gas.

For further improvement of the FLNR cyclotrons CIAE we have made multigap and polyharmonic bunching systems.

One more way of the CIAE improvement is to increase energy of injected ions, we are planning to apply the method for our new DC280 cyclotron [4].

MULTIGAP BUNCHING SYSTEMS

Multigap Buncher for the U400

As a variant of a multigap system we have unilized two single gap bunchers. The bunchers have been situated at different distances from the U400 CMP. We use combination of linear buncher and existing sine buncher (Fig. 1). The linear buncher has been situated at 4.4 m from the CMP [5]. The system has been developed for RF frequency range of 5.4÷12 МГц and U_{inj}=13÷15 kV (βλ=80 mm). The voltage amplitudes at grids were about 180 V (linear) and 650 V (sine). The U400 CIAE without bunchers is over 5%. The system allowed us to reach 23÷38% of CIAE, depending on ion current [6]. The contribution of the linear buncher to the CIAE was about 1.4.

Multigap Buncher for the DC110

The similar system has been installed at the D110 cyclotron injection [7]. The system was developed for RF frequency of $7.65^{\pm 0.16}$ МГц and U_{inj}=20 kV (βλ=98 mm). The bunchers have been situated at 0.8 m (sine) and 2.45 m (linear) above the CMP. The calculated phase distribution after bunched beam drifting for 2.45 m and corresponding distribution of the particle density in the bunch of $_{132}Xe^{20+}$ ions at the DC110 CMP are shown in Fig. 2. The calculations have been carried out with the use of the large particle method without account for the space charge effects and other effects mentioned above. The voltage amplitudes was 700 V for linear buncher (with ideal saw tooth voltage) and 300 V for sine one. The calculated CIAE was about 61% for the CPA value of 30°.

† kalagin@jinr.ru

ISBN 978-3-95450-181-6

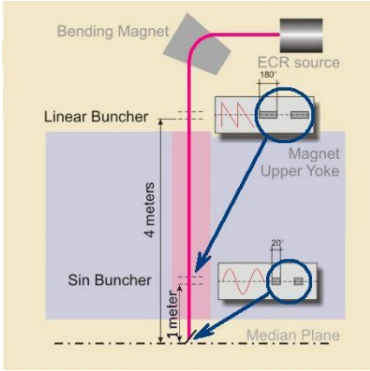

Figure 1: Layout of two bunchers system at the U400. Where: the linear buncher forms bunches with phase extent of 180° before the sine one. The sine buncher forms bunches before the CMP with phase extent of 20°.

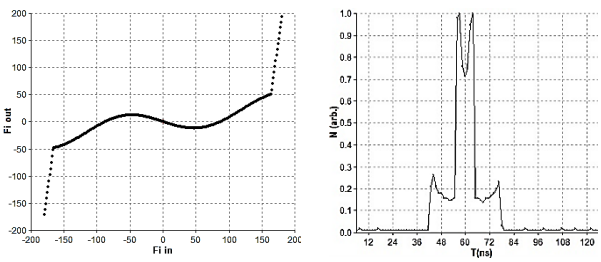

Figure 2. Left: Calculated dependence of the ion phases (after drifting for 2.45 m) at the buncher output *Fi* out on the phases at the buncher input *Fi* in for $A/Z = 6.6$. Right: Calculated distribution of the particle density in a bunch at the DC110 CMP.

To create saw-tooth voltage in the gap of the linear buncher, the special modulator has been developed. The maximal peak to peak voltage was up to 700 V which was created with using transistor modulator. The modulator allows us to form bipolar saw-tooth voltage ±350 V at the buncher grids. The maximal pick-to-pick voltage in the gap is ±700 V. The experimental signal of the grid voltage has distortions caused by operation of transistors (Fig. 3).

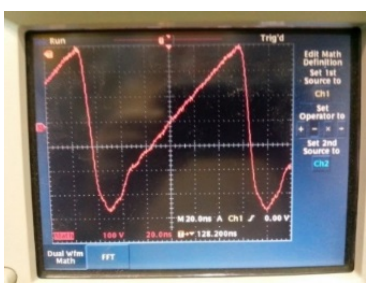

Figure 3. The experimental shape of saw-tooth voltage at the linear buncher grid.

The experimental CIAE for the system was 34÷38% for ion currents in the region from 20 to 100 μA. The corresponding experimental gap voltage amplitudes were about 700 V (linear) and over 430 V (sine). The CIAE without bunchers was about 9%. The linear buncher contribution to the CIAE was about 1.4.

POLYHARMONIC BUNCHING SYSTEMS

Creation of linear bunchers for cyclotrons is accompanied by some technical difficulties. For example, installation of the buncher near the CMP is restricted by possibility to translate saw-tooth voltage from a generator to a buncher at the distance of few meters without signal distortions. Another problem is creation of voltage amplitudes higher than 1 kV because of necessity to use lamp schematics instead of transistor one in presence of cyclotron fringing magnetic field. Therefore, we have started to develop polyharmonic bunchers. The type of bunchers was successfully used for linacs at fixed RF frequencies, but for cyclotrons it has to be tunable in RF frequency range. The problem is hardly solved for single gap polyharmonic bunchers and can be simplified a bit for multigap ones.

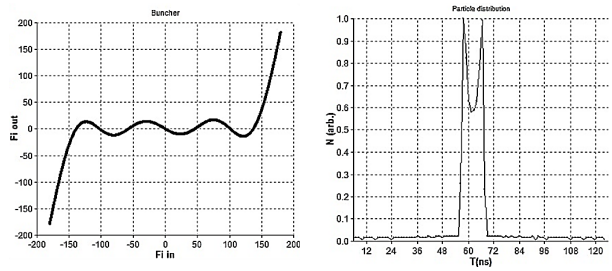

Figure 4. Left: Calculated dependence of the ion phases (after drifting for 3.8 m) at the buncher output *Fi* out on the phases at the buncher input *Fi* in for $A/Z = 7$, f=7.68 MHz. Right: Calculated distribution of the particle density in a bunch at the DC280 CMP.

Polyharmonic Multigap Buncher for the DC280

The DC280 cyclotron will be equipped with HV injection [4]. The injection voltage will be up to 80 kV (βλ=157 mm). If we will use a linear buncher, the maximal voltage amplitude in the gap will be about 5 kV. The estimated power of the saw-tooth voltage generator is more than 10 kW. Therefore using of a polyharmonic buncher with a resonant feeding system looks like more attractive. To simplify the system turning to DC280 frequencies (7.3÷10.4 MHz) we will use only three RF harmonics.

The buncher consists of a drift tube with a length of βλ/2, which allows us to decrease the RF voltage amplitude of first harmonic in two times to 1.2 kV (the harmonic corresponds to the cyclotron accelerating frequency). The second harmonic with maximal amplitude of 1 kV will be applied to the wolfram grid located before the drift tube. The third one with maximal amplitude of 0.6 kV will be applied to the grid located after the drift tube. Grounded grids are mounted between the drift tube and the harmonic grids in order to exclude the mutual influence of the harmonics. The total power of resonant feeding system (three separated tunable resonators) is estimated not more than 250 W.

The calculated phase distribution after bunched beam drifting for 3.8 m and corresponding distribution of the particle density in a bunch at the DC110 CMP are shown in Fig. 4. The calculated CIAE was about 80 % for the CPA value of 40°. The loses of ions at the buncher grids was estimated as 8÷10%. The calculated phase spread after the

ISBN 978-3-95450-181-6

helical inflector is ±15°, which can be a reason of the CIAE decreasing too. We plan to reach more than 50% of the CIAE with the buncher.

Single Gap Polyharmonic Bunchers

To minimise ion losses at the buncher grids we are planning to use a single gap polyharmonic buncher. In this case, we need to sum few harmonics at a gap as it was made in [8], for example. The method of turning of a special resonant system has been proposed in [9]. To test of the system workability we have created a model of a single gap buncher with two harmonics.

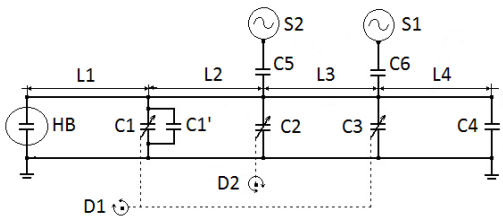

Figure 5. Principal scheme of resonant system of the double harmonic buncher. Where: HB is the buncher, L1÷L4 are coaxial cables (L=1 m); C1,C3 are variable capacitors for the 1-st harmonic (12÷495 pF); C1'is the compensation capacitor (60 pF); C2 are variable capacitors for the 2-nd harmonics (12÷495 pF); C5,C6 are coupling capacitors (22 pF and 64 pF); S1,S2 are RF generators for 1-st and 2-nd harmonics; D1,D2 are motor drives.

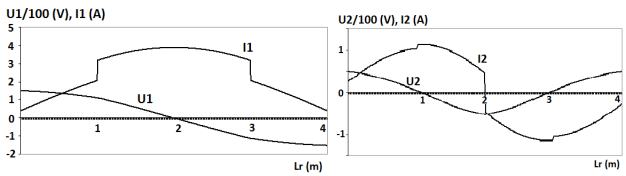

Figure 6. Typical voltage (U) and current (I) distribution along the resonant system (Lr=L1+L2+L3+L4, Fig. 5) for the first (1) and the second (2) harmonics.

The buncher has been installed into the axial injection of the U400M cyclotron at 4.4 m above the U400M CMP. The U400M RF frequency range is 11.5÷24 МГц, U_{inj}=18 kV (βλ=45 mm). The buncher has been utilized in combination with the sine buncher, situated at 0.75 м above the CMP. The CIAE with the sine buncher was 13÷15%, that is lower than one for the U400. The reason of it can be lower βλ that leads to bunch squeezing to a shorter length in presence of the same debunching factors. In 2015, the system has been tested with the RF frequencies of 14.68 MHz (1-st harmonic, U1=140 V) and 29.36 MHz (2-nd harmonic, U2=70 V). The regime has been used for acceleration of $_{48}Ca^{+6}$ and $_{40}Ar^{+5}$ ions. The CIAE without bunchers was about 5%.

The experimental CIAE after addition the upper double harmonic buncher was about 19% at the ion current is about 70 μA. The contribution of the double harmonic buncher to the CIAE was over 1.35, that is comparable with contribution of the linear buncher for the U400. The buncher resonant system (Fig. 5) allows us to carry out the buncher turning in the U400M RF frequency range. The 2-nd harmonics signal applied to the point where the 1-st harmonics has the maximal voltage (Fig. 6). For the U400M, the scheme has been modernized to form voltages at both grids in anti-phases. The similar principle will be used for a single gap polyharmonic buncher at the D280.

CONCLUSION

The multigap and polyharmonic bunching systems are efficiently utilized at the FLNR cyclotrons. The experimental CIAE value is in 1.5÷2 times lower than the calculated one for ion injection voltage up to 20 kV. The experimental CIAE depends on βλ value (Table 1). Increasing the ion injection energy and using polyharmonic bunchers can improve the CIAE.

Table 1: Parameters of the FLNR Bunchers

Cyclotron	βλ mm	Type	CIAE %	Notes
U400M	45	Multigap polyharm.	19	Testing
U400	80	Multigap	23÷38	Linear+Sine
DC110	98	Multigap	34÷38	Linear+Sine
DC280	157	Multigap polyharm.	>50	Expected

REFERENCES

[1] A. Chabert et al. “The linear buncher of SPIRAL.Beam test of a prototype”, Nucl. Instr. and Meth. In Phys.Research. A423, pp. 7÷15 (1999).
[2] Yu.Ts.Oganessian et al.,”Axial injection system for the U-400 cyclotron with the ECR-4M ion source”, in JINR FLNR sci. rep.1995-1996, Heavy Ion Physics, Dubna, pp. 270÷276 (1997).
[3] I.Kalagin, I. Ivanenko, G.Gulbekian “The experimental investigation of the beam transportation efficiency through the axial injection system of the U400 cyclotron”, Proc. of the 2001 Particle Accelerator Conf., Chicago, pp. 1568÷157 (2001).
[4] G.G.Gulbekian et al., “Proposed Design of Axial Injection System for the DC_280 Cyclotron”, Physics of Particles and Nuclei Letters, Vol. 11, No. 6, pp. 763–773 (2014).
[5] O. Borisov et al., “Optimisation of the axial injection system for U-400 cyclotron (linear buncher)”, Proc. of EPAC2000, Vienna, Austria, pp. 1468-1470 (2000).
[6] Yu. Ts. Oganessian et al., “Status report of the U400 cyclotron at the FLNR JINR”, Proc. of APAC2004 Int. Conf., Gyengju, Korea, pp 52÷54 (2004).
[7] B.N.Gikal et al., “Dedicated DC-110 heavy ion cyclotron for industrial production of track memebranes”, Proc. of RUPAC-2014, Obninsk, Russia, pp. 333÷335 (2014).
[8] F.J. Lynch et al. “Beam buncher for heavy ions”, Nucl. Instr. and Methods 159, pp. 245÷263 (1979).
[9] S.V.Prokhorov, “The method of RF resonator turning to resonant frequencies with given multiplicity”, Patent N RU 2601539.

ISBN 978-3-95450-181-6

NEW TECHNIQUES FOR OPERATION AND DIAGNOSTICS OF RELATIVISTIC ELECTRON COOLERS

M. W. Bruker, A. Hofmann, E. Riehn, T. Weilbach, K. Aulenbacher, J. Dietrich
Helmholtz Institute Mainz, Germany

W. Klag
Institute for Nuclear Physics Mainz, Germany

M. I. Bryzgunov, V. Parkhomchuk, V. B. Reva
BINP SB RAS, Novosibirsk, Russia

Abstract

The Helmholtz Institute Mainz (HIM) performs experiments related to possible improvements of high-energy d.c. electron coolers. Results and activities concerning non-invasive beam diagnostics and beam control at large operating currents will be shown. Furthermore, progress of our project to use turbo generators as a means for potential-free power generation in high-energy electron coolers is presented.

INTRODUCTION

High-intensity electron beams are getting more and more popular (e.g. in planned electron cooling devices) but make high demands on diagnostics and power supplies. With an energy of several MeV and a current of amperes, the use of conventional destructive diagnostic tools is very limited just as the use of conventional power supplies is. In this paper we present three experimental set-ups connected to high-energy electron coolers: non-invasive beam diagnostics, the impact of secondary electron emission in energy recovery machines and turbine-driven power supplies for focusing magnets. All experiments have been performed at the Institute of Nuclear Physics and the Helmholtz Institute in Mainz.

EXPERIMENTAL SET-UP FOR MEASUREMENT OF SECONDARY CURRENT

The energy recovery method used in electron coolers results in secondary electrons emitted from the collector surface being re-accelerated, possibly harming operational stability. Research done by BINP indicates that a Wien filter as part of the collector optics is a suitable means to suppress electron backflow, increasing the total recuperation efficiency by a factor of 100 [1]. However, stopping these particles in turn creates new secondaries with a different energy and angle distribution. This gives rise to a cascade that depends heavily on the geometry of the electrodes and the vacuum chamber.

HIM operates a test set-up capable of providing a magnetized 17 keV, 0.5 A electron beam and measuring the currents flowing onto the relevant aperture plates independently. A sketch of the device including the distribution of electric potentials is shown in Fig. 1.

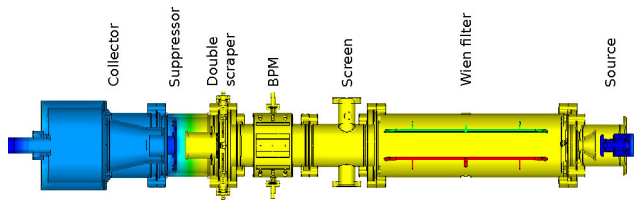

Figure 1: Schematic view of the vacuum chamber. Blue: $U < 0$. Yellow: $U = 0$.

The potential minimum inside the suppressor electrode results in secondary electrons with an energy $E_{\mathrm{kin}} < e\left|U_{\mathrm{col}} - U_{\mathrm{sup}}\right|$ being reflected to the collector. By varying this potential, secondary losses can be distinguished from primary losses. In the absence of primary losses, the integrated energy spectrum of secondary electrons exiting the collector can be obtained except for the elastic peak. Figure 2 shows that while the shape of the spectrum is what can be expected [2], several surfaces contribute to the total losses because of higher generations of secondary electrons emitted from the deceleration aperture plate and the Wien filter collector plate.

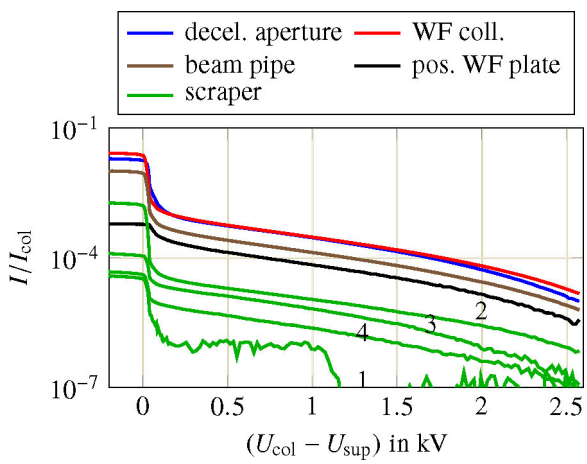

Figure 2: Secondary currents vs. suppressor voltage. $I_{\mathrm{col}} = 20\,\mathrm{mA}$.

These losses are irrelevant to the cooler as long as the particles cannot enter the high-energy section. To determine the possible trajectories of higher-generation secondary elec-

ISBN 978-3-95450-181-6

trons that can cause a non-zero current out of the Wien filter given a suitable aperture, detailed computer simulations were performed. These show that the total secondary current exiting the collector optics can be estimated to be of the order of $10^{-9}\, I_{\mathrm{col}}$, rendering the problem negligible in comparison with other unwanted effects such as residual gas ionization. More details can be found in [3].

TURBINE-DRIVEN POWERING OF HV COMPONENTS

One of the challenges in the development of a relativistic electron cooler is the powering of components, e.g. HV solenoids, which sit on different high potentials within a high voltage vessel and therefore need a floating power supply. A modular power supply with two cascade transformers per module would overcome the many disadvantages of a conventional setup. Either the transformers that power the HV solenoids or the solenoids themselves are then fed by a turbo generator powered by pressurized gas. A promising candidate for the needed turbo generator could be the Green Energy Turbine (GET) designed by company DEPRAG, which works with dry air and delivers a power of 5 kW. At the Helmholtz Institute Mainz (HIM) two of these generators have been tested for performance and durability. Figure 3 gives an overview of the experimental setup.

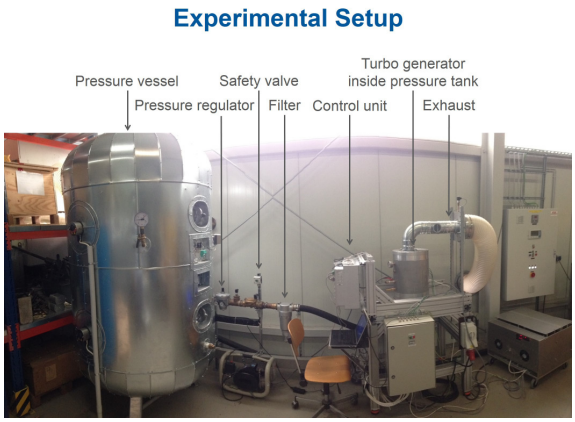

Figure 3: First set-up of the GET test facility at HIM. The main components are (from left to right): a pressure vessel, pressure regulators and safety valves, a control unit, the turbo generator itself and the exhaust.

Since the turbo generator will be placed inside an SF_6 vessel later, all experiments have been performed with the GET inside a pressurized tank with 10 bar. The relation between the inlet pressure (or the revolution speed, respectively) and the delivered DC power can be found in Fig. 4.

NON-DESTRUCTIVE DIAGNOSTIC METHODS

Two different methods to measure the beam profile will be presented in the following section, namely Thomson Laser Scattering (TLS) and Beam-Induced Fluorescence (BIF).

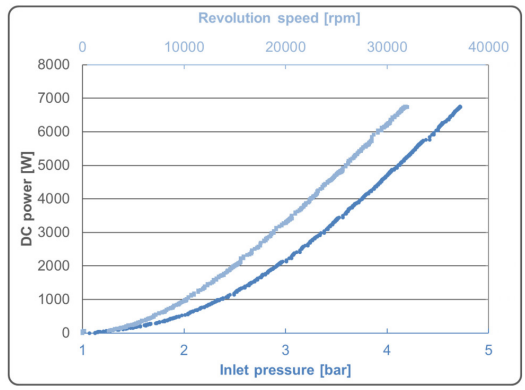

Figure 4: DC power versus revolution speed / inlet pressure of the green energy turbo generator.

Thomson scattering describes elastic scattering of a photon off a free electron and is basically the low-energy limit of the Compton scattering process. A photon λ_{L} hits the electron beam at an angle Θ and is scattered with the scattering angle Θ'. Due to the Doppler shift the scattered photon λ_{S} gains energy. The wavelength of the scattered photon as a function of the angle between the incident photon and electron and the angle between scattered photon and electron can be evaluated by

$$\lambda_{\mathrm{S}} = \lambda_{\mathrm{L}} \frac{(1 + \beta \cos \Theta')}{(1 + \beta \cos \Theta)} \tag{1}$$

where β is the electron velocity in units of the speed of light. The number of scattered photons can be calculated by using the following equation:

$$R = \frac{1}{2} r_e^2 \left(1 + \cos^2 \Theta'\right) N_L n_e P \epsilon \Delta\Omega l \frac{(1 + \beta \cos(\Theta))}{(1 + \beta \cos(\Theta'))\gamma} \tag{2}$$

with r_e = classical electron radius, N_L = number of incident photons per Joule, n_e = electron density, P = laser power, ϵ = detector system efficiency, $\Delta\Omega$ = detector solid angle, l = interaction length, $\frac{(1+\beta\cos(\Theta))}{(1+\beta\cos(\Theta'))\gamma}$ = factor resulting from Lorentz transformation.

In our experiment we set Θ to be 90° and Θ' to be 135°. With an electron energy of 100 keV, a current of 25 mA, P = 130 W, ϵ = 0.17, $\Delta\Omega$ = 0.01, l = 3 mm (beam diameter), the count rate is expected to be 5 Hz. Because of the low count rate, reducing or at least controlling the background is crucial. By carefully adjusting the beam optics, blackening the beam pipes and using a coincidence unit, the background has been reduced from 200 Hz to below 10 Hz, making TLS profile measurements possible in the first place.

Figure 5 shows a half section of the CAD model of the TLS chamber. The paths of the electron beam, the incident Laser beam, and the scattered photons are indicated. Due to the limited space, the detector cannot be placed in the scattering plane. Therefore, an imaging system consisting of a lens and a parabolic mirror images the interaction region onto the PMT passing two bandpass filters that reduce the background created by the laser.

ISBN 978-3-95450-181-6

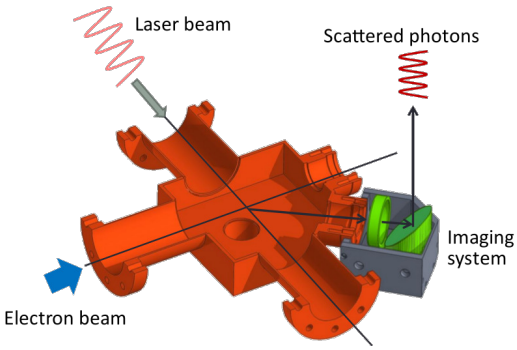

Figure 5: Half section of the TLS chamber (orange) and the detector system. The angle between laser and electron beam is $\Theta = 90°$ whereas $\Theta' = 135°$ is the angle between electron beam and scattered photons. The imaging system (green) consists of a lens and a parabolic mirror.

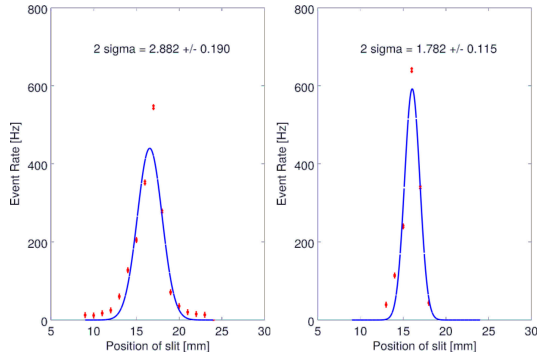

Figure 6: BIF measurement with statistical errors for different focusing strengths of the solenoid in front of the BIF chamber. The measurement is shown in red and the Gaussian fit in blue. Left: Solenoid current 50 mA, right: Solenoid current 500 mA.

The rate of the scattered photons is proportional to the integrated electron density along the path of the laser through the electron beam. By moving the laser beam through the electron beam vertically, a profile measurement can be done. Due to the low cross section, which is mostly dominated by the classical electron radius squared, the required laser power is very high (150 W). The electron beam to be measured is generated by illuminating a photocathode with a second laser system. In order to achieve the required peak current of about 30 mA, the latter has to be pulsed, making it necessary to synchronize both laser systems.

For protons and ions, beam profile measurement based on beam-induced fluorescence is a common technique [4]. The idea is to image the fluorescing residual gas on a photo detector with a spatial resolution. Instead of a detector with a spatial resolution, a photomultiplier tube (PMT) with a movable slit in front of it can be used.

The intensity of the photons is proportional to the pressure and the beam current. A gas dosing valve is used to insert N_2 gas into the vacuum system, which then converts 3.6 keV of average energy loss into one visible photon [5]. Since N_2 can be pumped out of the vacuum system very easily, residual gas pressures of 10^{-5} mbar can be generated in the BIF chamber without impacting other parts of the apparatus.

Figure 6 shows typical experimental results from a measurement with a beam current of 75 µA and two different settings of a focusing solenoid. It can clearly be seen that the width of the beam changes with respect to the focusing strength of the solenoids. A Gaussian function (blue) is fitted to the measured values including statistical errors (red) to extract the beam width.

CONCLUSIONS

Simulations of secondary electron trajectories using CST have been performed and are in very good agreement with experimental data. It could be shown that using a Wien filter and suitable collector optics, secondary emission from the collector surface poses no concern to the operation of future electron coolers. The turbo generator GET has been shown to deliver the sufficient power of 5 kW over a period of more than 1000 h without maintenance. An even further improvement regarding the lifetime would be a turbine with air bearings, which is under development at the moment. The laser system and the electron gun for both the TLS and the BIF measurements have been installed. With a signal-to-noise ratio of 50 %, the measurement still seems challenging but possible.

REFERENCES

[1] M. Bryzgunov et al., "Efficiency Improvement of an Electron Collector Intended for Electron Cooling Systems Using a Wien Filter", Technical Physics Vol. 58 No. 6, 2013.

[2] H. Bruining, "Physics and applications of secondary electron emission", 1954.

[3] M. Bruker, "Untersuchung der Rückgewinnungseffizienz eines Kühlerelektronenstrahls in longitudinalem Magnetfeld" (in German), PhD thesis, University of Mainz, Germany, 2016.

[4] F. Becker, "Beam Induced Fluorescence Monitors", WEODO1, Proceedings of DIPAC 2011, Hamburg, Germany.

[5] M.A. Plum et al., Nucl. Instr. Meth. A 492 (2002), p. 74.

ISBN 978-3-95450-181-6

COMMISSIONING OF THE 60 KEV ELECTRON COOLER FOR THE NICA BOOSTER

A. Bubley, M. Bryzgunov, A. Denisov, A. Goncharov, V. Panasyuk, V. Parkhomchuk, V. Reva,
BINP SB RAS, Novosibirsk, Russia

Abstract

The 60 keV electron cooler for the NICA booster was designed and constructed at BINP SB RAS. The article describes results of various measurements obtained during its commissioning. Also some details of design and construction of the cooler are discussed.

INTRODUCTION

NICA collider contains a big number of complicated systems and subsystems. One of them is gold ion booster, which is located at the existing hall of former synchrophasotron, and new superconductive magnets sit inside old giant iron yokes [1]. Low energy cooler is one of the elements of the booster those provides sufficient improvement of the ion beam quality.

Main specifications of the cooler are listed below:

ions type	p+ up to $^{197}Au^{31+}$
electron energy, E	1,5 ÷ 50 keV
electron beam current, I	0,2 ÷ 1,0 Amp.
energy stability, $\Delta E/E$	$\leq 1\cdot10^{-5}$
electron current stability, $\Delta I/I$	$\leq 1\cdot10^{-4}$
electron current losses, $\delta I/I$	less than $3\cdot10^{-5}$
longitudinal magnetic field	0,1 ÷ 0,2 T
inhomogeneity of the field, $\Delta B/B$	$\leq 3\cdot10^{-5}$
transverse electron temperature	≤ 0,3 eV
ion orbit correction:	
displacement	≤ 1,0 mm
angular deviation	≤ 1,0 mrad

The requirement for vacuum condition is usual for heavy ion accelerators $\leq 1\times10^{-11}$ mbar [1].

MEASUREMENTS OF THE ELECTRON GUN PERVEANCE

After long term training of the electron gun cathode, efficiency of the cathode increased and behavior of the perveance became similar to that of the electron gun being used in the electron cooler for COSY (Fig.1).

The main source of the current losses in the electron cooler is the secondary emission of electrons from the collector. In order to reduce losses, the suppressor placed before the collector creates a potential barrier that constrains the secondary emission. However, the magnitude of this barrier depends on the distance from the vacuum pipe axis and reaches its minimum at the center of the beam electron. The space charge of the electron beam produces the potential, which behaves the opposite way – the farther from the beam's axis, the lower the potential created by beam's space. With growth of the electron beam current the resulted potential barrier can lock the secondary emission and decrease the current losses (Fig.2). However, further increase of the beam current is limited as the beam's space charge can form an electrostatic mirror and lead to the breakdown.

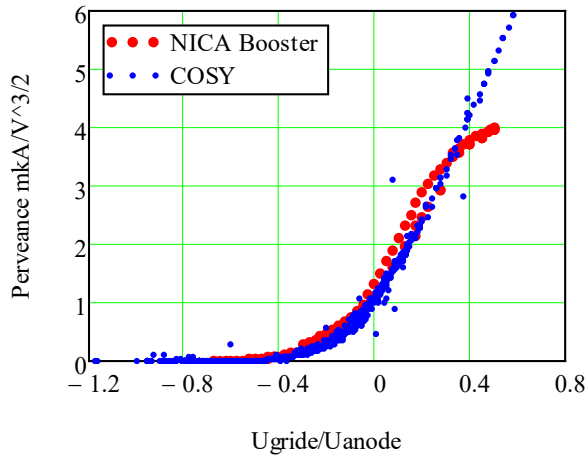

Figure 1: Electron gun perveance.

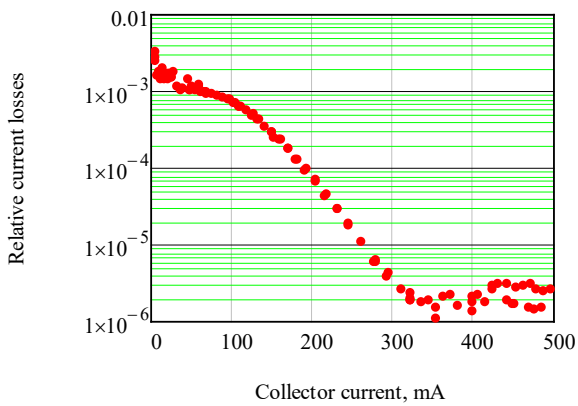

Figure 2: Electron current losses at collector.

VACUUM GENERATION

The vacuum system of the cooler has a volume approximately $0.2m^3$ .On the other hand the internal surface of the vacuum chamber is very advanced as it contains bending plates and other various electrodes. That leads to rather high outgassing rate. The scheme of the vacuum system is shown in Fig.3.

ISBN 978-3-95450-181-6

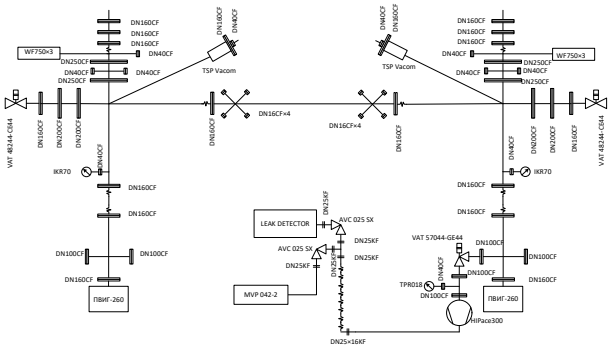

Figure 3: Scheme of the vacuum system.

For the obtaining the required vacuum condition as $\leq 1\times10^{-11}$ mbar following pumping equipment was includes into the system.

1. Ion pump combined with TPS "PVIG – 260" is most efficient in the range 1×10^{-6} to $1{,}5\times10^{-8}$Pa,total highest pumping speed 630 l/s.
2. Titanium sublimation pump TSP-IPG ("Vacom") is used with special ambient screen with surface area 1320 m^2, which corresponds to approximately 2000 l/s of pumping speed.
3. Every getter pump contains three modules of WP750-ST707. Data for one module: stripe surface 870 cm^2 , stripe thickness 0.2 mm, resistance 0.16 ohm, size 207×50×30 mm, pumping speed (H_2 - 330 l/s, CO - 130 l/s), sorption capacity (H_2-660 $torr^{-1}$, CO - 75 $torr^{-1}$, activation current (450ºC) is 27 amps.

All components of the vacuum system were baked out up to 300ºC for about two days with back pumping (300 l/s turbopump). The heating as well as cooling speed was about 0.5 ºC/min to protect numerous electric feedthroughs and other components contained ceramics. During cooling of the vacuum system the oxide cathode activation was performed and the NEG pump activation was done. After all those procedures were completed the system was closed from back pumping and ion pumps were turned on. Finally the required vacuum condition was obtained (see Fig.4).

Figure 4: Vacuum in the cooler vacuum chamber.

OXIDE CATHODE ACTIVATION

The oxide cathode, as required, was activated during the vacuum system bake-out with back pumping (see Fig. 5). The activation process is very sensitive to the vacuum condition when the cathode surface is overheated to provide necessary temperature. If the pressure is over required threshold so called, 'cathode poisoning' may occur. This leads to dramatic decrease of the emission ability of the cathode.

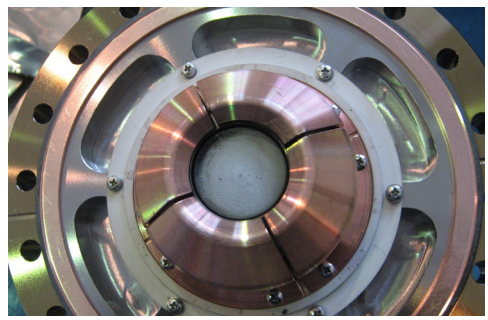

Figure 5: Oxide cathode (at the centre).

Gray and dark grey areas on the cathode surface show 'cathode poisoning'.

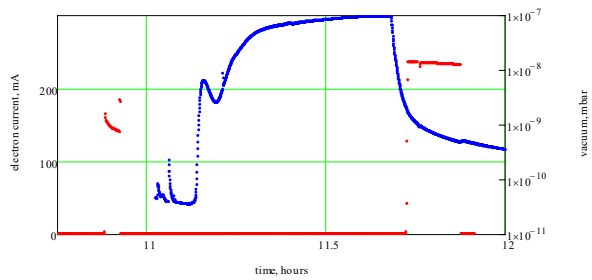

Figure 6: Electron current (red) and residual gas pressure (blue).

This experiment aimed at study the influence of the residual gases released during NEGs regeneration on oxide cathode properties. The electron current vas measured before and after regeneration process (Fig. 6). Cathode filament was on during the experiment. Pressure measurement plotted as a blue curve while electron current is red. Surprisingly the current significantly increased, that means the cathode surface was 'cured' with the hydrogen released from the NEGs.

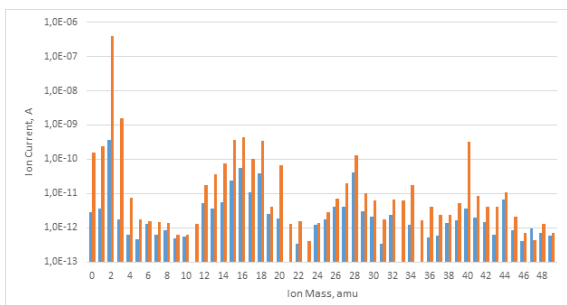

Figure 7: Residual gas mass spectrogram.

ISBN 978-3-95450-181-6

Mass spectrogram of the residual gas composition is shown on the figure 7. Blue bars correspond to the ions current at the cooler vacuum chamber; those are proportional to the partial pressure of the correspondent gas components. Red bars show the condition during NEGs regeneration. One may conclude that the hydrogen has pressure higher by 1000 times in comparison with other components.

HIGH VOLTAGE TEST

Figure above shows electron current leakage dependence on voltage for the HV terminal when its vessel was filled with air (red) and SF6 gas (blue). Sharp increase of the losses near 20 kV was observed due to the corona discharge (see photo on the Fig.8 upper left corner). SF_6 gas filling at atmosphere pressure suppress the corona discharge. This experiment shows that no extra pressure of the SF_6 is needed so the HV vessel design may be simplified.

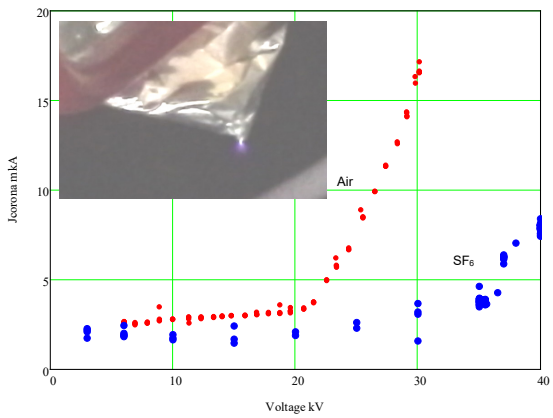

Figure 8: Electron current leakage.

SUMMARY

The 60 keV Electron Cooler for the NICA Booster [2 – 5] was successfully commissioned at BINP. At the moment of writing this article it is disassembled and prepared for the shipping to JINR.

ACKNOWLEDGMENT

Authors thank the people from laboratories 6-0, 6-2 of the BINP help in design and production various electronics.

REFERENCES

[1] N.Agapov, A.Butenko, et al. “Booster synchrotron for NICA collider”, Physics of Particles and Nuclei Letters, 2010, Vol. 7, No. 7, pp. 723–730.

[2] A.Bublei, A.Goncharov, A.Ivanov, et al. “The electron gun with variable beam profile for optimization of electron cooling” Proceeding of EPAC 2002, Paris, France, p.1357 - 1358.

[3] V.Bocharov, A.Bubley, Yu. Boimelstein, et al. “Electron Cooler Commissioning”. Nuclear Instruments and Methods in Physics Research, A 532 (2004) p.144-149

[4] A. Bubley, V. Parkhomchuk, V. Reva et al. “Commissioning of the LEIR electron cooler with Pb^{+54} ions”. Proceedings of XX Russian Accelerator Conference (RuPAC2006) Novosibirsk, Russia, September 10 - 14, 2006, WEBO01.PDF

[5] M. I. Bryzgunov, A. V. Bubley, A. D. Goncharov, et al. “Status of Construction of the Electron Cooling Systemfor the NICA Booster” Physics of Particles and Nuclei Letters, 2016, Vol. 13, No. 7, pp. 792–795. © Pleiades Publishing, Ltd., 2016.

ISBN 978-3-95450-181-6

STOCHASTIC COOLING SYSTEM AT NICA PROJECT

I. Gorelyshev#, N. Shurkhno, A. Sidorin, G. Trubnikov, VBLHEP, JINR, Dubna, Russia

Abstract

Stochastic cooling system is one of the crucial elements for luminosity preservation at NICA accelerator-collider complex. The foundation of main parameters of the stochastic cooling system is provided. The preparatory experimental work for longitudinal stochastic cooling was performed at Nuclotron accelerator. The description of Nuclotron system components, adjustment algorithms and remote control is given.

INTRODUCTION

NICA accelerator-collider complex is under construction in JINR [1]. One of the challenging technologies of the collider project is the stochastic cooling. It is required for beam accumulation and luminosity preservation. Stochastic cooling is developed in Russia for the first time and operational regimes differ from those used before in the world. So before the run of NICA a test channel was put into operation at Nuclotron.

GENERAL SCHEME

Stochastic cooling is a microwave broadband system with feedback via the beam. The working principle is the following: pickup electrodes detect noise from the beam, signal propagates through the system and applies on the kicker. For effective operation signal has to be properly amplified and delayed. If delay and amplification are correctly adjusted one has the reduction of betatron amplitudes in case of transverse cooling or momentum spread in case of longitudinal cooling. General scheme of Nuclotron stochastic cooling system is presented at the figure 1. This system has bandwidth 2-4 GHz and 60 W maximum output power. It consists of pickup with preamplifiers, notch filter, block of switches, variable delay and attenuation and diagnostic devices to maintain different modes of operation, main amplifier and kicker.

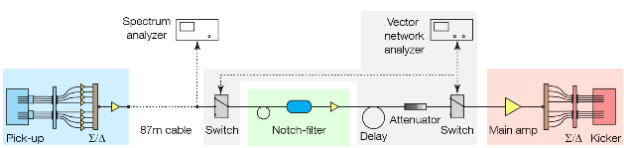

Figure 1: General scheme of the Nuclotron stochastic cooling system.

Pickup and Kicker

Pickup and kicker are HESR type ring-slot couplers which were designed and constructed in FZ Jülich [2]. Pickup is installed in vacuum chamber and has 8 outputs from 8 azimuthal positions around the beam (fig. 2a). Signals from outputs are amplified and can be combined into transverse horizontal, transverse vertical and longitudinal common signals (figure 2b).

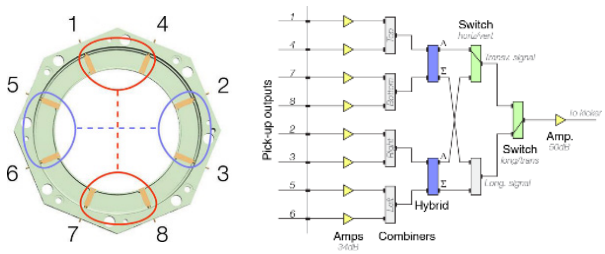

Figure 2: Pickup transverse cross section (left) and commutation scheme (right).

Kicker is the same device as pickup. It has identical commutation scheme with no amplifiers. The difference is that common signal splits to 8 signals at kicker.

Notch Filter

Notch filter (figure 3) receives RF signal from pickup. The signal is modulated by infrared laser and is divided into two lines.

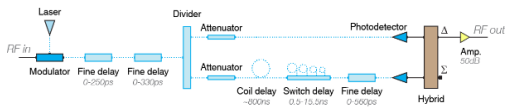

Figure 3: Scheme of optical notch filter.

Part of the signal from the short line passes directly to the output, another part from the long line passes through coil delay, switch delay and fine delay. Each line has photodetector demodulating optical signals to RF at its end. Signals from two lines are combined with 180° phase shift and outgoing signal is enlarged by 50 dB amplifier. To realize time-of-flight method the long line of the filter has to be switched off.

Variable Delay and Attenuation

These simple devices are manipulated by a set of switches. Each switch contacts either short line or modified (delay or attenuation) line (figure 4).

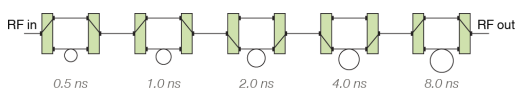

Figure 4: Scheme of variable delay.

Variable delay has 0.5, 1, 2, 4, 8 ns modified lines and range of manipulation 0-16 ns. Variable attenuation has 1, 2, 4, 8, 16, 24 dB lines and range of manipulation 0-55 dB.

ivan_v_gorelyshev@mail.ru

ISBN 978-3-95450-181-6

Main Amplifier

For stochastic cooling system it is required to have approximately frequency independent amplitude and phase response. Amplitude and phase response of main 60 W amplifier was measured and the result is given on figure 5. For bandwidth 2-4 GHz amplifier has excellent amplitude response, phase response is good enough, but has to be improved by phase equalizer.

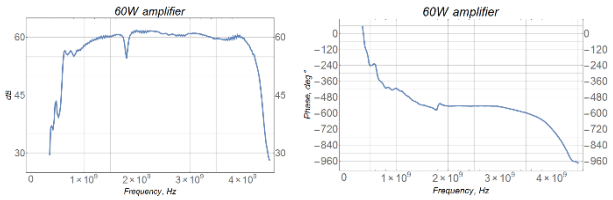

Figure 5: Amplitude (left) and phase response (right) of main 60 W amplifier.

REMOTE CONTROL AND MODES OF OPERATION

While system is in operation it needs to be quickly adjusted and remotely controlled. Thus application for remote control and automatic adjustment was developed (figure 6).

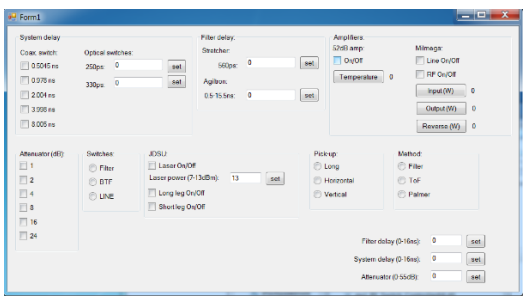

Figure 6: Interface window of the application for remote control and automatic adjustment.

Stochastic cooling system at Nuclotron has 3 modes of operation: filter adjustment, measurement of beam transfer function – BTF (system delay adjustment) and cooling. Commutation between these regimes is provided by block of switches (figure 7).

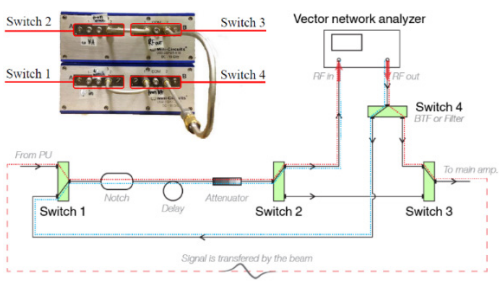

Figure 7: Operational regimes of stochastic cooling system at Nuclotron.

Adjustment in first two modes is supported by network analyzer measurements. In the first mode signal from network analyzer passes only through notch filter, variable delay and attenuation. In BTF mode the signal from the analyzer is transferred via the beam, and returns through the system. In the cooling regime the loop consisting of system components and the beam is closed.

EXPERIMENTAL RESULTS

Nuclotron stochastic cooling system was developed, assembled, adjusted and tested. The momentum cooling of bunched and coasting beam of D^+ and C^{6+} was obtained during several runs at Nuclotron [3]. As an example the momentum cooling of coasting deuteron beam is presented at the figure 8a. The beam intensity was 2×10^9 and energy 3 GeV/u. The RMS momentum spread was reduced by approximately a factor of 2.2 within 480 s. This process of longitudinal cooling was also calculated by solving the Fokker-Planck equation [4]. The simulation and experimental results are in reasonable agreement (figure 8b).

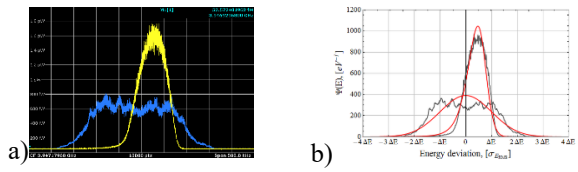

Figure 8: Reduction of beam energy spread: a) experimental result, b) comparison with simulation.

IBS CALCULATION

To preserve luminosity in the NICA collider the stochastic cooling system has to counteract the dominating heating process of intra-beam scattering (IBS). IBS rates calculations were performed in BETACOOL. Structures with β*=35, 70, 100 cm, where β^* is the β-function in collision point, were compared. While horizontal emittance was fixed and equal to 1.1 π mm. mrad., vertical emittance and momentum spread were chosen to match the equilibrium of heating rates between all three degrees of freedom.

If RF voltage is chosen to provide RMS bunch length σ_s=60 cm, then its maximum is less than the project limitation VRF_{max}=1 MV. Bunch intensity was matched in order not to exceed the acceptable betatron tune shift $\Delta Q=0.05$ and the project luminosity $L=10^{27}$ cm^{-2}s^{-1}.

The project luminosity in the structure with β^* = 35 cm is achieved at energy 3 Gev/u and bunch intensity 2.4×10^9. In structures with β^* = 70 and 100 cm the required luminosity is achieved at 3.2 and 3.4 Gev/u at 1.2 and 1.4 larger bunch intensity respectively. IBS rates for compared structures were calculated considering forgoing data and its values are about equality in the energy range between 3.3 and 4.5 GeV/u. The results of IBS calculation for different structures are presented at figure 9.

ISBN 978-3-95450-181-6

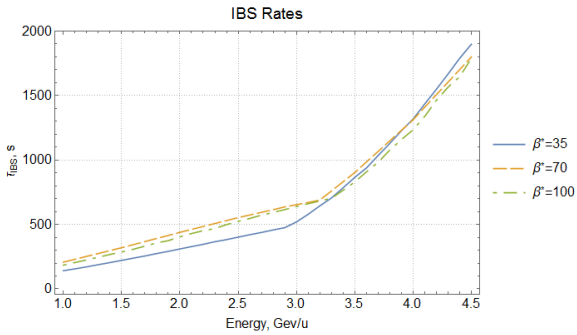

Figure 9: Rates of intra-beam scattering for different structures.

PARAMETERS OF THE COLLIDER STOCHASTIC COOLING SYSTEM

One of the limitations for the stochastic cooling system is the Shottky band overvap in the passband. The passband has to be the widest octave band with no or small Shottky band overlap. The project energy range for stochastic cooling in the collider is above 3 GeV/u. The convenient passband for this energy range is 2-4 GHz.

Another critical parameter is acceptance of the system. To avoid parasitic bunches and particle losses the acceptance of a cooling method must be larger than the separatrix height.

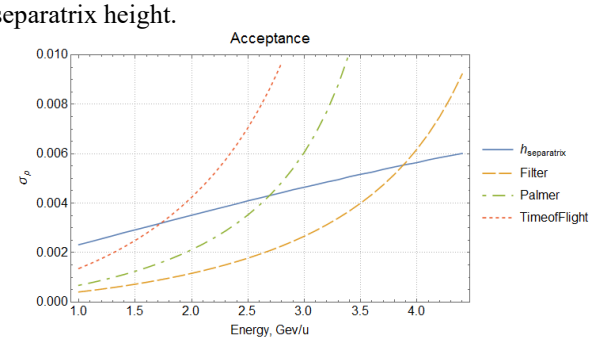

Figure 10: Acceptances of stochastic cooling methods.

In figure 10 it is seen that the filter method does not cover the whole separatrix at energies below 3.9 GeV/u.

We assume that the cooling method is applicable if its rates for the optimal gain is at least two times faster than equilibrium IBS rates.

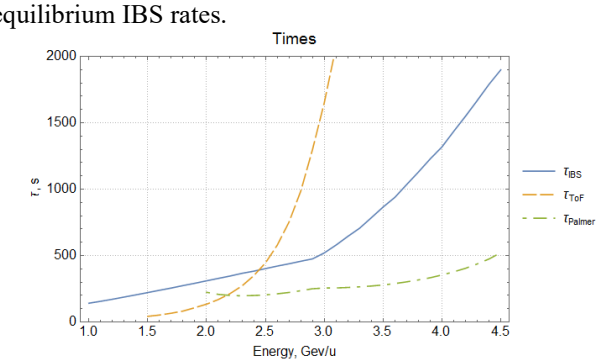

Figure 11: Cooling rates in comparison with IBS rates.

In figure 11 cooling rates for the rest methods are presented in comparison with IBS rates. It is seen that the ToF method does not provide required rates. So the only method which satisfies all conditions is Palmer. The ratios of heat/cool for compared structures is presented in table 1.

Table 1: Comparison of heat/cool ratios for different structures.

E=3Gev/u	β*=35 cm	β*=70 cm	β*=100 cm
IBS/Palmer	2,034152	2,54291	2,464272

CONCLUSION

New developed scheme was set in operation. All system components proved to be reliable and effective. With the developed software for remote control and adjustments the system can be easily operated and adjusted. Coasting and bunched beam cooling was obtained in Russia for the first time. Nuclotron experiments provided the basis for developing a stochastic cooling system of NICA collider and showed appropriateness of HESR type kicker for NICA and FAIR. Based on experience with stochastic cooling at Nuclotron the CDR for the NICA stochastic cooling system had been worked out, development of the TDR is in progress.

REFERENCES

[1] A. Sisakian et al., XXIII Int. Symposium. on Lepton and Photon Interactions at High Energy, LP07, Daegu, Korea, (2007).

[2] R. Stassen et al., “The stochastic cooling system of HESR”, COOL’11, Alushta, Ukraine, September 2011, p.191.

[3] A. O. Sidorin, G. V. Trubnikov, N. A. Shurkhno, “Experimental and theoretical studies at JINR dedicated to development of stochastic cooling of charged particle beams”, Phys. Usp. 59 (3) (2016).

[4] T. Katayama, N. Tokuda, “Fokker-Planck Approach for the Stochastic Momentum Cooling with a notch filter”, Part. Accel. 1987. V. 21. P. 99.

ISBN 978-3-95450-181-6

COMMISSIONING OF ELECTRON COOLING DEVICES AT HIRFL-CSR*

X. D. Yang†, L. J. Mao, J. Li, X. M. Ma, T. L. Yan, G. H. Li, M. T. Tang, Institute of Modern Physics, CAS, Lanzhou, 730000，China

Abstract

Electron cooling plays an important role in the Heavy Ion Research Facility of Lanzhou cooler storage ring (HIRFL-CSR). Two electron coolers were equipped in main ring (CSRm) and experimental ring (CSRe) in HIRFL-CSR respectively.

Two electron cooling devices have commissioned for twelve years since they were installed and completed in 2004.

The function and operation procedure of electron cooler were presented in this report. Their performance and the highlights of experiments results were described. Their commission and optimization were summarized here. The issues and troubles during the commission were enumerated and collected in this presentation. The future upgrade and improvement were suggested, and the new operation scenario and requirement were proposed.

INTRODUCTION OF HIRFL-CSR

HIRFL-CSR (Heavy Ion Research Facility at Lanzhou---Cooling Storage Ring) is multi-purpose accelerator complex [1], it is consisted two storage ring, the heavy ion beam with energy range 8-50 MeV/u from HIRFL—composed two existing cyclotron SFC(K=69) and SSC (K=450) is used as injector, will be accumulated, cooled and accelerated to the high energy range of 100—400 MeV/u in the main ring (CSRm), then extracted fast to produce RIB or highly charged heavy ions. The secondary beams will be accepted and stored by experimental ring (CSRe) for many internal target experiments or high precision spectroscopy with beam cooling, On the other hand, the beam with energy range of 100-900 MeV/u will also be extracted from CSRm with slow and fast extraction.

Accelerated ion beam from the CSRm through the radioactive beam separator line with the length of 100m was injected into the CSRe. Generally the CSRe operated with the DC mode. A gas jet internal target was installed in the opposite side of electron cooler.

ELECTRON COOLING FOR CSR

In CSRm, the electron cooling device [2, 3, 4, 5, 6] plays an important role in the heavy ion beam accumulation at injection energy. The new state-of-the-art electron cooling device was designed and manufactured in the collaboration between BINP and IMP, it has three distinctive characteristics, namely high magnetic field parallelism in cooling section, variable electron beam profile and electrostatic bending in toroids.

Each ring was equipped an electron cooling device, the electron energy in the main ring is 35 keV and 300 keV for the experimental ring.

The electron cooling device plays an important role in HIRFL-CSR experimental ring for the heavy ion beam. Continuous electron cooling is applied to the stored ion beam for the compensation of the heating by various scattering. The most important is the ability to cool ion beams to highest quality for physics experiments with stored highly charged ions.

STATUS OF HIRFL-CSR

In the past several years, more than 7000 operational hours was scheduled yearly for HIRFL-CSR, half of them were provided by the storage ring. Most beamtime was dedicated to the mass measurement experiments, recombination of ion with the free electron of cooler and the internal target experiments. The other beamtime was devoted to the cancer therapy and related experiments. More than 100 patients were treated in CSRm with the carbon beam. However, the extremely heavy ion beam like Bi and U were successfully cooled and accumulated with very low injection energy and weak intensity. A few times commission for accumulation of proton with the help of electron cooling were performed in CSRm, including instead of proton with H_2^+, these commission were not successfully completed carried out up to now due to the mismatching parameters between injector and storage ring.

COMMISSIONING AND OPERATION OF ELECTRON COOLING IN CSR

About kind of ion beam was accumulated with the help of electron cooling in CSRm. The ion species from H to Uranium, and the energy range from to 1.2MeV/u to 21.7MeV/u. The experiments and operation results were reported in the workshop on the beam cooling and related topics from 2005 to 2013 [7, 8, 9, 10, 11] and RuPAC 2010 [12], RuPAC 2012 [13]. One can find the related papers in the references. Some investigation and optimization experiments [14, 15] were completed in CSR. Some accumulation experiments in CSRm, cooling force measurement, optimization of electron cooling and bunch length measurement in CSRe were implemented.

WHAT WE HAVE DONE

Temperature Stabilization System

During the operation, we found the tunnel temperature have the influence on the stability of high voltage output of cooler system, it presented a sine wave in the day and

* Work supported by The National Natural Science Foundation of China, NSFC (Grant No. 11375245, 11475235, 11575264)

† yangxd@impcas.ac.cn

ISBN 978-3-95450-181-6

night. In order to decrease this effect, a special room was established to keep the constant temperature for the electronic system of the high voltage terminal of the electron cooler.

Electric and Magnetic Screen

Due to the electronic system of the high voltage terminal of the electron cooler was placed in the outside of tunnel and some place as the other power supplies for dipoles and quadrupoles magnets etc. The spatial electromagnetic wave had the influence on the stability of high voltage output of cooler system. With the help of a special shielding room, the electronic system of the high voltage terminal of the electron cooler was well screened, and the stability of output was improved.

Electrical Network Voltage Stabilization

Because of the CSRm ring operated in the pulse mode, a voltage sudden drop appeared during the ramping time in the input of power network due to huge load. A voltage stabilizer for the amplitude regulation was installed before the input of high voltage terminal.

Improvement of HV Stability

In the initial design, there were some electronic elements with low temperature coefficient, these elements were replaced by some with the higher temperature coefficient.

Screen of Amplifier of BPM

The signal from the beam position monitors in the cooler was influenced by the spatial electromagnetic wave from the power supplies of dipoles and other system, this noise became serious in the case of low intensity of stored ion beam. A screen box was designed and used for the preamplifiers of BPM systems the beam position measurement procession was improved.

CAMAC into NI Card in the BPM

In the initial design, a CAMAC system was established for beam position monitor, this system was replaced by 8-Channel Digitizers NI PCI-5105 card, and a new measurement interface based on LabVIEW was established. This made the measurement more convenient.

Replace the Correction Coils Power Supplies

There are twelve pair coils in the cooler in order to adjust the electron beam position and angle. These coils were powered individually. The current output stability had the influence on the measurement results of the electron beam position. The old analog electronics power supplies were replaced by the new digital controlled systems. The vibration of electron beam position was improved.

Drying of SF_6

Due to there was water vapour in the SF_6, the higher voltage output was not approached because of spark, a special drying system was used to remove the water vapour in SF_6, 285kV output was achieved after high voltage training.

ISSUES DURING OPERATION

Issues for Cooling Water

The trouble from deionized water for collector cooling lasted for long time. This problem influenced the operation of the electron cooling devices. At the beginning, the cooler did not work at higher voltage due to lower resistance. After some period operation, the water tube had to be cleaned by special acidic liquid due to the residual oil form the copper winding wire of various coils in the storage ring. As a result, some components were corroded by this liquid. The leakage happened in some weaker position at the connector of cooling water system. Specially, in the ceramic insulator section, the surface of collector was covered by the ferrugineous rust caused by the leakage. During the period of operation, spark happened due to the worst insulation. The current load became bigger than normal situation, and the power supply of collector was destroyed finally.

Issues form Control System

The control program for CSRm electron cooling devices was developed in the environment of Windows 98 system in the initial design. It was based on the LabWindows/CVI and LabVIEW. A special card named PCI-7841 was used for the communication between computer and electron cooling devices. The communication was based on the CAN bus. The PCI-7841 is a Controller Area Network (CAN) interface card. It supports a dual-port CAN's interface that can run independently or bridged at the same time. The built-in CAN controller of this card is Philips SJA1000, which provides bus arbitration and error detection with auto correction and re-transmission function. This needs special drive of DOS libraries and Windows DLLs (95, 98, NT, 2000, XP).

Up to now, the control system of electron cooling devices has not combined into the global control system of HIRFL-CSR. The electron cooling devices was controlled by the independent subsystem. As the upgrade of Windows system, The DOS libraries and Windows DLLs (95, 98, NT, 2000, XP) for PCI-7841 card had to been upgraded accordingly. At the same time, the different version of operation system existed small different. This factor made the operation inconvenient in the commission of electron cooling devices.

Issues form Beam Diagnostics System

In order to measure the profile of ion beam in the storage ring, a magnesium vapour profile monitor was installed in the upstream of electron cooling device in CSRm. At the beginning of this monitor operation, the temperature was not controlled well, some magnesium vapour escaped form monitor chamber and entered the vacuum chamber of cooling section. As a consequence, the insulator surface of beam position monitor in the cooling section was polluted by the magnesium vapour,

ISBN 978-3-95450-181-6

the insulation became weaker and worse. After some spark treatment, this situation became better, but the beam position monitor did not worked stably.

Issues of stability

It was important for mass measurement high voltage stability of electron cooling devices, it determined the final resolution.

In the case of atomic physics experiment, the stability of electron beam position was required in some position sensitive experiments, especially recombination experiment.

In the experiments of recombination, the electron beam current stability was also a focus point.

The stability of high voltage will be an issue for long-term effort and related many aspects from point of view of improvement and upgrade in the aspects of performance of electron cooling devices.

IMPROVEMENTS AND UPGRADE

- Real-time monitoring of ion beam position.
- Real-time monitoring of electron beam position.

In order to improve the performance of electron cooling system, a real-time monitoring system of the position of electron and ion beam was taken into account,

- Automatically ion beam orbit correction.
- Automatically electron beam orbit correction.

Based on the BPM real-time monitoring system, a automatically orbit correction of electron and ion beams was taken into account.

NEW REQUIREMENTS

- Switch on and off electron beam momentarily.

The electron beam was required to turn on and off in the different period of the atomic physics experiments.

- Change the energy of electron beam momentarily.

The energy of the electron beam was required to change in the different cases of the atomic physics experiments.

- Energy modulation of electron beam.

The energy of the electron beam was required to modulate in the different cases of the atomic physics experiments.

- Density modulation of electron beam.

The radial density distribution of the electron beam was required to modulate in the different cases of the atomic physics experiments.

- Electron beam bunch

In order to demonstrate the cooling of bunched electron beam, the formation of electron beam bunch was taken into account recently.

SUMMARY

From 2006, the electron cooler have operated well for ten years. Electron cooling, ion beam accumulation and electron cooling experiments were performed in HIRFL-CSR. Several physics experiments were completed with the help of electron cooling in CSR. The results show the electron cooling had well performance in the commission. In the future, the application of electron cooling should be extended according to the physics experiments. The performance of electron cooling should be improved carefully, and the reliability and stability of electron cooling should be upgraded in the future.

REFERENCES

[1] http://english.imp.cas.cn/rh/.

[2] X.D. Yang, et al., “HIRFL-CSR Electron cooling devices”, Cyclotrons and their Applications 2001, Sixteenth International Conference, East Lansing, Michigan 2001, paper P1-09, pp.186-188.

[3] YANG Xiao-Dong, et al., “Test results of HIRFL-CSR main ring electron cooling device”, *High Energy Physics and Nuclear Physics* (in Chinese) Vol. 27, no. 8, pp. 726-730. 2003.

[4] Xiaodong Yang, “Electron cooling at IMP”, Beam Dynamics Newsletter, No. 65, pp. 55-67, 2015.

[5] YANG Xiao-Dong, et al., “Commissioning of electron cooling in CSRm”, *Chinese Physics C (HEP & NP)* Vol.33 no. SII pp. 18-21, 2009.

[6] Yang Xiao-Dong, et al, “Commissioning of electron cooling in CSRe”, *Chinese Physics C (HEP & NP)*,Vol. 34, no.7, pp. 998-1004, 2010.

[7] Xiaodong Yang, et al., “Commissioning of HIRFL-CSR and its electron coolers”, “AIP conference proceedings 821”, 2006, paper TUM1I02, pp. 65-74.

[8] X.D. Yang, et al., “ Commissioning of electron cooling in CSRm”, Proceedings of COOL2007, paper TUM1I02, pp. 59-63.

[9] X.D. Yang, et al., “Commissioning of electron cooling in CSRe”, Proceedings of COOL 2009, Lanzhou, China, paper FRM1MCIO02, pp. 173-177.

[10] Xiaodong Yang, et al., “Electron cooling performance at IMP facility”， Proceedings of COOL’2011, Alushta, Ukraine，2011, paper MOIO01，pp. 1-5.

[11] Xiaodong Yang, et al., “Influence of electron energy detuning on the lifetime and stability of ion beam in CSRm”, Proceedings of COOL’2013, Murren, Switzerland, 2013, paper WEAM1HA02, pp. 84-88.

[12] Xiaodong Yang, et al., “Electron cooling experiments in CSR”, Proceedings of RuPAC-2010, Protvino, Russia, 2010, paper WECHZ05, pp. 161-165.

[13] Xiaodong Yang, et al., “Beam instability phenomena observed at HIRFL-CSR in the presence of electron cooler”, Proceedings of RuPAC-2012, St. Petersburg, Sept. 24-28 2012, paper MOZCH01, pp.33-37.

[14] YANG XiaoDong, et al., “Electron cooling performance at HIRFL-CSR”, *High Power Laser and Particle Beam* (in Chinese), Vol.24, no.10, pp. 2435-2440, 2012.

[15] YANG XiaoDong, et al., “Beam instability phenomena observed at HIRFL-CSR in the presence of electron cooler”, *Sci Sin-Phys Mech Astron*, Vol. 43, no. 1, pp. 76-84, 2013.

ISBN 978-3-95450-181-6

DESIGN AND CALCULATION OF CYLINDRICAL ELECTROSTATIC DEFLECTOR FOR THE TRANSPORT CHANNEL OF THE HEAVY ION BEAM

N.Kazarinov#, I.Kalagin, S.Zemlyanoy, JINR, Dubna, Russia

Abstract

The cylindrical electrostatic deflector is used in the beam transport channel of GALS spectrometer that is created at U400M cyclotron in Flerov Laboratory of Nuclear Reaction of Joint Institute for Nuclear research. The design and calculation of the deflector are presented in this report. The angular length of the electrodes and gap between potential electrode and screen are found by using of the minimization procedure.

INTRODUCTION

GALS is the experimental setup for selective laser ionization with gas cell [1] that will be created at U400M cyclotron in FLNR JINR [2]. The cylindrical electrostatic deflector is the optical element of the part of the channel intended for transportation of the secondary ion beam. The deflector rotates the researched ion beam from the focal plane of the spectrometric magnet onto the particle detector.

The design of the deflector is proposed in this report. In accordance with results of works [3,4] the deviation of the trajectory of the beam center of mass from the designed orbit have been minimized by appropriate choice of angular length of the deflector electrodes. The influence of the nonlinearities of the transverse electric field on the dynamics of the particles have been reduced by means of variation of angular distance between electrodes and grounded screen.

The beam dynamics simulations were performed by using the MCIB04 program code [5]. 2D field map of the deflector electric field calculated with the help of POISSON program code [6] was used in the simulations.

2D MODEL OF THE DEFLECTOR

The scheme of the deflector is shown in Fig.1.

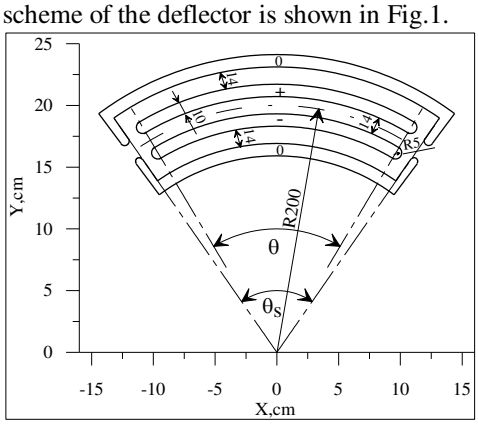

Figure 1: Scheme of deflector GALS

The deflector consists of two electrodes under potentials U_1 (-), U_2 (+) and two grounded screens (0). The design bending radius R = 20 cm, design bending angle φ = 67 degrees and the gap between the electrodes d = 14 mm. The optimal value of the angular size of the electrodes θ is equal to 62.6 degrees. The optimal angular distance between the inner end face of the screens is equal to $\theta_s = \theta + 8^0$. The vertical size of the electrodes (in the Z axis direction) is 80 mm.

2D computational models of the GALS deflector are shown in Fig.2. The first one (Fig.2a) corresponding to cylindrical system of coordinates (r,z≥0) has been used for evaluation of the electric field inhomogeneity inside the deflector aperture. The second one (Fig.2b) corresponding to Cartesian frame (X≥0,Y≥0) was used during determination of the optimum angular dimensions of the electrodes.

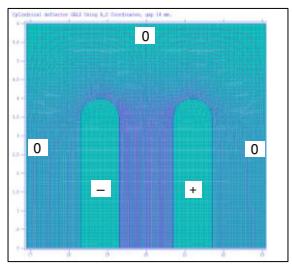

Figure 2a: 2D model in cylindrical frame

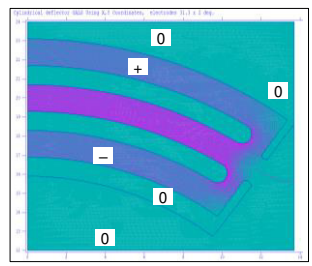

Figure 2b: 2D model in Cartesian frame

Two independent distributions of the electric field of the deflector were found for each of the potential electrodes. The electric field strength of the deflector for arbitrary voltages at the electrodes was calculated as a superposition of these distributions.

The inhomogeneity of the bending electric field within the working aperture of the deflector is shown in Fig.3,4.

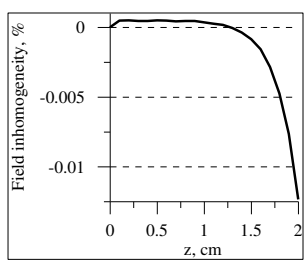

Figure 3: Inhomogeneity of bending electric field in Z-direction

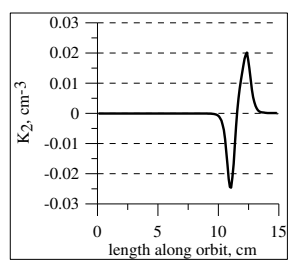

Figure 4: Sextupole coefficient K_2 of bending electric field

#nyk@jinr.ru

ISBN 978-3-95450-181-6

As may be seen from Fig.3 the inhomogeneity in Z-direction is less than 0.0125% at the edge of the working area of the deflector z = ±2 cm.

The dependence of the sextupole coefficient K_2 on length along orbit is shown in Fig.4. The chosen angular distance between potential electrodes and grounded screen $\Delta\theta$ = 8 degrees gives the possibility to minimize the average value of sextupole coefficient at level $K_2 = 8.4\times10^{-5}$. It is more than three hundred times less than maximum of the absolute value of K_2.

CALCULATED EQUILIBRIUM ORBIT

In the calculations using MCIB04 program [5] the half orbit ($X_0(s)$, $Y_0(s)$), corresponding area $X_0 \geq 0$, was considered. The initial conditions in this case were defined as follows:

$$X_0(0)=0;\ X_0'(0)=1;\ Y_0(0)=R_i;\ Y_0'(0)=0 \qquad (1)$$

Calculated equilibrium orbit was found by means of varying the values of the voltages at the electrodes $U_{1,2}$ and the initial radius R_i of the orbit. The matching condition is the coincidence of the calculated and the design orbits and its angles at the edge of the electric field map L_E:

$$\begin{aligned} X_0(L_E)Sin(\varphi/2)+Y_0(L_E)Cos(\varphi/2)&=R\\ X_0'(L_E)Sin(\varphi/2)+Y_0'(L_E)Cos(\varphi/2)&=0 \end{aligned} \qquad (2)$$

Due to existence of three variable parameters, we can add the condition of minimum of the root mean square deviation δ between the calculated and the design orbits:

$$\delta=\left[\frac{1}{L_E}\int_0^{L_E}\Delta^2(s)ds\right]^{1/2}=\min, \qquad (3)$$

where deviation Δ(s) is defined by formula

$$\Delta(s)=\begin{cases} R-\sqrt{X_0^2(s)+Y_0^2(s)} & ,\varphi_p\le\dfrac{\varphi}{2}\\ R-X_0(s)Sin(\dfrac{\varphi}{2})-Y_0(s)Cos(\dfrac{\varphi}{2}), & \varphi_p>\dfrac{\varphi}{2}\end{cases} \qquad (4)$$

Here φ_p is the current value of the angle of the reference particle.

In the non-relativistic approximation value of R_i is independent on the reference ion parameters (charge to mass ratio Z/A and accelerating voltage U_p). Thereby the orbit depends on only the electrodes geometry. The voltages at the electrodes $U_{1,2}$ in this case are proportional to U_p.

ELECTRODE ANGULAR SIZE

The minimum of expression (3) is strongly depended on the angular size of the potential electrodes θ. The angle θ was varied in the range of 59.0-62.6 degrees to determine it optimal value. The dependences of the ratio of the bending electric field $E_n(s)$ to its value at the deflector center $E_n(0)$ for the three values of angle θ are shown in Fig.5. The angular distance Δθ between electrodes and screen was not changed.

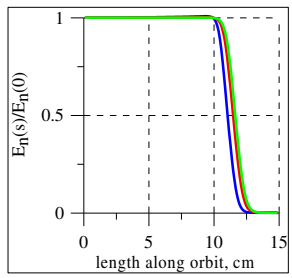

Figure 5: Bending electric field. θ = 59⁰ – blue line; θ = 61.6⁰ – red line; θ = 62.6⁰ – green line

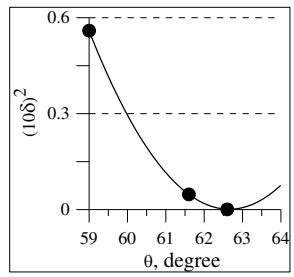

Figure 6: RMS deviation between design and calculated orbits.

The dependence of the rms deviation δ (3) on angle θ is shown in Fig.6. The dots mark the calculation results for the three field maps. The global minimum is corresponded to angle θ = 62.6⁰.

DEFLECTOR BASIC PARAMETERS

The calculated orbit and deviation Δ(s) (4) for the optimum value of the angle θ =62.6⁰ are shown in Fig.7.

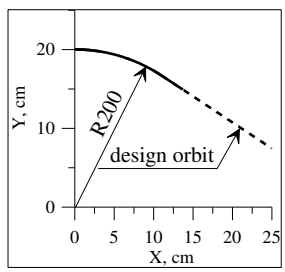

Figure 7a: Calculated orbit

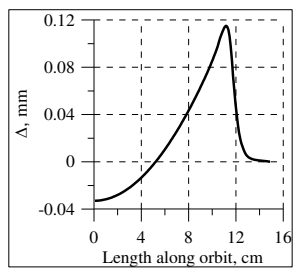

Figure 7b: Deviation between orbits

As may be seen from Fig.7b the maximal deviation does not greater than 0.12 mm. The maximum accelerator voltage of GALS setup U_p = 40 kV and corresponding voltages at the electrodes are U_1 = -2.866 kV and U_2 = 2.754 kV. The distributions of bending $E_n(s)$ and tangent $E_t(s)$ electric fields at calculated orbit are shown in Fig.8.

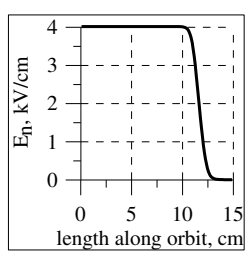

Figure 8a: Bending electric field at orbit

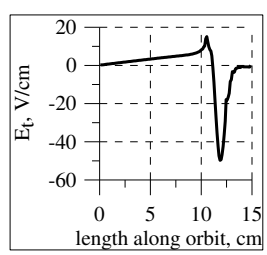

Figure 8b: Tangent electric field at orbit

ISBN 978-3-95450-181-6

The effective radius R_{eff} of the deflector was evaluated also. It defines the horizontal focusing of the beam and may be used in calculation of the beam transport line.

The effective quadrupole coefficient $K_1(s)$ of the cylindrical electrostatic deflector is equal to [7]:

$$K_1(s) = K(s)\left(3K(s) + \frac{1}{E_n}\frac{\partial E_n}{\partial x}\right) \qquad (5)$$

Here K(s) is curvature of the orbit and differentiation is carried out in the direction perpendicular to the orbit. The dependence of coefficient $K_1(s)$ on distance along the calculated orbit is shown in Fig.9.

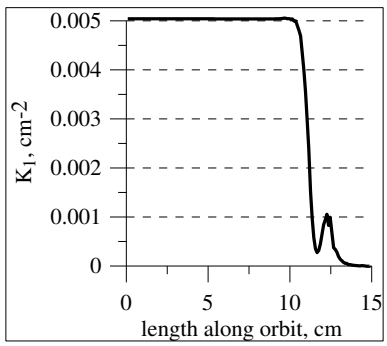

Figure 9: Quadrupole coefficient $K_1(s)$

The effective radius of the deflector may be introduced in accordance with the formula:

$$R_{eff} = \frac{\varphi}{< K_1 > L_E} \quad , \qquad (6)$$

where $< K_1 >$ is average value of the quadrupole coefficient (5) along the orbit.

The calculation with the help of formula (6) gives the value of the effective radius of the deflector R_{eff} = 20.8 cm.

REFERENCES

[1] S. Zemlyanoy, V. Zagrebaev, E. Kozulin, Yu. Kudryavtsev, V. Fedosseev, R. Bark and Z. Janas, "GALS – setup for production and study of multi-nucleon transfer reaction products: present status", Journal of Physics: C. S. 724 (2016) 012057

[2] B. Gikal et al., "The JINR FLNR Heavy Ion Cyclotron Complex", WEYMH03, these proceedings.

[3] H. Hubner and H. Wolnik, "The Design of Magnetic Field Elements," Nucl. Instrum. Methods 86, 141 (1970).

[4] I.A.Ivanenko, N.Yu.Kazarinov, "Optimization of the Magnetic Field in the Analyzing Magnet of the Axial Injection Beam Line of the Cyclotron DC-280, "Physics of Particles and Nuclei Letters, 2014, Vol. 11, No. 6, pp. 756–762, ISSN 1547-4771.

[5] V. Alexandrov, N. Kazarinov, and V. Shevtsov, "Multi-Component Ion Beam code – MCIB04," Proc. of XIX-th Russian Part. Accel. Conf. RUPAC2004. Dubna, Russia. 4-9 October 2004.

[6] Reference Manual for the POISSON/SUPERFISH Group of Codes, Los Alamos National Laboratory Report LA-UR-87-126 (1987)

[7] N.Kazarinov, I.Ivanenko, "Electrostatic Deflector of the Cyclotron DC-280 Axial Injection Channel", Proceedings of the 13th International Conference on Heavy Ion Accelerator Technology, HIAT2015, September 7-11, Yokohama, Japan, p.71.

ISBN 978-3-95450-181-6

THE WAY TO IMPROVE CONFORMITY OF PROTON THERAPY

I.A. Yakovlev, S.V. Akulinichev, Yu.K. Gavrilov, INR RAS, Moscow
R. D. Ilić, VINCA, Belgrade

Abstract

In the case of small tumors, the pencil beam width may be comparable with the target size. In these cases, the application of classic method of passive beam scattering with a one-stage formation of dose distribution may be reasonable. However, the last method in its standard implementation fails to provide the dose conformity: either the maximal dose exceeds the tumor volume on its proximate site or the dose deviates too much within the tumor. In order to overcome this shortcoming of the passive scattering method, we suggest a new construction of a two-component ridge filter (the corresponding patent is pending). We have performed a series of calculations with the Monte-Carlo code SRNA in order to find the optimal construction from the point of view of dose delivery accuracy and of the device manufacturability. With that ridge filter the 95% isodose does not notably leave the tumor volume. The usual "wings" of isodoses on proximate side are now absent and the volume of irradiated healthy tissue is significantly reduced. The experimental tests with proton beams are now in progress.

PROTON THERAPY AND DOSE FORMATION METHODS

Proton therapy has remarkable advantages over conventional photon radiation therapy. The depth dose distribution shows the increase with penetration depth leading to a maximum energy deposition near the end of range in matter (Bragg peak). This feature allows to spare healthy tissue while delivering maximal dose to the tumor [1].

Today proton therapy is represented by two techniques of dose formation: methods of passive spreading, mostly known as passive scattering and of active spreading or scanning. The first one implies installation of various beam-forming devices on the beam path. These devices alter the width of the beam by scattering and modify its energy spectrum. This method also implies the use of custom-made collimators and compensators for conforming the dose to the target volume. The active scanning technique uses magnets for deflecting and steering the proton beam. The depth of penetration can be varied by adjusting the beam energy. Thus, voxel by voxel, target volume can be covered by maximum dose.

Both methods of formation have their pros and cons. The letter one is considered as more advantageous as it provides the conformance of dose delivery to a tumor of any size with no significant radiation damage to healthy surrounding tissues. Also, due to absence of scattering materials fewer amount of stray radiation is generated. However, this method has the risk of target voxel misses because of organ motion. Small targets with the size comparable to the beam's width can be an additional difficulty for this technique. In these cases, the "old" method of proton scattering may be more effective as it allows to irradiate the whole target volume simultaneously. But in this case, distal edge formation by compensators of standard type inevitably leads to the emergence of hot lesions in the proximal region, beyond the borders of the target volume. Thereby, for better conformity the target has to be irradiated from multiple directions which themselves demand additional forming devices (i.e. custom-made collimators and compensators).

OUR PREVIOUS EXPERIMENTS

In our earlier study the technique of passive spreading was tested on proton beams of INR linac. The system of double scattering for the beam widening and a ridge filter for spread-out Bragg peak (SOPB) formation was used (see Fig. 1).

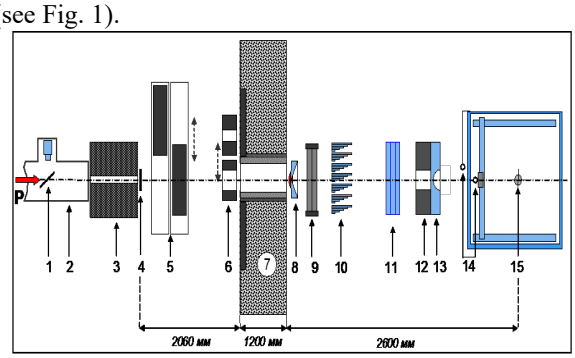

Figure 1: Formation system of INR medical proton beam. 1 – luminophor with TV-camera, 2 - beam channel; 3 - graphite collimator, 4 - the primary scatterer (S1), 5 – beam stop, 6 – beam aperture collimators of 40 and 70 mm, 7 - shielding, 8 – secondary scatterer (S2), 9 - ion chamber, 10 - ridge filter, 11 - energy degrader, 12 – individual collimator, 13 – bolus, 14 - ion chambers in a water phantom, 15 – target isocenter.

A number of measurements with the beams of 160 and 209 MeV was carried out, some results are presented in figs. 2-4.

In order to form a wider beam, we used scatterers S1 and S2 which are represented by copper foils and contoured scatterer with Lucite compensator. This formation system was calculated with the program NEU [2].

ISBN 978-3-95450-181-6

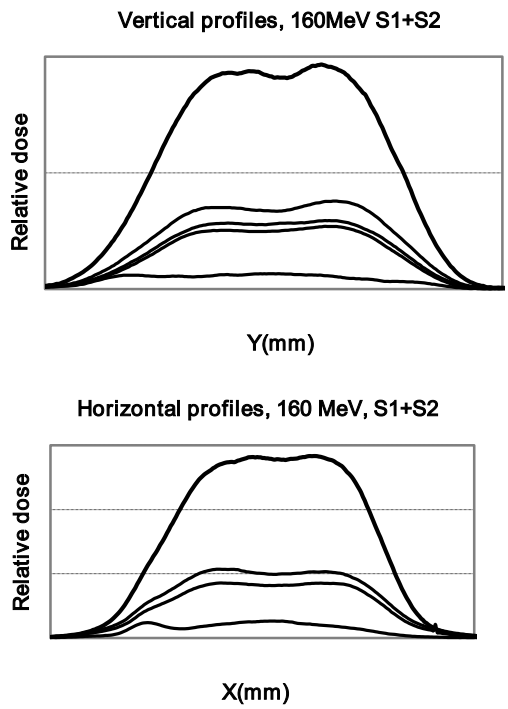

Figure 2: Vertical and horizontal profiles of the 160 MeV proton beamwith scatterers S1, S2.

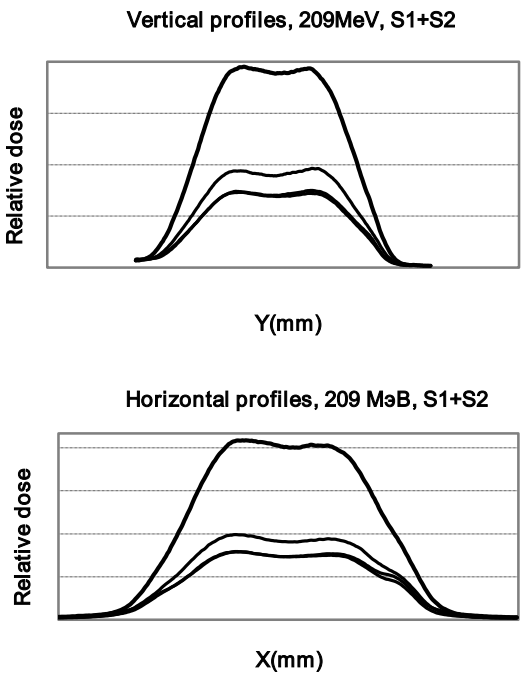

Figure 3: Vertical and horizontal profiles of the 209 MeV proton beam with scatterers S1, S2.

The depth dose distribution generator was a number of degraders with different width and thickness. The combination of which gives us SOBP with a rated modulation width. The results of measurements are presented in figs. 4-5.

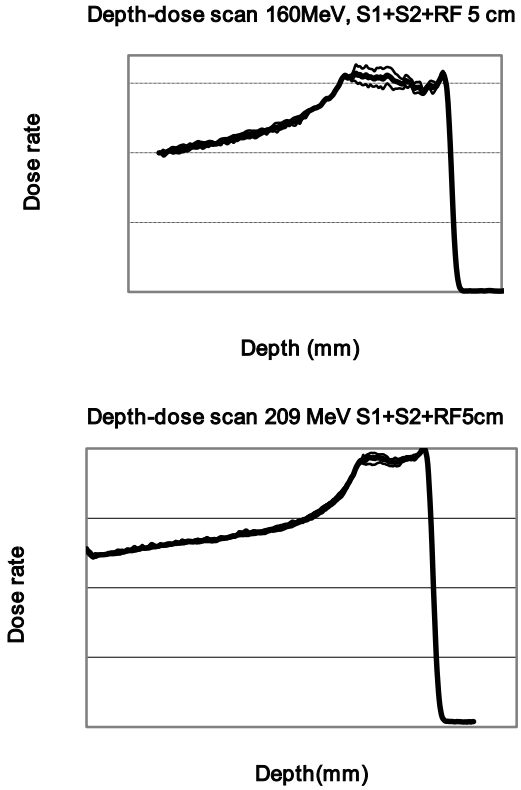

Figures 4 (above) and 5 (bottom): The depth dose distribution for the ridge filters with 5 cm modulation for 160 MeV and for 209 MeV.

For the energy160 MeV the dose deviation on the plateau is within 10 %. For the energy 209 MeV the dose deviation on a plateau is within 6 %, but a small overestimation of the high-energy components of a proton beam is observed. Measurements with other filters have shown an increase of up to 20 % of high-energy components and required insignificant adjustments.

TWO COMPONENT RIDGE FILTER

As mentioned before, traditional scattering techniques of dose formation with a standard ridge filter, a compensator and a collimator fails to provide the conformal dose distribution: either the maximal dose exceeds the tumor volume on its proximate site or the dose changes too much within the tumor volume. To solve this problem, we suggest a new construction of two component ridge filters. It is supposed to eliminate maximal dose exceeding the limits of target volume. We have performed a series of calculations with the help of the original Monte-Carlo code SRNA [3] in order to find the optimal construction from the point of view of dose distribution accuracy and of the device manufacturability.

Some examples of dose distributions calculated with the SRNA program are presented in the figs. below.

ISBN 978-3-95450-181-6

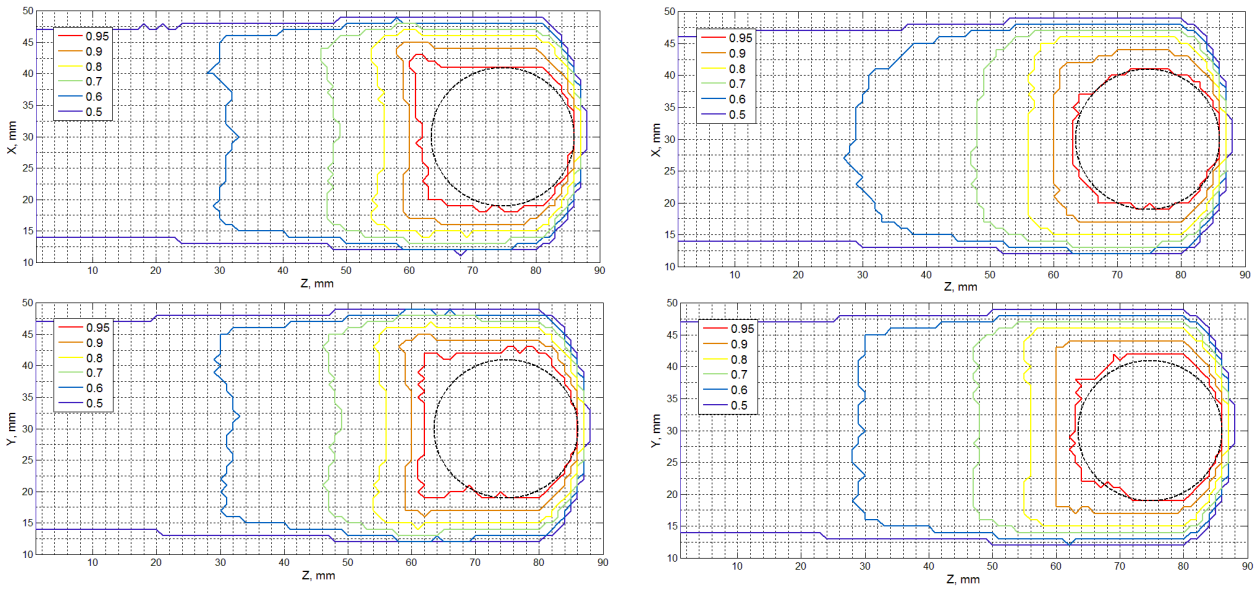

Figure 6: The dose distributions of 110 MeV protons in water, calculated with the Monte-Carlo code SRNA on horizontal (upper plots) and vertical (lower plots) planes. The dose distributions, obtained with conventional ridge filter (left) are compared with the same distributions, obtained with the new two component ridge filter (right). The target is represented by black circle.

As follows from fig. 6, the 95% isodose lines with the new ridge filter do not notably exceed the tumor volume. The usual "wings" of high-dose distributions on their proximate side, seen on the left plots, are absent on right plots. We conclude that new construction of ridge filters allows to improve the proton/ion therapy quality, especially in case of small targets, as e.g. eye tumors or small brain metastasis. The experimental tests of this method with proton beams are now in progress.

REFERENCES

[1] H. Paganetti, T. Bortfeld "Proton Radiotherapy" New Technologies in Radiation Oncology, 2005 p 345-363.

[2] B. Gottschalk, "NEU User Guide", Laboratory for Particle Physics and Cosmology, 2006.

[3] R. D. Ilić, D. Lalić, S.J. Stanković. "SRNA – Monte Carlo codes for proton transport simulation in combined and voxeled geometries", Nuclear Technology & Radiation Protection, 1-2 / 2002.

ISBN 978-3-95450-181-6

A CYCLOTRON COMPLEX FOR ACCELERATION OF CARBON IONS

V. Smirnov* and S. Vorozhtsov, Joint Institute for Nuclear Research, Dubna, Russia

Abstract

An accelerating complex for hadron therapy is proposed. Facility consists of two superconducting cyclotrons and is aimed to produce beams of $^{12}C^{6+}$ ions with energy of 400 MeV/nucleon. Accelerator-injector is a compact 70 MeV/nucleon cyclotron. Main machine is separated sector cyclotron consisting of six magnets. Basic features of the main cyclotron are high magnetic field, compact size, and feasible design of a magnetic system. The advantages of the dual cyclotron design are typical of cyclotron-based solutions. The first design studies of the sector magnet of the main cyclotron show that the beam dynamics is acceptable with the obtained magnetic field. Due to its relatively compact size (outer diameter of 12 m) the complex can be an alternative to synchrotrons. Design study of the main cyclotron is described here.

INTRODUCTION

Development of accelerators for producing carbon beams with the energy of 400–450 MeV/nucleon for hadron therapy appears to be an increasingly important issue today. The existing facilities for producing these beams are mainly based on synchrotrons. It seems interesting to use isochronous cyclotrons instead, as is the case in proton therapy. However, the developed designs of compact superconducting cyclotrons have some disadvantages in addition to their advantages [1]. An alternative solution can be a facility based on a superconducting sector cyclotron justified in detail in [2]. The design of this facility should comply with a number of conditions. First, the size and weight of the accelerator must be as small as possible, which makes it expedient to use the maximum high magnetic field. Second, the injection energy should be low enough for the injector to be of tolerable size. Third, the magnetic system design should be feasible, that is, the parameters of the superconducting coil (engineering current density, acting forces) should be adequate and the space between the sectors should be large enough to accommodate accelerating elements, inject a beam, etc. [3]. A separate task is to develop a system such that both maintains isochronism of the magnetic field and allows beam acceleration with a minimum number of resonance crossings.

INJECTION SYSTEM

The injection energy is chosen to be 70 MeV/nucleon because the accelerator with this final energy can be also used to accelerate H_2^+ ions. Their subsequent stripping allows obtaining protons of the appropriate energy suitable for medical applications. This cyclotron can be used for treating eye melanomas and also for producing radioisotopes.

A compact superconducting cyclotron seems to be the most optimal option. The optimum solution is a cyclotron with a central field of 2.4 T operating at the fourth harmonic of the accelerating field. The magnetic field is formed by four spiral sector shims (Fig. 1). With an acceptable spiral angle of 50°, the external diameter of the accelerator will be no larger than 3 m and the weight will be about 100 t.

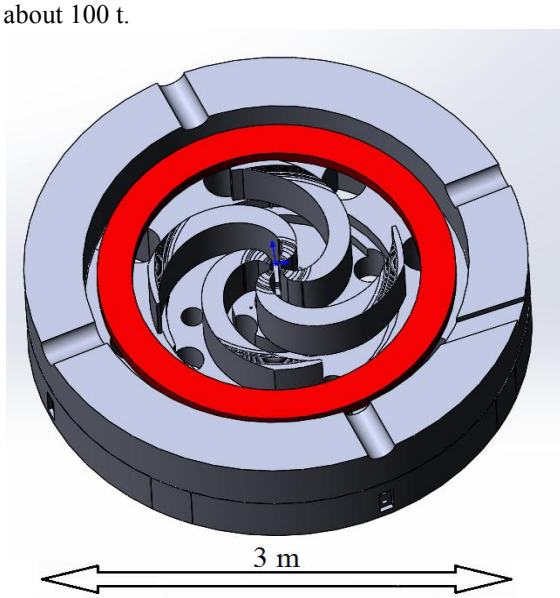

Figure 1: Cyclotron-injector.

The magnetic rigidity of 70-MeV/nucleon C^{6+} ions is about that of 250-MeV protons in the Varian cyclotron [4]. So, some technical solutions of the Varian machine can be applicable to the injector.

The system for injection in the main cyclotron consists of four magnetic channels and an electrostatic deflector (Fig. 2, Fig. 3).

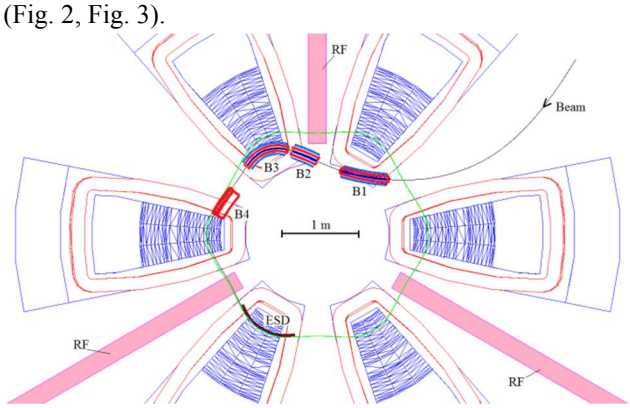

Figure 2: Injection system.

*vsmirnov@jinr.ru

ISBN 978-3-95450-181-6

The central fields in the channels are 1.2, 1.4, 1.4, and 0.8 T. The fourth magnetic channel comprises a septum. The strength of the electric field on the electrostatic deflector (ESD) is 80–90 kV/cm and can be slightly varied to ensure good beam centering. As far as possible, the channels are arranged in the region of the magnetic field with a large gradient. The channel structure made such as to provide increasing or decreasing magnetic fields allows compensating for the negative effect of the main field on the transverse emittance of the beam.

The axial distance between the coils with their cryostats in the beam injection region is ~400 mm, which is enough to house the magnetic channels. In addition, the distance between the pole tips of the sector magnet in the area intended for the third magnetic channel is large enough to install this channel. No problem arises with the formation of the required isochronous field since the major contribution to the cyclotron magnetic field can be from the superconducting coils.

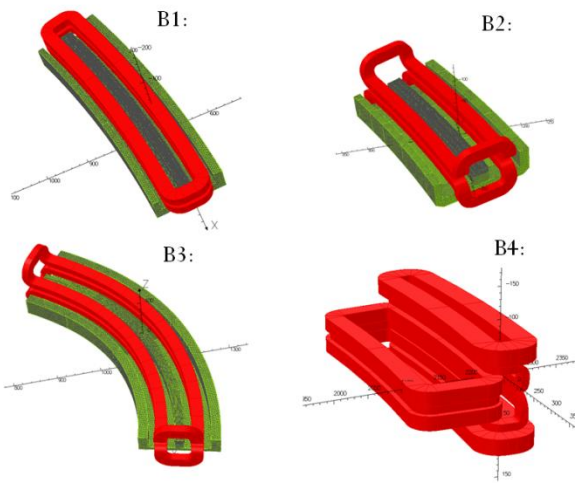

Figure 3: Magnetic dipoles of injection system.

The negative magnetic induction in the valley is the highest at medium radii, amounting to 1.4 T. At the center of the accelerator it is also high, being 1.2 T. The beam path in the valley is not linear. Passing through the valley, the beam moves alternately in the increasing and decreasing magnetic field, which leads to the alternating ion focusing.

For injection, the beam should be shaped at the entrance to the valley so as to have the smallest spread in angles. The following parameters of the beam at the entrance to the valley near the final radius were chosen for the dynamics analysis: transverse emittances 2 π mm mrad, transverse size 5 mm, and the Twiss parameter $\alpha = 0$. The spread in angles is below ±1 mrad. The orbit separation at the location of the electrostatic deflector is ~4 mm. The beam losses on the ESD septum are only ~15% with the septum thickness increasing along its length from 0.2 to 0.5 mm. During the beam tracing, the transverse size of the injected beam is no larger than ±6 mm. The size of the beam passing through the ESD is acceptable (±4 mm). With the deflector aperture of 10 mm, there should be no beam guiding problems.

MAIN CYCLOTRON

The magnetic rigidity of the carbon ions extracted from the main cyclotron with energy 400 MeV/nucleon is about 2.4 times that at injection. Therefore, the accelerator cascade could have an external size of about 12 m (Fig. 4), noticeably smaller than that of the synchrotron-based facilities currently used for hadron therapy. The main parameters of the accelerator are presented in Table 1.

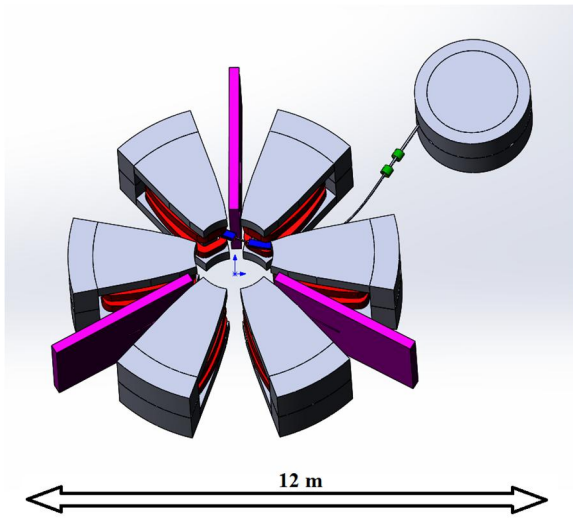

Figure 4: Acceleration complex including injector.

Table 1: Basic Cyclotron Parameters

Parameter	Value
Ion type	$^{12}C^{6+}$
Number of sectors	6
RF system	3 × 200 kV
RF frequency	73.56 MHz
RF mode	6
Average magnetic field: injection/extraction	1.64/2.11 T
Maximal magnetic field: injection/extraction	4.22/6.40 T
Energy: injection/extraction	70/400 MeV/u
Radius: injection/extraction	143/278 cm
Air gap between sectors	88-135 mm
Dimensions: diameter × height	8 m × 2.2 m
Total weight (sectors + coils)	310 t

Injection at a relatively low energy leads to a considerable decrease in the magnetic field flutter from the initial to the final radius, which makes the working point to cross dangerous resonances. To increase the flutter near the final radius, the axial distance between the upper and lower coils in this region should be decreased. This coil arrangement causes a decrease in the mean field

ISBN 978-3-95450-181-6

at small radii. An increase in the azimuthal size of the sectors can compensate for the missing magnetic field. The space between the neighboring sectors should be large enough to accommodate cryostats with coils and accelerating systems. According to some data, the critical engineering current density can be brought up to 150 A/mm^2. However, the operational value is considered to be 50–70 A/mm^2.

All the magnetic field calculations were performed on a three-dimensional basis using the Opera3D code. It was found out from a series of calculations that for the above requirements to be fulfilled, the central magnetic field that governs the particle circulation frequency should be no higher than 1.6 T. With this field, the extraction radius of ions with the energy of 400 MeV/nucleon is 278 cm, and the external diameter of the cyclotron is as large as 8 m. Desired minimization of the variation in the frequency of axial free oscillations entails a necessary increase in the magnetic field flutter at medium radii, where the superconducting coil must thus be convex. This shape allows avoiding additional problems with forces acting on the coil. The magnetic induction in the region of the coil is as high as 7.2 T. The maximum field is 7 T in the hills, 2.7 T in the yoke, and 8 T in the pole tips.

The yoke of a sector externally measures 3.2 × 2.0 × 2.2 m^3. The sector weighs 50 t. The operational engineering current density in the superconducting coil is 62 A/mm^2, and its cross section is 170 × 330 mm^2. The coils are tilted with respect to the median plane at angles of ±4°. Axial profiling of both the pole tip and the pole itself is used to shape the isochronous field (Fig. 5).

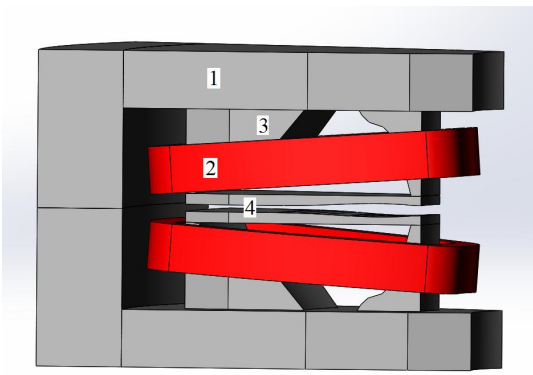

Figure 5: Magnet sector: 1 – yoke, 2 – superconducting coil, 3 – pole, 4 – pole tip.

Additional space between the neighboring sectors allows the azimuthal size of the sector to be varied, which combined with variation of the position of the coil permits producing the required field shape. Thus, it is possible to select a structure in which flutter increases with the radius and the variation range of the frequency Qz is the smallest (Fig. 6). A change in the azimuthal size of the coil leads to a shift of the frequency in the entire range of radii, and it becomes possible to prevent the working point from crossing dangerous resonances associated with the axial frequency of betatron oscillations (Qz = 1, 2Qz = 3, Qr − Qz = 0). Unfortunately, the crossing of the 2Qz − Qr = 1 and 2Qr − Qz = 2 resonances cannot be avoided. Their danger is to be investigated later.

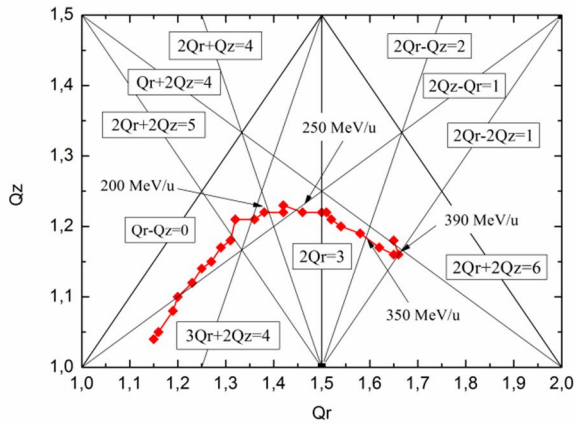

Figure 6: Tune diagram.

Using magnetic field isochronization algorithm from [5] we managed to keep the deviation of the beam phase from the optimum value within ±30°. The deviation of the magnetic induction from the required one along the central line of the sector varies within ±20 Gs. The 3D calculations of the field revealed that in order to keep the beam phase within the given limits, the axial profiles of the pole shim and the pole must be manufactured with the respective accuracy of ±0.2 mm and ±1 mm. In the beam phase calculations, the energy gain was given analytically in accordance with the accelerating voltage and the particle phase during the crossing of the accelerating gap. The acceleration is supposed to be performed by the RF field of three cavities located in the valleys with the accelerating voltage amplitude of 200 kV. In this case, the central particle makes 1240 revolutions to reach the final energy.

CONCLUSIONS

This design study has been carried out to show that a coupled superconducting cyclotron complex is a serious candidate for a light-ion medical facility. The cyclotron is more compact than the synchrotron and simpler to operate. The cyclotron elements specified in the current design are realistically achievable. The short-term activity on the project development includes:

- Concept of beam extraction from the cyclotron.
- Configuration of the accelerating system.
- Calculation of forces acting on the superconducting coil.
- Injector design and beam transport to the injection point of the separated sector cyclotron.

REFERENCES

[1] V. L. Smirnov and S.B. Vorozhtsov, “Modern compact accelerators of cyclotron type for medical applications”, *Physics of Particles and Nuclei*, vol. 47, no. 5, pp. 863–883, 2016.

ISBN 978-3-95450-181-6

[2] J. M. Schippers *et al.*, "A novel design of a cyclotron based accelerator system for multi-ions therapy", in *Proc. Heavy Ion Accelerator Technology (HIAT'09)*, Venice, Italy, Jun. 2009. pp.74-78
[3] S. Sanfilippo *et al,* "Design study of a 3.5 T Superconducting Sector Magnet in a 450 MeV/nucl Booster Cyclotron for Carbon Ion Therapy", *IEEE Transactions on Applied Superconductivity*, vol. 21, no 3, pp. 1838-1843, 2011.
[4] A. E. Geisler *et al*., "Commissioning of the ACCEL 250 MeV proton cyclotron", in *Proc. 18th Int. Conf. on Cyclotrons and their Applications (CYCLOTRONS'07)*, Giardini Naxos, Italy, Oct. 2007, pp. 9–14.
[5] V. Smirnov and S. Vorozhtsov, "A coupled cyclotron solution for carbon ions acceleration", in *Proc. 21th Int. Conf. on Cyclotrons and their Applications (CYCLOTRONS'16)*, Zurich, Switzerland, 2016.

ISBN 978-3-95450-181-6

BEAM SHAPING ASSEMBLY OPTIMIZATION FOR BORON NEUTRON CAPTURE THERAPY*

T. Sycheva#, S. Frolov, S. Lezhnin, S. Taskaev,
Nuclear Safety Institute, RAS, Moscow, Russia,
Novosibirsk State University, Novosibirsk, Russia,
BINP SB RAS, Novosibirsk, Russia

Abstract

Epithermal neutron source based on vacuum insulation tandem accelerator and lithium target has been developed and is now in use in the Budker Institute of Nuclear Physics. Neutrons are generated by $^{7}Li(p,n)^{7}Be$ reaction with proton beam energies from 2 to 2.5 MeV. A beam shaping assembly (BSA) for therapeutic neutron beam forming is used. It includes moderator, reflector, and absorber. In this work the simulation results of the depth dose rate distribution in modified Snyder head phantom for a range of neutron energies are presented and discussed. Variants of BSA optimization depending on tumor depth are proposed. The calculations were carried out by Monte-Carlo neutron and photon transport code NMC that was developed in NSI RAS. Our research reveal that high quality neutron beam generation may be obtained with proton energy of 2.3 MeV. Discovered optimal schemes of BSA including sizes and materials are presented and discussed.

INTRODUCTION

The main requirements to neutron source for BNCT is to generate epithermal neutron beam with neutron flux density more than 10^{9}n/cm^{2}s for treatment time less than 1 hour. Neutrons with energies from 0.5 eV to 10 keV are considered to be epithermal. The results of recent research clarified the requirements to the neutron spectrum and the range of neutron energies of 1 to 30 keV was established as the most suitable for BNCT [1].

For the therapy and determination of optimal treatment conditions such parameters as dose rate in healthy tissue and tumor, advantage ratio (AR, the ratio of maximum dose in tumor and healthy tissue), advantage depth (AD, the distance from the surface of the tissue in which the dose in tumor equals the dose in healthy tissue) are principal.

Minimum required values of these parameters are the following [1]:

- tumor dose rate 1 Gy/min;
- AD is 8 cm;
- AR is 4.

*The work supported by Russian Science Foundation (project N 14-32-00006), Budker Institute of Nuclear Physics and Novosibirsk State University
sychevatatyanav@gmail.com

DETERMINATION OF THE OPTIMAL RANGE OF NEUTRON ENERGIES

To determine the range of neutron energies that are optimal for BNCT we performed the simulations of the depth dose rate distribution in the healthy tissue and in the tumor in modified Snyder head phantom for monodirectional, monoenergetic from 0.025 eV to 100 keV neutron beams with the diameter of 10 cm.

All calculations were carried out by Monte-Carlo neutron and photon transport code NMC that was developed in NSI RAS using cross sections from the ENDF-VII.0 nuclear database [2].

Code validation was performed using benchmarks of the thermal, intermediate and fast spectral regions as well as shielding experiments from the International Criticality Safety Benchmark Evaluation Project (ICSBEP) [3].

The simulation results of the dose rates in tumor and healthy tissue and therapeutic ratio are shown in Fig. 1 and 2. The results are given for neutron and photon flux 10^{10}particles/cm^{2}s. In the calculations ^{10}B concentrations in tumor and in healthy tissue were set to 52.5 ppm and 15 ppm, respectively. It can be seen that the values of dose rate, depth and therapeutic ratio most suitable for therapy are achieved with neutron energies from 1 eV to 10 keV.

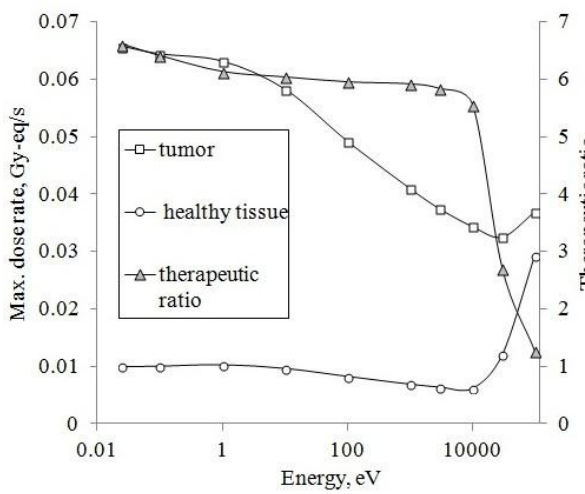

Figure 1: The dose rates in tumor and healthy tissue and therapeutic ratio for neutron beams with different energies.

ISBN 978-3-95450-181-6

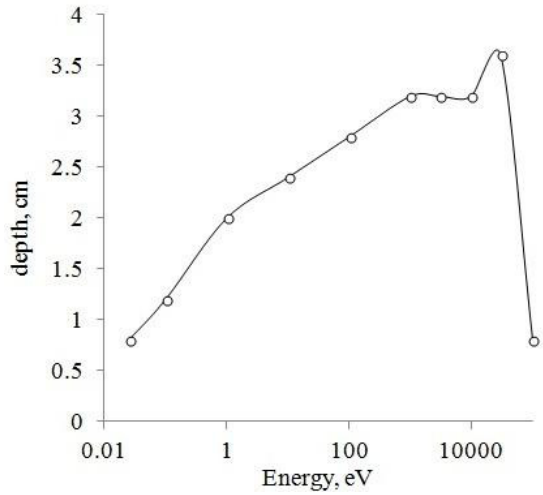

Figure 2: The dependence of the depth of the maximum dose in tumor on the neutron beam energy.

SELECTION OF OPTIMAL PROTON ENERGY

In the BINP neutron source the neutrons are generated with $^{7}Li(p,n)^{7}Be$ reaction under proton beam energies from 2 to 2.5 MeV. A beam shaping assembly (BSA) for therapeutic neutron beam forming is used. It includes moderator, reflector, and absorber.

To determine the optimal range of proton energies for neutron generation we performed simulations of dose rates and therapeutic ratio for proton energies from 1.9 to 2.5 MeV, moderator radius of 15 cm and heights from 15 to 30 cm.

The results of calculations are given in Fig. 3, 4, 5.

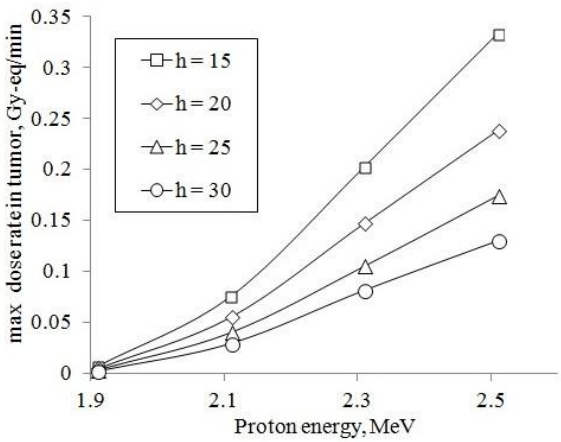

Figure 3: The dependence of the dose rate in tumor, on proton energy at different moderator heights (h) in cm.

It can be seen, that with increase of proton energy dose rate in tumor also increases, but therapeutic ratio decreases. This is due to the growth of fast neutron component with higher proton energy. Figures show, that the best values of dose rate, depth and therapeutic ratio are achieved at proton energy of 2.3-2.5 MeV and moderator height of 25-30 cm. The maximum value of the depth for the maximum dose rate in tumor is 3.6 cm.

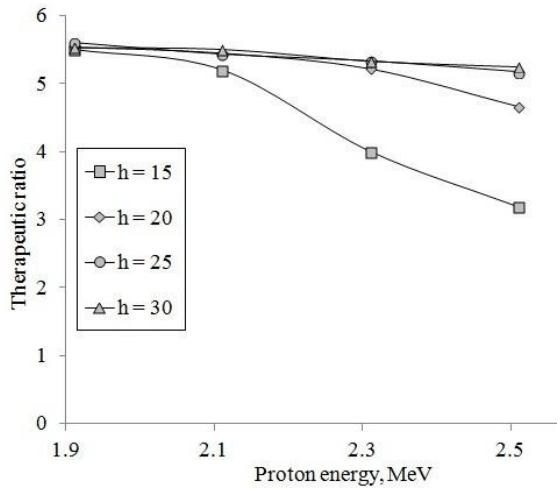

Figure 4: The dependence of the therapeutic ratio on proton energy at different moderator heights (h) in cm.

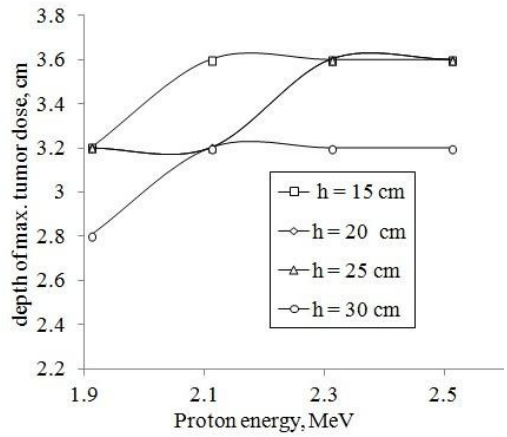

Figure 5: The dependence of the depth of the maximum dose in tumor on the proton beam energy.

OPTIMAL BSA

With the results of our simulations we designed model of the optimal BSA as shown in Fig.6 [1]. Distinctions of this model are composite moderator with MgF_2 near the target and AlF_2 near the beam outlet and composite reflector from graphite in the front hemisphere and lead in the back hemisphere. Besides, we propose to use proton energy of 2.3 MeV to generate optimal therapeutic beam, instead of commonly used range of 2.5-2.8 MeV. The reason is demonstrated in Fig.7. As it can be seen the attempt to reduce fast neutron component by increasing moderator height gives us the same neutron spectrum as with smaller moderator height and proton energy of 2.3 MeV. Moreover, at 2.5 MeV proton energy there is a significant neutron flux with neutron energies more than 500 keV.

ISBN 978-3-95450-181-6

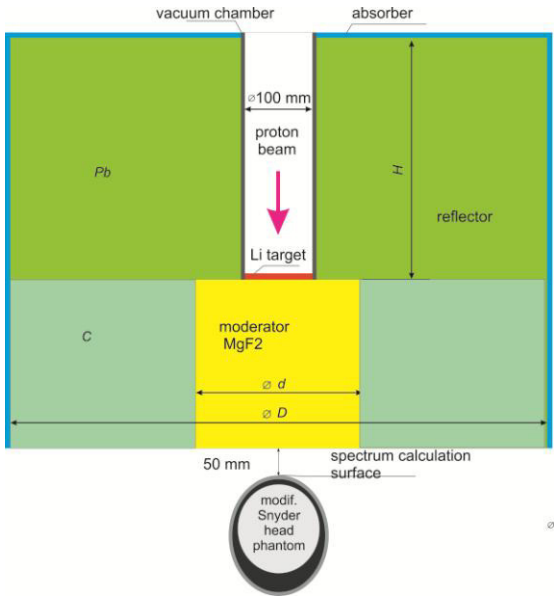

Figure 6: Optimal BSA.

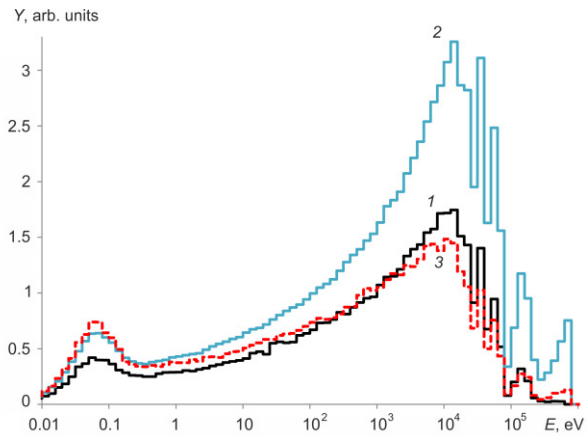

Figure 7: Neutron spectrum for BSA: 1 - proton energy is 2.3 MeV, moderator height is 21 cm, 2 - proton energy is 2.5 MeV, moderator height 21 is cm, 3 - proton energy is 2.5 MeV, moderator height is 26 cm.

The BSA has been manufactured, it is shown in Fig.8.

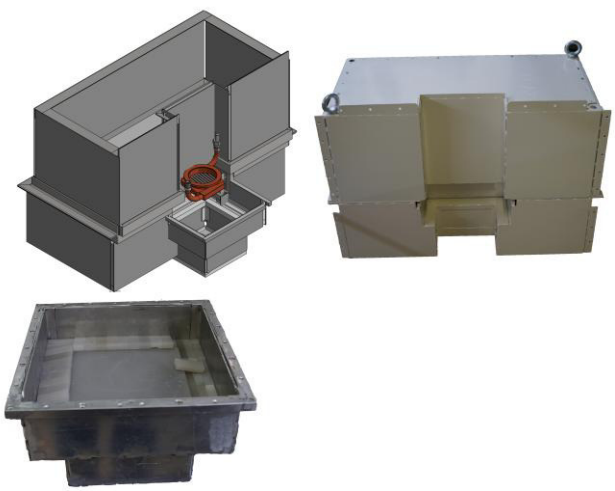

Figure 8: The appearance of manufactured BSA.

CONCLUSION

We demonstrated that neutrons with energies from 1 eV to 10 keV are the most suitable for BNCT. The BSA has been designed and manufactured, it was shown, that the best beam parameters are achieved with proton energies 2.3-2.5 MeV with moderator height of 25-30 cm. Our research revealed that high quality beam generation may be obtained with proton energy of 2.3 MeV.

REFERENCES

[1] S.Taskaev, Phys. Part. Nucl. 46(2015) 956.
[2] M. Chadwick et al., Nucl.Data Sheets 107(2006) 2931.
[3] http://icsbep.inel.gov/

ISBN 978-3-95450-181-6

TEMPERATURE CONTROL SYSTEM FOR THERMORADIOTHERAPY FACILITIES

A.M. Fadeev, S.M. Ivanov[1], S.M. Polozov
National Research Nuclear University - Moscow Engineering Physics Institute, Moscow, Russia
[1] and N.N. Blokhin Russian Oncological Research Center, Moscow, Russia
E.A. Perelstein, Joint Institute for Nuclear Research, Dubna, Russia

Abstract

As known, thermoradiotherapy and hyperthermia are widely used to improve the efficiency of cancer treatment.

Whole-body hyperthermia is used to treat metastatic cancer that has spread throughout the body, regional is used to treat part of the body (for instance leg or abdominal cavity). Local hyperthermia permits to heat tumour without overheating of healthy tiisues. It was proposed to use an array of eight independently phased dipoles operating on 100-150 MHz to focus the RF energy in deep-situated volume of 30-50 mm size. But the problem of non-invasive temperature measurement should to be solved for correct operation of the local thermoradiotherapy system. Conventional invasive thermometry devices as thermocouples, thermistors or Bragg optical sensors can not be widely used because of serious risk of the cancer cells transport to healthy tissues. Radiothermometry or acoustic thermometry can not be used for tissues located deeper than 5-7 cm. As known electrodynamics characteristics of tissues are sufficiently depends on temperature. It was proposed to use this effect for active radiothermometry in local hyperthermia. Two opposite RF dipoles can be used as generator and receiver of pick-up signal. It was shown by simulations that such method can be used for thermometry of deep-situated tissues and this method produces high resolution. Results of simulation will present in report.

INTRODUCTION

Hyperthermia is an adjuvant methods of cancer treatment in which tumour temperature is increased to high values (40-44 °C). It is usually used in combination with radiotherapy (thermoradiotherapy, TRT). The most evident approach is using an RF applicator(-s) situated around the patient body. RORC clinical studies demonstrate improving results of treatment by combined using of hyperthermia and radiation for the several tumour localizations. But only applicators for superficial hyperthermia were used in RORC. Common RORC-MEPhI-JINR project is pointed to expand the range of utilizing devices, i.e. using of devices for the regional hyperthermia gives more advantages for an oncological diseases treatment [1-6].

It was shown by many sets of simulations and experiments that such termoradiotherapy facility can provide the effective RF power focusing by means of amplitude and phase control for each applicator and effective local hyperthermia can be provided. As one example, the array of dipoles operating on 150 MHz with aperture diameter of 60 cm can provide RF power focusing wherever of patient body with spot diameter about 30 mm. A 450 MHz system can be used for hyperthermia of head and neck tissues with heated volume size of 15-20 mm.

Thermometry into heating volume is one of the major hyperthermia tasks. It is more difficult for deep-situated tissues. It is possible to use invasive or contact thermometry systems as thermistors and thermo-couples for deep-situated tissues and tumours. Russian hyperthermia protocol permits installation of thermocouples inside the patient body. But this causes pain and temperature probe can transport tumor cells to the healthy region of the patient body. European hyperthermia protocol forbids installation any temperature probes inside the patient body. They prefer to simulate any radiation process with phantoms. Moreover noninvasive thermometry of human tissues is important for other cases. It is suggested to determine tissues temperature by means of measurements effects that could be observed during heating. Optical fiber sensors based on Bregg grids became more popular last years. The measured parameter as temperature or mechanical displacement is coverts to the length of the light shift. But all of such sensors (thermo-couples, thermistors or optical fiber sensors) provide only invasive temperature measurement. Noninvasive control is possible by using of the magnetic resonance imaging (MRI) as it is proposed and realized by BSD Medical Systems (now Pyrexar Medical). But such way has serious difficulties and the price of MRI system is higher than the same of the hyperthermia system. Acoustic thermometry is one of new technologies. 2D and 3D temperature distributions were successfully imaged by means of acoustic thermometry experiments. But such technique can be used only for tissues located not deeper than 3-5 cm (for mammography as an example). Well-known radiothermometry (RTM) also can be used for deep-situated tissues. As known, the specific heat release of tumour is directly proportional to its growth velocity. More fast growth tumours will be “hotter” and will be brighter on the thermograph. The possibility to find the fast growth tumours is an unique advantage of the RTM. Main sufficient disadvantage is inherent as for acoustic thermometry: RTM can not be used for the deep suited tissues. The depth of temperature anomaly localization will not be greater than 3-7 cm depending of the tissues humidity.

ISBN 978-3-95450-181-6

THERMOMETRY IN PROCESS OF THE THERMORADIOTHERAPY

As known dielectric properties of the tissues (complex dielectric permittivity and tangent of the dielectric loses) depend of temperature. It is suggested to determine tissues temperature by means of measurements effects that could be observed during heating process. Thus dielectric properties of the human tissues sufficiently varies with temperature increasing (fat tissue and skin are not heated during hyperthermia with the phased array). This thermometry system could be used as addition to the other regional or local hyperthermia facilities. For example, the real part of dielectric permittivity of the muscle tissue or tumour tissue growths by 0.2-0.5 per 1 degree (absolute value is 70-100). It leads to the special absorption rate variation and to RF power scattering modification in tissues. Such variation can be registered. Detail review of experimental data, a number of theoretical models and results of numerical simulations are given in [7-9] for temperature dependences of electrodynamics characteristics for different tissues and organs. Two examples of real ε' and imaginary ε'' components of the complex dialectical permittivity $\varepsilon=\varepsilon'-i\varepsilon''$ are shown in Figure 1. Dependences are modeled for muscle tissue and liver using data from [8-9]. The operating frequency is 150 MHz. It is clear that such dependences are close to linear for temperature range 36-43°C which is used for thermoradiotherapy. The analyses of experimental and simulated data form [7-9] shows that for operating frequency of 150 MHz absolute values of ε' and ε'' are close for all tissues. Only dielectric properties of skin and fat tissues differ very significantly.

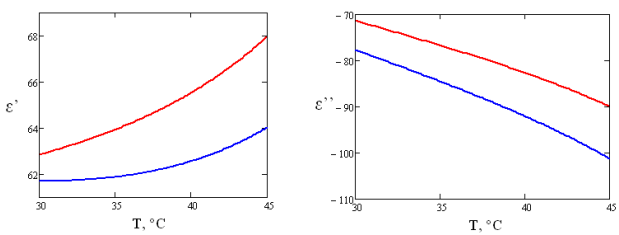

Figure 1: Dependences of real ε' and imaginary ε'' components of the complex dialectical permittivity for muscle tissue (blue) and liver (red). The operating frequency is 150 MHz.

Each dipole antennae feeds independently in the hyperthermia facility proposed in [1-6]. Each feeding channel includes RF circulator (see Fig. 2) to prevent the back wave penetration to the other feeding channels. Such system with minor modifications can be also used for thermometry. In the temperature measurement regime two feeding channels (RF input #1 and #5 in Fig. 2) will switch to low RF power regime and the feeding of all other dipoles turns off. The output of the circulator directs the transmitted back wave to the band-pass filter and further to the measuring PIN-diode. PIN-diode measures the time dependence of the RF power flux for further A/D conversion. Digital signal processes by the especially developed Fourier analyses code and time dependences of Fourier coefficients define. Current spectral series compares with "non-perturbed" signal which was previously defined for not heated patient body. Proposed radiothermometry technique differs very sufficiently from the conventional one: i) the thermometry system is combined with hyperthermia one and dipole antennae are used both for heating and thermometry; ii) the thermometry can be realized for deep situated tumours and tissues; iii) the noninvasive thermometry can be realized and the active tissues scanning can be used for the 2D temperature imaging.

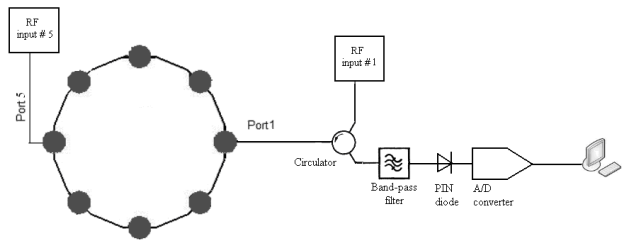

Figure 2: The scheme for measurement and analysys of the transmitted signal.

The simulation of the heating process with temperature control was done to verify the proposed thermometry technique. To define the spectral distribution of the transmitted signal as the function of temperature we do the fast Fourier analysis by the especially designed code. The main signal harmonic amplitude was controlled and the temperature distribution and its time dependence were calculated. The TRT facility was developed to heat only limited volume inside the patient's body. Only characteristics of such local area will influence to the transmitted signal. Its harmonic distribution and temperature control will be also provided for local volume where heating is taking place.

Numerical simulations show that the amplitude of the main Fourier harmonic of the transmitted signal depends of the temperature linearly. The analysis was done using the experimental and simulated data form [7-9] for the operating frequency of 150 MHz. The simulation model is shown in Figure 3, it includes voxel model of the human body with a number of tissues and organs. The dielectric characteristics of tissues were varied during simulation with the temperature increases. The temperature distribution is also shown in Figure 3. The detected transmitted signal is shown in Figure 4. Such detected signal expands to the Fourier series and its coefficients are compare with the "base" distribution which was done and safe for non-perturbed (hot heated, T=37°C) model. It is clear from Figure 4 that the main signal harmonic amplitude depends vs. temperature linearly. Such result simplifies the back problem of the temperature reconstruction for heated volume.

About 90 % of RF power absorbs by patient body while local or regional hyperthermia as it was shown by numerical simulation. The RF power necessary for effective treatment is up to 100 W/dipole for facility

ISBN 978-3-95450-181-6

proposed in [1-6]. The simulation of the heating process with temperature control shows that for the first Fourier harmonic of the transmitted signal the variation is about ~10^{-3} form coefficient value for the local hyperthermia and ~10^{-2} for the regional one. Temperature increasing range is about 37-43°C. It is clear that the transmitted power measurement accuracy should be better than 100 μW (if measurement signal power is ~1 W). The accuracy of the temperature measurement for the local heated volume will be better than 0.3°C due to such RF power accuracy measurement. Such result is better than for conventional radiothermometry and close to tolerance for invasive thermo-couples or thermistors. The process of local thermoratiotherapy takes 15-30 minutes usually and it is quite enough to measure the temperature 1-3 times/minute.

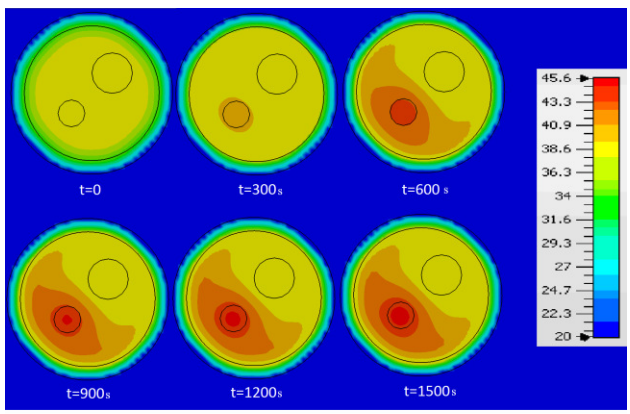

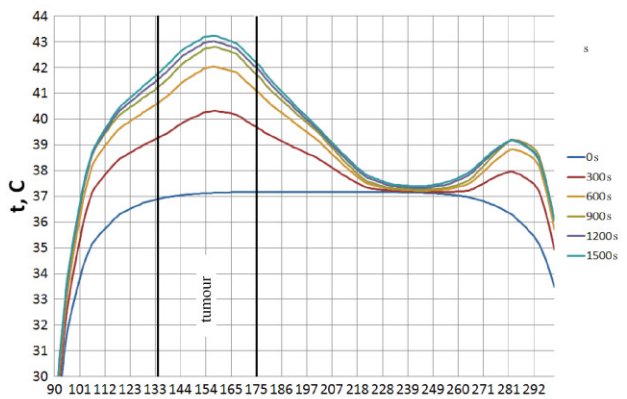

Figure 3: Temperature distributions in tissues for a set of times after termoradiotherapy start: cross-sections of tissue equivalent model (top) and distributions along of the axe pass though centers of two opposite dipoles.

CONCLUSION

It was shown that modified active radiothermometry technique can be used for temperature control during the thermoradiotherapy of the deep-situated tumours. Dipole antennae of the TRT facility can be used both for heating and for temperature measurement. The accuracy of the temperature measurement for the local heated volume will be better than 0.3°C with low (~1 W) measuring signal value.

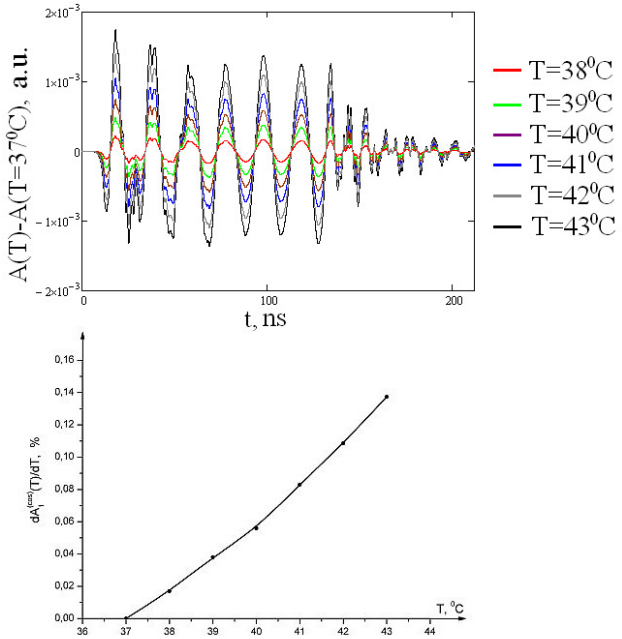

Figure 4: Temperature dependence of the difference (a.u.) of transmitted signal amplitudes for current and "base" (T=37°C) temperatures into the heated volume (top) and the temperature dependence of the first Fourier harmonic amplitude.

REFERENCES

[1] Ivanov S.M. et al., Problems of Atomic Science and Technology. Series: Nuclear Physics Investigations, 3 (79), 191-194 (2012).
[2] Fadeev A.M. et al., Proc. of RuPAC'12, 521-523 (2012).
[3] Polozov S.M. et al., Proc. of RuPAC'12, 524-525 (2012).
[4] Ivanov S.M. et al., Problems of Atomic Science and Technology. Series: Nuclear Physics Investigations, 6 (88), 220-224 (2013).
[5] Fadeev A.M. et al., Proc. of RuPAC'14, 240-242 (2014).
[6] Fadeev A.M. et al., Journal of Physics: Conference Series, 747, 012076 (2016).
[7] C. Gabriel, S. Gabriel, E. Corthout, Phys. Med. Biol., 41, 2231–2249 (1996).
[8] S. Gabriel, R.W. Lau, C. Gabriel. Phys. Med. Biol., 41, 2251–2269 (1996).
[9] S. Gabriel, R.W. Lau, C. Gabriel. Phys. Med. Biol., 41, 2271–2293 (1996).

ISBN 978-3-95450-181-6

LABORATORY MODEL OF THERMORADIOTHERAPY FACILITY: EXPERIMENTAL RESULTS

A.M. Fadeev, S.M. Ivanov[1], S.M. Polozov
National Research Nuclear University - Moscow Engineering Physics Institute, Moscow, Russia
[1] and N.N. Blokhin Russian Oncological Research Center, Moscow, Russia
E.A. Perelstein, Joint Institute for Nuclear Research, Dubna, Russia

Abstract

Hyperthermia and its combination with radiotherapy (thermoradiotherapy) or with chemotherapy is one of promising ways to improve cancer treatment efficiency. The treatment of deep-situated tumors is sufficient problem which can not be solved by means of traditional facilities developed for whole-body or regional hyperthermia because of overheating of healthy tissues and blood. A cylindrical array of independently phased dipoles was proposed to focus electromagnetic energy in deep-situated tumors. Early it was shown by simulations that array of eight independently phased dipoles operating on 100-150 MHz is able to focus energy in an ellipsoid of 30-50 mm in size. Later the laboratory model of thermoradiotherapy facility was developed and constructed and a series of experiments were carried out. Experimental results and its comparison with simulation will discussed in report.

INTRODUCTION

Hyperthermia is an adjuvant method of cancer treatment in which tumor temperature is increased to high values (40-44 °C). Many researches have shown that high temperature can damage and kill tumor cells, thus reduces tumor size. However the main advantage is that hyperthermia is a promising approach to increase efficiency of chemotherapy or radiation therapy. Under hyperthermia some tumor cells become more sensitive to the radiation and anticancer drugs. The effect on surviving fraction depends both on the temperature increase and on the duration of the expose. The main mechanism for cell death is probably protein denaturation at temperatures above 40 °C, which leads to changes in molecular structures such as cytoskeleton and membranes, and changes in enzyme complex for DNA synthesis and repair [1]. Heat also enhances the cytotoxicity of X-rays. Increased cytotoxicity is maximized when radiation and hyperthermia are given simultaneously. The combined effect decreases with time when the treatments are separated by more than one hour [2]. When cells are exposed to increased temperatures to anticancer drugs, their response is often different from the one at normal temperature. Drugs whose rate-limiting reaction is primarily chemical are expected to be more efficient at higher temperatures. Thus the combination of chemotherapy with hyperthermia has high potential in clinical practice [3].

The thermal therapy combined with the radiation (thermoradiotherapy, TRT) has been successfully applied in N.N. Blokhin Russian Oncological Research Center (RORC) since 1980th [4]. More than 1000 patients have been treated to date. Such program allows to sufficient and authoritative reduce of the regional cancer recrudescence and metastases comparatively to the surgery or independently radiotherapy (RT) [5].

One of the major problems of the devices mentioned above is the limited depth of penetration due to the principle of skin-effect. Only tumors located 2-3 cm (7-8 cm for the contact flexible microstrip applicator) from the surface can be heated by these applicators. To increase sufficient specific absorption rate (SAR) value in the tumors situated deeper than 10 cm relative to the surface SAR value it is necessary to focus energy of electric fields produced by an array of applicators. It consists of several antennae surrounding the patient and emitting radio-waves. Single antenna or groups of antennae are fed separately. Thus by proper selection of amplitudes and phases the interference patterns of the produced fields can be focused to create desirable temperature distribution [5]. Significant research successes have been obtained for the deep hyperthermia with the phased array. Simulation and measurements results are presented in [6].

FACILITY FOR TRT BASED ON ANTENNAE ARRAY

The most evident approach is using an antennae array of applicator situated around the patient body. Top view of this structure is shown in Figure 1. Arrays of applicators with variations in frequency, phase, amplitude and orientation in space give more possibilities to control heating pattern during hyperthermia treatment [6]. RF power feeding scheme is presented in [7]. Thus the phased array provides deeper tissue penetration of electromagnetic waves in comparison with single applicator, reduces undesirable heating of healthy tissues situated between applicator and tumour and improve local control for heating area. Also using array of applicators gives ability to control and to plan heating process without changing of patient position. Suggested phased array consists of eight copper dipoles, attached on the inner side of the dielectric cylinder, and surrounds a patient body. The aperture radius is up to 60 cm which can be applied in more cases. Dipoles are fed independently; this approach permits to control wave's phases and amplitudes. Space between dipoles and the patient body is filled by deionised water (conductivity $\sigma \approx 0.001$ S/m and $\varepsilon \approx 80$). Thus applicators are squeezed from the inner side by lossy medium with high permittivity (deionised water), and from the outer side by

ISBN 978-3-95450-181-6

medium with low permittivity (air ε=1). The conducting elements of antenna are isolated from lossy medium by thin layer of an insulator (thickness h≈1 mm). Because of energy density of electrical fields ($\vec{E}\vec{D}/2$) inside the dielectric tank is higher by a factor of ε (the relative dielectric constant of medium), energy is mainly concentrated inside the array. Thus deionised water not only cools body surface and superficial tissues but is also a matching medium. Electric field lines inside the phased array are parallel to the axis of dipoles. That's why heat absorption in the surface and superficial tissues (such as skin and fatty tissue) which is proportional to tissue conductivity (σ, these values for fat and skin are significant lower than for muscle or tumour tissue) will be substantially lower than in deeper tissues. Thus skin and fatty tissue overheating is reduced in comparison with the using capacitive applicators. So E_z (z is direction along of the patient body) is the only component, which may be able to control by shifting the amplitudes and phases of eight dipoles. E_x and E_y components are not under control. E-field generated by each of the dipoles is given by $E_j = A_j E_{j,0}(x,y)\cdot\exp(-i(\omega t - \Phi_j))$, where $E_{j,0}$ – is the complex E-field for A_j=1, Φ_j=0, and A_k=1 for $j\neq k$, A_j – is a scaling factor of amplitude, Φ_j – wave phase, j and k are numbers of dipoles, i is imaginary unit. It is possible to move peak of interference pattern and to focus it into the tumor site with the variation of these two parameters (phase and amplitude). The measure of the rate at which energy is absorbed by the body when exposed to a radio frequency (RF) electromagnetic field is a SAR. It is defined as the power absorbed per mass of tissue and has units of watts per kilogram (W/kg): $SAR = (\sigma\vec{E}^2)/\rho$, ρ – is the density of the tissue (kg/m^3), E – is the root of mean square electric field.

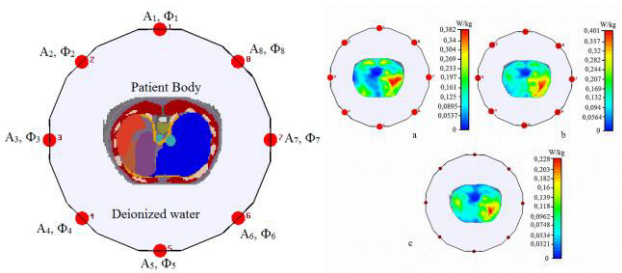

Figure 1: Top view of phased array surrounding patient body (left) and cross-section patterns of the SAR distribution with different operation frequencies (a) 150 MHz; (b) 100 MHz; (c) 80 MHz and with input phases of 50°, 50°, 50°, 50°, 0°, -30°, -40°, -10° applied to channels 1, 2, …, 8 respectively.

It was shown by many sets of simulations that such termoradiotherapy facility and RF power focusing by means of amplitude and phase control for each applicator can provide effective local hyperthermia. For example, the array of dipoles operating on 150 MHz and having aperture diameter of 60 cm can provide RF power focusing wherever of patient body with focusing volume diameter ~30 mm. A 450 MHz system can be used for hyperthermia of head and neck with heated volume size of 15-20 mm.

EXPERIMENTAL RESULTS

Based on previous simulations and RF feeding system design the first experimental prototype was developed and constructed. It consists of two RF dipoles and one feeding system. In such prototype temperature peak can move along the line connecting these dipoles and experiment will demonstrates 2D facility only. Water is used as an absorbing medium because it has dielectric properties and density similar with the muscle tissue. Pictures of laboratory prototype of the TRT facility, RF power feeding device and dipoles array are shown in Figure 2.

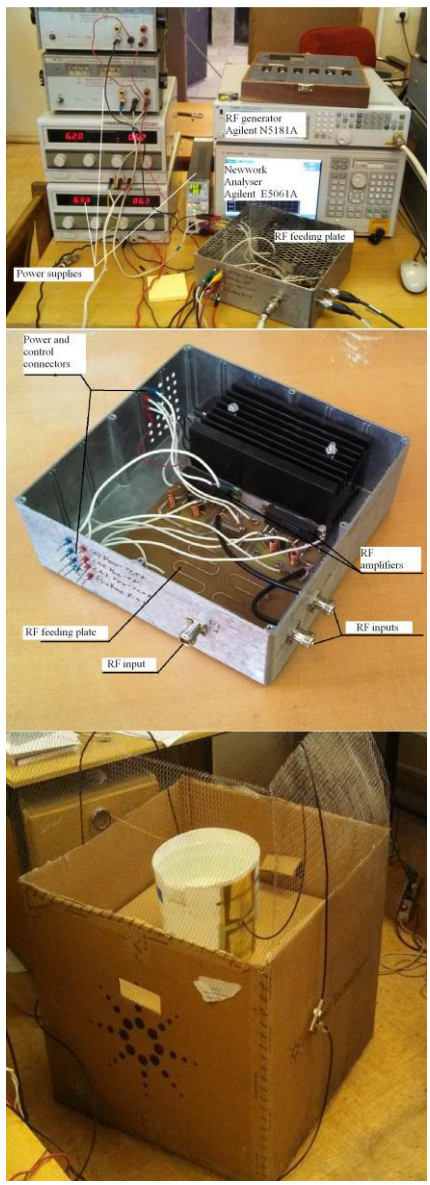

Figure 2: Laboratory prototype of the TRT facility: power feeding and measurement devices (top), RF power feeding device and dipoles array into Faraday cage.

ISBN 978-3-95450-181-6

Series of local heating experiments were done using such prototype. Experimental demonstration of the local energy distribution maximum and its moving versus of phase and amplitudes variation were the main goals of such experiments. Two dipoles were mounted on external side of a dialectical cylinder which was filled by deionised water. The tissue-equivalent phantom was prepared using a number of thin-walled dielectric tubes filled by salt water which permittivity and conductivity are close to human tissues. A number of dielectric tubes were positioned along the line connecting dipoles like it is shown in Figure 3 to prevent water blending during heating. Tubes are made of aluminum oxide (permittivity ε=9.4 and density ρ=3990 kg/m^3). Tubes diameter is 10 mm and wall thick is 2 mm. Tubes were placed on line connects centers of RF dipoles. Such phantom correctly imitates the deep suited tissue and can be easily used in temperature control which was realized by means of a number of thermocouples which were placed into all thin-walled tubes. The initial temperature was constant for all system points. Water starts the energy absorption after RF power on and the temperature in the local heating volume starts growth. Temperature distributions after heating are shown in figure 4 for in-phase dipoles on (a) and for 60 degrees phase shift (b). The heating was provided 20 minutes for in-phase experiments and 12 minutes for experiments with phase-shift. Zero-point on x-axe corresponds to the center of main cylinder. As if follows from figures 50 mm localization can be achieved in hyperthermia system proposed. Experimental heating results are compared with CST Studio Suite simulations (dot curves in Figure 4) and have very good accuracy.

Thermocouple-sensing element ATE-9380 was used to perform temperature measurement. Whereas it has metallic compounds TSE introduce alternations in electric distribution when RF is on. Thus temperature measurement was carried out after switching RF off.

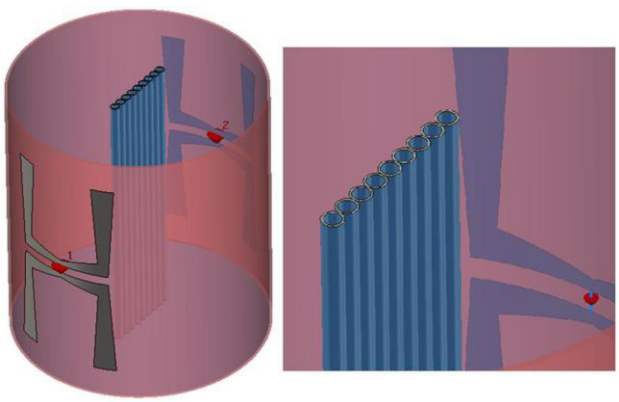

Figure 3: Experimental setup schematic view.

CONCLUSION

It was shown by means of electrodynamics and thermal simulations and experiment that system of a number of independently phased dipoles is suitable for TRT of deep suited tissues and tumors. The first experimental prototype was constructed and numbers of heating localization experiments were carried out. Comparison of simulation and experiments shows that the phased array solves the local heating problem and deep suited tumorous can be successfully heated without overheating of healthy tissues.

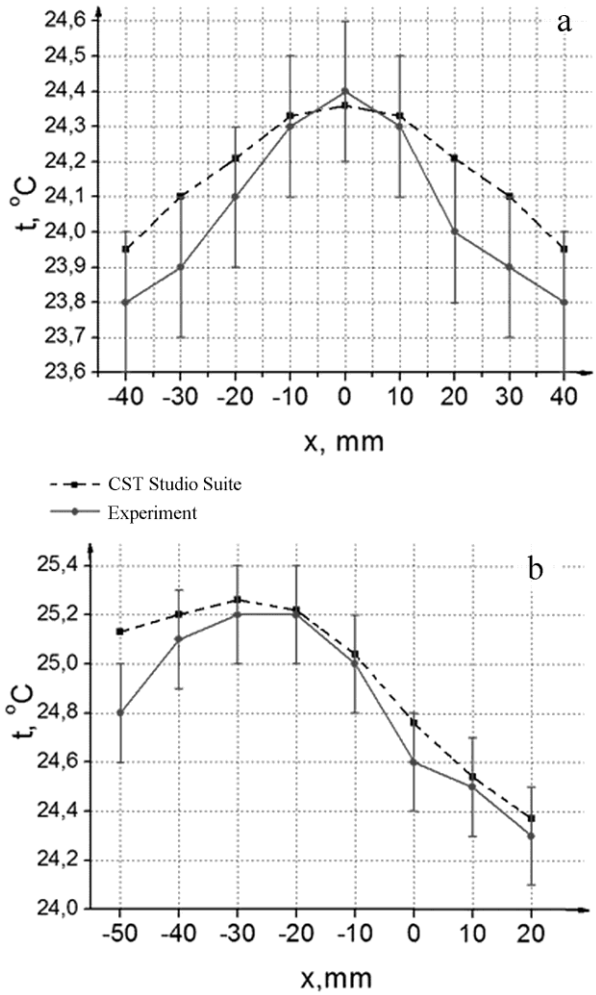

Figure 4: Temperature distributions after heating for in-phase dipoles on (a) and for 60 degrees phase shift (b).

REFERENCES

[1] Dewey W.C.. Int. J Hyperthermia 10, 457–83 (1994).
[2] Hahn G.M., Hyperthermia and cancer. New York: Plenum (1982).
[3] Kampinga H.H.,. Int. J Hyperthermia 22, 191–196 (2006).
[4] Tkachev S.I., Barsukov Y.A., Gordeyev S.S., Eur. Journal of Surgical Oncology 36(9), 877 (2010).
[5] Ivanov S.M. et al., Problems of Atomic Science and Technology. Series: Nuclear Physics Investigations, 3 (79), 191-194 (2012).
[6] Fadeev A.M. et al., Proc. of RuPAC'12, 521-523 (2012).
[7] Polozov S.M. et al., Ibid., 524-525.

ISBN 978-3-95450-181-6

MATHEMATICAL AND COMPUTER METHODS OF DATA PROCESSING IN NUCLEAR MEDICINE STUDIES

E.D. Kotina, A.V. Babin, P.V. Bazhanov, D.A. Ovsyannikov, V.A. Ploskikh, A.Yu. Shirokolobov, St. Petersburg State University, 7/9 Universitetskaya nab., St. Petersburg, 199034 Russia

Abstract

Currently nuclear medicine is a high-tech field. Its development requires solutions of problems related both to the improvement of hardware and computer processing of the information obtained in the course of study. The basic types of hardware of nuclear medicine are gamma cameras and single photon emission computed tomography (SPECT) [1], positron emission tomography (PET) and hybrid scanners (SPECT/CT, PET/CT).

The methods of SPECT data processing include analysis of static, dynamic, tomographic and ECG-gated images [2-9].

The PET data reconstruction software restores the three-dimensional distribution of the radiopharmaceutical in the body. Performance of iterative methods increases with the use of modern graphics processors [10]. Three-dimensional imaging allows a detailed analysis of the study area. The software also implements a fusion imaging of SPECT/CT, PET/CT scans performed in the same coordinate system.

An application of data flow model in medical software development is considered. Web-based imaging front-end of storage and processing system is presented.

DATA PROCESSING

The flexible platform with batch execution support and imaging elements is required during the process of development and testing new processing algorithms.

Mathematical modelling software such as MatLab is usually used for this purpose. But it makes harder to integrate the solutions into data processing applications as it often require redevelopment for application native platform.

Dataflow Programming

An approach to efficient development of data processing algorithms on .NET Framework is considered: program is represented as dataflow graph.

Dataflow consists of set of simple processing units called activities and connections. Activities represent simple operations such as data acquisition, reconstruction, volume transformations, ROI extraction, dynamic curves computation and analysis, etc. Each activity define a list of Inputs (or Attributes), a list of Outputs (or Results) and the Execution method, which supports cancellation and progress reporting. Dataflow connections bind activities outputs to inputs. Unbound inputs' data can be set from UI or file.

Dataflow are presented as an XML files. Activities are classes implementing interface *IActivity* and marked with *Activity* attribute. Its writable public properties define list of inputs, and read-only properties of generic type *ActivityResult* represent list of outputs. Sample dataflow graph is presented on fig. 1.

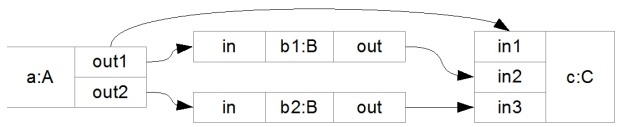

Figure 1: Example of dataflow application.

Basic dataflow execution environment (DEE) is developed. It supports running dataflow programs in interactive and batch modes. In interactive mode DEE dynamically loads user interface from a XAML file and binds UI components to inputs and outputs. Batch mode allows running dataflow with different input values provided from text files.

Reconstruction

Using dataflow approach we conducted series of experiments in tomographic reconstruction of PET data. Its goal was determination of correction parameters which adjust reconstructed values to physical units (Bq/ml).

Mathematical modeling of PET acquisition was performed. Cylindrical phantom (radius – 100 mm, length – 190 mm) with variable activity (10^5, 10^6 and 10^7 Bq) was used as positron source. Time of acquisition was selected in inverse ratio to activity (1000, 100 and 10 sec).

Ring detector configuration (radius – 410 mm) with different axial field of view (FOV) (50, 100, 150 and 200 mm) and number of detectors (720, 360, 240 and 144) was used.

The above experiments were repeated with photon attenuation in phantom volume.

Total of 96 sinograms were calculated.

Tomographic reconstruction of the sinograms was performed using 15 iterations of MLEM [10]. The iterative process is described by formula

$$x_j^{k+1} = \frac{x^k}{\sum_i m_i A_{ij}} \sum_i \frac{A_{ij}\, p_i}{\sum_l A_{il}\, x_l^k}, \qquad (1)$$

where x – reconstructed image in vector form, p – sinogram in vector form, A – system matrix, m – correction vector.

Images were reconstructed with three different resolutions: 32x32 (pixel size – 10 mm), 64x64 (5 mm) and 128x128 (2.5 mm).

ISBN 978-3-95450-181-6

System matrix values A_{ij} were calculated as normalized intersection area of j-th image pixel with i-th line of response. Uniform images ($x^0_j=1$) were used as initial estimation. No multiplicative correction was performed ($m_i=1$). For each image the average pixel value was calculated in central 110 mm square region.

Data analysis shows dependency of average values on acquisition and reconstruction parameters (fig. 2, 3).

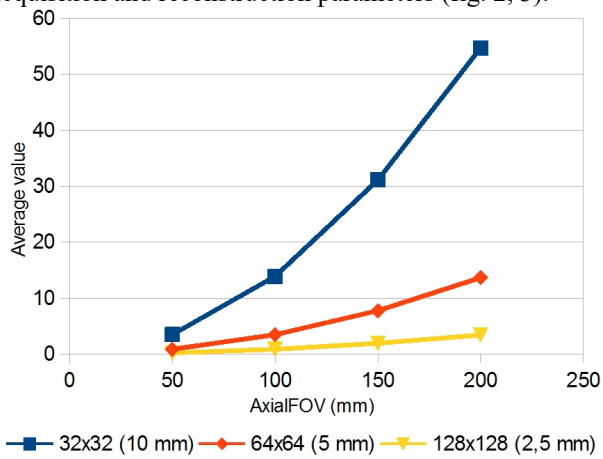

Figure 2: Quadratic dependency of reconstructed values on axial FOV and pixel size (volume activity – 10^6, 720 detectors, no attenuation).

The correction formula was derived as follows

$$m_i = \frac{1}{1000}\frac{X^2 Z^2}{4 R N_d}\frac{T_{1/2}}{\ln 2}\left(1-2^{-\frac{T}{T_{1/2}}}\right)e^{-\int_{L_i}\mu\, dl}, \quad (2)$$

where X – pixel size (mm), Z – axial FOV(mm), R – detector ring radius (mm), N_d – number of detectors, $T_{1/2}$ – radiopharmaceutical half-life (sec), T – time of acquisition (sec), μ – linear attenuation coefficient (1/mm), L_i – i-th line of response.

Reconstruction was performed second time using correction calculated by formula (2). Comparison of corrected average values with phantom activity was made (fig. 4).

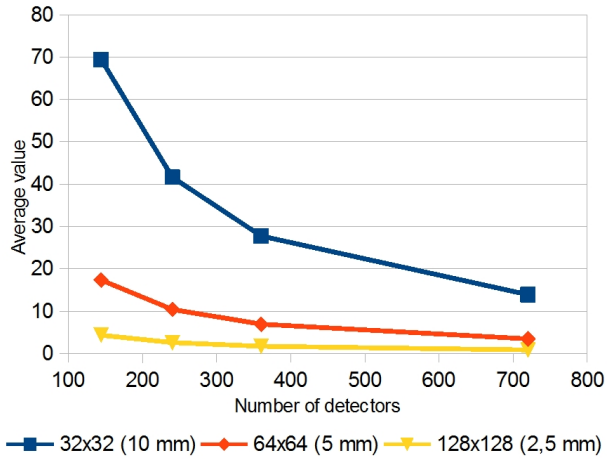

Figure 3: Inverse relation of reconstructed values and number of detectors (volume activity – 10^6, axial FOV – 100 mm, no attenuation).

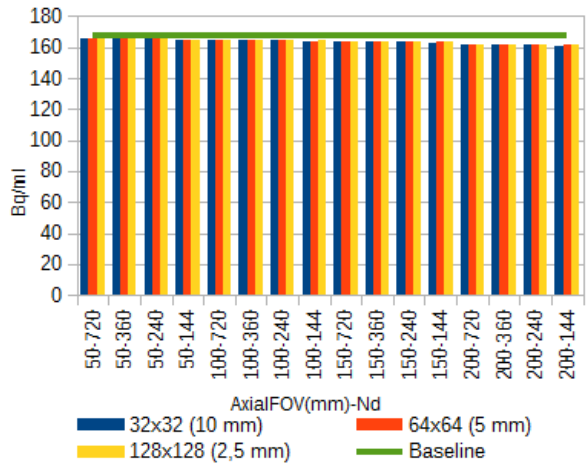

Figure 4: Reconstructed values compared to theoretical baseline (volume activity - 10^6, attenuation is present).

Figure 5 shows diagram of dataflow program used for reconstruction.

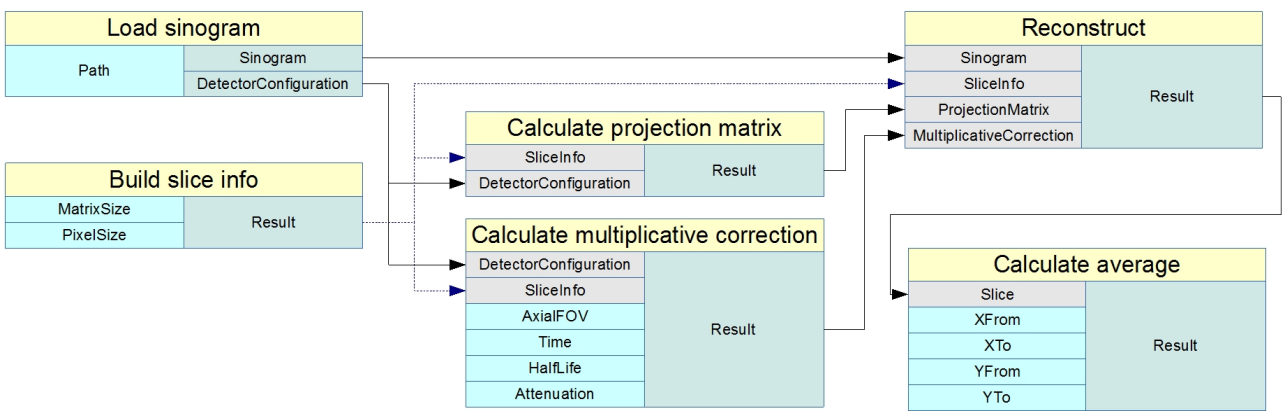

Figure 5: Reconstruction dataflow.

ISBN 978-3-95450-181-6

IMAGING TECHNIQUES

Besides data processing imaging plays important role in development of medical software. Basic imaging techniques (2D and 3D imaging, multiplanar reconstruction) have been presented in previous works [11, 12].

Fusion

Fusion is the technique of simultaneous imaging of anatomic (CT or MR) and functional (PET or SPECT) 3D data. These images have different resolution and common approach use data rescaling.

We have developed fusion imaging software which uses GPU to perform computation-heavy tasks (fig. 6).

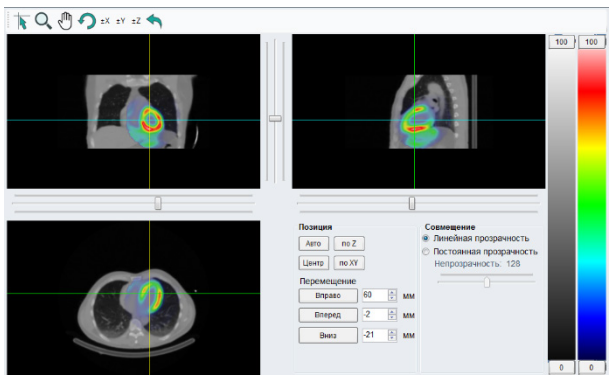

Figure 6: SPECT/CT fusion imaging.

Software automatically aligns images using DICOM (Digital Imaging and Communications in Medicine) metadata. It is also possible to perform value alignment manually. Two fusion modes are available: constant and progressive alpha.

Web Imaging

Evolution of web-technologies (HTML5, JavaScript, AJAX and WebGL) made it possible to create rich interactive applications executed in client browser. Such applications are high-portable. It also allows constructing distributed applications: heavy data processing is performed on server backend; imaging is done by client web-application.

To access possibilities of web imaging we have developed software capable of visualization of 2D medical images, multiplanar reconstruction and basic topographic processing (fig. 7).

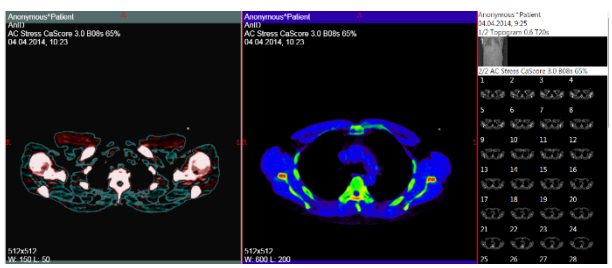

Figure 7: CT data imaging using WebGL.

REFERENCES

[1] M.A. Arlychev, V.L. Novikov, A.V. Sidorov, A.M. Fialkovskii, E.D. Kotina, D.A. Ovsyannikov, V.A. Ploskikh. EFATOM two-detector one-photon emission gamma tomograph // Technical Physics, 2009, Vol. 54, No. 10, pp. 1539–1547.

[2] E.D. Kotina, E.N. Ostroumov, V.A. Ploskikh. Left and Right Ventricular Phase Analysis of Gated SPECT Myocardial Perfusion // European Journal of Nuclear Medicine and Molecular Imaging. 2012, v. 39, № 2, p. 213.

[3] E.D. Kotina., G.A. Pasechnaya. 3D velocity field for heart tomography. International Conference on "Stability and Control Processes" in Memory of V.I. Zubov, SCP 2015 – Proceedings, 2015, 7342231, pp. 646-647.

[4] E.D Kotina, D.A Ovsyannikov, V.A. Ploskikh, V.N. Latipov, A.V. Babin, A.Y. Shirokolobov. Data processing in nuclear medicine. 20th International Workshop on Beam Dynamics and Optimization, BDO 2014, 2014, 6890037, p. 90.

[5] D.A. Ovsyannikov, E.D. Kotina, Determination of velocity field by given density distribution of charged particles // Problems of Atomic Science and Technology. 2012, (3), pp. 122-125.

[6] E.D. Kotina. Data processing in radionuclide studies // Problems of Atomic Science and Technology. 2012, (3), pp. 195-198.

[7] D.A. Ovsyannikov, E.D. Kotina, A.Y. Shirokolobov. Mathematical methods of motion correction in radionuclide studies // Problems of Atomic Science and Technology. 2013, 88 (6), pp. 137-140.

[8] Y.E. Balykina, E.P. Kolpak, E.D. Kotina. Mathematical Model of Thyroid Function // Middle - East Journal of Scientific Research. 2014, 19 (3), pp. 429-433.

[9] A.V. Babin, E.D. Kotina. Mathematical data processing of gated spect myocardial perfusion imaging with using wavelet analysis. International Conference on Computer Technologies in Physical and Engineering Applications, ICCTPEA 2014 – Proceedings, 6893254, pp. 19-20, 2014.

[10] E.D. Kotina, V.N. Latypov, V.A. Ploskikh. Universal system for tomographic reconstruction on GPUs // Problems of Atomic Science and Technology. 2013, 88 (6), pp. 175-178.

[11] E.D. Kotina, V.A. Ploskikh. Data processing and quantitation in nuclear medicine. RuPAC 2012 Contributions to the Proceedings - 23rd Russian Particle Accelerator Conference, 2012, pp. 526-528.

[12] E.D. Kotina, V.A. Ploskikh, A.V. Babin. Radionuclide methods application in cardiac studies // Problems of Atomic Science and Technology. 2013, 88 (6), pp. 179-182.

ISBN 978-3-95450-181-6

THE USE OF GRAPHENE AS STRIPPER FOILS IN SIEMENS ECLIPSE CYCLOTRONS

S. Korenev, R. Dishman, Siemens Healthineers, Knoxville, TN 37932, USA
A.M. Yerba, Siemens PETNET Solutions, Denver, CO 80210, USA
N. Mesheriakov, Siemens LLC, Moscow, Russia
I. Smirnov, Siemens LLC, Ekaterinburg, Russia
I. Pavlovsky, R.L. Fink, Applied Nanotech Inc., Austin, TX 78758, USA

Abstract

This paper presents the results of an experimental study for the use of graphene foils as an extractor (stripper) foil in the 11-MeV Siemens Eclipse Cyclotron. The main advantage of graphene foils compared with carbon is very high thermal conductivity. The graphene also has significant mechanical strength for atomically thin carbon layers. The life time of these foils is more than 16,000 μA*H. The graphene foils showed a significant increase in the transmission factor (the ratio of the beam current on the stripper foil to the current on the target), which was approximately more 90%. The technology in fabricating these graphene foils is shown. The pros and cons of using the graphene material as a stripper foil in cyclotrons are analysed.

INTRODUCTION

The use of stripper foils in the cyclotrons with negative hydrogen ions allows for easy output of the proton beam from the cyclotron into the target [1]. The 11-MeV Eclipse Cyclotron [2] uses this approach for the production of medical isotopes. The standard stripper foils based on carbon materials are widely used for these goals. The discovery of graphene [3] and the unique properties of graphene have created a large interest in this material as a stripper foil compared to the standard graphite and carbon foils. The main difference is the thermal conductivity of graphene which is up to 20 times higher than that of polycrystalline graphite. This gave interest for the application of graphene as a stripper foil in accelerators of charged particles and especially in commercial cyclotrons, such as the Eclipse cyclotron. The preliminary application of graphene foils from Applied Nanotech [4] as a stripper foil shows the main advantages of this material in comparison with the standard carbon and graphite foils. The main focus of this study was to determine the lifetime of stripper foils and to understand any cyclotron operating performance improvements. One the main questions was to characterize the radiation damage of graphene under irradiation by negative hydrogen ions with a kinetic energy of 11 MeV and current up to 100μA.

THE TECHNOLOGY OF FABRICATION FOR GRAPHENE FOILS

The technology for the fabrication of graphene foils is described in more detail in [5]. The foil fabrication method is based on the controlled reduction of graphene oxide by hydrazine with addition of ammonia in an aqueous dispersion. The dispersion of graphene oxide with loading of 0.5% wt. in water was obtained from Angstron Materials. The dispersion was reduced for 4 hours at 95°C and then cooled down to room temperature. The thickness of graphene foils was controlled by using a calculated volume of graphene dispersion knowing the loading of graphene. A commercially available stainless steel filter holder was used to make graphene foils by pressure filtration. The diameter of the fabricated foils was 13 cm. The filter holder allowed increasing the differential pressure across the filter. A compressed air line with a pressure regulator was connected to the filter holder to pressurize the air space above the graphene dispersion. Pressure up to 300 kPa was used to filter the dispersion. Commercially available polymer filter membranes with a diameter of 142 mm were used for the filtration. After filtration, graphene foils still on the filter membrane were removed from the filter holder and peeled off the filter membrane to obtain free-standing graphene foils. The described process can be adapted to fabricate foils with a wide range of foil thickness and using different isotopes of carbon.

EXPERIMENT

The experiments with graphene foils with a thickness of about 3μm (0.5mg/cm^2) were conducted on four Siemens Eclipse cyclotrons. The graphene foils were installed on the carousels of the Eclipse cyclotron. The general picture of the graphene material is shown in Figure 1.

a) b)

Figure 1: General view of graphene foils: a) fabricated foil; b) graphene cross section.

ISBN 978-3-95450-181-6

The dimension of graphene stripper on the carousel of Eclipse cyclotrons is 10mm x 10mm.

Experiments were conducted on the Siemens Eclipse Cyclotron [2], an example of is shown in Figure 2.

Figure 2: View of the Eclipse cyclotron.

The main experiments were conducted with main parameters of Eclipse cyclotrons:

1 Energy of negative hydrogen ions is 11 MeV.
2. Beam current on the foils ranged from 30 to 100 μA.
3. Beam current on the Faraday Cups (target) ranged from 25 to 80 μA.
4. Beam diameter of negative hydrogen ions is about 10 mm.

EXPERIMENTAL DATA

The experimental data was collected from four Eclipse cyclotrons. The summary of data for the transmission factor measurements is given in Table 1. The experimental study of high current mode of Eclipse cyclotrons with dual proton beam 80 μA on each target showed a decreasing level of the ion source current (arc current); see the plot in Figure 3. The bias current level was also observed to decrease during the experiments. The main experimental result of testing of cyclotron with graphene stripper foils is high transmission factor allowing the decreasing of ion source current. The good experimental correlation is decreasing of thickness with high thermal conductivity and ion source current permits us to work with a relative low current ion source. This in turn increases the life time of ion source.

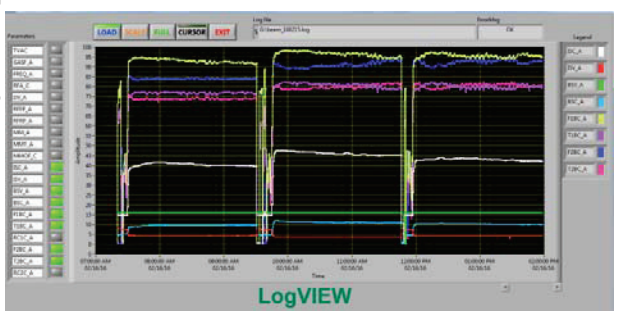

Figure 3: The log file display.

Table 1: Experimental Data

Cyclo-tron	Proton Beam Current (μA)	Transmission Factor (*) (%) Reg/Gr		Ion Source Current (*) (mA) Reg/Gr
1	2 x 55	86/75	92/78	230/192
2	2 x 25	80/81	88/89	120/90
3	2 x 60	75/88	89/90	340/250
	2 x 75	70/72	87/92	500/300
4	2 x 60	73/82	82/90	320/220
	2 x 80	70/85	82/93	600/450

(*) for Regular/Graphene stripper foils

LIFE TIME OF GRAPHENE FOILS

The lifetime of stripper foils is determined by 2 main mechanisms: radiation defects and sublimation [6, 7]. The experiments with graphene foils on the Eclipse cyclotron showed the radiation defects and sublimation have place. The lifetime of graphene foils determined by beam losses of the transmission factor and the mechanical destruction of graphene foil. The main contribution to lifetime is temperature from dissipation of beam energy. Typically considering dissipated power of the beam in the stripper is 1%, we have total dissipated power for beam in the Eclipse cyclotron of about 10 W for a 90 μA beam into the foil (for production of dual beam 2x80 μA). The distribution of temperature in graphene foil using Comsol Multiphysics package is shown in Table 2.

The lifetime test of the graphene foils on one of the Eclipse Cyclotrons was tested and resulted in a lifetime of 16,000 μA*Hours, which is 60% higher than the existing specification.

Table 2: Temperature Distribution in Stripper Soil

Dissipation Beam Power (W)	T_{min} Graphene (°C)	T_{max} Graphene (°C)	T_{min} Graphite (°C)	T_{max} Graphite (°C)
10	355	552	251	706

Figure 4 shows a picture of damaged graphene foil as observed at the end of this lifetime test.

Figure 4: A damaged graphene foil.

ISBN 978-3-95450-181-6

DISCUSSION ABOUT USING OF GRAPHENE AS A STRIPPER FOILS

The use of Graphene as a stripper foil shows benefits in comparison to the regular polycrystalline graphite foils. The main pros and cons of graphene compared with the standard stripper foils are provided in Table 3.

Table 3: Comparison of Strippers

Stripper Foil Type	Pros	Cons
Carbon	Low cost	Lifetime Thermal conductivity Foil ablation
DLC	Lifetime Small thickness	High cost Fabrication technology
Polycrystalline graphite	Low cost	Lifetime Thermal conductivity Foil ablation
Graphene	High thermal conductivity Small thickness Lifetime	Fabrication technology Limited suppliers

RECOMMENDATIONS

The graphene foils can be competitors to other carbon foils that are used as stripper foils, such as a DLC or polycrystalline graphite. Our investigations showed the benefits of using the graphene stipper foils. The question remains as to whether the technology to fabricate the graphene foils will continue to develop as well as the resulting cost.

CONCLUSIONS

In conclusion we can say that graphene stripper foils have a future that will require additional testing on diffrenet types of accelerators with stripper foils. The main advantuge of the graphene stripper foils is their unique properties, such as a high thermal conductivity and high mechanical strength compared to the standard carbon and graphite type foils.

ACKNOWLEDGMENT

Authors want to say thanks to James Hinderer, J. Bret Miller from Siemens Healthineers and Leif Thuesen from Applied Nanotech for their support and help with this work.

REFERENCES

[1] A.I. Papash, Yu.G. Alenitcki, "Commercial Cyclotrons Part 1. Commercial cyclotrons in energy range 10-30 MeV for isotope production", *Physics of Elementary Particles and Atomic Nuclei,* vol. 39, pp. 1150-1214, 2008.
[2] Siemens, http://www.siemens.com/mi
[3] Wikipedia, https://en.wikipedia.org/wiki/Graphene
[4] Applied Nanotech, http://www.appliednanotech.net
[5] I. Pavlovsky and R.L. Fink, "Graphene stripper foils", *J. Vac. Sci. Technol.,* B 30, 03D106 , 2012.
[6] E.A. Koptelov, S.G. Lebedev, and V.N. Panchenko, "A model of carbon stripper target failure under ion beam bombardment", *Nucl. Instr. Meth.*, vol.256, pp.247-250, 1987
[7] B. Gikal *et al*., "Calculation of lifetime of charge-exchanging carbon target in intense heavy ion beams", *Communication of JINR*, No: P9-2005-110, 2005.

ISBN 978-3-95450-181-6

THE PROBLEMS OF ACCELERATOR-DRIVER DESIGN FOR ADS

A. G. Golovkina*, I. V. Kudinovich[1], D. A. Ovsyannikov, Yu. A. Svistunov[2]
Saint Petersburg State University, St. Petersburg, Russia
[1]also at Krylov State Research Center, St. Petersburg, Russia
[2]also at JSC "NIIEFA", St. Petersburg, Russia

Abstract

Main problems of accelerator-driver design for ADS are considered. Accelerator-driver should meet additional requirements in comparison with accelerators for other purposes: - high neutron production rate; - higher reliability; - continuous operation for more than 5000 hours; - possibility of accelerator parameters adjustment to regulate ADS power level. Different types of accelerators were analyzed taking into account the mentioned features and the fact that the most prospective way of ADS application nowadays is transmutation. It's shown that the most preferable accelerator type is proton linac. Also it's marked that for demonstration facilities accelerators with lower requirements and correspondingly cost can be used.

INTRODUCTION

In contrast to traditional critical reactors, where the control on reactor power rate is fulfilled with neutron absorbing rods, in ADS subcritical reactor is controlled by charged particle accelerator [1]. Reactivity coefficient decreases as a result of nuclear fuel burning and fission products and actinide accumulation during reactor operation. So to maintain fixed ADS power-level dynamics of subcritical reactor driven by accelerator should be investigated [2].

ADS is most perspective for effective actinide transmutation, because it allows safely load large amount of transuranic elements to the reactor core in contrast to traditional critical reactors. However, it should be noted that construction of high power ADS will require to use accelerators also with high beam power not less than 10 MW. It is obvious, that such facilities are very expensive and the necessity of their construction as the alternative to fast reactors requires serious justification.

Nowadays R&D activities on ADS are focused on demonstration and experimental low-power facilities construction and also design of industrial ADS conceptual projects. In this paper the possibility of low-power ADS construction based on the proton linac is considered. The choice of such accelerator type as an ADS driver is justified. Also the problem of subcritical reactor control via accelerator is discussed.

THE CHOICE OF ACCELERATOR-DRIVER TYPE FOR ADS

There are three main accelerator types that are considered as drivers for ADS: proton [3] and electron linac [4] and cyclotrons [5]. In the majority of works devoted to the transmutation of nuclear waste using ADS RF proton accelerator is considered as a driver. It can be explained by the fact that neutron production per watt of beam power for heavy elements targets (Pb, W, U etc) reaches a plateau just above energy 1 GeV (Fig. 1) [3]. That allows achieve necessary for transmutation neutron fluxes $10^{17} \div 10^{18}$ n/s with the beam power 10 MW. At energy 1 GeV, it corresponds to a relatively low average current of 10 mA. For electron beam, neutron yield growth as a result of photo-nuclear reaction practically stops at energy of 50-60 MeV (Fig. 2) [6], and even at the average current of 200 mA neutron flux does not exceed 10^{16} n/s.

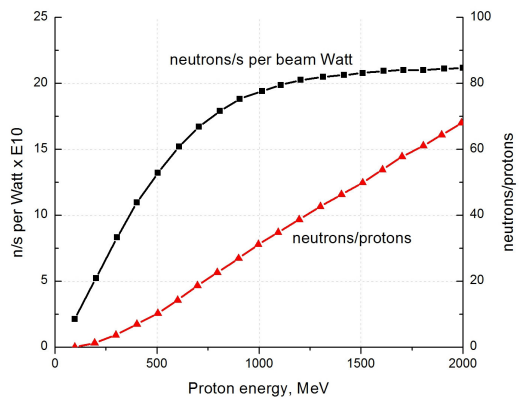

Figure 1: Neutrons/s per beam Watt, neutrons per proton, for a beam incident on axis of cylindrical W target 50-cm diam. x 100-cm long.

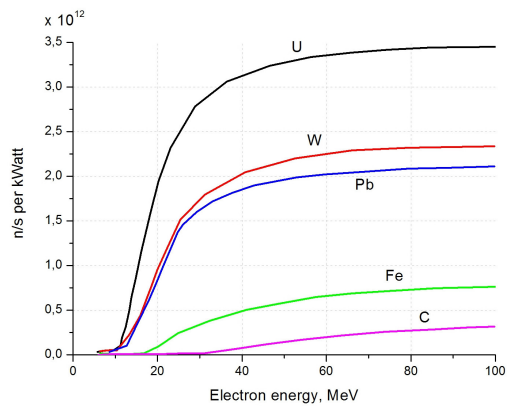

Figure 2: Neutrons/s per beam kWatt in photonuclear and photo fission reactions from Bremsstrahlung photons for an electron beam.

* a.golovkina@spbu.ru

ISBN 978-3-95450-181-6

In the energy and current range of ordinary proton and electron accelerators for industrial applications (50–100 MeV, the average current of 5-10 mA), the cost of one beam Watt for p-linac is 6–8 times higher than for e-linac. However the construction of e-linac providing neutron flux 10^{18} n/s by photo-nuclear reactions will require the output energy of 50 MeV with an average current of 10 A. Such accelerator would be far more difficult to create than p-linac with beam energy of 1 GeV and average current of 5–10 mA. It is shown, for example, in [4], where electron linac with an output energy of 100 MeV, the average current of 0.1 A and an accelerating system of racetrack microtron (RTM) type is offered as ADS driver. The authors expect to get 98% efficiency for RF power. Total efficiency, of course, will not exceed 40-50% [6].

The proof of possibility to construct proton linear accelerator with an energy of 1 GeV and average current of 2–3 mA is SNS accelerator working at ORNL Laboratory since 2006 [7].

There are also ideas to design accelerator-driver based on several circular RF accelerators. But even JINR offer to create cyclotron complex with an output energy of 600 MeV and a current of 10 mA looks not realistic, because in modern cyclotrons the output current is limited by 2 mA. It will take years of research to increase this limit to 5 times.

Deuteron linac isn't considered as ADS driver in this paper. Comparison of proton and deuteron beams as neutron producers was given in [8]. In range from 1 to 3.7 GeV under bombarding target the most essential difference are: (i) deuteron gives higher neutron yield by factor 1–1.15 than proton with the same energy; (ii) deuteron generates neutrons with smaller mean energy in comparison with proton. In the same time high energy d-linac design has essential additional problems in comparison with p-linac. So in this paper p-linac was decided to consider as an ADS driver. Conceptual scheme of proton accelerator proposed by Lawrence didn't change practically until the present time.

To accelerate particles to energy 2–3 MeV RFQ resonator, which allows to carry out almost 100% capture of particles in the acceleration, is used; to accelerate protons from 3 to 100 MeV — resonator with Alvarez-type drift tube with an additional beam focusing by quadrupole lenses, located in drift-tubes (not necessary in every one). The frequency of accelerating field can be 432, 350 or 216 MHz in the depenance of impulse current value. After the energy of 200 MeV is reached the further acceleration can be carried out in resonators with higher working frequency, for example, 864, 700 or 432 MHz. The accelerator length can be reduced at the expense of isochronous turn of the beam through 180° at the definite energy level. If account for an average accelerating field gradient of 3 MeV/m in prospect, then the length of accelerating tract will be 400–500 m.

NEUTRON PRODUCING TARGET

An electronuclear neutron source intensity is defined by the expression

$$S = \frac{I_p m_0}{e}, \quad (1)$$

where I_p — average beam current, m_0 — neutron yield (average neutron number generating by an accelerated particle in the target), e — accelerated particle charge.

Neutron yield from the target irradiated by charge particles depends on parameters of particle beam, target composition and it dimensions.

In ADS with targets of non fissile materials (Pb, Bi, etc.) the external neutron source intensity is specified by the spallation neutrons leakage from the target surface.

For small size targets a significant part of secondary particles that can induce nuclear fissions leave the target. For large size — radioactive capture of neutrons by the target plays an important role. Because of an anisotropy of non-elastic proton scattering the target length should in several times be greater than its radius, meanwhile the L value has weak influence on neutron yield if the following condition $L > D > \lambda_{in}$ is fulfilled. A great part of neutron leakage comes from the target face from the side of beam falling. So the neutron yield is maximal with some beam entry point deepening.

The optimal dimensions of cylindrical targets are presented in Table 1, and neutron yields from these targets irradiated by proton beam of different energies — in Fig. 3. The presented results were obtained using GEANT-4.9.5 code. Possible targets construction is presented in [9].

Table 1: Optimal Dimensions of Cylindrical Not Fssile Targets

Material	D_{opt}, cm	Z_{opt}, cm	L_{opt}, cm
Pb	66	31	76
Bi	95	49	105
W	7	2	10
Ta	7	2	10

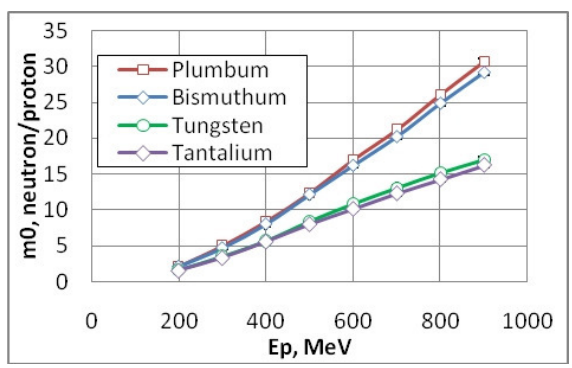

Figure 3: Neutron yield from target with the optimal sizes.

In ADS with fissionable targets (for example, U) as initial neutrons are to be considered only spallation neutrons, because the neutron multiplication due to fission reactions

ISBN 978-3-95450-181-6

are accounted in neutronics calculation of the reactor core with the target as a part of it.

The spallation neutron yields in the infinite uranic target in dependence of the protons energy are approximately in twice more than for non fissile targets.

From the presented results it is followed that for an ADS with 300 MeV proton energy beam it is reasonable to use fissile targets.

POSSIBLE CONTROL SCHEMES FOR ADS WITH PROTON LINAC

Thermal power for the reactor core is defined by the following formula [10]

$$N_T = \frac{E_f S k_{\text{ef}}}{\nu(1 - k_{\text{ef}})},$$

where E_f — energy, released per a fuel nuclei fission, k_{ef} — effective multiplication factor, S – external neutron source generation intensity defined by Eq. (1).

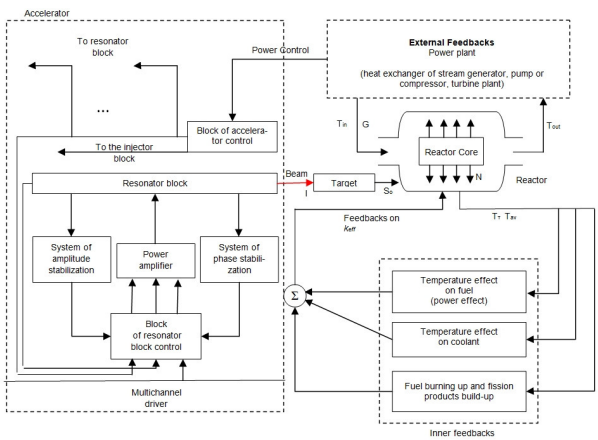

Figure 4: ADS structural scheme with feedbacks.

In traditional nuclear reactors k_{ef} and the core are maintained critical by control system with neutron-absorbing rods which are mechanically introduced and withdrawed from the core. In ADS for the nuclear safety reasons neutron-absorbing rods are not used, that eliminate the possibility of accidents with unauthorized multiplication factor growth. So durting ADS operation external neutron source intensity should be variable to compensate possible reactivity changes. Reactivity is determined by the physical characteristics of the core and depends on the temperature, reactor fuel burn up and the accumulation of fission products and actinides.

ADS Power Level Regulation

The ADS power level control can be realized by variation of external neutron source generation intensity which depends on the average accelerator current and charged particles beam energy [11].

The average current regulation is possible because of pulse current value or pulse repetition rate variation.

Pulse current can be increased by rising current at the exit of plasma ion source (for example, because of increasing the emissive aperture diameter), but the beam emittance grows meanwhile, system of beam formation for injection to the acceleration channel gets more complicated, transient processes in resonators and beam dynamics change. That is the accelerator design and adjustment becomes more complicated in comparison to accelerator with fixed output parameters.

Increasing of average current by increasing pulse repetition rate is a simpler decision because particle dynamics in accelerating tract isn't changed. The effect is achieved due to the control system of RF and injector feed lines.

Increasing of proton energy can be fulfilled by activating additional resonators at the end of the accelerating channel. In should be noted that when the resonators are turned off, the beam output characteristics will get worse.

Thus, the most suitable way to control ADS is the accelerator average current variation by pulse repetition rate change.

Subcritical Reactor Feedbacks

The ADS subcritical reactor dynamics depends on outer and inner feedbacks (Fig. 4). The inner feedbacks are determined by the reactor core physical characteristics, the external ones reflect the reactor connection with the power plant (coolant flow, coolant temperature at the entrance).

For stable ADS working at the constant power level, the reactor core should have the negative fuel and coolant temperature inner feedback and the negative mean reactivity coefficient. These conditions ensure the reactor self-control and the average temperature maintenance.

CONCLUSION

To maintain ADS power-level it is necessary to regulate the external neutron source intensity and therefore charged particles beam characteristics. The most convenient way to control ADS is the average current variation by pulse repetition rate change. This control scheme doesn't depend on the used type of accelerator-driver, but it's shown that proton linac is more preferable for this purpose.

REFERENCES

[1] F. Carminati *et al.*, "An energy amplifier for cleaner and inexhaustible nuclear energy production driven by a particle beam accelerator", CERN, Geneva, Switzerland, Rep. CERN/AT/93-47, 1993.

[2] A. Golovkina, I. Kudinovich and Y. Svistunov, "The problem of ADS power-level maintenance", *Cybernetics and Physics*, vol. 5, no. 2, pp. 52–58, 2016.

[3] G. P. Lawrence, "Transmutation and energy production with high power accelerators", in *Proc. Particle Accelerator Conf. (PAC'95)*, Dallas, TX, USA, 1995, pp. 35–39.

[4] G. I. Batskikh, B. V. Bekhtev, V. A.Boiko, V. V. Elian and A. V. Mitshenko, "Electron accelerator for transmutation of fission products and nuclear fuel cycle actinides", in *Proc.*

ISBN 978-3-95450-181-6

Particle Accelerator Conf. (PAC'91), San Francisco, CA, USA, 1991, vol. 4, pp. 2601–2603.

[5] Y. G. Alenitskii *et al.*, "High current cyclotron as a driver for electronuclear assembly", *Phys. of Particles and Nuclei Lett.*, vol. 7, no. 7, pp. 529–533, 2010.

[6] K. C. Mittal *et al.*, "Electron linacs as possible ads drivers", in Proc. 1st Int. Work. on Accelerator Driven Subcritical Systems & Thorium Utilization, Blacksburg, VA, USA, 2010.

[7] N. Holtkamp, "Status of the SNS linac: an overview", in *Proc. European Particle Accelerator Conf. (EPAC'06)*, Edinburgh, Scotland, 2006, pp. 29–33.

[8] V. I. Yurevich, V. A. Nikolaev and R. M. Yakovlev, "Fission of ^{232}Th in spallation neutron field", *Phys. of Particles and Nuclei Lett.*, vol. 13, no. 2, pp.244-248, 2016.

[9] Y. A. Svistunov *et al.*, "Characteristics of ads target irradiated by 200...400 MeV proton beam", *Problems of Atomic Science and Technology*, vol. 91, no. 3, pp. 64–69, 2014.

[10] A. G. Golovkina, I. V. Kudinovich, D. A. Ovsyannikov and A. A. Bogdanov, "Power plant based on subcritical reactor and proton linac", in *Proc. 5th Int. Particle Accelerator Conf. (IPAC'14)*, Dresden, Germany, Jun. 2014, pp. 2224–2226.

[11] A. G. Golovkina, I. V. Kudinovich, D. A. Ovsyannikov and Y. A. Svistunov, "Dynamics of processes in subcritical reactor driven by linear accelerator", in *Proc. 24th Russian Particle Accelerator Conf. (RuPAC'14)*, Obninsk, Russia, Oct. 2014, pp. 467–469.

ISBN 978-3-95450-181-6

STUDY OF OIL WELLS WITH THE USE OF ACCELERATOR TUBES, TIME AND ENERGY SPECTROMETERS OF NEUTRONS AND GAMMA RAYS IN A SINGLE GEOPHYSICAL COMPLEX

B.Yu. Bogdanovich, E.D. Vovchenko, A.V. Ilinskij, K.I. Kozlovskij, A.A. Isaev, A.V. Nesterovich, A.E. Shikanov, National Research Nuclear University "MEPhI" (Moscow Engineering Physics Institute), Moscow, Russia

Abstract

The report discusses the finding of the coefficient of oil saturation of the reservoir by of nuclear methods. For this purpose, the data about pulse and the activation neutron logging and spectral logging of natural gamma activity are used in a single geophysical complex. As sources of neutron radiation can been applied accelerating tube (AT) based on different ion sources, such as plasma discharge with oscillating electrons (gas AT), vacuum arc and laser-plasma (vacuum AT). For investigation of the oil reservoir, in particular with heavy oil, we discuss the prospects of using vacuum accelerating tube based on a laser-plasma source of deuterons with coaxial acceleration geometry and pulsed magnetic isolation of electrons.

INTRODUCTION

The coefficient of oil saturation $k_н$ (i.e. the relative volume of the pores in oil collector occupied with a productive fluid) is the most important criterion that shows a technical condition of a working oil well. It is determined by the properties of the reservoir, which can also contain water and clay. Between k_n, volumetric content of the solid phase (skeleton) – k_{sk}, relative water content in the pores (water saturation coefficient) – k_w and the relative content of clay in the pores (coefficient of clay content) – k_c installed connection [1]: $k_{sk} + k_c + k_w + k_n \approx 1$.The sum of k_w and k_n is the porosity coefficient: $k_p = k_w + k_n$. The information for the evaluation of k_n can be obtained by using combinations of different nuclear-geophysical methods, such as pulsed neutron lodding (PNL), activation logging, wells logging of natural γ-activity (JCC), laboratory nuclear techniques, well as the classical methods of petrophysics [1].

Method PNL gives information about the state of the forwation developed in the presence of the casing of the well, creating inconvenience for other "opaque" geophysical methods [2 − 3]. In the process of implementing a temporary field, analysis PNL thermal neutrons or γ-quanta of radiation capture (RC) generated in the borehole accelerator (AT). Their temporary structure is determined by the sum of the exponentials:

$$n(t,z) = A_п(z)\exp(-\lambda_п t) + A_c(z)\exp(-\lambda_c t),$$

$n(t,z)$ − spatial density of neutrons or γ-quanta; z − coordinate, set along the wellbore; λ_n и λ_c – decrements recession of density radiation field in the reservoir and wellbore respectively as a result of the RC.

The mathematical apparatus of separation exhibitor at wireline signal received as a result of the interim analysis [4] makes it possible to determine the parameter λ_n, as well as amplitude $A_n(z)$. In Fig. 1 is shown a typical example of computer processing logging signal.

Using the additivity rule, you can set up a relationship between the λ_n and radiation capture sections based on its individual components using the ratio:

$$\lambda = (\Sigma_{ск}k_{ск} + \Sigma_н k_н + \Sigma_в k_в + \Sigma_{гл}k_{гл})(1+\varepsilon),$$

$\Sigma_{с,н,в,гл}$ − macroscopic cross-section of RC in the skeleton, in reproductive fluid, in water and clay, respectively; $\varepsilon \approx 0.1$ − dimensionless correction option, resulting in model experiments.

This formula allows to judge quality of reservoir fluid saturation and determine the position of the boundary water-productive fluid because of the cross-section of RC in water significantly more than the hydrocarbons due to the presence of salt, and, hence, chlorine whose nuclei are abnormally high micro-cross RC.

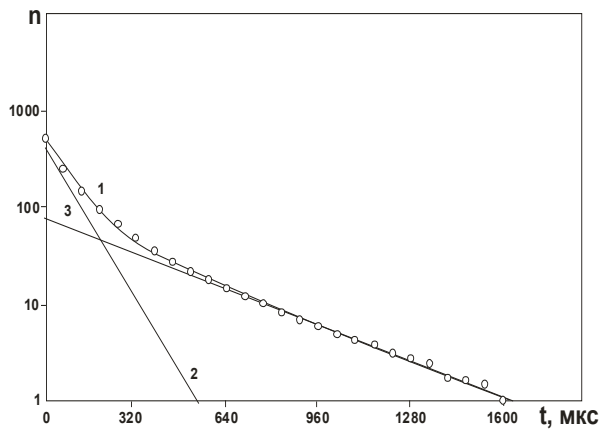

Figure 1: An example of splitting the Exhibitor in a logging signal. Slopes define by the direct signal λ_n (3) and λ_c (2).

The ratio $A_п(z_1)/A_п(z_2)$ carries information about slowing down and diffusive properties of formation, which are determined by the content of hydrogen there [2]. The relative content of hydrogen in water and hydrocarbons are close enough, so one could argue that this attitude will clearly depend on porosity ratio and will serve as a device for its definition.

ISBN 978-3-95450-181-6

One of the problems of interpreting data of INL is related to ambiguity of presence of clay in the pores, the amount of which may vary. One of the possible version of its solution is associated with additional information by method of JCC.

Another problem occurs when low mineralization, reduces contrast PNC to the level when the method ceases to be effective. In this case, you must use direct methods for determination of hydrocarbons.

Currently, the direct method is widespread enough γ-spectrometric method for the determination of carbon and oxygen (C/O logging) [5]. However, the equipment for its implementation is difficult to operate, has great size and commercial value.

As an alternative is suggested methods for determination of oxygen isotope activation ^{16}O and carbon isotope ^{12}C in the forwation using nuclear reactions ^{16}O(n, p)^{16}N and ^{12}C(n, p)^{12}B (oxygen and carbon logging) [6].

Consider two modes of implementation of the activation methods on the example of oxygen logging. In the first mode, the generation frequency of the neutron flares accelerating tube (AT) $f \leq 100$ Hz, in the second – $f = (300 - 1000)$ Hz.

Low frequency mode lets you start registration system after γ-quanta RC density will drop to a level more than 10 times lower level of external γ-radiation. Interfering background noise other radionuclides clipped the establishment of appropriate energy threshold, beyond which is carried out by γ-quanta emitted by excited nuclei of oxygen ($E_\gamma = 6.13$ MeV), formed in β-decay nuclei ^{16}N.

The second mode involves the generation of neutron flares with actuation frequency $f = 300 - 1000$ Hz. Use for the gas-filled AT have high pulse stability, allows you to simplify the system of registration, excluding monitor the neutron flux.

The difficulty of implementing the method of activation of oxygen in specified frequency mode is a small (~1 ms) time interval between the neutron flares, which does not allow to allocate to measure induced γ-activity time interval at which there is no radiation. While a constant stream of γ-quanta emitted by excited nuclei ^{16}O inevitably superimposed pulse-periodic flow of γ-quanta RC, against which you want to select continuous signal. To highlight it sponsored was a method of processing, in which the separation of alternating and direct signal similar methodology [4] and simultaneously obtained information, as activation effect and as decrement decline γ-quanta fields RC. Example of this separation is shown in Fig. 2.

In order to effectively determine the oxygen reaction ^{16}O(n, p)^{16}N accelerating tube should generate $\geq 10^8$ n/c with the energy of 14-MeV. Such AT successfully developed in VNIIA [7]. The first mode can be used with AT vacuum-arc sources of deuterons and for a second mode can be used gas-filed AT based on Penning discharge source.

When determining carbon AT should generate neutrons also the reaction T(d, n)^{4}He when accelerating deuterons to energy $T_d \geq 0.3$ MeV, predominantly in the direction perpendicular to the wellbore. Neutron flux should exceed 10^{10}n/c. Modern AT with vacuum-arc sources deuterons do not allow to achieve such parameters of radiation.

In addition, to the effective implementation of the activation methods of logging high stability play neutron flares from impulse to impulse at the level < 5%.

Operating experience with ARC-AT sources revealed substantial instability of deuterons, output associated with the characteristics of the source of deuterons. It can reach 50%. This requires, as noted above, involving of pulsed neutron flux monitor, which greatly complicates the logging facility.

The above-mentioned shortcomings could be eliminated when using AT laser-plasma source deuterons, diode system with radial acceleration and magnetic isolation accelerating gap [7].

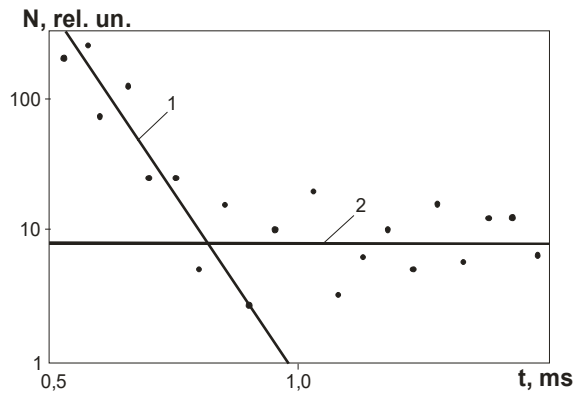

Figure 2: Logging signal decomposition. 1 − intensity radiation RC; 2 − the intensity of radiation nuclei of oxygen (points marked with the values measured in individual account temporary channels).

The accelerating voltage sources based on of generators Arkadiev-Marks allows creating on the led gap AT impulses of the acceleration (duration ≤ 100 ns) with amplitude up to 500 kV. Due to the low pulse duration combined with magnetic system suppressing electronic conductivity of diode systems, you can significantly reduce the requirements for high-voltage insulation in device in well.

In the experiment with the layout well neutron generator (SGBV) on the acceleration gap AT has been able to generate pulses of voltage with amplitude up to 350 kW and generate up to $2 \cdot 10^8$ n /impulse when using deuterons source based on Nd:YAG laser, generating pulses with energy up to 50 mJ.

Application of suppression the electrons from the cathode by magnetic elements placed in a working volume of AT [8], small lasers generated pulses of radiation with an energy of up to 1 J and frequency up to 100 Hz, as well as new high-power pulsed sources the accelerating voltage, makes a real creation of efficient and high-stability of SGBV. Such neuron generator allowing for its output parameters implement techniques for neutron activation logging with direct determination of carbon and oxygen.

ISBN 978-3-95450-181-6

This is confirmed by the results of recent experiments that was made in NRNU MEPHI [9, 10].

The work regarding the establishment of a gas-filled AT (as effective neutron source) with a frequency up to 1 kHz should be designed to increase their thermostability (heat stability). The benchmark should be considered temperature ~150 C, due to the increased depth of field wells in the process of development of new oil fields.

As noted above, to overcome difficulties associated with the presence of clay, JCC method should be involved. It gives additional information about a parameter k_c because clay have γ-activity at the expense of the nuclides ^{208}Th in the thorium series (line with E_γ = 2.62 MeV) and ^{40}K (line with E_γ = 1.46 MeV).

The intensity of these lines with the appropriate calibration allows to determine the concentration of thorium C_{Th} and potassium C_K withto study geophysical Wednesday [11].

It was found that value $G = 10^6 C_{Th} C_K$ potassium-thorium index) weakly depends on the mineral composition of clay and can serve as a yardstick for measuring the k_c. An analysis of the experimental data was obtained by the least squares method approximate empirical dependence: $k_c(G) = 1.294G - 0.965G^2$, which lets you remove marked above the ambiguity.

To implement these studies on geophysical sites with different geological structure and thermal conditions with the participation of the authors developed a simple to operate, dampen downhole γ-spectrometer [12], mastered at the pilot plant of JINR.

CONCLUSION

1. The solution to the problems of increasing the contrast of the dimensions and impact of exceptions results clay logging oil and gas wells with difficult geological conditions seen in the way of integrated management methods INL with the methods of neutron activation and MLK.

2. Attention should be drawn to the prospect of using AT with a laser source of deuterons and magnetic isolation due to the possibility of obtaining large neutron output combined with high impulse stability.

3. Work done in the framework of agreement No. 15-19-00151 between RNF, NRNU MEPHI and A.V. Nesterovich project leader of the grant for research.

REFERENCES

[1] Pearson S.D. Teachings on the oil reservoir. Leningrad, 1961, 571s.

[2] Shimelevich Yu.S., Cantor S.A., Cedars A.J., etc. Physical basis of Pulsed Neutron techniques. M., Nedra, 1976, 17 Celsius degrees.

[3] Zamyatnin Yu.S., Shikanov A.E. 50 years pulse neutron (1955-1958, G.n. Flerov). Message JINR, R3-2007-151, Dubna, 2007, 35.

[4] Startsev A.A. Fedyna, E.A., Shikanov A.E. Algoritm for Decomposition of PNL Response. Appl. Radiat. Isot. Vol. 48, No. 10-12, 1997, pp. 1329-1330.

[5] Modern nuclear geophysics in search, exploration and development of oil and gas fields, m., IAGO-AIS, 2004, pp. 324-329.

[6] Ilyinsky A.V., Cedars A.I., Mikhailov V.O., Shikanov A.E. apparatus-method complex oil and gas well logging method for activation of oxygen. Nuclear energy, vol. 97, 5, 2004. p. 355-361.

[7] Sat. materials of the international scientific and technical conference "portable generators neutrons and technology on their basis". M., VNIIA, 2005.

[8] Vovchenko E.D., Kozlovsky K.I., Shikanov A. E., etc. Ion diode for the generation of neutrons. The RF patent № 140351, Published: 10.05.2014. Newsletter. No. 13.

[9] Kozlovsky V.I. Ryzhkov V.I., Shikanov A. E., etc. Experimental study of small-sized layout generator with pulse neutron magnetic isolation. Nuclear energy, vol. 112, ISS. 3, 2012,ps. 182-184.

[10] Shikanov A.E. Vovchenko A.E., e.d., Kozlovsky K.I. Neutron generation in plasma diode electron insulated field permanent magnet. Nuclear energy, vol. 119, ISS. 4, 2015, p. 210-215.

[11] Urmanov E.G. Spectrometric gamma ray logging oil and gas wells. M., VNGIIOJENG, 1984, 81p.

[12] Urmanov E.G., Martyanov I.A., Shikanov A. E. etc. Avtostabilizirovannaja spectrometric apparatus γ-logging wells. Atomic Energy, vol. 83, vol. 5, 1997, pp. 358-362.

ISBN 978-3-95450-181-6

BEAM DYNAMICS IN NEW 10 MEV HIGH-POWER ELECTRON LINAC FOR INDUSTRIAL APPLICATION

S.M. Polozov, V.I. Rashchikov National Research Nuclear University – Moscow Engineering Physics Institute, Moscow, Russia
M.I. Demsky, CORAD Ltd., Saint-Petersburg, Russia

Abstract

Beam dynamics simulation in electron gun, bunching and accelerating cells of new 10 MeV high-power electron linac was fulfilled with the help of developed at MEPhI SUMA [1] and BEAMDULAC-BL [2] codes. Three-electrode electron gun was used to obtain up to 400-450 mA of pulse beam current which is necessary to produce 300 mA of the accelerated beam. Precise gun simulation was conducted to satisfy all necessary output beams characteristics, such as profile, energy spectrum, phase space size etc. Some additional calculation was conducted to provide wide range of gun output beam parameters which will be used for subsequent accelerator modification. The conventional biperiodical accelerating structure (BAS) based on disk loaded waveguide (DLW) was used in linac. Beam dynamics optimization was pointed to obtain effective beam bunching for all energy range and to achieve narrow energy spectrum. Simulation results shows that linac provides effective beam bunching and acceleration for wide bands of beam currents and energies.

ELECTRON GUN SIMULATION

PIC code SUMA was used for beam dynamics simulation in the electron gun. The traditional three-electrode gun with cathode-grid voltage 1-1.3 kV, emission current 0.5-0.7 A, cathode-anode voltage 50 kV was investigated. Fig. 1 shows computer simulation result for cathode-grid voltage 1 kV and emission current 0.7 A.

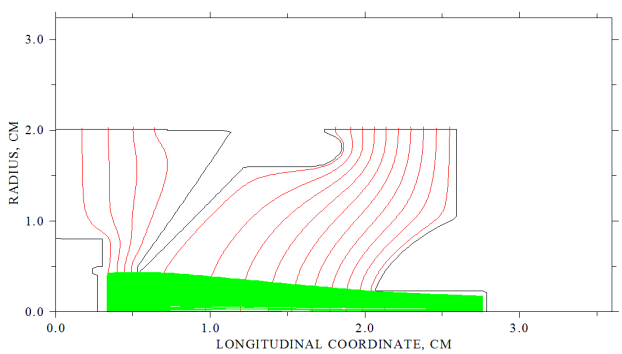

Figure 1: Electron trajectories (green lines), electric field equipotential lines (red lines) and boundary (black lines).

Output energy spread is 1.2% and transverse emittance 2.5 cm·mrad.

For code testing some experiments were conducted. Beam envelope was measured by collimated diaphragm current collector on different distance from gun anode. Fig.2 shows beam envelope dependence on anode distance for different gun currents and cathode – anode voltage is 20 kV, greed - anode microperveance is 0.078. SUMA simulation results for this case are presented in Fig. 3.

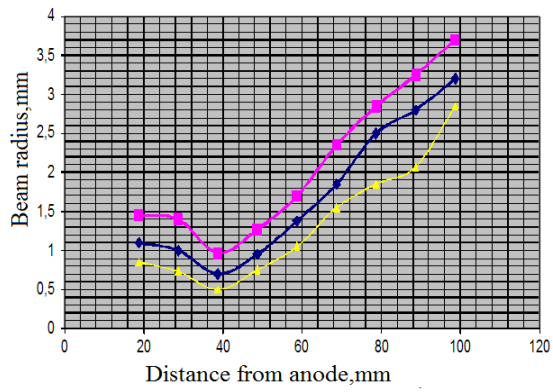

Figure 2: Beam envelope for different current values: red-0.222 A, blue-0.19 A, yellow-0.16 A, cathode-anode voltage 20 kV.

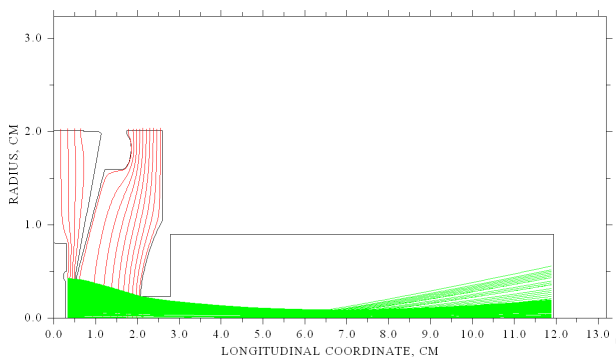

Figure 3: Electron trajectories (green lines), electric field equipotential lines (red lines) and boundary (black lines). Current value -0.222 A.

We obtain a good experimental and calculated results agreement for the beam emittance equals 2.42 cm·mrad and taking into account that distance between cathode and anode equals 25 mm.

For further accelerator modification program it might be necessary to increase output beam diameter from 2 to 3.5 – 4.0 mm or even more. For this purpose some new gun modifications were fulfilled. The main aim was to obtain necessary result with a few changes as possible. First step in this way is to increase the anode hole. Output beam radius rises due to potential sage on the anode hole. Fig. 4 shows beam profile for anode hole radius equals 3 mm (initial value 2.25 mm).

ISBN 978-3-95450-181-6

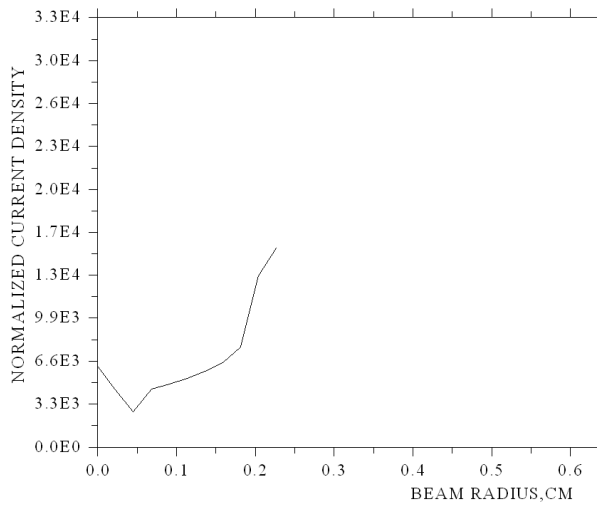

Figure 4: Beam profile.

Another way to increase the beam radius is to straighten equipotential lines in greed – anode gap. Easiest way to do this is to remove anode flange. Electron trajectories for this case are shown in Fig. 5.

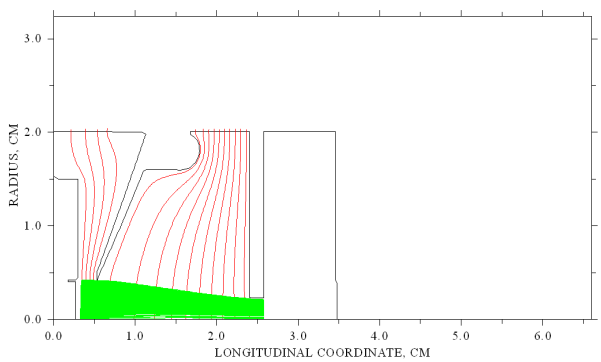

Figure 5: Electron trajectories (green lines), electric field equipotential lines (red lines) and boundary (black lines).

Beam profile is practically the same as at Fig. 4, but emittance decreased to 1.56 см·мрад. If we increase anode gap to 3 mm in last case we obtain emittance 1.26 см·мрад and low energy spread 500 eV. This results seems quite reasonable for further accelerating structure simulation.

ACCELERATING STRUCTURE OPTIMIZATION

Beam dynamics simulation was done using BEAMDULAC-BL code developed at MEPhI for simulations taking into account the beam loading and the Coulomb field effects self-consistently [2]. Beam dynamics optimization was pointed to obtain effective beam bunching for all energy range and to achieve narrow energy spectrum. Both requirements were met using sixperiod gentle buncher proposed. The phase velocities v_{ph} and RF field amplitudes are rising for effective beam bunching. The linac consists of 28 accelerating and 27 coupling cells, its total length is 143 cm. Maximal on-axis RF field amplitude was chosen about 200 kV/cm, it is enough for effective bunching and acceleration up to 13 MeV. One of the middle cells is used as RF power coupler.

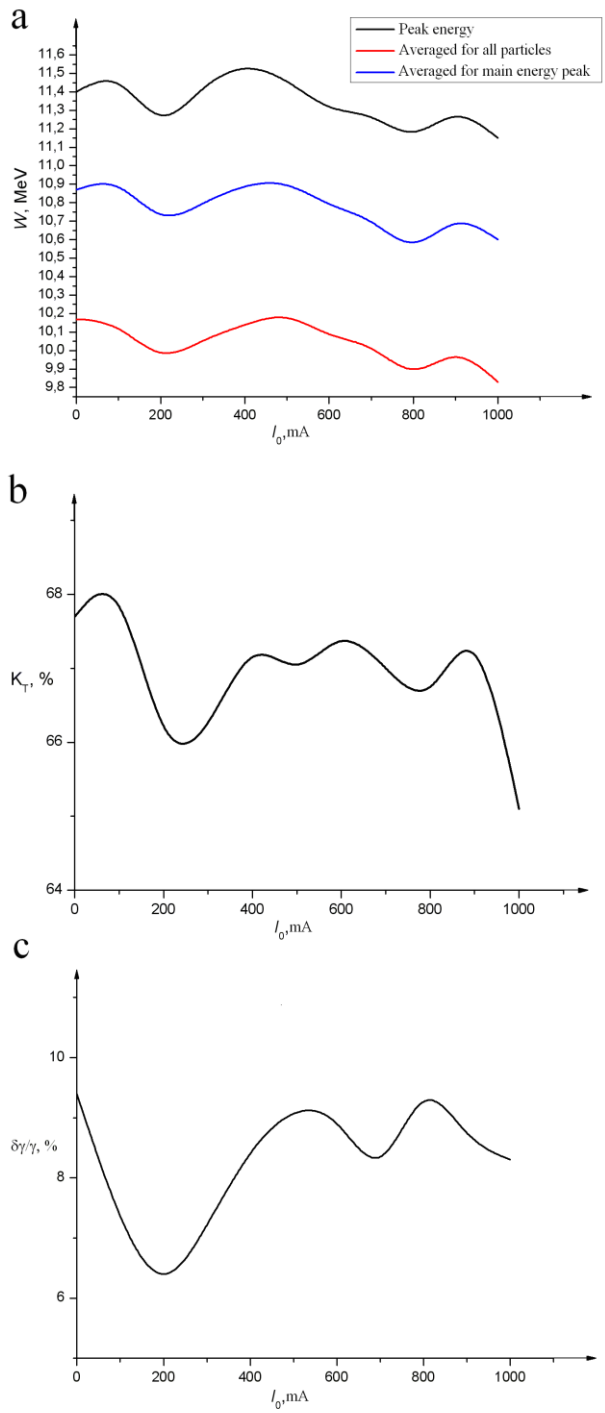

Figure 6: Output beam energy W (a), current transmission coefficient K_T (b) and output energy spectrum measured for full width $\delta\gamma/\gamma$ on the distribution base (c) vs. injection current for E_{max}=160 kV/cm.

Short (~20 cm) focusing magnetic coils are used for beam focusing. Finally three coils were installed before coupler and one after it. Magnetic field of 30 mT on the

ISBN 978-3-95450-181-6

linac axis is necessary for the effective beam focusing. Some main beam dynamics simulation results are presented in Figure 6. It is clear that linac provides effective beam bunching and acceleration for wide bands of beam currents and energies. The current transmission coefficient is not lower than 65 % for all operating modes [3]. It was shown that chosen accelerating structure gives very high quality beam in wide band of energies from 7 to 12 MeV (see Fig. 7 and Table 1). The energy spread measured for total width of the main peak of electron energy distribution is not higher than ± 5 %.

Table 1: Beam Output Parameters vs. RF Field Amplitude

E_{max}, кV/cm	Most probably energy, MeV	Average energy, MeV	Output beam current, mA	K_T, %	δγ/γ on the distribution base, %
70	1.93	1.60	110	24.4	± 3.6
80	4.44	3.86	157	34.9	± 9.0
90	6.19	5.91	198	44.0	± 7.5
100	7.05	7.20	217	48.2	± 4.6
110	7.86	7.94	234	51.9	± 4.9
120	8.61	8.68	256	56.8	± 4.8
130	9.03	9.28	275	61.2	± 4.9
140	9.73	9.89	293	65.2	± 3.8
150	10.34	10.45	306	67.9	± 3.4
160	11.04	11.02	320	71.2	± 3.4
170	11.71	11.62	326	73.4	± 4.9
180	12.33	12.22	316	70.3	± 5.0
190	13.00	12.83	306	68.0	± 6.6
200	13.58	13.43	294	65.3	± 5.2

CONCLUSION

Beam dynamics simulation results in electron gun, bunching and accelerating cells of new 10 MeV high-power electron linac were discussed. It was shown than used three-electrode gun can be effective used to generate high-quality beams having different beam sizes and low energy spread and transverse emittance. It was also shown that accelerating structure with gentle buncher and solenoid focusing can accelerate beams in wide energy band 7-13 MeV with low output energy spread < ± 5 %. Such section was manufactured and commissioned [3] and the base beam dynamics simulations results were confirmed.

REFERENCES

[1] V.I. Rashchikov, Problems of Atomic Science and Technology. Series: Nuclear Physics Investigations, 10 (18), 50 -53 (1990).

[2] T.V. Bondarenko, E.S. Masunov, S.M. Polozov, Problems of Atomic Science and Technology. Series: Nuclear Physics Investigations, 6 (88), 114-118 (2013).

[3] M.I. Demsky, S.M. Polozov, V.I. Rashchikov et al., Proc. of IPAC'16, pp. 1794-1796.

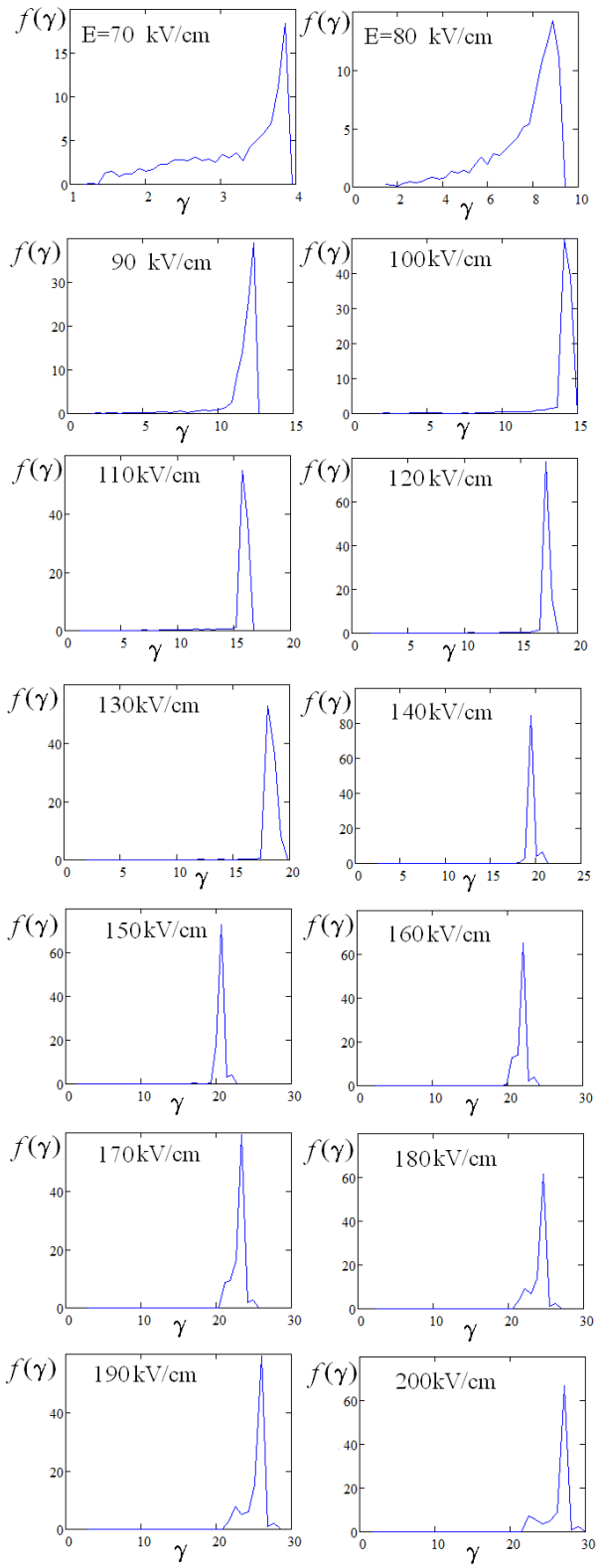

Figure 7: The energy spread measured for total width of the main peak of electron energy distribution vs. RF field amplitude in the range of 70-200 kV/cm.

ISBN 978-3-95450-181-6

REALIZATION OF POSITRON ANNIHILATION SPECTROSCOPY AT LEPTA FACILITY

K. Siemek, E.V. Ahmanova, M.K. Eseev, V.I. Hilinov, P. Horodek, A.G. Kobets, I.N. Meshkov, O.S. Orlov, A.A. Sidorin, JINR, Dubna, Russia

Abstract

The Positron Annihilation Spectroscopy (PAS) unit was created as a part of LEPTA project at JINR in Dubna. Currently works performed in PAS laboratory focus on studies of defects in solid state, especially on studying radiation damages in novel materials and semiconductors as a part of the international project "Novel Semiconductor for Fundamental and Applied Research". This report aims to present a current status of realization and progress in PAS methods at LEPTA facility at JINR.

INTRODUCTION

Positrons are used in materials science to study open volume defects such as vacancies, vacancy clusters and dislocations. Several positron annihilation spectroscopy (PAS) techniques exist. These methods are based on detection of the 511 keV gamma quantum. The first method is the analysis of the Doppler broadening of annihilation line and provides information about defect concentration. Both annihilation quanta can be observed. Coincidence observation of two quanta gives additional information about the environment around defect. The second method is based on lifetime concept, which allows us to distinguish type of defects. Nowadays, positron beams are of great interest for materials science. Using a low energy, monoenergetic beam it is possible to control the positron penetration depth, see Fig. 1, from the sample surface to a depth of several microns. Thus, the beam can be used to characterize thin films, analysis of surface modification, studying influence of ions on matter etc.

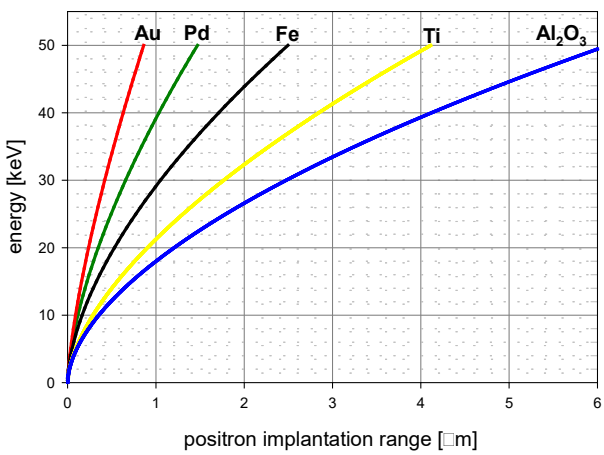

Figure 1: Dependency of positron energy on mean positron implantation depth [1].

THE DOPPLER BROADENING OF ANNIHILATION GAMMA LINE

The basics of method rely on registration energies of annihilation quanta. Due to Doppler's phenomenon quantum energies are changed according to the formula:

$$E_\gamma \cong mc^2 + E_B \pm \frac{p_\parallel c}{2}, \qquad (1)$$

where E_b is the energy of positron-electron pair coupling and $p_{||}$ is a component longitudinal to annihilation quanta direction of the pair's momentum. It is worth emphasising that positron's momentum is negligibly small in relation to electron's momentum, therefore it is usually omitted in deliberations.

The heart of Doppler broadening spectroscopy is a detector which requires a high energetic resolution. Typical available germanium detectors allow us to take measurements with resolution equal to 1-2 keV around 511 keV energy. The scheme of Doppler broadening spectrometer unit working in PAS laboratory at JINR is shown in Fig. 2. The important parameters of high purity germanium Detector (HPGe) made by Baltic Scientific Instruments working at LEPTA facility is gathered in Table 1. Next year also the second detector should appear in PAS laboratory, which will allow to perform coincidence measurements.

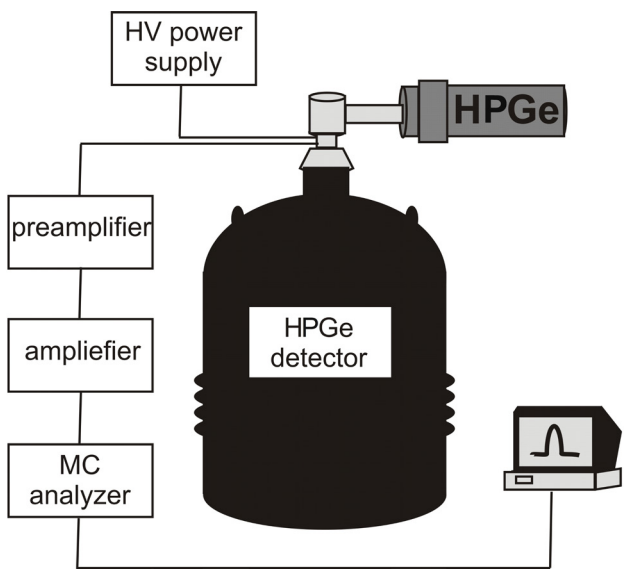

Figure 2: The scheme of Doppler broadening of annihilation gamma line 511 keV spectrometer.

ISBN 978-3-95450-181-6

Table 1: Main Parameters of HPGe Detector

Feature	Value
relative registration efficiency at 1.33 MeV-photon	30%
energy resolution FWHM for energy 511 keV	<1250 eV
peak to Compton ratio	58:1
energy range of detector operation intensity	40 ÷ 10 000 keV

In practice, information about concentration of defects is received from analysis of the shape of annihilation line, by calculating two important shape parameters, called S and W. Exemplary annihilation line as well as the rule for calculating both parameters are presented in Fig. 3.

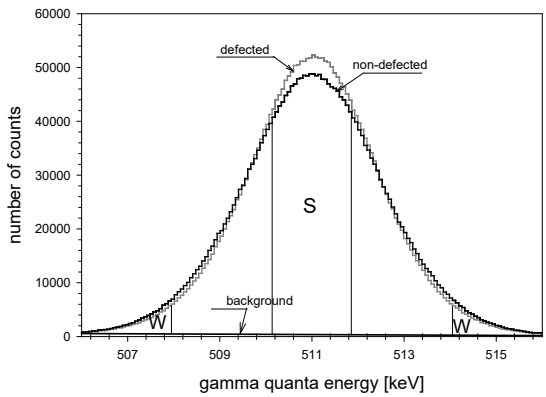

Figure 3: The annihilation lines with marked areas defining parameters S and W measured in stainless steel. The grey line comes from the defected (by sliding) sample, while the black line represents the non-defected sample.

S parameter defines proportion of annihilation of positrons with low-momentum electrons. It is closely related to concentration of defects in a material. It is defined as ratio of surface area under the central part of the 511 keV line to total surface area under this line. Areas are usually selected so that their ratio was approximately 0,5. Value of S parameter for trapped in defect positron is smaller than for a non-defected sample due to lower probability of annihilation with high-momentum core electrons during occupying vacancy position. In other words, less defected sample gives smaller broadening of the 511 keV line and bigger S parameter value. The second parameter, the so called W parameter is defined as ratio of surface area under the wing part of 511 keV line to total surface area. It is related to annihilation of positrons with high-momentum electrons and it provides information about chemical environment of the defect. Both S and W parameters are calculated after background reduction. Calculations are made by special computer software.

This method could be used to obtain information about defect concentration, its profile and defected zones range. In case of surface damaged in dozens of micrometres, i.e during cutting process standard measurements including isotope ^{22}Na could be used. Such results for cutting with various techniques, using milling, laser and water stream, AISI 304 austenitic stainless steel is presented in Fig. 4 [2]. It this case decreasing dependency of S parameter could be observed, which means that the defect profile in sample also decreases. For milling and water stream cutting defect profile is almost linear. However, the determined damaged zone range, the region where S parameter is bigger than value of S parameter obtained for well annealed sample, strongly depends on used cutting techniques and for water cutting is equal about 50 μm and for milling 150 μm. In case of laser cutting bulk value was not reached, despite 350 μm of the sample was etched. It turns out that positron spectroscopy is very useful in such studies.

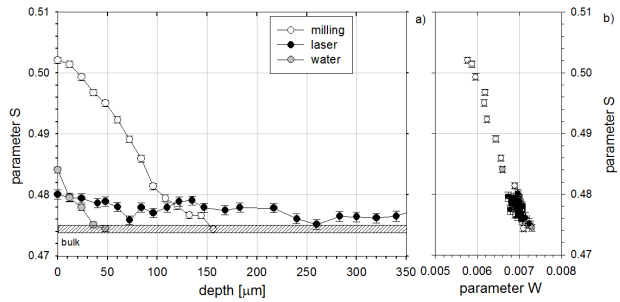

Figure 4: Dependency of S parameter on the depth below the surface for the 304 AISI stainless steel samples cut with various techniques: milling, laser and water stream. The hatched region represents the bulk value of S parameter obtained for the well-annealed RF sample. On the right, S parameter versus W parameter values from the Doppler broadening spectra are depicted. [2]

To study thin films, radiation damages a standard technique employing fast positrons implanted directly from isotope ^{22}Na source could not be used because most of positrons will penetrate the deeper, not interesting region of sample. For this case a slow positron beam with several keV energies should be applied. Slow positrons can be obtained through moderation of fast positron emitted from ^{22}Na. At JINR the moderation process is done using frozen neon. The exemplary studies of radiation damages for the iron samples irradiated with 167 MeV Xe^{26+} heavy ions with different doses from 10^{12} to 10^{14} ions/cm^2 is shown in Fig. 5 [3]. Characteristic decreasing from surface to deeper region dependency of S parameter could be observed. It is linked with diffusion of positrons to surface, which has a higher value of S parameter due to presence of oxide and surface imperfection. In deeper region, i.e. over 400 nm, the saturation of S parameter dependency could be observed. Increment of ions dose implanted to the samples gives higher value of the S parameter saturation value. The full analysis of these results is available in work [3]. It should be highlighted that positron spectroscopy is also very important in such studies.

ISBN 978-3-95450-181-6

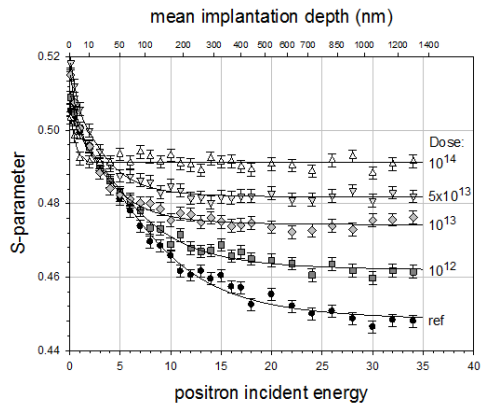

Figure 5: Variable energy positron measurements for the iron samples irradiated with 167 MeV Xe^{26+} heavy ions with different doses from 10^{12} to 10^{14} ions/cm^2 [3].

THE POSITRON LIFETIME SPECTROSCOPY

Positron lifetime spectroscopy measures the elapsed time between the implantation of the positron into the material and the emission of annihilation radiation. It is related with local electron density n_e and could be estimated as:

$$\overline{\tau} = \frac{1}{\pi r_0^2 c n_e}, \qquad (2)$$

where c is light velocity, r_0 electron radius. When positrons are trapped in open-volume defects, such as vacancies and their agglomerates, positrons stay in the locally reduced electron density of the defect. This gives longer positron lifetimes. The calculations of positron lifetime for metals and other materials show a link between number of vacancies in a cluster and measured positron lifetime. When number of vacancies rises, the positron lifetime increases too. This relation one can obtain using ab initio theoretical calculations. The performed calculations using ABINIT program for zirconium are shown in Fig. 6 [4]. Such results allow to assign the type of defect to measured experimental positron lifetime.

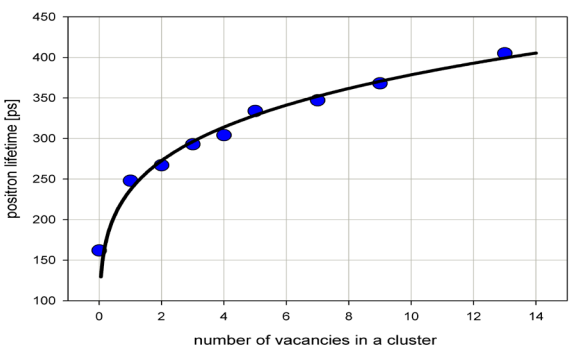

Figure 6: Positron lifetime as a function of the number of vacancies in a cluster Zr calculated using ABINIT code [3].

The positron lifetime spectroscopy measurements will start at JINR until year 2017. The collected equipment includes digital single processor APU-8002-RU and two photomultiplayers PMT H3370-50 with BaF_2 monocrystals. The scheme of positron lifetime measurements system is shown in Fig. 7.

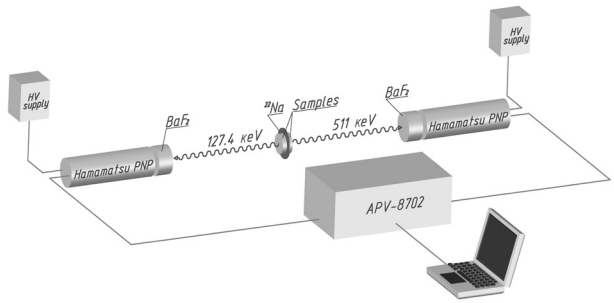

Figure 7: Scheme of positron lifetime measurement system.

SUMMARY

Positron annihilation spectroscopy measurements constitute an effective way to study surface and subsurface defects. It could be used for determination of the concentration and determination of the defect type. Currently installed apparatus allows to perform standard Doppler broadening and Variable Positron Beam measurements. Until next year positron lifetime measurements will start at LEPTA facility. In the nearest future we intend to expand our measuring system on Coincidence Doppler Spectroscopy, which would significantly reduce the background in the spectrum.

REFERENCES

[1] J. Dryzek and P. Horodek, Nucl. Instrum. Meth. B 266 (2008) 4000.
[2] P. Horodek, J. Dryzek, M. Wróbel, Tribol. Lett. 45 (2012) 341.
[3] P. Horodek, J. Dryzek, V.A. Skuratov, Rad. Phys. Chem. 122 (2016) 60.
[4] J. Dryzek and K. Siemek Tribol. Lett. 64 (2016) 15.

ISBN 978-3-95450-181-6

DEVELOPMENT OF POSITRON ANNIHILATION SPECTROSCOPY AT THE LEPTA FACILITY

I.N. Meshkov#,[1], E.V. Ahmanova, V.I. Hilinov, O.S. Orlov, A.A. Sidorin, Joint Institute for Nuclear Research, Dubna, Moscow region, Russian Federation
M.K. Eseev, Joint Institute for Nuclear Research, Dubna, Moscow region, Russian Federation and Northern (Arctic) Federal University, Arkhangelsk, Russian Federation
P. Horodek, K. Siemek, Joint Institute for Nuclear Research, Dubna, Moscow region, Russian Federation and Institute of Nuclear Physics of the Polish Academy of Sciences, Cracow, Poland
A.G. Kobets, Joint Institute for Nuclear Research, Dubna, Moscow region, Russian Federation and Institute of Electrophysics and Radiation Technologies NAS of Ukraine, Kharkov, Ukraine
[1]also at Saint Peterburg University, Saint Petersburg, Russian Federation

Abstract

The report aims to present the status of the development of the LEPTA facility for further enhancement of the positron annihilation spectroscopy (PAS) method application at the LEPTA facility. The research in solid state physics performed currently is based on slow monochromatic positron flux from the injector and Doppler PAS.

The new positron transfer channel being under construction at the LEPTA allows us to develop more advanced PAS method – so called "Positron Annihilation life-time spectroscopy" (PALS). It will enrich significantly the research program at the LEPTA. PAS method is sensitive to microdefects in solids. A pair of gamma quanta, born as a result of positron-electron annihilation carries information about the density of the defects that have the size less than 10 nm and are located at the depth from the surface of the material depending on the positron energy.

New monochromatic positron source construction supplied with the autonomous cooling system with emitter-source of the activity of 30 mCi (iThemba LABS production) and new positron transfer channel are presented in report.

DESIGN AND CONSTRUCTION OF THE TRANSFER CHANNEL

The new positron transfer channel (Fig. 1, 2) has been assembled at the LEPTA facility. It allows us to develop the advanced PAS method — so called «Positron Annihilation Life-time Spectroscopy» (PALS).

Positron lifetime spectroscopy measures the elapsed time between the implantation of the positron into the material and the emission of annihilation radiation. When positrons are trapped in open-volume defects, such as in vacancies and their agglomerates, the positron lifetime increases with respect to the defect-free sample. This is due to the locally reduced electron density of the defect. This method allow to determine defect concentration and its type.

#meshkov@jinr.ru

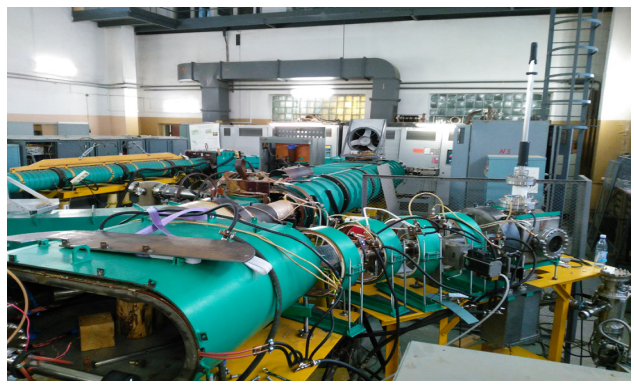

Figure 1: Positron transfer channel.

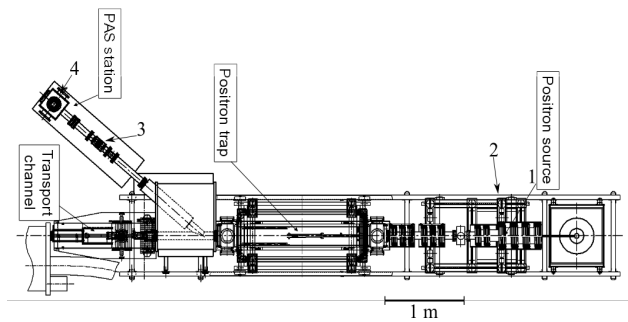

Figure 2: Scheme of the positron transfer channel.

The channel comprises four parts: cryogenic positron source equipped with closed loop LHe supply system (Fig. 3, pos. 1), pulsed voltage gap (Fig. 3, pos. 2), electrostatic acceleration gap (Fig 3, pos. 3), and the target box (Fig 3, pos. 4) containing samples to be studied by PALS method.

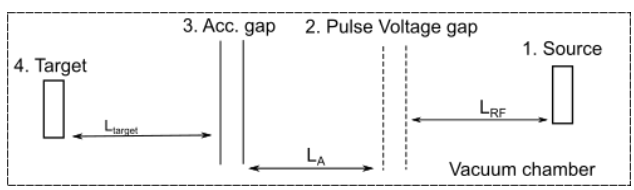

Figure 3: Scheme of the PALS method, with formation of the ordered positron flux: 1. Cryogenic positron source (Fig. 3); 2. Pulsed voltage gap; 3. Acceleration gap (electrostatic field); 4. Target — a sample for PAS studies.

ISBN 978-3-95450-181-6

The implemented method allows us to scan simply the sample in depth. Depending on the energy applied to the sample changes the depth where the positron annihilates, it gives the possibility to scan the sample thickness (Fig. 4).

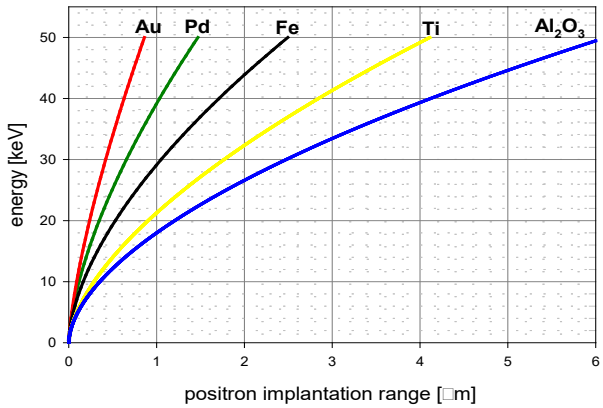

Figure 4: Dependency of positron energy on mean positron implantation depth.

In mid-November there was a beam of slow positrons at the exit of the positron channel (Fig. 5). The positron beam parameters are shown in Table 1.

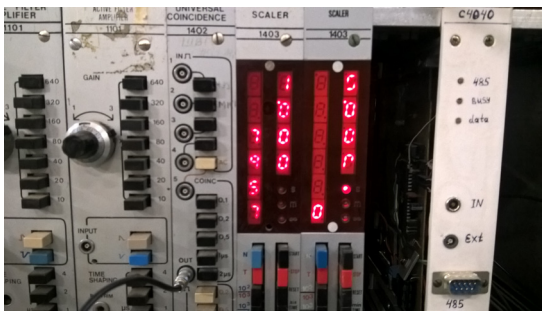

Figure 5: Positron counts at the transfer channel exit.

Table 1: General Parameters of Positron Beam

Feature	Value
Activity of ^{22}Na tablet	30 mCi
Moderator	Frozen Ne (7K) at 10^{-8}
Longitudinal magnetic	100 Gs
Vacuum conditions	10^{-6} Pa
Intensity	10^{6} e^{+}/s
Energy range	50 eV ÷ 35 keV
Diameter of the flux	3 mm

CALCULATION FOR THE TRANSFER CHANNEL

Было проведено математическое моделирование поведения позитронов в канале для PALS метода. Были определены параметры элементов канала вывода.

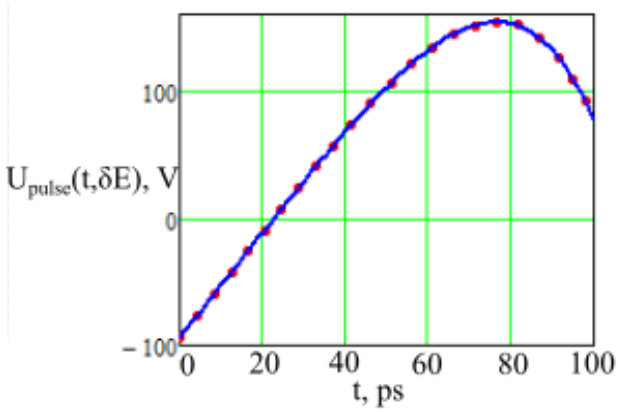

Figure 6: The pulsed voltage vs time. e+ average energy: 950 eV e+ energy spread: ··· 0; − 1.0 eV.

Figure 6 shows the voltage pulse in Voltage Pulse Gap (Fig. 3 Pos. 2) required to obtain the minimum time delays of arrival on target of the two positrons with various initial energies (Fig. 7).

The voltage pulse form V(t) (Fig. 6) is chosen as a result of numerical simulation for generation of an equidistant positron flux.

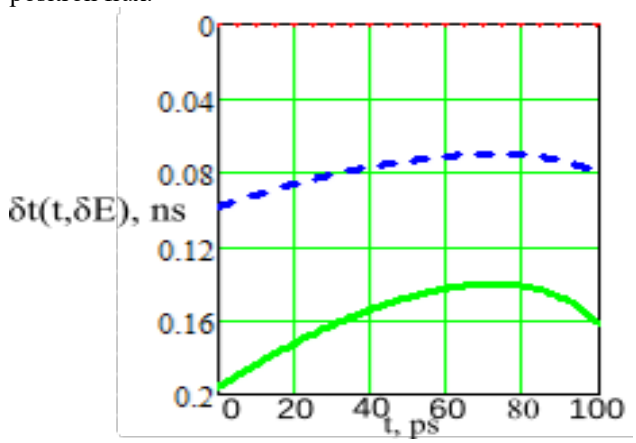

Figure 7: The difference of arrival time at the target of two positrons having different start energy eV: ••• 0; – – – 0.5; − 1.0.

New monochromatic positron source on the closed loop LHe system is based on 22Na isotope tablet of the activity of 30 mCi (iThemba LABS SAR) and cryocooler of the Sumitimo Co production. Presently the source is assembled, cooled down to 5.3 K and tested (Fig. 8). The positron flux of 10^{6} e^{+}/s is routinely generated. The flux was transported through the transfer channel in November 2016 (Fig. 5).

ISBN 978-3-95450-181-6

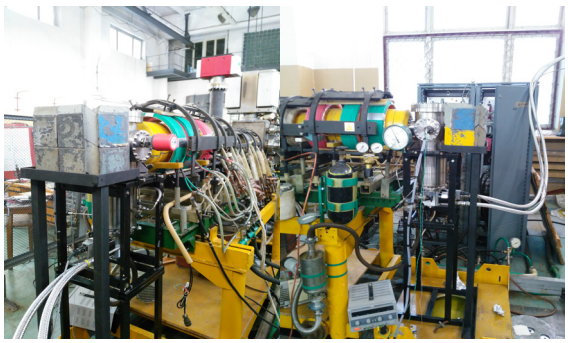

Figure 8: The autonomous cooling system.

PLANS

The next stage is experiments with a positron beam pass along the transport channel using the method of Doppler. Design and creation elements for the PALS system.

ISBN 978-3-95450-181-6

NEUTRON GENERATORS OF THE NG-10 SERIES FOR METROLOGY

D.A. Solnyshkov, G.G. Voronin, A.V. Kozlov, A.N. Kuzhlev, N.P. Mikulinas, A.V. Morozov
JSC "NIIEFA", St. Petersburg, Russia

Abstract

Neutron generators NG-10 and NG-10M with a neutron yield of $1 \cdot 10^{10}$ n/s and $2 \cdot 10^{11}$ n/s respectively have been designed in the JSC "NIIEFA". The generators are high-voltage accelerators with target devices, in which Ti-T/Ti-D targets of different diameters are used. A duoplasmotron allowing a beam current up to 5 mA to be obtained is used in the NG-10 generator, and the NG-10M employs a microwave ion source providing the beam current up to 10 mA. The power supplies, which are under a high voltage, are controlled via fiber-optic communication lines. A beam of ions produced in the ion source is accelerated up to 150 keV in a sectionalized accelerating tube, separated in mass with an electromagnetic mass-separator and focused onto a target with a doublet of electromagnetic quadrupole lenses.

The generators are equipped with several lines to transport the beam to target devices, which can be placed in separate rooms. In addition to a high and stable yield of neutrons when operating continuously, the generators can provide the pulsed mode with a time from 2 μs up to 100 μs and pulse repetition rate from 1 Hz up to 20 kHz.

INTRODUCTION

Neutron generators NG-10 [1] and NG-10M designed in NIIEFA are intended for application in metrological laboratories as apparatus generating reference neutron fluxes and can be also used for neutron-activation analysis in different fields of science and engineering. The machines are designed for neutron yields up to 10^{11} n/s in the continuous operating mode. The generators consist of a deuterium ion accelerator with an accelerating voltage continuously adjustable in the range of 120-150 keV, beam current of atomic deuterium ions on a target up to 2 mA and a series of target devices, in which Ti-T and Ti-TD targets of different diameters are used. In addition to a high and stable in time neutron yield in the continuous mode, such generators provide pulse neutron fluxes with pulse durations and pulse repetition rates varying over a broad range [2, 3].

The ion beam produced by the ion source is accelerated up to 150 keV in a sectionalized accelerating tube, separated in mass with an electromagnetic mass-separator and then focused to a target by a doublet of quadrupole electromagnetic lenses. The generators can be equipped with lines to transport beams to target devices placed in separate rooms.

VERSIONS OF ION SOURSE

A duoplasmatron-type source is used in the NG-10 generator. Duoplasmatron is the most widely used ion source applied in neutron generators. However, poisoning of the used heated cathode as a consequence of a micro leakage appeared in the discharge chamber or gas-supply system of the source makes necessary its cleaning or replacement, which requires opening of the vacuum volume and results in long-term shutdowns of the generator. The general view of the NG-10M generator is shown in Fig. 1.

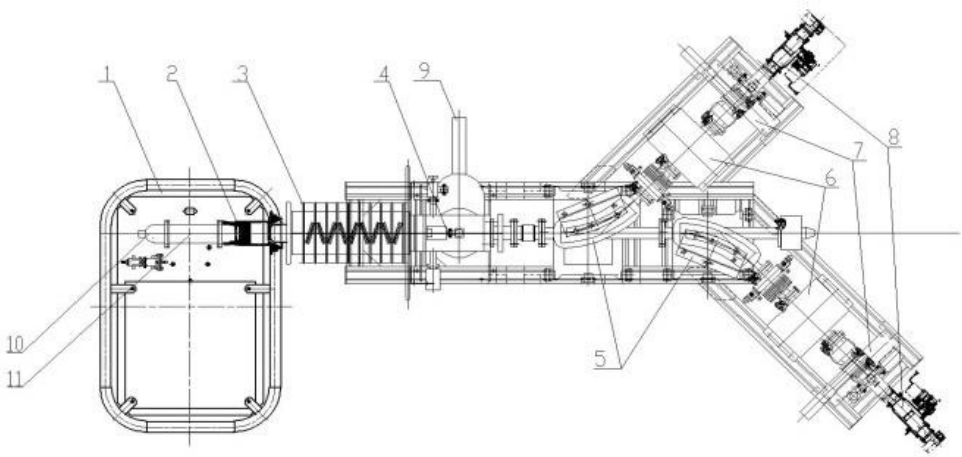

Figure 1: The NG-10M ion accelerator. General View. 1 - high-voltage terminal, 2 - ion source, 3 - accelerating tube, 4 - vacuum chamber, 5 - electromagnetic mass-separator, 6 - quadrupole lens, 7 - gate valve, 8 - target device, 9 - gate valve, 10 - magnetron, 11 - circulator.

ISBN 978-3-95450-181-6

This machine employs an ECR ion source, which in addition to highly reliable operation makes possible producing of ion beams with high optical characteristics and offers high gas and energy efficiency. The atomic component content in the beam produced by a source of similar type attains 80%.

The ECR source consists of a cylindrical discharge chamber with a dielectric window to input the microwave energy, magnetic coils intended to form a magnetic field along the chamber axis, 3-electrode "accel-decel" system for ions extraction and a system of microwave power supply. The discharge chamber is made of non-stainless steel; a movable diaphragm installed in front of the plasma electrode serves to tune the microwave system to a minimum standing wave coefficient. The microwave energy inputs the ion source chamber from a magnetron with an operating frequency of 2.45 GHz through a dielectric window. This window is made of 3 layers: a quartz disc to provide vacuum sealing, disc of silicon nitride preventing the window against back scattered electrons accelerated in the extraction gap and disk of aluminium dioxide to match the dielectric constant with the system.

To supply power to devices under high voltage, a compact isolation transformer was designed. The secondary winding of the transformer consists of 4 turns of a hv cable with an insulation designed for 160 kV placed inside ferrite cores located uniformly around the winding perimeter. The transformer operates at a frequency of 50 kHz, and its design allowed its overall dimensions and weight to be significantly reduced. Photo of the NG-10M neutron generator at a test-facility in NIIEFA is shown in Fig. 2.

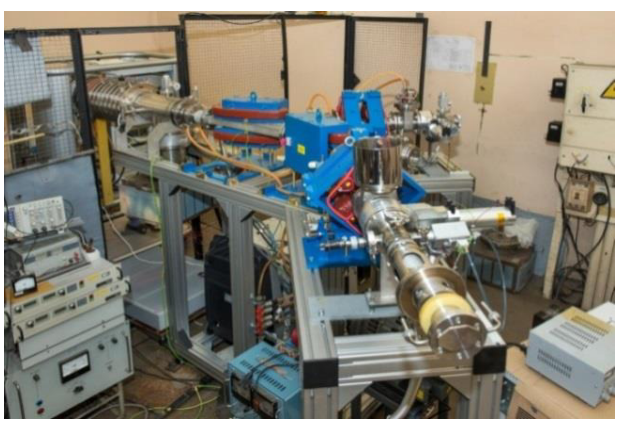

Figure 2: Neutron generator at a test facility.

VACUUM SYSTEM

The vacuum system of generators is based on the HMD-0.4 ion pump. A dry forevacuum pump is used for preliminary pumping. The HMD-0.4 pump is separated from the vacuum volume of the accelerator with a fast gate valve. The target device is connected to the accelerator vacuum system through a fast vacuum valve, which allows replacement of targets without the vacuum break in the accelerator. All vacuum valves are pneumatically driven; the process is controlled from the operator workstation. Necessary pressure in the pneumatic line is provided with a compressor, a part of the facility.

A set of targets devices, in which targets with diameter of 10, 16, 18, 23 mm can be used, was designed for the generators. Targets with the 45 mm diameter, which can be used at a high beam power, are installed in a special target device, which performs circular travel of a target relative to the ion beam.

AUTOMATIC CONTROL SYSTEM

The automatic control system performs acquisition of the data on the status of the neutron generator and its separate devices and systems and their display on the operator workstation as well as solves routine tasks of setting operating modes of the accelerator and tuning of the working parameters of separate devices. The automatic control system consists of a control cabinet, units for data receiving and transfer and operator workstation. The control cabinet houses controller blocks with expansion modules, input/output analog modules, transmitter-receiver of the optical channel for data transfer and power supply units for electronics. The unit for data receiving and transfer houses a controller with expansion modules, galvanic isolations of analog signals and transmitter-receiver of the optical communication link. The operator workstation consists of a personal computer with a monitor. The automatic control system allows the generator interaction with systems for measuring the neutron flux parameters.

The automatic control system of the neutron generator is built on the basis of the Fastwel CPM713 controller, which is the master of the Modbus TCP network, three Fastwel IO CPM713 controllers operating in the slave mode and a personal computer. All key units of the system are networked through an Ethernet switch HP 1410-16G. The software of the automatic control system consists of the five following programs:

- Program of the master controller (Fastwel CPM713).
- Program to control the injector (Fastwel IO CPM713).
- Program to control the vacuum system of the neutron generator (Fastwel IO CPM713).
- Program to control the neutron generator (Fastwel IO CPM713).
- Program of the computerized operator workstation (PC).

The Fastwel CPM713 controllers programs are developed in a special IDE Codesys v 2.3. The computerized operator workstation functions under operational system MS Windows 7. Fig. 3 shows the architecture of the automatic control system.

Controllers' programs are automatically loaded and are not directly controlled by the operator. Information about their states and control commands are transmitted in the network based on the Modbus TCP protocols via the

ISBN 978-3-95450-181-6

computerized operator workstation program. The ion source controller is placed in the high-voltage terminal cabinet, therefore an interface media converter SF-100-11S5 is used for galvanic isolation. Vacuum in the system is measured with the Meradat-manufactured measuring instrument VIT19IT2.

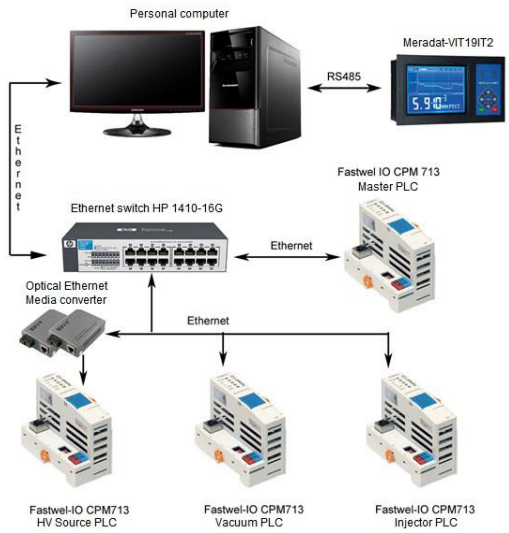

Figure 3: Architecture of the automatic control system.

The computerized operator workstation program is intended for:

- Setting the operation mode of the neutron generator.
- Control and preventing of accidents when the neutron generator is brought to its operating conditions and in the process of its operation.
- Keeping constant output parameters of the neutron generator in the process of operation.

The program is loaded automatically after the loading of the computer operational system or, if necessary, by an icon located on the desktop of MS Windows 7. General view of the user interface is given in Fig. 4.

Figure 4: The main window of the program.

The main window of the program consists of two sections. In the upper part of the window there are a panel to change-over pages of the control systems, setting buttons, unlocking buttons, buttons for logbook and exit. In the lower panel are located digital indicators of the main parameters of the neutron generator and indicators of the door and water interlocks. The most part of the window is occupied by the panel with switched-over pages of the NG sub-systems.

REFERENCES

[1] D.A. Solnyshkov et al., "The NG-10 Neutron Generator for Production of Neutron Fluxes in Continuous and Pulse Modes", RuPAC2014, Obninsk, October 2014, THPSC53, pp. 450-452.

[2] G.G. Voronin et al., "The NG-12-2 Neutron Generator", Proceed. of the 11th Intern. Conf. on Charged Particle Accelerators Applied in Medicine and Industry, St. Petersburg, October 2005, pp. 378-381.

[3] V.P. Bagrievich et al., "Neutron Generators for Production of Neutron Fluxes in Continuous and Pulse Modes", Voprosy Atomnoi Nauki i Tekhniki, series "Electrofizicheskaya apparatura", V. 5 (31), St. Petersburg, 2010, pp. 155-159.

ISBN 978-3-95450-181-6

MODIFICATIONS OF ELECTRON LINEAR ACCELERATORS PRODUCED IN NIIEFA FOR STERILIZATION

Yu.V. Zuev, A.P. Klinov, A.S. Krestianinov,O.L. Maslennikov, V.V. Terentyev
JSC NIIEFA, St. Petersburg, Russia

Abstract

The paper analyses modifications of electron linear accelerators equipped with one and the same accelerating structure produced in NIIEFA. The structure operates in the standing-wave mode at a frequency of 2856 MHz. The accelerators are designed for electron beam processing and provide beam energies in the range of 8-11 MeV and beam average powers up to 10-12 kW.

INTRODUCTION

A variety of facilities for radiation sterilization with a beam of accelerated electrons was designed and manufactured in NIIEFA [1,2].The paper outlines features of UELR-10-10S [2,6], UELR-10-10T [3], UELR-10-15S [4], LAE10/15 [5] accelerators, in which one and the same accelerating structure is used. The accelerators differ in microwave power sources, electron guns, beam scanning and extraction devices, composition and arrangement of auxiliary systems, consequently, in operational parameters and cost.

ACCELERATING STRUCTURE

All the listed above accelerators employ a biperiodic electrodynamic structure, which consisting of forty five cells placed on one axis, Fig. 1. The first ten cells form a 5-gap buncher, which provides high capture of beam in the acceleration (up to 85% of the continuous beam) and implements the beam focusing with the RF field.

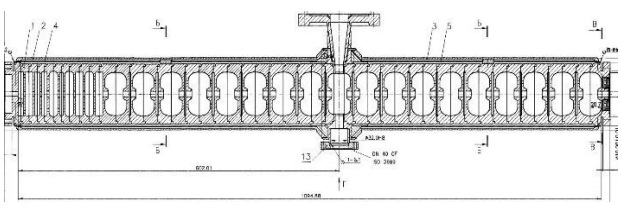

Figure 1: Layout of the accelerating structure.

Cells of the bunching part are cylindrical and U-shaped with a 3.5 mm-thick separating wall. The diameter of beam apertures in the first 4 cells of the buncher is 8 mm, and that in all the rest cells of the structure is 10 mm.

A regular part of the structure consists of Ω-shaped accelerating cells alternating with short (4 mm long) cylindrical coupling cells. Calculated values of the Q-factor and shunt-impedance of the accelerating cells are 14800 and 2.9 MΩ, respectively.

RF coupling of the cells is carried out by pairs of azimuthal slots. The working, π/2, mode of the accelerating field oscillations is excited at a frequency of fo=2856 MHz. The RF power is input to the structure through cell # 27, matching iris aperture and wave transformer. The accelerating structure length is 1.1m.

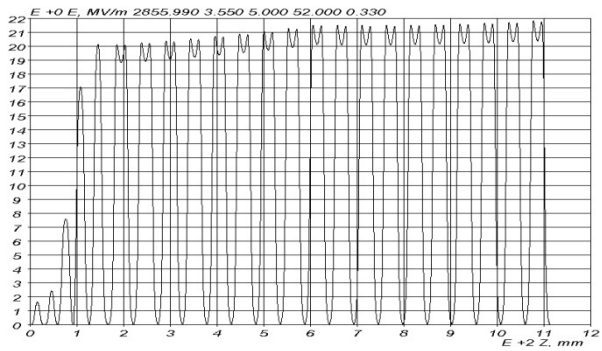

Figure 2: Field distribution on the structure axis.

The nominal distribution of the electric field in the structure is shown in Fig. 2, the energy spectrum corresponding to this field is given in Fig. 3. The electron spectrum width is not more than ±3%. The designed beam injection energy is 50 keV.

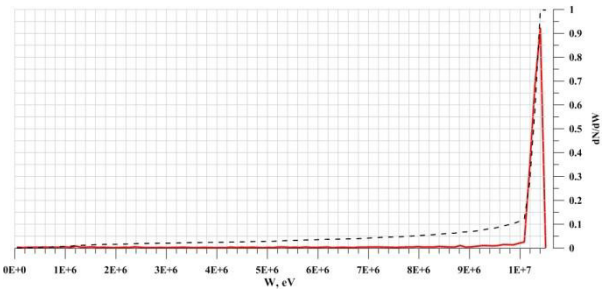

Figure 3: Energy distribution of electrons at the structure output (red solid line) and its integral (black dashed line).

THERMAL LOAD OF THE STRUCTURE

Thermal stability of the structure is maintained by a cooling jacket made of non-stainless steel and welded to the structure. To compensate the temperature non-uniformity along the structure, the cooling jacket is made double with oppositely directed water flows.

Table 1 demonstrates results of thermal and structural analysis of the structure for 2 values of the average RF power, P_W^{avr}, dissipated on the walls. Data in the table were calculated for water input temperature of 20°C and are designated as follows: Q_W is the cooling water flow rate, ΔT_W is the water heating, ΔP_W is the pressure drop, T_{MAX} is the maximum temperature and ΔL_{MAX} is the maximum displacement (strain).

ISBN 978-3-95450-181-6

Table 1: Thermoanalysis Data

P_W^{avr}, kW	7.44	11.16	11.16
Q_W, l/min	50	50	75
ΔT_W, °C	2.1	3.2	2.1
ΔP_W, atm	0.2	0.2	1.0
T_{MAX}, °C	48.2	61.5	54.4
ΔL_{MAX}, μ	19	28	22

The distribution of the maximum temperature over the structure cells is given in Fig. 4. The highest level of temperature and thermal deformations can be seen in the area of the maximum heat load and occurs in the 4th cell of the buncher [7]. Typical distributions of temperature and thermal deformations within Ω-shaped cell of the structure are shown in Fig. 5.

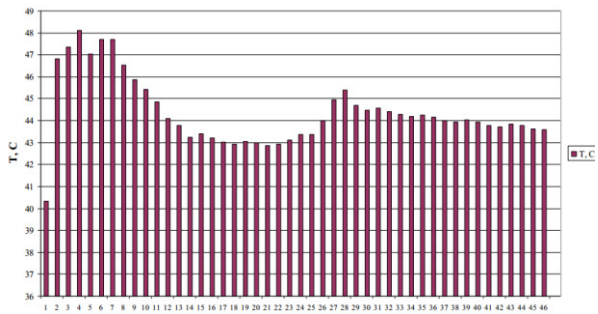

Figure 4: T_{MAX} distribution over the structure cells at P_W^{avr}=7.44 kW и Q_W=50 l/min.

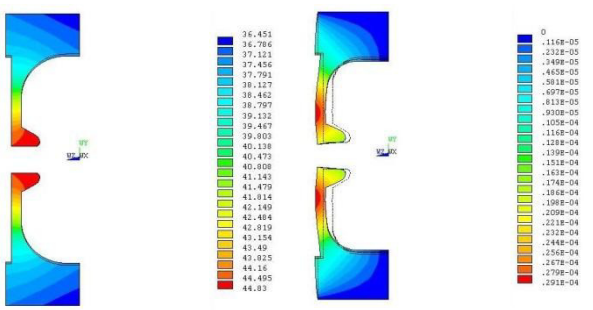

Figure 5: Typical distributions of temperature (left) and thermal deformations (right, 100:1 scale) within 1 cell of the structure.

RF POWER SYSTEMS

Table 2 shows parameters of RF power sources, which can be used for excitation of our structure and have been previously used in the accelerators. Only one device from the listed makes possible feeding the accelerator gun from the klystron modulator, hence, saving on cost. The preference of the other devices is higher average RF power, P_{RF}^{avr}, but high anode voltage, U_A, requires an additional expense for providing the breakdown strength.

The composition, arrangement, operating parameters and cost of an accelerator mostly depend on a chosen microwave source and accelerating structure.

Table 2: Klystrons with fo=2856 MHz

Model / manufacturer	**P_{RF}^{puls}, MW**	**P_{RF}^{avr}, kW**	**T^{puls}, μs**	**U_A, kV**
KIU-147A “Toriy”, Russia	6	25	16	50
“Belka” “Toriy”, Russia	6	60	10	120
TH-2158 THALES, France	5	45	25	122
TH-2173F THALES, France	5	36	26	122
VKS-8262F CPI, USA	5	36	16.3	125

Table 3 shows the accelerator design data in relation to the microwave source used. Operating parameters are designated as follows: W_B is the beam energy, P_B^{avr} is the average power of an accelerated beam; P_{INP}^{puls} (P_{INP}^{avr}) is the pulse (average) power supplied to the accelerating structure input; T_{RF} (T_B) is the RF (beam current) pulse duration, $f_П$ is the pulse repetition rate, I_B^{acc} (I_B^{inj}) is the pulse current of an accelerated (injected matched) beam.

Table 3: Accelerator Design Data

Klystron	TH-2158	KIU-147A
P_B^{avr}, kW	10-15	≥10
W_B, MeV	10	10
P_{INP}^{puls}, MW	3.7	4.7
P_{INP}^{avr}, kW	27.8	22.5
T_{RF}, μs	25	16
T_B, μs	23	≥14
$f_П$, Hz	300	300
I_B^{acc}, mA	210	300
I_B^{inj}, mA	280	350

In all the accelerators an AFC circuit is used to keep the operating frequency of the klystron tuned to the resonant frequency of the accelerating structure. The circuit is connected to a port of a ferrite circulator, which protects the klystron against the RF power reflected from the structure.

PULSE MODULATOR SYSTEMS

The high-voltage pulses necessary to drive the klystron and the accelerator gun are provided by both a solid-state modulator and a conventional line-type modulator on the basis of thyratron and PFN. The quality of formed pulses (top flatness, rise and fall time, remaining ripple, reliability and rightness of synchronization) affects significantly the accelerator performance, including an effective (time-averaged) electron energy spectrum, heat loss and background radiation.

ISBN 978-3-95450-181-6

If a klystron and accelerator diode gun have a common modulator, the head and rear parts of the beam pulse are injected to the structure with an improper accelerating field. As a result, an appreciable part of electrons does not acquire a required energy and strikes the vacuum chamber walls, notably, in the vicinity of the beam scanner magnet. The relative contribution from this phenomenon to energy loss depends on the ratio of the transient processes time to the pulse duration.

ELECTRON SOURCES

First accelerators for sterilization were equipped with diode guns followed by a beam current regulator (a short shielded solenoid, behind which a beam-limiting diaphragm was installed). Later on, diode guns were replaced for standard triode-type sources. The triode guns produced electron beam with an excess of current, but the beam was not well matched with the accelerating structure. This caused an increased loss of electrons both in the accelerating structure and in the gap of the beam scanning magnet. We had to install solenoidal lenses for additional beam focusing in the initial part of the structure and to solve the problem with the magnet vacuum chamber cooling.

At the present time the accelerators intended for sterilization are equipped with specially designed diode or triode electron sources. The sources provide an optimal injection into the structure and a minimum emittance of the beam, Fig. 6 [8]. The accelerators have no need of any external devices for beam focusing.

BEAM SCANNING SYSTEMS

In the most facilities considered in the paper, the accelerated beam extracted into the atmosphere is scanned over an area 800x20 mm in size. The scanning action results from passing the beam through the gap of a dipole magnet driven by a current waveform repeated in time with a frequency of 1-5 Hz. As a rule the scanning magnet is added with a device based on electric or permanent magnets to compensate the beam angular divergence. In special cases a two-sided irradiation is provided, for example in [4].

CONCLUSION

To date, nine accelerating structures under discussion have been manufactured. The accelerators equipped with these structures, Fig.7, are compact, have rather low manufacturing, operation and service costs. These machines have been used for electron beam sterilization of medical disposables and food processing over ten years. This year the latest accelerator in question was delivered for exploitation.

Figure 7: The UELR-10-10S accelerator in an assembling room.

REFERENCES

[1] M. Vorogushin et al., Problems of atomic science and technology. 2004. №2. Series: Nuclear Physics Investigation (43), p.208-211.

[2] M. Vorogushin et al., RuPAC'04, Dubna, THJO04, p.112 (2004); http://www.JACoW.org.

[3] M. Demsky et al., RuPAC'06, Novosibirsk, MOLP19, p.372 (2006); http://www.JACoW.org.

[4] M. Demsky et al., RuPAC'12, St. Petersburg, WEPPC052, p.547 (2012); http://www.JACoW.org.

[5] Z. Zimek et al., IAEA Publication SM-EB-31, Vienna (2009); http://www-pub.iaea.org/

[6] M. Vorogushin et al., RuPAC'12, St. Petersburg, FRXCH01, p.167 (2012); http://www.JACoW.org.

[7] V. Tanchuk, S. Grigoriev, NIIEFA Internal Report, St. Petersburg (2003).

[8] Yu. Zuev, IVECS-ICEE'14, St. Petersburg, p.308 (2014); IEEE Catalog number CFP14VES-PRT.

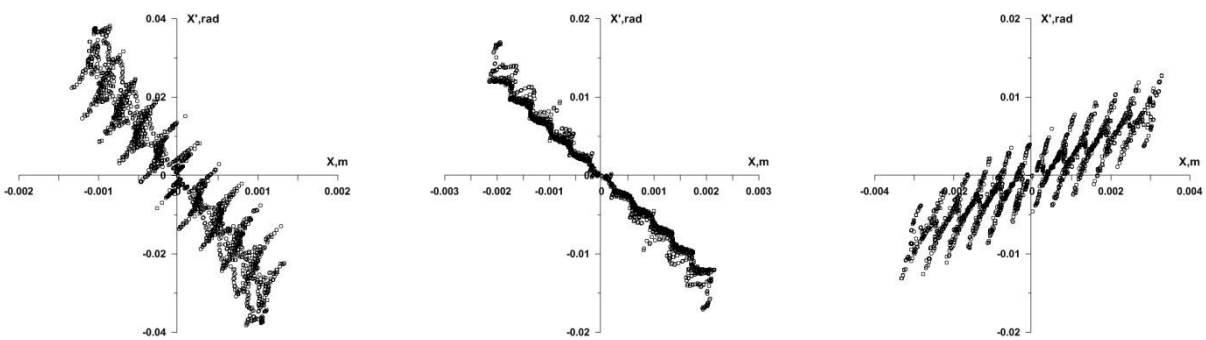

Figure 6: The beam-phase-space portraits at the output of the grid-controlled gun; I_B^{inj}=140, 350 700 mA (from left to right).

ISBN 978-3-95450-181-6

DEVELOPMENT OF THE BEAM DIAGNOSTIC SYSTEM FOR THE RADIOBIOLOGICAL RESEARCH AT THE PROTON LINEAR ACCELERATOR I-2*

A.V. Bakhmutova, N.V. Markov, A.V. Kantsyrev, A.A. Golubev,
Institute for Theoretical and Experimental Physics NRC «KI», Moscow, Russia

Abstract

At the present time at ITEP there is a possibility to investigate the biological mechanisms of the low energy protons on living systems on linear accelerator I2. The unique high current linear accelerator allows to obtain 20 MeV intense proton beams. They could be used for the radiobiological research in a wide range of absorbed doses and for different cell types. Currently some preliminary experiments were made to specify diagnostic equipment required for further investigations. This work presents the main results on the proton beam parameters measurements such as beam current, beam cross section dimension as well as the measurements of the absorbed dose and depth dose distribution using different types of detectors.

INTRODUCTION

For the last few years the distant radiation therapy with 70-230 MeV proton beam are on the rise in the world. According to PTCOG report 13 centers for proton radiation therapy are put into operation for last two years. Besides the general number of centers where the patients are irradiated, do not exceed 60 [1]. Though the amount of information has been collected for more than a half-century' history of the radiation therapy there are a set of questions needed further radiobiological investigations [2]. Now besides medical application the radiobiological research with low energy proton and ion beam of micron and submicron size develop worldwide (so-called microbeam) [3]. The main goal of this research is the biological effect investigation of charged particles on the level of single cell. It allows developing a deeper understanding of the ionizing radiation biological effect. Now at ITEP it is possible to provide the above-mentioned radiobiological research on proton linear accelerator I-2. The accelerator parameters allow to obtain high intensity proton beam with the energy approximately 20 MeV thus radiobiological investigations in the wide range of absorbed doses for different types of cells could be carried out. In this article, the made experimental setup for further radiobiological research and diagnostics system is described. Also the main results on the proton beam parameters measurements such as beam current, beam cross section dimension using different types of detectors and the measurements of the absorbed dose and depth dose distribution.

EXPERIMENTAL SETUP

For the experiment the proton beam with the energy of 24.6 MeV was used. Figure 1 gives the overview of the experimental scheme.

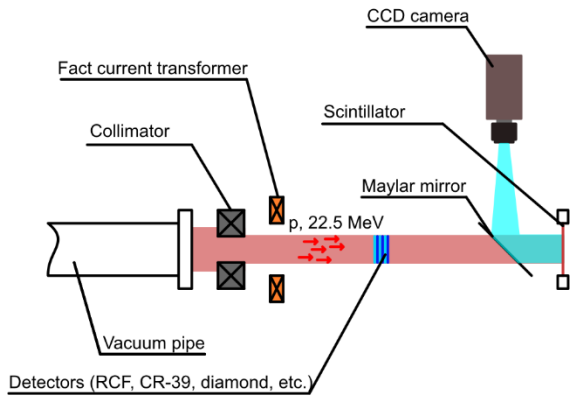

Figure 1. The view of the experimental setup.

The lateral size of the beam field in the area of measuring equipment is given by collimating system consisting of different sizes of brass collimator. The fast current transformer FCT-082 (Bergoz, France) was used as the main monitor to measure the number of particles. This detector is a broadband transformer of AC current with bandwidth of 700 MHz. The signal of current transformer is read off by oscilloscope DPO-3034 Tektronix (USA). The view is shown in Fig.2. The digitized signal send to software PTEK and the number of particles was calculated [4].

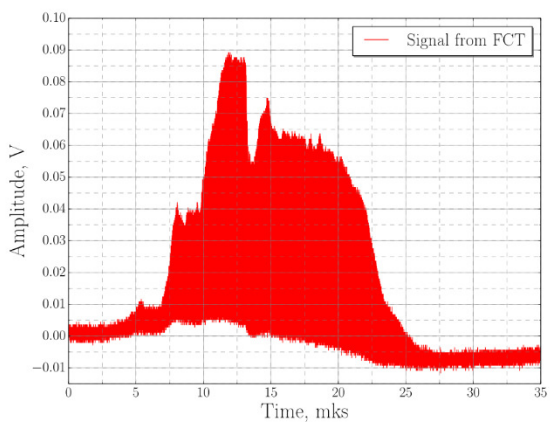

Figure 2. The output signal of FCT.

*Work supported by by the Russian Foundation for Basic Research, project no. 16-32-00393.

ISBN 978-3-95450-181-6

The particles spatial distribution in the beam cross-section was registered by optical system consists of the ceramic scintillator and CCD camera (SDU-285). The mirror made of thin metallized Mylar was used for image projection. Figures 3a and 3b give an image of the beam on scintillator with 12 mm collimator in diameter and without accordingly.

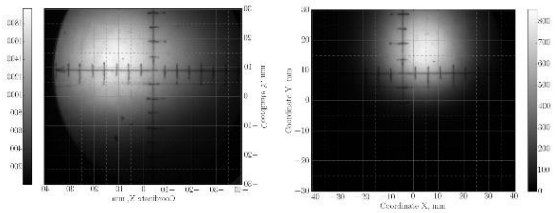

(a) (b)

Figure 3: The images of a beam on scintillator without (a) and with (b) 12 mm collimator.

The two types of radiochromic films (MD-55-2 and HD-810, GafChromic, USA) were used to measure dose depth distribution curve. This films change their color caused by irradiation. The color depth depends of absorbed dose value which is proportional to particle energy deposit. The homogenous field was formed with 12 mm diameter collimator. Two different assemblies consist of MD-55-2 and HD-810 films were irradiated. The assemblies were positioned each after each (the first one was MD-55-2).

RESULTS

Figure 4 gives a fragment of oscillograph image of output signal from FCT. The peaks locations allow determining the pulse period of micro bunches and it is 6.7 ns. The frequency of 148 MHz corresponds to this period value. This frequency is in good agreement with one of the cavity accelerating field.

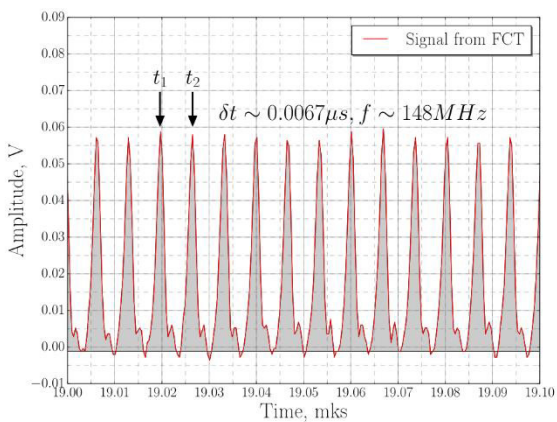

Figure 4: The image of output FCT signal.

Also the correlation between the integral value of scintillator light output and the intensity of the incoming beam were defined (Fig. 5). The beam intensity has been changing by adjusting the beam current in magnet elements of the beampipe [5].

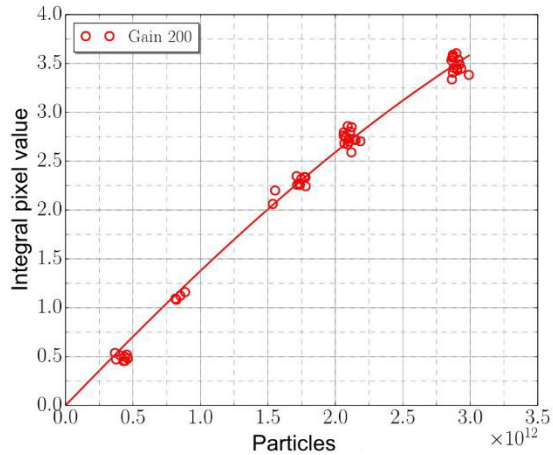

Figure 5: The relation the integral value of scintillator light and number of particles.

As it says above the radiochromic films were used to get the proton depth dose distribution. The flatbed scanner (Epson Perfection V700 Photo) was used for films digitization. The following mode was chosen: 48 bit color mode (by 16 bit for red, green, blue components), the resolution of 300 PPI, no image correction adjustment. The images are saved in TIFF (Tagged Image File Format). The irradiated scanned films of MD-55-2 and HD-810 are shown in Fig. 6a and 6b.

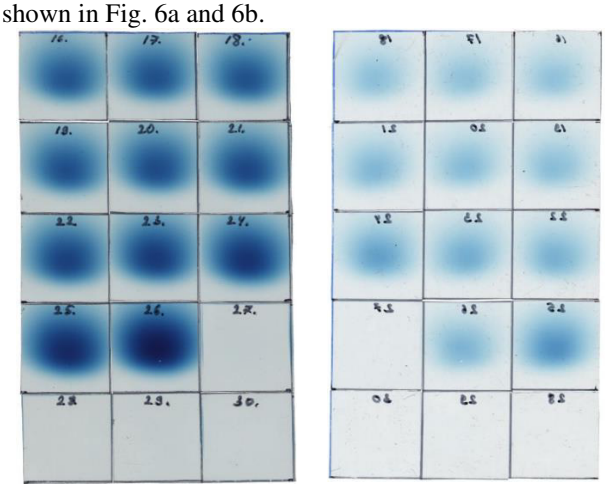

(a) (b)

Figure 6: The digitized images of MD-55-2 (a) and HD-810 (b) films.

The relation between the films optical density and the proton penetration depth is shown in Fig. 7. The width of films was recalculated to tissue equivalent one. The obtaining results were brought into comparison with calculating ones by Monte Carlo method in SRIM. At first, the proton energy at the diagnostics equipment point was determined (after 30 cm of air) as 21.5 MeV. Then using this value the relation between proton energy loss and penetration depth were obtained.

ISBN 978-3-95450-181-6

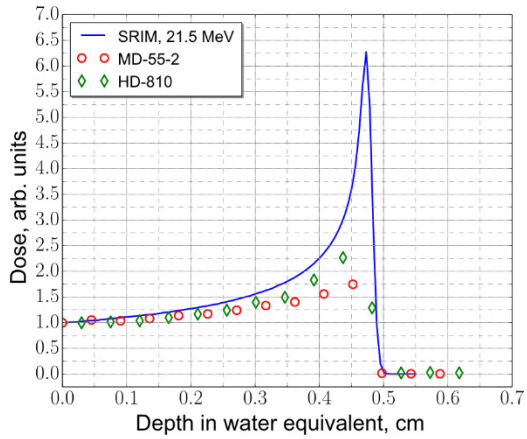

Figure 7: The energy deposition curve in water equivalent matter.

The presented results show that the Bragg Peak height is 2.25 for HD-810 and 1.75 for MD-55-22. These values differs because of films positioning in scanner and different films sensitivity. The difference is due to location of the films and sensitivity of these types of films. Though even the maximum values of the Bragg peak height obtained from HD-810 is more than double undervalue with the calculated results of the energy loss for 21.5 MeV proton in the water. The difference between experiment and calculation is due to a sensitivity reduction of the radiochromic films by increasing the proton energy deposit – Bragg peak range. The similar effect was obtained by several other experiments [6]. However, the presented results show that the location of the Bragg curve back for the calculation and experiment matches with good accuracy. Thus, we can say the beam energy defined correctly.

CONCLUSION

The obtaining experimental results show the possibility in principle of using the proton linear accelerator I-2 for radiobiological research. The design and creation of the facility with diagnostic system for further investigation has started. The homogeneous field of proton beam for different sizes was formed with the collimating system. The optical registration system based on scintillator and CCD camera was developed. The curve of energy depth distribution was measured with radiochromic films in tissue equivalent material. Also we used track detectors (CR-39) to measure the particles distribution in the beam cross section. But in view of the necessity of irradiated detectors chemical etching, the analysis of the results will be presented later.

ACKNOWLEDGMENT

Authors would like to thank the ITEP Linear accelerator I-2 group for technical support.

Work supported by the Russian Foundation for Basic Research, project no. 16-32-00393.

REFERENCES

[1] Particle Therapy Patient Statistics (per end of 2015) (2016);https://www.ptcog.ch/archive/patient_statistics/Patientstatistics-updateDec2015.pdf.
[2] Paganetti H., Phys. Med. Biol. 59. (2014) 22.
[3] Durante, M., Friedl, A.A., Radiat. Environ. Biophys. 50 (2011)3.
[4] F Markov N et al. Instr. and Exp. Techniques 57 (2014) 1.
[5] Batalin V.A. et al. Pribory i Tekhnika Eksperimenta (1967) 5.
[6] Kirby D. et al. Phys. Med. Biol. 55 (2010) 2.

ISBN 978-3-95450-181-6

MODELING OF ADSR DYNAMICS WITH PROTON LINAC IN MULTI-POINT APPROXIMATION

A. G. Golovkina*, Saint Petersburg State University, St. Petersburg, Russia

Abstract

The mathematical model of multi-point kinetics is proposed in the paper. The transients in subcritical reactor driven by proton linac taking into account the fuel and coolant temperature feedbacks are analyzed using this model. In contrast to the widely used point kinetics model, the proposed model makes it possible to more accurately take into account the heterogeneity of the material composition in the core. That is the one of the main features of transmutation systems with accelerator-driver.

INTRODUCTION

Accelerator Driven System (ADS) is a combination of high-power electronuclear neutron source with subcritical reactor [1]. In such systems external neutrons comes from the interaction of high energy proton beam with a heavy atom nucleus (spallation). ADS is of interest nowadays due to its prospects in long-living radionuclides transmutation [2], also subcritical condition in ADS provides advantages from safety standpoint in comparison with regular critical nuclear reactors.

Due to development of subcritical reactor technology for transmutation of long-living radionuclear waste, reactor cores with significant fuel spacial inhomogeneity are widely considered. Cascade system consisting of fast neutron section (plutonium fuel) and thermal neutron section (uranium fuel) can be treated as an example of such core [3,4]. During dynamical processes analysis in the reactor with fuel inhomogeneity it is necessary to calculate kinetics characteristics (prompt mean lifetime, delayed-neutron fraction) correctly [5]. These parameters depend on fission nuclides and neutron spectrum in the reactor core [6]. In this paper multi-point kinetics model is proposed. This model allows to estimate the influence of fuel inhomogeneity in the reactor core on the kinetics characteristics better, than the well-known point kinetics model [7]. It is compared with well-known point kinetics model in dynamics analysis of subcritical reactor with homogeneous and heterogeneous fuel composition driven by proton linac.

MULTI-POINTS KINETICS EQUATIONS DERIVATION

In the general case nonstationary neutron distribution in the reactor core is described by the following set of integro-differential equations [8]

$$\frac{1}{v}\frac{\partial F(\mathbf{r},E,\mathbf{n},t)}{\partial t} = -\mathbf{n}\nabla F(\mathbf{r},E,\mathbf{n},t) + \int_0^{E_0} dE' \int (1-\beta)\nu_{E'}(\mathbf{r})\Sigma_f(\mathbf{r},E')\frac{\chi(E)}{4\pi}F(\mathbf{r},E,\mathbf{n},t)d\Omega' - \Sigma_{ais}(\mathbf{r},E)F(\mathbf{r},E,\mathbf{n},t) + \sum_{i=1}^{6}\lambda_i C_i(\mathbf{r},t)\frac{\chi_{di}(E)}{4\pi} + \int_0^{E_0} dE' \int \omega(E,E',\mathbf{n}\cdot\mathbf{n}',\mathbf{r})F(\mathbf{r},E,\mathbf{n},t)d\Omega' + q(\mathbf{r},E,\mathbf{n},t), \quad (1)$$

$$\frac{\partial C_i(\mathbf{r},t)}{\partial t} = \int_0^{E_0} dE' \int \beta_i\Sigma_f(\mathbf{r},E')F(\mathbf{r},E,\mathbf{n},t)\nu_{E'}(\mathbf{r})d\Omega' - \lambda_i C_i(\mathbf{r},t).$$

Here $F(\mathbf{r},E,\mathbf{n},t)$ — neutron flux, $C_i(\mathbf{r},t)$ — concentration of the i-th energy group delayed neutron precursors, $q(\mathbf{r},E,\mathbf{n},t)$ — external source, λ_i — decay constant of i-th energy group delayed neutrons, β_i — i-th energy group delayed neutron fraction, $\beta = \sum_{i=1}^{6}\beta_i$, $\Sigma_{ais}(\mathbf{r},E)$ — macroscopic loss cross-section, $\Sigma_f(\mathbf{r},E)$ — macroscopic fission cross-section, $\nu_{E'}(\mathbf{r})$ — average number of neutrons produced per fission under the interaction of neutrons with energy E', $\omega(E,E',\mathbf{n}\cdot\mathbf{n}',\mathbf{r})$ — probability of neutrons of state $(E',\mathbf{n}')$ to move to state $(E,\mathbf{n})$ in elastic and inelastic scattering. Functions $\chi(E)$ and $\chi_i(E)$ describe normed delayed and prompt neutrons energy respectively.

Function $F(\mathbf{r},E,\mathbf{n},t)$ and $C_i(\mathbf{r},t)$ satisfy the following initial and boundary conditions

$$F(\mathbf{r}_b,E,\mathbf{n}_{in},t) = 0, \quad C_i(\mathbf{r}_b,t) = 0,$$
$$F(\mathbf{r},E,\mathbf{n},0) = \tilde{F}_0(\mathbf{r},E,\mathbf{n}), \quad C_i(\mathbf{r},0) = c_{i0}(\mathbf{r}). \quad (2)$$

Widespread point kinetics method supposes separation of spatial and temporal variables:

$$F(\mathbf{r},E,\mathbf{n},t) \approx \tilde{F}(\mathbf{r},E,\mathbf{n})\phi(t),$$

where $\tilde{F}(\mathbf{r},E,\mathbf{n})$ is a solution of corresponding stationary equation with boundary condition like Eq. (2).

Point kinetics equations are the following:

$$\frac{d\phi(t)}{dt} = \frac{\phi}{l}\left(\frac{k_{\text{eff}}-1}{k_{\text{eff}}} - \beta_{\text{eff}}\right) + \sum_{i=1}^{6}\lambda_i C_{\text{eff}i}(t) + q_{\text{eff}}(t),$$
$$\frac{dC_{\text{eff}i}(t)}{dt} = \frac{\beta_{\text{eff}i}\phi(t)}{l} - \lambda_i C_{\text{eff}i}(t), \quad (3)$$

where l — prompt average lifetime, β_{eff} — effective delayed neutron fraction, $C_{\text{eff}i}(t)$ — effective concentration of the i-th group delayed neutron precursors, $q_{\text{eff}}(t)$ — effective external neutron source intensity [9].

* a.golovkina@spbu.ru

ISBN 978-3-95450-181-6

Multi-point kinetics equation can be derived using "method of coupled zones" [10], based on the idea that neutron field in the reactor core is considered as a superposition of neutron fields produced by fission neutrons in inner and outer sections.

If we split the reactor core into n zones with fissile materials, then due to linearity the Eq. (1) can be presented as a system of n equations ($k, j = 1..n$, $k \neq j$) [7]

$$\frac{1}{v}\frac{\partial F_k(\mathbf{r},E,\mathbf{n},t)}{\partial t} = -\mathbf{n}\nabla F_k(\mathbf{r},E,\mathbf{n},t)+$$
$$\int_0^{E_0} dE' \int (1-\beta_k)\nu_{E'k}(\mathbf{r})\Sigma_{fk}(\mathbf{r},E')\frac{\chi_k(E)}{4\pi}F_k(\mathbf{r},E,\mathbf{n},t)d\Omega' -$$
$$\Sigma_{ais}(\mathbf{r},E)F_k(\mathbf{r},E,\mathbf{n},t) + \sum_{i=1}^{6}\lambda_i C_{ki}(\mathbf{r},t)\frac{\chi^k_{di}(E)}{4\pi} + \quad (4)$$
$$\int_0^{E_0} dE' \int (1-\beta_k)\nu_{E'k}(\mathbf{r})\Sigma_{fk}(\mathbf{r},E')\frac{\chi_k(E)}{4\pi}F_j(\mathbf{r},E,\mathbf{n},t)d\Omega' +$$
$$\int_0^{E_0} dE' \int \omega(E,E',\mathbf{n}\cdot\mathbf{n}',\mathbf{r})F_k(\mathbf{r},E,\mathbf{n},t)d\Omega' + q_k(\mathbf{r},E,\mathbf{n},t),$$
$$\frac{\partial C_{ki}(\mathbf{r},t)}{\partial t} = \int_0^{E_0} dE' \int \beta_{ki}\Sigma_{fk}(\mathbf{r},E')F_k(\mathbf{r},E,\mathbf{n},t)\nu_{E'k}(\mathbf{r})d\Omega' +$$
$$\int_0^{E_0} dE' \int \beta_{ki}\Sigma_{fk}(\mathbf{r},E')F_j(\mathbf{r},E,\mathbf{n},t)\nu_{E'k}(\mathbf{r})d\Omega' - \lambda_i C_{ki}(\mathbf{r},t).$$

where $F_k(\mathbf{r},E,\mathbf{n},t)$ — neutron field in the reactor core, generated by neutrons $\nu_{E'_k}(\mathbf{r})\Sigma_{fk}$, produced in k-th zone. Then Eq. (1) solution can be represented in the following form

$$F(\mathbf{r},E,\mathbf{n},t) = \sum_{k=1}^{n} F_k(\mathbf{r},E,\mathbf{n},t).$$

The same representation can be done for stationary Boltzman equation solution: $\tilde{F}(\mathbf{r},E,\mathbf{n}) = \sum_{k=1}^{n}\tilde{F}_k(\mathbf{r},E,\mathbf{n})$.

The main assumption of two-point kinetics model (deducted by analogy with point kinetics model) is the possibility of phase and time variables separation for function $F(\mathbf{r},E,\mathbf{n},t)$:

$$F_k(\mathbf{r},E,\mathbf{n},t) \approx \tilde{F}_k(\mathbf{r},E,\mathbf{n})\phi_k(t). \quad (5)$$

The system of equations adjoint to Eq. (4) can be written in the following form:

$$0 = \mathbf{n}\nabla\tilde{F}^+_k(\mathbf{r},E,\mathbf{n}) - \Sigma_{ais}(\mathbf{r},E)\tilde{F}^+_k(\mathbf{r},E,\mathbf{n}) +$$
$$+\int_0^{E_0} dE' \int \omega(E,E',\mathbf{n}\cdot\mathbf{n}',\mathbf{r})\tilde{F}^+_k(\mathbf{r},E,\mathbf{n})d\Omega' + \quad (6)$$
$$+\frac{1}{k_k}\int_0^{E_0} dE'\left((1-\beta_k)\frac{\chi_k(E')}{4\pi} + \sum_{i=1}^{6}\beta_{ki}\frac{\chi^k_{di}(E')}{4\pi}\right)\cdot$$
$$\cdot\int \nu_{E'_k}(\mathbf{r})\Sigma_{fk}(\mathbf{r},E')\tilde{F}^+_k(\mathbf{r},E,\mathbf{n})d\Omega'.$$

Here k_k — multiplication factor in k-th zone. Functions $\tilde{F}^+_k(\mathbf{r},E,\mathbf{n})$ satisfy the boundary conditions

$$\tilde{F}^+_k(\mathbf{r}_b,E,\mathbf{n}_{out}) = 0. \quad (7)$$

The traditional procedure, described in [8], is used to derive two-point kinetics equations: Eq. (4) are multiplied by $\tilde{F}^+_k(\mathbf{r},E,\mathbf{n})$ and Eq. (6) — by $F_k(\mathbf{r},E,\mathbf{n},t)$ correspondingly, then subtract the obtained expressions and integrate the result over the entire reactor volume, energy and neutrons velocity directions. Through the conjugacy of Eqs. (1) and (6), the terms taking into account neutron absorption and moderation are reduced and through boundary conditions (2) and (7) — terms describing neutron transport. As a result, taking into account assumption Eq. (5) two-point equations in similar to Eq. (3) form can be obtained ($k, j = 1..n$, $k \neq j$):

$$\frac{d\phi_k(t)}{dt} = \frac{\phi_k}{l_k}\left(\frac{k_k-1}{k_k} - \beta^k_{\text{eff}}\right) + \frac{\phi_j(t)}{l_k}\left(\varepsilon_{kj} - \beta^{kj}_{\text{eff}}\right) +$$
$$+\sum_{i=1}^{6}\lambda_i c_{ki}(t) + Q_k(t), \quad (8)$$
$$\frac{dc_{ki}(t)}{dt} = \frac{\beta^k_{\text{eff}i}\phi_k(t)}{l_k} + \beta_{\text{eff}}i^{kj}\frac{\phi_j(t)}{l_k} - \lambda_i c_{ki}(t).$$

Introduced in the Eq. (8) parameters are defined by these expressions

$$l_k = \frac{1}{\text{FNI}_k}\int_0^{E_0}\int\int dE\ d\Omega\ dV\frac{\tilde{F}_k(\mathbf{r},E,\mathbf{n})\tilde{F}^+_k(\mathbf{r},E,\mathbf{n})}{v},$$
$$Q_k(t) = \frac{1}{\text{FNI}_k l_k}\int_0^{E_0}\int\int\int dE\ d\Omega\ dV\tilde{F}^+_k(\mathbf{r},E,\mathbf{n})q(\mathbf{r},E,\mathbf{n},t),$$
$$Q_k(t) = \frac{1}{\text{FNI}_k l_k}\int_0^{E_0}\int\int\int dE\ d\Omega\ dV\ \tilde{F}^+_k(\mathbf{r},E,\mathbf{n})C_{ki}(\mathbf{r},t)\frac{\chi^k_{di}}{4\pi},$$
$$\varepsilon_{kj} = \frac{1}{\text{FNI}_k}\int_0^{E_0} dE\int d\Omega\int dV\ \tilde{F}^+_k(\mathbf{r},E,\mathbf{n})\frac{\chi_k(E)}{4\pi}\cdot$$
$$\cdot\int_0^{E_0} dE'\int \Sigma_{fk}(\mathbf{r},E')\nu_{E'_k}(\mathbf{r})\tilde{F}_j(\mathbf{r},E',\mathbf{n}')d\Omega',$$
$$\beta^{kj}_{\text{eff}i} = \frac{1}{\text{FNI}k}\int_0^{E_0} dE\int d\Omega\int dV\ \tilde{F}^+_k(\mathbf{r},E,\mathbf{n})\frac{\chi^k_{di}(E)}{4\pi}\cdot$$
$$\cdot\int_0^{E_0} dE'\int \beta_{ki}\Sigma_{fk}(\mathbf{r},E')\nu_{E'_k}(\mathbf{r})\tilde{F}_j(\mathbf{r},E',\mathbf{n}')d\Omega',$$
$$\beta^{kj}_{\text{eff}} = \sum_{i=1}^{6}\beta^{kj}_{\text{eff}i},$$

ISBN 978-3-95450-181-6

$$\mathrm{FNI}_k = \int_0^{E_0} \int \int dE\, d\Omega\, dV \tilde{F}_k^+(\mathbf{r}, E, \mathbf{n}) \cdot$$
$$\cdot \int_0^{E_0} dE' \left((1-\beta_k) \frac{\chi_k(E')}{4\pi} + \sum_{i=1}^{6} \beta_{ki} \frac{\chi_{di}^k(E')}{4\pi} \right) \cdot$$
$$\cdot \int \Sigma_{fk}(\mathbf{r}, E') \nu_{E_k'}(\mathbf{r}) \tilde{F}_k(\mathbf{r}, E', \mathbf{n}') d\Omega'.$$

Function $\tilde{F}_k(\mathbf{r}, E, \mathbf{n})$ and $\tilde{F}_k^+(\mathbf{r}, E, \mathbf{n})$ here are the solutions of stationary Boltzman equation and Eq. (6). These equations are solved numerically (Monte-Carlo method for multidimentional case or discrete ordinates method for one-dimensional). In this paper as an example one-dimensional multi-group diffusion transport model is used.

RESULTS AND ANALYSIS

To illustrate the proposed multi-point kinetics model, dynamics of ADS with homogeneous and heterogeneous reactor cores was calculated in two-point and point [11] approximation. Homogeneous reactor core with ^{235}U-fuel without moderator was divided into two sections with the same fuel composition. Heterogeneous reactor core already consists of two sections with different fuel: the inner section — ^{239}Pu-fuel and the outer one — ^{235}U-fuel with moderator ($\rho(^{12}\mathrm{C})/\rho(^{235}\mathrm{U}) = 10$). Physical characteristics of considered reactor cores are presented in Table 1 (index 0 corresponds to the whole reactor core, and indexes 1, 2 are related to the respective sections).

Table 1: Reactor Cores Main Physical Characteristics

Characteristics	Homogeneous	Heterogeneous
k_{eff}	1.0013	1.0013
k_1	0.625	0.613
k_2	0.610	0.646
β_{eff}	0.0068	0.0045
β_{eff1}	0.0068	0.00215
β_{eff2}	0.0068	0.0068
l, sec	$6.4{\cdot}10^{-7}$	$8.5{\cdot}10^{-6}$
l_1, sec	$9{\cdot}10^{-7}$	$4{\cdot}10^{-6}$
l_2, sec	$9{\cdot}10^{-7}$	$2{\cdot}10^{-5}$

In Fig. 1 functions ϕ, ϕ_1, ϕ_2 change in time for homogeneous and heterogeneous reactor core respectively using point and two-point kinetics models is shown. Figure 2 illustrates average fuel temperature change in time. From calculation result it could be seen that for homogeneous reactor cores two-point kinetics model has no advantages over point model, but in case of heterogeneous reactor cores significant difference as in flux time-component as in average temperature is observed. It can be explained by the

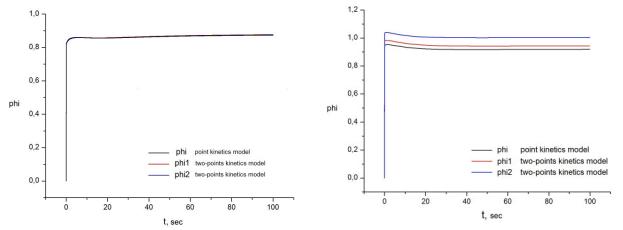

a) b)

Figure 1: Time dependence of functions ϕ, ϕ_1, ϕ_2 for reactor cores with a) homogeneous b) heterogeneous fuel composition.

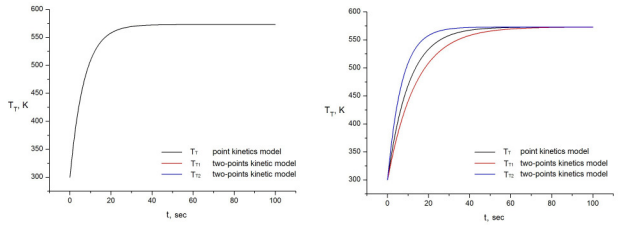

a) b)

Figure 2: Time dependence of average fuel temperature for reactor cores with a) homogeneous b) heterogeneous fuel composition.

fact, that in two-points model kinetics parameters averaging is fulfilled more accurately than in the point model (see Table 1).

CONCLUSION

Multi-point kinetics model, that can describe non-stationary processes in the reactor cores with spacial irregularity as in fuel composition as in energy neutron spectrum, is proposed. Homogeneous and heterogeneous reactor cores dynamics calculated via point and two-point kinetics models are compared. Good results agreement in case of homogeneous reactor core and significant disagreement in case of heterogeneous core are shown. The mentioned difference is explained by insufficiently correct averaged values of kinetics parameters in point model. The proposed multi-point kinetics model can be recommended for dynamical processes calculation in hybrid cascade subcritical reactors.

REFERENCES

[1] F. Carminati *et al.*, "An energy amplifier for cleaner and inexhaustible nuclear energy production driven by a particle beam accelerator", CERN, Geneva, Switzerland, Rep. CERN/AT/93-47, 1993.

[2] "Accelerator-driven Systems (ADS) and Fast Reactors (FR) in Advanced Nuclear Fuel Cycles", Tech. rep., OECD Nuclear Energy Agency, 2002.

[3] A. Golovkina, I. Kudinovich, and D. Ovsyannikov, "Power of ads with low-energy accelerator and fissionable target", *Problems of Atomic Science and Technology*, no. 4, pp. 328–332, 2013.

ISBN 978-3-95450-181-6

[4] V. Kolesov and B. Guzhovskii, "Increase of the efficiency of an electronuclear transmutation system due to a multi-sectional blanket structure", *Atomic Energy*, vol. 76, no. 2, 1994.

[5] A. Golovkina, I. Kudinovich, and D. Ovsyannikov, "Dynamics of accelerator driven subcritical reactor", in *Proc. 20th International Workshop on Beam Dynamics and Optimization (BDO'14)*, St. Petersburg, Russia, Jun.-Jul. 2014, p. 6890020.

[6] R. Avery, "Theory of Coupled Reactors", in *Proc. Second United Nations Int. Conf. on peaceful uses of atomic energy*, Geneva, Switzerland, Sept. 1958, vol. 12, pp. 182–191.

[7] A. Golovkina, "Two-point kinetics model for hybrid cascade subcritical reactor", in *Proc. Int. Conf. on "Stability and Control Processes" in Memory of V.I. Zubov (SCP'15)*, St. Petersburg, Russia, Oct. 2015, pp. 165–168.

[8] L. Usachev, "Equation for neutron importance, reactor kinetics and perturbation theory", in Proc. Int. Conf. on Peaceful Uses of Atomic Energy, Geneva, Switzerland, 1955, vol. 5, pp. 598–600.

[9] G. Keepin, *Physics of nuclear kinetics*, MA, USA: Addison-Wesley, 1965.

[10] V. Seliverstov, "Multiplication of external source neutrons in subcritical cascade systems with onedirectional neutron coupling", *Atomic Energy*, vol. 81, no. 5, pp. 378–390, 1996.

[11] A. G. Golovkina, I. V. Kudinovich, D. A. Ovsyannikov and Y. A. Svistunov, "Dynamics of processes in subcritical reactor driven by linear accelerator", in *Proc. 24th Russian Particle Accelerator Conf. (RuPAC'14)*, Obninsk, Russia, Oct. 2014, pp. 467–469.

ISBN 978-3-95450-181-6

RADIATION FROM OPEN-ENDED FLANGED WAVEGUIDE WITH DIELECTRIC LOADING *

V.V. Vorobev, S.N. Galyamin†, A.A. Grigoreva, A.V. Tyukhtin
St. Petersburg State University, 7/9 Universitetskaya nab., St. Petersburg, 199034 Russia

Abstract

Terahertz radiation is considered as a promising tool for a number of applications. One of the possible ways to emit THz waves is to pass short electron bunch through a waveguide structure loaded with dielectric [1]. Previously we considered the extraction of radiation from the open end of the waveguide with dielectric loading in both approximate and rigorous formulation [2]. We also developed a rigorous approach based on mode-matching technique and modified residue-calculus technique for the case when the waveguide with dielectric is co-axial with infinite waveguide with greater radius [3]. The study presented here is devoted to the case when the waveguide with open end has a flange and enclosed into another waveguide with a greater radius. The case of the flanged waveguide in the unbounded vacuum space can be described as the limiting case of the problem under consideration. We perform analytical calculation (based on mode-matching technique and modified residue-calculus technique) for the case of vacuum waveguide with a flange (dielectric with very high permittivity instead of flange is also considered), direct numerical simulation for this case and compare results. The case of inner waveguide with flange and dielectric filling is investigated numerically.

ANALYTICAL RESULTS

In this report, we consider 3 problems (Fig. 1). In problem (a), a semi-infinite ideally conducting ($\sigma = \infty$) cylindrical waveguide with radius b enclosed into a concentric infinite waveguide with radius $a > b$. Coaxial domain (2) is filled with a homogeneous dielectric ($\varepsilon_0 > 1$). In problem (b), coaxial part is terminated by ideally conducting flange. Problem (c) differs from (b) by filling the inner waveguide with dielectric ($\varepsilon > 1$). All structures are excited by a single TM_{0l} mode propagating from the inner waveguide. Below we present rigorous theory for the problem (a), which can be easily modified for problem (b). Problem (c) is investigated numerically. Incident field in cylindrical frame ρ, ϕ, z is

$$H_{\omega\phi}^{(i)} = J_1(\rho j_{0l}/b)e^{-\gamma_{zl}^{(1)}z}, \qquad (1)$$

where $J_0(j_{0l}) = 0$, $\gamma_{zl}^{(1)} = \sqrt{j_{0l}^2 b^{-2} - k_0^2}$, $\mathrm{Re}\gamma_{zl}^{(1)} > 0$, $k_0 = \omega/c$. The reflected field in the domain (1) is

$$H_{\omega\phi}^{(1)} = \sum_{m=1}^{\infty} B_m J_0(\rho j_{0m}/b)e^{\gamma_{zm}^{(1)}z}. \qquad (2)$$

* Work supported by Russian Foundation for Basic Research (grant No. 15-02-03913) and Government of Saint Petersburg.
† s.galyamin@spbu.ru

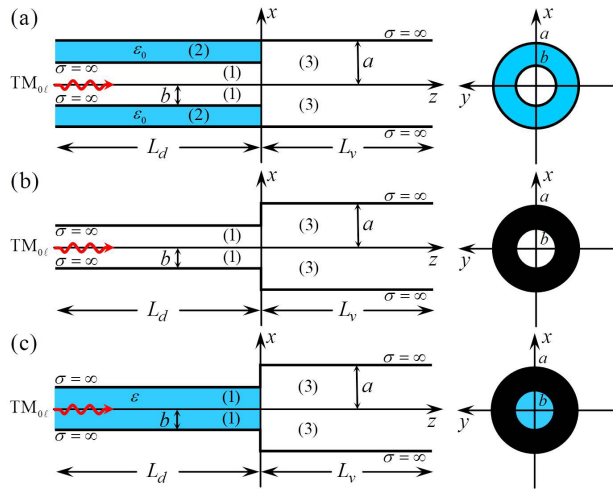

Figure 1: Geometry of the problems.

Fields generated in domains (2) and (3) are:

$$H_{\omega\phi}^{(3)} = \sum_{m=1}^{\infty} A_m J_0(\rho j_{0m}/a)e^{-\gamma_{zm}^{(3)}z}, \qquad (3)$$

$$H_{\omega\phi}^{(2)} = C_0\rho^{-1}e^{\kappa_{z0}^{(2)}z} + \sum_{m=1}^{\infty} C_m Z_m(\rho\chi_m)e^{\kappa_{zm}^{(2)}z}, \qquad (4)$$

where $\gamma_{zm}^{(3)} = \sqrt{j_{0m}^2 a^{-2} - k_0^2}$, $\kappa_{z0}^{(2)} = -ik_0\sqrt{\varepsilon_0}$, $\kappa_{zm}^{(2)} = \sqrt{\chi_m^2 - k_0^2\varepsilon_0}$, $\mathrm{Re}\gamma_{zm}^{(3)} > 0$, $\mathrm{Re}\kappa_{zm}^{(2)} > 0$,

$$Z_m(\xi) = J_1(\xi) - N_1(\xi)J_0(a\chi_m)N_0^{-1}(a\chi_m), \qquad (5)$$

χ_m is solution of dispersion relation for domain (2),

$$J_0(b\chi_m)N_0(a\chi_m) - J_0(a\chi_m)N_0(b\chi_m) = 0. \qquad (6)$$

Performing matching of $H_{\omega\phi}$ and $E_{\omega\rho} = c(i\omega\varepsilon)^{-1}\partial H_{\omega\phi}/\partial z$ for $z = 0$, and integrating separately over $0 < \rho < b$ and $b < \rho < a$ with eigenfunction of domains (1) and (2) correspondingly, we can obtain the following infinite systems for unknown coefficients:

$$\sum_{m=1}^{\infty}\left(\frac{\tilde{A}_m}{\gamma_{zm}^{(3)} - \gamma_{zn}^{(2)}} + \frac{\tilde{A}_m q_n}{\gamma_{zm}^{(3)} + \gamma_{zn}^{(2)}}\right) = 0, \qquad (7)$$

$$\sum_{m=1}^{\infty}\left(\frac{\tilde{A}_m q_n}{\gamma_{zm}^{(3)} - \gamma_{zn}^{(2)}} + \frac{\tilde{A}_m}{\gamma_{zm}^{(3)} + \gamma_{zn}^{(2)}}\right) = \frac{-4\tilde{C}_n\gamma_{zn}^{(2)}\kappa_{zn}^{(2)}}{\kappa_{zn}^{(2)} + \varepsilon_0\gamma_{zn}^{(1)}}, \qquad (8)$$

$$\sum_{m=1}^{\infty}\frac{\tilde{A}_m}{\gamma_{zm}^{(3)} - \gamma_{zp}^{(1)}} = -\delta_{lp}bJ_1(j_{0p})\gamma_{zl}^{(1)}, \qquad (9)$$

ISBN 978-3-95450-181-6

$$\sum_{m=1}^{\infty} \frac{\tilde{A}_m}{\gamma_{zm}^{(3)} + \gamma_{zp}^{(1)}} = 2\tilde{B}_p \gamma_{zp}^{(1)}, \quad (10)$$

$\gamma_{z0}^{(2)} = -ik_0$, $\gamma_{zp}^{(2)} = \sqrt{\chi_m^2 - k_0^2}$, $p = 1, 2, ..., n = 0, 1, ...,$

$$q_p = \left(\varepsilon_0 \gamma_{zp}^{(2)} - \kappa_{zp}^{(2)}\right)\left(\varepsilon_0 \gamma_{zp}^{(2)} + \kappa_{zp}^{(2)}\right)^{-1}, \quad (11)$$

$$\frac{\tilde{A}_m}{A_m} = J_0\left(\frac{b j_{0m}}{a}\right)\frac{j_{0m}}{a}, \quad \frac{\tilde{B}_p}{B_p} = \frac{bJ_1(j_{0p})}{2}, \quad (12)$$

$$\frac{\tilde{C}_0}{C_0} = \ln\left(\frac{a}{b}\right), \quad \frac{\tilde{C}_n}{C_n} = \frac{a^2}{2b}\frac{Z_n^2(a\chi_n)}{Z_n(b\chi_n)} - \frac{b}{2}Z_n(b\chi_n). \quad (13)$$

According to the residue-calculus technique [3, 4], in order to solve systems (7)–(9) one should construct the function $f(w)$ which satisfies the following conditions: (i) $f(w)$ is regular in complex plane w excluding first-order poles $w = \gamma_{zp}^{(3)}$; (ii) has first-order zeros for $w = \gamma_{zp}^{(1)}$ excluding $p = l$; (iii) $f(w) \xrightarrow[|w|\to\infty]{} w^{-(\tau_0+1/2)}$ with $\sin(\pi\tau_0) = (\varepsilon_0 - 1)/(2\varepsilon_0 + 2)$; (iv) $f(w)$ satisfies the relation $f(\gamma_{zn}^{(2)}) + q_p f(-\gamma_{zn}^{(2)}) = 0$ (v) and normalized so that $f(\gamma_{zl}^{(1)}) = bJ_1(j_{0p})\gamma_{zl}^{(1)}$. Asymptotic (iii) follows from Meixner's edge condition for $\rho = b$, $z \to +0$. It follows from (iii) and (iv) that $f(w)$ has first-order zeros $\Gamma_n^{(2)} = \gamma_{zn}^{(2)} + \pi/d\Delta_n^{(2)}$ shifted with respect to $\gamma_{zn}^{(2)}$. Considering integrals over circle C_∞ with infinite radius

$$\oint_{C_\infty} \frac{f(w)}{w - \gamma_{zp}^{(1)}} dw = \oint_{C_\infty} \left(\frac{f(w)}{w - \gamma_{zn}^{(2)}} + \frac{q_n f(w)}{w + \gamma_{zn}^{(2)}}\right) dw = 0, \quad (14)$$

$$\oint_{C_\infty} \frac{f(w)}{w + \gamma_{zp}^{(1)}} dw = \oint_{C_\infty} \left(\frac{q_n f(w)}{w - \gamma_{zn}^{(2)}} + \frac{f(w)}{w + \gamma_{zn}^{(2)}}\right) dw = 0, \quad (15)$$

we obtain $\tilde{A}_p = \mathrm{Res}\, f(\gamma_{zp}^{(3)})$, $\tilde{B}_n = -f(-\gamma_{zp}^{(1)})(2\gamma_{zp}^{(1)})^{-1}$,

$$\tilde{C}_n = \frac{\left(q_n f(\gamma_{zn}^{(2)}) + f(-\gamma_{zn}^{(2)})\right)}{4\gamma_{zn}^{(2)}\kappa_{zn}^{(2)}}\left(\varepsilon_0 \gamma_{zn}^{(2)} + \kappa_{zn}^{(2)}\right). \quad (16)$$

Function $f(w)$ can be constructed in the form

$$f = P_0 \frac{\left(w - \Gamma_0^{(2)}\right)\prod_{n=1}^{\infty}\left(1 - \frac{w}{\Gamma_n^{(2)}}\right)}{\prod_{m=1}^{\infty}\left(1 - \frac{w}{\gamma_{zm}^{(3)}}\right)} \prod_{\substack{s=1, \\ s\neq l}}^{\infty}\left(1 - \frac{w}{\gamma_{zs}^{(1)}}\right) G(w), \quad (17)$$

$$G(w) = \exp\left[-\frac{w}{\pi}\left(b\ln\left(\frac{b}{d}\right) + a\ln\left(\frac{d}{a}\right)\right)\right], \quad (18)$$

where $d = a - b$ and P_0 is chosen so that (v) is fulfilled. Condition (iii) dictates that $\Delta_n^{(2)} \xrightarrow[n\to\infty]{} \pi\tau_0/d$. Values $\Delta_n^{(2)}$ are obtained from (iv) using iteration process (see [4, 3, 5] for details).

In order to obtain solution for the problem (b), one should put $q_n = 1$ in the condition (iv) and find the shifted zeros again. In this case $C_n = 0$, and other coefficients are determined by the same formulas.

NUMERICAL CALCULATIONS AND DISCUSSION

Direct numerical simulations (using Comsol Multiphysics package) were performed in order to verify developed analytical algorithm. Moreover, in numerical simulations we consider dielectric loaded waveguides as well.

For each simulation the 3D model consists of two cylindrical "tubes" with different radii, which are connected with a flange. The length of each part is set to be ten times greater than the wavelength in the filling medium (dielectric or vacuum). The incident mode is launched and reflected/transmitted modes are received at the outer edge of each waveguide piece. Desired eigenmodes are calculated using pre-defined out-of-plane wave numbers.

Table 1: Comparison of the fractions of the transmitted W_t and reflected W_r power for the problem (b). Incident mode is TM_{01}, $\omega = 2\pi \cdot 80$ GHz, $b = 2.4$ mm.

Outer radius a	**Comsol** W_t	**Analytic** W_t	**Comsol** W_r	**Analytic** W_r
4.8 mm	93.0%	93.0%	7.0%	7.0%
9.6 mm	99.2%	99.2%	0.8%	0.8%
19.2 mm	96.8%	98.4%	3.2%	1.6%

Firstly, we compare numerical (Comsol) and analytical results for the problem (b). In the Table 1, we compare the ratios of the transmitted/reflected power to the power of the incident field for the launched TM_{01} mode with frequency 80 GHz and for different outer waveguide radius (small waveguide radius is b=2.4mm). Small waveguide has single propagating mode, while the larger waveguide can possess up to ten propagating modes depending on a. As one can see, results of both methods are in a good agreement. In addition, top plot of Fig. 2 represents distribution of the electric field absolute value for the case where a=2b=4.8mm.

Table 2: Comparison of the fractions of power transmitted into coaxial area (2) $W_t^{(2)}$, into vacuum area (3) $W_t^{(3)}$ and reflected power W_r for the problem (a) with $\varepsilon_0 = 5000$. Incident mode is TM_{01}, ω=2$\pi \cdot$ 80 GHz, b=2.4 mm.

a	$W_t^{(2)}$	$W_t^{(3)}$	W_r	Balance
4.8 mm	1.4%	91.6%	7.0%	100.0%
9.6 mm	1.0%	98.1%	0.9%	100.0%
19.2 mm	2.0%	96.8%	1.7%	100.5%

We also briefly discuss numerical results for the problem (a). It seems that for $\varepsilon_0 \to \infty$ problem (a) transforms to problem (b). Strictly speaking, this is generally not the case due to certain difference in field behavior near the edge $\rho = b$, $z \to +0$ (see [4] for details). Moreover, based on the above formulas, we have developed numerical algorithm which allows calculating mode structure for arbitrary ε_0 including very large values.

ISBN 978-3-95450-181-6

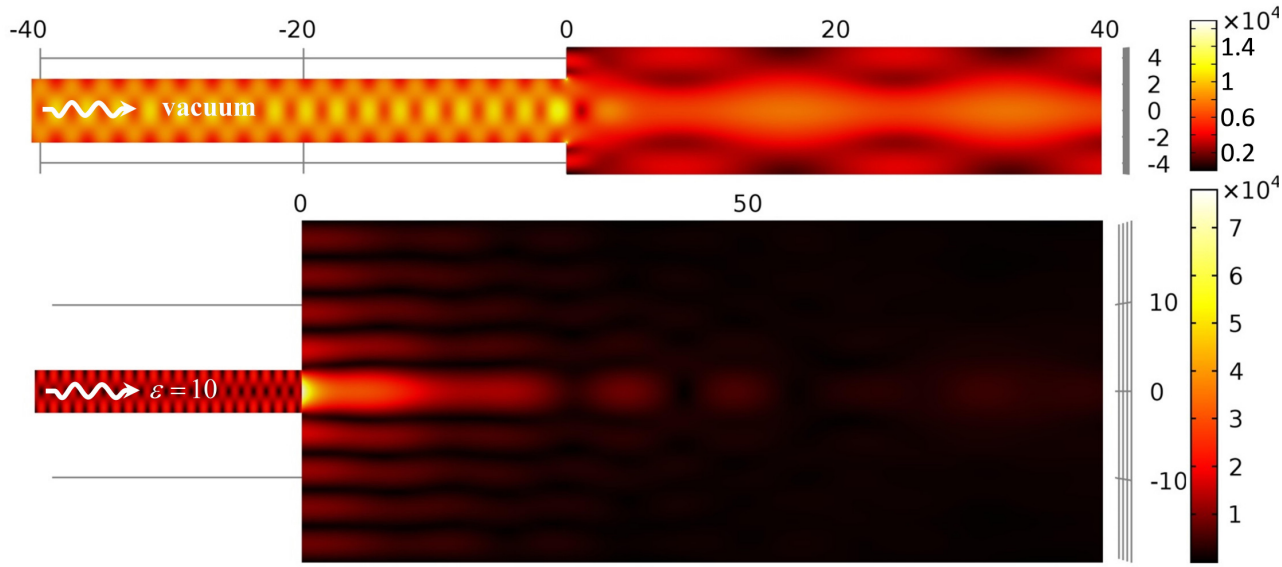

Figure 2: Distribution of the electric field absolute value for the case of the mode launching from the empty waveguide (top) and dielectric loaded waveguide (bottom), both with flanges. Structure parameters: $b = 2.4$ cm, $a = 2b$ (top), $a = 8b$, $\varepsilon = 10$ (bottom). Incident mode is TM_{01}, distances are in mm, electric field is in V/m.

Table 2 shows transmitted and reflected powers for the case (a) with $\varepsilon_0 = 5000$. Reflected power is close to that in problem (b), but power transmitted into area (3) is slightly smaller because $1-2\%$ of power goes in the coaxial waveguide despite of very high permittivity.

In numerical simulations, we also analyzed flanged waveguide with dielectric loading (problem (c)). As an example we consider material with permittivity $\varepsilon = 10$. At frequency $\omega = 2\pi \cdot 37$ GHz the dielectric waveguide has two propagating modes for $b = 2.4$ mm. In Table 3 comparison of the percentages of the reflected and transmitted power is given for different numbers of launching mode and radii a. As one can see, at a higher number of launching mode, the output power sufficiently decreases. The same situations was observed for the case of flange absence [3]. An illustration of the electric field distribution inside considered structure is given in Fig. 2, bottom row. We can see a strong evanescent field excitation near the conjunction, but the total output power is only 11% from the power of the launched mode.

CONCLUSION

We have developed rigorous theory for describing mode transformation at the discontinuity of cylindrical waveguide with dielectric layer and ideally conducting flange. For the case of vacuum flange, analytical results were in very good agreement with direct simulation using Comsol package. Moreover, analytical approach allows consideration of cases with very high permittivity (several thousands and larger). Using simulations, the case with flange and smaller radius waveguide filled with dielectric was also investigated. Compared to the case without flange, transmitted power is larger.

Table 3: Comparison of the fractions of the transmitted W_t and reflected W_r power depending on a and launching mode for problem (c); $\omega = 2\pi \cdot 37$ GHz, $b = 2.4$ mm, $\varepsilon = 10$.

Outer radius a	**Launching mode**	**Reflected power** W_r	**Transmitted power** W_t
4.8 mm	TM_{01}	82.9%	17.1%
9.6 mm	TM_{01}	85.1%	14.9%
19.2 mm	TM_{01}	89.1%	10.9%
4.8 mm	TM_{02}	99.8%	0.2%
9.6 mm	TM_{02}	99.9%	0.1%
19.2 mm	TM_{02}	99.9%	0.1%

REFERENCES

[1] S. Antipov et al., Appl. Phys. Lett. 100, 132910 (2012).

[2] S.N. Galyamin, A.V. Tyukhtin, S.S. Baturin, S. Antipov, Opt. Express 22(8), 8902 (2014).

[3] S. N. Galyamin, A. V. Tyukhtin, S. S. Baturin, V. V. Vorobev and A. A. Grigoreva, in Proc. IPAC'2016. pp. 1617-1619.

[4] R. Mittra and S. W. Lee, *Analytical techniques in the theory of guided waves* (Macmillan, 1971).

[5] S.N. Galyamin, A.V. Tyukhtin, A.M. Altmark, S.S. Baturin, WEPSB069, these proceedings.

ISBN 978-3-95450-181-6

RADIATION OF A BUNCH FLYING FROM THE OPEN END OF A WAVEGUIDE WITH A DIELECTRIC LOADING*

S.N. Galyamin†, A.V. Tyukhtin, Saint Petersburg State University, St. Petersburg, Russia
A.M. Altmark, S.S. Baturin, Saint Petersburg Electrotechnical University "LETI", St. Petersburg, Russia

Abstract

In this paper we proceed with our investigation of Terahertz emission from beam moving in waveguide structures with dielectric layer [1]. Recently we have considered an open-ended waveguide (with uniform dielectric filling) placed inside regular vacuum waveguide of a larger radius and excited by a single incident waveguide mode [2]. Here we present analytical results for the case where the structure is excited by a moving charge. We also perform simulations using CST® PS code and compare results.

THEORY

Analytical methods for investigation of various waveguide discontinuities have been developed several decades ago [3, 4]. However, the number of problems analysed by rigorous methods is quite limited; as a rule, they belong to the situation where the structure is excited by a specified waveguide mode.

Here we apply the modified residue-calculus technique to investigation of radiation from a charge (or Gaussian bunch) moving along the axis of a semi-infinite cylindrical waveguide with uniform dielectric filling and having an open end. We consider this waveguide to be placed inside coaxial infinite vacuum waveguide. This problem is of interest in the context of development of Terahertz radiation source based on waveguide structures loaded with dielectric and excited by short electron bunch [5].

Geometry of the problem under consideration is shown in Fig. 1. A semi-infinite ideally conducting ($\sigma=\infty$) cylindrical waveguide with radius b filled with a homogeneous dielectric ($\varepsilon>1$) is put into a concentric infinite waveguide with radius $a>b$. A point charge q moves along the axis with constant velocity $\vec{V}=\beta c\vec{e}_z$. Fourier harmonic of the magnetic component of the incident field has the following form (cylindrical frame r,φ,z is used):

$$H^{(i)}_{\omega\varphi}=\frac{iq\tilde{s}}{2c}\left[H_1^{(1)}(r\tilde{s})-\frac{H_0^{(1)}(\tilde{r}\tilde{s})}{J_0(\tilde{r}\tilde{s})}J_1(r\tilde{s})\right]e^{i\omega z/V}, \quad (1)$$

where $\tilde{r}=b$, $\tilde{s}=s=\sqrt{\omega^2V^{-2}(\varepsilon\beta^2-1)}$ for $z<0$, and $\tilde{r}=a$, $\tilde{s}=s_0=\sqrt{\omega^2V^{-2}(\beta^2-1)}$ for $z>0$ ($\operatorname{Im}\tilde{s}>0$). The reflected field in the domain (1) is

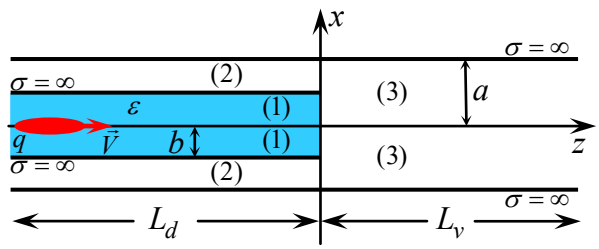

Figure 1: Geometry of the problem.

$$H^{(1)}_{\omega\varphi}=\sum_{m=1}^{\infty}B_mJ_0(rj_{0m}/b)e^{\kappa^{(1)}_{zm}z}, \quad (2)$$

where $J_0(j_{0m})=0$, $\kappa^{(1)}_{zm}=\sqrt{j_{0m}^2b^{-2}-k_0^2\varepsilon}$, $\operatorname{Re}\kappa^{(1)}_{zm}>0$, $k_0=\omega/c$. The fields generated in domains (2) and (3) can be presented by the following series:

$$H^{(3)}_{\omega\varphi}=\sum_{m=1}^{\infty}A_mJ_0(rj_{0m}/a)e^{-\gamma^{(3)}_{zm}z}, \quad (3)$$

$$H^{(2)}_{\omega\varphi}=C_0r^{-1}e^{\gamma^{(2)}_{z0}z}+\sum_{m=1}^{\infty}C_mZ_m(r\chi_m)e^{\gamma^{(2)}_{zm}z}, \quad (4)$$

where $\gamma^{(3)}_{zm}=\sqrt{j_{0m}^2a^{-2}-k_0^2}$, $\gamma^{(2)}_{z0}=-ik_0$, $\gamma^{(2)}_{zm}=\sqrt{\chi_m^2-k_0^2}$, $\operatorname{Re}\gamma^{(2,3)}_{zm}>0$,

$$Z_m(\xi)=J_1(\xi)-N_1(\xi)J_0(a\chi_m)N_0^{-1}(a\chi_m), \quad (5)$$

χ_m is the solution of the dispersion relation for the domain (2),

$$J_0(b\chi_m)N_0(a\chi_m)-J_0(a\chi_m)N_0(b\chi_m)=0. \quad (6)$$

Performing the matching of the components $H_{\omega\varphi}$ and $E_{\omega r}=c(i\omega\varepsilon)^{-1}\partial H_{\omega\varphi}/\partial z$ for $z=0$, and integrating these relations separately over $0<r<b$ with $J_0(rj_{0m}/a)$ and over $b<r<a$ with $Z_m(r\chi_m)$, after cumbersome calculations we obtain the following infinite systems for unknown coefficients:

$$\sum_{m=1}^{\infty}\left(\frac{\tilde{A}_m}{\gamma^{(3)}_{zm}-\gamma^{(1)}_{zp}}+\frac{\tilde{A}_m\rho_p}{\gamma^{(3)}_{zm}+\gamma^{(1)}_{zp}}\right)+\frac{q}{4j_{0p}cJ_1(j_{0p})}\times$$
$$\times\left[\left(\pi bs_0^2J_1(j_{0p})h_0-2ij_{0p}b^{-1}\right)\left(F^-_{vp}+\rho_pF^+_{vp}\right)+\right. \quad (7)$$
$$\left.+F^+_{dp}+\rho_pF^-_{dp}\right]=0,$$

*Work supported by the Grant of the President of Russian Federation (No. 6765.2015.2) and the Grants from Russian Foundation for Basic Research (No. 15-32-20985).
† s.galyamin@spbu.ru

ISBN 978-3-95450-181-6

$$\sum_{m=1}^{\infty}\left(\frac{\tilde{A}_m\rho_p}{\gamma_{zm}^{(3)}-\gamma_{zp}^{(1)}}+\frac{\tilde{A}_m}{\gamma_{zm}^{(3)}+\gamma_{zp}^{(1)}}\right)+\frac{q}{4j_{0p}cJ_1(j_{0p})}\times$$

$$\times\left[\left(\pi bs_0^2J_1(j_{0p})h_0-2ij_{0p}b^{-1}\right)\left(\rho_pF_{vp}^{-}+F_{vp}^{+}\right)+\right. \quad (8)$$

$$\left.+\rho_pF_{dp}^{+}+F_{dp}^{-}\right]=4\gamma_{zp}^{(1)}\kappa_{zp}^{(1)}\tilde{B}_p\Big/\left(\kappa_{zp}^{(1)}+\varepsilon\gamma_{zp}^{(1)}\right),$$

$$\sum_{m=1}^{\infty}\frac{\tilde{A}_m}{\gamma_{zm}^{(3)}-\gamma_{zn}^{(2)}}+\frac{iq}{2c}\frac{s_0^2h_0}{\omega/(iV)-\gamma_{zn}^{(2)}}=0\,, \quad (9)$$

$$\sum_{m=1}^{\infty}\frac{\tilde{A}_m}{\gamma_{zm}^{(3)}+\gamma_{zn}^{(2)}}+\frac{iq}{2c}\frac{s_0^2h_0}{\omega/(iV)+\gamma_{zn}^{(2)}}=-2\tilde{C}_n\gamma_{zn}^{(2)}\,, \quad (10)$$

$$h_0=H_0^{(1)}(bs_0)-H_0^{(1)}(as_0)J_0(bs_0)\Big/J_0(as_0)\,, \quad (11)$$

$$F_{dp}^{\pm}=\frac{2ij_{0p}}{\pi b}\left(\frac{\omega}{iV\varepsilon}\pm\gamma_{zp}^{(1)}\right)\left[s^2-(j_{0p}/b)^2\right]^{-1}, \quad (12)$$

$$F_{vp}^{\pm}=2ij_{0p}(\pi b)^{-1}\left(\omega/(iV)\pm\gamma_{zp}^{(1)}\right)^{-1}, \quad (13)$$

$$\rho_p=\left(\varepsilon\gamma_{zp}^{(1)}-\kappa_{zp}^{(1)}\right)\left(\varepsilon\gamma_{zp}^{(1)}+\kappa_{zp}^{(1)}\right)^{-1}, \quad (14)$$

$$\frac{\tilde{A}_m}{A_m}=J_0\left(\frac{bj_{0m}}{a}\right)\frac{j_{0m}}{a}\,,\quad \frac{\tilde{B}_p}{B_p}=\frac{bJ_1(j_{0p})}{2}\,, \quad (15)$$

$$\frac{\tilde{C}_0}{C_0}=\ln\left(\frac{a}{b}\right),\quad \frac{\tilde{C}_n}{C_n}=\frac{a^2}{2b}\frac{Z_n^2(a\chi_n)}{Z_n(b\chi_n)}-\frac{b}{2}Z_n(b\chi_n)\,. \quad (16)$$

According to the residue-calculus technique [2, 3], in order to solve the systems (7)–(10) one should construct the function $f(w)$ regular in the complex plane w (excluding first-order poles $w=\omega/(iV)$, $w=\gamma_{zm}^{(3)}$), having certain first-order zeros and satisfying condition $f(w)\xrightarrow[|w|\to\infty]{}w^{-(\tau+1/2)}$ with $\sin(\pi\tau)=(\varepsilon-1)/(2\varepsilon+2)$ (consequence of Meixner's edge condition [3] for $r=b$, $z\to+0$). Considering the integrals over the circle C_∞ with infinite radius

$$\oint_{C_\infty}\frac{f(w)}{w\pm\gamma_{zn}^{(2)}}dw=\oint_{C_\infty}\left(\frac{f(w)}{w\mp\gamma_{zp}^{(1)}}+\frac{\rho_pf(w)}{w\pm\gamma_{zp}^{(1)}}\right)dw=0\,, \quad (17)$$

calculating them using residue theorem and comparing the result with (7)–(10), we obtain

$$\tilde{A}_p=\mathrm{Res}\,f(\gamma_{zp}^{(3)})\,,\quad \tilde{C}_n=f(-\gamma_{zn}^{(2)})(2\gamma_{zn}^{(2)})^{-1}, \quad (18)$$

$$\tilde{B}_p=\left(\varepsilon\gamma_{zp}^{(1)}+\kappa_{zp}^{(1)}\right)\Big/\left(4\gamma_{zp}^{(1)}\kappa_{zp}^{(1)}\right)\left(\frac{iq}{2cb}\left(\rho_pF_{dp}^{+}+F_{dp}^{-}\right)-\right.$$

$$\left.-\rho_pF_{vp}^{-}-F_{vp}^{+}-\rho_pf(\gamma_{zp}^{(1)})-f(-\gamma_{zp}^{(1)})\right). \quad (19)$$

Function $f(w)=Pg(\omega)$, where

$$g(w)=\frac{(w-\gamma_{z0}^{(2)})\prod_{n=1}^{\infty}\left(1-\frac{w}{\gamma_{zn}^{(2)}}\right)}{\prod_{m=1}^{\infty}\left(1-\frac{w}{\gamma_{zn}^{(3)}}\right)}\prod_{s=1}^{\infty}{}^{(l)}\left(1-\frac{w}{\Gamma_s}\right)Q(w)\,, \quad (20)$$

$$Q(w)=\exp\left[-\frac{w}{\pi}\left(b\ln\left(\frac{b}{a-b}\right)+a\ln\left(\frac{a-b}{a}\right)\right)\right], \quad (21)$$

$P=iqs_0^2h_0[2cg(-i\omega/V)]^{-1}$ and shifted zeros $\Gamma_s=\gamma_{zs}^{(1)}+\pi\Delta_s/b$ are found by iterations from

$$f(\gamma_{zp}^{(1)})+\rho_pf(-\gamma_{zp}^{(1)})=$$

$$=iq\left(F_{dp}^{+}+\rho_pF_{dp}^{-}-F_{vp}^{-}-\rho_pF_{vp}^{+}\right)\Big/\left(2cbJ_1(j_{0p})\right), \quad (22)$$

which result in nonlinear infinite system

$$\frac{\pi}{b}\Delta_p=\frac{G_pu_p\left[\Gamma_p-\omega/(iV)\right]-2\gamma_{zp}^{(1)}\rho_p}{\upsilon_{p+}+\rho_p\upsilon_{p-}}\,, \quad (23)$$

$$u_p=g(w)\frac{w-\omega/(iV)}{1-w/\Gamma_p}\bigg|_{w=\omega/(iV)}\,,\quad \upsilon_{p\pm}=\frac{g(\pm\gamma_{zp}^{(1)})}{1\mp\gamma_{zp}^{(1)}/\Gamma_p}\,, \quad (24)$$

$$G_p=\left(F_{dp}^{+}+\rho_pF_{dp}^{-}-F_{vp}^{-}-\rho_pF_{vp}^{+}\right)\Big/\left(bJ_1(j_{0p})s_0^2h_0\right). \quad (25)$$

Meixner's edge condition dictates that $\Delta_s\to\tau$ for $s\to\infty$, which gives convenient zero-order approximation for Δ_s and allows controlling the iteration process convergence. The described approach gives the modes excitation coefficients for the given frequency ω. It should be also noted that the substitution $q\to q\exp(-\omega^2\sigma_g^2V^{-2})$ in the formulas above gives the result for the case of Gaussian bunch of length σ_g.

RESULTS

The key problem of the described theoretical approach is the determination of the shifted zeros Γ_m from the relation (23). Iteration process is organized as follows. We fix quantity N of Δ_m to be found. For the zero-order approximation, we put $\Delta_m=\tau$ for all m and calculate first-order approximation for Δ_m, $m=1,2,...N$. Then we substitute found Δ_m in the right-hand side of (23) and calculate second-order approximation, etc. After iterations have converged, we compare Δ_N with τ: if $\Delta_N=\tau$ within accepted accuracy, process is stopped, otherwise we change N and/or accuracy of calculations and repeat.

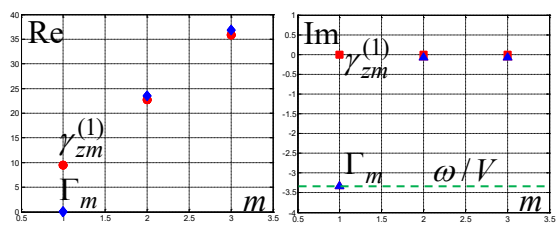

Figure 2: Shifting for first 3 zeros.

For the numerical simulation in CST® PS suite [6], we have chosen the following parameters: $b=0.24$cm, $\varepsilon=10$, $a=0.90$cm, $\beta=0.9999$, 1nC Gaussian bunch with

ISBN 978-3-95450-181-6

$\sigma_g = 0.5\text{cm}$. In this case, the incident field (1) in dielectric waveguide contains only first Cherenkov mode with frequency $\omega_{1\text{Cher}} = 2\pi \cdot 16\,\text{GHz}$ (for this frequency $s = j_{01}/b$), other modes are suppressed by the factor $\exp(-\omega^2\sigma_g^2 V^{-2})$. The reflected (2) and transmitted (3), (4) fields contain a single propagating mode, other modes are evanescent. Analytical calculations have been performed for $\omega = \omega_{1\text{Cher}}$. We used $N = 80-100$, and system (23) got converged at around 10 iterations with 0.001 accuracy.

Figure 2 shows how the first 3 zeros Γ_m are shifted with respect to $\gamma_{zm}^{(1)}$: essential shift appears for Γ_1 only, Γ_1 is purely imaginary (while $\gamma_{z1}^{(1)}$ was purely real) and $\Gamma_1 \approx \omega/(iV)$. As one can show, $P \sim g^{-1}\left(\omega/(iV)\right) \sim \left(1-\omega/(iV\Gamma_1)\right)^{-1}$, therefore frequency

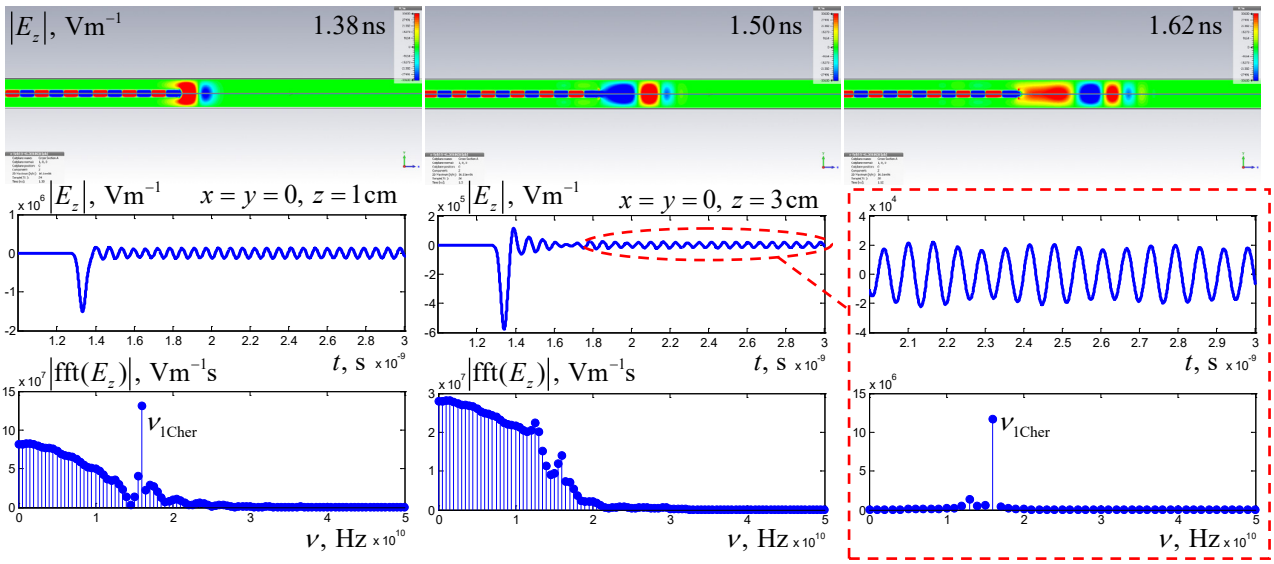

Figure 3: Simulated field distribution (top), signals from probes located on $z-$axis (middle) and spectra of these signals (bottom). Structure lengths for simulations are $L_d = 35\,\text{cm}$, $L_v = 50\,\text{cm}$. Full time of bunch propagation through the structure is $3\,\text{ns}$.

spectrum of coefficients A_m, B_m and C_m contains pole which corresponds to $\omega_{1\text{Cher}}$. Contribution of this pole describes reflected and transmitted Cherenkov wave.

Figure 3 shows the results of simulations. From two-dimensional field distribution (upper row) we can see some wave process in the domain (3) (larger radius vacuum waveguide). Field dependencies obtained from two probes (middle row) show relatively weak quasi-harmonic signal after strong peak which presents Coulomb field. Fast Fourier transforms of these signals (lower row) show that a harmonic $\omega_{1\text{Cher}} = 2\pi \cdot \nu_{1\text{Cher}}$ is clearly expressed in the signal from the first probe. Signal from the second probe contains a lot of secondary harmonics, and Cherenkov harmonic can be clearly seen in the reduced signal (from 2ns to 3ns).

CONCLUSION

In this report, we have presented rigorous theory for describing radiation from the open end of a cylindrical waveguide with dielectric filling in the case where it is enclosed in vacuum waveguide with larger radius and is excited by the charge (or Gaussian bunch) passing along the structure axis. In particular, we have shown that spectra of transmitted and reflected modes contain frequency corresponding to Cherenkov radiation in dielectric waveguide. We have also performed direct numerical simulation of electromagnetic field excitation in such structure using CST® PS code. Results are in qualitative agreement since the simulated signal contains Cherenkov frequency obtained theoretically.

REFERENCES

[1] S.N. Galyamin, A.V. Tyukhtin, S.S. Baturin, S. Antipov, Opt. Express 22(8) 8902 (2014).
[2] S.N. Galyamin, A.V. Tyukhtin, S.S. Baturin, V.V. Vorobev, A.A. Grigoreva, in Proc. IPAC'16, pp. 1617-1619.
[3] R. Mittra and S. W. Lee, *Analytical techniques in the theory of guided waves* (Macmillan, 1971).
[4] L. Weinstein, *The Theory of Diffraction and the Factorization Method* (Golem Press, 1969).
[5] S. Antipov et al., Appl. Phys. Lett. 100, 132910 (2012).
[6] http://www.cst.com

ISBN 978-3-95450-181-6

CHARGED BEAMS OPTICAL PROPERTIES OF SCATTERING MEDIA

V.G.Kurakin, P.V.Kurakin, Lebedev Physical Istitute, Moscow, Russia

Abstract

Distribution function for scattering angle and transverse displacement is used to derive the phase-plane portrait transformation in scattering medium for incoming charged particle beam. The phase-plane portrait of scattered beam depends strongly on incoming beam ellipse proportions and orientation, and simple matching conditions and expression has been derived. It is shown as well that in heterogeneous medium incident beam experiences trajectory refraction and reflection at the out coming medium border. Reflection criterion had been derived. This feature of scattering media may be used for beam control in accelerator based application.

INTRODUCTION

Metallic foil and dielectric films on charged particle beam path are quit natural elements of accelerators, storage rings and beam lines. These used for example for vacuum volumes separation, may serve as beam targets for various functions, as extraction window. Together with desired functionality, beam emittance growth is usually undesired consequent of beam-target interaction. For some application detail beam characteristic after its interaction with target are quit necessary. For example, this is true in the case when extracted beam is directed to experiment area and has to be matched with beam line optics. Another example is a target in tagged photons experiment in ecologically clean energy recovery accelerator [1]. Here electrons directed to accelerator after target and precise tuning of scattered beam is necessary to avoid particle losses. Charge exchanged injection into ion accelerator or storage ring is accompanied by multiple interaction of stored bunches with stripping target and bunch phase portrait evolution is desired for adequate storage process description.

Multiple Coulomb scattering of moving charges is the main process in media that results in emittance growth. We use classical distribution function for charged particle being scattered in media to explore particle dynamics, phase space concept being used. The concept of beam matching with scattering media is introduced and formula for beam emittance growth for matched beam has been derived. Distribution function for scattering in homogeneous infinite media is used to explore off normal incidence of a charge on a scattering plate. Formula connecting critical angle and media and particle parameters for the reflection phenomena is derived.

PHASE PORTRAIT OF SCATTERED BEAM

Let us imaging needle-shaped charged particle beam that moves in x direction and traverses a plate (target) from homogeneous material, placed perpendicular to x axis. Beam particles interact with target nuclei and change there impulses. We neglect energy lost and concentrating ourselves on transverse motion. One may consider particle motion the same for any transverse coordinate for homogeneous infinite scattering media. In such assumptions a probability to find a charge at depth x with any transverse coordinate y moving at angle θ relative direction of motion of incident needle-shaped beam in plane (x,y) is described by the formula [2,3]

$$P(x,y,\theta)dyd\theta = \frac{2\sqrt{3}}{\pi}\frac{1}{\Theta_s^2 x^2}\exp\left[-\frac{4}{\Theta_s^2 x}\left(\theta^2 - \frac{3y\theta}{x} + \frac{3y^2}{x^2}\right)\right]dyd\theta \quad (1)$$

Here Θ_s is physical quantity integrating scattering media and moving charge properties:

$$\Theta_s^2 = \left(\frac{E_s}{\beta cp}\right)^2 \frac{1}{X_0}, \quad (2)$$

where β, p, c are relative particle velocity $\beta = v/c$, particle impulse and light velocity respectively, v is particle velocity, X_0 - radiation length, E_0 is the constant with energy dimension:

$$E_s = \left(\frac{4\pi}{\alpha}\right)^{1/2} m_e c^2 = 21 \text{ MeV} \quad (3)$$

Here $\alpha = e^2/\hbar c = 1/137$ - is fine structure constant, e, m_e are electron charge and its mass respectively, $\hbar$ is Planck constant.

According to relation (1) scattered beam is described by Gaussian low in coordinate system $y/x;\theta$. The lines of equal probabilities are similar ellipses tilted at angle $\approx 1.08 \cong 62$ degrees to axis $\eta = y/x$. The tilted ellipse reflects those evident fact that transverse displacement of scattered particle and its direction of motion are not statistically independent. The relative number of particles enveloped by ellipse

$$3\eta^2 - 3\eta\theta + \theta^2 = F = const \quad (4)$$

depends on F value. Its average value is

$$\langle F \rangle = \frac{2\sqrt{3}}{\pi}\frac{1}{\Theta_s^2 x}\int \exp\left[-\frac{4}{\Theta_s^2 x}(3\eta^2 - 3\eta\theta + \theta^2)\right]^{(3\eta^2 - 3\eta\theta + \theta^2)\times} d\eta d\theta = \frac{1}{4}\Theta_s^2 x \quad (5)$$

Let us call the ellipse of equal probability (4) with $F = \langle F \rangle$ by "elementary scattering ellipse" while the area ε_s enveloped by this ellipse by "elementary scattering emittance". Taking into account that ellipse area described by equation (4) (emittance normalized by target thickness) is equal to $S = 2\pi F/\sqrt{3}$ we arrive at relation

$$\varepsilon_s = \frac{\pi}{2\sqrt{3}}\Theta_s^2 x^2 \quad (6)$$

One has to keep in mind that the emittance defined over average value encloses definite part of scattered particle

ISBN 978-3-95450-181-6

and perhaps multiple of this value describes scattered beam more precisely.

Let us derive distribution function for a particle entering scattering media at an angle Θ and transverse position Y. Choosing new coordinate system with the origin at point $(Y,0)$ turned around old one at angle Θ, we find that new and old particle coordinates are related as

$$x' = h\cos\Theta + (y-Y)\sin\Theta \quad y' = -h\sin\Theta + (y-Y)\cos\Theta \quad (7)$$

That gives for small angles

$$x' = h + (y-Y)\Theta, \quad y' = -h\Theta + (y-Y), \quad \theta' = \theta - \Theta \quad (8)$$

where h is target thickness. Thus we arrive at relation

$$Pdyd\theta = \frac{2\sqrt{3}}{\pi}\frac{1}{\Theta_s^2[h+(y-Y)\Theta]^2}\times \quad (9)$$

$$\exp\left\{-\frac{4}{\Theta_s^2}\left[\frac{(\theta-\Theta)^2}{h+(y-Y)\Theta} - \frac{3(y-Y-h\Theta)(\theta-\Theta)}{(h+(y-Y)\Theta)^2} + \frac{3(y-Y-h\Theta)^2}{(h+(y-Y)\Theta)^3}\right]\right\}$$

Neglecting the term $(y-Y)\Theta << h$ that is valid for beam with small divergence we find that to any element Y,Θ corresponds the same elementary scattering ellipse located at point $Y+h\Theta,\Theta$ of phase space.

MATCHING OF CHARGE PARTICLE BEAM WITH SCATTERING MEDIUM

Envelope to family of elementary scattering ellipses with the centers on ellipse

$$A(H-\Theta)^2 + B(H-\Theta)\Theta + C\Theta^2 = F1, \quad (10)$$

form the border of the beam phase portrait after its scattering on a target. Here

$$AH^2 + BH\Theta + C\Theta^2 = F1 \quad (11)$$

is the border of phase portrait of incident beam in normalized phase variables $(\eta = y/h, \theta)\, H = Y/h$. The area between the border (10) and the envelope is increase of emittance of incident beam and can be calculated. To do this let us subject (η,θ) plane to compression in direction of large elementary scattering ellipse axis up to value when ellipse becomes circle. Area element of compressed area to be calculated is equal

$$dS = rdl + \frac{1}{2}r^2 d\alpha, \quad (12)$$

where $dl, d\alpha$ are the differentials of compressed ellipse (10) arc and the angle of the perpendicular to this ellipse border, r is the circle radius. Thus the increase of beam emittance in compressed plane is

$$\Delta\varepsilon' = \oint_{L'} rdl + \int_0^{2\pi}\frac{1}{2}r^2 d\alpha = rL' + \pi r^2, \quad (13)$$

L' being compressed ellipse perimeter. It follows from (13) that $\Delta\varepsilon'$ has a minimum value when perimeter smallest. Among the family of ellipses with equal area circle has a minimal perimeter. So

$$\Delta\varepsilon'_{\min} = rL'_{\min} + \pi r^2 = 2\pi rR + \pi r^2 = 2\frac{r}{R}\varepsilon' + \varepsilon'_s = 2\sqrt{\varepsilon'\varepsilon'_s} + \varepsilon'_s \quad (14)$$

where R is the radius circle with the area equal to transformed emittance of incident beam. It follows from last formula that the smallest emittance increase is

$$\Delta\varepsilon_{\min} = 2\sqrt{\varepsilon\varepsilon_s} + \varepsilon_s \quad (15)$$

We say that an incident beam is matched with scattering media when condition (15) takes place. In general case we have the next formula that bind emittances of incident and scattered beam

$$\sqrt{\varepsilon_{out}} \geq \sqrt{\varepsilon_{in}} + \sqrt{\varepsilon_s} \quad (16)$$

Fig. 1 is illustration to just discussed. While (15) expresses minimal emittance growth over primary beam emittance and elementary scattering emittance relation below describes the ellipse of matched beam

$$3H^2 + 3H\Theta + \Theta^2 = F1 \quad (17)$$

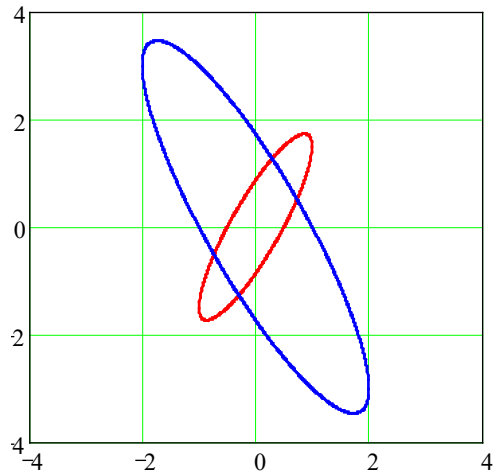

Figure 1: An example of beam-target matching.

This relation can be easily derived from relations (4),(10) if one keep in mind that matched scattered beam as it follows from previous discussion has to be similar to elementary scattering ellipse.

To have some reference points we list some formulae that one can derive from distribution function or take from the reference [2,3] and make some estimations. Mean-square for scattering angle and transverse displacement are

$$\langle\theta^2\rangle = \frac{1}{2}\Theta_s^2 x, \quad \langle y^2\rangle = \frac{1}{6}\Theta_s^2 x^3 \quad (18)$$

If Aluminum is used as scattering material then $X_0 \approx 27$ g/cm^2 = 10 cm and for a target with thickness 1 mm and for electron with energy 21 MeV we have $\Theta_s^2 \approx 0{,}1$ cm^{-1}, $\sqrt{\langle\theta^2\rangle} \approx 0{,}07$, $\sqrt{\langle y^2\rangle} \approx 0{,}4\times10^{-2}$ cm, $\varepsilon_s \approx 0{,}3\pi$ cm*mrad.

OFF-NORMAL INCIDENCE OF NEEDLE SHAPED BEAM ON A TARGET

Distribution function (1) is the steady state solution of differential equation for infinite homogeneous media and for charge starting from origin of coordinate system. One may suppose that it is still strict solution in the

ISBN 978-3-95450-181-6

special case of finite scattering media with the border that is normal to starting charge velocity. Outside the target in the forward direction a probability to find charge with coordinates y and $x>h$ moving at angle θ to x-axis is defined by (1) with the next exchange

$$y \to y-\theta(x-h),\ x \ge h\,. \tag{19}$$

One has the following distribution function in free space after such substitution

$$P(\xi,\eta,\theta)dyd\theta = \frac{2\sqrt{3}}{\pi}\frac{1}{\Theta_s^2 h}\times \tag{20}$$
$$\exp\left[-\frac{4}{\Theta_s^2 h}\left(\theta^2\left(1-3\xi+3\xi^2\right)-3\theta\eta(2\xi-1)+3\eta^2\right)\right]d\eta d\theta$$

where $x = h\xi, \xi > 1$.

If the out coming interface is described by relation

$$x = h + ky \tag{21}$$

a probability to find a charge with coordinate y,θ on interface surface (21) is

$$P_b(x,y,\theta)dyd\theta = \frac{2\sqrt{3}}{\pi}\frac{1}{\Theta_s^2(h+ky)^2}\times \tag{22}$$
$$\exp\left[-\frac{4}{\Theta_s^2}\left(\frac{\theta^2}{h+ky}-\frac{3y\theta}{(h+ky)^2}+\frac{3y^2}{(h+ky)^3}\right)\right]dyd\theta$$

The average of scattering angle $\langle\theta\rangle$ on interface surface that might be associate with direction of motion of scattered beam is determined by integral

$$\langle\theta\rangle = \iint \theta P_b dyd\theta = \frac{2\sqrt{3}}{\pi}\iint \theta\frac{1}{\Theta_s^2(h+ky)^2}\times \tag{23}$$
$$\exp\left[-\frac{4}{\Theta_s^2}\left(\frac{\theta^2}{h+ky}-\frac{3y\theta}{(h+ky)^2}+\frac{3y^2}{(h+ky)^3}\right)\right]dyd\theta$$

that after appropriate calculations may be reduced to

$$\langle\theta\rangle = \frac{3\sqrt{3}}{2\sqrt{\pi}\Theta_s\sqrt{h}}\int_{-1/k}^{b}\frac{\eta}{(1+k\eta)^{5/2}}\exp\left[-\frac{3\eta^2}{\Theta_s^2 h(1+k\eta)^3}\right]d\eta \tag{24}$$

Integration limits are dictated by problem conditions. Lower limit is determined by condition $x \ge 0$, while scattering plate dimensions determine upper integration limit. By analogy with light optics we call this mean value refraction angle. Introducing $\langle\theta\rangle = \gamma(\alpha)$; $\tan\alpha = k$ we arrive at formula

$$\gamma(\alpha) = \frac{3\sqrt{3}}{2\sqrt{\pi}\Theta_s\sqrt{h}}\times \tag{25}$$
$$\int_{-1/\tan\alpha}^{b}\frac{\eta}{(1+\eta\tan\alpha)^{5/2}}\exp\left[-\frac{3\eta^2}{\Theta_s^2 h(1+\eta\tan\alpha)^3}\right]d\eta$$

As in traditional light optics the phenomenon of partial beam reflection from outside target border may take place as it demonstrated on fig. 2.

Due to more tight bend of scattered beam envelope (18) compared with linear dependence of target border (21) one (of two) beam border does not intersect interface, target thickness being sufficient large. In this case part of particles flow leaves the target from its front side – the beam reflection takes place. Simple calculations result in formula $\Theta_s^2 h\tan^2\alpha = 8/9$ for reflection threshold

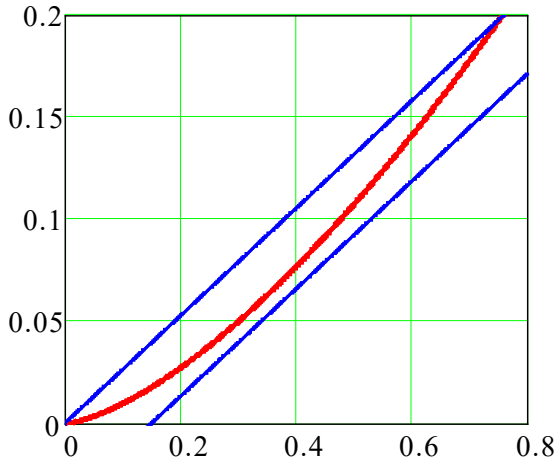

Figure 2: A plot illustrating beam reflection. Strait lines are target borders, the curve is beam envelope. $\Theta_s^2 = 0.55cm^{-1}, h = 0.15cm, k = 3.8 (t = h/\sqrt{1+k^2} \approx 0.04)cm$, target material is aluminium.

Taking into account the indistinct beam border envelope we rewrite reflection condition in the form

$$\Theta_s^2 t\tan^2\alpha\sqrt{1+\tan^2\alpha} \ge 1 \tag{26}$$

t being scattering target thickness.

CONCLUSION

Basing on distribution function for a charge Coulomb scattering the number of features and mechanisms of charged particles propagation in scattering medium has been established. Among these are matching condition and appropriate formula for beam emittance growth, the mechanisms of beam refraction and reflections.

REFERENCES

[1] V.G.Kurakin, A.V.Koltsov. Ecologically Clean Accelerator for Nuclear Physics Research. Proceedings of RuPAC 2008, Zvenigorod, Russia, September 28 – October 3, 2008, p. 376-378.

[2] B.Rossi. High energy particles. Prentice-Hall, Englewood Cliffs, NJ, 1952.

[3] S. Belenkiy. Avalanche processes in cosmic rays. GITTL, Moscow-Leningrad, 1948. 244 pp. In Russian.

ISBN 978-3-95450-181-6

DESIGN STUDY OF THE PROTON LINAC FOR RADIOPHARMACEUTICALS PRODUCTION

G. Kropachev, A. Balabin, D. Seleznev, and A. Sitnikov, T. Kulevoy, ITEP, Moscow, Russia

Abstract

The 8 MeV 200 MHz linac for acceleration of quasi cw 0.2 mA proton beam is under development at ITEP. The linac is designed for radiopharmaceuticals production which will be used in the Positron-Emission Tomography. The linac includes RFQ and DTL sections with 6D-beam matching between them. The DTL section has modular structure and consists of separated individually phased IH-cavities with beam focusing by permanent magnet quadrupoles located between the cavities. This DTL structure provides linac compactness and enables its tuning and commissioning cavity by cavity. Results of beam dynamic simulation and electrodynamics characteristics of linac cavities are presented.

INTRODUCTION

The 8 MeV 200 MHz linac for acceleration of 20 mA/pulse (0.2 mA average current at duty cycle 1%) proton beam is under development at ITEP. The linac is designed for radiopharmaceuticals production which will be used in the Positron-Emission Tomography. Such beam parameters provides generation of ^{18}F production and they should be obtained without activation of linac materials.

The linac consists of RFQ and DTL with 6D-beam matching between them. We proposed the modular DTL structure consisting of a number of separate individually phased accelerating cavities with beam focusing by permanent magnet quadrupoles (PMQs) located between them. The cavities are placed in the separate vacuum tanks with the identical length. PMQs can have the modular construction with constant gradient which greatly simplifies the manufacturing [9]. The linac basic parameters are shown in Table 1.

Table 1: The Linac Basic Parameters

Ions	H^+
Operating frequency	200 MHz
Beam energy	0.07÷8 MeV
Injection current	20 mA
Normalized beam emittance	0.2 π cm mrad
Normalized acceptance	0.5 π cm mrad
Transmission	> 90 %
Pulse power losses	< 1 MW
Maximum field strength	1.8 Kp
Length	~5 m

We proposed to use duoplasmatron as ion source for the linac. This ion source can provide the required beam current of 20 mA with normalized emittance lower than 0.2 π cm mrad (see Table 1).

The operating frequency equal to 200 MHz is determined by following factors:

- required acceptance (which should be higher than the beam emittance at least in 2.5 times [1]);
- accelerator compactness (the linac has to be located both in standard hospital office and in the transport unit [8]
- soft requirements to the RF structure manufacturing and adjustment.

The maximum strength of the electric field on the surface is limited by E_{smax} = 1.8* Kp = 270 kV/cm, where Kp is the Kilpatrick limit.

LINAC MAIN PARAMETRS

The layout of the medical linac and some of its parameters are given in Fig. 1. Below these parameters will be discussed.

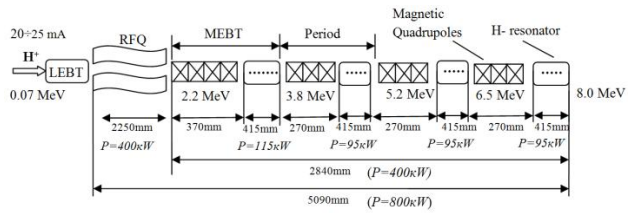

Figure 1: Layout of the medical linac.

RFQ Parameters

The RFQ consists of the matching, bunching, and regular acceleration sections. The 6D-beam matching is realized in the initial matching section. The adiabatic beam bunching is carrying out at quasi-stationary bunch mode [1]. In the regular acceleration section the protons are accelerated at constant synchronous phase of -35 degrees which achieved at intervane voltage of 147.5 kV.

To choose the injection voltage U_{inj} the following features should be taking into account. From one side to decrease the bunching section length U_{inj} should be decreased. From other side, increase of U_{inj} simplifies the vane manufacturing. The increase U_{inj} also reduces the space charge effects in the LEBT. Taking into account all these features the injection voltage U_{inj} was chosen equal to 70 kV (Fig. 1). The main RFQ parameters are presented in Table 2.

Transverse matching of continuous beam from the duoplasmatron with RFQ is realized in LEBT (Fig. 1) by two electrostatic einzel lenses with voltage ≤ 50 kV.

ISBN 978-3-95450-181-6

Table 2: The Main RFQ & DTL Design Parameters

	RFQ	DTL
Ions	H^+	
Operating frequency, MHz	200	200
Beam energy, MeV	0.070÷2.2	2.2÷8.0
Injection current, mA	20	~20
Normalized emittance, π cm mrad	0.2	~0.2
Pulse current limit, mA	200	200
Normalized acceptance, π cm mrad	0.5	0.6
Synchronous phase, deg.	-90÷-35	-35
Intervane voltage, kV	147.5	
Maximum field strength, Kp	1.8	1.8
Average radius, mm	7	
Vane radius of curvature, mm	5.6	
Maximum vane modulation	2.35	
Aperture radius, mm	18.3÷7.1÷4.2	10
Pulse RF power losses, kW	400	400
Length, m	2.25	2.84
Number of cavities	1	4
Lengths of gaps, mm		40

DTL Parameters

The necessary condition of the 6D matching between RFQ and DTL is longitudinal and transverse acceptances of the DTL not lower than the same acceptances of the RFQ. In the given linac for 6D matching between RFQ and DTL the four PMQs are used (matching quadruplet) as well as 7-gaps matching cavity which also used for beam acceleration (see Fig. 1). The electric field strength at the center of the accelerating gaps in DTL was chosen equal to 110 kV/cm, then the strength of the electric field at the DTL surface equal to 270 kV/cm which is equivalent to 1.8 Kp (Kilpatrick criteria) for resonant frequency of 200 MHz.

Focusing periods with different configuration for high acceleration gradient and required acceptance were investigated. The FDFOOOOO focusing period (Fig. 1) was chosen. Each FDFOOOOO focusing period has length of 685 mm and consists of PMQ triplet (270 mm), 5-gaps accelerating cavity (415 mm) and allows to achieve the average accelerating gradient not lower than 2 MeV/m and normalized acceptance higher than in RFQ. Total length of all three DTL focusing periods is ~2.8 m (see Fig. 1). All lenses have lengths of 70 mm and aperture radii of 15 mm. Magnetic lens gradients G are practically achievable ($G \leq 45$ T/m).

The longitudinal field distribution on axis of cavity at the first DTL period is presented in Fig. 2. The given accelerating cavity has the equal to each other length of the accelerating gaps. The electric field amplitudes in the gaps are also equal to each other except the first and the last gaps where electric field amplitude are two times lower than at center. Others periods have the same field distributions which allow to simplify cavities adjustment. Parameters of the accelerating cavities are presented in Tables 2&3.

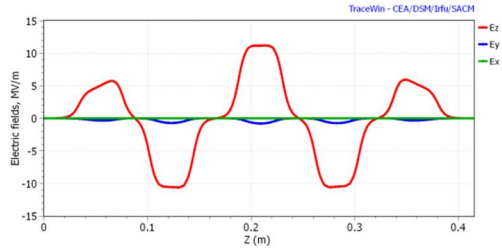

Figure 2: Distributions of the longitudinal and the transverse fields on the axis of the IH-cavity.

CHOICE OF RF STRUCTURE

According to the chosen accelerator scheme (Fig.1) the DTL should accelerate the proton beam from energy 2.2 MeV to 8 MeV (β=0.068-0.13).

The Alvarez structure has a 2π operating mode and thus it at 2 times longer compared to π- structures. Therefore the Alvarez structure was excluded from the consideration. The λ/2 & λ/4 coaxial accelerating cavities consume a high RF power, have great transverse sizes and challenge cooling systems. Such cavities are useful only under superconducting conditions [2].

The conventional IH- & CH-cavities were investigated in paper [3]. Such structures allow to achieve the acceptable accelerating gradient. These structures were compared to each other and it was found that the CH-structure consumes approximately 2 times more RF power than IH-structure [3]. Thus the IH-cavity (Fig. 3) was chosen for the DTL. This cavity is cheap and easily adjustable. The main parameters of IH-cavity are presented in Table 3.

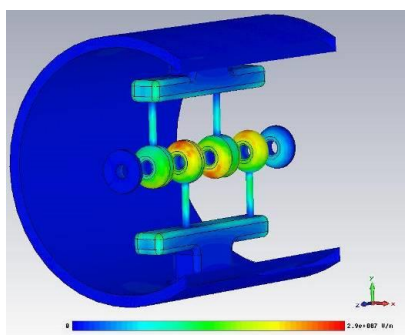

Figure 3: IH-cavity and electric field distribution

Table 3: Main Parameters of 5-gap IH-cavity

Resonant frequency	200 MHz
Field strength in accelerating gaps	110 kV/cm
Quality factor	8400
Maximum field strength	266 kV/cm
Pulse RF power losses	95 kW
Length	0.415 m
Diameter	0.3 m

The IH-cavity disadvantage is a transverse electric field on the axis [4]. The longitudinal E_z (accelerating) and

ISBN 978-3-95450-181-6

transverse E_y (deflecting) electric field distributions on axis are presented in Fig. 2.

The E_{ymax} (the maximum value of the transverse electric field on the cavity axis) can reach up to 5-10% to E_{zmax} (the maximum value of the longitudinal electric field on the cavity axis) and depends on cavity design. Since the IH-cavity operates on π mode the transverse electric field on the cavity axis has an opposite direction in time at each accelerating gap. Therefore the transverse electric field influence on the beam is mostly compensated.

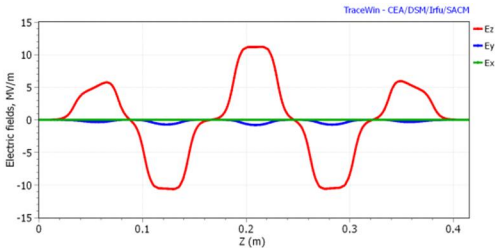

Figure 3: Distributions of the longitudinal and the transverse fields on the axis of the IH-cavity.

NUMERICAL SIMULATION OF BEAM DYNAMICS IN THE LINAC

Numerical simulation of the beam dynamics in the medical linac was carried out by macro particles method using RFQDYN, DYNAMION [4], and LIDOS [5] codes. Graphical representation of simulation results is performed by PlotWin code [6].

The beam transmission in the RFQ is equal to 95% for injection current of 20 mA .

The results of end-to-end particles dynamics simulation in the linac are presented in Fig. 4. As seen from Fig. 4 the rms-envelopes have a periodic character with increased up to 2 times the transverse beam sizes in the DTL compared to beam sizes in the RFQ. It should be mentioned that the aperture size in the DTL is larger up to 2.4 times than the RFQ.

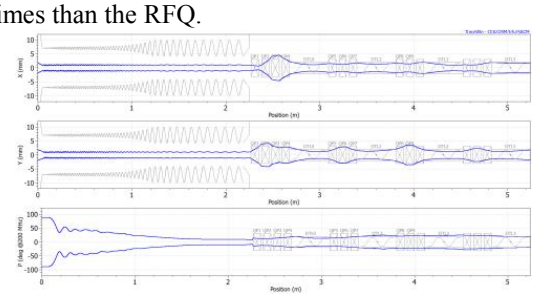

Figure 4: Rms-envelopes of the beam in the linac.

The phase spaces for accelerated 20 mA proton beam at DTL output are presented in Fig. 5. Particle losses in DTL are negligible and total transmission is about 95%. The emittance growth at RFQ & DTL less than 20 %.

The particles dynamics simulation with transverse electric field (deflecting) on the axis was carried out. The simulation shows that the transmission is reduced by 0.5% while emittance is increased by 5%. According to that the transverse electric field has no influence on beam dynamics in this case.

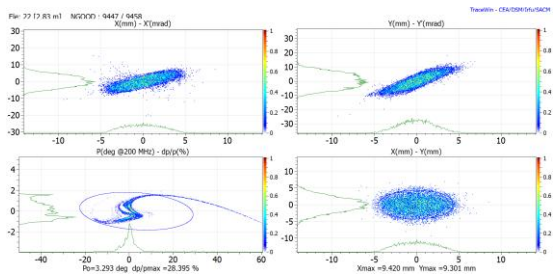

Figure 5: Phase spaces at the DTL output.

CONCLUSION

The scheme of the medical linac (Fig.1) consisting of RFQ and DTL including a number of separate individually phased accelerating cavities with beam focusing by PMQs is proposed.

The linac provides a high particle transmission about 95% for proton injection current of 20 mA. The PMQs minimize the electric power consumption. Magnetic lens gradients are practically achievable for the permanent magnet assembly. PMQs can have the modular construction with constant gradient which greatly simplifies the manufacturing.

The complexity of the DTL supply system by individual RF generators is compensated by simplicity of fabrication and tuning of cavities. The modular DTL structure is flexible and allows tuning and commissioning section by section. Moreover the modular structure can be used for other applications such as BNCT, neutron generator, semiconductor industry etc. The proposed scheme of the medical linac can be used as a base for a serial compact accelerator production.

REFERENCES

[1] I. M. Kapchinskij, Theory of Resonance Linear Accelerators, Harwood, 1985.

[2] S. Kurennoy, J. O'Hara, L. Rybarcyk, «Compact Linac for Deuterons (Based on IH Structures with PMQ Focusing)» HB 2008, August 27,2008 LANL, Los Alamos.

[3] S.S. Kurennoy, L.J. Rybarcyk, and T.P. Wangler, «AN H-MODE ACCELERATOR WITH PMQ FOCUSING AS A LANSCE DTL REPLACEMENT». Proceedings of IPAC2011, San Sebastián, Spain WEPS067 LANL, Los Alamos, NM 87545, U.S.A.

[4] V. Andreev, N.N. Alexeev, A. Kolomiets, V. Koshelev, A. Plastun, «NOVEL DTL SECTION FOR ITEP-TWAC HEAVY ION INJECTOR» Proceedings of RUPAC2012, Saint|-|Petersburg, Russia WEPPC013

[5] A.Kolomiets, et al., DYNAMION – The code for beam dynamics simulation in high current ion linac, Proc. Of EPAC-98, Stockholm, Sweden, 1998, pp. 1201-1203.

[6] B.I.Bondarev, A.P.Durkin, et al. LIDOS Unconventional, Helper for Linac Beam Designing. Computational Accelerator Physics Conference, AIP, Conference Proceedings 297, Los Alamos, NM 1993, pp.377-384.

[7] http://irfu.cea.fr/Sacm/logiciels/

[8] Pulsar TM 7 PET Isotope Production System, AccSys Technology, inc.

[9] V.S. Skachkov et al. RSI 87,023303 (2016)

ISBN 978-3-95450-181-6

HIGH-CURRENT PULSING DEUTERON ACCELERATOR WITH ENERGY OF 500 KeV

K.I. Kozlovskij, E.D. Vovchenko, A.A. Isaev, M.I. Lisovskij, A.E. Shikanov, National Research Nuclear University "MEPhI" (Moscow Engineering Physics Institute), Moscow, Russia

Abstract

In this work it is reported about development of compact prototype of fast ions and deuterons accelerator with next parameters: energy is up to 400 keV, electric current is more than 1 kA and current density is more than 20 A/sm^2 in pulses with duration up to 0,5 μs and repetition frequency is equal to 1 Hz. Method of electron magnetic insulation in accelerating gap was applied and optimized in the accelerator; intensive laser-plasma ion source was used.

INTRODUCTION

Researches in the area of magnetic insulation applied to compact diode systems for neutrons generation initially are introduced in the work [1]. Two possible schemes of electronic conductivity dampening exist. In the first case, the field of constant magnets with azimuthal symmetry is used [2,3]. In the second case pulsing helix magnetic field is applied [2,4]. However, it is experimentally established, that electronic conductivity dampening by the field of constant magnets [3] has a series of significant shortcomings. These shortcomings are connected with complex configuration of magnetic field and its inhomogeneity.

It was established by authors, that similar shortcomings to a lesser extent appears in diodes with pulsing magnetic insulation. In this work results of experimental investigation of similar diodes were set out.

EXPERIMENT

For the plasma production, YAG laser, activated by neodymium, generating pulses of infrared rays in modular Q mode with wave length of 1.06 μm, energy ≤ 0.85 J and duration is about 10 ns. was used.

Magnetic field in the diode configured with the help of helix, which forming surface had a frustaconical shape. Critical distinction between this experiment and experiment, conducted earlier is in the use of more powerful laser, high-stable PVG with characteristics, mentioned above and original scheme of start on the basis of laser controllable arrester (LCA).

An important aspect is the use of high-voltage pulse generator according to the scheme of Arkadyev-Marx, generating at idling conditions with amplitude of 400 kV and first half wave duration of 1 μs, in which original scheme of its start, based on LCA, is applied.

A laser target in the form of a tablet made of TiD was placed on the anode. Deuterons are extracted from the laser plasma in an electric field formed by a positive high-voltage pulse on the anode.

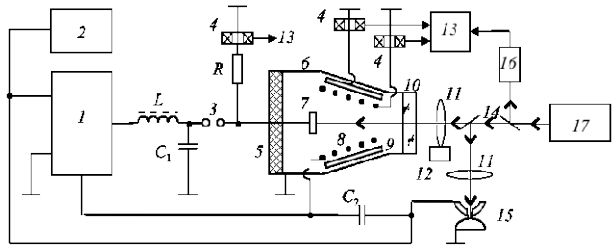

Figure 1: Scheme of experiment “Formation of deuteron flux”: 1 – PVG (2–30 cascades); 2 – PVG charging unit; 3 – arrester-peaker; 4 – Rogowski coils; 5 – insulator; 6 – vacuum chamber; 7 – plasma forming target; 8 – helix; 9 – ion collector (cathode); 10 – optical window; 11 – focusing lens; 12 – scanning device; 13 – oscillograph; 14 – partially transparent mirror; 15 – LCA; 16 – Photoelectronic coaxial converter PCC; 17 – laser.

We applied a pulsed magnetic isolation for suppression of parasitic electron current due to secondary electron emission at the cathode. Conical spiral is placed in the diode gap in front of the cathode, which also had a conical shape (Fig. 1). In addition, conical surface of the cathode and conical spiral are parallel. Diode system placed in a vacuum chamber pumped to a pressure of 10^{-2} Pa.

A laser plasma emission is accompanied by its expansion in the radial direction. The flow of deuterons reaches the conical spiral with a delay $\tau_P \approx 250 - 300$ ns.

Estimation of the efficiency of generating the magnetic field showed that current in the conical spiral achieved 60% from its maximum value after 300 ns from the beginning of the expansion of a laser plasma (i.e. when the flow of deuterons reaches the conical spiral).

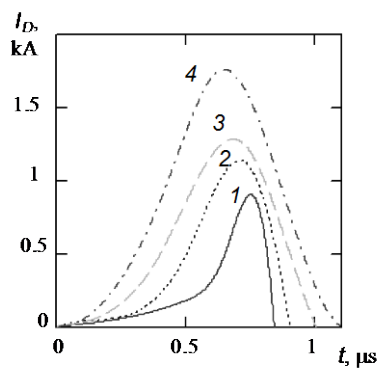

Figure 2: Diode current $I_D(t)$ at laser energies: *1* – 80 mJ, *2* – 200 mJ, *3* – 380 mJ, *4* – 750 mJ.

ISBN 978-3-95450-181-6

Accelerated deuterons current and current in helix circuit were measured by oscillograph with the help of Rogowski coils. On the Fig. 2 pulses of deuteron current at various energies of laser radiation are presented. They were obtained in the result of experimental oscillogram processing using method of cubical interpolation. It is needed for theoretical analysis of possible neutron yield. Obtained experimental data allows us to evaluate perspectives of neutron generation in considered diode system. Neutron yield per pulse is determined by equation:

$$Q(W) \approx \frac{n}{e}\int_0^{\tau} dt \cdot I_D(W,t) \int_0^{eU(t)} dE \frac{\sigma(E)}{F(E)},$$

where is n – concentration of reagent nuclei in the plasma forming target, e – elementary electric charge, τ – pulse duration of deuteron current, $U(t)$ – time dependence of accelerating-voltage, $F(E)$ – Deuteron energy loss per unit target length, $\sigma(E)$ – micro-cross section of nuclear reaction.

Dependences of deuteron current and electric potential on time were taken from oscillograms, obtained from the results of experiment. Evaluations of neutron yield were obtained for following nuclear reactions $T(d,n)^4He$ and $D(d,n)^3He$, usually used in compact neutron generators. Calculation results of neutron yield are shown in Table 1.

Table 1. Calculation Results – $Q(W)$ Neutrons/Pulse

W, mJ	Nuclear reaction	
	$T(d,n)^4He$	$D(d,n)^3He$
80	$2 \cdot 10^{10}$	$1.5 \cdot 10^{8}$
200	$4 \cdot 10^{10}$	$3 \cdot 10^{8}$
380	$6 \cdot 10^{10}$	$4 \cdot 10^{8}$
750	$8 \cdot 10^{10}$	$6 \cdot 10^{8}$

CONCLUSION

Experimental investigation of diode for neutron generation with laser-plasma deuteron source and pulsing magnetic insulation by helix of conical shape at laser pulse energy and amplitude of accelerating-voltage correspondingly equal to $W = 0.75$ J and $U_0 = 300$ kV was carried out.

It was shown, that within stated limits of W and U_0 proportion between amplitude of deuteron current and laser pulse energy is held.

Calculations for given ranges of W and U_0 showed that the neutron yield to full solid angle when using nuclear reaction $T(d,n)^4He$ could reach 10^{11} neutrons/pulse.

REFERENCES

[1] D.F. Bespalov, K.I. Kozlovskii, A.S. Tsybin, and A.E. Shikanov, Pulsed neutron tube: A. S. 766048 of the USSR, 1979.

[2] A.N. Didenko, A.E. Shikanov, K.I. Kozlovskii, V.L. Shatokhin, and D.D. Ponomarev, Plasma physics report, **40**, 1025-1034 (2014).

[3] A.E. Shikanov, E.D. Vovchenko, K.I. Kozlovskii, and V.L. Shatokhin, Tech. Phys. Lett. **41**, 511 (2015).

[4] Gulko V. M., Dydychkin V. N., Kozlovsky K. I., Kolomiets N. F., Mikhailenko B., Shikanov, A. E., and K.I. Yakovlev, Pulsed neutron tube: A. S. 1468275 of the USSR, 1985.

ISBN 978-3-95450-181-6

BEAM INJECTOR FOR VACUUM INSULATED TANDEM ACCELERATOR*

A. Kuznetsov#, A. Gmyrya†, A. Ivanov, A. Koshkarev‡, A. Sanin, D. Kasatov, K. Blokhina†,
BINP SB RAS, Novosibirsk, Russia

Abstract

The Vacuum Insulated Tandem Accelerator (VITA) is built at the Budker Institute of Nuclear Physics. The accelerator is designed for development of the concept of accelerator-based boron neutron capture therapy of malignant tumours in a clinic [1]. In the accelerator the negative hydrogen ions are accelerated by the high voltage electrode potential to the half of required energy, and after conversion of the ions into protons by means of a gas stripping target the protons are accelerated again by the same potential to the full beam energy. The epithermal neutrons generation reaction is $^{7}Li(p,n)^{7}Be$, and the estimated proton current for minimal therapeutic neutron flux should be higher than 3 mA @ 2.5 MeV energy [2] meanwhile about 10 mA required for comfortable BNCT treatment. During the facility development, the proton beam was obtained with 5 mA current and 2 MeV energy [3]. To ensure the beam parameters and reliability of the facility operation required for clinical applications, the new injector was designed based on the ion source with a current up to 15 mA [4], providing the possibility of preliminary beam acceleration up to 120-200 keV. The paper presents the status of the injector construction and testing.

INTRODUCTION

The VITA facility design is shown at Fig. 1. The first stage of acceleration – acceleration of ions – takes place in the area between the entrance volume of the accelerator and the high voltage electrode and the second stage – acceleration of protons – between the high voltage electrode and the beginning of high energy beam line. The gas stripping target is located inside the high voltage electrode and inflates up to 0.23 l×Torr/s into the accelerator volume to provide up to 99% conversion of ions into protons. Several innovative ideas were realized in the accelerator design to allow stable acceleration of intense beam in a compact facility.

The initial ion beam is produced by the injector composed of the ion source, low energy beam line and magnetic elements providing focusing and correction of the beam. Series of investigations have revealed the limitations of injecting current. The main problems are the ions loss due to high residual gas concentration and the ability of the stripping gas to rich the injector and corrupt the stability of the ion source [4]. To provide a reliable H- beam for clinical application of the facility the new injector is designed.

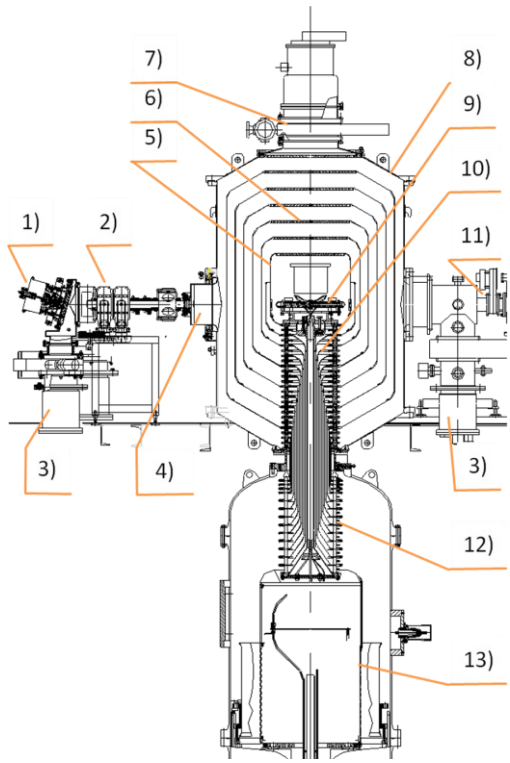

Figure 1. Scheme of the VITA facility: 1 – H ion source; 2 – low energy beam line; 3 - turbomolecular pump; 4 – entrance volume of the accelerator; 5 – high voltage electrode; 6 – electrode shutters; 7 – cryo pump; 8 – accelerator vacuum volume; 9 – stripping target; 10 – feedthrough insulator (vacuum part); 11 – high energy beam line; 12 – feedthrough insulator (gas part); 13– high voltage source.

INJECTOR DESIGN

The new injector proposed for the VITA facility [5] is under construction at BINP. The final design scheme of the injector is presented at Fig. 2. The surface-plasma ion source with Penning discharge and with hollow cathode (1) is used to generate the 15 mA H^- beam with energy up to 32 keV. The generated beam is bent by the magnet (4) and directed into the pre-accelerating tube. The usage of this magnet allows solving several tasks: splitting the beam from the gas and caesium flux, additional beam focusing to ensure axially symmetric parallel beam with round profile in the output, protect the ion source from the back streaming particles from the accelerator channel. The diaphragm with the beam diagnostics is located between the magnet and the accelerator tube. Measuring

* Applied research is carrying out with the financial support of the Russian Federation represented by the Ministry of Education and Science of Russia (unique identifier RFMEFI60414X0066)
#A.S.Kuznetsov@inp.nsk.su
† Second affiliation: NSTU, Novosibirsk, Russia
‡ Second affiliation: NSU, Novosibirsk, Russia

ISBN 978-3-95450-181-6

the temperature profile of the diaphragm provide feedback information about the beam position which allows to tune the magnet. The diaphragm makes possible differential pumping of the ion source.

The injector design does not implement focusing lenses or correctors to tune the beam convergence and direction in the input of the accelerator, but the injector support provides an adjustment of the device as a whole to direct the output beam to the accelerator axis precisely. The accelerator tube also operates as focusing lens to make the beam match the accelerator acceptance.

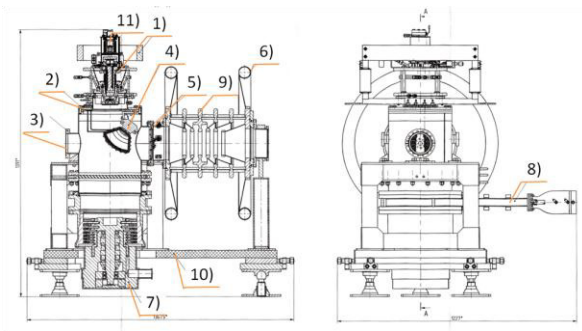

Figure 2. New injector design: 1 –15 mA H- ion source; 2 – positioning flange; 3 – vacuum chamber; 4 – beam magnet; 5 – diaphragm with the beam diagnostics; 6 – high voltage screen; 7 – turbomolecular pump; 8 – vacuum valve; 9 – pre-acceleration tube; 10 – insulated support; 11 – Cs heater.

The estimation of the H^- beam stripping by the residual gas demonstrates higher efficiency of beam delivery using this design of the injector in comparison to existing version.

Operation of the injector will require additional equipment including Faraday cages for high voltage part of the injector system and isolating transformer to provide 5 kW electric feeding to the 120-150 kV potential. The VITA facility arrangement with the injector equipment is presented at Fig. 3.

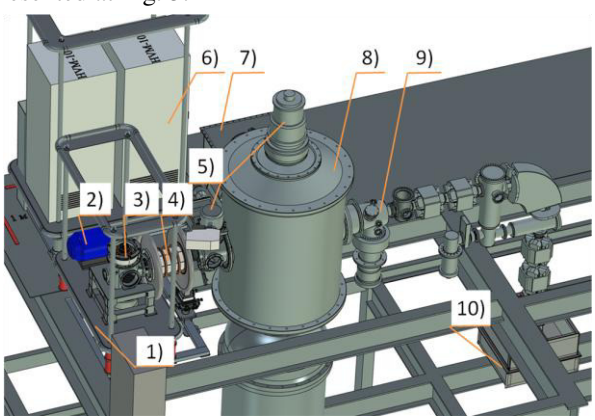

Figure 3. Facility arrangement with the beam injector equipment: 1 – Faraday cage with the injector, 2 – for-pump, 3 – H- ion source, 4 – pre-acceleration tube, 5 – cryo pumps, 6 – Faraday cage with the injector power and control cabinets, 7 – isolating transformer, 8 – vacuum insulated tandem accelerator, 9 – high energy beam line, 10 – neutron beam shaping assembly.

COMPUTER SIMULATIONS

Computer simulations of the beam transportation through the pre-acceleration tube and VITA were carried out using UltraSAM code developed at BINP [6-7]. Computation was made considering the temperature of the beam and space charge. It was demonstrated that 120 keV pre-acceleration provides very fast shrinking of the beam that leads to significant grows of the chaotic angles of the beam trajectories, so the transportation of the beam through the stripping target becomes problematic. Acceptable pre-acceleration energies have lower values with the optimum about 75 keV which corresponds to 105 keV of total injecting beam energy.

Transportation of the beam with 1 mA current through the pre-accelerator tube and the VITA is shown at Fig. 4 Coordinate Z=0 mm corresponds to the input flange of the accelerator tube, area of Z between 800 and ~1000 mm – 1-st accelerator gap of the VITA, and coordinates between ~1500 and ~2000 mm – the area of stripping target. The voltage of pre-acceleration is 75 kV and VITA voltage is 1 MV. The effects of input focusing and output defocusing of the pre-accelerator tube could be seen by the beam trajectories as well as focusing effect of the 1-st accelerator gap of VITA. The beam crossover is located near the 3 electrode of VITA (Z=1200 mm).

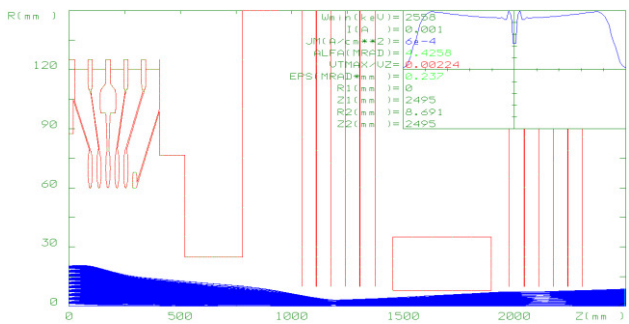

Figure 4. Transportation of 1 mA beam through the pre-accelerator tube and the VITA.

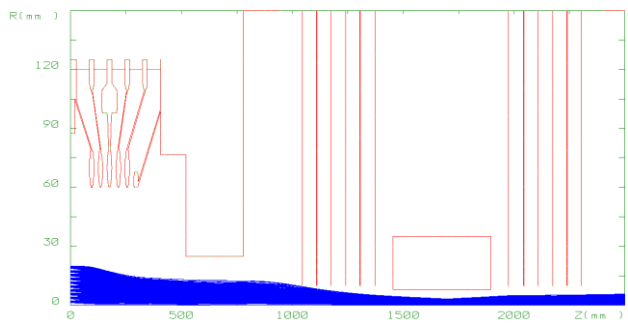

Figure 5. Transportation of 10 mA beam through the pre-accelerator tube and the VITA.

The trajectories of 10 mA beam demonstrate the effect of space charge (Fig. 5). The beam has bigger diameter and the crossover is inside the stripping tube. The beam

ISBN 978-3-95450-181-6

diameter is close to the diameter of the 1-st VITA aperture, which means necessity to choose the electrodes diaphragms diameters carefully. The output beam is almost parallel with the diameter less than 16 mm. One can see that space charge provides better beam parameters inside the stripping tube and in the output of the accelerator, that should be took into account while projecting the vacuum system to avoid space charge compensation by ionized residual gas.

As the main parts of the injector are already fabricated and the Faraday cages and some other equipment are still in fabrication it is possible to carry out preliminary injection of the beam using the pre-accelerator tube as an electrostatic lens. When the input and output electrodes of the tube has ground potential and the central electrodes has +60 kV potential the focusing provide ideal injection into the VITA with 1 MV potential at the high voltage electrode (Fig. 6). Computation proves that the beam space charge provides better transportation of the beam through the entrance electrostatic lens of the VITA. This experiment could prove the ability of the VITA to operate with more than 5 mA beam current.

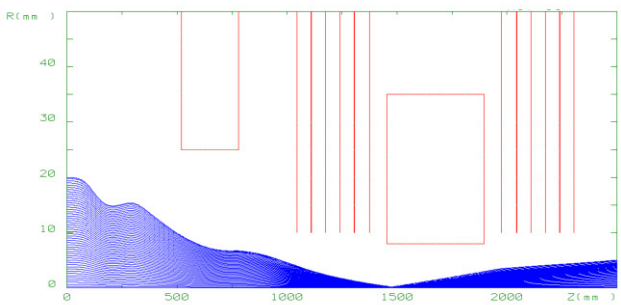

Figure 6. Transportation of 5 mA beam through the pre-accelerator tube (used as electrostatic lens) and the VITA.

BEAM DIAGNOSTICS

To check the beam quality at the VITA input it was decided to measure the beam emittance using pepper-pot method. The pepper-pot matrix will be located at the output of the pre-accelerator tube and the ceramics screen will be placed in the entrance volume of the VITA where the image could be registered using CCD camera. The converging beam makes compact beam picture at the screen surface, so it is necessary to provide high space resolution of the beam image to get sufficient angle measurement accuracy. With the convergence of the beam ~25 mrad, the necessary angle accuracy should be at least ~2 mrad or better.

PRELIMINARY TESTING

The stand was constructed for high voltage training of the accelerator tube with the ion beam (Fig. 7). The beam propagates from the ion source through the accelerator tube into the Faraday cup directly without bending. The tantalum foil is located at the bottom of the Faraday cup, and it is possible to register the total beam current and the light from the foil using vacuum window and CCD camera during the experiments. The profiles of the beam are presented without correction of the angle view. The tube was trained up to 80 kV.

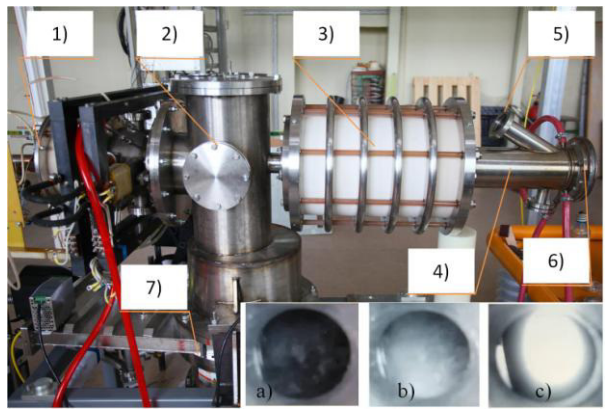

Figure 7. Stand for preliminary accelerator tube testing: 1 – 15 mA H^- ion source; 2 -vacuum chamber; 3 – accelerator tube; 4 – Faraday cup; 5 – view port; 6 – location of the tantalum foil; 7 – vacuum valve and pumping. Photo of the tantalum target: a) no beam; b) 6 mA, no acceleration; c) 6 mA @ 50.5 kV acceleration (82 keV total energy).

SUMMARY

The injector for VITA facility is under construction now at BINP. Preliminary testing of the ion source and accelerator tube is carried out. Optimal voltages for pre-acceleration tube are determined by computer simulation. Before the Faraday cage will be constructed it is possible to test the ability of VITA power system to operate with more than 5 mA beam currents by injecting the H- beam without acceleration. It is possible if we use the accelerator tube as an electrostatic lens. According to computer simulation 60 kV voltage at the central electrodes of the tube provide perfect injection of the beam into the accelerator.

REFERENCES

[1] B.F.Bayanov, et al. Nuclear Instr. and Methods in Physics Research A 413/23 (1998) 397426.
[2] A.Kuznetsov, et al. 4 International Particle Accelerator Conference Proceedings , 12-14 May 2013, Shanghai, China, p. 3693-3695.
[3] A. Ivanov, et al. Journal of Instrumentation 11 (2016) P04018.
[4] Yu. Belchenko, et al. AIP Conference Proceedings 1097, 214 (2009); doi: 10.1063/1.3112515
[5] A. Kuznetsov, et al. Proceedings of RuPAC2014, Obninsk, Russia, p.191-193.
[6] Ivanov A.V., Tiunov M.A. ULTRASAM-2D Code for Simulation of Electron Guns with Ultra High Precision // Proc 8th European Particle Accelerator Conference, Paris, 2002, 1634-1636.
[7] Ivanov A.V. Raschet elektronno-opticheskih system novih poklenii elektronnih ohladitelei. PhD, Diss. [Computation of the electron optics for the new generation electron cooling devises. PhD, Diss.]. Novosibirsk, 2008, 152 p.

ISBN 978-3-95450-181-6

HIGH SPEED CRYOGENIC MONODISPERSE TARGETS FOR HIGH INTENSITY CYCLIC AND LINEAR ACCELERATORS

A.Boukharov, E.Vishnevkii, NRU MPEI, Moscow, Russia

Abstract

The basic possibility of creation of high speed cryogenic monodisperse targets is shown. According to calculations at input of thin liquid cryogenic jets with a velocity of bigger 100 m/s in vacuum the jets don't manage to freeze at distance to 1 mm and can be broken into monodisperse drops. Drops due to evaporation are cooled and become granules. High speed cryogenic monodisperse targets have the following advantages: direct input in vacuum (there is no need for a chamber of a triple point chamber and sluices), it is possible to use the equipment of a cluster target, it is possible to receive targets with a diameter of D < 20 μk from various cryogenic liquids (H2, D2, N2, Ar) with dispersion less than 1%, the high velocity of monodisperse granules(> 100m/s), exact synchronization of the target hitting moment in a beam with the moment of sensors turning on

Development of accelerating technique made possible receiving the high-energy beams of elementary particles. Interaction between such beams and cryogenic monodisperse targets will allow to solve fundamental problems of nuclear physics.

The cryogenic monodisperse target is the most perspective target for future experiment of "PANDA" [1-3]. "PANDA" is a unique experiment within the project of the new European accelerator FAIR in Darmstadt (Germany). The physical program of the experiment is research of fundamental problems of nuclear physics, finding of new extremal matter forms.

Cryogenic monodisperse targets have the following unique properties:

1. The small size of monodisperse targets – diameter is from 20 micron to 100 microns. Targets can be received from hydrogen or its isotopes, nitrogen, argon, neon, krypton and xenon.
2. High luminosity of targets and a possibility of registration of particles dispersion at angle of 4π.
3. Renewability – targets pass through a beam during small time.

Cryogenic monodisperse targets represent the flow of solid monodisperse granules of the small sizes received from liquefied gas. The liquid cryogenic jet follows from the generator of monodisperse drops in the vacuum chamber. Under the influence of special perturbation the jet breaks up to drops .Because pressure in the vacuum chamber is smaller than pressure about drops surface, there is intensive evaporation of liquid. As a result drops are cooled, freeze and become solid granules. Passing through system of sluices the granules accelerate and come to the working camera where there is an interaction to an accelerating beam or laser ray. For reduction of leaking and increase of granules speed it is possible to use two and more vacuum chambers divided by sluices. After interaction with high-energy beam the granules get to the cooled trap and deposit on its walls.

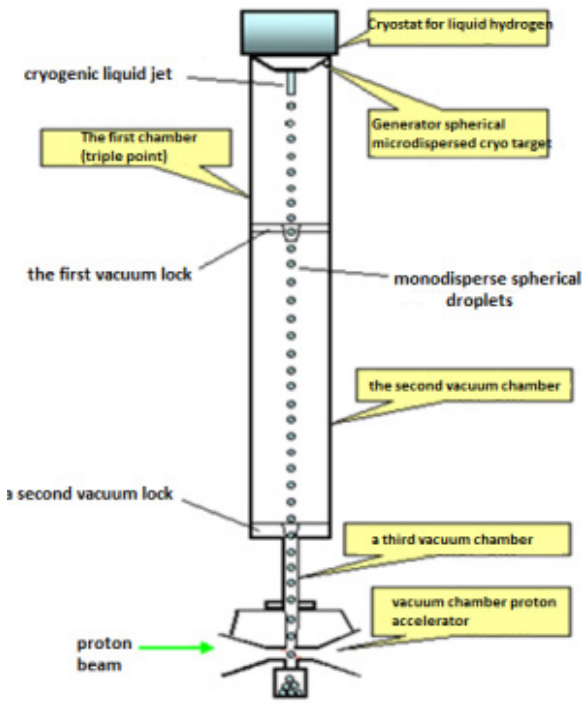

Figure 1: The detailed description cryogenic corpuscular targets.

The detailed description of the operation of installations on receiving cryogenic corpuscular targets is provided in [4-5] and fig. 1.

The important effect on stability of targets flow have sluices and especially the first sluice connecting the triple point camera to other vacuum chambers. If to remove the first sluice, not to allow to a liquid cryogenic jet to freeze and directly to send drops to the second vacuum chamber, then it is possible to simplify construction of installation and to reduce its sizes.

Operation purpose: to prove the possibility of application without sluice method of receiving monodisperse cryogenic targets.

For realization of purpose the model of the expiration of a jet to the low pressure area was created in the software PHOENICS and distribution of temperature to jet surfaces is investigated by the numerical method.

ISBN 978-3-95450-181-6

PROBLEM IN THE MEDIUM PHOENICS

When the geometric calculations and temporary space is divided into a finite number of small control volumes, with the help of the grid in the Cartesian coordinate system. PHOENICS automatically places the system of differential equations in a conservative system of algebraic equations in accordance with the selected grid. "Conservatism" of the system of algebraic equations means that when it is receiving the physical meaning of the original differential equations persists.

It is known that the differential equations that describe the processes of heat and mass transfer and fluid dynamics are subject to a generalized conservation law [6]. For the state variable F generalized differential equation takes the following form:

$$\frac{\partial}{\partial \tau}(\rho\Phi)+\frac{\partial}{\partial x_i}(\rho v_i\Phi)=\frac{\partial}{\partial x_i}\left(\Gamma_\phi\frac{\partial\Phi}{\partial x_i}\right)+S_\phi \qquad (1)$$

where: t, x_i – temporal and spatial coordinates, ρ – density, v_i – the components of the velocity vector, Γ_ϕ – transfer coefficient (eg, Γ_ϕ – turbulent viscosity coefficient, thermal conductivity, diffusion, etc.), S_ϕ – source term. In particular, S_ϕ may include inflow (outflow). In equation (1) and summation over index i. In solving three-dimensional problems i = 1,2,3.

Construction of a discrete analogue to the type of equation (1) was based on control volume method. The computational domain was divided into a number of non-overlapping control volumes so that in one control volume contained only one anchor point.

The differential equations are integrated by the control each volume. To calculate integrals used piecewise profiles that describe the variation of the function F between nodes [7]. Practice has shown that the best in terms of accuracy and efficiency in the numerical implementation are polynomial profiles.

RESULTS OF PAYMENTS

Numerical calculations were carried out changing the temperature of liquid jets of hydrogen, nitrogen and argon for jet length and the radius of the jet depending on the diameter, speed, temperature and initial jet pressure in the working chamber. The results of some calculations are presented in Fig. 2–6.

Figure 2 shows the temperature change of hydrogen jet: diameter 10 μm, velocity 100 m/s, chamber pressure 100 Pa.

Figure 3 shows the temperature change of hydrogen jet: diameter 10 μm, velocity 130 m/s, 150 m/s, 180 m/s and 200 m/s, chamber pressure 100 Pa.

Figure 4 shows the temperature change of hydrogen jet: diameter 20 μm, velocity 130 m/s, 150 m/s, 180 m/s and 200 m/s, chamber pressure 100 Pa

Figure 5 presents the temperature change of nitrogen jet: diameter 5 μm, 10 μm and 20 μm, velocity 10 m/s, chamber pressure 100 Pa. Figure 6 shows the temperature change of nitrogen jet: diameter 10 μm, velocity 10 m/s, 100 m/s, chamber pressure 100 Pa.

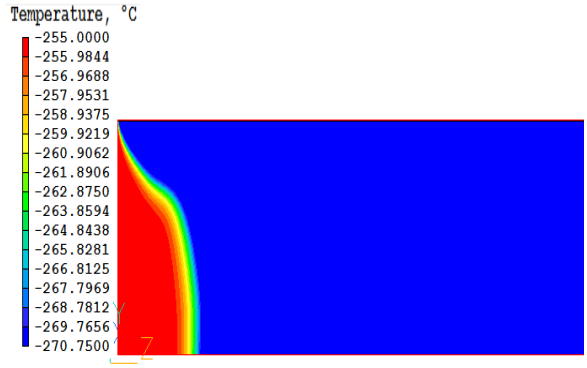

Figure 2: The temperature of the jet.

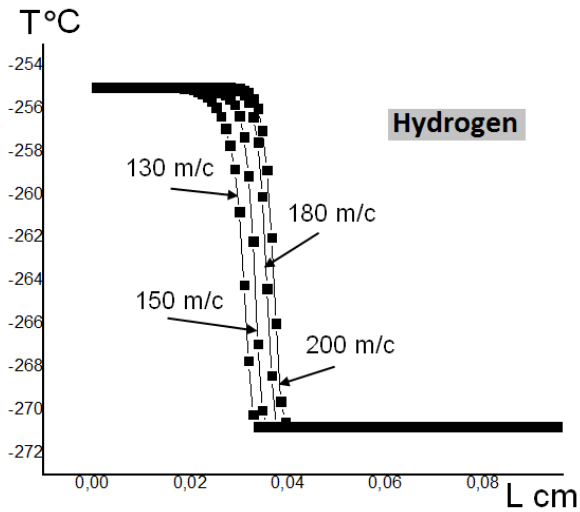

Figure 3: The temperature of the jet.

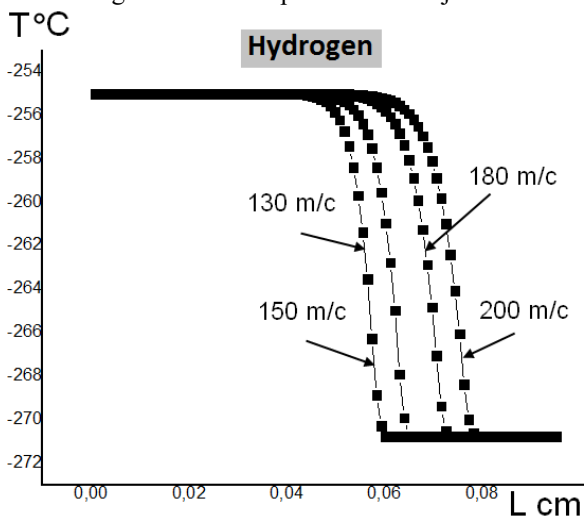

Figure 4: The temperature of the jet.

ISBN 978-3-95450-181-6

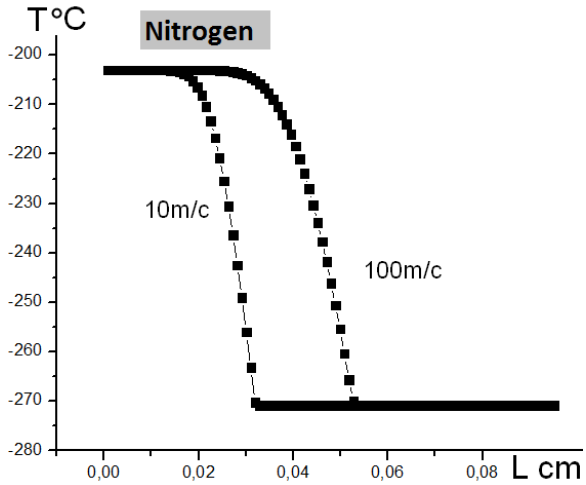

Figure 5: The temperature of the jet.

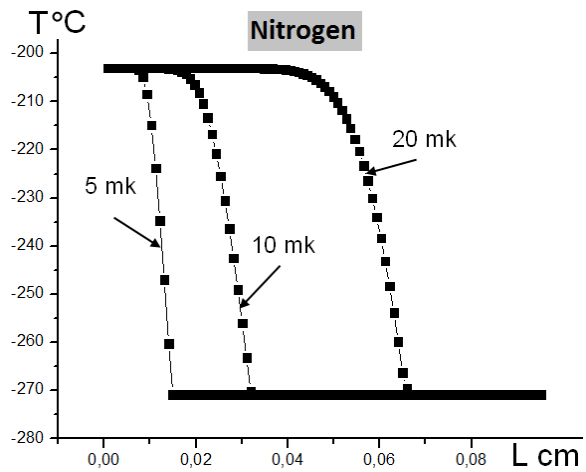

Figure 6: The temperature of the jet.

ACKNOWLEDGMENT

According to calculations at input of thin liquid cryogenic jets with a velocity of bigger 100 m/s in vacuum the jets don't manage to freeze at distance to 1 mm and can be broken into monodisperse drops. Drops due to evaporation are cooled and become granules.

High speed cryogenic monodisperse targets have the following advantages: direct input in vacuum (there is no need for a chamber of a triple point chamber and sluices), it is possible to use the equipment of a cluster target, it is possible to receive targets with a diameter of D < 20 μk from various cryogenic liquids (H2, D2, N2, Ar) with dispersion less than 1%, the high velocity of monodisperse granules(> 100m/s), exact synchronization of the target hitting moment in a beam with the moment of sensors turning on.

REFERENCES

[1] Technical Design Report for the PANDA (Antiproton Annihilations at Darmstadt) Straw Tube Tracker / W. Erni, I. Keshelashvili, A. Aab et al. // The European Physical J.A – Hadrons and Nuclei. – 2013. – V. 49. – № 2 . – P. 25.

[2] Search for New Forms of Matter in Antimatter–matter Interactions in the PANDA Experiment / A.V. Boukharov, A.N. Vasiliev, D.A. Morozov et al. //Atomic Energy.– 2012.– V. 112. – № 2. – P. 129–138.

[3] FAIR CDR - An International Accelerator Facility for Beams of Ions and Antiprotons // Conceptual Design Report, 2001. – 695 p.

[4] Trostell B. Status of the Hydrogen Micro-Sphere Target Development / B. Trostell // Univ. of Uppsala. – Sweden, 1992. – 08-18. – P.1–20.

[5] Cryogenic corpuscular target. Concept and the basic model / A.V. Bukharov, A.F. Ginevskii, V.P. Chernyshev, etc. – Preprint – number 17-17. M:. Publishing house of the Moscow Power Engineering Institute, 2002. – 35 p.

[6] Official site of company CHAM / Products, 2013. – URL: www.cham.co.uk.

[7] Official site of company CHAM / FLAIR. User Guide CHAM Technical Report TR 313. – URL: www.cham.co.uk/phoenics/d_polis/d_docs/tr313/tr313.htm

ISBN 978-3-95450-181-6

THE MULTIPOLE LENS MATHEMATICAL MODELING

E.M. Vinogradova*, A.V. Starikova,
Saint Petersburg State University,
7/9 Universitetskaya nab., St. Petersburg, 199034 Russia

Abstract

In the present work the mathematical model of the multipole system is presented. The multipole system is composed of arbitrary even number of the uniform electrodes. Each of the electrodes is a part of the plane. The potentials of the electrodes are the same modulus and opposite sign for neighboring electrodes. The variable separation method is used to solve the electrostatic problem. The potential distribution is represented as the eigen functions expansions. The boundary conditions and the normal derivative continuity conditions lead to the linear algebraic equations system relative to the series coefficients.

INTRODUCTION

Electrostatic multipole systems are widely used in the accelerator technology for the charged particle beams transport [1]– [3]. In this paper the mathematical modeling of the electrostatic multipole system is presented. The multipole system consist of the even number uniform plate electrodes of the same shape and size. Fig. 1 shows a schematic representation of the multipole system. The similar system was investigated in [4]. A quadrature expression was obtained for the field potential and the constraints imposed on the electrode potentials, under which such a solution is possible, were determined. In our work a system with an arbitrary even number $2N$ of electrodes is modeled. The variable separation method [5]– [7] is used in plane polar coordinates (r, α) to solve the boundary-value problem for the Laplace equation [8].

The multipole potential distribution has the planes of symmetry $\alpha = (\pi k)/N$ and planes of antisymmetry $\alpha = \pi/(2N) + (\pi k)/N$, $k = \overline{0, N-1}$. An additional plane $r = R_2$ can be introduce to limit the area of the problem under consideration without loss of generality. Thus it suffices to consider sector $0 \le \alpha \le \pi/2N$, $0 \le r \le R_2$ to find the electrostatic field. Schematic diagram of the multipole system sector is presented on Fig. 2 ($\alpha_1 = \pi/2N$).

The problem parameters are:

$(R_1, 0)$ — the coordinate position of the multipole electrode's edge,

R_2 — the radius of the area,

$\alpha_1 = \pi/2N$ — the boundary of the area (the plane of antisymmetry),

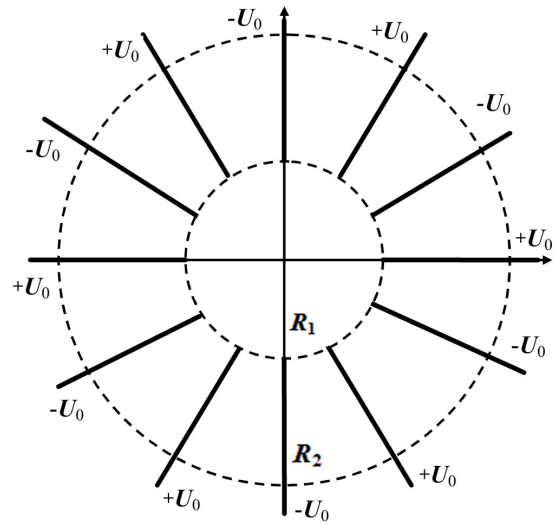

Figure 1: Schematic representation of the multipole system.

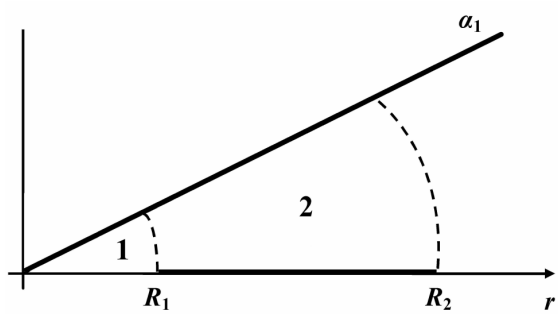

Figure 2: Schematic representation of the multipole system sector.

U_0 — the multipole electrode potential ($\alpha = 0$, $R_1 \le r \le R_2$).

MATHEMATICAL MODEL

The electrostatic potential distribution $U(r, \alpha)$ in the area $(0 \le r \le R_2, 0 \le \alpha \le \alpha_1)$ satisfies the Laplace equation and the boundary conditions

* e.m.vinogradova@spbu.ru

ISBN 978-3-95450-181-6

$$
\begin{aligned}
&\triangle\, U(r,\alpha) = 0, \quad 0 \le r \le R_2,\ 0 \le \alpha \le \alpha_1;\\
&U(R_1,0) = U_0, \quad R_1 \le r \le R_2;\\
&U(R_2,\alpha) = 0, \quad 0 \le \alpha \le \alpha_1;\\
&U(r,\alpha_1) = 0, \quad 0 \le r \le R_2;\\
&\left.\frac{\partial U}{\partial \alpha}\right|_{\alpha\,=\,0} = 0, \quad 0 \le r \le R_1,
\end{aligned}
\tag{1}
$$

where

$\alpha = 0$ — the plane of symmetry,

$\alpha = \alpha_1$ — the plane of antisymmetry.

SOLUTION OF THE BOUNDARY – VALUE PROBLEM

The variable separation method is used to solve the boundary-value problem (1). The interior of the multipole system sector domain ($0 \le r \le R_2$, $0 \le \alpha \le \alpha_1$) can be divided into two subdomains:

subdomain 1: ($0 \le \alpha \le \alpha_1$, $0 \le r \le R_1$);

subdomain 2: ($0 \le \alpha \le \alpha_1$, $R_1 \le r \le R_2$).

The potential distribution function $U(r,\alpha)$ can be presented as

$$
U(r,\alpha) = \begin{cases} U_1(r,\alpha), & 0 \le \alpha \le \alpha_1,\ 0 \le r \le R_1;\\ U_2(r,\alpha), & 0 \le \alpha \le \alpha_1,\ R_1 \le r \le R_2. \end{cases}
\tag{2}
$$

Then functions $U_1(r,\alpha)$, $U_2(r,\alpha)$ (2) are represented as a Fourier series:

$$
U_1(r,\alpha) = \sum_{n=1}^{\infty} a_n \left(\frac{r}{R_1}\right)^{\mu_n} \cos(\mu_n \alpha),
\tag{3}
$$

$$
\begin{aligned}
U_2(r,\alpha) = \sum_{k=1}^{\infty} b_k \frac{\left(\frac{r}{R_2}\right)^{\nu_k} - \left(\frac{R_2}{r}\right)^{\nu_k}}{\left(\frac{R_1}{R_2}\right)^{\nu_k} - \left(\frac{R_2}{R_1}\right)^{\nu_k}} \times\\
\times \cos(\nu_k \alpha) +\\
+ \sum_{m=1}^{\infty} c_m \frac{\sinh(\lambda_m(\alpha_1 - \alpha))}{\sinh(\lambda_m \alpha_1)} \sin\left(\lambda_m \ln\frac{r}{R_2}\right),
\end{aligned}
\tag{4}
$$

where

$$
\begin{aligned}
\mu_n &= \frac{\pi(2n+1)}{2\alpha_1},\\
\nu_k &= \frac{\pi\, k}{2\alpha_1},\\
\lambda_m &= \frac{\pi\, m}{\ln\frac{R_1}{R_2}}.
\end{aligned}
\tag{5}
$$

The potential distribution functions (2)–(5) are the Laplace equation solutions for each subdomain ($i = 1, 2$). The boundary conditions (1) are satisfied for $\alpha = \alpha_1$ ($0 \le r \le R_2$), $r = R_2$ ($0 \le \alpha \le \alpha_1$), $\alpha = 0$ ($0 \le r \le R_1$).

The coefficients c_m in expansion (4) can be calculated in an explicit form with the boundary conditions (1) $\alpha = 0$ ($R_1 \le r \le R_2$):

$$
c_m = \frac{U_0}{\pi\, m}(1 - (-1)^m).
\tag{6}
$$

The continuity condition for the potential distribution $U_1(R_1,\alpha) = U_2(R_1,\alpha)$ for $0 \le \alpha \le \alpha_1$ leads to the relation between the coefficients a_n and b_k:

$$
\begin{aligned}
a_n &= \frac{2}{\alpha_1} \sum_{k=1}^{\infty} b_k \frac{\nu_k}{\nu_k^2 - \mu_n^2} =\\
&= \frac{8}{\pi} \sum_{k=1}^{\infty} b_k \frac{k}{4k^2 - (2n+1)^2}.
\end{aligned}
\tag{7}
$$

The normal derivative of the electric displacement vector continuity conditions can be written as

$$
\left.\frac{\partial U_1(r,\alpha)}{\partial r}\right|_{r\,\le\,R_1} = \left.\frac{\partial U_2(r,\alpha)}{\partial r}\right|_{r\,\le\,R_1},
\quad 0 \le \alpha \le \alpha_1.
\tag{8}
$$

Equation (8) establishes another relation between the coefficients a_n and b_k:

$$
\begin{aligned}
a_n = \frac{2}{\alpha_1\, \mu_n} \times\\
\times \left[\sum_{k=1}^{\infty} b_k \frac{\nu_k^2}{\nu_k^2 - \mu_n^2} \frac{\left(\frac{R_2}{R_1}\right)^{\nu_k} + \left(\frac{R_1}{R_2}\right)^{\nu_k}}{\left(\frac{R_2}{R_1}\right)^{\nu_k} - \left(\frac{R_1}{R_2}\right)^{\nu_k}} + \right.\\
\left. + \frac{U_0}{\ln\frac{R_1}{R_2}} \sum_{m=1}^{\infty} \frac{(1 - (-1)^m)\lambda_m}{\lambda_m^2 + \mu_n^2} \coth \lambda_m \alpha_1 \right].
\end{aligned}
\tag{9}
$$

Then, in consequence of the formulas (7) and (9) the coefficients b_k are the solutions of the linear algebraic equations system:

$$
\begin{aligned}
\sum_{k=1}^{\infty} b_k \frac{\nu_k}{\nu_k^2 - \mu_n^2} \times\\
\times \left[\frac{\nu_k}{\mu_n} \frac{\left(\frac{R_2}{R_1}\right)^{\nu_k} + \left(\frac{R_1}{R_2}\right)^{\nu_k}}{\left(\frac{R_2}{R_1}\right)^{\nu_k} - \left(\frac{R_1}{R_2}\right)^{\nu_k}} - 1 \right] =\\
= \frac{U_0}{\mu_n \ln\frac{R_1}{R_2}} \sum_{m=1}^{\infty} \frac{(1 - (-1)^m)\lambda_m}{\lambda_m^2 + \mu_n^2} \coth \lambda_m \alpha_1.
\end{aligned}
\tag{10}
$$

ISBN 978-3-95450-181-6

CONCLUSION

In this article a mathematical model of the electrostatic multipole system is considered. The multipole system electrodes are the the uniform plate electrodes of the same shape and size. The variable separation method is applied to calculate the electrostatic potential distribution for the boundary-value problem (1) in plane polar coordinates. The potential distribution function is represented as Fourier series (3)–(5). Some of the coefficients (6) are determined from the boundary conditions (1) in an explicit form. The continuity conditions for the potential distribution and normal derivative of the electric displacement vector continuity conditions makes it possible to reduce the original boundary value problem (1) to the system of the linear algebraic equations with the constant coefficients (7), (10). All geometric dimensions and potential of the multipole system electrodes are the parameters of the problem.

REFERENCES

[1] H. Liu et al., "Design and Optimization of Multipole Lens and Wien Filter Systems," Nucl. Instrum. Methods Phys. Res. A 645 (2011) 300.

[2] P.W.Hawkes, "The Correction of Electron Lens Aberrations," Ultramicroscopy 156 (2015) A1.

[3] H. Sawada, "Aberration Correction in STEM (Book Chapter)," *Scanning Transmission Electron Microscopy of Nanomaterials: Basics of Imaging and Analysis*, (2014) 283.

[4] I.F. Spivak-Lavrov, "Solution of the dirichlet problem for the Laplace equation for a multiply connected region with point symmetry," Technical Physics 44(3) (1999) 223.

[5] N.V. Egorov and E.M. Vinogradova, "Mathematical modeling of the electron beam formatting systems on the basis of field emission cathodes with various shapes," Vacuum 72 (2) (2004) 103.

[6] E.M. Vinogradova et al., "Mathematical simulation of a diode system with a cylindrical field-emission tip," Technical Physics 60(2) (2015) 176.

[7] E.M. Vinogradova et al., "Mathematical modeling of field emitter array," Vacuum 127 (2016) 45.

[8] E.M. Vinogradova and A.V. Listrukova, "The Electrostatic Quadrupole Lens Mathematical Modeling," International Conference on "Stability and Control Processes" in Memory of V.I. Zubov, SCP 2015, Saint Petersburg, October 2015, p. 214 (2015).

ISBN 978-3-95450-181-6

USE OF STRUCTURAL-VARIATIONAL METHOD OF R-FUNCTIONS IN MATHEMATICAL MODELING OF MAGNETIC SYSTEMS

O.I. Zaverukha, M.V. Sidorov
Kharkiv National University of Radioelectronics, Ukraine

Abstract

Magnetic systems are widespread in nature and technics. It is atoms in crystal grid of ferromagnetic, magnets of accelerating installations, space satellites stabilization systems etc. Due to high cost of full-scale study of such systems during last decades mathematical modeling and numerical analysis with computer started to come to the fore. The methods of finite differences, finite element, boundary integral elements and others are mainly used for the numerical analysis of the magnetic systems. Each of mentioned methods has its own advantages and disadvantages [1]. The main shortcoming of all listed methods is necessity in generation and adjustment new computational grid according to characteristics of each area. The structural-variational method of R-functions [5,6,8], proposed by Rvachev V.L., academician of National Academy of Sciences of Ukraine, is an alternative to all existing methods of numerical calculation of magnetic particles. In the context of solving mathematical physical problems the *R*-function method allows to create the structures for solving the boundary value problems – the bundles of functions that exactly meet the boundary conditions of the problem. With this approach the geometry of the area is accurately taken into account. So, the development of existing methods of numerical analysis of magnetic systems with *R*-function methods is the scientific problem of current interest.

PROBLEM DEFINITION

Consider a magnetic system (figure 1), consisting of ferromagnetic Ω_f and vacuum Ω_v with closed current windings Ω_c. Magnetostatic problem is stated – find the magnetic field distribution, that created by steady currents and magnetization of isotropic ferromagnetics [2,3]. Let's assume that lengthwise cut is substantially larger than the transverse. Then vector potential of magnetic induction vector will have only one nonzero coordinate $u = u(x, y)$ and we can proceed from Maxwell's system of equations for stationary magnetic field to scalar equation

$$\frac{\partial}{\partial x}\left(\frac{1}{\mu}\frac{\partial u}{\partial x}\right)+\frac{\partial}{\partial y}\left(\frac{1}{\mu}\frac{\partial u}{\partial y}\right)=-\mu_0 J_z(x, y),\ (x, y)\in\mathbb{R}^2. \quad (1)$$

Here μ is function of the permeability of a ferromagnetic, which is known in Ω_f nonlinear function from magnetic field intensity vector (for nonmagnetic environment $\mu = 1$), μ_0 is vacuum magnetic permeability, $J_z(x, y)$ is z component of volumetric current density vector, that is different from 0 only in Ω_c and satisfies the equation $\iint_{\Omega_c} J_z(x, y)dxdy = 0$,

$$u(x, y)=\begin{cases} u_f(x, y), & (x, y)\in\Omega_f, \\ u_v(x, y), & (x, y)\in\Omega_v. \end{cases}$$

Equation (1) should be supplemented with conjugation conditions at the border $\partial\Omega_{fv}$ that separates ferromagnetic and vacuum

$$u_f\big|_{\partial\Omega_{fv}} = u_v\big|_{\partial\Omega_{fv}},\ \frac{1}{\mu}\frac{\partial u_f}{\partial \mathbf{n}}\bigg|_{\partial\Omega_{fv}} = \frac{\partial u_v}{\partial \mathbf{n}}\bigg|_{\partial\Omega_{fv}}, \quad (2)$$

where $\mathbf{n}$ is the unit vector normal to $\partial\Omega_{fv}$, and with conditions on infinity:

$$\lim_{x^2+y^2\to+\infty} u = 0. \quad (3)$$

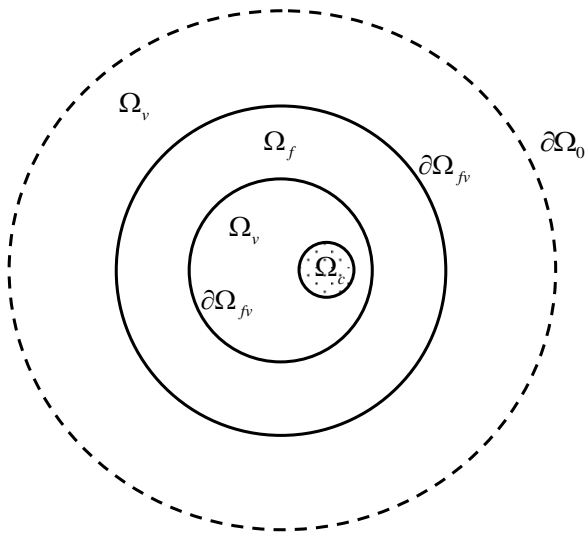

Figure 1: Magnetic system.

BUILDING OF SOLVING STRUCTURE

Let's replace condition on infinity (3) with other condition

ISBN 978-3-95450-181-6

$$u\big|_{\partial\Omega_0} = 0, \tag{4}$$

where circuit $\partial\Omega_0$ is far enough from Ω_f (figure 1). For instance, we can select circle $x^2 + y^2 = R_0^2$ as a $\partial\Omega_0$ with sufficiently large R_0.

Supposing Ω_0 as the computational domain of problem (1), (2), (4).

Assume that $\omega_0(x, y)$ has the following properties

1) $\omega_0(x, y) > 0$ in Ω_0;
2) $\omega_0(x, y) = 0$ on $\partial\Omega_0$.

Function $\omega_0(x, y)$ with mentioned properties can be built as a single analytical expression using structural unit of *R*-functions [8].

Then bundle of functions $u = \omega_0\Phi$ will meet the condition (1) for any choice of indefinite component Φ [4,8].

To meet the transmission conditions (2), we should use the following approach [9]. The function $u(x, y)$ will be sought in the form:

$$u(x, y) = \begin{cases} u_f(x, y) = \omega_0\Phi - A\omega_{fv} D_1^{fv}(\omega_0\Phi), \\ u_v(x, y) = \omega_0\Phi, \end{cases} \tag{5}$$
$$(x, y) \in \Omega_f, (x, y) \in \Omega_v.$$

where $\omega_{fv} = 0$ is normalized equation of the boundary $\partial\Omega_{fv}$ and $\omega_{fv} > 0$ in Ω_f and operator D_1^{fv} determined by following equation

$$D_1^{fv} = \frac{\partial\omega_{fv}}{\partial x}\frac{\partial}{\partial x} + \frac{\partial\omega_{fv}}{\partial y}\frac{\partial}{\partial y}.$$

Operator D_1^{fv} has property $D_1^{fv} u\big|_{\partial\Omega_{fv}} = \left.\frac{\partial u}{\partial \mathbf{n}}\right|_{\partial\Omega_{fv}}$, where $\mathbf{n}$ is unit vector normal to $\partial\Omega_{fv}$ inward Ω_f. Then

$$D_1^{fv}\omega_{fv}\big|_{\partial\Omega_{fv}} = \left.\frac{\partial\omega_{fv}}{\partial \mathbf{n}}\right|_{\partial\Omega_{fv}} = 1.$$

Notice, that function of the form (5) with any choice of constant A meets the first conjugation condition (2). So, we should choose function A to meet the second conjugation condition (2).

We have:

$$\left.\frac{1}{\mu}\frac{\partial u_f}{\partial \mathbf{n}}\right|_{\partial\Omega_{fv}} = \frac{1}{\mu} D_1^{fv} u_f\big|_{\partial\Omega_{fv}} =$$

$$= \frac{1}{\mu} D_1^{fv}[\omega_0\Phi - A\omega_{fv} D_1^{fv}(\omega_0\Phi)]\big|_{\partial\Omega_{fv}} =$$

$$= \left.\frac{1}{\mu}(1 - A) D_1^{fv}(\omega_0\Phi)\right|_{\partial\Omega_{fv}},$$

$$\left.\frac{\partial u_v}{\partial \mathbf{n}}\right|_{\partial\Omega_{fv}} = D_1^{fv} u_v\big|_{\partial\Omega_{fv}} = D_1^{fv}(\omega_0\Phi)\big|_{\partial\Omega_{fv}}.$$

So, the second conjugation condition (2) will be met, if $\frac{1}{\mu}(1 - A) = 1$, i.e $A = 1 - \mu$.

Summarizing, the problem (1), (2), (4) solving structure will be:

$$u(x, y) = \begin{cases} \omega_0\Phi - (1 - \mu)\omega_{fv} D_1^{fv}(\omega_0\Phi), & (x, y) \in \Omega_f, \\ \omega_0\Phi, & (x, y) \in \Omega_v. \end{cases} \tag{6}$$

CONSTRUCTION OF THE APPROXIMATE SOLUTION

To build an approximate solution for problem (1) – (3) the undefined component Φ in structure (6) should be approximated with following expression

$$\Phi_n = \sum_{i=1}^{n} c_i \tau_i, \tag{7}$$

where $\{\tau_i\}$ is complete in $L_2(\Omega_0)$ system of functions (trigonometric or exponential polynomials, splines etc.), $c_1, ..., c_n$ are unknown coefficients. Substituting (7) into (6) wiw i will show us that approximate solution of the problem (1) – (3) sought in the form

$$u_n(x, y) = \sum_{i=1}^{n} c_i \varphi_i, \tag{8}$$

where

$$\varphi_i = \begin{cases} \omega_0\tau_i - (1 - \mu)\omega_{fv} D_1^{fv}(\omega_0\tau_i), & (x, y) \in \Omega_f, \\ \omega_0\tau_i, & (x, y) \in \Omega_v. \end{cases}$$

We can use variational or projectional methods to find $c_1, ..., c_n$ coefficients. For instance, following the Galerkin method, we can find $c_1, ..., c_n$ from orthogonal residuals condition by substituting (8) into (1) to functions $\varphi_1, ..., \varphi_n$ [7]. This will lead us to the system of equations

$$\sum_{i=1}^{n} a_{ij} c_i = b_j, \quad j = 1, ..., n,$$

ISBN 978-3-95450-181-6

where

$$a_{ij} = \iint\limits_{\Omega_0} \left[\frac{\partial}{\partial x}\left(\frac{1}{\mu} \frac{\partial \varphi_i}{\partial x} \right) + \frac{\partial}{\partial y}\left(\frac{1}{\mu} \frac{\partial \varphi_i}{\partial y} \right) \right] \varphi_j \, dxdy \;\; i, j = 1, ..., n ,$$

$$b_j = -\mu_0 \iint\limits_{\Omega_c} J_z(x, y) \varphi_j \, dxdy , \;\; j = 1, ..., n .$$

COMPUTATIONAL EXPERIMENT

For the test problem as Ω_0 chose a circle of radius R_0 and a ferromagnetic also bound it with circles of radius r and R ($r > R$). Then functions ω_0 and ω_{fv} could be taken in like

$$\omega_0(x, y) = R_0^2 - x^2 - y^2 ,$$

$$\omega_{fv}(x, y) = \left[\frac{1}{2r}(x^2 + y^2 - r^2) \right] \wedge_0 \left[\frac{1}{2R}(R^2 - x^2 - y^2) \right],$$

Where $\wedge_0$ — is a R_0-conjunction symbol [8]:

$$g_1 \wedge_0 g_2 \equiv g_1 + g_2 - \sqrt{g_1^2 + g_2^2} .$$

Computational experiment was conducted for next values $R_0 = 20$ m, $R = 10$ m, $r = 3$ m, $\mu_0 = 4\pi \cdot 10^{-7}$ H/m, $\mu = 700$ H/m, Ω_c it is described by next inequality $1 - (x-1)^2 - y^2 > 0$, $J_z(x, y) = 10^8 \, y(1 - (x-1)^2 - y^2)$ A/m.

Chose system of harmonic polynomials as the functions of the system $\{\tau_i\}$ in the implementation of the Galerkin method. On figure 2, 3 is a represented received component surface $B_x = \frac{\partial u}{\partial y}$, $B_y = -\frac{\partial u}{\partial x}$ an magnetic induction vectors.

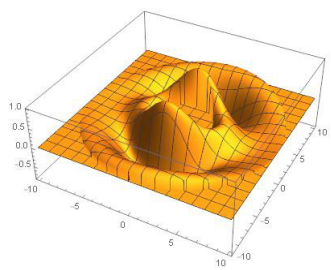

Figure 2: Surface B_x.

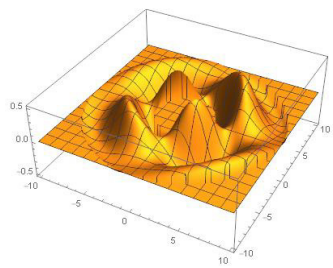

Figure 3: Surface B_y.

CONCLUSIONS

In the work, for the first time the structural method of R-functions was used for the numerical analysis of the magnetic system, which simulates the work of accelerator facility. It allowed us to build numerical method, which counts the geometric and analytic information from the problem input accurately, and allows to obtain an approximate solution analytically, that facilitate finding different characteristics of magnetic system.

REFERENCES

[1] Ayryan E.A., Zhidkov E.P., Fedorov A.V., Horomskiy B.N., Shelaev I.A., Yudin I.P., Yuldashev O.I. Chislennyie algoritmyi rascheta magnitnyih sistem uskoriteley zaryazhennyih chastits // Fizika elementarnyih chastits i atomnogo yadra. – 1990. – T. 21. – Vyip. 1. – S. 251 – 307.

[2] Baldin A.A., Voloshina I.G., Perepelkin E.E., Polyakova R.V., Ros-siyskaya N.S., Shavrina T.V., Yudin I.P. Chislennoe modelirovanie ras-predeleniya polya magnita SP-40 ustanovki "MARUSYa" i sravnenie re-zultatov s eksperimentalnyimi dannyimi // Zhurnal tehnicheskoy fiziki. – 2007. – T. 77. – № 11. – S. 7 – 16.

[3] Zhidkov E.P., Voloshina I.G., Polyakova R.V., Perepelkin E.E., Ros-siyskaya N.S., Shavrina T.V., Yudin I.P. Kompyuternoe modelirovanie magnitnyih sistem nekotoryih fizicheskih ustanovok // Kompyuternyie issledovaniya i modelirovanie. – 2009. – T. 1. – № 2. – S. 189 – 198.

[4] Kantorovich L.V., Akilov G.P. Funktsionalnyiy analiz. – SPb.: BHV-Peterburg, Nevskiy Dialekt, 2004. – 816 s.

[5] Kravchenko V.F., Rvachev V.L. Algebra logiki, atomarnyie funktsii i veyvletyi v fizicheskih prilozheniyah. – M.: Fizmatlit, 2006. – 416 s.

[6] Maksimenko-Sheyko K.V. R-funktsii v matematicheskom modelirovanii geometricheskih ob'ektov i fizicheskih poley. – H.: IPMASh NAN Ukrainyi, 2009. – 306 s.

[7] Mihlin S.G. Variatsionnyie metodyi v matematicheskoy fizike. – M.: Nauka, 1970. – 512 s

[8] Rvachev V.L. Teoriya R-funktsiy i nekotoryie ee prilozheniya. – K.: Nauk. dumka, 1982. – 552 s.

[9] Temnikov A.V., Slesarenko A.P. Sovremennyie priblizhennyie ana-liticheskie metodyi resheniya zadach teploobmena. – Samara: Izd-vo Samar. politehn. in-ta, 1991. – 92 s.

ISBN 978-3-95450-181-6

THE DESIGN OF PERMANENT MAGNET SPREAD SYSTEM FOR 0.5 MeV IRRADIATION ACCELERATOR

J. Huang†, M.W. Fan, L.G. Zhang, C. Zuo, Y.Q. Xiong, T.Q. Yu, J. Yang, K.J. Fan, W. Qi, School of Electrical and Electronic Engineering, Huazhong University of Science and Technology, Wuhan, 430074, P. R. China

Abstract

The traditional electron beam scanning magnet has many disadvantages, for example, the regulatory of excitation current is very complex and the irradiation uniformity as well as the irradiation area is very difficult to improve and expand. Thus, the author of the paper proposes an innovative technology of a permanent magnet spread system for 0.5MeV irradiation accelerator which uses a special configuration of the magnetic field to spread electron beam bunch directly and would remarkably improve the spread uniformity, simplify the accelerator and would be helpful to protect the titanium window and expand the irradiation area. Also, the technology could as well be used on the electron beam irradiation of those irregular structured objects of large size.

INTRODUCTION

Irradiation processing has been widely applied in industries of manufacture, agriculture, bio-medicine and environmental protection because of its energy saving and environmentally friendly advantages [1, 2]. An electron irradiation accelerator, with its benefits of controllable energy, operational efficiency, no radioactive pollution source, and no energy consumption when the machine is cut off, etc, has been widely adapted in the irradiation processing industry [3, 4].

A high voltage electron accelerator mainly consists of an electron gun and an accelerator tube that is followed by a scanning magnet system, which usually uses a dipole electromagnet with a saw tooth wave energy supply [5], as shown in Fig. 1. When the electron beam passes through this system, the dipole electromagnet scans the beam in the transversal direction like the row scanning of a TV set [6].

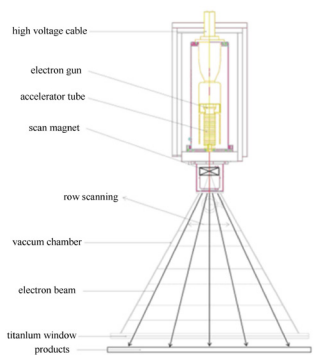

Figure 1: High voltage electron accelerator with a beam scanning device.

However, its shortcomings are as follows:

1. When the electron beam moves along a linear line, it tends to become overheated in some areas and burn the titanium film [7].
2. It also causes "Tail sweep" phenomenon and uneven irradiation.
3. The excessive use of electricity is liable to lead malfunction in the power system [8].
4. the speed of the conveyer belt has negative effects on the even distribution of irradiation.

The lab's invention to directly spread the electron beam with multi-pole magnetic field of specially constructed permanent magnets has perfectly addressed the inherent shortcomings of the conventional electromagnet scanning method.

THEORETICAL PRINCIPLE

Considering the relativistic effect, an electron's mass is decided by Eq. (1).

$$m = \frac{m_0}{\sqrt{1-\beta^2}} = m_0\gamma \tag{1}$$

According to the charged particle dynamics,

$$\frac{d(m\vec{V})}{dt} = e\vec{B} \times \vec{V} \tag{2}$$

Where B refers to the density of magnetic induction, e refers to the electron charge and, V refers to the electron velocity. If a Cartesian coordinate is used, Eq. (2) will be written as

$$\begin{cases} d(mv_x)/dt = qv_yB_z - qv_zB_y \\ d(mv_y)/dt = qv_zB_x - qv_xB_z \\ d(mv_z)/dt = qv_xB_y - qv_yB_x \end{cases} \tag{3}$$

In Eq. (3), the subscript refers to x, y and z components. By applying four order Ruge-Kutta's numerical integration, the equation can be solved numerically.

The deflecting distance S of electrons will be calculated by Eq. (4),

$$\begin{aligned} &\vec{F} = m\vec{a} \\ &S = \int_{t1}^{t2} atdt \\ &t = \frac{L}{V_z} \end{aligned} \tag{4}$$

In this equation, a is the acceleration of electron, L the height of scanning box, and V the velocity along the z-axis direction. The velocity changes in a limited region, which means the distance of the electron deflection is limited in a small region. This theoretically justifies that a permanent magnet combination may satisfy the requirements of different energies. To prove the com-

ISBN 978-3-95450-181-6

patibility of the proposed spread system, the low energy accelerators are divided into three groups (300keV/400keV, 400-600keV, 600-1000keV), which are based on 5% of different V.

NUMERICAL SIMULATION OF PERMANENT MAGNET SPREAD SYSTEM

If the energy of accelerated electron beams is to be spread is 0.5 MeV with 1 cm radius cross section, and 22.5 πmm·mrad emittance, which is the most common case for low energy electron irradiation accelerators at present. A Cartesian coordinate system is used. The Z direction refers to the mean direction of propagation of the electron beams pointing out of the paper. Both the Gaussian and uniform distributions of initial electron beam bunch are supposed in the simulation. The beam bunch is located in the center of the magnet equipment and enters the magnetic field at the very beginning. The Gaussian and uniform distributions of the electron are respectively shown in Fig.2.

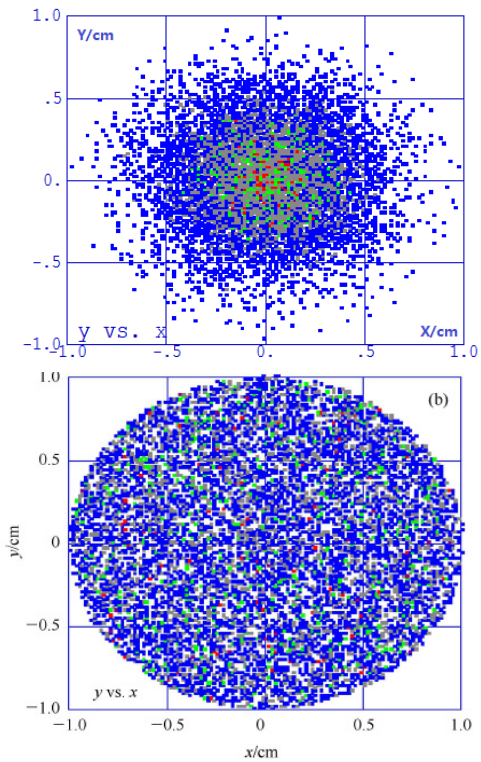

Figure 2: The electrons' Gaussian and Uniform distributions.

The Magnetic Field Analysis of Permanent Magnet Spread System

The spread system consists of 2 permanent magnets. They are 1 cm apart. The first magnet is used to spread the electron beam bunch. The second one is used to improve the distribution in four-corner areas of the bunch. The first magnet consists of 4 poles. The second magnet consists of 8 poles. DT4 pure iron is used for the magnetic yoke and rare earth permanent magnet material Nd-Fe-B for the poles, as shown in Fig.3 and Fig.4.

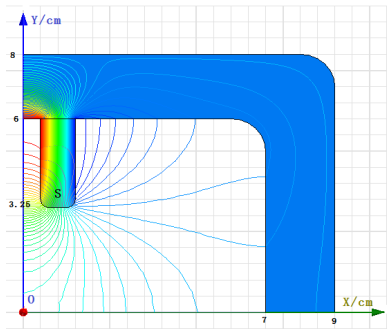

(a) The magnetic field distribution

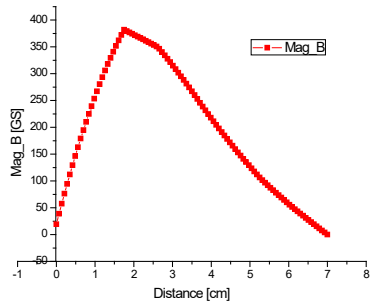

(b) The magnetic field distribution curve

Figure 3: The magnetic field of the first magnet.

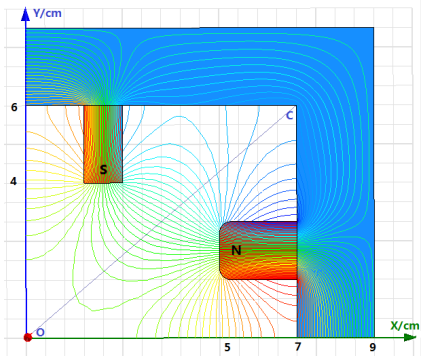

(a) The magnetic field distribution

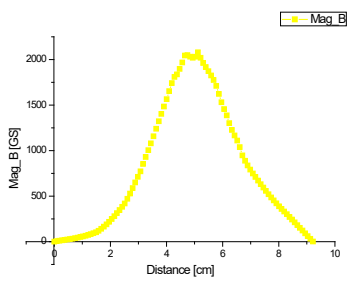

(b) The magnetic field distribution of segment EF on the second supplementary magnet.

Figure 4: The magnetic field of the second magnet.

The ideal distribution of electrons requires the poles of both the right and left side have minimized clearance. However, if the two poles were too close, the magnetic flux leakage (MFL) would increase through the magnet sides,

ISBN 978-3-95450-181-6

thus the peak field would be reduced. According to theoretical analysis, the changes of clearance and length of the poles will cause remarkable effect on the magnetic field.

Beam Dynamics Analysis

The distribution of electrons after the electron bunch passed through two magnets is showing in Fig. 5.

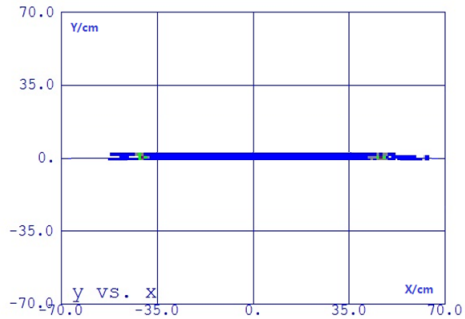

Figure 5: The beam distribution after the first and second set of magnets respectively.

The result shows that the electrons are uniformly distributed in a rectangle area with a length of 1.1m and a width of 0.2m, the lateral uniformity is ≤6.7%.

CONCLUSIONS

The proposed permanent magnet spread system remarkably improves the spread uniformity. As the spread area in the longitudinal direction could be enlarged, it might be used not only for wires, strips and panels irradiation, but also for irregular structured objects of large size.

This paper verified the excellence of the proposed system in improving the spread width and uniformity. Thus, the permanent magnet spread system is both practicable and applicable for 0.5MeV irradiation accelerators and could be used for irradiation processing.

REFERENCES

[1] Chmielewski A G, Haji-Saeid M. Radiation Physics and Chemistry, 2014, 71(1–2): 17–21.
[2] Emerging Applications of Radiation Processing. IAEA-TECDOC-1386, April, 2003.
[3] ZHENG Shu-Xin, TANG Chuan-Xiang et al. Chinese Physics C, 2008, 32(3): 228.
[4] LIU Hua-Chang, WANG Xiu-Long, FU Shi-Nian. High Energy Physics and Nuclear Physics, 2006, 30(6): 581 (in Chinese).
[5] WANG Xiang-Qi, XU Yu-Cun et al. Nuclear Techniques, 2008, 31(6): 441; YANG Jun, LI Dong et al. Calculation and De- sign of a High Voltage Electron Accelerator. Proceedings of IPAC'10, Kyoto, Japan, MOPEB074.
[6] Sanelli C, Voelker F et al. Specification of Power Supplies for Eight Scanning Dipole Magnets of the CNAO Project. CNAO internal Spec., CNASP-DF-007WXX-03018.
[7] FENG De-Ren, WANG Xiang-Qi et al. High Power Laser and Particle Beams, 2008, 20(4) 593–596 (in Chinese).
[8] REN Xiu-Yan, LU Yu-Zhu. Atomic Energy Science and Tech- nology, 2011, 45(7): 868 (in Chinese).

ISBN 978-3-95450-181-6

MEASURING SYSTEM FOR FLNR CYCLOTRONS MAGNETIC FIELD FORMATION

I.A. Ivanenko, G.N. Ivanov, V.V. Aleinikov, V.V. Konstantinov, FLNR, JINR, Dubna, 141980, Russia

Abstract

Since beginning of millennium, three new heavy-ion isochronous cyclotrons, DC72, DC60 and DC110, were created in FLNR, JINR. At the present time the activities on creation of the new cyclotron DC280 for Super Heavy Facility are carried out. The one of the main problem of cyclotron creation is a formation of the isochronous magnetic field. The FLNR measuring system bases on Hall probes and provide the measuring accuracy 10^{-4}. The paper presents the features, measuring and exploitation results of FLNR cyclotrons magnetic field formation.

INTRODUCTION

During the last twenty years the series of magnetic field measurements for FLNR new and operated cyclotrons were carried out. The purpose of these measurements were the increasing of the efficiency of operated cyclotrons U400, MC400 and IC100 and magnetic field formation for new cyclotrons DC72, DC60 and DC110 [1, 2]. This experience formed a general approach to mapping system creation and measurement philosophy. The common feature is a measuring in a polar coordinate system with the several, 8 or 14, Hall probes. The probes number depends on the cyclotron pole radius and extremely decreases the measuring time. The another feature is a usage of a toothed belt around the pole for azimuthal moving. For radial and azimuthal stepping motion of the magnetometer bar the pneumatic engines are used. Because presented cyclotrons have different parameters of the magnetic structures, such as pole diameter, sectors and pole gaps, the magnetometer bar is created separately for each cyclotron. The magnetometer electronics and pneumatic system of bar stepping motion are unificated and stay the same with minimal changing.

MECHANICAL SYSTEM

For magnetic field measurements at FLNR cyclotrons the polar coordinate mapping system was chosen. The mechanical part of magnetometers consists of the bar for radial motion of Hall probes and the system of bar azimuthal motion. Hall probes are placed at the plank that is moved radially along bar with a step 10mm. The usage of several probes decreases the number of radial steps of the plank and, as a result, a time of mapping. At the table 1 the number of probes - Nh, number of plank steps - Ns, the radiuses of mapping Rb and pole Rpole for FLNR new cyclotrons are presented. To control the coherence of the measuring data between the probes, the additional radial step is used. Then the total plank steps equal Ns+1. At the additional step the previous probe at its last position stands at the first position of the next probe. As a rule this difference is very small, some gausses, and can be corrected numerically in the processing program.

Figure 1: DC72 magnetometer with gear wheel.

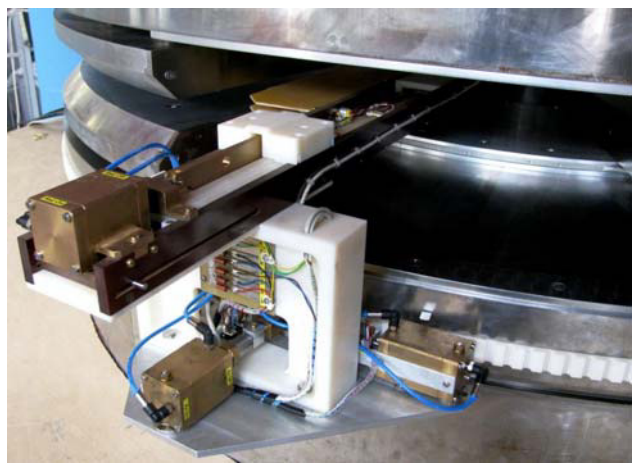

Figure 2: DC110 magnetometer with toothed belt.

The earlier versions of FLNR magnetometers used gear wheel for azimuthal motion, figure 1. The problem was that for each cyclotron the individual gear wheel must be created. It increase the price of magnetometer manufacturing dramatically. For DC110 and DC280 cyclotrons we refused to use the wheel and replaced it by a toothed belt, figure 2.

Table 1: Mapping System Radial Parameters

cyclotron	Nh	Ns	Rb	Rpole
DC280	14	16	2240mm	2000mm
DC110	8	16	1280mm	1000mm
DC60	8	14	1120mm	810mm
DC72	8	20	1600mm	1300mm

ISBN 978-3-95450-181-6

As radial and azimuthal motions are carried by the pneumatic engines, figures 2 and 3. It exclude the engines dependence on magnetic field. The air pressure provides by compressor with receiver and supplied to engines by a thin ∅4-6mm polyurethane tubes. Each step is controlled by optical probes and is counted by control program.

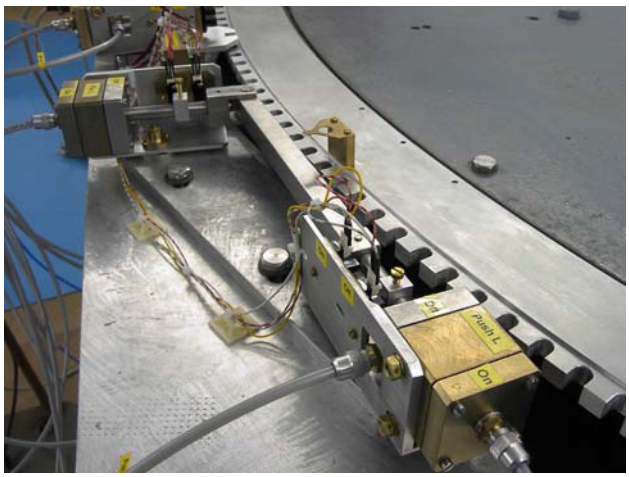

Figure 3: DC72 azimuthal step pneumatic engines.

The mechanical system of FLNR magnetometers, as with gear wheel and with toothed belt, provides the accuracy of probes positioning in radial direction ±0.02mm and in azimuthal direction ±0.01°. At this case the measuring errors, caused by mechanical inaccuracy, are no more than $\Delta B/B=10^{-4}$.

HALL PROBES

FLNR magnetometers use the series of InSb Hall probes with approximately the same parameters:

- Dimension of crystal 3x3x0.6mm.
- Dimension of working area 1.5x0.5mm.
- Nominal current 100mA.
- Magnetic sensitivity 90mkV/mT.
- Temperature coefficient -10^{-5} V/K.
- Upper level of magnetic field 10T.

Because the temperature variation during a map is not more then a few degrees and probes temperature coefficients are very small, so voltage correction due to temperature variations are negligible.

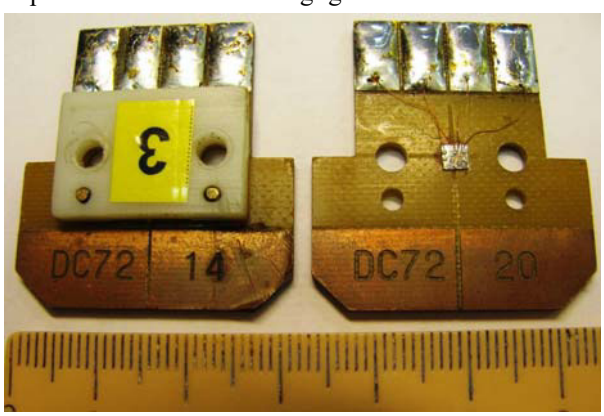

Figure 4: Hall probe at the substrate.

The crystals are placed at the substrate with the markers for correct placing at the magnetometer bar, figure 4.

All Hall probes were calibrated at the range 0.2 – 2.8T. The result of calibration of each probe are submitted by third-degree polynomial.

CONTROL SYSTEM

FLNR magnetometers control system is unified and consists of standard measuring and motion control parts. SPLC type controller provides the control of radial and azimuthal motions. Keithley 2701 multichannel voltmeter reads Hall probes voltages. The communication between apparatuses drivers and control program is based on Publish-Subscribe Protocol and uses Ethernet and RS-485 interface. The reading of Hall probes voltages takes about 2 seconds. Control program writes the voltages data to output file and in parallel demonstrates it in a form of graphics on monitor, figure 5. Each step of radial and azimuthal motions is controlled during the measuring. At the case of accidence the program stops the mapping and show the error message.

Figure 5: DC60 magnetometer control program interface.

Control program provides different mapping options:

- 360° or 90° of azimuthal range.
- 1° or 2° of azimuthal steps.
- 10mm or 20mm of radial steps.

Optionally one radius or one azimuth modes can be used. It is convenient for a quick testing of a magnetic field level and for a local area mapping.

The different mapping options lets to decrease the measuring time. The mapping of 90° azimuthal range with 2° and 20mm steps is taken for a quick analysis of average magnetic field of 4-sector magnetic structure and takes about 40 minutes. The mapping of 360° azimuthal range with 1° and 10mm steps is taken for field harmonic analysis and for final measuring, and takes more than 6 hours.

Control program provides as program and hand managing of magnetometer motion. The hand managing is used for calibration of magnetometer mechanism.

The magnetometer uses the monitor Hall probe. The monitor probe is placed stationary at the mapping area, usually on the pole surface between the sectors, and collect the information about the main field stability during the measuring process. This data is shown

ISBN 978-3-95450-181-6

graphically at the control program interface, as well as the time distribution of current of Hall probes power supply.

FIELD MEASHUREMENTS

The stability of magnetic field, temperature variation, stability of current of Hall probes power supply are important factors for accuracy of the magnetic field measurements. At the figure 6 the relative readings of the monitor probe during 6 hours of DC110 cyclotron mapping are presented. The absolute readings of the monitor probe for the present case was about 1.23T. The probe noise is about ±0.05Gs and the field instability during the measurements no more than 0.15Gs which are under the specified measurement accuracy.

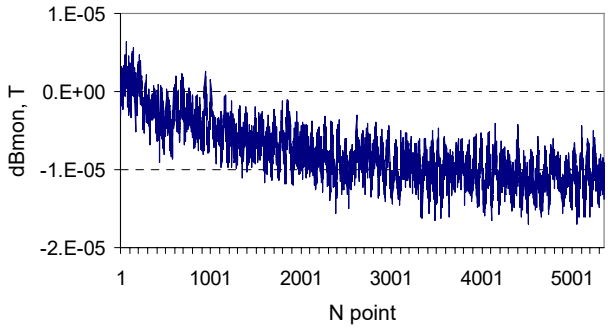

Figure 6: The relative readings of the monitor probe

The main topics of magnetic field formation are the average magnetic field for a range of levels, the compensation of parasitic field harmonics, radial and azimuthal correcting coils operation modes. The total time The results of magnetic field measuring are processed by a handle made program BCalc [3]. The program presents the main parameters of cyclotron magnetic field in a form of 2D and 3D graphics, figure 7.

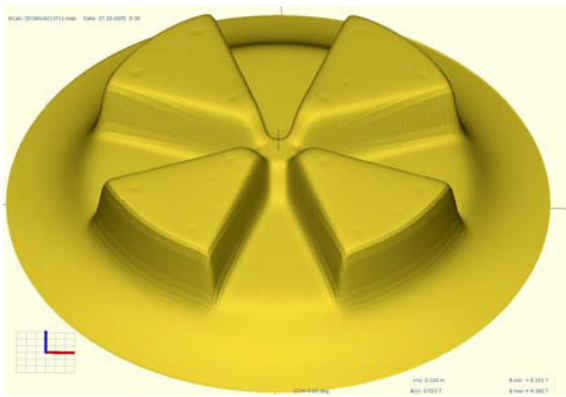

Figure 7: 3D visualisation of the measured field map.

As an example of measurements and formation of the magnetic field, the comparison of calculations and results of final measurements at three levels of DC 60 cyclotron magnetic field are presented at figure 8. The difference between calculations and measurements no more than 4 Gauss for the main acceleration area and about 10 Gauss for the areas of sector screws positions. Finally, the cyclotron commissioning shows the efficiency of the beam transition during acceleration up to 98%, that is a criteria of a quality of field mapping and formation [1]. Figure 9 demonstrates the experimental resonance characteristics, the dependence of beam current at different radiuses on the changing of magnetic field level. The concentric position of resonances shows the minimum deviation of magnetic field from isochronous. Similar results were obtained for other FLNR new cyclotrons, DC72 and DC110 [2].

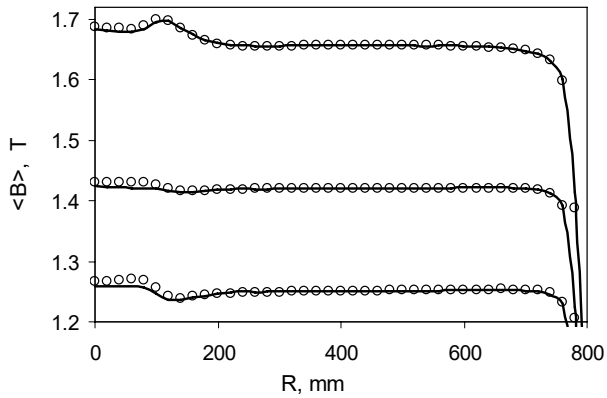

Figure 8: DC60 magnetic field calculations (circles) and results of final measurements (lines).

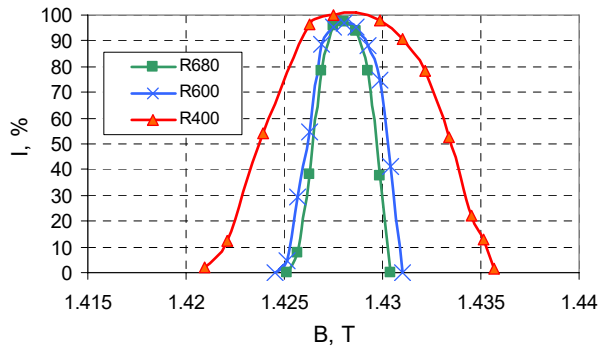

Figure 9: DC60 magnetic field resonance characteristic for $14N^{2+}$ acceleration mode.

REFERENCES

[1] B.N.Gikal, et al., "The method and results of formation of the DC-60 cyclotron magnetic field", In: Proceedings of the 18th Conference on Cyclotrons and Their Applications, 1 – 5 October 2007, Giardini Naxos, Italy, p.p. 432 - 434.

[2] E.V.Samsonov, et al., "Numerical simulation of Ion Acceleration and Extraction in Cyclotron DC110", Part. Nucl. Lett. 11, 2(186),2014, p.p.264 - 276.

[3] I.A.Ivanenko, et al., "BCalc – Software for Analysis and Vizualization of the Results of Measured Isochronous Cyclotron Magnetic Field", P9-2003-162, JINR, Dubna, 2003.

ISBN 978-3-95450-181-6

MAGNETIC MEASUREMENT SYSTEM FOR THE NICA COLLIDER DUAL DIPOLES

M. Shandov, V. Borisov, A Bychkov, O. Golubitsky, H. G. Khodzibagiyan, S. Kostromin, M. Omelyanenko, A. Schemchuk, Veksler and Baldin Laboratory of High Energy Physics, Joint Institute for Nuclear Research, Dubna, Russia

Abstract

NICA collider magnetic system consists of 80 dual-aperture dipole superconducting magnets. Measurement of magnetic field parameters is assumed for each collider's magnet. This paper describes magnetic measurements methods and developing of dedicated system.

INTRODUCTION

NICA (Nuclotron-based Ion Collider fAcility) is a new accelerator complex presently under construction at the Joint Institute for Nuclear Research (JINR) in Dubna, Russia to study properties of dense baryonic matter. NICA booster and collider composed more than 250 superconducting (SC) magnets [1]. These magnets will be assembled and tested at a new test facility in the Veksler and Baldin Laboratory of High Energy Physics (VBLHEP) JINR. The program for magnets testing includes warm and cold magnetic measurements (MM). The some of the details for measuring system for carrying out MM of a twin-aperture dipole magnet of collider is made and tested. Full-scale prototype of measurement shaft and plain bearing with teflon liner were tested in cold MM of quadrupole lens of NICA and sextupole lens SIS100. The basis of design laid down to magnetic measurement system for dipole magnets of NICA booster [2].

TWIN-APERTURE (DUAL) DIPOLE MAGNET FOR THE NICA COLLIDER

The Nuclotron-type design based on a cold (4.5K) window frame iron yoke and a saddle-shaped SC winding cooled with a two-phase helium flow has been chosen for the NICA booster and collider magnets. Main characteristic of the NICA twin-aperture dipole collider magnets are given in [1]. The twin-aperture dipole collider magnets with installed magnetic measuring system (MMS) is shown in Fig. 1. The general view of magnet is shown in Fig. 2.

Reference Magnet Field

Each magnet has an additional winding (see Fig. 1 Pos. 6) consisting of 4 conductors located in the corners of magnet yoke. This winding generate the reference magnetic field, directed parallel to the magnet poles, which used for positioning of measuring coils of separate sections relatively each other and magnet median plane.

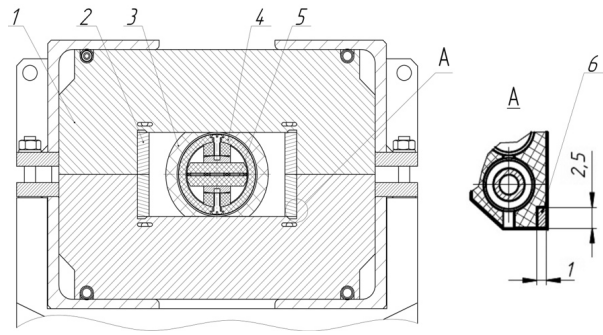

Figure 1: Cross-section view of dipole magnet for the NICA collider with MMS: 1. Yoke, 2. Main coil, 3. Plain bearing of measurement shaft, 4. Measurement shaft, 5. PCB with harmonic coils, 6. Reference coil.

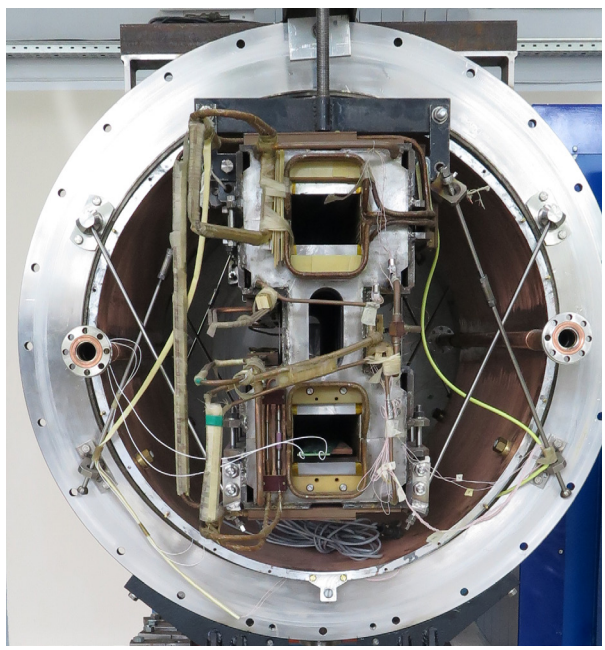

Figure 2: The twin-aperture dipole magnet mounted in a cryostat.

THE MAGNETIC MEASUREMENT SYSTEM

According to the technical specification the following parameters of dipole collider magnet have been measured:

- field at the center of magnet;
- magnetic field integral;
- effective length;

ISBN 978-3-95450-181-6

- angle between magnetic and mechanical median plane;
- integrated harmonics of a magnet field up to the 7th.

It is necessary to meet the following requirement by the developed system:

- system is designed for serial measurements and will be used for all magnets of this type;
- cold measurement of all parameters for each aperture must be carried out at one cooling session;
- small size of aperture (120×70mm) precludes the use of anti cryostat.

Mechanical Design

Measurement system for warm MM (Fig. 3) consist of two measurement shafts (Fig. 4), each comprising three identical section, fixed on plain bearings on the bottom yoke and driven by two servomotor.

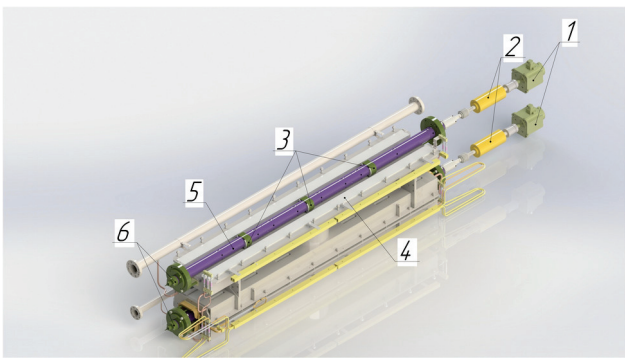

Figure 3: Layout of equipment for warm MM: 1. Servomotor, 2. Slip rings, 3. Plain bearings with teflon liner, 4. Bottom part of yoke, 5. Measurement shaft, 6. Angle encoder.

Measurement shaft composing three identical section, glued together. To eliminate the relative rotation of parts, pins are also installed in the place of gluing. Each section – glas-cloth-base laminate cylinder with an installed frame with a mounted multilayer printed-circuit measurement coil (Fig. 6).

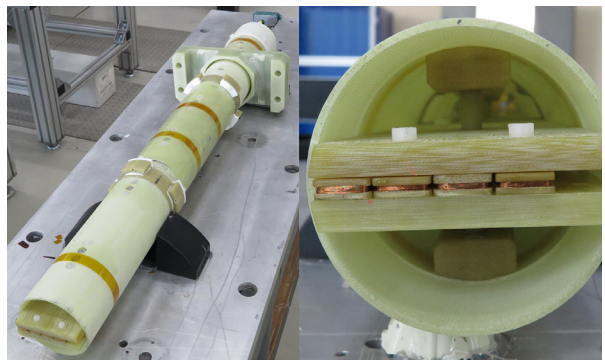

Figure 4: Measurement shaft (prototype).

Plain bearing includes housing from glas-cloth-base laminate and teflon liner. After assembly, the teflon liner connect to the housing by screws to avoid displacement. In the bearing seat on the shaft applied the epoxy resin layer, which reduce friction.

Precision fabrication of a yoke pole surface, plain bearings and base frame determines the accuracy of positioning of measuring system in a magnet aperture. For the connection of the signal cable used sliding connectors (slip rings) with 18 contacts. From the one side the system via the coupling connect to servomotor shaft, from the other side – connect to angular encoder (system accuracy is 5 arc. sec.).

Design of measuring system for cold MM (Fig. 5) is slightly different by location of main assembly parts. This is due to the fact that minimum operating temperature of slip rings is -40°C, angle encoder is -20°C and therefore it is necessary to place the devices in front of a nitrogen-screen. Also, organized additional insulation of devices and supply of heat through the mounting bracket.

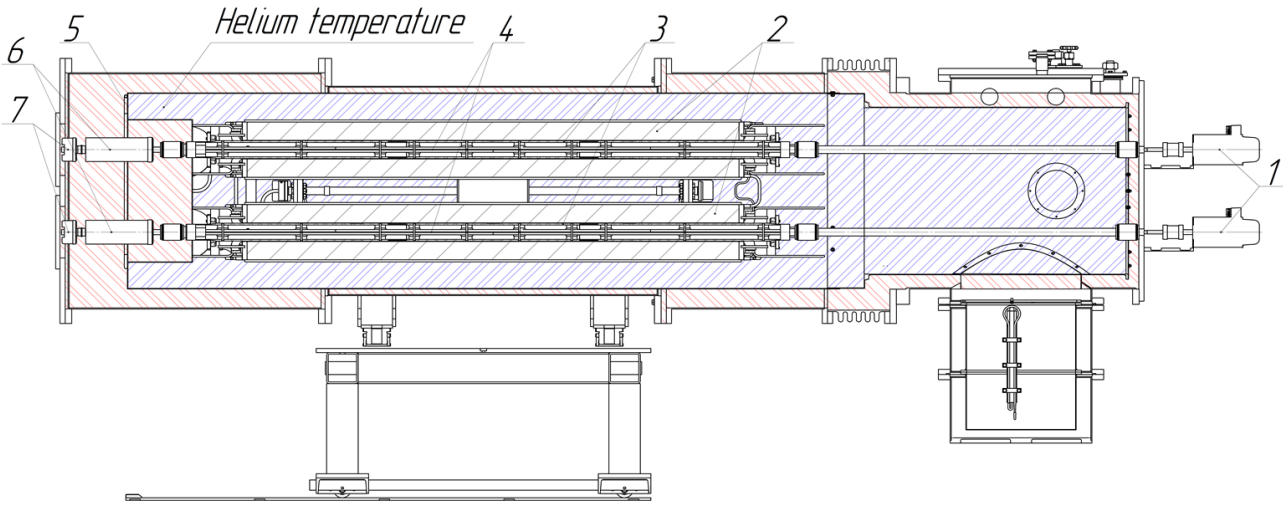

Figure 5: Layout of equipment for cold MM: 1. Servomotor, 2. Magnet, 3. Measurement shaft, 4. PCB, 5. Nitrogen-screen, 6. Slip rings, 7. Angular encoder.

ISBN 978-3-95450-181-6

Structure of Harmonics Coil

Measurement coils sets are made as the multilayered printed-circuit board (PCB). PCB contains three identical radial coils. Coils consist of 400 turns created from 20 layers, each of which contains 20 turns. Parameters of PCB are specified in the Table I. Print PCB are made to order in China. The central coil is symmetric to a rotation axis, i. e. is the dipole one. The sample coils of shorter length, were tested 50 times thermo cycled by cooling down to the LN2 temperature. The sample wasn't destructed.

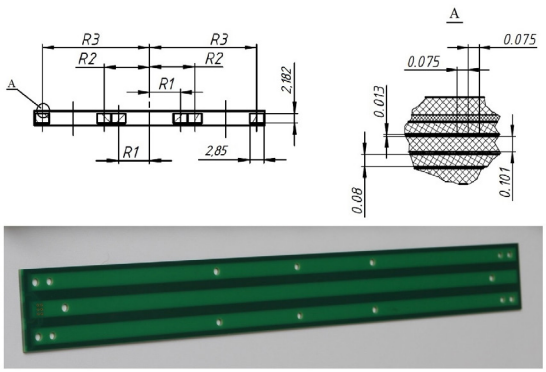

Figure 6: Cross section view of PCB with harmonics coils and photo of PCB.

Table 1: Main Parameters of the Harmonics Coils

Length, mm	730
Width, mm	53.4
Height, mm	2.4
R1, mm	7.325
R2, mm	10.325
R3, mm	24.975
Number of turns	400

Data Acquisition

The data acquisition system (Fig. 7) is developed on the basis of the hardware NI PXI platform and the environment of LabVIEW system. The form and parameters of operating signal for power supply generate in NI PXI 4461 DAC channel. Servomotor control is carried out by NI cRIO-9031. Measured signals from harmonic coils and magnet current sensor are digitized in NI PXI 4464 blocks with sample rate 204.8 kS/s [3]. Software in the LabVIEW environment is developed for acquisition data processing.

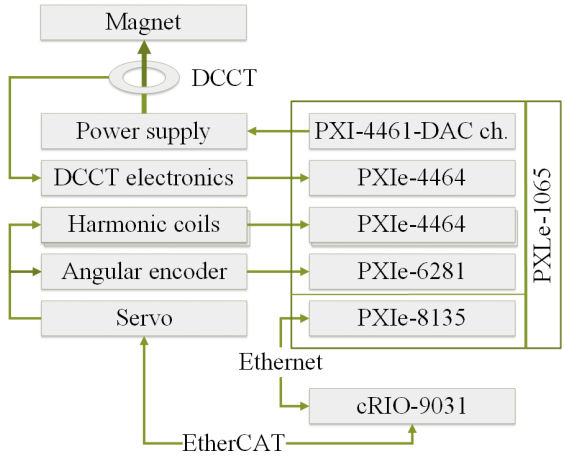

Figure 7: Data acquisition and controls schematic diagram.

Analyze of Raw-Data

Each measurement consist of reading of a reference, main and compensated signals delivered by rotating coils over complete forward and backward rotation. The coils angular position is read by angular encoder. Measurement cycle consist of: start rotation; generation of an operating signal for power supply; digitization of signals of EMF, from DCCT and angular encoder; data recording; stop rotation.

The main and reference signals are obtain from the reading of a single coil, and is used for determination of the main field component. The compensated signal is obtained as a combination of the signals of different coil and used for determination of the field errors.

Further is used the procedure for standard analysis of measurements taken with constant current in the measured magnets [4].

CONCLUSION AND FUTURE PLANS

The previous experience got in the establishing and operating of MMS for magnets of NICA booster was taken into account in the development of the MMS. Next our steps are executing of first warm testing, cold MM with full current, calibration of MMS, development of MMS for quadrupole magnets of NICA collider.

REFERENCES

[1] H. G. Khodzibagiyan et al, "Superconducting magnets for NICA accelerator-collider complex", IEEE Trans. Appl. Supercond, 3 (2014), 4001304.

[2] V. Borisov et al, "Series magnetic measurements of NICA booster dipoles", RuPAC'16, this conference.

[3] http://www.ni.com

[4] A. K. Jain, "Measurements of Field Quality Using Harmonic Coils", US Particle accelerator school on superconduction magnets 2001.

ISBN 978-3-95450-181-6

SIMULATION OF PRECISION MAGNETIC SHIELDING SYSTEM FOR BEAM INJECTORS IN TOKAMAKS

A. Bazarov, V. Amoskov, E. Gapionok, V. Kukhtin, E. Lamzin, D.V. Efremov Scientific Research Institute of Electrophysical Apparatus, 3 Doroga na Metallostroy, St.Petersburg, 196641, Russian Federation
V. Belyakov, S. Sytchevsky, St.Petersburg State University, 7/9 Universitetskaya embankment, St.Petersburg, 199034, Russian Federation
Yu. Gribov, ITER Organization, Route de Vinon-sur-Verdon, CS 90 046, 13067 St Paul Lez Durance Cedex, France

Abstract

Beam injectors in tokamaks are utilized for plasma heating and diagnostics. Due to the relatively large distance between the injectors and plasma, the tokamak stray magnetic field inside injectors during the operation should be very low (down to the tenths of Gauss) to avoid the deflection of the ion beams. The Magnetic Field Reduction System (MFRS) should be used to reduce the stray magnetic field produced by the tokamak EM systems and plasma to an acceptable level inside the injectors. In total, the complex MFRS can consist of a passive magnetic shield and active coils to provide the strict design criteria during a plasma scenario.

To provide precise computations, detailed numerical models of MFRS should have the dimensions up to several tens of millions of degrees of freedom. Such problem could be solved only with the use of high-efficiency vector algorithms and parallel computations.

The paper is dedicated to simulation of MFRS for beam injectors in tokamaks.

INTRODUCTION

High-energy neutral beams (NB) are used in present-day tokamaks for additional heating to provide plasma burn and current drive [1]. The heating is the most effective when the NBs are injected into plasma in the direction of the plasma current.

NB injection is also one of the basic techniques of plasma diagnostics. It allows detection of plasma particles and measurement of local plasma parameters from the plasma response to the injected beams.

The NBs are produced by neutralization of accelerated ions. The main components of an NB injector are a beam source, a gap where the beams are extracted, formed and accelerated, a neutralizer, commonly with a gas target, and a residual ion dump.

The paper describes the model and computational results for the Diagnostic Neutral Beam Injector (DNBI) of ITER tokamak.

The residual field inside ITER DNBI during operation should be as low as 0.2 Gs in the Neutralizer region and 0.5 Gs in the Gap region to avoid the deflection of the ion beams. The Magnetic Field Reduction System (MFRS) should be used to reduce the stray field produced by the tokamak EM systems and plasma [2, 3, 4], reaching 150-500 Gs at the injector location, to an acceptable level inside the injectors. The DNBI MFRS consists of a passive magnetic shield (PMS) and active correction and compensation coils (ACCC) to provide the strict design criteria during a plasma scenario. A CATIA model of ITER DNBI PMS is shown in Fig. 1.

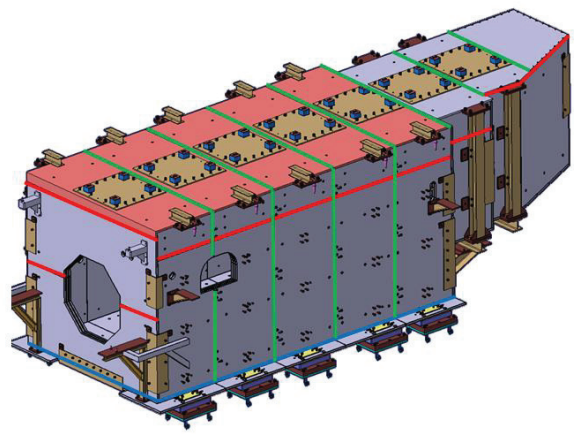

Figure 1: CATIA model of ITER DNBI PMS. Colored lines show 1 mm construction air gaps locations.

MAGNETIC MODEL

The tokamak is modeled as a set of PF coils, central solenoid (CS) and plasma, presented with a circular moveable current filament. The stray field of the tokamak is calculated with the code KLONDIKE [5] that implements integral volume elements and the Biot-Savart integration.

The FE approach is used for modeling the PMS. PMS is a bolted assembly of panels composed of three 50 mm thick low carbon steel (S235) plates with a 25 mm air gap between the plates. Also, the model includes the Neutralizer case made of 35 mm thick soft iron sheets to provide an additional shield for stray field reduction in the Neutralizer as the most magnetically crucial component. Circular holes in PMS are modeled as rectangular ones with the same area. The FE model and the computations were performed with the code KOMPOT [6].

ISBN 978-3-95450-181-6

COMPUTATIONAL RESULTS

Several models have been built for the study of DNBI MFRS. The Model A (Fig. 2) is a gapless model of PMS with the Neutralizer case which has about $4.2 \cdot 10^7$ elements. In the Model B, possible horizontal construction air gaps were implemented between the side/front/rear and top/bottom PMS panels to assess their impact on the residual field inside the PMS. Computations have demonstrated an increase in field up to 17% in the Gap region due to the increased magnetic reluctance of the path for magnetic flux through PMS (see Fig. 4). Thus, the construction gaps should be taken into consideration for the PMS magnetic model.

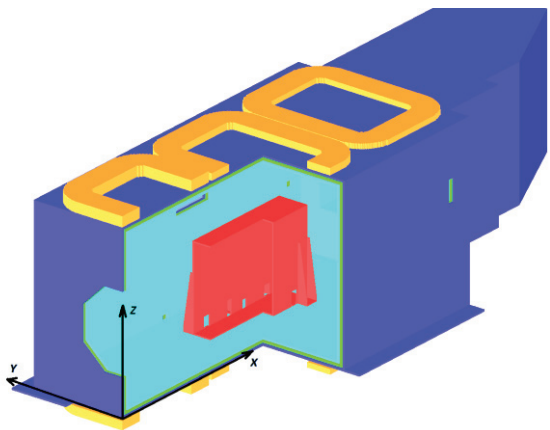

Figure 2: Cross-section of Model A and coordinate system (mesh is not shown).

The Model C (Fig. 3) has a full set of construction air gaps. It has about $5 \cdot 10^7$ finite elements in which the air gaps are modeled via the filling factor and equivalent magnetic permeability with a spacing of 10 mm.

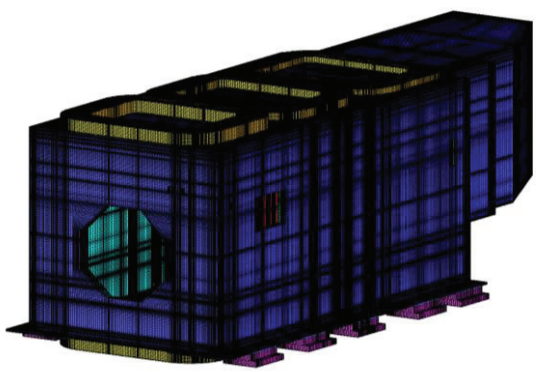

Figure 3: Model C.

Finally, a detailed model of about $6 \cdot 10^7$ finite elements, Model D, with the 1 mm air has been developed. As Model D demands high computational resources, it is used only to validate the results obtained with the Model C.

Fig. 4 shows a residual field inside the PMS (along the central line of the beam aperture) for the EOB time point of the operation scenario when the peak stray field occurs.

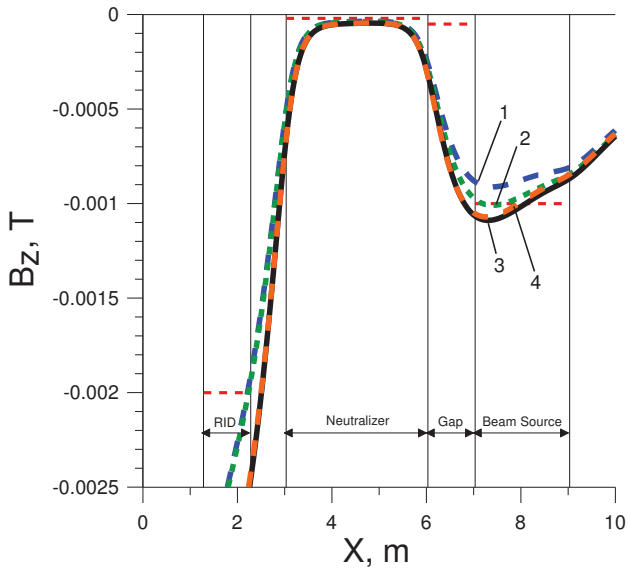

Figure 4: B_z component along center of aperture. EOB state. 1 – Model A, 2 – Model B, 3 – Model C, 4 – Model D. Dashed lines correspond to field design criteria.

With the use of Model C, a DNBI MFRS Controller has been designed supposing a linear dependence between the ACCC currents and the CS, PF and plasma currents during the operation scenario. The Controller allows control of the driving currents in the ACC coils using a single matrix so that to keep the residual field inside the DNBI close to the design field criteria. The Controller with the desired performance was achieved via an iterative procedure utilizing influence functions for the ACCC currents. As an example, a residual field along the center of the aperture with Controller ACCC currents is shown in Fig. 5.

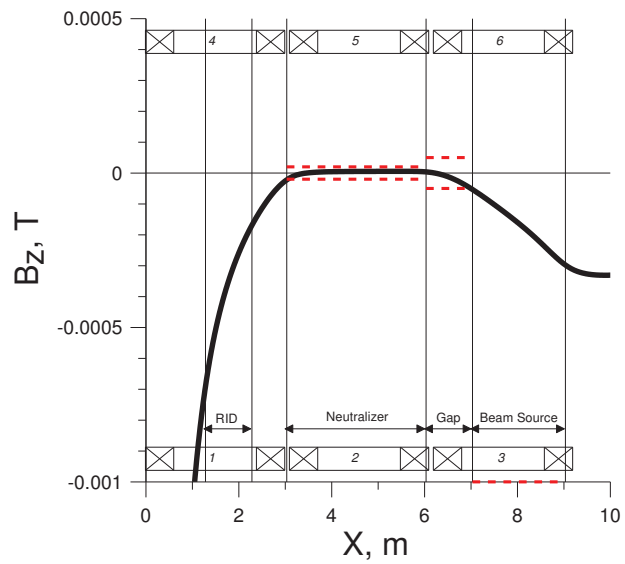

Figure 5: B_z component along center of aperture. Model C. EOB state, ACCC currents obtained with Controller. Dashed lines correspond to design field criteria.

ISBN 978-3-95450-181-6

SOLUTION CONVERGENCE

To study the EM effect of eddy current induced in PMS at the reference scenario, Model E with $4 \cdot 10^6$ DOF was developed (see Fig 6).

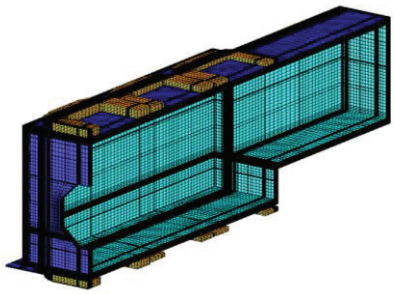

Figure 6: Model E.

Models C and E were used to investigate convergence at different DOFs. To make Model C close to Model E, the side holes, construction air gaps, the Neutralizer case were excluded.

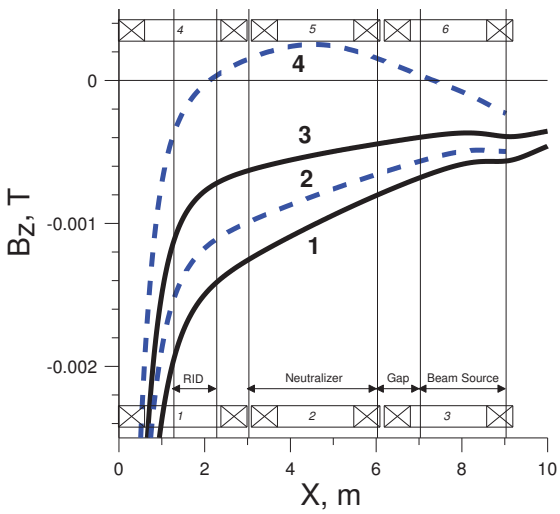

Figure 7: B_z component along center of aperture. 1, 3 – Model C with no Neutralizer case, side wall holes and air gaps, 2,4 – Model E; 1,2 – zero ACCC currents, 3,4 – energized ACCC.

As seen from Fig. 7, the results differ depending on the number of DOFs.

The shielding efficiency of MFRS depends on its magnetic permeability. The higher is permeability, the more efficient is the PMS. Local saturated zones would reduce the shielding efficiency. Particularly, saturated zones in PMS (2 T, μ_r = 100) are observed below ACC coils that produce high field gradients. In numerical computations, the permeability is determined through a field averaged within a finite element and assumed to be constant. As a result, the average field is found by means of integration of the gradients over an FE volume. In the saturated zones the integrations always gives overestimation for the permeability. The bigger is the FE size, the higher is overestimation of the shielding effect of PMS.

A comparison of the results demonstrates that the ACC coil currents evaluated with the $4 \cdot 10^6$ DOF and $5 \cdot 10^7$ DOF models diverge significantly with underestimated ACC coil currents for the first model. Further mesh refinement implies high computational cost, however, does not guarantee desired precision. For such EM analyses a validation is strongly recommended by a comparison between calculations performed on different models and experimental data to make sure that a particular model and solution strategy provide required accuracy.

CONCLUSION

To provide required accuracy, computational models (FE meshes) for DNBI MFRS should have at least tens of millions of DOF for correct estimation of magnetic permeability distribution in the PMS that has drastic effect on PMS shielding efficiency in computations.

REFERENCES

[1] A. Belov, E. Lamzin, N. Maximenkova, B. Mingalev, S. Sytchevsky, Numerical optimization of neutral beam magnetic field reduction system of the ITER, Plasma Devices and Operations, 2005, Vol. 13, No. 4, pp.225-233.

[2] V. Amoskov, A. Belov, V. Belyakov, Y. Gribov, V.Kukhtin, E.Lamzin, N.Maximenkova, S.Sytchevsky, Assesment of error field from ferromagnetic surrounding of ITER tokamak: ferromagnetic rebar of tokamak complex building, Plasma Devices and Operations, 2008, Vol. 16, No. 4, pp.301-316.

[3] V.Amoskov, A.Belov, V.Belyakov, Y.Gribov, V.Kukhtin, E.Lamzin, N.Maximenkova, S.Sytchevsky, Stray magnetic field produced by ITER tokamak complex, Plasma Devices and Operations, 2009, Vol. 17, No. 4, pp. 230-237.

[4] V.Amoskov, A.Belov, V.Belyakov, Y.Gribov, A.Kavin, V.Kukhtin, E.Lamzin, K.Lobanov, N.Maximenkova, A.Mineev, S.Sytchevsky, Stray magnetic field at plasma initiation produced by ferromagnetic elements of the ITER tokamak complex, Plasma Devices and Operations, 2009, Vol. 17, No. 4, pp. 238-249.

[5] A.V. Belov, T.F. Belyakova, I.V. Gornikel, V.P. Kukhtin, V.G. Kuchinsky, E.A. Lamzin, A.G. Semchenkov, N.A. Shatil, S.E. Sytchevsky, 3D Field Simulation of Complex Systems With Permanent Magnets and Excitation Coils, IEEE Transact.on Appl. Supercond. 2008, Vol. 18 No. 2, pp. 1609-1612.

[6] V.M. Amoskov, A.V. Belov, V.A. Belyakov, T.F. Belyakova, Yu.V. Gribov, V.P. Kukhtin, E.A. Lamzin, S.E. Sytchevsky, Computation technology based on KOMPOT and KLONDIKE codes for magneto static simulations in tokamaks, Plasma Devices and Operations, 2008, Vol. 16, No. 2, pp. 89-103.

ISBN 978-3-95450-181-6

MODELING MAGNETIC EFFECTS OF STEEL REBAR OF CONCRETE SURROUNDINGS FOR ELECTROPHYSICAL APPARATUS

V. Amoskov#, A. Bazarov, M. Kaparkova, V. Kukhtin, E. Lamzin, B. Lyublin, JSC «NIIEFA», St.Petersburg, Russia
V. Belyakov, S. Sytchevsky, St.-Petersburg State University, Russia
Y. Gribov, ITER IO, France

Abstract

The article describes an advanced approach to modelling magnetic properties of reinforced concrete structures taking into account the anisotropic effect due to rod layers orientations. The equivalent model has been validated in the computation of a test problem. For comparison, simulations have been carried out with a detailed 3D FE model that describes each of the steel rods. The equivalent model has required a few times less finite elements than the detailed model. A comparison of the fields obtained has demonstrated a very good match, even for the distances comparable with the rebar rod gaps.

INTRODUCTION

Buildings for large electrophysical apparatus, such as accelerators, experimental fusion devices, customs examination equipment, industrial and medical tomography systems etc, are typically constructed of reinforced concrete with steel rebar. Particularly, the ITER Tokamak Complex has steel rebar with a complex pattern [1, 2]. The rebar is arranged as a stack of criss-cross layers of steel bars filling from 1.5% to 12% of the structures [1]. Some of the reinforced structures are located as close as 5 – 10 m to the tokamak. The steel rebar in concrete are magnetized by the stray fields generated by the plasma and tokamak magnets (EMS ITER) up to saturation.

Previous studies have revealed a noticeable effect of the magnetized rebar on a field distribution in the plasma region [3] and outside the tokamak [4], thus making concern for performance, electromagnetic compatibility and safety. Strict design criteria are adopted for the acceptable level of field perturbations and efficiency of shielding the tokamak components, primarily injectors and analyzers.

Voluminous ferromagnetic structures may reduce the natural level of Earth's magnetic field (EMF) in the buildings. Russian safety standards for construction specify the acceptable EMF reduction as a half of the natural level [5]. For assessment of the interior EMF, mathematical modelling is applied with the use of simplified models for reinforced structures.

HOMOGENEOUS ISOTROPIC MODEL

Large electrophysical devices produce stray fields that are much higher than EMF, while massive ferromagnetic structures of the building affect the field distribution noticeably. This makes correct information about the stray field essential for the medical and safety engineering provisions as well as to ensure the normal operations of equipment sensitive to magnetic fields. The effect of the magnetized ferromagnetic structures can be evaluated with the use of solid steel models, models with effective volumetric steel fractions, or isotropic models for reinforced concrete. In particular, the authors have developed the Magnetic Model of the ITER Tokamak Complex, ver.1 (MMTC1) [6] that includes the bioshield with its lid, basemat, ceiling, walls, and seismic pit.

A challenging issue in modeling reinforced structures is to adequately describe the steel rebar arrangement. The layered pattern of the rebar produces a complicated field map inside the structures and near the tokamak building. However, at a distance comparable with a typical step of the rebar, contributions of separate steel bars are smoothed, and the reinforced concrete structure acts as a solid body with averaged magnetic properties. These properties are dictated by a magnetization curve of the steel and the layered pattern of the rebar.

In the MMTC1 each reinforced concrete structure was represented via a spatially homogeneous equivalent with isotropic magnetic properties [6]. The B-H characteristic of the equivalent was given as $B = 0.5 \cdot k \cdot f(H)$, where $B = f(H)$ is the magnetization curve of the steel rebar [7], k is the filling factor, 0.5 is the correction coefficient for the layered pattern. The correction coefficient is taken from the assumption that only 50% of bars which are co-directed with the magnetic field can effectively conduct the flux. $\eta = 0.5$ is applicable for any direction of the external field coplanar with the rebar layers. If the external field has a component normal to the rebar layers, the equivalent permeability and magnetization should be significantly lower as the bars are oriented normally to the field. The results obtained with the MMTC1 suggest that the normal field would have a weak effect on the rebar magnetization. However, more reliable modeling seems desirable.

ADVANCED LAYERED MODEL

Papers [1, 2] describe an advanced isotropic model for concrete structures with steel rebar that that takes into account anisotropic effects due to the rebar pattern. As compared to the homogeneous isotropic model, the proposed model provides more accurate assessment of the magnetic effect of the rebar with the same computational cost. For a detailed model describing every steel bar individually the computational cost is extremely high.

#sytch@sintez.niiefa.spb.su

ISBN 978-3-95450-181-6

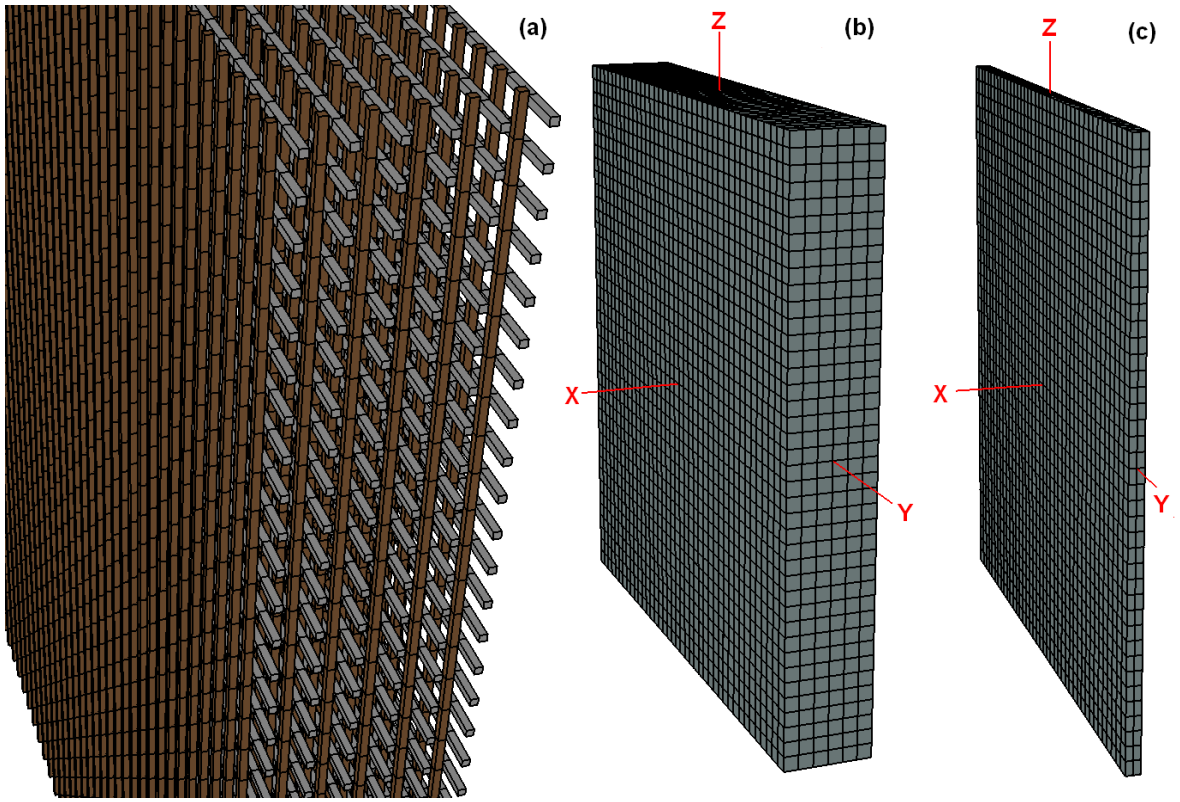

Figure 1: Computational models for test problem with a set of criss-cross rebar layer magnetized in parallel or perpendicular to layers external field: detailed (a), homogeneous isotropic (b) and single-layer (c) models, prepared for KLONDIKE code [8].

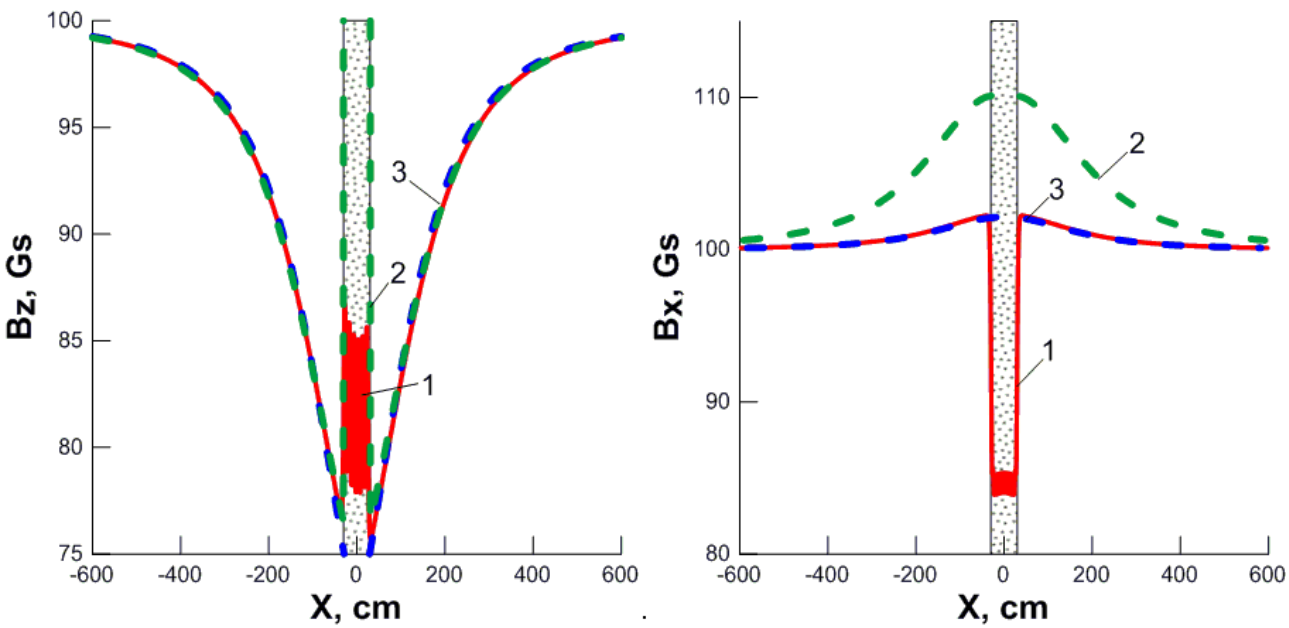

Figure 2: 100 Gs field disturbed by reinforced concrete structure. Field co-planar (B_z) or normal (B_x) to rebar. 1 – detailed models, 2 – homogeneous isotropic models, 3 – single-layer models.

ISBN 978-3-95450-181-6

In the advanced model, reinforced concrete is modelled as a layered structure formed with alternating magnetic and non-magnetic isotropic layers in the plane coplanar with the rebar layers. In the extreme case, the model is limited to a single isotropic layer. Geometry and effective properties of every layer are pre-determined in field simulations over a periodicity cell of the modeled structure.

The model has been validated in comparative simulations [1, 2] of the test problem with the use of 3 models (Fig. 1):

1) detailed 3D FE model with realistic description of the geometry, configuration and permeability of every bar (Fig. 1a);

2) isotropic model with a single homogeneous isotropic material, as in MMTC1 [6] (Fig. 1b);

3) advanced model representing a layered structure formed with alternating magnetic and non-magnetic isotropic layers, as described in [1], Fig 1c).

The study [2] has demonstrated that the layered model enables sufficient generality and is applicable for reinforced structures with a complex rebar pattern, non-linear magnetic properties, and non-uniform external field. A high accuracy of field evaluation is achieved, with a calculation error below 1%. The *optimized double-layer model* provides the error as low as 0.1%. For the majority of practical computations, the *single-layer model* gives sufficiently accurate predictions. The *double-layer model* is recommended for field simulation in the regions near the edges of reinforced structures where field behaviour is most complicated.

VALIDATION

The test simulations have been performed with the use of the finite-element code KOMPOT [8, 9] that utilizes differential formulation of the magnetostatic problem and enables high discretization of a calculated domain.

In order to ensure a smooth solution, the authors have carried out a benchmark with the code KLONDIKE [8] based on the integral formulation. The integral formulation of the magnetostatic problem provides a smooth solution for distant areas and is preferable for a range of applications.

The test problem represented concrete cuboid 60cm×400cm×400 cm reinforced with 12 criss-cross layers of steel bars each 400 cm long (Fig. 1a). The bar cross section was taken as 2cm × 2cm. The volumetric fraction of steel in the structure was 8%. For *homogeneous isotropic models* (Fig. 1b) an average filling factor $k = 8\%$ and isotropic correction coefficient $\eta=0.5$ were applied. The *layered models* (Fig. 1c) used the width contraction of 0.17 and filling factor of 0.24 pre-determined in field simulation in the periodicity cell.

A uniform external field distorted by this structure was simulated. Two options for the external field orientation were considered, (1) parallel and (2) normal to steel bars (Fig. 2). Numerical experiments have shown that *homogeneous isotropic models*, both finite-element and integral, overestimate magnetic effect of the rebar by several times if the external field is directed across steel bars. This leads to ~10% inaccuracy in the resulting field. On the other hand, the proposed *layered models* provide practically the same result, as the *detailed models*, for any field direction.

A discrepancy between results obtained with two codes is as low as 0.1%. This implies that the proposed approach of modeling reinforced structures can be utilized with any magnetostatic code and type of formulation.

REFERENCES

[1] V.Amoskov et al., “Modeling magnetic effect of steel rebar of buildings for electrophysical devices”, prepared for publication in Technical Physics.
[2] V. Amoskov et al., “Modeling magnetic effect of steel rebar of buildings for electrophysical devices with regard for non-linear properties”, prepared for publication in Technical Physics.
[3] V. Amoskov et al., Plasma Devices Oper. 17 (2009) 238.
[4] V. Amoskov et al., Plasma Devices Oper. 17 (2009) 250.
[5] RF Safety Standards for in-plant environment. SanPiN 2.2.4.1191-03 "Interior electromagnetic fields. – Moscow, 2003.
[6] V. Amoskov et al., Plasma Devices Oper. 16 (2008) 225.
[7] V. Amoskov et al., Plasma Devices Oper. 16 (2008) 171.
[8] V. Amoskov et al., Plasma Devices Oper. 16 (2008) 89.
[9] A. Belov et al., IEEE Transact.on Appl. Supercond. 18 (2008) 1609.

ISBN 978-3-95450-181-6

MAGNETIC SYSTEMS FOR BEAM TRANSPORT AT EXTRACTION CHANNELS OF ILU ACCELERATORS

V. Bezuglov, A. Bryazgin, B. Faktorovich, E. Kokin, V. Nekhaev, A. Panfilov, V. Radchenko, E. Shtarklev, V. Tkachenko, A. Vlasov, L. Voronin, BINP SB RAS, Novosibirsk

ABSTRACT

This paper is devoted to magnetic systems for beam transport at extraction channels of electron industrial accelerators of the ILU type. The extraction systems meant for energy of the accelerated electrons up to 10 MeV and beam power up to 100 kW are described. Special attention is paid to forming of the dose field in a radiation zone. In paper the magnetic system for bending of the nonmonochromatic beams is offered to application. The essence of the described device consists in application of two identical magnetic mirrors in which distribution of magnetic field on depth is formed so that natural rise of magnetic field intensity on an entrance to a mirror is followed by decrease of this field under a certain law [1]. In the issue of impact on charged particles of forces arising in cylindrical lenses of each mirror is possible to compensate angular divergence of strongly nonmonochromatic beams in gaps of magnetic mirrors and to receive after bending a beam with parameters close to phase characteristics of an input beam.

BEAM EXTRACTION SYSTEMS

Radiation technologies reached now such wide application in the industry that became its separate branch. And improvement of generators of electron beams occurs at the same time to high-quality improvements of extraction devices. Rigid modern requirements to uniformity of dose fields of electronic accelerators demand detailed consideration of the questions connected with operation of extraction devices. The extraction systems of ILU accelerators are meant for energy of the accelerated electrons up to 10 MeV and beam power up to 100 kW. The received nonuniformity of the dose field in radiation zone is up to ±5%. The most optimal for application in radiation technologies are ILU-10 accelerator (5 MEV, 50 kW) and ILU-14 accelerator (10 MEV, 100 kW).

The accelerated beam at ILU is scanned on the required sizes of the irradiated object in the triangular metal vacuum chamber (bell), the scanning electromagnet is located in triangle peak, and an extraction window from a titanic foil 50 microns thick on the opposite side. The power supply system of the scanning electromagnet forms a current pulse, in a form reminding piece of a sinusoid with duration of 0.5 ms and adjustable amplitude. The current density at edges of a foil increases, and for achievement of the dose uniformity the speed of beam scanning to edges should be raised. Necessary uniformity of output current density is reached by installation before a scanning electromagnet of the system for scanning magnetic field correction. The additional correcting field leads to equalizing of beam scanning speeds along the output bell (see figure 1).

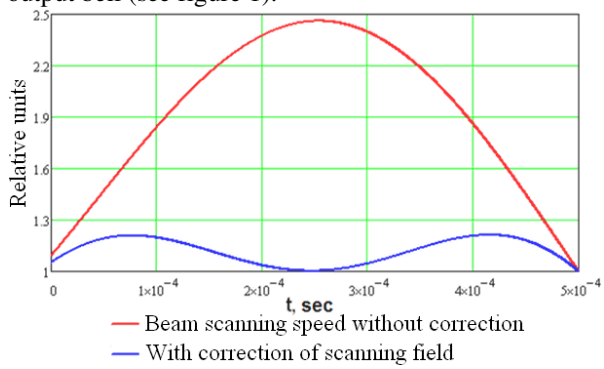

Figure 1: Beam scanning speed along the extraction window during the pulse.

The correction system of the scanning field was tested on the ILU-10 accelerator. For the distribution received without scanning correction, nonuniformity of a dose was ±13%. The optimum form of correction of the scanning magnetic field providing nonuniformity of distribution of a beam current density of ±5% was selected (figure 2).

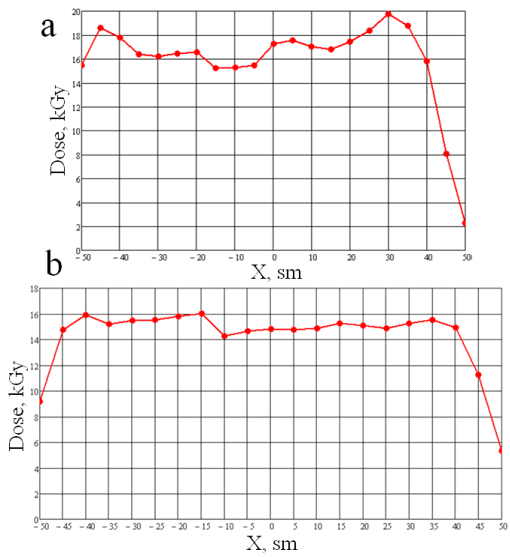

Figure 2: Dose field distribution along extraction window without correction of scanning (a) and with correction (b).

To provide the maximum penetration depth of electrons in material the beam should pass to atmosphere perpendicular to the irradiated production on all length of the accelerator extraction window. For this purpose near extraction window are set two bending electromagnets (Panofsky's lenses). In figure 3 electron trajectories at the extraction channel using the bending electromagnets and without them are given.

ISBN 978-3-95450-181-6

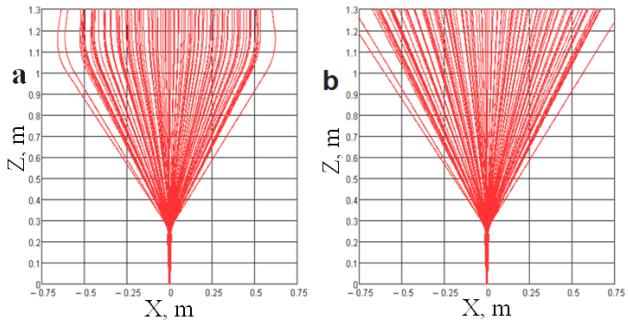

Figure 3: Electron trajectories of scanned beam: a – with using of Panofsky' lenses, b – without additional bending of beam.

In the ILU-14 accelerator along with the described elements of extraction system additional electromagnets for centering and focusing of a beam are used. To control beam position after the exit of accelerating structure with respect to the central axis of the output channel the additional magnet was entered. There is two-coordinate corrector of electron trajectories in the range ± 5 sm. For beam focusing at output channel of the accelerator the quadrupole doublet was installed.

SYSTEM OF BEAM BENDING

Extraction of the electron beam in the atmosphere not vertically, and under a certain corner, in particular, horizontal extraction is in certain cases of material radiation demanded. For bending of the accelerated electron beam it is offered to use system of two magnetic mirrors (M1 and M2). The task of use of a magnetic electron mirror as system for bending of the nonmonochromatic beams was considered for a long time [2]. However, practical implementation of these schemes (with formation by charged particles in a mirror of trajectories in the form of loops and without circumscribing of loops) for various reasons wasn't widely disseminated (complexity of receiving the required distributions of magnetic fields, narrow range of bending angles). At magnetic mirrors with electron trajectories without formation of loops input magnetic field is defocusing. This effect of beam widening on width of a mirror gap has stopped application of such scheme of bending. In connection with this, the subsequent achromatic bending or displacing magnetic systems began to contain flat bending magnets and the focusing systems of the quadrupoles. This scheme allows to reduce angular divergence of a beam after bending [3, 4], but has many permanently controlled variables. Considering the previous experience, authors suggest to use magnetic mirrors with such characteristic of magnetic field distribution on depth with which directly increase of magnetic intensity on the magnet input is followed by its recession under a certain law. Thus, the defocusing action of the growing field on an input to a mirror is compensated by the focusing area of the field recession (because of change of a sign of the first derivative of magnetic field).

The magnetic mirror represents the bending system with two-dimensional magnetic field. There are so-called flat or cylindrical fields. In such fields the method of approximation of this field in the symmetry plane by pieces of curves of the second order is applied to definition of three-dimensional distribution of magnetic field [5]. According to this work components of magnetic field in any point (x, y, z) for M1 and M2 have an appearance:

$$BX(x,y,z) = y \cdot B'(x);$$

$$BY(x,y,z) = B(z) + B(x) - \frac{y^2 \cdot B''(x)}{2} - \frac{y^2 \cdot B''(z)}{2};$$

$$BZ(x,y,z) = y \cdot B'(z).$$

Where BX, BY, BZ – components of a vector of magnetic field induction in any point of a magnet, B(z) and B(x) – the preset distributions of magnetic field in the symmetry plane: for M1 on z, for M2 on x. B' and B" – respectively the first and second derivative of these distributions of fields in the symmetry plane. System of the equations for the electron movement in the Cartesian coordinates:

$$\frac{d}{dt}vx = \eta \cdot (vy \cdot BZ(x,y,z) - vz \cdot BY(x,y,z));$$

$$\frac{d}{dt}vy = \eta \cdot (-vz \cdot BX(x,y,z) + vx \cdot BZ(x,y,z));$$

$$\frac{d}{dt}vz = \eta \cdot (vx \cdot BY(x,y,z) - vy \cdot BX(x,y,z)).$$

Where η – the electron charge relation to his relativistic mass, vx, vy and vz – a projections of speeds of particles.

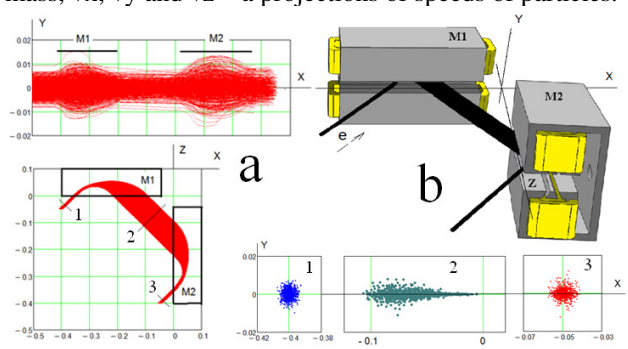

Figure 4: Calculation of beam bending on 180°.

By consideration of the three-dimensional movement of particles in a mirror it is convenient to divide it into two groups of projections of trajectories, as well as it is accepted for dipole magnets. The first group in the radial plane of symmetry (for M1 it is zx) represents bending of a beam on 90 degrees, the second group in the axial plane (xy for M1 magnet gap) describes focusing and defocusing of an electron beam (see figure 4a). For the first time the problem of a beam input taking into account the dispersion field at edges of a magnetic dipole has been considered in Ya. L. Hurgin's paper in 1939 [6].

ISBN 978-3-95450-181-6

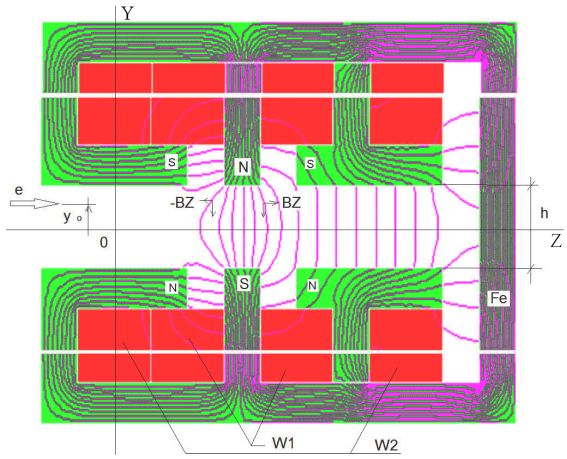

Figure 5: Construction of the magnetic mirror with two pairs of coils.

In this paper dynamics of the movement of particles in the growing flat fields has been for the first time considered. The proof that the growing fields of a magnet edge are cylindrical lenses which depending on the direction of a beam entrance can be collecting or dispersing was the main physical conclusion of this article. In the same place it has been shown that fields near the median plane (for M1 it is the zx plane at y = 0) are equal to the product of a particle coordinate from this plane y at a value of a derivative of magnetic field distribution on depth (for M1 on z).

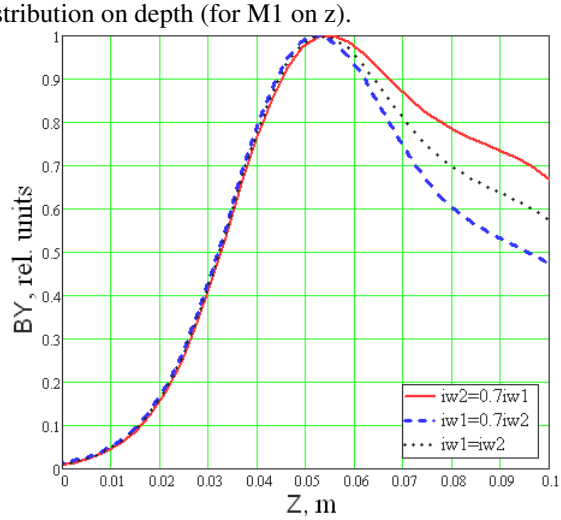

Figure 6: Adjustment of the magnetic field back front at different ratios of ampere-turns of internal (iw1) and external (iw2) coils of a mirror.

Results of calculation of beam bending on 180° are given as an example, the beam enters the first magnet at an angle 45 (see figure 4). Electron energy was 2.5 MeV and beam nonmonochromacity was 50%. The calculated radial projection of a beam to the median plane (xz plane), an arrangement of mirrors of M1 and M2 and an axial projection of path of trajectories to the xy plane are shown in figure 4a.

The scheme of the beam bending, and also beam cross-sections on the way of bending are provided on figure 4b.

The design of a magnetic mirror represents an E-shaped magnetic core with two pairs of coils – internal and external (see figure 5). Distributions of magnetic field in the median plane of this electromagnet for different ampere-turns of coils are provided in figure 6 (h=5sm). The general view of experimental installation for beam bending on 180° is also given in figure 7.

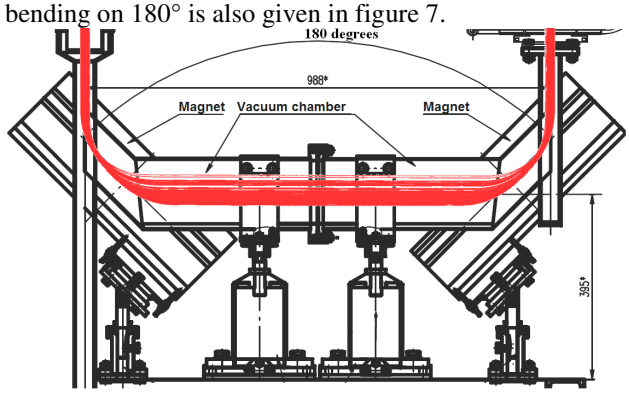

Figure 7: The general view of experimental installation for beam bending on 180° and the scheme of beam motion at the system of two magnetic mirrors.

RESULTS

The system of correction of the scanning magnetic field for electron energy up to 10 MeV providing nonuniformity of the absorbed dose up to ±5% has successfully tested. Calculations of bending of a nonmonochromatic beam with energy of 2.5 MeV on 180º are made, the design of magnetic mirrors and experimental installation for checking of these calculations are developed.

REFERENCES

[1] Bryazgin A.A. et al, “The device for bending of achromatic beams of charged particles”, Patent for the invention No. 2463749, request No. 2011115741, invention priority on April 20, 2011. It is registered in the State register of inventions of the Russian Federation on October 10, 2012.

[2] Kelmam V.M. et al, “Achromatic magnetic mirrors”, JTP, volume 30, issue 2, page 129-137, 1960.

[3] Panofsky Wolfgang K.H., McIntyre J.A., “Achromatic beam translation systems for use with the linear accelerator”, The review of scientific instruments, vol. 25, num. 3, p. 287-290, 1954.

[4] Vladimirskiy V.V., Koshkarev D.G., “Achromatic bending magnetic system”, IET, №6, 1958.

[5] Bleyvas I. M. et al, “The program for the decision on ECVM BESM-6 of three-dimensional problems of electronics”, Works of the third All-Union seminar, Novosibirsk, 1970.

[6] Hurgin Ya. L., “About vertical focusing of a beam of charged particles at its deviation in magnetic field”, JETP, volume 9, issue 7, p. 824-825, 1939.

ISBN 978-3-95450-181-6

MAGNETIC MEASUREMENT SYSTEM FOR THE NICA QUADRUPOLE MAGNETS

A. Shemchuk, V. Borisov, A. Donyagin, O. Golubitsky, H.G. Khodzhibagiyan,
M. Shandov, LHEP, JINR, 141980, Dubna, Moscow Region, Russia

Abstract

NICA is a new accelerator collider Nuclear Research (JINR) in Dubna. More than 250 superconducting magnets need for the NICA booster and collider. These magnets will be assembled and tested at the new test facility in the Laboratory of High Energy Physics JINR. A method of measuring of the quality of the magnetic field in the aperture of the quadrupole magnet for the booster synchrotron is described. Commissioning of equipment for magnetic measurements in the aperture of the doublet of quadrupole lenses is described.

INTRODUCTION

At the Laboratory of High Energy Physics (LHEP) creation of the first stage of technical complex [1] for assembly and testing of SC magnets for the NICA and FAIR project is finished. The program of testing of magnets includes «warm» and «cold» magnetic measurements. It is necessary to assemble and test 48 quadrupole magnets for NICA booster synchrotron. For measurement of characteristics of the quadrupole magnets two main sensors are used.

QUADRUPLE MAGNET FOR THE NICA BOOSTER

The quadrupole magnet consists of the focusing and defocusing lenses which are rigidly connected among themselves. The parameters of the quadrupole magnet are presented in [2] and Table 1. 3D view of the magnet shown in Figure 1.

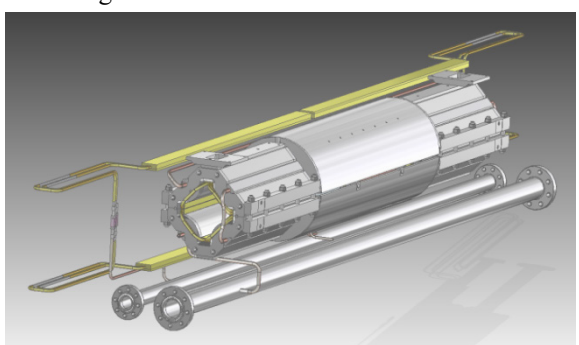

Figure 1: 3D view of the quadrupole magnet.

REQUIREMENTS FOR COMPOSITION OF MAGNETIC MEASUREMENTS

Requirements

- ✓ For all quadrupole lenses before the magnetic test in a superconducting mode, it is necessary to make measurements at normal (room) temperature. Thus, there is no need for magnetic measurements in the lenses with obviously unacceptable characteristics at 4.5 K temperature.
- ✓ The parameters of the harmonic coils must provide measurement accuracy according to specifications (see Table 1) during tests at 4.5 K.
- ✓ Both cold and warm serial measurements of the magnets are carried out without the vacuum chamber of the beam.
- ✓ For the 3-5 quadrupole lenses serial measurements should be supplemented by studies not included in a standard set of procedures:
  - The study of the effects (both static and dynamic) distortion values of the harmonics of the magnetic field associated with the presence of the vacuum chamber
  - Study of hysteresis effects
  - To study the influence of Assembly/disassembly of the lens on the measured parameters
  - The study of the dependence of field harmonics from the current. In particular, the necessary measurement of harmonics with a maximum field installation, field injection and 5-7 intermediate values. This task necessarily involves the need to accurately determine the values of the current in the main windings corresponding to three values of the fields.

Values which are Necessary to Measure

Based on the requirements for the creation of the measuring bench formulated the table 1. It contains both relative and absolute error.

It is necessary to measure the next parameter, quadrupole magnet:

- The gradient in the center of the magnet
- Integral gradient
- The effective length
- The offsets of the magnetic axis of the magnet, with respect to the geometric axis.
- The angle of rotation of the magnetic field relative to the yoke
- The relative Central and integral harmonics, to 6 inclusive

METHODS AND IMPLEMENTATION OF MEASUREMENTS

In accordance with the requirements specified in Table 1 was chosen 2 methods of measurement. The first method of harmonic coils [4], the second method of tangential coils.

ISBN 978-3-95450-181-6

Table 1: Relative Errors of the Parameters of the Magnet

Value	Precision
The gradient in the center of the magnet, G0	
Integrated gradient, GL	0.01%
The effective length, Leff	0.01%
The offset of the axis of the magnet, Δx	0.1 mm
The offset of the axis of the magnet, Δy	mm
The angle of rotation	rad
Higher harmonics	

For all quadrupole lenses were developed two sensors, corresponding to these two methods in front of the magnetic test of a superconducting mode, it is necessary to take measurements at normal (room) temperature. Thus, there is no need for magnetic measurements in the lenses with obviously unacceptable characteristics in a much more difficult technical conditions (cryogenic temperatures).

The Design of the Measuring System

Reference Magnetic Field. It is necessary to measure the orientation of all the sections of the sensor relative to each other. For the realization of this problem in measured magnets the reference magnetic field [3] from an additional winding (see Fig. 2) consisting of 4 conductors located in corners of the magnet yoke was used. This winding generates a magnetic field directed parallel to the magnet poles. The direction of this magnetic field, due to small sizes of a winding, is defined by the accuracy of fabrication of the magnet yoke. In view of the high mechanical accuracy of manufacturing of a yoke, it is possible to consider that a reference magnetic field is parallel to magnet poles. We will notice that this additional reference winding can be used also, as the detector of the quench in a SC magnet.

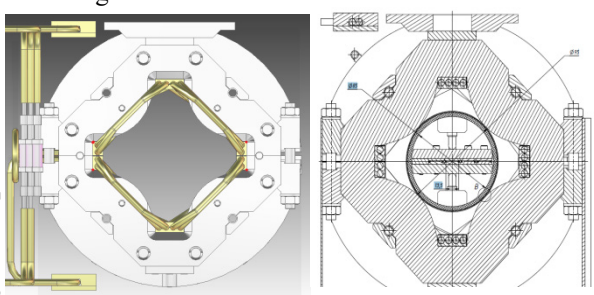

Figure 2: The location of the reference winding (left). In the lens F, and D, the magnetic field vector has opposite direction. The cross section of the quadrupole magnet is installed the harmonic sensor (right).

Mechanical Design. For measuring quadrupole magnet uses two types of sensors:

- With Tangential Coil (further TC)
- With Harmonic Coil (further HC)

In a tangential sensor used two sections (in the lens F and D, respectively) connected by two bellows couplings, and a common hollow shaft. Sections (see Fig. 3 pos.5) are made of fiberglass , after the processing - stoving varnish, in order to avoid adsorption pores of the fiberglass with water. Each section contains two ceramic bearing, which, in turn, planted in glass fibre laminate holders. The assembled structure is mounted in a long box, whose ends are reference plane. After the introduction of TC in the quadrupole magnet, the box is fixed with brackets (see Fig. 3 pos.4) to reference plates (see Fig. 3 pos.3) of the magnet. In each section, in a special way, set for 8 coils with different geometrical dimensions.

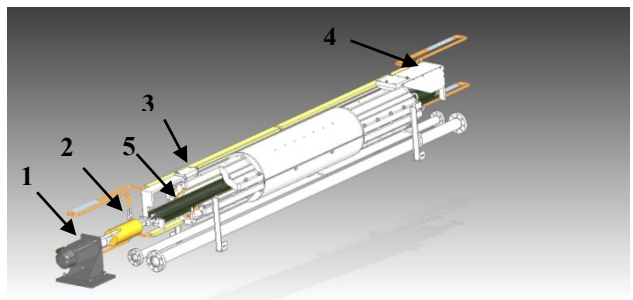

Figure 3: Quadrupole magnet with installed tangential sensor. In the front section made the cut.

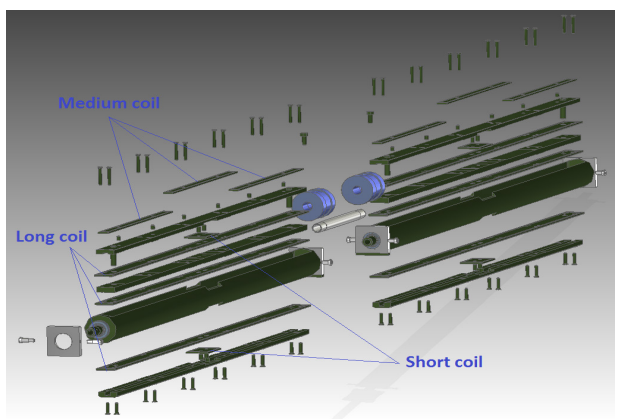

Figure 4: The composite tangential sensor elements.

For accurate assembly of the sensor used measurement arm that allows accurately set the coils according to the model. The sensor uses three types of coils (Fig. 4): 1, Long; 2 - Short; 3 - Medium.

In order to measure the specified value, the coil is included as a counter and sequentially. To measure the displacement of the magnetic axis using the center of a long coil (see Fig. 5, pos. 1). To measure the effective length and gradient fields are applied "quadrupole" long coil (see Fig. 5, pos. 2,3) plus a short coil in the center. To measure higher harmonics are used all the long coil (Fig. 5, pos 1,2,3), and all medium coil (Fig. 5, pos. 6,7,8).

In the prototype harmonic of the sensor, use a hollow tube of fiberglass, in which, on the adjustment screws to set the plate. On the plate are attached to the prototype coil with 193 turns. Figure 6 shows the assembled prototype of

ISBN 978-3-95450-181-6

the future sensor. The prototype is half working sensor, other words, it is possible to measure only the lens F or D.

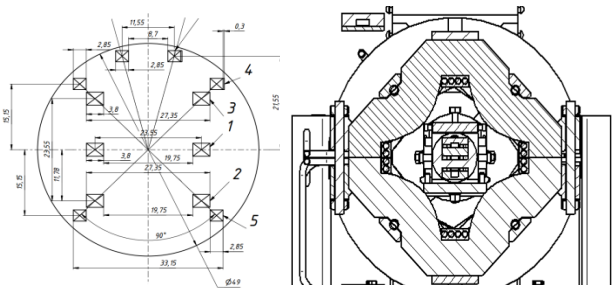

Figure 5: Scheme of the cross section of the measuring section (left). The cross section of the quadrupole magnet is installed the tangential sensor (right).

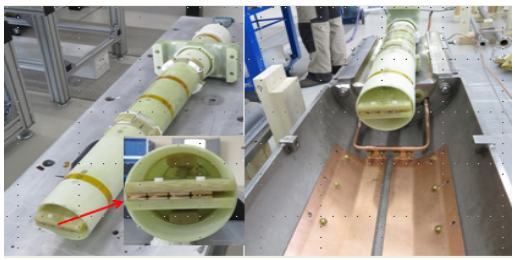

Figure 6: The prototype harmonic sensor.

In contrast to tangential - in a harmonic gauge is used sliding bearings (see Fig. 7, right). On the hollow pipe, in place of the slip applied epoxy resin, subsequently treated on a lathe. The bearing has a PTFE liners that provide the best glide.The advantage of such complex structures is the lack of deflection of the sensor along the entire length. Figure 7 left presents the 3D model of the harmonic full-size sensor. The numbers indicate the following elements: 1 - Doublet quadrupole lenses; 2 - Bracket for mounting the sensor magnet; 3 - Multipole corrector; 4 - Motor; 5 - Lens F; 6 - D Lens; 7 - glass fibre laminate tube; 8 - Slip rings; 9,10 - Sets tangentially coils.

Both sensors are driven by servo motors, with the parameter of the encoder is 2^{20} pulses per revolution. The signals from the coils and in that and in other case transmitted via a sliding contact. For more precise control of the position of the coils relative to the magnet, encoder mounted at the end of the sensor is used. This decision will allow to track possible backlash in the mechanics of the sensor.

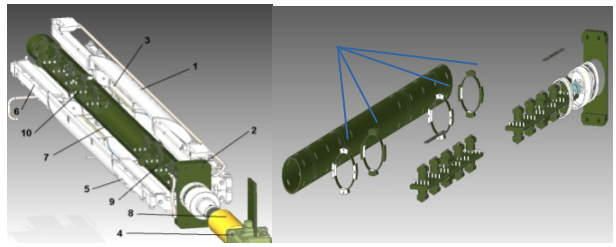

Figure 7: 3D model of a tangential sensor installed in the magnet (left) and its constituent elements (right).

Structure of harmonic and tangential coil. Tangential coils are made as the multilayered printed-circuit board (PCB). Coils consist of 400 turns created from 20 layers, each of which contains 20 turns. Production of PCB was ordered in China. The sample of PCB was tested cyclically by cooling down to the LN2 temperature. The sample wasn't destruction.

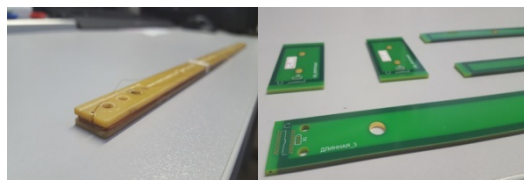

Figure 8: The measuring coil of tangential (right) and prototype of harmonic sensors (left).

Prototypes of harmonic coils(see Figure 8, left) are made from two bonded between a glass fibre laminate conductors to which a coil to a coil wound around a thin conduit with polyamide insulation. In operating the sensor, will be used coils made on PCB technology.

RESULTS AND FUTURE PLANS

Started mass measurements quadrupole magnets. At the moment, held the "warm" test, made a tangential sensor. The results of the measurements are presented in Table 2. The plans in the near future is to build the full harmonic sensor, as well as the launch of the stand string methods to determine the magnetic axis of quadrupole magnets.

Table 2: The Results of the Warm Measurements of the Tangential Sensor

№ of series		L_{eff} [mm]		G [mm]		ΔX [mm]		ΔY [mm]	
		F	D	F	D	F	D	F	D
1		490.106	491.18	0.21538	0.21866	-0.412	-0.4051	5.92E-4	-4.38E-4
	σ	0.009	0.01	6E-6	7E-6	4E-4	5E-4	6E-6	7E-6
2		491,20	490,058	0,21859	0,21532	-0,337	-0.327	-6.5E-4	2,08
	σ	0.02	0.007	3E-5	3E-5	0.001	0.002	4E-5	0.01
Average		490.65	490.62	0.21699	0.21699	-0.375	-0.366	-2,9E-5	1,040
	σ	0.02	0.01	3E-5	3E-5	0.001	0.002	3.3E-5	0.007

ISBN 978-3-95450-181-6

REFERENCES

[1] Khodzhibagiyan H. et al., Facility for Superconducting Magnet Assembling and Serial Testing, Proc. of the 13th Cryogenics, Prague, April 2014, 036.
[2] Khodzhibagiyan H. et al., Superconducting Magnets for the NICA Accelerator-Collider Complex, IEEE Trans. Appl. Supercond., vol.24, N3, pp. 4001304, June 2014.
[3] Borisov V. et al Magnetic Measurement System for NICA Booster Magnets, Proceedings of IPAC2014, Dresden, Germany (2014).
[4] Kostromin S. et al Measurements of Magnetic Field Parameters of NICA Booster Dipole Magnet, XI international seminar on charged particle accelerators memory Sarantseva V. P.,Alushta, Russia (2015).

ISBN 978-3-95450-181-6

FIRST EXPERIENCE OF THE HTS-II DIPOLE TYPE MAGNETS DEVELOPMENT AT NIIEFA

I. Rodin#, E. Andreev, V. Amoskov, V. Glukhich, A. Dyomina, V. Kukhtin, E. Lamzin, E. Zapretilina, JSC «NIIEFA», St.Petersburg, Russia
V. Belyakov, S. Sytchevsky, St.-Petersburg State University, Russia
S. Samoilenkov, JSC "SuperOx", Moscow, Russia

Abstract

The possibility to design, manufacture and test the dipole type magnets from the second generation high-temperature superconductors (HTS-II like YBCO and ReBCO) was demonstrated at the Efremov Institute. The paper describes available computation techniques, design approaches and manufacturing equipment, which could be used to meet the modern requirements for the magnets of accelerators, research equipment, magnet levitation systems etc. The manufacturing equipment comprises the winding lines and insulating devices to provide different configurations and insulating schemes of coils. Additionally, an equipment to produce the Roebel-cable for high current applications was procured and put in operation. As an example, the results of development of the HTC-II dipole type magnets for the different kind dummies of maglev systems are presented. The ReBCO tapes produced by JSC "SuperOx" (Moscow) were used. Up to 0.5 T magnets cooled by liquid nitrogen were designed as a part of levitation system consisting of permanent, HTS-II and normal conductive magnets. Comprehensive tests verified the computation results and demonstrated the readiness to develop HTS-II dipole magnets under the customer requirements.

INTRODUCTION

Over the last fifty years the Efremov Institute holding leading position in design and production of large-scale superconducting magnets was successfully developing low temperature superconductor technology (LTS). However, progress in high temperature superconductivity (HTS) urged the Efremov magnet department to apply considerable efforts to that new area. Starting with measurements of YBCO monocrystals [1], and testing HTS-I current leads it gradually turned to HTS-II tapes, cables and windings. When looking at the critical characteristic of the ReBCO tape (Fig. 1), three specific regions of HTS application could be distinguished:

- Low temperature and high or extra high field – magnets for NMR spectrometry.
- When operating temperature ranges from 20 to 40 K, the HTS can replace LTS in their traditional 5 to 15 T applications – dipoles, magnetic lens etc.
- Low field and LN temperature (the most attractive region from cryogenic point of view) – current leads, power cables, small coils (<0.5 T), bias coils for electromagnets etc.

Some aspects of the work, which seem prospective for accelerator magnets, research equipment, levitation systems and other applications, are reported below.

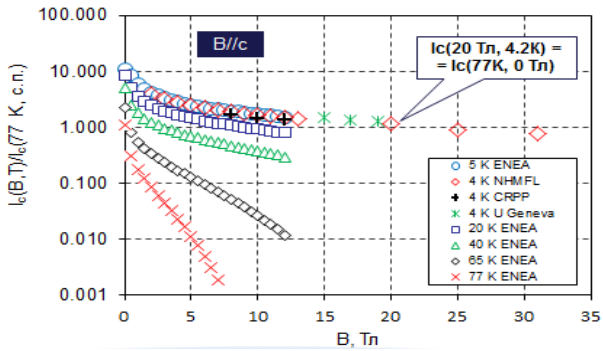

Figure 1: Critical characteristic of ReBCO tape.

WINDING AND INSULATING EQUPMENT

The HTS-II conductors suitable for coil winding are thin multilayer tapes. Typical dimensions of the tape are - width from 4 to 40 mm and thickness for 40 to 600 μm. A special insulating and winding equipment is needed to handle such a delicate conductor. The necessary equipment has been designed, manufactured, procured and put in operation in the Efremof Institute. The equipment allows winding of round, racetrack and saddle-shape coils up to 1.5 diameters. It can work with tapes, flat cables (Roeble or Rutherford type) and round wires with thickness ranges from 10 μm to 1.5 mm. The winding machine can get wire supply form nine delivery spools, so it can perform winding following "n-in-hand" technique. The optimal n in this scheme is two or three "elements", where an "element" is a composition of two or three tapes, for example, HTS tape, hastelloy tape and insulation tape. The machine can produce a pulling force up to 12 kg per spool. When performing racetrack or saddle winding the pulling force should vary with angle of the spin-table rotation. A special system controls the machine operation and the pulling force variation can be pre-programmed. Main parameters of the winding process are set form the touch panel and displayed at the monitor of the control console. The winding machine is shown in Fig. 2. At the rotating table in Fig. 3 is a coil in process of winding and assembly. The coil is 400 mm round section of the SMES model. It is designed to operate at

#rodin@sintez.niiefa.spb.su

ISBN 978-3-95450-181-6

20- 40 K and carry current over 600 A. The coil can work in liquids or be cooled by thermoconduction.

Figure 2: Winding machine at work.

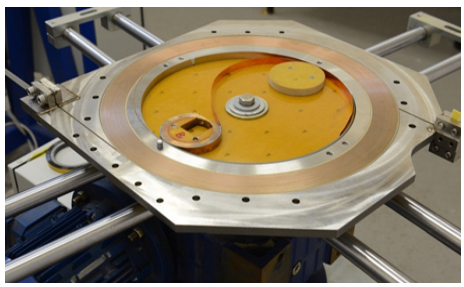

Figure 3: Pancake winding for HTS-II SMES.

FLAT TRANSPOSED CABLE WITH HTS-II STRANDS

While small coils and lab magnets can be wound with tapes carrying hundreds of amperes the large-scaled magnets require conductors with higher currents. Among the current carrying elements made of HTS-II tapes a flat transposed cable of Roeble-type seems the most compact and applicable for the purpose. Equipment to manufacture a flat transposed cable has been deigned, produced, procured and put in operation. It includes a punching machine (press) for cutting a meander shaped elements ("strands") and a planetary winding system to put the elements into a cable. The punching machine can produce strands up to 400 m long from 12 mm wide tape. The machine cuts strands from a bare (without stabilizing Cu) tape. Then bare strand goes to Cu electroplating. Usually thickness of the plated layer is about 20 μm. The Cu-plated strands should pass the Jc control and go to cable winding. A planetary winding system can produce up to 400 m cable with number of strands up to 26. Punching and planetary winding machines at work are shown in Fig. 4.

A short sample of Roeble cable (Fig. 5) has been produced and tested in LN. The cable was 3m long and consisted of 10 strands. Special design of the sample joint ensured uniform current distribution among the strands. The sample has shown the value of the critical current Ic (77 K, s.f) close to 1100 A.

Since current at the HTS–II tape flows through a thin 1 - 1.5 μm ReBCO layer a number of effects can be observed in cables and windings. A mathematical model has been developed to simulate characteristics of the complex tape-like current carrying elements [2]. The model allows performing analysis of the fine structure of magnetic field with a very good accuracy.

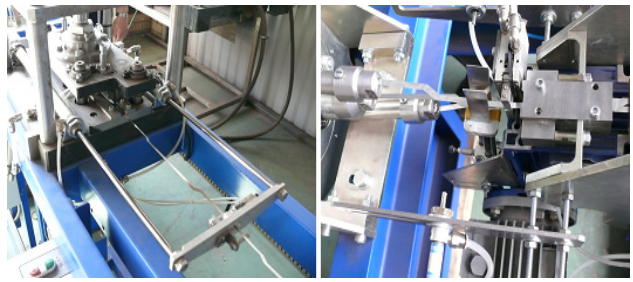

Figure 4: Punching (press) machine (left) and planetary winding system (right).

Figure 5: Insulated Roeble-type cable.

LN COOLED HTS-II COILS FOR MAGNET LEVITATION

A computation technique developed in the Efremov Institute for electromagnetic simulations of various devices related to accelerators, particle physics and fusion has been adapted for modeling and optimization of the maglev transport systems. Different principle types of maglev system have been analyzed [3-6]. The 3-D model gives detailed description of eddy currents, electromagnetic load, includes edge effects, takes into account all important elements and structures and can simulate various scenarios and regimes of vehicle motion. For verification of the modelling results and experimental check of electrodynamic suspension (EDS) performance a maglev dummy has been built. The dummy allows simulating distribution of electromagnetic force similar to that at the maximum vehicle velocity. The maglev dummy includes a guideway – stationary structure constructed from blocks of permanent magnets and a "vehicle" – suspended platform with a pair of permanent magnets or HTS blocks. The HTS block is shown in Fig. 6. It consists of the HTS-II racetrack coil placed into a compact cryostat. The coil – two-sectioned winding with dimension of 480×170×9 mm, made of 4mm insulated ReBCO tape was cooled with LN (77K). The coil winding was performed with insulation and winding equipment described above. The HTS blocks assembled at the platform have been successfully tested [7]. It should be mentioned that presence of permanent magnets, ferromagnetic materials and coils makes system non-linear and pooling force acting on the block in a complicated way depends on levitation gap and coil

ISBN 978-3-95450-181-6

current. A specially designed feed-back system was responsible for gap and current control and coil positioning. During the tests, HTS blocks were exposed to magnetic field equivalent to that of a real EDS system and have shown stable performance at nominal and maximum current up to 55 A. The module during the test is shown in Fig. 7.

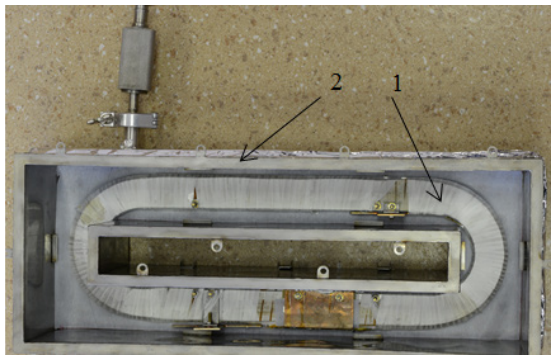

Figure 6: HTS-II block: racetrack coil (1) fixed into a compact cryostat (2) – double-wall stainless steel box providing vacuum insulation for the block.

Figure 7: The HTS-II module during tests: maximum levitation gap ~ 40 mm; total current – 14 kAt; total weight of the platform (two HTS blocks with cryostat filled with LN) – 48 kg.

The HTS-II coils are employed as support- magnets in the model of electromagnetic suspension (EMS) system, which is a part of combined magnetic suspension concept [3-6]. A schematic view of the test facility is given in Fig. 8.

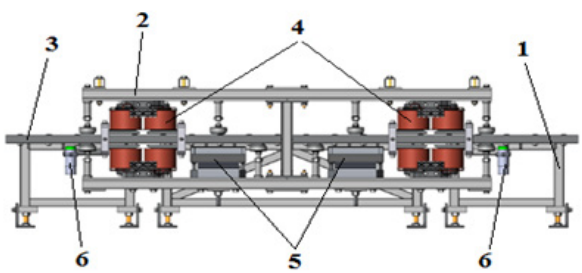

Figure 8: Facility to test elements of EMS system as a part of combined magnetic suspension concept: 1 – carrying frame; 2 – levitating platform; 3 – ferromagnetic guides; 4 – electromagnets; 5 – support- magnets; 6 – gap sensors.

A HTS-II coil replaces a block of permanent magnets. The coil current should remain constant or change slowly when operating. The coil for that model is a three-sectioned winding made of 12 mm tape, placed into a compact cryostat and assembled at the ferromagnetic core. Coil winding and magnet assembly is show in Fig. 9 Two coils have been successfully tested in LN: the coil current reached 120 A and pulling force was over 50 kg.

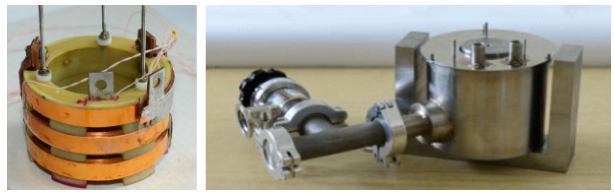

Figure 9: HTS-II support- magnet: HTS coil and assembly (coil, cryostat on the ferromagnetic core).

CONCLUSION

All necessary components to design and build HTS-II dipole magnets are concentrated in the Efremov Institute: the team of professionals able to perform a comprehensive analysis and numerical simulations of electromagnetic, mechanical and thermo-hydraulic processes and carry out design and technological support of the projects, modern engineering equipment, technology and mechanical production. The experimental equipment and test facilities allow conducting a wide range of research works from wire characterization to life test of the machine.

REFERENCES

[1] H. Araseki at all, IEEE Transactions on Applied Superconductivity, 18.N2 (June 2008), pp 1585-1588.
[2] M.Astrov, M.Chernogubovsky, I.Rodin, “Field features of the current-carrying bifilar block for Superconducting Fault Current Limiter”, Abstracts of 26th International Cryogenic Engineering Conference & International Cryogenic Materials Conference 2016 (ICEC26-ICMC2016), India, New-Delhi, March 7-11(2016) 10-P3-252.
[3] V.Amoskov at al, Vestnik of State Petersburg University, Ser.10 (Applied Mathematics), 4 (2014) 5.
[4] V.Amoskov at al, Vestnik of State Petersburg University, Ser.10 (Applied Mathematics), 3 (2015) 4.
[5] V.Amoskov at al, Vestnik of State Petersburg University, Ser.10 (Applied Mathematics),2 (2015) 17.
[6] V.Amoskov at al, Vestnik of State Petersburg University, Ser.10 (Applied Mathematics), 3 (2016) 4.
[7] I. Rodin, E. Zapretilina, O. Kovalchuk, A. Dyomina, A.Safonov, "Development and testing prototype of HTS module for the system of magnetic levitation of vehicle", Proc. 3d Int.Sci.Conf. MTST 2015.

ISBN 978-3-95450-181-6

THE NONSYMMETRICAL VARIANT OF THE NONFERROMAGNETIC EXTRACTION KICKER MAGNET OF THE NICA BOOSTER

V. S. Aleksandrov†, A.V.Tuzikov, A. A. Fateev, Joint Institute for Nuclear Research, Dubna, Moscow Region, Russian Federation

Abstract

Development and creation of the NICA acceleration complex are continued at JINR (Dubna). One of the main facilities of the complex is the Booster in which preliminary acceleration and cooling of an ion beam is performed. Further acceleration is fulfilled in the circular accelerator NUCLOTRON. The beam transfer from the Booster into the NUCLOTRON is provided by means of the fast extraction system and one of its central elements is the kicker magnet. For the beam deflecting into the extraction septum-magnet it is supposed to use the nonferrous kicker magnet consisting of two couples of conductors. Recent changes made in configuration of the Booster extraction section demand decrease of the kicker magnet length that leads to change of the beam extraction scheme. This report is devoted to the choice of the alternative design of the magnet (the nonsymmetrical variant).

INTRODUCTION

Within the NICA [1] project creation and development not only traditional, but also new transition systems of a beam is supposed. In article [2] the kicker magnet consisting of two couples of conductors in which the ferromagnetic yoke is not used is offered.

According to [3] extraction of ions from the Booster it is supposed to carry out in 2 stages. At the first stage the circulating beam is brought to a septum-magnet knife by means of a bump subsystem of a closed orbit. At the second stage an extraction of ions from the Booster is carried out actually. The kicker magnet represents two couples of conductors established inside vacuum box parallel to an axis of driving of a beam. Maximal magnetic field – 0.13 T, the corresponding current in conductors of a magnet – 15 kA. Inhomogeneity of a magnetic field in the area occupied by a bunch does not exceed ±1 %.

THE EXPECTED BEAM PARAMETERS

Calculated parameters of a beam in the location of a kicker magnet on energy of injection and the maximal energy are given in Table 1. The option of an extraction called in Table 1 "initial" was assumed at the time of the publication of article [2].

Table 1: Beam Parameters

	injection	extraction options	
		initial [2]	new [3]
ε_x, π mm · mrad	150	15	3
ε_y, π mm · mrad	10	2	1.5
Max β_x, mm / mrad	12	12	12
Max β_y, mm / mrad	12	12	6.5
D_x, m	1	1	0.1
$\Delta p/p$	$\pm 5 \cdot 10^{-4}$	$\pm 3.6 \cdot 10^{-3}$	$\pm 5 \cdot 10^{-4}$
Max A_x, mm	43	17	6
Max A_y, mm	11	5	3.3

NONSYMMETRICAL VARIANT OF THE KICKER MAGNET

New parameters of a bunch at the maximal energy, in particular, considerably smaller cross sectional dimensions, and also pulse character of a magnetic field, give the possibility to offer a kicker magnet consisting of one couple of conductors and the copper screen replacing the second couple of conductors with an opposite direction of current (Fig. 1).

As a current pulse length in a kicker magnet is about one microsecond, the strong skin effect takes place, and numerical simulation of magnetic fields can be carried out in the following approach. The magnetic field in conductors is absent, current is distributed on a surface of conductors. In model of an infinitely long magnet a current is directed along a longitudinal axis. Respectively the vector potential of a magnetic field has only a longitudinal component. In such approaching the problem of calculation of a pulse magnetic field is equivalent to an electrostatic task. It allows to carry out calculations for the choice of a configuration of couple of conductors and the screen by means of a POISSON [4] package in twodimensional model, trying to obtain the required distribution of a horizontal component of an electric field.

In calculations the following main variants of a magnet were considered: variant with the flat screen and variants with screens arched in the vertical plane with various radii of curvature. For expansion of area of uniformity of the field the distances between main elements were increased from 40 to 50 mm.

In Fig. 2 corresponding distributions of the field are shown.

† aleks@jinr.ru

ISBN 978-3-95450-181-6

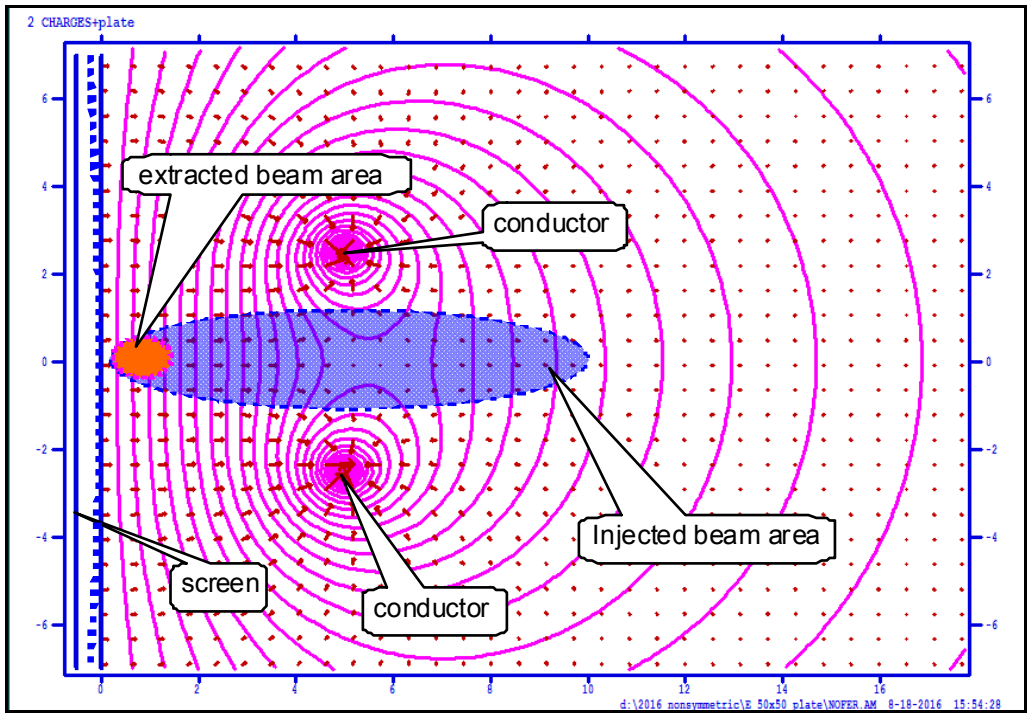

Figure 1: Arrangement of elements of a kicker magnet.

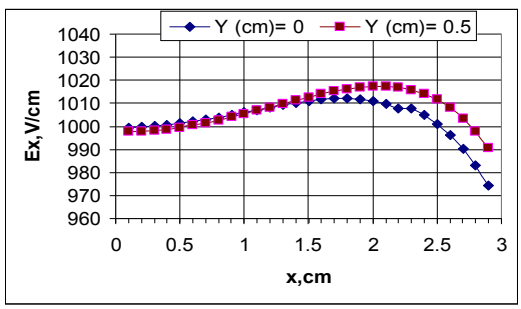

Flat screen: ±1.0 %

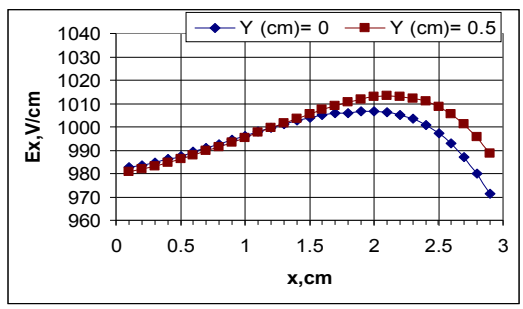

Concave screen: R=1000 mm, ±1.6 %

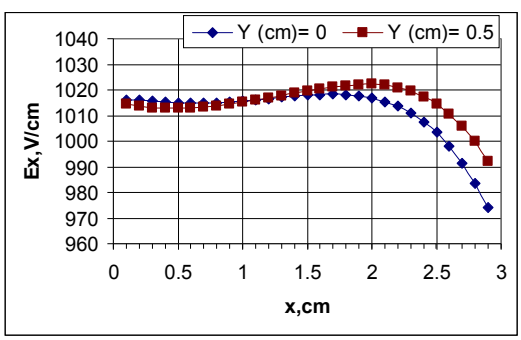

Convex screen: R=1000 mm, ±0.9 %

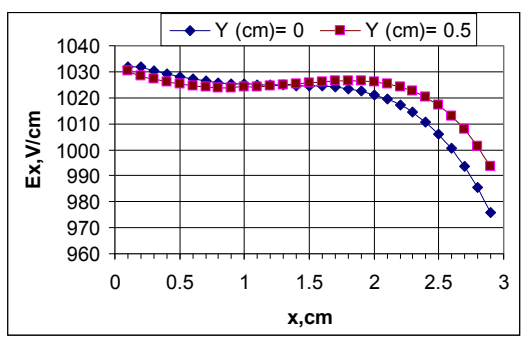

Convex screen: R=500 mm, ±0.5 %

Figure 2: Distributions of the field between the screen and conductors, inhomogeneity of the field in the area x = 0...20 mm is specified as a percentage.

CONCLUSION

The nonsymmetrical variant of a kicker magnet consisting of one couple of conductors and the copper screen is offered. The distance between axes of conductors is 50 mm. The copper screen is installed in 50 mm from the plane of couple of conductors. Screen parameters: thickness is 3 mm, width is about 180 mm. Such kicker magnet can provide uniformity of the field in the extraction region not worse than 0.5 % at the suitable

ISBN 978-3-95450-181-6

choice of radius of curvature. The required current in conductors of a magnet is about 20 kA.

REFERENCES

[1] G.Trubnikov et al., "NICA Project at JINR", Proc. of IPAC'13, Shanghai, China, 2013. P. 1343-1345.

[2] V. S. Alexandrov, E. V. Gorbachev, A. V. Tuzikov, and A. A. Fateev. Choosing the Power_Supply System and Construction of the Extraction Kicker Magnet of the NICA Booster, in Proc. of the 9th International scientific workshop to the memory of Professor V.P. Sarantsev, Alushta, Ukraine, 2011. Physics of Particles and Nuclei Letters, 2012, Vol. 9, No. 4–5, pp. 425–428, 2012.

[3] A. V. Butenko et al., "Channels of transportation, systems of injection and extraction of the bunch in the accelerating complex NICA", in Proc. of the XIth International scientific workshop to the memory of Professor V.P. Sarantsev, Alushta, Russia, 2015.

[4] POISSON Program, Los Alamos Acc.Group, LA-UR-87-115, 1987.

ISBN 978-3-95450-181-6

FAST KICKER FOR HIGH CURRENT ELECTRON BEAM MANIPULATION IN LARGE APERTURE

V. Gambaryan, A. Starostenko, BINP SB RAS, Novosibirsk, Russia

Abstract

Pulsed deflecting magnet (kicker) project was worked out in BINP (Budker Institute of Nuclear Physics). The kicker design task is: impulsive force value is 1 mT*m, pulse edge is 5 ns, and impulse duration is about 200 ns. The unconventional approach is for plates to be substituted by a set of cylinders. Obtained magnet construction allows controlling field homogeneity by changing currents magnitudes in cylinders. Furthermore we demonstrated the method of field optimization. In addition the harmonic components measurement technique was considered and the possibility to control harmonic components value was shown.

THE KICKER CONCEPT DESIGN

The kicker design should accept several requirements. The first one is vacuum chamber and kicker symmetry axis coincidences. The second one is that central angel should be about 90˚. The optimisation parameter is magnetic field homogeneity in centrally located square area (2 cm x 2 cm).

THE KICKER ACTUAL DESIGN

Taking into account the kicker design optimization results described in [1], the BINP designers developed a kicker prototype. The kicker dimensions were selected based on measurements. The magnet cross section is shown in Fig. 1. The physical magnet length is about 650 mm. The magnet aperture is 100 mm. The vacuum chamber diameter is 164 mm. The cylinder diameter is 28 mm. The cylinders are made of steel, as well as the body of the magnet. The ceramic feedthrough also was developed in BINP.

For the simulation of dynamics of charged particles beams the CST Studio is used. These simulations are in the initial stage. Only preliminary calculations have been held. One of the first results is shown in Fig. 2.

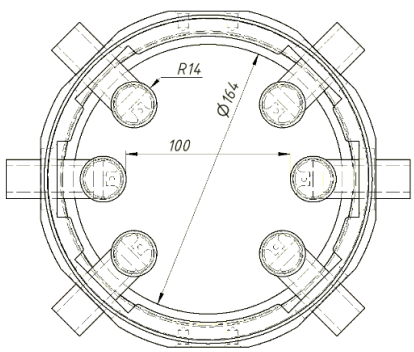

Figure 1: The kicker actual design (all dims are in mm).

MAGNETIC FIELD MEASUREMENTS

To control magnetic field quality the experimental measurements was carried out.

Experimental Stand Description

Experimental stand shown in Fig. 3 consists of the following parts:

1. Kicker
2. Pulse generator
3. The induction coil magnetometer
4. VSDC2 - Precision digital signal integrators with an accurate synchronization [2]
5. Hand caliper
6. Step motors with controllers
7. PC with a special software

The kicker is fixed on a metal frame. Step motors provide the movement in the horizontal plane. The vertical displacement of step motors is realized only by screws turning by hand. For both step motors we have to control vertical position using hand caliper. All of the stand components were precisely aligned with the help of BINP geodesy group.

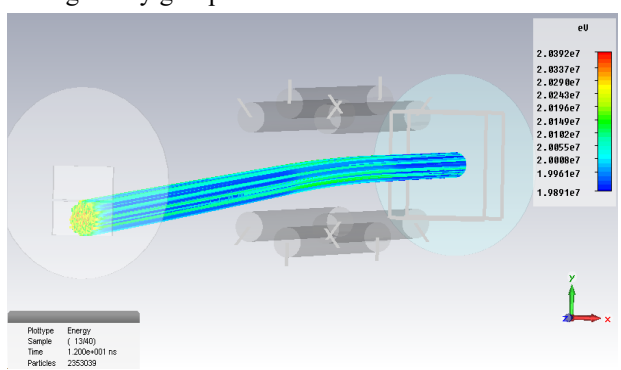

Figure 2: Beam dynamics simulation in CST.

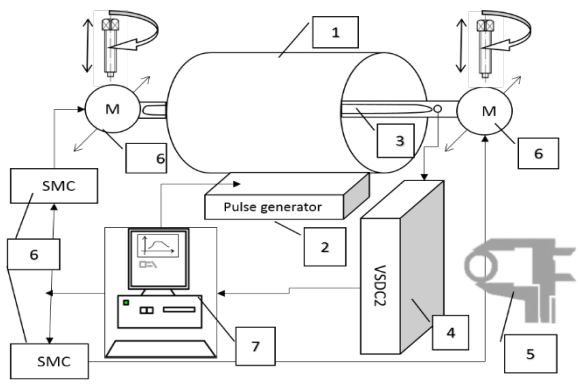

Figure 3: The principal scheme of magnetic field measurement stand: 1) kicker, 2) pulse generator, 3) the induction coil magnetometer, 4) VSDC2, 5) hand caliper, 6) step motors with controllers, 7) PC with special software.

ISBN 978-3-95450-181-6

The Induction Coil Magnetometer

The induction coil consists of five wire turns ($N=5$). It has the width w=5 mm and the length l=1000 mm. The wire diameter is 0.2 mm. The coil base is made of the fiberglass plastic strip. Induction coil principle is derived directly from the Faraday's law:

$$E(t) = -\frac{d\Phi_B(t)}{dt}, \quad (1)$$

where E is the electromotive force (EMF) and Φ_B is the magnetic flux. The EMF time integration gives us magnetic the flux. From magnetic flux definition we get the maximal magnetic field value:

$$B_{\max} = \frac{-\int_0^{T_0} E(t)dt}{N \cdot w \cdot l}, \quad (2)$$

where T_0 is the integration time chosen such to provide a maximum integral value, N, w and l described upper are the coil geometrical parameters.

For example, in Fig. 4 one can see typical signals. The first channel (grey dashed curve) is a signal from the coil and the second channel (black curve) is a current monitor signal.

We supply the coil signal to VSDC2. The software "S-Wire Kicker" created at BINP is close integrated in the experimental stand. The program can control step motors, pulse generator and store results of measurements on HDD.

Magnetic field distribution was measured in central part of the kicker. The exploring area is almost 2x2 cm square. Measurements were carried out in the five vertical positions: -2 cm, -1 cm, 0 cm, 1 cm and 2 cm. Horizontal shift was realized by the program "S-Wire Kicker" automatically within the range from -1.8 cm to 1.8 cm with a step of 0.1 cm. In each point five measurements were done and then they were averaged. Using obtained values we form the magnetic field distribution map. To compare experimental results with calculation we simulated FEMM task with the same current value as we get from the current monitor.

Magnetic Field Measurements

To measure the magnetic field distribution in experiment we used a single generator. With the aim to control a current in the separate cylinders the Variable Resistance Unit (VRU) was made. The commutation scheme with VRU is shown in Fig 5. To anticipate we can get the better magnetic field distribution as a result of using this scheme.

Experimental Results

In this part we present the results of magnetic field measurements. The experimental data in comparison with calculated once in FEMM are shown in Fig. 6 ((a) – experimental, (b) – calculation in FEMM).

We can see that the measurement results with a sufficiently high accuracy agree with the simulation results.

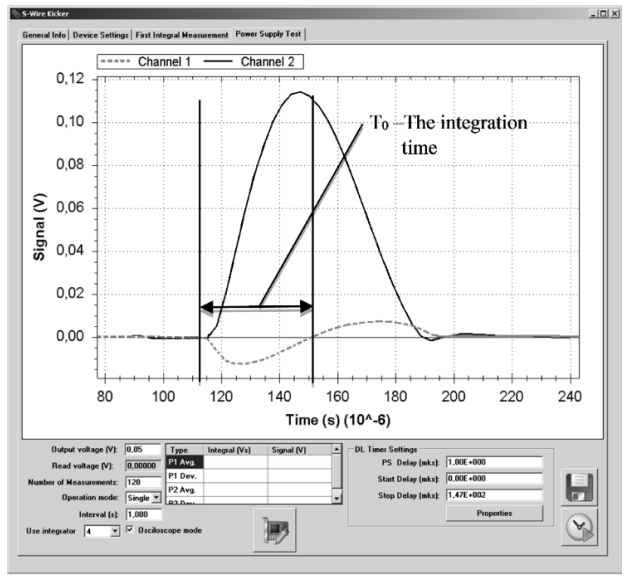

Figure 4: Typical signal from magnetometer (Channel 1) and current wave form (Channel 2).

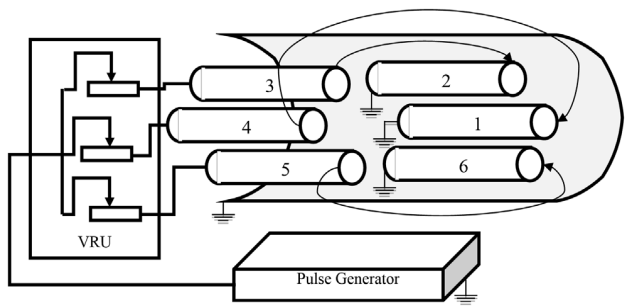

Figure 5: The kicker commutation diagram with Variable Resistance Unit (VRU).

We have an opportunity to control a magnetic field distribution and homogeneity. To implement this we need to set the specific current values in each conductor. The parametric optimization simulation was done in FEMM. We consider upper and lower conductors current value to be I_0 A. The current value in central conductor is $k \cdot I_0$ A, where k is optimizing parameter:

$$I_2 = I_6 = -I_3 = -I_5 = I_0, \; I_1 = -I_4 = k \cdot I_0.$$

The optimization goal is to minimize ΔB – field quality indicator:

$$\Delta B = \frac{B_{\max} - B_{\min}}{B_{\min}} \cdot 100\% \quad (3)$$

As a result of the optimization we have the following ratio: the first and fourth currents must be one point five times greater than others, i.e. k=1.5.

By means of VRU mentioned above the current in each conductor was tuned in accordance with optimization results. After this measurement was repeated. Obtained results are shown in Fig.7.

ISBN 978-3-95450-181-6

The magnetic field measured experimentally turned out non-symmetric. However we see that the homogeneity value is close to calculated one. The reasons of this non-symmetry is not completely explored.

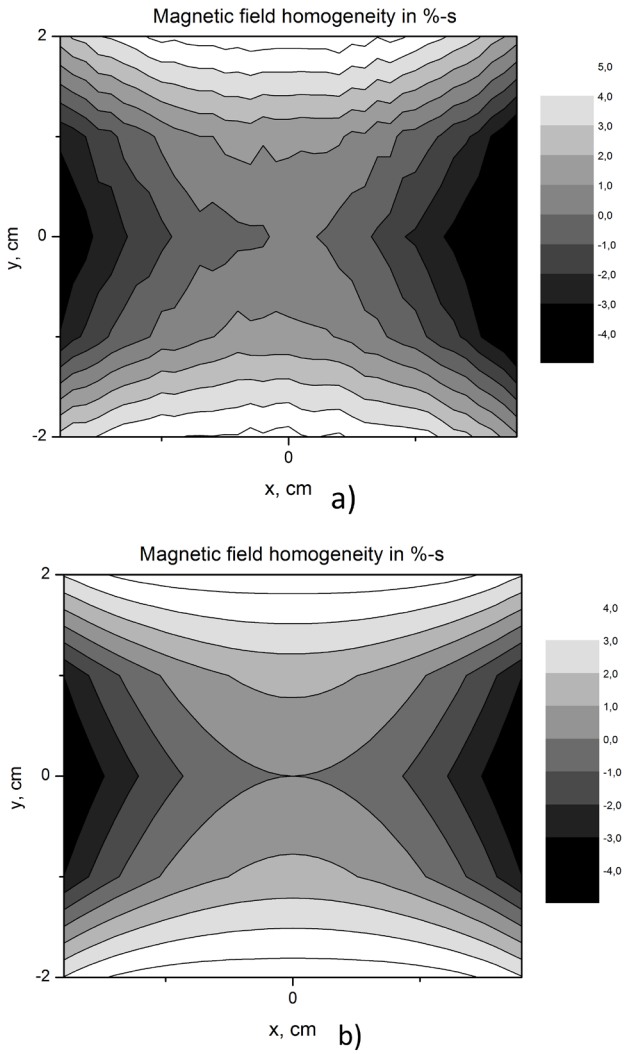

Figure 6: Magnetic field homogeneity: a) measured, b) calculated.

We have a number of assumptions, but they need to be checked. One of them is the limited induction coil magnetometer accuracy and other is some imperfections in electrical contacts. We plan to repeat measurements to provide more accurate results.

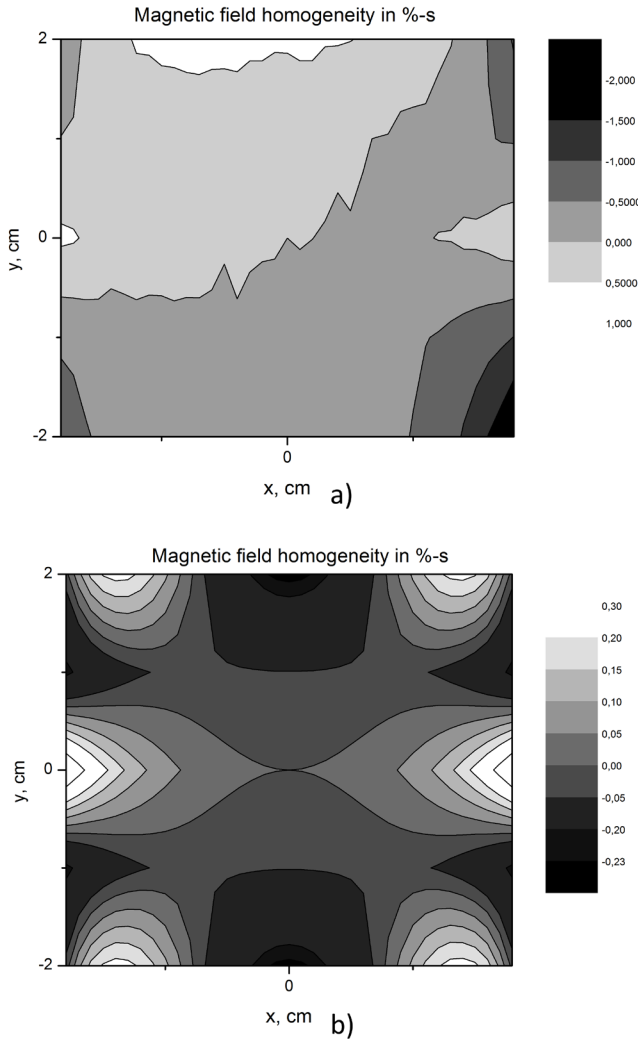

Figure 7: Magnetic field homogeneity: a) measured, b) calculated.

SUMMARY

The design of non-conventional kicker was developed in BINP. The kicker was manufactured. We carried out the magnetic field measurements. For this purpose the magnetic measurement stand was created and tested. We have plane to improve our measurements in future.

REFERENCES

[1] V.V. Gambaryan and A.A. Starostenko, Fast kicker, in Proc. 6th International Particle Accelerator Conference, Richmond, VA, USA, paper MOPTY033, pp. 1001-1003, ISBN: 978-3-95450-168-7, http://jacow.org/IPAC2015/papers/mopty033.pdf, 2015.

[2] A.M. Batrakov, I.V. Il'yin, & A.V. Pavlenko. (2015). Precision digital signal integrators with accurate synchronization. Optoelectronics, Instrumentation and Data Processing, 51(1), 51-57, DOI:10.3103/S8756699015010082.

ISBN 978-3-95450-181-6

A SYNCHROTRON RADIATION BEAMLINE INSTALLED AT BINP TO STUDY THE HIGH LUMINOSITY LHC VACUUM SYSTEM

A. Krasnov[1*], V. Anashin, A. Semenov[2], D. Shwartz[1], BINP SB RAS, Novosibirsk, Russia
V. Baglin, P. Chiggiato, B. Henrist, CERN, Geneva, Switzerland
[1] also at NSU, Novosibirsk, Russia
[2] also at NSTU, Novosibirsk, Russia

Abstract

In the framework of the HL-LHC project, the vacuum performance of new surface material needs to be studied. In particular, a-C coating is proposed as an anti-multipactor surface for the HL-LHC superconducting final focusing system. Since the protons will generate synchrotron radiation (SR) with ~ 10 eV critical energy and ~10^{16} ph/m/s flux, it is therefore of great importance to study the impact of such photons on a-C coating held at room and cryogenic temperature and compares the results against present LHC material. This paper describes the construction and the parameters of the experimental set-up based on a new Synchrotron Radiation beamline of the BINP booster synchrotron, BEP. The experimental program done in collaboration between CERN and BINP, to perform measurements of photon stimulated gas desorption, photon distribution and photo-electron emission provoked by synchrotron radiation is also presented.

INTRODUCTION

The CERN Large Hadron Collider (LHC) is currently operating at nominal luminosity with proton-proton collisions at 13 TeV in the center of mass. Its upgrade, the High Luminosity LHC (HL-LHC), is designed to provide about 10 times more integrated luminosity with the aim to achieve ~3000 fb^{-1} by the mid-2030ies [1]. To do so, the circulating current is doubled, the beam size and the crossing angle at the collision point are further reduced to achieve a desired levelled luminosity five times larger than the LHC nominal luminosity.

In these storage rings, the vacuum system is subjected to synchrotron radiation (SR) and electron bombardment due to the build-up of an electron cloud. In particular, the vacuum level in the vicinity of the experimental areas should be kept to a minimum in order to maintain the beam induced background to acceptable values. In HL-LHC, the final focusing system consists of three superconducting quadrupoles, so called “Inner Triplets”. The vacuum system houses a shielded beam screen, operating in the ~60 K range, which intercepts the debris produced at the interaction point, thereby protecting the 1.9 K cold mass from radiation damage.

In the context of the HL-LHC project, the vacuum performance of new surface material needs to be studied in details. In particular, amorphous carbon (a-C) coating [2,3] is proposed as an anti-multipactor surface with the objective to minimize the heat load induced by the electron cloud on the shielded beam screen and the background to the experiment due to proton scattering onto the residual gas. Since the protons in the HL-LHC Inner Triplets generates SR with ~ 10 eV critical energy and ~ 10^{16} ph/m/s flux, it is therefore of great importance to study the impact of such photons on a-C coating held at room and cryogenic temperature and compare the results against present LHC material.

The new beam line facility, presently under construction at BEP, BINP, provides SR irradiation at ~10 mrad grazing angle with 10-1300 eV critical energy and ~$5 \cdot 10^{16}$ ph/m/s flux. It is designed to study photon stimulated molecular gas desorption, photo-electron emission and photon reflectivity of candidate HL-LHC materials held at room and cryogenic temperature.

SR BEAM LINE

BEP is the booster synchrotron of the collider VEPP-2000. The machine is part of the new injection complex at BINP. BEP was re-designed and reconstructed to operate with electron or positron at energies in the range 50 ÷ 1000 MeV, with a nominal operation at 300 MeV. Nevertheless, a continuous operation is possible up to 900 MeV. The main SR parameters of a BEP dipole magnet at electron energies 200, 300 and 900 MeV are shown in Table 1. They cover the range of parameters for LHC and HL-LHC.

Table 1. SR Parameters at Different Particles Energy in BEP

Parameter	min	nominal	max
E [MeV]	200	300	900
Beam current [A]	0.5	0.5	0.5
Bending magnet radii [mm]	1280		
SR critical energy [eV]	14	47	1260
SR flux [ph/mrad/s]	1.1E15	1.8E16	5.6E16
SR power [W/mrad]	0.009	0.045	3.6
SR vertical divergence [mrad] at Ec	2.5	1.7	0.56

EXPERIMENTAL INSTALLATION

A schematic diagram of the experimental set-up on the BEP SR Beam Line is shown in Figure 1. The main elements are: “P” – a pivot point to allow a precise tuning

*a.a.krasnov@inp.nsk.su

ISBN 978-3-95450-181-6

of the irradiation at grazing incidence angle; "C" – a cone with a thermo-cathode to allow conditioning of measuring port [4]; EC – an end collector for the measurements of specular scattering; V – an all metal gate valve to isolate the beam line equipment from the experimental set-up; LV –a leak valve to perform gas injection for RGA calibration; RA&M – a movable radiation absorber and a mirror for interrupting and monitoring the SR beam. The SR Beam Line will also contain a collimator to control the horizontal and vertical sizes of SR beam.

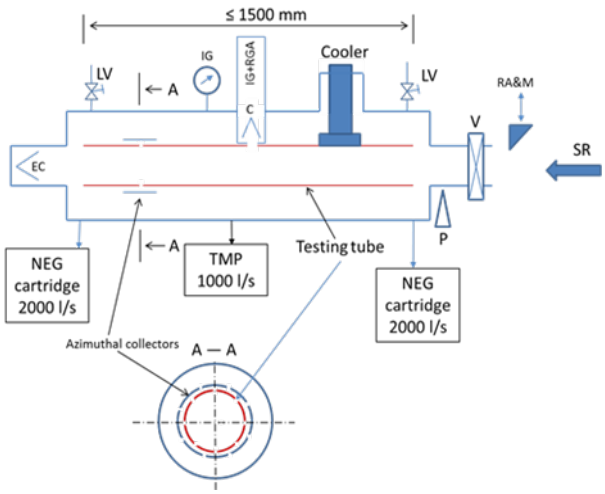

Figure 1: Experimental set-up.

The tested chamber is installed coaxially inside a tube with larger diameter. A pumping system consisting of two NEG cartridge pumps and a turbomolecular pump provides a very large pumping speed which simulates the large pumping speed of the Cold Bore (CB) in the 1.9 K cold beam pipes of HL-LHC. The objective is to achieve pressure level in the range 10^{-8} Pa or even less without baking.

Table 2. Parameters of the experimental set-up installed on the BEP SR Beam Line.

Parameter	value		
Max SR horizontal angle [mrad]	10		
Testing chamber max length [m]	1500		
Length of irradiated part of testing chamber	1300		
Coordinate of testing chamber inlet* [mm], pivot point	2100		
Horizontal SR beam size at testing chamber inlet [mm]	5	13	21
SR max. flux at Ec=47 eV	4.5E16	1E17	1.8E17
Incident angle [mrad]	5 ± 1.2	13 ± 3	21 ± 5

*relatively to SR generation point.

The chosen geometry allows a simple exchange of the tested chamber. The system is equipped with azimuthal collectors (10 pieces) placed behind holes produced in the tested chamber. The collectors allow for the measurements of azimuthal distribution of diffusely scattered photons (or distribution of photoelectrons in case of positive bias of the collectors relatively to testing tube). The system allows to cool the testing tube down to at least 60K (at least) with the use a standard cryo-cooler. Table 2 contains the main parameters of the experimental set-up.

EXPERIMENTAL PROGRAM

The first phase of the experimental program consist in the quantitative measurement of:

- photon stimulated molecular gas desorption with a calibrated residual gas analyser (RGA);
- photo-electron yield;
- forward reflectivity in SR power and photon flux units;
- azimuthal distribution of photoelectrons and azimuthal distribution of diffusely scattered photons.

The measurements will be produced in the following conditions:

- up to an accumulated photon dose > 10^{23} ph/m,
- with a SR incident angle of 10 mrad,
- at a SR critical energy in the accumulated photon dose mode in the range 40 ÷ 50 eV,
- scanning over SR critical energy at 10, 25, 50, 100, 200, 400, 800, 1300, 1700 eV at selected doses of 10^{21}, 10^{22}, 10^{23} ph/m,

These measurements will be performed at room temperature for two samples: uncoated and a-C coated OFE-Cu tubes. The geometrical dimensions are: inner diameter = 40.5 mm, thickness 2.5 mm, length 1500 mm. The followed experimental program and system parameters will be the same for both sample.

A second round of experiment will be later repeated for some of the most interesting measurements in the temperature range 60 ÷ 300K.

CONCLUSION

A new experimental set-up produce on the new BEP SR Beam Line will provide detailed investigation of vacuum properties of prototypes subjected to high intensity SR. With this device, the accumulated photon dose will be comparable with SR dose expected in the HL-LHC experimental areas after about one-year operation.

ACKNOWLEDGMENT

The authors would like to thank J-M. Jimenez, O.B. Malyshev, Yu. Rogovsky for helpful discussions and support to the project. They would like also to warmly acknowledge P. Costa-Pinto and A. Sapountzis for the a-C coating of the tested tube.

ISBN 978-3-95450-181-6

REFERENCES

[1] “High-Luminosity Large Hadron Collider (HL-LHC)”: Preliminary Design Report, CERN-2015-005, CERN, Geneva.

[2] P. Costa Pinto et al., “Thin film coatings for suppressing electron multipacting in particle accelerators”, Proceedings of 2011 Particle Accelerator Conference, New York, NY, USA.

[3] P. Costa Pinto et al., “Carbon coatings with low secondary electron yield”, Vacuum 98 (2013), p.p. 29-36.

[4] V. Anashin et al., "A photodesorption study of a TiZrV coated stainless steel vacuum chamber" - EPAC-2002, Paris, France, June 2002 // Proceeding of EPAC-2002, p.p. 2550-2552.

ISBN 978-3-95450-181-6

ACHIEVEMENT OF NECESSARY VACUUM CONDITIONS IN THE NICA ACCELERATOR COMPLEX

A.V. Smirnov#, A.M. Bazanov, A.V. Butenko, A.R. Galimov, H.G. Khodzhibagiyan, A.V. Nesterov, A.N. Svidetelev, A.M. Tikhomirov, JINR, Dubna, 141980, Russia

Abstract

NICA is the accelerator collider complex under construction at the Joint Institute for Nuclear Research in Dubna. The facility is aimed at providing collider experiments with heavy ions up to Gold in a center of mass energy range from 4 to 11 GeV/u and an average luminosity up to 10^{27} cm^{-2} s^{-1}. The collisions of polarized deuterons are also foreseen. The facility includes two injector chains, a new superconducting booster synchrotron, the existing superconducting synchrotron Nuclotron, and a new superconducting collider consisting of two rings, each of about 500 m in circumference [1].

Vacuum volumes of the accelerator booster and Nuclotron and the superconducting collider are divided into volumes of superconducting elements thermal enclosure and beam chambers. The beam chambers consist regular cold periods, which are at a temperature of 4.2K to 80K, and warm irregular gaps at room temperature. Operating pressure in thermal enclosure vacuum volumes have to maintained in the range of 1×10^{-7} to 1×10^{-4} mbar, in the beam chamber cold and warm areas – not more than 2×10^{-11} mbar. The description of way to achievement and maintenance of the working vacuum in the NICA project are presented.

GAS COMPOSITION OF THE VACUUM VOLUMES

Gas composition in vacuum volumes depending on many factors: choice of material, purity, heating of vacuum system, type of pumps, temperature mode, photon, electron or ion bombardment of the surface, etc.

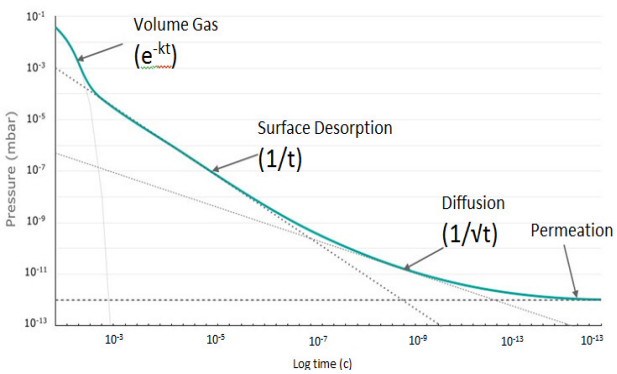

Figure 1 : Pump-down diagram.

The main gas constituents of the atmosphere are nitrogen and oxygen. Other gases, such as argon, carbon dioxide and water steam are less than 1% of the total volume of air.

Water is the main component in the unheated metal vacuum chambers. Degassing of water is not significantly dependent on the nature of the metal, surface treatment, and temperature conditions (at temperatures less than 110°C). Currently there are practically no methods other than baking to remove water from the metal surfaces. Diagram of achieving extreme-high vacuum is shown in Figure 1.

Hydrogen is the main residual gas, which is desorbed from the metal surface, when obtaining an ultra-high vacuum. The process of hydrogen degassing depends on the properties of the metal and capacity of the surface at a constant temperature. Heating at a high temperature (up to 900°C) reduces the content of hydrogen on the surface by more than two orders of magnitude [2].

VACUUM VOLUMES OF THE NICA

NICA complex consists of two warm linear injectors, two superconducting synchrotron (Nuclotron and booster), one superconducting collider and warm transport beam channels.

All vacuum volumes can be divided on three different types. The first type is volumes without beam, for example the thermal enclosure vacuum volumes. The second type is the volumes, through which beam passes one time. It is the vacuum chambers of linear accelerators and transport channels between accelerators and areas of experiment. The third type is the volumes, through which beam passes many times. It is the volumes of booster, Nuclotron and collider.

The linear accelerators' volumes of LU-20 and LUTI (Linear accelerator of heavy ions) are required vacuum not worth then 1×10^{-7} mbar. Such value is more determined by resistance to high-voltage breakdown and less by accelerating particles.

The vacuum degree in transport channels depends on adjacent vacuum volumes. For example, the vacuum value for transport channel of the beam transfer from LUTI to booster needs to be not more than 1×10^{-7} mbar from the one side and not less than 1×10^{-11} mbar from the another side. And the channel must have high resistance to residual gas migration from LUTI to booster. For the transfer beam channel from Nuclotron to experimental building is enough roughing vacuum (1×10^{-2} mbar).

Requirements for vacuum in booster, Nuclotron and collider are the highest. At the same time the booster requirements are higher than in collider at the expense of low beam energy – 1×10^{-11} mbar. Vacuum in collider must be better than 1×10^{-10} mbar because of prolonged being of particles inside the vacuum chamber – about one

#smirnov@jinr.ru

ISBN 978-3-95450-181-6

hour. The Nuclotron requirements are the lowest – 1×10^{-9} mbar, because beam energy is enough for minimization beam lost residual gas [3].

PUMPING SYSTEMS OF LINEAR ACCELLERATORS AND TRANSFER CHANNELS

The vacuum system of the LUTI is divided into three sections by gate vacuum valves (Figure 2). The vacuum equipment is designed for reaching the working vacuum at a level of 1×10^{-7} mbar.

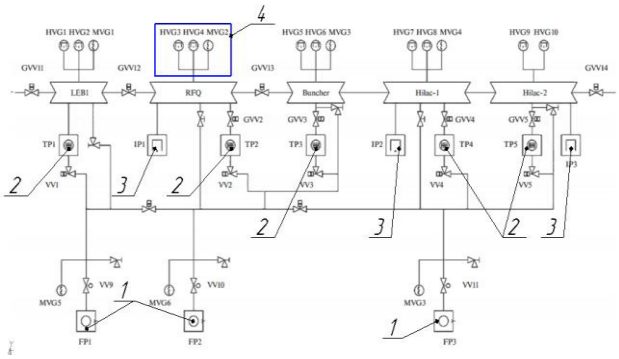

Figure 2: Principle vacuum system scheme of LUTI. 1 – scroll pumps, 2 - turbomolecular pumps, 3 - ion pumps, 4 – cold cathode and Pirani gages.

For reaching working vacuum the turbo-molecular pumps and ion pumps were chosen. For roughing vacuum scroll pumps were used. Cold cathode and Pirani gages were mounted for pressure measure in required range.

Pumping vacuum volumes of LU-20 is realized by two HiPace 2300 (Pfeiffer Vacuum) turbo-pumps (Figure 3).

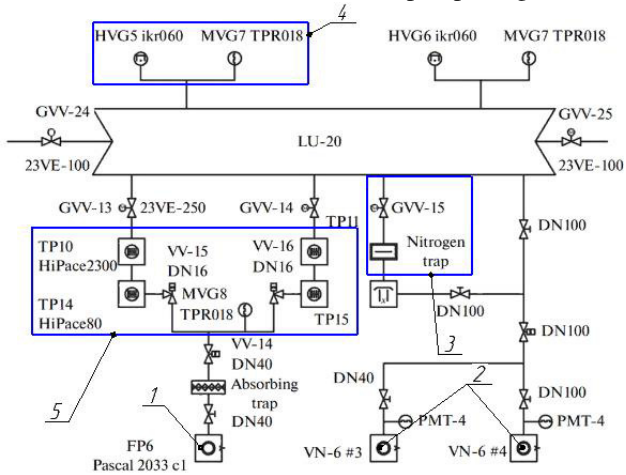

Figure 3: Principle vacuum system scheme of LU-20 injecting complex. 1 – double stage rotary vane pump, 2 - plunger pumps, 3 - diffusion pumps, 4 - cold cathode and Pirani gages, 3 - liquid nitrogen cryogenic pump.

The volume of LU-20 contains mainly water vapor. To pump the water out, a KN-20 000 cryogenic pump cooled by liquid nitrogen was mounted.

Its expected operation rate in the molecular regime is 20 000 L/s, which made it possible to significantly decrease the time of pumping and it takes to reach the working vacuum on the order of 1×10^{-7} mbar.[4]

For pumping beam channels standard scheme with turbopumps are used. Vacuum system of beam transport channel from LU-20 to Nuclotron is shown on Figure 4.

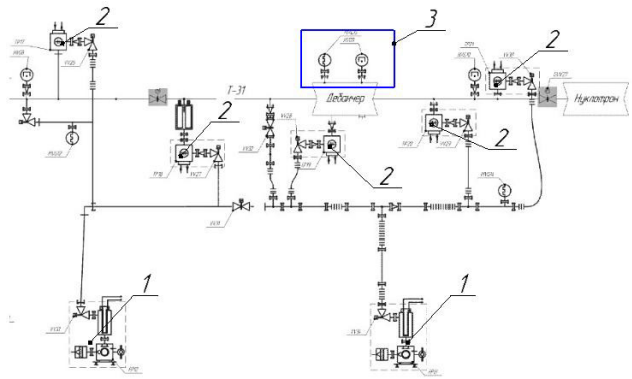

Figure 4: Principle vacuum system scheme of beam transport channel from LU-20 to Nuclotron. 1 – double stage rotary vane pumps, 2 - turbomolecular pumps, 3 - ion pumps, 3 – cold cathode and Pirani gages

PUMPING SYSTEM OF SUPERCONDUCTING BOOSTER SYNCHROTRON

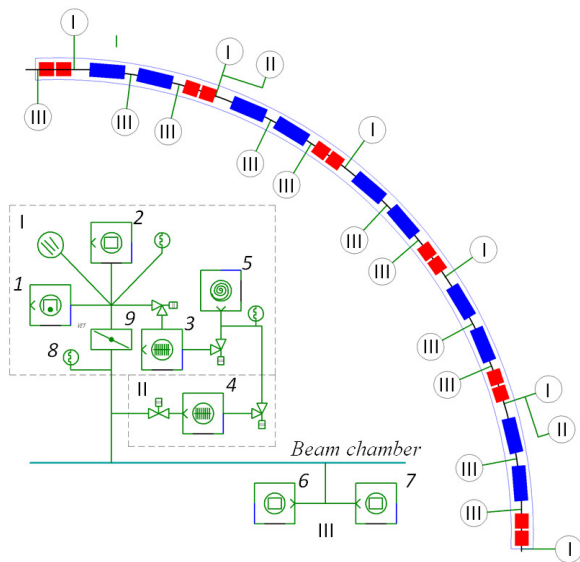

Figure 5: Principle vacuum system scheme of beam chamber`s cold part. I – XHV plant, II - rough evacuation plant, III – chambers with NEG or titan-sublimation pumps, 1 - ion pump, 2 - NEG pump, 3, 4 - turbomolecular pump, 5 - Dry scroll pump, 6,7 - Titan-sublimation or NEG pumps, 8 - UHV and XHV gauges, 9 - all metal gates

The main task for the achievement of working vacuum in the beam chamber will be the hydrogen control. For this goal we will use NEG pumps which are highly recommended in such conditions. For pumping out another gases which cannot be evacuated by NEG, turbomolecular and ion pumps will be situated on vacuum pumping station. Turbomolecular pump will use only for the prepa-

ISBN 978-3-95450-181-6

ration of pumping plant to work. This pump will cut off by all-metal valve (Figures 5, 6).

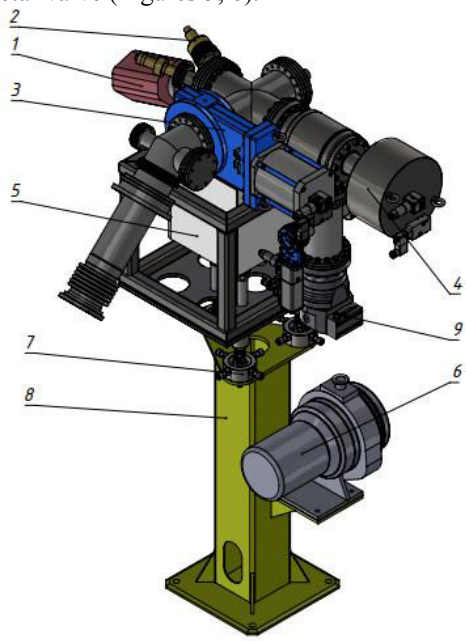

Figure 6: View of XHV station for cold parts. 1- mass-spectrometer, 2 – cold or hot cathode and Pirani vacuum gages, 3 – all-metal gate, 4 – all-metal valve, 5 – ion pump, 6 – scroll pump, 7 - adjustment jack, 8 – upright with frame, 9 – turbomolecular pump

Because of big distance between main pumping stations of cold chamber (around 9 m), in gaps between magnets we will install auxiliary pumps for evacuation hydrogen. Now we are considering three variant of such pumps: 1 – NEG, 2 – titan sublimation pump, 3 – carbon activated adsorption cryopump [5].

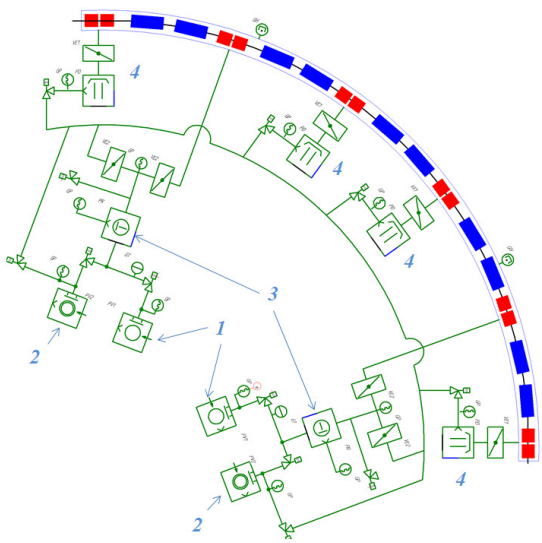

Figure 7: Vacuum system principle scheme of thermal enclosure volume of booster's one quadrant. 1 – single stage rotary vane pumps, 2 - double stage rotary vane pumps, 3 - Roots pumps, 4 - diffusion pump.

The working vacuum of warm gaps will reached by the same set of equipment. There is no problem to warm up and placement of pumps in warm gaps and there is the opportunity to install efficient evacuation systems.

For obtaining the preliminary vacuum in the isolation volume (1×10^{-3} mbar) we want to use tandem with Roots' and rotary-vane pumps. The working vacuum (1×10^{-6} mbar) will reached by diffusion pumps (Figures 7, 8).

This equipment will be working to the reach of helium temperatures in the accelerator in the absence of helium leaks in the isolation volume. After that the pumps will be shut down. The pumping will be continue at the expense of advanced cryosurfaces.

All pumping stations are designed in the form of modules for the purpose of equipment unification and service simplification. Assembly, setup and preparation of modules to work are realizing outside of accelerator ring.

There is the same set of equipment for collider. More detailed configuration of pumping stations will be determinate after the final design of vacuum chamber.

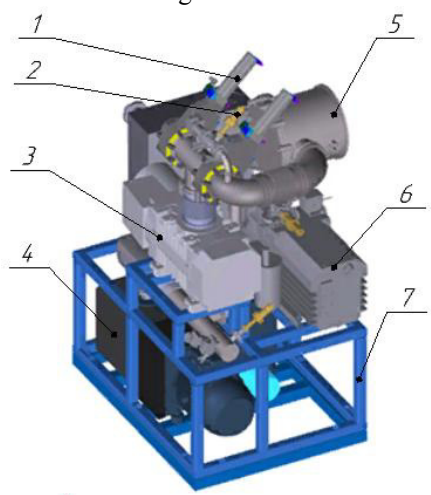

Figure 8: Roughing pumping plant. 1 – vacuum gates, 2 – Pirani gage, 3 – Root's pump, 4 – single stage rotary vane pump, 5 – inlet port DN250, 6 – double stage rotary vane pump, 7 – frame.

REFERENCES

[1] G. Trubnikov, et al. "The NICA project at JINR", Proceedings of IPAC2016, Busan, Korea, 2016, pp. 2061-2065.

[2] P.A.Redhead, "Hydrogen in Vacuum Systems; an Overview". Proceedings of CIRCA 2002.

[3] A.V.Smirnov et al. "Ultrahigh vacuum in superconducting synchrotrons", Proceedings of RUPAC2014, Obninsk, Russia, 2014, pp. 23-25.

[4] A.V.Smirnov et al. "Vacuum Systems of Linear Accelerators of the NICA Injection Complex", Physics of Particles and Nuclei Letters, 2016, Vol.13, No.7, pp.942–948.

[5] A.V.Smirnov et al. "Ultra-High Vacuum in Superconducting Accelerator Rings", Physics of Particles and Nuclei Letters, 2016, Vol. 13, No. 7, pp. 937–941.

ISBN 978-3-95450-181-6

HARDWARE FOR INCREASING RELIABILITY OF THE POWER SUPPLY SYSTEM FOR CORRECTOR MAGNETS OF THE EUROPEAN XFEL

O. Belikov, V. Kozak, E. Kuper, A. Medvedko, BINP, Novosibirsk, Russia
H.-J. Eckoldt, N. Heidbrook, DESY, Hamburg, Germany

Abstract

The modern linear accelerators, which are quite long, need a lot of electromagnets to correct the position of beam of charged particles. Typically, each corrector electromagnet shall be powered by a separate high-precision current source. Using a large number of high-precision power supplies reduces the reliability of the power supply system. To avoid this we have developed a system of "hot" replacement of power supply, which enables remote replacement of a faulty power supply with a backup one.

INTRODUCTION

The total length of the European XFEL is 3.4 km. 296 corrector electromagnets correct the electron beam position, each magnet powered by an individual high-precision current source [1]. Main parameters of the sources are listed in Table 1.

Table 1: Parameters of power supplies for corrector magnets.

Parameter	Specified Value	Units
Output current, max.	± 5 / 10	A
Output voltage, max.	± 70 / 60	V
Short-term current deviations (up to 1 sec)	< 10	ppm
Long-term current deviation (1 sec to several years)	< 100	ppm
Mean time between failures (MTBF)	≥ 100 000	hrs

A failure even in a single power supply for the corrector magnets significantly affects the electron beam quality. In continuous operation of the XFEL, the estimated amount of faults will be 1 failure per 14 days. The power supplies are distributed along the length of the complex, and it takes quite a time to replace a faulty crate. Given the estimated time for troubleshooting, these time losses are considered as inadmissible.

STRUCTURE OF POWER SUPPLY MODULE

To minimize the downtime at the European XFEL, it was decided to use a redundancy system, i.e. to complement the power supply group with a backup source module, which may be switched on instead of any other. The structure of such a module is shown in Fig. 1. In normal operation, seven power supplies feed the corrector magnets. The eighth power supply (the backup one) is switched to an equivalent load, which enables monitoring of its operability. If one of the normal sources fails, the control system can switch the respective correction magnet to the backup power supply, and the power supply system will continue normal operation.

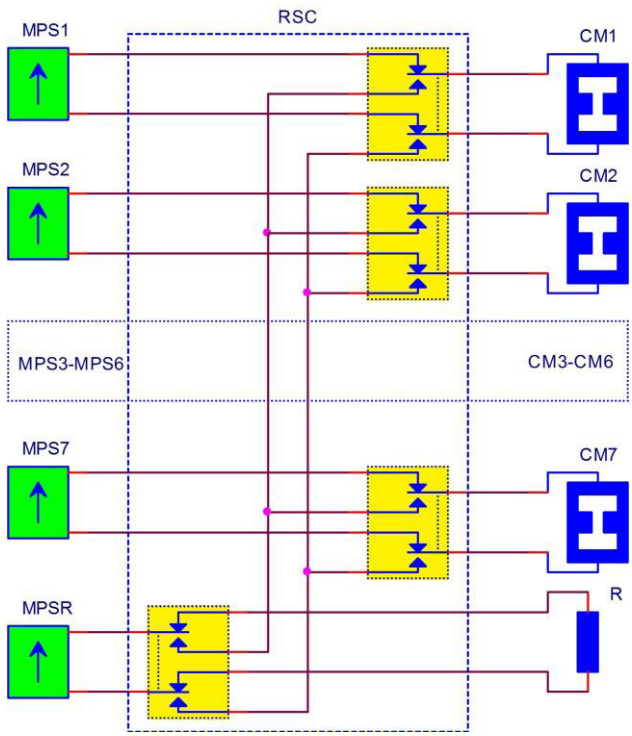

Figure 1: Function chart of power supply module. MPS – Magnet power supply; RSC – Redundancy system crate; CM – Corrector magnet; R – Dummy load.

INCREASING POWER SUPPLY SYSTEM RELIABILITY

48 power modules feed the corrector magnets of the European XFEL, each module having a backup power source. Increase in the number of the power supplies will result in a bigger estimated number of failures. With the redundancy system, a power supply failure that requires operating personnel intervention may occur only in the case of breakage of two or more sources from one module. If maintenance works to replace faulty power supplies are carried out once a month, one can calculate the probability of failure of the power supply system per year by the following formula:

$$P = \frac{N \cdot (n-1) \cdot P_i^2}{12},$$

ISBN 978-3-95450-181-6

where $N = 344$ is the total number of the power supplies; $n = 7$ is the number of power sources in a single module (without backup ones); $P_i \approx 0.088$ is the probability of failure of a single power supply per year. So, $P \approx 1.32$.

With the redundancy system and maintenance performed once a month, the probability of failure of the power system will be 1 time per 9 months, and the estimated time between failures of the power system will increase twenty-fold.

It should be noted that the fundamental simplicity of the solution is complicated by a variety of technological features. For example, a faulty power supply may turn out to be uncontrollable and operate with the maximum output current in the load. The energy stored in the magnet (inductance of 15 H) is quite high and has to be released from the load, otherwise an arc will occur. To this end, a semiconductor switch is provided, as well as a number of other protective circuits.

The semiconductor switch shortened main power supply up to reconnection of load. The output voltage of power supply is shown on Fig.2 (Channel 1). Then programmable delay (6 second, typical) followed. During this time the current in load (Channel 2 on Fig.2) is decreased up to safe value allowing reconnect the load. At the moment of reconnection the voltage on load was 7 V. It is quite acceptable.

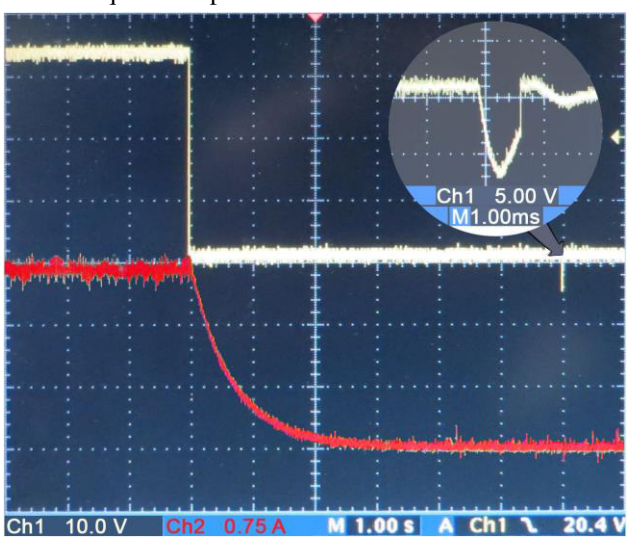

Figure 2: Transient waveform.

ASSEMBLING POWE SUPPLY MODULE

The redundancy system is implemented in a 432×355×133 mm^3 Euromechanics crate (Fig. 3).

Figure 3: Redundancy system crate.

The Power Supply System Module is located in 2000×800×600 mm^3 Euromechanics cabinet (Fig. 4). The module includes up to 7 power supplies for the corrector magnets, a backup power supply and the redundancy system crate. Control and monitoring of the power supply module are performed in accordance with the CANbus standard [2].

Figure 4: Magnet power supply cabinet.

CONCLUSION

Fifty power modules have been delivered to the European XFEL. About 40 power modules have been connected to the control system of the installation and are

ISBN 978-3-95450-181-6

in the trial operation mode. The first year of operation of the system has not revealed any serious problems, which confirms the calculations.

ACKNOWLEDGMENT

This work was supported by grant 14-50-00080 of the Russian Science Foundation.

REFERENCES

[1] O. Belikov, et al., “Corrector magnet power supplies of the European XFEL”, THPSC021, these proceedings.
[2] V. Kozak, O. Belikov, “Controller of Power Supplies for Corrector Magnets of European XFEL”, THPSC078, these proceedings.

ISBN 978-3-95450-181-6

ELECTROMAGNETIC COMPATIBILITY OF THE POWER SUPPLY SYSTEM FOR CORRECTOR MAGNETS OF THE EUROPEAN XFEL

O. Belikov, V. Kozak, BINP, Novosibirsk, Russia
H.-J. Eckoldt, N. Heidbrook, B. Moelck, DESY, Hamburg, Germany

Abstract

The power supply system for the corrector electromagnets of the European XFEL includes over 300 precision current sources with an output power of up to 600 W. BINP developed, manufactured and supplied the power sources for the corrector magnets. For reliable operation of the physical installation, at the design stage it was necessary to ensure electromagnetic compatibility of the power supplies with other electronic equipment of the European XFEL.

INTRODUCTION

During the development of high-precision power supplies for electromagnets, it is necessary to ensure compliance of the precision and stability of the power supply parameters. This is a challenge on large physical installations because the power supplies shall work in contact with a variety of other electronic devices. It is therefore necessary to make the power supplies capable to work in a specific electromagnetic environment, while maintaining the stability of their parameters and without creating intolerable electromagnetic disturbances to other electronic devices.

BINP members developed MPS-10-60, a prototype of the power supplies for the corrector magnets [1]. This prototype was verified in relation to compliance with certain directives of the EMC international standard: EN 61000-4, EN 61000-6, EN 55011, and EN 61326-1. The tests were conducted at the EMC Laboratory "TÜV NORD" (Hamburg). Upon successful completion of all the tests, the production of 400 power supplies for the corrector electromagnets of the European XFEL started.

GENERIC EMISSION OF THE POWER SUPPLIES

For the sake of convenience of arrangement and maintenance of the power supply system, all the sources were made with natural air cooling. The cases of the power supplies are heated during operation, which results in output current instability caused by temperature drift. Therefore, high-precision power supplies should have high efficiency. Reducing the dynamic losses in switching elements often leads to an increase in the radiated power of electromagnetic interference. Electromagnetic shielding of the units of the power supply inverter would not be effective in this case since the screens hinder cooling. The largest emission amplitudes were in the frequency ranges of 30 ÷ 60 MHz (interference from the rise/fall of the fast switches mosfet of the inverter) and 100 ÷ 200 MHz (interference from the CAN line). Additional low-pass filters turned out to be helpful in both cases. A graph of the radiated emission of power supply for the corrector magnets in the frequency range from 30 MHz to 1 GHz is shown in Fig. 1.

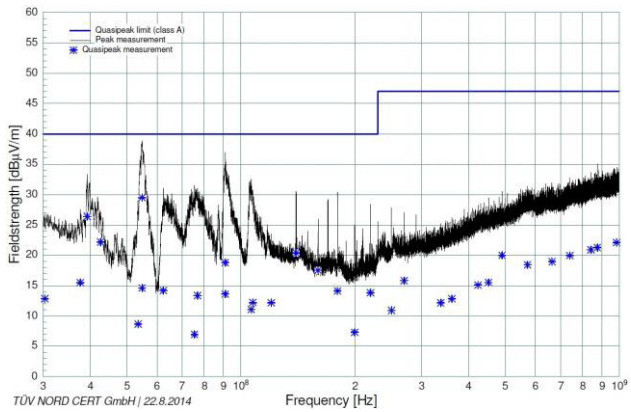

Figure 1: Radiated emission. Vertical antenna polarization.

In addition to the radiated emission, we measured the amplitude of the conducted emission of power supply to a 230 VAC mains in the frequency range from 150 kHz to 30 MHz. The maximum amplitudes of the emission were observed at the switching frequencies of the power switches. The emission decreased after addition of a CM/DM power line filter. A graph of the conducted emission is shown in Fig. 2.

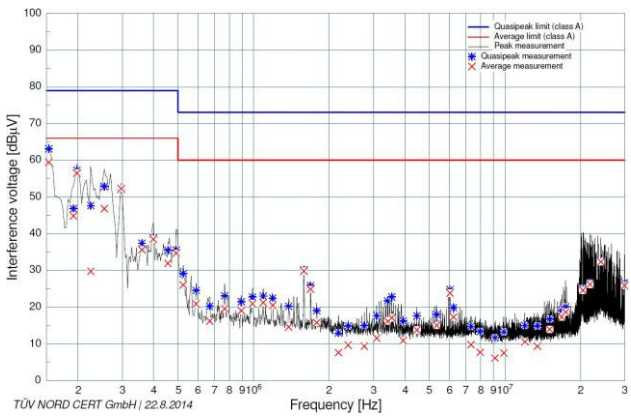

Figure 2: Conducted emission. Disturbing voltage on conductor L.

IMMUNITY TO INDUCED DISTURBANCE

Below are described tests that were carried out for verification of the immunity of the power supply output parameters to the effects of conducted and inducted interference. During the tests, external devices were controlling the stability of the power supply parameters.

ISBN 978-3-95450-181-6

The first test was to check immunity to electrostatic discharges. Selected points (marked with arrows in Fig. 3) were subjected to an electrostatic discharge via pulses of different polarity and an amplitude of 2, 4, and 8 kV (air discharge), as well as an amplitude of 4 kV (contact discharge). The stability of the output current and of the operation of the CANbus and the external indication was controlled.

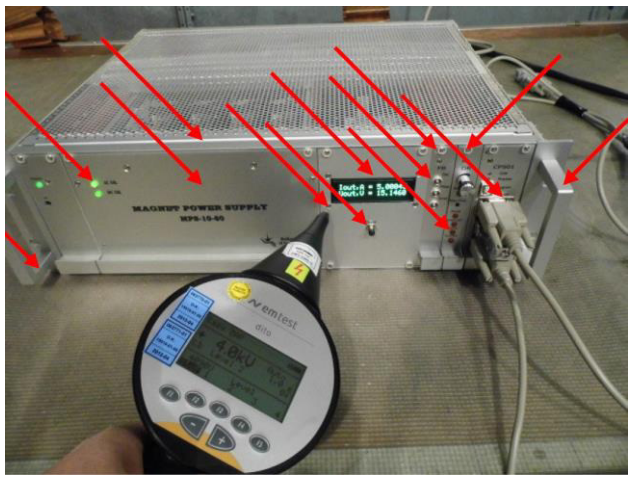

Figure 3: Test set-up for ESD testing.

In the next test, we were checking the immunity of power supply to impact noise. The amplitude of the noise was ± 2 kV on the AC power lines and ± 1 kV on the DC output, Interlocks connector and CANbus cable. The duration of the pulses was 50 ns; the pulse rise time was 5 ns; the repetition frequency was 5 kHz. Like in the previous tests, we controlled the output current stability.

In addition to the previous test, we were checking the power supply immunity to impact noise in the 230 VAC mains. During operation of the power supply, single pulses with an amplitude of 0.5 kV and 1 kV (line to neutral) and 0.5 kV, 1 kV and 2 kV (line to earth) were applied to the mains input. The pulse duration was 50 μs and the period was 1 min. The pulses were applied synchronously with the mains frequency and with phase shifts of 0^0, 90^0, 180^0, and 270^0. The entire test lasted for 2 h 40 min. An external device was monitoring the stability of the output current of the power supply.

In the fourth test, we were checking immunity to conducted disturbance induced by radio frequency fields. The coupling was performed with a coupling network into the power leads and a coupling clamp into the data lines. An electromagnetic field was induced on the AC power lines, DC output and CANbus cable. The amplitude of the induced field was 3 V; the frequency was 150 kHz to 80 MHz. During the experiment, we controlled the stability of the output current of the power supply.

In the fifth test, we were checking immunity to power frequency magnetic field. An operating power supply was placed in a frame with a variable magnetic field with an amplitude of 30 A/m and a frequency of 50 Hz (Fig. 4). As in the previous test, the stability of the output current of the power supply was monitored.

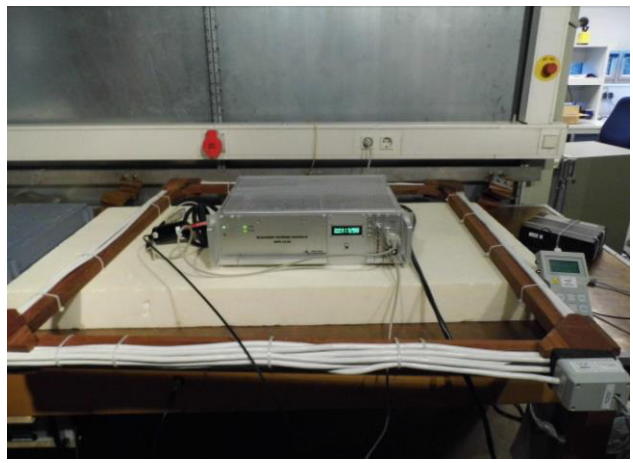

Figure 4: Test was performed with frame-coil.

In the sixth test, we were checking the immunity of power supply to electromagnetic field effects. The tests were carried out in an anechoic chamber (Fig. 5). In the frequency range of 80 MHz to 1 GHz we used a horizontally- and vertically-polarized log-periodic antenna with an amplitude of 10 V/m. In the frequency range of 1.4 GHz to 2.7 GHz we used a horizontally- and vertically-polarized horn antenna with an amplitude of 3 V/m. The immunity of the output current of the power supply to electromagnetic field effects was monitored.

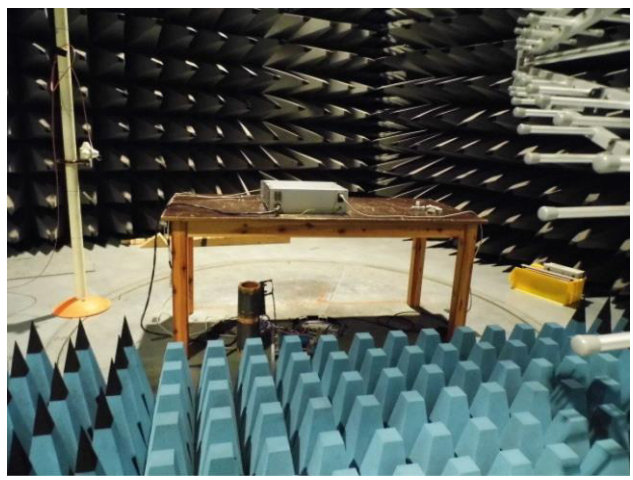

Figure 5: Test set-up for radiated susceptibility.

In addition to the above tests, we carried out additional tests with the 230 VAC mains and checked immunity to voltage dips, short interruptions, voltage variations, etc. All the tests were successfully completed in September 2014.

CONCLUSION

Developing power sources in accordance with the above-mentioned European directives makes it possible to avoid mutual interference of electronic devices and prevent a lot of start-up problems. Successful completion of tests at specialized laboratories enables supply of the power sources to any European research center. By the moment of this writing, most power supplies for the

ISBN 978-3-95450-181-6

corrector magnets were delivered to the European XFEL and commissioned.

ACKNOWLEDGMENT

This work was supported by grant 14-50-00080 of the Russian Science Foundation.

REFERENCES

[1] O. Belikov, et al., "Corrector magnet power supplies of the European XFEL", THPSC021, these proceedings.

ISBN 978-3-95450-181-6

CORRECTOR MAGNET POWER SUPPLIES OF THE EUROPEAN XFEL

O. Belikov, V. Kozak, A. Medvedko, D. Skorobogatov, R. Vahrushev, BINP, Novosibirsk, Russia.
H.-J. Eckoldt, N. Heidbrook, DESY, Hamburg, Germany.

Abstract

The total length of the European XFEL is 3.4 km. The electron beam parameters are corrected by about 300 corrector magnets, each powered by an individual power supply. BINP performed the development, production and delivery of the power supply system for the corrector magnets. For the powering of the corrector magnets, seven types of precision power supplies with output currents of up to 10 A and output voltages of up to 70 V were developed.

INTRODUCTION

The European X-ray Free-Electron Laser (XFEL) is designed for generation of synchrotron radiation with an intensity of 27 000 bunches per second, a wavelength of 0.05 to 4.7 nm, and a peak brightness of $5 \cdot 10^{33}$ ph/(s·mm^2·mrad^2·0.1% bandwidth). To attain the above parameters it is necessary to have an electron beam of extreme quality [1]. The XFEL structure comprises a linear superconducting accelerator with a maximum electron energy of 17.5 GeV, several photon tunnels with undulators, and experiments halls. The total length of the tunnels is 5.77 km (Fig. 1). The XFEL magnetic system structure includes 296 corrector electromagnets:

- Injector tunnel (XTIN) – 13 pcs.
- Entrance shaft (XSE) – 12 pcs.
- Linac tunnel (XTL) – 122 pcs.
- Shaft 1 (XS1) – 35 pcs.
- Distribution tunnel 1 (XTD1) – 32 pcs.
- Distribution tunnel 2 (XTD2) – 44 pcs.
- Distribution tunnel 3 (XTD3) – 22 pcs.
- Distribution tunnel 4 (XTD4) – 7 pcs.
- Distribution tunnel 5 (XTD5) – 9 pcs.

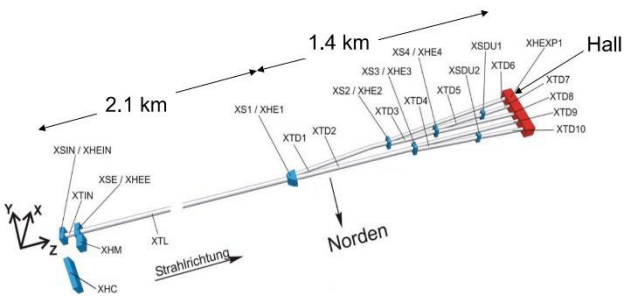

Figure 1: XFEL nomenclature.

In accordance with the requirements to the magnetic system, each corrector electromagnet shall be powered by a separate precision current source (magnet power supply, MPS). The MPS required parameters are given in Table 1.

Table 1: Requirements to Corrector Power Supplies

Parameter	Specified Value	Unit
Output current, max.	± 5 / 10	A
Output voltage, max.	± 70 / 60	V
Minimum current setting step	< 4	ppm
Short-term current deviations (up to 1 sec)	< 10	ppm
Long-term current deviation (1 sec to several years)	< 100	ppm
Temperature coefficient of output current drift	< 6	ppm/K
Output current non-linearity	< 20	ppm
Efficiency of power part	> 90	%
Mean time between failures (MTBF)	> 100 000	hrs

STRUCTURE OF POWER SUPPLIES

The power supplies for the XFEL corrector magnets are divided into two groups, with maximum output currents of 5 A and 10 A. Since the corrector electromagnets have different resistances, power supplies with different maximum output voltages were required. The result is seven types of the power supplies, the maximum values of their output parameters shown in Table 2.

Table 2: Maximum output currents and voltages of power supplies.

Power supply	Maximum output current, A	Maximum output voltage, V
MPS-5-24	5	24
MPS-5-48	5	48
MPS-5-72	5	72
MPS-10-15	10	15
MPS-10-30	10	30
MPS-10-45	10	45

The circuitry design relies on double pulse conversion (Fig. 2).

ISBN 978-3-95450-181-6

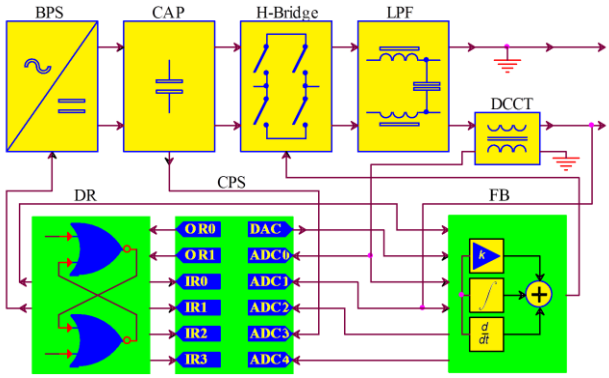

Figure 2: MPS structure. BPS – Bulk power supply, CAP – Capacitor, H-Bridge – H-Bridge inverter, LPF – Low-pass filter, DCCT – Direct Current-Current Transformer, DR – Digital Regulator, CPS – Controller Power Supply, FB – Feedback module, OR – Output register, IR – Input register, DAC – Digital-to-analog converter, ADC – Analog-to-digital converter.

The alternating voltage of the mains is converted into a DC voltage using a BPS, which consists of several Alternating current - Direct current (AC-DC) converters. The maximum output voltage of the power supply is set by the BPS module. The output current regulation is performed via pulse-width modulation of the output voltage of the H-Bridge inverter with a frequency of 100 kHz. The carrier frequency ripples are suppressed by a passive second-order filter, LPF. There is a Direct Current-Current Transformer, which is used in the main loop of the current feedback. The required accuracy of the output current is provided by the Feedback module, which includes a proportional link and an integral one. Mains ripples (50 ÷ 300 Hz) are suppressed with an additional loop of the voltage feedback. The output current regulation constants are set using a mezzanine in dependence on the power supply load parameters. The inductance of the coils of the XFEL corrector magnets varies from 100 mkH to 15 H. Four types of mezzanines were selected for this range of loads; they are installed in the Feedback module.

The DR module is used to generate the PWM signal. The value of the output voltage of the H-Bridge inverter is defined by two PWM channels: the first and second PWM channels set the high pulse and low pulse duration, respectively. Therefore, we have three voltage values in the H-Bridge Inverter output voltage oscillogram (Fig. 3): $+U_{BPS}$, $-U_{BPS}$ and 0 V. This method of forming a PWM signal allows us to have low ripples of the power supply output voltage at low output currents.

The power supply is controlled by an embedded controller CPS [2] via the CANbus interface. The controller includes an 18-bit digital-to-analog converter (DAC), a 6-channel 24-bit analog-to-digital converter (ADC), and input and output registers of discrete signals.

Figure 3: Oscillogram of H-Bridge Inverter output voltage.

CONSTRUCTIVE OF SUPPLY SYSTEM FOR CORRECTOR MAGNETS

All the power supplies are implemented in 432×355×133 mm^3 Euromechanics crates (Fig. 4).

Figure 4: Magnet power supply.

The structural parts are designed as modular devices. Some modular devices are made as universal, for different types of power supplies. The commutation of the modular devices is done by the Motherboard.

The power supply system for the XFEL corrector magnets consists of 48 2000×800×600 mm^3 Varistar racks (Pentair/Schroff). One rack comprises up to seven power supplies for the corrector magnets, a reserved power supply, and a redundancy system crate. The redundancy system [3] is intended to reduce XFEL downtimes caused by malfunction of the power supplies. The redundancy system crate enables remote replacement of any of the seven power supplies by the spare one.

CONCLUSION

The Power Supply Prototypes were successfully tested in Novosibirsk and Hamburg. The compliance with the requirements to power supplies for the XFEL corrector magnets was tested at BINP and DESY. The compliance with CE certification standards was checked at the EMC Laboratory "TUV NORD" (Hamburg) [4]. After all the

ISBN 978-3-95450-181-6

tests, a permit to manufacture the power supplies was signed.

387 power supplies for the corrector magnets have been produced, tuned and delivered to XFEL:

- 296 power supplies to feed corrector magnets.
- 48 power supplies to work in the redundancy system
- 43 spare power supplies

The power supply system for the corrector magnets has been assembled and tested.

ACKNOWLEDGMENT

This work was supported by grant 14-50-00080 of the Russian Science Foundation.

REFERENCES

[1] W. Decking, et al., "European XFEL construction status", FEL-2014, Basel, Switzerland, August 2014, WEB03, p.623.

[2] V. Kozak, O. Belikov, "Controller of Power Supplies for Corrector Magnets of European XFEL", THPSC078, these proceedings.

[3] O. Belikov, et al., "Hardware for Increasing Reliability of the Power Supply System for Corrector Magnets of the European XFEL", THPSC019, these proceedings.

[4] O. Belikov, et al., "Electromagnetic Compatibility of the Power Supply System for Corrector Magnets of the European XFEL", THPSC020, these proceedings.

ISBN 978-3-95450-181-6

HIGH-VOLTAGE POWER SUPPLY FOR GOG-1001

V. Dokutovich†, D. Senkov, A. Chernyakin,
Budker Institute of Nuclear phisics SB RAS, Novosibirsk, Russia

Abstract

The submitted report contains the description of the high-current high-voltage quasipulse four-channel laser pumping power supply. Channels are the completely identical. It is possible to feed up to 10 kJ on each channel with up to 5 kA of output current. Source controller is developed with PLM, Atmega MCU and ARM type CPU which allows to optimize operations of device, and also to make a number of calculations. The controllers are connected by internal control network for more flexibility and efficiency. The description of the source and the test results are presented.

INTRODUCTION

At the present stage of development of systems of deduction of high-temperature plasma the question of stability of walls of a vacuum chamber remains very urgent. One of the key problems is firmness of diverter plates during the pulse. The particle fluxes influence on them and energy leading to formation of serious defects, melting and intensive evaporation of material. The studying of these processes demands carrying out dynamic measurements directly during intensive radiation of material. It is for this purpose offered to use the measuring technique of scattering of synchrotron radiation, and for model operation of thermal influence to use a laser radiation [1]. The laser impulse with energy of 1000 J is formed by GOG 1001. This is the optically-excited laser. There are four flashlight gas-discharge valves are used for laser pumping.

The high-voltage quasipulse source which would perform not only function of supply, but also monitoring of lamps status during the pulse. It is necessary for a delivery of system of pump excitation. The source offered below which has the following parameters was developed for these purposes:

- An opportunity to feed at the same time up to four lamps
- Peak energy to 10 kJ on one lamp
- Amplitude of output current to 5 kA.

DESCRIPTION

The block diagram of a source is shown on Fig.1. The source consists of the discharge circuit giving to lamps energy from accumulative capacity and the parallel scheme of ignition of an arch in a lamp [2]. In total 4 channels are executed equally and are started synchronously. Charging of capacity of a discharge circuit is carried out by the linear charger. The power supply controller allows both manual control from the forward panel of a source and removed from the workstation. The management of charging, with start-up and monitoring of work of a source is also provided.

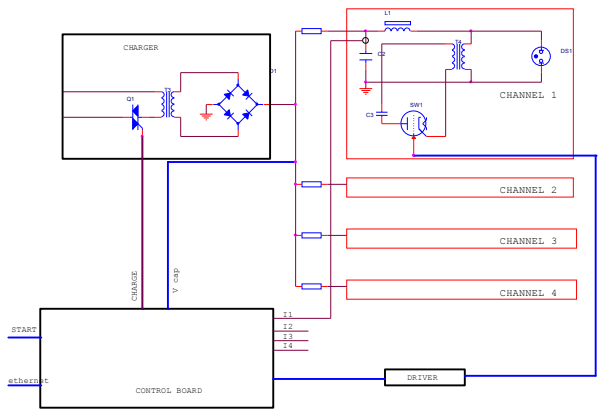

Figure 1: Block diagram of a source.

Charger

The charger represents a step-up transformer with the bridge rectifier and the current-limiting resistor at the output. At achievement by tension on the storage capacitance bank voltage of the assigned level the charging source is disconnected by a TRIAC switch. For compensation of an electrostatic leakage when maintaining the given tension on capacity the switch carries out short-term (on 50 ms) ON-state of the charging source.

Discharge Circuit

The bank of k75-100 750 μF type capacitors everyone with an operating voltage up to 6 kV are used as the store of energy. Each capacitors connected through the throttle to the load. Switching is carried out by a path of ignition of the electrical discharge in the lamp. The discharge caused by voltage pulse produced with the parallel contour representing a step-up transformer with 3 μF capacity switching to the primary winding with the thyratron-based switch. The capacitance charged up to the voltage of 3 kV. The low-current small-size high-voltage converter is used for charging of this capacity. Application of the described scheme of start allows changing the energy of flash in very wide limits: beginning from 1% of rated power that favourably distinguishes the described source created for the same purposes before.

ISBN 978-3-95450-181-6

Controller

The controller which carries out the following functions was developed for management and monitoring of a source

- Monitoring of tension of charging of capacities of a discharge circuit
- Management of an arson of lamps
- Monitoring of impulse currents
- Manual and remote control by a source
- Protection of a source and laser

The programmable logical matrix responsible for processing of signals of protection and start is the cornerstone of a source. By means of the microprocessor on the basis of the Atmel family realise a feed-back on charging of storage capacity to the necessary level, and also is carried out manual control and a conclusion to information to the graphic touch display.

The microprocessor on the basis of ARM is responsible for communication with a higher control system on ethernet networks, processing of signals of the impulse currents removed by means of Rogovsky's belts established on each capacity and for data processing.

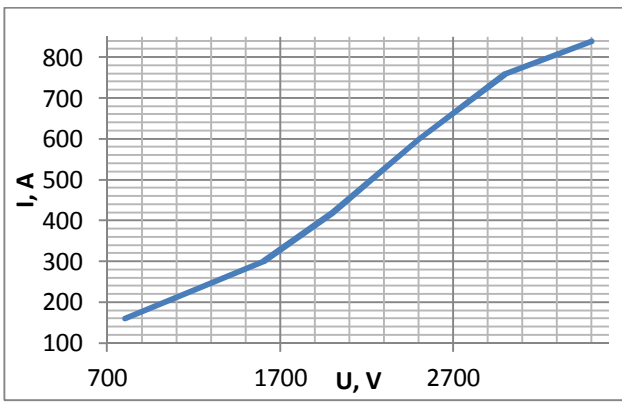

Figure 2: Pumping lamp current vs capacitance bank voltage.

CONCLUSION

The current source was made and fully tested. The Fig.2 presents the dependence of the current proceeding through lamps vs voltage on storage capacitance.

REFERENCES

[1] A. Arakcheev et al., AIP Conf. Proc. 1771 (2016) 060003 http://dx.doi.org/

[2] I. Volkov,V. Vakulenko “Power supplies of lasers” (in Russian, 1976).

ISBN 978-3-95450-181-6

AUTOMATED SYSTEM FOR PRECISION CURRENT SOURCES TESTING

E. Bykov, O. Belikov, A. Batrakov, E. Gusev, V. Kozak, BINP, Novosibirsk, Russia

Abstract

The beam correction system for European XFEL includes about 400 precise current sources. The every current source must tested and verified in concordance with specifications before including in XFEL equipment. For this purpose there was developed the automated system that allowed to test up to 7 current sources simultaneously. The system consists hardware stand and software that written for Linux OS. The stand was equipped emulated real load test loads, with precise DCCT and by precise analog-to-digital converters with CANbus interface. During testing the current in each current source was changed and digitized in concordance with different algorithms. The duration of typical session was 25 hours. The specific software was developed for this stand. It provides testing process, collecting and storing the primary information and displaying the first information. There are addition utilities which allows to make different analyzes in off-line mode using data accumulated during tests. The article provides a detailed description of the stand and main results.

INTRODUCTION

In 2009 at the DESY (Deutsches Elektronen-Synchrotron) research center, construction of the world's largest free-electron laser was started. The project was called XFEL (X-ray free-electron laser).

The realization of this international project will make it possible to observe molecules in dynamics while they are involved in chemical reactions.

The XFEL has a total length of 3.4 km and consists of a linear accelerator and a complicated magnetic focusing system. The XFEL beam correction system consists of almost 400 corrective dipole magnets. To ensure the power supply for these magnets, the BINP has been contracted to design and provide four hundred precision current sources. The sources have to meet a number of requirements, some of which are listed below:

- The RMS noise of output current in the frequency range from 0 Hz to 1 kHz should not exceed 10 ppm.
- The deviation of the absolute value during long-term use should be not more than 100 ppm.
- To control a number of parameters, each precision source must be tested during 25 hours with a gain of statistical data.

Considering the above requirements, it is reasonable to create an automated system that would be able to perform the real time test for several precision current sources simultaneously.

Physically, the automated system consists of a stand, to which seven precision current sources can be connected, and the software that automatically controls the stand.

BLOCK DIAGRAM OF THE STAND

Figure 1 shows a block diagram of the stand. The stand has seven independent channels, which provide a non-contact method of measuring current in a range of ± 10 amps. The channel has a power input for connecting a precision power source and output for connecting an equivalent load. In the figure, the precision sources are indicated as MPS, and the equivalent load is shown as a series connection of resistance and inductance. Furthermore, each channel has two additional analog outputs: **C** (Current) for indicating the measured current equivalent (in volts) and **T** (Temperature) for indicating the temperature equivalent (in volts) from the temperature sensor in the channel. Current and temperature values are measured by six-channel ADC of CPS01 controller. CPS01 controllers and MPS precision sources are controlled via CANbus.

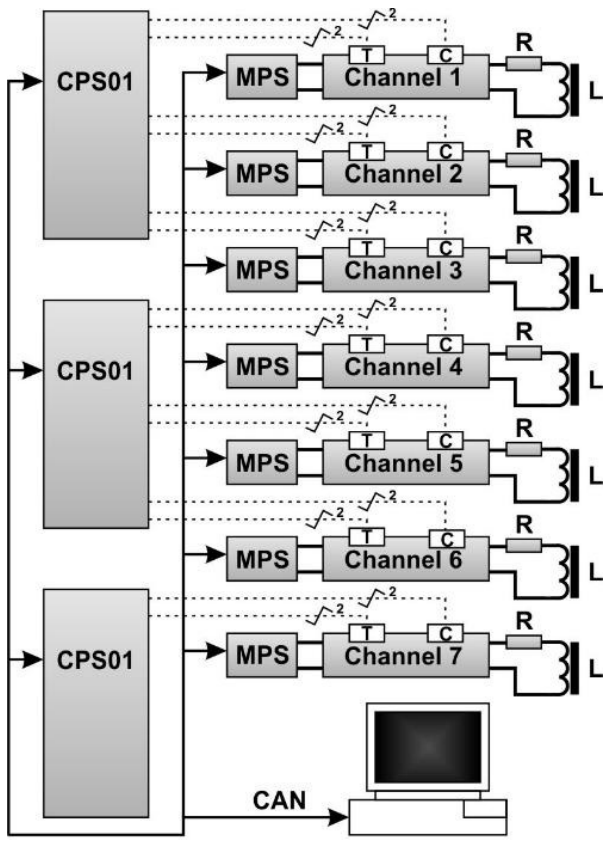

Figure 1: Block diagram of the stand.

ISBN 978-3-95450-181-6

BLOCK DIAGRAM OF THE CHANNEL

Figure 2 shows a block diagram of the channel. Its detailed description is given below.

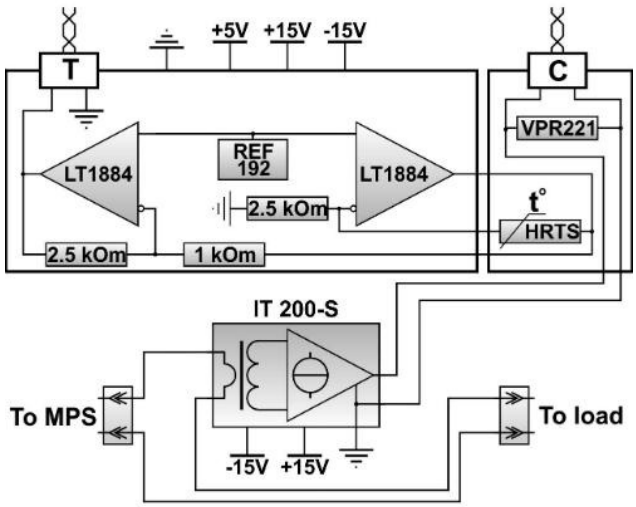

Figure 2: Block diagram of the channel.

A precision non-contact sensor IT200-S (LEM production) is used for the measurement of the source current. The sensor is a DC current transformer with a transformation ratio of 1:1000. The current output of the sensor is loaded on the precision resistance VPR221 (Vishay production), the voltage on which indicates the current value in the channel. VPR221 resistor body is attached to the radiator for temperature stabilization. In addition, the temperature monitoring of the precision resistor is performed. In Fig. 2, the temperature sensor indicated as HRTS. Operational amplifiers shown in the figure, provide a linear dependence between the output voltage and the temperature. The precision resistance and the temperature sensor are attached to the radiator using a copper plate and located tightly to each other. The copper plate ensures a low gradient in temperature distribution over the surface. This allows the temperature of the precision resistor to be measured with a good accuracy.

RESULTS

Defining the Parameters

Before testing precision current sources, some parameters of the stand have been determined, in particular:

- the warm-up time of the stand required to ensure the thermal equilibrium with the environment.
- the temperature drift.

Figure 3 shows the time dependence of the measured current values on all channels of the stand during the warm-up period. The current was passed consistently through all channels of the stand and set by the same MPS source. It should be noted that the current curves show a summarized drift from the precision current source and DCCT precision meter.

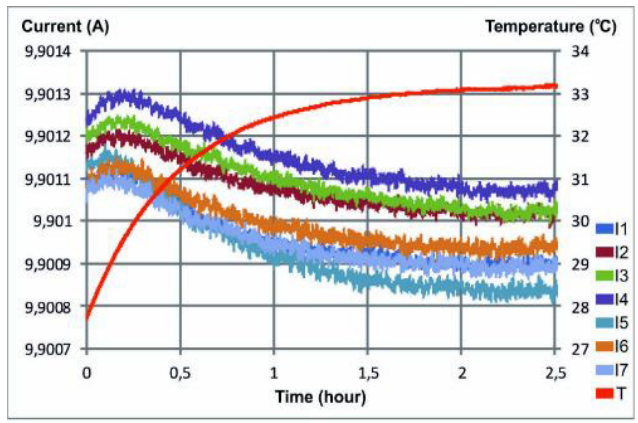

Figure 3: Warm-up.

Warm-up time was determined at a current of 9.9 amperes. The diagram shows that the greatest change in the current occurs between 1 and 1.5 hours after turning on. Based on this result, it was concluded that daily testing of the sources makes sense after at least one hour of the stand warming up.

To determine the temperature drift of the stand a Fluke 5730A current calibrator, which had its own temperature drift of ~5mka/^0C, was used. The current was passed through all channels of the stand consistently and set by the calibrator. The measurements were performed for both polarities of the current and for each polarity statistic has been acquired during the day. The data processing showed that when the current is positive, some channels have a positive drift, while others have a negative one. When the current is negative, all channels have a drift of the same sign.

Figure 4 shows the drifts of two channels at positive current that have the greatest temperature dependence. Black lines along the graphs are the trend lines calculated using Microsoft Excel. According to the diagram, the channel with positive drift has a drift value of 17.9 mka/^0C, while the channel with negative drift has 7.1 mka/^0C.

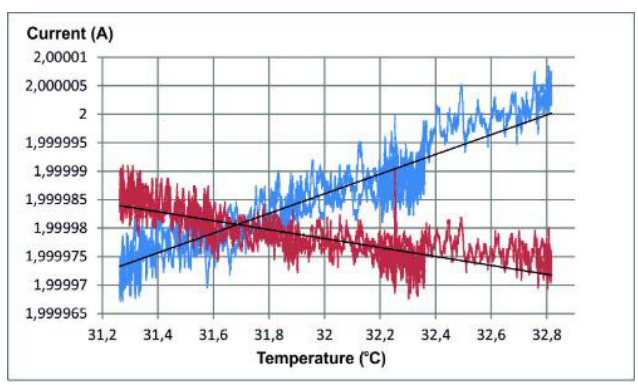

Figure 4: Current temperature drift. Positive current.

ISBN 978-3-95450-181-6

Figure 5 shows a drift of one of the channels with the greatest temperature dependence at the negative current. Simple calculations show that the maximum drift at the negative current is equal to 13.2 mka/ ^0C .

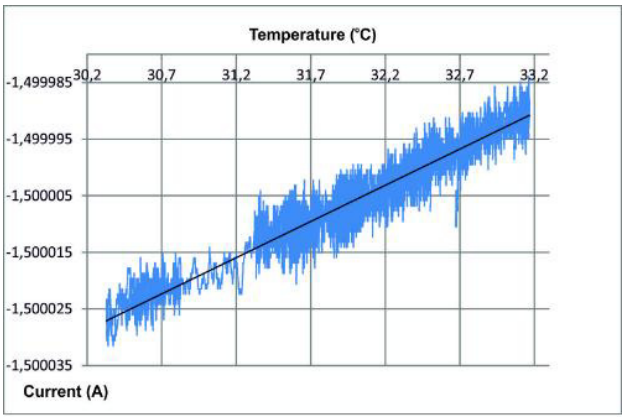

Figure 5: Current temperature drift. Negative current.

Unfortunately, it is difficult to say how the drift of the calibrator affected the results. But even if the calibrator moved down the positive drift at the positive current, then compensating for the drift decrease, we obtain: 17.9 + 5 = 22.9 mka/ ^0C . Therefore, the maximum possible drift of the current due to the temperature changes is almost 23 mka/ ^0C or 2,3ppm/ ^0C .

The Stand Calibration

All channels of the stand have been calibrated before testing the sources. Calibration is needed to compensate inaccuracy of absolute measurement of the real current. To calibrate the stand, an MPS precision current source and an external DCCT precision non-contact current meter were additionally used, The latter has been preliminary configured and calibrated to measure the absolute value of the current with an accuracy of 10^{-5}. The source current was passed through all channels of the stand consistently and controlled additionally using an external high-precision measuring instrument. The measurements were carried out at two current values, 9.5 A and -9.5 A. These currents were displayed by the external current meter. After the data were acquired, the current measured on the channels was compared with that measured by the external DCCT meter. The real current on the channels is calculated by the formula (1):

$$J = a + b * I \quad (1)$$

Where ***J*** is the real current, ***I*** is current measured on the channel, ***a*** is DC offset and ***b*** is correction factor to the measured current. Correction factors ***a*** and ***b*** are selected for each channel of the stand so that the current ***J*** corresponds to the readings of the external DCCT precision current meter. The program that controls the stand takes into account these correction factors and displays current ***J***.

The Process of the Sources Testing

Daily testing of precision sources consists of two stages. The first stage is the Ramp Test, figure 6 shows a small interval of this test during the real test of one of the sources.

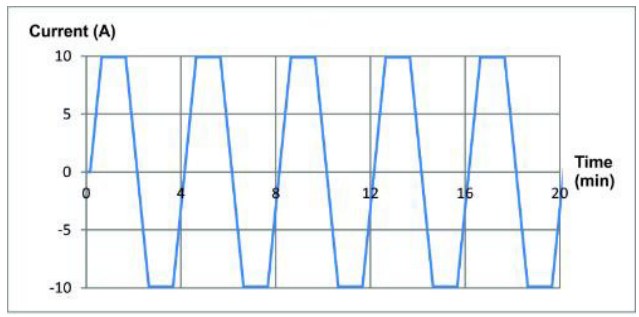

Figure 6: Ramp test.

Within 24 hours, the program performs the switching between the maximum current values of the source as follows:

- the transition from the maximum current value of one sign to a maximum current value of the other sign is performed during one minute.
- the sources are working at the maximum currents during one minute.

The RMS noise calculation is performed by the program at maximum currents, but for the calculations only the last 30 seconds are considered, not the whole one minute interval. This is due to the fact that immediately after reaching the maximum current, during the first few seconds, a transition process takes place.

The second stage of the testing is called the Full Power Test. This test is automatically started immediately after the end of the Ramp Test and lasts for one hour. During this test, the sources work 30 minutes at + Imax and 30 minutes at -Imax. Similarly as in the previous stage, the RMS noise is calculated at the maximum currents, but in this case during 29.5 minutes. The first 30 seconds of the plateau, similarly as in the Ramp Test, are not taken into account due to the transition process.

During the testing, the measured data is written in the text files in the real time mode. Seven text files are created after completing the test for each source: three files with the Ramp Test data, one of which contains all data, and other two files contain the data for selected intervals. The same algorithm is for three files of the Full Power Test. The last file is the log file. The data from this file provide the basis for making a conclusion whether the the source passed the test or not.

ISBN 978-3-95450-181-6

THE PULSED HIGH VOLTAGE POWER SUPPLY FOR THE NICA BOOSTER INJECTION SYSTEM

V.A.Bulanov, A.A. Fateev†, E.V. Gorbachev, H.P. Nazlev, Joint Institute for Nuclear Research, Dubna, 141980, Russia

Abstract

Three pairs of electrostatic deflecting plates will be used in the injection system of booster ring. The electric circuit and design of the power supply system for one plate are presented in the report. The experimental results of testing are also presented.

INTRODUCTION

The NICA ion collider [1] is currently under construction at Joint Institute for Nuclear Research. The booster of the main accelerator NUCLOTRON is used for initial acceleration and cooling of ion beams.

Electrostatic septum and three deflecting devices will be used in the booster injection system [2]. Electric plates are used as actuating elements. Hydrogen thyratrons are used as switches.

PARAMETERS OF ELECTRIC PULSES

The number of supplied plates and amplitude of applied voltages depend on type of injection [2]. All electrical plates are supplied with identical pulses that differ in amplitude of the applied voltage. Main parameters of electric pulse with maximum amplitude are shown in Table 1.

Table 1: Main Characteristics of Electric Pulse

Maximum electrical potential on the plate	60 kV
Duration of pulse plateau at least	30 us
Nonuniformity of voltage on the plateau	≤ 1%
The discharge time	≤ 0,1 us
Residual voltage	≤ 0,5 kV

The parameter values given in Table 1 are generally achieved without major difficulties except for residual voltage value.

To reduce residual voltage and improve reliability of high voltage components, it was decided to use a pulse charging.

The conceptual version of such scheme was tested and results were published [3]. Then the parameters of main elements were optimized and device was designed and manufactured.

THE POWER SUPPLY SCHEME AND DESIGN

PSPICE model of the power supply circuit is presented in Fig.1.

The initial pulse of the thyristor generator is applied to the primary winding of the step-up transformer. We use industrial measuring transformer GE-36. Thyratron is triggered near the top of the pulse when the current in the primary winding of the transformer crosses zero value.

The discharge chain C_1, R_2-R_3 maintains the discharge current through the thyratron in a few tens of microseconds, thereby preventing fast afterpulses. Slow processes are suppressed by leakage of charges through the secondary winding of transformer. Besides that the reversal magnetization of the transformer produces negative potential of several tens of volts at the diode set.

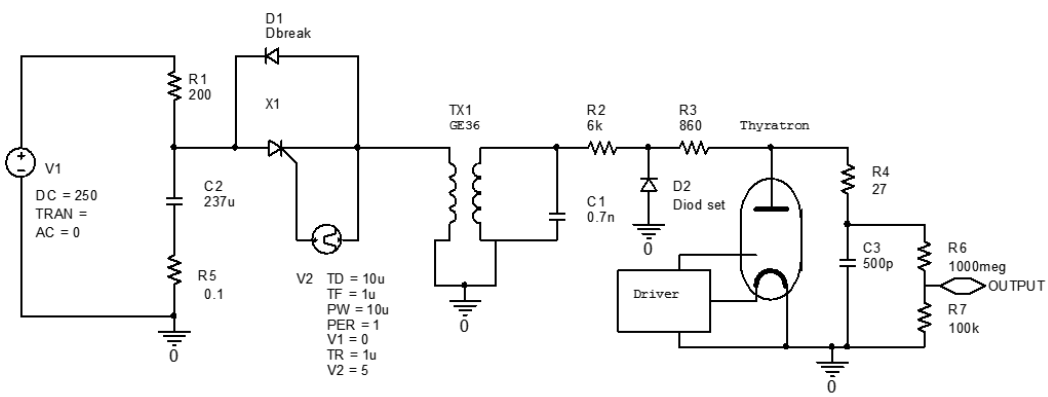

Figure1: PSPICE model of the power supply circuit.
C_3-equivalent load, R_6-R_7 – divider VD-60

† fateev@sunse.jinr.ru

ISBN 978-3-95450-181-6

This variant of scheme was designed and manufactured. The view of device is presented in Fig.2.

Figure 2: The photo of device at testing bench.

This pulse power supply was tested at different output voltages up to maximum working parameters. The oscillograms are presented in fig.3.

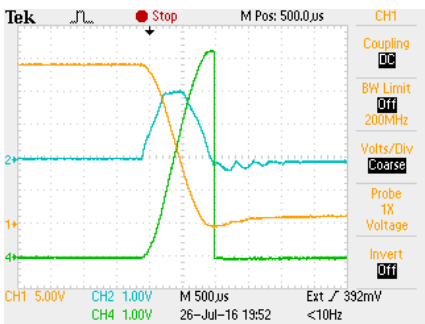

Figure 3: Measurement results. Voltage (10 kV/div) at the equivalent capacitance (green), input current (40 A/div) of the transformer (blue) and voltage at C_2 (50 V/div).

CONTROL SYSTEM INTEGRATION

The power supply is controlled by system based on National Instruments hardware – CompactRIO [4] controller with few acquisition modules for analog and digital input and output, CAN interface module and FPGA for timing control.

The control unit communicates with NICA control system by means of TANGO Controls [5] device servers and provides synchronization with the booster injection and setting of power supply parameters.

CONCLUSIONS

The pulse power supply for deflecting plate was developed, manufactured and tested at working parameters. The test results put in a strong performance. The device is ready to use at booster injection system.

ACKNOWLEDGMENT

Authors express thanks Bochkov Viktor Dmitrievich for seminal discussion and useful remarks.

REFERENCES

[1] G.Trubnikov et al., "NICA Project at JINR", Proc. of IPAC'13, Shanghai, China, 2013. P. 1343-1345.
[2] V. A. Bulanov, E. V. Gorbachev, N. I. Lebedev et al., "A Conceptual Design of a Power Supply System of Deflecting Plates for Multivariate Injection into the NICA Accelerator Complex Booster", Physics of Particles and Nuclei Letters, 2014, Vol. 11, No. 5, pp. 695–698.
[3] V.A.Bulanov, A.A. Fateev, E.V. Gorbachev, N.I. Lebedev, "The Power Supply System of Electrostatic Deflecting Plates for Accelerating Complex NICA", Proceedings of RuPAC2014, Obninsk, Kaluga Region, Russia, TUPSA34.
[4] The CompactRIO Platform, http://www.ni.com/compactrio
[5] TANGO Controls, http://www.tango-controls.org.

ISBN 978-3-95450-181-6

GENERATOR OF HIGH-VOLTAGE PULSE FOR HIGH-CURRENT ACCELERATOR OF DEUTERON WITH LASER STARTS

A.A. Isaev, E.D. Vovchenko, K.I. Kozlovskij, A.E. Shikanov, National Research Nuclear University "MEPhI" (Moscow Engineering Physics Institute), Moscow, Russia

Abstract

The report deals with the source of pulsed high voltage, and simultaneously, source of the pulsed current for the magnetic insulation of electrons near the cathode that was developed for a high-current accelerator of deuterons with laser-plasma anode. The accelerating voltage up to 400 kV and ion current about 1 kA have been achieved. The current in the spiral inductor has reached 5 kA and it excludes breakdown between the cathode and anode for 0.5 μs. For synchronization of physical processes in accelerator of deuterons with pulsed power, the laser control is applied.

INTRODUCTION

Currently for a number of applied problems of geophysics are used small-size pulse neutron generators [1]. The sources of neutrons with gas-filled or vacuum accelerating tubes are most developed and used in such researches. The alternative schemes of the neutron generator based on vacuum diode with coaxial electrode geometry and laser plasma as an efficient source of deuterons [2, 3] are developing in addition to these researches. In this diode is used the direct acceleration of deuterons to cathode and isolation of the electron current by using magnetic field. The laser plasma is generated by using of Nd: YAG laser with a wavelength of 1.06 μm and contains deuterons produced from TiD target placed at the anode. Diode system is placed in a vacuum chamber with a residual pressure of 10^{-2} Pa.

For diodes with coaxial geometry of electrodes, there are two possible schemes of suppression of electron current: a field of permanent magnets with azimuthal symmetry [4] and pulsed magnetic field of the spiral inductor [5]. Analysis of computer experiment showed that a permanent ring magnet does not provide the reliable insulation of electronic current near the poles. This leads to a rapid breakdown of the diode gap and decreasing the accelerating voltage.

In diodes with pulsed magnetic insulation, these problems occur to a lesser extent. In this case, for effective magnetic insulation it is necessary to synchronize three processes: expansion of a laser plasma, the formation of accelerating voltage and generation of the increasing magnetic field. To solve this problem the authors have developed the original scheme of the pulsed power supply, in which the laser-triggered gap runs Marx generator of the high voltage (U ≈ 400 kV) and the magnetic field generator with high current (I ≈ 10 kA). The features of the coordinated work of these generators with physical processes in the accelerator diode is considered in this article.

THE MARX GENERATOR

A high-voltage Marx generator is the main part of the pulsed power supply. The generator is made according to the scheme with unipolar charging and without change of the polarity of the output voltage. It consists of 30 stages (n = 30), each of them uses two capacitors K15-4 connected in parallel with a total capacitance of C_0 = 2 x 4700 = 9400 pF. In the charging circuits is used a high-voltage resistor with resistance R_0 = 16 kΩ. Each of stages stored 1.0 – 1.7 J of energy at a charging voltage of 15 –18 kV. Open circuit voltage is 400 kV, capacitance in peak is $C_{marx} = C_0 / n$ = 310 pF.

In the first stage of the Marx generator is applied the laser-triggered gap, the second stage uses the field distortion gap. In the rest stages of the Marx generator installed uncontrolled spark gaps. All gaps operate in air at atmospheric pressure.

Stable running of the laser-triggered gap (*LG*) with a time delay of not more than 50 ns is obtained at energies of laser are more W ≥ 80 mJ. In this case, the main energy of the laser pulse (85− 90%) is directed to the laser target. Note that the use of laser control greatly simplifies the synchronization of Marx generator with a laser plasma.

The field distortion gap (*FDG*) provides reliable switching of the second stage. To run this gap in the first stage of the Marx generator attached simple high-voltage generator. Its principle of operation is based on fast discharge of the capacitance (C = 470 pF) on the pulse transformer because of the switching of the laser-triggered gap (Fig. 1). Transformer is made on a rod core of ferrite M400HH. The number of turns in the primary and secondary windings of the transformer is equal to w_1 = 5 and w_2 = 25, respectively.

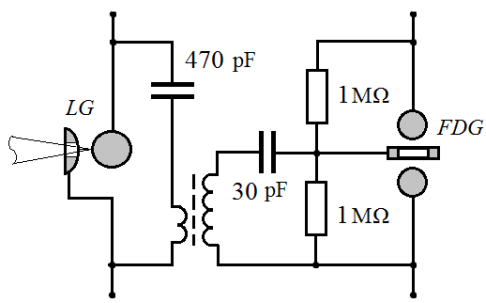

Figure 1: Electrical circuit of the simple high-voltage generator for switching field distortion gap (*FDG*).

In addition, more stable running was observed when the low-voltage electrode of gaps in the second, third and fourth stages of Marx generator was connected to the

ISBN 978-3-95450-181-6

grounded conductor via capacitors with capacitance $C_{cor} \sim 7$ pF and working voltages of 40, 60 and 80 kV, respectively.

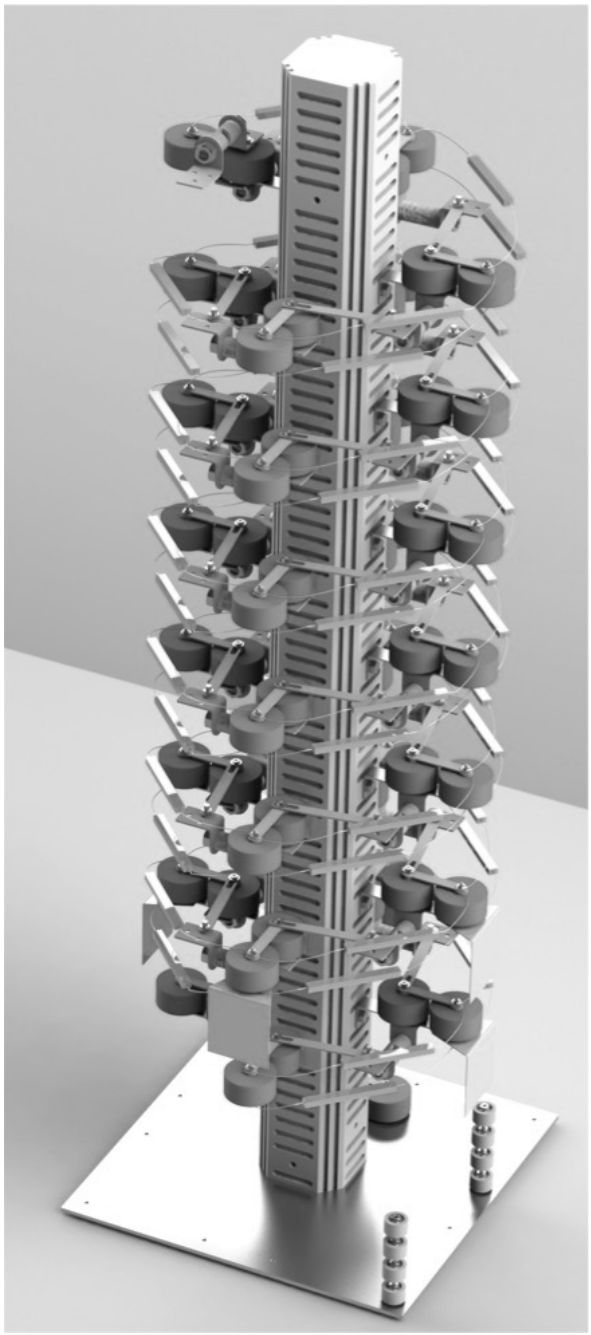

Figure 2: The Marx generator with a helical geometry.

The stages of Marx generator are mounted around the central cylindrical pillar (a height is 0.9 m, a diameter is 0.07 m), made from dielectric. The lateral surface of the cylinder-pillar are made with complex profile in order to enhance the dielectric strength of the insulation between the stages. A chain of capacitors and the spark gaps is located along a helix, which surrounds the central pillar.

The diameter of the helix is 0.15 m and the step is 0.1 m. At each full turn of the helix is used 4 spark gap. The generator has a size of 0.2 x 0.2 x 0.9 m. The appearance and the geometry of the Marx generator elements are shown in Fig. 2.

To analyze the inductance of the Marx generator we have considered a model in the form of a cylindrical helix with a radius of r = 0.075 m. The step of helix is equal to p=0.1 m, number of turns is equal to N = 7.5. The inductance of such cylindrical helix can been estimated according to the formula [6]

$$L = \mu_0 \cdot N^2 \cdot K \cdot (S/H) - \mu_0 \cdot r \cdot N \, (G^* + N^*) \approx 5 \text{ мкГн},$$

Where $S = \pi r^2 = 0.07$ м^2 is square round inside turn; $H = N \cdot p = 0.75$ м is the height of the helix; $K = f_1 (H/2r)$, $G^* = f_2 (2 \cdot r/p)$ и $N^* = f_3 (N)$ is correction factors, depending on the geometry of the helix and number of turns. For our geometry $K(5) = 0.9$; $G^*(1.5) = 1$; $N^*(7.5) = 0.25$. For capacitance in peak $C_{marx} = C_0 / n = 310$ pF and inductance $L \approx 5$ мкГн it is possible to estimate the period of oscillation $T = 2 \pi (L \cdot C_{marx})^{1/2} \approx 250$ нс. This value is in good agreement with the experimental data obtained from the oscillogram for open circuit voltage.

CURRENT GENERATOR

The insulating magnetic field to be generated by increasing pulse current. The generator is performed according to scheme with the discharge of the capacitor ($C_M = 0.25$ μF) on an inductive load. An inductor ($L_M = 0.65$ μH) is made in form of conical spiral. The rise time of current (i.e. magnetic field) is

$$\tau_M = \sqrt{L_M C_M} \approx 400 \text{ нс}.$$

The same laser-triggered gap *LG* is used for switching the capacitor C_M. Such technique is provided a reliable synchronization the pulse of current with the pulse of the high-voltage Marx generator. The start of the current pulse coincides with the moment of breakdown of *LG*.

The capacitor C_M stored energy of 25 – 40 J. The maximum current reached in the inductor can be estimated from energy balance

$$I_{max} = U \sqrt{C_M / L_M} \approx 9 \text{ кА}.$$

The corresponding estimate of a magnetic field in the center on the axis of the conical spiral gives

$$B_{max} \approx 0.5 - 0.6 \text{ Тл}.$$

It should be noted that the induction of magnetic field is $B \approx 0.7 \, B_{max}$ after a quarter of a period from start of current pulse.

EXPERIMENT AND SYNCHRONIZATION OF GENERATORS

The experimental setup for accelerating deuterons with using Marx generator (1), current generator and a vacuum diode with laser-plasma ion source and a magnetic insulation of the electrons is shown in Fig. 3. A laser target in the form of a tablet made of TiD was placed on the

ISBN 978-3-95450-181-6

anode (2). Deuterons are extracted from the laser plasma in an electric field formed by a positive high-voltage pulse on the anode.

We applied a pulsed magnetic isolation for suppression of parasitic electron current due to secondary electron emission at the cathode. Conical spiral (3) is placed in the diode gap in front of the cathode (4), which also had a conical shape. In addition, conical surface of the cathode and conical spiral are parallel. Diode system placed in a vacuum chamber pumped to a pressure of 10^{-2} Pa.

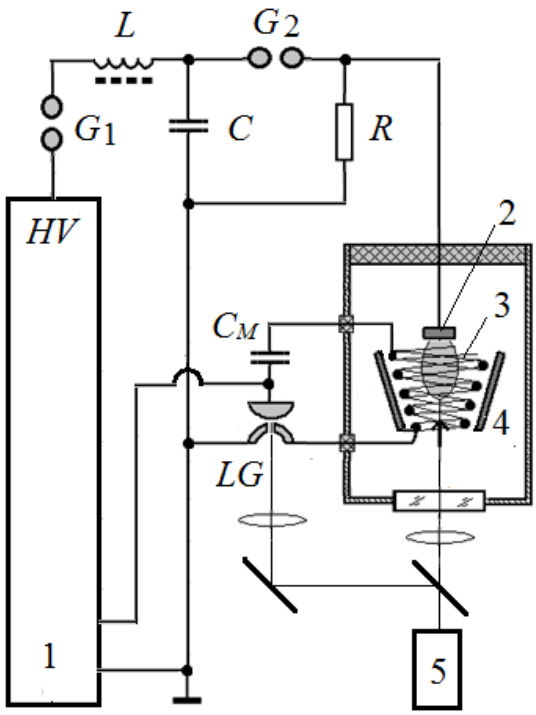

Figure 3: Scheme of the experimental set-up for the acceleration of deuterons in the diode with the laser plasma on the anode and magnetic insulation of electrons: 1 – anode; 2 –conical spiral; 3 – cathode; 4 – laser; 5 – Marx generator (L = 400 – 700 μH, R =100 kΩ, C = 30 pF, C_M = 0.25 μF).

To obtain a laser plasma, we used Nd: YAG laser (5) with wavelength λ = 1.06 μm (energy $W \leq 0.85$ J, duration is about10ns). The main part of the laser beam (85-90%) is focused on the anode target. Radiation intensity on the target is equal to $q \approx 10^{11}$ W/cm^2. The remaining energy of the laser pulse is focused to the laser-triggered gap LG. The breakdown of LG runs the first stage of the Marx generator and the discharge circuit of the current generator. This allowed us to synchronize three processes: expansion of a laser plasma, the formation of accelerating voltage and generation of the increasing magnetic field.

A laser plasma emission is accompanied by its expansion in the radial direction. The flow of deuterons reaches the conical spiral with a delay $\tau_P \approx 250 - 300$ ns.

To coordinate the work between the deuteron accelerator and pulse generators we have added a circuit of inductance L = 400 – 700 μH and capacitance $C \approx 30$ pF (time constant $\sqrt{LC} \approx 110 - 150$ ns) and the spark gap G_2. In this case, the total delay of the high-voltage pulse relative to the laser pulse is equal to $\tau_{HV} \approx 200$ ns.

The inductance L is a cylindrical spiral (the number of turns is 20) with a core made of ferrite M400HH (diameter 70 mm, length 500 mm). The spark gap G_1 separates the delay LC-circuit from the charging voltage of the Marx generator.

Estimation of the efficiency of generating the magnetic field showed that current in the conical spiral achieved 60% from its maximum value after 300 ns from the beginning of the expansion of a laser plasma (i.e. when the flow of deuterons reaches the conical spiral).

In our experiment, we measured the currents in the accelerator diode and a conical spiral by using of Rogowsky coil operating in the regime of current transformer. The peak diode current achievable with the magnetic insulation was about 1 kA when the energy of radiation on the laser target was 0.75 J and accelerating voltage up to 400 kV. The current in the conical spiral reached 5 kA, and its impedes the breakdown between the cathode and anode for 500 ns.

CONCLUSION

We showed the possibility of synchronization of the physical processes between the laser-plasma source of ions with pulse generators of voltage and of current. In the diode with magnetic insulation was achieved the fulfillment of a condition $\tau_{HV} \leq \tau_P \leq \tau_M$ what is important to effective acceleration of deuterons. This requires a compromise in the selection of the parameters of the LC-circuit in the delay line and the parameters of the L_M and C_M in generator of current. Running process in the diode system by using of a laser-triggered gap limits the possibility of optimizing the temporal characteristics, however, significantly simplifies the experiment.

This work is supported by the Ministry of education and science of Russian Federation according to the agreement № 14.575.21.0049 (RGMEFI 57514X0049).

REFERENCES

[1] Portable generators of neutrons and technology on their basis / Reports edited by Yu.N. Barmakov. Moscow: VNIIA, 2013, − 620 pages.
[2] A.N. Didenko, A.E. Shikanov, K.I. Kozlovskii, V.L. Shatokhin, and D.D. Ponomarev, Plasma physics report, **40**, 910–918 (2014).
[3] A.E. Shikanov, E.D. Vovchenko, and K.I. Kozlovskii, At. Energy **119,** 258–264 (2016).
[4] A.E. Shikanov, E.D. Vovchenko, K.I. Kozlovskii, and V.L. Shatokhin, Tech. Phys. Lett. **41**, 511 (2015).
[5] K.I. Kozlovskii, D.D. Ponomarev, V.I. Ryzhkov, A.S. Tsybin, and A.E. Shikanov, At. Energy **112**, 218–221 (2012).
[6] Heinz Knoepfel. Pulsed high magnetic fields. London, North-Holland publishing company, 1970. – 391 P.

ISBN 978-3-95450-181-6

THE AUTOMATION OF ENERGY RAMPING FOR THE MAIN STORAGE RING OF KSRS

Y. Krylov, E. Kaportsev, K. Moseev, N. Moseiko, A. Valentinov, NRC Kurchatov Institute,
1 Kurchatov sq., 123182 Moscow, Russia

Abstract

Kurchatov Synchrotron Radiation Source (KSRS) is the complex of electron synchrotrons specialized as a source of synchrotron radiation. The running cycle of KSRS main storage ring includes the energy ramping from 450 MeV up to 2.5 GeV. Fast and reliable energy ramping algorithm was developed and implemented at KSRS main storage ring. Using the hardware decisions on the basis of the NI units and CAN-bus interface, the control system is developed and launched for the power supplies of magnetic elements.

ENERGY RAMPING PROCESS

Magnetic system of KSRS main ring includes one family of bending magnets, 6 families of quadrupole lenses, two families of sextupole lenses for chromaticity correction [1]. The supply current of the bending magnets varies from 1270 A up to 7200 A, it determines the machine energy. The currents of the quadrupole power supplies vary from 80 A up to 760 A depending on the energy and number of the family. The currents of sextupole power supplies vary from 0.4 A up to 8 A. As a result saturation of iron exists at high energy, while residual magnetization manifests at low energies. Thus, a simple proportional increase of the currents will lead to the betatron tune shifts during energy ramping.

The process of energy ramping between injection energy 0.45 GeV and working energy 2.5 GeV consists in proportional change of magnetic field in bending magnets, field gradients in quadrupole and sextupole lenses. To facilitate the energy ramping process, 9 intermediate regimes were introduced at a distance of 10 - 20% in energy one from another. The regime means list of power supply settings. Magnetic measurements were conducted to determine right currents for all power supply families in each regime. Field in bending magnets was measured with an accuracy of 0.00001 using NMR sensor. For the quadrupole lenses measurements were carried out by Hall effect sensor with an accuracy of 0.001. Relative changes of the field gradients in each family in all intermediate regimes were measured [2].

Complicated algorithm with 9 intermediate regimes (collections of power supplies settings) was developed to produce fast and efficient energy ramping. The correction of closed orbit, betatron tunes and chromaticity is accomplished in each regime in static conditions. Special file is used to provide acceleration or deceleration of power supplies in dynamic conditions. This scheme allows to compensate betatron tune shifts during energy ramping. Power supplies are not stopped on intermediate regimes; speed of current changing is continuous function of time.

Fast and reliable energy ramping algorithm was developed and implemented at KSRS main storage ring [2]. Whole process takes 2 minutes and 40 seconds, beam losses doesn't exceed 2 – 3 %, betatron tune shifts are less than 0.015.

For more accurate reproduction of the results standard demagnetization cycle was introduced. After the work on the energy of 2.5 GeV currents of power supplies of the magnetic elements rise above the maximum working value, then gradually, over 80 seconds, fall below the minimum values of the injection energy, then regime of injection is restored. In every state a 30 seconds pause is maintained. The practice showed that after this demagnetization cycle betatron tunes returned to its initial values with a good accuracy of about 0.003.

KSRS MAIN RING CONTROL SYSTEM

KSRS control system (CS) is the multilayer and multiprocessor design consisting of three levels: executive, server and operator (see in Figure 1).

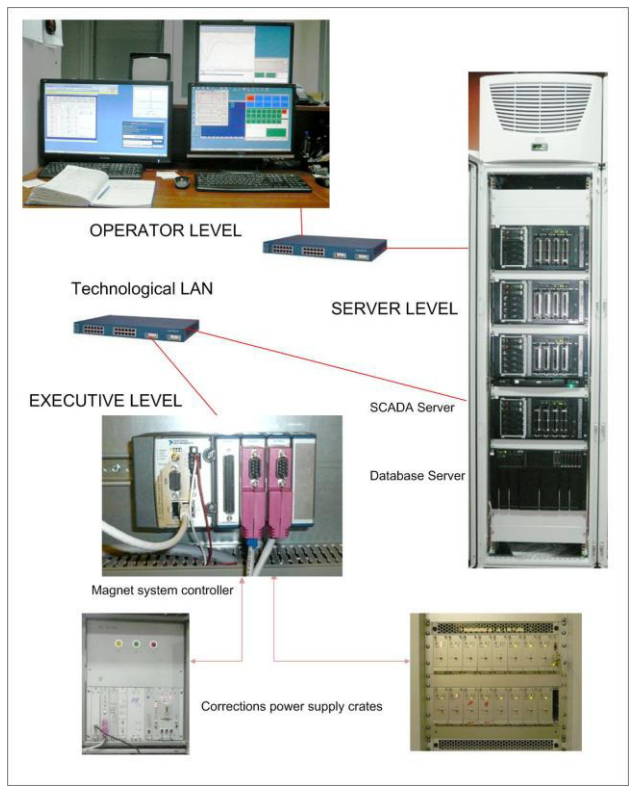

Figure 1: KSRS magnet system control.

ISBN 978-3-95450-181-6

All equipment is connected by two local area networks: public and technological. The magnet subsystem controls a high-current power supply of linear optic elements and a low-current power supply of bending magnets and nonlinear optic elements. The process control subsystem realizes a direct control of all subsystems. For example, it controls electron beam energy ramping process or beam transfer between accelerators. Any control algorithms (global or local electron beam orbit correction, photon beam stabilization at user's beam lines, etc.) or mathematical data processing are performed by this subsystem [3].

The CS server level consists of application servers and database server, which are operated under Microsoft Windows Server 2008 operating system. The full-featured system for monitoring, control and data acquisition CitectSCADA is operated on applications servers. We have two application servers combined into redundant cluster. This cluster controls vacuum, magnetic, thermo control subsystems. The functional structure of the CS you can see at Figure 2.

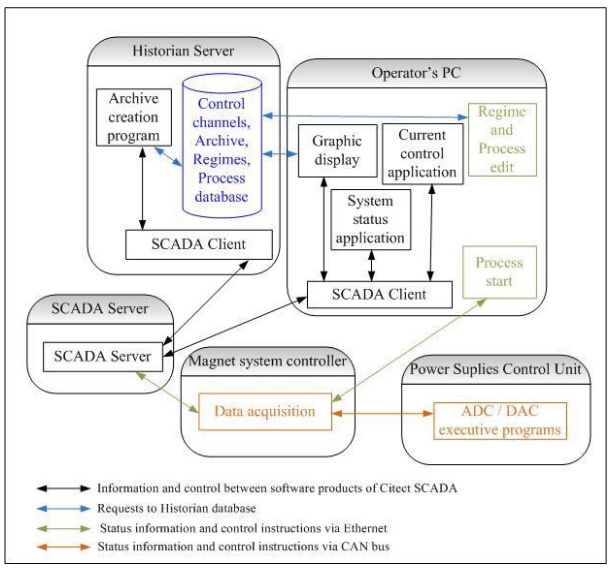

Figure 2: Functional structure of software.

To store the data about state of the accelerators, the data acquisition and reporting system Citect Historian v.4.3 is used. This system based on database management system (DBMS) MS SQL Server. In addition, this DBMS is used to store information about input/output channel parameters and description (for example, critical values, conversion factors, sampling rate, etc.). At this server level the following are realized:

- algorithms assignment;
- the data exchange between controllers, servers and operator's workstations;
- monitoring of the facility operation and some mathematical data processing;
- data storing into the database, acquisition and processing on user's requests.

The CS upper level includes automated operator's workstations, workstations of technology services staff and the facility users. At this level, as well as server level, the system CitectSCADA is operated. But at this level the CitectSCADA has other tasks, namely:

- the processes visualization in graphical mode and alarms control;
- the detailed reports preparation and statistical process control.

The executive level includes magnet system controller (NI platform) and embedded controllers in power supply, which operates as a node of CAN field bus. Specialized tool kit was developed for adjustment and calibration of power sources [4].

Operator's Interface

The video frame of the operator's program of the magnet system is shown in a Figure 3. This program solves following tasks:

- representation on the monitor of the circuit and the status of magnet system of main ring KSRS;
- display of preventive and alarm messages;
- control of tuning of power supply units of magnet systems;
- operator's authorization.

By clicking on the element of listing of power supply units one can control of this element. The technical status of power supply is shown on the screen and is highlighted a colour warning in case of a deviation from a normal mode of operation.

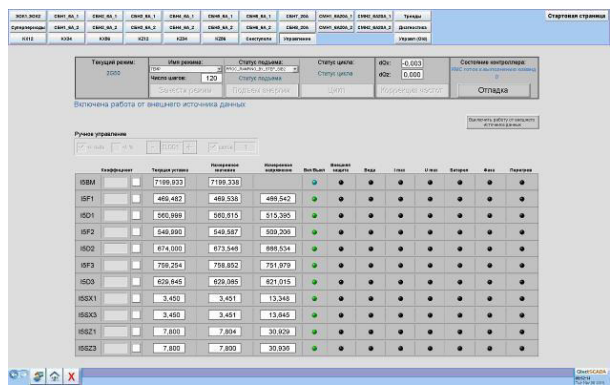

Figure 3: The video frame of operator's program.

This program has additional functions:

- job of the regimes – collection of power supplies settings;
- launch of energy ramping;
- start of a magnetization cycle;
- support of useful applications such, as local electron beam orbit correction, photon beam stabilization at user's beam lines.

The video frame of the history trends program of the magnet system is shown in a Figure 4.

ISBN 978-3-95450-181-6

Figure 4: The video frame of history trends program.

This program represents of archive and current parameter values in the form of diagrams. The graphic interface allows the user to choose control channels and the form of graphic representation.

Work in Progress

This upgrade of the magnet system control is a part of the project of modernization of KSRS control system. In the first phase is created test stand, which is designed to develop and debug software for local subsystems and CAN-bus equipment [5]. By the present moment the control of magnet system is tested, collected and launched, the moment of tests of energy ramping is recorded on the diagram in Figure 4.

REFERENCES

[1] V.Korchuganov, et al., "The Status Of The Facilities Of Kurchatov Synchrotron Radiation Source", Proceedings of RuPAC 2014, Obninsk, Russia, 2014. http://accelconf.web.cern.ch/AccelConf/rupac2014/papers/thy02.pdf

[2] A.Valentinov, et al., "Energy Ramping At Siberia-2", Proceedings of RuPAC 2012, Saint-Petersburg, Russia, 2012. http://accelconf.web.cern.ch/AccelConf/rupac2012/papers/weppd008.pdf

[3] V.Dombrovsky et al., "Modernization Of The Automated Control System In The Kurchatov Synchrotron Radiation Source Using SitectSCADA." Proceedings of RuPAC 2014, Obninsk, Russia, 2014. http://accelconf.web.cern.ch/AccelConf/rupac2014/papers/thpsc42.pdf

[4] N. Moseiko, et al., "The Power Supply System For Electron Beam Orbit Correctors And Focusing Lenses Of Kurchatov Synchrotron Radiation Source", Proceedings of ICALEPCS 2013, San Francisco, 2013. http://accelconf.web.cern.ch/AccelConf/ICALEPCS2013/papers/thppc049.pdf

[5] Y. Fomin, et al., "New Automated Control System At Kurchatov Synchrotron Radiation Source Based On SCADA System Citect", Proceedings of ICALEPCS 2013, San Francisco, 2013. http://accelconf.web.cern.ch/AccelConf/ICALEPCS2013/papers/moppc020.pdf

ISBN 978-3-95450-181-6

SOLID-STATE MODULATORS FOR PARTICLE ACCELERATORS

A. A. Zavadtsev†, D. A. Zavadtsev, D. V. Churanov, D. A. Zybin,
Nano Invest, LLC, Moscow, Russia

Abstract

A series of the wide parameter range solid-state high-voltage modulators has been developed and built as a power supplies for the magnetrons and the klystrons in the particle accelerators. The series includes 60 kV/100 A/6 μsec modulator with pulse transformer for 3 MW magnetron, 60 kV/300 A/6 μsec direct switch modulator for 6 MW multi-beam klystron, 110 kV/80A/6 μsec direct switch modulator for 3 MW klystron, 130 kV/100 A/6 μsec modulator with pulse transformer for 5 MW klystron, 250 kV/250 A/6 μsec modulator with pulse transformer for 20 MW klystron. The last modulator is under construction. All other modulators have been supplied to customers in Russia as well as in Europe.

INTRODUCTION

The solid-state modulators are used to feed klystrons and magnetrons in the particle accelerators more and more often. These modulators include the semiconductor HV switch (IGBT or MOSFET) instead of the tube one in traditional modulators. The main advantages of the solid-state modulator are low voltage on each switch connected in series, long lifetime, and easy control.

Several schemes of the solid-state modulator are used at the modulator building.

The first modulator type is a series switch. It includes serial IGBT switches discharging the full-voltage capacitor to the load (klystron) [1, 2].

The second modulator type is a high-voltage pulse generator with parallel charging of the capacitors and discharging them to the load in serial circuit. V. K. Arkadiev and N. V. Baklin have built this generator with mechanical switch in 1904. E. O. Marx suggested the use of the discharger as a switch in this generator in 1924. IGBT is used as a switch in this generator now [3]. The voltage in the load is a sum of the capacitor voltages.

These modulator types can be used with the pulse transformer.

The next modulator type includes a number of modules, each of which includes the capacitor, the switch and the pulse transformer [2]. The secondary windings of these pulse transformers are connected in series, so the load voltage is a sum of module voltages.

Another approach is used in the modulator including one complex pulse transformer with several primary windings and one secondary one [4]. The modules are connected to the primary windings. The magnetic flows of the primary windings are added in the pulse transformer core. So the secondary voltage is a sum of primary voltages times transformer ratio.

MODULATOR WITH ADDING MAGNETIC FLOW

The modulator with adding magnetic flow in the pulse transformer has been built for HV feeding of 2.5-3 MW S-band magnetron in the electron linac [5].

Eleven 1 kV modules are connected to eleven primary windings of the pulse transformer. All equipment is located in the oil-tank as this is shown in Figure 1.

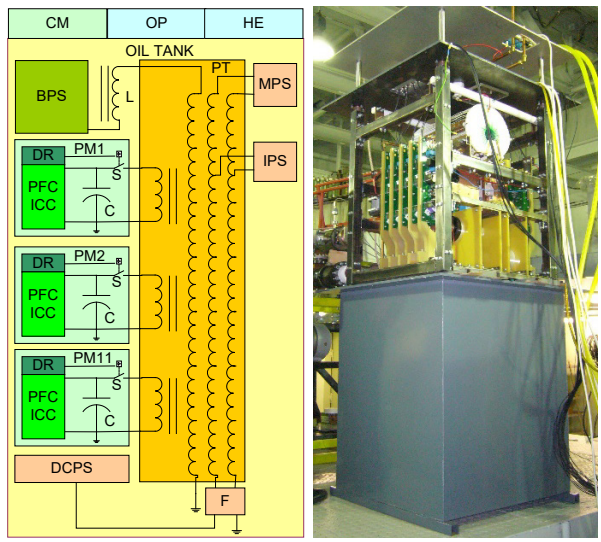

Figure 1: Modulator with adding magnetic flow.

Main modulator parameters are

- voltage 55 kV;
- current 100 A;
- pulse length 0-6 μsec;
- average power 4.5 kW;
- bifilar secondary winding for power supply of magnetron filament;
- terminals at secondary winding for reduced injector voltage.

DIRECT SWITCH 60 KV MODULATOR

The direct switch solid-state Arkadiev type modulator has been developed for 6 MW multi-beam klystron. Two modulators have been built for the 40 MeV electron linac [6]. Each modulator includes 6 modules with 10 levels of the Arkadiev generator. The modulator is shown in Figure 2, in the cabinet, where the klystron is located too.

Main parameters of the modulator are:

- voltage 60 kV;
- current 300 A;
- pulse length 0-6 μsec.

† azavadtsev@yandex.ru

ISBN 978-3-95450-181-6

Figure 2: Direct switch solid-state 60 kV modulator.

The voltage and current pulse shapes are shown in Figure 3. The modulator allows switching off the load voltage within the pulse with limitation of the current in case of break-down. The oscillograms corresponding to this fast interlock are shown in Figure 4.

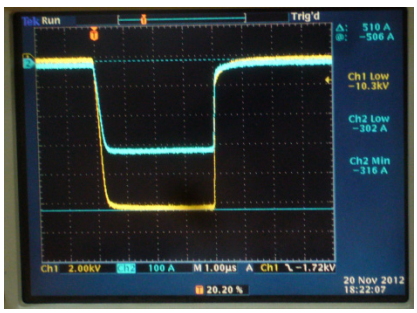

Figure 3: Voltage and current pulse shape.

Figure 4: Voltage and current pulse shape in case of the fast interlock event (break-down).

DIRECT SWITCH 110 KV MODULATOR

Another direct switch solid-state Arkadiev type modulator has been developed and built for 3 MW klystron [7]. It is shown in Figure 5.

Eleven modules with ten levels in each are located in the oil-tank. The klystron is located on the top of the oil-tank.

Main parameters of the modulator are:

- voltage 110 kV;
- current 80 A;
- pulse length 0-6 μsec.

Figure 5: Direct switch solid-state 110 kV modulator:
- out of oil-tank with test resistive load on the left and
- in the oil-tank with the klystron on the right.

The pulse shape in the modulator is shown in Figure 6.

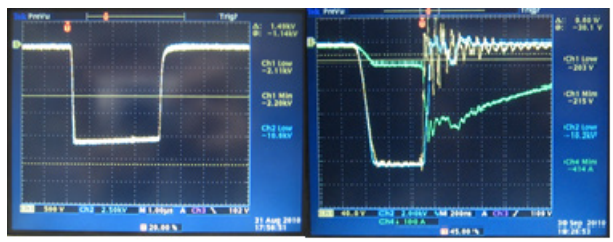

Figure 6: The pulse shape in 110 kV modulator (normal and in case of interlock event).

130 KV MODULATOR WITH PULSE TRANSFORMER

130 kV modulator has been developed and built for the 3-5 MW klystron. The modulator includes six 10 kV modules in the cabinet, producing dual output voltage ±24 kV, which is transmitted to the transformer primary (48 kV). Figure 7 shows (from left to right) the pulse transformer in the oil-tank (with klystron and local shielding on the top), the modulator cabinet and the control cabinet.

Figure 7: 130 kV modulator with pulse transformer.

ISBN 978-3-95450-181-6

Measured parameters of the modulator&transformer are:

- voltage 130 kV;
- current 100 A;
- pulse length 0-6 usec;
- pulse-to-pulse output voltage instability (peak-to-peak) 0.19%;
- RMS voltage fluctuation 0.03%;
- flat-top voltage non-uniformity <1%.

The pulse shape in the modulator is shown in Figure 8.

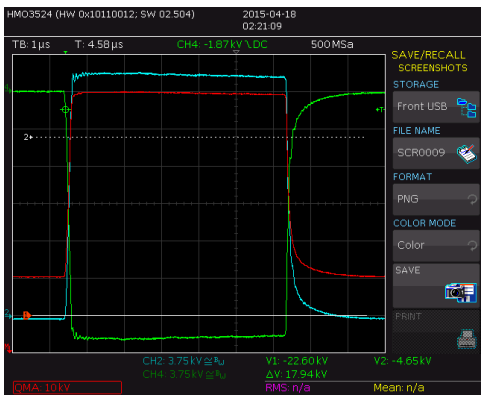

Figure 8: The pulse shape in 110 kV modulator (BLUE is positive voltage, GREEN is negative voltage, RED is differential voltage).

The modulator operates as a part of the complex equipment in Europe.

250 KV MODULATOR WITH PULSE TRANSFORMER

The next modulator has been developed to feed 24 MW S-band klystron. It consists of two dual 22 kV modules in the cabinet and the pulse transformer in the oil-tank with the klystron on the top. 3D design of the modulator and the pulse transformer in the oil tank with the klystron is shown in Figure 9.

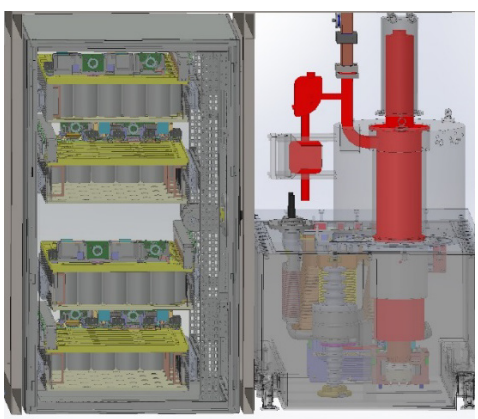

Figure 9: 250 kV modulator with pulse transformer and klystron.

Main parameters of the modulator are:

- voltage 250 kV.
- current 250 A.
- pulse length 0-6 µsec.

The modulator is under construction now.

CONCLUSION

A number of solid-state modulators have been developed and built for klystrons and magnetrons.

The modulators cover a wide range of the parameters: voltage up to 250 kV, current up to 300 A, pulse length up to 6 µsec.

The solid-state modulators have been built with different schematics: direct switch, with adding the magnetic flow, with or without pulse transformer. Therefore, any customer requirements can be fulfilled on base of developed and built modulator series.

The solid-state modulators have following advantages over the tube-based modulators:

- module type of the building;
- easy parameter scaling on base of module type;
- low voltage of the single switch;
- long lifetime of the semiconductor switch;
- easy control of the voltage, pulse length, rise time;
- availability of the fast break-down interlock, switching off the voltage on the klystron within the pulse with limitation of the klystron current.

REFERENCES

[1] M.P.J. Gaudreau et al., “Solid-State Modulator Applications in Linear Accelerators”. Proceedings of the 1999 Particle Accelerator Conference, New York, 1999, p.1491-1493.

[2] E. G. Cook, “Review of Solid-State Modulators”. XX International Linac Conference, Monterey, California, p. 663-667.

[3] J. Casey et al., “Solid-State Modulators for the International Liner Collider”. In Proceedings of 2005 Particle Accelerator Conference, Knoxville, Tennessee, 2005, p.2998-3000.

[4] D.A.Zavadtsev et al., “Compact Electron Linear Accelerator RELUS-5 for Radiation Technology Application”. Proceedings of EPAC 2006, Edinburgh, Scotland, p.2385-2387.

[5] D. Churanov et al., “Solid State Modulator for Linear Accelerators”. Proceedings of RuPAC 2008, Zvenigorod, Russia, p.175-177.

[6] E.A. Savin et al., “Design and tuning of a 40-MeV electron linear accelerator”. Instruments and Experimental Techniques, 2013, 56 (5), p. 506-515.

[7] L. Kravchuk et al., “Layout of the PITZ Transverse Deflecting System for Longitudinal Phase Space and Slice Emittance Measurement”. Proceedings of Linear Accelerator Conference LINAC2010, Tsukuba, Japan, 2010, p. 416-418.

ISBN 978-3-95450-181-6

SWITCHING NETWORK UNITS FOR HIGH CURRENTS AND VOLTAGES OR PLASMA APPLICATIONS

F. Burini, M. Pretelli, G. Taddia, S. Tenconi, OCEM Power Electronics, Bologna, Italy
A. Lampasi, P. Zito, National Agency for New Technologies, Energy and Sustainable Economic Development (ENEA), Frascati, Italy

Abstract

OCEM and ENEA gained a wide experience in the design and experimental characterization of fast and accurate switching systems for high DC currents, as required to control magnets and superconductors. The exploited idea consists in inserting an electronic switch in parallel to a fast electromechanical switch in air, to combine the benefits of both devices. The electronic switch is turned on and off to support the electromechanical commutations, reducing the jitter to tens microseconds and limiting the arcs that would reduce the system lifetime. During the performed tests, DC currents up to 20 kA were diverted in less than 100 μs with good repeatability. In case of emergency, the current can be interrupted in few tens of milliseconds. If necessary, a resistor can be inserted in parallel to the switch to dissipate the energy trapped in inductive loads or to produce desired overvoltages (a voltage up to 5 kV was reached in this configuration). Specific circuits were designed to preserve the components from transient voltage overshoots. This switching system is expected to work for 10000 operations without major maintenance. The developed solutions may be extended to many relevant applications as particle accelerators and HVDC networks.

INTRODUCTION

The poloidal field (PF) coils, as the central solenoid (CS), of a new Tokamak generally consist of a number of superconducting coils, each connected to a dedicated power supply (PS) circuit. To initiate the plasma breakdown, an abrupt current derivative shall be produced almost simultaneously in all the PF coils, to produce an adequate voltage transient across them [1], [2]. As the power and voltage ratings of the PSs are limited, to about 20÷30 MVA and ±1 kV dc, a Switching Network Unit (SNU) is put in series to each of the poloidal circuits. An interruption nominal voltage up to 5 kV, a DC current up to 20 kA and an opening/closing time lower than 1 ms are required. The simultaneous opening of the SNUs shall be synchronized within 0.5 ms. The coil inductance is normally very high (up to tens of mH), so the current must be diverted into resistor banks R1 (the R1 resistance value can be pre-adjusted by selectors, in order to match the maximum current to be interrupted). After plasma breakdown and current ramp-up, the SNU hybrid switch shall be reclosed and from this time on the PSs will control the current in the circuit. The basic circuit diagram of Hybrid Switching Unit is reported in Fig. 1.

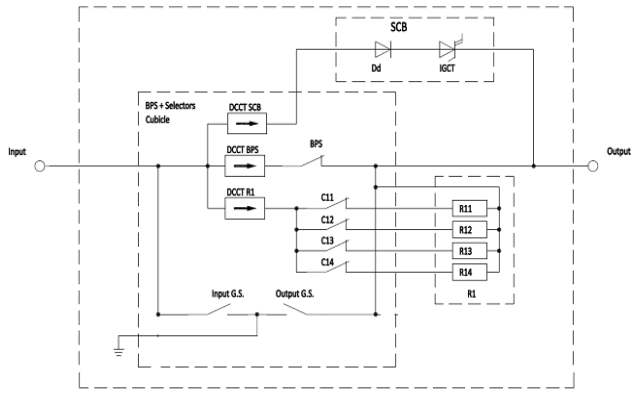

Figure 1: Functional Scheme of the hybrid SNU.

CHARACTERISTICS AND OPERATION OF THE HYBRID SWITCHING CIRCUIT

Operation and Ratings of the Switching Network Unit

Table 1 reports the main SNU parameters, whose detailed power circuit diagram is reported in Fig. 2. The opening and re-closing of the hybrid switch (hereafter referred to as SS) can be repeated every thirty minutes, generally for about ten hours per day; the SS structure improves and adapts the use of a solid state Static Circuit Breaker (SCB), in parallel with the main electromechanical By-Pass Switch (BPS). The use of a hybrid circuit breaker for DC applications is in principle not new and has been proposed and developed in the past for some Tokamak and Naval applications [3], [4].

When applied to Tokamaks, the reasons of the hybrid configuration come from the specific working cycle: the central solenoid current is ramped up for a maximum of 60 s and then, at a predefined time, the voltage across them is abruptly reversed. So, while the mechanical BPS carries the current for most of the operational time, the SCB "masks" the inadequate velocity and repeatability of the BPS in commutation, giving the hybrid switch the precision timing and velocity of solid state devices; moreover, the power dissipated in the arcing across the BPS contacts is greatly reduced and the operational life of mechanical contacts is correspondingly increased.

The Hybrid SNU detailed circuit diagram is reported in Fig. 2. It is worth pointing out that even though the Base Power Supplies are normally able of four-quadrant operation, the SCB are unidirectional devices, since they operate at the beginning of the tokamak current pulse; but

ISBN 978-3-95450-181-6

the BPS mechanical switch is obviously bidirectional, so the SNU as a whole is also bidirectional. As said before, during the current ramp-up, the BPS is closed and the current flows through it only. When the plasma breakdown is required, the hybrid switch is opened. The sequence is reported in Fig. 3.

Table 1. SNU Main Operational Parameters

Description	Value
Nominal Current	± 20 kA
SS Maximum conducting Current	± 23 kA
SS Maximum Interrupting Current	20 kA
Maximum Pulse Length	250 s
Minimum repetition time	1800 s
Current Interruption	Unidirectional
Rated Voltage	5 kV
Reference highest voltage for equipment (IEC 60071)	7.2 kV
SS maximum switch-on/off time	≤ 1.0 ms
SS operation accuracy/repeatability	≤ 1.0 ms
Accuracy of each breakdown resistor (at 20 °C)	±2%
Maximum variation of resistors with temperature	±10%
Number of operations without maintenance (excluding sacrificial contacts)	10000

The SCB is activated, but the current still flows in the BPS, until the mechanical contacts begin to open. Across the opening contacts, an electrical arc develops and this voltage forces the current into the activated SCB; correspondingly, the conduction voltage across the SCB (a few volts) limits the arcing voltage to some tens of volts and greatly reduces the corresponding dissipated power in the contacts.

After a time margin ensuring the completion of the current transfer and the de-ionization of the air across the BPS contacts, the SCB can be opened, producing across the resistors R1 the high voltage necessary to ignite the plasma breakdown (from a minimum of 4.4 kV to a max of 5.5 kV).

The energy ratings of resistor R1 have been designed in order to match the insertion time of about 300 ms. When the SS hybrid switch must be closed again: first the SCB is turned on and most current returns to flow through it; then the BPS contacts close, while the voltage across its closing contacts has come down to a few volts and the arc, if any, sets in when the contacts are so close that duration and energy are negligible.

IMPLEMENTATION AND TESTS RESULTS

In order to test the SCB design in the most critical conditions, concerning specifically the steady state current balance and the behavior of the devices at turn-off, two SCB modules (S/N 001 and S/N 002) were first assembled. The IGCTs and the associated decoupling diodes Dd were selected in order to obtain the worst possible situation concerning voltage drop in conduction and turn-on /turn-off delay times.

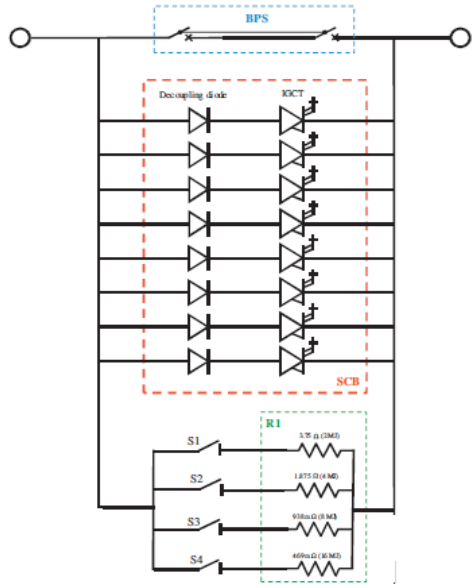

Figure 2: Functional Scheme of the hybrid SNU with emphasis on the main semiconductor components [5].

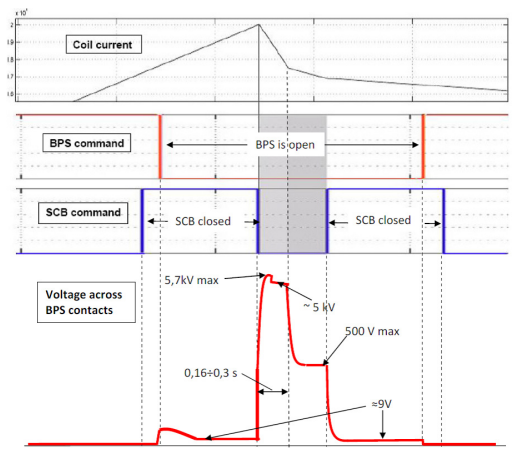

Figure 3: Operational sequence of the SS hybrid Switch, with the expected current and voltage across it.

The test circuit used a capacitor bank of 1.2 mF, which is discharged through a 70 μH inductor into the two SCB modules in parallel; the starting voltage of the capacitor bank was adjusted to achieve the desired peak current at turn-off of 4200 A. The test was first simulated using a PSIM model, which took all the circuit elements into account, including the stray inductances (Fig. 4); the waveforms resulting from the test are in very good agreement with them (Fig. 5).

ISBN 978-3-95450-181-6

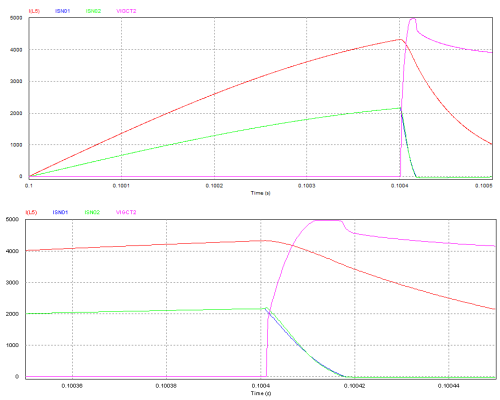

Figure 4: Simulation results of the parallel testing of the two SCB modules. Time scales: 0.1 ms /div (upper) and 20 µs/div (lower).

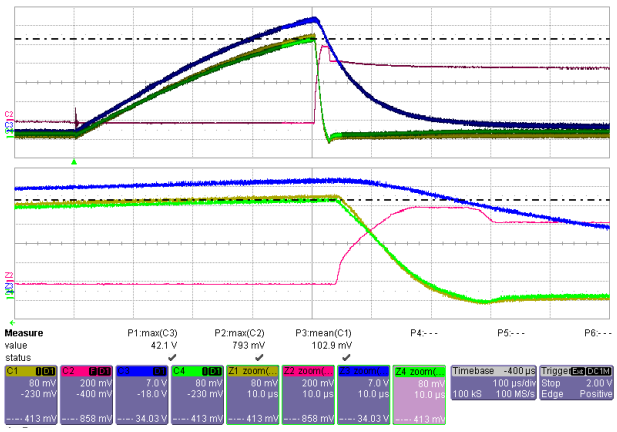

Figure 5: Test results of module 001 and 002 in par.: blue trace=total current: 700 A/div; yellow trace (S/N002), green trace (S/N001) = module current, 400 A/div; red trace = IGCT Voltage 1.25 kV/div.Time scale:0.1 ms/div and 10 µs/div [6].

The complete hybrid SNU was then built and tested. The most relevant tests were performed by inserting a complete single SNU in a PS circuit of the ENEA Frascati Tokamak Upgrade (FTU). The total inductance of this circuit is about 80 mH, and the test scenarios were adapted to perform the BPS closure at significant currents.

Fig. 6 summarizes the experimental characterizations of the BPS opening, showing the SNU voltage curves when the whole current is diverted to R1 for the two extreme cases producing 5 kV at the breakdown: the maximum nominal current 20 kA (for R1=250 mΩ) and 1333 A (for R1=3.75 Ω). At 20 kA, the measured SNU opening time was about 80 µs. Since the specific snubbers were introduced to shape the voltage derivative and the transient overshoots. Due to these snubbers, the opening is slower at lower currents. Then, the maximum possible opening time is slightly higher than that observed at 1333 A (≈700 µs), since the snubber effect is negligible at lower currents and voltages.

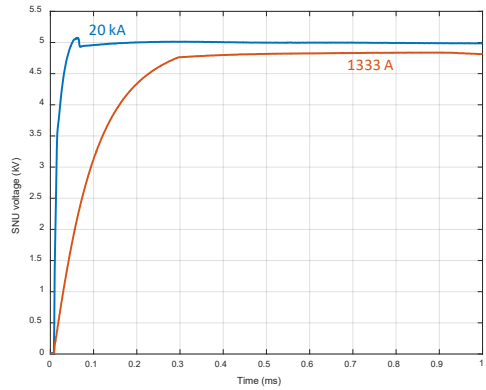

Figure 6: Voltage measured at the SCB opening during two full voltage tests (20 kA with R1=250 mΩ and 1333 A for R1≈3.75, respectively).

CONCLUSIONS AND PERSPECTIVES

A high power DC hybrid circuit breaker, capable of 20 kA for 5 minutes and able to commutate in less than 1 ms with extremely precise repeatability and low maintenance (in spite of the required 20 cycles per day) has been designed, built and tested. The overall footprint is 7.3 m x 4.2 m (excluding the local control cubicle). Four identical SNUs were then built and are now being installed.

Although designed and produced for a tokamak, possible applications include medium voltage DC networks (either naval or land based). The possibility to put several solid-state devices in series or even several static circuit breakers in series make the extension to higher DC voltages viable.

REFERENCES

[1] A. Coletti, et al., “JT-60SA power supply system”, Fusion Eng. Des. 86 (2011) 1373–1376.

[2] F. Milani, et al., “Fusion applications of large DC-current interruption units”, Fusion Sci. Technol. 61 (January (1T)) (2012) 83–88.

[3] E. Gaio, et al., “Final design of the quench protection circuits for the JT-60SA superconducting magnets”, IEEE Trans. Plasma Sci. 40.

[4] B. Roodenburg, A. Taffone , E. Gilardi, S.M. Tenconi, B.H. Evenblij, M.A.M. Kaanders, “Combined ZVS–ZCS topology for high-current direct current hybrid switches: design aspects and first measurements”, Journal of Electric Power Applications, 1, 2, 183-192, 2007.

[5] A. Lampasi, et al. A. Coletti, L. Novello, M. Matsukawa, F. Burini, G. Taddia, S. Tenconi, "Final design of the Switching Network Units for the JT-60SA Central Solenoid", Elsevier Fusion Engineering and Design, 89 (2014), 342-348.

[6] A. Lampasi, A. Coletti, L. Novello, M. Matsukawa, F. Burini, Y. Kuate Fone, G. Taddia, S. Tenconi, "Design and Implementation of Four 20 kA, 5 kV Hybrid Switching Networks for plasma ignition in the Japanese Tokamak JT-60SA", Proc. 40th IECON-2014, Pages 5036-5040.

ISBN 978-3-95450-181-6

300 kV HIGH-VOLTAGE SOURCE WITH UP TO 15 kW OUTPUT POWER

D.V. Senkov, I.A. Gusev, A.Yu. Protopopov, D.N. Pureskin, M.A. Scheglov,
Budker INP, Novosibirsk, Russia

Abstract

The presented report contains the description of high-voltage source with output voltage up to 300 kV and output current up to 50 mA. The source consist of the chopper with IGBT switches working with a principle of pulse-width modulation and the full H-bridge converter with IGBT switches, both working on programmed from 15 to 25 kHz frequency, and the high voltage transformer powering the eight-stage multiplier with the additional capacity filter at output. The transformer and multiplier both are made in common volume separated on oil tank part with silicon oil for transformer and SF6 part for multiplier. The additional capacity filter provides low ripple and noise level in working range of output currents. The source can operate in normal mode with series of high-voltage breakdown in output voltage. In the high-voltage breakdown the released in load and matching circuit energy is less than 40 J at maximum operating voltage 300 kV. The efficiency of system is more than 80% at the nominally output power 15 kW. The description of the source and the test results are presented.

DESCRIPTION

The presented source was designed for accelerator electron gun of Siberian Synchrotron and Terahertz Radiation Centre. That was reason for some specific terms like: strong reliability to high-voltage breakdown, low energy dissipated in high voltage breakdown, low voltage ripple for maximal power operation. The energy is dissipated in components of source and in the load during the high voltage breakdown less than 30 J for 260 kV operations. The basic characteristics of high-voltage source are shown in Table 1.

OVERVIEW

The circuit diagram of power part of high-voltage source is shown in Fig.1. The high-voltage source consists of the 20 kHz power converter with insulated gate bipolar transistors (IGBT) as switches (part A) and high-voltage transformer with the four-stage multiplier (part B). The power converter consists of 3-phase rectifier VD1, electromagnetic (EMI) filter F1, switch SW1, rectifier's filter capacitors C1-C2, 20 kHz chopper with IGBT switch Q1, 20 kHz inverter with IGBT switches Q3-Q6, output filter circuit L2 C5 C6, and isolation transformer T1.

Input Rectifier

EMI filter is used to eliminate high-frequency noise to the power line from the source. 3-phase rectifier and filter C1-C2 is used to convert input AC 3-phase voltage 380 V 50 Hz to DC-link 550-600 V voltage. Contactor SW1 consists of 2 groups of contact: the first is used for soft start of converter and another is used for normal operations.

Table 1. Basic Characteristics of High-Voltage Source

Parameter	Unit			
		Min	Nom	Max
Output voltage	kV	10	260	300
Output current	mA		15	50
Output power	kW			15
Voltage ripple (full load)	%			0.2
Long term stability	%			0.1
Transient time	ms		50	
Converter frequency	kHz	15	20	25

Chopper

The chopper switch Q1 is operated with principle of pulse-width modulation on programmed from 15 kHz to 25 kHz frequency synchronously with inverter. The output voltage of chopper is changed from 10 to 450 volts DC by control circuit to obtain the required output high voltage of source.

Inverter

Full-bridge inverter Q3-Q6 converts DC voltage from chopper's capacitors C3-C4 to AC voltage with programmed from 15 to 25 kHz frequency.

Filter Circuit

The matching circuit consists of elements C5 and L2 and low pass filter L2 C6 are used for minimizing transient process and for improving efficiently of design. The matching circuit is used for protection reasons. When there is a high voltage breakdown or over current the matching circuit limits the rate of current rise in the inverter. Magnetising inductance of high voltage transformer, its capacitance calculated to primary side in parallel with C6 and the matching circuit organize low-pass filter for all high harmonics of inverters rectangular waveform voltage. That way, sinusoidal voltage is feed in the high-voltage transformer, because all high harmonics are filtered. In other case, the presence of high harmonics causes power dissipation in the coils because of skin-effect. Also this harmonics can induce the singing in the winding of high-voltage transformer and this effect increases the output zero load voltage and complicates the reduction transient over voltage.

ISBN 978-3-95450-181-6

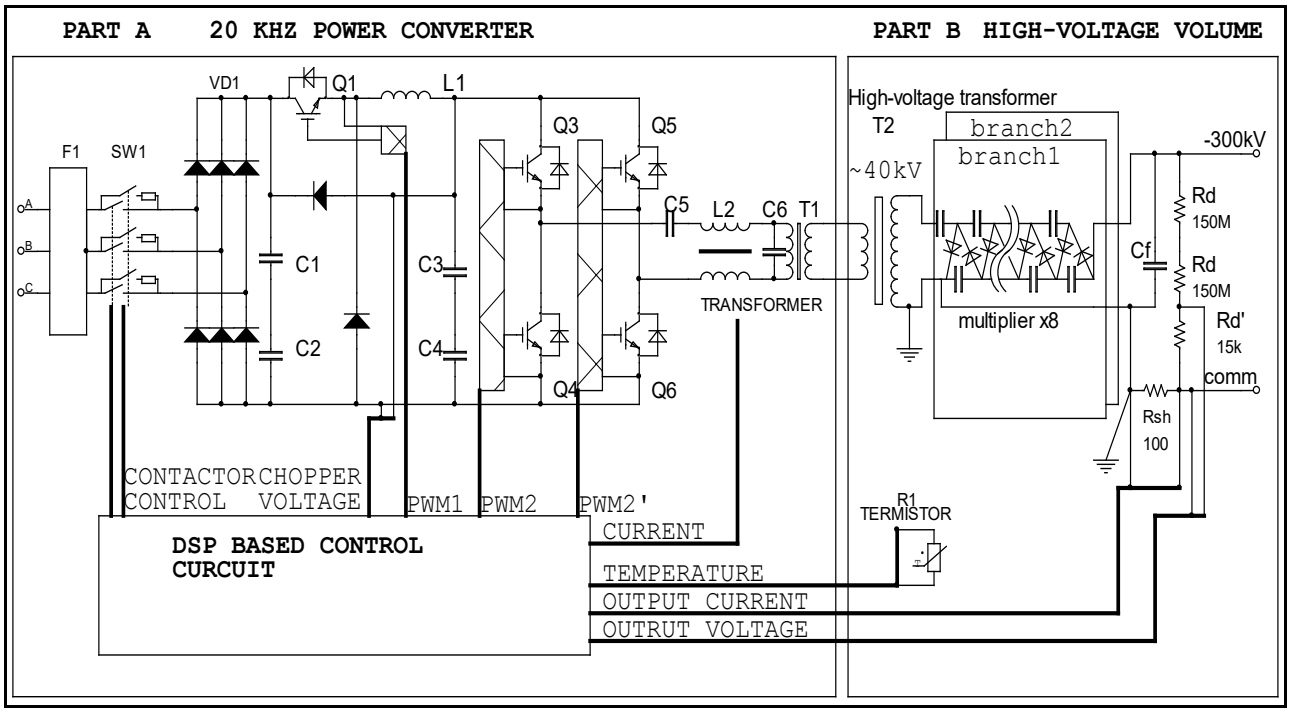

Figure 1: The high-voltage source block-diagram.

High-Voltage Transformer and Multiplier

Sectioned high-voltage transformer consists of two high voltage sections, joined in series. The nominal output voltage of transformer is 40 kV. The transformer is designed in oil-filled tank. The silicon oil [1] is used. This tank is located in the top part of high voltage volume. In the bottom part of the volume is located eight stage multiplier. The multiplier has two parallel connected brunches. Each brunch is the same.

The multiplier brunch is complete design and it includes multiplier, output filter capacitors, output current sensor and voltage divider resistors Rd, Rd`. Output filter capacity is chosen to decrease output voltage 40 kHz ripples less than ±0.1% for full load operation. The sulfur hexafluoride (SF6) is used as insulator is this part of the high voltage volume.

Design

The converter is made in one 4U and three 6U crates in the rack of 19" Euromechanics standard. There are distilled water is used for power converter elements cooling. The Fig. 2 presents converter rack view.

Control Circuit

The control circuit is realised in digital signal processor (DSP), programming logic matrix array (PLM), and analogue input buffers. The control and analogue grounds are isolated from external signals and grounds and, that way, in control circuit has obtained low noise level. It allows operation with better then 0.1% accuracy. All the IGBT switches are protected from short circuit and overcurrent. The controller measured seven analogue channels with 12-bits resolution. The controller has CAN-bus interface which is used to link with an external control system. The used data rates are 125, 250 and 500 Kbits in second. The protocol of CAN-bus interface is compatible with devises produced in the BINP [2]. This controller circuit is an improved development of previous version used high voltage source [3].

Protections and Interlocks

There are two level of overcurrent protection: programmable and circuitry one. Rigid protection has a 55 mA threshold level, if the output current increases up to 55 mA or higher the all converter switches OFF. The programmable threshold level is tunable. If output current is higher then programmable threshold level (from 5 to 55 mA) the converter first tries to limit current on this level than in case of failure all converter switches OFF. Switching OFF time is less then 50 ms. The converter tries to switch on output voltage after 100 milliseconds with rise speed 100 V/ms. High-voltage transformer protection measures the temperature of transformer and the transformer's input current. In case the input current of transformer rises up to 250 A that matter the short circuit in transformer. In this case the converter is OFF.

RESULTS

The high-voltage source was designed tested and now it operates with 300 keV electron gun at Siberian Synchrotron and Terahertz Radiation Centre. The tests are shown high reliability, efficiency better than 85% for full load operations. The long time stability of output voltage was better than 0,1% at 260 kV output voltage.

ISBN 978-3-95450-181-6

Figure 2: Power converter rack.

REFERENCES

[1] http://www.sofex.ru/pdf/SOFEXIL-TCJ.pdf. Transformer fluid technical manual.

[2] V. R. Kozak, M. M. Romakch "The devices vith CANBUS interface for automatic control systems of physical complexes" pre-print BINP 2004-68, 2004.

[3] I.A.Gusev, A.S.Medvedko, A.Yu.Protopopov, D.N.Pureskin, D.V.Senkov. "High-Voltage Source with Output Voltage up to 110 kV with Output Current up to 100 mA", Proceedings of RUPAC2012, Saint-Petersburg, Russia, 2012, P506.

ISBN 978-3-95450-181-6

HIGH-PRECISION RAMPED HIGH-VOLTAGE SOURCE WITH UP TO 50 kV OUTPUT VOLTAGE

D.V. Senkov, I.A. Gusev, A.A. Zharikov, A.M. Batrakov, A.Yu. Protopopov,
Budker INP, Novosibirsk, Russia

Abstract

This report describes the precision high-voltage ramped high-voltage power system. The output voltage up to 50 kV with 10 ppm precision. The power system consists of the 3 kW high-voltage source based on multiplier, precision high-voltage divider with digital interface and high-voltage discharge switch to provide low ramp-down time for output voltage. The power system is planned to use in the NIKA booster electron cooler project. The description and test results are presented.

DESCRIPTION

The presented source was designed as part of electron cooler for booster ring of NIKA project (JINR, Dubna). The booster operating circle scenario is shown on Fig. 1. The electron cooling is planned to use at the injection plato and at the extraction plato. That was reason for some specific terms like: low transient process time after voltage increase, high voltage stability (10 ppm) in the full range of output voltage. The high-voltage terminal (see cooler electrical diagram Fig. 2) is the sourse of 2-3 mA current ripples at 150 and 300 Hz. So the high-voltage source have to suppress load voltage variation generated by this ripples to the 10ppm level. The basic characteristics of high-voltage source are shown in Table1.

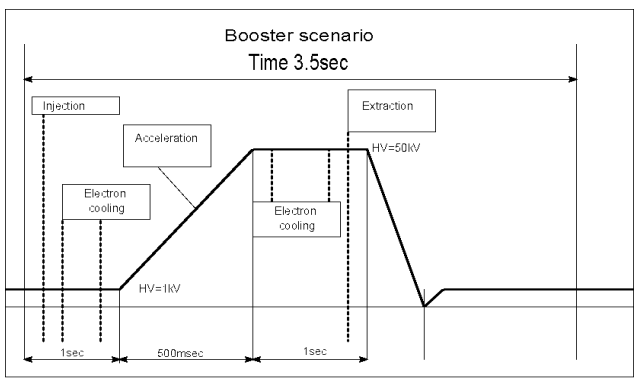

Figure 1: Booster operating cycle scenario.

Overview

The high-voltage source consists of the 20 kHz power converter, high-voltage transformer with the two-stage multiplier (part B) the separate precision high-voltage divider with digital output (Part C) and the ripple suppressor (Part D). The power converter with high-voltage multiplier generates 0-50 kV output voltage. The precision high-voltage divider is used for feedback loop. The analogue ripple suppressor is used to decrease output voltage variations at 150 and 300 Hz caused by the external (from load) current ripples. The suppressor increase effective gain of feedback system at these frequencies.

Table 1. Basic Characteristics of High-Voltage Source

Parameter	Unit			
		Min	Nom	Max
Output voltage	kV	0.5	50	55
Output current	mA		0.2	10
Output power	kW			3
Voltage ripples(nom load)	ppm			10
Long term stability	ppm			10
Transient time	ms		100	
Converter frequency	kHz		20	

Power Converter

The power converter uses two DC-link stage to decrease voltage ripples. First AC-DC converter supply its output with stabilized 50 VDC voltage. The boost stage can increase this voltage to level 50-250 V in depends on specified power source output voltage. This boost stare feeds the 20 kHz full-bridge inverter operates with PWM modulation to precision regulate the output voltage.

High-Voltage Transformer and Multiplier

Sectioned high-voltage transformer consists of two high voltage sections, joined in series. The nominal output voltage of transformer is 30 kV. The multiplier has two parallel connected brunches. Each brunch is the same.

The multiplier brunch is complete design and it includes multiplier, output filter capacitors, output current sensor and protection system voltage divider resistors. Output filter capacity is chosen to decrease output voltage 40 kHz ripples less than ±0.01% for full load operation, and 10ppm ripples at nominal output current. The silicon oil [1] is used as insulator the high voltage volume.

High-Voltage Divider

The separate precision high voltage divider is used for feedback system. This divider is located is separate oil tank heated to 40 °C. Its consists of two independent divider with and precision ADC board. The fiber link is used for output voltage data transmit to power source feedback system. In addition, the voltage information

ISBN 978-3-95450-181-6

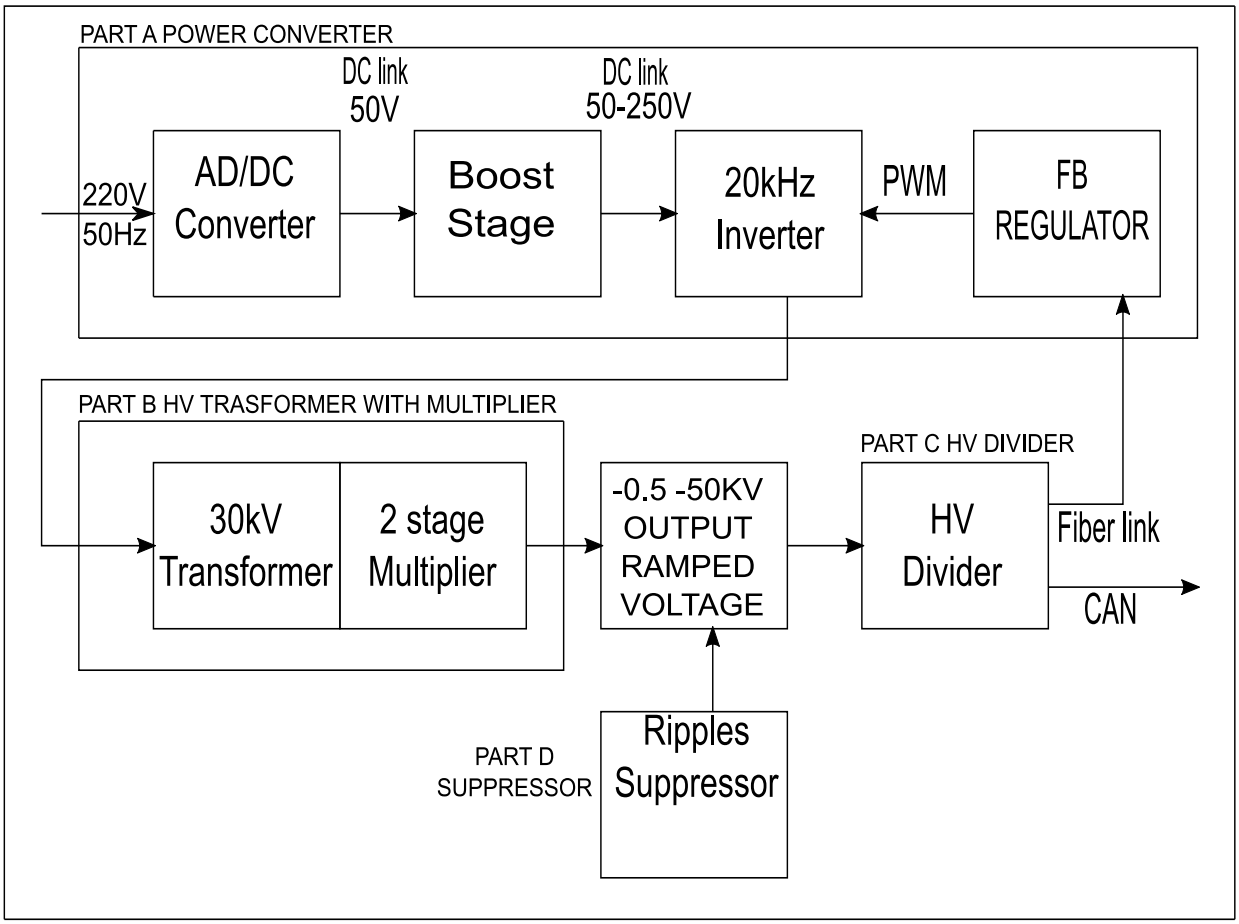

Figure 2: The high-voltage source block-diagram.

controller send with CAN-bus interface the cooler control system. The used data rates are 125, 250, 500 and 1000 Kbits in second. The protocol of CAN-bus interface is compatible with devises produced in the BINP [2].

Ripples Suppressor

During the tests was discovered that the cooler high-voltage terminal produce the 2-3 mA current ripples with 50, 150 and 300 Hz frequencies (Fig.3). The power converters feedback system dynamic diapason cants decrease the high-voltage terminal voltage variations, produced by this ripples the 10 ppm level. So the additional suppressor was designed and tested. This suppressor operates at injection and extraction plato and increase effective gain twenty thirty times depends on frequency.

Design

The high voltage source is made in one 4U crate in the rack of 19" Euromechanics standard, two high-voltage volumes with oil isolation, one for multiplier and one for high-voltage divider and separate suppressor located near the load. The high-voltage divider operates with heated to 40°C oil to the compensate ambient temperature variation.

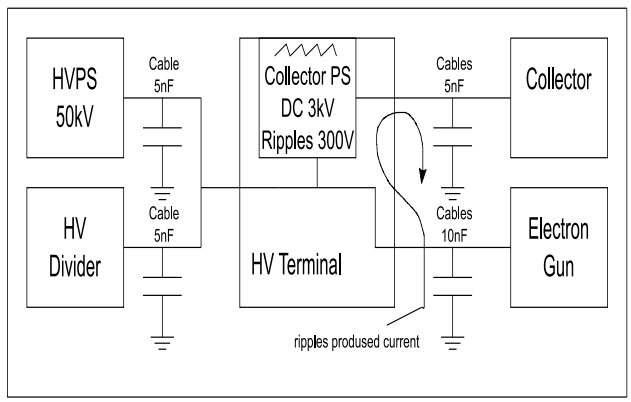

Figure 3. The Cooler high-voltage terminal.

RESULTS

The high-voltage source was designed tested and now it ready to use at JINR. The tests are shown high reliability, long term stability better than 5 ppm and voltage ripples level less than 10ppm during the operating cycle (see fig. 4).

ISBN 978-3-95450-181-6

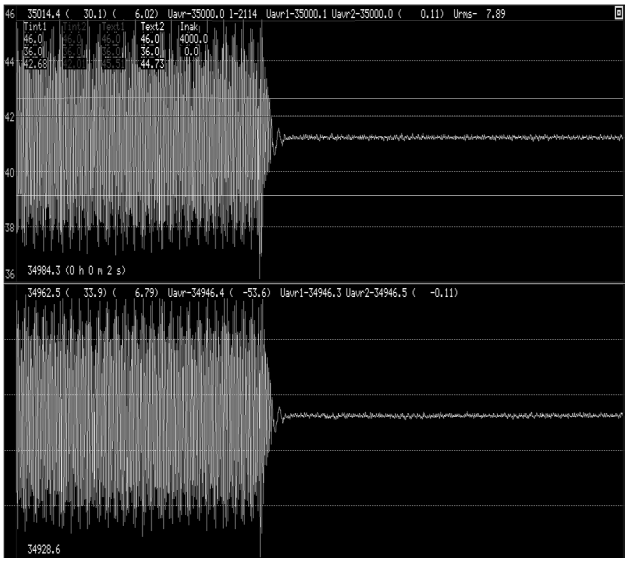

Figure 4: Suppressor operates. Decrease Cooler HV terminal voltage ripples from 100 ppm to 10 ppm.

REFERENCES

[1] http://www.sofex.ru/pdf/SOFEXIL-TCJ.pdf. Transformer fluid technical manual.

[2] V. R. Kozak, M. M. Romakch “The devices vith CANBUS interface for automatic control systems of physical complexes” pre-print BINP 2004-68, 2004.

ISBN 978-3-95450-181-6

POWER SUPPLIES FOR IHEP NEGATIVE HYDROGEN IONS SOURCE

B.A. Frolov, National Research Centre "Kurchatov Institute" State Research Center of Russian Federation – Institute for High Energy Physics, Protvino, Moscow Region, Russia
V.S. Klenov, V.N. Zubets, Institute for Nuclear Research, Russian Academy of Science, Moscow, Russia

Abstract

The source of negative hydrogen ions is constructed at IHEP for the implementation of multiturn charge-exchange injection to increase the intensity of IHEP buster. Surface-plasma ion source (SPS) with Penning discharge is selected as source of H-minus ions. A set of power supplies for SPS which includes the extraction voltage power supply, the discharge power supplies, the hydrogen gas pulse valve power supply, cesium oven and cesium storage device temperature controllers was designed, constructed and tested on the equivalent loads. This set of power supplies will allow to commission and test the ion source with the beam extraction energy up to 25 keV and repetition rate of 25 Hz.

INTRODUCTION

For injection into IHEP LU-30 RFQ the source of H-minus ions should generate the beam with current not less than 50 mA, pulse duration up to 200 mks, repetition rate - 25 Hz, normalized rms emittance no more then 0,25 mm*mrad, e/H^- ratio < 5 providing a long-term stability and reproducibility of the parameters [1]. To provide these requirements surface-plasma ion source based on the Penning discharge cell with an axially symmetric emission aperture the two-stage system of cesium supply and pulsed gas valve is developed.

A power supply system which includes the extraction voltage power supply, the Penning gas discharge power supplies, the hydrogen gas pulse valve power supply, cesium oven and cesium storage device temperature controllers should provide the operation of the ion source.

GAS DISCHARGE POWER SUPPLIES

Gas discharge power supplies must provide the ignition of discharge, burning high-current pulsed glow discharge with a current up to 150 A in the conditions when the internal resistance of the discharge is less than 1 ohm with pulse durations of 25 up to 200 microseconds and pulse repetition rate of 25 Hz.

Gas discharge power supply consists of the following components: a thyristor unit, transistor unit, power supply, isolation transformer. The external view of the front panel is shown in Fig. 1.

Thyristor unit generates pulses with fixed amplitude of 800 V. These pulses are applied through the 30 ohms limiting resistance to the primary winding of the output isolation transformer for "ignition" of the high-current discharge which afterwards is picked up by the stabilized current of the transistor block.

Transistor unit generates amplitude-adjustable powerful current pulses with the stabilization on pulses top in the primary winding of output isolation transformer. The regulating element is the transistor MG400H1FK1.

Power supply unit is the power source for the transistor unit with the ability to turn off on the "alarm" signal received from the transistor unit. The power supply unit provides also the voltage for ± 12 V transistor and thyristor units.

Thyristor unit, transistor unit and power supply unit are designed in the same construction design «Vishnya»

Figure 1: General view of the gas discharge power supplies.

Discharging current generator prototype tests on the equivalent load were carried out. The 0.5 Ohm, 1 Ohm, 3 Ohms resistances of appropriate power were used as equivalent load. Tests were conducted at the pulses repetition rate of 25 Hz. The waveform of the output current on resistance of 1 Ohm is shown in Fig.2.

Tests of the gas discharge power supplies prototype were also conducted when working with the H-minus ion source of injector INR RAS linac. The waveforms of the ion source operating parameters are shown in Fig.3. The top beam (blue) is the voltage at the discharge, the lower beam (yellow) is the discharge current.

These tests demonstrated the ability of gas discharge power supply to provide the required parameters in various modes of source operation including the discharge ignition, the transition to a low-voltage (cesium) regime and work in conditions of intensive breakdowns in the 15 kV extraction gap.

ISBN 978-3-95450-181-6

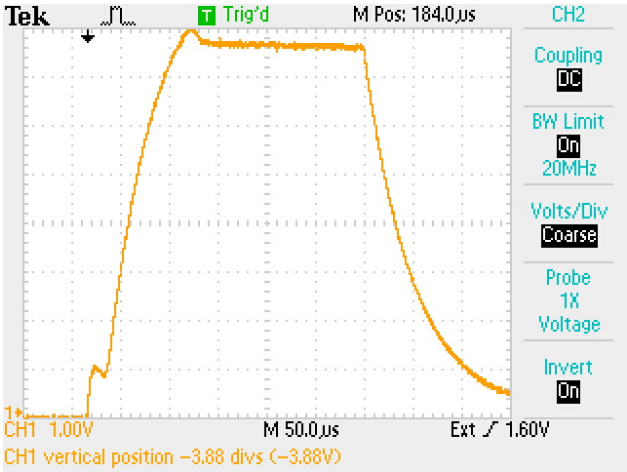

Figure 2: The output current of gas discharge power supplies. Vertical scale – 20 A/div, horizontal scale – 50 µs/div.

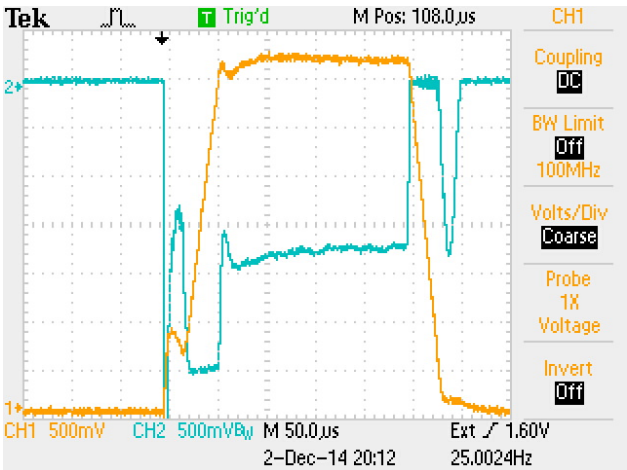

Figure 3: The oscillograms of voltage and discharge current of the H-minus ion source. The top beam (blue) is the voltage at discharge, 50 V/div. The lower beam (yellow) is the discharge current, 10 A/div. Horizontalscale - 50 µs/div.

GAS VALVE POWER SUPPLY UNIT

Gas valve power supply unit is designed for pulsed opening of solenoid valve for hydrogen gas feed into the discharge chamber of the H-minus ion source. This unit should provide the valve actuations with the pulse repetition rate of 25 Hz and should give the current pulses with the adjustable value of 50 A, duration of about 200 µs and stability no worse than ± 0,5%. The unit can control output current from the external reference of 0...+ 5 V value (with conversion scale 1V/10 A) and with the potentiometer installed on the gas valve power supply unit front panel.

The unit provides the current pulses monitoring through the valve with a scale of 1V/10 and the valve voltage monitoring with scale 1 V/10 V. This unit power consumption does not exceed 20 W with the network supply of 220 V 50 Hz.

The designed prototype was tested on the equivalent load (the resistance value of 1 Ohm) and on the acting gas valve. The current waveform for the unit tested on the acting gas valve is shown in Fig.4.

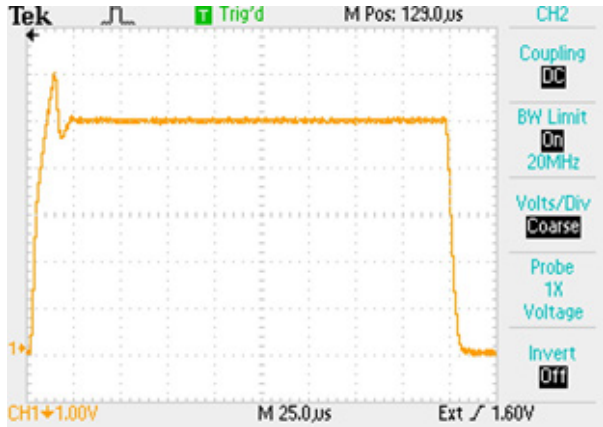

Figure 4: The waveform of the valve power supply output current. The vertical scale is 10 A/div, horizontal scale – 25 µs/div.

EXTRACTION VOLTAGE POWER SUPPLY

Extraction voltage power supply should provide pulses of the voltage amplitude Uo = 0 ... 25 kV with the extraction voltage instability no worse than ± 0,5 kV and the pulse repetition rate of 25 Hz. The extraction voltage power supply must withstand operation with frequent (continuous) breakdowns in the extraction gap at the current limitation less than 1 A in the breakdowns. The extraction voltage pulses of the 25 kV amplitude are formed at the pulse step-up transformer output at the forming line discharge with a characteristic impedance of 40 Ohms through the thyristor in the primary winding of the transformer. The transformer was made on the core with cross-section 25 cm2 with the number of turns in the primary winding W1 = 72 turns, in the secondary winding W2 = 2100 turns.

Output pulse amplitude stabilization is provided by capacitive – diode limiter made on 2 capacitors K75-15 with the capacitance of 0.1 µF connected in parallel, and 2 diodes КЦ201Е connected in series which are charged from the reference voltage rectifier to 25kV.

The short-circuit current magnitude on the load in this scheme is limited by the characteristic impedance of the forming line in the primary circuit. For the selected parameters of the characteristic impedance of 40 Ohm and the transformation ratio k = 29, the short-circuit current does not exceed 0.75 A in the secondary circuit.

The extraction voltage power supply consists of two units: thyristor unit and transformer unit. A thyristor unit contains the forming and the switching thyristor with a thyristor triggering device. The thyristor triggering device provides also the interlocking function. The transformer unit contains a pulse step-up transformer with the

ISBN 978-3-95450-181-6

secondary voltage pulse amplitude of 25 kV and the capacitive – diode limiter of output voltage.

The tests of extraction voltage power supply were conducted at the pulse repetition rate of 25 Hz and the load resistance value of 100 kOhms. The waveforms of the extraction voltage output pulses are shown in Fig. 5 and Fig. 6. The waveforms in Fig. 5 shows that the amplitude of the output pulse is 25 kV.

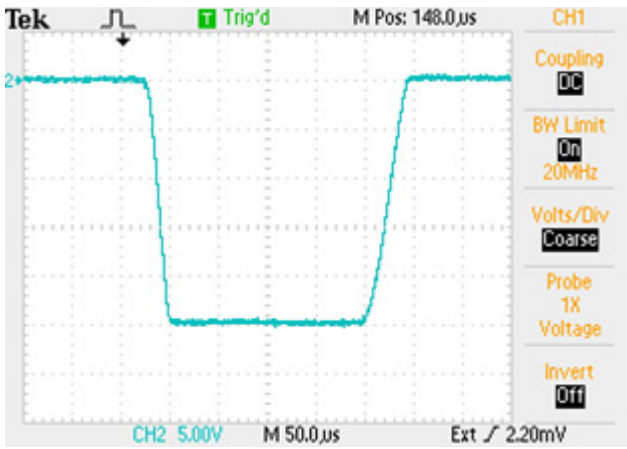

Figure 5: The waveform of the output pulse of extraction voltage power supply. Vertical scale - 5 KV/div, horizontal scale - 50 µS/div.

The pulse top in scale 500 V/div. given in Fig.6 shows that the instability of pulse peak is 200 V, or ± 100 V. This value of instability completely satisfies the requirements for the negative ion source power supply system.

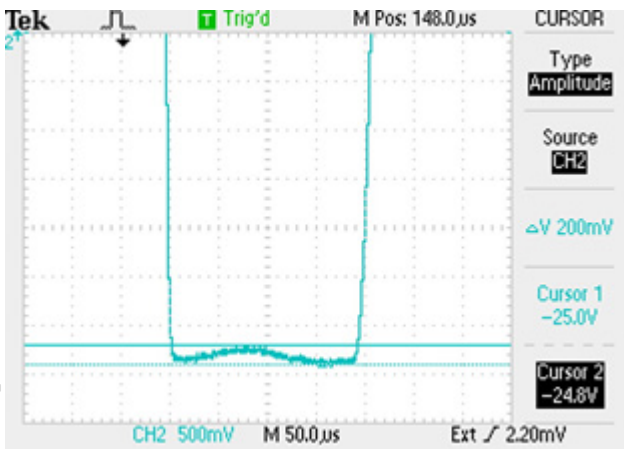

Fig. 6. Waveform of the output pulse top of extraction voltage power supply. Vertical scale - 500 V/div, horizontal scale - 50 µS/div.

CESIUM SUPPLY CONTROL SYSTEM

Cesium supply control system consists of two blocks. The first block controls the heater of the reservoir with cesium dichromate and titanium mixture and second controls heater of the cumulative volume in which the metal cesium predetermined vapor pressure is maintained directly at the gas-discharge entrance of H-minus ion source The heating of reservoir with tablets of cesium dichromate is performed up to the temperature that ensures the cesium dichromate decomposition and the metallic cesium release in the form of vapors to enter in the cumulative volume.

Tests on maximum current were performed on load equivalent – active resistance equivalent to the resistance of the heater element in the heated state. The tests were performed in long mode corresponding to the mode of cesium output in the gas discharge which has the time interval to two hours. During the tests load current instability did not exceed ± 0,4% with the input voltage change in the range 198...242 V.

CONCLUSION

The designed, constructed and tested ion source power supplies form the union required for autonomous operation of the H-minus ion source and beam generation with ion energy up to 25 keV and repetition rate 25 Hz.

REFERENCES

[1] B.A.Frolov, V.S.Klenov, V.N.Mihailov, O.M. Volodkevich «SIMULATION AND OPTIMIZATION OF ION OPTICAL EXTRACTION, ACCELERATION AND H- ION BEAM MATCHING SYSTEMS», Proceedings of RuPAC2014, THPSC46, Obninsk, Russia, pp.429-431.

ISBN 978-3-95450-181-6

THE STUDY OF THE ELECTRICAL STRENGTH OF SELECTED INSULATORS WITH A DIFFERENT SHAPE OF THE SURFACE

Ya.A. Kolesnikov#, A.A. Gmyrya, D.A. Kasatov, A.M. Koshkarev, A.S. Kuznetsov, A.N. Makarov, E.O. Sokolova, I.N. Sorokin, I.M. Shchudlo, S.Yu. Taskaev, Budker Institute of Nuclear Physics, SB RAS, Novosibirsk, 630090 Russia

Abstract

In the BINP SB RAS was proposed and created a source of epithermal neutrons for BNCT. The proton beam obtained on a tandem accelerator with vacuum insulation. Sectionalized demountable feed through insulator is an integral part of the accelerator. Voltage from the high voltage source distributed to the electrodes via resistive divider. Because of the small amount of current (hundreds of microamperes) flowing through the divider, dark currents that occur in the accelerating gaps, can significantly affect the uniform distribution of the potential along the accelerating channel, and, consequently, on the beam transportation. Therefore there is a need to change the design of the feed through insulator which will allow to set potentials at the electrodes directly from the high voltage rectifier sections.

To study the feasibility of such changes has been designed and built an experimental stand, in which a single insulator with double height subjected to the same conditions as in accelerator. On the experimental stand was studied electrical strength of ceramic and polycarbonate insulators with a different shape of the surface. The paper presents the results of experimental studies of insulators. Their application will get rid of the voltage divider inside the feed through insulator and realize the scheme which allows to set potential on the electrode gaps directly from the rectifier section. This will increase the operating voltage of the accelerator and its reliability.

INTRODUCTION

In 1998, for high-current proton beams BINP proposed a new type of accelerator - tandem accelerator with vacuum insulation. At present, on the accelerator neutron source there were conducted various experiments for the development of Boron Neutron Capture Therapy (BNCT) [1]. The principle of BNCT technique is simple and elegant: a boron-containing agent is injected in patient's blood, and then part of the body with tumor is irradiated with neutrons. During the nuclear reaction $n(^{10}B, ^{7}Li)\alpha + \gamma$ most of the energy (84%) is allocated within $3 \div 10$ μm, which matches with the size of the mammalian cells. Illustration of BNCT idea is presented in Figure 1.

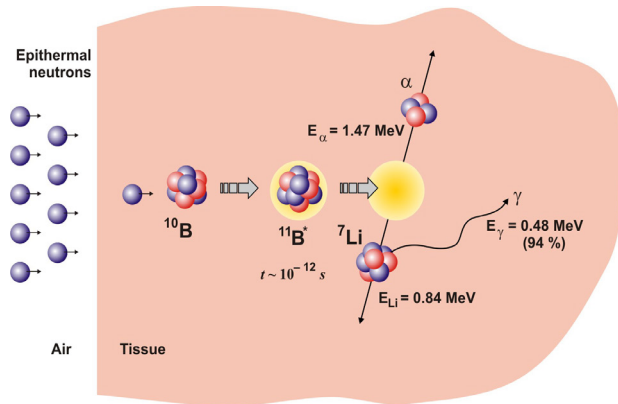

Figure 1: Principle of BNCT.

DESIGN OF THE ACCELERATOR

Figure 2 presents the scheme of the tandem accelerator with vacuum insulation. The outgoing beam from the source of negative hydrogen ions *1* with 23 keV energy and 5 mA current is rotated by 15° in a magnetic field , focused by a pair of magnetic lenses *2*, injected into the accelerator and accelerated up to 1 MeV. In the argon stripping target *7*, mounted inside the high voltage electrode *5*, negative hydrogen ions are converted into protons. Then protons are accelerated by the same potential 1 MV up to 2 MeV. The potential at the high voltage electrode *5* and five intermediate electrodes *6* of accelerator supplied from the high voltage source *10* using a feedthrough insulator *9*, wherein the ohmic divider is installed. Pumping of the gas is maintaining by turbo-molecular pumps *8* installed on the ion source chamber and at the exit of the accelerator, and a cryogenic pump *4* via jalousies [2].

Accelerator produces a stationary proton beam with 2 MeV energy and 5 mA maximum current with 0.1% high energy monochromaticity and 0.5% current stability [3]. On the accelerator the generation of neutrons is achieved and the effect of neutron radiation on cell cultures is studied [4]. For the therapy it is necessary to increase the voltage up to 1.15 MV and is desirably to increase proton beam current to the value 10 mA.

Figure 3 shows one of the main elements of the accelerator – sectioned assembled feedthrough insulator using which voltage from the high voltage rectifier is applied to the central electrode and the intermediate electrodes.

#i.kolesnikov@g.nsu.ru

ISBN 978-3-95450-181-6

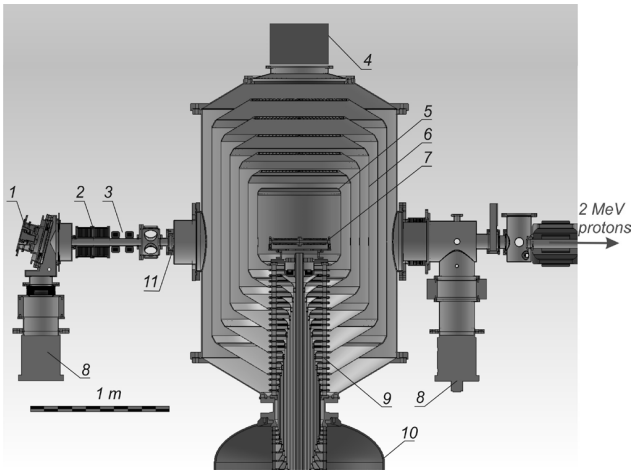

Figure 2: Tandem accelerator with vacuum insulation: *1* - source of negative hydrogen ions, *2* - magnetic lenses, *3* - correctors, *4* - cryogenic pump, *5* - high voltage electrode, *6* - intermediate electrodes, *7* - the gas stripping target, *8* - turbo molecular pump, *9* – feedthrough insulator, *10* – high voltage source, *11* - inlet diaphragm.

The insulator is situated outside of the beam accelerating channel. The insulator consists of two parts - a SF_6 gas-filled (bottom) part, and vacuum (top) part.

The top part of the feedthrough insulator assembled from 24 circular glass insulators, vacuum-tightly fastened together with intermediate electrodes through the rubber seals. Height of the glass rings is 35 mm.

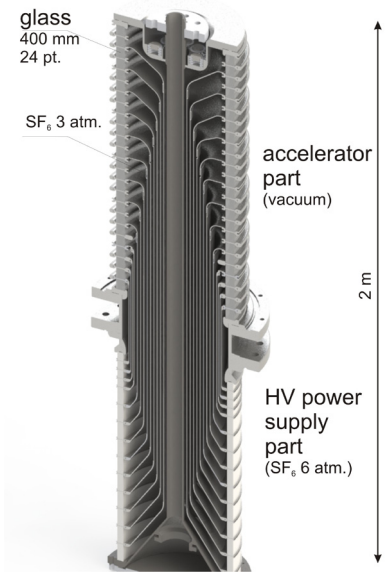

Figure: 3: Scheme of the high-voltage feedthrough insulator.

The bottom gas part of the feedthrough insulator, located in the tank of high-voltage rectifier, consists of 14 ceramic rings glued with their electrodes. The height of the ceramic rings are 30 and 60 mm. The diameter of the ceramic rings as the diameter of the glass rings is about 400 mm.

The potential distribution on the electrodes is set by a resistive divider located inside the top and outside of the bottom part of the feedthrough insulator using a system of inner coaxial cylinders, connecting the electrodes with the equal potential gas and vacuum parts of the feedthrough insulator.

The potential distribution on the electrodes of the vacuum insulator, which are not electrically connected with the coaxial tubes is set by resistors, located inside the vacuum part of the feedthrough insulator.

Dark currents in the accelerating gaps can significantly affect on the uniform distribution of the potential in the accelerating gaps, and, consequently, on the beam transportation, due to the use of low power voltage divider and low value of the current (hundreds of microamperes), flowing through the divider.

EXPERIMENTAL STAND

The aim of experiments was to study the electrical strength of the double-heighted (73 mm) insulators, made of different materials (polycarbonate and ceramics), and various outer surface shapes (ribbed and smooth) an experimental stand was created (Figure 4).

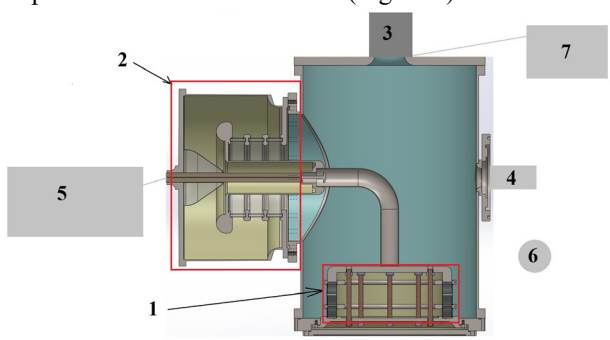

Figure 4: The scheme of the experiment: *1* - test module, *2* - high voltage input, *3* – turbomolecular pump, *4* - vacuum gauge, *5* - high voltage source, 6 – spherical dosimeter, 7 - backing pump.

Test module *1*, which contains an insulator, situated inside the vacuum volume. Voltage on insulator is put on by high voltage source 5 through the input *2*. Vacuum system *3, 4* and *7* provides necessary conditions as in vacuum insulated tandem accelerator.

The major aim of experiments is to study the electrical strength of insulators and possibility of one hour exposure without breakdowns at 100 kV.

RESULTS OF EXPERIMENTS

The first training session of smooth ceramic insulator have been running for 3 hours and ended at 105 kV. During this time there were about 220 breakdowns, more than half of which were in the range from 83 to 95 kV. Subsequent training gives as a result exposure over 1.5 hour of the insulator at a voltage of 100 kV (corresponding to the electric field strength of 13.7 kV/cm).

ISBN 978-3-95450-181-6

A month later, a second experiment was conducted with the insulator. Raising the voltage to 104 kV lasted 20 minutes, as shown in Figure 5. It is 9 times faster than the first training. Considering the time of voltage rise, insulator stood for about an hour without breakdowns. Voltage rise rate was 1 kV/min. At each step power of X-ray radiation dose increased, and by the end of minute fell to 0.5 μSv/h. This is shown in Figure 6.

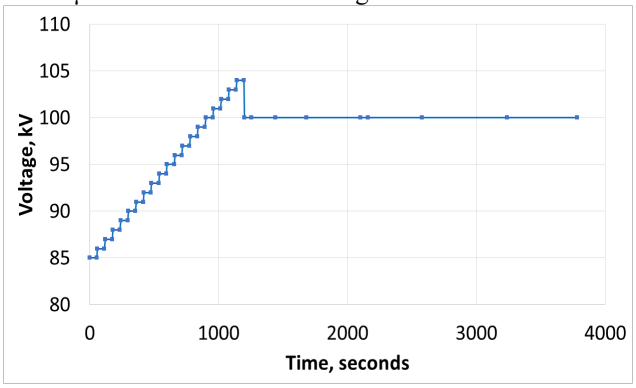

Figure 5: The dependence of voltage from time while training and exposuring of smooth ceramic insulator at 100 kV voltage.

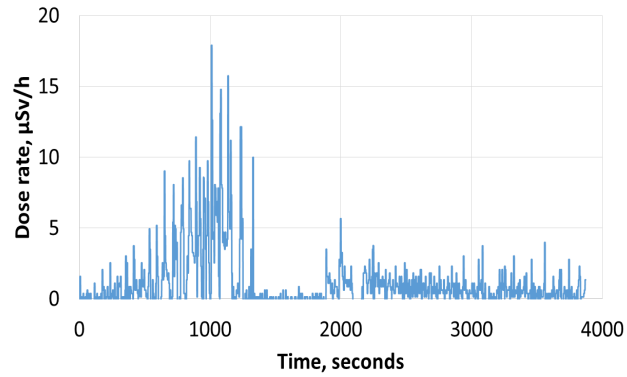

Figure 6: The dependence of the dose rate from time while training and exposuring smooth ceramic insulator at 100 kV voltage.

The second series of experiments has been carried out with a ribbed ceramic insulator. In 40 minutes of training voltage raised up to 83.2 kV. After a 40-minute of break in 15 minutes 100 kV was achieved. Next training gave 110 kV on insulator in 20 minutes. Insulator stood for 80 minutes without breakdowns at a voltage of 100 ÷ 105 kV. This is shown in Figure 7.

The third series of experiments has been conducted for ribbed polycarbonate insulator. The first training session was held to 105 kV for 30 minutes. Figure 8 shows decreasing of radiation over time while exposuring of the insulator at a voltage of 100 kV during an hour. Also, the vacuum level in these experiments was 10 times higher, than in experiments with ceramic insulators.

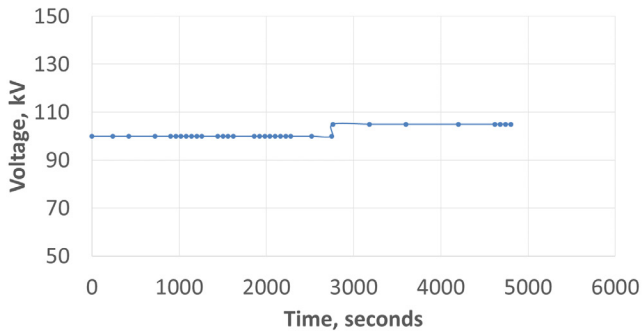

Figure 7: The dependence of voltage from time for training and exposure of ribbed ceramic insulator at 100÷105 kV voltage.

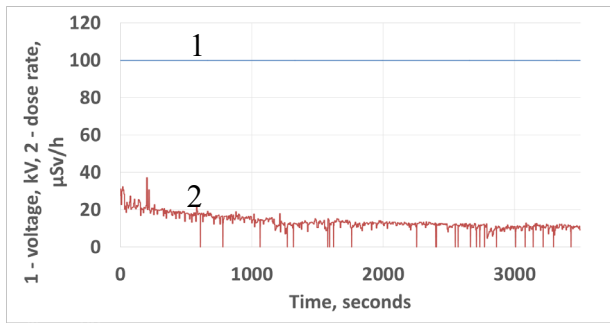

Figure 8: The dependence of the voltage and dose rate from time while training and exposuring ribbed polycarbonate insulator at 100 kV voltage.

CONCLUSION

Experiments showed, that the best double-height insulator for a tandem accelerator is ceramic insulator with a ribbed outer surface, because its reliability higher, than reliability of others insulators.

Polycarbonate insulators with ribbed inner surface can be used in new scheme of feedthrough insulator also, but then it should be upgraded the vacuum pumping.

ACKNOWLEDGMENT

This work was supported by the Ministry of Science of the Russian Federation, unique identifier of applied research RFMEFI60414X0066.

REFERENCES

[1] W. Sauerwein et al., *Neutron Capture Therapy. Principles and Applications*, (Springer, 2012), 553.
[2] B. Bayanov et al., Nucl. Instr. Meth. Phys. Research 413 (1998) 397.
[3] A. Ivanov et al., Jour. Instr. 11 (2016) 4018.
[4] O. Volkova et al., Jour. Rad. 97 (2016) 283.

ISBN 978-3-95450-181-6

OBTAINMENT OF 5 mA 2 MeV PROTON BEAM IN THE VACUUM INSULATION TANDEM ACCELERATOR*

I. Shchudlo#, D. Kasatov, A. Koshkarev, A. Makarov, Yu. Ostreinov, I. Sorokin, S. Taskaev,
BINP and Novosibirsk State University, Novosibirsk, Russia

Abstract

In BINP the neutron source for BNCT based on proton accelerator was designed and built. It is necessary for the therapy to ensure a stable proton beam current of not less than 3 mA with energy 2 MeV. During the injection of negative hydrogen ion beam into the accelerator the unwanted charged particles are produced, affecting the stability of beam parameters. The article describes methods of suppression of undesirable charged particles and the results of experiments.

INTRODUCTION

Boron-neutron capture therapy (BNCT) [1] is a promising method of malignant tumours treatment. For implementation the technique in clinical practice the accelerator based compact epithermal neutron sources with energy of protons from 2 to 3 MeV and a current at least of 3 mA are required. To solve this problem in BINP a new type of particle accelerator was proposed and developed – vacuum insulation tandem accelerator. In the accelerator construction the high rate of acceleration of ions and the insulator placed remote from acceleration channel are implemented [2]. After reducing of dark current to an acceptable level [3], optimizing of injection of negative hydrogen ion beam into the accelerator [4] and optimizing of stripping gas target [5], the proton beam current increased from initial values of approximately 140 μA [6] to a value 1.6 mA [7], stable over time more than hour. While explaining the causes of the current limitation in the acceleration channel a significant flow of electrons and the counter-flow of positive ions generated in the accelerating channel and in the stripping target were detected and measured [8]. The paper describes details of further modernization of the accelerator and presents experimental results on the suppression of unwanted fluxes of charged particles and increasing proton beam current.

EXPERIMENTAL RESULTS

Scheme of the vacuum insulation tandem accelerator is shown at Fig. 1. Negative hydrogen ion beam with an energy of 23 keV and current of 6 mA leaves the source *1*, after that it is rotated in magnetic field at an angle of 15°, focused by a pair of magnetic lenses *2*, injected into the accelerator and accelerated to an energy of 1 MeV. In the gas (argon) stripping target *7* mounted inside the high-voltage electrode *6*, negative hydrogen ions are converted into protons, which are accelerated to an energy of 2 MeV by the same potential. To the high-voltage *6* and five intermediate electrodes *5* the potential is supplied from a high voltage power supply (sectional rectifier) *9* (most of the source is not shown) through the insulator with resistive divider *8*. Turbo molecular pumps *10* installed in the ion source chamber and in the output of the accelerator, and a cryogenic pump *4* through the blinds in high-voltage electrodes provide vacuum pumping.

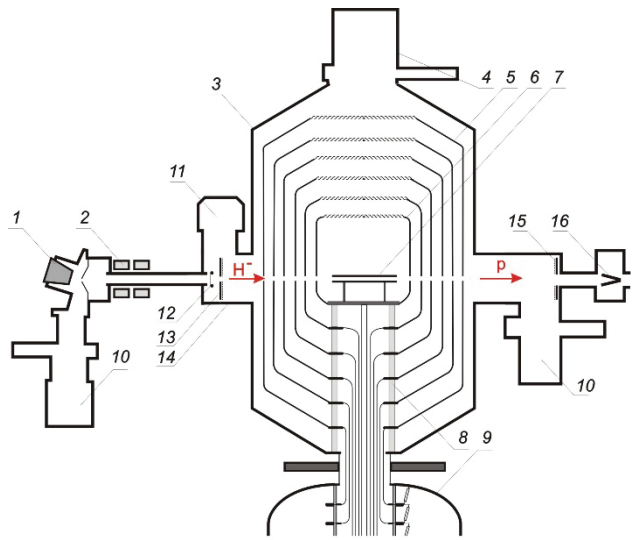

Figure 1: Vacuum insulation tandem accelerator. *1* - negative hydrogen ion source, *2* - magnetic lenses, *3* - accelerator, *4* - cryogenic pump, *5* - intermediate electrodes, *6* - high-voltage electrode, *7* - gas stripping target, *8* – insulator, *9* - high voltage power supply, *10* - turbo molecular pump, *11* - cryogenic pump, *12* – ring, *13* - metal cooled aperture and detector with a grid, *14* - input vacuum volume, *15* - detector with a grid, *16* - Faraday cup. The arrows indicate the direction of the negative hydrogen ion beam (H^-) and protons (p).

Modernization of the accelerator was as follows. The water-cooled metal diaphragm *13* with a 20 mm hole with possibility of centring along the beam axis was installed in the vacuum chamber *14* at the accelerator input. That aperture is considered to reduce the flow of gas and ultraviolet from the source of negative hydrogen ions in the accelerating channel. At the upper flange of input vacuum volume through the slide valve DN 250 the cryopump On-Board 250F (CTI-Cryogenics, USA) *11* was installed. This should improve the vacuum conditions in the beam-transporting channel and in the accelerating channel. In front of the cooled diaphragm a metal ring *12* was installed. Negative potential applied on this ring should suppress the flow of electrons that accompany the beam of negative

* The study was funded by the grant from the Russian Science Foundation (Project No.14-32-00006) with support from the Budker Institute of Nuclear Physics and Novosibirsk State University.
#Cshudlo.i.m@gmail.com

ISBN 978-3-95450-181-6

hydrogen ions. Surface of cooled aperture *13* was covered by the wired tantalum grid for suppressing the secondary electrons produced by irradiation of metal surface by positive ions. Between the grid and the diaphragm an insulated metal plate for current measurement was placed. In addition, on the surface of the vacuum chamber at the output of the accelerator the similar grid and plate *15* were installed.

Fig. 2a shows that when voltage is applied to the grid at the entrance of the accelerator, bremsstrahlung dose rate (caused by the absorption of electrons in the metal, accelerated to 1 MeV [9]) is significantly reduced. Presented at Fig. 2b the current-voltage characteristic of the detector at the entrance of the accelerator indicates that the coefficient of secondary electron emission formed under the influence of positive ions is ~ 10 (high secondary electron emission coefficient is typical for many-electron atoms and ions with energies above 100 keV [10].

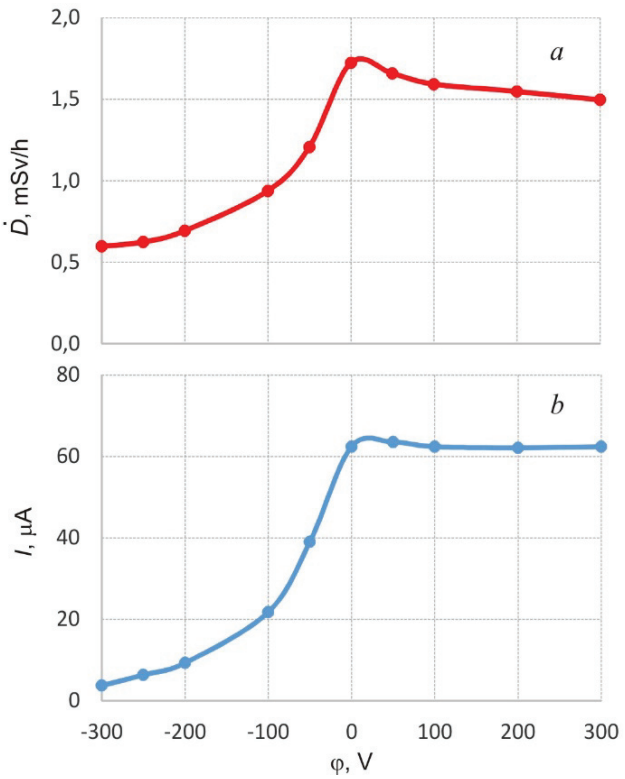

Figure 2: Dependence of the gamma radiation dose rate *D* (*a*) and current on the detector mounted at the accelerator input from grid potential φ (*b*).

After installation of the diaphragm, the cryogenic pump, rings and grids it was achieved a significant reduction of unwanted flows of charged particles. In particular, the flow of electrons accelerated to full voltage was reduced 20 times to a value of about 0.5% of the ion beam current. Suppression of undesired flows of charged particles in the accelerator improved accelerator operation resistant to breakdowns of the total voltage and significantly increased the proton beam current. Fig. 3 shows the oscillograms of current and energy of the proton beam. Measured by Faraday cup (*16* in Fig. 1) proton beam current for one hour exceeds 5 mA, the average value is 5,120 ± 0,060 mA, max value is 5.327 mA.

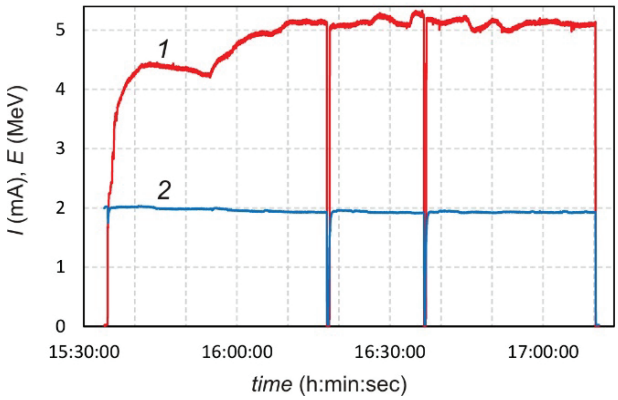

Figure 3: Proton beam current *I* (*1*) and energy *E* (*2*) oscillograms.

CONCLUSION

As a result of the modernization of the accelerator flows of undesired charged particles was effectively suppressed. It is allowed to reduce the level of gamma radiation from accelerator and increase proton beam current up to 5 mA Obtaining of a stationary proton beam with a current of 5 mA has actually solved a problem of neutron source for BNCT - irradiating of a lithium target by this beam provides the desired flux of epithermal neutrons.

REFERENCES

[1] W. Sauerwein et al., *Neutron Capture Therapy. Principles and Applications*, (Springer, 2012), 553.
[2] B. Bayanov et al., Nucl. Instr. and Meth. in Phys. Res. A. 413 (1998) 397.
[3] V. Aleinik et al., Instrum. Exp. Tech. 56 (2013) 497.
[4] A. Makarov et al., "Optimization of the negative hydrogen ion beam injection into the tandem accelerator with vacuum insulation", RUPAC'2012, Saint-Petersburg, Russia, Sept. 2012, WEPPD038, p. 623 (2012).
[5] A. Kuznetsov et al., "Calibration testing of the stripping target of the vacuum insulated tandem accelerator", RUPAC'2012, Saint-Petersburg, Russia, Sept. 2012, WEPPC057, p. 560 (2012).
[6] A. Kuznetsov et al., Tech. Phys. Lett. 35 (2009) 346.
[7] D. Kasatov et al., JINST 9 (2014) 12016.
[8] D. Kasatov et al., Tech. Phys. Lett. 41 (2015) 139.
[9] I. Shchudlo et al., "Measurement of the spatial distribution of gamma radiation at tandem accelerator with vacuum insulation", RUPAC'2014, Obninsk, Russia, Oct. 2014, TUPSA37, p. 116 (2014).
[10] U. Arifov et al., Proc. of the Academy of Sciences of USSR, series: Physical 26 (1962) 1398.

ISBN 978-3-95450-181-6

LOSS ANALYSIS OF INSULATED CORE TRANSFORMER HIGH VOLTAGE POWER SUPPLY*

Y.F. Zhang, M.K. Li, H. Liang, T.Q. Yu, J. Yang#, J. Huang, Y.Q. Xiong,
W. Qi, C. Zuo, L.G. Zhang, T. Liu
School of Electrical and Electronic Engineering, Huazhong University of Science and Technology,
Wuhan, 430074, P. R. China

Abstract

Insulated core transformer (ICT) electron accelerator is an ideal prototype in low energy radiation processing industry, and ICT high voltage power supply is the essential apparatus. Conventional ICT high voltage power supply uses laminated silicon steel sheets as magnetic cores and works at 50 Hz. In a novel design of the ICT high voltage power supply, the magnetic cores made of ferrite material are adopted to increase the frequency and improve the performance. Focusing on the new scheme, the loss calculation of the high voltage power supply was carried out. The loss of ferrite magnetic cores and the windings was analysed and simulated.

INTORDUCTION

Insulated core transformers (ICT) are widely used in electron accelerators in irradiation processing industry [1]. Conventional ICT high voltage power supply uses laminated silicon steel sheets as magnetic cores and works at 50Hz. At present, the rapid developments of the fields of power electronics, electrical materials and high voltage technology make it possible to adopt new technologies and designs in ICT high voltage power supply, and a novel design of high frequency ICT high voltage power supply was proposed (see Fig. 1): ferrite magnetic cores, 4-phase structure and 5 kHz square wave as the excitation source are adopted [2]. As the frequency of the ICT is raised, the volume and the weight of the ICT high voltage power supply will be improved, and the output voltage will be more stable.

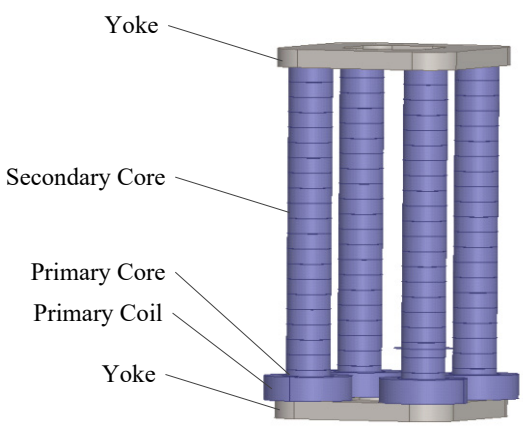

Figure 1: The 3D model of the 4 phase high frequency ICT.

*Work supported by National Natural Science Foundation of China (11305068)
#jyang@mail.hust.edu.cn

The high frequency ICT consists of 4 phases and each phase has a primary core and 20 secondary cores. There are insulated sheets to isolate the potential of the magnetic cores. Each secondary core has a rectifier circuit, and all rectifier circuits are connected in series to get the high DC voltage. With the existence of the insulated sheets, the leakage magnetic flux cannot be ignored. The induced voltage will be lower in the coils, which are further from the primary coil. The total number of the cores is 84 and there are also two yokes. The loss of magnetic cores cannot be neglected. The eddy current loss of the coils should also be considered with the high frequency of the excitation source and the leakage magnetic flux acts on the coils. These two kinds of loss need to be calculated when analyzing high frequency ICT efficiency.

FERRITE MAGNETIC COER LOSS

The magnetic core loss includes eddy current loss, hysteresis loss and excess loss. The rapidly changing magnetic flux density dB/dt will cause the induced voltage E(r, t), where r is the radius of the magnetic core. Because of the resistance of the ferrite core, the eddy current exists, which causes the eddy current loss per unit volume:

$$P_e = \frac{1}{V}\cdot\frac{1}{T}\int_0^T\int_0^{r_0} dP_e dr dt \tag{1}$$

Where V is the volume of the ferrite core, T is the time period, r_0 is the radius of the ferrite core, and dP_e is the instantaneous power which given by

$$dP_e = \frac{E(r,t)^2}{R} \tag{2}$$

R is the equivalent resistance of the instantaneous induced current.

Using (1) and (2), we can obtain:

$$P_e = \frac{1}{2\rho r_0 T}\int_0^T\int_0^{r_0} r^3\cdot\left(\frac{dB}{dt}\right)dr dt \tag{3}$$

Transform the formula (3), the eddy current loss per unit volume is obtained finally by:

$$P_e = \frac{U_1^2}{8\pi\rho N^2 A} \tag{4}$$

Where U_1 is the input excitation voltage, ρ is the resistivity of the ferrite core, A is the area of the cross section of the magnetic core, N is the number of turns. For the high frequency ICT, the waveform of the input excitation voltage is square, so the eddy current loss can be presented by [3]:

ISBN 978-3-95450-181-6

$$P_E = \frac{2A}{\pi\rho} \cdot B_m{}^2 f^2 \cdot V \quad (5)$$

B_m is the peak value of the magnetic flux density, and f is the frequency of the excitation voltage.

Hysteresis loss is also caused by the rapidly changing of the magnetic flux in the magnetic core. There is no accurate numerical computation suit for different kinds of materials to obtain the hysteresis loss. Therefore, the experimental method is adopted to obtain the hysteresis loop of the ferrite material which used in the high frequency ICT, then the hysteresis loss can be calculated from the hysteresis loop by [3]

$$P_H = V \cdot f \cdot \oint HdB \quad (6)$$

V is the volume of the ferrite core. According to the experimental method, the hysteresis loop is shown in Fig. 2. The value of the maximum working flux is 0.08 T, so the hysteresis loss can be calculated precisely.

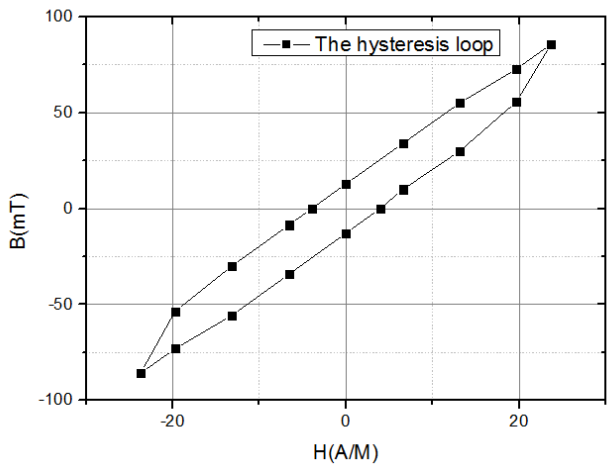

Figure 2: The hysteresis loop of the ferrite core working at 0.08 T.

The computation of the excess loss uses the formula in [4]:

$$P_{EX} = 8\sqrt{\frac{A\alpha n_0}{\rho}}(B_m f)^{3/2} \cdot V \quad (7)$$

Finally the magnetic core loss is obtained by adding the three kinds of magnetic core loss:

$$P_{core} = P_E + P_H + P_{EX} \quad (8)$$

WINDING LOSS

The winding loss mainly includes exciting current loss and eddy current loss. In the high frequency ICT, the eddy current loss caused by exciting current and leakage flux due to air gap between upper core and lower core. For the secondary winding, the induced current is so small that the loss of the winding is negligible, so the primary winding loss is the main loss. Before computing the winding loss, the right size of the wire of the primary winding should be selected. First, the skin depth of the wire at the frequency of 5 kHz is calculated by

$$\Delta = \sqrt{\frac{\rho}{\pi\mu_0\mu_r f}} \quad (9)$$

Where ρ is the resistivity of the copper wire, μ_r is the relative permeability of the copper wire, and f is the frequency of the exciting current. The skin depth of the copper wire at 5 kHz is 0.935 mm. In order to reduce the eddy current loss caused by skin effect, the diameter of the wire must less than 1.87 mm. The wire size should be analysed by taking the leakage magnetic flux into account, as shown in Fig.3 there are large leakage flux getting through the primary winding, which will cause the eddy current loss in the primary winding [5].

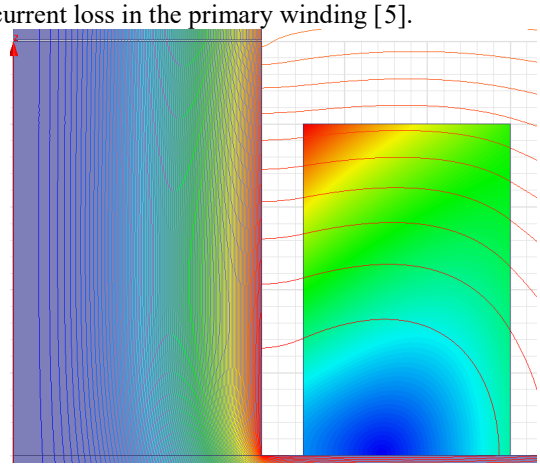

Figure 3: The magnetic flux density distribution nearby the primary winding.

To reduce the eddy current of the primary winding, the stranded wire is adopted under the circumstance of the same cross-section of the winding. In this case, different number of the parallel wires corresponds to certain size of the wires. Fig.4 shows the eddy current loss of the windings when working without a load, the diameter and paralleled number of which is 1 mm and 9 respectively.

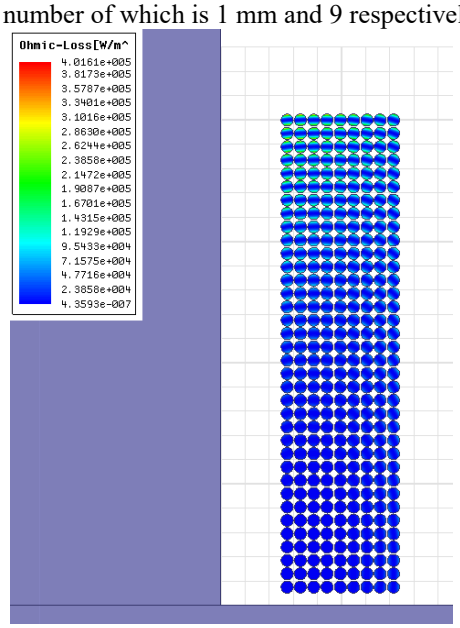

Figure 4: The distribution of eddy current loss in primary winding at the size of 1 mm.

ISBN 978-3-95450-181-6

The exciting current of the primary winding is triangular wave as the exciting voltage is square waveform, so the magnetic flux density in the magnetic core is also triangular waveform, the eddy current loss can be computed when the exciting current changes to 0, at which time the current in the primary winding is produced by the changing leakage flux, so the eddy current loss is obtained individually which is shown in Fig.4.

To verify the correctness of the FEM result in calculating the eddy current loss, the numerical method [6] is adopted, which can be calculated by

$$P_e = \frac{(4fBd)^2}{12\rho} V \qquad (10)$$

Where f is the frequency, B is the peak value of the leakage magnetic flux density, d is the diameter of the wire, and V is the volume of the winding. The results of the eddy current loss calculated by FEM and numerical method are shown in Fig.5, which shows that there is little difference between the two methods. Fig.6 shows the computation results of the eddy current loss in different size of the wire by finite element method (FEM).

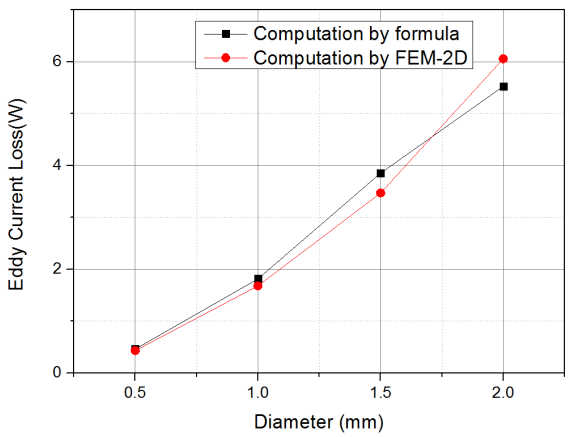

Figure 5: The eddy current loss in different size of the wire by two different method.

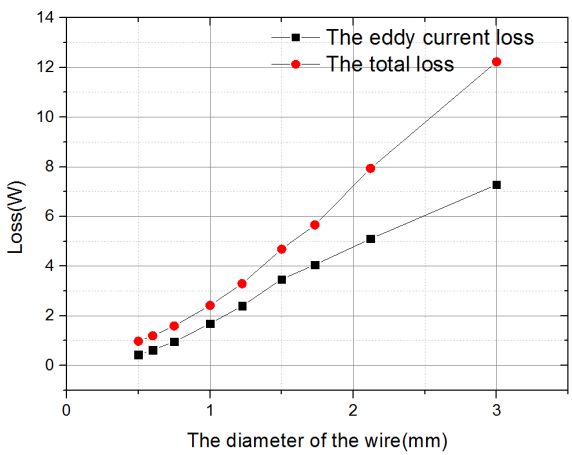

Figure 6: The eddy current loss in different size of the wire.

As shown in Fig.6 the eddy current loss decreases as the diameter of the wire raises, and the decreasing speed of the eddy current loss and the total loss become slow as the size of the wires less than 1 mm, in this case the eddy current loss and the total loss are both rather small. Moreover, as the size of the wire decreases, the cost and the difficulty of production will increase, but there is less contribution to reducing the loss. Above all, 1 mm is selected as the size of wire for the primary winding.

CONCLUSION

High frequency ICT has better performance than conventional ICT, but the leakage flux cannot be neglected as well. Furthermore, with the increasing of the frequency and the current, the eddy current in primary winding should be paid more attention. The magnetic core loss was calculated by numerical method, then the primary winding loss was analysed by FEM. According to the computation result, the design of the primary coil was optimised. This paper analysis the two kinds of loss in high frequency ICT, a loss calculation method for the high frequency ICT is completed. The total core loss of the high frequency ICT is less than 60 W, and the total primary winding loss of the high frequency ICT is less than 10 W when working without a load, which meet the design requirement and it is practicable in engineering.

REFERENCES

[1] Gracheova, A Yu, et al. “Accelerators Application for Radiation Processing of Foodstuffs,” 24-Th Russian Particle Accelerator Conference 2014.

[2] Mengkui Li, et al. “A novel design of insulated core transformer high voltage power supply,” RuPAC’16, November 2016.

[3] Zhi Cun Liu. Research and application of hysteresis loss characteristics of ferrite material. Journal of Northwest University. 4 (2003) 394.

[4] W. A. Roshen. A practical, accurate and very general core loss model for non-sinusoidal waveforms. IEEE Transactions on Power Electronics, 2 (2007) 30.

[5] Yang, L., et al. “Study On Eddy Current Power Losses In Insulated Core Transformer Primary Coil,” Diss. IPAC, 2012.

[6] Cheng Zhiguang et al., Electromagnetic and Thermal Field Modelling and Application in Electrical Engineering, (Beijing: Science Press, 2009), 373.

ISBN 978-3-95450-181-6

A NOVEL DESIGN OF INSULATED CORE TRANSFORMER HIGH VOLTAGE POWER SUPPLY*

M.K. Li, M.W. Fan, Y.F. Zhang, H. Liang, L. Yang, T.Q. Yu, J. Yang#, J. Huang, K.J. Fan, Y.Q. Xiong, W. Qi, C. Zuo, L.G. Zhang, T. Liu
School of Electrical and Electronic Engineering, Huazhong University of Science and Technology, Wuhan, 430074, P. R. China

Abstract

Insulated core transformer (ICT) high voltage power supply is an ideal model for industrial radiation accelerator at energy below 1MeV. Compared to the traditional scheme, a novel ICT high voltage power supply was put forward. Conventional silicon steel sheets were replaced with manganese zinc ferrites, raising working frequency from 50Hz to thousand hertz. Magnetic structure was changed from three-phase structure to four-phase structure. Accordingly, excitation voltage was changed from three-phase sinusoidal wave to square wave. Polyimide was chosen as insulation material instead of teflon or mica. A prototype of 400kV/50mA was designed, simulated and verified with the aid of finite element analysis software. To optimize the voltage distribution, corresponding flux compensation methods were raised to solve the problem of flux leakages.

INTRODUCTION

ICT high voltage power supply has been widely used in electron accelerator [1][2]. ICT is the kernel component of the accelerator, and its conventional magnetic core structure is shown in Fig.1. There are three groups of cores between the top yoke and the bottom yoke. Each group consists of a primary core and a plurality of segmented secondary cores. Each primary core is wound with primary coil. Each secondary core is wound with secondary coil and then connected to corresponding voltage doubler rectifier circuit, which converts AC voltage to DC voltage. Finally, all rectified voltages are connected in series to obtain the desired high voltage. Between all neighbouring cores are gaps filled with insulation materials of high dielectric strength. For the purpose of clarity, coils and circuits are not shown in Fig.1.

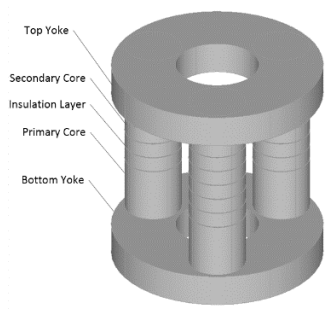

Figure 1: Structure of conventional ICT.

*Work supported by National Natural Science Foundation of China (11305068)
#jyang@mail.hust.edu.cn

The conventional design is as follows [3][4]: silicon steel sheets are selected as magnetic materials; three-phase sinusoidal wave with the working frequency of 50Hz is selected as excitation voltage; teflon or mica sheets with a thickness of several millimeters are selected as insulation material. When in operation, three-phase AC voltage (380V) is connected to delta-connected primary coils through a three-phase column type variable transformer, which controls the output voltage.

With the rapid development of power electronics, magnetic materials and insulation materials, new materials and technology can be introduced to improve the performance of ICT high voltage power supply, and the new design was proposed. Compared to the traditional scheme, it can effectively improve the efficiency of energy transfer, and reduce the volume of power supply and the requirement of rectified capacitance. It can finally achieve fast and precise control of the high-voltage output, and it's also stable and easy to maintain.

GENERAL DESIGN

Magnetic Material

Raising working frequency is an effective method to reduce the volume of ICT. As frequency increases, however, eddy-current loss of the silicon-steel sheet increases sharply, resulting in severe Joule heat and low efficiency. To solve this problem, manganese zinc ferrite is introduced. Compared to silicon steel, although the relative permeability and saturation magnetic flux density of manganese zinc ferrite fall, its electrical resistivity increases greatly, which effectively restrain the eddy-current loss and enable it to function well at high frequency.

Magnetic Structure

The magnetic structure of designed ICT is shown in Fig.2. To increase the breakdown voltage, the whole power supply is enclosed in an airtight steel barrel, fulfilled with sulfur hexafluoride at certain pressure. The working frequency can reach thousand hertz as manganese zinc ferrite is introduced. Consequently, the size of magnetic cores and the capacity of the rectifier capacitors decrease greatly. As magnetic structure is changed from three-phase structure to four-phase structure, excitation voltage is changed from three-phase sinusoidal wave to square wave consequently. This kind of structure improves the utilization of space and further reduces the volume of ICT.

ISBN 978-3-95450-181-6

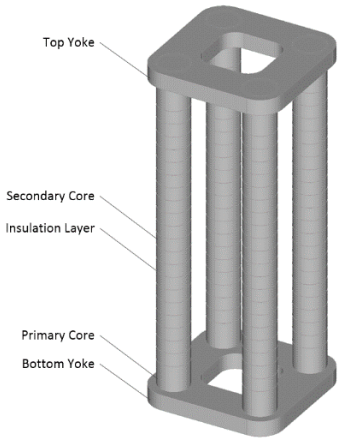

Figure 2: Structure of new ICT.

Insulation Material

Insulation layer between segmented secondary cores greatly reduces the difficulty of insulation, which effectively improves the level of output voltage. However, the reluctance increases a lot, since the permeability of insulation material is nearly the same as that of air. As a result, flux leakage is not negligible. Consequently, the induced output voltages of secondary coils taper off as the stage increases. Conventionally, teflon or mica sheet is selected as insulation material with a thickness of several millimeters. Decreasing the thickness of the insulation layer will effectively reduce the reluctance, and the flux leakage will reduce as well. However, high voltage of each stage and dielectric strength of the insulation material restrict the thickness from decreasing. As insulation technology develops, new materials can be introduced. A kind of polyimide film, the dielectric strength of which is as high as 3MV/cm [5], is a good choice. Considering that thicker film results in lower dielectric strength, the thickness of polyimide film is usually set to less than one millimeter. Although the number of stages increases, the total thickness decreases a lot, resulting in less flux leakage.

Output Voltage Control

As mentioned before, the output voltage in conventional ICT is controlled through a three-phase column type variable transformer. The transformer is bulky and the control accuracy is not continuous since the number of turns of the coil is limited. In the designed ICT high voltage power supply, a programmable DC power supply and a square wave inverter is used to obtain the square wave excitation voltage. Then the output voltage can be controlled through the programmable DC power supply, which is faster, more accurate and more continuous.

DESIGN CASE

Dimension Parameters

The general design scheme of ICT (400kV/50mA) is presented. The output voltage in each stage is set to 20kV, and then the number of stages is 20. Considering that the dielectric strength of polyimide film is about 3MV/cm, the thickness of polyimide film should be at least 0.067mm. To ensure safety, the thickness of polyimide film is set to 0.125mm. The diameter of primary core and secondary core is 60mm. The height of primary core and secondary core is 50mm and 25mm respectively. The whole power supply is enclosed in a grounded airtight steel barrel, fulfilled with sulfur hexafluoride of about 0.5-0.6MPa. The diameter and height of steel barrel is about 700mm and 1100mm respectively.

Electrical Parameters

The constructed magnetic circuit model is shown in Fig.3. Here, F is the magnetomotive force provided by corresponding primary coil. R_1 is the total reluctance of each group of cores, including primary cores, secondary cores and gaps between neighbouring cores. Each yoke is divided into four parts by magnetic cores, and R_2 is the reluctance of each part. Considering that the thickness of the insulation is much smaller than that of the cores, it is acceptable to ignore leakage reluctance. The working frequency is f. The magnetic flux density in magnetic core is B. The sectional area of magnetic core is S. The following formula can be concluded from Fig.3:

$$F = (R_1 + 0.5R_2)BS \quad (1)$$

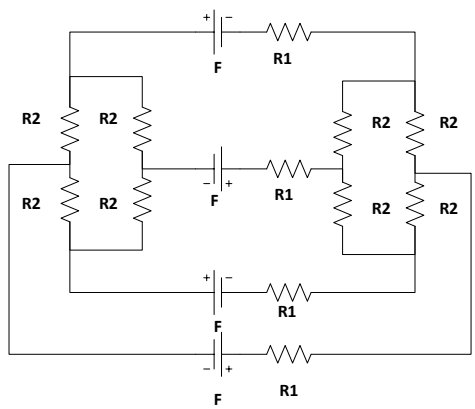

Figure 3: Magnetic circuit model.

The selected manganese zinc ferrite is PC44 (relative permeability 2400, saturation magnetic flux density 0.51T at 25℃,1194A/m). B is set to 0.08T, f is set to 5kHz. It can be concluded from formula (1) that F equals to187A.

RESULT AND DISCUSSION

The three-dimensional model of ICT is built (Fig.2). The induced voltage in each secondary core mainly depends on the magnetic flux density in corresponding core. Fig.4 shows magnetic flux density distribution of the power supply. Considering its symmetry, only one group of cores need to be studied. Choose one group of cores, and choose the axis of the cores as a path. Fig.5 shows the magnetic flux density mapped to the axis from

ISBN 978-3-95450-181-6

bottom yoke to top yoke. The average value of magnetic flux density is approximate to the designed value 0.08T. However, magnetic flux density decreases as the secondary cores goes far away from the primary core. On the top secondary cores, it falls to about 0.06T. The flux leakage will lead to the inhomogeneity of the induced voltage and a decrease of output voltage. Compensation methods should be taken to improve the voltage uniformity of each layer.

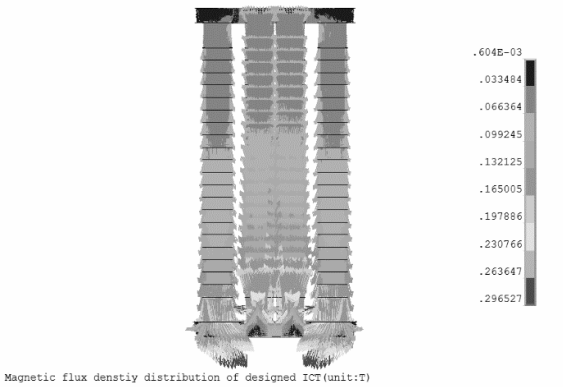

Figure 4: Magnetic flux density distribution.

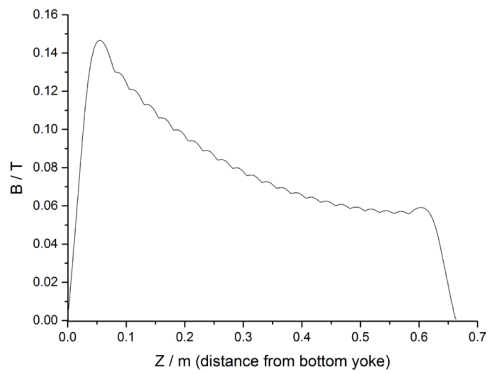

Figure 5: Magnetic flux density distribution on the chosen path.

There are different kinds of methods to compensate the magnetic flux leakage. One method is to increase the turns of the secondary coils to keep each coil at the same induced voltage. Another method is to use capacitors. Compensation capacitors are connected to primary coils or secondary coils in parallel. Capacitive current flows through the corresponding coils and the induced magnetic flux density has the same direction as the main flux, thus compensating the flux leakage.

In this design, an additional layer of cores together with specific turns of coils and paralleled capacitors are introduced on the top secondary cores. The additional coils can serve as a new excitation coil, the capacitive current of which will compensate the flux leakage. Choose proper capacitor and proper number of turns, the introduced excitation coils will provide the same magnetomotive force as the primary coils. With two excitation coils up and down, the excitation current needed will halve in an ideal case. Fig.6 shows the magnetic flux density (after compensation) on the same path as that of Fig.5. It can be seen that the flux leakage decreases a lot after compensation. To keep the induced voltage in each stage the same, the number of turns of secondary coils in the middle should be a little more than that of the two sides.

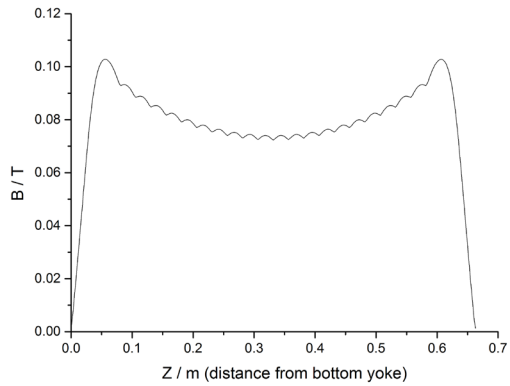

Figure 6: Magnetic flux density distribution on chosen path (after compensation).

CONCLUSION

A novel ICT type high voltage power supply was put forward to overcome the disadvantages of conventional one. And specific design process was given. By finite element simulation software, the rationality of the scheme was verified and the methods of flux leakage compensation were given.

REFERENCES

[1] Zimek, Zbigniew, G. Przybytniak, and A. Nowicki. "Optimization of electron beam crosslinking of wire and cable insulation." Radiation Physics & Chemistry 81.9(2012):1398-1403.

[2] Kurucz, Charles N., et al. High Energy Electron Beam Irradiation of Water, Wastewater and Sludge. Advances in Nuclear Science and Technology. Springer US, 1991:1-43.

[3] Graaff, Robert Van De. J. "High voltage electromagnetic apparatus having an insulating magnetic core." US, US3187208. 1965.

[4] Yang, L., et al. "A combined compensation method for the output voltage of an insulated core transformer power supply. " Review of Scientific Instruments 85.6(2014):063302-063302-6.

[5] Diaham, S., et al. "Dielectric breakdown of polyimide films: Area, thickness and temperature dependence." IEEE Transactions on Dielectrics & Electrical Insulation 17.1(2010):18-27.

ISBN 978-3-95450-181-6

NEW SUPERCONDUCTING LINAC INJECTOR PROJECT FOR NUCLOTRON-NICA: CURRENT RESULTS

A.V. Butenko, A.O. Sidorin[1], G.V. Trubnikov[1],
Joint Institute for Nuclear Research, Dubna, Moscow Region, Russia,
M.A. Gusarova, T.V. Kulevoy[2], M.V. Lalayan, S.M. Polozov[2], A.V. Samoshin, S.E. Toporkov, V.L. Zvyagintsev[3], National Research Nuclear University – Moscow Engineering Physics Institute, Moscow, Russia
M.A. Batouritski, S.A. Maksimenko, Institute for Nuclear Problems, Belarusian State University, Minsk,
A.A. Marysheva, V.S. Petrakovsky, I.L. Pobol, A.I. Pokrovsky, D.A. Shparla, S.V Yurevich, Physical-Technical Institute, National Academy of Sciences of Belarus, Minsk,
[1]also at Saint-Petersburg State University, Saint-Petersburg, Russia
[2]also at Institute of Theoretical and Experimental Physics of NRC "Kurchatov Institute", Moscow, Russia
[3] also at TRIUMF, Vancouver, Canada

Abstract

The joint collaboration of JINR, NRNU MEPhI, INP BSU, PTI NASB, BSUIR and SPMRC NASB started in 2015 a new project on the development of superconducting cavities production and test technologies and new linac-injector design. This linac intend for the protons acceleration up to 25 MeV (up to 50 MeV after upgrade) and light ions acceleration up to ~7.5 MeV/u for Nuclotron-NICA injection. Current status of linac general design and results of the beam dynamics simulation and SRF technology development are presented in this report.

INTRODUCTION

Nuclotron-based Ion Collider fAcility (NICA) is new accelerator complex developing and constructing at JINR [1-4]. The injection system of operating Nuclotron and new NICA is under upgrade now. It was consisted of old Alvarez-type DTL called LU-20. The pulse DC forinjector was replaced by new RFQ linac which was developed and constructed by joint team of JINR, ITEP and MEPhI [5] and commissioned on December, 2016. The first technical session was done on May-June, 2016, with new injector [6] and the first experimental session is under operation at present (November, 2016). The other heavy ion linac for beams with charge-to mass ration Z/A=1/8-1/6 was developed by joint team of JINR, Frankfurt University and BEVATECH and it is under installation and commissioning at present.

The possibility of LU-20 replacement by new superconducting (SC) linac of 25 MeV for protons [7, 8] and up to 7.5 MeV/nucleon for deuterium beam is discussed now. Project should also include upgrade option up to 50 MeV for the proton beam. Beam intensity and quality could be sufficiently increased in Nuclotron and NICA after new linac commissioning.

Technologies which are necessary for serial SC cavities manufacturing are now absent in Russia. JINR in cooperation with the INP BSU and the PTI NASB done the pilot project of elliptical cavities fabrication and testing [9-11]. Now a new collaboration of the JINR, the NRNU MEPhI, the ITEP NRC "Kurchatov Institute", the INP BSU, the PTI NASB, the Belarusian State University of Informatics and Radioelectronics and the Scientific and Practical Material Research Center of NAS of Belarus is established. The new collaboration declares two main aims of cooperation: development of technologies for SC cavities production and construction of the new linac – the injector for the Nuclotron-NICA complex. The first results of the linac general layout development and beam dynamics simulation are presented in the paper.

NEW SUPERCONDUCTING LINAC GENERAL SCHEME AND THE FIRST VERSIONS OF LAYOUT

Superconducting linac would to be consisting of a number of superconducting independently phased cavities and focusing solenoids. Low to mid-energy linear accelerator development is challenging because of serious limitations imposed on non-relativistic beam accelerating and focusing systems. This task could be solved using RF accelerator with identical short SC cavities with independent phase control for high energy gain and focusing solenoids. This design is economically allowable in the case of identical cavities, otherwise the total accelerator cost dramatically increases. Such linac design was called modular. It means that RF wave for all cavities will have the same phase velocity value. Wave and particle synchronous motion will be not observed here due to of particles reference phase slipping. The slipping value should not exceed some allowable limits otherwise the rate of the energy gain decreases, both transverse and longitudinal beam stability disturbs and current transmission decreases [12-13].

Starting 2014 two SC linac designs were proposed, discussed and simulated [7]. The first preliminary design was done with the following assumptions: the injection

ISBN 978-3-95450-181-6

energy of proton beam after new RFQ for-injector is 1.6 MeV (particles velocity is 0.058c), total length of linac not higher than 20 m and accelerating gradient not higher than 3 MV/m in the low energy part and <10 MV/m in medium energy one. For the chosen type of accelerating elements and the admissible slipping factor < 20%, it was determined that the accelerator should be divided into five groups of cavities with the geometric velocity β_G = 0.072, 0.105, 0.15, 0.217, and 0.314. The analysis of the stability conditions for longitudinal and transverse oscillations showed that, for example, for the first group of cavities, the stability is achieved for the field strength E=2.26 MV/m, entrance phase φ = –20°. Such field limitation is caused by transverse and longitudinal stability but not by RF limitations for the cavities. Solenoid field amplitude not higher than ≈3 T is necessary for the effective beam transverse focusing with such RF field limitations. Cavities types for all groups were not choused in [7] but QWR or HWR were discussed for the first two or three groups of cavities and CH- or Spoke cavities were discussed for the other groups.

The second version of linac layout was done on first half 2016 [8]. The ion beam motion stability analysis show that with the slipping factor about 17.5% the new SC linac will consists of four groups of cavities having geometrical velocities of β_g=0.07, 0.141, 0.225 and 0.314. The first two groups of cavities should be two-gap QWR's and the other – four-gap CH-cavities or Spoke-cavities. Using transfer matrix calculation method and smooth approximation [12-14] the preliminary SC linac parameters were defined for minimal linac length and lowest cost. The total length of the linac was reduced from 17.8 to 15.5 m and the number of cavities was also reduced from 32 to 28.

CURRENT SC LINAC LAYOUT AND BEAM DYNAMICS

After a number of meetings the linac general layout was sufficiently modified. At the first it was stated that the injection energy for SC part of linac will increased up to 5 MeV (as it is for LU-20 at present), the normal conducting part will consist of 2.5 MeV proton linac (which also should be designed for beams with charge-to-mass ratio Z/A<1/3 acceleration up to 2.5 MeV/nucleon) and a number of identical cavities for acceleration from 2.5 to 5 MeV. The RF field was limited by 4.5 MV/m for QWR (and HWR if they will be necessary) and by 7.5 MV/m for CH- and Spoke cavities designed. The solenoid field limitation was contrariwise increased to 2.5 T and a beam envelope limitation was also increased form 3 to 5-6 mm.

For the chosen types of accelerating elements and the assumptions noted above the third version of SC linac design was developed. The slipping factor should be not higher than 24% (see Figure 1) and the accelerator should be divided into three groups of cavities with the geometric velocity β_G = 0.12, 0.21 and 0.314. Current characteristics of the SC linac are shown in Table 1. Note that now only one group of QWR is necessary and correct choice of cavities of 2nd and 3rd groups (CH-cavities, Spoke-cavities or HWR) should be done. The proton beam dynamics in the polyharmonic field was simulated basing on the chosen parameters (see Fig. 2). We choose initial beam parameters (Fig. 2a) that provide particles matching with the longitudinal channel acceptance without dissipative effects (blue curve) and taking into account oscillations decay (magenta curve). Initial beam radius was taken equal to 3 mm, beam current being not taken into account. The protons beam acceleration, the oscillations decay and the slipping factor of the RF phase in dependence of the ratio between the particle velocity β and the phase velocity of the wave β_g should be taken into account for correct beam dynamics simulation. Results of beam dynamics simulation are presented in Figure 2 (b–e).

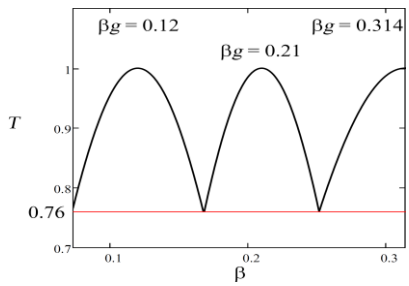

Figure 1: The slipping factor T for each cavity group.

Table 1: Current Parameters of the SC Linac

Cavity Group	0 *	1	2	3
β_g	0.12	0.12	0.21	0.314
W_{in}, MeV	2.50	4.90	13.47	31.00
β_{in}	0.073	0.102	0.168	0.251
W_{out}, MeV	4.90	13.47	31.00	50.00
β_{out}	0.102	0.168	0.251	0.314
T, %	24	24	24	24
K_T, %	100	100	100	100
F, MHz	162	162	324	324
N_{gap}	2	2	4	4
Φ, deg	–20	–20	–20	–20
L_{res}, m	0.222	0.222	0.39	0.58
E. MV/m	4.50	7.52	7.70	7.76
U_{res}, MV	1.0	1.67	3	4.32
B, T	1.35	1.4	1.9	2.3
L_{sol}. m	0.2	0.2	0.2	0.2
L_{gap}, m	0.1	0.1	0.1	0.1
L_{per}, m	0.622	0.622	0.79	0.98
N_{per}	3	5	7	5
L, m	1.87	3.11	5.53	4.90

* 0th group cavities are normal conducting.

SC CAVITIES DESIGN

The operating frequency of the linac was chosen equal to 162 MHz with further increase twice to 324 MHz for CH- or Spoke cavities. QWR and CH-cavities were simulated (see more in [15]).

ISBN 978-3-95450-181-6

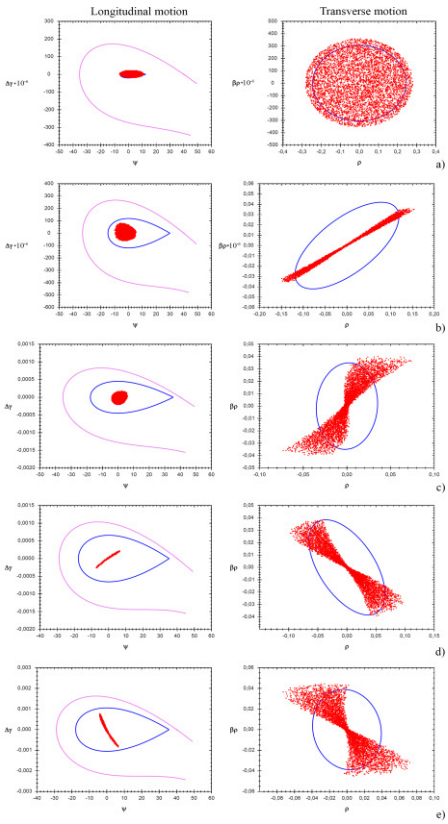

Figure 2: The longitudinal and transverse phase spaces after each section.

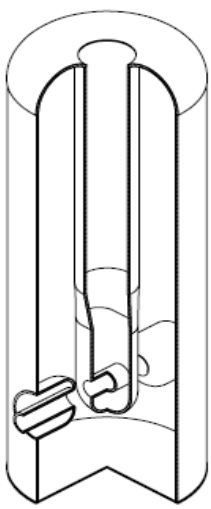

Figure 3: Model of QWR.

SC CAVITIES FABRICATION TECHNOLOGY

SC cavities fabrication technologies are under development in PTI NASB and BSU last years [9-11] but it were developed for 1300 MHz elliptical SC cavities.

Now we start to develop fabrication technologies for 162 MHz quarter-wave resonators. Preliminary QWR construction has been developed based on the simulated model. Then we identified the key units in the construction of a QWR and divided them into elementary components in terms of the possibility of their production. The QWR components were analyzed for the ability to use semi-finished products that are produced in the industry (tubes having a required diameter, sheets, etc.) to reduce the cost of the resonator fabrication. For the resonator components high requirements to quality of the internal surface, purity of a superconducting niobium, accuracy of geometrical parameters are imposed. The best way to ensure these requirements is impact hydroforming technology. A feature of the method is use of liquid as the forming tool that ensures absence of damage and contamination of the surface and high precision of stamping [16]. Current version of the QWR design for 162 MHz and β_G=0.07 is shown in Figure 3.

CONCLUSION

Corrent results of new SC proton linac development for JINR LU-20 upgrade were discussed. Beam dynamics simulation and preliminary design of SC cavities results were presented and problems of SC cavities production technologies were discussed.

REFERENCES

[1] G. Trubnikov, N. Agapov, V. Alexandrov et al., Proc. of IPAC'10, 693 (2010).
[2] O. Kozlov, H. Khodzhibagiyan, S. Kostromin et al., Proc. of IPAC'11, 1108 (2011).
[3] A.V. Butenko, E.E. Donets, E.D. Donets et al., Proc. of IPAC'13, 3915 (2013).
[4] A.V. Butenko, E.E. Donets, E.D. Donets et al., Proc. of IPAC'14, 2103 (2014).
[5] V.A. Andreev, A.I. Balabin, A.V. Butenko et al., Problems of Atomic Science and Technology. Series: Nuclear Physics Investigations, 6 (88), 8-12 (2013).
[6] A.V. Butenko et al., Proc. of RuPAC'16, FRCAMH02.
[7] G.V. Trubnikov, T.V. Kulevoy, S.M. Pololzov et al. PEPAN Letters, 13, 7, 943-946 (2016).
[8] G.V. Trubnikov, T.V. Kulevoy, S.M. Pololzov et al. Proc. of IPAC'16, 941-943 (2016).
[9] N. Azaryan, Ju. Boudagov, D. Demin et al., Proc. of RuPAC'12, 602–604 (2012).
[10] N. Azaryan, Ju.A. Budagov, D.L. Demin et al., Proc. of IPAC'13, 2393–2395 (2013).
[11] S.E. Demyanov, E.Ju. Kanjukov, I.L. Pobol et al., Low Temp. Phys., 41, 671-678 (2015).
[12] E. S. Masunov, A. V. Samoshin, Technical Physics, 55, Issue 7, 1028-1035 (2010).
[13] A.V. Samoshin, Problems of atomic science and technology, 4 (80), 78 – 82 (2012).
[14] E. S. Masunov, A. V. Samoshin, Atomic Energy, 108, Issue 2, 141-153 (2010).
[15] M.A. Gusarova et al., Proc. Of. RuPAC'16, THPSC028 (2016).
[16] M.A. Batouritski, A.V. Butenko, V.A. Monchinsky et al., Proc. of IPAC'16, 944-946 (2016).

ISBN 978-3-95450-181-6

SERIES MAGNETIC MEASUREMENTS OF NICA BOOSTER DIPOLES

V. Borisov, A. Bychkov, A. Donyagin, O. Golubitsky, H. Khodzhibagiyan,
S. Kostromin, M. Omelyanenko, M. Shandov, A. Shemchuk, Laboratory of High Energy Physics,
Joint Institute for Nuclear Research, Dubna, Russia

Abstract

NICA booster magnetic system consists of 40 dipole and 48 quadrupole superconducting (SC) magnets. Measurement of magnetic field parameters is assumed for each booster magnets. At the moment six series dipole magnets are assembled and have passed all tests. Booster dipole magnets are 2.14 m-long, 128 /65 mm (h/v) aperture magnets with design similar to Nuclotron dipole magnet but with curved (14.1 m radius) yoke. They will produce fields up to 1.8 T. The magnetic field parameters will be measured at "warm" (300 K) and "cold" (4.5 K) conditions. The obtained results of magnetic measurements of first five magnets are summarized here.

INTRODUCTION

At the Laboratory of High Energy Physics (LHEP) the technical complex [1] for assembly and testing of SC magnets for the NICA and FAIR project is lunched for pass whole cycle operating at assembling and series testing mode. Five magnets were done. The testing program of magnets includes "warm" and cold magnetic measurements (MM).

DIPOLE MAGNET FOR THE NICA BOOSTER

The Nuclotron-type design based on a window frame iron yoke and a saddle-shaped SC winding has been chosen for the NICA booster and collider magnetic system. A cross-section view of the booster dipole magnets with installed magnetic measuring system (MMS) is shown on Fig. 1.

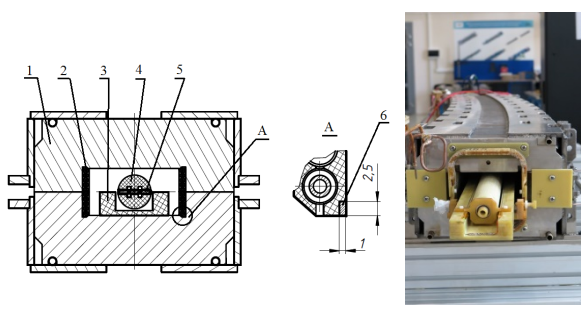

Figure 1: Cross-section view of the bent dipole magnet for the NICA booster with magnetic measurement system. 1. Yoke, 2. Main coil, 3. Base of MMS frame, 4. MMS frame, 5. PCB with harmonic coils, 6. Reference coil.

The NICA Booster operating cycle consists of stages of linear field ramping up and down with a ramp rate of 1.2 T/s and two stages with a constant field. Injection magnetic field is 0.11 T, at electron cooling is 0.56 T.

SPECIFICATION FOR MAGNETIC MEASUREMENTS

According to the specification following parameters of Booster dipole magnets have to be measured:

- Relative variation of effective lengths

$$L_{eff} = \frac{\int_{-\infty}^{\infty} B_y ds}{B_y(0)} \qquad \delta L_{eff} = \frac{\Delta L_{eff}}{< L_{eff} >} \le 5 \cdot 10^{-4}$$

- Angle between the magnetic and mechanical median plane (Dipole angle)

$$\alpha_1 = -arctg(\frac{a_1}{b_1}) \quad \delta(\alpha_1) \le 0.1\,\text{mrad}$$

- Relative integrated harmonics up to the 5th

b_2^*	$5 \cdot 10^{-4}$
a_2^*	$5 \cdot 10^{-4}$
b_3^*	10^{-3}
b_n^* , a_n^* , $n>3$	10^{-4}

THE MAGNETIC MEASUREMENT SYSTEM

Magnetic measurements were carried out by means of the rotating harmonic coils probes. Detailed description of magnetic measurement system and methods was done in papers [2], [3].

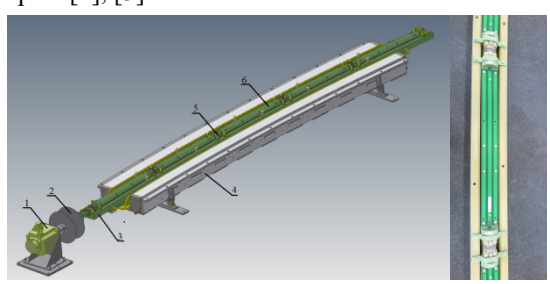

Figure 2: Layout of bottom part of magnets yoke with installed MMS: 1. Servomotor, 2. Bobbin for the cable, 3. Base of frame, 4. Bottom part of yoke, 5. Flexible coupling, 6. Measuring section.

ISBN 978-3-95450-181-6

The measuring system (Fig. 2) consists of five identical sections connected by bellow couplings. Each section has inside three measuring coils made as multilayered printed-circuit board. The base frame is fixed on the bottom pole of a magnet yoke. Coils consist of 400 turns created from 20 layers, each of which contains 20 turns. Dipole component suppression

$$\frac{cmp_{\Psi_1}}{ncmp_{\Psi_1}} \cdot 10^4 = 2.6 \div 11$$

THERMAL CONTRACTION OF PCB

Temperature of magnetic measurement probe is controlled by TVO sensors (Fig. 3). If measuring time from start of cooling differs for magnets, probe temperature will be too various in range 100-70 K and the calculated effective length should be corrected on a thermal contraction. Magnetic measurement probe contraction by cooling was measured in CERN (Fig. 4). Typical value of the contraction is 2.6-3.2 mm/m.

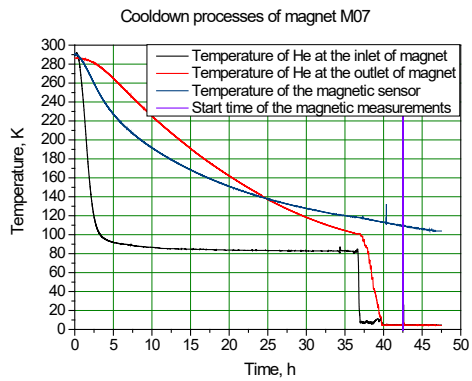

Figure 3: Cooling down processes of NICA Booster dipole magnet.

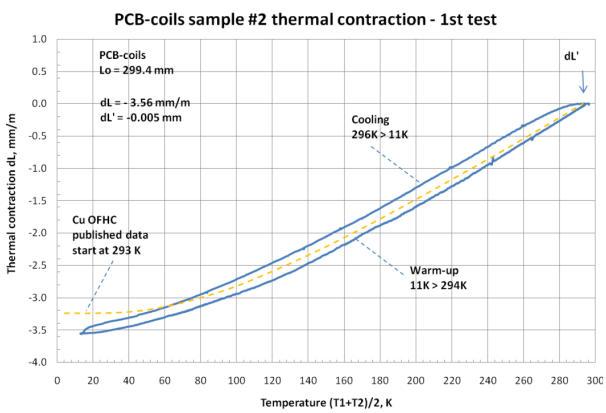

Figure 4: Thermal contraction of PCB.

MAGNETIC MEASUREMENT RESULTS

At the moment five dipole magnets are assembled and have passed all tests, including “warm” and “cold” magnetic measurements. Results are presented on Figures 5-11.

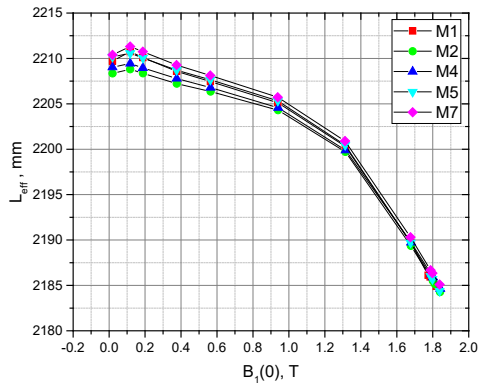

Figure 5: Effective lengths vs. the magnetic field intensity in the center of magnet.

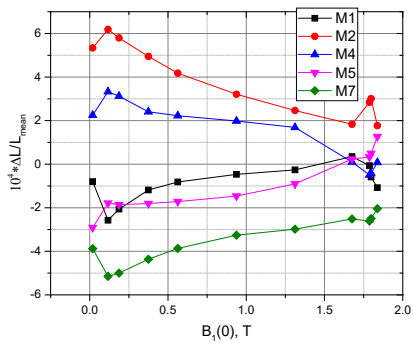

Figure 6: Relative variation of effective lengths vs. the magnetic field in the center.

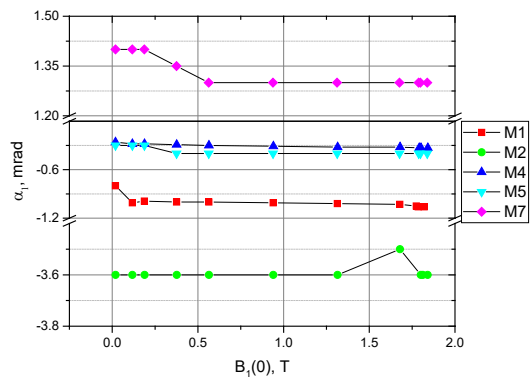

Figure 7: Dipole angle vs. the magnetic field intensity in the center. Accuracy of the measurements is equal 0.5 mrad.

Dipole angle doesn’t depend on a magnetic field Fig.7.

ISBN 978-3-95450-181-6

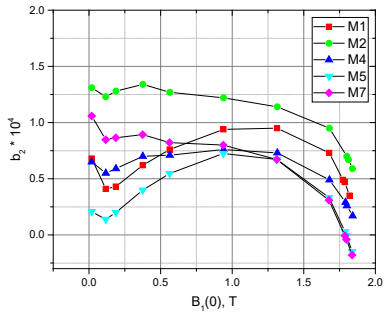

Figure 8: b_2 harmonic vs. the magnetic field intensity in the center.

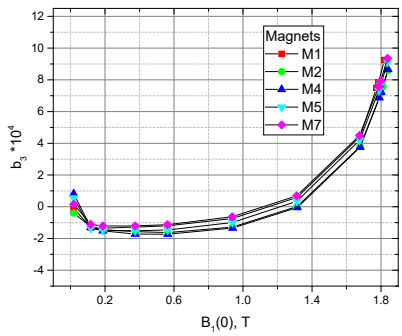

Figure 9: b_3 harmonic vs. the magnetic field intensity in the center.

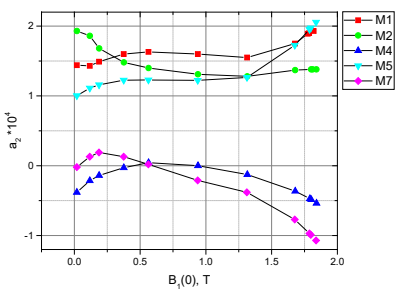

Figure 10: a_2 harmonic vs. the magnetic field intensity in the center.

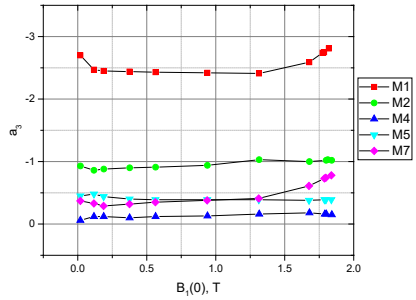

Figure 11: a_3 harmonic vs. the magnetic field intensity in the center.

CONCLUSION

First magnets are released on series testing. Magnetic measurements showed good agreement with the specification.

ACKNOWLEDGMENT

Authors would like to thank to those who support our tests at JINR, especially to the staffs of the SC-magnets Department of LHEP. Special thanks are given to V.Datskow (GSI), F.-O. Pincot, G.Kirby and O. Dunkel (CERN) for the thermal contraction measurement.

REFERENCES

[1] H.G. Khodzhibagiyan et al., Progress on manufacturing and testing of the SC magnets for the NICA Booster synchrotron, this conference.

[2] V. Borisov, et al., "Magnetic measurement system for the NICA booster magnets," in Proceedings of the 5th International Particle Accelerator Conference IPAC 2014, Dresden, Germany, June 15–20, 2014, p. 2696, WEPRI088.

[3] S. A. Kostromin, et al., Measurement of the Magnetic-Field Parameters of the NICA Booster Dipole Magnet, Physics of Particles and Nuclei Letters, 2016, Vol. 13, No. 7, pp. 855–861.

ISBN 978-3-95450-181-6

HIGH-POWER HIGH-TEMPERATURE GRAPHITE BEAM DUMP FOR E-BEAM IRRADIATION TEST OF PROTOTYPE IF TARGET IN RISP

K.V. Gubin, ILP SB RAS, Novosibirsk, Russia
Yu.I. Maltseva, P.V. Martyshkin, BINP, Novosibirsk, Russia
J.-W. Kim, J.Y. Kim, Y.-H. Park, IBS, Daejeon, Korea

Abstract

Nowadays project RISP is developed in IBS, Daejeon [1,2]. One of the main project device is graphite target system meant for production of rare isotopes by means of the in-flight fragmentation (IF) technique. The power inside the target system deposited by the primary beam with energy of 200 MeV/u is estimated to be around 100 kW [3]. The target represents rotating multi-slice graphite disc cooled by thermal radiation [4]. Necessary step of target development is integrated test of target prototype under high power electron beam modelling real energy deposit into target. This test is planned to be held in BINP, Novosibirsk, with the use of ELV-6 accelerator [5-7]. Heavy-ion beam will be modelled by the e^- beam of ELV-6 accelerator with diameter down to ~1 mm and energy 800 keV (minimum possible).

IF target is not full stopping target for an electron beam with energy 800 keV. Considerable part of beam energy will be not absorbed by a target material and must be deposited into special beam dump. In this paper the design of beam dump of the graphite cone geometry cooled by thermal irradiation is described.

BEAM DUMP PURPOSE AND LAYOUT

Beam dump is mainly purposed for utilization of electrons passed through the rotating target and removing the excess energy from experimental area. Beam dump is insulated from installation body. Simultaneously it means prevention the direct passing of high-energy electrons into metal surfaces. Moreover, it is specified using of current signal from beam dump for fast interlock unit. These tasks cause general layout of beam dump devise is shown in Fig. 1.

- Graphite conical beam dump with thickness 2 mm absorbs most part passed electrons and removes its energy by the thermal irradiation. The thickness of graphite is enough for electron beam full stopping.
- Cylindrical graphite blanket protects the outlet metal devices from electrons scattered with high angles. This device also is cooled by thermal irradiation.
- Water beam dump and additive cooling panel removes heat by water cooling channels. Also this devices saves overheat of the different parts of installation against of direct graphite thermal irradiation.
- Ceramic insulator gives possibility to measure electron beam current through graphite cone.

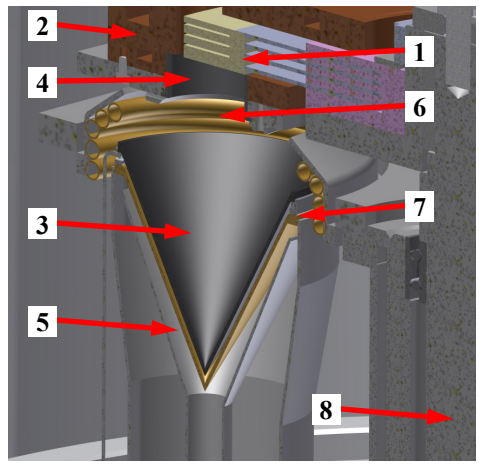

Figure 1: Layout of beam dump: 1 – multi-slice rotating target, 2 – cooling panel, 3- graphite cone beam dump, 4 – graphite blanket, 5 – water beam dump, additive cooling panel, 7 – ceramic insulator, 8 – target shaft.

Main problem of beam dump development is optimization of device size and placement. First of all, beam dump must have enough large size for providing high flow of thermal irradiation without overheat of graphite more than 1900-2000 °C. In other hand, a beam dump size is limited by maximum sizes of installation: distance between target shaft and electron beam axis is ~ 10 cm. Also, operational conditions of beam dump will determine maximum possible electron beam power during experiment

Principal subtasks of target development are next:

- simulation of electron beam scattering and passing through rotated target,
- estimation of beam dump heating, temperature and thermal stress distribution, ultimate parameters of electron beam,
- estimation of heat removal by external cooling channel,
- optimization of beam dump design and operational conditions,
- definition of ultimate experimental regime for the next prototype test [4, 7].

SIMULATION OF ELECTRON BEAM SCATTERING

Simulation of electron beam passing through the rotating target was performed by G4beamline code based on GEANT4 by means of Monte Carlo method. Main

ISBN 978-3-95450-181-6

parameters of simulation were:

- Thin graphite target. 3 layers with thickness 0.2 mm, diameter is 20 mm, distance between layers is 2 mm, graphite density is 1.85 g/cm^3.
- Beam dump axis is normal to target, thickness of wall was 2 mm, graphite density is 1.85 g/cm^3.
- Electron beam is normal to target (along to the beam dump axis), zero transverse size, monoenergetic, with kinetic energy 800 keV was taken.

Computed energy-radial and energy-angular distributions of electrons passed through the target are presented in Fig. 2. Number of back scattered electrons is negligibly small. Results of simulation follow next conclusions:

- Passed beam has enough small size (greatly less than typical size of beam dump devices). Electron beam after passing through a target can be considered as a point size beam for a next beam dump optimization.
- For following step of modelling only one dimension angular distribution of passed beam power density was used.

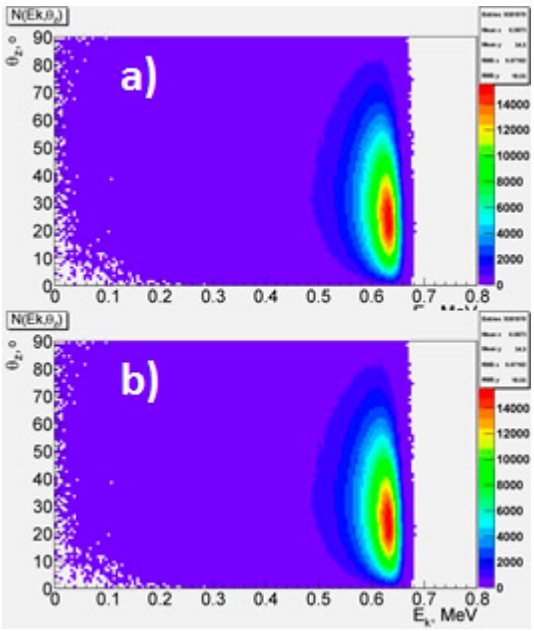

Figure 2: Energy-radial (a) and energy-angular (b) distribution of electrons at outlet of rotating target.

OPTIMIZATION OF BEAM DUMP GEOMETRY

Applying a simple graphite disk shape as a beam dump is not suitable, because the square of surface is not enough to absorb significant power flux of electron beam. Due to this reason and reducing transverse size of a beam dump unit as smaller as possible the conical shape with thin wall was taken for a beam dump particular design. Angular electrons distribution defines a minimum transverse size of cone base and a distance between graphite target and a cone. Also it is strongly important to make a correct shielding all other vacuum chamber elements against of electron flux.

The cone height was varied to have a moderate value of energy deposition in beam dump wall. Otherwise, the temperature of wall should be extremely high. It is well known, graphite can operate long time with temperature about 1900-2000 °C and short time (several tens hours) with a temperature up to 2100-2150 °C. In case, a temperature is higher graphite material degradation and evaporation came too fast. Due to maximum temperature we estimate the ultimate heating power density and temperature distribution in graphite cone and blanket.

Procedure of optimization consists of temperature distributions for varied parameters (cone diameter and heights, blanket diameter and length, distance between cone and target) and definition of minimum acceptable overall dimensions with a maximum acceptable electron beam power.

As a result, optimal geometry of cone beam dump and blanket is shown in Fig. 3. Temperature and heating power distributions for these parameters are presented in Fig. 4-5. Due to very small thickness of graphite, temperature difference through wall depth is negligible small as well as thermal flux along graphite surfaces.

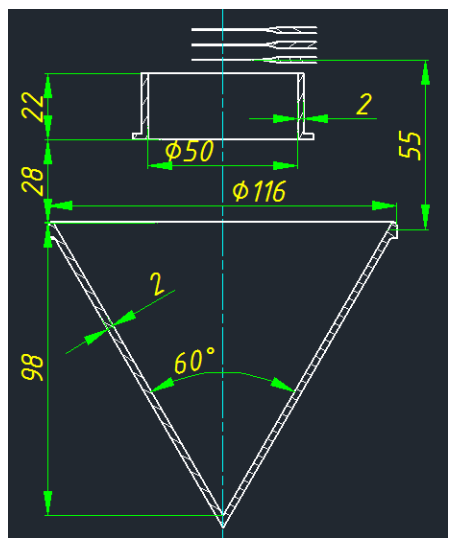

Figure 3: Geometry of graphite beam dump recommended for fabrication.

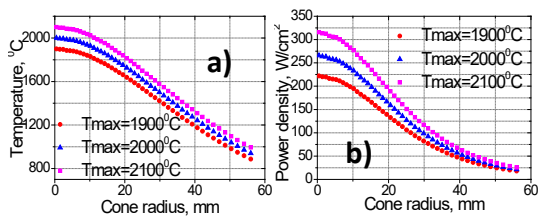

Figure 4: Temperature (a) and accepted heating power (b) distributions over cone for geometry Fig. 3.

ISBN 978-3-95450-181-6

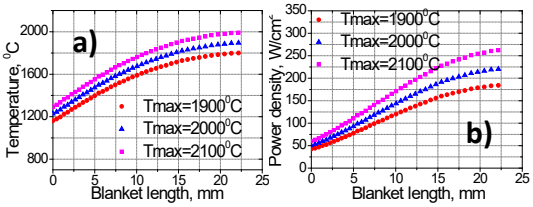

Figure 5: Temperature (a) and accepted heating power (b) distributions over blanket for geometry Fig. 3.

In addition, energy deposit into different graphite parts of prototype for optimal beam dump geometry via different maximum temperature was calculated. Results are presented in Table 1.

Table 1: Energy deposit into different graphite parts of prototype for different maximum acceptable temperature.

Maximum temperature		1900°C	2000°C	2100°C
Total beam power, kW	100%	27.3	32.6	38.8
Energy deposit in 1st layer, kW	8.4%	2.29	2.74	3.26
Energy deposit in 2nd layer, kW	10.6%	2.90	3.46	4.11
Energy deposit in 3rd layer, kW	16.1%	4.40	5.26	6.25
Energy deposit in blanket, kW	16.2%	4.42	5.29	6.29
Energy deposit in cone, kW	48.7%	13.3	15.9	18.9

CONCLUSION

As it is shown, maximum reachable energy deposit in single layer consist about 3÷6 kW, on the contrary, nominal energy deposit in single layer of real IF target must be in range 4÷10 kW [4]. But we cannot increase size of beam dump. It means for achievement of higher energy deposit we must use additive layer purposed to absorb additive beam energy. Of course this variant does not abolish principal scientific and technical decisions for beam dump.

By now, experimental testing of IF prototype planned at spring of 2017 in BINP, experimental installation is designed. Most part of equipment and devices is fabricated or purchased.

Experiments with 3 layers as well as 4 layers are discussed. In first case main goal is accurate checkup of device in principal include correspondence between simulations and real working conditions. In second case we can test of different units at conditions most closed to planned conditions of IF target.

REFERENCES

[1] http://risp.ibs.re.kr/
[2] Y. K. Kwon et al., Status of Rare Isotope Science Project in Korea, Few-Body Syst (2013) 54:961–966.
[3] K. Tshoo et al., Experimental systems overview of the Rare Isotope Science Project in Korea, Nuclear Instruments and Methods in Physics Research B 317 (2013) 242–247.
[4] S.G. Hong et.al., Design and test of a graphite target system for in-flight fragment separator, Nuclear Instruments and Methods in Physics Research A 752 (2014) 1–5.
[5] R.A. Salimov et. al.; DC High Power Electron Accelerators of ELV-series: Status, Development, Applications, Radiation Physics and Chemistry, 2000, Vol.57, Iss. 3-6, pp. 661-665.
[6] Yu.I. Golubenko et al. “Electron accelerator of ELV-type and their worldwide application”, Proc of APAC 2007.
[7] K.V. Gubin et al., “Experimental facility for e-beam irradiation test of prototype IF target in RISP.” Proc. of this conf.

ISBN 978-3-95450-181-6

A FARADAY CUP FOR A LOW CHARGE LWFA ELECTRON BEAM MEASUREMENT

K.V. Gubin, V.I. Trunov, ILP SB RAS, Novosibirsk, Russia
V.V. Gambaryan, A.E. Levichev, Yu.I. Maltseva, P.V. Martyshkin, A.A. Pachkov, S.N. Peshekhonov, BINP SB RAS, Novosibirsk, Russia

Abstract

Nowadays laser wakefield acceleration (LWFA) is considered as one a perspective method for GeV electron beam production. Combination of laser accelerated electrons and Compton backscattering of probe light beam opens possibility to create the table top source of femtosecond light beam in x-ray and gamma range. Project of laser-driven Compton light source started in ILP SB RAS in collaboration with BINP SB RAS. Production of 1-10 pC electron beams sub-ps time range duration with energies up to 100 MeV is expected as a result of the first stage of the project. Since energy of electrons does not exceed of 100 MeV, it allows using Faraday cup (FC) with reasonable dimensions, instead of commonly used integrating current transformer (ICT). Geometry of the FC was optimized taking into account of beam stopping simulation as well as low capacity requirement. RF properties, simulation of the system operation were carried out. System has been tested at the VEPP-5 electron linac. Results of development and testing of this FC are presented.

INTRODUCTION

At the present time, the impressive progress in laser wakefield acceleration (LWFA) of charged particles gives grounds to consider LWFA as a perspective method of electron beam production in the GeV energy range [1,2].

LWFA experiments are currently prepared at the Institute of Laser Physics (ILP) in collaboration with Budker INP. The experiments are based on the two-channel multi-terawatt femtosecond high contrast, high angle stability laser system with the pulse repetition rate of 10 Hz, which is developed at ILP [3].

To pursue further studies of laser-based acceleration techniques, a specialized experimental facility was designed. A sketch of the experimental stand is shown in Fig. 1. Scenario and design of stand are traditional for LWFA devices: sub-PW high-contrast femtosecond laser pulse will be responsible for gas ionization and formation of the plasma channel inside the supersonic gas jet, wakefield excitation, and trapping of plasma electrons by the wave.

General parameters of the LWFA stand are [4]:

- laser system: repetition rate is 10 Hz, pulse energy is 100÷300 mJ, pulse duration is ~20 fs, central wavelength is 810 nm;
- acceleration area: diameter is ~ 10÷15 μm, length is ~ 0.5 mm;
- supersonic He jet: diameter is ~1.2 mm, gas density is 10^{18}÷10^{19} cm^{-3}, Mach number is 3.5÷4, gas backpressure is 5÷10 atm;
- expected parameters of the electron beam are: up to 50-100 MeV of energy, 1-10 pC of charge, 1-10 mrad of angular divergence, ≤ 0.1 ps of beam duration.

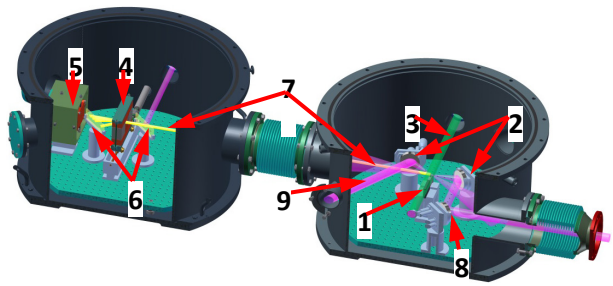

Figure 1: Two experimental chambers (without the compressor chamber): 1 – supersonic gas jet, 2 – focusing mirrors, 3 – laser beam for diagnosing the jet density, 4 – electron spectrometer magnet, 5 – Faraday cup, 6 – luminophor screens, 7 – electron beam, 8 – driving laser beam, 9 – scattered laser beam.

FC PURPOSE AND REQUIREMENTS

Beam current measurement is a necessary constituent of any accelerator facility. Usually the ICT (Integrating Current Transformer) device is used as a detector of charge in LWFA electron bunch [2,5-7]. This method has the principal difficulties:

- ICT is indirect diagnostic;
- ICT demands periodic recalibration of complicated equipment set;
- ICT system is expensive (tens of thousands euro).

However, in our case of intermediate energy range (10÷100 MeV) we can use alternative variant of diagnostic. It is Faraday cup (FC). FC gives us a possibility to have direct current measurements with high accuracy and reliability without any additional complicated electronics and does not need special recalibration procedures. Moreover, FC can be used for calibration of more complicated systems in future.

The FC development is constrained by the conflicting demands:

- Compact size (boundary dimensions 20-25 cm). Device must be placed inside limited volume of experimental vacuum chamber.
- Small capacity, not more than 10-30 pF (several tens pF including output circuit). It is caused by small

ISBN 978-3-95450-181-6

bunch charge and by requirement to register the signal with sufficiently high precision.

- FC materials have to be nonactivated, nonmagnetic, vacuum usable.
- FC has to provide full stopping of primary beam as well as secondary charged particles. It means the total charge and particle losses should be less than 1%.

In this way, for FC development the following tasks have to be solved:

- Electron beam stopping simulation for energy up to 100 MeV taking into account electron scattering, absorption, reflection and electromagnetic showers.
- FC design and optimization subject to minimize FC size as well as FC capacity simultaneously.
- Final testing of fabricated device under real electron beam with closed to necessary parameters.

ELECTRON BEAM STOPPING SIMULATION

Charge losses of a beam stopping region were simulated using GEANT4 code. Charge losses can occur due to electron backscattering and penetration of electromagnetic shower or incident beam through the beam dump. Electron beam has normal direction to target, point size and monoenergetic.

Fig. 2 presents results of backscattering simulations for long tungsten beam dump with front face aluminium layer of different thickness. Simulations were performed for electrons with energy 10, 50 and 100 MeV. As it is shown, part of backscattered particles reaches the acceptable level ~ 0.5 % at layer thickness 10 mm. Further increase of Al is meaningless.

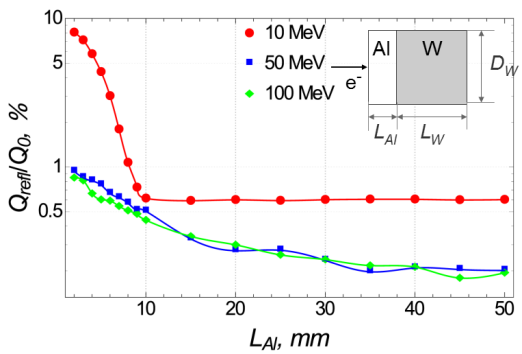

Figure 2: Dependence of charge reflection on thickness of Al layer for 10, 50, 100 MeV electron beam.

In order to optimize the total size of FC central part (subsequently beam dump) it was performed simulation of charged particles passed through the rear and lateral surfaces of beam dump with different proportions. Simulations were carried out for 100 MeV electron energy as maximum possible, since maximum electron energy defines beam dump size. Particles with lower energies will be fully stopped all the more.

Fig. 3 presents results of performed beam stopping simulations for long tungsten beam dump of different sizes. Simulations were performed for electrons energy 10, 50 and 100 MeV. It is shown, using of FC with simple cylindrical geometry of 60 mm diameter and 60 mm of length, particles losses are less than 1 %.

According to the calculations, the FC geometry was chosen to be a 90x60x60 mm^3 tungsten parallelepiped with a 10 mm thick aluminum layer at front to minimize electron backscattering. Beam dump width of 90 mm is due to large horizontal beam size after spectrometer magnet.

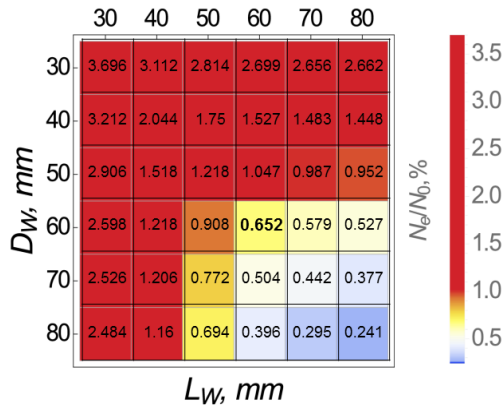

Figure 3: Number of penetrated particles for different W cylinder sizes, %. Primary beam energy is 100 MeV.

FC DESIGN AND PARAMETERS

Based on the simulations the FC construction has the following parameters (see Fig. 4):

- Beam dump is tungsten parallelepiped with thickness 60 mm, width 90 mm, height 60 mm assembled from 10 mm slices. Front face aluminium layer has 10 mm thickness.
- Grounded external shield made from duralumin, vacuum gap between the target and external shield equals to 30 mm.
- FC has self-capacity of 14.5 pF that is optimal for given problem.
- Charge drain and signal output are made through the R ~ 100 kOhm and low-capacitance connectors. It follows time of discharge $\tau = RC \sim 1\text{-}3$ μs.
- Possible excitation of RF electromagnetic fields attenuates output signal duration less than 100-200 ns ($<<\tau$) and can be unconsidered.

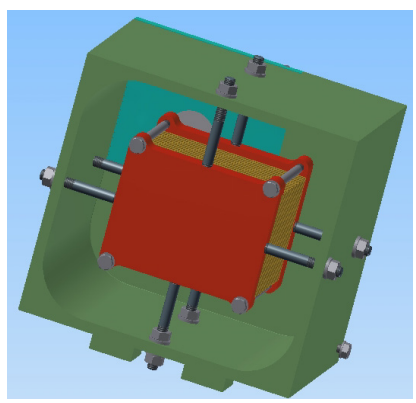

Figure 4: Construction of the FC

ISBN 978-3-95450-181-6

FC BEAM TEST

The FC was tested at electron linac of Injection Complex VEPP-5, BINP [8-10]. Sketch of experiment is presented in Fig. 5. Beam energy at the FC point was 120-125 MeV, bunch duration was ~ 1 ns, tunable bunch charge was in the range between 4.8 nC ($3 \cdot 10^{10}$ e^-, nominal operational condition of VEPP-5 Injection Complex) and practically down to zero, repetition rate was 2 Hz.

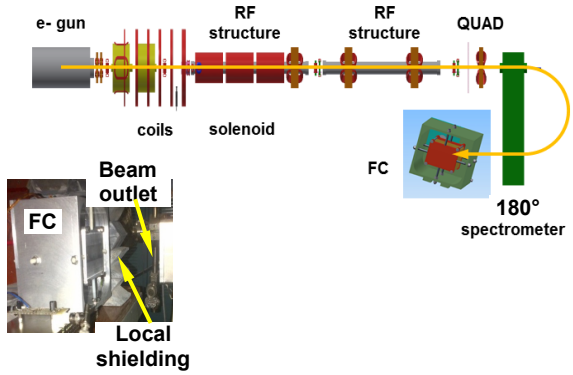

Figure 5: Electron beam line layout of VEPP-5 Injection Complex and the FC in experimental area.

Experimental results are presented in Fig. 6. Measured signal was provided from VEPP-5 beam line to control room and was registrated by the usual oscilloscope without any additive amplifiers. The stable work of the device with low bunch charge ~ 10 pC, was observed that practically equals to expected parameters.

Experimental data are in a good agreement with one of the standard beam diagnostics in Injection Complex VEPP-5.

CONCLUSION

This FC allows measuring the charge of ultrashort electron bunch ($\tau \leq 0.1$ ps) with high precision (≤ 1 pC) without any additional complicated electronics and does not need special calibration procedures.

The Faraday cup is fabricated and successfully tested under 120 MeV beam of VEPP-5 accelerator complex at Budker INP, Novosibirsk.

This work was partially supported by RAS Program "Extreme laser radiation: physics and fundamental applications" (project N0. 115113010008) of ILP and by The Federal Agency for Scientific Organizations "New method of charged beam accelerating" N305-2014-0016 of BINP.

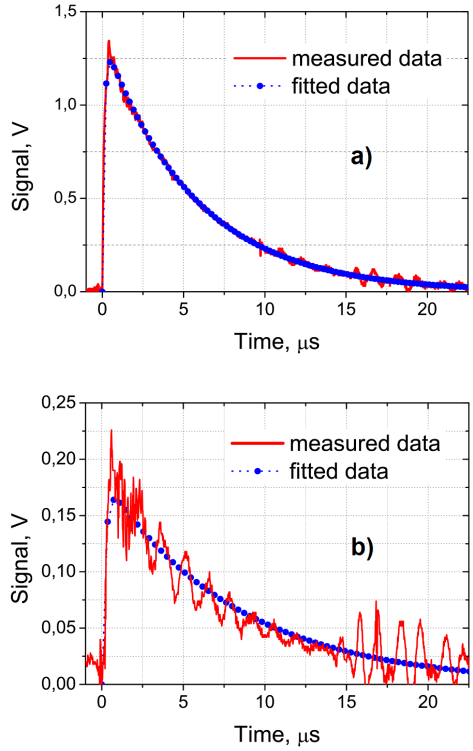

Figure 6: Beam charge measurements at e-linac. (a) is 72.3 pC ($4.52 \cdot 10^8$ e^-), (b) is 16.0 pC ($1 \cdot 10^8$ e^-).

REFERENCES

[1] W. P. Leemans et al. *Phys. Rev. Lett.* 113 245002, (2014).
[2] Hyung Taek Kim et al. *Phys. Rev. Lett.* 111 165002, (2013).
[3] V E Leshchenko et al. *Laser Phys. Lett.* 11 095301, (2014).
[4] V.I.Trunov et al. Proc. of VII International Symposium and School for Young Scientists "MPLP-2016", August 22-27, 2016, Novosibirsk, Russia.
[5] K. Nakamura et al. *Phys. Plasmas* 14, 056708, (2007).
[6] Mengze Tao et al. *Phys. Plasmas* 21, 073102 (2014).
[7] www.bergoz.com
[8] A.V. Alexandrov et al. Proc. LINAC96, Geneva, Switzerland, August 26- 30, 1996, pp.821-823 (CERN-1996-007).
[9] M.S. Avilov et al. *Atomic Energy* 94.No.1 (Jan 2003): 50-55.
[10] M.S. Avilov et al. Proc. of LINAC2002, Gyeongju, Korea.

ISBN 978-3-95450-181-6

MEASUREMENT OF GAMMA BEAMS PROFILE BY CHERENKOV RADIATION IN FIBERS*

A.V. Vukolov†, A.I. Novokshonov, A.P. Potylitsyn, S.R. Uglov, E.N. Shuvalov
National Research Tomsk Polytechnic University, Tomsk, Russia

Abstract

Results of γ-beam profile experimental investigations measuring of Cherenkov radiation [1] generated in an optical fiber with 0.6 mm and 5 mm diameter are presented. These experiments were carried out on γ beams of the linac "Philips SL-75" and the betatron, both with 6 MeV energy. In works [2,3] authors have showed feasibility of Cherenkov radiation applying for high energy beam diagnostics. In our work the Cherenkov radiation yield dependence on the fiber orientation with respect to the beam axis was investigated and showed that the maximal light yield corresponds to the angle between fiber and beam axes closed to the Cherenkov angle [1]. Proposed technique for measurements of γ and electron [4] beam profiles is insensitive to low energy part of the bremsstrahlung spectrum and to undesirable background in contrast with well-known technique based on ionization chambers. Using such a technique it is possible to construct compact and noise insensitive device. It is also possible to reach submillimeter spatial resolution.

INTRODUCTION

A wide application of γ beams in different fields requires beam profile measurement with a good accuracy. The most wide-spread technique of beam profile measuring is based on its detection by ionization chamber or by scintillator. But these techniques have spatial resolution exceeding 1 mm. One can also use X-ray films [5] to reach submillimeter resolution, but such a technique is an off-line one. All these disadvantages indicate a necessity of new, alternative device development.

In works [1–3] a feasibility of Cherenkov radiation applications for high-energy beams diagnostics is shown. In this work a diagnostic technique for γ-beams with MeV energies and mm sizes is suggested. This technique is based on detection of Cherenkov radiation, generated by γ or electron beams, passing through the optical fiber.

Cherenkov radiation is emitted in cone with the opening angle [1]:

$$\cos\theta_{ch}(\lambda) = \frac{1}{\beta n(\lambda)} \qquad (1)$$

where $\beta = v/c$, λ - wavelength, n - refractive index.

Number of photons, emitted by an electron, can be estimated from [1]:

$$\frac{d^2N}{dxd\lambda} = 2\pi\alpha\left(1 - \frac{1}{\beta^2 n^2}\right)\frac{1}{\lambda^2} \qquad (2)$$

where x - passed by a particle distance, α - thin structure constant, z - particle charge. The estimation of Cherenkov photons yield in glass for the $\lambda = 400 \div 700$ nm gives result about 20 photons per 1 mm. The outgoing angle for photons in glass ($n = 1.47$) is $\theta_{ch} \approx 46^o$.

MEASUREMENTS OF THE LINAC GAMMA BEAM

Experimental setup

A schematic of experimental setup is shown in Fig. 1. The γ-beam generated by the linear accelerator "Philips SL-75" was registered by the optical fiber with 0.6 mm diameter, which was connected to the silicon photomultiplier (PMT). The fiber length was about few meters, this allowed the locate PMT far from the beam. The accelerator has 6 MeV energy, 1 GHz frequency and 4 μs duration. The dose rate at 0.5 m distance from collimator was 4 Gr/min. The fiber was located at 20 cm distance from the collimator. An orientation dependence of intensity on angle θ between a beam axis and fiber was measured for angular range $0^o \div 180^o$.

The PMT has 6×6 mm^2 active area, 300÷800 nm spectral range, 47% photon registration efficiency at 420 nm wavelength, 10^6 gain coefficient and low supply voltage - 24.5 V. Additional advantages of the PMT are its compact size, insensibility to influence of magnetic fields, mechanical reliability, weak reaction on ionization radiation and possibility of operation in vacuum.

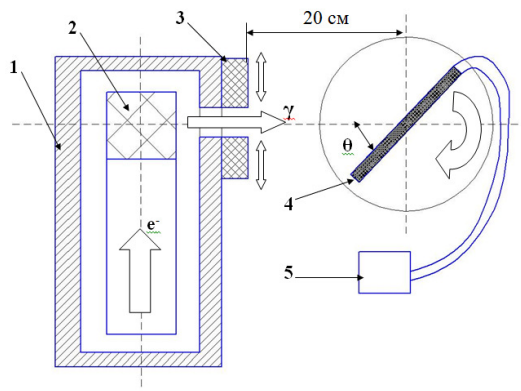

Figure 1: Schematic of experimental setup. 1 - radiation shielding, 2 - linear accelerator, 3 - collimator, 4 - optical fiber, 5 - silicon PMT.

Results

In Fig. 2 the orientation curves for different collimator sizes are shown. These curves were measured by the fiber

* This work was partially supported by the Russian Ministry of Education and Science within the program "Nauka" Grant # 3.709.2014/K
† vukolov@tpu.ru

ISBN 978-3-95450-181-6

for changing collimator sizes from 35 mm up to 120 mm. Cherenkov angle for glass (n = 1.47) is ≈46^o, the experimental outgoing photon angle is about 46^o±3^o in good agreement with estimations.

The decreasing of collimator slit size gives distortion of characteristic picture of Cherenkov radiation. When a collimator slit size is less than ≈10 mm the surface of the fiber rotated at angle more than ≈10^o does not give significant contribution in the measurement and the maximal photon yield corresponds to the zero angle, therefore there is no need to use the fiber rotated at 45^o for scanning of γ beam with sizes less than 40 mm.

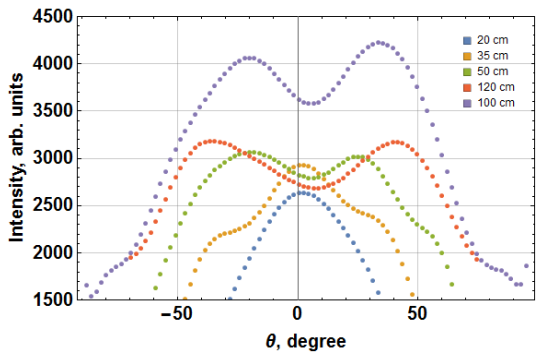

Figure 2: Orientation dependencies for different sizes of collimator.

A vertical profile of the beam at 350 mm distance from the collimator, measured by the fiber, is shown in Fig. 3. The collimator size was 4 cm. This profile was compared with the same one measured by UNIDOS detector [6], which is shown in Fig. 4. One can see that results of both measurements agree good. The technique based on fibers provides spatial resolution ≈0.6 mm, whereas the UNIDOS detector resolution is in the range of a few mm.

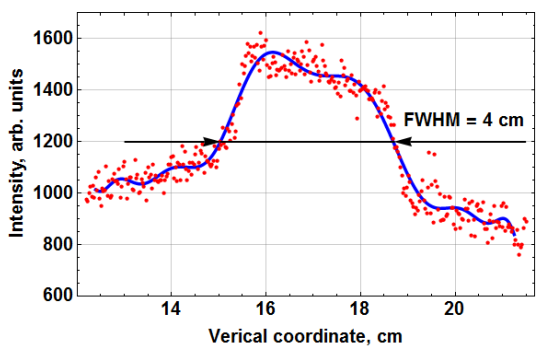

Figure 3: Vertical profile of the γ beam, measured by the fiber. Points - experiment, curve - smoothed dependence.

MEASUREMENTS OF THE BETATRON GAMMA BEAM

Experimental setup

The schematic of the experiments is shown in Fig. 5. In this case we used a glass rod with 5 mm diameter and 200 mm length instead the fiber, because the betatron dose rate (1.2 mGr/min at 1 m distance from the injector) is too weak for registration by the 0.6 mm glass fiber. The rod was always inclined relatively to the beam axis, otherwise the PMT could be on the beam way. Inclination angle was ≈30^o. The energy of electrons was 6 MeV.

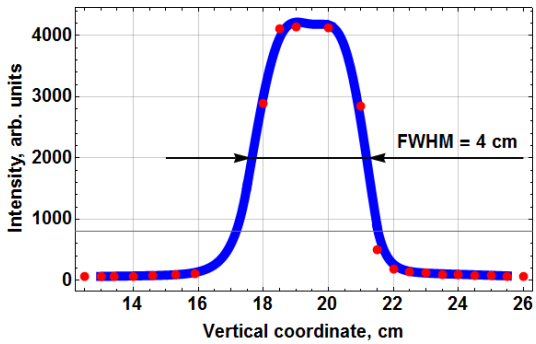

Figure 4: Vertical profile of the γ beam, measured by the UNIDOS detector. Points - experiment, curve - smoothed dependence.

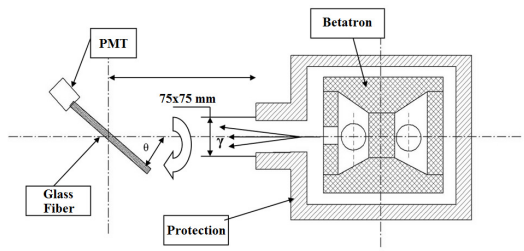

Figure 5: The schematic of betatron experiments.

Results

In Fig. 6 one can see the orientation curve measured with the glass rod. The collimator size was 75 mm. There is no Cherenkov radiation observed within small dose rates (about mGr/min) at the rotation angles close to θ = 0.

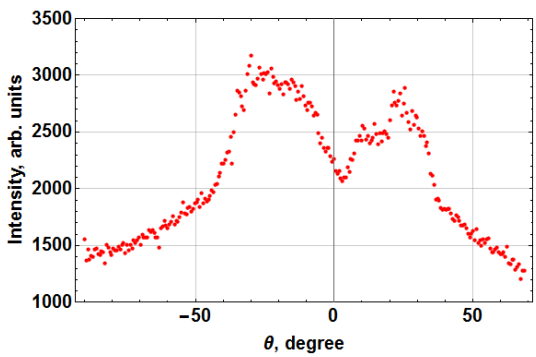

Figure 6: The orientation dependence for the betatron γ beam.

Fig. 7 demonstrates horizontal profile measured with the rod after 10 mm collimator at 125 mm distance. The size was determined only by the "plate" part, as one can see, because

ISBN 978-3-95450-181-6

of the 5 mm diameter of the rod: when the rod is completely irradiated by the γ beam it gives constant intensity, but when it begins to go out of the field the intensity decreases, therefore we have to take into account only "plate" part. And of course the rod inclination distorts the measurement.

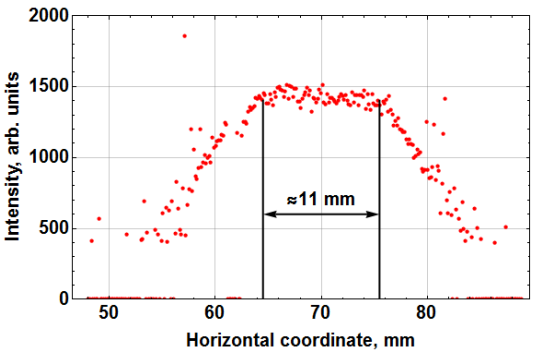

Figure 7: The γ beam profile after 10 mm collimator at 120 mm distance.

CONCLUSION

- A dose rate less than 10 mGr/min doesn‘t allow to measure Cherenkov radiation using 0.6 mm glass fiber;
- Measurements of the γ beam profile with size less than 1 cm can be carried out, when the fiber is located parallel to the beam axis;
- Measurements with 0.6 mm fiber, rotated at small angles relatively to the beam axis, give maximal yield of Cherenkov radiation within dose rates larger than Gr/min.
- During several days of measurements on the linac there were not found any changes of optical properties of the fiber.

The experimental results demonstrate a feasibility of transverse γ beam profile measurements with mm sizes and MeV energy with a help of optical fibers. Proposed technique has simple realization, small sizes, and high signal/noise ratio. The main advantage of the proposed technique is parallel location of the fiber relatively to the beam direction.

REFERENCES

[1] J.V. Jelley, *Cherenkov Radiation and its Application*, (Pergamon Press, 1958)

[2] F. Wulf, M. Körfer, ”Beam Loss and Beam Profile Monitoring with Optical Fibers”, DIPAC’09, Basel, WEOA01, p. 411, http://www.JACoW.org

[3] A. Murokh, etc., in *Proc.* IPAC’12, T03 Beam Diagnostics and Instrumentation, New Orleans, Louisiana, USA, p. 996, 2012

[4] A.V. Vukolov, A.I. Novokshonov, A.P. Potylitsyn, S.R. Uglov, J. Phys.: Conf. Ser., 732, (2015), pp. 1-7

[5] P. Schiaparelli, D. Zefiro, F. Massone and G. Tacichi, J. Med. Phys., 37, (2010)

[6] //www.ptw.de/products_solutions.html

ISBN 978-3-95450-181-6

DIELECTRIC CHART AS A TOOL FOR DIAGNOSIS OF DIELECTRIC MATERIALS

V.A.Klemeshev*, A.G.Karpov†, Saint-Petersburg State University,
7/9 Universitetskaya emb., St. Petersburg, 199034, Russia

Abstract

One of the most informative diagnostic methods dielectric materials is the analysis of the complex permittivity depending on the frequency of the electric field [1]. Dielectric chart is the dependence of the imaginary part of the complex permittivity of its real part. Thus, difference between the real dielectric chart from the reference or change it during the operation can be a means of diagnostics of dielectric materials. Dielectric chart in the classical theory of Debye is a semicircle with its center lying on the real axis. For solid dielectric the dielectric chart deviation from the semicircle can be quite large, but it still remains a circular arc. This deviation is characterized by parameter α (in the case of the Debye $\alpha = 0$). To clarify the physical meaning of the deviations of the experimental data on the Debye theory, expressed in the value of α, several possible causes have been considered: the effect hindered reorientation of dipoles, the effect of the non-sphericity of the molecules, the complex nature of viscosity. However, the main cause of deviations, in our opinion, is the availability of the distribution of relaxation times around a central relaxation time, in particular, due to defects in the sample. Gaussian distribution width increases rapidly with increasing α. In this paper we propose an algorithm for calculating α, allowing you to quickly determine the condition of the sample on a single parameter.

INTRODUCTION

One of the most informative diagnostic methods for dielectric materials is the analysis of the complex permittivity ε^* depending on the frequency of the electric field [1, 2]. But the presentation in the form of frequency dependency does not allow to easily analyze data and assess the significance of the deviation from the expected relationship. A more appropriate presentation is a dielectric diagram (Argand diagram) in the complex plane when built dependence of the imaginary part of the complex permittivity ε'' of the real part of it ε', and each point is characterized by individual frequency (Fig. 1). Difference between the real dielectric chart from the reference or change it during the operation can be a means of diagnostics of dielectric materials.

DIELECTRIC DIAGRAM

Dielectric diagram according to the classical equations of Debye is a semicircle with its center lying on the real axis (ε'), and crosses the real axis at the points ε_0 and ε_∞ (see Fig. 1). We introduce the notation

$$\begin{aligned} u &= \varepsilon^* - \varepsilon_\infty, \\ v &= (\varepsilon^* - \varepsilon_\infty) i\omega\tau_0, \\ u + v &= \varepsilon_0 - \varepsilon_\infty, \end{aligned}$$

where τ_0 — relaxation time, ε_0 — the value of the real part of the dielectric permittivity at a frequency $\omega = 0$, ε_∞ — the value of the real part of the dielectric permittivity at a frequency $\omega \to \infty$, the difference between ε_0 and ε_∞ attributed to dipole.

The values v and u may be considered as vectors in the complex plane, and in Debye case they are perpendicular, and their sum is constant and equal to the real value of $\varepsilon_0 - \varepsilon_\infty$.

The deviation from the semicircle can be very large for solid dielectrics. Nevertheless, depending on ε' ε'' still represent circular arcs.

In equivalent circuit for the experimental dependence the impedance is $Z = \tau_0 (i\omega\tau_0)^{-\alpha}/(\varepsilon_0 - \varepsilon_\infty)$, and the phase angle between the active and reactive components does not depend on the frequency and is equal to $\alpha\pi/2$. Since the angle between the axis ε' and the radius vector to the point ε_∞ on diagram arc circle in the complex plane is also equal to $\alpha\pi/2$, it is reasonable to assume that the properties of the dielectric are determined by the value α. Angle $(1-\alpha)\pi/2$ (between the vectors v and u in the complex plane) does not depend on the frequency and is equal to half of the arc angle. Consequently,

$$u + v = u[1 + f(\omega) e^{i(1-\alpha)\pi/2}] = \varepsilon_0 - \varepsilon_\infty,$$

where $f(\omega)$ — real function of frequency and other parameters. Since $e^{i(1-\alpha)\pi/2} = i^{(1-\alpha)}$, then

$$\varepsilon^* - \varepsilon_\infty = (\varepsilon_0 - \varepsilon_\infty)/[1 + i^{(1-\alpha)} f(\omega)].$$

From general considerations, it can be assumed that this relationship will look $\omega^{(1-\alpha)}$, when the complex form ε^* is the result of the initial hypothesis that the applied field is given by $E = E_0 e^{i\omega t}$. If ω is the result of linear operations over the exponent, the dependence on ω is identical to depending on the imaginary unit i, so that

$$\varepsilon^* - \varepsilon_\infty = (\varepsilon_0 - \varepsilon_\infty)/[1 + (i\omega\tau_0)^{1-\alpha}].$$

for $0 < \alpha < 1$.

The dependence of $\ln|u/v|$ on $\ln\omega$:

$$\ln|u/v| = (1-\alpha)\ln\omega\tau_0 = (1-\alpha)\ln\omega + (1-\alpha)\ln\tau_0,$$

* v.klemeshev@spbu.ru
† a.g.karpov@spbu.ru

ISBN 978-3-95450-181-6

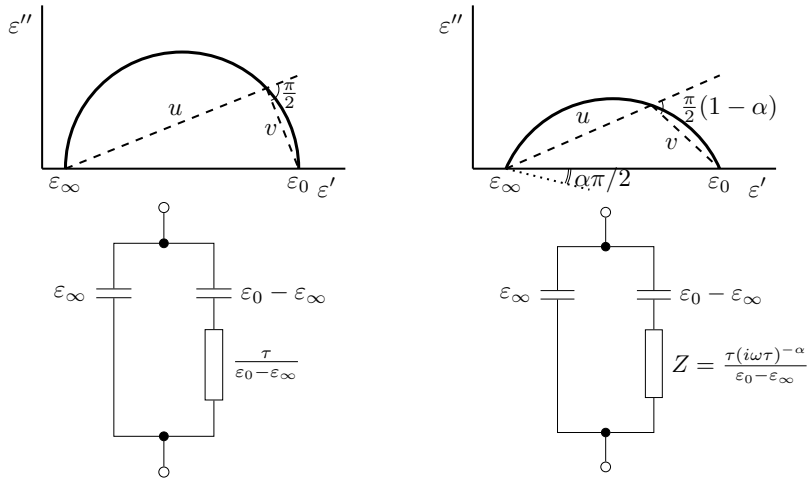

Figure 1: Dielectric diagrams and respective equivalent circuits.

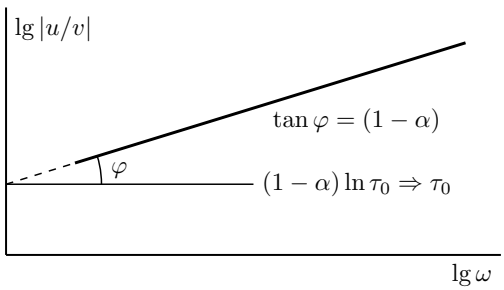

Figure 2: The dependence of $\ln|u/v|$ on $\ln\omega$.

is a linear function of which can be determined α and τ_0 (see Fig. 2).

Then

$$\varepsilon' - \varepsilon_0 = \frac{\varepsilon_0 - \varepsilon_\infty\left[1 + (\omega\tau_0)^{1-\alpha}\sin\frac{1}{2}\alpha\pi\right]}{1 + 2(\omega\tau_0)^{(1-\alpha)}\sin\frac{1}{2}\alpha\pi + (\omega\tau_0)^{2(1-\alpha)}} = \frac{1}{2}(\varepsilon_0 - \varepsilon_\infty)\left[1 - \frac{\sinh(1-\alpha)x}{\cosh(1-\alpha)x + \cos\frac{1}{2}\alpha\pi}\right],$$
$$\varepsilon'' = \frac{(\varepsilon_0 - \varepsilon_\infty)(\omega\tau_0)^{1-\alpha}\cos\frac{1}{2}\alpha\pi}{1 + 2(\omega\tau_0)^{1-\alpha}\sin\frac{1}{2}\alpha\pi + (\omega\tau_0)^{2(1-\alpha)}} = \frac{1}{2}(\varepsilon_0 - \varepsilon_\infty)\frac{\cos\frac{1}{2}\alpha\pi}{\cosh(1-\alpha)x + \sin\frac{1}{2}\alpha\pi}, \quad (1)$$

where $x = \ln\omega\tau_0$. These expressions are reduced to the case of Debye when $\alpha = 0$. If $\alpha > 0$ $(0 \leqslant \alpha \leqslant 1)$ the range of variation of ε^* is expanding, and the maximum of ε'' (at $\omega = 1/\tau_0$) decreases.

Expressions (1) provide the following maximum value ε'' at the point $\omega = 1/\tau_0$:

$$\varepsilon''_{max} = \frac{1}{2}(\varepsilon_0 - \varepsilon_\infty)\tan[(1-\alpha)\frac{\pi}{4}].$$

At very low frequencies (see (1))

$$\varepsilon = (\varepsilon_0 - \varepsilon_\infty)(\omega\tau_0)^{2-\alpha}\cos\frac{1}{2}\alpha\pi.$$

If $\omega \ll 1/\tau_0$, then admittance $\sigma \sim \omega^\gamma$ $(1 \leqslant \gamma \leqslant 2)$, corresponding $0 \leqslant \alpha \leqslant 1$.

EVALUATION OF DEFECTS IN THE DIELECTRIC MATERIAL

To clarify the physical meaning of the deviations of the experimental data from Debye theory, expressed in the value of α, several possible causes have been considered: the effect of dipoles hindered reorientation, the effect of the non-sphericity of the molecules, the complex nature of viscosity. However, the main cause of deviations, in our opinion, is the availability of the distribution of relaxation times around a central τ_0, in particular, due to defects in the sample. Here we are not talking about different phenomena of polarization or non-homogeneity of the material. The distribution of the relaxation times, proposed by Wagner [3], is given by the logarithmic Gaussian type distribution

$$F(s)ds = (b/\sqrt{\pi})\exp(-b^2s^2)ds,$$

where $s = \ln(\tau/\tau_0)$, parameter b determines the width of the distribution. If we use the expression (1) for ε'', we obtain a different distribution function $F(s)$ for relaxators:

$$F(s)ds = \frac{1}{2\pi}\frac{\sin\alpha\pi}{\cosh(1-\alpha)s - \cos\alpha\pi}ds.$$

If we define the ε' and ε'' using numerical integration of this expression it is possible to find b, which most closely matches a given α. For example, if $\alpha = 0.23$, found by the above procedure b is equal to 0.6. Obviously, the Gaussian distribution requires too high a concentration of the relaxation times nearby τ_0, and distribution using α much wider (see Fig. 3). Distribution width increases rapidly with increasing α, and Gaussian distribution is getting worse approximation. For $\alpha = 0.5$ 95% of relaxation times are in the range $0.001 < \tau/\tau_0 < 1000$ whereas only $\alpha = 0.75$ only 72% of relaxation times are in the specified range.

ISBN 978-3-95450-181-6

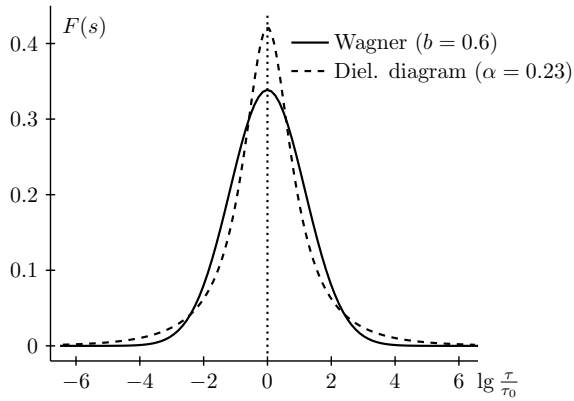

Figure 3: Comparing the distributions of relaxation times, obtained by Wagner and dielectric diagrams.

CONCLUSION

The paper deals with the application of the dielectric diagram as a tool for processing of dielectric information. It has been shown that its study allows to characterize the material under test by parameter α, associated with the emergence of the distribution of relaxation times around the classic Debye relaxation time τ_0. It should be noted that the proposed method is limited to processing of dielectric diagrams representing symmetrical arcs. Also the difficulties of the physical explanation of relaxation time distribution $F(s)$ remain. In addition, the physical sense of the real and imaginary parts of the impedance of the equivalent electrical circuit $Z = \tau(i\omega\tau)^{-\alpha}/(\varepsilon_0 - \varepsilon_\infty)$ are unclear.

REFERENCES

[1] P.J. Hyde, “Wide-frequency-range dielectric spectrometer,” Proc. IEEE. — 1970. — Vol. 117. — N 9. — pp. 1891–1901.

[2] A.G. Karpov, N.V. Egorov, “Automated dielectrometer,” Pribory i tehnika eksperimenta. — 1999.- N 6.— pp. 63–67.

[3] A.P. Aleksandrov et al., *Fizika dielektrikov*; pod red. prof. A.F. Waltera, (M.-L .: GTTI, 1932) 176.

ISBN 978-3-95450-181-6

POSSIBILITIES OF DIFFRACTION RADIATION NON-DESTRUCTIVE DIAGNOSTICS FOR NON- AND MODERATELY RELATIVISTIC BEAMS*

D. A. Shkitov#, A. P. Potylitsyn, Tomsk Polytechnic University, Tomsk, Russia

Abstract

In this report the estimations of diffraction radiation yield from a slit target for European Spallation Source proton beam parameters is given. The possibilities of the non-destructive bunch length diagnostics using the diffraction radiation for non- and moderately relativistic beams of this accelerator are investigated.

INTRODUCTION

Diffraction radiation (DR) in mm wavelength region from relativistic electrons was first observed in 1995 [1]. Since then, the development of new approaches using the DR for charged particle beam diagnostics is continued. The DR is a radiation which occurs when charged particle moves near the media and only the electromagnetic field of particle interacts with the media. One significant advantage of DR diagnostics in contrast with transition radiation (TR) is its non-destructive character.

For instance, a rather well-known in scientific accelerator community the non-destructive diagnostic method of transversal bunch size determination is to use a slit target with optical diffraction radiation (ODR) [2]. Another examples are to use the radiation interference in order to determine such parameters as a bunch emittance based on system of two slit target [3] and a bunch length based on double DR target (where one plate is movable) [4].

However, all of these approaches were tested on the electron accelerators. For proton accelerators the studies of TR/DR application for diagnostics were conducted much less than for electron accelerators. There are a few articles which dedicated to the transverse beam shape measurements of relativistic proton beams using optical transition radiation (OTR) [5-7]. The possibilities of DR transverse size diagnostics for relativistic proton beams were discussed in [8] in optical wavelength range as well.

In this report we present the estimations and simulation results characterizing the DR applicability for non-destructive diagnostics of non- and moderately relativistic proton beams with the parameters of European Spallation Source (ESS) [9].

THEORY BACKGROUND

For the DR simulation we have used the generalized surface current method [10]. This method can be applied for the transition radiation and diffraction radiation calculations from different surfaces and for arbitrary particle energy. However, the only ideal conductivity of the target may be considered.

In our geometry a charged particle moves in the center between two semi-infinite plates through the slit. Using the formula obtained in Ref. [11], we may calculate the spectral-angular distributions in the single particle approximation from the slit target. In Fig. 1 the scheme of DR generation from this target is shown.

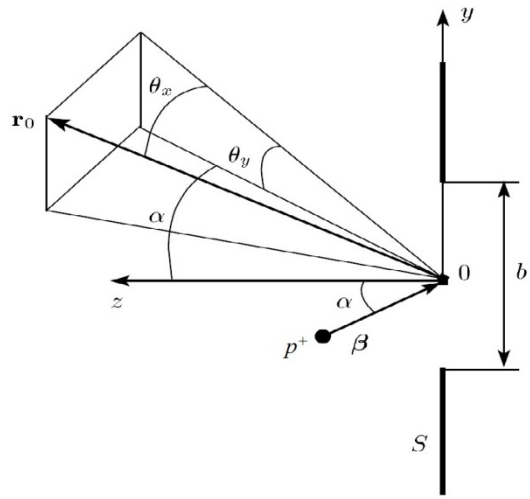

Figure 1: The scheme of DR generation by charged particle [11].

Here β is a particle velocity (in units of the light speed c), α is incidence angle, b is the slit width, S is an area of target surface, r_0 is a distance to observation point, θ_x and θ_y are the observation angles and γ is the Lorentz factor. Hereinafter in our calculations, we will assume that the angle $\alpha = 0°$.

DR YIELD ESTIMATIONS

The ESS is a multi-disciplinary research facility based on the world's most powerful neutron source [9]. The facility includes the most powerful linear proton accelerator ever built. The construction of the facility began in the summer of 2014. In Table 1 the main parameters of ESS proton beam are listed. In this facility the accelerator up to 90 MeV (γ = 1.1) of protons is normal and up to 2 GeV (γ = 3.1) is superconductive.

Table 1: Simulation Parameters

Name	Value
Proton energy, E_e	up to 90 MeV "warm" up to 2000 MeV "cold"
Bunch length, σ_z (r.m.s.)	~1 – 4 mm
Bunch size, σ_t (r.m.s.)	~0.5 – 4.5 mm
Bunch population, N_e	$\sim 1.83 \cdot 10^8$
Bunches in macro-pulse, N_b	$\sim 6.13 \cdot 10^6$
Repetition rate, f	14 Hz
Macro-pulse duration	2.86 ms

* Work was partially supported by the RFBR grant No 15-52-50028.
# shkitovda@tpu.ru

ISBN 978-3-95450-181-6

As we see the amplification of DR spectral-angular intensity due to the coherent effect will be about 10^8 times larger than incoherent radiation from the same beam. Note that in ESS case the coherent radiation appears when observed radiation wavelength $\lambda > 5 - 20$ mm and the impact parameter should be $\geq 4\sigma_t$ (~2 – 18 mm). An exact value of these quantities depends on the bunch length and size.

For the brief estimations we may use the total energy formula [12] of backward DR (BDR) from slit target for single non-relativistic and relativistic particle with charge "e" $W = \frac{3}{4}\left(\frac{e^2}{\hbar c}\right)\beta^2\hbar\omega_c$, where $\omega_c = \frac{\gamma c}{2h}$ is the characteristic frequency of radiation, h is the impact parameter. We assume that a slit width $b = 2h$ ($\alpha = 0°$). These estimations are presented in Table 2 for $\gamma = 1.1$, for higher γ the values of radiation energy will be more.

Table 2: Total Radiation Energy Estimations

h, mm	5	10
b, mm	10	20
ω_c, GHz	33	16
$WN_e^2N_b$ (one macro-pulse)	~4 mJ	~2 mJ
$WN_e^2N_b$ (per second)	~60 mJ	~30 mJ

One of the commercially available detector is MD902 [13] with working frequency range 10 MHz – 40 GHz (wavelength > 7.5 mm) and input signal dynamic range from -40 to +20 dBm (0.1 μW to 100 mW). Assuming uniform distribution of BDR throughout the solid angle of half space, we may estimate the average energy passing through the detector aperture per one second as $WN_e^2N_b \cdot f \cdot \frac{\Delta\Omega}{2\pi} \approx 10$ μW, where $\Delta\Omega = S/r_0^2$, $S = 50\times20$ mm^2 is the detector aperture and $r_0 = 1$ m and b was equal to 10 mm (see Table 1 and 2). We see that 10 μW is reliable value.

We have to note that these estimations were done based on the formula for single particle. For the bunch of particles we need to take into account the longitudinal form factor (see Fig. 2) because of its influence to the radiation spectrum. Even if we will detect 1% from obtained energy (see Table 2) it is enough for the modern detector.

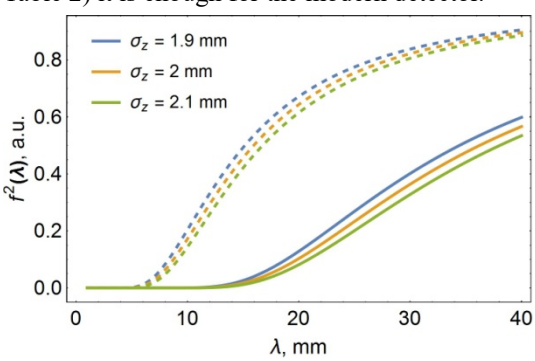

Figure 2: Gaussian longitudinal bunch form factor calculated for different bunch lengths σ_z and energies $\gamma = 3.1$ (dashed lines above) and $\gamma = 1.1$ (solid ones below).

The approach how to detect the TR (or DR) in mm wavelength range is presented in Ref. [14].

SIMULATION RESULTS AND DISCUSSION

Further the results of angular and spectral distribution calculations are described. In this section all simulations were conducted with taking into account the form factor (Fig. 2). The reading direction from top to bottom (↓) of legends and curves in all graphs is matched. Figure 3 shows the DR spectral-angular distributions for two cases of proton energies.

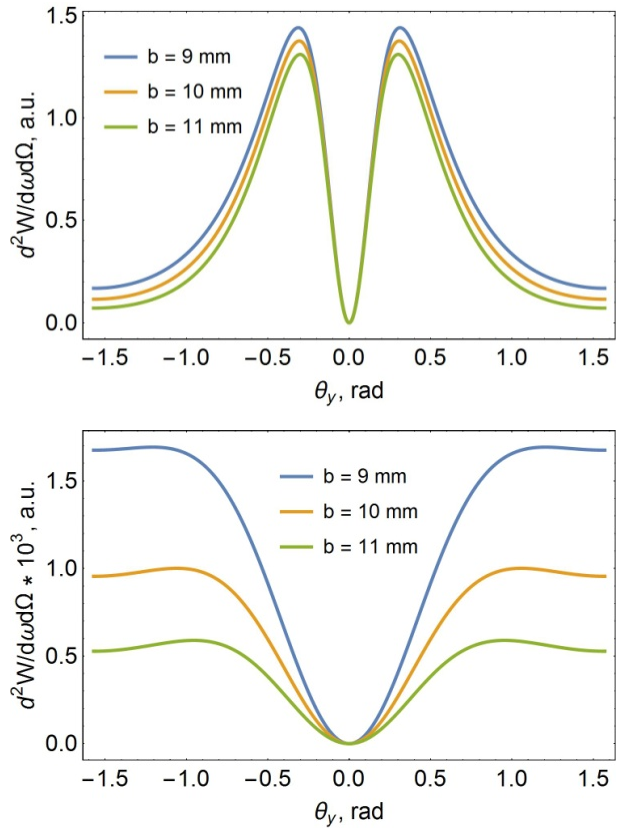

Figure 3: Cross-section of the spectral-angular of DR distributions for two energies $\gamma = 3.1$ (top picture) and $\gamma = 1.1$ (bottom one) with different slit widths. Simulation parameters are $\sigma_z = 2$ mm, $\theta_x = 0$, $\lambda = 25$ mm.

One may clear see these two distributions are significantly different in shape. The quantity $1/\gamma$ for both of the cases is equal to 0.32 rad / 18.5° ($\gamma = 3.1$) and 0.91 rad / 52.1° ($\gamma = 1.1$). It means that the directions of radiation maxima are different for them. This fact should be appreciated in the measurements. Note that in the presented data the relative changes of spectral-angular distributions by reason of the slit width variation are greater for lower energies. These changes depend on the chosen wavelength.

Figure 4 presents the DR spectral distributions for two cases of proton energies as in Fig. 3. These spectral calculations were done in the maxima of above DR distributions. As we observe from these pictures, the DR spec-

ISBN 978-3-95450-181-6

trum is changed with the bunch length. For this reason, after measuring the spectrum we may reconstruct the lengths of bunches in the certain points of accelerator.

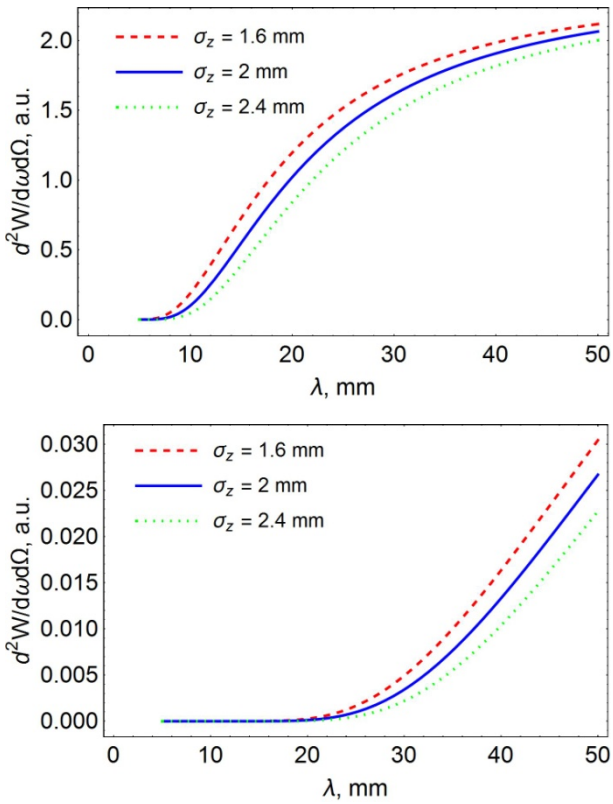

Figure 4: Spectral distributions in the peaks for two energies $\gamma = 3.1$ (top picture) and $\gamma = 1.1$ (bottom one) with different bunch longitudinal sizes σ_z (r.m.s.). Simulation parameters are b = 10 mm, $\theta_x = 0$, $\theta_y = 1/\gamma$.

CONCLUSION

We may conclude the following:

- We propose to consider the DR technique for non-destructive diagnostics of non-relativistic and moderately relativistic ESS proton beams.
- The DR yield from ESS proton beam can achieve the level of 10 μW ($\gamma = 1.1$) and more (in average) which can be detected without problem.
- Technique based on DR may be considered as a diagnostic tool for determination of the bunch length in proton accelerators using coherent radiation measurements. For this purpose we may suppose to use the approach applied in [4] (double DR target) or with the help of interferometer (e.g. Michelson, Martin-Puplett).
- In future studies to analyze the DR properties from non-relativistic beam in more detail is essential. We need to take into account the influence of such beam parameters as transversal size, target tilt angle, beam divergence and so on.

REFERENCES

[1] Y. Shibata et al., "Observation of coherent diffraction radiation from bunched electrons passing through a circular aperture in the millimeter- and submillimeter-wavelength regions", Phys. Rev. E, vol. 52, p. 6787, 1995.

[2] P. Karataev *et al.*, "Beam-Size Measurement with Optical Diffraction Radiation at KEK Accelerator Test Facility", *Phys. Rev. Lett.*, vol. 93, p. 244802, 2004.

[3] A. Cianchi *et al.*, "Nonintercepting electron beam size monitor using optical diffraction radiation interference", *Phys. Rev. ST Accel. Beams*, vol. 14, p. 102803, 2011.

[4] D. A. Shkitov *et al.*, "Non-invasive bunch length diagnostics based on interferometry from double diffraction radiation target", in *Proc. IPAC'13*, Shanghai, China, May 2013, paper MOPME067, p. 583.

[5] S. D. Borovkov *et al.*, "On studying a possibility to use optical transition radiation for proton beam diagnostics", *NIM A*, vol. 294, pp. 101-107, 1990.

[6] V. E. Scarpine *et al.*, "OTR imaging of intense 120 GeV protons in the NuMI beamline at FNAL", in *Proc. PAC'07*, Albuquerque, USA, 2007, paper THOAC02, p. 2639.

[7] V. E. Scarpine, "Transverse beam shape measurements of intense proton beams using optical transition radiation", *Physics Procedia*, vol. 37, pp. 2123-2128, 2012.

[8] T. Sen *et al.*, "Prospects of diagnostics with optical diffraction radiation in hadron colliders", in *Proc. PAC'07*, Albuquerque, USA, 2007, paper TUPAS032, p. 1721.

[9] ESS Technical Design Report, https://europeanspallationsource.se.

[10] D. V. Karlovets, A P. Potylitsyn, "Generalized surface current method in the macroscopic theory of diffraction radiation", *Phys. Lett. A*, vol. 373, pp. 1988-1996, 2009.

[11] D. V. Karlovets, A. P. Potylitsyn, "On the theory of diffraction radiation", JETP, vol. 107, p. 755, 2008.

[12] A. P. Potylitsyn, M. I. Ryazanov, M. N. Strikhanov, A. A. Tishcenko, Diffraction Radiation from Relativistic Particles, Berlin, Springer, 2010.

[13] http://www.micran.com/sites/micran_eng/data/UserFile/pdf/mmic/MD902.pdf.

[14] B. N. Kalinin *et al.*, "Measurement of the angular characteristics of transition radiation in near and far zones", *JETP Letters*, vol. 84, pp. 110-114, 2006.

ISBN 978-3-95450-181-6

THE MAGNETIC ENERGY ANALYZER FOR ELECTRON BEAM OF LUE-200 LINAC OF IREN FACILITY

A.P. Sumbaev, N.I. Tarantin, V.I. Shokin, JINR, Dubna, Moscow region, 141980 Russia

Abstract

Theses for a base substantiation, results of the calculation for the electron optical parameters and design features of the magnetic energy analyzer for the beam of the LUE-200 electron linac are presented. The static dipole magnet with homogeneous transverse field and with a combined function (the function of a spectrometer and of a spectrograph) established after the second accelerating section, allows to spend measurements in a wide energy range of the analyzed particles up to 224 MeV with the instrumentation resolution not worse ±7 %.

INTRODUCTION

IREN Facility [1,2] of the Joint Institute for nuclear research as a particle energy analyzer uses the static analyzer with magnetic spectrometer and functions as a spectrograph. Feature LUE-200 is the vertical axis of the accelerator and beam transport channel to the target, so convenient for hosting and maintenance analyzer configuration is in the form of a dipole magnet with rotation sector beam at an angle of close to $\Phi = \pi/2$, set so that the longitudinal axis of the accelerator tract passes through the magnet median plane. The energy of the accelerated electrons can vary from 15 to 100 MeV, with the one accelerating sections, and up to 100 - 200 MeV when accelerator is operating in full. When you select the main axis provide turning radius analysing magnet R_0 = 0.5 m its magnetic rigidity BR [Tm] = E [MeV]/300 should vary within 0.05 – 0.66 Tm.

ANALYZER DESIGN

The analyzer consists of an electromagnet, the vacuum chamber and the detector - registrar. The principle circuit of the analyzer is presented at Fig. 1. The analyzer electromagnet is made in the “Ш” shape. The yoke of the magnet is mounted on one of the "racks", "beams" of the yoke form the side walls and the median plane of the poles is aligned with the axis of the accelerator. The analyzer is installed in the channel of beam transportation between the second accelerating section and a target (Fig. 2). The magnet is mounted on the rails on which the magnet can be rolled horizontally away from the accelerator (Fig. 3). When the beam is transported to the target, the analyzer is disabled, and the residual magnetization of the yoke is removed by the powering of the magnet from the low current power supply. The current value is selected by the absence of deflection of the beam passing through the analyzer.

To control the position of the beam at the input and output of the vacuum chamber of the analyzer using a “beamviewers”. The analyzer can operate in two modes. When changing beam energy analyzer mode of the spectrometer, the changing of the level of the magnetic field is adjusted for accepting of particles with energies E_0 from 10 MeV to 200 MeV. In the mode of the spectrograph at a fixed level of the field corresponding to the electron energy E_0, the analyzer has ability to simultaneously register particles in the energy range $E_0 \pm 0.5E_0$.

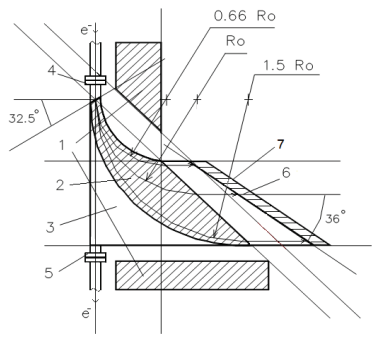

Figure 1: The principle circuit of the analyzer - axial section on median magnet plane. 1 – yoke of the electromagnet, 2 - electromagnet pole, 3 - the vacuum chamber, 4 and 5 - entrance and target branch pipes, 6 - detector window, 7 - the detector - registrar.

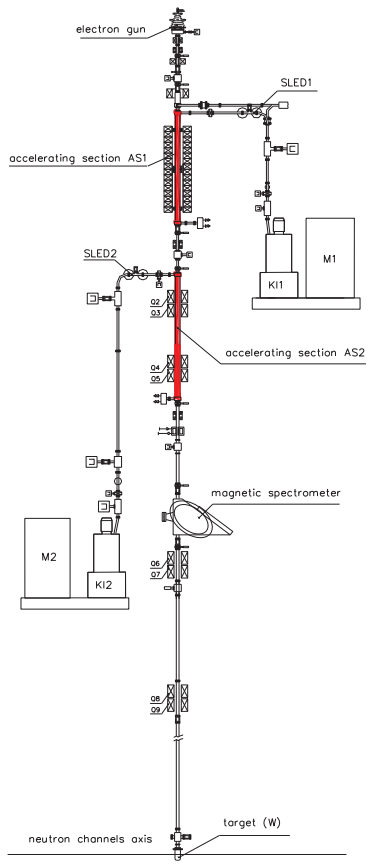

Figure 2: Scheme of the accelerator.

ISBN 978-3-95450-181-6

Figure 3: Layout of the magnet.

CALCULATION OF THE ANALYZER PARAMETRES

Calculation of parameters of magnetic analyzer is performed using the method of matching the initial and final parts of the trajectories of charged particles [3,4]. For numerical simulations, the following beam parameters are used: the beam radius r_1 = 6 mm, beam divergency $\Delta\alpha_1$=1.7 x 10^{-3}. The subscript "1" means input parameter value, and the i subscript "2" means the value of the parameter at the output of the analyzer. According to the Liouville theorem, the magnitude of the emittance of the beam when the dispersion is stored by the analyzer, eliminating the dependence of the size of the focused beam from the largest component of its initial emittance. In this case, "the relative transverse size" of the electron beam $\Delta y_1 = 2r_1/R_0$ = 2.4 x 10^{-2} is substantially more deflection of the particle from the "ideal trajectory" due to the angular divergence of the beam $\Delta\alpha_1$, so of the two types of conversion of the beam magnetic field analyzer "point in point" and "parallels in point" dealt with the latter providing a narrower radial "image" of the beam at the output boundary of the analyzer in its median section and consequently a higher energy resolution. The deflection angle of the optical axis defined by place of the analyzer placement on the beam and placing the device, registering the analyzed electrons is assumed to be π/2. In this case, the axial defocusing effect of the exit boundary of the magnet does not take place and the electrons, crossing the exit border, continue to move in straight lines with no additional discrepancies.

The terms linear radial type conversion "parallels in point" in the magnetic sector analyzer in accordance with [3,4] are of the form

$$\text{tg } p\Phi_1 = \text{tg } \varepsilon_1/p \text{ and tg } p\Phi_2=\text{tg}(\varepsilon_2 + L_2/R_0)/p, \qquad (1)$$

where ε_1 and ε_2 - the angles of the input and output boundaries of the analyser, L_2 - distance from the exit boundary of the analyzer to the radial focal surfaces, Φ_1 and Φ_2 - auxiliary angles that define the plane of matching of the input and output parts of the trajectories in the analyzer, $\Phi_1 + \Phi_1 = \Phi$ - a full deflection angle of the main optical axis of the analyzer, p is the index of the radial decline of the magnetic field. In our case, the analyzing magnetic field made homogeneous (i.e., the simplest formation) with index p = 1.

From (1) follows that the input field of the analyzer will provide an axial type conversion “parallels in point” when the deviation of the electrons in the median plane at an angle of $\Phi = 90^O$, if the angle of inclination of the entrance boundary of the analyser is $\varepsilon_1 = +32.5^O$.

A similar situation holds for the auxiliary optical axes of the analyzer, which illustrate two extreme trajectories with radii of curvature $R_{max} = 1.5R_0$ and $R_{min} = R_0/1.5=0.67\ R_0$. In this case, the exit of the magnetic analyzer boundary is a straight line inclined to the main optical axis and to the auxiliary optical axis at an angle $\varepsilon_2 = -45.0^O$. The auxiliary optical axis parallel to the main optical axis at $\Phi = 90^O$. Local angular dispersion analyzer at the exit boundary is zero on the main and auxiliary optical axis [3,4]:

$$A_\delta = (1/p)\ [(1-\cos p\Phi)\ \text{tg}\ \varepsilon_2 + p \sin p\Phi] = 0.$$

From the condition of the radial transform with $\varepsilon_1 = +32.5^O$ should $\Phi_1 = +32.5^O$, $\Phi_2 = +57.5^O$ and $L_2/R = 0.39$, where R takes the values R_0, R_{max} and R_{min}. In this case the focal surface is a plane inclined in the radial cross-section to the main and auxiliary optical axes at an angle $\gamma = -54.0^O$. The length of the focal plane between the outermost auxiliary optical axes is equal to 0.70 m. The coefficient of linear radial dispersion is equal, according to [3, 4],

$$Y_\delta = L_2(\sin p\Phi_1+\sin p\Phi_2)/pR\ \cos p\Phi_2 = 1.0\ R \qquad (2)$$

normal to the optical axis, and

$$Y_\delta/\cos\gamma = 1.70\ R \qquad (3)$$

along the focal plane. This means that the absolute value of the dispersion along the focal plane are Y_δ = 12.8, 8.5 и 5.7 mm for 1% relative change in the pulse of electrons, respectively for the three electron - optical axes of R_{max}, R_0, and R_{min}. If the value of the magnetic induction = 1.0 T energy values of electrons moving along the three optical axes are equal to 224.4, 149.4 и 98.4 MeV, respectively. While reducing the magnetic induction up to B = 0.447 T the maximum energy of the electrons coming to a focal plane is reduced to 100 MeV, the minimum energy of the electrons is 44.2 MeV. Thus, for two successive cycles of measurements can be analyzed a full range of electron energies from 44 MeV to 224 MeV.

The size of the focal spot along the focal plane is determined by the conversion factor [3,4]

$$Y_\alpha = L_2 \cos\Phi_1/R\cdot\cos\Phi_2 \cdot \cos\gamma \qquad (4)$$

ISBN 978-3-95450-181-6

and the value of the initial angular divergence of the beam $\Delta\alpha_1$. These two values determine the specific sizes of the spots on the focal plane 1.17, 0.71 and 0.48 mm for the three axes R_{max}, R_0 and R_{min}.

The resolution of the magnetic field of the analyzer, determined by the ratio of the coefficient of dispersion (3) to the size of the image (4),

$$R.P. = Y_{\delta}/ Y_{\alpha} \cos\gamma \Delta\alpha_1, \quad (5)$$

is 1190 in the entire focal plane. The reciprocal of the relative energy resolution is $\Delta E/E=8 \times 10^{-4}$.

Technical characteristics of the electromagnet:
- relative magnetic permittivity of μ=1000,
- maximum magnetic induction of 1.0 T,
- the turning radius along the central axis, R_o = 0.5 m,
- inside turning radius R_{min} = 0.66 R_o, = 0.33 m,
- outside turning radius R_{max} = 1.5, R_o = 0.75 m,
- the sector angle along the central axis is π/2,
- interpolar gap of 43 mm,
- the weight of the magnet ~ 1.5 t.

The winding of the electromagnet is made of copper tube with square cross section of 12.5 x 12.5 mm with hole Ø 7.5 mm. Winding parameters:
- number of coils - 2,
- the number of turns in the coil - 49 (7 x 7),
- the average length of the turn - 1.5 m,
- single coil resistance (at 200 C) - 0.03 Ohm,
- the current density in the winding ≤ 5.5 A/mm^2,
- adjustment range current - 0 ÷ 700 A.

THE VACUUM CHAMBER OF THE ANALYZER

Analyser vacuum chamber (Fig. 4) is made of stainless steel flat vacuum cavity, covering the trajectories of particles with energies in the range of $E_0 \pm 0.5 E_0$. Chamber is installed in the interpolar gap of the electromagnet. Chamber has the input flange (1) and output flange (2), the output window to release the beam detector (3), tube for the pumping (4) and detector window (5). The detector window has a rectangular cross section and closes the stainless steel foil with a thickness of 50 μm.

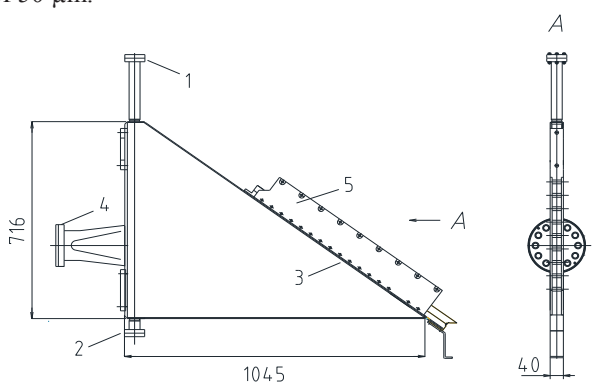

Figure 4: The sketch of the vacuum chamber of the analyser.

THE ANALYZER DETECTOR

The detector is a lamella collector is composed of 37 lead lamellas with dimensions 10 x 40 x 40 mm eacch, installed in the line close to the output window of the vacuum chamber. The lamellas are separated from each other by an insulating plate with a thickness of 1.66 mm. Thus, the step sequence of the lamellas 10 mm + 1.66 mm = 11.66 mm. The input of the detector is set on the "focal plane" of the analyzer magnet at a distance of 0.39R from the edge of the poles of the magnet. The angle of inclination of the plane of the entrance of the detector to the axis of the central trajectory of particles equal 36°. Full size range of the lamellas covers the trajectories of electrons having a radius of 0.33 m to 0.75 m. The amplitude of the electrical signal with separate lamella is proportional to the proportional to the number of particles with energy E_L[MeV] = 300·B·R_L where R_L is the position of the lamella along the radius. The electrical signals of the lamellas are measured in every cycle and processed in mode “off line”.

Design features of the analyzer detector allow to measure energy spectra with a relative accuracy of ΔE/E is not worse than ± 7% with a frequency of cycles not more than 5 Hz. If necessary, the lamellas can be combined in groups of 2, 3 or 4 lamellas. Energy spectrum of an electron beam, when lamellas are combined in groups of 4 is presented at Fig. 5.

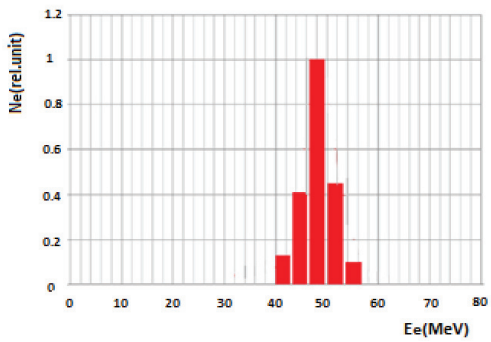

Figure 5: Energy spectrum of an electron beam, measured in process of adjustment of the LUE-200 linac.

REFERENCES

[1] A.V. Novokhatski et al., “Linear accelerator for Intense Resonance Neutron source (IREN)”. Proc. of the 2nd Workshop on JINR Tau-Charm Factory, JINR, D1,9,13-93-459, p. 197, Dubna, 1994.

[2] Boettcher Ju., et al., “LUE-200 Accelerator Of IREN Facility: Current Status And Development”, Physics Of Elementary Particles And Atomic Nucl. Lett. 2014. V. 11, N 5, P. 1029-1039.

[3] N.I. Tarantin, Journal of technical physics, 1979, V. 49, p. 251 - 263.

[4] N.I. Tarantin, “Magnetic static analyzers of charged particles. Fields and linear optics”. Moscow, Energoatomizdat, 1986.

ISBN 978-3-95450-181-6

THE LONGITUDINAL BROADBAND IMPEDANCE AND ENERGY SPREAD MEASUREMENTS AT VEPP-4M

V. M. Borin[1], V. L. Dorokhov, V. A. Kiselev, G. Ya. Kurkin, O. I. Meshkov[1], S. A. Nikitin, M. A. Skamarokha, Budker Institute of Nuclear Physics, Novosibirsk, Russia
[1]also at Novosibirsk State University, Novosibirsk, Russia

Abstract

The paper presents studies of the longitudinal broadband impedance of VEPP-4M and measurements of its bunch energy spread at different energies in range of 1.45 – 3.5 GeV. In order to measure the longitudinal bunch size at different currents we used "PS-1/S1" streak camera with picosecond temporal resolution. Considering that influence of collective effects is negligible at low currents we determined bunch energy spread from its length at low currents. Collected bunch length data demonstrate microwave instability thresholds and potential well distortion lengthening. Potential well distortion was studied at 3 GeV and 3.5 GeV. Measured potential well distortion lengthening was used to estimate a value of the reactive part of the longitudinal impedance. Observed microwave instability thresholds was used to measure the value of broadband impedance. Measured value of the VEPP-4M is 7.9 ± 1.5 Ω.

ELECTRON BUNCH LENGTH

Natural Length

A length of the electron bunch is determined by synchrotron oscillations and has no current dependence if collective effects are negligible [1]. While the energy spread is determined by the balance between quantum excitation and synchrotron damping, so longitudinal bunch size σ_S and its relative energy spread σ_E / E are:

$$\sigma_S = \frac{\sigma_E}{E}\frac{\alpha c}{\omega_S}, \qquad (1)$$

where α is the momentum compaction factor, c is the speed of light, ω_s is the synchrotron oscillation frequency.

Intrabeam Scattering

With the increasing of electrons density in the bunch the effects of the intrabeam scattering (or multiple Touscheck effect) becomes significant. The effect is based on transferring of momentum from transverse plane of motion to the longitudinal that leads to growth of bunch energy spread and bunch lengthening [2]. Growth of energy spread can be obtained as a solution of (2-4):

$$\left(\frac{\sigma_{ET}}{E}\right)^6 = \frac{N r_0^2 \beta_x \tau_E \omega_S f(x_m)}{2^5 \pi \gamma^3 \left(\beta_x U_x + \eta^2\right)\sqrt{k\beta_z U_x}\alpha}; \qquad (2)$$

$$\chi_m = \frac{N^{1/3} r_0 \beta_x^2 Q_s^{1/3} \left(\sigma_{ET}/E\right)^{-3}}{2\sqrt{\pi}\gamma^2 \left(\beta_x U_x + \eta^2\right)^{7/6} \left(k\beta_z U_x\right)^{1/6} (\alpha R)^{1/3}}; \qquad (3)$$

$$f(\chi_m) = \int_{\chi_m}^{\infty} \frac{1}{\chi} \ln\left(\frac{\chi}{\chi_m}\right) e^{-\chi} d\chi. \qquad (4)$$

Where N is a number of particles in the bunch, βx, βz is a horizontal and vertical beta functions, τ_E is a synchrotron damping time, γ is the Lorentz factor, η is a dispersion function, k is a betatron coupling, r_0 is the classical electron radius, Q_s is a synchrotron tune, σ_{ET} is the energy spread induced by intrabeam scattering, U_x is determined by (5).

$$U_x = \frac{\tau_x}{\tau_E} < \frac{1}{\beta_x}\left[\eta^2 + \left(\beta_x \eta' - \frac{1}{2}\beta_x' \eta\right)^2\right] > \qquad (5)$$

Where τ_x is horizontal betatron damping time and the averaging is made in bending magnets only. Since these effects are independent then the total bunch length is quadratic sum of lengths.

Wake Field Interactions

There are two effects appearing due to interaction of the bunch with induced wake fields. First is the effect of potential well distortion that leads to bunch lengthening or shortening depending on the value of impedance. The synchrotron frequency shifts due to this effect also. The effect can be observed even at low bunch currents. Lengthening caused by this effect is expressed by (6).

$$\left(\frac{\sigma_s}{\sigma_{s_0}}\right)^3 - \left(\frac{\sigma_s}{\sigma_{s_0}}\right) + I_b \frac{\alpha Im\left[\left(z_\square / n\right)_{eff}\right]}{\sqrt{2\pi} E Q_{s_0}^2}\left(\frac{R}{\sigma_{s_0}}\right)^3 = 0 \qquad (6)$$

Where I_b is the bunch current, E is a bunch energy, R is an average radius of accelerator, $Im\left[\left(z_\square / n\right)_{eff}\right]$ is an imaginary part of the longitudinal effective impedance and subscript 0 stands for values at low currents where the effect is negligible.

As bunch current increase, as we can observe a threshold of the microwave instability. The effect leads to a growth of a length and energy spread of the bunch but the synchrotron frequency of the bunch remains undisturbed [3]. Microwave instability threshold is determined by (7).

$$I_{th} = \frac{\sqrt{2\pi}\alpha E \sigma_s}{R\left|z_\square / n\right|_{BB}}\left(\frac{\sigma_E}{E}\right)^2 \qquad (7)$$

Where I_{th} is the threshold current and $\left|z_\square / n\right|_{BB}$ is an absolute value of the longitudinal broadband impedance.

ISBN 978-3-95450-181-6

Above the threshold we have an influence of both effects on the bunch length and the lengthening is described by Eq. (8) [3].

$$\sigma_s^3 = \frac{R^3 \alpha I_b}{\sqrt{2\pi} E Q_{S0}^2} \left(\left| z_\square / n \right|_{BB} - Im\left[\left(z_\square / n \right)_{eff} \right] \right) \qquad (8)$$

EXPERIMENTS

For our purposes we need to measure a bunch length and synchrotron damping time. Other parameters of the VEPP-4M are known and presented in the Table 1 and Table 2.

Table 1: VEPP-4M Parameters

Parameter	Value
Momentum compaction factor	0.016
Circumference	366 m
U_x	25 cm
Optical functions $\beta_x/\beta_z/\eta$	4.4/12.9/0.82 m
e	0.04
Revolution frequency	818.924 kHz

Table 2: Synchrotron Tune

Energy, MeV	Synchrotron tune
1558	0.0091
1865	0.0103
3000	0.0125
3500	0.0140

The "PS-1/S1" streak camera was implemented into optical diagnostics of the VEPP-4M for measurements of the longitudinal bunch size [5, 6]. The camera had a temporal resolution about 3 ps. The example of longitudinal profile of the bunch acquired by the camera is shown in Fig. 1.

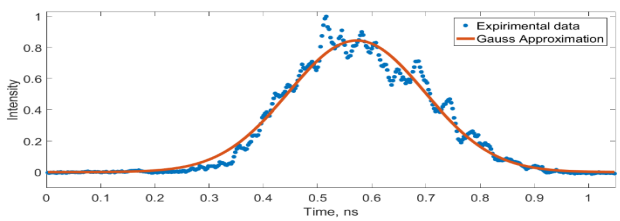

Figure 1: The longitudinal profile obtained by the streak camera.

Besides the longitudinal size we need to measure the synchrotron damping time in order to calculate the energy spread induced by intrabeam scattering.

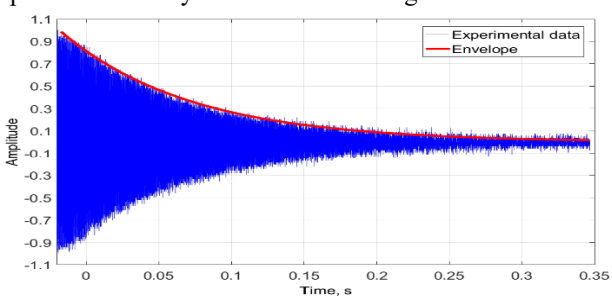

Figure 2: Synchrotron damping time measurements.

For these measurements we applied the fast phase detector which is used in the longitudinal feedback system of the VEPP-4M [4]. The acquired data are presented in Fig. 2.

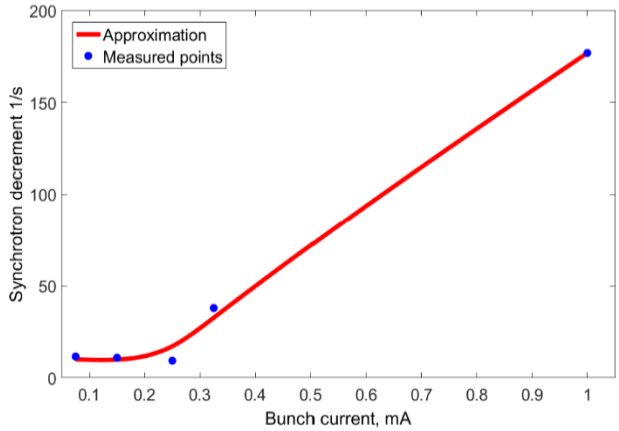

Figure 3: A dependence of the damping time vs bunch current.

We have measured the synchrotron damping time only at the energy of E = 1865 MeV. The experiments revealed the current dependence of the damping time (Fig. 3). We believe that it's caused by collective effects. The measured value of the damping time is τ_E = 94±11 ms and calculated value is $\tau_E \approx$ 100 ms. We have used the beam current less than 250 μA (Fig. 3) for these calculations.

Longitudinal Impedance

The next step was the measurements of the longitudinal bunch size at different currents and energies of the accelerator. At energy of 1865 MeV we can observe the thresholds of microwave instability (Fig. 4, 5).

Using measured data and Eq. (7) we measured longitudinal broadband impedance $\left| z_\square / n \right|_{BB}$ from thresholds of microwave instability at different energies (Table 3).

Table 3: Impedance Measurements

Energy, MeV	Threshold, mA	Impedance, Ohm
1558	0.3±0.1	7.7±1.4
1865	0.5±0.1	7.3±1.4
3000	1.7±0.3	8.8±1.7

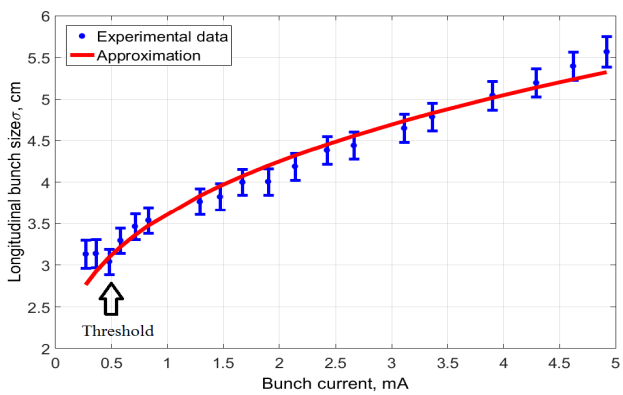

Figure 4: The bunch length at the energy E= 1865 MeV.

ISBN 978-3-95450-181-6

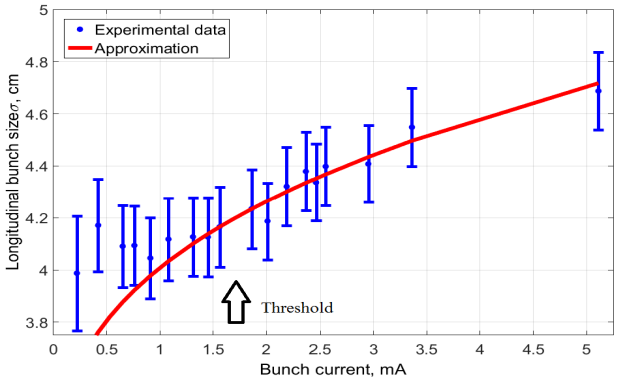

Figure 5: The bunch length at the energy $E = 3000$ MeV.

The average value of impedance is 7.9±1.5. Unfortunately we can't observe the influence of potential well distortion. We can only estimate maximum value of imaginary part of the longitudinal effective impedance which is $\mathrm{Im}(z_0/n)_{\mathrm{eff}} \approx -1$ ohm. The estimation was made using Eq. (6) with the assumption that the lengthening is smaller than the instrumental function of the streak camera. The estimation is in a good agreement with lengthening fitted by Eq. (8). The fit was performed at the bunch current superior the threshold.

Energy Spread

We have measured a relative energy spread σ_E / E using bunch length data at beam currents less than 0.3 mA applying Eq. (1). As we know a natural bunch length is proportional to the bunch energy. Thus it's expected that if we exclude energy spread induced by intrabeam scattering then the energy spread will be fitted by linear approximation. We were able to determine the intrabeam scattering effect only at the energy of 1865 MeV. The total energy spread was $\sigma_E / E = 3.2 \cdot 10^{-4}$ and impact of intrabeam scattering obtained as a solution of (2-4) was $0.74 \cdot 10^{-4}$ thus we conclude that natural energy spread is $3.1 \cdot 10^{-4}$. From Eq. (2) we see that intrabeam scattering effect is inversely proportional to bunch energy. Using this fact, we can expect that at the energies of 3 and 3.5 GeV this effect is negligible. Then we can assume that measured energy spread at these energies is natural energy spread. Using values of energy spread at $E = 1865$, 3000 and 3500 MeV we made linear fit of energy spread. The results are presented in Fig. 6.

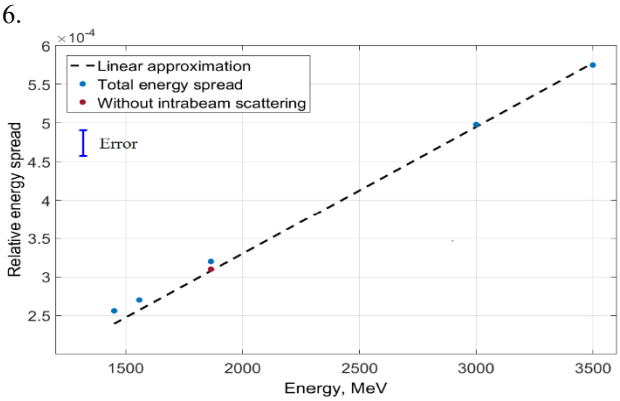

Figure 6: The measured energy spread.

Here we can see that the total energy spread is deviated from this fit. This deviation is due to the intrabeam scattering. Using the deviation, we can estimate energy spread of this effect at lower energies. The results of this estimation are presented in the Fig. 7.

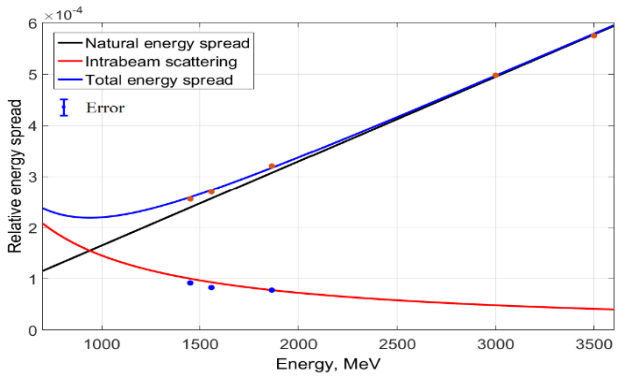

Figure 7: An expected behaviour of the energy spread.

CONCLUSION

We have observed the effect of intrabeam scattering and the microwave instability measuring dependence of beam length on the beam current. To complete this study, we are going to measure a bunch length and synchrotron tune at lower range of energies to prove the existence of minimum of the energy spread of a beam as it is shown in Fig. 7.

ACKNOWLEDGMENTS

The presented experimental results were implemented due to financial support of the Russian Science Foundation (Projects N 14-29-00295).

REFERENCES

[1] M. Sands, "The physics of Electron Storage Rings, An Introduction", SLAC Report 121 (1971), pp. 128-129.

[2] J. Le Duff, "Single and Multiple Touschek Effects" in *Proc. of CERN Accelerator School*, CERN 89-01, 1995.

[3] A. Chao, "Wake Fields and Impedances" in *Physics of Collective Beam Instabilities*. New York: Wiley, 1993, pp. 38-126.

[4] G. Kurkin, et al., "Commissioning of the VEPP-4M Longitudinal Feedback System", *ICFA Beam Dynamics Newsletter*, No 48, (2009) pp. 191-195.

[5] S.G. Garanin et al., PS-1/S1 picosecond streak camera application for multichannel laser system diagnostics, Quantum Electron. 44 (2014) 798.

[6] O. I. Meshkov et al. The upgraded optical diagnostics of the VEPP-4M collider. Proceedings of EPAC 2004, Lucerne, Switzerland, pp. 2739-2741.

ISBN 978-3-95450-181-6

THE PEPPER-POT EMITTANCE MEASURING DEVICE AT THE 400 keV H-MINUS LEBT CHANNEL

V.S. Klenov, S.E. Bragin, O.T. Frolov, S.E. Golubovski, O.V. Grekhov, O.M. Volodkevich, V.N. Zubets, Institute for Nuclear Research Russian Academy of Sciences, Moscow, Russia

Abstract

The emittance measuring device has been developed for operational control of INR RAS linac 400 keV H-minus injector beam parameters. It includes the "pepper-pot", the quartz screen, the CCD camera, PC, the software for camera data processing and beam phase portrait formation. The device has been mounted at the first straight section extension of H-minus LEBT after 45 degree bending magnet. When the bending magnet is switched off the device is possible to measure and to represent single shot beam phase portrait. The results of the H-minus beam emittance measurements and the device performance have been discussed.

INTRODUCTION

Registration of light, received on the scintillator after passing the ion beam through mask with a set of holes ("pepper-pot"), allows, in principle, to measure the emittance of the ion beam in a single shot beam pulse.This method of measuring the emittance associated with the interception of the beam, and is usually implemented by inputting the emittance measuring device into the beamline [1-2]. The H-minus LEBT of INR RAS linac contains 45 degree bending magnet, this allowed to mount an emittance measuring device at the straight extension after bending magnet (Fig. 1). Aiming beam at device is possible to produce by switching off the bending magnet, and the parameters of beam emittance at the entrance to the bending magnet can be calculated from the experimentally obtained values by the reverse linear transformation for a drift length through the magnet.

EQUIPMENT, CALIBRATION AND EXPOSURE REDUCING

For testing of this emittance measuring device in the H-minus LEBT channel of INR RAS linac was assembled the system, which included "pepper-pot", the quartz screen and the CCD-camera type "VIDEOSCAN-415-USB".

Diagram of this emittance measuring device is shown in Fig.2 The camera uses CCD-matrix SONY ICX415AL with 780*582 pixels image format and 12-bit digitization. "Pepper-pot" had a set of holes with a diameter of 0.2 mm, arranged with a pitch of 3 mm for a field of approximately 100x100 mm^2. Distance from "pepper-pot" to the screen was 200 mm.

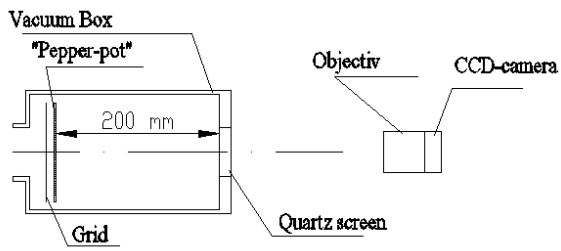

Figure 2: Diagram of emittance measuring device.

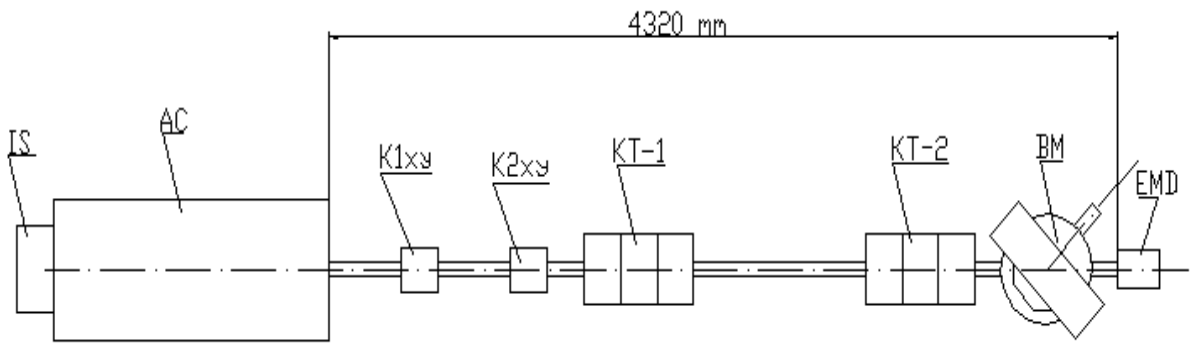

Figure 1: Scheme of the beam line channel with the emittance measuring device. IS – H-minus ion source, AC – 400 keV acceleration column, K1xy, K2xy – steering magnets, KT-1, KT-2 - quadrupole triplets, BM – bending magnet, EMD - emittance measuring device.

ISBN 978-3-95450-181-6

A camera calibration by irradiation of "pepper-pot" with parallel beam light is performed before emittance measurement. As a result of calibration the "binding" of the image is performed, i.e. the pixel in the matrix of the camera corresponding to the center of axial hole of "pepper-pot" is located.

Figure 3: Example photo of the beamlets after "pepper-pot" on the quartz screen.

Then the calibration coefficient Kc has been determined. This coefficient Kc is the ratio of the distance between the centers of two adjacent holes of "pepper-pot" (which is equal to 3 mm for our “pepper-pot”) to the number of pixels separating this images on the camera. Kc~0.232 mm/pix has been obtained in the result of calibration.

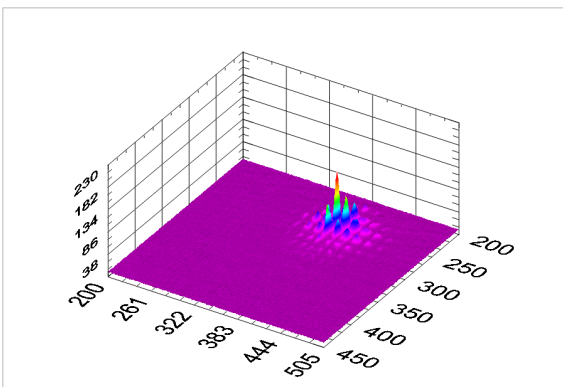

Figure 4: The intensity distribution obtained from the processing of image Fig.3 (after the subtraction of the data file without illumination by ion beam).

Fig. 3 shows an example of illumination of the screen, obtained with a beam of H-minus ions with energy of 400 keV. File of 12-bit data values from the array pixels were saved in bmp format for later processing.

A file of values pixels of CCD- matrix was recorded without ion beam to reduce the influence of background lighting of the screen. Then these values were subtracted from values obtained with the ion beam on the screen. Fig.4 shows an example of intensity distribution, obtained after this procedure of subtraction.

THE ALGORITHM OF DATA PROCESSING AND DETERMINATION OF BEAM EMITTANCE

Integrating the distribution function f(x,y), shown in Fig.4, on the Y or X direction, the resulting we get intensity distributions along the X or Y axis respectively. To exclude the effect of the remaining noise on data processing, we subtract from the obtained data of the function f(x,y) the value, equal to 0.1 of the maximum value of the function f(x,y). As a resultwe obtain intensity distribution with clearly separated " spikes", which corresponds to the holes of the "pepper-pot" (Fig. 5). Square of the "spikes" is proportional to the fraction of the beam passing through vertical or horizontal rows of "pepper-pot" holes.

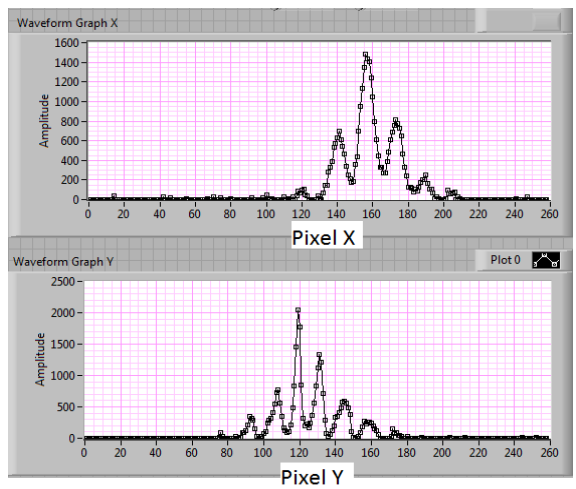

Figure 5: Intensity distributions along the X or Y axis.

Consider the intensity distribution of the beam along the X axis. Each separate n–th "spike", corresponding to the fraction of the beam that passes through an n–th vertical row of holes of "pepper-pot", has a width of N_n pixels. Each point of the n-th "spike" can be assigned in accordance the angle of the particle in a beam X'_m and the level of intensity of w_m, where $m=1,2,...,N_n$. The results of the calibration of the camera were used to calculate the angles of deviation X'_m. Thus, we obtain the intensity distribution in the coordinate X and angle X' for the entire beam at the "pepper-pot". It is the input data array to determine the configuration and parameters of the beam emittance in XX' plane. First and second moments of the beam intensity distribution w(x,x') are calculated based on these data. N is the total number of points.

ISBN 978-3-95450-181-6

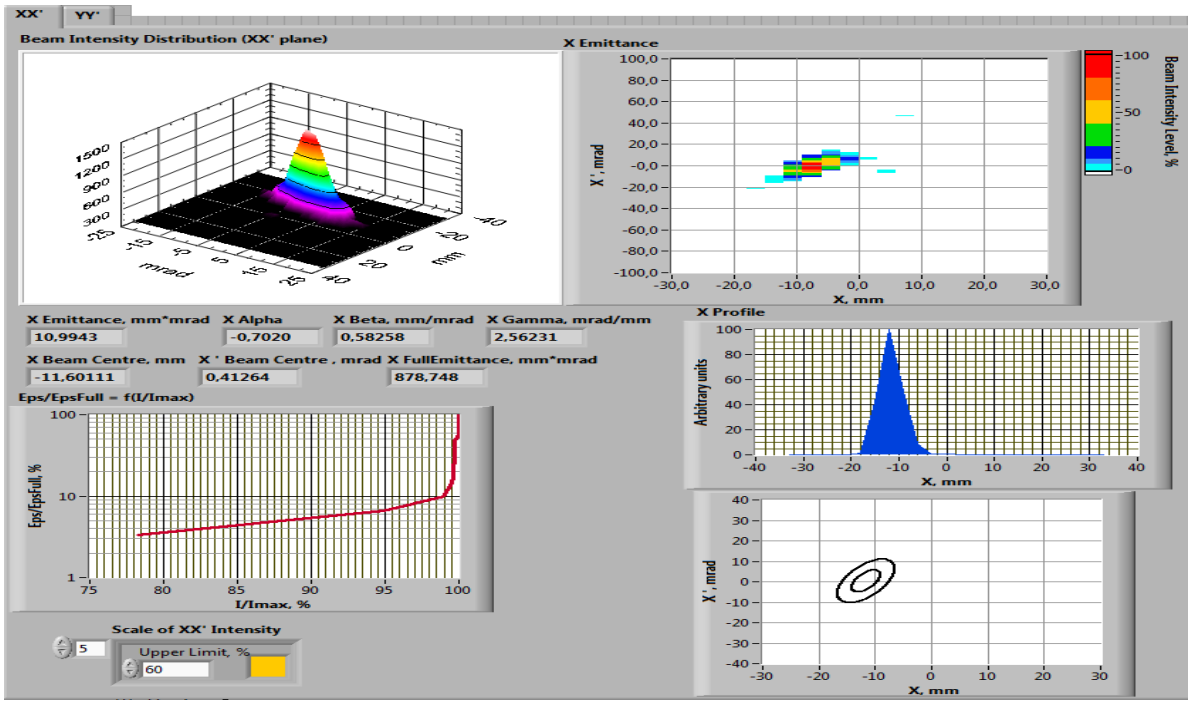

Figure 6: Data processing results.

$$\bar{x} = \frac{\sum_{i=1}^{N} x_i \cdot w_i}{\sum_{i=1}^{N} w_i} \; ; \; \bar{x}' = \frac{\sum_{i=1}^{N} x_i' \cdot w_i}{\sum_{i=1}^{N} w_i} \; ;$$

$$\langle x^2 \rangle = \frac{\sum_{i=1}^{N} (x_i - \bar{x})^2 \cdot w_i}{\sum_{i=1}^{N} w_i} \; ;$$

$$\langle x'^2 \rangle = \frac{\sum_{i=1}^{N} (x_i' - \bar{x}')^2 \cdot w_i}{\sum_{i=1}^{N} w_i} \; ;$$

$$\langle xx' \rangle = \frac{\sum_{i=1}^{N} (x_i - \bar{x})(x_i' - \bar{x}') \cdot w_i}{\sum_{i=1}^{N} w_i} \; ;$$

The value of RMS emittance is determined by:

$$\varepsilon_{Xrms} = \sqrt{\langle x^2 \rangle \langle x'^2 \rangle - \langle xx' \rangle^2} \; ;$$

And calculated Twiss-parameters of the ellipse:

$$\alpha_X = -\frac{\langle xx' \rangle}{\varepsilon_{Xrms}} \; ; \; \beta_X = \frac{\langle x^2 \rangle}{\varepsilon_{Xrms}} \; ; \; \gamma_X = \frac{\langle x'^2 \rangle}{\varepsilon_{Xrms}}$$

Fig.6 shows the following results of the date processing: 3-dimensional beam intensity distribution, diagram of the intensity of the beam (X Emittance) at selected beam intensity level, the beam profile obtained by integrating values of the intensity distributions over the angles for each coordinate, the dependence of the beam emittance on the share of current, phase ellipses for $\varepsilon_{x\,rms}$ and for $4 \cdot \varepsilon_{x\,rms}$.

Here the parameters of the emittance obtained at the position of "pepper-pot". Parameters of the emittance at the entrance to the bending magnet prior to the "pepper-pot" on the drift distance L, can be recalculated as follows:

$$\beta_{X0} = \beta_X + 2L\alpha_X + L^2\gamma_X \; ;$$

$$\alpha_{X0} = \alpha_X + L\gamma_X \; ;$$

$$\gamma_{X0} = \gamma_X$$

For the YY' plane, all parameters are calculated similarly.

CONCLUSION

The pepper-pot emittance measuring device has been tested at the 400 keV H-minus LEBT channel of the INR RAS linac and the possibility to measure the emittance of the ion beam in a single shot beam pulse was demonstrated.

REFERENCES

[1] A. Pikin, A. Kponou, J. Ritter, V. Zajic "Pepper-Pot Emittance Meter" C-A/AP/#244 (2006), Brookhaven National Laboratory.

[2] Min Zhang, "Emittance Formula for Slits and Pepper-pot Measurement", FERMILAB·TM-1988, (1996).

ISBN 978-3-95450-181-6

MODERNIZATION OF THE ELECTRON BEAM STABILIZATION SYSTEM IN THE KSRS

K. Moseev#, E. Kaportsev, Y. Krylov, A.Valentinov,
NRC Kurchatov Institute, Moscow, Russia

Abstract

The stabilization system is designed to prevent drift of the spot SR at the experimental stations by local changes of the orbit. This system was developed and implemented about twelve years ago as an element of the ACS and worked well. Produced by modernization has led to the need of adaptation of the system of stabilization not only in hardware but also in software. Work on updating of the stabilization system and will be shown next.

The running cycle of Kurchatov Synchrotron Radiation Source (KSRS) includes the injection of electrons with energy 80 MeV from the linear accelerator in the booster storage ring Siberia-1, the accumulation of a electron current up to 400 mA and, then, electron energy ramping up to 450 MeV with the subsequent extraction of electrons in the main ring, storage ring Siberia-2, and accumulation there up to 300 mA, and at last the energy ramping up to 2.5 GeV. [1] This mode is the basic mode for obtaining SR by users of the experimental stations. The high stability of the x-ray beam at the entrance of the experimental station is one of the most important conditions for the successful functioning of the SR source. (Fig.1)

LOCAL FEEDBACK SYSTEM TO CORRECT SYNCHROTRON RADIATION BEAM POSITION AT SIBERIA-2 STORAGE RING

Stabilization system (SS) is part of a control system of accelerator complex and is designed to prevent drift of the spot SR at the experimental stations by local changes of the orbit [2].

Stabilization system provides feedback spot position SR at the experimental stations and the current in the correctors. Information about the position of the spot SR is obtained from the video camera, then it is calculated the deviation from the nominal position and the value of the required correction. Needed position of the beam in the area of the controlled channel is provided specific for this channel set, containing 3 or 4 corrector, so that the changes don't affect the orbit outside the correction area (Fig.2).

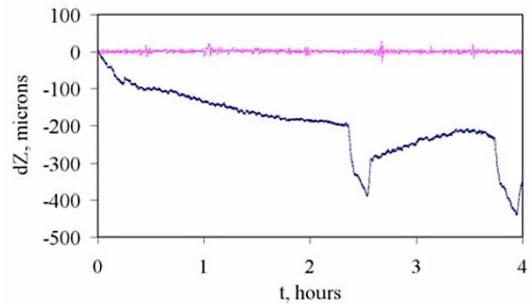

Figure 1: SR beam position at an entrance of experimental station. Bottom line – feedback system is switched off, top line – feedback is switched on. Standard deviation from initial position in last case was 4.5 microns.

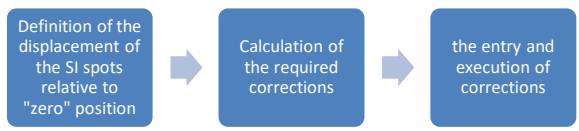

Figure 2: The principle of the stabilization system.

LOCAL FEEDBACK SYSTEM. REALIZATION AND MODERNIZATION

SR beam position monitor is a stripe of phosphor using side part of SR beam. A few dozen frames of digital image exposure is processed to determine the center of the spot of SR. The output of the program is the value of deviation of the beam from the nominal position. This value is written to the database table. Further there is a similar process the next channel. The operator at any time has the ability not only to enable or disable the stabilization, but also to adjust the position of the SR spots. In addition, there is the ability to accurately define the area of illumination to reduce the impact of probable defects of the camera and the phosphor (Fig.3).

The program calculate the necessary correction values, referring to the database, receives the position deviation of the beam from the nominal position and the set of coefficients for the calculation, selected in advance. The result of this program is the set of values of the currents of the correctors are also recorded in the database table. Further, similarly calculated for other stations (Fig.4).

#kirit@yandex.ru

ISBN 978-3-95450-181-6

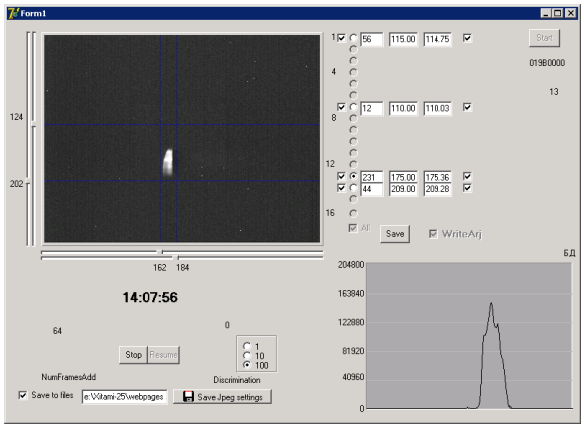

Figure 3: Program of determination of the spot position SR.

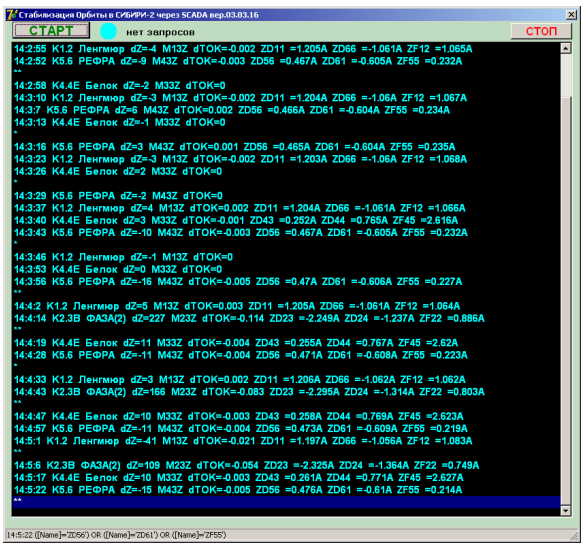

Figure 4: The program of calculate the necessary corrections.

Program designed for entering setpoints (BANK), taking data from the database, puts the calculated currents in the DAC power sources of the correctors by using the programmable controller K167.

The division of the system into blocks and use database tables allows you to add new stabilized channels and change the stabilization settings simple edit the appropriate fields in the database without making any changes to the program code. This system was developed and implemented about twelve years ago as an element of ACS and well-proven. Started a few years ago the modernization of the automated control systems of accelerator complex has led to necessity of adaptation of the stabilization system both in hardware and software.

The introduction of the SCADA system of the company Citect changed the organization of data exchange. The replace the power supply UM-6 and TIR-25 to PCS-6A and PCS-20A and using the power control correction (BUK) required the use of a controller of the magnetic system (CCMS) NI cRIO-9081 [3-5].

The updated system of the stabilization program the deviation of spot position SR is used with minimal changes.

The program calculate the necessary correction values, referring to the database, receives the position deviation of the beam from the set and the set of coefficients to calculate, chosen in advance, however, the output from this program is used by the SCADA system, which creates a boot table for the controller of the magnetic system. Next, the CCMS, based on the values obtained, generates commands for the BUK, which directly controls the power supplies of correctors.

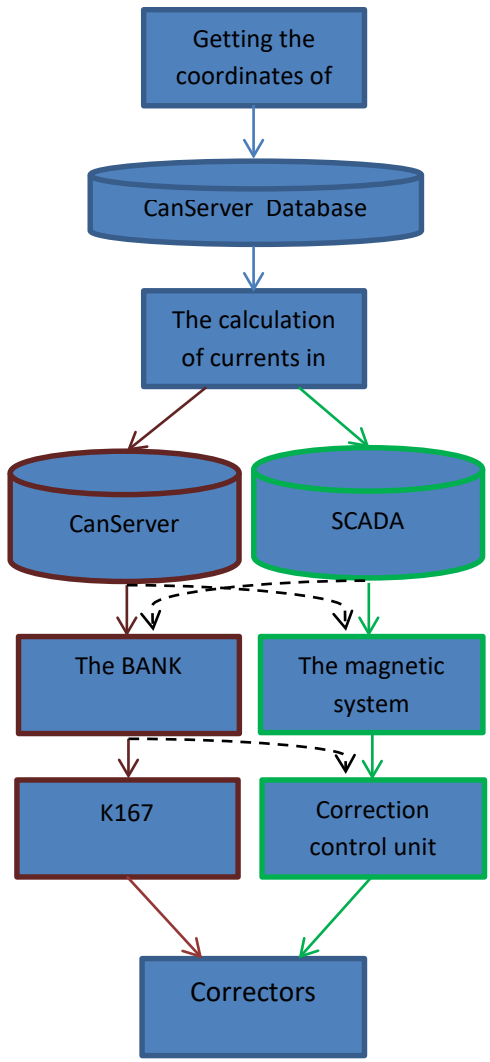

Figure 5: The old and the new stabilization system.

The upgrade is performed without stopping complex, so it is important to maintain compatibility of software and hardware units of the old and updated control systems. To achieve compatibility, the program calculating the correction value, outputs the result of calculation in the database, and SCADA. Program BANK got the opportunity to take source data not only from databases, but also from the SCADA and to operate not only K167, but BUK (Fig.5).

ISBN 978-3-95450-181-6

This approach leads to redundancy, however, allows the use of both new and old components and software modules in almost any combination, which in turn allows you to debug new and modified during technological breaks in the work setting.

REFERENCES

[1] V.Korchuganov et al., Kurchatov Synchrotron Radiation Source Facities Modernization. Proceedings of RuPAC XXII, Protvino, Russia, 2010.

[2] A.Valentinov et al., Local feedback system to correct synchrotron radiation beam position at Siberia-2 storage ring. Proceedings of RuPAC XIX, Dubna 2004.

[3] V. Dombrovsky et al., New automated control system at Kurchatov Synchrotron Radiation Source based on SCADA system Citect. Proceedings of ICALEPCS2013, San Francisco, CA, USA.

[4] E. Kaportsev et al., Modernization of the automated control system in the Kurchatov Synchrotron Radiation Source, Proceedings of RUPAC2012, Saint-Petersburg, Russia.

[5] E. Kaportsev et. Al, Modernization of the automated control system in the Kurchatov Synchrotron Radiation Source using SitectSCADA , Proceedings of RuPAC2014, Obninsk, Kaluga Region, Russia.

ISBN 978-3-95450-181-6

ELECTRODYNAMIC CHARACTERISTICS OF RF-DEFLECTOR FOR BUNCH SHAPE MONITOR

D. Chermoshentsev[†1], A. Feschenko, S. Gavrilov, Institute for Nuclear Research of the Russian Academy of Sciences, Moscow, Russia and Moscow Institute of Physics and Technology, Moscow, Russia
[1] also at Skolkovo Institute of Science and Technology, Skolkovo, Russia

Abstract

Bunch shape monitors, based on a transverse RF-scanning of secondary electrons, are used for measurements of particles longitudinal distribution in bunches at different linear ion accelerators. The phase resolution of such monitors depends crucially on accuracy of fabrication and tuning of RF-deflector, thus preliminary simulations of its electrodynamic characteristics are of importance for subsequent commissioning of the monitor. Simulations of basic operational electrodynamic parameters and some experimental results are presented.

INTRODUCTION

Bunch shape monitor (BSM) [1] uses the technique of coherent transformation of a temporal bunch structure into a spatial charge distribution of low energy secondary electrons through RF-modulation [2]. The main part of BSM is RF-deflector. The deflector is combined with electrostatic lens, thus enabling simultaneous focusing and RF-scanning of the electrons. Typically, BSM deflectors are RF-cavities based on parallel wire lines with capacitive plates. Electrical length of the deflectors is usually λ/4 or λ/2 (Fig. 1). The electrodes with deflecting plates 1 are supported by ceramic insulators. Focusing potentials are supplied at a zero electrical field points via ceramic resistors 4, which are used to diminish the influence of external connections.

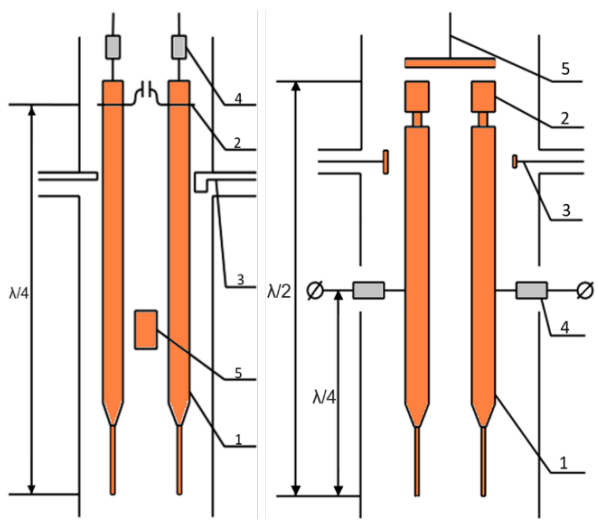

Figure 1: Scheme of λ/4 (left) and λ/2 (right) RF-deflectors.

In λ/4-type deflector resonant frequency is adjusted by moving jumper 2. The jumper consists of two collets connected by ceramic capacitors. Coupling loops 3 are used to drive the cavity and to pick up the RF-signal.

In λ/2-type deflector resonant frequency is adjusted by changing the length of the electrodes with screws 2. Capacitive couplers 3 are used for driving and control.

Tuners 5 with different geometries are intended for fine frequency tuning of both cavity types from outside vacuum. Tuning of RF-deflectors includes adjustment of resonant frequency and input matching of RF-couplers to minimize reflections.

For proper operation, a deflector development should begin from preliminary calculations of its electrodynamic parameters, such as: resonant frequency, quality factor and equivalent impedance as well as S-parameters.

RESONANT FREQUENCY

Development process of BSM is based on COMSOL Multiphysics, that provides comprehensive simulations of all characteristics, including RF-parameters [3].

A frequency of RF-deflecting field should be equal or multiple to the RF-field frequency in the accelerator. Geometry of the RF-cavity can be simply calculated via Eigenfrequency solver. However these simulations should take into account positions of ceramic insulators (electrode holders), which change the resonance frequency crucially, because of rather high relative permittivity (about 10).

If the deflector is tuned in the air, it needs extra tuning from outside vacuum after pumping, due to the shift of resonance frequency. The exact values depend on the temperature and humidity of the air, but the difference is rather small (less than 100 kHz for operational frequencies) and can be easily compensated (Fig. 2) by fine tuner, which geometry and stroke can be simulated preliminarily.

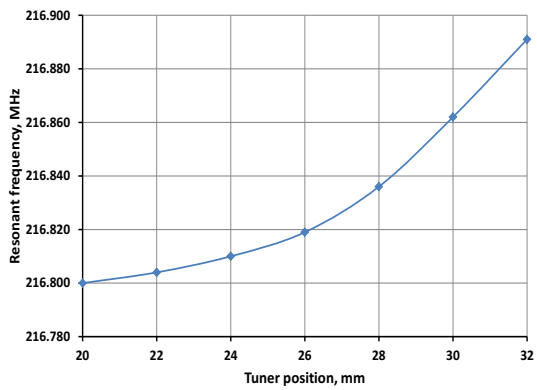

Figure 2: Example of experimental dependence between resonant frequency and tuner position in the λ/4-type deflector with operational frequency 216.816 MHz.

† dmitriy.chermoshentsev@phystech.edu

ISBN 978-3-95450-181-6

STANDING WAVE RATIO

S11-parameter, defining standing wave ratio (SWR), depends on geometry and position of coaxial RF-couplers: washer for capacitive drive (Fig. 3) and loop for inductive drive (Fig. 4).

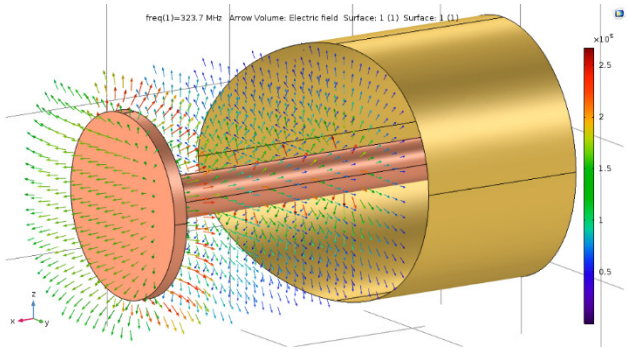

Figure 3: Electric field of capacitive coupler (washer).

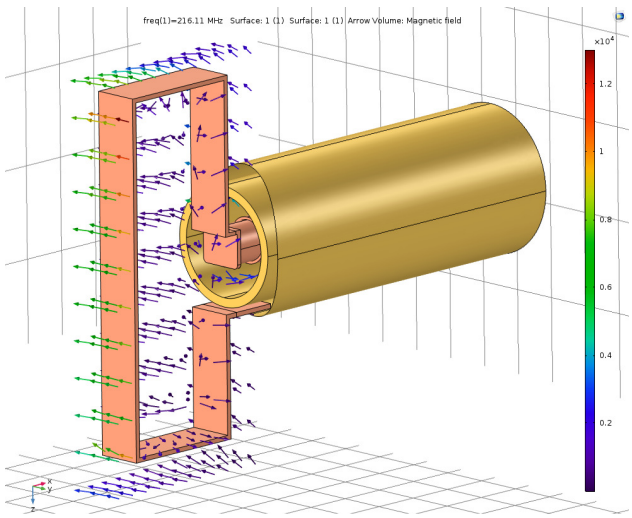

Figure 4: Magnetic field of inductive coupler (loop).

SWR can be tuned by adjusting of the distance between the electrode and coupler. However the geometry of a loop or diameter of a washer should be preliminarily simulated to find optimum values for fabrication (Fig. 5).

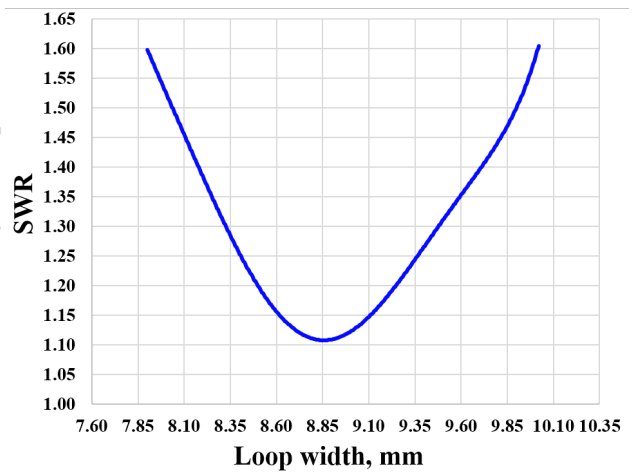

Figure 5: Simulated dependence SWR vs. coupling loop width (with constant length 27 mm).

EQUIVALENT IMPEDANCE, Q-FACTOR & INSERTION LOSS

The RF-cavity parameter of importance for electron deflection is an equivalent impedance $R_e = U_d^2/2P$, where U_d is the amplitude of RF-deflecting voltage between the plates and P is RF-power dissipated in the deflector. Simulations and real operation show, that the power, required for typical U_d = 1 kV, is less, than 10 W, that can be provided easily by relatively compact RF-amplifier [4].

Typical value of unloaded simulated Q-factor is about 1000 ÷ 1500 and depends on positions of ceramic insulators (Fig. 6) in electrical field because of non-zero dielectric loss tangent. Positions of insulators is mainly defined by their function as mechanical holders and cannot be changed arbitrarily.

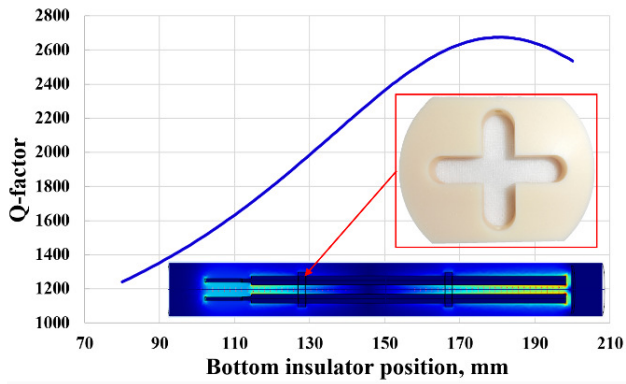

Figure 6: Q-factor vs. insulator position in λ/2 deflector (color shows amplitude of electric field in the deflector).

Loaded Q-factor as well as insertion loss, can be measured by network analyzer in terms of S21-parameter (Fig. 7) due to the presence of the special pick-up coupler.

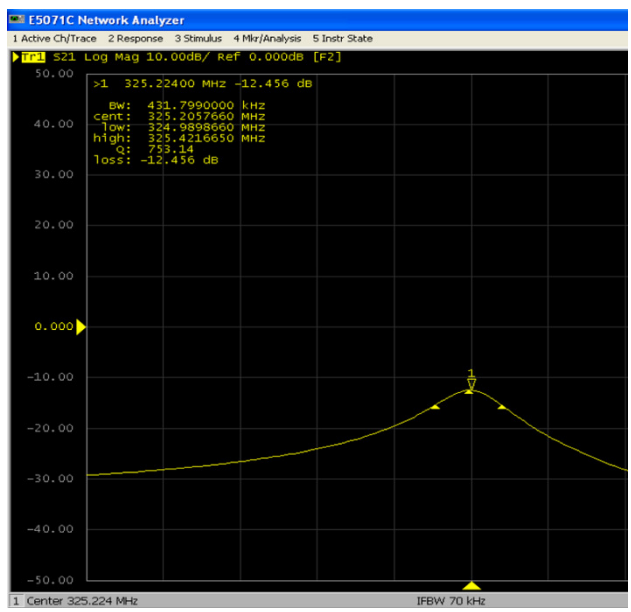

Figure 7: S21 measurements by network analyzer.

One should note, that neither insertion loss nor standing wave ratio is changed when the resonant frequency of the deflectors is adjusted.

ISBN 978-3-95450-181-6

RF-SIMULATION FEATURES

There are two main problems in RF-simulation of BSM deflector. The first one is the presence of ceramic parts: capacitors in λ/4-deflector (Fig. 8) and isolating holders. RF-characteristics of ceramic depend on the frequency of electromagnetic field and may vary from part to part significantly due to fabrication and storage conditions. It means, that only experimental measurements at given frequency for parts from the same consignment can give relevant calibration curve for the model.

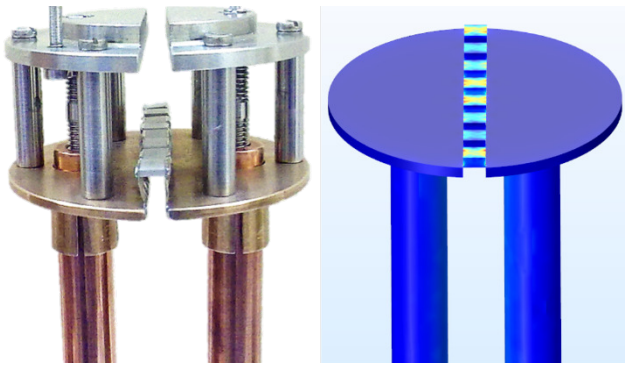

Figure 8: Jumper with ceramic capacitors in λ/4-deflector: photo (left) and simplified model (right).

The second problem is a big discrepancy (up to 10^3 times) between sizes of various deflector parts, that leads to problems in meshing for finite element model. Some effects in transition zones between different parts (Fig. 9) can be lost in this case, that results in inaccurate numerical values even for basic RF-parameters, like resonant frequency or Q-factor. The efficient solution is an adaptive mesh with manual meshing for separate parts and tuning the order of finite elements.

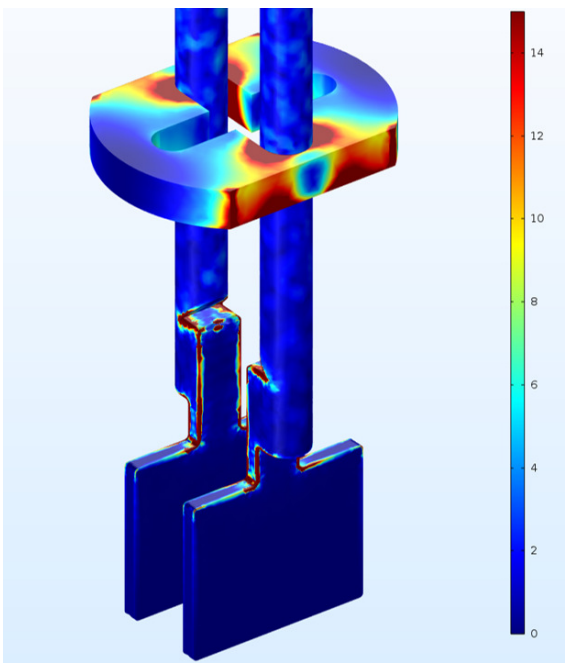

Figure 9: Simulated distribution (in a. u.) of electromagnetic power loss density in ceramic isolator and electrodes with plates at adaptive mesh.

CONCLUSION

A number of electrodynamic parameters of BSM RF-deflector: resonant frequency and quantities derived from S-parameters – should be calculated before its fabrication. Simulated results, based on finite element model in COMSOL Multiphysics, are in a good agreement with experimental measurements.

The final values are defined by many unpredictable conditions. For example, there is a slight change of the resonant frequency due to connection of the cables supplying focusing high voltage. This change is within 20 kHz and depends on the length of the connecting cables. However such small discrepancies can be adjusted by fine tuners foreseen in the deflectors.

Simulations of loss parameters are rather sensitive to a mesh quality, so manual meshing with control of transition zones between deflector parts may be determinative for precise relevant calculations.

REFERENCES

[1] A. Feschenko, "Technique and instrumentation for bunch shape measurements", in *Proc. RUPAC2012*, Saint-Petersburg, Russia, Oct. 2012, pp. 181-185.

[2] R. Witkover, "A non-destructive bunch length monitor for a proton linear accelerator", *Nucl. Instr. Meth.*, vol. 137, no. 2, pp. 203-211, 1976.

[3] www.comsol.com/rf-module

[4] www.svpa.com/labamps.html

ISBN 978-3-95450-181-6

PROPOSAL TO SYMMETRIC QUENCH DETECTION AT SUPERCONDUCTING ELEMENTS BY BRIDGE SCHEME USAGE

E.V. Ivanov, A.O. Sidorin, A.L. Svetov, JINR, Dubna, Moscow Region

Abstract

In the frame of the NICA project [1] two new superconducting accelerators will be constructed – the Booster and the NICA collider. Specialized facility for manufacturing and testing of the SC magnets for the NICA and FAIR projects is under development at JINR [2]. Proposal to quench detection system for these and similar facilities is described in this paper.

INTRODUCTION

Currently to detect the active phase on the superconducting elements of modern accelerator complexes widely used method of active phase voltage selection out of the total voltage drop at the controlled element and further analysis to meet the criteria of the quench.

The voltage on the inductive superconducting element is described by the formula:

$Vm = Lm\frac{dI}{dt}$, where Vm – voltage at inductance element, Lm – inductance of a magnet. Voltage at the beginning of quench is Vsm=Rq*I+$Lm\frac{dI}{dt}$ =Rq*I+Vm, where Rq- is resistance of a region with active phase.

Selected quench voltage is Vq=Vsm-Vm is analyzed by the detector logic to meet the criteria of exceeding the voltage threshold Vth by amplitude during predefined time Tv. Exceeding of these thresholds is a condition to turn protective systems on and start energy evacuation from the magnetic system of the accelerator.

It should be noted that the quench voltage Vq is typically ≈100÷200 mV, and voltage Vsm and Vm change dynamically during acceleration cycle in the range from –10V to +10V depending on the rate of change of the magnetic field and of the element inductance.

Thus, the detection scheme must reliably identify the voltage Vq over a wide dynamic range regardless of the instantaneous voltage on the element at each moment of time [3].

Basically bridge scheme is used to select quench signal Vq. This method of detection is widely used due to its undeniable advantages that are missed in other solutions. So, the bridge is completely passive element, so it can detect the signal of any dynamic range in amplitude. The signals from the magnetic elements in the bridge scheme are differential, thus making the bridge scheme insensitive to induced noise. And moreover the bridge scheme is pretty simple, cheap in realization and very robust.

While using the bridge scheme, it is very important that arms of the bridge – that is controlled inductance - have a minimum length. Otherwise due to phase shifts to obtain the bridge scheme being balanced is possible only at one fixed frequency. Herewith any change of the voltage (rise and/or decline) will result in short-term dynamic disbalancing.

So the optimal usage of the bridge scheme to protect quench of a superconducting accelerator elements is to use it in schemes with mid-point connection. In such a solution the scheme logic compares signals from two halves of a magnet. Such a bridge scheme should use the minimum possible inductance, and the shortest linear connections.

Some publications (TEVATRON [4], LHC [5], and the latest SIS 100 documents) indicate the possibility of the so-called "symmetric quench" to occur while using the protection system with mid-point connection scheme. That is the appearance of the active area at the mid-point connection and its symmetric uniform propagation resulting in the bridge scheme disbalancing not happened. Earlier to exclude this situation the sensors with group of magnets bridging were mostly used. Recently some attempts are made to measure the quench by non-bridge sensors.

Unfortunately, the comparison of signals without using the bridge scheme implies necessity to use a very accurate differential amplifier with large dynamic ranges of input voltage and low drift in both measurement channels. Today such devices appear in catalogues of some manufacturers, although usage of these amplifiers in real accelerators is still very difficult to be widely used. In addition, for comparison of the real and reference signals you need to have the reference signal exactly copying the controlled signal and having no phase shift and noise. This fact is the main difficulty to implement such methodology. Realization of such a reference signal is quite difficult structurally.

As an alternative, at the LHC obtaining the derivative is implemented by measuring the current in the circuit before and after the controlled magnet with the subsequent differentiation and averaging. This method is very complex and expensive, and is used in circuits with currents less than 700A and very large (~1V) threshold.

SIS 100 proposes to use one supplementary superconducting filament as a reference winding. The method is also very complex and difficult in design.

In this paper we propose a solution for a problem of the symmetric quench detection while using a bridge detector for the magnetic elements of the NICA accelerator complex, LHEP, and the like [3].

ISBN 978-3-95450-181-6

BRIDGE SCHEME OF THE QUENCH DETECTION WITH ADDITIONAL SENSOR

Usually, talking about usage of the bridge scheme with the mid-point connection means a circuit as in Fig. 1:

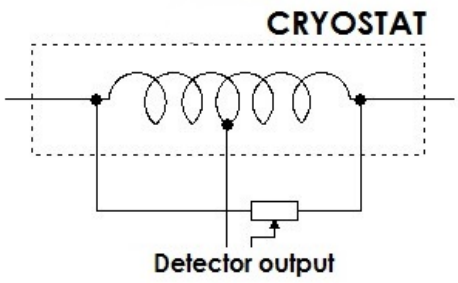

Figure 1: Idealized scheme with mid-point connection.

It is assumed that may be such a situation when the active phase appears and the bridge scheme with mid-point connection does not disbalance. True, it is really so. But in practice the real implementation of the bridge scheme looks like this (Fig. 2):

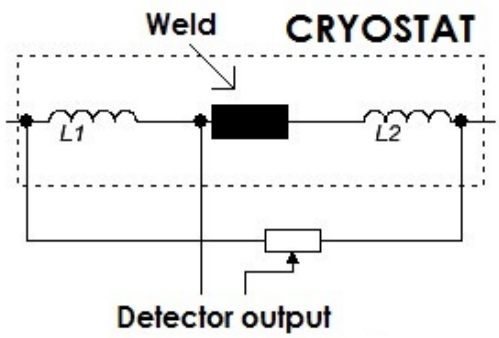

Figure 2: Real scheme of mid-point bridge connection.

There is a weld at the junction point of magnet winding halves. And the mid-point of the bridge is connected to one of the weld edges. It is hardly possible to imagine a situation when the active phase there will be symmetrically and evenly spread through a pure superconductor and the weld. With that any fears of a "symmetric quench" is unlikely to have any reason. Moreover the publications mentioned above clearly state that such cases have never been observed.

Despite the optimism of this view, the theoretical possibility of such a situation still remains. Additionally, there may be a real situation when the magnet completely loses superconducting state. In this case the bridge does not work either.

So we propose the solution to this problem of the symmetric quench as shown in the Fig. 3.

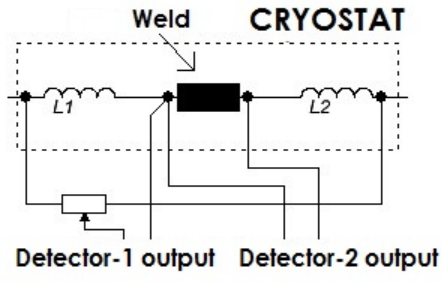

Figure 3: Scheme of total protection for a magnetic element.

A separate sensor is connected to both sides of the weld between winding halves to monitor superconductivity at the weld by absolute value.

Thus, with such an arrangement of the detection scheme a quench, wherever it occurred, will be clearly detected. Even in case of total loss of superconductivity inside controlled volume this separate sensor will show quench, because it compares voltage at weld with absolute value “0 V”.

From the design point of view this solution will require only some extra sensors to be installed. All sensors in this solution are designed identically. Their work has already been tested many times in practice at NUCLOTRON accelerator runs [6].

CONCLUSION

In this paper we propose a solution for a problem of the symmetric quench detection while using a bridge detector with one additional sensor connected to both sides of the weld between winding halves. The sensors required for such a scheme was designed and tested at JINR.

REFERENCES

[1] G.Trubnikov, NICA project, these proceedings.
[2] H. Khodzhibagiyan et.al, The Progress on manufacturing and Testing of the SC Magnets for the NICA Booster Synchrotron, these proceedings.
[3] Ivanov E.V. et al, “System of Quench Detection in Superconducting Magnets of the Nuclotron Accelerator Complex”, Physics of Particles and Nuclei Letters, 2013, Vol. 10, No. 4.
[4] Robert H. Flora et al, “Doubler-TEVATRON mP Quench Protection System”, https://accelconf.web.cern.ch/accelconf/p79/PDF/PAC1979_3451.PDF
[5] K. Dahlerup-Petersen, et al, “The protection system for the superconducting elements of the Large Hadron Collider at CERN”, http://accelconf.web.cern.ch/AccelConf/p99/PAPERS/THP105.PDF
[6] E.Ivanov et. al. Quench Detector for Superconducting Elements of the NICA Accelerator Complex, Proceedings of RuPAC-2014, Obninsk, Russia.

ISBN 978-3-95450-181-6

APPLICATION OF MODEL INDEPENDENT TECHNIQUES AT VEPP-2000 AND SIS100

D. Rabusov, Yu. Rogovsky, BINP, Novosibirsk, Russia

Abstract

In order to exploit an accelerator successfully all parameters should be set correctly. To check and fix errors in the accelerator lattice measurements of parameters of the betatron motion and measurements of optical functions of the accelerator lattice are used. Due to Model Independent Analysis it is possible to carry out measurements of the beta-function and the phase advance fast. Using NAFF technique lets us compute betatron tune with good precision. Limiting capabilities of the MIA at SIS100 project are discussed, implementation of the MIA and the NAFF techniques at booster VEPP-5 and at collider VEPP-2000 are shown.

INTRODUCTION

In order to receive the information about settings of an accelerator we can use MIA (Model Independent Analysis) [1] and NAFF (Numerical Analysis of Fundamental Frequencies) [2]. These techniques demand beam histories — arrays of data from BPMs (Beam Position Monitors), which have the information about the betatron motion of the beam. We don't have enough possibilities to describe these methods, but full specification you can find in the references.

SIS100. THE RESULTS OF SIMULATIONS

SIS100 is a future synchrotron for acceleration of high intensity and high energy ion beams with primary significance in the FAIR project. In its design the synchrotron has six equivalent sectors and is served by 84 BPMs.

To examine the limiting capabilities of the future diagnostic system of SIS100 and the MIA technique, numerical simulations were applied. At first, particle tracking with MADX [3] was used, then simulated "beam histories" were filtered and analyzed with MIA. Received results (shown on Figure 1 and 2) were compared with the beta-function and the phase advance, that are calculated using MADX. For all these calculations parameters were applied: $n = 200$ turns, the level of the noise $\Delta x = 100$ μm; amplitudes of the simulated betatron oscillations were ≈ 1 mm. The error of MIA calculations is determined as:

$$\delta = 100\% \cdot \frac{1}{m} \sum_{i=1}^{m} \left| \frac{f_i^{MADX} - f_i^{MIA}}{f_i^{MADX}} \right| \qquad (1)$$

where f is β or ϕ, $\phi_i = \Psi_i - \Psi_{i-1}$. The difference between the model beta-function in positions of BPMs and measured by MIA is less than 2 %. For the phase advance precision is better than 1 %. Also the relative error of calculations raises almost linearly in the observed range of noise-amplitude ratio. Furthermore the MIA error decreases when n raises. These results are shown on the Figure 3.

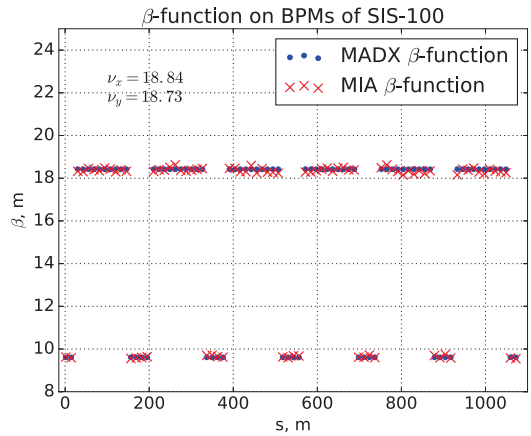

Figure 1: Values of β-function at BPMs for SIS100.

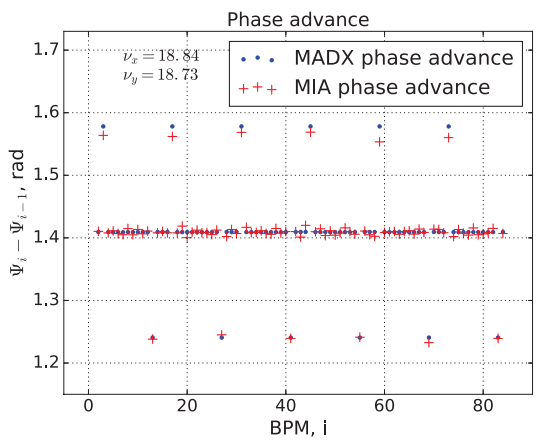

Figure 2: The phase advance between neighboring BPMs.

Finally, we tested limiting capabilities of MIA using the "beta-beating" task. We applied the unrealistically big gradient error at the level equal to 5%. Results are shown on the Figure 4. Green triangles are the distorted beta functions at the BPMs, blue points are the ideal beta-functions at the BPMs, red crosses are β calculated by MIA. Here we found that calculations of the β-function are very sensitive for varying scaling factor (J^{-1}).

ISBN 978-3-95450-181-6

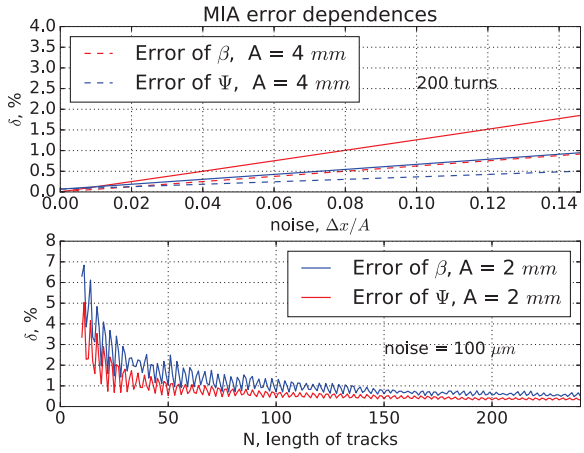

Figure 3: MIA error dependence: a) on the number of turns b) on the noise-amplitude ratio.

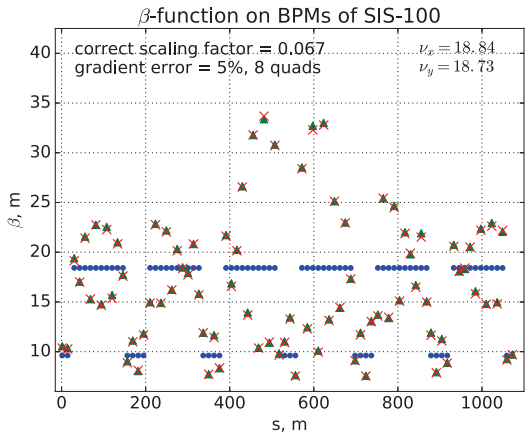

Figure 4: Beating of the beta-function of the SIS lattice.

THE RESULTS OF MEASUREMENS AT VEPP-5 AND VEPP-2000

VEPP-5 Damping Ring

The damping ring of Injection Complex (VEPP-5 at BINP) is an accelerator which stores and cools down both of electron and positron beams. The accelerator ring consists of four cells, each cell includes: two dipole bending magnets, five quadrupole lenses and sextupole lenses between bending magnets. The circumference of the ring is 27.4 meters, the project energy is 510 MeV, the detailed description is given in [4]. The damping ring is served by 16 beam position monitors as the main tool of diagnostic system.

The number of experiments with electron bunch with different initial states was carried out. The bunch of electrons had the betatron oscillations which were implemented by the horizontal kick excitation. The intensity of the bunch was varied in the range from 1 mA to 25 mA. The amplitude of the kick was chosen to produce betatron oscillations with an amplitude $\approx$ 5 mm. Simultaneously with the kick recording at the BPMs was initialized. The energy of the beam was 390 MeV, betatron tunes were calculated using NAFF and they corresponded to their project values: $\nu_x = 4.44, \nu_z = 2.65$ (the fractional part of $\nu_x = 0.43794 \pm 9 \times 10^{-6}$).

However several BPMs for the some reasons aren't able to be used in the experiment. The 13-th and 15-th BPMs have problems with the ADC and the line delay, 5-th and 14-th monitors had strong a electromagnetic noise in the signal.

After preliminary analysis the phase advance and the beta-function were computed using MIA. Results obtained with different beam intensities differ less than experimental error (as the results of MIA and NAFF for the phase advance), thus 4 mA results are shown at the Figure 6 and 5. The difference between the model and experiment might be described: the model of the damping ring was made in 2015, but then values of magnetic fields were significantly changed in order to obtain a successful injection of the electron bunch into the damping ring from linac.

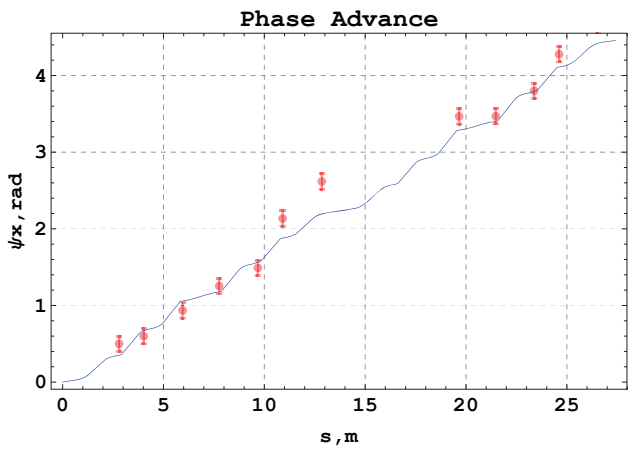

Figure 5: The horizontal phase advance at the damping ring.

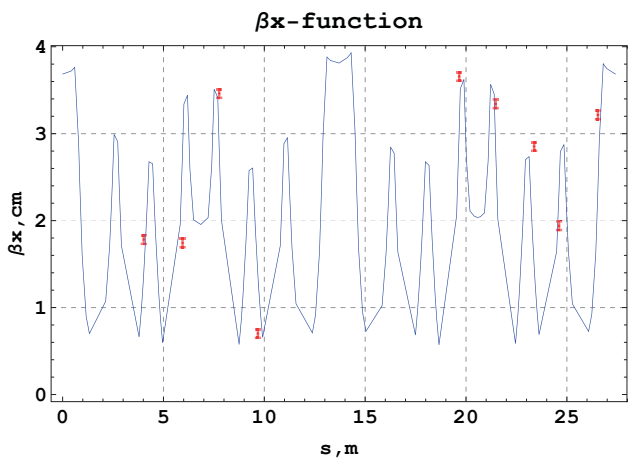

Figure 6: The horizontal beta-function at the damping ring.

ISBN 978-3-95450-181-6

VEPP-2000

Collider VEPP-2000 at BINP is an accelerator with a symmetric magnet structure which is divided on four sectors. The sector consist of two bending magnets, five quadrupole lenses and few sextupoles. As well there are superconductive solenoids for the final focusing and the realization of the round beam concept of the machine. The circumference of the collider is 24.38 meters, the project energy is 1 GeV, full description of the accelerator see here [5]. To obtain data about equilibrium orbit and to carry out turn-by-turn measurements four electrostatic BPMs are used.

This experimental work has been done directly after the modernization of the booster (BEP) and VEPP-2000. In order to set all systems of the accelerator correctly using the beam, the magnet system of the collider was changed to the "warm optics" mode, which means that solenoids of final focusing were switched off and the gradients of all lenses were reduced.

The range of experiments with electron bunch was carried out. The intensity of the bunch was varied in the range from 1 mA to 3 mA. In order to excite betatron oscillations with the variable amplitude the horizontal kick with suitable amplitude was implemented. The amplitude of betatron oscillations was varied in the range from 1 mm to 5 mm. Simultaneously with the kick beam histories at the BPMs were recorded. Computed by NAFF the value of the fractional part of $\nu_x = 0.431876 \pm 4 \times 10^{-6}$

Results obtained with varied intensities and amplitudes differ less than experimental error, thus results of the experiment where intensity was 1 mA and amplitude of betatron oscillations was 1 mm are discussed below.

For the sake of computing the phase advance between BPMs MIA was applied, results are shown on the Figure 7. Red dots are the array of the experimentally measured betatron phase, the blue curve is the model phase advance for "warm optics" mode. Next result is beta-function which is shown on the Figure 8. As for the phase advance red dots is the array of the experimentally measured beta-function at BPMs, the blue curve is the model beta-function for "warm optics" mode.

CONCLUSIONS

Beta-function at the BPMs and the phase advance was measured at the collider VEPP-2000 and the damping ring of VEPP-5 during the experimental research. Also simulations for SIS100 were made, there is the result — MIA is available for applying at SIS100. Aims of further studies are: to measure the optic functions with better accuracy at the damping ring, to reduce different noises and to improve the diagnostic system of accelerator. Now on-line measurements of the optic functions are available at VEPP-2000 and next step is to calculate the beta-function and the phase advance in "hard focusing" mode with turned solenoids on.

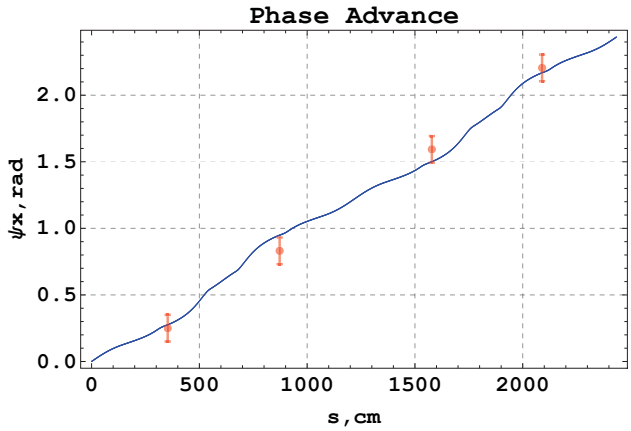

Figure 7: The horizontal phase advance at the VEPP-2000

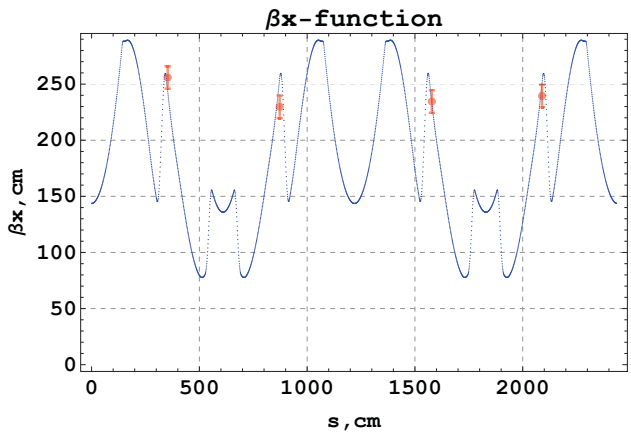

Figure 8: The horizontal beta-function at the VEPP-2000

ACKNOWLEDGMENTS

I'd like to thank Dr. V. Kornilov for the opportunity to work with SIS100 project. I'm particularly grateful for the assistance with MADX which Dr. Stefan Sorge and Ivan Karpov did for me. I would also like to thank all VEPP-2000 team

REFERENCES

[1] Chun-xi Wang, Vadim Sajaev, and Chih-Yuan Yao, Phase advance and β-function measurements using model-independent analysis, The American Physical Society, Argonne National Laboratory, Illinois, USA, (Received 20 December 2002; published 22 October 2003)

[2] Laskar, J., Froeschle, C., Celletti, A., The measure of chaos by the numerical analysis of the fundamental frequencies. Application to the standard mapping, Physica D, 56, (253-269) (1992)

[3] http://madx.web.cern.ch/madx/

[4] P.V.Logatchev et al, Status of VEPP-5 Injection Complex, Proc.RuPAC-2006

[5] Yu. M. Shatunov et al., Project of a New Electron-Positron Collider VEPP-2000, in: Proc. 7th European Particle Accelerator Conf. (EPAC 2000), Vienna, Austria, p. 439.

ISBN 978-3-95450-181-6

BEAM DIAGNOSTICS AND INSTRUMENTATION UPGRADE FOR MULTIPURPOSE RESEARCH COMPLEX OF INR RAS

S. Gavrilov†, V. Gaydash, V. Gorbunov, Y. Kalinin, Y. Kiselev, P. Reinhardt-Nickoulin, I. Vasilyev
Institute for Nuclear Research of the Russian Academy of Sciences, Moscow, Russia

Abstract

Accelerated proton beam of INR linac is used for various facilities in multipurpose research complex of INR RAS, including experiments of neutron investigations and medical physics laboratories. In recent years beam instrumentation for transport channels of the complex has been upgraded and supplemented. Electrostatic pick-ups, beam current transformers, ionization chambers, multiwire SEM-grids, as well as its front-end and processing electronics were developed and combined to improve beam diagnostics. Some technical details and available results of beam measurements are presented in the paper.

INTRODUCTION

Multipurpose research complex (MRC) [1] of INR RAS includes four beam outlets (Fig. 1): three neutron facilities of neutron investigations laboratory (time-of-flight RADiation Experiment, pulse neutron source IN-06, lead neutron slowing-down spectrometer LNS-100) and research Complex of Proton Therapy, which is a part of medical physics laboratory.

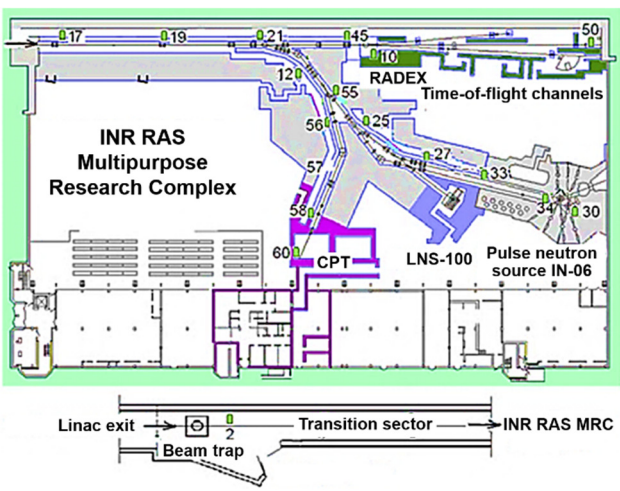

Figure 1: Layout of INR RAS MRC.

Depending on beam user requirements INR RAS linac has to provide beam parameters in a wide range of values: beam energy 100÷209 MeV, pulse current 0.01÷15 mA, pulse repetition rate 1÷50 Hz, pulse duration 0.3÷180 μs. Moreover, these parameters can be changed several times during a shift for different research groups, that needs not only reliable operation of the linac in different duty cycles, but also a universal beam instrumentation available for routine beam control in the whole range of parameters.

† s.gavrilov@gmail.com

DIAGNOSTICS AT THE LINAC EXIT

Beam emittance and position measurements at the linac exit are of importance for proper matching with the linac-MRC transition sector. In-flight beam diagnostics before a beam trap is provided by Beam Cross Section Monitor (BCSM) [2]. The monitor, utilizing a residual gas ionization, enables to observe 2D beam cross section, beam position and profiles, as well as transverse emittance ellipses (Fig. 2), which can be reconstructed [3] from beam profiles data during linear transformations in phase space by variation of fields in upstream quads.

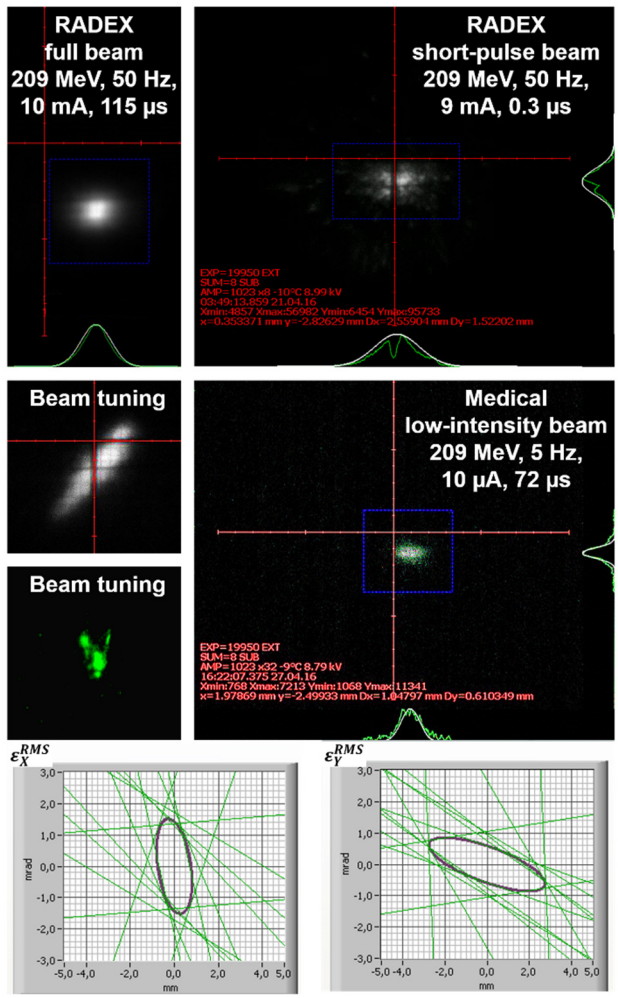

Figure 2: BCSM results for different beam parameters.

Now BCSM is a reliable tool for efficient beam tuning and an accurate non-destructive diagnostics at the linac exit in the whole required range of beam parameters.

ISBN 978-3-95450-181-6

ELECTROSTATIC PICK-UPS

Beams with given energies are transported about 400÷500 m to the research facilities without acceleration. Due to the momentum spread ($\Delta p/p \approx \pm 3.5 \cdot 10^{-3}$ at the base) a beam bunch structure ($T_{Bunch} \approx 200$ ps, $f_{RF} = 198.2$ MHz) is lost and the measurements are done for debunched coasting beams. For a bunched beam a measurement is performed by radio frequency methods, but in case of a debunched beam it is transformed into measurement of quasi-steady-state charge during the whole macropulse.

Ten linear-cut electrostatic pick-ups (Fig. 3) upstream and downstream of elements with reduced aperture are installed for non-destructive measurements of beam position and tilt in a wide range of beam intensity.

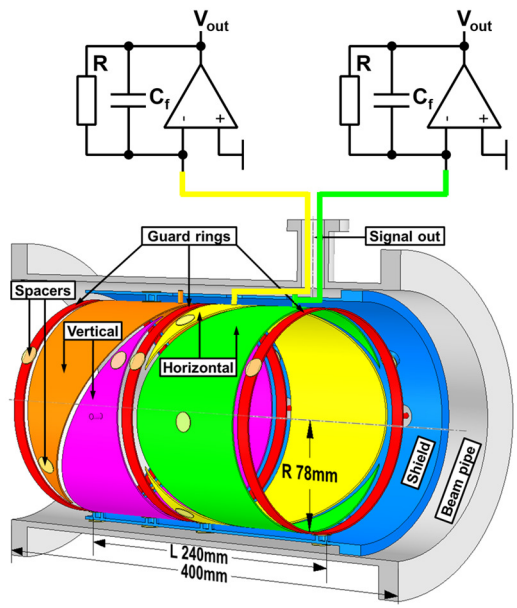

Figure 3: Pick-up scheme with charge amplifiers.

The design and operation principles of used pick-ups are discussed completely in [4]. Signal-to-noise ratio is limited by a total capacitance C_t which is the sum of plate-to-ground $C_{pg} = 110$ pF, plate-to-plate $C_{pp} \approx 2 \div 3$ pF and capacitance C_c of an interconnecting cable. The main implemented feature is a charge amplifier based on operational amplifier with JFET inputs and $C_f = 10$ pF, $R = 100$ MΩ. In this case an output signal is practically independent of a total detector capacitance, so pick-up calibration can be performed with arbitrary cable length. With second stage gain of 10 and input referred noise of 16 nV/√Hz, the output noise is 15 mV peak-to-peak.

High value resistor R defines DC gain and provides a path for the bias current to flow. In parallel with C_f it forms a high pass filter that causes pulse droop. Small droop can be assumed as linear for compensation by simple baseline restoration algorithm after digitization.

Signals from pick-up plates during a beam pulse as well as beam position calculated from a difference-over-sum measurement are shown in Fig. 4. Unfortunately, a bandwidth of used processing electronics, based on National Instruments modules, is insufficient for diagnostics of pulse durations less than about 10 μs.

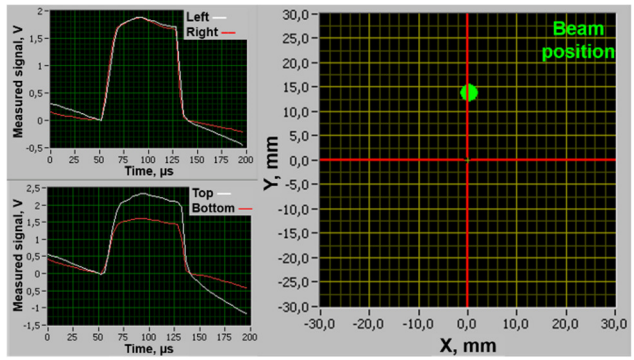

Figure 4: Pick-up signals and calculated beam position.

BEAM CURRENT TRANSFORMERS

Operation with high-intensity beams for RADEX and IN-06 requires protection systems, based on beam losses control. One of them, so-called ΔBCT, is based on beam current transformers (BCT) and registers an absolute value of beam losses by a beam current difference between the linac exit and entrances to the research facilities.

BCT signals from every beam macropulse are read-out and compared by special electronics, which turns off a beam directly in case of specified difference threshold (1÷5 % typically) is exceeded in three successive pulses. In addition, this system holds on 1 Hz tuning mode as long as the difference remains.

There are nine BCTs, based on ferrite rings installed in vacuum, with different design and electronics. Two standard BCTs with preamplifiers, based on AD810 op-amps, are used for routine range of beam parameters. Three sensitive BCTs with OPA827 and ADA4627 – for medical beams with pulse currents down to 10 μA. Four fast BCTs measure short-pulse beams (Fig. 5) for RADEX and LNS-100. Fast BCTs have 10÷15 turns in signal windings and low input impedance preamplifiers, based on AD844.

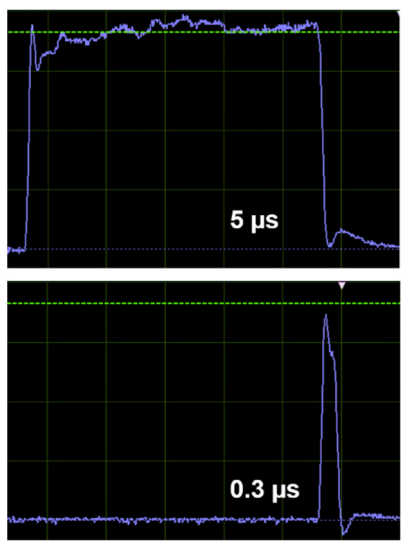

Figure 5: BCT signals from short-pulse beams.

Current signals and calibration signals of all BCTs are transmitted in differential mode by twisted-pair cables, so interferences are minimized, and preamplifiers can be distant for hundreds meters from a control room.

ISBN 978-3-95450-181-6

IONIZATION CHAMBERS

Ionization chambers (IC) [5] form another system for beam losses control. There are 32 double IC fixed on the outside of beam pipes from the beam trap to the research facilities: inside quadrupole doublets and near steering magnets generally. Protons and neutrons from beam losses ionize air in a volume, enclosed by comb electrodes with 600 V potential difference, that produces a current between the electrodes proportional to the dose rate.

A new electronics allows to control beam losses in every macropulse, but only in a relative manner, because of the absence of any proper calibration mechanism. One another drawback is a small value of signal currents for beam losses during routine linac operation. The comb electrodes form a condenser, which is a high responsive to an external electrical noise, so signal-to-noise ratio decreases crucially at acceptable beam losses.

Nevertheless, IC system plays a significant role during a beam tuning process, indicating critical points, like in Fig. 6, where chambers # 2, 8, 9 show heightened levels of beam losses due to not so good correction of a beam position after the beam trap and near two lifting magnets at the beginning of the transition sector correspondingly. Also ICs can be used as a fast emergency protection system, like ΔBCT, but pointwise distributed across the whole MRC.

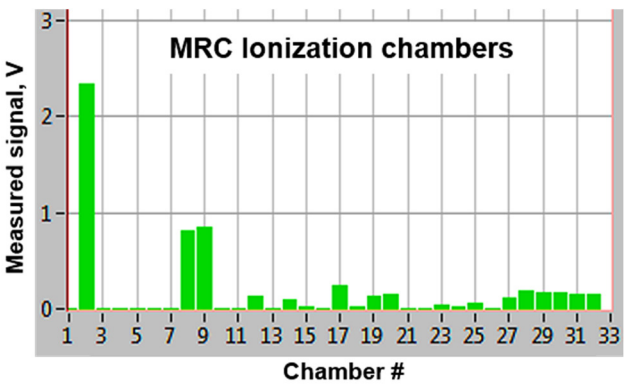

Figure 6: IC signals along MRC channels.

MULTIWIRE SEM-GRIDS

Multiwire SEM-grids are used to control beam profiles and position at inlets of the research facilities. There are 16 gilded tungsten wires 100 μm diameter with 4 mm spacing in each horizontal X- and vertical Y-plane of the grid. Polarization grids are not used.

A plate with a grid can be moved in/out a beam by a DC-actuator, but such grid is practically transparent for operational beam energies, besides the total designed aperture lets through beams with the sizes up to 120 mm at the base. Thus it can be used for continuous in-flight control during the whole accelerator run without an appreciable influence on a beam. Dosimetric measurements after several runs confirm this assumption.

A beam current signal from every wire is integrated in a separate channel during each beam macropulse, then the signal readout is done by time multiplexing with channel switching time equal to 10 μs.

Such coarse grids are proved to be sufficient, because it needs to retain beam transverse sizes as big as possible with RMS value about 10 mm (Fig. 7) for a thermal load reduction of the neutron production targets. For IN-06 beam sizes should be made asymmetric due to X-stretched rectangle inlet window.

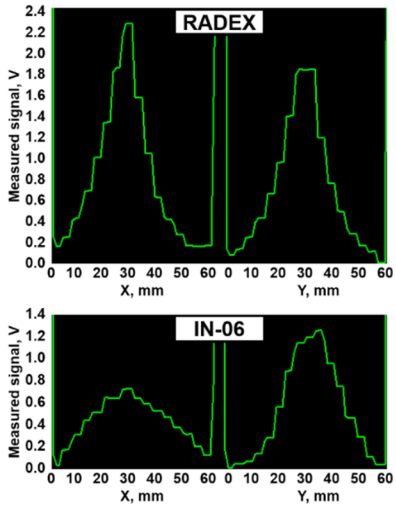

Figure 7: Beam profiles at RADEX and IN-06 inlets.

CONCLUSION

All beam instrumentation systems at MRC transporting channels were recalibrated and upgraded by extra new units and/or electronics. Data from electrostatic pick-ups, beam current transformers, ionization chambers, multiwire SEM-grids is gathered now in the central control room for in-flight diagnostics in a wide range of beam parameters. Also a protection system ΔBCT of beam losses control by beam currents difference is implemented.

Operation in different extreme modes with high and low beam intensities as well as long and short pulse durations reveals some drawbacks, such as: a lack of the electronics bandwidth, excessive susceptibility to an external noise or wires overheating in the SEM-grids in case of high-intensity beams, that leads to profile distortions.

Beam diagnostics and instrumentation development will be continued during the next maintenance periods with the view of enhancement of MRC INR RAS resources.

REFERENCES

[1] A. Feschenko et al., "Multipurpose research complex based on INR high intensity proton linac", in *Proc. RUPAC2012*, Saint-Petersburg, Russia, pp. 90-94.

[2] S. Gavrilov et al., "Two-dimensional non-destructive diagnostics for accelerators by Beam Cross Section Monitor", 2014 *JINST* 9 P01011.

[3] P. Reinhardt-Nickoulin et al., "Emittance measurements at the exit of INR linac", in *Proc. RUPAC2012*, Saint-Petersburg, Russia, pp. 668-670.

[4] S. Gavrilov et al., "Electrostatic pick-ups for debunched beams", 2014 *JINST* 9 T10007.

[5] Y. Davydenko et al., "Registration of losses of protons with energy 200-600 MeV", in *Proc. XVII Conf. on Charged Particle Accelerators*, Protvino, Russia, pp. 220-224.

ISBN 978-3-95450-181-6

THERMAL LOADS OF WIRE-BASED BEAM INSTRUMENTATION AT ION LINACS

M. M. Churaev†[1], S. A. Gavrilov, Institute for Nuclear Research of the Russian Academy of Sciences, Moscow, Russia and Moscow Institute of Physics and Technology, Moscow, Russia
[1] also at Skolkovo Institute of Science and Technology, Skolkovo, Russia

Abstract

Wire-based beam instrumentation remains a reference for calibration of many other instruments, providing direct and accurate measurements with high resolution. However increasing of a beam power of existing and forthcoming ion linacs results in strict constraints on operation modes acceptable for control and diagnostics. Relevant simulations of wire thermal loads are necessary not only for a mode choice, but also for a preliminary design of such instrumentation. Simulations for different wire materials and various beam parameters are made. Features of the model are discussed. Numerical estimations and conclusions are presented in comparison with some experimental results.

INTRODUCTION

Beam ionization losses are the main target heating mechanism at ion linacs. In wire-based instrumentation excessive heating may cause different problems. Firstly, temperature increase results in rise of thermionic emission, that makes additional electric noise, and accuracy in case of secondary emission based measurements goes down. Secondly, overheating can change metal structure of wire or result in wire breakage. Moreover, thermal expansion affects accuracy.

MODEL

Calculations were done using finite elements analysis in COMSOL Multiphysics package. For the computing geometrical mesh with 1/10 of wire radius in cross-section and 1/50 of wire length in longitudinal direction was chosen.

Temperature dependences of thermal conductivity, heat capacity and total hemispherical emissivity of wire material are taken into account (Figs. 1-3).

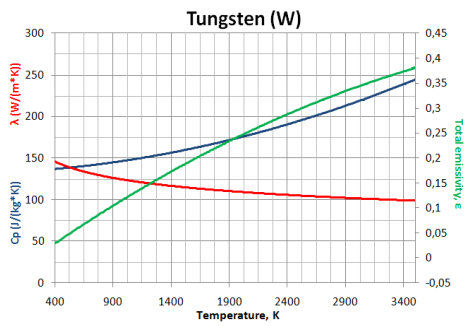

Figure 1: Thermal properties of tungsten.

† churaev@phystech.edu

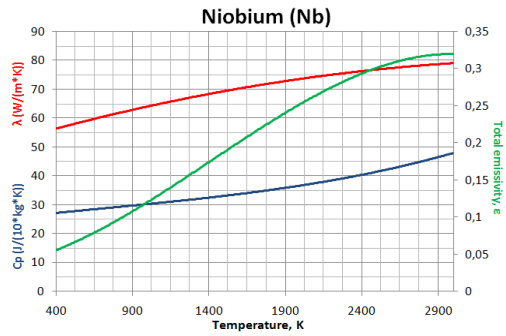

Figure 2: Thermal properties of niobium.

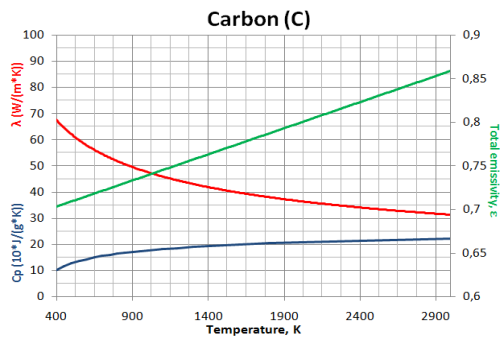

Figure 3: Thermal properties of carbon.

Ambient temperature and initial wire temperature assumed to be 293 K. Considering wire holder being well thermal conductive, boundary conditions can be set as constant temperature 293 K at the wire edges.

Beam is described by: ion parameters, energy, pulse current and duration, pulse repetition frequency, RMS transverse sizes. The wire center supposed to be in the beam center. Function of ionization losses of projectiles are taken from SRIM tables [1]. Volume density of ionization losses (Fig. 4) in the wire is used further as a heat source.

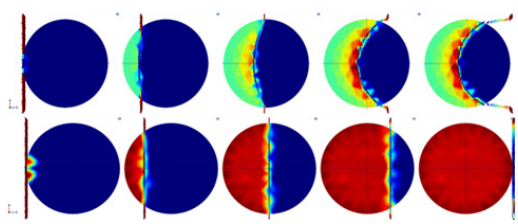

Figure 4: Density of ionization losses for low-energy and high-energy proton beam across the tungsten wire.

The most results are given for tungsten wire with diameter d=100 um in proton beam with RMS size 2x2 mm, unless otherwise specified.

ISBN 978-3-95450-181-6

COOLING BY DELTA-ELECTRONS

One of the possible cooling effects is delta-electrons producing [2]. Delta-electrons are knocked out of wire material and can take away a part of deposited energy of ionisation losses.

Total energy of escaped electrons as well as total energy of ionisation losses was calculated in different cases using self-made code. It was estimated that for low-energy beams cooling effect due to delta-electrons is very small. But for thinner wires this effect increases (Fig. 5): delta-electrons need less energy to reach wire boundary and leave the material.

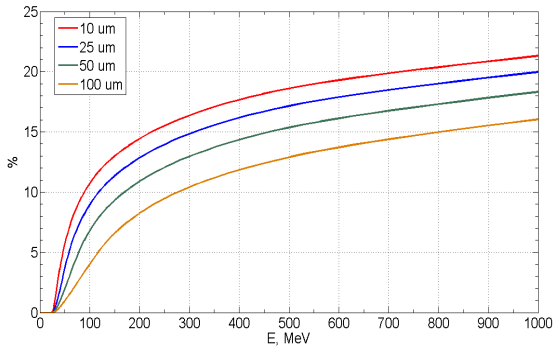

Figure 5: Percentage of deposited proton beam energy removed by delta-electrons for tungsten wires with different diameter.

For tungsten, carbon, and niobium wires results are quite similar (Fig 6). Therefore modeling of wire heating in proton beams with energy less than 100 MeV can be made without considering cooling by delta-electrons at all in order to simplify the model. For higher energy beams this percentage is included in model as a factor in heat source.

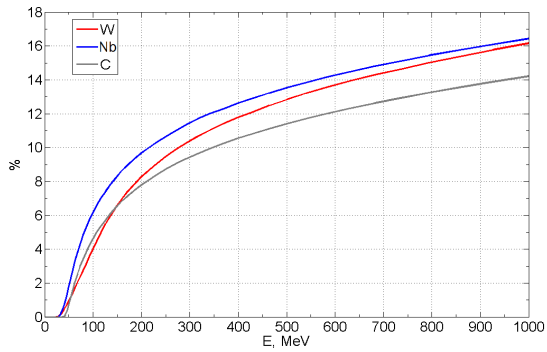

Figure 6: Percentage of deposited proton beam energy removed by delta-electrons for different wire materials.

RESULTS

According to calculations, dependence of maximum wire temperature on beam pulse current, duration and RMS transverse size can be determined as $T \sim \left(\frac{I_{current} \cdot \tau_{current}}{RMS_x \cdot RMS_y}\right)^a$, where index a takes on value between 0.3 and 0.6 (Fig. 7).

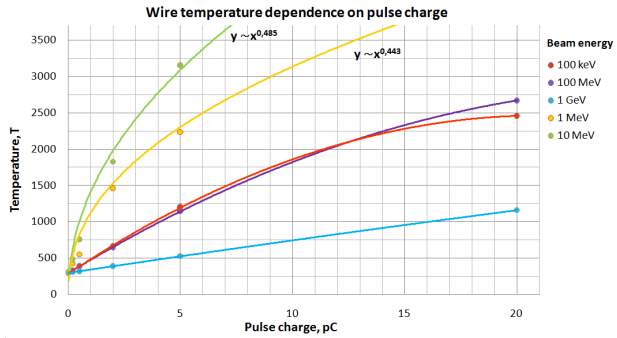

Figure 7: Wire maximum temperature dependence on beam pulse charge.

Choice of wire material and diameter is crucial for preliminary design of beam instrumentation. Materials with high melting point should be chosen for wires. Besides, material atomic charge number is important. Therefore three typical materials can be considered: low-z carbon, mid-z niobium and high-z tungsten. Estimations for different wire materials and diameters are shown at Fig.8.

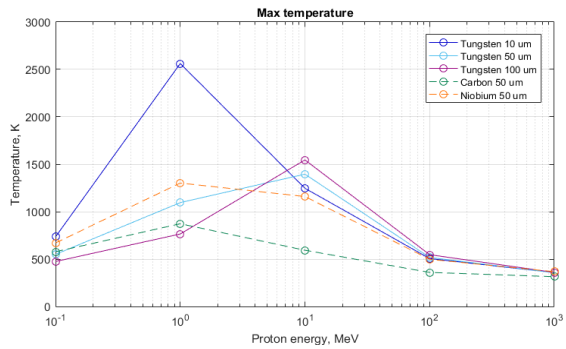

Figure 8: Wire temperature dependence on the material and diameter for proton beam 1 Hz, 10 mA, 200 us.

According to results, thin wires are heated more than thick ones for low energy beams. But for energy beams with energy more than 100 MeV, dependence on wire radius can be neglected. At high energies distribution of ionization losses becomes uniform enough heating power is proportional to d^2 as well as cooling power. Moreover, for niobium and tungsten heating is almost the same: high ionization losses in tungsten are compensated by better thermal parameters. For carbon temperature is lower for all beam energies.

Results for different ion types are given at Fig. 9.

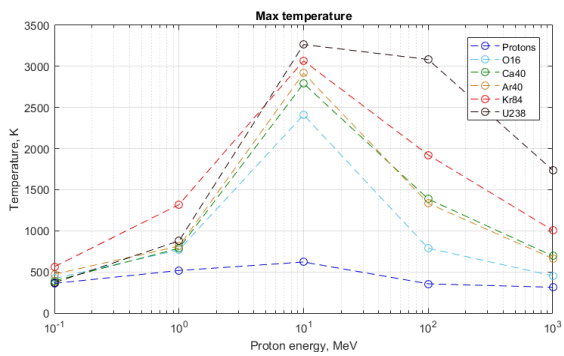

Figure 9: Wire heating for different ion types.

ISBN 978-3-95450-181-6

For higher beam pulse frequency thermal processes don't have enough time to cool the wire between successive beam pulses, thus temperature increases (Fig. 10).

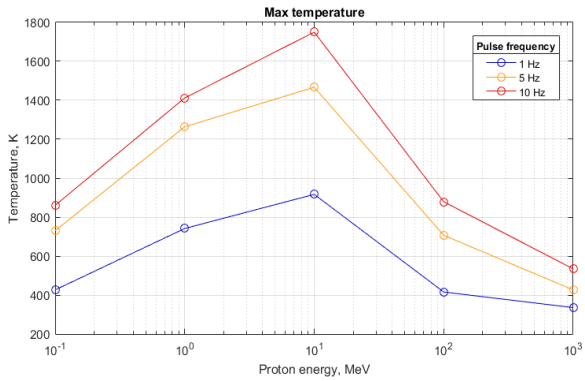

Figure 10: Wire heating for different pulse repetition frequency.

In the model pulses supposed to be debunched, because bunch repetition period is much smaller than typical time of thermal processes, therefore pulse microstructure does not matter.

The feature of wire heating model is that time steps should be inconstant: during the pulse passing through a wire time steps should be less than beam pulse duration. Beam pulse duration can be less than repetition period by several orders of magnitude. Small constant time steps require high computing resources. One of the possible ways to reduce computing time is to use average beam current as constant heating source instead of pulse current.

This approach reduces number of time steps but have an error which depends on pulse repetition frequency. An example for 10 Hz is given on Fig. 11. In this case error is about 180 K, but for the same parameters and frequency 50 Hz this error is less than 80 K. It means that approach of average current is acceptable for maximum temperature estimations for high frequency.

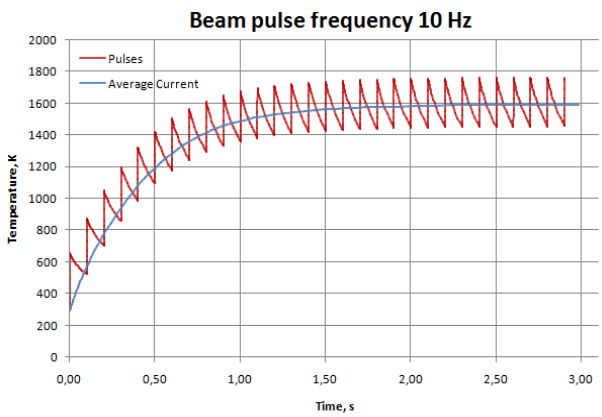

Figure 11: Heating in assumptions of average current and pulses, pulse duration and current are 100 us, 100 mA.

CONCLUSION

The model of wire heating due to ionization losses has been built. Several cooling mechanisms were considered. Less than 25 % of ionization losses energy is removed by delta-electrons for energies below 1 GeV in wide range of wire diameters. Heating rate doesn't depend on wire diameter for high energy beams. But for low energy, massive wires are more preferable in terms of heating. Low-density materials such as carbon are heated significantly less than hard metal wires. Wire temperature is proportional to beam intensity, but dependence is not linear, because thermal processes in wire are not linear.

REFERENCES

[1] James F. Ziegler, M.D. Ziegler, J.P. Biersack // SRIM – The stopping and range of ions in matter, 2010, 19th International Conference on Ion Beam Analysis, Volume 268, Issues 11–12, June 2010, p. 1818–1823.

[2] C. Fischer // Ionisation losses and wire scanner heating: evaluation, possible solutions, application to the LHC, CERN, 1999.

[3] M.J. Berger, J.S. Coursey, M.A. Zucker and J. Chang // Stopping-Power and Range Tables for Electrons, Protons, and Helium Ions, NIST, Physical Measurement Laboratory, 2009.

[4] M. Sapinski // Model of Carbon Wire Heating in Accelerator Beam, CERN-AB-2008-030.

ISBN 978-3-95450-181-6

THE LONGITUDINAL DISTRIBUTION AND BUNCH LENGTH MEASUREMENTS AT VEPP-2000 COLLIDER*

Yu. Rogovsky#, E. Perevedentsev, Yu. Zharinov, V. Volkov,
Budker Institute of Nuclear Physics, Novosibirsk, 630090, Russia
A. L. Romanov, Fermi National Laboratory, Batavia, IL 60510, USA

Abstract

The paper describes the bunch length measurement system for VEPP-2000 collider, equipped with optical analysers based on LI-602 dissector, which provides permanent measurements of the longitudinal beam profile. Potential well distortion lengthening was measured at different bunch currents for the energies below 500 MeV. First measurements reveals the presence of microwave instability with turbulent emittance growth. The thresholds of these processes was used to estimate the values of reactive part of the longitudinal impedance. Measured energy loss factors was compared with computer simulations for the RF cavity. All results will be discussed and further estimations will be given.

VEPP-2000 OVERVIEW

The VEPP-2000 collider [1] exploits the round beam concept (RBC) [2]. This approach, in addition to the geometrical factor gain, should yield the significant beam–beam limit enhancement.

Collider itself hosts two particle detectors [3], Spherical Neutral Detector (SND) and Cryogenic Magnetic Detector (CMD-3), placed into dispersion-free low-beta straights. The density of magnet system and detectors components is so high that it is impossible to arrange a beam separation in the arcs. As a result, only a one-by-one bunch collision mode is allowed at VEPP-2000.

Table 1: VEPP-2000 Main Parameters @ E = 1 GeV

Parameter	Value
Circumference (C)	24.3883 m
Energy range (E)	150÷1000 MeV
Number of bunches	1 × 1
Number of particles per bunch (N)	1×10^{11}
Betatron functions at IP ($\beta^*_{x,y}$)	8.5 cm
Betatron tunes ($\nu_{x,y}$)	4.1, 2.1
Beam emittance ($\varepsilon_{x,y}$)	1.36×10^{-7} m rad
Beam–beam parameters ($\xi_{x,y}$)	0.1
Luminosity (L)	1×10^{32} cm^{-2} s^{-1}

The layout of the VEPP-2000 collider as it worked until 2013 is presented in Figure 1. The main design collider parameters are listed in Table 1.

*Work supported by the Ministry of Education and Science of the Russian Federation, Nsh-4860.2014.2
#rogovsky@inp.nsk.su

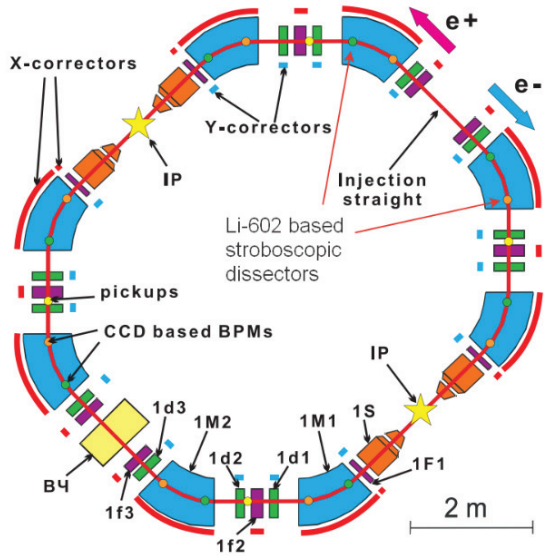

Figure 1: VEPP-2000 collider layout.

BEAM DIAGNOSTICS

Diagnostics is based on 16 optical CCD cameras that register the visible part of synchrotron light from either end of the bending magnets and give full information about beam positions, intensities and profiles. In addition to optical beam position monitors (BPM) there are also four electrostatic pickups installed in the technical straight sections, two photomultipliers for beam current measurements via the synchrotron light intensity, and one beam current transformer as an absolute current monitor.

In 2013 VEPP-2000 was equipped with two phi-dissectors [4] – stroboscopic image dissector with electrostatic focusing and deflection, that gives information about e+/e− longitudinal distribution of particles and bunch length.

In general, the instrumental temporal resolution of the dissector is determined by a set of different factors. The most important ones: energy and angular distribution of the photoelectrons emitted by a photocathode; quality of the electron image in the plane of the slit aperture; light image size at the photocathode; amplitude and frequency of sinusoidal sweep voltage; slit aperture size.

The contribution to the instrumental temporal resolution of the first factor is estimated as equal (or less) to 1.0 ps. value and contribution of other factors can be measured. For this purpose a point-like image of the continuous light source is projected onto photocathode and the signal

ISBN 978-3-95450-181-6

duration with the switched on and off RF sweeping voltage is determined [4].

The width of the technical instrumental function for first prototype of the dissector is close to 30-40 ps. FWHM. The typical longitudinal bunch distribution measured during routine operations with a single beam at VEPP-2000 collider is shown on Figure 2, where dashed blue curve is a Gaussian fit of the raw data.

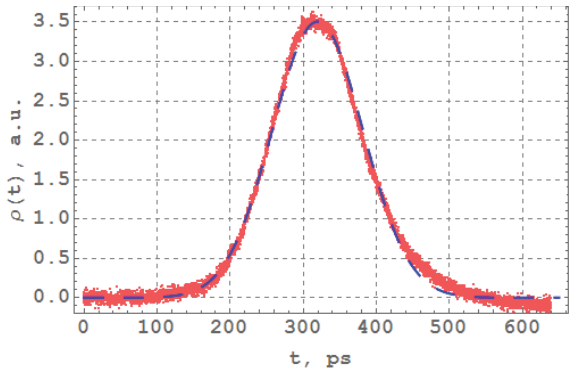

Figure 2: The longitudinal bunch distribution at low bunch intensity (~1 mA).

The control system of the VEPP-2000 collider allow us to measure and even store (for offline analysis) almost all parameters of magnetic system, RF system, timings and measured beam parameters. The most of these parameters can be measured with frequency 1-5 Hz. The resolution of beam current measurement is equal to 0.1 mA and of the RF cavity voltage – 0.2 kV.

BUNCH LENGTHENING

The length of an electron bunch in a storage ring depends on the peak current of the bunch. The two effects that alter the length are potential well distortion and microwave instability. For potential well distortion bunch length varies due to the electro-magnetic fields induced by the electrons, that modify the RF voltage seen by the bunch. This effect is present even at very low currents. The second effect, microwave instability, is only observed after a certain threshold current has been reached. Above this threshold energy spread of the beam increases until the peak current of the bunch reduces to equal the threshold current again.

Direct observation of the onset of microwave instability in the VEPP-2000 was possible at an intermediate energy. Measurements have been carried out for electrons, with intensities up to 50 mA at energy equal to 478 MeV with different values of RF voltages, in presence of positrons with infinitesimal intensity. In these experiments all beam dimensions were recorded as a function of bunch current. A subsequent experiment for positrons shows the same dependencies of lengthening behaviour and threshold values as for electrons.

Throughout the experiment σ_x remained constant below certain threshold (see Figure 3, where blue dots show bunch size below threshold, red ones – above), confirming that the beam was indeed below the threshold of microwave instability. The variation of the bunch length with the beam current is given in Figure 4. One can clearly see that the microwave instability threshold appears at around 24.5 mA and 32 mA for RF voltages equal 9.2 kV and 18.5 kV respectively.

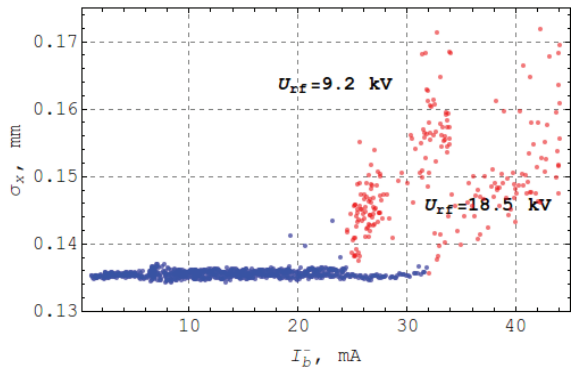

Figure 3: Horizontal beam size on 4M1L CCD (in place with non-zero dispersion) as a function of beam current at energy E=480 MeV.

The bunch length data below threshold has been fitted to the model [5] described by equation:

$$\sigma_z^3 - \sigma_{z0}^2 \sigma_z = \frac{\alpha_p \left| Z/n \right|_{eff} R^3}{\sqrt{2\pi}(E/e)\nu_s^2} I_b,$$

where I_b is the average beam current, e is the electron's charge, R is the ring average radius, E is the beam energy and ν_s is the synchrotron tune. The magnitude of the effect depends on the reactive part of the effective longitudinal coupling impedance |Z/n|. The dashed lines on the figure is a curve derived using equation above for |Z/n| = 2.32 Ohm.

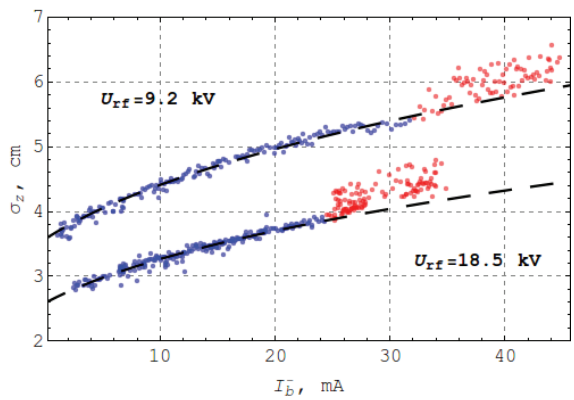

Figure 4: Bunch length as a function of beam current at energy E=480 MeV.

Our capabilities do not allow to measure the energy spread directly, but estimation can be done by methods developed [6] during VEPP-2000 operations. These methods based on measurements of beam transverse sizes along the ring with further fitting the emittances end effective beta functions to known optical model of the ring assuming that there is no focusing perturbations other than those caused by collisions. In Figure 5, one can find beam energy spread is estimated in such a way.

Longitudinal Loss Factor

The energy loss in accelerator rings due to impedance is proportional to the longitudinal loss factor as an integral over the real (or resistive) part of longitudinal impedance

ISBN 978-3-95450-181-6

times the bunch spectrum. Vacuum chamber itself and RF cavity [7], were considered as the major contributors to the impedance in VEPP-2000.

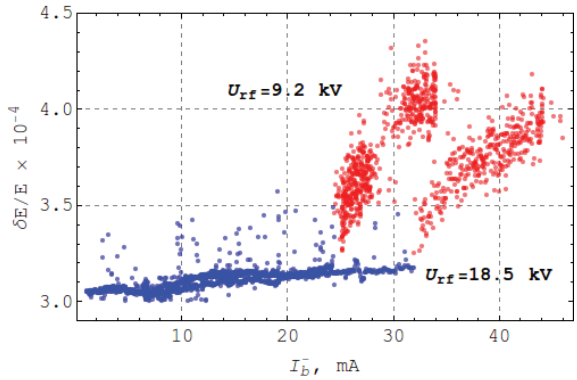

Figure 5: Beam energy spread as a function of beam current at energy E=480 MeV.

The synchronous phase shift is being determined as a difference between phase of beam longitudinal distribution centre of mass and phase of RF system reference signal. Dependence of synchronous phase on beam current allow to determinate a value of a bunch coherent energy loss.

$$k_l = f_0 \cdot U_{rf} \cdot Cos(\varphi_s) \cdot {}^{d\varphi_s}/_{dI_b} \text{ and } \Delta E = -k_l \cdot q^2,$$

where f_0 – revolution frequency, φ_s – synchrotron phase, U_{rf} – RF voltage and I_b – beam current.

The coherent energy losses of the beam is caused by the interaction with the RF cavity – the beam itself excite the electromagnetic field on frequencies proportional f_0 – was calculated (SLANS и CLANS2 code at BINP) [8].

Results are shown in Figure 6, where dashed line corresponds to coherent energy loss caused only by RF cavity HOM frequencies. As one can see from the pictures the contribution of the RF cavity is comparable (or slightly less) with the contribution of the net vacuum chamber in the ring (k_l = 0.15÷0.7 V/pC for U_{rf} = 10÷30 kV, while σ_z = 2.5÷6 cm, what corresponds to I_b = 0÷50 mA).

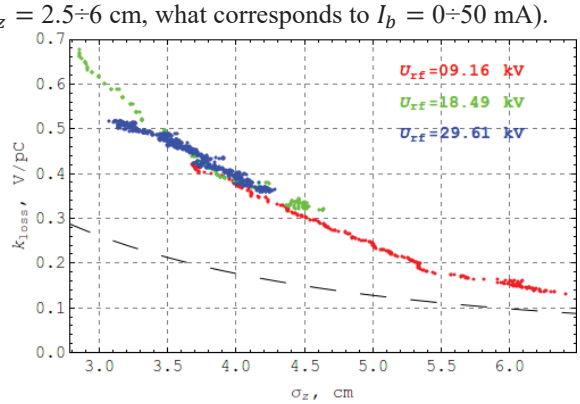

Figure 6: Longitudinal loss factor at energy E=480 MeV.

FUTHER ESTIMATIONS

If the values of effective longitudinal impedance obtained, then one can estimate the behaviour of the bunch length with beam current variance, for the case |Z/n| has no frequency dependence (pure inductance). The results of such naïve estimation is shown on Figure 7. Different lines corresponds to energies: 480 MeV – black, 500 MeV – red, 700 MeV – brown, 990 MeV – blue.

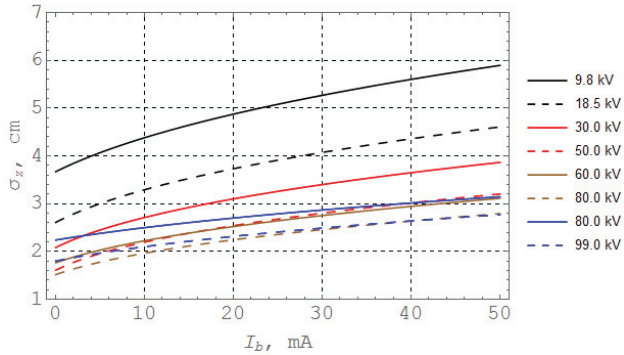

Figure 7: Bunch length as a function of beam current at different energies and RF voltages.

CONCLUSION

The current dependence of bunch length was measured at beam energy level E = 400-500 MeV. This dependence is in a good agreement with that obtained from the solution of balance equation. Estimated longitudinal impedance is |Z/n| = 2.32 Ohm and |Z/n| = 5.2 Ohm below and above the threshold accordingly. Measured dependence of the bunch length on bunch current on the threshold of microwave instability is linear.

The longitudinal loss factor integrated over the ring is a twice bigger than value predicted by the interaction with single mode RF cavity only. We strongly believe that this difference partially caused by interaction of the beam with dipole HOM in RF (1 mm transverse beam shift in RF cavity gives 20% gain in energy losses). Moreover, the net vacuum system also gives its influence on the common longitudinal impedance at the same level as RF cavity.

At high bunch current the longitudinal shape changes from Gaussian to parabolic profile. Besides an asymmetry of bunch shape takes place. It is believed this asymmetry provided by the contribution of real part of impedance.

REFERENCES

[1] Yu. Shatunov et al., "Project of a New Electron-Positron Collider VEPP-2000", EPAC'2000, Vienna, Austria, p.439.

[2] V.V. Danilov et al. "The Concept of Round Colliding Beams", Proc. EPAC'96, Sitges, p. 1149 (1996).

[3] T.V. Dimova *et al.*, "Recent Results on e^+e^-→hadrons Cross Sections from SND and CMD-3 Detectors at VEPP-2000 collider", *Nucl. Part. Phys. Proc.*, vol. 273-275, pp. 1991-1996, 2016.

[4] E.I. Zinin, PhD Thesis, Budker Institute of Nuclear Physics, 1984 (in Russian)

[5] A. Hoffman and J.R. Maidment, "Current dependent phenomena in LEP", CERN, LEP Note-168 (1979).

[6] A. Romanov et al. "Status of the Electron-Positron Collider VEPP-2000", Proc. NaPAC'13, Pasadena, p. 14 (2013).

[7] V.Volkov et al., "Single mode RF cavity for VEPP-2000 storage ring based collider", in: Proc. of EPAC 2004, Lucerne, Switzerland, 2004.

[8] V. Volkov, D. Janssen, High order mode analyses for the Rossendorf SRF gun. FEL2007

ISBN 978-3-95450-181-6

BEAM DIAGNOSTICS OVERVIEW FOR COLLECTOR RING AT FAIR*

Yu.A. Rogovsky†, D.B. Shwartz, Budker INP SB RAS, Novosibirsk, Russia and Novosibirsk State University, Novosibirsk, Russia and FSBI "SSC RF ITEP" of NRC "Kurchatov Institute", Moscow, Russia
E.A. Bekhtenev, O.I. Meshkov, Budker INP SB RAS, Novosibirsk, Russia and Novosibirsk State University, Novosibirsk, Russia
M.I. Bryzgunov, Budker INP SB RAS, Novosibirsk, Russia
O. Chorniy, GSI Helmholtzzentrum für Schwerionenforschung, Darmshtadt, Germany

Abstract

The Collector Ring (CR) [1] is an essential ring of the new international accelerator Facility of Antiproton and Ion Research (FAIR) [2] at Darmstadt, Germany. It will operate with antiproton energy of 3 GeV and has a complex operation scheme and several types of operational cycles. In this paper, we present an overview of all diagnostic systems, which are planned for commissioning and operations. Challenges and solutions for various diagnostic installations will be given.

INTRODUCTION

The main emphasis of the CR is laid on the effective stochastic precooling of intense Rare Isotope Beams (RIBs), secondary stable beams and/or antiproton as well. Special task – mass and half-life measurements of very short-lived nuclides (down to few tens μs) will be performed in the CR operated in isochronous mode [3].

Table 1: Main Parameters of the CR

Parameter	Value		
Circumference	221.45 m		
B ρ	13 Tm		
Mode	**p-bar**	**RIB**	**Isochronous**
Max. intensity	10^8	10^9	1-10^8
Particl. charge	1	40-100	40-100
Repetit. rate	1	1	—
Kinetic energy	3 GeV	740 MeV/u	400-790 MeV/u
Lorentz γ	4.20	1.79	1.43 – 1.84
Transition γ_{tr}	4.83	2.727	1.43 – 1.84
Slip factor $\lvert\eta\rvert$	0.014	0.1776	0
Acceptance	240	200	100
RF freq., MHz	1.315	1.124	0.968-1.137
RF harmonic	1	1	—
Betatron tunes	4.39/3.42	3.40/3.44	2.21/4.27
Bunch length	50 ns	50 ns	—

There are several types of operational cycles with beams in CR starting from injection and finishing with extraction, and beam parameters (see Table 1) change significantly during the cycles. The momentum spread is largest at injection, when very short bunches of several tens ns from the production targets (either RIBs or antiprotons) are injected. At this instant, the horizontal aperture of the ring is filled.

After a 1.5 ms bunch rotation and a 150 ms adiabatic debunching, the momentum spread is decreased, whereas this process leaves the transverse emittance unchanged in both directions. After these procedures the bunch fills all the perimeter of the CR. The reduced momentum spread is a necessary prerequisite for stochastic cooling. The cooling time for the antiprotons is 10 s and is estimated as 5 s after further CR upgrade. The cooling time for highly charged RIBs is much shorter (1.5 s). After the procedure of stochastic cooling, all phase subspaces are strongly reduced. The cooling is followed by the re-bunching procedure in 130 ms and further extraction of the beam.

Beam parameters changes significantly during the cycles as well as along the ring [4]. This demands an exceptional high dynamic range for the beam instrumentation and non-destructive methods are mandatory for high currents as well as for the low current secondary beams due to the low repetition rate. Precise measurements of all beam parameters and automatic steering with short response time are required due to the necessary exploitation of the full ring acceptances.

BEAM DIAGNOSTICS SUITE

The beam diagnostic systems are designed to provide a complete characterization of the beam properties including beam closed orbit, size, tune, circulating current, fill pattern, lifetime, chromaticity, beam loss pattern, beam density distribution, emittance, and bunch length. A large number of beam monitors and will be installed in the ring (see Table 2).

Electrostatic Pick-ups (18 combined and 1 vertical) measure the beam centre-of-charge transverse position in a non-interceptive way. In normal operation mode, the Pick-up signals are averaged for orbit corrections [5]. Alternatively, a subset of the monitors can be read out turn-by-turn, synchronized to the bunch passage for tune measurements, etc.

A Fast Current Transformer provides the longitudinal structure with turn-by-turn resolution during bunch rotation in longitudinal phase space. A DC Current provides the total number of ions circulating in the ring. Both Fast CT and DC Current Transformers will have calibration coils

* The work is carried out with the financial support of FAIR-Russia Research Center
† rogovsky@inp.nsk.su

ISBN 978-3-95450-181-6

implemented. To determine the circulating current of low intensity beam, one Cryogenic Current Comparator (CCC) will be installed with a detection limit of few nA, well below the threshold of regular transformers.

Table 2: List of Beam Diagnostics at CR

Beam Monitor	Amount
Position Pick-up	19
DC Current Transformer	1
Fast Current Transformer	1
Residual Gas Profile Monitor	2
Broadband Schottky Pick-up	1
Beam Stopper	2
Scintillating Screen	5
Beam Scrapper	20
Cryogenic Current Comparator	1
BTF Exciter	1

A combined Schottky Pick-up measure the relative momentum spread Δp/p, the non-integer part of the betatron tune Q, the tune spread and the transverse velocity spread. These monitors are of special interest as CR will have almost coasting beam during the cooling process.

An array of scintillating screens is deployed to provide transverse profiles at strategic locations throughout the ring.

A combined Residual Gas Monitors (RGM) measure transverse beam profile in a non-interceptive way, thus giving us an important tool for determination of the beam emittance and its evolution during the acceleration and cooling process.

Beam Position

The BPM system based on linear-cut type electrodes (see Figure 1) will measure the beam position as well as an approximate beam current. As far as possible, BPM sensors will be physically located near quadrupoles, since the goal of beam steering normally is to center the beam in the quadrupoles.

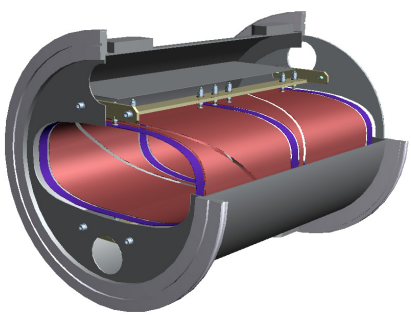

Figure 1: A large (400 mm) aperture, super-elliptical, split plate BPM design in dispersive section provides a larger linear response aperture.

The linear-cut electrodes geometry is designed to fit the beam without losses: in straight section beam has almost equal sizes less than 80 mm, but in arcs beam has horizontal size 360 mm, while vertical size less than 80 mm. Such a geometry is believed to be linear in response. Additional "groundings" electrodes introduced to vanish parasitic influence between pairs of electrodes. Polynomial correction removes geometric nonlinearities from the difference-over-sum algorithm, providing position error less than 100 μm over ~90% of the BPM aperture.

The CR has quite limited space for beam diagnostics installations. Despite this fact, the BPMs will be installed between the main magnetic elements but will be integrated with its vacuum chamber into vertical dipole corrector (see left side in Figure 2) which can adopt quite huge aperture. There will be 4 "small" BPMs in the straight sections (shown on right side in Figure 2) and 6+7 "big" BPMs in arcs of the CR. Additional "big" BPM will be installed just after injection where TCR1 and CR vacuum chambers combines to measure the position during injection or during stable operations. One more "big" BPM will be installed just before extraction line where beam orbit will be shifted towards the extraction [6].

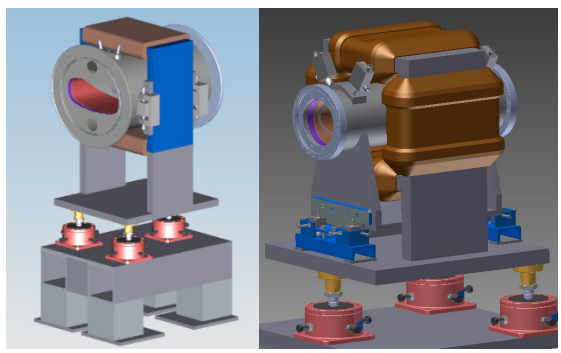

Figure 2: BPM installed in vertical (left) and combined (right) dipole corrector.

Beam Profile

An RGM principle (fig. 3) of operation is based on measuring the profile of secondary ions appeared in the process of ionization of residual gas by the main beam. For the collection of secondary ions in the profile monitor a transverse electric field is applied, which sends positively charged ions to the detector. Uniformity of the electric field should be sufficient to provide the required spatial resolution of profile measurement. The position-sensitive optical particle detector measures density distribution of secondary particles, which is proportional to transverse beam profile in one direction.

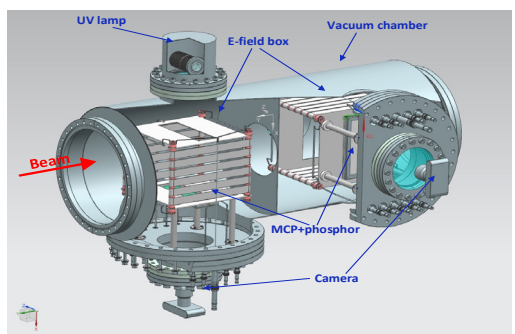

Figure 3: Combined RGM and its components.

ISBN 978-3-95450-181-6

This monitor is designed for high-current operation where conventional intercepting diagnostics will not withstand high-intensity ion beams.

The system in principle can operate with different detector where electrons, which appear at the exit of MCP, go directly to resistive plate, thus locally charging it. Measuring the charge flows from both ends of the plate, you can determine where electronic avalanche hits the plate. The advantage of this approach is a total elimination of the transformation of particle flux to light, which, due to the reflections can lead to spurious peaks in the measured profile.

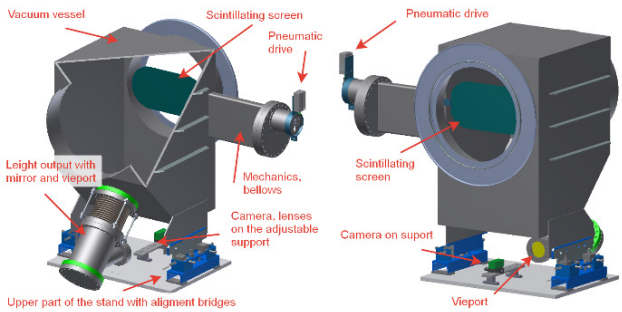

Figure 4: Scintillating screen and its cross section.

For the same purpose of beam profile measurements, five scintillating screen monitors (see fig. 4) are installed in the injection/extraction area, downstream of the electrostatic injection septum and in arcs centres. One of the screens observes the beam directly after injection and after the first turn in the machine in principle.

Beam Intensity

During the commissioning and tuning phase of the CR ring, insertable Faraday cups (or Beam Stoppers) (fig. 5) will measure current, while isolating the downstream accelerator components from the beam.

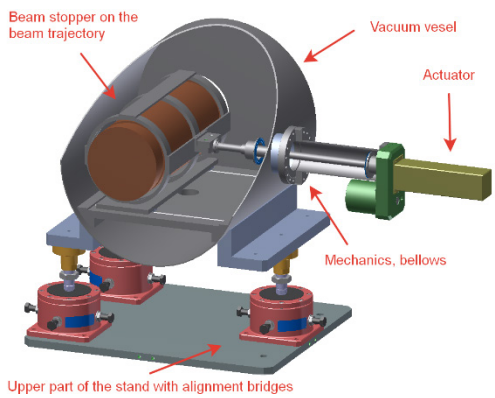

Figure 5: Faraday cup with longitudinally sectioned body.

The main requirements for this device in CR is to full stop of incoming ions and partial stop of antiprotons (with kinetic energy losses up to 10%). The body of FC will consist of two pars – relatively short part ~1/3 from Cu (for stopping ions and measuring intensity) and ~2/3 part from Pu (for stopping antiprotons). Preliminary simulations shows that ions are stopped at the first 2-3 cm of the stopper body (Z=40, E=750 MeV/nucleon), and 40 cm of Pb in length is excessive for reasonable design of the stopper.

Beam Tunes

Schottky Pick-up consists of four cylindrical stripline type electrodes connected to vacuum chamber and feedthrough to provide signal for further processing. This assembly is a part of beam line. These electrodes in combination with vacuum chamber are considered as transmission line. The pick-up geometry should be an object of optimization where two most important criteria are field homogeneity and matching of the signal path to 50 Ohm.

Beam Loss Detection

The beam loss monitoring (BLM) has the dual purpose of keeping the machine safe from beam - induced damage and avoiding excessive machine activation by providing critical input to the machine protection system. Thus, the system must be designed complete coverage of possible loss scenarios. In addition, as the BLM system will be a major tool for beam tune-up, it should also be designed in a way that enables it to pin-point the loss location as precisely as possible. The optimal location of detectors will be determined by simulations in nearest future.

Other Diagnostics

Five sets of scrapers with four blades in each planned, to provide several functions: 1) control the loss point for beam aborts or dumps, 2) limit the particles losses that create radiation on RF cavities with quite small cross section, and 3) for diagnostics and physics studies of the dynamic and momentum aperture of the ring.

Several other diagnostics systems are also in a mature stage but are not discussed here. These systems include CCC current measurement, BTF exciter, and 2-position scintillating screen, beam loss detector, commercially available FCT and DCCT devices from Bergoz Instrumentation [7].

CONCLUSION

An overview of the proposed beam diagnostics concept for CR given in this paper. The results from ongoing research, developments and preliminary design work of BINP and GSI teams have been shown. The design level of subsystems is now very good and provides a firm basis to meet challenging requirements of diagnostics relating to the all requirements of CR.

REFERENCES

[1] P. Shatunov et al., “Collector Ring Project at FAIR: Present Status”, in Proc. RUPAC’16, St. Petersburg, Russia, Nov. 2016, paper WECBMH02, this conference.
[2] FAIR, http://www.fair-center.eu
[3] A. Dolinskii et al., NIM A 574, 207-212 (2007).
[4] D. Shwartz et al., “Beam dynamics at CR”, in Proc. International Workshop on Antiproton Physics and

ISBN 978-3-95450-181-6

Technology at FAIR (FAIR'15, fair15.inp.nsk.su), Novosibirsk, Russia, Nov. 2015.

[5] O. Gorda et al., "Beam Dynamics and Closed Orbit Correction at the Collector Ring", presented at IPAC'16, Busan, Korea, May 2016, paper THPMB002.

[6] P. Shatunov et al., "The Injection Septum Magnet for the Collector Ring", presented at IPAC'16, Busan, Korea, May 2016, paper TUPMB017, this conference.

[7] Bergoz Instrumentation, http://bergoz.com

ISBN 978-3-95450-181-6

SYSTEM OF THERMOMONITORING AND TERMOSTABILIZING OF KURCHATOV SYNHROTRON RADIATION SOURSE

N. Moseiko, E. Kaportsev, K. Moseev, Y. Krylov, A. Valentinov, Y. Efimov, National Research Centre Kurchatov Institute, Moscow, Russia

Abstract

The modern system of thermomonitoring and thermostabilizing of KSRS is described. The system provides: a monitoring of temperatures of the magnets and RFresonators of KSRS; informing operator on violations of the course of technological process; data protection from illegal access; archiving and displaying of archive data in a trend type. The system includes 480 temperature sensors of the AD592 type, providing the accuracy of measurements 0, 2 C^0. System of thermo stabilizing of the linear accelerator the proportional integral differentiating regulator for support of stability of temperatures at the level of 0, 05 C^0 .

INTRODUCTION

The National Research Centre Kurchatov Institute, completed work on the creation of a new automated control system (ACS) accelerator-storage complex (ASC) "Siberia" [1-5] on the basis of modern servers, network equipment, the VME hardware, National Instruments company modules and new power ASC equipment (with built-in controllers). It uses software tools: Citect SCADA 7.2 (full version), Lynx OS Runtime, LabVIEW-2013 development environment Thursday PK-166 software, OS ARTX166, PCAN-Evaluation, and others. As part of a new ACS was developed modern system of temperature control and temperature stabilization of ASC "Siberia".

APPLICATIONS

TERMOCS operator's application consists of a set of video imaging that are designed to display information about the temperature adjustment is-ditch, lenses and bending magnets ASC "SIBERIA" [1-5]. In this video frame (Fig. 1) shows designed to display the current temperature correctors, lenses and bending magnets of a linear accelerator, a small storage, the EOC-1 and the EOC-2.

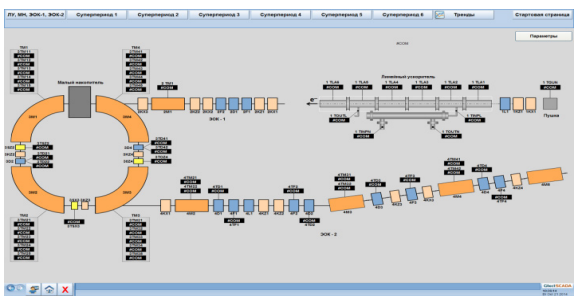

Figure 1: Video frame "LU, PL, EOC-1 and EOC-2".

In this video frame (Fig. 2) shows display the current temperature correctors, lenses and bending magnets in each superperiod Accumulate large-telja.

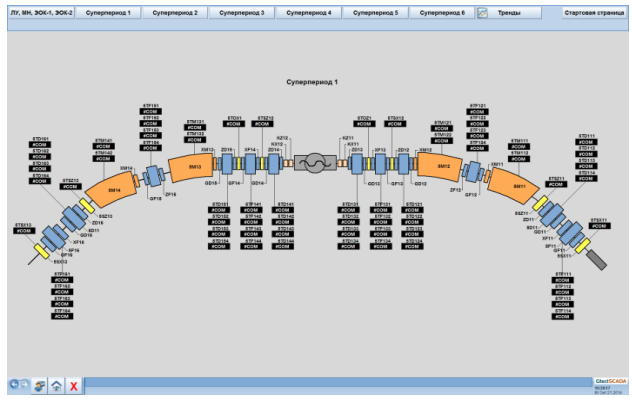

Figure 2: Video "Superperiod 1"- "Superperiod 6".

In this video frame (Fig. 3) shows intended to display archival temperatures in graphs.

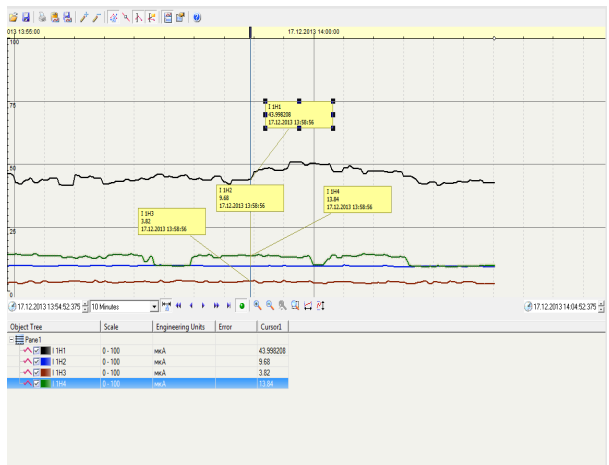

Figure 3: Video frame "Trends".

WORKING WITH TREND

To work with the current and historical trends using «Process Analyst» (Fig. 4). The horizontal axis of the graph is the time axis, which is equal to the selected interval, co-tory user-configurable. The vertical axis represents the values of technological parameters imposed on the chart. Setting trends and management is carried out by the following elements:

- Addition and removal of curves with the trend;

ISBN 978-3-95450-181-6

• Coupling / decoupling curves (if the curves are linked, then all actions affecting the display of time intervals in the chart, are performed with all the curves);
• Show / hide the point plotting;
• Show / hide the arrow mark;
• Show / hide the curves.

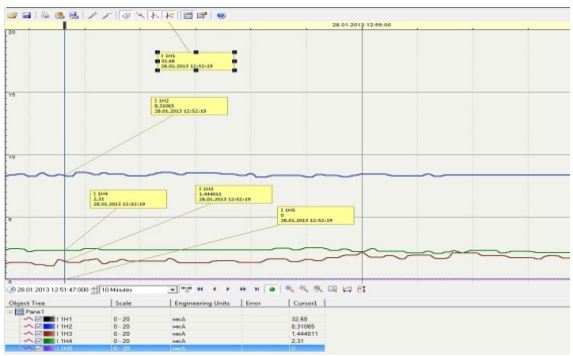

Figure 4. «Process Analyst».

With the help of these buttons you can save the desired presentation of graphs and Liu-bout time to load it from the file.
• In this field specify a time period for which the values are displayed graphs on the screen (the default interval is 10 minutes, but the User The-Telem can be changed) ;
• The initial time interval of the current screen (can be changed by the user);
• Final torque (can be changed by the user) of the current time interval on the screen;
• Enable / disable auto-scroll mode, all curves;
• Zoom in / out 2 times along both axes;
• Single arrow moves the chart on the floor of the interval forward;
• backward double arrow shifts the graph of a range;
• Curves in the plots shifted to a point on the axis of the date and time corresponding to the currently-th time;
• Activate zoom separate part of the graphs. By pressing this button the mouse cursor changes to a crosshair with which, the area on the chart. Cancel this mode can be with help of pressing the right mouse button again or by pressing the button ;
• Set acustom duration of the interval display time;
• Change the scale of the vertical spine;
• Adding new graphs is done by pressing the corresponding button.

In the window that appears (Fig. 4) must be from the dropdown list box in the Connection (connection) to select Port-tion with CitectHistorian Knop and click Search (search), select the list that appears necessary parameters to display by double-clicking the left mouse button. After selecting an optionally-sary settings you must press the "OK" button. To remove the scheduling is required in the "tree of objects" to select the schedule you want to delete and press on the appropriate button.

EQUIPMENT

Lower level equipment of the "TEMOKS" system is built based on the standard equipment of NationalInstruments company. Measuring and control is performed by NIsRIO-9073 Integrated 266 MHz Real-Time Controller and 2M Gate FPGA. The thermal control system uses AD592 temperature sensors (error 0.2 C^0) and AD590 (error 0.5 C^0) . These advanced sensors replaced KT904 sensors that are not manufactured anymore. The temperature sensors (480 pcs.) use a 2-wire connection scheme. A new board was developed -16-channel multiplexer with a common signal amplifier to convert these signals into a voltage(0 –10 V).

Let us briefly review the TERMOKS system. From the database of the new ACS system configuration of an each temperature control sensor and its alarm settings get loaded into the NI cRIO-9073 controller : 1 lower to detect when a sensor is off and 2 upper - emergency and critical. When each of these levels is exceeded, high-current power supplies the magnetic system ASC "Siberia" is disconnected. Measuring signals from multiplexers are done by using two NI 9205 AI Differential / 32 AI Single-Ended, ± 10 V, 16 Bit Module and NI 9401 5 V / TTL, Bidirectional Digital I / O, 8 Ch Module. Then averaging over several points, translating into a temperature value, comparison with the settings and output signals of the relay interlocking is being performed using NI 9476 24 V, Sourcing Digital Output, 32 Ch Module. The acquisition cycle of all sensors including filtering and averaging is 2 s

To measure temperature in the thermal stabilization system we use conversion board that converts Pt100 sensor signals into signals of 0-20 mA and NI 9203 8-Channel, ± to 20 mA, 16-Bit Analog Input Module. Temperatures are read by the controller NI cRIO-9073, then calculated output value of the heating element is transmitted (using the NI 9265 4-Channel 16-Bit Analog Output Module) to the E5AN-H Omron module to control heating element's thyristors . Work cycle of thermal stabilization - 2. Temperature stability in the linear accelerator is 0,05 C^o

In video frame (Fig. 5.) shows a diagram of the system of thermal stabilization, the state is turned off, teley QF1 and QF2, contactors KM1 and KM2. With a given video system operator controls the heat setting.

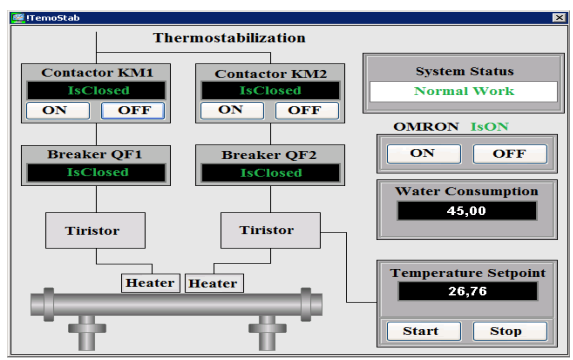

Figure 5: Control Window thermal stabilization system.

ISBN 978-3-95450-181-6

The graphs (Fig. 6) of the measured values of the water temperature at the inlet of the copper (TSX12) and aluminum (TSX11) circuits at the input (T1NPN) and output (T1OUTN) from the heater, as well as the average temperature of the linear accelerator structure (T linac average temperature). The latter varies between 0.05 ° C.

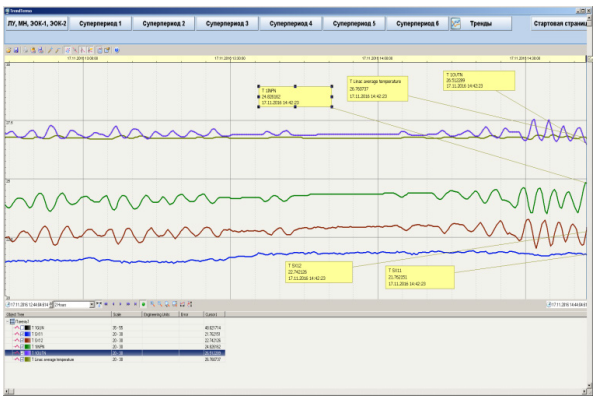

Figure 6. A screen shot of the archival program thermal stabilization system.

CONCLUSION

As a result of this work, a modern thermal control system and temperature stabilization by the use of new sensors, control and measuring equipment. Improve the reliability of the system and the ability to more effectively manage the accelerating-storage complex "Siberia, promptly obtain complete and accurate information from the server system. The system has the ability to improve the accuracy of temperature stabilization system of measurement to 0.01 C^0.

REFERENCES

[1] Y.Fomin, V.Dombrovsky, Y.Efimov et al. “New Automated Control System At Kurchatov Synchrotron Radiation Source Based On SCADA System Citect”, Proceedings of ICALEPCS 2013, San Francisco, CA, USA, MOPPC020, pp.97-99, www.JACoW.org

[2] N.Moseiko, A.Valentinov, V.Korchuganov et al. “The Power Supply System For Electron Beam Orbit Correctors And Focusing Lenses Of Kurchatov Synchrotron Radiation Source”. Proceedings of ICALEPCS2013, San Francisco, CA, USA, pp.1180-1182, THPPC049,www.JACoW.org

[3] N.Moseiko, V. Dombrovsky, V.Korchuganov, et al. “Upgrate System Of Vacuum Monitoring Of Synchrotron Radiation Sources Of National Research Centre Kurchatov Institute”. Proceedings of ICALEPCS2013, San Francisco, CA, USA Control System, THPPC050, pp.1183-1185, www.JACoW.org

[4] Y.Krylov, Y. Fomin, ,E. Kaportsev et al. “RF-Generators Control Tools For Kurchatov Synchrotron Radiation Source”. Proceedings of ICALEPCS2013, San Francisco, CA, USA, MOPPC107, pp.359-361, www.JACoW.org

[5] Y.Fomin, V. Korchuganov, N. Moseiko et al. “First Operation Of New Electron Beam Orbit Measurement System At Siberia-2”. Proceedings of ICALEPCS2013, San Francisco, CA, USA, pp.1186-1188, THPPC051, www.JACoW.org

ISBN 978-3-95450-181-6

MONITORING OF LOW INTENSITY ION BEAMS AT FLNR ACCELERATOR COMPLEX

Yu.G. Teterev, S.V. Mitrofanov and A.I. Krylov, Flerov Laboratory of Nuclear Reactions, Joint Institute for Nuclear Research, Dubna, Moscow Region, Russia

Abstract

Detectors are developed to diagnose ion beams inside the accelerator, during beam transportation, and to control beam in the user area. The intensity of beam in the range from several ions per second up to pnA, the energy, the density distribution and the grade of the beam are monitored by the detectors. Depending on the operating conditions the ionization chambers, the proportional counters, the scintillation detectors and lamellar sensors with dual screen are used. The main criteria for the detector design are the reliability in long time operation under radiation, in magnetic fields and in rapidly changing vacuum conditions, and the possibility of quick repair or replacement. The diagnostic detectors are located in the channels to study the radiation resistance of electronics, and in the channel for the biological research.

INTRODUCTION

Beams of accelerated ions of low intensity are required for applied research, e.g., research of radiation resistance of electronics [1] or in biology. The intensity of these beams is less at three or more orders of magnitude than those used at the FLNR accelerator complex traditionally. There is a need to create a new set of diagnostic tools with greater sensitivity. A new set based on the detectors that are traditionally used in physical experiments. When choosing the detectors the conditions in which they will operate are taken into account. For example, detectors placed inside the cyclotron are exposed to a strong magnetic field, high radio frequency field and x-radiation. The detectors operate in high vacuum, which must not be spoiled. It is not always possible to remove the detector from the vacuum chamber. It can only be moved to the periphery, if the cyclotron works on the traditional beams. The detector should be reliable and resistant to radiation.

MEASUREMENT OF BEAM CURRENT INSIDE THE CYCLOTRON

Two different detectors operating in the current mode are designed and tested to work inside the cyclotron. First one is the detector based on secondary emission; the second one is the air filled ionization chamber with a thin metallic entrance window. Currents produced by these detectors are measured by means of amplifiers, the minimum value of the input current which is 1 pA.

The detector based on secondary emission consists of three lamellae, one of which is located in the center perpendicularly to the beam axis, the other two above and below, respectively. The width of each lamella is 8 mm, the thickness is 1 mm, and the distance between the centers of the lamellae is 11 mm. Each lamella is surrounded by a screen. The screen is open only from the side of the ion beam. Voltage +9 V from a battery is fed to the screen. The emission electrons arising from the bombardment of ion beam are collected by the screen. This screen is surrounded by second screen which is grounded. Dual screening reduces noise level to less than 1 pA. Current from each of the lamella is measured.

The described detector allows measuring the ion current only in arbitrary units. The output of the secondary electron emission depends on the type of ion, its energy and is proportional to the differential energy loss in the material of the lamella. The experiment on the calibration of the detector by the external beam of argon with energy of 32 MeV/nucleon shows that the detector can be used on the beam intensities higher than10^4 ions/s.

In the same calibration experiment it was shown that a detector with ionization chamber can be used on the beam intensities by three orders of magnitude lower. Special measures are adopted to prevent x-ray radiation from dees on the readings of the detector. Current from ionization chamber is measured on collector, in front of which there are two identical electrodes. The voltage on these two electrodes is supplied with the opposite polarity. Currents in the chamber compensate each other in the absence of the beam. The beam is passed only through space between the collector and one of the opposite electrodes. In spite of the high sensitivity, the camera has some disadvantages. One of them is the presence of the entrance window, which limits the application of the detector for measuring the intensity of ions having a small path length. Another disadvantage is the presence of gas in the volume of the ionization chamber inside a cyclotron that can create an emergency situation.

THE DETECTOR TO MEASURE THE BEAM CURRENT AFTER THE EXIT FROM THE CYCLOTRON

Gas-filled detector is mounted directly after the beam extraction from a cyclotron. The working gas of the detector is air. The input window of the detector with a diameter of 60 mm is closed by a foil of stainless steel with a thickness of 6 μm. The detector can operate in two modes: proportional counter and ionization chamber. The detector is a set of interleaved grids, the anodes and cathodes. The anodes are coiled from a wire thickness of 20 μm, and the cathodes from wire thickness of 100 μm. Voltage 1800-2100 V is supplied to the counter. Its efficiency is nearly 100% for all ions. Similar proportional counter filled with air is described in [2].

ISBN 978-3-95450-181-6

The detector in the mode of a proportional counters suits for measuring the beam intensity in the range from single up to10^5 ions/s. The detector is switched into the mode of ionization chamber at higher beam intensity. The transition from mode to mode is caused by reducing the voltage to 300 V. Ionization chamber current depends not only on the beam intensity but also on the species and energy of the ion beam. The measured current can be correlated with the intensity of the ion beam in the overlapping range of the ionization chamber and proportional counter. The detector in the mode of ionization chamber can measure the beam intensity in the range from 10^2 to10^8 ions/s. The described detector helps in the extraction of a beam even at low intensity within a cyclotron. With their help, can be controlled the acceleration and extraction of ions, when the traditional ECR sources produce ions with a low yield. The possibility appears to expand the variety of beams and energies.

DETECTORS TO MEASURE THE BEAM PROFILE DURING TRANSPORTATION OF THE BEAM TO USER AREA

Multi-channel secondary emission detectors are used for the diagnosis during transport of beams to user area. Detectors are of two kinds: with 13 and 25 lamellae. The first is to monitor the transverse distribution of the beam in a region with a diameter of 80 mm, the second - in square 80 x 80 mm. The detectors are made on the same principle as the detector with three lamellas, described above, that is, have dual screening. The currents from all of the lamellae are measured by multichannel current amplifier. A fragment of the detector is presented on Fig.1, which shows the location of one of the lamellae and of the screens. Multi-channel detectors are an alternative to phosphors and can be used for a beam with flux density above 10^4 ions/s cm^2. The readings of the detectors are linearly proportional to the current of the incident beam, in contrast to the phosphors.

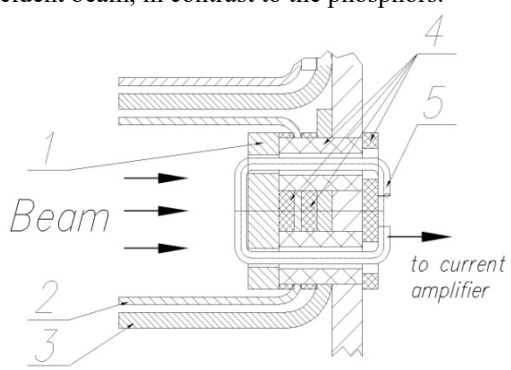

Figure 1: Location of the lamellae and of the screens. 1-lamella, 2 - the first screen, 3- the second screen, 4 – isolators made from Al2O3 , 5 - copper wire

DETECTORS TO MEASURE THE ENERGY OF ION BEAM DURING THE TRANSPORTATION TO THE USER AREA

Energy beam is measured on the straight section of the beam transport line. Time-of-flight method is used to measure energy. The time of flight is determined by registering the induced one and the same beam microbunch signals from two scintillation detectors separated by path length. Microbunches are a natural time structure of ion beams accelerated in the circular accelerator. Detectors with a substantially smaller size compared with the scanning beam cross section are used. They are mounted on the periphery of the scanning ion beam in such a way that they don't overshadow each other and the device under test. Method allows working with beams of low intensity. More detail concerning the method are described in [3]. The created detectors based on organic scintillators and photosensory modules of the firm "HAMAMATSU".

The diagnostic system has a function of identifying the ion. For its implementation the system uses a detector with a thick CsI scintillator which is inserted into the beam. The total energy of the studied ion is measured using this detector. The total energy and time-of-flight can definitely identify the ion. This feature is rarely used.

DETECTORS TO MEASURE BEAM PARAMETERS AT THE TARGET OF THE USER

Control of the irradiation of the user objects is carried out using the detectors of the two appointments. The intensity and homogeneity of the beam at the object is controlled by one set of detectors. The given beam intensity and exposure time is controlled with the help of other set installed on the periphery of the object. Detectors based on organic scintillators and photosensory modules of the firm "HAMAMATSU" use on beams for studies of radiation resistance of electronics. The registration efficiency is 100%. The detectors operate in the counting mode [3]. Due to low radiation hardness of the organic scintillators the possibility of fast them replacement is provided.

The homogeneity of the distribution and the intensity of the beam at the object are controlled in advance. The readings of detectors in the target region correlate with the readings of the detectors located at the periphery. The detectors controlling the uniformity of the beam are removed out and control is carried out by detectors at the periphery. Nine detectors are now used to control the homogeneity of the beam. There is a need to increase their number.

The ion beam at the channel for biological studies is controlled by five ionization chambers, Fig. 2 [4]. The cameras are thin and the beam passes through them. The biological object is positioned immediately behind the central camera. The other four cameras are used to control the homogeneity of the irradiation field.

ISBN 978-3-95450-181-6

Central camera is calibrated in units of absorbed dose rate. Ionization chamber can measure the dose rate in the range from 10^{-3} to10^{2} Gy/s.

All service for detectors, signal processing and presentation of the results are carried out by electronic components conforming by the standard "Euromechanics". Communication with a computer located on the remote accelerator, goes via Ethernet.

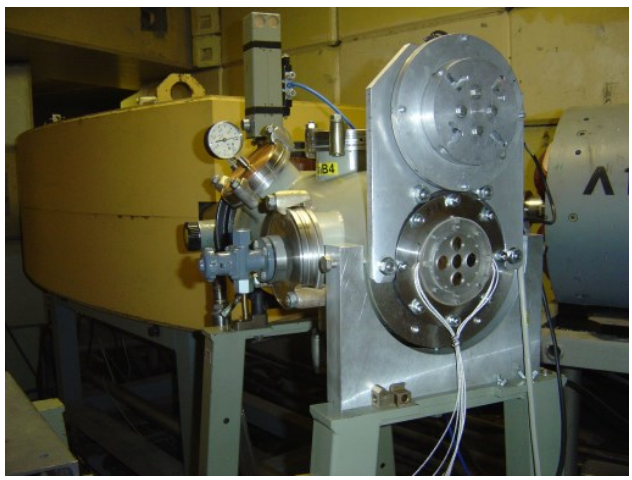

Figure 2: Five-channel ionization chamber for monitoring the irradiation of biological objects

CONCLUSIONS

A new set of diagnostic tools with increased sensitivity is created for applied research. A new set based on the detectors used traditionally in physical experiments. Detectors are developed to diagnose ion beams inside the accelerator, during beam transportation, and to control beam in the user area. The beam intensity in the range from several ions per second up to pnA, the energy, the density distribution and the grade of the beam are monitored. Depending on the operating conditions the ionization chambers, the proportional counters, the scintillation detectors and lamellar sensors with dual screen are used. The main criteria for the detector design are the reliability in long time operation under radiation and the possibility of quick repair or replacement. The diagnostic detectors are located in the channels to study the radiation resistance of electronics, and in the channel for the biological research.

REFERENCES

[1] V. A. Skuratov et al. Ion Beam Diagnostics for SEE Testing at U400M FLNR JINR Cyclotron**.** RADECS 2012 Proceedings.

[2] Yu. G. Teterev and G. A. Kononenko, Instruments and Experimental Techniques, 2011, Vol. 54, No. 4, pp. 585–589, published in Pribory i Tekhnika Eksperimenta, 2011, No. 4, pp. 148–152.

[3] V. A. Skuratov et al. Instruments and Experimental Techniques, 2014, Vol. 57, No. 1, pp. 11–16. Published in Pribory i Tekhnika Eksperimenta, 2014, No. 1, pp. 15–21.

[4] A.A. Besbach et al, Physics of Particles and Nuclei Letters 2013, v.10, No. 2, pp. 274-280.

ISBN 978-3-95450-181-6

DIAGNOSTICS OF ACCELERATOR BEAMS BY THE DEPENDENCE OF THE VAVILOV-CHERENKOV RADIATION INTENSITY ON THE REFRACTIVE INDEX OF THE RADIATOR "*n*"

K. A. Trukhanov†, SSC RF Institute of Biomedical Problems, RAS, Moscow, Russia
A. I. Larkin, Moscow Engineering Physics Institute, Moscow, Russia
V. I. Shvedunov, Skobeltsyn Institute of Nuclear Physics Institute MSU, Moscow, Russia

Abstract

The report presents the methods for finding of the particle velocity (energy) distribution of accelerator beams. Velocity distribution is deduced from the Volterra integral equation of the first kind with the right part, which is defined by the dependence of Cherenkov radiation (CHR) intensity on *n*, experimentally obtained for the given beam. Velocity distribution is the second derivative of CHR intensity. The problem of stability of the second derivative is solved by attracting a priori information. Using of optical dispersion of radiator is discussed. It enables to find velocity distribution even for the single bunch of particles. The method also enables to find velocity distribution for beams with a noticeable transverse velocity of the particles. The method is virtually non-destructive in many cases.

INTRODUCTION

The development of the non-intercepting methods for finding a velocity (energy) distribution of particles in accelerator beams is of great importance for irradiation process control in industry, medicine and science.

Existing methods of charged particle beam diagnostics have well-known disadvantages especially in the case of high energy beams. The non-traditional method of accelerator beam diagnostics based on the use of the CHR is considered below.

CHR angular distribution is used for a long time for determination of the velocity or the energy spectra of the charged particles [1]. However application of this method for the accelerator beams and especially for the electron beams of the high intensity industrial accelerators is limited by an essential transverse velocity component of the particles in the beam "smearing" the angular distribution of the radiation. Addition difficulty consists in superimposing of a transition radiation at radiator boundaries on the CHR angular distribution.

We consider two methods for finding a velocity (energy) particle distribution of beams based on the dependence of the CHR intensity and its spectral distribution on the phase velocity of the electromagnetic waves in the optical ranges (Fig. 1). The methods are practically non-intercepting and may be convenient for the energy and the energy spectrum measurements of beams including high intensity electron beams.

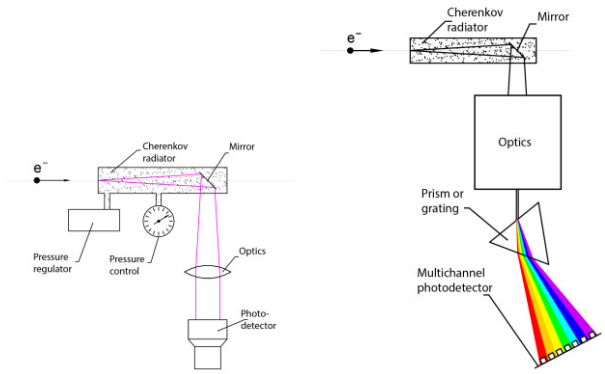

(a) (b)

Figure 1: Two methods for finding a velocity (energy) particle distribution with CHR. (a) The photons yield is registered by a photodetector depending on gas pressure. (b) The photons spectrum is recorded by the spectrum analyzer.

THEORETICAL BASES AND RESULTS

For the first time the possibility of determination of average electron velocity in the beam of the electron accelerator (the 4.5 MeV microtron) by the measurements of CHR intensity dependence on a radiator refraction index *n* in an optical range was demonstrated in [2, 3].

CO_2 was used as a radiator. The gases, which refraction index *n* varies with pressure *p* as $n(p) = 1 + kp$ at $kp << 1$, are natural choice of the CHR medium in this case. Once *p* passes the threshold of CHR for the maximum electron beam velocity in the detector ($1/\beta_{max} = 1+kp$) the CHR intensity *I* grows nonlinearly as more and more particles produce the CHR. Beginning from point where the minimal electron velocity β_{min} of beam particles becomes equal to the phase light velocity in the gas -radiator an intensity *I* of CHR in the detector is dependent on *kp* linearly. The intersection of the extrapolated CHR linear part with a background level corresponds to the average electron velocity in the beam [2, 3].

The same method was proposed in the work [4, 5] carried out 15 years later without reference to [2, 3]. No nonlinear part in *I(n)* dependence was noted.

In works of one of us (K.T.) [6] it was shown that nonlinear part of the intensity curve can be used for obtaining the velocity distribution and the energy distribution of the particles in the beam.

† trukhkt@com2com.ru

ISBN 978-3-95450-181-6

If the same part of the CHR light is registered by the photodetector independently of the position and the direction of a particle (electron, nucleus etc.) passing through radiator (as in the spherical Cherenkov detector for example) then the velocity distribution of particles and the energy spectrum can be obtained for the arbitrary angular distribution of the particles. In the case under consideration (the accelerator monitoring), this condition can be easily fulfilled.

In further consideration, we will follow [6]. If $n = n(\lambda)$ (λ is wavelength) a number of the CHR photons $N_{ph}(n(\lambda))$ in a unit wavelength band reaching the photodetector can be written as:

$$N_{ph}(n(\lambda)) = g \int_{1/n}^{\beta_{max}} \left(1 - \frac{1}{n(\lambda)^2 \cdot \beta^2}\right) \cdot f(\beta) d\beta \cdot \lambda^{-2} \qquad (1)$$

where $f(\beta)$ is a particle velocity distribution, $g = 2\pi\alpha N_e k L$, where α is the fine structure constant, N_e – the number of the electrons, L- the length of particle path in detector, k – the photon collection factor.

By successively differentiating (1) with respect to $(1/n^2)$ we obtain the solution in the form of the first and the second derivative of N:

$$f(\beta_\lambda) = \frac{\lambda^2}{2g}\{(\beta_\lambda)^2 \frac{d^2}{d\beta_\lambda^2} N_{ph,\lambda} - \frac{d}{d\beta_\lambda} N_{ph,\lambda}\} \qquad (2)$$

where $\beta_\lambda = 1/n(\lambda)$ (Fig. 2).

The equation (1) is Volterra integral equation of the first kind with the right part having experimental errors. Its solution is ill - posed task. Finding derivatives from experimental data containing errors is ill - posed task too. There are several methods for solution of the problems. The stabilization is based on using a priory information about peculiarity of the solution. In this case, the main peculiarities are the next: number of CHR photons is greater or equal to zero, the first derivative is less or equal to zero, the second derivative is greater or equal to zero.

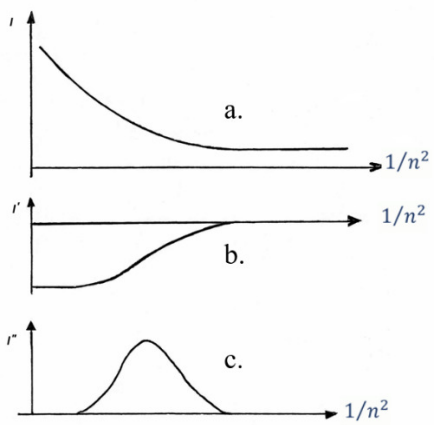

Figure 2: Dependence of CHR intensity on $1/n^2$ (a) and its first (b) and second (c) derivatives.

The equation (1) can be reduced to equation of convolution type [7]. Let us change variables:

$$\beta = y^{1/2}; \quad \Psi(y) = \frac{f(y^{1/2})}{2y^{3/2}}; \quad \frac{1}{n(\nu)} = z^{1/2} \qquad (3)$$

Then

$$g \int_{z}^{z_{max}} (y - z(\nu))\Psi(y) dy = N_{ph}(z(\nu)) \qquad (4)$$

By successively differentiating (4) we obtain the solution as:

$$\Psi(z^{1/2}) = \frac{1}{g} \frac{d^2 N_{ph}(z)}{dz^2} \qquad (5)$$

Of course, the equation (4) is also Volterra integral equation of the first kind with the right part having experimental errors.

The proposed method can be used not only for diagnostics of charged particle fluxes but also for diagnostics of powerful uncharged particles fluxes (neutrons, γ and bremsstrahlung radiation) with the help of the secondary charged particles.

To avoid the gas dissociation by the beam usage of the single atomic gases is preferable. For the narrow energy spectra typical for microtron beams, beams from the high brightness accelerators and for high energy beams the required change of the pressure will not large. The narrow band filter before the photodetector and measurement of gas refraction index with a build-up interferometer can decrease sufficiently the experimental errors. The instant gas expansion by high power beam pulses can be neglected if a pulse is very short ($\leq 10^{-8}$ s).

The yield of the CHR near the threshold for the most accelerators is more than sufficient for the reliable intensity registration with the photodetectors (photomultipliers). The energy loss fluctuations in the CHR detector should be taken into account in estimation of a device resolving power.

Consider now the second method based on the analyses of a spectral distribution of CHR photons (Fig. 1b). It is important that this method does not require sequential measurement of the yield of CHR photons with changing the gas pressure in the radiator. All measurements are performed at the single selected gas pressure. It also allows finding the velocity distribution of charged particles for non-repetitive "bursts" and, in principle, even for a single high power event.

Dependence of refraction index on the wavelength causes known trouble in Cherenkov counter methods. However, it becomes “friendly” phenomena in that variant of the method. The essence of method consists in following. CHR photons from the radiator is directed to a spectral

ISBN 978-3-95450-181-6

device (grating, prism etc.) decomposing CHR into spectrum. CHR spectrum is registered with the line of photodetectors or with multichannel spectrum analyzer. Because of refraction index for any medium depends on a wavelength, the CHR threshold has such dependence also. Thus, the measurements at the different wavelengths are analogous to the measurements with variable gas pressure described above or to measurements with a large number of the threshold counters with different thresholds.

In the visible light range the refraction index decreases with the wavelength increase. Thus, the higher is the particle velocity, the longer the wavelength of CHR threshold. The number of the CHR photons having a wavelength λ in the unit wavelength range may be written as:

$$N_{ph,\lambda} = g \int_{\beta_\lambda}^{\beta_{max}} f(\beta) \cdot (1 - \frac{\beta_\lambda^2}{\beta^2}) \cdot \lambda^{-2} \cdot d\beta \qquad (6)$$

(β_λ is the velocity threshold at the wavelength λ, g is as in (1)).

Using known formula by Cauchy $n(\lambda) = a + b\lambda^{-2}$, where a and b are the constants for given gas we obtain the threshold wavelength for given β_λ:

$$\lambda^{-2} = (\beta_\lambda^{-1} - a)/b \qquad (7)$$

Substituting (7) into (6), converting this one, performing the differentiation with respect to β_λ, transforming, performing the differentiation with respect to β_λ, converting again, we obtain:

$$f(\beta_\lambda) = \frac{\beta_\lambda^2}{2g} \frac{d}{d\beta_\lambda} (\frac{1}{\beta_\lambda} \cdot \frac{d}{d\beta_\lambda} (\frac{b}{\beta_\lambda^{-1} - a} \cdot N_{ph,\lambda})) \qquad (8)$$

The equation (6) can be reduced as above (the equation (3)) to the equation of the convolution type also (the designations are the same):

$$\int_z^{z_{max}} (y - z(\lambda)) \Psi(y) dy = \frac{\lambda}{g}^2 N_{ph,\lambda}(z(\nu)) \qquad (9)$$

Its solution can be found by successive differentiating as described above.

Thus, to get a beam velocity distribution it is necessary to measure the number of photons in different wavelength ranges and to get their first and second derivatives with respect to the wavelength. The number of photons is known with error and this procedure is ill -posed task, so appropriate methods to obtain stable solution must be applied.

The proposed method is convenient for the accelerator beam monitoring especially in the case of the narrow energy spectra. As an example, at the bean energy 30 MeV and the energy spread 0.5 MeV the spectral interval in the case of xenon is from 400 nm to 600 nm. As already noted it seems likely that the method will permit to measure the energy and the energy distribution at the single and non-repeating powerful pulse fluxes of the charged and non-charged particles. If the photodetectors (or special optical shutter built-in between CHR detector and the photodetectors) are high – speed then it is possible to measure the energy and the energy distribution within the pulse (the bunch).

At Fig. 3 we illustrate energy spectrum measurements for race-track microtron [9] done by first method.

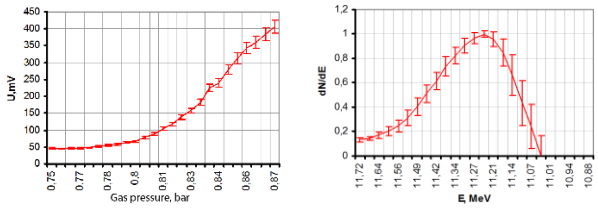

(a) (b)

Figure 3: Energy spectrum measurements for race-track microtron by first method: (a) is photodetector signal dependence on gas pressure; (b) is reconstructed energy spectrum.

REFERENCES

[1] Zrelov V.P. Vavilov - Cherenkov radiation and its applications at high energy physics. V. I, V. II. M. Atomizdat. 1968.

[2] Bhiday M.R., Jennings R.E., Kalmus P.I.P. Measurement of electron beam energy using a gas Cerenkov detector. Proc. Phys. Soc., 72, 973 - 980, 1958.

[3] Jennings R.E., Kalmus P.I.P. A gas Cerenkov detector for the accurate determination of electron beam energy. Nucl. Instr. Meth., 6, 209 – 212. 1960.

[4] De Almeida C.E., Almond P.R. Energy calibration of high energy electrons using a gas Cerenkov detector and a comparison with different methods. Phys. Med. Biol., 19, N. 4, 476 – 483. 1974.

[5] De Almeida C.E., Almond P.R. In Proc. Amer. Assoc. Phys. in Med. A. Cerenkov detector for the energy calibration of electron beams from 9-22 MeV. Phys. Med. Biol., 17, N. 6, 870. 1972.

[6] Trukhanov K.A. Measurement of particle energy by the dependence intensity of Vavilov - Cherenkov radiation on the phase velocity. In Proc. of seminar “Cherenkov detectors and their applications in science and technique” (1984). M. Nauka. 380 –383. 1990.

[7] Trukhanov K.A., Shvedunov V.I. Measurements of accelerator beam spectrum through dependence of Cherenkov radiation intensity on phase velocity of electromagnetic waves in optical and microwave ranges // Rad. Phys. and Chem. 2006. V. 75. N. 8. P. 899-902.

[8] Trukhanov K.A., Larkin A.I., Shvedunov V.I. Measuring the distribution of particles according to their velocity in accelerator beams on the basis of Cherenkov radiation in the optical and microwave range. Bulletin of the Russian Academy of Sciences: Physics: 2010, Vol. 74, № 11, pp. 1600-1603.

[9] V.I. Shvedunov, R.A. Barday, D.A. Frolov, et al, Racetrack Microtron with High Brightness Beams, Nucl. Instrum. Meth. A531 (2004) 346-366

ISBN 978-3-95450-181-6

COAXIAL QUARTER WAVELENGTH IMPEDANCE CONVERTER FOR COUPLING CONTROL OF TRIODE CAVITY

K. Torgasin†, H. Zen, K.Morita, S.Suphakul, T. Kii, K. Nagasaki, K. Masuda and H. Ohgaki
Institute of Advanced Energy, Kyoto University, Kyoto, Japan

Abstract

In this work we describe the development of a coaxial quarter wavelength impedance transformer. The transformer is used for coupling control of a pre-bunching cavity for a triode type thermionic RF gun in Kyoto University Free Electron Laser (KU-FEL) facility. The application of prototype of impedance transformer could convert the coupling situation of the triode cavity from undercoupled to overcoupled state. The advantage of tested prototype is high power tolerance and out vacuum application. Further development of the prototype should ensure coupling control for beam loading compensation.

INTRODUCTION

The KU-FEL (Kyoto University Free Electron Laser) facility uses an S-band 4.5 cell thermionic RF gun as an electron source [1]. The gun is strongly suffering from back-bombardment effect, which causes decrease of beam energy during the macropulse. A promising cure for the electron back-bombardment problem is an introduction of triode configuration. In the triode structure a small pre-bunching cavity is set prior to the main accelerating body for controlling of injection timing. For the triode configuration the reduction of the back streaming electron energy for more than 80% is expected [2].

We have designed a small coaxial cavity as the pre-buncher of thermal emitted electrons. Figure 1 shows the longitudinal and cross sectional view on the triode cavity for the 4.5 cell triode type thermionic RF gun as designed for KU-FEL facility.

The cavity contains thermionic cathode for electron beam generation. For sake of compactness the cavity is coupled to RF power by longitudinal coaxial waveguide. The cathode was designed for overecoupled conditions. The overcoupling is intended to compensate for power absorption by the electron beam. For higher beam current higher overcoupling condition is required. The pre-bunching cavity was fabricated and cold tests at low and high power conditions were performed. However the fabricated cavity was revealed to be in underecoupled conditions [3].

In order to change the coupling conditions of the triode cavity we have developed an external quarter wavelength coaxial impedance transformer. We have applied a prototype of the impedance transformer with successful conversion of the undercoupled conditions to overcoupled. Further development could allow us selective adjustment of the coupling.

In this work we report about coupling conversion for triode cavity applying λ/4 impedance transformer.

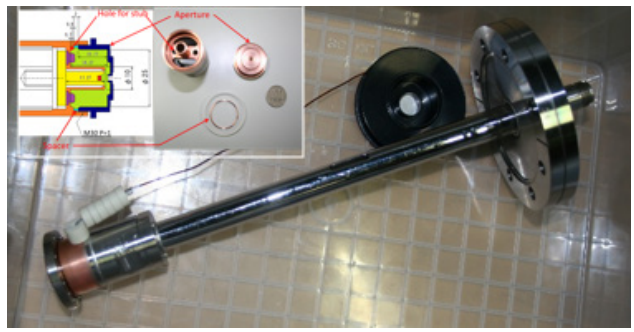

Figure 1: Pre-bunching triode cavity with longitudinal power coupling for a triode type thermionic RF gun.

CAVITY RF COUPLING

Coupler can be defined as a network that allows to transfer power from an RF source to the cavity. Due to impedance and frequency mismatch between the RF power generator and the cavity load some power might be reflected at the coupler. The impedance mismatch is characterized by reflection coefficient Γ. In steady-state case without frequency mismatch the Γ is determined by coupling coefficient κ.

$$\kappa = \frac{1+\alpha|\Gamma|}{1-\alpha|\Gamma|}\begin{cases}\alpha = +1\ overcoupled\\ \alpha = -1\ undercoupled\end{cases}$$

The coupling coefficient represents the ratio of the impedances from the transmission line and the cavity on resonance

$$\kappa = \frac{Z_L}{Z_0}\begin{cases}1 > overcoupling\\ 1 = critical\ coupling\\ 1 < undercoupling\end{cases}$$

In general the reflection coefficient is the ratio of complex amplitudes of inputted and reflected waves. Thus it can be determined from inputted and reflected power ratio at resonance $\Gamma=(P_{ref}/P_{in})^{1/2}$. The corresponded coupling conditions are evaluated from the power transient signal. Figure 2 shows the scheme of transient signals for different coupling conditions.

The triode cavity was evaluated by low power test, which has revealed the undercoupled conditions [3]. For high beam current generation overcoupling conditions are required in order to compensate for beam loading effect. Due to geometrical limitations the coupling change of the cavity is not possible [4]. In order to change the coupling condition we develop an external impedance transformer for the triode cavity.

[1†] konstant@iae.kyoto-u.ac.jp

ISBN 978-3-95450-181-6

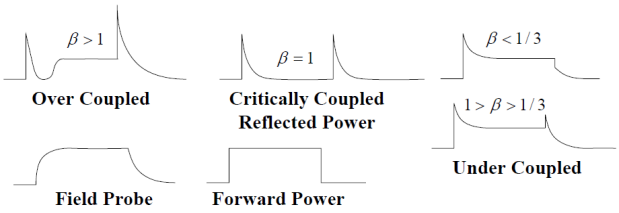

Figure 2: Coupling conditions according to the transient signal of inputted and reflected power [5].

IMPEDANCE TRANSFORMER

The simplest impedance transformer is a waveguide. The impedance of a coaxial waveguide is described by transmission line impedance equation:

$$Z_{in} = Z_0 \frac{Z_L + jZ_0 \tan(\beta l)}{Z_0 + jZ_L \tan(\beta l)}$$

with β=2π/λ and transmission line length *l*. The Z_L is cavity load and Z_0 the characteristic impedance of the transmission line (waveguide).

We are interested in modification of impedances to establish overcoupled conditions ($Z_0 < Z_L$). For this reason we apply a technique of λ/4 transformer [6]. By insertion of λ/4 long section with different impedance Z_b the transmission line equation is simplified to

$$Z_{in}(l = \frac{\lambda}{4}, Z_0 = Z_b) = \frac{Z_b^2}{Z_L}$$

For proper choice of the Z_b the coupling coefficient can be modified. Our system is operated at resonance frequency of f_0=2856 MHz, which correspond to the wavelength of λ=10.5 cm and λ/4=2.6 cm respectively. The impedance Z_b of the λ/4 section can be varied by change of the radius of the waveguide.

The λ/4 impedance transformer has a disadvantage of frequency specification. The load impedance can be transformed efficiently only at a single wavelength.

Impedance Transformer Model

The cavity has longitudinal coupling through a coaxial waveguide (see Fig. 1). The impedance of the waveguide might have an imaginary part $Z_0=R_0+jX_0$. Since this imaginary part jX_0 is unknown we introduce a 2nd section in the λ/4 impedance transformer. The first section is for impedance transformation and the second section with variable length is for compensation of the imaginary part of coaxial waveguide between the transformer and the triode cavity. The imaginary part disappears when the length of the second section would correspond to *l*=λ(n+1/4), λ(n+1/2), λ(n+3/4), where n is a natural number. In order to build a prototype of 2-section impedance transformer we need to determine the shortest *l* which would correspond to the λ/4 position. The 2-section model is illustrated in Fig. 3. According to the Fig. 3 the modified reflection coefficient depends on the impedance ratio of $Z_2(Z_b)$ and Z_0. Which is calculated as follows:

$$\left.\begin{aligned} Z_1\left(l = \lambda\left(n + \frac{1}{4}\right)\right) &= \frac{Z_0^2}{Z_L} \\ Z_2\left(l = \lambda\left(n + \frac{1}{4}\right)\right) &= \frac{Z_b^2}{Z_1} \end{aligned}\right\} \Rightarrow Z_2\left(\frac{\lambda}{4}\right) = \frac{Z_b^2}{Z_0^2} Z_L$$

The coupling coefficient of the undercoupled triode cavity is κ=0.7. By application of the 2- section impedance transformer with Z_b =96.4 Ω the reflection coefficient is Γ=0.4 and modified coupling coefficient is κ=2.3. This result corresponds to overcoupled conditions.

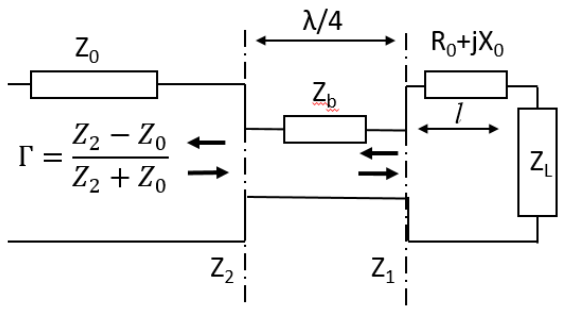

Figure 3: Two-section model of λ /4 impedance transformer.

Prototype

For prototype we have taken an external matched coaxial section (Z_0=50 Ω) and introduced a movable λ/4 (2.6 cm) long section with specific diameter *a* on the inner conductor of the coaxial waveguide. In order to mitigate arcing and to make the transformer suitable for high input power, the movable section was made with a smaller diameter than the usual inner conductor. Due to geometrical limitations the diameter of the movable section was set to *a*=4 mm which corresponds to the impedance of Z_b=96.4 Ω. Figure 4 shows the photo of the prototype of the impedance transformer.

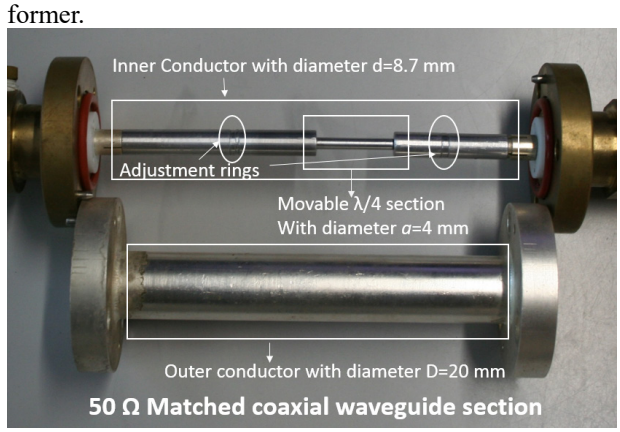

Figure 4: Prototype of the 2-section quarter wavelength impedance transformer.

ISBN 978-3-95450-181-6

The distance *l* to the cavity load Z_L was found experimentally as a shortest distance at which the cavity resonance is maintained (no influence from imaginary part).

COPLING CONVERSION

Figure 5 shows the transient signals of the cavity with and without impedance transformer. Comparing with the Fig. 2 the signals demonstrate the onversion of coupling conditions from undercoupled to overcoupled state. Thus the transformer is shown to work properly. Evaluation of coupling coefficient from the transient signal gives κ(undercoupled)=0.7 and κ(overcoupled)=2.1. There is a deviation of 10% of calculated and estimated value.

The high power tolerance of the impedance transformer was experimentally checked by feeding high RF power to the system. As the result, we did not detect arcing by input power up to 20 kW. It was demonstrated that the impedance transformer has enough high power tolerance for practical application.

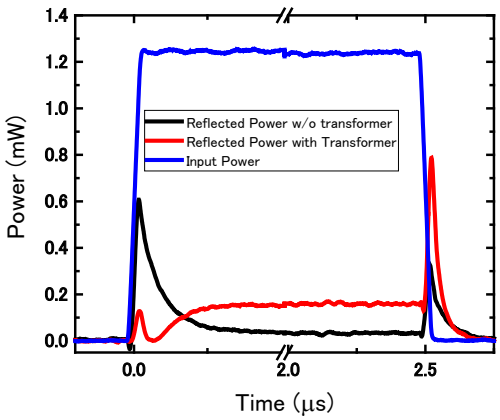

Figure 5: Transient signal of the triode cavity with and without impedance transformer.

Prototype's Uncertainty

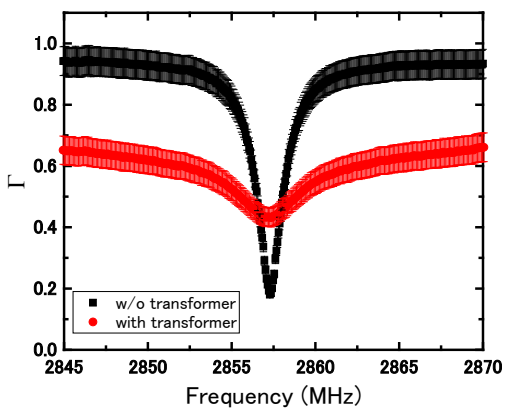

Figure 6: Resonance curve of the triode cavity with and without impedance transformer.

Figure 6 shows the resonance curves of the triode cavity with and without the impedance transformer. The curve with impedance transformer shows power loss of about 40% at off resonance condition. Such power loss is not expected according to calculations shown in the Fig. 7. We suggest that the power loss is caused by low precision of fabrication of the impedance transformer. The impedance transformer used in this experiment is wavelength specific, however the resonance of the cavity may change with environmental conditions. Another point are the rings used for position adjustment (see Fig.4), they might cause additional reflections.

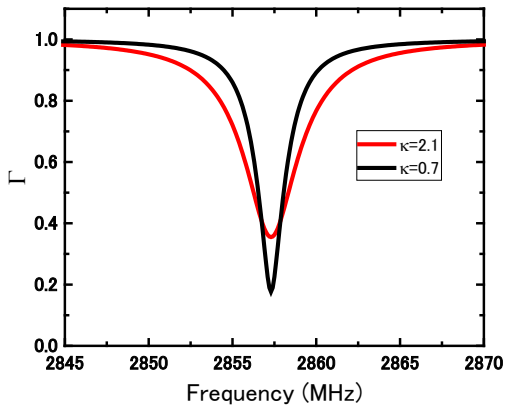

Figure 7: Resonance curve of the triode cavity as calculated for κ(undercoupled)=0.7 and κ(overcoupled)=2.1.

SUMMARY

We have successfully built an external coaxial impedance transformer, which allows us to change coupling from undercoupling to overcoupling condition. The coupling conversion was demonstrated on the triode cavity. The advantage of the proposed transformer design is a tolerance of high input power. Another advantage of the application of impedance transformer is that it could be integrated into the power line as a waveguide without modification of the cavity and breaking the vacuum. However, the prototype we used requires further improvement in order to mitigate power losses.

REFERENCES

[1] H.Zen et al., "Present Status of Kyoto University Free Electron Laser", Proceedings of FEL 2013, pp.711-714

[2] T.Shiyama et al. "A Triode –Type Thermionic RF Gun for Drastic Reduction of Back-Streaming Electrons", Proceedings of FEL 2007, pp. 398-401

[3] K.Torgasin et al.,"Beam Test of the Coaxial Cavity for the Thermionic Triode Type RF Gun", Presentation at IVESC 14, unpublished.

[4] Dr. Kanno, private communication, Oct.2014.

[5] T. Powers, "Theory and Practice of Cavity RF Test Systems",12th International Workshop on RF Superconductivity, Ithaca, NY, USA, 2005.

[6] David M. Pozar, "Microwave Engineering", 3rd Edition, NY,USA. Wiley, 2005, pp.73-74.

ISBN 978-3-95450-181-6

INTEGRATED INSPECTION METHOD OF MOTOR TRANSPORTS BASED ON ACCELERATION TECHNOLOGY

A.M. Fialkovsky, T.R. Virkunen, P.O. Klinovsky, K.V. Kotenko, V.P. Malyshev,
NIIEFA, St. Petersburg, Russia

Abstract

Integrated inspection method of motor transports was suggested based on linear electron accelerator and neutron generator, which helps to detect substances forbidden for carrying, including explosives, narcotic drugs and fissionable materials. The linear high-frequency electron accelerator is a source of X-ray bremsstrahlung. The result of scanning is an introscopical image of a motor transport with color-selected suspicious substances. The neutron activation analysis of these substances with neutron generator as a neutron source lets detect elemental substance composition as well as identify explosives or narcotic drugs. This article contains accelerator specifications, which lets implement suggested method.

PURPOSE

The purpose of the inspection system (IS) is an examination of motor transports. IS lets detect and identify substances forbidden for carrying including explosives, narcotic drugs and fissionable materials. Integrated informational and technical system of the IS aims to let the operator make valid decision on the presence or absence of the transportation rules violation signs.

IS provides:

- Visualization of inspected object contents.
- Recognition of the different devices located therein, objects and substances.
- Determining load merchandise volume of the container and inspect the contents of the spatial location.
- Coordinate attachment of the detected items to their location.
- Ability to recognize items of different materials (metals, organic substances, including elemental analysis).
- Ability to view the structural cavities and spaces between walls, ceilings and container floors, car components.

Additional specialized process equipment of the IS allows inspection of the driver and the persons accompanying the vehicle.

All information contributes to the overall control of cargo, identifying caches and prohibited substances.

The complex information technology tools of the IS are placed in a one-story industrial building (customs examination hall) and in the control room unit. The walls of the inspection hall are made of reinforced concrete, weighing not less than 2350 kg / m^3. The IS contains all necessary systems to ensure efficient functioning and safety management system. The basis of the IS is the system of inspection of containers loaded and trucks using the accelerator, which is the source of the X-ray bremsstrahlung with 6 MeV energy in the normal mode and an additional method for the implementation of the dual energy – 9 MeV.

General view of the IS is shown in Fig. 1.

Figure 1: General view of the IS building.

INTEGRATED METHOD

To solve the problem of identification and detection of the prohibited items in the inspected vehicle there is provided an integrated method comprising applying the following techniques:

αβγ Channel

Detection system of radioactive and fissile materials monitors the vehicle for the presence of radioactive and fissile materials.

X-Ray Channel

Scans the vehicle and gets its picture at two radiation energies; displays images on the screen completely without loss of visual information with a quality that allows the detection of hidden places, objects and substances under control; identifies suspicious areas for the presence of hazardous (explosive) substances by dual-energy and transmits their coordinates to the neutron - sensing module for detailed substance identification.

n-Neutron Channel

Neutron - sensing system conducts the spectral analysis of the selected areas and performs identification of substances, including drugs and explosives.

ISBN 978-3-95450-181-6

Block diagram of the IS is presented in Fig. 2.

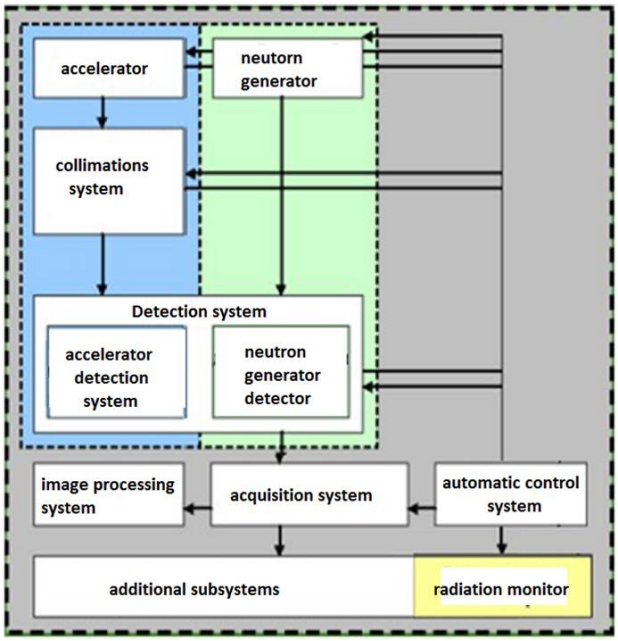

Figure 2: Block diagram of the IS.

INTEGRATED INSPECTION SYSTEM

According to structural features and control technology, IS is the second-type stationary inspection accelerator complex containing an electron accelerator with energies up to 10 MeV (according to SanPiN 2.6.1.2369-08). The second-type IS includes fixed and mobile IS with a stationary object and moving control source of ionizing radiation. IS produces a flat beam of bremsstrahlung, which scans a stationary inspected object when moving the portal parallel to the longitudinal axis of the object. IS general characteristics are shown in Table 1.

Radiating and receiving systems comprising the portal, the linear electron accelerator and the system receiving the detectors is shown in Fig. 3.

Figure 3: Radiating and receiving systems of the IS.

Table 1: IS General Characteristics

Characteristic	**Value**
Bremsstrahlung energy	6/9 MeV
Dose rate	2-5 Gy / min 1 m
Steel Penetration	400 mm
Detection of steel wire diameter without barriers	0.8 mm
Detection of steel wire diameter with 100 mm steel barrier	mm
Detection of steel wire diameter with 250 mm steel barrier	8 mm
Contrast sensitivity	0.5 %
Scanning height	4.5 m
ADC capacity	20 bit
Capacity	Up to 25 vehicles per hour
The maximum dimensions of the inspected vehicle	20 m (L)×3 m(W)×4,5 m (H)
Continuous duty	7/24
Radiation safety	SanPiN 2.6.1.2369-08
Operating ambient temperature	
• for apparatus inside the IS building	+5°C to +45°C
• for apparatus outside the IS building	-45°C to +50°C
Humidity	Up to 95% at +25°C
Presence of condensable atmospheric precipitation	frost, dew
Rain intensity	Up to 40 mm/h
Snowfall intensity	Up to 10 mm/h
Wind gusts at speeds	Up to 30 m/s
Snow cover thickness	Up to 2 m
Static and dynamic dust	+
Solar radiation	+
Power consumption	Less than 70 kVA

ISBN 978-3-95450-181-6

Receiving detector system provides bremsstrahlung intensity conversion to an analog electrical signal, the analog signal into the digital form, and transfers the obtained values to the computer. The sensitivity and dynamic range of the detection system determines the quality of the images and, therefore, the operator's ability to control the vehicle and the cargo. The detector module is shown in Fig. 4.

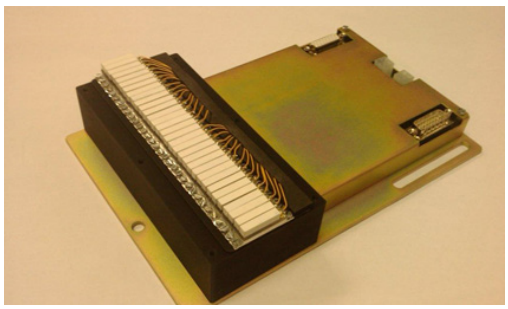

Figure 4: The detector module of the IS receiving systems.

Detection ability of the IS X-Ray channel is shown in Fig. 5.

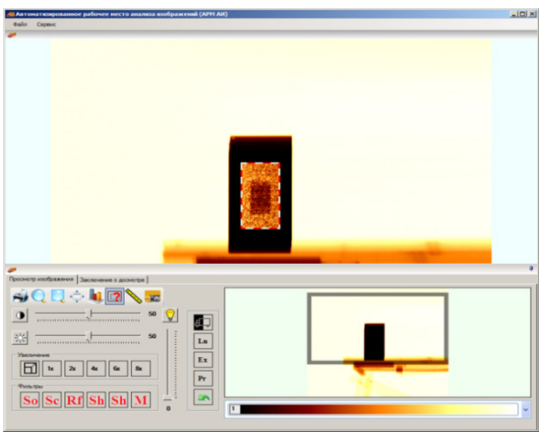

Figure 5: Measurement of the maximum penetrating power of the IS. Image of the lead brick behind the steel barrier at the image analysis operator workstation.

n-Neutron Channel

Main characteristics of the neutron channel are shown in Table 2.

Table 2: Main Characteristics of the IS Neutron Channel

Characteristic	**Value**
Neutron energy, MeV	14.1
Maximum neutrons flux, n/s	Up to 10^8
Technology used	Method of tagged neutrons
Transverse object dimensions (W×H) (mm, up to)	2900×4000
Probability of explosives detection (% ,at least)	90
Probability of false positives, (%, not more than)	15
Localization resolution of explosives in each orthogonal direction (cm, not more than)	15
The list of detected explosives trinitrobenzene, dazin, geksonitrostilben, PVV-5A, TC, TATB, RDX, okfol, okfol-3.5, TG-50, A-the IX-3T, HL-24, izopropilnitrat, okfel-20, OLA-8T, still-smon, LD-70, Pentol, POE-85, TGA-16, TM, tokaf, tetra, nitrate, ammonium-19 POE-7, TEN, TA-23	

Features of the neutron channel are:

- Determination of the three-dimensional distribution of substances in the volume of the inspection object.
- Automated algorithm for unattended identifying hazardous substances.

αβγ Channel

Detection of fissile and radioactive materials based on the use of transport radiation monitors by registration of penetrating gamma and / or neutron radiation accompanying radioactive conversion of nuclear materials and radioactive substances.

CONCLUSION

Integrated inspection method of motor transports was suggested, which helps the detection of substances forbidden for carrying, including explosives, narcotic drugs and fissionable materials. The combination of solutions is unique.

ISBN 978-3-95450-181-6

MEASUREMENT OF THE ION BEAM PROFILE WITH THE D-PACE WIRE SCANNER*

E.O. Sokolova#, D.A. Kasatov, A.M. Koshkarev, A.N. Makarov, I.N. Sorokin, I.M. Shchudlo, S.Yu. Taskaev, BINP SB RAS, Novosibirsk, Novosibirsk State University, Russia
A.A. Gmyrya, Ya.A. Kolesnikov, A.S. Kuznetsov, BINP SB RAS, Novosibirsk, Russia

Abstract

In The Budker Institute of Nuclear Physics the accelerator-based source of epithermal neutrons was invented and now operates to be used in the Boron Neutron Capture Therapy (BNCT) [1]. For several reasons the real beam flow in the facility differs from the calculated one. To take into account this distinction it is necessary to provide continuous monitoring of the beam parameters. This paper describes the method of diagnostics of the ion beam with the D-pace wire scanner and the results, which were obtained, using this method.

INTRODUCTION

The principle of operation of the facility is as follows. The negatively charged ion beam is generated on the ion source, then it is injected in the tandem accelerator with vacuum insulation. After a recharge of negatively charged ions of hydrogen into positively charged protons in the gas stripper a proton beam is formed, which is accelerated to the doubled potential of the high voltage electrode. On the lithium target, as a result of a threshold reaction ^{7}Li(p,n)^{7}Be, the neutron flux is generated [2].

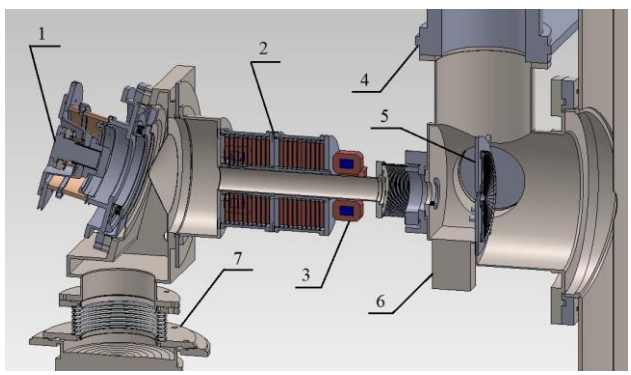

Figure 1: Low-energy part of accelerator. 1 – H^- ion source, 2 – magnetic lenses, 3 – corrector, 4 – cryosorption pump, 5 – cooled diaphragm, 6 – D-Pace wire scanner, 7 – differential pumping system.

Figure 1 shows the view of low-energy part of the facility, where the measurement of the beam profile was carried out. Between the diaphragm and the first electrode the beam is accelerated by the electromagnetic field. In the area of the diaphragm the powerful electrostatic lens is formed, also the accelerating field falls into the collimator of the diaphragm, as it could be seen in the figure 2. This phenomenon could lead up to the refocusing of the beam, in this way it could become strongly divergent and the emittance could increase significantly. Moreover, a huge part of the beam could be lost, as it wouldn't fall into the gap of electrodes, setting on their surface, which could lead up to redistribution of voltage and to electrical breakdown as a result [3].

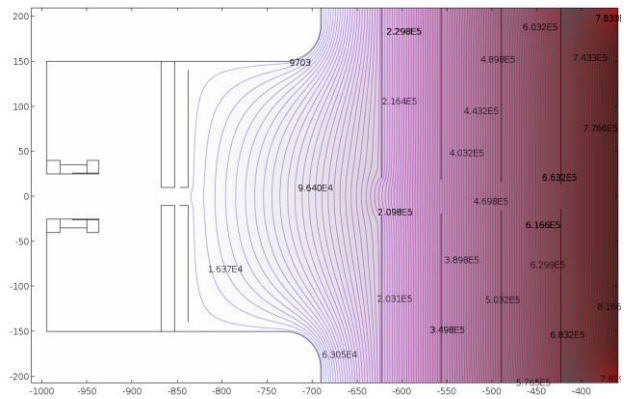

Figure 2: Calculated field distribution inside the vacuum chamber at the entrance to the accelerator.

In order to take into account the described phenomena it is necessary to monitor the beam thoroughly, since the beam should be led with minimal losses. In this way, it was proposed to install The D-Pace OWS-30 Oscillating Wire Scanner Probe (TRIUMF-Licenced) inside the vacuum chamber before the diaphragm. For this purpose the necessary changes of the design of the vacuum chamber were implemented, which allow to set the device with the possibility of adjustment of its position.

RESULTS OF EXPERIMENTS

The experiments were carried out under different conditions of focusing and current of the ion beam. In the standard mode the current is supplied to the lenses is 54 A, to the corrector 2.4 A.

* The study was supported by grants from the Russian Science Foundation (Project no. 14-32-00006), the Budker Institute of Nuclear Physics and the Novosibirsk State University.
#e-mail: buiya@bk.ru

ISBN 978-3-95450-181-6

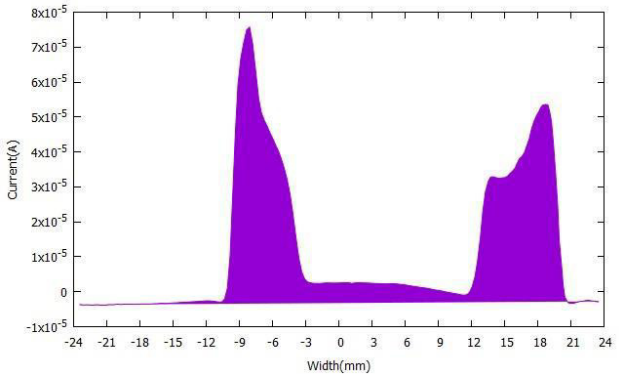

Figure 3: Readings of the wire scanner in the standard mode.

In the figure 3 there are two distinct peaks, each of which is a result of scanning by a single wire. One peak is the X-beam profile, measured by one wire, and the other is the Y-profile, which is obtained by the second wire. The center of the distance between the peaks characterizes the position of the beam relatively to the horizontal axis of the installation. Under constant conditions of the focusing relative distance between the peaks will characterize the displacement of the beam along the vertical axis.

The current density in the ion beam of 5 mA with the cross-section of 3 cm^2 ~ 1.5 mA/cm^2. Thus, the current on the wire with a cross section of 0.5 mm, is equal to 0.45 mA. The estimation of the maximum temperature of tungsten wires with a current of 5 mA was obtained by the condition of the thermodynamic equilibrium of the wire radiation. The estimation gives a value of about 1000 K.

Using the experimental data and the assumption of the Gaussian form of the beam shape, an approximate profile was restored as it is shown in the figure 4. The point [0;0] in the figure corresponds to the central position of the scanning wires.

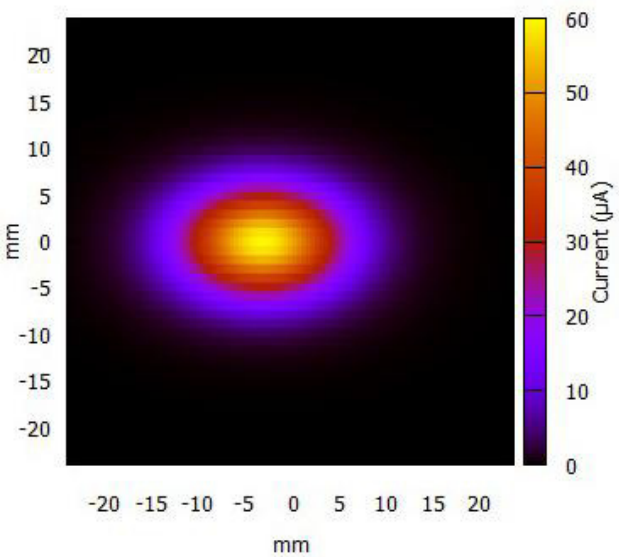

Figure 4: Profile of the ion beam.

During the experiments it was found that in the low energy part the beam is elliptical with the lengths of the major and minor axes 15 and 10 mm, respectively. The relative displacement of the device axis was 3 mm.

IMPROVEMENTS

In an effort to supress a secondary emission from the wires of the scanner it was proposed to install a ring with the cut-off potential inside the vacuum chamber. Volt-ampere characteristics of the wire scanner is shown in the figure 5. It reveals the maximum signal, registered by the wire scanner, plotted against the voltage, which is set on the ring.

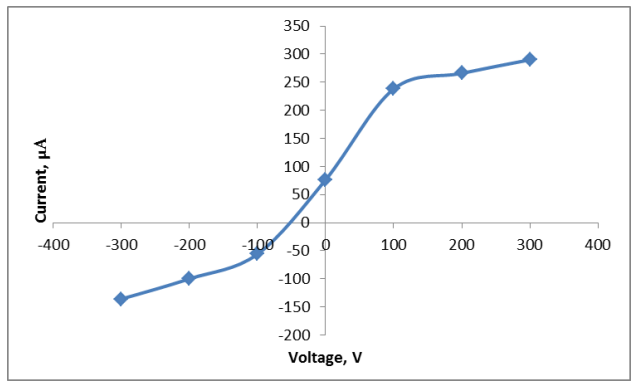

Figure 5: Volt-ampere characteristics of the wire scanner.

In this way, applying a cut-off potential to the ring, secondary electrons would not leave wires of the scanner, and the device would register only the readings of the ion beam, as it is shown in the figure 6. An integrated current, falling on the wires, which is actually a full current of the ion beam, thus is equal to 5.54 mA.

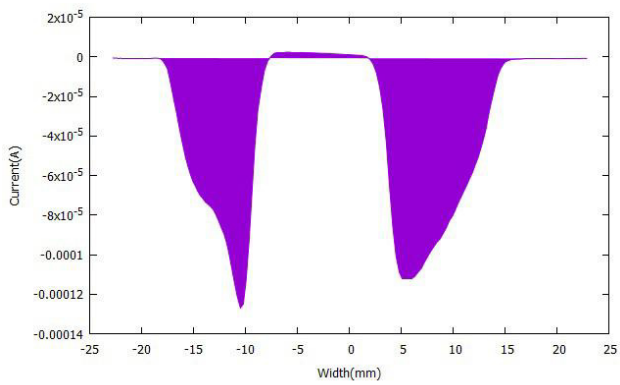

Figure 6: Readings of the wire scanner with suppressed secondary emission.

CONCLUSION

In The Budker Institute of Nuclear Physics the research to obtain a high-current proton beam is pursued in the tandem accelerator with vacuum insulation. For the diagnostics of the ion beam in the low energy part The D-Pace OWS-30 Oscillating Wire Scanner Probe (TRIUMF-Licenced) was installed.

ISBN 978-3-95450-181-6

The experiments were carried out under different conditions of focusing and current. In this way, the possibility to control the focusing and the position of the beam, using the magnetic correcting elements was clearly demonstrated. For the first time the elliptical shape of the beam was realized. Using the experimental data, the profile was restored, also its sizes and position were determined. Moreover, the secondary emission from wire scanner was suppressed, that allows to measure the full current of the ion beam.

The application of the wire scanner allows to operatively monitor and correct the beam injection into the accelerator.

REFERENCES

[1] "Neutron Capture Therapy: Principles and Applications", W. Sauerwein, A. Wittig, R. Moss, Y. Nakagawa, Eds.: Springer, 2012.

[2] S. Yu. Taskaev, "Accelerator Based Epithermal Neutron Source", *Phys. Part. Nuclei*, Vol. 46, no. 6, pp. 956–990, 2015.

[3] S. Yu. Taskaev, V. V. Kanygin, "Boron Neutron Capture Therapy", Novosibirsk, Russia: Publisher of SB RAS, 2016.

ISBN 978-3-95450-181-6

MEASUREMENT OF THE PROTON BEAM PROFILE VIA AN ACTIVATION METHOD OF DIAGNOSTICS*

E.O. Sokolova#, D.A. Kasatov, A.N. Makarov, I.M. Shchudlo, S.Yu. Taskaev, BINP SB RAS, Novosibirsk, Russia and Novosibirsk State University, Russia
Ya.A. Kolesnikov, BINP SB RAS, Novosibirsk, Russia

Abstract

In The Budker Institute of Nuclear Physics the accelerator-based source of epithermal neutrons was invented and now operates to be used in the boron neutron capture therapy. Neutrons on the facility are generated during the threshold reaction ^{7}Li(p, n)^{7}Be which occurs when the proton beam is thrown on the lithium target. To control the neutron output it is necessary to monitor the parameters of the accelerated proton beam. The spatial distribution of the accelerated proton beam was measured exactly on the lithium target, using an activation method of diagnostics.

INTRODUCTION

The principle of operation of the facility is as follows. The negatively charged ion beam is generated on the ion source, then it is injected in the tandem accelerator with vacuum insulation. After a recharge of H^- beam into positively charged protons in the recharging gas target a proton beam is formed, which is accelerated to doubled potential of the high voltage electrode. On the lithium target as a result of a threshold reaction ^{7}Li(p, n)^{7}Be the neutron flux is generated [1]. General view of the accelerator is shown in fig. 1.

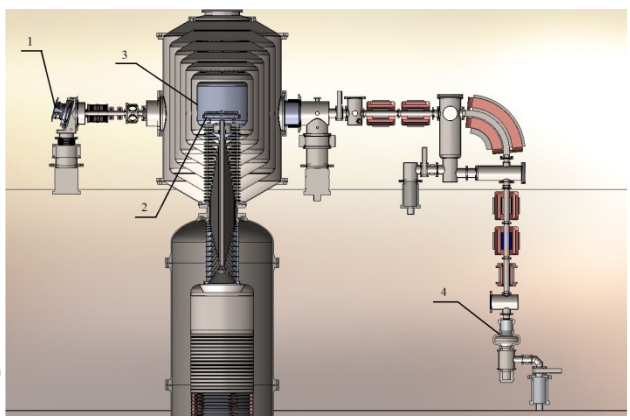

Figure 1: Vacuum insulation tandem accelerator. 1 – H^- ion source, 2 – gas recharging target, 3 – high voltage electrode, 4 – lithium neutron-generating target.

As a result of an interaction between protons and lithium on the neutron-generating target an accumulation of the radioactive isotope of beryllium takes place. It was proposed to track down an area of the beryllium storage in order to restore a profile of the proton beam.

THEORETICAL FOUNDATION

The neutrons are generated during an inelastic scattering of 2 MeV proton beam on the lithium nuclei according to the reactions [2]:

$$^{7}Li + p \rightarrow {}^{7}Be + n - 1{,}646 \text{ MeV},$$
$$^{7}Li + p \rightarrow {}^{7*}Be + n - 2{,}076 \text{ MeV } (\sim 10\%),$$
$$^{7*}Be = {}^{7}Be + \gamma + 430 \text{ keV}.$$

The process of an inelastic scattering is characterized by the resonance energies: 1.05, 2.05, 2.25 MeV, which are close to the threshold reaction of the neutron generation 1.882 MeV. The flux of gamma-quants with the energy of 0.478 MeV is equal to the flux of neutrons. To decrease the gamma-quants flux the thin layer of lithium is sprayed to the copper substrate.

After an experiment there is a radioactive isotope ^{7}Be is accumulated, which has a half-life of 53.6 days. The tracking of gamma-quants with the energy of 478 keV, released during the beryllium decay, could serve an alternative way of the proton beam profile measurement in an accelerating part of the facility. To implement such a method the gamma-spectrometric complex was involved, that consists of the scintillation NaI-detector, which was pre-calibrated for energy, and the lead shielding with the collimation hole of 8 mm. The measurement of gamma-radiation is carried out after an experiment, remotely from the facility.

With the penetration of ionizing particles in the scintillator material the flash of luminescence occurs, then it is converted into a pulse of electrical current by the photomultiplier, finally the electronic system records it.

RESULTS OF EXPERIMENTS

For the restoring of the beam profile the neutron-generating target was imposed a proton beam influence during 25 minutes. The measurement of gamma-radiation was carried out one week later after an experiment, in order to exclude the short-lived gamma-quants.

The lithium target substrate is moved in increments of 1 cm before the collimation hole of the lead shielding (the center of the target is the point [0;0] in the figure 2), in this way the counting speed was determined in the line of a full absorption. The luminescence intensity distribution on the target surface, defined as the number of recorded events to the time of statistics collecting, is shown in fig.2.

* The study was supported by grants from the Russian Science Foundation (Project no. 14-32-00006) and the Budker Institute of Nuclear Physics and Novosibirsk State University.
#e-mail: buiya@bk.ru

ISBN 978-3-95450-181-6

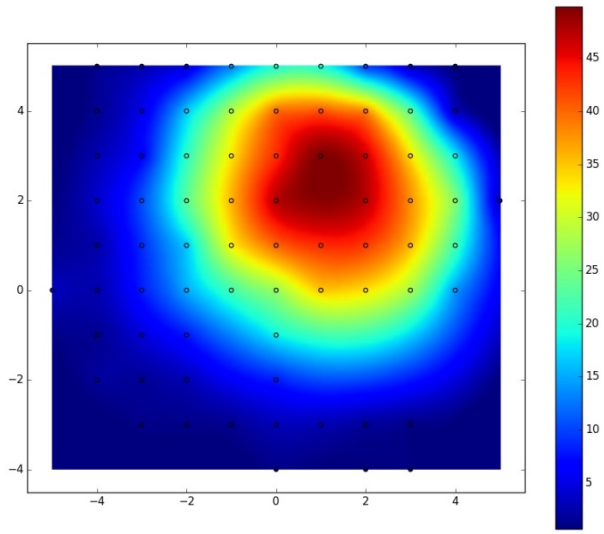

Figure 2: Ttransverse beam profile, registered on the lithium target.

As it follows from the obtained distribution, the proton beam shape is round. The width on the level of "e" times decrease of the luminescence intensity is about 48 mm. This result is in a good agreement with the results of numerical calculation, in which the focusing element is a bending magnet in the transport part of the facility. The beam with 1 cm radius and maximum angles of 1.6 mrad was used as a source. Also the calculation takes into account the same conditions, as it is on the real facility. According to the calculation, made by A.M. Dolgov and V.A. Kiselev, transverse beam size was about 40 mm at the distance of 200 cm to the bending magnet. The result of calculations is shown in the figure 3.

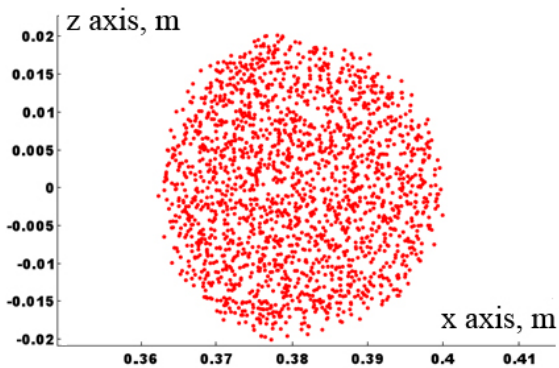

Figure 3: Transverse beam profile at the distance of 200 cm to the bending magnet.

CONCLUSION

In The Budker Institute of Nuclear Physics the research to obtain a high-current proton beam is pursued in the tandem accelerator with vacuum insulation.

The innovative diagnostics on the gamma-spectrometric complex was implemented in order to monitor the proton beam profile on the lithium neutron-generating target. The shape, size and profile of the beam were successfully determined, also this result corresponds to the numerical calculation.

Such method of diagnostics could allow to estimate the full neutron flux, the amount of neutrons, judge the target state and restore the proton beam profile. According to the attractive capabilities, the prospects are to develop this method and apply it continuously.

REFERENCES

[1] S. Yu. Taskaev, "Accelerator Based Epithermal Neutron Source", *Phys. Part. Nuclei*, Vol. 46, no. 6, pp. 956–990, 2015.

[2] "Tables of physical quantities", Acad. I.K. Kikoin, Ed., Moscow: Atomizdat, 1976.

ISBN 978-3-95450-181-6

DIGITAL-TO-ANALOG BEAM ENERGY AND CURRENT STABILIZATION OF ELV ELECTRON ACCELERATORS

D.S. Vorobev, E.V. Domarov, S.N. Fadeev, N.K. Kuksanov, A.V. Lavrukhin, P.I. Nemytov,
Budker Institute of Nuclear Physics, SB RAS, Lavrentyev av. 11, Novosibirsk, 630090, Russia

Abstract

The methods of links between technology line and ELV accelerator control system are described. accelerator control system are described. The problems of the fast control of the beam current are revised. The method of improving the rising of beam current and stability of electron energy is shown.

INTRODUCTION

ELV industrial electron beam accelerator is effective instrument for radiation treatment applications. Especially frequently it is used in cable and heat shrink tube manufacturing. Accelerator is only a part of technology line. There are underbeam transportation line, take-up and pay-off systems, safety system etc… All of them are controlled by signals from ELV control system, which are generated on base of the values as electron energy and beam current. There are 2 well-known methods of controlling the transportation line. The first: there ELV is master, line is slave (see Fig. 1). What things are the most important for this method?

For accelerator:

- stable parameters (better stability – less inhomogeneity of absorbed dose);
- smooth beam operation (except dose inhomogeneity, fast beam current changes can break treated cable or tube).

For technology line:

- quick response for incoming parameters changes;

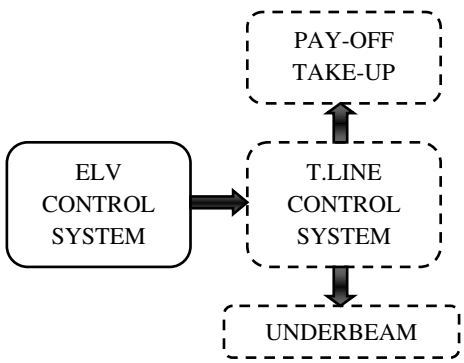

Figure 1: Accelerator is master.

Other method, where the accelerator is a slave, the technology line is a master, and accelerator parameters (beam current) follow production line velocity (see Fig. 2). Unlike the first method, here the most important things will be:

For accelerator:

- stable parameters (better stability – less inhomogeneity of absorbed dose);
- quick response for incoming parameters changes;

For technology line:

- smooth velocity;

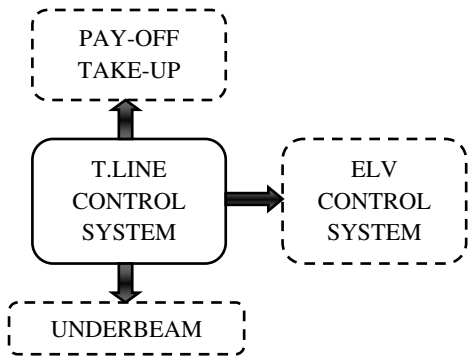

Figure 2: Technology line is master.

For second method the accelerator should provide enough performance and quick response.

New technologies of rubber component irradiation treatment are increasing the performance of technology lines, so they are using second method of links the accelerator to technology line. It led us to find possibility to increase the velocity of beam current control (speed of ascending/descending of beam current value).

STABILIZATION SYSTEMS

Systems of energy and current stabilization are based on analog PID-controllers. They provide good stability at sufficient speed-work. Energy stabilization system separated from current stabilization. It is enough fast (time constant is 0.5 sec) for 100 kW accelerator. Energy stabilizer output is directly connected to Pulse Width Modulator of power supply cabinet, and has feedback from energy sensor (it can be resistive divider or rotary voltmeter).

Current stabilizer is mix of analog PID and digital matrix. Current stabilizer is controlling heating of electron gun filament (heater of cathode), and has feedback from beam current sensor. Cathode heater has a big inertia, so time constant of analog PID should be about 3-5 sec. Low speed of PID is good for steady state, but seriously increases time of transient process. Digital matrix is software part of current stabilizer. Each matrix elements is delay, between present and next (or previous) moments of setting the beam current value to input of current stabilizer. Then during the beam ascend or

ISBN 978-3-95450-181-6

descend, the matrix will set step by step all his elements to input of analog PID. This works well, while we operate with velocities about 0.5-1 mA per sec, but for fast beam ascending we should add in current stabilizer some module, which will have possibility influent (accelerate or decelerate) matrix.

Concerning energy stabilization: if the beam current is rising the accelerator energy is falling. It is due to the parameters of high voltage transformer and rectifiers. If energy decreases, energy stabilizer tends to return this to reference. So energy became stable. It was experimentally determined: more current speed caused more fall of energy (formula 1). Other words: the energy curve approximately follows to derivative of beam current (see Fig. 3 and 4).

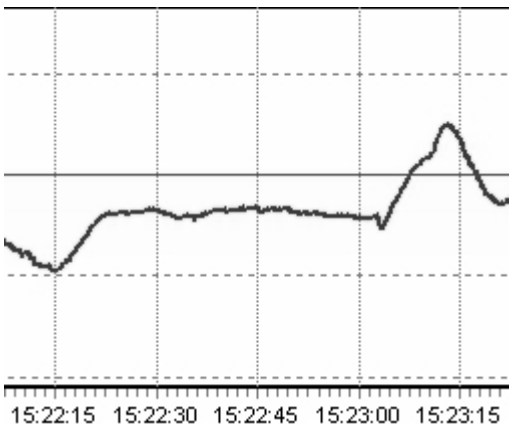

Figure 3: Accelerator energy curve.

Figure 4: Current velocity curve.

UPGRADE

Finally, for accelerate beam current velocity we added three modules into accelerator software. First module is derivative calculator. Each 0.01 - 0.1 second this module calculate difference from previous and present beam current value. Output value is a beam current velocity, which is to be used in other two modules (see Fig. 5, new modules inside dotted line).

Second module is energy compensator. Using formula 1 and current velocity as an argument, module generates offset that will be mixed with energy DAC signal. . So the signal on input of energy stabilizer E will be in accordance with formula 1. This provides better stability of accelerator energy during beam current ascending or descending.

$$E = E_{ref} - V_{bc} * k \qquad (1)$$

Eref – reference energy;
Vbc – beam current velocity;
k – coefficient.

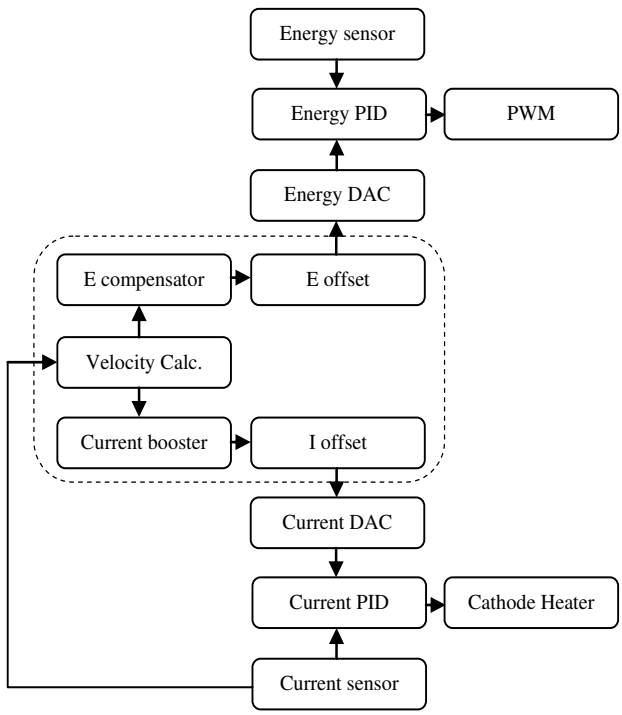

Figure 5: Schematic diagram of stabilization systems.

Third module is current velocity booster. This module controls beam current velocity by generating offset for input of current stabilizer PID. Algorithm keep the velocity in predefined range, for example between 2 mA/sec and 3 mA/sec. If the velocity is not enough, the function will increase the beam current offset, which will be mixed with the current DAC signal. If the velocity is too high, the offset will be decreased. Adjusting this range, we can increase or decrease beam current ascending speed.

RESULTS

Improved stabilization systems provide current velocity up to 5 mA per sec. Modern ELV accelerators can work in a slave mode as part of technology lines with strict requirements to performance and response.

Present system passed through the testing and it is already installed onto ELV-0.5 (0.5MeV 100mA) accelerator in Qingzhou (automobile tire production) and onto ELV-8(2.5MeV 40mA) accelerators in China for cable insulation treatment.

ISBN 978-3-95450-181-6

DEVELOPMENT OF THE HARDWARE-SOFTWARE COMPLEX PIRS-5 FOR FIELD MEASUREMENTS IN ACCELERATING STRUCTURES

G. Pomogaybo, S. Toporkov, M. Lalayan, National Research Nuclear University MEPhI, Moscow, Russia

Abstract

Hardware-software complex «PIRS-5» was developed to make measurements in warm accelerating structures. The idea was to create full-automatic measuring system, which can measure electrical field at the bead position with non-resonant and resonant pull techniques. PIRS-5 has postprocessor, which calculate electrical component from the frequency, reflection or transmission coefficient, shunt and effective shunt impedance. This work describes the construction of this complex, its mathematical part and possible future modifications.

PIRS-5 LAYOUT AND SCHEMATICS

Measurement setup PIRS-5 is software and hardware complex developed for electrodynamical characteristics measurements of accelerating structures. “PIRS” is acronym for Russian “facility for resonator parameters measurements” initially developed at MEPhI by Prof. A.Ponomarenko and his research team. After series of renovations and upgrades it became powerful tool for accelerating structures research nad development led by RF lab tem at MEPhI. Vector network analyzer being the key element of this setup is able to measure resonant frequencies and quality factors without any additional hardware or software involved. But field distribution inside accelerating structure and corresponding parameters like shunt impedance are not so easily acquired. In this paper new upgraded version is described. Algorithms and software part were substantionally altered and redesigned. Both resonant and non-resonant measurements of electromagnetic fields became possible using this implementation. New software allows computation of shunt impedance and effective shunt impedance computation based on electric field measured.

Measurement setup schematics is illustrated on Fig. 1. It is quite ordinary hardware for this kind of measurements based on small perturbation technique. It includes Vector network analyzer Agilent 8753ET (1), control PC (2), accelerating structure under test (3), coupling antenna (4), small dielectric or metal bead (5), bead moving and positioning system (6) actuated by step motor (7). Latter is powered and PC controlled via step motor controller (8).

It was already mentioned, that Agilent VNA is the main RF measuring device able to acquire accelerating structure parameters operated up to 6 GHz. Bidirectional GPIB interface connects it to PC and provides VNA control and data transfer. Accelerating structure under test is connected to VNA port by one or two coupling pickups chosen accordingly to particular measurement task. Small dielectric or metal perturbing bead attached to nylon string is travelling along cavity axis. Mechanical system allows precise string alignment and bead position determination. Computer controls all the hardware, provides data storage and user interface.

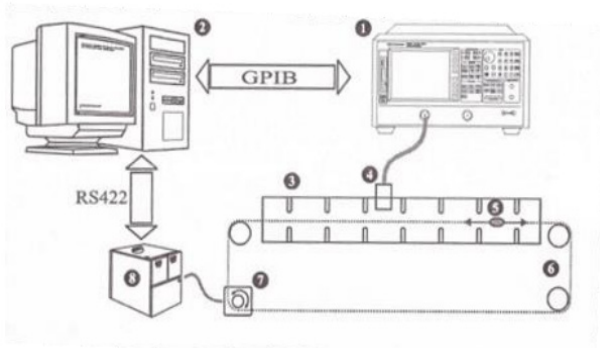

Figure 1: PIRS-5 layout.

PIRS-5 SOFTWARE

Control software developed for PIRS-5 consists of two main algorithms (see Fig.2).

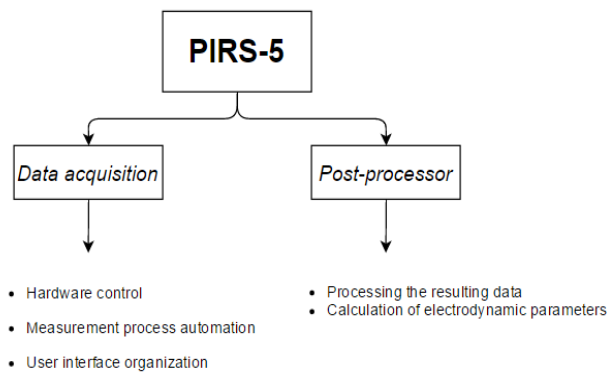

Figure 2: PIRS-5 software.

They are algorithm of data acquisition and post-processor. Let us consider algorithm features paying brief attention to the user interface implementation details. After user enters cavity length, measured quality factor and bead form-factor program starts measurement. This algorithm is illustrated on Fig. 3.

ISBN 978-3-95450-181-6

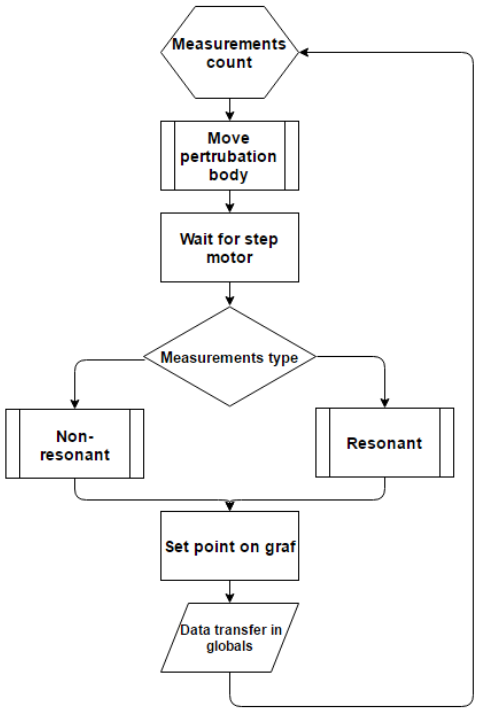

Figure 3: Field measurement algorithm.

Dedicated subroutine for data acquisition and step motor control algorithm is shown on Fig.4. There are several operations repeated in loop in this algorithm. At first step VNA is addressed to make measurement and transfer data to PC. Then it is analyzed converted from raw string to real type.

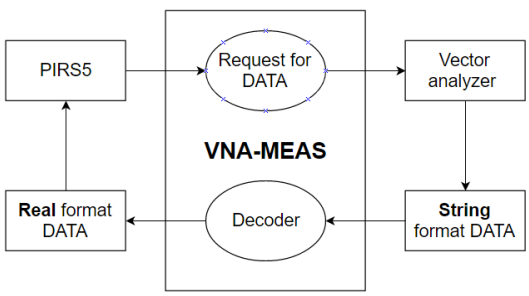

Figure 4: Subroutine for data acquisition algorithm.

FIELD DISTRIBUTION BASED ON FREQUENCY MEASUREMENTS

As it was mentioned earlier measurement setup allows to perform measurements of electric field longitudinal component E_z. Resonant frequency variation under perturbing bead influence was initially used as basic method of E_z computation. Well-known Slater formula [2] was used for field computation

$$\frac{\Delta f}{f_0} = \frac{f_p - f_0}{f_0} = -k_{\Delta f}^{E} |E|^2 / U \,. \tag{1}$$

rewritten as

$$\xi_z = \sqrt{\frac{\Delta f}{2\pi k_{\Delta f}^{E} f_0^2}} \frac{\Omega^{1/2}}{m} \,. \tag{2}$$

where f_0 (f_p) – unperturbed / perturbed cavity frequency, |E| - field strength in bead location, U – electromagnetic field stored energy, ξ_z – field strength factor equal to $E/\sqrt{PQ}$, $k_{\Delta f}$ – bead form-factor.

Later additional algorithms were added allowing one to measure E_z via real and imaginary parts of reflection coefficient.

FIELD DISTRIBUTION BASED ON REFLECTION FACTOR MEASUREMENS

Field amplitude and phase in n-th cell could be directly calculated using recurrent formulas [3]:

$$E_{n+1} = E_n \sqrt{\left| \frac{\Delta \dot{S}_{11}^{(n+1)}}{\Delta \dot{S}_{11}^{(n)}} \right|}, E_1 = 1; \,. \tag{3}$$

$$2\left(\varphi_{n+1} - \varphi_n\right) = \arg\left(\frac{\Delta \dot{S}_{11}^{(n+1)}}{\Delta \dot{S}_{11}^{(n)}} \right), \varphi_0 = 0. \,. \tag{4}$$

It is supposed that at the first cell field amplitude is 1 and phase to zero. This generic normalization becomes a problem while shunt impedance computation. Therefore we chose another approach for absolute field strength values computation based on raw acquired data processing.

In [1] the bead form-factor difference for TW and SW modes is discussed. It was shown that these two values necessary for E_z calculation are defined as

$$k_{\Delta f} = \frac{|\Delta f|}{f_0 \frac{|E|^2}{U}} \,;\; k_{\Delta S11} = \frac{\left|\Delta \dot{S}_{11}\right|}{\left(1 - \left|\dot{S}_{11}^{0}\right|^2\right) Q_0 \frac{|E|^2}{U}} \tag{5}$$

and their relationship could be derived:

$$k_{\Delta S11} = \frac{\left|\Delta \dot{S}_{11}\right| f_0}{\left(1 - \left|\dot{S}_{11}^{0}\right|^2\right) Q_0 |\Delta f|} k_{\Delta f} \,. \tag{6}$$

Using latter equation substituted in (2) we obtain

$$\xi_z = \sqrt{\frac{\left|\Delta \dot{S}_{11}\right|}{2\pi f_0 k_{\Delta S11} \left(1 - \left|\dot{S}_{11}^{0}\right|^2\right) Q_0}} \frac{O_M^{1/2}}{M} \,. \tag{7}$$

where $|\Delta S_{11}|$ reflection absolute value alteration caused by perturbing bead, f_0 and $|(S_{11}{}^0)^{\cdot}|$– resonant frequency and reflection without perturbation, Q_0 – cavity quality factor.

ISBN 978-3-95450-181-6

FIELD DISTRIBUTION BASED ON PHASE MEASUREMENTS

This algorithm used as n option is based on known approach used for example by Jefferson Lab. We adopted it for our case and finally equations

$$\Delta f / f_0 = \frac{\tan\left(\Delta \arg\left(S_{21}\right)\right)}{2Q} \quad . \tag{8}$$

and

$$\xi_z = \sqrt{\frac{\tan\left(\Delta \arg\left(S_{21}\right)\right)}{4\pi k^E_{\Delta f} f_0 Q}} \frac{Ом^{1/2}}{м} \quad . \tag{9}$$

were used in algorithm.

Executable code consisting of user interface and service subroutines with all algorithms discussed above was developed using LabView environment.

PIRS5 TESTING

Wideroe based cavity with modified drift tubes stems which is under development at lab was used for testing of measurement setup. This cavity and field distribution along cavity axis obtained earlier using numeric simulation are presented on Fig. 5.

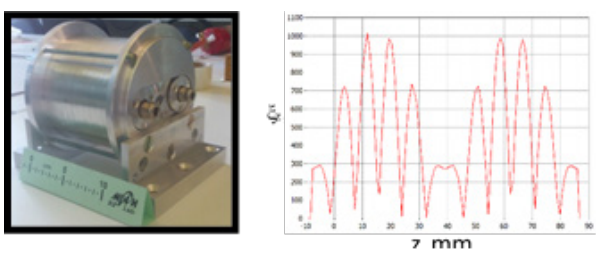

Figure 5: Cavity used for measurement setup tests and simulated Ez(z) field distribution.

Results of field measurements using the same hardware (including bead) but with different methods discussed above are presented on Fig. 6.

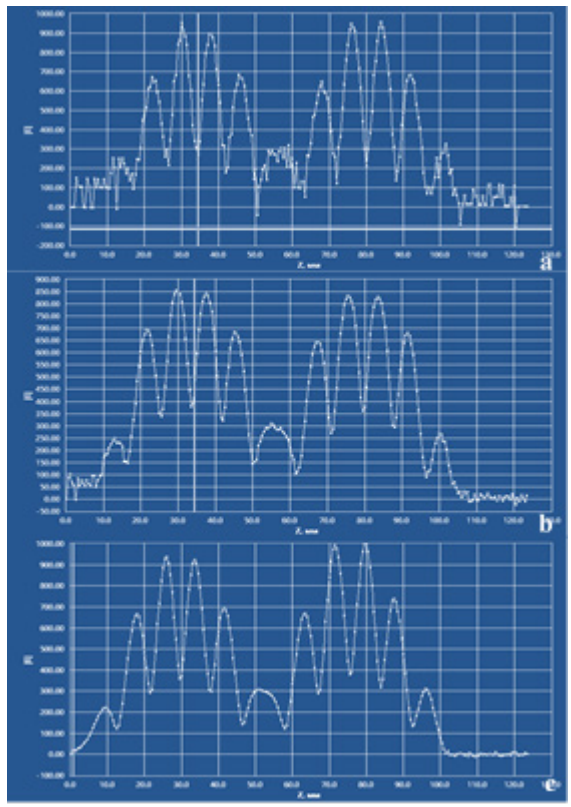

Figure 6: Cavity Ez(z)distributions acquired using easurements of: frequency variation (a), reflection (b) and phase (c).

CONCLUSIONS.

PIRS5 measurement setup used at MEPhI RF laboratory for accelerating cavities low power measurements was considerably upgraded. New algorithms of field strength computation based on different electrodynamical characteristics measured were implemented. After tests it is used as multipurpose tool for low power measurements of accelerating structures under development.

REFERENCES

[1] M.V. Lalayan, A. Yu. Smirnov, N.P. Sobenin, Form-factor of Beads for SW and TW Perturbation Field Measurement Analysis / Problems Of Atomic Science And Technology, I. 3, 2012.

[2] D. Alesini et al, About Non Resonant Perturbation Field Measurement In Standing Wave Cavities // EPAC08, Genoa, Italy, 2008.

[3] B.V. Zverev, N.P. Sobenin. Electrodynamics characteristics of accelerating resonators. M. Energoatomizdat, 1993. In Russian.

ISBN 978-3-95450-181-6

LONGITUDINAL BEAM DISTRIBUTION MEASUREMENTS IN DAMPING RING OF VEPP-5 INJECTION COMPLEX

V.V. Balakin†[1], D.E. Berkaev, O.V. Anchugov, O.I. Meshkov[1], V.L. Dorokhov, G.Ya. Kurkin, F.A. Emanov[1],
Budker Institute of Nuclear Physics, Novosibirsk, Russia
[1]also at Novosibirsk State University, Novosibirsk, Russia

Abstract

Injection Complex VEPP-5 was turned into operation in the end of 2015 in the Budker Institute of Nuclear Physics (Novosibirsk, Russia). The main task of the facility is production, acceleration and transportation of high intensity electron and positron beams for two BINP's colliders. Now, VEPP-5 successfully delivers electron and positron beams to VEPP-2000 and ready to start operation with VEPP-4M. Beam diagnostics issues are very important for VEPP-5 facility tuning during the operation. Longitudinal beam diagnostic based on synchrotron radiation in the VEPP-5 Damping Ring is presented in the article. Equipment operation principle, main measurement results and future prospects are presented in this paper.

IC VEPP-5 OVERVIEW

Injection complex (IC) VEPP-5 [1] was constructed for production, acceleration and transportation of high intensity electron and positron beams for two BINP's colliders – VEPP-4M [2] and VEPP-2000 [3]. IC [4] consists from thermionic electron gun, two linear accelerations, conversion system, damping ring (DR) and transporting channels (transfer line K-500).

DISSECTOR OPERATION PRINCIPLE

One of the main method of measurement of fast processes is electro-optical chronography. Stroboscope method is used in the circular accelerators, where dissector is used as converter (Figure 1).

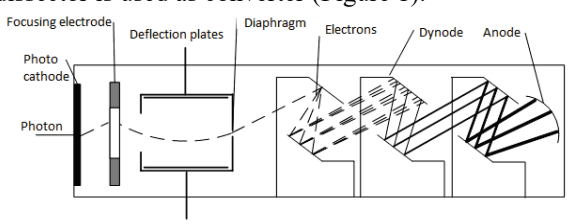

Figure 1: Dissector structure.

Let the light signal reached the dissector photocathode has time distribution $I(t)$. If high frequency sweep and incoming light impulses are synchronized, electron distribution $q(x)$ occurs in the plane of the diaphragm seal. Distribution $q(x)$ precisely imitates time distribution of light signal $I(t)$. Average anode current of photomultiplier $I_a(t)$ is proportional to light intensity falling onto photocathode. It is possible to shift different parts of distribution $q(x)$ on diaphragm seal changing voltage phase on dissector's deflection plates (see on Figure 2). Thus, photomultiplier's anode current will follow the shape of studied signal $I(t)$, if the parameters of incoming photocathode light signal be stable.

All temporal characteristics are true for distribution $q(x)$, but system applying dissector has some features:

- Researched object's information represented as electrical signal;
- Electrical signal precisely imitates temporary structure of light impulse, because there is no phosphor and microchannel decay;
- There is possibility to observe fast shape and duration changes of researched signal (the scale of hundreds synchrotron oscillations).

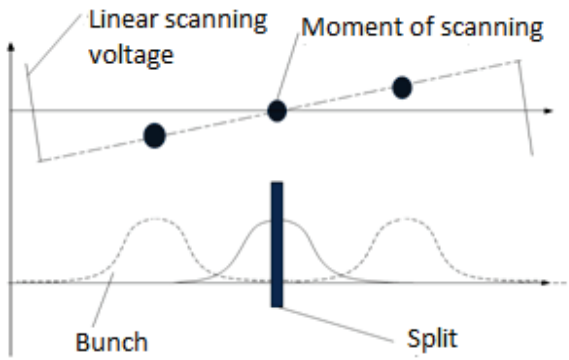

Figure 2: Scanning process.

Electron bunch length is far less than the perimeter of DR ($\sigma_z \ll \Pi$). Thus, it is necessary to scan distribution $q(x)$ with low frequency voltage applied to the deflection plates synchronously with high frequency voltage (see on Figure 3).

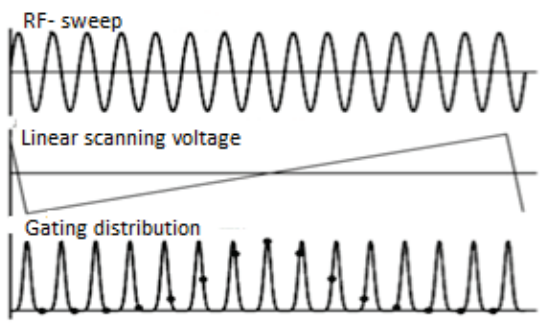

Figure 3: Synchronously scanning process.

† balakinvitalyv@gmail.com

ISBN 978-3-95450-181-6

Exceptional performance of the device allows using dissector for precise measurement of longitudinal bunch structure and monitoring occurrences of longitudinal oscillations.

DISSECTOR ON THE DAMPING RING

The dissector is installed in the synchrotron radiation (SR) bunker. Optical channel delivers the SR from damping ring to bunker (Figure 4).

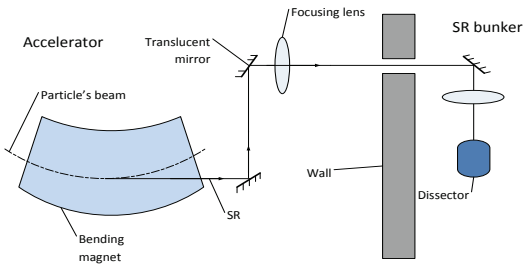

Figure 4: Optical channel to dissector.

The main dissector's characteristics are given in Table1 and the instrumental function is given on Figure 5.

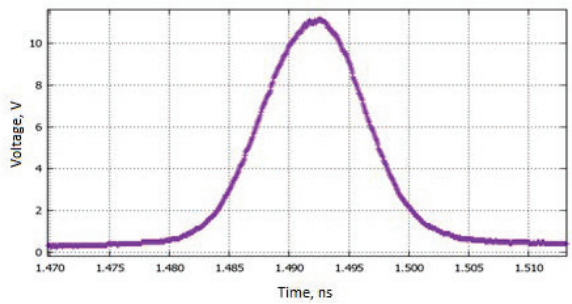

Figure 5: The dissector instrumental function.

The instrumental function defines precision of the measurements.

Table1: The Dissector Parameters

Photocathode voltage, kV	12
Grid voltage, kV	10
Focusing electrode voltage, kV	9
Photomultiplier voltage, kV	2
Frequency, MHz	78.6
Dissector resolution, ps	4.88

LONGITUDINAL BEAM STRUCTURE

Damping ring has high frequency cavity (700 MHz). Frequency of beam circulation is 10.9 MHz. Consequently, there are 64 buckets in the DR and only filled buckets can be detected by the dissector. At this moment Damping Ring operates with 3 filling mode buckets (Figure 6)*.

Moreover, it is possible to measure dependence of bunch size from parameters of DR, such as beam current, cavity voltage, lattice function of Damping Ring, etc.

Such difference between experimental result and model function in both cases (Figure 7, Figure 8) is explained by multibunched beams structure. Model function is proportional to $I^{1/3}$ and $U^{-1/2}$ for beams current and cavity voltage respectively in the one-bunched approximation. But discrepancy appear in experimental results due to neighbor bunches interaction.

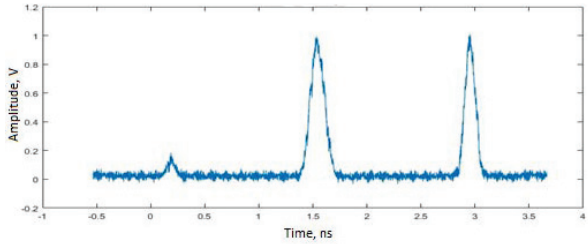

Figure 6: Damping ring beam structure.

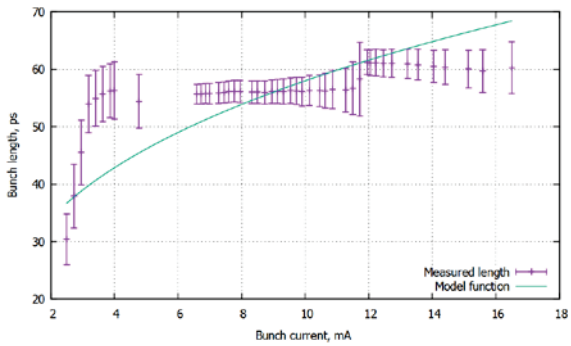

Figure 7: Bunch length vs beam current.

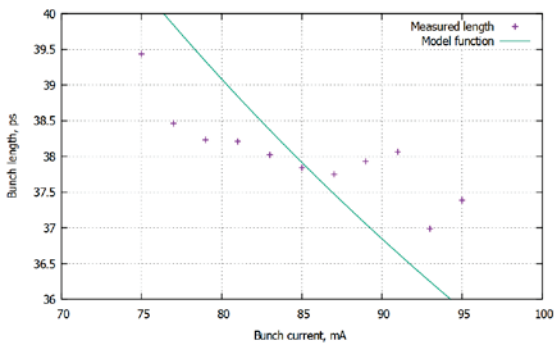

Figure 8: Bunch length vs cavity voltage.

Another application of the dissector is observing the phase oscillations (Figure 9). If phase oscillations excite, injection complex won't be able to transport electron or positron beams to colliders VEPP-4M and VEPP-2000. That's why, appearing of oscillations should be monitored.

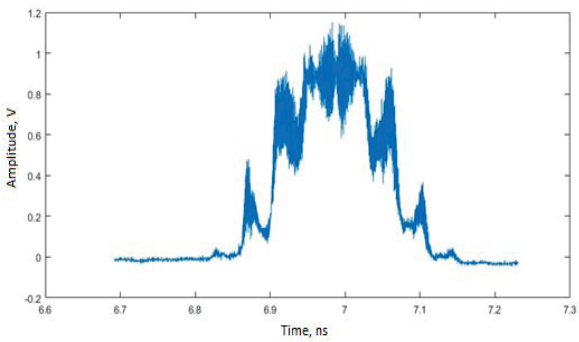

Figure 9: Phase oscillation observed by the dissector.

* Such filling of buckets defines by beam length injecting from linear accelerator.

ISBN 978-3-95450-181-6

ANOTHER APPLICATIONS ON DAMPING RING

The dissector has a lot of applications on damping ring. First of all, it is opportunity to observe the DR beams structure during the operation of accelerator complex. It is possibility to observe the whole evolution of bunch train parameters in during of injection cycle (Figure 10).

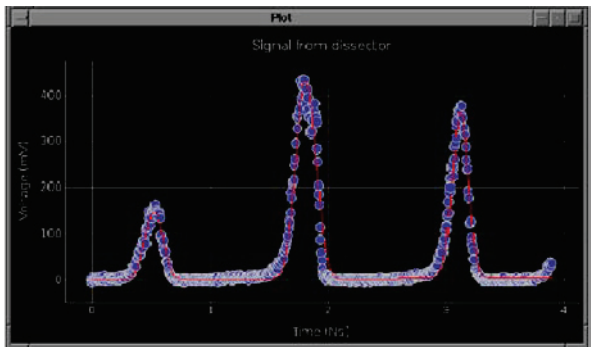

Figure 10: Signal from dissector and fitting Gaussian curves.

Secondly, there are a few methods of measuring the longitudinal and transverse impedance of accelerator vacuum chamber [5].

The bunch length above longitudinal mode coupling instability threshold is given by (for Gaussian beams shape):

$$\left(\frac{\sigma_z}{\sigma_{z0}}\right)^3 - \left(\frac{\sigma_z}{\sigma_{z0}}\right) = -\frac{\alpha I_b \mathrm{Im}\{[Z_{||}/n]_{eff}\}}{\sqrt{2\pi}(E/e)Q_s^2}\left(\frac{R}{\sigma_{z0}}\right)^3$$

Where σ_z is the rms bunch length, I_b is the average bunch current, $[Z_{||}/n]_{eff}$ is the longitudinal coupling impedance, R is the average accelerator radius, α is the momentum compaction factor, Q_s is the synchrotron frequency.

$\sigma_{z0} = \frac{\alpha R}{Q_s}\frac{\sigma_E}{E}$ is the zeros bunch length, $\frac{\sigma_E}{E}$ is the energy spread.

Below longitudinal mode coupling instability threshold is described by this equation:

$$\left(\frac{\sigma_z}{R}\right)^3 = \frac{\alpha I_b}{\sqrt{2\pi}(E/e)Q_s^2}\left[\left(\frac{Z_{||}}{n}\right) - \mathrm{Im}\left(\frac{Z_{||}}{n}\right)_{eff}\right]$$

Thus, after approximation $\sigma_z(I_b)$ of necessary functions longitudinal impedances can be calculated.

Moreover, it is possible to measure azimuthally impedance distribution. If bunch is deposed from equilibrium orbit transverse shift is expressed by formula:

$$\Delta x(z) = \frac{\Delta I_p}{\sqrt{2}E/e}\mathrm{Im}Z_\perp x_0 \frac{\sqrt{\beta(x_0)\beta(z)}}{2\sin(\pi Q_b)}\cos(\Delta\varphi - \pi Q_b)$$

$$I_p = \frac{\sqrt{2\pi}R}{\sigma_z}I_b$$

Where φ is the betatron phase, Q_b is the betatron frequency, β is the beta function, x_0 is the value of bump, and $\mathrm{Im}Z_\perp$ is the transverse localized impedance.

It is necessary to take into consideration contribution of dispersion function $D(z)$ in orbit distortion during horizontal measuring:

$$\Delta x_D(z) = \Delta x' \frac{D(z_0)D(z)}{\alpha\Pi}$$

$$\Delta x' = x\frac{I_p}{\sqrt{2}E/e}\mathrm{Im}Z_\perp$$

Using data from beam position monitors azimuthally impedance distribution will be calculated.

Another application of dissector is studying the condition of phase oscillations raising. It helps to tune linear accelerator, damping ring and their timing system more precisely for operation under absence phase oscillations. The estimated value of $\left[\left(\frac{Z_{||}}{n}\right) - \mathrm{Im}\left(\frac{Z_{||}}{n}\right)_{eff}\right]$ is about 10 Ohm.

One more application of the dissector is the Wakefield accelerating experiments (Figure 11). This outcast pipe is intended for transporting channel to Wakefield section on IC VEPP-5.

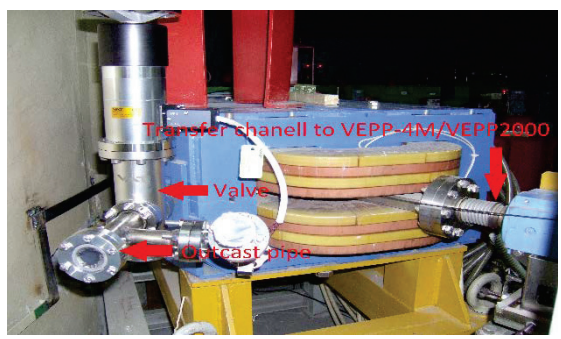

Figure 11: Outcast pipe for Wakefield section.

SUMMARY

The usage of the dissector and results of longitudinal beam size measurements are presented in this paper. Such type of diagnostic is everyday routine on Damping Ring now. It is possible to monitor bunches length and DR beam structure on-line. Operating staff are able to observe the changing in beam or bunches structure in each injection cycle. It is the opportunity for fast estimating the stability of injection process.

Moreover, the dissector gives an opportunity to estimate the longitudinal coupling impedance and azimuthally impedance distribution. And the method of measuring frequency of phase oscillation by analyze of the bunch structure modulation was suggested

Finally, the dissector measured data can be used for simulating and developing the Wakefield accelerating in Injection Complex.

ISBN 978-3-95450-181-6

REFERENCES

[1] P. Logatchev et al. “Status of Injection Complex VEPP-5”, Proceedings of RuPAC2014, Obninsk, Kaluga Region, p.11-13, TUY02.

[2] E. B. Levichev, et al. “Status of VEPP-4M collider”. IPAC-16, Busan, Korea, paper THPOR020.

[3] D.E. Berkaev, et al. “Commissioning of upgraded VEPP-2000 injection chain”. IPAC-16, Busan, Korea. paper THPOR018.

[4] “Physical project VEPP-5”, BINP SB RAS, 1995.

[5] V.V. Smaluk. Diagnostics of charged particles beams in accelerators. / Novosibirsk, Russia. 2009. p. 294.

ISBN 978-3-95450-181-6

HOST-BASED SYSTEM TO CONTROL THE ACCELERATOR

V.N. Zamriy, JINR, Dubna, Russia

Abstract

The report discusses development of the host-based system to control the accelerator. We consider modes of timing and allocation of operations of the system node. The time of any working cycle, rate of a data flow and an amount of serviced tasks are coordinated with characteristics of the node. Estimations of the readout rate of the data and the waiting time demonstrate the system efficiency. The data acquisition technique has been developed to provide checking of pulse parameters and control the linac LUE-200 of the neutron source IREN.

STATEMENTS OF A PROBLEM

Considered technique of synchronized data acquisition has been developed to control the linear accelerator of electrons LUE-200 of the neutron source IREN [1].

A multiplex system of timed data acquisition for monitoring parameters of the working cycle (at time period T, from one pulse of the electron beam up to another one, and cycle repetition rate – $1 / T \leq 150$ per second) has been offered and tested while the linac LIU-30 and full-scale test facility IREN were equipped with instruments [2].

Timed procedures of data acquisition are applied in the host-based solutions for a group of tasks to supervise process variables and control pulsed facilities [3].

The advanced system is aimed at carrying out several (up to N) tasks simultaneously. For this purpose it require to apply groups of N (an order 10) channels, one able to complete up to K (~100) measurements during the given time interval of the period T.

Some timed operations of the channels are assumed to be fulfilled by means of common nodes (with the timing controller) of the system. A link exchange of a node supports reading the data (at rate n) to feedback control.

Then procedure flowcharts of the engineering with the timed data interchange on the base of the system node allows one finding more efficient structural solutions.

Characteristics of operations of the channels and node should be coordinated and high enough to provide the minimum waiting time of service, taking into account the time period and rate of the data flow.

Key characteristics of channels and system node are coordinated to minimize a service time. Their idle time factors (P_1 and P_2) are examined, and also at possible queue of service requests.

The timing controller and link exchange of the node integrate the HB system, started at a working cycle. Diagnostics of process variables is complete for the cycle to feedback control.

Performance and number of serviced channels at chosen sync modes for such system are examined further.

The further analysis of operations forms requirements and approaches to develop system engineering.

THE PROCEDURE OF HOST-BASED DATA ACQUISITION

The host-based solutions of the type A, B and C for comparison are shown (Fig. 1).

The operations of the channels include groups of synchronized measuring and quantization of the process variables. Timed data acquisition and exchange of links (communication channels) for data processing provide the feedback control.

Levels of the main operations are applicable for the solutions based on the host with the link exchange. In the developed circuit (at first, type A, then B and C as the next step) the main operations of the channels are fulfilled simultaneously in the assemblies connected via the link exchange of the node.

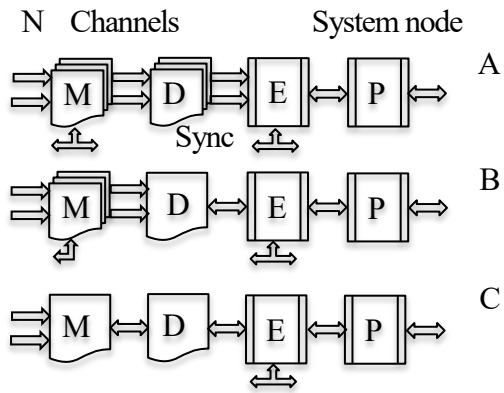

Figure 1: Procedure flowcharts of A, B and C type.

The operations M, D, E and P represent timed measuring of process variables, data acquisition and link exchange with interface to control.

The conditions of parallel operations lead to more sophisticated modes of the timing. Problems of the traffic of the data from all channels require coordination of the data readouts and of the data flow for the link exchange.

Estimations of the data readout rate and amount of data from the channels have been considered, first of all, under conditions of levels of A and advanced type B.

The procedures at the node levels cause timing problems to be solved and also put the requirements to the node. Development of the system on purpose to increase a data flow has led to higher requirements, especially when the data convenient for feedback control, are necessary.

Performance of operations at various timing modes of system is examined at complex requirements to pulsed facilities of the linac.

The amount and rate of the data gained during the accelerating cycle, attained number of channels which should be serviced, and also possible waiting time of operations, both for channels and node, will be considered

ISBN 978-3-95450-181-6

PERFORMANCES OF THE HB SYSTEM

For the cyclic run of measuring and data acquisition the lower limited rate of the data flow for the system is sufficient if the time of data readout does not exceed the specified part of the period of time T.

System characteristics define possible rate n of data readout just as amount K of the data of one channel and also the number N of serviced channels.

Performance of the system and the number of its channels are considered further for the selected timing modes, taking into account the specified key characteristics and estimated factors of an idle time for the channel and a node ((P_1 and P_2).

Timed Readout of Group of the Data of Channel

Plain read-out of K data from one channel is fulfilled during period T, when service time $t < T$ and its factor $m = t / T$.

At the given values of T and K and service factor $m = 0.1$, the lower limited rate of data readout is calculated as $n_1 \geq K / mT$. Idle time factors $P_1 = m$, but P_2 are estimated as $(1 - m)$.

Then the equipment is used inefficiently.

Simultaneous Data Readout of the Channels

The data transmission rate in comparison with the above-specified speed should be increased according to the following expression: $n \geq n_1 N / A$.

Coefficient $A < 1$ denotes a part of the operating time T (within the interval between two runs) which depends on the time of the link exchange and preparation for data reading. If the read-out time is $t = m T$, the rate is determined as $n \geq K N / m T A$. From this one can see what requirements are necessary at given key parameters.

The coefficient of the idle time (the ratio of waiting time to period T) of the channel is defined as $P_1 \leq (N - 1) m / N$. The idle time coefficient for the node: $P_2 = 1 - m A$, remains significant.

Thus the equipment is used further with modest efficiency.

Successive Data Readout of the Channels

Service of each subsequent channel having the order number of $M \leq N$ will start with a delay $(M - 1) t$, where t is the service time for the channel. The number of the channels working simultaneously with a node service can be estimated as $N \leq (T - t_1) / (t_2 + t_3)$.

In this case the times t_1 and t_3 are introduced to take into account a time of preparation of data readout for all channels and each channel. The time t_2 is readout time of the data of the channel at the estimated rate of reading.

Taking into account the conditions $(t_2 + t_3) = m T$ and $t_1 << T$, we have the modest rate $n = \sim n_1$ at the number N (< 18). Then the channels can work with one node even at the modest rate.

For the channel expecting service the coefficient P_1 defined by the ratio of time t_3 to period T, at $t_3 < N t_2$, is small. For the node the coefficient of the idle time is $P_2 = (t_1 + N t_3) / T$.

Taking into account requirements $t_3 << t_2$ and $t_2 = m T$ we gain the coefficient $P_2 = 1 - N m$. That is much less than in the previous mode. In particular, it shows the significance of time t_3 reducing.

This mode in comparison with the previous one is more efficient.

A Possible Queue of Requests of Servicing

It is of interest to consider the case when the request of service of the channel can arrive while the node is busy with service of another channel. Such situation when requests can occur at arbitrary time is characteristic for the system in the same "queuing" mode.

The system efficiency is considered for a limited flow of requests [4].

The parameter m is equal to the ratio of an average time of service to the average time between the requests of the channels. And also P_0 is meaning a probability that the node is not engaged in servicing, and k is the number of the appeared requests.

Figure 2 shows the dependence of the idle time factors on the number of the channels.

$$P_1 = \frac{1}{N} \sum_{k=2}^{N} \frac{(k-1)N!}{(N-k)!} P_0 m^k \qquad P_2 = 1 \Big/ \sum_{k=0}^{N} \frac{N!}{(N-k)!} m^k$$

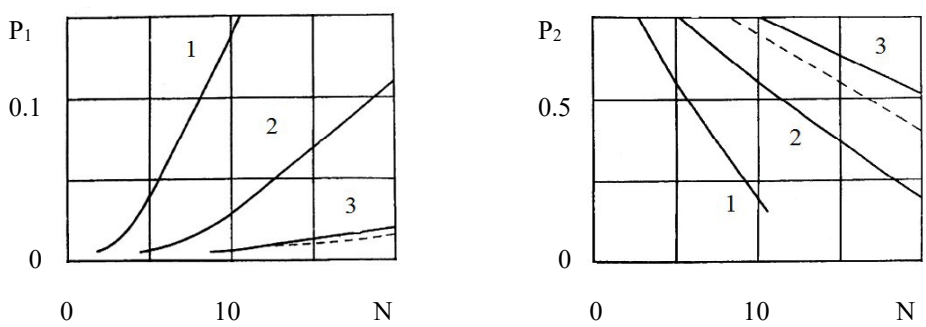

Figure 2: Idle time of channel (P_1) and node (P_2) depending on the number N of channels, the graphs 1, 2 and 3 are shown at the factor m to 0.1, 0.05 and 0.025, respectively.

ISBN 978-3-95450-181-6

When the factor m is reduced, the waiting time is shorten and thus does not exceed service time for bigger number of the channels (to 8, 13 and 21, accordingly).The estimates help one to select the key parameters.

Performance and Quantity of the System Nodes

Requests of service form queue if their number at the same time exceeds number of nodes. The nodes should be reserved for parallel operations to increase performance just as reliability of system. Possibilities of service in case of a node failure also are in view.

At using the doubled nodes the general characteristics accordingly change (the graph 1, in a Fig. 2, comes nearer to the graph 2); however, waiting time does not exceed servicing time for a greater number N (to 20). The dashed curves show efficiency of usage of three nodes. Efficiency of use (it concerns idle time at the chosen timing for the solution) grows under the given conditions.

The sent data is accompanied by signs to identify process variables and thus to reduce time of data exchange and preliminary operations (t_3 etc.). It allows reduce "dead times" of each cycle which are a key problem for timing under conditions of feedback control.

ADVANCED HB SYSTEM

The HB system includes the N channels and a node (as shown in Fig. 3) to monitor the process variables and control pulsed facilities. Embedded channels for a consecutive sample of pulse parameters and for check of parameter deviations extend the system opportunities.

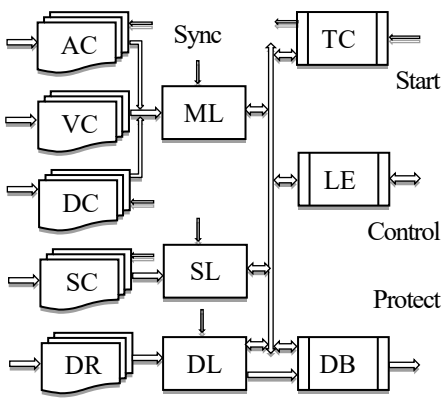

Figure 3: The system to control and protect the linac.

The system includes the next units:
TC, LE - timing controller and link exchange of a node;
ML - timed multiplex logger (one unit for 32 tasks);
AC, DC, VC - converters of amplitude, a delay and value;
SC, SL - sample-hold converters and serial logger;
DR, DL - a register of identification and deviation logger;
DB - logics of protection and lock a working cycle, etc.

Timed Data Acquisition to Feedback Control

The units of the node (with the data processing interface) are started at running of a cycle. They integrate the HB system (of type B). The data interchange has sync with timing controller of the system and pulsed facilities.

The converters start sample (with a nanosecond timing), then transform and keep pulse parameters for the period of logging. Also the conditioners of value normalize the low-level signals.

The multiplex logger records group of the data in a given time (to a millisecond). Remaining time of a cycle is reserved for data exchange and diagnostics to obtain a decision and control the cycles.

Consecutive Sample of Pulse Parameters

After the beginning of the working cycle, the strobes of sample-hold converters are started and repeatedly follow. The sequence of K values of amplitude with nanosecond discrete timing is registered.

Record of series of parameters of trailing pulse (its shape etc.) or pulse sequences is fulfilled for fast diagnostics of a series of pulse parameters, to control the mode of pulsed facilities.

Tracking of Deviation to Protect Cycle Mode

The identifying registers and the logger of the channels for monitoring the parameter deviations can directly control the protection logics. The state transition is registered when the alarm levels are defined.

The protection logic allows to lock of a working cycle immediately and then to change operating conditions under emergency.

Besides, the data recorded in the logger will be transferred via the link exchange interface into the process controller for subsequent diagnostic and control.

CONCLUSION

The developed HB technique allows one to coordinate the timed procedures of measuring and data acquisition, to control the linac. Efficiency of the HB system has been gained at selected modes of timing of the channels and link exchange of the node. The performances of the advanced system match the available conditions of the running cycle of the linac. The examined system parameters take into account doubling of accelerating sections. The presented solutions and characteristics are developed taking into account further reduction of the time period of repetition and duration of the beam pulse.

REFERENCES

[1] Ju. Becher *at al.*, "The LUE-200 accelerator at the IREN facility: current status and development", *Physics of Particle and Nuclei Letters*, vol. 11, no. 5, pp.1029-1039, 2014.

[2] V.N. Zamriy, "Study of automation sources of data acquisition", *Nuclear Electronics and Computing*, Proc. of the XXI International Symposium, Varna, Bulgaria, 2007. JINR, E10,11-2008-37. Dubna, 2008, pp. 455-460.

[3] V.N. Zamriy, "Host-based data acquisition system to control pulsed facilities of the accelerator", *Physics of Particles and Nuclei Letters*, vol. 13, no. 5, pp. 601-604, 2016.

[4] V. Ja. Rosenberg and A.I. Prokhorov, *The Theory of Mass Servicing*, Moscow, Soviet Radio, 1962, 254 p.

ISBN 978-3-95450-181-6

CONTROL SYSTEM FOR THE 1 MW NEUTRAL BEAM INJECTOR*

V.V.Oreshonok[†1], V.V.Kolmogorov, Budker INP, Novosibirsk, Russia
A.N.Karpushov, Swiss Plasma Center – EPFL, Lausanne, Switzerland
[1]also at Novosibirsk State University, Novosibirsk, Russia

Abstract

This paper presents general description of hardware and software of the neutral beam injector control system. The system is developed for control of the neutral beam injector which operates with 15-25 keV deuterium and hydrogen beams of 2 s maximum duration. It performs injection parameters calculation according to the desired beam power vs time curve, synchronizes and protects the injector subsystems and acquires its data during the shot. It also controls the injector operation between the shots.

The system is based on an industrial computer with National Instruments PCIe boards: two PCIe-7842R reconfigurable input-output modules and a PCIe-6323 data acquisition module. An in-house developed interfacing module (cross-box) as well as serial to fiber optic converters are used for galvanic isolation and electrical compatibility with the injector subsystems. User interface software and PCIe boards programmable logic firmware are implemented in LabVIEW. Injection calculations and results acquired are represented with MATLAB.

INTRODUCTION

An 1 MW neutral beam injector has been designed and built by the Budker Institute of Nuclear Physics (Novosibirsk, Russia) for the TCV tokamak of the Swiss Plasma Center (Lausanne, Switzerland) [1]. The injector parameters are shown in the Table 1. It operates in the pulsed mode and is aimed to produce deuterium and hydrogen neutral beams with an ability of the beam on/off modulation with millisecond resolution and of gradually varying the power injected into tokamak.

Table 1: Neutral Beam Injector Parameters

Parameter	Value
Max power injected in tokamak	1 MW
Beam power range	30 – 100 %
Beam power stability	± 5 %
Beam energy range	15 – 25 keV
Max injection pulse duration	2 sec.
Time delay between consecutive pulses	5 – 30 min.

The injector consists of an ion source connected to a vacuum tank where the gas neutralizer, bending magnet, residual ion dumps and moving calorimeter are mounted. The injector subsystems are located in two areas: gas system, ignition system, vacuum system, thermocouple modules of movable calorimeter and ion dumps and some parts of the RF supply are mounted near the injector in the tokamak zone. The rest parts including high-voltage supply system, power supplies for the ion source grids and bending magnet, RF supply electronics as well as control system equipment are located in the electronics zone being 50 meters away.

CONTROL SYSTEM

The system to control the injector was decided to be based on an industrial computer with a set of embeddable input-output modules. As injector operates in pulsed mode all its subsystems must be synchronized carefully during the injection pulse (shot). Also care should be taken of monitoring the subsystems status between the shots. Total number of channels required to control the injector operation is as follows:

- 24 analog input channels with the rate of 5 kSamp/s for monitoring the subsystems operation during the shot;
- 8 analog output channels with 10 kSamp/s rate to control subsystems parameters during the shot;
- 16 digital output channels with the maximum rate of 10 kSamp/s used for subsystems synchronization during the shot;
- 16 digital input channels with 10 kSamp/s maximum rate used as interlocks during the shot and between the shots as well;
- up to 40 digital input/output channels with the rate of less than 1 Samp/s to control and monitor the injector subsystems between the shots.

Since the control system equipment is distanced from the injector itself and partly from its subsystems, it was decided to isolate the system galvanically and connect with distant injector elements using optical lines and communication interfaces to avoid interference and cross-talks from injector and tokamak operation.

Hardware

Shown on the Fig. 1 is the injector control system block diagram. A SuperLogics industrial computer SL-3U-H77EB-GK with Windows 7 OS is chosen to run the control system software. It uses three PCI Express data acquisition modules by National Instruments as peripherals. Two of them are PCIe-7842R [2]: these reconfigurable input-output modules are based on a user-programmable Virtex-5 FPGA. Each module also has 16-bit resolution analog outputs with independent rate of up to 1 MSamp/s and analog inputs up to 200 kSamp/s. Another module used is PCIe-6323 data acquisition device [3] with 32 analog inputs of 16-bit resolution and 250 kSamp/s rate. Synchronization between PCIe modules is implemented by means of RTSI bus.

* This work supported in part by the Swiss National Science Foundation.
†V.V.Oreshonok@inp.nsk.su

ISBN 978-3-95450-181-6

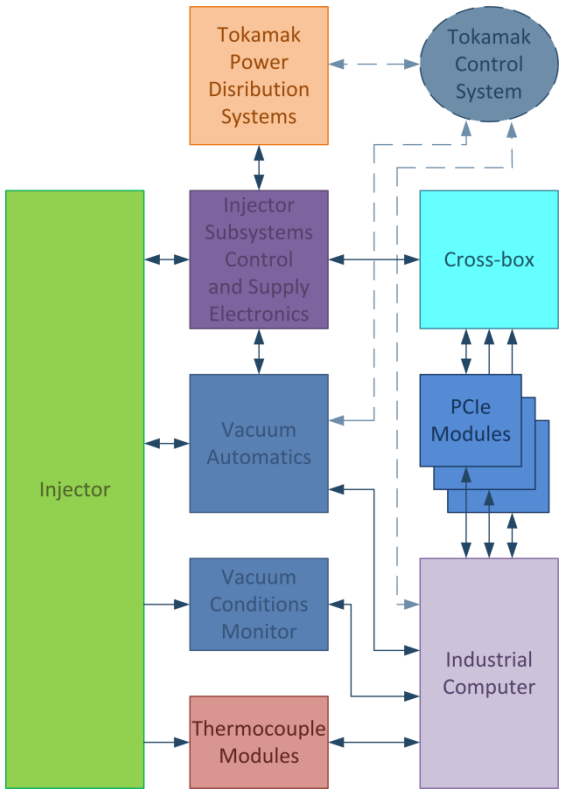

Figure 1: Control system block diagram.

All modules are connected to the interfacing device (cross-box) which is responsible for galvanic isolation and electrical compatibility between the control system equipment and the injector elements. The cross-box was in-house designed, its parameters are listed in Table 2.

Table 2: Cross-box Parameters

Parameter	Value
Analog channels	
Number of channels, input/output	24/8
Input and output voltage range	0 – 10 V
Input and output voltage accuracy	1 %
Channels bandwidth	50 kHz
Isolation voltage	1.5 kV
Digital channels	
Number of channels, input/output	
electrical	16/16
optical	32/32
Channels bandwidth	80 kHz
Isolation voltage	5 kV

The cross-box converts timing and interlock signals to/from optics. Also several signals of distant injector subsystems are transmitted via optical lines while electrical digital channels as well as analog input and output channels are used for communication with subsystems in electronics zone. The system analog outputs are used to control such injector parameters as ion source high-voltage supply values, RF system output power range, bending magnet current settings and others. For monitoring the analog subsystems parameters such as power supplies characteristics and beam position monitors data analog channels are used.

Another way of connecting the injector zone elements to the control system is via serial communication interfaces. The data is also transmitted with fiber optics to minimize losses and crosstalks and provide galvanic isolation and is converted to RS-232/RS-485 physical layers at the ends. Four serial channels applied are connected to the control system industrial computer as virtual COM ports. These channels are used for acquiring the injector thermocouple modules measurements, monitoring vacuum conditions and communication with the liquid nitrogen refilling system [4].

Software

The system software and firmware for the reconfigurable PCIe modules is designed in LabVIEW. The software is intended to perform several tasks as listed:

- analog control signals shapes and values calculation;
- timing signals synchronization sequences calculation;
- uploading sequences calculated into reconfigurable modules, checking its consistency;
- injector subsystems monitoring and control between shots;
- data acquisition and collection during and between shots;
- communication with the tokamak control system and its database.

The latter task features description is not an aim of this paper.

Control signals as well as estimated beam energy and ions and neutrals current calculation is performed with help of the MATLAB software using the MATLAB script nodes in LabVIEW based on the user defined power vs time curve. All data calculated and acquired during the shot (from data acquisition device and reconfigurable module internal memory as well) is then saved in a global structure along with shot parameters and settings to log the history.

The control system user interface with injector mimic panel opened is shown on Fig. 2. Different pages of the interface tab are displaying the injector subsystems information: moving calorimeter and ion dumps temperature measurements, vacuum conditions, interlocks and timers status and settings, power supplies characteristics and others. Each shot graphical results, including neutral beam power, energy, current vs time curves and subsystems parameters are displayed with MATLAB plots.

Firmware

System firmware is implemented in reconfigurable PCIe modules FPGAs to perform real-time operations during the shot. Four main tasks are of its responsibility:

- synchronization sequences generation;
- generation of analog control waveforms;
- monitoring of interlocks;
- acquisition of analog subsystems parameters.

ISBN 978-3-95450-181-6

As control signals and synchronization sequences calculated are uploaded to the FPGA internal memory and its consistency is checked by the system software, FPGA state machine is set ready for the injection shot. When injection is initiated all timers and DACs outputs are started to update according to the waveforms data loaded. Also interlocks inputs are monitoring during the shot. Should any interlock signal occur, synchronization sequences generation will be stopped thus aborting the shot process.

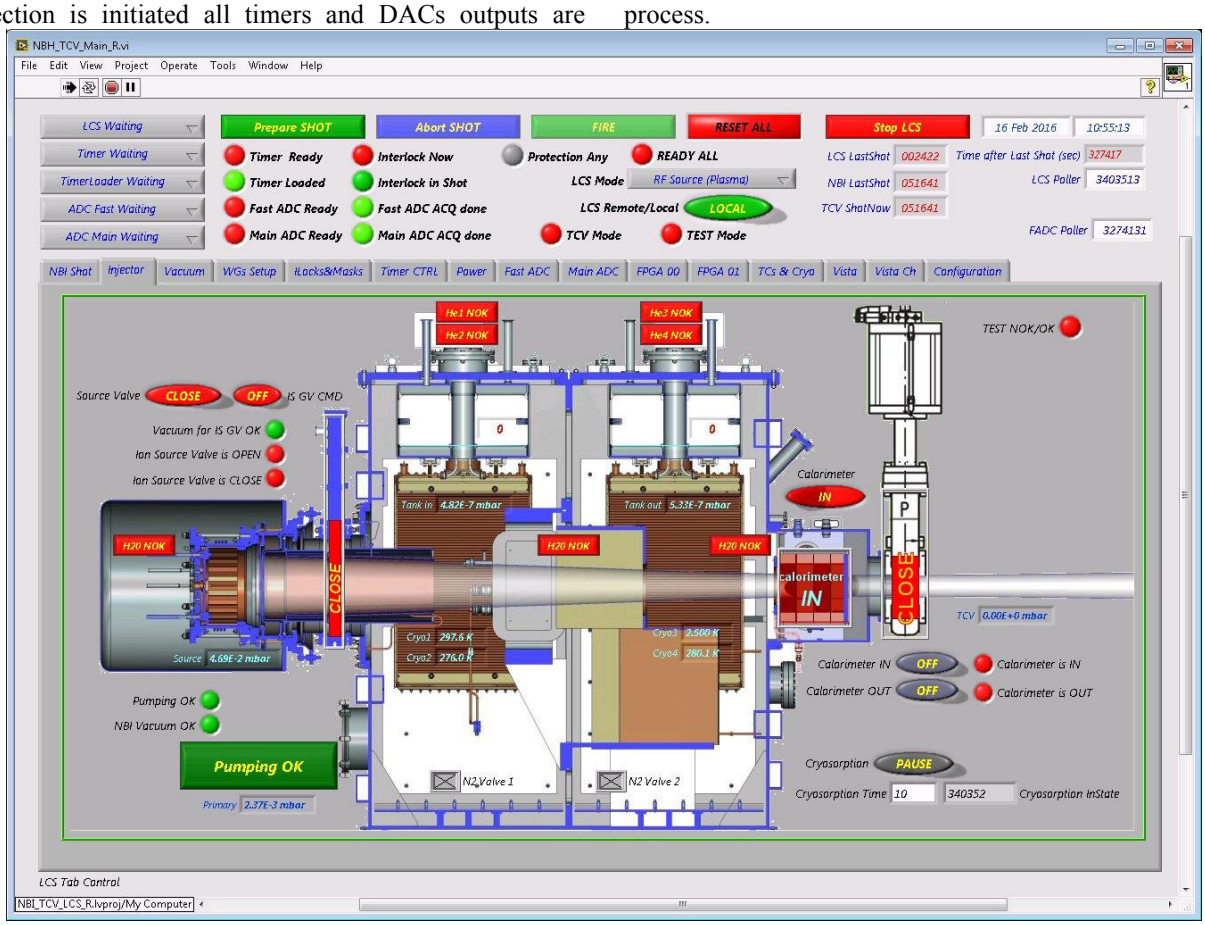

Figure 2: User interface.

COMMISSIONING

The system presented was commissioned during the injector assembling and tests performed at the Swiss Plasma Center in July-August and November-December 2015. In the late January 2016 the first neutral beam injector heated plasma was obtained at TCV tokamak.

REFERENCES

[1] TCV tokamak, http:// spc.epfl.ch/research_TCV

[2] NI PCIe-7842R, http://sine.ni.com/nips/cds/view/p/lang/en/nid/207369

[3] NI PCIe-6323, http://sine.ni.com/nips/cds/view/p/lang/en/nid/207406

[4] A. N. Dranitchnikov and V. V. Oreshonok, "An automated liquid nitrogen refilling system for cryopumps in the 1-MW heating neutral-beam injector of the TCV tokamak", *Instruments and Experimental Techniques*, vol. 59, no. 5, pp. 775-779, 2016.

ISBN 978-3-95450-181-6

CONTROLLER OF POWER SUPPLIES FOR CORRECTOR MAGNETS OF EUROPEAN XFEL

V. Kozak, O. Belikov, BINP, Novosibirsk, Russia

Abstract

The European XFEL is under construction now in Hamburg [1]. It is a big international project. Budker Institute of Nuclear Physics (BINP) developed, produced and delivered power supplies for corrector magnets of XFEL. A controller for these power supplies was developed. It provides an 18 bits resolution of digital-to-analog converter and 6 channels of precise analog-to-digital converter with high accuracy and resolution. A combination of the general-purpose functions with the specific function for power supplies allowed using the same controller for different equipment of corrector magnet subsystem. Here is described the controller, its properties and main applications.

INTRODUCTION

The European XFEL is 3.4-kilometre-long facility, which is located mainly in underground tunnels. It consists of a linear accelerator, undulators, electron and photon beam transport system. Eleven countries make the joint efforts for this international project. The Budker Institute of Nuclear Physics (BINP) takes participation in creating the European XFEL. BINP produces and delivers warm magnets, vacuum chambers, some cryogenic equipment and so on.

In frame of this works the BINP develops, builds and commissions the family of power supplies for corrector magnets. The family consists of models with output current 5 and 10 Amperes and with different output voltages. The quantity of power supplies to be 330 pieces [2]. Really the quantity should be above 400 pieces, it will be explained below. The Fig.1 shows the power supply.

Figure 1: The power supply for corrector magnets.

The requirements to power supplies includes high accuracy (less than 100 ppm), low output ripples (less than 10 ppm) and high reliability (MTBF >100000 hrs). The high reliability is required to reduce the pause in XFEL operation during replacing failed power supply by spare one. To reduce this time there is used the same trick like in most DESY installations- each rack with power supplies (up to 7) is equipped by spare power supply and controlled switch. When control software detects a failed power supply it tries to restart it and this attempt was not successful it replaces a failed power supply by spare one.

CONTROLLER OF POWER SUPPLIES

There was decided to use analog regulation for power supplies. That means we need a precise digital-to-analog (DAC) channel, a few of precise analog-to-digital (ADC) channels and discrete input/outputs. Using a modular approach in developing power supply we can implement the controller as a universal module (Fig.2.) which may be used in different applications.

Figure 2: Controller CPS01.

The second possible application is providing an interface for the controlled switch. All power supplies for corrector magnets are located in 48 euro-racks. So, we have 48 controlled switches (one per rack). For this purpose is suited more simple device which have not ADC and DAC. But even the simple device should have network interface, microcontroller and something else. And more important we should have separate documentation, separate production order and separate certification for European standards. More cheap way is to increase total quantity of identical controllers.

Most power supplies for magnet system in XFEL use CANbus as lowest level network. So, it is the reason for our choice of the same interface.

The controller was implemented using typical structure for similar applications (Fig.3.).

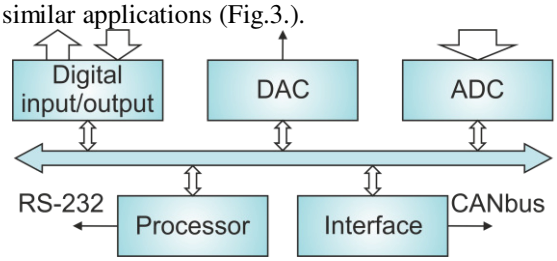

Figure 3: The structure of controller CPS01.

As for DAC, there is used chip AD5781- 18-bits DAC (Analog Devices). We use circuitry recommended by producer. The parameters of this chip satisfy the specification requirements. When we choose DAC chip

ISBN 978-3-95450-181-6

we kept in mind that Analog Device has AD5791 chip which is pin-to-pin and bit-to-bit compatible but it provides resolution 20 bits. So, if we would need in increasing DAC resolution for some power supplies we could replace the DAC chip only. The firmware of microcontroller will work with this chip without any changes.

As for ADC, we need to satisfy specifications for power supply:

- DC accuracy better than 100 ppm
- output noise less than 10 ppm (rms) in bandwidth 0÷2kHz

Choosing ADC chip and schematics we kept in mind that for mass production of 400 power supplies we need a lot of precise equipment. We need to have a few precise stands for testing and tuning power supplies and we need a multichannel system for 24 hour burn-in test. It means to have ≈10 amperemeters with accuracy at least 20 ppm. Using industrial voltmeter for these stands is expensive choice and it means many problems with integration this equipment in united measurement system.

We considered as an optimal choice to make this equipment with DCCT as sensor and ADC of controller as digitizer.

To provide high DC resolution the sigma-delta ADC is more suitable. Here was chosen ADS1255 chip (Texas Instruments). It provides high resolution and acceptable rate of measurements. Fig.4 shows structure of ADC.

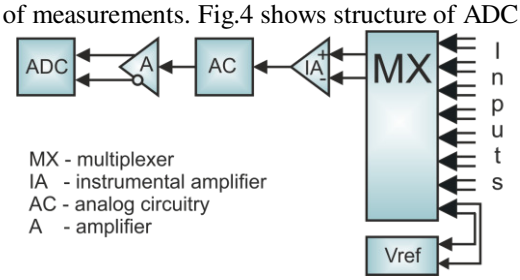

Figure 4: Structure of ADC.

The device works with differential input signals. After two-wire multiplexer the selected signal accepted by instrumental amplifier. Then common-mode signal is processed by analogue circuitry. Here the signal is converted from ±10 V range to 0,5÷4,5 V range. The circuitry suppresses high frequency components of signal. And then the signal is converted to differential mode. It allows to reduce the noise of ADC (using full input range of chip) and to improve linearity of digitizing.

Input multiplexer provides 8 inputs. 6 from them are used for measurement of external signals. Two inputs are used for calibration of system and are connected with ground and the precise reference source (AD688, Analog Devices) with typical drift near 1 ppm/°C. In main (multichannel) mode ADC digitizes predefined input channels (from 0 to 5, for example). Before each scanning these channels the microcontroller performs calibration of zero and range for all system. It consumes some time of course but it ensured the accuracy.

Described schematic provides high DC parameters and acceptable AC parameters. For low data rate (from 2,5 to 50 measurements/second) it has linearity 10 ppm and noise from 1 to 5 ppm (peak-to-peak).

For measurements of ripples we need a highest data rate. ADC has data rates 1, 2 and 3.75 kHz. On highest data rate the ADC noise is 30÷35 ppm (peak-to-peak). This resolution is enough for detecting ripples out of specification. Additionally the power supply circuitry extracts the error signal from output current, amplifies it by 100 and connects this signal with ADC input.

For measurements of ripples the oscilloscope mode of ADC is recommended. It this mode the microcontroller performs one calibration cycle and then digitizes a signal without time losses.

Controller has digital inputs and outputs. Outputs are used to switch bulk power supply on or off, reset the circuitry. Inputs are used to inform control system about status of power supply (overload, over temperature and so on).

Controller has two interfaces. One of them is CANbus and the second is RS-232. Users like to have a display which shows the output current at the moment. Usually developers use one from two ways. The first way is to use a cheap voltmeter with digital indication. The second way is to have display controlled by microcontroller of power supply. In this case the firmware of microcontroller should know which model of power supply it serves (or which device).

We have chosen the compromising approach. Most properties of controller are independent from controlled equipment. For example, range of ADC and DAC is always ±10 V. All measurement data is transmitted through RS-232 to smart module with OLED display and microcontroller. This module is part of power supply and it knows which equipment it serves. It allowed making important part of firmware more conservative. Any possible improving of user interface (accumulating data, additional processing, graphics etc.) may be done with intact firmware of controller.

The CANbus is used for interaction with control system. The firmware of microcontroller provides the following functions:

- control and monitoring components of power supply including some high level functions
- interaction with the control system providing a flexible set of functions. The command set was created in collaboration with XFEL people from software department
- low level primitives which allows for control software to use resources of controller as general purpose independent devices

APPLICATION OF CONTROLLER

It was mentioned above that we have chosen the one universal controller for different applications. Here we use it for replacing failed power supply («hot swap»). In this application only digital input/output ports are used. Usually we call it «redundancy system». It is shown in

ISBN 978-3-95450-181-6

fig.5a. The reserved power supply is located in lowest floor and controlled switch is located in highest floor.

The second additional application is the final acceptance test. It performed with special test rack (fig.5b). Instead of controlled switch the measurement crate is installed here (top floor in rack).

Figure 5: Racks with power supplies: with redundancy system at XFEL (left) and the burn in rack with the measurements crate (right).

The measurement crate has 7 home-made precise amperemeters. There are 7 sensors based on DCCT (Ultrastab, LEM) and precise shunts VPR221 (Vishay). As digitizers here are used 3 controllers. They measure 7 voltages on shunts (actually it is current) and temperatures of shunts.

All components of measurement circuitry have high linearity and low drift (1÷2 ppм/°C). But we checked stability with calibrator 5730A (Fluke). It provides 2 A maximal output current only. Fig.6 shows deviation of output current from reference (error signal) and temperature of shunt (ambient temperature) for one channel.

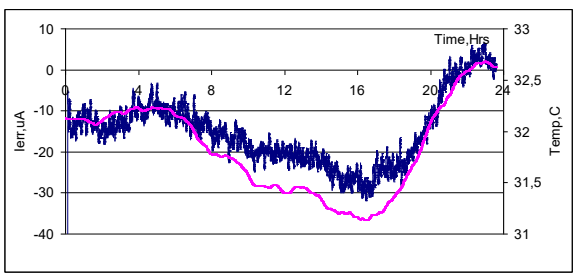

Figure 6: Error of current measurement (blue) for channel 4 and ambient temperature (red).

The graphics shows that the drift of measurement is 30 μA when temperature is changed on 1,5°C. The measurements for negative current and zero current confirmed that the drift for all measurement channels is less than 3 ppм/°C.

The measurement of current inside the power supply is built with the similar components and circuitry. So, it means we can rely on stability both power supply and measurement system.

CONCLUSION

At the moment all power supplies are produced, tested and delivered to XFEL. Most of power supplies passed acceptance tests at installation already. The control system of XFEL serves first racks more than 1 year [3]. No ideological problems were detected. Commissioning full system will be completed at end of 2016.

ACKNOWLEDGMENT

We thank Hans-Joerg Eckoldt and Piotr Karol Bartkiewicz (DESY) for fruitful discussions of requirements to controller.

This work was supported by grant 14-50-00080 of the Russian Science Foundation.

REFERENCES

[1] W.Decking et al., European XFEL construction status.// FEL-2014, Basel, Switzerland, August 2014, WEB03, p.623.

[2] Hans-Joerg Eckoldt. Specification of Power supplies at DESY.// 5th Workshop on Power Converters for Particle Accelerators, 24-26 May 2016, Madrid, Spain.

[3] L.Fröhlich, P.Bartkiewicz, M.Walla. Magnet server and control system database infrastructure for the European XFEL //ICALEPCS 2015, 17-23 October 2015, Melbourne, Australia, pp. 701-704.

ISBN 978-3-95450-181-6

DATA PROCESSING AUTOMATIZATION FOR GAMMA-SPECTROMETRY DIAGNOSTICS OF NEUTRON ACCELERATOR BNCT*

T.A. Bykov, Novosibirsk State University, Novosibirsk, Russia
D.A. Kasatov, Budker Institute of Nuclear Physics, Novosibirsk, Russia

Abstract

There is the accelerator-tandem at the Nuclear physics institute in Novosibirsk which is suitable for malignancies treatment such as glioblastoma and melanoma using BNCT methods.

There are different gamma spectrometry diagnostics which apply under this project. One of these is used to determine the parameters of the neutron beam. The method is to irradiate a set of activation foils with neutrons. Then measure the gamma-spectrum of foils using gamma detector. Based on these data it can be calculated the activity of foil, as well as the amount and the energy of neutrons.

For data processing of these diagnostics there was developed software which is used for convenient display of gamma-spectrometer data and the activity of the foil. Software allows setting a canal calibration and the sensitivity calibration which is needed to calculate the foil activity.

INTROCUTION

One of the most important and still unsolved problems is dosimetry of BNCT on all the stages of treatment. [1] Experiments are carried out to determine the parameters of generated neutron flow, using activation methods, and accompanying gamma-radiation. In this experiments it was used the spectrometric complex with NaI scintillator which must have automatic and operative data processing. The data processing task include automatic calibration, noise reduction, determination of the energy of the peak and the substance activity.

For these tasks the software was developed which allows processing the data in semi-automatic mode.

SUBJECT AREA

Activation method is used for determination of the current and the spectrum of neutrons. The special set of foils is used for the experiments (Au, Co, Cu, Fe, In, 5.2% Lu-Al, 81.3% Mn-Cu, Mo, NaCl, Sc, W). These foils are irradiated with neutrons during the experiment. Then the gamma-spectrum of foils using gamma detector is measured. Output spectrum data and period of measurement are saved into special file with specified format. As a result of the experiment there is a set of files with the spectrum data for every foil. These files are the input data for developed program.

These data have the following features. The graph of the spectrum has a shape of decaying exponent with a peak in the Gaussian form for some energy, and also the noise which has about the same amplitude on the entire spectrum (see Fig. 1).

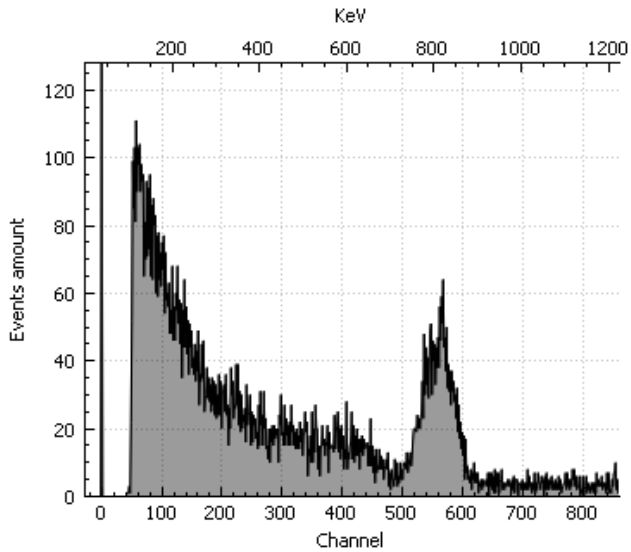

Figure 1: The graph of the spectrum of manganese isotope (^{56}Mn).

The noise amplitude in the spectrum is depends on the period of measurement and background during the measurement.

The number of peaks may be different and depends on the substance.

DATA PROCESSING

In the program the data processing consists of the following steps performed sequentially.

Noise Reduction

This module uses discrete wavelet transform.[2] The obtained spectrum data are represented as a mathematical function of amplitude by time i.e a signal with amplitude by time. The wavelet transform converts the signal from the time-amplitude representation to the time-frequency representation. In this subject area the useful information in the signal is a low-frequency component with large amplitude, i.e, trend, while noise is a high-frequency component and has a small amplitude.

The signal is decomposed into transform coefficients, then the coefficients with the amplitude below a user-specified values are reset to zero. and then performed the inverse wavelet transform. As a result, all of the useful low-frequency component of the signal remains, and small high-frequency noise is removed.

*Work supported by a grant from the Russian Science Foundation (Project No.14-32-00006) with support from the Budker Institute of Nuclear Physics and Novosibirsk State University.

ISBN 978-3-95450-181-6

Biorthogonal spline wavelet was selected as a mother wavelet, which provides the necessary smoothness of the result signal. The user must enter a value that is a percentage of the noise in the signal. (see Fig. 2)

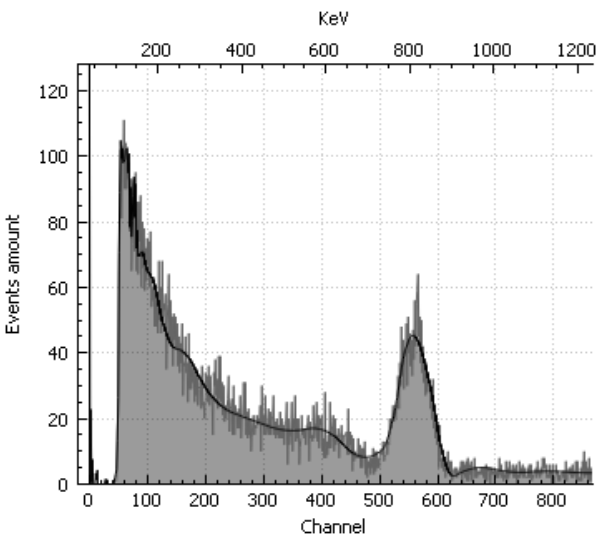

Figure 2: The result of smoothing using wavelet transform with the noise threshold of 6%.

Calibration

To display the data by values of energy, calibration needed. It is assumed that the energy values are linearly dependent on the channel values. So coefficients of the calibration are sets with the coefficients of line function. The user can enter the coefficients of the calibration line, also he has the opportunity to enter the channel values and the energy values, so the calibration coefficients will be calculated by the least squares method. In the figure one the upper horizontal scale shows the energy, and the bottom shows the channels.

Peak Determination and Activity Calculation

The measured isotopes have known parameters such as: the number of emitted gammas, their energy, their percentage and isotope's half-life. All these parameters are stored in the program, and it is possible to edit them.

Gamma detector saves in the file number of registered events for each channel. And the actual number of the emitted gammas is much different from that which records the detector due to imperfections of the detector. Part of gammas just does not hit the detector. The part that reaches the detector is scattered on adjacent channels. Thus in Figure 3 it is shown a normal distribution of the detected gammas. So the number of events is calculated as the integral of a gauss for a given energy.

In the Figure 4 the inputs are: the "Peak channel", the "Probability", it is the probability the gamma-quantum to emit, and the "Window", it is the maximum Gauss width.

The field "Events amount" displays value of the integral. This value divided by the duration time displays into the field "Real activity". This is the activity measured by the detector, but without taking into account the sensitivity calibration. Activity multiplied by the sensitivity calibration coefficients displayed into the field "True active".

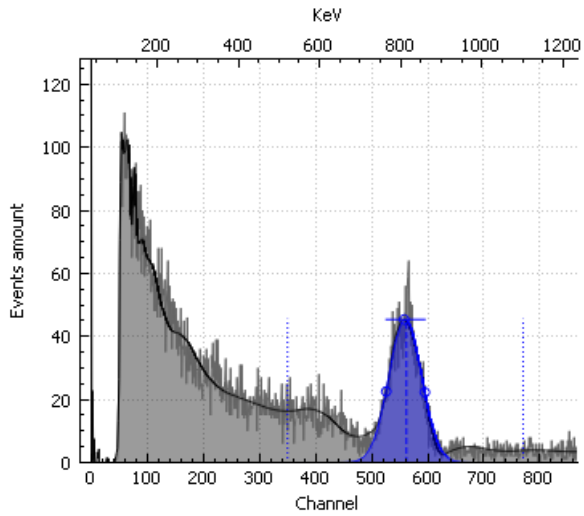

Figure 3: The Gaussian function is fitted in a peak of energy 847 KeV for ^{56}Mn.

The program calculates the Gauss by three points: the top which can be set by the user, and the two values in the middle of the height of Gauss.

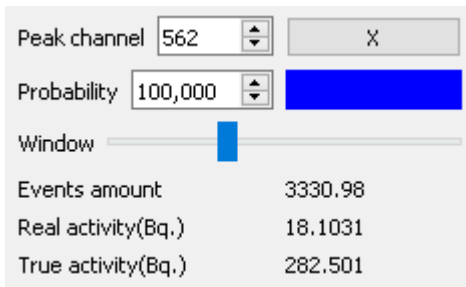

Figure 4: The user interface for the input of the peak parameters.

Sensitivity Calibration

Sensitivity in the channel - it is the true activity ratio, i.e. the activity that should be for that substance, to the activity measured by the detector. As in the case of calibrating the channels it is assumed that the channel sensitivity dependence is linear. So coefficients are sets with the coefficients of line function. It is possible to input these coefficients, or to calculate these coefficients, using the least squares method for channels values and the sensitivity values. The sensitivity values represented by the real activity and the true activity.

Restoring the Initial Activity

Substance activation - is the number of active cores obtained after irradiation. The resulting isotope begins to decay immediately after irradiation emitting gamma rays. And different substances have different half-life. At the moment, there is no way to measure all foils at the same time, so foils are measured separately and while measured

ISBN 978-3-95450-181-6

the first foils, the rest decay before the start of measurement. So the measured foil activity will be less than after the neutron irradiation. Substance activity decreases exponentially with time. Figure 5 is a graph of substance decay. Knowing the start and end of the measurement, and activity it is not difficult to restore the initial activity.

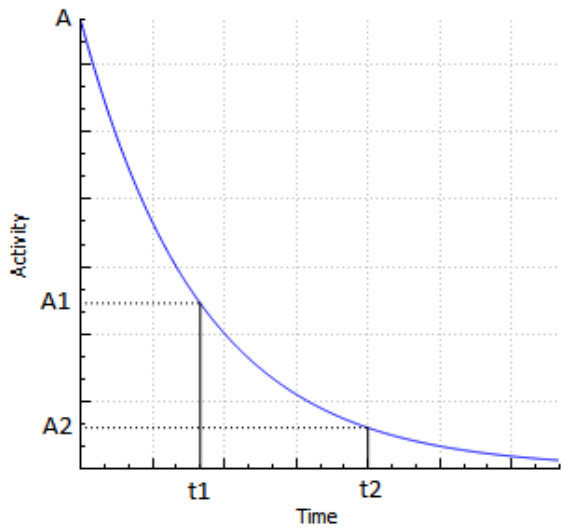

Figure 5: Graph of radioactive decay. Where the time t1 and t2 are the time of the start and the end of measurement, A1, and A2 - the activity at this time.

Activity measured by the detector and calculated by the program is ΔA = A1 - A2. The initial activity is restored with the equation (see Eq. 1)

$$A = \frac{\Delta A}{2^{-\frac{t1}{T}} - 2^{-\frac{t2}{T}}} \quad (1)$$

In equation 1 A is the amount of the resulting isotope after irradiation, or activity, ΔA is the activity resulting from the measurement, t1 - start time measurement, t2 - time measurement end, T - the half-life.

Restoration of the Neutron Spectrum by Activity

To restore the neutron spectrum used SAND II (Spectrum Analysis by Neutron Detectors). One of the input parameters for the calculation is the initial activity of the substance which is already calculated, and many other parameters. All these parameters are automatically passed from the main program to this program. Currently, this module is not implemented.

USED TOOLS

The program is implemented in C++ using the Qt 5.7 framework for the user interface. To display graphs used QCustomPlot library. For wavelet transform and calibration calculation used GSL library.

CONCLUSION

Currently developed program allows the processing of data only in semi-automatic mode. This means that after measurements on spectrometric complex, it is necessary to collect information and enter it into the program. It does not allow to see the result of the measurement real time. As a result of this work it is planned to develop a fully automated gamma spectrometric complex where data processing will take place without user participation. Implemented modules: noise reduction, channel and sensitivity calibration, the determination and calculation of peak activity. the modules of restoring the original activity and neutron spectrum calculation is not implemented.

REFERENCES

[1] S. Taskaev, V. Kanygin, Boron neutron capture therapy, (Novosibirsk: Russian Academy of Sciences, 2016), 216.
[2] A. N. Yakovlev Introduction to wavelet transform, (Novosibirsk: Publishing House of Novosibirsk State Technical University, 2003), 104

ISBN 978-3-95450-181-6

VME BASED DIGITIZERS FOR WAVEFORM MONITORING SYSTEM OF LINEAR INDUCTION ACCELERATOR LIA-20

E.S. Kotov, A.M. Batrakov, G.A. Fatkin, A.V. Pavlenko, K.S. Shtro, M.Yu. Vasilyev,
Budker Institute of Nuclear Physics SB RAS, Novosibirsk, Russia

Abstract

The Linear Induction Accelerator LIA-20 is being created at the Budker Institute of Nuclear Physics. Waveform monitoring system (WMS) is an important part of LIA-20 control system. WMS includes "slow" and "fast" monitoring subsystems. Three kinds of digitizers have been developed for WMS.

"Slow" subsystem is based on ADCx32. This digitizer uses four 8-channel multiplexed SAR ADCs (8 μs conversion cycle) with 12 bit resolution. Main feature of this module is program configurable channel sequencing, which allows to measure signals with different timing characteristics.

Two types of digitizers are involved in “fast” subsystem. The first one, ADC4x250-4CH, is 4-channel 250 MSPS digitizer. The second one, ADC4x250-1CH, is single channel digitizer with sample rate of 1 GSPS. Resolution of both devices is 12 bit. “Fast” modules are based on the common hardware.

This paper describes hardware and software architecture of these modules.

INTRODUCTION

The linear induction accelerator with energy of 20 MeV (LIA-20) intended for pulsed X-ray radiography with high space resolution is under development in the BINP (Novosibirsk, Russia). In the total control system one of the most important is the waveform monitoring system. For linear induction accelerators which are high-power, high-voltage pulsed installations, waveform monitoring, i.e. registration of waveforms of signals received from a wide range of sensors in each operating cycle, is the most informative, although very expensive way to control the normal operation of equipment [1, 2].

It is assumed that in the final version the WMS will enable the registration of two thousand waveforms with different durations. Analysis of the data obtained immediately at the end of the operating cycle will make a conclusion about the current condition of the installation elements and their operation in the last cycle. At the same time, data archiving, performed for many operating cycles, and their appropriate processing will allow to identify and study in detail trends in the equipment, the evolution of their parameters and thus to predict possible failures.

Operating cycle of the LIA-20 can be divided into three phases: a preparatory, acceleration phase and an experimental phase. The typical duration of the processes in the preparatory phase are in the range of 0.2 – 20 ms, in the acceleration phase – 100 – 400 ns, and in the experimental phase, when the beam is directed into several routes, the signal durations are 20 – 50 ns. The signal bandwidth in the first phase does not exceed 10 – 20 kHz, in the second it is 30 – 40 MHz, and in the third – 200 MHz.

Thus, three types of modules are required for arranging the waveform monitoring. The first one is to have the sampling rate 50 – 100 kSPS and can be built based on the multiplexed ADC chips. The second one must provide the sampling rate of 3 – 5 ns/sample. The fastest module should have a speed not less than 1 ns/sample. Note that for a full-scale waveform monitoring is necessary to record signals for the first phase in 1563 channels, for the second – in 840 channels and for the third – in 18 channels.

The following describes structural schemes of modules used in the WMS, discusses the features of the chosen solutions, ways of errors minimizing. Some details of schemes and the resulting device parameters are presented.

SLOW WMS DIGITIZERS ADCX32

"Slow" WMS subsystem provides data acquisition of Pulsed HV System (PHVS) signals (see Fig. 1). PHVS includes 27 HV chargers, 480 pulse modulators with Pulse Forming Networks (PFN) for supplying accelerating inductors, 64 pulsed demagnetizer and 32 magnetic lens supply units. Such parameters as HV charger voltage, PFN voltage, demagnetizer current and magnetic lens current should be measured with an error not exceeding 0.1%. The durations of PHVS elements processes differ significantly as shown in timing diagram of PHVS operation (see Fig. 1). Thus, "slow" WMS should be able to digitize 1563 signals in time range 500 us – 20 ms.

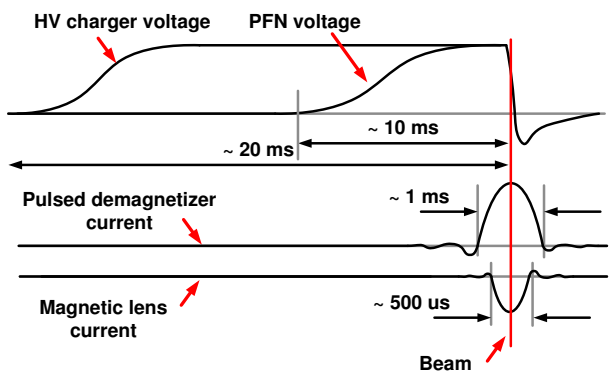

Figure 1: PHVS timing diagram.

The basic idea of "slow" WMS digitizer design is using four 8-channel multiplexed 1 MSPS SAR ADCs with

ISBN 978-3-95450-181-6

programmable channel sequencing. Channel sequence configuration determines sampling rate for each ADC channel individually. That allows sampling channels with shorter time duration faster than channels with longer time duration. This approach is illustrated in Fig. 2. Sequence example is shown in timing diagram for the case, when CH.0 of ADC records fast process with twice higher sampling rate than CH.1 and CH.2.

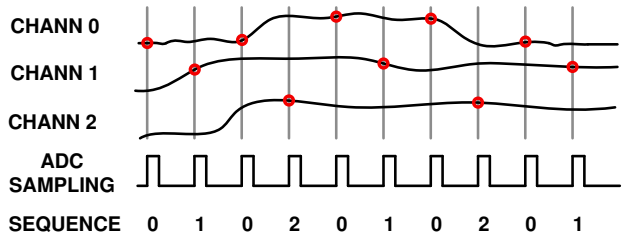

Figure 2: ADC channel sequencing.

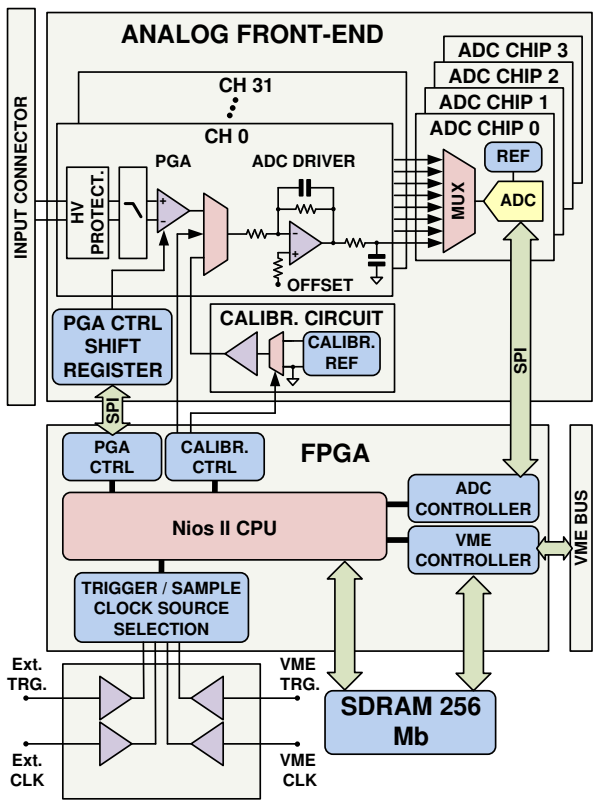

Figure 3: ADCx32 block diagram.

ADCx32 is 32-channel VME digitizer based on channel sequencing technique designed for "slow" WMS subsystem. ADCx32 block diagram is shown in Fig. 3. Core of the digitizer is Nios II embedded CPU implemented in a Cyclone III (Altera FPGA). Core provides VME interface support, driving of SDRAM memory, trigger and sample clock sources selection and analog front-end control. Front-end is built on four ADC chips and 32 input channels circuits. Digitizer inputs equipped with HV protection (100 V), 50 kHz filtering and PGAs. See Table 1 for ADCx32 specifications.

Necessary precision was achieved by using calibration procedure, which includes measurements of zero and scale errors of drivers and ADCs and applying built-in data correction algorithm.

Table 1: ADCx32 Specifications

Sampling rate	1 MSPS (max)
Bandwidth, -3dB	50 kHz
Ranges	±1 V, ±2 V, ±4 V, ±8 V
Resolution	12 bit
Absolute error	$\pm 3*10^{-4}$ FS
Total noise (RMS)	< 0.7 LSB
SNR	75.3 dB_{FS} in the operating band
Buffer size	524 288 samples per channel

FAST DIGITIZERS FAMILY ADC4X250

A relatively small number of signals recorded in the third phase, makes uneconomical the development of the device with 1 GSPS sample rate, if take into account labour expenditures. On the other hand, the purchase of a number of modules, each of which costs about $ 12,000, not a satisfactory one. However, it is clear that the structural schemes of modules of the second and third types (ADC4x250-4CH, ADC4x250-1CH) are identical and include fast ADCs, buffer memory, accurate synchronization elements and VME interface. In this regard, it looks attractive variant when first developed slower module type, and then based on it is realized the fastest device.

Let us discuss the structural scheme which allows realizing proposed method. It is shown in Fig. 4.

The module consists of an input (replaceable) and common parts. The marked by dashing part of the structure in the figures is a uniform hardware platform. This part remains unchanged for both modules and contains four 250 MSPS 12-bit ADCs with their drivers, synchronization and timing circuit as well as digital equipment. These parts implemented as a separate PCBs and stacked with each other by mezzanine way.

It the case of four-channel device (ADC4x250-4CH) replacement part consists of four input amplifiers. Each amplifier corresponds to one channel. In this case all ADCs are driven by synchronous clocks. Therefore, the sample rate of such device coincides with the sample rate of one ADC and equals 250 MSPS. The bandwidth of the ADC4x250-4CH is determined by the input amplifiers and ADC and equals 75 MHz.

One-channel device is obtained by replacing the input amplifier and program reconfiguration of a clock circuit. To increase the high sample rate of A/D conversion it is needed to drive ADCs by clock signals with a phase shift of 90° (Fig. 5). ADCs work sequentially in time. Therefore, sample rate for one input is quadrupled and eventually equals 1000 MSPS.

ISBN 978-3-95450-181-6

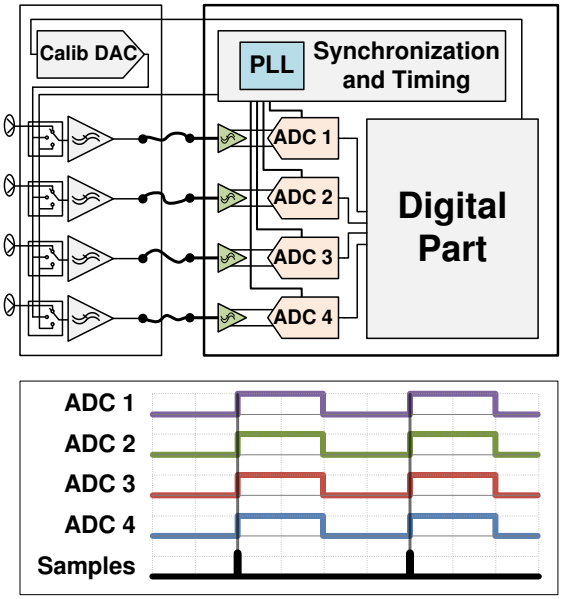

Figure 4: The structure of ADC4x250-4CH and its clock sequence.

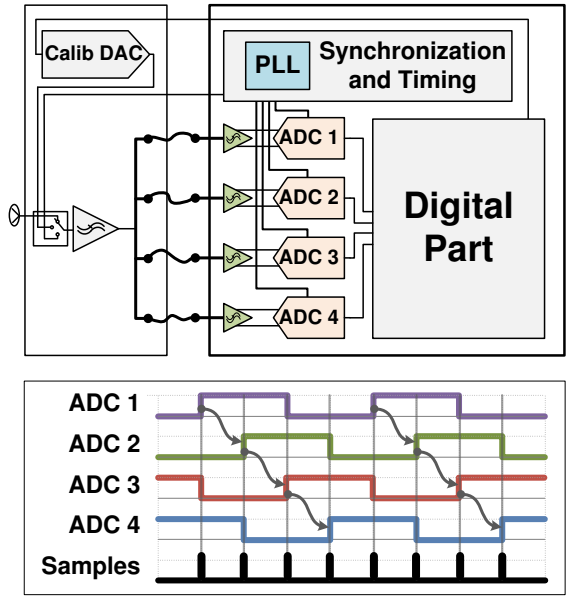

Figure 5: The structure of ADC4x250-1CH and its clock sequence.

Following this way, two-channel device with 500 MSPS may be easily made if it will be needed.

The advantages of this approach are the same circuit solutions, unified element base, tracing the multilayer PCB. It is important to say that LIA-20 control system including WMS using of VME64x standard with advanced extensions that providing inter-module synchronization in VME crate [3]. A necessary of supporting this quite complex interface and the need to develop devices that provide such synchronization are additional reasons for creating uniform hardware platform.

Of course, the proposed approach has the additional charges, which require more complex "firmware" for PLDs, additional calibration procedures and specific signal processing. For one-channel device in addition to standard static (zero and scale) calibration, dynamic calibration are implemented which allow to measure difference of channels delays. A number of signal correction methods based on dynamic calibration are added as part of signal processing.

Characteristics of the ADC4x250 family digitizers are specified in Table 2.

Table 2: ADC4x250 Family Specifications

	ADC4x250-4CH	ADC4x250-1CH
Sample rate	250 MSPS	1000 MSPS
Bandwidth, -3dB	75 MHz	300 MHz
Voltage ranges	±0.5 V, ±1 V, ±2 V, ±4 V	
Resolution	12 bit	
Buffer length	786 432 samples/ch	3 145 728 samples/ch
Static noise (RMS)	< 0.8 LSB	< 1 LSB
Phase noise (RMS)	< 0.7 ps	< 0.7 ps
Crosstalk @ 50 MHz	< -60 dB	—
SNR	62.7 dB_{FS} @ 11 MHz	62 dB_{FS} @ 110 MHz
SINAD	61.8 dB_{FS} @ 11 MHz	45.6 dB_{FS} @ 110 MHz

CONCLUSION

Three kinds of VME-based waveform digitizers have been developed. These modules are intended for creating Waveform Monitoring System of the Linear Induction Accelerator LIA-20, but can be used in other VME-based systems to arrange multichannel recording signals in wide time range.

A pilot batch of modules is produced and tested in real experiments. Currently it is prepared serial production of all three models of digitizers.

REFERENCES

[1] P.A. Bak et al., “Control system of a linear induction accelerator of an X-ray complex: Structure, hardware, and test performance“, Optoelectron. Instrument. Proc., 2011, Vol. 47, No. 3, pp. 303-312.

[2] D.A. Starostenko. et al., “Results of operating LIA-2 in radiograph mode”, Phys. of Particles and Nuclei Letters, 2014, Vol.11, No. 5, pp. 660-664.

[3] G. Fatkin et al., “Structure and Hardware of LIA-20 Control System”, RuPAC’2016, Saint Petersburg, Russia, 2016, THCBSH02, these proceedings.

ISBN 978-3-95450-181-6

SYSTEM OF GEODETIC MEASUREMENTS FOR LIA-20.

A.G.Chupyra, E.A.Bekhtenev[1], G.V.Karpov,
Budker Institute of Nuclear Physics, Novosibirsk, Russia,
[1] also at Novosibirsk State University, Novosibirsk, Russia.

Abstract

The system of geodetic measurements for accelerator LIA-20 is presented in this paper. The system consists of two subsystems. The first one is hydrostatic level system and the second one is system with the stretched wire. The system of geodetic measurements controls vertical and horizontal shifts of the accelerating structures, and also their inclinations in the longitudinal and cross directions.

INTRODUCTION

LIA-20 is a new accelerator for radiography which is now under development and construction. It consists of the injector and a number of accelerating modules placed on girders. Total length of the accelerator is about 70 meters. The accelerator is designed to provide a electron beam with energy up to 20 MeV, current 2 kA and lateral size of beam less than 1 mm. The last condition requires a careful alignment of the accelerator's elements and further monitoring of their positions. It is necessary to control change of the accelerating module's position less than 0,1 mm on height and less than 1 milliradian on angle. System for geodetic measurements is developed for this purpose.

The system consists of two subsystems. The first one is hydrostatic level system and the second one is system with the stretched wire. The system of geodetic measurements controls vertical and horizontal shifts of the accelerating structures, their inclinations in the cross directions and its rotation angle around the longitudinal axis (Fig.1).

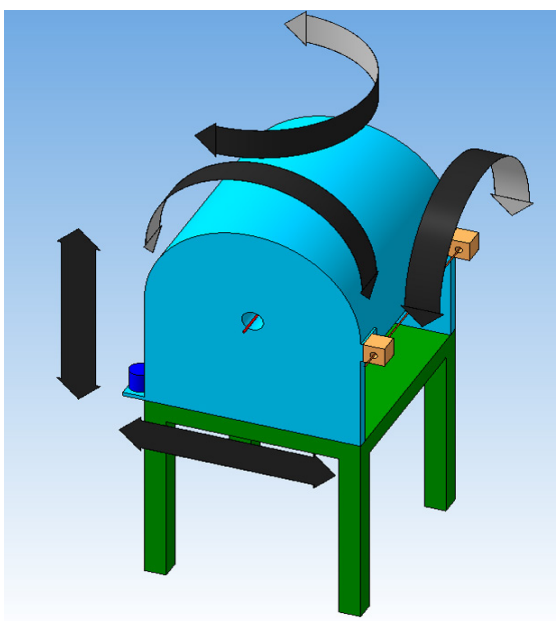

Figure 1: Movement types measured by the system.

HYDROSTATIC LEVEL SYSTEM

General Description

Hydrostatic level system is based on principle of communicating vessels. All water level measuring sensors are linked to its neighbours by a system of tubes. So the principle is based on the equilibrium of the pressure of liquid in communicating vessels (see Fig. 2).

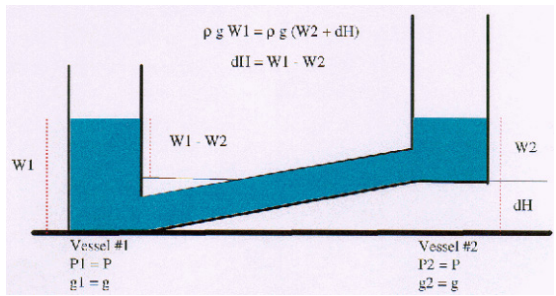

Figure 2: The principle of communicating vessels.

Ultrasonic level sensor

Ultrasonic Level Sensor (ULS) is designed to work into the hydrostatic level system for monitoring of vertical position of the accelerating modules. The resolution of the ULS is 0.2 μm and the accuracy is 5 μm in measurement range of 5 mm.

A pulse-echo method is used in ULS for water level measurements. The ultrasonic hydro-location is well known and widely distributed method of distance measurements for many applications. One of precise methods was described by Markus Schlösser and Andreas Herty [1]. Their idea is to locate not only the water surface in a vessel, but also two addition surfaces with calibrated distance between them (D1) and at the calibrated distance to alignment reference target (D2), see Fig. 3.

The pulse-echo ultrasonic measurements can determine the location of free water surface in a vessel or location of reflective surface into water by accurately measuring the time required for a short ultrasonic pulse generated by a transducer to travel through a thickness of water, reflect from the free water surface or from the reflective surface, and be returned to the transducer. The two-way transit time measured is divided by two to account for the down-and-back travel path and multiplied by the velocity of sound in the test material.

$$d = v \cdot t / 2 \quad (1)$$

Here ***d*** is the distance from the surface of transducer to the reflective surface or to free water surface, ***v*** is the

ISBN 978-3-95450-181-6

velocity of sound waves in water, and ***t*** is the measured round-trip transit time.

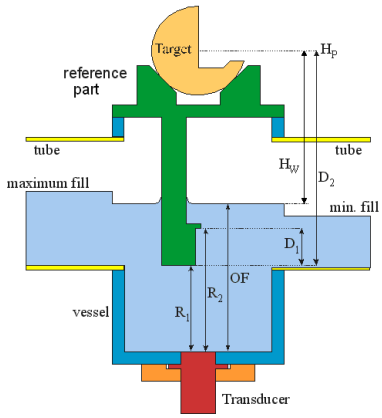

Figure 3: Principle of organizing the reference surfaces at the ultrasonic sensor.

Usually it is necessary to determine vertical distance between the free water surface and centre of alignment ball (Hw). It is easy to do by next formula:

$$H_W = D_2 - D_1 * \frac{t_{OF} - t_{R_1}}{t_{R_2} - t_{R_1}} \quad (2)$$

Here D_1 and D_2 are linear dimensions of the reference part. They can be measured with high accuracy after their fabrication. So ULS has self-calibrating capability and as result there is a possibility to make measurements of absolute water level position with high accuracy. Because of self-calibrating capability one can eliminate any electronics drifts.

On each girder it will be installed three Ultrasonic Level Sensors (ULS).For the placement of the sensors on the girders special brackets will be used. All sensors will be connected into the hydrostatic level system with pipes half-filled with water.

Fig.4 presents general view of the ULS installed on prototype of the girder. ULS has special nest for a 1.5 inch ball to provide alignment survey.

Figure 4: The general view of the ULS installation.

ULS electronics

The ULS electronics is located in separate module of Euromechanics 1U size. One module encloses electronics for three ULS sensors. The goal of the ULS electronics is to measure time intervals and to transfer them to the operating computer for calculation of actual accelerator module's positions.

Experimental Results

Test results of the ULS sensitivity are presented on Fig.5. For two sensors connected in hydrostatic level system test with dosed addition of water has been carried out. As result level steps of about 0.5μm were performed which were measured by the sensors (curves L1 and L2 on Fig.5). In calculated level difference signal there are only noise and spikes at moments of water addition.

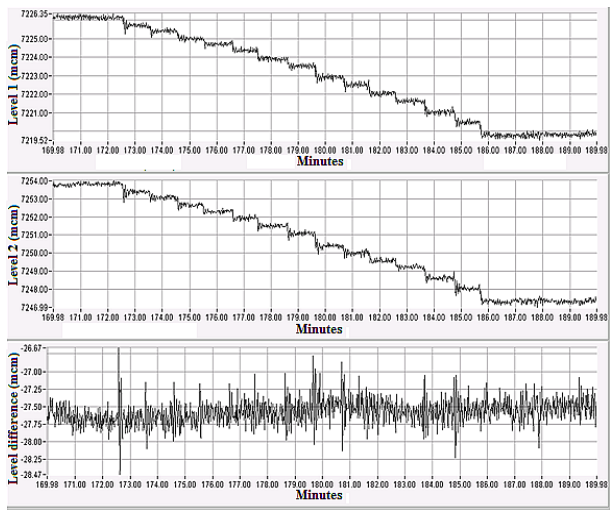

Figure 5: Test of the ULS sensitivity.

STRETCHED WIRE SYSTEM

General Description

Stretched wire system consists of stretched wire, wire position monitors and electronics. 150 m long stretched wire is passed through 140 wire position monitors attached with the accelerating modules and transportation line magnets. One end of the wire is loaded with a weight of 50 kG via roller installed in special girder (Fig.6).

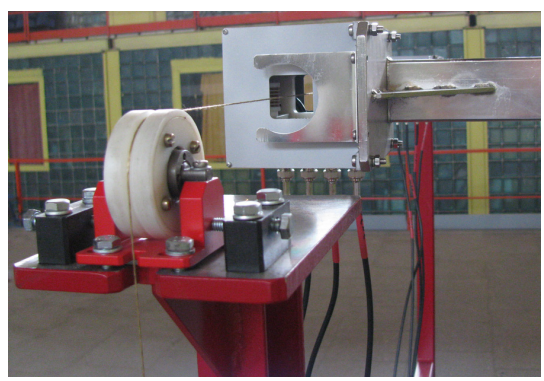

Figure 6: Load at the stretched wire end.

ISBN 978-3-95450-181-6

The wire is made of aramid thread (Fig.7). This material is able to withstand the load approximately the same as steel.

Figure 7: Stretched wire material.

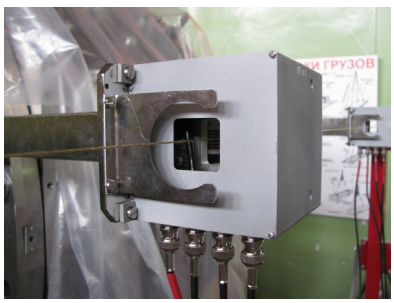

Figure 8: Wire position monitor on the acceleration module.

But its weight in 5 times less than steel. As a result wire sag in the middle of the 150 m long wire is only ~50 mm. 1 MHz sinusoidal current of 20-40 mA goes through the wire.

Two wire position monitors are attached to each acceleration module (Fig.8). Wire positions measurement relatively of these monitors gives us not only position of the acceleration module but its inclination angles in the cross directions and its rotation angle around the longitudinal axis.

Wire Position Monitor

The wire position monitor (WPM) consists of body, 4 coils located in horizontal and vertical planes and 4 BNC connectors (Fig.9).

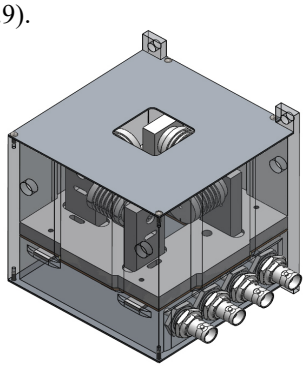

Figure 9: Wire position monitor.

An amplitude of 1 MHz signal induced in the coil ends is proportional to distance between the coil and stretched wire. After measurement of four coil voltages V_i then wire position is calculated with formulae:

$$X = K_{X0}\frac{V_1 - V_3}{V_1 + V_3}, \qquad Y = K_{Y0}\frac{V_2 - V_4}{V_2 + V_4},$$

where K_{X0}, K_{Y0} are WPM geometric coefficients.

Wire Position Electronics

Functional diagram of the wire position electronics is represented in Fig.10.

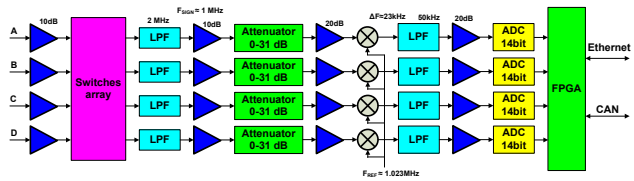

Figure 10: Functional diagram of the WPM electronics.

Electronics for one WPM consists of Switches array, 4 identical signal processing channels, FPGA Cyclone-3 of Altera firm, Ethernet interface and CAN interface. Use of the Switches array allows us to eliminate measurement error caused by inequality of the channels transmission coefficients.

Experimental Results

Two WPMs were installed on the accelerating module prototype. Continuous wire position measurements had been performed during a few days. Some results of these measurements are represented in Fig.11.

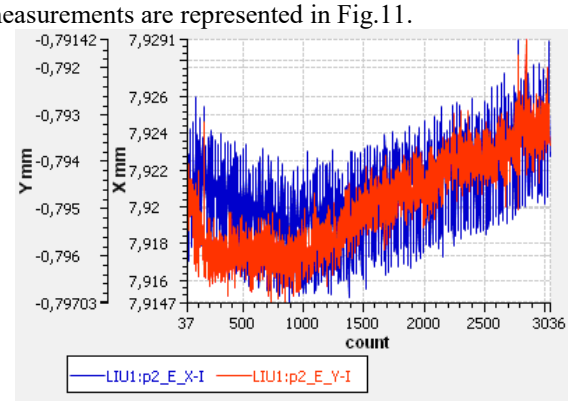

Figure 11: Results of continuous wire position measurements during ~1 hour.

An achieved resolution of the wire position measurements is about 1 micron.

SUMMARY

At present prototype of the accelerating module with installed on it hydrostatic level sensors and wire position monitors is successfully tested in BINP. The system demonstrates required accuracy parameters.

REFERENCES

[1] M. Shlösser, A. Herty, "High precision accelerator alignment of large linear colliders – vertical alignment". Proceedings of the 7th IWAA, Spring-8, 2002.

ISBN 978-3-95450-181-6

THE NEW CONTROL FOR MAGNET SYSTEM OF KSRS

E. Kaportsev, A. Valentinov, Yu. Krylov, K. Moseev, N. Moseiko, RRC Kurchatov Institute, Moscow, Russia

Abstract

The running cycle of Kurchatov Synchrotron Radiation Source (KSRS) includes the injection of electrons with energy 80 MeV from the linear accelerator in the booster storage ring Siberia-1, the accumulation of a electron current up to 400 mA and, then, electron energy ramping up to 450 MeV with the subsequent extraction of electrons in the main ring, storage ring Siberia-2, and accumulation there up to 300 mA, and at last the energy ramping up to 2.5 GeV. [1]

Several years ago, a modernization of the current system of automated control systems (ACS) has started. Modernization has affected the most important parts of the system - the system of data collection and monitoring system. Used advanced solutions based on CAN and VME and modular complexes National Instruments.

This article describes some of the features of the most important part of the control system - the controller of the magnetic system and software management environment.

APPOINTMENT OF ACS

The existing automated control system (ACS) accelerator-storage complex (UNK) "Siberia" - synchrotron radiation source and center of collective use NRC "Kurchatov Institute" was established over 20 years ago on the basis of the control equipment in the CAMAC standard. Currently, there is an active modernization and replacement of outdated equipment with new, modern and more productive. [2]

The control apparatus of the new ACS with integrated processors, as well as acquired powerful servers, the operator's computer and network equipment has developed software (software) at all levels of the ACS.

The control system of the magnetic system is one of the most important parts of the ACS. So far, the management system used obsolete equipment in the CAMAC standard, as well as outdated transformer type current sources controlled by the analogue signal.

We have improved the management of the magnetic system, setting a new high-performance controller, and using a new, more accurate current sources, controlled by a digital signal on the CANOpen standard.

CONTROL OF THE MAGNETIC SYSTEM

The magnetic system is controlled by a controller NI cRIO-9081 (Figure 1). In the chassis of the controller is installed one discrete I/O module NI 9425 and two double-channel CAN module NI 9853. To control the high-current and the low-current magnets control module uses two CAN network. One CAN network connected to smart crate-controller K167 [3] and CAN-DAC power supply units of the quadrupole lens and bending magnets of the accelerator. The second network, connect the power supply control units of the correction magnets of the accelerator.

Smart crate-controller K167 used to translate commands transmitted from magnetic controller via the CAN bus system into CAMAC commands. Management of the high-current sources of bending magnets and quadrupole lenses is performed by using a 20-bit DAC-20. Measurement of currents on the buses is performed by means of 20-bit ADC 20. All these units are installed in the CAMAC crate. For transmitting diagnostic signals (interlocks, errors) used CEDAC20 units installed in the power supply cabinet.

To control the current sources of the electron beam orbit correction system uses specialized correction control units (CCU). These blocks have been specifically designed by our employees. CCU provides translation of commands transmitted from the controller of the magnetic system via the CAN bus into CANOpen command. Each CCU manages the 16 th power supplies developed by a third party specifically for the needs of Kurchatov Institute.

DAC and ADC management teams made directly via the CAN bus, ie, values of DAC and ADC values are transmitted via the CAN bus. The mechanism works as follows: during the execution mode (magnetization reversal, injection, energy recovery) is carried out pre-entry table the estimated current values in the controller's memory. Then, on command from the old system, a magnetic system controller begins to record currents in the DAC current sources corresponding channels. Recording is carried out simultaneously with the record values RF parameters of the system, connected to the old control system.

SYNCRONIZATION WITH OLD ACS.

To synchronize the operation of the controller of the magnetic system with the old control system, we using one channel of the controlled registers in the crate CAMAC, and one channel of discrete input NI9425. The operator selects the desired mode of operation using the appropriate snap-in of the CitectSCADA system [4]. This command is transmitted to the RF generator control system, as well as the program for calculating of currents table. After all preliminary calculations have been made, the controller of the magnetic system is commanded to start through the channel of the register, and the process entering the into the synchronous mode.

ISBN 978-3-95450-181-6

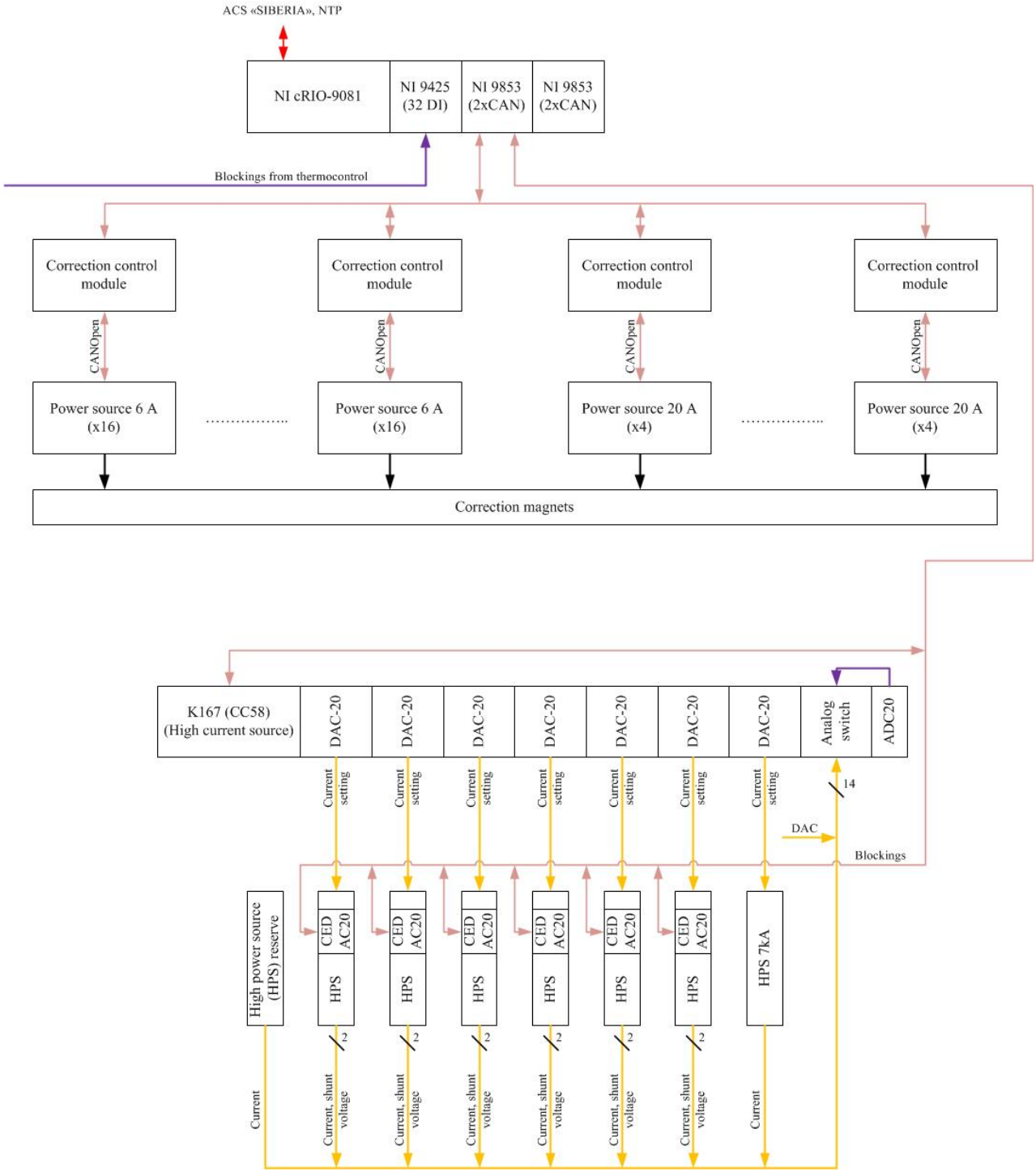

Figure 1: Block diagram of the magnetic system.

SOFTWARE

Low level Software of the magnetic system controller NI cRio-9081 is developed using an integrated development environment LabView (National Instruments). Management and integration of all the individual components of ACS is implemented by using CitectSCADA. The operator selects the desired screen form, in this case, "magnetic system", and make the necessary action - entry mode or manual control sources. Also here are displayed all the possible diagnostic and measuring channels are connected to the sources of supply of the accelerator magnets.

ISBN 978-3-95450-181-6

CONCLUSION

The new control system based on high-performance controller that allows you to simultaneously control the currents in power supplies, as well as to diagnose, measure currents on the buses, process the signals and blocking errors. In addition, this controller is modular, which allows to increase its capacity and number of controlled channels. It is planned to upgrade the RF generator control system, and the abandonment of the old system completely.

REFERENCES

[1] V.Korchuganov et al., The status of the facilities of Kurchatov's synchrotron radiation cource. Proceedings of RuPAC2014, Obninsk, Kaluga Region, Russia.

[2] E.Kaportsev et al., Modernization of the automated control system in the Kurchatov synchrotron radiation source. Proceedings of RuPAC XXIII, S.-Petersburg, Russia, 2012.

[3] L.Moseiko et al. INTELLECTUAL CRATE-CONTROLLER K167. Proceedings of RuPAC 2008, Zvenigorod, Russia.

[4] E.Kaportsev et al. Modernization of the automated control system in the Kurchatov synchrotron radiation source. Using SitectSCADA. Proceedeings of RuPAC XXXIV, Obninsk, Kaluga Region, Russia, 2014.

ISBN 978-3-95450-181-6

PRESENT STATUS OF VEPP-5 INJECTION COMPLEX CONTROL SYSTEM

F. Emanov*, D. Berkaev, D. Bolkhovityanov, P. Cheblakov , BINP, Novosibirsk, Russia

Abstract

VEPP-5 injection complex is being put into operation as beam source of VEPP-2000 and VEPP-4 colliders at the end of 2016. Its control system is being upgraded in order to reliably work with beam users and increase its manageability computer infrastructure was reconsidered to provide high availability and flexibility through virtualization of control servers. The paper presents architecture and implementation of complex computer infrastructure. A control software set based on CXv4, EPICS and VCAS frameworks under operating system Linux deals with a set of CAN, CAMAC and Ethernet specialized hardware. The software and hardware architecture and implementation is described.

INTRODUCTION

VEPP-5 injection complex [1] (IC) is linear accelerator based e+/e- beam source with a damping ring and transfer lines. IC is now being put into operation to provide beams for VEPP-2000 and VEPP-4 colliders. This requires continuous functioning of control system infrastructure and development of software for joint operation with colliders.

In order to ensure reliability of control system infrastructure and hence on the whole injection complex it is proposed to deploy separated network infrastructure and high availability cluster of control servers based on modern virtualization techniques.

Software structure principles for joint operation with beam users was proposed earlier [2] and then corrected according to development and operation experience.

CONTROL SYSTEM INFRASTRUCTURE INITIAL STATE

There is the following set of control system hardware at the beginning of work:

- 126 CAN DAC/ADC and other devices developed in BINP [4, 5, 6] connected via CANGW [3] embedded computers or dedicated desktop PC,
- 17 CAMAC crates with specialized electronic modules and fast ADCs, 1 cPCI crate with ADC200me [7]
- 8 Ethernet photo-cameras
- 15 Ethernet BPM processors [8]
- 5 RS-485 controllers connected via Moxa UC-7112-lx plus embedded computer
- 2 former control room workstations working as control system servers, 3 main control room workstations and 6 old PCs as control system terminals

All the Ethernet controllers are connected to dedicated controllers network, which is also connected to control system servers. PCs are connected to BINP network, which is currently used for communication between IC and colliders control systems. Hardware related issues are the following: lack of CANGW performance for some tasks, no reliability assurance for mission-critical devices and network connections (control servers, vacuum control, communications with beam users), complexity of infrastructure service and deployment of new devices. Historically injection complex computers were bare metal with Linux OS installed, and there were no network infrastructure services. Therefore, additional difficulty was to work around maintenance or failure of institution network infrastructure services.

INFRASTRUCTURE UPGRADE

The project

In order to solve the described above problems control system infrastructure upgrade was proposed with following outline:

- Replace network switches with managed ones and build VLANs for BINP network, controllers, computers and IPMI.
- Add direct optical links from IC network to beam users networks for operation data exchange.
- Deploy infrastructure servers for internal networks: 2 servers as hosts for general services, network boot servers and remote storage for operating systems, 2 Firewall servers.
- Create high-availability cluster of 4 control servers based on virtualization platform. 2 CAN servers (with 5 PCI/PCIe slots for CAN adapters) connected to the same CAN lines for reliability assurance, 2 Main control system servers directly connected to high volume shared storage for operation history data or other big data volume applications.
- Replace CAMAC-based stepper motor controllers with CAN ones. This is required due to incompatibility of old CAMAC controllers with managed switches.
- Replace old PC terminals with thin clients in order to reduce maintenance requirements.

The resulting sketch of control system infrastructure is shown on Fig. 1.

The implementation

In order to reduce the range of equipment we decided to use close Supermicro platforms for servers and control room workstations. Since some of servers have 10G

* F.A.Emanov@inp.nsk.su

ISBN 978-3-95450-181-6

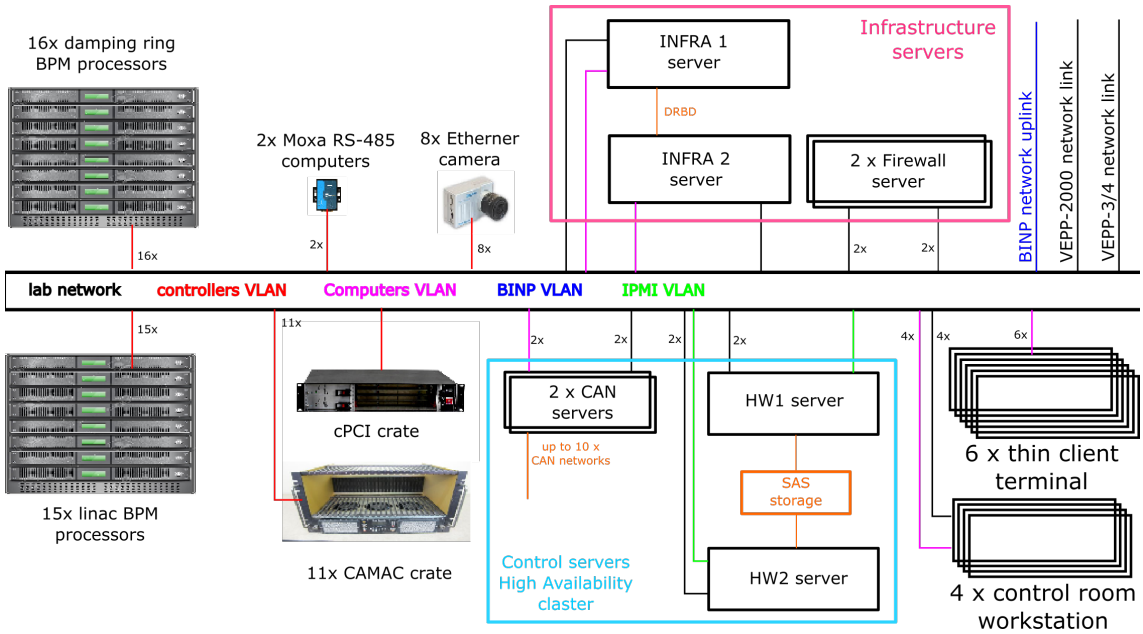

Figure 1: Injection complex control infrastructure layout.

network interfaces, 3 HPE-1950-24 are selected to build the network base, HPE-1920 series is used as peripheral switches. Raspberry Pi 2 is successfully tested for remote terminal role. Proxmox VE is selected as virtualization platform due to authors experience and easy enough management. KVM virtual machines are used now due to available live migration and authors experience while Linux Containers have better performance in some cases [10]. Virtual machines are deploying on per service group basis. There are 7 virtual machines now. Described infrastructure is under construction and only partially in operation.

CONTROL SYSTEM SOFTWARE

Injection complex software is currently based on three control system frameworks:

- CXv4 [11] serves most of complex equipment and transfers messages between applications.
- EPICS [12] serves some of complex equipment.
- VCAS [13] works with beam transfer lines hardware.

Injection complex software was earlier a set of CX and EPICS servers, drivers and basic GUI applications separately for each framework. In order to start regular operation a set of common instruments is required. Since all the mentioned above frameworks can run client software under Qt main loop common tools currently based on Qt framework.

CXv4 client libraries Python bindings were implemented in Cython in a high-level object-oriented way. Resulting Python module can run native CX main loop or use Qt 4/5 one (from PyQt). EPICS Python bindings working with PyQt4 were developed in Diamond Light Source [9]. Both these bindings are used to implement common CXv4 and EPICS control system applications.

CXv4 was selected for interprocess communications since it is easier to deploy than other used frameworks and we do not want to increase the range of used protocols.

The following control system tools were implemented:

- Configuration database and Django based management tools for simplification of software configuration.
- Machine mode service as joint tool to saving/restoring complex state to database.
- GUI tool for injection complex mode control.
- Machine loop service automating injection/extraction and based on synchronization hardware functions and machine mode service.

These instruments allowed us to start semi-automatic operation with colliders: automatic beam storage-transfer loop and manual particle type or beam consumer switching. This operation way is acceptable for initial injection complex and beam transfer lines tuning and collecting data for future automatic work. In order to implement fully automatic work it is required to create machine scheduler service, which will accept beam user requests and command by other services according to the most effective schedule. The resulting injection complex software structure is shown on Fig. 2.

There are two database tasks now: structured configuration information storage for different software and machine mode storage. First PyCDB [14, 15] was considered as a tool for configuration information management. Since PyCDB is not supported centralized configuration tools for high-level software were implemented with Django framework and Postgresql databases. Hardware and its servers and hardware control applications are now configured separatly in decentralized way.

ISBN 978-3-95450-181-6

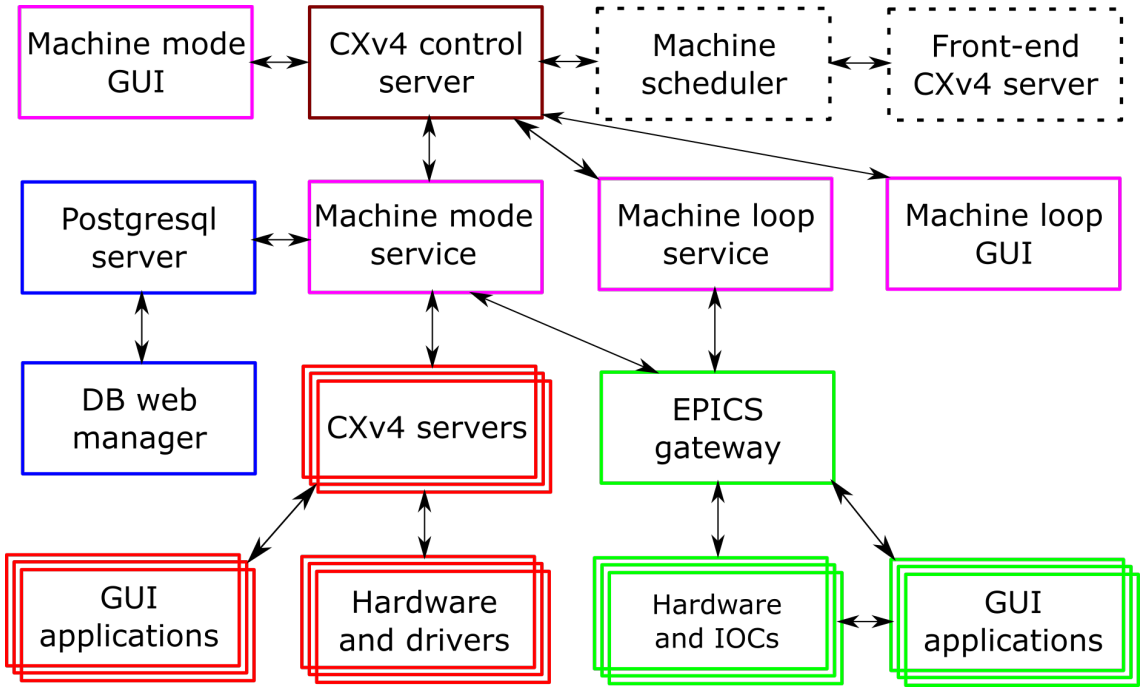

Figure 2: Injection complex software structure layout

CONCLUSION

Proposed and implemented control infrastructure and software is sutable for semiautomatic operation of VEPP-5 injection complex and data accumulation for further automatic techniques development.

REFERENCES

[1] Physical project VEPP-5. BINP SB RAS. 1995.

[2] F.A. Emanov et al., "Extending VEPP-5 control system by middleware for injection/extraction automation," Proceedings of RuPAC2014, Obninsk, Kaluga Region, Russia, THPSC25.

[3] V.R.Mamkin, P.A.Selivanov, "Can Bus Gateway For Data Acquisition And Control," RUPAC 2006, Novosibirsk, MODP01.

[4] V. Kozak, "Embedded device set for control systems. Implementation and applications," RUPAC 2006, Novosibirsk, THDO05.

[5] V.R. Kozak at el., "CEAC Controllers Family for Control of Power Supplies of Accelerator Facilities," Vestnik NSU. Series: Physics. 2012. V7, i 4.

[6] A. Batrakov at el., "Multimode Digital Integratiors for Precise Magnetic Measuremente" RUPAC 2012, Saint-Petersburg, Russia, WEPPD032.

[7] P. A. Bak at al., "Control System of a Linear Induction Accelerator of an X-Ray Complex: Structure, Hardware, and Test Performance," Optoelectron. Instrument. Proc., 2011, Vol. 47, No. 3, pp. 303312.

[8] G.V. Karpov, A.S. Styuf, "New Beam Position Monitor System for injection complex preinjector," Proceedings of the Russian Higher School Academy of Sciences, 2013, 2, p. 110-117.

[9] M. G. Abbott, T. M. Cobb, I. J. Gillingham, M. T. Heron, "Diverse Uses Of Python At Diamond," PCaPAC08, Ljubljana, Slovenia, TUP024.

[10] W. Felter, A. Ferreira, R. Rajamony, J. Rubio, "An Updated Performance Comparison of Virtual Machines and Linux Containers", IBM Research Report, RC25482 (AUS1407-001) July 21, 2014, Computer Science.

[11] D. Bolkhovityanov, P.B. Cheblakov, F.A. Emanov, "CXv4, a Modular Control System," ICALEPCS2015, Melbourne, Australia, WEPGF093.

[12] L.R. Daleslo et al., "The Experimental Physics and Industrial Control System architecture: past, present and future," ICALEPCS 1993, Berlin, Germany.

[13] A.Senchenko et al., "VEPP-2000 Collider Control System," Proceedings of PCaPAC2012, Kolkata, India, FRCB04.

[14] A. Makeev et al., "Centralized software and hardware configuration tool for large and small experimental physics facilities," Proceedings of ICALEPCS2013, San Francisco, CA, USA, TUPPC022.

[15] P.B. cheblakov, S. Karnaev, "Applicatin of PyCDB for K-500 beam transfer line," Proceedings of ICALEPCS2015, Melbourne, Australia, WEPGF095.

ISBN 978-3-95450-181-6

DEVELOPMENT AND IMPLEMENTATION OF THE AUTOMATION SYSTEM OF THE ION SOURCE FOR BNCT*

A.M. Koshkarev#, S.Yu. Taskaev, Budker Institute of Nuclear Physics, Novosibirsk, Russia and Novosibirsk State University, Novosibirsk, Russia
A.S. Kuznetsov, A.L. Sanin, V.Ya. Savkin, P.V. Zubarev, Budker Institute of Nuclear Physics, Novosibirsk, Russia

Abstract

To operate a source of negative hydrogen ions an automatic distributing control system was developed. This system consists of master controller (Slab C8051F120) and a set of peripheral local controllers (PLC) based on microcontroller Slab C8051F350. Using an optical link between PLC and master controller there was created a system resistant to high-voltage breakdown of the ion source.

To control the system, a special programming language has been created. It includes procedures for checking the necessary parameters, setting the value of the physical quantities to simplify the experiment, verifying the lock status and protection. This system provides two programmable timers, as well as procedures in emergency situations, such as: lack of water, poor vacuum. It can be operated in semi-automatic mode, if the script asks operator about preferable actions and then continues the script depending on the response. All scripts are performed in master controller, and this makes system very rapid (for example system response time is 1 ms).

INTRODUCTION

One of the most important stages in the development of new facilities is to automate and connect all control units together. To achieve this goal, the automation of power supply units in the new ion source injector was carried out. The ion source injector is located in a research facility BNCT [1]. This method of treatment is very effective against a number of currently incurable radioresistant tumors, such as glioblastoma multiforme and metastatic melanoma [2, 3]. Frequent changes of control commands and their parameters during experiments cause serious problems. Therefore, the scripting language consisting of control commands was developed. It allows operator to implement all sorts of automatic control algorithms and conduct experiments with minimal outer control. Automation, conducted within the framework of this work, simplifies significantly the operation of the facility.

SUBJECT AREA

The ion injector comprises several high-voltage power sources, temperature and vacuum level nodes, requiring remote control and data capture.

*Work supported by part by the Russian Science foundation (project no. 14-32-00006), the Budker Institute of Nuclear Physics and Novosibirsk State University.
#koshkarev_al@mail.ru

Power sources are controlled by identical and interchangeable modules of programmable logic controller (PLC), receiving commands from a personal computer through a switch. Each PLC has a microcontroller and several analog and digital channels, which are connected via serial interfaces SPI & I2C with the PLC microcontroller. The microcontroller allows operator to test devices on the board if they are connected with each other. In conditions of high electromagnetic noise the distributed control system with sufficient independence of modules increases the reliability of the entire control system.

The structure of the control system is shown in Fig. 1.

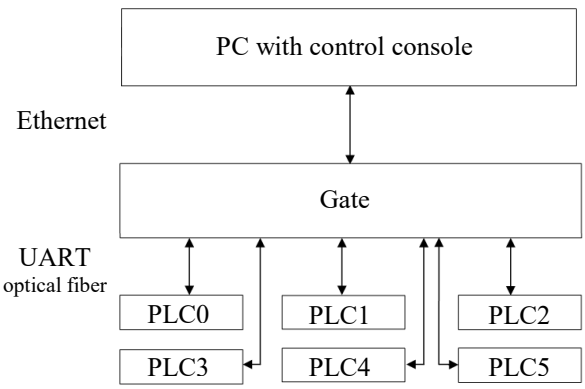

Figure 1: Structure of the control system.

ALGORITHMS

Commands are usually repeated during the experiment and for convenience to operator algorithm scenarios have been developed. Operator can create a certain set of commands once and then these commands can be repeatedly applied. Command can be as unconditional execution of some action, and also it can be a check of channel status. After checking it is possible to jump to another line in the scenario.

The switch algorithms allows user to apply two modes: manual and automatic. In manual mode, the operator can change the values of PLC. On the other hand, automatic mode allows user to run the script, which will perform the control over the experiment without operator. A block diagram of the basic algorithm is presented in Fig. 2.

The developed switch algorithms allow user to control automatically the ion source. Link between the management console and the switch is not required. Accordingly, if the operator console suddenly loses contact with the switch, the experiment will not stop, and the switch will continue to capture the critical parameters

ISBN 978-3-95450-181-6

of the experiment. If these values are exceeded, the switch takes some measures that were initially set by the user.

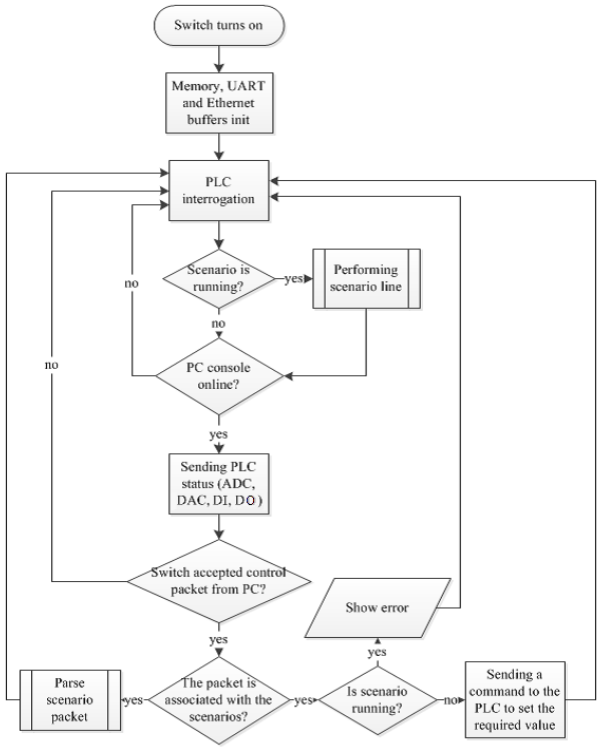

Figure 2: The basic algorithm of the switch.

SCENARIO

Scenarios – a set of strings that contain parameters such as the block number, channel number, the command, the value of the team and its priority.

The sequence of operations required depends on checking of states and transitions. Therefore, an internal control programming language was created – scripting language. To measure the time intervals the internal timer of microcontroller was used, which hosted four logical timers with a period of one millisecond. All script parameters are translated into physical quantities, so the operator can control experiment simply. Scenarios allow us to describe the action in emergency situations, such as a lack of cooling water, poor vacuum, etc. If this happens, the console informs the operator about the error. Scenario processes by the switch and that allows user to instantly respond to emergencies and not waste time waiting for a response from the PC.

Block number denotes the index card PLC, which will use certain equipment. The channel number indicates what kind of equipment can be used. User can choose ADC, DAC, digital inputs (DI, 1 bit ADC) or digital outputs (DO, 1 bit DAC). The command can be either set the value or values of the comparison device with the parameters specified by the user. Execution priority specifies how the command will be executed: normally, rapid or emergency. After the command with normal priority it is exhibited a delay in one second. Rapid command is executed without delay. Command checking emergency are executed before each execution line in the script: on stage startup script host controller stores the row numbers and emergency script before executing the next line in the script ensures rapid implementation of all emergency lines.

User has an opportunity to write the values in the array of intermediate calculations, for example for the implementation of various filters.

Automatic control is realized by algorithms which are stored as data files in the controller memory. Microcontroller has built-in memory, but depending on the complexity of the scenarios it may not be enough. To solve this problem, the anchor controller is equipped with an external memory to 32 KB.

For transmission lines in the script, you must first compile them using the built-in compiler, and only then operator can transmit control commands to the switch. All lines of the script have the same number of parameters. Each parameter – a signed 32-bit number.

HARDWARE

The programming code implements the developed algorithms and allows switch to receive pre-programmed in the console operator scenarios, to change values on the PLC through the console and send the values of recorded parameters to the operator. Program code was written in C language with the help of SiLabs utility.

THE SWITCH

The switch is a "bridge" between the Ethernet channel and the UART interface. It also processes its own programming language, which allows operator to organize the automatic control equipment. Switch hardware:

- microcontroller C8051F120;
- RAM memory K6X4008T1F 32 KB;
- Internet module CP2201;
- two-channel UART buffer SC16IS752.

THE PCL

The PLC board is used as a direct control unit, which interacts with high-voltage power sources. Every PLC contains 8 ADC (16 bit, 0-5 V), 4 DAC (16 bit, 0-10 V), 8 DI and 8 DO. Every PLC communicates with a switch through opto fiber lines. After the switch is turned on, it queries all PLC one by one. All data transfers between these devices according to a certain algorithm, which allows switch to send the unlimited length of the packet data. PLC hardware:

- microcontroller C8051F350;
- 8 16-bit ADC with a range from 0 to 5 V;
- 4 16-bit DAC with a range from 0 to 10 V;
- 16 optocouplers SFH628A;
- Instrumentation amplifiers INA129;
- 16 I / O ports I2C PCA9539.

ISBN 978-3-95450-181-6

PC CONSOLE

Control of source of negative ions is performed using the program created in LabView environment.

The program allows user to work on manual and automatic control. The user is provided with a special language that provides the implementation of various management scenarios, as well as the handling of emergencies.

The attendant console is implemented so-called "scenario editor", allowing user to create scenarios. The editor allows you to save the script in computer memory and load them into the program. It also allows you to select a control channel by its name. All names must be assigned to a special configurator, which is composed of the management console. Before sending the script to the switch user have to compilated it by program means. During compilation program check all the lines in the script, conversion of physical quantities in the codes for DAC / ADC and the conversion of all the rows in a clear view of the switch.

IMPLANTATION

The developed system has been successfully tested on stand without high voltage. Designed scenario worked for 3 hours. Testing algorithm consisted in that the inputs are shorted to the outputs. When value on output is set, program checks the value of the input.

However, after mounting the system showed some problems. Raising the voltage to 22 kV, switch starts to hang out.

The first step was connecting high frequency noise filter to avoid noise on power rail. It did not help, and on the next step the switch connected to the DC-AC converter from an external battery. It helped, but not much.

After the diagnosis of board components, has been found a fault in the quartz generator: its timing diagrams were very noisy and the component was soldered with nearby components. It also didn't get good result.

Because of features of media converter switch board has been connected to it via an Ethernet-switch, which was powered from the rack without filters. It was suspected that power noise passed through a switch to a switch via Ethernet cable. However, after connecting to an external periphery of the battery much change has not occurred.

The next step was to design grounded box for peripherals and switch board. But placing the apparatus into it allow operator to work twice longer. After that, in the switch watchdog timer have been activated, but it also does not give much result.

For further possibilities of the experiment it was proposed and implemented following solution: in the absence of a signal from the switch control program sends a reboot signal to the remote relay module ADAM 6066, connected to the switch. This solution is not ideal, because operator loses control of the experiment within 1-2 seconds, but it takes place, while our laboratory is looking for other solutions.

Now we are working on integration of hydrogen diagnostics and control.

RESULTS AND DISCUSSION

The developed and tested control system allows operator to perform experiments with minimal operator control. It improves the operational characteristics of the facility, including the protection of the patient from operator errors. At the same time this system allows operator to interact with the elements of the installation without much effort.

This system is easy to operate, so it is possible to integrate it into other hardware and control systems. Simplicity of replacing of burned-out modules allows to repair the ion source in a few minutes. Also, when you connect the adapter for PLC, which was developed earlier [4], it is possible to apply this management system in any other assigned. To control high voltage sources created and integrated system need to be upgraded. We are looking for opportunities to fix high voltage noise problem. With the help of temporary solution experiment can be carried out.

REFERENCES

[1] S. Taskaev, Phys. Particl. Nuclei 46 (2015) 956.
[2] W. Sauerwein et al., Neutron Capture Therapy: Principles and Applications, (Springer, 2012) 533.
[3] S. Taskaev, V. Kanygin, Boron Neutron Capture Therapy, (Novosibirsk: Publisher of SB RAS, 2016), 216.
[4] A.M. Koshkarev et al., "Development of automation system of the ion source", RUPAC 2014, Obninsk, Russia, Oct. 2014, THPSC28, p. 380 (2014).

ISBN 978-3-95450-181-6

STABILIZATION OF THE EQUILIBRIUM POSITION OF A MAGNETIC CONTROL SYSTEM WITH DELAY*

A.Yu. Aleksandrov†, A.P. Zhabko, I.A. Zhabko, Saint Petersburg State University, Saint Petersburg, Russia
A.A. Kosov, Matrosov Institute for System Dynamics and Control Theory of Siberian Branch of Russian Academy of Sciences, Irkutsk, Russia

Abstract

A model of magnetic suspension control system of a gyro rotor is studied. A delay in the feedback control scheme and dissipative forces occurring due to energy losses at the interaction of the magnetic field with currents in the control loops are taken into account. Two approaches to the synthesis of controls stabilizing the equilibrium position of the considered system are proposed. The results of a computer simulation are presented to demonstrate effectiveness of the approaches.

INTRODUCTION

Nonlinear oscillatory systems are widely used for the modeling charge particles motions in cyclotrons in neighborhoods of equilibrium orbits [1–3]. They are also applied for the analysis and synthesis of magnetic control devices [4, 5]. In particular, magnetic systems of retention of power gyro rotors are used in modern control systems of spacecraft orientation with long periods of autonomous operation. An actual problem for such systems is stabilization of their operating modes.

It is worth mentioning that realistic models of numerous control systems should incorporate delay in feedback law [6]. It is well-known that delay may seriously affect on system's dynamics. Therefore, it is important to obtain restrictions for delay values under which stability can be guaranteed.

In this paper, analytical and numerical investigations of stability of the equilibrium position for a nonlinear oscillatory system are presented. The system can be treated as a mathematical model of magnetic suspension control system of a gyro rotor [5]. A delay in the feedback control scheme and dissipative forces occurring due to energy losses at the interaction of the magnetic field with currents in the control loops are taken into account.

Two approaches to the synthesis of stabilizing controls are proposed. With the aid of a computer simulation of dynamics of closed-loop systems, a comparison of these approaches is fulfilled, and their features and conditions of applicability are determined.

* The research was partially supported by the Saint Petersburg State University (project No. 9.37.157.2014), and by the Russian Foundation for Basic Research (grant Nos. 15-08-06680-a and 16-01-00587-a).

† a.u.aleksandrov@spbu.ru

ISBN 978-3-95450-181-6

STATEMENT OF THE PROBLEM

Consider the control system

$$\begin{cases} \ddot{x}(t) - p(x(t), y(t))y(t) = u_x, \\ \ddot{y}(t) + p(x(t), y(t))x(t) = u_y. \end{cases} \quad (1)$$

Here $(x(t), y(t))^T$ is the state vector, u_x and u_y are control variables, and function $p(x, y)$ is defined by the formula

$$p(x, y) = \alpha + \beta(x^2 + y^2),$$

where α and β are constant parameters. Thus, the considered system is affected by non-conservative forces and control ones. Equations of the form (1) are used, for instance, for modeling rotor dynamics in magnetic suspension system [5].

In the present paper, we will assume that $\alpha = 0$, and non-conservative forces are generated in the electromechanical system with a certain delay $\tau \geq 0$. The reason for arising the delay is an inertia in response of the magnetic suspension control system on rotor deviations from the equilibrium position. It should be noted that the value of delay might be unknown. In addition, we will assume that the system is affected by a dissipative force $(F_x, F_y)^T$ depending only on the velocities.

Thus, the rotor dynamics is described by the equations

$$\begin{cases} \ddot{x}(t) - \beta\left(x^2(t-\tau) + y^2(t-\tau)\right) y(t-\tau) \\ \qquad + F_x(\dot{x}(t), \dot{y}(t)) = u_x, \\ \ddot{y}(t) + \beta\left(x^2(t-\tau) + y^2(t-\tau)\right) x(t-\tau) \\ \qquad + F_y(\dot{x}(t), \dot{y}(t)) = u_y. \end{cases} \quad (2)$$

We assume that initial functions for solutions of (2) belong to the space $C^1([-\tau, 0], R^2)$ of continuously differentiable functions $\varphi(\theta) = (\varphi_x(\theta), \varphi_y(\theta))^T : [-\tau, 0] \to R^2$ with the uniform norm

$$\|\varphi\|_\tau = \max_{\theta \in [-\tau, 0]} \left(\|\varphi(\theta)\| + \|\dot{\varphi}(\theta)\|\right),$$

and $\|\cdot\|$ denotes the Euclidean norm of a vector.

For the desired position of the rotor axis we have $x = y = 0$. It is known, see [7], that if $\tau = 0$ and $u_x = u_y = 0$, then the equilibrium position

$$x = y = \dot{x} = \dot{y} = 0 \quad (3)$$

of system (2) is unstable. Therefore, we should to design a feedback control law stabilizing the equilibrium position.

In the present paper, we will study the stabilization problem for two types of dissipative forces:

(i) linear forces;

(ii) nonlinear homogeneous forces.

SYNTHESIS OF STABILIZING CONTROLS

First, consider the case where dissipative forces are linear ones. Then system (2) takes the form

$$\begin{cases} \ddot{x}(t) - \beta\left(x^2(t-\tau)+y^2(t-\tau)\right)y(t-\tau) \\ \qquad +b_{11}\dot{x}(t)+b_{12}\dot{y}(t)=u_x, \\ \ddot{y}(t) + \beta\left(x^2(t-\tau)+y^2(t-\tau)\right)x(t-\tau) \\ \qquad +b_{21}\dot{x}(t)+b_{22}\dot{y}(t)=u_y. \end{cases} \quad (4)$$

Here $b_{11}, b_{12}, b_{21}, b_{22}$ are constant coefficients such that the matrix $B = \{b_{ij}\}_{i,j=1}^{2}$ is positive definite.

With the aid of the approach proposed in [8, 9], we obtain that the following theorem is valid.

Theorem 1 *Let*

$$u_x = -\frac{\partial \Pi(x(t),y(t))}{\partial x}, \quad u_y = -\frac{\partial \Pi(x(t),y(t))}{\partial y}. \quad (5)$$

Here $\Pi(x,y)$ *is an arbitrary positive definite homogeneous form of the forth order. Then the equilibrium position* (3) *of system* (4) *is asymptotically stable for any* $\tau \geq 0$.

Remark 1 Theorem 1 remains valid in the case where there is a delay in the feedback law, i.e., where

$$u_x = -\frac{\partial \Pi(x(t-\tau_1),y(t-\tau_1))}{\partial x},$$

$$u_y = -\frac{\partial \Pi(x(t-\tau_1),y(t-\tau_1))}{\partial y}.$$

Here $\tau_1 = \text{const} > 0$.

Next, consider the case where system (2) is of the form

$$\begin{cases} \ddot{x}(t) - \beta\left(x^2(t-\tau)+y^2(t-\tau)\right)y(t-\tau) \\ \qquad +b_1\left(\dot{x}^2(t)+\dot{y}^2(t)\right)^{\gamma}\dot{x}(t)=u_x, \\ \ddot{y}(t) + \beta\left(x^2(t-\tau)+y^2(t-\tau)\right)x(t-\tau) \\ \qquad +b_2\left(\dot{x}^2(t)+\dot{y}^2(t)\right)^{\gamma}\dot{y}(t)=u_y. \end{cases} \quad (6)$$

Here b_1, b_2 and γ are positive parameters. Thus, we assume that dissipative forces are essentially nonlinear and homogeneous ones.

Using the results of [8–10], we arrive at the following theorem.

Theorem 2 *Let*

$$u_x = g\beta\dot{y}(t), \qquad u_y = -g\beta\dot{x}(t), \quad (7)$$

where $g = \text{const} > 0$. *If* $0 < \gamma < 1$, *then the equilibrium position* (3) *of system* (6) *is asymptotically stable for any* $\tau \geq 0$.

Remark 2 Condition $0 < \gamma < 1$ of Theorem 2 is essential one. Really, if $\gamma = 1$, $\tau = 0$, and $b_1 = b_2 = \beta = 1/g > 0$, then the corresponding system (6) closed by control (7) admits the following family of solutions:

$$x(t) = c\sin t, \quad y(t) = c\cos t,$$

where c is an arbitrary constant. Hence, the equilibrium position (3) of the system is not asymptotically stable.

RESULTS OF A NUMERICAL SIMULATION

The results of a computer simulation are presented in Figs. 1–4. It is assumed that $\beta = 1$, $b_{11} = b_{22} = 1$, $b_{12} = b_{21} = 0$, $b_1 = b_2 = 1$, $\gamma = 1/2$, $\tau = 1$. Initial conditions of solutions are chosen as follows: $t_0 = 0$, $\varphi_x(\theta) = \varphi_y(\theta) = 0.25$, $\dot{\varphi}_x(\theta) = \dot{\varphi}_y(\theta) = 0$ for $\theta \leq 0$.

First, consider system (4) closed by the control

$$u_x = -10x^3(t), \qquad u_y = -10y^3(t). \quad (8)$$

According to Theorem 1, Fig. 1 illustrates stabilization process.

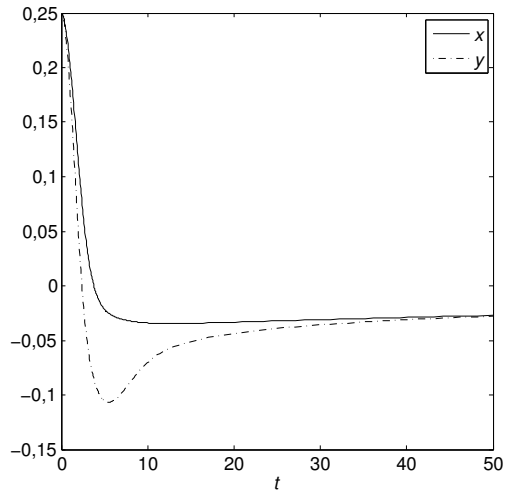

Figure 1: State response of system (4) closed by control (8).

Next, consider system (4) with a control of the form (7). Let

$$u_x = 0.242\dot{y}(t), \qquad u_y = -0.242\dot{x}(t). \quad (9)$$

In this case, Fig. 2 demonstrates unstable behavior of the solution.

In Fig. 3, trajectory of the solution of system (6) closed by the control

$$u_x = \dot{y}(t), \qquad u_y = -\dot{x}(t) \quad (10)$$

is shown. The figure demonstrates the effectiveness of Theorem 2.

Finally, consider system (6) closed by a control of the form (5) with a delay in the feedback law. Let

$$u_x = -100x^3(t-1.05), \quad u_y = -100y^3(t-1.05). \quad (11)$$

Figure 4 shows that the corresponding solution does not converge to the origin as $t \to +\infty$.

ISBN 978-3-95450-181-6

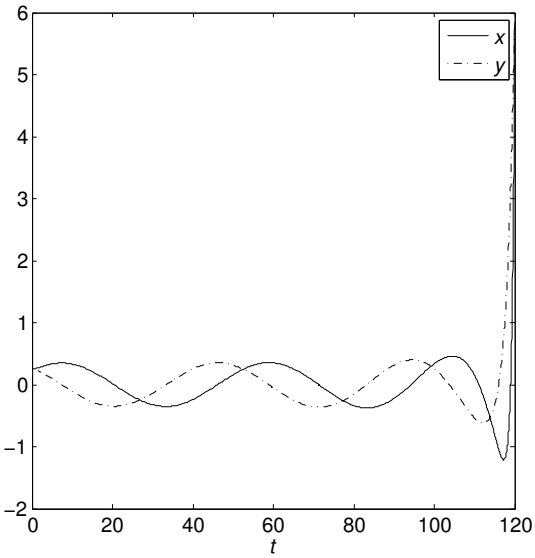

Figure 2: State response of system (4) closed by control (9).

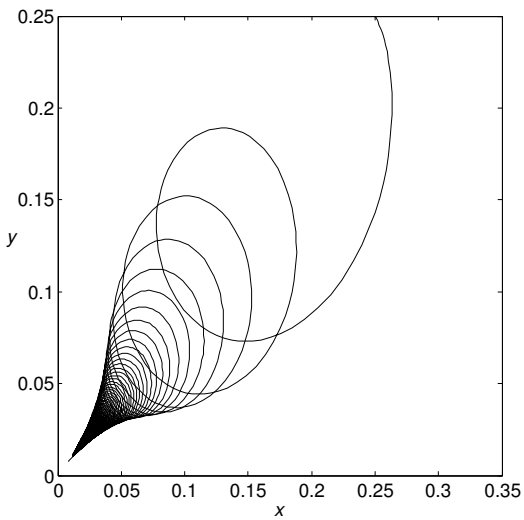

Figure 3: The trajectory of system (6) closed by control (10).

CONCLUSION

In the paper, two approaches to the synthesis of stabilizing controls are proposed for a nonlinear oscillatory system with time delay. The first one is based on the using of potential control forces. It is applicable in the case of linear dissipative forces. The second approach is efficient for systems with essentially nonlinear homogeneous dissipative forces. For this case, gyroscopic control forces are constructed. It should be noted that the application of the proposed approaches provides asymptotic stability of the corresponding closed-loop systems for any nonnegative delay.

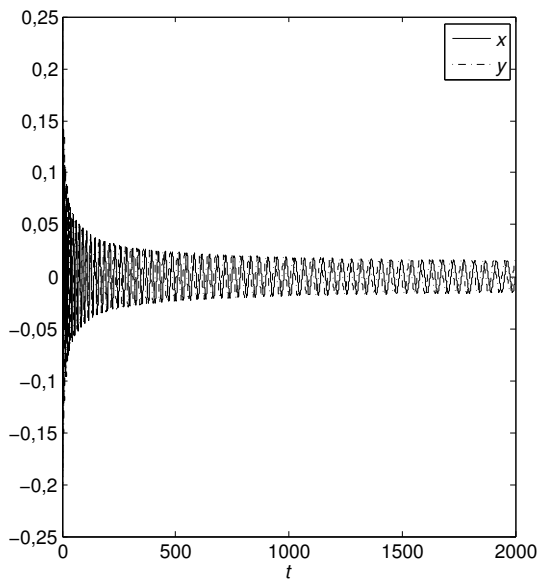

Figure 4: State response of system (6) closed by control (11).

REFERENCES

[1] R.C. Davidson and H. Qin, Physics of Intense ChargedParticle Beams in High Energy Accelerators, (Singapore: World Scientific, 2001).

[2] A. Blaquiere, Nonlinear Systems Analysis, (New York: Academic Press, 1966).

[3] D.A. Ovsyannikov, Modeling and Optimization of Charged Particle Beam Dynamics, (Leningrad: Leningrad State University, 1990).

[4] K. Halbach, "Application of permanent magnets in accelerators and electron storage rings," J. App. Phys. 57 (1985) 3605.

[5] R.F. Post, "Stability issues in ambienttemperature passive magnetic bearing systems," Lawrence Livermore National Laboratory, Technical Information Department's Digital Library, February 17, 2000, http://e-reports-ext.llnl.gov/pdf/237270.pdf

[6] K. Gu, V.L. Kharitonov and J. Chen, Stability of Time-Delay Systems, (Boston, MA: Birkhauser, 2003).

[7] V.M. Matrosov, The Method of Vector Lyapunov Functions: Analysis of Dynamical Properties of Nonlinear Systems, (Moscow: Fizmatlit, 2001).

[8] A. Aleksandrov, G.-D. Hu and A. Zhabko, "Delay-independent stability conditions for some classes of nonlinear systems," IEEE Transactions on Automatic Control 59 (2014) 2209.

[9] A. Aleksandrov, E. Aleksandrova and A. Zhabko, "Asymptotic stability conditions and estimates of solutions for nonlinear multiconnected time-delay systems," Circuits, Systems, and Signal Proc. 35 (2016) 3531.

[10] A. Y. Aleksandrov, A. P. Zhabko and A. A. Kosov, "Analysis of stability and stabilization of nonlinear systems via decomposition," Siberian Math. J. 56 (2015) 968.

ISBN 978-3-95450-181-6

SOFTWARE AND COMPUTATIONAL INFRASTRUCTURE OF LIA-20 CONTROL SYSTEM

A. Senchenko#, G. Fatkin, S. Serednyakov, BINP SB RAS and Novosibirsk State University, Novosibirsk, Russia
P. Selivanov, BINP SB RAS, Novosibirsk, Russia

Abstract

The linear induction accelerator LIA-20 for radiography is currently under construction at Budker Institute of Nuclear Physics.

This paper presents software architecture and computational infrastructure for the accelerator controls. System and application software are described. Linux operating system is used on PC and embedded controllers. Application software is based on TANGO. Overall data transfer rate estimations are provided.

LIA-20 PROJECT

Linear Inductor Accelerator LIA-20 is designed to provide three electron bunches with energy up to 20 MeV, current up to 2 kA and lateral size after focusing on the target less than 1 mm. It is planned to provide three consecutive bunches, with one of them divided into 9 angles. The accelerator will be used for the flash X-Ray radiography.

LIA-20 consists of the injector, 30 "short" accelerating modules (SAM) and 12 "long" ones (LAM). Injector generates beam with the energy up to 2 MeV. SAM increases the energy by 0.33 MeV and LAM increases the energy by 0.66 MeV. The total length is about 75 meters. Structure is described in detail in [1].

Control units are placed along the installation. All units are based on uniform VME crate and connected via Ethernet.

DATA RATES

All channels could be divided into following groups:

Fast. All measurements faster than 10 us: voltage on inductor, currents on lenses and beam position monitor.

Slow. This group includes measurements with duration up to several milliseconds (charging device, degaussing current).

Timing. These channels provide all devices with proper start pulse.

Interlock. These channels belong to subsystem that prohibit experiment in case of component malfunction or failure.

Technological controls. This group incorporates vacuum controls, optical system alignment [4], control of power supplies.

First four groups are bound to machine cycles, while the last one is continuous.

Tables 1 present the summary of channels and data rates. Estimations are provided for one-bunch cycle.

COMPUTATIONAL INFRASTRUCTURE

Computational infrastructure components are distribute across two areas: control room and experimental hall (see Fig.1). Control rack and operators PC are located in control room. Control rack is equipped with two server, UPS and 24 port switch. The switch provides connectivity between server, UPS, operator's PC and experimental hall switch. All VME crates are located in experimental hall and connected via two switches. Description of components are provided below.

Server:

- CPU 2.0 GHz, Cores 4
- Intel x86-64
- RAM 32GB
- Gigabit Ethernet
- 4TB SCSI
- RAID 5

VME Crate Controller:

- PowerPC - based
- Diskless network boot

Operator's PC:

- CPU 2.2, Cores 4
- Intel x86-64
- RAM 4GB
- Up to 4 monitors

Table 1: Data Rates Estimation

Channel type	Number of channels		Data rate	
	whole system	per VME crate	whole system	per VME crate
Fast	594	22	5.7 MB/cycle	214 KB/cycle
Slow	1485	55	13.5 MB/cycle	0.5 MB/cycle
Timing	1485	55	13.5 KB/cycle	0.5 KB/cycle
Interlock	1485	55	13.5 KB/cycle	0.5 KB/cycle
Technological control	1000	~40	513 KB/min	19 KB/min
	6000	~280	19.3 MB/cycle + 540 KB/min	3.5 MB/cycle + 19.5 KB/min

#a.i.senchenko@inp.nsk.su

ISBN 978-3-95450-181-6

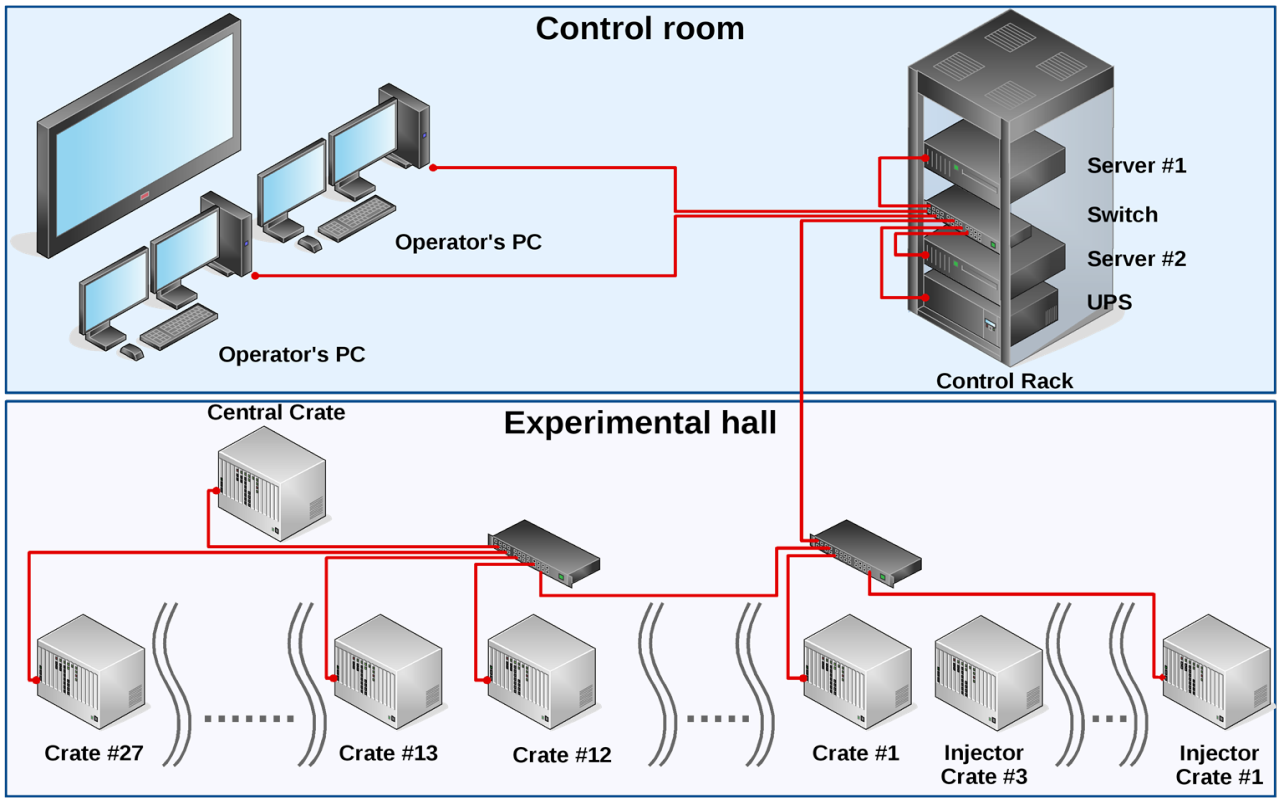

Figure 1: LIA-20 computational infrastructure layout.

SYSTEM AND APPLICATION SOFTWARE

System Software

Experience of BINP facilities shows that use of isolated virtual environment facilitate maintenance while keeping resources overhead at acceptable level. It was decided to provide dedicated virtual machines(VMs) for different services and subsystems.

VM#1 is used for network boot. Kernel image is served via TFTP. Controller' file systems exported on NFS.

VM#2 hosts Tango(see below) specific services: TANGODB and Sardana.

Additional VM could be easily provided on demand.

It is necessary to reduce number of upgrades during development phase and to freeze changes before commission. That why it seems rational to use OS distribution with long term support (LTS).

Server:
Ubuntu LTS
VM:
Ubuntu LTS
Operator's PC:
Ubuntu LTS
Controller:
Debian

Application Software

Experience of LIA-2[2] shows that use of widely-used control system software could reduce costs. Taking into account that LIA-20 is more sophisticated than LIA-2 it could crucial.

After some studies it was decided to use TANGO controls. A lot tools (like rapid UI prototyping, Archive service, macros) are available out-of-the-box or in the form external library.

Application software consists of following layers:

IO abstraction layer. The bottom layer. There are libraries that provide access to CANBus, VME and hide implementation details.

Device Driver layer. This layer is a set of libraries (user-space drivers) that implement interaction with particular device and facilitate re-use.

Low-Level TangoDevices. This layer consists of TangoDevices that wrap Device Drivers and expose them to Tango. They are arranged in tango servers by underlying bus type.

High-level TANGO devices. The topmost layer. Tango Devices and user applications that control subsystems rather than particular device.

There are two types of user application: “engineer” and “operator's”. The first one provides access to “raw” tango-device. It is designed for developing and testing purposes. The second one is high-level application that interacts with multiple tango-devices and hides implementation details. The software scheme is illustrated in Fig. 2.

ISBN 978-3-95450-181-6

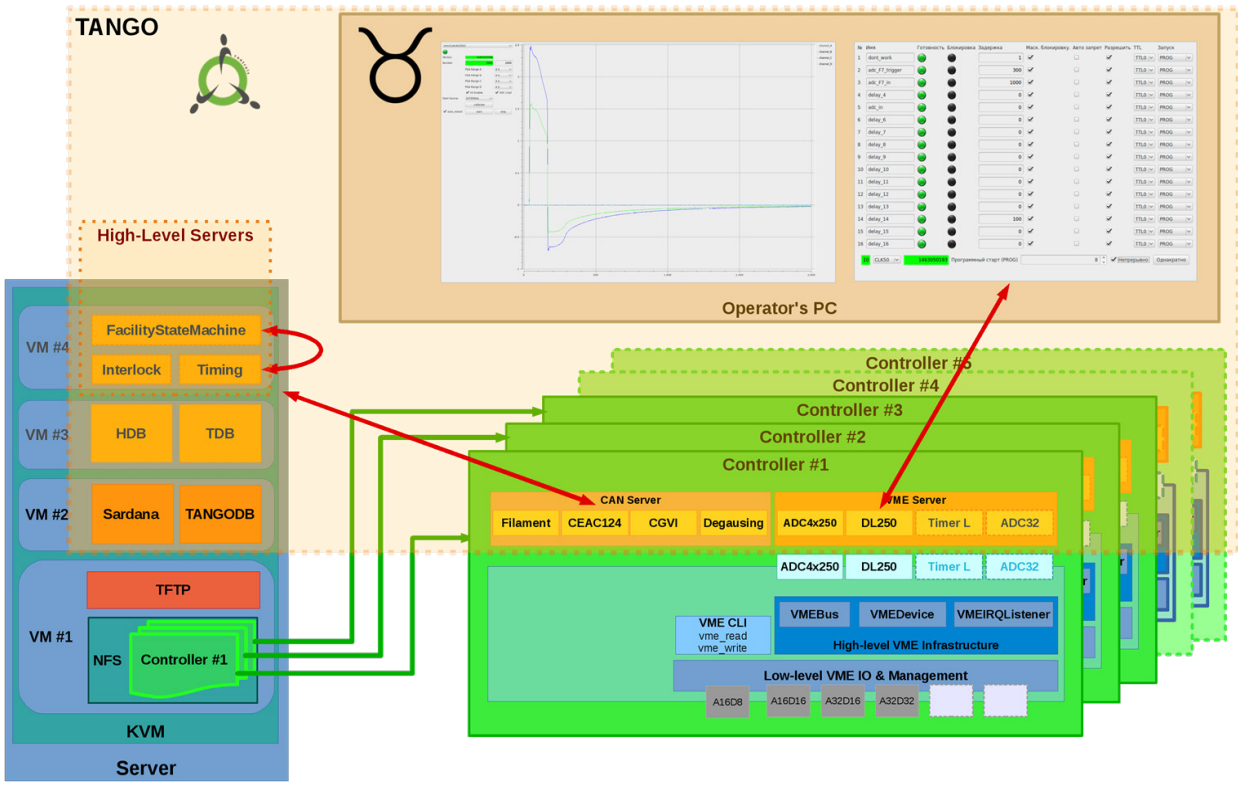

Figure 2: LIA-20 software scheme.

To date, tango-devices (with underlying drivers) and engineering user application are provided for ADC4x250VME [3], DL-250VME, and for majority of CANBus devices.

CONCLUSION

Next step is assembling of LIA-5 – the 5 MeV linear accelerator with all control system elements. It requires to not only minimal viable software but high-level tango-devices also. Other important tasks arise – infrastructure management software (cabling database), machine modelling software and integration of proven LIA-2 data analysis system [5].

REFERENCES

[1] G. Fatkin et al. "Structure and hardware of LIA-20 control system" THCBSH02, these proceedings.
[2] Bak P. A. et al., "Control system of a linear induction accelerator of an X-ray complex: Structure, hardware, and test performance", Optoelecron. Instrument. Proc., 2011, Vol. 47, No. 3, pp. 303-312.
[3] E. Kotov et al. "VME Based Digitizers for Waveform Monitoring System of Linear Induction Accelerator (LIA-20)", THPSC081, these proceedings.
[4] A. Chupyra and E. Bekhtenev "System of Geodetic Measurements for LIA-20" THPSC083, these proceedings.
[5] Data analysis system of a radiographic complex based on a LIA-2 accelerator Fatkin, G.A. 2015 Optoelectronics, Instrumentation and Data Processing.

ISBN 978-3-95450-181-6

THE STOCHASTIC CHARACTERISTICS STABILITY IN THE PROBLEM OF OBSERVATION AND ESTIMATE OF THE CHARGED PARTICLES MOVEMENT

M. Chashnikov, Saint Petersburg State University, Saint-Petersburg, Russia

Abstract

The charged beam moving in the accelerator is modelled by particle-in-cell method. The control with delay in the connection canal is simulated by the after-effect. Thus, the model is described by system of the differential equations with delay. We observe and estimate changes of particles coordinates in the cross-section of the accelerator. It is supposed that initial conditions are the set with random error and we have chance of updating the solution in periodic timepoints with the same error. The dependence between the estimate dispersion and the measuring error dispersion is recieved.

INTRODUCTION

Consider a beam of charged particles, moving in the accelerator. We research them by particle-in-sell method. Suppose that the problem is to calculate the coordinates in the transverse section of the accelerator.

We'll linearize the equations, describing one of the large particles movement. Herewith we add a delay in the system. In such way we'll simulate the control with delay in the connection canal [1].

Thus the dynamic of the beam coordinates will be described by the linear equations system with delay:

$$\dot{z}(t) = Az(t) + Bz(t-h), \qquad (1)$$

where A, B nonsingular 2x2 constant matrices,

$$z(t) = \begin{pmatrix} x_1(t) \\ x_2(t) \end{pmatrix}$$

is the vector of the beam coordinates in the cross-section of the accelerator. The solution of the equation is uniquely determined by the initial function $\varphi(t)$, defined on the interval $[-h; 0]$.

Suppose we can measure the initial position of the beam with some error. We'll designate by $\hat{z}(t)$ the solution with measured initial values $\hat{\varphi}(t)$, $t \in [-h; 0]$, and consider its difference with the exact solution.

$$\bar{z}(t) = z(t) - \hat{z}(t)$$

The value of the error is obviously depending on the measuring error of the initial value, which is equal

$$\bar{\varphi}(t) = \varphi(t) - \hat{\varphi}(t)$$

We suppose that the measuring error is a centered random variable and that the errors of the components measuring aren't depending on each other. Thus, $\bar{\varphi}(t)$ on $[-h; 0]$ is a centered random vector with the covariation matrix $\sigma^2 I$.

Now we'll build the upper limit of the covariation matrix $D(\bar{z}(t))$ as a function of t for $t > 0$. We note, that for each A, B, z there is

$$\left\|\sqrt{AA^{\mathrm{T}}}z\right\| \geq \|Az\|, \left\|\sqrt{BB^{\mathrm{T}}}z\right\| \geq \|Bz\|.$$

Because of the positive definiteness of the matrices $\sqrt{AA^{\mathrm{T}}}$ and $\sqrt{BB^{\mathrm{T}}}$, if we put them into (1) instead of A, B, then each component $\dot{z}(t)$ will have the same sign as the corresponding component $z(t)$, and it means that the module of each component is monotonicaly increasing on $t > 0$, and $\|z(t)\|$ is increasing too. Thus, if we change the equation (1) with

$$\dot{w}(t) = \left(\sqrt{AA^{\mathrm{T}}} + \sqrt{BB^{\mathrm{T}}}\right)w(t), \qquad (2)$$

we get the function, which is the upper limit of the solution of the system (1). At each moment it will be a random vector, and its covariation matrix norm will be larger than the covariation matrix norm of the system (1) solution.

OBSERVATION WITH CORRECTION

Consider the set of the moments $n\tau$, then the solution of (2) at these moments is given by the formula $w(n\tau) = \Phi_n w(0)$, where $\Phi_n = e^{\left(\sqrt{AA^{\mathrm{T}}}+\sqrt{BB^{\mathrm{T}}}\right)n\tau}$.

The covariation matrix of $w(n\tau)$ is:

$$D\big(w(n\tau)\big) = \Phi_n \sigma^2 I \Phi_n^{\mathrm{T}} = \sigma^2 \Phi_n \Phi_n^{\mathrm{T}} = \sigma^2 \Phi_n^2$$

because of the symmetry of the matrix Φ_n. Because of the positive definiteness of the matrix Φ_n^2 matrix its spectral norm is equal its largest eigenvalue $e^{2\lambda n\tau}$, where λ is the largest eigenvalue of the matrix $\sqrt{AA^{\mathrm{T}}} + \sqrt{BB^{\mathrm{T}}}$. If we want to bound the error dispersion of $\bar{z}(t)$, we can bound the function $M(t) = \left\|D\big(w(t)\big)\right\|$.

Suppose on each segment $[n\tau - h, n\tau]$, $\tau = const$, $\tau > h$, $n = 1,2, \ldots$, we can measure the values of $z(t)$ with the error dispersion σ^2. Then we have 2-dimensional case of the dynamic filtration, described in [2].

Suppose this correction will be made not surely, but with the probability, which means that $M(t)$ will be a stochastic function. At each moment $n\tau$ we can calculate its expectation value $E\big(M(n\tau)\big)$ and the dispersion $D\big(M(n\tau)\big)$. Thus, the function $M(t)$ is left-continuous function and it increases on each segment $(n\tau, (n+1)\tau]$, and then it begin to increase from the value σ^2.

Let p is chance of correction response at any moment $n\tau$, $n = 1,2, \ldots$ Denote $q = 1 - p$, $E_n = E\big(M(n\tau)\big)$, $D_n = D\big(M(n\tau)\big)$, $Y_n = \sigma^2 e^{2\lambda n\tau}$. It is obvious that the set of possible values E_n is $\{Y_i\}_{i=1}^n$.

STOCHASTIC CHARACTERISTECS STABILITY

Lemma 1

E_n is monotonically increasing by n.

ISBN 978-3-95450-181-6

Proof

Notice that expectancy $P\{M(n\tau-0)=Y_i\}$ is $q^{i-1}p$ for $i=\overline{1,n-1}$ and it equals q^{i-1} for $i=n$.

Therefore,

$$E_n = q^{n-1}Y_n + \sum_{i=1}^{n-1} q^{i-1}p\,Y_i$$

$$= q^{n-1}\sigma^2 e^{2\lambda n\tau} + p\sigma^2 e^{2\lambda\tau}\sum_{i=0}^{n-2}\left(qe^{2\lambda\tau}\right)^i$$

Hence,

$$E_{n+1}-E_n = \sigma^2\left(q^n e^{2\lambda(n+1)\tau} - q^{n-1}e^{n\alpha\tau} + pe^{2\lambda\tau}\left(qe^{2\lambda\tau}\right)^{n-1}\right)$$

$$= \sigma^2\left(q^n e^{2\lambda(n+1)\tau} - e^{2\lambda n\tau}(-q^{n-1}+pq^{n-1})\right).$$

Having regard to $q^{n-1}+pq^{n-1}=q^n$ and $a\tau>0$, we arrive to

$$E_{n+1}-E_n = \sigma^2 q^n e^{2\lambda n\tau}\left(e^{2\lambda\tau}-1\right) > 0. \blacksquare$$

Lemma 2

D_n is monotonically increasing by n.

Proof

We have

$D_n = \sum_{i=1}^{n-1} q^{i-1}p\,(Y_i-E_n)^2 + q^{n-1}(Y_n-E_n)^2$,

hence

$D_{n+1}-D_n = \sum_{i=1}^{n} q^{i-1}p\,(Y_i-E_{n+1})^2 + q^n(Y_{n+1}-E_{n+1})^2 - \sum_{i=1}^{n-1} q^{i-1}p\,(Y_i-E_n)^2 - q^{n-1}(Y_n-E_n)^2$

$$= \sum_{i=1}^{n-1} q^{i-1}p\,(Y_i-E_n)^2 + q^{n-1}(Y_n-E_n)^2$$

$$+ \sum_{i=1}^{n} q^{i-1}p\;\Delta E^2 - 2\sum_{i=1}^{n} q^{i-1}p(Y_i-E_n)\Delta E$$

$$+q^n(Y_{n+1}-E_{n+1})^2 - \sum_{i=1}^{n-1} q^{i-1}p\,(Y_i-E_n)^2$$

$$-q^{n-1}(Y_n-E_n)^2$$

Since

$2\Delta E[\sum_{i=1}^{n} q^{i-1}p(Y_i-E_n) + q^{n-1}(Y_n-E_n)] = 0$,

and

$\sum_{i=1}^{n} q^{i-1}p\;\Delta E^2 = \Delta E^2(1-q^n)$,

where $\Delta E = E_{n+1}-E_n$, we have

$D_{n+1}-D_n = \Delta E^2(1-q^n) + q^n\Delta E^2 - 2q^n(Y_{n+1}-E_n)\Delta E + q^n(Y_{n+1}-E_n)^2 + q^{n-1}p(Y_n-E_n)^2$

$$+2\Delta E q^n(Y_n-E_n) - q^{n-1}(Y_n-E_n)^2$$

$$= q^n[(Y_{n+1}-E_n)^2 - (Y_n-E_n)^2]$$

$$-2q^n\Delta E[(Y_{n+1}-E_n)-(Y_n-E_n)] + \Delta E^2$$

$$= q^n(Y_{n+1}-Y_n)(Y_{n+1}+Y_n-2E_n) - \Delta E^2$$

$$= \Delta E(Y_{n+1}+Y_n-2E_n-\Delta E)$$

$$> \Delta E(Y_{n+1}-E_n-\Delta E) = \Delta E(Y_{n+1}-E_{n+1}) > 0. \blacksquare$$

Theorem

The sufficient condition for the stability of the solutions $E\big(M(t)\big)=0$ and $D\big(M(t)\big)=0$ for $\sigma^2=0$ on $[0,\infty)$ is the inequality $4\lambda\tau < \ln\frac{1}{q}$.

Proof

For any t exists such n that $E\big(M(n\tau)\big) > E\big(M(t)\big)$ and $D\big(M(n\tau)\big) > D\big(M(t)\big)$. That's why we consider only the moments $n\tau$.

If $2\lambda\tau < \ln\frac{1}{q}$, then $\lim_{n\to\infty} E\big(M(n\tau)\big) = \frac{\sigma^2 pe^{2\lambda\tau}}{1-qe^{2\lambda\tau}} = \bar{E}$.

If $4\lambda\tau < \ln\frac{1}{q}$, then

$\lim_{n\to\infty} D\big(M(n\tau)\big) = \sigma^4\left(\frac{pe^{4\lambda\tau}}{1-qe^{4\lambda\tau}} - \frac{p^2e^{4\lambda\tau}}{\left(1-qe^{2\lambda\tau}\right)^2}\right) = \bar{D}$, as it was shown in [3].

According to Lemma 1 and Lemma 2, $E\big(M(t)\big) < \bar{E}$ and $D\big(M(t)\big) < \bar{D}$. That's why for any ε if $\sigma^2 < \min\left\{\frac{\varepsilon}{\bar{E}}, \sqrt{\frac{\varepsilon}{\bar{D}}}\right\}$, then $E\big(M(t)\big) < \varepsilon$ and $D\big(M(t)\big) < \varepsilon$. ■

Example

In Fig. 1 we see the example of concrete realization of stochastic process for values $\sigma^2=1$, $\tau=1$, $\lambda=1/2$. Correction works at points $t=1$, $t=3$.

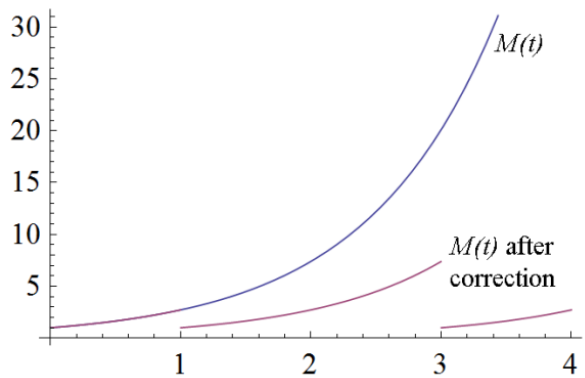

Figure 1: Plot of $M(t)$ before and after correction.

CONCLUSION

We obtain the sufficient conditions of the stochastic characteristics stability for system (1). If this inequality is satisfied, then our estimate is not far from the exact solution.

REFERENCES

[1] A.P. Zhabko, O.N. Chizhova, "Razumikhin Approach to Analyses of the Differential-difference Systems with Linearly Increasing Time-delay", 20th International Workshop on Beam Dynamics and Optimization, 2014.

[2] P. Eiyasberg, "Solution of Motion after Measuring Results", Moscow: Nauka, 1978 (Russian).

[3] V. Chashnikova, "The Statistic Model of the Complex Measuring System", Dep. VINITI no. 7604-B at 31.10.1985 (Russian).

ISBN 978-3-95450-181-6

ISBN 978-3-95450-181-6

List of Authors

Bold papercodes indicate primary authors

— A —

Abbaslou, M. **TUPSA057**
Afonin, A.G. **MOZMH02**
Agapov, N.N. THCDMH03, FRCAMH01
Ageev, A.I. THZMH01
Agguiaro, D. TUZMH03
Ahmanova, E.V. WEPSB059, WEPSB060
Akishin, P.G. THCDMH03
Aktershev, Yu. TUPSA001
Akulinichev, S.V. WEPSB045
Aleinikov, V.V. THPSC004
Aleksandrov, A.Yu. **THPSC087**
Aleksandrov, V. **THPSC013**
Alexandrenko, V.V. TUPSA058
Alexeev, N.N. **WEYMH01**, TUPSA060
Alexey, P.G. TUPSA027
Alfeev, A.V. FRCAMH01
Alimov, A.S. WECDMH01
Altmark, A. **WEPSB018**, WEPSB069
Altsybeyev, V.V. WECAMH05, **TUPSA062**, **WEPSB001**, WEPSB013
Amberg, M. WECBMH01
Amerkanov, D.A. THCAMH01, TUCASH04, THPSC075
Amoskov, V.M. THPSC006, **THPSC007**, THPSC012
Anashin, V.S. WECDMH02, THCAMH01
Anashin, V.V. TUYMH03, WECBMH02, TUPSA001, THPSC017
Anchugov, O. FRCAMH05, THPSC074
Andelkovic, Z. WEPSB002
Andreev, A. WEYMH01
Andreev, E.N. THPSC012
Andreev, V. FRCAMH01
Andreeva, T.A. **THPSC066**
Andreeva, Z. WECDMH03
Andrianov, A.V. WEXMH01, TUPSA001
Andrianov, S.N. **WECAMH01**, **WEPSB023**
Andrighetto, A. WEYMH02
Ang, Z.T. THZMH02
Anghel, A. THCDMH01
Anthony, L.S. WEYMH02
Antipkin, N.R. WEPSB053
Antipov, Y. **THYMH01**
Antoniazzi, L. TUZMH03
Antonov, A.V. TUCASH05
Antonov, A.Yu. **TUPSA063**
Antropov, I.V. **TUPSA017**, **WEPSB024**
Arbuzov, V.S. TUXMH02, TUCAMH02
Artamonov, S.A. **THCAMH01**, **TUCASH03**, TUCASH04
Artemenko, S.N. TUPSA031
Aseev, V.N. **TUPSA016**
Asfari, Z. TUPSA059
Ashanin, I.A. THCAMH05, WEPSB053
Astrelina, K.V. WEXMH01
Au, T. TUPSA034
Aulenbacher, K. WECBMH01, WEPSB039
Averyanov, G.P. **WEPSB003**, **WEPSB004**
Avreline, N.V. **TUPSA027**, **TUPSA034**
Avvakumova, I.L. WEPSB024, WEPSB028
Azaiez, F. WEYMH02
Azaryan, N.S. THCBSH04

— B —

Baard, S. WEYMH02
Babin, A.V. WEPSB051
Baglin, V. THPSC017
Bagrov, V.G. **TUCBMH02**
Bakhmutova, A.V. **WEPSB065**
Bakirov, L.R. THCAMH01
Balabaev, A. TUPSA060
Balabanov, M.Yu. **WEPSB011**
Balabin, A.I. WEPSB073
Balakin, V.V. WEXMH01, **THPSC074**
Balalykin, N. TUPSA003
Baldin, A.A. WEPSB078
Baldo, A. TUZMH03
Baluev, A.O. THCBSH02
Barabin, S.V. FRCAMH02
Bark, R.A. WEYMH02
Barminova, H.Y. WEPSB008, WEPSB009
Barnard, A.H. WEYMH02
Barnyakov, A.M. WEXMH01, **TUPSA068**
Barth, W.A. WECBMH01, TUPSA026
Bartlett, C.D. TUPSA034
Barzakh, A.E. THCAMH03
Bashmakov, Y.A. WEPSB032
Basten, M. WECBMH01
Batin, V. FRCAMH01
Batist, L.Kh. THCAMH03
Batrakov, A.M. THCBSH02, TUPSA001, THPSC023, THPSC030, THPSC081
Battistello, A. TUZMH03
Baturin, S. WEPSB069
Baturitski, M.A. THPSC041
Bazanov, A.M. THPSC018, FRCAMH02, FRCAMH03
Bazarov, A.M. **THPSC006**, THPSC007
Bazhanov, P. V. WEPSB051
Bazyl, D.B. TUCASH02
Beck, D. WEPSB002
Bedrina, M.E. THPSC066
Bekhtenev, E.A. WECBMH02, THCBSH02, THPSC061, THPSC083
Belikov, O.V. WEXMH01, TUPSA001, **THPSC019**, **THPSC020**, **THPSC021**, THPSC023, THPSC078
Belkov, A. TUCBMH01

ISBN 978-3-95450-181-6

Belonogaya, E.S. TUPSA049
Belov, A. FRCAMH01, FRCAMH02
Belyakov, V.A. THPSC006, THPSC007, THPSC012
Benedikt, M. **TUYMH01**
Benediktovitch, A.I. **TUPSA052**
Berkaev, D.E. TUYMH03, WEXMH01, WECBMH02, TUPSA001, THPSC015, THPSC016, THPSC074, THPSC085
Berlev, A.I. WEPSB078
Bezuglov, V.V. THCAMH02, **THPSC008**
Bleile, A. THCDMH04
Blinov, M.F. WEXMH01, TUPSA001
Blokhina, K.A. WEPSB075
Boettcher, J. THPSC082
Bogdanov, A.V. TUPSA020
Bogdanov, I. THZMH01
Bogdanovich, B.Y. WEPSB056
Bogomolov, A.S. TUPSA032
Bogomolov, S.L. WEYMH03, TUPSA059
Boimelshtain, Y.M. WEXMH01
Bolkhovityanov, D. WEXMH01, THPSC085
Bondarchenko, A.E. **TUPSA058**, **TUPSA059**
Bondarenko, T.V. TUCASH02, TUPSA025, TUCBSH01
Borin, V.M. **THPSC052**
Borisov, V.V. THCDMH03, THPSC005, THPSC010, THPSC042, **THPSC043**
Borotto Dalla Vecchia, F. TUZMH03
Bottin, P. TUZMH03
Boudagov, Ju. THCBSH04
Bräuning-Demian, A. WEPSB002
Bragin, S. TUPSA016, THPSC053
Brüning, O.S. TUYMH02
Broodryk, J.I. WEYMH02
Brovko, O.I. FRCAMH01, FRCAMH05
Bruker, M.W. WEPSB039
Bryazgin, A.A. THCAMH02, THPSC008
Bryzgunov, M.I. WECAMH04, WECBMH02, WEPSB039, WEPSB040, THPSC061
Bubley, A.V. **WEPSB040**
Budkin, V.A. WEPSB003, WEPSB004
Bugaev, V.V. FRCAMH01
Bukharov, A.V. **WEPSB077**
Bulanov, A.V. **TUPSA009**, **TUPSA010**
Bulanov, V. A. THPSC024
Burini, F. THPSC028
Burov, A.V. WEPSB022
Busch, M. WECBMH01
Butenko, A.V. FRCAMH01, FRCAMH05, FRCAMH07, TUPSA028, TUPSA038, WEPSB037, THPSC018, THPSC041, **FRCAMH02**, **FRCAMH03**
Bychkov, A.V. THCDMH03
Bychkov, A.V. THPSC005, THPSC010, THPSC043
Bykov, E.V. **THPSC023**
Bykov, T.A. THCEMH01, **THPSC080**
Bylinskii, I.V. TUPSA034

— C —

Calzolaio, C. THCDMH01
Cao, L. TUPSA047
Chai, W.P. FRCAMH06
Chakin, I. TUPSA018, THPSC035
Chashnikov, M.V. **THPSC090**
Cheblakov, P.B. THPSC085
Chen, Q.S. **TUPSA047**, WEPSB043, THPSC003, THPSC044, **THPSC045**
Chepurnov, A.S. TUPSA071, THPSC036
Cherepkov, V.G. THPSC035
Chermoshentsev, D.A. **THPSC055**
Chernousov, Y.D. **TUPSA006**, **TUPSA007**, **TUPSA008**
Chernov, A.N. TUCASH03
Chernov, K.N. TUXMH02
Chernyakin, A.D. THPSC022
Chiggiato, P. THPSC017
Chikhachev, A.S. **WEPSB008**, **WEPSB009**
Chizhova, O.N. **TUPSA024**
Chorniy, O. THPSC061
Chubunov, P.A. THCAMH01
Chupyra, A.G. WEXMH01, THCBSH02, **THPSC083**
Churaev, M.M. **THPSC059**
Churanov, D. THPSC027
Colombo, A.G. TUZMH03
Conradie, J.L. **WEYMH02**
Cornell, J.C. WEYMH02

— D —

Danilova, I. THPSC071
Davidyuk, I.V. TUXMH02, **TUPSA054**
De Villiers, J.G. WEYMH02
Deichuli, O.I. TUXMH02
Dementiev, E.N. THPSC062
Dementyev, E.N. TUXMH02
Demsky, M.I. TUCASH02, WEPSB057
Denisov, A.P. WEPSB040
Di Girolamo, B. **TUYMH02**, **THCBSH04**
Dietrich, J. **WEPSB039**
Dikansky, N.S. WEXMH01
Dishman, R. WEPSB052
Dmitriev, S.N. WEYMH03
Dokutovich, V. **THPSC022**
Dolbilov, G.V. **WEPSB033**
Domarov, E.V. THPSC035, THPSC072
Donets, D.E. FRCAMH01
Donets, D.E. FRCAMH02, FRCAMH03
Donyagin, A.M. THCDMH03, THPSC005, THPSC010, THPSC042, THPSC043
Dorokhov, V.L. THPSC052, THPSC074
Dovbnya, A.N. **WEPSB047**
Dovzhenko, B.A. TUXMH02, TUPSA001
Drivotin, O.I. **TUPSA013**, **TUPSA014**, **WEPSB020**
Drozdovsky, A.A. **TUPSA020**
Drozdovsky, S.A. TUPSA020

ISBN 978-3-95450-181-6

Du Plessis, H. WEYMH02
Duckitt, W. WEYMH02
Dughera, G. TUZMH03
Dulatov, I.T. TUPSA014
Durkin, A.P. TUPSA015, WEPSB001
Dyomina, A.A. THPSC012
Dyubkov, V.S. **TUPSA011**, **WEPSB032**
Dziuba, F.D. TUPSA026, **WECBMH01**

— E —

Eckoldt, H.-J. THPSC019, THPSC020, THPSC021
Edamenko, N.S. WECAMH01, WEPSB015, WEPSB023
Efanov, M.V. **THCEMH20**
Efanov, V.M. THCEMH20
Egorov, N.V. TUPSA064, TUPSA066, TUPSA067
Eliseev, A.A. TUCASH02
Eliseev, A.V. FRCAMH01, FRCAMH05
Emanov, F.A. **WEXMH01**, TUPSA001, THPSC074, **THPSC085**
Emeljanov, M.A. THCAMH05, TUCASH05
Engelko, V.I. TUPSA062
Ermakov, A.N. **WECDMH01**
Esakov, I.I. WEPSB063
Eseev, M.K. **WECAMH02**, WEPSB059, WEPSB060, WECAMH03

— F —

Fadeev, A.M. WEPSB049, WEPSB050
Fadeev, S. TUPSA018, THPSC035, THPSC072
Fagotti, E. **TUZMH03**
Faillace, L. TUCASH01
Faktorovich, B.L. THCAMH02, THPSC008
Fan, K. TUPSA047, THPSC003, THPSC038
Fan, M. WEPSB043, THPSC003, THPSC038, THPSC045
Fateev, A.A. FRCAMH05, WEPSB037, THPSC013, **THPSC024**
Fatkin, G.A. **THCBSH02**, THPSC081, THPSC088
Fatkina, A.I. **WEPSB025**
Fedorov, D.V. THCAMH03
Fedorova, A.N. **WEPSB019**, **WEPSB026**
Fedotova, S. WEPSB002
Feng, G. WEPSB043
Ferrari, L. TUZMH03
Feschenko, A. THXSH01, **TUZMH02**, THCBSH01, TUPSA004, THPSC055
Fetzer, R. TUPSA062
Fialkovsky, A.M. **THPSC068**
Filippovich, V.P. **WEPSB063**
Fimushkin, V.V. FRCAMH01, FRCAMH02
Fink, R.L. WEPSB052
Fischer, E.S. **THCDMH04**
Fomin, Y.A. TUCBMH01, **WEPSB010**, WEPSB016
Fong, K. THZMH02
Fourie, D.T. WEYMH02
Frolov, A.R. WEXMH01, WEZMH02
Frolov, B.A. **TUPSA061**, **THPSC031**
Frolov, O.T. THPSC053
Frolov, S.A. WEPSB048

— G —

Gaidash, V. THPSC058
Galchuck, A.V. THCAMH05, TUCASH04, TUCASH05
Galimov, A.R. THCDMH03, THPSC018, THPSC042
Gall, B.J.P. TUPSA059
Galyamin, S.N. **TUPSA049**, WEPSB034, WEPSB068, **WEPSB069**
Gambaryan, V.V. TUPSA001, **THPSC014**, THPSC047
Gao, J. **MOZMH01**
Gapionok, E.I. THPSC006
Gardiner, P.G. WEYMH02
Gavrilin, R. TUPSA020
Gavrilov, S.A. **THCBSH01**, TUPSA016, THPSC055, **THPSC058**, THPSC059
Gavrilov, Y.K. WEPSB045
Gavrish, Yu.N. THCAMH04, THCAMH05, **TUCASH04**, TUCASH05
Gayde, J. THCBSH04
Geithner, W. WEPSB002
Gerbershagen, A. THCDMH01
Getmanov, Ya.V. TUXMH02, **TUPSA050**
Gettmann, V. WECBMH01
Giacchini, M.G. TUZMH03
Gikal, B. **WEYMH03**, WECDMH02, WEPSB038
Giraudo, G. TUZMH03
Gitman, D.M. TUCBMH02
Glagolev, V.V. THCBSH04
Glukhih, V.A. THPSC012
Glukhov, S.A. **FRCAMH08**, **WEPSB014**
Gmyrya, A.A. THPSC032, WEPSB075
Gnutov, P.A. THCAMH05, WEPSB053
Golkovsky, M. TUPSA018
Golovenskiy, B.V. FRCAMH02, FRCAMH03
Golovkina, A.G. **WEPSB055**, **WEPSB067**
Golubenko, Yu.I. THPSC035
Golubev, A. WEPSB065
Golubitsky, O. THCDMH03, THPSC005, THPSC010, THPSC042, THPSC043
Golubkov, E.A. TUPSA002, TUPSA019, THPSC082
Golubovski, S.E. THPSC053
Goncharov, A.D. WEZMH02, WEPSB040
Gorbachev, E.V. FRCAMH01, THPSC024
Gorbachev, Ya.I. TUXMH02
Gorbunov, V.A. THCAMH02
Gorbunov, V.K. THPSC058
Gorelyshev, I.V. FRCAMH01, **WEPSB041**
Gorev, S.A. **TUPSA031**
Gorev, V.V. **WEPSB070**
Gorkin, G.I. THPSC075
Gotman, V. THPSC079
Govorov, A. FRCAMH01, FRCAMH02, FRCAMH03
Gracheova, A.Yu. WEPSB063

ISBN 978-3-95450-181-6

Grebentsov, A.Yu. FRCAMH01
Grekhov, O.V. THPSC053
Grespan, F. TUZMH03
Gribov, Y. THPSC006, THPSC007
Grigorenko, S.V. THCAMH04, THCAMH05, TUCASH04, TUCASH05
Grigoreva, A.A. TUPSA049, WEPSB068, **WEPSB034**
Grigoriev, V.I. THCAMH04, THCAMH05, TUCASH05
Grigoryev, I.P. THCAMH05, WEPSB053
Gromov, M.B. TUPSA071
Gryzlov, A.V. TUPSA010
Gubin, V. **TUPSA018**, **THPSC046**, **THPSC047**
Guchkin, A.S. THCAMH05, **WEPSB053**
Gulbekyan, G.G. WEYMH03, WECDMH02, WEPSB038
Gurov, D. WECBMH02
Gurskiy, S. THYMH02
Gusarova, M. TUCASH02, **TUPSA028**, THPSC041
Gusev, I.A. THPSC029, THPSC030
Gusev, Ye.A. WEXMH01, THPSC023

— H —

Harisova, A.E. TUPSA051
He, X.Y. WEPSB043
Heidbrook, N. THPSC019, THPSC020, THPSC021
Heilmann, M. WECBMH01
Henrist, B. THPSC017
Herfurth, F. WEPSB002
Hess, R. WEPSB002
Hilinov, V.I. WEPSB059, WEPSB060
Hoeltermann, H. FRCAMH03
Hofmann, A. WEPSB039
Hogan, M.E. WEYMH02
Hong, Y. WEPSB043
Horodek, P. WEPSB060, WEPSB059
Hu, T. TUPSA047, WEPSB043, THPSC044, THPSC045
Huang, G. WEPSB043
Huang, J. **THPSC003**, THPSC037, THPSC038, THPSC045

— I —

Iakushkin, O.O. WEPSB025
Igumnov, V.S. TUPSA031
Ikryanov, I.M. TUPSA007
Il'inskiy, A.V. WEPSB056
Ilich, R.D. WEPSB045
Iluhina, N.V. WEPSB063
Ionidi, V.Y. TUPSA071, THPSC036
Isaev, A.A. WEPSB056, **WEPSB074**, THPSC025
Isaev, I.I. TUPSA035
Ivanenko, I.A. **THPSC004**
Ivanov, A.A. THCEMH01
Ivanov, A.V. WEPSB075
Ivanov, E.M. THPSC075
Ivanov, E.M. WEZMH01, THCAMH01, TUCASH03, TUCASH04
Ivanov, E.V. FRCAMH01, **THPSC056**
Ivanov, G.N. THPSC004
Ivanov, I.A. TUPSA058
Ivanov, Ivanov, N.A. THPSC075
Ivanov, S.M. WEPSB049, WEPSB050
Ivanov, S.V. **TUZMH01**
Ivanov, V.S. THCAMH03
Ivashchuk, O.O. THPSC036

— J —

Jakovljevic, B. TUPSA034
Jia, D. WEPSB043
Jin, K. WEPSB043
Junginger, T. THZMH02

— K —

Kalagin, I.V. WEYMH03, WECDMH02, **WEPSB038**, WEPSB044
Kalaturskaja, E.V. TUPSA064
Kalinichenko, M.A. WECDMH03
Kalinin, Y.Z. TUPSA004, THPSC058
Kalinina, Z.A. WEPSB063
Kalmykov, A.V. THPSC082
Kamerdzhiev, V. WECAMH04
Kanareykin, A. WEPSB018
Kantsyrev, A.V. TUPSA020, WEPSB065
Kaparkova, M. THPSC007
Kaplii, A.A. THPSC036
Kaportsev, E.V. TUCBMH01, THPSC026, THPSC054, THPSC063, **THPSC084**
Karamyshev, O. THYMH02
Karamysheva, G.A. THYMH02
Karpinsky, V. THCDMH03, FRCAMH01, FRCAMH05
Karpov, A.G. THPSC049
Karpov, G.V. WEXMH01, THPSC083
Karpushov, A.N. THPSC077
Kasaev, A.S. TUYMH03, WEXMH01, WECBMH02, **THPSC015**, **THPSC016**
Kasatov, D.A. THCEMH01, WEPSB075, THPSC032, THPSC033, THPSC034, THPSC069, THPSC070, THPSC080
Kashtanov, E. THZMH01
Kats, M.M. **THCAMH06**
Kayukov, A.S. TUPSA002, THPSC082
Kazarinov, N.Yu. **WEPSB044**
Keir, J.J. THZMH02
Kenzhebulatov, E. TUCAMH02, TUYMH03
Khankin, V.V. WECDMH01
Khodzhibagiyan, H.G. **THCDMH03**, THCDMH04, FRCAMH01, FRCAMH05, FRCAMH07, THPSC005, THPSC010, THPSC018, THPSC042, THPSC043
Khomutova, V.O. WEPSB024
Khrisanov, I.A. TUPSA060
Khrushchev, S.V. TUCAMH01
Kii, T. THPSC067

ISBN 978-3-95450-181-6

Kim, J.-W. TUPSA018, THPSC046
Kim, J.Y. TUPSA018, THPSC046
Kirichenko, A. FRCAMH01
Kiselev, V.A. FRCAMH05, TUPSA001, THPSC052
Kiselev, Yu.V. THPSC058
Kishin, I.A. THPSC036
Klag, W. WEPSB039
Kleffner, C.M. WEPSB002
Klementiev, V.V. WECDMH01
Klemeshev, V.A. **THPSC049**
Klenov, V.S. TUPSA061, THPSC031, **THPSC053**
Klinov, A.P. WECDMH03, WEPSB064
Klinovsky, P.O. THPSC068
Kliuchevskaia, Yu.D. TUCASH02
Klopenkov, M.L. THCAMH04, THCAMH05, WEPSB053
Klopenkov, R.M. THCAMH04, **THCAMH05**, WEPSB053
Klyuev, V. WEZMH02
Klyuyev, A.S. TUPSA071, THPSC036
Knyazev, B.A. TUXMH02
Kobets, A.G. WEPSB059, WEPSB060
Kobets, V. FRCAMH01, FRCAMH02, FRCAMH03, TUPSA002, **TUPSA003**, TUPSA019, THPSC082
Kobylyatskiy, A.V. WEPSB004
Kogut, D.A. **THPSC035**
Kohler, I.H. WEYMH02
Kokin, E.N. THPSC008
Kokoulin, V.I. WEXMH01
Kolesnikov, S.Yu. WEPSB037
Kolesnikov, Ya.A. **THPSC032**, THPSC069, THPSC070, THCEMH01
Kolmogorov, V.V. WECBMH02, TUPSA029, THPSC077
Kolobanov, E.I. TUXMH02, TUCAMH02
Kolomiets, A. WEYMH01
Kondakov, A.A. TUXMH02, TUCAMH02, WEXMH01
Kondo, K. TUZMH03
Kondratenko, V.V. WEPSB063
Kondratiev, B.Yu. THCDMH03, THPSC042
Konstantinov, E.S. WEZMH02
Konstantinov, V.V. THPSC004
Konyashin, A.V. THCBSH03
Koop, I. TUYMH03, WEXMH01, WECBMH02, TUPSA001, WEPSB017
Korchagin, A.I. THPSC035
Korchuganov, V. **TUXMH03**, TUCBMH01, WEPSB010, WEPSB016
Korenev, S. **WEPSB052**
Korobeynikov, M.V. THCAMH02
Korolev, L.E. THCAMH05, TUCASH05
Korovkin, S.A. THCDMH03, THPSC042
Koshkarev, A.M. WEPSB075, THPSC032, THPSC033, THPSC069, **THPSC086**, THCEMH01
Kosov, A.A. THPSC087
Kostromin, S.A. THCDMH03, THCDMH04, FRCAMH05, FRCAMH07, THPSC005, THPSC010, **THPSC042**, THPSC043
Kotanjyan, A. **TUPSA053**
Kotenko, K.V. THPSC068
Kotina, E.D. **WEPSB051**
Kotov, E.S. THCBSH02, **THPSC081**
Kovalenko, A.D. FRCAMH01, **WEPSB028**, THPSC009, FRCAMH02, FRCAMH03
Koveshnikov, A.N. THZMH02
Kozak, V.R. TUXMH02, THPSC019, THPSC020, THPSC021, THPSC023, **THPSC078**
Kozienko, M.T. TUCASH05
Kozin, S.G. TUPSA058
Koziukov, A.E. THCAMH01
Kozlov, A.V. FRCAMH02, TUPSA038
Kozlov, A.V. WEPSB061
Kozlov, O.S. FRCAMH01, **FRCAMH07**, WEPSB024
Kozlovskiy, K.I. WEPSB056, WEPSB074, THPSC025
Kozub, S. **THZMH01**
Kozynchenko, S.A. WEPSB012
Kozynchenko, V.A. TUPSA017, WEPSB012, WEPSB024
Kozyrev, E.V. TUCAMH02
Kozyrev, E.V. TUXMH02
Krasnov, A.A. TUYMH03, WECBMH02, TUPSA001, **THPSC017**
Krasnov, A.A. TUCBSH01
Krasnykh, A. THPSC071
Kraus, I. WEPSB002
Kravchuk, L.V. TUZMH02, TUPSA004
Krestianinov, A.S. WECDMH03, WEPSB064
Kriklenko, A.V. THCEMH20
Krishnagopal, S. TUPSA021
Kropachev, G. FRCAMH02, **WEPSB073**
Krotov, S.A. **THCAMH03**
Krotov, V.V. TUCASH02
Krutikhin, S.A. TUXMH02, TUCAMH02
Krylov, A.I. THPSC064
Krylov, Y.V. TUCBMH01, THPSC054, **THPSC026**, THPSC063, THPSC084
Kubankin, A.S. TUPSA071, THPSC036
Kubarev, V.V. TUXMH02
Kudashkin, A.V. THCDMH03
Kudinovich, I.V. WEPSB055
Kukhtin, V.P. THPSC006, THPSC007, THPSC012
Kuksanov, N.K. THPSC035, THPSC072
Kulabukhova, N.V. **WEPSB030**
Kulevoy, T. **TUCDMH01**, FRCAMH02, TUPSA026, TUPSA038, WEPSB073, TUPSA028, THPSC041
Kulipanov, G.N. TUXMH02
Kuper, E.A. TUXMH02, THPSC019
Kuptsov, I.V. TUXMH02, TUCAMH02, WEXMH01
Kurakin, P.V. TUPSA012, WEPSB071
Kurakin, V.G. **TUPSA012**, **WEPSB071**
Kurkin, G.Y. TUXMH02, TUCAMH02, TUYMH03, WEXMH01, THPSC052, THPSC074
Kutnykova, L.A. WEZMH02
Kutsaev, S.V. TUCASH01

ISBN 978-3-95450-181-6

Kuzhlev, A.N. THCAMH05, TUCASH04, TUCASH05, WEPSB053, WEPSB061
Kuzmenkov, K.I. TUPSA059
Kuzmichev, V.G. FRCAMH02, **TUPSA038**
Kuznetsov, A.S. **WEPSB075**, THPSC032, THPSC069, THPSC086
Kuznetsov, G.L. THCDMH03, THPSC042
Kuznetsov, S.V. **WEPSB027**
Kvasha, A.I. **THXSH01**, **TUPSA037**
Kyrpotin, A.N. TUYMH03

— L —

Laforge, C. THZMH02
Lalayan, M.V. TUCASH02, TUPSA028, TUPSA032, TUPSA046, THPSC041, THPSC073
Lampasi, A. THPSC028
Lamzin, E.A. THPSC006, THPSC007, THPSC012
Lang, D. THZMH02
Lapik, R.M. WEXMH01
Larkin, A.I. THPSC065
Lavrukhin, A. THPSC035, THPSC072
Lawrie, J. WEYMH02
Laxdal, R.E. THZMH02
Lebedev, N.N. WEXMH01
Lebedev, V.Ya. TUPSA059
Lebedeva, J.S. THCAMH01
Leontiev, V.N. TUPSA004
Lestinsky, M. WEPSB002
Levichev, A.E. WEXMH01, TUPSA068, THPSC047
Levichev, E.B. FRCAMH08
Levin, A.D. TUCBMH02
Levterov, K.A. FRCAMH01, FRCAMH02, FRCAMH03
Lezhnin, S.I. WEPSB048
Li, G.H. WEPSB042
Li, J. WEPSB042
Li, M.K. THPSC037, **THPSC038**
Liakin, D.A. FRCAMH03
Liang, H. THPSC037, THPSC038
Liang, Z.K. THPSC044
Litvinov, S.A. **WEPSB002**
Liu, K.F. **THPSC044**
Liu, X. THPSC044
Lobanov, O.V. THPSC075
Lobov, I. **THPSC079**
Logatchov, P.V. WEXMH01
Loginov, A.S. TUCBMH02
Loginov, V.N. TUPSA058, TUPSA059
Losev, A.A. **TUPSA060**
Lotov, K.V. **MOYMH02**
Lozeev, Y. TUPSA026, WEPSB032
Lu, P. WEPSB043
Lussi, C. WEYMH02
Lyablin, M.V. THCBSH04
Lysenko, A.P. TUYMH03
Lyublin, B.V. THPSC007
Lyuosev, D.A. FRCAMH02, FRCAMH03

— M —

Ma, X.M. WEPSB042
Ma, Y. THZMH02
Macheret, Ya.M. THCBSH02
Macri, E.A. TUZMH03
Makarov, A.N. THCEMH01, THPSC032, THPSC033, THPSC034, THPSC069
Maksimenko, S.A. THPSC041
Malafeyev, O.A. WEPSB035
Maltseva, M.V. TUPSA068
Maltseva, Yu. WEXMH01, TUPSA018, THPSC046, THPSC047
Malyshev, V.P. THPSC068
Mamkin, V.R. THCBSH02
Mantengu, N.R. WEYMH02
Mao, L.J. WEPSB042
Markov, N.V. WEPSB065
Martin Yebra, A. WEPSB052
Martynov, A.A. FRCAMH02, FRCAMH03
Martyshkin, P.V. WEXMH01, TUPSA018, THPSC046, THPSC047
Marysheva, A.A. THPSC041
Maslennikov, O.L. WECDMH03, WEPSB064
Masuda, K. THPSC067
Matsievskiy, S.V. TUPSA009
Mayzel, A.V. THCBSH03
McAlister, R.H. WEYMH02
Medvedev, L.E. TUXMH02
Medvedko, A.S. THPSC019, THPSC021
Meier, J.P. THCDMH04
Mereu, P. TUZMH03
Mergelkuhl, D. THCBSH04
Meshcheryakov, N.D. WEPSB052
Meshkov, I.N. **WECAMH03**, WECAMH04, FRCAMH05, FRCAMH07, WEPSB037, WEPSB059, WEPSB060, WECAMH02
Meshkov, O.I. WECBMH02, THPSC052, THPSC061, THPSC074
Mezentsev, N.A. **TUCAMH01**
Mialkovskiy, V.V. FRCAMH02, FRCAMH03
Mickat, S. WECBMH01
Mierau, A. THCDMH04
Mihailov, K.I. **TUPSA019**
Mikhailov, V.A. FRCAMH01
Mikhaylov, V.A. FRCAMH05, WEPSB024, WEPSB028, WEPSB037
Mikheev, G.F. WEZMH01, THCAMH01
Mikheev, I.A. TUPSA001
Mikulinas, N.P. WEPSB061
Miloichikova, I.A. **THPSC071**
Minashkin, V.F. TUPSA002, TUPSA003, **THPSC082**
Mira, J. WEYMH02
Miroshnichenko, A.G. THCAMH05, TUCASH05
Mishunin, M.V. THPSC036
Miski-Oglu, M. WECBMH01

ISBN 978-3-95450-181-6

Mitrofanov, S. **WECDMH02**, **THPSC064**
Mizintseva, M.A. **WEPSB005**
Moelck, B. THPSC020
Moiseev, V.I. TUCBMH01
Molkanov, P.L. THCAMH03
Monchinsky, V.A. FRCAMH01, FRCAMH02, FRCAMH03
Monetti, A. WEYMH02
Montis, M. TUZMH03
Morita, K. THPSC067
Moroz, F.V. THCAMH03
Morozov, A.V. WEPSB061
Morozov, N.A. THYMH02
Moseev, K. TUCBMH01, THPSC026, **THPSC054**, THPSC063, THPSC084
Moseiko, N.I. TUCBMH01, THPSC026, **THPSC063**, THPSC084
Mostert, H.W. WEYMH02
Motygin, S.V. TUXMH02, TUCAMH02, TUYMH03
Mudrolyubov, V.G. THCAMH04, THCAMH05, TUCASH04, **TUCASH05**
Müller, G. TUPSA062
Muller, N. THZMH02
Murasev, A.A. TUCAMH02, WEXMH01
Muraviov, G.V. THCAMH04, THCAMH05, TUCASH05
Mustapha, B. TUCASH01

— N —

Naboka, A.N. TUPSA004
Nagaitsev, S. WEPSB021
Nagasaki, K. THPSC067
Nagimov, R.R. THZMH02
Naidoo, C. WEYMH02
Nassiri, A. TUCASH01
Naumenko, G.A. THPSC071
Nazhmudinov, R.M. THPSC036
Nazlev, H.P. THPSC024
Nekhaev, V.E. THCAMH02, THPSC008
Nemnyugin, S.A. **WEPSB035**
Nemulodi, F. WEYMH02
Nemytov, P.I. THPSC035, THPSC072
Nesterov, A. FRCAMH01, THPSC018
Nesterovich, A. WEPSB056
Nikiforov, D.A. WEXMH01, TUPSA001, TUPSA068
Nikiforov, D.N. THCDMH03, THPSC042
Nikiforov, K.A. **TUPSA067**, **TUPSA065**, **TUPSA066**
Nikishkin, V.I. THCAMH04, THCAMH05, TUCASH05
Nikitin, S.A. THPSC052
Nikolaev, V.I. WEYMH01
Nikulin, I.S. THPSC036
Nolden, F. WEPSB002
Novokshonov, A.I. THPSC048
Nozdrin, M.A. TUPSA003
Nozhenko, Yu.M. FRCAMH01

— O —

Odintsov, D.G. TUCBMH01
Oganessian, Y.T. WEYMH03
Ohgaki, H. THPSC067
Oleinik, A.N. **TUPSA071**, **THPSC036**
Omelyanenko, M.M. THPSC005, THPSC010, THPSC043
Oreshonok, V.V. **THPSC077**
Orlov, A. TUPSA046
Orlov, O. WEPSB059, WEPSB060
Orlov, S.Yu. THCAMH03
Osadchuk, I.O. WEPSB003, WEPSB004
Osipenkov, A.L. FRCAMH01
Osipov, N.F. WECDMH02
Osipov, V.N. TUXMH02
Ostreinov, Y.M. THCEMH01, THPSC033, **THPSC034**
Ostroumov, P.N. TUCASH01
Otboev, A.V. TUPSA001
Ottmar, A.V. THCBSH02
Ovchar, V.K. TUXMH02, TUCAMH02
Ovchinnikova, L. WECDMH01, **TUPSA040**
Ovsyannikov, A.D. WECAMH03, **TUPSA015**, TUPSA017, TUPSA062, **WEPSB012**
Ovsyannikov, D.A. WECAMH03, **WECAMH05**, TUPSA015, TUPSA017, TUPSA062, WEPSB001, WEPSB024, WEPSB051, WEPSB005, **WEPSB015**, WEPSB020, WEPSB055

— P —

Pachkov, A.A. THPSC047
Pakhomov, N.I. WECDMH01
Panasyuk, V.M. WEPSB040
Panero, R. TUZMH03
Panfilov, A.D. THCAMH02, THPSC008
Panov, A. THCBSH02
Panteleev, V.N. THCAMH03
Panyushkin, V.A. TUPSA020
Paraipan, M. **WEPSB078**
Paramonov, V.V. **THCASH01**, TUPSA004, TUPSA036, **TUPSA069**
Park, Y.H. TUPSA018, THPSC046
Parkhomchuk, V.V. WECAMH04, WEZMH02, WEPSB039, WEPSB040
Paschenko, S.V. WECDMH02
Pashuk, V.V. **THPSC075**
Pathak, A. **TUPSA021**
Pavlenko, A.V. WEXMH01, THCBSH02, TUPSA001, THPSC081
Pavlov, V.M. WEXMH01, TUPSA019
Pavlov, Y.S. WEPSB063
Pavlovsky, I. WEPSB052
Pavshenko, Yu.N. WECDMH01
Pchelkin, N.N. WEPSB038
Pei, Y.J. **WEPSB043**, THPSC044, THPSC045
Pepato, A. TUZMH03
Perelstein, E.A. WEPSB049, WEPSB050
Perepelkin, E.E. THPSC009
Perevedentsev, E. TUYMH03, THPSC060
Peshekhonov, S.N. THPSC047

ISBN 978-3-95450-181-6

Pesterev, S.G. TUCBMH01
Petrakovsky, V.S. THPSC041
Petrenko, A.V. WEXMH01, **TUPSA041**
Petrischev, N. WEZMH02
Petrov, G.A. WEZMH01
Petrov, V.M. TUXMH02, TUCAMH02
Petrozhitskii, A.V. WEZMH02
Philippov, A.V. FRCAMH01, **WEPSB036**
Pikalov, V.A. THYMH01
Pilan, A.M. TUXMH02, TUCAMH02
Pisent, A. TUZMH03
Plastun, A.S. TUCASH01
Ploskikh, V.A. WEPSB051
Pobol, I.L. THPSC041
Podlech, H. FRCAMH03, WECBMH01
Podlevskih, V. WEXMH01
Pokrovsky, A.I. THPSC041
Pokrovsky, V.A. THZMH01
Polikhov, S.A. TUCBSH01
Polozov, S.M. TUPSA011, **TUPSA026**, TUPSA038, FRCAMH02, **TUCASH02**, **TUPSA025**, TUPSA027, TUPSA028, **WEPSB049**, **WEPSB050**, **WEPSB057**, **THPSC041**
Polyakova, R.V. **THPSC009**
Pomogaybo, G.S. TUPSA032, **THPSC073**
Ponkin, D.O. FRCAMH02
Ponomarenko, V.I. THCAMH04, THCAMH05, TUCASH05
Ponomarev, I.D. THPSC082
Ponomarev, V.A. WECAMH03, TUPSA062
Popeko, A.G. **MOYMH01**
Popik, V.M. TUXMH02
Popov, D.V. THYMH02
Potylitsyn, A. THPSC048, THPSC050
Prete, G.P. WEYMH02
Pretelli, M.P. **THPSC028**
Prianishnikov, K.E. TUPSA011
Prokhorov, S.V. WEPSB038
Prokopenko, A.V. WEPSB063
Prosvetov, V.P. TUYMH03, TUPSA001
Protopopov, A.Yu. THPSC029, THPSC030
Puchkov, S.N. WEPSB063
Pureskin, D.N. THPSC029
Pushkar, R.G. FRCAMH02
Pyataev, V.G. TUPSA002, THPSC082

— Q —

Qi, W. THPSC003, THPSC037, THPSC038
Qin, B. TUPSA047, WEPSB043, THPSC044, THPSC045
Qu, G.F. FRCAMH06

— R —

Rabusov, D.V. **THPSC057**
Radchenko, V.M. THCAMH02, THPSC008
Rahighi, J. TUPSA057
Ramina, L. TUZMH03
Rashchenko, V.V. WEXMH01, TUPSA001
Rashchikov, V.I. TUCASH02, WEPSB057
Rastigeev, S. **WEZMH02**
Ratzinger, U. FRCAMH03
Reinhardt-Nickoulin, P.I. THCBSH01, TUPSA016, THPSC058
Repkin, A.N. TUPSA002, TUPSA019
Repkov, A.V. TUCAMH02
Repkov, V.V. TUXMH02
Reva, V.B. **WECAMH04**, WEPSB039, WEPSB040
Riabov, G.A. WEZMH01, THCAMH01, TUCASH03, TUCASH04
Riehn, E. WEPSB039
Rodin, I.Yu. **THPSC012**
Rogovsky, Yu. A. **TUYMH03**, WECBMH02, TUPSA001, THPSC016, THPSC057, **THPSC060**, **THPSC061**, WEXMH01
Romanov, A.L. WEXMH01
Romanov, S. FRCAMH01
Rossi, L. TUYMH02
Rossignoli, M. WEYMH02
Roudskoy, I. TUPSA020
Rubtsova, I.D. **WEPSB006**, WEPSB007
Rukojatkin, P.A. FRCAMH01
Ryabov, A. TUPSA040
Rybakov, I.V. **TUPSA004**, **TUPSA035**, **TUPSA036**
Rybitskaya, T.V. WECBMH02
Ryskulov, A.E. TUPSA058

— S —

Sabirov, B.M. **THCDMH02**
Saeidi, F. TUPSA057
Saharian, A.A. TUPSA053
Sakildien, M. WEYMH02
Salikova, T.V. TUXMH02
Salimov, R.A. THPSC035
Sambayev, Y.K. TUPSA058
Samoilenkov, S.V. THPSC012
Samoshin, A.V. THPSC041
Samoylov, S.L. WEXMH01
Samsonov, E.V. THYMH02
Sanfilippo, S.T. **THCDMH01**
Sanin, A.L. WEPSB075, THPSC086
Saprykin, A.D. TUCBMH02
Sasorov, P.V. TUPSA020
Satov, Yu.A. WEYMH01, TUPSA060
Savin, E.A. **TUCASH01**, TUCASH02, TUPSA009, TUPSA010
Savin, S.M. TUPSA020
Savkin, V.Ya. THPSC086
Scantamburlo, F. TUZMH03
Scarpa, D. TUZMH03
Schaumann, M. THCBSH04
Scheglov, M.A. TUXMH02, TUCAMH02, THPSC029, THPSC062
Schempp, A. FRCAMH03
Schippers, J.M. THCDMH01

ISBN 978-3-95450-181-6

Schnizer, P. THCDMH04
Schwarz, M. WECBMH01
Sedaghatizadeh, M. TUPSA057
Sedlyarov, I.K. TUXMH02, TUCAMH02
Selesnev, D.N. TUPSA038, WEPSB073
Seleznev, V.V. FRCAMH02, FRCAMH03
Selivanov, A.N. THCBSH02
Selivanov, P.A. THCBSH02, THPSC088
Semenov, A.M. THPSC017
Semenov, A.V. TUYMH03, WECBMH02, TUPSA001, THPSC035
Senchenko, A.I. TUYMH03, THCBSH02, **THPSC088**
Senichev, V. **MOZMH03**
Senkov, D.V. THPSC022, **THPSC029**, **THPSC030**
Serednyakov, S.S. THCBSH02, **THPSC062**, THPSC088
Serednyakov, S.S. TUXMH02, TUCAMH02
Serochkina, T.E. THPSC042
Serov, V.L. TUZMH02, THXSH01, TUPSA004, TUPSA037
Shabratov, V. TUPSA003, TUPSA002
Shandov, M.M. **THPSC005**, THPSC010, THPSC043
Shang, L. WEPSB043
Sharkov, G.B. **TUCBSH01**
Shashkov, Ya.V. **TUPSA046**
Shatunov, P.Yu. TUYMH03, **WECBMH02**, TUPSA001, WEPSB017, THPSC016
Shatunov, Y.M. TUYMH03, WECBMH02, TUPSA001
Shchagin, A.V. THPSC036, TUPSA071
Shcherbakov, O.A. **WEZMH01**, THCAMH01
Shcherbakov, P.A. THZMH01
Shchudlo, I.M. THCEMH01, THPSC032, **THPSC033**, THPSC034, THPSC069, THPSC070
Shebolaev, I.V. TUPSA007, TUPSA008
Sheinman, I.L. TUPSA041, **TUPSA042**, **TUPSA043**
Sheinman, Yu.S. TUPSA043
Shemchuk, A.V. THCDMH03, THPSC005, **THPSC010**, THPSC042, THPSC043
Shen, L.G. WEPSB043
Sheshin, E.P. **TUPSA070**, **WEPSB076**
Shevchenko, K.V. FRCAMH02, FRCAMH03
Shevchenko, O.A. TUXMH02, TUCAMH02, TUPSA050, TUPSA054
Shikanov, A.E. **WEPSB056**, WEPSB074, THPSC025
Shinya, T. TUZMH03
Shirikov, I.V. FRCAMH02, FRCAMH03
Shirkov, G. **THYMH02**, THCBSH04, TUPSA003
Shirkov, S.G. THYMH02
Shirokolobov, Yu. WEPSB051
Shirshov, L.S. THZMH01
Shishanin, O.E. **WEPSB031**
Shiyankov, S.V. WEXMH01, WECBMH02
Shkaruba, V.A. TUCAMH01
Shkitov, D.A. **TUPSA051**, **THPSC050**
Shokin, V.I. THPSC051
Shparla, D.A. THPSC041
Shtarklev, E.A. THCAMH02, THPSC008
Shtro, K.S. THCBSH02, THPSC081
Shubin, E. **TUPSA029**
Shumshurov, A. WEYMH01, TUPSA060
Shurkhno, N. WEPSB041
Shurygin, A.A. FRCAMH01
Shuvalov, E. THPSC048
Shuvalov, V.I. THZMH01
Shvedov, D.A. FRCAMH05
Shvedunov, N.V. WECDMH01
Shvedunov, V.I. WECDMH01, TUPSA030, TUPSA040, THPSC065
Shvetsov, V.N. TUPSA002, THPSC082
Shvetsov, V.S. WEPSB037
Shwartz, D.B. TUYMH03, WECBMH02, TUPSA001, **WEPSB017**, THPSC015, THPSC016, THPSC017
Sidorin, A.A. WEPSB059, **WEPSB060**
Sidorin, A.O. **FRCAMH01**, FRCAMH05, FRCAMH07, TUPSA028, WEPSB037, THPSC041, FRCAMH02, FRCAMH03, WEPSB024, WEPSB041, THPSC056
Sidorov, A.I. FRCAMH05, WEPSB037
Sidorov, A.V. THCAMH02
Sidorov, M.V. THPSC002
Siemek, K. WEPSB060, **WEPSB059**
Simonov, A.S. WECDMH01
Singatulin, S.R. THCBSH02
Sitnikov, A. WEPSB073
Skamarokha, M.A. THPSC052
Skasyrskaya, A.K. TUPSA036
Skorobogatov, D.N. WECAMH04, THPSC021
Skrinsky, A.N. TUXMH02, TUYMH03, WEXMH01
Skudnova, I. **WEPSB013**
Skuratov, V.A. WECDMH02
Slabodchikov, I. THZMH01
Slepnev, I. FRCAMH01
Slepnev, V. FRCAMH01
Smetanin, M.L. **TUCASH07**
Smirnov, A.V. FRCAMH01, FRCAMH02, FRCAMH03, FRCAMH05, **FRCAMH06**, **THPSC018**
Smirnov, I.B. WEPSB052
Smirnov, K.E. THCAMH05, TUCASH05
Smirnov, S.A. THCDMH03
Smirnov, V.L. **WEPSB046**
Smolyakov, N.V. **TUPSA056**, **TUPSA055**
Smygacheva, A.S. TUCBMH01, WEPSB010, **WEPSB016**
Sobenin, N.P. TUPSA009, TUPSA010, TUPSA028, TUPSA046
Sokolova, E.O. THPSC032, **THPSC069**, **THPSC070**, THCEMH01
Solnyshkov, D.A. **WEPSB061**
Sorokin, I.N. THCEMH01, THPSC032, THPSC033, THPSC069
Sotnikov, A.V. THPSC036
Spiller, P.J. THCDMH04
Starikov, A.Y. THCDMH03, THPSC042

ISBN 978-3-95450-181-6

Starikov, D.A. TUPSA013
Starikova, A.V. THPSC001
Starostenko, A.A. WEXMH01, WECBMH02, TUPSA001, THPSC014
Stasevich, Yu. TUPSA038
Steck, M. WEPSB002
Steyn, G.F. WEYMH02
Stirin, A.I. TUCBMH01
Stodart, N. WEYMH02
Stogov, Yu.I. THCAMH05, TUCASH05
Stolbunov, V. WEYMH01
Storey, D.W. THZMH02
Strokach, A.P. **THCAMH04**, THCAMH05, TUCASH05
Stuchebrov, S. THPSC071
Styuf, A.S. TUPSA029
Sugita, K. THCDMH04
Sukhanov, A.V. WECBMH02
Sukhanov, D.P. WEXMH01
Sumbaev, A.P. **TUPSA002**, TUPSA019, **THPSC051**, THPSC082
Sun, B.G. WEPSB043
Suphakul, S. THPSC067
Surkov, D.V. TUPSA028
Svetov, A.L. THPSC056
Svidetelev, A.N. THPSC018
Svistunov, Y.A. WEPSB001, WEPSB055, TUPSA015
Sycheva, T. THCEMH01, **WEPSB048**
Syresin, E. FRCAMH01, FRCAMH03, FRCAMH05, FRCAMH07
Syrovatin, V.M. TUCAMH01
Sytchevsky, S.E. THPSC006, THPSC007, THPSC012
Sytnik, V. THZMH01
Sytova, S.N. **WEPSB029**

— T —

Taddia, G.T. THPSC028
Tan, P. TUPSA047, WEPSB043, THPSC044, THPSC045
Tanchuk, A.V. WECDMH03
Tang, M.T. WEPSB042
Tang, Zh. X. WEPSB043
Tarantin, N.I. THPSC051
Tararyshkin, S.V. TUXMH02, TUCAMH02
Taskaev, S.Yu. **THCEMH01**, WEPSB048, THPSC032, THPSC033, THPSC069, THPSC070, THPSC086
Tcheskidov, V.G. TUXMH02, TUPSA054
Telnov, A.V. **TUCASH06**
Tenconi, S.M. THPSC028
Terekhov, S.A. TUPSA028
Terentyev, V.V. WECDMH03, WEPSB064
Teterev, Yu.G. WECDMH02, THPSC064
Thoeng, E. THZMH02
Thomae, R.W. WEYMH02
Tikhomirov, A. THPSC018, THPSC042
Tikhonov, N.O. WEPSB025
Tkachenko, L. THZMH01
Tkachenko, V.O. **THCAMH02**, THPSC008
Tonkikh, V.A. TUCASH03
Toporkov, S.E. TUPSA028, **TUPSA032**, THPSC041, THPSC073
Torgasin, K. **THPSC067**
Tribendis, A.G. TUXMH02, TUCAMH02, WEXMH01
Trifonov, D.E. TUCASH02
Trofimchuk, S.G. WECDMH03
Trubnikov, G.V. THYMH02, THCDMH03, THCDMH04, FRCAMH01, FRCAMH02, FRCAMH03, FRCAMH05, FRCAMH07, TUPSA028, WEPSB037, WEPSB041, THPSC041, **FRXMH01**, THCBSH04, WEPSB024
Trukhanov, K.A. **THPSC065**
Trunov, V.I. THPSC047
Trusov, O.V. THZMH01
Tsukanov, V.M. TUCAMH01
Tsvetkov, I.I. WECDMH03
Tsygankov, S.S. THCAMH05, TUCASH05
Tsyganov, A.S. WEXMH01, WECBMH02
Tuzikov, A. FRCAMH01, **FRCAMH04**, **FRCAMH05**, **WEPSB037**, THPSC013, WEPSB036
Tyukhtin, A.V. TUPSA049, WEPSB034, WEPSB068, WEPSB069
Tyutyunnikov, S.I. WEPSB078

— U —

Uchida, M.A. **MOYMH03**
Udovichenko, K.V. TUPSA002, THPSC082
Uglov, S.R. THPSC048
Usenya, A.S. **THCBSH03**
Ushakov, V. TUCBMH01
Ushkov, V.L. TUCBMH01
Utkin, A.V. WECBMH02

— V —

Vahrushev, R. THPSC021
Valentinov, A.G. **TUCBMH01**, THPSC026, THPSC054, THPSC063, THPSC084
Van Niekerk, M.J. WEYMH02
van Schalkwyk, P.A. WEYMH02
Varajun, M.I. TUPSA063
Vasichev, S.S. TUPSA001
Vasiliev, S.V. WEXMH01, THPSC015
Vasilishin, B. FRCAMH01
Vasilyev, A.A. TUPSA060
Vasilyev, I.V. THPSC058
Vasilyev, M.Yu. THCBSH02, THPSC081
Veresov, O.L. THCAMH05, TUCASH05
Vernov, A. TUCBMH01
Vinogradova, E.M. **TUPSA064**, **THPSC001**
Vinokurov, N.A. **TUXMH02**, TUCAMH02, TUPSA050, TUPSA054
Virkunen, T.R. THPSC068
Vishnevskii, E.V. WEPSB077

ISBN 978-3-95450-181-6

Vladimirova, L.V. **WEPSB007**
Vlasov, A. YU. THCAMH02, THPSC008
Vobly, P. TUXMH02
Vokhmyanina, K.A. TUPSA071, THPSC036
Volkov, V. TUXMH02, **TUCAMH02**, THPSC060
Volkov, V. FRCAMH01, FRCAMH05, WEPSB037
Volkov, Yu.M. THCAMH03
Volodkevich, O. TUPSA016, THPSC053
Vorobev, D.S. THPSC035, **THPSC072**
Vorobev, V.V. TUPSA049, WEPSB034, **WEPSB068**, WEPSB069
Vorobyev, A.S. WEZMH01, THCAMH01
Vorobyev, G. WEPSB002
Voronin, G.G. WEPSB061
Voronin, L.A. THCAMH02, THPSC008
Vorozhtsov, S.B. WEPSB046
Vovchenko, E.D. WEPSB056, WEPSB074, **THPSC025**
Vukolov, A.V. **THPSC048**

— W —

Wang, W. THPSC044
Waraich, B.S. THZMH02
Wei, W. WEPSB043
Weilbach, T. WEPSB039
Weise, H. **TUXMH01**
Wenninger, J. THCBSH04

— X —

Xiong, Y.Q. TUPSA047, WEPSB043, THPSC003, THPSC037, THPSC038, THPSC044, THPSC045
Xuan, K. WEPSB043

— Y —

Yakovlev, I.A. **WEPSB045**
Yakushkin, A.E. TUPSA042
Yan, T.L. WEPSB042
Yanenko, V.V. TUPSA020
Yang, J. THPSC003, THPSC037, THPSC038, THPSC044, THPSC045
Yang, L. THPSC038
Yang, X.D. **WEPSB042**
Yao, L.P. FRCAMH06
Yao, Z.Y. THZMH02
Yaramyshev, S. WECBMH01, TUPSA026
Yarosh, V.E. WEPSB053
Yu, T. THPSC003, THPSC037, THPSC038, THPSC045
Yudin, I.P. THPSC009, **WEPSB054**
Yudin, V.D. WEXMH01, TUPSA001
Yurchenko, V.I. TUCASH04
Yurevich, S.V. THPSC041
Yurov, D.S. **TUPSA030**

— Z —

Zamriy, V.N. **THPSC076**, THPSC082
Zapretilina, E.R. THPSC012
Zarubin, A. WEYMH01
Zavadtsev, A.A. **THPSC027**, **THXSH02**
Zavadtsev, D.A. THPSC027
Zaverukha, O.I. **THPSC002**
Zavialov, M.A. WEPSB063
Zazulin, S.V. THCEMH20
Zdorovets, M.V. TUPSA058
Zeitlin, M.G. WEPSB019, WEPSB026
Zemlyanoy, S.G. WEPSB044
Zemlyansky, I.M. TUYMH03, WEXMH01, **TUPSA001**
Zen, H. THPSC067
Zhabko, A.P. TUPSA024, THPSC087
Zhabko, I.A. THPSC087
Zhang, L.G. THPSC003, THPSC037, THPSC038
Zhang, Y.F. **THPSC037**, THPSC038
Zhao, Z. WEPSB043
Zharikov, A.A. THPSC030
Zharinov, Yu.M. TUYMH03, TUPSA001, THPSC060
Zheng, Q. THZMH02
Zhironkin, I.S. THPSC082
Zhuravlev, A.N. FRCAMH05
Zimek, Z. **WEPSB058**
Zinchenko, S. THZMH01
Zito, P. THPSC028
Zolkin, T. **WEPSB021**, **WEPSB022**
Zubarev, P.V. THPSC086
Zubets, V. THPSC031, THPSC053
Zuev, Yu. **WECDMH03**, **WEPSB064**
Zuo, C. THPSC003, THPSC037, THPSC038
Zvyagintsev, V. TUPSA028, THPSC041, **THZMH02**, TUPSA034
Zybin, D.A. THPSC027

ISBN 978-3-95450-181-6

ISBN 978-3-95450-181-6

Institutes List

Allrussian Electrotechnical Institute
Moskow, Russia
- Chikhachev, A.S.

ANI
Austin, USA
- Fink, R.L.
- Pavlovsky, I.

ANL
Argonne, Illinois, USA
- Mustapha, B.
- Nassiri, A.
- Ostroumov, P.N.
- Plastun, A.S.

BARC
Mumbai, India
- Krishnagopal, S.
- Pathak, A.

Belarussian State University, Scientific Research Institute of Nuclear Problems
Minsk, Belarus
- Sytova, S.N.

BelSU/LRP
Belgorod, Russia
- Kishin, I.A.
- Klyuyev, A.S.

BelSU
Belgorod, Russia
- Ivashchuk, O.O.
- Kaplii, A.A.
- Kubankin, A.S.
- Mishunin, M.V.
- Nazhmudinov, R.M.
- Nikulin, I.S.
- Oleinik, A.N.
- Shchagin, A.V.
- Sotnikov, A.V.
- Vokhmyanina, K.A.

BEVATECH
Frankfurt, Germany
- Hoeltermann, H.
- Podlech, H.
- Ratzinger, U.
- Schempp, A.

BINP & NSTU
Novosibirsk, Russia
- Gmyrya, A.A.

BINP SB RAS
Novosibirsk, Russia
- Aktershev, Yu.
- Anashin, V.V.
- Anchugov, O.
- Andrianov, A.V.
- Arbuzov, V.S.
- Astrelina, K.V.
- Balakin, V.V.
- Baluev, A.O.
- Barnyakov, A.M.
- Batrakov, A.M.
- Bekhtenev, E.A.
- Belikov, O.V.
- Berkaev, D.E.
- Bezuglov, V.V.
- Blinov, M.F.
- Blokhina, K.A.
- Boimelshtain, Y.M.
- Bolkhovityanov, D.
- Borin, V.M.
- Bryazgin, A.A.
- Bryzgunov, M.I.
- Bubley, A.V.
- Bykov, E.V.
- Chakin, I.
- Cheblakov, P.B.
- Cherepkov, V.G.
- Chernov, K.N.
- Chernyakin, A.D.
- Chupyra, A.G.
- Davidyuk, I.V.
- Deichuli, O.I.
- Dementyev, E.N.
- Denisov, A.P.
- Dikansky, N.S.
- Dokutovich, V.
- Domarov, E.V.
- Dovzhenko, B.A.
- Emanov, F.A.
- Fadeev, S.
- Faktorovich, B.L.
- Fatkin, G.A.
- Frolov, A.R.
- Gambaryan, V.V.
- Getmanov, Ya.V.
- Glukhov, S.A.
- Gmyrya, A.A.
- Golkovsky, M.
- Golubenko, Yu.I.
- Goncharov, A.D.
- Gorbachev, Ya.I.
- Gorbunov, V.A.
- Gurov, D.

ISBN 978-3-95450-181-6

- Gusev, I.A.
- Gusev, Ye.A.
- Ivanov, A.A.
- Ivanov, A.V.
- Karpov, G.V.
- Kasaev, A.S.
- Kasatov, D.A.
- Kenzhebulatov, E.
- Khrushchev, S.V.
- Kiselev, V.A.
- Klyuev, V.
- Knyazev, B.A.
- Kogut, D.A.
- Kokin, E.N.
- Kokoulin, V.I.
- Kolesnikov, Ya.A.
- Kolmogorov, V.V.
- Kolobanov, E.I.
- Kondakov, A.A.
- Konstantinov, E.S.
- Koop, I.
- Korchagin, A.I.
- Korobeynikov, M.V.
- Koshkarev, A.M.
- Kotov, E.S.
- Kozak, V.R.
- Kozyrev, E.V.
- Krasnov, A.A.
- Krutikhin, S.A.
- Kubarev, V.V.
- Kuksanov, N.K.
- Kulipanov, G.N.
- Kuper, E.A.
- Kuptsov, I.V.
- Kurkin, G.Y.
- Kutnykova, L.A.
- Kuznetsov, A.S.
- Kyrpotin, A.N.
- Lapik, R.M.
- Lavrukhin, A.
- Lebedev, N.N.
- Levichev, A.E.
- Levichev, E.B.
- Logatchov, P.V.
- Lotov, K.V.
- Lysenko, A.P.
- Macheret, Ya.M.
- Makarov, A.N.
- Maltseva, Yu.
- Mamkin, V.R.
- Martyshkin, P.V.
- Medvedev, L.E.
- Medvedko, A.S.
- Meshkov, O.I.
- Mezentsev, N.A.
- Mikheev, I.A.
- Motygin, S.V.
- Murasev, A.A.
- Nekhaev, V.E.
- Nemytov, P.I.
- Nikiforov, D.A.
- Nikitin, S.A.
- Oreshonok, V.V.
- Osipov, V.N.
- Ostreinov, Y.M.
- Otboev, A.V.
- Ottmar, A.V.
- Ovchar, V.K.
- Pachkov, A.A.
- Panasyuk, V.M.
- Panfilov, A.D.
- Panov, A.
- Parkhomchuk, V.V.
- Pavlenko, A.V.
- Pavlov, V.M.
- Perevedentsev, E.
- Peshekhonov, S.N.
- Petrenko, A.V.
- Petrischev, N.
- Petrov, V.M.
- Petrozhitskii, A.V.
- Pilan, A.M.
- Podlevskih, V.
- Popik, V.M.
- Prosvetov, V.P.
- Protopopov, A.Yu.
- Pureskin, D.N.
- Rabusov, D.V.
- Radchenko, V.M.
- Rashchenko, V.V.
- Rastigeev, S.
- Repkov, A.V.
- Repkov, V.V.
- Reva, V.B.
- Rogovsky, Yu. A.
- Rybitskaya, T.V.
- Salikova, T.V.
- Salimov, R.A.
- Samoylov, S.L.
- Sanin, A.L.
- Savkin, V.Ya.
- Scheglov, M.A.
- Sedlyarov, I.K.
- Selivanov, A.N.
- Selivanov, P.A.
- Semenov, A.M.
- Semenov, A.V.
- Senchenko, A.I.
- Senkov, D.V.
- Serednyakov, S.S.
- Shatunov, P.Yu.
- Shatunov, Y.M.
- Shchudlo, I.M.
- Shevchenko, O.A.
- Shiyankov, S.V.
- Shkaruba, V.A.
- Shtarklev, E.A.
- Shtro, K.S.
- Shubin, E.
- Shvedov, D.A.
- Shwartz, D.B.
- Sidorov, A.V.

ISBN 978-3-95450-181-6

- Singatulin, S.R.
- Skamarokha, M.A.
- Skorobogatov, D.N.
- Skrinsky, A.N.
- Sorokin, I.N.
- Starostenko, A.A.
- Sukhanov, A.V.
- Sukhanov, D.P.
- Sycheva, T.
- Syrovatin, V.M.
- Tararyshkin, S.V.
- Taskaev, S.Yu.
- Tcheskidov, V.G.
- Tkachenko, V.O.
- Tribendis, A.G.
- Tsukanov, V.M.
- Tsyganov, A.S.
- Utkin, A.V.
- Vahrushev, R.
- Vasichev, S.S.
- Vasiliev, S.V.
- Vasilyev, M.Yu.
- Vinokurov, N.A.
- Vlasov, A. YU.
- Vobly, P.
- Volkov, V.
- Vorobev, D.S.
- Voronin, L.A.
- Yudin, V.D.
- Zemlyansky, I.M.
- Zharikov, A.A.
- Zharinov, Yu.M.
- Zhuravlev, A.N.
- Zubarev, P.V.

BINP
Novosibirsk, Russia
- Dorokhov, V.L.

BSU
Minsk, Belarus, Belarus
- Benediktovitch, A.I.

Budker INP & NSU
Novosibirsk, Russia
- Bykov, T.A.
- Dementiev, E.N.
- Rogovsky, Yu. A.
- Sokolova, E.O.

CERN
Geneva, Switzerland
- Baglin, V.
- Benedikt, M.
- Brüning, O.S.
- Chiggiato, P.
- Di Girolamo, B.
- Gayde, J.
- Henrist, B.
- Mergelkuhl, D.
- Petrenko, A.V.
- Rossi, L.
- Schaumann, M.
- Wenninger, J.

CHTD
Moscow, Russia
- Antipkin, N.R.
- Ashanin, I.A.
- Grigoryev, I.P.
- Guchkin, A.S.

CORAD Ltd.
St. Petersburg, Russia
- Demsky, M.I.
- Eliseev, A.A.
- Krotov, V.V.
- Trifonov, D.E.

DESY Zeuthen
Zeuthen, Germany
- Isaev, I.I.

DESY
Hamburg, Germany
- Eckoldt, H.-J.
- Feng, G.
- Heidbrook, N.
- Moelck, B.
- Weise, H.

DICP
Dalian, People's Republic of China
- Tang, Zh. X.

ENEA C.R. Frascati
Frascati (Roma), Italy
- Lampasi, A.
- Zito, P.

Euclid TechLabs, LLC
Solon, Ohio, USA
- Kanareykin, A.

Fermilab
Batavia, Illinois, USA
- Burov, A.V.
- Nagaitsev, S.
- Romanov, A.L.
- Zolkin, T.

ISBN 978-3-95450-181-6

FZJ
Jülich, Germany
- Kamerdzhiev, V.
- Senichev, V.

GSI
Darmstadt, Germany
- Andelkovic, Z.
- Barth, W.A.
- Beck, D.
- Bleile, A.
- Bräuning-Demian, A.
- Chorniy, O.
- Dziuba, F.D.
- Fedotova, S.
- Fischer, E.S.
- Geithner, W.
- Heilmann, M.
- Herfurth, F.
- Hess, R.
- Kleffner, C.M.
- Kraus, I.
- Lestinsky, M.
- Litvinov, S.A.
- Meier, J.P.
- Mickat, S.
- Mierau, A.
- Nolden, F.
- Schnizer, P.
- Spiller, P.J.
- Steck, M.
- Sugita, K.
- Vorobyev, G.
- Yaramyshev, S.

HIM
Mainz, Germany
- Amberg, M.
- Aulenbacher, K.
- Barth, W.A.
- Bruker, M.W.
- Dietrich, J.
- Dziuba, F.D.
- Gettmann, V.
- Hofmann, A.
- Miski-Oglu, M.
- Riehn, E.
- Weilbach, T.

Huazhong University of Science and Technology, State Key Laboratory of Advanced Electromagnetic Engineering and Technology,
Hubei, People's Republic of China
- Yu, T.
- Zuo, C.

HUST
Wuhan, People's Republic of China
- Cao, L.
- Chen, Q.S.
- Fan, K.
- Fan, M.
- Hu, T.
- Huang, J.
- Li, M.K.
- Liang, H.
- Liang, Z.K.
- Liu, K.F.
- Liu, X.
- Qi, W.
- Qin, B.
- Tan, P.
- Xiong, Y.Q.
- Yang, J.
- Yang, L.
- Zhang, L.G.
- Zhang, Y.F.
- Zuo, C.

IAP
Frankfurt am Main, Germany
- Amberg, M.
- Basten, M.
- Busch, M.
- Podlech, H.
- Schwarz, M.

IBS
Daejeon, Republic of Korea
- Kim, J.-W.
- Kim, J.Y.
- Park, Y.H.

ICKC SB RAS
Novosibirsk, Russia
- Ikryanov, I.M.
- Shebolaev, I.V.

ICKC
Novosibirsk, Russia
- Chernousov, Y.D.

IERT
Kharkov, Ukraine
- Kobets, A.G.

IFJ-PAN
Kraków, Poland
- Horodek, P.
- Siemek, K.

IFMIF/EVEDA
Rokkasho, Japan
- Scantamburlo, F.

ISBN 978-3-95450-181-6

IFUSP
Sao Paulo, Brazil
- Gitman, D.M.
- Levin, A.D.

IHEP
Moscow Region, Russia
- Afonin, A.G.
- Ageev, A.I.
- Antipov, Y.
- Bogdanov, I.
- Frolov, B.A.
- Gao, J.
- Gotman, V.
- Ivanov, S.V.
- Kashtanov, E.
- Kozub, S.
- Lobov, I.
- Pikalov, V.A.
- Pokrovsky, V.A.
- Ryabov, A.
- Shcherbakov, P.A.
- Shirshov, L.S.
- Shuvalov, V.I.
- Slabodchikov, I.
- Sytnik, V.
- Tkachenko, L.
- Trusov, O.V.
- Zinchenko, S.

IKP
Mainz, Germany
- Aulenbacher, K.
- Klag, W.

ILSF
Tehran, Iran
- Rahighi, J.
- Saeidi, F.

IMP/CAS
Lanzhou, People's Republic of China
- Chai, W.P.
- Li, G.H.
- Li, J.
- Ma, X.M.
- Mao, L.J.
- Qu, G.F.
- Tang, M.T.
- Yan, T.L.
- Yang, X.D.
- Yao, L.P.

Imperial College of Science and Technology, Department of Physics
London, United Kingdom
- Uchida, M.A.

INFN- Sez. di Padova
Padova, Italy
- Agguiaro, D.
- Colombo, A.G.
- Pepato, A.
- Ramina, L.

INFN-Torino
Torino, Italy
- Borotto Dalla Vecchia, F.
- Dughera, G.
- Giraudo, G.
- Macri, E.A.
- Mereu, P.
- Panero, R.

INFN/LNL
Legnaro (PD), Italy
- Andrighetto, A.
- Antoniazzi, L.
- Baldo, A.
- Battistello, A.
- Bottin, P.
- Fagotti, E.
- Ferrari, L.
- Giacchini, M.G.
- Grespan, F.
- Monetti, A.
- Montis, M.
- Pisent, A.
- Prete, G.P.
- Rossignoli, M.
- Scarpa, D.

INP BSU
Minsk, Belarus
- Baturitski, M.A.
- Maksimenko, S.A.

INP NNC RK
Almaty, Kazakhstan
- Alexandrenko, V.V.
- Ivanov, I.A.
- Kozin, S.G.
- Ryskulov, A.E.
- Sambayev, Y.K.
- Zdorovets, M.V.

Institute of Laser Physics, SB RAS
Novosibirsk, Russia
- Gubin, V.
- Trunov, V.I.

Institute of Nuclear Chemistry and Technology
Warsaw, Poland
- Zimek, Z.

ISBN 978-3-95450-181-6

IPCE RAS
Moscow, Russia
- Pavlov, Y.S.

IPHC
Strasbourg Cedex 2, France
- Asfari, Z.
- Gall, B.J.P.

ISDCT SB RAS
Irkutsk, Russia
- Kosov, A.A.

ISDE
Moscow, Russia
- Chubunov, P.A.

ITEP
Moscow, Russia
- Alexeev, N.N.
- Andreev, A.
- Bakhmutova, A.V.
- Balabaev, A.
- Balabin, A.I.
- Barabin, S.V.
- Bogdanov, A.V.
- Drozdovsky, A.A.
- Drozdovsky, S.A.
- Gavrilin, R.
- Golubev, A.
- Kantsyrev, A.V.
- Kats, M.M.
- Khrisanov, I.A.
- Kolomiets, A.
- Kozlov, A.V.
- Kropachev, G.
- Kulevoy, T.
- Kuzmichev, V.G.
- Liakin, D.A.
- Losev, A.A.
- Markov, N.V.
- Nikolaev, V.I.
- Panyushkin, V.A.
- Polozov, S.M.
- Roudskoy, I.
- Satov, Yu.A.
- Savin, S.M.
- Selesnev, D.N.
- Shumshurov, A.
- Sitnikov, A.
- Stasevich, Yu.
- Stolbunov, V.
- Vasilyev, A.A.
- Yanenko, V.V.
- Zarubin, A.

ITER Organization
St. Paul lez Durance, France
- Gribov, Y.

iThemba LABS
Somerset West, South Africa
- Anthony, L.S.
- Azaiez, F.
- Baard, S.
- Bark, R.A.
- Barnard, A.H.
- Broodryk, J.I.
- Conradie, J.L.
- Cornell, J.C.
- De Villiers, J.G.
- Du Plessis, H.
- Duckitt, W.
- Fourie, D.T.
- Gardiner, P.G.
- Hogan, M.E.
- Kohler, I.H.
- Lawrie, J.
- Lussi, C.
- Mantengu, N.R.
- McAlister, R.H.
- Mira, J.
- Mostert, H.W.
- Naidoo, C.
- Nemulodi, F.
- Sakildien, M.
- Steyn, G.F.
- Stodart, N.
- Thomae, R.W.
- Van Niekerk, M.J.
- van Schalkwyk, P.A.

JIHT RAS
Moscow, Russia
- Kuznetsov, S.V.

JINR/DLNP
Dubna, Moscow region, Russia
- Hilinov, V.I.
- Horodek, P.
- Meshkov, I.N.
- Popov, D.V.
- Siemek, K.

JINR/FLNP
Moscow Region, Russia
- Mihailov, K.I.
- Shvetsov, V.N.

JINR/FLNR
Moscow region, Russia
- Konstantinov, V.V.
- Krylov, A.I.
- Pchelkin, N.N.
- Popeko, A.G.
- Zemlyanoy, S.G.

ISBN 978-3-95450-181-6

JINR/VBLHEP
Dubna, Moscow region, Russia

- Avvakumova, I.L.
- Bazanov, A.M.
- Bulanov, V. A.
- Butenko, A.V.
- Donets, D.E.
- Gorelyshev, I.V.
- Kovalenko, A.D.
- Levterov, K.A.
- Lyuosev, D.A.
- Martynov, A.A.
- Mialkovskiy, V.V.
- Philippov, A.V.
- Ponkin, D.O.
- Pushkar, R.G.
- Seleznev, V.V.
- Serochkina, T.E.
- Shabratov, V.
- Shemchuk, A.V.
- Shevchenko, K.V.
- Shirikov, I.V.
- Sidorin, A.O.
- Svetov, A.L.
- Trubnikov, G.V.
- Tuzikov, A.
- Yudin, I.P.

JINR
Dubna, Moscow Region, Russia

- Agapov, N.N.
- Ahmanova, E.V.
- Akishin, P.G.
- Aleinikov, V.V.
- Aleksandrov, V.
- Alfeev, A.V.
- Andreev, V.
- Azaryan, N.S.
- Balalykin, N.
- Baldin, A.A.
- Batin, V.
- Bazanov, A.M.
- Berlev, A.I.
- Boettcher, J.
- Bogomolov, S.L.
- Bondarchenko, A.E.
- Borisov, V.V.
- Boudagov, Ju.
- Brovko, O.I.
- Bugaev, V.V.
- Butenko, A.V.
- Bychkov, A.V.
- Dmitriev, S.N.
- Dolbilov, G.V.
- Donets, D.E.
- Donyagin, A.M.
- Eliseev, A.V.
- Eseev, M.K.
- Fateev, A.A.
- Fimushkin, V.V.
- Galimov, A.R.
- Gikal, B.
- Glagolev, V.V.
- Golovenskiy, B.V.
- Golubitsky, O.
- Golubkov, E.A.
- Gorbachev, E.V.
- Govorov, A.
- Grebentsov, A.Yu.
- Gulbekyan, G.G.
- Gurskiy, S.
- Ivanenko, I.A.
- Ivanov, E.V.
- Ivanov, G.N.
- Kalagin, I.V.
- Kalmykov, A.V.
- Karamyshev, O.
- Karamysheva, G.A.
- Karpinsky, V.
- Kayukov, A.S.
- Kazarinov, N.Yu.
- Khodzhibagiyan, H.G.
- Kirichenko, A.
- Kobets, A.G.
- Kobets, V.
- Kolesnikov, S.Yu.
- Kondratiev, B.Yu.
- Korovkin, S.A.
- Kostromin, S.A.
- Kovalenko, A.D.
- Kozlov, O.S.
- Kudashkin, A.V.
- Kuzmenkov, K.I.
- Kuznetsov, G.L.
- Lebedev, V.Ya.
- Levterov, K.A.
- Loginov, V.N.
- Lyablin, M.V.
- Meshkov, I.N.
- Mikhailov, V.A.
- Mikhaylov, V.A.
- Minashkin, V.F.
- Mitrofanov, S.
- Monchinsky, V.A.
- Morozov, N.A.
- Nazlev, H.P.
- Nesterov, A.
- Nikiforov, D.N.
- Nozdrin, M.A.
- Nozhenko, Yu.M.
- Oganessian, Y.T.
- Omelyanenko, M.M.
- Orlov, O.
- Osipenkov, A.L.
- Osipov, N.F.
- Paraipan, M.
- Paschenko, S.V.
- Perelstein, E.A.
- Perepelkin, E.E.
- Polyakova, R.V.
- Ponomarev, I.D.
- Prokhorov, S.V.

ISBN 978-3-95450-181-6

- Pyataev, V.G.
- Repkin, A.N.
- Romanov, S.
- Rukojatkin, P.A.
- Sabirov, B.M.
- Samsonov, E.V.
- Shabratov, V.
- Shandov, M.M.
- Shemchuk, A.V.
- Shirkov, G.
- Shirkov, S.G.
- Shokin, V.I.
- Shurkhno, N.
- Shurygin, A.A.
- Shvetsov, V.S.
- Sidorin, A.A.
- Sidorin, A.O.
- Sidorov, A.I.
- Skuratov, V.A.
- Slepnev, I.
- Slepnev, V.
- Smirnov, A.V.
- Smirnov, S.A.
- Smirnov, V.L.
- Starikov, A.Y.
- Sumbaev, A.P.
- Svidetelev, A.N.
- Syresin, E.
- Tarantin, N.I.
- Teterev, Yu.G.
- Tikhomirov, A.
- Trubnikov, G.V.
- Tuzikov, A.
- Tyutyunnikov, S.I.
- Udovichenko, K.V.
- Vasilishin, B.
- Volkov, V.
- Vorozhtsov, S.B.
- Yudin, I.P.
- Zamriy, V.N.
- Zhironkin, I.S.

JSC FID Technology
Saint Petersburg, Russia
- Efanov, M.V.
- Efanov, V.M.
- Kriklenko, A.V.
- Zazulin, S.V.

JSC SuperOx
Moscow, Russia
- Samoilenkov, S.V.

Keldysh Institute of Applied Mathematics
Moscow, Russia
- Sasorov, P.V.

KIT
Karlsruhe, Germany
- Fetzer, R.
- Müller, G.

KNTU
Tehran, Iran
- Abbaslou, M.
- Sedaghatizadeh, M.

KSRC
St. Petersburg, Russia
- Kudinovich, I.V.

Kyoto University
Kyoto, Japan
- Kii, T.
- Masuda, K.
- Morita, K.
- Nagasaki, K.
- Ohgaki, H.
- Suphakul, S.
- Torgasin, K.
- Zen, H.

Laboratory of Electron Accelerators MSU, Ltd, Physics Department, Lomonosov Moscow State University
Moscow, Russia
- Gromov, M.B.

LEA MSU
Moscow, Russia
- Alimov, A.S.
- Ermakov, A.N.
- Khankin, V.V.
- Klementiev, V.V.
- Ovchinnikova, L.
- Pakhomov, N.I.
- Pavshenko, Yu.N.
- Shvedunov, N.V.
- Shvedunov, V.I.
- Simonov, A.S.

LETI
Saint-Petersburg, Russia
- Altmark, A.
- Baturin, S.
- Belonogaya, E.S.
- Nikiforov, K.A.
- Sheinman, I.L.
- Sheinman, Yu.S.
- Varajun, M.I.
- Yakushkin, A.E.

LPI
Moscow, Russia
- Bashmakov, Y.A.
- Kurakin, P.V.
- Kurakin, V.G.

ISBN 978-3-95450-181-6

M.V. Lomonosov Moscow State University (MSU), Skobeltsyn Institute of Nuclear Physics
Moscow, Russia
- Ionidi, V.Y.

MEPhI
Moscow, Russia
- Alexey, P.G.
- Averyanov, G.P.
- Barminova, H.Y.
- Barth, W.A.
- Bashmakov, Y.A.
- Bazyl, D.B.
- Bogdanovich, B.Y.
- Bogomolov, A.S.
- Bondarenko, T.V.
- Budkin, V.A.
- Bulanov, A.V.
- Dyubkov, V.S.
- Fadeev, A.M.
- Gusarova, M.
- Il'inskiy, A.V.
- Isaev, A.A.
- Ivanov, S.M.
- Kliuchevskaia, Yu.D.
- Kobylyatskiy, A.V.
- Kozlovskiy, K.I.
- Kulevoy, T.
- Lalayan, M.V.
- Lozeev, Y.
- Matsievskiy, S.V.
- Nesterovich, A.
- Osadchuk, I.O.
- Polozov, S.M.
- Pomogaybo, G.S.
- Prianishnikov, K.E.
- Prokopenko, A.V.
- Rashchikov, V.I.
- Samoshin, A.V.
- Savin, E.A.
- Shashkov, Ya.V.
- Shikanov, A.E.
- Sobenin, N.P.
- Surkov, D.V.
- Terekhov, S.A.
- Toporkov, S.E.
- Vovchenko, E.D.
- Yanenko, V.V.
- Yaramyshev, S.
- Zvyagintsev, V.

MIPT
Dolgoprudniy, Moscow Region, Russia
- Chermoshentsev, D.A.
- Churaev, M.M.
- Feschenko, A.
- Sheshin, E.P.
- Smolyakov, N.V.

Moscow State Academy of Water Transport
Moscow, Russia
- Shishanin, O.E.

MPEI
Moscow, Russia
- Bukharov, A.V.
- Vishnevskii, E.V.

MRTI RAS
Moscow, Russia
- Durkin, A.P.
- Esakov, I.I.
- Puchkov, S.N.

MSU SINP
Moscow, Russia
- Chepurnov, A.S.

MSU
Moscow, Russia
- Chepurnov, A.S.
- Shvedunov, V.I.
- Yurov, D.S.

NAFU
Arkhangelsk, Russia
- Eseev, M.K.

Nano
Moscow, Russia
- Churanov, D.
- Zavadtsev, A.A.
- Zavadtsev, D.A.
- Zybin, D.A.

NArFU
Arhangelsk, Russia
- Eseev, M.K.

National Instruments
Moscow, Russia
- Konyashin, A.V.
- Mayzel, A.V.
- Usenya, A.S.

NIIEFA
St. Petersburg, Russia
- Amoskov, V.M.
- Andreev, E.N.
- Andreeva, Z.
- Antonov, A.V.
- Bazarov, A.M.
- Belyakov, V.A.
- Dyomina, A.A.
- Emeljanov, M.A.

ISBN 978-3-95450-181-6

- Fialkovsky, A.M.
- Galchuck, A.V.
- Gapionok, E.I.
- Gavrish, Yu.N.
- Glukhih, V.A.
- Gnutov, P.A.
- Grigorenko, S.V.
- Grigoriev, V.I.
- Kalinichenko, M.A.
- Kaparkova, M.
- Klinov, A.P.
- Klinovsky, P.O.
- Klopenkov, M.L.
- Klopenkov, R.M.
- Korolev, L.E.
- Kotenko, K.V.
- Kozienko, M.T.
- Kozlov, A.V.
- Krestianinov, A.S.
- Kukhtin, V.P.
- Kuzhlev, A.N.
- Lamzin, E.A.
- Lyublin, B.V.
- Malyshev, V.P.
- Maslennikov, O.L.
- Mikulinas, N.P.
- Miroshnichenko, A.G.
- Morozov, A.V.
- Mudrolyubov, V.G.
- Muraviov, G.V.
- Nikishkin, V.I.
- Ponomarenko, V.I.
- Rodin, I.Yu.
- Smirnov, K.E.
- Solnyshkov, D.A.
- Stogov, Yu.I.
- Strokach, A.P.
- Svistunov, Y.A.
- Sytchevsky, S.E.
- Tanchuk, A.V.
- Terentyev, V.V.
- Tsygankov, S.S.
- Veresov, O.L.
- Virkunen, T.R.
- Voronin, G.G.
- Zapretilina, E.R.
- Zuev, Yu.

NIITFA
Moscow, Russia
- Bondarenko, T.V.
- Krasnov, A.A.
- Polikhov, S.A.
- Sharkov, G.B.
- Yarosh, V.E.

NRC
Moscow, Russia
- Belkov, A.
- Fomin, Y.A.
- Gorev, V.V.
- Kaportsev, E.V.
- Korchuganov, V.
- Krylov, Y.V.
- Moiseev, V.I.
- Moseev, K.
- Moseiko, N.I.
- Odintsov, D.G.
- Pesterev, S.G.
- Smolyakov, N.V.
- Smygacheva, A.S.
- Stirin, A.I.
- Ushakov, V.
- Ushkov, V.L.
- Valentinov, A.G.
- Vernov, A.

NRNU
Moscow, Russia
- Larkin, A.I.
- Orlov, A.

NSC/KIPT
Kharkov, Ukraine
- Dovbnya, A.N.
- Shchagin, A.V.

NSI RAS
Moscow, Russia
- Frolov, S.A.
- Lezhnin, S.I.

NSTU
Novosibirsk, Russia
- Blokhina, K.A.
- Gmyrya, A.A.
- Tribendis, A.G.

NSU
Novosibirsk, Russia
- Bekhtenev, E.A.
- Davidyuk, I.V.
- Fatkin, G.A.
- Getmanov, Ya.V.
- Ivanov, A.A.
- Kasatov, D.A.
- Knyazev, B.A.
- Kolesnikov, Ya.A.
- Koshkarev, A.M.
- Kotov, E.S.
- Kozyrev, E.V.
- Krasnov, A.A.
- Maltseva, M.V.
- Oreshonok, V.V.
- Pavlenko, A.V.
- Rogovsky, Yu. A.
- Senchenko, A.I.

ISBN 978-3-95450-181-6

- Serednyakov, S.S.
- Shwartz, D.B.
- Sokolova, E.O.
- Starostenko, A.A.
- Styuf, A.S.
- Taskaev, S.Yu.
- Vasilyev, M.Yu.
- Vinokurov, N.A.

NURE
Kharkov, Ukraine
- Sidorov, M.V.
- Zaverukha, O.I.

OCEM
Valsamoggia, Italy
- Burini, F.
- Pretelli, M.P.
- Taddia, G.T.
- Tenconi, S.M.

Physical-Technical Institute of the National Academy of Sciences of Belarus
Minsk, Belarus
- Marysheva, A.A.
- Petrakovsky, V.S.
- Pobol, I.L.
- Pokrovsky, A.I.
- Shparla, D.A.
- Yurevich, S.V.

PNPI
Gatchina, Leningrad District, Russia
- Amerkanov, D.A.
- Artamonov, S.A.
- Barzakh, A.E.
- Batist, L.Kh.
- Chernov, A.N.
- Fedorov, D.V.
- Gorkin, G.I.
- Ivanov, E.M.
- Ivanov, Ivanov, N.A.
- Ivanov, V.S.
- Krotov, S.A.
- Lebedeva, J.S.
- Lobanov, O.V.
- Mikheev, G.F.
- Molkanov, P.L.
- Moroz, F.V.
- Orlov, S.Yu.
- Panteleev, V.N.
- Pashuk, V.V.
- Petrov, G.A.
- Riabov, G.A.
- Shcherbakov, O.A.
- Tonkikh, V.A.
- Volkov, Yu.M.
- Vorobyev, A.S.
- Yurchenko, V.I.

PSI
Villigen PSI, Switzerland
- Anghel, A.
- Calzolaio, C.
- Gerbershagen, A.
- Sanfilippo, S.T.
- Schippers, J.M.

QST
Aomori, Japan
- Kondo, K.
- Shinya, T.

RadiaBeam
Marina del Rey, California, USA
- Faillace, L.
- Kutsaev, S.V.

RAS/INR
Moscow, Russia
- Akulinichev, S.V.
- Aseev, V.N.
- Belov, A.
- Bragin, S.
- Chermoshentsev, D.A.
- Churaev, M.M.
- Feschenko, A.
- Frolov, O.T.
- Gaidash, V.
- Gavrilov, S.A.
- Gavrilov, Y.K.
- Golubovski, S.E.
- Gorbunov, V.K.
- Grekhov, O.V.
- Kalinin, Y.Z.
- Kiselev, Yu.V.
- Klenov, V.S.
- Kravchuk, L.V.
- Kvasha, A.I.
- Leontiev, V.N.
- Naboka, A.N.
- Paramonov, V.V.
- Reinhardt-Nickoulin, P.I.
- Rybakov, I.V.
- Serov, V.L.
- Skasyrskaya, A.K.
- Vasilyev, I.V.
- Volodkevich, O.
- Yakovlev, I.A.
- Zavadtsev, A.A.
- Zubets, V.

RAS/IPME
St. Petersburg, Russia
- Fedorova, A.N.
- Zeitlin, M.G.

ISBN 978-3-95450-181-6

RRC
Moscow, Russia
- Kaportsev, E.V.
- Krylov, Y.V.

RRICT
Vidnoye, Russia
- Filippovich, V.P.
- Gracheova, A.Yu.
- Iluhina, N.V.
- Kalinina, Z.A.
- Kondratenko, V.V.
- Zavialov, M.A.

Saint Petersburg State University
Saint Petersburg, Russia
- Aleksandrov, A.Yu.
- Altsybeyev, V.V.
- Andreeva, T.A.
- Antropov, I.V.
- Babin, A.V.
- Balabanov, M.Yu.
- Bazhanov, P. V.
- Bedrina, M.E.
- Belyakov, V.A.
- Chashnikov, M.V.
- Chizhova, O.N.
- Edamenko, N.S.
- Engelko, V.I.
- Fatkina, A.I.
- Galyamin, S.N.
- Grigoreva, A.A.
- Iakushkin, O.O.
- Kalaturskaja, E.V.
- Khomutova, V.O.
- Kotina, E.D.
- Kozynchenko, S.A.
- Kozynchenko, V.A.
- Malafeyev, O.A.
- Meshkov, I.N.
- Nemnyugin, S.A.
- Ovsyannikov, A.D.
- Ovsyannikov, D.A.
- Ploskikh, V.A.
- Ponomarev, V.A.
- Shirokolobov, Yu.
- Sidorin, A.O.
- Skudnova, I.
- Starikov, D.A.
- Starikova, A.V.
- Svistunov, Y.A.
- Sytchevsky, S.E.
- Tikhonov, N.O.
- Trubnikov, G.V.
- Tyukhtin, A.V.
- Vorobev, V.V.
- Zhabko, A.P.
- Zhabko, I.A.

Saint-Petersburg State University
Saint-Petersburg, Russia
- Grigoreva, A.A.
- Vinogradova, E.M.

Siemens Healthcare
Moscow, Russia
- Meshcheryakov, N.D.
- Smirnov, I.B.

Siemens Medical Solutions Molecular Imaging
Knoxville, TN, USA
- Dishman, R.
- Korenev, S.
- Martin Yebra, A.

SINP MSU
Moscow, Russia
- Alimov, A.S.
- Ermakov, A.N.
- Khankin, V.V.
- Ovchinnikova, L.
- Pakhomov, N.I.
- Shvedunov, N.V.
- Shvedunov, V.I.

Skoltech
Moscow, Russia
- Chermoshentsev, D.A.
- Churaev, M.M.

SPC-EPFL
Lausanne, Switzerland
- Karpushov, A.N.

SSC RF- IBMP RAS
Moscow, Russia
- Trukhanov, K.A.

St. Petersburg State University
St. Petersburg, Russia
- Andrianov, S.N.
- Antonov, A.Yu.
- Drivotin, O.I.
- Dulatov, I.T.
- Egorov, N.V.
- Golovkina, A.G.
- Karpov, A.G.
- Klemeshev, V.A.
- Kudinovich, I.V.
- Kulabukhova, N.V.
- Mizintseva, M.A.
- Nikiforov, K.A.
- Ovsyannikov, D.A.
- Rubtsova, I.D.
- Vladimirova, L.V.

ISBN 978-3-95450-181-6

St. Petersburg University
St. Petersburg, Russia
- Sidorin, A.O.

Tomsk State University
Tomsk, Russia
- Bagrov, V.G.
- Loginov, A.S.
- Saprykin, A.D.

TORIY
Moscow, Russia
- Gryzlov, A.V.

TPU
Tomsk, Russia
- Artemenko, S.N.
- Danilova, I.
- Gorev, S.A.
- Harisova, A.E.
- Igumnov, V.S.
- Krasnykh, A.
- Miloichikova, I.A.
- Naumenko, G.A.
- Novokshonov, A.I.
- Potylitsyn, A.
- Shkitov, D.A.
- Shuvalov, E.
- Stuchebrov, S.
- Uglov, S.R.
- Vukolov, A.V.

TRIUMF, Canada's National Laboratory for Particle and Nuclear Physics
Vancouver, Canada
- Ang, Z.T.
- Au, T.
- Avreline, N.V.
- Bylinskii, I.V.
- Fong, K.
- Jakovljevic, B.
- Junginger, T.
- Keir, J.J.
- Koveshnikov, A.N.
- Laforge, C.
- Lang, D.
- Laxdal, R.E.
- Ma, Y.
- Muller, N.
- Nagimov, R.R.
- Storey, D.W.
- Thoeng, E.
- Waraich, B.S.
- Yao, Z.Y.
- Zheng, Q.
- Zvyagintsev, V.

United Rocket and Space Corporation, Institute of Space Device Engineering
Moscow, Russia
- Anashin, V.S.
- Bakirov, L.R.
- Koziukov, A.E.

University of Victoria
Victoria BC, Canada
- Bartlett, C.D.

USTC/NSRL
Hefei, Anhui, People's Republic of China
- Feng, G.
- He, X.Y.
- Hong, Y.
- Huang, G.
- Jia, D.
- Jin, K.
- Lu, P.
- Pei, Y.J.
- Shang, L.
- Sun, B.G.
- Tang, Zh. X.
- Wang, W.
- Wei, W.
- Xuan, K.
- Zhao, Z.

USTC/PMPI
Hefei, Anhui, People's Republic of China
- Shen, L.G.

VINCA
Belgrade, Serbia
- Ilich, R.D.

VNIIEF
Sarov, Russia
- Smetanin, M.L.
- Telnov, A.V.

VNIIM
St.Petersburg, Russia
- Trofimchuk, S.G.
- Tsvetkov, I.I.

YSU
Yerevan, Armenia
- Kotanjyan, A.
- Saharian, A.A.

ISBN 978-3-95450-181-6

ISBN 978-3-95450-181-6